AD-A247 540

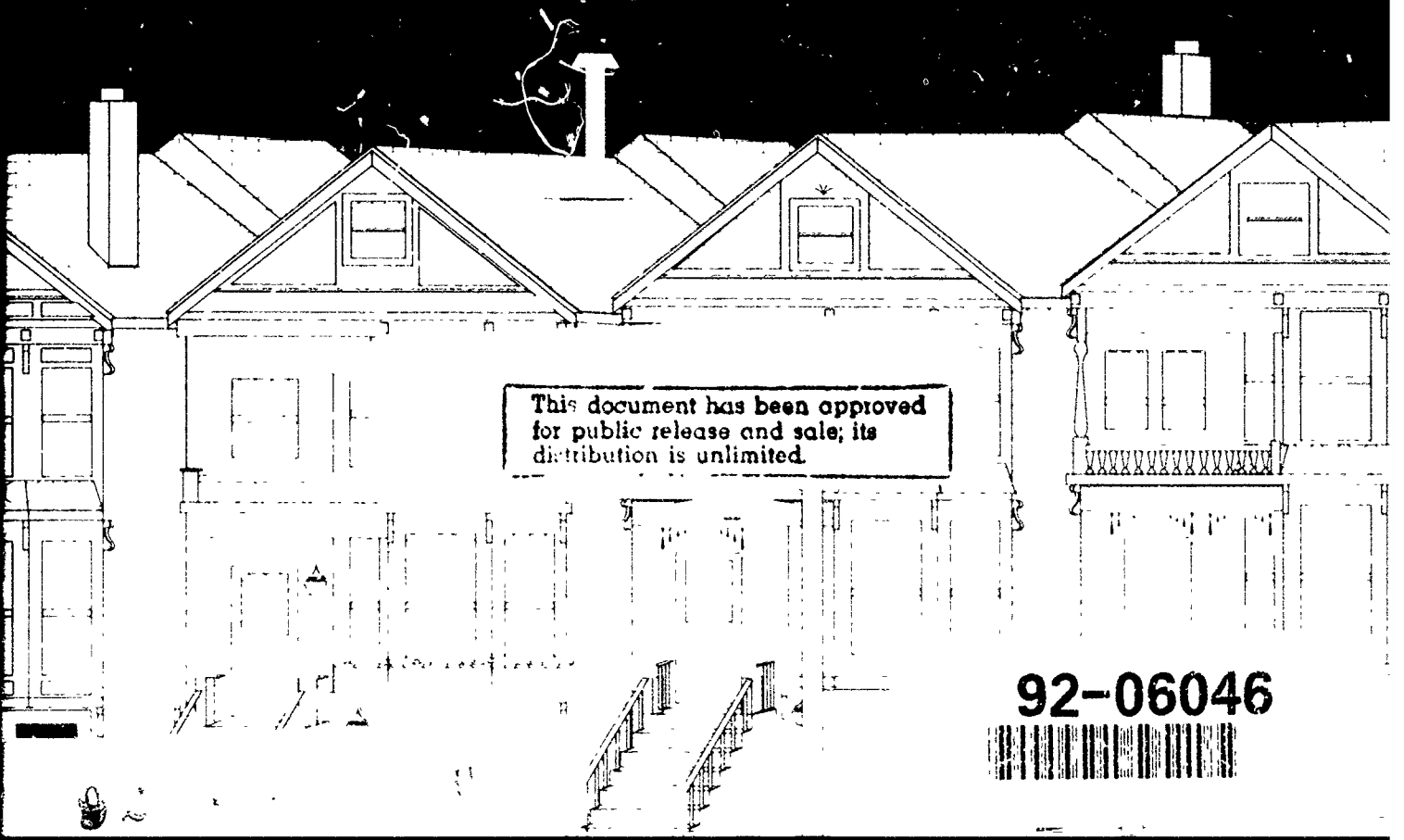
91CH3038-7
Conference Record

1991 IEEE Particle Accelerator Conference

May 6–9, 1991
San Francisco, California

DTIC
ELECTE
MAR 11 1992
S D

Accelerator Science and Technology
Volume 5 of 5



This document has been approved for public release and sale; its distribution is unlimited.

92-06046



Conference Record of the 1991 IEEE Particle Accelerator Conference

DTIC
COPY
INSPECTED
6

Accesion For
NTIS CRA&I ☑
DTIC TAB ☐
Unannounced ☐
Justification .....
By .....
Distribution /
Availability Codes
Dist | Avail and / or Special
A-1 | 21

Accelerator Science and Technology

May 6–9, 1991
San Francisco, California

Volume 5 of 5

IEEE Service Center
445 Hoes Lane
P.O. Box 1331
Piscataway, N.J. 08854-1331
212.00 per set Vol. 1,2,3,4&5
NWW 3/10/92

Organized by
Lawrence Berkeley Laboratory
Stanford Linear Accelerator Center
with Assistance of
Los Alamos National Laboratory

Under the Auspices of
Institute of Electrical and Electronics Engineers—
Nuclear and Plasma Sciences Society

Sponsored by
Department of Energy
Offices of High Energy and Nuclear Physics
Superconducting Super Collider
Basic Energy Sciences
National Science Foundation
Office of Naval Research

IEEE Catalog Number 91CH3038-7
ISBN 0-7803-0135-8 (Softbound)
ISBN 0-7803-0136-6 (Casebound)
ISBN 0-7803-0137-4 (Microfiche)
Library of Congress Number 88-647453

Additional copies are available from

IEEE Service Center
445 Hoes Lane
P.O. Box 1331
Piscataway, NJ 08854-1331
1-800-678-IEEE

Copyright and Reprint Permission: Abstracting is permitted with credit to the source. Libraries are permitted to photocopy beyond the limit of U.S. copyright law for private use of patrons those articles in this volume that carry a code at the bottom of the first page, provided the per-copy fee indicated in the code is paid through Copyright Clearance Center, 27 Congress Street, Salem, MA 01970. Instructors are permitted to photocopy isolated articles for non-commerical classroom use without fee. For other copying, reprint or republication permission, write to Director, Publishing Services, IEEE, 345 47th Street, New York, NY 10017. All rights reserved. Copyright © 1991 by The Institute of Electrical and Electronics Engineers, Inc.

Cover Artwork by Sylvia MacBride, SLAC
Conference Photos by Tom Nakashima, SLAC

TABLE OF CONTENTS

Volume 1

Conference Organizations ..... Volume 1 v
Comments on the Conference ..... Volume 1 vii
Conference Highlights Photo Section ..... Volume 1 xlv
List of Attendees ..... Volume 5 ix

Opening Plenary Session

Chairman: K. Berkner

Physics and technology challenges of BB factories *(Invited Paper)* — *Michael S. Zisman* 1
Charged particle accelerators for inertial fusion energy *(Invited Paper)* — *Stanley Humphries, Jr.* 6
Physics and technology challenges of ultra low emittance synchrotron light sources *(Invited Paper)* — *S. Krinsky* 11

Accelerator Technology III–Superconducting Components, Magnets

Chairman: P. Mantsch

Superconducting accelerator cavities on a large scale *(Invited Paper)* — *Yuzo Kojima* 16
Microscopic examination of field emission areas in superconducting Nb cavities — *D. Moffat, T. Flynn, L. Hand, J. Kirchgessner, R. Noer, H. Padamsee, D. Rubin, J. Sears, and Q. Shu* 21
Issues confronting vacuum system design for e^+e^- storage rings *(Invited Paper)* — *Nari B. Mistry* 24
APS storage ring vacuum system development — *R. C. Niemann, R. Benaroya, M. Choi, R. J. Dortwegt, R. Ferry, G. A. Goeppner, J. D. Gonczy, C. Krieger, J. Howell, R. W. Nielsen, B. Roop, and R. B. Wehrle* 29
Design of superconducting magnets for the SSC — *R. B. Palmer* 32
Field quality issues in superconducting magnets — *P. Schmüser* 37
A comparison of calculations and measurements of the field harmonics as a function of current in the SSC dipole magnets — *R. C. Gupta, J. G. Cottingham, S. A. Kahn, G. H. Morgan, and P. Wanderer* 42
Analysis of magnetic field measurement results for the AGS booster magnets — *E. Bleser and R. Thern* 45

Low- and Medium-Energy Accelerators and Rings

Chairman: R. Richardson

Some recollections on the story of the cyclotron and comments on higher degrees *(R. R. Wilson Prize Lecture)* — *J. Reginald Richardson* 48
Construction and early commissioning results of the AGS booster *(Invited Paper)* — *W. T. Weng, L. Ahrens, R. Damm, and A. J. McNerney* 52
The TRIUMF KAON factory *(Invited Paper)* — *M. K. Craddock* 57
The Superconducting Super Collider low energy booster: A status report — *R. C. York, W. Funk, A. Garren, S. Machida, N. K. Mahale, J. Peterson, F. Pilat, X. Wu, and U. Wienands* 62

Commissioning and first operation of a 500 μA, 30 MeV, H⁻ cyclotron: The TR30 — *B. F. Milton, G. Dutto, P. W. Schmor, H. R. Schneider, R. Dawson, K. L. Erdman, W. Gyles, J. Sample, and Q. Walker* 65
DAΦNE: The Frascati Φ-factory — *G. Vignola* 68
CW racetrack microtrons *(Invited Paper)* — *M. A. D. Wilson* 71
Present status of ion cooler rings *(Invited Paper)* — *Takeshi Katayama* 76

High Energy Accelerators and Colliders

Characteristics of the new Tevatron lattice — *S. Y. Hsueh, D. Finley, N. M. Gelfand, G. Goderre, B. Hendricks, D. Herrup, D. E. Johnson, R. P. Johnson, R. Joshel, K. Koepke, S. Saritepe, and D. Siergiej* 81
PEP-II: An asymmetric *B* factory based on PEP — *A. Hutton and M. S. Zisman* 84
Early operating experience with the new TEVATRON low-β insertion — *D. A. Herrup, C. Ankenbrandt, G. Annala, D. Finley, N. Gelfand, G. Goderre, B. Hendricks, D. E. Johnson, R. P. Johnson, R. Joshel, K. Koepke, S. Pruss, S. Saritepe, and D. Siergiej* 87
Prospects for tunes near the integer at the Fermilab PBAR-P collider — *D. Siergiej, C. Ankenbrandt, D. Finley, G. Goderre, R. P. Johnson, and P. Zhang* 90
Common mode noise on the main Tevatron bus and associated beam emittance growth — *P. Zhang, R. P. Johnson, M. Kuchnir, D. Siergiej, and D. Wolff* 93
Design and multiparticle simulation of the half integer slow extraction system for the main injector — *D. Trbojevic and M. Harrison* 96
Modification of the horizontal dispersion in the Fermilab main ring with additional quadrupoles — *D. Trbojevic, I. Kourbanis, and C. Ankenbrandt* 99
Computation of the TEVATRON luminosity using measured machine parameters — *N. M. Gelfand* 102
Characteristics of the beam during the second Fermilab collider run — *Norman Gelfand* 105
Energy and energy width measurement in the FNAL antiproton accumulator — *M. Church, S. Y. Hsueh, P. A. Rapidis, and S. Werkema* 108
Experimental study of the main ring transition crossing — *Ioanis Kourbanis, Keith Meisner, and King-Yuen Ng* 111
Lattice function perturbations caused by the beam-beam interaction — *D. E. Johnson, N. Gelfand, R. P. Johnson, and S. Saritepe* 114
Evolution of SSC collider design — *M. J. Syphers* 117
Design description of the SSC high energy booster — *D. E. Johnson* 120
The medium energy booster at the SSC laboratory — *Cleon Manz and Rod Gerig* 123
Physics issues of the synchrotron radiation intercept at the Superconducting Super Collider — *Weiren Chou* 126
Planning and development of underground facilities for the SSC — *T. K. Lundin, C. Laughton, D. L. Earsom, and M. J. Syphers* 129
CESR-B, upgrading the CESR facility to B-factory capability — *M. Tigner* 132
A B-factory in the PETRA tunnel — *F. Willeke* 135
Accelerator design of the KEK B-factory — *Shin-ichi Kurokawa, Kotaro Satoh, and Fumihiko Takasaki* 138
Decay rates and average luminosity in a B-factory — *H. Braun, W. Joho, and K. Hübner* 141
Single interaction point operation of CESR — *D. L. Rubin and Louis A. Schick* 144
Observation of transverse polarization in LEP — *J. Badier, A. Blondel, M. Crozon, B. Dehning, L. Knudsen, J.-P. Koutchouk, M. Placidi, and R. Schmidt* 147
The LEP energy upgrade project — *Carlo Wyss* 150
Proton antiproton collisions at a finite crossing angle in the SPS — *K. Cornelis, W. Herr, and M. Meddahi* 153
An optimized e-p insertion for LEP and LHC — *A. Verdier* 156
A transitionless lattice for the Fermilab main injector — *K. Y. Ng, D. Trbojevic, and S. Y. Lee* 159
Examination of the stability of the advanced imaginary γ_t lattice — *K. Y. Ng, D. Trbojevic, and S. Y. Lee* 162
A preliminary design of the PS collider — *Y. Mori, M. Yoshii, T. Toyama, I. Sakai, T. Shintomi, T. Suzuki, S. Ninomiya, A. Takagi, H. Sato, S. Hiramatsu, and E. Takasaki* 165

'Siberian Snake' solenoid for the AGS — *L. G. Ratner* 168
The CERN PS complex as part of the LHC injector chain — *R. Cappi, R. Garoby, S. Hancock, M. Martini, N. Rasmussen, T. Risselada, J. P. Riunaud, K. Schindl, H. Schönauer, and E. J. N. Wilson* 171
Mixed ion beams near transition energy — *S. Hancock* 174
Crystal optics of high energy beams — *M. D. Bavizhev, V. M. Biryukov, A. I. Drozhdin, K. P. Myznikov, Y. S. Fedotov, I. A. Yazunin, A. R. Dziba, A. M. Taratin, and S. A. Vorobiev* 177
The BEPC storage ring— *Status and prospects* — *Y. Wu* 180
Status of the Novosibirsk phi-factory project — *L. M. Barkov, S. A. Belomestnykh, V. V. Danilov, N. S. Dikansky, A. N. Filippov, B. I. Grishanov, P. M. Ivanov, I. A. Koop, O. B. Malyshev, S. S. Nagaitsev, I. N. Nesterenko, E. A. Perevedentsev, D. V. Pestrikov, L. M. Schegolev, I. K. Sedlyarov, Y. M. Shatunov, E. A. Simonov, A. N. Skrinsky, I. B. Vasserman, V. G. Vescherevich, P. D. Vobly, and E. I. Zinin* 183
Compensation of the chromatic effects in the Novosibirsk Φ-factory lattice — *V. V. Danilov, A. N. Filippov, P. M. Ivanov, I. A. Koop, and E. A. Perevedentsev* 186
On using bent single crystals for proton extraction from IHEP accelerator — *A. A. Asseev, M. D. Bavizhev, E. A. Ludmirsky, V. A. Maisheev, E. A. Mjae, and Y. S. Fedotov* 189
Bent single crystals to form high energy particle beams — *N. A. Galyaev, V. N. Zapol'sky, V. I. Kotov, S. V. Tsarik, and Y. A. Chesnokov* 192
JINR tau-charm factory design considerations — *V. S. Alexandrov, V. K. Antropov, O. V. Arkhipov, P. F. Beloshitsky, L. V. Bobyleva, D. I. Kaltchev, V. I. Kazacha, N. Y. Kazarinov, A. K. Krasnykh, V. I. Mironov, L. M. Onischenko, E. A. Perelstein, A. N. Sissakian, Y. I. Smirnov, and T. D. Vylov* 195

Beam Dynamics II

Geometrical (Lienard–Wichert) approach in accelerator physics — *S. G. Arutunian and M. R. Mailian* 198
Simulation of a storage ring free electron laser with a mapping algorithm for distribution functions — *V. Ziemann* 201
Particle orbit tracking on a parallel computer: Hypertrack — *B. Cole, G. Bourianoff, F. Pilat, and R. Talman* 204
Lattice parameters database and operational simulation at FNAL and SSCL — *Eric Barr, Steve Peggs, Leo Michelotti, Al Russell, Selcuk Saritepe, C. G. Trahern, and J. Zhou* 207
Effects of errors on the dynamic aperture of the advanced photon source storage ring — *H. Bizek, E. Crosbie, E. Lessner, L. Teng, and J. Wirsbinski* 210
Parasitic crossing at an asymmetric B factory, apiary — *Y. H. Chin* 213
Effect of RF phase noise on the SSC beam — *J. A. Ellison, B. S. Newberger, and H.-J. Shih* 216
Optimizing a nonlinear collimation system for future linear colliders — *N. Merminga, J. Irwin, R. Helm, and R. D. Ruth* 219
Simulation of high energy beam focusing by a plasma — *S. Rajagopalan and P. Chen* 222
Separation criterion and scaling law for long-range beam–beam interactions in the Tevatron — *S. Saritepe* 225
Observation and analysis of time-dependent closed orbit motion in the LAMPF proton storage ring — *R. Hutson, D. Fitzgerald, and R. Macek* 228
Quantum variances for transverse SSC injection dynamics — *T. Garavaglia* 231
Relativistic acceleration and retardation effects on photoemission of intense electron short pulses, in RF-FEL photoinjectors — *J.-M. Dolique and M. Coacolo* 233
Transverse emittance of an intense electron short pulse just emitted by the cathode of a RF-FEL photoinjector: Influence of electrodynamic effects — *J.-M. Dolique and M. Coacolo* 236
Observation of plasma wakefield effects during high-current relativistic electron beam transport — *J. D. Miller, R. F. Schneider, K. T. Nguyen, G. Joyce, D. J. Weidman, J. Goldhar, and H. S. Uhm* 239
Beam dynamics in the spiral line induction accelerator — *S. Slinker, J. Krall, M. Lampe, and G. Joyce* 242
Upgrade of the PHERMEX accelerator — *T.P. Hughes, D. C. Moir, and R. L. Carlson* 245
Experimental studies of emittance growth due to initial mismatch of a space charge dominated beam in a solenoidal focusing channel — *D. Kehne, M. Reiser, and H. Rudd* 248

Simulation studies of emittance growth in RMS mismatched beams — *A. Cucchetti, M. Reiser, and T. Wangler* 251
The incoherent beam–beam effect in linear-on-ring colliders — *C. D. Johnson* 254
Nonlinear dynamics of electrons in alternating-sign toroidal magnetic field — *Y. L. Martirosian and M. L. Petrosian* .. 257
Transport and error sensitivity in a heavy-ion recirculator — *W. M. Sharp, J. J. Barnard, and S. S. Yu* 260
3d and *r, z* particle simulation of beams for heavy ion fusion: The WARP code — *A. Friedman, D. P. Grote, D. A. Callahan, A. B. Langdon, and I. Haber* 263
Canonical particle tracking in undulator fields — *G. Wüstefeld and J. Bahrdt* 266
The spin motion calculation using lie method in collider nonlinear magnetic field — *Y. Eidelman and V. Yakimenko* .. 269
ASAP— *A symbolic algebra package for accelerator design* — *Eva Bozoki, Aharon Friedman, and Ilan Ben-Zvi* 272
Digital computer simulation of three-dimensional ion beam extraction and transport systems — *Jack E. Boers* 275
Digital computer simulation of axisymmetric electron beams and guns of any energy — *Jack E. Boers* 278
Using MOTER to design PILAC — *H. S. Butler, Z. Li, and H. A. Thiessen* 281
ELISE, a code for intensity dependent effects — *Mark Q. Barton* 284
Program DIMAD: Vectorization, links with DA, LIELIB and COSY-∞ — *Roger V. Servranckx* 287
Aperture determination by long term and multiparticle tracking — *G. F. Dell and G. Parzen* 288
A different approach to beam–beam interaction simulation — *Stephen Milton* 291
Chromaticity modelling in the Fermilab main ring — *J. E. Goodwin and S. M. Pruss* 294
Turnplot—A graphical tool for analyzing tracking data — *V. Paxson and L. Schachinger* 297
RAMPRF: A program for synchronous acceleration — *Miguel A. Furman* 300
Application of differential-and-lie algebraic techniques to the orbit dynamics of cyclotrons — *W. G. Davies, S. R. Douglas, G. D. Pusch, and G. E. Lee-Whiting* 303
Recovering phase density distribution from line density — *Joseph M. Kats* 306
DIMAD based interactive simulation of the CEBAF accelerator — *M. H. Bickley, D. R. Douglas, and R. V. Servranckx* . 309
A high-order moment simulation model — *K. T. Tsang, C. Kostas, D. P. Chernin, J. J. Petillo, and A. Mondelli* 312
LEBT modeling with ARGUS — *J. J. Petillo and A. A. Mondelli* 315
Model performance of the new Tevatron Collider lattice — *S. Saritepe and S. Peggs* 318
Conformal FDTD modeling of 3-D wake fields — *T. G. Jurgens and F. A. Harfoush* 321
First polarization calculations in MAD — *Hans Grote* 324
Improvements in MAD in view of LHC design — *F. Christoph Iselin* 327
Space-charge calculation for bunched beams with 3-D ellipsoidal symmetry — *R. W. Garnett and T. P. Wangler* 330
ZLIB: A numerical library for differential algebra and lie algebraic treatment of beam dynamics — *Yiton T. Yan* 333
Applications of ZMAP to the SSC — *A. W. Chao, T. Sen, Y. T. Yan, and E. Forest* 336
Implementation of one-turn maps in SSCTRK using ZLIB — *S. K. Kauffmann, D. M. Ritson, and Y. T. Yan* 339
LIEMAP: A program for extracting a one-turn single exponent lie generator map — *Tanaji Sen, Y. T. Yan, and J. Irwin* . 342
Effect of tune modulation on the dynamic aperture of the SSC lattice — *Tanaji Sen, A. W. Chao, and Y. T. Yan* 345
Closed orbit correction in the SSC — *G. Bourianoff, B. Cole, H. Ferede, and F. Pilat* 348
Design characteristics of the Linac–LEB transfer line for the SSC — *R. K. Bhandari, E. Seppi, and S. Penner* 351
The code COSY INFINITY — *M. Berz* 354
Collimator simulation for the TRIUMF KAON factory using DIMAD — *U. Wienands, C. P. Parfitt, and F. W. Jones* . 357
Dynamic aperture and extraction studies for the SSC high energy booster — *S. K. Dutt, A. W. Chao, D. E. Johnson, T. Sen, and Y. T. Yan* 360
Dynamic aperture and performance of the SSC low energy booster lattice — *F. Pilat, G. Bourianoff, B. Cole, R. Talman, and R. York* 363
The extension of the OSCAR2D code to compute azimuthally dependent modes of axially symmetric cavities — *P. Fernandes, G. Sabbi, and R. Parodi* 366
The HIF transport code FOCI — *D. W. Hewett and R. O. Bangerter* 369
Comparison of binning and sorting of magnets in the SSC high energy booster — *Mingyang Li and Shorokou Ohnuma* . 371
The beam dynamics study in a compact synchrotron — *Yunxiang Huang and Shoroku Ohnuma* 374
Compensation of RF transients during injection into the collector ring of the TRIUMF KAON factory — *Shane R. Koscielniak and Tai-Sen Wang* 377

Diffraction radiation by a charge sheet moving past a conducting wedge — *H. Henke* 380
Space charge effects in the SSC low energy booster — *S. Machida, G. Bourianoff, N. K. Mahale, N. Mehta, F. Pilat, R. Talman, and R. C. York* 383
Debunching and capture in the LEB for the SSC — *N. K. Mahale and Miguel A. Furman* 386
Longitudinal matching between the LEB and the MEB for the SSC — *N. K. Mahale and A. Maschke* 389
Constant of motion and dynamic equations for one dimensional autonomous system, and radiation damping — *G. López* . 392
Beam dynamics of multi-tank DTL and CCL designs — *C. C. Paulson, A. M. M. Todd, and S. L. Mendelsohn* 395
Electron density enhancement in a quasi isochronous storage ring — *C. Pellegrini and D. Robin* 398
Simultaneous acceleration of H^+ and H^- in RFQ linacs — *K. R. Crandall* 401
Limiting density distribution for charged particle beams in free space — *James S. O'Connell* 404
Phase space distribution of particles near an isolated difference resonance — *Jicong Shi, Yunxiang Huang, and Shoroku Ohnuma* 407
Transient beam loading reduction during multi-batch coalescing in the Fermilab main ring — *D. Wildman* 410
First turn around strategy for RHIC — *J. Milutinovic and A. G. Ruggiero* 413
Properties of the longitudinal equilibrium distribution in a storage ring — *V. Ziemann* 416
A study of misalignment effects of the ANL-APS electron linac focusing system — *A. Nassiri and G. Mavrogenes* ... 419
Hourglass effects for asymmetric colliders — *Miguel A. Furman* 422
IONSCAN: A program for optimizing charge-state combinations and calculating operating parameters for the Chalk River Superconducting Cyclotron — *Helena Lindqvist* 425
A study for lattice comparison for PLS 2 GeV storage ring — *M. Yoon* 428
Simulation of accelerating structures with large staggered tuning — *K. A. Thompson and J. W. Wang* 431
Tracking with space charge in the Fermilab booster — *S. Stahl and C. Ankenbrandt* 434
Emittance measurement in a magnetic field — *J. K. Boyd* 437
Collective effects in single bunch mode at the photon factory storage ring — *N. Nakamura, S. Sakanaka, K. Haga, M. Izawa, and T. Katsura* 440
Error analyses and modeling for CEBAF beam optical systems: Beam line element specifications and alignment error tolerances — *D. R. Douglas, J. Y. Tang, and R. C. York* 443
The CEBAF beam transport system lattice design — *B. Bowling, D. R. Douglas, L. H. Harwood, J. Kewisch, D. V. Neuffer, J. Y. Tang, and R. C. York* 446
Chromatic correction in the CEBAF beam transport system — *David R. Douglas* 449
Impedance for a multi-cell, multi-block structure — *I. Gjaja, R. Li, and R. L. Gluckstern* 452
Theory of relativistic electron beam bunching by the wakefield effects of a background plasma — *Han S. Uhm* 455
On the impedance due to synchrotron radiation — *S. Heifets and A. Michailichenko* 458
Transverse phase space in the presence of dispersion — *N. Merminga, P. L. Morton, J. T. Seeman, and W. L. Spence* .. 461
Measurements of synchro-betatron coupling by an RF cavity in CESR — *D. Rice, S. Greenwald, Z. Greenwald, and S. Peck* 464
Nearly equal β at CESR — *P. Bagley, M. Billing, S. Krishnagopal, D. Rubin, R. Siemann, and J. Welch* 467
Beam–beam performance as a function of β_v at CESR — *Louis A. Schick and D. L. Rubin* 470
Tune modulated beam–beam resonances in the Tevatron — *S. Saritepe and S. Peggs* 473
Is beta modulation more or less potent than tune modulation? — *T. Satogata and S. Peggs* 476
Root-mean-square emittance analysis of a multiple beam system — *K. A. Boulais and M. J. Rhee* 479
Coherent beam-beam interaction in DAΦNE — *Kohji Hirata and Eberhard Keil* 482
Longitudinal tune-up of the SSC drift-tube and coupled cavity linac sections — *S. Nath and G. Neuschaefer* 485
A new approach to potential well bunch deformation — *J. Hagel and B. Zotter* 488
A new wake-potential calculation method using orthogonal polynomials — *Tai-Sen F. Wang and Bruno Zotter* 491
Transverse wake field characteristics of the KEK positron generator linac — *Yujiro Ogawa, Tetsuo Shidara, Masaru Takao, and Akira Asami* 494
Longitudinal wake field characteristics of the KEK positron generator linac — *M. Takao, Y. Ogawa, T. Shidara, and A. Asami* 497

Isochronous 180° turns for the SLC positron system — *R. H. Helm, J. E. Clendenin, S. D. Ecklund, A. V. Kulikov, and R. Pitthan* 500
Chromatic correction in the SLC bunch length compressors — *C. E. Adolphsen, P. J. Emma, T. H. Fieguth, and W. L. Spence* 503
Estimation of the longitudinal impedance of the ATF damping ring — *M. Takao, T. Higo, K. Kanazawa, H. Nakayama, J. Urakawa, K. Yokoya, and K. L. F. Bane* 506
Beam pulse shorting phenomena in a rf electron gun — *Y. Huang* 509
Beam emittance and the effects of the RF, space charge and wake fields— *Application to the ATF photoelectron beam* — *Zohreh Parsa* 511
On the low-beta optics for round and flat beams in colliders — *D. Möhl* 514
Synchrotron radiation perturbations in long transport lines — *G. Leleux, P. Nghiem, and A. Tkatchenko* 517
Beam-breakup calculations for the DARHT accelerator — *Paul Allison, Michael J. Burns, George J. Caporaso, and Art G. Cole* 520
Incoherent beam–beam effects for round beams in the Novosibirsk phi-factory project — *N. S. Dikansky, P. M. Ivanov, D. V. Pestrikov, and E. A. Simonov* 523
Longitudinal beam–beam effects for an ultra-high luminosity regime — *V. V. Danilov, P. M. Ivanov, E. A. Perevedentsev, and E. A. Simonov* 526
Compensation of coherent tune shift of betatron oscillation in storage rings — *V. V. Parkhomchuk, A. A. Sery, and V. D. Shiltsev* 529

Applications and New Methods of Acceleration

Applications Chairman: R. W. Hamm

Developing a clinical proton accelerator facility: Consortium-assisted technology transfer *(Invited Paper)* — *James M. Slater, Daniel W. Miller, and Jon W. Slater* 532
Progress in light ion fusion *(Invited Paper)* — *D. L. Cook* 537
Overview of X-ray lithography at IBM using a compact storage ring *(Invited Paper)* — *Juan R. Maldonado* 542
Use of a high-current accelerator (CWDD) for neutron radiography — *C. L. Fink, D. L. Smith, and J. W. Meadows* ... 547

New Methods

New Methods Chairman: D. Sutter

The BNL accelerator test facility and experimental program *(Invited Paper)* — *Ilan Ben-Zvi* 550
An update on Argonne's AWA — *M. Rosing, E. Chojnacki, W. Gai, C. Ho, R. Konecny, S. Mtingwa, J. Norem, P. Schoessow, and J. Simpson* 555
A new look at inverse Cerenkov acceleration and vacuum laser acceleration — *L. C. Steinhauer, W. D. Kimura, and R. D. Romea* 558
Pulse power driven high power traveling wave tube amplifiers — *J. A. Nation, J. D. Ivers, G. S. Kerslick, L. Schachter, and D. Shiffler* 561
Laser wakefields at UCLA and LLNL — *W. B. Mori, T. Katsouleas, C. B. Darrow, C. E. Clayton, C. Joshi, J. M. Dawson, C. B. Decker, K Marsh, and S. C. Wilks* 564

Linear Accelerators and Pulsed Power Devices

Chairman: B. Jameson

The IH-structure and its capability to accelerate high current beams *(Invited Paper)* — *U. Ratzinger* 567

Design of the SSC linac — *J. Watson, R. Bhandari, C. Chang, Cutler R., L. Funk, G. Leifete, D. Raparia, T. Bhatia, R. Garnett, S. Nath, G. Neuschaefer, and L. Young* 572
Status of PLS 2 GeV linac project — *W. Namkung, M. Cho, I. S. Ko, Y. X. Luo, C. Ryu, S. Won, and T. N. Lee* 575
Beam-dynamics design and performance of the RF deflector in the Los Alamos single-beam funnel experiment — *F. W. Guy, K. F. Johnson, and O. R. Sander* 578
Control of energy sweep and transverse beam motion in induction linacs *(Invited Paper)* — *William C. Turner* 581
Emittance variations in current-amplifying ion induction linacs *(Invited Paper)* — *Thomas J. Fessenden* 586
Fast risetime BLT switches for accelerator applications — *G. Kirkman-Amemiya, N. Reinhardt, M. S. Choi, and M. A. Gundersen* 591

Accelerator Technology II–RF, Power Supplies, Operations

The SISSI project: An intense secondary ion source using superconducting solenoid lenses — *A. Joubert, E. Baron, C. Grunberg, J. D. Larson, W. Mittig, and F. Ripouteau* 594
Application of carbon fibre composite materials for the collision sections of particle accelerators — *H. Betzold and G. Lippmann* 598
Energy compression system design for the MIT-Bates Accelerator Center — *J. B. Flanz, P. T. Demos, K. D. Jacobs, and A. Zolfaghari* 601
The Brookhaven ATF low-emittance beam line — *X. J. Wang and H. G. Kirk* 604
First-, second-, and third-order achromatic bend systems for free-electron laser applications — *D. P. Usthoi and E. A. Wadlinger* 607
Commissioning results of the LLUMC beam switchyard and gantry — *M. E. Schulze* 610
SLIA beam line design — *J. J. Petillo, C. Kostas, D. P. Chernin, and A. A. Mondelli* 613
Induction accelerator test module for HIF — *Andris Faltens* 616
Plasma lenses for SLAC final focus test facility — *D. Betz, P. Chen, D. Cline, M. Gundersen, C. Joshi, T. Katsouleas, J. Norem, S. Rajagopalan, J. Rosenzweig, J. J. Su, and R. Williams* 619
Direct observation of plasma wakefield caused by a train of LINAC bunches — *A. Ogata, Y. Yoshida, N. Yugami, Y. Nishida, H. Nakanishi, K. Nakajima, H. Shibata, T. Kozawa, T. Kobayashi, and T. Ueda* 622
The SSC collider beam halo scraper system — *R. Soundranayagam, N. V. Mokhov, M. A. Maslov, and I. A. Yazynin* ... 625
Alignment of the SLC final focus system using beam orbits — *Y. Chao, F. LeDiberder, P. Burchat, W. Kozanecki, and N. Toge* 628
A laser alignment system for low beta quadrupoles — *C. Moore and H. Jostlein* 631
Fiducialization of magnets for the MIT-Bates SHR — *M. Farkhondeh, S. P. Holmberg, W. W. Sapp, and J. D. Zumbro* . 634
Efficiency and frequency stability in a high power microwave gap — *Y. Y. Lau and D. G. Colombant* 637
Fields and trajectories in the magnicon — *Paul Tallerico and Daniel Rees* 640
Proton synchrotron RF cavity mode damper tests — *W. R. Smythe, C. C. Friedrichs, and L. S. Walling* 643
A chopper driven 11.4-GHz traveling-wave RF generator — *G. Westenskow, J. Boyd, T. Houck, D. Rogers, R. Ryne, J. Haimson, and B. Mecklenburg* 646
High-current relativistic klystron amplifier development for microsecond pulse lengths — *M. V. Fazio, B. E. Carlsten, R. Faehl, T. J. Kwan, D. G. Rickel, R. M. Stringfield, and P. J. Tallerico* 649
High-power radio-frequency binary pulse-compression experiment at SLAC — *T. L. Lavine, Z. D. Farkas, A. Menegat, R. H. Miller, C. Nantista, G. Spalek, and P. B. Wilson* 652
Ferrite tuned cavity as possible source of bunched beam instability — *M. Popovic* 655
Amplification studies of a multi-megawatt two-cavity X-band gyroklystron — *W. Lawson, J. Calame, P. E. Latham, B. Hogan, C. D. Striffler, M. E. Read, V. Specht, W. Main, M. Reiser, and V. L. Granatstein* 658

Overview of the Superconducting Super Collider RF systems — *Jimmy D. Rogers and Jim H. Ferrell* 661
Use of Ferrite-50 to strongly damp higher order modes — *D. Moffat, P. Barnes, J. Kirchgessner, H. Padamsee, D. Rubin, J. Sears, and Q. Shu* 664
Current status of RF system for the SPring-8 — *K. Inoue, T. Nakamura, Y. Kawashima, and M. Hara* 667

Volume 2

Recycling of a LAMPF klystron — *Paul J. Tallerico and Robert L. Cady* 670
A new approach in simulating RF linacs using a general, linear real-time signal processor — *Andrew Young and Stephen P. Jachim* 672
Modeling of a 1700-MHz cluster cavity of planar triodes — *Daniel E. Rees and Carl Friedrichs* 675
Prototype 500 MHz planar RF input window for a B-factory accelerating cavity — *J. Kirchgessner, P. Barnes, R. Gerlack, D. Moffat, H. Padamsee, D. Rubin, and Q. S. Shu* 678
The AGS booster high frequency RF system — *R. T. Sanders, P. Cameron, W. Eng, M. A. Goldman, E. Jablonski, D. Kasha, J. Keane, A. McNerney, M. Meth, M. Plotkin, M. Puglisi, A. Ratti, and R. Spitz* 681
A fast amplitude and phase modulated RF source for AmPS — *F. B. Kroes, E. Heine, and T. G. B. W. Sluijk* 684
Higher order mode damping in a pill box cavity — *F. Voelker, G. Lambertson, and R. Rimmer* 687
RF impedance measurements of the various vacuum chambers for the Advanced Photon Source (APS) — *J. J. Song, J. W. Howell, R. L. Kustom, and J. F. Bridges* 690
Measurements on prototype cavities (352 MHz) for the Advanced Photon Source (APS) — *J. F. Bridges, J. M. Cook, R. L. Kustom, and J. J. H. Song* 693
Calculation of required tuner accuracy and bandwidth with and without fast feedback — *S. R. Koscielniak* 696
Analysis of eddy currents in the walls of the ferrite tuned rf cavity for the TRIUMF Kaon Factory Booster Synchrotron — *I. B. Enchevich, M. J. Barnes, and R. L. Poirier* 699
Power-combining and injection-locking magnetrons for accelerator applications — *Todd A. Treado, Todd A. Hansen, and David J. Jenkins* 702
Performance characteristics of the CEBAF klystron amplifier — *E. W. McCune and R. A. Fickett* 705
Development of 5-cell rf cavity for SPring-8 booster synchrotron — *H. Suzuki, T. Harami, Y. Miyahara, T. Rizawa, S. Satoh, Y. Tanabe, K. Yoshiyuki, T. Nagafuchi, S. Kawazu, and M. Nakano* 707
Status report on the ELETTRA R.F. system — *A. Massarotti, G. D'Auria, A. Fabris, C. Pasotti, C. Rossi, and M. Svandrlik* 710
Component development for X-band above 100 MW — *W. R. Fowkes, R. S. Callin, and M. Studzinski* 713
Comparison of SW and TW non-synchronous accelerating cavities as used in electron beam storage rings — *A. Zolfaghari, P. T. Demos, J. B. Flanz, and K. Jacobs* 716
A high power cross-field amplifier at X-band — *K. Eppley, J. Feinstein, K. Ko, N. Kroll, T. Lee, and E. Nelson* 719
A 2d field solver for periodic structures with special corner elements — *E. Nelson* 722
Gated field-emission cathodes for microwave devices — *P. M. McIntyre, H. P. Demroff, S. M. Elliott, B. Lee, J. D. Legg, Y. Pang, D. L. Parker, M. Popovic, M. D. Stewart, M. H. Weichold, W. Yu, and W. K. Yue* 725
High power X-band coaxial amplifier experiments — *T. J. Davis and J. A. Nation* 728
Studies of an X-band three-cavity gyroklystron with penultimate cavity tuning — *S. Tantawi, W. Main, P. E. Latham, H. Matthews, W. Lawson, C. D. Striffler, and V. L. Granatstein* 731
A second harmonic amplifier for accelerator applications — *P. E. Latham, W. Lawson, C. D. Striffler, and W. Main* ... 734
RF breakdown test of SiO_2 coated copper electrodes — *D. Sun, P. Datte, W. W. MacKay, and F. R. Huson* 736
The AGS booster low frequency RF system — *R. T. Sanders, P. Cameron, W. Eng, M. Goldman, D. Kasha, A. J. McNerney, M. Meth, A. Ratti, and R. Spitz* 739
Bevalac injector final stage RF amplifier upgrades — *D. Howard, J. Calvert, R. Dwinell, J. Lax, A. Lindner, R. Richter, and W. Ridgeway* 742

RF drivers for the Bevalac injector final stage RF amplifiers — *D. Howard, J. Calvert, M. Hui, A. Lindner, N. Kellogg, W. Ridgeway, and K. Woolfe* 745
New design concepts for ferrite-tuned low-energy-booster cavities — *Georg Schaffer* 748
Injection locking of a long-pulse relativistic magnetron — *S. C. Chen, G. Bekefi, and R. J. Temkin* 751
Cyclotron autoresonance maser (CARM) amplifiers for RF accelerator drivers — *W. L. Menninger, B. G. Danly, C. Chen, K. D. Pendergast, R. J. Temkin, D. L. Goodman, and D. L. Birx* 754
Analysis and optimisation of RF power-klystrons by FCI-code — *E.-G. Schweppe, E. Demmel, H. Seifert, S. Isagawa, T. Shintake, and M. Yoshida* 757
Numerical simulation of the SLAC X-100 klystron using RKTW2D — *Robert D. Ryne and Arnold E. Vlieks* 760
250 GHz cold tests for the LLNL CARM experiment — *B. Kulke, M. Caplan, and R. Stever* 763
Test results from the LLNL 250 GHz CARM experiment — *B. Kulke, M. Caplan, D. Bubp, T. Houck, D. Rogers, D. Trimble, R. VanMaren, G. Westenskow, D. B. McDermott, and N. C. Luhmann, Jr.* 766
The linac and booster RF systems for a dedicated injector for SPEAR — *J. N. Weaver, S. Baird, M. Baltay, M. Borland, H.-D. Nuhn, J. Safranek, C. Chavis, L. Emery, R. D. Genin, R. Hettel, H. Morales, J. Sebek, J. Voss, D. Wang, H. Wiedemann, B. Youngman, and R. H. Miller* 769
A high-power free-electron maser for RF acceleration — *F. Hartemann, T. S. Chu, P. Papavaritis, B. G. Danly, R. J. Temkin, G. Faillon, G. Mourier, T. Trémeau, and M. Bres* 772
Fast ferrite tuner for the BNL synchrotron light source — *E. Pivit, S. M. Hanna, and J. Keane* 774
Copper plating the ground test accelerator RFQ — *Henry Mignardot and Joseph Uher* 777
Idle superconducting RF cavities for bunch focusing — *P. Marchand and L. Rivkin* 780
Sliding mode controller for RF cavity tuning loop — *L. K. Mestha and K. S. Yeung* 783
Accelerating cavity development for the Cornell B-factory, CESR-B — *H. Padamsee, P. Barnes, C. Chen, W. Hartung, M. Hiller, J. Kirchgessner, D. Moffat, R. Ringrose, D. Rubin, Y. Samed, D. Saraniti, J. Sears, Q. S. Shu, and M. Tigner* 786
Beam impedance measurements— *Coaxial wire method* — *Giuseppe Di Massa and Maria Rosaria Masullo* 789
A simple analytical estimate of the loss parameter of a large tapered chamber — *James J. Welch* 792
Measurements of high-temperature rf and microwave properties of selected aluminas and ferrites used in accelerators — *R. M. Hutcheon, M. S. de Jong, P. Lucuta, J. E. McGregor, B. H. Smith, and F. P. Adams* 795
100 MW Klystron development at SLAC — *A. E. Vlieks, R. S. Callin, G. Caryotakis, K. S. Fant, W. R. Fowkes, T. G. Lee, and E. L. Wright* 798
Computer determination of HOM damping for a prototype JLC accelerator cavity and a prototype B factory cavity — *Norman M. Kroll and Robert Rimmer* 801
SXLS RF cavity and system — *M. Thomas, R. Biscardi, R. D'Alsace, J. Keane, P. Mortazavi, and J. Rose* 804
Low power RF system for the ALS Linac — *C. C. Lo, B. Taylor, and H. Lancaster* 807
Initial operating experience with the auxiliary accelerating cavity for the TRIUMF cyclotron — *R. E. Laxdal, K. Fong, G. H. Mackenzie, V. Pacak, J. B. Pearson, L. Root, and M. Zach* 810
CONDOR simulation of an 11.4-GHz traveling wave output cavity — *Y. Goren and D. Yu* 813
Switchable 10 Hz/1 Hz LEB magnet power supply system — *Cezary Jach* 816
An RF cavity for the B-factory — *R. Rimmer, F. Voelker, G. Lambertson, M. Allen, J. Hodgeson, K. Ko, R. Pendleton, H. Schwarz, and N. Kroll* 819
Survey and alignment of an MLI model 1.2–400 synchrotron light source — *W. J. Pearce* 822
Correlation of beam loss to residual activation in the AGS — *K. A. Brown* 825
The condition of γ-ray emission by electrons interacting with the wall in medium energy electron storage rings — *Y. Gomei and M. Kawai* 828
Gamma ray activation of the Fermilab Pbar target — *C. M. Bhat and J. Marriner* 831
Recent experience with backgrounds at the SLC — *R. Jacobsen, H. Band, T. Barklow, A. Bazarko, K. Brown, D. Burke, D. Coupal, H. DeStaebler, D. Fujino, C. Hearty, S. Hertzbach, J. Jaros, T. Maruyama, T. Tauchi, N. Toge, J. Turk, S. Wagner, and C. Zeitlin* 834
Analysis of uptime efficiency of the SLC as measured by pulse accounting — *D. Bernstein, A. Gromme, D. Ohman, and N. Spencer* 836

First results of proton injection commissioning of the AGS booster synchrotron — *R. K. Reece, L. Ahrens, J. Alessi, E. Bleser, J. M. Brennan, A. Luccio, J. Skelly, A. Soukas, W. van Asselt, W. T. Weng, and R. Witkover* 839
Multi-beamlet injection to the RFQ1 accelerator— *A comparison of ECR and duopigatron proton sources — G. M. Arbique, T. Taylor, M. H. Thrasher, and J. S. C. Wills* 842
Beam transmission and emittance measurements of the RFQ1 accelerator — *G. M. Arbique, B. G. Chidley, W. L. Michel, G. E. McMichael, and J. Y. Sheikh* 845
First two years operational experience with LEP — *R. Bailey, T. Bohl, F. Bordry, H. Burkhardt, K. Cornelis, P. Collier, B. Desforges, A. Faugier, V. Hatton, H. Laeger, J. Miles, J. Poole, G. de Rijk, H. Schmickler, and D. Vandeplassche* 848
Accelerator energy conservation at Fermilab — *James P. Morgan* 851
Designing high energy accelerators under DOE's 'New Culture' for environment and safety: An example, the Fermilab 150 GeV main injector proton synchrotron — *William B. Fowler* 854
Installation of the superconducting magnets in the HERA tunnel — *I. Borchardt, D. Brauer, S. Chermenin, D. Degèle, K. Escherich, H. J. Fiebig, H. Grabe, J. Holz, D. Hubert, R. Kus, M. Leenen, H. Maywald, O. Peters, B. Petersen, K. Pieczora, U. Riemer, Z. Sanok, P. Schmüser, S. Schollmeier, W. Schwarz, G. Tödten, D. Trines, and S. Wolff* . 857
Stripping foil losses and space charge blowup in the FNAL booster — *C. Johnstone, D. Bogert, J. Lackey, and R. Tomlin* 860
Fast kicker requirements for the SSC's low and medium energy boosters — *M. Wilson, L. Schneider, D. Anderson, and C. Pappas* 863
A pinger system for the Los Alamos proton storage ring — *T. W. Hardek and H. A. Thiessen* 866
Electrical performance of the injection system kickers at the Saskatchewan Accelerator Laboratory — *C. Figley* 869
PSR switchyard kicker system improvements — *T. W. Hardek* 872
Slow beam extraction experiments at TARN II — *M. Yoshizawa, A. Ando, K. Chida, M. Kanazawa, T. Hattori, H. Muto, A. Noda, K. Noda, M. Tomizawa, and J. Yoshizawa* 875
A triple-isotope injector for accelerator mass spectrometry — *R. J. Schneider, K. F. von Reden, and K. H. Purser* 878
Beam induced heating of ferrite magnets — *W. K. van Asselt and Y. Y. Lee* 881
On-line correction of aberrations in particle spectrographs — *M. Berz, K. Joh, J. A. Nolen, B. M. Sherrill, and A. F. Zeller* 884
The ELETTRA linac to storage ring transfer line — *D. Einfeld and R. Richter* 887
Test and calibration beams at the Superconducting Super Collider — *Frank Stocker, Howard Fenker, and Ron Schailey* . 890
Upgrade of LAMPF's 750-keV, H^+ transport — *J. W. Hurd, A. A. Browman, K. W. Jones, and M. J. Jakobson* 893
User control of the proton beam injection trajectories into the AGS booster — *T. D'Ottavio, A. Kponou, A. Luccio, J. G. Alessi, R. K. Reece, and J. Skelly* 896
Zero-degree injection line for PILAC, the proposed Los Alamos Pion Linac — *Barbara Blind* 899
The APS transfer line from linac to injector synchrotron — *R. K. Koul and E. Crosbie* 902
Dispersion and betatron matching into the linac — *F.-J. Decker, C. E. Adolphsen, W. J. Corbett, P. Emma, I. Hsu, H. Moshammer, J. T. Seeman, and W. L. Spence* 905
Upgrade of the main ring magnet power supply for the KEK 12 GeV proton synchrotron — *H. Sato, T. Sueno, T. Toyama, M. Mikawa, T. Toda, and S. Matsumoto* 908
Correction magnet power supplies for APS machine — *Y. G. Kang* 911
Circuit description of the power systems for pulsed septum magnets at APS — *D. G. McGhee* 914
Design and simulation of high accuracy power supplies for injector synchrotron dipole magnets — *Masoud Fathizadeh* . 917
Power supply system for the TRIUMF KAON factory — *K. W. Reiniger* 920
Problems with tap-changing power supplies — *John Budnick and Robert Forgas* 923
The 10 Hz resonant magnet power supply for the SSRL 3 GeV injector — *R. Hettel, R. Averill, M. Baltay, S. Brennan, C. Harris, M. Horton, C. Jach, J. Sebek, and J. Voss* 926
Magnet power supply as a network object — *S. Cohen and R. Stuewe* 929
Active filter for the DESY III dipole circuit — *W. Bothe* 932
Precision power supply control module — *N. Dobeck, B. Lamora, J. Larkin, M. O'Sullivan, and C. Sharp* 935
Measurements of crowbar performance of the 20 kV 130 A dc power supply of the TRIUMF rf system — *A. K. Mitra* . 938

Transient analysis of the AGS-booster ring dipole and quadrupole magnet system — *W. Zhang, A. V. Soukas, and S. Y. Zhang* 940
Operational results of an improved regulator and trigger system for the 'Fast' Raster Scanning Power Supply system constructed at the Bevalac Biomedical Facility — *G. Stover, J. Halliwell, B. Ludewigt, M. Nyman, and R. Stradtner* 943
Precision current regulation of multipole magnets using commercial SMPS — *Coles Sibley, Oscar Calvo, and Tomás Russ* 946
Principles and theory of resonance power supplies — *A. Sreenivas and G. G. Karady* 949
Control theory: A practical approach — *Mike Anderson and Tom Bertuccio* 952
Theoretical study of H^- stripping with a wiggler magnet — *R. Hutson* 955
The AGS new fast extraction system for the g-2 experiment and RHIC injection — *M. Tanaka and Y. Y. Lee* 958
The Frascati Φ-factory injection system — *R. Boni, S. Kulinski, M. Preger, B. Spataro, M. Vescovi, and G. Vignola* ... 961
Prototype studies of a 1 MHz chopper for the KAON factory — *G. D. Wait, M. J. Barnes, D. Bishop, G. Waters, and C. B. Figley* 964
Results of calculations on the beam deflection due to the 1 MHz chopper for the kaon factory — *M. J. Barnes and G. D. Wait* 967
Construction of a new Tevatron Collider beam abort dump — *B. Hanna and C. Crawford* 970
The SSRL injector kickers — *H.-D. Nuhn, R. Boyce, J. Cerino, and T. Hostetler* 973
Design and performance of the traveling-wave beam chopper for the SSRL injector — *M. Borland, J. N. Weaver, M. Baltay, L. Emery, A. S. Fisher, P. Golceff, R. Hettel, H. Morales, J. Sebek, H. Wiedemann, B. Youngman, R. Anderson, and R. H. Miller* 976
Electrostatic deflector development—At the Chalk River superconducting cyclotron — *V. T. Diamond, G. R. Mitchel, J. Almeida, and H. Schmeing* 979
The proposed injection system for an asymmetric B factory in the PEP tunnel — *E. Bloom, F. Bulos, G. Loew, R. Miller, B. Sukiennicki, T. Mattison, and W. Barletta* 982
HEB to Superconducting Super Collider transfer lines — *F. Wang and R. Schailey* 985
The ELETTRA gun trigger module — *G. Roberto Aiello and Maurizio Bossi* 988
POISSON study of electrostatic septa for the MIT-Bates SHR — *Manouchehr Farkhondeh* 990
The ultra-fast injection kicker for SXLS — *Thomas J. Romano and Richard Heese* 993
SLC kicker magnet limitations — *R. Cassel, A. Donaldson, T. Mattison, G. Bowden, J. Weaver, F. Bulos, and D. Fiander* . 996
The booster-to-AGS beam transfer fast kicker modulators — *W. Zhang, J. Bunicci, W. W. Frey, A. V. Soukas, and S. Y. Zhang* 999
On the design of beam absorbers for the SSC — *Brett Parker* 1002
Thyristor converter simulation and analysis — *S. Y. Zhang* 1005
Applications of the hot isostatic pressing (HIP) for high gradient accelerator structure — *Hiroshi Matsumoto, Mitsuo Akemoto, Hitoshi Hayano, Atsushi Miura, Takashi Naito, and Seishi Takeda* 1008
X-band accelerating structure for Japan linear collider — *T. Higo, M. Takao, K. Kubo, and K. Takata* 1011
Method of longitudinal impedance measurement for accelerator elements in wide frequency region using double Fourier transform — *P. Reinhardt-Nickulin, N. Ilinsky, and S. Bragin* 1014
Prototype of the accelerating resonator for the superconducting sector deuteron cyclotron — *N. V. Vasiliev, A. A. Glazov, E. N. Zaplatin, V. A. Kochkin, and D. L. Novikov* 1017
Design of an accelerating cavity for the Superconducting Super Collider Low-Energy Booster — *C. C. Friedrichs, L. Walling, and B. M. Campbell* 1020
Superconducting niobium sputter-coated copper cavity modules for the LEP energy upgrade — *C. Benvenuti, P. Bernard, D. Bloess, G. Cavallari, E. Chiaveri, E. Haebel, N. Hilleret, J. Tückmantel, and W. Weingarten* 1023
A new main control room for the AGS Complex — *P. F. Ingrassia, R. M. Zaharatos, and O. H. Dyling* 1026
Personnel protection and beam containment systems for the 3 GeV injector — *R. Yotam, J. Cerino, R. Garoutte, R. Hettel, M. Horton, J. Sebek, E. Benson, K. Crook, J. Fitch, N. Ipe, G. Nelson, and H. Smith* 1028
A cooling-water system for the Accelerator Test Facility — *Mitsuo Akemoto, Yutaro Nishinomiya, and Akio Suyama* . 1031

Blumlein-type X-band klystron modulator for Japan Linear Collider — *Tetsuo Shidara, Mitsuo Akemoto, Masato Yoshida, Seishi Takeda, Koji Takata, Iwao Ohshima, and Tsuneharu Teranishi* 1034
High-power input coupler with a cylindrical alumina window — *Mitsuo Akemoto* 1037
X-band klystron modulator for the accelerator test facility — *Mitsuo Akemoto, Tetsuo Shidara, Seishi Takeda, and Junji Urakawa* 1040
Performance test of a 65-MW klystron unit relevant to the microwave source upgrade of the KEK 2.5-GeV linac — *Tetsuo Shidara, Hiroyuki Honma, Katsumi Nakao, Shozo Anami, and Akira Asami* 1043
Superconducting cavity development at Los Alamos National Laboratory — *B. Rusnak, E. R. Gray, R. G. Maggs, D. L. Schrage, A. H. Shapiro, G. Spalek, and P. Wright* 1046
RF pulses with flat output waveform generator in RF power upgrade system — *B. Y. Bogdanovich, A. P. Ignatyev, and V. A. Senyukov* 1048
Tuning and coupling mismatch tolerance in cavities driven by a quadrature hybrid — *Arthur M. Vetter* 1051

Beam Dynamics II

Chairman: R. Gluckstern

On sustaining short, intense bunches in linear and circular accelerators *(Invited Paper)* — *Joseph J. Bisognano* 1054
Acceleration of polarized proton in high energy accelerators *(Invited Paper)* — *S. Y. Lee* 1059
Longitudinal instability in HIF beams *(Invited Paper)* — *Lloyd Smith* 1064
Computer simulation of the coherent beam–beam effect in the LHC — *W. Herr* 1068
The coherent beam–beam interaction — *S. Krishnagopal and R. Siemann* 1071
Effect of non-planar undulators on beam dynamics in ELETTRA — *Lidia Tosi and Ryutaro Nagaoka* 1074
Calculations of the conditions for bunched-beam e-p instability in the Los Alamos Proton Storage Ring (PSR) — *David V. Neuffer* 1077
Measurement of octupole induced decoherence at CESR — *John M. Byrd and David Sagan* 1080

Synchrotron Radiation Sources/FELs

Chairman: H. Winick

New developments on the generation of arbitrary polarized radiation from insertion devices *(Invited Paper)* — *Pascal Elleaume* 1083
Rapidly-modulated variable-polarization crossed-undulator source — *Michael A. Green, Kwang-Je Kim, Walter S. Trzeciak, and P. James Viccaro* 1088
Magnetic field tolerances for insertion devices on third generation synchrotron light sources *(Invited Paper)* — *P. J. Viccaro, R. Savoy, and D. W. Carnegie* 1091
NSLS prototype small-gap undulator (PSGU) — *P. M. Stefan, L. Solomon, S. Krinsky, and G. Rakowsky* 1096
Operation of synchrotron light sources with multiple insertion devices *(Invited Paper)* — *John Galayda and Anne-Marie Fauchet* 1099
Low-emittance in SPEAR — *J. Safranek and H. Wiedemann* 1104
Commissioning of the phase I superconducting X-ray lithography source (SXLS) at BNL — *J. B. Murphy, R. Biscardi, J. Bittner, L. N. Blumberg, E. Bozoki, E. Desmond, H. Halama, R. Heese, H. Hsieh, J. Keane, S. Kramer, R. Nawrocky, T. Romano, J. Rothman, J. Schuchman, M. Thomas, J. M. Wang, J. Krishnaswamy, W. Louie, and R. Rose* 1107
Short wavelength FELs — *Richard L. Sheffield* 1110
Initial operation of the Vanderbilt Free Electron Laser — *Perry A. Tompkins, Foorood Amirmadhi, K. Becker, C. A. Brau, W. D. Andrews, Marcel R. Marc, and J. Kiaie* 1115

Spectrum of coherent sychrotron radiation — *T. Nakazato, M. Oyamada, N. Niimura, S. Urasawa, Y. Shibasaki, R. Kato, S. Niwano. M. Ikezawa, T. Ohsaka, Y. Shibata, K. Ishi, T. Tsutaya, T. Takahashi, H. Mishiro, F. Arai, and Y. Kondo* 1118

Accelerator Technology I—Instrumentation, Control, Feedback

Theoretical studies on the beam position measurement with button-type pickups in APS — *Y. Chung* 1121
A beam position detector for SSC collider rings — *Donald J. Martin* 1124
Beam detector impedance calculation using circuit models — *Donald J. Martin* 1127
Monitoring system to permit accurate alignment of beams at collision in CESR — *J. P. Sikora and R. Littauer* 1130
Development of a wall current beam position monitor for a kaon factory ceramic chamber — *Yan Yin, Bill Rawnsley, George Mackenzie, Dave Pearce, and John Worden* 1133
Measurements and performance of a microstrip beam probe system — *J. D. Gilpatrick, K. F. Johnson, S. Lloyd, D. Martinez, R. Meyer, G. Neuschaefer, J. Power, R. B. Shurter, and F. D. Wells* 1136
Log-ratio circuit for beam positior monitoring — *F. D. Wells, J. D. Gilpatrick, R. E. Shafer, and R. B. Shurter* 1139
Capacitive beam position monitors and automatic beam centering in the transfer lines of GANIL — *P. Gudewicz and E. Petit* 1142
Operational amplifier based stretcher for stripline beam position monitors — *W. C. Sellyey and R. W. Kruse* 1145
A beam position monitor for AmPS — *J. Noomen, J. Bijleveld, F. Kroes, T. Sluijk, and H. Verkooijen* 1148
The SSRL injector beam position monitoring systems — *W. Lavender, S. Baird, S. Brennan, M. Borland, R. Hettel, H.-D. Nuhn, R. Ortiz, J. Safranek, J. Sebek, C. Wermelskirchen, and J. Yang* 1151
DELTA beam position monitor — *S. Brinker, R. Heisterhagen, and K. Wille* 1154
Beam position measurement system for SRRC — *G. J. Jan and K. T. Hsu* 1157
The LEP synchrotron light monitors — *C. Bovet, G. Burtin, R. J. Colchester, B. Halvarsson, R. Jung, S Levitt, and J. M. Vouillot* 1160
A CCD camera probe for a superconducting cyclotron — *F. Marti, R. Blue, J. Kuchar, J. A. Nolen, B. Sherrill, and J. Yurkon* 1163
High-sensitive remote diagnostics of the accelerated particles' beam cross section — *P. Y. Komissarov, V. G. Mikhailov, V. A. Rezvov, A. A. Roschin, V. I. Sclyarenko, and L. I. Judin* 1166
Intensity interferometry and its application to beam diagnostics — *Efim Gluskin* 1169
H^- beam characterization using laser-induced neutralization — *V. W. Yuan, R. Garcia, K. F. Johnson, K. Saadatmand, O. R. Sander, D. Sandoval, and M. Shinas* 1171
Upgrades to the Fermilab flying wire systems — *J. Zagel, A. A. Hahn, G. Jackson, T. Johnson, K. Martin, J. Misek, X. Q. Wang, and W. Ye* 1174
Results from a prototype beam monitor in the Tevatron using synchrotron light — *A. A. Hahn and P. Hurh* 1177
Design and commissioning of flying wires in the Fermilab Accumulator — *X. Q. Wang, T. Groves, A. A. Hahn, G. Jackson, J. Marriner, K. Martin, and J. Misek* 1180
Beam structure and transverse emittance studies of high-energy ion beams — *K. Saadatmand, K. F. Johnson, and J. D. Schneider* 1183
Wire scanners at LEP — *B. Bouchet, C. Bovet, A. Burns, J. Camas, G. Ferioli, C. Fischer, R. Jung, Q. King, K. H. Kissler, J. Koopman, J. Mann, H. Michel, R. Schmidt, and L. Vos* 1186
Design of the AGS Booster Ionization Profile Monitor — *A. N. Stillman, R. E. Thern, R. L. Witkover, and W. H. Van Zwienen* 1189
Beam size measurement at high radiation levels — *Franz-Josef Decker* 1192
Beam emittance measurement technique for PLS-IM-T linac — *Y. X. Luo, W. Namkung, C. Ryu, and I. S. Ko* 1195
A carbon jet beam profile monitor for LEAR — *R. Galiana, D. Manglunki, and C. Mazeline* 1198
Wire scanners for beam size and emittance measurements at the SLC — *M. C. Ross, J. T. Seeman, E. Bong, L. Hendrickson, D. McCormick, and L. Sanchez-Chopitea* 1201

Emittance measurements of FEL accelerators using optical transition radiation methods — *R. B. Fiorito, D. W. Rule, A. H. Lumpkin, R. L. Tokar, D. H. Dowell, W. C. Sellyey, and A. R. Lowrey* 1204
Beam spot size measurement using beamstrahlung signals at the SLC interaction point — *E. Gero, W. Kozanecki, and P. Chen* 1207
Beam diagnostic systems in the IUCF Cooler and cyclotron — *Mark S. Ball, Timothy J. P. Ellison, and Brett J. Hamilton* 1210
The commissioning of the LEP polarimeter — *J. Badier, A. Blondel, M. Crozon, B. Dehning, C. Bovet, P. Castro-Garcia, J. De Vries, G. P. Ferri, M. Glaser, C. Grunhagel, R. Jung, L. Knudsen, F. Lemeilleur, J. Mann, M. Placidi, R. Schmidt, and K. Unser* 1213
AGS booster tune meter kickers — *W. Zhang, J. Bunicci, P. R. Cameron, A. V. Soukas, and W. van Asselt* 1215
Mechanical design of the beam current transformers for the HERA proton ring — *W. Schütte* 1219
Betatron tune measurement system for the HERA proton storage ring — *S. Herb* 1222
Real time spectrum analyzer — *M. Bergher, E. Jules, and A. Louis-Joseph* 1225
A frequency tracking synthesizer for beam diagnostic systems — *D. Peterson and J. Marriner* 1228
The AGS booster beam loss monitor system — *E. R. Beadle, G. W. Bennett, and R. L. Witkover* 1231
A wide band slot-coupled beam sensing electrode for the advanced light source (ALS) — *J. Hinkson and K. Rex* 1234
A real-time longitudinal phase-space measurement technique for H^- beams — *R. C. Connolly and D. P. Sundoval* ... 1237
Fast ion chambers for SLC — *D. McCormick* 1240
Diagnostic instrumentation for the SSRL 3 GeV injector — *J. Sebek, M. Baltay, M. Borland, J. Cerino, L. Emery, R. Hettel, H. Morales, D. Mostowfi, M. Rowen, J. Safranek, J. Voss, J. N. Weaver, H. Wiedemann, Y. Yin, B. Youngman, J.-L. Pellegrin, and V. Smith* 1243
Bunch length measurement using beam spectrum — *Z. Greenwald, D. L. Hartill, R. M. Littauer, S. B. Peck, and D. H. Rice* 1246
Beam diagnostics for the 400 MeV Fermilab linac — *Elliot S. McCrory, Fady Harfoush, G. Jackson, Glenn Lee, and Dennis McConnell* 1249
Tune trackers for the Fermilab Tevatron — *J. Fitzgerald and R. Gonzalez* 1252
Coupled bunch dipole mode measurements of accelerating beam in the Fermilab Booster — *D. McGinnis, J. Marriner, and V. Bharadwaj* 1255
Beam transfer function measurements of accelerating beam in the Fermilab Booster — *D. McGinnis, J. Marriner, and V. Bharadwaj* 1258
Diagnostics for the MLI Model 1.2-400 Synchrotron Light Source — *Dan Y. Wang and Robert Legg* 1261
The design and packaging of the instrumentation electronics for the AGS booster, a generic approach — *G. A. Smith, E. Beadle, V. Castillo, W. Sims, A. Stillman, T. Tallerico, R. L. Witkover, and E. Zitvogel* 1264
Beam current monitoring in the AGS Booster and its transfer lines — *R. L. Witkover, E. Zitvogel, and V. Castillo* 1267
A Faraday Cup with high frequency response for a 200 MeV LINAC proton beam — *M. S. Zucker and J. W. Bittner* . 1270
The tune meter systems at the AGS complex — *W. K. van Asselt, L. A. Ahrens, P. R. Cameron, S. Mandell, G. A. Smith, and W. Zhang* 1273
Betatron tune measurement and control in the PETRA proton ring — *S. Herb* 1276
Prompt diagnostics of the cyclotron dees shift — *N. I. Karpov, Y. M. Krasnikov, I. V. Naumov, S. T. Latushkin, and L. I. Judin* 1279
Instrumentation for SSC test beams — *Howard Fenker, Frank Stocker, and Ron Schailey* 1281
Orbit monitoring in the SLC — *L. Sanchez-Chopitea, P. Emma, and D. Van Olst* 1284
Program for automatic control of beam transfer lines — *S. H. Ananian and R. H. Manukian* 1287
Embedded software for the CEBAF RF control module — *G. Lahti, I. Ashkenazi, C. West, and B. Morgan* 1290
The Tevatron orbit program — *B. Hendricks, R. P. Johnson, R. Joshel, E. Martensson, and D. Siergiej* 1293
Control of the time and energy dependent parameters of the upgraded Tevatron Collider — *D. E. Johnson, G. Goderre, B. Hendricks, R. P. Johnson, and R. Joshel* 1296
Development and application of general purpose data acquisition shell (GPDAS) at Advanced Photon Source — *Youngjoo Chung and Keeman Kim* 1299
UNIX data acquisition system — *I. Kourbanis, S. Peggs, T. Satogata, G. Tsironis, and G. Bourianoff* 1302

Control system user interface for accelerator commissioning and operation — *D. Dobrott, D. Keeley, G. Kolte, Z. Mikic, M. Lee, J. Corbett, S. Howry, and A. King* 1305
Overview of real-time kernels at the Superconducting Super Collider Laboratory — *K. Low, S. Acharya, M. Allen, E. Faught, D. Haenni, and C. Kalbfleisch* 1308
A new man–machine-interface at BESSY — *R. Müller, H.-D. Doll, I. J. Donasch, H. Marxen, and H. Pause* 1311
Alarm handler for the Advanced Photon Source control system — *Martin R. Kraimer, Ben-chin K. Cha, and Mark Anderson* 1314
Correlation plot facility in the SLC control system — *L. Hendrickson, N. Phinney, and L. Sanchez-Chopitea* 1317
Indirect phase locking of RF clock to the beam for BNL booster BPM system — *T. Hayes and A. Zaltsman* 1320
Feed forward rf control system of the Accelerator Test Facility — *Ilan Ben-Zvi, Jialin Xie, and Renshan Zhang* 1323
Progress on bunch lengthening at the NSLS VUV ring — *R. Biscardi, W. Broome, S. Buda, J. Keane, G. Ramirez, J. Wachtel, and J. M. Wang* 1326
Design of a multivariable RF control system using gain-shaping in the frequency domain — *Christopher D. Ziomek, Stephen P. Jachim, and Eckard F. Natter* 1329
Synchronization of a variable frequency source with a fixed frequency source using a sliding-mode controller — *L. K. Mestha and K. S. Yeung* 1332
Phase and amplitude stabilization of short-pulsed, high-power microwave amplifiers — *D. Hopkins, D. Yu, T. Orzechowski, G. Westenskow, and S. Yu* 1335
Measurement of bunch time-structure in KEK PF — *M. Tobiyama, T. Kasuga, T. Obina, T. Takeo, and T. Katsura* ... 1338

Volume 3

Beam diagnostics at the COSY injection beamline — *F. Anton* 1341
Design and testing of the AGS booster BPM detector — *R. Thomas, D. J. Ciardullo, and W. Van Zwienen* 1344
The AGS booster beam position monitor system — *D. J. Ciardullo, A. Abola, E. R. Beadle, G. A. Smith, R. Thomas, W. Van Zwienen, R. Warkentien, and R. L. Witkover* 1347
Contemporary approaches to control system specification and design applied to KAON — *George A. Ludgate, Edwin A. Osberg, and Don A. Dohan* 1350
Rejuvenation of the CPS control system: The first slice — *G. Benincasa, G. Daems, B. Frammery, P. Heymans, F. Perriollat, C. Serre, and C.-H. Sicard* 1353
The UNK control system — *V. N. Alferov, V. L. Brook, A. F. Dunaitsev, S. G. Goloborodko, P. N. Kazakov, V. V. Komarov, A. F. Lukyantsev, M. S. Mikheev, N. N. Trofimov, V. P. Sakharov, E. D. Scherbakov, V. P. Voevodin, S. A. Zelepoukin, and B. Kuiper* 1356
Control system specification for a cyclotron and neutron therapy facility — *Jonathan Jacky, Ruedi Risler, Ira Kalet, Peter Wootton, Alexandra Barke, Stan Brossard, and Ralph Jackson* 1359
The COSY control system, a distributed realtime operating system: First practical experience at the COSY-injector — *M. Stephan, U. Hacker, K. Henn, A. Richert, K. Sobotta, and A. Weinert* 1362
Initial control of the H^- ion source at the Superconducting Super Collider Laboratory — *G. Martinsen, S. Acharya, M. Allen, E. Faught, K. Low, and J. Sage* 1365
PLS linac instrument and control system — *C. Ryu, S. S. Chang, J. H. Kim, M. S. Kim, D. K. Liu, S. Won, and W. Namkung* 1368
Control system for the MLI Model 1.2-400 Synchrotron Light Source — *B. Ng, R. Billing, R. Legg, K. Luchini, D. Meaney, S. Pugh, and Y. Zhou* 1371
Control system of the superconducting X-ray lithography (SXLS) at Brookhaven — *E. Desmond, J. Galayda, W. Louie, B. Martin, and R. Rose* 1374
An inexpensive PC-based ion linac control system — *M. E. Hamm and J. M. Potter* 1377
Control system at the Synchrotron Radiation Research Center — *G. J. Jan* 1380

The SSRL injector control system — *C. Wermelskirchen, S. Brennan, T. Götz, W. Lavender, R. Ortiz, M. Picard, and J. Yang* 1383
Longitudinal damping system for the Fermilab Booster — *I. Haberman and I. Rypshtein* 1386
Design of 4–8 GHz bunched beam stochastic cooling arrays for the Fermilab Tevatron — *D. McGinnis, J. Budlong, G. Jackson, J. Marriner, and D. Poll* 1389
Design of 4–8 GHz stochastic cooling equalizers for the Fermilab Accumulator — *D. McGinnis and J. Marriner* 1392
Bulk acoustic wave (BAW) devices for stochastic cooling notch filters — *Ralph J. Pasquinelli* 1395
Design and operational results of a 'one-turn-delay feedback' for beam loading compensation of the CERN PS ferrite cavities — *F. Blas and R. Garoby* 1398
Improvement of the time structure and reproducibility of the Bevalac spill — *C. M. Celata, M. J. Bennett, D. N. Cowles, B. Feinberg, Robert Frias, M. A. Nyman, G. D. Stover, M. M. Tekawa, and R. Salomons* 1401
Prompt bunch by bunch synchrotron oscillation detection via a fast phase measurement — *D. Briggs, P. Corredoura, J. D. Fox, A. Gioumousis, W. Hosseini, L. Klaisner, J.-L. Pellegrin, K. A. Thompson, and G. Lambertson* 1404
Computer modelling of bunch-by-bunch feedback for the SLAC B-factory design — *D. Briggs, J. D. Fox, W. Hosseini, L. Klaisner, P. Morton, J.-L. Pellegrin, K. A. Thompson, and G. Lambertson* 1407
A longitudinal multibunch feedback system for PEP — *H.-D. Nuhn, Y. Sun, H. Winick, W. Xie, R. Yotam, H. Schwarz, and P. Friedrichs* 1410
Energy feedback system for the SSRL injector linac — *L. Emery* 1413
Design of VAX software for a generalized feedback system — *F. Rouse, S. Castillo, T. Himel, B. Sass, and H Shoaee* 1416
General, database-driven fast-feedback system for the Stanford Linear Collider — *F. Rouse, S. Allison, S. Castillo, T. Gromme, B. Hall, L. Hendrickson, T. Himel, K. Krauter, B. Sass, and H. Shoaee* 1419
The transverse damper system for RHIC — *J. Xu, J. Claus, E. Raka, A. G. Ruggiero, and T. J. Shea* 1422
The stochastic-cooling system for COSY-Jülich — *P. Brittner, R. Danzglock, H. U. Hacker, R. Maier, U. Pfister, D. Prasuhn, H. Singer, W. Spiess, and H. Stockhorst* 1425
Beam position monitoring in the AGS linac to booster transfer line — *T. J. Shea, J. Brodowski, and R. Witkover* 1428
Design of the AGS Booster Beam Position Monitor electronics — *D. J. Ciardullo, G. A. Smith, and E. R. Beadle* 1431
Modeling in control of the Advanced Light Source — *J. Bengtsson, E. Forest, H. Nishimura, and L. Schachinger* 1434
Accelerator and feedback control simulation using neural networks — *D. Nguyen, M. Lee, R. Sass, and H. Shoaee* ... 1437
Optimal, real-time control–colliders — *J. E. Spencer* 1440
Accelerator simulation and operation via identical operational interfaces — *J. Kewisch, A. Barry, R. Bork, B. Bowling, V. Corker, G. Lahti, K. Nolker, J. Sage, and J. Tang* 1443
The estimation and control of closed orbit in fast cycling synchrotron — *S. H. Ananian, R. H. Manukian, A. R. Matevosian, V. T. Nikogossian, and A. R. Tumanian* 1446
MARCO—Models of accelerators and rings to commission and operate—*L. Catani, G. Di Pirro, C. Milardi, A. Stecchi, L. Trasatti, and M. J. Lee* 1448
Use of digital control theory state space formalism for feedback at SLC — *T. Himel, L. Hendrickson, F. Rouse, and H. Shoaee* 1451
A database for modeling the Brookhaven AGS Booster — *E. H. Auerbach* 1454
A 256 channel digital filter for a data acquisition system — *W. Roberts and B. Aikens* 1455
Proposed data acquisition system for the Fermilab Booster — *V. Bharadwaj, S. Peggs, G. Wu, and C. Saltmarsh* 1458
Arbitrary function generator for APS injector synchrotron correction magnets — *Oscar D. Despe* 1461
Energy feed forward at the SLC — *R. Keith Jobe, Mike J. Brown, Ian Hsu, and Ed Miller* 1464
BPM data acquisition system for the Bates pulse stretcher ring — *O. Calvo, T. Russ, and J. Flanz* 1467
The CEBAF frequency distribution system — *A. Krycuk, J. Fugitt, K. Mahoney, and S. Simrock* 1470
Generalized emittance measurements in a beam transport line — *J. Skelly, C. Gardner, A. Luccio, A. Kponou, and K. Reece* 1473
The control and operation of the programmable wave form generator for the SSRL injector — *S. Brennan, S. Baird, W. Lavender, H.-D. Nuhn, C. Wermelskirchen, and J. Yang* 1476
Triggers and timing system for the SSRL 3 GeV injector — *R. Hettel D. Mostowfi, R. Ortiz, and J. Sebek* 1478
Main cycle controls for the AGS Booster synchrotron — *B. B. Culwick and S. Yen* 1481

Smart Rack Monitor for the Linac control system — *S. Shtirbu, R. W. Goodwin, E. S. McCrory, and M. F. Shea* 1484
SLC's adaptation of the ALS high performance serial link — *K. Krauter* 1487
Use of Ethernet and TCP/IP socket communications library routines for data acquisition and control in the LEP RF system — *E. Ciapala, P. Collier, and P. Lienard* 1490
Fiber optics in the BNL booster radiation environment — *E. R. Beadle* 1493
I/O subnets for the APS Control System — *N. D. Arnold, G. J. Nawrocki, R. T. Daly, M. R. Kraimer, and W. P. McDowell* 1496
The trajectory control in the SLC Linac — *I. C. Hsu, C. E. Adolphsen, T. M. Himel, and J. T. Seeman* 1499
Machine protection schemes for the SLC — *M. C. Ross* 1502
A programmable beam intensity display system for the Fermilab accelerators — *S. Johnson and D. Capista* 1505
An automated RF control and data acquisition system for testing superconducting RF cavities — *C. Reece, T. Powers, and P. Kushnick* 1508
A new data acquisition and control system for the power amplifier test station — *Mark S. Champion* 1511
Vacuum control system for the MLI Model 1.2-400 Synchrotron Light Source — *S. Pugh and B. Ng* 1514
The new vacuum control system for the SPS — *Detlef Swoboda* 1516
Vacuum and beam diagnostic controls for ORIC beam lines — *B. A. Tatum* 1519
An automated vacuum system — *W. H. Atkins, G. D. Vaughn, and C. Bridgman* 1522
Open loop compensation for the eddy current effect in the APS storage ring vacuum chamber — *Y. Chung, J. Bridges, L. Emery, and G. Decker* 1525
Automatic local beam steering systems for NSLS X-ray storage ring— *Design and implementation — O. V. Singh, R. Nawrocky, and J. Flannigan* 1528
Controls and interlocks for a prototype 1 MHz beam chopper — *G. Waters, D. Bishop, M. J. Barnes, and G. D. Wait* . 1531
Beam diagnostics using transition radiation produced by a 100 MeV electron beam — *M. Jablonka, J. Leroy, X. Hanus, J. C. Derost, and L. Wartski* 1534
Intelligent power supply controller — *R. S. Rumrill and D. J. Reinagel* 1537
History data facility in the SLC control system — *Ralph G. Johnson and Gregory R. White* 1540
A beam diagnostic system for ELSA — *M. Schillo, K. H. Althoff, W. v. Drachenfels, T. Goetz, D. Husmann, M. Neckenig, M. Picard, F. J. Schittko, W. Schauerte, and J. Wenzel* 1543
A table driven database and applications generator for accelerator control systems — *Anthony Carter, Coles Sibley, and Tomás Russ* 1546
Grid scans: A transfer map diagnostic — *P. Emma and W. Spence* 1549
Fiber optic communications links for the Main Ring Control System upgrade — *Robert J. Ducar* 1552
The improvement of TRISTAN timing system — *J. Urakawa and T. Kawamoto* 1555
Bunch monitor for an *S*-band electron linear accelerator — *Yuji Otake and Kazuo Nakahara* 1558
C++ objects for beam physics — *Leo Michelotti* 1561
Beam steering using quadrupoles as position monitors — *Jean-Yves Hémery and Thomas Pettersson* 1564
Optical fiber Cherenkov detector for beam current monitoring — *I. V. Pishchulin, N. G. Solov'ev, and O. B. Romashkin* 1567
Electron beam pumped semiconductor laser for particle beam diagnostics — *O. V. Garkusha, I. V. Pishchulin, and O. V. Romashkin* 1570
Method and apparatus for multifunctional nonperturbing diagnostics of H^- beam — *A. S. Artiomov, N. G. Vaganov, A. K. Gevorkov, V. V. Limar, and V. P. Sidorov* 1573
Correlation method of nonperturbing measurements of ion beam energy spectra — *A. S. Artiomov* 1576
Specialized microprocessor modules for the synchrotron automatic control system — *A. G. Agababian, S. H. Ananian, A. A. Kazarian, M. Yu Khoetsian, and A. R. Matevosian* 1579
The pulsers of the damping injection oscillation — *I. N. Ivanov, N. A. Malachov, V. A. Mel'nikov, N. V. Pilyar, A. S. Shcheulin, V. V. Akimov, V. B. Ermakov, T. A. Latypov, and G. L. Mamaev* 1582

Beam Dynamics I

Particle amplitude growth due to single or repetitive resonance crossing — *S. R. Mane and W. T. Weng* 1585

Construction of high order maps for large proton accelerators — *John Irwin* 1588
Refinement of the Hamilton–Jacobi solution using a second canonical transformation — *W. E. Gabella, R. D. Ruth, and R. L. Warnock* 1591
Tracking studies for the Oxford Instruments Compact Electron Synchrotron — *Chas N. Archie and Jan Uythoven* ... 1594
Suppression of single bunch beam breakup by autophasing — *R. L. Gluckstern, J. B. J. van Zeijts, and F. Neri* 1597
Longitudinal coupling impedance of a thin iris collimator — *R. L. Gluckstern and W. F. Detlefs* 1600
Study of loss factor for slots in the vacuum chamber — *Yong-chul Chae and Lee C. Teng* 1603
Bunched beam longitudinal stability — *R. Baartman* 1606
Reduction of beam breakup growth by bleeding cavities in linear accelerators — *D. G. Colombant and Y. Y. Lau* 1609
Observation of magnetized cooling in the IUCF cooler — *Timothy J. P. Ellison* 1612
Tune splitting in the presence of linear coupling — *G. Parzen* 1615
The WKB approximation and the traveling-wave acceleration cavity — *David C. Carey* 1618
Kick factorization of symplectic maps — *A. J. Dragt, I. M. Gjaja, and G. Rangarajan* 1621
Non-linear resonance studies at the Synchrotron Radiation Center, Stoughton, Wisconsin — *E. Crosbie, J. Bridges, Y. Cho, D. Ciarlette, R. Kustom, Y. Liu, K. Symon, L. Teng, and W. Trzeciak* 1624
Correction of skew-quadrupole errors in RHIC — *G. F. Dell, H. Hahn, S. Y. Lee, G. Parzen, and S. Tepikian* 1627
Invariant metrics for Hamiltonian systems — *Govindan Rangarajan, Alex J. Dragt, and Filippo Neri* 1630
Further dynamic aperture studies on a wiggler-based ultra-low-emittance damping ring lattice — *L. Emery* 1633
Analytic closed orbit analysis for RHIC insertion — *S. Y. Lee and S. Tepikian* 1636
Beam–beam interaction and high order resonances — *S. Tepikian and S. Y. Lee* 1639
Single beam crab dynamics — *T. Chen and D. Rubin* 1642
Emittance growth due to beam motion — *King-Yuen Ng and Jack M. Peterson* 1645
Adiabatic invariance for spatially dependent accelerating structures — *John R. Cary and David L. Bruhwiler* 1648
Particle tracking and map analysis for compact storage rings — *Michael F. Reusch, Etienne Forest, and James B. Murphy* 1651
Symplectic full-turn maps in a Fourier representation — *J. S. Berg and R. L. Warnock* 1654
Comments on the behavior of α_1 in main injector γ_t jump schemes — *S. A. Bogacz and S. Peggs* 1657
A comparison of transition jump schemes for the main injector — *S. Peggs, A. Bogacz, and F. Harfoush* 1660
Normalization of the parameterized Courant–Snyder matrix for symplectic factorization of a parameterized Taylor map — *Yiton T. Yan* 1663
LEP dynamic aperture with asymmetrical RF distribution — *Francesco Ruggiero* 1666
Long-term stability studies for the Large Hadron Collider — *F. Galluccio, Z. Guo, W. Scandale, F. Schmidt, and A. Verdier* 1669
Compensation of linear lattice imperfections in the Large Hadron Collider — *F. Galluccio, Z. Guo, T. Risselada, W. Scandale, and F. Schmidt* 1672
High-luminosity insertion for a B-meson factory — *Bruno Autin* 1675
Diffusive transport enhancement by isolated resonances and distribution tails growth in hadronic beams — *A. Gerasimov* 1678
Evaluation of the synchrotron close orbit — *Yu A. Bashmakov and V. A. Karpov* 1681
Phase trajectory analysis at the nonlinear resonances — *Yu A. Bashmakov* 1684
Emittance calculation using Liouville's theorem for a diagonalized Hamiltonian — *H. Heydari* 1687
Method for calculating strong synchrotron tune modulation of depolarizing resonances in storage rings — *S. R. Mane* 1690
First turn beam correction for the advanced photon source storage ring — *Y. Qian, E. Crosbie, and L. Teng* 1692
Uniform beam distributions using octupoles — *N. Tsoupas, R. Lankshear, C. L. Snead, Jr., T. E. Ward, M. Zucker, and H. A. Enge* 1695
Sensitivity reduction against misalignment of quadrupole and sextupole magnets — *K. Tsumaki, H. Tanaka, and N. Kumagai* 1698
Dynamic aperture of low beta lattices at Tevatron collider — *Vladimir Višnjic* 1701
Adaptive method of closed orbit correction — *Yao Cheng and Chen-Shiung Hsue* 1704
Perturbation treatment of the longitudinal coupling impedance of a toroidal beam tube — *H. Hahn and S. Tepikian* .. 1707

Impact of cross-sectional changes in a beam tube on beam dynamics — *Weiren Chou* 1710
Coupled-bunch instabilities in the APS ring — *L. Emery* 1713
Damping of higher-order modes in a threefold symmetry accelerating structure — *D. Yu and N. Kroll* 1716
Wakefield suppression using beatwave structures — *D. Yu and J. S. Kim* 1719
Measurement of longitudinal impedance for a KAON test pipe model with TSD-calibration method — *Y. Yin, C. Oram, N. Ilinsky, and P. Reinhardt-Nikulin* 1722
Calculation of seed values for longitudinal coupled bunch dipole instability due to uneven bucket population — *S. R. Koscielniak* 1725
Simulation of hollow beams with cancellation of steady state non-linear space-charge — *Shane R. Koscielniak* 1728
Stationary longitudinal phase space distributions with space charge — *R. Baartman* 1731
Characterization and monitoring of transverse beam tails — *J. T. Seeman, F. J. Decker, I. Hsu, and C. Young* 1734
Analysis of resonant longitudinal instability in a heavy ion induction linac — *Edward P. Lee and L. Smith* 1737
An investigation of the source of a low-Q, low-frequency impedance disrupting bunch coalescing in the Fermilab main ring — *P. L. Colestock, J. Griffin, X. Lu, G. Jackson, C. Jensen, and J. Lackey* 1740
A critical survey of stretched-wire impedance measurements at Fermilab — *P. L. Colestock, P. J. Chou, B. Fellenz, M. Foley, F. Harfoush, K. Harkay, G. Jackson, Q. Kerns, D. McConnell, and K. Y. Ng* 1743
Longitudinal instability in the Fermilab accumulator during slow transition crossing — *X. Q. Wang and G. Jackson* .. 1746
Results from longitudinal impedance measurements in the Fermilab Tevatron — *G. Jackson, A. Bogacz, P. J. Chou, P. Colestock, F. Harfoush, X. Lu, K. Y. Ng, W. Pellico, T. Sullivan, and X. Q. Wang* 1749
Measurement of the Fermilab Main Ring longitudinal impedance — *X. Lu and G. Jackson* 1752
Measurement of the resistive wall instability in the Fermilab Main Ring — *G. Jackson* 1755
A test of bunched beam stochastic cooling in the Fermilab Tevatron collider — *G. Jackson, E. Buchanan, J. Budlong, E. Harms, G. Lee, J. Marriner, D. McGinnis, R. Pasquinelli, D. Peterson, D. Poll, D. Rohde, P. Seifrid, and D. Voy* 1758
The self-cooling of charged particle beams in a straight line — *Y. S. Derbenev* 1761
Laser cooling of stored beams in ASTRID — *J. S. Hangst, K. Berg-Sørensen, P. S. Jessen, M. Kristensen, K. Mølmer, J. S. Nielsen, O. Poulsen, J. P. Schiffer, and P. Shi* 1764
Theoretical studies of the ultra slow extraction for the cooler synchrotron COSY-Jülich — *K. Bongardt, D. Dinev, S. Martin, P. F. Meads, H. Meuth, D. Prasuhn, H. Stockhorst, and R. Wagner* 1767
Beam property measurements in the IUCF cooler ring — *M. Ball, D. D. Caussyn, J. Collins, D. DuPlantis, V. Derenchuk, G. East, T. Ellison, D. Friesel, B. Hamilton, B. Jones, S. Y. Lee, M. G. Minty, and T. Sloan* 1770
Intrabeam scattering in the Fermilab antiproton accumulator — *C. M. Bhat and J. Marriner* 1773
Ion clearing by cyclotron resonance shaking — *P. Zhou and J. B. Rosenzweig* 1776
Envelope instability in the Fermilab booster — *P. Zhou, J. B. Rosenzweig, and S. Stahl* 1779
Multibunch instability investigation on a cavity — *E. Karantzoulis* 1782
Beam breakup in recirculating linacs — *B. C. Yunn* 1785
Electromagnetic instability of an intense beam in a quadrupole focusing system — *Cha-Mei Tang and Jonathan Krall* 1788
Instability calculations for the MIT-Bates South Hall Ring — *K. D. Jacobs, P. T. Demos, J. B. Flanz, A. Zolfaghari, J. Wurtele, X. T. Yu, and K. Balewski* 1791
Diagnosis and cure of a transverse instability in the NSLS VUV ring — *J. Rose, R. Biscardi, W. Broome, R. D'Alsace, J. Keane, and J. M. Wang* 1794
Modified octupoles for damping coherent instabilities — *M. Cornacchia, W. J. Corbett, and K. Halbach* 1797
Simulation of longitudinal phase space in the SLC — *Karl L. F. Bane* 1800
Bench measurements of coupling impedance of AGS booster components — *A. Ratti and T. J. Shea* 1803
A feedback for longitudinal instabilities in the SLC damping rings — *Y. Chao, P. Corredoura, T. Limberg, H. Schwarz, and P. Wilson* 1806
Beam breakup with finite bunch length — *C. L. Bohn and J. R. Delayen* 1809
Beam breakup with longitudinal halo — *J. R. Delayen and C. L. Bohn* 1812
Microwave instability at transition—Stability diagram approach — *S. A. Bogacz* 1815
Electron beam injector for longitudinal beam physics experiments — *J. G. Wang, D. X. Wang, and M. Reiser* 1818

Analysis of the longitudinal instability in an induction linac — *J. G. Wang and M. Reiser* 1821
Shielded coherent synchrotron radiation and its possible effect in the next linear collider — *Robert L. Warnock* 1824
Experiments on the beam breakup instability in long-pulse electron beam transport through RF cavity systems — *R. M. Gilgenbach, P. R. Menge, R. A. Bosch, J. J. Choi, H. Ching, and T. A. Spencer* 1827
Studies of coupled-bunch modes in the Fermilab booster — *K. C. Harkay, V. K. Bharadwaj, and P. L. Colestock* 1830
Simulation of multibunch instabilities in the damping ring of JLC — *Kiyoshi Kubo* 1833
Construction of an RF quadrupole magnet for suppressing transverse coupled-bunch instabilities — *Shogo Sakanaka and Toshiyuki Mitsuhashi* 1836
Ion trapping in the CESR B-factory — *David Sagan and Yuri Orlov* 1839
Longitudinal beam response measurements at CESR — *John M. Byrd* 1842
Nonlinear effects in the SLC e^+ transport line — *H. Braun, A. Kulikov, R. Pitthan, and M. Woodley* 1845
Head–tail stability and linear coupling in the Tevatron — *G. P. Goderre, S. Peggs, G. Annala, S. A. Bogacz, D. Herrup, S. Saritepe, T. Sullivan, and T. Williams* 1848
Low loss parameter for new CESR electrostatic separators — *James J. Welch and Zhong Xiong Xu* 1851
Coupled bunch motion in large size rings — *P. L. Morton, R. D. Ruth, and K. A. Thompson* 1854
Simulation and stability of a crab cavity — *Z. Greenwald, S. Greenwald, and D. H. Rice* 1857
Effects of quadrupole wake field on RF focusing in linear colliders — *A. N. Didenko, V. N. Gusarov, and G. A. Kuzmenko* 1860
Realistic modeling of microwave instability effects on the evolution of the beam energy-phase distribution in proton synchrotrons — *J. A. MacLachlan* 1863
Comparison between coasting and bunched beams on optimum stochastic cooling and signal suppression — *J. Wei* .. 1866
Beam life-time with intrabeam scattering and stochastic cooling — *J. Wei and A. G. Ruggiero* 1869
Beta functions in the presence of linear coupling — *G. Parzen* 1872
Dynamic aperture effects due to linear coupling — *G. Parzen* 1875
Brown's transport up to third order aberration by artificial intelligence — *Xia Jiawen, Xie Xi, and Qiao Qingwen* 1878
Resonance seeding of stability boundaries in two and four dimensions — *Leo Michelotti* 1881
Beam dynamics design of an RFQ for the SSC laboratory — *T. S. Bhatia, J. H. Billen, A. Cucchetti, F. W. Guy, G. Neuschaefer, and L. M. Young* 1884
On dynamic aperture — *Zohreh Parsa* 1887
Modelling of space charge effects in the CERN proton synchrotron — *Michel Martini and Oleg Ponomarev* 1890
Observation of space-charge effects in the Los Alamos Proton Storage Ring — *D. Neuffer, D. Fitzgerald, T. Hardek, R. Hutson, R. Macek, M. Plum, H. Thiessen, and T.-S. Wang* 1893
Observations of the PSR transverse instability — *E. Colton, D. Fitzgerald, T. Hardek, R. Macek, M. Plum, H. Thiessen, T. Wang, and D. Neuffer* 1896
Nonlinear dynamics in the booster of the Moscow Kaon Factory — *N. I. Golubeva, A. I. Iliev, and Yu V. Senichev* ... 1899
How to get a separatrix branch with low divergence at a 1/3-integer resonant beam slow extraction — *S. P. Volin* 1902
Racetrack lattices for low-medium-energy synchrotrons — *A. I. Iliev and Yu V. Senichev* 1904
Analytic approach to design of high transition energy lattice with modulated β-function — *A. I. Iliev* 1907

Ion Sources and Injectors

A compact RF driven H^- ion source for linac injection — *J. Patrick Rymer, G. A. Engeman, R. W. Hamm, and J. M. Potter* 1910
The BNL toroidal volume H^- source — *J. G. Alessi and K. Prelec* 1913
Laser diagnostics of H^- formation in a magnetic multicusp ion source — *A. T. Young, P. Chen, W. B. Kunkel, K. N. Leung, C. Y. Li, and G. C. Stutzin* 1916

Optimization of an RF driven H^- ion source — *K. N. Leung, W. F. DiVergilio, C. A. Hauck, W. B. Kunkel, and D. S. McDonald* 1919
IUCF high intensity polarized ion source — *M. Wedekind, R. Brown, J. Collins, V. Derenchuk, D. Dale, D. DuPlantis, T. Ellison, D. Friesel, J. Hicks, D. Jenner, A. Pei, H. Petri, P. Schwandt, and J. Sowinski* 1922
Operational experience with the TRIUMF optically pumped polarized H^- ion source — *P. W. Schmor, L. Buchmann, K. Jayamanna, C. D. P. Levy, M. McDonald, and R. Ruegg* 1925
Operation of the optically pumped polarized H^- ion source at LAMPF — *R. L. York, D. Tupa, D. R. Swenson, and O. B. van Dyck* 1928
Optical pumping of the polarized H^- ion source at LAMPF — *D. R. Swenson, D. Tupa, O. B. van Dyck, and R. L. York* 1931
Installation of the Legnaro ECR ion source — *M. Cavenago, G. Bisoffi, G. Carugno, F. Cervellera, G. Fortuna, M. F. Moisio, V. Palmieri, and K. Rudolph* 1934
Design aspects for a pulsed-mode, high-intensity, heavy negative ion source — *G. D. Alton* 1937
Current density calculation of a high frequency ion source — *H. Heydari* 1940
Review of Mevva ion source performance for accelerator injection — *I. G. Brown, X. Godechot, P. Spädtke, H. Emig, D. M. Rück, and B. H. Wolf* 1943
An antiproton target design for increased beam intensity — *K. Anderson, C. M. Bhat, J. Marriner, and Z. Tang* 1946
Project of complex tandem—RF linear postaccelerator — *O. A. Valdner, V. P. Gass, A. D. Koljaskin, A. N. Pronin, and P. B. Shurupov* 1949
An induction linac injector for scaled experiments — *H. L. Rutkowski, A. Faltens, C. Pike, D. Brodzik, R. M. Johnson, D. Vanecek, and D. W. Hewett* 1952
Testing of a high current DC ESQ accelerator — *J. W. Kwan, G. D. Ackerman, O. A. Anderson, C. F. Chan, W. S. Cooper, G. J. deVries, W. B. Kunkel, L. Soroka, W. F. Steele, and R. P. Wells* 1955
Transport properties of a discrete helical electrostatic quadrupole — *C. R. Meitzler, K. Antes, P. Datte, F. R. Huson, and L. Liu* 1958
Low energy H^- beam transport using an electrostatic quadrupole focusing system — *S. K. Guharay, C. K. Allen, M. Reiser, and V. Yun* 1961
SLC polarized beam source electron optics design — *K. R. Eppley, T. L. Lavine, R. A. Early, W. B. Herrmannsfeldt, R. H. Miller, D. C. Schultz, C. M. Spencer, and A. D. Yeremian* 1964
Observations on field-emission electrons from the Los Alamos FEL photoinjector — *Alex H. Lumpkin* 1967
An RF modulated electron gun pulser for linacs — *Robert Legg and Robert Hartline* 1970
Scaling study of pseudospark produced electron beam — *K. K. Jain, B. N. Ding, and M. J. Rhee* 1972
Low-emittance uniform-density Cs^+ sources for heavy ion fusion accelerator studies — *S. Eylon, E. Henestroza, T. Garvey, R. Johnson, and W. Chupp* 1975
Preliminary design for a thermionic R.F. gun — *G. D'Auria, J. Gonichon, and T. Manfroi* 1978
Applications of diamond films to photocathode electron guns and accelerators — *C. P. Beetz, B. Lincoln, K. Segall, D. Wall, M. Vasas, D. R. Winn, D. Doering, and D. Carroll* 1981
Development of laser optics for the AWA photocathode — *J. Norem and W. Gai* 1984
Flat-beam RF photocathode sources for linear collider applications — *J. B. Rosenzweig* 1987
Electron beam generation from a superemissive cathode — *T.-Y. Hsu, R.-L. Liou, G. Kirkman-Amemiya, and M. A. Gundersen* 1990
Quantum yield measurements of photocathodes illuminated by pulsed ultraviolet laser radiation — *A. T. Young, P. Chen, W. B. Kunkel, K. N. Leung, C. Y. Li, and J. M. Watson* 1993
3D numerical thermal stress analysis of the high power target for the SLC positron source — *Eric M. Reuter and John A. Hodgson* 1996
Mechanical design and development of a high power target system for the SLC positron source — *Eric Reuter, Dean Mansour, Tom Porter, Werner Sax, and Anthony Szumillo* 1999
Channeling crystals for positron production — *Franz-Josef Decker* 2002
SLC positron source pulsed flux concentrator — *A. V. Kulikov, S. D. Ecklund, and E. M. Reuter* 2005
Progress in H^- ion source development at TAC — *J. Culver, K. Antes, F. R. Huson, A. Larsson, C. R. Meitzler, and L. Xiu* 2008

Volume 4

Investigation of an intense H^- ion beam produced by a volume source — *M. Bacal, P. Devynck, C. Michaut, Z. Sledziewski, and F. P. G. Valckx* 2011
Single bunched beam generation using conventional electron gun for JLC injector — *T. Naito, J. Urakawa, M. Akemoto, and H. Akiyama* 2014
Measures to alleviate the back bombardment effect of thermionic RF electron gun — *Y. Huang and J. Xie* 2017
Development of thermionic-cathode RF electron gun at IHEP — *Jialin Xie, Jie Gao, Yongzhang Huang, Renshan Zhang, Hongxiu Liu, and Youzhi Wang* 2020
Characteristics of the H^- /D^- beam extracted from an RF-driven volume source — *G. Gammel, T. Debiak, J. Sredniawski, K. Leung, and D. McDonald* 2023
Design and modeling of a 17 GHz photocathode RF gun — *C. L. Lin, S. C. Chen, J. S. Wurtele, R. Temkin, and B. Danly* 2026
Strain enhanced electron spin polarization observed in photoemission from InGaAs — *T. Maruyama, E. L. Garwin, R. Prepost, G. H. Zapalac, J. S. Smith, and J. D. Walker* 2029
Development of polarized electron sources using AlGaAs–GaAs superlattice and using strained GaAs — *T. Nakanishi, Y. Kurihara, T. Omori, H. Aoyagi, T. Baba, T. Furuya, H. Horinaka, K. Itoga, Y. Kamiya, T. Kato, M. Mizuta, S. Nakamura, T. Saka, Y. Takeuchi, M. Tsubata, and M. Yoshioka* 2032
Magnetic ring for transformation of the heavy ions charge states — *V. P. Kukhtin, Yu P. Servergin, and I. A. Shukeilo* 2035

Linear Colliders

Chairman: C. Pellegrini

Emittance control in linear colliders *(Invited Paper)* — *Ronald D. Ruth* 2037
Application of superconducting RF to linear colliders *(Invited Paper)* — *H. Padamsee* 2042
Accelerator test facility for the JLC project — *Seishi Takeda* 2047
The CERN study of a 2 TeV e^+e^- collider CLIC — *CLIC Study Group* 2052
The final focus test beam project — *David Burke* 2055
The optics of the final focus test beam — *J. Irwin, K. Brown, F. Bulos, D. Burke, R. Helm, G. Roy, R. Ruth, N. Yamamoto, and K. Oide* 2058
High gradient experiments by the ATF — *Seishi Takeda, Mitsuo Akemoto, Hitoshi Hayano, Hiroshi Matsumoto, and Takashi Naito* 2061
Summary of emittance control in the SLC linac — *J. T. Seeman, C. Adolphsen, K. L. F. Bane, P. Emma, F. J. Decker, I. Hsu, T. Limberg, L. Merminga, M. Ross, and W. Spence* 2064
Chromaticity corrections in the SLC final focus system — *N. Toge, K. Brown, D. Burke, R. Jacobsen, P. Krejcik, and V. Ziemann* 2067
An active alignment test facility for the CERN linear collider — *W. Coosemans, I. Wilson, and P. Poirier* 2070
Emittance growth in TESLA — *G. A. Krafft, M. Fripp, and J. J. Bisognano* 2073

Ion Sources and Injectors

Chairman: R. Stevens

State of H^- source development *(Invited Paper)* — *K. N. Leung* 2076
H^- temperature measurements by a slit diagnostic technique — *Joseph D. Sherman, H. Vernon Smith, Jr., Carl Geisik, and Paul Allison* 2080
Recent developments in intense polarized hydrogen and deuterium ion sources *(Invited Paper)* — *Thomas B. Clegg* .. 2083

Ion sources for commercial ion implanter applications *(Invited Paper)* — *S. R. Walther, B. O. Pedersen, and C. M. McKenna* 2088
High-current CW RFQ's *(Invited Paper)* — *G. E. McMichael* 2093
SLC positron source—Simulation and performance — *Rainer Pitthan, Hans Braun, J. E. Clendenin, S. D. Ecklund, R. H. Helm, A. V. Kulikov, A. C. Odian, G. X. Pei, M. C. Ross, and M. D. Woodley* 2098
Overall simulation of a positron beam generated by photons from channeled multiGeV electrons — *X. Artru, R. Chehab, A. Jejcic, J. Maillard, and J. Silva* 2101
Electron emission from ferroelectric ceramics — *J. D. Ivers, R. Advani, J. A. Nation, and L. Schachter* 2104
Time-resolved emittance measurements of an excimer-laser-driven metal photocathode — *T. Kauppila, R. Carlson, D. Moir, and R. Ridlon* 2107

Accelerator Technology III—Superconducting Components, Magnets

Magnet design for the DARHT linear induction accelerators — *Michael Burns, Ken Chellis, Cathy Mockler, Tom Tucker, George Velasquez, and Roger Van Maren* 2110
Magnetic data analysis for the ALS lattice magnets — *Roderich Keller* 2113
Magnetic measurements of the XLS magnets — *L. Solomon, J. Galayda, and C. Sylvester* 2116
Magnetic measurements of the 12-pole trim magnets for the 200 MeV compact synchrotron XLS at the National Synchrotron Light Source — *J. Krishnaswamy, Swarn Kalsi, and Hank Hsieh* 2119
Determination of the particle momentum in LEP from precise magnet measurements — *J. Billan, J. P. Gourber, and K. N. Henrichsen* 2122
Measurements of quadrupole magnets for the MIT-bates SHR — *J. D. Zumbro, P. Bonneau, M. Farkhondeh, J. B. Flanz, S. P. Holmberg, T. Russ, W. W. Sapp, and C. Sibley* 2125
Harmonic analysis of Fermilab main ring quadrupoles — *B. C. Brown, P. O. Mazur, J.-F. Ostiguy, S. M. Pruss, and F. Turkot* 2128
Three-dimensional field map of the Fermilab DO detector — *Jean-François Ostiguy and Ryuji Yamada* 2131
Software design for a database driven system for accelerator magnet measurements — *B. C. Brown, M. E. Bleadon, H. D. Glass, R. Glosson, R. W. Hanft, D. J. Harding, P. O. Mazur, J. E. Pachnik, J. W. Sim, K. Trombly-Freytag, and D. G. Walbridge* 2134
Modification of LAMPF's magnet-mapping code for offsets of center coordinates — *J. W. Hurd, S. Gomulka, F. Merrill, and B. L. Weintraub* 2137
A new 3-D integral code for computation of accelerator magnets — *L. R. Turner and L. Kettunen* 2140
The physical way of standardizing magnets — *Franz-Josef Decker* 2143
Septum magnet for electron slow extraction from the Yerevan synchrotron — *A. Z. Babaian, G. B. Bagdasarian, V. T. Nickogosian, A. R. Toumanian, A. G. Zacharian, E. A. Ludmirsky, and J. Rummler* 2146
Observation of a periodic pattern in the persistent-current fields of the superconducting HERA magnets — *H. Brück, D. Gall, J. Krzywinski, R. Meinke, H. Preissner, M. Halemeyer, P. Schmüser, C. Stolzenburg, R. Stiening, R. ter Avest, and L. J. M. van de Klundert* 2149
New final focus system for the SLAC linear collider — *N. Toge, W. W. Ash, H. Band, A. O. Bazarko, Y.-C. Chao, R. Erickson, R. Gray, S. S. Hertzbach, R. R. Kofler, D. Mansour, C. M. Spencer, J. Turk, C. Zeitlin, and V. Ziemann* 2152
Recent improvements in superconducting cable for accelerator dipole magnets — *Ronald M. Scanlan and John M. Royet* 2155
Correction of magnetization sextupole and decapole in a 5 centimeter bore SSC dipole using passive superconductor — *Michael A. Green* 2158
Preliminary study of an integral harmonic analysis magnetic field measurement system for long SSC magnets — *Michael I. Green* 2161

Experiments with all-Kapton insulation and axial prestress in 1.8 m-long SSC R&D magnets — *P. Wanderer, M. Anerella, G. Cottingham, G. Ganetis, M. Garber, A. Ghosh, C. Goodzeit, A. Greene, R. Gupta, J. Herrera, S. Kahn, E. Kelly, A. Meade, G. Morgan, J. Muratore, A. Prodell, P. Radusewicz, M. Rehak, E. Rohrer, W. Sampson, R. Shutt, P. Thompson, and E. Willen* 2164
Construction and results of the 50 mm short R&D dipole magnets — *G. H. Morgan, M. Anerella, J. Cottingham, G. Ganetis, M. Garber, A. Ghosh, C. Goodzeit, A. Greene, R. Gupta, J. Herrera, S. Kahn, E. Kelly, A. Morgillo, J. Muratore, A. Prodell, P. Radusewicz, M. Rehak, E. P. Rohrer, W. Sampson, R. Shutt, P. Thompson, P. Wanderer, and E. Willen* 2167
Magnetic properties of iron yoke laminations for SSC dipole magnets — *S. A. Kahn and G. H. Morgan* 2170
Tests of 1.5 meter model 50mm SSC collider dipoles at Fermilab — *M. Wake, R. Bossert, J. Carson, K. Coulter, S. Delchamps, S. Gourlay, T. S. Jaffery, W. Kinney, W. Koska, M. J. Lamm, J. Strait, R. Sims, and M. Winters* 2173
Mechanical design of the 2D cross-section of the SSC collider dipole magnet — *J. Strait, J. Kerby, R. Bossert, J. Carson, G. Spigo, and J. R. Turner* 2176
Tests of 40 mm SSC dipole model magnets with vertically split yokes — *W. Koska, R. Bossert, K. Coulter, S. Delchamps, S. Gourlay, W. Kinney, T. S. Jaffery, M. J. Lamm, J. Strait, and M. Wake* 2179
Coil end design for the SSC collider dipole magnet — *J. S. Brandt, N. W. Bartlett, R. C. Bossert, J. A. Carson, J. J. Konc, G. C. Lee, and J. M. Cook* 2182
SSC collider dipole magnet end mechanical design — *S. W. Delchamps, R. C. Bossert, J. Carson, K. Ewald, H. Fulton, J. Kerby, W. Koska, J. Strait, M. Wake, and K. K. Leung* 2185
Optimization of the end winding geometry of dipole magnets — *Michael F. Reusch, Don W. Weissenburger, and James C. Nearing* 2188
Bipolar and unipolar tests of 1.5m model SSC collider dipole magnets at Fermilab — *M. J. Lamm, J. P. Ozelis, S. Delchamps, K. J. Coulter, T. S. Jaffery, W. Kinney, W. Koska, J. Strait, M. Wake, D. Fortunato, and D. E. Johnson* 2191
Coil shapes towards pure multipoles in circular regions (a numerical approach) — *V. Thiagarajan* 2194
A software package linking PE2D and ANSYS for SSC magnet design — *Nick Kallas, Chris Haddock, Jay Jayakumar, David Orrell, Greg Snitchler, Giancarlo Spigo, and Jon Turner* 2197
Cooldown stresses on the coldmass of SSC dipole magnets — *B. Aksel and K. Leung* 2200
Divergent quench velocity expression and 4-cm SSC R&D dipole magnets — *G. López* 2203
Mechanical analysis of beam tube assemblies for SSC dipoles during a quench — *S. A. Smith, C. Haddock, R. Jayakumar, J. Turner, and J. Zbasnik* 2206
Hydraulic quench simulations in SSC dipole magnets — *G. Snitchler and B. Aksel* 2209
Quench analysis of the energy deposition in the SSC magnets and radiation shielding of the low-β IR quadrupoles — *G. López* 2212
SSC dipole quench protection heater test results — *C. Haddock, R. Jayakumar, F. Meyer, G. Tool, J. Kuzminski, J. DiMarco, M. Lamm, T. Jaffery, D. Orris, P. Mazur, R. Bossert, and J. Strait* 2215
The SSC collider correction system — *S. R. Stampke, Y. Cai, and J. Skaritka* 2218
Superferric correction magnet test results — *R. Rocha, J. Colvin, F. R. Huson, W. W. MacKay, Y. Miao, S. Pissanetzky, G. Shotzman, and J. Zeigler* 2221
Quench simulation studies of the TAC jelly roll superferric dipole corrector elements for the SSC — *G. López* 2224
Quench performance of superconducting quadrupole magnets for the new Fermilab low beta insertion — *S. A. Gourlay, J. A. Carson, R. Hanft, T. S. Jaffery, K. Koepke, M. J. Lamm, F. M. Mantsch, A. D. McInturff, A. Mokhtarani, D. Orris, and T. Peterson* 2227
Production measurements on the quadrupole correctors for the new low-beta system for the Tevatron collider — *A. Mokhtarani, B. C. Brown, R. Hanft, A. R. Oleck, T. Peterson, and F. Turkot* 2230
Magnetic performance of new Fermilab high gradient quadrupoles — *R. Hanft, B. C. Brown, J. A. Carson, S. A. Gourlay, M. J. Lamm, A. D. McInturff, A. Mokhtarani, and A. Riddiford* 2233
Fabrication and performance of a new high-gradient trim quadrupole for the Fermilab luminosity upgrade — *P. M. Mantsch, J. A. Carson, S. A. Gourlay, M. J. Lamm, and A. W. Riddiford* 2236

RHIC insertion magnets — *R. C. Gupta, J. Cottingham, G. Ganetis, M. Garber, A. Ghosh, A. Greene, H. Hahn, J. Herrera, S. Kahn, E. Kelly, E. Killian, G. Morgan, A. Meade, J. Muratore, A. Prodell, M. Rehak, E. Rohrer, W. Sampson, R. Shutt, P. Thompson, P. Wanderer, and E. Willen* 2239
Iron saturation control in RHIC dipole magnets — *P. A. Thompson, R. C. Gupta, S. A. Kahn, G. H. Morgan, P. J. Wanderer, E. Willen, and H. Hahn* 2242
Revised cross section for RHIC dipole magnets — *P. A. Thompson, R. C. Gupta, S. A. Kahn, G. H. Morgan, P. J. Wanderer, E. Willen, and H. Hahn* 2245
Superconducting magnet program for X-ray lithography source at Brookhaven National Laboratory — *H. Hsieh, R. Blumberg, R. Heese, J. Murphy, S. Pjerov, S. Sharma, E. M. W. Leung, S. Kalsi, and M. F. Reusch* 2248
A dipole magnet model for compact synchrotron light source — *M. Kitamura, H. Yamamoto, H. Tomeoku, and N. Maki* 251
The superconducting Tritron magnets — *R. Kratz, G. Hinderer, J. Junger, J. Labedzki, and U. Trinks* 2254
Superconducting quadrupole magnet system for TRISTAN mini-beta insertions — *K. Endo, K. Egawa, H. Fukuma, A. Kabe, T. Kubo, S. Kuroda, S. Kurokawa, Y. Morita, Y. Ohsawa, N. Ohuchi, T. Ozaki, R. Sugahara, and K. Tsuchiya* 2257
A design concept for the LHC insertion quadrupoles — *W. Scandale and T. Taylor* 2260
A guideline for design, analysis, and fabrication of vacuum vessels for cryogenic accelerators — *Robert C. Gentzlinger and Kirk E. Christensen* 2263
Instrumentation and control of the AGS booster vacuum system — *J. Gabusi, J. Geller, H. C. Hseuh, P. Rosas, J. Sandburg, B. Shen, P. Stattel, and R. Zapasek* 2266
Pumping mechanisms in sputter-ion pumps low pressure operation — *Kimo M. Welch* 2269
Ceramic beam pipe for the TRIUMF KAON factory synchrotron rings — *T. Hodges, R. Langstaff, C. Oram, M. Featherby, and C. Planner* 2272
Vacuum chamber of the injector synchrotron for the advanced photon source — *R. Benaroya and R. Dortwegt* 2275
Vacuum chamber for the 3 GeV SPEAR injector synchrotron — *H. Morales, N. Hower, U. Cummings, P. Golceff, W. Li, J. Safranek, J. Voss, and H. Wiedemann* 2278
Design considerations for beam tube penetration of a liquid argon collider detector — *Keith Primdahl and Hans Jöstlein* 2281
SLC polarized beam source ultra-high-vacuum design — *T. L. Lavine, J. E. Clendenin, E. L. Garwin, E. W. Hoyt, M. W. Hoyt, R. H. Miller, J. A. Nuttall, D. C. Schultz, and D. Wright* 2284
Photon stimulated desorption of neutral species from aluminum — *T. S. Chou* 2286
Modeling photo-desorption in high current storage rings — *William A. Barletta* 2289
Processing and evaluation of the AGS booster ultra-high vacuum system — *H. C. Hseuh, M. Mapes, P. Schnitzenbaumer, B. Shen, R. Sikora, and P. Stattel* 2292
Calculation of pressure distribution in vacuum systems using a commercial finite element program — *J. Howell, B. Wehrle, and H. Jostlein* 2295
Performance estimation of vacuum system components including crotch and absorber — *T. Nishidono, S. H. Be, H. Daibo, T. Hanasaka, Y. Hirano, S. R. In, Y. Oikawa, H. A. Sakaue, S. Takahashi, S. Yokouchi, and K. Watanabe* 2298
ANL advanced photon source crotch absorber design — *M. Choi, J. D. Gonczy, J. W. Howell, and R. C. Niemann* ... 2301
UHV seal studies for the advanced photon source storage ring vacuum system — *J. D. Gonczy, R. J. Ferry, R. C. Niemann, and B. Roop* 2304
Vacuum design for a superconducting mini-collider — *William A. Barletta and Sergio Monteiro* 2307
Design of the vacuum system for the high energy ring of an asymmetric B-factory based on PEP — *William A. Barletta, Manuel Calderon, Robert Wong, and Theodore Jenkins* 2310
Ion clearing and photoelectron production in the 200 MeV SXLS ring — *H. Halama and Eva Bozoki* 2313
SXLS phase II vacuum system — *J. C. Schuchman, T. S. Chou, H. Halama, H. Hsieh, T. Kim, S. Pjerov, and F. Staicu* 2316
The cryogenic operation of the superconducting magnet system in the HERA proton storage ring: Cool down, steady state operation, quench recovery processes — *G. Horlitz, M. Clausen, H. Lierl, R. Lange, and H. Herzog* 2319
Magnetic permeability of stainless steel for use in acclerator beam transport systems — *Norman Wilson and Paul Bunch* 2322
A closed cycle cryogenic system for testing superconducting RF cavities — *C. Reece, J. Susta, T. Powers, and B. Almeida* 2325
Extraction septum magnet for the SSRL SPEAR injector — *J. Cerino, M. Baltay, R. Boyce, S. Harris, R. Hettel, M. Horton, and K. Zuo* 2328

Operational experience with SLC damping ring kicker magnets — *T. Mattison, R. Cassel, A. Donaldson, G. Gross, and A. Harvey* 2331
Development of epoxy potting for high voltage insulation at SLAC — *G. Gross, R. Cassel, and T. Mattison* 2334
Development and performance of electrostatic deflector insulators for the Chalk River superconducting cyclotron — *C. R. Hoffmann and J. F. Mouris* 2337
A design for a beam halo scraper system for the Tevatron collider — *S. M. Pruss* 2340
Synchrotron radiation masking on asymmetric 6.5 × 4.3-GeV B-factory — *V. E. Blinov, V. A. Lebedev, A. V. Matveev, V. A. Tayursky, and A. A. Zholents* 2342
Engineering design of the PLS 2 GeV storage ring dipole magnet — *E. S. Park, Y. G. Nah, H. S. Han, and Y. M. Koo* 2345
Low-sextupole steering dipoles for the MIT-Bates SHR — *M. Farkhondeh, R. J. Averill, W. W. Sapp, and J. D. Zumbro* 2348
Permanent magnet-based dipole for a small storage ring — *Firas Putris and Wayne Vernon* 2351
Magnet end design: The main injector dipoles — *Jean-François Ostiguy* 2354
Effects of the SRRC second prototype dipole magnet on the SRRC ring — *J. C. Lee* 2357
A radiation-hardened pulsed magnet for the Tevatron-I target station — *P. Hurh, M. Gormley, J. Hangst, S. O'Day, and J. Howell* 2360
Magnets for TRIUMF's KAON factory — *A. J. Otter and P. A. Reeve* 2363
Magnetic devices of the Amsterdam pulse stretcher ring AmPS — *H. Boer Rookhuizen, J. Bijleveld, A. van der Linden, G. Luijckx, R. Maas, and Y. Wu* 2366
The ring magnets for the SSRL SPEAR injector — *M. M. Baltay, J. Cerino, R. Hettel, J. Safranek, J. Voss, H. Wiedemann, and K. Zuo* 2369
The ELETTRA transfer line magnets — *M. Begg, D. Einfeld, and D. Tommassini* 2372
Fabrication and tests of prototype quadrupole magnets for the storage ring of the Advanced Photon Source — *S. H. Kim, K. M. Thompson, E. L. Black, and J. M. Jagger* 2375
A quadrupole magnet for the Fermilab Linac Upgrade — *T. Kroc* 2378
CEBAF cryomodule testing — *Kevin Jordan, Rich Bundy, I. E. Campisi, Ken Crawford, Mike Drury, J. Patrick Kelley, Tim Lee, Jim Marshall, Joe Preble, John Robb, William J. Schneider, Ed Stitts, Ronald M. Sundelin, Henry Whitehead, and Mark Wiseman* 2381
Performance of superconducting cavities for CEBAF — *Peter Kneisel, John Mammosser, Ganapati Rao, Kenji Saito, and Ron Sundelin* 2384
Q degradations in superconducting niobium cavities — *Kenji Saito and Peter Kneisel* 2387
Production of superconducting niobium cavities for CEBAF — *M. Dzenus, K. Iversen, M. Peiniger, and D. Kiehlmann* 2390
First operation of MACSE the Saclay pilot superconducting electron linac — *B. Aune, C. Antoine, B. Bonin, P. Bosland, J. M. Cavedon, S. Chel, C. Chianelli, A. Curtoni, M. Desmons, J. Fagot, J. Gastebois, A. Godin, F. Gougnaud, J. F. Gournay, G. Gourcy, F. Guemas, X. Hanus, C. Henriot, J. Jablonka, J. M. Joly, M. Juillard, E. Klein, F. Koechlin, P. Leconte, A. Mosnier, Phung Ngoc B., M. Promé, H. Safa, T. Tourrette, A. Veyssière, S. Buhler, M. Fouaidy, and T. Junquera* 2393
Superconducting RF activities at Peking University — *Chia-erh Chen, Zui Zhao, Baocheng Zhang, Guangwei Wang, Lifang Wang, and Jinhu Song* 2396
First test of a 1.5 GHz single cell accelerating cavity obtained by magnetron sputtering of niobium — *G. C. Gualco, A. Matrone, S. Rizzo, F. Rosatelli, R. Parodi, P. Fabbricatore, G. Gemme, R. Musenich, and Bi Zhang* 2399
Fabrication techniques and RF properties of niobium thin wall cavities — *M. Sakano, S. Mukoyama, T. Shimano, H. Matsuba, M. Ikeda, T. Fujino, A. Yamamoto, and H. Hirabayashi* 2402
Operational experience with the TRISTAN superconducting RF system — *K. Akai, T. Furuya, E. Kako, K. Kubo, S. Noguchi, and T. Shishido* 2405
Long term performance of the TRISTAN superconducting RF cavities — *E. Kako, K. Akai, T. Furuya, K. Kubo, S. Mitsunobu, H. Nakai, S. Noguchi, T. Shishido, T. Tajima, and T. Takahashi* 2408
High peak power RF processing studies of 3 GHz niobium cavities — *J. Graber, P. Barnes, J. Kirchgessner, D. Moffat, H. Padamsee, D. Rubin, J. Sears, and Q. S. Shu* 2411
Increase in RF surface resistance of niobium as a result of acid treatment — *D. Moffat, P. Barnes, J. Kirchgessner, H. Padamsee, J. Potts, D. Rubin, J. Sears, Q. Shu, and D. Proch* 2414

Test results on 3 GHz structures for a superconducting linear collider — *R. W. Röth, V. G. Kurakin, G. Müller, H. Piel, J. Pouryamout, D. Reschke, H. Padamsee, J. Graber, J. Kirchgessner, D. Moffat, D. Rubin, J. Sears, and Q. S. Shu* 2417
Field emission studies of heat treated and chemically treated superconducting cavities — *H. Padamsee, P. Barnes, J. Kirchgessner, D. Moffat, D. Rubin, J. Sears, and Q. S. Shu* 2420
Crab cavity development for the Cornell B-factory, CESR-B — *H. Padamsee, P. Barnes, C. Chen, J. Kirchgessner, D. Moffat, D. Rubin, Y. Samed, J. Sears, Q. S. Shu, M. Tigner, and D. Zu* 2423
Development and test of an accelerating cavity shape for a superconducting linear collider — *J. Kirchgessner, P. Barnes, M. Hiller, D. Moffat, H. Padamsee, D. Rubin, D. Saraniti, J. Sears, Q. S. Shu, and W. Hartung* 2426
Status of the superconducting cavity program for HERA — *B. Dwersteg, G. Enderlein, W. Körber, A. Matheisen, W.-D. Möller, D. Proch, D. Renken, and J. Sekutowicz* 2429
Investigations on hydrogen contamination of superconducting cavities — *G. Enderlein, W. Körber, A. Matheisen, D. Proch, and F. Schölz* 2432
Transient heat conduction analysis in superconducting cavities — *Xiaoping Cao and D. Proch* 2435
Analysis of the radiofrequency dipole and quadrupole effects in a QW resonator — *A. M. Porcellato, A. Battistella, G. Bisoffi, and M. Cavenago* 2438
Recent developments in high-current superconducting ion linacs — *J. R. Delayen, C. L. Bohn, W. L. Kennedy, C. T. Roche, and L. Sagalovsky* 2441
Status of the SUNY superconducting RFQ — *A. Jain, I. Ben-Zvi, P. Paul, H. Wang, and A. Lombardi* 2444
RF power requirements for a high intensity proton collider— *Part I* — *D. Boussard* 2447
The superconducting cavities for the TRITRON — *P. Schütz, T. Grundey, J. Labedzki, and U. Trinks* 2450
Applied geometric tolerancing in accelerator component design — *Richard E. Lujan and Kirk E. Christensen* 2453
Considerations for design of a micropositioner for cryogenic accelerators — *Stephen C. Lloyd and Robert C. Gentzlinger* 2456
Cryogenic gas disconnect joints used in cryogenic accelerator cold-gas distribution systems — *Norman G. Wilson, Clark Bridgman, and Robert J. Grieggs* 2459
Field measurement of superconducting quadrupole magnets for TRISTAN mini-beta insertions — *K. Egawa, K. Endo, T. Kubo, Y. Morita, Y. Ohsawa, N. Ohuchi, T. Ozaki, R. Sugahara, and K. Tsuchiya* 2462
Design of the magnet for the SPring-8 storage ring — *N. Kumagai, J. Ohnishi, H. Takebe, K. Kumagai, and S. Motonaga* 2465
One-dimensional time-independent conduction states and temperature distribution along a normal zone during a quench — *G. López* 2468
Non similarity solution approximation to the thermal hydraulic quenchback in superconductors — *G. López* 2471
Development of non-ferrous superconducting magnets — *Frank Krienen, Dinesh Loomba, and Wuzheng Meng* 2474
Design considerations and prototype performance of the Fermilab main injector dipole — *D. J. Harding, M. E. Bleadon, B. C. Brown, E. Desavouret, J. D. Garvey, H. D. Glass, F. A. Harfoush, S. D. Holmes, J. C. Humbert, J. M. Jagger, G. R. Kobliska, A. Lipski, P. S. Martin, P. O. Mazur, F. E. Mills, D. F. Orris, J.-F. Ostiguy, S. G. Peggs, J. E. Pachnik, E. E. Schmidt, J. W. Sim, S. C. Snowdon, and D. G. Walbridge* 2477
Time decay measurements of the sextupole component of the magnetic field in a 4-cm aperture, 17-m-long SSC dipole magnet prototype — *A. Devred, J. DiMarco, J. Kuzminski, R. Stiening, J. Tompkins, Y. Yu, H. Zheng, T. Ogitsu, R. Hanft, P. O. Mazur, D. Orris, and T. Peterson* 2480

Beam Dynamics I

Chairman: A. Chao

The impact of persistent current field errors on the stability of the proton beam in the HERA proton ring *(Invited Paper)* — *F. Willeke and F. Zimmermann* 2483
Tuning of final focus system for future linear colliders *(Invited Paper)* — *Katsunobu Oide* 2488
Beam dynamics of cooled heavy ion beams *(Invited Paper)* — *Ingo Hofmann* 2492
Emittance growth in mismatched charged particle beams — *M. Reiser* 2497

Correction of the first order beam transport of the SLC arcs — *N. Walker, T. Barklow, P. Emma, and P. Krejcik* 2500
A new method of correcting the trajectory in linacs — *T. O. Raubenheimer and R. D. Ruth* 2503
Energy change of a depolarizing resonance due to a type-3 Siberian snake — *M. G. Minty, T. J. P. Ellison, J. E. Goodwin, S. Y. Lee, P. V. Pancella, T. Rinckel, M. A. Ross, F. Sperisen, E. J. Stephenson, B. von Przewoski, R. Baiod, Y. S. Derbenev, A. D. Krisch, R. A. Phelps, T. Roser, B. S. van Guilder, B. Vuaridel, E. D. Courant, and L. G. Ratner* 2506
Impedance measurements with strongly cooled beams at LEAR — *J. Bosser, M. Chanel, D. Manglunki, D. Möhl, F. Pedersen, G. Tranquille, D. Vandeplassche, and M. Gurevitch* 2509
Visualization of wake fields in 3-D — *F. A. Harfoush and T. G. Jurgens* 2512

Accelerator Technology I—Instrumentation, Control, Feedback

Chairman: J. Hinkson

RF control system for CEBAF *(Invited Paper)* — *S. Simrock* 2515
Modern computer networks and distributed intelligence in accelerator controls *(Invited Paper)* — *C. Briegel* 2520
Modern operators' consoles for accelerator control at Fermilab — *P. Lucas, K. Cahill, R. Peters, and J. Smedinghoff* . 2523
The advanced photon source control system — *Martin J. Knott, William P. McDowell, Frank R. Lenkszus, Martin R. Kraimer, Ned D. Arnold, Robert T. Daly, Gary R. Gunderson, Ben-Chin K. Cha, and Mark D. Anderson* 2526
Measurement of longitudinal emittance growth using a laser-induced neutralization method — *V. W. Yuan, R. Garcia, K. F. Johnson, K. Saadatmand, O. R. Sander, D. Sandoval, and M. Shinas* 2529
Bunched beam stochastic cooling *(Invited Paper)* — *G. Jackson* 2532
Control of coupled-bunch instabilities in high-current storage rings *(Invited Paper)* — *G. Lambertson* 2537
Real time global orbit feedback system for NSLS X-ray ring — *L. H. Yu, R. Biscardi, J. Bittner, A. M. Fauchet, S. Krinsky, R. J. Nawrocky, J. Rothman, O. V. Singh, and K. M. Yang* 2542
Progress on the development of APS beam position monitoring system — *Glenn Decker and Youngjoo Chung* 2545

Applications and New Methods of Acceleration

RF transfer in the coupled-cavity free-electron laser two-beam accelerator — *Michael A. Makowski* 2548
Beam dynamics and RF evolution in a multistage klystron-like free-electron laser — *Ken Takayama* 2551
Modelling of the transverse mode suppressor for dielectric wake-field accelerator — *Wei Gai and Ching-Hung Ho* .. 2554
Accelerating field step-up transformer in wake-field accelerators — *E. Chojnacki, W. Gai, P. Schoessow, and J. Simpson* 2557
Suitability of tunneling ionization produced plasmas for the plasma beat wave accelerator — *W. P. Leemans, C. E. Clayton, K. A. Marsh, A. Dyson, and C. Joshi* 2560
Vlasov–Maxwell simulations of nonlinear plasma dynamics in the plasma wakefield accelerator — *Jonathan Krall, Glenn Joyce, and Eric Esarey* 2563
High accelerating-gradient accelerator based on magnetic field decay mechanism — *Han S. Uhm* 2566
An active particle accelerator — *T. Goldman* 2569
Design of micrograting structures for laser acceleration of electrons — *Ira S. Lehrman, Michael J. Arida, Richard C. Fernow, and Harold G. Kirk* 2572
An electrostatic accelerator FEL amplifier as a possible microwave power source for linear colliders — *L. R. Elias, D. J. Larson, and I. Boscolo* 2575
Studies of ion acceleration in a one meter laser controlled collective accelerator — *W. W. Destler, J. Rodgers, C. D. Striffler, and R. L. Yao* 2578
Particle trajectories through MIRRORTRON configurations — *D. J. Larson and D. W. Hewett* 2581
Preliminary design of a dedicated proton therapy linac — *R. W. Hamm, K. R. Crandall, and J. M. Potter* 2583
Intensity possibilities for the Loma Linda medical accelerator — *P. E. Young and P. L. Morton* 2586
Heavy ion, recirculating linac, design optimization — *D. W. Hewett and T. F. Godlove* 2589

Physics issues in the design of a recirculating induction accelerator for heavy ion fusion — *J. J. Barnard, M. A. Newton, L. L. Reginato, W. M. Sharp, H. D. Shay, and S. S. Yu* 2592
Engineering systems designs for a recirculating heavy ion induction accelerator — *M. A. Newton, J. J. Barnard, L. L. Reginato, and S. S. Yu* 2595
High-power proton linac for transmuting the long-lived fission products in nuclear waste — *G. P. Lawrence* 2598
Electron accelerator for transmutation of fission products and nuclear fuel cycle actinides — *G. I. Batskikh, B. V. Bekhtev, V. A. Boiko, V. V. Elian, and A. V. Mishchenko* 2601
Radioactive beams with the HHIRF accelerators — *D. K. Olsen, G. D. Alton, C. Baktash, H. K. Carter, D. T. Dowling, J. D. Garrett, D. L. Haynes, C. M. Jones, R. C. Juras, S. N. Lane, I. Y. Lee, M. J. Meigs, G. D. Mills, S. W. Mosko, B. A. Tatum, and K. S. Toth* 2604
Accelerated radioactive beams at TRIUMF — *J. D'Auria, L. Buchmann, J. S. Fraser, and H. Schneider* 2607
Acceleration and mass-separation of radioactive ion beams in an isochronous cyclotron — *G. Berger, T. Daras, M. Loiselet, N. Postiau, and G. Ryckewaert* 2610
Linear resonant accelerators for industrial applications — *O. A. Waldner, V. G. Gass, A. A. Glaskov, V. D. Danilov, B. V. Zverev, A. A. Il'in, A. D. Koljaskin, A. I. Krivonosov, V. N. Leonov, N. R. Lobanov, O. S. Milovanov, A. A. Mishukov, A. N. Fronin, A. A. Revkov, N. P. Sobenin, Y. I. Tlekhas, and P. B. Shurupov* 2613
The test run of the AMS system at Peking University — *Chia-erh Chen, Zhiyu Guo, Shangqing Yan, Min Xiao, Zhengfang Zhang, Fengling Yang, Renxing Li, Jingxiang Yu, Kun Li, Hongtao Liu, Dongxing Jiang, Ruju Zhang, Xiangyang Lu, Bin Li, Weishu Qian, Jinglin Yuan, Zheng Yang, Kexin Liu, and Houzhi Si* 2616
The Ghent State University linear electron accelerator facilities: Status and perspectives — *W. Mondelaers* 2619
EXDEP/CTX—An explosive detection system for screening luggage with high energy X-rays — *Kerry W. Habiger, Jerome R. Clifford, R. Bruce Miller, and William F. McCullough* 2622
CW 100MW microwave power transfer in space — *K. Takayama, S. Hiramatsu, and M. Shiho* 2625
Ion accelerators for space — *R. J. Slobodrian and L. Potvin* 2628
Performance of the CERN plasma lens in laboratory and beam tests at the antiproton source — *R. Kowalewicz, M. Lubrano di Scampamorte, S. Milner, F. Pedersen, H. Riege, J. Christiansen, K. Frank, M. Stetter, R. Tkotz, and E. Boggasch* 2631

Synchrotron Radiation Sources/FELs

Progress with ELETTRA, the synchrotron light source in Trieste — *M. Puglisi and A. Wrulich* 2634
The advanced light source— *Status report* — *Alan Jackson* 2637
The ALS— *A high-brightness XUV synchrotron radiation source* — *A. L. Robinson and A. S. Schlachter* 2640
Aladdin II$^+$ — *Walter S. Trzeciak and Dornis C. Morin* 2643
Status of the SPring-8 project (storage ring) — *M. Hara, H. Kamitsubo, and N. Kumagai* 2646
Status of compact synchrotron light source work at TAC — *C. A. Swenson, F. R. Huson, R. Rocha, and Y. Huang* ... 2649
The DARPA compact superconducting X-ray lithography source features — *Richard Heese, Swarn Kalsi, and Eddie Leung* 2652
The superconducting compact storage ring NIJI-III — *Y. Tsutsui, K. Emura, F. Miura, H. Takada, and T. Tomimasu* . 2655
Calculation of eddy-currents induced in a compact synchrotron superconducting magnet structure during a current ramp — *Swarn Kalsi and Richard Heese* 2658
Orbits, tunes and chromaticities for the BNL SXLS storage ring — *L. N. Blumberg, J. B. Murphy, and S. Sharma* 2661
Lattice properties of the phase I BNL X-ray lithography source obtained from fits to magnetic measurement data — *L. N. Blumberg, J. B. Murphy, and M. F. Reusch* 2664
Beam dynamics of the SRRC 1.3 GeV storage ring — *C. C. Kuo, C. S. Hsue, J. C. Lee, M. H. Wang, and H. P. Chang* 2667
Lattice design of the SRRC 1.3 GeV storage ring — *C. S. Hsue, C. C. Kuo, J. C. Lee, and M. H. Wang* 2670

Volume 5

Magnet lattice of the Pohang Light Source — *J. Choi, T. Lee, K. Nam, and M. Yoon* 2673
Undulator based synchrotron radiation source in the 5–30 eV spectral region — *Xiaohao Zhang, James B. Murphy, and Samuel Krinsky* 2676
Theoretical minimum emittance lattice for an electron storage ring — *S. Y. Lee and L. Teng* 2679
Orbit distortion due to the floor displacement in the light source building under climatic thermal stress — *T. Katsura, Y. Kamiya, and Y. Fujita* 2682
Beam lifetime investigations at BESSY — *L. Schulz, E. Weihreter, and H. Lehr* 2685
The 3 GeV synchrotron injector for SPEAR — *H. Wiedemann, M. Baltay, J. Voss, K. Zuo, C. Chavis, R. Hettel, J. Sebek, H. D. Nuhn, J. Safranek, L. Emery, M. Horton, J. Weaver, J. Haydon, T. Hostetler, R. Ortiz, M. Borland, S. Baird, W. Lavender, P. Kung, J. Mello, W. Li, H. Morales, L. Baritchi, P. Golceff, T. Sanchez, R. Boyce, J. Cerino, D. Mostowfi, D. F. Wang, D. Baritchi, G. Johnson, C. Wermelskirchen, B. Youngman, C. Jach, J. Yang, and R. Yotam* 2688
Commissioning experiences of the ALS booster synchrotron — *Charles H. Kim* 2691
A high energy electron beam facility for industrial research — *S. Okuda, T. Nakanishi, K. Ikegami, S. Nakata, T. Nakagawa, C. Tsukishima, A. Maruyama, H. Tanaka, S. Nakamura, I. Kodera, S. Yamamoto, T. Matsuda, S. Fujimura, H. Itagaki, T. Yamada, and M. Iwamoto* 2694
The booster to storage ring transport line for SRRC — *M. H. Wang, C. C. Kuo, and C. S. Hsue* 2697
Design of beam transfer line and injection system of Pohang Light Source — *In Soo Ko and M. Yoon* 2700
Beam transport to the SXLS ring — *Eva Bozoki* 2703
Design and simulation of fast pulsed kicker/bumper units for the positron accumulator ring at APS — *Ju Wang and Gerald J. Volk* 2706
Magnets with full apertures for extracting synchrotron radiation at the photon factory ring — *Yukinori Kobayashi, Akira Araki, and Yukihide Kamiya* 2709
Status of development of the insertion devices for ELETTRA — *C. Poloni, R. Bracco, B. Diviacco, R. P. Walker, and D. Zangrando* 2712
A wedged pole hybrid type undulator as a synchrotron radiation source — *Shigemi Sasaki, Takeo Takada, Nobuo Matsuki, Shigeki Sasaki, and Hideo Ohno* 2715
Design considerations for a fast modulator in a 'crossed undulator' — *Roland Savoy and Klaus Halbach* 2718
The U5.0 undulator for the ALS — *E. Hoyer, J. Chin, K. Halbach, W. V. Hassenzahl, D. Humphries, B. Kincaid, H. Lancaster, and D. Plate* 2721
Fast excitation variable period wiggler — *A. van Steenbergen, J. Gallardo, T. Romano, and M. Woodle* 2724
Incorporation of a 5 T superconducting wiggler in an MLI synchrotron light source — *Dan Y. Wang, F. C. Younger, and H. Wiedemann* 2727
Ion channel focusing in FEL wigglers — *John Vetrovec* 2730
Performance of rocketdyne phase-optimized pure permanent magnet undulator — *G. Rakowsky, B. Bobbs, J. Brown, P. Kennedy, and G. Swoyer* 2733
Design and test of a model pole for the ALS U5.0 undulator — *W. V. Hassenzahl, E. Hoyer, and R. Savoy* 2736
ALS insertion device block measurement and inspection — *S. Marks, J. Carrieri, C. Cork, W. V. Hassenzahl, E. Hoyer, and D. Plate* 2739
Ion beam probe for measurement of wiggler errors — *John Vetrovec, Bradley Bobbs, and Michael Lampel* 2742
FEL design using the CEBAF linac — *G. R. Neil, J. J. Bisognano, H. F. Dylla, G. A. Krafft, C. W. Leemann, C. K. Sinclair, and B. Yunn* 2745
Coherent X-rays from PEP — *Simon Baird, Heinz-Dieter Nuhn, Roman Tatchyn, Herman Winick, Alan S. Fisher, Juan C. Gallardo, and Claudio Pellegrini* 2748
SATURNUS: The UCLA infrared free-electron laser project — *J. W. Dodd, S. C. Hartman, S. Park, C. Pellegrini, J. B. Rosenzweig, J. A. Smolin, G. Hairapetian, J. Kolonko, W. A. Barletta, D. B. Cline, J. G. Davis, C. J. Joshi, N. C. Luhmann, Jr., S. N. Ivanchenkov, A. S. Khlebnikov, Y. Y. Lachin, and A. A. Varfolomeev* 2751

Performance of the photoinjector accelerator for the Los Alamos free-electron laser — *P. G. O'Shea, S. C. Bender, B E. Carlsten, J. W. Early, D. W. Feldman, R. B. Feldman, W. J. D. Johnson, A. H. Lumpkin, R. L. Sheffield, R. W. Springer, W. E. Stein, and L. M. Young* 2754
CFEL-I: A compact free electron laser — *L. R. Elias, D. R. Anderson, A. L. Centore II, Hua Bei Jiang, I. Kimel, D. J. Larson, M. Tecimer, and Zhong Zhefu* 2757
Design, manufacturing and first measurements of a hybrid permanent magnet undulator for free electron laser — *F. Rosatelli, L. Barbagelata, F. Crenna, M. Grattarola, G. Gualco, A. Matrone, G. B. Ottonello, F. Ciocci, and A. Renieri* 2760
Pulsed undulators for high efficiency FEL oscillators usable in the visible spectrum — *Hubert Leboutet* 2763
Reduction of undulator radiation and FEL small gain due to wiggler errors — *Aharon Friedman* 2766
Heating of the LSS wiggler beam tube due to induced surface current — *W. C. Sellyey and C. G. Parazzoli* 2769
A new possibility of coherent microwave radiation by relativistic particles — *A. N. Didenko* 2775
Effects of construction and alignment errors on the orbit functions of the Advanced Photon Source Storage Ring — *H. Bizek, E. Crosbie, E. Lessner, L. Teng, and J. Wirsbinski* 2778
A low vertical β mode for the LNLS UVX electron storage ring — *Liu Lin and P. Tavares* 2781
Injection into the LNLS UVX electron storage ring — *Liu Lin* 2784
The transport line from MAIRA to the LNLS UVX electron storage ring — *Liu Lin, L. Jahnel, P. Tavares, and R. H. A. Farias* 2787
An active interlock system for the NSLS X-ray ring insertion devices — *R. J. Nawrocky, R. Biscardi, J. Dabrowski, J. Flannigan, S. Ramamoorthy, J. Rothman, J. Smith, I. So, M. Thomas, and G. Decker* 2790
A bypass for synchrotron radiation experiments at the storage ring PETRA II — *W. Brefeld and P. Gürtler* 2793

Low- and Medium-Energy Accelerators and Rings

Beam acceleration in the LBL 88-inch cyclotron with injection from the AECR source — *D. J. Clark, C. M. Lyneis, and Zuqi Xie* 2796
Recent improvements and new possibilities of the GANIL facility — *M. Bajard* 2799
Superconducting booster cyclotron studies at GANIL — *Chabert A., C. Bieth, P. Bricault, M. Duval, J. Fermé, A. Joubert, M. H. Moscatello, F. Ripouteau, and Q. V. Truong* 2802
Developing the Chalk River Superconducting Cyclotron for operation in π-mode — *J. A. Hulbert and X.-H. Zhou* ... 2805
The COSY-Jülich project April 1991 status — *R. Maier, U. Pfister, and J. Range* 2808
ASTRID— *A storage ring for ions and electrons* — *Søren Pape Møller* 2811
Status of the CRYRING project — *K.-G. Rensfelt* 2814
Advanced stacking methods using electron cooling at the TSR Heidelberg — *M. Grieser, D. Habs, R. v. Hahn, C. M. Kleffner, R. Repnow, M. Stampfer, E. Jaeschke, and M. Steck* 2817
The ADRIA project — *A. Dainelli, A. Lombardi, A. Ratti, and A. G. Ruggiero* 2820
The proposal of the accelerator complex of the Moscow kaon factory — *V. V. Balandin, A. G. Chursin, G. A. Dubinsky, S. K. Esin, N. I. Golubeva, A. I. Iliev, L. V. Kravchuk, V. A. Matveev, V. V. Paramonov, A. S. Pashenkov, Y. V. Senichev, E. N. Shaposhnikova, S. P. Volin, V. P. Belov, V. A. Glukhikh, N. D. Malitskiy, Y. P. Severgin, M. N. Tarovik, I. A. Shukeilo, G. I. Batskikh, Y. D. Ivanov, Y. S. Ivanov, V. A. Konovalov, R. A. Meshcherov, B. P. Murin, and Y. F. Semunkin* 2823
Application of a new scheme for passing through transition energy to the Fermilab main ring and main injector — *J. A. MacLachlan and J. E. Griffin* 2826
Low momentum compaction lattice study for the SSC low energy booster — *E. D. Courant, A. A. Garren, and U. Wienands* 2829
Operational aspects of electron cooling at the Low Energy Antiproton Ring (LEAR) — *J. Bosser, M. Chanel, R. Ley, D. Möhl, J. C. Perrier, G. Tranquille, and D. J. Williams* 2832
A combined symmetric and asymmetric B-factory with monochromatization — *A. N. Dubrovin and A. A. Zholents* .. 2835

B-factory optics and beam–beam interaction for millimeter β and locally shortened bunches — *Yuri F. Orlov, Christopher M. O'Neill, James J. Welch, and Robert H. Siemann* 2838
Apiary B Factory lattice design — *M. H. R. Donald and A. A. Garren* 2841
Apiary B-Factory separation scheme — *A. Garren and M. Sullivan* 2844
Feasibility of a φ factory in KEK — *Kohji Hirata and Kazuhito Ohmi* 2847
DAΦNE storage rings — *S. Bartalucci, M. Bassetti, M. E. Biagini, C. Biscari, R. Boni, A. Gallo, S. Guiducci, M. R. Masullo, L. Palumbo, M. Serio, B. Spataro, and G. Vignola* 2850
Conceptual design of a high luminosity 510 MeV collider — *C. Pellegrini, D. Robin, and M. Cornacchia* 2853
A high luminosity superconducting mini collider for phi meson production and particle beam physics — *C. Pellegrini, D. Robin, D. Cline, J. Kolonko, C. Anderson, W. Barletta, A. Chargin, M. Cornacchia, G. Dalbacka, K. Halbach, E. Lueng, F. Kimball, D. Madura, and L. Patterson* 2856
DELTA optics — *D. Schirmer and K. Wille* 2859
Status of DELTA and design of its vacuum system — *Niels Marquardt* 2862
Commissioning the SSRL injector — *S. Baird and J. Safranek* 2865
An isochronous lattice for PEP — *W. J. Corbett, M. H. R. Donald, and A. A. Garren* 2868
Lattice studies for a small storage ring — *Philip Kiefer and Wayne Vernon* 2871
High frequency betatrons — *David R. Winn* 2874
Improvement of 150 MeV racetrack microtron — *T. Hori, M. Sugitani, T. Mitsumoto, and Y. Sasaki* 2877
Measurement and tuning of beam parameters in the heavy ion storage ring ESR — *F. Nolden, S. Baumann, K. Beckert, H. Eickhoff, B. Franczak, B. Franzke, O. Klepper, W. König, U. Schaaf, H. Schulte, P. Spädtke, M. Steck, and J. Struckmeier* 2880
Algorithm for the deflector plates of the 1 MHz chopper for the Kaon Factory — *M. J. Barnes and G. D. Wait* 2883
Conception of the 200 MeV/u booster for the Nuclotron — *I. B. Issinsky and V. A. Mikhailov* 2886
The project of the heavy ion storage rings complex of the JINR at Dubna — *O. N. Malyshev, I. N. Meshkov, R. T. Oganessian, Y. T. Oganessian, V. V. Parkhomchuk, P. Pokorny, A. A. Sery, S. V. Stepantsov, Y. A. Syresin, G. M. Ter-Akopian, and V. A. Timakov* 2888

High-Energy Accelerators and Colliders

Chairman: W. Wallenmeyer

Performance of LEP and future plans *(Invited Paper)* — *Jean-Pierre Koutchouk* 2891
Achieving high luminosity in the Fermilab Tevatron *(Invited Paper)* — *Stephen D. Holmes* 2896
RHIC project *(Invited Paper)* — *Satoshi Ozaki* 2901
The status of HERA *(Invited Paper)* — [illegible] 2905
An electron–proton collider in the TeV range — *M. Tigner, B. Wiik, and F. Willeke* 2910
The status and development of the UNK project *(Invited Paper)* — *V. A. Yarba* 2913

Accelerator Technology II, RF, Power Supplies, Operations

Chairman: R. L. Kustom

High frequency cascaded resonant transformer rectifier power supply for neutral beam injection *(Invited Paper)* — *Louis L. Reginato* 2918
Switching power supply regulation of storage ring magnets *(Invited Paper)* — *M. G. Billing* 2923
Multimegawatt RF power sources for linear colliders *(Invited Paper)* — *G. Caryotakis* 2928
The magnicon: A new RF power source for accelerators *(Invited Paper)* — *Oleg A. Nezhevenko* 2933
AC bias operation of the perpendicular biased ferrite tuned cavity for the TRIUMF Kaon Factory Booster Synchrotron — *R. L. Poirier, T. A. Enegren, and I. B. Enchevich* 2943
RF reference generation for the ground test accelerator — *Amy H. Regan and Peter M. Denney* 2946

Alignment issues of the SLC linac accelerating structure — *J. T. Seeman, C. Adolphsen, F. J. Decker, G. Fischer, J. Hodgson, R. Pennacchi, C. Perkins, and M. Pietryka* 2949
Operational history of the SPS collider 1981-1990 — *V. Hatton* 2952
Status of the SLC damping ring kicker systems — *T. Mattison, R. Cassel, A. Donaldson, D. Gough, G. Gross, A. Harvey, D. Hutchinson, and M. Nguyen* 2955

Linear Accelerators and Pulsed Power Devices

Cell design for the DARHT linear induction accelerators — *M. Burns, L. Allison, L. Earley, D. Liska, C. Mockler, J. Ruhe, H. Tucker, and L. Walling* 2958
Transverse impedance measurements of prototype cavities for a dual-axis radiographic hydrotest (DARHT) facility — *L. Walling, Paul Allison, M. Burns, D. J. Liska, D. E. McMurry, and A. H. Shapiro* 2961
A new front-end for the LEP Injector Linac — *Jean-Claude Godot, Louis Rinolfi, Andrea Pisent, and Hans Braun* ... 2964
Photocathode driven linac at UCLA for FEL and plasma wakefield acceleration experiments — *S. Hartman, F. Aghamir, W. Barletta, D. Cline, J. Dodd, T. Katsouleas, J. Kolonko, S. Park, C. Pellegrini, J. Rosenzweig, J. Smolin, J. Terrien, J. Davis, G. Hairapetian, C. Joshi, N. Luhmann, Jr., and D. McDermott* 2967
Status of the LISA superconducting linac project — *F. Tazzioli, A. Aragona, R. Boni, M. Castellano, G. Di Pirro, S. Faini, M. Ferrario, A. Gallo, S. Kulinski, C. Marchetti, M. Minestrini, P. Patteri, C. Sanelli, M. Serio, A. Stecchi, L. Trasatti, M. Vescovi, L. Catani, S. Tazzari, N. Cavallo, and F. Cevenini* 2970
Status of the ARES R&D program — *R. Boni, M. Castellano, P. Fabbricatore, M. Ferrario, A. Gallo, P. Michelato, M. Minestrini, F. Musenich, C. Pagani, R. Parodi, P. Patteri, L. Serafini, S. Tazzari, and F. Tazzioli* 2973
Preliminary conceptual design for a 510 MeV electron/positron injector for a UCLA ϕ factory — *Glen Dahlbacka, Robert Hartline, William Barletta, and Claudio Pellegrini* 2976
Operating experience with the ALS linac — *F. Selph and D. Massoletti* 2978
Commissioning of the new heavy ion injector at GSI — *N. Angert, L. Dahl, J. Glatz, J. Klabunde, U. Ratzinger, H. Schulte, B. Wolf, H. Deitinghoff, J. Friedrich, H. Klein, and A. Schempp* 2981
Development of a radioactive nuclides accelerator at the Moscow meson factory — *V. A. Andreev, V. A. Bomko, G. N. Vjalov, S. K. Esin, D. V. Gorelov, J. D. Ivanov, A. S. Iljinov, A. A. Kolomiets, V. A. Moiseev, B. P. Murin, P. N. Ostroumov, and A. N. Zelenskiki* 2984
Status of the uranium upgrade of ATLAS — *L. M. Bollinger, P. J. Billquist, J. M. Bogaty, B. E. Clifft, P. Markovich, F. H. Munson, R. C. Pardo, K. W. Shepard, and G. P. Zinkann* 2987
45 MeV linac for the 800 MeV synchrotron radiation light source — *N. Kaneko, M. Y. Yamamoto, O. Azuma, H. Iwata, T. Nakashizu, and Y. Hoshi* 2990
Design studies of SSC coupled cavity linac — *C. R. Chang, R. Bhandari, W. Funk, D. Raparia, and J. Watson* 2993
Tuning of the first 805 MHz side-coupled cavity module for the Fermilab upgrade — *Zubao Qian, Mark Champion, Thomas G. Jurgens, Harold W. Miller, Alfred Moretti, and René Padilla* 2996
Beam loading in a high current accelerating gap — *M. J. Rhee and B. N. Ding* 2999
An interactive code SUPERLANS for evaluation of RF-cavities and acceleration structures — *D. G. Myakishev and V. P. Yakovlev* 3002
The $3\pi/4$ backward TW structure for the ELETTRA 1.5 GeV electron injector — *P. Girault* 3005
A new electron linac injector design up to 200 MeV — *D. Tronc* 3008
Quadrupole effects in on-axis coupled linacs — *F. P. Adams, R. J. Burton, and J. Ungrin* 3011
Cavity shape and beam dynamics design for a linac for pions — *G. Swain* 3014
Characterization of a ramped gradient DTL: Experiment and theory — *K. F. Johnson, E. A. Wadlinger, O. R. Sander, G. P. Boicourt, G. O. Bolme, C. M. Fortgang, J. D. Gilpatrick, J. Merson, D. P. Sandoval, and V. Yuan* 3017
High order calculation of the multipole content of three dimensional electrostatic geometries — *Martin Berz, William M. Fawley, and Kyoung Hahn* 3020
Measurements on iris-structures with rectangular holes — *M. Kurz, P. Hülsmann, H. Klein, and A. Schempp* 3023
RF tests of a band overlap free DAW accelerating structure — *R. Parodi, A. Stella, and P. Fernandes* 3026

Transient analysis of beam-loaded standing wave accelerator cavities — *Tom Buller* 3029
Three-dimensional space charge and image charge effects in radio-frequency-quadrupole accelerators — *F. W. Guy* . 3032
Acceleration tests of the INS 25.5-MHz split coaxial RFQ — *S. Arai, A. Imanishi, T. Morimoto, S. Shibuya, E. Tojyo, and N. Tokuda* 3035
Numerical simulation of a short RFQ resonator using the MAFIA codes — *H. Wang, I. Ben-Zvi, A. Jain, P. Paul, and A. Lombardi* 3038
Deceleration of antiprotons with a RFQ — *A. Schempp, H. Deitinghoff, A. Firjahn-Andersch, H. Vormann, M. de Saint Simon, J. Y. Hemery, C. Thibault, and F. Botlo-Pilat* 3041
Properties of the GSI HLI-RFQ structure — *J. Friedrich, A. Schempp, H. Deitinghoff, U. Bessler, H. Klein, R. Veith, N. Angert, and J. Klabunde* 3044
New vanes for RFQ1: Fabrication, installation, and tuning — *B. G. Chidley, G. E. McMichael, and T. Tran-Ngoc* 3047
Progress of the 473 MHz four-rod RFQ — *Reza Kazimi, F. R. Huson, and W. W. MacKay* 3050
Development of a variable energy RFQ for cluster acceleration — *A. Schempp, J. Madlung, J. Dehen, H. Deitinghoff, J. Friedrich, A. Kipper, H. O. Moser, G. Hadinger, M. J. Gaillard, R. Genre, and J. Martin* 3053
Least-squares fitting procedure for setting RF phase and amplitude in drift-tube-linac tanks — *F. W. Guy and T. P. Wangler* 3056
Production of tightly focused E-beams with high-current accelerators — *J. W. Poukey, M. G. Mazarakis, C. A. Frost, and J. J. Ramirez* 3059
Longitudinal emittance measurement of the 100 MeV proton beam — *Y. V. Bylinsky, A. V. Feschenko, and P. N. Ostroumov* 3062
The delta-t tuneup procedure for the Fermilab linac upgrade — *Thomas L. Owens and Elliott S. McCrory* 3064
Proton beam acceleration up to 160 MeV at the Moscow meson factory linac — *G. I. Batskich, Y. V. Bylinsky, S. K. Esin, A. P. Fedotov, A. V. Feschenko, Y. D. Ivanov, O. S. Korolev, L. V. Kravchuk, A. I. Kvasha, V. A. Matveev, V. N. Michailov, A. N. Mirzojan, N. P. Murin, P. N. Ostroumov, S. A. Petronevich, B. A. Rubtsov, V. L. Serov, S. I. Scharamentov, N. I. Uksusov, S. Z. Zyarylkapov, and I. A. Sagin* 3067
Drift compression experiments on MBE-4 and related emittance growth phenomena — *S. Eylon, A. Faltens, W. Fawley, T. Garvey, K. Hahn, E. Henestroza, and L. Smith* 3070
Transverse emittance studies of an induction accelerator of heavy ions — *T. Garvey, S. Eylon, T. J. Fessenden, K. Hahn, and E. Henestroza* 3073
Funneling study with a low energy proton beam — *W. Barth and A. Schempp* 3076
LIAM—A linear induction accelerator model — *H. Brand, G. Caporaso, D. Lager, F. Coffield, and F. Chambers* ... 3079
Artificial intelligence techniques for tuning linear induction accelerators — *Darrel L. Lager, Hal R. Brand, William J. Maurer, Fred Coffield, Frank Chambers, and William Turner* 3082
Diagnostics and data analysis for the ETA-II linear induction accelerator — *F. W. Chambers, S. L. Allen, F. J. Deadrick, W. E. Nexsen, A. C. Paul, V. L. Renbarger, and W. C. Turner* 3085
Modeling of switching cores for induction accelerators — *Henry D. Shay, John F. DeFord, and George D. Craig* ... 3088
Modeling magnetic pulse compressors — *Anthony N. Payne* 3091
Measurements of reduced corkscrew motion on the ETA-II linear induction accelerator — *A. L. Allen, H. R. Brand, F. W. Chambers, Y.-J. Chen, F. E. Coffield, F. J. Deadrick, L. V. Griffith, D. L. Lager, W. J. Mauer, W. E. Nexsen, A. C. Paul, S. Sampayan, and W. C. Turner* 3094
Performance characteristics of an induction linac magnetic pulse compression modulator at multi-kilohertz pulse repetition frequencies — *S. Sampayan, F. W. Chambers, F. J. Deadrick, W. A. Niven, C. W. Ollis, A. N. Payne, V. L. Renbarger, E. T. Scharlemann, W. C. Turner, and J. A. Watson* 3097
Degradation of brightness by resonant particle effects — *Y.-J. Chen, G. J. Caporaso, A. G. Cole, A. C. Paul, and W. C. Turner* 3100
Reduction of energy sweep of the ETA-II beam — *W. E. Nexsen, S. L. Allen, F. W. Chambers, R. A. Jong, A. C. Paul, S. E. Sampayan, and W. C. Turner* 3103
ETA-II beam brightness measurement — *A. C. Paul, S. L. Allen, F. W. Chambers, Y.-J. Chen, F. J. Deadrick, and W. C. Turner* 3106

Development of RFQ accelerator for the MMF linac — *V. A. Andreev, S. K. Esin, I. M. Kapchinskij, D. A. Kashinskij, A. M. Kozodaev, A. A. Kolomiets, P. N. Ostroumov, A. M. Raskopin, N. V. Schachrai, and R. M. Vengrov* 3109
High power microwave generation in virtual cathode systems — *A. N. Didenko and V. I. Rashchikov* 3111
Experimental tests of the power supply and prototype cell for the 1.5 MeV SLIA acceleration unit — *P. Corcoran, B. Bowen, V. Bailey, V. Carboni, J. Fockler, B. Chugg, and H. Nishimoto* 3114
Beam breakup considerations in the design of multiple off-axis gaps in an induction accelerator cell for SLIA — *John Edighoffer* 3117
Experimental observations of beam transport in twisted quadrupole fields — *J. P. Lidestri, V. L. Bailey, Jr., J. A. Edighoffer, S. D. Putnam, M. G. Tiefenback, and D. Wake* 3120
Magnet design for SLIA proof-of-concept experiment — *V. Bailey, D. Wake, R. Curry, J. Lidestri, and M. Tiefenback* 3123
Experiments investigating the effects of the accelerating gap voltage pulse on the ion focused (IFR) high current electron recirculators — *M. G. Mazarakis, D. L. Smith, J. W. Poukey, J. S. Wagner, L. F. Bennett, W. R. Olson, B. N. Turman, K. R. Prestwich, and J. Wells* 3126
RADLAC II/SMILE performance with a magnetically insulated voltage adder — *S. L. Shope, M. G. Mazarakis, C. A. Frost, C. E. Crist, J. W. Poukey, K. R. Prestwich, B. N. Turman, K. Struve, and D. Welch* 3129
A novel concept for a lithium lens exciter — *G. G. Karady and H. A. Thiessen* 3132
High-intensity flash X-ray source for HERMES III — *T. W. L. Sanford, J. A. Halbleib, W. H. McAtee, and R. C. Mock* 3135
SLC positron source flux concentrator modulator — *J. de Lamare, A. Kulikov, R. Cassel, and V. Nesterov* 3138
Fast risetime magnetic field coil for electron beam propagation studies — *D. J. Weidman, W. C. Freeman, J. D. Miller, M. J. Rhee, R. F. Schneider, K. T. Nguyen, and R. A. Stark* 3141
Long pulse electron beams — *J. R. Smith, I. R. Shokair, and K. W. Struve* 3144
Kicker pulser charger — *R. Cassel and M. Nguyen* 3147
PSR extraction kicker system improvements — *T. W. Hardek* 3150
Fast thyratron driver — *M. N. Nguyen and R. L. Cassel* 3153
Pulse shape adjustment for the SLC damping ring kickers — *T. Mattison, R. Cassel, A. Donaldson, H. Fischer, and D. Gough* 3156
High voltage pulse cable and connector experience in the kicker systems at SLAC — *K. Harris, M. Artusy, A. Donaldson, and T. Mattison* 3159
Kicker prepulse canceler — *R. L. Cassel and T. S. Mattison* 3162
Kicker thyratron experience from SLC — *A. R. Donaldson, R. L. Cassel, T. S. Mattison, and L. L. Reginato* 3165
The timing and diagnostic systems of the kicker magnet pulsers for the Stanford Linear Collider — *D. E. Gough, R. L. Cassel, A. R. Donaldson, D. P. Hutchinson, and T. S. Mattison* 3168
Fast power supplies for kicker and thin septum magnets in a 1.2 GeV synchrotron radiation source — *B. E. Strickland, G. L. Schofield, B. L. Thomas, W. P. White, B. Ng, and D. Meaney* 3171
Fast TEM kicker with MOSFET solid state driver — *Alfredo Saab, Michael Kogan, and Tomás Russ* 3174
Application of electrostatic undulators for acceleration of intense ion beams — *E. S. Masunov and A. P. Novicov* 3177
The ELETTRA 1.5 GeV electron injector — *D. Tronc, D. T. Tran, C. Bourat, P. Girault, P. Letellier, G. Meyrand, S. Sierra, and A. Massarotti* 3180
Microwave and beam optics design features of a preinjector linac for a synchrotron radiation source — *J. Haimson and B. Mecklenburg* 3183
Electron preinjector for Siberia-2 SR source — *O. A. Nezhevenko, G. N. Ostreiko, B. Z. Persov, S. I. Ruvinsky, G. V. Serdobintsev, E. N. Shaimerdenov, M. A. Tiunov, V. P. Yakovlev, and I. A. Zapryagaev* 3186
Fermilab linac upgrade side coupled cavity temperature control system — *J. Crisp and J. Satti* 3189
Electron-beam generation, transport, and transverse oscillation experiments using the REX injector — *R. L. Carlson, P. W. Allison, T. J. Kauppila, D. C. Moir, and R. N. Ridlon* 3192
Matching and transport of beams in a continuously twisted quadrupole channel — *M. G. Tiefenback, J. P. Lidestri, V. L. Bailey, Jr., and S. D. Putnam* 3195
PILAC: A pion linac facility for 1-GeV pion physics at LAMPF — *Henry A. Thiessen* 3198
High voltage, high power nested high voltage accelerator — *R. J. Adler and R. J. Richter-Sand* 3201

LELIA: An induction linac developed for FEL application — *P. Eyharts, J. Bardy, P. Anthouard, P. Eyl, and M. Thevenot* 3204
A traveling wave accelerator with HOM outcouplers for FEL's — *R. Miller and M. Lampel* 3276

Linear Colliders

Effect of wakefields on first order transport in the SLC linac — *Chris Adolphsen, Karl L. F. Bane, and John T. Seeman* 3207
Multibunch energy and spectrum control in the SLC high energy linac — *J. T. Seeman, F. J. Decker, R. K. Jobe, and I. Hsu* 3210
Review of tolerances at the Final Focus Test Beam — *F. Bulos, D. Burke, R. Helm, J. Irwin, G. Roy, and N. Yamamoto* 3213
Beam-based alignment and tuning procedures for e^+e^- collider final focus systems — *F. Bulos, D. Burke, R. Helm, J. Irwin, A. Odian, G. Roy, R. Ruth, and N. Yamamoto* 3216
Wakefield measurements of SLAC linac structures at the Argonne AATF — *J. W. Wang, G. A. Loew, J. Simpson, E. Chojnacki, W. Gai, R. Konecny, and P. Schoessow* 3219
Maintaining micron-size beams in collision at the interaction point of the Stanford Linear Collider — *F. Rouse, T. Gromme, W. Kozanecki, and N. Phinney* 3222
Transverse equilibria in linear collider beam–beam collisions — *J. B. Rosenzweig and Pisin Chen* 3225
Progress on the CLIC final focus system — *O. Napoly, P. Sievers, T. Taylor, and B. Zotter* 3228
Optimizing energy spread in the CLIC main linac — *G. Guignard and C. Fischer* 3231
Investigations on beam damping simulations and the associated model of CLIC — *G. Guignard, C. Fischer, and A. Millich* 3234
Microwave quadrupole structures for the CERN linear collider — *W. Schnell and I. Wilson* 3237
Design calculations of the CLIC transfer structure — *Erk Jensen* 3240
Model work on a transfer structure for CLIC — *L. Thorndahl* 3243
Higher order effects in beam–beam deflection — *Yu-Chiu Chao and Pisin Chen* 3246
Beam–beam deflection and beamstrahlung monitor response for tilted elliptic beams — *V. Ziemann* 3249
Simulations on pair creation from beam–beam interaction in linear colliders — *P. Chen, T. Tauchi, and K. Yokoya* ... 3252
Differential luminosity under beamstrahlung — *Pisin Chen* 3255
A practical algorithm for chromaticity correction in linear collider final focus systems — *P. Krejcik* 3258
Linear e^+e^- colliders above 1 TeV (CM) — *Alfred A. Mondelli* 3261
Linac-ring colliders with high disruption parameters— A first test of principle — *J. R. Boyce, S. Jin, J. Kewisch, R. Li, P. K. Kloeppel, B. Niczyporuk, R. Rossmanith, N. Sereno, and R. Whitney* 3264
Misalignment study of NLC bunch compressor — *R. P. Rogers and S. A. Kheifets* 3267
High brightness sources for colliders — *J. E. Spencer* 3270
Investigation of seismic vibrations and relative displacements of linear collider VLEPP elements — *B. A. Baklakov, P. K. Lebedev, V. V. Parkhomchuk, A. A. Sery, A. I. Sleptsov, and V. D. Shiltsev* 3273

Closing Plenary Session

Chairman: J. O'Fallon

CERN plans for the future *(Invited Paper)* — *Carlo Rubbia* 3279

Author Index Follows Pages 699
..... 1340
..... 2010
..... 2672
..... 3283

LIST OF PARTICIPANTS

STEVEN R. ABBOTT
LBL
ONE CYCLOTRON RD,
MS-64/121
BERKELEY CA 94720
USA

RAFAEL C. ABELA
PSI
5232 VILLIGEN PSI
SWITZERLAND

DAN ABELL
UNIV. OF MARYLAND
DEPARTMENT OF PHYSICS
COLLEGE PARK MD 20742
USA

E. K. ABOLEMOVA
INSTITUTE OF NUCLEAR PHYSICS
NOVOSIBIRSK BRANCH AT SERPUKHOV
142 284 PROTVINO MOSCOW REGION
USSR

MICHEL ABS
ION BEAM APPLICATIONS SA
CHEMIN DU CYCLOTRON, 2
B-1348 LOUVAIN-LA-NEUVE
BELGIUM

FRED P. ADAMS
CHALK RIVER LABS
AECL RESEARCH
CHALK RIVER ONTARIO KOJ1JO
CANADA

GARY ADAMS
US ARMY-SMC
ATTN CSSD-DE-T
P. O. BOX 1500
HUNTSVILLE AL 35807-3801
USA

RICHARD ADLER
NORTH STAR RESEARCH CORP.
5555 ZUNI S.E., STE. 345
ALBUQUERQUE NM 87108
USA

CHRIS ADOLPHSEN
SLAC
P.O.B. 4349, BIN 95
STANFORD CA 94305
USA

ROBERTO AIELLO
SSC
2550 BECKLEYMEADE AVENUE, MS 1046
DALLAS TX 75237
USA

MITSUO AKEMOTO
KEK
1-1 OHO,
TSUKBA-SHI
IBARAKI-KEN
JAPAN

RON A AKRE
IRT LINAC
7695 FORMULA PLACE
SAN DIEGO CA 92121
USA

BULENT AKSEL
SSC
2550 BECKLEYMEADE AVE.,
MS 1005
DALLAS TX 75237
USA

JAMES G. ALESSI
BROOKHAVEN NATL LAB
BLDG. 930
UPTON NY 11973
USA

RUDULFO A. ALFORQUE
BROOKHAVEN NATL LAB
BLDG. 725-C, NSLS
UPTON NY 11973
USA

NICOLA ALLA
INFN-NAPLES
ITALY

MATTHEW A. ALLEN
SLAC
P.O. BOX 4349, BIN 33
STANFORD CA 94309
USA

MIKE ALLEN
SSC
2550 BECKLEYMEADE STE. 125
MS 1045
DALLAS TX 75237
USA

S. E. ALLEN
VARIAN ASSOC.
811 HANSEN WAY, B209
PALO ALTO CA 94303
USA

STEVEN ALLEN
LLNL
P. O. BOX 5511, L-637
LIVERMORE CA 94551
USA

PAUL W. ALLISON
LOS ALAMOS NATL LAB
P.O. BOX 1663
AT-10, MS H818
LOS ALAMOS NM 87545
USA

JOSE R. ALONSO
LBL
BLDG. 51, RM 208
BERKELEY CA 94720
USA

GERALD D. ALTON
OAK RIDGE NATL LAB
P.O. BOX 2008, BLDG. 6000
OAK RIDGE TN 37831
USA

ABDUL ALWANI
ATOMIC ENERGY CONTROL BOARD
P O BOX 1046, STATION B
OTTAWA CANADA K1P559
CANADA

KRIS ANDERSON
FERMILAB
BOX 500, MS 340
BATAVIA IL 60510
USA

OSCAR A. ANDERSON
LBL
ONE CYCLOTRON RD, BLDG 4-111
BERKELEY CA 94720
USA

NORD ANDRESEN
LBL
1 CYCLOTRON ROAD
BERKELEY CA 94720
USA

TIMOTHY A. ANTAYA
NATL. SUPERCON. CYCLO. LAB
S. SHAW LANE
EAST LANSING MI 48824
USA

ARMANDO ANTILLON
UNIVERSITY OF MEXICO, UNAM
LABORATORIO DE CUERNAVACA
APDO. POSTAL 20-364
01000 MEXICO, D.F., MEXICO

FRANK ANTON
INTERATOM
FRIEDRICH-EBERT-STR.
5060 BERGISCH-GLADBACH
GERMANY

GARY M. ARBIQUE
CHALK RIVER LABS
AECL RESEARCH
CHALK RIVER ONTARIO KOJ1JO
CANADA

SOAM ARCHARYA
SSC
2550 BECKLEYMEADE AVE., MS 1046
DALLAS TX 75237
USA

CHAS N. ARCHIE
IBM RESEARCH
T. J. WATSON RESERCH CENTER
P. O. BOX 218
YORKTOWN HEIGHTS NY 10527
USA

BERNARD ARFIN
590 EMERALD
SAN CARLOS CA 94070
USA

NED D. ARNOLD
ARGONNE NATL LAB
9700 S. CASS AVENUE
ARGONNE IL 60439
USA

MAX ARTUSY
SLAC
BIN 49
2575 SAND HILL ROAD
MENLO PARK CA 94025
USA

WES ASHER
SLAC
BIN 49
2575 SAND HILL ROAD
MENLO PARK CA 94025
USA

ISAAC ASHKENAZI
CEBAF
12000 JEFFERSON AVE.
NEWPORT NEWS VA 23602
USA

GARY ASKE
SLAC
BIN 49
2575 SAND HILL ROAD
MENLO PARK CA 94025
USA

ALEXEY A. ASSEEV
INSTITUTE FOR HIGH ENERGY PHYSICS
SERPUKHOV
142284 PROTVINO
MOSCOW USSR
USSR

WILLIAM H. ATKINS
LOS ALAMOS NATL LAB
AT-8, MS H820
LOS ALAMOS NM 87545
USA

MARK AUGUSTINE
CEBAF
12000 JEFFERSON AVENUE
NEWPORT NEWS VA 23606
USA

BERNARD AUNE
CEA
DPHN/STAS
91191 GIF/YVETTE CEDEX
FRANCE

ROBERT AVERILL
MIT-BATES LAB
MIDDLETON MA 01949
USA

HENRIK AYVAZIAN
#47, KASHANI STREET, KABOLI STREET,
RESALAT AVE.
TEHRAN 16316
IRAN

RICHARD A. BAARTMAN
TRIUMF
4004 WESBROOK MALL
VANCOUVER B.C. V6T
CANADA

MARTHE BACAL
ECOLE POLYTECHNIQUE
LABO P.M.I., ECOLE POLYTECHNIQUE
PALAISEA 91128
FRANCE

GERARD BACHY
CERN
LEP DIVISON
CH-1211 GENEVA 23
SWITZERLAND

PETER P. BAGLEY
CORNELL UNIV/PPB
ITHACA NY 14853
USA

VERNON BAILEY
PULSE SCIENCES, INC.
600 MCCORMICK ST.
SAN LEANDRO CA 94577
USA

SIMON BAIRD
SSRL/CERN
CH-1211 GENEVA 23
SWITZERLAND

MARCEL BAJARD
GANIL
BP 5027
14021 CAEN CEDEX
FRANCE

VLADIMIR E. BALAKIN
INP., USSR
INSTITUTE OF NUCLEAR PHYSICS
PROTVINO MOSCOW 142284
USSR

MARK BALL
INDIANA UNIVERSITY
CYCLOTRON FACILITY
2401 MILO B. SAMPSON LANE
BLOOMINGTON IN 47405
USA

MICHAEL BALTAY
SLAC
P.O.B. 4349, BIN 99
STANFORD CA 94309
USA

ROSE MARY BALTRUSAITIS
EG&G ENERGY MEASUREMENTS
130 ROBIN HILL ROAD
GOLETA CA 93117
USA

KARL L. F. BANE
SLAC
P.O. BOX 4349, BIN 26
STANFORD CA 94309
USA

KENNETH BAPTISTE
LBL
MAILSTOP 46-125
BERKELEY CA 94720
USA

LOY BARKER
SLAC
P. O. BOX 4349
BIN 50
STANFORD CA 94309
USA

WILLIAM A BARLETTA
LLNL
P O. BOX 808, L-626
LIVERMORE CA 94550
USA

JOHN J. BARNARD
LLNL
P. O. BOX 808, L626
LIVERMORE CA 94550
USA

MICHAEL J. BARNES
TRIUMF
4004 WESBROOK MALL
VANCOUVER B.C. V6T2A3
CANADA

WALTER BARRY
CEBAF
12000 JEFFERSON AVE.
NEWPORT NEWS VA 23602
USA

DONALD S. BARTON
BROOKHAVEN NATL LAB
BLDG. 911B
UPTON NY 11973
USA

MARK Q. BARTON
IBM RESEARCH
THOMAS J. WATSON RESEARCH
RM 19-223, P. O. BOX 218
YORKTOWN HEIGHTS NY 10598
USA

GEORGE BASBAS
PHYSICAL REVIEW LETTERS
P. O. BOX 1000
1 RESEARCH ROAD
RIDGE NY 11961
USA

SANDRA BASS
SLAC
P. O. BOX 4349
BIN 50
STANFORD CA 94309
USA

KEN BATCHELOR
BROOKHAVEN NATL LAB
NSLS BLDG. 725A
UPTON NY 11973
USA

MUKHAMMED D. BAVIZHEV
INSTITUTE FOR HIGH ENERGY PHYSICS
SERPUKHOV
142284 PROTVINO
MOSCOW USSR
USSR

OLIVIER BAYARD
CERN
CH-1211
GENEVA 23
SWITZERLAND

SUCK HEE BE
RIKEN
WAKO-SHI
SAITAMA 351-01
JAPAN

EDWARD BEADLE
BROOKHAVEN NATL LAB
BLDG. 911B
UPTON NY 11973
USA

VOLKER BECHTOLD
ZYKLOTRONLABORATORIUM
POSTFACH 3640
D-7500 KARLSRUHE
GERMANY

JUERGEN BEDAU
BRUKER PHYSIK AG
13 WIKINGER STREET
7500 KARLSRUHE 21
GERMANY

MICHAEL BEGG
TESLA ENGINEERING
WATER LANE
STORRINGTON RH203EA
BRITAIN

SYEDA BEGUM
LITTON ELECTRON DEVICES
960 INDUSTRIAL ROAD
SAN CARLOS CA 94070
USA

GERD BEHRSING
LBL
1 CYCLOTRON RD., 71-259
BERKELEY CA 94720
USA

ROBERT A. BELL
SLAC
P.O. BOX 4349, BIN 95
STANFORD CA 94309
USA

ILAN BEN-ZVI
BROOKHAVEN NATL LAB
725C BNL
UPTON NY 11973
USA

RALPH BENAROYA
ARGONNE NATL LAB
9700 S. CASS AVE, BLDG 360
ARGONNE IL 60439
USA

JOHAN BENGTSSON
LBL
MS B71-259
1 CYCLOTRON ROAD
BERKELEY CA 94720
USA

RICHARD BENSON
LECROY CORPORATION
5912 STONERIDGE MALL ROAD #150
PLEASANTON CA 94588
USA

VICTOR BENVENISTE
EATON CORPORATION
108 CHERRY HILL DR.
BEVERLY MA 01915
USA

JOHN BERCOVITZ
LBL
ONE CYCLOTRON RD, MS 64/121
BERKELEY CA 94720
USA

J. S. BERG
SLAC
BIN 26
P. O. BOX 4349
STANFORD CA 94309
USA

WILLIAM J. BERG
ARGONNE NATL LAB
BUILDING 371T
9700 S. CASS AVENUE
ARGONNE IL 60439
USA

JULIEN BERGOZ
BERGOZ, INC.
01170 CROZET
FRANCE

KLAUS H. BERKNER
LBL
1 CYCLOTRON RD, BLDG B50,149
BERKELEY CA 94720
USA

MARTIN BERNDT
SLAC
P.O. BOX 4349, BIN 51
STANFORD CA 94309
USA

KIRK BERTSCHE
LLNL
P. O. BOX 808, L-397
LIVERMORE CA 94551
USA

MARTIN M. BERZ
MICHIGAN STATE UNIVERSITY
DEPT PHYSICS & ASTRONOMY
EAST LANSING MI 48824
USA

HUGO BETZOLD
DORNIER GMBH
P. O. BOX 1420, DEPT. TMSW
7990 FRIEDRICHSHAFEN 1
GERMANY

RAKESH K. BHANDARI
SSC
2550 BECKLEYMEADE AVE.
DALLAS TX 75237
USA

VINOD BHARADWAJ
FERMILAB
P.O.B. 500
BATAVIA IL 60510
USA

C. M. BHAT
FERMILAB
P.O.B 500, MS 341
BATAVIA IL 60510
USA

TARLOCHAN BHATIA
LOS ALAMOS NATL LAB
P.O.B. 1663, MS H817
LOS ALAMOS NM 87545
USA

MARIA ENRICA BIAGINI
INFN, LAB NAZIONALI FRASCATI
C.P. 13
00044 FRASCATI
ITALY

M. BICKLEY
CEBAF
12000 JEFFERSON AVE.
NEWPORT NEWS VA 23606
USA

ROBERT BIERI
MIT/LBL
LBL
MAIL STOP 47-112
BERKELEY CA 94708

JAN BIJLEVELD
NIKHEF-K
P. B. 41882
AMSTERDAM, 1009DB
NETHERLANDS

JACQUES BILLAN
CERN
CH-1211 LEP DIVISION
GENEVA 23
SWITZERLAND

JAMES H. BILLEN
LOS ALAMOS NATL LAB
P.O. BOX 1663, AT-1, H817
LOS ALAMOS NM 87545
USA

MICHAEL G. BILLING
CORNELL UNIV
WILSON LAB., DRYDEN RD
ITHACA NY 14853
USA

ROY BILLINGE
CERN
PS DIVISION
CH-1211 GENEVA 23
SWITZERLAND

ALAN BIOCCA
LBL
MAILSTOP 50B-4235
BERKELEY CA 94720
USA

JOSEPH J. BISOGNANO
CEBAF
12000 JEFFERSON AVENUE
NEWPORT NEWS VA 23606
USA

EDGAR L. BLACK
ARGONNE NATL LAB
9700 SOUTH CASS AVENUE
ARGONNE IL 60439
USA

EWART B. BLACKMORE
TRIUMF
4004 WESBROOK MALL
VANCOUVER B.C. V6T
CANADA

DIETHER BLECHSCHMIDT
CERN
CH-1211 GENEVA 23
SWITZERLAND

E. J. BLESER
BROOKHAVEN NATL LAB
BLDG. 911B
UPTON NY 11973
USA

JOHN P. BLEWETT
310 WEST 106 STREET
NEW YORK NY 10025
USA

BARBARA BLIND
LOS ALAMOS NATL LAB
P.O. BOX 1663, AT-3, H811
LOS ALAMOS NM 87545
USA

KENNETH BLISS
ROCKWELL INTERNATIONAL
90 NORTH CENTER ST.
WELLSVILLE UT 84339
USA

ELLIOTT BLOOM
SLAC
P. O. BOX 4349, BIN 98
STANFORD CA 94309

HANS BLUEM
LSU-CAMD
60 UNIVERSITY LAKESHORE DRIVE
BATON ROUGE LA 70808
USA

LEROY N. BLUMBERG
BROOKHAVEN NATL LAB
NATL. SYNCH. LIGHT SOURCE
BLDG. 725C
UPTON NY 11973
USA

V.I. BOBLYEV
INST. THEOR. & EXPER PHYS
B. CHEREMUSHKINSKAYA 25
MOSCOW USSR 117259
USSR

HERMAN BOERROOKHUIZEN
NIKHEF
POB 4395, 1009 A. J.
AMSTERDAM
NETHERLANDS

JACK E. BOERS
THUNDERBIRD SIMULATIONS
626 BRADFIELD DRIVE
GARLAND TX 75042-6005
USA

COURTLANDT BOHN
ARGONNE NATL LAB
9700 S. CASS AVE., EP-207
ARGONNE IL 60439
USA

ERIC L. BONG
SLAC
2575 SAND HILL ROAD
MENLO PARK CA 94025
USA

ROBERTO BONI
INFN
C.P. 13
00044 FRASCATI
ITALY

INGE BORCHARDT
DESY-HERAP
NOTKESTR. 85
2000 HAMBURG 52
GERMANY

ROLF BORK
CEBAF
12000 JEFFERSON AVE
NEWPORT NEWS VA 23602
USA

MICHAEL BORLAND
ANL
BUILDING 360
9700 S. CASS AVENUE
ARGONNE IL 60439
USA

JEREMY BORRETT
NUCLEAR EFFECTS DIRECTORATE
FTEWS-NE
WHITE SANDS MISSILE RANGE NM 88002
USA

WERNER BOTHE
DESY
NOTKESTRASSE 85
D-2000 HAMBURG 52
GERMANY

FULVIA C. BOTLO-PILAT
SSC
2550 BECKLEYMEADE AVE., MS 1046
DALLAS TX 75237
USA

CHRISTOPHE BOURAT
GENERAL ELECTRIC CO.
551 RUE DE LA MINIERE BP 34
78530 BVC
FRANCE

GEORGE BOURIANOFF
SSC
2550 BECKLEYMEADE AVE.
DALLAS TX 75237
USA

BRUCE BOWLING
CEBAF
12000 JEFFERSON AVENUE
NEWPORT NEWS VA 23606
USA

JOHN K BOYD
LLNL
P. O BOX 808, L-626
LIVERMORE CA 94550
USA

EVA S. BOZOKI
BROOKHAVEN NATL LAB
BLDG. 725C
UPTON NY 11973
USA

JOSEPH BRADLEY
UNM
EECE BUILDING
ALBUQUERQUE NM 87171
USA

JEFFREY S. BRANDT
FERMILAB
P. O. BOX 500, MS 315
BATAVIA IL 60510
USA

JEAN PIERRE BRASILE
THOMSON CSF
SAINT AUBIN BP 150
BAGNEUX 92223
FRANCE

HANS H. BRAUN
SLAC-PSI
PSI WEST BG-C-41
CH 5332
VILLIGEN PSI
SWITZERLAND

WERNER BREFELD
DESY
NOTKESTR. 85
D-2000 HAMBURG 52
GERMANY

BRENT BRENTNALL
ROCKWELL INTERNATIONAL
ROCKETDYNE DIVISION
6633 CANOGA AVENUE, FA15
CANOGA PARK CA 91303
USA

JAMES F. BRIDGES
ARGONNE NATL LAB
9700 S CASS Bldg. 360
ARGONNE IL 60439
USA

CLARK BRIDGMAN
LOS ALAMOS NATL LAB
AT-10, MS H818
P. O BOX 1663
LOS ALAMOS NM 87545
USA

CHARLES BRIEGEL
FERMILAB
P. O. BOX 500, MS 347
BATAVIA IL 60510
USA

RICHARD BRIGGS
SSC
2550 BECKLEYMEADE AVE
DALLAS TX 75237
USA

WILLIAM BROBECK
MAXWELL LABS
4905 CENTRAL AVE
RICHMOND CA 94804
USA

ETIENNE BROUZET
CERN
CH-1211 GENEVA 23
SWITZERLAND

BRUCE C. BROWN
FERMILAB
P.O. BOX 500, MS 316
BATAVIA IL 60510
USA

HUGH BROWN
BROOKHAVEN NATL LAB
ACCELERATOR DEPT, BLDG 911B
UPTON NY 11973
USA

IAN G. BROWN
LBL
1 CYCLOTRON RD, BLDG. 53-103
BERKELEY CA 94720
USA

KARL BROWN
SLAC
P.O. BOX 4349
STANFORD CA 94309
USA

KEVIN A. BROWN
BROOKHAVEN NATL LAB
BLDG. 911A
UPTON NY 11973
USA

MICHAEL J. BROWNE
SLAC
P.O. BOX 4349, BIN 12
STANFORD CA 94309
USA

DAVID L. BRUHWILER
U. OF COLORADO
CAMPUS 391
BOULDER CO 80309
USA

JOHN E. BUDNICK
INDIANA UNIVERSITY
2401 MILO SAMPSON LANE
BLOOMINGTON IN 47408
USA

NATHAN BULTMAN
LOS ALAMOS NATL LAB
P.O. BOX 1663, AT-4, H821
LOS ALAMOS NM 87545
USA

ROBERT BURKE
ROCKWELL INT.
ROCKETDYNE DIVISION
6633 CANOGA AVENUE FA60
CANOGA PARK CA 91303
USA

PAUL J. BURNHAM
BURLE INDUSTRIES INC
1000 NEW HOLLAND AVENUE
LANCASTER PA 17601
USA

M. J. BURNS
LOS ALAMOS NATL LAB
MS P940
LOS ALAMOS NM 87545
USA

HAROLD S. BUTLER
LOS ALAMOS NATL LAB
P.O. BOX 1663, MP-DO, H832
LOS ALAMOS NM 87545
USA

JOHN BYRD
CORNELL UNIV
WILSON LABORATORY
ITHACA NY 14853
USA

ROD BYRNS
LBL
2457 MARIN AVENUE
BERKELEY CA 94708
USA

YUNHAI CAI
SSC
MS 1047
2550 BECKLEYMEADE
DALLAS TX 75237
USA

LUCIANO CALABRETTA
I.N.F.N.-LNS
LABORATORIO NAZIONALE DEL SUD
VIALE A. DORIA ANG. S. SOFIA
CATANIA I-95125
ITALY

JEFFREY CALAME
UNIV. OF MARYLAND
LAB. FOR PLASMA RESEARCH
COLLEGE PARK MD 21403
USA

MANUEL CALDERON
LLNL
P. O. BOX 5511
L-644
LIVERMORE CA 94550
USA

RICHARD S. CALLIN
SLAC
BIN 30
P.O. BOX 4349
STANFORD CA 94309
USA

JACK CALVERT
LBL
MAILSTOP 64-121
BERKELEY CA 94720
USA

OSCAR A CALVO
MIT
P.O. BOX 846
MIDDLETON MA 01949
USA

I. E CAMPISI
CEBAF
12000 JEFFERSON AVE
NEWPORT NEWS VA 23606
USA

DAVID CAPISTA
FERMILAB
P. O. BOX 500, MS 306
BATAVIA IL 60510
USA

MALCOLM CAPLAN
LLNL
4219 GARLAND DRIVE
FREMONT CA 94536
USA

GEORGE J. CAPORASO
LLNL
P.O. BOX 808, L-626
LIVERMORE CA 94550
USA

RUBEN CARCAGNO
SSC
2550 BECKLEYMEADE STE 125
MS 1045
DALLAS TX 75237
USA

LAWRENCE S. CARDMAN
UNIVERSITY OF ILLINOIS
23 STADIUM DRIVE
CHAMPAIGN IL 61820
USA

DAVID C. CAREY
FERMILAB
P.O.BOX 500
BATAVIA IL 60510
USA

RANDOLPH L. CARLSON
LOS ALAMOS NATL LAB
P.O. BOX 1663, M4, P940
LOS ALAMOS NM 87545
USA

BRUCE E. CARLSTEN
LOS ALAMOS NATL LAB
P.O. BOX 1663, AT-7, H825
LOS ALAMOS NM 87545
USA

ROGER CARR
SSRL
P. O. BOX 4349, BIN 69
STANFORD CA 94309
USA

JOHN CARSON
FERMILAB
P.O.B. 500
BATAVIA IL 60510
USA

JOHN R. CARY
U. OF COLORADO
APAS DEPT., CAM. BX 391
BOULDER CO 80309
USA

GEORGE CARYOTAKIS
SLAC
P.O.BOX 4349, BIN 33
STANFORD CA 94309
USA

SHLOMO CASPI
LBL
1 CYCLOTRON RD, BLDG 46/161
BERKELEY CA 94720
USA

RICHARD L. CASSEL
SLAC
P.O. BOX 4349, BIN 49
STANFORD CA 94309
USA

MICHELE CASTELLANO
INFN-LNF
C. P. 13
FRASCATI ITALY 00044
ITALY

MARCO CAVENAGO
LAB NAZ LEGNARO
VIA ROMEA N 4
I 35020 LEGNARO PD
ITALY

ROBERT J CAYLOR
LBL
1 CYCLOTRON RD., 46-161
BERKELEY CA 94720
USA

CHRISTINE M. CELATA
LBL
1 CYCLOTRON RD, BLDG 47, 112
BERKELEY CA 94720
USA

FEDERICO CERVELLERA
INFN
LABORATORI DI LEGNARO
L.N.L.V. ROMEA, 4 35020
LEGNARO (PD)
ITALY

BEN-CHIN K. CHA
ARGONNE NATL LAB
9700 S. CASS AVENUE
ARGONNE IL 60439
USA

ANDRE CHABERT
GANIL
BP 5027
F 14021 CAEN
CEDEX
FRANCE

YONG-CHUL CHAE
UNIV. OF HOUSTON
ANL
BUILDING 362
ARGONNE IL 60437
USA

FRANK W. CHAMBERS
LLNL
P. O. BOX 808, L626
LIVERMORE CA 94550
USA

MARK CHAMPION
FERMILAB
P. O. BOX 500, MS 306
BATAVIA IL 60510
USA

MICHEL CHANEL
CERN
PS DIVISION
CH 1211
GENEVA 23
SWITZERLAND

CHU RUI CHANG
SSC
2550 BECKLEYMEADE STE 125
MS 1045
DALLAS TX 75237
USA

ALEX CHAO
SSC
2550 BECKLEYMEADE STE 125
MS 1045
DALLAS TX 75237
USA

YU-CHIU CHAO
SLAC
P.O.B. 4349
STANFORD CA 94309
USA

ANTHONY K. CHARGIN
LLNL
P.O. BOX 808, L-123
LIVERMORE CA 94550
USA

SWAPAN CHATTOPADHYAY
LBL
1 CYCLOTRON RD, BLDG 47/112
BERKELEY CA 94720
USA

CHIA-ERH CHEN
PEKING UNIVERSITY
OFFICE OF THE PRESIDENT
PEKING UNIVERSITY
BEIJING 100871
P.R. CHINA

CHIPING CHEN
MIT
NW16-264
CAMBRIDGE MA 02139
USA

CHRISTOPHER CHEN
STANFORD UNIVERSITY
HANSEN LABS
STANFORD CA 94305
USA

FELIX K. CHEN
SCHLUMBERGER-DOLL
OLD QUARRY ROAD
RIDGEFIELD CT 06877
USA

PISIN CHEN
SLAC
P O B. 4349, BIN 26
STANFORD CA 94309
USA

SHIAW-HUEI CHEN
INST. OF NUCLEAR ENERGY RES.
P. O. BOX 3-4
LUNG-TAN
ROUTAN TAIWAN
PR CHINA

SHIEN-CHI CHEN
MIT
NW16-176
CAMBRIDGE MA 02139
USA

TONG CHEN
LNS/CORNELL UNIVERSITY
WILSON LAB
CORNELL UNIVERSITY
ITHACA NY 14853
USA

YU-JIUAN CHEN
LLNL
P.O. BOX 808, L626
LIVERMORE CA 94550
USA

WEN-HAO CHENG
UNIVERSITY OF MARYLAND
DEPT. OF PHYSICS
COLLEGE PARK MD 20742
USA

RON CHESTNUT
SLAC
P. O. BOX 4349
BIN 50
STANFORD CA 94309
USA

MICHAEL J. CHIN
LBL
1 CYCLOTRON RD., 46-125
BERKELEY CA 94720
USA

Y. H. CHIN
LBL
1 CYCLOTRON ROAD
MS 71-259
BERKELEY CA 94720
USA

MOO-HYUN CHO
POSTECH
PHYSICS DEPT.
P. O. BOX 125
POHANG 790-600
S. KOREA

YANGLAI CHO
ARGONNE NATL LAB
9700 S.CASS AVE,BLDG 362, D-360
ARGONNE IL 60439
USA

LEONG-SIK CHOI
LBL
MS 71J
ONE CYCLOTRON RD.
BERKELEY CA 94720
USA

MANSOO CHOI
SEOUL NATIONAL UNIV.
DEPT. OF MECHANICAL ENG.
SHINLIMDONG, KWANAKKU
SEOUL
KOREA

ERIC P. CHOJNACKI
ARGONNE NATL LAB
9700 SOUTH CASS AVENUE
ARGONNE IL 60439
USA

YEE PING CHONG
LLNL
P.O. BOX 808, L-390
LIVERMORE CA 94551
USA

TZI-SHAN CHOU
BROOKHAVEN NATL LAB
BLDG. 535C
UPTON NY 11973
USA

WEIREN CHOU
SSC
2550 BECKLEYMEADE AVE.
MS 1042
DALLAS TX 75237
USA

KIRK CHRISTENSEN
LOS ALAMOS NATL LAB
P.O.B. 1663, MS H821
LOS ALAMOS NM 87545
USA

MIKE CHRISTIANSEN
SSC
2550 BECKLEYMEADE AVE., MS 1046
DALLAS TX 75237
USA

YOUNGJOO CHUNG
ARGONNE NATL LAB
C-165, BUILDING 362
9700 S. CASS AVENUE
ARGONNE IL 60439
USA

MICHAEL D. CHURCH
FERMILAB
P. O. BOX 500, MS 341
BATAVIA IL 60510
USA

PAOLO CIRIANI
CERN
ST. DIVISION
1211 GENEVA 23 CH
SWITZERLAND

DAVID J. CLARK
LBL
1 CYCLOTRON RD, BLDG 88
BERKELEY CA 94720
USA

SPENCER CLARK
SLAC
P. O. BOX 4349
BIN 50
STANFORD CA 94309
USA

JAMES CLARKE
DARESBURY LAB
SERC
DARESBURY LABORATORY
WARRINGTON WA44AD
ENGLAND

CHRISTOPHER CLAYTON
UCLA
56-125B ENGINEERING IV
LOS ANGELES CA 90024
USA

MARSHALL CLELAND
RADIATION DYNAMICS, INC.
151 HEARTLAND BLVD.
EDGEWOOD NY 11717
USA

JAMES E. CLENDENIN
SLAC
P.O. BOX 4349, BIN 12
STANFORD CA 94309
USA

ELON R. CLOSE
LBL
1 CYCLOTRON RD, BLDG 47/112
BERKELEY CA 94720
USA

PETER N. CLOUT
VISTA CONTROL SYSTEMS, INC.
134B EASTGATE DRIVE
LOS ALAMOS NM 87544
USA

STAN COHEN
LOS ALAMOS NATL LAB
MP-6, MS H852
LOS ALAMOS NM 87545
USA

BEN COLE
SSC
2550 BECKLEYMEADE STE 125
MS 1045
DALLAS TX 75237
USA

FRANK COLE
511 AURORA AVENUE #301
NAPERVILLE, IL 60540-6290

DALE COLEMAN
SSC
2550 BECKLEYMEADE AVE.
MS 1049
DALLAS TX 75237
USA

PATRICK COLESTOCK
FERMILAB
P. O. BOX 500, MS 306
BATAVIA IL 60510
USA

DENIS COLOMBANT
NAVAL RESEARCH LAB
CODE 4790
WASHINGTON DC 20375
USA

EUGENE P. COLTON
U.S. DEPT. OF ENERGY
ER-24, GTN
WASHINGTON DC 20545
USA

EMILE P. CONARD
ION BEAM APPLICATIONS SA
2, CHEMIN DU CYCLOTRON
1348 LOUVAIN LA NEUVE
BELGIUM

MANOEL E. CONDE
MIT
ROOM 36-213
CAMBRIDGE MA 02139
USA

ROGER CONNOLLY
LOS ALAMOS NATL LAB
AT-3, MS H808
LOS ALAMOS NM 87545
USA

THEODORE N. CONSTANT
SLAC
P.O. BOX 4349, BIN 50
STANFORD CA 94309
USA

DONALD L. COOK
SANDIA NATL LAB.
P.O.B. 5800, ORG. 1260
ALBUQUERQUE NM 87185
USA

RAYMOND COOPERSTEIN
U. S. DEPT OF ENERGY
MS DP 132
WASHINGTON DC 20545
USA

WILLIAM CORBETT
SLAC
P. O. BOX 4349
BIN 39
STANFORD CA 95014
USA

PATRICK CORCORAN
PULSE SCIENCES, INC.
600 MCCORMICK ST.
SAN LEANDRO CA 94577
USA

CARL W. CORK
LBL
1 CYCLOTRON RD., MS 46-161
BERKELEY CA 94720
USA

JOHN CORLETT
DARESBURY LAB
SERC
KECKWICK LANE
WARRINGTON WA44AD
UNITED KINGDOM

MAX CORNACCHIA
SSRL
P. O. BOX 4349, BIN 99
STANFORD CA 94309-0210
USA

WAYNE CORNELIUS
SAIC
4161 CAMPUS POINT COURT
SAN DIEGO CA 92121
USA

PAUL LEWIS CORREDOURA
SLAC
P.O.B. 4349, BIN 33
STANFORD CA 94309
USA

W. CLAY CORVIN
SLAC
P..O.BOX 4349
STANFORD CA 94309
USA

LOUIS COSTRELL
NATIONAL BUREAU OF STANDARDS
RT 270, 245/B119
GAITHERSBURG MD 20899
USA

DON COWLES
LBL
1807 DRAKE DR.
OAKLAND CA 94611
USA

PETER J. CRACKNELL
TECHNICAL SYSTEMS LTD.
SIMMS LANE
MORTIMER
READING RG72JP
UNITED KINGDOM

MICHAEL CRADDOCK
TRIUMF
4004 WESBROOK MALL
VANCOUVER BC V6T
CANADA

BENJAMIN C. CRAFT
LOUSIANA STATE UNIVERSITY
3990 W. LAKESHORE DR
BATON ROUGE LA 70803
USA

GEORGE D. CRAIG
LLNL
P.O BOX 808, L-826
LIVERMORE CA 94550
USA

A. CRAMETZ
COMM. EUROPEAN COMMUNITIES
CENTAL BUREAU FOR NUCLEAR
MEASUREMENTS
2440 GEEL
BELGIUM

KENNETH CRANDALL
ACCSYS TECHNOLOGY, INC.
1177A QUARRY LANE
PLEASANTON CA 94566
USA

KENNETH CRAWFORD
CEBAF
12000 JEFFERSON AVE.
NEWPORT NEWS VA 23606
USA

NIGEL CROSLAND
OXFORD INSTRUMENTS, LTD.
OSNEY MEAD
OXFORD OXLODX
ENGLAND

ANTONELLA CUCCHETTI
LOS ALAMOS NATL LAB
AT-1, MS H817
P. O. BOX 1663
LOS ALAMOS NM 87545
USA

JOHN M. CULVER
TEXAS ACCEL CENTER
4802 RESEARCH DR., BLDG. 2
THE WOODLANDS TX 77381
USA

CURTIS CUMMINGS
LBL
MS 4-161
1 CYCLOTRON ROAD
BERKELEY CA 94720
USA

GENE CUNNINGHAM
SSC
2550 BECKLEYMEADE AVE , SUITE 125 MS 1005
DALLAS TX 75237
USA

RANDY CURRY
PULSE SCIENCES, INC.
600 MCCORMICK ST.
SAN LEANDRO CA 94577
USA

ROY CUTLER
SSC
2550 BECKLEYMEADE STE 125
MS 1045
DALLAS TX 75237
USA

JOHN M. D'AURIA
TRIUMF
4004 WESBROOK MALL
VANCOUVER B C. V6T
CANADA

LUDWIG DAHL
GSI DARMSTADT
POSTFACH 110541
D-6100 DARMSTADT
GERMANY

PER F. DAHL
SSC
2550 BECKLEYMEADE AVE STE 125
MS 1090B
DALLAS TX 75237
USA

GLEN DAHLBACKA
MAXWELL LABS
BROBECK DIVISION
4905 CENTRAL AVE
RICHMOND CA 94804
USA

ANTONIO DAINELLI
INFN
LABORATORI DI LEGNARO
V. ROMEA, 4 LEGNARO
(PADORA) I-35020
ITALY

L. ROBERT DALESIO
LOS ALAMOS NATL LAB
P.O.B. 1663, MS H820
LOS ALAMOS NM 87545
USA

GORDON T. DANBY
BROOKHAVEN NATL LAB
AGS DEPT., BLDG. 911B
UPTON NY 11973
USA

WALTER G. DAVIES
ATOMIC ENERGY OF CANADA
CHALK RIVER NUCLEAR LABORATORY
CHALK RIVER ONTARIO K0J
CANADA

TIMOTHY J. DAVIS
CORNELL UNIV
909 MITCHELL ST.
ITHACA NY 14850
USA

REMY DAWSON
EBCO TECHNOLOGIES, INC.
4004 WESBROOK MALL
VANCOUVER B.C. V6T
CANADA

JEAN PIERRE DE BRION
CEA
SCE PTN, BP12
91680 BRUYERES-LE-CHATEL
FRANCE

JEFF DE LAMARE
SLAC
BIN 49
2575 SAND HILL ROAD
MENLO PARK CA 94025
USA

DAVID DEACON
DEACON RESEARCH
2440 EMBARCADERO WAY
PALO ALTO CA 94303
USA

FRED DEADRICK
LLNL
MS L-627
LIVERMORE CA 94550
USA

HELEN DEAVEN
LOS ALAMOS NATL LAB
AT-7, MS H829
P. O BOX 1663
LOS ALAMOS NM 87545
USA

PHILIP H. DEBENHAM
U. S. DEPT OF ENERGY
ER-224/GTN
WASHINGTON DC 20585
USA

FRANZ-JOZEF DECKER
SLAC
P.O.BOX 4349, BIN 66
STANFORD CA 94309
USA

GLENN DECKER
ARGONNE NATL LAB
BUILDING 362
9700 S. CASS AVENUE
ARGONNE IL 60439
USA

CHRIS DEENEY
PHYSICS INTERNATIONAL COMPANY
2700 MERCED STREET
SAN LEANDRO CA 94577
USA

JOHN DEFORD
LLNL
P.O.B. 808, L626
LIVERMORE CA 94550
USA

RUSSELL A. DEHAVEN
LOS ALAMOS NATL LAB
P.O. BOX 1663, MP-11, H823
LOS ALAMOS NM 87545
USA

BERND DEHNING
MAX-PLANCK-NUNICH
B. DEHNING, CERN
GENEVA
SWITZERLAND

JEAN-PIERRE DELAHAYE
CERN, PS DIVISION
CH-1211 GENEVA 23
SWITZERLAND

STEPHEN DELCHAMPS
FERMILAB
P. O. BOX 500, MS 316
BATAVIA IL 60510
USA

G. FRITZ DELL
BROOKHAVEN NATL LAB
UPTON NY 11793
USA

DOMENICO DELL'ORCO
LBL
MAILSTOP 46-161
BERKELEY CA 94720
USA

JEAN-CLAUDE DENARD
SINCROTRONE TRIESTE
PADRICIANO 99
34012 TRIESTE
ITALY

YAROSLAV DERBENEV
UNIV. OF MICHIGAN
RANDALL LABORATORY OF PHYSICS
500 EAST UNIVERSITY
ANN ARBOR MI 48109-1120
USA

VLADIMIR PETER DERENCHUK
INDIANA UNIVERSITY
2401 MILO B. SAMPSON LANE
BLOOMINGTON IN 47408
USA

HANK DERUYTER
SLAC
2575 SANDHILL RD.
MENLO PARK CA 94309
USA

EDMOND J. DESMOND
BROOKHAVEN NATL LAB
BUILDING 725B
UPTON NY 11973
USA

OSCAR D. DESPE
ARGONNE NATL LAB
9700 S. CASS AVE
ARGONNE IL 60439
USA

HOBEY DESTAEBLER
SLAC
P. O. BOX 4349, MAIL BIN 96
STANFORD CA 94309
USA

WILLIAM W. DESTLER
UNIVERSITY OF MARYLAND
DEPT. OF ELECT. ENGINEERING
COLLEGE PARK MD 20742
USA

ARNAUD DEVRED
SSC
2550 BECKLEYMEADE, MS 1002
DALLAS TX 75237
USA

JOSEPH DI MARCO
LOS ALAMOS NATL LAB
P. O. BOX 1663
AT-1, MS H817
LOS ALAMOS NM 87545
USA

WILLIAM T. DIAMOND
CHALK RIVER LABS
CHALK RIVER ONTARIO KOJ1JO
CANADA

CARL DICKEY
FERMILAB
P. O. BOX 500, MS 361
BATAVIA IL 60510
USA

A. DIDENKO
MOSCOW INSTITUTE OF PHYSICAL
ENGINEERING
KASHIRSKOE SHOSSE 31
115409 MOSCOW
USSR

JOHN A. DINKEL
FERMILAB
P O BOX 500, MS-308
BATAVIA IL 60510
USA

N. DOBECK
CEBAF
12000 JEFFERSON AVE.
NEWPORT NEWS VA 23602
USA

DONALD DOBROTT
SAIC
2200 POWELL STREET, SUITE 715
EMERYVILLE CA 94608
USA

JAMES W. DODD
U. CAL. LOS ANGELES
PHYSICS DEPARTMENT
LOS ANGELES CA 90024-1547
USA

DONALD A. DOHAN
SSC
MS 1049
2550 BECKLEYMEADE AVE.
DALLAS TX 75237
USA

JEAN M. DOLIQUE
UNIVERSITE DE GRENOBLE I
LAB. OF PHYSICS
JOSEPH FOURIER-GRENOBLE I
BP 53X GRENOBLE CEDEX 38061
FRANCE

MARTIN H. R. DONALD
SLAC
P.O. BOX 4349, BIN 26
STANFORD CA 94309
USA

ANTHONY R. DONALDSON
SLAC
P O. BOX 4349, MS 49
STANFORD CA 94309
USA

RENE DONALDSON
SLAC
P.O.BOX 4349, BIN 70
STANFORD CA 94309
USA

JONATHAN DORFAN
SLAC
BIN 95, P. O BOX 4349
STANFORD CA 94309
USA

JOSEPH A. DOUCET
SCHLUMBERGER-DOLL
OLD QUARRY ROAD
RIDGEFIELD CT 06877
USA

DAVID R DOUGLAS
CEBAF
12070 JEFFERSON AVE
NEWPORT NEWS VA 23606
USA

WILLIAM F DOVE
US-DOE
ER-543, ADVANCED CONCEPTS BRANCH
WASHINGTON DC 20545
USA

ALEX J. DRAGT
UNIVERSITY OF MARYLAND
DEPT. PHYSICS & ASTRONOMY
COLLEGE PARK MD 20742
USA

GILBERT DROUET
CERN
AC DIVISION
CH-1211
GENEVE 23
SWITZERLAND

MICHEL DROUIN
CEA
CEA MORONVILLIERS
PONT FAVERGER L 51490
FRANCE

ROBERT J. DUCAR
FERMILAB
P.O.B. 500, MS 307
BATAVIA IL 60510
USA

ALAN DUDAS
SIEMENS MEDICAL LABS
4040 NELSON AVE.
CONCORD CA 94520
USA

GERALD F. DUGAN
FERMILAB
P.O. BOX 500, MS-306
BATAVIA IL 60510
USA

DEREK C. DUPLANTIS
INDIANA UNIVERSITY
2401 MILO B. SAMPSON LANE
BLOOMINGTON INDIANA 47408
USA

SAMIR DUTT
SSC
2550 BECKLEYMEADE
MS 1042
DALLAS TX 75237
USA

GERARDO G. DUTTO
TRIUMF
4004 WESBROOK MALL
VANCOUVER BC V6T2A3
CANADA

ROGER D. DWINELL
LBL
1 CYCLOTRON RD, BLDG 64-121
BERKELEY CA 94720
USA

F. DYLLA
CEBAF
12000 JEFFERSON AVE
NEWPORT NEWS VA 23606
USA

RICHARD A EARLY
SLAC
P.O.B. 4349, BIN 26
STANFORD CA 94309
USA

GARY EAST
INDIANA UNIVERSITY
CYCLOTRON FACILITY
2401 MILO B. SAMPSON LANE
BLOOMINGTON IN 47405
USA

LAWRIE EATON
LOS ALAMOS NATL LAB
P.O. BOX 1663, MS H827
LOS ALAMOS NM 87545
USA

STAN D. ECKLUND
SLAC
2575 SAND HILL RD.
MENLO PARK CA 94309
USA

JOHN EDIGHOFFER
PULSE SCIENCES, INC.
600 MCCORMICK ST.
SAN LEANDRO CA 94577
USA

DONALD EDWARDS
SSC
2550 BECKLEYMEADE STE 125, MS 1045
DALLAS TX 75237
USA

HELEN EDWARDS
SSC
2550 BECKLEYMEADE STE 125, MS 1045
DALLAS TX 75237
USA

G. V. EGAN-KRIEGER
BESSY GMBH
LENTZEALLEE 100
W-1000 BERLIN 33
GERMANY

YURY EIDELMAN
INP-NOVOSIBIRSK
LAVRENTEVA ST. 11
NOVOSIBIRSK 630090
USSR

DIETER EINFELD
FACHHOCHSCHULE OSTFRIESLAND
CONSTANTIA PLATZ 4
EMDEN 2970
GERMANY

VLADIMIK ELIAN
MOSCOW RAD. INS.
132, WARSHAVSKOE SHOSSE
MOSCOW 113519
USSR

LUIS R. ELIAS
U OF CENTRAL FLORIDA
CREDL
ORLANDO FL 32816
USA

TOM ELIOFF
LBL
1 CYCLOTRON RD., BLDG 47-112
BERKELEY CA 94720
USA

PASCAL ELLEAUME
ESRF
BP220
GRENOBLE 38043
FRANCE

WILLIAM ELLIS
EBASCO SERVICES, INC.
TWO WORLD TRADE CENTER- 89TH FLOO
NEW YORK NY 10048
USA

TIMOTHY ELLISON
INDIANA UNIVERSITY
2401 MILO B. SAMPSON LANE
BLOOMINGTON IN 47405
USA

LOUIS EMERY
ARGONNE NATL LAB
BLDG. 360, RM. 141, APS ACCEL DIV.
9700 SOUTH CASS AVE.
ARGONNE IL 60439
USA

PAUL J. EMMA
SLAC
P.O.B. 4349, BIN 55
STANFORD CA 94309
USA

IVAN ENCHEVICH
TRIUMF
4004 WESBROOK MALL
VANCOUVER B.C. V6T2A3
CANADA

KENNETH R. EPPLEY
SLAC
P.O. BOX 4349, BIN 26
STANFORD CA 94309
USA

ROGER A. ERICKSON
SLAC
P.O. BOX 4349, BIN 55
STANFORD CA 94309
USA

SERGEI K. ESIN
INSTITUTE FOR NUCLEAR RESEARCH
60TH OCTOBER PROSPECT 7A
MOSCOW USSR 117312
USSR

LYNDON R. EVANS
CERN
SPS DIVISION
CH-1211 GENEVA 23
SWITZERLAND

PHILIPPE EYHARTS
CEA/CESTA
BPN 2
LEBARP 33114
FRANCE

SHMUEL EYLON
LBL
1 CYCLOTRON ROAD, 47/112
BERKELEY CA 94720
USA

MICHAEL FAHMIE
LBL
MAILSTOP 46-125
BERKELEY CA 94720
USA

ANDRIS FALTENS
LBL
1 CYCLOTRON RD, BLDG 47-112
BERKELEY CA 94720
USA

KAREN S. FANT
SLAC
BIN 30
P.O. BOX 4349
STANFORD CA 94309
USA

ZOLTAN D. FARKAS
SLAC
P.O. BOX 4349, BIN 26
STANFORD CA 94309
USA

MASOUD FATHIZADEH
ARGONNE NATL LAB
9700 S. CASS AVENUE
APS/360, RM. C141
ARGONNE IL 60439
USA

ANNE MARIE FAUCHET
BROOKHAVEN NATL LAB
BLDG. 726
UPTON NY 11973
USA

JEAN FAURE
CEA/CEN
LABORATOIRE NATIONAL SATURNE
91191 GIF SUR YVETTE CEDEX FRANCE
FRANCE

ANTHONY J. FAVALE
GRUMMAN CORP
111 STEWART AVENUE
BETHPAGE NY 11714
USA

WILLIAM M. FAWLEY
LBL
MAIL STOP 47/112
BERKELEY CA 94720
USA

MICHAEL V. FAZIO
LOS ALAMOS NATL LAB
P.O. BOX 1663
AT-9, H851
LOS ALAMOS NM 87545
USA

BENEDICT FEINBERG
LBL
1 CYCLOTRON RD, MS 71-259
BERKELEY CA 94720
USA

HAREGEWEYN FEREDE
SSC
2550 BECKLEYMEADE AVE , MS 1046
DALLAS TX 75237
USA

FRITZ FERGER
CERN
CH-1211
GENEVA 23
SWITZERLAND

RICHARD C. FERNOW
BROOKHAVEN NATL LAB
PHYSICS, 510D
UPTON NY 11973
USA

JIM FERRELL
SSC
2550 BECKLEYMEADE AVE., MS 1049
DALLAS TX 75237
USA

THOMAS J. FESSENDEN
LBL
1 CYCLOTRON RD, BLDG 47-112
BERKELEY CA 94720
USA

DAVID FICKLIN
SLAC
BIN 33
P. O. BOX 4349
STANFORD CA 94309
USA

THEODORE H. FIEGUTH
SLAC
P.O. BOX 4349
STANFORD CA 94309
USA

CURTIS B. FIGLEY
SASK. ACCEL. LAB
UNIVERSITY OF SASKATCHEWAN
SASKATOON SASK S7N0W0
CANADA

CHARLES L. FINK
ARGONNE NATL LAB
9700 S.CASS AVE,BLDG 207/ENG
ARGONNE IL 60439
USA

DAVID A. FINLEY
FERMILAB
P.O. BOX 500 MS 306
BATAVIA IL 60510
USA

MARC A. FIRESTONE
MISSION RESEARCH CORP.
735 STATE ST., P. O. DRAWER 719
SANTA BARBARA CA 93102-0719
USA

GERHARD E. FISCHER
SLAC
P.O. BOX 4349, BIN 1.
STANFORD CA 94309
USA

ALAN S. FISHER
BROOKHAVEN NATL LAB
PHYSICS, 510D
UPTON NY 11973
USA

JAMES FITZGERALD
FERMILAB
P.O. BOX 500, MS 308
BATAVIA IL 60510
USA

JOHN FLANNIGAN
BROOKHAVEN NATL LAB
BLDG. 725B
UPTON NY 11973
USA

JACOB B. FLANZ
MIT BATES ACCELERATOR
P.O. BOX 846
MIDDLETON MA 01949
USA

ISMAEL FLORES
LBL
MAILSTOP 64-121
BERKELEY CA 94720
USA

JAMES FOCKLER
PULSE SCIENCES, INC.
600 MCCORMICK ST.
SAN LEANDRO CA 94577
USA

CRAIG FONG
LBL
1 CYCLOTRON ROAD, 47/112
BERKELEY CA 94720
USA

EDGAR FONG
LBL
MS 46-161
1 CYCLOTRON ROAD
BERKELEY CA 94720
USA

MARTIN FONG
LBL
MS 47-112
1 CYCLOTRON ROAD
BERKELEY CA 94720
USA

JORGE R. FONTANA
U. CAL. -SANTA BARBARA
4375 VIA GLORIETA
SANTA BARBARA CA 93110
USA

ETIENNE FOREST
LBL
MS 71-268
1 CYCLOTRON ROAD
BERKELEY CA 94720
USA

CLAUDE FOUGERON
CEA/CEN
LABORATOIRE NATIONAL SATURNE
91191 GIF SUR YVETTE CEDEX
FRANCE

RANDY FOWKES
SLAC
P.O. BOX 4349, BIN 30
STANFORD CA 94309
USA

BILL FOWLER
FERMILAB
P.O.B. 500
BATAVIA IL 60510
USA

JOHN D. FOX
SLAC
BIN 33
P. O. BOX 4349
STANFORD CA 94309
USA

BERNHARD FRANZKE
GSI-DARMSTADT
POSTFACH 110 541
D-6100 DARMSTADT
GERMANY

PAUL FREDA
LBL
1 CYCLOTRON RD, 64-121
BERKELEY CA 94720
USA

ROBERT FRIAS
LBL
1 CYCLOTRON RD., MS 64-121
BERKELEY CA 94720
USA

AHARON FRIEDMAN
BROOKHAVEN NATL LAB
BUILDING 725C
UPTON NY 11973
USA

ALEX FRIEDMAN
LLNL
L472
P. O. BOX 808
LIVERMORE CA 94550
USA

CARL C. FRIEDRICHS
LOS ALAMOS NATL LAB
P.O. BOX 1663, AT-5, H827
LOS ALAMOS NM 87545
USA

PAUL FRIEDRICHS
SIEMENS MEDICAL LABS
4040 NELSON AVENUE
CONCORD CA 94520
USA

DENNIS L. FRIESEL
INDIANA UNIVERSITY
2401 MILO B. SAMPSON LANE
BLOOMINGTON IN 47408
USA

MATTHEW FRYER
LBL
6401 BROADWAY TERRACE
OAKLAND CA 94618
USA

JOCK F. FUGITT
CEBAF
12070 JEFFERSON AVE
NEWPORT NEWS VA 23602
USA

BOB FULLER
SLAC
P. O. BOX 4349
BIN 50
STANFORD CA 94309
USA

ROBERT FULTON
LBL
MAILSTOP 90-2148
BERKELEY CA 94720
USA

L. WARREN FUNK
SSC
2550 BECKLEYMEADE AVE.
DALLAS TX 75237
USA

MIGUEL FURMAN
LBL
MAIL STOP 71-H
BERKELEY CA 94720
USA

WILLIAM E. GABELLA
SLAC
P.O.B. 4349, BIN 26
STANFORD CA 94309
USA

GEORGE GABOR
LBL
1 CYCLOTRON ROAD
MS 46-125
BERKELEY CA 94720
USA

JOHN NICOLAS GALAYDA
ARGONNE NATL. LAB
9700 S. CASS AVENUE
ARGONNE IL 60439
USA

JUAN C. GALLARDO
BROOKHAVEN NATL LAB
PHYSICS DEPT. 510D
UPTON NY 11973
USA

GEORGE GAMMEL
GRUMMAN
MS B29-25
BETHPAGE NY 11714
USA

T GARAVAGLIA
SSC
2550 BECKLEYMEADE AVE MS-1047
DALLAS TX 75237
USA

CHRISTINA GARDEN
SLAC
P. O. BOX 4349
BIN 66
STANFORD CA 94309
USA

CHRISTOPHER GARDNER
BROOKHAVEN NATL LAB
BLDG 911B
UPTON NY 11973
USA

JAMES GARNER
SMC TECHNOLOGY
7180 LAMPSON AVE.
GARDEN GROVE CA 92641
USA

JAMES BRANT GARNER
U.S. ARMY STRATEGIC DEF. COMMAND
ATTN: CSSD-DE-N
P. O. BOX 1500
HUNTSVILLE AL 35807-3801
USA

ROBERT W. GARNETT
LOS ALAMOS NATL LAB
AT-1, MS H817
LOS ALAMOS NM 87545
USA

ROLAND GAROBY
CERN
PS DIVISION
CH-1211 GENEVA
SWITZERLAND

AL GARREN
SSC
2550 BECKLEYMEADE STE 125, MS 1045
DALLAS TX 75237
USA

PETER GARRETT
METHODIST HOSP.
RADIATION THERAPY
1701 N. SENATE BLVD.
INDIANAPOLIS IN 46202
USA

TERENCE GARVEY
LBL
1 CYCLOTRON ROAD, MS 47/112
BERKELEY CA. 96720
USA

EDWARD L. GARWIN
SLAC
P.O. BOX 4349, BIN 72
STANFORD CA 94309
USA

BRUCE GEE
LBL
1 CYCLOTRON RD., 46-161
BERKELEY CA 94720
USA

DONALD GEILER
MAXWELL LABS
BROBECK DIVISION
4905 CENTRAL AVE.
RICHMOND CA 94804
USA

WILLIAM GELBART
TRIUMF
4004 WESBROOK MALL
VANCOUVER BC V6T2A3
CANADA

NORMAN M GELFAND
FERMILAB
P.O BOX 500
BATAVIA IL 60510
USA

LEN GENOVA
SLAC
BIN 49
2575 SAND HILL ROAD
MENLO PARK CA 94025
USA

ROBERT GENTZLINGER
LOS ALAMOS NATL LAB
AT-4, MS H821
P. O. BOX 1663
LOS ALAMOS NM 87545
USA

ANDREI GERASIMOV
FERMILAB
P. O. BOX 500, MS 345
BATAVIA IL 60510
USA

EARL C. GERO
UNIV. OF MICHIGAN
3170 BRAEBURN CIRCLE
ANN ARBOR MI 48108
USA

WOLFGANG S. GIEBELER
INTERATOM
WERK II POSTFACH
5060 BERGISCH GLADBACH 1
GERMANY

WILLIAM S. GILBERT
LBL
1 CYCLOTRON RD, BLDG 46-161
BERKELEY CA 94720
USA

RONALD M. GILGENBACH
U. OF MICHIGAN, NUCLEAR ENERGY
COOLEY BLDG., NORTH CAMPUS
ANN ARBOR MI 48109
USA

EDWARD GILL
BROOKHAVEN NATL LAB
AGS DEPT., BLDG. 911A
UPTON NY 11973
USA

J. DOUG GILPATRICK
LOS ALAMOS NATL LAB
P.O. BOX 1663, AT-3, H808
LOS ALAMOS NM 87545
USA

GIRAULT
GENERAL ELECTRIC CO.
551, RUE DE LA MINIERE, BP 34
NBUC 78533
FRANCE

IVAN GJAJA
UNIV. OF MARYLAND
DEPARTMENT OF PHYSICS
COLLEGE PARK MD 20742
USA

HENRY GLASS
FERMILAB
P. O. BOX 500, MS 316
BATAVIA IL 60510
USA

A. A. GLAZOV
JINR DUBNA
P.O. BOX 79
MOSCOW USSR 101000
USSR

JOSEPH W. GLENN
BROOKHAVEN NATL LAB
BLDG. 911-A
UPTON NY 11973
USA

ROBERT L. GLUCKSTERN
UNIVERSITY OF MARYLAND
DEPT. OF PHYSICS
COLLEGE PARK MD 20742
USA

VASILY A. GLUKHIKH
EFREMOV RESEARCH INST. OF ELEC. & PHYSICS
APPARATUS
LENINGRAD
USSR

EFIM GLUSKIN
ARGONNE NATL LAB
9700 S. CASS AVE.
ARGONN E IL 60439
USA

GLENN P. GODERRE
FERMILAB
P.O.B. 500, MS 306
BATAVIA IL 60510
USA

TERRY F. GODLOVE
FM TECHNOLOGIES
9713 MANTEO CT
FT. WASHINGTON MD 20744
USA

DONALD A. GOER
SCHONBERG RADIATION CORP
3300 KELLER STREET
SANTA CLARA CA 95054
USA

THOMAS GOETZ
UNIV. BONN
PHYSIKALISCHES INSTITUT
NUSSALLEE 12
5300 BONN 1
GERMANY

OMER F. GOKTEPE
US-DOE
DIV. OF HIGH ENERGY PHYSICS, ER-22 GTN
WASHINGTON DC 20585
USA

STEVEN GOLD
NAVAL RESEARCH LABORATORY
CODE 4793
WASHINGTON DC 20375
USA

DAVID A. GOLDBERG
LBL
1 CYCLOTRON RD, BLDG 47-112
BERKELEY CA 94720
USA

JEFFRY GOLDEN
BERKELEY RES. ASSOC.
P. O. BOX 852
SPRINGFIELD VA 22150
USA

LEONARD M. GOLDMAN
BECHTEL NATIONAL, INC.
P.O.BOX 193965
SAN FRANCISCO CA 94119
USA

TERRENCE GOLDMAN
LOS ALAMOS NATL LAB
P.O. BOX 1663, MS-B283
LOS ALAMOS NM 87545
USA

YOSHIO GOMEI
TOSHIBA CORP
4-1 UKISHIMA CHO
KAWASAKI KU 210
JAPAN

JOHN D. GONCZY
ARGONNE NATL LAB
9700 S. CASS AVENUE
ARGONNE IL 60439
USA

CYLON GONGALVES DA SILVA
LNLS
CX. P. 6192
CAMPINAS SP 13083
BRAZIL

ROBERT W. GOODWIN
FERMILAB
P.O. BOX 500, MS-307
BATAVIA IL 60510
USA

YEHUDA GOREN
SSC
2550 BECKLEYMEADE AVE., MS 1-49
DALLAS TX 75237
USA

ANTHONY GORSKI
ARGONNE NATL LAB
9700 S. CASS AVENUE
ARGONNE IL 60439
USA

DAVID E. GOUGH
SLAC
P.O. BOX 4349, BIN 49
STANFORD CA 94309
USA

RICHARD A. GOUGH
LBL
1 CYCLOTRON RD., BLDG 71-259
BERKELEY CA 94720
USA

STEVE GOURLAY
FERMILAB
P.O BOX 500, MS 316
BATAVIA IL 60510
USA

JOEL GRABER
CORNELL UNIVERSITY
111 NEWMAN LABORATORY
ITHACA NY 14853
USA

M. I. GRACHEV
INSTITUTE FOR NUCLEAR RESEARCH
PROFSOJUZNAJA 7A
MOSCOW 117 3123
USSR

PIERRE GRAND
AMPARO CORPORATION
P. O. BOX 2687
SANTA FE NM 87504
USA

WILLIAM GRAVES
UW-MADISON
PHYSICS DEPT.
1150 UNIVERSITY AVENUE
MADISON WI 53706
USA

EDWARD R. GRAY
LOS ALAMOS NATL LAB
P.O. BOX 1663, AT-1, H817
LOS ALAMOS N.M. 87545
USA

MICHAEL GREEN
U.OF WISCONSIN,SYNCROTRON
3731 SCHNEIDER DR.
STOUGHTON WI 53589
USA

MICHAEL A. GREEN
LBL
1 CYCLOTRON ROAD
BUILDING 90/2148
BERKELEY CA 94720
USA

MICHAEL I. GREEN
LBL
MAILSTOP 7-222
BERKELEY CA 94720
USA

MANFRED GRIESER
MPI FUR KERNPHYSIK
P. O. BOX 103980
D6900 HEIDELBERG
GERMANY

JAMES E. GRIFFIN
FERMILAB
P.O. BOX 500, MS-341
BATAVIA IL 60510
USA

ALEX GRILLO
SLAC
P. O. BOX 4349
BIN 50
STANFORD CA 94309
USA

DAVID GROTE
LLNL
P. O. BOX 808
L-637
LIVERMORE CA 94550
USA

HANS GROTE
CERN
SL DIVISION
CH-1211
GENEVA 23
SWITZERLAND

HERMANN A. GRUNDER
CEBAF
12000 JEFFERSON AVE.
NEWPORT NEWS VA 23606
USA

PIERRE GUDEWICZ
GANIL
BP 5027
14021 CAEN
CEDEX
FRANCE

SAMAR GUHARAY
UNIV. OF MARYLAND
LAB. FOR PLASMA RESEARCH
COLLEGE PARK MD 20742
USA

PHILIPPE J. GUIDEE
THOMSON CSF
38 RUE VAUTHIER, BOX 305,92102
BOULOGNE
FRANCE

SUSANNA GUIDUCCI
INFN-LNF
CP 13
00044 FRASCATI
ITALY

GILBERT F. GUIGNARD
CERN
LEP DIVISION
CH-1211 GENEVA 23
SWITZERLAND

MARTIN GUNDERSEN
UCLA
DEPT. OF ELEC. ENGR.-EP
SSC-420, MC-0484
LOS ANGELES CA 90089-0484
USA

LI GUONGXIAO
IHEP-BEIJING
P. O. BOX 918
BEIJING
P.R. CHINA

RAMESH C. GUPTA
BROOKHAVEN NATL LAB
BLDG. 902-B
UPTON NY 11973
USA

DAVID GURD
SSC
2550 BECKLEYMEADE AVE , MS 1046
DALLAS TX 75237
USA

FRANK W. GUY
SSC
2550 BECKLEYMEADE AVE.
DALLAS TX 75237
USA

IRVING HABER
NAVAL RESEARCH LAB.,CODE 4790
4555 OVERLOOK AVE.
WASHINGTON DC 20375
USA

ISRAEL HABERMAN
FERMILAB
P. O. BOX 500
BATAVIA IL 60510
USA

KERRY HABIGER
TITAN/SPECTRON DIV.
P. O. BOX 9254
ALBUQUERQUE NM 87119
USA

CHRISTOPHER HADDOCK
SSC
MS 1005
2550 BECKLEYMEADE AVE.
DALLAS TX 75237
USA

DAVID HAENNI
SSC
2550 BECKLEYMEADE AVE., MS 1046
DALLAS TX 75737
USA

ALAN HAHN
FERMILAB
P.O.B. 500
BATAVIA IL 60510
USA

HARALD HAHN
BROOKHAVEN NATL LAB
BLDG. 1005-4
UPTON NY 11973
USA

KYOUNG HAHN
LBL
1 CYCLOTRON ROAD, 47/112
BERKELEY CA 94720
USA

JACOB HAIMSON
HAIMSON RESEARCH CORP.
4151 MIDDLEFIELD RD
PALO ALTO CA 94303
USA

HENRY J. HALAMA
BROOKHAVEN NATL LAB
BLDG. 728
UPTON NY 11973
USA

KLAUS HALBACH
LBL
1 CYCLOTRON RD, BLDG 2-400
BERKELEY CA 94720
USA

ROBERT HAMM
ACCSYS TECHNOLOGY, INC.
1177A QUARRY LANE
PLEASANTON CA 94566
USA

WILLIAM HAMMER
GRUMMAN
MS B29-025
BETHPAGE NY 11714
USA

KYUNG HAN
POHANG ACCELERATOR LAB
POSTECH
P. O. BOX 125
POHANG KYUNGBUK 790-600
KOREA

RAYMOND W. HANFT
FERMILAB
P.O. BOX 500, MS 316
BATAVIA IL 60510
USA

JEFF S. HANGST
FERMILAB
P.O.B. 500, MS 341
BATAVIA IL 60510
USA

BRUCE M. HANNA
FERMILAB
P.O. BOX 500, MS 500
BATAVIA ILL. 60510
USA

SAMY M. HANNA
BROOKHAVEN NATL LAB
NSLS BUILDING 725C
UPTON NY 11973
USA

SIGMUND HANSEN
CERN, DIV. LEP
1211 GENEVA
SWITZERLAND

MASAHIRO HARA
RIKEN
HONKOMAGOME 2-28-8, BUNKYO-KU
TOKYO 113
JAPAN

THOMAS W. HARDEK
LOS ALAMOS NATL LAB
P.O. BOX 1663, MS H852
LOS ALAMOS N.M. 87545
USA

ROBERT A. HARDEKOPF
LOS ALAMOS NATL LAB
P.O. BOX 1663, AT-DO, H804
LOS ALAMOS NM 87545
USA

DAVID J HARDING
FERMILAB
P.O.B. 500, MS 341
BATAVIA IL 60510
USA

LAURENT HARDY
ION BEAM APPLICATIONS SA
CHGEMIN DU CYCLOTRON,2
B-1348 LOUVAIN-LA-NEUVE
BELGIUM

FADY ADEL HARFOUSH
FERMILAB
P.O.B. 500, MS 345
BATAVIA IL 60510
USA

KATHERINE HARKAY
PURDUE U/FERMILAB
P.O.B. 500
BATAVIA IL 60510
USA

MICHAEL R. HAROLD
RUTHERFORD APPLETON LABORATORY
CHILTON DIDCOT
OXON
ENGLAND

CLARENCE HARRIS
SLAC
1121 RUSSELL AVENUE
LOS ALTOS CA 94024
USA

KEVIN HARRIS
SLAC
BIN 49
2575 SAND HILL ROAD
MENLO PARK CA 94025
USA

MICHAEL HARRISON
FERMILAB
P.O. BOX 500, MS-306
BATAVIA IL 60510
USA

FREDERIC HARTEMANN
THOMSON TUBES
MIT
PFC NW 16-170
CAMBRIDGE MA 02139
USA

SPENCER HARTMAN
UCLA
CENTER FOR ADVANCED ACCELERATORS
405 HILGARD AVE.
LOS ANGELES CA 90034
USA

ALEXANDER HARVEY
SLAC
P.O. BOX 4349 BIN 26
STANFORD CA 94309
USA

EVERETT HARVEY
LBL
MAILSTOP 46A-1123
BERKELEY CA 94720
USA

LEIGH H HARWOOD
CEBAF
12000 JEFFERSON AVE
NEWPORT NEWS VA 23602
USA

HELMUT D HASEROTH
CERN
1211 GENEVA 23
SWITZERLAND

WILLIAM V. HASSENZAHL
LBL
1 CYCLOTRON RD, BLDG 46-161
BERKELEY CA 94720
USA

VINCENT HATTON
CERN - SPS DIVISION
CH-1211 GENEVA 23
SWITZERLAND

CHERYL HAUCK
LBL
MS 46-161
1 CYCLOTRON ROAD
BERKELEY CA 94720
USA

REINHARD HAUERT
UNIVERSITY OF DORTMUND
POSTFACH 500 500
D-4600 DORTMUND
GERMANY

JAMES M. HAUGHIAN
LBL
BLDG. 90, ROOM 2148
BERKELEY CA 94720
USA

HITOSHI HAYAYNO
SLAC
P. O. BOX 4349
STANFORD CA 94309
USA

HELGA HAYSE
ETM ELECTROMATIC INC.
35451 DUMBARTON COURT
NEWARK CA 94560
USA

JAY HEEFNER
CEBAF
12000 JEFFERSON AVENUE
NEWPORT NEWS VA 23602
USA

RICHARD N. HEESE
BROOKHAVEN NATL LAB
BLDG. 725C
UPTON NY 11973
USA

SAMUEL HEIFETS
SLAC
BIN 26
P. O. BOX 4349
STANFORD CA 94309
USA

RICHARD H HELM
SLAC
P.O BOX 4349, BIN 26
STANFORD CA 94309
USA

JY HEMERY
CERN
CH-1211
GENEVA 23
SWITZERLAND

GUENTER HEMMIE
DESY
NOTKESTRASSE 85
D-2000 HAMBURG 52
GERMANY

LINDA HENDRICKSON
SLAC
P. O. BOX 4349
BIN 50
STANFORD CA 94309
USA

ENRIQUE HENESTROZA
LBL
1 CYCLOTRON ROAD, MS 47/112
BERKELEY CA 96720
USA

HEINO HENKE
CERN
LEP DIVISION
CH-1211 GENEVA 23
SWITZERLAND

MICHAEL F. HENNELLY
AMER. INST. OF PHYSICS
335 E. 45TH STREET
NEW YORK, NY 10017

KNUD N. HENRICHSEN
CERN
CH-1211
GENEVA 23
SWITZERLAND

DAVE HENRY
TENNELEC/NUCLEUS, INC.
2302 BASSWOOD CIRCLE
TUSTIN CA 92680
USA

STEPHEN W. HERB
DESY
NOTKESTRASSE 85
D-2000 HAMBURG 52
GERMANY

HAROLD HERMAN
ARGONNE NATL LAB
9700 S.CASS AVE,BLDG 207/EP
ARGONNE IL 60439
USA

STEVEN HERNANDEZ
LBL
MS 46-161
1 CYCLOTRON ROAD
BERKELEY CA 94720
USA

WERNER F. HERR
CERN
SL DIVISION
CH-1211
GENEVA 23
SWITZERLAND

WILLIAM B HERRMANNSFELDT
SLAC
P O BOX 4349, BIN 26
STANFORD CA 94309
USA

DAVID A. HERRUP
FERMILAB
P.O.B. 500, MS 306
BATAVIA IL 60510
USA

ROBERT O. HETTEL
SLAC
P.O. BOX 4349, BIN 69
STANFORD CA 94309
USA

DENNIS HEWETT
LLNL
P O.B. 808
LIVERMORE CA 94550
USA

TOM HIMEL
SLAC
P. O. BOX 4349
BIN 50
STANFORD CA 94309
USA

JAMES A. HINKSON
LBL
1 CYCLOTRON RD, BLDG 46-125
BERKELEY CA 94720
USA

KOHJI HIRATA
KEK
OHO
TSUKUBA IBARAKI 305
JAPAN

CHING-HUNG HO
ARGONNE NATL LAB
9700 S CASS AVE,BLDG 362
ARGONNE IL 60439
USA

DARWIN D. HO
LLNL
P O BOX 3162
LIVERMORE CA 94550
USA

HAROLD A. HOAG
SLAC
P.O. BOX 4349, BIN 33
STANFORD CA 94309
USA

TERRY HODGES
TRIUMF
4004 WESBROOK HALL
VANCOUVER B C. V6T2A3
CANADA

JOHN HODGSON
SLAC
BIN 96
P O BOX 4349
STANFORD CA 94309
USA

CLARENCE R HOFFMANN
ATOMIC ENERGY OF CANADA
CHALK RIVER NUCLEAR LABS
CHALK RIVER ONTARIO J0J
CANADA

ALBERT J. HOFMANN
CERN
CERN, SL-DIV
CH-1211 GENEVA 23 SWITZERLAND
SWITZERLAND

INGO HOFMANN
GSI-DARMSTADT
P. O. BOX 110552
6100 DARMSTADT
GERMANY

PAUL HOLIK
SLAC
P. O. BOX 4349
BIN 50
STANFORD CA 94309
USA

STEPHEN D. HOLMES
FERMILAB
P.O. BOX 500, MS-306
BATAVIA IL 60510
USA

RONALD F. HOLSINGER
FIELD EFFECTS, INC.
6 EASTERN ROAD
ACTON MA 01720
USA

TOSHITADA HORI
SUMITOMO HEAVY IND.
2-1-1 YATO-CHO, TANASHI-CITY
TOKYO 188
JAPAN

G. HORLITZ
DESY
NOTKESTR. 85
2 HAMBURG 52
GERMANY

WALID HOSSEINI
SLAC
2575 SAND HILL ROAD
MENLO PARK CA 94301
USA

TIMOTHY HOUCK
LLNL
P. O. BOX 808, L626
LIVERMORE CA 94550
USA

CURT HOVATER
CEBAF
12000 JEFFERSON AVE
NEWPORT NEWS VA 23602
USA

DONALD HOWARD
LBL
1 CYCLOTRON RD, BLDG 64-121
BERKELEY CA 94720
USA

JOSEPH W HOWELL
ARGONNE NATL LAB
9700 S CASS AVENUE
ARGONNE IL 60439
USA

SAM HOWRY
SLAC
P. O. BOX 4349
BIN 50
STANFORD CA 94309
USA

EGON HOYER
LBL
1 CYCLOTRON RD, BLDG 46-161
BERKELEY CA 94720
USA

EARL HOYT
SLAC
P. O. BOX 4349, BIN 74
STANFORD CA 94309
USA

HSIAO-CHAUN HSEUH
BROOKHAVEN NATL LAB
BLDG. 911B
UPTON NY 11973
USA

HANK HSIEH
BROOKHAVEN NATL LAB
NSLS, BLDG. 725C
UPTON NY 11973
USA

IAN C. HSU
SLAC
P.O.BOX 4349, BIN 55
STANFORD CA 94309
USA

TSENG-YANG HSU
UNIV. OF SO. CALIF.
DEPT. OF ELEC. ENGINEERING
LOS ANGELES CA 90007
USA

CHEN-SHIUNG HSUE
SYNCH. RAD. RES. CEN-TAIWAN
HSINCHU SCIENCE INDUSTRIAL PK
HSINCHU 30077
TAIWAN, ROC

SHAO-YUAN HSUEH
FERMILAB
P. O. BOX 500, MS 341
BATAVIA IL 60510
USA

YUN-XIANG HUANG
UNIV. OF HOUSTON/TAC
DEPT. OF PHYSICS
UNIVERSITY OF HOUSTON
HOUSTON TX 77204-5504
USA

EDWARD L. HUBBARD
GENERAL ATOMICS
5527 CHELSEA AVE
LA JOLLA CA 92037
USA

ROBERT E HUBBARD
MEDI-PHYSICS INC
3350 N RIDGE AVE
ARLINGTON HEIGHTS IL 60004
USA

GLEN HUFFMAN
VARIAN
811 HANSEN WAY
PALO ALTO CA 94304
USA

THOMAS P. HUGHES
MISSION RESEARCH CORP.
1720 RANDOLPH RD, S.E.
ALBUQUERQUE NM 87106
USA

LANNY R. HUGHEY
NATL INSTI OF STD & TECH
BLDG 245, RM B119
GAITHERSBURG MD 20899
USA

RUSTY HUMPHREY
SLAC
P. O. BOX 4349
BIN 50
STANFORD CA 94309
USA

DAVID HUMPHRIES
LBL
1 CYCLOTRON RD., MS-46-161
BERKELEY CA 94720
USA

STANLEY, JR. HUMPHRIES
UNIVERSITY OF NEW MEXICO
EECE BLDG., RM 110
ALBUQUERQUE NM 87131
USA

DONALD B HUNT
LBL
1 CYCLOTRON RD, BLDG 64-121
BERKELEY CA 94720
USA

JAMES W. HURD
LOS ALAMOS NATL LAB
P.O. BOX 1663, MP-2, H812
LOS ALAMOS NM 87545
USA

PATRICK HURH
FERMILAB
P.O B 500, MS 340
BATAVIA IL 60510
USA

RICHARD L. HUTSON
LOS ALAMOS NATL LAB
MP-5, MS H838
LOS ALAMOS NM 87545
USA

ANDREW HUTTON
SLAC
P.O BOX 4349, BIN 12
STANFORD CA 94309
USA

JEAN-PIERRE ICHAC
THOMSON TUBES ELECTRONIQUES
38 RUE VAUTHIER-BP 305
F-92102 BOULOGNE-BILLANCOURT
FRANCE

HIRO IKEZI
GENERAL ATOMICS
P. O. BOX 85608
SAN DIEGO CA 92138
USA

PETER F. INGRASSIA
BROOKHAVEN NATL LAB
AGS DEPARTMENT, BUILDING 911A
UPTON NY 11973
USA

K. INOUE
RIKEN
HONKOMAGOME 2-28-8
BUNKYO-KU
TOKYO, 113
JAPAN

ANDREW INTRATER
ADVANCED TECHNOLOGY, INC.
2110 RINGWOOD AVENUE
SAN JOSE CA 95131
USA

JOHN IRWIN
SLAC
P.O.B. 4349
STANFORD CA 94309
USA

I. ISSINSKI
JINR DUBNA
P.O. BOX 79
MOSCOW USSR 101000
USSR

PETR IVANOV
NOVOSIBIRSK
LAURENTEVA ST 11 630090
USSR

JAMES IVERS
CORNELL UNIV
909 MITCHELL ST.
ITHACA NY 14850
USA

YOSHIHISA IWASHITA
KYOTO UNIVERSITY
ACCELERATOR LAB,
INST. FOR CHEM. RES , GOKANOSHO, UJI
KYOTO 611
JAPAN

CEZARY JACH
SSC
MS 1044
2550 BECKLEYMEADE AVE.
DALLAS TX 75237
USA

ALAN A JACKSON
LBL
1 CYCLOTRON RD
B80-101
BERKELEY CA 94720
USA

GERALD P JACKSON
FERMILAB
P.O BOX 500, MS 308
BATAVIA IL 60510
USA

JOHN W. JACKSON
BROOKHAVEN NATL LAB
BLDG. 911C
UPTON NY 11973
USA

JONATHAN JACKSON
CEBAF
12000 JEFFERSON AVENUE
NEWPORT NEWS VA 23606
USA

LESLIE JACKSON
LBL
MAILSTOP 46-125
BERKELEY CA 94720
USA

KEN JACOBS
MIT BATES ACCELERATOR
P.O. BOX 846
MIDDLETON MA 02148
USA

ROBERT JACOBSEN
SLAC
P. O. BOX 4349, BIN 95
STANFORD CA 94309
USA

TARIQ JAFFERY
FERMILAB
P. O. BOX 500, MS 346
BATAVIA IL 60510
USA

ANIMESH JAIN
SUNY AT STONYBROOK
DEPT. OF PHYSICS, SUNY
STONY BROOK NY 11776-3800
USA

ROBERT A. JAMESON
LOS ALAMOS NATL LAB
P.O. BOX 1663, AT-DO, H811
LOS ALAMOS NM 87545
USA

GEORGES E. JAMIESON
SSC
2550 BECKLEYMEADE AVE.
MS 1046
DALLAS TX 75237
USA

GUO-JEN JAN
SYNCH. RAD. RES. CEN-TAIWAN
HSINCHU SCIENCE INDUSTRIAL PK.
HSINCHU 30077
TAIWAN, ROC

DAVID JENNER
INDIANA UNIVERSITY
CYCLOTRON FACILITY
2401 MILO B. SAMPSON LANE
BLOOMINGTON IN 47405
USA

R. KEITH JOBE
SLAC
P O BOX 4349
STANFORD CA 94309
USA

KJELL JOHNSEN
CERN
LEP DIVISION
CH-1211 GENEVA 23
SWITZERLAND

DAVID E. JOHNSON
SSC
2550 BECKLEYMEADE
DALLAS TX 75237
USA

JIMMIE K. JOHNSON
LBL
1 CYCLOTRON RD,BLDG. 47/112
BERKELEY CA 94720
USA

KENNETH F. JOHNSON
LOS ALAMOS NATL LAB
P.O.BOX 1663
AT-10, H818
LOS ALAMOS NM 87545
USA

RAY M. JOHNSON
E M DESIGN
4009 CRATER LAKE ROAD
MEDFORD OR 97504
USA

ROLLAND P. JOHNSON
MAXWELL LABS
BROBECK DIVISION
4905 CENTRAL AVE.
RICHMOND CA 94804
USA

RUDI JOHNSON
LBL
1 CYCLOTRON ROAD, 47/112
BERKELEY CA 94720
USA

STANLEY R. JOHNSON
FERMILAB
P. O. BOX 500, MS 306
BATAVIA IL 60510
USA

WALTER C. JOHNSON
BURLE INDUSTRIES INC.
53 WILDWOOD ROAD
LACONIA NH 03246
USA

WERNER JOHO
PSI
CH-5232 VILLIGEN
SWITZERLAND

SERGE JOLY
CEA
SCE PTN, BP12
91680 BRUYERES-LE-CHATEL
FRANCE

ALAN A. JONES
SSC
2550 BECKLEYMEADE AVE.
DALLAS TX 75237
USA

KEVIN JONES
LOS ALAMOS NATL LAB
MP-6, MS H812
P. O. BOX 1663
LOS ALAMOS NM 87545
USA

WILLIAM P. JONES
INDIANA UNIVERSITY
2401 MILO B. SAMPSON LANE
BLOOMINGTON IN 47405
USA

YVES JONGEN
ION BEAM APPLICATIONS SA
CHEMIN DU CYCLOTRON, 2
B - 1348 LOUVAIN-LA-NEUVE
BELGIUM

STEVE JORDAN
CMI TECHNOLOGY INC.
3411 LEONARD COURT
SANTA CLARA CA 95054
USA

KEVIN JORDON
CEBAF
12000 JEFFERSON AVE.
NEWPORT NEWS VA 23606
USA

A. JOUBERT
GANIL
B.P. 5027
14021 CAEN CEDEX
FRANCE

•DAVID JUDD
LBL
1 CYCLOTRON ROAD, 47/112
BERKELEY CA 94720
USA

JAMES JUDKINS
SLAC
P.O BOX 4349, BIN 33
STANFORD CA 94309
USA

ROLAND R. JUNG
CERN - LEP DIVISION
CH-1211 GENEVA 23
SWITZERLAND

THOMAS G. JURGENS
FERMILAB
P.O. BOX 500 MS 308
BATAVIA IL 60510
USA

EMMANUEL KAHANA
ARGONNE NATL LAB
APS 362
9700 S. CASS AVENUE
ARGONNE IL 60539
USA

STEPHEN KAHN
BROOKHAVEN NATL LAB
BUILDING 902-A
UPTON NY 11973
USA

CARL KALBFLEISCH
SSC
2550 BECKLEYMEADE AVE., MS 1046
DALLAS TX 75237
USA

GREGORY KALKANIS
VARIAN MEDICAL EQUIP
911 HANSEN WAY, MS C-077
PALO ALTO CA 94303
USA

NICHOLAS KALLAS
SSC
2550 BECKLEYMEADE AVE.
MS 1005
DALLAS TX 75237
USA

SWARN S. KALSI
GRUMMAN CORP
MS B29-25
BETHPAGE NY 11714
USA

NAMIO KANEKO
ISHIKAWAJIMA-HARIMA HEAVY IND. CO., LTD.
1-15, 3-CHOME, LOTO-KU
TOKYO
JAPAN

CHRISTOS A. KAPETANAKOS
NAVAL RESEARCH LAB.
CODE 4710
WASHINGTON DC 20375
USA

GEORGE KARADY
ARIZONA STATE UNIVERSITY
ELEC. & COMP. ENG. DEPT.
TEMPE AZ 85287
USA

JEFF KARN
CEBAF
12000 JEFFERSON AVE.
NEWPORT NEWS VA 23606
USA

TAKESHI KATAYAMA
INS, UNIV. TOKYO
3-2-1 MIDORICKO
TANASHI TOKYO 188
JAPAN

S. KATO
OSAKA UNIVERSITY
LABORATORY OF NUCLEAR STUDIES
TOYONAKA, OSAKA 560
JAPAN

TADAHIKO KATOH
KEK
1-1, OHO
TSUKUBA, IBARAKI 305
JAPAN

THOMAS C. KATSOULEAS
UCLA PHYSICS DEPARTMENT
56-125B ENGINEERING IV
LOS ANGELES CA 90024
USA

TOMOTARO KATSURA
KEK
TSUKUBA
IBARAKI KEN 305
JAPAN

STEVEN KAUFFMANN
SSC
MS 1041
2550 BECKLEYMEADE AVE.
DALLAS TX 75237
USA

JURIS KAUGERTS
U. S. DEPT OF ENERGY
ER-224
WASHINGTON DC 20585
USA

TODD J. KAUPPILA
LOS ALAMOS NATL LAB
P.O. BOX 1663, MS P940
LOS ALAMOS NM 87545
USA

REZA KAZIMI
TEXAS ACCEL CENTER
4802 RESEARCH FOREST DR., BLDG. 2
THE WOODLANDS TX 77381
USA

JOHN T. KEANE
BROOKHAVEN NATL LAB
BLDG. 725C
UPTON NY 11973
USA

DAVID M. KEHNE
UNIV. OF MARYLAND
3109 ROSEMARY LANE
HYATTSVILLE MD 20783
USA

EBERHARD K. KEIL
CERN
LEP DIVISION
CH-1211 GENEVA 23
SWITZERLAND

RODERICH KELLER
LBL
1 CYCLOTRON ROAD
B80-101
BERKELEY CA 94720
USA

KURT D. KENNEDY
LBL
1 CYCLOTRON RD, BLDG 46-161
BERKELEY CA 94720
USA

ARDITH KENNEY
LBL
ONE CYCLOTRON RD., 50-149
BERKELEY CA 94720
USA

JORG KEWISCH
CEBAF
12000 JEFFERSON AVENUE
NEWPORT NEWS VA 23606
USA

SEMYON A. KHEIFETS
SLAC
2575 SAND HILL ROAD
MENLO PARK CA 94025
USA

PHILIP KIEFER
UC SAN DIEGO
B-019, MAYER HALL
LA JOLLA CA 92093
USA

DIETMAR KIEHLMANN
INTERATOM
P. O. BOX 100351 FRIEDRICH-EBERT-STR.
BERGISCH GLADBACH1 D5060
GERMANY

CHARLES H. KIM
LBL
1 CYCLOTRON RDB80-101
BERKELEY CA 94720
USA

KEEMAN KIM
ARGONNE NATL LAB
APS-362
ARGONNE IL 60429
USA

KWANG-JE KIM
LBL
MAILSTOP 71-259
BERKELEY CA 94720
USA

SUK HONG KIM
ARGONNE NATL LAB
9700 S.CASS AVE, BLDG 360
ARGONNE IL 60439
USA

YOSHITAKA KIMURA
KEK
OHO, TSUKUBA-SHI
305
JAPAN

HANS-PETER KINDERMANN
CERN
SPS DIVISION
CH-1211 GENEVA 23
SWITZERLAND

H L. KINNEY
BROOKHAVEN NATL LAB
DIRECTOR'S OFFICE
UPTON NY 11973
USA

JOHN KINROSS-WRIGHT
LOS ALAMOS NATL LAB
MS H851
P O BOX 1663
LOS ALAMOS NM 87545
USA

R E KIRBY
SLAC
P O BOX 4349, BIN 74
STANFORD CA 94309
USA

JOSEPH KIRCHGESSNER
CORNELL UNIV
124 NEWMAN LABORATORY
ITHACA NY 14853
USA

BILL KIRK
SLAC, BIN 80
P.O. BOX 4349
STANFORD, CA 94309

HAROLD G. KIRK
BROOKHAVEN NATL LAB
BLDG. 510D
UPTON NY 11973
USA

GEORGE KIRKMAN
INTEGRATED APPLIED PHYSICS
50 THAYER ROAD
MALTHAN MA 021LL54
USA

MASASHI KITAMURA
HITACHI, LTD.
4029 KUJI
KUJI/HITACHI/IBARAKI
JAPAN

LOWELL KLAISNER
SLAC
P. O. BOX 4349
STANFORD CA 94309
USA

HANS U. KLEIN
INTERATOM
FRIEDRICH-EBERT-STR.
5060 BERGISCH-GLADBACH
GERMANY

J. DENNIS KLEIN
BROOKHAVEN NATL LAB
BUILDING 725A, NSLS
UPTON NY 11973
USA

THOMAS KNIGHT
SLAC
BIN 26
P. O. BOX 4349
STANFORD CA 94309
USA

MARTIN J KNOTT
ARGONNE NATL LAB
9700 S.CASS AVE,BLDG 360,FPP
ARGONNE IL 60439
USA

HARROLD B. KNOWLES
ARINC RESEARCH CORP
4030 HILLCREST ROAD
EL SOBIZANTE CA 94803
USA

IN KO
POSTECH
DEPT OF PHYSICS
P. O. BOX 125
POHANG KYUNGBUK 790-600
KOREA

KWOK C. KO
SLAC
P.O.B. 4349 BIN 26
STANFORD CA 94309
USA

YUZO KOJIMA
KEK, NATL LAB FOR HIGH ENERGY
1-1 OHO TSUKUBA
IBARAKI 305
JAPAN

RICHARD KONECNY
ARGONNE NATL LAB
9700 SOUTH CASS AVENUE
ARGONNE IL 60439
USA

GERHARD T. KONRAD
SIEMENS MEDICAL LABS
4040 NELSON AVENUE
CONCORD CA 94520
USA

YANG KOO
POSTECH
P. O BOX 125
POHANG KYUNGBUK 790-600
KOREA

ROLAND F. KOONTZ
SLAC
P.O. BOX 4349
STANFORD CA 94309
USA

SHANE R. KOSCIELNIAK
TRIUMF
4004 WESBROOK MALL
VANCOUVER BC V6T
CANADA

WAYNE A. KOSKA
FERMILAB
P. O. BOX 500
MS 316
BATAVIA IL 60510
USA

CHRISTOPHER KOSTAS
SAIC
1710 GOODRIDGE DR.
P. O BOX 1303, MS II-3-1
MCLEAN VA 22102
USA

RABINDER KOUL
ARGONNE NATL LAB
APS-362
9700 S CASS AVE
ARGONNE IL 60439
USA

JOANIS KOURBANIS
FERMILAB
P. O BOX 500, MS 306
BATAVIA IL 60510
USA

JEAN-PIERRE KOUTCHOUK
CERN
SL DIVISION
CH-1211
GENEVA 23
SWITZERLAND

ROLAND KOWALEWICZ
UNIV ERLANGEN-NURNBERG
ROLAND KOWALEWICZ
GENEVA 23
SWITZERLAND

ANDREW KOZUBEL
LOS ALAMOS NATL LAB
P. O. BOX 1663
AT-8, MS H820
LOS ALAMOS NM 87545
USA

GEOFFREY A. KRAFFT
CEBAF
12070 JEFFERSON AVE
NEWPORT NEWS VA 23606
USA

STEPHEN F. KRAL
ASTRO. CORP. OF AMERICA
5800 COTTAGE GROVE RD.
MADISON WI 53716
USA

JONATHON KRALL
NAVAL RESEARCH LAB
CODE 4790
WASHINGTON DC 20375
USA

ROBERT KRAUS
LOS ALAMOS NATL LAB
AT-3, MS H808
LOS ALAMOS NM 87545
USA

K. KRAUTER
SLAC
P. O. BOX 4349
BIN 50
STANFORD CA 94309
USA

LEONID V. KRAVCHUK
INSTITUTE FOR NUCLEAR RESEARCH
60TH OCTOBER PROSPECT 7A
MOSCOW USSR 117312
USSR

GARY F KREBS
LBL
1 CYCLOTRON RD, BLDG 51-208
BERKELEY CA 94720
USA

P KREJCIK
SLAC
P O BOX 4349, BIN 66
STANFORD CA 94309
USA

SAMUEL KRINSKY
BROOKHAVEN NATL LAB
BLDG. 725B
UPTON NY 11973
USA

SRINIVAS KRISHNAGOPAL
LBL
MS 71H
1 CYCLOTRON ROAD
BERKELEY CA 94720
USA

JAYARAM KRISHNASWAMY
GRUMMAN SPACE & ELEC. DIV.
725C NSLS
BROOKHAVEN NATL. LAB
UPTON NY 11972
USA

FRANZ KRISPEL
SIEMENS MEDICAL LABS
4040 NELSON AVENUE
CONCORD CA 94520
USA

TOM KROC
FERMILAB
P.O.B. 500
BATAVIA IL 60510
USA

FRANS KROES
NIKHEF-K
P.O. BOX 4395
1009 AJ AMSTERDAM
NETHERLANDS

NORMAN M. KROLL
UNIV. OF CALIF., SAN DIEGO
DEPT. OF PHYSICS 0319
9500 GILMAR DRIVE
LA JOLLA CA 92093-0319
USA

JAMES KRUPNICK
LBL
MAILSTOP 46-161
BERKELEY CA 94720
USA

A. KRYCUK
CEBAF
12000 JEFFERSON AVE.
NEWPORT NEWS VA 23602
USA

MOYSES KUCHNIR
FERMILAB
P.O. BOX 500, MS-316
BATAVIA IL 60510
USA

BEREND KUIPER
CERN
PS DIVISION
CH-1211 GENEVA 23
SWITZERLAND

A\ \TOLY A. KULAKOV
SLAC
BIN 33
P. O. BOX 4349
STANFORD CA 94309
USA

ARTEM KULIKOV
SLAC
P.O.B. 4349
PALO ALTO CA 94309
USA

CHIN-CHENG KUO
SYNCH RAD. RES CEN-TAIWAN
NO 1 R&D ROAD VI
HSINCHU SCIENCE-BASED INDUSTRIAL PARK
HSINCHU, TAIWAN 30077
CHINA

THOMAS KUO
MICHIGAN STATE UNIV.
NATIONAL SUPER COND.
EAST LANSING MI 48824
USA

SHIN-ICHI KUROKAWA
KEK
1-1, OHO
TSUKUBA, IBARAKI 305
JAPAN

MARTIN D. KURZ
INST FUR ANGEWANDTE PHYSIK
ROBERT-MAYER-ST. 2-4
D-6000 FRANKFURT A M. GERMANY
GERMANY

ROBERT L. KUSTOM
ARGONNE NATL LAB
9700 S.CASS AVE, BLDG 360
ARGONNE IL 60439
USA

NIVOLAI KUZNEZOV
INP-NOVOSIBIRSK
630080 NOVOSIBIRSK
USSR

JOE W. KWAN
LBL
1 CYCLOTRON RD., BLDG 4/230
BERKELEY CA 94720
USA

KENNETH LA MON
LBL
MAILSTOP 71/259
BERKELEY CA 94720
USA

DARREL LAGER
LLNL
BOX 808, L-156
LIVERMORE CA 94550
USA

TERRY LAHEY
SLAC
P. O BOX 4349
STANFORD CA 94309
USA

G. LAHTI
CEBAF
12000 JEFFERSON AVE
NEWPORT NEWS VA 23602
USA

GLEN R. LAMBERTSON
LBL
1 CYCLOTRON RD, BLDG 47-112
BERKELEY CA 94720
USA

SERGE Y LAMISSE
ION BEAM APPLICATIONS SA
CHEMIN DU CYCLOTRON 2
1348 LOUVAIN-LA-NEUVE
BELGIUM

MICHAEL LAMM
FERMILAB
P. O. BOX 500, MS 346
BATAVIA IL 60510
USA

MICHAEL C. LAMPEL
ROCKETDYNE DIV-ROCKWELL INTL
6633 CANOGA AVE. MS FA38
CANOGA PARK CA 91303
USA

HENRY D. LANCASTER
LBL
1 CYCLOTRON RD, BLDG 46-125
BERKELEY CA 94720
USA

FRITZ LANGE
FERMILAB
P.O.B. 500, SM 340
BATAVIA IL 60510
USA

DAVID C. LARBALESTIER
UNIVERSITY OF WISCONSIN
919 ENGINEERING RESEARCH BLDG
MADISON WI 53706
USA

ROBERT J. LARI
VECTOR FIELDS INC.
1700 N. FARNSWORTH AVE.
AURORA IL 60505
USA

DAVID LARSON
LLNL
MS L-472
7000 EAST AVENUE
LIVERMORE CA 94550
USA

DELBERT J. LARSON
CREOL
12424 RESEARCH PARKWAY
ORLANDO FL 32826
USA

PETER E. LATHAM
UNIV OF MARYLAND
LAB FOR PLASMA RES.
COLLEGE PARK MD 20742
USA

Y Y LAU
NAVAL RESEARCH LAB
CODE 4790
WASHINGTON DC 20375
USA

EUGENE J LAUER
LLNL
P O BOX 808, L-626
LIVERMORE CA 94550
USA

RON LAUZE
CEBAF
12000 JEFFERSON AVENUE
NEWPORT NEWS VA 23606
USA

WILLIAM LAVENDER
SSRL
P. O. BOX 4349, BIN 99
STANFORD CA 94309
USA

CHARLES LAVERICK
16 ROSLYN COURT
PATCHOGUE NY 11772
USA

THEODORE L. LAVINE
SLAC
P.O.B. 4349, BIN 26
STANFORD CA 94309
USA

GEORGE P. LAWRENCE
LOS ALAMOS NATL LAB
P.O. BOX 1663, AT-DO, H817
LOS ALAMOS NM 87545
USA

WESLEY G. LAWSON
UNIVERSITY OF MARYLAND
EE DEPARTMENT
COLLEGE PARK MD 20742
USA

ROBERT E. LAXDAL
TRIUMF
4004 WESBROOK MALL
VANCOUVER B.C. V6T
CANADA

P. HUBERT LEBOUTET
CEA-DAM
PTN, 16 RESIDENCE BEAUSOLEIL
92210 SAINT CLOUD
FRANCE

LEON M. LEDERMAN
FERMILAB
P.O. BOX 500
BATAVIA IL 60510
USA

EDWARD P. LEE
LBL
1 CYCLOTRON RD, BLDG 47/112
BERKELEY CA 94720
USA

HEON-JU LEE
LBL
1 CYCLOTRON ROAD, 47/112
BERKELEY CA 94720
USA

MARTIN J. LEE
SLAC
P.O. BOX 4349, BIN 12
STANFORD CA 94309
USA

SHYH-YUAN LEE
INDIANA UNIVERSITY
DEPARTMENT OF PHYSICS
BLOOMINGTON IN 47405
USA

TONG NYONG LEE
POHANG INSTI. OF SCIENCE & TECH
P. O BOX 125
POHANG KYUNGBUK 790-600
KOREA

YONG YUNG LEE
BROOKHAVEN NATL LAB
ACCEL. DEPT.
BLDG 911B
UPTON NY 11973
USA

CHRISTOPH LEEMANN
CEBAF
12070 JEFFERSON AVENUE
NEWPORT NEWS VA 23606
USA

ROBERT LEGG
MAXWELL LABS
BROBECK DIVISION
4905 CENTRAL AVE.
RICHMOND CA 94804
USA

IRA S. LEHRMAN
GRUMMAN SPACE SYSTEMS
PRINCETON CORP. CTR.
4 INDEPENDENCE WAY
PRINCETON NJ 08540
USA

GORDON LEIFESTE
SSC
2550 BECKLEYMEADE AVE
DALLAS TX 75237
USA

CARLOS LEITAO
SLAC
P. O. BOX 4349
BIN 50
STANFORD CA 94309
USA

WILLIAM J. LEONHARDT
BROOKHAVEN NATL LAB
BLDG. 911A
UPTON NY 11973
USA

ELIANE S. LESSNER
ARGONNE NATL LAB
APS BLD 360
9700 S. CASS AVENUE
ARGONNE IL 60539
USA

EDDIE LEUNG
GENERAL DYNAMICS
8828 GREENBERG LANE
SAN DIEGO CA 92129
USA

KA-NGO LEUNG
LBL
MS 4-230
BERKELEY CA 94720
USA

KENT LEUNG
SSC
2550 BECKLEYMEADE AVE.
DALLAS TX 75237
USA

STEPHEN LEWIS
LBL
BLD. 64, ROOM 121
BERKELEY CA 94720
USA

MINGYANG LI
SSC
MS 1049
2550 BECKLEYMEADE AVE.
DALLAS TX 75237
USA

RUI LI
CEBAF
12000 JEFFERSON AVENUE
NEWPORT NEW VA 23606
USA

JOSEPH LIDESTRI
PULSE SCIENCES, INC.
600 MCCORMICK ST.
SAN LEANDRO CA 94577
USA

TORSTEN LIMBERG
SLAC
P. O. BOX 4349, BIN 66
STANFORD CA 94309
USA

CHIA-LIANG LIN
MIT
NW16-223
CAMBRIDGE MA 02139
USA

HELENA E LINDQUIST
CHALK RIVER LABS
CHALK RIVER LAB
CHALK RIVER ONTARIO KOJ1JO
CANADA

PHILIP LINDQUIST
CEBAF
12000 JEFFERSON AVENUE
NEWPORT NEWS VA 23606
USA

CARL LIONBERGER
LBL
MAILSTOP 46A-1123
BERKELEY CA 94720
USA

RONGLIN LIOU
UNIV SO. CALIF.
ROOM 410
LOS ANGELES CA 90089-0484
USA

JAMES LIPARI
SLAC
BIN 49
2575 SAND HILL ROAD
MENLO PARK CA 94025
USA

DR. GERHARD LIPPMANN
DORNIER GMBH
7990 FRIEDRICHSHAFEN 1
P.O.B. 1420, DEPT. MCF
GERMANY

VLADIMIR LITVINENKO
DUKE UNIVERSITY
FEL LABORATORY
LA SALLE ST. EXT.
DURHAM NC 27706
USA

STEPHEN LLOYD
LOS ALAMOS NATL LAB
P. O. BOX 1663
AT-8, MS H820
LOS ALAMOS NM 87545
USA

C. C. LO
LBL
1 CYCLOTRON RD., 46-125
BERKELEY CA 94530
USA

GARY LODA
6921 JOHNSTON ROAD
PLEASANTON CA 94588
USA

GEORGE LOEGEL
SSC
2550 BECKLEYMEADE AVE., MS 1046
DALLAS TX 75237
USA

GREGORY A. LOEW
SLAC
P.O. BOX 4349, BIN 33
STANFORD CA 94309
USA

MORE LOISELET
UNIV. LOUVAIN
2, CHEMIN DU CYCLOTRON
B1348 LOUVAIN-LA-NEUVE
BELGIUM

AUGUSTO LOMBARDI
INFN
LABORATORI DI LEGNARO
VIA ROMEA #4
LEGNARO 3502
ITALY

ALEXANDRE LOOLERGUE
SLAC
679 STANFORD AVENUE
PALO ALTO CA 96301
USA

GUSTAVO LOPEZ
SSC
2550 BECKLEYMEADE DR.
DALLAS TX 75237
USA

FRED H. G. LOTHROP
LBL
1 CYCLOTRON RD, BLDG 51-208
BERKELEY CA 94720
USA

KENG M. LOW
SSC
2550 BECKLEYMEADE AVE
MS 1046
DALLAS TX 75237
USA

ROBERT R. LOWN
FIELD EFFECTS, INC.
6 EASTERN ROAD
ACTON MA 01720
USA

XIANPING LU
FERMILAB
P.O.BOX 500, MS 308
BATAVIA IL 60510
USA

PETER W. LUCAS
FERMILAB
P.O. BOX 500, MS-307
BATAVIA IL 60510
USA

ALFREDO LUCCIO
BROOKHAVEN NATL LAB
BLDG. 911A
UPTON NY 11973
USA

KENNETH S. LUCHINI
LBL
1 CYCLOTRON RD. MS 46-125
BERKELEY CA 94720
USA

BERNHARD A. LUDEWIGT
LBL
1 CYCLOTRON ROAD
BUILDING 64
BERKELEY CA 94720
USA

G. LUDGATE
TRIUMF
4004 WESBROOK MALL
VANCOUVER B.C. V6T2A3
CANADA

DON LUDWIG
WESTERN BIOMEDICAL RESEARCH
401 W. ASPEN STREET
FLAGSTAFF AZ 86001
USA

GUY LUIJCKX
NIKHEF K
P. B. 4395
1009 AJ AMSTERDAM
NETHERLANDS

RICHARD E LUJAN
LOS ALAMOS NATL LAB
P. O BOX 1663
AT-4, MS H821
LOS ALAMOS NM 87545
USA

ALEX H. LUMPKIN
LOS ALAMOS NATL LAB
P O BOX 1663, P-15, D406
LOS ALAMOS NM 87545
USA

CESAR LUONGO
STONER ASSOCIATES
388 MARKET ST, SUITE 250
SAN FRANCISCO CA 94111
USA

ROB MAAS
NIKHEF-K
P. O. BOX 41882
1009 DB AMSTERDAM
THE NETHERLANDS

ROBERT J. MACEK
LOS ALAMOS NATL LAB
P.O. BOX 1663, MP-DO, H848
LOS ALAMOS NM 87545
USA

SHINJI MACHIDA
SSC
MS 1049
2550 BECKLEYMEADE AVE.
DALLAS TX 75237
USA

JAMES A. MACLACHLAN
FERMILAB
P.O. BOX 500, MS-341
BATAVIA IL 60510
USA

DAVE MACNAIR
SLAC
BIN 49
2575 SAND HILL ROAD
MENLO PARK CA 94025
USA

JOHN MAENCHEN
SANDIA NATL LABS
P.O. BOX 5800, DIV 1263
ALBUQUERQUE NM 87185
USA

CHRISTIAN MAENNEL
THOMSON TUBES
38 RUE VAUTHIER, BP 305
BOULOGNE BILLANCOURT 92100
FRANCE

NARAYAN K. MAHALE
SSC
2550 BECKLEYMEADE AVE.
DALLAS TX 75237
USA

WILLIAM T MAIN
UNIV. OF MARYLAND
LAB FOR PLASMA RESEARCH
COLLEGE PARK MD 20742
USA

MICHAEL MAKOWSKI
LLNL
L-637
P O BOX 808
LIVERMORE CA 94550
USA

JEROME MALENFANT
PHYSICAL REVIEW LETTERS
1 RESEARCH ROAD
RIDGE NY 11961
USA

JEAN CH. MALGLAIVE
GENERAL ELECTRIC CO.
BP 34
BUC 78530
FRANCE

JOHN MAMMOSSER
CEBAF
12000 JEFFERSON AVE.
NEWPORT NEWS VA 23606
USA

S. R. MANE
BROOKHAVEN NATL LAB
BLDG. 911B
UPTON NY 11973
USA

JOH N MANGINO
SSC
2550 BECKLEYMEADE AVE., MS 1046
DALLAS TX 75237
USA

PAUL M. MANTSCH
FERMILAB
P.O BOX 500, MS-316
BATAVIA IL 60510
USA

WILLIAM A. MANWARING
INDIANA UNIVERSITY
2401 MILO B. SAMPSON LANE
BLOOMINGTON IN 47405
USA

CLEON B. MANZ
SSC
2550 BECKLEYMEADE, MS 1047
DALLAS TX 75237
USA

NAIFENG MAO
LOS ALAMOS NATL LAB
MP-14, MS H847
LOS ALAMOS NM 87545
USA

J. STEPHEN MARKS
LBL
ONE CYCLOTRON RD
MS 2-400
BERKELEY CA 94720
USA

KRISTA MARKS
LBL
MAILSTOP 46A-1123
BERKELEY CA 94720
USA

NIELS MARQUARDT
UNIV. DORTMUND, INST F PHYSIK
POSTFACH 500 500
D-4600 DORTMUND
GERMANY

FELIX MARTI
MICHIGAN STATE UNIV.
CYCLOTRON LABORATORY
EAST LANSING MI 48824
USA

DON MARTIN
SSC
2550 BECKLEYMEADE STE 125, MS 1045
DALLAS TX 75237
USA

JOHN A. MARTIN
9623 TUNBRIDGE LANE
KNOXVILLE TN 37922
USA

PHILIP S. MARTIN
FERMILAB
P O. BOX 500, MS 306
BATAVIA IL 60510
USA

RONALD L. MARTIN
ACCTEK ASSOC. INC.
901 S KENSINGTON AVE.
LAGRANGE IL 60525
USA

RICK L. MARTINEAU
LOS ALAMOS NATL LAB
AT-4, MS H821
P. O. BOX 1663
LOS ALAMOS NM 87545
USA

GARTH MARTINSEN
SSC
2550 BECKLEYMEADE AVE., MS 1046
DALLAS TX 75237
USA

TAKASHI MARUYAMA
SLAC
BIN 78
P. O. BOX 4349
STANFORD CA 94309
USA

XAVIER K MARUYAMA
NAVAL POSTGRADUATE SCHOOL
CODE 61MX, DEPT PHYSICS
MONTEREY CA 93943
USA

M MARZIALE
SIEMENS MEDICAL LABS
4040 NELSON AVE.
CONCORD CA 94520
USA

ANDRE MARZIALI
STANFORD FEL/SCA
HANSEN LAB
STANFORD CA 94305
USA

ANNE MASON
SLAC
P O BOX 4349
BIN 50
STANFORD CA 94309
USA

ANTONIO MASSAROTTI
SINCROTRONE TRIESTE
PADRICIANO 99
TRIESTE 34012
ITALY

DEXTER MASSOLETTI
LBL
B80-101
1 CYCLOTRON ROAD
BERKELEY CA 94720
USA

MARIA MASULLO
INFN
80125 NAPOLI
ITALY

GIOVANNI MATARRESE
S R L IMPIANTI
VIA DEI GUARNERI 14
I 20141 MILANO
ITALY

AXEL MATHEISEN
DESY
NOTKESTR. 85
HAMBURG, D2000
GERMANY

THOMAS MATTISON
SLAC
BIN 95
P. O. BOX 4349
STANFORD CA 94305
USA

CHARLES MATUK
LBL
MS 46-161
1 CYCLOTRON ROAD
BERKELEY CA 94720
USA

MICHAEL G. MAZARAKIS
SANDIA NATL LABS
P.O. BOX 5800, DIV 1272
ALBUQUERQUE NM 87185
USA

PETER O. MAZUR
FERMILAB
P O BOX 500, MS 316
BATAVIA IL 60510
USA

GARY A McCARTHY
UNIVERSITY OF NEW MEXICO
EECE BUILDING
ALBUQUERUE NM 87196
USA

DOUGLAS J McCORMICH
SLAC
2575 SANDHILL ROAD
BIN 66
MENLO PARK CA 94309
USA

MARVIN MCCOY
SLAC
2575 SAND HILL ROAD, BIN 49
MENLO PARK CA 94025
USA

ELLIOTT S MCCRORY
FERMILAB
P O BOX 500, MS 307
BATAVIA IL 60510
USA

EARL W. MCCUNE
VARIAN ASSOCIATES
611 HANSEN WAY
PALO ALTO CA 94303
USA

DOUGLAS S. McDONALD
LBL
1 CYCLOTRON ROAD
BUILDING 4
BERKELEY CA
USA

WILLIAM P. MCDOWELL
ARGONNE NATL LAB
APS 360
ARGONNE IL 60439
USA

THOMAS K. MCGATHEN
LBL
MAILSTOP 50B-4235
BERKELEY CA 94720
USA

DONALD G. MCGHEE
ARGONNE NATL LAB
9700 S. CASS AVE, 360
ARGONNE IL 60439
USA

JOHN A. MCGILL
SSC
MS 1049
2550 BECKLEYMEADE AVE.
DALLAS TX 75237
USA

EDWARD K. MCINTYRE
EATON CORPORATION
108 CHERRY HILL DRIVE
BEVERLY MA 01915
USA

PETER M MCINTYRE
TEXAS A&M UNIV
DEPARTMENT OF PHYSICS
COLLEGE STATION TX 77843
USA

RAYMOND MCINTYRE
VARIAN ASSOC.
611 HANSEN WAY, MS C-077
PALO ALTO CA 94303
USA

KENNETH F. MCKENNA
LOS ALAMOS NATL LAB
P O BOX 1663, DRA/APO, MS F688
LOS ALAMOS NM 87545
USA

PEGGY MCMAHAN
LBL
MS 51-208, 1 CYCLOTRON ROAD
BERKELEY CA 94720
USA

GERRY E MCMICHAEL
CHALK RIVER LABS
ONTARIO
CHALK RIVER ONTARIO K0J
CANADA

PHILIP F. MEADS, JR.
7053 SHIRLEY DRIVE
OAKLAND CA 94611
USA

BEVERLY MECKLENBURG
HAIMSON RESEARCH CORP.
4151 MIDDLEFIELD ROAD
PALO ALTO CA 94303-4793
USA

GARD MEDDAUGH
VARIAN ASSOCIATES
611 HANSEN WAY, MS C077
PALO ALTO CA 94303
USA

NARESH MEHTA
SSC
2550 BECKLEYMEADE
MS 1042
DALLAS TX 75237
USA

RAINER MEINKE
SSC
2550 BECKLEYMEADE AVE , MS 1046
DALLAS TX 75237
USA

CHARLES R. MEITZLER
TEXAS ACCEL CENTER
4802 RESEARCH FOREST DR., BLDG. 2
THE WOODLANDS TX 77381
USA

WUZHENG MENG
BROOKHAVEN NATL LAB
BUILDING 911B
UPTON NY 11973
USA

NIKOLITSA MERMINGA
SLAC
P O.B. 4349, BIN 26
STANFORD CA 94309
USA

BILL MERZ
SSC
MS 1044
2550 BECKLEYMEADE AVE
DALLAS TX 75237
USA

L K MESTHA
SSC
2550 BECKLEYMEADE
DALLAS TX 75237
USA

ROBERT B MEUSER
LBL
1 CYCLOTRON RD , BLDG 47-112
BERKELEY CA 94720
USA

HENRY MIGNARDOT
LOS ALAMOS NATL LAB
P O BOX 1663, MS H821
LOS ALAMOS NM 87545
USA

MIKHAIL S. MIKHEEV
INSTITUTE FOR HIGH ENERGY PHYSICS
SERPUKHOV
142 284 PROTVINO
MOSCOW REGION
USSR

CATIA MILARDI
INFN
VIA E. FERMI
P O. BOX 13
FRASCATI ROMA
ITALY

ED MILLER
SLAC
P. O. BOX 4349
BIN 50
STANFORD CA 94309
USA

JOEL D. MILLER
NAVAL SURFACE WARFARE CENTER
10901 NEW HAMPSHIRE AVE.,
CODE R42
SILVER SPRING MD 20903-5000
USA

ROGER H MILLER
SLAC
P.O BOX 4349, BIN 26
STANFORD CA 94309
USA

FRED E. MILLS
ANL/FERMILAB
40W665 GRAND MONDE DR.
ELBURN IL 60119
USA

DAVE MILLSOM
SLAC
P. O BOX 4349
BIN 50
STANFORD CA 94309
USA

BRUCE F MILTON
TRIUMF
4004 WESBROOK MALL
VANCOUVER B.C V6T2A3
CANADA

STEPHEN V MILTON
PAUL SCHERRER INSTITUTE
CH-5232 VILLIGEN PSI
SWITZERLAND

M. MINESTRINI
INFN-LNF
C P 13
00044 FRASCATI (RM)
ITALY

JERRY MINISTER
SLAC
BIN 49
2575 SAND HILL ROAD
MENLO PARK CA 94025
USA

MICHIKO MINTY
INDIANA UNIVERSITY
2401 MILO B SAMPSON LANE
BLOOMINGTON IN 47408
USA

SAKANO MISAO
FURUKAWA ELECTRIC CO.
2-4-3 OKANO NISHI-KU
YOKOHAMA KANAGAWA 220
JAPAN

GARY R. MISCIKOWSKI
HIGH VOLTAGE TECHNOLOGY GROUP
4040 GROS VENTRE
SAN DIEGO CA 92117
USA

NARI MISTRY
CORNELL UNIV
214 NEWMAN LAB
ITHACA NY 14853
USA

AMIYA K. MITRA
TRIUMF
4004 WESBROOK MALL
VANCOUVER B.C. V6T2A3
CANADA

SHINJI MITSUNOBU
KEK
1-1 OHO, TSUKUBA-SHI
IBARAK-KEN 305
JAPAN

MASAHIRO MIYABAYASHI
SUMITOMO HEAVY IND.
WUANTUM EQUIP. DIV.
151 HEARTLAND BLVD.
EDGEWOOD NY 11717
USA

YOSHIKAZU MIYAHARA
3-2-1, MIDORI-CHO
TANASHI
TOKYO 188
JAPAN

TATASURO MIYATAKE
FURUKAWA ELECTRIC CO.
900 LAFAYETTE ST., SUITE 401
SANTA CLARA CA 95050
USA

AKIRA MIZOBUCHI
INS-UNIV. TOKYO
3-2-1 TANASHI,
TOKYO 188
JAPAN

JONAS H. MODEER
SCANDITRONIX AB
HUSBYBORG
UPPSALA 755
SWEDEN

DAVID L. MOFFAT
CORNELL UNIV
NEWMAN LAB
ITHACA NY 14853
USA

DAVID C. MOIR
LOS ALAMOS NATL LAB
P.O BOX 1663, M-4, P940
LOS ALAMOS NM 87545
USA

NIKOLAI MOKHOV
SSC
2550 BECKLEYMEADE AVE.
MS 1041
DALLAS TX 75237
USA

AKBAR MOKHTARANI
FERMILAB
P.O B. 500, MS 316
BATAVIA IL 60510
USA

SOREN P. MOLLER
ISA INST. FOR SYNCH. RAD.
AARHUS UNIV., NYMUNKEGADE
DK-8000 ARHUS C
DENMARK

WIM K. MONDELAERS
GHENT UNIV
PROEFTERINSTRAAT 86
B9000 GHENT
BELGIUM

ALFRED A. MONDELLI
SAIC
1710 GOODRIDGE DRIVE
MCLEAN VA 22102
USA

MICHAEL MONSLER
W. J. SCHAFER
6140 STONERIDGE MALL ROAD
PLEASANTON CA 94566
USA

MELVIN MONTH
BROOKHAVEN NATL LAB
BLDG. 902-A
UPTON NY 11973
USA

CRAIG D. MOORE
FERMILAB
P.O. BOX 500, MS-306
BATAVIA IL 60510
USA

MICHAEL MORAN
LLNL
P O. BOX 808, L-41
LIVERMORE CA 94550
USA

GERRY H. MORGAN
BROOKHAVEN NATL LAB
BLDG 902B
UPTON NY 11973
USA

JAMES P MORGAN
FERMILAB
110 JANET AVE.
DARIEN IL 60559
USA

WARREN B MORI
UCLA
56-125B ENGINEERING IV
LOS ANGELES CA 90024
USA

DORNIS C. MORIN, JR.
UNIVERSITY OF WISCONSIN, SRC
622 JACOBSON AVE
MADISON WI 53714
USA

JONATHAN MORROW-JONES
MISSION RESEARCH CORP.
735 STATE ST.
P. O. DRAWER 719
SANTA BARBARA CA 93102-0719
USA

PAYMAN MORTAZAVI
BROOKHAVEN NATL LAB
BLDG. 725C
UPTON NY 11973
USA

PHIL MORTON
SLAC
BIN 26
P. O. BOX 4349
STANFORD CA 94309
USA

HERBERT MOSHAMMER
SLAC
BIN 26
P. O. BOX 4349
STANFORD CA 94309
USA

SIGMUND W. MOSKO
OAK RIDGE NATL LAB
P.O. BOX 2008, BLDG. 6000
OAK RIDGE TN 37831
USA

DARIUS MOSTOWFI
SSRL
P. O. BOX 4349, BIN 69
STANFORD CA 94309
USA

MIKE MOUAT
TRIUMF
4004 WESBROOK MALL
VANCOUVER B C. V6T2A3
CANADA

ROLAND MUELLER
BESSY
BERLIN
GERMANY

SAM MUKHERJEE
LBL
1 CYCLOTRON ROAD, 47/112
BERKELEY CA 94720
USA

JAMES B MURPHY
BROOKHAVEN NATL LAB
BLDG 725C
UPTON NY 11973
USA

KENICHI MUTO
KEK
1-1 OHO
TSUKUBA IBARAKI 305
JAPAN

GANAPATI RAO MYNENI
CEBAF
12000 JEFFERSON AVE.
NEWPORT NEWS VA 23606
USA

YASUCHIKA NAGAI
HITACHI CABLE AMERICA, INC.
50 MAIN STREET
WHITE PLANS NY 10606
USA

DAVY N. NAKADA
NISSEI SANGYO AMERICA, LTD.
460 E. MIDLEFIELD ROAD
MOUNTAIN VIEW CA 94043
USA

NORIO NAKAMURA
KEK
OHO 1-1, TSUKUBA
IBARAKI 305
JAPAN

TOSHIHARU NAKAZATO
TOHOKU UNIV.
1-2-1 MIKAMINE
SENDAI JAPAN 982
JAPAN

SANG HOON NAM
POS TECH
P. O. BOX 125
POHANG KYUNGBUK 790-600
SOUTH KOREA

WON NAMKUNG
POSTECH
PLS PROJECT POB 125
POHANG 790-600
KOREA

ALIREZA NASSIRI
ARGONNE NATL LAB
BUILDING 371T
9700 S. CASS AVENUE
ARGONNE IL 60439
USA

SUBRATA NATH
LOS ALAMOS NATL LAB
AT-1, MS H817
LOS ALAMOS NM 87545
USA

JOHN A. NATION
CORNELL UNIV
UPSON HALL
ITHACA NY 14853
USA

ROMAN J. NAWROCKY
BROOKHAVEN NATL LAB
BLDG. 725B
UPTON NY 11973
USA

JOHN L. NEED
DUKE MEDICAL CENTER
P.O. BOX 3808
DURHAM NC 27710
USA

J. R. NEIGHBOURS
NAVAL POSTGRADUATE SCHOOL
PHYSICS DEPARTMENT
MONTEREY CA 93940
USA

GEORGE NEIL
CEBAF
ACCEL. DIV.
12000 JEFFERSON AVENUE
NEWPORT NEW VA 23606
USA

V. KELVIN NEIL
LLNL
P.O. BOX 808, L626
LIVERMORE CA 94550
USA

ERIC NELSON
SLAC
P.O.B. 4349 BIN 26
STANFORD CA 94309
USA

R. NELSON
CEBAF
12000 JEFFERSON AVE.
NEWPORT NEWS VA 23602
USA

VALERY NESTEROV
SLAC
BIN 49
2575 SAND HILL ROAD
MENLO PARK CA 94025
USA

DAVID NEUFFER
CEBAF
12000 JEFFERSON AVENUE
NEWPORT NEWS VA 23606
USA

BARRY NEWBERGER
UNIVERSITY OF TEXAS
INST. FOR FUSION, RLM 11.222
AUSTIN TX 78712
USA

BARRY P. NEWTON
EEV LTD
WATERHOUSE LANE
CHELMSFORD ESSEX
ENGLAND

MARK A NEWTON
LLNL
P O BOX 808, L-627
LIVERMORE CA 94550
USA

WILLIAM E. JR. NEXSEN
LLNL
P.O BOX 808, L626
LIVERMORE CA 94550
USA

OLEG A. NEZHEVENKO
INSTIT NUCLEAR PHYSICS
NOVOSIBIRSK 630090
USSR

BRIAN NG
MAXWELL LABS
BROBECK DIVISION
4905 CENTRAL AVE.
RICHMOND CA 94804
USA

CHO-KUEN NG
SLAC
P. O. BOX 4349
STANFORD CA 94309
USA

KING-YUEN NG
FERMILAB
P.O. BOX 500, MS 345
BATAVIA IL 60510
USA

PHI NGHIEM
CEA/CEN/SACLAY
LABORATOIRE NATIONAL SATURNE
91191 GIF SUR/YVETTE CEDEX
FRANCE

DERRICK HUY NGUYEN
STANFORD
3782 CORINA WAY
PALO ALTO CA 94303
USA

K. T. NGUYEN
NAVAL SURFACE WEAPONS CENTER
10901 NEW HAMPSHIRE AVE.
SILVER SPRING MD 20903
USA

MINH NGUYEN
SLAC
BIN 49
2575 SAND HILL ROAD
MENLO PARK CA 94025
USA

VIET NGUYEN
CEBAF
12000 JEFFERSON AVENUE
NEWPORT NEWS VA 23606
USA

BJARNE NIELSEN
GMW ASSOCIATES
P. O. BOX 2578
REDWOOD CITY CA 94064
USA

RALPH C. NIEMANN
ARGONNE NATL LAB
9700 S CASS AVENUE
ARGONNE IL 60439
USA

VALERIJ NIKOGOSSIAN
YEREVAN PHYSICS
ALIKHANIAN BROTHERS ST 2
YEREVAN ARMENIA 375036
USSR

MASATSUGU NISHI
ENERGY RESEARCH LAB, HITACHI
1168 MORIYAMACHO
HITACHI, IBARAKI
JAPAN

TOSHIROU NISHIDONO
HONKOMAGOME 2-88-8
BUNKYO-KU
TOKYO, 113
JAPAN

YOSHIAKI NISHIHARA
SUMITOMO HEAVY IND.
RPC INDUSTRIES
21325 CABOT BLVD.
HAYWARD CA 94545
USA

HIROSHI NISHIMURA
LBL
1 CYCLOTRON ROAD, B71-259
BERKELEY CA 94720
USA

FRITZ NOLDEN
GSI-DARMSTADT
POSTFACH 110552
PLANCKSTR.
DARMSTADT
GERMANY

JACOB G. NOOMEN
NIKHEF-K
P.O. BOX 4395
1009 AJ AMSTERDAM
NETHERLANDS

JAMES H. NOREM
ARGONNE NATL LAB
9700 SOUTH CASS AVE., BLDG 360
ARGONNE IL 60439
USA

G. GORDON NORTH
LLNL
P. O. BOX 808, L-281
LIVERMORE CA 94550
USA

WILLIAM R. NORTH
LOS ALAMOS NATL LAB
MS H827
P. O. BOX 1663
LOS ALAMOS NM 87545
USA

HEINZ-DIETER NUHN
STANFORD SYNCHRO RAD LAB
P.O B 4349, BIN 69
STANFORD CA 94309
USA

CRAIG S. NUNAN
VARIAN ASSOCIATES
611 HANSEN WAY
PALO ALTO CA 94303
USA

MARK A NYMAN
LBL
1 CYCLOTRON RD, BLDG 46A, 1123
BERKELEY CA 94720
USA

JAMES S. O'CONNELL
BOOZ, ALLEN & HAMILTON
1725 JEFF DAVIS HWY.,
CRYSTAL SQ 2, SUITE 1100
ARLINGTON VA 22202
USA

STEPHEN O'DAY
FERMILAB
P. O. BOX 500, MS 341
BATAVIA IL 60510
USA

JOHN R O'FALLON
U. S. DEPT. OF ENERGY
ER-22 GTN
WASHINGTON DC 20545
USA

PATRICK O'SHEA
LOS ALAMOS NATL LAB
MAIL STOP J579
LOS ALAMOS NM 87545
USA

M. O'SULLIVAN
CEBAF
12000 JEFFERSON AVE.
NEWPORT NEWS VA 23602
USA

MASATOSHI ODERA
SUMITOMO HEAVY IND.
1, KANDA MITOSHIRO-CHO
CHIYODA-KU, TOKYO 101
JAPAN

ALLEN ODIAN
SLAC
P. O. BOX 4349
STANFORD CA 94305
USA

BRIAN OERTER
BROOKHAVEN NATL LAB
BUILDING 911C
UPTON NY 11973
USA

IOURI OGANESSIAN
JINR DUBNA
BOX 79, DUBNA HEAD POST OFFICE
101000 MOSKOW
USSR

RUBEN OGANESSIAN
JINR, DUBNA
BOX 79
101000 MOSCOW
USSR

SHOROKU OHNUMA
UNIVERSITY OF HOUSTON
PHYSICS DEPT
HOUSTON TX 77204
USA

KATSUNOBU OIDE
KEK
OHO, TSUKUBA
IBARAKI 305
JAPAN

SOICHIRO OKUDA
MITSUBISHI
DEN3, CRL, 101 TSUKAGUCHI HONMACHI8
AMAGASAKI HYOGO 661
JAPAN

DAVID K. OLSEN
OAK RIDGE NATL LAB
P.O. BOX 2008, BLDG. 6000
OAK RIDGE TN 37830
USA

YURI F. ORLOV
CORNELL UNIV
NEWMAN LAB OF NUCLEAR STUDIES
ITHACA NY 14853
USA

JOHN H. ORMROD
CHALK RIVER LABS
ACCELERATOR PHYSICS
CHALK RIVER ONTARIO KOJ
CANADA

DARRYL ORRIS
FERMILAB
P.O.B. 500, MS 316
BATAVIA IL 60510
USA

THADDEUS J. TED ORZECHOWSKI
LLNL
P.O BOX 808, L-626
LIVERMORE CA 94550
USA

EUGENE OSTER
ADVANCED TECHNOLOGY, INC.
2110 RINGWOOD AVENUE
SAN JOSE CA 95131
USA

JEAN-FRANCOIS OSTIGUY
FERMILAB
P. O. BOX 500, MS 345
BATAVIA IL 60510
USA

ALAN J. OTTER
TRIUMF
4004 WESBROOK MALL
VANCOUVER B.C. V6T
CANADA

THOMAS L. OWENS
FERMILAB
631 SYLVAN COURT
BATAVIA IL 60510
USA

SATOSHI OZAKI
BROOKHAVEN NATL LAB
BLDG 1005
UPTON NY 11973
USA

JOSEPH OZELIS
FERMILAB
P. O. BOX 500, MS 346
BATAVIA IL 60510
USA

HASAN PADAMSEE
CORNELL UNIV
NEWMAN LABORATORY
ITHACA NY 14853
USA

CARLO PAGANI
UNIVERSITY OF MILANO
VIA CELORIA 16
20133 MILANO
ITALY

ROBERT PALMER
SLAC
BIN 26
P. O. BOX 4349
STANFORD CA 94309
USA

KIRIL A. PANDELISEV
HORIBA CRYSTAL PRODUCTS
2520 SOUTH INDUSTRIAL PARK DRIVE
TEMPE AZ 85282
USA

WOLFGANG PANOFSKY
SLAC, BIN 76
P.O. BOX 4349
STANFORD, CA 94309

G. CHRIS PAPPAS
SSC
2550 BECKLEYMEADE
DALLAS TX 75237
USA

RICHARD C. PARDO
ARGONNE NATL LAB
9700 S.CASS AVE, BLDG 203
ARGONNE IL 60439
USA

SANGHYUN PARK
U. CAL. LOS ANGELES
PHYSICS DEPARTMENT
LOS ANGELES CA 90024-1547
USA

SOO Y. PARK
POSTECH
POSTECH
POGANG KYUNGBUK
KOREA

BRETT L. PARKER
SSC
MAIL STOP 1041
2550 BECKLEYMEADE AVE.
DALLAS TX 75237
USA

RENZO F. PARODI
INFN - ITALY
VIA DODECANESO 33
16146 GENOVA
ITALY

GEORGE PARZEN
BROOKHAVEN NATL LAB
ACCEL. DEPT, BLDG 1005-S
UPTON NY 11973
USA

RALPH J. PASQUINELLI
FERMILAB
P O BOX 500, MS-341
BATAVIA IL 60510
USA

JAMES PATERSON
LBL
BUILDING 46
1 CYCLOTRON ROAD
BERKELEY CA 94720
USA

JAMES M. PATERSON
SLAC
P.O. BOX 4349, BIN 26
STANFORD CA 94309
USA

ARTHUR C. PAUL
LLNL
P. O. BOX 808, L626
LIVERMORE CA 94550
USA

CARL PAULSON
GRUMMAN SPACE SYSTEMS
PRINCETON CORP. CTR.
4 INDEPENDENCE WAY
PRINCETON NJ 08540
USA

VERN PAXSON
LBL
MAILSTOP 46A-1123
BERKELEY CA 94720
USA

ANTHONY N. PAYNE
LLNL
P.O. BOX 808
L-627
LIVERMORE CA 94550
USA

JOHN B. PEARSON
TRIUMF
4004 WESBROOK MALL
VANCOUVER B.C. V6T2 A3
CANADA

ZHANG PEILEI
FERMILAB
P. O. BOX 500, MS 306
BATAVIA IL 60510
USA

MICHAEL PEINIGER
INTERATOM
PA114 ACCEL TECHNOLOGY
D-5060 BERGISCH GLADBACH 1
GERMANY

JEAN-LOUIS PELLEGRIN
SLAC
P.O BOX 4349, BIN 21
STANFORD CA 94309
USA

CLAUDIO PELLEGRINI
UCLA
DEPARTMENT OF PHYSICS
405 HILGARD AVENUE
LOS ANGELES CA 90024-1547
USA

RAND PENDLETON
SLAC
BIN 33
P. O. BOX 4349
STANFORD CA 94309
USA

ROZ PENNACCHI
SLAC
P. O. BOX 4349
STANFORD CA 94309
USA

ELKUNO PERELSTEIN
JINR, DUBNA
P.O. BOX 101000
MOSCOW USSR
USSR

FABIEN PERRIOLLAT
CERN
PS DIVISION
CH-1211 GENEVA 23
SWITZERLAND

DMITRI PESTRIKOV
SLAC
P. O BOX 4349
STANFORD CA 94309
USA

GERALD J. PETERS
U.S DEPT. OF ENERGY
HIGH ENERGY PHYS., ER-224GTN
WASHINGTON D C. 20585
USA

JACK PETERSON
SSC
2550 BECKLEYMEADE STE 125, MS 1045
DALLAS TX 75237
USA

THOMAS J. PETERSON
FERMILAB
P O.B. 500
BATAVIA IL 60510
USA

JOHN J. PETILLO
SAIC
1710 GOODRIDGE DR.,G-81
MCLEAN VA 22170
USA

ERIC PETIT
GANIL
BP 5027
14021 CAEN CEDEX
FRANCE

UWE PFISTER
KFA JULICH
D-5170 JUELICH
PRG BOX 1913
GERMANY

PAUL L. PHELPS
LLNL
P O BOX 808, L-156
LIVERMORE CA 94550
USA

NANETTE PHINNEY
SLAC
P.O. BOX 4349, BIN 12
STANFORD CA 94309
USA

ANDREA PISENT
INFN
LABORATORI DI LEGNARO
VIA ROMEA 4
LEGNARO (PD) I-35100
ITALY

MOHANAN PISHARODY
CORNELL UNIV
WILSON LAB
CORNELL UNIVERSITY
ITHACA NY 14850
USA

RANIER PITTHAN
SLAC
P.O. BOX 4349, BIN 96
STANFORD CA 94309
USA

MASSIMO PLACIDI
CERN
SL DIVISION
CH-1211
GENEVA 23
SWITZERLAND

GUNTHER PLASS
CERN
LEP DIVISION
CH-1211 GENEVA 23
SWITZERLAND

DAVID W. PLATE
LBL
1 CYCLOTRON RD., 46-161
BERKELEY CA 94720
USA

MICHAEL A PLUM
LOS ALAMOS NATL LAB
P.O.BOX 1663, MS H848
LOS ALAMOS NM 87545
USA

ROGER L POIRIER
TRIUMF
4004 WESBROOK MALL
VANCOUVER B.C. V6T2A3
CANADA

CARLO POLONI
SINCROTRONE TRIESTE
PADRICIANO 99
TRIESTE ITALY 34012
ITALY

ALEXANDER S POPP
INVERPOWER CONTROLS, LTD
835 HARRINGTON COURT
BURLINGTON ONTARIO L7N3P3
CANADA

JAMES POTTER
ACCSYS TECHNOLOGY, INC
1177A QUARRY LANE
PLEASANTON CA 94566
USA

ROBERT J. POWERS
POWERS ASSOC. INC.
57 WEATHERLY DRIVE
SALEM MA 01970
USA

TOM POWERS
CEBAF
12000 JEFFERSON AVE.
NEWPORT NEWS VA 23606
USA

KRSTO PRELEC
BROOKHAVEN NATL LAB
BLDG. 911B
UPTON NY 11973
USA

RICHARD PREPOST
UNIV. OF WISCONSIN
SLAC
BIN 94
P.O. BOX 4349
STANFORD CA 94309
USA

KENNETH R. PRESTWICH
SANDIA NATL LABS
P.O. BOX 5800, DEPT. 1240
ALBUQUERQUE NM 87185
USA

KEITH PRIMDAHL
FERMILAB
P. O. BOX 500, MS 340
BATAVIA IL 60510
USA

PETER P. PRINCE
LOS ALAMOS NATL LAB
P. O. BOX 1663, MS H821
LOS ALAMOS NM 87545
USA

DIETER PROCH
DESY, NOTKESTRABE 85
2000 HAMBURG 52
GERMANY

MICHEL PROME
CEA
DPHN/STAS
91191 GIF/YVETTE CEDEX
FRANCE

DONALD PROSNITZ
LLNL
P.O. BOX 808, L-626
LIVERMORE CA 94550
USA

IGOR PROTOPOPOV
INP, NOVOSIBIRSK
INSTITUTE OF NUCLEAR PHYSICS
NOVOSIBIRSK, 63009 USSR
USSR

STANLEY M PRUSS
FERMILAB
P O BOX 500, MS-306
BATAVIA IL 60510
USA

MARIO PUGLISI
SINCROTRONE TRIESTE
PADRICIANO 99
TRIESTE ITALY 34012
ITALY

SIDNEY D. PUTNAM
PULSE SCIENCES, INC.
600 MCCORMICK ST.
SAN LEANDRO CA 94577
USA

FIRAS PUTRIS
UCSD
3738 AVE. JOHANNA
LA MESA CA 91941
USA

ZUBAO QIAN
FERMILAB
P.O. BOX 500, MS 307
BATAVIA IL 60510
USA

JEAN-YVES RAGUIN
THOMSON TUBES
SLAC BIN 33
P. O. BOX 4349
STANFORD CA 94309
USA

PANTALEO RAIMONI
SLAC
P. O. BOX 4349
STANFORD CA 94305
US

SANKARANARAYANAN RAJAGOPALAN
UCLA/SLAC
BIN 26
STANFORD CA 94309
USA

EUGENE C. RAKA
BROOKHAVEN NATL LAB
BLDG. 911-B
UPTON NY 11973
USA

GEORGE RAKOWSKY
ROCKWELL INTERNATIONAL
6633 CANOGA AVE, MS-FA38
CANOGA PARK CA 91303
USA

ROY E. RAND
IMATRON INC.
389 OYSTER POINT BLVD
S SAN FRANCISCO CA 94080
USA

GOVINDAN RANGARAJAN
LBL
1 CYCLOTRON RD, MS 71H
BERKELEY CA 94720
USA

DEEPAK RAPARIA
SSC
2550 BECKLEYMEADE STE 125, MS 1045
DALLAS TX 75237
USA

VLADIMIR RASHCHIKOV
BARVIHINSKAYA 4-1-40
121596 MOSCOW
USSR

SYED RASHID
ION BEAM APPLICATIONS SA
CHEMIN DU CYCLOTRON, 2
B-1348 LOUVAIN-LNEUVE
BELGIUM

LAZARUS G. RATNER
BROOKHAVEN NATL LAB
BLDG. 911B
UPTON NY 11973
USA

ALESSANDRO RATTI
BROOKHAVEN NATL LAB
BLDG 911A
UPTON NY 11973
USA

DR. ULRICH RATZINGER
GSI-DARMSTADT
POSTFACH 11 0552
61 DARMSTADT 11
GERMANY

TOR O. RAUBENHEIMER
SLAC
P.O.B. 4349, BIN 26
STANFORD CA 94309
USA

RAYMOND RAUSCH
CERN
SPS DIVISION
CH-1211 GENEVA 23
SWITZERLAND

BILL REASS
LOS ALAMOS NATL LAB
AT-5, MS H827
P. O. BOX 1663
LOS ALAMOS NM 87545
USA

CHARLES E. REECE
CEBAF
12000 JEFFERSON AVE
NEWPORT NEWS VA 23606
USA

R. KENNETH REECE
BROOKHAVEN NATL LAB
BLDG 911A
UPTON NY 11973
USA

DANIEL E. REES
LOS ALAMOS NATL LAB
MS 827
P O BOX 1663
LOS ALAMOS NM 87545
USA

GRAHAME H. REES
RUTHERFORD APPLETON LAB, R2
SERC, CHILTON DIDCOT
OXON OX110QX
ENGLAND

J. R. REES
SLAC
P.O.B. 4349 BIN
STANFORD CA 94309
USA

AMY H. REGAN
LOS ALAMOS NATL LAB
P. O. BOX 1663
MS H827
LOS ALAMOS NM 87545
USA

LOU REGINATO
LLNL
117 LOMBARDY LANE
ORINDA CA 94563
USA

DON W. REID
LOS ALAMOS NATL LAB
P.O. BOX 1663, AT-DO, H804
LOS ALAMOS NM 87545
USA

JOHN REID
UNITED MAGNET TECHNOLOGIES
P. O. BOX 77
NEWARK CA 94560
USA

RICHARD M REIMERS
LBL
1 CYCLOTRON RD, BLDG 46-161
BERKELEY CA 94720
USA

KLAUS W. REINIGER
TRIUMF
4004 WESBROOK MALL
VANCOUVER BC V6T2A3
CANADA

MARTIN P. REISER
UNIVERSITY OF MARYLAND
LAB FOR PLASMA RESEARCH
COLLEGE PARK MD 20742
USA

DAG REISTAD
SVEDBERG LAB
BOX 533
S-75121 UPPSALA
SWEDEN

TIM R. RENNER
LBL
1 CYCLOTRON RD, 64-121
BERKELEY CA 94720
USA

K-G RENSFELT
MANNE SIEGBAHN
INST. OF PHYSICS
FRESCATIVAGEN 24
S 10405 STOCKHOLM
SWEDEN

MICHAEL RESCH
GRUMMAN SPACE SYSTEMS
4 INDEPENDENCE WAY
PRINCETON NJ 08540
USA

KENNETH R. REX
LBL
ONE CYCLOTRON ROAD
BERKELEY CA 94720
USA

MOON-JHONG RHEE
UNIVERSITY OF MARYLAND
PASMA AND FUSION ENERGY
COLLEGE PARK MD 20742
USA

DAVID H RICE
CORNELL UNIV
WILSON LABORATORY
ITHACA NY 14853
USA

J. REGINALD RICHARDSON
TRIUMF
4004 WESBROOK MALL
VANCOUVER B.C. V6T
CANADA

BURTON RICHTER
SLAC
P.O BOX 4349, BIN 80
STANFORD CA 94309
USA

LARRY RIEDEL
SSC
2550 BECKLEYMEADE AVE
MS 1045
DALLAS TX 75237
USA

JEFFREY RIFKIN
SLAC
2575 SAND HILL ROAD
MENLO PARK CA 94025
USA

ROBERT RIMMER
LBL
1 CYCLOTRON ROAD, 47/112
BERKELEY CA 94720
USA

RICHARD L. RINEY, III
MARTIN MARIETTA ASTRONAUTICS
P. O BOX 179
MAILSTOP DC6100
DENVER CO 80127
USA

LOUIS RINOLFI
CERN
CH 1211
GENEVA 23
SWITZERLAND

MICHAEL RIORDAN
UNIVERSITIES RESEARCH ASSOCIATION
1111 NINETEENTH STREET, NW #400
WASHINGTON DC 20036
USA

LEONID Z RIVKIN
PAUL SCHERRER INSTITUTE
CH-5232 VILLIGEN PSI
SWITZERLAND

ALAN W. ROBB
LBL
1 CYCLOTRON RD.
MS 46-125
BERKELEY CA 94720
USA

CHARLES W. ROBERSON
OFFICE OF NAVAL RESEARCH
800 N. QUINCY STREET
ARLINGTON VA 22217
USA

THOMAS ROBERTS
TECHNOCO
2815 BENTLEY STREET
HUNTSVILLE AL 35801
USA

RALPH ROBERTSON
SLAC
BIN 49
2575 SAND HILL ROAD
MENLO PARK CA 94025
USA

DAVID SETH ROBIN
UCLA
DEPARTMENT OF PHYSICS
CENTER FOR ADVANCED ACCELERATORS
LOS ANGELES CA 90024
USA

ARTHUR ROBINSON
LBL
MS 46-161
1 CYCLOTRON ROAD
BERKELEY CA 94720
USA

BARRY W. ROBINSON
REALTIME CONTROLS
49 QUAIL HILL LANE
RICHMOND CA 94803
USA

KEM ROBINSON
SIT OPTRONICS
2755 NORTHUP WAY
BELLEVUE WA 98004
USA

RICHARD ROCHA
TEXAS ACCEL CENTER
4800 RESEARCH FOREST DR., BLDG 2
THE WOODLANDS TX 77381
USA

CHARLES T. ROCHE
ARGONNE NATL LAB
9700 S CASS AVE. BL 207
ARGONNE IL 60439
USA

ROLF ROETH
UNIV OF WUPPERTAL
GAUSS-STRASSE-20
D-5600 WUPPERTAL 1
GERMANY

DOYLE ROGERS
LLNL
P O BOX 808, L-627
LIVERMORE CA 94550
USA

JIMMY ROGERS
SSC
2550 BECKLEYMEADF AVE
MS 1049
DALLAS TX 75237
USA

SAYED ROKNI
SLAC
P. O. BOX 4349, BIN 20
STANFORD CA 94309
USA

THOMAS ROMANO
BROOKHAVEN NATL LAB
BLDG. 725A
UPTON NY 11973
USA

MICHAEL T. RONAN
LBL
M/S 50B-5239
BERKELEY CA 94720
USA

FRANCO ROSATELLI
ANSALDO RICHERCE
CORSO PERRONE 25
16152 GENOVA
ITALY

JAMES B. ROSENZWEIG
UCLA
DEPT OF PHYSICS
405 HILGARD AVENUE
LOS ANGELES CA 90024
USA

MIKE G. ROSING
ARGONNE NATL LAB
BLD. 207/ENG.
ARGONNE IL 60439
USA

MARC C. ROSS
SLAC
P.O BOX 4349, BIN 55
STANFORD CA 94309
USA

ROBERT ROSSMANITH
CEBAF
12070 JEFFERSON AVE
NEWPORT NEWS VA 236
USA

CYROUS ROSTAMZADEH
SSCL
2550 BECKLEY MEADE AVE
MS 1044
DALLAS TX 75237
USA

JEFFREY L ROTHMAN
BROOKHAVEN NATL LAB
NSLS
UPTON NY 11973
USA

THEODORE ROUMBANIS
SCHONBERG RADIATION CORP
3300 KELLER ST, #101
SANTA CLARA CA 95054
USA

FOREST R. ROUSE
1275 BONITA
BERKELEY CA 94709
USA

SANDRA ROVANPERA
SIEMENS MEDICAL LABS
4040 NELSON AVE.
CONCORD CA 94520
USA

EDNOR M. ROWE
UNIVERSITY OF WISCONSIN, SRC
3731 SCHNEIDER DRIVE
STOUGHTON WI 53589
USA

GHISLAIN ROY
SLAC
P.O.B. 4349 BIN 26
STANFORD CA 94309
USA

JOHN ROYET
LBL
MAILSTOP 46-161
BERKELEY CA 94720
USA

CARLO RUBBIA
CERN
DG DIVISION
CH-1211
GENEVA 23
SWITZERLAND

DAVID L. RUBIN
CORNELL UNIV
NEWMAN LAB
ITHACA NY 14853
USA

TOMAS RUSS
MIT BATES ACCELERATOR
21 MANNING ROAD
MIDDLETON MA 01949
USA

THOMAS J RUSSELL
VARIAN ASSOCIATES
2085 R 4675
SALT LAKE CITY UTAH 84117
USA

DANIEL P. RUSTHOI
LOS ALAMOS NATL LAB
P.O BOX 1663, AT-2, H818
LOS ALAMOS NM 87545
USA

RONALD D RUTH
SLAC
P O BOX 4349, BIN 26
STANFORD CA 94309
USA

HENRY L RUTKOWSKI
LBL
1 CYCLOTRON ROAD, 47/112
BERKELEY CA 94720
USA

WILLIAM A. RYAN
BROOKHAVEN NATL LAB
BUILDING 1005S
UPTON NY 11973-5000
USA

J. PATRICK RYMER
ACCSYS TECHNOLOGY, INC.
1177A QUARRY LANE
PLEASANTON CA 94566
USA

ROBERT D. RYNE
LLNL
P. O. BOX 808, L626
LIVERMORE CA 94550
USA

ISAC RYPSHTEIN
FERMILAB
P. O. BOX 500, MS 341
BATAVIA IL 60510
USA

ALFREDO H. SAAB
SLAC
2575 SAND HILL ROAD
BIN 49
MENLO PARK CA 94025
USA

KOUROSH SAADATMAND
LOS ALAMOS NATL LAB
AT-10, MS H818
P. O BOX 1663
LOS ALAMOS NM 87545
USA

M SABADO
SAIC
4161 CAMPUS POINT COURT
SAN DIEGO CA 92121
USA

JAMES SAFRANEK
SLAC
P.O.B. 4349, BIN 99
STANFORD CA 94309
USA

DAVID C. SAGAN
CORNELL UNIV
WILSON LAB
ITHACA NY 14853
USA

JOAN SAGE
SSC
2550 BECKLEYMEADE
DALLAS TX 75237
USA

RICHARD C. SAH
MAXWELL LABS
BROBECK DIV 4905 CENTRAL AVE
RICHMOND CA 94804
USA

SHOGO SAKANAKA
KEK
OHO 1-1, TSUKUBA
IBARAKI 305
JAPAN

KOICHI SAKURAI
MITSUBISHI
8-1-1 TSUKAGUCHI-HONMACHI
AMAGASAKI HYOGO 661
JAPAPN

REUBEN SALOMONS
LBL
1 CYCLOTRON ROAD, BLDG. 64-121
BERKELEY CA 94720
USA

ARTHUR SALOP
VARIAN ASSOC.
611 HANSEN WAY, MS C-077
PALO ALTO CA 94303
USA

CHRIS SALTMARSH
SSC
2550 BECKLEYMEADE STE 125, MS 1045
DALLAS TX 75237
USA

STEPHEN E SAMPAYAN
LLNL
P.O. BOX 808
L-627
LIVERMORE CA 94550
USA

JOHN T. SAMPLE
EBCO TECHNOLOGIES, INC
4004 WESBROOK MALL
VANCOUVER B. C. CANADA V6T2A3
CANADA

OSCAR R. SANDER
LOS ALAMOS NATL LAB
P.O. BOX 1663
AT-10, H818
LOS ALAMOS NM 87545
USA

RALPH T. SANDERS
BROOKHAVEN NATL LAB
ACCELERATOR DEPT, BLDG 911
UPTON NY 11973
USA

THOMAS W. L. SANFORD
SANDIA NATL LABS
P.O BOX 5800, DIV 1231
ALBUQUERQUE NM 87185
USA

JAMES R SANTANA
SSC
2550 BECKLEYMEADE AVE, MS 1046
DALLAS TX 75237
USA

SELCUK SARITEPE
FERMILAB
P O B 500, MS 306
BATAVIA IL 60510
USA

BOB SASS
SLAC
P O BOX 4349
BIN 50
STANFORD CA 94309
USA

HIKARU SATO
KEK
ACC. DIV. 1-1 OHO
TSUKUBA-SHI IBARAKI-KEN 305
JAPAN

TODD SATOGATA
FERMILAB
P. O. BOX 500, MS 345
BATAVIA IL 60510
USA

JOHN A. SATTI
FERMILAB
P.O. BOX 500
BATAVIA IL 60510
USA

TIMOTHY J. SAVORD
SSC
2550 BECKLEYMEADE AVE
MS 1044
DALLAS TX 75237
USA

ROLAND SAVOY
ARGONNE NATL LAB
APS/360
ARGONNE IL 60439
USA

Z. PIOTOR SAWA
SAIC
2950 PATRICK HENRY DR.
SANTA CLARA CA 95054
USA

YOSHIO SAWADA
TOSHIBA CORP.
2-4 SUEHIRO-CHO TSURUMI-KU
YOKOHAMA KANAGAWA 230
JAPAN

WERNER A. SAX
SLAC
2575 SAND HILL ROAD
MENLO PARK CA 94025
USA

GODFREY SAXON
32 THORN ROAD
BRANHALL STOCKPORT SK71H
UNITED KINGDOM

RONALD SCANLAN
LBL
MS 46-161
1 CYCLOTRON ROAD
BERKELEY CA 94720
USA

ALBERTO SCARAMELLI
ST DIVISION-CERN
1211 GENEVE 23
SWITZERLAND

LINDSAY C SCHACHINGER
LBL
MS 71-259
ONE CYCLOTRON ROAD
BERKELEY CA 94720
USA

GEORG SCHAFFER
SSC
2550 BECKLEYMEADE AVE
MS 1049
DALLAS TX 75237
USA

STUART C. SCHALLER
LOS ALAMOS NATL LAB
P.O. BOX 1663, MP-6, H852
LOS ALAMOS NM 87545
USA

ERNST T. SCHARLEMANN
LLNL
P. O. BOX 808, L626
LIVERMORE CA 94550
USA

LOUIS A. SCHICK
CORNELL UNIVERSITY
WILSON LAB
CORNELL UNIVERSITY
ITHACA NY 14853
USA

DETLEV SCHIRMER
UNIVERSITY OF DORTMUND
OBERE HUSEMANNSTR. 3
4750 UNNA
DORTMUND
GERMANY

ROSS SCHLUETER
LBL
MS 2/400
1 CYCLOTRON ROAD
BERKELEY CA 94720
USA

CHARLES W. SCHMIDT
FERMILAB
P.O. BOX 500, MS-307
BATAVIA IL 60510
USA

FRANK SCHMIDT
CERN
GENEVA NETHERLANDSA
SWITZERLAND

PAUL W. SCHMOR
TRIUMF
4004 WESBROOK MALL
VANCOUVER B C. V6T2A3
CANADA

PETER SCHMUSER
DESY
NOTHESLVASSE
D200 HAMBURG 52 GERMANY
GERMANY

HARVEY R. SCHNEIDER
TRIUMF
4004 WESBROOK MALL
VANCOUVER B C V6T2A3
CANADA

J. DAVID SCHNEIDER
LOS ALAMOS NATL LAB
P.O BOX 1663
AT-10, H818
LOS ALAMOS NM 87545
USA

LARRY X. SCHNEIDER
SSC
MS 1050
2550 BECKLEYMEADE
DALLAS TX 75237
USA

RALPH F SCHNEIDER
NAVAL SURFACE WEAPONS CENTER
10901 NEW HAMPSHIRE AVE
SILVER SPRING MD 20903
USA

ROBERT SCHNEIDER
WOODS HOLE OCEANOGRAPHIC
MCLEAN LABORATORY/WHOI
WOODS HOLE MA 02543
USA

WOLFGANG SCHNELL
CERN
CH-1211 PS DIVISION
GENEVA 23
SWITZERLAND

RUSSELL SCHONBERG
SCHONBERG RADIATION CORP
3300 KELLER ST
SANTA CLARA CA 95054
USA

DAVID SCHRAMM
U OF CHICAGO
5640 S. ELLIS AAC-140
CHICAGO IL 60637
USA

STAN O. SCHRIBER
LOS ALAMOS NATL LAB
P O. BOX 1663 MS H811
LOS ALAMOS NM 87545
USA

JOSEPH C SCHUCHMAN
BROOKHAVEN NATL LAB
BLDG 725C
UPTON NY 11973
USA

LOTHAR SCHULZ
BESSY GMBH
LENTZEALLEE 100
W-1000 BERLIN 33
GERMANY

MARTIN E SCHULZE
SAIC
RESEARCH PARK, 227 WALL ST
PRINCETON NJ 08540
USA

WINFRIED SCHUTTE
DESY-HAMBURG 52
NOTKESTR 85/F-DIV
D2000
GERMANY

PETRA D SCHUTZ
TECHNISCHE U
PHYSIK DEPARTMENT E12
D8046
GARCHING D8046 GERMANY
GERMANY

PETER SCHWANDT
INDIANA UNIVERSITY
MILO SAMPSON LANE
BLOOMINGTON IN 47408
USA

HEINZ D SCHWARZ
SLAC
P.O. BOX 4349, BIN 33
STANFORD CA 94309
USA

ERNST-GUNTER SCHWEPPE
PHILIPS GMBH
ROHREN- UND HALBLEITERWERKE
STRESEMANNALLEE 101
POSTBOX 54-02-40
2000 HAMBURG 54
GERMANY

H. Alan SCHWETTMAN
STANFORD
PHYSICS DEPARTMENT
STANFORD UNIVERSITY
STANFORD CA 94305
USA

JAMES J. SEBEK
SLAC
P O.BOX 4349, BIN 99
STANFORD CA 94309
USA

JOHN T. SEEMAN
SLAC
P.O. BOX 4349, BIN 12
STANFORD CA 94309
USA

BILL SELLYEY
BOEING AEROSPACE CO
P. O BOX 3999
SEATTLE WA 98124
USA

FRANK B SELPH
LBL
1 CYCLOTRON RD, BLDG B80-101
BERKELEY CA 94720
USA

TANAJI SEN
SSC
2550 BECKLEYMEADE
MS 1042
DALLAS TX 75237
USA

YURIJ V SENICHEV
INSTITUTE FOR NUCLER RESEARCH
MOSCOW 117 312
USSR

NICHOLAS S SERENO
CEBAF
12000 JEFFERSON AVENUE
NEWPORT NEWS VA 23606
USA

VICTOR SERLIN
NAVAL RESEARCH LABORATORY
CODE 4732
WASHINGTON DC 20375-5
USA

ROGER V. SERVRANCKX
TRIUMF
BOX 40
GABRIOLA ISLAND B. C. VOR 1XO
CANADA

ANDREI A. SERY
INSTITUTE FOR NUCELAR PHYSICS
PROTVINO
MOSCOW REGION 142284
USSR

ANDREW M. SESSLER
LBL
1 CYCLOTRON RD, 71-259
BERKELEY CA 94720
USA

IOURI P. SEVEKGIN
INST. OF ELECTRO-PHISICAL EQUIPMENT
EPHREMOV RESEARCH INSTITUTE
LENINGRAD 189631 USSR
USSR

ROBERT E. SHAFER
LOS ALAMOS NATL LAB
P.O. BOX 1663, AT-3, MS H808
LOS ALAMOS NM 87545
USA

HOWARD W. SHAFFER
WESTINGHOUSE ELECTRIC
1310 BEULAH ROAD
PITTSBURGH PA 15235
USA

SUSHIL K. SHARMA
BROOKHAVEN NATL LAB
BLDG 725D
UPTON NY 11973
USA

WILLIAM M. SHARP
LLNL
BOX 808, L-626
LIVERMORE CA 94550
USA

HENRY D. SHAY
LLNL
P.O. BOX 808, L-626
LIVERMORE CA 94550
USA

THOMAS SHEA
BROOKHAVEN NATL LAB
BLDG. 1005S
UPTON NY 11973
USA

KENNETH L. SHEARER
MARTIN MARIETTA
M.S. DC6069
P. O. BOX 169
DENVER CO 80201
USA

JOSEPH SHEEHAN
BROOKHAVEN NATL LAB
BUILDING 725 C
UPTON NY 11973
USA

RICHARD L. SHEFFIELD
LOS ALAMOS NATL LAB
P.O. BOX 1663, AT-7, H825
LOS ALAMOS NM 87545
USA

BOB SHELDON
SSC
2550 BECKLEYMEADE STE 125, MS 1045
DALLAS TX 75237
USA

RON SHELDRAKE
EEV CO. LTD
WATERHOUSE LANE SEC. 9
CHELMSFORD, ESSEX
ENGLAND

KENNETH W. SHEPARD
ARGONNE NATL LAB
9700 S.CASS AVE, BLDG 203
ARGONNE IL 60439
USA

JOHN C SHEPPARD
SLAC
P.O. BOX 4349, BIN 12
STANFORD CA 94309
USA

JICONG SHI
UNIVERSITY OF HOUSTON
DEPARTMENT OF PHYSICS
UNIVERSITY OF HOUSTON
HOUSTON TX 77204
USA

TETSUO SHIDARA
KEK
1-1 OHO,TSUKUBA-SHI
IBARAKI, 305
JAPAN

JENG SHIH
SSC
2550 BECKLEYMEADE AVE.
DALLAS TX 75237
USA

HAMID SHOAEE
SLAC
P O BOX 4349, BIN 50
STANFORD CA 94309
USA

STEVEN L. SHOPE
SANDIA NATL LABS
P O. BOX 5800, DIV. 1242
ALBUQUERQUE NM 87185
USA

MERRALD B. SHRADER
VARIAN ASSOCIATES
301 INDUSTRIAL WAY
SAN CARLOS CA 94070
USA

SORIN SHTIRBU
FERMILAB
P O BOX 500, MS 347
BATAVIA IL 60510
USA

QUAN SHENG SHU
SSC
2550 BECKLEYMEADE AVE
MS 1002
DALLAS TX 75238
USA

R. COLES SIBLEY
MIT BATES LINAC
MANNING ROAD
MIDDLETON MA 01944
USA

DONNA SIEGIET
FERMILAB
P. O. BOX 500, MS 306
BATAVIA IL 60510
USA

R. SIEMANN
SLAC
P. O. BOX 4349
BIN 26
STANFORD CA 94309
USA

SERGE SIERRA
GENERAL ELECTRIC CO
551, RUE DE LA MINIERE, BP 34
BUC 78533
FRANCE

JOHN SIKORA
CORNELL UNIV
WILSON LABORATORY
ITHACA NY 14853
USA

STEFAN SIMROCK
CEBAF
12000 JEFFERSON AVENUEW
NEWPORT NEWS VA 23602
USA

WILLIAM P. SIMS
BROOKHAVEN NATL LAB
BLDG 911-B
UPTON NY 11973
USA

CHARLES K. SINCLAIR
CEBAF
12000 JEFFERSON AVE.
NEWPORT NEWS VA 23606
USA

OM VIR SINGH
BROOKHAVEN NATL LAB
NSLS, BLDG. 725-C
UPTON NY 11973
USA

RAJINDER SINGH
LBL
MAILSTOP 46A-1123
BERKELEY CA 94720
USA

DIXIE G. SINKOVITS
THE CARBOUUNDAM CO
P O BOX 664
NIAGARA FALS NY 14302
USA

JOSEPH F. SKELLY
BROOKHAVEN NATL LAB
AGS DEPT., BLDG., 911C
UPTON NY 11973
USA

ALEXANDER SKRINSKI
ACADEMY OF SCIENCES-USSR
SIBERIAN DIVISION
NOVOSIBIRSK
USSR

JAMES M. SLATER
LOMA LINDA UNIV.
DEPT. OF RADIATION MEDICINE
11234 ANDERSON STREET
LOMA LILNDA CA 92354
USA

WILLIAM T. SLOAN
INDIANA UNIVERSITY
2401 MILO B. SAMPSON LANE
BLOOMINGTON IN 47401
USA

RODOLFO J. SLOBODRIAN
UNIVERSITE LAVAL
DEPARTEMENT DE PHYSIQUE
STE. FOY QUEBEC G1K
CANADA

THEODORUS J. SLUYTERS
BROOKHAVEN NATL LAB
AGS DEPT., BLDG. 911B
UPTON NY 11973
USA

IOURI S SMIRNOV
COUNCEL OF MINISTERS OF THE USSR
MOSCOW USSR
USSR

CARL H. SMITH
ALLIED SIGNAL INC
CTC-1
MORRISTOWN NJ 07902
USA

DAVID L. SMITH
SANDIA NATL LABS
P.O BOX 5800, DIV. 1272
ALBUQUERQUE NM 87185
USA

GARY A. SMITH
BROOKHAVEN NATL LAB
BLDG. 923
UPTON NY 11973
USA

H VERNON SMITH
LOS ALAMOS NATL LAB
P O BOX 1663
AT-10, H818
LOS ALAMOS NM 87545
USA

JOHN R. SMITH
TITAN COMPANY
P O BOX 9254
ALBUQUERQUE NM 87119
USA

LLOYD SMITH
LBL
1 CYCLOTRON RD., BLDG 47-112
BERKELEY CA 94720
USA

PATRICK SMITH
SLAC
P.O BOX 4349, BIN 55
STANFORD CA 94309
USA

SALLY SMITH
SSC
2550 BECKLEYMEADE AVE., SUITE 125
DALLAS TX 75237
USA

STEVE SMITH
SLAC
P. O. BOX 4349
BIN 50
STANFORD CA 94309
USA

TAB J SMITH
US NAVAL RSCH. LAB
4555 OVERLOOK AVE. SW
WASHINGTON DC 20375
USA

W RODMAN SMYTHE
U. OF COLORADO
CAMPUS BOS 446
BOULDER CO 80309
USA

SUNG-LEUNG ZVAN SO
BROOKHAVEN NATL LAB
BLDG 725B
UPTON NY 11973
USA

LORRIANE SOLOMON
BROOKHAVEN NATL LAB
BLDG 725B
UPTON NY 11973
USA

JOSHUA JAI-HO SONG
ARGONNE NATL LAB
BLDG 371T
9700 S CASS AVE.
ARGONNE IL 60439
USA

LUDMILLA SOROKA
LBL
1 CYCLOTRON RD, BLDG 4-230
BERKELEY CA 94720
USA

ANDY SOUKAS
BROOKHAVEN NATL LAB
BLDG 911B
UPTON NY 11973
USA

RAYAPPU SOUNDRANAYAGAM
SSC
MS 1041
2550 BECKLEYMEADE AVE.
DALLAS TX 75237
USA

BRIAN SOUTHWORTH
CERN
DOCUMENTATION DEPT.
CH-1211 GENEVA 23
SWITZERLAND

GEORGE SPALEK
LOS ALAMOS NATL LAB
P O. BOX 1663, AT-1, H817
LOS ALAMOS NM 87545
USA

JAN B. SPELT
N I K H E F-K
P.O.B 4395
1009 A J AMSTERDAM
NETHERLANDS

CHERRILL M. SPENCER
SLAC
2575 SAND HILL ROAD
MENLO PARK CA 94025
USA

JAMES E SPENCER
SLAC
P O. BOX 4349, BIN 26
STANFORD CA 94309
USA

NANCY SPENCER
SLAC
P O.BOX 4349, BIN 55
STANFORD CA 94309
USA

STEVE J. ST LORANT
SLAC
P O. BOX 4349
STANFORD CA 94309
USA

STEVE M. STAHL
FERMILAB
P O BOX 500, MS 306
BATAVIA IL 60510
USA

MARCEL T. STAMPFER
MAX PLANCK INST. FOR NUCLEAR PHYS
SAUPFERCHECKWEG
6900 HEIDELBERG GERMANY
GERMANY

STUART R STAMPKE
SSC
MS 1047
2550 BECKLEYMEADE
DALLAS TX 75237
USA

MICHAEL STANEK
SLAC
2575 SAND HILL ROAD, BIN 55
MENLO PARK CA 94025
USA

JOHN W STAPLES
LBL
1 CYCLOTRON RD, 64-RM 224A
BERKELEY CA 94720
USA

PETER M. STEFAN
BROOKHAVEN NATL LAB
BUILDING 725D
UPTON NY 11973
USA

ROBERT E. STEGE
SLAC
BIN 39
P.O. BOX 4349
STANFORD CA 94309
USA

CHARLES P. STEINBACH
CERN
CH-1211
GENEVE 23
SWITZERLAND

LOREN C. STEINHAUER
SPECTRA TECHNOLOGY, INC.
2755 NORTHUP WAY
BELLEVUE WA 98004
USA

MARTIN STEPHAN
KFA JEULICH/IKP
P. O. BOX 9 3
D-5 FO JUELICH GERMANY
GERMANY

RALPH R., JR. STEVENS
LOS ALAMOS NATL LAB
P.O B. 1663, MS H818
LOS ALAMOS NM 87545
USA

ALEXANDER G. STEWART
5506 HARVEST SCENE LN
COLUMBIA MD 21044
USA

JOHN J. STEWART
LLNL
P. O. BOX 808, L626
LIVERMORE CA 94550
USA

ARNOLD STILLMAN
BROOKHAVEN NATL LAB
BUILDING 911-B
UPTON NY 11973
USA

JAMES E. STOVALL
LOS ALAMOS NATL LAB
P.O. BOX 1663, AT-1, H817
LOS ALAMOS NM 87545
USA

GREGORY STOVER
LBL
1 CYCLOTRON RD, BLDG 64-121
BERKELEY CA 94720
USA

RONALD STRADTNER
LBL
1 CYCLOTRON RD
MS 46A-1123
BERKELEY CA 94720
USA

JAMES STRAIT
FERMILAB
P.O.B 500, MS 316
BATAVIA IL 60510
USA

BRUCE P. STRAUSS
POWERS ASSOCIATES, INC.
P.O.B 235
NEWTON MA 02160
USA

BORIS STRONGIN
VARIAN ASSOC. INC.
3075 HANSEN WAY, MS K-312
PALO ALTO CA 94304-1025
USA

KAZUO SUGAYA
HITACHI CABLE, LTD
3550 KIDAMARI
TSUCHIURA IBARAKI 300
JAPAN

VICTOR SULLER
DARESBURY LAB
SERC
DARESBURY LABORATORY
WARRINGTON WA44AD
ENGLAND

MICHAEL SULLIVAN
SLAC
BIN 43
P. O. BOX 4349
STANFORD CA 94309
USA

DING SUN
TEXAS A&M UNIV
4802 RESEARCH FOREST DR., BUILDING 2
WOODLANDS TX 77380
USA

RONALD M. SUNDELIN
CEBAF
12000 JEFFERSON AVE.
NEWPORT NEWS VA 23606
USA

JOZEF SURA
LNS-CATANIA
CATANIA 95-123
ITALY

DAVID F SUTTER
U S DEPT OF ENERGY
ER-224,
WASHINGTON DC 20545
USA

GEORGE R SWAIN
LOS ALAMOS NATL LAB
P O BOX 1663, MP-14, H847
LOS ALAMOS NM 87545
USA

J A SWEGLE
LLNL
P O BOX 808, L-389
LIVERMORE CA 94550
USA

CHARLES A. SWENSON
TEXAS ACCEL CENTER
4802 RESEARCH FOREST DR. , BLDG 2
THE WOODLANDS TX 77381
USA

DAVID R. SWENSON
LANL
MP-5
H838
LOS ALAMOS NM 87545
USA

DONALD A SWENSON
SAIC
2109 AIR PARK ROAD SE
ALBUQUERQUE NM 87106
USA

D. SWOBODA
CERN
1211 GENEVA 23
SWITZERLAND

COSMORE SYLVESTER
SSC
2550 BECKLEYMEADE AVE.
MS 1048
DALLAS TX 75237
USA

KATO SYOHEI
OSAKA UNIVERSITY
LABORATORY OF NUCLEAR STUDIES
TOYONAKA, OSAKA 560
JAPAN

MIKE SYPHERS
SSC
2550 BECKLEYMEADE STE 125
MS 1045
DALLAS TX 75237
USA

EUGENIO TACCONI
SSCL
2550 BECKLEMEADE AVE.
DALLAS TX 75237
USA

KEN TAKAYAMA
TEXAS ACCEL CENTER
4802 RESEARCH FOREST DR , BLDG 2
THE WOODLANDS TX 77381
USA

SEISHI TAKEDA
KEK
OHO 1-1
TSUKUBA 305 JAPAN
JAPAN

PAUL J. TALLERICO
LOS ALAMOS NATL LAB
P O. BOX 1663, AT-5, H827
LOS ALAMOS NM 87545
USA

THOMAS TALLERICO
BROOKHAVEN NATL LAB
BUILDING 911-B
UPTON NY 11973
USA

EIJI TANABE
AET ASSOCIATES, INC.
20370 TOWN CENTER LANE, STE. 260
CUPERTIN CA 95014
USA

CHA-MEI TANG
NAVAL RESEARCH LABORATORY
CODE 4790 NAVAL RES LAB
WASHINGTON DC 20375
USA

ROMAN TATCHYN
SLAC BIN 69
P.O. BOX 4349
STANFORD CA 94309
USA

B ALAN TATUM
OAK RIDGE NATL LAB
P.O. BOX 2008, MS 6368
OAK RIDGE TN 37831
USA

ROBERT TAUSSIG
BECHTEL CORP.
MS 50/17/C5
P. O. BOX 193965
SAN FRANCISCO CA 94119
USA

STANLEY R. TAWZER
FERMILAB
P.O. BOX 500, MS 306
BATAVIA IL 60510
USA

ANTHONY TAYLOR
ARGONNE NATL LAB
9700 S. CASS, EP/207
ARGONNE IL 60439
USA

BRIAN TAYLOR
LBL
1 CYCLOTRON ROAD
MS 46-125
BERKELEY CA 94720
USA

CLYDE E. TAYLOR
LBL
1 CYCLOTON RD, BLDG 46-161
BERKELEY CA 94720
USA

RICHARD E. TAYLOR
SLAC
P. O. BOX 4349, MAIL BIN 96
STANFORD CA 94309
USA

THOMAS M. TAYLOR
CERN
LEP DIVISION
CH-1211 GENEVA 23
SWITZERLAND

FRANCO TAZZIOLI
INFN
LAB NAZIONALI DI FRASCATI
C P. 13, 00044 FRASCATI
ITALY

YURI A. TCHESNOKOV
INSTITUTE FOR HIGH ENERGY PHYSICS
SERPUKHOV
142284 PROTVINO
MOSCOW
USSR

MARSH M. TEKAWA
LBL
1 CYCLOTRON RD., 51-200B
BERKELEY CA 94720
USA

L. E. TEMPLE, JR.
U S. DEPT OF ENERGY
ER 65, GTN
WASHINGTON DC 20545
USA

PETER TENENBAUM
UNIV. CA-SANTA CRUZ
BOARD OF STUDIES IN PHYSICS
1156 HIGH STREET
SANTA CRUZ CA 95060
USA

LEE C. TENG
ARGONNE NATL LAB
9700 S. CASS AVENUE
ARGONNE IL 60439
USA

JEFFREY L. TENNYSON
SLAC
BIN 26
P. O. BOX 4349
STANFORD CA 94309
USA

STEVEN TEPIKIAN
BROOKHAVEN NATL LAB
BLDG 1005S-4
UPTON NY 11973
USA

VLADIMIR E. TERIAEV
INSTITUTE OF NUCLEAR PHISICS
PROTVINO MOSCOW REGION 142284
USSR

EDWARD THEIL
LBL
1 CYCLOTRON RD, BLDG 46A-1123
BERKELEY CA 94720
USA

V THIAGARAJAN
SSC
MS 1047
2550 BECKLEYMEADE AVE.
DALLAS TX 75237
USA

PETER THIEBERGER
BROOKHAVEN NATL LAB
PHYSICS DEPT.,BLDG 510
UPTON NY 11973
USA

HENRY A THIESSEN
LOS ALAMOS NATL LAB
P O BOX 1663, MP-14, H847
LOS ALAMOS NM 87545
USA

LESTER THODE
LOS ALAMOS NATL LAB
P.O.BOX 1663, MS E527
LOS ALAMOS NM 87545
USA

BRIAN L. THOMAS
MAXWELL LABS
9244 BALBOA AVENUE
SAN DIEGO CA 92123-1506
USA

KENNETH M. THOMAS
MAXWELL LABS
4905 CENTRAL AVE.
BERKELEY CA 94804
USA

MANFRED G. THOMAS
BROOKHAVEN NATL LAB
BLDG. 728
UPTON NY 11973
USA

KATHLEEN A. THOMPSON
SLAC
P O BOX 4349, BIN 26
STANFORD CA 94309
USA

PATRICK THOMPSON
BROOKHAVEN NATL LAB
BUILDING 902-B
UPTON N.Y. 11973
USA

MICHAEL THUOT
LOS ALAMOS NATL LAB
P O.B. 1663, MS H820
LOS ALAMOS NM 87545
USA

MICHAEL TIEFENBACK
PULSE SCIENCES INC.
600 MCCORMICK STREET
SAN LEANDRO CA 94577
USA

MAURY TIGNER
CORNELL UNIV
NEWMAN LABORATORY
ITHACA NY 14853
USA

CHRISTOPHER A TIMOSSI
LBL
1 CYCLOTRON RD, 46-125
BERKELEY CA 94720
USA

MAKOTO TOBIYAMA
HIROSHIMA UNIVERSITY
1-1-89, HIGASHISENDA-MACHI
NAKA-KU
HIROSHIMA 730
JAPAN

ALAN M TODD
GRUMMAN SPACE SYSTEMS
4 INDEPENDENCE WAY
PRINCETON NJ 08540
USA

NOBU TOGE
SLAC
P. O. BOX 4349, BIN 66
STANFORD CA 94309
USA

PERRY TOMPKINS
VANDERBILT UNIVERSITY
DEPARTMENT OF PHYSICS
NASHVILLE TN 37235
USA

SATOSHI TONEAWA
NEC CORP
MS 22-27241
1753 SHIMONUMABE NAKAHARA
KAWASAKI KANAGAWA 211
JAPAN

SATOSHI TONEGAWA
NEC CORPORATION
MS 22-27241
1753 SHIMONUMABE NAKAHARA
KAWASAKI KANAGAWA 211
JAPAN

GERRY TOOL
SSC
2550 BECKLEYMEADE STE 125, MS 1045
DALLAS TX 75237
USA

LIDIA TOSI
SINCROTRONE TRIESTE
PADRICIANO 99
TRIESTE ITALY 34012
ITALY

CHRISTIAN TOURNES
THOMSON CSF
6767 OLD MADISON PIKE, SUITE 200
HUNTSVILLE AL 35976
USA

CHARLES TRAHERN
SSC
2550 BECKLEYMEADE AVE., MS 1046
DALLAS TX 75237
USA

MARK TRAIL
VARIAN MEDICAL EQUIP
911 HANSEN WAY, MS C-077
PALO ALTO CA 94303
USA

GERARD TRANQUILLE
CERN
PS DIVISION
CH-1211
GENEVA 23
SWITZERLAND

DEJAN TRBOJEVIC
FERMILAB
P.O.BOX 500, MS 306
BATAVIA IL 60510
USA

TODD A TREADO
VARIAN ASSOCIATES
150 SOHIER ROAD
BEVERLY MA 01915
USA

DIETER TRINES
DESY-HERAP
NOTKESTR. 85
2000 HAMBURG 52
GERMANY

UWE TRINKS
TECH. UNIV MUNCHEN, PHYSIK E12
JAMES FRANCK STRASSE
D-8046 GARCHING
GERMANY

DOMINIQUE TRONC
G E-CGR-MEV
B.P. 34
78530 BUC
FRANCE

RICHARD TRUE
LITTON SYSTEMS
960 INDUSTRIAL ROAD
SAN CARLOS CA 94087
USA

WALTER S. TRZECIAK
U OF WISCONSIN, SRC
3731 SCHNEIDER DR
STOUGHTON WI 53589
USA

KANG T. TSANG
SAIC
1710 GOODRIDGE DR
MCLEAN VA 22102
USA

EUGENE TSIANG
IMATRON, INC.
389 OYSTER PT. BLVD.
SOUTH SAN FRANCISCO CA 94080
USA

GEORGE P TSIRONIS
UNIV OF NORTH TEXAS
PHYSICS DEPT
P O BOX 5368
DENTON TX 76201
USA

NICHOLOAS TSOUPAS
BROOKHAVEN NATL LAB
BLDG. 830
UPTON NY 11973
USA

YASUMITSU TSUTSUI
SUMITOMO ELEC
1-1-3, SHIMAYA, KONOHANA
OSAKA JAPAN 554
JAPAN

J. E TUOZZOLO
BROOKHAVEN NATL LAB
BLDG 911-B
UPTON NY 11973
USA

FRANK T TURKOT
FERMILAB
P O BOX 500, MS 316
BATAVIA IL 60510
USA

LARRY R. TURNER
ARGONNE NATL LAB
9700 S. CASS AVE, BLDG 360
ARGONNE IL 60439
USA

WILLIAM C. TURNER
LLNL
P.O. BOX 808, L-626
LIVERMORE CA 94550
USA

DAVID V. TURNQUIST
IMPULSE ENGINEERING INC.
27 VILLAGE LN, POB 5037
WALLINGFORD CT 06492
USA

ERIK UGGERHOJ
ISR-DENMARK
AARHUS UNIVERSITY
NY MUNKEGADE
8000 AARHUS
DENMARK

HAN S UHM
NAVAL SURFACE WARFARE CENTER
10901 NEW HAMPSHIRE AVE.
SILVER SPRINGS MD 20903-5000
USA

KUNIHIKO UKENA
NISSEI SANGYO
1-24-15 NISHI SHINBASHI MINATOKU
TOYKO JAPAN
JAPAN

JAN UYTHOVEN
OXFORD INSTRUMENTS LTD.
SYNCHROTRON DIVISION
OSNEY MEAD
OXFORD OX2ODX
ENGLAND

WILLEM VAN ASSELT
BROOKHAVEN NATL LAB
BLDG 911B
UPTON NY 11973
USA

SYBILLE VAN DEN HOVE
ION BEAM APPLICATIONS SA
CHEMIN DU CYCLOTRON, 2
B-1348 LOUVAIN-LA-NEUVE
BELGIUM

ROELOF VAN DER VEER
HIGH VOLTAGE ENGINEERING
70 TUFTSTREET
ARLINGTON MA 02174
USA

OLIN B. VAN DYCK
LOS ALAMOS NATL LAB
P O. BOX 1663, MP-DO, H844
LOS ALAMOS NM 87545
USA

ROGER VAN MAREN
LLNL
P O BOX 808, L-547
LIVERMORE CA 94550
USA

HANS VAN OORT
LBL
MS 46-161
1 CYCLOTRON ROAD
BERKELEY CA 94720
USA

PETER K. VAN STAAGEN
G. H. GILLESPIE ASSOC
P. O. BOX 4640
HUNTSVILLE AL 35803
USA

ARIE VAN STEENBERGEN
BROOKHAVEN NATL LAB
BLDG. 725B
UPTON NY 11973
USA

JOHANNES VAN ZEIJTS
UNIVERSITY OF MARYLAND
PHYSICS DEPARTMENT
COLLEGE PARK MD 20742
USA

DAVID L. VANECEK
LBL
1 CYCLOTRON RD., BLDG 58-113
BERKELEY CA 94720
USA

ANDRE P.M. VERDIER
CERN
LEP DIVISION
CH-1211 GENEVA 23
SWITZERLAND

WAYNE VERNON
UCSD
B-019 PHYSICS
LA JOLLA CA 92093
USA

JOHN VERTREES
LBL
MS 46-161
1 CYCLOTRON ROAD
BERKELEY CA 94720
USA

ARTHUR M VETTER
BOEING AEROSPACE CO.
P O BOX 3999, MS 1E-86
SEATTLE WA 98124
USA

P. JAMES VICCARO
ARGONNE NATL LAB
9700 S CASS AVE, 360
ARGONNE IL 60439
USA

VLADIMIR VISNJIC
FERMILAB
P.O.BOX 500, MS 345
BATAVIA IL 60510
USA

ARNOLD E. VLIEKS
SLAC
P.O. BOX 4349
STANFORD C[illegible]
USA

FERDINAND VOELKER
LBL
1 CYCLOTRON RD, BLDG 46-161
BERKELEY CA 94720
USA

HANSPETER VOGEL
INTERATOM
5060 BERGISCH
GLADBACH GERMANY
GERMANY

MARK E. VOGT
ARGONNE NATL LAB
BLDG. 376
9700 SOUTH CASS AVENUE
ARGONNE IL 60439
USA

GERALD J. VOLK
ARGONNE NATL LAB
9700 S CASS AVE, BLDG 360
ARGONNE IL 60439
USA

JOHN VOSS
SLAC
P.O.B 4349, BIN 69
STANFORD CA 94309
USA

DUANE VOY
SSC
MS 1044
2550 BECKLEYMEADE AVE.
DALLAS TX 75237
USA

G. WAIT
TRIUMF
4004 WESBROOK MALL
VANCOUVER B C V6T2A3
CANADA

DANIEL WAKE
PULSE SCIENCES, INC.
600 MCCORMICK ST.
SAN LEANDRO CA 94577
USA

MASAYOSHI WAKE
FERMILAB
P O BOX 500, MS 316
BATAVIA IL 60510
USA

WILLIAM A. WALLENMEYER
SURA
1709 NEW YORK AVE, NW
SUITE 32D
WASHINGTON DC 20006
USA

LINDA WALLING
LOS ALAMOS NATL LAB
P O BOX 1663
AT-1, MS H817
LOS ALAMOS NM 87545
USA

DAVE WALLIS
SSC
2550 BECKLEYMEADE AVE, MS 1046
DALLAS TX 75237
USA

PETER WALSTROM
LOS ALAMOS NATL LAB
P O.BOX 1663, AT-3, H808
LOS ALAMOS NM 87545
USA

STEVEN R. WALTHER
VARIAN ION IMPLANT SYSTEMS
BLACKBURN INDUSTRIAL PARK
GLOUCESTER MA 01930
USA

JAMES T. WALTON
FERMILAB
P.O. BOX 500, MS 340
BATAVIA IL 60510
USA

DIETER R. WALZ
SLAC
P.O BOX 4349
STANFORD CA 94309
USA

DAN WANG
MAXWELL LABS
BROBECK DIVBISION
4905 CENTRAL AVE.
RICHMOND CA 94804
USA

FUHUA WANG
SSC
MS 1047
2550 BECKLEYMEADE
DALLAS TX 75237
USA

HAIPENG WANG
STATE U OF NEW YORK
PHYSICS DEPARTMENT
STORY BROOK NEW YORK 11794-3800
USA

JIA-QUANG WANG
UNIV. OF MARYLAND
LAB. FOR PLASMA RESEARCH
COLLEGE PARK MD 20742
USA

JU WANG
ARGONNE NATL LAB
9700 S CASS AVENUE
APS 360
ARGONNE IL 60439
USA

JUWEN W WANG
SLAC
P O. BOX 4349, BIN 26
STANFORD CA 94309
USA

TAI-SEN F WANG
LOS ALAMOS NATL LAB
P O BOX 1663, AT-6, H829
LOS ALAMOS NM 87545
USA

XIAO-QING WANG
FERMILAB
P O B 500, MS 308
BATAVIA IL 60510
USA

THOMAS P. WANGLER
LOS ALAMOS NATL LAB
P.O. BOX 1663, AT-1, H817
LOS ALAMOS NM 87545
USA

ROBERT L. WARNOCK
SLAC
P.O.B. 4349, BIN 26
STANFORD CA 94309
USA

JOHN WARREN
SSC
2550 BECKLEYMEADE STE 125, MS 1045
DALLAS TX 75237
USA

GRAHAM WATERS
TRIUMF
4004 WESBROOK MALL
VANCOUVER B.C. V6T2A3
CANADA

JERRY WATSON
SSC
2550 BECKLEYMEADE STE 125, MS 1045
DALLAS TX 75237
USA

JAMES N. WEAVER
SSRL
P. O. BOX 4349, BIN 69
STANFORD CA 94309
USA

ROBERT C. WEBBER
SSC
2550 BECKLEYMEADE AVE
MAIL STOP 1046
DALLAS TX 75237
USA

MOIRA K. WEDEKIND
INDIANA UNIVERSITY
2401 MILO B SAMPSON LN
BLOOMINGTON IN 47405
USA

ALAN WEGER
OXFORD INSTRUMENTS, LTD
1167 ROUTE 52, STE 222
FISHKILL NY 12524
USA

JIE WEI
BROOKHAVEN NATL LAB
BUILDING 1005S
UPTON NY 11973
USA

PAUL WEIDLER
SFSU
1600 HALLOWAY AVE
SAN FRANCISCO CA 94132
USA

JULIA WEILER
SLAC
2575 SAND HILL ROAD, BIN 13
MENLO PARK CA 94025
USA

WOLFGANG WEINGARTEN
C[illegible]
CH-[illegible]1 13 DIVISION
GENEV[illegible] 23
SWITZE[illegible]LAND

MIKE WEISS
MDC VACUUM PROD. CORP.
23842 CABOT BLVD
HAYWARD CA 94545
USA

JAMES J WELCH
CORNELL UNIV
WILSON LABORATORY
ITHACA NY 14853
USA

KIMO WELCH
BROOKHAVEN NATL LAB
BUILDING 1005S
UPTON NY 11973-5000
USA

FRANK D. WELLS
LOS ALAMOS NATL LAB
P.O BOX 1663, AT-3, H808
LOS ALAMOS NM 87545
USA

WILLIAM (WU-TSU WENG
BROOKHAVEN NATL LAB
BUILDING 911-A
UPTON NY 11973
USA

JOHANNES WENZEL
PHYSIKALISCHES INS. -bONN
NUSSALLEE 12
5300 BONN
GERMANY

CLEMENS WERMELSKIRCHEN
SSRL
SLAC
BIN 99, BOX 4349
STANFORD CA 94309
USA

WAYNE WESELOH
POWER SPECTRA, INC
42660 CHRISTY STREET
FREMONT CA 94538
USA

GLEN WESTENSKOW
LLNL
P O BOX 808, L-626
LIVERMORE CA 94550
USA

GREG WHITE
SLAC
P. O BOX 4349
BIN 50
STANFORD CA 94309
USA

KENNETH WHITHAM
TITAN BETA
6780-R SIERRA COURT
DUBLIN CA 94568
USA

DAVID WHITTUM
KEK
1-1 OHO, TSUKUBA
IBARAKI 305
JAPAN

HELMUT WIEDEMANN
STANFORD UNIV
P.O BOX 4349
BIN 69
STANFORD CA 94309
USA

ULRICH WIENANDS
TRIUMF
4004 WESBROOK MALL
VANCOUVER B C V6T
CANADA

BJORN H WIIK
DESY
NOTKESTRASSE 85
D-2000 HAMBURG 52
GERMANY

DAVID W. WILDMAN
FERMILAB
P.O BOX 500, MS 306
BATAVIA IL 60510
USA

FERDINAND WILLEKE
DESY
MPY NOTKESTV 85
2000 HAMBURG 52
GERMANY

IAN WILSON
CERN
SL DIVISION, CERN
1211 GENEVA 23 SWITZERLAND
SWITZERLAND

MARK A WILSON
NATL INSTI STD & TECH
BLDG. 245, ROOM B-119
GAITHERSBURG MD 20899
USA

MIKE WILSON
SSC
2550 BECKLEYMEADE AVE
MS 1044
DALLAS TX 75237
USA

NORMAN G. WILSON
LOS ALAMOS NATL LAB
P O BOX 1663
AT-4, MS H821
LOS ALAMOS NM 87545
USA

PERRY B. WILSON
SLAC
P O BOX 4349, BIN 26
STANFORD CA 94309
USA

HERMAN WINICK
STANFORD SYNCHRO RAD LAB
P O BOX 4349, BIN 69
STANFORD CA 94309
USA

RUSSELL A. WINJE
SSC
2550 BECKLEYMEADE AVE
MS 1044
DALLAS TX 75237
USA

DAVID R. WINN
FAIRFIELD U
DEPT. OF PHYSICS
FAIRFIELD CT 06430-7524
USA

SANGCHUL WON
POSTECH
EE DEPT. POSTECH
P. O. BOX 125
POGANG KOREA 790-600
KOREA

MERVYN WONG
LBL
MS 50A-2129
BERKELEY CA 94720
USA

RICHARD WOOD
LOS ALAMOS NATL LAB
AT-1, MS H817
P. O. BOX 1663
LOS ALAMOS NM 87545
USA

MIKE WOODS
SLAC
P. O. BOX 4349
STANFORD CA 94305
USA

RICHARD WOODS
U. S DEPT OF ENERGY
GTN, ER-65
WASHINGTON DC 20585
USA

DANIEL WRIGHT
SLAC
2575 SAND HILL ROAD, BIN 13
MENLO PARK CA 94025
USA

EDWARD L. WRIGHT
SLAC
BIN 33
P. O BOX 4349
STANFORD CA 9430)
USA

ALBIN WRULICH
SINCROTRONE TRIESTE
PADRICIANO 99
34012 TRIESTE
ITALY

DANDAN WU
STANFORD U
STANFORD SYNCHROTRON RADIATION LAB
STANFORD CA 94309
USA

J-LIANG WU
WESTINGHOUSE S&T
1310 BEULAH RD
PITTSBURGH PA 15235
USA

GODEHARD WUESTEFELD
KFA JULICH
POSTFACH 1913
D-5170 JUELICH
GERMANY

JONATHAN S. WURTELE
MIT
NW16-258
CAMBRIDGE MA 02139
USA

MELINDA W. YLIE
SSC
2550 BECKLEYMEADE AVE , MS 1046
DALLAS TX 75237
USA

JIALIN XIE
BROOKHAVEN NATL LAB
NSLS 725B
UPTON NY 11973
USA

MING XIE
LBL
1 CYCLOTRON ROAD
MS 714
BERKELEY CA 94720
USA

RATHNAKAR YADAMA
LBL
MAILSTOP 46-125
BERKELEY CA 94720
USA

TADATOSHI YAMADA
MITSUBISHI ELEC
1-1, TSUKAGUCHI-HONMACHI 8-CHOME
AMAGASAKI JAPAN 661
JAPAN

NOBORU YAMAMOTO
SLAC
BIN 26
P. O BOX 4349
STANFORD CA 94309
USA

YITON YAN
SSC
2550 BECKLEYMEADE
DALLAS TX 75. 37
USA

TSUN NENG YANG
INST OF NUCLEAR RESEARCH
P O BOX 3-4 LUNG-TAN
TOUYAN TAIWAN
REPUBLIC OF CHINA

C Y YAO
SYNCROTRON RADIATION LAB
U SCI & TECHNOLOGY
HEFEI, ANHUI 230029
P R. CHINA

VICTOR A YARBA
INSTITUTE FOR HIGH ENERGY PHYSICS
SERPUKHOV
142284 PROTVINO
MOSCOW
USSR

KOJIMA YASUAKI
NEC
1753 SHIMONUMABE NAKAHARA-KU
KAWASAKI KANAGAWA-KEN
JAPAN

DONALD P. YEE
LBL
1 CYCLOTRON RD. 46-161
BERKELEY CA 94720
USA

EDWARD YEN
SYNCH. RAD. RES. CEN.-TAIWAN
HSINCHU SCIENCE INDUSTRIAL PK.
HSINCHU 30077
TAIWAN, RO CHINA

ANAHID DIAN YEREMIAN
SLAC
P. O. BOX 655
MENLO PARK CA 94026
USA

Y YIN
TRIUMF
4004 WESBROOK MALL
VANCOUVER B C. V6T2A3
C A N A D A

WU YINGZHI
IHEP-BEIJING
P O. BOX 918
BEIJING
P R. CHINA

KAORU YOKOYA
NAT LAB FOR HIGH ENERGY PHYSICS
TSUKUBA-SHI IBARAKJKEN 305
JAPAN

MOOHYUN YOON
POHANG INSTI. OF SCI & TECH
DEPT OF PHYSICS
POHANG
KOREA

RICHARD C YORK
SSC
2550 BECKLEYMEADE AVE
MS 1049
DALLAS TX 75237
USA

MORIO YOSHIZAWA
U OF TOKYO
3-2-1 MIDORIMACHI
TANASHI TOKYO 188
JAPAN

REUBEN YOTAM
SLAC
BIN 68
STANFORD CA 94305
USA

ANDREW YOUNG
LOS ALAMOS NATL LAB
MS H827
P O BOX 1663
LOS ALAMOS NM 87545
USA

ANTHONY YOUNG
LBL
MS 4/230
BERKELEY CA 94720
USA

[illegible]CE YOUNG
[illegible]BL
MAILSTGOP 46-125
BERKELEY CA 94720
USA

LLOYD M. YOUNG
LOS ALAMOS NATL LAB
P.O. BOX 1663, AT-1, H817
LOS ALAMOS NM 87545
USA

PHILLIP YOUNG
SAIC
4161 CAMPUS PT COURT MS 53J
SAN DILGO CA 92121
USA

RON YOURO
LBL
MS 46-161
1 CYCLOTRON ROAD
BERKELEY CA 94720
USA

DAVID YU
DULY CONSULTANTS
1912 MACARTHUR ST.
RANCHO PALOS VERDES CA 90732
USA

SIMON YU
LLNL
P.O. BOX 808, L-626
LIVERMORE CA. 94550
USA

XIAO-TONG YU
MIT
NW16-223
CAMBRIDGE MA 02139
USA

VINCENT YUAN
LOS ALAMOS NATL LAB
P.O BOX 1663
AT-10, H818
LOS ALAMOS NM 87545
USA

BYUNG C. YUNN
CEBAF
12070 JEFFERSON AVENUE
NEWPORT NEWS VA 23607
USA

FUJITA YUTAKA
SHIMIZU CORP.
NO 2-3 SHIBAURA
1-CHOME
MINATO-KU TOKYO
JAPAN

MILOS ZACH
TRIUMF
4004 WESBROOK MALL
VANCOUVER B.C. V6T2A3
CANADA

JAMES R. ZAGEL
FERMILAB
P.O.B. 500, MS 308
BATAVIA IL 60510
USA

EMERY ZAJEC
LBL
1 CYCLOTRON RD., 51-208
BERKELEY CA 94720
USA

ALEXANDER ZALTSMAN
BROOKHAVEN NATL LAB
BLDG 911-B
UPTON NY 11973
USA

SHOLEH ZAMINI
#47, KASHANI STREET, KABOLI STREET,
RESALAT AVENUE
TEHRAN 16316
IRAN

ANTHONY ZANTE
TITAN BETA
6780-R SIERRA COURT
DUBLIN CA 94569
U.S.A

GEORDIE ZAPALAC
SLAC
BIN 94
P.O. BPX 4349
STANFORD CA 94309
USA

SIMON ZAREMBA
ION BEAM APPLICATIONS SA
CHEMIN DU CYCLOTRON, 2
B-1348 LOUVAIN-LA-NEUVE
BELGIUM

MIKE ZELAZNY
SLAC
P. O. BOX [illegible]
BIN 50
STANFORD CA 94309
USA

JAN-MARK ZENTLER
LLNL
P. O BOX 808, L-153
LIVERMORE CA 94550
USA

A V ZHAKOVSKY
USSR ATOMIC ENERGY
MOSCOW
USSR

RENSHAN ZHA[illegible]
BROOKHAVEN NATL LAB
BUILDING 725B, NSLS
UPTON NY 11973
USA

XIAOHAO ZHANG
BROOKHAVEN NATL LAB
NSLS 725C
UPTON NY 11727
USA

YAN ZHANG
SSC
2550 BECKLEYMEADE AVE.
DALLAS TX 75237
USA

YONG XIANG ZHAO
LAB. NACIONAL DE LUZ SINCROTRON
LNLS, CX P. 6192
CAAMPINAS S.P. CEP 13081
BRAZIL

ALEXANDER ZHOLENTS
INSTITUTE OF NUCELAR PHYSICS
630090 NOVOSIBIRSK USSR
USSR

PING ZHOU
FERMILAB
P O BOX 500, MS 341
BATAVIA IL 60510
USA

VOLKER ZIEMANN
SLAC
P.O. BOX 4349, BIN 66
STANFORD CA 94309
USA

CHRISTOPHER D. ZIOMEK
LOS ALAMOS NATL LAB
P. O. BOX 1663
AT-5, MS H827
LOS ALAMOS NM 87545
USA

MICHAEL ZISMAN
LBL
1 CYCLOTRON RD, BLDG 47/112
BERKELEY CA 94720
USA

ABBASALI ZOLFAGHARI
MIT
P.O BOX 846 MANNING RD.
MIDDLETON MA 01949
USA

BRUNO W ZOTTER
CERN
LEP DIVISION
CH-1211 GENEVA 23
SWITZERLAND

HENRI ZYNGIER
LURE, BATIMENT 209
CENTRE D'ORSAY
F-91405 ORSAY CEDEX
FRANCE

Magnet Lattice of the Pohang Light Source

J. Choi, T. Lee, K. Nam, and M. Yoon
Pohang Accelerator Laboratory, Pohang Institute of Science and Technology
Pohang, Korea 790-600

Abstact

Features of the 2 GeV Pohang Light Source Accelerator are described. The lattice type is Triple Bend Achromat (TBA). The whole circumference of 280.56 m is composed of 12 cells each of which has 12 quadrupoles. The harmonic number is 468 ($= 2^2 \cdot 3^2 \cdot 13$) and the corresponding RF frequency is 500.082 MHz. The aimed natural emittance is 12 nm-rad. The description is mainly concerned with lattice poperties and Insertion Device (ID) effects.

I. LATTICE PROPERTIES

The Pohang Light Source (PLS) has a storage ring of 12 period mirror-symmetric TBA lattice. Its relatively long length of 280.56 m can accomodate 12 quadrupoles in each cell. This large number of quadrupoles provides flexibilities and a number of varieties. A standard β function plot is given in Fig. 1. Triplets of quadrupoles in the straight sections will be used for ID matching and triplets of quadrupoles in the achromat section are used for the control of dispersion function and phase advance as well as matching η_x'. Lattice specifications and beam parameters are listed in Table I. The bending magnets are rectangular and separated functioned. With the energy of 2 GeV, the rigidity $B\rho$ is 6.67 T-m. Magnet specifications are listed in Table II. Two pairs of sextupoles, one focusing and one defocusing, are used for chromaticity correction. The sextupole strength is low compared with other third generation machines.

Sextupoles have additional trim windings to correct the closed orbit distortions. Of the whole 48 sextupoles, 16 have another windings to control the skew quadrupole components arising from both quadrupole rotation error and vertical closed orbit distortion at the location of the sextupoles. The tune versus momentum plot resulting from chromaticity correction is shown in Fig. 2. As usual in TBA lattices, no harmonic correction sextupole is employed. Harmonic correction sextupoles improve dynamic aperture to some extent, but not as much as to justify the complexities and higher order fields induced by their presence.

For the analysis of multipole error sensitivity, we used essentially the same data as the one used in ALS of LBL[1].

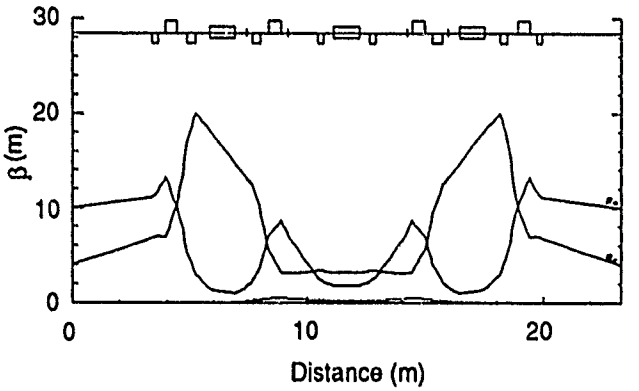


Figure 1: PLS Lattice

Critical Photon Energy (E_c)	2.8 keV
Natural emittance (m-rad)	1.21×10^{-8}
Natural energy spread, rms	6.8×10^{-4}
Bunch length, rms, natural (mm)	4.78
RF Voltage (MV)	1.8
Insertion straight length (m)	6.8
Bending radius (m)	6.303
Sextupole Strength ($1/m^2$)	
SF	4.49
SD	-6.48
Betatron tunes	
Horizontal (ν_x)	14.28
Vertical (ν_y)	8.18
Synchrotron tune (ν_s)	0.0115709
Natural chromaticities	
Horizontal (ξ_x)	-23.36
Vertical (ξ_y)	-18.19
Maximum beta functions (m)	
Horizontal (β_x)	13.17
Vertical (β_y)	20.0
Beta functions at ID center (m)	
Horizontal (β_x)	10.0
Vertical (β_y)	4.0
Maximum dispersion, η_x (m)	0.46464
Radiation loss per turn, dipoles (keV)	225

Table 1: PLS Parameter List

0-7803-0135-8/91S01.00 ©IEEE

Element	Length(m)	Strength
Q1	0.24	-4.28 T/m
Q2	0.53	10.13 T/m
Q3	0.35	-11.30 T/m
B	1.1	1.06 T
SD	0.2	-6.48 m^{-2}
Q4	0.35	-9.71 T/m
Q5	0.53	12.14 T/m
SF	0.2	4.49 m^{-2}
Q6	0.24	-5.30

Table 2: PLS Magnet Parameters

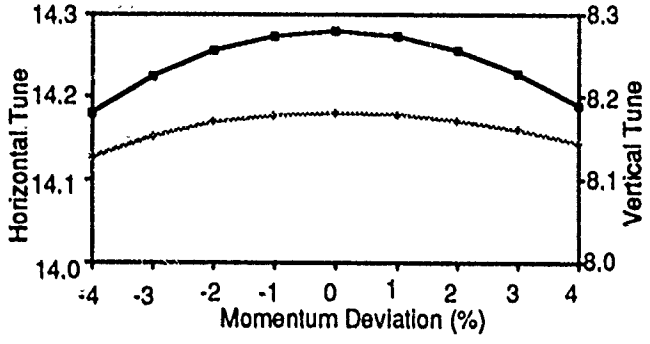


Figure 2: Momentum versus Tune

The notation we use is defined by the expansion

$$B_y(x) = B\rho \sum_n \frac{k_n x^n}{n!}, \qquad k_n = \frac{d^n B_y}{dx^n}. \qquad (1)$$

The dynamic aperture with and without multipole errors is ploted in Fig. 3, which is the output of MAD6 after 300 turns. The graph shows that the PLS lattice has fairly strong rigidity against multipole components. Also more detailed analysis indicated that the random quadrupole component is dominantly influent on the dynamic aperture among multipoles. The random decapole components arising from corrector windings of sextupoles are not serious in our case, which gave negative effects in Elettra of Trieste[2].

II. CLOSED ORBIT CORRECTION

The closed orbit correction scheme is a key issue in the machine operation. In PLS, each cell has 9 beam position monitors, 8 horizontal correctors and 7 vertical correctors. Among them, 6 correctors are horizontal and vertical combined ones. These correctors can be used for global and local orbit correction. The maximum kick angle of correctors is designed to be 2.0 mrad. However, for the operation, 1.3 mrad is set to be the maximum by power supply. Additional corrector windings of the four sextupoles in a cell will be activated, two of them horizontally and the other

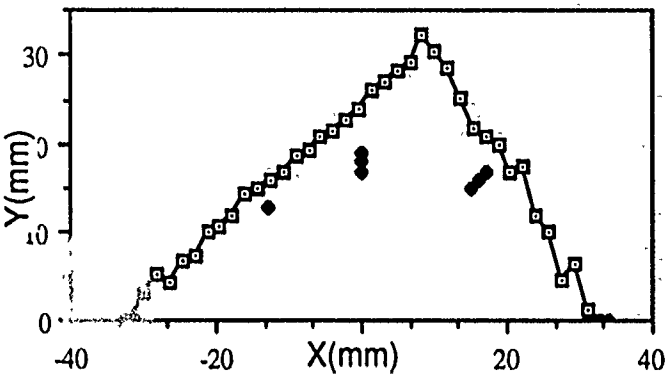


Figure 3: PLS Dynamic Aperture

two vertically. Because of this separation of sextupole correctors, their multipole effects are not so harmful.

The rms orbit distortion can be computed analytically as follows

$$x_{rms} = \frac{\sqrt{\beta_x}}{2\sqrt{2}\sin\pi\nu_x}\left[\theta_B^2\left(\frac{\Delta B}{B}\right)^2_{rms}\sum_i \beta_{x_i} + (\Delta x_Q)^2_{rms}\sum_i (kl)_i^2\beta_{x_i}\right]^{\frac{1}{2}}, \qquad (2)$$

$$y_{rms} = \frac{\sqrt{\beta_y}}{2\sqrt{2}\sin\pi\nu_y}\left[\theta_B^2(\Delta\phi)^2_{rms}\sum_i \beta_{y_i} + (\Delta y_Q)^2_{rms}\sum_i (kl)_i^2\beta_{y_i}\right]^{\frac{1}{2}}, \qquad (3)$$

where $\Delta B, \Delta\phi$, are bending magnet field error and bending magnet rotation error respectively. Also $\Delta x_Q, \Delta y_Q$ are horizontal and vertical misalignment errors of quadrupoles respectively. With errors of

$$\frac{\Delta B}{B} = 0.001, \Delta\phi = 0.5mrad, \Delta x_Q = \Delta y_Q = 0.15mm, \qquad (4)$$

the above formula gives

$$x_{rms} \approx 4\text{mm}, \qquad y_{rms} \approx 9\text{mm}. \qquad (5)$$

These analytic results are a little bit higher than computer calculation of MAD6. Higher value of y_{rms} than x_{rms} is a consequence of higher average value of β_y than β_x. After correction, these numbers are reduced to values less than 0.1 mm without monitor error. Fig. 4 and 5 display the typical closed orbit distortion before and after correction respectively.

III. INSERTION DEVICE EFFECTS

Insertion Devices not only break the linear optics of the lattice but also introduce higher order field components that may excite non-systematic resonances. The linear optics

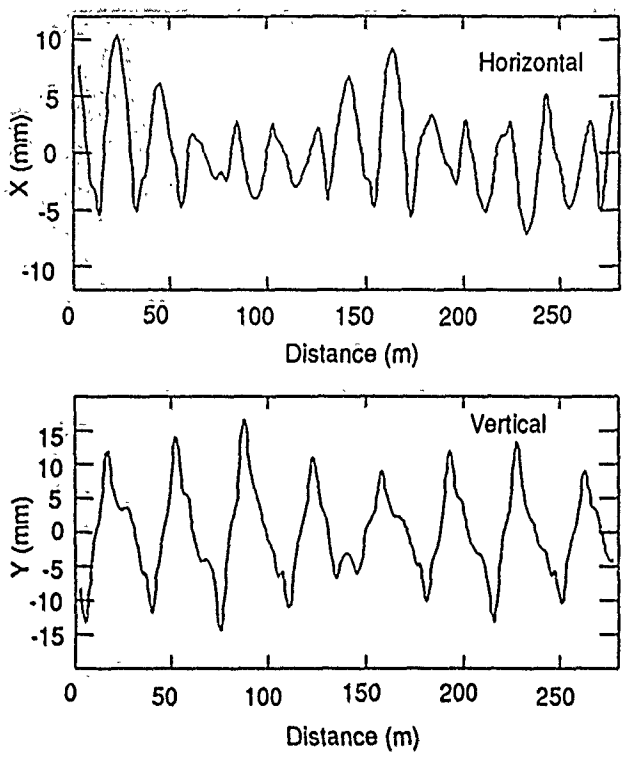


Figure 4: Closed Orbit Distortion Before Correction

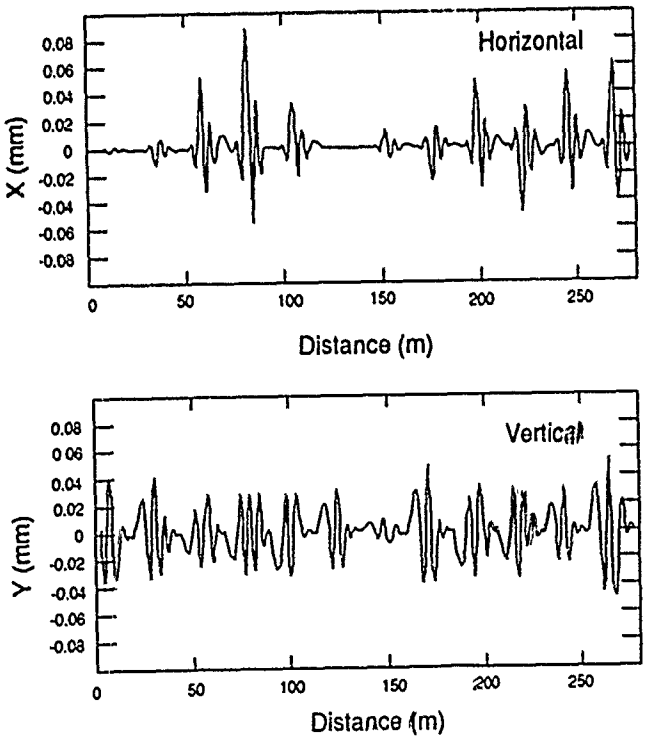


Figure 5: Closed Orbit Distortion After Correction

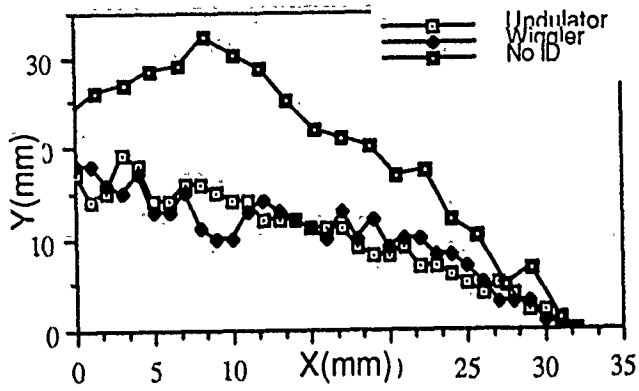


Figure 6: Dynamic Aperture with ID's

break comes from the vertical focussing of the ID's, which modifies the vertical tune and breaks the $\alpha = 0$ condition necessary to guarantee the closed orbit formation. This linear disturbances can be repaired to a certain degree by readjusting the three pairs of quadrupoles surrounding an ID. In PLS, each pair of quadrupole located on each side of the nondispersive region is connected in series to the power supply. The two pairs of quadrupoles are readjusted to reset $\alpha = 0$. This step is called 'α matching'. The remaining pair was chosen to be used for minimizing $\sqrt{\Delta\nu_x^2 + \Delta\nu_y^2}$, where $\Delta\nu_x$ and $\Delta\nu_y$ are tune changes due to ID's. This might be called 'tune matching'.

Even though the linear perturbations can be cured to some extent, the higher order perturbations can not be controlled and can not be estimated analytically. The only way we have is computer tracking. The code, *Racetrack*, was used for this purpose. Fig. 6 shows dynamic apertures for a single wiggler and an undulator respectively. The number of numerical integration steps were 100 for the wiggler and 50 for the undulator. We tracked two particles symmetrically at the same time, one in the positive x and the other one in the negative x. The resulting dynamic aperture is symmetric. In the figure this symmetric dynamic apertures are compared with the right half of the ideal case that is larger than the left half. Therefore the insertion devices reduce the dynamic apertures not as much as it looks in the figures. The dynamic apertures are reduced but still fairly large enough. The figure shows tune matching only.

IV. REFERENCES

[1] Alan Jackson, ESG Tech Note-103 NSAP-56

[2] F. Iazzourene, Sincrotrone Trieste, ST/M-TN-89/6

Undulator Based Synchrotron Radiation Source in the 5-30 eV Spectral Region *

Xiaohao Zhang, James B. Murphy and Samuel Krinsky
National Synchrotron Light Source
Brookhaven National Laboratory
Upton, NY 11973

Abstract

There has been recent interest in the utilization of high intensity radiation in the 5-30 eV spectral region. Applications include angle resolved photoemission, photochemistry, and radiation oncology. Here we present the design of a 500 MeV electron storage ring with long insertions for undulators. The ring is designed to provide an emittance of 0.1 mm-mrad, an average current of 1 Amp and an electron beam lifetime of greater than 3 hrs. The undulators operating near K=1, yield 10^{15} ph/sec/0.1% bandwidth in the fundamental.

I Introduction

Existing second-generation and planned third-generation synchrotron radiation facilities do not provide optimum undulator sources of soft photons in the energy range 5-30 eV. In this note we discuss the design of a low energy storage ring with long dispersion free straight sections for soft photon undulators. The electron energy is chosen to be 500 MeV. Lower energy leads to shorter undulator period length and hence higher brightness, but at the cost of reduced tunability of the undulator radiation wavelength. We have taken a relatively large value of the electron emittance, 0.1 mm-mrad. Reduced emittance leads to higher brightness, but at the cost of a shorter Touschek lifetime. The storage ring is designed with 3 superperiods of an expanded Chasman-Green design. With this choice the emittance of 0.1 mm-mrad is achieved with a simple, natural optics. With 4 superperiods, the ring tends to have smaller emittance requiring a more difficult optics to raise the emittance while maintaining the proper β-function structure for efficient chromaticity correction. In addition the 3 superperiod ring is smaller and more economical.

*This work was performed under the auspices of the U.S. Department of Energy.

0-7803-0135-8/91$01.00 ©IEEE

II Undulators

The fundamental photon energy produced by an undulator is given by the electron beam energy E, the period λ_u and the magnetic parameter K ($K = .934 B_u[T]\lambda_u[cm]$) of the undulator [1, 2]. For permanent-magnet undulators, the magnetic field B_u is determined by the choice of material and the undulator gap. The tunability of the radiated photon energy is obtained by varying either the electron energy or the gap of the undulator.

Since the required spectrum (5-30eV) is too wide to be spanned in the first harmonic by a single undulator, we use two undulators with different periods to cover the desired spectral region. Even so, the K value for high photon energy is still low. In fact, at this case we can increase electron energy to yield higher photon flux. For the 500 MeV electron storage ring, the periods of undulators are chosen to be $\lambda_u = 7.5$ cm and $\lambda_u = 10$ cm respectively. The magnetic parameters K and the gap of the undulators are plotted in Fig. 1 as functions of the fundamental photon energy ϵ_1. The main parameters of the undulators are listed in Table 1.

Table 1: Undulator Parameters ($SmCo_5$)

λ_u [cm]	7.5	10
Photon Energy [eV]	$15 \sim 30$	$5 \sim 15$
N_u	100	75
L_u [m]	7.5	7.5
K	$.331 \sim 1.49$	1.08~2.738
B_u[T]	$.047 \sim .213$	.116~.293
Full Gap [cm]	$4.7 \sim 8.2$	$5.3 \sim 8.2$

Since the photon energy of the undulator radiation is related to the magnetic parameter K, the number of photons at different energy varies due to the change of the gap. To make sure that there is a enough photon flux, we need to estimate the values at $\epsilon_1 = 30$ at which, the photon flux is a minimum for the fundamental. Using the parameters of the case 30 eV given above, we find flux integrated over

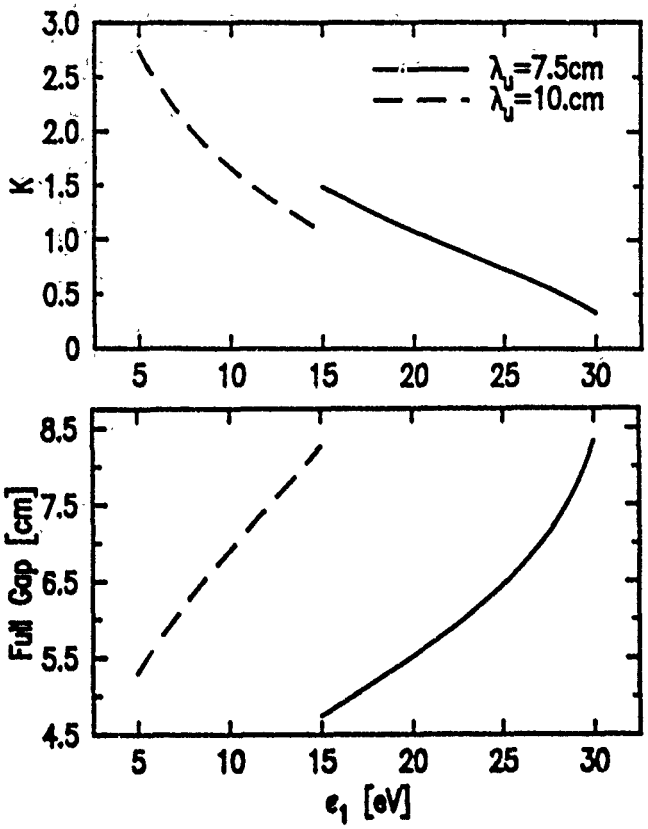


Figure 1: Undulator parameter K and gap vs fundamental photon energy.

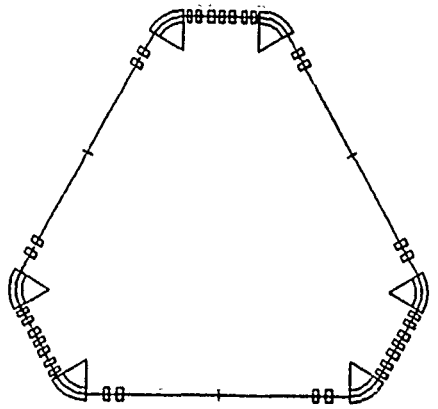


Figure 2: Schematic layout of the electron storage ring with 8 m straights for undulator radiation.

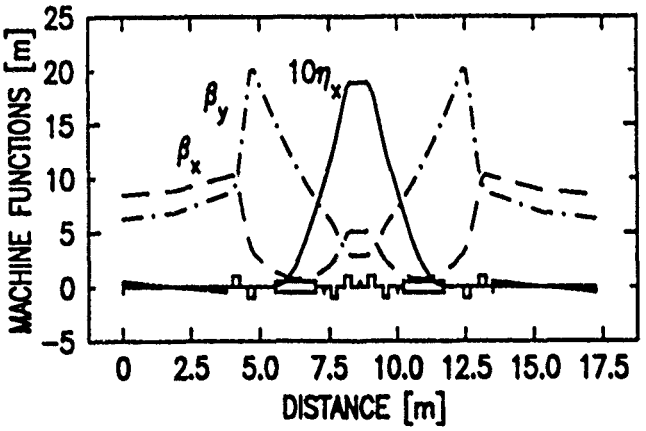


Figure 3: Lattice functions in one superperiod of the ring.

the central cone $N_1 = 1.45 \times 10^{15}$ ph/sec/0.1%/Amp.

In previous discussion, all parameters are based on the fundamental (n=1). In fact, we can also use the third harmonic to generate the desired photon spectrum. For example, an undulator of $\lambda_u = 10$ cm can be used to generate 15-30 eV photon radiation in the third harmonic. The corresponding K value in the region $1.65 \sim 2.74$ in which the photon flux is expected to be near peak in the third harmonic.

III Storage Ring

For our photon energy range, the electron storage ring is chosen to operate at 500 MeV. To obtain a dispersion free straight section in the undulator region, we use a Chasman-Green structure. The ring consists of 3 superperiods containing 8 meter straights with room to accommodate two different 7 5 meter undulators and a shorter undulator in the injection section. The schematic layout of the electron storage ring is shown in Fig. 2. The betatron and dispersion functions for one superperiod of the lattice without undulators are shown in Fig. 3. The expanded Chasman-Green structure (includes defocussing quadrupoles between the bending magnets) provides better value of the dispersion and betatron functions to facilitate chromaticity correction We list the main ring parameters in Table 2 and 3.

The undulators break the symmetry of the ring, since they have different periods λ_u and magnetic parameters K. The effects on the ring due to the undulators are investigated at the case in which the maximum designed K values are reached. After adjusting the strength of the quadrupoles, the distortions of betafunction are confined to the insertions.

IV Lifetime

The lifetime of a stored beam is determined from a combination of the gas scattering lifetime and the Touschek lifetime [3]. The total gas scattering lifetime depends on Coulomb scattering and Bremsstrahlung scattering. For our ring, assuming the pressure of the residual diatomic gas in the ring is 1 ntorr with the average atomic number Z=7, these lifetimes are 9.70 and 53.88 hours respectively. The total gas scattering lifetime is about 8.22 hours. Touschek lifetime with 1 Amp of beam is computed using ZAP code [4] taking into account bunch lengthening and intrabeam scattering which has small effects. Assuming $Z_{eff} = 5\Omega$, the bunch length is about 3.15 times higher than natural value and Touschek half-life is 7.06 hours. If $Z_{eff} = 2\Omega$, the bunch lengthens about 2.32 times the natural value

Table 2: Storage Ring Parameters

Energy, E [MeV]	500
Superperiod, N_s	3
Circumference, C [m]	51.635
Lattice Structure	Chasman-Green
Dipole Field, B_0 [T]	1.2
Bending Radius, ρ [m]	1.3903
Horizontal Betatron Tune, ν_x	3.175
Vertical Betatron Tune, ν_y	1.125
Uncorrected Chromaticity, ξ_x, ξ_y	-3.82, -5.84
Momentum Compaction, α	2.927×10^{-2}
Emittance, ϵ [m-rad]	7.309×10^{-8}
Energy Loss/Turn [KeV]	3.977
Natural Energy Spread	3.636×10^{-4}
Natural Bunch Length [cm]	3.022
Average Ring Current [mA]	1000
Average Current/Bunch [mA]	111.2
Peak Current/Bunch [A]	24.68
Coupling Coefficient, χ	0.1
Harmonic Number, h	9
RF Frequency, [MHz]	52.254
RF Acceptance, ϵ_{RF} [%]	2.13

and Touschek half-life is 4.55 hours. For the latter, The overall beam half-life from gas and Touschek scattering is 3.29 hours. The lifetime could be increased with the addition of a fourth harmonic cavity to further lengthen the bunch.

V Dynamic Aperture

The natural chromaticities of the ring are corrected to zero by the sextupoles in the achromatic bend which have strengths $SF = 12.52\ m^{-3}$ and $SD = -14.82\ m^{-3}$. The dynamic aperture of the ring is examined numerically by particle tracking, and is shown in Fig. 4, which is found using the computer code Krackpot [5]. Krackpot which uses an explicit sympletic integrator based on the exact Hamitonian for the drift and isomagnetic combined function bending magnets can track particles without large storage ring approximations. An arbitrary order Taylor map through a succession of elements can be generated by the code through the numerical differential algebra. The resulting geometric aberration coefficients are $\pi_{xx} = -2.47$, $\pi_{yy} = -119.26$ and $\pi_{xy} = 5.24$. Synchrotron oscillations are taken into account in the particle tracking. This aperture is obtained at the center of the insertion and is larger than the assumed physical size of the chamber. Therefore the effects due to the chromaticity-correcting sextupoles are acceptable.

To find the effects of the undulator on the dynamic aperture, we need to track the electrons with the undulators. This is one of the future works we are going to do. The nonlinear effects due to the sextupoles are expected to not be very important, but the effects due to the undulators have to be investigated. In addition, the breaking of symmetry of the lattice may reduce the aperture. The closed orbit error may also reduce the aperture. For the real aperture, we need to take them all into account.

Table 3: Lattice Parameters

Component	Length (m)	Strength
D1	4.000	
Q1	.250	3.433 $[m^{-2}]$
D2	.300	
Q2	.250	-3.311 $[m^{-2}]$
D3	.750	
B	1.456	1.2 $[T]$
D4	.150	
SD	.200	-14.82 $[m^{-3}]$
D5	.200	
Q3	.200	-1.310 $[m^{-2}]$
D4	.300	
Q4	.250	2.609 $[m^{-2}]$
D4	.200	
SF/2	.100	12.52 $[m^{-3}]$

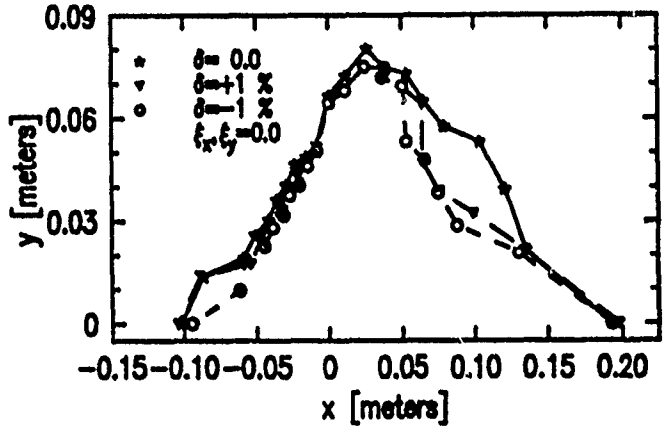


Figure 4: Dynamic aperture from Krackpot 1000 turns.

References

[1] J. B. Murphy, BNL Report 42333 (1990).

[2] S. Krinsky, IEEE Trans. on Nucl. Sci. NS-30 3078 (1983).

[3] J. Leduff, Nucl. Inst. & Meth. **A239** 83 (1985).

[4] M. S. Zisman, S. Chattopadhyay, and J. J. Bisognano, LBL Report 21270 (1986).

[5] M. F. Reusch, E. Forest, and J. B. Murphy, 1991 IEEE Particle Accelerator Conference, San Francisco, May 6-9, 1991.

Theoretical Minimum Emittance Lattice for an Electron Storage Ring

S.Y. Lee
Department of Physics, Indiana University, Bloomington, IN 47405
L. Teng
APS, Argonne National Laboratory, Argonne, IL 60439

Abstract

A theoretical minimum emittance lattice for an electron storage ring is derived, where the dispersion function at the entrance to the dipole is varied to minimize the $< H >$ function in the dipole. We find that the achievable minimum emittance is about 1/3 that of the equivalent Chasman-Green lattice. The interesting aspect is that the optimal minimum β^* value in the minimum emittance lattice is 4/3 times larger than that of the corresponding Chasman-Green Lattice. Therefore it may be easier to achieve the minimum emittance with this lattice. However, the theoretical minimum emittance lattice does not have a zero dispersion straight section.

1. Introduction

In recent years, electron storage rings have frequently been used as light sources for research in atomic, molecular, condensed matter and solid state physics, chemistry, cell biology, microbiology, and electronic technologic processing etc.. For many experiments, it is desirable to use high brightness light, which requires a high brightness electron beam. The synchrotron light emitted from a storage ring dipole spans vertically an rms angle of $1/\gamma$ around the beam trajectory at the point of emission, where γ is the Lorentz factor. Horizontally, the synchrotron light fans out an angle equal to the bending angle of the dipole magnet. The synchrotron light spectrum is continuous with a critical energy of $h\nu_c = \frac{3}{4\pi}\lambda_c m_e c^2 \frac{\gamma^3}{\rho}$, where λ_c is the Compton wave length of the electron.

The amplitudes of the betatron and synchrotron oscillations are determined by the equilibrium processes of the quantized emission of photons and the rf acceleration fields used in compensating the energy loss of the synchrotron radiation[1]. The horizontal emittance is given by

$$\epsilon_x = C_q \gamma^2 \frac{< H >_{dipole}}{J_x \rho} , \qquad (1)$$

where $C_q = 3.84 \cdot 10^{-13}$ m, $J_x \approx 1$ is the damping partition number and $< H >$ is averaged over the dipole for the function,

$$H = \frac{1}{\beta_x}(\eta_x^2 + (\alpha_x \eta_x + \beta_x \eta_x')^2) , \qquad (2)$$

where α_x, β_x are the Courant-Snyder[2] betatron amplitude functions; η_x, η_x' are the dispersion functions.

The design of low emittance optics is an important task in achieving high brighness electron bunches. There are several important ways to obtain small $< H >$ using the Chasman-Green lattice[3-5] and/or FODO cells[6]. FODO cells, composed of interspacing quadrupole and dipole magnets units, are used most often in the collider design due to their simplicity and high packing factor. A Chasman-Green (CG) lattice is composed of cells with two bend achromats, which connect zero dispersion straight sections. Because of its unique properties, the CG lattice has been widely used in the design of synchrotron light sources[7]. An alternative method in achieving a small emittance would be using a wiggler or an undulator to increase the radiation loss at the zero dispersive straight section.

In this paper we shall study the theoretical minimum emittance obtainable in the storage ring without using wigglers or undulators. Minimum emittance can be contemplated through minimizing the $< H >$ function with respect to the dispersion functions, η_x and η_x'.

2. Minimum Emittance Chasman-Green

A *half* cell of the Minimum Emittance Chasman-Green (MECG)[4] lattice is made of a single dipole with a set of quadrupoles on both sides such that (1) the dispersion function, η_x, is zero on one side and finite on the other side; (2) $\eta_x' = 0$ at the reflection symmetric point; and (3) the betatron amplitude function, β_x, is shaped to have a minimum in the dipole region. The choice of the dispersion function gives rise to a zero dispersion straight section, which is beneficial for the rf cavities and insertion devices. With this choice of dispersion functions, we obtain[4] the minimum betatron function location at $s^*_{MBCG} = \frac{3}{8}\ell_B$ with $\beta^*_{MBCG} = \frac{\sqrt{3}}{8\sqrt{5}}\rho\theta$ where ℓ_B is the length of the dipole, ρ and θ are respectively the bending radius and the bending angle of the dipole. The final average value of the H-function is

$$< H >_{MBCG} = \frac{1}{4\sqrt{15}}\rho\theta^3 \qquad (3)$$

The corresponding H-function at the ends of the dipole is given by $H(0) = 0$ and $H(\ell_B) = \rho\theta^3\{\frac{\sqrt{5}}{8\sqrt{3}} + \frac{\sqrt{3}}{8\sqrt{5}}\}$.

3. Emittance Minimization Procedure

To obtain a minimum emittance, we have to minimize the average value of $H(s)$ in the dipole region. Since the betatron amplitude function is shaped mainly by the quadrupoles, we shall assumed certain desired properties for the betatron function in the dipole. Since the betatron amplitude functions outside the dipole region do not affect the emittance to first order, we can concentrate our discussion in the dipole region. There we shall solve for the dispersion function, which obeys the equation

$$\eta_x'' + \frac{1}{\rho^2}\eta_x = \frac{1}{\rho} , \qquad (4)$$

where the primes denote the derivative with respect to the longitudinal coordinate, s, and ρ is the radius of the

0-7803-0135-8/91$01.00 ©IEEE

curvature for the dipole magnet. Thus the general solution for the dispersion function is given by

$$\eta_x = \rho(1 - a\cos\phi + b\sin\phi) \;\; ; \;\; \eta'_x = a\sin\phi + b\cos\phi \;,$$

where $\phi = s/\rho$. We have chosen $s = 0$ at the entrance of the dipole. The initial values of the dispersion function are given by $\eta_x(s = 0) = 1 - a$ and $\eta'_x(s = 0) = b$.

To minimize $< H >$ in the dipole, we assume β_x to be

$$\beta_x = \beta^* + \frac{(s - s^*)^2}{\beta^*},$$

which can be obtained by a proper arrangement of the quadrupoles. Other betatron functions are then given by, $\alpha_x = -\frac{1}{2}\beta'_x = -(s - s^*)/\beta^*$ and $\gamma_x = 1/\beta^*$. Averaging the function $H(s)$ of Eq.(2) in the dipole, we obtain

$$\begin{aligned} < H > = \; & \frac{\rho^2}{\beta^*}\{(1-a)^2 - \frac{1}{3}a(1-a)\theta^2 + \frac{1}{4}(1-a)b\theta^3 \\ & + \frac{1}{20}a^2\theta^4 - \frac{1}{12}ab\theta^5 + \frac{1}{28}b^2\theta^6 + [b^2 + ab\theta + \frac{1}{3}(a^2 - b^2)\theta^2 \\ & - \frac{1}{4}ab\theta^3 + \frac{1}{20}b^2\theta^4](\frac{\beta^*}{\rho})^2 + [2b(1-a)\theta + a(1-a)\theta^2 \\ & - \frac{1}{3}b\theta^3 - \frac{1}{4}(a^2 - b^2)\theta^4 + \frac{3}{10}ab\theta^5 - \frac{1}{12}b^2\theta^6]\frac{s^*}{\ell_B} + \theta^2[b^2 \\ & + ab\theta + \frac{1}{3}(a^2 - b^2)\theta^2 - \frac{1}{4}ab\theta^3 + \frac{1}{20}b^2\theta^4](\frac{s^*}{\ell_B})^2\}, \end{aligned} \quad (5)$$

where ℓ_B is the length of the dipole and $\theta = \ell_B/\rho$ is the corresponding bending angle. $< H >$ can be minimized with respect to s^*. We obtain with $s^* = s_m$ where $s_m = \ell_B[-b(1-a)\theta - \frac{1}{2}a(1-a)\theta^2 + \frac{1}{6}b\theta^3 + \frac{1}{8}(a^2-b^2)\theta^4 - \frac{3}{20}ab\theta^5 + \frac{1}{24}b^2\theta^6] \times [\theta^2(b^2 + ab\theta + \frac{1}{3}(a^2 - b^2)\theta^2 - \frac{1}{4}ab\theta^3 + \frac{1}{20}b^2\theta^4)]^{-1}$. The resulting value of $< H >$ is then given by

$$< H >= \frac{\rho^2}{\beta^*}[\mathrm{A} + \mathrm{B}\cdot(\frac{\beta^*}{\rho})^2], \quad (6)$$

where the coefficients A and B can be obtained easily from Eq.(4), i.e. $\mathrm{A} = (1-a)^2 - \frac{1}{3}a(1-a)\theta^2 + \frac{1}{4}(1-a)b\theta^3 + \frac{1}{20}a^2\theta^4 - \frac{1}{12}ab\theta^5 + \frac{1}{28}b^2\theta^6 - \mathrm{B}\theta^2(\frac{s_m}{\ell_B})^2$ and $\mathrm{B} = (b^2 + ab\theta + \frac{1}{3}(a^2 - b^2)\theta^2 - \frac{1}{4}ab\theta^3 + \frac{1}{20}b^2\theta^4)$. Varying β^*, we obtain the minimum of $< H >$ as

$$< H >_m = 2\mathrm{B}\cdot\beta^*_m = 2\rho\sqrt{\mathrm{AB}} \quad (7)$$

with $\beta^*_m = \rho\cdot\sqrt{\frac{\mathrm{A}}{\mathrm{B}}}$. Eq.(7) indicates that the achievable minimum emittance is proportional to the product of the coefficients A and B. Therefore we will minimize the product of AB with respect to the dispersion functions in the dipole region The Chasman-Green lattice corresponds to $a = 1$ abd $b = 0$. In the following, we shall study some other cases.

3.1 Special case: $b = \eta'_x(s = 0) = 0$

If we relax the constraint $a = 1$ but keep $b = 0$, we obtain a solution by minimizing the product of AB with respect to a, i.e.

$$a = \frac{180 - 15\theta^2 + \sqrt{3600 - 600\theta^2 - 135\theta^4}}{240 - 40\theta^2 + 3\theta^4} \approx \frac{1}{1 - \theta^2/12}\,.$$

It is interesting to note that the solution $a = 1/(1 - \frac{\theta^2}{12})$ corresponds to the condition $s^*_m = \frac{1}{2}\ell_B$, i.e. the optimal location of the β^* is located at the center of the dipole. The optimal β^* value is $\beta^*_m = \frac{2}{3}\cdot\frac{\sqrt{3}}{8\sqrt{5}}\rho\theta$, which is 2/3 of the corresponding value of β^* in a MECG lattice. Because of the location of β, the aperture requirement is about the same. Thus it is advantageous to obtain the minimum β^* at the center of the dipole. The maximum values of the betatron function on both side of the dipole will have the same magnitude. We will thus assume the approximate solution of $a = 1/(1 - \frac{\theta^2}{12})$ and obtain then $< H >_{b=0} = \frac{2}{3(1-\theta^2/12)^2}\cdot\frac{1}{4\sqrt{15}}\rho\theta^3$ The result can be interpreted easily. The minimum $< H >$ is obtained from a slightly negative initial dispersion function, $\eta_x(s = 0) = 1 - a = -\rho\frac{\theta^2}{12-\theta^2}$. The resulting emittance equals approximately 2/3 that of the corresponding MECG lattice. The difficulty in obtaining the minimum betatron amplitude function is the same as that with the Chasman-Green lattice. The H-function at the ends of the dipole is given by $H(0) = \rho\theta^3\frac{1}{(1-\theta^2/12)^2}\{\frac{\sqrt{5}}{12\sqrt{3}}\}$ and $H(\ell_B) = \rho\theta^3\frac{1}{(1-\theta^2/12)^2}\{\frac{\sqrt{5}}{12\sqrt{3}} + \frac{\sqrt{3}}{12\sqrt{5}}\}$. Thus the dispersion function outside the dipole remains small.

3.2 General case:

If we also relax the condition $\eta'_x(s = 0) = b = 0$, the emittance can be minimized further. Constraining the minimum β^* at the location $s^*_m = \frac{1}{2}\ell_B$, we obtain from Eq.(7)

$$\begin{aligned} & \theta(1 - \frac{\theta^2}{12})a^2 - (-2b + \theta + b\theta^2 + \frac{1}{20}b\theta^4)a \\ & - b(2 + b\theta - \frac{1}{3}\theta^2 - \frac{1}{12}b\theta^3 - \frac{1}{30}b\theta^5) = 0. \end{aligned} \quad (8)$$

Table 1. Minimum emittance vs. initial dispersion functions with $\theta = 2\pi/100$ radians

b	a	$\beta^*_{min}/\beta^*_{\mathrm{MBCG}}$	$\epsilon_{min}/\epsilon_{\mathrm{MBCG}}$
0.00	1.00032	0.6667	0.6671
-0.01	1.00001	0.8620	0.5162
-0.02	0.99967	0.9890	0.3942
-0.03	0.99938	1.3316	0.3347
-0.04	0.99907	1.2068	0.3687
-0.05	0.99875	0.9328	0.4767

Table 1 lists the improvement factor, $\epsilon_{min}/\epsilon_{\mathrm{MBCG}}$, for an accelerator composed of 100 half cells, i.e. $\theta = 2\pi/100$ for the storage ring. Note that the emittance is reduced when the constraints of $a = 1, b = 0$ are relaxed. When the dipole bending angle θ is varied, the optimal a, b values are also changed. We found that the optimal b value is about $-\theta/2$. The resulting minimum emittance is about 1/3 of the corresponding Chasman-Green lattice. The above statement can be proved easily as following: Up to the lowest order in θ, Eq.(8) gives

$$b = -\theta/2, \;\; a = 1 - \theta^2/6\,. \quad (9)$$

where we obtain also $s_m^* \approx \frac{1}{2}\ell_B$, $A = \frac{1}{720}\theta^4 + O(\theta^6)$ and $B = \frac{1}{12}\theta^2 + O(\theta^4)$. From Eq.(7), we obtain

$$< H >_m = \frac{1}{3} < H >_{\rm MECG} \; ; \; \beta_m^* = \frac{4}{3}\beta^*_{\rm MECG} \cdot \qquad (10)$$

The H-function at the ends of the dipole are given by

$$H(0) = \frac{1}{3\sqrt{15}}\rho\theta^3; \quad H(\ell_B) = \frac{1}{3\sqrt{15}}[1 + 2\theta^2 + \frac{17}{12}\theta^4]\rho\theta^3.$$

Note that the values of the H-function at both ends of the dipole are small.

4. Beam Dynamics Properties

Finally, let us study the properties of the dispersion function outside the dipole region. The dispersion function outside the dipole region satisfies the same equation of motion as that of the horizontal coordinate. Thus the $H(s)$ function is invariant. This means that η_x and η_x' are located on an invariant ellipse. Thus the only important quantities are the invariants at $H(s=0)$ and $H(s=\ell_B)$. Maintaining a small value for these two quantities will guarantee a reasonable dispersion function in the quadrupole matching section.

For the maximum brilliance of the photon beam from an undulator located in the straight section at the entrance end of the dipole, one wnats to minimize the beam width and not just the emittance. Let us discuss the general minimum emittance lattice discussed in section 3.2. The emittance is given by

$$\epsilon_\beta = C_{\rm q}\frac{\gamma^2}{J_x\rho} < H >_{dipole} = \frac{1}{12\sqrt{15}}C_{\rm q}\frac{\gamma^2}{J_x\rho}\rho\theta^3. \qquad (11)$$

The corresponding dispersion emittance, which should be defined as

$$\epsilon_\eta \equiv \gamma_x(\eta_x\delta)^2 + 2\alpha_x(\eta_x\delta)(\eta_x'\delta) + \beta_x(\eta_x'\delta)^2 = H(0)\delta^2, \quad (12)$$

where $\delta^2 = (\frac{\sigma_E}{E})^2 = C_{\rm q}\frac{\gamma^2}{J_E\rho}$ is the equilibrium energy spread in the beam. Thus substituting $H(0)$ of section 3.2 into Eq.(12), we obtain then

$$\epsilon_\eta = \frac{1}{3\sqrt{15}}C_{\rm q}\frac{\gamma^2}{J_E\rho}\rho\theta^3. \qquad (13)$$

For a separated function lattice, $J_E \approx 2$, $J_x \approx 1$ or $J_E \approx 2J_x$. The total emittance for a bi-Gaussian distribution is given by

$$\epsilon = \epsilon_\beta + \epsilon_\eta = \frac{1}{4\sqrt{15}}C_{\rm q}\frac{\gamma^2}{J_x\rho}\rho\theta^3 = \epsilon_{\rm MBCG}. \qquad (14)$$

Thus the decrease in the betatron emittance is taken up by the dispersion beam size. The brillance of the photon beam (namely the size of the electron beam in the "dispersion free" straight section) is not affected by the dispersion introduced to minimize the betatron emittance. The total electron beam size in the straight section remains unchanged. Thus the minimization procedure does not impair the function of undulators. On the other hand, larger β^* may be helpful in the chromatic correction of the lattice.

5. Conclusion

In conclusion, we have relaxed the constraints of the lattice design to obtain a minimum emittance lattice for electron storage rings. We derived general properties of the minimum emittance lattice and compared them to that of the Chasman-Green lattice. We found that an emittance of about 1/3 of the equivalent Minimum Emittance Chasman-Green lattice can be obtained. Table 1 shows that optimal emittances are derived at β^* values larger than those of the Chasman-Green. The beam size in the straight section should remain the same as that of the MECG lattice. Thus the brillance of the photon beam is not affected. Due to a smaller emittance, the photon brillance should be greater in the dipole region.

Note however, the small β^* value remains to be an essential element in achieving a small emittance. The lattice would still be sensitive to errors. Thus careful studies are needed to evaluate the feasibility. Problems, such as chromaticity correction, sensitivity of the lattice perturbations, stopband widths, tunablity, and stability arise in any lattice with small betatron amplitude functions. Careful studies of these problems are needed to understand the applicability of this minimum emittance concept. Possible retuning of the existing synchrotron radiation sources can be used to test the feasibility of the minimum emittance lattice.

Reference

1. M. Sands, ed. B. Touschek, "Physics with Intersecting Storage Rings" , (Academic Press, N.Y. 1971).
2. E.D. Courant and H.S. Snyder, Ann. Phys. 3,1(1958).
3. G.K. Green, "Spectra and Optics of Synchrotron Radiation", BNL-50522 (1976).
4. R. H. Helm, M.J. Lee and P.L. Morton, "Evaluation of Synchrotron Radiation Integrals", IEEE Trans. NS-20 (No. 3), 900 (1973); M. Sommer, Internal report DCI/NI/20/81 (1981); D. Potaux, Internal report DCI/NI/30/81 (1981); Y. Kamiya and M. Kihara, KEK 83-16 (1983); H. Wiedemann, Report ESRP-IRM-71/84 (1984); L. Teng, "Minimum Emittance Lattice for Synchrotron Radiation Storage Rings", LS-17, Argonne Report (1985).
5. see e.g. S. Tazzari, "Electron Storage Rings for the Production of Synchrotron Radiation", in CERN school proceedings, CERN 85-19, pp 566-585 (1985).
6. H. Wiedemann, Nuclear Instrument and Methods, 172,33(1980).
7. J. Murphy, "Synchrotron Light Source Data Book", BNL-42333 (1989).

Orbit Distortion due to the Floor Displacement in the Light Source Building Under Climatic Thermal Stress

T. Katsura, Y. Kamiya and Y. Fujita†
National Laboratory for High Energy Physics
1-1 Oho, Tsukuba 305, JAPAN
†Nuclear Power Division Shimizu Corporation
No. 2-3, Shibaura 1-Chome, Minato-ku, Tokyo 105 JAPAN

Abstract

Diurnal orbit drift in the storage ring was found resulting from the floor displacement of the building distorted under climatic thermal stress. The building distortion was both simulated by using a computer model and measured with a leveling system. Both simulation and measurement gave a good evaluation of the floor displacement. The orbit drift calculated from the measured floor displacement agreed well with that actually measured with beam position monitors. In consequence, it was decided to insulate the roof, which made the building distortion much smaller and the orbit drift minimal.

I. INTRODUCTION

The Light Source Building distorted under climatic thermal stress was found mainly responsible for the diurnal aggravation of vertical closed orbit distortion (COD) in the storage ring. This was recognized first by the fact that COD measured at the beginning of a day was not conserved for the rest of the day, and at the same time by the fact that experimenters often found it difficult to keep track of synchrotron radiation photon beams coming from the storage ring to their stations.[1] Efforts were paid first to identify the origin of this cause, and second to reduce its effect on the storage ring. This report covers studies on the mechanism of building distortion and its correlation to the vertical orbit drift.

Building distortion was evaluated both by employing a model simulation based on the finite element method and by directly measuring the displacement of the ring floor with a hydrostatic leveling system (HLS).

Vertical orbit drift was then calculated by using both simulated and measured floor displacements along the ring and compared with the orbit drift actually measured with beam position monitors (BPM). The comparison was made both before and after the roof was insulated to reduce the thermal stress from the solar irradiation.

II. EVALUATION OF FLOOR DISPLACEMENT

Figure 1 shows a plan view of the Light Source Building having two stories above and one below the ground to enclose an elliptical storage ring of which minor axis points almost the north. Location of some quadrupole magnets (quads) are shown as Q042-Q241.

To understand the mechanism of the floor displacement, a model simulation study was carried out assuming the building as a simple ellipse although the real building has an injection line. It was shown that the simulation produced about the order of floor displacements which would give the same amount of orbit drift as that observed with BPM. However, the shape of the observed orbit distortion could not be predicted well from the simulation results. This led us to actually measure the floor displacement and to see if such orbit drift can be obtained from the measured floor displacements. The floor displacement was measured at the location of quadrupole magnets.

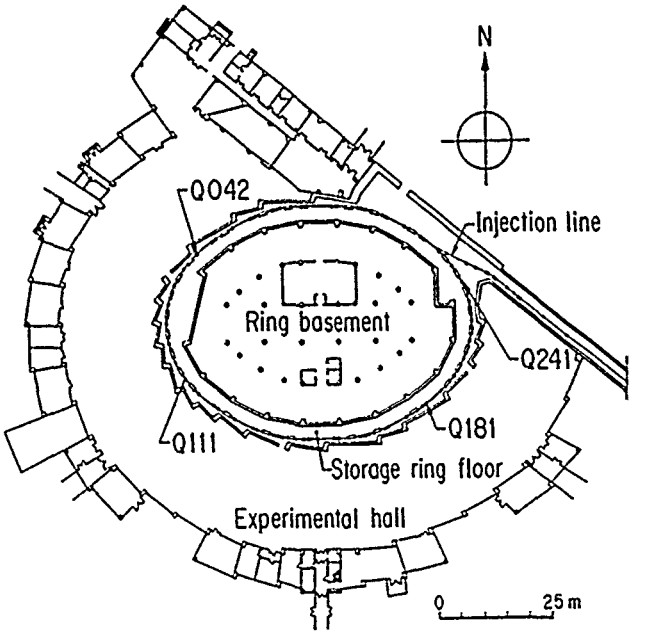


Fig. 1 Plan view of the Light Source Building.

Part of this work was supported by a collaboration program between National Laboratory for High Energy Physics and the Nuclear Power Division, Shimizu Corporation.

0-7803-0135-8/91$03.00 ©IEEE

A. Model simulation

The model structure used for the simulation analysis is shown in Fig. 2. The whole building shape was made elliptic with no injection region. Structural elements used in the modeling are the walls, columns, beams and piles of the real building. Symmetry of the ellipse is partially broken because the sizes and numbers of elements are different between the opposite ends of the major axis of the ellipse. The axis lies almost along the east-west direction. Simulated results are available on the mesh points.

The simulation program was supplied with data of temperatures measured both on the roof and in the surrounding atmosphere as a thermal stress loading. The building distortion was simulated both before and after insulation. The floor displacement was expressed as a relative value by choosing the mesh point at Q181 as reference. Simulation results are expressed both in the floor displacement versus time of day for each quad location and in the floor displacement versus distance along the ring for every hour of day.

In the top of Fig. 3, the simulated relative floor displacement along the ring is shown by a dotted line for the time of day at 15:00 before insulation. It is fundamentally symmetric but slightly different for its peak value at north and south points along the ring as the sun shines southerly. The west and east points differ because of the difference in column and wall strengths between them.

In the bottom of Fig. 3, the simulated floor displacement after insulation is shown by a dotted line. The difference in peaks between north and south or between east and west originates from the same cause as before insulation although the peak heights were greatly reduced compared to those before insulation.

B. Measurement of floor displacement

The displacement of the storage ring floor was measured by using a hydrostatic leveling system so designed to work as a water level of the size of the storage ring. Before a full-size leveling system was actually installed in the storage ring tunnel, the characteristics of this scheme was tested using a prototype system of three water tanks connected in series with water pipes.[2,3] The full-size system was composed of twelve tanks, each of which was located at the foot of a quad. Each tank has about 5 μm of measuring error.

As detailed description of the system was already reported,[2,3] only the results of the floor displacement measured with the system are given in Fig. 3 to be compared with the simulated results.

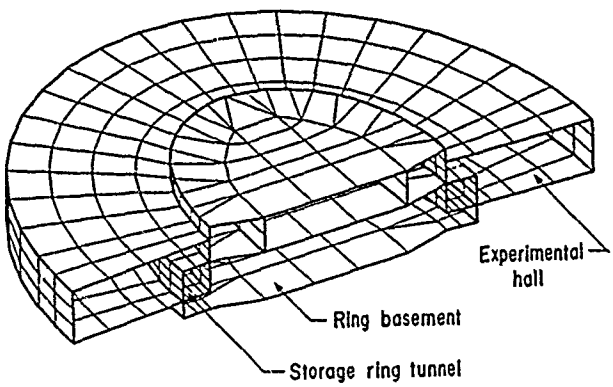


Fig. 2 Simulation model for the structure analysis.

C. Comparison of simulation and measurement

Before insulation, both simulation and measurement of relative floor displacement agreed quite well in both magnitude and phase along the ring, except near the injection region. The reason for the exception can naturally be understood as the injection region was not included in the simulation model.

After insulation, both simulation and measurement gave about 1/3 of the floor displacement obtained before insulation and agreed with each other within the measuring limit of the HLS system. This proved that simulation can describe well the general tendency of the building distortion.

III. Evaluation of Orbit Drift

Orbit drift was calculated by using the data of the floor displacement either simulated from the model or measured with the HLS, and compared with that measured with beam position monitors along the ring.

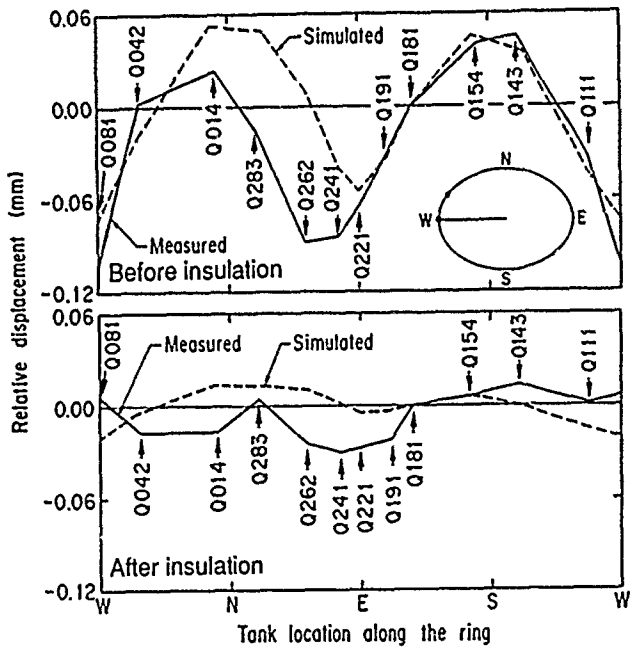


Fig. 3 Relative floor displacements both simulated and measured along the ring at 15:00 of one day before and after insulation.

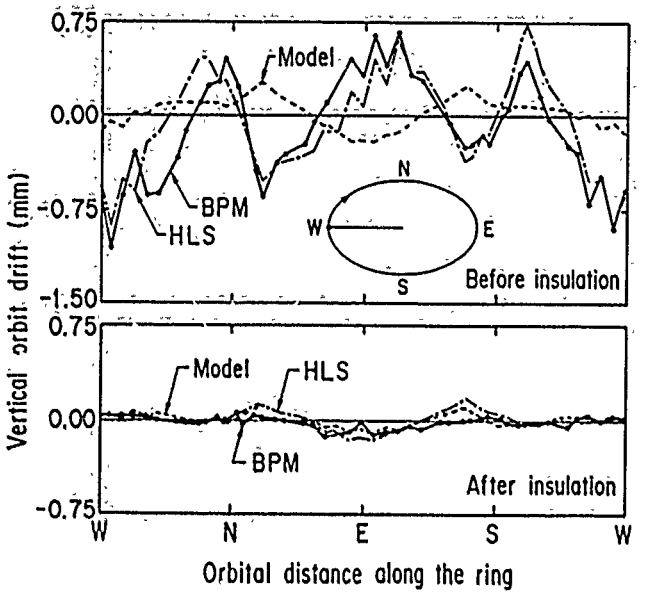


Fig. 4 Orbit drift measured with BPMs, calculated from the HLS measurement and model simulation.

A. Calculation and measurement of orbit drift.

Figure 4 shows the orbit drift calculated from the model simulation by a dotted line and that from the HLS measurement by a broken line. The amount of diurnal floor displacement was first obtained as a difference between floor level measured at 6:00 and 16:00 and then given to the orbit calculation program.

The orbit drift directly measured with BPMs is also shown by a solid line with circles indicating where BPMs are located along the ring. The BPM system has about 7 μm rms of error for each BPM and the curve shown here is a difference between two COD data taken at 6:00 and 16:00. The error in the difference accordingly becomes about 10 μm.

B. Comparison of the three kinds of evaluation

Before insulation, both BPM and HLS results are in good agreement within the measurement errors. The results from the model simulation, however, do not agree with those from BPM and HLS; neither in magnitude nor in phase along the ring.

After insulation, all three results became close each other within the measurement errors. The orbit drift was reduced to 1/6 of that before insulation.

IV. DISCUSSIONS

The comparison made above shows that the building distortion was mainly responsible for the diurnal drift of the closed orbit.

Before insulation, the simple modeling expressed well the gross feature of the building distortion. The model suited well to express the magnitude but not the phase of the floor displacement because of the existence of the injection line. The roof behaved just as one single piece of an elliptical plate when irradiated by the sun and was the major factor of the floor displacement. The building was thus distorted quadratically with mode 2 along the ring, having peaks either at north and south or at west and east depending on what time of day it was observed. However, the vertical tune of the storage ring is close to 3 and the orbit calculation picks up selectively the component of mode 3. The orbit drift calculated from the results of the model therefore became smaller compared to that calculated from the HLS data.

After insulation, on the other hand, the major factor of distortion was shifted from the roof to other part of building such as walls and columns and induced more of other modes than only mode 2. This may be the reason why the measured orbit and the orbit calculated using either simulation or measurement of floor displacement became close each other.

V. SUMMARY

Diurnal drifting of the vertical closed orbit in the storage ring was quantitatively investigated by using a model simulation of the building distorted under climatic thermal stress and by employing a hydrostatic leveling system to measure the displacement of the storage ring floor. It was proved that building distortion was largely responsible for the diurnal orbit drift. After the building was insulated on the roof, the orbit drift was reduced to about 1/6 of that before insulation.

The model simulation proved to be a useful tool to analyze the building distortion in high precision and will be confidently used for designing a storage ring building. The orbit drift calculated from the HLS results of the vertical floor displacement was consistent with that calculated from the BPM results both before and after insulation. This report has dealt with the vertical floor displacement. The horizontal displacement is also of our current concern.

VI. ACKNOWLEDGMENTS

The authors express their sincere thanks to Prof. H. Kobayakawa, head of the Light Source Division of the Photon Factory, KEK for his useful advice and suggestions and to the staff of the Division who conveyed continuous cooperation. They are also indebted to the staff of the Nuclear Power Division, Shimizu Corporation for their valuable cooperation.

VII. REFERENCES

1. T.Katsura, Y. Kamiya, K. Haga, and T. Mitsuhashi, Proc. of the IEEE Particle Accel. Conf., p.538(1987).
2. T. Katsura, KEK Internal report 90-32, and 90-33,(in Japanese) Jan. 1991.
3. T. Katsura and Y. Fujita, to be published in Rev. of Sci. Instr.

Beam Lifetime Investigations at BESSY

L.Schulz, E.Weihreter, H. Lehr

Berliner Elektronenspeicherring-Gesellschaft
für Synchrotronstrahlung m.b.H. (BESSY)
Lentzeallee 100, 1000 Berlin 33, FRG

Abstract

Lifetime measurements are reported for different operating conditions of the BESSY I storage ring. These experiments have been performed in an attempt to identify the relative contributions of different lifetime limiting processes as a basis for lifetime optimisation. Broadening of the beam using white noise excitation has proved to be a helpful tool to obtain quantitative information on the relative strength of the contributions due to gas scattering and the Touschek effect.

Introduction

For a synchrotron radiation source used as a tool in the field of fundamental and applied research, besides brilliance, source stability and up-time, the beam lifetime is an important figure of merit. In the present paper we describe measurements and calculations to determine the relative importance of the different lifetime limiting processes of the BESSY storage ring under the typical conditions of high brilliance operation [1]. This information is also helpful in the planning of a reasonable and cost effective component replacement and improvement program, which is under way at BESSY, to keep the machine running at high performance for the next decade after the first ten years of very successful user's operation.

For an electron machine in the energy range around 1 GeV the most important processes affecting the lifetime are i) Coulomb scattering between the electrons and the gas molecules in the vacuum chamber, ii) scattering between individual electrons in a bunch (Touschek effect) and iii) interaction of the electrons with the ion cloud captured by the beam. Assuming that these processes are statistically independent, the total loss rate is $1/\tau_{tot} = 1/\tau_{Coul} + 1/\tau_T + 1/\tau_{ion}$.

Measurements

We have measured the lifetime as a function of beam current for various operation modes, which are possible using the two rf-systems of the BESSY-ring, a 500 MHz (h = 104) system and a 62.4 MHz (h = 13) system. As can be seen in Fig. 1, the lifetimes observed with the 62.4 MHz rf-system in single bunch and multi bunch operation follow the same power law, $\tau \sim I^{-a}$ with a = 0.52. In the normal high brilliance user operation mode (500 MHz rf-system, partial filling of the storage ring with N ≅ 64 buckets) the lifetime shows roughly the same characteristic for higher single bunch currents, whereas at lower currents a slightly stronger dependence is observed.

If all 104 buckets of the 500 MHz rf-system are filled, the current dependence of the lifetime is less pronounced (a = 0.2) with the same current dependence as observed at low currents in single bunch operation with the 500 MHz system. For single bunch currents above 7 mA, however, the decrease in beam lifetime with increasing current is much stronger (a = 0.85).

Some features of these observations can be explained qualitatively by ion effects: if no filling gap is used, ion trapping is most effective and the transverse beam size is enlarged, which leads to a longer Touschek lifetime. When operating the ring with a filling gap a significant fraction of the ions can leave the capture potential. This ion clearing effect is particularly strong in single bunch operation with the 500 MHz rf-system above the clearing threshold of about 7 mA. Practically no difference is observed in the lifetime between single bunch and

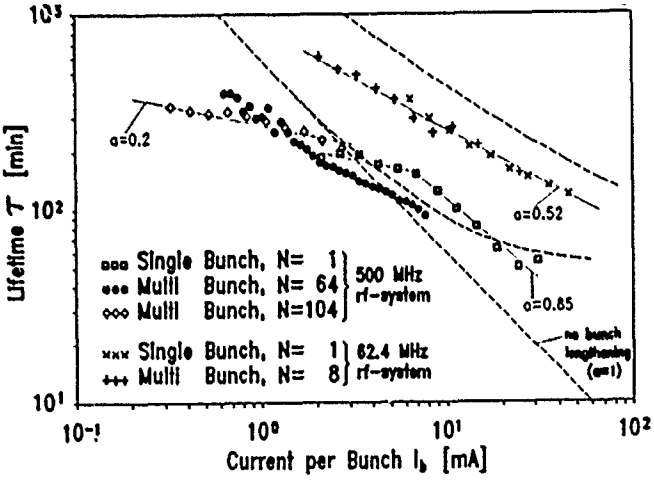


Figure 1: Beam lifetime measured for different operation modes as function of the current per bunch. N = number of buckets filled with electrons. The dotted lines show the theoretical Touschek lifetime taking bunchlengthening with a broadband impedance of Z/n = 7 Ω and ΔE/E = 1% into account.

0-7803-0135-8/91$03.00 ©IEEE

multi bunch operation (N = 8) with the 62.4 MHz rf-system in Fig. 1, which indicates that there is not much variation in the ion behaviour of the two operation modes.

The situation changes when the lifetimes of the single bunch and multi bunch mode with the 500 MHz rf-system are compared. The obvious difference of the current dependence must be attributed to a different ion trapping behaviour of the single bunch mode which shows the strongest current dependence (a = 0.85) above the trapping threshold around 7 mA. However, the maximum value a = 1 is not reached, which could be expected in the limit of zero bunchlengthening, when the Touschek effect dominates the lifetime and other contributions can be neglected.

For the user operation mode (500 MHz rf-system, N = 64) it is most interesting to get quantitative information on the relative contributions from Coulomb-scattering and from the Touschek effect. The observed lifetime τ_{exp} in the partial filling

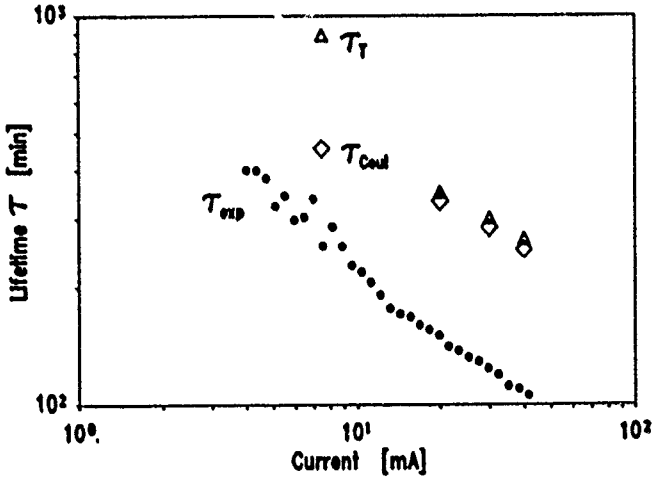


Figure 2: Beam lifetime τ_{exp} measured in the multibunch user operation mode. The data for the Coulomb lifetime τ_{Coul} and the Touschek lifetime τ_T are extracted from Fig. 3

mode as function of the stored current is shown in fig. 2 (circles). The rhomboidal symbols denote the Coulomb lifetime τ_{Coul} and the triangles the Touschek lifetime extracted from the data of fig. 3. As can be seen, the Coulomb scattering process dominates the loss rate at smaller beam current, whereas both lifetime limiting processes are comparable at higher currents.

Utilizing white noise excitation, the vertical beam size σ_z has been varied for different stored currents resulting in a strong lifetime enhancement with increasing beam size up to approximately $\sigma_z = 1mm$ (fig. 3). A further beam size enlargement has a negligible effect on the beam lifetime, which may be attributed to a strong increase of the Touschek lifetime

$$\tau_T \propto \frac{\left(\frac{\Delta E}{E}\right)^3 \sigma_x \sigma_y \sigma_s}{I_b} \qquad (1)$$

and a correspondingly small contribution to the total loss rate. This justifies to take the saturation values for the beam lifetimes in fig. 3 as an approximation for the Coulomb scattering

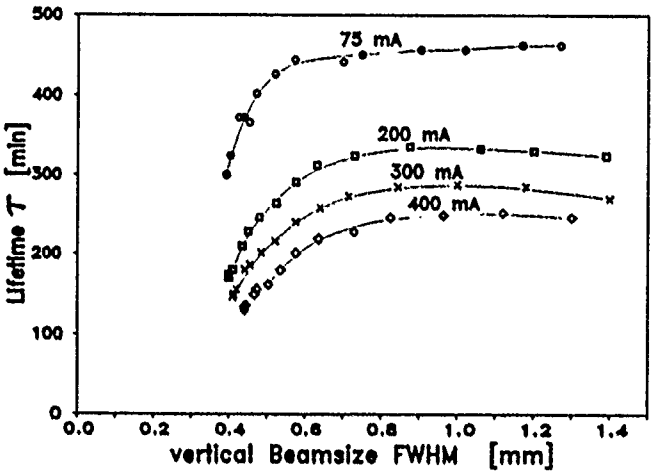


Figure 3: Beam lifetime in the multi bunch mode (500 MHz rf-system, N = 64) as a function of vertical beam size σ_z

lifetime only (triangles in fig. 2). Assuming furthermore that the loss rate due to Coulomb scattering is independent of the beam size, the values obtained for τ_{Coul} may be used to extract τ_T using $1/\tau_{exp} = 1/\tau_{Coul} + 1/\tau_T$, where τ_{exp} corresponds to the experimental values from fig. 3 without beam excitation.

Possible improvements

The measurements and the extracted data show that an improvement of the lifetime may be obtained by i) improving the vacuum conditions at large beta values as indicated by Wiedemann [2] due to $\tau_{Coul} \propto 1/ < p \cdot \beta >$ ii) reduction of the Touschek loss rate by an improvement of the energy acceptance as given in the above expression for τ_T.

Concerning the gas scattering process, the dominant contribution is expected to be concentrated on the inner dipole magnet vacuum chambers of the BESSY TBA structure due to an increased pressure caused by synchrotron radiation induced desorption and large beta values. A new and simple vacuum chamber was constructed, taking advantage of simple forming techniques and utilizing NEG pumps which are integrated in the vacuum chamber.

To determine the limiting energy acceptance we measured the lifetime of the stored beam as function of the 500 MHz cavity voltage (fig.4). The strong increase of the lifetime corresponds roughly with $\tau_T \propto (\Delta E/E)^3$, up to a saturation value, which is approximately obtained at 250 KV. The comparison with the theoretical energy acceptance curve (full drawn line) results in an energy acceptance of 1%. The saturation indicates that the energy acceptance is transversely limited. A detailed analysis of the non-linear dynamics for off momentum particles indeed demonstrates a limitation of the transverse energy acceptance to about 0.8% due to an unsymmetrical sextupole scheme in the ring [3]. Therefore symmetrized correction schemes have been worked out to improve the energy acceptance.

Another way to overcome the Touschek effect induced life-

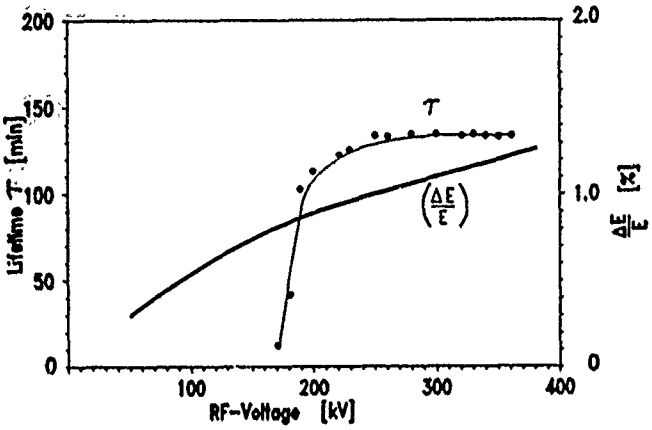


Figure 4: Measured beam lifetime τ and theoretical longitudinal energy acceptance as a function of the cavity voltage for operation with the 500 MHz (N = 62, I ≈ 300 mA) rf-system.

time limitation is to increase the bunch volume by lengthening the bunches with a higher harmonic cavity, provided that the time structure of the beam is not a concern. This method has been applied successfully at the NSLS-VUV ring. First experiments at BESSY to improve the lifetime using the existing double rf-system have shown, that longitudinal oscillations which are always excited at high currents in multibunch operation [4] play an important role in the loss process. Further studies are necessary to understand this mechanism.

Conclusion

Lifetime measurements under different operation conditions of the BESSY I storage ring have shown that Touschek and Coulomb scattering loss rates are comparable at high intensities in the low emittance user operation mode. Broadening of the beam using white noise excitation proved to be a helpful tool to obtain quantitative information on the relative strength of the contributions from beam-gas interaction and the Touschek effect. The results also indicate that the energy acceptance of the machine is transversely limited. Symmetrisation of the sextupole compensation scheme and bunch lengthening using a higher harmonic cavity are promising countermeasures to overcome this limitation.

Acknowledgements

We would like to thank W. Anders, T. Westphal, and the machine group for assistence in the single bunch measurements. Helpful discussions with P. Kuske are gratefully acknowledged.

References

[1] G. Mülhaupt et al: Proceedings of the conference on Insertion Devices for Synchrotron Radiation Sources, Stanford, USA, Oct. 1985

[2] H. Wiedemann: ESRF Internal Report ESRF-IRM-10/83 (1983)

[3] B. Kuske: Untersuchungen zur Energieakzeptanz des BESSY- Speicherrings BESSY TB 162/91

[4] E. Weihreter et al.: IEEE Trans. NS-32, No. 5, 2317(1985)

The 3 GeV Synchrotron Injector for SPEAR*

H. Wiedemann, M. Baltay, J. Voss, K. Zuo, C. Chavis, R. Hettel, J. Sebek, H.D. Nuhn, J. Safranek, L. Emery, M. Horton, J. Weaver, J. Haydon, T. Hostetler, R. Ortiz, M. Borland, S. Baird, W. Lavender, P. Kung, J. Mello, W. Li, H. Morales, L. Baritchi, P. Golceff, T. Sanchez, R. Boyce, J. Cerino, D. Mostowfi, D.F. Wang, D. Baritchi, G. Johnson, C. Wermelskirchen, B. Youngman, C. Jach, J. Yang, R. Yotam
Stanford Synchrotron Radiation Laboratory, P.O. Box 4349, Bin 69, Stanford, CA 94309-0210

Abstract

A dedicated 3 GeV injector synchrotron for the storage ring SPEAR has been constructed at the Stanford Synchrotron Radiation Laboratory, SSRL, and has become operational by November 1990. The injector consists of an rf-gun, a 120 MeV linear accelerator, a 3 GeV booster synchrotron and associated beam transport lines. General design features and special new developments for this injector are presented together with operational performance.

I. Introduction

The 3 GeV storage ring SPEAR is fully dedicated to the production of synchrotron radiation since 1990. To eliminate the need to fill SPEAR from the SLAC linear accelerator causing significant interruption of SLC operation SSRL proposed in 1987 to DOE to construct a 3 GeV full energy dedicated electron injector for SPEAR [1](Fig.1). This

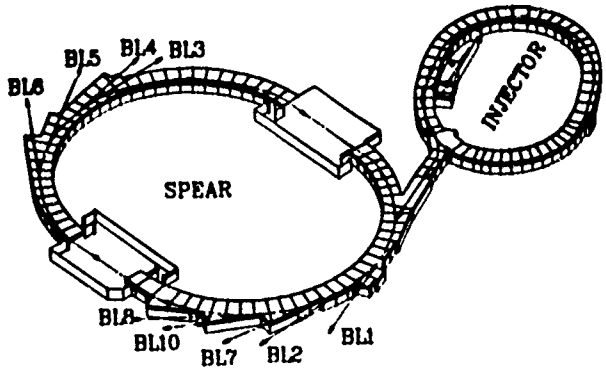


Figure 1
3 GeV SPEAR injector

proposal was approved and construction begun in February of 1988. By mid of 1990 most component had been constructed and installed and commissioning begun. First beam tests to the booster started on July 20 with successful capture the same day. After a summer shut down to complete installation, first acceleration occurred on September 6 and beam was stored in SPEAR the first time from the new injector on November 21, 1990.

II. General Injector Facility

A. Basic Design Goals

The basic goals for the design of all components was to produce an electron beam for injection into SPEAR with an energy of 3 GeV and an intensity which would allow to fill SPEAR to 100 ma in less than 5 minutes. The electron source is a 2.5 MeV rf-gun and after acceleration to 120 MeV in a linear accelerator the particles follow a short beam transport line to the booster synchrotron. The booster magnets are energized by a White circuit cycling at 10 Hz. After reaching the SPEAR injection energy the beam is kicked out of the booster into a beam transport line to SPEAR.

B. Parameters

The lattice of the booster synchrotron is based on a simple FODO structure of 20 cells. To accommodate the rf system, instrumentation and injection and ejection components a missing bending magnet scheme was employed without interrupting the FODO focusing. This scheme depresses the dispersion function at the bending magnet free sections where the rf cavity is installed. In Fig.2 the magnet structure and lattice functions are shown for one

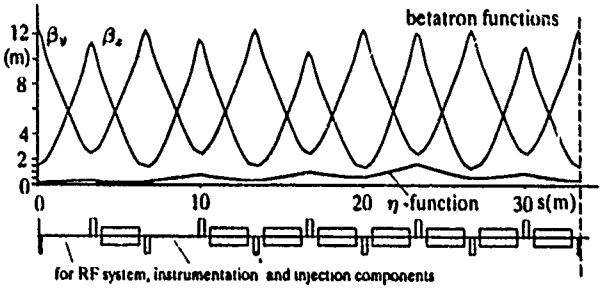


Figure 2
Magnet structure and lattice functions

quadrant of the ring and in Table 1 basic design parameters are compiled.

Table 1
Basic Design Parameters

Energy	E	3.0	GeV
Circumference	C	133.4	m
Cycling Rate	R	10	Hz
Intensity	N	$\geq 1.0\ 10^{10}$	ϵ^-/sec
Tunes:	ν_x/ν_y	6.25/ 4.18	
Linac Energy	E_{linac}	≥ 120	MeV
Linac Frequency	f_{linac}	2856	MHz
Linac Intensity	$\dot{N}_{linac}$	$\geq 2.0\ 10^{10}$	ϵ^-/sec

*Work supported by the Department of Energy, Office of Basic Energy Sciences, Division of Material Sciences.

0-7803-0135-8/91$03.00 ©IEEE

III. COMPONENTS

A. Preinjector

To simplify the source components for the electron beam it was decided to use a thermionic rf gun [2],[3] being powered by 5 MW split off from the second linac klystron by a 7db coupler. The maximum pulse current from the rf gun has been measured at 1.5 ampere. Simulations of the gun design show that back bombardment is minimized to a level where the cathode temperature is determined by external heating as has been observed experimentally. After acceleration in the gun to 2.5 MeV the electrons pass through an alpha magnet for energy selection and bunch compression. The energy filter in the alpha magnet is set to about 15 to 20 % and from measurements at the end of the linac we conclude that the bunch becomes compressed to less than 1 psec. The energy spread of the beam at 120 MeV is reduced by adiabatic damping to abut 0.4%. A

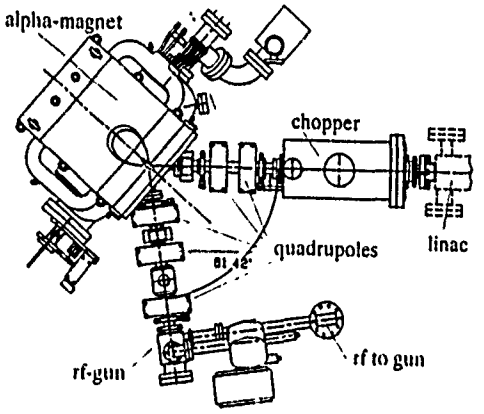


Figure 3
Rf gun, compressor and chopper unit

chopper unit [4] is installed between the alpha magnet and linac to facilitate the selection of only 3 S-band bunches. The beam is swept vertically across a small slit by a travelling wave allowing the passage of only 3 S-band bunches. Acceleration to 120 MeV occurs in three ten foot long linac sections. Each section is driven by a 35 MW modulator and klystron[5]. The rf power for the gun is split off the second klystron rather than from the first section to allow maximum acceleration to relativistic energies in the first section. This combination of an rf gun and a beam chopper eliminates the need for prebuncher, buncher sections and elaborate solenoid focusing along the linac sections. No such focusing is employed in this preinjector due to the significant energy of 2.5 MeV which greatly reduces the sensitivity of the beam to stray fields. The component arrangement of the electron source is shown in Fig.3.

B. Magnets

The booster magnets are designed for a cycling operation at 10 Hz and maximum field strength of 1.39 Tesla for future operation at 5 GeV [6]. The magnets must be constructed from laminated steel to avoid eddy current effects and heating. After R&D with different steel qualities, US1005 steel was used because of it's excellent magnetic qualities. At 10 Hz measurements did not indicate significantly higher AC or eddy current losses compared to transformer steel. Each coil includes 19 turns for the main current and a pair of trim coils for orbit correction and compensation of induced voltages from the main coil. To simplify installation and alignment the bending magnet cores are constructed in five short pieces set directly on precision drilled pins on a single steel girder such as to form a "curved" magnet following the beam path (see Fig.4). The quadrupoles are constructed in four quadrants from US1005 steel and are powered in series with the bending magnets. Extra computer controlled trim coils are used to adjust the quadrupole strength.

C. Vacuum

The vacuum chambers in a synchrotron must be fabricated in such a way as to avoid eddy current losses and allow the magnetic field to penetrate the chamber wall to reach the beam orbit without distortion. Following the pioneering design for the DESY synchrotron [7], a stainless steel tube with a wall thickness of 0.3 mm was used for the booster vacuum chamber. Strengthening ribs surrounding the chamber every inch along the chamber prevent collapse of the chamber [8]. Pressure tests demonstrated stability of the chamber in excess of 10 atmospheres. The eddy current heating is negligible and the chamber temperature does not exceed measurably the ambient temperature within the magnets. No detrimental effect of eddy currents on beam dynamics has been observed. The vacuum chambers are constructed in 40 cm straight pieces and welded together at the correct angle to form a "curved" chamber 2.5 m long and reaching through bending magnet, quadrupole and sextupole instrument modules are installed between individual chambers to accommodate pump port, beam position monitor, bellows and an isolating ceramic ring.

D. RF System [5]

Acceleration of the electrons is accomplished in a 5-cell rf cavity at 358.4 MHz The cavity voltage must be controlled during acceleration to avoid too high synchrotron oscillation frequencies and amplitudes at low energy. The computer control allows to adjust the rf voltage at any point along the acceleration cycle for best beam stability.

E. Instrumentation and Control

Beam position monitors and orbit correction coils are installed [9] for beam control during ramping although orbit correction is done in DC mode and compensates for remnant field errors only. Diagnostic instrumentation [10] and timing systems[11] complement the electronic controls of the injector. The computer software [12] allows the control of all systems from a terminal. Specifically, magnet currents can be adjusted by pointing and moving the cursor to screen sliders. Time dependent adjustments necessary during energy ramping can be preprogrammed as well on

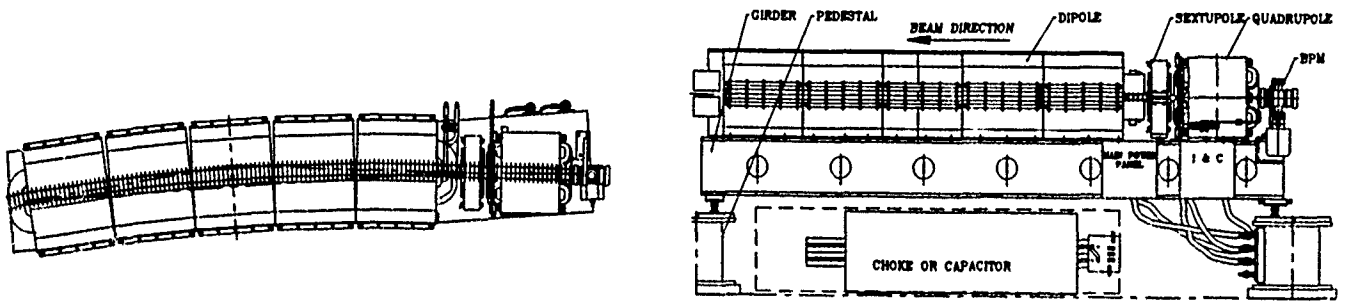


Figure 4
Top and side view of magnet girder

by adjusting function values on a diagram.

F. Power Supplies

The main magnets, bending magnet and quadrupoles, are powered from a single White circuit [13]. The specific field requirements of the focusing (QF) and defocusing quadrupoles (QD) are met by constructing both magnets in different length to produce the proper focusing to within 1 to 2 %. For fine adjustments all quadrupoles contain trim coils which are separately powered by computer controlled power supplies. This feature allows free adjustment of the quadrupole strengths and betatron tunes during the accelerating cycle for maximum beam stability. Horizontal and vertical beam steering is accomplished by trim coils in the bending magnets and in the quadrupoles. These corrections are static to correct mostly for remnant field errors. No orbit correction is provided for higher energies where orbit distortions are determined mostly by alignment errors. Due to the low sensitivity of the orbit to alignment errors in this lattice no such correction is necessary.

G. Injection/Ejection

A beam transport line from the linac to the booster ring includes energy analyzing equipment as well as capabilities to measure the beam emittance. Injection into the booster is performed on axis with a horizontal septum magnet and a pulsed kicker magnet[14]. A peaking strip signal from one of the bending magnets is used to trigger the kicker magnet at the correct field level. Ejection occurs at the end of the acceleration cycle by firing a kicker magnet guiding the beam into a Lambertson septum [15] and through vertical bending magnets into the beam transport line to SPEAR located in it's first section atop the booster ring.

IV. Performance

The injector project has been completed by the end of November 1990 ahead of schedule and within budget. All design beam parameters have been achieved, specifically an intensity of more than 1.0^{10} electrons per second can be delivered to SPEAR[16]. This is sufficient to fill SPEAR to the nominal current of 100 mA in less than five minutes.

V. Acknowledgements

It is a pleasure for the injector group to thank SSRL administration and staff members, SLAC and outside consultants for their contributions to this project.

VI. References

[1] "3 GeV SPEAR Injector", *Conceptual Design Report*, SSRL Report 88/ 03, July 1988.
[2] M. Borland et. al., "Performance of the 2 MeV Microwave Gun for the SSRL 150 MeV Linac", 1990 Linac Conf. in Albuquerque.
[3] M. Borland, "A High Brightness Thermionic Microwave Electron Gun. PhD, Stanford University, 1991.
[4] M. Borland et.al., "Design and Performance of the Traveling Wave Beam Chopper for the SSRL Injector", this Conference
[5] J.N. Weaver et.al., "The Linac and Booster RF Systems for a Dedicated Injector for SPEAR", this Conf.
[6] M. Baltay et.al., "The Ring Magnets for the SSRL SPEAR Injector ", this Conference
[7] J. Kouptsidis et.al., "A Novel Fabrication Technique for Thin Vacuum Chambers with Low Eddy Current Losses", IEEE, Vol. NS-32, No. 5, Oct. 1985
[8] H. Morales et.al., "Vacuum Chamber for the 3 GeV SPEAR Injector Synchrotron ", this Conference
[9] W. Lavender et.al., "The SSRL Injector Beam Position Monitoring Systems", this Conference
[10] J. Sebek et.al., "Diagnostic Instrumentation for the SSRL 3 GeV Injector for SPEAR", this Conference
[11] R. Hettel et.al., "Triggers and Timing System for the SSRL 3 GeV Injector", this Conference
[12] C. Wermelskirchen et.al., "The SSRL Control System", this Conference
[13] R. Hettel et.al., "The 10 Hz Resonant Magnet Power Supply System for the SSRL 3 GeV Injector", this Conference
[14] H.D. Nuhn et.al., "The SSRL Injector Kickers", this Conference
[15] J. Cerino et.al., "Extraction Septum Magnets for the SSRL Injector", this Conference
[16] S. Baird, J. Safranek, "Commissioning the SSRL Injector", this Conference

Commissioning Experiences of the ALS Booster Synchrotron

Charles H. Kim
Lawrence Berkeley Laboratory
M/S 80-101
Berkeley, CA 94720

Abstract

Installation of the ALS booster synchrotron proper was completed on April 30, 1991, and commissioning has just begun. Circulating beam around the booster was observed on the first day of operation, May 3, 1991. The beam was visible for about 400 turns. In this paper we describe the status and commissioning experience of the 1.5–GeV electron synchrotron accelerator.

I. Introduction

Construction of the Advanced Light Source (ALS), a third-generation synchrotron radiation source for the UV and soft X-ray region at LBL [1], entered a new phase recently with beneficial occupancy of the building and with the start of commissioning of the booster. The ALS injector consists of a 50–MeV S-band linac and a 1.5–GeV booster synchrotron [2]. Commissioning of the linac is described elsewhere in these proceedings [3].

The booster consists of 24 dipole and 32 quadrupole magnets in a missing-magnet FODO-lattice configuration with a superperiodicity of 4. The booster also has 20 sextupole magnets for chromaticity corrections and 32 corrector magnets for orbit corrections. The synchrotron was designed to accelerate a current of 20 mA (5 nC) in the multibunch mode and 4 mA (1 nC) in the single-bunch mode. Full energy injection into the 1.5–GeV storage ring is expected to take few minutes. Lattice parameters are summarized in Table 1.

Table 1
Booster Lattice Parameters

Energy	1.5 GeV
Circumference	75 m
Rf Frequency	499.7 MHz
Harmonic Number	125
Revolution Frequency	3.997 MHz
Radiation Loss	112 keV
Natural Energy Spread	0.064%
Radiation Damping [msec]	
Horizontal	6.68
Vertical	6.72
Energy	3.37

II. Fabrication

The prototype dipole and quadrupole magnets have been fabricated, measured for multipole errors, and qualified for production [4, 5, 6]. The production magnets have been measured for their magnet-to-magnet reproducibility [7]. These errors were controlled such that the dynamic aperture is larger than the vacuum chamber aperture [8].

The booster vacuum chamber is made of stainless-steel pipes, 30 mm in radius and 1 mm in wall thickness. Pipes in the dipole magnets were flattened to ±20 mm to fit the gap and bent to the proper radius. Average booster vacuum pressure reached lower than 5×10^{-8} Torr after a few days of pumping.

Eddie currents, induced on the vacuum chamber wall when the dipole magnetic fields are ramped, generate defocusing sextupole fields whose magnitudes are proportional to dB/dt. The sextupole fields reduce the dynamic aperture severely if the repetition rate is higher than 4 Hz [8]. The repetition rate of the booster is limited by the dipole power supply to 1 Hz.

II. Installation

All magnets, vacuum chambers, and instrumentation in the bends were preassembled on 12 girders. When placing the dipoles, the magnet with the most positive error and most negative error were paired and placed adjacent to each other to minimize the closed-orbit distortion. Each magnet was then prealigned with respect to the girder on which it was mounted and the girders were transported to the accelerator building and lowered into the booster cave. Straight sections (injection, extraction, diagnostic, and rf straight sections) were installed subsequently in the tunnel. After utility connections were made, the magnets were aligned again with respect to the girder and the girder with respect to the ALS coordinate system. We have finished aligning most of the girders at the present time with alignment errors < ±300 μm, which is better than the specifications (300 μm rms) [9].

Dipole magnets are connected in series to an SCR-switched power supply [10]. (We used a small dc power supply for the dipoles in the initial injection study.) The focusing (and likewise the defocusing) quadrupoles are connected in series to a power supply which tracks the dipole-magnet excitation current. Sextupole- and corrector-magnet power supplies also track the dipole current. Current tracking alone does not insure that the magnetic fields will track the dipole field because of the nonlinearities such as the residual fields and core saturation. Therefore, provisions are made in the control system to add small corrections of arbitrary shape to all magnet power supplies that track the dipole power supply.

III. Operation

The booster is controlled by the ALS control system [11] using intelligent local controllers (ILCs), which are highly distributed and centrally connected to collector micro-modules via fiber-optical links. Operator interface is via a number of personal computers (six 486/PCs at present) using mostly commercially available software and development tools. Applications are being developed jointly by the ALS control systems group and the accelerator systems group.

U.S. Government work not protected by U.S. Copyright.

Because of the construction and installation activities during normal working hours, injector commissioning activities have been limited to the evenings.

IV. Injection Studies

Parameters of the injected beam are summarized in Table 2. Linac operation is very reliable at these operating conditions. Energy spread is mainly due to the energy droop in the subsequent bunches and is high because (1) the beam loading compensation has not been implemented, and (2) the bunching system has not been fully optimized yet. We have a beam collimator for energy selection in the linac-to-booster transfer line. The collimator was left wide open in the present experiment for the initial tuning purpose.

Table 2
Injected Beam Parameters

Beam energy	45 MeV
Charge per bunch	0.1 nC
Separation between bunches	8 ns
Number of bunches	20 pulses
Energy spread	±2%
Repetition rate	1 Hz

The booster lattice was set up according to the "nominal tune" column in Table 3.

Table 3
Two Typical Operating Points of the Booster

	nominal tune	low tune
Betatron Tune		
Horizontal	6.264	5.764
Vertical	2.789	2.480
Momentum Compaction	0.0408	0.0466
Chromaticity		
Horizontal	-11.2	-8.31
Vertical	-4.79	-4.69
Emittance [nm, unnorm]	0.15	0.18
Quadrupole kL [1/m]		
Focusing	0.830	0.787
Defocusing	0.504	0.471
Sextupole kL [1/m^2]		
Focusing	0.971	0.867
Defocusing	1.183	0.989

for quadrupoles $k = (dB/dx) / [B\rho]$
for sextupoles $k = (d^2B/dx^2) / 2 [B\rho]$

Injection from the 50–MeV linear accelerator is via a fast kicker magnet [12] utilizing the well-established single-turn, on-axis injection technique. The fast kicker consists of two 25–cm modules and provides a 60–mrad kick to the injected beam onto the booster beam axes. The injection kicker has a 150–nsec flat top, with rise and fall times of about 100 nsec. Each module has a pulse flatness of ±0.5 %. When fully commissioned, the entire 150 nsec period will have a flatness of < ±0.5 %.

Booster instrumentation includes 5 TV monitor stations, 32 beam-position monitors (BPMs), travelling wave electrodes (TWEs) [13], and one beam-intensity monitor (DCCT). A TV monitor station consists of a Chromox 6 fluorescent screen and a CCD camera. A BPM utilizes 4 button monitors and is similar to the ALS storage ring BPM system [14].

We first observed the injected beam on the fluorescent screen located on the down-stream side 1005 mm from the center of the kicker magnet where the dispersion is still very small. (The lattice functions at the screen are: horizontal α = 3.93; β =8.45 m; η = 0.12 m; vertical α =-1.53; β =3.37 m.) The beam centroid moved about 6 mm as expected when the kicker amplitude was varied by about 10%.

Next, we observed the beam with one of the BPMs located 5586 mm from the center of the kicker magnet. This BPM is located immediately after the focusing quadrupole in which the dispersion function is very large (z = 5.3425 m; horizontal α = 4.23; β =9.17 m; η = 1.05 m; vertical α =1.98; β =6.07 m.) We observed that more than half of the 20 bunches were already lost at this location.

Finally, we observed the circulating beam using one of the TWEs in the third quadrant. Figure 1 shows that only the first 3 bunches survived up to the third quadrant. It also shows that about half of the beam intensity was lost by the next turn.

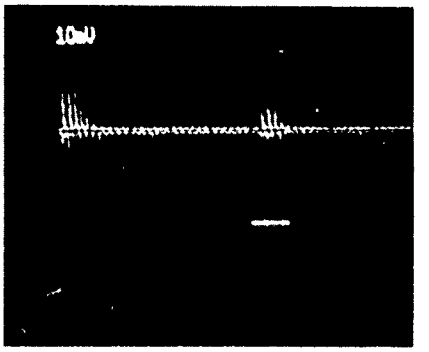


Figure 1. TWE signal showing electron bunches for the first two turns. [XBB 915-3445]

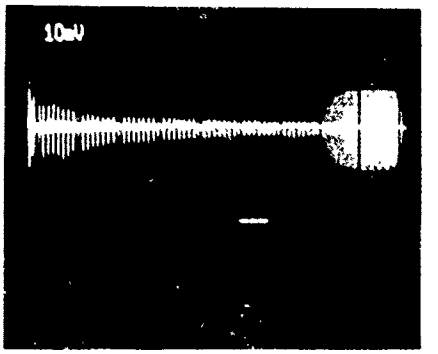


Figure 2. TWE signal showing electron bunches for the first 20 μsec. [XBB 915-3446]

Figure 2 shows the TWE signal for the first 20 μsec. It shows that the rapid beam loss during the first few turns is followed by a slower beam decay. Circulating beam was visible for about 400 turns.

V. Summary and Discussions

We were actually surprised to observe that the beam survived as long as it did with neither steering magnets nor the rf cavity energized. Rapid beam loss was expected from the beginning because of (1) the large energy spread in the injected beam; (2) large closed-orbit distortion; and (3) imperfect flatness of the injection kicker wave form. Our beam stay-clear specifications are summarized in Table 4.

Table 4
Beam Stay-Clear Specifications
[mm rms]

	At 50 MeV	At 1.5 GeV
Beam Size	3.6	1.3
Dispersion	3.5	0.7
Energy Spread [%]	(0.3)	(0.06)
Closed Orbit distortion		
before correction	6.0	6.0
after correction§	0.3	0.3
Quadratic Sum		
before correction	7.8	6.2
after correction§	5.0	1.5
Pipe Size	±30.0	±30.0

§ requires corrector strength of 0.5 rmad rms

We expect the specifications will be met in the near future as we finish aligning the rest of the magnets, execute beam loading compensation, tune the linac for a smaller energy spread, and flatten the kicker pulse. We will be able to implement orbit corrections and tune fitting as soon as the rf system and the timing system come on line.

Components necessary for beam acceleration are to be in place by late June. The extraction system is expected to be on line in September, and the booster-to-storage-ring transfer line in October 1991. Storage ring injection is expected to occur in Spring 1992.

Acknowledgements

Material presented in this paper is the result of a cooperative effort by many groups of the ALS project team, whose personal commitment and unselfish cooperation are gratefully acknowledged. Only some of the groups are listed below: Magnet design and fabrication efforts led by Jack Tanabe, vacuum system by Kurt Kennedy, mechanical installation by Tom Henderson, electrical installation by Ivan Lutz, survey and alignment by Ted Lauritzen, beam diagnostics by Jim Hinkson, injection-extraction mechanical system by John Milburn, kicker and fast magnets by George Gabor, power supply by Terry Jackson, controls group by Steve Magyary, analysis of the magnet measurements and survey and alignment data by Rod Keller. Special thanks are due to Alan Jackson for his guidance and encouragement and ALS operations group for the long evening shifts.

This work was supported by the Office of Energy Research, Office of Basic Energy Sciences, US Department of Energy, under Contract No. DE-AC03-76SF00098.

References

1. A. Jackson, "The Advanced Light Source: Status Report," in these proceedings.
2. F. Selph, A. Jackson, and M. S. Zisman, "Injector System Design," Proc. of the 1987 IEEE Particle Accelerator Conference, Washington, D. C., p. 446.
3 F. Selph and D. Mossoletti, "Operating Experience with ALS Linac," in these proceedings
4. J. Tanabe et al., "Fabrication and Test of Prototype Ring Magnets for the ALS," Proceedings of the 1989 IEEE Particle Accelerator Conference, March 20-23, 1989, Chicago, IL p. 566
5. R. Keller et al., "Magnetic Properties of the ALS Booster Synchrotron Engineering Model Magnets," Proceedings of the 1989 IEEE Particle Accelerator Conference, March 20-23, 1989, Chicago, IL p. 1966.
6. M. I. Green, E. Hoyer, R. Keller, and D. H. Nelson, "AC Magnetic Measurements of the ALS Booster Dipole Engineering Model Magnets," Proceedings of the 1989 IEEE Particle Accelerator Conference, March 20-23, 1989, Chicago, IL p. 1969.
7. R. Keller, "Magnetic Data Analysis for the ALS Multipole Magnets," in these proceedings.
8. C. Kim and H. Nishimura, "Dynamic Aperture for the ALS Booster Synchrotron," Proceedings of the 1989 IEEE Particle Accelerator Conference, March 20-23, 1989, Chicago, IL p. 1328.
9. R. Keller, C. Kim, and H. Nishimura, "Alignment Tolerances for the ALS Storage Ring and Booster Synchrotron," LBL ALS Report LSAP-70 (1989)
10. L. T. Jackson and I. C. Lutz, "Magnet Power Supplies for the Advanced Light Source," Proceedings of the 1989 IEEE Particle Accelerator Conference, March 20-23, 1989, Chicago, IL p. 74.
11. S. Magyary et al., "Advanced Light Source Control System," Proceedings of the 1989 IEEE Particle Accelerator Conference, March 20-23, 1989, Chicago, IL p. 74.
12. G. Gabor and F. Voelker, "Kicker Magnets for ALS" Proceedings of the 1989 IEEE Particle Accelerator Conference, March 20-23, 1989, Chicago, IL p 405.
13. J. H. Hinkson and K. Rex, "A Wide band slot coupled beam sensing electrode for ALS," in these proceedings.
14. J. Hinkson, J. Johnston, and I. Ko, "ALS Beam Position Monitor," Proceedings of the 1989 IEEE Particle Accelerator Conference, March 20-23, 1989, Chicago, IL, p. 1507.

A High Energy Electron Beam Facility for Industrial Research

S.Okuda, T.Nakanishi, K.Ikegami, S.Nakata, T.Nakagawa, C.Tsukishima, A.Maruyama, H.Tanaka
S.Nakamura, I.Kodera, S.Yamamoto, T.Matsuda, S.Fujimura, H.Itagaki, T.Yamada, M.Iwamoto
Central Research Laboratory, Mitsubishi Electric Corporation
1-1, Tsukaguchi honmachi 8, Amagasaki, *Japan* 661

Abstract

A high-energy electron beam facility is under commission at the Mitsubishi Electric Corporation. This facility consists of a $20MeV$ linac and a $1GeV$ synchrotron. The synchrotron is designed to act as a storage ring as well as an injector to a compact storage ring.

1 Introduction

A high-energy electron beam facility is under commission at the Mitsubishi Electric Corporation.

Basic research for industrial applications is planned with this facility. The applications include synchrotron radiation (SR) for lithography and material analysis, generation and measurement of positrons, and free electron lasers.

The building containing this facility was completed at the end of 1989, and initial operation of the system has begun.

In this paper we describe the high-energy electron beam facility. The main subject is the design of the booster synchrotron.

2 Description of Facility

The configuration of the system is shown in figure 1[1]. It consists of a $20MeV$ linac, a $1GeV$ booster synchrotron, beam transport lines, and an $800MeV$ storage ring.

The linac, the synchrotron, and the beam transport lines have been installed and the electron beam is under commission.

2.1 Linac

The linac was built in the Communication Equipment Works of the Mitsubishi Electric Corporation. The main parameters of the linac are shown in table 1.

2.2 Storage Ring

An $0.8GeV$ storage ring of racetrack shape has been designed. This ring has a pair of superconducting bending

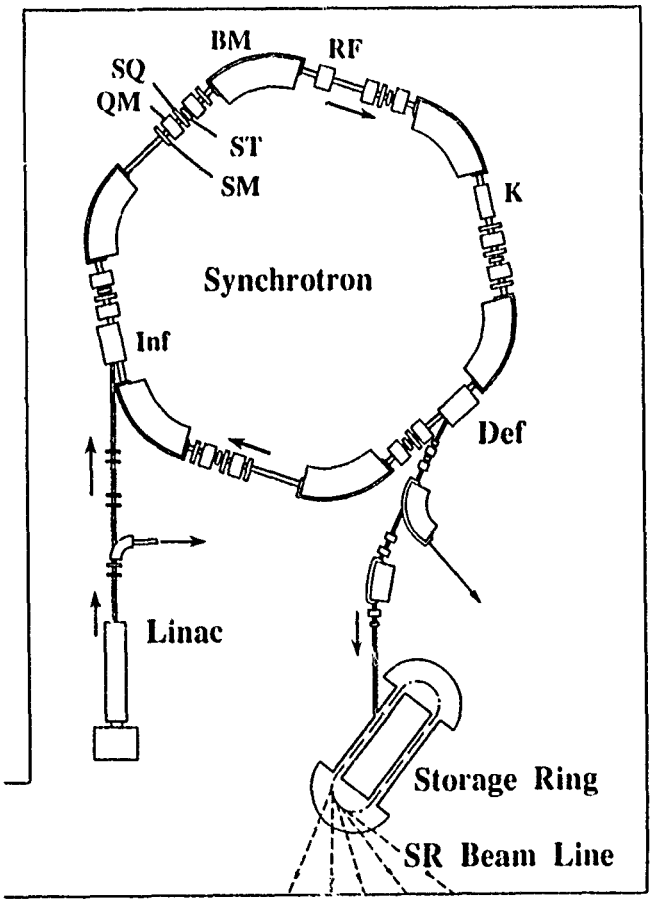


Figure 1: The high-energy electron beam facility and the synchrotron layout. BM: bending magnet, QM: quadrupole magnet, SM: sextupole magnet, ST: steering magnet, SQ: skew quadrupole magnet, RF: RF cavity, Inf: inflector, K: kicker, Def: Deflector

0-7803-0135-8/91$03.00 ©IEEE

Table 1: Main parameters of the linac

Energy	$20MeV$
Current	$100mA$
Pulse width	$2.5\mu sec$
Repetition	$3Hz$
Energy spread	$\pm 0.5\%$
Emittance	$1.3\pi mm \cdot mrad$
Tube length	$1.6m$
Acceleration Frequency	$2.856GHz$

Table 2: Main parameters of the storage ring

Energy	$0.8GeV$
Current	$220mA$
Bending field	$4.5T$
Critical Wavelength	$0.7nm$

magnets with iron shields. The main parameters of the storage ring are shown in table 2.

The beam is mainly injected at the maximum energy ($0.8GeV$), while a beam injected at a lower energy may be accelerated as an option. The magnets and other components are currently being fabricated.

2.3 Synchrotron

The principal function of the booster synchrotron is to provide the accelerated electron beam ($0.8GeV$) to the storage ring. The second function is to store the beam and use it as an SR source.

The layout of the components are shown in figure 1, and the main parameters are shown in table 3.

2.3.1 Lattice

The lattice type is FODO. In order to install sextupole magnets (SM) in every other straight section, the quadrupole magnets (QM) have to be located away from the bending magnet (BM). Hence, a superperiod requires two straight sections resulting in a lattice structure of three sperperiods.

The lattice parameters are summarized in table 4.

2.3.2 Magnets

In addition to the bending, quadrupole, and sextupole magnets, vertical-steering magnets (ST) and skew quadrupole magnets (SQ) are installed. In order to steer the beam horizontally, the trim coils of the bending magnets (BMT) are excited.

Table 5 summarizes the number, strength, and operational mode of each magnet.

Table 3: Main parameters of the synchrotron

Energy	E	1	GeV
Current	I_b	200	mA
Harmonic number	h	15	
Circumference	C	34.59	m
Bending field	B	1.5	T
No. Bends	n_B	6	
Bending radius	ρ	2.22	m
Repetition		2	Hz
Radiation loss	U_0	40	$keV/turn$
Acceleration frequency	f_{RF}	130	MHz
RF Voltage	V_{RF}	100	kV
Coupling factor	κ	0.1	

Table 4: Lattice parameters of the synchrotron

Tune	ν_x	2.23	
	ν_y	1.21	
Strength of quads	K_f	2.39	m^{-2}
	K_d	2.12	m^{-2}
Emittance	ϵ_{x0}	0.405	$\pi mm \cdot mrad$
Energy dispersion	σ_E	0.053	%
Momentum compaction	α_p	0.146	
Beam size	$\sigma_{x max}$	1.73	mm
	$\sigma_{x min}$	0.86	mm
	$\sigma_{y max}$	0.60	mm
	$\sigma_{y min}$	0.32	mm
Bunch length	σ_z	76.9	mm
Quantum lifetime	τ_Q	203	hr

Table 5: Magnet parameters of the synchrotron

	Number	Strength		Mode
BM	6	1.5	T	AC
QM	12	9.5	T/m	AC
SM	6	140	T/m^2	AC
ST	6	0.05	T	DC
SQ	6	1.7	T/m	DC
BMT	6	0.015	T	DC

Table 6: Synchrotron injection and extraction devices

Device	Beam energy		Deflection angle		Pulse width	
Inflector	20	MeV	12	deg		DC
Perturbator	20	MeV	20	$mrad$	3	μs
Kicker	1	GeV	15	$mrad$	0.2	μs
Deflector	1	GeV	21.5	deg	3	ms

Table 7: Design parameters of RF cavity

Cavity inner radius	600	mm
Drift-tube radius	160	mm
Cavity length	350	mm
Acceleration gap	12.2	mm
Q	19700	
Shunt impedance	1.46	$M\Omega$
Maximum field	11	kV/mm
Coupling coefficient	1.80	
Phase angle	$0 \sim -51$	deg
Output power	20	kW

2.3.3 Injection and Extraction

The linac beam is injected through an electrostatic inflector with the aid of three magnetic perturbators. With these devices, eight turns of electrons are captured in a ring acceptance.

The accelerated beam is extracted by a septum magnet (deflector) with the aid of a kicker magnet. For this small synchrotron with a turning time of $115ns$, it is a requirement that the kicker is excited in a short risetime of $40ns$. This fast rise has been achieved by use of a double-ended Blumlein circuit[2]. Table 6 summarizes these injection/extraction devices.

2.3.4 RF system

The design parameters (calculated) of the RF system are shown in table 7.

2.3.5 Vacuum

A pumping system is installed such that a pressure of $10^{-7}Pa$ is maintained when the beam is stored, and a pressure of $10^{-4}Pa$ is maintained for the acceleration mode.

While bellows chambers are currently used for acceleration experiments, flat thin chambers mechanically strengthened with rib structures will be substituted for future storage.

2.3.6 Beam Monitors

The beam monitors installed in the synchrotron are as follows:

- two fast beam current monitors with risetimes of $0.1\mu sec$,
- a direct beam current monitor of one core type,
- a wall current monitor with a risetime of $5ns$,
- six beam-position monitors of $0.1mm$ spatial resolution,
- a betatron-frequency monitor with six knockout electrodes,
- an SR monitor installed in a thin flat chamber in a bending section,
- four screen-monitors,
- a beam scraper with four blades,
- eight gamma-ray monitors distributed around the chamber.

2.3.7 Control System

The beam signals are recorded by computers via CAMAC, GPIB, and RS-232C interfaces. These interfaces are connected to local personal computers and a host computer. All computers are networked using Ethernet.

Two console computers independently work as man-machine interfaces. One can operate the accelerator from the main console, from local stations in the control room, or on-site.

3 Summary

The high-energy electron beam facility of Mitsubishi Electric Corporation consists of a $20MeV$ linac, a $1GeV$ synchrotron, and a superconducting storage ring. The lattice, magnets, injection/extraction, RF system, vacuum, beam monitors, controls of the $1GeV$ synchrotron are presented.

References

[1] S.Okuda, S.Nakamura, T.Yamada, and M.Iwamoto. A high-energy beam facility of Mitsubishi Electric Corporation. In *Topical Symposia on Synchrotron Radiation, Part 1, Status and Prospects of Compact Synchrotrons*, pages 53–54, The Japanese Society for Synchrotron Radiation, 1991.

[2] C.Tsukishima and S.Nakata. Experiment of double-ended blumlein line modulator. In *Proceedings of the General Meeting of the Institute of Electrical Engineers of Japan*, page 7.20, IEEJ, 1989.

The Booster to Storage Ring Transport Line for SRRC

M. H. Wang, C. C. Kuo, C. S. Hsue*

Synchrotron Radiation Research Center
P.O. Box, 19-51, Hsinchu 300, Taiwan, R. O. C
and
*Department of Physics, National Tsing Hua Univ.
Hsinchu 300, Taiwan, R.O.C.

Abstract

A 70 m long booster to storage ring (BTS) transport line has been designed for the SRRC to transport the beam extracted from the booster to the storage ring at 1.3 GeV. The booster is outside the main ring and has a vertical level difference of 4.15 m relative to the ring. The design has been optimized to reach small beam size and to reduce the effects of magnet errors. In total, two families of bending magnets and 17 quadrupoles are used in the BTS line. Diagnostic instruments and correctors are equipped to measure the beam intensity, position, emittance, energy spread and to steer the beam. A method of injection into the storage ring is also presented.

I: Introduction

The injector of SRRC is a 1.3 GeV booster synchrotron. The energy of the booster is ramped from 50 MeV to 1.3 GeV in 10 Hz. The emittance of the beam from the booster is below 3×10^{-7} m·rad and the energy spread is less than 5×10^{-4}. The BTS transport line will transfer the the beam extracted from the booster to the storage ring. The beam size in the transport line should be as small as possible in order to reduce the loss of the beam in the transport line.

II: Design of Transport Line

The layout of the storage ring[1], BTS transport line and the booster are shown in Fig.1. There is a level difference of 4.15 m between main ring and the booster. The beam is extracted from the booster, through the transport line and injected into the ring in the horizontal plane from the inside of the storage ring. The whole BTS transport line is about 70 m long which includes one 9° extraction septum (B1), four horizontal bending magnets (B2,B3,B6,B7) with length of 0.8 m and bending angle ≈10°, two vertical bending magnets (B4,B5) with length of 1.2 m and bending angle of 15°, 17 quadrupoles (Q1~Q17) with length of 0.21 m and one 10° injection septum (B8). The bending magnets are classified into two families which can be powered in series respectively. This will save the cost of construction. The BTS transport line is separated into three achromats and two dispersion free sections. The beam parameters coming from the booster can be matched by using the four quadrupoles (Q1~Q4) in the horizontal achromat between the extraction septum and B3. The beam parameters at the end of the BTS are calculated basing on Tazzari's report "Aperture for Injection" [2]. The β_X is 3 m for a three standard deviation up right elliptical injected beam (α_i=0). It is matched by using the quadrupoles Q14, Q15 and Q16, Q17 in the horizontal achromat between B6 and B8. Special care should be taken in the vertical achromat between B4 and B5 because there is a 7 m long sleeve tunnel which can not be equipped with any

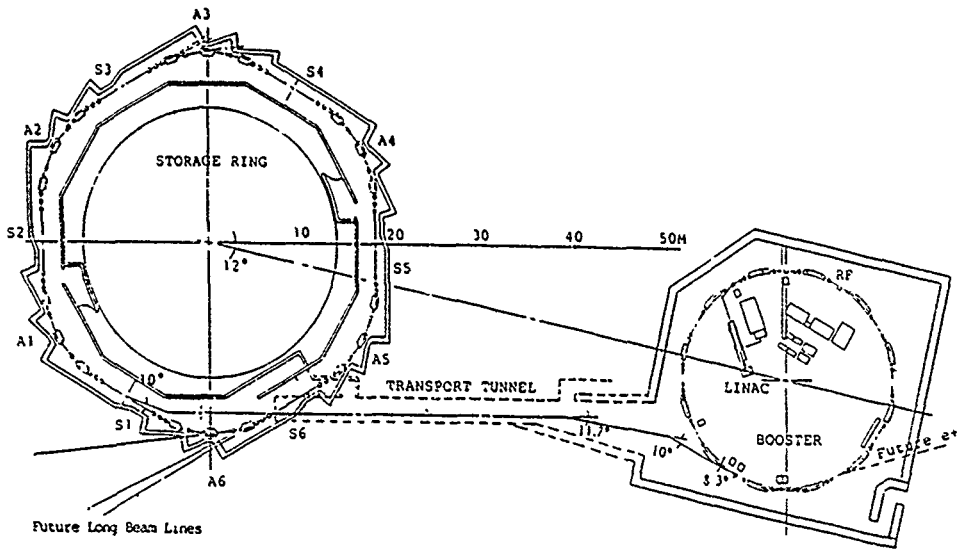


Fig. 1 SRRC Synchrotron Layout

0-7803-0135-8/91$03.00 ©IEEE

components. The optics of BTS transport line has been carefully managed s.t. the β function of the whole line are below 100 m. The maximum β value occurs before Q14 with value of 81 m which corresponds to the beam size of $3\sigma_X$, about 15 mm, with $\varepsilon_X = 3 \times 10^{-7}$. The β_X at the exit of B5 is 57 m which determines the minimum dipole magnet gap. The value of the half magnet gap is 16 mm by taking $3\sigma_X$ plus 3mm for the thickness of vacuum chamber and assembly error. The maximum dispersion function occurs at Q2 with η = -2 m and β = 37 m. The beam size of $3\sigma x$ is 16 mm for $\Delta p/p = 10^{-3}$. All these numbers are well accommodated with dipole gap of 36 mm and quadrupole bore radius of 30 mm. The horizontal and the vertical beam profiles of 3 $\sigma_{x,y}$ with and without dispersion function are shown in Fig.2.

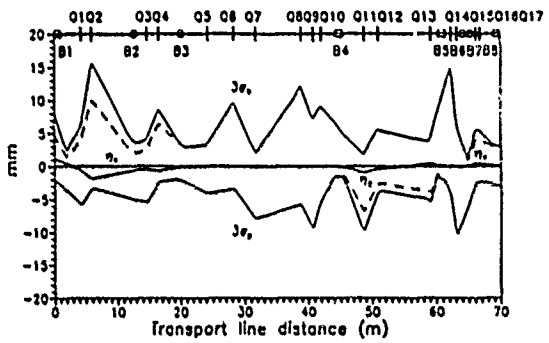


Fig. 2 The horizontal and vertical beam profile of 3 $\sigma_{x,y}$

III: Diagnostic and Correction Scheme

The main task of the diagnostic and the correction scheme in BTS transport line are:

1. Beam position measurement.
2. Energy, energy spread measurement.
3. Emittance measurement.
4. Beam steering.

There are 5 screen monitors and 6 button position monitors in this transport line for beam position measurement. The reason why we use two kinds of monitors is that there are different requirements on commissioning and routine operation and the construction cost can be reduced in this way. The screen monitor, which is a destructive monitor, is mainly used in commissioning stage. Two screen monitors are put between extraction septum and B2 to "see" the beam extracted from the booster and to measure the profile and position of the beam. For the same reason two screen monitors are put between B5 and the injection septum to adjust the beam launch condition. Using any three beam profiles read from screen monitors the emittance of the beam can be calculated. The energy of the beam is obtained by changing the strength of bending magnets and measuring the movement of the orbit. For energy spread measurement the optics are changed by tuning Q1, Q2 and Q3 to blow up the dispersion function and the slit before Q4 is used to measure the beam. The resolution of the energy spread is about 8×10^{-4}. A gap monitor is used to measure the time structure of the beam. Three current transformers are inserted after extraction septum, before Q12 and before injection septum to measure the intensity of the beam. Trim coils in the bending magnet and independent trim magnet after every bending magnet are put as a pair of horizontal and vertical correctors to steer the beam. These correctors combined with the BPM or screen monitors right before the next bending magnet work as a set to correct the orbit. The maximum strength of the corrector is 2 mrad. The location of the diagnostic and the correction elements are shown in Fig.3. A set of typical errors with dipole field error $\Delta B/B = 10^{-3}$,quadrupole displacement error $\Delta x,y = 0.3$ mm and dipole rotation error $\alpha = 0.5$ mrad are put into simulation using application code O.C. developed by ourselves. The results of the beam with these errors before and after corrections are shown in Fig.4.

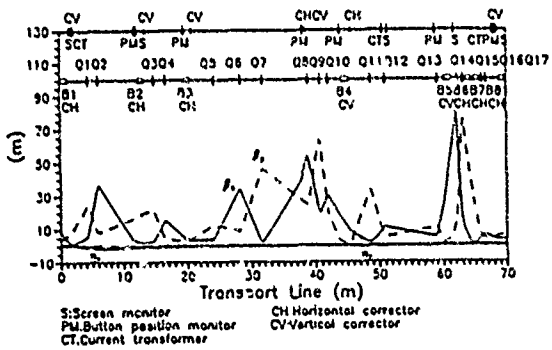


Fig. 3 The diagnostic and corrective scheme

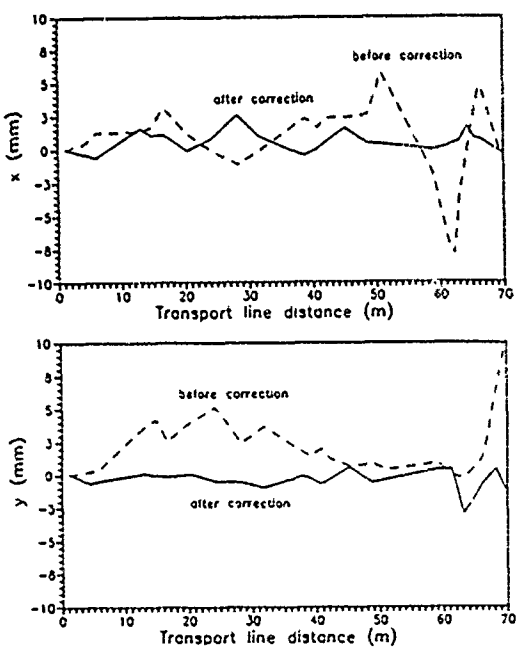


Fig. 4 Orbit distortion before and after correction

A beam dump are reserved after B4. The beam will go straight to the beam dump by turning off the power of the dipole B4. With the screen monitor, BPM and CT placed in the beam dump the beam properties can be studied without interacting with the main storage ring.

IV: Injection Scheme

The injection section is placed in one of the six long straight section of storage ring. The scheme is composed of four 40 cm long fast bumpers and a 1 meter long 2 mm thick septum magnet. The four fast bumpers are symmetrically positioned with respect to the middle point of the long straight section. In this way, all fast bumpers can be of the same strength, independent of the tune, to form a local bump. The septum is located between the two inner bumpers. A schematic layout of the scheme is shown in Fig.5. The oscillation amplitude A at injection is estimated to be $A= 8\ \sigma_0 + ES + 3\ \sigma_i = 14.2$ mm[3]. Where σ_0, σ_i are the stored beam size and the injected beam size at the injection point. ES is the effective septum thickness which includes fringe field effect, vacuum chamber wall and high permeability material for leakage field shielding. It turns out that the aperture required at the injection point determines the Beam Stay Clear (BSC) of the main ring. The BSC at the injection point is 21 mm from the center. Fig.6 illustrate the horizontal phase space acceptance defined by the effective septum position, the bumped ring acceptance, the vacuum chamber wall, the stored beam, the bumped beam, and the injected beam etc. It is shown that the injected beam is accepted by inwardly bumping the stored beam by 17.3 mm. The corresponding strength and field of fast bumper are 11.93 mrad and 1.29 KGauss.

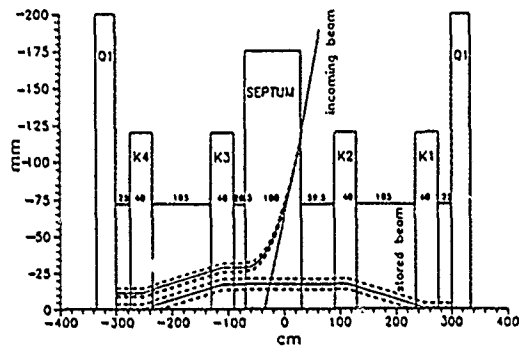


Fig. 5 Schematic layout for injection elements

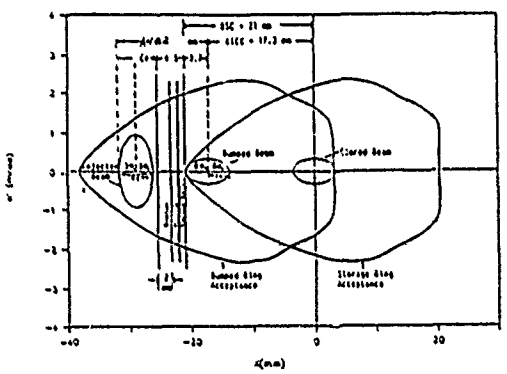


Fig. 6 Horizontal phase space acceptance at injection point

Conclusion:

The design goal of this BTS transport line is to transfer the beam at 1.3 GeV from booster to storage ring efficiently. With the design of the arrangment of the magnets and diagnostic elements this goal can be achieved easily.

Acknowledgement:

We would like to thank Dr. Arie van Steenbergen and Prof. Helmut Wiedemann for their helpful discussions during the design studies of this BTS transport line.

Reference:

[1]: C. S. Hsue, C. C. Kuo, J. C. Lee and M. H. Wang," Lattice Design of the SRRC 1.3 GeV Storage Ring", also presented in this conference.

[2]: S. Tazzari,"Apertures for injection", ESRF-IRM-4/83, 1983.

[3]: C. C. Kuo, S. T. Chou, M. H. Wang and C. S. Hsue," Storage Ring Injection Scheme and Booster to Storage Ring Transport Line", SRRC/BD/89-7, 1989.

Design of Beam Transfer Line and Injection System of Pohang Light Source*

In Soo Ko and M. Yoon
Pohang Accelerator Laboratory/POSTECH
Pohang, Korea 790-600

Abstract

The 2 GeV electron (or positron) beam provided by full energy linac is injected into the storage ring after passing about 100 m long beam transfer line. Since the linac is located outside and 6 m below the ring, the injecting beam is approached to the ring in the vertical plane by Lambertson magnet. Prior to the injection, the orbit of stored beam is deflected toward the septum by using four bump magnets. The injection rate is 10 Hz.

I. Introduction

The injection system of 2 GeV Pohang Light Source (PLS) is a full energy linear accelerator. This 150 meter-long linac is placed at the underground tunnel located 6 meters below the ground level in order to achieve enough shielding at the klystron gallery. The storage ring (SR) is placed on the ground level. The electron beam path is located 1.4 meter above the floor for both linac and storage ring, so the vertical distance of beam paths remains 6 meters. Major change after conceptual design report [1] published January 1990 is that the injection of storage ring is taken place in vertical plane by Lambertson magnet instead of horizontal plane. This vertical injection scheme saves about 45 meters of beam transfer line from previous design. It is also very important that the design and the manufacturing of thin and thick septa and their vacuum chambers are avoided.

The normalized emittance for the electron beam of the linac is 0.015 π *MeV/c cm rad.* It corresponds the emittance at 2 GeV is 7.5×10^{-8} π *m rad.* The energy spread of the electron beam is $\pm$ 0.6% at FWHM. The above values are, in fact, measured at BEPC and found to be well in agreement with the calculation.

II. Beam Transfer Line

The beam transfer line (BTL) provides a dispersion-free, focused beam that is matched to the displaced storage ring acceptance. The BTL consists of three major sections: vertical section, horizontal section, and linac-side section. The horizontal section is bent by 20 degree from the direction of linac. The electron beam goes to the beam dump straightforwardly when the linac is commissioning or testing. Two 10 degree bending magnets and one quadrupole between them are used to form an achromatic section so there is no horizontal dispersion beyond this section. There are 6 quadrupole pairs in the dispersion free space.

The vertical section is made of three vertical bending magnet and a Lambertson magnet, so all the bending is taken place in the vertical plane. The bending angle of these magnets is 8 degrees. The two vertical magnets are formed an achromatic section like the horizontal section with one quadrupole. Another achromatic section is by the Lambetson magnet and nearest vertical bending magnet. In the latter case, two quadrupoles are used instead of one. There are four quadrupoles placed in the dispersion-free space in the vertical section. These quadrupoles are used to match beta and alpha functions at the injection point.

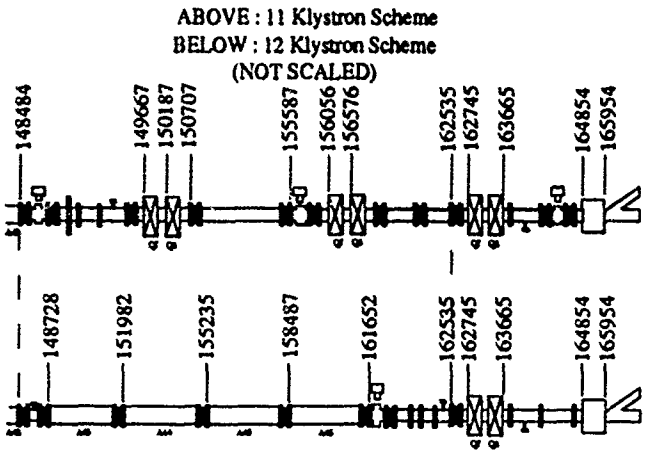


Figure 1. Linac-side BTL. The elements between lines can be replaced for future upgrade.

The linac-side section is shown in Figure 1. Most of this drift section is actually the reserved space for future upgrade of the linac. The distance between the end of

*Supported by POSCO and MOST, Korea

0-7803-0135-8/91$01.00 ©IEEE

42nd accelerating column and the 3rd quadrupole pair is about 14 meters. Four accelerating column will be located in this space when the future upgrade is necessary. This layout provides minimum effort and material loss in case of future upgrade.

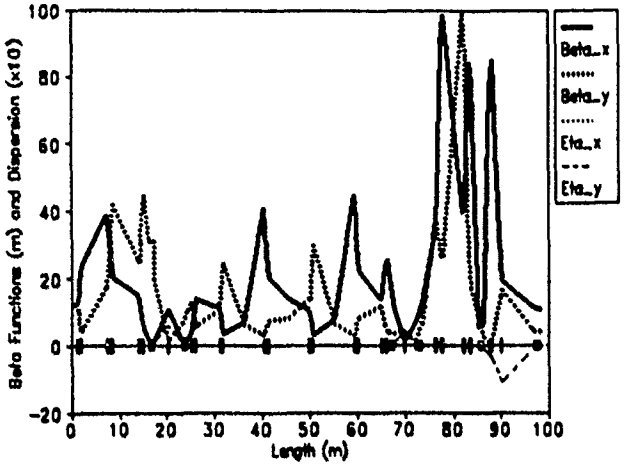


Figure 2. Beta functions and dispersions for BTL lattice.

The lattice functions and the beam envelopes are shown in Figures 2 and 3. Maximum beta function and dispersion are roughly 100 m and 1 m, respectively. The beam envelope is within 8 mm for the electron. Since the positron injection is one of future options, the positron beam is also considered. In this case, the emittance of positron is assumed to be $7.5 \times 10^{-7} \pi$ *m rad* and the maximum beam envelope is about 8 mm.

Table 1. PLS Beam Transfer Line Magnets

Type	Length (m)	Bending Angle	Strength	Units
Bend (H)	1.1	10°	1.0582 T	2
Bend (V)	1.1	8°	0.8465 T	3
Lambertson Septum	1.17	8°	0.8 T	1
Quad	0.4		13 T/m	26

The information of BTL magnet is summarized in Table 1. Maximum quadrupole strength is 13 T/m. BTL vacuum chamber will be made by simple stainless tube. Its outer diameter is 50 mm and, thus, the pole gap of the bending magnet and the aperture of quadrupole are 54 mm.

III. Injection into Storage Ring

A. Bumped Orbit

The length of the injection straight is 6.8 meters. Along this straight, we place four bump magnets and one Lambertson magnet, a typical arrangement for the off-axis, vertical injection scheme. The electron beam passing the last vertical bending magnet is in parallel in horizontal direction with the storage ring bump orbit and it is injected with 8 degrees vertically. The Lambertson magnet then bends this beam by -8 degrees vertically to make it on the same level with the bumped orbit. The schematic diagram of this vertical injection scheme is shown in Figure 4. Here we take the bumped orbit to be 21 mm. This particular value was chosen by considering the injection system hardware arrangement (i.e. space requirement) as well as the good field region requirement for the bump magnets and the storage ring quadrupole magnet.

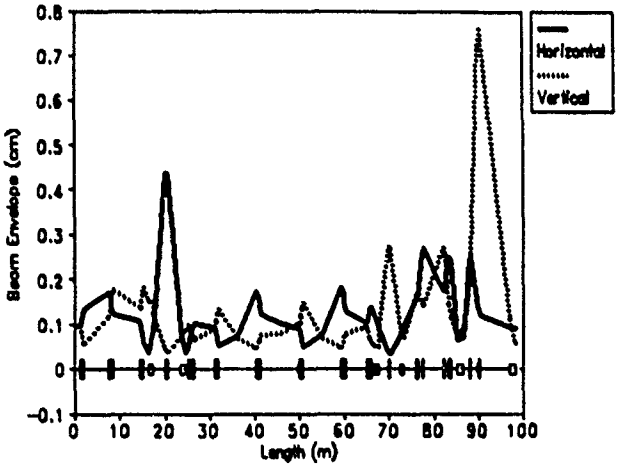


Figure 3. Beam envelopes for BTL. The momentum spread is assumed to be 0.6%.

The clearance between the center of the bumped orbit to the storage ring vacuum chamber is taken to be 4 mm at the position of the Lambertson magnet. Therefore, the physical aperture at this point is 25 mm from the center of the stored beam. This location of the chamber wall seems to be reasonable considering the reduction in dynamic aperture due to various errors in the ring.

The coherent betatron oscillation amplitude, the distance between the center of the bumped orbit to the edge of the injected orbit, was chosen to be 15 mm. This means that the horizontal good field region of the bump magnet should be ±36 mm because the good field region of the bump magnet has to include the injected beam from the beam transfer line. In the vertical direction, the good field region of the bump magnet is taken to be ±9 mm.

Unlike thin or thick septum, the septum wall of the Lamberson magnet is located in the air, so the vacuum chamber thickness of both BTL and SR must be included for

the effective septum thickness. The effective thickess is 4 mm including gaps between chambers and the Lambertson magnets. Figure 5 shows this thickness and other dimensions at the injection point.

The horisontal phase space acceptance of the storage ring is given by

$$A_x = \frac{(x_b + 4\sigma_o)^2}{\beta_{x_o}},$$

where x_b is the bumped orbit (=21mm) and σ_o is the *rms* value of the horisontal beam size at the injection point which is 0.387 mm. β_{x_o} is the horisontal beta function at the injection point ($\approx$ 10 m). Substituting these values yields $A_x = 50\ mm\ mrad$ which is sufficient to accept the injected beam. In the vertical direction, the acceptance is $A_y = 40\ mm\ mrad$.

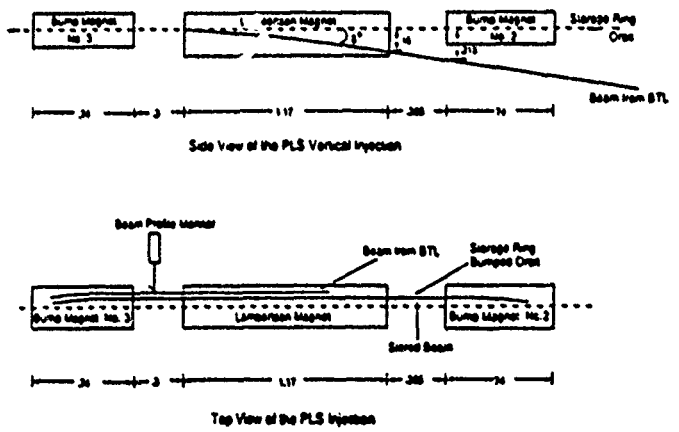


Figure 4. Schematic diagram of vertical injection.

B. *Injection Hardwares*

The required magnitide of the kick for 4 bump magnets is obtained from

$$x_b = L \times \tan\left(\frac{B_b l_b}{B\rho}\right),$$

where L is the distance between the centers of the first two bump magnets. B_b and l_b are the magnetic field and the length of the bump magnet, respectively. $B\rho$ is the usual magnetic rigidity in Tesla-meter which is 6.67 for a 2 GeV electron. By taking 0.74 m for the effective length of the bump magnet and 1.26 m for L, the required magnetic field for a bump magnet to produce 21 mm bumped orbit is found to be 1.5 kG at 2 GeV. The kick angle of the bump magnet is then 16.64 mrad.

The bump magnet is operated with 10 Hz repetition rate. Therefore, the pulse to pulse seperation is 100 msec which is about 6 damping times of the storage ring. The excitation of the bump magnet has a 4 μsec half-sine waveform so the rize and fall time are respectively 2 μsec. Thus, the injected beam will restore the original stored orbit in less than three orbital turns (the revolution time of the storage ring beam is 0.94 μsec).

For bump magnet power supply, the required peak current is 4,775 A when the gap height of the bump magnet is 40 mm and the required peak voltage per each magnet is 8.33 kV.

The Lambertson magnet is 1.17-m long and the maximum field is 8 kG. Since the bending angle of the Lambertson magnet is 8 degrees, the distance between the stored beam orbit and the injecting beam path is 16 cm at the entrance of the Lambertson magnet and 21.5 cm at the nearest bump magnet. Thus the bottom of this bump magnet must clear the BTL vacuum chamber. In the drift space between the Lambertson magnet and the bump magnet located at the downstream, the injected beam profile can be measured by using a destructive profile monitor. The enclosure for the placement of this monitor will be kept at low vacuum. The BTL vacuum and the storage ring vacuum will be separated by thin foils at this low vacuum enclosure.

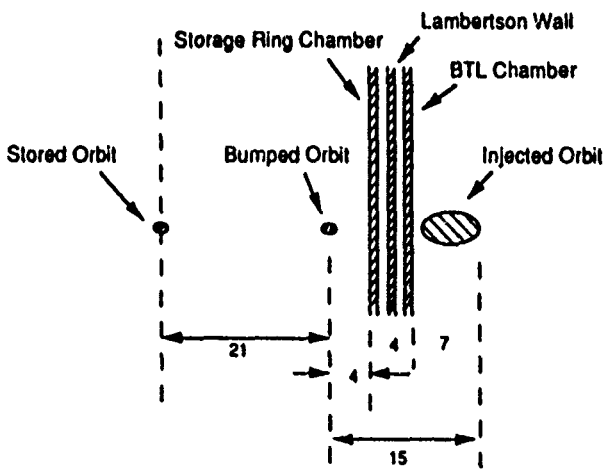


Figure 5. Schematic diagram of cross section at the injection point.

Four photon stoppers are allocated in order to prevent the photon beam from hitting the ceramic vacuum chamber walls of the bump magnet. A number of smooth transition pieces are also placed between various vacuum chambers in order to reduce the RF impedance seen by a beam. Two pneumatic gate valves are placed at each side of the straight section to seperate the remaining storage ring section from injection region.

IV. References

1. Conceptual Design Report of Pohang Light Source, January 1990, POSTECH.

Beam transport to the SXLS ring

Eva Bozoki*
National Synchrotron Light source, BNL, Upton, NY, 11973.

Abstract

Design of a transport line with highly restrictive space and beam size requirements and with flexibility in the orientation of the injector is presented. An analytic method, based on symbolic algebra is used to find optimal regions of the design parameters. The fine tuning of the parameters were then performed with a standard matrix program. Special interest was paid to the question of dispersion vector matching large angle bend with very small bending radius using non-iron bending magnets with very small gap area.

1. Introduction

The SXLS ring [1] is a superconducting compact synchrotron/storage ring of 8.5 m circumference, runing at 696 MeV and providing $\lambda_{critical}$=10 A for x-ray lithography. It is a two superperiod machine consisting of two superconducting combined function bending magnets, four warm quadrupoles and four warm sextupoles. Injector is a 200 Mev LINAC [2]. Injection takes places at one of the straight sections immediatelly before the ring quadrupole (see Fig. 1). It has to fit into the small space left by the beam line, the cryostat and other elements of the densely packed compact ring. On the other hand, the presence of iron close to the superconducting ring dipoles has to be avoided.

The transport line consists of a triplett, followed by an achromatic bend (29°) with horizontal/vertical waist in the middle to allow matching of 1% momentum spread from the LINAC to the 0.1% momentum spread in the ring. This is followed by a quintuplett, which basically serves to match the phase space ellipses into the ring, and finally a total of 151° bend. This last bend consists of two combined function bending magnets with small radius of curvature (B≥2 T) and a septum. There is also a quadrupole between the two bending magnets, separated by drift spaces from them. This last 151° bend will bring the beam parallell with the stored beam as well as match the dispersion and its derivative into the ring. The high field bending magnets and quadrupole will be pulsed non-iron magnets. The design, as shown on Fig. 1, is such, that by reversing the direction of a 29° achromatic bend in the transport line, the LINAC can be lined up either with the long axis of the ring or with the closest beam line, thus making future installation flexible.

*Work performed under the auspices of the U.S. Department of Energy, contract DE-AC02-76CH00016.

0-7803-0135-8/91S03.00 ©IEEE

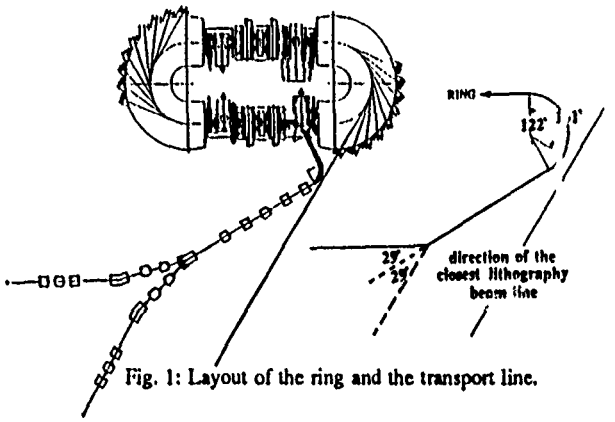


Fig. 1: Layout of the ring and the transport line.

2. Geometry considerations

The septum magnet is in one of the straight sections immediatelly before the ring quadrupole. From the values of the machine parameters at that point of the ring, the matching conditions can be obtained.

It is desirable to limit the presence of iron in the proximity of the superconducting coils of the 180° ring dipole. The only element, where iron is needed (to confine the flux) is the pulsing septum. The maximum achievable bending field in the septum is 1.1 - 1.3 T, and this dictates a minimum bend of 9° to clear the vacuum pipe.

To establish the geometry of the injection into the ring let us imagine to proceed in the reverse direction, from the septum towards the linac, bending the beam to the right, away from the ring. After the septum (in the reverse direction), the *minimum bending field, in order to clear elements in the ring as well as the cryostat itself, is 2.5 - 2.0 T*, the lower field corresponding to the higher operating field in the septum. The larger the bending field is, the more compact the final injection can be made and the easier it is to clear all ring elements as well as the lithography beam lines. From purely geometrical considerations, *to keep as far as possible from the lithography lines, B = 3 T would be preferable to 2 T.* Calculations in the following sections will be shown for both, B = 2 and 3 T.

The minimum total bend (including the septum) is 122°, dictated by the closest lithography beamline. Instead, we chose this bend to be 151° for the following two reasons. Since the SXLS machine is a prototype, it will be more flexible if the design allows future installations at the customer's site with two different linac orientation. This can be achieved if the magnitude of the total final bend (θ_{tot}), and the momentum spread matching achromatic bend (θ_{achr}), are chosen such that: $\theta_{tot} \pm$

θ_{achr}=180° or 122°. These conditions yield θ_{tot} = 151° and θ_{echr} = 29°. The second reason is that, as it will be discussed later, the larger the total bend is, the easier is to match the dispersion vector into the ring.

3. Dispersion matching bend

The final 151° bend has to provide dispersion vector matching into the ring besides bending the injected beam parallell with the stored beam. As a consequence, the bend after the septum (still in reverse direction) is broken into two bending magnets with a horizontally focusing quadrupole between them. The strength (k_q) and location (i.e. the θ_3, θ_4 split of the total $\Theta=\theta_{tot}-\theta_{septum}$=142° bend) of the quadrupole is chosen to match the $\eta_T = \eta_T' = 0$ in the transport line with η_R = -1.2, η_R' = -.6 in the ring. One would like to make the bend as compact as possible (no or very short drift spaces and short quadrupole) in order to clear the closest lithography beam line. It turns out, however, that *it is impossible to match the dispersion vector without drift space* with either B = 3 T or with B = 2 T.

Consider a horizontal composite bend (vertical can be treated similarly), consisting of two bending magnets with bending fields B_3 and B_4, bending angles θ_3 and θ_4 ($\theta_3+\theta_4=\Theta$) and field indices of n_3 and n_4 with a horizontally focusing quadrupole between them. The quadrupole is separated from the dipoles by L_3 and L_4 drift spaces. The length and the strength of the quadrupole is l_q and k_q (=B'/Bρ). Calculating the standard second order transport matrix of the bend as:

$$M=M^{B_2}\,M^{L_1}\,M^{Q}\,M^{L_2}\,M^{B_1},$$

the resulting η and η' will be:

$$\eta = \eta_a + q_{12}b_{11}\eta'_b + q_{21}(L_1\eta'_b + \eta_b)(b_{11}L + b_{12}) +$$
$$q_{11}[b_{11}\eta_b + (b_{11}(L_1 + L_2) + b_{12})\eta'_b] \qquad (1a)$$

$$\eta' = \eta_a + q_{12}b_{21}\eta'_b + q_{21}(L_1\eta'_b + \eta_b)(b_{21}L_2 + b_{22}) +$$
$$q_{11}[b_{21}\eta_b + (b_{21}(L_1 + L_2) + b_{22})\eta'_b] \; . \qquad (1b)$$

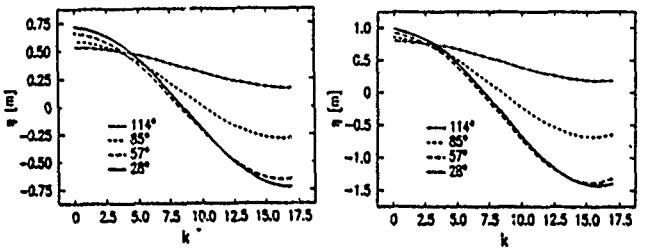
In eqs.(1) q_{ij} are the quadrupole matrix elements and a_{ij}, η_a and η'_a are the matrix elements representing the B_1 dipole. The b index refers to the B_4 dipole.

Eqs.(1) can be written in a simple format if $L_1=L_2=0$, $\rho_3=\rho_4$, $n_3=n_4$ and if the thin lens approximation for the quadrupole is valid ($q_{11}=q_{22}=1$, $q_{12}=0$ and $q_{21}=-\delta=-1/f_x$):

$$\eta=\frac{\rho}{h^2}\left\{1 - \delta\,\frac{\rho}{h}[1 - C(h\theta_3)]S(h\theta_4) - C(h\Theta)\right\} \qquad (2a)$$

$$\eta'=\frac{1}{h}\left\{-\delta\,\frac{1}{h}[1 - C(h\Theta)]S(h\theta_4) + 1 - C(h\Theta)\right\} \qquad (2b)$$

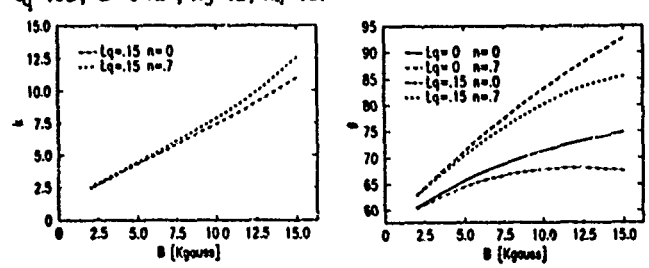
η was calculated from eq.(1a) at $B_3=B_4$=3 and 2T, and is plotted on Figs.2 as a function of k_q for $L_1=L_2=0$, $n_3=n_4$=.5, Θ=142°, l_q=.15m and different values of θ_4.



Figs. 2: η as a function of the quadrupole strengths for different values of θ_4 at (a) B=3T and (b) B=2T.

One can see, that there is a minimum value of the $\eta(k_q)$ function which can be reached with a given set of parameters. *The minimum and the location of the minimum (k_q) sligthly depends on the gradient in the bending magnet but strongly depends on the bending field, on the θ_3, θ_4 split of the total bending angle and on the quadrupole lengths:* It can be shown, that (a) lower bending field or larger field index help in lowering η_{min} and k_q, (b) longer quadrupole results in weeker quadrupole, but increases η_{min}, (c) smaller θ_4 results in strongly lower η_{min}, and slightly weeker quadrupole, and (d) η (and η') has a minimum as a function of Θ, and this minimum is reached at 180°.

Let us now consider the conditions of dispersion vector matching. The eqs.(1) nonlinear equations have to be solved for the strength (k_q) and location (θ_4) of the quadrupole with a given set of the remaining eight parameters; Θ, ρ_3, ρ_4, n_3, n_4, l_q, L_1 and L_2. First, we will explore the most compact geometry, when $L_1=L_2=0$. The solutions can be seen on Figs.3, where k_q and θ_4 are plotted as a function of the B bending field with n=.0 and .7 field indices and l_q=.15m quadrupole length. One can see, that already at B=1.5T strong quadrupole (k_q >10) is needed. For higher bending fields, drift spaces have to be allowed. On Figs. 4, k_q and θ_4 are plotted as a function of the L_1 drift space with L_2 as parameter and with B=3T, l_q=.15, Θ=142°, n_3=.8, n_4=.6.



Figs.3: Location (θ_4) and strengths (k_q) of the matching quad is shown as a function of the B bending field for Θ=142°, l_q=.15m. and n=.0, .7

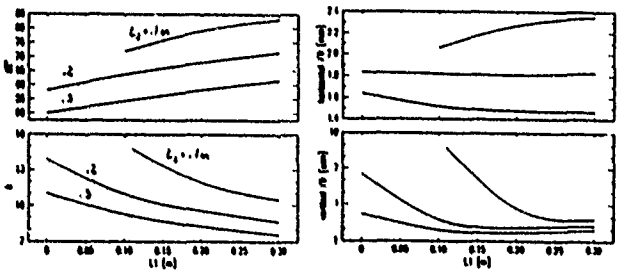
In addition to matching the beam into the ring, the beam size have to fit within the very small aperture (≈1.0-1.5cm^2) of the pulsing bending magnets. The beam size, divergence and orientation of the phase space ellipse are given by the matrix elements as:

$$x=\sqrt{\Sigma_{x,11}},\quad x'=\sqrt{\Sigma_{x,22}},\quad \alpha=\frac{r}{\sqrt{(1-r^2)}},\quad \text{where } r=\frac{\Sigma_{x,12}}{\sqrt{\Sigma_{x,11}\Sigma_{x,22}}}$$

and similar expressions for the vertical case. The Σ matrix transforms as

$$\Sigma = M\,\Sigma^0\,M^T.$$

Proceeding in the reverse direction, that is starting with the desired horizontal and vertical phase space ellipses at injection, the Σ matrix was calculated before the B_3 bending magnet using the previously obtained solutions for the strengths and location of the dispersion matching quadrupole. The calculated H and V beam sizes are also plotted on Figs. 4 as a function of L_1 with L_2 as parameter for Θ=142°, B=3T, l_q=.15m and n_1=n_2=.6. One can see, that only solutions with $L_2 \geq .2$m and $L_1 \geq .1$m yield reasonably small horizontal and vertical beam sizes at the same time.



Figs. 4: θ_4, k_q, and the horizontal/vertical beam sizes, calculated to match the dispersion vector are shown as a function of L_1, while L_2 is used as parameter. Θ=142° n_3=.8, n_4=.6, and l_q=.15 m.

One can see from the above analysis, that *at B=3T either the beam size can be kept small* (≈1cm²) *or all beam lines can be cleared, but it is difficult to satisfy both criteria at the same time.* The solutions which clear the beam lines require stronger quadrupoles (therefore the resulting beam size is larger). By increasing the length of the quadrupole the strengths is decreasing, (but of course, at the same time the length of the bend is also increasing). By lowering the bending field to B=2T, weeker ($\delta \approx 1/\rho$) quadrupole is needed to match the dispersion vector, and therefore the horizontal focusing/vertical defocusing will be less. However, this is more then compensated for by the increase in the length ($l \approx \rho$) of the bending magnet. As a net result, the $\sigma_{x,y}$ beam size will even slightly increase. However, the gap area of the non-iron dipoles can be increased by the same ratio as the bending field is decreased.

In Table-1, three cases of the 142° bend are presented. The first case cuts one beam line, the second barely and the third safely avoids all of them.

Table-1
Parameters of different dispersion matching bends with Θ = 142°.

$L_{1,2}$ m	$B_{3,4}$ T	θ_4	$n_{3,4}$	B' T/	l_Q m	σ_x cm	σ_y cm	$(3\sigma)^2$ cm²
.10-.3	3	48	.8-.60	29	.25	.28	.43	1.08
.15-.2	3	58	.8-.60	51	.15	.34	.38	1.16
.10-.2	2-3	62	.8-.55	54	.15	.42	.45	1.70

4. Achromatic bend / Momentum dispersion matching

The 29° achromatic bend serves to match the original 1% momentum dispersion to that of .1% in the ring. It consists of two 14.5° bending magnets operating at .582 T bending field (l=.29 m, ρ=1.146 m) and two 15 cm long quadrupoles separated from each other by 30 cm to accomodate the aperture (on which the beam is focused). The quadrupoles are separated from the dipoles by 25 cm drift spaces.

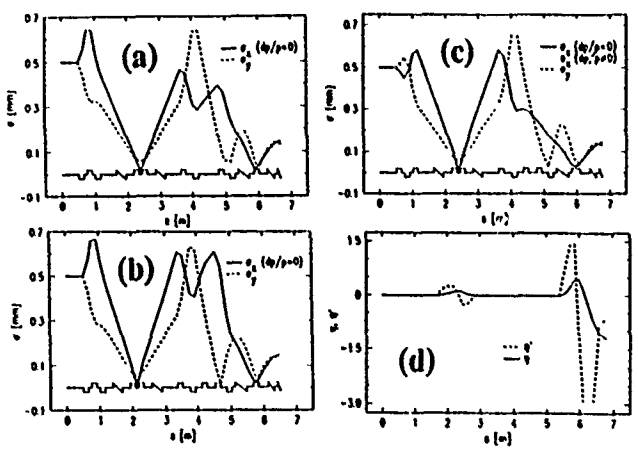
The beam is focused at the middle of the achromatic bend with the help of the $Q_{1,2,3}$ quadrupole triplett after the linac.

5. Phase space ellipse matching

After the achromatic bend, a quadrupole quintuplett is used to match the horizontal and vertical phase space ellipses from the slit through the second half of the achromat and through the 151° dispersion matching bend into the ring.

6. Beam envelope and accuracy of matching

The location and the strengths of the quadrupoles as well as the beam envelope through the whole transport line for the three cases presented in Table-1 are shown on Figs. 5. The quadrupole strengths are somewhat different for the three cases, but the quadrupole locations were kept the same. In all three cases the match of the dispersion vector and the phase space ellipses into the ring are good to the third decimal place The dotted line on Fig. 5b shows the effect of δp/p=1% in the 29° achromatic bend and the effect of the δp/p=.1% in the 151° final bend. The dispersion and its derivative is shown of Fig. 5d. The effect of $\delta p/p \neq 0$ and the behaviour of η and η' are very similar for all cases.



Figs.5: Horizontal and vertical beam envelopes through the whole transport line, for cases presented in Table-1.

7. References

[1] J.Murphy et all,"Comissioning of the SXLS ring at Brookhaven", *These Proceedings.*

[2] P.Letellier et all., "Comissioning of the 200 MeV Injector Linac", *Proc. IEEE Conf. on Accelerator Physics, 1989.*

Design and Simulation of Fast Pulsed Kicker/Bumper Units for the Positron Accumulator Ring at APS*

Ju Wang and Gerald J. Volk
Argonne National Laboratory
9700 South Cass Avenue
Argonne, Illinois 60439

Abstract

In the design of fast pulsed kicker/bumper units for a positron accumulator ring (PAR) at APS, different pulse forming networks (PFN) are considered and different structures for the magnet are studied and simulated. This paper describes some design considerations and computer simulation results of different designs.

I. INTRODUCTION

Three fast pulsed kicker/bumper magnets are required in PAR for the beam injection and/or extraction at 450 MeV. These magnets have the same design because they have identical specifications and are expected to produce identical magnetic fields. Each kicker/bumper magnet is required to generate a magnetic field of 0.06 T with a rise-time of 80 ns, a flat-top of 80 ns and a fall-time of 80 ns.

A fast pulsed magnet system normally consists of a high voltage dc power supply, charging/discharging switches, a PFN, and a magnet assembly consisting of a ferrite magnet, a matching capacitor or capacitors and a load (termination) resistor. The primary objective of this study is the design of the PFN and magnet assembly.

II. PULSE FORMING NETWORK

There are various configurations for pulse forming networks [1]. The simplest one is to use coaxial cables (transmission lines) as the PFN. For this kind of PFN, the duration of the pulse waveform is equal to twice the cable length divided by the propagation velocity of the cable. It is usually used for pulses with durations under 100 ns.

The second way is to use equal inductors and capacitors to construct PFNs. This type of PFN is actually a lumped equivalent to coaxial cables and, hence, behaves similarly to coaxial cables. They are normally used to generate pulses with durations over several hundred nanoseconds.

Another type of PFN is called a type-C Guillemin network. For a type-C Guillemin network, Fourier analysis is used to calculate the frequency components of the desired waveform. Then multiple L-C branches are connected in parallel with each L-C branch generating one frequency component. The number of the L-C branches depends on the requirement of the waveform. There are other types of Guillemin networks. Some of them are different variations of the type-C network.

Among many types of PFNs, the best candidates for the PAR kicker/bumper are coaxial cables and the equal L-C network. In the design, a combination of coaxial cables and an equal L-C network with damping resistors is used. The cable section of the PFN consists of two 12 meter paralleled cables. The cable impedance is approximately 13 Ω, the inductance is 101.7 nH/m and the capacitance is 377.3 pF/m. The propagation velocity of the cable is 0.161 m/ns. The equal L-C section of the PFN is made of the magnet and the matching capacitors. Since a capacitor or capacitors have to be added to the magnet to match the cable impedance in order to minimize the reflections between the cables and the magnet, it will be advantageous if the magnet can contribute to the pulse forming network. With the capacitors matching the above cables, the magnet is equivalent to two 4.15 meter paralleled cables. It takes 25.7 ns for the current and voltage to pass through the magnet.

III. MAGNET

A window-frame magnet has been proposed in the design. This magnet is 35 cm long and has an air gap of 11 cm by 5.3 cm. The air gap size is determined by the sizes of the vacuum chamber and copper conductors with the insulations. The cross section of the magnet is shown in Figure 1.

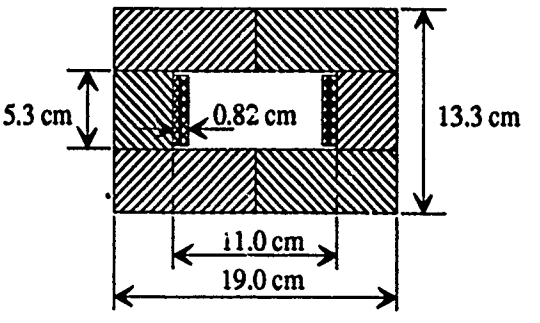


Figure 1. Cross section of the PAR kicker/bumper magnet

Assuming that the magnetic field inside the air gap is uniform and the magnetic field intensity inside the ferrites is negligible compared with that in the air gap, the flux density, **B**, in the air gap can be calculated as

* Work supported by U.S. Department of Energy, Office of Basic Energy Sciences under Contract No. W-31-109-ENG-38.

U.S. Government work not protected by U.S. Copyright.

$$B = \frac{\mu_0 I}{g} \quad (1)$$

where I is the current in the coil and g is the air gap length. Equation (1) can be solved for I when B is given. For the magnet in Figure 1, to generate a magnetic field of 0.06 T, the required current will be 2530.56 A.

The inductance of the coil can be calculated as

$$L = \frac{\mu_0 w l}{g} \quad (2)$$

where w is the air gap width, the distance between the centers of two conductors, and l is the magnet length if the end effect is ignored. For the given geometry, the magnet inductance, L, is equal to 844.8 nH.

Since the rise-time of the current, hence the rise-time of the magnetic field, mostly depends on the magnitude of the inductance, the inductance of the magnet needs to be as small as possible. The total inductance is fixed for the given geometry of the magnet. The only way to reduce the inductance is to divide the single-turn coil into two half-turn coils. In doing so, the inductance seen by the cables is reduced to one half. However, the number of required cables is increased by a factor of two.

The magnet will be constructed with ferrite CMD5005, by Ceramic Magnetics, Inc. The thickness of the ferrite blocks is selected as 4 cm. This results in a magnetic field of about 764 Gauss inside the ferrites, below its saturation field. Thin copper films will be inserted into the top and the bottom ferrites to completely decouple two half-turn coils.

IV. Impedance Match of the Magnet and the Coaxial Cables

To match the magnet with the cables, the ideal way is to build the magnet with a coaxial structure. However, the size of the required aperture for the beam is relatively large and the cable impedance is relatively small, so it is very difficult to build a coaxial magnet that has a large air gap and a small impedance. Therefore a window-frame magnet is chosen and a lumped capacitor or capacitors will be added to the magnet to match the cable impedance. Since the magnet is a lumped element, to better match the cables the magnet can be divided longitudinally into several sections with multiple capacitors. Ideally, the more sections the magnet is divided into, the better it matches the cables. However, the number of sections cannot be very large due to the limitation of the physical sizes of the magnet and the capacitors. In this design, the magnet is divided into 4 sections.

Now that the magnet is divided by the capacitors, it can be part of the pulse forming network and is precharged to the PFN voltage. When the discharge switch (thyratron) is closed, the current will travel through the magnet back to the input of the PFN. The minimum rise-time of the current in the termination resistor is approximately equal to

$$T_{r,term} = \frac{\pi\sqrt{L_{1/2}C}}{8} \quad (3)$$

where $L_{1/2}$ is the half-turn magnet inductance and C is the total capacitance of the capacitors added to one half of the magnet. With the given cable and magnet parameters, a total capacitance of 6.26 nF will be required. Each capacitor is 1.56 nF and each section of the magnet is 105.6 nH.

Substituting $L_{1/2}$ and C into equation (3) gives the minimum rise-time of the current in the termination resistor as 20.2 ns. The minimum rise-time of the magnetic field of the whole magnet will be the sum of $T_{r,term}$ and the time required for the current to pass through the magnet, and will be 45.9 ns.

Even if the magnet is divided into multiple sections, it still cannot match the cables perfectly. There exist voltage and current oscillations between the capacitors and the magnet, which destroy the flat-top of the magnetic field. Hence, resistors need to be added to the capacitors to damp the oscillations. But, the damping resistors slow down the rise-time of the current, especially when the circuit is critically damped. Because the damping resistors are unavoidable, a compromise has to be made between the rise-time and the flat-top. According to the computer simulations, the best result is obtained when the circuit is slightly under damped and the corresponding resistance of the damping resistors is 6.5 Ω.

V. Computer Simulation of the Circuit

A basic circuit diagram of the kicker/bumper unit is shown in Figure 2. This circuit has been simulated with PSpice program, by MicroSim Corporation, Irvine, CA.

In the simulation two different cases were considered for the cables. One assumed that the cables were lossless. The other took into consideration the copper losses of the cables. In the case of the copper losses, the skin effect was taken into account by using equation (4) to estimate the resistance [2].

$$r = 8.3(f)^{1/2}\left(\frac{1}{d}+\frac{1}{D}\right) \quad \mu\Omega/m \quad (4)$$

In equation (4), f is the frequency, d and D are the cable diameters in centimeters at the inner conductor and the outer conductor, respectively. According to the required pulse width, f is approximately 4 MHz. Diameters d and D are 3.64 and 2.25 cm, respectively. The estimated cable resistance is 0.0119Ω/m, about five times the dc resistance.

The simulations show no significant effect on the rise-time and the flat-top due to the copper losses. Only the PFN voltage needs to be slightly higher when the copper losses are considered. The losses in the dielectrics could not be included in the simulation because no data are available.

The thyratron is represented by a 100V dc voltage source and a 20 nH inductor (suggested by the manufacturer). This may have over simplified the turn-on process of the

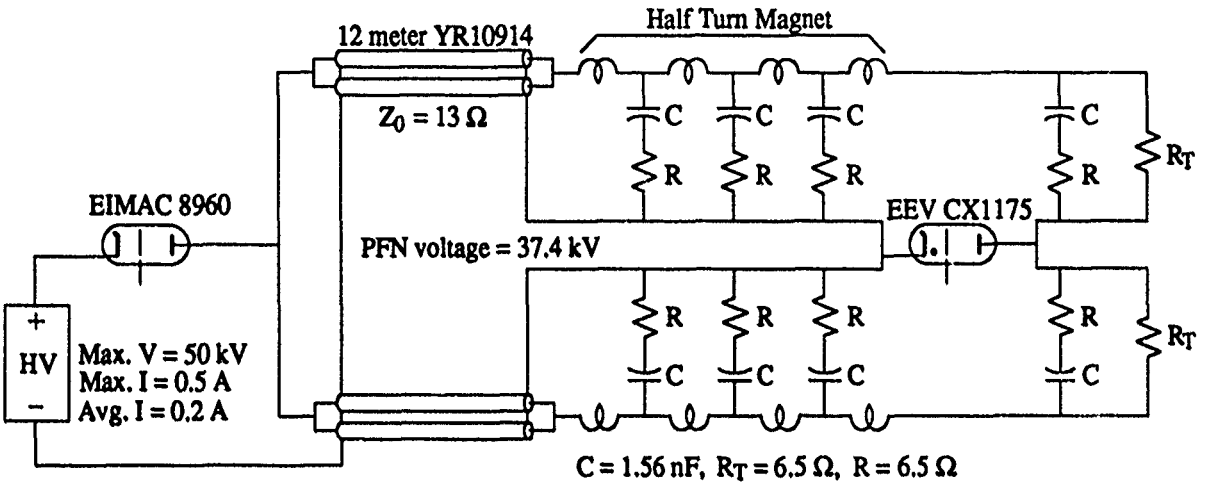


Figure 2. Circuit diagram of the kicker/bumper unit for PAR

thyratron. In reality, the turn-on process may take a longer time than that due to a 20-nH inductor. If a longer turn-on process does happen, a saturable magnet can be added to the anode (or cathode) of the thyratron. This technique can significantly reduce the turn-on time. Furthermore, it may also extend the life time of the thyratron [3,4].

The simulations were also done for the circuit with only one matching capacitor for each half-turn magnet, and the circuit with the magnet divided by multiple capacitors but no damping resistors. The results show that the circuit shown in Figure 2 produces the best current waveform.

Figures 3 through 6 show some simulation results.

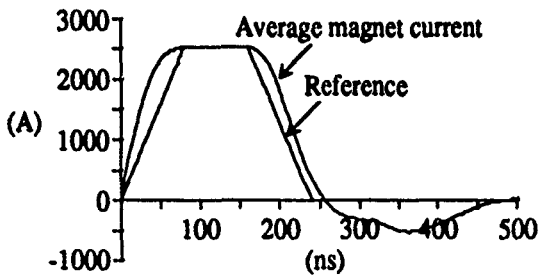


Figure 3. Simulation result for the circuit in Figure 2.

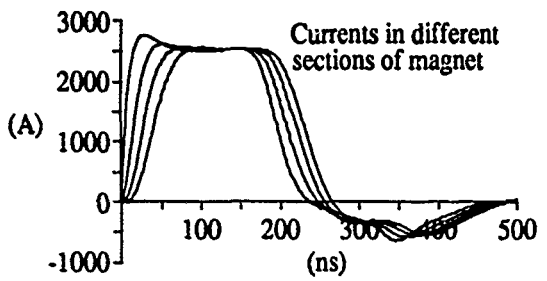


Figure 4. Simulation result for the circuit in Figure 2.

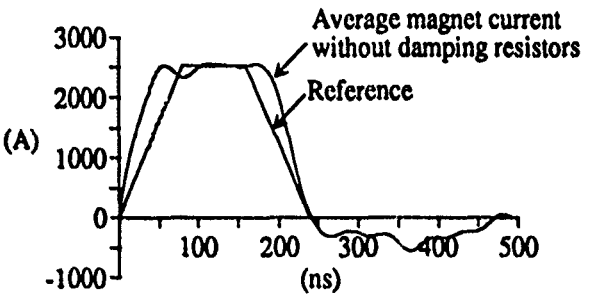


Figure 5. Average magnet current for magnet without damping resistors.

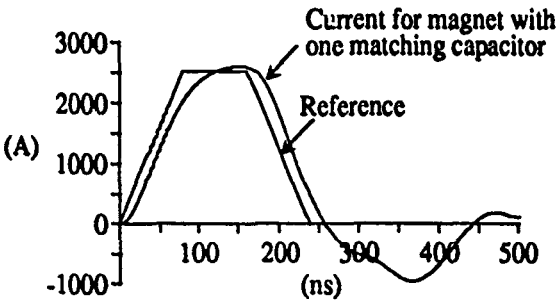


Figure 6. Currents for one half-turn magnet with only one matching capacitor.

VI. REFERENCES

[1] Sarjeant, James W. and Dollinger, R. E., *"High-Power Electronics,"* TAB BOOKS Inc., 1989.

[2] Giacoletto, L. J., *"Electronics Designers' Handbook,"* Second Edition, McGraw-Hill Book Company.

[3] Ducimetière, L. and Fiander, D. C., "Commutation Losses of a Multigap High Voltage Thyratron," *19th Power Modulator Symposium*, San Diego, CA, June 26-28, 1990.

[4] Rust, Ken and McDuff, Glen, "Life Extension of Thyratrons in Short Pulse Circuits with the Use of Saturable Magnetic Sharpeners," *19th Power Modulator Symposium*, San Diego, CA, June 26-28, 1990.

Magnets with Full Apertures for Extracting Synchrotron Radiation at the Photon Factory Ring

Yukinori KOBAYASHI, Akira ARAKI and Yukihide KAMIYA

Photon Factory, KEK, 1-1 Oho, Tsukuba-shi, Ibaraki-ken, 305 Japan

I. Introduction

For the next-generation synchrotron radiation (SR) sources, ring magnets should be designed to accommodate the vacuum chamber such as an antechamber, which lets intense synchrotron radiation from an insertion device to pass through and can reduce gas load produced by the photodesorption due to synchrotron radiation. Such kinds of magnets with iron yokes of largely deformed shape or with a missing part of yoke have been widely adopted in the SR rings planned or being constructed[1].

At the Photon Factory, we designed a set of magnets with apertures enough to extract almost all synchrotron radiation from the upstream bending magnet. These magnets are a quadrupole, a sextupole and a vertical steering. After the field measurement in the summer shutdown of 1990, they were positioned in the lump on a common magnet-base in the ring, taking the place of the then-existing magnets (see Fig. 1). On the restart of the ring operation in the following autumn, no harmful effect was observed on the circulating beam and since then the magnets are being operated without any trouble. In this paper, we will report the magnet designs, the field measurement and the effects of the magnets on the beam orbit.

II. Design Specifications

Before constructing the magnets, calculations of magnetic field were made using the program LINDA[2] for various types of the magnets, particularly, for those of the quadrupole, because it might have an effect on the beam more dangerous than the others; the sextupole and the vertical steering.

Quadrupole Magnet

For the quadrupole, we first investigated several types of magnet that simply had a deformed part of iron yoke not so as to interfere with SR being extracted. The field calculation showed that these types had quite the same field quality as usual types at a lower field, while at a higher field, i.e., when the iron yoke began to saturate, the quality got worse and the magnetic center moved sideways. Therefore, we next considered to attach correction coils wound on to the yoke, but found it complicated to make this method work well. Then we finally adopted a Collins' type, for which the magnetic center does not move because of its geometrical symmetry.

The designed magnet is shown in Fig. 2. Since it was planned to replace with a focusing magnet (called Type I) in a normal cell and to excite in series with several magnets of the same type, the thickness of the iron yoke was increased to 100 mm, two times thicker than that of Type I, in order to make the excitation curve at a higher field agree with each other as far as possible. In addition, two pairs of correction coils that can be excited by an independent small power supply were attached on the iron yoke to compensate for the difference in field excitation.

In order to study the structural strength under magnetic stress, a simple program using the method BEM (Boundary Element Method) was written to compute a magnetic field of the quadrupole with assuming μ infinite in iron and the structural distortion by induced magnetic stress. An example of the computed results is shown in Fig. 3. From such results, we adopted a structure of magnet with stainless steel sections in the yoke. With the magnet yoke having a protrudent portion of 100 mm-thick stainless steel, the magnetic center was expected to shift the order of a few tens μm at a current of 500 A. On the other hand, the thickness of the opposite portion made of stainless steel is constrained to allow the existing alignment instrument to use. The principal parameters of the quadrupole together with those of the sextupole and the vertical steering are listed in Table I.

Sextupole Magnet

For the sextupole, the magnetic field were also calculated by LINDA and the results showed that the whole yoke made only of iron has a relatively good field quality, though the horizontal field distribution is inclined at a high field and the sign of field within ± 5 mm around the center of magnet becomes opposite to that of the other region. This change of sign was estimated to give little effect on the beam orbit. Thus we adopted a simple structure for the sextupole as shown in Fig. 4.

Vertical Steering

In order to hold the symmetry of the magnetic structure, we

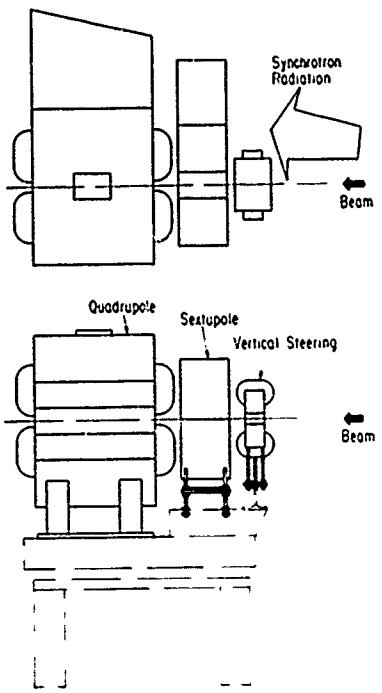


Fig. 1 Schematic view of the magnet arrangement in the ring.

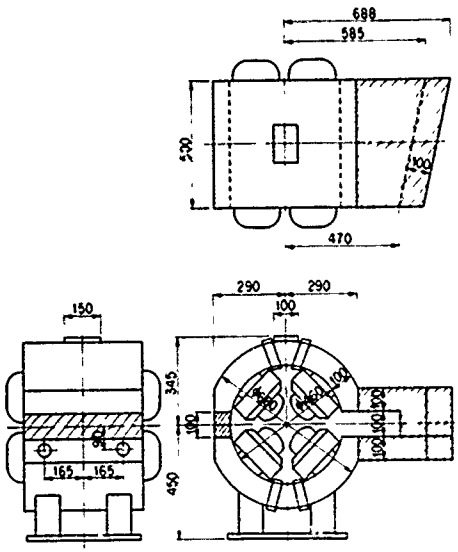


Fig. 2 Design sketch of the quadrupole. The shaded portions are made of stainless steel.

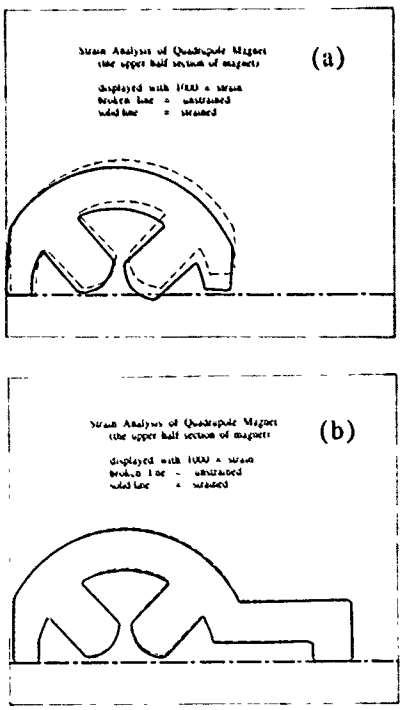


Fig. 3 Structural distortion of the quadrupole at a current of 500 A. (a): the case without stainless-steel yoke, (b): the case with a 100 mm-thick stainless-steel yoke. The minimum gap at right has a displacement about 30 μm in the case of (a) and about 4 μm in the case of (b).

0-7803-0135-8/91$01.00 ©IEEE

adopted a type of structure as shown in Fig. 5, much similar to the type adopted for the quadrupole. Differing from the quadrupole, however, the mechanical structure of the vertical steering is not necessarily so strong as the quadrupole is, so that one of the side yokes is made open to let SR pass through. Two-dimensional calculation of LINDA implied that the field degraded by splitting the side yokes could be restored by attaching four rectangular shims, each about 10 mm wide and 10 mm high, to the inside wall of the iron yokes. As the length of magnet is shorter than the transverse dimensions, however, various sizes of shims were prepared to choose an optimum size in the field measurement.

Table I. Principal parameters of the magnets

Qauadrupole	
gradient (B')	9.5 T/m
main coil current	500 A
turn number of coil	23 per pole
bore radius	55 mm
length of iron core	0.5 m
width of iron yoke	100 mm
electric resistance	32 mΩ
cooling water	5 *l*/min.
power dissipation	8 kW
correction coil current	4.5 A (max.)
number of correction coils	4
turn number of correction coil	100 per coil
Sextupole	
sextupole gradient (B")	29 T/m^2
current	3 A (max. 5 A)
turn number of coil	436 per pole
bore radius	70 mm
length of iron core	0.2 m
electric resistance	9.5 Ω
power dissipation	85 W (max. 240 W)
diameter of conductor	1.8 mmφ
Vertical steering	
field (B)	380 G
current	3 A
turn number of coil	2100 per pole
length of iron core	80 mm
electric resistance	14 Ω
power dissipation	127 W
diameter of conductor	1.6 mmφ

III. Field Measurement

The magnetic field measurements were carried out mainly using the following two methods; (1) a moving induction coil for the quadrupole and (2) harmonic coils for the sextupole and the vertical steering. Furthermore, a rotating coil was used for quadrupole and sextupole to check the reliability of measurement made by the above methods, and also used was a colloidal instrument to measure the magnetic centers[3]. In the method (1), at the same time that a horizontal position of the moving coil was measured with a precision of 50 μm by a Nikon position scale, the voltage induced by the quadrupole field was also measured with 1×10^{-4} accuracy by VFC (Voltage to Frequency Converter) connected to a CAMAC scaler system.

For the quadrupole, a good field region (about ±40 mm) of the integrated gradient distribution as shown in Fig. 6 was obtained by attaching a pair of end shims at each end of the pole pieces. The thickness of the end shims was chosen to be 4 mm. The excitation curve was measured up to 800 A (beyond a maximum-allowed current of 500 A), and compared with that of an existing quadrupole of Type I (see Fig. 7). The difference in excitation that became apparent above 300 A (0.7% at 300 A and 4.0% at 800 A) was compensated for by exciting the correction coil. The correction current required for compensation is plotted with respect to the main current in Fig. 8, and it is only 1.0 A at the ring energy of 2.5 GeV. The magnetic center was checked using a colloidal instrument[4] and agreed with a geometric center less than 50 μm below a current of 400A, though it was slightly deviated with the correction coil current as shown in Fig. 9. A large deviation seen in the figure at a high current that had also been observed for the existing Type I quadrupoles is due to the iron support legs, which give rise to an asymmetry in the magnetic circuit of the quadrupole.

The mechanical distortion due to magnetic stress was measured by strain gauges directly stuck on the magnet and by those stuck on pieces of aluminum that were in turn fixed between the minimum gaps in the magnet. The latter gauges had a better sensitivity and gave the same order of strain as predicted. Temperature rise and flow rate of the cooling water were measured simultaneously, and the flow rate was observed to increase with the current due to the

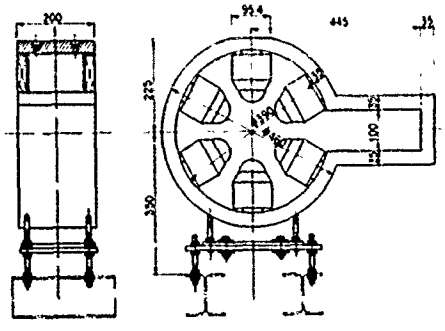


Fig. 4 Design sketch of the sextupole. The whole yoke is made of iron.

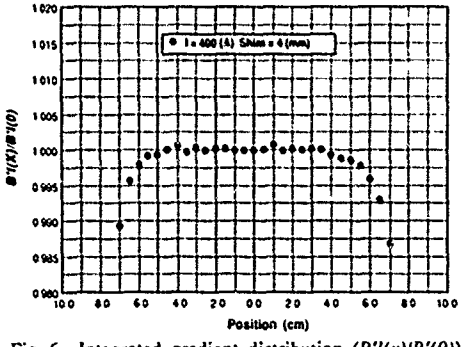


Fig. 6 Integrated gradient distribution ($B'l(x)/B'(0)$) versus the horizontal position (x) of the quadrupole at a current of 400 A with 4 mm-thick end shims.

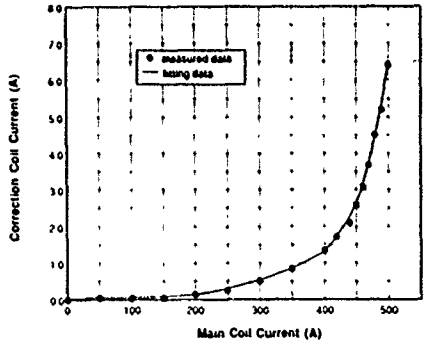


Fig. 8 Correction coil current required to compensate for the difference in excitation.

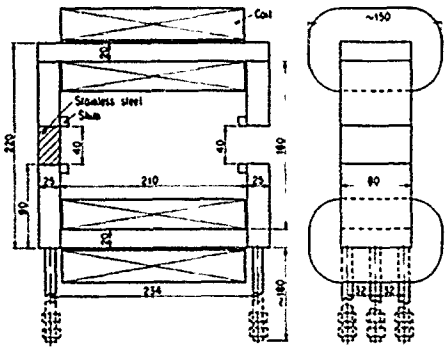


Fig. 5 Design sketch of the vertical steering. The shaded portion is made of stainless steel

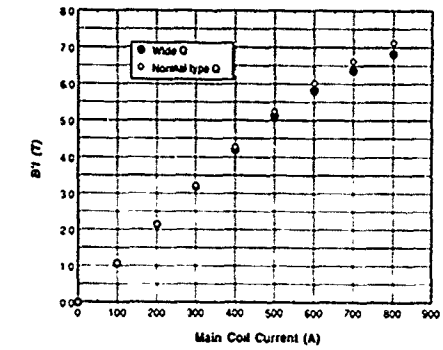


Fig. 7 Comparison of the excitation curves between the quadrupole and one of the existing quadrupoles (Type I). Wide Q and Normal type Q in the figure indicate the designed magnet and a magnet of Type I, respectively.

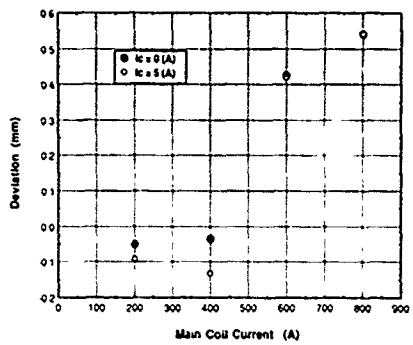


Fig. 9 Deviation of the magnetic center of the quadrupole versus the main coil current.

temperature dependence of the viscosity of water. The details of both strain and temperature measurements will be reported elsewhere.

The field strength of the sextupole measured by a harmonic coil is B"l = 10.13 T/m at 4.5 A, and the field distribution measured by a rotating coil is shown in Fig. 10. Further the field around the center of magnet was finely measured and found that the field has an opposite sign to that of the outer region, just as predicted by the field calculation.

For the vertical steering, the 10 mm-thick end shims were as optimum in the field measurement as in the two-dimensional calculation. The distribution of the integrated field is shown in Fig. 11 and the field strength is Bl = 73.4 G·m at a current of 3.0 A.

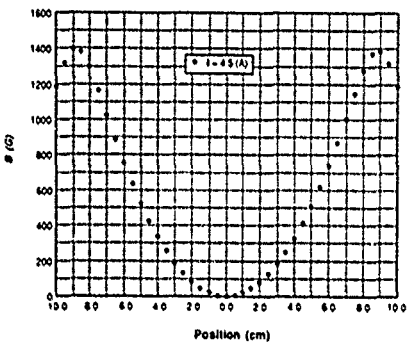


Fig. 10 Field distribution at the center of the sextupole measured by a rotating coil.

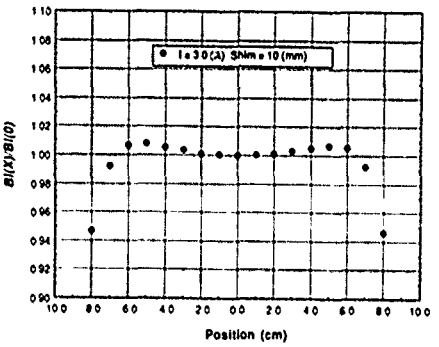


Fig. 11 Integrated field distribution of the vertical steering.

IV. Effects on Beam Orbit

The effects of the magnets on the beam orbit were studied after installing the magnets at the downstream of a bending magnet called B22, which was actually impossible to use for SR experiment because of the building structure. Since the quadrupole is a horizontally focusing magnet, the effects on the tune shift and the distortion of betatron function appeared more clearly in the horizontal direction than in the vertical direction, when the current of the correction coil in the quadrupole was set to a value different from the nominal one determined by the field measurement. Figure 12 shows the measured beta functions for three different values of the correction coil current (1.0, 2.5 and -4.5 A) and Fig. 13 shows the tune shifts with respect to the correction current. The method of measuring beta function is described in Ref. 4. At the nominal current of 1.0 A, both horizontal and vertical beta functions agreed well with the design values and any appreciable tune shifts were not observed. As shown in Fig. 14, the beta distortion measured at the other values of the correction coil current was also in good agreement with the distortion predicted from the data of field measurement.

The closed orbit distortion produced by the deviation of the magnetic centers in the quadrupole and in the sextupole was found to be negligibly small. The chromaticities were also measured and any appreciable change from the previous values was not found.

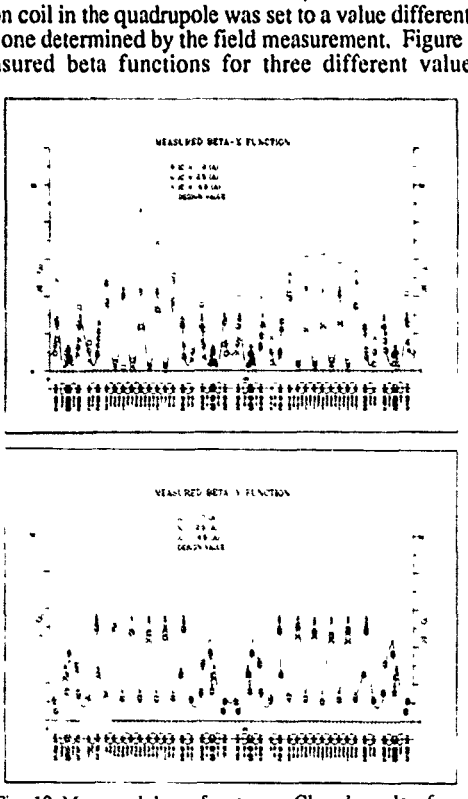


Fig. 12 Measured beta functions. Closed circles for a correction coil current of 1.0 A, open squares for 2.5 A, cross symbols for -4.5 A and the solid line for the design value.

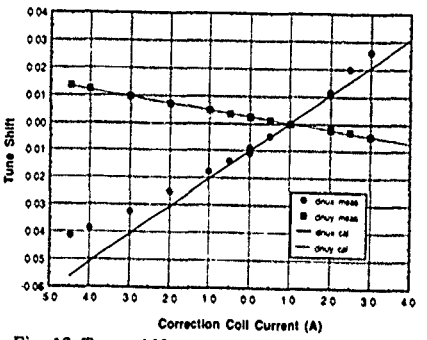


Fig. 13 Tune shift versus the correction coil current. Closed circles denote the measured values and solid line the expected value.

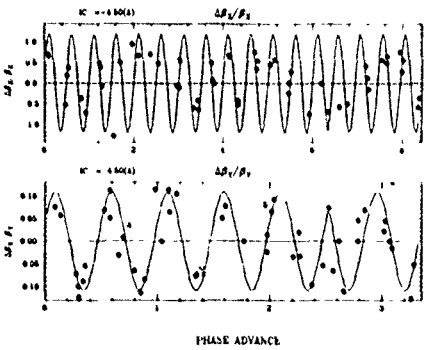


Fig. 14 Fractional changes of the beta functions at -4.5 A for the correction coil. Closed circles denote the measured values and solid lines the expected values.

V. Summary and Acknowledgements

The magnets described here are being operated without any trouble until now, while a kind of antechamber appropriate for the magnets will be installed within a few years [5]. If the magnets and vacuum chamber together achieve their design specifications, next step is probably "the full moon project" which will utilize the unused bending magnets in the injection region for supplying SR with extraction angles much wider than previously available.

We would like to thank all staff of the Light Source Division of the Photon Factory, in particular, Prof. M. Kobayashi and Dr. Y. Hori for their discussion about the vacuum chamber yet to be installed in the magnets. We also thank Prof. R. Sugahara of the Accelerator Department for kindly lending us his colloidal instrument.

References

(1) for example see the ESRF Design Report "RED BOOK", January 1987, the ALS Conceptual Design Report, July 1986 and so on.

(2) KEK version of the program LINDA, and also see K. Endo and M. Kihara,"Manual of Magnetostatic program LINDA", KEK ACCELERATOR-1, 1972 (in Japanese).

(3) R. Sugahara, T. Kubo and Y. Oosawa, "A Colloidal Solution of Fe_3O_4 Crystallites to Optically Locate the Magnetic Center of Multipole Magnets", KEK Report 89-9, September 1989.

(4) I. Honjo, M. Katoh, A. Araki, Y. Kamiya, and M. Kihara, "Measurement of Betatron Function at the Photon Factory", in Proc. of the 1987 IEEE Part. Accel. Conf., p. 1272, 1987.

(5) M. Kobayashi and Y. Hori, private communication.

Status of Development of the Insertion Devices for ELETTRA

C.Poloni, R.Bracco, B.Diviacco, R.P.Walker and D.Zangrando
Sincrotrone Trieste, Padriciano 99, 34012 Trieste, Italy

Abstract

The status of development of insertion devices for the 1.5-2 GeV synchrotron radiation source ELETTRA is described, including details of the prototype undulator, multipole wiggler, mechanical support structure and vacuum chamber. Plans for a novel source of circularly polarized radiation are also presented.

I. INTRODUCTION

A 1.5-2 GeV third generation synchrotron radiation source, ELETTRA, is under construction in Trieste, Italy [1,2]. The storage ring design has been optimized for the inclusion of up to 11 insertion devices (IDs), which will provide high brightness radiation from pure permanent magnet undulators (U), hybrid multipole wigglers (W), and special sources of circularly polarized radiation. Table 1 summarizes the main parameters of the devices presently forseen for the initial phase of operation.

Table 1. Preliminary ELETTRA insertion device parameters.

Beamline	Type-Period (cm)	Field (T)	No. of Periods
Superesca	U 5.6	0.60	81
Surface diffraction	U 7.3	0.77	63
Spectromicroscopy	U 7.3	0.77	63
Photoemission	U 12.5	0.49	36
Diffraction	W 14.0	1.55	30

II. INSERTION DEVICE SUPPORT STRUCTURE

For reasons of ease of construction, flexibility in use and cost, a standard mechanical support structure for both undulators and wigglers will be used [3,4]. The structure is 1.5 m long, so that each of the 11 ID straight sections in ELETTRA will accommodate up to 3 such structures. Following a design study made by Sincrotrone Trieste [4], a prototype carriage was constructed by CONTEK, Italy, and delivered in June 1990 (see fig. 1). Since then, a series of detailed measurements has been carried out to assess the mechanical performance, including the effect of a magnetic load, as well as further finite element structural calculations. The mechanical measurements were made using a HP 5528A laser interferometer and two Heidenhain optical rulers. The following values, that are within the specification, have been measured independent of magnetic load : gap setting accuracy ±10 μm, gap reproducibility < 10 μm, flatness of the reference surfaces 30 μm, parallelism of the I-beams 60 μm (for gaps between the I-beams ≤ 550 mm).
The measured deformation of the structure due to the magnetic load of the undulator prototype has been found to be significantly larger (5 times) than the value foreseen with the first structural model used during the design stage (using beam elements) [4] but in good agreement (7% of difference including the load determination error) with a more detailed finite element model prepared to take into account the true 3D geometry of the structure [5]. A gap variation along the beam axis of 1.4 μm/kN and a parallelism error of 12.7 μrad/kN in the plane normal to the beam axis are induced by the magnetic force. This leads to a total gap error of ± 5.5 μm in the case of the undulator prototype which is higher than the specified value but is still acceptable. Calculations made with the accurate structural model have shown that a vertical thermal gradient of 1 °C/m and an ambient temperature stability of ± 2.5 °C do not cause unacceptable deformations of the insertion device support structure.

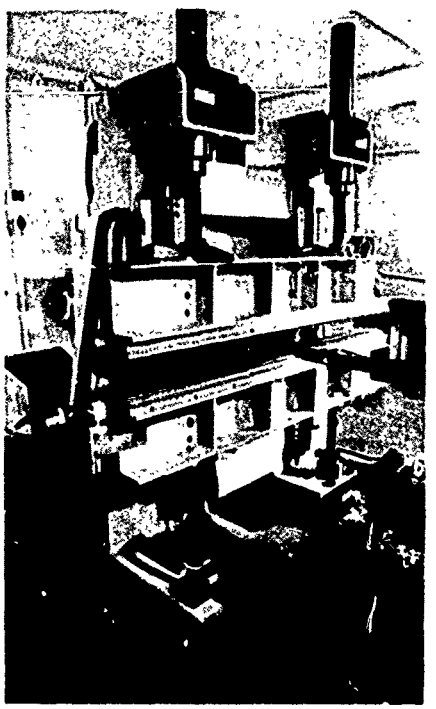


Figure 1. Prototype of ELETTRA insertion device support structure and undulator magnet.

III. UNDULATOR PROTOTYPE

Initial measurements of the NdFeB blocks for a 56 mm period pure permanent magnet undulator, using a Helmholtz coil system to determine the total block magnetizations and a Hall plate system to make point measurements, were described previously [6]. It was clear from the results of these and later measurements that to the level of accuracy required the blocks could not be modelled as ideal CSEM material, even if different magnetization values were used for the upper and lower faces of the blocks. Instead a purely empirical approach had to be adopted, but still relying on the fact that to a good approximation the field from different blocks superimposes

0-7803-0135-8/91$03.00 ©IEEE

linearly. In order to allow the main field component in the undulator to be calculated at the peaks and zeros each block has been measured at 21 points above and below the block, with a spacing of one quarter of the period along the beam direction, at a distance corresponding to the minimum magnetic gap (20 mm). In addition a new stretched-wire flipping coil bench has been used to measure the field integrals in both planes, above (u) and below (d) the blocks, along the beam direction and displaced transversely by ± 15 mm. The average time required per block was 14 min. for the Hall plate and 30 min. for the flipping coil. Table 2 shows the results from the flipping coil for "A" and "C" blocks (vertical magnetization) and for "B" blocks (horizontal magnetization) [6].

Table 2. Results of measurements of the field integrals for the prototype undulator blocks, in units of μTm.

	A (111 blocks)		B (117 blocks)		C (24 blocks)	
	mean	rms	mean	rms	mean	rms
Ix^u-Ix^d	2.0	18.1	-39.2	60.4	-2.3	10.2
$(Ix^u+Ix^d)/2$	-2.2	68.5	-8.7	71.4	-1.3	16.0
Iy^u-Iy^d	17.1	236.9	0.7	216.4	-1.5	151.0
$(Iy^u+Iy^d)/2$	2956.1	28.5	0.3	51.1	1474.1	8.3

A computer program has been written to arrange the blocks in the structure using a simulated annealing algorithm [7] involving the following components to the "cost function" that was minimized: (a) rms field error at the peaks (ΔB/B) and crossing-points, (b) first and second field integrals, (c) horizontal trajectory 'straightness' and (d) rms vertical displacement. A total cpu time of 5 hours was required for calculating the arrangement of the 222 blocks in the 1.5 m undulator.

The undulator was constructed according to the specified arrangement and then measured using both benches. Figure 2 shows the measured field and trajectory at minimum gap, and Table 3 summarizes various parameters as a function of magnet gap.

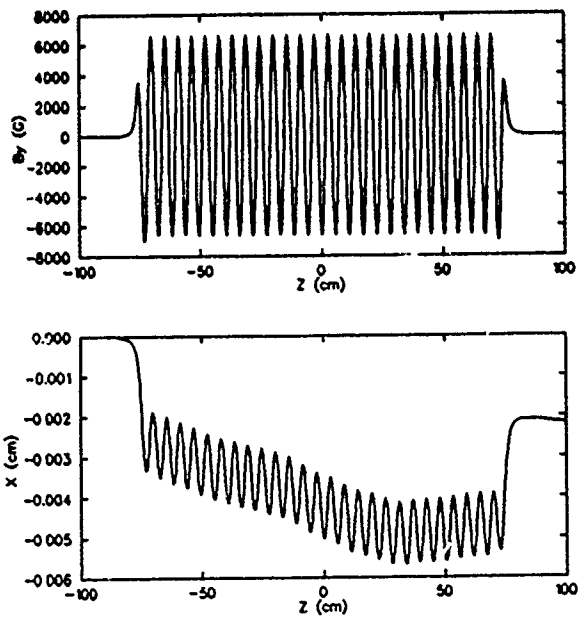


Figure 2. Measured magnetic field (upper) and trajectory (lower) in the prototype undulator at minimum gap (2 GeV).

Compared to a random configuration of the blocks the performance is very much better, at least an order of magnitude for ΔB/B, but not as good as predicted, particularly for the field integrals. A factor which probably contributed to this error is the variation in temperature during the block measurements (±4.5 °C). Attempts to measure and correct for the temperature variation have been unsuccessful, possibly due to the thermal time constant of the blocks, about 20 minutes, which means that the surface temperature can be different from the bulk. Use of a temperature stabilized laboratory in the future should eliminate this error.

Table 3. Results of initial measurements of the ELETTRA prototype undulator.

gap (mm)	Bo(T)	ΔB/B rms %	Ix (μT m)	Iy (μT m)
20	0.66	0.34	398.	70.5
30	0.37	0.41	306.	35.
50	0.12	0.84	178.	-15.6

To improve the quality of the undulator field experiments are presently being carried out using shims made from Fe-Si laminations, placed on the surface of the blocks. So far, very good agreement has been obtained between measured changes in both field amplitude and field integral and model calculations [8]. Efforts are presently being directed towards compensation of residual errors over a range of operating gap. Correction coils for fine adjustment of field integrals have also been fabricated and will soon be tested.

IV. MULTIPOLE WIGGLER PROTOTYPE

The optimization of the wiggler parameters to give the maximum field level with the given constraints on gap and radiation opening angle resulted in a period of 125 mm, with a predicted field of 1.48 T [3]. Since then the plan to include an additional experimental station on the wiggler beamline which will take radiation from the outer part of the radiation fan has necessitated a modification of the parameters, to take into account the effect of the third harmonic field component on the critical energy of the radiation emitted off-axis [9]. Figure 3 shows the relation between field and angle, calculated using POISSON, for the original design which has a third harmonic component (B3/B0) of 12 %.

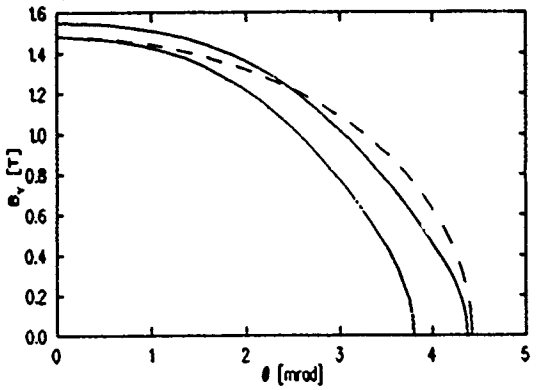


Figure 3. Field amplitude as a function of horizontal emission angle for the previous multipole wiggler design (lower solid curve), a sinusoidal model with the same field amplitude (dotted) and the present design (upper solid curve).

It can be seen that the field (and hence critical energy) is significantly reduced for angles above about 2.5 mrad, and that the total radiation angle is reduced by a factor 0.87, compared to the case of a purely sinusoidal field distribution. To overcome these effects the period length has been increased to 140 mm and the field to 1.55 T, keeping the same transverse block dimensions. Figure 4 shows that the modified design gives significantly improved performance at off-axis angles. The increase in field compensates the reduction in number of full poles from 21 to 19 per section at energies above 10 keV. Components to construct a 0.5 m prototype will be delivered by the end of May, to test design calculations, assembly procedures, and different end configurations.

V. CIRCULARLY POLARIZED RADIATION SOURCE

Various schemes have been studied for the production of circularly polarized radiation [3,10], in particular those that satisfy users' demands for a relatively broad spectral range (200 eV - 1 keV) with a rapid variation of the helicity (> 20 Hz). The solution favoured at present is a novel electromagnetic elliptical wiggler (see fig. 4), similar to the elliptical wiggler of ref. [11], except that the horizontal field component is generated by an a.c. electromagnet in order to modulate the helicity of the on-axis radiation.

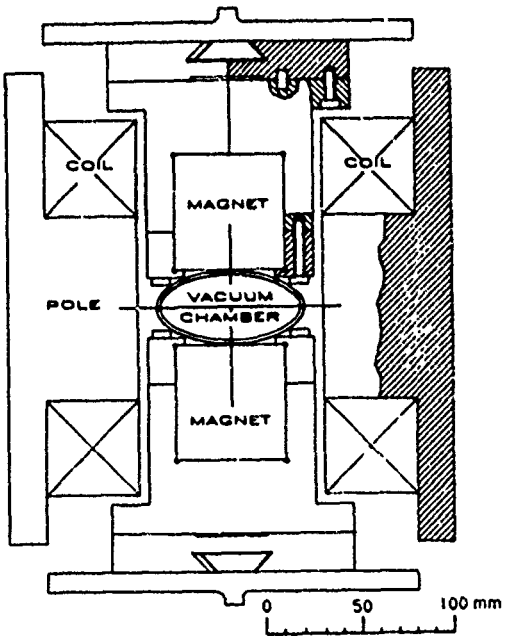


Figure 4. Preliminary design of an electromagnetic elliptical wiggler source of circularly polarized radiation.

The horizontal gap is necessarily large in order to allow space for the pure permanent magnet structure which produces the vertical wiggler field, and so a relatively large period has been chosen (230 mm) to reduce power supply demands. With this period a maximum field of 0.6 T, in order to restrict the opening angle of the radiation, gives an acceptable critical energy of up to 1.6 keV (2 GeV). Table 3 gives preliminary parameters for the device, which using a special ID support structure 3m long will give 25 times the flux of a bending magnet source with a modulation rate up to 100 Hz. POISSON calculations have been carried out to calculate field amplitude and inductance. A prototype will be constructed in the following months using existing permanent magnet blocks and an a.c. power supply.

Table 3. Preliminary parameters for an electromagnetic elliptical wiggler, at 100 Hz excitation.

Period	0.23	m
Number of full poles	25	
Bx, By	0.0466, 0.61	T
Kx, Ky	1.0, 13.2	
Inductance, total	2.5	mH
Ampere-turns per pole, peak	5000	A
Current, peak	250	A
Voltage, peak	432	V

The effect of the device on the dynamic aperture of the storage ring has been calculated and is tolerable [12].

VI. INSERTION DEVICE VACUUM CHAMBER

Following the design and specification of a narrow gap (15 mm internal, 20 mm external) vacuum chamber employing NEG pumping [4,13], an order for the construction of a 2.4 m half-length prototype vacuum chamber has been placed with E.ZANON, Italy, including a tapered section 240 mm long which incorporates a pumping tee. The chamber will be constructed from stainless steel 316 LN. The elliptical beam chamber will be obtained by deformation of a 54 mm diameter circular pipe, formed from 1.5 mm thick sheet material, with machined pumping slots 16 mm long x 10 mm high spaced every 40 mm. The ante-chamber will be formed from 3.5 mm sheet, machined then TIG welded to the beam chamber. After delivery in May 1991 and subsequent installation of the NEG pumping strips it will then undergo a thorough series of tests in the Vacuum Laboratory.

VII. REFERENCES

[1] A.Wrulich, this Conference
[2] ELETTRA Conceptual Design Report, April 1989, Sincrotrone Trieste
[3] B.Diviacco and R.P.Walker, Proc. 2nd European Particle Accelerator Conference, Nice, June 1990, p. 1359
[4] C.Poloni and R.P.Walker, ibid, p. 1362
[5] C.Poloni, Report in preparation
[6] D.Zangrando and R.P.Walker, ibid, p. 1365
[7] A.D.Cox and B.P.Youngman, Proc. SPIE 582, p. 91
[8] J.Chavanne et. al., European Synchrotron Radiation Facility Report ESRF-SR/ID-89-32, Nov. 1989.
[9] W.Hassenzahl, private communication
[10] B.Diviacco and R.P.Walker, Nucl. Instr. Meth. Phys. Res. A292 (1990) 517.
[11] S.Yamamoto and H.Kitamura, Jpn. J. Appl. Phys. 26 (1987) L1613.
[12] L.Tosi and R.Nagaoka, this conference
[13] T.Monaci and C.Poloni, Sincrotrone Trieste Report ST/M-TN-90/18, Sep. 1990

A Wedged Pole Hybrid Type Undulator as a Synchrotron Radiation Source

Shigemi Sasaki, Takeo Takada*, Nobuo Matsuki, Shigeki Sasaki*
and
Hideo Ohno
Office of Synchrotron Radiation Facility Project
Japan Atomic Energy Research Institute
Tokai-mura, Naka-gun, Ibaraki 319-11, Japan
*Institute of Physical and Chemical Research (RIKEN)
Honkomagome, Bunkyo-ku, Tokyo, Japan

Abstract

An undulator of wedged-pole-hybrid type has been constructed. This undulator was designed as a prototype undulator for the SPring-8 Project. The magnetic period of this device is 33 mm, and the number of period is 61.5. It generates 0.59 T for the maximum magnetic field at the minimum gap width (13.5mm). This device is expected to generate brilliant photon beams of energy ranges around 10 keV by installing into the low emittance high energy storage ring such as the SPring-8.

I. INTRODUCTION

The third generation synchrotron radiation source in the x-ray regime is now under construction in Japan as well as in USA and Europe. The aim of this project, which is called the SPring-8 Project, is to construct a large synchrotron radiation facility to provide highly brilliant x-ray beams for synchrotron radiation users. The 8 GeV SPring-8 storage ring has 44 straight sections including 4 long (30 m) sections. Most of all straight sections, except the injection section and the RF-cavity sections, are expected to be used for insertion devices. The length of normal straight section is longer than 6 m. However, at present, the length of insertion device is planned not to exceed 4 m because both upper and downstream parts of vacuum chambers are occupied by electron beam position monitors, tapered sections, valves and flanges.

We have constructed an undulator of wedged-pole-hybrid type as a prototype but a half length version for the SPring-8 insertion device. In this paper, the magnetic characteristics of this undulator is described, and the Halbach type semi-empirical equation for WPH undulator is proposed. Also included are expected spectral characteristics of the undulator radiation.

II. UNDULATOR

The characteristics of the undulator radiation depends on the peak magnetic field, the magnetic period length of undulator and the electron energy of the storage ring. Since changing the electron energy is not plausible during the dedicated run for synchrotron radiation user's experiments, the magnetic field of insertion device required to be changed widely in order to obtain a wide range of tunability of photon energy. Usually, the magnet gap width is controllable for changing the magnetic field. Smaller gap width gives larger magnetic field providing lower photon energy for the fundamental peak of undulator radiation. The fundamental energy on the beam axis is given by;

$$\varepsilon[\mathrm{keV}] = \frac{0.950E^2[\mathrm{GeV}]^2}{\{\lambda_u[\mathrm{cm}](1+K^2/2)\}},$$

where E is the electron energy, λ_u is the magnetic period and K is the deflection parameter described as follows by using the peak magnetic field B_0;

$$K = 0.934B_0[\mathrm{T}]\lambda_u[\mathrm{cm}].$$

In order to meet the synchrotron radiation users' needs, the strongest magnetic field at minimum magnet gap is desirable.

The permanent magnet hybrid undulator was proposed by Halbach for obtaining higher on-axis magnetic field compared with pure magnet undulator [1]. Lately, a wedged-pole hybrid undulator was proposed by Quimby [2]. The wedged-pole configuration is expected to generate the strongest on-axis field. It softens a trade-off relation between the physical aperture of electron beam and the tunability of photon energy to some extent. Therefore, we chose a wedge-pole configuration for the prototype undulator. Table 1 shows the undulator parameters. The design parameters of this device is quite similar to the APS prototype undulator except the magnet design [3].

Table 1
Parameters of a wedged-pole hybrid undulator.

Magnet material,	Nd-Fe-B
Undulator period, λ_u(cm)	3.3
Magnet gap range (cm)	1.35-30
Maximum peak field on-axis, B_0(T)	0.59
Deflection parameter range, K	≤1.8
Peak field error, $\Delta B/B$(%)	0.4
Transverse rolloff at ±1 cm (%)	≤0.09
Total steering error (G-cm)	-11
Number of periods	61.5

0-7803-0135-8/91$01.00 ©IEEE

This undulator was built by Spectra Technology Inc. Figure 1 shows the whole view of this device with the magnetic measurement system.



Figure 1. The prototype undulator under the magnetic measurement. The wedged-pole hybrid undulator was built by Spectra Technology Inc.

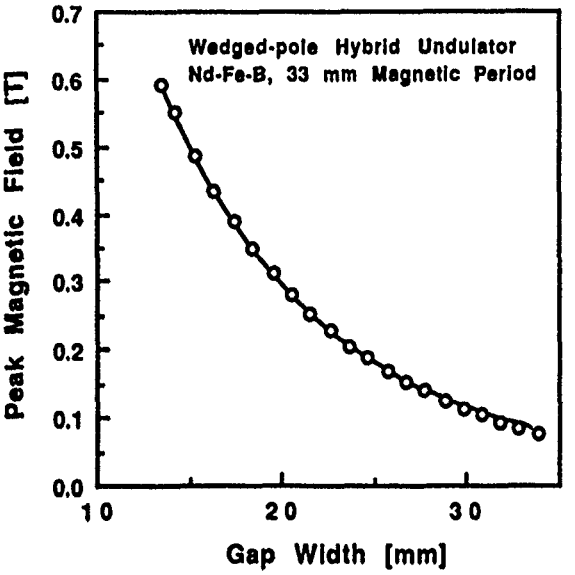


Figure 2. Maximum peak magnetic field on-axis as a function of magnet gap. Measured data (open circle), and calculated values (solid line) are presented.

III. MAGNETIC MEASUREMENTS

The precise magnetic measurements at minimum gap was carried out before shipping to Japan. The measured on-axis peak magnetic field was in good agreement with the design value. The integrated steering errors measured along the beam axis -11 Gauss-cm, which is extremely good compared with the design value (<100 G-cm), was achieved by the shimming technique [4]. The transverse field rolloff at ± 1.0 cm from the centerline was less than 0.09 %. All these measurements were confirmed after the device was installed at JAERI site.

A series of measurements of the magnetic field was carried out on the magnet at various gap settings using a Hall probe magnetic measurement system. Hall probe output voltages were converted to digital data using 16 bit A/D board and acquired in a 32 bit personal computer as a function of Hall probe position. The position measurements were carried out using an optical linear encoder with the resolution of 10 μm. The average peak field value, B_0, was calculated for the central periods excluding 3 poles values of each end of undulator.

Figure 2 shows the measured peak field on-axis as a function of magnet gap. The results can be well represented by the Halbach type equation as follows;

$$B_0 = 2.87\exp\left\{-\frac{g}{\lambda_u}\left(4.12-0.63\frac{g}{\lambda_u}\right)\right\},$$

where g is the magnet gap width. This equation seems to be valid within the range of gap to period ratio, g/λ_u, less than 0.7.

Originally, above equation was proposed by Halbach for Sm-Co hybrid undulator and modified for Nd-Fe-B hybrid undulator by himself [5, 6]. Only the difference between original Halbach equations and the present equation is the numerical constants. These constants were determined from the measured magnetic peak fields for this particular device. The calculated result using above equation is also shown in figure 2 (solid line). Furthermore, it may worth noting that the measured peak field data are in good agreement with the computed values using 2D-finite-element method [7].

IV. EFFECT ON ELECTRON BEAM

The undulator introduces some vertical focusing effect on the electron beam when it is installed in the storage ring, and therefore changes the vertical tune slightly. This tune shift is given simply by the following equation [8];

$$\Delta Q = \frac{1}{4\pi}\beta_y\left(\frac{0.3}{E}\right)^2\frac{B_0^2 L_u}{2},$$

where β_y is the betatron function of undulator straight section in m, E is the electron energy in GeV, B_0 is the peak magnetic field in T and L_u is the length of the undulator in m. For the SPring-8 storage ring, the electron energy is 8 GeV, the β_y of undulator straight section is 10.0 m and the maximum peak field of undulator is 0.59 T. Therefore, the above equation gives a tune shift of 3.9×10^{-4}. Tune shifts of this magnitude can be easily corrected by the quadrupole trim coil windings.

One of the other effects on the electron beam due to the undulator installation might be a reduction of the beam lifetime. Although the vertical physical aperture is limited around 10 mm or so by the undulator vacuum chamber, the physical aperture of this order would not affect the lifetime because the vertical electron electron beam size is small enough in the low-emittance storage ring such as the SPring-8 storage ring. Only the problem that would be happen is the reduction of dynamic aperture due to the destruction of the lattice symmetry. However, solving this problem is not the case in this paper, and the similar problem was already solved elsewhere [9].

V. UNDULATOR SPECTRUM

The expected spectral brightness of the undulator radiation was calculated. Figure 3 shows the on-axis spectral brightness of the prototype undulator installed in the symmetry straight section in the PEP storage ring at the Stanford Linear Accelerator Center. For the calculation, PEP was assumed to be operated 8 GeV, 50 mA low-emittance mode. The machine parameters for the low-emittance operation are listed elsewhere [10].

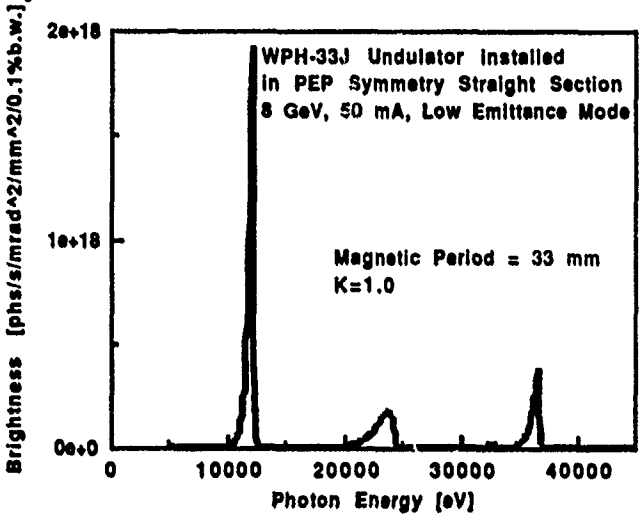


Figure 3. Spectral brightness of wedged-pole hybrid undulator installed in PEP, 8 GeV, low-emittance mode operation.

Figure 4 also shows the on-axis spectral brightness of the undulator installed in SPring-8. An undulator of 3.3 cm magnetic period at 8 GeV operation energy of SPring-8 provides first harmonic radiation within the energy between 7 keV and 16 keV while changing the deflection parameter K from 1.8 to 0.5. The expected brightnesses of the first-harmonic radiations are of the order of 10^{18} photons/s/mm^2 /mrad^2/0.1%b.w. Vertical and horizontal emittance coupling in SPring-8 is assumed to be 10 % for the calculation.

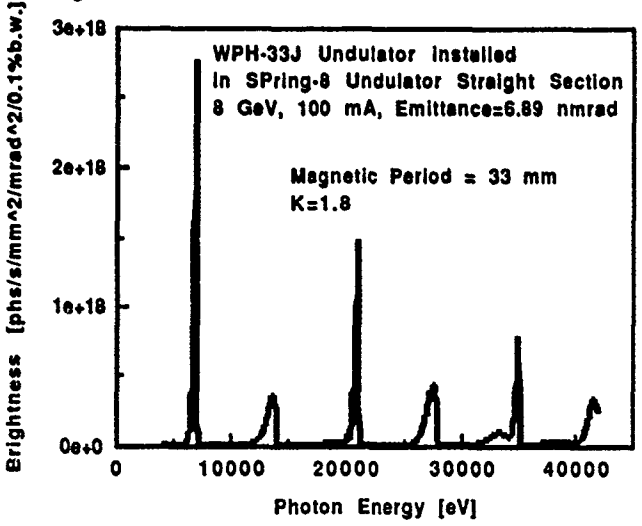


Figure 4. Spectral brightness of wedged-pole hybrid undulator installed in SPring-8. K=1.8 correspond to the minimum gap.

As is shown in figure 3, PEP has an excellent capability if it is operated in low-emittance mode and the undulator is installed at a symmetry straight section. The calculated brightness shows that PEP is comparable with the other so-called "the third generation" synchrotron radiation sources. Looking forward to the future, ESRF will be commissioned in three years, APS in five years and SPring-8 in seven years. In all these rings, it seems that the wedged-pole hybrid permanent magnet undulator would be one of the standard insertion device for obtaining a wide tunability of photon energy.

VI. ACKNOWLEDGEMENTS

One of the authors (Sm.S.) would like to thank Dr.s J.Slater, K.Robinson, S.C.Gottschalk and D.Jander of Spectra Technology Inc. for their many useful suggestions. He also wishes to thank Dr. R.P.Walker for allowing him to use the code URGENT for the calculation of undulator radiation.

The authors are grateful to the members of FEL group, Department of Physics, JAERI for helpful discussions.

VII. REFERENCES

[1] K.Halbach, J. Phys. (Paris) 44, C1-211 (1983)
[2] D.C.Quimby and A.L.Pindroh, Rev. Sci. Instrum. 58, 339 (1987).
[3] D.H.Bilderback, B.W.Batterman, M.J.Bedzyk, K.Finkelstein, C.Henderson, A.Merlini, W.Schildkamp, Q.Shen, J.White, E.B.Blum, P.J.Viccaro, D.M.Mills, S.Kim, G.K.Shenoy, K.E.Robinson, F.E.James, and J.M.Slater, Rev. Sci. Instrum. 60, 1419 (1989).
[4] S.G.Gottschalk, D.C.Quimby, K.E.Robinson, and J.M.Slater, to be published.
[5] K.Halbach, J. Appl. Phys. 57, 3605 (1985).
[6] S.H.Kim and Y.Cho, IEEE Trans. Nucl.Sci. NS-32, 3386 (1985).
[7] K.Miyata:Shin-Etsu Chemical Co. Ltd., private communication.
[8] M.W.Poole and R.P.Walker, IEEE Trans. Nucl. Sci. NS-32, 3374 (1985)
[9] R.Nagaoka, K.Yoshida, H.Tanaka, K.Tsumaki, and M.Hara, Proc. IEEE Particle Accelerator Conference, Chicago (March 1989).
[10] S.Sasaki, B.Youngman, and H.Winick, Nucl. Instrum. Methods A291, 401 (1990).

Design Considerations for a Fast Modulator in a 'Crossed Undulator'

Roland Savoy, Advanced Photon Source, APS/360,
Argonne National Laboratory, Argonne, IL 60439
and
Klaus Halbach, Advanced Light Source, Ms.2-400,
Lawrence Berkeley Laboratory, Berkeley, CA 94720

Abstract

The modulator, a short electromagnetic wiggler, can be used to generate a phase shift between the synchrotron radiation of the two undulators in a crossed undulator. The switching frequency between two polarization states can be as high as 10 Hz. This paper discusses some physical requirements for the modulator and a conceptual design of the magnet for a crossed undulator at the Aladdin storage ring (Synchrotron Radiation Center, University of Wisconsin, Madison) as a prototype development for the Advanced Light Source (ALS) and the Advanced Photon Source (APS).*

I. INTRODUCTION

Third generation synchrotron light sources, like the ALS at Berkeley and the APS in Argonne, currently under construction, can be powerful sources of X-ray radiation with adjustable polarization state, especially by utilizing the small design emittance of these machines. A device to produce radiation with any desired polarization state is the crossed undulator [1,2] in which the electron beam travels through: first, an undulator; second, a phase shifter; and, third, another undulator. The on-axis radiation from a planar undulator by a zero emittance electron beam observed through an infinitely small pinhole is linearly polarized. The direction of the magnetic field in the first undulator is perpendicular to the field orientation in the second (a schematic drawing of the device is found in [3]). Therefore, the polarization vectors of the radiation from the two undulators are orthogonal. The radiation from the two undulators is mixed in a monochromator to produce the desired polarized radiation. The polarization state can be selected by changing the phase of the radiation from the upstream undulator with respect to the downstream undulator. One way of adjusting the phase is to introduce a drift space of variable length between the two undulators. However, this procedure results in a rather slow (some ten seconds) change of the polarization. Another difficulty is that the drift space between the two undulators enhances the depolarization due to the finite emittance of the electron beam [2]. A more elegant approach without physically moving a magnet is to utilize an electromagnetic wiggler as a phase shifter [2]. The magnetic field within the wiggler forces the electrons on a path that is longer than that for the electromagnetic radiation. This phase shift is, in a saturation-free magnet, determined by the current through the wiggler coils. The switching frequency is limited by the eddy current effects in both the wiggler laminations and the walls of the vacuum chamber. Recently, a polarizer of this kind utilizing two hybrid undulators and a dc modulator was installed on the BESSY-1 storage ring [4].

II. THE MODULATOR

A. General Description

The modulator is a five pole wiggler with a fixed gap. The magnet is constructed from thin stamped steel laminations that are electrically insulated for each other to suppress eddy current effects in the steel. Figure 1 shows a longitudinal section through the modulator. The center pole and the two side poles can be energized with water-cooled coils. The end poles have no coil and serve as field clamps to reduce the stray field of the modulator and the sextupole coefficient of the field integral.

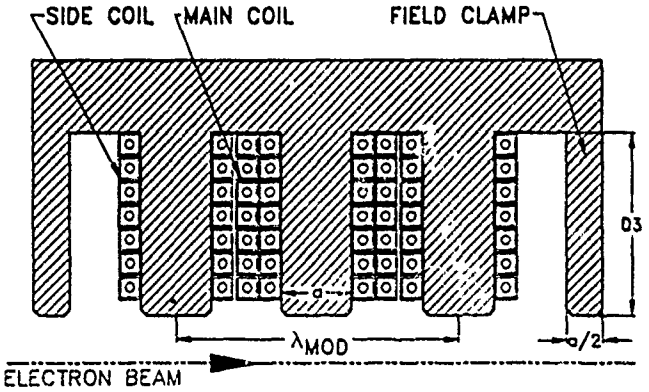


Fig. 1: Longitudinal section through a modulator. The upper half of the magnet is shown. The period length for the SRC magnet is 10 cm, the overall length is 20 cm. The full gap is 3.0 cm, a=2.5 cm and D_3=6.1cm.

In a saturation-free magnet of this geometry, the first (steering) and second (displacement) field integral of the

*Work sponsored by U.S. Department of Energy, BES-Materials Sciences under Contract W-31-109-ENG-38.

U.S. Government work not protected by U.S. Copyright.

wiggler field are approximately zero when the current through the center coil is twice the current through the side coils [5], i.e., the scalar potential of the center pole is $2V_0$ (side pole - V_0). Therefore, if the center coil has twice as many windings as the side coil, the magnet could be driven by one power supply. One condition for proper functioning of the device is to keep steering and displacement as small as possible. Therefore, correction coils may be necessary to dynamically adjust the steering.

B. Magnetic Design

The modulator shall be able to change the phase of the longest wavelength of interest λ_R by up to 2π without perturbing the storage ring. The magnetic design procedure as outlined in [6] consists of two steps. First we determine the necessary current that will produce a phase shift of at least 2π. Second, the pole height D_3 [see Fig. 1] is determined. The highest magnetic field in the modulator occurs at the base of the center pole. The magnetic field at the base of the side poles is considerably lower. This could result in steering due to saturation at the base of the center pole. Saturation in the center pole can be minimized by carefully specifying D_3. In the following paragraphs we describe the design process.

The time of flight difference Δt between the photon and the electron beam is approximately:

$$\Delta t \approx \frac{1}{c}\left[\frac{L}{2\gamma^2} + s\right] = \frac{m\lambda_R}{c} \qquad (1)$$

where L is the spacing between the two undulators, c the speed of light, γ the energy of the electrons in units of the rest energy, λ_R the wavelength of the radiation and m the phase shift in fractions of a wavelength λ_R. The adjustable path difference s between the electron beam path length and the radiation path length is calculated by:

$$s = \int_{-\infty}^{\infty} (\sqrt{1 + x'^2} - 1)dz \approx \frac{1}{2}\int_{-\infty}^{\infty} x'^2 dz \qquad (2)$$

A standard coordinate system is used: z is measured along the (ideal) average electron beam, x is the horizontal and y the vertical distance from z. The prime symbolizes a derivative with respect to z. The equation of motion of an electron in a weak wiggler field is in good approximation:

$$x'' = \frac{B(z)}{B\rho} \text{ and } x' = \frac{A(z)}{B\rho} \qquad (3)$$

where B(z) is the magnetic field as a function of z, A(z) the vector potential, and $B\rho$ the rigidity of the electron beam. Combining Eq. 2 and 3 results in:

$$s = \frac{1}{(B\rho)^2}\int_0^{\infty} A^2(z)dz \qquad (4)$$

Using a 2D computer program that solves Maxwell's equations (like POISSON [7]), it is straightforward to numerically calculate the integral in Eq. 4 for a given scalar potential $V_{0,2D}$. The scalar potential is related to the current by $3V_{0,2D}=\mu_0 I_{tot,2D}$, where $I_{tot,2D}$ are the total Ampere-turns about the center pole used in the computer run.

However, we want to invert the problem and calculate the scalar potential $V_{0,d}$ for a given path difference s_d. We define the dimensionless quantity *S*:

$$S = \frac{\int_0^{\infty} A^2(z)dz}{V_{0,2D}^2\,\lambda_{mod}} \qquad (5)$$

where λ_{mod} is defined in Fig. 1. Writing $s=m_d\lambda_R$ and using Eqs. 4 and 5 we obtain:

$$V_{0,d} = \sqrt{\frac{m_d\,\lambda_R}{S\,\lambda_{mod}}}\,B\rho \qquad (6)$$

The next step is to calculate the average magnetic field at the base B_{base} of the center pole. The derivation of Eq. 7 [6] is beyond the scope of this paper. The result is:

$$\overline{B_{base}} = \frac{2V_{0,d}}{p}\left(3E_B + E_0 + \frac{3D_3}{2\,h_2}\right) \qquad (7)$$

where p is the pole thickness in z direction, $2h_2 = 0.5\lambda_{mod}-p$, D_3 the pole height and E_B and E_0 are excess flux coefficients. The concept of excess flux coefficients is discussed in [8]. However, we will give a recipe for determining E_B and E_0.

E_B can be determined with a POISSON run. A typical field line plot is shown in Fig. 2a.

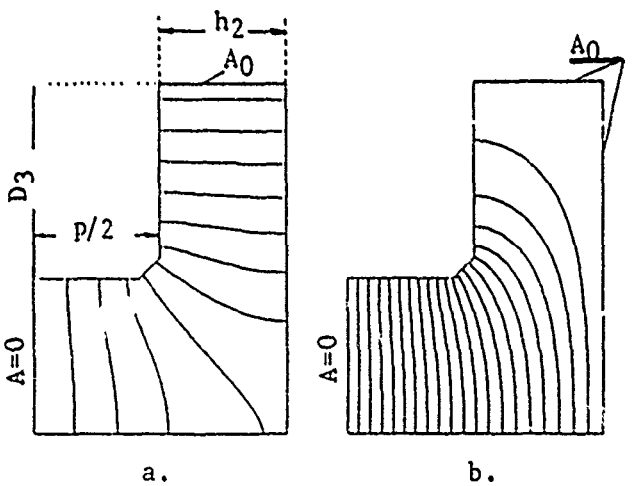


Fig. 2: Field line plots of POISSON runs that are used to determine the excess flux coefficients E_B (Fig. 2a) and E_0 (Fig. 2b). For details see text.

Only the upper half of a quarter period of the magnet is shown. The bottom boundary is the midplane. A constant vector potential A_0 is assigned to the top boundary.

POISSON calculates the current in each node of the mesh on the top boundary that is necessary to satisfy this boundary condition. These currents are added and multiplied by μ_0 to get the scalar potential of the pole V_{EB}. The other boundaries are obvious from the field line plot. The coefficient E_B is determined with:

$$E_B = \frac{A_0}{V_{EB}} \cdot \frac{D_3}{h_2} \qquad (8)$$

E_0 is determined with another POISSON run. Now the top and right boundary are set to a fixed vector potential A_0. The scalar potential of the pole V_{E0} is again calculated by adding the currents that POISSON places in the nodes on the boundary and multiplying them by μ_0. A typical field line plot is shown in Fig. 2b.

$$E_0 = \frac{A_0}{V_{E0}} \qquad (9)$$

III. THE SRC MODULATOR

A. Design Parameters

A crossed undulator that will deliver polarized radiation between 8 and 40 eV using an 800 MeV electron beam is being proposed for the Synchrotron Radiation Center (SRC) in Madison-Wisconsin. The horizontal rms electron beam divergence at the location of the device is about 140 μrad, whereas the vertical divergence is 15 μrad.

The two hybrid undulators will both have five periods. A period length of 10.5 cm results in a K_{max} of about 3.70 at a magnetic gap of 5.0 cm [9]. The synchrotron radiation opening angle $1/(\gamma\sqrt{N})$ is 280 μrad.

The modulator will have a λ_{mod} of 10 cm and a gap of 3.0 cm. We are designing the wiggler for a maximun phase shift m_d of 1.5 at a wavelength of 1550 Å. The tolerance on the steering integral of the modulator is completely determined by the storage ring. A steering error of only 3 μrad will produce a beam displacement of 10 μm (and interfere with experiments) at a bending magnet port [10].

B. Results of Calculations

The parameter S (Eq. 5) for the specified geometry is 1.735. Using Eq. 6, the necessary scalar potential of the pole is calculated to be 3075 G-cm resulting in a total current of 7340 A-turns. The pole height D_3 is determined using Eq. 7 assuming that B_{base} should not be larger than 1.5 T. The excess flux coefficients were determined to be: E_B = 1.328, E_0 = 1.437. The resulting pole height is 5.64 cm. A slightly taller pole (D_3=6.10 cm) is required to accommodate the coil; the average field at the base of the center pole increases to 1.57 T, which is still acceptable. This result was independently confirmed with a POISSON run using a "real" B-H curve. These results indicate that a slight steering of about 30 μrad is introduced for m=1.5. It is larger than the allowable steering, but can be compensated by using trim coils. The maximum magnetic field in the midplane is 0.38 T, corresponding to a K_{mod} of about 3.5.

C. Coil Design

The coil [11] can be constructed with a standard square hollow core conductor (min. bore 3.05 mm, effective copper area 31 mm^2, outer dimensions including insulation 7.95 mm). The maximum current in the conductor is about 370 A; the current density is 11.3 A/mm^2.

The dissipated power is about 1400 W if we assume that the coils are excited with a dc current of 370 A. An analysis of the cooling requirements [12] showed that a modest water flow (29.2 cm^3/s at a pressure drop of <5 bar) will cool the magnet efficiently. The temperature rise of the cooling water is less than 4 K and the temperature gradient over the water metal interface is less than 1 K.

Additional heat is dissipated when the modulator is energized with 10 Hz alternating current with an amplitude of 185 A. The power dissipation due to eddy currents in the conductor, the steel laminations and the hysteresis losses is quite small (total <20 W). The total voltage in the ac case is less than 12 V.

IV. FUTURE RESEARCH

Field pertubations at the location of the electron beam caused by eddy currents in the vacuum chamber will be studied next.

V. REFERENCES

[1] M.B. Moiseev, M.N. Nikitin, N.I. Fedosov, Sov. Phys. J. 21, 332, 1978.

[2] K.-J. Kim, NIM 219, 425, 1984.

[3] M.A. Green, W.S. Trzeciak, K.J. Kim, P.J. Vicarro, "Rapidly-Modulated Variable-Polarization Crossed-Undulator Source," Proc. this conference.

[4] Ch. Wang, J. Bahrdt, A. Gaupp, W. Peatman, Th. Schroeter, "Magnetic Measurements on U-2," Internal Report BESSY, Berlin 1991.

[5] K. Halbach, NIM A 250,1986, pg. 95-99.

[6] K. Halbach, presentation at the 3rd CUA Workshop at LBL, Feb. 23, 1990.

[7] POISSON is a improved version of TRIM (A.M. Winslow, J. Computer Phys. 1, 149, 1967), dev. by K.Halbach et al.

[8] K. Halbach, "Design of Hybrid Insertion Devices", 16 Lectures, LBL, Oct 1988 - March 1989, Pub. V8811.1-16.

[9] R. Savoy, "Magnetic Design of the Undulators for the SRC crossed undulator," to be published as ANL LS Note.

[10] M.A. Green, personal communication.

[11] We thank E.Hoyer (LBL) for his help in the coil design.

[12] R. Savoy, ANL LS Note 151 (1990).

THE U5.0 UNDULATOR FOR THE ALS*

E. Hoyer, J. Chin, K. Halbach, W. V. Hassenzahl, D. Humphries, B. Kincaid,
H. Lancaster, D. Plate

Lawrence Berkeley Laboratory, University of California
Berkeley, California 94720

Abstract

The U5.0 Undulator, an 89 period, 5 cm period length, 4.6 m long insertion device has been designed and is in fabrication. This undulator will be the first high brightness source, in the 50 to 1,500 eV range, for the Advanced Light Source (ALS) and is scheduled for completion in 1992. A modular hybrid configuration utilizing Nd-Fe-B permanent magnet material and vanadium permendur is used that achieves 0.837 Tesla effective peak field. Correction of the vertical field integral is with permanent magnet rotors at the ends. Gap adjustment is with an arrangement of roller screws, chain drives, a gear reduction unit and a stepper motor driven by a closed loop control system. The vacuum chamber design is a two-piece, machined and welded 5083-H321 aluminum construction of 5.1 m length. Magnetic design, subsystem design and fabrication progress are presented.

I. INTRODUCTION

The Advanced Light Source (ALS), a third generation synchrotron radiation source, is currently under construction at the Lawrence Berkeley Laboratory.[1] This facility consists of a 50 MeV linac, a 1 Hz, 1.5 GeV booster synchrotron and a low-emittance electron storage ring optimized for the use of insertion devices at 1.5 GeV. The use of insertion devices in the storage ring will produce high brightness beams in the UV to soft X-ray range.

The U5.0 Undulator will be the first high brightness source in the 50 to 1,500 eV range. It is scheduled for completion in 1992. To achieve high brightness, the U5.0 undulator design must meet the stringent requirements derived from the need for rapid scanning of narrow spectral features and the need to avoid perturbing the electron beam in the storage ring.[2]

The engineering parameters, shown in Table I for the U5.0 Undulator, are derived from operating constraints and spectral and storage-ring requirements. Figure 1 shows an end view of the U5.0 Undulator with most major subsystems identified.

II. MAGNETIC STRUCTURE

The magnetic structure provides the required magnetic fields and includes the periodic magnetic structure, end magnetic structures, backing beams and if required auxiliary tuning coils.

The ALS insertion devices incorporate hybrid magnetic configurations consisting of Nd-Fe-B magnetic blocks and vanadium permendur poles. The hybrid design was chosen because there are several advantages over the pure current sheet equivalent material (CSEM) design.[3]

U.S. Government work not protected by U.S. Copyright.

Table I. U5.0 Undulator engineering design parameters

Parameter	Value
Maximum peak field (@ 1.4 cm magnetic gap)	0.89 T
Effective peak field (@ 1.4 cm magnetic gap)	0.837 T
Period length	5 cm
Number of periods	89
Number of full field poles	179
Nominal entrance sequence	0,-1/2,+1,-1
Overall length	455.8 cm
Pole width	8 cm
Pole height	6 cm
Pole thickness	0.8 cm
Number of blocks per half-period (one side of pole)	6
End correction range (B_y)	1,500 G cm
End correction range (B_x)	None
Steering coils (short)	~ 25 cm
Dipole trim coils (long)	4.5 m
Steering and trim field strength	± 5 G
Systematic gap variation	58 μm

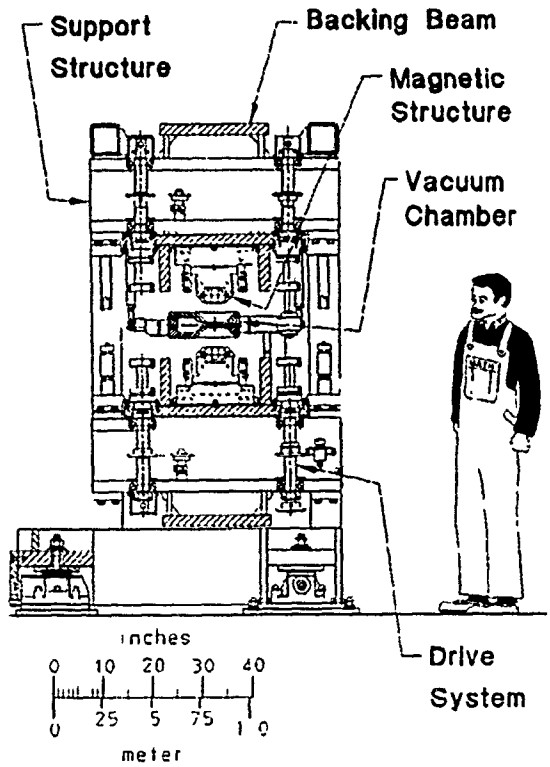


Fig. 1. U5.0 Undulator Design.

For undulators, the objective of the magnetic design is to develop a magnetically well behaved structure which yields a high value of B_{eff} for mid-plane fields. B_{eff} is given by

$$B_{eff}^2 = \sum_{i=0}^{\infty} \left(\frac{B_{2i+1}}{2i+1} \right)^2 \qquad (1)$$

where B_1 is the amplitude of the fundamental, B_3 is the amplitude of the third harmonic, etc.

The magnetic configuration is based on 2-D modeling with the computer code PANDIRA and a 3-D Hybrid theory for hybrid CSEM insertion devices.[4,5] To verify the magnetic design for U5.0, a model was built and tested under a variety of conditions.[6] The undulator performance criteria are met by tolerances based on the hybrid CSEM insertion device theory. The tolerances established for U5.0 are given in Table II.[7]

Figure 2 shows the U5.0 magnetic structure, which is made of: a) half-period pole assemblies, that include an aluminum keeper, a vanadium permendur pole pinned into the keeper and six Nd-Fe-B blocks (3.5 cm square by 1.7 cm thick in the magnetization direction) bonded into the assembly[8] (this design allows for accurate vertical and longitudinal pole tip placement); b) assembly sections that consist of an aluminum pole mount onto which 35 half-period pole assemblies are mounted and accurately positioned; c) stress relieved steel backing beams that are 4.5 m long, 81 cm deep, and 89 cm wide[9] (each beam provides magnetic shielding and holds five assembly sections and two end sections); and d) dipole and steering coils, if needed.

Table II. U5.0 Magnetic Structure tolerances

Error Type	Total Tolerance	Error (%)
Spacing CSEM to pole	102 μm	0.08
Pole thickness	50 μm	0.03
Vertical pole motion (gap)	22 μm	0.05
Pole width	100 μm	0.03
Surface easy axis orientation	± 2.3 degrees	0.16
	Total:	0.19

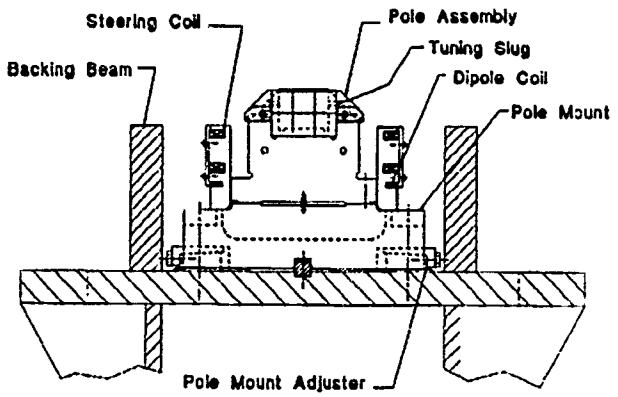


Fig. 2. U5.0 magnetic structure assembly section

The upper and lower backing beams are tied together with low reluctance Ni-Fe linkages to reduce the effect of environmental fields on the electron beam trajectory.[10]

To avoid steering the beam as it travels through the insertion device, it is necessary to control the configuration of the fields at the ends. Figure 3 shows the end magnetic structure that utilizes a system of Nd-Fe-B rotors to fine-tune the fields at the ends of the insertion device. There are four rotors at each end, and a fixed quantity of Nd-Fe-B at each rotor location. In the absence of significant gap-dependent field errors in the periodic structure, a single set of orientations for the rotors should minimize steering over the entire range of gaps.

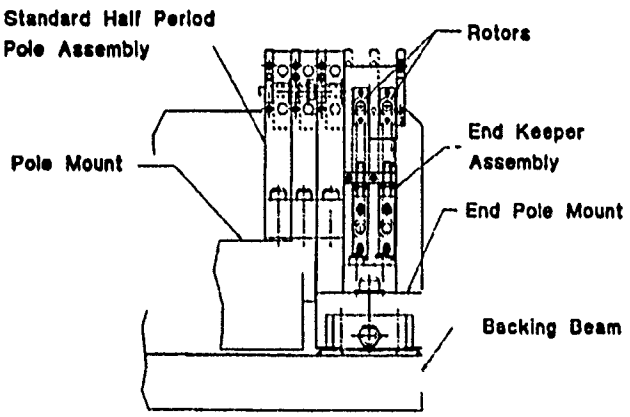


Fig. 3. End pole assembly.

III. SUPPORT AND DRIVE SYSTEMS

The support and drive systems include the support structure that provides the framework for holding the magnetic structure and the drive system that opens and closes the magnetic gap. Requirements for the support structure include: supporting a maximum magnetic load of 84,000 lb; maintaining a magnetic gap variation of 58 μm at the smallest gap (14 mm); meeting the ALS storage ring, tunnel and adjacent beamlines space requirements; accommodating the vacuum system and its support structure; and, being capable of installation, alignment and servicing in the storage ring.

The support structure is of rigid construction consisting of a base onto which two lower horizontal members are mounted. Four vertical posts are in turn attached to the lower horizontal members and the two upper horizontal members are attached to the tops of these posts. The four horizontal beams pass thru the webs of the backing beams to limit the overall height of the support structure to less than the 8 ft tunnel height.

A magnetic-load compensating spring system is provided to counteract the gap-dependent magnetic load.[11] Each of the eight spring assemblies consist of two helical compression springs connected in series to match the gap dependent magnetic load to within 20%.

The drive system requirements are set by the spectral requirements and include: the capability of opening the magnetic gap with an 84,000 lb magnetic load; a step resolution of 1 μm; a maximum scanning speed of 2.3 mm/s; a magnetic gap range of 1.4 cm to 21.6 cm; an opening or closing time of five minutes or less and determination of gap position by an absolute encoder.

Changing the magnet gap in an insertion device requires moving the backing beams. This is accomplished by rotating the 2 mm pitch Transrol roller screws that are mounted to the horizontal beams and support the backing beams. Specifically, the four right-handed roller screws attach to the upper backing beam and the four left-handed roller screws attach to the lower backing beam. They are connected by a shaft coupling and combine to provide equal and opposite vertical motion when rotated. Gap motion is provided by the rotation of a stepper motor which is transmitted through a gear box and a series of sprocket wheels and roller chains to the roller screws. An absolute rotary encoder is coupled to one of the Transrol roller screw shafts to read the absolute position of the magnet gap.

Undulator temperature control is important. A vertical temperature gradient of greater than 0.1 degree C in the undulator backing beams produces excessive spectral broadening. The U5.0 Undulator will have an enclosure, and the temperature in the enclosure will be maintained by circulating the air.

IV. CONTROL SYSTEM

The insertion device control systems are designed to provide sufficient position accuracy, resolution, velocity and range information for the motors and encoders for all anticipated insertion devices. In addition, the control system must control and monitor the dipole and steering correction power supplies, as well as controlling gap dependent rotator positioning, if required. The insertion device control systems are to be integrated into the overall accelerator computer control system.

A Compumotor system has been selected for the gap control and is currently undergoing tests.

V. VACUUM SYSTEM

The objective of the vacuum system is to provide a 10^{-9} Torr vacuum at the insertion device beam aperture. Figure 4 shows a plan view of an undulator vacuum system. Two vacuum chambers are required for ALS operation, one for commissioning and one for dedicated operation.[12] The commissioning chamber has an elliptical beam aperture of dimensions 1.8 cm vertical x 6.2 cm horizontal. The chamber for dedicated operation has a rectangular beam aperture of dimensions 1.0 cm vertical x 6.2 cm horizontal.

The 5.1 m long undulator vacuum chambers will be made of two pieces of machined 5083-H321 aluminum alloy. Both chambers have a total horizontal aperture of 21.8 cm, the inner 6.2 cm provides the circulating beam aperture and the outer aperture allows the bending-magnet synchrotron radiation to pass through the chamber. The radiation is then absorbed by the photon stop located at the exit end of the chamber. External surfaces of the chambers have pockets machined into them for the magnet poles. The shape allows a minimum magnetic gap of 2.2 cm for commissioning and 1.4 cm for dedicated operation.

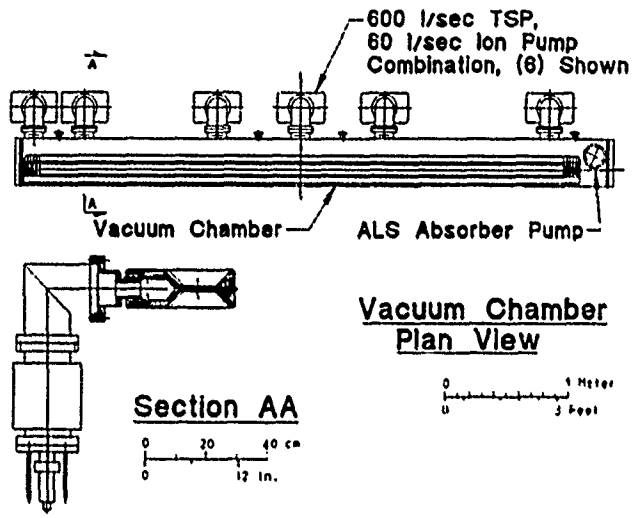


Fig. 4. Undulator vacuum system layout.

The vacuum system consists of six combination 600 l/s titanium sublimation and 60 l/s ion pumps (which give a net pumping speed of 173 l/s each at the antechamber) and an ALS absorber pump of 1450 l/s capacity giving a total antechamber pumping speed of 2500 l/s.

VI. ACKNOWLEDGMENT

***This work was supported by the Director, Office of Energy Research, Office of Basic Energy Sciences, Materials Sciences Division of the U.S. Department of Energy, under Contract No. DE-AC03-76SF00098**

VII. REFERENCES

1. "1-2 GeV Synchrotron Radiation Source," LBL PUB-5172, Rev. (July 1986)
2. "U5.0 Undulator Conceptual Design Report," LBL PUB-5256 (November 1989).
3. W.V. Hassenzahl, et al., "Insertion Devices for the ALS at LBL," IEEE Particle Accelerator Conference, 89CH2669-0, Page 1222 (March 1989).
4. K. Halbach, et al., developed PANDIRA, an improved version of POISSON which allows solution of permanent magnet and residual field problems; POISSON is an improved version of TRIM [A. Winslow, J. Computer Phys. 1, 149 (1967)].
5. K. Halbach, "Insertion device Design: 16 Lectures Presented from October 1988 to March 1989," LBL Publication V 8811-1.1-16.
6. W.V. Hassenzahl, E. Hoyer, and R. Savoy, "Design and Test of a Model for the ALS Undulator," to be published at this conference, LBL-29921 (May 1991).
7. R. Savoy, et al., Calculation of Magnetic Error Fields in Hybrid Insertion Devices, LBL-27811.
8. E. Hoyer, "Magnetized Neodymium-Iron-Boron Blocks," LBL Specification 734D (April 1989).
9. E. Hoyer, "Backing Beam Design Calculations," LBL Engineering Note M6834 (May 1989).
10. E. Hoyer, "Flexible Yoke Design," LBL Engineering Note M7039B (July 1990).
11. J. Chin, "Magnetic Load Compensating Springs," LBL Engineering Note M6829 (April 1989).
12. E. Hoyer, "Vacuum Chamber Design," LBL Engineering Note M6806 (February 1989).

Fast Excitation Variable Period Wiggler*

A. van Steenbergen, J. Gallardo, T. Romano, M. Woodle
National Synchrotron Light Source and Physics Department
Brookhaven National Laboratory
Upton, New York 11973

Abstract

The design of an easily stackable, variable period length, fast excitation driven wiggler, making use of geometrically alternating substacks of Vanadium Permandur ferromagnetic laminations, interspaced with conductive, non magnetic, laminations which act as eddy current induced "field reflectors", is discussed and experimental results obtained with short wiggler models are presented.

I. INTRODUCTION

As part of the program of Inverse Free Electron Laser (IFEL) Accelerator Development [1-4], the development of planar wigglers with high K magnitude has been pursued. The IFEL accelerator, as parameterized, makes use of a quasi-sinusoidal magnetic field, with constant maximum field magnitude, and varying wiggler period length, as shown in Fig. 1. Related to the beam injection energy into this accelerator, this period length may vary from a few cm's in length to tenth of cm's. Such a structure could be constructed using presently known techniques employing permanent magnet material. It would, however, be very high in cost because of the nonrepeat feature of the wiggler period length. The use of conventional dc electromagnetic excitation of the wiggler, by means of a multiplicity of individual pole coils, is excluded for the objective of a high field wiggler because of the small value of the period length at beam injection for a typical set of IFEL accelerator parameters. Hence, for the present objective, a new design approach has been pursued, which makes use of easily stackable, geometrically alternating substacks of identical ferromagnetic material (VaP) laminations, which is driven in a fast excitation mode and which makes use of interleaving of conductive, non magnetic, laminations, which act as eddy current induced "field reflectors" [5,6]. In the following, the design approach is given, and experimental results, obtained with short model wigglers, are presented.

II. TECHNICAL APPROACH AND EXPERIMENTAL RESULTS

For the ferromagnetic laminations for this wiggler design a number of basic configurations have been studied by means of two dimensional mesh computations (POISSON) and by means of actual short wiggler model measurements. The adopted configuration is shown in Fig. 2. The laminations are assembled in substacks, and stacked, separated by non-magnetic material laminations. Four straight current conductors, in parallel to the axis of the composite assembly and interconnected only at the ends of the total assembly, constitute the single current excitation loop for the wiggler, permitting ease of stack assembly, compression of the stacks by simple tie rods, and ready adoption of either constant period length or sequentially varying period length.

Initial experimental results obtained with short wiggler models, without conductive material interleaving, indicated expected behavior of maximum on axis field magnitude when varying the period length towards smaller values. It also showed, however, that for these configurations the required field magnitude of B = 12.5 kG. could not be obtained, with a gap value of 4 mm, for a period length of less than approximately 5 cm.

Subsequent to those early trials of a fast excitation driven wiggler, the use of eddy current induced "field reflectors" in the laminated wiggler core, was initiated. This is illustrated in Fig. 3. This led to dramatic enhancement of maximum on axis field magnitude, for a specific wiggler period length and gap value, as shown by the experimental data given in Fig. 4. Field saturation is evident in these results for higher excitation current values. The onset of field saturation is clearly discernible with the onset of distortion of the magnetic measurement probe voltage versus time display. The field value corresponding to the onset of saturation, for a sequence of model measurements with different period length values, was obtained, both for the case of wiggler models without field reflection and with field reflection. This is summarized in Fig. 5. As is evident from these results the specification of 12.5 kG., for a 2.9 cm period length wiggler, with gap value of 4 mm, can readily be met for the fast excitation wiggler with field reflection.

It is of interest to compare the achievable B(max) vs (λ_o/g) for this wiggler, with the permanent magnet "driven" wiggler, such as the classical Halbach hybrid $SaCo_5$-VaP wiggler and the "pure" $SaCo_5$ permanent magnet wiggler. This is shown in Fig. 6. Clearly, the fast excitation wiggler, as presently executed, compares favorably, in terms of B vs λ_o/g behavior, with state of the art hybrid wigglers.

The median plane field versus wiggler longitudinal coordinate was also measured for a number of wiggler models. An example of this, with tapered period length, and a nominal

*This work was performed under the auspices of the U.S. Department of Energy.

0-7803-0135-8/91$01.00 ©IEEE

λ_o = 28.5 mm., is shown in Fig. 7. In this case also, the harmonic content (harmonic and non-sinusoidal content) of the central section of the wiggler models was measured and found to be acceptably small.

III. SUMMARY AND CONCLUSIONS

It is evident from the foregoing that fast excitation driven, laminated Vanadium-Permandur wigglers or undulators, with periodic interleaving of conductive "field reflectors", can provide state of the art (in terms of B(max) vs λ_o/g) wigglers or undulators, which may be optimum for specific applications, such as, for example, the IFEL accelerator module, for which a tapered period length is required.

It is worthwhile to note that similar maximum field on axis versus λ_o/g enhancement as achieved here for the fast excitation wiggler, should be obtainable for a dc electromagnetic wiggler or permanent magnet wiggler with the periodic interleaving ($\lambda_o/2$ separation) of superconducting field exclusion sheets*. The possible maximum enhancement achievable in this case is given by the limiting value of $B_{max}=B_s/\cosh\zeta$ with $\zeta = (\pi g/\lambda_o)$ [7], i.e. making use of periodic superconducting "field reflectors" could, for example, for the case of a λ_o/g value = 3, yield a factor of two enhancement in the wiggler B_{max} versus λ_o/g value, when compared with a room temperature hybrid $SaCo_5$-VaP.

Taking advantage of inherent symmetry, the fast excitation, Cu sheet interlaced, undulator/wiggler can be constructed in the form of a passive septum bounded periodic magnet [5]. As such, it may find also application as a small gap, large number of periods, undulator in conjunction with a storage ring without the need for a bypass configuration.

IV. REFERENCES

[1] C. Pellegrini, P. Sprangle, W. Zakowicz, Intern. Conf. on He Accelerators, 1983.

[2] E. Courant, C. Pellegrini, W. Zakowicz, Phys. Rev. A 32, 1985.

[3] E. Courant, J. Sandweiss, BNL Report 38915.

[4] A. van Steenbergen, in Exp. Progr., ATF, BNL 42664, 1988; and "IFEL Accelerator Demonstration Stage," ATF, BNL 43702, 1989.

[5] A. van Steenbergen, J. Gallardo, T. Romano, M. Woodle, "Fast Excitation Wiggler Development," Proc. Workshop 1 Angstrom FEL, Sag Harbor, NY, 1990, Editor J. Gallardo, p.79, BNL 52273.

[6] A. van Steenbergen, Patent Application 368618, June 1989 (issued August 1990).

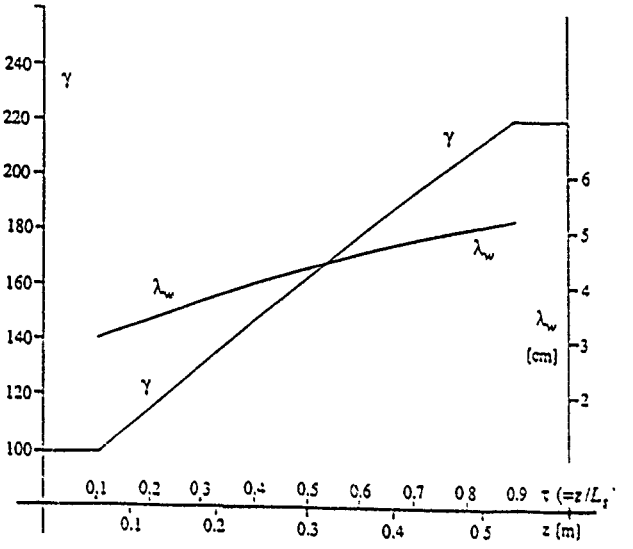
[7] K. Halbach, priv. comm., Workshop 1 Angstrom FEL, April, 1990.

*Note added in proof: The suggested use of periodic located superconducting laminations in a dc electromagnetic wiggler is mentioned by R. Tatchyn, et al. in the Proc. Workshop "PEP as a Synchrotron Radiation Source", SSRL, p. 229, Oct. 1987.22

IFEL ACCELERATOR DEMONSTRATION STAGE*
γ *vs* z; λ_w *vs* z
[B = constant accelerator, B_{max}(wiggler) = 1.25 T.]
[Dielectric coated guide laser transport, α = 0.05 m^{-1}]

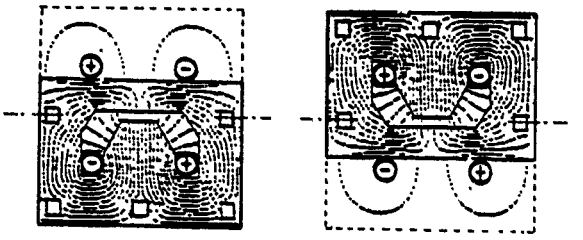
$[\gamma_r^{4/3} = 1.8\ 10^3\ \tau\ L_s\ \exp\text{-}(\alpha\tau L_s) + \gamma_0^{4/3}]$

Fig. 1



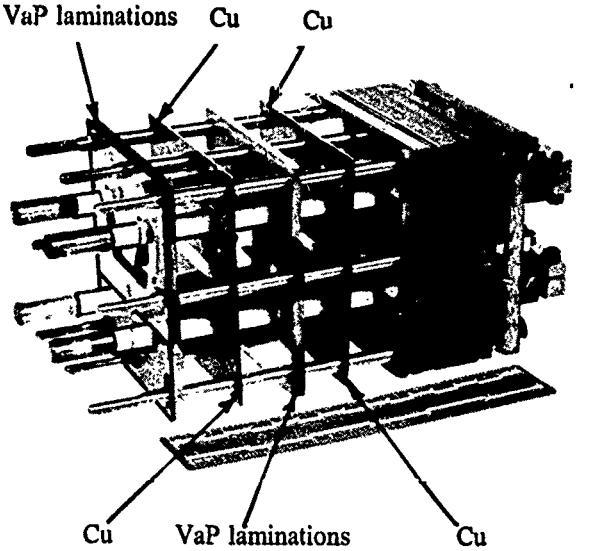
Computed 2D Field Distribution (Excit.current 10 kA)

Fig. 2

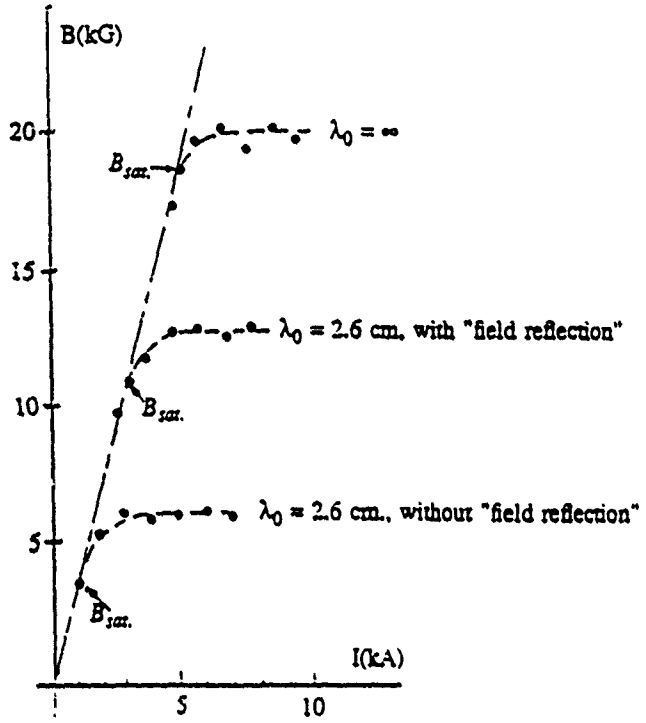


Fast Excitation Variable Period Wiggler

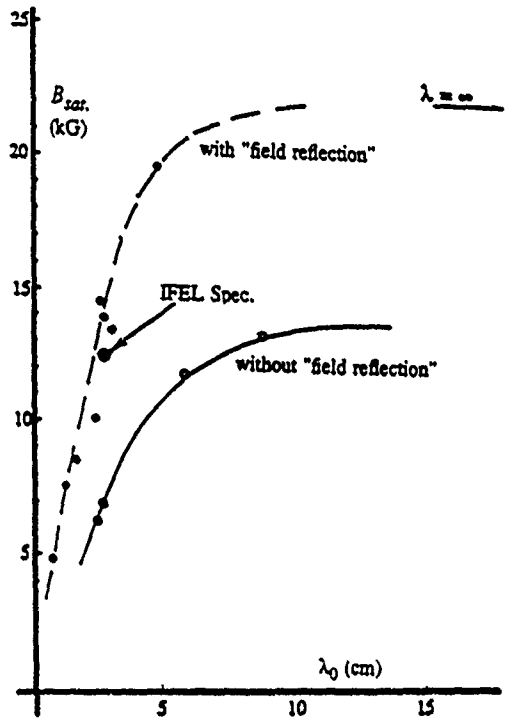
Fig. 3



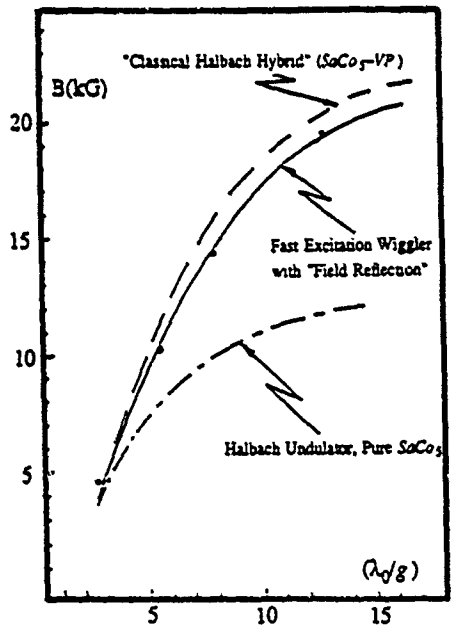
FAST EXCITATION WIGGLER, B vs I
Fig. 4



FAST EXCITATION WIGGLER, $B_{sat.}$ vs λ_0
(Gap = 4.0 mm)
Fig. 5

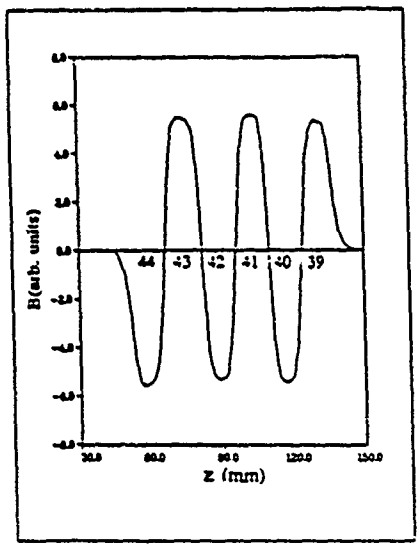


PULSED EXCITATION WIGGLER
Fig. 6



Relative Performance B(max) vs (λ_0/g) for a Permanent Magnet Hybrid ($SaCo_5$–VP), a "pure" $SaCo_5$ Undulator and the Fast Excitation Wiggler with Field Reflection

FAST EXCITATION WIGGLER, B vs z
[With Field Reflection]
Fig. 7



Tapered Period Length Wiggler
I = 4.8 kA; B(max) = 14.85 kG; K(w) = 4.0
$\lambda_0(42)$ = 28.5 mm (Cu = 3.6 mm, d(lam) = 0.254 mm)

Incorporation of a 5 T Superconducting Wiggler in an MLI Synchrotron Light Source

Dan Y. Wang and F.C. Younger
Maxwell Laboratories, Inc., Brobeck Division
4905 Central Avenue
Richmond, California 94804

H. Wiedemann
Stanford Synchrotron Radiation Laboratory

Abstract

The MLI Model 1.2-400 synchrotron light source employs a Chasman-Green lattice with room temperature dipoles producing synchrotron radiation with a critical wavelength of 9.5 Å at 1.2 GeV. To perform angiography studies and micromachining research, the radiation spectrum must be shifted towards shorted wavelength. In this paper it is shown that a 5 pole, 5 T wiggler can be incorporated into the lattice in one of the 3.2 meter long straight sections to obtain a critical wavelength of 2 Å at 1.4 GeV without jeopardizing beam stability.

I. Introduction

The MLI Model 1.2-400 Synchrotron Light Source was optimized for x-ray lithography research. With a view towards other applications, the ring magnets were designed such that they are capable of operation up to 1.4 GeV. Moreover, there are free 3-meter straight sections. Therefore it is of interest to consider incorporating a 5 pole, 5 T superconducting wiggler in one of these straights. With a beam energy of 1.4 GeV, the critical wavelength becomes 2 Å, and the resultant radiation is suitable for micromechanics research as well as for angiography studies.

A 5 pole, 5 T wiggler introduces a significant perturbation to the beam dynamics of the storage ring. In terms of linear optics, wiggler fields add to the vertical focusing, causing a potentially unacceptably large vertical tune shift. In terms of non-linear optics, the higher order fields of the wiggler serve to reduce the dynamic aperture and thus limit the beam lifetime. Both these effects are discussed in section IV. It will be shown that tune compensation can be achieved, and that after including the combined effects of wiggler non-linearities, ring magnet non-linearities and orbit distortions, the dynamic aperture is roughly the same size as the physical aperture.

II. Wiggler Magnetic Fields

The characteristics of the 5 tesla superconducting wiggler for use in the MLI storage ring are shown in table 1. This wiggler is based on a cold iron core and Nb-Ti superconductor. The design uses three full-field poles and two half-field poles to give the field profile shown in figure 1. This profile resulted from a 2D calculation. The field profile is symmetrical and has a zero field integral, so the exit angle equals the entrance angle. The second integral is also zero to give zero net deflection of an on-axis on-angle electron. The calculated path for the on axis beam is shown in figure 2. As can be seen, the displacement at the center of the wiggler is 11.5 mm, and the peak displacement is 17.2 mm.

Table 1. Key Parameters

Maximum field strength	5 tesla
Number of poles	3 full strength, 2 half strength
Pole axial spacing	180 mm
Magnetic gap	70 mm
Rated coil current at 5 tesla	250 amperes
Superconductor	NbTi : Cu :: 1 : 1.8
Size	1.7 × 0.85 mm
Number of turns: large coil	2400
Number of turns, small coil	800
Total photon power at 400 mA	7.8 kW
Peak power per unit length	24.8 W/mm
Heat load to liquid helium	5 W

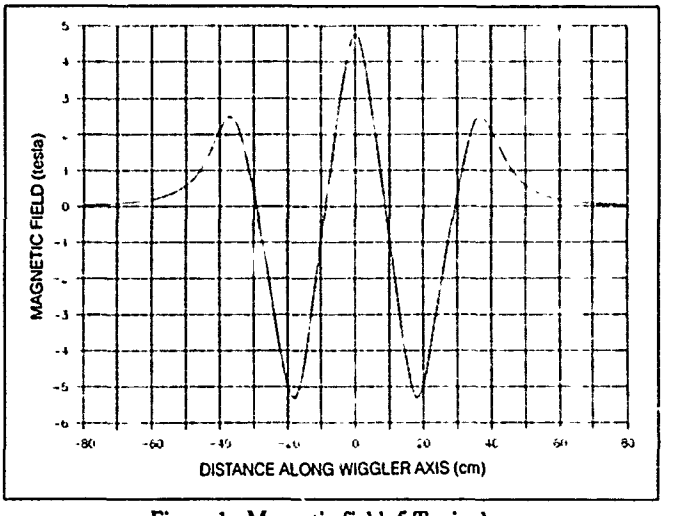


Figure 1. Magnetic field, 5 T wiggler.

The wiggler has five coils per half, arranged in the conventional manner. Zero-field clamps at each end limit the extent of the fringe fields. The iron core provides strength and stiffness in addition to providing a highly saturated flux path. All of the cold portions of the wiggler are cooled by liquid helium and are supported in a cryostat with suitable insulation and current leads. A persistent current switch is not included because the magnetic

0-7803-0135-8/91S03.00 ©IEEE

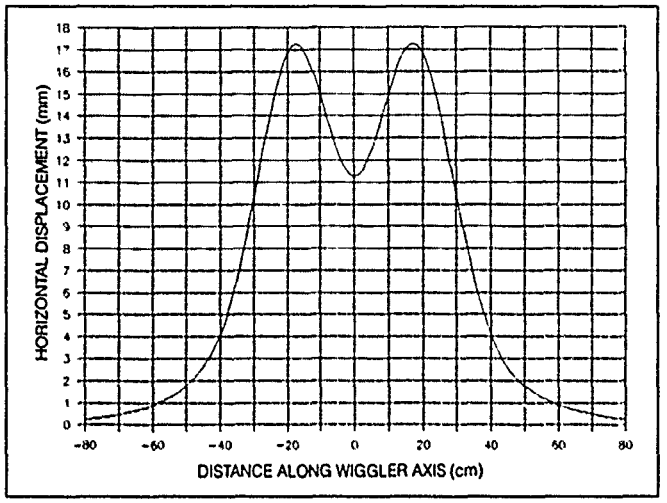


Figure 2. Beam displacement through 5 T wiggler.

field must be reduced during injection. The cycling of the magnetic field is inconsistent with the use of a persistent current switch.

For the purposes of the beam dynamics calculation, a pure sinusoidal field distribution was assumed. In addition, it is assumed that the field is completely uniform in the midplane of the wiggler. The fields can be written approximately as:

$$B_y = B(m) \sin(k_p(z-(m-1)A_p/2))\,(1+\{(k_py)^2/2! + (k_py)^4/4!\})$$
$$B_z = B(m) \cos(k_p(z-(m-1)A_p/2))\,(k_py + \{(k_py)^3/3!\}) \quad (1)$$

where B(m) is given by

m	1	2	3	4	5
B(m)	$B_0/2$	$-B_0$	B_0	$-B_0$	$B_0/2$

The terms outside of braces contribute to linear optics perturbations due to the wiggler. The first term in B_y gives the deflection in the trajectory, while the first term in B_z causes vertical focusing. The terms within braces contribute to non-linear perturbations of the beam dynamics from the wiggler.

III. Tune Compensation

A series of hard-edged rectangular magnets were used to model the additional vertical focusing caused by the wiggler. To define each rectangular pole, two conditions were used: the net deflection angle and the net vertical focusing had to equal that resulting from the sinusoidal field distribution (1). Using the hard-edge model, lattice matching was performed using the program COMFORT with the wiggler inserted in the middle of a straight section. Local compensation was sought whereby only the Q_d's and Q_f's bracketing the straight section containing the wiggler were adjusted. This is preferable to global tune compensation from a synchrotron user viewpoint since the beam conditions in other superperiods are left nominally untouched. Due to the strong effect of the wiggler, local compensation alone led to a vertical tune shift of 0.04 which was deemed too large. To bring the tunes back to the original horizontal/vertical values of 3.264/1.168 (within ±20.004), small global adjustments of quadrupoles in all superperiods were made.

Two quadrants of the lattice functions of the resultant solution are shown in figure 3. With the wiggler included, for the same tune, the quadrupoles bracketing the wiggler are significantly reduced in strength, especially Q_d. The vertical focusing otherwise supplied by Q_d has been replaced by that of the wiggler. From a practical viewpoint, the reduction in quadrupole strengths is advantageous since no new quadrupoles are required. The small change in quadrupole strengths in non-wiggler quadrants changes the beam sizes by no more than 2.5%.

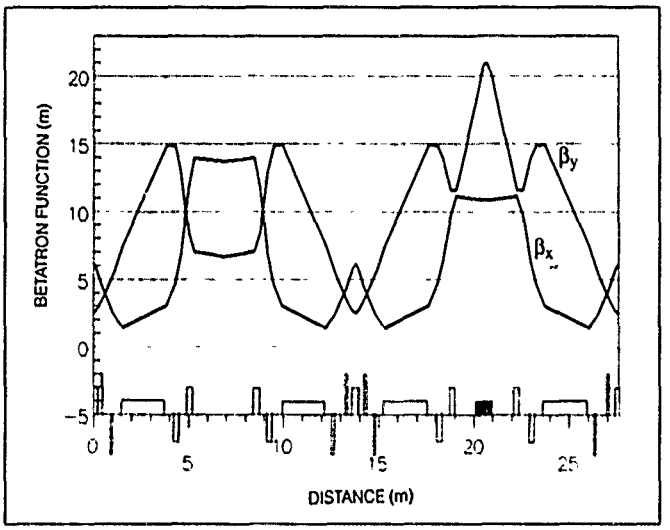


Figure 3. Betatron functions for quadrants without and with 5 T wiggler.

IV. Dynamic Aperture

All calculations of dynamic aperture were performed using an extended version of PATPET. The wiggler was represented as a series of rectangular magnets as described in section III for the purposes of modeling its beam deflection and focusing behavior. The effect of the non-linear fields which are shown within braces in equation (1) was modeled as concentrated kicks on the beam found by integration of the momentum changes caused by these fields along the first order beam path, over which the betatron phase advance is only a couple of degrees in either plane.

To obtain the most realistic estimate of the dynamic aperture (DA) in the presence of the wiggler, other effects which have an impact on the DA were included in this study: the higher order multipoles of the magnets (the strengths of which were found by measurement) and orbit distortions caused either by misalignment or magnet strength errors (the magnitudes of which were based on survey/alignment and power supply tolerances). The magnitudes of these terms are summarized as follows:

Multipole errors: All multipole strengths are defined as the magnetic multipole field at a radius of 1 cm relative to the field of associated main magnet at this radius.

Dipole: main magnet strength = 3.69249 T-m

order	6	8	10
strength	-1.18×10^{-4}	4.76×10^{-6}	-7.39×10^{-6}

Quadrupole: main magnet strength = 3.68 T/m-m (Q_a)

order	6	10	12
strength	4.82×10^{-4}	2.00×10^{-5}	-2.95×10^{-5}

Misalignment/strength errors: all quantities quoted are rms values of Gaussian distributions with a 2σ cutoff.

	x	y	ANGLE	STRENGTH
Quadrupoles, Sextupoles	0.3 mm	0.3 mm	0.05 deg	0.1%
Monitors	1 mm	1 mm	0.5 deg	NA
Dipole	NA	NA	0.1 deg	0.1%

Figure 4 shows the DA computed in units of beam sigma for a variety of circumstances. The baseline reference (curve I) is the DA for a ring with a bare lattice, a single "linear" wiggler insertion and sextupole correction to obtain a chromaticity of +1 in both planes. As seen, when the non-linear fields of the wiggler are included (curve II), the DA is reduced mostly in the vertical, as expected. The net reduction is about 30%. Adding the non-linear terms of the ring magnets (curve III) reduces the DA by another 60%. A further comparable reduction in DA is caused by misalignment and strength errors, as seen from curve IV. For curve IV, even though orbit errors were generally allowed throughout the ring, the orbit error at the wiggler was kept to no more than 0.5 mm. From this study it may be concluded that while wiggler non-linearities do have a significant negative impact on the DA, it is not the dominant one for the lattice studied.

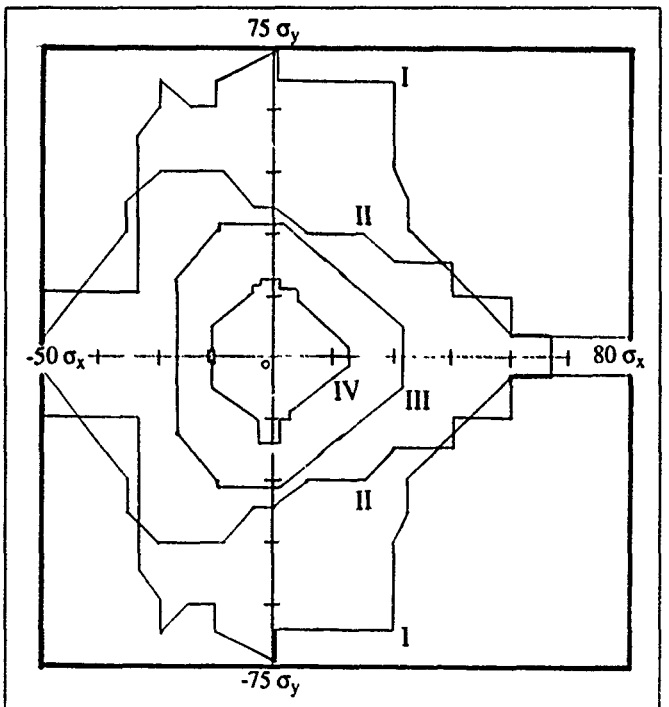


Figure 4. Dynamic aperture reduction from various sources.

Curve IV is a realistic representation of the DA when all non-linearities and orbit distortions are included. A few studies of the DA were made using different starting locations around the ring, effectively changing the sequence of random magnet misalignments. Two examples are shown in figure 5, with starting locations at the midpoint of Q_a and at the wiggler. As expected, the results are comparable in units of sigma, though in absolute space, the values of sigma are quite different (at Q_a, σ_x=1.33 mm, σ_y=0.60 mm; at the wiggler midpoint, σ_x=1.78 mm, σ_y=1.74 mm).

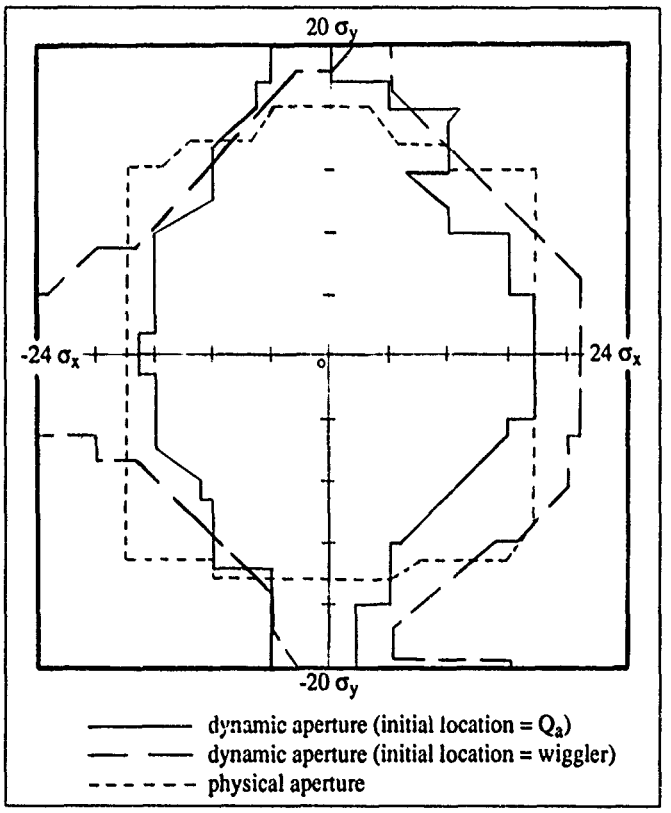


Figure 5. Dynamic aperture with magnet non-linearities, misalignments, and strength errors compared with physical aperture.

The DA can be compared to the physical aperture, which is defined to be the DA for the baseline reference with all real physical limits caused by the vacuum enclosure included. These limits were set at 35 mm × 35 mm for all quadrupoles and sextupoles, and 35 mm × 22 mm for the dipole. The DA with all non-linearities and orbit distortions included is approximately equal to the physical aperture, which is greater than ±10σ in both planes, thus ensuring adequate quantum lifetime.

V. Conclusion

It has been shown that the MLI 1.2-400 light source operated at 1.4 GeV can accommodate a 5 pole, 5 T wiggler which serves to increase the critical energy of the synchrotron radiation to 6.5 keV. While the wiggler non-linearities do reduce the dynamic aperture by some 30%, the resultant dynamic aperture with all non-linearities and orbit distortions included is still equal to the physical aperture so that beam lifetime is not degraded.

Ion Channel Focusing in FEL Wigglers

John Vetrovec
Rockwell International, Rocketdyne Division
6633 Canoga Ave.
Canoga Park, Calif. 91304, (818) 700-4875

Abstract

Accumulation of ions inside FEL wigglers can significantly alter electron beam transport and lead to a reduction of laser gain. This is of particular importance to devices driven by RF accelerators with continuous operation and with long wigglers. We show that while the mechanism for ion channel formation is the same as in electron beam storage rings, the problem appears less severe because the electron beam makes only a single pass through the system. In addition, the electric field of the beam together with the magnetic field of the wiggler cause an *ExB* drift which can provide effective mechanism for ion removal.

INTRODUCTION

The Ground Based Free Electron Laser Technology Integration Experiment (GBFEL-TIE) planned for White Sands, New Mexico, has a continuously operating RF accelerator. Electron beam transport in this system is subject to ion trapping often found in electron storage rings. The problem appears to be most severe in the wiggler where spatial constraints impede vacuum pumping and reduce effectiveness of ion clearing electrodes. In addition, ions have been suspected to accumulate inside wigglers by magnetic mirror effect. Even a small amount of ions trapped inside storage ring beams is highly undesirable because they cause a reduction of beam lifetime and brightness. This problem is unique to cyclic devices where effects of repeated interactions between the beam and trapped ions are cumulative. Ion population in storage rings is controlled by operating the beamline at a very high vacuum, typically in the range of 10^{-10} Torr, and by ion extraction electrodes.

Typical FEL has a single pass electron beam system and, therefore, is not susceptible to cumulative effects. However, for practical reasons the GBFEL-TIE beamline is designed to operate at a higher pressure (about 10^{-7} - 10^{-8} Torr) resulting in higher ionization rates. In addition, the wiggler, which is 15 m long, has a small beam aperture with poor side access for vacuum pumping. That leads not only to additional increase in pressure, but also makes ion extraction electrodes less effective. In absence of efficient ion loss mechanism, a dense ion channel may form inside the wiggler, potentially causing focusing mismatch and emittance growth. As a result, the FEL gain could be compromised. This work investigates criteria for beam neutralization, ion motion in the combined wiggler field and electrostatic potential well, and the impact of beam neutralization on transport as applied to the 15 m GBFEL-TIE wiggler. Our analysis indicates that the magnetic mirror trapping may not be very strong, and that the ions are subject to *ExB* drift which may provide an effective ion removal mechanism. This result is also supported by computer models.

ION CHANNEL FORMATION

An electron beam propagating through the vacuum tube collides with and ionizes molecules of the residual gas. Electrons born in the ionization process are ejected while the ions are trapped by the electric field of the beam. In the absence of an efficient loss mechanism the ion plasma density in the channel can exceed that of the background gas. An electron beam of average current I_{avg} propagating through background gas of density n_o produces ions at a rate

$$\frac{dN_i}{dt} = \frac{I_{avg}}{e}\,\sigma_{01}\,n_o \qquad (1)$$

where e is the elementary charge and σ_{01} is the ionization cross section. At the 100 MeV electron beam energy the cross-section does not vary significantly for the gases of interest [1] and the value of 1.5×10^{-18} cm^{-2} has been used in all calculations. With the background gas at 10^{-8} Torr pressure and 0.23A average current the ion production rate in the GBFEL-TIE wiggler can be as high as 7.6×10^{9} ions cm^{-1} sec^{-1}.

In the absence of a magnetic field the transverse motion of an ion of charge ze and mass M immersed in the beam is described by

$$\ddot{r} - \frac{ze}{M}[E_i + E_b\,P(t)] = 0 \qquad (2)$$

where r is the radial coordinate, t is time, E_i and E_b are respectively the instantaneous electric fields produced by the ion and electron space charges, and $P(t)$ is the micropulse format function. To simplify this analysis, we assume that both the electron beam and the trapped ions have a uniform transverse density distribution. Let b be the beam radius, T_1 the beam bunch length in seconds, F_1 the bunch frequency, $<z>$ the average degree of ionization of the ion plasma, and N_i the ion line density. Then, $E_i(r) = <z>\, e\, N_i\, r/(2\pi\epsilon_o b^2)$ and $E_b(r) = -I_{avg}\, r/(2\pi\epsilon_o c\beta b^2 F_1 T_1)$ where ϵ_o is the permittivity of free space, c the speed of light, and β the relativistic factor.

To find the limiting ion line density we note that if the beam is completely neutralized, ion motion is barely stable. From eq. (2) it is seen that this happens when $<z>\, e\, N_i = I_{avg}/(c\beta)$, i.e., when the ion line charge is same as the time averaged line charge of the electron beam. We define the average fractional neutralization f_{avg} as the ratio of the ion line density and the average electron line density, i.e., $f_{avg} = <z>\, e\, N_i\, c\beta/I_{avg}$. When the beam is completely neutralized, $f_{avg} = 1$. This translates to a line

0-7803-0135-8/91S01.00 ©IEEE

density $N_i = 4.8 \times 10^7$ cm^{-1}, which is about an order of magnitude higher than the density of the background neutral gas at 10^{-8} Torr. It is also useful to define the instantaneous neutralization f_1 as the ratio of the ion line density and the instantaneous electron line charge, i.e., $f_1 = < z > e\, N_i\, c\beta\, T_1 F_1 / I_{avg}$. Using the GBFEL-TIE operating parameters, $F_1 = 54$ MHz and $T_1 = 18$ ps, we get $f_1 = 0.00097\, f_{avg}$.

Except for well neutralized beams, the kinetic energy of a newly born ion is not sufficient to climb out of the potential well presented by the beam space charge and the ion is trapped. However, as the ions accumulate, the potential well becomes more shallow and some of the previously trapped ions escape. Again, assuming a uniform beam density, the time dependent potential inside the beam can be expressed as

$$U(r,t) = \frac{1}{4\pi\epsilon_o}\left[< z > e\, N_i\,(t) - \frac{I_{avg}}{c\beta}\right]\left(1 - \frac{r^2}{b^2}\right) \quad (3)$$

Combining eq. (1) and (3) it can be shown that the time dependent average neutralization fraction is then

$$f_{avg}(t) = \left[1 + (c\beta\sigma_{01} n_o t)^{-1}\right]^{-1} \quad (4)$$

This means that at 10^{-8} Torr (and in absence of other ion loss mechanism) the electron beam would be 50% neutralized in about 60 ms and 90% neutralized in about 650 ms. Evidently, unless ions are efficiently removed, continuous operation of the accelerator leads to a fully neutralized beam.

EFFECTS ON ELECTRON BEAM TRANSPORT

Dense ion channel present in the wiggler partially neutralizes the electron beam which upsets the Lorentzian cancellation of beam self fields and the beam tends to focus. This changes the acceptance of the wiggler and produces a mismatch to the injection optics. In particular, the beam envelope inside the wiggler satisfies the equation [2]

$$\frac{d^2 b}{ds^2} + k_\beta^2\, b - \frac{\epsilon_{rms}^2}{b^3} - \frac{K_f}{b} = 0 \quad (5)$$

where s is the beam propagation path, k_β is the wiggler betatron wave number, ϵ_{rms} is the rms emittance, and K_f is the generalized perveance

$$K_f \equiv \frac{2 I_{avg}\, r_c\, (1 - \beta^2 - f_1)}{ec\beta^3\gamma} \quad (6)$$

with r_c being the classical particle radius, and γ the relativistic factor. Equation (5) has been numerically solved for various levels of neutralization and the results are plotted in Figure 1. As the neutralization sets in, the envelope of the beam starts to oscillate. Changing the cross section of the electron beam reduces the overlap between the electron and the FEL laser beam, which results in a loss of FEL gain. At 100% neutralization, the rms beam radius drops to about 65% of its nominal value which translates to well over 50% loss of FEL power. This problem is potentially correctable by changing the setting on wiggler injection optics.

In the simple analysis above it is assumed that both the beam and ion channel densities are uniform. Such simplification is highly optimistic for realistic electron beams. Moreover, there is little guarantee that the spatial distributions of the beam and the ions are even similar. As a result, the trapped ion plasma could present the electron beam with a highly nonlinear focusing channel. Such conditions are known to produce emittance growth [3]. While the analysis of this phenomenon is beyond the scope of this article, it is recognized that such effects could be of overriding importance [4].

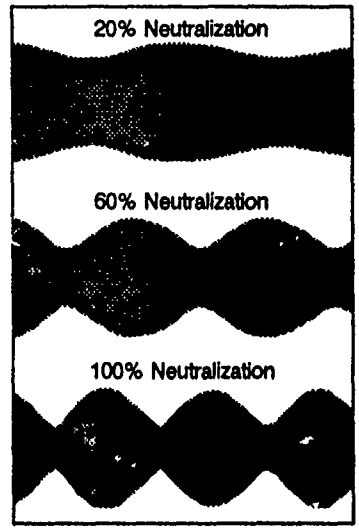


Figure 1. Beam envelope oscillations caused by neutralization driven mismatch into wiggler focusing channel

ION LOSS BY *ExB* DRIFT

The magnetic field of the wiggler has a profound effect on the motion of trapped ions. First, we note from eq. (2) that the ions execute transverse oscillations at a frequency roughly an order of magnitude lower than the beam bunch frequency. So a test ion reacts only to the time averaged electric field of the combined electron and ion plasma space charge. At the edge of the beam this field has a maximum value E_{avg} of about 28 kV/m. In the wiggler plane an ion born at a location x_o is subjected to an *ExB* drift

$$v_E = \frac{E_{avg}}{B_y}\,\frac{x_o}{b} \quad (7)$$

where B_y is the local magnetic field which is assumed to be roughly constant over one cyclotron gyration, Figure 2.

This simple model is verified by numerical simulations using a fully 3-dimensional model of magnetic field and particle transport, with a temporal resolution sufficient to track individual 18 ps micropulses of the beam. A sample plot of computed ion trajectory presented in Figure 3 exhibits the characteristic cycloid shape of a particle subjected to *ExB* drift. The orientation of the cycloid flips as the magnetic field switches polarity. It is important to note that in a single gyration the ion generally remains in a constant magnetic field which validates our simple analysis.

In a wiggler field of 0.5 T an ion born at the edge of the beam drifts at an average velocity of 5.6×10^4 m/s. So the av-

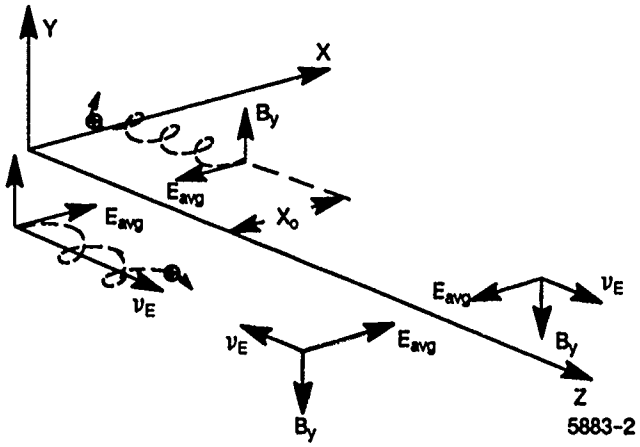


Figure 2. *EXB* drifts in wiggler field

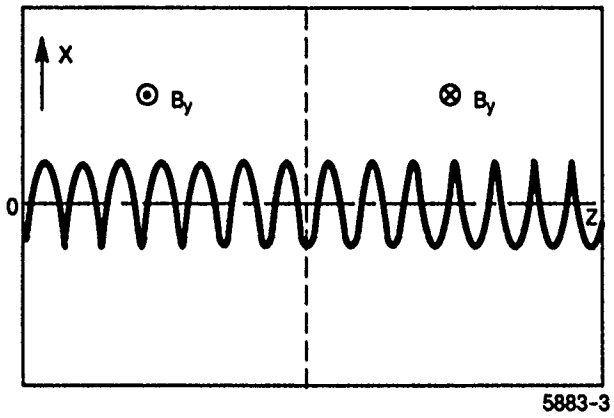


Figure 3. Computer simulation of ion drift

erage ion lifetime τ_i in a wiggler 15 m long is about 130 μs. At 10^{-8} Torr background pressure this suggests an ion line density $N_i = (dN_i/dt)\ \tau_i$ of about 1 x 10^6 ions/cm which translates to average neutralization f_{avg} of 0.2%. Admittedly, this kind of analysis is exceedingly optimistic. Ions born closer to the beam center see a lower electric field and those born between wiggler poles see a reduced magnetic field. Also, as the ions start to accumulate, the electric field of the beam is partially canceled. In either case, the drift velocity is reduced. To account for such nonoptimistic situations we estimated the average drift velocity to be a factor of 10 lower then above. Happily, this still translates to a relatively low neutralization of 2%.

Despite the fact that electric and the magnetic field have significant spatial variations, our computer simulations failed to detect ion trapping by magnetic mirror effects as seen by our colleagues [5]. We intend to perform a more thorough investigation of this phenomenon in the future.

CONCLUSION

We presented our initial analysis of the trapped ion problem expected in the GBFEL-TIE wiggler. In the absence of an effective ion removal mechanism, the electron beam is fully neutralized. While catastrophic beam pinching does not take place, the focusing mismatch could significantly reduce FEL power. In addition, emittance growth is strongly suspected and warrants further study. However, the *ExB* drift promises to be very effective for removing of trapped ions and reducing the neutralization to a tolerable level. Additional work is needed to to analyze this phenomenon under all operational conditions.

REFERENCES

1. F. F. Rieke and W. Prepejchal, "Ionization Cross-Sections of Gaseous Atoms and Molecules for High Energy Electrons and Positrons," Phys. Rev. A, Vol. 6, No.4, 1972.
2. J. D. Lawson, "Space Charge Optics," in the "Applied Charged Particle Optics," part C, ed. by Septier, Academic Press, New York, 1983.
3. J. D. Lawson, "The Physics of Charge Particle Beams," Clarendon Press, Oxford, 1988, Sect. 2.2 and 4.4.
4. L. Thode, LANL, personal communications, September 1989.
5. Y. H. Chin, LBL, personal communications, March 1990.

Performance of Rocketdyne Phase-optimized Pure Permanent Magnet Undulator,

G. Rakowsky, B. Bobbs, J. Brown, P. Kennedy and G. Swoyer
Rockwell International, Rocketdyne Division
6633 Canoga Avenue, Canoga Park, CA 91303

Abstract

Preliminary results of magnetic measurements of a high field, pure permanent magnet (PPM) undulator are presented. A two-step optimization process, using simulated annealing, was applied to reduce the RMS field error and to minimize RMS phase shake, trajectory walkoff and integrated dipole and multipole field errors by optimally arranging the magnets. The field-terminating end module design is a novel implementation of Halbach's displacement-free termination scheme. Simulations of entry/exit trajectories for this termination are compared to trajectories computed from field measurements.

I. INTRODUCTION

A high-field, pure permanent magnet (PPM) undulator design [1] has been under development at Rocketdyne with the objective of delivering optimal performance in free electron lasers (FEL's) and in synchrotron radiation (SR) sources. The iron-free structure allows construction of field models by superposition of measured fields of individual magnets or modules, and permits evaluation of the performance of any given arrangement of magnets. An optimization algorithm such as simulated annealing [2] may then be used to select and sort magnets or modules to minimize various errors and to optimize device performance. The effectiveness of SA in minimizing trajectory wander has been demonstrated in Rocketdyne's Wiggler I, [3] an 80-period PPM device with a low field, "classical" 4-block-per-period geometry. Wiggler II was constructed to implement the high field, 6-block design and to demonstrate the higher level of optimization possible with this structure. This paper reviews the design of Wiggler II and discusses the results obtained from initial field mappings

The last section describes the novel, non-steering, displacement-free end sections installed on Wiggler II. Entry/exit trajectories computed from the field maps are compared with simulations.

II. WIGGLER II DESIGN

The basic design, shown in Figure 1, is an implementation of the Halbach PPM wiggler concept [4] and has been described previously. It employs 6 magnets per period in two opposing arrays forming a planar wiggler or undulator. The magnetic structure uses two basic magnet types: Type A with vertical magnetization and Type B magnetized at 60° from the vertical. Magnet dimensions have been optimized to achieve 93% of the theoretical maximum on-axis field obtainable in a planar Halbach PPM structure.

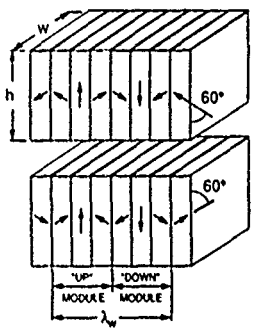


Figure 1. High field PPM structure.

Each half-period triplet module consists of an A magnet flanked by two B magnets, clamped in an aluminum holder. There are two types of modules, "up" and "down", which alternate to form the periodic structure (Figure 1). The magnet holders are located by dowel pins in the I-beam-supported aluminum magnet trays. Independent stepper motor drives allow tapering of the magnetic gap in FEL's. The mechanical design is shown in Figure 2. Table 1 lists the key parameters.

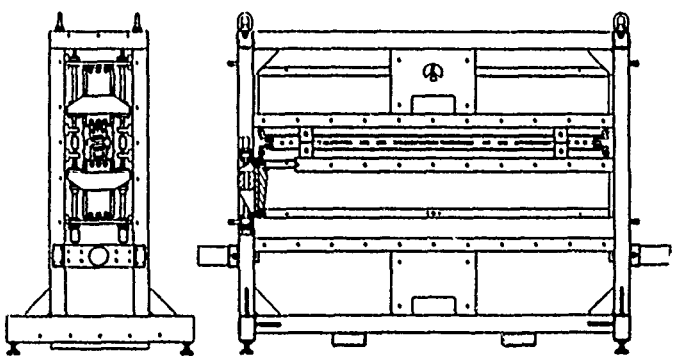


Figure 2. Wiggler II mechanical design.

Table 1

Rocketdyne High Performance Undulator
Design Parameters

Type	Pure Permanent Magnet
Structure	6 Magnets/period
Period	2.4 cm
No. Periods	82
Length	2 m
Taper	Variable, linear gap
Magnet Material	$SmCo_5$
Remanent Field	0.97 T
Minimum Gap	0.76 cm
Peak Field (max)	0.65 T
K_w(max)	1.47

0-7803-0135-8/91$01.00 ©IEEE

The 2m long trays were designed for an 83-period structure plus half-strength end modules as well as rotatable trim magnets. However, the structure was shortened to 78 periods to accomodate the new, displacement-free terminations, and to permit adequate mapping of the entry/exit regions by the externally-mounted, dual Hall probe field mapper, whithin the travel limits imposed by the wiggler frame.

III. OPTIMIZATION

The natural modularity and symmetry of the 6-block geometry lends itself to a two-step optimization process. A total of 1245 magnets (415 Type A and 830 Type B) were purchased and individually characterized in each orientation, using the Hall probe scanning technique. Effects of ambient temperature and probe drift were accounted for by scanning a reference magnet along with the magnet under test. This resulted in a repeatability error of 0.04%. The integrated field "kick" values, were input to a "Stage 1" version of the SA code which selected and arranged magnets to form an optimized set of 190 "up" and 190 "down" triplets with minimized variation in triplet strength. The modules were assembled as prescribed and recharacterized. With magnet tolerances of ±2% on remanence and ±1° on magnetization angle, the code predicted a variation of triplet strength of σ=1.25% for random selection of magnets, while for the annealed set the prediction was σ=0.19%. The actual measured variation was σ=0.23%.

For the next stage of optimization, the 380 triplet modules were remapped for both x and y field components, on- and off-axis. The on-axis By scan data were used to set up the modified Kincaid-type, quasi-sinusoidal field and trajectory models described by Bobbs et al.[5] This model takes into account the field overlap among neighboring modules and distributes the errors associated with each triplet among neighboring intervals. The transverse (Bx) field components were modeled as a sequence of point-kicks, and the out-of-plane (y-z) trajectory was then represented by a simpler, piecewise-linear model.

The algorithm for Stage 2 optimization selects and arranges triplet modules with appropriate orientation in the wiggler array, then evaluates the RMS walkoff and phase shake in x and y from the models desribed above. In addition, the on-axis and off-axis field integrals of the individual triplets in the array are summed to compute the predicted normal and skew dipole, quadrupole and sextupole errors for the given configuration. The total "cost function" is a weighted sum of these 10 error terms, which is evaluated for each iteration. The SA algorithm provides a systematic search for an arrangement which produces a global minimum of the cost function.

Preliminary Results

Initial field maps have been taken of the 78-period structure for both the normal (By) and transverse (Bx) field components, on and off-axis. The structure includes the displacement-free terminations, discussed in the next section. Data were taken at a gap of 11mm. Analysis shows that the measured peak field of 0.42 Tesla agrees with the value predicted by the Halbach formula to better than 1%. As expected, the field of the 6-block geometry has very low harmonic content, with only 0.25% measured third harmonic. The RMS field errors are 0.83% for By and 0.34% for Bx. Comparison of the By field error with the 0.23% RMS variation of triplet strength found earlier, suggests that the bulk of the error probably comes from construction errors.

Integrating the fields twice and scaling to an electron gamma of 80 yields the trajectory in the x-z wiggle plane shown in Figure 3. In the calculation we subtracted a DC field offset of 0.25 Gauss. The RMS walkoff in the x-z plane is 0.32 of the wiggle amplitude, well within target and similar to that obtained in Wiggler I . Walkoff (Xerr), which is computed as the difference between the trajectory and a best-fit sinusoid over the core of the undulator, is also plotted in Figure 3

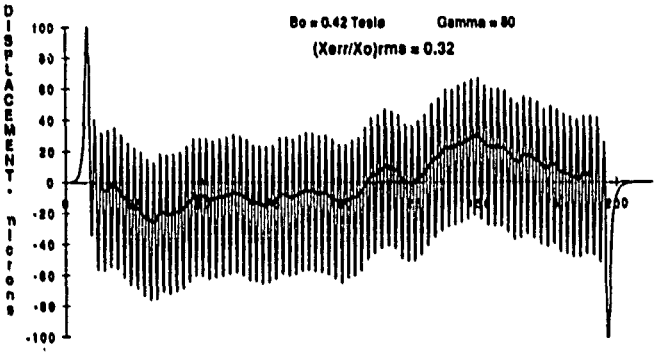


Figure 3. Trajectory in wiggle plane and walkoff error.

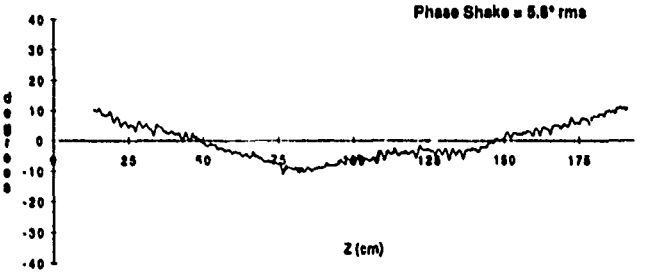


Figure 4. Phase error in x-z plane.

Phase error was computed by numerically integrating the path lengths along both the wiggle trajectory and the best-fit sinusoid and expessing the difference in degrees of phase at the resonant optical wavelength. A plot of the phase error is shown in Figure 4. Overall, the RMS value of the phase error (phase shake) is 5.8°. According to statistical studies by Kennedy et al.,[6] this should assure small-signal FEL gain or fundamental spectral brightness of better than 90% of ideal. However, the gross feature of the plot is a bow, indicating a long-range, systematic field variation, which may be removed by adjusting the gap taper. The remaining phase variations due to local magnet errors are then quite small, on the order of 1-2°, as expected.

Calculation of the y-z trajectory form the Bx field data showed a severe walkoff, indicating that perhaps the Bx field errors were accumulating instead of cancelling. Indeed, it was found that the formulation of the y-z walkoff erroneously

included an alternating negative sign. One could correct this error by simply rotating every other module 180° about the vertical axis. However, such a reversal would also affect the quadrupole cost function, which is sensitive to module orientation. It appears then, that the best solution would be to disassemble the arrays and redo Stage 2 annealing.

Another source of error was the fact that the trays were fabricated separately from the support beams, resulting in peak gap variations of up to 40 microns and a twist of about 1°. We attempted to compensate for the gap errors by introducing a field scaling correction factor in the formulation of the cost function. From the plot of trajectory error it appears that the compensation was only partially successful. Clearly, the better approach would be to eliminate the problem by regrinding the trays mounted on their support beams.

Quadrupole and sextupole errors were not minimized adequately either. Again, this may be due in large part to the gap errors.

IV END SECTION DESIGN

Two different termination schemes have been considered for Wiggler II. The first was a non-steering termination using half-strength end modules. In the 6-block geometry such a module is easily realized with just a single Type A magnet flanked with nonmagnetic "dummy" blocks. The arrangement is illustrated in Figure 5a. The magnets could be selected to cancel any residual trajectory steering. Since the terminating magnets are the same size and type, and are at the same gap as the core of the structure, their fields should track with gap changes and the trajectory should remain true. This scheme does, however, produce a small trajectory displacement, on the order of a wiggle amplitude.

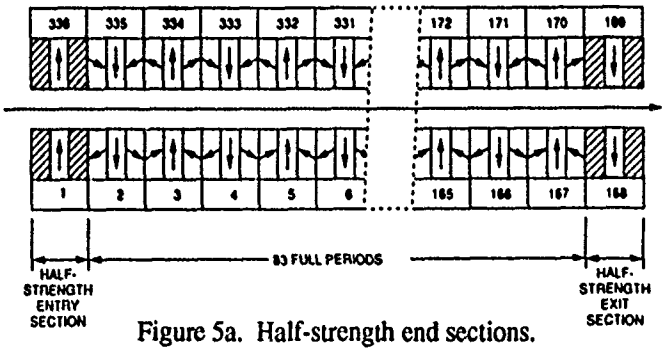


Figure 5a. Half-strength end sections.

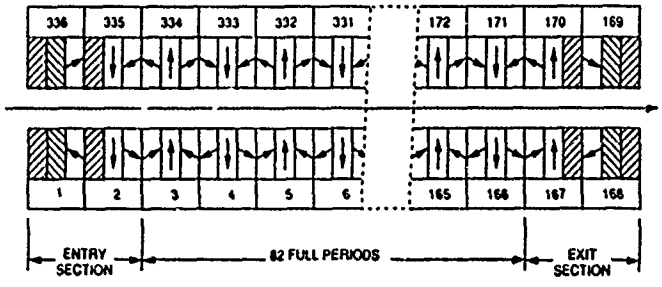


Figure 5b. Non-steering, dispplacement-free termination.

Recently Klaus Halbach suggested a *displacement-free*, non-steering termination scheme for PPM structures analogous to the arrangement he devised for hybrids.[7] We developed a variant of the scheme which again uses only standard magnets and modules, with one or two magnets replaced by dummy blocks. This termination, shown in Figure 5b, has been implemented in Wiggler II.

To simulate the trajectory through the new end section, field scan data of a typical A-type and B-type magnet were used to construct by superposition the fields in the entry region. These were then twice integrated numerically to obtain the plots shown in Figures 6 . The form of the trajectory shown in Figure 3 agrees well with the simulation. The 12 magnets used in the terminations were initially chosen at random to confirm the validity of the termination design. Final selection will be done by a Stage 3 optimization process, to cancel any remaining trajectory or multipole errors.

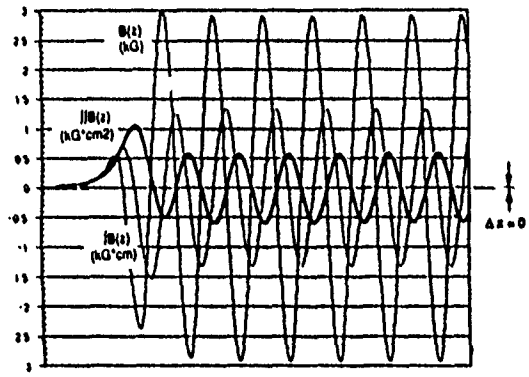


Figure 6. Simulation of fields and trajectories through entry region with displacement-free termination.

V. ACKNOWLEDGEMENT

The authors thank Cynthia Todd and Youssef Kohanzadeh for their assistance in hardware assembly, mapping and data reduction

VI. REFERENCES

[1] G. Rakowsky *et al.*, "High Performance Pure Permanent Magnet Undulators," *Proc. 11th Int'l. FEL Conf.*, Nucl. Inst. Meth. ,vol. A296, pp. 597-602, 1990.

[2] A. Cox and B. Youngman, "Systematic Selection of Undulator Magnets Using the Technique of Simulated Annealing," Proc. SPIE, vol. 582, p.91, 1986.

[3] M. Curtin *et.al.*, "A High Quality Permanent-Magnet Wiggler for the Rocketdyne/Stanford Infrared Free Electron Laser", Proc. IX Int'l. Free Electron Laser Conf., Nucl. Inst. Meth. vol. A272, pp. 187-191, 1988.

[4] K. Halbach, "Physical and Optical Properties of Rare Earth Cobalt Magnets," Nucl. Inst. & Meth., vol. 187, pp. 109-117, 1981.

[5] B. Bobbs *et al.*, "In Search of a Meaningful Field Error Spec for Wigglers", *Proc. 11th Int'l. FEL Conf.*, Nucl. Inst. Meth. ,vol. A296, pp. 574-578, 1990.

[6] P. Kennedy *et al.*, "Statistical Variation of FEL Performance Due to Wiggler Field Errors," *Proc. 11th Int'l. FEL Conf.*, Nucl. Inst. Meth. ,vol. A296, pp. 607-610, 1990.

[7] Klaus Halbach, private communication, August 24, 1990.

DESIGN AND TEST OF A MODEL POLE FOR THE ALS U5.0 UNDULATOR

W. V. Hassenzahl and E. Hoyer

Accelerator and Fusion Research Division, Lawrence Berkeley Laboratory,
University of California, Berkeley, California 94720

R. Savoy

Argonne National Laboratory, Argonne, Illinois 60439-4814

Abstract

The ALS insertion devices must meet very tight requirements in terms of field quality and field strength. Even though the ability to calculate the performance of a hybrid insertion device has improved considerably over the past few years, a model pole was assembled to test the ALS U5.0 undulator geometry and to verify the calculations. The model pole consists of a half period of the periodic structure of the insertion device, with mirror plates at the midplane and at the zero-field, half-period planes. A Hall probe was used to measure the vertical component of the field near the midplane of the model as a function of gap and transverse position. Field quality requirements demand that the ALS insertion devices be designed to permit several types of correction, including the capability of adding magnetic material or iron at several locations to boost or buck the field. This correction capability was evaluated during our tests. The model is described and the test results are discussed, including the fact that the measured peak field is several percent higher than the calculated value, which is based on the measured magnetization of the blocks used in the model.

I. INTRODUCTION

Insertion devices for the Lawrence Berkeley Laboratory (LBL) Advanced Light Source (ALS) and other third generation synchrotron light sources must meet more stringent tolerance requirements than insertion devices built to date for existing light sources. Considerable effort has been dedicated to the development of requirements for the U5.0, a 5 cm period undulator,[1] the first insertion device for the ALS. The preferred design choice for high performance devices is a hybrid configuration with vanadium permendur poles and neodymium-iron-boron (Nd-Fe-B) permanent magnets. The performance of a device is determined by the peak field at minimum gap and the magnetic field errors. The peak field as a function of gap can be calculated with a three dimensional theory of hybrid devices[2]. An extension of this theory[3] was used to estimate the field errors due to various material and assembly tolerances in the U5.0. To ensure peak field performance of the U5.0 undulator, a half-period model of the magnetic structure was constructed and tested to determine the peak field at the midplane and the transverse variation of the vertical field for the nominal design. This paper addresses the peak field characteristics.

U.S. Government work not protected by U.S. Copyright.

II. DESCRIPTION OF THE U5.0 MODEL POLE ASSEMBLY

The U5.0 model pole assembly shown in Fig. 1 consists of: 1. a vanadium permendur pole; 2. eight Nd-Fe-B blocks that are 0.85 cm thick (half the thickness of the U5.0 blocks); 3. a keeper that holds the pole and blocks in place and allows iron and permanent magnet material, sometimes called Current (or Charge) Sheet Equivalent Material (CSEM) inserts or studs to be placed close to the pole; 4. a set of three mirror plates that define the magnetic symmetry of the device (one is at the midplane and one at each of the 1/4 period planes); and 5. a mounting fixture, which simulates the backing beam-including the side pieces. This fixture allows the pole to be positioned at distances above the midplane corresponding to various half gaps. The pole and the eight CSEM blocks form half of a U5.0 half period, the smallest unit of the periodic magnetic structure that can be modeled.

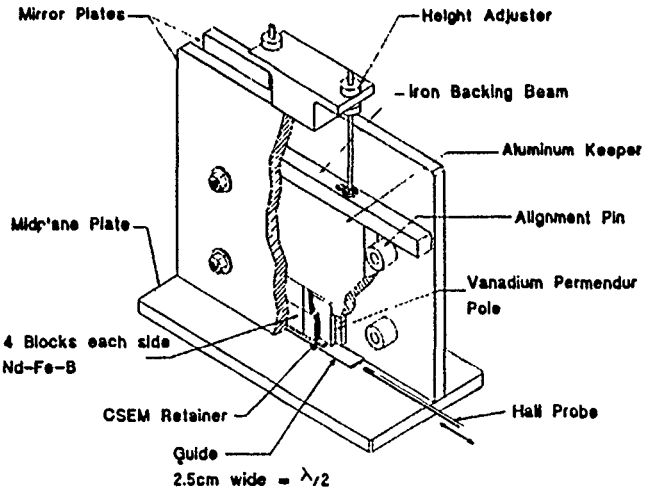


Figure 1. Cutaway View of the U5.0 Model Pole Showing the Major Components.

To study magnetic field tuning the aluminum pole keeper was constructed with three tapped holes on each side to hold iron or CSEM inserts. The inserts were all 5.6 mm (0.220") in diameter and were held in threaded brass rods that accurately position them close to the pole. Both types of inserts were made in lengths of 11.2 and 20.6 mm.

III. The Gap Dependence of the Magnetic Field

The peak field was measured at several gaps. This field is the algebraic sum of all the spatial field harmonics.

$$B_p = \sum_{i=1}^{\infty} B_{2i+1}$$

The quantity of interest, however, is the effective field, B_{eff}, which enters into the calculation of the spectrum of the light emitted by the undulator. B_{eff} is given by

$$B_{eff} = \left\{ \sum_{i=1}^{\infty} [B_{2i+1}/(2i+1)]^2 \right\}^{1/2}$$

The relationship between the peak field and the effective field depends on the geometry of the device and can be found from the spatial field distribution, i.e. the magnitude of the spatial field harmonics. The gap dependence of each spatial harmonic of the field is given by

$$B_{2i+1}(g1) = B_{2i+1}(g2)\exp(2\pi\{2i+1\}\{g2-g1\}/\lambda_u)$$

The spatial field distribution can be calculated accurately by POISSON using the geometry and measured permeability of the pole. The theory of hybrid insertion devices, developed by K. Halbach,[3] can then be combined with these POISSON results to predict the peak field. The measured and calculated gap dependence of the peak field is given in Fig. 2.

The calculated fields are slightly smaller than the measured values. This difference varies from about 3% for the smallest gap to 10% for the largest gap. The source of this discrepancy is not understood at this time. Fortunately, the measured fields are larger. At a 7.0 mm half gap the measured peak field is 1.03 T, which yields an effective field of about 0.96T, which is well above the design goal of 0.88 T.

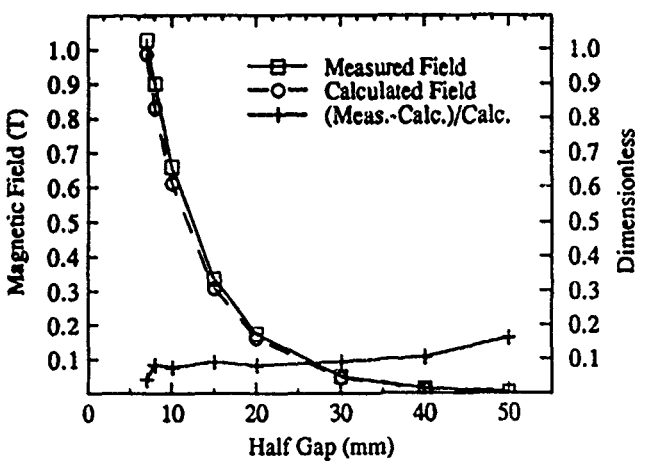


Figure 2. Measured and Calculated Peak Field as a Function of Half Gap.

IV. Magnetic Field Variation in the X Direction

Transverse (x) profiles of B_y were obtained by scanning the Hall probe from the field-free region on one side of the pole, x ≈ +100 mm, to an equivalent position on the other side, x ≈ -100 mm. The field was measured with a Hall probe at discrete transverse locations (usually every 2 mm). Figure 3 shows the normalized magnetic field near the center of the device for half gaps of 7, 10, 15 and 20 mm.

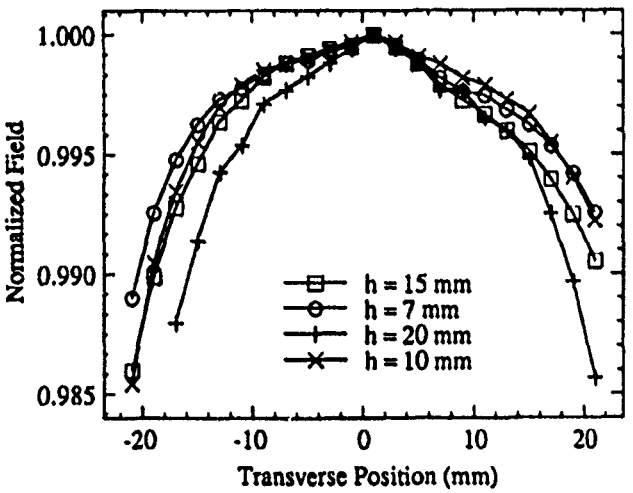


Figure 3. Transverse Profile of the Field for Different Half Gaps.

V. Field Modifications Due to Shimming"

A major concern in the design of an insertion device is that the magnitude and/or distribution of the error fields exceeds the specifications. The underlying philosophy in ALS insertion device design is to limit errors by assigning tight tolerances. But, as a fall back position, the ALS insertion device design includes several methods of local field correction. We used the U5.0 model pole assembly to evaluate two methods of adjusting the field; either CSEM or iron studs were placed on the sides of the pole. Because of the model geometry, the effect of any pole modification is the same as if all poles had received the same change in scalar potential.

The CSEM inserts were magnetized along the length (or axis) of the cylinder, and could be oriented to either boost or reduce the central magnetic field.

Two typical difference maps, with one and two CSEM studs in the bottom position, are shown in Fig. 4. The pair of studs boosted the field under the pole by about 0.35%. The large field excursions near ± 60 mm are caused by flux that goes directly from the "magnetic charge" at the end of the stud to the midplane, which is a graphic example of the direct field[3]. The field in the center of the device is boosted twice as much for two studs as it is for one, which suggests that saturation does not degrade the effect of the inserts.

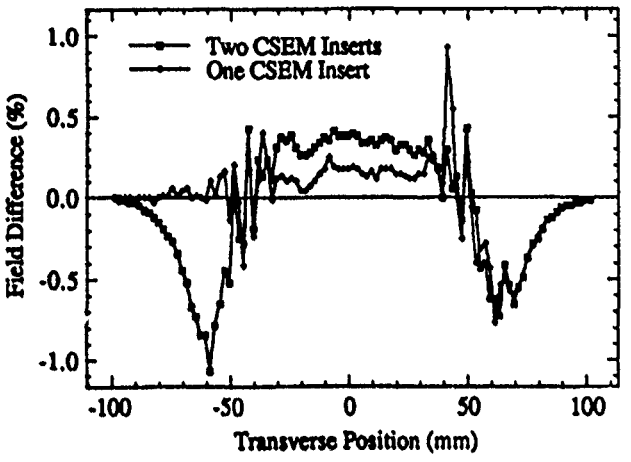


Figure 4. Field Change due to CSEM Inserts

The change of center field as a function of the CSEM distance from the pole is plotted in Fig. 5. One turn of the screw that captures the CSEM insert increases the distance from the pole by 1.81 mm. The figure shows that 50% of the effect occurs within the first two turns of the screw. The effect on the central field of the long CSEM stud pairs in the bottom and middle positions was studied as a function of gap. The results of these measurements are shown in Fig. 6.

Except for small gaps, the field produced by the inserts tracks that produced by the main CSEM. Our suspicion is that the differences are caused by saturation effects in the pole. There is a significant variation in the normalized change of the central field and the field difference from a 0.7 cm gap to a 1.0 cm gap.

The effect on the transverse field distribution of an iron stud on one side is given in Fig. 7. The large peak at -50 mm is caused by the direct fields of the stud. The field change under the pole exhibits a gradient, showing that there is a potential drop along the pole, which is a sign of pole saturation.

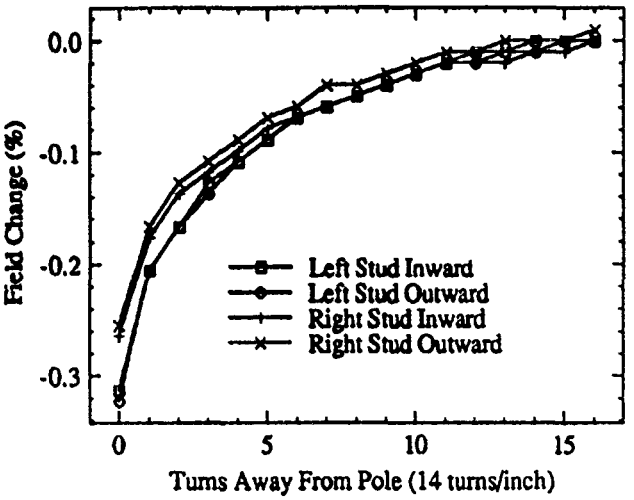


Figure 5. Variation of Central Field as a Function of Insert Location

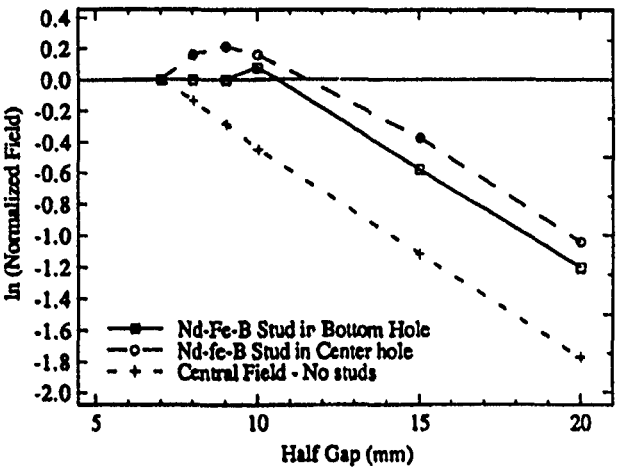


Figure 6. Half Gap Dependence of Field and Field Variation Due to CSEM Inserts.

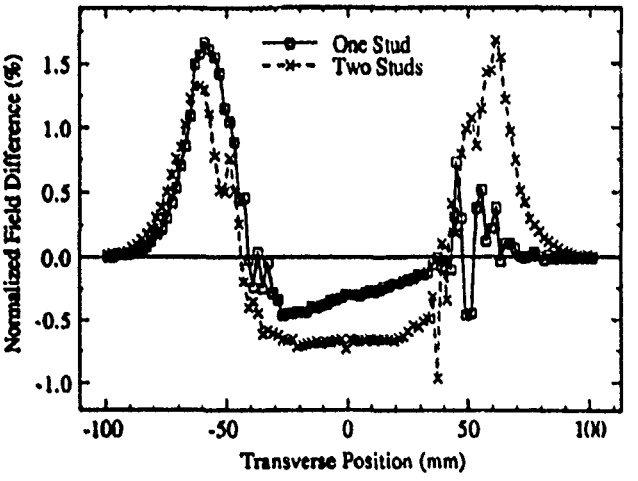


Figure 7. Transverse Scan Showing the Effect of Iron Inserts.

The effect of a pair of studs has no gradient, as shown in Fig. 7. We observe no measurable direct fields in the midplane for the studs in the higher positions.

VI. Acknowledgment

***This work was supported by the Director, Office of Energy Research, Office of Basic Energy Sciences, Materials Sciences Division of the U.S. Department of Energy, under Contract No. DE-AC03-76SF00098**

VII. References

1. "U5.0 Conceptual Design Report" LBL Report PUB-5256, November, 1989.
2. K. Halbach, "Design of Magnets" videotape lecture series Jülich, Germany, May-June, 1985.
3. K. Halbach, "Design of Hybrid Insertion Devices", videotape lecture series, LBL Report V-8811, October, 1988 - March, 1989.
4. R. Savoy, personal notes.

ALS Insertion Device Block Measurement and Inspection

S. Marks, J. Carrieri, C. Cork, W.V. Hassenzahl, E. Hoyer, and D. Plate

Accelerator and Fusion Research Division, Lawrence Berkeley Laboratory
University of California, Berkeley, California 94720

Abstract

The performance specifications for ALS insertion devices require detailed knowledge and strict control of the Nd-Fe-B permanent magnet blocks incorporated in these devices. This paper describes the measurement and inspection apparatus and the procedures designed to qualify and characterize these blocks. A detailed description of a new, automated Helmholtz coil facility for measurement of the three components of magnetic moment is included. Physical block inspection and magnetic moment measurement procedures are described. Together they provide a basis for qualifying blocks and for specifying placement of blocks within an insertion devices' magnetic structures.

I. INTRODUCTION

The Advanced Light Source (ALS) at the Lawrence Berkeley Laboratory will use insertion devices, wigglers and undulators, to produce intense photon beams. These insertion devices are designed as hybrid structures that include Nd-Fe-B blocks as the source of magnetic field that energizes vanadium permendur poles. The basic structure is illustrated in Figure 1, which shows a pole assembly including six magnetic blocks. Each insertion device typically contains between 1,000 and 3,000 blocks. The block specifications are summarized below :

- Nominal Principal Magnetic Moment per Unit Volume M_z = 10.6 kOe or greater
- Minimum allowed M_z =10.4 kOe
- Allowed variation in M_z = +/- 2.5%
- Alignment of magnetic axis = +/- 3° .

The midplane magnetic field of an insertion device, which determines the spectral performance, is dominated by the shape and placement of the poles and the total flux entering the poles due to the adjacent Nd-Fe-B blocks. Therefore, the primary requirements for the blocks are on the principal magnetic moment, M_z. The peak midplane magnetic field determines the nominal value of this moment. The allowable block to block variation is determined by the acceptable variation in the midplane field. For previous insertion devices designed at LBL, this was the only requirement. Experience with previous designs and increased performance specifications led to additional block specifications for ALS insertion devices. New considerations concern the off axis components of the magnetic moment, which cause beam steering, and the distribution of flux perpendicular to the beam direction, which is associated with quadrupole and higher order multipoles. These affects are most significant near the midplane where they have the greatest effect on the beam.

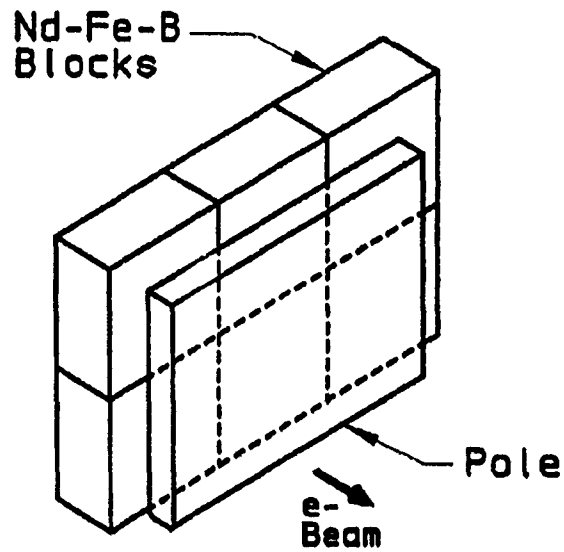


Fig. 1. Insertion Device Pole Structure for ALS U5.0.

II. PHYSICAL INSPECTION

The first step in block qualification is a physical inspection. This includes a visual inspection, dimensional checks, and a qualitative magnetic field check using magnaview film (Edmund Scientific stock number 33447). The visual inspection screens the blocks for flaws in the plating, cracks and surface voids larger than 2 mm. The block width and thickness are checked by passing the blocks through two "go"/"no-go" gauges. Blocks that fall within the tolerance fit through the "go" part of the gauge, indicating that it is not too large, but do not fit through the "no-go" part of the gauge, indicating that it is not too small.

The magnaview film consists of an emulsion of fine iron grains contained between two translucent plastic sheets. When exposed to a magnetic field the metal grains align themselves with the local field direction. When held under a light source, the grains aligned in the plane of the paper reflect and this region appears light. Other regions appear dark. By putting a sheet of the magnaview film in contact with a block and viewing under a light, one can get a picture of the magnetic quality of the block.

III. HELMHOLTZ COIL SYSTEM

After the blocks have been examined by the procedure described above, the Helmholtz coil system is used to measure magnetic moment. The following objectives were established for a new Helmholtz coil system.

U.S. Government work not protected by U.S. Copyright.

1) The system must measure three components of magnetic moment to an accuracy of +/- 0.1% of the main component, M_z.
2) The system must be fast; capable of processing at least 20 blocks per hour.
3) The system must be easy to use and must minimize the possibility of human error.
4) The system must store data in a standard, secure and accessible format.

The first three requirements, coupled with the need to measure upwards of 10,000 blocks, motivated the design of an automated system. This was based on the recognition that the manual procedure used previously was slow, extremely tedious and prone to operator error, and would be incompatible with the construction schedule and the large number of blocks to be measured. The fourth requirement motivated the incorporation of a standard commercial data base system into the data acquisition software.

The Helmholtz coil functions in the following way. When a block at or near the center of a Helmholtz coil is rotated continuously, a periodic voltage is induced according to Equation (1) below.

$$V(t) = \frac{N\omega}{RG}[m_y\cos(\omega t) + \{m_z\cos(\chi) + m_x\sin(\chi)\}\sin(\omega t)], \quad (1)$$

where N is the number of turns in each of the two coils, R is the radius of the coils (m), G = 1.3975 is the geometry factor for a Helmholtz coil pair [1], and ω is the rotation rate (radians per second) for the block. The angle χ corresponds to the angular orientation of the block with respect to the spin axis. The three components of magnetic moment are determined by first rotating the block about an axis parallel to m_z, $\chi = 0°$, and then flipping the block so that it rotates about m_z, $\chi = 90°$. A Fourier decomposition of the sampled voltage for the first orientation determines m_z and m_y. Components m_x and m_y are determined from the second orientation (note the redundant measurement of m_y).

The Helmholtz coil voltage is sampled 256 times per revolution, for 10 revolutions, for both configurations, $c = 0°$ and $c = 90°$. The voltage is corrected for the instantaneous velocity and the values from each revolution are Fourier analyzed separately. The average of the 10 resulting amplitudes is used for the vaule of the moment and the variation as a measure of the error.

A. Hardware

Figure 2 is a photograph of the Helmholtz coils and the associated mechanical hardware. The system consists of two 60 cm diameter coils and a rotating block holder driven by a servo motor. A linear actuator is coupled to the head assembly and produces the 90° block flip. The magnetic blocks are secured in the head with a keyed fixture. An incremental rotary disk encoder is attached directly to the spin axis.

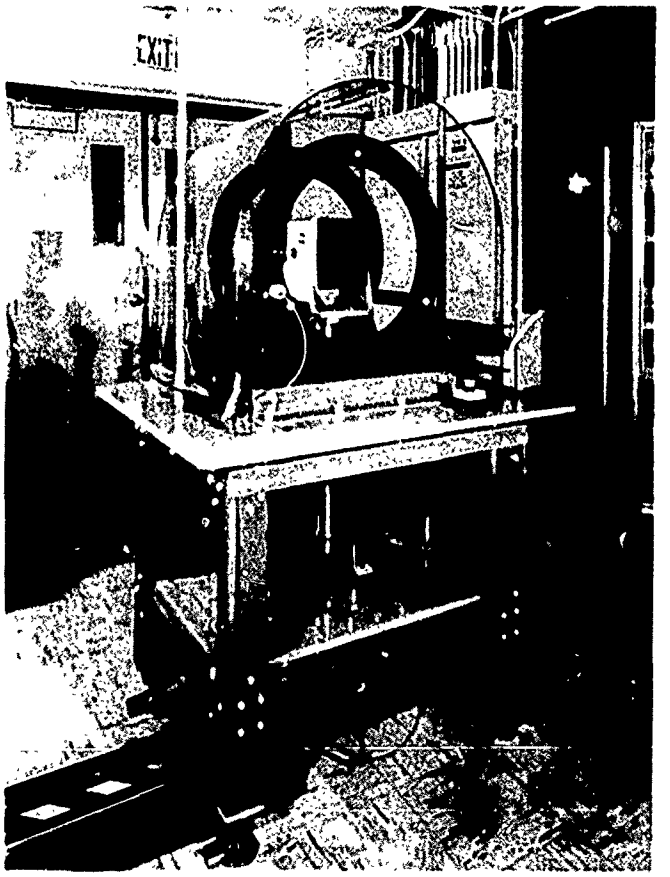


Figure 2. Helmholtz Coil and Mechanical Hardware

The magnetic moment measurement system also includes an operator interface stand and an electronics rack. The operator stand includes a Sun 3/80 workstation and an operator "keystation." The workstation is the operator interface during measurements; it performs all the data processing, database storage and access to measurement results. The "keystation" is a safety feature that prevents access to the block holder while it is rotating. When the key that is used to lock the block into the holder is inserted into the "keystation", a Lexan shield is lowered, the head is allowed to rotate, and the test begins.

The electronics rack contains various instruments and a real-time subsystem for fast data collection and instrument control. The equipment includes a VME crate, a Hewlett Packard 3458A digital voltmeter (DVM), a Compumotor KHX-250 servo driver/controller for the block rotation motor, and a Compumotor AX driver/controller for a linear actuator that executes the block flip. The VME crate includes a Motorola MVME-147 real time central processing unit (CPU), a Burr Brown MPV991 timer/counter module, and a Motorola MVME-300 GPIB controller.

The MVME-147 provides real-time data collection and instrument control. The DVM samples the coil voltage, which is stored in internal memory. Sampling occurs when triggers are received from the timer/counter module, which processes 1024 pulses per revolution from the Teledyne Gurley model 8708 ring encoder. Time between pulses is measured to provide angular velocity information.

Figure 3 is a logical block diagram of the hardware components and their interconnections. The DVM is controlled and its data is retrieved via GPIB. The motor driver/controllers are connected to the MVME-147 via RS-232 ports. Communication between the MVME-147 and the Sun 3/80 workstation occurs over an Ethernet interface.

B. Software

The software is divided into two major subsystems that correspond to the real-time hardware and the operator workstation. Coordination between the subsystems is provided by using the Sun remote procedure call (RPC) mechanism. Figure 4 is a block diagram of the software modules.

The *Mv300* module controls the MVME-300 GPIB control board. The *Dvm* interface module is for communication with the DVM via the IEEE-488 interface bus and the *Mv300* device handlers. The device handler for the MPV991 timer/counter module, *Mpv991*, provides services for access and control of the parallel counter channels and interrupt controller. *Encoder* is an interface module for setup, initiation, and sampling of the MPV991 timer/counter with the specific hardware interconnections for our system where it is interfaced with the spin axis incremental encoder. *Flip* is an interface module for communication with the flip axis motor driver. The module is used to initialize and calibrate the flip axis positioner as well as toggle between the two measurement configurations. *Scan_svc* is the top level server task on the real-time subsystem that provides remote procedure call service to client tasks. This task is spawned during system initialization and it listens to the network for service requests. *Scan_clnt* is the client interface module. It resides on the operator workstation as a subroutine library that coordinates network connections, RPC access, and disconnection to the server module. *ScanMaster* is the routine that runs on the operator workstation and provides basic coordination of the measurement, user prompts and information, retrieves and processes data, and stores measurement results. Results are stored in an Informix database; access to the database is provided by structured query language subroutine calls embedded in *ScanMaster*.

IV. CONCLUSIONS AND OBSERVATIONS

The Helmholtz coil system described above has been operational since January 1991. A total of 4866 Nd-Fe-B blocks have been successfully measured. An average measurement rate of 20 blocks per hour was sustained while it was in operation, and peak measurement rates were as high as 40 blocks per hour. Repeatability of measurements was verified by remeasurement of a reference block before and after each day's sequence of measurements. This block was measured over 100 separate times during this period. The standard deviation of these measurements was +/- 0.04%, some of which is due to temperature variation that can be corrected for.

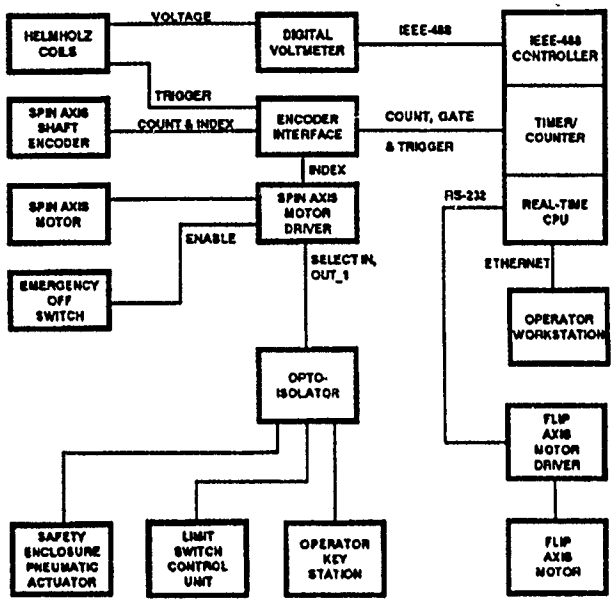


Figure 3. Block Diagram of Helmholtz Coil Hardware Components

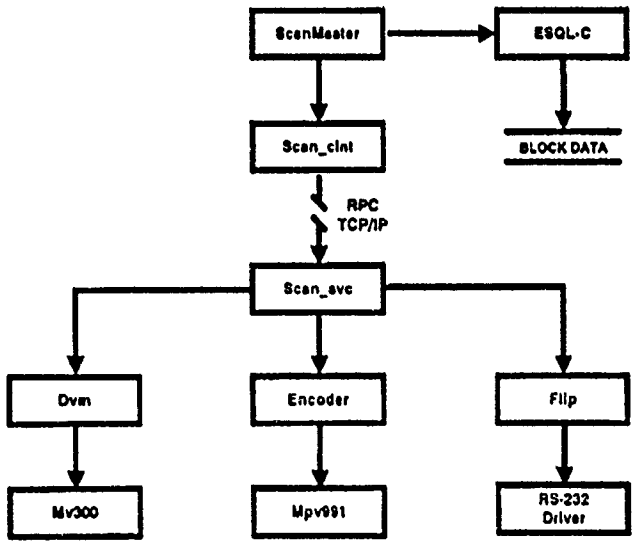


Figure 4. Block Diagram of Software for Helmholtz Coil Automated Block Measurements

V. ACKNOWLEDGMENT

This work was supported by the Director, Office of Energy Research, Office of Basic Energy Sciences, Materials Sciences Division of the U.S. Department of Energy, under Contract No. DE-AC03-76SF00098

V. REFERENCES

[1] D. H. Nelson, F. H. Pao, R. L. Schermer, and D. A. Van Dyke, "Magnet Moment Measurements of Permanent Magnet Blocks by the Lawrence Berkeley Laboratory Magnet Measurement Engineering Group", MT400, December, 1989

Ion Beam Probe for Measurement of Wiggler Errors

John Vetrovec, Bradley Bobbs, and Michael Lampel
Rockwell International, Rocketdyne Division
6633 Canoga Ave.
Canoga Park, Calif. 91304, (818) 700-4875

Abstract

Precise characterization of wiggler field errors is needed in order to perform compensations. Traditional method, which relies solely on Hall probe data acquired from a field map, suffers due to cumulative noise effects and is inadequate for long wigglers. The proposed instrument avoids this problem by directly measuring an equivalent trajectory of a low energy ion beam which is momentum and emittance matched to the electron beam. The ion beam is injected into the wiggler where it is imaged onto the screen of a miniature CCD camera which travels through the wiggler bore. By combining data from the camera and the Hall probe, the instrument achieves a resolution superior to a Hall probe alone.

INTRODUCTION

The Ground Based Free Electron Laser Technology Integration Experiment (GBFEL-TIE) in White Sands, NM, calls for a wiggler 400 periods long. Strong concerns exist over the cumulative effects of wiggler field errors on the trajectory and the phase of the electron beam. Several correction schemes using 20 pairs of beam position monitors (BPMs) and steering correctors are being considered [1]. However, BPMs provide only a discrete sampling (every 20 periods) of the trajectory at a rather low resolution (100 μ m). Since this data appears insufficient for wiggler tuning, other, more reliable means for trajectory analysis are sought. This article describes the Ion Beam Probe System (IBPS) which promises to provide reliable trajectory measurements.

INSUFFICIENCY OF HALL PROBE DATA

Traditionally, the magnetic field of the wiggler is mapped by a Hall effect probe and this data is used to reconstruct the electron beam trajectory, which, in turn, is used to tune wiggler taper and steering correctors. While this technique is entirely sufficient for short wigglers, accumulation of the residual Hall probe sampling errors (largely due to mechanical alignment of the probe) along the 400-period wiggler becomes intolerable. The most severely affected is the estimate of the phase of the electron motion with respect to the optical wavefronts. As the FEL performance shows a strong correlation to the phase [2], this problem is of major importance.

ION BEAM PROBE SYSTEM (IBPS)

Accuracy of phase error measurements can be greatly improved with the proposed IBPS. Instead of reconstructing electron beam trajectory solely from Hall probe data, this instrument directly measures the trajectory as simulated by a beam of low energy ions having the same momentum as the electrons. Ions are injected into the wiggler bore where they are intercepted by a fluorescent screen on a CCD array mounted in a movable carriage (Figure 1). At the same time a pilot laser beam from a stable source is injected coaxially into the wiggler and used as an alignment reference. Transverse position of the ion beam is then determined as a separation of the two beam spots viewed by the CCD chip (Figure 2). As the carriage is moved through the wiggler bore, the entire ion beam trajectory is resolved.

While the spatial resolution of the CCD limited by the noise in the optical signals to about 10 μ m, the error in measured transverse position is not cumulative. Still, the raw trajectory data is too noisy to be useful for phase calculations, and must be locally smoothed. This process makes use of complementary Hall probe data also obtained by the instrument [3], thus combining the best qualities of the two data sets: global accuracy of the ion trajectory detector and local accuracy of the Hall probe. This reduces error accumulation and produces more reliable data which can be used for

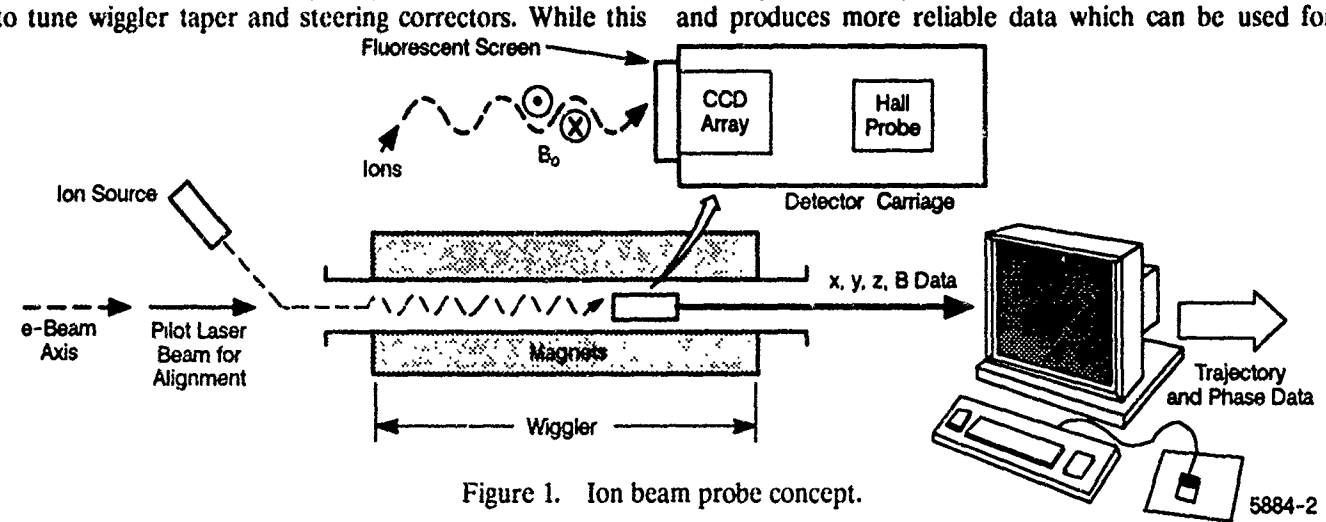


Figure 1. Ion beam probe concept.

0-7803-0135-8/91$01.00 ©IEEE

wiggler tuning, thereby improving the performance of the FEL.

The electron-ion momentum matching condition leads to a trade between ion mass and acceleration voltage. Required ion energy T_i can calculated as $T_i = T_e m_e/M_i (\gamma/2 + 1)$ where T_e is the electron energy, m_e/M_i is the ratio of electron and ion (rest) masses, and γ is the relativistic factor. Since heavy ions have the least acceleration voltage requirements, the most abundant Xe(132) isotope was selected as a working specie. At the design electron beam energy of 100 MeV, momentum matched singly charged xenon ions are required to have an energy of only 41 keV.

In order to produce an ion beamlet of the same size as the electron beam, the ion beam emittance is matched by apodizing. Unfortunately, this also reduces the available beam current and the optical signal at the CCD. Although negative ions would follow exactly the same trajectory as electrons, negative ion sources typically produce a substantially lower current than their positive counterparts. As a result, the DanFysik positive ion source model 920 was selected [4]. This device is capable of extracting a 10 mA xenon beam of 15π mm-mr rms emittance through a 10 mm diameter aperture. While positive ions follow a trajectory which is a mirror image of the electron trajectory, this data contains all the necessary information to calculate the phase. A 45 deg bending magnet working in conjunction with a small defining aperture is used to filter out unwanted xenon isotopes and other impurities. The aperture is sized to extract a beamlet with (unnormalized) emittance of 0.046π mm-mr which, inside the wiggler, results in a beam spot diameter of about 1 mm.

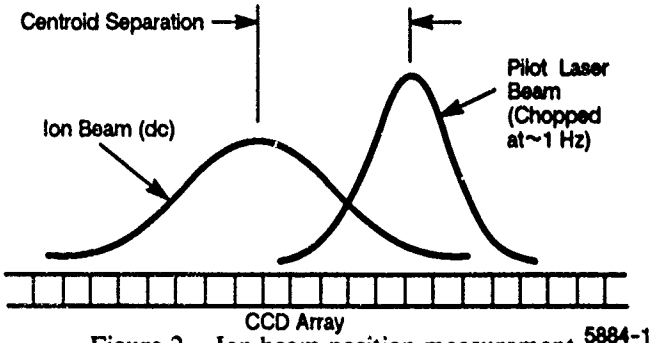


Figure 2. Ion beam position measurement.

Inside the wiggler the ion beamlet is intercepted by a detector slowly moving through the bore. A possible detector is the Texas Instrument TC210 196x165 planar CCD array with approximate pixel size of about 14 μm. This sensor is specifically packaged to allow mounting on a tip of small cross-section insertion probe. A layer of phosphorus coated over the protective glass window of the CCD sensor converts the kinetic energy of incident ions into an optical signal. Current density of the ion beam is about 65 nA/mm^2, which is roughly the same as in a conventional cathode ray tube (CRT). It is somewhat conservatively assumed that using available phosphorus material the conversion efficiency of 41 keV ions into visible spectrum light is about 100 times less effective then for 5-10 keV electrons (such as in a CRT). The intensity of light produced by the phosphorus screen is then about 0.032 μW/mm^2. The CCD array has a typical 1000:1 dynamic range and, when scanned at 30 Hz, it saturates at about 0.08 μW/mm^2. This leads to about 400:1 signal to noise ratio, which appears quite satisfactory. In practice, the optimum signal-to-noise ratio in the CCD can be found by adjusting the scan rate.

OPERATIONAL CONSIDERATIONS

The IBPS is designed to operate in situ as a part of the electron beam line. It collects data needed to tune the wiggler prior to each FEL run. When inoperational, the detector carriage is hidden in an alcove at the downstream end of the wiggler (Figure 3). Radiation shield protects the CCD and Hall probe sensors from destruction when the electron beam is on. Since the alcove is evacuated, the carriage can be inserted into the wiggler without a vacuum break. The insertion process as well as the travel through the wiggler is under computer control. The carriage is mechanically propelled by a system of pulleys and wires hidden in longitudinal slots extruded into the vacuum tube bore. Longitudinal

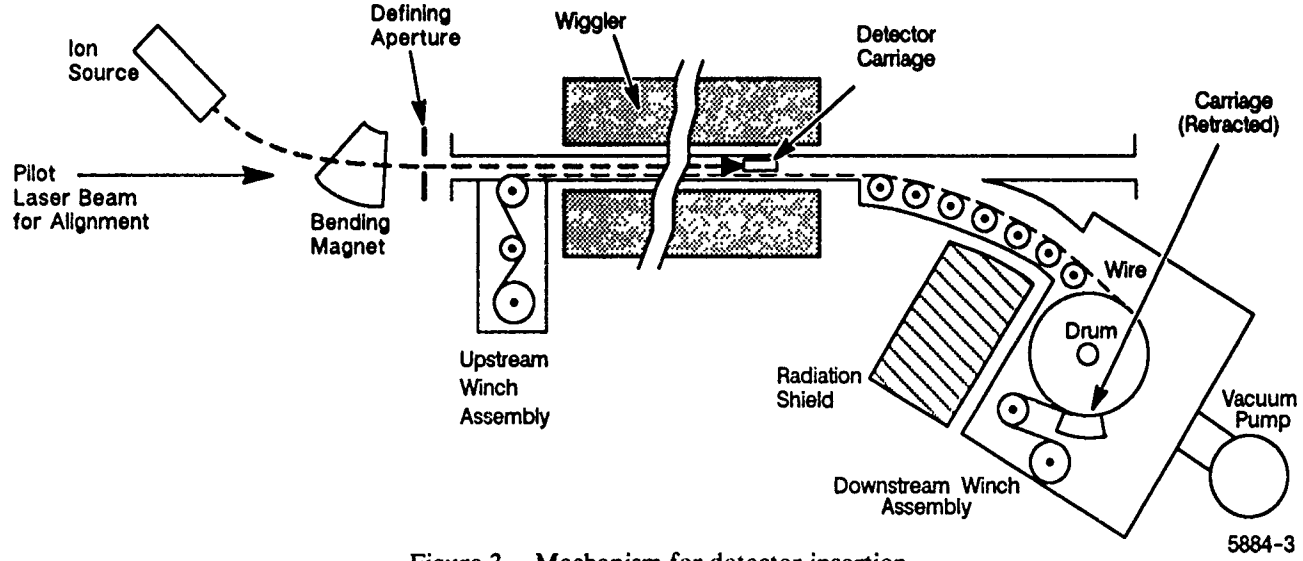


Figure 3. Mechanism for detector insertion.

slots extruded into the vacuum tube bore. Longitudinal position of the carriage is inferred from a magnetic field profile monitored by a the Hall sensor contained within the carriage. This technique avoids the complexity of alternate mechanical or optical schemes while providing an accuracy of about 100th of wiggler wavelength.

The detector carriage also contains the drive and the output signal electronics for both the CCD and the Hall sensor. The magnetic field of the wiggler is understood to have negligible impact on the function of the carriage-mounted electronics. The CCD video signal with a bandwidth 1 to 10 MHz (depending on the scan rate) is transmitted from the carriage to an external processing unit via 75 ohm coaxial cable wound on the same drum as the motion wires. After digitizing, the CCD image is subjected to standard image processing techniques to determine the transverse position of the ion beam. Typically, 10-20 samples per wiggler period are taken. These data together with the Hall probe signal are sufficient to reconstruct the local trajectory of the ion beam.

SIMULATED PHASE MEASUREMENTS

Performance of the IBPS has been evaluated using a one-dimensional model of the wiggler field and a particle transport simulator. General parameters are set to reflect the GBFEL-TIE wiggler design. Local magnetic field errors with the cosine half-wave spatial form suggested by Kincaid [5] are generated automatically by the computer to conform to a statistical model with Gaussian distribution. Field errors are unique to each run. Spatial resolution of the CCD system is primarily limited by the noise in the optical signals and it is conservatively assumed to be 10 μ m. It is slightly less than 1 pixel size, and it represents about 20% of the wiggle amplitude $K/(k_w\gamma)$, where K is the wiggler parameter and k_w is the wiggler wave number.

An example computer run (Figure 4) shows the trajectories and phase retardations as calculated from the Hall probe data alone, from the IBPS data, and the actual (synthesized, error-free) conditions for the first 100 periods of the wiggler. Transverse displacement of the electron beam centroid measured by the ion beam sensor is shown before spatial smoothing. Clearly, despite a significant (10 μm) local noise, the trajectory detected by the CCD array system faithfully follows the actual path. After smoothing, the two curves almost coincide. However, the trajectory calculated from Hall probe data alone drifts away after about 60 periods. Phase profile along the wiggler calculated from a smoothed trajectory also shows a good agreement with the actual data, while that based on Hall probe data exhibits large deviations.

CONCLUSION

The ion beam probe system promises to be a very accurate instrument which can be useful both during the initial commissioning as well as operational maintenance of the wiggler. Data obtained by the IPBS permits fine tuning of the wiggler and optimization of FEL performance. In addition, as the tuning is completed before the electron beam is injected, electron beam transport risk is reduced.

ACKNOWLEDGMENTS

A similar, but simpler, ion beam probe was used earlier at LLNL to analyze field errors in the 5 m sections of the Paladin wiggler before installation into the ATA beam line. We wish to thank to H. Shay, B. Kulke, and G. Deis for providing us with information about the LLNL device.

REFERENCES

[1] C.J. Elliott, B.D. McVey, and D.C. Quimby, "Field Error Lottery," in proc. from the *12th Intl. FEL Conf.*, Paris, September 1990, North-Holland Elsevier, 1991, also to appear in *Nucl. Instr. and Meth.*, 1991.

[2] J. Vetrovec, "Performance Model for FEL Wigglers," in proc. from the *12th Intl. FEL Conf.*, Paris, September 1990, North-Holland Elsevier 1991, also to appear in *Nucl. Instr. and Meth.*, 1991.

[3] B. Bobbs and J. Vetrovec, "Characterizing Wiggler Phase Errors with an Ion Beam Probe," paper TC.7, in proc. from the *Lasers '90 Conference*, San Diego, CA, December 1990.

[4] High Current Ion Source Model 920 data sheets, DanFysik A/S, DK-4040 Jyllinge, Denmark, also available from GMW Associates, Redwood City, CA 94064.

[5] B. Kincaid, "Random Errors in Undulators and their Effect on the Radiation Spectrum," *J. Opt. Soc. Am.* B/Vol. 2, No. 8, pp. 1294-1306, August 1985.

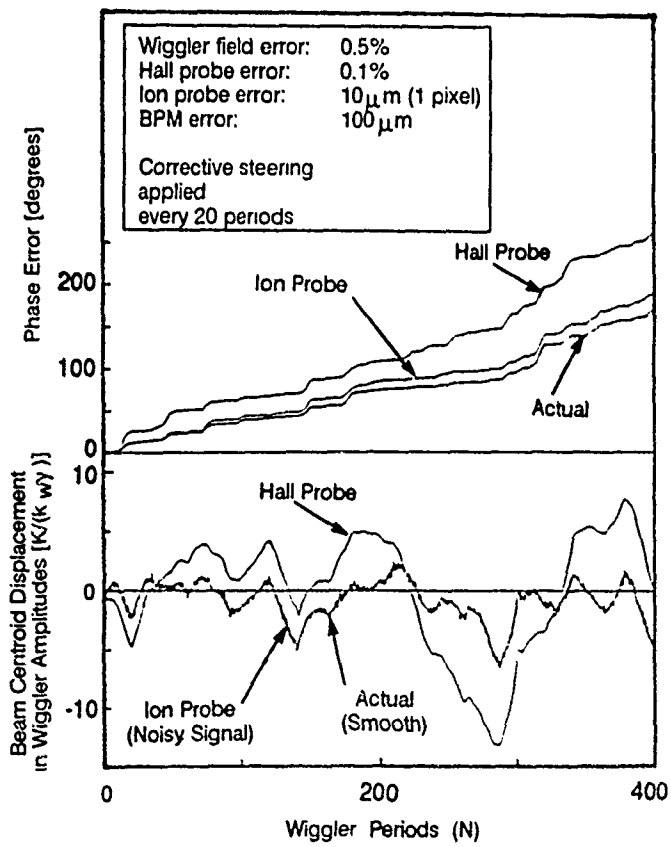


Figure 4. Comparison of measurements obtained by Ion and Hall probes (based on 1-D computer simulations).

FEL Design Using the CEBAF Linac*

G. R. Neil, J. J. Bisognano, H. F. Dylla, G. A. Krafft
C. W. Leemann, C. K. Sinclair, and B. Yunn
Continuous Electron Beam Accelerator Facility
12000 Jefferson Avenue
Newport News, VA. 23606

ABSTRACT

The approaching availability of a high quality, continuous electron beam from the CEBAF accelerator presents the opportunity to explore regimes of free electron laser (FEL) physics and photon production heretofore unapproachable. Using a 3 cm wavelength hybrid wiggler with 200 MeV from the North Linac and a new photoinjector, output powers exceeding 1 kW CW could be achieved at wavelengths from 200 to 700 nm. A simple electromagnetic wiggler utilizing the output of the CEBAF injector could provide an early test of operation and ultimately simultaneous output in the 0.7 to 3 micron range. Details of the design and performance analyses will be discussed.

INTRODUCTION

The CEBAF accelerator will be a 4 GeV, 200 μA CW electron accelerator for basic research in nuclear physics[1]. It achieves continuous operation through the use of superconducting RF cavities operating with helium refrigeration at 2K. The projected electron beam quality and energy spread are excellent with a design edge emittance of 2π nm at 1 GeV and a energy spread of better than 10^{-4}. The machine uses five passes through two antiparallel linacs to achieve full energy. The five-cell superconducting cavities were originally designed at Cornell and are manufactured by Interatom. Processing, assembling the cavities into dewars, and testing is performed at CEBAF. Of the > 110 cavities manufactured to date, all have met the specification for gradient (5 MV/m) and most meet the Q specification of 2.4×10^9 at 5 MeV. In fact, the average gradient is close to 10 MV/m with the best cavities exceeding three times baseline gradient.

The stability and beam quality required by high resolution nuclear scattering experiments are also necessary requirements for short wavelength operation of FELs. With this in mind we have explored the possibility of utilizing the early phases of the CEBAF linac operation for tunable coherent light generation. A natural consequence of the CW nature of the linac is the projected high average power that could be produced. We have explored two possible locations for FELs; one is at the output of the CEBAF Front End where the beam has energies of up to 45 MeV single pass or 85 MeV with a single recirculation. The other is located at the end of the North Linac. Energies up to 445 MeV could be possible. In either case a new injector for the FEL would be required since the FEL requires high peak current for sufficient gain. The new injector in this study is presumed to be a photoinjector with the capability of providing up to 110 A of peak current in a 2 ps micropulse (.23 ncoul) at a normalized RMS emittance of 15 π mmmrad. These pulses would be delivered at the 200th subharmonic of the CEBAF's fundamental frequency of 1497 MHz, 7.485 MHz.

OPERATIONAL LIMITATIONS

Operation of FELs at CEBAF would be subject to several constraints including available RF power, induced wakefields, and, after physics commissioning in 1994, constraints deriving from the need for simultaneous operation of an undegraded electron beam for nuclear physics. An example of this would be beam loading induced energy droop which must remain below a $\Delta E/E$ of 10^{-4}. In this section we briefly explore the most significant of these.

In dedicated FEL operation, the proposed design allows an average current of 1.7 mA to be accelerated using the available 4 kW at reduced gradient. Full current nuclear physics operation at 200 μ A at 4 GeV requires 1 mA (five passes of 200 μA) to be accelerated at full gradient. At 4 kW/cavity only an additional 450 μA can be accelerated, which is equivalent to only a 60 pC bunch charge or 30 A peak current unless a dispersion section is used to compress the pulse length.

There is neither RF power nor RF control bandwidth to compensate for the instantaneous gradient decrease from the high charge bunches at the 200th subharmonic. Due to the high gradient and Q of the superconducting cavity the fractional fundamental voltage droop would be 5×10^{-5} which would act on the nuclear physics pulses which follow (the voltage gradually recovers its original value by the arrival of the 200th micropulse only to receive another high charge load).

An additional 5×10^{-5} of energy jitter could be induced from high-Q HOMs. Using previous estimates of the impedance[2] for bunches of 60 pC the HOM power is conservatively estimated to be

$$P_{hom} = q^2 k_l f = 0.5 \text{ W/cavity}$$

where k_l is the loss factor of the cavity, q is the charge in the bunch and f is the bunch repetition frequency. Since the fundamental mode cooling power is 5.4 W/cavity dissipation in the helium cooled HOM loads should not be a problem.

*Supported by Virginia Center for Innovative Technology

0-7803-0135-8/91$01.00 ©IEEE

1-D PERFORMANCE ESTIMATES

Using the characteristics of the electron beam described above we examined possible operation at two wavelength ranges using the 1-D formula for FEL gain[3]. Although the small signal gain formula cannot correctly predict effects such as performance degradation due to energy spread, emittance, etc., and does not handle saturation or effects on the optical mode, it does serve as a useful figure of merit for comparison of various designs. The actual gain may be expected to be within a factor of a few of such predictions.

Table 1. A summary of the parameters of four wigglers considered in the design study.

Type	Electromagnetic		SmCo/Iron Hybrid	
Configuration	Uniform planar		Planar optical klystron	
Periods	30	30	50 + 400 effective	same
Length (m)	1.5	1.5	2 × 1.5	2 ×1.5
Wavelength (cm)	3	5	3	5
Peak B (kG)	2.1	3.8	5.1	9.4
K	0.4	1.2	1.0	3.1
Gap (cm)	1.0	1.0	1.0	1.0
ΔB/B (%)	0.2	0.2	0.5	0.5

Four wigglers were examined utilizing electromagnetic technology and REC-iron hybrid technology. Their parameters are given in Table 1. None of the wiggler designs is believed to stress the state of the art in any area. Although the UV wiggler is configurable as an optical klystron, no credit has been taken for the enhancement of gain.

Assuming rather short wiggler lengths and optical cavities with 30% outcoupling the output was estimated using 1/2N as the saturation efficiency, where N is the number of wiggler periods. Higher efficiency could be produced by tapering the wiggler[4]. The wavelength performance for the four wigglers in each case is shown in Figure 1a) and 1b) for the IR and UV respectively. The power outputs are considerable, exceeding that available from all tunable and most fixed wavelength lasers by several orders.

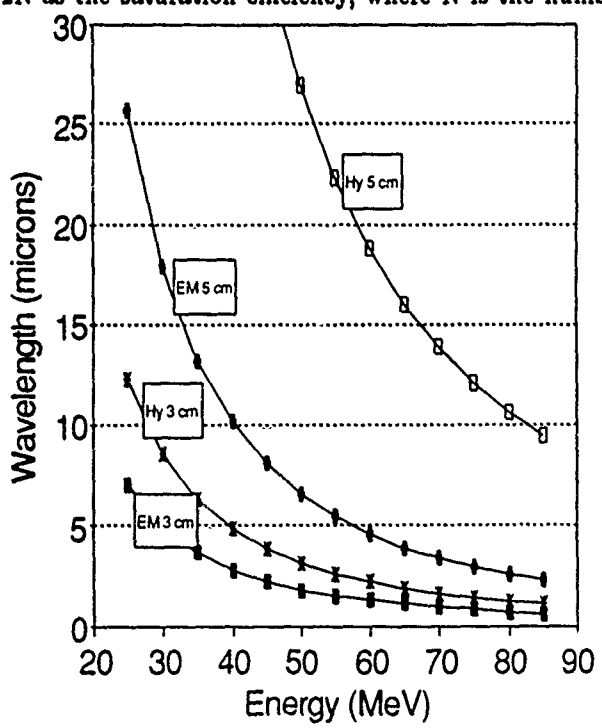


Figure 1a. IR performance of the four wigglers listed in Table 1.

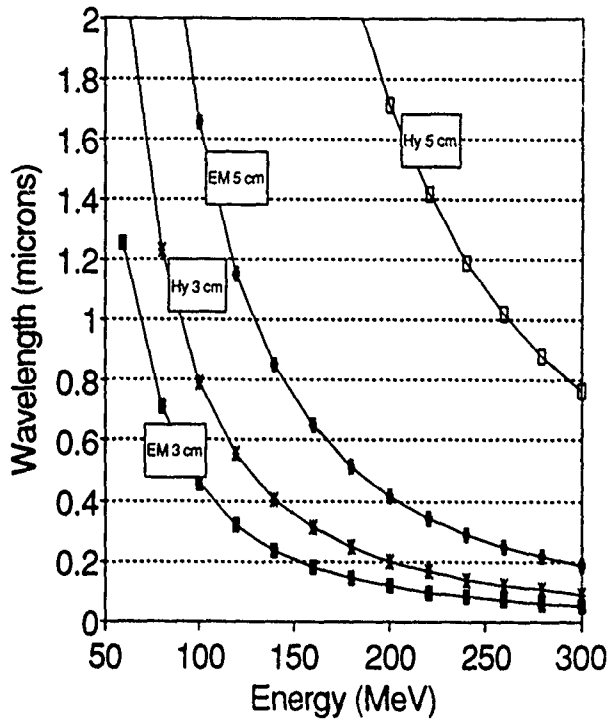


Figure 1b. UV performance of the four wigglers in Table 1.

It is worth noting that the energy and beam quality available is similar to that at VEPP3 which currently holds the world's record for short wavelength FEL lasing[5]. Moreover, the CEBAF peak current (which is proportional to small signal gain) is 20 times higher and optical cavity reflectivities could be comparable. During operation the FEL induces significant growth in energy spread highlighting the potential advantage of a linac configuration over a storage ring: new, unperturbed electrons are used each time.

The optical cavity deserves careful consideration in view of the high optical power predicted. In the IR region sufficient capability exists to manage the high powers with metal mirrors. The long wavelengths give a relative insensitivity to thermally induced distortion. Further, the relatively bright beam gives significant gain estimates in 1-D analytic formulas (Figure 2). The gains are so high in some cases that the performance estimates are significantly in error since they presume slow changes of the optical field and weak interactions with the pondermotive potential well. In addition, during growth of the optical mode to saturation the optical mode can be expected to distort due to gain guiding[6]. This leads to even higher effective gains but mismatch between the optical cavity and the mode during growth to saturation. Such effects would not be expected to hamper operation of a CW system.

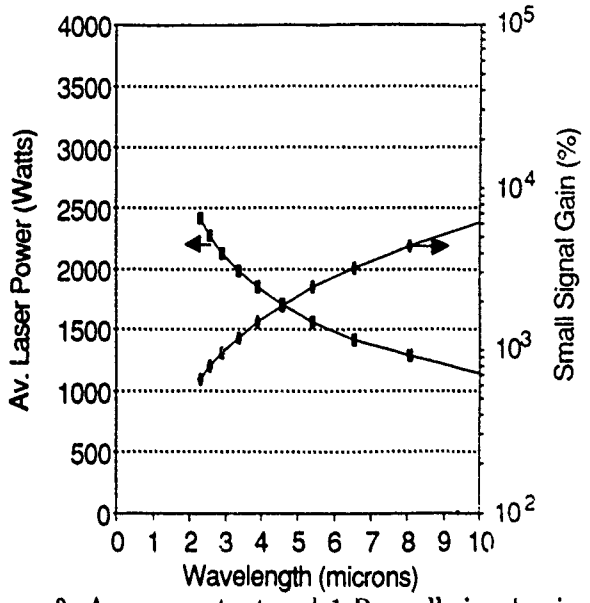


Figure 2. Average output and 1-D small signal gain for the IR FEL under dedicated FEL operation.

In the UV region the longer Rayleigh range and the desire to push operation to as short a wavelength as possible suggests that use of a novel resonator design such as that proposed by Shih, *et al.*,[7] see Figure 3. This resonator has the interesting property that it is extremely insensitive to alignment errors and jitter, permitting the mirrors to be placed very far away from the wiggler. The calculated 1-D optical gain in the UV region is also quite large (Figure 4).

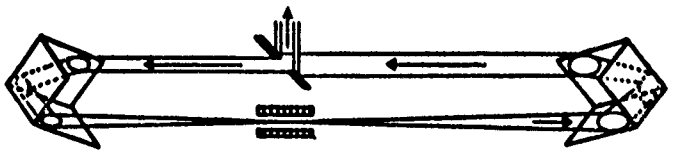


Figure 3. A schematic of the re-imaged retro-reflective ring resonator.[7]

Table 2 shows a possible hardware implementation of such resonators. Virtually all the parameters are achievable with inexpensive, off-the-shelf components with the possible exception of the mirror power loading which is close to the maximum specifications and the sensitivity of the cavity to proper mirror curvature. As shown in Figure 1b the higher energy available at the end of the North Linac yields wavelengths with the proposed wigglers that are shorter than conventional optics can handle. Several

Table 2. Possible resonator design parameters.

Outcoupling (%)	30	20
Length (m)	20.04	60.12
Rayleigh range (m)	0.75	1.5
Radi of Curve (m)	10.076	30.079
w_0 (mm) @ λ (nm)	0.66 @ 1850	0.32 @ 210
Fresnel #	8.5	25.5
Configuration	Near concentric	Re-imaged retro ring
Outcoupling	Hole/Partial refl.	Scraper
Substrate	Copper/ZnSe	Sapphire

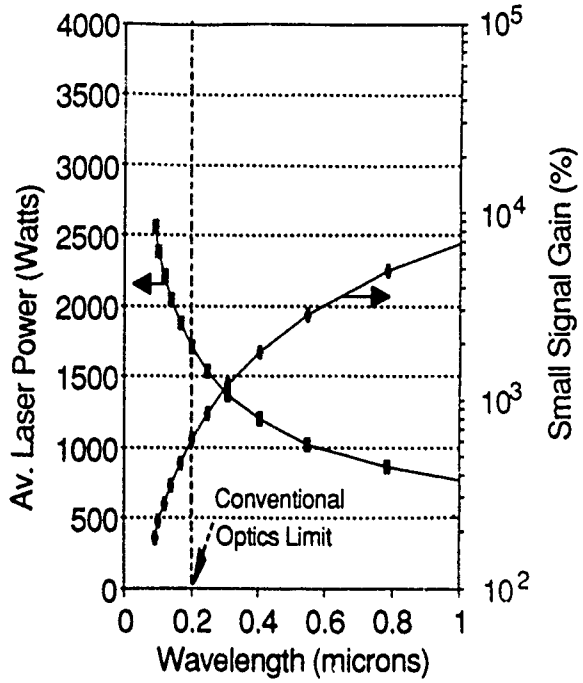


Figure 4. Average laser output and 1-D small signal gain for the UV FEL. With simultaneous nuclear physics operation the FEL performance would be reduced due to lower current. Mirror technology limits operation below about 200 nm.

resonators/mirrors have been proposed for this region[8]. Further research will be required to determine if any are practical for use with the proposed high power UV FEL.

SUMMARY

In summary, we have performed conceptual studies of a pair of FELs located at the output of the Front End and North Linac of the CEBAF accelerator. The high average beam power coupled with the superior electron beam quality produced by the linac yield projections of tunable output power that substantially exceed existing and most proposed sources. The tolerances for most FEL components are not severe but the high optical power requires careful consideration and, perhaps, special optical cavity arrangements and mirror designs.

REFERENCES

[1] H. A. Grunder, in *1988 Lin. Acc. Conf. Proc.* CEBAF-Report-89-001, 3(1988).

[2] J. J. Bisognano, *et al.*, CEBAF Technical Note CEBAF-TN-90-189.

[3] L. R. Elias, *et al.*, Phys. Rev. Lett. **38**, 892(1977).

[4] J. A. Edighoffer, *et al.*, Phys. Rev. Lett **52**, 344(1984).

[5] V. N. Litvinenko, Synch. Rad. News **1** (5), 18(1988).

[6] E. T. Scharlemann in Free Electron Lasers, Critical Rev. of Optical Science and Tech., SPIE 738, (1988).

[7] Shih, *et al.* in *Proc. 12th Int. FEL Conf.*, Paris(1990).

[8] J. C. Goldstein, *et al.*, Nucl. Inst. and Meth. in Phys. Rsch. A296 288 (1990).

Coherent X-Rays from PEP*

Simon Baird†, Heinz-Dieter Nuhn, Roman Tatchyn, Herman Winick
Stanford Synchrotron Radiation Laboratory, SLAC, Bin 69, P.O. Box 4349, Stanford, CA 94309-0210
Alan S. Fisher, Juan C. Gallardo
Brookhaven National Laboratory, Upton, NY 11973
Claudio Pellegrini
Department of Physics, University of California, Los Angeles, CA 90024-1547

Abstract

This paper explores the use of a large-circumference, high-energy, electron-positron collider such as PEP to drive a free-electron laser (FEL), producing high levels of coherent power at short wavelengths. We consider Self-Amplified Spontaneous Emission (SASE), in which electron bunches with low emittance, high peak current and small energy spread radiate coherently in a single pass through a long undulator. As the electron beam passes down the undulator, its interaction with the increasingly intense spontaneous radiation causes a bunch density modulation at the optical wavelength, resulting in stimulated emission and exponential growth of coherent power in a single pass. The need for optical-cavity mirrors, which place a lower limit on the wavelength of a conventional FEL oscillator, is avoided.

We explore various combinations of electron-beam and undulator parameters, as well as special undulator designs and optical klystrons (OK), to reach high average or peak coherent power at wavelengths around 40 Å by achieving significant exponential gain or full saturation. Examples are presented for devices that achieve high peak coherent power (up to about 400 MW) with lower average coherent power (about 20 mW) and other devices which produce a few watts of average coherent power.

I. Introduction

The relevant features of PEP are the long straight sections (117 m) in its 2.2-km circumference, the large RF voltage (up to 40 MV), and the low bending-magnet field (0.07 T at 3.5 GeV). The electron-beam emittance required for an FEL is given by $\epsilon_x \lesssim \lambda/(2\pi)$. At 40 Å, the requirement of 0.64 nm·rad can be reached by operating PEP at 3 — 4 GeV, a fraction of its 16-GeV maximum energy, with low-emittance optics, and with extra emittance reduction from damping wigglers and/or the long FEL undulator itself. Radiation produced by damping wigglers and the FEL undulator reduces the damping time, facilitating operation of PEP at low energy.

II. Characteristics of PEP

Instead of the 14.5 GeV typically used in collider experiments, the FEL requires energies as low as 3 GeV, taking advantage of the fact that the transverse emittance scales quadratically with energy in a storage ring. Successful beam storage has been achieved at 4.5 GeV [1], but lower-energy operation has not yet been tried. Low-emittance optics [2] have been tested, giving $\epsilon_x = 5.3$ nm·rad [3] at 7.1 GeV (compared to 30 nm·rad with colliding-beam optics). Scaling this value down to 3 GeV gives an emittance only a factor of 1.5 above the FEL requirement. The measured vertical emittance was 4% of the horizontal. Thus the horizontal emittance could be cut in half by coupling the two dimensions. The fractional rms energy spread σ_ϵ in a storage ring, determined by synchrotron-radiation losses in the bending magnets, is proportional to beam energy and so favors low energy for the FEL. Without damping wigglers [4], $\sigma_\epsilon = 6.6 \cdot 10^{-5} \cdot E\,[\mathrm{GeV}]$, giving an energy spread of 2×10^{-4} at 3 GeV. Synchrotron radiation from a wiggler increases the beam's energy spread and changes its emittance [5]. Damping wigglers, in low or zero dispersion locations, reduce emittance but increase energy spread.

FEL gain requires a high peak current, I_p. The peak single-bunch current in a storage ring is limited by the microwave instability. Adding charge results in lengthening of the bunch, with no increase in I_p. Transversely, there is a similar fast blow-up. The instability growth rates are short compared with the period of synchrotron oscillation. The threshold for the longitudinal instability in PEP will be reached long before the transverse. To estimate this limit, we use the ZAP code [6] and an extrapolation of bunch-length measurements made on the SPEAR ring and scaled to fit PEP data [7-8]. For PEP's low-emittance mode and an energy of 3 GeV, this gives a maximum peak current of 17.6 A.

To increase this peak current, we considered compressing the circulating bunch over a half turn [2,4], in order to reach a high peak current only when the beam passes through the FEL, thereby avoiding bunch-lengthening instabilities. However, the phase-space rotation that compresses the bunch longitudinally and so increases the peak current, is accompanied by an increase in energy spread by the same factor. If the FEL gain is not close to the energy-spread limit (see below), then the half-turn compression would be helpful. However, this tolerance for extra energy spread would be put to better use by arranging an equilibrium state with a higher energy spread, since the peak-current limit scales with σ_ϵ^2. Reasonable damping-wiggler parameters ($B_w = 1.26$ T, $\lambda_w = 12$ cm, $K = 14.1$, and $L_w = 9$ m at 3 GeV, or $L_w = 18$ m at 3.5 and 4 GeV) can increase the energy spread by a factor of three, increasing the peak current attainable by nine. For the same increase in energy spread, bunch compression would gain only a factor of three in peak current.

The radiation damping time and the beam lifetime are of concern at the very low energy necessary for the FEL. Lifetimes of over 30 hours have been observed in PEP at 8 GeV and low current with low-emittance optics [9]. Assuming that the beam lifetime is determined by Coulomb scattering, which scales with the inverse square of the beam energy, we expect lifetimes of more than 5.7 and 4.2 hours for 3.5 and 3 GeV, respectively. These lifetimes are sufficient for FEL operation. The radiation damping times for PEP at 3 GeV, without damping wigglers and in the low emittance mode, are $\tau_{x,y} = 1.02$ s and $\tau_s = 0.51$ s. With the damping

0-7803-0135-8/91$01.00 ©IEEE

Table 1: Parameters for various FEL's on PEP. Lines 1-4 describe conventional permanent-magnet undulators, located in a bypass and used once every $3\tau_x$. A 100% duty cycle is assumed in lines 5-7 (but see text for line 6). The Paladin undulator is in lines 5 and 6, without and with an optical klystron configuration, respectively. The cusp-field undulator in line 7 is helical; the effective K is shown. Single-bunch operation of all undulators is assumed.

E GeV	λ Å	λ_u cm	g cm	B_u T	K	ϵ_x Å·rad	β_x m	z_R m	σ_ϵ 10^{-4}	I_p A	ρ 10^{-4}	$\rho_{\rm eff}$ 10^{-4}	L_G m	L_u m	τ_x ms	σ_s mm	$P_p^{\rm coh}$ MW	$P_{\rm av}^{\rm coh}$ mW	$P_p^{\rm spon}$ MW	$P_{\rm av}^{\rm spon}$ mW
3.0	35.8	3.70	1.0	0.98	3.37	1.96	8.5	5.8	6.3	144	7.0	4.1	4.1	89	550	3.3	180	4	70	1.2
3.5	37.9	4.00	1.0	1.06	3.97	2.05	5.5	3.7	7.2	219	9.1	6.0	3.1	67	230	4.2	460	28	130	5.1
3.0	36.2	2.85	0.5	1.48	3.94	1.96	8.0	5.5	6.3	144	6.6	3.7	3.6	77	550	3.3	160	3	140	2.3
3.5	37.8	3.10	0.5	1.58	4.57	2.05	5.0	3.4	7.2	219	8.7	5.5	2.6	57	230	4.2	420	26	240	9.7
3.0	40.7	8.00	3.0	0.30	2.24	1.96	9.1	6.2	6.3	144	8.7	6.1	6.0	25.6	550	3.3	879W	3.3	1.9	7.1W
3.0	40.7	8.00	3.0	0.30	2.24	1.96	9.1	6.2	6.3	144	8.7	6.1	N/A	25.6	550	3.3	1.0	3.7W	6.8	26W
4.0	37.9	27.0	N/A	0.034	1.2	2.71	15.0	13.5	7.4	327	11.8	9.0	13.9	100	100	5.1	0.043	250	1.5	3.5W

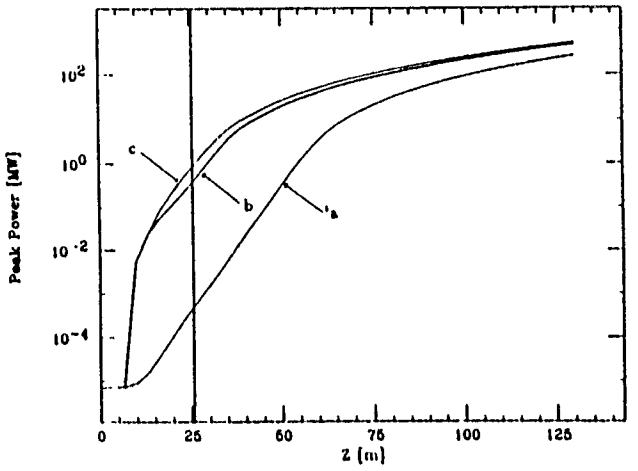


Figure 1: Power emitted as the beam passes through the Paladin undulator. The vertical line marks Paladin's true length, which has been extended here to the saturation length. (a) Without OK. (b) With one 1-m dispersion section ($B = 1$ T for 25 cm, -1 T for 50 cm, 1 T for 25 cm) in the first break between undulator sections. (c) With a 1-m dispersion section in the first break, and a 0.25-m dispersion section in the second break.

wigglers described above, they are reduced to $\tau_{x,y} = 0.55$ s and $\tau_s = 0.23$ s.

III. FEL Designs for PEP

A. Conventional Permanent Magnet Undulators

These considerations, and the formulas [10-12] for the exponential gain parameter ρ, the power e-folding length $L_G = \lambda_u/\left(4\pi\sqrt{3}\rho\right)$, and the undulator length for saturation of $L_{\rm sat} = \lambda_u/\rho$ in an SASE FEL, lead (without attempting a full optimization) to the first four examples in Table 1. In all cases, the wavelength has been held near 37 Å, in the "water window" between the oxygen and carbon K edges (23 and 44 Å) to permit the study of organic compounds in solution.

The first four examples use neodymium-iron hybrid undulators with $B_u\,[\mathrm{T}] = 3.44\exp\left[-(g/\lambda_u)(5.08 - 1.54g/\lambda_u)\right]$, periods of 2.85 to 4 cm, and saturation lengths of 57 to 89 m. The undulator lengths $L_{\rm sat}$ and L_G were calculated using $\rho_{\rm eff}$, which includes the correction for energy spread [13],

$$\frac{\rho_{\rm eff}}{\rho} = \frac{\exp\left[-0.136\,(\sigma_\epsilon/\rho)^2\right]}{1 + 0.64\,(\sigma_\epsilon/\rho)^2}. \qquad (1)$$

We use the damping wigglers described above and assume full coupling between horizontal and vertical emittance. The lower beta values (with $\beta_x = \beta_y$) will require periodic refocusing along the undulator.

The peak coherent x-ray power, $P_p^{\rm coh}$, ranges from 160 to 460 MW. Perturbation of the beam parameters by the saturated FEL [14], as well as the reduction in beam lifetime by the narrow undulator gap, require placing these FEL's in a bypass to the main ring. The average coherent power, $P_{\rm av}^{\rm coh}$, is calculated assuming that the bunch is switched into the bypass once every three transverse damping times τ_x. The 460 MW case has a peak and average spectral brilliance of 4×10^{29} and 2.3×10^{19} photons $\cdot\, s^{-1} \cdot mm^{-2} \cdot mrad^{-2} \cdot (0.1\%\text{bandwidth})^{-1}$ respectively. Total peak and average spontaneous powers are also given in Table 1. Comparisons of these with the coherent power should take their significantly larger bandwidths ($\approx$100%) and opening angles ($1/\gamma$) into account. To indicate how in-band levels of spontaneous coherent power would compare to the amplified levels listed in the table, calculations for the first four devices (assuming a 100 % duty cycle and complete suppression of SASE) yield 140, 100, 141, 107 W peak, and 0.52, 0.5, 0.52, 0.51 mW average, respectively.These figures are for a spectral bandwidth of $\lambda_u/2L_u$ and an opening angle of $\approx \frac{1}{2}\sqrt{\lambda/L_u}$.

B. The Paladin Undulator with an Optical Klystron

The long undulators discussed above would be expensive and difficult to build. Here we consider using a long, existing undulator. The Paladin undulator [15] was used at the Lawrence Livermore National Laboratory for FEL experiments with the 50-MeV ATA induction linac. It is a DC iron-core electromagnetic undulator with a length L_u of 25.6 m, made in five 5.12-m sections, and a period λ_u of 8 cm. Fields B_u of up to 0.32 T have been attained. Here we use a 0.3-T field, giving a K of 2.24. The fifth line of Table 1 shows the result, using the same 3-GeV parameters as before. The wavelength, $\lambda = 40.7$ Å, and gain, $\rho = 8.7 \times 10^{-4}$, are similar to the previous cases, but the power gain length has gone up to 6.0 m due to the longer undulator period. A length of 131 m would be needed for saturation, as curve (a) of Fig. 1 shows. Refocusing quadrupoles in the breaks

between the five sections are needed to obtain the lower β_x. Although too short to saturate, the existing four gain lengths are sufficient to demonstrate exponential growth at x-ray wavelengths. Because Paladin's gap is 3 cm, it could be placed on the main PEP ring, rather than a bypass, without limiting beam lifetime.

An optical klystron (OK), formed by placing dispersive sections in one [16] or more [17] of the breaks between the Paladin sections, can improve substantially on this result. The calculations of Table 1 use a 1D simulation code, including energy spread and emittance [16], to find the increase in output power obtained by inserting dispersive sections in the first one or two section breaks, which are approximately one gain length apart (see Fig. 1). Line 6 of Table 1 gives the values for curve (c) at the true 25.6-m length. The peak power increases by over three orders of magnitude due to the optical klystron, but is still over two orders short of saturation. The average power is impressive, with the assumption of a 100% duty cycle (undulator in the main ring); this exceeds the Renieri limit [14], and further work will be required to find optimal dispersion parameters for average power. For maximum peak power, the dispersive section can be pulsed on, avoiding the need for a bypass.

The second dispersive section brings the FEL to saturation slightly more quickly, but contributes only a factor of 2 in the 25.6-m length of the actual device. The increasing energy modulation of the beam as it travels requires less dispersion in successive sections. The parameters are not fully optimized, but demonstrate decreasing benefit from successive dispersion sections. Longer sections or a third section would overbunch and decrease the output.

C. The Cusp-Field Undulator

Several alternative approaches to insertion device design for PEP based on weak-field, long-period undulators have been introduced in recent years [18-19]. These focus on the maximization of time-averaged (as opposed to peak) coherent power through a single-pass device. A "Cusp-Field" undulator [20-21] of this class has been explored by one of us (R.T.). It is an iron-free structure consisting of two axisymmetric arrays of circular coils with displaced parallel axes producing a helical field on the electron orbit which runs parallel to the coil axes. The main features of a cusp-field device are 1) a sparse copper coil construction, whose long period facilitates the use of refocusing elements along its length; 2) a simply-configured helical structure; and 3) a built-in provision for orbit deflection along the entire undulator length, allowing continuous control of coherence gain, including switching in and out of the FEL mode in one orbital period. It is expected that the field quality of this structure should be very high, and that its versatile selection of field configurations will enable a wide range of x-ray research, including systematic studies of coherence growth and modulation in particle beams, to be performed.

A cusp-field device appears suitable for use as an unsaturated SASE undulator (see last line of Table 1). The power gain g for the indicated 100m may be calculated with the formula [22] $g \approx 0.11\exp(\lambda_u/L_g)$. For the parameters shown, the length required for full saturation would be 300 m, corresponding to a peak coherent power of 1.2 GW. Note the rather high value of average coherent power, due to the 100 % duty cycle in a steady state mode. At the listed levels of peak coherent output power, the perturbation of PEP's beam is estimated to be still negligible, whereas operation at levels an order of magnitude higher would begin reducing the coherent power gain due to increasing beam energy spread. The calculations done here followed those of Renieri [14].

Due to its modular structure, the cusp-field undulator is particularly suited for being configured as an optical klystron with a flexible number of modulation/dispersion sections. This would permit the systematic study of OK configurations ranging from a minimum of one dispersion section to the recently-proposed "distributed-OK" structure [17]. Calculations based on the parameters in Table 1 [16] indicate that the first 50 meters of the device could be replaced by one 14 meter gain length + 4 meters of dispersion, and that two or more such sections would enable gain saturation to be attained in less than 100 m. For equal numbers of gain lengths in the OK mode, the net power gain attained by the cusp-field device would be about twice as much as Paladin's (see Fig. 1), based on the ratio of their operating peak currents, energies, and effective gain parameters ρ_{eff}.

IV. REFERENCES

1. M. Donald et al., LEP Note 553 (1986).
2. A Bienenstock, G. Brown, H. Wiedemann, and H. Winick, Rev. Sci. Instr. **60**, 1393 (1989).
3. M. Borland and M. Donald, Proc. IEEE Part. Acc. Conf., Chicago, IL, March 1989.
4. A. Hofmann, SSRL ACD Note 39, Nov. 1986.
5. H. Wiedemann, NMI **A266**, 24 (1988).
6. M.S. Zisman, S. Chattopadhyay, and J.J. Bisognano, "ZAP User's Manual," LBL 21270, 1986.
7. A. Chao and J. Gareyte, SPEAR 197, PEP 224 (1976).
8. M. Month, SPEAR 198, PEP 227 (1976).
9. G. Brown et al., Proc. 1987 IEEE Part. Accel. Conf., **461-663**, (1987).
10. C. Pellegrini, NMI **A272**, 364 (1988).
11. J. Bisognano et al., Part. Acc. **18**, 223 (1986).
12. M. Cornacchia et al., Nucl. Instrum. Methods **A250**, 57 (1986).
13. G. Dattoli et al., Nuovo Cimento **11D**, 393 (1989).
14. A. Renieri, IEEE Trans. Nucl. Sci. **26**(3), 3827 (1979).
15. G.A. Deis et al., Proc. 10th Int. Conf. Magnet Technology, Boston, MA, Sept. 1987.
16. J. Gallardo, C. Pellegrini, Optics Commun. **77**, 45 (1990).
17. V. N. Litvinenko, INP, submitted.
18. R. Tatchyn, Proc. Workshop on PEP as an SR Source, SSRL, 10/21-21/87, 97-113.
19. R. Coisson, Rev. Sci. Instr. **60**(7), 1426(1989).
20. T. Cremer and R. Tatchyn, unpublished.
21. R. Tatchyn, T. Cremer, P. Csonka, SR-90 Synchrotron Radiation Conference, Moscow, (1990).
22. A. Jackson et al., SPIE Proceedings 582, 131(1985).

*The U.S. Department of Energy supported this research, through the Office of Basic Energy Sciences, Division of Material Sciences for SSRL, and under contract DE-AC02-76-CH0016 for BNL.

†Permanent address: CERN, Geneva, Switzerland.

SATURNUS: The UCLA Infrared Free-Electron Laser Project

J.W. Dodd, S.C. Hartman, S. Park, C. Pellegrini, J.B. Rosenzweig, J.A. Smolin, G. Hairapetian,
J. Kolonko, W.A. Barletta, D.B. Cline
Center for Advanced Accelerators, Department of Physics, U.C.L.A., Los Angeles, CA, 90024-1547

J.G. Davis, C.J. Joshi, N.C. Luhmann Jr.
Department of Electrical Engineering, U.C.L.A., Los Angeles, CA 90024-1594

S.N. Ivanchenkov, A.S. Khlebnikov, Yu.Yu. Lachin, A.A. Varfolomeev
I.V. Kurchatov Institute of Atomic Energy, Moscow, 123182, U.S.S.R

ABSTRACT: A compact 20 MeV linac with an RF laser-driven electron gun will be used to drive a high-gain (10cm gain length), 10.6μm wavelength FEL amplifier, operating in the SASE mode. Saturnus will mainly study FEL physics in the high-gain regime, including start-up from noise, optical guiding, sidebands, saturation, and superradiance, with emphasis on the effects important for future short wavelength operation of FEL's. The hybrid undulator was designed and built at the Kurchatov Institute of Atomic Energy in the U.S.S.R. The primary magnetic flux is provided by C-shaped iron yokes, where between the poles thin blocks of neodymium-iron-boron magnets are placed to provide additional magnetic flux along the undulator axis. The field strength is adjusted by moving the thin Nd-Fe-B blocks on a set-screw mount. The initial assembly will have forty periods, each 1.5cm long. The gap distance between the "yoke" pole-pieces is fixed at 5mm. The undulator field has been measured, yielding an on axis peak value of 6.6kGauss, which closely matches computer simulations.

Table 1. Saturnus design parameters.

ELECTRON BEAM	
Energy, nominal	16.5MeV
Energy spread, r.m.s.	0.2%
Peak current	200A
Klystron frequency	2.865GHz
Pulse repetition rate	5Hz
Macropulse duration	3.5μsec
micropulse duration, r.m.s.	≈1.6psec
Charge per bunch	≈1nC
Normalized emittance, r.m.s.	8mm-mrad
UNDULATOR	
Drift tube I.D. within undulator	4mm
Electron beam diameter in undulator	0.4mm
Period	1.5cm
Length	60cm
Fixed gap between pole pieces	5mm
Field on axis	6.6kGauss
FEL OUTPUT RADIATION	
Wavelength	10.6μm
Gain length	10cm
Saturation length	130cm
Peak saturated power	50MW

ACKNOWLEDGEMENTS: Our group appreciates the help received from H. Kirk, K. Batchelor, J. Xie, J. Sheehan, G. Bennett, J. Wurtele, M. Allen, G. Loew, M. Baltay, and H. Hoag. This work is supported by DOE Grant No. DOE-DE-AS-3-90ER-40583.

I. INTRODUCTION

A compact 16.5 MeV linac with an RF laser-driven electron gun[1] is being built at UCLA (See S.C. Hartman, *et al.*, this Conf.). This linac will be used to study the production of high-brightness electron beams, and to drive a high gain, 10.6μm wavelength FEL amplifier, capable of operating in the SASE mode. Saturnus will use a 1.5cm period, 6.6kG peak field undulator developed and built at the I.V. Kurchatov Institute of Atomic Energy. Table 1 shows beam parameters.

Saturnus will mainly study FEL physics in the high-gain regime, including start-up from noise, optical guiding, sidebands, saturation, and superradiance, with emphasis on the effects important for future short wavelength operation of FEL's.[2] For the electron beam we will study ways to improve the beam brightness and peak current. We will have two beam lines, one leading straight into the undulator, the other designed for beam diagnostic and longitudinal bunch compression. This second beam line will also be used for other particle beam physics experiments, including plasma wakefield acceleration.[3]

II. FEL OUTPUT: SIMULATIONS AND DIAGNOSIS

The FEL performance in SASE is evaluated using the TDA code developed by Tran and Wurtele at MIT.[4] TDA predicts a gain length of 10cm, with a saturation power of 50MW. This assumes that a full 200A peak current is achievable. Fig. 1(a) graphs the power versus distance along the undulator as projected by TDA. Fig. 1 uses an input power of 40nW, corresponding to the spontaneous radiation emitted in one gain length, within an angle $\Theta = 1/(\gamma\cdot\sqrt{N})$ and a line width $1/(2N)$. This radiation is assumed to be focused to a spot radius $(\lambda L_{UNDUL.})^{1/2}/4\pi$ at the centre of the first gain length.

Fig. 1(b) plots the calculated r.m.s. optical beam radius versus the distance along the undulator. Notice that once growth occurs the optical beam collapses and remains in the vicinity of the electron beam as it propagates down the entire undulator. It is interesting to note that the optical beam radius and the gain length depend on the extent of detuning the electron beam energy from the resonant energy.

The FEL's output wavelength will closely match the 10.6μm radiation which CO_2 lasers produce, simplifying the diagnosis of the output radiation by allowing the possibility to inject the FEL with an external CO_2 laser. For cryogenic

0-7803-0135-8/91$01.00 ©IEEE

infrared detectors sensitive to 10μm wavelengths, the expected power output from spontaneous emission in the FEL (excluding gain) is marginally detectable. For 1nC charge per bunch, $1.2 \cdot 10^7$ photons per micropulse are expected from spontaneous emission within the angle and linewidth given above over a 10cm distance. For smaller charges one may need to integrate the signal over many pulses. As seen from fig. 1(a) at the end of the undulator section, roughly 3kW of power occurs from exponential gain. This power level corresponds to 10^{12} photons per micropulse and is easily detected.

III. HYBRID UNDULATOR

The hybrid undulator was designed and constructed at the Kurchatov Institute of Atomic Energy in the U.S.S.R. The primary magnetic flux is provided by $SmCo_5$ magnets placed in the middle of C-shaped vanadium-permendur yokes. Thin blocks of neodymium-iron-boron magnets are placed between the poles to provide additional magnetic flux. The field strength is adjusted by moving the thin Nd-Fe-B blocks towards or away from the axis on a set-screw mount. Fig. 2 is a schematic diagram of the Kurchatov undulator. The initial assembly has forty periods, each period being 1.5 cm long. The gap distance between the "yoke" pole-pieces is fixed at

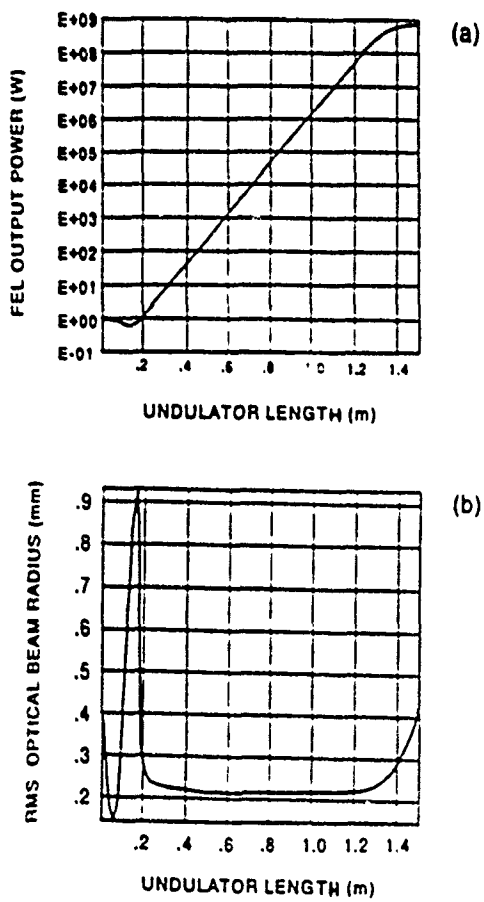


Figure 1. TDA simulations of SASE using the parameters in table 1: (a) power growth through the undulator and (b) radius of the optical beam within the undulator. Optical guiding is evident since the optical beam remains confined near the electron beam, once power growth predominates.

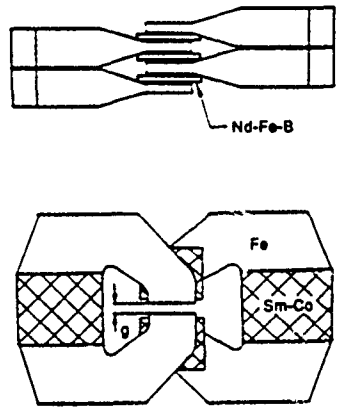


Figure 2. The Kurchatov hybrid undulator (g = 5mm).

5mm. The complete undulator was measured and yielded an average peak field on axis of 6.6kGauss. A computer simulation using the TOSCA[5] code gave similar results. The deviation of the peak field within the undulator has been controlled within a tolerance of 0.5%.

Fig. 3 shows the measured values of the perpendicular magnetic field as measured along the undulator's axis. The 600mm end includes a compensating taper by tilting the endmost Nd-Fe-B magnets 45°. The zero millimeter end shows the field distribution without this compensation.

The first phase of construction consists of this single 60cm undulator section. The second phase of construction will have two separate 60cm undulator sections with a dispersive array installed in between the other sections. The dispersive section provides a shorter distance for the velocity modulation induced by the first section to enhance the bunching of the electron stream in the ponderomotive well.[6]

IV. ELECTRON BEAM DIAGNOSTICS

A. Current and Position:

The electron beam position diagnostic is based upon a design used on ATF at BNL. Each monitor consists of four stripline electrodes placed symmetrically around the electron beam, inside and electrically isolated from the vacuum vessel via ceramic, vacuum feed throughs. The total signal induced on the four striplines is proportional to the total charge in a bunch. The difference of the signals between two diametrically opposed striplines determines the relative position of the

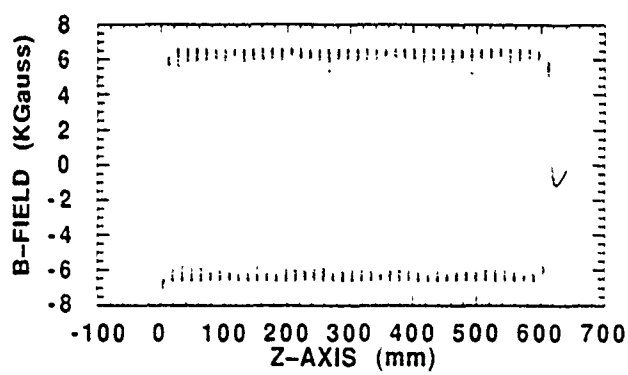


Figure 3. Measured B-field configuration along the axis of the Kurchotov undulator.

electron bunch from the geometric center of the four striplines. The sum and difference signals are subsequently sent to a heterodyne receiver with local oscillator at 2.856GHz, in order to rectify the signal sent to the preamplifier. Each microbunch generates a positive and negative signal of equal magnitude on the electrode, separated by twice the transit time of the electrode's length (i.e., 500psec).[7] The heterodyning process reverses the polarity of the second pulse, therefore the net integrated charge is doubled instead of cancelled in the preamp.

B. Emittance, Energy Spread, and Overall Energy:

Accurate measurements of the electron beam properties are important to understand the FEL behavior. The beam emittance will be measured using a technique similar to that developed at ATF.[8] A phosphor screen is placed to intercept the electron beam. The spot size is reflected into an optical camera. The emittance can be unfolded from the comparison of the spot sizes at two different settings of the beam transport system.[9]

In the dispersive region between two dipole magnets, the energy and energy spread of the electron beam can be measured by placing the phosphour screen at the the beam focus. Since the beam emittance is expected to be low, an angular spread in the spot size at the focus (as seen on the charge-coupled camera viewing the phosphour screen) can by and large be attributed entirely to the energy spread in the beam. The average energy of the beam can be determined from locating the centroid of the electron spot as seen on the phosphour screen and comparing to the calculated trajectory.

C. Temporal Pulse Duration:

The time duration of the electron pulse will be measured by passing the electron beam through a thin plate of dielectric material, then sweeping the Cerenkov radiation thereby produced, on the picosecond time scale using a streak camera.

V. REFERENCES

[1] K. Batchelor, H. Kirk, J. Sheehan, M. Woodle, and K. McDonald, *Proc. European Particle Accel. Conf.*, Rome, Italy, June 7-12, 1988; also, K. Batchelor, *et al.*, *Proc. 1989 Particle Accel. Conf.*, Chicago, IL, p. 273.

[2] C. Pellegrini, *Nucl. Instr. & Meth. Phys. Res.* **A272** (1988) 364.

[3] J. Smolin, T. Katsouleas, C. Joshi, P. Davis, C. Pellegrini, "Design of a plasma wakefield accelerator experiment at UCLA," *Bul. Am. Phys. Soc.* to be publ. Nov, 1990. Cf., T. Katsouleas, J.J. Su, W.B. Mori, C. Joshi, J.M. Dawson, "A compact 100MeV accelerator based on plasma wakefields," *Microwave and Particle Beam Sources and Directed Energy Concepts*, H.E. Brandt, ed., Proc. SPIE 1061, pp. 428-433 (1989).

[4]T.M. Tran and J.S. Wurtele, "Free-electron laser simulation techniques," *Physics Reports* **195** (1990) 1-21.

[5]IEEE Proc. Vol. 127, Pt. B, No. 6 (1980).

[6]J. Gallardo and C. Pellegrini, *Optics Comm.*, **77** (1990) 45.

[7]K.-Y. Ng, "Fields, Impedances, and Structures," in *Phys. of Part Accelerators*, Vol. One, eds., M. Month and M. Dienes, AIP Conf. Proc. No. 184 (Am. Inst. of Physics, New York, 1989), pp. 472-524; especially §4.3 on beam position monitors.

[8]D.P. Russell, and K.T. McDonald, "A beam-profile monitor for the BNL Accelerator Test Facility (ATF)," *Proc. 1989 IEEE Particle Accel. Conf.*, Vol. 3, eds., F. Bennett and J. Kopta, Chicago, IL., pp. 1510-1512.

[9]K.T. McDonald and D.P. Russell, "Methods of Emittance Measurement," in the *Proc. of the Jont US-CERN School on Observation, Diagnosis and Correction in Part. Beams*, Capri, Italy, October 20-26, 1988.

PERFORMANCE OF THE PHOTOINJECTOR ACCELERATOR FOR THE LOS ALAMOS FREE-ELECTRON LASER

P.G. O'Shea, S.C. Bender, B.E. Carlsten, J.W. Early, D.W. Feldman, R.B. Feldman, W.J.D. Johnson, A.H. Lumpkin, R.L. Sheffield, R.W. Springer, W.E. Stein, L.M. Young
MS J579, Los Alamos National Laboratory, Los Alamos NM 87544

Abstract

The Los Alamos free-electron laser (FEL) facility has been modified by the replacement of the thermionic electron gun and bunchers with a 1300 MHz RF photoinjector. Two more accelerator tanks have been added to increase the beam energy to 40 MeV. Preliminary studies at 15 MeV have demonstrated excellent beam quality with a normalized emittance of 40 π mm-mrad. The beam quality is now sufficient to allow harmonic lasing in the visible. At present we are beginning FEL experiments at a wavelength near 3 μm. In this paper we report on the performance of our photoinjector accelerator.

I. Introduction

Free-electron laser oscillators operating at high power and short wavelength (λ) require high-current, low-emittance electron beams. The gain of an FEL increases with beam current subject to the constraint that

$$\varepsilon_n < 4\beta\gamma\lambda.$$

In this context high current implies I»100A and low emittance implies ε_n « 100 π mm-mrad (normalized). Very low emittance allows the possibility of accessing short optical wavelengths at low beam energy, by lasing on harmonics of the fundamental FEL wavelength.

High quality electron beams must not only be generated, but must also be transported to the wiggler without loss of beam quality. Previously such beams have been produced by thermionic high-voltage guns, with emittances near the source thermal limit. Before being accelerated in an RF linac the beam is typically passed through subharmonic bunching cavities at non-relativistic energies. Nonlinear forces from space-charge and RF fields of the bunchers generally cause emittance growth and result in diminished FEL performance.

For a number of years we have been developing photocathode RF guns for high-brightness electron beam applications [1]. In a photoinjector, a laser driven photocathode is placed directly in a high-gradient RF accelerating cavity. This system allows unsurpassed control over the spatial and temporal profiles, and current of the beam. In addition the "electrodeless emission" avoids many of the difficulties associated with multi-electrode guns, i.e. the electrons are accelerated very rapidly to relativistic energies, and there are no electrodes to distort the accelerating fields.

We have installed and tested a high-gradient (26 MV/m at the cathode) 1300 MHz, π/2-mode photoinjector, that is 0.6 m long and produces 6 MeV, 300 A, 15 ps electron pulses at a 22 MHz rep. rate. Figure 1 shows a cutaway view of the photoinjector. Table 1 gives the specifications for the photoinjector.

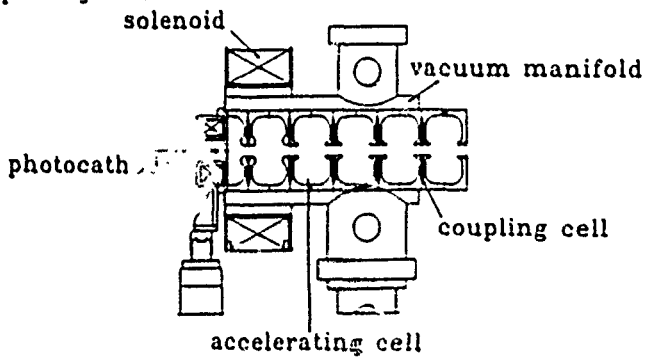


Figure 1. Photoinjector

Table 1 Photoinjector specifications

Frequency	1300 MHz
Accelerating gradients:	
cell 1	26.0 MV/m
cell 2	14.4 MV/m
cell 3-6	10.0 MV/m
Measured Q	18500
Shunt impedance	35 MΩ/m
Copper power	1.8 MW
Output energy	6 MeV
Micropulse length	15 ps
Micro pulse charge	5nC
Micropulse rep. rate	21.7 MHz
Peak current	300 A
Macropulse length	100 μs
Macropulse rep. rate	1 Hz
Macropulse ave. current	0.1 A
Emittance (4rms, normalized)	< 50 π mm-mrad

Following the photoinjector the electron beam is accelerated to 40 MeV by three additional side-coupled linac tanks. RF power is provided by Thomson CSF klystrons (TH2095A), with one klystron per accelerator tank.

The FEL configuration is a single-accelerator master-oscillator power-amplifier (SAMOPA) [2]-[4] configuration as shown in figure 2. Resonator optics are often the limiting factor in high average power FELs. In the SAMOPA concept

Work performed under the auspices of the Department of Energy for the United States Army.

0-7803-0135-8/91$01.00 ©IEEE

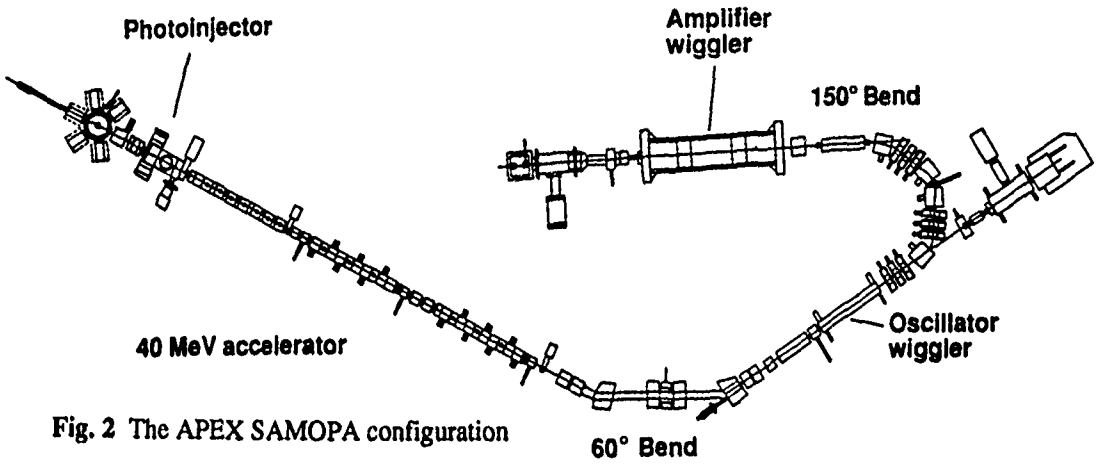


Fig. 2 The APEX SAMOPA configuration

the electrons first pass through a low power oscillator and then through a high gain amplifier. The light from the oscillator is fed into the amplifier. Since the power in the oscillator is low, and there are no resonator optics in the amplifier, the optical damage difficulty is removed. We are studying the physics issues associated with SAMOPA operation as part of the Boeing/Los Alamos collaboration to build the Average Power Laser Experiment (APLE). Los Alamos will perform the APLE prototype experiments and will be known by the acronym APEX.

In 1990 we completed experiments that characterized the photoinjector operation and beam transport through one additional accelerator tank at an energy of 15 MeV.

II. Drive Laser and Photocathode

The performance of our FEL depends critically on our photocathode and its drive laser. Phase and amplitude jitter in the drive laser result in energy and current jitter in the electron beam. We require the phase and amplitude jitter to be <1 ps and <1 % respectively. Table 2 gives the measured performance of the drive laser and photocathode.

Table 2 Drive laser and photocathode performance

Drive laser:	Doubled Nd-YLF
Wavelength	527 nm
Micropulse width	7-15 ps
Micropulse rep. rate	21.7 MHz
Micropulse energy	12 μJ (5-6 μJ at cathode)
Macropulse length	0-200 μs
Phase jitter	< 1 ps
Amplitude jitter	< 1%
Photocathode:	CsK_2Sb
Radius	4 -5 mm
Peak quantum efficiency	8 %
1/e lifetime in operating accelerator	10-15 hrs at 2 x 10^{-9} Torr

The fundamental relationship between drive laser micropulse energy (E), photocathode quantum efficiency (Q) and charge (C) per micropulse is given by:

$$C\ (nC) = 4.5[Q\ (\%) \times E(\mu J)]$$

Since the type of cathode material used (CsK_2Sb) produces prompt electrons, the current may be approximately calculated by multiplying the charge by the laser pulse FWHM. Typically Q is greater than 6% at the start of an accelerator run. The 1/e lifetime is greater than 10 hrs when the accelerator is operating. Since our design value of C is 5 nC, we require our QxE product to be greater than 1.1 for effective operation.

To improve our operating time on a single cathode we are endeavoring to a) reduce the quantum efficiency decay rate; and b) increase the energy delivered by the drive laser to the photocathode.

Reducing the decay rate of Q implies improving the vacuum conditions in the accelerator. Studies have shown that CO_2 and H_2O can contaminate the cathode and reduce its effective lifetime [5]. Since a standard bake at 250-350°C imparts « 1 eV to surface adsorbed molecules, it is not effective in removing those adsorbed gases that are bound with binding energies » 1 eV. In the non-operating accelerator (no RF, no beam) such a bake produces a vacuum of 5 x 10^{-10} torr. In the operating accelerator there are many electrons with energies » 1 eV that induce electron stimulated desorption (ESD) of gases from the cavity walls and cause the pressure to rise to the mid 10^{-9} torr range. To improve this situation we have initiated an RF generated glow discharge cleaning technique [6]. Using 200 W CW 1.3 GHz RF, fed into the photoinjector cavity through the waveguide, we generated a glow discharge with approximately 10^{-2} torr of hydrogen. By varying the RF frequency (1.3 ±0.03 GHz) the glow could be initiated in one or more cells of the photoinjector. During the discharge the photoinjector was maintained at a temperature of 130 °C. The discharge was run for 48 hours, followed by a 24 hour bake at only 130 °C. The immediate result was to reduce the pressure to 1 x 10^{-10} torr at room temperature. Preliminary results indicate that the pressure during high power RF operation has been reduced to the low 10^{-9} torr range. Because we are now recommissioning the accelerator after a

long shutdown, we do not yet have data on enhanced photocathode lifetimes

We have implemented a drive laser upgrade which has increased the deliverable optical energy to the photocathode from 1 to 5 μJ per micropulse. This will allow the nominal 5 nC per micropulse to be produced with a Q as low as 0.22 %

III. RF Controls

The stability of the RF phase and amplitude is as critical to the FEL performance as is that of the drive laser. We have replaced our old RF feedback control system with a novel system using state-feedback [7]. The system in its present form is significantly smaller and produces better RF stability than our old system. Table 3 gives the performance of the state-feedback system over a 100-μs macropulse on the photoinjector.

Table 3 RF phase and amplitude stability

	Amplitude (%)	Phase (ps)
Jitter	0.03	0.1
Slew	0.25	1

We will be testing the effectiveness of the feedback system on all four accelerator tanks shortly.

IV. Operational Experience

Measurements on the electron beam produced by the photoinjector have been made after post acceleration to 14 MeV by an additional side coupled tank. Of particular interest has been the comparison between the design code (INEX) predictions and actual performance. Details of the comparison between INEX and measurements are presented elsewhere in these proceedings [8].

The performance of the photoinjector has proven to be excellent in the areas of most importance to FEL operation, i.e. reduced emittance and reduced energy spread as indicated in table 4.

Table 4 Comparison of the performance of the old vs. new injector at the Los Alamos FEL

Electron source	Thermionic gun	Photoinjector
Emittance	160 π mm-mrad	40 π mm-mrad
Energy spread	0.5%	0.3%
Charge per bunch	5 nC	5 nC

A visual example of our beam quality is shown in fig. 3. The letters **FEL** were cut from a mask that was placed in the drive laser beam. The **FEL** was then imaged on the cathode with a dimension of 2x3 mm. The electron beam (in the shape of **FEL**) was accelerated to 15 MeV, focused on an insertable screen 7 m downstream of the cathode, and imaged by optical transition radiation. The letters **FEL** were clearly visible on the screen.

There were three unanticipated effects observed during operation of the photoinjector:



Fig 3. Electrons make an "FEL"

1)Multipactoring in one or more coupling cells produced coherent 7 MHz oscillations in both phase (±1°) and amplitude (±1%) of the RF in the tank. The problem was solved by detuning the photocathode cell (the end wall was pulled by a couple of tenths of mm) so as to raise the fields in the coupling cells above the multipactoring limit.

2) The electron beam was observed to have an elliptical crossection before passing through any quadrupole magnets. The source of this effect was RF quadrupole focusing resulting from the number and location of the coupling slots in the accelerator. This problem is being partially corrected by placing a small quadrupole magnet between the photoinjector and the next tank. For more detail see ref. [8].

3) A small field-emission electron current (~1 mA) was observed with the drive laser off. The intensity of this field emission current is not sufficient to significantly affect our operation. For more details see ref. [9].

V. Present Status

We are at present commissioning the complete 40 MeV linac and the oscillator leg of the SAMOPA. We have successfully accelerated beam to 40 MeV and transported it around the 60° bend to the beam dump beyond the oscillator. Later this year we will install the 150° bend and amplifier legs of the system.

VI. References

1. R.L. Sheffield, E.R. Gray, J.S. Fraser "The Los Alamos Photoinjector Program" Nucl. Inst. Meth. A272 222, (1988)
2. D.W Feldman, W.D. Cornelius, S.C. Bender, B.E. Carlsten, P.G. O'Shea, R.L Sheffield, Free-Electron Lasers and Applications, D. Prosnitz, Ed., Proc. SPIE 1227, 2, (1990)
3. B.E. Carlsten, L.M. Young, M.E. Jones, B. Blind, E.M. Svaton, K.C.D. Chan, L.E. Thode, Nucl. Inst. Meth., A296, 687, (1990)
4. J.C. Goldstein, B.E. Carlsten, B V. McVey, Nucl. Inst. Meth., A296, 273, (1990)
5. R.L. Sheffield, Proc. 1990 LINAC Conf, Albuquerque NM, Page 269, Los Alamos Pub. # LA-12004-C (1991)
6. "Surface Conditioning of Vacuum Systems", R. Langley Ed., American Vacuum Soc. Series, Vol. 8, AIP, (1990)
7. W.J.D. Johnson, C.T. Addallah, Proc. 1990 LINAC Conf page 487 (1991)
8. B.E. Carlsten, L.M. Young, M.J. Browman,"Comparison of INEX Simulations and Experimental Measurements at the Los Alamos FEL Facility", these proceedings.
9. A.H. Lumpkin, "Observations on Field-Emission Electrons from the Los Alamos FEL Photoinjector", these proceedings

CFEL-I : A Compact Free Electron Laser

L.R. Elias, D.R. Anderson, A.L. Centore II, Hua Bei Jiang,
I. Kimel, D. J. Larson, M. Tecimer and Zhong Zhefu
Center for Research in Electro Optics and Lasers (CREOL) and
Physics Department, University of Central Florida
12424 Research Parkway
Orlando, FL 32826

Abstract

We discuss the design and predicted performance of the CREOL - UCF Compact Free Electron Laser (CFEL-I). This device will consist of a 1.7 MV Pelletron electrostatic accelerator that will be able to provide electron beam energies between 800 keV and 1.7 MeV. A 200 milliamp electron beam will be used to achieve output laser power up to 1 kW. Highly efficient electron beam transport and collection will enable this device to have a large duty cycle, and eventually it may operate on a CW basis. Construction of a microundulator is underway. The 8 millimeter microundulator period will allow device operation between 250 microns and one millimeter.

I. INTRODUCTION

The CREOL-UCF Compact Free Electron Laser (CFEL-I) has been designed to operate in the sub-millimeter region with an order of magnitude more compact technology, three orders of magnitude higher average power and efficiency and two to three orders of magnitude better time-averaged laser spectral purity than that of any existing FEL. These improvements stem mainly from the utilization of short-period magnetic undulators (microundulators) and from the unique advantage possessed by electrostatic accelerators to generate very high optical quality electron beams.

CFEL-I will build on the success of both the UCSB FEL and the UW-NEC electron cooler prototype development. The UCSB FEL has shown reliable operation in the FIR-sub-millimeter region using a 6 MeV Pelletron that was modified for ampere-level *pulsed* electron beam recovery[1]. The UW-NEC experiment demonstrated *continuous* generation of a 2 MeV, 100 mA electron beam[2]. Both experiments demonstrated that electrostatic accelerators are uniquely suited to produce the very high optical quality electron beams demanded not only by FELs using long microundulators, but most importantly, the stringent beam quality requirements imposed by the electron beam recovery system.

CFEL-I represents a major step in technology and size improvement of FELs. The successful demonstration of CFEL-I will pave the way for the development of low-cost, compact, small-laboratory-size FELs, capable of operating in other spectral regions, such as the FIR, IR, visible, and possibly the soft X-ray.

II. ELECTRON BEAM OPTICS

CFEL-I is shown in Figure 1. All ninety degree bends are designed to have zero dispersion by using a quadrupole singlet placed between the two 45 degree dipole magnets. The electron optics for CFEL-I were calculated using the TRANSPORT[3] and SCAT[4] computer codes. Tables I and II present parameters of the CFEL-I dipoles and quadrupoles.

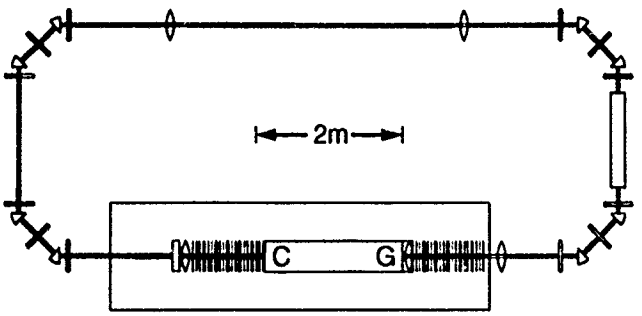


Figure 1. Diagram of the CREOL Compact FEL. Electron beam is formed in an electron gun (G) located in the terminal (inner rectangle) of a 1.7 MeV electrostatic accelerator, focused by a solenoid (lens shaped object), accelerated in the acceleration tube (hashed lines), focused by a solenoid, matched and bent into the undulator (long rectangular box) by quadrupoles (thin rectangles) and dipoles (pie shaped pieces), matched and bent into a long drift return, bent by a 180 degree bend, focused, sent into the deceleration tube and collected (C) in the terminal of the electrostatic accelerator The outer rectangle is the high pressure SF_6 containment vessel.

0-7803-0135-8/91$01.00 ©IEEE

Table I. CFEL-I Dipole Magnets	
Bend Angle	45°
Magnetic Field	719 Gauss
Gap	1 Inch
Physical length	2 Inches
Effective Mag. Length	3 Inches
Entrance Edge Angle	22.5°
Exit Edge Angle	22.5°
Integrated $\Delta B/B_0$ @ .25"	.0004
Height, Width	6.25, 8.25 Inches
Power Consumption	22.5 Watts

Table II. CFEL-I Quadrupole Magnets	
Magnetic Field Gradient	250 Gauss/Inch
Gap	1.25 Inch
Physical length	1 Inch
Effective Mag. Length	1.66 Inches
Height, Width	5.7, 5.7 Inches
Power Consumption	22.5 Watts

The electron gun for CFEL-I is shown in Figure 2. The electron gun has been designed to produce an electron beam with an emittance equal to the thermal limit. The gun uses a standard Pierce geometry. The anode voltage of 20 KV was chosen so that the beam has a sufficiently high energy upon its return to the terminal to assure a large collection efficiency. An intermediate electrode will be used to control the current output of the gun. The multistage collector designed for CFEL-I is shown in Figure 3. A small (two millimeter diameter) beam size at the entrance to the collector should result in excellent collector operation. A magnetic trap located at the input to the collector will reduce backstreaming. Table III presents design parameters of the electron gun and collector.

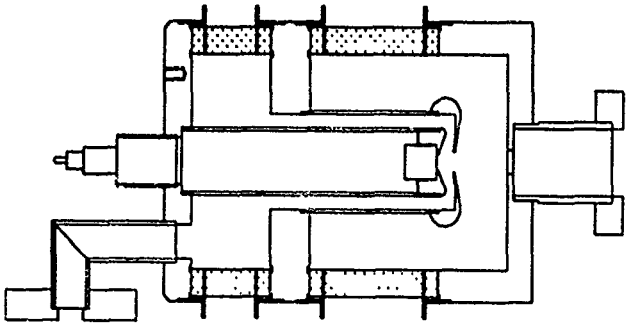


Figure 2. CFEL-I Electron Gun. The gun uses a standard Pierce geometry to acheive a beam emittance close to the thermal limit. The 3.2 mm diameter cathode produces the 200 mA beam with a cathode loading of 0.7 A/cm^2.

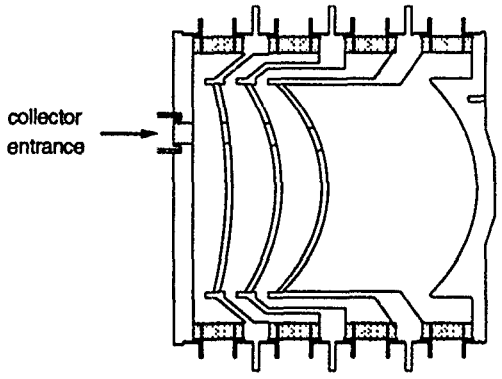


Figure 3. CFEL-I Electron Beam Collector. The collector uses three collection plates and one repulser plate to efficiently collect the electron beam.

Table III. CFEL-I Electron Gun and Collector	
Gun Parameters	
Perveance	.071 μPervs
Anode Voltage	20 KV
Output Current	0-200 mA
Normalized Emittance	2 π mm-mr
Grid Voltage (Gun On)	4 KV
Grid Voltage (Gun Off)	-2 KV
Collector Parameters	
# of collecting plates	3
Collection Voltage 1	14 KV
Collection Voltage 2	6.8 KV
Collection Voltage 3	2 KV
Suppressor Voltage	-4 KV
Input aperture	1 cm diameter

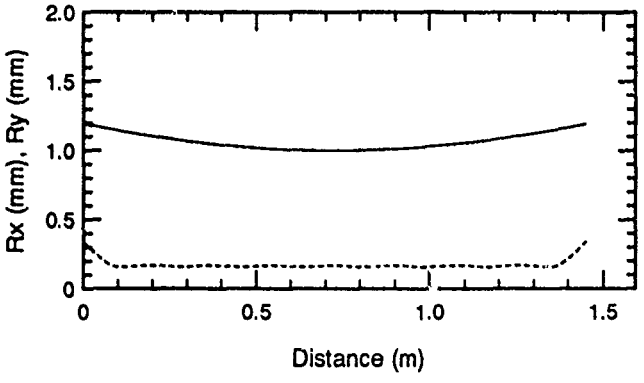


Figure 4. Electron optics in the undulator. Careful matching of the input beam optics results in very smooth beam transmission through the undulator. The natural focusing of the undulator in the vertical direction has been matched by the defocusing caused by space charge and emittance, resulting in beam transmission without a large betatron motion of the beam envelope

The electron optics of the beam in the undulator were calculated by SCAT and are shown in Figure 4. The beam

size in the vertical direction must have a half width less than 0.6 mm so that the nonlinear magnetic fields of the undulator are not appreciable. The beam has been designed to match ideally into the undulator so that the space charge and emittance defocusing are exactly cancelled by the magnetic focusing of the undulator in the vertical direction, resulting in a beam with half width equal to 0.2 mm vertically.

III. UNDULATOR AND RESONATOR DESIGN

Table IV lists the operating parameters of CFEL-I. An important advance in undulator parameters is the use of a very short period (8 mm) undulator. A hybrid configuration was considered for the undulator, but it was decided that a Halbach arrangement will be easier to assemble. (The Halbach arrangement will be made by gluing magnets together.) The individual magnets are plates of Neodymium-Iron-Boron. A representation of the undulator is shown in Figure 5.

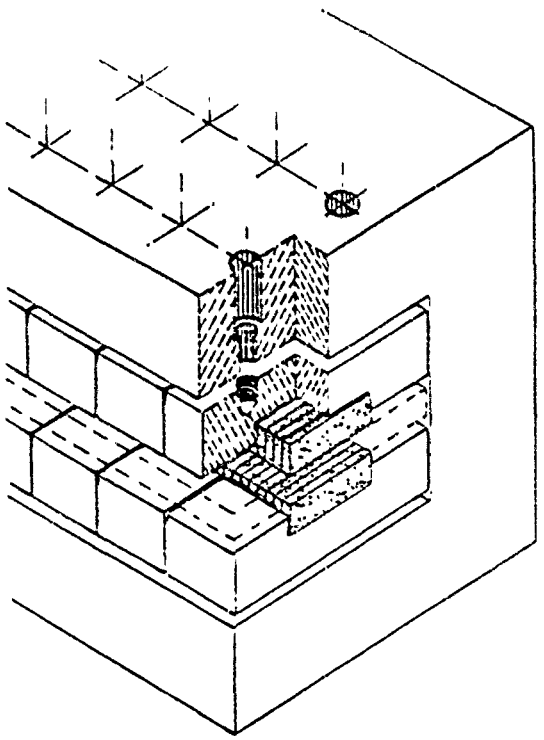


Figure 5. Halbach microundulator with supporting structure.

The resonator is rectangular with the width much larger than the height. In this way the optical modes are hybrid: the modes are guided vertically but free horizontally. The electromagnetic fields are extremely small at the top and bottom walls due to boundary conditions, and they are practically zero at the side walls because the Gaussian spot size is much smaller than the width of the undulator. The small values of the fields near the conductors will lead to very small propagation losses for the modes, while simultaneously allowing for a small enough guide height to obtain large undulating magnetic fields. This type of resonator was first used with the UCSB FEL[5].

Table IV. CFEL-I Design Parameters		
Accelerator Voltage (MV)	1.7	0.9
Gamma	4.33	2.76
Beam Current (A)	0.2	0.2
Undulator Period (mm)	8	8
Number of Periods	156	156
Undulator Length (m)	1.248	1.248
Peak Magnetic Field (G)	1800	1800
Undulator Parameter	0.13	0.13
Wavelength (μm)	233	640
Frequency (THz)	1.29	0.469
Gain per Pass (%)	15.33	35.48
Loss per Pass (%)	2.11	6.18
Net Gain per Pass (%)	13.22	29.30
Max. Power Output (kW)	1.09	0.58

IV. ACKNOWLEDGEMENTS

The design of CFEL-I has involved outside experts from national labs and industry. Richard Hechtel designed the electron gun and collector and Ron Van Iderstine prepared mechanical designs for gun and collector construction. Stan Snowdon designed dipole and quadrupole magnets for use in CFEL-I. The Pelletron electrostatic accelerator for CFEL-I has been purchased from the National Electrostatics Corporation.

V. REFERENCES

[1] L.R. Elias, et al., Phys. Rev. Lett., Vol. 57, 424 (1986).

[2] J.R. Adney, et al., "Successful DC Recirculation of a 2 MeV Electron Beam at Currents More than 0.1 Ampere", IEEE Proceedings of the 1989 Particle Accelerator Conference, 348-350, (1989).

[3] K.L. Brown, F. Rothacker, D.C. Carey and Ch. Iselin "TRANSPORT", SLAC-91, Rev. 2, UC-28.

[4] D.J. Larson, "A Modified Twiss Parameter Optical Treatment for Space Charge Dominated Electrostatic Accelerator Free Electron Lasers", Proceedings of the Eleventh International Free Electron Laser Conference held in Naples, Florida, North Holland publishers, 732-735, (1990).

[5] L.R. Elias and J. Gallardo, Appl. Phys. B31 (1983) 229; L.R. Elias, J. Gallardo and I Kimel, Appl. Phys. 57 (1985) 4870.

Design, Manufacturing and First Measurements of a Hybrid Permanent Magnet Undulator for Free Electron Laser

F. Rosatelli, L. Barbagelata, F. Crenna, M. Grattarola, G. Gualco
A. Matrone, G.B. Ottonello
Ansaldo Ricerche, Corso Perrone 25, 16161 Genova, Italy

F. Ciocci, A. Renieri
ENEA, Dipartimento Sviluppo Tecnologie di Punta, PO Box 65, 00044 Frascati, Italy

Abstract

The hybrid permanent magnet undulator for the LISA-FEL experiment (INFN, Frascati, Italy) [1] has been designed and manufactured under a collaboration between Ansaldo Ricerche and ENEA (Fig. 1). A computerized driving system has been developed in order to ligthen the mechanical structure and gain accuracy in positioning of the jaws during gap variation. The NdFeB permanent magnet blocks have been measured and sorted in order to reduce magnetic field errors along the undulator axis. The field integrals are minimized by the electronic control which feeds the correction coils with a gap dependent current.The first results of mechanical tests and magnetic field measurements confirm the good performances and reliability of the device.

I. INTRODUCTION

The requirements on the field quality of permanent magnet undulators for Synchrotron Radiation Sources and Free Electron Lasers can be satisfied by performing a precise magnetic and dimensional characterization and sorting of the magnetic elements (permanent magnets and poles). It is also important to have a mechanical structure which can accurately position the jaws carrying the magnetic arrays at each gap. The tolerance for the jaws positioning compatible with the magnetic specifications is typically 0.01 mm. A purely mechanical approach in the design of the carriage leads to the manufacturing of components with very high dimensional tolerances. The stiffness must be high enough to keep displacements due to elastic deformations below 0.01 mm at the maximum value of the attractive magnetic force (minimum gap). Systems to control the clearances of the driving system must be foreseen. This solution is expensive and the device is very heavy. A different approach, based on an electronic system which actively controls the parallelism between the jaws during gap variations, has been developed. This system gives a high positioning accuracy of the jaws in spite of a light mechanical structure and a reduction in manufacturing tolerances of the driving components.

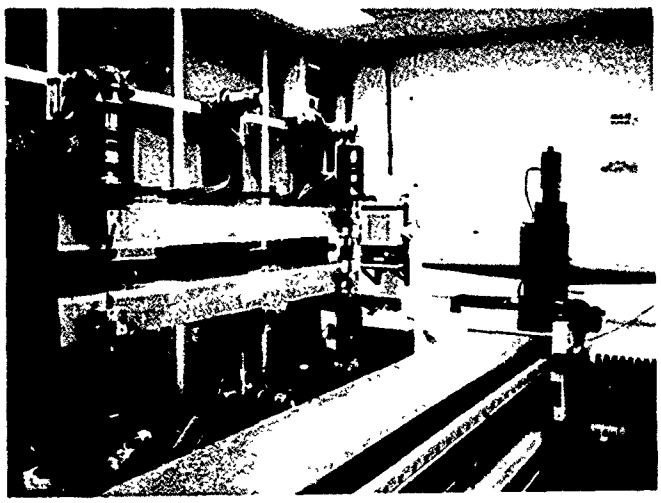


Fig. 1 - Hybrid undulator ON1 and positioning device.



Fig. 2 - ON1 magnetic arrays.

II. DRIVING SYSTEM DESIGN

An innovative design of the mechanical structure and electronic control system for a permanent magnet undulator have been developed in order to have an high accuracy in positioning of the jaws with a simplified mechanical structure [2]. The amount of structural material is minimized and the manufacturing tolerances for the driving components could be relaxed where ever possible so that the weigth and the cost are reduced. Each jaw can be independently displaced by means of three supporting screws which constrain

0-7803-0135-8/91S01.00 ©IEEE

the jaws isostatically. Any rotation of screws is converted into a rigid body motion. This allows a complete freedom in the positioning of the jaws so that the parallelism between the magnetic arrays can always be restored. The current position of each jaw is acquired from three linear optical encoders having a resolution of 0.005 mm and sent to the electronic control system. The electronic system is based on a PLC (Programmable Logic Controller) which controls the motors

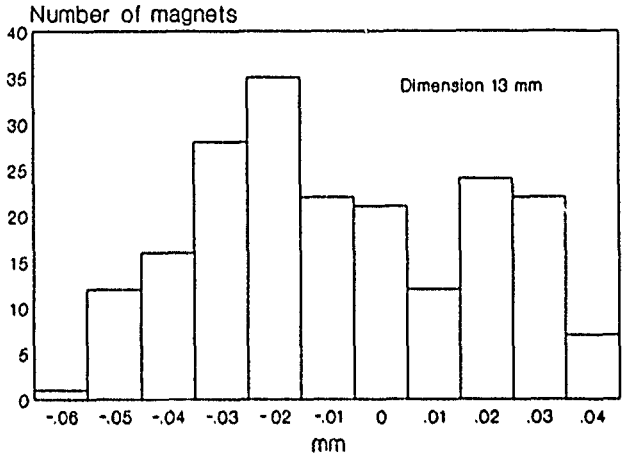


Fig. 3 - Deviation from the nominal dimension (200 magnets).

connected to the supporting screws. This system compensates for the mechanical clearances and small deformations of the mechanical structure arising from the attractive force between the jaws. This active electronic control allows to keep the parallelism between the magnetic arrays during gap variations within the resolution of the optical encoders by means of a PID control of the axis velocities. The system provides also the correction currents, according to the actual gap, during the motion of the jaws.

III. PERMANENT MAGNETS AND POLES ASSEMBLY

The undulator megnetic array has the following main features:

Number of periods	50
Period length	44 mm
Magnets (NdFeB)	13 x 30 x 60 mm
Poles	9 x 26 x 50 mm

The dipole moment of each permanent magnet block has been measured by means of an equipment developed at Ansaldo Ricerche and sorted in order to compensate for the differences in magnetization [3].Each period is assembled by keeping together magnet blocks and poles in an aluminium alloy (ERGAL) holder which is then inserted in to the jaw with a dovetail coupling. The dimensional tolerances of permanent magnets and poles can produce cumulative errors which must be minimized in order to prevent misalignment of the corresponding lower and upper poles. Then both permanent magnets and poles have been measured and the dimensional tolerances have been compensated by means a proper sorting of the poles and exchanging magnets with similar dipole moment in such a way to maintain the average period length. The correct phasing of upper and lower magnetic arrays is verified during assembly by means of a positioning device (Figs. 1 and 2). Figs. 3 and 4 show the results of the dimensional measurements on magnets and poles.

IV. CHARACTERIZATION OF THE PERMANENT MAGNETS

Permanent magnets usually show differences of magnetization which can significantly modify the shape of the magnetic field along the undulator axis. Hence, it is very important to measure these differences of magnetization with high precision and then properly arrange the magnets in the undulator. The equipment set up at Ansaldo Ricerche allows to measure the angular deviation ϑ of the magnetic dipole m from the nominal direction and the strength ε relative to a reference magnet with magnetic dipole m_r [3]:

$$\varepsilon = \frac{|m_r| - |m|}{|m_r|}$$

The results of the measurements on NdFeB permanent magnets are shown in Figs. 5 and 6. The sorting software determines the arrangment of the magnets looking for the best compensation of the measured magnetization differences.

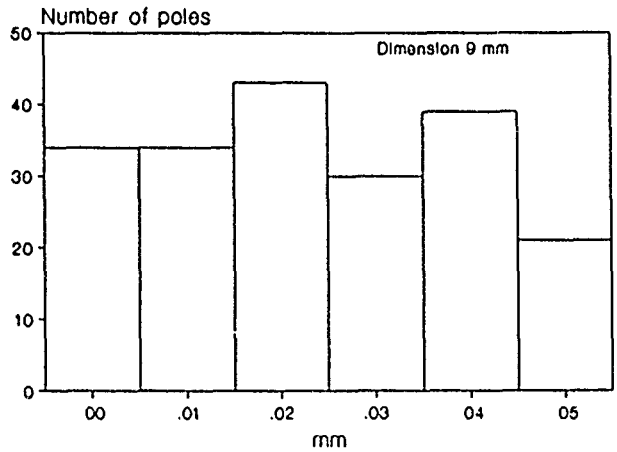


Fig. 4 - Deviation from the nominal dimension (201 poles).

V. MECHANICAL MEASUREMENTS ON THE JAWS

The deformation of the jaws due to magnetic forces at the minimum gap is the most critical parameter in the design of

than 0.01 mm. The final mechanical measurements on the undulator have confirmed the FEM calculations.

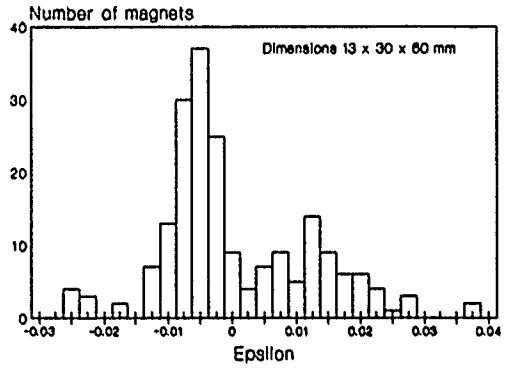


Fig. 5 - Measurements of strength on 200 magnets.

VI. FIRST MAGNETIC MEASUREMENTS

A sistematic campaign of magnetic measurements has been started on ON1 ondulator. A F.W.Bell Gaussmeter (mod. 9900) is used with the Hall probe (mod. HTR 99-0608) mounted on a high precision positioning device (1μm positioning resolution). A first scan along the mechanical axis is presented in Fig. 7 with a spacing step of 2.1mm. The measurement has been carried out also using a finer step. The results of these measurements for the central region and the end one, are presented in Fig. 8-9. From these data we have evaluated a rms variation in field amplitude of 0.3%.

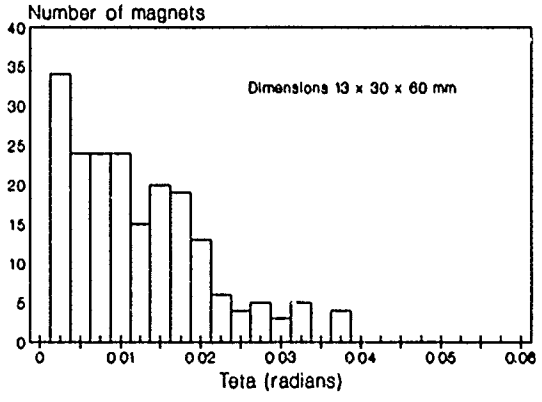


Fig. 6 - Measurements of angular deviation on 200 magnets.

VII. REFERENCES

[1] M. Castellano et al., "The LISA Project in FRASCATI INFN Laboratories" 11th FEL Conference, Naples, Florida, August 28 - September 1, 1989.

[2] F. Rosatelli, F. Ciocci et al., "Advanced Concept in Mechanical Design and Computerized Control System for a Hybrid Permanent Magnet Undulator" 12th FEL Conference, Paris, France, September 17-21, 1990.

[3] F. Rosatelli, F. Ciocci et al., "Development of a Hybrid Permanent Magnet Undulator Prototype for Free Electron Lasers" 11th FEL Conference, Naples, Florida, August 28 - September 1, 1989.

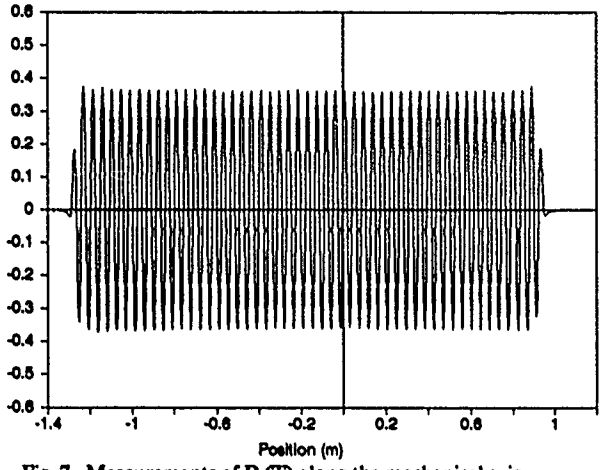


Fig. 7 - Measurements of B (T) along the mechanical axis.

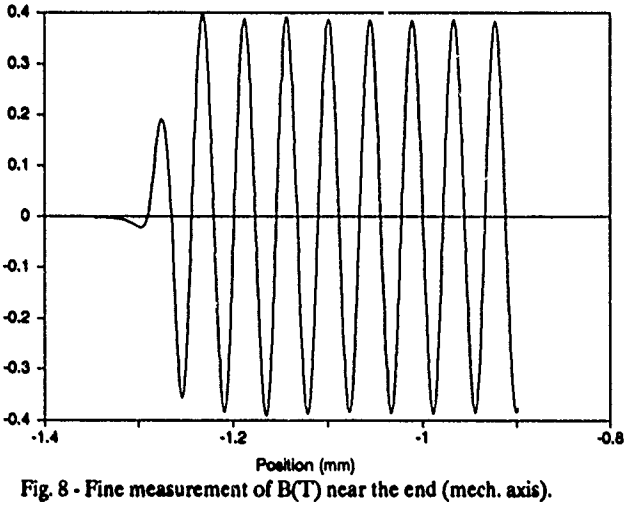


Fig. 8 - Fine measurement of B(T) near the end (mech. axis).

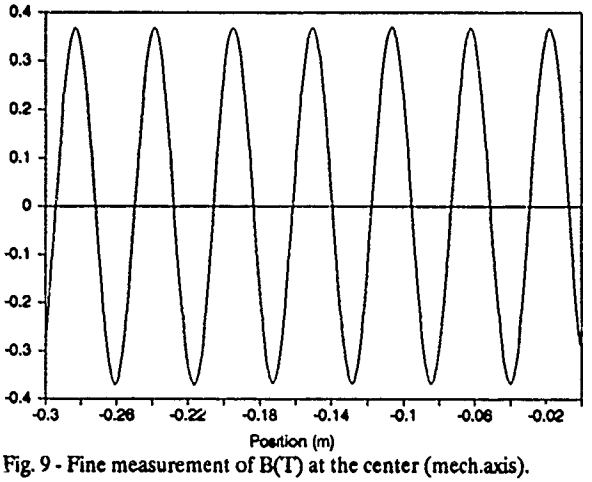


Fig. 9 - Fine measurement of B(T) at the center (mech.axis).

PULSED UNDULATORS FOR HIGH EFFICIENCY FEL OSCILLATORS USABLE IN THE VISIBLE SPECTRUM

Hubert LEBOUTET
c/o CEA-DAM (Service PTN) BP 12 91680 Bruyeres le Chatel

ABSTRACT The problem for reaching high efficiencies in RF-linac driven FEL's , is to cross the perturbed region between the small signal and the large-signal operation due to large phase shifts variations.

We consider the FEL as a Traveling-Wave-Tube (TWT) or the reverse of a tapered buncher as in an electron accelerator The equivalent transverse gradient is

$$E_{\parallel} = \frac{K}{2\gamma} E_{\perp}$$

.The difference with a TWT is that the EM beam instead of being guided inside a waveguide , is in free space

A- ASSUMPTIONS :

1-multi-pass operation : the build-up of the oscillation requires 100 to 200 turns (order of 1µs)

2-gain per pass 1.02-1.03 in gradient to compensate losses and useful power : E=Const

3-efficiency : energy transfer - electrons-to-EM - at each pass: For a 20% efficiency , the product $p(1+\frac{K^2}{2})$ has to change about 40-50% in value along the undulator during the steady-state operation .

4-spontaneous emission does not contribute to a substantial amount to the exchange of energy between the electron beam and the EM wave. Harmonics can be considered , eventually as a nuisance for the mirrors ,or as a low power source .

5-Coupling impedance :

Two conditions are necessary for a substantial exchange of energy between beam and RF :

a/ the beam current must carry a large component at the frequency of operation , -means good bunching-

b/ the line must create a coupling impedance Z which ,in the case of a perfect undulator and a transverse wave , in ideal conditions , is simply

$$Z = \frac{K}{\gamma}\sqrt{\frac{\mu_o}{\varepsilon_o}} = \frac{K}{\gamma}\,\eta$$

This is true as well for the fondamental or harmonics if we would like to generate them with an acceptable efficiency.

B-EQUATIONS

p is the period and K (.94 B.p) the conventional undulator factor . They are defined for one full period

Since the period and the magnetic field may vary , we introduce a coefficient proportional to the inverse of phase velocity , versus a reference given by p_0 and K_0 :

$$\alpha^2 = p_o(1+\frac{K^2}{2o}) \;/\; p\,(1+\frac{K^2}{2})$$

The abscissa is refered to the period or fraction of period : x is the independant variable

$$dz = p(x)\,dx$$

and we use the two equations for phase and energy along the line :

$$\frac{d\Psi}{dx} = 2\pi\left[(\alpha - 1 + \alpha u)\frac{\alpha+1+\alpha u}{\alpha^2(1+u)^2}\right]$$

$$\frac{du}{dx} = -\frac{K}{1+\frac{K^2}{2}}\cdot\frac{E\lambda}{m_o c^2}\cdot\frac{1}{\alpha^2(1+u)}\cdot\sin\Psi \qquad u = \frac{\gamma}{\gamma_o} - 1$$

In these equations , the wavelength enters as the scaling parameter $E_0\lambda$.

The "transfer coefficient" a is the sum of the values of u over all phases calculated at each period .

C- UNIFORM UNDULATOR and UNIFORM-TAPERED :

Fig 1 and 2 summarize the results in those two conventional situations . The data come in two sets of curves : evolution of phase and energy along the line for each value of the RF level (Eλ) , and value of the transfer efficiency v Eλ.

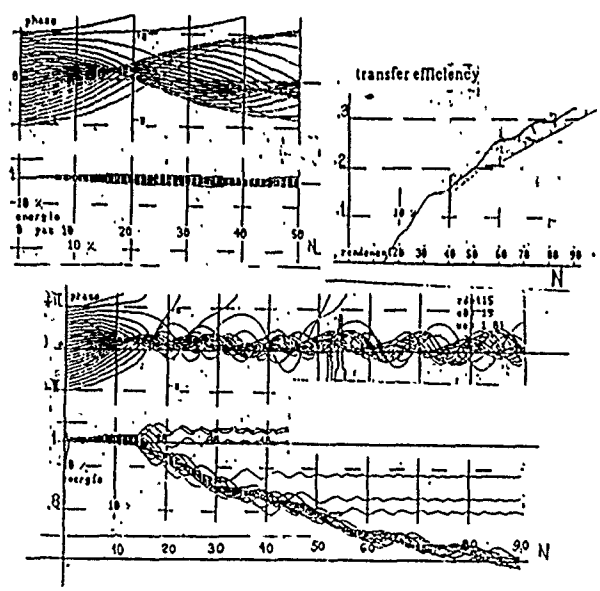


FIG 1 . Phase and energy diagrams .
TOP : uniform undulator Eλ =1kV
BOTTOM : Buncher +tapered undulator Eλ =15kV
the efficiency displayed here is 33% with a 90 periods undulator , including 14 periods for the buncher

For the uniform undulator ,and Eλ < .5 kV ,the transfer coefficient is in $(E\lambda)^2$,(slope 2 on the graphic Fig 2) as in the conventional small-signal theory .

0-7803-0135-8/91S01.00 ©IEEE

The efficiency levels off at about 1-1.5% and starts to drop if the RF level is made to increase above 1 kV.

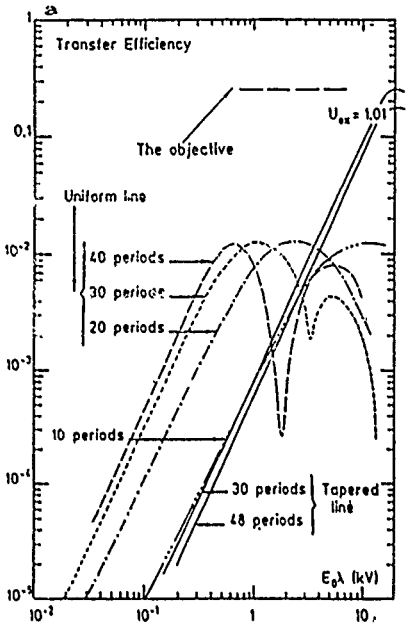


FIG 2 Transfer coefficient vs (Eλ)

With the tapered undulator ,and values of the parameter Eλ above a few kVolts , we are in the "large-signal" conditions . The bunching is nearly complete . The efficiency of transfer is then roughly proportional to Eλ instead of $(E\lambda)^2$ as in the small signal situation .

The beam intensity which can sustain the oscillation is:

$$I_{(Amp)} = \frac{b}{\zeta} \cdot \frac{1}{4\eta} \cdot \frac{e}{m_o c^2} \cdot \frac{2}{1+\frac{K^2}{2}} \cdot \gamma \cdot \frac{n\epsilon_n}{\gamma\lambda} \cdot ff \qquad \zeta = \frac{a}{N(E\lambda)^2}$$

ff : form factor of the RF beam (order of 1.4)

b : loss coefficient per turn of the RF (3-5%)

It is well known and can be seen on Fig 2 , that such a tapered line has no gain at small signal (slope below .5 kV larger than 2) : oscillation does not start !

D- BUNCHER+STRONG TAPER +UNIFORM+SLIGHT TAPER

A high gain structure must be added , of course not *ahead* of the tapered part (it would behave as above)! , but *after* . And we arrive at a geometry similar to the one already described and tested°.

At small signal , the tapered part acts as a delay line between the buncher and the uniform line . The small signal coming out of the buncher is amplified and must arrive at the correct phase in the line . In the large signal operation , buncher + tapered portion behave as previously.

However there are very strict limitations in this operation : The number of periods of each part is critical , in order to get the optimum phase shift.

For monoenergetic electrons , there always remains a "hole" in the efficiency curve ,between .5 to 1 kV, and the system would stop building up . Fortunately , this hole is not exactly at the same place for different electron energies ,within 0.4% . So, if the available current in the beam were sufficient , this critical transition could be passed

E- PROGRAMMING THE PROFILE DURING BUILD UP OF OSCILLATION

This will be the correct solution : change the line profile , so that the profile is continuously adjusted to the level of RF power . In a TWT , this , of course , is impossible . But here , the build up covers 100 turns or more , which represents a duration of one , or a few , microseconds which is enough to program the currents which create the magnetic field in the undulator .

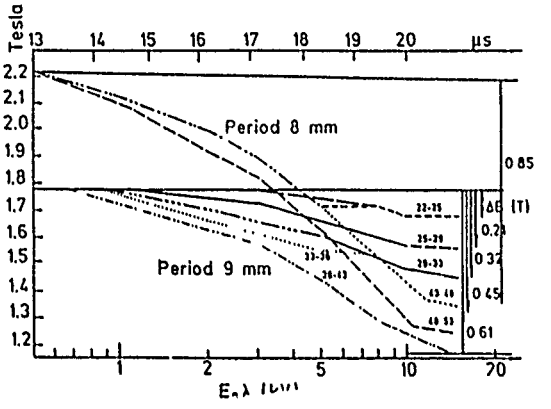


FIG 3 Variation of the magnetic field *vs* (Eλ) and N.
For (Eλ)< .5 kV , there is no taper
above .5 kV, the diagram is swept during the few microseconds of rise time .
Tapering starts just one or two periods after the buncher .

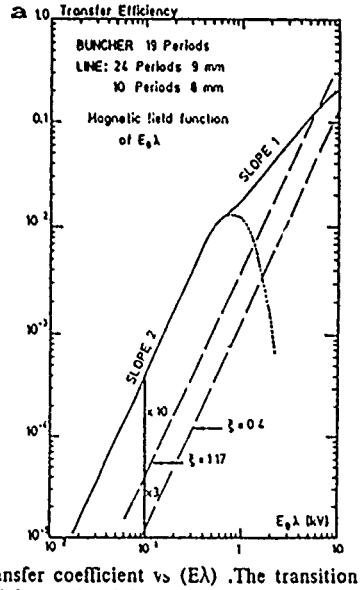


FIG 4 Transfer coefficient vs (Eλ) .The transition between small and large signal is smooth , and efficiencies larger than 20% can theoretically be obtained with 35 - 40 periods (not including the buncher).

Of course , this implies that the undulator has no magnetic material , and is short enough so that the reactances are kept small .

Fig 3 gives the slopes of the taper *vs* the RF level .

In the large signal region , (Eλ) increases of an equal amount per turn , and since each turn has the same duration , dE/dt is a constant .

Fig 4 is a typical plot of the transfer coefficient , for a 34 period-line preceeded by a 19 period-buncher , which shows a 20% efficiency at a value of (Eλ) not too high for the mirrors .

It can be seen that the bunching is of the order of 80% , so that side-bands excitation has a very low efficiency [∞] and the bunches are 30-40 degrees in phase so that the space-charge fields stay below a few percent of the main RF field [∞∞]. The "transfer coefficient" can be of the order of .4-.5 % per period

F- TECHNOLOGY

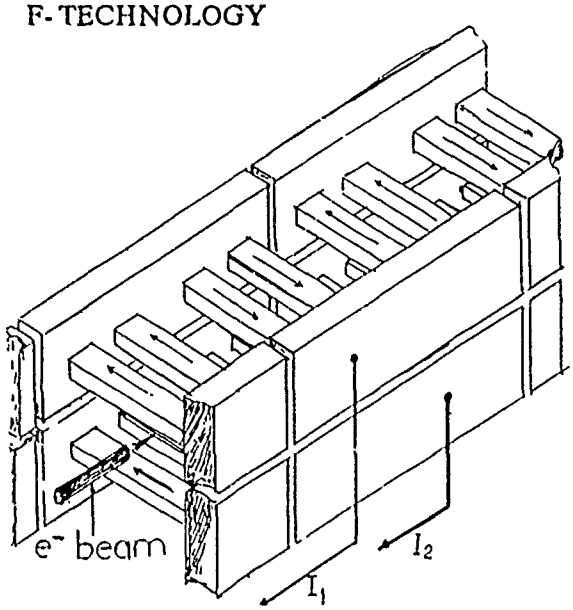


FIG 5 Schematic vue of an undulator
I1 and I2 : Derivation currents to control B(z) *vs* time.

The major difficulty is obviously to provide sufficient cooling capacity . The undulator presents itself as two layers of " bars " (1 or 2 mm cross-section ,and 10 to 20 mm long) . Copper bars can be cooled at the two ends if 100-150 degrees C can be tolerated between the middle and the ends . The cooling pipes are four- titanium or stainless steel -spirals , cooling the four ends of the successive bars . The period of the spirals is the same as for the undulator . Pipes are available down to 2 mm in diameter , so that the mechanical limit of this type of technology is around 2.5 mm period for the undulator.

The maximum current which can be passed through such a "bar" is

$$I_{(Amp)} \simeq 433 \cdot \frac{S}{l} \cdot \sqrt{\frac{\Delta T}{f\tau}}$$

where : s and l are the cross-section and length of the bar (mm)

fτ. is the duty factor

ΔT is the maximum temperature difference.

for a temperature difference of 100 °C and a duty factor of 1/100 ,the period is limited down to 7 mm for K=1.4 and 3mm with 200 °C and 1/300 duty factor

In the end , the major difficulty will be in the mirrors

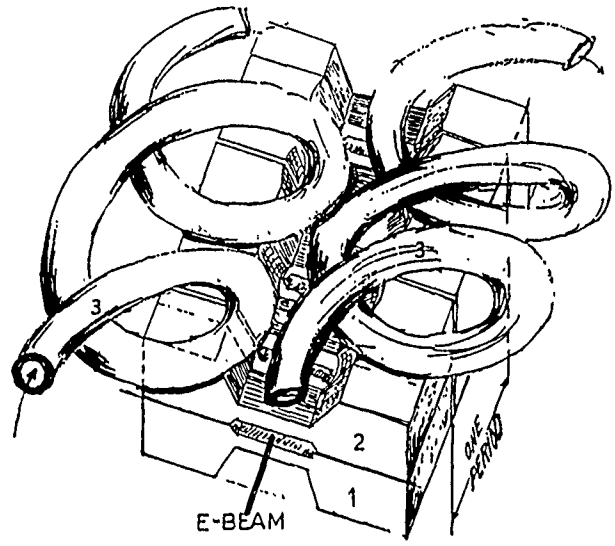


FIG 6 Arrangement of the cooling pipes

G- HARMONICS ENHANCEMENT

If the "bars" corresponding to each half period are divided into two or more "sub-bars" in parallel , as in Fig 5 , it is possible , by changing the relative distances , to have a Kn value of the coupling parameter even larger for the harmonics than for the fondamental as it is shown in Fig 7 .

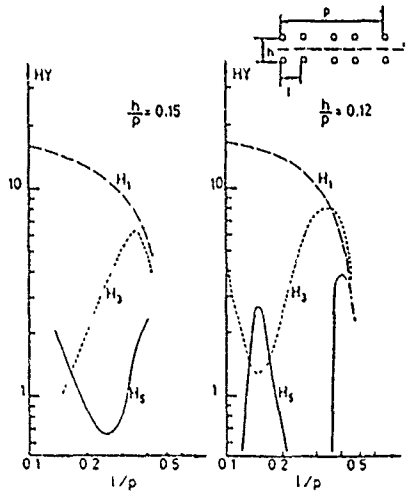


FIG 7 Coupling factor K for the fundamental and harmonics 3 and 5 , for the structure represented on Fig 5 : Two bars in parallel for each half period .

* Variable-Wiggler FEL oscillator
J.A. EDIGHOFFER, G.R. NEIL, C.E. HESS, T.L. SMITH , S W. FORNACA and H.A. SCHWETTMANN
Phys.Rev.Letters Vol 52 Nr 5 Jan84

** Development of side-bands in tapered and untapered FEL's
B.Hafizzi,A.Tang *et al* PHYS REV.July 1 1988

*** Density and Deceleration limits in tapered FEL's
Thomas M Antonsen PHYS REV LETTERS Jan 18 1967

REDUCTION OF UNDULATOR RADIATION AND FEL SMALL GAIN DUE TO WIGGLER ERRORS*

Aharon Friedman
National Synchrotron Light Source
Brookhaven National Laboratory
Upton, NY

Abstract

A deterministic approach is taken to study the effect of errors in the wiggler magnet field on the spontaneous emission and the gain of Free Electron Lasers. A 3D formulation is used to derive the reduction in spontaneous emission due to changes in the time of flight of the electrons. A generalization of Madey's theorem to 3D is then used to calculate the reduction in the FEL small gain.

I. INTRODUCTION

The conventional approach taken in order to study the effect of wiggler errors on radiometric parameters is statistical in its nature [1,2]. This approach is good at the design stage of the device when tolerance must be specified for the construction of the wiggler. However, once the wiggler is constructed, its errors can be measured and the radiometric parameters for that particular wiggler can be calculated. These parameters may differ significantly from those calculated at the design phase. A deterministic approach is, thus called for in order to evaluate the expected radiometric parameters and to decide how much effort is needed to correct the wiggler errors.

II. REDUCTION IN SPONTANEOUS EMISSION (UNDULATOR RADIATION)

The spectral radiant intensity of a charged particle is given by [3]:

$$\frac{dP}{d\omega d\Omega} = \frac{e\eta_o}{4\pi}\frac{I}{\lambda^2}\cos^2\theta\ |I_e|^2 \qquad (1)$$

where θ is the view angle and

$$I_e=\int_{-\infty}^{\circ} dt\vec{v}(t).\hat{e}_o e^{i\vec{k}\vec{r}(t)-i\omega t} \qquad (2)$$

In equation 2 v(t), r(t) are the particle velocity and its respective trajectory e_o, k are the polarization of the electromagnetic field and its wave vector respectively.

In the undulator approximation [3] the electron trajectory is assumed to be a straight line and the synchronization of the electron with the EM wave is through the transverse velocity imposed on it by the wiggler. For a highly relativistic electron this velocity is:

$$\vec{\beta} = \frac{1}{\gamma} K\,[1+s(z)]\cos k_w z \hat{e}_x \qquad (3)$$

where

$$K=\frac{1}{2\pi}\frac{e}{mc}B\lambda_w \qquad (4)$$

is the wiggler strength parameter and s(z) is the error in the wiggler field. Substituting equation (4) into equation (2) yields.

$$I_e=\frac{K}{2\gamma}e_x \cdot e_o \int_o^L dz\,[1+s(z)]e^{i\theta_w z} \qquad (5)$$

where

$$\theta_w=\frac{2\pi}{\omega}\left(\frac{1}{\beta_z}-\hat{e}_k\cdot\hat{e}_e-\frac{\lambda}{\lambda_w}\right) \qquad (6)$$

is the detuning parameter [4]. One can see that in equation (5) the effect of the wiggler error on the radiation path integral I_e can be distinguished from the total path integral. Thus, the path integral may be written as:

$$I_e = I_{eo} + \Delta I_e \qquad (7)$$

where I_{eo} is the path integral of a perfect wiggler and ΔI_e is the contribution of the wiggler errors. Explicitly, the perfect wiggler path integral is:

$$I_{eo}=\frac{K}{2\gamma}e_x \cdot e_o L e^{i\bar{\theta}/2}\,\mathrm{sinc}\frac{\bar{\theta}}{2} \qquad (8)$$

*Work performed under the auspices of U.S. DOE.

0-7803-0135-8/91$01.00 ©IEEE

where

$$\bar{\theta} \equiv \theta_u L \tag{9}$$

and

$$sinc\ x \equiv \frac{sinx}{x} \tag{10}$$

In order to calculate the wiggler error contribution, it is assumed that s(z) is constant along half a wiggler period of this assumpti . may not hold if the wiggler has multi-poles per half per . S(z) can then be

$$s(z) = s_n\ ;\ for\ n\frac{\lambda w}{2} < z < (n+1)\frac{\lambda w}{2}\ ;\ 0 < n < 2N \tag{11}$$

In equation (11) $N=L/\lambda_w$ is the total number of wiggler periods. To simplify the calculation we assume that s_n averages to zero over the wiggler length. Note that this assumption does not reduce the generality of the treatment, since the value of K can always be modified to accommodate it. Substituting equation (11) in equation (5) results in:

$$\Delta I_e = \frac{K}{L\gamma}\hat{e}_x \cdot \hat{e}_o \lambda_w e^{i\theta_w/4}\ sinc\frac{\theta_w}{4}\sum_{n=0}^{2n-1} s_n e^{i n\theta_w/2} \tag{12}$$

where

$$\theta_w \equiv \lambda_w \theta_u = \frac{\bar{\theta}}{N} \tag{13}$$

We now can calculate the spectral radiant intensity by substituting equations (8, 9) into equation (1). Here again we express the total spectral radiant intensity as a sum of the radiation from a perfect wiggler and the modification of the wiggler errors.

$$\frac{d^2P}{d\omega d\Omega} = \frac{d^2P_o}{d\omega d\Omega} - \frac{d^2(\Delta P)}{d\omega d\Omega} \tag{14}$$

It is preferable to express the wiggler errors term as a subtracting term, since one can hardly expect them to increase the radiation. The perfect undulator spectral radiant intensity is:

$$\frac{d^2P_o}{d\omega d\Omega} = \frac{e\eta_o}{16\pi}\frac{I}{\lambda^2}\frac{K^2}{\gamma^2}\cos^2\theta\,|\hat{e}_x \cdot \hat{e}_o|^2 L^2 sinc\frac{\bar{\theta}}{2} \tag{15}$$

The wiggler error term is

$$\frac{d^2(\Delta P)}{d\omega d\Omega} = \frac{e\eta_o}{4\pi}\frac{I}{\lambda^2}\frac{K^2}{\gamma^2}\cos^2\theta\,|e_x\ e_o|L^2 sinc\frac{\theta_w}{4}\left(sinc\frac{\bar{\theta}}{2}mM_s + \frac{1}{2}sinc\frac{\theta_w}{4}R_s\right) \tag{16}$$

where

$$M_s \equiv \frac{1}{2N}\sum_{n=0}^{2n-1} s_n \sin^2\frac{\theta_w}{4}(N-n-\frac{1}{2}) \tag{17}$$

$$R_s \equiv \frac{1}{(2N)^2}\sum_{n=0}^{2n-1}\sum_{m=0}^{2n-1} s_n s_m \sin^2(n-m)\frac{\theta_w}{4}$$

It is constructive to calculate the relative reduction of radiation due to wiggler errors. This is achieved by dividing equation (16) by equation (15):

$$\frac{d^2(\Delta P)/(d\omega d\Omega)}{d^2P_o/(d\omega d\Omega)} = 4\frac{sinc\frac{\theta_w}{4}\left(sinc\frac{\bar{\theta}}{2}M_s + \frac{1}{2}sinc\frac{\theta_w}{4}R_s\right)}{sinc^2\frac{\bar{\theta}}{2}} \tag{18}$$

From equation (18) one can see that the relative reduction of spontaneous radiation of an undulator is independent on its length. The correlation functions M_s and R_s have in them the total number of magnets poles. However, assuming that the errors have the same statistical behavior throughout the wiggler, this dependence cancels out. This fact leads to the important conclusion that one does not have to change the tolerances of a designed undulator when changing its length if its only purpose is to produce undulator radiation (e.g. an insertion device in a storage ring).

III. REDUCTION IN SMALL GAIN

The small gain in Free Electron Lasers can be calculated from the spontaneous emission of an undulator with the use of the generalized Madey's Theorem. This Generalization of Madey's Theorem [4,5] is described in reference [6]. In this paper the relation between spontaneous emission and gain was derived from first quantum electrodynamics principles and selection rules for electron-photon-wiggler interaction. The gain dependence on the spontaneous spectral radiant intensity is given in reference [6] by:

$$G = \frac{4\pi^2}{mc^2}\frac{L\lambda}{A_{em}}\frac{1}{\gamma}\left(\frac{1}{\gamma^2} + tg^2\theta_{rec}\right)\left(\frac{d^2P}{d\Omega d\omega}\right)_{\omega}\frac{1}{F(\bar{\theta})}\frac{d}{d\bar{\theta}}F(\bar{\theta}) \tag{19}$$

where the gain G is defined as $G = (P_{out} - P_{in}) / P_{in}$, A_{em} is the effective area of the electromagnetic mode being amplified and

$$\cos\theta_{rec} = \hat{e}_e \cdot \frac{\vec{k} + \hat{e}_z k_w}{|\vec{k} + \hat{e}_z k_w|} \tag{20}$$

is the recoil angle of the electron. In most practical cases $k_w << k$, hence, $\cos\theta_{rec} \sim e_e . e_k$. In equation (19), $F(\theta)$ is the lineshape function of the spontaneous emission. For a perfect

wiggler this function is

$$F(\bar{\theta}) = sinc^2\frac{\bar{\theta}}{2} \tag{21}$$

Since the Generalized Madey's Theorem as described in equation (19) is based on Q.E.D. first principles, it is valid also for the case of a non-perfect wiggler. However, for a non-perfect wiggler the spontaneous emission can no longer be described as having a single lineshape function. Instead, each term in the spontaneous emission has its own lineshape function. This problem can be easily solved when one realizes that the derivative of the lineshape function in equation (20) is due to the fact that the emission and absorption control frequency are slightly displaced from each other. Thus, Madey's Theorem holds for each of the spontaneous emission terms independently. The total gain is, thus, the sum of the applications of Madey's Theorem to each of the spontaneous emission terms. The gain can also be written as the sum of the gain of a perfect wiggler minus wiggler errors contribution.

$$G = G_o - \Delta G \tag{22}$$

The gain of a perfect wiggler FEL is given in reference [6]

$$G_o = \frac{\pi}{4}\frac{e\eta_o}{mc^2}\frac{L^3}{\lambda A_{em}} \cdot \frac{K^2}{\gamma^3}\left(\frac{1}{\gamma^2} + tg^2\theta_{ave}\right)\cos^2\theta|\hat{e}_x \cdot \hat{e}_o|^2\frac{d}{d\bar{\theta}}sinc^2\frac{\bar{\theta}}{2} \tag{23}$$

The reduction of the gain due to wiggler errors is calculated by applying equation (19) to eqs. (17).

$$\Delta G = \pi\frac{e\eta_o}{mc^2}\frac{L^2\lambda_w}{\lambda A_{em}} I \cdot \frac{K^2}{\gamma^3}\left(\frac{1}{\gamma^2}+tg^2\theta_{ave}\right)\cos^2\theta|\hat{e}_x \cdot \hat{e}_o|^2$$

$$\times\ sinc\frac{\theta_w}{4} \times \left(M_G+\frac{1}{2}\ sinc\ \frac{\theta_w}{4}R_G\right) \tag{24}$$

where

$$M_G \equiv \frac{1}{2N}\sum_{n=0}^{2n-1} s_n\frac{d}{d\theta_w}\left[sinc\frac{N\theta_w}{2}\sin^2\frac{\theta_w}{4}(N-n-\frac{1}{2})\right]$$

$$R \equiv \frac{1}{(2N)^2}\sum_{n=0}^{2n-1}\sum_{m=0}^{2n-1} s_n s_m\frac{d}{d\theta_w}\left[\sin^2(n-m)\frac{\theta_w}{4}\right] \tag{25}$$

In equations (25), it was assumed that $N>>1$. It is again, interesting to calculate the relative reduction in gain:

$$\frac{\Delta G}{G_o} = 4\frac{\lambda_w}{L}\frac{M_G+\frac{1}{2}R_G}{\frac{d}{d\bar{\theta}}sinc^2\frac{\bar{\theta}}{2}} \tag{26}$$

Note that for a consistent statistics of the wiggler poles the correlation functions M_G and R_G are expected to behave linearly in N. Thus, canceling the λ_w/L factor in equation (26). Hence, the relatively reduction in gain is expected to be weakly coupled to the wiggler length.

IV. CONCLUSION

The small gain and spontaneous emission reduction due to wiggler errors was calculated, including some 3D effects. This formulation only takes into account the effect on the phase between the electron and the electromagnetic wave. However, there is another important effect to be taken into account that that is the effect of the "random walk" of the electrons from the axis. It seems, that the formulation used in this paper can be extended to include "random walk", and it is the intention of the author to pursue this course of action.

V. REFERENCES

1. B.M. Kincaid, Nuclear Inst. and Meth. Phys. Res. A-291 p.363 (1990).
2. J. Gallardo, BNL Report #45798 (1991).
3. A. Gover and A. Friedman - to be published.
4. J.M.J. Madey, JAP 42, p. 1906 (1971).
5. S. Krinsky, J.M. Wang and P. Luchini, JAP 53, p.5453 (1982).
6. A. Friedman, A. Gover, G. Kurizki, S. Ruschin and A. Yariv, Reviews of Modern Physics 60, #2, p. 471 (1988).

Heating of the LSS Wiggler Beam Tube Due to Induced Surface Current

W. C. Sellyey and C. G. Parazzoli
Boeing Aerospace and Electronics Division
Boeing Defense and Space Group
PO Box 2499
Seattle, WA 98124, USA

I. INTRODUCTION

During 1990, The Boeing Company was designing a high-power, free-electron laser, referred to as the Laser Subsystem (LSS). Among the considerations determining the wiggler beam tube cooling requirements, was the heating caused by induced surface currents flowing on the inside of the beam tube.

The expected heating is calculated here. Additionally, the effect of pulse shape and length on the heating is investigated.

Two methods are used to evaluate the power dissipated in the LSS wiggler beam tube. The first is an expansion of methods used in reference 1. In this method, the beam charge is assumed to be uniformly distributed in a cylinder of length l and radius r_0. The beam center is taken as the z axis. The moving beam induces currents in the beam tube wall, resulting in the heating of the wall. This heating is given by

$$P(\zeta) = 2\pi\sigma \int_b^{inf} E_z^2(r,\zeta) r dr \qquad (1)$$

Here ζ = z-ct, z = longitudinal distance, t=time, r=distance from beam tube center, E_z=longitudinal component of the electric field, b=beam tube radius and σ = conductivity. It is assumed that the radial part of the E-field is unimportant.

Following reference 1, E_z and the charge distribution are Fourier transformed.

$$E_z(r,\zeta) = \int_{-inf}^{inf} \tilde{E}_z(r,k) e^{ik\zeta}\, dk \qquad (2)$$

$$\rho(r,\zeta) = \int_{-inf}^{inf} \tilde{\rho}_z(r,k) e^{ik\zeta}\, dk \qquad (3)$$

ρ=charge distribution and the wiggle indicates the Fourier transform. These are inserted into Maxwell's equations, and a new set of equations results. These are solved for E_z in three regions $r<r_0$, $r_0<r<b$ and $r>b$. The solutions are Hankel and Bessel functions, but only their asymptotic forms are needed. Boundary conditions are applied and E_z in the metal wall is determined.

Inserting this result for E_z and equation (2) into (1), simplifying, performing the integration over r, and averaging over the pulse length, one obtains

$$P = \frac{8\pi\sigma q^2 \beta^4}{b(RL)^2} \sum \sqrt{2Rk_n} \left\{ \frac{\sin[k_n(L+l)/2] - \sin[k_n(L-l)/2]}{k_n l} \right\}^2 \qquad (4)$$

$$R = 4\pi\beta\sigma/c \quad k_n = \pi n/L \quad \beta = v/c \qquad (5)$$

Here P=average power dissipated per unit length, q=charge per bunch and L=separation between bunches.

The second method is largely based on eq 1.55 from reference 2. This is the energy loss of beam through an arbitrary, transverse-charge multiple moment. It is assumed that all particles travel at c. For a cylindrically symmetric beam, only the zeroth moment contributes and it reduces to

$$P = 2\pi c^2 f \int_{-inf}^{inf} d\omega \left|\tilde{\rho}(\omega)\right|^2 R_e Z_o''(\omega)/D \qquad (6)$$

$$\tilde{\rho}(\omega) = \frac{1}{2\pi c} \int_{-inf}^{inf} e^{-i\omega z/c} \rho(\rho) dz \qquad (7)$$

Here $\rho(z)$ is the longitudinal charge distribution and fL=c. $Z_0(\omega)/D$ is the zeroth order longitudinal impedance of the beam pipe per unit length. In general, Z is a difficult quantity to evaluate. However, for a smooth, cylindrical beam pipe, this can be easily evaluated by combining equations 1-48, 1-36, 1-14, 1-7 and 1-9 of Ref. 2. The result is:

$$\frac{Z_o''}{D} = \frac{2}{cb} \frac{1}{\sqrt{\frac{2\pi\sigma}{c|k|}} + i\left[\sqrt{\frac{2\pi\sigma}{c|k|}} s_k - \frac{kb}{2}\right]} \qquad (8)$$

s_k=sign of k, k=ω/c

The only approximation used in deriving the above result is that wavelengths of about 1km or greater are ignored. The predominant wavelength will be concentrated around distances which describe the beam-pulse structure. These are about a cm

0-7803-0135-8/91S01.00 ©IEEE

and shorter, so the neglected part of the impedance should be unimportant.

II. SOFTWARE

A short program was written to evaluate the terms of the expression for P of method 1. It was found that 40,000 terms allow evaluation of the beam power to a few percent.

The program for method 2 accepts input specifying the beam-pipe characteristics and the charge distribution. One possible way of specifying the charge distribution is by reading it in from a file. A different option instructs the software to generate a gaussian which can be symmetrically cut off at any distance from the centroid. An additional option allows the first gaussian to be continued by another gaussian of different width. The two gaussians are matched in slope and vertical height at the cut in the first gaussian.

A fast Fourier transform (FFT) of up to 65536 points is performed on the charge distribution. The number of points and the spatial interval used for the transform can be specified as input. Once the transform is done, a Simpson's rule integration is used to obtain the power dissipation.

III. RESULTS

The following input was used in all calculation, unless otherwise noted:

- 5.7 mm = beam tube radius
- 3.43×10^7/(ohm.m) = conductivity of aluminum
- 10nc = microbunch charge
- 27.088 MHz = micropulse rate

Figure 1 shows the PARMELA-predicted[3] charge distribution at the entrance to the LSS wiggler. Using method 2, the calculated heating will be 90 watts/m. The numerical integration is a possible source of error. To check how serious this might be, the integration is done using different Fourier spatial intervals (S), and different numbers of points (N). Some results are shown in Table 1. If N is kept at 65536, the calculation should be accurate to better than 1%.

TABLE 1 Effect of number of points (N) and Fourier interval (S), on calculated results.

S(m)	N	Heating (w/m)
.1	4096	90.23
1	4096	90.84
10	4096	95.13
.1	65536	90.23
1	65536	90.87
10	65536	90.10

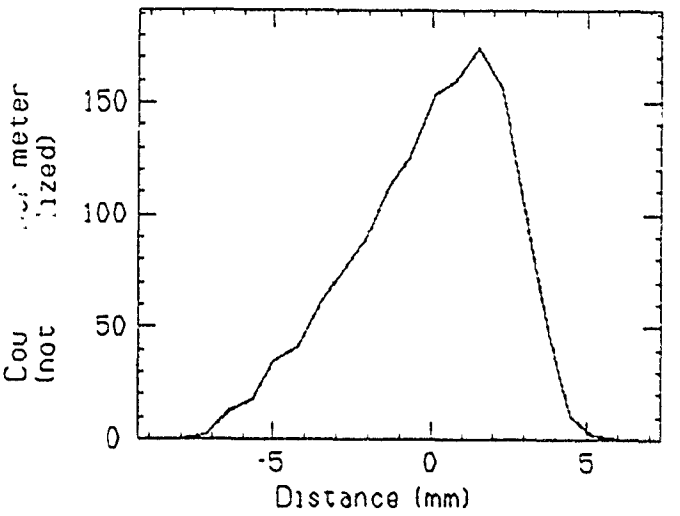


Figure 1. LSS wiggler longitudinal charge density.

Consider the imaginary term in equation (8). Letting

$$\frac{kb}{2} = \sqrt{\frac{2\pi\sigma}{c|k|}}$$

one gets $k = 6.74 \times 10^4$/m for beam-pipe parameters used here. The r.m.s. width of the charge distribution used above is a = 2.43mm. Taking ka = 1 gives $k = 4.12 \times 10^2$mm. Thus if one uses a gaussian charge distribution of r.m.s. width around 2.43mm, the kb term in the impedance can be ignored. When this is done, equation (6) can be integrated to give (in MKS):

$$P = 1.27 \times 10^8 \frac{q^2 f}{b\sigma^{1/2} a^{3/2}}$$

This gives 85.9w/m at a 27.088Mhz pulse rate. The program of method 2 gives the same result for the same gaussian distribution. This verifies that the program is working correctly. It also indicates that -3/2 scaling of the bunch length can be used to estimate power dissipation for LSS-type beam pulses.

To investigate the effect of pulse shape, figure 2 was produced. The lowest point at 85.3 watts is generated using a gaussian with the same r.m.s. width (a = 2.43mm) as the PARMELA prediction. The gaussian FWHM = 5.71mm. The remaining points are generated by using a wide central gaussian (a = 30mm). It is cut off and a second gaussian is appended to give the indicated rise and fall length. The FWHM is kept at 5.71mm. All calculations use a spatial interval of 5cm and 65536 points. Because of the short, spatial interval, low-frequency components are underestimated and all results are about 1% low.

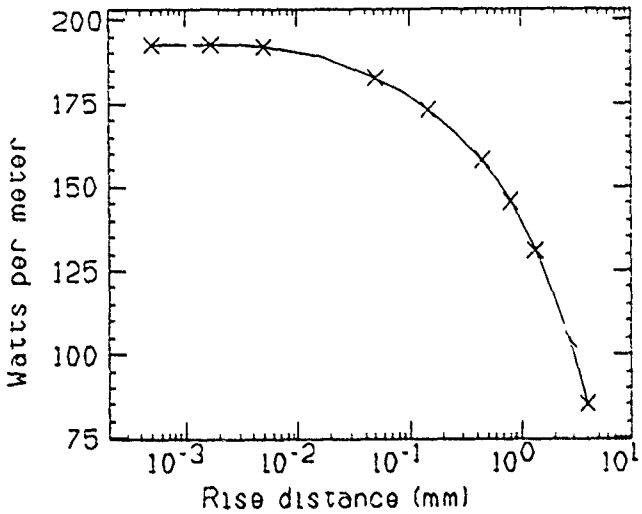


Figure 2. Dissipated power vs rise distance.

The interesting features of this graph are that the power dissipation increases until a rise distance of about .01mm is reached. For shorter distance, the dissipation does not increase. This can be understood in the following way. It is shown in reference 2 that in a beam bunch, charges separated less than about

$$d=x^{1/3}b \qquad x=1/(b\sigma\mu_0 c)$$

the leading charge repels the trailing charge, while the trailing charge has no effect on the leading charge. Thus, the trailing charge loses energy. If the trailing charge is further behind than d, it is attracted to the leading charge, and thus gains energy. A charge well within a long, uniform cylinder of charge will be about equally repelled and attracted by leading charges, and thus, will gain or lose little energy. This is approximately the situation inside gaussian distribution, whose width is much greater than d. For a finite cylinder of charge with zero-rise and fall distances at the two ends, charges within a few times d of the ends will be strongly decelerated. These charges will lose orders of magnitude more energy than the charges in the cylinder interior.

For the situation considered here, d = .014mm. If the rise distance is long compared to this, all charges will lose small amounts of energy. As the rise distance is reduced, more charges will have large, decelerating forces and power dissipation increases. If rise distance is short compared to .014mm, then no more increase in power loss should be expected.

Figure 3 shows the heating as a function of pulse length for the cylindrical pulse shape of method 1. Also shown, are calculations done with method 2, for a pulse-rise distance of .0005mm. The solid curve is $Aa^{-3/2}$, where A was adjusted so the curve falls near the data for both methods. This indicates that the $a^{-3/2}$ dependence arrived at using the gaussian pulse shape is approximately valid for a rectangular charge distribution. Since the rectangular shape is drastically different from the gaussian distribution, it seems reasonable to use a $^{-3/2}$ scaling to estimate beam-tube heating for most pulse shapes.

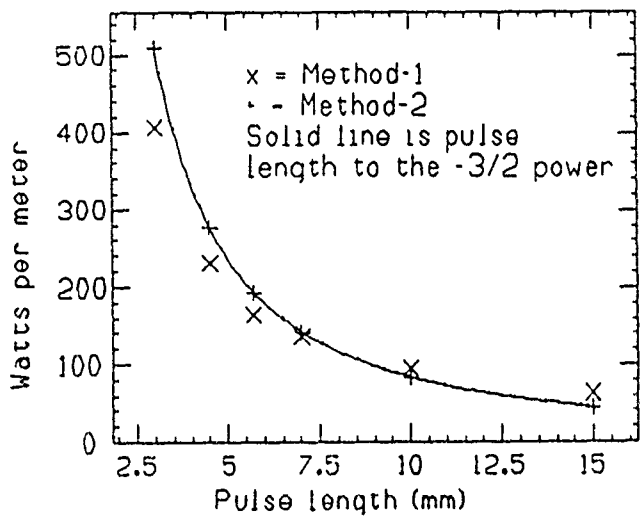


Figure 3. Dissipated power vs pulse length for a cylindrical charge bunch.

IV. CONCLUSIONS

The expected heating in the LSS wiggler beam tube will be 90 watts per meter. If the pulse rise and fall times are shortened, the heating will increase, but this increase will be limited to a factor of three. If the pulse length is shortened, the increase in heating can be estimated using a -3/2 scaling. Thus, a 10% shortening of the pulse length will result in a 15% increase in beam-tube heating.

It would be conceivable to have much greater heating than 200 watts per meter if the beam pulse becomes chopped up with many, rapidly rising and falling edges.

V, REFERENCES

(1) P.L. Morton, V.K. Neil, A.M. Sessler, *App. Phys.*, 37, p. 3875, 1966.
(2) A.W. Chao "SLAC-PUB-2946", June, 1982.
(3) B. McVay, Los Alamos National Laboratory, Private Communication.

Heating of the LSS Wiggler Beam Tube Due to Induced Surface Current

W. C. Sellyey and C. G. Parazzoli
Boeing Aerospace and Electronics Division
Boeing Defense and Space Group
PO Box 2499
Seattle, WA 98124, USA

I. INTRODUCTION

During 1990, The Boeing Company was designing a high-power, free-electron laser, referred to as the Laser Subsystem (LSS). Among the considerations determining the wiggler beam tube cooling requirements, was the heating caused by induced surface currents flowing on the inside of the beam tube.

The expected heating is calculated here. Additionally, the effect of pulse shape and length on the heating is investigated.

Two methods are used to evaluate the power dissipated in the LSS wiggler beam tube. The first is an expansion of methods used in reference 1. In this method, the beam charge is assumed to be uniformly distributed in a cylinder of length l and radius r_0. The beam center is taken as the z axis. The moving beam induces currents in the beam tube wall, resulting in the heating of the wall. This heating is given by

$$P(\zeta) = 2\pi\sigma \int_b^{inf} E_z^2(r,\zeta) r dr \qquad (1)$$

Here ζ = z-ct, z = longitudinal distance, t=time, r=distance from beam tube center, E_z=longitudinal component of the electric field, b=beam tube radius and σ = conductivity. It is assumed that the radial part of the E-field is unimportant.

Following reference 1, E_z and the charge distribution are Fourier transformed.

$$E_z(r,\zeta) = \int_{-inf}^{inf} \tilde{E}_z(r,k) e^{ik\zeta}\, dk \qquad (2)$$

$$\rho(r,\zeta) = \int_{-inf}^{inf} \tilde{\rho}_z(r,k) e^{ik\zeta}\, dk \qquad (3)$$

ρ=charge distribution and the wiggle indicates the Fourier transform. These are inserted into Maxwell's equations, and a new set of equations results. These are solved for E_z in three regions $r<r_0$, $r_0<r<b$ and $r>b$. The solutions are Hankel and Bessel functions, but only their asymptotic forms are needed. Boundary conditions are applied and E_z in the metal wall is determined.

Inserting this result for E_z and equation (2) into (1), simplifying, performing the integration over r, and averaging over the pulse length, one obtains

$$P = \frac{8\pi\sigma q^2 \beta^4}{b(RL)^2} \sum \sqrt{2Rk_n} \left\{ \frac{\sin[k_n(L+l)/2] - \sin[k_n(L-l)/2]}{k_n l} \right\}^2 \qquad (4)$$

$$R = 4\pi\beta\sigma/c \quad k_n = \pi n/L \quad \beta = v/c \qquad (5)$$

Here P=average power dissipated per unit length, q=charge per bunch and L=separation between bunches.

The second method is largely based on eq 1.55 from reference 2. This is the energy loss of beam through an arbitrary, transverse-charge multiple moment. It is assumed that all particles travel at c. For a cylindrically symmetric beam, only the zeroth moment contributes and it reduces to

$$P = 2\pi c^2 f \int_{-inf}^{inf} d\omega \left|\tilde{\rho}(\omega)\right|^2 R_e Z_o''(\omega)/D \qquad (6)$$

$$\tilde{\rho}(\omega) = \frac{1}{2\pi c} \int_{-inf}^{inf} e^{-i\omega z/c} \rho(\rho) dz \qquad (7)$$

Here $\rho(z)$ is the longitudinal charge distribution and fL=c. $Z_0(\omega)/D$ is the zeroth order longitudinal impedance of the beam pipe per unit length. In general, Z is a difficult quantity to evaluate. However, for a smooth, cylindrical beam pipe, this can be easily evaluated by combining equations 1-48, 1-36, 1-14, 1-7 and 1-9 of Ref. 2. The result is:

$$\frac{Z_o''}{D} = \frac{2}{cb} \frac{1}{\sqrt{\frac{2\pi\sigma}{c|k|}} + i\left[\sqrt{\frac{2\pi\sigma}{c|k|}} s_k - \frac{kb}{2}\right]} \qquad (8)$$

s_k=sign of k, $k=\omega/c$

The only approximation used in deriving the above result is that wavelengths of about 1km or greater are ignored. The predominant wavelength will be concentrated around distances which describe the beam-pulse structure. These are about a cm

0-7803-0135-8/91$01.00 ©IEEE

and shorter, so the neglected part of the impedance should be unimportant.

II. SOFTWARE

A short program was written to evaluate the terms of the expression for P of method 1. It was found that 40,000 terms allow evaluation of the beam power to a few percent.

The program for method 2 accepts input specifying the beam-pipe characteristics and the charge distribution. One possible way of specifying the charge distribution is by reading it in from a file. A different option instructs the software to generate a gaussian which can be symmetrically cut off at any distance from the centroid. An additional option allows the first gaussian to be continued by another gaussian of different width. The two gaussians are matched in slope and vertical height at the cut in the first gaussian.

A fast Fourier transform (FFT) of up to 65536 points is performed on the charge distribution. The number of points and the spatial interval used for the transform can be specified as input. Once the transform is done, a Simpson's rule integration is used to obtain the power dissipation.

III. RESULTS

The following input was used in all calculation, unless otherwise noted:

5.76mm = beam tube radius
3.43×10^7/(ohm.m) = conductivity of aluminum
10nc = microbunch charge
27.088 MHz = micropulse rate

Figure 1 shows the PARMELA-predicted[3] charge distribution at the entrance to the LSS wiggler. Using method 2, the calculated heating will be 90 watts/m. The numerical integration is a possible source of error. To check how serious this might be, the integration is done using different Fourier spatial intervals (S), and different numbers of points (N). Some results are shown in Table 1. If N is kept at 65536, the calculation should be accurate to better than 1%.

TABLE 1 Effect of number of points (N) and Fourier interval (S), on calculated results.

S(m)	N	Heating (w/m)
.1	4096	90.23
1	4096	90.84
10	4096	95.13
.1	65536	90.23
1	65536	90.87
10	65536	90.10

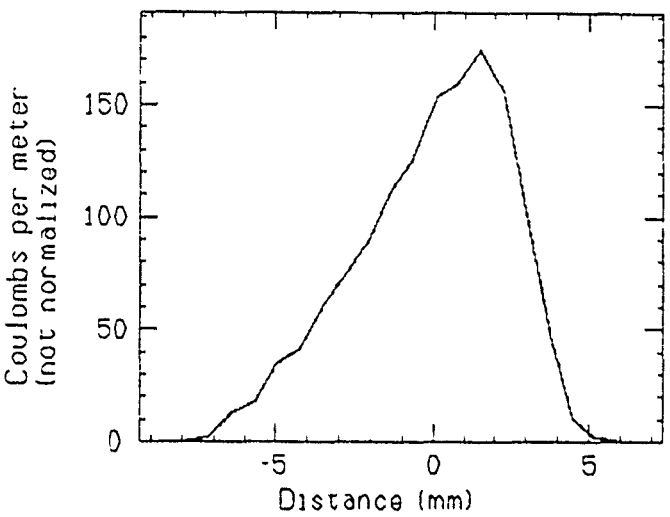


Figure 1. LSS wiggler longitudinal charge density.

Consider the imaginary term in equation (8). Letting

$$\frac{kb}{2} = \sqrt{\frac{2\pi\sigma}{c|k|}}$$

one gets $k = 6.74 \times 10^4$/m for beam-pipe parameters used here. The r.m.s. width of the charge distribution used above is a = 2.43mm. Taking ka = 1 gives $k = 4.12 \times 10^2$mm. Thus if one uses a gaussian charge distribution of r.m.s. width around 2.43mm, the kb term in the impedance can be ignored. When this is done, equation (6) can be integrated to give (in MKS):

$$P = 1.27 \times 10^8 \frac{q^2 f}{b\sigma^{1/2} a^{3/2}}$$

This gives 85.9w/m at a 27.088Mhz pulse rate. The program of method 2 gives the same result for the same gaussian distribution. This verifies that the program is working correctly. It also indicates that -3/2 scaling of the bunch length can be used to estimate power dissipation for LSS-type beam pulses.

To investigate the effect of pulse shape, figure 2 was produced. The lowest point at 85.3 watts is generated using a gaussian with the same r.m.s. width (a = 2.43mm) as the PARMELA prediction. The gaussian FWHM = 5.71mm. The remaining points are generated by using a wide central gaussian (a = 30mm). It is cut off and a second gaussian is appended to give the indicated rise and fall length. The FWHM is kept at 5.71mm. All calculations use a spatial interval of 5cm and 65536 points. Because of the short, spatial interval, low-frequency components are underestimated and all results are about 1% low.

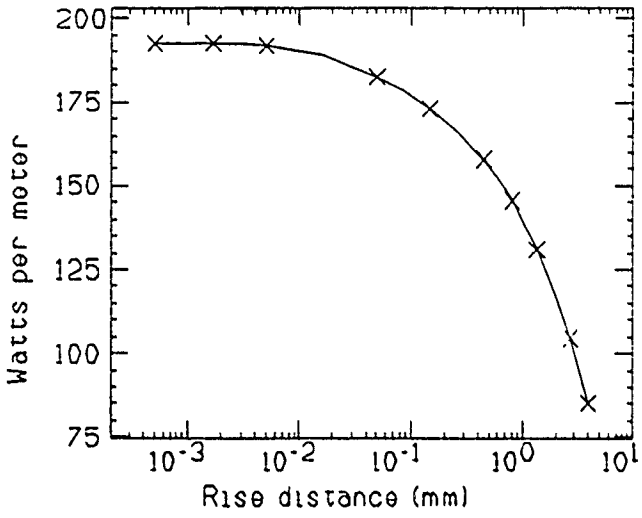


Figure 2. Dissipated power vs rise distance.

The interesting features of this graph are that the power dissipation increases until a rise distance of about .01mm is reached. For shorter distance, the dissipation does not increase. This can be understood in the following way. It is shown in reference 2 that in a beam bunch, charges separated less than about

$$d=x^{1/3}b \qquad x=1/(b\sigma\mu_o c)$$

the leading charge repels the trailing charge, while the trailing charge has no effect on the leading charge. Thus, the trailing charge loses energy. If the trailing charge is further behind than d, it is attracted to the leading charge, and thus gains energy. A charge well within a long, uniform cylinder of charge will be about equally repelled and attracted by leading charges, and thus, will gain or lose little energy. This is approximately the situation inside gaussian distribution, whose width is much greater than d. For a finite cylinder of charge with zero-rise and fall distances at the two ends, charges within a few times d of the ends will be strongly decelerated. These charges will lose orders of magnitude more energy than the charges in the cylinder interior.

For the situation considered here, d = .014mm. If the rise distance is long compared to this, all charges will lose small amounts of energy. As the rise distance is reduced, more charges will have large, decelerating forces and power dissipation increases. If rise distance is short compared to .014mm, then no more increase in power loss should be expected.

Figure 3 shows the heating as a function of pulse length for the cylindrical pulse shape of method 1. Also shown, are calculations done with method 2, for a pulse-rise distance of .0005mm. The solid curve is $Aa^{-3/2}$, where A was adjusted so the curve falls near the data for both methods. This indicates that the $a^{-3/2}$ dependence arrived at using the gaussian pulse shape is approximately valid for a rectangular charge distribution. Since the rectangular shape is drastically different from the gaussian distribution, it seems reasonable to use a $^{-3/2}$ scaling to estimate beam-tube heating for most pulse shapes.

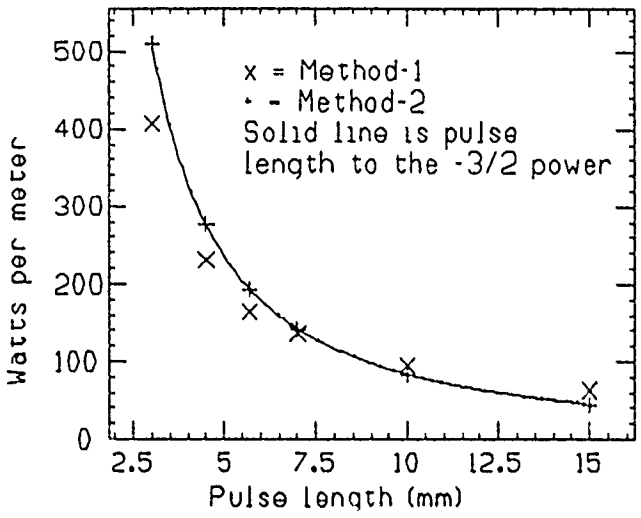


Figure 3. Dissipated power vs pulse length for a cylindrical charge bunch.

IV. CONCLUSIONS

The expected heating in the LSS wiggler beam tube will be 90 watts per meter. If the pulse rise and fall times are shortened, the heating will increase, but this increase will be limited to a factor of three. If the pulse length is shortened, the increase in heating can be estimated using a -3/2 scaling. Thus, a 10% shortening of the pulse length will result in a 15% increase in beam-tube heating.

It would be conceivable to have much greater heating than 200 watts per meter if the beam pulse becomes chopped up with many, rapidly rising and falling edges.

V. REFERENCES

(1) P.L. Morton, V.K. Neil, A.M. Sessler, *App. Phys.*, 37, p. 3875, 1966.
(2) A.W. Chao "SLAC-PUB-2946", June, 1982.
(3) B. McVay, Los Alamos National Laboratory, Private Communication.

A NEW POSSIBILITY OF COHERENT MICROWAVE RADIATION BY RELATIVISTIC PARTICLES

A.N.Didenko
Moscow Physical Engineering Institute
Moscow, 115409, USSR

Many scientists are interested nowadays in the problem of high power sharp-directed microwave radiation production. It is generally admitted that submillimeter and shorter wave (up to light) range radiation may be produced by means of relativistic and ultrarelativistic electron beams provided that Doppler shift permits radiation wavelengths essentially smaller than generating system characteristic size.

Undulator-based free electron lasers (FEL) are the most promising among facilities of this type [1].

The first impressive results produced by superconducting linac in the USA [2] and electron storage rings in the USSR [3] raised hopes of a rapid and large scale implementation of such facilities. However, the further detailed theoretical consideration revealed [4] that radiation generation needed a special accelerating facility construction since low current densities and wide energy spread of now existing accelerators could not provide proper conditions for FEL generation based on such facilities. Complex is also the problem of small period (less than 1 cm) magnetic field production.

This paper shows that normally crossing constant or pulsed magnetic and electrical fields can provide the condition to start generation using the beams of already operating accelerators.

Nonrelativistic particle moving in crossing electrical E and magnetic H fields, its trajectory is known [5] to depend on the particle initial velocity to drift velocity $v_{dr} = cE/H$ relation. The same picture will also be valid in relativistic case.

In view of the possible practical application the case of small drift velocity particle movement, that is, trochoidal movement, will be of the most interest. That is exactly why such device may be called a relativistic trochotron or creditron (Crossfield Relativistic Electron Drift Interaction). Similar to undulator based FEL relativistic case radiation in the direction of drift velocity will be increased by that from the corresponding parts of circumferences shifted relatively each other; differing, however, from undulator case, the number of such trajectories, hence the efficiency, may reach a high value, the length of the device being rather small.

Let us consider the angular and spectral characteristics of such device radiation in detail.

If $\beta_{\parallel} = v_{dr}/c \ll 1$, radiation characteristics of a trochoidally moving particle will be approximately the same as those of a circumferentially moving electron [6], that is, the radiation angle $\theta \sim 1/\gamma$, radiation power $W \sim 2e^2c\gamma^4/3R^2 = 2e^2c(eH/m_0c)^2\gamma^2/3$, radiation approaching its maximum value at a frequency $\omega \cong 3\omega_0\gamma^3/2 \sim 3eH\gamma^2/2m_0c$.

To define creditron generated oscillation spectrum it is necessary to find increments of instability development for each harmonic. The main instability for relativistic particle beams has bean shown to be [7] the radiation one, its increment at n-th harmonic being

$$\alpha_n = I_m\left\{-(tN|K|n\omega_0 W_n/2\mathcal{E}+n^2\omega_0 K^2(\Delta\mathcal{E}/\mathcal{E})^2\right\}^{1/2} =$$

$$= \omega_0\left\{\left[\left(N^2K^2n^2W_n^2/4\omega_0^2\mathcal{E}^2\right)+K^4n^4\left(\Delta\mathcal{E}/\mathcal{E}\right)^4\right]^{1/2}/2-\right.$$

$$\left.-K^2n^2\left(\Delta\mathcal{E}/\mathcal{E}\right)^2/2\right\}^{1/2} \qquad (1)$$

Energy spread of particles is taken into account. Here N is number of particles inhabiting one circumference, ω_0 - revolution frequency of a particle, W_n - radiation power at n-th harmonic, $K=\frac{1}{\beta^2}\left(\frac{1}{\gamma^2}-\frac{1}{\gamma_r^2}\right)$, where γ_r -

0-7803-0135-8/91$01.00 ©IEEE

betatron oscillation number (in case presented $\nu_r \sim 1$), while $\gamma = \mathcal{E}/m_o c^2$-relativistic factor.

Making use of [6]

$$W_n = dW/dn \quad \text{and} \quad nW_n = n\,dW/dn = y\,dW/dy =$$

$$= \left(3^{3/2} e^2 c\gamma^4 y^2/4\pi R^2\right)\left[2K_{2/3}(y) - \int_y^\infty K_{1/3}(x)dx\right] \quad (2)$$

where $y = 2n/3\gamma^3$, $K_{1/3}$ and $K_{2/3}$-McDonald functions, the expression for α may be transformed to

$$\alpha(y) = \left(3Nr_o\gamma^3/8R\right)^{1/2}\left[\left(f^4+\delta^4y^4\right)^{1/2} - \delta^2y^2\right]^{1/2} \quad (3)$$

where $r_o = e^2/m_o c^2$ is the classical radius of electron, $\delta = \left(3\gamma^3\right)^{1/2}\left(\Delta\mathcal{E}/\mathcal{E}\right)/\left(Nr_o/R\right)^{1/2}$ and

$$f(y) = \left\{3^{1/2} y^2\left[2K_{2/3}(y) - \int_y^\infty K_{1/3}(x)dx\right]/2\pi\right\}^{1/2}$$

It is evident that the function $f(y)$ defining the increments of various harmonics at $\delta = 0$ reaches its maximum value at $y = 4/3$. This means that the maximum increment corresponds to the frequency

$$\omega = 2\gamma^3\omega_o = 2\gamma^2 eH/m_o c$$

its wavelength being

$$\lambda = 2\pi m_o c^2/2\gamma^2 eH = \lambda_o/2\gamma^2,$$

where λ_o-dipole radiation wavelength of a rotating nonrelativistic particle. This result means that with the particles moving along circumference oscillations are most probably excited with the frequency, like in the case of a relativistic particle moving along sine curve in FEL, increased, as compared to a certain characteristic frequency, by the factor of $2\gamma^2$. This fact underlines the deep community of the two movements.

The energy spread of particles differing from zero, that is $\delta \neq 0$, $\alpha(y)$ reaches its maximum value at y, defined from equation

$$f^3\,\frac{\partial f}{\partial y} + \delta^4y^3 - \delta^2y\left(f^4+\delta^4y^4\right)^{1/2} = 0 \quad (4)$$

From this expression follows that increase of δ results in $y(\alpha=\alpha_{max})$ decreasing, the latter approaching $y=1/3$ at $\delta \Rightarrow \infty$.

Function $F(y,\delta) = \left[\left(f^4+\delta^4y^4\right)^{1/2} - \delta^2y^2\right]^{1/2}$ characterizes oscillation increment dependence on y. It shows that growth of δ results in, first, increment decrease and, second, that it will be maximal at lower y value.

Besides that, if more than one bunch rotates along each of the shifted circumferences, radiation angular distribution of such a system will differ from that of a single electron, becoming sharply elongated along and against drift velocity, it will result in the growth of the part of radiated energy that will be transformed into coherent radiation energy.

The above said shows that radiation characteristics of creditron are similar to these of undulator, both devices having similar dependence of angle, power and frequency of radiation on energy. However, expressions for W and ω including magnetic field dependent factors, creditron admits sufficiently higher field strength values. This might result in rather essential differences: on one hand, radiation power of creditron increases at the same energy, and, on the other hand, that very same radiation frequency may be obtained, the energy of electrons being sufficiently less, since at the values of external magnetic field $H \geq$ 10 kOe the value of $\lambda_o < 1$ cm, while in undulators, due to the specificity of alternating field structure this value can never be less than some centimeters. And here is the promise of creditron.

At the same time the equation obtained implies that the energy spread requirements increase with gamma. Physically it follows from the fact that the higher the energy the higher the number of the harmonic at which radiation instability develops.

Energy spread resulting in additional particle movement in azimuthal direction and hence to partial mixing of particles originating from different bunches, that in its turn causes steep decrease of oscillation

increments and coherent oscillation power generated, this spread should be diminished. Nevertheless, creditron's efficiency

$$G = \left(1/v_{dr}\right)\int_{0}^{L}\alpha dl = \alpha L/\beta_{\parallel} c = 2\pi\alpha R N_{eff}/c =$$

$$= 2\pi\alpha N_{eff}/\omega_{o} \gg 1 \qquad (5)$$

even at high enough δ values (about 10 and more), where N_{eff} is the effective number of interaction periods.

This signifies that in such devices up to light range the requirements to energy spread and density of particles used might be less strict than those in undulator based FEL.

REFERENCES

[1] T.C. Marshall, Free-Electron Lasers. NY-London:Mc-Millan Publ.Co,1985

[2] .D.A.G Deacon, L.R. Elias, J.M.J. Madey, G.J. Ramian G.J., H.A Schwettman, T.L. Smith, Phys. Rev. Lett., 1987, 38, p.892

[3] .N.A. Vinokurov, E.S Gluskin, G.A. Kornyukhin, V.A Kochubei, G.N Kulipanov, N.A. Mezentsev, V.F.Pindyurin, A.N. Skrinski, V.M. Khorev, Nucl. Inst. and Meth., 1980, 177, p.239

[4] P. Sprangle, C.M. Tang, I. Bernstein, Phys. Rev. Lett., 1983,50, p.1775; Phys. Rev. A, 1983, 28, p.2300

[5] L.D. Landau, E.M. Lifschitz, Teoriya Polya, Moscow, GITTL,1960

[6] A.A.Sokolov, I.M. Ternov, Relyativistski Elektron, Moscow, Nauka, 1974

[7] .A.N. Didenko, V.P. Grigoryev, Yu.P. Usov Moshchnyye Elektronnyye Puchki i Ikh Primeneniye, Moscow, Atomizdat, 1977

EFFECTS OF CONSTRUCTION AND ALIGNMENT ERRORS ON THE ORBIT FUNCTIONS OF THE ADVANCED PHOTON SOURCE STORAGE RING

H. Bizek, E. Crosbie, E. Lessner,
L. Teng, and J. Wirsbinski
Argonne National Laboratory
Advanced Photon Source
9700 South Cass Avenue
Argonne, IL 60439

Abstract

The orbit functions for the Advanced Photon Source Storage Ring have been studied using the simulation code RACETRACK. Non-linear elements are substituted into the storage ring lattice to simulate the effects of construction and alignment errors in the quadrupole, dipole, and sextupole magnets. The effects of these errors on the orbit distortion, dispersion, and beta functions are then graphically analyzed to show the rms spread of the functions across several machines. The studies show that the most significant error is displacement of the quadrupole magnets. Further studies using a 3 bump correction routine show that these errors can be corrected to acceptable levels.

I. INTRODUCTION

The Advanced Photon Source (APS) will be a third generation, 7-GeV synchrotron radiation source. The storage ring will contain 80 dipole bending magnets and 400 focusing quadrupole magnets in a Chasman-Green type lattice. It will also contain 120 chromaticity sextupoles, 160 harmonic sextupoles, and 40 dispersion free straight sections for a total circumference of 1104 m. Figure 1 shows where these components, as well as the beam position monitors and orbit correcting magnets are located in the storage ring lattice.

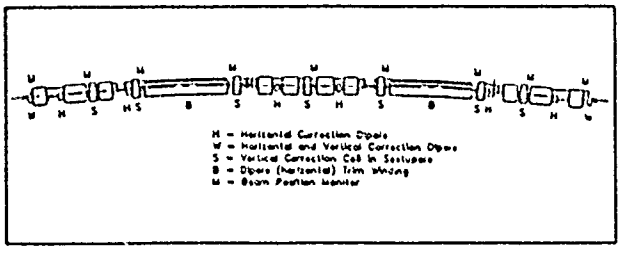


Figure 1: APS Storage Ring Cell Without Straight Sections

*Work supported by U.S. Department of Energy, Office of Basic Energy Sciences under Contract No. W-31-109-ENG-38.

U.S. Government work not protected by U.S. Copyright.

Errors in the construction and alignment of the magnets adversely affect the orbit functions of the storage ring. These effects are computed and studied in order to set tolerances for the construction and installation of the magnets.

The orbit simulation code RACETRACK with Orbit Corrections was used. RACETRACK with Orbit Corrections is a version of the program RACETRACK, modified by Hiroshi Nishimura and Albin Wrulich [1] to include orbit corrections. Both programs track transverse nonlinear particle motion in accelerators; multipoles up to 20-pole are included and treated as thin elements.

In addition, once a stable closed orbit is established, RACETRACK with Orbit Corrections has the ability to correct orbit distortions using the correcting dipoles. It accomplishes this reduction using a local three dipole bump correcting routine.

II. PROCEDURE

The following steps were followed to conduct the study of the orbit functions:

1. An error type and level was chosen.
2. Generally 10 different random seeds were run for each error level to generate 10 different random distributions of errors.
3. The values, both horizontal and vertical, of the beta functions, orbit distortion and dispersion were then graphed using the spreadsheet 2020.
4. For the quadrupole misalignments, 22 seeds were run and the correction routine was activated to verify that the effects of this error could be reduced to within acceptable values.

III. RESULTS

Of all the errors studied, the one that produced the greatest orbit distortion was the transverse misalignment of the quadrupole magnets. The distorted orbits, the beta functions, and the dispersion functions are shown in Figures 2, 3, and 4 for an rms quadrupole misalignment of 0.1 mm.

Orbit correction was studied with RACETRACK with Orbit Corrections. After correction, the spread of the distortions of the orbit, the beta functions, and the dispersion functions were greatly reduced as shown in Figures 5, 6, and 7.

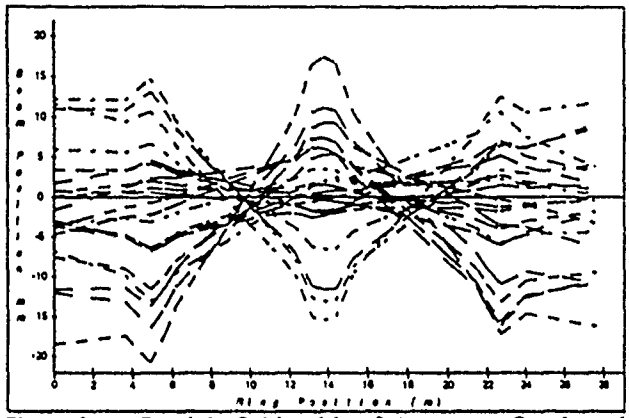


Figure 2: Particle Orbit with a 0.1 mm rms Quadrupole Misalignment

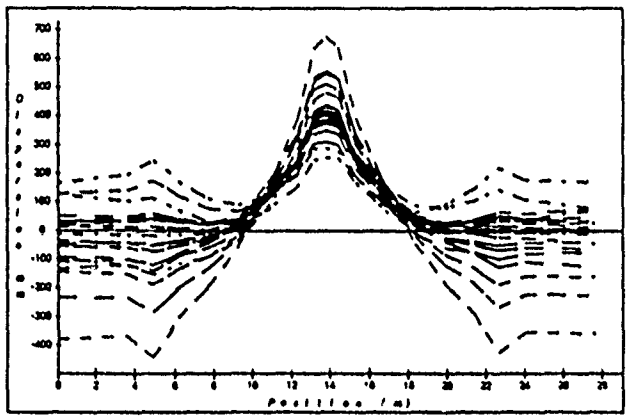


Figure 3: Horizontal Dispersion with a 0.1 mm rms Quadrupole Misalignment

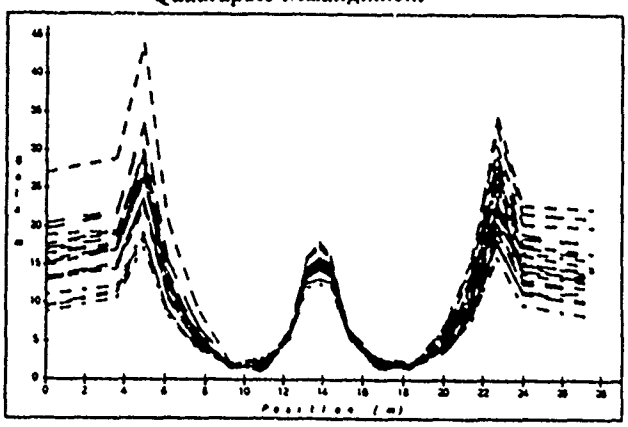


Figure 4: Horizontal Beta Functions with a 0.1 mm rms Quadrupole Misalignment

Random field errors in the dipole magnets (ΔB/B) did not have any effect on the vertical orbit distortion or the vertical dispersion. They did, however, distort the horizontal orbit and dispersion function, as well as both the horizontal and vertical beta functions.

The roll misalignment errors had minimal effect on the orbit functions. The three functions most distorted were the vertical orbit and the horizontal and vertical dispersion functions.

Transverse displacement of the sextupole magnets had no effect on the orbit and minimal effect on the dispersion. The distortion of the beta function is shown in Figure 8.

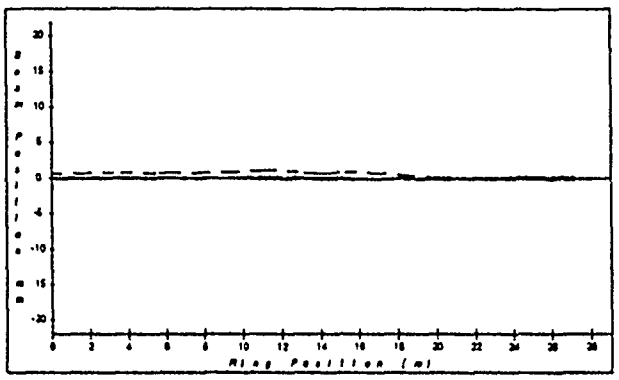


Figure 5: Particle Orbit after Correction of a 0.1 mm rms Quadrupole Misalignment

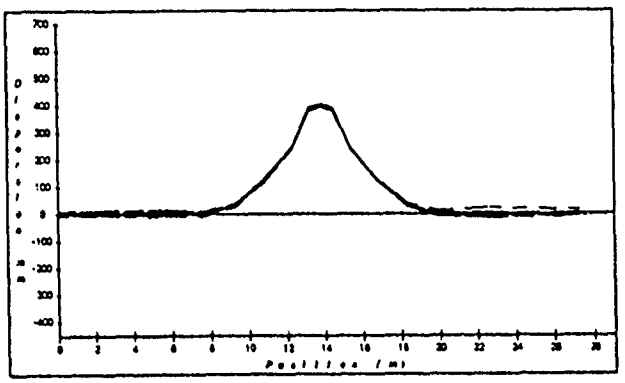


Figure 6: Horizontal Dispersion after Correction of a 0.1 mm rms Quadrupole Misalignment

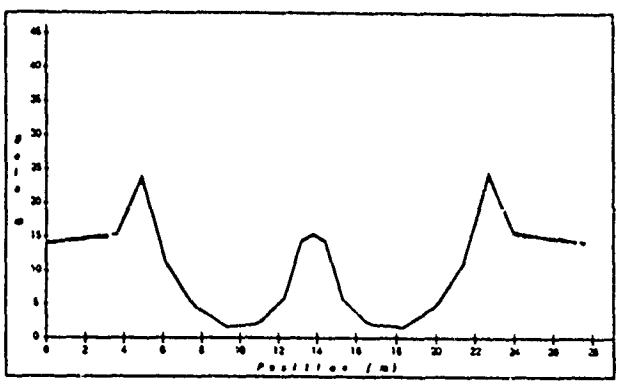


Figure 7: Horizontal Beta after Correction of a 0.1 mm rms Quadrupole Misalignment

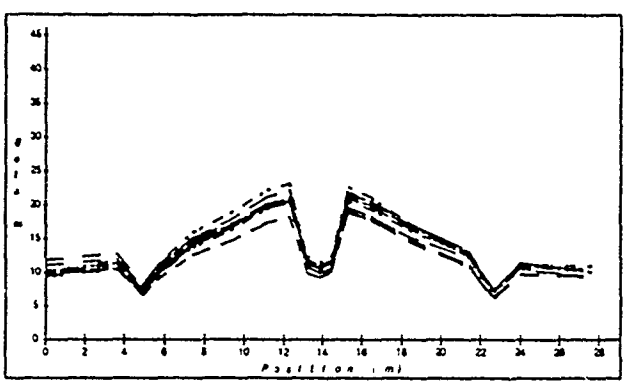


Figure 8: Vertical Beta Function with a 0.1 mm rms Displacement of the Sextupole Magnets.

The field gradient errors in the quadrupole magnets ($\Delta B'/B'$) distorted the beta functions and the horizontal dispersion, while the particle orbits and the vertical dispersion were unaffected. Figures 9 and 10 show the distortions of the dispersion and beta functions due to an rms error magnitude of 1%.

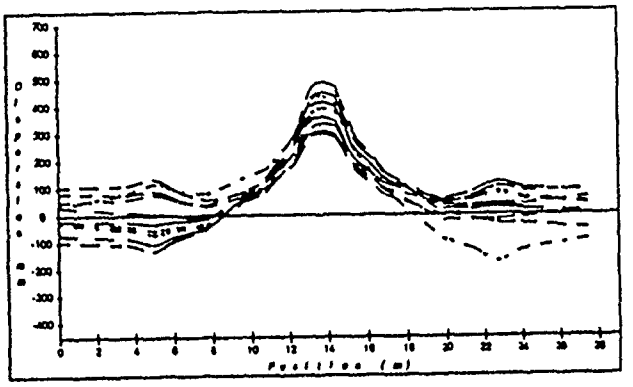


Figure 9: Horizontal Dispersion Function with a Gradient Field Error of 1% in the Quadrupole Magnets

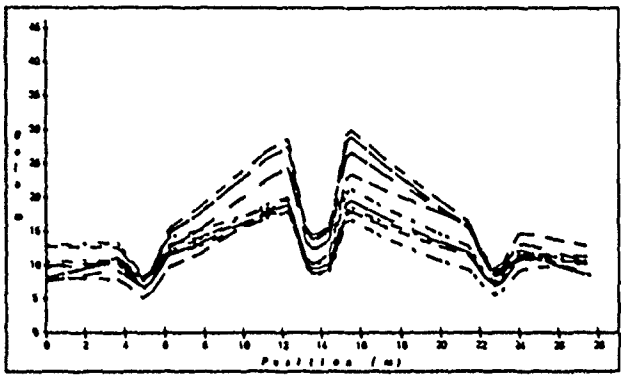


Figure 10: Vertical Beta Function with a Gradient Field Error of 1% in the Quadrupole Magnets

The distortions caused by the transverse misalignment of sextupoles and the quadrupole field gradient errors cannot be corrected using the local bump method found in RACETRACK with Orbit Corrections; however, these distortions can be minimized by tuning the quadrupole magnets.

For random errors the orbit function distortions can be evaluated analytically. These are

Orbit distortion

$$\frac{\delta z}{\sqrt{\beta}} = \frac{1}{2|\sin\pi\nu|} \begin{cases} \sqrt{\sum_Q \beta k^2}\ \Delta z_{qrms} \\ \sqrt{\sum_D \beta\theta^2}\ \left[\left(\frac{\Delta B}{B}\right)_{rms} \text{ or } \phi_{rms}\right] \end{cases}$$

β-function distortion

$$\frac{\delta\beta}{\beta} = \frac{1}{2|\sin 2\pi\nu|} \begin{cases} \sqrt{\sum_S \beta^2 s^2}\ \Delta z_{srms} \\ \sqrt{\sum_Q \beta^2 k^2}\ \left(\frac{\Delta B'}{B'}\right)_{rms} \end{cases}$$

where $\Theta \equiv B\ell/B\rho$ = dipole strength, $k \equiv B'\ell/B\rho$ = quadrupole strength, $s \equiv B''\ell/B\rho$ = sextupole strength, ϕ ≡ dipole roll error, $\Delta z_q \equiv$ quadrupole misalignment, $\Delta z_s \equiv$ sextupole misalignment, and $\sum_D$, $\sum_Q$ and $\sum_S$ denote summations over all dipoles, quadrupoles and sextupoles respectively; and the formulas apply to both the horizontal ($z \to x$) and the vertical ($z \to y$) planes. In APS the numerical results are given in Table 1.

Table 1
Orbit and β-distortion due to various random errors derived analytically

Errors	Orbit distortion $\delta z/\sqrt{\beta}$	β-distortion $\delta\beta/\beta$
Δx_{qrms}=0.1 mm	0.00236 $m^{1/2}$	
Δy_{qrms}=0.1 mm	0.00167 $m^{1/2}$	
$\left(\frac{\Delta B}{B}\right)_{rms} = 10^{-2}$	0.00885 $m^{1/2}$	
$\phi_{rms}=10^{-2}$	0.0178 $m^{1/2}$	
Δx_{srms}=0.1 mm		0.0211
Δy_{srms} = 0.1 mm		0.0460
$\left(\frac{\Delta B'}{B'}\right)_{rms} = 10^{-2}$		0.00628

We see that the analytical results agree approximately with the numerical results.

IV. CONCLUSION

The results of this study show that the most severe effects on the orbit functions are caused by transverse misalignments of the quadrupole magnets, but they can be effectively corrected with the correction dipole system as designed.

V. REFERENCES

[1] "RACETRACK with Orbit-Corrections", H. Nishimura, A. Wrulich, 1986, private communication.

A Low Vertical β Mode for the LNLS UVX Electron Storage Ring

Liu Lin and P. Tavares
LNLS - Laboratório Nacional de Luz Síncrotron
Cx. Postal 6192 - Campinas - SP - Brazil

Abstract

An operation mode with low vertical betatron function in one of the long dispersion free straight sections of the LNLS UVX Electron Storage Ring is studied for applications with small gap insertions. The flexibility of this lattice is analyzed regarding two aspects: the range of variation of the vertical betatron tune and the ability to set the betatron functions to high/low values in the insertion straights.

1. INTRODUCTION

The LNLS UVX electron storage ring is a 1.15 GeV six fold symmetric double bend achromat lattice[1]. Some of its parameters for the nominal operation mode are given in table 1. To meet the need of different kinds of experiments, other operation modes are foreseen, including a low vertical beta mode envisaging the use of micro-undulators or other devices with very small gaps.

Table 1: Main Parameters of the UVX storage ring for nominal operation mode.

Energy	1.15	GeV
Current	100	mA
Circumference	77.3977	m
Magnetic Structure	CG-6-fold	
Revolution Frequency	3873.17	kHz
Harmonic Number	129	
RF-Frequency	500	MHz
Natural Emittance	63.4	nm.rad
Horizontal betatron tune	5.23	
Vertical betatron tune	2.12	
Synchrotron tune	4.054	1/1000 (@108 kV)
Momentum Compaction	0.010	
Natural energy spread	0.059	%
Nat. hor. chromaticity	-8.3	
Nat. vert. chromaticity	-6.2	
Hor. betatron damping time	11.0	ms
Ver. betatron damping time	10.5	ms
Synchrotron damping time	5.1	ms
Dipoles		
Bending radius	2.735	m
Bending field	1.4	Tesla
Number	12	
Quadrupoles		
Number of families	4	
Number	42	
Sextupoles		
Number of families	4	
Number of sextupoles	42	

2. LOW VERTICAL β MODE

We have investigated an operation mode with low vertical beta function in one of the long dispersion-free straight sections that could be achieved by continuously transfering the configuration of the lattice from the normal operation mode. This requires that no resonance lines are crossed during the process. This scheme has the advantage of circumventing the need to establish new injection conditions in this mode.

The proposed mode can be accomplished in this lattice by independently powering the quadrupole doublets adjacent to the low β straight. The lattice functions for 3 superperiods of the ring are shown in figure 1. The vertical beta is matched to 0.69 m in the small gap insertion straight, a factor of 10 smaller than the value for the normal operation mode. Both the vertical and the radial tunes, as well as the emittance are kept the same as in the normal operation mode. The reduction in the vertical beta in the insertion straight causes the vertical phase advance to increase across this region. To keep the same tune, the vertical phase advance over the achromat must be reduced. This is not the case in the horizontal plane: the change in horizontal beta is very small, not significantly affecting the horizontal phase advance in the achromat, and this is the reason why the emittance of the lattice in this mode (ε_0=6.4 x 10^{-8} rad.m.) does not change.

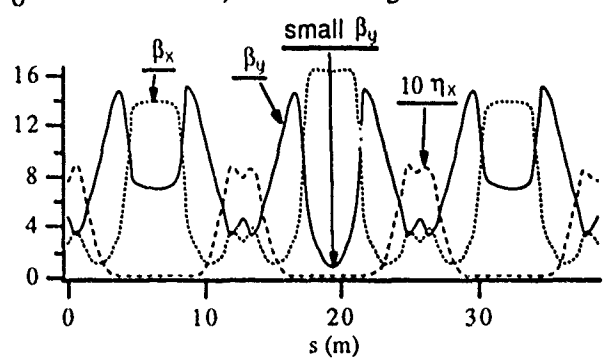


Figure 1: Lattice functions for three superperiods of UVX in the low vertical β mode.

We look now at the various dimensions at the point where β=0.69 m. The residual vertical emittance after closed orbit correction in ten simulations for the normal operation mode [1] is ε_y=(0.10±0.11) x 10^{-9} rad.m. and the maximum residual vertical orbit distortion y_{max}=0.19±0.06 mm. We assume the mean values plus 3 standard deviations, i.e, ε_y=0.43 nm.rad and y_{max}=0.37 mm. With these values the vertical beam size is σ_y=0.017 mm giving for a very small gap insertion, say, 2 mm, a distance of 95 σ from the center of the displaced closed orbit to the insertion wall. At 69 cm

0-7803-0135-8/91S01.00 ©IEEE

from this point of minimum, the vertical betatron function doubles its value and the beam size increases by a factor of 1.4. It is also interesting to note that the β scaled physical aperture at the small β symmetry point is 1.3 mm; thus any gap greater than this value will not limit the vertical acceptance of the ring.

Dynamic aperture studies are performed with the code PATPET[2]. The two families of sextupoles placed in the dispersion-free region are used to improve the dynamic aperture, which can be made as large as the dynamic aperture of the normal mode. Particles are tracked for 500 turns. The effect of systematic and random multipole errors and random strength and alignment errors are simulated. The tolerances and error distributions are the same as the ones used in the normal operation mode. Figure 2 shows the dynamic aperture at the midpoint of the long dispersion-free, high beta straight section. The hatched regions correspond to the uncertainty area of dynamic aperture for 5 different sequences of random errors.

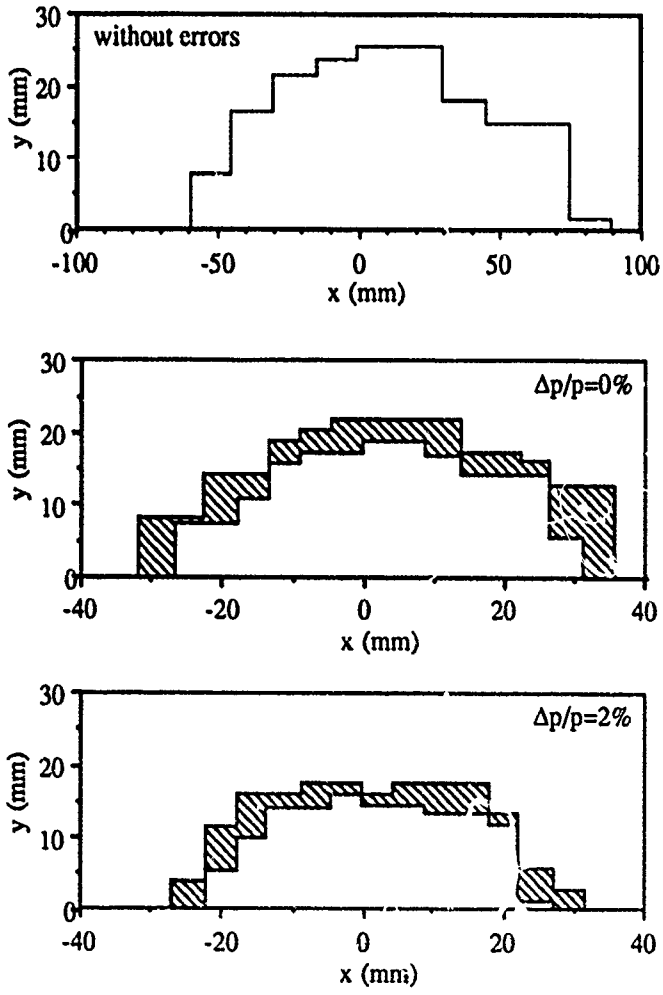


Figure 2. Dynamic aperture at the midpoint of the dispersion-free, high beta straight section for the low vertical beta mode. The upper graphic shows the dynamic aperture for the machine without errors and the other two show the dynamic aperture including the errors described in the text. The last figure also includes 2 % momentum deviation.

Since a large dynamic aperture is not required for injection in this mode, we analyse it from the viewpoint of the beam lifetime.

2.1 Beam Lifetime

A thorough analysis of collective effects and lifetime limitations for the low-ß operation mode has not been carried out yet. Nevertheless, we do not expect to observe significant deviations from the characteristics of the normal operation mode, since all lattice parameters (momentum compaction, damping times, natural emittance, average beta functions) for both modes are quite similar, so that instability thresholds and equilibrium bunch dimensions should not vary much. The main difference lies in a slightly reduced dynamic aperture and a slightly smaller physical vertical acceptance(essentially due to the higher values of the vertical ß function in the bending magnets). The former can significantly alter the Touschek contribution to the overall lifetime, whereas the latter only influences the lifetime due to elastic scattering of residual gas molecules. Since the cross-section for this process decreases sharply with energy, it should not be very important at full energy. In order to check these assertions, a calculation that consistently takes into account bunch lengthening due to microwave instability and potential-well distortion for an assumed 13 Ω ring broadband impedance and emittance growth due to intrabeam scattering was carried out with the computer code ZAP[3] to determine the expected overall lifetime for one single set of operating parameters (RF voltage = 600 kV, bunch current = 3 mA, emittance coupling = 10%). The Touschek lifetime is reduced from 80 hours (normal mode) to 59 hours, whereas the gas scattering contribution remains essentially constant, the overall lifetime being in both cases ~ 18 hours.

3. FLEXIBILITY OF THE UVX LATTICE

The flexibility of the UVX lattice is analyzed regarding two aspects: the range of variation of the vertical betatron tune and the ability to set the betatron functions to high/low values in the insertion straights.

The inclusion of insertion devices in the ring affects the beam in various aspects. In the case of wigglers and undulators with plane poles, the edge-focussing of these poles produces a vertical betatron tune shift which must be compensated to ensure operation far from resonances. A plane pole insertion device with length L and bending radius ρ produces a vertical tune shift

$$\Delta\nu_y = \frac{1}{4\pi}\beta_y \frac{L}{\rho^2}$$

where β_y is the betatron function at the wiggler position, assumed to be constant over the length of the magnet. A 1 m, 2 Tesla wiggler increases the vertical tune by 0.14; and a 25 cm, 5 Tesla one by 0.22. Let us take a worst case estimate of $\Delta\nu_y$=0.4. The UVX lattice can be tuned to compensate this vertical tune-shift without changing the horizontal tune. Larger tune shifts were not investigated up to now.

It is always desirable to set the betatron values in the insertion straights to values suitable for particular applications. Compared to a previous design (VUV-III) [4], UVX has an extra quadrupole family in the dispersive region. This allows for the changing of the betatron function in the insertions while keeping the same tune. An example is the low vertical beta mode described above. Lowering the horizontal beta while keeping the tune has the price of increasing the emittance. Further flexibility to tailor the beta values can be achieved using quadrupole triplets to match the betatron functions in the insertion regions.

4. REFERENCES

[1] Liu Lin, L. Jahnel and P. Tavares, "A Magnet Lattice for the LNLS Soft X-Ray Source", in *EPAC*90.

[2] L. Emery, H. Wiedemann and J. Safranek, "User's Guide for the PATPET Version 88.2", SSRL ACD-NOTE 36, 1988.

[3] M. S. Zisman, S. Chattopadhyay, J. J. Bisognano, "ZAP User's Manual", LBL Report - 21270, 1986.

[4] Liu Lin and L. Jahnel, "VUV-III Structure", LNLS Internal Report MP009/89.

Injection into the LNLS UVX Electron Storage Ring

Liu Lin
LNLS - Laboratório Nacional de Luz Síncrotron
Cx. Postal 6192 - Campinas - SP - Brazil

Abstract

To inject the 1.15 GeV electron storage ring - UVX - a beam from a linear accelerator - MAIRA - is used. The electrons are injected and accumulated at low energy (100MeV) until the nominal current of 100 mA is reached and then are ramped to the nominal energy. A study on a conventional injection scheme has been carried out. Two injection modes are investigated: injection with the phase ellipse parameters matched and mismatched to the ring's acceptance. The mismatched mode is optimized to fit the maximum of the injected beam into the acceptance.

1. INTRODUCTION

To inject the 1.15 GeV electron storage ring - UVX[1] - a beam from a linear accelerator - MAIRA[2] - is used. The electrons are injected and accumulated at low energy (100 MeV) until the nominal current of 100 mA is reached and then are ramped to the nominal energy. The low energy injection presents some problems that make it more difficult than the high energy injection: short beam lifetime, long betatron oscillation damping time and enlargement of beam dimensions due to the intra-beam scattering effect (IBS); on the other hand it has the advantage of requiring a less expensive injector system. Two injection schemes are being used in this case: conventional injection and injection with anomalous repetition rate[3].

In the conventional injection, the linac pulses are injected at a rate determined by the stored beam oscillation damping time, whereas in the injection with anomalous repetition rate the pulses are injected at a much faster rate and the stored beam does not damp.

In this report a study on the conventional injection into UVX is described.

2. INJECTION SCHEME

The injection into the UVX storage ring takes place in one of the long straight sections, in the radial plane and from the inner side of the circumference. The electron beam from the linac is transported by an underground transfer line and is brought into the storage ring by two horizontal deflection septa. The beam is injected into the storage ring's acceptance which is locally deflected in the radial plane by three fast kickers.

The beam from the linac has the following characteristics:

- Energy = 100 MeV
- Macropulse current = 200 mA
- Pulse length = 200 ns
- r.m.s. emittance = 6.7 x 10^{-7} rad.m. ,

and the UVX storage ring running at 100 MeV has the following ones:

- Circumference = 77.3977 m
- Revolution period = 258 ns
- Harmonic number = 129
- RF frequency = 500 MHz
- Horizontal betatron damping time = 16.7 s
- Vertical betatron damping time = 16.0 s
- Synchrotron damping time= 7.8 s
- Equilibrium r.m.s. emittance = 1.0 x 10^{-6} rad.m

The equilibrium r.m.s. emittance of the stored beam at 100 MeV is calculated including IBS, which is, at this energy, the dominating excitation effect. The calculations show[4] that in the range of considered values, the equilibrium emittance increases with the current per bunch and with peak RF voltage. As the greater the emittance the more critical the injection, we assume a worst case condition of 5 mA per bunch, 600 kV peak RF voltage and 13 Ω ring impedance with Spear scaling. These result in the value of emittance given above. The radial r.m.s. stored beam size at the injection point (end of septum) is then, σ^S_x= 3.8 mm.

At the injection point the deflected closed orbit is 15 mm from the central orbit and at an angle of -0.95 mrad with respect to it. The distance from the vacuum chamber wall corresponds to 4 σ^S_x. The radial stability limit (dynamic aperture) assumed for the calculations is ±29 mm[1]. 5 mm are reserved for the septum wall thickness. After the injection point the deflected orbit goes through a focussing quadrupole, a defocussing quadrupole, a dipole and finally crosses the central orbit at 57 cm from the last element, where it is kicked again to the central orbit. The position of the elements, the bumped stored beam and the injected beam are shown in figure 1. Table I lists the kicker strengths necessary to deflect the closed orbit by the amplitude A at the injection point.

Two injection modes were studied: injection with the phase ellipse parameters matched and mismatched to the ring's acceptance. The mismatched mode is optimized to fit the maximum of the injected beam into the available bumped acceptance region. Figures 2 and 3 show the injected beam and the bumped acceptance in the radial phase space at the injection point, illustrating the difference between the two injection modes.

The kickers must be turned off in 4 turns to prevent the injected beam from colliding with the vacuum chamber wall. Figure 4 shows the evolution of the injected beam, the bumped acceptance and the stored beam for the mismatched injection mode, assuming that the kicker strengths fall linearly to zero in three turns.

This process is repeated after damping of the beam with the injection of a new pulse from the linac.

0-7803-0135-8/91$01.00 ©IEEE

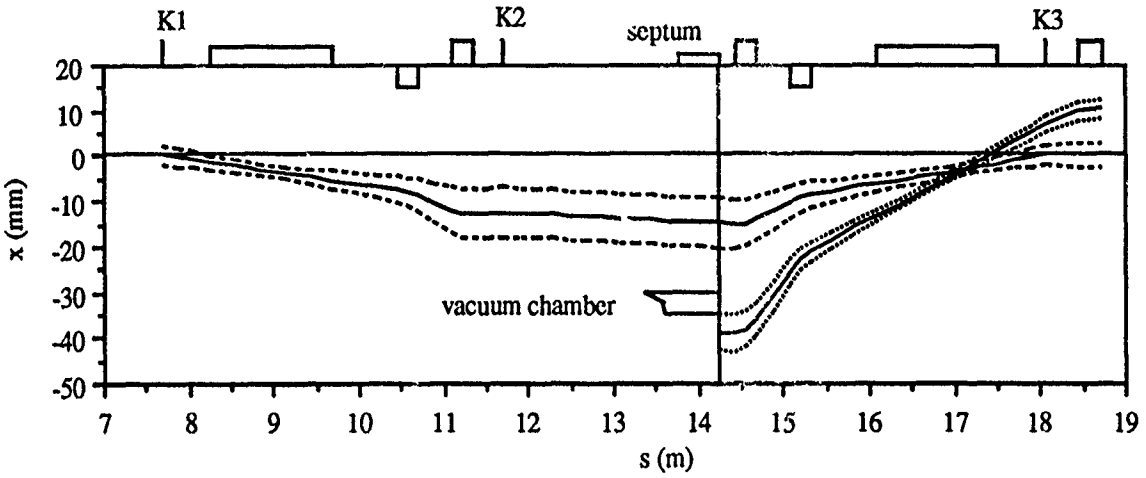


Figure 1: Schematic injection process showing the kickers position and the trajectories of the injected and stored beams. The envelope enclosing a phase space area of 2 times the r.m.s. stored beam emittance and the envelope of the injected beam are shown in dotted lines.

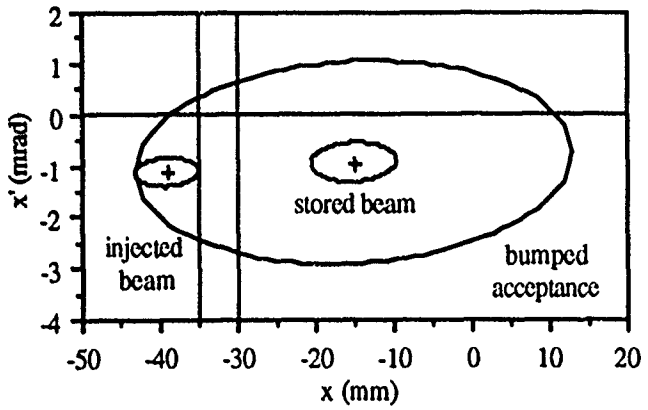


Figure 2: Bumped acceptance, injected and stored beams in the radial phase space, at the injection point (end of septum), for the matched injection mode. The area of the stored beam in the figure is two times the equilibrium emittance of the ring at 100 MeV, and that of the injected beam is 1.7 times the linac r.m.s. emittance.

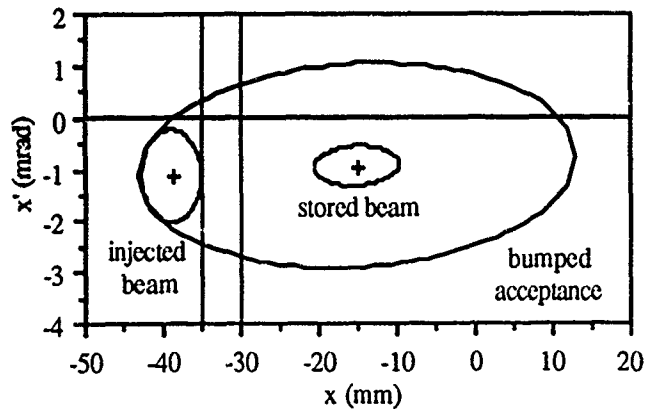


Figure 3: Bumped acceptance, injected and stored beams in the radial phase space, at the injection point (end of septum), for the mismatched injection mode. The area of the stored beam in the figure is two times the equilibrium emittance of the ring at 100 MeV, and that of the injected beam is 5.1 times the linac r.m.s. emittance.

Table I : Kicker strengths for 15 mm and 30 mm bump amplitudes at the injection point.

	A = 15 mm	A = 30 mm
θ kicker1 (mrad)	-2.8	-5.6
θ kicker2 (mrad)	-1.8	-3.5
θ kicker3 (mrad)	-3.3	-6.6

The parameters of the injected beam for the two injection modes are shown in table II.

Table II: Parameters of the injected beam for the two injection modes.

	Matched injection	Mismatched injection
x centroid (mm)	-39.0	-38.8
x' centroid (mrad)	-1.14	-1.14
β_x (m)	14.20	4.25
α_x	-0.096	0.0
A* (rad. m)	1.1×10^{-6}	3.4×10^{-6}
F** (%)	56	92

*A is the phase ellipse area of the injected beam contained in the ring's acceptance, as shown in figures 2 and 3.

**F is the fraction of the injected beam contained in the ellipse described above. Note that the fraction contained in the acceptance is greater than F, we have thus taken a conservative value.

3. INJECTION TIME

The time needed to accumulate 100 mA in the storage ring in a multi-bunch mode is estimated. The linac provides a 200 ns and 200 mA pulse. Only the electrons injected into the storage ring's RF buckets are captured in a bunch. The phase trajectories of the electrons for the UVX operating at 100 MeV with 600 kV peak RF voltage are shown in figure 5. The period in the graph, determined by the RF system, is 2 ns and

the injected pulse fills 100 buckets (out of 129). The maximum amplitude of a stable oscillation of τ is τ_{max}= 1 ns and the RF energy aperture is ε_{max}= 5.4 %. Figure 5 also shows the energy deviation limit of ±3 % due to physical aperture. We observe that a small fraction of the beam is injected outside the stable region. We recall that distribution of the injected particles is gaussian in energy with 2 % standard deviation (beam from the linac).

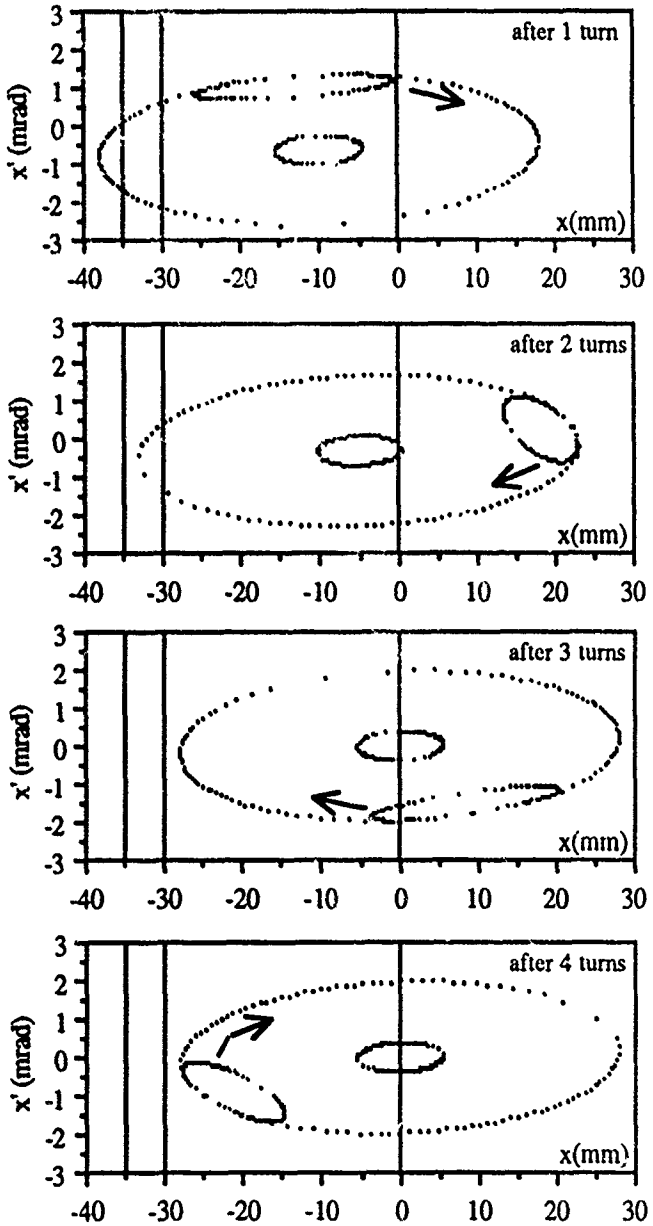


Figure 4: Evolution of the injected beam and bumped acceptance in the mismatched injection mode.

The efficiency η of the injection process depends on the efficiency in the various stages of the process. Table III shows the calculated and supposed values in the various stages.

Table III: Efficiency at the various stages of the injection process.

	Matched injection	Mismatched injection
Transport line[5] (η_{a1})	87 %	86 %
Inj. into acceptance (η_{a2})	56 %	92 %
Other* (η_b)	25 %	25 %
η**	14 %	21 %

* Safety factor, fraction outside the RF buckets, losses in the ramping process, etc.

** $\eta = \eta_a \cdot \eta_b$, where η_a is the smaller of η_{a1} and η_{a2}.

The accumulated current in one linac pulse is:

$$I_0 = \eta \frac{T_L}{T_{ring}} I_L$$

where T_L and I_L are the linac macro-pulse length and current, respectively, and T_{ring} is the storage ring revolution period. For the matched injection mode I_0 = 21.7 mA and 5 pulses from the linac are needed to store 100 mA. Injecting the pulses at intervals equal to the betatron damping time gives a injection time of 1.4 minutes. For the mismatched injection mode I_0 = 32.5 mA and the injection time falls to 1.0 minute. These injection times are less than the beam lifetime at 100 MeV, which is about 20 minutes.

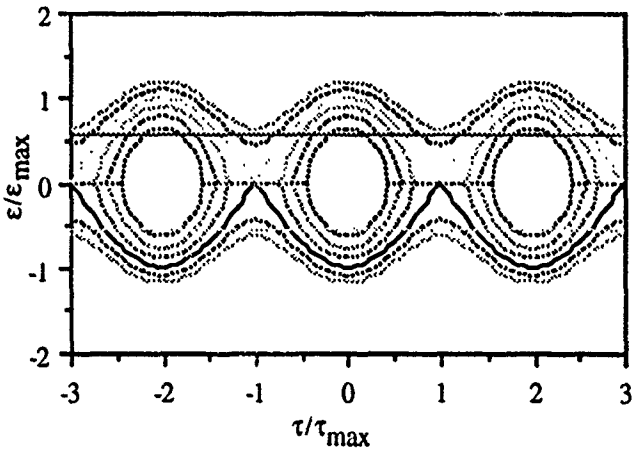


Figure 5: RF buckets for the UVX ring at 100 MeV and with 600 kV peak RF voltage. We have τ_{max}= 1 ns and ε_{max}= 5.4 %. The two horizontal lines indicate ε= ±3 %. The separatrix is shown in solid line.

4. REFERENCES

[1] L. Lin, L. Jahnel and P. Tavares, "A Magnet Lattice for the LNLS Soft X-Ray Source", in 1990 EPAC.

[2] A. R. D. Rodrigues and D. Wisnivesky, "Commissioning of the LNLS Injector Linac", in 1990 EPAC.

[3] E. M. Rowe, "Synchrotron Light Source Experiments: Bringing Aladdin on Line", NIM B24/25 (1987) p 414-416.

[4] "Collective Effects in the LNLS Soft X-Ray Source", LNLS internal report.

[5] Liu Lin, L. Jahnel, P. Tavares and R. H. A. Farias, "The Transport Line from MAIRA to the LNLS UVX Electron Storage Ring", these proceedings.

The Transport Line from MAIRA to the LNLS UVX Electron Storage Ring

Liu Lin, L.Jahnel, P.Tavares and R.H.A.Farias
LNLS - Laboratório Nacional de Luz Síncrotron
Cx. Postal 6192 - Campinas - SP - Brazil

Abstract

The magnet lattice of the transport line from the 100 MeV linear accelerator (MAIRA) to the LNLS UVX electron storage ring is described. Two operation modes of the transport line to match the phase ellipse parameters for the matched and mismatched injection modes are calculated. Orbit distortion and correction have also been simulated.

I. INTRODUCTION

The electron beam from the linear accelerator MAIRA[1] is transported by an underground transfer line - MU - and is brought into the LNLS UVX[2] storage ring by a 14° horizontal thick septum magnet and a 2.9° horizontal thin septum magnet.

The linac building is outside the ring building and the linac centre is 1.2 m above the ground, whereas the UVX beam centre is 20 cm higher. In order to keep the experimental hall free, the beam is transfered through a tunnel 4 meters under the ring.

The proposed line is composed of a quadrupole triplet after MAIRA, an achromatic system to transfer the beam to underground level, a FODO section, one horizontal achromatic system to rotate the line 90° anticlockwise, a quadrupole triplet, another achromatic system to bring the beam up to the storage ring level, a quadrupole doublet and finally another horizontal achromatic system to match the phase ellipse parameters of the beam to the injection parameters. See fig. 1.

Two operation modes, for the matched injection and the mismatched injection[3], are presented.

II. BEAM DIMENSIONS

The maximum values of the optical function in MU were determined to ensure a good transmission of the beam. The following parameters were used to calculate the transmission efficiency:

- Diameter of the vacuum chamber: 36 mm
- linac r.m.s. emittance, $\varepsilon_L = 6.7 \times 10^{-7}$ rad.m.
- r.m.s. energy dispersion, $\Delta p/p = 2\%$.

The r.m.s. beam envelope is given by:

$$\sigma = \sqrt{\beta\varepsilon_L + \eta^2(\frac{\Delta p}{p})^2}$$

The first term is the emittance contribution and the second is the dispersion contribution to the envelope σ.

A maximum of 35 m for the β functions in both planes and of 60 cm for the dispersion functions guarantees the transmission of 3 standard deviations of the beam, the limitation being in the dispersive regions of the lattice. This corresponds to about 85% transmission efficiency.

III. MAGNET LATTICE

MU matches the phase ellipse parameters at the end of MAIRA and at the injection point of UVX for two injection modes. Table 1 gives some parameters of the line.

Table 1: Main parameters of MU

	Matched	Mismatched
Length (m)	86.592	
# of dipoles	11	
# of quadrupoles	34	
# of septa	2	
Horizontal phase advance (2π)	3.000	3.864
Vertical phase advance (2π)	3.213	3.875

The β-functions for the two operation modes (matched and mismatched injection) are shown in figures 1 and 2. Figure 3 shows the dispersion function (for x and y direction), for both modes.

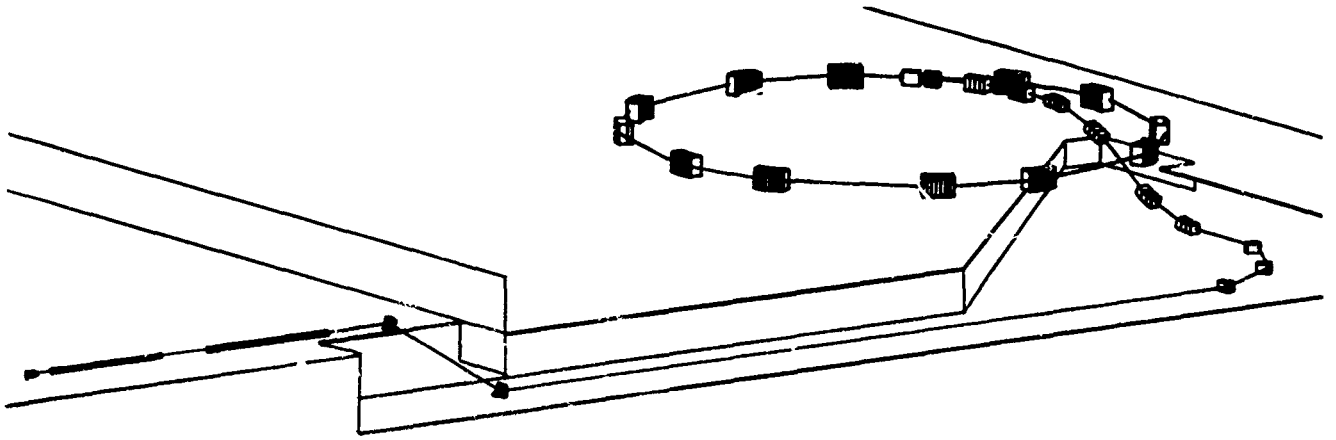


Figure 1. Layout of the transport line - MU .

0-7803-0135-8/91S01.00 ©IEEE

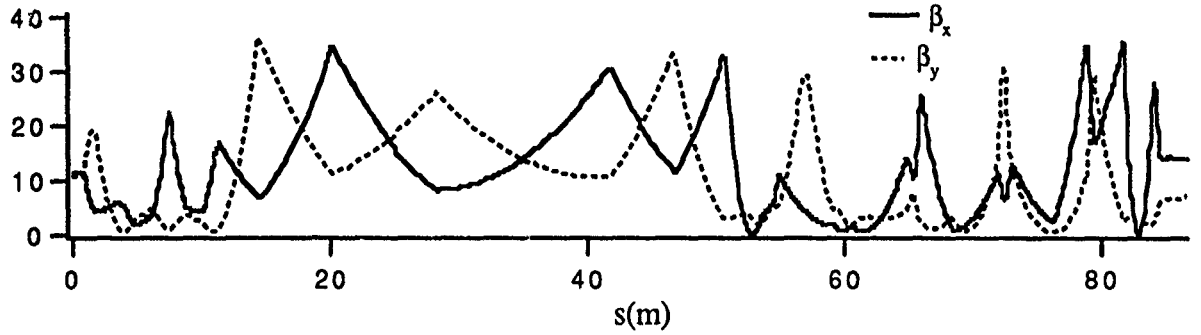


Figure 2. β-Functions for MU in the matched injection mode

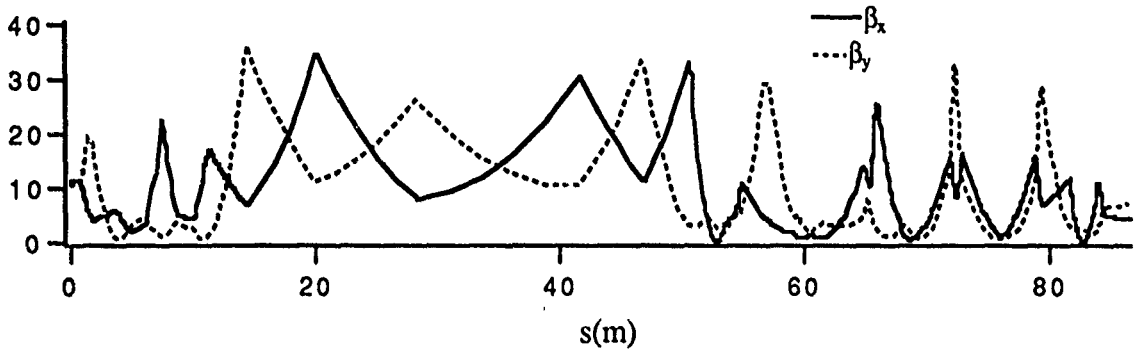


Figure 3. β-Functions for MU in the mismatched injection mode

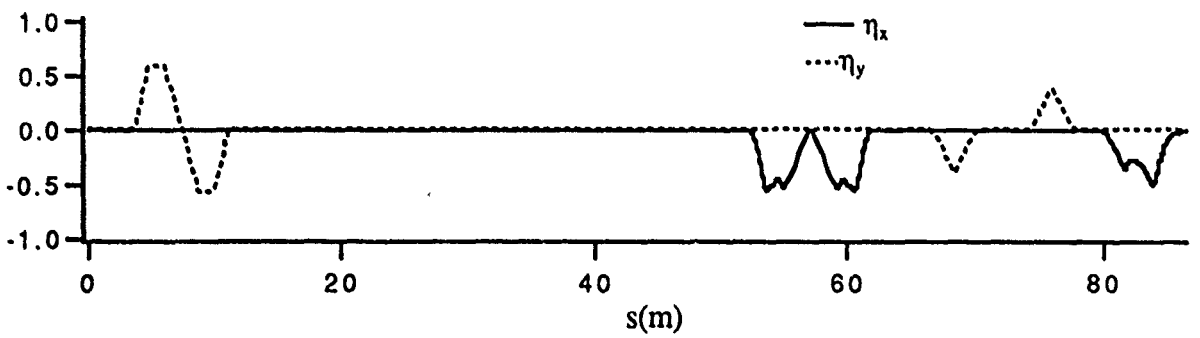


Figure 4. $\eta_{x,y}$-Functions for MU in the matched and mismatched injection modes

IV. ORBIT DISTORTION AND CORRECTION

We have simulated orbit distortion in MU to determine the number and distribution of monitors and correctors, as well as the necessary strengths of these elements. The simulation was done for the matched injection mode.

The correction scheme is straightforward: the orbit displacement is corrected exactly at the monitor position by a steering dipole (corrector) upstream of it. The horizontal and vertical planes are independent for correction elements.

Care has been taken to position the elements for the best sensitivity. The monitor controlling a corrector is placed approximately a quarter betatron wavelength downstream. All correctors are inside the quadrupoles and dipoles. The monitors can perform both horizontal and vertical readings. We have 10 horizontal correctors, 12 vertical ones and 17 position monitors.

Alignment errors and relative field errors are assumed to follow random Gaussian distribution truncated at two standard deviations. One standard deviation of the errors distribution in all dipoles and quadrupoles are given in table 2.

Table 2: Alignment and strength random errors (one standard deviation) in magnetic elements.

Alignment errors		$\frac{\Delta S}{S}$
$\sigma_x = \sigma_y$	σ_α	
0.2 mm	0.02°	0.02%
0.2 mm	0.02°	0.02%

The correction of orbit distortion uses a new procedure that was developed for transport lines[4]. The basic idea is to use a transformation matrix that can represent the motion from s=0 to s including the distorted central orbit. Considering the uncoupled case, the vector (x,x',1) is transported by the matrix:

$$M = \begin{pmatrix} S & C & p \\ S' & C' & p' \\ 0 & 0 & 1 \end{pmatrix},$$

where p represent a particular solution of the inhomogeneous equation of motion in presence of alignment errors.

A table of central orbit distortions, without correction, for 3 independent initial conditions is given by MAD[5]. This

table is used to obtain the matrix M between the position of all monitors and correctors and the value of the correctors is evaluated to correct exactly the orbit distortion at the monitors. This uncoupled first order matrix approach is iterated 3 times to give zero distortion at monitors within the accuracy used by MAD.

Ten different sequences of random values have been generated; for each sequence orbit correction has been simulated. A statistical analysis of the results is presented in table 3. Note that multipole errors have not been considered.

Table 3: Maximum absolute and average value of the correctors for ten simulations

$\langle C_x \rangle$	0.07±0.67	mrad
$\lvert C_x \rvert_{max}$	1.41±0.77	mrad
$\langle C_y \rangle$	-0.01±0.51	mrad
$\lvert C_y \rvert_{max}$	1.26±0.37	mrad

Figure 5 shows the distorted and corrected orbit in horizontal and vertical planes before and after correction in MU for one of the sequence of random errors.

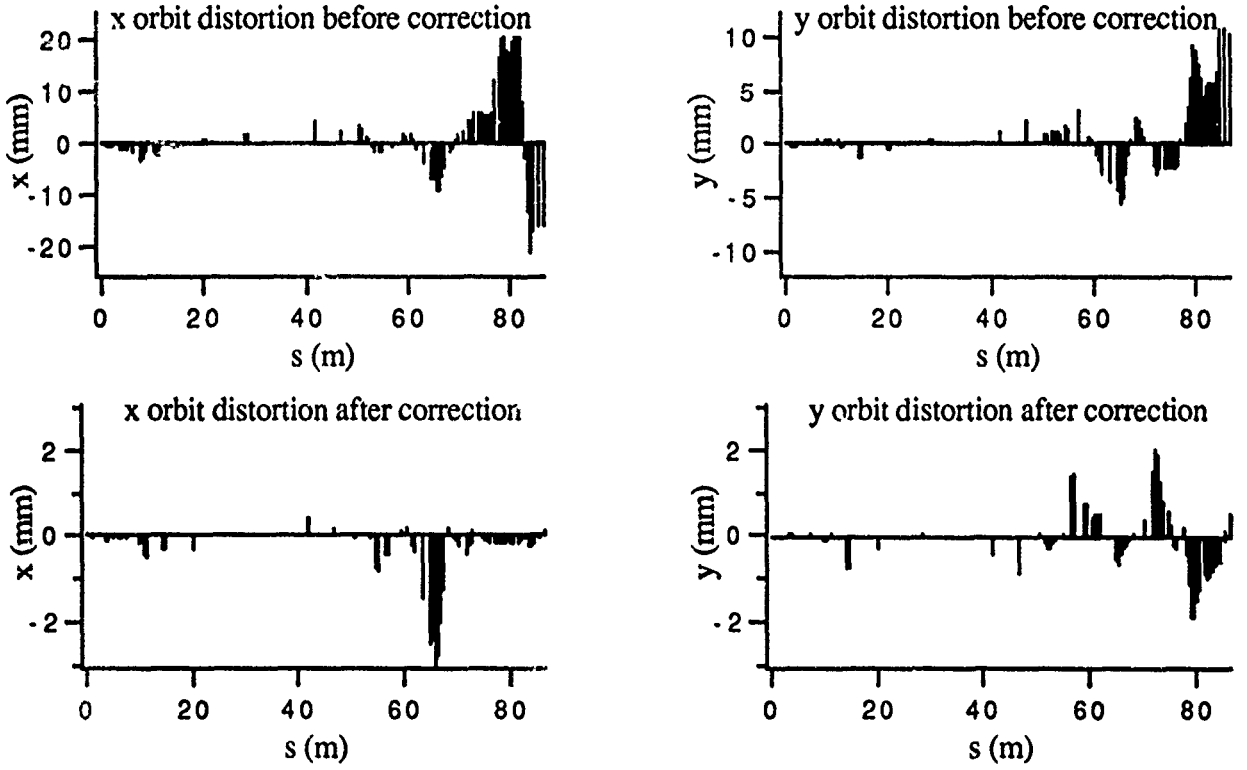


Figure 5. Distorted and corrected orbit in horizontal and vertical planes before and after correction in MU.

V. REFERENCES

[1] A. R. D. Rodrigues and D. Wisnivesky, 'Commissioning of the LNLS Injector Linac', 1990 EPAC.

[2] L. Lin, L. Jahnel and P. Tavares, 'A Magnet Lattice for the LNLS Soft X-Ray Source', 1990 EPAC.

[3] Liu Lin, 'Injection into UVX', presented at this conference.

[4] Liu Lin,'Orbit Correction in Transfer Line', to be published.

[5] F.C.Iselin and J.Niederer,'The MAD Program', CERN/LEP-TH/88-38.

An Active Interlock System for the NSLS X-Ray Ring Insertion Devices

R.J. Nawrocky, R. Biscardi, J. Dabrowski, J. Flannigan
S. Ramamoorthy, J. Rothman, J. Smith, I. So, M. Thomas
Brookhaven National Laboratory
Upton, New York 11973
and
G. Decker
Argonne National Laboratory
Argonne, IL 60439

Abstract

This paper describes the design and operation of an active interlock system which has been installed in the NSLS X-ray electron storage ring to protect the vacuum chamber from thermal damage by mis-steered high power photon beams from insertion devices (IDs). The system employs active beam position detectors to monitor beam motion in the ID straight sections and solid state logic circuitry to "dump" the stored beam in the event of a fault condition by interrupting the RF. To ensure a high degree of reliability, redundancy and continuous automatic checking has been incorporated into the design. Overall system integrity is checked periodically with beam at safe levels of beam current.

I. INTRODUCTION

The NSLS X-ray electron storage ring operates with several insertion devices (IDs) which generate high power photon beams sufficiently intense to cause severe thermal damage to the machine aluminum vacuum chamber if mis-steered. Presently, the IDs consist of two hybrid wigglers (HBW) at X-21 and X-25 and a 5 Tesla superconducting wiggler (SCW) at X-17, all located in their respective straight-sections. Power density in the X-25 HBW photon beam is of the order of 1.75 kW/mrad^2 at 250 mA. The power carried by a photon beam from an insertion device varies as $i\gamma^2K^2$, where i is the beam current, γ is the energy and K is the ID field factor. In the low beta ID straight sections, the beam may be deflected by as much as $\pm$ 8 mrad and still survive in the machine. Due to various reasons it was not possible to design the X-ray ring vacuum chamber to be safe under all possible operating conditions, however, the chamber is safe for $i < 7.0$ mA, all horizontal beam deflection angle (except in the case of the SCW) and for vertical angles $< \pm$ 2.5 mrad. Vertical deflections $> \pm$ 2.5 mrad could expose parts of the vacuum chamber to incident radiation and must be avoided.

To protect the machine chamber from damage due to mis-steered beams, an interlock system has been developed and installed in the ring. This system utilizes active beam position detectors which continuously monitor beam motion in each of the ID straight sections and logic circuitry which interrupts the RF and dumps the stored beam in the case of a fault. The time interval within which the system must respond to an out-of-range beam has been calculated for worst case to be $\approx$ 30 msec. A portion of a typical straight section vacuum chamber protected by the interlock is shown in Fig. 1.

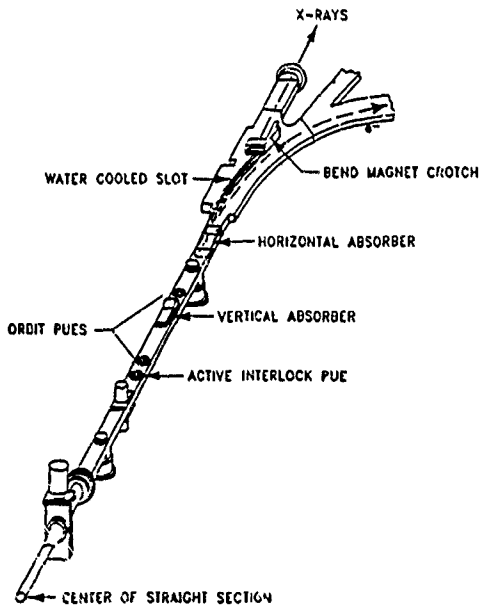


Fig. 1. Vacuum Chamber in a Straight Section

In the design of the system, various beam position monitors have been considered, including such devices as thermal and pressure sensors, radiation monitors as well as the NSLS developed RF BPMs. After careful consideration, it was decided that the BPMs would be best suited for this application.

Reliability of the interlock is ensured by using two completely redundant channels starting from the BPMs all the way through to the low-level RF switches with all components hard-wired (i.e no software links). Each redundant circuit interrupts the low-level RF drive independently. Operation of critical system components is continuously monitored in the background by dedicated micro-computers which generate warning signals to the machine operator in case of a problem. The overall system is periodically tested with beam at safe levels of beam current using one of the main NSLS control

*Work performed under the auspices of the U.S. Department of Energy.

U.S. Government work not protected by U.S. Copyright.

computers. Test software has been written to automatically generate local orbit "bumps" and move the beam at each location until a trip level is reached and the RF is pulsed off. Such tests are routinely performed prior to normal machine fills. The software checks measured values against stored data to determine whether all criteria have been satisfied and generates a "PASS/FAIL" report at the end of the test.

II. SYSTEM DESCRIPTION

A design of an NSLS interlock prototype was described in [2]. Present system realization differs from the prototype in several aspects such as circuit topology, inhibit functions, testing philosophy, etc. The design and basic operation of the system presently installed in the machine will be described by referring to the block diagram in Fig. 2. In each of the straight sections containing an ID, vertical position of the stored beam is monitored both upstream and downstream of the device at the locations of the dedicated RF PUEs. For reliability, two BPMs are connected to each PUE, one from interlock channel "A" and the other from channel "B". The output of each BPM is monitored by a window comparator in the local logic chassis (LLC). The center of the window is set to match the offset voltage of the BPM if any, and the width of the window is adjusted for the allowable range of beam displacements at the PUE. If the comparator detects an out-of-range signal, it generates a fault bit which is transmitted to the Central Logic Chassis (CLC). After receiving a fault signal, CLC sends an interrupt request to the RF Interface Chassis (RFI) which then momentarily interrupts the low level RF drive signal to all RF systems (RF1, RF2, etc.). The RF interrupt pulse must be long enough to "dump" the beam (few milliseconds) yet short enough so as not to disturb the thermal equilibrium of the RF transmitters and accelerating cavities. The presence of beam in the machine is monitored independently by two detectors (log amps) and if the beam is present at the end of the interrupt interval, all high-level RF systems are crashed by crow-barring the plate power supplies. Response time of each interlock channel has been intentionally slowed down to approximately 20 ms to avoid false trips.

Each of the local nodes as well as the central node of the system contains a dedicated micro-computer. The computer hardware consists of a Motorola VME-133 CPU, battery backed up memory, GPLS board (NSLS General Purpose Interface Board), ADC and bit I/O boards- all housed in a VME-format crate. The central node micro also services the RFI. The function of each micro is to monitor the status of latches, set control bits, perform digital filtering, perform comparison tests between redundant detectors and to generate video displays. All of the dedicated micros communicate with the main NSLS control computers via Ethernet.

The following is a description of some of the more important features of the interlock system:

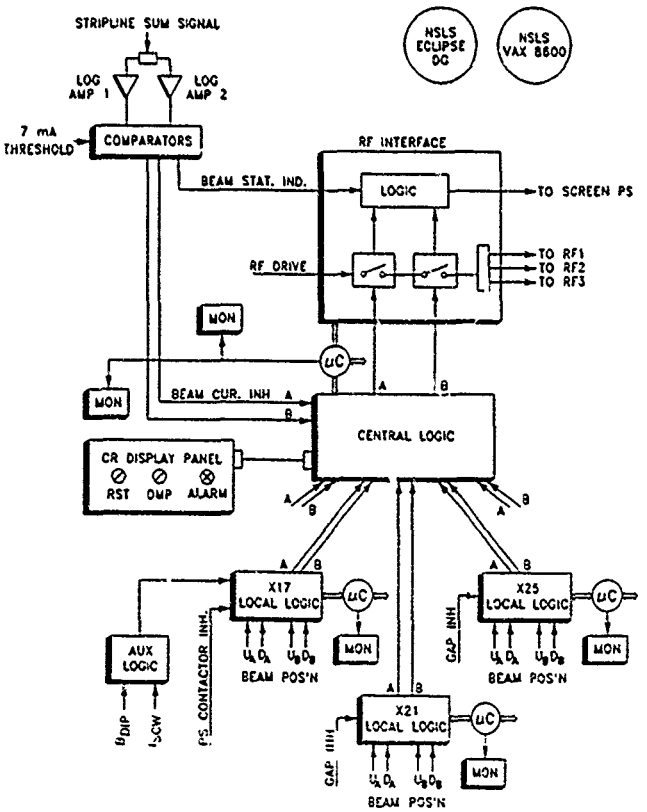


Fig. 2. System Block Diagram

First Event Latches

The LLCs and the CLC contain so-called first event latches to permit capturing of momentary window comparator fault signals. The first event latches can be made "transparent" by means of control bits which is useful in system testing.

Local and Global Inhibits

To permit testing of the individual blocks and of the overall system, local as well as global inhibits have been incorporated in the design. A local node may be automatically inhibited if either the gap of the insertion device is open or if the gap field is low. The entire system may be automatically inhibited for beam currents < 7 mA. Any of the inhibit signals may be overridden with control bits from the micro-computer to force-activate the interlock.

Fault Interrupt

Fault signals generated by comparators in the LLCs generate an interrupt to the local micro. The interrupt causes the last digitized output from each BPM prior to beam dump, which has been initiated by the interlock, to be saved in memory.

Automatic Testing

With micro-computers interfaced to the system, it is possible not only to monitor individual status bits and/or analog readbacks or to set control bits, but also to perform a whole range of automatic system tests. To ensure that all micros are alive and are performing the background comparison tests, "heartbeat" signals from the local and central micros are monitored by the LLCs and the CLC.

Status Display

The state of the interlock, status of the latches, inhibits and background faults are displayed on a display panel in the control room which is directly connected to the CLC. In addition to display lights, the panel contains two manual switches and a sonic alarm. One of the switches resets all latches (global reset) and the other dumps the beam. In addition to the display panel, a video monitor is used to display the overall status of the system including the RFI, the log amp detectors and the beam current transformer. The video display is generated by the central micro.

III. SYSTEM SOFTWARE

Software developed for the interlock system may be divided into the following three groups:

Local Micro Software (LMSoft)

LMSoft continuously monitors gap status bits, status of latches as well as the analog outputs of BPMs. It continuously compares BPM outputs in the A and B channels and generates background fault bits in case of a disagreement. This software also generates the gap inhibit override bits and the interlock branch test bits.

Central Micro Software (CMSoft)

CMSoft continuously monitors the status of the A and B latches in the CLC, status of the RFI latches, background fault and gap status from each local node as well as the analog outputs from the log amps and the ring current DCCT. It compares the analog signals and generates background faults, generates global current inhibit override and beam dump command bits and measures the time delay from beam dump command to actual beam dump.

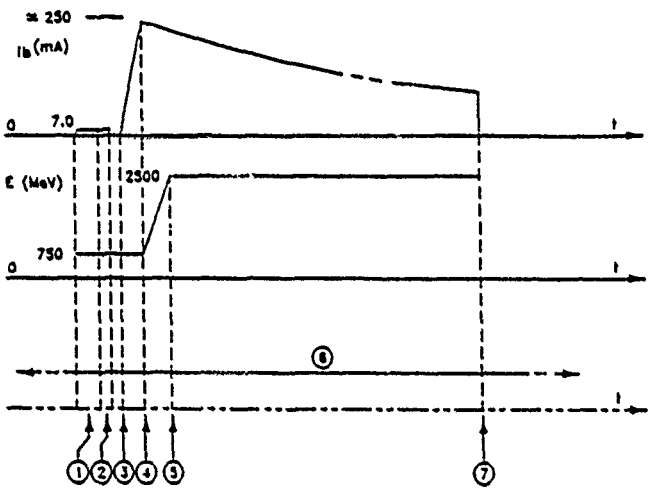
Host Computer Software (HCSoft)

HCSoft includes programs for measuring BPM output/orbit bump input transfer functions, and for measuring BPM gains and offsets. It also includes the pre-fill test programs to test the interlock system prior to each regular high current machine fill. A program is also available to generate a fault report after a beam dump.

IV. TYPICAL OPERATION

A typical operational cycle of the X-ray ring is shown in Fig. 3. As illustrated, an automatic test is performed at low current (<7mA) prior to a normal fill for operations. This "pre-fill" test checks the status of each BPM, bumps the orbit in the ID regions to test the window comparators in the LLCs with the global low-current inhibit activated, and then overrides the global inhibit to dump the beam. If the pre-fill test, having checked all the necessary criteria generates a "PASS" report, the operator proceeds with a normal fill for operations.

At all times, each of the local micros and the central micro perform comparison tests between the A and B channels and between the log amps and the ring current DCCT. A fault in any of the background tests generates a warning to the machine operator.



① LOW CURRENT PRE-FILL TEST (PARTS 1 & 2, NO BEAM DUMP)
② LOW CURRENT PRE-FILL TEST (PART 3, BEAM DUMP)
③ START OF NORMAL FILL FOR OPERATIONS
④ START OF RAMP
⑤ BEAM AVAILABLE
⑥ BACKGROUND COMPARISON TESTS
⑦ END OF FILL BEAM DUMP (COMMAND)

Fig. 3. A Typical Operational Cycle

V. ACKNOWLEDGEMENTS

The design of the system hardware and software evolved over a period of about a year with contributions from many individuals within NSLS as well as from other laboratories. Construction, installation and testing was performed by NSLS personnel, primarily by Jack Tallent.

VI. REFERENCES

[1] R. Biscardi and J. Bittner, "Switched Detector for Beam Position Monitor," *Proceedings of 1989 PAC*, IEEE Catalog No. 89CH2669-0, Vol. 3, pp. 1516-19.

[2] J. Rothman and R. Nawrocky, "Active Interlock For Storage Ring Insertion Devices," *Proceedings of 1989 PAC*, IEEE Catalog No. 89CH2669-0, pp. 266-67.

A BYPASS FOR SYNCHROTRON RADIATION EXPERIMENTS AT THE STORAGE RING PETRA II

W.Brefeld and P.Gürtler
Hamburger Synchrotronstrahlungslabor HASYLAB at DESY
Notkestrasse 85, D-2000 Hamburg 52, Germany

The electron positron collider PETRA now being reconstructed into a 14 GeV electron proton booster for HERA would be an excellent source for next generation synchrotron radiation experiments. Insertion devices in such a high energy storage ring would have unique properties in the photon energy range from 20 to 50 keV and open the possibility for new experiments above 100 keV. However, all plans have to take into account that PETRA II has primarily to be used as a booster. A bypass at PETRA II seems to be the way to use the ring also as a synchrotron radiation source without reducing the qualities of its booster functions. Results of first considerations, which lead to a bypass with two undulator beamlines, are presented.

I. INTRODUCTION

The number of synchrotron radiation users who want to do experiments with high photon energies increases steadily. Demand exists especially in the photon energy range between 20 and 50 keV and above 100 keV. Storage rings above 10 GeV like PETRA, PEP or TRISTAN are excellent tools to cover this field of synchrotron radiation research.

All these rings are originally built for high energy physics. Particularly PETRA has been reconstructed to an electron and proton booster for HERA, now named PETRA II [1]. Therefore all considerations have to take into account that the qualities of PETRA II as a booster have to be preserved, if the function is extended to a synchrotron radiation source.

Another important condition is a short time of reconstruction not disturbing the booster operations. The corresponding work has to fit into a normal shut down period. Investigations were concentrated on the modification of one of the four short straight sections of PETRA II. The section located in the northeast part is the most favorable place because of three reasons. This part is placed above ground, it has no injection or ejection elements, and the location of an experimental hall seems to create no special problems. What is the potential of such a straight section with regards to the number of suitable synchrotron radiation beamlines?

II. THE PETRA II-SR-BYPASS

For synchrotron radiation users an electron beam of 10 to 15 GeV and undulators with a length of about 5 meters would be desirable. To fulfil the magnetic field requirements for this scenario the undulator(s) have to be closed to a gap of 10 to 15 mm. However, the protons need a vacuum aperture of 30 to 40 mm. This problem can be solved either by a flexible vacuum chamber or by an electron bypass parallel to the straight section (Fig.1). The second way opens in addition the possibility for more than one photon beam and the vacuum

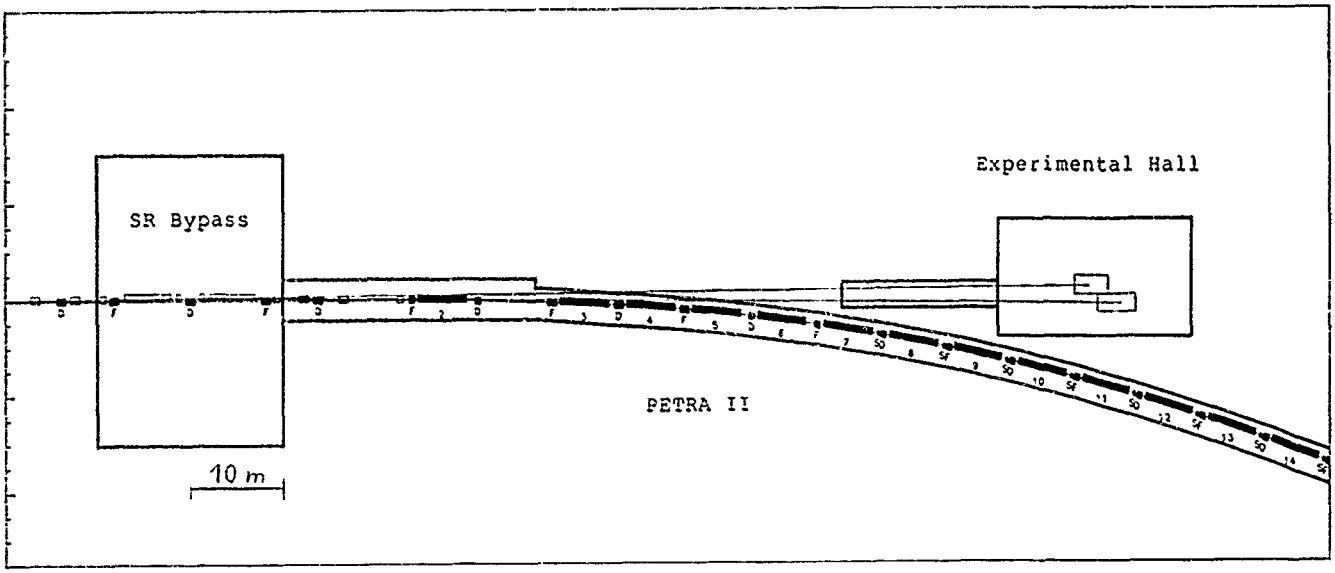


Figure 1. PETRA II with bypass, undulator beams and experimental hall.

0-7803-0135-8/91$01.00 ©IEEE

system should will be less complicated since no flexible vacuum chambers are needed.

A. Geometry

PETRA II has a harmonic number of 3840 and uses a 500 MHz RF system for the electrons. Normally a bypass has to add an integer to the harmonic number so that the particles can run on the design orbit with the same frequency. This is not possible in our case, because the bypass would become much more extended than the short straight section itself. Therefore PETRA II together with the electron bypass has to keep the harmonic number. As a consequence the RF is a little too high for the longer design orbit. A frequency increase of not more than about 5 kHz in comparison to the design frequency should cause no problems for PETRA, because the electron beam is still damped. That means a maximum additional length of the bypass of 23 mm is allowed. As PETRA II is already running at 1.7 kHz above its design frequency for electrons because of HERA reasons, an additional length of 15 mm should be the limit for a bypass design. The bypass shown in Fig. 2 has a length of 60.3 meters and increases the circumference of PETRA II by only 2.3 mm. So there are reserves for more bypasses or a different bypass design.

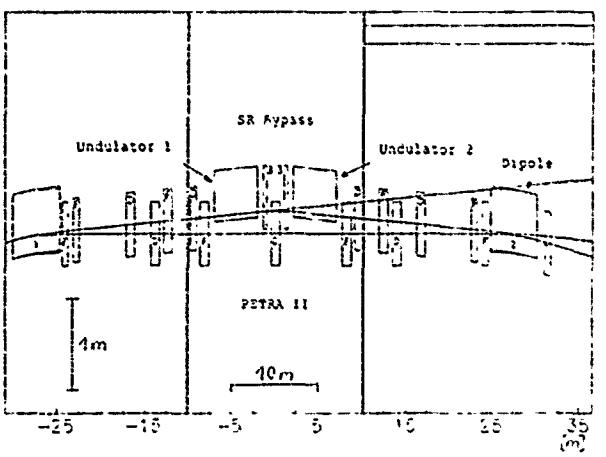


Figure 2. The PETRA II bypass for synchrotron radiation.

For the realization of this bypass two dipoles which are nearest to the former interaction point (IP) and which were needed to protect the IP from synchrotron radiation of the strong bending magnets have to be removed. To bring the electrons into the bypass 2 of the 6 windings of the first strong dipole at each end of the straight section are shunted. The reduction of field will be compensated by the field of two central bypass dipoles. By this method a maximum distance of 245 mm between ring and bypass can be achieved (Fig. 2). This seems to be enough to install two 5 m long undulators with their narrow bypass vacuum chambers next to the large chambers for the protons. However, it is not large enough to put a bypass quadrupole besides a normal ring quadrupole. Probably the concept of interleaved quadrupoles has to be used (Fig. 2).

Because of the central dipoles there is an angle of 1.87 mrad between the two undulator beams. This leads to a beam separation of nearly two meters in a distance of 100 meters, which is large enough for the installation of experiments. This number fulfils also the condition that the beams have to be separated from the storage ring by a reasonable value (Fig. 1).

B. Electron optics

The experiments which are proposed for the undulator beamlines would already take big advantage of the emittance of the existing electron booster optics, which is 79 nmrad at 13 GeV. Therefore as a first step the optical functions in the bypass were fitted to this optics. The resulting optics including the bypass has the possibility to be used as the electron booster optics as well. This would be an attractive scenario for the operation of PETRA II.

Beta and dispersion functions in the bypass are shown in Fig. 3. In the case of photon energies of several ten keV the beam divergence are dominated by the electron divergence at the source point. Therefore large beta functions in both directions were aspired. However, in the vertical direction the aperture for the electrons must remain big enough. It should be mentioned that also an optics with much smaller emittance can be achieved in PETRA II.

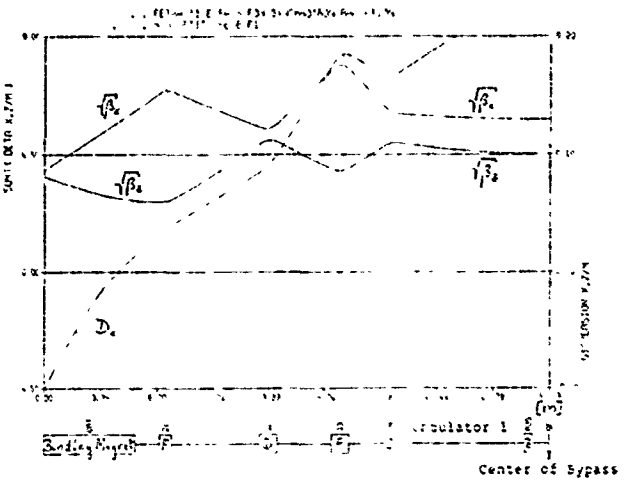


Figure 3. Optical functions of the bypass.

C. Energy and ramp procedure

Due to the 16 seven cell cavities the maximum energy of electron PETRA II is 13 GeV for 60 mA electron current. These cavities are located parallel to the proton bypass in the long straight section "South". There is room for additional cavities to obtain 14 GeV.

As long as PETRA II is running also as a proton booster no cavities can be installed outside the proton bypass region, because the proton beam would become unstable passing the electron cavities. By replacing all the normal conducting cavities by superconducting ones the electron energy could be increased up to about 18 GeV and this was already taken into consideration for the design of the synchrotron radiation bypass.

It is expected to have lifetimes of about 3 hours in electron HERA and 12 hours in proton HERA. To ramp electrons and protons in PETRA II from 7 GeV to 13 GeV and from 7 GeV to 40 GeV respectively 5 to 7 minutes are estimated. To fill the two HERA rings three booster ramp cycles of each type are needed. If HERA and PETRA II would work routinely with these numbers, a timegap of more than 2 hours could be used for a synchrotron radiation run after every ramp procedure. If HERA could be supplied with electrons using the synchrotron radiation bypass optics, only one additional electron ramp cycle would be neccessary to supply PETRA II with electrons for a synchrotron radiation run. Following this procedure PETRA II would be used most effectively.

At last one important point should be mentioned. Already at storage rings with full energy injection a photon beam position control system is very useful. For undulator beams at PETRA II such a system is absolutely neccessary, because prior to every synchrotron radiation run at least a ramp procedure or even a change of the optics has taken place.

III. UNDULATORS FOR THE BYPASS

As mentioned above, there is an increasing demand of high intensity synchrotron radiation above 20 keV. For example ultra high resolution backscattering experiments can best be done above 15 keV. Experiments in the energy range from 100 to 200 keV open new fields in solid state research. A high intensity synchrotron radiation beam of such high photon energy can only be obtained at high energy storage rings in combination with undulators.

To generate high energy photons in an undulator, a short periodic length is required and to have a sufficiently high magnetic field on orbit with such a short period a small gap is essential. On the other hand, large beta functions are needed to have a well collimated beam. With the beta functions choosen, a magnetic gap of the undulator of 11 mm is possible and can technically be realized [3]. The beam divergence would be 0.053 mrad horizontal and 0.012 mrad vertical and would give a beam dimension at the experiment in 100 m distance of 12 x 2.7 mm.

A proposed undulator in hybrid technology [4] with a periodic length of 3.35 cm and a gap of 11 mm emits its first harmonic at 20 keV. By opening the gap the energy can be scanned up to 50 keV with nearly constant intensity. The third harmonic is covering the energy range from 60 to 130 keV and the fifth harmonic from 100 to 200 keV. So the whole range from 20 to 200 keV is covered by one device. The parameters of the undulator are listed in the table.

Gap height	11 mm
Periodic length	3.35 cm
Number of periods	149
Undulator parameter	1.88
Magnetic Field	0.60 Tesla

Fig. 4 shows the brightness of the PETRA II undulator in comparison with a DORIS bending magnet and a DORIS III wiggler. The gain in brightness amounts to 2 orders of magnitude between 20 and 50 keV and about 4 orders of magnitude at 150 keV. Such a synchrotron radiation source will have unique properties in this energy range and will open complete new possibilities for synchrotron radiation experiments.

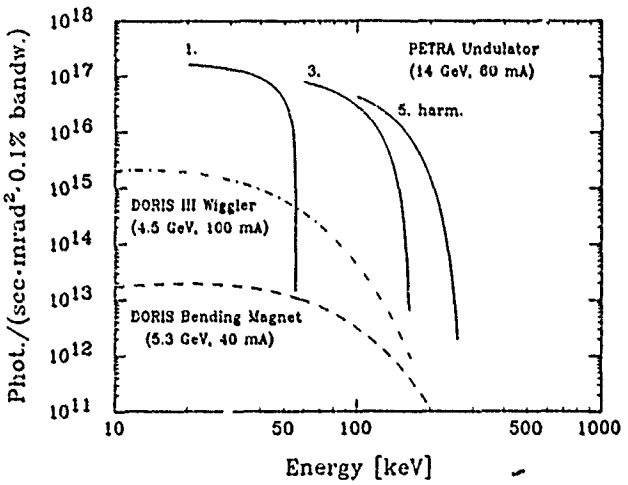


Figure 4. Central brightness of the bypass undulator.

IV. CONCLUSIONS

First considerations show that it should be possible to use PETRA II as a booster for HERA and as a synchrotron radiation source in a time sharing mode. An electron bypass with two undulators seems to be a promising tool for the realization of this scenario. Already an electron beam with the emittance of the normal booster optics will produce undulator radiation of very good quality.

IV. REFERENCES

[1] J. Rossbach, DESY HERA Report 87-06, March 1987

[2] W. Brefeld, R. Brinkmann, and J. Rossbach, 1987 Part. Acc. Conf., Washington, USA

[3] J. Pflüger and P. Gürtler, Nucl. Inst. and Meth. A287 (1990) 628

[4] K. Halbach, J. Phys. Coll. C1, Suppl. no. 2, vol. 44 (1983)

Beam Acceleration in the LBL 88-Inch Cyclotron with Injection from the AECR Source*

D.J. Clark, C.M. Lyneis and Zuqi Xie
Nuclear Science Division, Lawrence Berkeley Laboratory
1 Cyclotron Road, Berkeley, CA 94720, U.S.A.

Abstract

The new Advanced ECR (AECR) source is being developed [1] for the 88-Inch Cyclotron at Lawrence Berkeley Laboratory. It operates at 14.5 GHz, compared to 6.4 GHz for the present LBL ECR source [2]. An electron gun [3] injects electrons into the plasma chamber to increase the production of high charge state ions. The first AECR beams were injected into the cyclotron in June of 1990 and since then a variety of ion species from the AECR have been accelerated, including beams from oxygen at 32 MeV/u to bismuth at 4.6 MeV/u. A Xe^{32+} beam of 1054 MeV or 8 MeV/u was accelerated.

I. INTRODUCTION

The system used to inject beams from the ECR sources into the cyclotron is shown in Fig. 1. Either the LBL ECR or the AECR can be used to inject the cyclotron. There are several advantages of adding the AECR source. The new AECR source operates at 14.5 GHz, compared to 6.4 GHz for the LBL ECR, to take advantage of the demonstration by Geller's group in Grenoble that both higher intensities and higher charge states could be produced by operating at higher frequency. A higher charge state, Q, produces higher cyclotron energy as Q^2. Also the flexibility of the system is increased by having two sources and analyzing systems, because one source can be used for cyclotron injection while the other is used for development, maintenance or atomic physics experiments. The LBL ECR source has injected beams for regular operation since 1985. The AECR source was completed in Dec. 1989 and is now undergoing testing. This paper describes the AECR source, its high charge state beam performance with an electron gun, the injection system into the cyclotron and the acceleration of beams from the AECR through the cyclotron.

II. THE AECR SOURCE

Figure 2 illustrates the design of the AECR. A single 14.5 GHz 2.5 kW klystron supplies microwave power to the source. The independent coils make it easy to vary the axial magnetic field. An iron yoke around the coils increases the axial field at each end while the iron plates between coils 2 and 3 reduce the axial field in the center to achieve the required mirror ratio. Pumping for the plasma chamber and extraction regions is provided by a 240 l/s and a 500 l/s turbomolecular pumps, respectively. In May 1990, we developed an electron gun [3], which injects cold electrons on axis into the plasma. The electron gun is shown at the left side of Fig. 2. As shown in Table I, the AECR can produce much higher charge state ion beams than the LBL ECR, and the maximum ion currents are much higher than those from the LBL ECR for the same charge state ion beams. The best results to date were obtained with electron currents between 20 and 100 mA at bias voltages between 50 and 150 V. With the electron gun, the optimum microwave power and total extracted currents were typically 2 kW and 2 to 3 mA, respectively. The lifetime of the first LaB_6 cathode was about 600 hours. To improve the operational stability of the AECR source a new sextupole magnet is being built, with stronger field at the chamber walls.

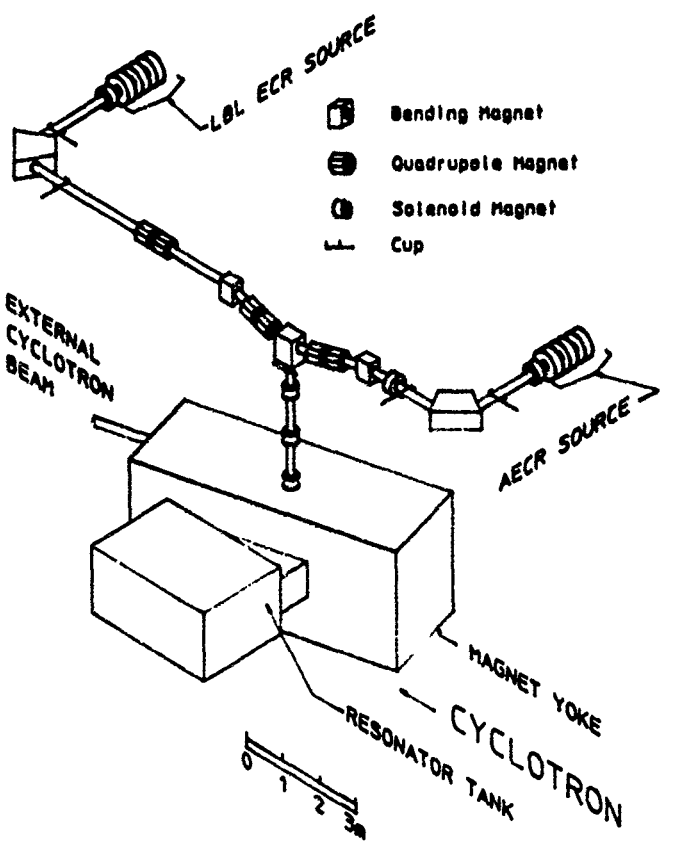


Fig. 1. Schematic view of the injection beam transport lines for the 88-Inch Cyclotron, from the LBL ECR and the AECR sources. Either of these two ion sources can inject beams into the cyclotron.

0-7803-0135-8/91$01.00 ©IEEE

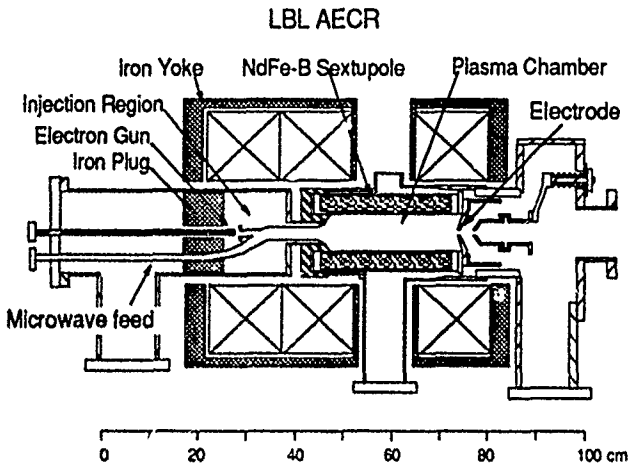


Fig. 2. Schematic drawing of the AECR. The axial magnetic field is produced by copper coils in an iron yoke. The iron plug on the injection side was added to increase the axial magnetic field. Electrons from a LaB_6 filament flow along the axial magnetic field lines into the plasma chamber.

III. THE INJECTION SYSTEM

The LBL ECR source uses 10 meters of horizontal beamline for injection, Fig. 1. The AECR is placed opposite the LBL ECR, and uses 7 meters of horizontal beam line. The two horizontal beamlines meet in a common 4 meter long vertical transport line to the cyclotron. Magnetic rather than electrostatic bending, focusing and steering elements were chosen because of better space charge neutralization, fewer vacuum penetrations and better long term reliability. Focusing is done with quadrupoles and Glaser lenses (magnetic solenoids with iron return yokes). Coils mounted on the beam pipe provide steering. To minimize beam steering due to the stray field of the cyclotron, nickel plated magnetic steel beam pipes were used where possible.

The AECR and LBL ECR sources use the same design for analyzing systems. A Glaser focuses the source beam at the analyzing system entrance slits. The beam is then analyzed and focused by the initial 90 degree magnet. The resolution is 1/100 in mass for full transmission, and 1/200 with narrower slit settings. The new section of horizontal beamline for the AECR, from the analyzing magnet to the vertical line, uses a Glaser and a quadrupole doublet to match the beam through the 90 degree bend into the vertical line. The sections of the beamline between the source analyzing magnets and the vertical axial injection line are commonly powered for the LBL ECR and the AECR beamlines, which not only reduces the cost but also simplifies the control system.

The vacuum system uses cryo-pumps and turbo-pumps and all metal seals. The typical beam line pressure is 5×10^{-8} Torr which is sufficiently low so that beam loss due to charge exchange with residual gas is negligible.

Table I. Comparison of ion currents in eμA from the AECR and LBL ECR sources. All measurements reported were done with a source extraction aperture of 8 mm diameter and 10 kV of beam acceleration.

ION	AECR with E. Gun	LBL ECR
O^{6+}	475	90
O^{7+}	131	20
O^{8+}	~13	~0.95
Ar^{11+}	141	18
Ar^{13+}	34	7
Ar^{16+}	1.4	0.03
Kr^{19+}	36*	2
Kr^{22+}	10*	0.1
Kr^{25+}	2.2*	
Kr^{28+}	0.25*	
Xe^{24+}	30*	2
Xe^{27+}	12*	0.3
Xe^{31+}	1*	
Bi^{28+}	6	2.5
Bi^{31+}	4.5	0.56
Bi^{34+}	1.5	0.05
Bi^{38+}	0.2	

* Isotopically enriched gas used.

Beam diagnostics along the injection beam line consist of fixed four jaw collimators with beam readouts before each set of lenses, where the beam is large. Beam current can be read on several Faraday cups along the line.

A gridded buncher is placed 2.1 m above the cyclotron midplane. At the cyclotron center the beam from the injection system is bent through 90 degrees by a gridded electrostatic mirror with a transmission of 90%. Beam current can be read on the mirror with the voltage off, a useful diagnostic for low level beams.

In our non-scaling mode of operation the requirement for beam centering is that the dee voltage should be approximately 5 times the injection voltage. The usual operating values are 10 kV for the injection voltage and 50 kV for the dee voltage. The advantage of operating in this non-scaling mode is that the dee voltage can be operated near its maximum for all beams, giving the minimum number of particle turns and thus high center region acceptance and low beam loss due to stripping during acceleration. Also, keeping the injection voltage high reduces the emittance in the transport line to increase transmission.

IV. PERFORMANCE OF THE 88-INCH CYCLOTRON WITH THE AECR

The cyclotron accelerates protons to 55 MeV, ions with Q/A = 1/2 to 32.5 MeV/u, and heavier beams to E/A = K Q^2/A^2, where the maximum K = 140. The transmission from source to external beam has been typically 3-20% with the LBL ECR source. The loss of beam due to charge exchange during acceleration ranges from 10% for highly stripped light ions to over 50% for heavy ions such as xenon.

With the higher charge state ion beams produced by the AECR, the performance of the 88-Inch Cyclotron has been greatly enhanced. The AECR source can inject beams of higher intensity and higher charge state than those available with the LBL ECR source. Table II shows the ion beams injected from the AECR and accelerated by the 88-Inch Cyclotron. The "BS" column indicates the first beam stop for external beam. A wide variety of ions at high charge states has been accelerated, including Ar^{16+}, Kr^{25+}, Xe^{32+} and Bi^{38+}. The low temperature oven was used for bismuth production.

These high charge state ions have a large electron pick-up cross-section at the low energy region in the center of the cyclotron. Although the pressure is $1\text{-}2\times10^{-6}$ torr near the vacuum tank outer wall, it is higher in the center region and there is still significant beam loss during acceleration for these beams. For the xenon beams of Table II the beam loss is a factor of 2-5, for pressures in the above range. For the bismuth beams the loss is a factor of 5-40. So a better vacuum is very important for higher transmission of these beams.

The injection efficiency has been similar to that with the LBL ECR, with about 10% transmission from source to external beam for typical first harmonic beams. The 160 MeV oxygen beam of Table II is a typical high intensity beam, with 6 μA on the beam stop. The maximum K of 140 was used for most of the beams to study the performance at maximum energy. The beams use first harmonic acceleration, except for those below 6 MeV/u, which use third harmonic. Fig. 3 shows the best performance of the cyclotron with the AECR and the performance with the LBL ECR.

A useful technique for rapid charge state and energy variation [4] has been used for runs with both the LBL ECR and AECR sources. The charge state from the source is changed, and the injection voltage is also changed to keep it proportional to charge state, so the injection line magnet settings are unchanged. The cyclotron K is constant, which eliminates the settling time of the main magnet. This technique was useful for changing charge states of the high charge state beams in Table II.

Table II. AECR Beams Accelerated by the 88-Inch Cyclotron.

Ion	Charge State	K	E (MeV)	E/A (MeV/u)	BS (nA)
^{16}O	6	71	160	10	6200
^{16}O	8	130	520	32	200
^{20}Ne	10	130	650	32	90
^{40}Ar	14	140	686	17	320
^{40}Ar	16	140	896	22	30
^{86}Kr	23	140	861	10	60
^{86}Kr	25	140	1017	12	8
^{136}Xe	29	140	865	6.4	30
^{136}Xe	30	140	926	6.8	20
^{136}Xe	31	140	990	7.3	8
^{136}Xe	32	140	1054	7.8	3
^{209}Bi	35	138	809	3.9	1.4
^{209}Bi	36	138	856	4.1	1.1
^{209}Bi	37	138	904	4.3	0.3
^{209}Bi	38	138	954	4.6	0.1

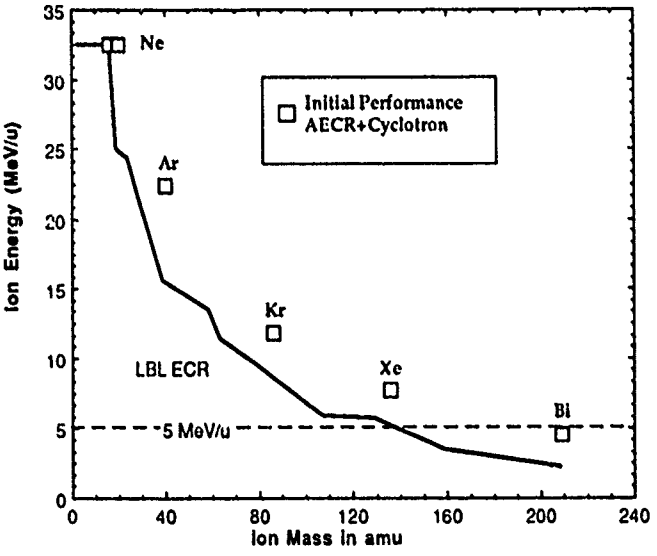


Fig. 3. The best performance of beams accelerated by the LBL ECR and the AECR sources in the 88-Inch Cyclotron.

V. REFERENCES

[1] C. M. Lyneis, Zuqi Xie, D. J. Clark, R. S. Lam and S. A. Lundgren, Proc. 10th Int'l Workshop on ECR Ion Sources, Knoxville, Tenn., Nov. 1990.

[2] D. J. Clark and C. M. Lyneis, Proc. 12th Int'l Conf. on Cyclotrons and Their Applications, Berlin, FRG, May 1989, LBL-26401.

[3] Zuqi Xie, C. M. Lyneis, R. S. Lam and S. A. Lundgren, Rev. Sci. Instr. 62 (3), Mar. 1991.

[4] D. J. Clark and G. J. Wozniak, Nucl. Instr. & Meth., A295 (1990) p.34.

*This work was supported by the Director, Office of Energy Research, Division of Nuclear Physics of the Office of High Energy and Nuclear Physics of the U.S. Department of Energy under Contract DE- AC03-76SF00098.

RECENT IMPROVEMENTS AND NEW POSSIBILITIES OF THE GANIL FACILITY

M. BAJARD and GANIL Group

GANIL - B.P. 5027 - F-14021 Caen Cedex

Abstract

The results of the machine improvements recently achieved : ECR source, new injector[1], and medium energy output are presented . The measured characteristics of all the recently accelerated beams are summarized, featuring results obtained with metallic ions : ^{40}Ca, ^{48}Ca, ^{58}Ni, ^{64}Zn, ^{157}Gd, ^{238}U. Specific beams can be tuned : very short bunch length, parallel beam for channeling experiments, special beam line focusing for secondary particles. Finally, new developments are mentioned : axial injection at 100 kV, high intensity secondary beam production and new operational facilities are described.

I. INTRODUCTION

The GANIL (Grand Accélérateur National d'Ions Lourds) is beeing operated at Caen since 1983. This national facility is widely opened to the International Nuclear Physics Community.

The accelerating system provides the physicists with ion beams from carbon (E_{max} = 100 MeV/u) up to uranium (E_{max} = 25 MeV/u) . The intensity varies from 1.5×10^{12} p.p.s for carbon to 7×10^{8} p.p.s for uranium (see below).

In conjonction with the upgrading of the accelerator, much efforts have been put in the design and the construction of major experimental set-ups: two Spectrometers SPEG and LISEIII and several 4 π detectors for neutrons, gammas and charged particles (ORION, TAPS, NAUTILUS, INDRA)(figure 1).

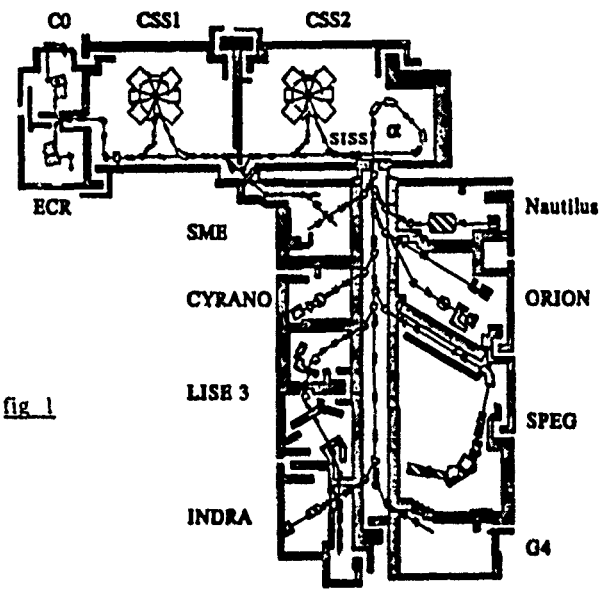


fig 1

II. RECENT IMPROVEMENTS

After the O.A.E. modification (Opération Augmentation d'Energie)[2] energy and intensity have been increased.

ION/M	Charge state before and after stripping	RF Frequency (MHz)	Maximum energy (MeV per nucleon)	Maximum intensity on target (6) (measured)			Beam characteristics (measured)	
				pps x 10^{11}	enA	± ΔW/W half height (10^{-3})	Bunch timing half height ns	Intensity enA
O 16	4/8	13.45	95	15.6	2000			
(1)O 18	4/8	12.2	76	16.4	2100	0.64	0.2	6
Ne 20	3/10	9.893	48	21.87	3500	0.32		
(1)Ar 36	10/18	13.45	95	2.8	800		0.3	10
Ar 40	7/17	11.77	70	3.67	1000	0.79	0.5	340
Ca 40	6/19	10.1347	50.4	1	300			
(2)Ca 48	8/19	11	60.3	2.78	800		0.3	360
Ni 58	10/26	11.651	68.5	1.92	800		< 1	180
(5)Ni 64	10/26	11.061	61	0.72	300			
(4)Zn 64	11/29	12.42	79	0.2	100		< 0.8	10
(3)Kr 84	14/33	11	60	2.8	1500	0.59	0.6	900
(1)Kr 86	14/34	11	60	1.10	600			
(2)Xe 129	18/44	9.52	44	1.09	800	0.90	0.2	18
(2)Xe 132	18/45	9.649	45.4	0.61	440	0.6		
(4)Gd 155	19/47	8.672	36.1	0.05	40	0.5		
(4)Gd 157	19/47	8.562	35.1	0.03	25	0.5		
(4)Ta 181	23/57	9.055	39.5	0.044	40	0.64	1.4	40
(4)Pb 208	23/56	7.82	29	0.049	45	0.61	< 1.9	30
(4)U 238	24/59	7.13	24	0.0068	6.4		< 1.7	5

(1) enriched 99% ; (2) enriched 70% ; (3) enriched 90% ; (4) natural ; (5) enriched 50% ; (6) for light ion beams, the intensity is voluntarily reduced according to the radiation level

Table 1

0-7803-0135-8/91$01.00 ©IEEE

Table 1 shows the ion beams and their characteristics accelerated up to April 1st, 1991 with the source called ECR3 (CAPRICE IIB). For light ion beams, the intensity is voluntarily reduced according to the radiation level and allowed beam power (400 watts).

The beam time devoted to the heavy and specially heavy metallic elements occupies the main part of the total beam time (64%).

1. *Medium-energy beam facility* (S.M.E.)[3]

An unused charge state of the beam stripped between SSC1 and SSC2 can be directed into a new experiment room dedicated to atomic and solid state physics.

In 1990 approximately 1400 hours of beam have been delivered consisting of :
$^{16}O^{7+}$, $^{16}O^{8+}$, $^{36}Ar^{17+}$, $^{40}Ar^{14+}$, $^{40}Ca^{18+}$, $^{48}Ca^{18+}$, $^{58\text{-}64}Ni^{25+}$, $^{64}Zn^{27+}$, $^{84\text{-}86}Kr^{32+}$, $^{129\text{-}132}Xe^{42+}$, $^{208}Pb^{53+}$.
energy range : 3.5 to 13.5 MeV/u
emittance : 10 π.mm.mrad in both planes
number of experiments : 38

2. *New radiation safety control system*

A new control system called UGSII (Unité de Gestion des Sécurités) which is more flexible and more evolutive than the old one has been installed and is working satisfactorily since February 1990. The system is VME processed.

3. *Mass measurements with the GANIL cyclotrons*[4]

An original method of mass measurements using the GANIL cyclotrons as an Accelerator-Mass Spectrometer System was suggested in order to reach a higher level of resolution. The main idea is to make use of the specific features of the GANIL cyclotron SSC2 to extend the time of flight. Secondary nuclei are produced by nuclear reactions between SSC1 and SSC2 and reaccelerated in SSC2.

4. *Time structure of the beam*[5]

A new method is being developed to reduce the length of the pulses. It consists in tuning SSC2 as a rebuncher, by increasing the magnetic field over the last 50 turns, with one or two trim-coils.

Due to the drift to the experimental room, the longitudinal emittance ellipsoid rotates and reaches its minimum phase length (chromatic width) when arriving in the room(the drawback of this method is of course an increase of the energy dispersion, the total area of the longitudinal emittance ellipsoid remaining constant). For example, the pulse length decreases from 400 ps (FWHM) in the spectrometer (see fig 1) to 215 ps in LISE, that is a 60 m drift length.

Evidence of the stability of such a tuning was established but a reproducible procedure has to be developed by calculation of the parameters taking into account the room where the beam is sent.

5. *Pencil beam*

A pencil beam with low divergence and cross section can be obtained by reducing emittance (0.05 π..m.mrad in both planes). The intensity can be also reduced to a few p.p.s by closing energy spread slits. The beam diameter is less than 0.5 mm on target.

6. *Acceleration of uranium ions*

$^{238}U^{25/58+}$ was accelerated at 24 MeV/u for the first time before OAE. The beam characteristics are presented below.

ECR3 source (CAPRICE IIB)	Material UO_2 Gas : neon
Intensity before analysis in axial injection	2.6 eμA U^{25+}
Energy before SSC1	3.72 MeV/u
Charge state in SSC2	58
Carbon stripper	150 μg/cm^2
Intensity before SSC2	8.5 x 10^8 p.p.s
Half bunch length	less than 1.7 ns

7. *Parallel beam for channeling*

GANIL is an unique tool to carry channeling experiments. Beams with a diameter of 3 mm and a divergence smaller than 0.1 mrad can be delivered. Channeling is directly observed by a decrease of nuclear reaction production when the beam is aligned with one of the crystal axes. In addition, two new objectives were recently reached using calibrated Al foils to strip the initial beam and/or to slow it down. These foils were placed before the emittance slits and the alpha spectrometer ; with a 3.x 10^{10} p.p.s incoming Xe beam, 3.x 10^5 p.p.s of Xe^{52+} are available, and the energy is varied from 42 MeV/u to 32 MeV/u by 0.4 MeV/u steps. Only half an hour is needed to change the energy and to reproduce the channeling conditions by an automatic procedure.

8. *Secondary beam production*

A 4.x 10^5 p.p.s , 70 MeV/u ^{14}O beam has been produced by fragmentation of 95 MeV/u, 1.5 x 10^{12} p.p.s ^{16}O ions traversing a 3.6 mm thick ^{12}C target.

The composition of the beam selected within the acceptance of the nigh resolution spectrometer was : ^{17}F - 12% ; ^{16}O - 25%, ^{15}O - 25% ; ^{14}O - 9% ; ^{14}N - 4%, ; ^{13}N - 3% ; C, Be, B - 21%.

During that experiment the primary beam power has been voluntarily limited to 400 W for the safety of the accelerator components.

III. NEW PROJECTS

In the near future four major improvements will be achieved in order to get a considerable increase of the intensity.

1. *New high intensity injection system*[6]

In order to increase the beam intensities for metallic and heavy ions delivered by the GANIL injectors, a new injection system has been designed. It consists of a new 14.5 GHz ECR source installed on a 100 kV platform. Injector C01 has also been modified. The ECR source is working now and the completion of this system is planned for July 1991.

2. *O.A.I operation* (Opération Augmentation d'Intensité)

The goal of this operation is to adapt all the accelerator components (vacuum chambers, septa, beam diagnostics, ...) to a beam power of about 5 to 10 kW.

3. *SISSI project*[7]

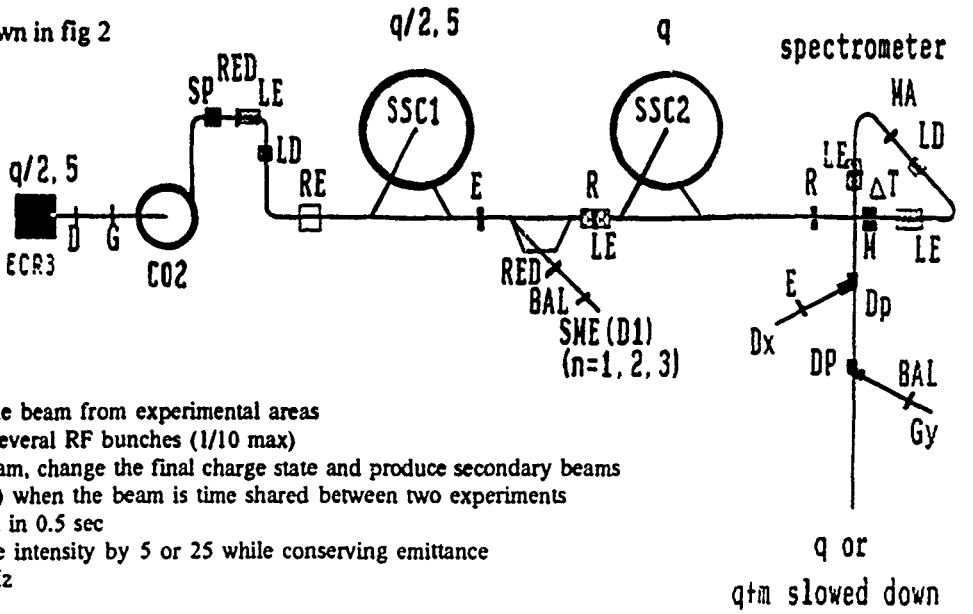
The objective of this project is to increase the transmission of the secondary products by a factor of 50 with respect to the present set-up ; the main component is a pair of high magnetic field solenoids (11 T) providing a large angular acceptance (80 mrad).

4. *Computer control system renewal*[8]

This control system is being renewed to meet the increasing demands of the accelerator operation. The new system is planned to be operational by the end of 1992. It is composed of distributed powerful processors (VAX 6410, μVAX 3800) federated through Ethernet and flexible network wide database access, VME standard front-end microprocessors, enhanced color graphic tools and workstation based operator interface.

IV. OPERATIONAL FACILITIES

The operational facilities are shown in fig 2



q : charge state
G : buncher
RE : rebuncher
E : stripper
MA : periodic beam stop

D : beam chopper to stop periodically the beam from experimental areas
SP : bunch suppressor to select one or several RF bunches (1/10 max)
R : energy degrader to slow down the beam, change the final charge state and produce secondary beams
M : intensity modulator (ratio up to 100) when the beam is time shared between two experiments
DP : pulsed dipole to establish the beam in 0.5 sec
RED : intensity reduction grid to reduce intensity by 5 or 25 while conserving emittance
BAL : beam sweeping from 4 Hz to 7 kHz
LD : energy spread limitation
LE : emittance limitation (down to 0.05 π.mm.mrad in both plans H and V)
Δt : time structure measurement

SME : medium energy beam facility with two beam lines in room D1 at SSC1 energy

fig 2

V. CONCLUSION

The number of additions, modifications and improvements shows that GANIL is in the process of a constant upgrade enlarging the field of physics which can be investigated with a cyclotron facility.

VI. REFERENCES

[1] M.P. Bourgarel, E. Baron et al "Modifications of the GANIL Injectors" 12th Int Conf. on Cycl. and their Applications , Berlin, 1989
[2] J. Fermé "Project OAE at GANIL", 11th Int. Conf. on Cycl. and their Applications, Tokyo, 1986
[3] R. Beck and SME Group, "Medium Energy Beam Facility at GANIL", 12th Int. Conf. on Cycl. and their Applications, Berlin, 1989
[4] G. Auger et al, "Mass Measurements with the GANIL Cyclotrons", "Les Nouvelles du GANIL n° 37", March 1991
[5] M.H. Moscatello to be published
[6] Ch. Ricaud and GANIL Group, S. Chel and R. Vienet from CEN/Saclay, "Status of the new high intensity injection system for GANIL", 2nd European Particle Accelerator Conf., Nice, June 1990
[7] A. Joubert et al, "The SISSI project : an Intense Secondary Ion Source using Superconducting Solenoid lenses, this conference
[8] L. David, E. Lécorché, T.T. Luong, M. Ulrich, "The GANIL Computer Control System renewal", 2nd European Particle Accelerator Conference, Nice, June 1990.

SUPERCONDUCTING BOOSTER CYCLOTRON STUDIES AT GANIL.

A. Chabert, C. Bieth, P. Bricault, M. Duval, J. Fermé, A. Joubert, M.H. Moscatello, F. Ripouteau, Q.V. Truong.

GANIL - B.P. 5027 - F-14021 Caen Cedex.

Abstract : The study of a booster cyclotron SSC3 giving a maximum energy around 500 MeV/A for light ions has been performed at GANIL. SSC3 is a separated sector cyclotron using separated superconducting coils. The results concerning these studies are reported.

Introduction : The GANIL facility provides ions from C to U at maximum energies and intensities ranging from 100 MeV/A, 10^{13} pps for light ions, down to 25 MeV/A, 10^{10} pps for the heaviest ones. Among various possible developments of our laboratory, it would be very fascinating to increase the maximum energy in the 500 MeV/A range while preserving the beam intensities and still improving its qualities. A new separated sector cyclotron is the booster suited to this goal.

I. Main parameters and description of SSC3.

The mean ejection radius ($\bar{r}_{out}$ = 3m) and the RF frequency range (f = 7 - 13.36 MHz, 2nd harmonic) of SSC2 being given, it turns out that the ratio of SSC3 ejection to injection radii has to be larger than 1.8 in order to reach 500 MeV/A. We have chosen $\bar{r}_{out} = 2\ \bar{r}_{in}$ and restricted the SSC2 frequency range to 7 - 12 MHz when injecting into SSC3. The SSC3 maximum energy will then be 490 MeV/A and will be reached at $\overline{B}.r$ = 7.144 Tm for ions of Q/A = 0.5, we will also limit the maximum SSC3 rigidity to this value.

From these choices, we deduce the SSC3 energy range versus Q/A as shown on figure 1.

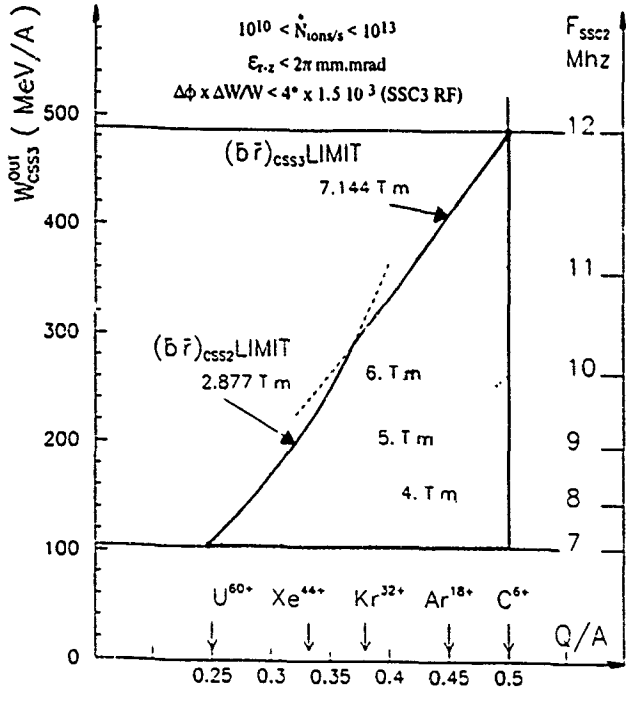
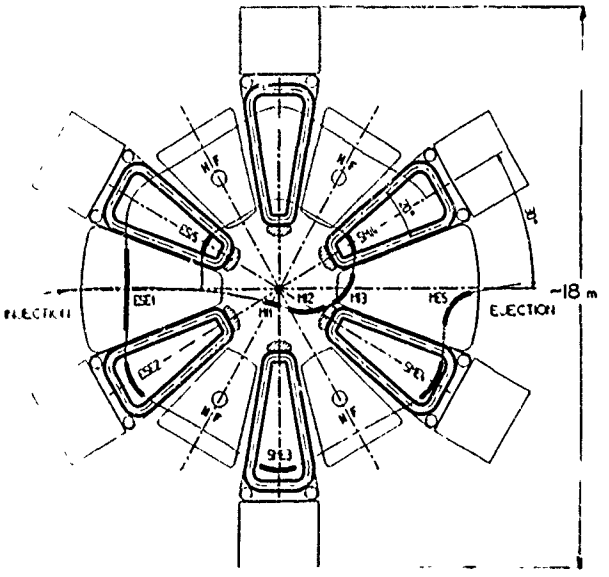


Figure 1 : SSC3 energy range versus Q/A.


~18 m
INJECTION
EJECTION
SSC1
SSC2
SSC3
HF
HF
HF

II. Magnetic structure.

Due to the large range of energy and ion species, the required field laws are very different and for the most difficult operating point, the induction in the sector between the injection and ejection radii raises by more than one Tesla. As a consequence, correction coils must provide a high field value and one peculiarity of the machine will be to work with superconducting trim coils.

A sector magnet has been designed according to the following main options as shown on figure 3 :

- room-temperature poles with a large yoke to reduce the stray-fields,
- main coil and superconducting trim coils related to one pole enclosed in the same cryostat, its vacuum tank being closed by the magnet circuit,
- direct mechanical link between the upper and lower main coils, through their cryostats,
- a separated vacuum chamber with 15 cm axial clearance to accommodate the injection and ejection elements,
- a set of warm conductors, located between the beam and the cryostat vacuum chambers to provide the necessary small adjustments of the field pattern.

A preliminary technological study of the cryogenic parts (coils and cryostat) has been performed in Saclay (Service des Techniques Instrumentales des Particules Elémentaires).

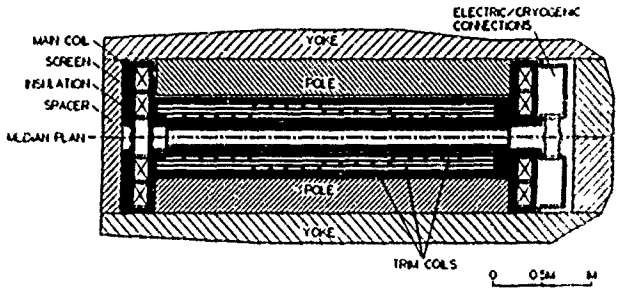


Figure 3 : Layout of the sector structure.

II.1. Main coils : We have chosen hollow conductors cooled by a forced flow of supercritical He so that a classical impregnated winding, more favourable than the bath system to hold the forces could be used. The overall maximum current density of 45 A/mm^2 is below the technological limits but was chosen for stability and protection reasons.

The magnetic forces, calculated with TOSCA, tend to make the coil circular and the strongest component integrated along the straight side reaches 12000 N as shown on figure 4.

The coil is placed inside a thick stainless steel box divided into two parts for strengthening and all along and between the straight sides of this box, a plate gives a maximum stiffness.

Computed mechanical behaviour with such a structure gives a maximum radial deformation of 3 mm. The tolerances haven't been studied yet. It will be necessary to find the field perturbations introduced by the geometrical defects and to determine their influence on the beam behaviour.

II.2 Correction coils : These coils are located inside the main coils, in three layers. In spite of a lower efficiency (smaller magnetic angle) this configuration is chosen in order to get the main coils as close as possible to the median plane.

The conductors are distributed according to the field variation law. This method is very attractive, minimizing the number of currents whose connexions require a lot of room. With only three independant currents we managed to fulfill the requested field pattern for any field level and energy. The residual corrections to be applied are small enough to be obtained with classical warm trim coils.

If necessary, a set of "nose" conductors could be added to compensate for both the negative return flux produced by the trim coils and the natural main field fall off.

Weight (iron only)	500 t
Stored energy - main coil	50 MJ
- trim coils	25 MJ
Main coil (one coil)	
Ampere turns	$< 3.10^6$ A
Max intensity	12000 A
Overall current density	< 46 A/mm^2
12 double pancakes of 2 x 10 turns (150 x 420 mm^2)	240 turns
Proposed conductor : 54 wires Cu-NbTi. Diameter 1 mm - Cu/Sc = 1.3 - around a rectangular tube 12.2 x 14.3 mm^2, cooling channel ϕ = 7 mm.	
Trim coils (one set)	
Ampere turns	6.10^5 A
Max intensity	2500 A
Overall current density	25 A/mm^2
3 layers of 10 conductors (20 x 40mm^2) each one made of 8 elementary conductors	240 turns
Proposed conductor : 14 wires (same type as for main coils) inside an Al stabilizer of 5 x 20 mm^2.	

Table 2 : Main characteristics of a sector magnet.

II.3. Field calculations : The field calculations are performed using the 3D code TOSCA. The 6 sectors are always introduced, their mutual influence being very important.

Exemples of the results are displayed on figures 4, 5, 6 which show clearly the characteristics of this magnetic structure : main field patterns, trim-coil contributions, isochronous field laws obtained. We can notice the reverse field outside the loops of the cryogenic coils and the isochronous field laws obtained which are within some tens of gauss from the theoritical ones (average field along the trajectories). This residual $\delta\overline{B}(\bar{r})$ shown on figure 7 can be reduced to the required level of some gauss using the warm trim coils.

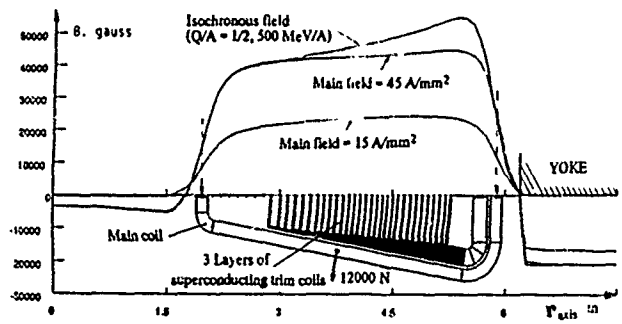


Figure 4 : Field along the sector axis and cryogenic trim coil setting on the 3 layers.

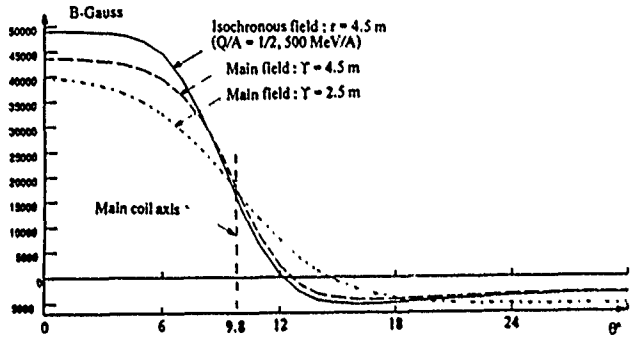


Figure 5 : Field at given radii from a sector axis to a valley axis.

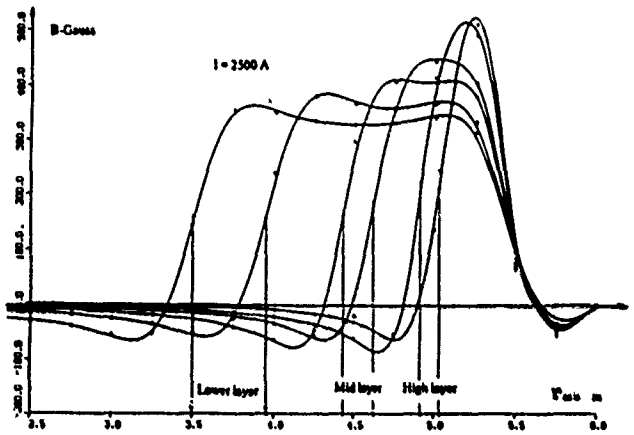


Figure 6 : Field added by a trim coil along a sector axis.

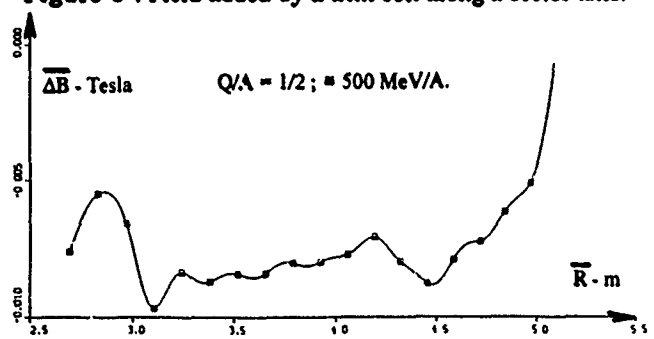


Figure 7 : Residual mean field error versus mean radius.

II.4. $\nu_r\nu_z$ curves : These curves are shown for the extreme cases on the figure 8 ; the hard edge results are also displayed for comparison. The high ν_z obtained are typical of the high flutter given by the superconducting coils : in such a geometry we can used straight poles at least up to ≈ 500 MeV/A.

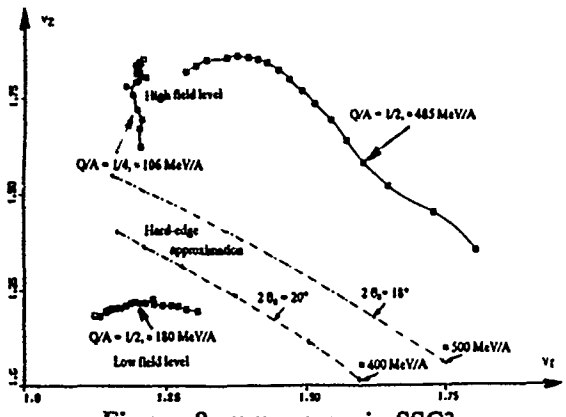


Figure 8 : $\nu_r\nu_z$ curves in SSC3.

III. Accelerating cavities.

We have chosen double gap cavities well adapted to the frequency range and able to sustain high voltages. The main tuning is provided by sliding short circuits, capacitive pannels being excluded at these voltage levels. The first calculations show no major problem to fulfill our requirements. A sketch of such a cavity is shown on figure 9.

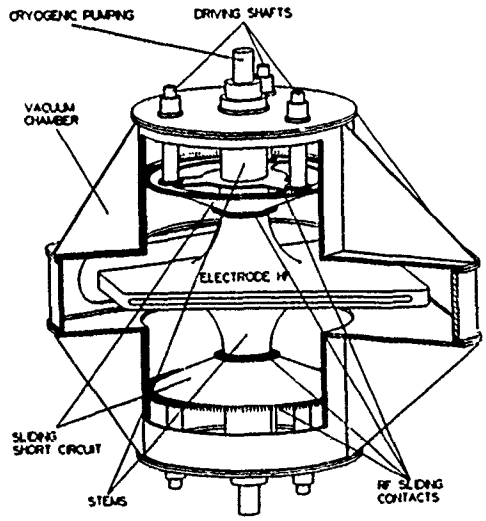


Figure 9 : Sketch of an accelerating cavity.

IV. Injection and ejection systems.

The use of 4 double gap cavities able to sustain 500kV and the large $\bar{r}_{in}$, $\bar{r}_{out}$ of the machine account for a rather large turn spacing. Nevertheless we have to use a precession effect in order to get enough turn separation for a single turn extraction.

The characteristics of the elements shown on figure 2 are given in table 3. Most of these elements must be movable (some cm), both in injection and ejection systems.

Injection	1	Superconducting Magnet	2.5 T
	2	Superconducting Magnet	2.5 T
	3	Superconducting Septum Magnet	1 T
	4	Magnetic Septum	0.25 T
	5	Electrostatic Septum	60 kV/cm
Ejection	1	Electrostatic Septum	70 kV/cm
	2	Electrostatic Septum	60 kV/cm
	3	Magnetic Septum	- 0.3 T
	4	Magnetic Septum	- 1 T
	5	Superconducting Magnet	$B\rho \leq 7.2$ Tm

Table 3 : Characteristics of injection and ejection elements.

V. Conclusion.

Our preliminary studies led us to the solution here exposed. Many detailed design questions and technological problems will have to be solved and the tolerances have to be determined. Anyway the feasibility of such a machine seems rather well established.

Developing the Chalk River Superconducting Cyclotron for Operation in π-Mode

J.A. Hulbert and X-H. Zhou[1]
AECL Research, Chalk River Laboratories
Chalk River, Ontario K0J 1J0, Canada

Abstract

The Chalk River Superconducting Cyclotron [1] operates in two rf modes. In the π-mode, the voltages on the four dees move in opposition in adjacent dees, giving rise to high rf surface currents in the cavity wall under the magnetic hills, and to vertical asymmetries in the dee excitation. Studies on a half-scale rf model of the accelerating cavity have confirmed the current distribution and the magnitude of the vertical asymmetries. Cavity cooling provided in the initial design required augmentation for π-mode operation, but the magnet cryostat prevents access to the outside of the cavity. Additional cooling has been installed with cooling lines passing through high-rf-field regions to demountable cooling plates. Concurrently, instrumentation leads have been added to provide extra diagnostics of beam trajectories entering the extraction system. The added cooling has enabled operation of the cyclotron up to 65% of design rf power at the highest π-mode frequency, permitting acceleration up to a specific energy of 50 MeV/u, close to the magnetic focussing limit of the cyclotron.

I. RF MODES

The four dees in the Chalk River Superconducting Cyclotron may be excited in two rf modes: the 0-mode, in which all four dees are in phase, and which is used to accelerate in the range of specific energies 5.2 - 21.5 MeV/u, at the fourth harmonic; and the π-mode, in which opposite dees are in phase and adjacent dees in anti-phase, and which is used at the sixth harmonic to accelerate in the range 3 - 5.2 MeV/u, and at the second harmonic to accelerate in the range 21.5 - 50 MeV/u.

II. OVERHEATING

The midplane rf cavity of the cyclotron is lined with copper sheet, which is stabilized mechanically by an external rough vacuum, to balance the internal high vacuum. Water-cooling pipes are attached to the outer surface of the copper liner, inside the rough vacuum space, according to the expected internal rf current distribution. However, for reasons of magnetic and cryogenic system space requirements, cooling pipes could not be located under the magnetic hills, either on the hill faces or at the outer wall of the midplane, except at Hill B (Figure 1) where the beam leaves the cyclotron along the extraction trajectory. Development tests of π-mode cavity operation, which were performed using a dummy supporting enclosure [2], seemed to indicate that thermal conduction along the cryostat wall would provide sufficient cooling for the areas not directly cooled. Estimates of heat load from heating rate measurements indicated a total midplane load of no more than 1% of the total cavity power. Separate tests using simulated heating on the cryostat inner wall showed the capability of each valley sector to cope with a load of 2 kW.

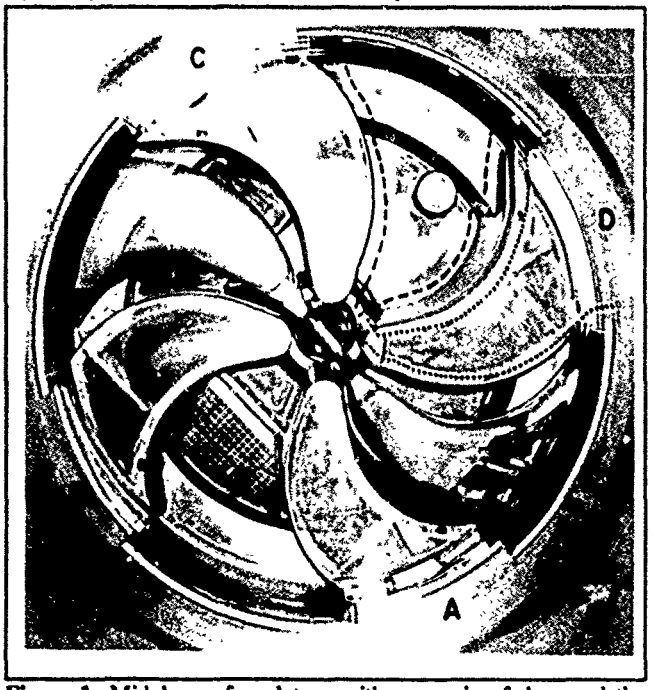


Figure 1. Midplane of cyclotron with one pair of dees and the lower pole removed. The dashed line shows the path of valley currents. The dotted line shows the current route along the hills in π-mode.

However, when the rf structure was installed in the magnet cryostat, operation in π-mode gave rise to overheating at the outer cavity wall, which threatened the integrity of midplane seals in the cryostat and the mechanical stability of the cryostat inner wall, even at an rf power level of only 15 kW.

[1] Now at HIRFL, Lanzhou, Gansu Province, Peoples' Republic of China.

0-7803-0135-8/91$01.00 ©IEEE

In 0-mode the charge on the dee-to-ground capacitance can change by a current that flows up the tuner stem and down the tuner outer conductor, across the valley floor to the midplane. To first order, the voltage on each dee pair oscillates with reference to the potential of its own valleys, with the small coupling capacitor C_c (shown in the equivalent circuit of Figure 2) maintaining the two dee pairs in phase, so that there is no current flow between top and bottom of the cavity. In

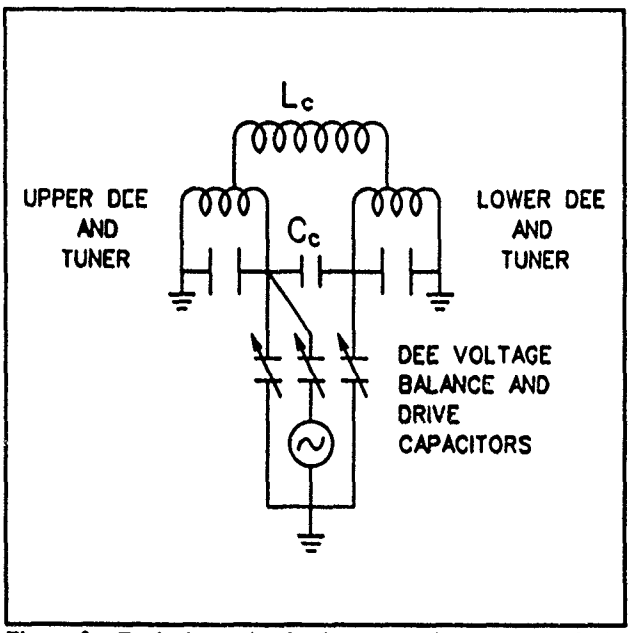


Figure 2. Equivalent circuit for 0- and π-modes of the accelerating cavity.

π-mode, charge has to flow from one dee pair to the other. The most direct path is along the edges of the hills, and down the outer cavity wall from one end of the structure to the other, represented as the inductor L_c. The current paths in the two modes are indicated in Figure 1. The cooling pipes on the outside of the cavity surface on the sides of the hills seem to provide sufficient cooling for the hill surface currents, but cooling on the cryostat wall around the valley panels was too remote from high-current areas on the vertical wall "under" the hills to be effective. The hill edge currents also coupled into the radial probe stems, causing disastrous overheating in the initial probe design, which had no effective stem cooling.

III. HALF-SCALE MODELING

A. Cavity Outer Wall Currents

A precise half-scale model of the accelerating cavity was constructed and wall currents measured to confirm the distribution of the heat sources in the outer cavity wall. Typical results of these measurements are shown in Figure 3. Using the tuner short-circuit current as a reference, valley currents near the convex dee-edge are similar in the two modes, but elsewhere, local surface current densities in π-mode can be five times higher than found anywhere in 0-

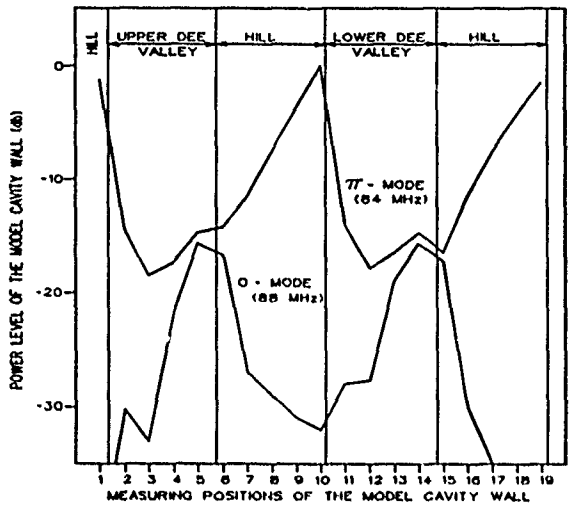


Figure 3. Loop probe measurements of cavity wall currents around the half-scale model circumference.

mode. In particular, the highest densities occur at the outer cavity wall, under the hills, and near the convex side of each hill, as indicated by thermometers inside the cryostat in the actual cyclotron. These locations are close to the radial probe ports and the hill lens #2 element of the extraction system.

B. Vertical Asymmetries in the Midplane

Measurements on the model with a capacitive probe show voltage differences, between the upper and lower edges of the dee gap at inner radii, in both 0-mode and π-mode, of as much as 20% of the mean dee voltage, caused by the vertical geometric asymmetry of the dees. In π-mode, an additional vertical voltage arises across the hill gap from the currents flowing between top and bottom of the cavity.

The resulting vertical field components in the accelerating gaps affect the beam motion, particularly at low radii. At optimum rf phase, the vertical impulses tend to be compensating, except for motion either side of the stripper foil. The effect is that the charge change causes the first turn to suffer a large vertical deflection with the motion damping in subsequent turns. This leads to a loss in injection efficiency by scraping on the vertical aperture.

IV. AUGMENTED CAVITY COOLING

The model measurements confirmed the intuitive analysis of the π-mode heating problem, but the magnet cryostat prevented access to the outside of the cavity for attaching additional cooling where indicated. A single access port to the midplane region remained unused, through the upper pole. Through this port (on the floor of the valley between hills marked "A" and "D" in Figure 1) a four-branch water

manifold was introduced. Demountable supply-and-return connectors, sealed with O-rings, were set on the manifold at valley floor level, and were shielded from rf with a grounded copper dome. Cooling lines were then run within the cavity, from the manifold, to four locations where extra cooling was most critically required. Ideally, the cooling lines would have been fastened to the cavity surface to eliminate induced rf currents, but the vulnerability of the cavity liner made this hazardous. Instead, the lines were carefully separated and positioned about 6 mm from the cavity surface, coming into contact only when they entered the midplane gap. Essential pipe-to-pipe contacts were stabilized by soldering with indium. Crossing the outer end of the hills, contact of the lines was maintained with the cavity surface. Lines passing round to the next hill sector crossed the valley at the low corner of the midplane region, well clear of the dees, and were firmly anchored at three locations. In close to 10 000 hours of rf operation there has been no sign of any rf action around these cooling lines.

The cooling was applied to silver-plated copper plates fitted with heavy contact springs, which bridged the cavity wall at the outer edges of the hills. These plates diverted the π-mode currents away from the areas where cavity wall heating had been excessive.

The four hill sectors (marked A,B,C and D in Figure 1) were treated differently in detail. Sectors C and D each contain one radial probe port. They were cooled in series by a single cooling branch having one bridge plate in each sector. The probes enter the midplane through ring-contact grounding springs. The springs were moved to the bridge plates to prevent rf currents being guided to the backs of the plates. The remounting lost the precision of the spring location, so probe guide bushings were incorporated in the spring mounts and the springs strengthened.

In sector A, two cooling streams were employed. One stream cooled the two hill lens mounting brackets, in series. The second stream was used to cool a short bridge plate, which protected instrumentation lines in the sector from rf currents. Radiofrequency heating of the hill lens was stabilised and a cooling path for the heat established, by replacing the detachable copper covers on the lenses with heavy silver plating. Further, the attachment of the lenses to their (now cooled) mounting brackets was modified, very simply, to ensure a good thermal path to the bracket. An additional benefit from this treatment was the elimination of arcing between the lenses and the hill surfaces.

Sector B, which contains the beam extraction port, had been cooled in the initial design, partly because access was possible from within the cryostat, as for the valley region cooling, but also because the wall in that sector protruded into the mid-plane. The remaining (fourth) cooling branch was therefore used to support and cool instrumentation lines to a set of beam scrapers situated round the extraction port.

The instrumentation signal lines, introduced as part of the cavity cooling modification, consisted of bundles of UT 34 semi-rigid coaxial cable encased in copper sleeves. The sleeves were thermally and electrically bonded to convenient cooling lines at intervals of 80 mm, with pure indium solder. The instrumentation lines carry signals from thermometers located on the hill lenses, and from beam scrapers at the extraction port, and at hill lens apertures. The beam scrapers have proved essential in locating and directing the accelerated beam through the extraction system.

With the added cooling at the cavity walls, hill lenses and probe ports, and with cooling added also to the electrostatic deflector electrode [3], operation of the cyclotron has been made possible in π-mode, at up to 65% of design specification power. With this capability, beams of 50 MeV/u ^{12}C, with currents up to 140 nA, have been extracted, proving the cyclotron to the maximum specific energy for the original design focussing limit specification.

V. ACKNOWLEDGEMENTS

Valuable discussions on solutions to the heating problems were contributed by C.B. Bigham and R.M. Hutcheon. Installation of the modifications was carried out with the patient assistance of R. Tremblay and R. Kelly. Radiofrequency power tests were performed by E. Stock and J.E. McGregor.

VI. REFERENCES

[1] C.B. Bigham, W.G. Davies, E.A. Heighway, J.D. Hepburn, C.R.J. Hoffmann, J.A. Hulbert, J.H. Ormrod, and H.R. Schneider, "First Operation of the Chalk River Superconducting Cyclotron," Nuclear Instrumentation and Methods, vol.A 254, pp 237 - 251, 1987.

[2] C.B. Bigham, "The Chalk River Superconducting Heavy-Ion Cyclotron RF Structure," IEEE Transactions on Nuclear Science, vol.NS-26, No.2, pp 2142 - 2145, 1979 April.

[3] W.T. Diamond, G R. Mitchel, J. Almeida and H. Schmeing, "Electrostatic Deflector Development at the Chalk River Superconducting Cyclotron," see Paper HTP 30 at this conference.

The COSY-Jülich Project April 1991 Status

R.Maier, U.Pfister and J.Range for the COSY-Team
Forschungszentrum Jülich GmbH.
Postfach 1913, D-5170 Jülich, Germany

Abstract

The cooler synchrotron COSY-Jülich, a synchrotron and storage ring for protons and light ions is at present being built in the Forschungszentrum Jülich GmbH (KFA). The facility will deliver protons in the momentum range from 270 to 3300 MeV/c. To increase the space density electron and stochastic cooling will be applied for experiments with internal and after slow extraction for external targets. The facility consists of different ion sources, the cyclotron JULIC as injector, the injection beamline with a length of 100 m, the ring with a circumference of 184 m and the extraction beamlines to the external experiments.

I. Introduction

The COSY ring consists of two 180 degree bending arcs and two straight sections. The two arcs are composed of six mechanically identical periods. Each of the mirror symmetric half cells is given a QF-bend-QD-bend structure leading two a six fold symmetry of the total magnetic lattice. By interchanging the focusing and defocusing properties additional flexibility for adjusting the tune is given. The momentum dispersion in the straights can be set to zero with the supersymmetry two. The straights are acting as 1:1 telescopes with a phase advance either π or 2 π. Bridged by four optical triplets each they provide free space for the RF stations, for phase space cooling devices and for internal target areas. The main machine and beam parameters are shown in table I, the layout of the total facility in figure 1.

Two cooling systems will be installed, the electron cooler being foreseen from the beginning of experimental operation. The transverse stochastic cooling system is built as a two band system with an overall bandwidth of 2 GHz [1] the bands extending from 1 two 1.7 GHz and 1.7 to 3 GHz respectively allowing cooling in the energy range of 0.8 to 2.5 GeV. The system offers a cooling rate of $7 \cdot 10^{-2}$ Hz for 10^{10} protons the lowest emittance being expected at 1 π mm mrad. It is foreseen not to cross the transition energy but to shift it slowly during ramping to energies above proton energy and decrease it after debunching prior to experiments.

The COSY control system is hierarchically organized and divided into three major layers [2]. Implementation of the control operations is made in the system layer, the work cells and the process I/O layer. The experimentators are offered to get access to the COSY databases and to use machine data for reduction of experimental data.

Table I
COSY Basic Parameters

momentum range	275-3300 MeV/c
max. no. of stored protons	$2 \cdot 10^{11}$
typical cycle	
injection	∼ 10 ms
ramp up/down	1.5 s/1.5 s
e-cooling	1-4 s
s-cooling	10-100 s
bending magnets, no./radius/ field at 3.5GeV/c	24/7 m/1.67 T
quadrupoles, no./no. of families/magnetic length/ max.grad. at 3.5GeV/c	
arc	24;6;0.29m;7.5 T/m
telescope	32;4;0.65m;7.65 T/m
focusing structure	6periods,sep.functions FoBoDoBooBoDoBoF
betatron wave no.	3.38/3.38
γ_{tr}	2.06
aperture limit hor/vert	70/27.5 mm
geom.acceptance hor/vert	130/35 π mm mrad
vacuum system pressure	10^{-10} - 10^{-11} hPa
RF system	
frequency range(h=1)	0.462 - 1.572 MHz
gap voltage (at duty cycle)	5kV(100%)/8kV(50%)

The diagnostic instrumentation will deliver measuring data of the beam intensity, the orbit deviation, the phase relationship between beam phase and RF [3]. The beam will be excited in vertical and horizontal direction by stripline units thus enabling fast measurements of the betatron tunes and evaluation of beam stability thresholds. The diagnostic devices of the beamlines in particular the transverse wire arrays as beam position and profile monitors have also been defined and partially ordered.

Acceleration of the injected particles to the required experimental energy, at maximum 2.5 GeV (per nucleon), will be achieved by the RF acceleration station. The revolution frequency changes from 460 kHz to 1.6 MHz. As the cavity will work at the first harmonic, this is also the frequency span to be covered by the acceleration system. The system is fabricated by a cooperation

0-7803-0135-8/91$01.00 ©IEEE

between the LNS SATURNE and Thomson Tubes Electronique, France.

In the first stage of development COSY will be filled with protons from the stripping reaction of H_2^+ via the injection beamline [4] from the upgraded isochronous cyclotron JULIC as injector. The beamline is designed for particles of a maximum rigidity of 2 T·m and has been ordered turn-key. Assembly of the components has just begun.

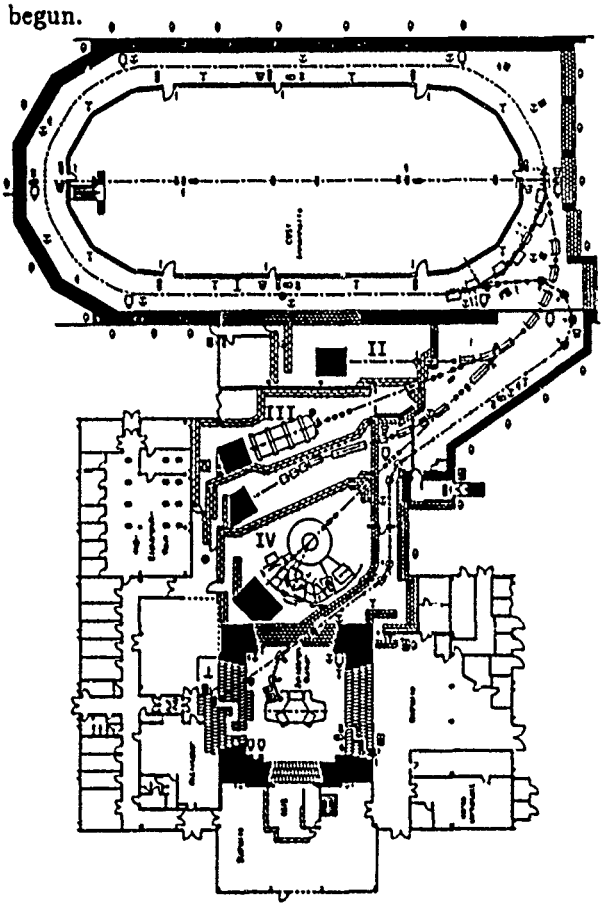


Figure 1. Layout of the COSY facility.

II. Accelerator Components

A. Magnets

All of the 25 dipole magnets of the COSY ring have been installed after measuring the field properties. As they will be fed by a single power converter in series the equality of magnetic length better than $2 \cdot 10^{-4}$ is needed for identical bending angles. Therefore precise measurements of the magnetic field have been made based on the use of long integrating coils moved stepwise on two 2D-tables along x and y axis of the magnet air gap. The integrated voltages over each step give the change of flux. The deviations of the effective lengths after adjusting with the removable endpieces were measured at a homogeneous field strength of 1 T. After the shimming procedure the excitation curves were measured. Saturation was found to appear around 1.1 T compared to the maximum field in COSY of 1.8 T. The relative deviation of bending angles at all field strengths is less than 0.2 mrad. Cycling procedures to measure hysteresis effects proved the reproducibility of the effective length within the tolerable limits. The series production of the 24 arc quadrupoles and 32 telescope cell quadrupoles has been delayed because the prototypes failed to fullfill the specifications. The prototypes from a new manufacturer are delivered in May this year. The sextupole magnets for the ring have been delivered and field measurements are running. The steering magnets are manufactured, too. Injection and extraction septum magnets are ready for testing.

B. Power Converters

Very stable power converters with a wide dynamic operation range and nominal outputs between 100 kW and several MW are required for most of the magnets in the COSY ring. The power converter feeding all 25 dipole magnets in series provides an output voltage of 1300V to produce a field slope of 1.6 T during 1.6 s particle acceleration phase. The required minimum current during injection and cooling is 235 A, the maximum current amounts to 5000 A. The stability requirement is 10^{-4} of the actual value. The converter will be tested under full load after finishing the assembly of the dipole magnets. Each of the 14 quadrupole families is fed by one power converter delivering a rated dc current of 520 A. Due to the different types of magnets the output voltages show different values of 188 V, and 270 V maximum value during acceleration. The tolerance margins during acceleration are equal to those of the dipole power converter but strongly reduced during injection and storage modes. The prototype converter has been tested successfully. The delivery of the converters in quantity has started. They will be tested under operation conditions after the delivery of the quadrupole prototypes. The power converters for the sextupole magnets, the steering magnets and of septa magnets have been ordered and partially manufactured.

C. Vacuum Components

The COSY vacuum system is specified to operate at an average pressure of 10^{-10} hPa in the ring. The total ring beampipe can be divided into 12 separate sections by vacuum valves. The assembly of the beampipe vacuum chambers of two sections has started in March this year. Prior to assembling in the ring and in the beamlines each vacuum exposed component is given to a final vacuum test run. The base pressure in the test facility is in the 10^{-12} hPa regime and the components are heated up to bakeout temperature of 300 centigrade. The ultra high vacuum test area contains also systems for the test of gauges, gas analysers, ceramic breaks and

linear motion feedthrougs. Up to now the vacuum chambers for more than 140 m length of the ring of totally 184 m were annealed and vacuum tested including the chambers for the kicker magnet and the electrostatic septum. The special chambers for H_0- and laser-diagnostics as well as the chambers at injection and extraction have been ordered. A further component in the manufacturing phase is the remote controlled multi stripper target with a 8-fold magazine. The self-controlling subsystems for the bake-out heating system and for vacuum control are just before completion including the software. These systems will be linked to the COSY main control system. Auxiliary components for the vacuum and heating system are ready for assembly.

D. Electron Cooler

The electron cooling in COSY was intended to prepare the beam prior to acceleration at proton injection energy of 40 MeV corresponding to an electron energy of 22 keV. By this a highest storable phase space density in a fast cycling operation can be achieved. The transverse emittance of the injected beam by phase space condensation is reduced down to the order of 1 π mm mrad and the momentum spread is reduced to appr. 10^{-4}. Meanwhile we succeeded in incorporating the planned second stage of extension to electron energies up to 100 keV corresponding to proton energies of 184 MeV into the first stage terminated at the beginning of experimental operation by reconstruction of gun and collector. The electron cooler has been detailed completely and ordered for machining. The active cooling length of 2 m will be built in into the 7.2 m long free section of the cooler telescope. The main magnets and coils and the main power converter are manufactured. Gun, collector, high voltage platform and transmission line for 100 kV are in the tendering phase. Field measurements in the single coils and in the assembly to adjust the correction coils are in preparation.

E. Ultra Slow Extraction

The users' requests for a low emittance beam together with the requested maximum duty cycle will be met by the method of the ultra slow extraction (USE). A third order resonance will be driven by a proper set of sextupoles to fulfil the conditions for resonance extraction. Additional sextupoles are needed for tuning chromaticity to optimal values while a cavity puts a RF noise onto the beam. This moves the particles chromatically to the extraction resonance. It is expected to extract a beam with an emittance of less than 1 π mm mrad at a momentum spread of less than $2 \cdot 10^{-4}$. The hardware is under construction following the LEAR design [5].

F. Extraction Beamlines

COSY will be used as a facility with internal and external targets. The internal targets in the ring serve mostly for high luminosity experiments in the recirculator mode. Most of the experimental proposals aim at using external targets. The beamlines to 3 external experimental areas are shown in figure 1 :
Area III serves the beam to a Time Of Flight spectrometer(TOF). Area IV will be used for the magnetic spectrometer BIG KARL, which is already existing and going to be upgraded. For the areas III and IV a beam with a minimum spot size (less than 1mm) and a high stability has been requested. Therefore these two beam lines have been designed like achromats with a demagnification of about a factor of 20. The main components for the beamlines have been ordered.

III. Summary

Approximately 85% of the components of the accelerator and storage ring COSY have been ordered or delivered. The assembly of components is in a progressive status. The cyclotron JULIC has been upgraded as injector and the injection beamline is in the assembly phase. The main components for the extraction beamlines to external target places have been ordered. For resolution of charged products with momenta $\leq$ 1.3 GeV/c the spectrometer BIG KARL will be available. Outside the present project an additional beamline for polarization experiments is under discussion and design. Start of users' operation of COSY-Jülich is aimed at April 1993.

IV. Acknowledgement

We are indebted to our colleagues from BESSY, CERN, DESY, GSI, CELSIUS, IUCF, LBL Berkeley, MPI Heidelberg, PSI, RWTH Aachen, SLAC, University of Dortmund and we wish to recognize cooperation with the CANU members.

V. References

[1] P. Brittner et al., this conference, paper KTH 14
[2] U. Hacker et al., this conference, paper KSC 8
[3] R. Maier et al., Non-Beam Disturbing Diagnostics at COSY-Jülich, Proc. EPAC 90, Nice, June 1990
[4] P. Jahn et al., Injection Beam Line, Annual Report 1990, Institute for Nuclear Physics, Forschungszentrum Jülich GmbH, p. 177
[5] S. Martin et al., this conference, paper LRA 72

ASTRID - a storage ring for ions and electrons

Søren Pape Møller
Institute for Synchrotron Radiation
University of Aarhus
DK-8000 Århus C, Denmark

Abstract

A small storage ring, ASTRID, for ions and electrons has been constructed in Aarhus. It is a dual-purpose machine, serving as a storage ring for either ions or electrons for synchrotron-radiation production. The ring has for more than one year been operational with ions and is presently being commissioned for electron storage. In the following both running modes will be described.

I. Introduction

The motivation for the storage ring ASTRID first came from the wish to store low-energy ions for laser and recombination experiments. Later it was realized that the requirements for ion operation could be fulfilled by a storage ring which also could serve as a competitive VUV/XUV synchrotron-radiation source [1]. Hence a relatively expensive piece of equipment could serve a wider user community.

II. The Facility

The storage ring with injectors and associated lab space is situated in a recently constructed laboratory in connection to the Institute of Physics, see fig. 1. The electron injector is placed in a separate well-shielded cave. There is no radiation shielding around the storage ring, and during filling of the ring with electrons, the ring hall is evacuated. When a beam is stored at high energy, researchers are allowed to reenter. Scrapers in the ring are left close to the beam to give a well-defined beam dump.

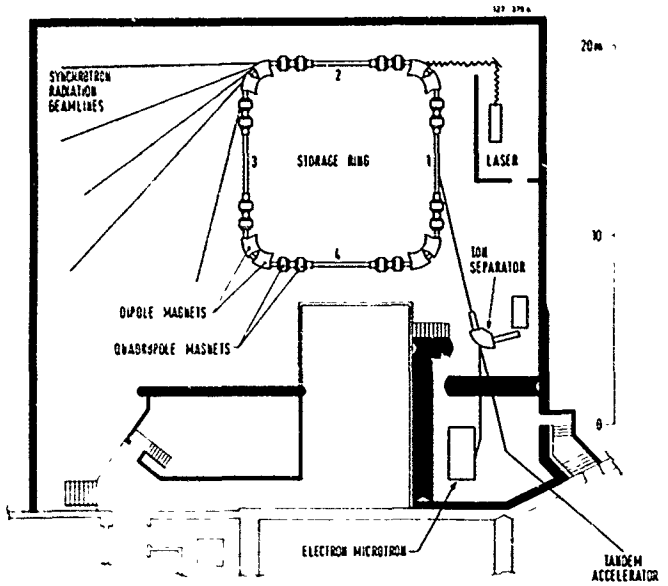


Figure 1. Layout of the ASTRID laboratory.

A. The ion injector

Ions are preaccelerated in an isotope separator using a very stable (RMS < 1 V) 200 kV high-voltage supply. A variety of ion sources can be used with the separator to produce singly-charged ions of almost any type. A sputter ion source has also been used to produce negative ions. A charge exchange cell is presently being installed after the separator magnet to increase the current of negative ions. Differential pumping is made in the injection beamline in order to separate the high-pressure ion source (10^{-2} torr) from the storage ring vacuum (10^{-12} torr).

B. The electron injector

A pulsed (10 Hz) race-track microtron [2] has been built to produce the 100 MeV electrons for the storage ring. The RF system is operating at 2998.6 MHz. The resonant energy gain is 5.3 MeV corresponding to 19 turns. Horizontal and vertical correctors are installed on every turn.

C. The storage ring

The "ring" is a square as formed by the two 45° bending magnets, excited by a common coil, in each corner. The lattice functions for ASTRID is shown in fig. 2. The quadrupoles are grouped in four families,

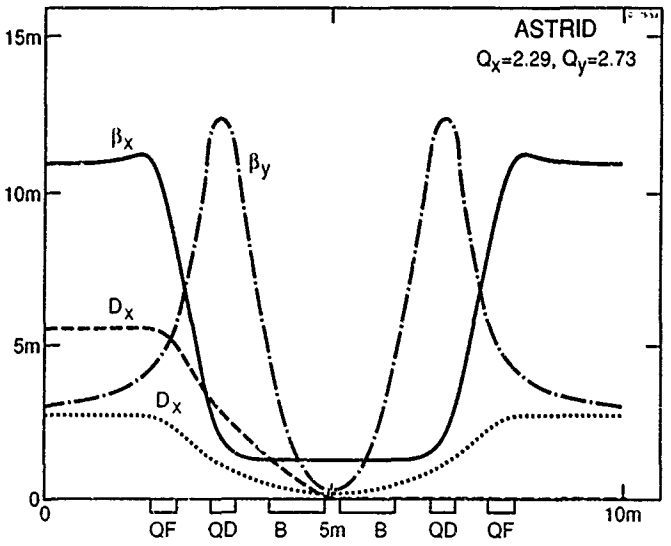


Figure 2. Lattice functions of ASTRID.

0-7803-0135-8/91$01.00 ©IEEE

so that the dispersion in two opposite straight sections can be varied continously between 0 and 6 m without change of the tunes. In fig. 2 is shown the dispersion in ASTRID with four superperiods, and with two superperiods giving two dispersion-free straight sections.

Two families of 8 sextupoles are available for chromaticity corrections. Superimposed on the air-cored sextupoles are 8 horizontal and 8 vertical

Table 1
Parameters of ASTRID

general	
Magnetic rigidity	1.87 Tm
Circumference	40 m
Hor., vert. tune	2.29, 2.73
Hor., vert. chromaticity	-3.4, -7.5
Momentum compaction	0.053
electrons	
Nominal current	200 mA
Electron energy	560 MeV
Horizontal emittance	0.17 mm mrad
Critical energy, wavelength	0.33 keV, 37 Å
Energy loss/turn	7.1 keV
Beam lifetime (Touschek)	24 hours
Number of bunches	14
RF system	105 MHz, 25 kV

correction dipoles. Furthermore 4 horizontal correctors are available as back-leg windings on the main dipoles.

The vacuum system is designed for the 10^{-12} torr region, as required for long storage times of the ions. Hence the system has been vacuum fired and is prepared for a 300° C in-situ bake-out. There is installed a total of 20 ion pumps and 24 sublimation pumps in the ring. Presently the system has only been baked to 150° C, resulting in an average pressure around 10^{-10} torr. A small leak is responsible for this pressure, and the minimum pressure in the ring is around 10^{-11} torr.

Two different RF systems are used. For the ions, a ferrite-loaded cavity operating in the 0.4-5 MHz region is available, giving a maximum voltage of 2 kV. For the electrons, a capacitively loaded coaxial TEM cavity operating at 104.9 MHz is used. This cavity was fabricated in steel, which was then copper plated. The obtained Q was around 8000.

Ions and electrons are injected with a magnetic septum (dc) and a kicker placed diametrically opposite. For the ions an electrostatic kicker excited by a square pulse injects one turn. For the electrons, a magnetic kicker excited by a half-sine pulse is used to accumulate electrons. The septum is also designed for extraction of a high-energy electron beam.

Clearing electrodes covering around half the circumference are installed in the ring to reduce ion-trapping effects.

The kicker and RF-system are the only hardware being exchanged when swapping between electron and ion operation.

A variety of diagnostics is installed, including 8 horizontal and vertical position pick-ups, scintillation screens, transverse and longitudinal Schottky pick-ups, beam-current transformer, beam scrapers and synchrotron-radiation detectors.

A control system based on a NORD main computer with PC's as consoles is used. Function generators are used for all dynamical parameters for acceleration and similar operations.

III. THE FIRST ION RUNS

Since the start up of the facility many different ions have been stored in the ring. The long physics runs

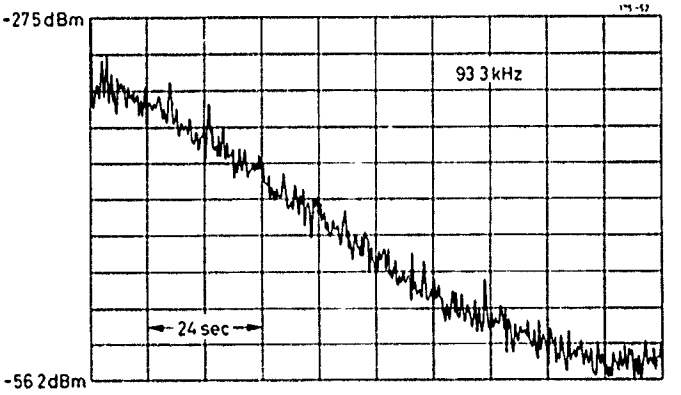


Figure 3. Decay of an $^{166}Er^{+}$ beam; the lifetime is 9 seconds.

have been with $^{7}Li^{+}$ and $^{166}Er^{+}$ for Laser-cooling experiments [3]. These ions were injected at an energy of 100 keV. The lifetime of the stored beam was limited by the vacuum, typically in the 10^{-10} torr region, giving lifetimes of some seconds. In fig. 3 is shown the decay of an Erbium beam as observed with a longitudinal Schottky pick-up electrode. Other runs included simultaneous storage of $^{20}Ne^{+}$ and $^{40}Ar^{+}$ ions. A test run with negative ions, $^{12}C^{-}$, has also been performed. The lifetime of the negative carbon beam was only around 20 msecs. owing to rest-gas stripping of the loosely bound outer electron. Stored currents were in the 1-10 μA range.

The observed closed-orbit deviations were less than 10 mm and could be corrected to less than 1 mm, limited by the position resolution, both horizontally and vertically by the correction magnets.

The ion cavity has only been used at a fixed frequency to bunch the beam for life-time measurements.

IV. THE FIRST ELECTRON RUN

The 100-MeV race-track microtron has been commissioned and routinely delivers 5-10 mA pulses of 1 μsec width. An example of an electron pulse from the microtron is shown in fig. 4. A few turns are injected into the ring and captured by the 105 MHz RF system. Around 0.3 mA has been captured in one shot, and several pulses has been accumulated to reach 1 mA. The electron beam has been accelerated to 500 MeV without significant losses. The decay of a stored

electron beam at 500 MeV is shown in fig. 5. The lifetime is around 15 hours at a pressure of 8 10^{-10} torr. Only a modest RF power (1.5 kW) was fed into the cavity during these runs. No detectable outgassing of the vacuum system was observed under these conditions.

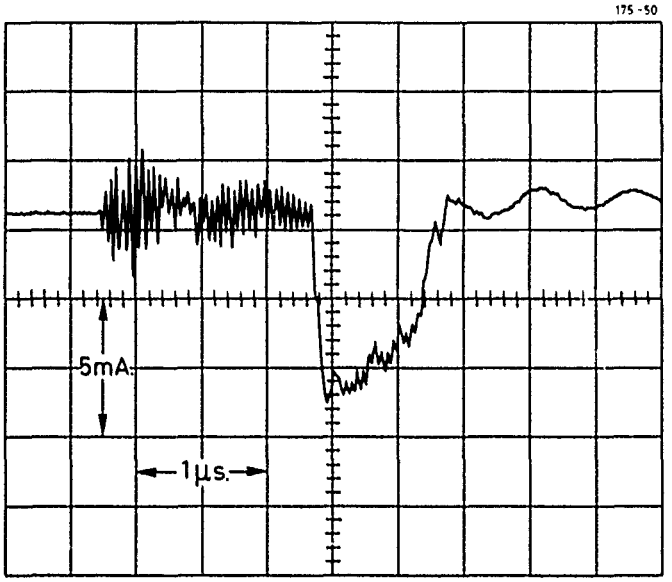


Figure 4. The microtron pulse.

V. FUTURE PLANS

The final step in the commissioning of the ion facility, namely acceleration, will be completed.

The future runs will include further $^{7}Li^{+}$ runs for laser cooling and also $^{6}Li^{+}$ for RF spectroscopy with laser detection.

Following the succesfull test run with negative ions, a sodium vapour cell is being installed after the isotope separator to produce a variety of negative ions. The first experiments with negative ions will simply consist of measuring the lifetimes of the metastable ions, which are completely unknown in most cases. A program for laser spectroscopy of H^{-} is also under development.

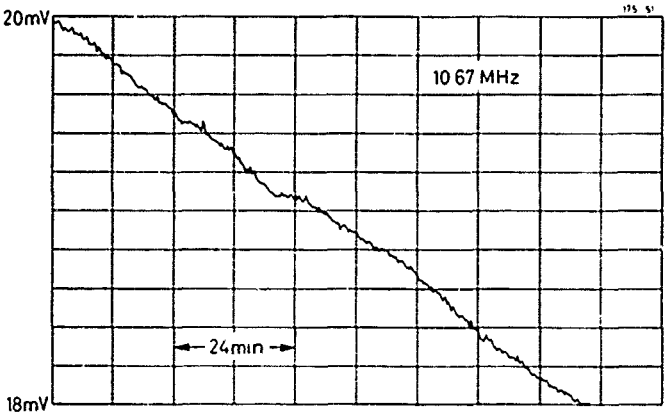


Figure 5. Decay of a stored electron beam; the lifetime is 17 hours.

Based on the first electron cooler, which has been operational at the Tandem accelerator at the Institute of Physics for several years [4] a new electron target (cooler) is being designed for the ring. The physics aim is electron recombination/detachment studies using positive/negative ions and molecules.

It is planned that the electron/ion operation will alternate approximately every six months. The next electron run will comprise commissioning of the synchrotron-radiation facility to full specifications, i.e. 200 mA electron beam at 560 MeV. Several improvements will be added to the electron facility, including full power (20kW) operation of the electron cavity and better focusing in the injection beamline. Three beamlines will then be ready, i.e. 1) an x-ray microscope, 2) an SGM monochromator operational in the 30-600 eV region for atomic physics and 3) an PGM monochromator (SX-700) for the 11-2300 eV range for surface physics.

VI. REFERENCES

[1] S.P. Møller, "ASTRID, a Storage Ring for Ions and Electrons", Proc. Eur. Part. Acc. Conf., Rome 1988, p. 112.

[2] M. Eriksson, "Race-track microtron injectors for SR-sources", Nucl. Instrum. Methods A 261 (1987) 39.

[3] J. Hangst et al., "Laser cooling of stored beams in ASTRID", these proceedings.

[4] L. H. Andersen, "State-selective dielectronic recombination measurements for He- and Li-like C and O ions", Phys. Rev. A 41 (1990) 1293.

Status of the CRYRING project

K.-G. Rensfelt for the CRYRING group
Manne Siegbahn Institute of Physics, S–104 05 Stockholm

Abstract—The status of the CRYRING project is reported. Results of the tests that began with the first beam in December 1990 are reviewed.

Introduction

This report summarizes the present status of the CRYRING project [1]. The project is centered around a synchrotron/storage ring of maximum rigidity 1.44 Tm, corresponding to an energy of 24 MeV per nucleon at a charge-to-mass ratio $q/A = 0.5$. It is mainly intended for highly charged, heavy ions produced by an electron-beam ion source (CRYSIS). Light atomic or molecular ions can also be injected from a small plasmatron source (MINIS). Ions from the ion sources are accelerated electrostatically to 10 keV per nucleon and transported to a radiofrequency-quadrupole linear accelerator (RFQ) which brings them to 300 keV per nucleon. The ions are inflected electrostatically into the ring where they are accelerated using a driven drift tube. The stored ions will be cooled by an electron cooler. Fig. 1 shows a layout of the CRYRING facility.

Ion sources

For the ring and RFQ tests performed so far the MINIS plasmatron ion source has been used. This source was originally intended for the initial tests only but will in an upgraded version also be used to run molecules and some light ions such as Li^+ for laser cooling. It will be provided with an analyzing magnet and will be made completely UHV compatible.

The CRYSIS electron-beam ion source [2], which gave the first beam to low-energy experiments in 1987, has since been continuously modified and improved. Electron-beam currents up to 250 mA have been propagated through the source. Typically currents of about 125 mA are used to produce highly charged ions up to Ar^{18+} (3×10^6 ions per pulse) and Xe^{44+}. The ion output has been stable during shifts lasting over 12 hours and changing between xenon and argon ions requires only a few hours. Recent work on the source has included a raising of the capacity of the liquid-helium system, implementation of full computer control of the source parameters, and insulation of

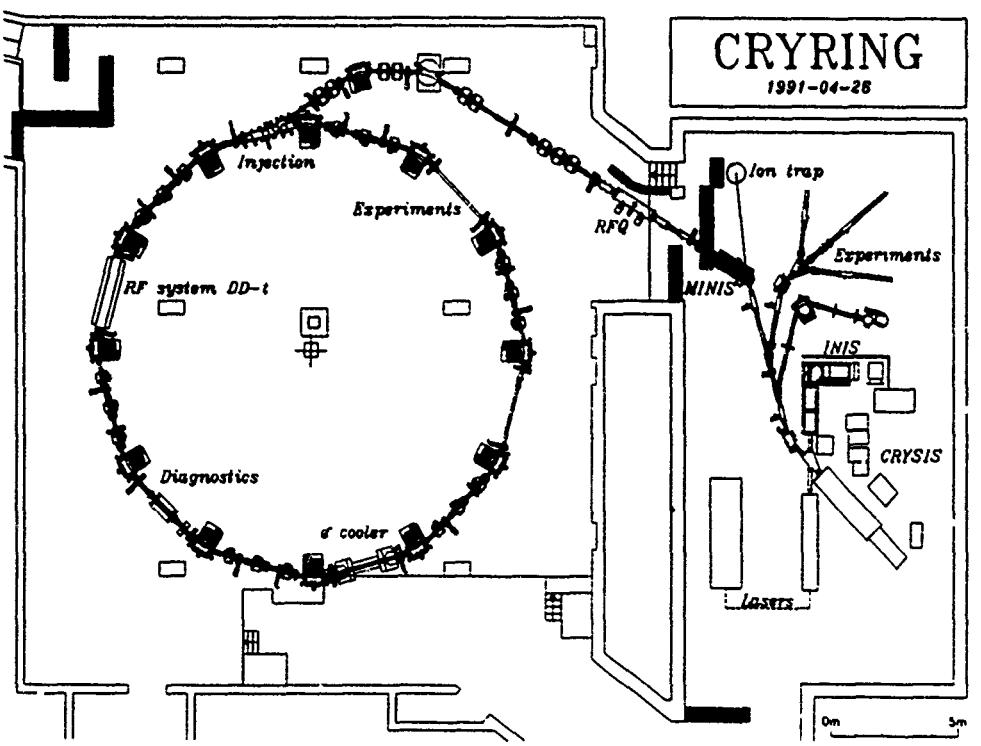


Fig. 1. Layout of the CRYRING facility.

0-7803-0135-8/91$03.00 ©IEEE

the entire source, including helium liquefier, for 50 kV as a preparation for injection of CRYSIS ions into the ring. The beamline connecting CRYSIS with the RFQ will be completed during the summer of 1991 and then tests with heavy ions in the ring will begin.

RFQ

The RFQ [3] has been used with an RF power of up to 30 kW and has successfully accelerated ions with $q/A \geq 0.33$. Due to the 30-kW limitation particles with lower q/A have not been used. The transmitter will, however, shortly be upgraded to deliver a pulsed RF power of 100 kW. Optimizing the low-energy (10 keV per nucleon) transport line to the RFQ has been difficult due to a mixture of ions in the beam from MINIS. This problem will be relieved when MINIS is rebuilt and an analyzing magnet has been installed or when CRYSIS ions are used.

Ring

The ring has so far been operated with dipole and quadrupole magnets only. Correction dipoles are ready for use but have not been needed yet—a first closed-orbit measurement at injection energy showed deviations of less than 10 mm. Sextupole magnets are mounted in the ring but their power supplies are not purchased. In the runs so far the regular working point of $Q_x = 2.30$ and $Q_y = 2.27$ has mostly been used but a higher working point with $Q_x = 3.4$ and $Q_y = 1.8$ has also been tried successfully.

The power supplies for dipole and quadrupole magnets have operated at DC currents for most of the runs but tests of the fast ramping (150 ms ramp time and 500 ms cycle time) have been performed and all data concerning stability, time response, etc. were found to lie within the specified values. The power supply for the electron cooler magnets has also been tested with a satisfactory result.

Since the injection energy from the RFQ is as low as 300 keV per nucleon the inflection of the injected ions and the closed-orbit displacement are made electrostatically [4]. The displacement is made locally, making the injection less sensitive to the choice of working point. The four pairs of plates displacing the orbit at injection are supplied by a single high-voltage supply with one positive and one negative output that is ramped from ± 30 kV to zero in 50–100 μs. This allows for a multiturn injection over about 10 turns which has been used all through the test of the ring. The fields between the plates can be adjusted by changing the distances between them using stepper motors.

The acceleration system, a driven drift tube [5], currently operates over its main frequency range (<150 kHz to 1.5 MHz) up to a peak to peak voltage of 1 kV, both at constant and ramped frequency, using a surplus test power tube. The full design voltage of 7 kV peak to peak, needed for fast acceleration of particles with low q/A, will be achieved after switching to a full-power tube already in house. To allow for bunching and acceleration of slow, low-charge ions such as molecular ions, the RF system has been designed to work at frequencies down to 10 kHz. This feature has been shown to work but is not yet fully operational.

The magnetic field in the electron cooler [6] has been measured using Hall probes for rough scans through all magnets and an electronic autocollimator for precision measurements of the straightness of the field in the cooling solenoid. Based on the results of the autocollimator measurements two sets of correction coils were made. As a result a field straightness of better than ± 0.1 mrad was achieved. The vacuum system, the gun and the collector is under manufacturing and we plan to install the cooler in the ring at the end of 1991.

The pressure in the ring is at present a few times 10^{-9} torr, maintained by twelve ion pumps with a total pumping speed of 1000 l/s. During the early autumn of 1991 60 NEG-pump modules, each one containing 2700 cm^2 NEG strips, will be installed. This is expected to reduce the pressure by about a factor of ten. The UHV system has not yet been baked although all critical components such as dipole and quadrupole chambers are fully prepared for bake-out.

Nine horizontal and nine vertical pickups are in use in the ring. The signals from these pickups can be processed either by a fast peak-detection system [7] or using synchronous rectifiers for low-bandwidth measurements. A system with flash ADCs for Q-value measurements over 128 turns is also under construction. A Schottky-noise detector consisting of four plates 135 cm long and 9 cm apart has been assembled and tested.

The first parts of the control system, controlling CRYSIS and its ion injector INIS have now been in use for two years. The different subsystems of the ring, such as beam lines, RFQ, injection, ring magnets and the acceleration have successively been connected to it. Local control of subgroups of parameters has been implemented using terminal stations with limited menues.

Results

The initial tests of the RFQ and the ring have been performed using the MINIS ion source and light ions such as H_2^+, D^+ and $^3He^+$. These beams have been accelerated through the RFQ and injected into the ring using multiturn injection over 10 turn During the first runs about 1×10^9 H_2^+ ions were stored, later that number was increased to 1×10^{10}. The D^+ current was somewhat smaller than the H_2^+ current since the ion source gives smaller amounts of atomic ions than of molecular ones. Also the transmission through the RFQ has not been fully optimized for all ions run so far.

The half-life of the H_2^+ beam was only ten milliseconds due to the large dissociation cross section at the injection energy of 300 keV per nucleon. The residual-gas pressure was around 2×10^{-9} torr. Running with D^+ the lifetime was increased and the beam has been seen for more than two seconds. In this case the lifetime is probably limited

by multiple scattering although an exact calculation is difficult due to the uncertainty in rest-gas pressure and composition.

During most of the runs the beam was bunched by an RF voltage of constant frequency and amplitude applied to the acceleration drift tube. The beam was then followed through the sum signal from one of the electrostatic position pickups. Fig. 2 shows a measurement during the injection phase with the beam of H_3^+ building up during the multiturn injection, getting bunched and decaying. Adiabatic trapping has also been used, leading to a considerable increase in the trapping efficiency. The lifetime of the beam was measured by monitoring the amplitude at the revolution frequency of the above beam signal as a function of time. Such a measurement for D^+ ions is shown in fig. 3.

The ramped operation of all parameters used during acceleration has been implemented and gradually tested. In a first step, the week before this conference, a D^+ beam was accelerated from the injection energy to 350 keV per nucleon and followed for one second at the higher energy.

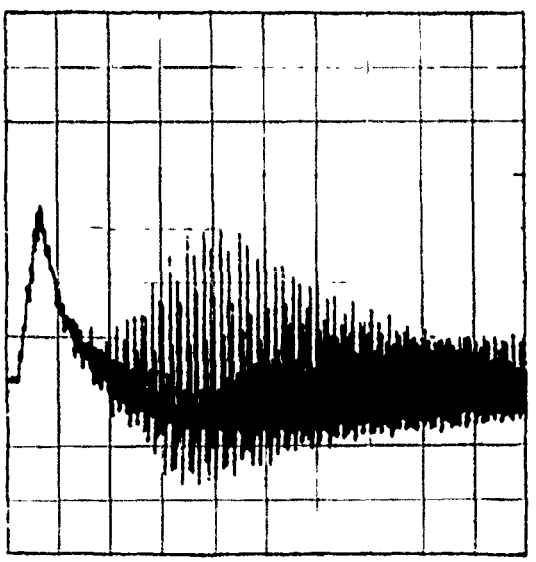


Fig. 2. Signal from H_3^+ beam. Sweep time is 1 ms.

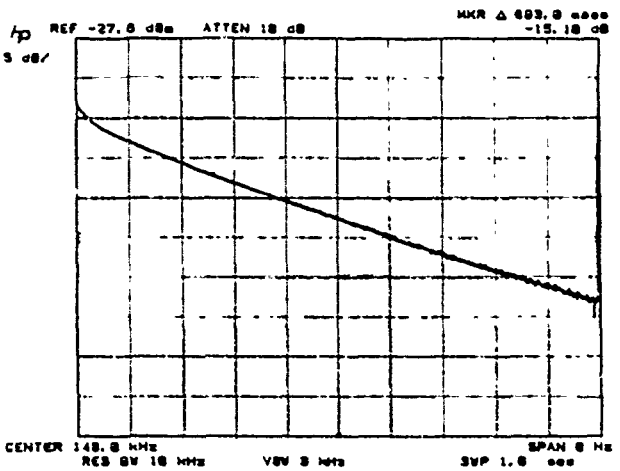


Fig. 3. Signal from D^+ beam. Sweep time is 1 s.

Experimental program

The first experimental device to be inserted into the ring will be a residual-gas-ionization detector. This system will allow the measurement of the position and profile of the stored beam through the coincident detection of recoil ions and electrons from ionization events. A resolution of better than 100 μm is expected.

After installation of the electron cooler during the autumn of 1991 experiments using the cooler as an electron target will start. These will include studies of dissociative recombination at very low relative velocities of light molecular ions such as H_3^+ or HeH^+ and x-ray spectroscopy of radiative recombination into highly charged ions. Also experiments on laser cooling of Li^+ and Be^{2+} are being prepared.

References

[1] C. J. Herrlander, K.-G. Rensfelt and J. Starker, "CRYRING—a heavy-ion synchrotron and storage ring," in *EPAC 88* Rome, June 7–11, 1988, p. 350; K.-G. Rensfelt, "Status of the CRYRING project," in *EPAC 90* Nice, June 12–16, 1990, p. 623; C. J. Herrlander, "CRYRING— a Low Energy Heavy Ion Facility", in *Cooler Rings and Their Applications*, Tokyo, November 5–8 1990, to be published.

[2] L. Liljeby and Å. Engström , "Status report on the Stockholm cryogenic electron beam ion source," in *Int. Symp. on Electron Beam Ion Sources and Their Appl.*, Upton, N.Y., 1988, p. 27.

[3] A. Schempp, H. Deitinghoff, J. Friedrich, U. Bessler, J. Madlung, G. Riehl, K. Volk, K. Langbein, A. Kipper, H. Klein, A. Källberg, A. Soltan, M. Björkhage, and C. J. Herrlander, "The CRYRING RFQ for heavy ion acceleration," in *EPAC 90* Nice, June 12–16, 1990, p. 1231.

[4] A. Simonsson, "Injection in CRYRING," in *EPAC 88* Rome, June 12–16, 1988, p. 1404.

[5] K. Abrahamsson, G. Andler, and C. B. Bigham, "A drift tube accelerating structure for CRYRING," *Nucl. Instrum. Methods*, vol. B31, p. 475, 1988.

[6] H. Danared, "The CRYRING electron cooler," in *ECOOL 90*, Legnaro, May 15–17 1990, to be published.

[7] S. Borsuk, K. Agehed, W. Klamra, and Th. Lindblad, "A peak detecting pulse height ADC system for beam diagnostic pick-up detectors in the CRYRING accelerator," *Nucl. Instrum. Methods*, vol. A284, p. 430, 1989.

Advanced Stacking Methods Using Electron Cooling at the TSR Heidelberg

M. Grieser, D. Habs, R.v. Hahn, C.M. Kleffner, R. Repnow , M. Stampfer
MPI für Kernphysik, D-6900 Heidelberg, FRG
E. Jaeschke
BESSY , D-1000 Berlin, FRG
and
M. Steck
GSI, D-6100 Darmstadt, FRG

Abstract

Using the new method of beam accumulation by stacking with electron cooling intensities were enhanced by factors of several thousands compared with single turn injection. With electron cooler stacking a current of 18 mA ($3 \cdot 10^{10}$ particles) for $^{12}C^{6+}$ ions (E = 73.3 MeV) was achieved.

Introduction

In order to accumulate heavy ions in the Heidelberg Test Storage Ring TSR [1], multiturn injection is used. With the application of multiturn injection, the horizontal machine acceptance can be filled in typically $200\mu s$. In order to inject more particles, the already filled phase space must be emptied of particles, which can be accomplished by phase space compression by electron cooling. Phase space needed for a new multiturn injection is thus made available (see fig. 1).

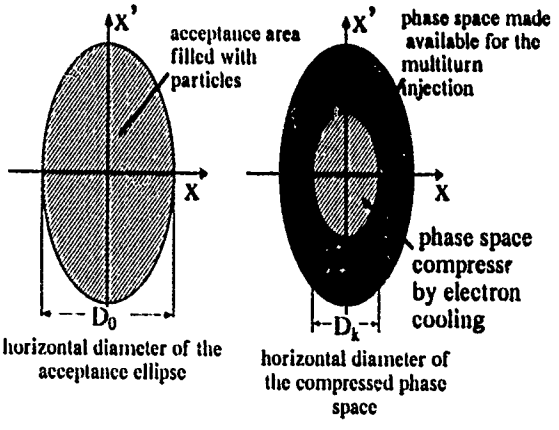


Figure 1: *Schematically the compressed phase space during multiturn injection with electron cooling and the phase space which is available for the multiturn injection is represented. D_0 gives the spatial diameter of the acceptance ellipse and D_k that of the compressed phase space.*

When this process is repeated several times, a large intensity multiplication factor is obtained. This intensity multiplication factor is defined as the ratio of the stored to the injected current. With the use of this stacking method - called ECOOL stacking hereafter - the stored intensity I increases with time as:

$$\frac{dI}{dt} = n_r I_m - \lambda I \qquad (1)$$

where n_r is the repetition rate, I_m the effectivly stored current of a multiturn injection and $1/\lambda$ is the beam lifetime. The solution of the differential equation (1) is:

$$\begin{aligned} I &= I_0(1 - e^{-\lambda t}) \\ I_0 &= n_r I_m / \lambda \end{aligned} \qquad (2)$$

The current I_m depends on the the injector current I_e with $I_m = M \cdot I_e$, where M is the intensity multiplication factor with multiturn injection. The total intensity multiplication factor $N = I_0/I_e$ is thus given by:

$$N = n_r M/\lambda \qquad (3)$$

In the following sections, parameters important for ECOOL-stacking will be discussed.

The Lifetime $1/\lambda$

In order to calculate the intensity multiplication factor N of ECOOL stacking, the beam lifetime of the ions must be known. The main processes which affect the lifetime of the ions are electron capture in the residual gas and in the electron cooler, as well as stripping reactions and single scattering. Multiple scattering does not play a role since it is compensated by electron cooling. Table 1 shows measured lifetimes. For protons a lifetime without electron cooling of 3 hours was reached whereas with electron cooling the lifetime increased to 36 hours. The cause for this increase by more than one order of magnitude is the compensation of multiple scattering. A lifetime of approximately 15 s was achieved with Li^+ and Be^+. The reason for these short lifetimes are stripping reactions in the residual gas. With increasing charge of the ions the cross sections of the capture processes increase. The main processes affecting the lifetime, for example with $^{35}Cl^{17+}$ ions, are electron capture in the residual gas and electron capture in the electron cooler.

0-7803-0135-8/91$03.00 ©IEEE

Table 1: *Measured lifetimes for cooled and uncooled ions.*

Ion	Energy [MeV]	Pressure 10^{-11} [mbar]	cooled [s]	uncooled [s]
p	21	8	130000	11000
$^{7}Li^{+}$	13	6	—	18
$^{9}Be^{+}$	7	6	16	16
$^{12}C^{5+}$	52	40	11	10
$^{12}C^{6+}$	73	6	7470	—
$^{16}O^{6+}$	54	20	16	14
$^{16}O^{8+}$	98	50	260	200
$^{28}Si^{14+}$	115	6	540	260
$^{32}S^{16+}$	196	5	450	—
$^{35}Cl^{17+}$	202	6	318	366
$^{63}Cu^{26+}$	510	6	122	—

The Intensity Multiplication Factor M

An intensity multiplication factor as large as possible is desirable with ECOOL stacking. The factor M depends on the phase space that is available for the multiturn injection (see fig.1). The spatial diameter of the electron cooler compressed phase space during multiturn injection is designated by D_k. D_0 is the maximum beam diameter which should be equal to the electron beam diameter (5 cm) at the position of the cooler. D_k is chosen using the following criterion: $D_k = D_0/2$. The filling of the phase space was investigated under this condition with a simulation program. A value for the emittance of the injected beam from the tandem- postaccelerator combination after three stripping processes of $5 \cdot \pi \cdot mm \cdot mrad$ was used in the calculations. The horizontal tune Q_x of the TSR was selected between 2.6 and 2.9. Investigations of the phase space filling were made for different tunes between 2.6 and 2.9 resulting in an average value of $M = 15$.

The Repetition Rate n_r

The repetition rate n_r for the multiturn injection depends on the time T which is necessary for the electron cooling to clear the available phase space for the multiturn injection ($n_r = 1/T$). T is the time necessary to reduce the beam cross section from D_O to D_k. In order to calculate T, the damping decrement $\lambda_\perp$ of the electron cooling is needed and defined by the following relation:

$$\frac{\mathrm{d}D}{\mathrm{d}t} = -\lambda_\perp D \qquad (4)$$

The damping decrement $\lambda_\perp$ was investigated by a Novosibirsk group [2]. They found the following semi-empirical formula for protons:

$$\lambda_\perp = \frac{12\,\pi\sqrt{\pi}\, r_e r_p \gamma n_e c^4 \eta}{\left((\alpha_0\beta_0 c)^2 + \sigma_{v\perp}^2 + 11\sigma_{v\parallel}^2\right)\sqrt{\Delta_e^2 + \sigma_{v\perp}^2 + \sigma_{v\parallel}^2}} \qquad (5)$$

$$\text{with} \qquad \Delta_e^2 = 2kT_e/m_e$$

where:

r_e	classical electron radius
r_p	classical proton radius
γ	relativistic mass increase (TSR energies, $\gamma = 1$)
n_e	electron density
η	ratio of the effective length of the electron cooling to the circumference of the storage ring
α_0	error in the alignment of the electron beam to the ion beam as well as magnetic field errors
$\beta_0 \cdot c$	particle velocity
$\sigma_{v\perp}$	transversal velocity spread of the ions
$\sigma_{v\parallel}$	longitudinal velocity spread of the ions
Δ_e	velocity spread of the electron beam
k	Boltzmann constant
m_e	electron mass
T_e	transversal electron temperature T_e is approximatly $930°C$ at the TSR.

In a theoretical description [3] of the cooling process $\lambda_\perp$ depends on the ion charge Z and mass number A as follows: $\lambda_\perp \sim Z^2/A$. This means that the cooling decrement $\lambda_\perp$ can be estimated for ions when the classical proton radius r_p is replaced by the classical ion radius r_i, with $r_i = Z^2/A \cdot r_p$. The transverse velocity spread $\sigma_{v\perp}$ of the ions in the electron cooler can be calculated approximately from the beam diameter D, the β–function in the cooler: β_{ecool} and the ion velocity $v_0 : \sigma_{v\perp} = v_0 \cdot D/(2 \cdot \beta_{ecool})$.
If one considers different bare ions with equal magnetic rigidity one finds that all ion species have the same velocity spread $\sigma_{v\perp}$ after multiturn injection. Since $A \approx 2 \cdot Z$, the cooling decrement as well as n_r scale with Z ($\lambda_\perp \sim Z, n_r \sim Z$). If the ions have a magnetic rigidity of 0.7 Tm, the electron density is $3.4 \cdot 10^{13}\ m^{-3}$ at an electron cooler perveance of $1.6\mu Perv$. With this, one obtains for $D_k = D_0/2$: $n_r \approx 0.15 \cdot Z$ Hz.

The Total Multiplication Factor N

Calculated values for the total intensity multiplication factor N are shown in curve a of figure 2 for bare ions ($A = 2 \cdot Z$) with $D_k = D_0/2$, $M = 15$, $p = 6 \cdot 10^{-11}$ mbar and $B \cdot \rho = 0.7$ Tm. For light ions one finds an intensity multiplication factor of the order of 10^5. This factor certainly cannot be reached since instabilities will occur. For example, with a $^{12}C^{6+}$ beam ($B \cdot \rho = 0.71$ Tm) instabilities were observed between 5 mA and 18 mA. N decreases continously with Z,because of the decreasing lifetime and should approach 10^4 at the atomic number $Z = 25$ ($p = 6 \cdot 10^{-11}$ mbar, $D_k = D_0/2$, $M = 15$). These intensity multiplication factors should in principle be achievable for an optimum setup of the machine parameters when no instabilities occur. A lower limit for N can be estimated if a value of $M = 1$ and the value n_r for $D_k = 0.05\ D_0$ are substituted into equation (4). Curve b of figure 2 shows the results of these calculations. N should reach a value of 10^4 for light ions and for $Z = 20$, a value of $N = 500$ at least should be obtainable.

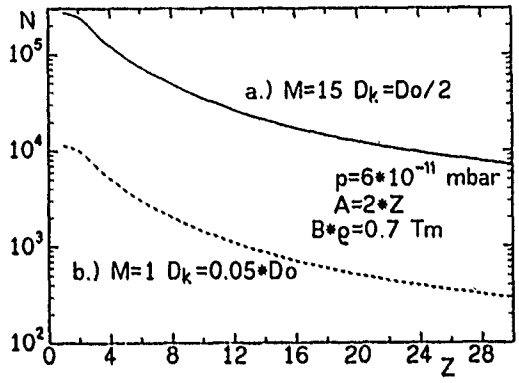


Figure 2: *a) Calculated intensity multiplication factor N with $A = 2 \cdot Z$, $M = 15$, $p = 6 \cdot 10^{-11}$ mbar $D_k = D_0/2$. b) calculated with the following parameters: $M = 1$, $p = 6 \cdot 10^{-11}$ mbar, $D_k = 0.05 \cdot D_0$.*

Experimental Results

Stacking experiments were carried out with the condition that the electron velocity was equal to the ion velocity, for example with $^{32}S^{16+}$ ($B \cdot \rho = 0.7$Tm) a factor $N \approx 4000$ was obtained. Besides the above described ECOOL stacking experiment, where the electron velocity is set equal to the ion velocity, other variations of the ECOOL stacking are used in the Heidelberg Test Storage Ring. In those experiments, the electron velocity is selected slightly lower than the ion velocity (typically $\Delta v/v = -0.5\%$).The ions will thus be pulled inwards because of the dispersion available at the injection point and the distance between the stack and the electrostatic septum (accumulated particles) will increase. Figure 3 shows a Schottky spectrum that was taken during this accumulation process. The successively injected multiturn batches are decelerated by the electron beam to the stack position. ECOOL stacking can also be

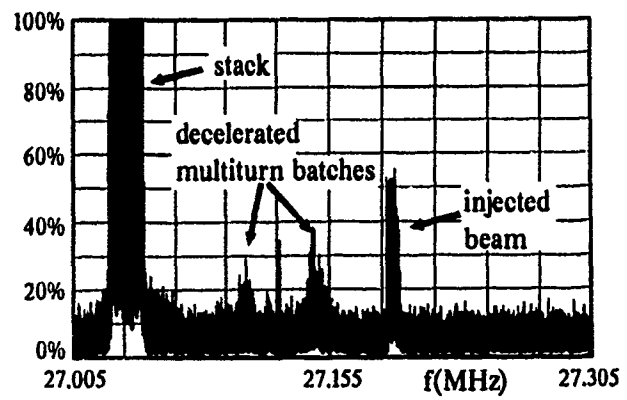


Figure 3: *Schottky-noise spectrum illustrating the process of beam accumulation of multiturn batches by deceleration and cooling with the electron beam.*

combined with RF stacking. With this method, a current of 18 mA for $^{12}C^{6+}$ ions ($E = 73.3$ MeV) was reached. The modulated frequency of the RF cavity decelerates the ions in this case filling the longitudinal phase space and bringing the ions closer to the detuned electron velocity (fig. 4). In table 2 the achieved intensities are listed for various ions,

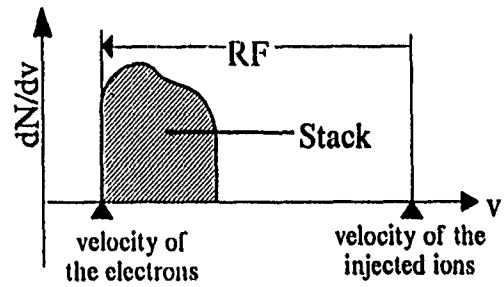


Figure 4: *Schematic description of the combination of ECOOL and RF stacking*

as well as the applied injection scheme: MU labels multiturn injection only, EC is ECOOL stacking and EC+RF is a combination of ECOOL and RF stacking. There is also listed whether an equilibrium has been reached between the injection rate and particle loss (EQ) or if an instability (IN) occured with the given current. One sees that with $^9Be^+$ and $^7Li^+$ only a relatively low current can be stored because ECOOL stacking can't be attempted with these ions due to the small lifetime and cooling force.

Table 2: *Achieved intensities for a few ion species with different methods of injection.*

Ion	Energy [MeV]	Intensity [μA]	Injection Method	Limitation
p	21	2400	EC	IN
$^7Li^+$	13	4	MU	-
$^9Be^+$	7	6	MU	-
$^{12}C^{6+}$	73	18000	EC+RF	IN
$^{32}S^{16+}$	195	1500	EC	EQ
$^{35}Cl^{15+}$	157	400	EC	EQ
$^{35}Cl^{17+}$	202	650	EC	IN
$^{63}Cu^{26+}$	510	110	EC	EQ

Acknowledgement

We gratefully acknowledge the skillful and enthusiastic work of the technicians of the Max-Planck-Institute.

References

[1] E. Jaeschke et. al., Part. Acc. 32 (1990) 97

[2] N.S. Dikansky, V.I. Kononov, V.J. Kudelainen, I.M. Meshkov, V.V. Parkhomchuk, D.V. Pestrikov, A.N. Skrinsky, B.N. Sukhina, The Study of fast electron cooling, INP Novosibirsk, preprint 79-56 (1979)

[3] Y.S. Derbenev, A.N. Skrinsky, Part. Acc. 8 (1978) 235

The ADRIA Project

A. Dainelli, A. Lombardi, A. Ratti*, A. G. Ruggiero*

INFN-LNL, Via Romea 4, Legnaro (PD) I-35020, Italy

Abstract

A proposal of accelerator complex for the Laboratori Nazionali di Legnaro is described. The main components are a Heavy Ion injection system, two rings, a Fast Synchrotron and an Accumulator, both with a maximum rigidity in excess of 22 Tm connected by a Transfer Line where unstable isotopes are produced and selected. The system is designed for the acceleration of heavy ions with specific energy in the range of few GeV/u, the production of unstable isotopes and their deceleration to specific energies around the Coulomb barrier. The unstable isotopes are produced by impinging the primary beam on a production target and collecting them in the Accumulator where electron and stochastic cooling techniques are applied to reduce the large phase space volume generated in the production process and during accumulation. At the repetition rate of 10 pulses per second, primary beam currents are in excess of 10^{11} ions/s.

I. INTRODUCTION

The proposed complex of accelerators has the main goal to accelerate broad range of ion species to specific energies of few GeV/u for direct experiments in nuclear physics on fix target and for unstable isotopes production. The beam quality (transverse and longitudinal spreads) has to be adequate for precise measurements typical of nuclear structure studies.

The ensemble of the following components are referred to as the ADRIA Complex:

- a Heavy Ion Injector (XTU tandem & ALPI);
- a Fast Cycling Synchrotron (Booster);
- a Slow Cycling Synchrotron (Accumulator);
- a Transfer Line;
- an Experimental Area.

The acceleration system consists of a heavy ion injector [1] and a Booster with a maximum magnetic rigidity of 22.25 Tm; the same rigidity has been fixed for the Accumulator. The two rings, with the same shape and circumference (267 m), are located in the same building stacked one on top of the other with 2.5 m of separation between the beam axis.

After the acceleration in the Booster, the primary ion beam is extracted and travels through the Transfer Line to a target where exotic fragments are produced and selected. The secondary beam is injected into the Accumulator where the momentum spread is reduced by bunch rotation [2] and cooling techniques.

After the accumulation of 12 subsequent pulses from the fast synchrotron, the beam is cooled and then bunched for the final deceleration to specific energies adequate to study nuclear interactions around the Coulomb barrier.

The system will be capable to deliver beams with intensities in excess of 10^{11} ions/s and specific energies ranging from 1 GeV/u (Uranium) to 2.5 GeV/u (Oxygen). With the addition of a proton linac it will be also possible to accelerate intense beams of protons to 8 GeV.

II. THE SYNCHROTRON LATTICES

The two rings, with the same rigidity and shape, have similar lattices with fourfold symmetry and the basic cell has standard FODO structure (Fig. 1). Each period, which has a mirror symmetry with respect to its mid point, is made of an arc (4 subsequent cells) and two half straight sections at the ends. The two half straight sections are obtained by removing the bending magnet from the standard cell. The total number of cell is 24 each about 11 m long.

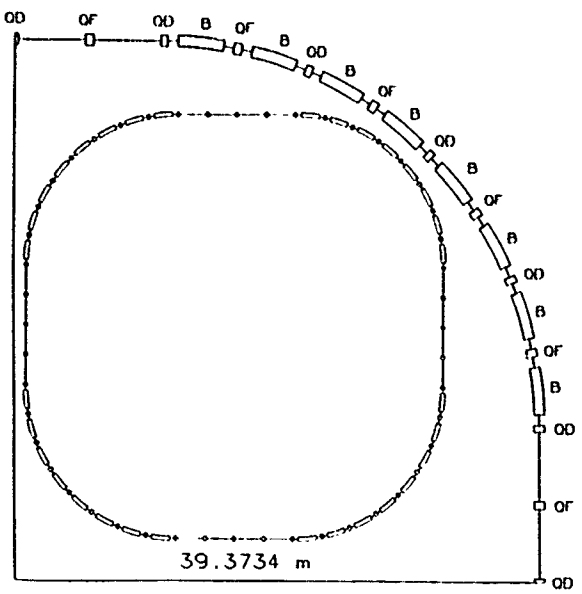


Figure 1: Booster Ring Lattice

The phase advance per cell is about 90° in the horizontal and 60° in the vertical plane; the betatron

* Brookhaven National Laboratory, Upton, N.Y. 11973, USA

0-7803-0135-8/91$01.00 ©IEEE

tunes are 5.8 and 3.8 respectively, away from any low-order systematic resonances.

The bending is provided by 32 curved dipoles 3.46 m long and a magnetic field of 1.3 T, for a maximum field variation of 40 T/s. The magnetic gap is 10 cm, whereas the bore radius of the focusing quadrupoles is 7 cm in both rings for the betatron acceptance of 140 π mm-mrad.

The horizontal betatron phase advance in each arc is 360° which enables zero dispersion values at the extremities. The dispersion function remains zero along the full length of the straight section. The transition energy (γ_t=4.6) is well above the maximum energy reached during the heavy ion acceleration cycle and it is crossed only in the proton cycle.

To provide space (~10 m) for the electron cooling system a different quadrupole arrangements have been chosen in the long straight section of the Accumulator. The phase advances per cell and the betatron tunes of the Accumulator are the same as in the Booster.

III. THE RF SYSTEM

To cope with the large frequency swing required for the acceleration of the wide mass range involved, the Booster rf system is made of two different groups of cavities. The first (LFRF, 6 cavities) sweeps from 5 to 32 MHz while the second (HFRF, 6 cavities) covers the frequencies ranging from 30 to 51 MHz.

Both LFRF and HFRF systems are made of double-gap cavities, tuned by longitudinally biased Ni-Zn ferrites. Table 1 summarizes the rf requirements for the acceleration of different ion species. The rf frequency at injection is 5 MHz for all kind of ions and equals the frequency of the low energy buncher of the ALPI injector. Since different ions are injected with different velocities, the proper harmonic numbers are chosen for each species.

The acceleration of protons to 8 GeV (10 Hz) is within the limits of the facility, provided that an additional rf system is built to deliver a total voltage of 270 kV in a frequency range from 50 to 56 MHz.

The rf system in the Accumulator fulfills three tasks, namely the capture and subsequent rotation in the longitudinal phase space of the secondary beam bunches, the rf stacking and the deceleration.

Two cavities with a gap voltage of 700 kV, tuned at fixed frequencies ranging from 26 to 47 MHz, are used for the bunch rotation [3]. The rf stacking is performed by a second system of two similar rf cavities which displace the beam by a 1.2 % momentum variation.

The third system of rf cavities is required for the deceleration at the end of the stacking and cooling processes. The rf is turned on to adiabatically bunch and capture the coasting beam, at the same harmonic number selected in the corresponding acceleration process in the Booster. The beam is decelerated to about 4÷10 MeV/u which corresponds to the Coulomb barrier. A total of 50 kV is needed. The deceleration stops at the lowest available rf frequency of 5 MHz, where a final momentum spread of about 0.02% is expected.

TABLE 1. RF parameters for heavy ion acceleration

	S	Cu	Au	
A	32	63	197	
Q	16	27	51	
Inj. Kin. Energy	16.40	10.39	4.58	MeV/u
Extr. Kin. Energy	2.53	2.08	1.03	GeV/u
Injection β	.185	.148	.098	
Extraction β	.963	.950	.880	
Harmonic Number	24	30	45	
	LFRF System			
Peak Voltage	195	200	210	kV
Trans. Time Fact.	.98	.96	.91	
Voltage/Gap	17.8	17.4	19.2	kV
	HFRF System			
Peak Voltage	-	-	210	kV
Trans. Time Fact.	-	-	.82	
Voltage/Gap	-	-	21.4	kV

IV. THE PRODUCTION OF EXOTIC BEAMS

The beam Transfer Line between the rings is also used for the production and the separation of exotic beams to be collected and decelerated in the Accumulator. Its layout consists in one half of a ring with some modifications of the insertion regions to accommodate the production target and the degrader station, used for the energy and mass analysis.

The Transfer Line and the collection system of fragments are designed for the capture of a full momentum spread of at least 0.7%; the production angle is chosen to be 7.5 mrad corresponding to a transverse momentum spread which matches the longitudinal momentum width. The expected yield can then be as large as one part in ten thousand and typically 10^6 fragments of assigned mass number and atomic number can be collected per every Booster pulse.

The production target is located in a dispersion free insertion of the Transfer Line where a waist with transverse betatron functions of the order of 1 m are designed in both planes.

The full beam emittance of the primary beam is around 5π mm-mrad and the beam size at the target is 2.3 mm. The emittance of the secondary beam is 17 π mm-mrad. Based on these figures, the betatron acceptance of the Transfer Line and of the Accumulator is set to 40 π mm-mrad and the momentum aperture to 2%. Momentum selection of the fragments is obtained using two pairs of collimators and slits in an

8 meter drift. A horizontal waist β^*=1 m is designed in the middle of the drift section, where the degrader target is also placed.

V. THE COOLING SYSTEMS

In the Accumulator both stochastic and electron cooling are planned in order to have manageable beam dimensions during the process of accumulation, capture and deceleration of fragments. The most demanding requirements are imposed by the accumulation process, when by setting the total cooling time to 150 ms. The average momentum spread in the stack is maintained to 0.3 %.

TABLE 2. Electron and Stochastic cooling parameters

Electron Cooling		
Kinetic Energy	1	GeV/u
β	0.8	
Mass	200	
Charge State	80	
Length of the e-Beam	8	m
Beam Transv. Dimension	10	mm
e-Beam Current	15.5	A
Cooling Time	0.3	s
e-Beam Energy	0.6	MeV
e-Beam Power	7.1	MW
Stochastic Cooling		
Number of ions	1×10^7	
Bandwidth	1-2	GHz
Method	Notch Filter	
No. of Pickups	16	
No. of Kickers	32	
Schottky Power	1	kW
Thermal Power	negligible	
Amplifier Gain	160	db

A second cooling period of 0.5 s, following the stacking cycle, reduces at the same rate the total beam momentum spread to $1\cdot10^{-1}$ (Fig. 2). Electron cooling alone is adequate for the reduction of the beam emittance. Betatron cooling proceeds at twice the rate of momentum cooling; thus, over a period of 0.5 s, the betatron emittance can be reduced by at least one order of magnitude.

The power required for the electron cooling is of the order of 7 MW, which indicates the need for a very efficient energy recovery system. Stochastic cooling can be implemented with a bandwidth of the order of 2 GHz and a power of 1 kW. Table 2 summarizes the cooling parameters.

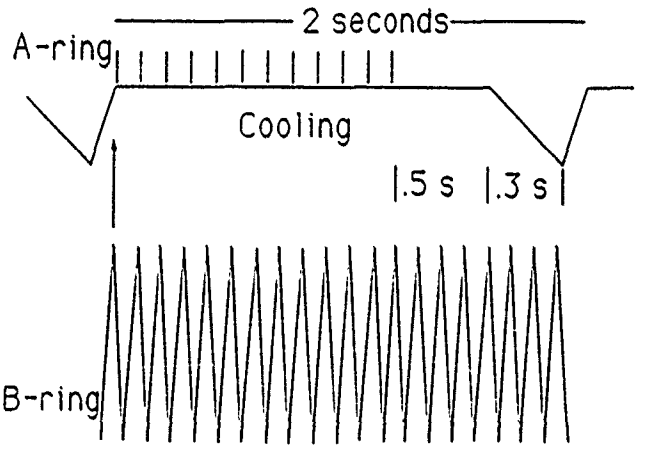


Figure 2: Magnetic cycle of the ADRIA Complex

VI. ACKNOWLEDGEMENTS

The authors would like to thank the EHF study group and the staff members of the Legnaro Laboratories for their help in preparing the ADRIA proposal. We are particularly grateful to J. Griffin and V. Vaccaro for their determinant contribution to the design of the rf system.

VII. REFERENCES

[1] G. Fortuna et al. "The ALPI project at the Laboratori Nazionali di Legnaro", Nucl. Instr. and Meth. A287 (1990) 253-256.
[2] J. E. Griffin et al. "Time and momentum exchange for production and collection of intense antiproton beams at Fermilab", IEEE Trans. on Nucl. Sc., NS-30, no. 4 August 1983, pag. 2630-2632
[3] J. E. Griffin et al. "RF exercise associated with acceleration of the intense antiproton bunches at Fermilab", IEEE Trans. on Nucl. Sc., NS-30, no. 4 August 1983, pag. 2627-2629

THE PROPOSAL OF THE ACCELERATOR COMPLEX OF THE MOSCOW KAON FACTORY

V. V. Balandin, A. G. Chursin, G. A. Dubinsky, S. K. Esin, N. I. Golubeva, A. I. Iliev, L. V. Kravchuk,
V. A. Matveev, V. V. Paramonov, A. S. Pashenkov, Yu. V. Senichev, E. N. Shaposhnikova and S. P. Volin
Institute for Nuclear Research of the Academy of Sciences of the USSR, Moscow
V. P. Belov, V. A. Glukhikh, N. D. Malitskiy, Yu. P. Severgin, M. N. Tarovik and I. A. Shukeilo
Scientific-Research Institute for Electro-Physical Equipment, Leningrad
G. I. Batskikh, Yu. D. Ivanov, Yu. S. Ivanov, V. A. Konovalov, R. A. Meshcherov, B. P. Murin and Yu. F. Semunkin
Moscow Radio-Technical Institute, Moscow

I. INTRODUCTION

The tuning of the linear accelerator of the present Moscow Meson Factory is about to be completed. We are going to get first 600 MeV protons this year. The Kaon Factory [1] is the next step after Meson Factory. In the Proposal of the Moscow Kaon Factory (*MKF*) the linear accelerator of the Meson Factory is to be used as the injector for the Booster [2]. Figure 1 shows the time-energy structure of the accelerator complex. Every second a $100\mu s$ long macropulse of $600 MeV$ H^-

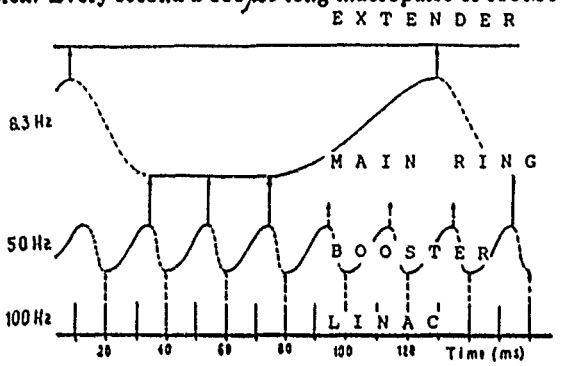


Figure 1: Time-energy structure

ions from the linac with $3.1 \cdot 10^{13}$ particles is injected into the $50\ Hz$ rapid-cycling Booster and are accelerated to $7.5\ GeV$. Then three out of six pulses are transferred to the Main Ring. An other three pulses of the beam are used in the experimental area of the Booster. The Main Ring is filled during the $40ms$ flat bottom magnetic field. The Main Ring accelerates $9.3 \cdot 10^{13}$ protons per pulse from $7.5\ GeV$ to $45\ GeV$ during $50ms$. The reset of the field in the Main Ring takes $30ms$, thus one cycle is $120ms$ long, for a repetition rate of $8.3\ Hz$. The Extender is need for slow extraction with 100% duty cycle. This accelerators complex can produce an average current of $125\ \mu A$ with slows extraction with the average current from linac being $500\ \mu A$. The program of physics research to be carried out at the $45\ GeV$ high-intensity proton beam was discussed at "The 5 All Union Seminar" [3].

II. INJECTION FROM THE LINAC

At injection into the Booster, the bunches follow with $198.2\ MHz$. The length of the bunch from the linac is about 3° at $33.03\ MHz$ and the momentum spread is 0.6%. Since the rf frequency of the Booster is $33.03\ MHz$, three out of six bunches are rejected, which is done before injection into the linac. The debuncher is used to transport bunches from linac to the Booster with simultaneous bunch rotation in the longitudinal phase space. A single bunch injected into the Booster has ±11° phase size and ±0.1% momentum spread. We have chosen the injection scheme to get the desired particle distribution in the longitudinal phase space [4]. The initial difference between synchronous momenta of the linac and of the Booster is $\Delta p/p = -0.055\%$. Painting is provided by shifting the bunch phase during the injection: $\phi_0 = \pi/16(1 - \cos(t/T_{inj}))$. Due to the small duration ($140\mu s$), injection is carried out without flat bottom magnetic field during the accelerating cycle that leads to the additional particle painting. This scheme provides ±0.33% momentum spread, 0.8 fill factor, phase size of ±106° and longitudinal emittance of $0.09\ eVs$. Numerical simulation of the longitudinal beam injection including coulomb interaction has been provided by program *LongBeD* [5].

III. RF VOLTAGE PROGRAM

To obtain $0.9\ eVs$ longitudinal emittance, rf voltage at injection in the Booster should be $780\ kV$. The voltage at extraction $660\ kV$ is determined by the condition of microwave stability and longitudinal matching of the Booster and Main Ring. Magnet waveform for the Booster is complicated and consists of three parts - harmonic, linear and harmonic [6]. The ratio of rising time to falling time equals to 1.5. This law was chosen in order to minimise the number of rf cavities which is determined by maximum gap voltage $80\ kV$ and rf power supply $220\ kW$. In this case the number of rf cavities equals to 21. In the Main Ring a maximum power supply per cavity is supposed to be $450\ kW$. The magnetic waveform with two harmonics allows to approximate the linear law and to have 42 rf stations. Assuming broadband impedance of the Main Ring and Extender to be 8Ω the rf voltage at the end of the acceleration in the Main Ring and in bunched beam mode of Extender has to be at least $1200\ kV$ to avoid microwave instability. Rf voltage program (see Fig. 2) keeps the ratio of bunch height to bucket height in both rings no more than 0.8.

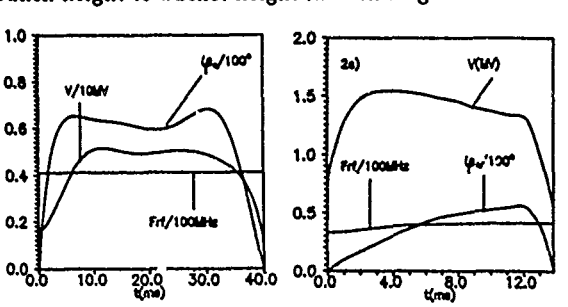


Figure 2: RF voltage program

IV. LATTICES

From the general consideration of lattice designs for low energy synchrotrons [7,8,9], a lattice with both modulation of the β-function and ρ is most suitable for Booster ring. The Booster has a racetrack shape with two 180° arc and two

0-7803-0135-8/91$01.00 ©IEEE

dispersion-free straight sections. The arcs have 8 superperiods. Each superperiod contains 4 *FODO* cells, two central halve-cells have not dipoles ('missing magnets'). The horizontal tune of arc equals to 3, that gives zero dispersion in long straight sections. The phase advance of the straight sections in the vertical plane is chosen to be $2 \times 2\pi$ for suppressing of spin-depolarization resonances and the vertical tune of arc is $6.25 \,/\, 2$ A high γ_t is obtained by the 'missing magnets' scheme and by using relatively small perturbations in the arc's quadrupoles. The Booster lattice functions are shown in Fig. 3.

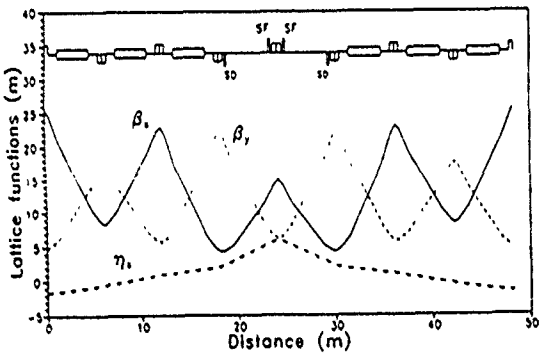


Figure 3: The Booster lattice functions

The Main Ring racetrack lattice has been designed using a regular *FODO* focusing structure with superperiodicity 2. The transition energy is determined by the horizontal tune and is below injection energy, $\gamma_t = 6.6$. The 180° arcs contain 18 cells with $\pi/3$ advanced phase for each cell in both planes. The dispersion in the straight sections is canceled by the 'missing magnet' dispersion suppressors placed at the arc ends. The rf cavities, the injection and extraction systems are placed in the straight sections of the length 178 m. The natural chromaticity is corrected by installing the sextupole magnets near to each quadrupole magnet in the arcs to positive value. The Extender occupies the same tunnel as the Main Ring and has the same lattice in arcs. Dipoles have a maximum field of 1.7 T and quadrupoles of 1 T at the pole tip. The Extender gives an almost continuous beam during the 120 ms cycle time with the extraction losses on low level — less than 0.1% via the combination of the resonant extraction mechanism and septa [10]. The extraction system itself includes two magnetic pre-septa, the electrostatic septum and the Lambertson magnetic septum and was designed in the one of the two long straight sections. Both magnetic pre-septa are identical. Each of them provides an angle of 0.5 $mrad$ between the circulated and the extracted beams and has a length of 0.5 m. That allows to decrease the particle losses at the electrostatic septum in 40 times. The electrostatic wire septum is 5 m long with a field of 80 kV/cm. It deflects the beam by 0.85 $mrad$. The thickness of the wires will be 50 mm. The Lambertson magnetic septum deflects the extracted beam into the derivation line. The thickness of the septum determined by the beam separation at the entrance of the magnet and is found to be 2.5 cm. The scheme of the beam separating along the extraction section is shown in the Fig. 4. Deeper hatching in the figure corresponds to more dense beam ($MPS1$, $MPS2$ — the first and the second magnetic pre-septa, ES and MS are the electrostatic and the magnetic septa)..

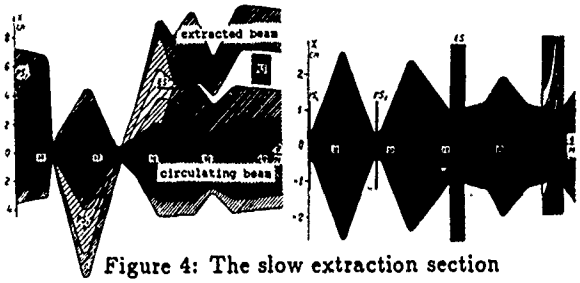


Figure 4: The slow extraction section

V. BEAM STABILITY

The space charge term of longitudinal impedance divided by mode number changes during acceleration in the Booster from $-i280$ to $-i10$. To avoid microwave instability the upper bound on the inductive wall term in the Booster with $\gamma_t = 18$ becomes 10 Ω. The Main Ring operates above the transition energy with $\gamma_t = 6.6$. Condition on longitudinal microwave stability is satisfied if inductive wall term of broadband impedance does not exceed 8 Ω. In both rings the worst situation for microwave instability occurs at the end of acceleration cycle. The high impedance parasitic modes of the rf cavities are serious sources of the longitudinal instability. Passive mode damping of the parasitics helps to control them by active damping. An upper limit for the parasitic shunt impedance increase with a frequency and for lowest modes has value of 4 $k\Omega$ for the Booster and 11 $k\Omega$ for the Main Ring. In the case when parasitic modes from different cavities overlap, this limit gives 0.25 $k\Omega$ per cavity. Landau damping of longitudinal modes is present only at the beginning of the accelerating cycle. Later on it is lost because the coherent frequency shift becomes larger than the half spread in incoherent frequencies. To provide transverse stability of low frequency coupled-bunch mode the special construction of vacuum ceramic chamber and broad-band feedback system are under development. In the Main Ring the natural chromaticity must be corrected to positive value.

VI. POLARIZED BEAM

The acceleration of polarized proton beam is intented up to the top energy [11]. During the acceleration in the Booster 14 imperfection and 13 intrinsic resonances will be encountered. The high-periodicity arcs of the Booster allow to reduce the number of intrinsic resonances by tuning the straight sections to an integer $\times 2\pi$ phase advance in the vertical plane making them "invisible" for spin. A partial snake with the stationary superconducting longitudinal magnetic field is proposed for the Booster. The spiraling motion and additional focusing of the solenoids are corrected by the special quadrupole system. The linear spin resonances are eliminated for the magnetic field integral 12.5 $T\,m$ in one straight section if the fractional part of the betatron tunes is less 0.2. Due to the low periodicity and large acceleration range the Main Ring has a high number of depolarizing resonances: 72 intrinsic and 71 imperfection. The Siberian Snakes adoption is planed to avoid the passage though all spin resonances. The length of the straight sections provides the space long enough for Siberian Snake.

VII. RF CAVITIES

Two types of tunable *RF* cavities, with inductive tuner us-

ing ferrites with perpendicular bias and capacitive one using magnetron as a varactor, are now under consideration. Ferrite tunable cavities were optimized [12] to provide parameters needed with reasonable consumption of RF power and power of the bias circuit, to have lowered R/Q (in comparison with the $LANL - TRIUMF$ cavities) values and relatively small amount of ferrite. RF parameters of the $USSR$ produced yttrium ferrites with saturation less then $800\,G$ were tested at low level RF signal. Ferrites with magnetic quality greater then 10^4 were chosen. Development of the process to provide large (outer diameter $850\,mm$) rings is under way now and first (technological) ring for Booster RF cavity is ready. RF cavity for the Main Ring is designed to test both ferrite and varactor tuners and is now under manufacturing. The varactor for Main Ring cavity is now under autonomous testing (Fig. 5). The RF cavity with varactor tuner (shorter

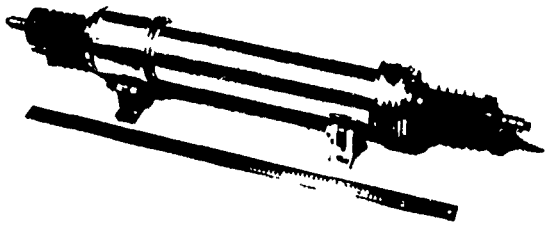


Figure 5: The varactor

and much more simpler in design then ferrite tunable one) for Booster is under development. An RF stands for full—scale testing are under construction.

VIII. VACUUM CHAMBER

The Booster and Main Ring magnets will have ceramic vacuum chamber (CVC) of high-density, high-purity alumina with very thin continuous conducting coating and overlaied metal strips with it to provide low eddy current heating, longitudinal impedance and low secondary emission yields simultaneously. The using of alumina ceramic provides an excellent vacuum and radiation properties for desired vacuum and radiation levels. The first stage of our investigations in the field of CVC was successfully completed in March, 1991. We have a ceramic segments with length $250\,mm$, accuracy of outside sizes $30\,\mu m$ and $4\,mm$ wall thickness. The design of the two types of the joints has been made - glazed joints with 450 or $1100C^\circ$ (strength about 0.6 of ceramic strength) and diffusive-pressure joints with strength 0.95 of ceramic strength. Extensive mechanical and vacuum tests have proven its a very good reliability for $KAON$ vacuum system. The investigations of the manufacturing silver/ceramic paste, Cu and Mo conducting RF-strips on the inside ceramic pipe surface has been made. The other materials for RF-shield (Al, $Stainless\ Steel$, Ni, Ti) will be considered. One of the main problem are the charging and the dynamic of the secondary electron emission in the ceramic vacuum pipe. This had led to interest in the properties of the ceramic surface. The apparatus for these investigations are using low intensity current and single-pulse methods. Maximum secondary emission yield (SEY) for our alumina was about 7.0 at the primary energies of the electrons $450 - 750\,eV$. With such SEY in accordance with our experimental results for all ceramic materials the $e - p$ instability may be possible. For $ISIS$ vacuum pipe design (Rutherford Laboratory, England) the RF-wire is the secondary emission shield. With the perspective using of the RF-shield on the ceramic surface - the minimum effective CVC wall thickness in magnet gap to achieve the desired field strengths we propose to cover all inside surface by very thin ($0.2\mu m$) conducting layer to damp the SEY up to $1.0 - 1.3$ (for Cu layer with thick 0.2 micron maximum SEY is 1.3). In this case such thin layer give us the additional eddy-current losses, but from our estimate this losses will be small part of the integral losses in the CVC. The next step of our investigation - the production of the curved ceramic segments with length $500\,mm$ and the same accuracy. We have a first good results in this direction. The range of materials for injection-extraction magnets and experimental area with a very high radiation levels and with possibility of direct interaction of the beam with ceramic surface should include a nitrid ceramics- view point supported by our preliminary experimental results. This ceramic is also competitive from a technology and cost points of view.

IX. REFERENCES

[1] M. K. Craddock, "The TRIUMF Kaon Factory Accelerators," in proc. of Intern. Sem. on Interm. En. Phys., INR, Moscow, November, 1990

[2] Yu. Senichev et al., "The proposal of the accelerator complex of the Moscow Kaon Factory," in proc. of AHF Accel. Design Workshop, LA-11684-C, vol. 1, 1989, pp. 207-219, February 1989

[3] V. A. Matveev, V. A. Rubakov,"Particle Physics at Kaon Factory — The Program of experimental research at the Moscow Meson Facility," The 5-th All Union Seminar, 1987

[4] G. Dubinsky, E. Shaposhnikova and Yu. Senichev ,"Longitudinal injection into the Booster of the Moscow Kaon Factory," Proc. of XII All Union Conf. on Charge Particle Accel., Moscow, 1990

[5] G. Dubinsky,"Program *LongBeD* for the simulation of the Longitudinal Beam Dynamics in synchrotrons," *ibid.*

[6] G. Dubinsky, E. Shaposhnikova and Yu. Senichev, "Acceleration cycles for Booster and Main Ring of the Moscow Kaon Factory," *ibid.*

[7] N. I. Golubeva, A. I. Iliev and Yu. V. Senichev, "The new lattices for the booster of Moscow Kaon Factory," in proc. of Intern. Sem. on Interm. En. Phys., INR, Moscow, November 1990

[8] A. I. Iliev and Yu. V. Senichev, "Racetrack Lattices for Low-Medium-Energy Synchrotrons," in this proceedings

[9] N. I. Golubeva, A. I. Iliev and Yu. V. Senichev, "The booster lattice for the Moscow Kaon Factory," Proc. of XII All Union Conf. on Charge Particle Accel., Moscow, 1990

[10] A. G. Chursin, Yu. V. Senichev, S. P. Volin,"Slow extraction from the Extender Ring of the Moscow Kaon Factory," *ibid.*

[11] N. I. Golubeva, Yu. V. Senichev,"The capability of polarized beam acceleration at the Moscow Kaon Factory," *ibid*

[12] Yu. D. Ivanov et al.,"RF system development for the Moscow Kaon Factory accelerators complex," *ibid.*

Application of a New Scheme for Passing Through Transition Energy to the Fermilab Main Ring and Main Injector

J. A. MacLachlan and J. E. Griffin
*Fermi National Accelerator Laboratory, Box 500, Batavia IL 60510**

Introduction

In the vicinity of the transition energy of an ion synchrotron the longitudinal oscillation frequency drops and the motion becomes non-adiabatic; the result is emittance dilution. Furthermore, because the synchrotron oscillation is too slow to average particle energy gain, particles off the synchronous phase get too much or too little acceleration depending whether they lead or lag; therefore, momentum spread is increased. In this regime rf focusing degrades beam quality. To confront these effects directly J. Griffin has proposed eliminating the rf focusing near transition by flattening the rf waveform with a second or third harmonic component.[1] The rf is phased so that all particles in the bunch are accelerated by the flattened portion, receiving just the acceleration required by the magnet cycle as illustrated in fig. 1(b). We will show by concrete examples related to the Fermilab Main Ring (MR) and Main Injector[2] (MI) that one can eliminate rf focusing sufficiently long before and after transition to reduce the maximum momentum spread and emmitance growth significantly. Additionally, the bunch has its maximum phase spread at transition so that the peak current and resulting microwave instability is mitigated, and the bunch above transition becomes a satisfactory match to an accelerating bucket. We call this procedure the "slide-under" technique to distinguish it from the single-frequency "duck-under" technique and simultaneously to recognize that there are ideas in common.

The process is illustrated schematically in fig. 1. A bunch is accelerated in a standard bucket to $\eta = \gamma_\tau^{-2} - \gamma^{-2} \approx -10^{-4}$ with a voltage program chosen to optimize the momentum spread for the next steps. The fundamental phase is moved to 90° and the harmonic system is turned on at about 28% of the fundamental for second harmonic or 13% for third harmonic. The width of the flattened region is about 70° for second harmonic or 54° for third. While the bunch is below transition it shears as shown in fig. 1(c) with lower momentum particles lagging those of higher momentum, reaching its greatest phase spread at transition. When $|\eta|$ returns to its initial value, the bunch is again upright, and a conventional accelerating bucket can be restored. The linearity of the shearing motion is affected by the "Johnsen parameter" α_2, the second order term in the dependence of orbit length on relative momentum offset.[3] The maximum phase drift is given by[1]

$$\Delta\varphi|_{\max} = \frac{\omega_{rf} t_o}{\gamma_\tau^2}\left[\frac{\dot\gamma t_o}{\gamma_\tau} - \alpha_2\frac{\Delta p}{p}\right]\frac{\Delta p}{p} ,$$

where t_o is the starting time relative to transition time for the synchronous particle. We infer from this equation and parameters for the MR and MI that for both it is possible to pass through the non-adiabatic time for all particle momenta with no rf focusing. The result should be brighter beams or higher intensity limits than possible with conventional technique. We present below results of modeling carried out with the ESME code[4] including space charge and nonlinearity in the equations of motion to order $(\Delta p/p)^2$. We also comment on hardware requirements.

A Main Ring Test

The Fermilab Main Ring has been converted from its original service as a high intensity source for a 400 GeV fixed target program to a 150 GeV injector for the Tevatron. Losses at transition have become a serious problem because non-planar bypasses and other modifications for collider operation have reduced the momentum aperture to $\sim 0.4\%$ and because the acceptable losses are governed by the close proximity of the superconducting Tevatron magnets. It is now difficult to exceed 0.2 eVs or $2.5 \cdot 10^{10}$ protons/bunch at transition. The slide-under technique is a direct attack on this limitation. The relevant MR parameters are

mean radius	1000.00	m
γ_τ	18.75	
$\dot\gamma$ at t_τ	88.7	s^{-1}
Johnsen parameter α_2	0.816	
harmonic number h	1113	
maximum rf volts	4.0	MV
accelerating volt. at trans.	1.75	MV
longitudinal emittance (95%)	0.2	eVs
protons per bunch	3	$\times 10^{10}$
coupling impedance $Z_{\|\|}/n$	9.0	Ω

The third harmonic scheme is favored because substantially less new hardware is needed; therefore an earlier test

*Operated by the Universities Research Association under contract with the U. S. Department of Energy

0-7803-0135-8/91$01.00 ©IEEE

of the concept is possible. The $\sim 54°$ flat on the rf waveform is narrower than desirable. It limits the emittance that can be handled and may shorten the time available for slide-under to somewhat less than the non-adiabatic time for the full momentum spread. Figure 2 shows the phasespace distribution for a MR bunch which has been carried through transition to $\gamma = 25$ with an optimized voltage-phase program (duck-under). Figure 3 is a comparable result from a 6.7 ms third harmonic slide-under starting at $\eta = -9 \cdot 10^{-5}$. Emittance growth of 45% vs. 8% clearly favors the new approach; more favorable comparison may be obtained by lengthening the slide-under slightly and optimizing other parameters.

A single 159 MHz cavity can provide the 250 kV required. The plan is to borrow a bare cavity, install a large enough Fe Yt garnet ferrite tuner to tune ~ 20 kHz, and excite it with a standard Fermilab PA running as a class C tripler. If the ferrite is unbiased during the greater part of the accelerating cycle when the cavity is not used, it may be lossy enough to make the unexcited cavity harmless.[5] If beam loading proves a problem it might be necessary to develop a PA with fast feedback to keep the fields under control. Because the amount of acceleration can not be controlled by adjusting the phase, both fundamental and third harmonic amplitudes must be controlled by radial position information.

The Main Injector

The Main Injector project is to replace the original 400 GeV ring with a 150 GeV ring in a new tunnel, optimized as an injector for the Tevatron. It will also have a high intensity fixed target mode at 120 GeV. The following parameters reflect the latter mode:

mean radius	538.302	m
γ_T	20.4	
$\dot{\gamma}$ at t_T	161.9	s^{-1}
Johnsen parameter α_2	0.0	
harmonic number h	588	
maximum rf volts	4.0	MV
accelerating volt. at trans.	1.68	MV
longitudinal emittance (95%)	0.5	eVs
protons per bunch	6	$\times 10^{10}$
coupling impedance $Z_{\|\|}/n$	5.0	Ω

At least four improvements over the MR make the MI a far better machine at transition, *viz.*, larger good field aperture, lower dispersion, faster ramp, and $\alpha_2 = 0$. The result shown in fig. 4 for emittance growth in a second harmonic slide-under is practically the same as for an optimum duck-under. If brighter beam is obtained from the Booster, however, the advantage of the slide-under in preserving that brightness would be apparent. At this time the utilization of the second harmonic scheme in the MI is provisional.[6] The choice to pursue the option will rest on further modelling and, it is hoped, observations in the MR or elsewhere.

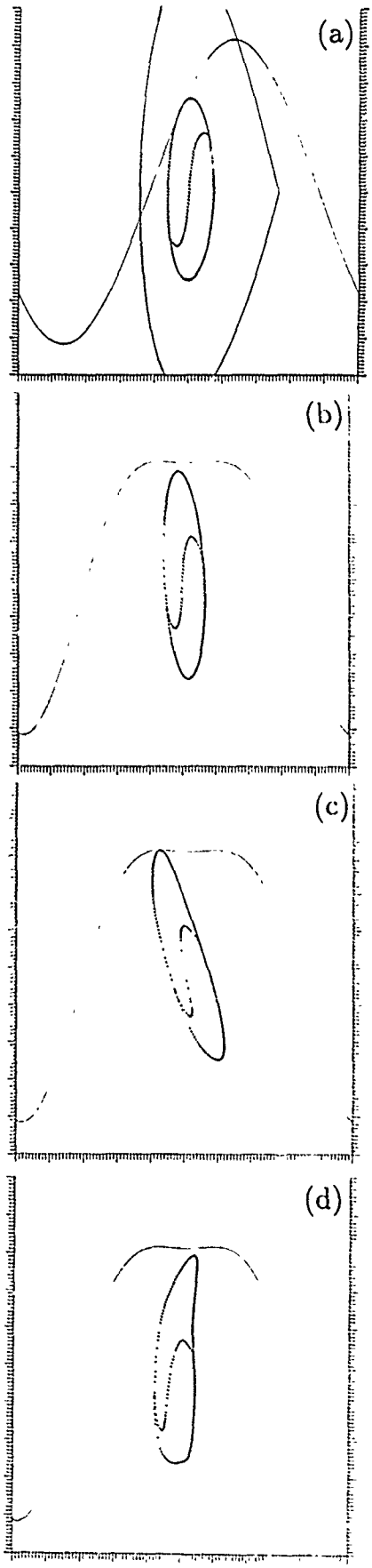


Figure 1: Steps in slide-under — see Introduction

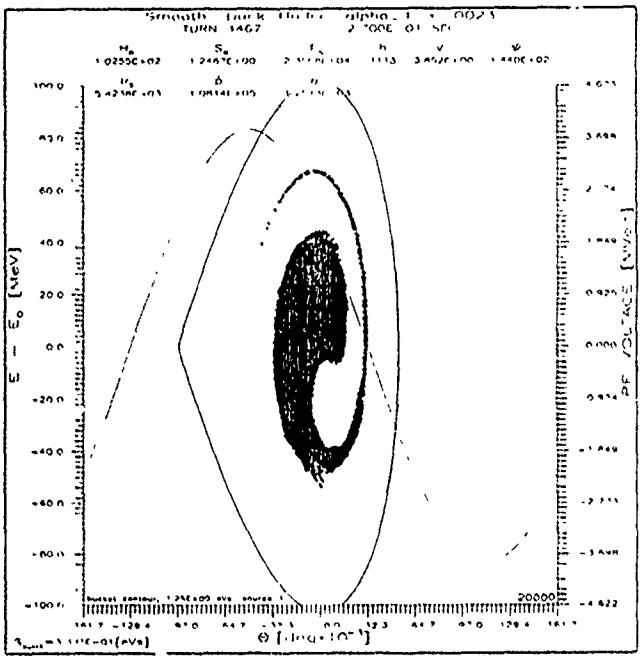


Figure 2: Main Ring bunch after duck-under transition crossing; note both mismatch and μ-wave instability.

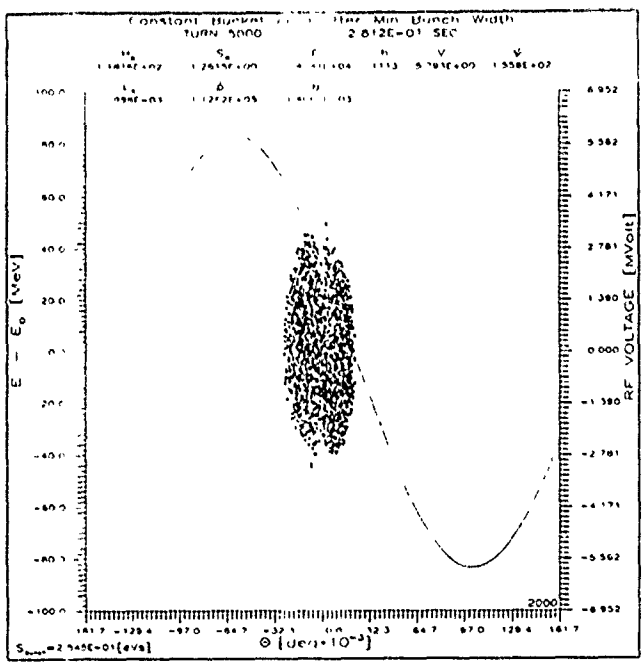


Figure 3: Main Ring bunch after slide-under transition crossing

Conclusions

The application of a novel technique for transition crossing to the Fermilab Main Ring and Main Injector project has been described on the basis of numerical modelling. The demonstrated reduction of momentum spread and peak beam current at transition contribute in several ways to reduced emittance blowup and beam loss during transition crossing. The fundamental idea of eliminating the detrimental effects of rf focusing during the few milliseconds of non-adiabatic particle motion is pleasingly direct. The details of optimizing the phase to account for higher order asymmetry in the bunch shearing, the choice of starting time and momentum spread, and the best bucket to match the distribution produced are the objects of an active modelling effort.

The tolerance of the Main Injector to conventional transition crossing results primarily from its fast ramp. An alternative scenario for antiproton acceleration uses a very slow ramp and depends critically on the slide-under technique, which was originally conceived in that context. The usefulness of the technique for the project depends on options now open. The utility and desirability of a timely experimental test is apparent.

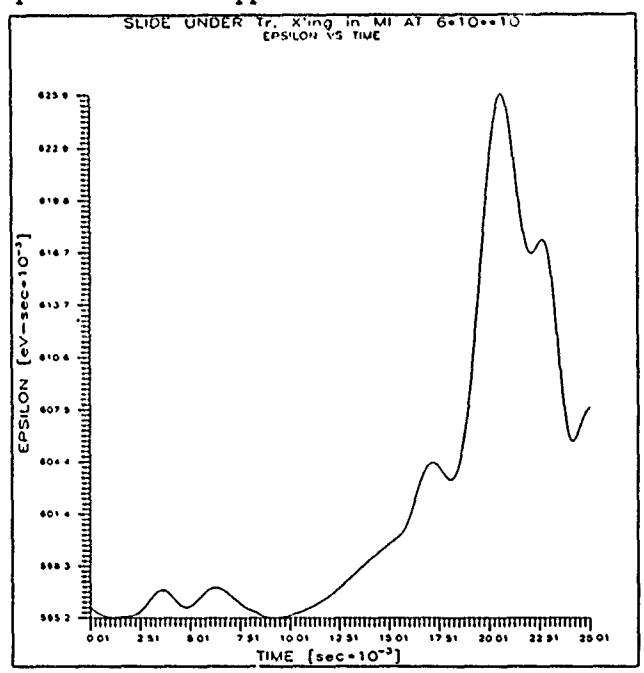


Figure 4: Longitudinal emittance ($6\sigma_{rms}$) vs. time for slide-under in MI

References

[1] J. E. Griffin, "Synchrotron Phase Transition Crossing Using an RF Harmonic", Fermilab internal note TM-1734 (March 91)

[2] "Fermilab Upgrade: Main Injector Conceptual Design Report", Rev. 2.3, Fermilab (April 90)

[3] K. Johnsen, "Effects of Non-Linearities on the Phase Transition", in *Proc. of the CERN Symposium on High Energy Accelerators and Pion Physics*, 1, 106, CERN (1956)

[4] S. Stahl and J. MacLachlan, "User's Guide to ESME v. 7.1", Fermilab internal note TM-1650 (Dec. 90)

[5] W. Funk, priv. comm. on HERA 53 MHz cavities built by AECL Chalk River Laboratory

[6] Conceptual Design Report Fermilab Main Injector Rev. 2.3 Addendum", Fermilab (March 91)

Low Momentum Compaction Lattice Study for the SSC Low Energy Booster

E. D. Courant and A. A. Garren
Superconducting Super Collider Laboratory*, 2550 Beckleymeade Av., Dallas, TX 75237
U. Wienands
TRIUMF, 4004 Wesbrook Mall, Vancouver, BC, Canada

Abstract

To avoid emittance growth from transition crossing it is desirable that the Low Energy Booster have a transition energy well above its extraction energy or even imaginary. A number of lattices have been designed with this feature. Examples will be given along with the general principles underlying their design. One of the lattices has been tentatively chosen as reference design.

I. Introduction

The SSC injector system consists of a linac and a chain of three booster synchrotrons. The first of these, the Low Energy Booster (LEB), will accelerate protons from 1.22 GeV/c to 12.5 GeV/c with a repetition rate of 10 Hz. The magnetic field and gradient are 1.3 T and 14.9 T/m, respectively, and the circumference is to be in the 500 m to 600 m range. The ring will contain proton bunches spaced at 5 m intervals, each containing 10^{10} protons for the nominal luminosity of $10^{33}\mathrm{cm}^{-2}\mathrm{s}^{-1}$. However, the machine must be capable of higher intensities for accelerating test beams.

In order to maximize performance and reliablility, the lattice should have the following properties:

- Transition energy γ_t either imaginary or well above the extraction energy;
- Low or zero dispersion function η in the straight sections;
- Adequate straight sections for rf, injection, extraction, etc.;
- Provision for acceleration of polarized beams.

In addition, the lattice should satisfy conventional requirements such as linear behaviour up to amplitudes of 4σ (for a test-beam emittance four times the nominal emittance of 0.6π mm-mr), moderate peak values of the orbit functions, and an area in tune space large enough to encompass the space-charge tune spread.

These design goals are not all obviously compatible. This paper contains a brief account of recent LEB lattice studies.

II. Obtaining high γ_t

Three methods have been explored for raising γ_t: these might be labeled the high-tune, harmonic, and modular methods.

The high-tune approach is to design a simple FODO-cell ring with sufficiently large cell number and phase advance to raise the tune to the value desired for γ_t , since these quantities are nearly equal in such lattices. This method leads to higher chromaticity and, at fixed circumference, to small peak dispersion values, both of which drive up sextupole strengths, possibly compromising single particle stability (cf. Talman [1]).

The harmonic approach involves enhancing a higher-order Fourier component of the momentum compaction α. The expression for α is given in [2]:

$$\alpha = \frac{\nu^3}{R}\sum_k \frac{|\alpha_k^2|}{\nu^2 - k^2},$$

where α_k^2 is nonzero only for $k = 0$ and k equal to multiples of the periodicity P of the quantity $\beta^{3/2}/\rho$. If ν is made close to, but less than, P the momentum compaction will be reduced and can even be made negative. This can be done in a FODO lattice by superposing a P^{th} harmonic perturbation in the gradient or bending distribution [3]. Two problems with this approach are that the η oscillations can be very large and that it is not obvious how to include dispersion-free straight sections.

The moduiar approach is to design simple modules or supercells that give negative η in some or all of the bending magnets. Sets of these modules are combined into an arc. This approach is convenient for conceptually separating the design of the supercells from that of the straight sections, each with desired characteristics. A drawback is that it sometimes leads to lattices with numerous magnet types.

III. Obtaining low η in the straight sections

We have constructed lattices with zero η in the straight sections in two ways. One way is to make the horizontal matrix of each arc be unity, leading to an integer tune across the arc. As a result the dispersion function will be identically zero in the straight sections.

The second way is to make the arc out of modules with unconstrained phase advance, bordered by dispersion suppressors. The suppressors should be designed so as not to raise the momentum compaction by an unacceptable amount.

IV. Polari o Beams

A polarized beam will tend to be depolarized as it crosses the energies corresponding to depolarizing resonances. These are of two kinds: intrinsic resonances, induced by betatron oscillations, occur at

*Operated by the University Research Association, Inc., for the U.S. Department of Energy under Contract No. DE-AC02-89ER40486.

U.S. Government work not protected by U.S. Copyright.

$$\gamma G = kP \pm \nu_y$$

with the relativistic energy factor γ, the magnetic moment anomaly $G = (g-2)/2$ (=1.7928 for protons), any integer k, the lattice periodicity P and the vertical betatron tune ν_y. A high periodicity will limit the number of intrinsic resonances to be crossed. Imperfection resonances are due to closed-orbit excursions and occur at integer values of the "spin tune," which measures the number of spin revolutions per turn.

A method used successfully to overcome intrinsic resonances is the tune jump. A set of very fast pulsed quadrupoles jumps the tune across the resonant value in approximately 1.5 μs, followed by a slow decay of the quadrupoles in about 3 ms [4]. Problems arise if the tune jump required is too large or the resonances follow each other too closely.

Imperfection resonances can be corrected by programmed orbit correctors, allowing different corrector settings as each resonance is crossed. A more elegant method has been developed in the form of a partial Siberian snake [5]. For LEB energies this would be a 4 Tm solenoid, rotating the spin by 10°...18°.

V. Examples

In this section we present four examples, each illustrating one or more of the design methods discussed above.

A. *SCDR Lattice*

The first example, demonstrating the high-tune approach, is the lattice designed by Y. Y. Lee for the SSC Site-Specific Conceptual Design Report [6]. This ring is made up of 54 FODO cells. Missing magnets give the ring six superperiods, one of which is shown in Figure 1. The

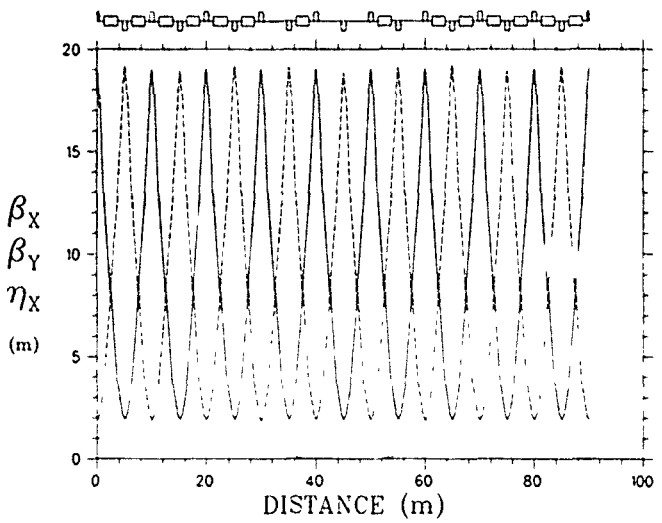


Figure 1: Lattice functions of the high-tune lattice.

number of cells and the phase advance per cell, 112°, together conspire to raise γ_t to 14.5, somewhat above the extraction energy, while the tune is 16.8. The missing-magnet half cells make straight section space for injection, extraction and rf, and their distribution serves to give nearly zero dispersion in the center empty cell of the superperiod. This design shows a very straightforward way to make a non-transition crossing LEB. The main reasons to explore other possibilities were that still higher γ_t values are desirable, and these could be made with this approach only by making the ring too crowded or too large in circumference.

B. *The $-I$ Straight Section Lattice*

This lattice is a simple example of the modular approach. The ring is made up entirely of modules, each consisting of two bending cells and two empty cells, the latter each having 90° phase advance. The two empty cells constitute a straight section with a $-I$ matrix, which transforms the momentum vector from $(0, \eta')$ at one end to $(0, -\eta')$ at the other, forcing η to have negative values in the bending cells (moreover, they are invisible to the β-functions of the bending cells). Hence α is negative and γ_t is i7.4. Figure 2 shows the half-superperiod of a three-

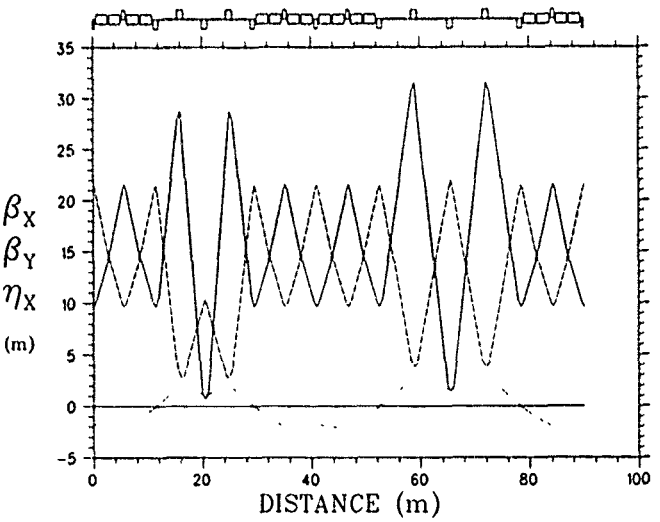


Figure 2: Lattice functions of the $-I$ straight-section lattice.

superperiod ring containing two module types that differ in the length of their empty cells. The short ones serve the purpose of reversing η' only, while the long ones are also used for injection, extraction and rf. Lattices of this type do not have zero η in the straight sections. Similar lattices have been devised by D. Trbojevic [7].

C. *Lattice with Low-α Modules and Dispersion Suppressors*

Here a more complex example of the modular method is given. The ring has three superperiods, each with a zero-η straight section and an arc. Figure 3 shows half of one reflection-symmetric superperiod, the left end is at the center of the straight section, the right end at the center of the arc. The half arc shown has a dispersion suppressor on the left, and one low-α module on the right. The module,

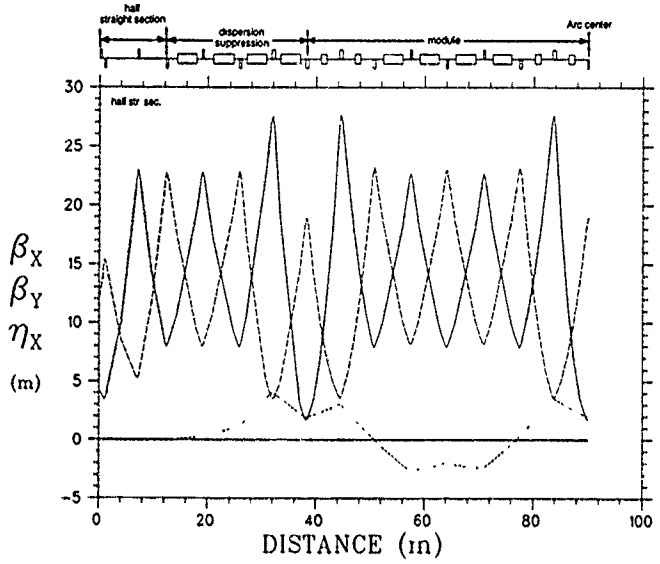


Figure 3: Lattice functions of the low-α lattice.

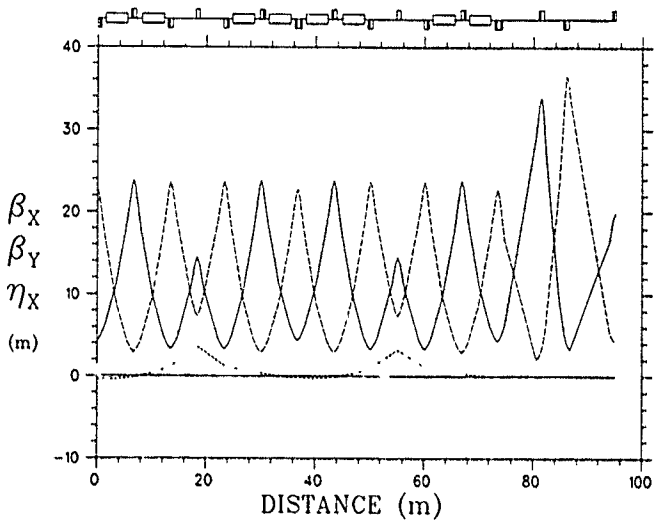


Figure 4: Lattice functions of the 4^{th} lattice example.

also symmetric, has four cells. The short cell at each end has about 90° phase advance and short dipoles, the two longer cells in the center each have 60° phase advance and long dipoles. This combination causes η to be negative on the average. The module has a phase advance $5/6 \times 2\pi$ in each plane. The sextupoles in one arc module are thus at a phase interval from the corresponding ones in the other, causing cancellation of the third-order resonances.

The dispersion suppressor has the same focusing structure as a half module, but the lengths of the dipoles in the two cells are different from the corresponding ones in the module. Unlike more standard suppressors in this one the bending is *increased* rather than decreased about a point 90° away from its end, to prevent η from becoming negative. Because the suppressor has the half-module structure, it has the same β-functions as the module.

The half straight section has four quadrupoles, which are adjusted to produce a waist at the center and give the ring the desired tune, 8.8. The γ_t value of this ring is 21.3.

D. *Lattice with reduced number of spin-resonance crossings*

The last example (Fig. 4) shows a threefold symmetric lattice designed using the harmonic method. The arcs by themselves are a FODO lattice with a superiodicity P of 12, introduced by the missing-magnet cells and enhanced by a modulation of the quadrupole strength. They are similar to structures proposed by Senichev *et al.* for the Moscow Kaon Factory [8]. The total horizontal phase advance is $9 \times 2\pi$, and thus, due to its reflection symmetry, each arc is a second-order pseudo-achromat in the horizontal plane, which suppresses *eta* in the straight sections. The insertion points for the straight sections are chosen to minimize $\hat{\eta}$ in the arcs. The straight sections are tuned to give the desired fractional tune in the horizontal plane. The same principles were used before in the design of some of the TRIUMF KAON Factory lattices [9].

In the vertical plane the arcs are used to achieve the desired fractional tune, while the straight sections are unit sections with a phase advance of 2π each. Thus they are transparent to both the particle orbit and the spin; the apparent symmetry w.r.t. first-order intrinsic depolarizing resonances is restored to be 12-fold, and only four such resonances are in the acceleration range. These are fairly evenly spaced and calculations show they can be crossed with reasonable tune-jumps of less than 0.2 in magnitude. The straight sections allow for inclusion of a partial snake.

The nominal tune of the machine is 11.60; γ_t was chosen to be about 22. The lattice can be tuned to any working point within the rectangle in tune space defined by $10.9 \leq \nu \leq 11.9$ in either plane.

This lattice has been tentatively adopted as reference design for the LEB.

VI. References

[1] R. Talman, "A 'Push-Pull' Low Energy Booster", SSC internal note, Dec. 1990.

[2] E.D. Courant and H.S. Snyder, Ann. Phys. **3**, 1 (1988).

[3] R.C. Gupta *et al.*, IEEE Trans. Nucl. Sci. **NS-32**, 2308 (1985).

[4] F.Z. Khiari *et al.*, Phys. Rev **D39**, 45 (1989).

[5] T. Roser, in *Proc. 8^{th} Int. Symposium on High Energy Spin Physics*, Minneapolis, MN, Sept. 1988.

[6] SSC Laboratory, "Site-Specific Conceptual Design Report", SSC Laboratory Report SSCL-SR-1056, Dallas, TX, July 1990.

[7] D. Trbojevic *et al.*, in *Proc. 2^{nd} European Particle Accelerator Conf.*, Nice, France, June 1990, p. 1536.

[8] Yu.V. Senichev *et al.*, private communication.

[9] R.V. Servranckx *et al.*, in *Proc. 1989 IEEE Particle Accelerator Conference*, Chicago, IL, March 1989, p. 1355.

Operational Aspects of Electron Cooling at the Low Energy Antiproton Ring (LEAR)

J. Bosser, M. Chanel, R. Ley, D. Möhl, J.C. Perrier, G. Tranquille, D.J. Williams
PS Division, CERN, CH-1211 Geneva 23

Abstract

This paper describes the major modifications made to the LEAR electron cooler for its reliable and effective use in every day operations. The transverse feedback system used to counteract the coherent instabilities observed with the dense beams obtained with electron cooling will also be discussed.

I. INTRODUCTION

The electron cooling device installed on the Low Energy Antiproton Ring (LEAR) at CERN has shown that electron cooling can be used as an effective method of phase space compression of a stored ion beam. The experiments performed with a variety of particles over the past three years [1,2,3] have enabled us to modify the cooler and the LEAR environment in order to use the apparatus on the different machine 'flat tops' at momenta below 308.6 MeV/c. In the past year different operational modes were investigated so that the cooler can be used routinely during particle physics runs this year.

II. HARDWARE MODIFICATIONS

Major improvements were made on the stability of the 40 kV high voltage (HT) power supply which was the cause of longitudinal instabilities in the early days of electron cooling. Rectifier circuits were developed and have given HT stabilities of the order of 10^{-4}. To further upgrade the stability a compensator was installed which corrects any drift with respect to a reference voltage given by a ratiometer signal.

For a better understanding of the loss mechanisms in the collector a number of analogue fibre optic cables were connected to the various elements of the collector. If the current loss on one or more of these elements increases above a certain threshold a specially developed module gives a visual indication of where the losses occured. During the annual shut downs the high voltage feedthroughs and connections inside the collector were modified in order to render the ensemble more reliable. However the operation of electron cooling at 27 keV is still problematic and it is for this reason that it was decided to build a new electron beam collector.

The new electron collector is the result of a collaboration between the electron cooling team at CERN and the Centre for Applied Physics and Technology (CAPT) at Lipetsk, USSR [4,5]. The design is very simple [Fig. 1] consisting of a Faraday cup with a repeller electrode at the collector entrance. As we would like to test a number of different types of collectors on the LEAR cooler a vacuum valve has been installed at the collector entrance. Computer simulations made at CERN [Fig. 2] have shown that with an extra coil after the valve, electron trajectories are acceptable and that a magnetic mirror is created at the entrance reflecting any secondary electrons that might be created at the collector surface. Initial tests made at Lipetsk indicated that a collection efficiency of 99.995% could be obtained for an electron beam having an intensity of 3.3 Amps and an energy of 35 keV.

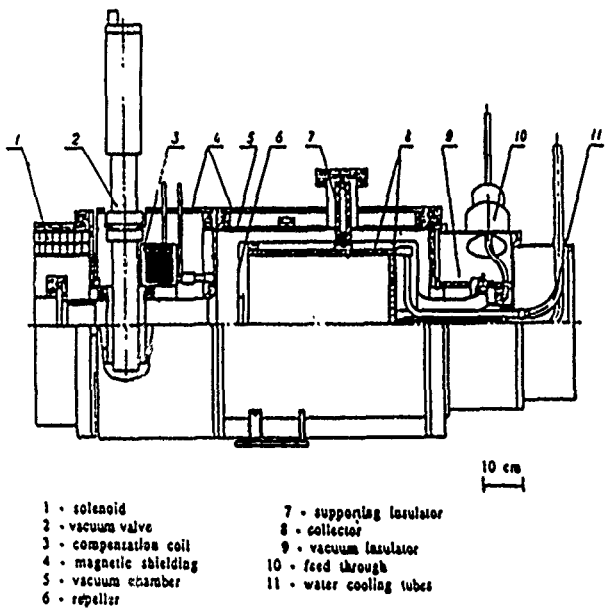


Fig. 1 : The new collector scheme

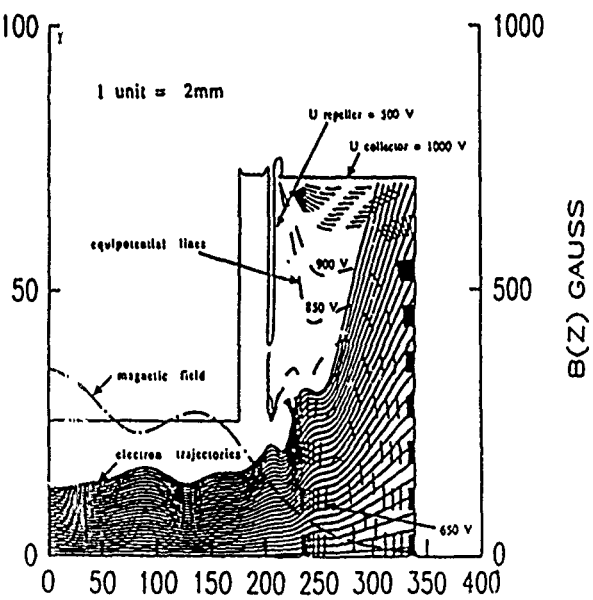


Fig. 2 : The electron trajectories with the equipotential lines and the corresponding magnetic field on axis (I coil = 1500 A)

0-7803-0135-8/91$01.00 ©IEEE

The 36° toroids of the cooler cause a deformation in the closed orbit of the circulating ion beam. In the past this has been corrected using the horizontal correction dipoles in the cooler vicinity. However a second perturbation is the coupling between the horizontal and vertical betatron oscillations of the ion beam due to the 1.5m long solenoid in the cooling section. This solenoid excites the coupling resonance $Q_h+Q_v=5$ and implies a fine tuning of the machine working point. Moreover polarized beams required for the FILTEX experiment will be depolarized after a number of passages through the solenoid if it is not compensated. For these reasons two tilted solenoids have been installed, one on each side of the cooler, which have the combined effect of correcting the orbit and compensating the coupling of the betatron motions. The solenoids are connected in series with the main solenoid so that when switched on the cooler will compensate itself. Figure 3 shows the closed orbit with and without the tilted solenoids.

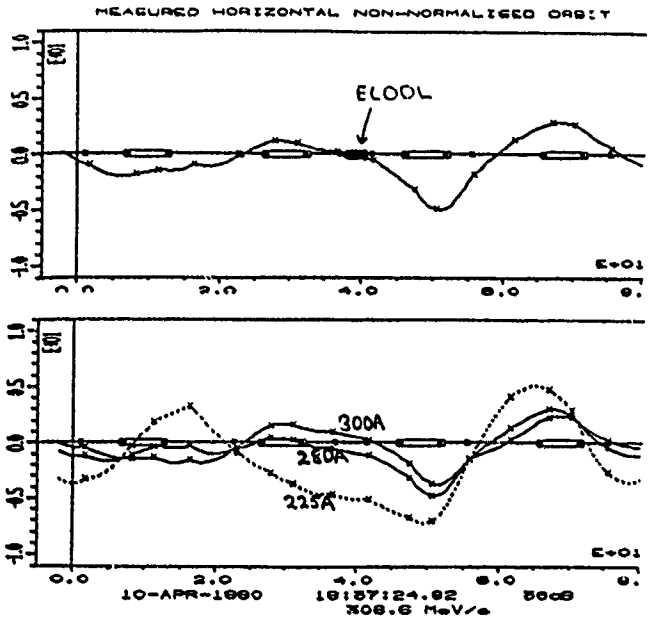


Fig. 3 : Compensation of the cooler toroid deflection with two tilted solenoids. The first trace shows the normal machine closed orbit. The second trace shows three orbits with the cooler solenoid at 100 A and the compensation solenoids at 300 A, 280 A and 225 A respectively.

III. THE TRANSVERSE FEEDBACK

During the cooling process the beam density increases and the beam can become unstable when this density reaches a given threshold. At lower intensities, a beam will resist coherent instabilities by virtue of Landau damping. Using the simple threshold criteria of refs. 6 and 7, we find that for a beam of 10^9 particles, loss of Landau damping can occur for a momentum spread $\Delta p/p$ of about 10^{-4}. The double peak structure regularly observed on longitudinal Schottky scans of an electron cooled beam [Fig. 4] is linked to the fact that the beam is near to this threshold.

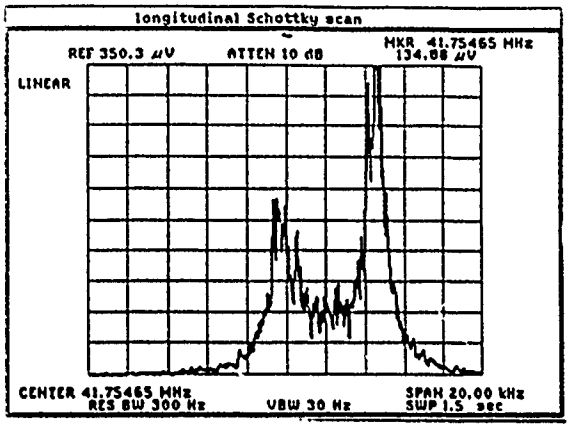


Fig. 4 : Longitudinal Schottky scan of an electron cooled beam of 2.2 10^9 protons. The two peak structure is characteristic of a beam near to the stability threshold.

Transverse instabilities can be observed on both Schottky noise and normal electrostatic position pick-ups. A spectrum analyzer is used to observe the variation in amplitude of an (n -q) sideband as a function of time. The instability manifests itself by an abrupt rise in the amplitude. This is followed by a cooling period of about 1 to 10 seconds in LEAR before the threshold is reached again. Usually, when instabilities occur, beam is lost until the intensity reaches 10^9 particles at 200MeV/c. At this intensity blow-up occurs without any appreciable loss in particle number.

The feedback system (or "damper") developed to counteract these coherent transverse instabilities consists of a horizontal and vertical electrostatic pick-up and a horizontal and vertical kicker placed at an odd number of quarter wavelengths of the betatron oscillation away from the pick-up. The position signal from the pick-ups is linearly amplified, delayed, and then applied to the kicker plates. The bandwidth of the system is determined by the number of modes to be corrected and the gain by the growth rate of the instability. In our case a band from 70kHz to 70MHz is desirable to cover the first 20 modes in the whole energy range at LEAR. The kick required corresponds to a beam displacement of up to 0.1mm per turn. At present only a prototype "damper" is installed, a definite version has been designed which will maintain damping during energy ramping. A closed orbit interference suppressor will be needed to reduce the strong signals observed when a bunched beam is not perfectly centred in a position pick-up.

IV. THE CONTROL SYSTEM

To be fully compatible with the LEAR environment the electron cooler control system also had to be revised. The new system uses a workstation and handles all CAMAC access through a dedicated microprocessor [8]. The CAMAC loop consists of three crates connected by fibre optic cables for data

transfer to and from the high voltage platform. In addition a new crate was inserted into the LEAR loop for the installation of the new generation function generators known as GFD-GOCT [9,10] and a timing event decoder. The function generators and the timing decoder are needed in order to run the cooler in the 'pulsed mode' which will be discussed later.

The serial CAMAC access is confined to a single board microprocessor acting as an intelligent controller. This controller is connected to a local area network, Ethernet, and any other computer in the same network may send requests to it. All parameters of the cooler are handled in databases which are interfaced to the control system via a limited number of subroutines. These environment routines cover the low level details of the operating system, details that the ordinary user does not wish to be confronted with when programming.

V. OPERATIONAL MODES

A number of operational modes were investigated in the past 18 months in order to determine the most effective manner in which electron cooling could be used at LEAR. With the introduction of digital function generators it has been possible to synchronize the electron cooler with the machine during deceleration and then 'switch on' the cooling process by pulsing the high voltage power supply to the desired value. However the beam loss mechanisms at the ultra low momenta of LEAR also become critical with the perturbations induced by the magnetic elements of the cooler. Therefore much machine study time was used to find acceptable working parameters (tune, chromaticity, closed orbit etc.) in order to obtain a deceleration cycle to 61.2 MeV/c with minimum losses. For operations two modes have been retained.

In the first scenario all the magnetic elements of the cooler are controlled via function generators which are synchronized with the LEAR magnetic cycle. Data relating the different electron energies needed in the cycle are down line loaded into the different GFD vector tables. An antiproton beam is injected at 609 MeV/c and is stochastically cooled for about 5 minutes. When the desired beam dimensions have been obtained, one decelerates the beam to 308.6 MeV/c, the highest momentum for which the cooler is designed to work. On this flat-top the beam is debunched and a trigger is sent from the timing event decoder to the GFD controlling the HT power supply which is ramped to the operational value in 120 msec. Cooling is kept on for typically 6 seconds and then the power supply is ramped back down to zero. The machine and the cooler are then ramped down to the next flat-top and the same cooling procedure is applied. In this way we have managed to decelerate beams to 105 MeV/c saving some 15 minutes in cooling time as compared to stochastic cooling.

The second mode is very much similar to the first with the exception that the magnetic elements as well as the HT power supply are ramped from zero to their operational values on each flat-top. In effect a current regulation system installed on the 1000 A power supply for the cooler solenoids will enable us to reduce the current to zero without any instabilites in the power supply. In this manner the beam sees the effects of the cooler magnets only during a 20 second period on each flat-top when the cooling process is active.

V. CONCLUSIONS

Electron cooling is an effective and rapid means of reducing the phase space dimensions of an ion beam at LEAR. However very high reliabilty and ease of operation are required to make its routine use profitable. Due to hardware bugs, insufficient long term stability and the need to redefine the control system, the full implementation at LEAR has been a gradual and painstaking process. Experience gained while using the cooler in a 'semi-operational' manner has enabled us to redesign the critical components. Supplemented by the active feedback system, electron cooling can now be used consistently between decelerating ramps to obtain beams of ultra low momenta with an appreciable gain in duty cycle and beam quality as compared to previous modes of operation.

ACKNOWLEDGEMENTS

We would like to thank the members of the LEAR and LINAC teams for their assitance and support. Special thanks to F. Ollenhauer, J.L. Vallet and M. LeGras for their efforts in the electronics developments.

REFERENCES

[1] H. Poth , W. Schwab, B. Seigmann, M. Wörtge, A. Wolf, S. Baird, M. Chanel, H. Haseroth, C. Hill, R. Ley, D. Manglunki, G. Tranquille, J.L. Vallet and P. Dittner, "First Results of Electron Cooling Experi-ments at LEAR", Zeitschrift für Physik, A332 (1987).

[2] H. Poth, W. Schwab, B. Seligmann, M. Wörtge, A. Wolf, S. Baird, J. Bosser, M. Chanel, H. Haseroth, C. Hill, R. Ley, D. Manglunki, D. Möhl, G. Tranquille, J.L. Vallet, "Further Results and Evaluation of Electron Cooling Experiments at LEAR", NIM A287 (1990).

[3] J..Bosser, R. Ley, F. Ollenhauer, G. Tranquille, "Status of Electron Cooling Experiments at LEAR", CERN/PS 90-43 (AR).

[4] V. Bikovsky, I. Meshkov, A. Rogozin, V. Sinitsky, E Syresin, V. Funtikov, J. Bosser, R. Ley, G. Tranquille, "The New Electron Beam Collector for LEAR", CERN/PS 90-44 (AR).

[5] J. Bosser, R. Ley, G. Tranquille, V. Bikovsky, V. Funtikov, I. Meshkov, A. Rogozin, V. Polyakov, I. Seleznev, V. Sinitsky, A. Smirnov, E. Syresin, "The New Collector for the Electron Cooling Device at LEAR", To be published.

[6] W. Schnell and B. Zotter, "A Simplified Criterium for Transverse Stability of a Coasting Beam", CERN/ISR-GS-RF 76-26 (1976).

[7] E. Keil and W. Schnell, "Concerning Longitudinal Stability in the ISR", CERN/ISR-TH-RF/69-48 (1969).

[8] T. Pettersson and G. Tranquille, "The New Control System for the LEAR Electron Cooler", CERN/PS 90-46 (OP).

[9] P. Liénard , "The LEAR GFD", CERN/PS, To be published.

[10] E.Tanke, "The LEAR GOCT", CERN/PS 87-04 (LI).

A Combined Symmetric and Asymmetric B-Factory with Monochromatization

A.N. Dubrovin and A.A. Zholents

Institute of Nuclear Physics, 630090 Novosibirsk, USSR

Abstract. A new approach to the design of a high luminosity electron-positron collider is considered. The distinctive feature of the approach is the use of a large dispersion function at the collision point. This fact allows us to have a high luminosity as well as a good monochromaticity of electron-positron collision energy. The application of the approach to the B-factory design is considered. We receive the luminosity of 5×10^{33} $cm^{-2}s^{-1}$ and c.m. energy spread of 1 MeV in a case of asymmetric 6.5x4.3-GeV beams. The symmetric variant with beam energies of 4.7x4.7-GeV will have the luminosity of $2\times10^{33}cm^{-2}s^{-1}$ and c.m. energy spread of 60 keV. Two variants differ mainly in the ways of the beam final focusing and in the method of the beam separation after collision.

I. INTRODUCTION

B-factory is a high luminosity electron-positron collider intended for operation in the c.m. energy W = 9.5 - 13 GeV. Design motivations are specified mainly by the desire for observation of *CP* violation in the B-meson system. Precise measurements of rare decay modes of *Y1S*, *Y2S*, *Y3S* resonances, B-mesons and B-barions are also considered as the primary goal.

The luminosity requirements for definitive *CP* violation measurement are minimized by having a moving c.m. at the peak of *Y4S*, which implies two rings with unequal beam energies. In spite of the relatively wide width of *Y4S* resonance a monochromatization is used here for better resolution of B-meson masses. We would expect to run the rings with the minimum asymmetry 6.5 GeV on 4.3 GeV that allows a good *CP* violation measurement [1], although a more costly choice 7 GeV on 4 GeV is also possible.

Y1S, *Y2S*, *Y3S* resonances are very narrow. Only few percents of the luminosity are used for generation of these resonances. The monochromatization is the only way to increase the useful luminosity here. We found that best results for the monochromatization level can be obtained in a symmetric variant of a B-factory. Maximum c.m. energy is also available easier in this case.

Our studies show that asymmetric rings have a potential to higher luminosity than symmetric rings. But there is no actual demonstration that it is true. If that fails, we would use the familiar symmetric mode 5.32 GeV on 5.32 GeV for *CP* violation measurements. Thus, our design provides for asymmetric and symmetric operations A requirement flexibility is achieved for a machine with one interaction point and two almost identical rings in the arcs. Two long straight sections are used for implementation of all distinctions in the variants (see Fig.1).

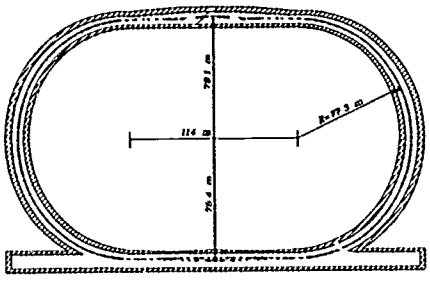


Fig.1 A layout of a B-factory

II. BASIC PRINCIPLES

We usually employ the term *monochromatization* in two senses. In the narrow sense the monochromatization means the reduction of the c.m. energy spread of e^+e^- collisions. In the wide sense it means a collection of certain principles of a collider design. They were already publicized in Refs.2-5. Here we emphasize only some of them.

a) *Large dispersion at the interaction point* (IP) *in one direction* (*e.g.*, D_x^*) *and small beta functions in two directions* β_x^*, β_y^*.

The function $H = (D_x^*)^2/\beta_x^*$ should be large to provide for a good energy resolution, σ_W :

$$\sigma_W = W\left[\left(\epsilon_{x1} + \epsilon_{x2}\right)/H\right]^{1/2} \qquad (1)$$

where ϵ_{x1}, ϵ_{x2} are horizontal beam emittanses.

(In the case of the vertical dispersion D_y^* one should substitute vertical dispersion and beta functions in H and vertical emittances in Eq.(1).)

An excitation of the synchrobetatron resonances in beam-beam effects is not seemed now a severe problem since there are suppressions of most resonances obliged to the effect of smallness of betatron oscillation amplitudes relative to the total transverse beam size at the IP [6].

b) *Very small emittances.*

Large emittances are not more needed for high luminosity since beam spots at the IP are mainly determined by beam energy spreads.

c) *Small synchrotron tunes even for very short bunches.*

The main reason for this is a small momentum compaction factor obtained due to the storng focusing in standard cells needed for small emittances.

d) *The very possibility to imply the chromaticity correction inside (or very close to) final focusing quads.*

It means that less sensitivity of a dynamic aperture to high beta functions in the final focus than in the conventional case is achieved.

e) *The independence of the energy resolution on energy spreads inside the beams.*

It means that a possible beam energy spread blowup due to the microwave instability is not more very dangerous. Moreover it can be accomplished by a gain in the luminosity if bunchlengthening is compensated with the implementation of an additional rf voltage.

III. ASYMMETRIC VARIANT

A. Layout

The layout of experimental and utility sections of a B-factory in the asymmetric variant is shown in Fig.2. The high energy beam (*HEB*) enters the experimental section (ex.s.) in a top position and leaves it in a bottom position. Then in the utility section (ut.s.) the *HEB* moves from the bottom to the top. An ongoing low energy beam (*LEB*) moves in a similar fashion in the opposite direction. The interaction region in the ex.s. and straight sections with rf cavities in the ut.s. lie in the middle plane.

Trajectories in the horizontal plane are mirror symmetrical relative to the line connected the IP and the central point of the ut.s. Such symmetry in the ex.s. is important for generation of the large dispersion at the IP by the same bends that used for the orbit separation. Due to the stronger bends the beamline of the *LEB* in the ex.s. is longer than the beamline of the *HEB*. It is compensated in the ut.s., so the circumferences of both rings are equal.

The *LEB* orbit deviation from a central line in the ut.s. is made in two steps with the wiggler magnets in

0-7803-0135-8/91$01.00 ©IEEE

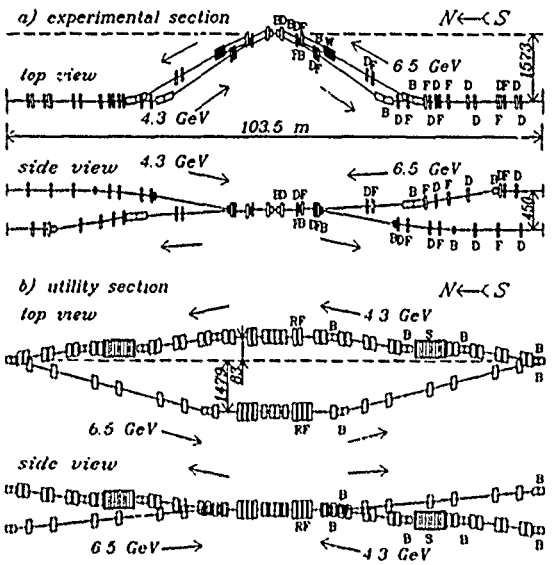


Fig.2 The layout of the experimental and utility sections of a B-factory in the asymmetric variant. B - bending magnet, F,D - quads, W - dipole-quadrupole wiggler, S - dipole wiggler.

between. An idea is to have two vertically separated x rays of wiggler radiation passed by the rf cavities. Their absorption should be made at a large distance as it is foreseen in the machine layout (see Fig.1).

B. Orbit separation and final focus design

An attractive feature of the asymmetric variant is the possibility to use magnets for a fast orbit separation. We begin the separation with the bending magnet and a common vertically focusing quad. The lens focuses too much the *LEB* and doesn't focus enough the *HEB*. This effect has to be compensated and it is done by a double lens (see Fig.3) [3] with the different gradient sign in two centers. The orbit separation at the entrance of the double lens should be sufficient for its installation. Therefore an additional magnet is placed between the main and compensating lenses and the main lens is placed offset. After the double lens there is enough orbit separation for independent beamlines. With this scheme we manage to get the fast orbit separation at the first parasitic crossing (2.1 m from the IP) that is equivalent to 18 horizontal sigma.

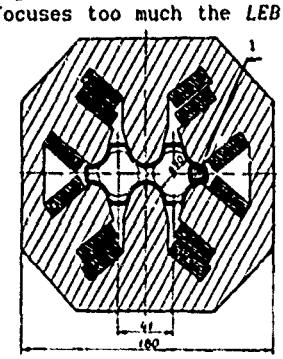


Fig.3 Double quadrupole. 1-SR absorber

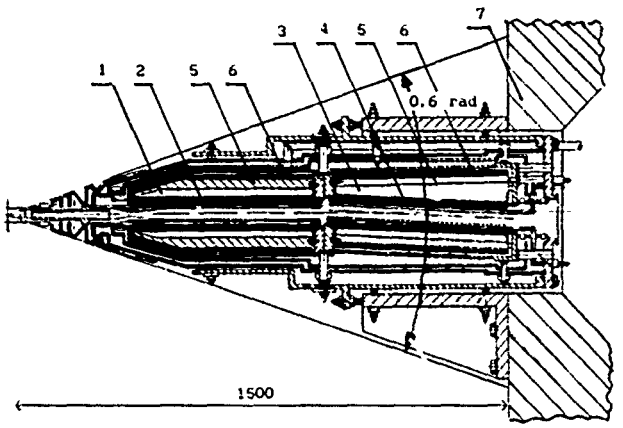


Fig.4 The arrangement of accelerator elements inside the detector.1- bending magnet iron,2- magnet superconducting coils, 3- iron of the Panofsky quad, 4- superconducting coils of the quad, 5 - iron of the screening solenoid, 6 - solenoid coils 7 - iron of the detector.

Since the first bending magnet and the first quad are placed inside the detector they need screening from the outer longitudinal field. It is done by their installation inside the iron shield with compensating superconducting coils around (see Fig.4). With the goal of the compact design of the magnet and quad they have superconducting coils and their irons are frozen at the helium temperature [5]. The quad is designed according to the Panofsky scheme.

A serious problem for a B-factory in the asymmetric variant is the IP beampipe masking from a synchrotron radiation (SR). A solution of this problem is described in the separate report of this conference [7].

IV. SYMMETRIC VARIANT

A. Beam optics and orbit separation

For the symmetric variant of a B-factory the final focus beam optics were designed to provide for $\beta x \ll \beta y$ and a large Dy with the opposite signs for each beam. So, nearest to the IP quad in the final doublet is the horizontal focusing quad while the second quad is the vertical focusing one. Therefore similar to Dubna-INP tau-charm factory design [8] we placed the first electrostatic separator ES1 between the quads to produce the initial horizontal separation (see Fig.5).

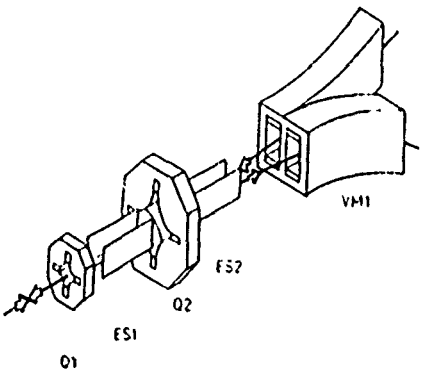


Fig.5 A schematic drawing of orbit separation scheme in the symmetric variant of a B-factory. Q1,Q2 - quads, ES1,ES2 - electrostatic separators, VM1 - magnets.

Then the separation is increased in the second quad and in the second electrostatic separator ES2.

Thus at the entrance into two vertical magnets VM1 placed in 8.2 m from the IP the horizontal orbit separation reaches 30 mm, then magnets turns beams vertically in opposite directions. They have a common iron pole of 3 mm thickness in between, that is enough for magnetic fields of ±0.5 kG. The horizontal beta function near the magnets falls already down to the values about 8 m, so the required horizontal aperture for 30 horizontal sigma at the entrance of VM1 is equal to 5 mm.

A small horizontal beta function is also favorable for beam-beam effects at parasitic crossing. Although we are thinking to have initially the first parasitic crossing in the place where beams are totally separated into two independent vacuum chambers, but the very possibility to place it closer to the IP is a very attractive for further improvements.

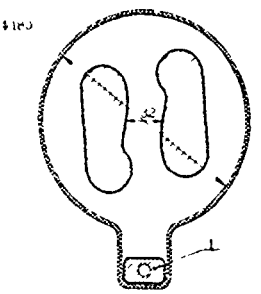


Fig.6 Electrostatic separator ES1 1-SR absorber

A designed value of the electric field in separators is 30 kV/cm. In addition the separator ES1 is made to provide for a sextupole

gradient of 3 kV/cm^3. It is needed for a simultaneous chromaticity correction in both rings in the case of dispersions of different signs. A schematic drawing of this separator is shown in Fig.5.

The evident benefit to begin with the horizontal orbit separation is the very possibility to through the SR from vertical bends between the electrostatic plates and to absorb it on the hidden SR absorber.

B. Layout

The layout of the ex.s. and ut.s. of a L-factory in the symmetric variant is shown in Fig.6. Beamlines of the rings are symmetric relatively to the horizontal and vertical planes. The requirement to have the rings in arcs in the top and bottom positions similar to the asymmetric variant force us to make additional transitions of the trajectories in the south part of the ex.s. It makes the ex.s. geometrically asymmetric relative to the IP while the beam optics remain almost symmetric.

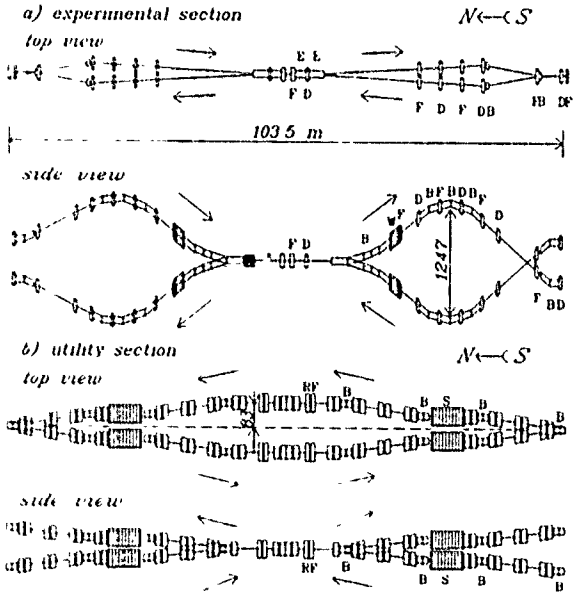


Fig.7 The layout of the experimental and utility sections of a B-factory in the symmetric variant. B - bending magnet, F,D - quads, W - dipole-quadrupole wiggler, S - dipole wiggler, E - separators.

V. STANDARD CELLS

Each arc of a B-factory is filled with 50 identical standard *FODO* cells for every ring. The standard cell (s.c.) is designed to satisfy the required flexibility to different variants and to different beam energies. Two bending magnets can be potentially placed between two neighboring lenses of the s c. They can be easily removed and installed. Therefore when the ring is operated at the beam energy below 5.32 GeV there are only two magnets in the s.c. placed symmetrically between the lenses. At the higher energies there are all four magnets. Orbit lengthening on 17 mm in the regime with two magnets is compensated by the length of the beamline in the ut.s.

There are at least two purposes for such a trick. One is to manage with better damping at lower energies another is the lowering of the synchrotron radiation at higher energies.

Since the beam emittances in all variants of a B-factory are very small the required aperture in s.c. is 25 mm in the horizontal direction and 15 mm in the vertical direction. Therefore all magnetic elements of the standard cell can be made very compact. We designed the s.c. magnet with the gap of 26 mm and the s.c. quad with the internal diameter of 34 mm.

VI. ACCELERATOR PARAMETERS FOR A B-FACTORY

Parameter	Asymmetric		Symmetric
beam energy, [GeV]	4.3	6.5	4.7
circumference, [m]	714	714	714
beam current, [A]	1	0.7	0.6
N [10^{11}] (e/bunch)	0.9	0.6	2
bunch spacing, [m]	4.2	4.2	15.6
horiz. emittance, [nm·rad]	4	5	3
vert. emittance, [nm·rad]	0.25	0.25	0.06
energy spread [10^{-3}]	1	1	1.1
damping time, $\tau_x/\tau_y/\tau_s$, [ms]	14/8/11	11/6/11	9/6/7
SR energy loss, [MeV/rev]	1.5	2.7	2
momentum compaction [10^{-3}]	1.6	1.6	1.1
bunch lenght, σ [mm]	7.5	7.5	7.5
betatron tunes, Q_x/Q_y	33/21	29/18	37/25
synchrotron tune, Q_s	0.023	0.023	0.019
rf frequency, [MHz]	1000	1000	1000
number of SC cavites	6	6	4
cavity voltage, [MV]	4.5	7	4.5
maximum rf power, [MW]	2.4	2.4	1.6
crossing param., β_x^*/β_y^*, [cm]	60/1	60/1	1/25
crossing param., Dx/Dy, [cm]	40/0	40/0	0/±42
beam-beam tune shifts, ξ_x	0.012	0.012	0.035
ξ_y	0.05	0.05	0.011
IP beam spot sizes, σ_x [mm]	0.4	0.4	0.006
σ_y [mm]	0.0016	0.0016	0.45
luminosity, [$10^{33}cm^{-2}s^{-1}$]	5		2
c.m. energy spread, σ_W, [MeV]	1		0.06
Υ1S generation rate, [kHz]			2.5

A designed luminosity and c.m. energy spread at different energies of interest and for a symmetric variant of a B-factory are shown below.

beam energy, [MeV]	5011 (Υ2S)	5178 (Υ3S)	5320
luminosity, [$10^{33}cm^{-2}s^{-1}$]	2.5	3	3
c.m. energy spread, σ_W, [MeV]	0.075	0.08	0.09

VII. REFERENCE

[1] "Feasibility Study for a B-Meson Factory in the CERN ISR Tunnel", ed. T.Nakada, CERN 90-02, 1990.

[2] A.N. Dubrovin *et al.* "Conceptual Design of a Ring Beauty Factory", EPAC-I, Rome 1989, v1, pp.467-469

[3] A.N. Dubrovin, A.M. Vlasov, A.A. Zholents, Annals of the New York Academy of Sciences, v.619, 1991, pp.193-201.

[4] A. Zholents, AIP Conf. Proc., 1990, v.214, p.592.

[5] A Dubrovin, A. Garren, A. Zholents, AIP Conf Proc.,1990, v.214, pp.347-363.

[6] A Gerasimov, D. Shatilov, A.A. Zholents, "Beam-Beam Effects with a Large Dispersion at the Interaction Point", to be published in NIM A.

[7] A.E. Blinov *et al.*, "Synchrotron Radiation Masking on Asymmetric 6.5x4 3-GeV B-Factory", Proc. of this Conf.

[8] Yu.I.Alexakhin, A.N.Dubrovin, A.A. Zholents, "Proposal on a Tau-Charm Factory with Monochromatization", to be published in Proc. of EPAC-II.

B Factory Optics and Beam-Beam Interaction for Millimeter β^* and Locally Shortened Bunches *

Yuri F. Orlov, Christopher M. O'Neill, James J. Welch, *Laboratory of Nuclear Studies*, Cornell University, Ithaca, NY 14853
Robert H. Siemann, *Stanford Linear Accelerator Laboratory*, Stanford, CA 94309

Abstract

To achieve the enormous luminosity required for B factories it is necessary to increase the factor $I\xi_y/\beta_y^*$. We have investigated the possibility of decreasing β_y^*, using locally shortened bunches. The lattice and optics were designed to accommodate the CESR tunnel. The beam-beam interaction was simulated for the following conditions: finite bunch length, longitudinal beam-beam kicks, and crossing angle collision geometry. Estimations and simulations show that using a method of local bunch shortening, it is possible to design the "after 10^{34}" generation of e^+e^- colliders with luminosities $\sim 10^{35}$.

Introduction

The next step in the development of extra high ($\sim 10^{35}$) luminosity for e^+e^- colliders can be made by decreasing both β_y^* and σ_L^* to the order of $1\,mm$. This step seems to be expensive and technically difficult but not unrealistic. In this paper, we have tried to explore the practical possibilities of a theoretical design of local bunch compression [1] that permits us to have a normal bunch size, σ_L, outside of the IR.

The basic idea of local bunch compression is first to deliver a powerful kick to the particles, producing a horizontal angle $\Delta x'(s)$ that depends on s, the longitudinal coordinate of the particle; and then to send the particles into a bending magnet, so that those with different s will move along different trajectories and will be focussed longitudinally. One needs for this a set of deflecting RF cavities and a rather large horizontal size Δx of all focussing elements: $\Delta x \sim 10\sigma_L\,(R/\ell)$, where $\ell/R = \phi$ is the rotation angle in the magnetic field. The further transverse focussing into the IP also requires a set of large and powerful elements, not only because of a small β_y^*, but also because of a large horizontal emittance, ϵ_x^*. In this design there is a chain of transformations between the entrance to and the exit from the interaction area:

$$\epsilon_L \to \epsilon_x^* \to \epsilon_L;\ \epsilon_x \to \epsilon_L^* \to \epsilon_x;\ \epsilon_L^* \ll \epsilon_L. \qquad (1)$$

It is convenient and probably useful to design this system in such a way that bunches will have a disk-like shape at the IP: $\sigma_L^* \approx \sigma_x^*$ (and $\sigma_L^* = \beta_y^*$). Such "disks" are almost insensitive to the crossing and crabbing angles. Besides that, if the lattice is designed properly in this system, the horizontal oscillations of the particles are almost insensitive to the beam-beam perturbations. The x-oscillations are perturbed only by longitudinal beam-beam kicks, which are relatively weak. Horizontal beam-beam kicks produce only longitudinal perturbations.

Our rough design and preliminary simulations (without taking into account the errors of the lattice) show that such a project is not unfeasible.

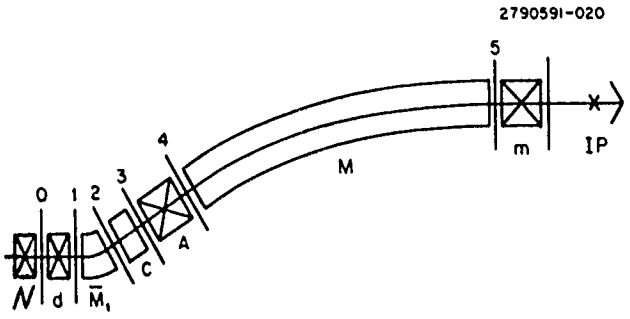


Figure 1: Lattice for Bunch Shortening

Lattice for Bunch Shortening

Fig. 1 shows the lattice needed for local bunch shortening. Particles first pass the thin defocussing lens, d, which eliminates the dependence of σ_L^* on σ_z,

$$\frac{1}{f} \approx \frac{Rb}{3L}\left(\frac{\ell}{R}\right)^2\left(1 + \frac{1}{2b\bar{R}}\right) \qquad (2)$$

where $\ell/R = \phi$ is the angle of the bending magnet mentioned above, b is the full strength of the deflecting RF cavities C (fig. 1)

$$\Delta x' = bs,\ b = \frac{2\pi U}{\lambda_{RF}\,\epsilon} = \frac{1}{L\sin\phi}, \qquad (3)$$

and l is the strength of the triplet A (fig. 1) of quadrupole lenses FDF with phase shifts $\pi/4$, $3\pi/4$, $\pi/4$, with 2×2

*Work supported by the National Science Foundation

0-7803-0135-8/91$01.00 ©IEEE

matrices

$$A_x = \begin{pmatrix} 0 & L \\ -1/L & 0 \end{pmatrix}, \quad A_y = \begin{pmatrix} 0 & -Le^{-3\pi/2} \\ e^{3\pi/2}/L & 0 \end{pmatrix} \tag{4}$$

Here $L = \exp(3\pi/2)\sqrt{\frac{BR}{\partial B/\partial R}}$, and $\overline{R}$ in (2) is the radius of the magnet (with an inverse field) next to lens d. This magnet eliminates the dependence of $\sigma_{l'}^*$ on σ_ϵ, its (inverse) angle $\overline{\alpha}$ and 4×4 matrix $\overline{M}$ are

$$\overline{\alpha} = \frac{\overline{\ell}}{\overline{R}} = \frac{R}{L}\frac{(\phi - \sin\phi)}{\sin\phi} \ll 1, \tag{5}$$

$$\overline{M} \approx \begin{pmatrix} 1 & \overline{R}\overline{\alpha} & 0 & 0 \\ -\overline{\alpha}/\overline{R} & 1 & 0 & -\overline{\alpha} \\ \overline{\alpha} & 0 & 1 & 0 \\ 0 & 0 & 0 & 1 \end{pmatrix}. \tag{6}$$

The main magnet, M, whose matrix is

$$M = \begin{pmatrix} \cos\phi & R\sin\phi & 0 & R(1-\cos\phi) \\ -\sin\phi/R & \cos\phi & 0 & \sin\phi \\ -\sin\phi & -R(1-\cos\phi) & 1 & -R(\phi - \sin\phi) \\ 0 & 0 & 0 & 1 \end{pmatrix} \tag{7}$$

transforms x deviations (which now depend on s after a particle has passed through the triplet A) into the deviations of s,

$$\Delta s = -\int_0^z dz\, x(z)/R. \tag{8}$$

Finally, lenses m form the dispersion function η^* at the IP (taking into account a given focussing system between m and the IP), and lenses N form the dependence of $\sigma_{l'}^*$ on $\sigma_{x'}$. (All sizes $\sigma_x, \sigma_{x'}, \sigma_s, \sigma_\epsilon$ are given at the entrance of the lattice.)

Multiplying all matrices, including the 4×4 matrix of the RF cavity,

$$C \approx \begin{pmatrix} 1 & 0 & 0 & 0 \\ 0 & 1 & b & 0 \\ 0 & 0 & 1 & 0 \\ b & 0 & 0 & 1 \end{pmatrix}, \tag{9}$$

we get the matrix for the transition from the entrance of the lattice to the IP in the horizontal plane

$$S = \begin{pmatrix} 0 & 0 & 0 & \eta^* \\ 0 & r/\eta^* & -1/\eta^* & 0 \\ 0 & r & 0 & 0 \\ 1/r & 0 & 0 & 1 \end{pmatrix} \tag{10}$$

$$S^{-1} = \begin{pmatrix} r/\eta^* & 0 & 0 & r \\ 0 & 0 & 1/r & 0 \\ 0 & \eta^* & 1 & 0 \\ 1/\eta^* & 0 & 0 & 0 \end{pmatrix} \tag{11}$$

The remarkable feature of the S^{-1} matrix is that it cancels the influence of the horizontal beam-beam kicks $(\delta x')^*$ on the x-movement $(S_{21}^{-1} = S_{22}^{-1} = 0)$. The kick $(\delta x')^*$ itself depends on y^* and on the deviation $\Delta p/p$ at the entrance of the lattice, because, according to (10), $S_{11} = S_{12} = S_{13} = 0$, $S_{14} = \eta^*$, and the x^*-coordinates at the IP depend only on $\Delta p/p$. Therefore, kick $(\delta s)_{exit}$ depends only on $(\Delta p/p)_{entrance}$ and y^*. The x coordinates link with the longitudinal coordinates through relatively small longitudinal kicks $(\Delta p/p)^*$ $(S_{14}^{-1} = r \neq 0)$. Four deflecting cavities with $\lambda_{RF} = 0.6\,m$ can give $b \approx 1.5 \times 10^{-2}\,m^{-1}$. With $L \approx 100$ condition (3) gives $\sin\phi \approx 0.65$. When $R = 40\,m$, $\ell = 26\,m$. When $\epsilon_x = 10^{-7}$ and $\epsilon_y = 0.25 \times 10^{-9}$, $\sigma_x < 1\,cm$ and $\sigma_y < 1.5\,mm$ over the entire lattice. If $\sigma_L = 0.5\,cm$ and $\sigma_\epsilon = 5.5 \times 10^{-4}$, then $\epsilon_y^* = 2.75 \times 10^{-6}$, $\sigma_x^* = 1\,mm$, and $\sigma_y^* = 5 \times 10^{-7}\,m$.

Interaction Region Optical Design

There are two very challenging problems in designing interaction region optics with $\beta_y^* \sim 1\ mm$ controlling the vertical chromaticity, and providing aperture for a large horizontal emittance. High chromaticity causes a reduction of the range of energies with stable focussing. Indirectly, it causes a reduction in the dynamic aperture through increased sextupole strengths that are required to compensate for the chromaticity . High chromaticity is basic to all millimeter β_y^* optics for B factories; focussing magnets simply cannot be made strong enough or fit close enough to the interaction point. The vertical beta function grows so rapidly with distance from the interaction point $(\beta_y \approx s^2/\beta_y^*)$ that the contribution to the vertical chromaticity, $\Delta\xi_y = \frac{1}{4\pi}\int K\beta_y ds$ becomes very large. Peak β_y of 500 m or more are unavoidable given a 'detector stay clear' cone of half angle 0.3 *radians*, an interaction point beam pipe radius of $\approx 2\ cm$, and the limits of magnetic materials.

The problem of finding an adequate aperture for high horizontal emittance is specific to the scheme described in this paper, where the horizontal emittance is locally enlarged in order to shorten the bunch length. An example of an engineered conceptual design of magnetic elements and vacuum chamber that would provide a 1 mm β_y^* is given in figure 2. The horizontal stay clear criterion is $X_{STAY\,CLEAR}\,[m] = 10\sigma_H + .005\sqrt{\beta_x\,[m]} + .10$ and is the same as that used in the Cornell B factory design. The vertical stay clear criterion is $Y_{STAY\,CLEAR} = X_{STAY\,CLEAR}$. The latter was chosen because the large local horizontal emittance dominates the aperture. In this interaction region design, the contribution to vertical chromaticity from each side of the interaction point is 62. With such a large chromaticity, adequate single beam stability is doubtful. There are a couple of ideas that could be used to reduce the effect of the chromaticity. One is to put sextupole components on the windings of the superconducting quadrupoles. Although there is no conventional η_x the effect of the bunch compression optics would correlate energy with horizontal position and could be used to cancel the chromaticity tuneshift locally. The other idea is to "tune out" the chromaticity using a series of optimized

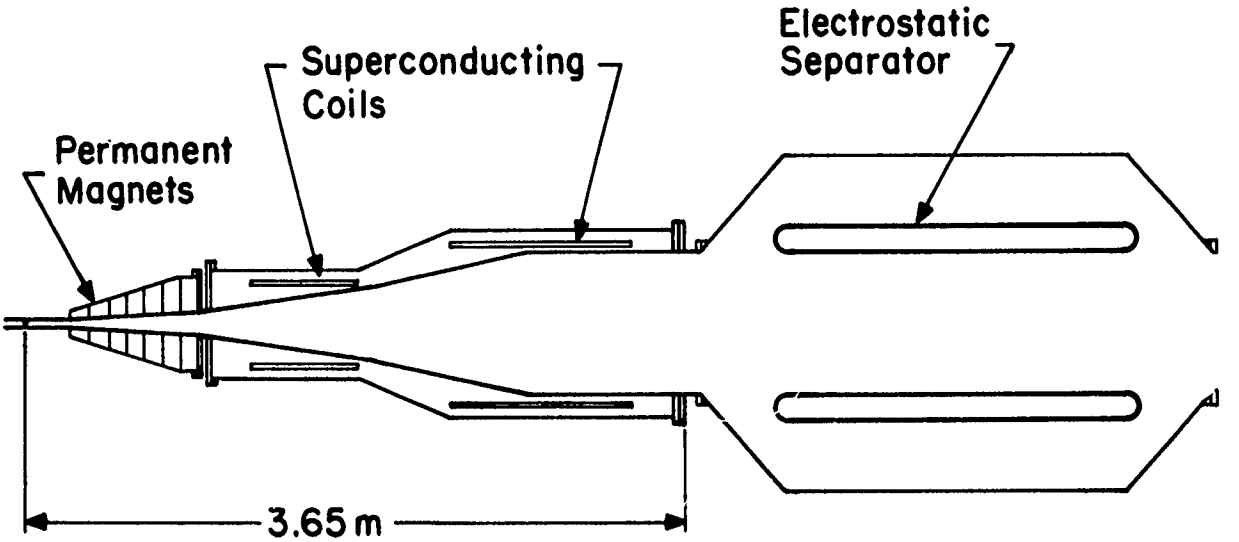


Figure 2: The interaction region quadrupoles and vacuum chamber are designed for 1 mm β_y^*, a crossing angle of ± 16.6 *milliradians*, and a (local) horizontal emittance $\epsilon_x = 2.75 \times 10^{-6}$ m. The electrostatic separator is used to further separate the beams into separate vacuum chambers.

quadrupoles.

Program Description and Simulation Results

In the simulation we have used 10^5 "particles" per bunch executing 5×10^3 turns. Only the symmetric case (equal energy beams) was considered. When treated as the "strong" beam, every bunch was divided into several equally charged slices. We have developed the basic program used in [2] for the flat beam in the following respects:

(a) Strong-strong collisions, in the approximation of unperturbed bunch shapes during a collision. In reality, the relative perturbation of vertical bunch size during one collision is about 10^{-3}.

(b) Longitudinal kicks, $\delta\varepsilon/\varepsilon$ They are essential in this design even without a crossing angle because of the relatively large angles $\sigma_{x'}^*$, $\sigma_{y'}^*$. In the presence of the crossing angle $\theta \ll 1$ (without crabbing), we simply use the angle $(x' + \theta)$ instead of x' when calculating the longitudinal kick. Neglecting quadratic terms $(\delta x')^2$ and $(\delta y')^2$, we have

$$\frac{\delta\varepsilon}{\varepsilon} = \frac{1}{2}\left[(x' + \theta)\,\delta x' + y'\delta y'\right]. \qquad (12)$$

(c) Crossing angle In addition to $\delta\varepsilon/\varepsilon$, θ changes the horizontal distance between the "weak" particle position x and the position x_c of the center of the strong bunch slice, at the moment of collision with this slice:

$$\Delta = (x - x_c) = x_{1p} + s^{(1)}\left(x'_{1p} + \theta\right) - \bar{s}_c\,\alpha, \qquad (13)$$

where $s^{(1)} = (s_{1p} - \bar{s}_c)/2$, x_{1p}, x'_{1p}, and s_{1p} are coordinates of the particle in the "weak"bunch system, $\bar{s}_c$ is the s-coordinate of the slice in the "strong" bunch system, and α is the crabbing angle; $\alpha = 0$ in our case. For the short disk-like bunch, $\sigma_l^* \approx \sigma_x^*$, we have $\sigma_l^*\theta \ll \sigma_x^*$, so the influence of the crossing angle on Δ is very small.

(d) Feedback dipole corrections. We have included such corrections in the program because without them some dipole beam-beam instabilities could develop.

The main preliminary result of the simulations is that the tune map of the luminosity, $\mathcal{L} = \mathcal{L}(\nu_x, \nu_y)$, in this design is at least as good as the maps of usual colliders.

ν_h	$\nu_v = 0.66$	$\nu_v = 0.67$	ν_h	$\nu_v = 0.68$	$\nu_v = 0.69$
	$K = 0.74$	$K = 0.71$		$K = 0.74$	$K = 0.59$
.70	$\mathcal{L} = 6.79$	$\mathcal{L} = 6.5$	.66	$\mathcal{L} = 6.96$	$\mathcal{L} = 0.54$
	$\mathbf{L} = 1.0$	$\mathbf{L} = 0.97$		$\mathbf{L} = 1.0$	$\mathbf{L} = 0.8$
	$K = 0.73$	$K = 0.75$		$K = 0.79$	$K = 0.61$
.71	$\mathcal{L} = 6.93$	$\mathcal{L} = 6.98$	.67	$\mathcal{L} = 7.08$	$\mathcal{L} = 5.7$
	$\mathbf{L} = 1.0$	$\mathbf{L} = 1.0$		$\mathbf{L} = 1.0$	$\mathbf{L} = 0.85$

Table 1: Examples of stable regions. $\mathcal{L}_0$ is the initial luminosity; $K = \mathcal{L}\left(10^{32}\right)/\mathcal{L}_0\left(10^{32}\right)$. $\mathbf{L} = \mathcal{L}n_B\left(10^{35}\right)$; $n_B = 150$; $I_B = 20\,mA$, $I = 3\,A$. $E = 5.3\,GeV$ (both beams); crossing angle $\theta = 33\,mradians$.

References

[1] Y. Orlov, "Bunch Length Compression Using Crab Cavities", *Proceedings of the Berkeley B Factory Workshop* (1990).

[2] S. Krishnagopal and R. Siemann, "Bunch-Length Effects in the Beam-Beam Interaction", Phys Rev. D 41 (1990), 2312.

Apiary B Factory Lattice Design*

M. H. R. Donald

Stanford Linear Accelerator Center Stanford, CA 94309

and

A. A. Garren

Lawrence Berkeley Laboratory Berkeley, California 94720

Abstract

The Apiary B Factory is a proposed high-intensity electron-positron collider. This paper will present the lattice design for this facility, which envisions two rings with unequal energies in the PEP tunnel. The design has many interesting optical and geometrical features due to the needs to conform to the existing tunnel, and to achieve the necessary emittances, damping times and vacuum. Existing hardware is used to a maximum extent.

I. Introduction

The Apiary B Factory consists of two equal-sized rings in the PEP tunnel with unequal energies, offset vertically except in the IR straight section where the beams are brought into head-on collision. The rings retain the general configuration of PEP, with a geometric 6-fold periodicity. The Apiary lattice resembles that of PEP in the arcs but is quite different in the straight sections. The design of the high and low energy rings (HER and LER) differ, especially in the straight sections, but in the arcs and in some of the straight sections the quadrupoles are directly above and below each other.

For each ring, all of the arcs are identical except that in the HER the dispersion suppressors of four of them are tuned to create a beat in the dispersion function through the arc. This 'mismatched' dispersion function serves to adjust the emittance of the HER to the desired value. Each arc consists of 16 cells; twelve cells in the center have the same length, two at each end are slightly longer.

The main differences between the sextants of the rings are occasioned by the different types of long straight sections, each of which has its orbit functions matched to those of the arcs at the boundaries.

Having touched on the common features of the rings, we will now discuss their individual features.

II. Low Energy Ring

A. Arcs

The center nine cells are regular 80° phase FODO cells, and the remaining 3-1/2 cells at each end are the dispersion suppressors. The phase was chosen to achieve a suitable momentum compaction and to make an achromat of the center nine cells. The dipoles are displaced upstream from the center of each half cell to give space to extract the synchrotron radiation.

Table I. Apiary Lattice Parameters

	Low Energy Ring	High Energy Ring	
Energy	3.1	9	GeV
Circumference	2199.32	2199.32	m
Vertical ring separation	0.895	m	
Collision mode		head on	
Luminosity		3 E 33	cm-2 s-1
Current	2.14	1.48	A
Emittance, epsx/epsy	96.5/3.9	48.2/1.9	nm-rad
Betas @ IP, $\beta x/\beta y$	37.5/1.5	75/3.0	cm
Bunch separation	1.26	1.26	m
Damping time, τe	18.4	18.4	ms
Number straight sections	6	6	
Arc length	245.553	245.553	m
Straight section length	121	121	m
Cell length - normal	15.125	15.125	m
Cell length - suppressor	16.0125	16.0125	m
Cell phase advance	80	60	deg

B. Normal Straight Sections

The LER has two normal sextants whose long straight sections consist of eight normal-length cells without dipoles, with phase advances of 90° in their normal state. However the central seven quadrupoles can be tuned with four independent power supplies to change the global tunes while retaining the overall matching to the arcs. RF cavities can also be installed in these straight sections.

C. Injection Straight Section

One long straight section has a 40 m long drift space for injection, with $\beta x = 80$ m at the center.

D. Wiggler Straight Sections

Two straight sections are configured to house wiggler magnets. These are used to adjust the emittance and damping time of the LER. They are placed on doglegs that direct the radiation away from the ring magnets.

* Work supported by Department of Energy contract DE AC03-76SF00515 and DE-AC03-76SF00098.

U.S. Government work not protected by U.S. Copyright.

E. IR Straight Section

The LER beamline is brought into colinearity with that of the HER at the IP by a combination of vertical and horizontal bends. The first separation of the beams leaving the IP is horizontal, and is done with a permanent-magnet dipole 20 cm from the IP and a triplet, whose quadrupoles are suitably offset to increase the separation. These are adjusted primarily to focus the low-energy beam. The triplet is followed by a septum quadrupole that focuses the HER beam only. Next the LER beamline is bent upwards by a septum dipole. The remainder of the IR straight section contains bends to bring the beamline to the arc at the right position and direction, and quadrupoles to match the beta functions and dispersion. The horizontal bending is antisymmetric about the IP, producing an S-bend that is favorable for masking.

III. HIGH ENERGY RING

A. Arcs

The center twelve cells are of a regular FODO structure with 60° phase advance per cell in each plane. The dipoles are centered between the QF and QD quadrupoles. At each end of each arc are 2-cell dispersion suppressors, each cell having close to 90° phase advance. In four of the arcs the dispersion suppressors are tuned so as to create a beat in the dispersion function through those arcs.

B. Straight Sections

The normal straight sections are filled with a regular FODO lattice. The length and phase advance of these cells is the same as that in the arcs In two of the straights the FODO lattice is tunable so as to adjust the overall betatron tune of the HER. In this case the center cells of the straight are tuned together and three quadrupoles at each end are adjusted to effect the match to the dispersion suppressor. The injection straight section is identical to that in the LER

C. Collision Straight Section

The collision straight of the HER, being in a plane, is much simpler than that of the LER. The common permanent magnet triplet provides some focusing for the high energy beam but the main interaction region focusing is provided by a doublet placed as close as possible to the IP. The first quadrupole of this doublet has to be of a septum design so as to not interfere with the low energy beam. The dispersion function caused by the separation of the beams is controlled by two strings of very weak dipoles and another quadrupole doublet completes the focusing into the dispersion suppressor. A pair of weak dipoles adjust the angle of the beam as it enters the arc.

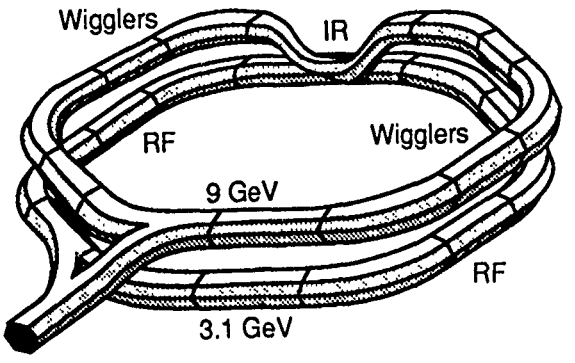


Fig. 1. Schematic of the two rings. The Low Energy Ring (LER) is elevated 0.895 m above the High Energy Ring (HER) which lies in the horizontal plane. The beams are brought into collision by a combination of vertical and horizontal bends. Wiggler magnets in some long straight sections serve to adjust the damping time and emittance of the LER.

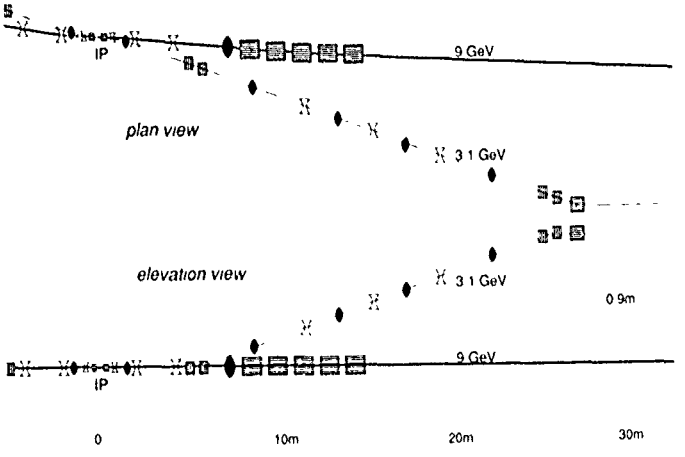


Fig. 2. Magnetic separation of the high and low energy beams. The initial horizontal separation is accomplished by a combination of a permanent magnet dipole followed by three offset permanent magnet quadrupoles. Separation is achieved by exploiting the energy difference between the beams. Once the beams are separated a system of vertically bending dipoles elevates the LER above the HER.

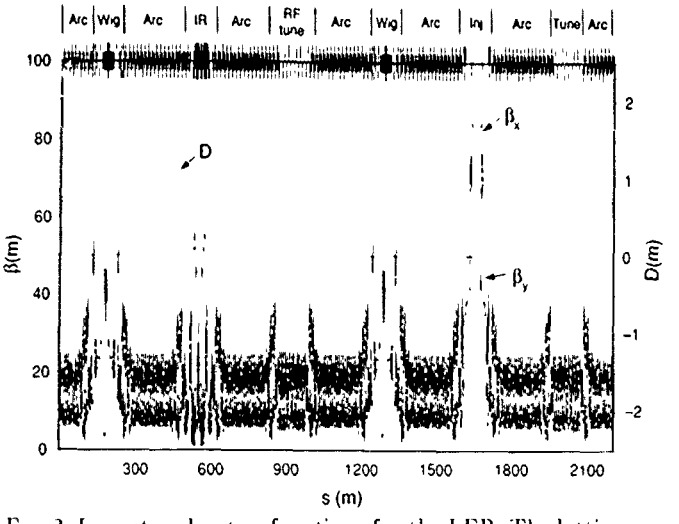


Fig. 3. Layout and optics functions for the LER. The lattice for the full ring is shown, starting and finishing at mid-arc in region 11.

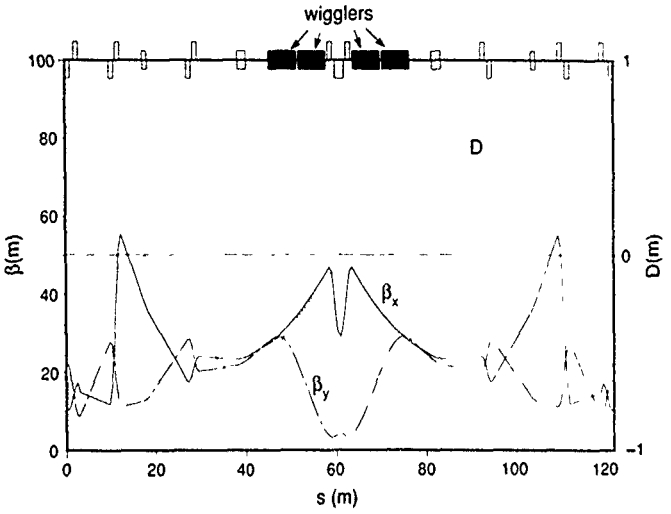


Fig. 4. Layout and optics functions for the wiggler straight sections of the LER. In conjunction with the dispersion function D, and its derivative, the wigglers increase the emittance of the low-energy beam. In addition, the wigglers can decrease the damping time of the low-energy beam so that it is equal to that of the high-energy beam.

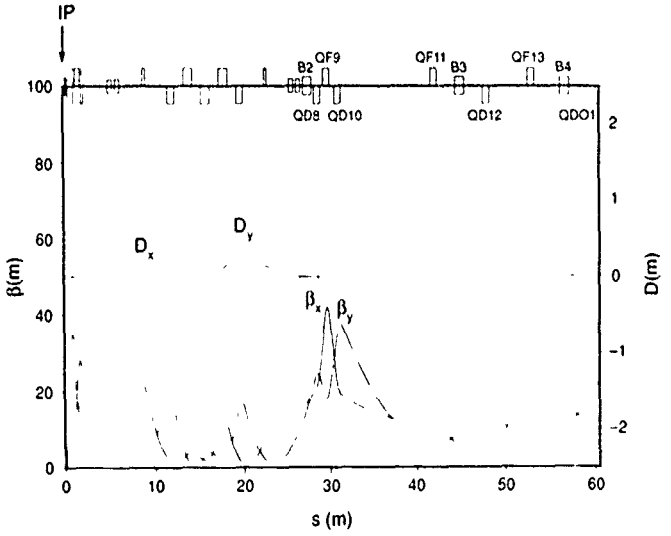


Fig. 5. Layout and optics functions for the right-hand half of the IR straight section of the LER. The quadrupoles QD8 through QF13 match the beta functions into the dispersion suppressor.

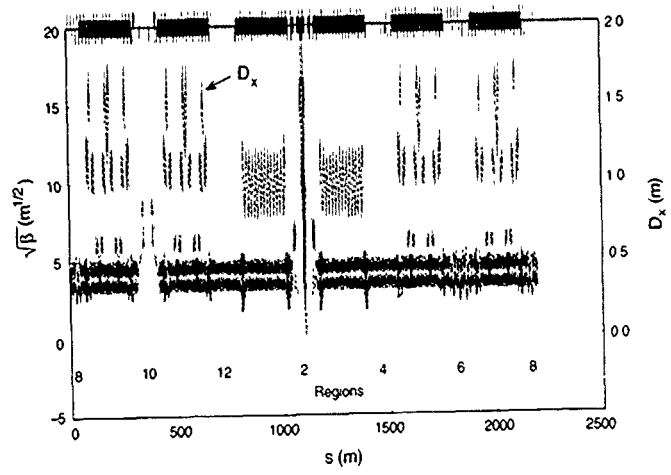


Fig. 6. Lattice functions $\sqrt{\beta_x}$, $\sqrt{\beta_y}$, and D_x (horizontal dispersion function) for the complete HER, starting at region 8. The collision region (region 2) is shown in the center of the figure.

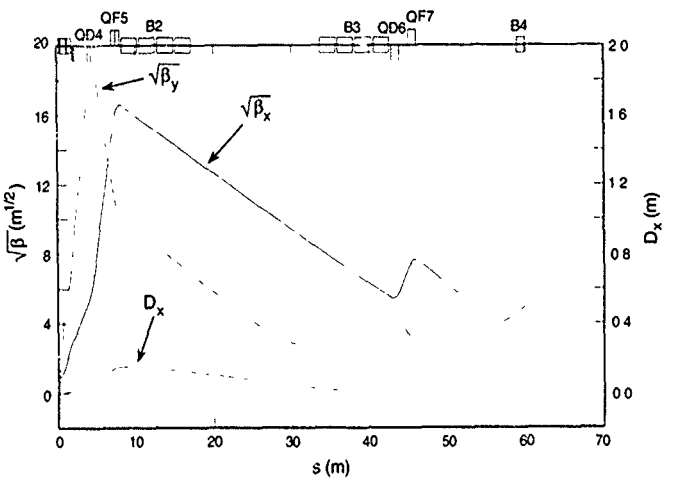


Fig. 7. Lattice functions for the first 60 m of the IR straight section of the HER. The B2 and B3 dipoles match the dispersion function to zero.

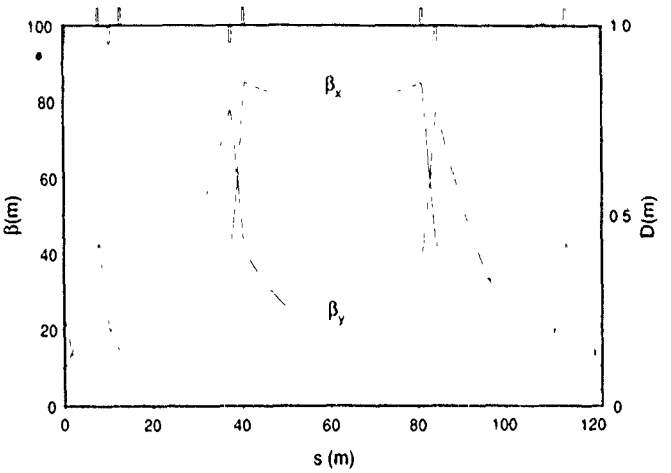


Fig. 8. Layout and optics functions for the injection straight section of the LER. The injection point is at the center of the figure, in the middle of the long straight section. Beta functions in this region are easily adjustable to match injection requirements.

APIARY B-Factory Separation Scheme*

A. GARREN

Lawrence Berkeley Labs, University of California at Berkeley, Berkeley, CA 94720
and
M. SULLIVAN

Inter-campus Institute for Research at Particle Accelerators—Stanford Linear Accelerator Center, Stanford, CA 94309

Abstract

A magnetic beam-separation scheme for an asymmetric-energy B-Factory based on the SLAC electron-positron collider PEP is described that has the following properties: the beams collide head-on and are separated magnetically with sufficient clearance at the parasitic crossing points and at the septum, the magnets have large beam-stay-clear apertures, synchrotron radiation produces low detector backgrounds and acceptable heat loads, and the peak β–function values and contributions to the chromaticities in the IR quadrupoles are moderate.

I. INTRODUCTION

The APIARY B-Factory design calls for electrons and positrons to be stored in two rings, separated vertically, and located in the PEP tunnel. The 2-ring system is forced by the high currents and small bunch spacing required for high luminosity. The parameters of the system are shown in Table 1.

Table 1. APIARY Parameters

	Low Energy Beam	High Energy Beam	
Energy	3.1	9.0	GeV
Current	2.14	1.48	A
Betas at IP, β_x/β_y	37.5/1.5	75.0/3.0	cm
Emittance, $\varepsilon_x/\varepsilon_y$	96.5/3.9	48.2/1.9	nm-rad
Bunch separation	1.26	1.26	m
Vertical separation	0.895		m
Collision mode	head on		
Separation scheme	magnetic: horizontal, then vertical		
IP aspect ratio, σ_x:σ_y	25:1		
Luminosity	3×10^{33}		cm^{-2} sec^{-1}

The separation scheme must solve three interwoven problems: to separate the beams and lead them into the two rings, to focus the beams without unacceptable β–function values or chromaticity contributions, and to control the quantity and distribution of synchrotron radiation (SR) produced so that sensitive components can be shielded by the masking system.

II. DESCRIPTION OF THE SEPARATION SCHEME

The separation scheme is briefly as follows: the beams collide head-on and are separated after leaving the interaction point (IP) by the dipole magnet B1 starting 20 cm from the IP, a triplet common to both beams with quadrupoles QD1, QF2, and QD3 centered alternately on the high, low and high energy beams to increase the separation, a septum quadrupole QD4 focussing the high-energy beam (HEB) only, and a vertical septum dipole that deflects the low-energy beam (LEB) upwards, see Figs. 1–3. This dipole together with three others beyond bring the LEB to a level 89.5 cm above the HEB. Seven quadrupoles between these vertical bends focus the LEB and bring the horizontal and vertical dispersions to zero. Just beyond the vertical septum, the quadrupole QF5 focusses the HEB horizontally (see Fig. 4), and bending magnets begin the steering of that beam toward the arc and contribute to the dispersion suppression. Additional horizontal dipoles and quadrupoles in both beamlines complete the steering, dispersion matching, and matching of the beams to the β functions in the arcs.

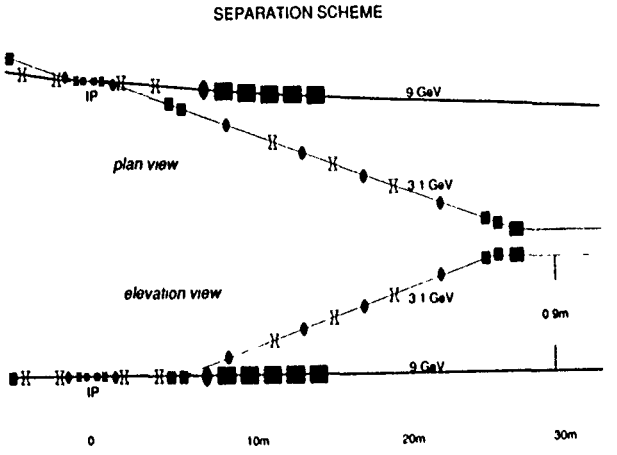


Figure 1. Schematic diagram of the APIARY separation scheme.

The system design satisfies the following constraints:

- The beam-stay-clear (BSC) in the interaction region (IR) magnets is defined to contain both beams with $15\sigma_{x,y}$ envelopes, plus 2 mm for orbit distortion, where σ_x, σ_y refer to uncoupled, fully-coupled beams respectively
- At least 2 mm spacing between SR fans and the nearest surface
- A 5 mm allowance for beam pipe, cooling, and trim coils between the BSC and SR fans and any magnetic material
- The ratio β_y^*/(distance to 1st quadrupole) $\sim$ 100, in order to keep the chromaticity reasonable
- 15 mm is allowed for the QF4 septum between the BSCs of the two beams

* Work supported by Department of Energy contract DE-AC03-76SF00515 and DE-AS03-76ER70285 and DE-AC03-76SF00098.

0-7803-0135-8/91$01.00 ©IEEE

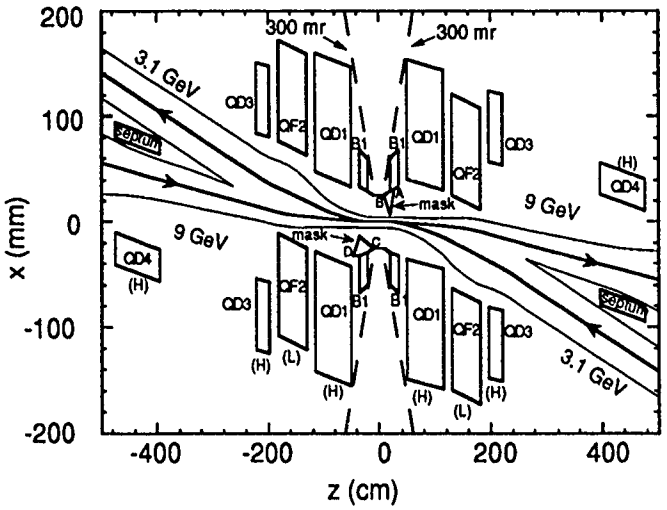


Figure 2. Plan view of the magnets and beamlines near the IP. Note the distorted scale.

III. Optics, Beam Matching and Steering

The four common elements B1, QD1, QF2, and QD3 are permanent magnets, with 1.05 T remnant fields, and inner radii satisfying the BSC and other constraints listed previously. Fig. 2 shows a diagram of the IR in plan view. The beamlines are shown as heavy lines, and the $15\sigma_x$ envelopes as light lines. The (H) or (L) near each magnet indicates on which beam (HEB or LEB) the quadrupole is centered.

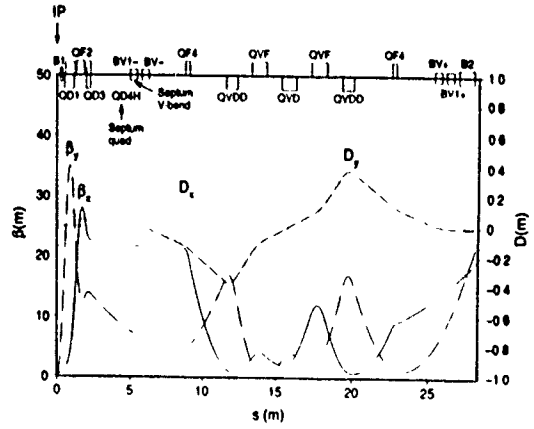


Figure 3. Lattice functions of the LEB from the IP to the end of the vertical step.

The triplet is adjusted to focus the LEB so that it is small at the QD4 septum and enters the vertical-step region in a nearly parallel state with small β–function values (see Fig. 5). The triplet is also quite useful for some initial focusing of the HEB. The quadrupole QD1, though centered on the HEB, is tilted with respect to it in order that one of the SR fans not strike its inner surface.

The first 'parasitic' bunch crossing point occurs 63 cm from the IP, just inside QD1, where the beamlines are separated by 7.5 times the largest σ-value of either beam (σ_x(LEB)).

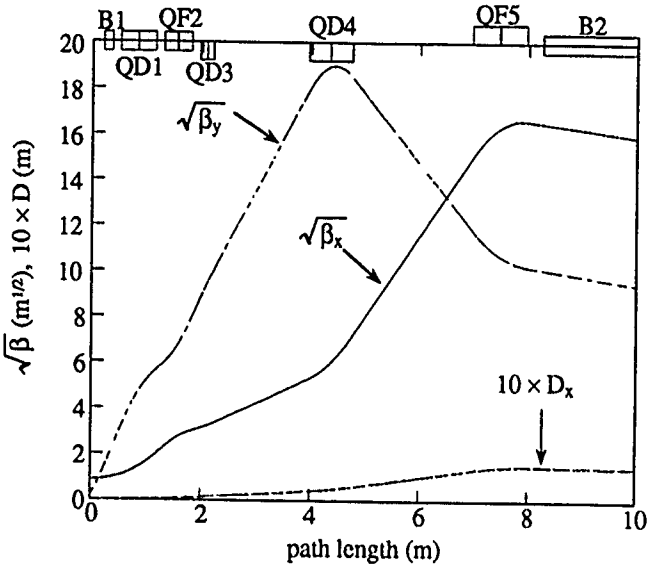


Figure 4. Lattice functions of the HEB within the first 10 m of the IP.

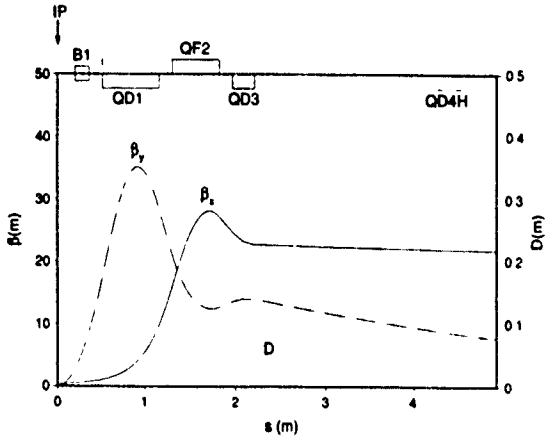


Figure 5. Lattice functions of the LEB through the common magnets and the septum quadrupole.

The horizontal bending pattern is antisymmetric about the IP, which produces an S-bend beamline—a geometry that is conducive to extracting the synchrotron radiation.

Figure 6 shows the first 60 m from the IP to the start of the arc for the HEB. The dispersion function D and its slope are brought to zero by the dipoles B2 and B3 whose bending is very weak ($\epsilon_{crit} \approx 1$ keV) to avoid problems with the SR in the IR. These dipoles are followed by quadrupoles QD6 and QF7 that match the β functions into the arc. Two additional dipoles in the dispersion suppressor at the end of the arc steer the HEB to the proper direction.

The strength of the B2 dipole of the LEB (originally set to bring D_x and its slope D_x' to zero at the end of B2), together with the strengths of three additional dipoles, are adjusted to steer the LEB from the arc to the IP with the correct radial position and slope, while preserving the dispersion matching. The remaining β–function matching for the LEB, is done with quadrupoles QD8-QF13, located between the end of the vertical step and the arc.

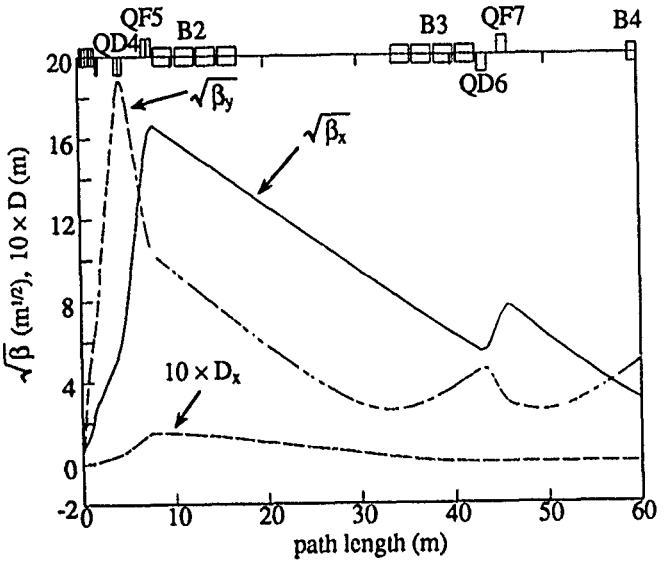


Figure 6. Lattice functions of the HEB from the IP to the begining of the arc.

IV. Control of the Synchrotron Radiation

The LEB generates SR fans as it passes through QD3, QD1 and B1 on its way to the IP. Figure 7 shows the LEB radiation fans near the IP. The mask labeled AB in Figs. 7 and 8 is designed to prevent any SR generated by the upstream magnets from directly striking the detector beam pipe. The QD1 magnet, in the LEB downstream direction, is tilted with respect to the HEB axis by 22 mrad, so that any SR generated by the LEB upstream magnets that goes by the AB mask tip clears the beampipe.

As can be seen in Fig. 7, the AB mask absorbs all of the fan radiation from the upstream QD3 magnet. The fans generated by the two B1 dipoles and by the downstream QD1 and QD3 magnets pass through the IR without striking any surfaces. The first surface that intercepts the QD1 fans is the "crotch mask" in front of the QD4 septum. Table 2 summarizes some of the properties of the LEB and HEB radiation fans.

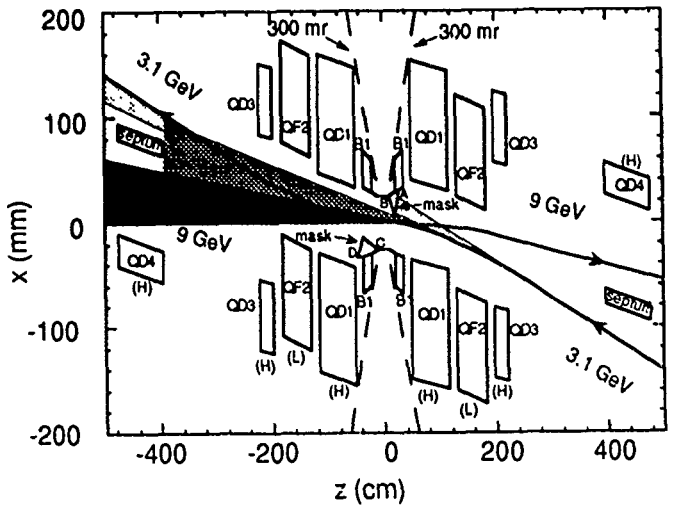


Figure 7 Radiation fans generated by the LEB near the IP Darker shading indicates higher radiation intensity.

Table 2. Properties of the synchrotron radiation generated within ±3 meters of the IP.

Magnet	Fan pwr (kW)	N_γ (10^{10})	ε_{crit}(keV)
LEB:			
Upstream QD3	0.84	3.1	2.3
Upstream QD1	0.83	5.4	1.3
Upstream B1	2.39	4.2	4.8
Downstream B1	2.39	4.2	4.8
Downstream QD1	0.96	5.2	1.4
Downstream QD3	0.91	3.1	2.4
subtotal	8.3	13	
HEB:			
Upstream QF2	28.3	7.5	32.1
Upstream QD1	2.3	2.7	7.3
Upstream B1	13.8	2.9	40.4
Downstream B1	13.8	2.9	40.4
Downstream QD1	1.1	1.8	5.1
Downstream QF2	26.1	7.3	30.5
subtotal	85.4	25	
Total	93.7	38	

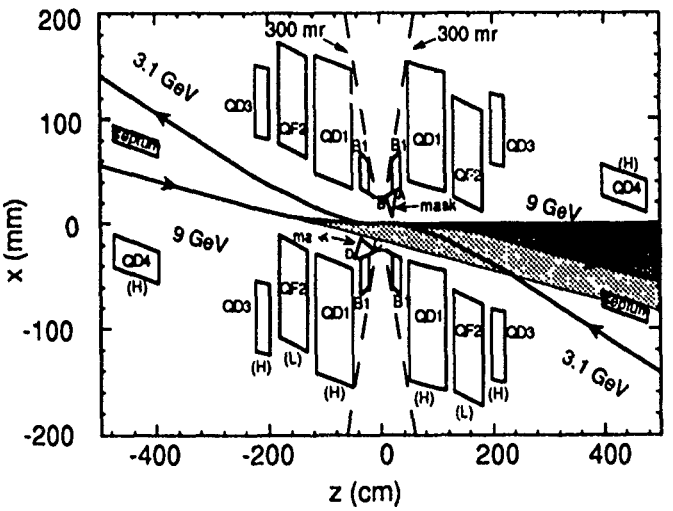


Figure 8. Radiation fans generated by the HEB near the IP.

The SR fans generated by the HEB as it passes through the QF2 and B1 magnets also pass through the detector region without striking any surfaces. Figure 8 shows the HEB radiation fans near the IP. The mask labeled CD in Figs. 7 and 8 is located to prevent quadrupole radiation produced by the HEB in QF5 and QD4 from directly striking the detector beam pipe. The CD mask tip is positioned 2 mm outside the upstream QF2 radiation fan that passes through the IR. The other QD1 magnet, in the HEB downstream direction, is tilted with respect to the HEB axis by 15 mrad, so that this fan clears the beampipe. Therefore the first surface struck by the upstream QF2 fan is the crotch mask in front of QD4.

Only 6% of the total generated SR strikes surfaces within 4 m of the IP: 4.3 kW on the crotch mask from the HEB and 1.2 kW on the AB mask from the LEB (see Table 2) This leads to an estimated detector background level that is 50 times lower than acceptable limits.

Feasibility of a ϕ Factory in KEK

Kohji HIRATA and Kazuhito OHMI
KEK, National Laboratory for High Energy Physics, Oho, Tsukuba, Ibaraki 305, Japan

Abstract

An e^+e^- two-ring collider is being considered in KEK with the beam energy of 0.51GeV and the peak luminosity of 3×10^{33} cm^{-2}s^{-1}. By making an example, it is shown that such a ring can be constructed in KEK, with its present and already planned facilities, in a short period and at small expense.

1 Introduction

We consider a ϕ factory. The aim is to study CP and CPT violations[1]. To this end, a huge luminosity, $L = 3 \times 10^{33}$cm^{-2}s^{-1}, is required.

As shown in Fig.1, the rings we employ have racetrack shapes: two rings will be superposed and cross each other horizontally at the interaction region (IR). In addition to four arcs (65.6m), there are two long straight sections (24m each: one for IR and the other for RF and possibly Damping wigglers) and two short straight sections (3.2m each: one for injection and the other for feed back systems).

We consider it first from beam-dynamics point of view and then from facility point of view.

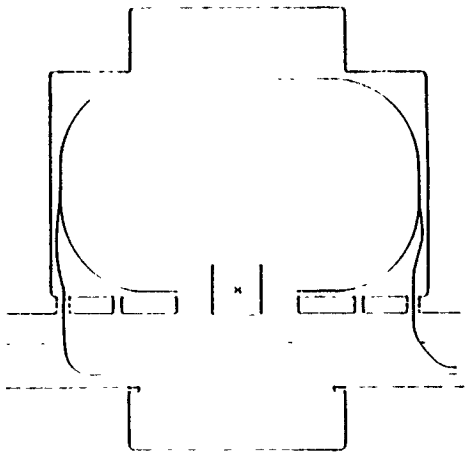


Figure 1: Configuration of the ϕ-Factory rings.

2 Beam Dynamics Consideration

We need a huge luminosity.

Based upon the assumption that horizontal and vertical beam-beam parameters (ξ) are equal (the optimal coupling), the maximum luminosity can be expressed as

$$L_{max}(\times 10^{33} cm^{-2} s^{-1}) = 0.2167 \times I_{max}(A) \times E(GeV) \times \frac{\xi_{max}}{\beta_y^{IP}(m)}(1+\kappa), \quad (1)$$

We first reject the idea of plural interaction points to maximize the ξ_{max}[2,3]. We, then, try to increase the ratio ξ_{max}/β_y^{IP} in order to achieve the luminosity with the least current. We assume $\xi_{max} \simeq 0.03$, (limited by the beam-beam interaction: see 2.1), and that β_y^{IP} is 1 cm (limited by the chromaticity correction: see 2.2). We choose a flat beam ($\kappa \simeq 0$) rather than a round one ($\kappa = 1$), since the former allows simpler final-focus and beam-separation systems and since there does not seem to be a large merit of using a round beam[4].

With these parameters, we need a huge current: $I_{max} =$ 9A. The number of particles per bunch N_b, then, is expressed as $N_b = IS_B/(ec)$, where S_B is the bunch spacing. The horizontal emittance, ε_x, is determined by ξ_x and N_b as

$$\varepsilon_x = \frac{r_e N_b}{2\pi\gamma\xi_x}. \quad (2)$$

Thus, when S_B, hence N_b is large, ε_x should also be large.

We adopt the 1.428 GHz RF system (see 2.3), since we can utilize some of the RF equipment which will be used in the damping ring, now being planned[5] for JLC[6]. We found it necessary to fill every two buckets (hence $S_B = 40cm$) to avoid too large value of ε_x. Since this bunch spacing is too short, we adopt a collision with a finite crossing angle (see 2.4). Since the lifetime of the beam is not long, we need an injection every 17 minutes (see 2.5).

2.1 Beam-Beam Interaction

The luminosity is limited by the beam-beam interaction[7, 4]. It is still difficult to accurately predict the limit. We had better assume an empirically safe value: $\xi_{max} = 0.03$.

0-7803-0135-8/91$01.00 ©IEEE

There is an empirical law for the maximum possible value of ξ[8], which fits the data surprisingly well: $\xi_{lim} \simeq 230/\sqrt{\gamma T_\epsilon}$, where $T_\epsilon \simeq E_0/U_0$. Assuming that $T_\epsilon \simeq 35000$, this gives $\xi_{max} \simeq 0.039$.

This applies, however, when $\sigma_s \ll \beta_y^*$[9]. If $\sigma_s/2\beta_y^*$ is large ($\gtrsim 0.1$), the experimental results drawn from various machines indicate that the disruption parameter defined by $D_y = 4\pi\xi\sigma_z/\beta_y^{IP}$ has a limit, which ranges between 0.25~0.3[10]. (A theoretical support was shown in Ref. [9]). Our value, $\xi = 0.03$, gives $D_y = 0.1884$.

The ξ_{max} ($\simeq 0.03$) is, thus, fairly below the empirical standard. The parameters related to the beam-beam interaction are listed below:

Beam-beam parameter	ξ_{max}	0.03
Betatron function at IP	$\beta_{x,y}^{IP}$	1m/1cm
Bunch Length	σ_s	4.7mm
Bunch spacing	S_B	40cm
Coupling	κ	0.01
Damping parameter	T_ϵ	3.5×10^4
Disruption parameter	D_y^{max}	0.19
Emittance	ε_x	1.14×10^{-6}m
Number of particles per bunch	N_b	6×10^{10}

2.2 Lattice Design

Emittance The ε_x due to Eq.(2) is a little too large for our E_0. In order to achieve this ε_x, we adopt a modified Chasman-Green lattice[11] and put wigglers at the central part, where the horizontal dispersion is large. Figure 2 shows the linear optics of a quadrant (an arc).

Chromaticity Correction The linear chromaticity due to the final focusing quadrupole, put at 30cm from the IP, is too large for our circumference.

We put S_F at a point where β_x is large and β_y is small and S_D at another point where β_x is small and β_y is large. The dispersions at these two points should be equally large. The differences between β_x's and β_y's between two points

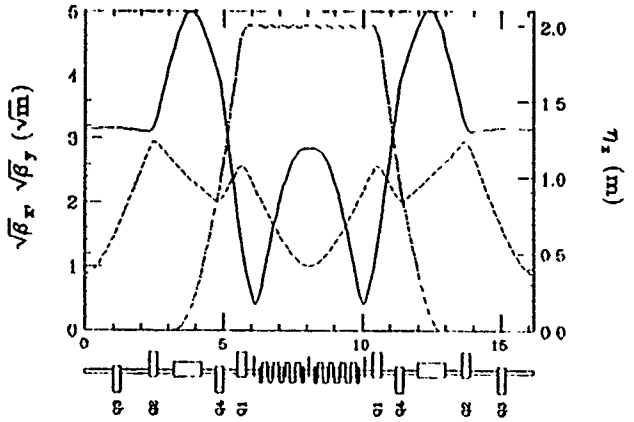


Figure 2: Optics in a quadrant.

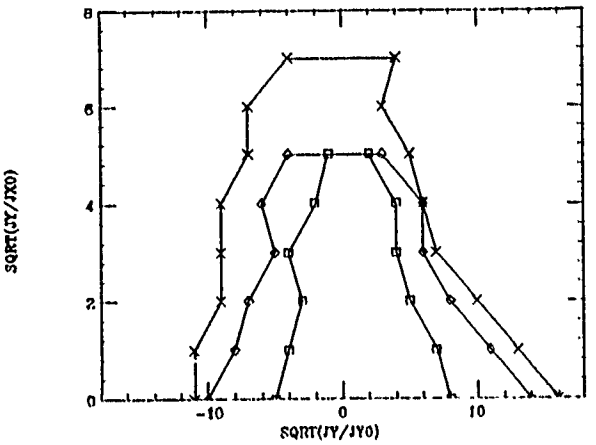


Figure 3: Dynamic aperture for a particle with 0, 10 and 20 σ_ϵ energy deviations.

should also be large. We make such points by use of the edge focus of the wigglers: β_x changes in the fashion of the drift space while β_y is affected by the focusing force of the edges.

The chromaticity correction scheme seems to work well. The tracking results, based on a 6-dimensional tracking code installed in SAD[12], are shown in Fig. 3. We have enough apertures. The main lattice parameters (without the damping wigglers) are given as follows:

Betatron tune	ν_x/ν_y	6.25/7.20	
Bucket height	A_E	0.5%	
Circumference	C	120	m
Energy	E_0	0.51	GeV
Energy loss/turn	U_0	14.5	KeV
Energy spread	σ_ϵ	0.042%	
Mean radius in the arc	ρ	10.4	m
Momentum compaction	α	7.43×10^{-3}	
Harmonic number	h	600	
RF frequency	f_{RF}	1.428	GHz
RF voltage	V_c	0.1	MV
Synchrotron tune	ν_s	0.011	

2.3 RF System

Since U_0 is small, the RF power is not the problem. One cell only (10.5cm long) can provide $V_c = 0.2$MV. We have assumed $V_c = 0.1$MV but larger V_c (hence more cavities) would have some merits. In particular, the bunch length σ_s is shorter. This increases the threshold current for the bunch lengthening[13]. On the other hand, it will enhance the coupled bunch instability, even if we employ the damped cavity[14,15]. We should find the optimum of V_c. We keep some room to use plural cavities.

Bunch Lengthening The N_b is limited by the single bunch instability. The Keil-Schnell criterion on the bunch lengthening tells us that our N_b exceeds the limit. Since,

however, σ_s is so small that the impedance Z_n/n should be replaced by[13] $|Z_n/n|_{eff} = (\omega_r\sigma_s)^2|Z_n/n|$, provided the short range wake function can be approximated by a single resonator. Here ω_r is the resonator angular frequency.

Our parameters, then, require

$$|\frac{Z_n}{n}|_{eff} < 0.018\Omega.$$

In LEP at the injection ($\sigma_s = 5$mm), $|Z_n/n|_{eff} = 0.02\Omega$ was observed[13,16]. We conclude that the bunch lengthening due to the short range wake is not serious.

Coupled Bunch Instabilities We have bad and good points: [Bad] The current is so large and the energy is so low that the beam is sensitive to the instability. [Good] RF cavities, the main source of the inter-bunch coupling, are so few. In addition, the feed-back is relatively easy, because of the low value of the energy. We can also introduce[17] a tune-spread between bunches and some vacant bunches, which seems helpful to reduce the difficulty.

2.4 Interaction Region

The final focus quadrupole is set at 30cm distant from the IP. The present-day permanent magnet has enough strength for this use.

We employed $S_B = 0.4$m so that the separation of beams around the IP is necessary to avoid additional peripheral collisions[18]. We need a crossing in an angle. According to a simulation[18] based on the rigid Gaussian model[4], 20 mrad (half angle) crossing angle is more than enough to avoid the dangerous long range beam-beam interaction due to the peripheral collisions.

From the synchro-betatron-resonances[19] point of view, σ_s/σ_x is small enough that the crossing is harmless.

2.5 Injection System

The lifetimes of the beams are limited by Touschek effect: $\tau \simeq 15$ minutes. Other, i.e., Bremsstrahlung, vacuum and quantum lifetimes are large enough. The present e^+ source[20] can provide enough number of particles. In order to make the injection easy, we will have another ring (the cooling ring), which accumulate e^+ from linac and cool its energy spread. With it, we can fill the ring in the rate of 1A per minutes[21]. Under assumptions that the injection efficiency is 100%, the operation time of 10 minutes requires the injection time to be 6.6 minutes. The average luminosity is then 1/3 of the L_{max}:

$$\bar{L} \simeq L_{max}/3.$$

3 Facility Consideration

Here, we will consider how the ϕ factory is suitable for KEK.

The second phase of TRISTAN will be completed in a few years. The experimental halls will not be used afterward. Since our ring is so small, we can use one of the experimental halls to set the rings. In Fig.1, the building wall imitates one of such halls.

In KEK, B factory is also being considered[22]. The upgrade of the positron source is seriously considered for this project. There is a plan to build similar cooling rings[21] for positron beam to raise the injection efficiency. The operation energy is around 0.5GeV. We can share them.

4 Conclusion

We have shown that the ϕ factory of the 3×10^{33}cm^{-2}sec^{-1} can be constructed without any serious problem almost within the presently available technology. Since we do not need any new tunnel, and since we do not anticipate any extremely new idea, we can finish the construction in a short period. More detailed and careful study should follow in order to fix the final design.

References

[1] M. Fukawa et.al., KEK report 90-12 (1990).
[2] E. Keil and R. Talman, Part. Acc. **14**109(1983).
[3] K. Hirata, Phys. Rev. **D37**, 1307(1988).
[4] K. Hirata, AIP Conf. Proc. 214, p175(1990).
[5] J. Urakawa et. al., KEK Preprint 90-118(1990).
[6] Y. Kimura, Proc. 2-nd. EPAC, Nice, France, June 12-16, 1990, p.23.
[7] A. W. Chao, SSCL-346(1991).
[8] J.T. Seeman, in Lecture Notes in Physics No.247, edited by J.M. Jowett, M. Month and S. Turner, Springer, Berlin Heiderberg New York Tokyo,1986.
[9] K. Hirata in Ref. [22].
[10] S. Milton, PSI Report PR-90-05, 1990.
[11] R. Chasman, G. K. Green and M. Rowe, IEEE Trans. Nucl. Sci. **NS22**(1975).
[12] For example, K. Hirata, CERN 88-04, p.62 (1988).
[13] B. Zotter, in KEK report 90-21, p.49 (1991).
[14] R. B. Palmar, SLAC-PUB-4542(1989).
[15] M. Suetake, T. Higo and K. Takata, KEK Preprint 89-164 (1989).
[16] D. Brandt et.al. LEP Commissioning Note 21 (1989).
[17] Y. H. Chin and K. Yokoya, DESY 86-097 (1986).
[18] K. Hirata, AIP Conf. Proc. 214, p.441, 1990.
[19] A. Piwinski, IEEE Trans Nucl. Sci. **NS-24** 1408 (1977).
[20] A. Enomoto et al, Nuclear Instrum. Methods in Phys. Res. **A281** ,1 (1989).
[21] K. Satoh, KEK B-Factory report, BF-0042 (1991).
[22] S. Kurokawa, K. Satoh and E. Kikutani Eds, KEK Report 90-24 (1991).

DAΦNE Storage Rings

S.Bartalucci, M.Bassetti, M.E.Biagini, C.Biscari, R.Boni,
A.Gallo, S.Guiducci, M.R.Masullo°, I. Palumbo*, M.Serio, B.Spataro, G.Vignola

INFN, Laboratori Nazionali di Frascati, C.P.13, 00044 Frascati (Roma), Italy
° INFN, Sezione di Napoli, Mostra d'Oltremare, Pad.20, 80125 Napoli, Italy
*Università di Roma 'La Sapienza', Dipartimento Energetica, Via A. Scarpa 14, 00161 Roma, Italy

Abstract

The lattice for the double ring e^+e^- collider DAΦNE, the Frascati Φ-factory project is presented. Electrons and positrons circulate in two horizontally separated storage rings and collide at a horizontal half angle θ=10 mrad in one or two interaction points. This allows a very short bunch distance and therefore a very high collision frequency (f ≤ 380 MHz). Due to the high number of bunches (120), the higher order modes (HOM's) in the RF cavities can excite multibunch instabilities. An R&D program on the suppression of the HOM's in the RF cavities is in progress.

I. INTRODUCTION

The general description of the machine is given elsewhere [1]. The two rings cross in the horizontal plane in two points and have a symmetry axis so that the two interaction regions have the same magnetic structure and the same optical functions. Each ring consists of two parts: an inner one, shorter, and an outer one, longer, which are symmetric and have a very similar structure. A crab-crossing [2] scheme is contemplated, if necessary.

A description of lattice and dynamic aperture is presented in Sections II and III. A summary of the preliminary results on cavity R&D is given in Section IV.

II. THE LATTICE

The lattice is a four-period modified Chasman-Green type. To increase the radiated energy per turn, a 2 m long, 1.9 T normal-conducting wiggler is incorporated into each achromat. The emittance value can be adjusted by tuning the dispersion function in the wiggler region.

Two different solutions have been designed, a higher emittance one with $\varepsilon = 10^{-6}$, and a lower emittance one with $\varepsilon = 5 \times 10^{-7}$. Moreover, a lattice with a high momentum compaction, useful to increase the threshold for the longitudinal microwave instability, is under study.

In the following the high emittance lattice [3] is described in detail. The optical functions of half ring are shown in Fig.1. A parameter list is given in Table I.

Table I - Single ring lattice parameters

Circumference (m)	94.56
Horizontal betatron tune Q_x	4.12
Vertical betatron tune Q_y	6.10
Horizontal natural chromaticity Q'_x	- 4.8
Vertical natural chromaticity Q'_y	- 17.8
Emittance ε (m-rad)	9.5×10^{-7}
Energy loss/turn with wigglers (keV)	13.75
Momentum compaction α_c	0.0068
Betatron damping time τ_x (msec)	24.0
Relative energy spread (rms)	4.3×10^{-4}

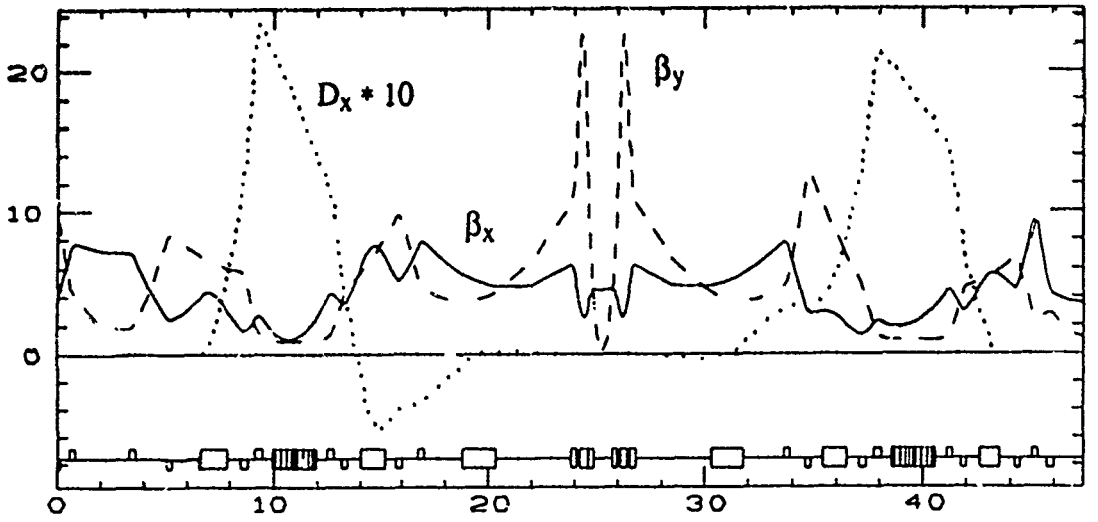


Figure 1. Optical functions of half ring.

0-7803-0135-8/91$01.00 ©IEEE

A. Low-β insertion

The low-β insertion is one of the most crucial parts of the Φ-Factory design because of the constraint imposed by the experimental apparatus, that is the requirement of a large unencumbered solid angle around the interaction point (IP). A tentative agreement has been reached with the users on a low-β insertion confined within a cone of half-aperture angle 8.5°, over a length of ± 5 m from the IP. The distance of the first quadrupole from the IP is 43.3 cm and the quadrupole maximum outer diameter $Ø_Q$ is 12.9 cm. Another constraint is the horizontal separation required at a short distance from the IP, to allow for a short bunch-to-bunch longitudinal distance L_b.

The optical parameters at the IP relevant to the luminosity are the following:

$$k_\beta = \frac{\beta_y^*}{\beta_x^*} = .01 \qquad \beta_y^* = .045 \text{ m} \qquad \beta_x^* = 4.5 \text{ m}$$

The low-β insertion consists of a quadrupole triplet followed by a long drift and a special designed split field magnet. The first quadrupole is rather weak and focussing in the horizontal plane. This provides better control over the β functions and keeps the horizontal beam size small inside the quadrupole triplet and along the rest of the insertion.

Let us point out that the low-β insertions give the largest contribution to the ring chromaticity; in particular the vertical chromaticity is $Q'_y = -10.32$ for the insertions compared with $Q'_y = -17.76$ for the whole ring.

The half separation Δ_x between the two beams along with the horizontal beam size in the low-β insertion are plotted in Fig.2. In the same figure the first parasitic crossing points for 30, 60, 120 bunches are indicated.

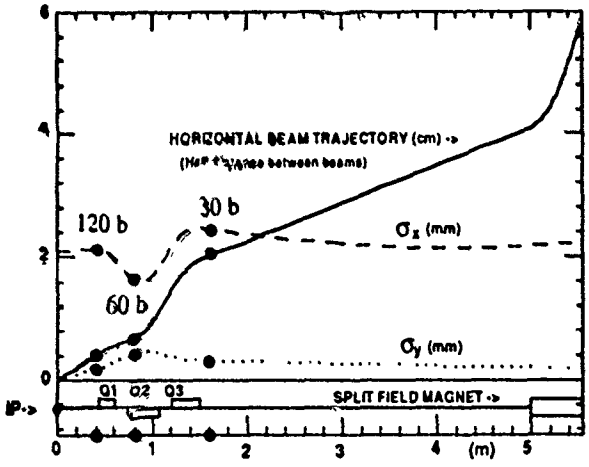


Figure 2. Beam half-separation and beam dimensions in the low-β region. The heavy dots mark the parasitic crossing points.

B. The achromats

The low-β insertion is connected to the main arcs by a matching section consisting of a long drift and two quadrupoles. The length of the drift is chosen in order to have a good separation between the first quadrupoles of the two rings. In this section, at π/2 horizontal betatron phase advance from the IP, there is room for the crab-cavity if necessary.

The dispersion and the horizontal β-function in the wiggler magnet are adjusted in order to tune the emittance, the contribution of the bending magnets to the emittance being negligible.

C. The zero dispersion insertions

Most flexibility in changing the betatron tunes is obtained in the zero dispersion insertions.

The short insertion has a 2.6 m long drift space with rather small β_x, suitable for the RF cavity. The long insertion provides space for injection septum and kickers, diagnostics and also free space for future developments.

III. DYNAMIC APERTURE

The study of the dynamic aperture has been performed with the computer code Patricia [4]. The strong sextupoles needed to correct the high vertical chromaticity are indeed the main limiting effects on the dynamic aperture.

To correct the tune-shift for particles with large oscillation amplitudes, a careful sextupole optimization in the dispersion-free regions has been performed.

The dynamic aperture is shown in Fig. 3, where the stable area for off-momentum particles, with a deviation $\Delta p/p = -.5\%$ (dashed line) and $\Delta p/p = +.5\%$ (dot-dashed line), are plotted for comparison on the unperturbed one (solid line).

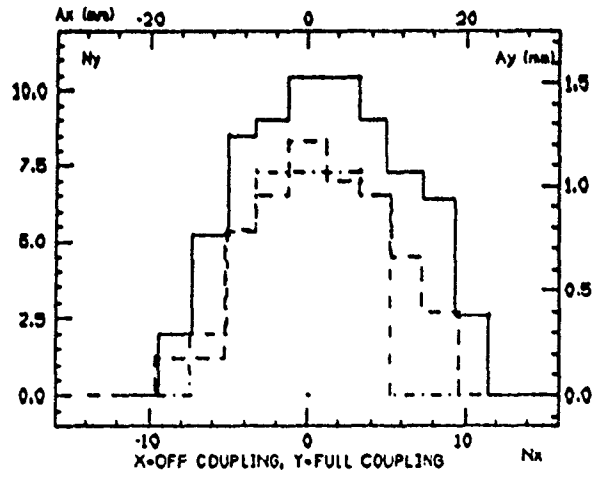


Figure 3. Dynamic apertures.

IV. CAVITY R&D

Due to the high number of bunches, the higher order modes (HOM) in the RF cavities can excite multibunch instabilities. An intense R&D program for the design of an RF cavity with the lowest interaction with the beam spectrum is in progress.

Two different approaches have been followed:

a) coupling off and damping the higher order modes (HOM's) with absorbers;
b) shifting the HOM's frequencies while keeping that of the fundamental mode constant.

One method which has been recently proposed for coupling off the HOM's [5-6] consists in connecting one or more waveguides to the lateral surface of the resonator. The waveguide cut-off wavelength has to be higher than the fundamental mode wavelength in order to let it trapped in the cavity, whereas the HOM's are free to propagate out. A 380 MHz brass cavity prototype has been tested. Two waveguides are connected to the resonator and a dissipative load is placed at the other end of each guide.

In Fig. 4, the measured frequencies and the quality factors Q's of the unperturbed prototype, and the spectrum of the waveguide-loaded cavity are compared. The measured reduction is 12 % for the fundamental mode frequency and 25 % for Q_0. The few remaining modes have a residual Q of some hundreds.

Some technological problems remain open: due to the pill-box shape that ensures the best coupling with the guides, the cavity is, in principle, prone to multipacting. Anyway, with appropriate surface coatings, multipacting can be inhibited. Furthermore, each damping load will dissipate a fraction (some kW's) of the parasitic beam losses and therefore adequate cooling must be provided. In alternative to the present design, the use of ridged waveguides will be investigated in order to reduce the overall size of the cavity.

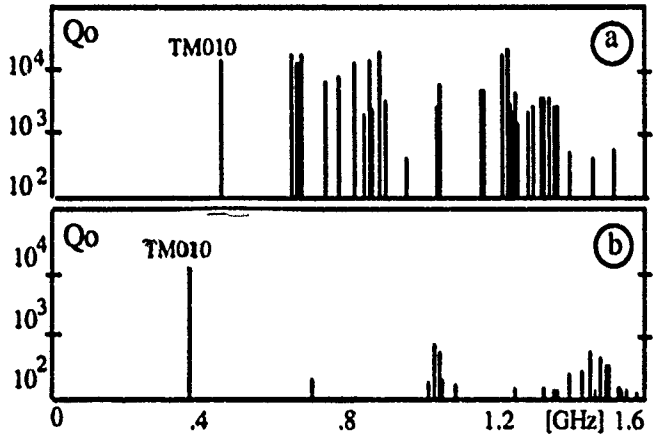


Figure 4. Spectrum of the uncoupled (a) and coupled (b) prototype cavity .

An other design for absorbing the cavity HOM's is being investigated. It consists of a resonator with relatively large beam holes, connected to the beam pipe with long tapered tubes which prevent trapping of parasitic modes in the resonator region [7]. In addition, the tapers reduce the cavity loss factor with beneficial effects on the broad-band impedance of the machine. However, the HOM's have to be damped by means of ferrites or other lossy materials located inside the tapered tubes and the heating produced by the parasitic beam losses has to be removed.

An optimization of the tapered profiles has been carried out on paper. Simulations with TBCI [8] give a loss factor of about 0.12 V/pC/cell. Two parasitic dipole modes, however, remain trapped in the resonator and, should they overlap the beam spectrum lines, detuning is required.

In Fig. 5 the long-tapered cavity profile is outlined along with the electric field lines of the fundamental mode.

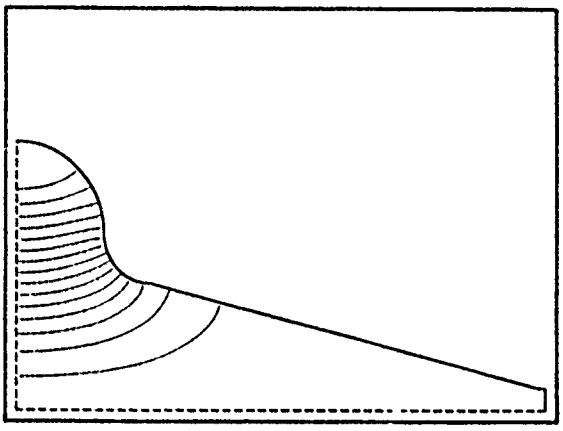


Figure 5. One quadrant of the long-tapered cavity.

An alternative way to fight collective coupled-bunch instabilities consists in shifting the HOM frequencies, without affecting the fundamental one, by means of perturbing metallic objects appropriately located [9]. Indeed, in small ring accelerators like DAΦNE, the spacing of beam spectrum lines is of the order of several MHz, so that the shift of a few offending HOM's can be a very powerful technique to decouple the beam oscillation modes from the cavity modes. The feasibility of this method is under study: one has to focus on the most dangerous cavity HOM's and to carefully consider the influence of the cavity tuning system at the injection.

V. REFERENCES

[1] G. Vignola, "DAΦNE. The Frascati Φ-Factory project", this conference.

[2] B. Palmer, SLAC-PUB 4707, (1988).

[3] M. Bassetti et al., DAΦNE Technical Note L-1, (1990).

[4] H. Wiedemann, SSRL ACD-Note 29, (1985).

[5] G. Conciauro, P. Arcioni, Proceedings of EPAC 90, Nice, France,1990, p. 149, (1990).

[6] A. Massarotti, M.Svandrlik, Sincrotrone Trieste, Note ST/M-90/5, (1990).

[7] T.Weiland, DESY 83-073, (1983).

[8] T.Weiland, DESY 82-015, (1982).

[9] S. Bartalucci et al., "A Perturbation Method for HOM Tuning in a RF Cavity", submitted for publication.

Conceptual Design of a High Luminosity 510 MeV Collider *

C. Pellegrini, D. Robin
UCLA Dept. of Physics 405 Hilgard Ave., Los Angeles, CA 90024
M. Cornacchia
Stanford Synchrotron Radiation Laboratory, Stanford, CA 94309

Abstract

We discuss the magnetic lattice design of a high luminosity 510 MeV electron-positron collider, based on high field superconduction bending dipoles. The design criteria are flexibility in the choice of the tune and beta functions at the interaction point, horizontal emittance larger than 1 *mm mrad* to produce a luminosity larger than $10^{32}cm^{-2}s^{-1}$, large synchrotron radiation damping rate, and large momentum compaction. The RF system parameter are chosen to provide a short bunch length also when the beam energy spread is determined by the microwave instability. A satisfactory ring dynamic aperture, and a simultaneous small value of the horizontal and vertical beta function at the interaction point, we expect will be achieved by using Cornacchia-Halbach modified sextupoles.

Introduction

In order to study CP violation in the Φ-meson system it is necessary to have a machine with a large luminosity. The luminosity in a collider is given by the expression

$$\mathcal{L} = \frac{fN^2}{4\pi\sigma_x\sigma_y} \qquad (1)$$

where f is the frequency of collisions, N is the number of particles in each bunch, σ_x and σ_y are the horizontal and vertical dimensions of the bunch respectively. Presently the largest luminosities which have been obtained in electron-positron machines is $10^{32}cm^{-2}s^{-1}$. In order to make interesting tests of the standard model it would be desirable to have luminosities in the range of $10^{33}cm^{-2}s^{-1}$ to $10^{34}cm^{-2}s^{-1}$. This is a very challenging accelerator problem.

At UCLA we are proposing to build an electron-positron storage ring at $510MeV$ per beam to be used as a Φ-factory. The name we have assigned to it is the Superconducting Mini Collider Φ-factory or the SMC/Φ-factory. In order to achieve large luminosities in a ring we have adopted a certain strategy. First we will build a storage ring whose luminosity is about $10^{32}cm^{-2}s^{-1}$. We will then employ new methods to increase the luminosity to the range of several times $10^{33}cm^{-2}s^{-1}$.

The collider will evolve in three phases. In phase one we will use conventional technology and methods which we expect will achieve an average luminosity greater than $2 \times 10^{32}cm^{-2}s^{-1}$. In phase two we would like to increase the luminosity to $10^{33}cm^{-2}s^{-1}$. To achieve this high luminosity we will have to use new ideas. One of our favorite ideas to go to this high luminosity is to run the machine in a quasi-isochronous mode [1]. The momentum compaction in the ring would be decreased by changing the strength of the quadrupoles. The bunch length would then decrease allowing for a more strongly focused beam at the interaction point. In phase three we plan to use a quasi-linear configuration where the bunches would be colliding outside the ring in a bypass. In this paper we will discuss only our phase one design.

Design Goals of Phase 1

As was mentioned in the previous section, the objective in phase one is to build a machine whose luminosity is $2 \times 10^{32}cm^{-2}s^{-1}$. We have several design goals in phase one and we list them here. The first goal is to design our ring with a small circumference. There are several reasons for doing this. First of all if one looks at the expression for the luminosity of a collider given in equation 1, the luminosity is proportional to the frequency of collisions, f. One can increase the frequency of collisions by either increasing the number bunches in the ring or making the ring smaller. The second reason is that if one has a small ring one then needs a large field in the dipoles to bend the beam, increasing the energy loss due to synchrotron radiation. This is an advantage. It will increase the damping time which will help to damp collective instabilities. Also the radiation which the dipole produces in dispersive regions will increase the transverse emittance of the beam allowing us to put more current in the beam. The current is also limited by the beam-beam interaction In our ring we have assumed a linear beam-beam tune shift of 0.05 The third reason for choosing a compact ring design is that a compact ring has a naturally large momentum compaction. The threshold peak current, I_p, for the longitudinal microwave instability which is the dominant coherent effect for small rings increases as the momentum

*Work supported by DOE contract DE-FG03-90ER 40565

0-7803-0135-8/91$01.00 ©IEEE

compaction goes up.

$$I_p \propto \alpha \tag{2}$$

where α is the momentum compaction of the ring. This is an approximate relation valid when the bunch length is on the order of the beam pipe radius.

There are two other reasons why we chose to build a small ring and they are practical reasons. The first of these two reasons is we are trying to make the machine as affordable as possible. By limiting the number of magnetic elements, we have decreased the cost. In particular if we did not have such strong bending dipoles, we might have to increase the emittance and reduce the damping time with wigglers as has been proposed in the Frascati machine [2]. The second of these practical reasons is that the building which is to be built to house this ring is not so large that it will be able to fit within its walls a machine of the size of that which is to be built in Frascati.

The second design goal is to have a machine which was flexible and that the control of the tune, the bending and the final focus system were decoupled. In other words we wanted the arc regions which are to bend the beam around 180 degrees to be unaffected by what was happening in the interaction region. We wanted to have the ability to adjust the tune without affecting the dispersion in the bends or the focussing in the interaction region. In other words we wanted to decouple all three of these functions so that we could adjust one parameter while minimizing the effects on the other parameters.

The third design goal is to build a machine whose dynamic aperture was large enough to give a good lifetime. This is somewhat difficult for machines like this because we have a large chromaticity in the ring which is a result of the large quadrupole strengths necessary to produce the small beam size at the interaction point. There will then have to be strong chromaticity correcting sextupoles in the ring in order to make the chromaticity zero. Also nonlinearities in the field are enhanced as a result of the small bending radius of the dipoles. We expect the Halbach-Cornacchia sextupoles to increase the dynamic aperture and they will be discussed later.

The fourth design goal is to build a ring which had the capability of decreasing the momentum compaction by several orders of magnitude with out significantly changing the configuration of the ring. What we mean by significantly is that we did not want to change the overall circumference of the ring. In addition we do not want to change the dipoles because they are the most complicated and expensive magnets in the ring and we want to build them so as to keep them at fixed strength.

Linear Lattice Design

As one can see from the artists conceptual design in Figure 1, the lattice consists of two straight sections and two 180 degree bending sections or arcs. In each of the 180 degree bends there are three dipoles which bend the beam 60 degrees each. Between the dipoles there is a quadrupole and a sextupole. In one of the two straight sections the

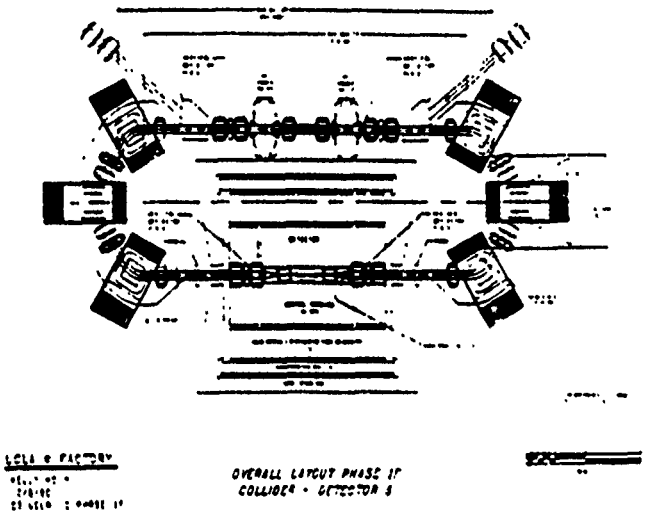


Figure 1: Conceptual Drawing of the UCLA SMC/Φ-Factory

detector will be placed In the interaction region a triplet is placed to provide a small beam size. In the other straight section the beam will be injected.

Arcs

The arcs consist of three dipoles and two quadrupoles and two sextupoles. Since we have zero dispersion in the straight sections the quadrupoles function is to bend the off energy particles back to the on energy ones when they reach the straight sections. They are thus both horizontally focussing.

The dipoles have a bending field of four tesla. They are parallel faced magnets to take advantage of the fact that edge focussing provides focussing in the vertical plane and helps to compensate for the defocussing in that plane due to the quadrupoles. Each dipole has small field gradient (n= 0.23) which also provides some vertical focussing. The magnets are H-type shaped for stability and have been designed by General Dynamics.

Straight Section

The interaction region consists of a triplet and controls the beta function at the interaction point. We can have $\beta_x = 19cm$ and $\beta_y = 3.9cm$. consistent with a bunch length of $3cm$. The quadrupole closest to the interaction point is $30cm$ away.

The fourth quadrupole farthest from the interaction region is used to vary the tune of the ring. It does not effect the dispersion and changes the final beta very little.

The reference parameters for the ring are given in Table 1. The current in the ring is $1.16A$ which is rather large. We have calculated with the help of ZAP[3] the lifetimes of the beam due to such things as Touschek scattering, intrabeam scattering, gas scattering and beam-beam lifetime. We have found that the limiting factor at this current is the gas scattering which for a pressure of $10^8 torr$ is $1.8 hours$.

Because of the size of the ring and the amount of synchrotron radiation, the vacuum system will be difficult.

Table 1

SMC Parameter List

Beam Energy, *MeV*	510
Luminosity, $cm^{-2}s^{-1}$	2×10^{32}
Circumference, *m*	17.4
Dipole bending radius, *m*	0.425
Horizontal betatron tune, *m*	2.1
Vertical betatron tune, *m*	3.85
Momentum compaction	0.11
Energy loss/turn, *KeV*	14.1
Horizontal damping time, *ms*	4.6
Vertical damping time, *ms*	4.2
Longitudinal damping time, *ms*	2.0
Natural emittance, *mm mrad*	3.2
Vertical/horizontal coupling	0.2
Number of particles/bunch	4×10^{11}
Number of bunches/beam	1
Collision frequency, *MHz*	17.2
β_x at IP, *cm*	19
β_y at IP, *cm*	3.9
σ_x at IP, *cm*	0.78
σ_y at IP, *cm*	0.071
$\delta\nu_x$,	0.05
$\delta\nu_y$,	0.05
RF frequency, *MHz*	500
Harmonic number,	29
RF voltage, *kV*	400
Synchrotron tune,	0.02
bunch length, *cm*	3
Average current, *A*	1.16
Peak current, *A*	269
Z/n, Ω	3
Lifetime: Beam-beam, *hours*	2.8
Lifetime: Touschek, *hours*	2.5
Lifetime: Gas, 10^{-8}*Torr*	1.8

Dynamic Aperture

The ring's small bending radius enhances nonlinearities in the fields. This fact and also the fact that the large natural chromaticity in the ring is quite large and has to be corrected for by strong chromaticity correcting sextupoles tends to leave the ring with a small dynamic aperture. In order to avoid a short lifetime due to quantum fluctuations, it is desirable to have a dynamic aperture which is at least ten times the rms bunch size in both planes.

A possible way to increase the dynamic aperture would be to use modified sextupoles whose strength is not a pure sextupole in place of a normal sextupole. This possibility has been proposed by M. Cornacchia and K. Halbach[4]. They have demonstrated that the dynamic aperture can be increased. In particular for a ring such as ours, Cornacchia did some calculations of the dynamic aperture for a sextupole whose fields expressed in complex notation are

$$B^* = -iz^2 e^{kz^2} \qquad (3)$$

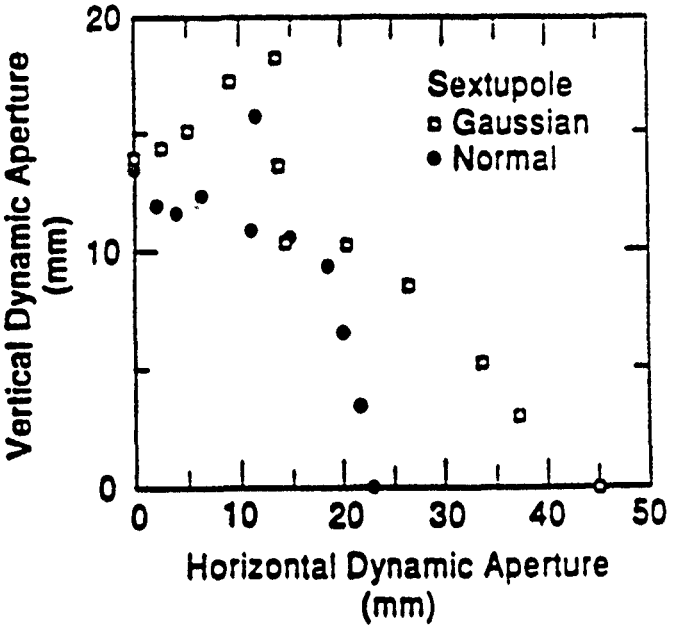


Figure 2: Dynamic aperture due to modified and normal sextupoles

where $B_x = \mathcal{R}e(B^*)$ and $B_y = -\mathcal{I}m(B^*)$. z is the coordinate in complex notation were $z = x + iy$. The results of his calculation can be seen in Figure 2.

These results are preliminary because the model in the computer code that was used does not provide the proper Hamiltonian for rings having a small bending radius. We think that the qualitative behavior is correct. The sextupoles do help increase the dynamic aperture.

We are now adapting a code Krakpot[5] in collaboration with E. Forest which was used to study the dynamic aperture of the SXLS ring at Brookhaven National Laboratory. This program has the ability of implementing these modified sextupoles in the lattice and also has the proper Hamiltonian.

References

[1] C. Pellegrini and D. Robin, "Quasi-Isochronous Storage Ring", *Nuclear Instruments and Methods*, A301 (1991) 27-36

[2] M.E. Biagini, C. Biscari, S. Guiducci and G. Vignola, "The lattice for DAΦNE, the Frascati Φ-Factory project",These proceedings

[3] M. Zisman, S. Chattopadhyay and J J Bisognano, "Zap Users Manual", Lawrence Berkeley Laboratory rep., LBL-21270, UC-28 (1986)

[4] M. Cornacchia and K. Halbach, Study of Modified Sextupoles for Dynamic-Aperture Improvement in Synchrotron Radiation Sources", *Nuclear Instruments and Methods*, A290 (1990)

[5] KRAKPOT was developed by E. Forest J Murray and M. Reusch to track particles in Brookhaven's SXLS ring

A High Luminosity Superconducting Mini Collider for Phi Meson Production and Particle Beam Physics

C.Pellegrini, D. Robin, D. Cline, J. Kolonko

University of California at Los Angeles, Department of Physics
405 Hilgard Avenue, Los Angeles, California 90024

C. Anderson, W. Barletta, A. Chargin
Lawrence Livermore National Laboratory
Livermore, California 94550

M. Cornacchia
Stanford Synchrotron Radiation Laboratory
P.O. Box 4349, Stanford, California 94309

G. Dalbacka
Maxwell Laboratories, Inc.
4905 Central Av., Richmond, California 94804

K. Halbach
Lawrence Berkeley Laboratory
1 Cyclotron Road, Berkeley, California 94720

E. Lueng, F. Kimball, D. Madura, L. Patterson
General Dynamics, Space Systems Division
P.O. Box 85990, San Diego, California 92186

Abstract

A 510 MeV electron-positron collider has been proposed at UCLA to study particle beam physics and Phi-Meson physics, at luminosities larger than 10^{32} cm^{-2} s^{-1}. The collider consists of a single compact superconducting storage ring (SMC), with bending field of 4 T and a current larger than 1 A. We discuss the main characteristics of this system and its major technical components: superconducting dipoles, RF, vacuum, injection.

Introduction

A high luminosity, low energy (510 MeV per beam), electron-positron collider is being proposed for construction at UCLA. The goals of this program are:
1. particle beam physics research;
2. phi meson physics, CP and CPT violation studies;
3. graduate student training.

The collider energy has been chosen to coincide with the phi resonance energy. To obtain the large luminosity and to keep the system cost and size to a level where it can be accomodated on a University campus, we have chosen a compact design, using superconducting magnets, shown in Fig. 1.

The choice of a compact design, about 17m circumference, maximizes the collision frequency, and the synchrotron radiation damping rates. Injection is done with a linac-positron accumulator complex, to keep the filling time at about one minute. The beam lifetime is about one hour and is dominated by the beam-beam bremstrahlung. The vacuum system requires the use of low desorption materials, and an antechamber design. The use of specially modified sextupoles is needed to provide a large enough dynamic aperture.

Designs for large luminosity Phi-Factories have been developed also at Novosibirsk, Frascati and KEK, and are described in other contributions to these Conference. The Novosibirsk design is also based on superconducting magnets, while the Frascati design uses room temperature magnets and high field wiggler to reduce the damping time. All these designs share some features, like large non linear beam dynamics effects,

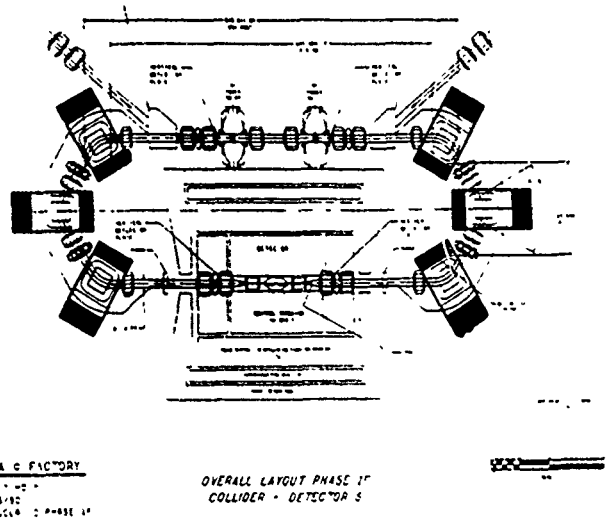


Figure 1· Conceptual Drawing of the UCLA SMC/Φ-Factory

Work supported by DOE contract DE-FG03--90ER40565

0-7803-0135-8/91$01.00 ©IEEE

large currents and short bunches, and the need to increase the damping rate, given the low beam energy, and the potential damage from intrabeam scattering. The SMC is the first step in a program to develop colliders of increasing luminosities and flexibility in the choice of the energy of the beams. Some of the future upgrades to increase the luminosity to the 10^{33} level are also discussed.

Storage Ring

A list of the main parameters of SMC is given in Table 1. The main advantages of the choice of superconducting dipoles and a compact ring are:
1. the high revolution frequency increases the luminosity for a given number of electrons and positrons and simplifies the positron injection system;
2. the large bending field and small radius of curvature maximizes the synchrotron radiation damping rates and produces a large momentum compaction, thus incresing the threshold fro the microwave instability;
3. the small circumference makes the system compact and reduces the cost.

The disadvantages are limited space for injection and instrumentation, larger non linear effects due to the small bending radius, and the large synchrotron radiation power density on the vacuum chamber walls.
The magnetic lattice design is discussed in another paper presented at this Conference [1]; this design was based on the requirements of flexibility in the choice of operating point and beam emittance, in addition to a dispersion free interaction region. The large non linearities present in the ring, because of the low beta and the small bending radius, tend to reduce the useful dynamic aperture. As shown in [1] we intend to solve this problem using the modified sextupoles proposed by Cornacchia and Halbach [2].

Superconducting Magnets

Several option are available in the construction of the superconducting dipoles. Configurations with and without enhancing permeable materials are possible. Because the storage ring will be operated essentially at fixed energy, the effects of highly non linear materials in the magnets are acceptable. For this reason a superferric (iron enhanced) design has been selected that utilizes superconducting coils in a racetrack dipole configuration with a room temperature iron yoke. This configuration has the advantage of reducing the criticality of the conductor placements, reducing the required amount of superconductor, and reducing structural material needed.

Table 1: SMC Parameters List	
Beam Energy, MeV	510
Luminosity, $cm^{-2}\ s^{-1}$	$2\ 10^{32}$
Circumference, m	17.4
Bending Radius, m	0.425
Momentum Compaction	0.11
Horizontal tune	2.1
Vertical Tune	3.85
Energy loss/turn, KeV	14.1
Damping time, horizontal, ms	4.6
Damping time, vertical, ms	4.2
Damping time, energy, ms	2.0
Emittance, mm mrad	3.2
Vertical/Horizontal coupling	0.2
Particles/bunch	$4\ 10^{11}$
Number of bunches/beam	1
Collision frequency, MHz	17.2
β_x at IP, cm	19
β_y at IP, cm	3.9
$\delta\nu_x$	0.05
$\delta\nu_y$	0.05
RF frequency, MHz	499
RF voltage, KV	400
Synchrotron tune	0.02
Bunch length, cm	3
Average current, A	1.2
Peak current, A	270
Z/n, Ω	3
Lifetime, beam-beam, hrs	2.5
Lifetime, Touschek, hrs	2.5
Lifetime, gas (10 nT), hrs	1.8

An additional design consideration is the cooling method and conductor to be employed. To minimize cost, a state of the art pool boiling conductor has been selected. Magnets built by this method simply immerse the conductor pack in liquid helium. Designed correctly, this a simple and reliable method.

There are six magnets in the ring, each bending the beam by 60^0. By designing magnets with a relatively large good field region, it is intended to produce magnets that require no curvature. The beam enters the dipole at an angle to the magnet centerline, and exits at a similar, although oposite, angle. By eliminating the magnet curvature, the manufacturing of these dipoles is simplified and cost is reduced.
Convential copper coils to produce the same field would require a power consumption of about 3 MW. Thus superconducting magnets (even with refrigeration power considered) are less expensive than conventional magnets when operation costs are included.

Beam Parameters and RF system

We assume as a design goal a peak luminosity of $3\,10^{32}$ $cm^{-2}\,s^{-1}$. To achieve this luminosity requires a beam current of 2A per beam, in a single bunch, with a bunch length not larger than 3 cm, and an energy spread not larger than 0.1%. The RF, vacuum and injection system are designed for these beam characteristics. The bunch length and energy spread is determined by the microwave instability and the RF system. To evaluate the RF voltage needed we estimate a longitudinal broad band impedance of 3 Ω, with contribution coming from the RF cavities, other ring elements, and the vacuum impedance. This last term is unusually large and is responsible for the emission of coherent synchrotron radiation. The threshold for the fast head-tail is larger than that of the microwave instability and has no effect on the design. Intrabeam scattering has been evaluated and is not important, because of the short damping times.

Table 2: RF Parameters	
Frequency, MHz	499
Voltage, KV	400
Shunt Impedance, MOhm	5
Synchrotron radiation losses (4 A), KW	56
HOM+BB losses (4A), KW	56
Cavity losses, KW	32
Total Power, KW	144

For the RF system we choose a 500 MHz cavity, based on the Daresbury design, for the avalaibility of the power sources, and to reduce the voltage needed to produce the short bunch length. We can use one or two cavities. A list of parameters is given in Table 2 for the one cavity case.

Vacuum and injection systems

These systems are discussed in more detail in other papers presented at this Conference [3], [4]. We only want to mention here that this design produces a very large synchrotron radiation load, up to 10 KW/m. It is shown in [3] that this can be controlled with an antechamber design.
The injection system is required to provide $6\ 10^{11}$ positrons, with an injection time shorter than 1 minute. We used a solution, [4], with electron positron conversion at 200 MeV, full injection energy of 510 MeV, and a positron accumulator ring. In this system we can reach our goal with a safety margin, usin an electron gun like the SLC gun built at SLAC.

Conclusions

We have established the feasibility of a 510 MeV electron-positron collider with luminosity larger than 10^{32} $cm^{-2}\,s^{-1}$, and the capability of testing the accelerator physics and technology relevant for large peak and average current operation. Further studies will be needed to optimize the system design and have a more detailed understanding of some of these effects. More work will also be needed to fully develop the design of the superconducting dipoles, the RF, and the vacuum systems.
We also intend to continue our work for the design of a higher luminosity collider, and the next step in our program is to study a system based on the Quasi Isochronous Ring concept [5,6].

References

1. M. Cornacchia, C. Pellegrini, D. Robin, Conceptual Design of a High Luminosity 510 MeV Collider, Proc. this Conf. (1991).
2. M. Cornacchia and K. Halbach, Nucl. Instr. and Meth., A290, 372 (1991).
3. W. A. Barletta and S. Monteiro, Vacuum Design for a Superconducting Mini Collider, Proc. this Conf. (1991).
4. G. Dalbacka, R. Hartline, W. Barletta, C. Pellegrini, A 510 MeV e^+-e^- Injection System for the UCLA Phi-Factory, Proc. this Conf. (1991).
5. C. Pellegrini and D. Robin, Nucl. Instr. and Meth. A301, 27 (1991).
6. C. Pellegrini and D. Robin, Electron Density Enhancement in a Quasi Isochronous Storage Ring, Proc. this Conf. (1991).

DELTA Optics

D. Schirmer, K. Wille
DELTA Group, Institute of Physics, University of Dortmund
P.O. Box 500 500, 4600 Dortmund 50, Germany

Abstract

DELTA (**D**ortmund **EL**ectron **T**est **A**ccelerator) is a new 1.5 GeV electron storage ring now under construction at the University of Dortmund [1]. The facility consists of a 100 MeV LINAC, the ramped booster synchrotron **BODO** (**BO**oster **DO**rtmund) and the main storage ring DELTA (see Fig.1).

One of the most important goals for the DELTA lattice and the corresponding optical functions is the requirement of extremly low emittance, to enable DELTA to serve as a driver for different FEL experiments and to make a photon source of special beam characteristics available for single user SR experiments. Furthermore, the storage ring is optimized to provide highly flexible optics, suitable for various applications. Therefore, the lattice is based on a triplet focusing structure. The optical properties of such a triplet cell are investigated.

Founded upon this magnetic structure optional lattice configurations and corresponding versions of optics for alternative applications are available and presented in this paper.

The influence of inserted sextupoles, necessary for chromaticity correction, on nonlinear beam dynamics and energy dependence is also investigated in a rough manner.

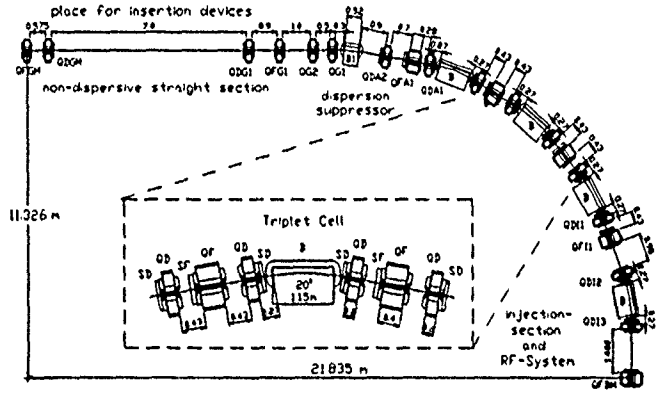


Figure 1: *One quarter of the basic magnetic lattice of DELTA and detailed view of the triplet cell structure*

1 The Triplet Cell

In general the 'basic cell structure' of accelerators determines the integral properties of the beam around the ring. In order to meet the requirements mentioned before, the lattice design based on a triplet focusing cell, consists of three quadrupoles located between two rectangular bending magnets. The layout of a basic triplet cell of the DELTA optics is shown in the insert of figure1.

In the bending magnets the beta functions and dispersion are quite small, yielding the required low emittance. Little additional focusing in the vertical plane is provided by the edge angles of the dipoles. The focusing quadrupole in the center of the triplet has twice the length of the defocusing one. The rectangular bendings, with 1.51 T field at maximum beam energy, have a magnetic length of 1.15 m providing a bending radius of 3.31 m , and a bending angle of 20° for each magnet. To obtain dispersion-free straight sections, two of these bendings are split into half magnets, located at the ends of each arc.

A criterion for the optical functions can be given, providing a minimum value of the emittance. In first order, assuming small bending angles and zero dispersion ($D_x = D'_x = 0$), the minimum emittance for an isomagnetic ring becomes [2]

$$\epsilon_{x_{min}}\,[rad \cdot m] \cong \frac{C_a}{4\sqrt{15}}\,E^2\,\Theta^3 \approx 9.475 \cdot 10^{-8}\,E^2\,[GeV^2]\,\Theta^3\,[rad^3] \quad (1)$$

With Θ=0.349 rad and E=1.5 GeV the corresponding emittance of DELTA becomes $\epsilon_{x_{min}}$=$9.06 \cdot 10^{-9}$ rad m. In order to reach the required emittance of $\epsilon_{x_0} \approx 1 \cdot 10^{-8}\ rad \cdot m$,the number of dipoles N_D is given by

$$N_D = \sqrt[3]{\frac{C_a\,E^2\,(2\pi)^3}{1 \cdot 10^{-8}\,4\sqrt{15}}} \cong 17.41 \quad (2)$$

with $\Theta = \frac{2\pi}{N_D}$. For DELTA a number of 18 bending magnets is chosen. With $\Theta = L/\rho$ we get the characteristic dimensions of the DELTA dipoles. Without approximations and considering the dispersion function, the optimum emittance for the rectangular DELTA dipole is minimized

0-7803-0135-8/91$01.00 ©IEEE

to be [3]

$$\epsilon_{x_{opt.}} = 2.95 \cdot 10^{-9}\ [rad \cdot m] \qquad \text{at E=1.5 GeV.} \qquad (3)$$

This calculated optimum value for the dipole represents a theoretical threshold. The actual design values of the lattice function differ from the optimum solutions, leading to a beam emittance which is larger by a factor of three to four than obtained theoretically. The reasons are higher-order chromatic and geometric aberrations, which can be very large for the ideal solution and would limit the dynamic aperture severely. To get more detailed information about

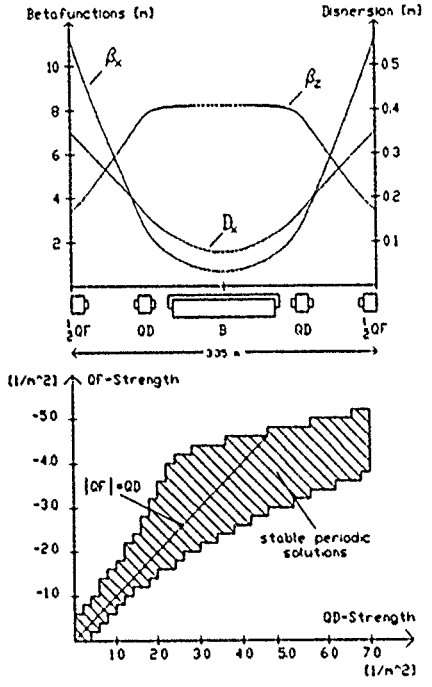


Figure 2: *Optical functions and range of stable solutions in dependence on the quadrupole strength of one triplet cell*

this particular optics, the exact triplet structure is calculated with the 'thick-lens matrix technique' using a computer code. The program calculates the periodic solution, determines the eigenvalues of the triplet transfer matrix $\tilde{M}_{Trip}$ and solves the main sychrotron-radiation integrals. Fig.2(bottom) depicts the range of periodic solutions of a triplet cell in dependence on the quadrupole strength (necktie stability diagram). The trace of the transfer matrix is $\tilde{M}_{Trip} \leq 2$, corresponding to stable solutions only in the framed area. The diagrams in fig.3 reveal the most important graphs and represent equivalent calculations for emittance, chromaticity and phase advance.

Based on the triplet structure, several lattice configuations and optics have been calculated. The lattice in fig.1 represents the basic version with three quads in the center of the straight sections. This magnetical configuration allows to adjust the emittance over a wide range from $5.0 \cdot 10^{-8}$ to $5.0 \cdot 10^{-9}$ rad m at 1 GeV. Because DELTA is a test storage ring, the philosophy is to adapt the straight sections to the requirements of the particular experiment

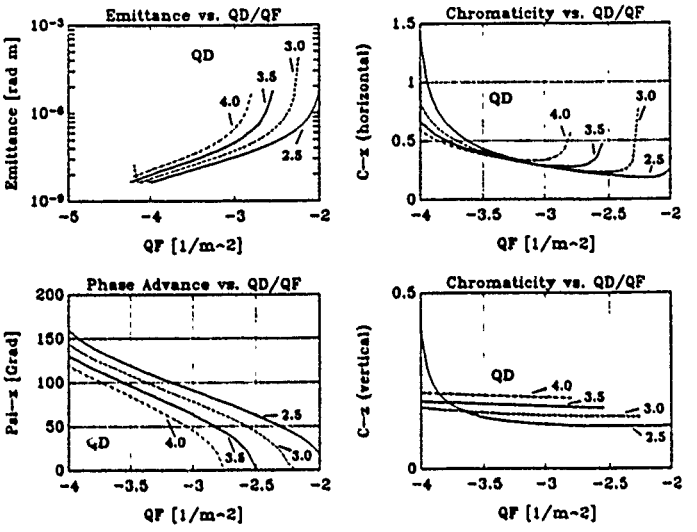


Figure 3: *Chromaticity, phase advance and emittance as dependent on the strength of QF and QD*

keeping the arcs unchanged. Therefore, the two 20 m long straights of the racetrack-shaped storage ring are available for insertion devices.

2 FELICITA II

FELICITA II will be the second FEL experiment at DELTA, operating in the wave length regime from 100 to 20 nm.

Because of the quads in the straights necessary for optical matching the available space for long undulators is limited to about 14 m.

The most important parameters of FELICITA II, which determine the influence on the optical functions are:

- undulator length $L = 13.97m$
- period length $\lambda_u = 3.4cm$
- number of periods $N_p = 411$
- peak field $B_0 = 1.07T$
- electron energy $E = 0.5 - 1.0GeV$

Picture 4 shows the focusing properties of the FEL undulator on the electron beam. In horizontal direction the undulator provides no focussing and acts just like a drift space, whereas, in vertical direction, there is a kind of quadrupole focussing, leading to two betatron oscillations over the whole undulator length. Thus, the undulator produces a tune shift of 1 for the storage ring optics. Accordingly only a little change of the optics without insertion is necessary. This is provided by the quads in the straights. Similar results have been obtained from a 3-dimensional numerical FEL simulation code [5].

3 Superconducting Wiggler

The demand for synchrotron radiation in the soft x-ray regime is increasing continuously. Unfortunately, the radi-

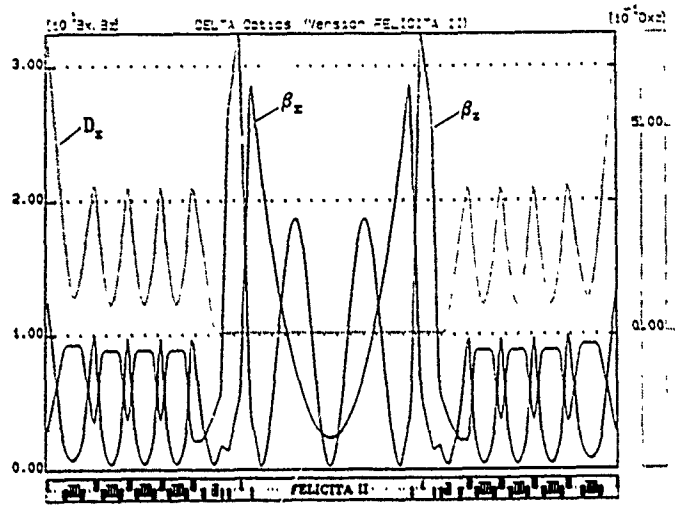


Figure 4: *Optics for FELICITA II calculated with an undulator of 411 periods*

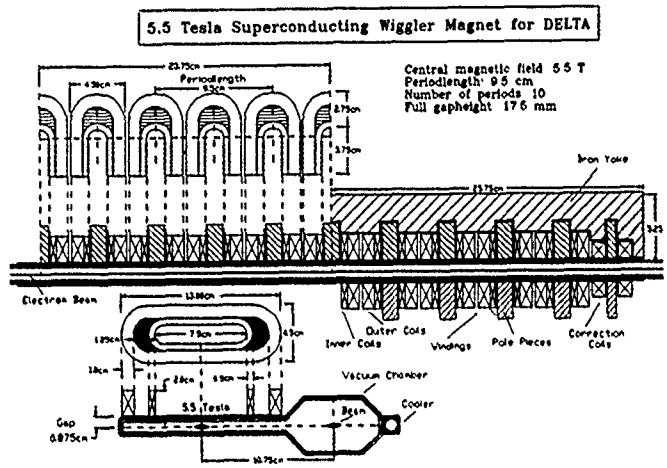


Figure 5: *Schematic view of the proposed 5.5T Wiggler*

ation from the DELTA bending magnets of 1.5T strength has a characteristic wave length of only 5.47 $\AA$. To enlarge the range of wave length of the machine for short-wavelength users, the installation of a superconducting wiggler is foreseen. The wiggler will be inserted in the straight section of the fourth quadrant, for which the effects on beam optics due to edge focussing are compensated by additional quads. The design parameters of the magnet are mainly defined by the SR properties determined by the experiments of the user. Some users are interested in photons with a critical wave length of 1 $\AA$ and a photon flux of about 10^{15} [photons/mA/0.1%BW] in a horizontal radiation fan of 10 mrad. As a consequence, the design must be optimized to provide extremly short period length and a small gap heigth, requiring superconducters with high critical currents. Fig. 5 shows a preliminary design for such a wiggler with 20 poles. The design field at the orbit is about 5.5 T, based on Nb-Ti superconducters with a critical current of $10^3 A/mm^2$ at $8T$ and $4.2°K$. Further studies on a detailed magnet design is under work.

4 Tracking Studies

An effective compensation of the chromaticity for low-emittance optics has been evaluated by testing various arrangements of sextupole families. Satisfactory results have been obtained with a correction scheme of four sextupole families regularly distributed over both arcs at positions with nonvanishing dispersion.

The sextupolar strengths are optimized to minimize the non linear effects, in accordance with energy dependence and dynamical aperture.

Some results of these investigations are given in fig.6 As can be seen, the relative variation of the tunes and the optical functions in the center of the arcs is sufficiently small the range of 3%. Also, the tunes do not approach any resonance of third, half or integer order.

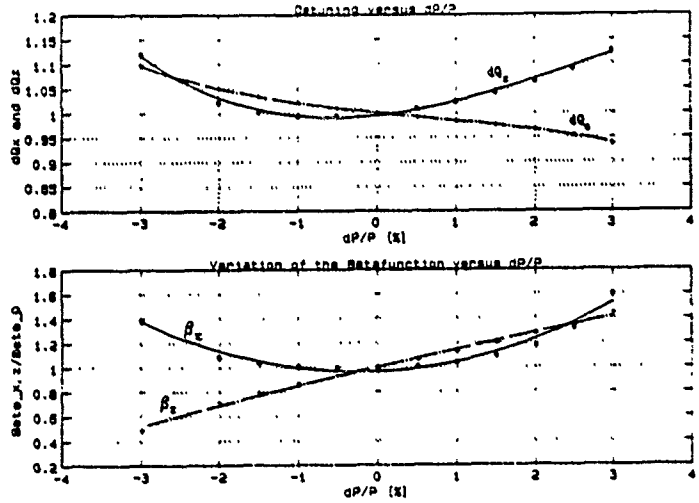


Figure 6: *Tracking results plotted as a function of the energy dependence*

References

[1] DELTA Group, *DELTA Status Report 1990*; University of Dortmund, 1990, unpublished

[2] H. Wiedemann, *Low-Emittance Storage Ring Design*; CERN Sommerschule (USA) 1987

[3] D. Schirmer, *Entwicklung von Strahloptiken für den Testspeicherring DELTA auf Basis der Triplett-Struktur*; Diploma Thesis 1989, unpublished

[4] D. Nölle et al, *DELTA, A new Storage-Ring-FEL Facility at the University of Dortmund*; Nucl. Instr. and Meth. A296 (1990) 263-269

[5] D Nölle, K Wille, *XUV FELs in Storage Rings*, to be plublished in AIP Conference Proceedings, 1991

Status of DELTA and Design of its Vacuum System

Niels Marquardt
DELTA Group, Institute of Physics, University of Dortmund
4600 Dortmund 50, Germany

Abstract

A status report of the Dortmund ELectron Test Accelerator DELTA [1], now under construction, is presented. This low-emittance storage ring is dedicated to FEL and accelerator-physics R & D. Preacceleration will be performed with a 100 MeV LINAC which is presently rebuilt from the old Mainz LINAC. Lattice designs of the 1.5 GeV booster (FODO structure) and storage ring (triplet structure) are completed [2] and prototypes of magnets and vacuum vessels, identical for both cyclic machines, are to be delivered end of 1991. A monitor development has been performed [3]. Commissioning of the machines is planned for end of 1993. - An overall description of the vacuum system is given with the design goal of achieving beam life times of >10 h at high currents. Low-impedance vacuum chambers made of 3 mm thick 316LN stainless steel have been designed. They consist of a small-aperture beam channel separated by a continuous slot from an antechamber equiped with DIP's and NEG pumps.

1 INTRODUCTION

The 1.5 GeV electron storage ring DELTA [1] of 115.2 m circumference is being built at the University of Dortmund, in the center of West-Germany. As a typical example of a third-generation synchrotron light source and as a machine dedicated to free-electron-laser (FEL) and accelerator physics research, DELTA is designed specifically to optimize the radiation from undulators. Correspondingly, it is aiming at a beam emittance as small as about 10 nm rad and large currents of 0.1 to 0.5 amperes for single- or multi-bunch ($\geq$12) operation, respectively. Due to its moderate design energy it will provide VUV and soft X-ray radiation. Since it is intended to represent a national test facility for R & D, DELTA will not serve primarily as an ordinary users machine.

2 LATTICE

To accomodate long undulators, two 20 m long straight sections with zero dispersion and nearly constant beta functions over a considerable length together with sufficient space for numerous monitoring and controlling devices [3] are foreseen. Other characteristics of the storage ring are its highly flexible and variable beam optics, its very stable electron beam of high quality and its short damping time and long beam life time. Whereas the long drift sections provide the space for insertions and experimental setups, the two arcs mainly determine the optical properties of the ring. As the best compromise between small emittance and short damping time requiring strong bending fields, qualities which contradict one another, a triplet focussing cell [2] has been found as the basic structure of the DELTA lattice. Each of these triplet cells (all together 18) consists of two short (20 cm) defocussing and one long (40 cm) focussing quadrupoles, installed between two rectangular bending magnets. These dipoles operate at 1.5 T for the maximum beam energy of 1.5 GeV. With their magnetic length of 1.15 m they are providing a bending angle of 20°, a bending radius of 3.31 m and a weak additional focusing caused by the angle of their edges.

Different versions of the optics have been obtained either for the original lattice of fourfold symmetry and different values of the emittance (low, standard, high) or for the same lattice but modified by adding different insertion devices in the straight sections, namely an optical-klystron electromagnetic undulator as an FEL device and a superconducting wiggler as an energy shifter. Besides these various results from optics calculations some design work has already been done for the beam-transfer channel between booster and storage ring.

3 STATUS

The present status of the DELTA project is the following. After approval of the facility by the German federal and provincial governments and after ground breaking end of 1989 and end of 1990, respectively, a 1-year construction period for the laboratory building starts in May 1991. The general layout of the laboratory is shown in figure 1 . The building consists of offices and workshops in one part and of a 40 m by 74 m large hall, housing storage ring and injector complex with LINAC and booster. All three machines are on ground level and surrounded by a 1 m thick,

0-7803-0135-8/91$01.00 ©IEEE

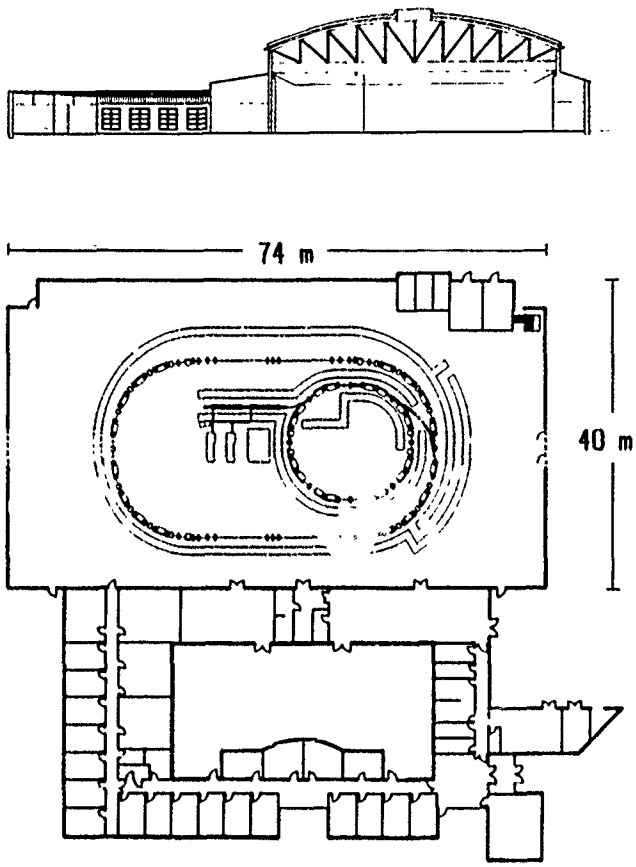


Figure 1: Floor plan of the DELTA facility with the accelerator hall, workshops and offices (lower part) and cross-section of the building (above).

3 m high concrete wall for radiation protection. Two accelerating sections of an old LINAC from the University of Mainz will serve as preinjector for DELTA. All parts of this machine were shipped already to Dortmund, and work on redesigning the LINAC has been started. After completing the construction work of the building in early summer 1992, installing of the 100 MeV LINAC will begin, followed successively by assembling booster and storage ring. The booster synchrotron with its rather simple FODO lattice has a circumference of 50.4 m and will be ramped slowly to the full injection energy of DELTA of 1.5 GeV. In another operational mode the booster can also be used as a storage ring with lower currents and 1 - 2 hours life time.

All main dipole and quadrupole magnets, which are for cost-saving arguments identical for booster and storage ring, are ordered already. Prototypes of magnets and of the vacuum vessels, which are also the same for booster and storage ring, are expected to arrive in late 1991 and will then be subjected to detailed measurements The low-emittance optics and the correspondingly strong focussing cause high chromaticities. Whereas these are compensated for DELTA by short sextupolar magnets, a prototype of which has already been built, investigations are in progress to compensate the chromaticity of the booster just by mounting small correction coils between the poles of the focussing magnets. The main magnet power supplies are just ready to order.

Some components of the RF system, using a frequency of 500 MHz, are also ordered. Both cavities obtained from the DESY laboratory at Hamburg, a 1-cell cavity for the storage ring and a 3-cell one for the booster, are already in house. The design of the beam-position monitors and the corresponding electronics, performed in close collaboration with the ESRF at Grenoble, has been finished and their detailed testing is well under way [3].

After finishing the construction work and commissioning of the accelerators at the end of 1993, routine machine operation and first experiments will begin in spring of 1994.

4 VACUUM SYSTEM

In order to guarantee for DELTA life times of the order of 10 - 20 hours under very stable beam conditions, the vacuum system has to provide a pressure of 10^{-7} Pa at most and a very low microwave impedance of the beam tube. As a consequence of the closely mounted DELTA magnets with small apertures (dipoles with 50 mm gap, quadrupoles with 35 mm radius of aperture), one has a low longitudinal conductance of the beam channel of relatively large impedance and, in particular, very little empty space between the magnets. Therefore, installing the many discrete vacuum pumps necessary to obtain ultra-high vacuum is impossible. Consequently continuous pumping of the beam channel all along the electron path is mandatory. For this purpose, a vacuum vessel has been designed with an antechamber at the inner side of the ring circumference for housing the distributed ion-getter pumps (DIP's). Electron channel and antechamber are connected with each other by a continuous slot of 8 mm height and about 30 mm width (fig. 2). This slot has been optimized to obtain lowest RF impedance together with highest possible gas-flow conductance to maintain a sufficiently large pumping capacity.

Because only about 20 % of the circumference of the storage ring has a strong and homogeneous magnetic field necessary for operating DIP's, it was decided to use non-evaporable getter (NEG) strips as the main integrated pumping elements. Since the booster is a machine with ramped magnetic fields not suitable for DIP's, it will be fully equipped with NEG pumps only. The NEG material chosen is the low-temperature getter (St 707 alloy from SEAS GETTERS S.p.A.). Whereas four strips will be installed more or less continuously in both machines, DIP's will be mounted additionally inside the dipole vessels of the main storage ring only. At these locations two DIP's, one on top of the other sharing the cathode in between, are mounted side by side with two NEG strips (fig. 2), thus providing sufficient pumping capacity for inactive gases. To further improve the pumping speed for noble gases and

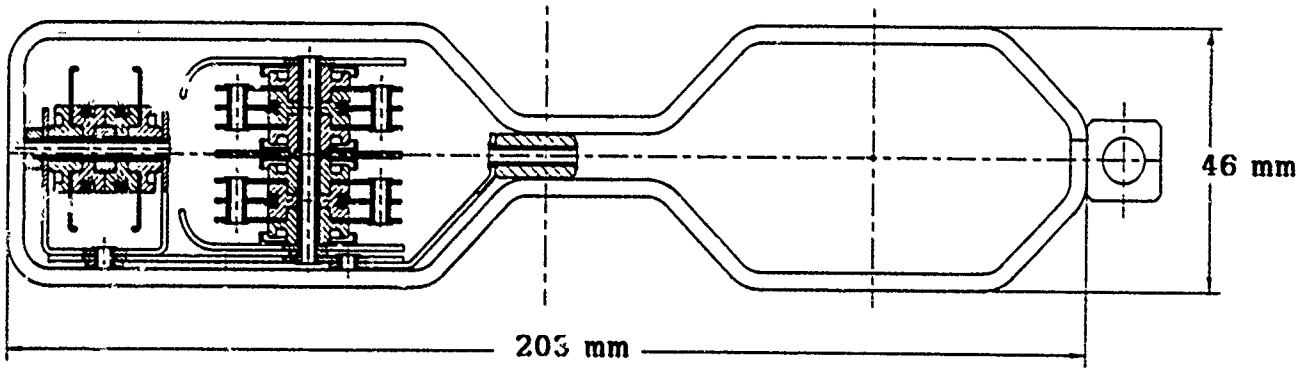


Figure 2: Cross-section of the DELTA vacuum vessel with the compact DIP-NEG pumping module mounted inside the antechamber and with the beam channel and its outer cooling tube to reduce the heat load caused by synchrotron radiation (about 1 kW/m in the arcs at an energy of 1.5 GeV and a beam current of 500 mA).

to reduce the phenomenon of the so-called "argon instability", the central cathode plate of this two-stage DIP is made from tantalum instead of titanium (which is used for the two other cathodes). This leads, however, to a somewhat lower total amount of hydrogen that can be pumped. The anodes are stainless steel sheets with holes of 6 mm diameter, optimized for an average magnetic field of 1 T.

The vacuum vessels for DELTA (curved and straight ones for the dipoles and quadrupoles, respectively) are made of cold-rolled stainless steel sheets of 316LN type of EFR quality. This rather low wall thickness with the correspondingly reduced mechanical stability of the chambers requires to insert spacers in longitudinal direction at about every other 30 cm into the slot to the antechamber. These spacers, to which the pump modules are rigidly fixed, guarantee a constant slot size and also keep the distributed pumps in position. Therefore, any welding or soldering at the inner surfaces of the chamber is avoided. The cross-section of the vacuum chamber with the rather compact pumping element of a combined DIP-NEG module is shown in figure 2 . Vacuum vessels of arcs and straight sections of the main storage ring are separated by four all-metal valves. Whereas, these sector valves and bellows are fabricated with the same cross-section as that of the beam channel, but without an opening for the antechamber, the cross-sections of flanges and monitors are identical to that shown in figure 2 for the standard vacuum vessel. Fabrication of this particularly shaped vacuum chambers from stainless steel is novel, but for a rather small machine like DELTA it is still considerably cheaper than making it from aluminum alloy. A novelty is also the type of flanges and seals we are going to use between beam chambers. It will be VATSEAL (trademark of VAT A.G.), a thin plate of a 20 μm silver-plated copper sheet with a narrow, rectangularly shaped sealing lip on both sides around a central hole, which has the form of the chamber cross-section. This particular seal has shown high tightness under thermal and mechanical strain, and its plain sealing surface can easily be machined afterwards when distorted by the manufacturing process. Conflat and Helicoflex seals are also used.

Only about 8 to 10 lumped pumping stations will be installed at both machines for roughing. Each of them is equipped with a turbo-molecular pump, an external ion-getter pump of 45 l/s, a titanium sublimation pump, a mass-spectrometer head and a connexion for a mobile leak detector. These ion-getter pumps together with the NEG pumps keep the pressure below 10^{-6} Pa, even if the magnets are switched off.

In conclusion, the total vacuum system of DELTA consists of about 110 DIP's each of a length of roughly 300 mm and a pumping speed of 100 l/s, and about 300 NEG pumps of 1 m length, 30 mm width and a pumping speed of 45 l/s at 10^{-6} Pa. Together with the extra pumping stations, this results in a total pumping speed of about 25000 l/s (=220 l/(s m)) with dipole fields on and 11000 l/s (=100 l/(s m)) with magnets switched off. The various pumps, ion gauges, vacuum accessories and prototype vessels are now in the process of being ordered.

References

[1] N. Marquardt et al., *DELTA, a Low-Emittance Storage Ring as Free-Electron-Laser Radiation Source* , Proc. 1989 IEEE PAC, Vol.2 of 3 (1989)780 ; N. Marquardt, *The Dortmund Electron Test Accelerator "DELTA", a New Low-Emittance Storage Ring of 1.5 GeV* , Part. Accel. (1990) Vol.33, p.27 ; DELTA Group, *DELTA Status Report 1990*, Univ. Dortmund, (1990) unpublished.

[2] D Schirmer, *DELTA Optics*, Contrib. USC9 to this Conference, Diploma Thesis, Univ. Dortmund, (1989) unpublished.

[3] R. Heisterhagen et al., *The Beam-Position Monitor for DELTA*, Contrib. KPH13 to this Conference.

Commissioning the SSRL Injector*

S. Baird† and J. Safranek
For the SSRL Injector Group
Stanford Synchrotron Radiation Laboratory, P.O. Box 4349, Bin 69, Stanford, CA 94309-0210

Abstract

Some results from the commissioning of the SSRL injector [1] for SPEAR are described.

I. Pre-Injector

A. Microwave Gun

The microwave gun is fed with a 2.5 μsec RF pulse (2856 MHz), which produces a 2 MeV electron pulse with a peak current of around 650 mAmps. The pre-injector is described in [2]. In order to obtain the optimum electron beam, in both intensity, energy and energy spread, careful attention must be paid to the Gun Cathode heater, which controls the intensity of the electron beam and thus the beam loading in the RF Gun. The balance between input RF power and beam intensity is monitored by observing the RF power reflected from the Gun.

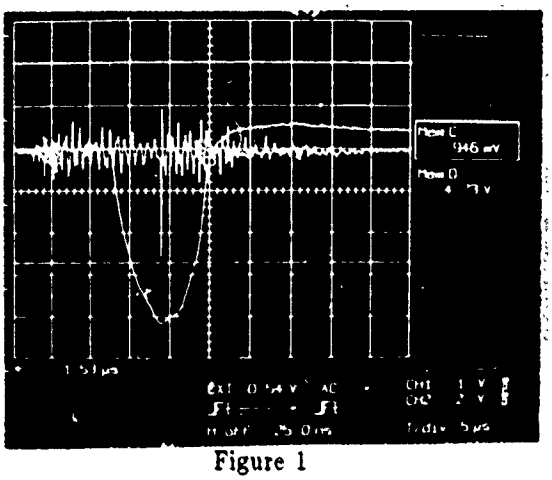


Figure 1
Pre-injector beam before and after the Chopper

B. Alpha Magnet

The 281 degree Alpha magnet shortens the individual micro-bunches and a movable scraper, placed inside the magnet, allows the low energy tail of the beam to be removed before it reaches the Linac. The beam intensities before and after the alpha magnet are measured on two identical current toroids [3]. The beam energy profile is measured from the incremental change in beam current as the scraper is moved through the beam. Then the scraper is positioned to remove the low energy tail of the beam, reducing the beam intensity by around 30%.

C. Fast Chopper

Since only a single bunch is accelerated on each Booster cycle, a fast chopper [4], consisting of two permanent magnets and a vertical kicker, lets only three 2856 MHz bunches into the Linac. The beam is steered so that the rising edge of the chopper pulse scans the beam vertically across a horizontal slit. The fast rise time of the chopper pulse allows only three pre-injector bunches into the Linac. Figure 1. This vertical steering through the chopper is very delicate as incorrect steering here allows secondary particles and scattered beam into the Linac. See section II. 2 10^9 electrons, pulse in three bunches are injected into the Linac.

II. Linac

The Linac has three accelerating sections [5] and operates at 2856 MHz, with a 10 Hz repetition rate. The Klystron for accelerating section 2 also supplies the RF drive for the microwave gun and the other Klystrons.

When accelerating the beam from the pre-injector, the phase of the RF in each accelerating section and the gun have to be optimised so that the bunches always travel on the peak of the accelerating wave all three sections. These phases are optimised by maximizing the beam energy and minimizing the energy spread, as measured in the high dispersion region after the first bending magnet in the Linac to Booster transport line. Here both beam position monitors and a luminescent screen are used for beam observation. The nominal Linac beam energy is between 120 and 130 MeV, with an energy spread given by: $\sigma = 0.25\%$.

Two current toroids monitor the beam intensity at the beginning and end of the Linac. Once the Linac is operating correctly, 100% transmission efficiency is routinely achieved. These toroids have been absolutely calibrated using a Faraday Cup at the end of the Linac. When the Injector is operating, the beam in the Booster must not exceed 3 10^{10} electrons sec. Therefore, if the integrated current read by these toroids exceeds 3 10^9 electrons, pulse, the beam is shut off [6]. So unwanted particles must not enter the Linac. See section IC.

III. Linac to Booster (LTB) transport line

The LTB transport line transports the 125 MeV beam from the Linac to the Booster. It consists of three main bending magnets and 6 quadrupoles. Corrector magnets and trim coils on the bending magnets and quadrupoles are used for fine steering. The beam position and intensity in the line are monitored using 5 Beam Position Monitors (BPM). As well as beam position the summed signals from all 4 individual BPM buttons are very useful for measuring beam intensity. Once the beam is well centered throughout the LTB line, 100% transmission is routinely achieved.

IV. Booster operation

A. Injection and Acceleration

Injection into the Booster uses a horizontal septum magnet and a horizontal kicker [7]. Early in the commissioning large position fluctuations at injection into the Booster made injection very difficult. They are caused by energy changes in the Linac beam due to small changes in the output of the Variable Voltage Transformer, which supplies high voltage to the three Linac Modulators. Modifications

*Work supported by the Department of Energy, Office of Basic Energy Sciences, Division of Material Sciences.

†Visiting SSRL from CERN

0-7803-0135-8/91$01.00 ©IEEE

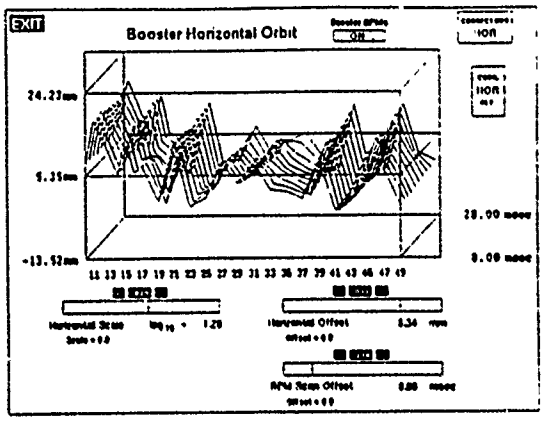


Figure 2
Evolution of the horizontal closed orbit over 20 msecs of acceleration

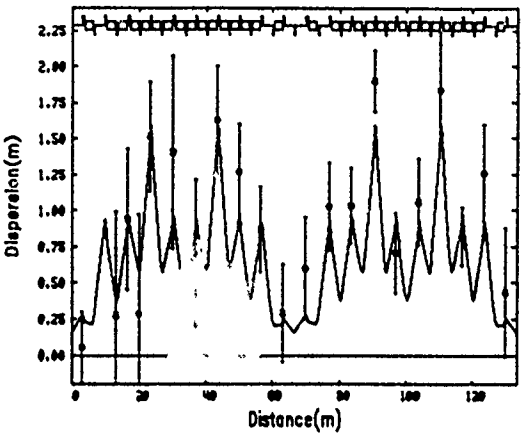


Figure 3
Dispersion function, the solid line is the theoretical curve

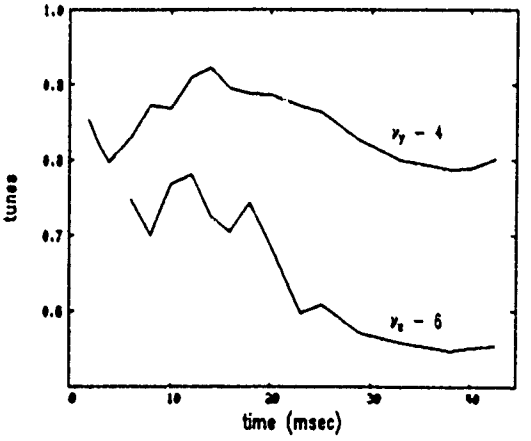


Figure 4
ν_x and ν_y during the acceleration. The design values were 6.25 and 4.18. Note the large change in ν_x shown here was part of a deliberate machine experiment

to the VVT are in progress, but a software feedback system [8], which monitors a BPM in a high dispersion region of the LTB line and corrects the Linac RF power to maintain constant beam energy, has greatly reduced the impact of this problem.

The Booster bending magnets and quadrupoles are part of a single 10 Hz resonant or "White" circuit [9]. The oscillating current passes from a small negative current to around +500 Amps peak value, which corresponds to an energy of 2.3 GeV. Injection occurs at about 27 Amps, and is triggered at a particular main magnet field level set for the incoming beam energy [10]. Accurate control of this field level is essential for reliable injection into the Booster. This trigger is also synchronised to the Booster RF frequency to ensure RF capture of the beam. In the early days of commissioning the Booster, DC injection, using a constant main field setting, was established first. However, since the remanent fields are completely different when ramping, DC injection is no longer used.

The beam intensity in the Booster is measured on a sensitive capacitive longitudinal pick-up. [3]. The captured beam intensity was found to be very sensitive to the horizontal orbit and the QF and QD settings at injection. Now a typical ramp shows no losses, except for a 10-20% during the first few turns after injection. To reduce this initial loss the matching of the beam from the LTB line into the Booster still needs some study. The Booster RF [5] system runs at 358 MHz to match exactly that of SPEAR, and all three 2856 MHz Linac bunches are injected into a single RF bucket. The RF voltage is ramped during acceleration according the relation:

RF Gap Voltage $\propto E^4 - dE/dt$. (E=beam energy)

B. Closed Orbits

Initially obtaining a first turn around the Booster required steering around the ring BPM by BPM. Now that the Booster orbit is better understood, injection RF capture and acceleration can usually be established in a few minutes. The closed orbits in the Booster are measured every 2 msec through the 45 msec ramp. Figure 2 [11]. Over the first 8 msec of the acceleration the distortion shrinks as the remanent field effects from different magnets wash out. The orbit then stays constant until around 4 msec before ejection, when the distortion increases slightly as the pulsed ejection septum magnet comes on. The large residual horizontal orbit distortion, is due to many small quadrupole misaligments and not a single large error. Short of a complete re-alignment this is proving very difficult to correct, and predictions for correction by moving single quadrupoles are shown in Table 1. The dispersion function around the Booster has been measured by analyzing the horizontal orbit as a function of RF frequency. Figure 3

Table 1
Horizontal orbit correction for displacement of different quadrupoles

Quad	Disp. (mm)	Initial rms orbit error	Final rms orbit error	ν_x
Q16	2.50	7.82	1.95	6.96
Q13	0.47	7.82	2.29	6.97
Q19	0.88	7.82	2.38	6.92
Q19	2.05	5.81	3.86	6.55
Q16	7.13	5.81	4.26	6.55
Q16	1.76	5.81	4.40	6.55

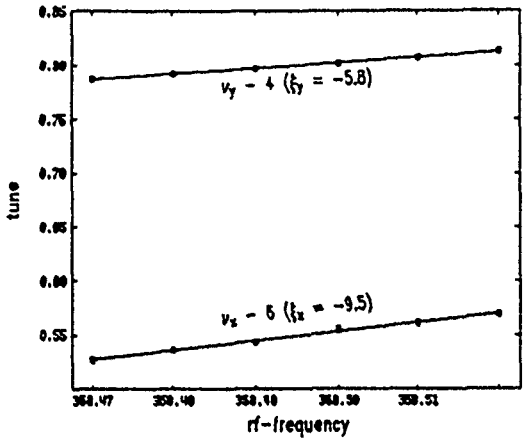


Figure 5
ν_x and ν_y vs. RF Frequency. This gives ξ_x = -9.1(-9.3) and ξ_y = -5.5(-6.5). Design values are given in brackets.

C. Betatron Tunes

Variation of horizontal and vertical tunes have been measured during the acceleration. Figure 4. Tunes are controlled by trim windings on the QF and QD quadrupoles, fed by a function generator [12], which is programmed for the required tune corrections. The beam is excited in both planes simultaneously using a pair of striplines driven at a variable frequency in the range 0-2 MHz. The beam response is observed, via a similar pair of strip lines, on a spectrum analyser, externally triggered to take data at a particular time in the acceleration. As the frequency is swept across the horizontal or vertical betatron sidebands a strong response is seen. By measuring the tunes at a fixed point in the ramp as a function of RF frequency. Figure 5, the chromaticities have been measured. The Booster has sextupoles, but they have not been powered, and there are no plans to use them. Horizontal tunes were also measured by observing the response of the beam after a single horizontal kick. No evidence was found that the horizontal tune varied measurably with the amplitude of the initial kick. It was not possible to observe any vertical excitation in this way, which suggests that horizontal, vertical coupling is small.

V. Booster to SPEAR (BTS) transport line

A horizontal kicker [7] and a vertical pulsed septum [13] eject the beam at the peak of the magnetic cycle into the BTS transport line. Due to the close proximity of the ejection line to both the Booster and the injection line, powering the BTS magnets perturbs the beam at injection in the Booster. These effects are corrected using two vertical dipole correctors in the Booster and two vertical steering magnets at the end of the LTB injection line. This line is matched to give the same injected beam parameters at SPEAR injection as the SLAC Linac. Three luminescent screens and 6 BPM's are routinely used for monitoring beam stability, position and transmission efficiency.

VI. Conclusions

In conclusion the SSRL injector has been commissioned and already fills SPEAR at rates which are comparable to those obtained using the SLAC Linac. Table 2 shows the design goals for the Injector, the best achieved performance levels, and routine performance levels.

Table 2
Injector performance: Intensity in 10^{10} electrons/sec

	Design	Best	Routine
Linac	2.00	2.50	2.00
Booster Inj.	2.00	1.60	1.10
Booster Acc.	1.25	1.50	0.70
Booster Ej.	0.60	1.00	0.60
SPEAR Inj.	0.15	0.22	0.15[1]

VII. References

[1] H. Wiedemann, "3 GeV Injector Sunchrotron for Spear." At this Conference.
[2] M. Borland, "A High-Brightness Thermionic Microwave Electron Gun." Stanford University Phd. Thesis, 1991.
[3] J. Sebek et al. "Diagnostic Instrumentation for the SSRL 3 GeV Injector for SPEAR." At this Conference.
[4] M. Borland et al. "Design and Performance of the travelling-wave beam chopper for the SSRL Injector." At this Conference.
[5] J.N. Weaver et al. "The Linac and Booster RF System for a dedicated Injector for SPEAR." At this Conference.
[6] R. Yotam et al. "Personnel Protection and Beam Containment Systems for the SSRL 3 GeV Injector." At this Conference.
[7] H-D. Nuhn et al. "The SSRL Injection Kickers." At this Conference.
[8] L. Emery, "Energy Feedback system for the SSRL Injector Linac." At this Conference.
[9] R. Hettel et al. "The 10 Hz Resonant Magnet Power Supply System for the SSRL 3 GeV Injector." At this Conference.
[10] R. Hettel et al. "Triggers and Timing System for the SSRL 3 GeV Injector." At this Conference.
[11] W. Lavender et al. "The SSRL Injector Beam Position Monitoring Systems." At this Conference.
[12] S Brennan et al. "The Control and Operation of the Programmable Waveform Generator for the SSRL Injector." At this Conference.
[13] J. Cerino et al. "Extraction Septum Magnet for the SSRL Injector." At this Conference.

[1] This corresponds to an accumulation rate of 20 mAmps/minute

An Isochronous Lattice for PEP*

W.J. Corbett and M.H.R. Donald

Stanford Linear Accelerator Center, Stanford, CA 94309

and

A. A. Garren

Lawrence Berkeley Laboratory, Berkeley, California 94720

Abstract

With e^+e^- storage rings operating in a quasi-isochronous mode, it might be possible to produce short bunches with length $\sigma_z < 1$ cm. The unique characteristics of the short bunches could then be utilized for synchrotron radiation applications or colliders with mm-scale β^*. In principle, the design of a quasi-isochronous storage ring is relatively straight-forward, but experimental studies with electron storage rings in this configuration have not been carried out. The purpose of this paper is to demonstrate that an isochronous lattice design is compatible with PEP given a minimum of hardware modifications.

I. Introduction

In addition to being a prime candidate for a B Factory, [1] PEP is well recognized as a high brilliance synchrotron radiation source. [2] To further explore new directions in B Factory design and the capabilities of PEP as a light source, [3] we have begun to investigate the potential for short bunch operation in a quasi-isochronous, or low momentum-compaction mode. Since we are working under the constraint that magnets may not be moved, the configuration requires periodically driving the dispersion function negative throughout the arcs to compensate for positive values. Using this approach, a preliminary solution has been found for the present PEP magnet arrangement. Following further refinement of the design, valuable short-bunch machine studies of interest to both the high energy physics and synchrotron radiation communities might be possible.

The principle behind using a low momentum-compaction lattice for bunch length compression proceeds from the observation that for high energy electron storage rings the bunch length scales as [4,5]

$$\sigma_l \propto \sqrt{\alpha} \tag{1}$$

for a given RF voltage and frequency. Here, the momentum compaction factor

$$\alpha = \frac{\Delta L}{L} \times \frac{p}{\Delta p} = \frac{1}{\gamma_t^2} = 1/(2\pi R) \oint D_x/\rho \, ds \tag{2}$$

gives (to lowest order) the path length deviation due to small energy excursions from the central value. If α is made sufficiently small, the phase slip factor

$$\eta = \frac{1}{\gamma^2} - \frac{1}{\gamma_t^2} \tag{3}$$

tends to zero and the synchrotron oscillation amplitude is reduced. For PEP, the lowest value achieved to date is $\alpha = 1 \times 10^{-3}$ in a low-emittance configuration. [6] The isochronous condition implies a lattice with $\alpha = 1/\gamma^2 \approx 5 \times 10^{-5}$ at 10 GeV. In the following Section, a solution for a low-α lattice in PEP which maintains the proper phase advance between chromaticity correction sextupoles is discussed, and a two-family solution for sextupole strengths is found. In Section III, the bunch length is estimated based on an analysis of the longitudinal acceptance for a small, energy dependent, momentum compaction factor. [7,8]

The results are summarized in Section V along with recommendations for future work.

II. Lattice Design

The PEP lattice consists of six long straight sections, connected by 2-cell dispersion suppressors to arcs containing 12 FODO cells. The regular FODO structure of each arc is broken at its center to accommodate a short 5 m "symmetry" straight. In the "colliding beams" mode the insertion quadrupoles, close to the center of each long straight, focus the beams to low β values, while in the "low emittance" light source mode weak focussing is used across the interaction points. The basic constraint in designing any alternative lattice for PEP is not to move any magnets in the arcs. It is also advantageous not to exceed the power dissipation of the present magnets.

One way to obtain a low momentum compaction lattice [9,10] is to force the dispersion function D_x to negative values through some of the dipoles to compensate for the positive values of D_x in other dipoles. The requirement is that $\alpha = 1/(2\pi R) \oint D_x/\rho \, ds$ be close to zero for the whole ring. We achieve this by making super-cells, consisting of several FODO cells, that repeat in regular fashion through the arcs. We have found (so far) that the most suitable arrangement for PEP is a super-cell made of three PEP FODO cells and having betatron phase advance $\mu_x/(2\pi) = 0.75$ and $\mu_y/(2\pi) = 0.25$. There are thus four super-cells in one PEP arc. The phase advance is arranged so that self-compensating pairs of chromaticity correcting sextupoles can be placed with a phase advance of $(2n+1)\pi$ between them. The basic super-cell is shown in Fig. 1.

It was found that this particular super-cell matched nicely into the symmetry section and, through the disper-

* Work supported by Department of Energy contract DE-AC03-76SF00515 and DE-AC03-76SF00098.

U.S. Government work not protected by U.S. Copyright.

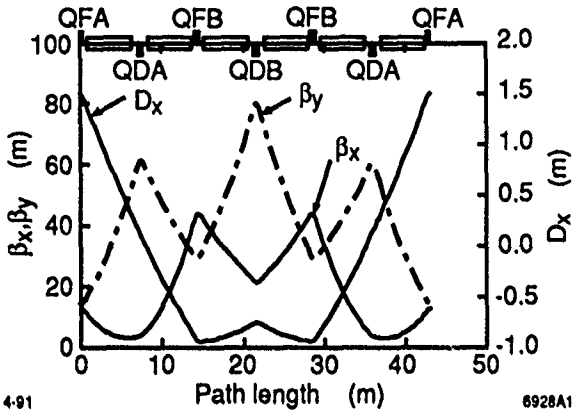


Figure 1. The standard supercell is made up of three FODO cells with symmetry about the middle of the center cell. The strong quadrupoles QFA drive the dispersion function through the center of QDA to negative values.

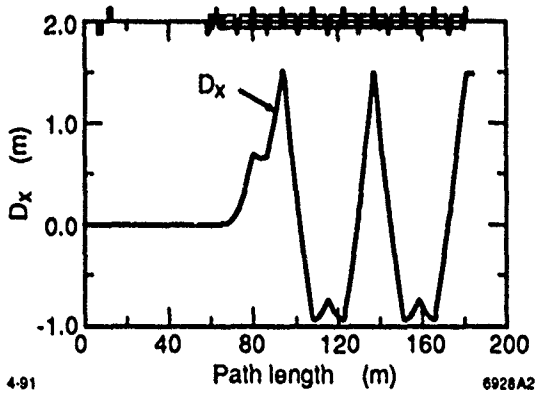


Figure 2. Dispersion Function for one half Superperiod.

sion suppressor, into the long straight sections (Figs. 2,3). The phase advance through the symmetry straight required an adjustment to the super-cell phase advance, so that the phase advance through the combination of super-cell and symmetry straight equalled $0.75(2\pi)$ and $0.25(2\pi)$. Figure 4 shows the phase advance between typical sextupole pairs.

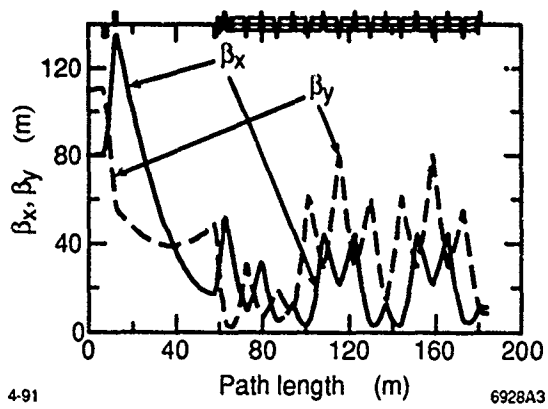


Figure 3. Beta Functions for one half Superperiod.The beta functions of the supercells match easily into the symmetry straight and into the long straight section.

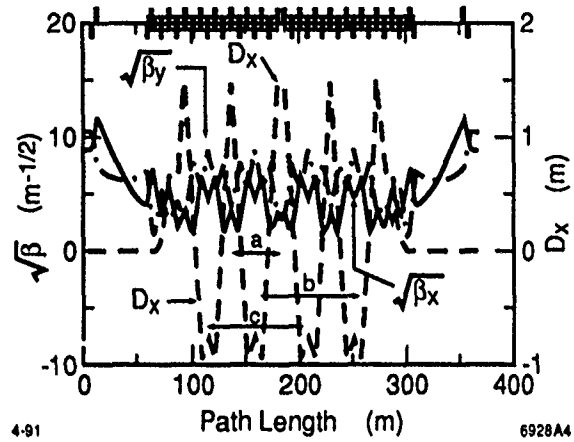


Figure 4. One of the six Sextants of PEP. (a) The phase advance is adjusted to be 90° and 270° across the supercell. (b, c) Chromaticity correcting sextupoles may be placed in pairs with phase advance of 0.5 and 1.5 times 2π.

Some lattice parameters for the 6 superperiod PEP ring are:

$P = 9$ GeV

$Q_x = 25.526$ $\quad Q_y = 15.861$ $\quad Q_s = 0.0022$

$\xi_x = -38.32$ $\quad \xi_y = -39.13$ (uncorrected)

$V_{RF} = 15\ MeV/rev$ $\quad \sigma_E = 0.06\% \left(\frac{dp}{p}\right)$

Preliminary particle tracking results are promising, showing a dynamic aperture of $12\sigma_\beta$ for both on-momentum particles and those undergoing synchrotron oscillations with 6σ momentum deviation. The chromatic properties $(d\beta)/\beta)/(dp/p)$ and $(d\nu_{x,y})/(dp/p)$ were also good.

The lattice as shown is more of a demonstration of a lattice with zero α than a finished design. As explained in the following section, a lattice with α this small would not be stable in synchrotron motion at this energy deviation. A more realistic lattice design would have a larger value of α. In addition, we must explore alternative ways of changing the betatron tune of the machine, either by adding quadrupoles in the long straight sections or by having a conventional FODO lattice in one or more of the arcs.

III. Bunch Length Scaling

Analysis of the longitudinal dynamics for short bunches is inherently a non-linear problem and has been discussed by Pellegrini and Robin.[4, 7] In principle, since the bunch length scales as $\sigma \propto \sqrt{\alpha}$, a factor of > 100 reduction in momentum compaction is required to compress a 5 cm bunch into the range of interest for short bunch B Factory designs, or advanced synchrotron radiation applications. Expanding the momentum compaction as a function of energy deviation, $\alpha = \alpha_1 + \alpha_2\delta$ where

$$\alpha_1 = \frac{1}{2\pi R}\int D_x/\rho ds \quad , \quad \alpha_2 \approx \frac{1}{2\pi R}\int \frac{\langle D_x^2\rangle}{\rho} ds$$

and $\delta = \Delta p/p$, the authors [4, 7] have found that the ratio α_1/α_2 gives a rough estimate of the longitudinal bucket

size along the energy axis. To estimate the lower bound on α_1, we assume the RF acceptance must exceed the energy spread of the bunch by a factor of 10 to preserve quantum lifetime.

Since D_x can be energy dependent, we use the computer program MAD[11] to find the off-energy closed-orbit and plot α as a function of energy deviation. For our lattice, including chromaticity sextupoles, we find $\alpha_2 = 0.027$, as shown in Fig. 5. Imposing the lifetime condition $\alpha_1/\alpha_2 \sim 10\delta$, the lower bound on α_1 is about 1.6×10^{-4}. The design bunch length is 3.3 mm for this lattice. By adding more families of sextupoles, it may be possible to reduce the longitudinal chromaticity (α_2) and thus obtain shorter bunches.

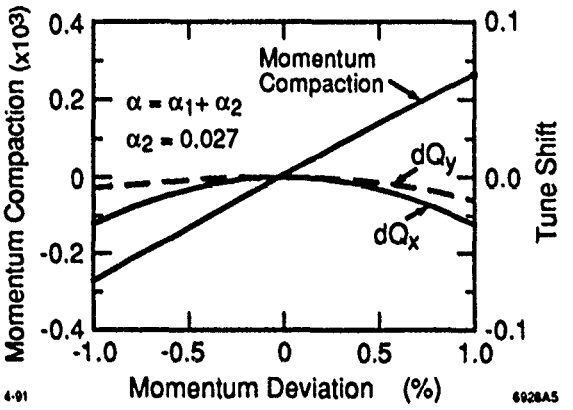


Figure 5. (1) α has an energy dependence $\alpha = \alpha_1 + \alpha_2 \frac{dp}{p}$ that governs the size of the RF bucket. (2) Two sextupole families (SD and SF) are used to correct chromaticity.

IV. Conclusions

We have demonstrated the design of a low momentum-compaction lattice for PEP. The configuration is based on a succession of supercells (3 FODO cells each) with regions of negative dispersion and betatron phase advance between pairs of compensating sextupoles fixed at $(2n+1)\pi$. Although the configuration must be regarded as preliminary, it requires no magnet re-locations, no quadrupole polarity reversals, and does not exceed power load ratings for a 9 GeV beam. Some new bus work is required. Prior to experimental verification of the low-α lattice, further study of chromatic properties (including tracking with synchrotron motion), injection and tuning procedures, and longitudinal dynamics would be required. At this stage, the theoretical bunch length is about 3.5 mm at 9 GeV (V_{RF} = 15 MV), but smaller values could in principle be reached by correcting the longitudinal chromaticity with additional sextupole families.

V. Acknowledgments

The authors would like to thank Max Cornacchia for initiating this study, and Claudio Pellegrini and David Robin for their non-linear bunch stability analysis. Heinz-Dieter Nuhn, Jim Spencer and Hermann Winick provided many useful comments throughout the course of this work.

References

[1] "An Asymmetric B Factory Based on PEP: Conceptual Design Report," LBL PUB-5303 (SLAC-372, CALT-68-1715, UCRL-ID-106426,UCIRRPA-91-01), 1991.

[2] A. Bienenstock, G. Brown, H. Wiedermann, H. Winick, "PEP as a Synchrotron Radiation Source," R. S. I. 60 (7), pp. 1393-1398, 1989.

[3] A. Fisher, et al., "Coherent Radiation for PEP," these proceedings.

[4] C. Pellegrini and D. Robin, "Quasi-Isochronous Storage Ring," NIM A301, pp. 27-36, 1991.

[5] M. Sands, "The Physics of Electron Storage Rings: An Introduction," SLAC-121, 1970.

[6] M. Donald, L. Rivkin, A. Hofmann, SSRL ACD Note 34, 1985.

[7] C. Pellegrini and D. Robin, "Quasi-Isochronous Storage Rings: A Possible Low Current High Luminosity Meson Flavor Factory," these proceedings.

[8] E. Ciapola, A. Hofmann, S. Myers, T. Risselada, "The Variation of γ_t with $\Delta p/p$ in the CERN ISR,' IEEE Trans. N. S., Vol. NS-26, 3, pp. 3571-3573, 1979.

[9] A. A. Garren, E. D. Courant, U. Wienands, "Low Momentum Compaction Lattice Study of the SSC Low Energy Booster," these proceedings.

[10] R. V. Servranckx, U. Wienands and M. K. Craddock, "Racetrack Lattices for the TRIUMF Kaon Factory," in Proc. IEEE PAC, Chicago, IL, pp. 1355-1357, 1989.

[11] H. Grote and F. C. Iselin, "The MAD Program (Methodical Accelerator Design)," Rev. 2, CERN/SL/90-13 (AP).

Lattice Studies for a Small Storage Ring *

Philip Kiefer and Wayne Vernon
Physics Department, University of California at San Diego
and
Intercampus Institute for Research at Particle Accelerators
B-019, UCSD, La Jolla, CA 92093

Abstract

We have studied configurations of magnetic elements in order to maximize the beam brightness of a small e^- storage ring for use as a component in a Compton scattered x-ray facility. The design goal was a single bunch current of 20 mA at a beam energy of 125 MeV. The design produced a low emittance beam ($\varepsilon_x = 10^{-7}$ m-rad) with a reasonable lifetime. We plan to use NdBFe permanent magnetic driven dipoles in an attempt to reduce the overall cost of the storage ring facility, and the design used their properties for the bends in the lattice. Parameters varied include RF voltage, lattice structure, number and size of bend elements. In particular, the effect of intrabeam scattering at such a low energy was studied.

I. Introduction

We are working on the design of a small storage ring as part of a Compton scattered photon source of high brightness x-rays for protein crystallography. When the 10.6 μm wavelength (or 0.12 eV) energy photons of a CO_2 laser are scattered at right angles with a 100 MeV electron beam, x-rays of 9 keV are emitted in the direction of the electron beam. If a variable energy storage ring (80 to 125 MeV electrons) is used, then x-rays with energies between 5.7 and 14 keV are emitted. Since the brightness of the x-rays is determined by a combination of laser focus spot size and reasonably low electron angular divergence (1 mrad), the emittance of the ring must be

$$\varepsilon_x < 10^{-7}\ \mathrm{m-rad}$$

in the horizontal bend plane; the units of ε_x are such that the x distribution has an rms value of $\sqrt{\beta_x \varepsilon_x}$ for the Twiss parameter β_x.

One of the main goals of this study is to keep the ring small so that it will be inexpensive to build and operate. A related study [1] has shown that inexpensive permanent magnet-based dipoles should work well as the bend elements in the ring lattice, and the properties of those magnets have been assumed here. Initially it appeared that we could design a high brightness ring with square magnets and allow the beam to enter the dipoles at some angle other than at 90° to the iron face. This would generate considerable focusing and, perhaps, would allow a reduction in the number of quadrupoles and sextupoles in the lattice. We became suspicious of the computer programs' abilties to handle these iron face problems correctly at low energy, and decided to concentrate on "high quality" rings because there has not been too much work done in this low energy regime where intrabeam scattering is so important. Therefore, we have used a traditional, many element lattice in order to establish what we hope is a nearly optimum machine that can be used as a basis for comparison when simpler designs are studied.

II. Ring Specifications

The desired/achieved ring and stored beam properties are enumerated in Table I. Brightness requirements dominate the design, and intra-beam scattering leads to a search for longer bunch lengths, if possible, because internal bunch density will decrease without a corresponding loss in brightness. On the other hand, we will see that schemes for increasing bunch length will tend to cause reduced beam lifetime. There is also a need for a small β_x and β_y (0.1 and 1 m) in the insertion region for generating a small spot size at the collision point with the laser.

0-7803-0135-8/91$01.00 ©IEEE

Table I

Small Ring Parameters		
Parameter	Desired	This Design
Bend radius (m)	1	1
Circumference (m)	8	19
Beam current (mA)	300	-
One bunch (mA)	20	20
e^- Eng., max. (MeV)	125	125
e^- Eng., min. (MeV)	80	-
Life time (hour)	1	0.8
Bunch Length (cm)	10	2.8
ϵ_x (mm-mrad)	0.1	0.2

III. The Design

The main tools for this design are GEMINI [2] and ZAP [3] , computer programs which have been used extensively to design the LBL Advanced Light Source and its injector synchrotron [4]. Gemini was used to obtain a closed orbit solution(dispersion and chromaticity fit) and the natural horizontal emittance. ZAP calculated the equilibrium emittance due to intra-beam scattering and the Touschek lifetime as a function of RF voltage and beam current. Things assumed were 2 Ω longitudinal impedance, an RF frequency of 193 MHz (12th harmonic), and an ϵ_x/ϵ_y ratio of 10:1.

The bend magnets were picked to be 0.4 m in length to acquire the appropriate deflection angle for the existing field strength in the dipole [1]. The pole faces were chosen perpendicular to beam to prevent problems with edge focusing effects at low energies. The actual lattice has 16 bends contained within a FODO lattice, and a quadrant is shown in Figure 1. The focusing quadrupoles are placed at each entrance to the insertion regions to obtain a small spot size. Table II lists the element parameters for the ring. The large strengths of the quadrupoles(k=20 and -15 m^{-1}) are used because of the small dimensions of the ring, and they produce large beta functions which deter intra-beam scattering. The beta functions and the dispersion are plotted in Figure 2 for a quadrant of the ring, staring at the insertion region. Sextupoles were placed to appropriately diminish any chromaticity present. Horizontal focusing sextupoles were placed where the ratio of the horizontal to vertical beta function is large and defocusing where the ratio is small. All other lattices tried did not have the small horizontal beta function at the insertion region.

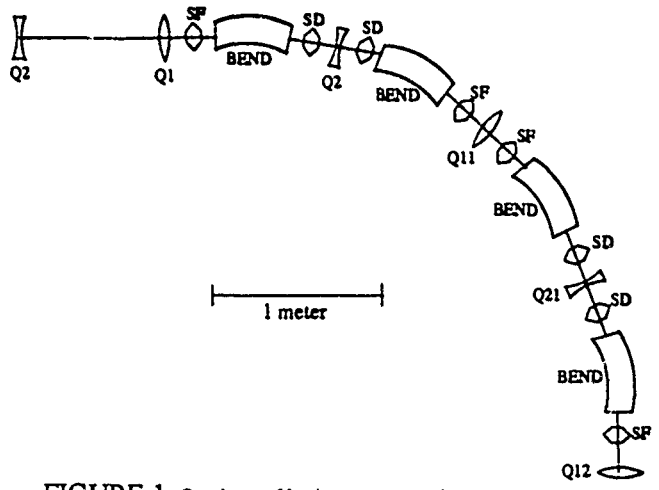


FIGURE 1. Quadrant of lattice starting at the insertion region. The distance between two quadrupoles is 0.85m.

Table II

Lattice Element Parameters		
Element	Length (m)	k (m^{-1})
Q_1 (=Q_{12})	0.1	20
Q_2 (=Q_{21})	0.1	-15
Q_{11}	0.1	20.6
SF	0.1	-3.4 m^{-2}
SD	0.1	2.7 m^{-2}
Bend	0.4	-0.41

IV. Results

One of the more interesting results of the study is shown in Figure 3. The horizontal emittance and the beam lifetime are plotted *vs* single bunch current for two RF cavity voltages. It is fairly clear that the low voltage, which allows a longer bunch length, will, however, lead to a significantly shorter beam lifetime. In the future we will try lower frequency RF solutions, but lower frequencies probably mean lower number of filled bunches in the ring and a lower total current.

We do not yet have a good solution for the insertion; the vertical size is too large ($\beta_y > 1$ m) and is located in the center of a quadrupole. Hopefully this can be fixed without too large an effect on the beam brightness. Overall, the ring looks quite promising for use as a Compton scattering x-ray source for protein crystallography, and future efforts should result in even simpler solutions with comparable brightness. We just

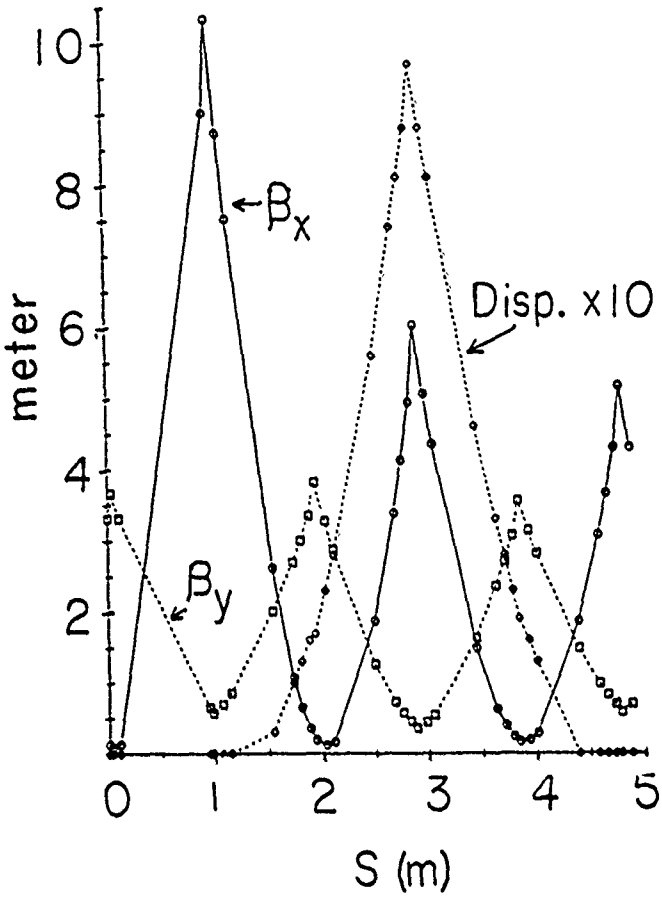


FIGURE 2. Horizontal, vertical beta functions, and 10xdispersion of quadrant starting at insertion region.

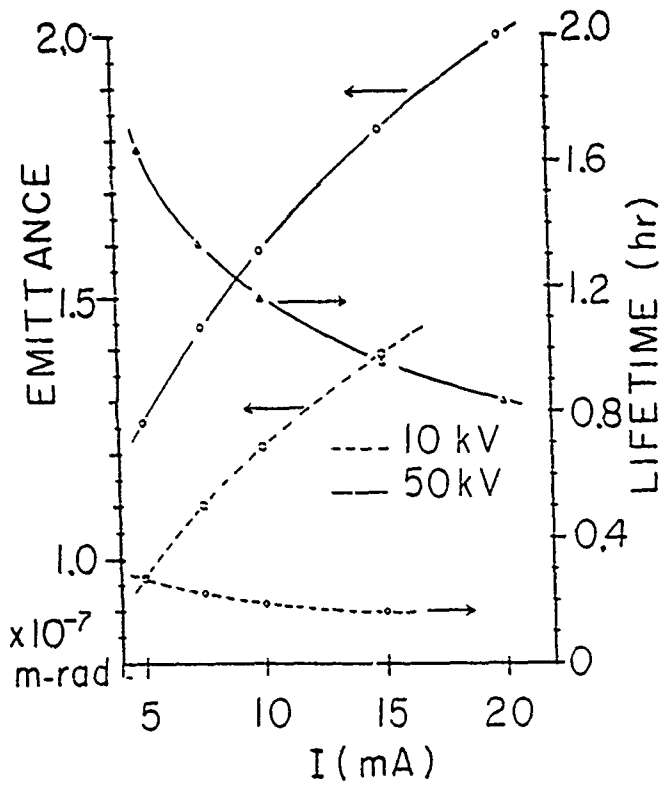


FIGURE 3. Emittance and Touschek lifetime vs. beam current for 50 & 10kV RF voltages.

learned of the SXLS project at BNL [5] in which 200 mA of current is being stored in a small ring at 80 MeV; if the emittance is low enough, that ring makes an excellent starting point for our needs.

V. Acknowledgements

We wish to thank Hiroshi Nishimura, Mike Zisman and Helmut Wiedemann for all of the time they spent answering our questions, providing programs and giving advice. They are not to blame for any mistakes we have made.

VI. References

[1] "Permanent magnet-based dipole for a small storage ring," F. Putris and W. Vernon, these proceedings.

[2] "GEMINI Manual," H. Nishimura, private communication.

[3] "ZAP Users Manual," M. S. Zisman, S. Chattopadhyay, J. J. Bisognano, LBL 21270 (1986).

[4] "1 – 2 GeV Synchrotron Radiation Source – Conceptual Design Report," PUB-5172 Rev. (1986).

[5] "Commissioning of the Phase I Superconducting X-Ray Lithography Source (SXLS) at BNL," J. B. Murphy, *et al*, these proceedings.

*Support provided by NIH/DRR (Grant 1R03RR060034-01) and DOE (Contract DE-AS03-76ER70285)

High Frequency Betatrons

David R. Winn
Department of Physics
Fairfield University
Fairfield CT 06430-7524

Abstract

We discuss the scaling of betatron technique with the use of high frequency, low-loss magnetic materials (ferrites, metglas, etc.). Because of synchrotron radiation, the maximum betatron energy E_{max}(GeV) scales as ~ 0.013 f(Hz)/B_S^2(T), where B_S is the maximum magnetic field on the orbit and f is the full-wave acceleration frequency. Eddy current losses in laminated iron limit f to ~120 Hz, thereby limiting E_{max} to 300-400 MeV for a classical betatron, with a low acceleration gradient, and low current. With low-loss, high frequency materials, one may consider f~1-100 kHz, and energies in the GeV regime, or betatrons with substantially higher current. We discuss practical considerations, potential advantages, and possible applications.

I. INTRODUCTION

The standard betatron[1] has many advantages for generating electron beams compared with other technologies. At energies below ~50 MeV betatrons have a much simpler power modulator and construction than either linear induction or RF linacs, and can be more compact for a given energy. On the other hand, the standard betatron is flux-limited compared with the linacs of similar energy. Compared with the synchrotron, both the energies obtainable and the large amounts of high μ material necessary lessen the the betatron from being the technology of choice in many applications. In this brief note, we point out that the inherent virtues in the betatron technique may be enhanced by the availability of modern high frequency magnetic materials[2]. We refer throughout to the excellent reviews in references [3], [4], [5], [6], [7] .

II. ENERGY LIMITS

The energy limit of a betatron is given to first order by synchrotron radiation. As was pointed out by Iwanenko and Pomeranchuk in 1944 [8], the maximum possible energy of a full core betatron scales as

$$E_{max}(GeV) \sim 0.013 f(Hz)/B_S^2(T), \qquad (1)$$

where B_S is the maximum magnetic guide field = 1/2 B_W, the average induction swing during acceleration, and f is the frequency of the full-wave acceleration cycle. Typical early large laminated iron core betatrons were limited by eddy current losses to low frequencies, typically ~120 Hz at 2 T maximum, thereby limiting E_{max} to about 400 MeV for a classical betatron. With modern high frequency low loss magnetic materials [7],[9] at frequencies f > 1-10 kHz one can therefore in principle consider betatrons in the multi-GeV regime.

The induction energy on the equilibrium orbit for relativistic electrons [7] is given by:

$$E=eV \le eB_S R c s^2. \qquad (2)$$

The constant s^2 is the fraction of the area of the orbit of radius R filled with core, introduced as a connection to large recirculating induction machines[7]. The limit of small cores on a circle is that of a recirculating induction linac. As usual in a full-core betatron, R~3.3 m at B_s= B_W/2=1 T, at E~pc=1 GeV. The energy under the betatron condition is constrained by half or less of the maximum magnetic field swing available in magnetic materials with low loss.

R is also constrained by

$$R = c/8\pi fn, \qquad (3)$$

where n is the number of turns per 1/4 cycle of the acceleration frequency f, for producing beams with small energy spread at maximum value. (The limit of n=1, single turn acceleration, is essentially the linear induction accelerator.)

Substituting, we find that the fn product

$$fn \le B_S c^2 s^2/8\pi E(eV), \qquad (4)$$

which for a field B=1 T and s^2=1 gives fn ~3.6 x 10^6 Hz-turns at 1 GeV. The fn product, scaling as 1/E, highlights that high frequency operation at a fixed energy requires a small number of turns in the acceleration cycle, implying a high acceleration gradient. The small number of turns lessen the orbit stability requirements, while the high gradient allows higher captured current. For other parameters fixed, the acceleration gradient F scales directly with f, and the turns per 1/4 cycle n with 1/f. A 1 T betatron at 300 MeV has a gradient of ~9 keV/Turn at 100 Hz, travelling 120,000 turns; a 1(5) kHz, 600 MeV betatron beam would travel only 6,000 (1,200) turns, with a gradient of 100(500) keV/turn; the electron energy gain exceeds the injection energy from a typical internal electron gun in less than 1 turn.

III. CURRENT LIMITS

If the injected charge in one cycle were independent of the acceleration mechanism, the time averaged current

0-7803-0135-8/91$01.00 ©IEEE

would simply increase with f. However, we note that the peak injection current limit scales roughly as $I_0 \sim F^{3/2} f(E_0)$ where F is the the acceleration gradient and $f(E_0)$ is a function that scales between linear-quadratic in the injection energy E_0[10]. Since F scales with f, the initial injected current scales as $I_0 \sim f^{3/2}$. However, to maintain a well-defined energy, the current is injected over a small fraction of the betatron cycle time T=1/f, typically about 0.1% to a few 2% of T, and therefore the average beam current I scales as $I \sim I_0 f^{-1} \sim f^{1/2}$ (averaged over a cycle).

The captured current limit in space charge equilibrium with a weak focussing force in a standard betatron also scales between B to B^2 at injection [6], [7], depending on the focussing gradients, implying that the highest practical injection energies and gradients are needed. In a large betatron, for example, a typical peak current limit at injection would be only ~1 A at 100 keV, but this limit rises to ~30 kA if it could reach ~1 GeV.

As an example of the potential of rapid acceleration, at 100 keV injection for acceleration to 1 GeV at 1 kHz , the energy after 1 turn is ~350 keV, increasing the equilibrium current limit averaged over the single orbit by a factor of ~2-6, depending on the weak focussing. The radius of the instantaneous orbit after 1 turn shrinks proportionally to the acceleration frequency (gradient), and beam avoidance problems of the injector could be made minimal at large gradients/high frequencies. However, normal betatron orbit solutions assume that the accelerating field does not change appreciably over 1 revolution, which for a 10-20 turn machine would not be as good an approximation.

Therefore, for similar focussing force betatrons, it is reasonable to expect at least a factor of x3-x10 in average current for every decade increase in the acceleration frequency. Typical weak-focussing betatrons injecting at ~100 keV over 2% of the cycle, accelerating to ~0.34 GeV, achieved 20 mA average current, averaged over over 1 cycle, at 60 Hz (and therefore an average circulating current of 2-10 mA if operated continuously - losses typically forced them to operate at a few Hz in pulsed mode). We would therefore expect classical betatrons could be designed for ~0.5-1 GeV at a few kHz to provide ~100-200 mA of average circulating current, a range useful to synchrotron radiation x-ray photolithography, [11] provided low loss material can be afforded.

IV. FREQUENCY LIMITATIONS

The frequency that a betatron is able to be driven is limited by practical considerations of: (1) the large inductance of the betatron core & guide fields, and (2) core losses. A resonant drive with the inductor and a series energy store capacitor avoids switching large amounts of power because the current and voltage are always 90° out of phase. However, besides the Wattless current which stores energy in the magnetic field, there is a working current proportional to the ampere-turns of an effective loss of magnetic field. This is given by: (1) eddy currents, and (2) the ampere-turns equivalent to the hysterisis phase shift. (Reviews of inductive drives at high frequencies are given in [12],[13], and in [9], [7], [3]). For simple estimates, we assume $\mu >> \mu_o$, and a gap height g much less than the length of the flux lines, about 5% of the beam radius, and make estimates based on the 340 MeV betatron made by Kerst [1]., [3] as in Figure 1[5]. Then the inductance L_g for the guide field magnet and L_C, the core inductance, are given approximately by $L_g \sim \mu_o A N^2/g$, $L_C \sim \mu A N^2/l$, where N, A are the respective coil turns and area, l is average length of a flux line in the core circuit, and μ is the core permeability. The guide magnetic field B is given by $B \sim \mu_o IN/g$. The energy is given by $1/2\ CV^2 \sim 1/2\ LI^2$, where C is the energy store, and V and I are the driving voltage and current. The resonant frequency $f_c = 2\pi/\sqrt{LC}$.

An interesting but extreme specific example of the above is to take f_c =1.2 kHz, E=1 GeV, g=8 cm, N=10, and B_S=1.5 T and metglas, $\mu \sim 10^3$. We assume a DC biased (B_W~3.3 T) betatron, like figure 1. We find that I_{peak} ~ 12 kA, L ~ 20 mH, 10 mH for the core and guide field respectively, C ~ 1.2 mF, and V_{peak}=50 kV for a 2.2 m radius electron beam. The energy store is prodigious, ~3 MJ. The volume of high μ~1,000, 1.5 T magnetic materials scales like $V \sim 12r^3$ where r is the beam radius. The metglas for this example would have a mass of ~10^6 kg. At 1.2 kHz (0.2 ms 1/4 cycle saturation time), the losses for typical 0.6 mil metglas with a 3.3 T saturation are measured to be ~10^{-4} J/kg, giving ~120 kW of loss which must be resupplied by a 1.2 kHz power source. Parasitic losses could be as small as ~1-2% of the RMS circulating power, ~50-100 kW, depending on the dielectric hysteresis of the energy store, and coil losses and resistance. If the magnet is driven by a 50Ω line, a shunt capacitance is ~4-8 μF. Using this beam as a light source would yield ~1 kW of x-ray power with a peak wavelength of ~2 nm at an average beam current of ~0.5 A.

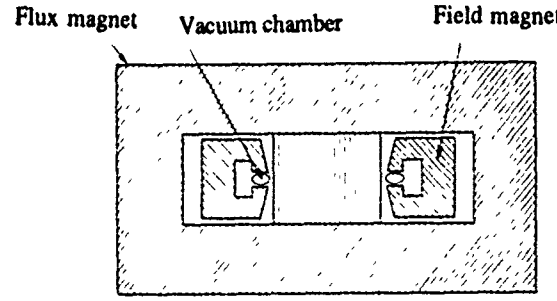


Figure 1. Betatron schematic with 2 independent magnetic circuits for the accelerating flux and guide field, from [5].

More practical applications (less extreme cases) might be in radiotherapy (10-30 MeV) or x-ray imaging of thick objects (1-10 MeV), where the increased performance of a betatron made with low loss ferrites or metglas might make betatrons again competitive with RF linacs, and the compact size and a modulator coupled by power lines may offer

advantages. In the case of smaller machines (<10 MeV) high frequency operation up to 100 kHz might be contemplated. At 20 MeV, we estimate core losses could be <1 kW at 10 kHz using the best available magnetic materials. Much higher frequencies may be contemplated with the best available ferrites, especially at lower energies where losses are not as important.

V. COMMENTS AND DISCUSSION

A fast-cycling betatron has many similarities with a recirculating induction linac[7].The demands on a modulator of a high-gradient betatron approaches that of an induction linac as the frequency increases, making the betatron technique more difficult, but offering higher energy and flux. Breaking the core into many sectors[7] offers the possibility of reducing the demands on an individual resonant power modulator, and decreases the individual inductance, allowing faster operation. Low-loss magnetic materials may make the trade-off between the flux, energy and modulator of a single pass induction linac relative to a betatron less distinct. A 10kHz, 1,000 beam-turn ferrite betatron operating at 0.2 T, R=75 cm, would give 45 MeV electrons at high average current; the modulator would have a risetime of 25 μsec over the acceleration cycle, less taxing than an induction linac of similar energy.

In practical terms, the high energy limit is the limit of the cost of large volumes of magnetic material, with $V \sim E^3$. A 1-GeV accelerator would cost ~$25 million US for cores of metglas alone, at $25/kg in large quantity. This probably exceeds the practical cost limit of the synchrotron/storage ring technique for light sources at ~1 GeV, for example. Furthermore, the capacitive store is expensive. However, strong focussing techniques, which would be feasible for such a large accelerator, may result in a large average circulating current. The region between 500 MeV-1 GeV is accessible, and sensitive to the cost of materials.

Although ferrite is a cheaper and a faster material than metglas, the saturation magnetic field is too low to be even remotely cost-effective for high energy. However, for low energy (~1-25 MeV), high frequency (> ~5 kHz) betatrons, ferrites would be the material of choice. We note that the steep scaling of core volume down with lower energy may make low-energy, fast-cycling betatrons attractive in many low energy applications when compared with commercial linacs.

Parasitic resistance, capacitance and inductance, and the overall energy budget, will require careful analysis. Driving the accelerator with high impedence (ferrite loaded) lines may be a possible way to reduce some of these effects. These problems may make superconducting techniques desirable for this application, and are especially appropriate for DC biasing the induction field. The potential to eliminate costly magnetic material with superconducting/superferric magnets can be considered if the conductors (filaments) are small enough to avoid quenching during the induction cycle. Operation of high-current superconductors at high (~0.5-1 kHz) frequencies is problematic but may be possible; for a discussion see [14].

VI. CONCLUSION

The extension of the betatron technique to high frequency magnetic materials has potential for improved betatron technology, allowing it to be extended to higher energies and to higher currents. We expect this possibility may be especially practical for machines with energies below 700 MeV.

VII. REFERENCES

[1] D. W. Kerst, Phys.Rev. 58, 841 (1940)
[2] Private Communication, Prof. W. Bertozzi, MIT (1984).
[3] D.W. Kerst, "The Betatron", Handbuch de Physik, Dd. XLIV, Springer (1959), and loc. cite.
[4] M.S. Livingston & J.P. Blewett, Particle Accelerators, McGraw-Hill, NY (1962)
[5] E. Persico, E. Ferrari, S. Segre, Principles of Particle Accelerators, Benjamin, NY (1968)
[6] W. Scharf, Particle Accelerators and Their Uses, Harwood Academic, NY 1985
[7] S. Humphries, Jr, Principles of Charged Particle Acceleration, Wiley, NY, (1986)
[8] D. Iwanenko and I. Pomeranchuk, Phys.Rev. 65, 343 (1944)
[9] D. Birx, "Induction Linacs", Lecture Notes, US Particle Accelerator School, BNL, M. Month, ed. (1989),
[10] S. Humphries, Charged Particle Beams, chapter 5, Wiley, NY (1990)
[11] D. Andrews and M. Wilson, J. Vac.Sci Tech.,B7 (6), 1696 (1989)
[12] J. Weaver et al., Design, Analysis and Measurement of Fast Kicker Magnets at SLAC, SLAC-Pub-4397, (1989)
[13] B. Brown, "Simply Physics Limitations on Pulsed Bending Magnets", Fermilab pub. TM-768, 0353.000 (1978)
[14] M. Wilson, Superconducting Magnets, Oxford, (1983).

Improvement of 150 MeV Racetrack Microtron

T. Hori, M. Sugitani, T. Mitsumoto, and Y. Sasaki

Quantum Equipment Division, Sumitomo Heavy Industries, Ltd.
2-1-1 Yato-cyo, Tanashi, Tokyo 188 Japan

Abstract- A 150-MeV pulsed racetrack microtron (RTM) which was developed as an injector of an electron storage ring, succeeded in first-beam acceleration in April 1989. However, the output beam current of the RTM was far less than the designed value, and insufficient for the storage ring to accumulate the designed current. Therefore, the improvement program of the RTM started soon and the remodeling was finished in Octorber 1990 which brought a quite good result. The essential features of the improvement are simplification of the injection system and focusing magnets in the recirculation system. The new RTM has achieved the design specification with ease, proving its reliability by very stable operation.

1. Introduction

A simplest and smallest synchrotron-radiation (SR) source has been developed by Sumitomo Heavy Industries, Ltd. for industrial use, especially for X-ray lithography. The storage ring consists of a single cylindrical superconducting weak-focusing magnet having the circular electron orbit of 1-m diameter. The system, called AURORA[1] parameters of which are listed in Table 1, consists of a 150-MeV RTM injector and 16 SR light channels at the maximum.

Table 1. Main parameters of the electron storage ring in the SR source system AURORA.

Energy	650	MeV
Beam currents	300	mA
Critical wavelength	1.02	nm
Beam lifetime	> 24	hours
Magnetic field	4.34	T
Vacuum pressure	6×10^{-10}	Torr

Generally, linacs or synchrotrons are used as injectors in conventional SR rings, especially for high-energy-beam injections. There are systems using RTM as an injector such as that of the University of Wisconsin (UW). The RTM has the advantages of good beam quality and small machine size. We adopted the concept of UW-RTM[2], but opted for an alternative cylindrical acceleration column and a permanent-magnet (PM) focusing system. This type of the 150-MeV RTM[3,4] succeeded in the first-beam extraction in April 1989[5], and the first SR light was observed from the storage ring in November 1989[6,7]. However, achievement of the AURORA's full specifications seemed difficult because of a lack of beam intensity from the injector RTM, normally ~10 μA and 0.1 mA at the maximum[5]. Therefore, the remodeling of the RTM was started, and completed in October 1990. The result was very successful. The RTM is routinely operated since then satisfying the needs of the storage ring.

2. Main Modifications

The essential features of the improvement are; 1) simplification of the injection scheme substituting DC 120 keV beam for RF preaccelerated one, and 2) removal of PM quadrupole-doublets (QD) from return paths to eliminate dispersion from the linac line. The parameters of the new RTM are listed in Table 2.

Table 2. Design parameters of the injector RTM in the SR source system AURORA.

Injection energy	120	keV
Final energy	150	MeV
Beam currents(peak value)	5	mA
Pulse width	0.5-3.0	μsec
Repetition rate	1-180	Hz
Emittance(ϵ_x, ϵ_y)	$<1\pi$	mm·mrad
Energy spread($\Delta E/E$)	0.2	%
Number of orbits	25	
Energy gain per pass	6	MeV
Main magnetic field	1.23	T
Main field gradient	0.14	T/m
Reverse magnetic field	0.29	T
RF frequency	2856	MHz
RF pulse width	6	μsec
Accelerating gradient	15	MV/m
Bore diameter	1	cm
Wall loss(peak)	<1.3	MW
Beam loading(peak)	~1.3	MW

Except the reverse magnetic field strength and energy spread, nothing has been changed since the old parameters were fixed[3]. However, the outlook of the new RTM (Figure 1) became fairly different due to the remodeled structure preventing leakage of magnetic flux effectively and more vacuum-tight constitution. The whole size shown in Figure 2 is almost the same as the old one.

2.1. Injection System

In the old system, the 20-keV gun and three cavities; prebuncher, preaccelerator and buncher, were aligned to boost a beam 100 keV up keeping the bunching effect simultaneously[3]. The old one had the advantages of compactness and easy-handling of the high voltage power supply. But the disadvantages such as diffi-

0-7803-0135-8/91$01.00 ©IEEE

cult clarification of the beam quality owing to the RF preacceleration and bunching, and a lack of stability derived from too many RF parameters were crucial.

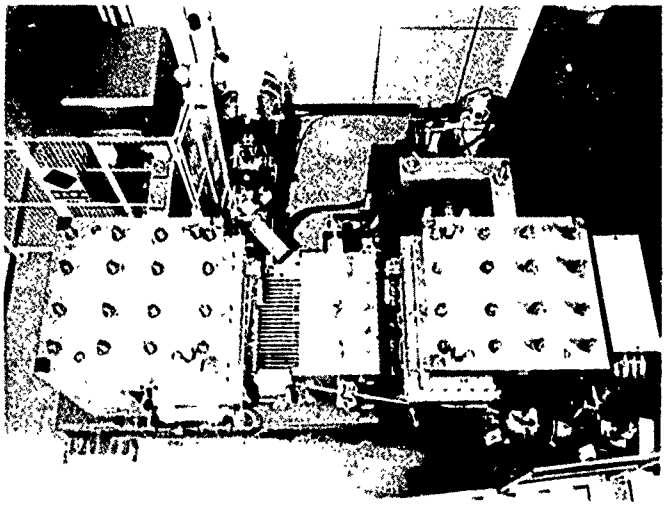


Figure 1. An overall view of the AURORA injector 150-MeV RTM after improvement.

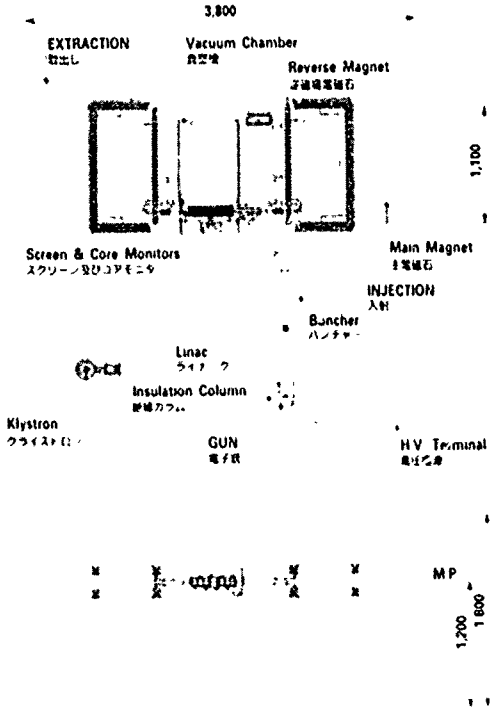


Figure 2. Schematic drawings of the new RTM with its outer dimensions.

The new system is designed to make the beam optics clear by simple DC acceleration. The parameters of both injection and recirculation systems are separated, and decided each other independently. Practically this makes the RTM tuning very easy, which was proved on the initial commissioning of the new RTM. Emittances of the new 120-keV gun were measured for the various cases and 80 mA was obtained within 60π mm-mrad for both ε_x and ε_y, as shown in Figure 3 for ε_x, and 220 mA in 100π mm-mrad at the entrance of the linac, where the beam size was restricted within $\phi 6$ mm. Actually 20 mA is enough to operate the RTM as the AURORA injector.

2.2. Recirculation System

The constitution of the auxiliary magnets in the recirculation system has been changed completely. The design strategy is to remove PMQD placed on every return paths, which makes the linac line dispersionless.

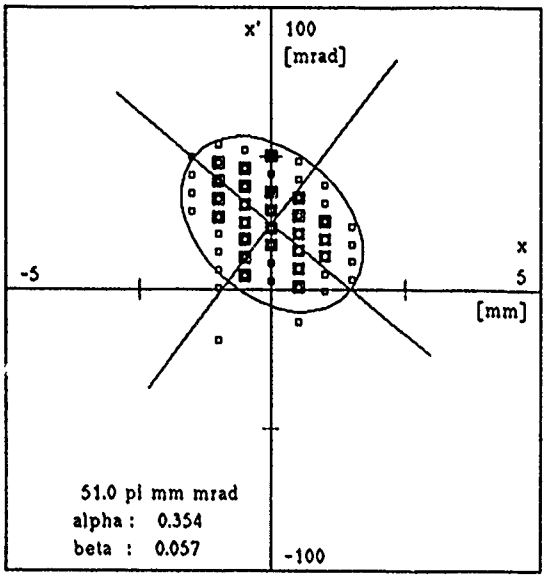


Figure 3. Measured horizontal emittance of 120-keV beam at the entrance of the linac.

Another advantage is simplification of the focusing parameters due to missing of all PMQD's. One can avoid confliction come from combined effect; focusing and steering of PMQD, which makes beam tuning very complicated. On the design stage, main concern was paid to vertical focusing, especially to the 6-MeV beam which is reflected back into the linac.

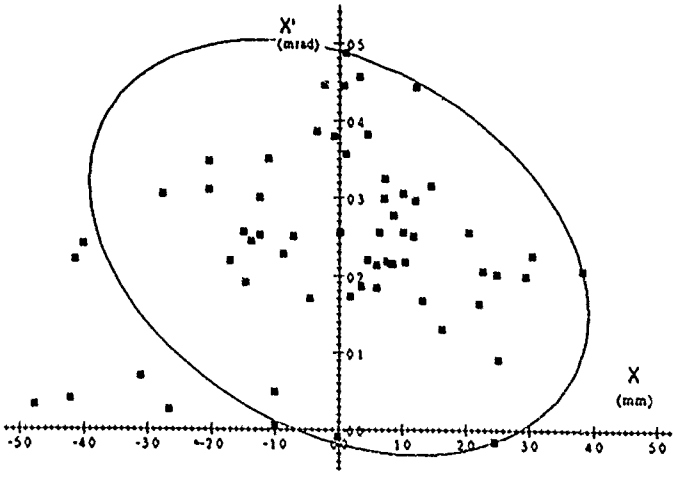


Figure 4. Calculated horizontal emittance of 150-MeV extracted beam. Ellipse of 1π mm-mrad is shown.

According to the careful beam simulation, it was found that horizontal focusing is achieved by the only Q-singlet placed on the linac line adjacent to the chi cane, and vertical focusing by the reverse field can compensate all the vertical defocusing in the low energy region. In the result, more than 100π mm mrad acceptances are obtained in the both horizontal and transverse directions, which are quite large compared

with the designed emittances of the injected beam. Calculated results of the 150-MeV extracted beam are shown in Figures 4 and 5. The horizontal emittance is less than 1π mm·mrad including the dispersion effect[7], that means it is reduced to about a half at the linac exit where no dispersion exists. The energy spread $\Delta E/E$ of the 80% beam is within $\pm 0.1\%$.

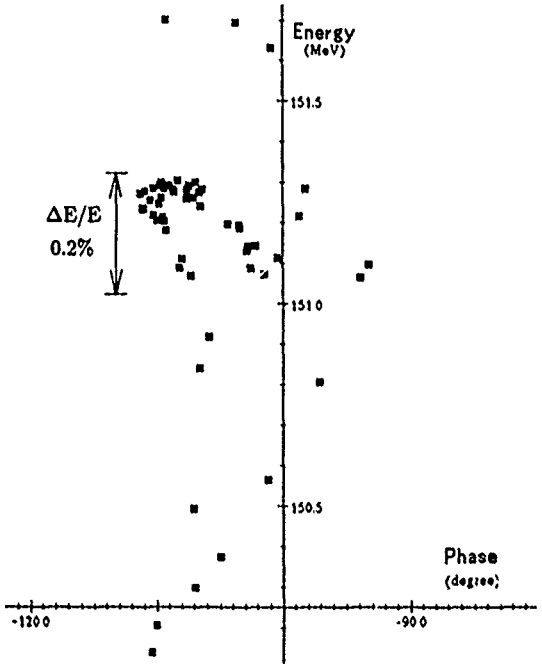


Figure 5. Calculated energy spread of 150-MeV extracted beam. About 80% of the beam are within 0.2% $\Delta E/E$.

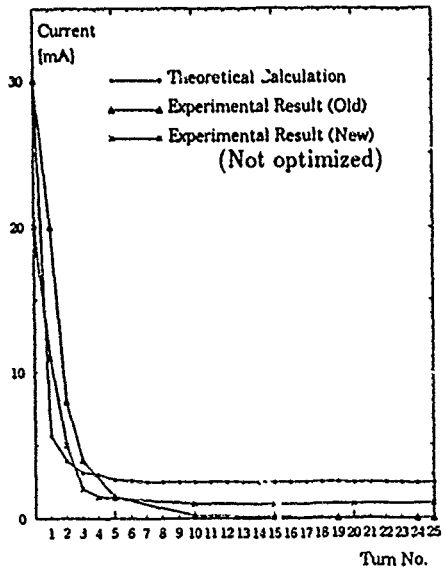


Figure 6. Transmission efficiency at each lap. Null turn no. correspondes to 120-keV injected beam and turn no. 25 to 150-MeV extracted one.

Various transmission efficiencies, calculated and measured ones, are seen in Figure 6. On the contrary to the old data, not so much decreasing after fifth lap appears in the new RTM's, which agrees well with the simulation result. A series of SR light spots from the RTM shown in Figure 7 is used as a powerful monitor whenever the RTM is tuned or operated[5].

3. Performance

The result of improvement is quite satisfactory. About 1 mA of a 150-MeV beam was extracted only after a-few-hours initial-tuning. This intensity is sufficient to accumulate the specified current in the storage ring, and the RTM is to be operated routinely as the AURORA injector with this rather-a-low intensity. Up to ~3 mA, the machine capability is proved without the buncher, and more than 7 mA with the buncher on the injection line. To achieve 10 mA is not difficult if the RF source could provide enough power to compensate the equivalent beam loading.

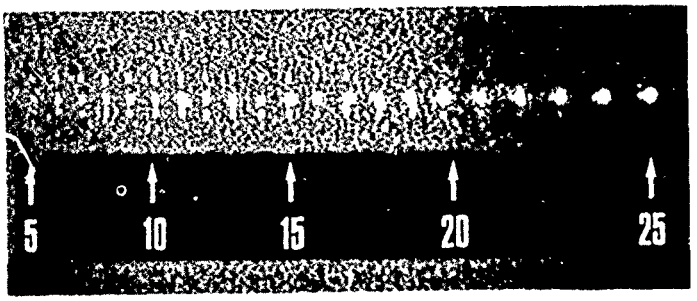


Figure 7. SR light spots emitted from the beam on the circular trajectories in the 180° end magnet, which are observed from the pole gap, 10 mm in width, through a view port. The spots from the fifth lap to twenty-fifth lap are seen from left to right in sequence.

Operability of the new RTM is so well-improved that the daily operation is on a full turnkey basis as the injector. Restoration of an operating condition is also well. Even when all the magnets are re-excited after shutdown, there is almost no need to change the magnets' parameters once they are determined. Thus the reliability of this stable machine is proved.

References

[1] e.g., N.Takahashi, "Compact Superconducting SR Ring for X-Ray Lithography", *Nucl. Instrum. Meth. Phys. Res.* vol. B24/25 1987 pp.425-428

[2] Roy E. Rand, *Recirculating electron accelerators*, New York: Harwood Academic Publishers 1984 pp.88-91

[3] M. Sugitani, "Design Study of 150-MeV Racetrack Microtron", in *Proc. of 6th Symp. on Accel. Sci. and Tech.* Tokyo, Japan, Oct. 1987 pp.186-188

[4] M. Sugitani, "Racetrack Microtron - 150 MeV Injector for Compact SR Ring", in *Proc. of EPAC'88* Rome, Italy, June 1988 pp.596-598

[5] T. Hori, "Status of Compact SR Light Source for X-Ray Lithography", in *Proc. of 1989 Internat. Symp. on MicroProcess Conf.* Kobe, Japan, July 1989 pp.108-112

[6] H. Yamada, "Commissioning of AURORA:The Smallest Synchrotron Light Source", *J. Vac. Sci. Technol.* Nov/Dec 1990 pp.1628-1632

[7] Y.toba, "A Compact SR Light Source for X-Ray Lithography", in *Proc. of 2nd Internat. Symp. on Advanced Nucl. Energy Res.* Mito, Japan, Jan. 1990 pp.590-595

Measurement and Tuning of Beam Parameters in the Heavy Ion Storage Ring ESR

F. Nolden, S. Baumann, K. Beckert, H. Eickhoff, B. Franczak, B. Franzke, O. Klepper, W. König, U. Schaaf, H. Schulte, P. Spädtke, M. Steck, J. Struckmeier,
GSI, Postfach 110552, D-6900 Darmstadt, Germany

Abstract

The ESR is a cooler ring with large momentum acceptance $\Delta p/p_0$ of about 2.5 %. We could bound the Q variation in both transverse planes to less than 0.02, thereby allowing for rf stacking over the large momentum range without crossing resonances up to the fifth order. Tunes are measured very accurately in cooled beams via the BTF technique. The field quality in the large dipole magnets was improved by the excitation of pole face windings, leading to an improved linearization of natural chromaticity. Linear coupling due to large solenoid fields in the electron cooler could be detected and was then corrected by auxiliary solenoids installed in the vicinity of the cooler. Momentum compaction was determined by comparison of the cooler voltage and the measured revolution frequency. Transverse beam dimensions are measured by means of position sensitive detection of ions that captured an electron in the cooler.

1 Introduction

The experimental storage ring ESR is dedicated to experiments with heavy ion beams [1]. Beams are accumulated via rf stacking of bunches from the heavy ion synchrotron SIS [2], cooled in an electron cooler [3], and are then used for several types of in-beam experiments. There will also be a slow extraction to the experimental areas at GSI and a fast reinjection back into the SIS.

Commisioning of the ESR began in early 1990. Here we report on how important beam parameters were measured and set.

2 Schottky and BTF Diagnostics Hardware

Schotkky and BTF diagnostics is employed as a tool for the measurement of longitudinal distribution functions, synchrotron frequencies, longitudinal and transverse machine impedances, and betatron tunes.

The necessity to observe low-velocity ($\beta < 0.1$) as well as moderately relativitic ($\beta = 0.75$) beams led to the choice of an electrostatic pick-up. By means of a tunable cable resonator, the signal-to-noise ratio of the Schottky signal can be enhanced in a chosen freqency band. The exciter is a quarter-wave kicker. It is used in the BTF measurements, as well as for beam excitation by rf noise with simultaneous electron cooling, in order to measure and optimize the cooling force. Typical frequencies are 30 MHz, the amplifiers work up to 100 MHz.

The instrumentation in the control room consists of an analog spectrum analyzer, a network analyzer, a digital Fast Fourier Transform analyzer (FFT), and various signal sources. All of these are connected to a computer providing automatic measurement procedures, data analysis, and graphic processing. The analog spectrum analyzer is a general, easy-to-use tool for the observation of processes like storing, stacking, energy-loss measurements with internal target, etc. The network analyzer is used for BTF measurements. For measurements with very good frequency resolution we use FFT processing. Image reject mixers (IRM) provide a unique mapping into the FFT working range of 100 kHz. FFT measurements are both faster and more sensitive than analog ones. The FFT is also used as a source of well-defined noise.

3 Tune Measurements with Cooled Beams

Tunes are measured via the technique of the tranverse BTF which has maxima at the first horizontal sidebands of the revolution frequency $\omega(p)$

$$\omega_{x,z}(m,p) = (m \pm Q_{x,z}(p))\,\omega(p) \qquad (1)$$

By means of electron cooling, the momentum width $\Delta p/p$ of the beams is easily cooled down to values

0-7803-0135-8/91$01.00 ©IEEE

of $2 \cdot 10^{-5}$. With the same precision the momentum can be set by variation of the cooler voltage. The revolution frequency $\omega(p)$ is determined by standard Schottky diagnosis. The error of the Q measurements is at most

$$\Delta Q_{x,z} = \sqrt{2} m \eta \frac{\Delta p}{p} \qquad (2)$$

if the BTF's and revolution frequencies are measured around the same harmonic m. Even for m=20, the typical error $\Delta Q_{x,z}$, measured with a beam cooled by electrons, is no larger than 10^{-4}, which is very convenient. The method still works at currents below 10μA. There is a computer-controlled semi-automatic searching procedure for a fast mapping of the working point in the interesting momentum range.

4 Quadrupoles, Sextupoles, and Pole Face Windings

The large ESR momentum acceptance ($\approx 3\%$) facilitates rf stacking, and it allows for the simultaneous storage of beams with different charge states, for example fully stripped and hydrogen-like beams of ions with $Z > 33$. To avoid beam loss, the machine must be operated over the full momentum range in a region free from disturbing betatron resonances.

The 20 quadrupole magnets of the ESR are fed in pairs by 10 different families of power supplies. Tunes and values of the dispersion function at important locations (i.e. at the internal target and the electron cooler) can be set independently, provided a correct ion optical model of the machine. One important mode of operation has a vanishing dispersion function at both the cooler section and the internal target. In that case we use the the neighbouring quadrupole dublets to change the working point without affecting the dispersion function elsewhere.

Chromaticity is corrected by means of 8 sextupoles, each with its own power supply.

The design width of the good field region in the dipole magnets is 220 mm. As we intend to operate the magnets at low excitation as well as close to saturation, the form of the remaining field error depends on the field level. In order to minimize higher order multipoles, the dipoles are equipped with 24 pole face windings which can be set independently.

5 Control of Betatron Tune Variation

In our first storage experiments, we excited neither the sextupoles nor the pole face windings. Due to

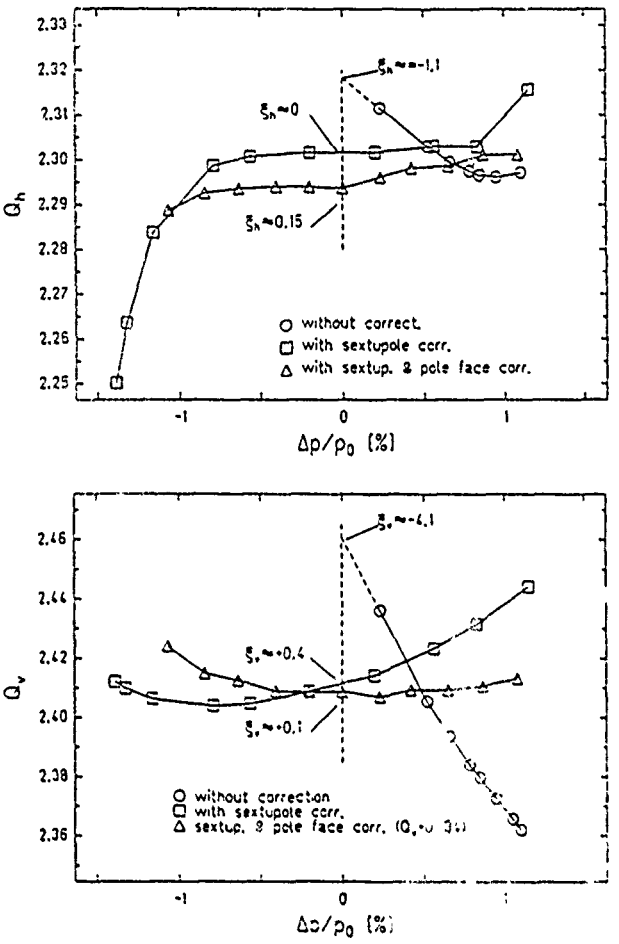


Figure 1: Q_x and Q_z vs. $\delta p/p_0$ measured with different settings

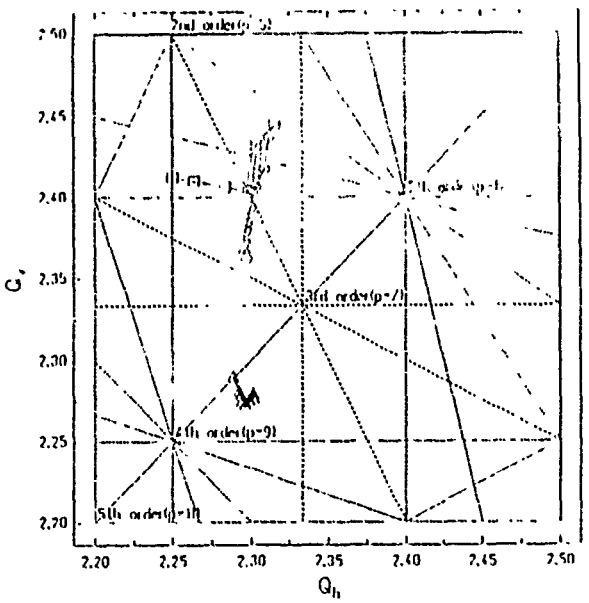


Figure 2: Resonance diagrams at the different settings

natural chromaticity, it turned out to be impossible to cover more than 1 % of momentum range without hitting fatal resonance lines (see fig. 1). With the notation (m, n, p) for the resonances

$$mQ_x + nQ_z = p \tag{3}$$

strong beam loss occurred around the third order sum resonances (3,0,7), (2,1,7), and (1,2,7). This is not surprising as the toroidal fields in the electron cooler section are considerably non-linear with respect to the ion beam closed orbit. With appropriate sextupole current settings, we reduced the chromaticities

$$\xi_{x,z} = \frac{\delta Q_{x,z}(p)/Q_{x,z}(p_0)}{\delta p/p_0} \tag{4}$$

to values $|\xi_{x,z}| < 0.1$ for orbits near the center of the horizontal aperture. However, there remained a considerable Q variation at the aperture limits. Using tables from magnetic measurements, by excitation of the pole face windings we limited the excursion of the working point over the momentum range of 2.2 % inside limits $|\Delta Q_{x,z}| < 0.02$ in a region which is free from resonances up to the fifth order. As soon as the working point approached the coupling resonance $Q_x = Q_z$, vertical betatron sidebands appeared in the horizontal BTF. We got rid of these lines by tuning the current in the solenoids installed closely in front of and behind the electron cooler. These solenoids correct for the coupling due to the main solenoid that guides the electron beam in the cooler.

6 Frequency Dispersion And Momentum Compaction

With beams cooled in an electron cooler, it is possible to determine experimentally the frequency dispersion η and the momentum compaction factor α_p to an absolute accuracy of better than 10^{-2}. The basic relationship involved relates the off-momentum $\delta p/p_0$ to both the variation of effective cooler voltage δU and the corresponding change $\delta\omega$ in revolution frequency

$$\frac{\delta p}{p_0} = \frac{1}{\beta^2}\frac{e\delta U}{\gamma m_e c^2} = \frac{1}{\eta}\frac{\delta\omega}{\omega} \tag{5}$$

where m_e is the electron rest mass. The momentum compaction factor is

$$\alpha_p = \eta - \gamma^{-2} \tag{6}$$

Typical α_p values in the ESR are around 0.16. The electron energy inside the beam depends on the degree of space charge depression, which can be deduced from measurements of the revolution frequency as a function of electron current.

7 Transverse Width of Cooled Beams

In beams cooled by electrons it is hardly possible to detect any tranverse Schottky signals. For the measurement of transverse beam dimensions we detect ions that captured electrons in the cooler by means of a position sensitive gas detector installed inside the chamber of the dipole after the cooler.

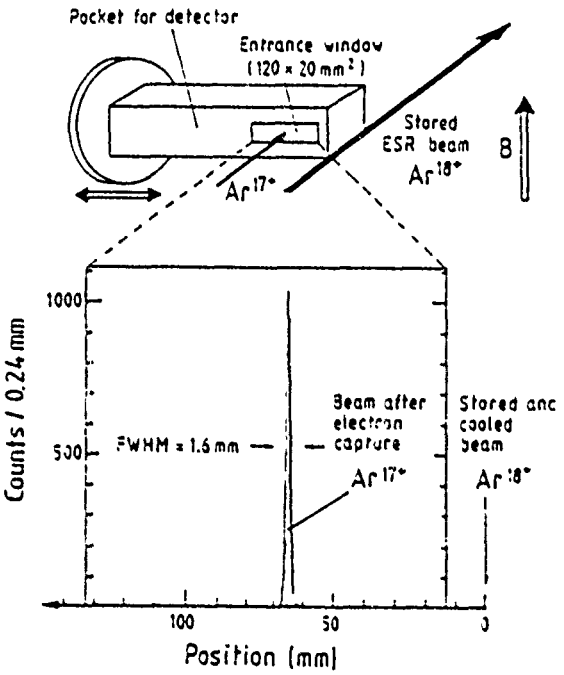


Figure 3: Measuring the Transverse Width of Cooled Beams

References

[1] B. Franzke, Nucl. Inst. Meth. B24/25 (1987) 18-25

[2] K. Blasche, D. Böhne, B. Franzke, H. Prange, IEEE NS-32 (5) (1985) 2657

[3] P. Spädtke et. al.; Status of the ESR Electron Cooler and First Results, Proc. of the 19th INS Symposium on Cooler Rings and their Applications, Tokyo 1990

Algorithm for the Deflector Plates of the 1 MHz Chopper for the Kaon Factory

M. J. Barnes, G. D. Wait
TRIUMF, 4004 Wesbrook Mall, Vancouver, B.C., Canada V6T 2A3

Abstract

The Kaon Factory at TRIUMF requires a 1 MHz chopper to create appropriate gaps in the extracted 1 GeV/c H^- beam from the cyclotron. Deflection of bunches to be eliminated by the 1 MHz chopper will be predominantly provided by an electric field between a set of deflector plates, although there will be a magnetic component of deflection too. Previous simulations to calculate angular deflection of beam particles in the deflector plates approximated the plates as 8 sections, and only considered plates of one length. This paper presents the results of time-domain mathematical simulations to assess errors introduced by approximating the deflector plates using a finite number of sections. In order to validate the mathematical model of the deflector plates the predictions are compared with analytical equations for angular deflection for the situation where centre-fed plates are energized by a 'step-function'. Predictions of angular deflection are presented for four configurations of deflector plates in order to confirm that centre-feeding is the best option considered.

I. Introduction

A novel design concept has been developed for a 1 MHz chopper for suppressing 5 bunches in the Kaon factory Accumulator injection line [1–5]. Deflection of the bunches to be eliminated is predominantly provided by an electric field between the deflector plates, although there will be a magnetic component of kick [2,6,7]. When the deflector plates are fully charged, with flat-top pulses, there is no net current flow in the plates, and thus the deflection of particles passing between the plates is totally attributable to the electric field. However while the plates are charging up, or there is ripple on the pulse, there is a current flow: this current flow results in a magnetic field which either assists or opposes the effect of the electric field [7]. In order to predict the effects of the electric and magnetic components of kick upon beam deflection it is necessary to simulate tracking of the beam bunches through the deflector plates of the chopper [8]: this has been achieved using version 4·03 of the circuit analysis package PSpice together with its Analog Behavioral Model option [9]. The quality of the predictions is related to the number of transmission line sections utilized to represent the deflector plates. Details of the mathematical model are given elsewhere [3,6,8].

II. Number of Sections used to Approximate Deflector Plates

Simulation of the deflector plates by a finite number of sections results in errors in the rising and falling edges of the predicted angular deflection. In order to assess the significance of these errors, which are themselves a function of deflector plate length and trapezoid rise [fall] time, sets of studies have been carried out where the physical length of the plates (ℓ) and trapezoid rise [fall] time ($t_{v(r/f)}$) have been systematically changed:

- ℓ = 3·78 m and $t_{v(r/f)[0\%\rightarrow 100\%]}$ = 20 ns;
- ℓ = 2 m and $t_{v(r/f)[0\%\rightarrow 100\%]}$ = 20 ns;
- ℓ = 3·78 m and $t_{v(r/f)[0\%\rightarrow 100\%]}$ = 6·67 ns.

During each of the above sets of studies the number of sections (N) used to represent the deflector plates was increased from 8 to 80 in increments of 8. The maximum relative error in the total angular deflection (i.e. sum of magnetic and electric components of angular deflection) between adjacent numbers of sections (e.g. maximum error of 8 section prediction w.r.t. 16 section prediction, and maximum error of 16 section prediction w.r.t. 24 section prediction, etc.) were noted, and normalized to the ideal flat-top total angular deflection. Figure 1 shows the relative errors between adjacent numbers of sections for each of the above three sets of simulations.

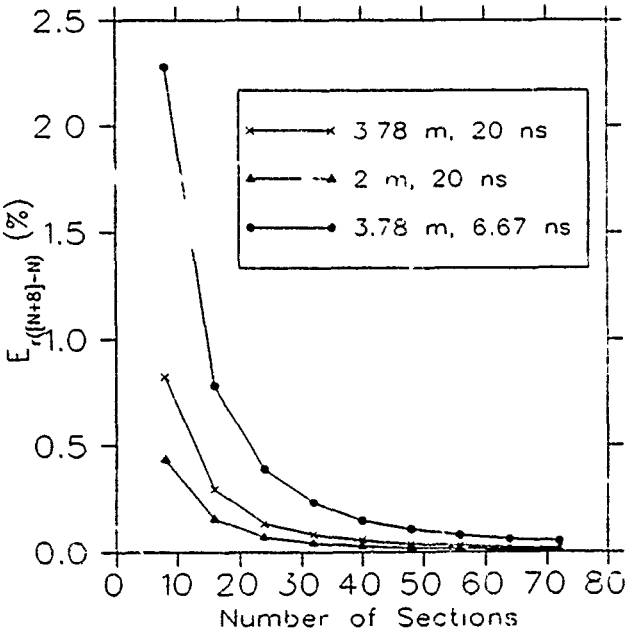


Figure 1. Dependence of maximum relative error ($E_{r[N+8]-N)}$) upon number of sections, length of plates, and trapezoid rise-time

In order to estimate the absolute error introduced when an 80 section representation is utilized it is necessary to curve fit to each of the individual curves shown in figure 1 [6]. For the case where the deflector plates are represented as having a physical length of 3 78 m, and voltage trapezoid rise-time (0 % → 100 %) of 20 ns, the data can

0-7803-0135-8/91$01.00 ©IEEE

be approximated by [6]:

$$\ln(100 \times E_{r([N+8]-N)}) = [-1 \cdot 7581 \times \ln(N)] + 8 \cdot 1664 \quad (1)$$

The absolute error in the 80 section representation ($E_{r(\infty-80)}$) can be approximately determined by assuming that the relative errors between adjacent numbers of sections are cumulative (this should be a worst-case assumption):

$$E_{r(\infty-80)} = \sum_{n=10}^{\infty} \left(\frac{e^{[(-1 \cdot 7581 \times \ln(8 \times n)) + 8 \cdot 1664]}}{100} \right) \quad (2)$$

Evaluation of equation 2 gives an estimated value, for the absolute error in the 80 section prediction, of 0·22 %. Similarly calculating $E_{r(\infty-80)}$ for the other two sets of studies results in values for $E_{r(\infty-80)}$ of 0·114 % (ℓ = 2m & $t_{v(r/f)[0\%\rightarrow 100\%]}$ = 20 ns) and 0·615 % (ℓ = 3·78m & $t_{v(r/f)[0\%\rightarrow 100\%]}$ = 6·67 ns), respectively.

Absolute error ($E_{r[\infty-N]}$) in the predicted total angular deflection, normalized to the ideal flat-top total angular deflection, for 'N' sections (where $N < 80$) is determined from the following equation:

$$E_{r(\infty-N)} = E_{r(\infty-80)} + E_{r(80-N)} \quad (3)$$

where $E_{r(80-N)}$ is the relative error of N sections w.r.t. 80 sections.

Fig. 2 shows a plot of the estimated absolute error in angular deflection, as a function of the number of sections, for the three cases studied. Thus for the first set of studies (ℓ = 3·78 m & $t_{v(r/f)[0\%\rightarrow 100\%]}$ = 20 ns) the absolute error in the angular deflection introduced by representing the deflector plates by 8 sections is about 1·7 %: in order to reduce the absolute error below say 0·5 % requires approximately 28 sections. However increasing the number of sections by a factor of 3, from 8 to 24, resulted in an increase in cpu time by a factor of about 5.

For the 2 m plates excited by a trapezoid with a rise-time (0 % → 100 %) of 20 ns, an 8 section representation of the deflector plates results in an absolute error in the angular deflection of about 0·9 %: a 16 section representation results in an absolute error of approximately 0·5 %.

For the 3·78 m plates excited by a trapezoid with a rise-time (0 % → 100 %) of 6·67 ns, an 8 section representation of the deflector plates results in an absolute error of about 4·5 %: a 42 section representation would be needed to reduce the absolute error below 1 %: 102 sections are required to reduce the absolute error to approximately 0·5 %.

For both a given driving voltage rise-time and number of sections, the absolute errors in the predicted angular deflection are proportional to the length of the deflector plates (see fig. 2) Similarly, for a given plate length and number of sections, the absolute error in the predicted angular deflection is approximately inversely proportional to the rise-time of the driving voltage (see fig. 2).

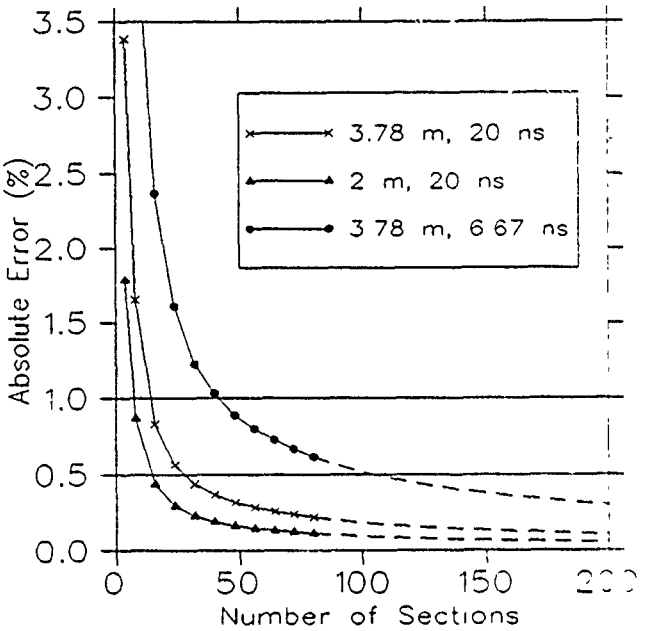


Figure 2: Dependence of estimated value of absolute error ($E_{[\infty-N]}$) upon number of sections, length of plates, and trapezoid rise-time

III. Validation of Mathematical Model

Analytical equations for the electric (Θ_e), magnetic (Θ_m) and total (Θ_t) angular deflection, for centre-fed deflector plates driven by an ideal step-function, have been derived [6]. Figure 3 shows the predicted components of angular deflection, obtained using PSpice, together with the components calculated from the analytical equations. For the PSpice simulation, the deflector plates were modelled using 80 sections and the rise-time of the driving voltage ($t_{v(r)[0\%\rightarrow 100\%]}$) was 0·3 ns. The predictions lag the results of the analytical equations by about 0·15 ns (i.e. $t_{v(r)[0\%\rightarrow 100\%]}/2$): the lag reduces to approximately 0 1 ns when $t_{v(r)[0\%\rightarrow 100\%]}$ is decreased to 0·2 ns.

IV. Methods of Feeding the Plates

In order to confirm that centre-feeding deflector plates is an optimum configuration for minimizing the rise-time of the total angular deflection, four configurations of deflector plates have been simulated:

- centre-fed plates;
- end-fed with the particle beam and initial switch-on wave propagating in the same direction;
- end-fed with the particle beam and initial switch-on wave propagating in opposing directions;
- plates fed from both ends simultaneously.

The total angular deflection for each of the above four configurations, is shown in figure 4. A minimum rise-time (10 % → 90 %) for the total angular deflection (20·7 ns) is achieved with the centre-fed plates [6]. For the centre fed configuration the magnetic angular deflection helps to improve the rise-time of the total angular deflection, by opposing the initial lead-in to the 'S-curve' electric angular deflection and adding to the top of the 'S-curve' electric angular deflection [$t_{\Theta_e(r/f)[10\%\rightarrow 90\%]} = 23 \cdot 5ns$].

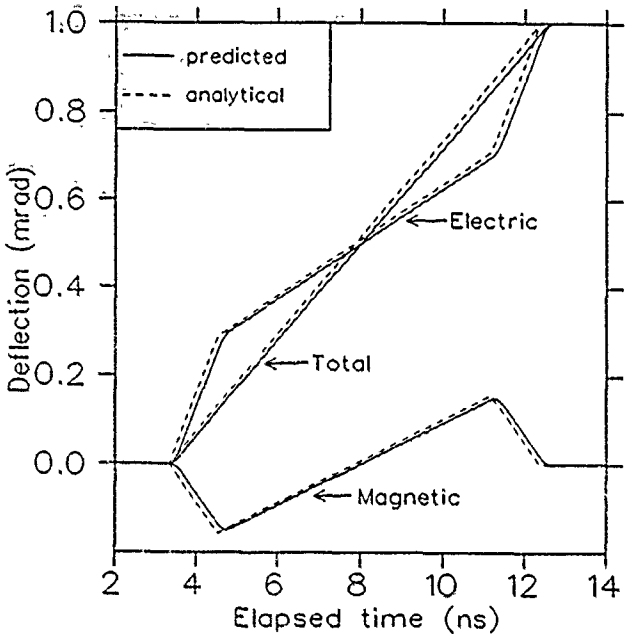


Figure 3: Angular deflection determined by equivalent circuit (PSpice) and analytical equations

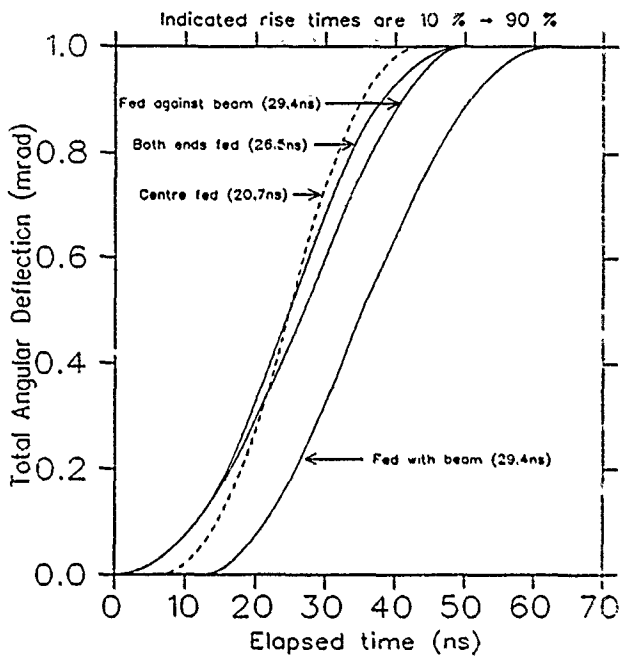


Figure 4: Dependence of rise time of total angular deflection upon method of feeding the deflector plates: ℓ = 3.8 m, $t_{v(r)[0\% \rightarrow 100\%]}$ = 20 ns

For the configuration where both ends of the plates are fed simultaneously, the magnetic angular deflection adds to the lead-in to the 'S-curve' electric angular deflection, and opposes the electric angular deflection at the top of the 'S-curve', therefore extending the total angular deflection rise-time to 26·5 ns [6].

For the configurations where the deflector plates are fed at only one-end, the magnetic angular deflection is unidirectional: hence if the magnetic angular deflection opposes the initial lead-in to the electric angular deflection it will also oppose the electric angular deflection at the top of the 'S-curve'. Similarly if the magnetic angular deflection adds to the electric angular deflection at the top of the 'S-curve' it will also add to the initial lead-in to the 'S-curve' [6]. In addition, if the electric component of angular deflection rise-time alone is considered (and the magnetic component neglected), the rise-time for the situations where the deflector plates are fed at one end only is significantly greater than that which results from centre-feeding the deflector plates (for both end fed configurations $t_{\Theta_e(r/\ell)[10\% \rightarrow 90\%]}$=28·7ns, c.f. 23·5 ns for the centre-fed configuration).

V. Conclusion

The mathematical representation developed for the purposes of tracking particles through the deflector plates of the 1 MHz chopper permits the angular deflection resulting from both the magnetic and electric components of the field to be predicted. The quality of these predictions is dependent upon the number of sections used to represent the deflector plates, the length of the deflector plates, and the maximum rate-of-change of the driving voltage waveform. The mathematical model has been shown to give predictions for angular deflection which are in good agreement with analytical equations.

Four different methods of feeding deflector plates have been considered: it is concluded that centre-feeding results in a minimum rise-time for total angular deflection.

VI. References

[1] G. D. Wait., M. J. Barnes, C. B. Figley "A 1 MHz Beam Chopper for the Kaon Factory". TRI-DN-89-K70.

[2] M. J. Barnes, G. D. Wait, D. C. Fiander "Mathematical Modelling of the 1MHz Beam Chopper for the Kaon Factory", (Proceedings of European Particle Accelerator Conference, June 1990).

[3] M. J. Barnes, D. C. Fiander, C. B. Figley, V. Rödel, G. D. Wait, G. Waters. "A 1 MHz Beam Chopper for the Kaon Factory", (Proceedings of European Particle Accelerator Conference, June 1990).

[4] TRIUMF KAON FACTORY STUDY, Accelerator Design Report, May 1990.

[5] G. D. Wait, M. J. Barnes, D. Bishop, G. Waters, C. B. Figley. "Prototype Studies of a 1 MHz Chopper for the Kaon Factory", Proceedings of this Conference.

[6] M. J. Barnes, G. D. Wait. "Simulation of Deflector Plates and Assessment of Rise-Times for the 1 MHz Chopper". TRI-DN-90-K149.

[7] D. C. Fiander, G. D. Wait, M. J. Barnes. "Advantages of Center Feeding the Deflector Plates for the 1MHz Chopper System". TRI-DN-89-K45.

[8] M. J. Barnes, G. D. Wait. "Results of Calculations on the Beam Deflection Due to the 1 MHz Chopper for the Kaon Factory", Proceedings of this Conference

[9] MicroSim Corporation, PSpice version 4 03, released January 1990.

CONCEPTION OF THE 200 MEV/U BOOSTER FOR THE NUCLOTRON

I.B.Issinsky and V.A.Mikhailov
Joint Institute for Nuclear Research, Dubna, USSR

Summary

The superconducting accelerator of heavy nuclei, Nuclotron /1/, which is now under construction, will have a linac as an injector in the first phase of operation. To increase substantially beam intensities, it is planned to construct a booster of a 200 MeV/u energy for nuclei (650 MeV for protons) (Fig.1). The Synchrophasotron should be replaced by this complex. The intensity of heavy ion beams has to be increased by more than a factor of 10 by means of multiturn injection into the booster and 5 injection cycles in the main ring. For protons and deuterons it will be up to 10¹³ ppp. One of long straight sections is designed for electron cooling which will decrease emittance by a factor of 10-100 and will give a momentum spread of 10^{-4} - 10^{-5}. Apart from the operation for the main ring, the booster can be used indepently for research on its inner, external (outer) targets.

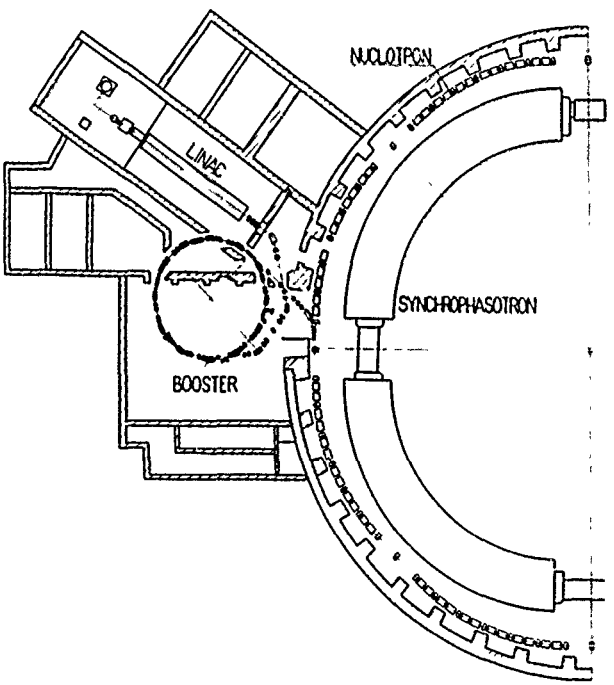


Fig.1. Layout of the booster

Operation and Main Characteristics of the Booster

A time diagram of the operation of the booster and the main ring is shown in Fig.2.

An ion beam from the linac is stored in the booster, and then after acceleration it is injected into the Nuclotron. The circumference of the booster constitutes 1/5 of the main ring one. This corresponds to five filling cycles in the Nuclotron. The repetition rate of the booster is fixed by the linac repetition rate which, in its turn, is determined by RF-power supply. After enlarging the latter, the repetition rate of the booster can be higher.

A simpler and frequently used method of ion storage in synchrotrons is the filling of its radial acceptance. The duration of injection, its efficiency and, respectively, the number of injected particles can be enlarged if a vertical acceptance is also used for partical storage.

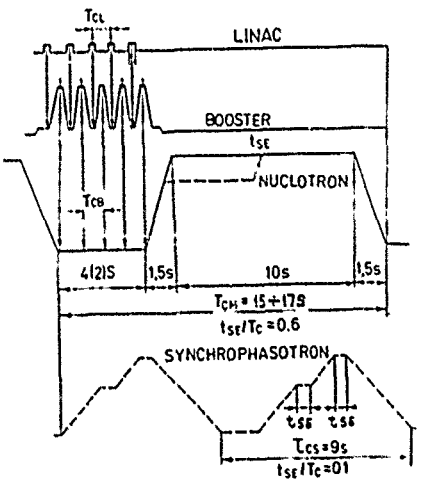


Fig.2. Time diagram of the operation of the accelerated complex.

In our case this advantage is realized by means of multiturn injection into the booster when a 4-dimensional phase volume is filled with the aid of the difference coupling resonance $Q_x - Q_z = 0$. When this resonance is excited by a longitudinal magnetic field, vertical and horizontal betatron oscillations are in phase. At a miximum of horizontal displacement of particles on the inflector azimuth their vertical displacement is maximum /2/ as well. If the inflector with a restricted vertical dimension is employed, the particles will go round it at more dangerous turns with large probability.

The time of multiturn injection is determined under the following conditions. The acceptance of the main ring matches a linac emittance of 40π mm·mrad. This means that the emittance of the beam ejected from the booster should be equal to or less than the linac emittance. Taking into account an adiabatic decrease of emittance during beam acceleration in the booster by K times, where $K=(B\rho)max / (B\rho)i$ is the ratio of magnetic rigidity for extraction and injection, the acceptance of the booster filled at multiturn injection should be $A_x = KE_x$, $A_z = KE_z$.

For a linac energy of 5 MeV/u it corresponds to K=6.65 and $A_x = A_z = 260\pi$ mm·mrad. Thus, for filling the booster acceptance, the storage of particles is possible during $K^2 = 44$ turns. For the period of particles turn T=1.6μs the time of injection is 70 μs (35μs for protons); this is much larger than the time of single turn

0-7803-0135-8/91$01.00 ©IEEE

injection into the Nuclotron which is equal to 8μs(4μs for protons, respectively).

The pulse duration of beams from the linac (which operates at the Synchrophasotron) using a laser source and an EBIS is equal to 10-25μs. This permits ions in the booster to be stored almost without losses. A considerable gain is also obtained by using a duaplasmatron and a polarized deuteron source which pulse duration is 400-500μs.

Table 1 gives pulse intensities of the Nuclotron for the linac and the booster as an injector and after the development of the ion sources. A planned layout of the booster-Nuclotron region is shown in Fig.1.

Table 1

Intensity of Nuclotron beams at various tapes of injection (ppp)

Beam	Sources	Injection form		
		Linac	Booster	Booster and developed ion sources
P	Duaplasmatron	$4\cdot10^{11}$	$1\cdot10^{13}$	$1\cdot10^{13}$
H_2^{1+}	Duaplasm.	$2\cdot10^{11}$	$5\cdot10^{12}$	$1\cdot10^{12}$
He_4^{2+}	Duaplasm.	$2\cdot10^{10}$	$5\cdot10^{11}$	$1\cdot10^{12}$
D	POLARIS	$5\cdot10^{8}$	$1\cdot10^{10}$	$5\cdot10^{10}$
C_{12}	Laser	$1\cdot10^{10}$	$1\cdot10^{11}$	$5\cdot10^{11}$
Mg_{24}	Laser	$6\cdot10^{8}$	$6\cdot10^{9}$	$3\cdot10^{10}$
Ar_{40}	EBIS	$2\cdot10^{5}$	$2\cdot10^{6}$	$1\cdot10^{7}$
Kr_{84}	EBIS	$4\cdot10^{4}$	$4\cdot10^{5}$	$2\cdot10^{6}$
Xe_{131}	EBIS	$2\cdot10^{4}$	$2\cdot10^{5}$	$1\cdot10^{6}$
U_{238}	EBIS	$1\cdot10^{4}$	$1\cdot10^{5}$	$5\cdot10^{5}$

The effective procedure improving significantly the parameters of a beam is electron cooling which makes it possible to reduce the pulse spread and emittance of circulating and extracted beams, to increase the efficiency of slow extraction at the Nuclotron and to provide better conditions for experiments on the beams of the booster.

The task of the acceleration of polarized deuterons will be decided comparatively easy since there are no depolarizing resonances up to the fourth order in that interval of energy and for betatron frequency oscillations $Q_x=Q_z=2.25$.

The acceleration of uranium ions specifies requirements for the pressure of residual gas which should be 10^{-10} Torr at beam losses of a few percent.

Machine Lattice

The booster lattice contains 6 cells (Fig.3). Each cell consists of a FOFDOD type quadrupole quartet and two sector dipole magnets. Two straight sections 2.6m and 0.9m in length are used to install the elements of the systems: injection, extraction, acceleration, correction, diagnostic and electron cooling.

The injection system includes a septum-magnet for preliminary bending of an injected beam, a septum-magnet, 4 bump-magnets to produce a local distortion of the orbit and a solenoid to excite the linear difference coupling resonance.

The fast one-turn extraction system consists of a 2m kicker and an extraction septum-magnet.

Taking into account the use of the vertical volume for storage, the apertures of the magnets are b x h = 192mm x 104mm for dipoles (Fig.4) and D=90mm for quadrupoles (D is inscribed circle radius).

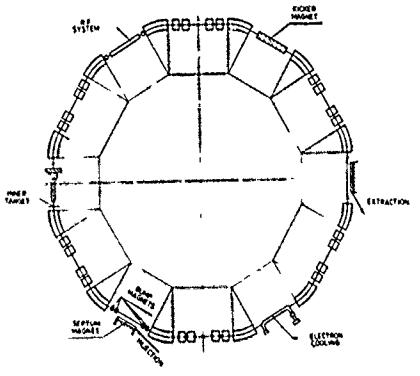


Fig.3. Lattice of the booster.

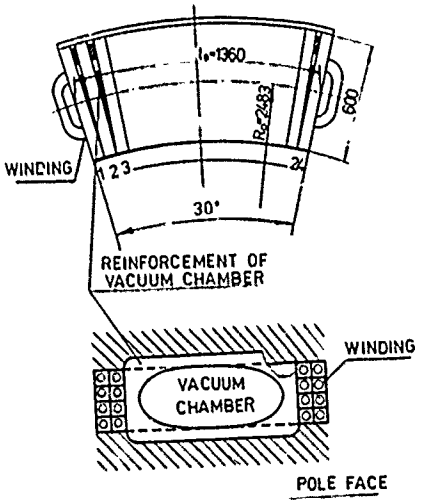


Fig.4. Draft of the dipole magnet.

The general booster parameters are given in Table 2.

Table 2

Injection energy	5 MeV/u
Max energy (q/A=0.5)	200 MeV/u
Charge limit	$2\cdot10^{12}A/q^2$ ppp
Injection time	70 μs
Circumference	50.52 m
Number of FOFDOD	6
Field in the dipoles (max)	1.73 T
Gradient in the quadrupoles(max)	7.74 T/m
Betatron frequency $Q_x \approx Q_z$	2.25
Acceptance $A_x = A_z$	260π mm·mrad
Emittance at extraction $E_x=E_z$	$<10\pi$ mm·mrad

References

1. A.M.Baldin et al. IEEE Trans.Nucl.Sci.NS-30, N°4, 1983, p.3247.
2. A.M.Gromov and P.A.Cherenkov. Proceedings of the IIId Allunion Part.Accel. Conference, v.II, p.110, Moscow 1973 (in Russian).

THE PROJECT OF THE HEAVY ION STORAGE RINGS COMPLEX OF THE JINR AT DUBNA

O.N.MALYSHEV[1], I.N.MESHKOV[2], R.Ts.OGANESSIAN[1], Yu.Ts.OGANESSIAN[1], V.V.PARKHOMCHUK[2], P.POKORNY[1], A.A.SERY[2], S.V.STEPANTSOV[1], Ye.A.SYRESIN[2], G.M.TER-AKOPIAN[1] and V.A.TIMAKOV[1]

[1]Joint Institute for Nuclear Research, Dubna

[2]Institute of Nuclear Physics, Novosibirsk, USSR

Abstract

Recently commissioned of Darmstadt SIS-ESR complex has started the new generation of Radioactive Ion Beams (RIB) facilities. We give in thes paper the brief description of the project of the heavy ion storage ring complex K4-K10 and discuss, for the specific case, methods which could provide the highest production rates of stored and cooled RIB's. Some numerical estimations are given for the processes of storing and cooling the primary and exotic beams.

I. Introduction

Soon after the invention of the electron cooling |1|, the potential of this method was recognized especially in that case when it is used as a means to maintain the high quality of the beam in experiments exploiting a thin internal target placed on the orbit of a storage ring |2|. Building the heavy ion storage and cooler rings formed, during the eighties, a considerable part of general trend towards developing new accelerator and experimental techniques for atomic and nuclear physics. Several projects are either accomplished or close to commissioning |3-10|.

We would like to discuss in this paper one of the possible future facilities, i.e. the project of heavy ion storage ring complex K4-K10 recently proposed in Dubna |11|. After the brief discription of the project, we shall present some considerations of proposed method of producing, storing and cooling the RIB's.

II. Brief discription of the project K4-K10

The layout of the storage ring complex K4-K10 is shown in Fig. 1 together with the heavy ion cyclotrons of the JINR (Dubna). The project includes two rings, K4 and K10*). The beam channels related to this project are also shown in Fig. 1. The most important of

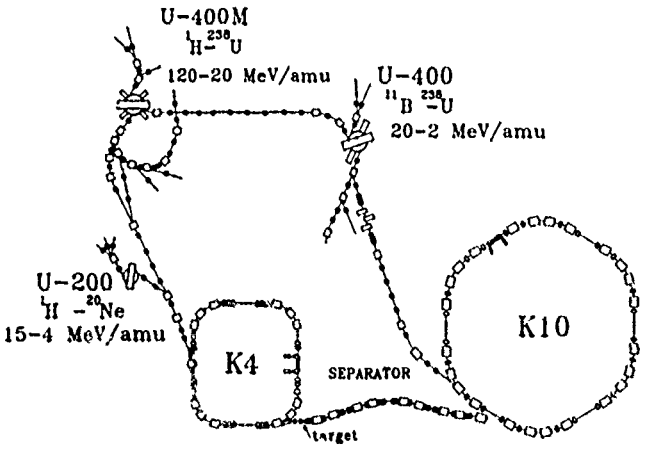


Fig. 1. The layout of the storage ring complex K4-K10.

them are the channel guiding from the U400M cyclotron to the injection section of the ring K4 and the fragment separation channel. The momentum loss achromat technique will be utilized in the design of this separator channel.

Two cyclotrons, i.e. U200 and U400, are the working accelerators whereas the third one, U400M, is at present at the stage of commissioning. The mass and energy ranges of heavy ion beams by the cyclotrons are given in Fig. 1. The main injector of the storage ring complex will be the U400M. The charge states and intensities of some representative ions which will be accelerated by this machine are given in Table 1.

Two modes of operation of the U400M cyclotron are foreseen. The beams ranging from hydrogen to krypton will be produced by exploiting an sources whereas, for heavier ions extending up to uranium, the tandem mode will be used, in which case the U400 cyclotron will serve as an injector for the U400M. The values of mean currents for ions with mass numbers $A \leq 20$ and $A > 100$ in Table 1 are anticipated by taking into account the long term experience of running the U400 cyclotron in combination with different modifications of the PIG ion source. For the ions ranging from magnesium to

*)We mark the rings K4 and K10 and the complex K4-K10 by taking the abbreviation from russian "koltso" (ring) and the numbers 4 and 10 giving the magnetic rigidity of the rings in T m.

0-7803-0135-8/91$01.00 ©IEEE

TABLE 1
Estimated intensities of U400M beams.

Ions	Mean current of beam (s^{-1})	Number of beam ions per time interval of 1 μs
H_2^{1+}	4×10^{13}	2×10^{8}
$^{4}He^{1+}$	6×10^{13}	3×10^{8}
$^{4}He^{2+}$	4×10^{13}	2×10^{8}
$^{7}Li^{2+}$	4×10^{13}	2×10^{8}
$^{18}O^{5+}$	2×10^{13}	1×10^{8}
$^{20}Ne^{5+}$	3×10^{13}	1.5×10^{8}
$^{48}Ca^{10+}$	3×10^{12}	3×10^{7}
$^{86}Kr^{18+}$	3×10^{11}	3×10^{6}
$^{136}Xe^{33+}$	2×10^{11}	1×10^{6}
$^{208}Pb^{44+}$	1×10^{11}	5×10^{5}
$^{238}U^{48+}$	1×10^{11}	5×10^{5}

krypton, the published results are used which illuminate the data obtained by the working groups at GANIL (Caen), MSU (East Lancing) and LBL (Berkeley) in the course of operation of their cyclotrons with the ECR ion source. We give in the last column of Table 1 the beam intensities of the terms of the ion numbers delivered by the cyclotron within one microsecond, the time interval cloce to the period of the beam revolution in a storage ring. These values are given for the pulsed operation mode of ion sources.

Table 2 gives the basic parameters of the storage rings K4 and K10. Apparently, such a pair of coupled storage rings both equipped with the electron cooling sections, the RF accelerating/deccelerating systems and having three injector cyclotrons will be capable of providing different options on selection of operational modes. We note that the highest energy

TABLE 2
Basic parameters of the rings K4 and K10.

Ring		K4	K10
$B\rho_{max}$,	T m	4	10
Circumference	m	70	140
Acceptance, ε_i	π mm mrad	50	25
$(\Delta p/p)_{max}$,	%	1.5	1.5
Maximum cooling electron energy,	keV	100	250
Length of the cooling section,	m	3	3
Maximum electron current,	A	5	5
Cathode diameter,	cm	3	3
Range of the RF frequency,	MHz	0.5-3.4	0.3-2.1

of heavy ions, 500-800 MeV/nucleon, will be achieved in the case when ions, after the U400M, are successively accelerated first in the ring K4 and than in K10 being stripped every time before injection into the ring. Fully stripped ions as heavy as zirconium and hafnium will be accessible in the rings K4 ans K10, respectively. Table 3 lists, for some typical beams, the ionic charges and maximum ion energies on the

TABLE 3.
Maximum energies (MeV/nucl.) of heavy ions of different charge states (q)

Ion	Cyclotron U400M Ion source or injector cyclotron U400		Ring K4 Injector cyclotron U400M		Ring K10 Injector ring K4	
	q	E/A	q	E/A	q	E/A
^{1}H	1	120	1	580	1	2200
^{4}He	1	30	2	170	2	830
^{7}Li	2	45	3	135	3	650
^{18}O	5	40	8	140	8	690
^{20}Ne	5	30	10	170	10	830
^{48}Ca	10	25	20	125	20	625
^{136}Xe	33	35	52	100	54	580
^{208}Pb	44	24	72	90	80	550
^{238}U	48	20	82	87	90	535

orbits of the rings.

III. The possibilities of generating storing and cooling the RIB's.

We suppose that projectile fragmentation will be used for generating the RIB's. Cooled and accelerated in the ring K4 up to the maximum energy, the heavy ion beam, after the fast extraction, will be focused onto a production target positioned at the source plane of the fragment separator (see Fig. 1). As a result of fast extraction, the primary beam can be delivered to the target in the form of short bursts having variable time structure. This will considerably facilitate conditions of accumulating and cooling the RIB's in the ring K10. In the following we shall present some estimations of luminosity values which will be attainable for the cooled RIB's on the orbit of the ring K10.

The injection method adopted for the ring K4 is of significance for the rate of generating the RIB's. Two different methods of injection will be employed. For lighter ions extending up to neon, this will be tne charge-exchange injection. In order to eliminate the transverce beam emittance blowing up during the injection the stripper will be positioned on the closed orbit bump generated on the nondispersive straight section of the ring.

Two typical situations are presented in Table 4 for $^{7}Li^{2+}$ and $^{18}O^{5+}$ beams accelerated in the U400M and injected by stripping in the ring K4. The limitation on the maximum number of the ions accumulated on the ring orbit occurs due to the space charge effect which sets automatically the minimum value of the transverse emittance of the stored and cooled beam.

The efficiency of the charge-exchange injection seems to be justified for ions not heavier than neon. It appears to be problematic for heavier beams due to

TABLE 4.
Charge-exchange injection in the ring K4.

Ion		^{7}Li	^{18}O
Injection energy,	MeV/nucl.	45	40
Thickness of the carbon stripper,	$\mu g/cm^2$	10	100
Number of ions injected per one microsecond		$2\cdot10^8$	$1\cdot10^8$
Number of ions on the ring orbit for which the transverse emittance $\varepsilon_\perp$=1π mm mrad is set after cooling		$1.6\cdot10^{10}$	$6\cdot10^9$
Cooling time,	ms	6	55
Maximum energy,	MeV/nucl.	135	140
Acceleration time,	ms	300	300
Total duration of the working cycle,	ms	330	360
Number of ions on the ring orbit limited by the transverse emittance $\varepsilon_\perp$=50π mm mrad		$8\cdot10^{11}$	$3\cdot10^{11}$

the increased target thickness needed for producing fully stripped ions. Therefore, we foresee for the beams of ions much heavier than neon the single turn injection which will be realized in the same straight section of the ring K4 where the charge-exchange injection is accomplished (see Fig. 1). We present some figures in Table 5 which illustrates the conditions of the single-turn injection for the case of the $^{48}Ca^{10+}$

TABLE 5.
Single-turn injection of $^{48}Ca^{20+}$ in the ring K4.

Injection energy,	MeV/nucl.	25
Revolution period in the ring K4,	μs	1.5
Number of ions injected per one turn		$3\cdot10^7$
Number of ions on the ring orbit for which the transverse emittance 1π mm mrad is set after injection and cooling		$1\cdot10^9$
Injection and cooling time,	ms	170
Number of ions on the ring orbit for which the transverse emittance 4π mm mrad is set after injection and cooling		$4\cdot10^9$
Injection and cooling time,	ms	1050
Maximum energy,	MeV/nucl.	125
Acceleration time,	ms	300
Total duration of the working cycle,	ms	1350

beam extracted from the U400M cyclotron. The ions should be stripped to the charge state 20+ before the injection in the ring. The accumulation of Ca ions on the ring orbit will be accomplished by cooling the newly injected beam and its adiabatic capture into the stationary RF bucket.

We give in Table 5 the number of accumulated by single turn injection and captured in the RF $^{48}Ca^{20+}$ ions ($N_i=10^9$) for which the transverse emittance $\varepsilon_\perp=1\pi$ mm mrad will be set as a result of manifestation of the space-charge instability. The accumulation and cooling time (170 ms) of such number of ions is also presented in Table 5. The number of accumulated ions of about 4×10^9 is of practical interest as the sum of accumulation cooling times aproaches one second for this case, i.e. a factor of two longer than the ion acceleration time up to the maximum energy of the ring K4.

Inspecting Tables 4 and 5 one can see that, in connection with the problem of the RIB's generation, we are interested in accumulation on the orbit of the ring K4 such a number of ions for which the space charge instability is actual. We considered also microwave beam instabilities and come to the conclusion that this effects either would be of minor importance or one would easily found the means to suppress this effects in our case.

Some calculating parameters of different type radioactive ions which will accumulated and cooled in the ring K10 are presented in Table 6.

TABLE 6.

Primary beam	RIB	$T_{1/2}$,s	N	L, $cm^{-2}s^{-1}$ (injection energy)	E_{max}	L, $cm^{-2}s^{-1}$ (maximum energy)
^{7}Li	^{6}He	0.8	$3\cdot10^7$	$2\cdot10^{27}$	430	$1\cdot10^{27}$
^{18}O	^{8}He	0.122	20	$2\cdot10^{21}$	260	$1\cdot10^{20}$
	^{11}Be	13.8	$4\cdot10^7$	$4\cdot10^{27}$	500	$2\cdot10^{27}$
	^{15}C	2.45	$3\cdot10^7$	$2\cdot10^{2}$	580	$\cdot10^{27}$
	^{16}C	0.747	$2\cdot10^6$	$2\cdot10^{26}$	520	$1\cdot10^{26}$
^{48}Ca	^{44}Ar	720	$3\cdot10^7$	$2\cdot10^{27}$	600	$1\cdot10^{27}$
	^{46}Ar	7.8	$4\cdot10^4$	$3\cdot10^{24}$	560	$2\cdot10^{24}$
	^{47}K	17.5	$5\cdot10^7$	$6\cdot10^{27}$	590	$3\cdot10^{27}$
	^{38}S	$1\cdot10^4$	$2\cdot10^8$	$2\cdot10^{28}$	630	$1\cdot10^{28}$

References

1. G.I.Budker, Atomnaja Energija 22, 346 (1967) (in Russian).
2. G.I.Budker and A.N.Skrinsky, Uspekhi Fiz. Nauk 142, 561 (1978) (in Russian).
3. R.E.Pollock. In Proceedings of the IEEE Accelerator Conference, Chicago, 1989. Edited by F.Bennett and J.Kopta (IEEE, New York, 1989), p.17.
4. D.Kraemer et al., Nucl. Instr. Meth. A287, 268 (1990)
5. P.Kienle, Nucl. Phys. A478, 847c (1988)
6. S.Kullander et al. In Proc. Int. School-Seminar on Heavy Ion Physics, Dubna, 1989. JINR D7-90-142, Dubna (1990), P.20.
7. A.Noda et al. IEEE Transactions on Nuclear Science, NS-32 (1985) 2684.
8. C.J.Herrlander et al., Phys.Scr. T22, 282 (1988).
9. R.Stensgaard, Phys.Scr. T22, 315 (1988).
10. S.A.Martin et al., Nucl.Instr.Meth. A236, 249 (1985).
11. Yu.Ts.Oganessian and G.M.Ter-Akopian, In: Heavy Ion Storage Rings with Electron Cooling (USSR Proposals and Projects Collection), I.V.Kurchatov Institute of Atomic Energy, Moscow, 1990, p.65.
12. H.Geissel et al., Projectile Fragment Separator, A Proposal for the SIS-ECR Experimental Program (1987).

PERFORMANCE OF LEP AND FUTURE PLANS

Jean-Pierre Koutchouk
CERN
CH-1211 Geneva 23

Abstract The performance of LEP has been steadily improving: 750,000 Z^0 were produced in 1990. Many of the design parameters have been reached separately, showing that the machine behaves basically as expected. In fact, some design parameters have been exceeded (β^*, emittance ratio) and a significant level of polarization was obtained. An improvement by a factor of up to four in integrated luminosity is still to be expected by overcoming the identifiable limitations : strong synchro-betatron resonances and blow-up of the beam due to the beam-beam effect. Solutions to these problems have been devised and will be tested in a vigorous machine study programme. The long term LEP Experimental Programme has been defined by the physics community: a pretzel scheme will be installed to increase the luminosity. It will be followed by the LEP 200 programme to increase the energy up to and beyond the W pair threshold. The production and installation of the required superconducting cavities are in progress and due to be finished in 1994. An active programme of polarization studies is undertaken with the objective of precision measurement of Z^0 mass and width. The feasibility of spin rotators is being assessed to provide longitudinally polarized beams.

1 INTRODUCTION

After reviewing the performance achieved, this paper presents the phenomenology of the beam dynamics in LEP, the present understanding of its limitations and the possible solutions. The future of LEP is contained in its acronym, i.e. Luminosity, Energy and Polarization. The status of the development programmes is presented.

2 PERFORMANCE

Operational performance

	Inj.	Ramp	Coast	Fault
average	2:42	0:55	7:52	1:31
rms	2:03	0:23	5:04	2:18
best	0:30	0:12	22:35	0:00

Table 1: Statistics on the LEP runs

LEP is operated 50 % of the time at the Z^0 peak and 50 % at intermediate energies within ±3 GeV of the peak. The integrated luminosity in 1990 (a total of 750000 Z^0) was 10 times larger than in 1989 (fig 1). During 1990, the integrated luminosity per week has been increasing steadily from 0.5 pb^{-1} to 1.4 pb^{-1}. The physics events were clean after automatic positioning of the 72 collimators. Very clean conditions were obtained by fine optimization.

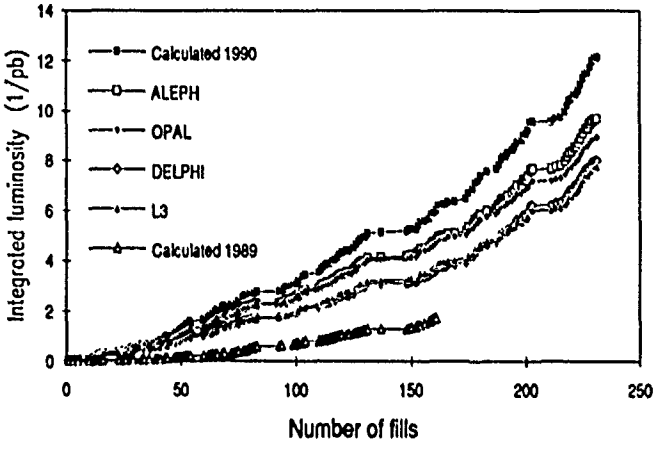


Figure 1: Integrated luminosity in 1989 and 1990

The availability of the machine was 50 % , partly due to the large number of machines in series and the size of LEP. It is actively worked up. The long set-up time (table 1) is compensated by the very long coasts [1].

Peak performance

The peak performance, often obtained during machine studies, is close to design, showing that the machine behaves basically as expected.

Parameter	Design	Achieved
Current per bunch (mA)	0.750	0.780
Current per beam (mA)	3.000	2.980
Current in both beams (mA)	6.000	4.700
V. beam beam parameter (ξ_y)	0.040	0.017
H. beam beam parameter (ξ_x)	0.040	0.035
Emittance ratio (ϵ_y/ϵ_x)	0.04	$\sim$ 0.01
Luminosity ($10^{30} cm^{-2} s^{-1}$)	16.0	$\sim$ 7.0
β function at the IP (β_y^*) cm	7.0	3.2

Table 2: Achieved (peak) and design LEP performance

0-7803-0135-8/91$01.00 ©IEEE

Energy calibration

An original method was developed [2] taking advantage of the availability of protons. If electrons and protons circulate on the *same* central orbit, the difference in revolution frequencies is an absolute measurement of the electron energy, to the accuracy of the knowledge of the particle masses. The central orbit can be accurately found by its insensitivity to the excitation of the sextupoles. The accuracy is ±1 MeV per beam at 20 GeV. Extrapolated at the Z^0 energy, it reaches ±20 MeV in the centre-of-mass.

3 MAGNETIC OPTICS

Description

The LEP optics is structured so as to separate its main functions: 8 arcs, 16 dispersion suppressors, 16 RF, 4 high-β and 4 low-β straight-sections. The cell phase advance in the arc is 60° and the chromaticity is corrected by six sextupole families. Since the switch-on of LEP, the optics has been modified twice. The integer parts of the betatron tunes were changed from 70/78 to 71/77 by rematching the four high-β insertions. The purpose was to avoid a very strong linear coupling resonance driven by an unexpected defect of the vacuum chamber [3]. The linear betatron coupling is now well compensated.Emittance ratios below design were observed (1%). The β_y^* in the low-β insertions was reduced from the nominal 7 cm to 5 cm for operation.

The optical model, in the MAD language, includes the nominal fields as well as the known field imperfections. Its predicts the important operational parameters (tunes, closed orbit, β^*, betatron coupling) very well. It partially fails in predicting the linear chromaticity, the parasitic dispersion and the dynamic aperture at injection.

Injection, ramp and squeeze

The LEP cycle from injection to physics consists of some 20 intermediate optics configurations. Apart from the synchronization of the insertion quadrupoles, no significant problems have been encountered in accelerating whatever current was accumulated. However the procedures are complex and time consuming. They are being improved by the introduction of new software, continuous monitoring of the tunes, tune loops, reactive feedback to maintain the coherent and incoherent tunes equal and, possibly, continuous monitoring of the chromaticity.

Observations and Developments

Vertical dispersion Surprisingly, the parasitic dispersions in LEP were 2 to 2.5 higher than expected. The search for the sources is made difficult by the resolution of the orbit measurement (100 μm), which may be limited by residual coherent oscillations and the small damping aperture (.2 % without beam loss). No strong defect was isolated. The fact that the dispersion is decreased by careful correction of the vertical orbit rather points to distributed sources. Antisymmetric orbit bumps in the insertions have been used to minimize it.

In 1991, an improvement of the beam monitor resolution is expected to yield dispersion measurements accurate to a few centimeters. Closed dispersion bumps in the RF straight-sections will be provided, using small skew quadrupoles in the lattice as well as a global correction scheme.

Chromaticity and dynamic aperture Two observations are still unexplained: the measured chromaticity disagrees by 15 % with the model, with opposite signs in the two planes; the horizontal dynamic aperture at injection is 3 times less than expected. At top energy, even after β squeezing, the latter discrepancy is reduced. In practice, the chromaticity is straightforwardly corrected, and the dynamic aperture is still enough (10 rms beam sizes). There is a suspicion that, combined with synchro-betatron resonances, it might limit the current at injection. The hunt for the missing multipoles opens in 1991.

Optics asymmetries The luminosities in the four insertions differ by up to 25 % (Figure 1). A β-beating was detected and eventually explained by a longitudinal misalignment of the superconducting coils and girders of some insertion quadrupoles, enhanced by the larger sensitivity of the very low-β optics. The alignment method, made difficult by the presence of the detectors, is being improved. The matching of the insertions has been modified to allow for asymmetric insertions.

Decrease of β^* At the Z^0 peak, some aperture is left to further squeeze β^*. Calculation of the higher-order chromatic effects [4] shows no pathological behaviour when β_y^* is reduced from the nominal 7 cm to 2.54 cm (the bunch length is 1.7 cm). Experiments have confirmed so far that 3.2 cm is possible, i.e. that non-linear phenomena do not perturb the dynamics. The machine is now routinely operated at $\beta_y^* = 5$ cm. The amplification of alignment and focusing errors may set a practical limit on the lowest β-value compatible with reliable operation.

90° lattice Stronger focusing is required to reach the beam-beam limit at higher energies (LEP Phase II). Some initial experiments were carried out to test this optics at injection energy. While injection and a good set-up were rapidly obtained, a few attempts to store high currents were not successful. The development of this high-tune lattice is being pursued with high priority.

New optics developments At injection, the low field level makes LEP sensitive to very small field imperfections. To compensate for the most significant, i.e. the skew gradient, an optics with unequal horizontal and vertical phase advances was designed. The betatron coupling is self-compensated within each arc. The integer part of the betatron tunes is optimum with respect to luminosity and polarization. Although the achromatic structure of the arc cannot be retained in both planes, the higher-order chromatic properties remain well behaved. Before this optics is shown to be viable, the 71/77 optics is modified by rematching the high-β insertions to yield the tunes 70/76.

The aim is to increase the beam-beam limit and prospects for polarization.

4 COLLECTIVE EFFECTS

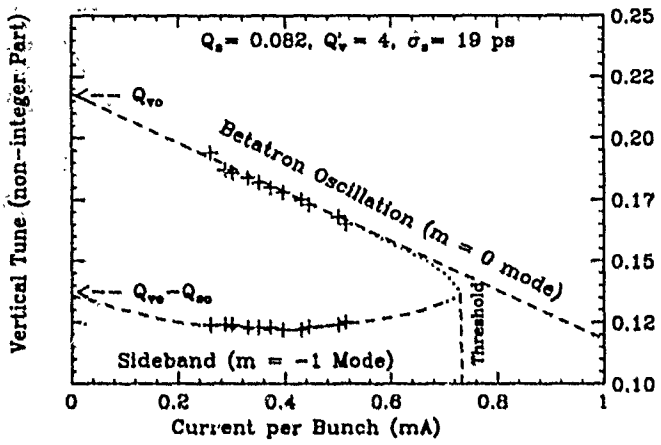


Figure 2: Observed transverse mode coupling

Transverse mode coupling instability The transverse mode coupling instability was predicted to be the most severe limitation of single bunch current in LEP. The transverse broad-band impedance of the LEP vacuum chamber was therefore minimized by very careful design. Experimental observations of the betatron frequencies of the two modes $m = 0$ and $m = -1$ (Figure 2), confirmed the impedance calculations (2.24 MΩ/m) [5]. The estimated threshold current of about 0.75 mA/bunch has been reached without instability, but at a higher Q_s (0.13).

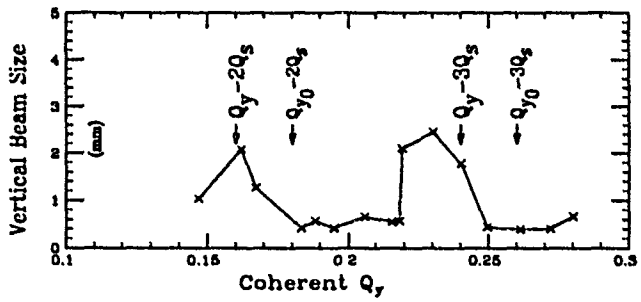


Figure 3: Synchro-betatron resonances

Synchro-betatron resonances In practice, the beam current is limited by synchro-betatron resonances. The dominant driving mechanism is the parasitic dispersion in the RF cavities. Measurements done so far indicate that the resonances are coherent (Figure 3) though incoherent ones are also present. The improvement of the optics and a betatron tune below the integer are expected to remove this limitation.

Longitudinal bunch oscillations The large spacing between bunches makes coupled bunch oscillations unlikely in LEP. However, longitudinal oscillations did indeed limit the current until a provisional longitudinal feedback was quickly installed. The absence of exponential growth and of transverse coherent oscillations, which are expected to have a relatively lower threshold, have oriented the studies towards a possible noise on the magnets or RF system. A dedicated 1 GHz feedback is under construction.

5 BEAM-BEAM EFFECT

The saturation of the beam-beam strength parameter at a value some 2.5 times lower than expected is the present major limitation (Figure 4); it causes the luminosity to

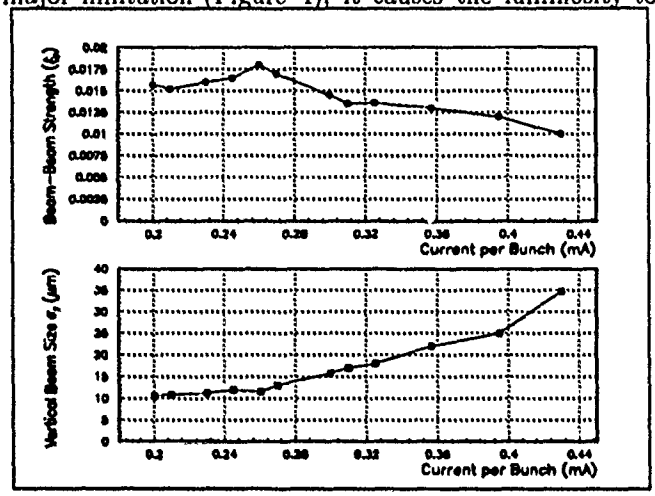


Figure 4: Beam blow-up due to the beam-beam forces

remain constant over the 5 first hours of the coasts or more.

A likely explanation, consistent with numerical simulations (fig 5) [6] and observations, is the presence of a systematic beam-beam difference resonance close to the working point ($Q_x = 71.28$, $Q_y = 77.18$):

$$2Q_x - 2Q_y = 4 \times 3$$

which reduces the luminosity by some 50 %. This harmful

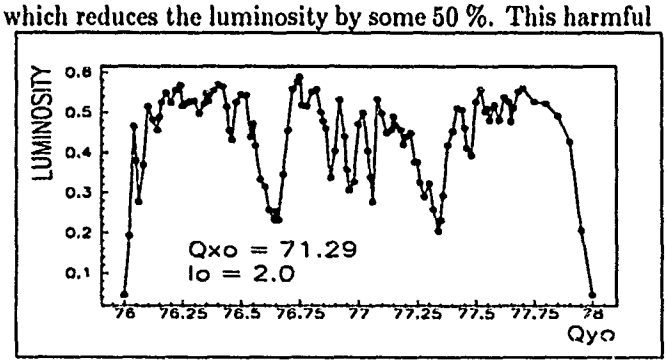


Figure 5: Simulation of the beam-beam effect

resonance will be avoided with the new 70/76 optics.

Other sources known to decrease the beam-beam limit are the optics imperfections. As already mentioned, the vertical dispersion is twice what was expected; large β-beating (20 %) and optics asymmetries (some 10 degrees in betatron phase) were identified. Numerical simulations show that improvements in the optics measurements and correction could yield a potential luminosity gain of more than 50 % . Automatic bunch equalization is as well expected to raise the beam-beam limit.

6 TRANSVERSE POLARIZATION

Transverse polarization allows the calibration of the energy to a few MeV. The capability of the LEP beams to spontaneously polarize has however been debated. The rise time of the polarization at the Z^0 peak is long (300 minutes); the depolarizing spin resonances are stronger ($\sim \gamma^2$) and denser than in other machines, to the extent that reliable predictions are difficult.

During the summer of 1990, a significant fraction of the machine study time was devoted to commissioning the Compton polarimeter, optimizing the parameters of the standard optics and refining the correction of its imperfections until a polarization degree of 10 to 20 % was predicted. After several attempts, an unambiguous asymmetry of the back-scattered photons was detected (figure 6 and [7]). The validity of the signal was assessed by internal on-line checks of the systematics and by the controlled excitation of spin resonances using a pattern of vertical orbit bumps. The polarization level, calculated in two independent ways, was found to be 9 % ± 2% systematic ± 2 % random. In 1991, this polarization, possibly increased, will be used to calibrate the Z^0 energy and width.

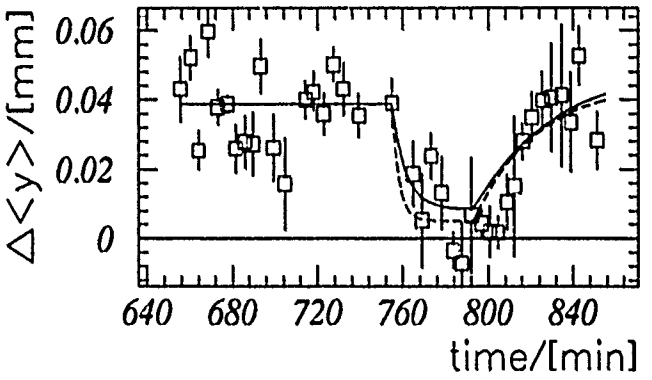


Figure 6: Observed polarization in LEP (plain line) compared to expectation (dotted line)

7 THE ENERGY UPGRADE

Parameters of Phase II

Phase 2 of the LEP programme is approved and will take the beams up to energies beyond the W pair threshold of 82 GeV [8]. With 192 additional superconducting cavities and a target operational gradient of 6 MV/m, an energy of 92 GeV can be reached. If the effective gradient was only 5 MV/m, the energy would be reduced to 89 GeV, i.e. still significantly above the threshold. The expected luminosity, limited by the beam current (2 × 4 × 0.750 mA), is about 2 10^{31} $cm^{-2}s^{-1}$ or more. It requires the stronger focusing of 90° per cell. The luminosity may be doubled by combining the energy and luminosity upgrades.

Superconducting cavities

Two lines of development have been followed to optimize the quench behaviour of the cavities: niobium sheet metal with improved thermal conductivity and sputtering the inside surface of copper cavities with niobium. The latter approach presents a higher performance potential and has therefore be retained for the series production of 160 cavities by industry. The complement will consist of 24 Nb sheet cavities made by CERN and industry, and 8 Nb sputtered cavities made at CERN. Two 4-cavity modules of each type are presently installed in the LEP ring. The first module has been used for physics runs in 1990 already; the operational gradient was limited to 4 MV/m because of difficulties in the adjustment of the RF power coupler of one cavity. Adjustable main couplers developed in the mean-time, clean room assembly and protection from synchrotron radiation by collimators will allow to get closer to the target gradient. Four cryogenic plants with an initial cooling power of 12 kW at 4.5°K, designed to be reusable for the LHC project, will be installed in the experimental points. The installation of the new cavities is planned over 3 years and due to be completed at the beginning of 1994.

Modifications to LEP 1

The optics of all the insertions was revised or redesigned to minimize the cost of the upgrade. A better chromatic correction using 4 sextupole families was found. It provides a large dynamic aperture and small chromatic variations of the important optical parameters. Studies are presently devoted to the robustness of the dynamic aperture with respect to magnetic imperfections and asymmetrical RF acceleration.

At present four out of the 16 available RF straight sections are equipped with copper cavities. To install the full complement of 192 new cavities, klystron galleries must be dug in points 4 and 8. The underground work is being carried out with special care to prevent dust from reaching the experiments. The energy upgrade requires changing the superconducting insertion quadrupoles, rebuilding many power converters, new klystrons, new electrostatic separators and new collimators to efficiently protect the superconducting cavities and the separators. The power distribution and cooling systems for LEP will also be upgraded to handle twice the presently installed power.

8 THE LUMINOSITY UPGRADE

A pretzel scheme to collide up to 36 bunches in LEP has been shown to be attractive [9]. A low cost version of this proposal is being implemented. 8 electrostatic separators become available from the $Sp\bar{p}S$, they allow for a 8 bunch pretzel scheme, doubling the luminosity without significant modifications to other systems.

The pretzel separation is provided by four horizontal bumps, each extending over most of a quadrant of the machine (figure 7). They are antisymmetrical about the

non-experimental insertions. This arrangement has the

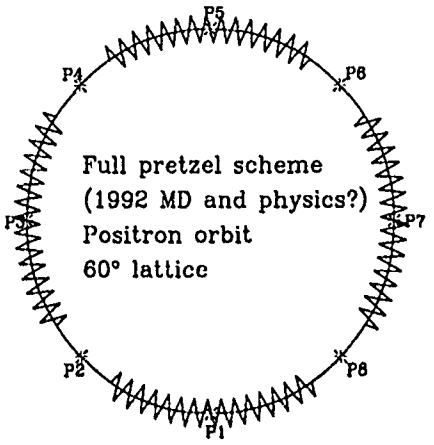


Figure 7: Pretzel separation

favourable feature of cancelling the differential optical effects. The polarity of the pretzel orbits can be chosen so that the extra separation due to the energy sawtooth effect (significant at 90 GeV) adds up. The beams are separated by 12 rms beam widths up to 90 GeV. The horizontal separation is not incompatible with polarization. The geometrical aperture of the LEP vacuum chamber and dynamic aperture around the pretzel orbits seem sufficient to ensure a good lifetime; a first experiment carried out on an orbit simulated with magnetic deflections showed no significant influence on the injection rate and maximum current.

Some copper cavities must be removed to make room for the separators, slightly reducing the maximum RF voltage. The HOM losses in the cavities and separators are calculated to be acceptable. Special care is taken to reduce the sparking rate of the separators with a low electric field (~2MV/m) and collimators to shield the electrodes from the direct synchrotron radiation. Four separators are now installed, allowing a partial pretzel scheme to be established for machine development purposes. The full complement of 8 separators will be installed in 1992 allowing further tests and, possibly, first operation with 8 bunches.

9 LONGITUDINAL POLARIZATION

To carry out precise tests of the Standard Model, the LEP physics community has made a strong case for obtaining collisions of longitudinally polarized beams in the four LEP experiments at the Z^0 energy. Meanwhile, studies have shown that the prospects for polarized beams are not as dark as often believed. The success of the transverse polarization experiment confirmed this. To run efficiently with polarized beams, the polarization degree must reach 50 % and the rise-time must be reduced. The former requires spin resonance compensation which will be tried this year. The rise-time can be reduced from 300 to 36 minutes by new asymmetrical wigglers just installed.

The polarization vector may be rotated at each crossing point by a Richter-Schwitters spin rotator. To minimize the depolarization due to the bending in the rotator, the fields have to be weak and the rotator insertion straddles many quadrupoles. The conditions for optical and spin transparency could nevertheless be fulfilled with only one additional quadrupole per half insertion. (Figure 8). A

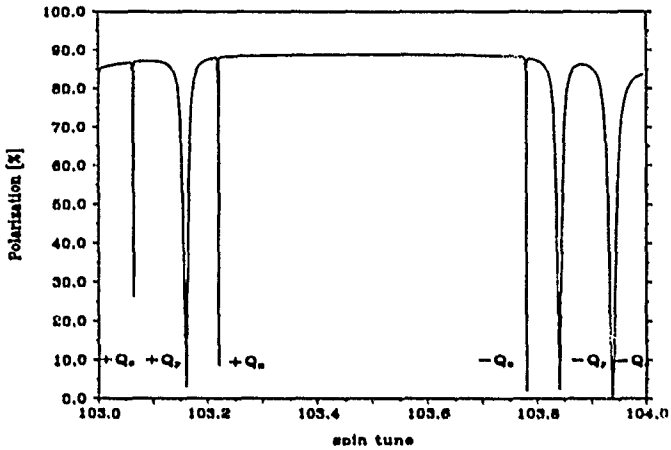


Figure 8: First-order polarization with spin rotators

collimator scheme to protect the machine and experiments from the synchrotron radiation generated by the rotator is under study with encouraging results.

Acknowledgements

The success of LEP and dynamism of its development programs is shared by the many colleagues of the Accelerator and Technical divisions of CERN.

References

[1] R. Bailey *et al.*,'First two years operational experience with LEP', this conference.

[2] A. Hofmann, T. Risselada, CERN LEP Note 383 (1982).

[3] J. Billan *et al.*, 'Measurement of the LEP coupling source', Proc. 2nd EPAC, Nice, 1990.

[4] J.P. Koutchouk, A. Verdier, 'Developments of the LEP low-β optics, Proc. 2nd EPAC, Nice 1990.

[5] D. Brandt *et al.*, 'Intensity Limitations and the Impedance of LEP', Proc. 2nd EPAC, Nice, 1990 and CERN SL-AP/90-55 (1990).

[6] E. Keil, LEP Performance Note 41 (1990) and S. Myers, private communications (1990,1991).

[7] J Badier *et al.*, 'First evidence of transverse polarization in LEP', 9th Int. Sym. on High-Energy Spin Ph., Bonn '990.

[8] C. Wyss, 'The LEP energy upgrade', this conference.

[9] J.M. Jowett, "More bunches in LEP", CERN LEP-TH/89-17 and PAC, Chicago 1989.

Achieving High Luminosity in the Fermilab Tevatron

Stephen. D. Holmes
Fermi National Accelerator Laboratory*
P.O. Box 500
Batavia, Illinois 60510

Abstract

Fermilab has embarked upon a program, christened Fermilab III, to raise the luminosity in the Tevatron proton-antiproton collider over the next five years by at least a factor of thirty beyond the currently achieved level of $1.6x10^{30}cm^{-2}sec^{-1}$. Components of the program include implementation of electrostatic separators, Antiproton Source improvements, installation of cold compressors, doubling the existing linac output energy, and the construction of a new accelerator--the Fermilab Main Injector. Basic limitations in the achievement of higher luminosity in the Tevatron, the strategy developed to achieve the Fermilab III goals, and the evolution of luminosity throughout the period will be discussed.

I. FERMILAB III GOALS

The Fermilab III program is designed to extend the discovery potential of the U.S. High Energy Physics program during the period leading up to the utilization of the SSC, and to ensure continued significant contributions from the Fermilab facility during the SSC era. Specifically, the g ..ls of Fermilab III are to assure discovery of the top quark in the present decade assuming our understanding of nature as described by the Standard Model is correct, to provide a factor of two increase in the mass scales characterizing possible extensions to the Standard Model, to provide B-factory capability in a hadron collider, and to support new initiatives in neutral Kaon physics and neutrino oscillations. In order to attain these goals Fermilab is planning to attain by mid-decade a luminosity in excess of $5x10^{31}$ $cm^{-2}sec^{-1}$ in the Tevatron Collider, supported by a new 150 GeV accelerator, the Fermilab Main Injector (FMI).

II. CURRENT PERFORMANCE LIMITATIONS

The Fermilab Tevatron is the highest energy particle collider in the world today. It will retain this position until the initial operation of either the Superconducting Super Collider (SSC) in the U.S. or the Large Hadron Collider (LHC) in Europe around the year 2000. At present in the Tevatron countercirculating proton and antiproton beams are brought into collision at 1800 GeV in the center-of-mass with a typical initial luminosity of $1.6x10^{30}$ $cm^{-2}sec^{-1}$. Averaged over a multi-month running period typical initial luminosity translates into integrated luminosity with about a 33% duty factor.

The luminosity in a proton-antiproton collider is given by the expression,

$$\mathcal{L} = \frac{3\gamma f B N_p N_{\bar{p}}}{\beta^*(\varepsilon_p+\varepsilon_{\bar{p}})} F(\sigma_z/\beta^*) \qquad (1)$$

where γ is the relativistic factor of the proton (1066 at 1000 GeV), f is the revolution frequency (47.7 kHz), B is the number of bunches, N_p and $N_{\bar{p}}$ are respectively the number of protons and antiprotons per bunch, β^* is the beta function at the interaction point (assumed equal for horizontal and vertical), ε_p and $\varepsilon_{\bar{p}}$ are the proton and antiproton 95% normalized emittances respectively, and F is a form factor associated with the ratio of the bunch length to beta function at the interaction point.

The operating conditions which led to a luminosity of $1.6x10^{30}$ $cm^{-2}sec^{-1}$ during the last collider run are given in the leftmost column of Table 1. The luminosity is limited by two quite different effects: 1)The beam-beam tune shift experienced by the antiprotons, which limits the useable phase space density, N_p/ε_p, of the proton beam; and 2)The availability of antiprotons, which is reflected in the product $BN_{\bar{p}}$. One can note by looking at equation (1) that as long as the proton and antiproton emittances are of comparable magnitude the luminosity achievable is proportional to the product of N_p/ε_p and $BN_{\bar{p}}$.

A. Beam-Beam Tune Shift

The beam-beam tune shift experienced by the antiprotons is given by,

$$\Delta\nu = .00733(N_p/\varepsilon_p)N_c \qquad (2)$$

where N_p is in units of 10^{10}, ε_p is in units of π mm-mr, and N_c is the number of bunch crossings per turn (=2B in the absence of orbit separation). As shown in Table 1 the achieved $\Delta\nu$ is .025. This is believed to be limited by the available working space in the tune diagram as delineated by the absence

* Operated by Universities Research Association under contract to the U.S. Department of Energy

0-7803-0135-8/91$01.00 ©IEEE

of resonances of ≤10th order. (The collider is operated with $\nu_x=\nu_y=19.42$, in a region bounded by the 5th order resonance 19.40, and the 7th order resonance, 19.428.) The Fermilab complex is actually capable of producing a proton phase space density approximately 60% larger than that reflected in the table. However, the use of such intense proton bunches has been found to have a deleterious effect on the antiproton bunches which makes the achievement of higher luminosities, accompanied by good lifetimes, impossible.

B. Space-charge at Booster Injection

Even if the proton phase space density were not limited by the tune shift experienced by the antiproton bunches, it would still be impossible to create a density more than about 60% above that listed in Table 1. This is because the fundamental limit on proton density in the Fermilab complex arises from space-charge forces at injection into the Fermilab Booster. With the present 200 MeV injection energy the smallest proton emittance which can be produced for injection into the Tevatron collider is about 15π mm-mr. Any planned improvements which reduce the antiproton beam-beam tune shift can only affect the luminosity in a significant manner if it allows the creation of higher phase-space densities at the upstream end of the accelerator complex.

C. Antiproton Availability

Antiproton availability is limited by two effects, one obvious and the other more subtle. The obvious constraint is the antiproton production rate. During 1988-89 a rate of $2\times10^{10}\bar{p}$/hour was achieved. The transfer efficiency of antiprotons from the Antiproton Accumulator to 900 GeV in the Tevatron was in the range 60-70%. Since the average store lasted 13 hours, a total of 1.7×10^{11} antiprotons were typically available in the Tevatron Collider. The antiproton production rate is limited by the proton beam intensity delivered from the Main Ring onto the $\bar{p}$ production target, by the Main Ring cycle rate, and by the admittance of the Antiproton Source rings. The Main Ring beam intensity itself is limited by the Main Ring admittance.

Table 1: Tevatron Luminosity Evolution through the 1990s

	88-89	Ia	Ib	II	
Energy (Center of Mass)	1800	1800	2000	2000	GeV
Protons/bunch	7.0×10^{10}	7.0×10^{10}	1.2×10^{11}	3.3×10^{11}	
Antiprotons/bunch	2.9×10^{10}	7.2×10^{10}	1.2×10^{10}	3.7×10^{10}	
Number of Bunches	6	6	36	36	
Total Antiprotons	1.7×10^{11}	4.3×10^{11}	4.3×10^{11}	1.3×10^{12}	
$\bar{p}$ Stacking Rate	2.0×10^{10}	4.0×10^{10}	6.0×10^{10}	1.7×10^{11}	$hour^{-1}$
ε_p	25π	15π	15π	30π	mm-mr
$\varepsilon_{\bar{p}}$	18π	18π	18π	22π	mm-mr
β^*	55	50	50	50	cm
Luminosity	$\mathbf{1.6\times10^{30}}$	$\mathbf{5.7\times10^{30}}$	$\mathbf{1.1\times10^{31}}$	$\mathbf{5.7\times10^{31}}$	$cm^{-2}sec^{-1}$
$\Delta\nu$/crossing ($\bar{p}$)	.002	.003	.006	.008	
Number of Crossings	12	2	2	2	
$\Delta\nu$ Total ($\bar{p}$)	.025	.007	.012	.017	
Bunch Separation	3000	3000	395	395	
Interactions/crossing (@45 mb)	0.3	0.9	0.3	1.5	
What's New?	---	Separators, $\bar{p}$ Source Improv.	Linac Upgrade	Main Inject.	
When?	1988	1991	1992,94	1996	

Figure 1 displays the correlation between intensity delivered from the 8 GeV Booster and the beam emittance. The correlation appears to be due to the space-charge effect mentioned earlier. As can be seen from the figure, the Main Ring is currently incapable of accelerating the full quantity of beam which the Booster is capable of delivering due to the restricted admittance. As a result the Booster is typically run at two-thirds of its ultimate capability for antiproton production.

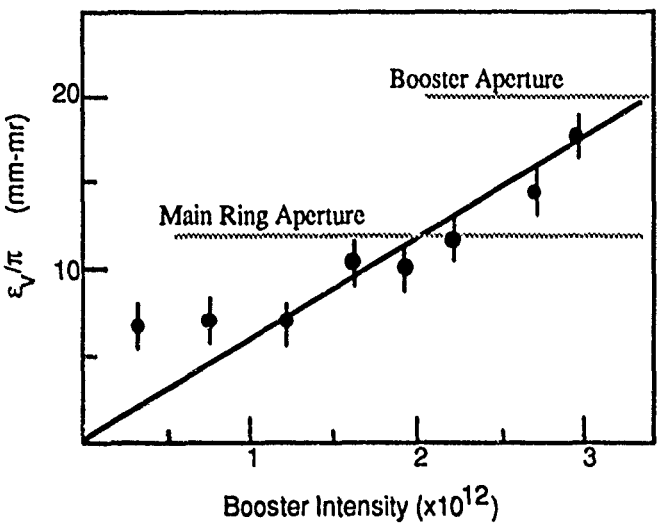


Figure 1: Transverse emittance delivered from the Fermilab Booster as a function of intensity.

Antiproton availability is also limited by a more subtle effect having to do with the correlation between the antiproton transverse beam emittance and stack size in the Accumulator. The beam emittance arises as a result of the attainment of equilibrium between intrabeam scattering and stochastic cooling. As the stack size increases, the heating due to intrabeam scattering increases, while the effectiveness of the cooling system decreases. The resultant antiproton beam emittance rises as the stack size increases. Unfortunately, the Main Ring admittance is less than the emittance emanating from the Accumulator at a stack size in excess of $6x10^{11}$. In general this guarantees that accumulated antiprotons in excess of $6x10^{11}$ will not be transmitted through the Main Ring on their journey to the Tevatron. Since we are currently capable of delivering about 40% of the antiproton stack from the Accumulator, with 60-70% transmission to the collider this also limits antiproton availability in the collider to $1.7x10^{11}$.

III. Luminosity Evolution Through the 1990s

Fermilab has initiated a series of improvements to the existing accelerator complex to provide a luminosity capability in excess of $5x10^{31}$ cm^{-2}sec^{-1} by 1996. These improvements are aimed at attacking the above-described limitations associated with the beam-beam tune shift, space-charge in the Booster, and antiproton availability. Specifically included are: 1)implementation of electrostatic separators in the Tevatron; 2) a series of Antiproton Source improvements; 3)upgrading the Linac energy from 200 MeV to 400 Mev; and 4)construction of a new accelerator, the Fermilab Main Injector, to replace the existing Main Ring.

The expected progression of luminosity throughout the decade is summarized in Table 1. Note that in addition to the items listed above the table reflects the implementation of cold compressors which will lower the operating temperature of the Tevatron magnets by about 0.5^{o}K and provide an energy of 1000 GeV per beam.

A. Electrostatic Separators

Electrostatic separators will create helically separated orbits in the Tevatron which will keep up to 36 proton and antiproton bunches separated everywhere but at the B0 and D0 collision points. This will reduce the total beam-beam tune shift, as given in equation (2), by providing N_c=2 with B up to 36.

Each separator is 3 meters in length and is capable of generating 250 kV over a 5 cm aperture. Twenty units are required to create the desired orbits. The peak field, 50 kV/cm, is required only during injection--during a proton-antiproton store no unit will be required to operate above 40 Kv/cm.

Several units have been tested in the Tevatron with protons and antiprotons stored at 150 GeV. These studies have shown no anomolous behavior, i.e. unexepcted tune shifts, emittance growth, or lifetimes, for separations as low as 1σ.

Thirteen of the required twenty units are installed at this time. The remaining units, which are located in the region currently occupied by slow extraction equipment, will be installed following the completion of the current fixed-target run. All separators will be in place and operational for the collider run scheduled to start in late 1991.

It should be noted that separators themselves do not create higher luminosity in the collider. They only create the potential for raising the luminosity if one has the capability of raising the proton phase space density and/or the number of antiprotons in the Tevatron.

B. Antiproton Source Improvements

Improvements implemented in the Antiproton Source since 1989 have beem aimed at increasing the accumulation rate and reducing the emittance characterstic of a given stack size. An enlargement of antiproton collection line and Debuncher ring apertures, and implementation of Debuncher momentum cooling are expected to increase the antiproton stacking rate by a factor of 2-3 beyond that achieved in 1988-89. A 4-8 GHz core cooling system has replaced the original 2-4 GHz system in the Accumulator Ring. The new system will reduce the emittance at a given stack size relative to that currently achieved. Future improvements to the targeting system and a

new Accumulator stack-tail system will be required for Main Injector operations, leading to an ultimate capability of of stacks containing $2x10^{12}$ antiprotons and stacking rates of $1.7x10^{11}$/hour.

C. The Linac Upgrade

The existing 200 MeV linac is in the process of being upgraded to 400 MeV by replacement of the second half of the existing drift tube linac with a side coupled structure generating 300 MeV in the same length. The result of the higher energy will be a reduction in the space-charge forces which lead to emittance dilution at injection into the 8 GeV Booster. It is anticipated that achievable proton transverse beam densities delivered from the Booster will increase by 75% following implementation of 400 MeV injection. This will benefit antiproton production by increasing the proton flux through the Main Ring, and will simultaneously allow for the creation of higher proton phase space densities in the Tevatron collider.

The Linac Upgrade was initiated in Fiscal Year (FY) 1990, and is schduled for completion in FY1992. Commissioning is expected to start in late summer of 1992.

D. The Main Injector

The Fermilab Main Injector is a proposed new 150 GeV accelerator which will replace the existing Main Ring. The purpose of the FMI is to remove forever the bottleneck that the Main Ring presents in the delivery of high intensity proton and antiproton beams to the Tevatron, and to increase the antiproton production rate sufficiently to be able to utilize this new capability.

The Fermilab Main Injector will be constructed tangent to the Tevatron in a separate tunnel on the southwest corner of the Fermilab site. The FMI will be roughly half the size of the existing Main Ring yet will boast greatly improved performance. The FMI will allow the production of about seven times as many antiprotons per hour ($1.7x10^{11}$/hour) as are currently possible using the Main Ring and will have a capability for the delivery of five times as many protons to the Tevatron (at least $3x10^{11}$ protons/bunch for collider operations). Additionally the FMI will support the delivery of very intense proton beams ($3x10^{13}$ protons every 2.9 seconds with a 33% duty factor) for use in state-of-the-art studies of CP violation and rare Kaon decays, and for experiments designed to search for transmutation between different neutrino generations. Low intensity proton beams emanating from the FMI will support test and calibration beams required for the development of new experimental detection devices which will be required both at Fermilab and at the SSC. In contrast to the present situation at Fermilab, simultaneous antiproton production and FMI slow spill operation will be possible under normal circumstances, as will simultaneous FMI and Tevatron fixed target operations.

The Fermilab Main Injector parameter list is given in Table 2. The FMI will perform at a significantly higher level than the existing Main Ring as measured either in terms of protons delivered per cycle, protons delivered per second, or transmission efficiency. For the most part expected improvements in performance are directly related to optics of the ring. The MI ring lies in a plane with stronger focussing per unit length than the Main Ring. This means that the maximum betas are half as big and the maximum (horizontal) dispersion a third as big as in the Main Ring, while vertical dispersion is nonexistent. As a result physical beam sizes associated with given transverse and longitudinal emittances are significantly reduced compared to the Main Ring. The elimination of dispersion in the RF regions, raising the level of the injection field, elimination of sagitta, and improved field quality in the dipoles will all have a beneficial impact on beam dynamics. The construction of new, mechanically simpler magnets is expected to yield a highly reliable machine.

The FMI is seven times the circumference of the Booster and slightly more than half the circumference of the Tevatron. Six Booster cycles will be required to fill the FMI and two FMI cycles to fill the Tevatron. The FMI is designed to have a transverse aperture of 40π mm-mr (both planes, normalized at 8.9 GeV/c). This is 30% larger than the expected Booster aperture following the 400 MeV Linac upgrade, and a factor of three to four larger than that of the existing Main Ring. A single Booster batch will be accelerated for antiproton production while six such batches are required to fill the FMI. Yields out of the FMI for a full ring are expected to lie in the range $3\text{-}4x10^{13}$ protons ($6\text{-}8x10^{13}$ delivered to the Tevatron.) By way of contrast the existing Main Ring is capable of accelerating $1.8x10^{13}$ protons in twelve batches for delivery to the Tevatron.

The power supply and magnet systems are designed to allow a significant increase in the number of 120 GeV acceleration cycles which can be run each hour for antiproton production, as well as to allow a 120 GeV slow spill with a 35% duty factor. The cycle time at 120 GeV can be as low as 1.5 seconds. This is believed to represent the maximum rate at which the Antiproton Source might ultimately stack antiprotons and is to be compared to the current Main Ring capability of 2.6 seconds.

The Total Estimated Cost of the Fermilab Main Injector is $177.8 M. The FMI is included in the President's proposed FY1992 budget with $43.4M of funding in the first year. This proposal is now before the Congress. With the proposed funding profile the FMI would become operational on or about January 1, 1996.

Magnet R&D was initiated on this project in 1990. A full-scale prototype was built and is undergoing measurement at the Fermilab Magnet Test Facility. Measurements show that this magnet is very well described by the computer models and satisfies the magnet field quality specification.

Environmental permitting is well advanced on this project. A Clean Air and Water, Section 404, joint permit application was submitted to the U.S. Army Corps of Engineers, Illinois Environmental Protection Agency, and the Illinois Department of Transportation in September of 1990. These permits are expected well in advance of construction. In addition an

Environmental Assessment has been prepared and is currently under review by the Department of Energy. A Finding of No Significant Impact (FONSI) is expected in late summer.

Table 2: Fermilab Main Injector Parameter List

Circumference	3319.419	meters
Injection Momentum	8.9	GeV/c
Peak Momentum	150	GeV/c
Minimum Cycle Time (@120 GeV)	1.5	sec
Number of Protons	3×10^{13}	
Harmonic Number (@53 MHz)	588	
Horizontal Tune	26.4	
Vertical Tune	25.4	
Transition Gamma	20.4	
Natural Chromaticity (H)	-33.6	
Natural Chromaticity (V)	-32.9	
Number of Bunches	498	
Protons/bunch	6×10^{10}	
Transverse Emittance (Normalized)	20π	mm-mr
Longitudinal Emittance	0.4	eV-sec
Transverse Admittance (at 8.9 GeV)	40π	mm-mr
Longitudinal Admittance	0.5	eV-sec
β_{max}	57	meters
Maximum Dispersion	2.2	meters
Number of Straight Sections	8	
Length of Standard Cell	34.3	meters
Phase Advance per Cell	90	degrees
RF Frequency (Injection)	52.8	MHz
RF Frequency (Extraction)	53.1	MHz
RF Voltage	4	MV
Number of Dipoles	216/128	
Dipole Lengths	6.1/4.1	meters
Dipole Field (@150 GeV)	17.2	kGauss
Dipole Field (@8.9 GeV)	1.0	kGauss
Number of Quadrupoles	128/32/48	
Quadrupole Lengths	2.1/2.5/2.9	meters
Quadrupole Gradient	196	kG/m
Number of Quadrupole Busses	2	

IV. SUMMARY

The Fermilab Tevatron Collider currently operates at a luminosity of 1.6×10^{30} $cm^{-2}sec^{-1}$. Luminosity limitations in the collider are well understood and a coherent plan has been formulated for increasing the luminosity by at least a factor of 30 in several steps over the next five years. All elements required for achievement of 5×10^{31} $cm^{-2}sec^{-1}$ are in place or funded with the exception of the Fermilab Main Injector which is currently before the Congress.

The research program based on the Fermilab III program will allow High Energy Physicists to extend their understanding of the basic structure of matter over the decade leading up to utilization of the SSC. In parallel many of the detector techniques required for utilization of the SSC will be developed and proven in the Tevatron Collider over the next decade. The construction and operation of the Fermilab Main Injector will leave Fermilab well positioned for continuing contributions to the field of High Energy Physics during the SSC era.

RHIC PROJECT*

Satoshi Ozaki
RHIC Project
Brookhaven National Laboratory
Upton, New York 11973

Abstract

With funding in place and governmental approval to begin the detailed design, as well as to proceed with the procurement of long lead-time items, the RHIC Project is now a *bona fide* construction project at Brookhaven National Laboratory. This paper will present an overview of the RHIC accelerator configuration, the collider design, and the present status of the Project.

I. INTRODUCTION

The scope of the RHIC Project at Brookhaven National Laboratory is to design, construct, and bring into operation a colliding beam facility and an initial complement of detectors dedicated to studies of nuclear phenomena in relativistic energy heavy ion collisions. Performance objectives call for the acceleration and storage of beams of ions as heavy as gold with a top energy of 100 GeV/u. The lower end of the energy is limited by the speed of emittance growth due to the intra-beam scattering and is envisaged to be about 30 GeV/u. The collider, which consists of two concentric accelerator/storage rings of superconducting magnets, will be constructed in the existing 3.8 km circumference ring tunnel in the northwest section of the BNL site. The operational flexibility derived from having two independent rings for the counter rotating beams allows collisions of unequal species of ions. The wide energy range available at the collider is expected to cover the transition from confined phase to plasma phase of the nuclear matter. These unique features meet experimental requirements which will be vital for the understanding of complex heavy ion collision phenomena, particularly those pertaining to the study of the on-set of a new phenomenon such as quark-gluon plasma formation.

The performance objectives for the collider were initially formulated in 1983 by a Task Force for Relativistic Heavy Ion Physics, and was endorsed by the DOE/NSF Nuclear Science Advisory Committee as early as December 1983. The present scope of the project was finalized with input from scientific and technical review committees.

*Work performed under the auspices of the U.S. Department of Energy under Contract No. DE-AC02-76CH00016.

The funding for the RHIC construction was proposed by the President and approved by the U.S. Congress for a Project start in FY 1991. Subsequently, after a review by the DOE Energy Systems Acquisition Advisory Board (ESAAB) in January 1991, the Project received approval to begin the detailed design and procurement of long lead-time items (e.g., superconducting cables). $11.3 million of the FY 1991 construction funds was released at that time, and the remaining $2.2 million is to be released after ESAAB approval for the full construction, anticipated in the July-August time frame. The construction funding for FY 1992 is expected to be $50 million. The total estimated cost (TEC) for construction is $397 million, to be distributed over six years. Approximately $97 million of the TEC is earmarked for the initial complement of detectors. The total project cost (TPC), which includes R&D and pre-operations cost, is estimated to be $499 million. With the funding in place, construction of RHIC began in full swing with the target date of completion in the spring of 1997.

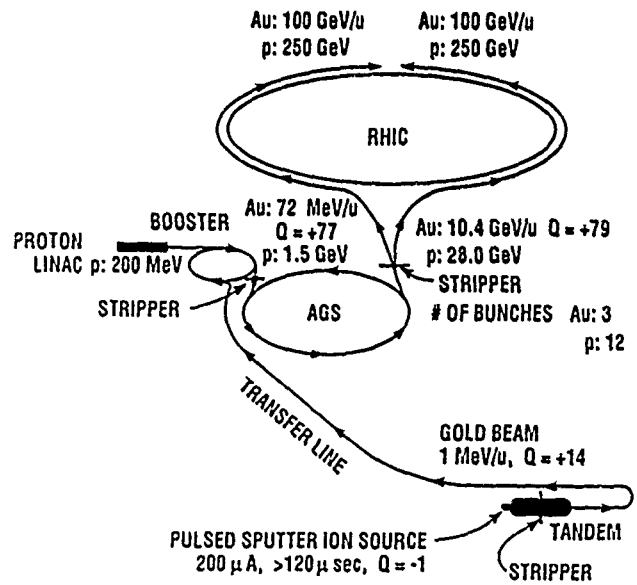


Figure 1. Overall configuration of accelerator complex for RHIC. An existing accelerator chain, which consists of the Tandem Van de Graaff, the Booster Synchrotron, and the AGS, serves as the injector to the RHIC collider.

0-7803-0135-8/91$01.00 ©IEEE

II. COLLIDER CONFIGURATION

Figure 1 illustrates the RHIC accelerator strategy, which includes the use of an existing chain of accelerators—Tandem Van de Graaff, Booster Synchrotron (to be commissioned in 1991), and AGS—as the injector to the RHIC collider. Using gold ions as an example, negative ions from a pulsed sputter ion source (200 μA, >120 μsec, Q = −1) are accelerated by the first stage of the Tandem Van de Graaff, stripped of atomic electrons by a foil at the high voltage terminal to reach the charge Q = +14 state, and then accelerated to about 1 MeV/u by the Tandem's second stage. The ions are then transported through a 540 m long transfer line for injection into the Booster without further stripping. After multi-turn injections, the beam of ions is grouped into 3 bunches and accelerated to 72 MeV/u. A foil at the Booster exit strips all but two K-shell electrons, forming Q = +77 gold ions. The AGS, with planned improvement of its vacuum, will accelerate these bunches 10.4 GeV/u with insignificant loss by further electron stripping. Ions are fully stripped at the exit of the AGS and injected into RHIC collider rings. Beam stacking is done in the box-car fashion by repeating this cycle 19 times to establish 57 bunches for each ring. Overall filling time for two rings should be about 1 minute.

The bunches are captured in stationary buckets of the "acceleration rf" system operating at ~26.7 MHz, corresponding to a harmonics h = 57 × 6. With the exception of protons, all ion species must be accelerated through the gamma transition. The time required for the acceleration to the top energy is also ~1 minute. When the operating beam energy is reached, the bunches are transferred to the "storage rf" at ~160 MHz (h = 57 × 6 × 6). This six times higher frequency was chosen to compress the stored bunch so that a short (22 cm rms) collision diamond can be obtained for head-on collisions, an advantage for experiments.

The layout of the collider is shown schematically in Figure 2. It consists of two quasi-circular concentric rings in a common horizontal plane, oriented to intersect with one another at 6 locations along the ring. Each ring consists of three inner and three outer arcs (each ~355.5 m long) and six insertions (each ~283.5 m long) connecting the inner and outer arcs. Each arc is composed of 12 FODO cells, i.e., 24 half cells each consisting of a dipole unit (9.46 m long), and a unit made up of a sextupole (0.75 m long), a quadrupole (1.13 m long), and a corrector assembly (0.58 m long), all superconducting. The corrector assembly contains co-axial layers of cylinders on which decapole, octupole, quadrupole, and dipole correction coils are fixed. In the arc sections, the counter rotating beams are separated by 90 cm horizontally. Beams are to cross each other at the middle of each insertion section (see Figure 3). Each half of the insertion contains 9 quadrupoles and 2 dipoles for dispersion matching and β-function manipulation. Although the geometry of the insertion sections allows beam crossings at an angle up to 7 mrad, head-on collisions will be used as the standard mode of operation to minimize the beam instability which might arise from coherent bunch-to-bunch interaction. Two dipoles closest to the interaction point are to steer beams to a collinear path for collisions. Most of the magnets have a large coil inner diameter of 80 mm to allow enough aperture for the emittance growth due to intra-beam scattering. Quadrupoles close to the interaction point have a 130 mm coil inner diameter, and the closest dipole 200 mm.

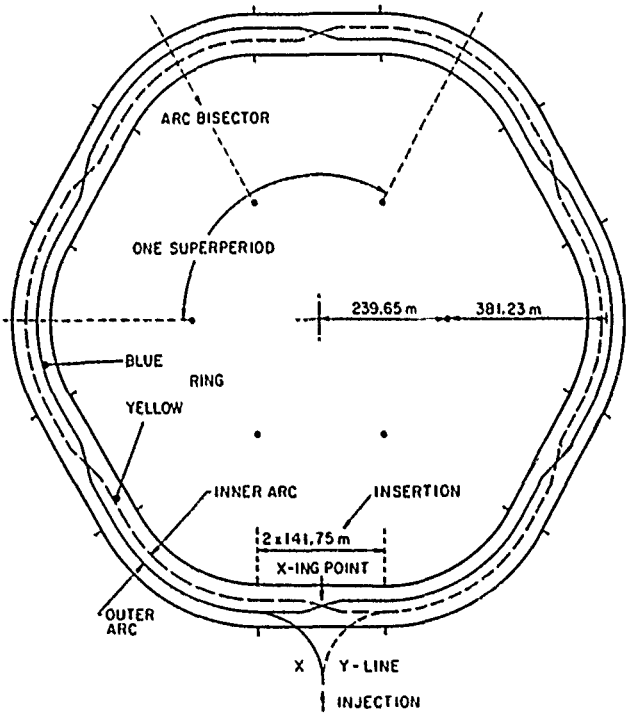


Figure 2. Layout of the RHIC collider.

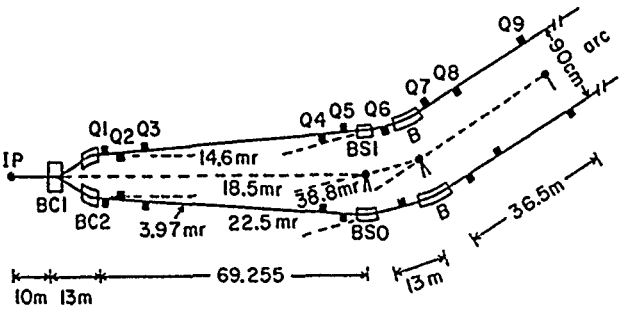


Figure 3. Layout of one half of the insertion section connecting inner and outer arcs of a ring.

III. EXPECTED PERFORMANCE

Major RHIC performance estimates are summarized in Table 1.

Table 1. RHIC Performance Estimates

No. bunches	57	
Bunch spacing (nsec)	224	
Collision angle	0	
Free space at crossing point (m)	±9	
	Au	p
No. particles/bunch	1×10^{9}	1×10^{11}
Top energy (GeV/u)	100	250
Emittance (π mm · mrad)	60	20
Diamond length (cm rms)	22	20
Beta* (m)	2	2
Luminosity ($cm^{-2}\ s^{-1}$)	$\sim 2 \times 10^{26}$	1.4×10^{31}
Lifetime (hr)	~10	>10
Beam-beam tune spread/ crossing	3×10^{-4}	4×10^{-3}

Energy: The top kinetic energy of each beam is designed to be 100 GeV/u for heavy ions, about 125 GeV/u for light ions, and 250 GeV for protons. The collider will be able to operate over a wide range of energy, typically from 30 GeV/u to the top energy.

Luminosity: The collider is designed for an Au-Au luminosity of about $2 \times 10^{26} cm^{-2}\ s^{-1}$, and for a proton-proton luminosity of $1.4 \times 10^{31} cm^{-2}\ s^{-1}$ at the top energy, while maintaining the option for future upgrades by an order of magnitude. The luminosity will be higher for light ions and is energy dependent, decreasing in first approximation proportional to the beam energy.

Ion Species: The collider will accommodate a range of ion species with mass number of about 200 (Au) to 1 (proton). Asymmetric operation with protons colliding with heavy ions is unique to RHIC. Uranium is a viable species and can be considered as a future upgrade but requires the development of a suitable ion source.

Luminosity Lifetime: The luminosity lifetime is expected to be about 10 hours for Au-Au operation at the top energy, and is believed to be limited by the emittance growth due to intra-beam scattering which is significant for heavy ions. Thus, the lifetime becomes shorter for lower energies and longer for light ions.

IV. PROJECT STATUS AND RECENT DEVELOPMENTS

During the past year, the layout of the rings was re-studied from the viewpoint of actual mechanical layout of ring components in the tunnel. The cost savings by a standardization of ring components, simplification of the ring installation, and the beam optics including tunability and correctability were the principal concerns in this study. The optimization in this study resulted in a number of small but significant modifications to the layout given in the Conceptual Design Report.[1]

The development of 8 cm bore superconducting arc dipole magnets has been a major emphasis in the RHIC R&D program. A relatively modest magnetic field of 3.45 T required for the arc dipoles makes the magnet design simple (see Figure 4). It has a single layer $\cos\theta$ coil design

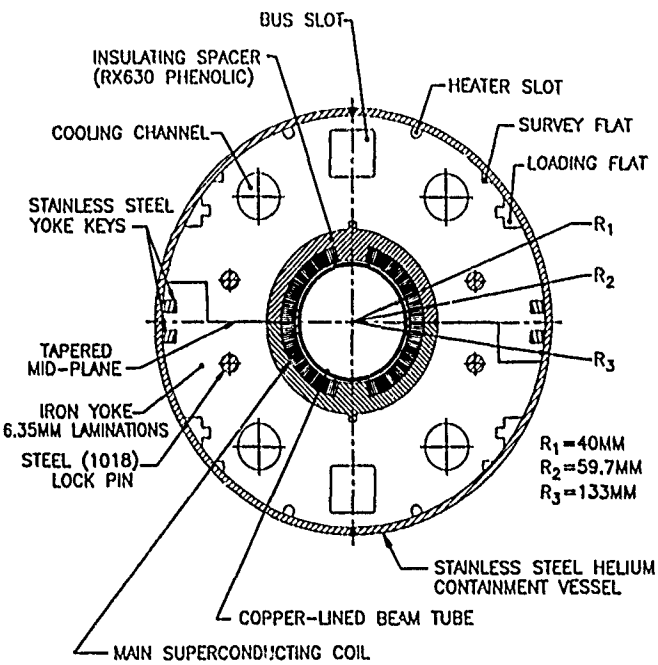


Figure 4. Cross section of RHIC arc dipole magnet.

with low carbor yoke iron lamination acting as a collar. A high-precision injection-molded mineral-loaded phenolic (RX 630) is used as the insulator/spacer between the coil and the yoke lamination. The superconducting cables used are similar to the Rutherford cables developed for the outer coil of the SSC 40 mm dipoles. Namely, they have a keystone angle of ~1.2° made up of 30 strands of 6 μm NbTi composite wires (0.648 mm diameter), but with a Cu to superconductor ratio of 2.25:1. Eight full-length model dipoles were built. These satisfied the RHIC requirement in the magnetic field strength with a comfortable margin (~30% for the last two R&D units). The field quality of these magnets almost satisfied the requirement, but with an error in the b_2 and b_4 harmonic components. This error is small enough to be easily adjusted by minor iteration of wedge dimension in the manufacturing process. After the eight, two additional dipoles were fabricated. The new

dipole design incorporates features suggested by industrial manufacturing studies which simplify manufacturing, thus reducing the cost. The dipoles are now close to the final design.

We intend to have industry build all 80 mm bore dipole, quadrupole, sextupole, and corrector magnets. An Industrial Technology Orientation session was held in October 1990 at BNL in preparation for the issuance of a Request for Proposal (RFP). The session was attended by ~80 participants representing 34 industrial firms, confirming industry's enthusiasm for this Project. Presently, the RFP for the development of the production tooling and manufacturing of 80 mm bore dipole magnets is in preparation. The anticipated release is May or June 1991, with contract award this fall. The RFP for the procurement of other magnets will follow. We plan to procure the total quantity of superconducting cable from one supplier to assure uniformity. The cable produced will be characterized at BNL and supplied to industry for the dipole and quadrupole manufacturing. A pilot program for cable production is in progress at three qualified suppliers (63,000 feet each). An order for the full quantity production (1.7 million feet) will be placed in the fall of 1991, after an evaluation of the cables manufactured in the pilot program.

One FODO-cell consisting of two dipole magnets and two sextupole/quadrupole/corrector magnet assemblies was assembled to test (1) the mechanical assembly scheme of a train of arc magnets, (2) the mechanical and electrical properties of the magnets under a number of thermal and electrical cycles, and (3) the behavior of the system, such as the pressure build-up under quench conditions. The tests were successful, confirming the soundness of the magnet design and also providing guides to improve the interconnect design.

In expectation of colliding beam operation beginning in the spring of 1997, the Laboratory has issued a call for letters of intent for initial experiments using RHIC. Nine letters of intent supported by ~300 enthusiastic physicists from the U.S. and abroad were received by the September 1990 deadline. Although RHIC storage rings intersect each other at 6 locations, the current scope of the RHIC Project calls for the use of 3 existing experimental halls and one open area for studies of nuclear phenomena. This, together with the limited funding (~$100 million) allocated to the construction of the initial complement of detectors, indicates that two, at most three, proposals of significant scale can be approved. An effort is underway to see if the experimental groups can be consolidated before going into the costly proposal formulation by each group. The Laboratory plans to select the first-round detectors before mid 1992 to allow sufficient time for their construction. Meanwhile, R&D for detector technology, which is essential to fully exploit the physics potential of RHIC, has been actively supported by the RHIC Project organization at the level of $1 million in FY 1990, $2 million in FY 1991 and hopefully ~$3 million in FY 1992.

The RHIC Project has taken significant steps forward in recent months. In the technical areas, key personnel responsible for most of the accelerator subsystems have been identified, and are working toward finalizing the detailed design. Further increases in the Project scientific and engineering staff level are expected for the next few years. In addition, the Project management organization has been strengthened by including the areas of environment, safety and health aspects and quality assurance.

On Friday, April 12, the Laboratory held a cerebration to mark the official beginning of the RHIC construction.

V. REFERENCES

[1] Conceptual Design of the Relativisitic Heavy Ion Collider, May 1989, Brookhaven National Laboratory, BNL 52195.

THE STATUS OF HERA

B.H.Wiik
II.Institut für Experimentalphysik, Univ. Hamburg, and
Deutsches Elektronen-Synchrotron DESY, Hamburg.

Abstract:

The preaccelerator chains are operational delivering 13 GeV electron (positron) and 40 GeV proton beams to the HERA rings. The electron ring has achieved 27.5 GeV at 5% of the design intensity and with a beam lifetime of several hours. The first octant of the proton ring was cooled down last summer, the quench protection was successfully tested and the optics was checked using a 7 GeV positron beam.

The HERA proton ring was completed in early November 1990 and it has been at cryogenic temperatures since mid December. The steady state condition at 4.4 K could easily be established and the measured cryogenic heat load of the ring is below the predicted value. Commissioning with beams started end of March with a 7 GeV positron beam and continued through April with the injection of single 40 GeV proton bunches. A stored beam was obtained just a few days after the first injection. Presently the lifetime is 30 min for single low intensity proton bunches at 40 GeV.

I. INTRODUCTION

The electron proton colliding beam facility HERA has two distinct features: it is the first electron-proton collider ever and it has been built in an international collaboration. Institutions in Canada, CSFR, France, Israel, Italy, The Netherlands, PR of China, Poland, United Kingdom and the USA have contributed either in kind or by delegating skilled manpower to the project. A picture of the two accelerators is shown in Fig. 1. The parameters of the collider and further details can be found in [1-4].

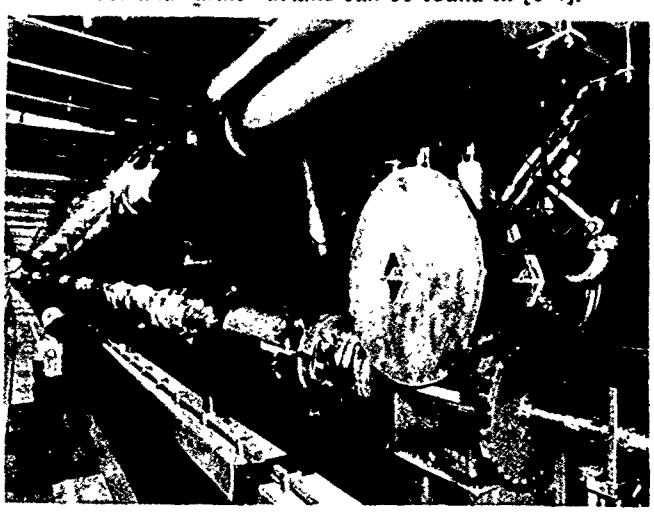


Fig. 1 - A view of the two rings at the end of a quadrant. The helium transferline and a feedbox are also shown.

0-7803-0135-8/91$01.00 ©IEEE

II. PREACCELERATORS

The electron (positron) and the proton injection chains have been described elsewhere [3]. The expected 6 min filling time of the electron ring is dominated by the 2 min cycle time of PETRA. Using a new longitudinal and transverse feedback system, the threshold for multibunch instabilities in PETRA has recently been raised from 2.6 mA to the design current of 60 mA [5].

The 50 MeV linear accelerator for negatively charged hydrogen ions is in routine operation and delivers a 6 mA beam with a normalized 95% emittance of 3.3 πmm mrad horizontally, 5.7 πmm mrad vertically, and a momentum spread of $\pm$ 0.1%.

The negatively charged hydrogen ions are stripped upon their injection into DESY III. After a multiturn injection, protons are captured into 11 buckets, spaced 28.8 m apart as in HERA, accelerated to 7.5 GeV, and transferred to PETRA II. The design intensity of 1.1·E12 protons can be injected and accumulated in DESY III with high efficiency, however, only 50% reach 7.5 GeV. The main loss occurs at flat bottom and is associated with space-charge blow up, field non-linearities and inefficiencies in the rf capture of the coasting beam. A transverse instability is also observed in the early part of the cycle. Associated with the early beam loss is a reduction in emittance. During acceleration the normalized transverse emittance grows by roughly a factor of 3. The longitudinal emittance at 7 GeV is 0.16eVs in rough agreement with the prediction.

The maximum number of 70 bunches at 10% of the design intensity has been accumulated in PETRA II and accelerated to the final energy of 40 GeV. The lifetime was 1 hr at 7.5 GeV and increased to more than 10 hrs at 40 GeV. The cycle time of 5 min is limited by the tune shift caused by eddy currents in the thick aluminium vacuum chamber. The tune shift is measured in real time using a fast Q-measuring system [6]. It is compensated by varying the current in two distributed quadrupole circuits.

III. THE ELECTRON RING

While the first run of the electron ring in August 1988 was mainly used to inject and store a beam, a second run in September 1989 focussed on the performance of the ring. The results are summarized below:

- The injection efficiency into HERA at 7 GeV and 13 GeV was 93%.
- The electron beam was ramped to 27.5 GeV without loss.
- The beam lifetime was 5 hrs at low current and high energy.

- The maximum single bunch current was 2.49 mA, nearly a factor of 10 above the design value.
- The maximum current in a multibunch mode was 2.87 mA or 5% of the design value. The main limitations were low accumulation rate, poor lifetime at high currents, but also horizontal instabilities.
- The measured luminosity optics was in good agreement with the predicted values.
- The vertical dispersion after orbit correction was 15 cm, corresponding to a 5% vertical coupling.
- The dynamical aperture was 9 π mm mrad, corresponding to 11.9 standard deviations at 35 GeV.

During the present six weeks' shutdown several new components will be installed in parallel to the effort needed to restore the integrity of the electron ring.

To reach the design current of 56 mA a longitudinal and transverse damping system [5] similar to the tested PETRA system will be installed.

The conventional rf system will be augmented by a set of 16 four-cell 500 MHz superconducting cavities [7], assembled pairwise into 8 cryostats. These cavities have been industrially produced from high purity niobium (RRR=300). At the design current of 58 mA the gradient is limited to 1.7 MV/m due to the 100 kW power rating of the high power couplers. The cavities reach 3 MV/m at Q = 3·E9. At higher gradients, Q drops below 1·E9 due to the presence of niobium-hydrogen compounds resulting from hydrogen dissolved in bulk niobium.

A picture of the first four cryostats installed in the HERA tunnel is shown in Fig. 2. These cryostats have been cooled down to the operating temperature of 4.2 K. Three more will be installed in May leaving the last one to search for remedies against the HNb_x problem. This system together with the conventional rf system is able to accelerate and store a beam up to the design energy of 30 GeV.

The transverse polarization of the circulating electron beam will be determined [8] by measuring the azimuthal asymmetry of a back-scattered polarized laser light. The components are ready for installation.

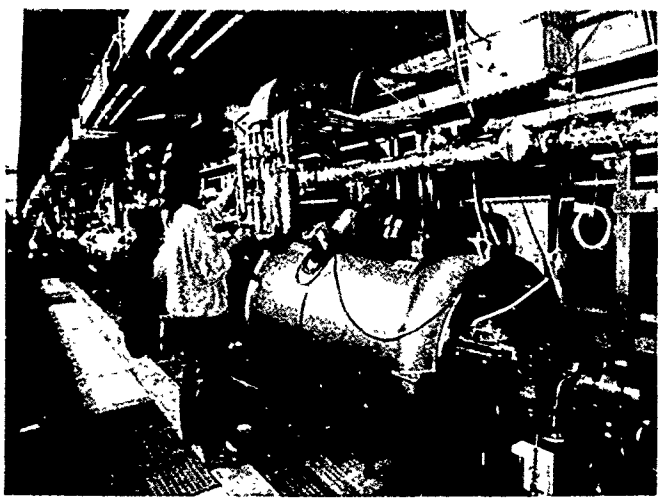


Fig. 2 - The first 4 cryostats installed in the HERA tunnel.

IV. THE HERA PROTON RING

The installation [9] of the proton ring components (including the helium distribution system) was completed by November 1990, roughly 6 1/2 year after authorization and in accordance with the original time schedule.The cryogenic system and the superconducting magnets are the most challenging components of HERA. I will first describe the status and the performance of these components and then discuss the results obtained during the first commissioning run.

IV.1 The Refrigeration System

The central refrigerator is located on the DESY site. It is subdivided into three identical plants each providing 6.6 kW isothermally at 4.3 K, 20.4 g liquid helium per second and 20 kW at 40 K to 80 K.

The cryogenic plant is very reliable, each of the three coldboxes has run for about 12000 hrs. Liquid helium and 40 K helium gas are supplied by a fourfold transferline to precoolers and feedboxes which are installed at the ends of each octant. The same transferline is used to return helium gas of 4.6 K and of 80 K to the refrigerator. In the case of a quench the warm gas from the quenched magnets is fed through a safety valve to a ring line which returns the gas to the storage vessels at a pressure up to 20 bar. A detailed description of the cryogenic system and its performance can be found elsewhere [10]. Here we only summarize the main results.

Of the 15 tons of helium stored in the magnets and in the transferlines some 5 tons have been consumed last year, mainly because of the testing of the superconducting magnets and of the helium distribution system.

The north half ring was cooled to the operating temperature of 4.4 K by mid October, the south half ring by mid December. The cooldown time of 140 hrs was determined by the condition that mechanical stresses caused by the temperature gradient within a magnet should be limited to 100 MPa - a factor of two below the critical values. All octants can be cooled down in parallel. A typical cooldown profile is shown in Fig. 3.

During Christmas the He plant was shut down and the magnet temperature rose from 4.4 K to 150 K. The proton ring has been kept at 4.4 K since the middle of January. Instabilities or pressure oscillations have not been observed during more than 3000 hours of operation of the complete ring.

Semiconductor temperature sensors are installed in the single-phase helium volume of each dipole, allowing to monitor the temperature with a precision of 0.02 K [11]. A first measurement of the heat load, using these monitors at

a known mass flow, yielded a heat leak of 5.1 kW at 4.4 K and 28.5 kW at the shield level for the whole ring, including transferlines and feedboxes. These values com-

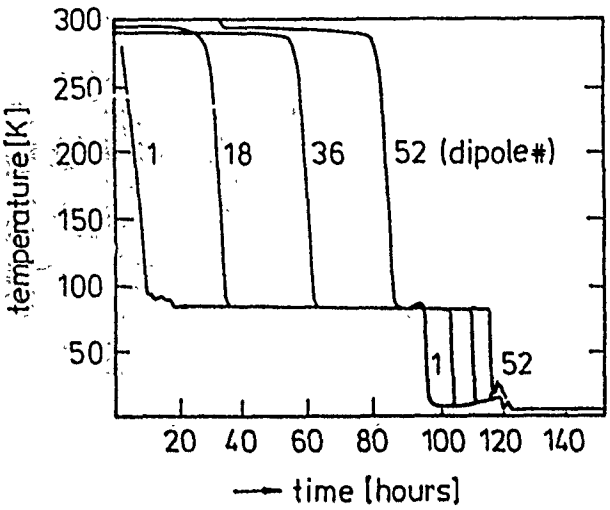


Fig. 3 - Cooldown profile of a HERA octant.

pare favourably to the proposal values. The heat leak of the magnets alone is 3.6 kW at 4.4 K and 19.6 kW at the shield level, in excellent agreement with heat leak measurements on single magnets.

At a current of 5020 A an additional heat load of 21 W at 4.4 K per octant was observed. Ramping the magnets at the nominal rate of 10 A/s led to a heat load of 80 W per octant at 4.4 K.

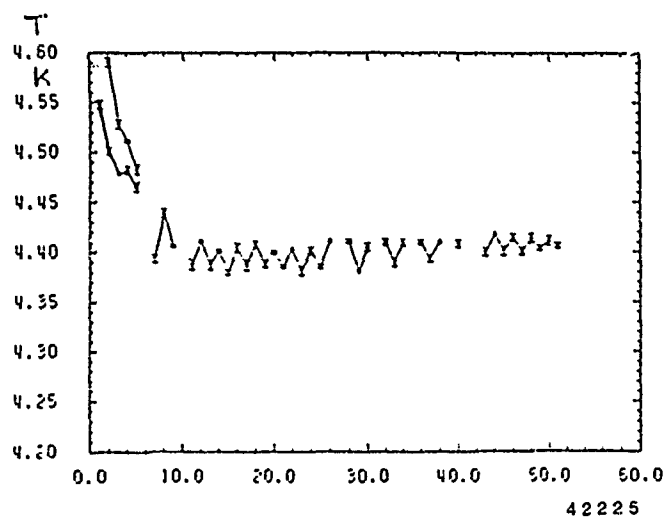


Fig. 4 - The temperature distribution measured in the dipoles along an octant. The re-cooling of the one-phase flow by heat exchange with the two-phase flow is clearly seen. The heat leak at the end of the octant is caused by the current leads.

IV. 2 The Superconducting Magnets

A total of 1819 superconducting magnets and correction coils has been installed in the HERA proton ring. In the arcs the superconducting magnets are arranged in 104 cells with an ordering shown in Fig. 5.

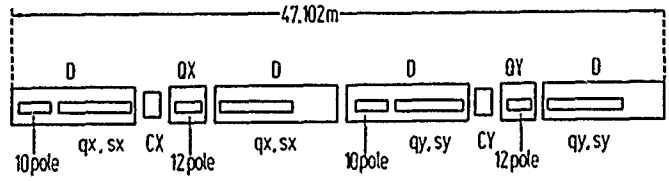


Fig. 5 - A unit cell of the proton ring. D: main dipole; QX, QY: main quadrupoles, qx,qy: quadrupole correction coils, sx, sy: sextupole correction coils, CX, CY: correction dipoles. In addition, there are 10-pole and 12-pole correction coils.

The design [12,13] and the performance [3,14] of the magnets have been reported elsewhere. Here we just summarize the main results. The industrial production of superconducting magnets was a success. During series production, DESY received an average of 8 dipoles and 6 quadrupoles per week, exceeding the contractual rates. Out of 449 dipoles and 246 quadrupoles, only 5 magnets were rejected, four of which had shortened windings and one a bad spot in the superconductor.

All magnets were tested [15] at liquid helium temperature and the results can be summarized as follows: Nearly 93% of the magnets reached the critical current at the first or second excitation. Adjusted to an operating temperature of 4.4 K the average quench current was (6900 ± 130) A for the dipoles and (7840 ±160) A for the quadrupoles. Only magnets with a quench current above 6600 A were installed in HERA. The field quality of both the dipole and the quadrupole magnets is better than specified. The field integrals of the dipole magnets produced in Italy and Germany differ systematically by 0.19%. Among the dipoles from one vendor the rms variation is 0.05%. The integrated quadrupole gradient has an rms spread of 0.085%.

The direction of the dipole field varies along the magnet by (0.5 ± 1.6) mrad. The dipole magnets are installed such that on the average the protons have no vertical deflection. The field direction of the quadrupoles with respect to gravity is (1.5 ± 1.1) mrad. The position of the quadrupole axis at 4.7 K agrees horizontally to (0.02 ± 0.36) mm and vertically to (-0.38 ± 0.32) mm with the positions as determined by the manufacturers at room temperature. The data from the magnetic measurements were used for the alignment in the tunnel.

At the low injection field of HERA the persistent current multipoles [14,15] are large. However, they vary little from magnet to magnet and are compensated by the multipole coils which are wound directly on the dipole and quadrupole beam pipes.

Caused by flux creep in the superconductor and other effects, the magnetization current decays with a

nearly logarithmic time dependence. This drift is also compensated using the correction coils.

In order to determine the required strength of the correction elements at injection and during acceleration, the dipole and sextupole fields will be measured continuously in cold "reference magnets", powered in series with the ring magnets.

IV. 3 Commissioning of the Proton Ring

During last summer the first octant was cooled down and operated at liquid helium temperature for several months. A 7 GeV positron beam was injected and passed through the 632 m long octant without the use of steering coils. To minimize the effects of the persistent-current sextupole the magnets were - prior to injection - cycled in temperature from 4.4 K to 20 K and back to 4.4 K and then excited to a predetermined maximum before setting the current corresponding to a 7 GeV beam. This procedure reduced the sextupole field in the dipoles by almost two orders of magnitude. The positron beam was used to calibrate the beam position monitors and to measure the optical parameters of the octant which were found to be in agreement with the predictions.

After a careful test of the quench protection system the magnets were powered to 6000 A which corresponds to a proton energy of 980 GeV. Induced quenches in single magnets at currents up to 5600 A and a current decay time of 18 s (300 A/s) did not cause the quench to propagate. The magnets could be ramped at the nominal rate of 10 A/s and be powered at 5027 A without a spontaneous quench. Finally, all magnets in the octant were quenched simultaneously at 6000 A. No helium was lost and operation continued after 6 hours.

The first test run with the completed proton ring started on March 4th and continued through April. The first three weeks in March were used to activate the interlock system and complete the first commissioning of the 400 power supplies needed to run HERA. In parallel a 40 GeV proton beam was extracted from PETRA and transferred to the injection septum magnet of HERA. In the last week of March a 7 GeV positron beam was injected into HERA and used to adjust the timing of the beam position monitors. The magnets were temperature- and current-cycled to erase any persistent-current sextupoles. The horizontal correction dipoles were used to compensate for the different bending strengths of the two groups of dipoles. After commissioning of the complex synchronization system between PETRA and HERA the beam was threaded around the HERA ring and several turns could be obtained using a few correctors only.

An image of the injected beam and the overlap of five turns on a screen positioned at the septum magnet is shown in Fig. 6.

A coasting beam was obtained after orbit correction. Turning on the 52 MHz rf system resulted in a stored beam with a lifetime of 30 s. The commissioning was greatly eased by the excellent performance of the beam position monitors [16]. The tune measurement system [6] and the beam profile monitors [17] worked immediately. Fig. 7 shows a measured beam profile.

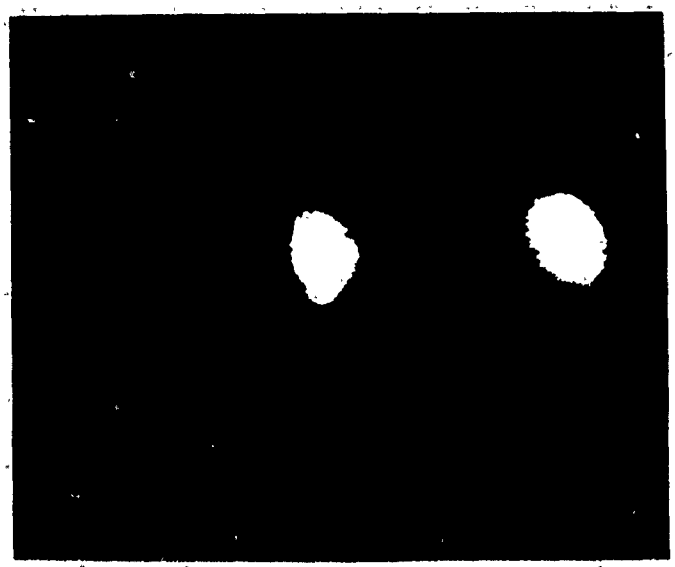


Fig. 6 - Images of the injected beam (right spot) and of 5 successive turns (left spot) on a screen close to the septum magnet. The distance between the spots is 3 cm.

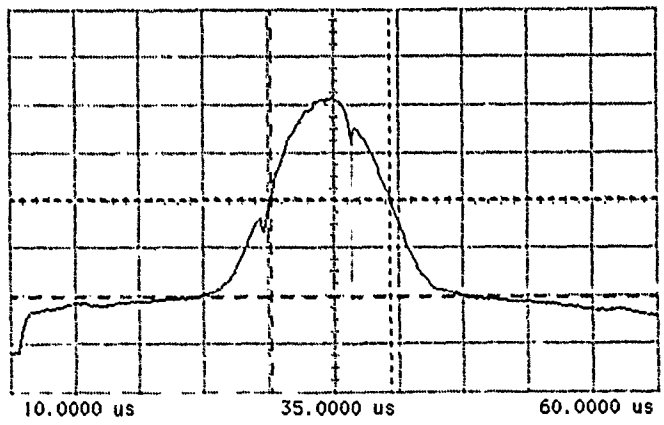


Fig. 7 - Beam profile measured with the residual gas monitor. Full width at half height is 13.8 mm.

The experience gained in the first run can be summarized as follows:

- Linac III and DESY III worked reliably during the whole period. The reliability of PETRA II as a 40 GeV proton accelerator must be improved.
- The complex timing and triggering system linking PETRA and HERA worked well in the single bunch mode. The multibunch mode was not yet available.
- The cryogenic system was very reliable. Some minor problems resulting from the process control computer have been corrected.
- The beam vacuum in the cold arcs was better than E-11 mbar. In the warm straight section East, which had been

baked out in situ at 250°C, the vacuum was a few E-11. In the remaining three straight sections the vacuum was a few E-8, leading to an average pressure of some E-9.

- The injection and the beam abort system worked reliably.
- After some initial problems the 400 power supplies including the control system were reliable and reproducible.
- The proton 52 MHz rf system worked reliably. The 208 MHz system could not be tested in the time available.

Preliminary information was also obtained on the performance of the accelerator. Only single bunches were injected and the number of protons was kept between E8 and E10 per bunch to avoid accidental quenches.

- The transfer efficiency of a single proton bunch between PETRA and HERA was as high as 90%.
- The measured injection optics is in agreement with predictions.
- The pathlength difference between electrons and protons agrees with the expectation to within 3 mm.
- The beam intensity at injection decays nearly exponentially with a time constant of at least 30 min (see Fig. 8). Beam-gas multiple scattering is one possible explanation of this behaviour. There is a hint that particles with large amplitudes have a shorter lifetime indicating some influence of non-linear resonances.
- Persistent current effects are not important at present lifetimes and intensities.
- Crossing the 4th order resonance leads to loss of beam.
- Crossing the 5th and 6th order resonance influences the beam lifetime.
- The acceptance of the proton ring was of the order of 1.5 πmm mrad.



Fig. 8 - Intensity versus time for a bunch of 5 · E9 injected protons. Total time range is 20 min. Visible at the left side are the extraction of the previous bunch and the new injection.

After the 6 weeks' shutdown which started on May 2nd, the commissioning will resume with an electron run. In parallel the quench protection system for the proton magnets will be checked at currents up to 5000 A. Late July the commissioning of the proton ring will continue with the aim of providing luminosity for the H1 and ZEUS experiments towards the end of the year.

V. REFERENCES

[1] HERA, A Proposal for a Large Electron-Proton Colliding Beam Facility at DESY, DESY HERA 81-10

[2] G.-A.Voss, Proceedings of the First European Accelerator Conference, Rome, June 1988

[3] B.H.Wiik, 1989 Particle Accelerator Conference Chicago, March 1989 and Proceedings of the Second European Accelerator Conference, Nice, June 1990

[4] H.Kumpfert and M.Leenen, Proc. of the 14th Int. Conf. on High Energy Accel., Tsukuba 1989, Part.Accel. 26, 97 (1990)

[5] D.Heins et al., DESY 89-151 and R.D.Kohaupt, private communication

[6] S.Herb, Papers submitted to this Conference

[7] B.Dwersteg et al., Papers submitted to this Conference

[8] D.Barber, private communication

[9] I.Borchardt et al., Paper submitted to this Conference

[10] G.Horlitz, Invited Paper to this Conference and references therein

[11] H.Lierl, private communication

[12] H.Kaiser, 13th Intern. Conf. on High Energy Accelerators, Novosibirsk, USSR, August 1986 and DESY HERA 86-14, S.Wolff, 10th Int.Conf. on Mag.Techn., Boston, USA, September 1981

[13] R.Auzolle et al., IEEE Trans. on Magnetism, Vol. 25, 1660, 1989.

[14] P.Schmüser, Invited Paper to this Conference

[15] H.Brück et al., Proceedings of the Second European Accelerator Conference, Nice, June 1990

[16] W.Schütte et al., IEEE 1987 Particle Accelerator Conference, Washington D.C.

[17] W.Hain et al., Proceedings of the Second European Accelerator Conference, Nice, June 1990

An Electron-Proton Collider in the TeV Range

M. Tigner, Cornell Univ., Ithaca, NY
B. Wiik, F. Willeke, DESY, Hamburg, FRG

Abstract

In ep colliding beam measurements, approximate equality of electron and quark energies is desirable for good detection efficiency. In the TeV CM energy regime, synchrotron radiation makes this requirement very expensive to meet using a storage ring for the electrons. Here we review a scheme,[1] that ameliorates this problem by using a superconducting linac for electron acceleration. Parameter lists show that such an approach may be practical for the next generation ep collider beyond HERA. An example of a 300 GeV electron beam colliding with the HERA p ring is shown in some detail. Examples up to $\sqrt{s} = 12$ TeV are given.

1 INTRODUCTION

Access to ep physics with ep colliders beyond HERA CM energies will require increase of the beam energy product as well as maintenance of a mainimum ratio of e to p energy to maintain reasonable production angles. Its inherent freedom from synchrotron radiation and its geometric flexibility suggest an electron linac on proton storage ring configuration for future, higher energy, ep colliders. The luminosity needed for useful physics together with the accelerator physics and technology limits to stored proton beam densities and interaction region optics work together to demand linac parameters that can be met only with rf superconductivity technology. A schematic layout of such a facility is shown in Figure 1 in which head-on collision of an electron and proton beam are arranged.

2 LUMINOSITY

As shown below, the achievable luminosity is constrained by the electron beam power, the intrabeam scattering limited emittance of the proton beam and the practical limits to focusing strength at the IP.

Assuming round beams and equal transverse beam sizes for e and p at the crossing point then

$$L = \frac{N_e N_p f_b \gamma_p}{4\pi\epsilon_p \beta^*} \qquad (1)$$

where ϵ_p is the normalized proton beam emittance or mean square beam size divided by betatron parameter, N_e, N_p the numbers of electrons and protons per bunch and f_b their collision frequency. γ_p is the proton Lorentz factor.

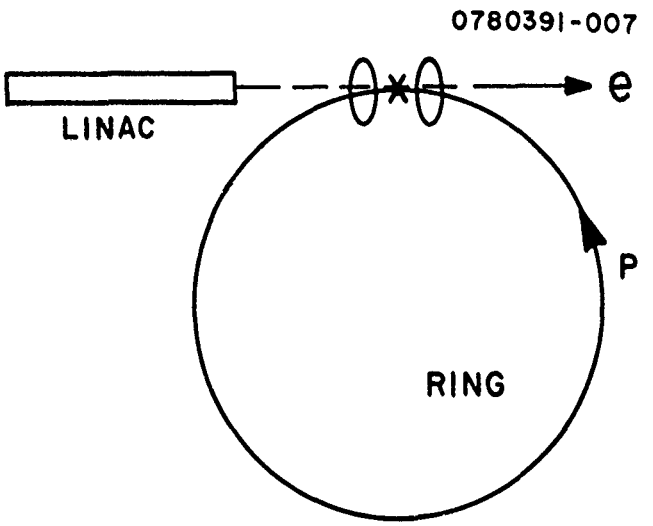


Figure 1: Layout of Linac on Ring e-p Collider

Once the e-beam energy is chosen, then the total electron beam current $I_e = N_e \cdot e \cdot f_b$ is, limited by the allowed electron beam power or $I_e = P_e/E_e$ and from (1), L is independent of N_e and f_b as long as their product is constant. Numerically

$$L = 1.66 \times 10^{31} s^{-1} cm^{-2} N_p/10^{11} \cdot P_e/10^8 \text{watt} \cdot 0.3\text{TeV}/E_e \cdot \gamma_p/1000 \cdot 10^{-6}\text{m}/\epsilon_p \times 10\text{cm}/\beta^* \qquad (2)$$

Table 1 displays some possible examples for future interest.

Table 1

E_p (TeV)	E_e (TeV)	$\sqrt{s}$ (TeV)	L ($10^{32} cm^{-2} s^{-1}$)
1.0	0.10	0.632	1.1
	0.20	0.894	0.56
	0.30	1.200	0.38
8.0	0.30	3.098	3.0
	0.50	4.000	1.75
	1.00	5.657	0.88
20.0	1.00	8.944	2.25
	2.00	12.649	1.13

Luminosities for various proton and electron energies. All have $N_p = 3 \times 10^{11}$, $P_e = 60$MW, $\epsilon_p = 0.8 \times 10^{-6}$m. $\beta^* = 10$cm.

0-7803-0135-8/91$03.00 ©IEEE

3 EXAMPLE USING HERA p RING

3.1 Proton Emittance

From (1) it is evident that a small proton emittance is desirable. For the 1 TeV proton beam of our example, the intra beam scattering dilution time of $\epsilon_p = 0.8 \times 10^{-6}$m is 5 hours. In future, this effective luminosity lifetime may be extended by use of bunched beam stochastic cooling.[2] At higher proton energies an even smaller emittance can, in principle, be used. Achievement of bunch intensities in excess of 10^{11} is regularly achieved in high energy proton colliders.[3] Achievement of the low emittances desired may require use of electron cooling in the lower energy stages.[4]Active feedback to damp injection oscillations will also be needed in the higher energy stages.

3.2 Interaction Region Layout

Small β^* are essential for high L. β^* is limited by chromaticity of the proton ring, and by proton bunch length. As chromaticity grows linearly with final focus quadrupole distance from the IP it is necessary to focus e and p simultaneously, thereby minimizing quadrupole distances. At 1 TeV proton energy the bunch length should be 10 cm or longer for adequate intrabeam scattering life time. In addition, avoidance of synchro-betatron excitation of the protons by the electrons requires a head on collision and hence the use of a beam separation technique. The large energy ratio of the beams makes soft magnetic separation a natural choice. Figure 2 shows a component layout and resulting envelope functions that meet the requirements.The e beam is focused by a sc quadrupole triplet and two doublets which give 10 cm β^* and also low β at 25 and 50 m from the IP. At these latter positions strong quadrupoles for the protons are placed which, because of the low electron betas there, have minimal influence on the electrons while effecting a β^* of 10 cm for the protons. A 100 meter long separator magnet acts to merge and separate the beams. This soft, defocusing quadrupole is aligned along the e orbit while the p pass off center and receive a deflection. A small preseparation prevents the first parasitic crossing at 25 m. The separation at the IP is minimized by strong electron focusing there. The average synchrotron power emitted by the e beam due to separation is 180W, half of which passes straight out of the IR through a 30 mm radius beam tube. Quadrupole gradients are 150 T M^{-1}. The exiting electron beam is focused by the beam-beam interaction at the IP as well as the out going lenses. Inclusion of the beam-beam interaction in the linear optics shows that the e beam is still well behaved on its way out. Full separation is achieved at 50 m from the IP.

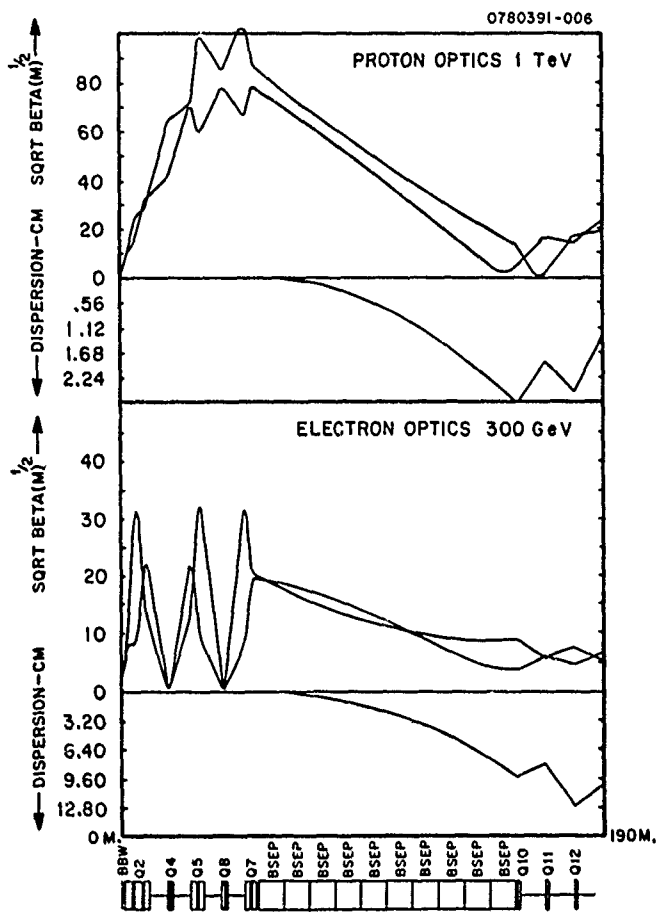


Figure 2: Component Layout and Envelope Functions - 1 TeV p, 0.3 TeV e.

3.3 Bunch Spacing and Linac Duty Factor

The bunch spacing is constrained by the allowed proton beam-beam tune spread and linac duty factor as long as the beam separation scheme employed permits no parasitic crossings. When the spacing is reduced to twice the separation length it probably cannot be reduced farther without decreasing the per bunch, allowed proton beam-beam parameter ΔQ_p.

$$\Delta Q_p = \frac{r_p N_e}{2\pi\epsilon_p(1+\kappa)} \qquad (3)$$

where r_p is the proton classical radius and κ is the beam aspect ratio at the crossing point which we have taken as 1. Introducing this relation into the electron beam power and current relation, including the linac duty factor, d, we can find the needed bunch spacing, expressed in time units, as

$$t_s = 118ns \cdot \frac{E_e}{0.3\text{TeV}} \cdot \frac{\Delta Q_p}{0.003} \cdot \frac{\epsilon_p}{10^{-6}m} \cdot \frac{d}{0.01} \cdot \frac{10^8 W}{P_e} \qquad (4)$$

d is to be selected as the result of an economic optimization balancing refrigerator operating and capital cost against the need for stronger higher mode damping as the bunches are closer together. About 1% appears reasonable.[2]

3.4 The Electron Linac

The requirement for high current subdivided into many bunches spaced relatively far apart with high duty factor in addition can be met only with a superconducting linac. The emittance and current requirements can be met with existing injectors.[5] High current polarized electron guns are also in development for the SLC and should be available in time for this application. Mass produced, multicell accelerating structures now being produced achieve 9 MeV per meter or more with standard chemical processing. Recent improvements in processing by vacuum heating have doubled this figure.[6] It is not unreasonable to expect that (at the present rate of improvement) 25 MeV/m will be available[7] at Q's of 5×10^9 though improved niobium purity and processing techniques. The choice of rf frequency is somewhat arbitrary at this stage. We have chosen 1.5 GHz for our example as a compromize between the beam stability, number of rf feeds and HOM couplers per unit length and low BCS wall losses all of which favor low frequencies, and fabrication lost, small surface area, short filling times and low stored energy which favor high frequency. Table 2 displays the principal parameters of such a linac.

Table 2-Electron Beam Parameters

Electron Energy	$E_e = 300$ GeV
Number of Electrons per bunch	$N_e = 2 \times 10^{10}$
Bunch length	$\sigma_L = 1$ mm
Invariant emmitance	$\epsilon_e = 2.2 \times 10^{-4}$ m
Beta function at IP	$\beta_{x/y} = 0.2$ m
Electron tune shift	$\Delta\nu = 0.3$
Disruption	$D = 0.02$
Bunch spacing	$t_{be} = t_{bp} = 156$ ns
RF frequency	$f = 1500$ MHz
Accelerating gradient	$g = 25$ MV/m
R/Q	R/Q = 10^3 Ohm/m
Unloaded quality factor	$Q_o = 5 \times 10^9$
Loaded quality factor	$Q_L = 1.25 \times 10^6$
Pulse length	$\tau = 1$ ms
Duty cycle	$d = 10^{-2}$
Repetition rate	prr = 10 Hz
Beam Power	$P_b = 60$ MW
Peak RF power	P_{rf} =6GW
Peak klystron power	$P_{klys} = 4$ MW
Static heat leak	$P_s = 17.2$ kW
Resistive wall loss	$P_w = 15$ kW
Higher order mode loss	$P_{HOM} = 17$ kW
Operating temperature	$T = 2$K
Refrigeration efficiency	$\eta = 1000$ W/W

4 Conclusion

As the era of e-p colliders begins we need to begin a search for practical schemes for increasing the available center of mass energies. The use of an SC linac on SC proton ring approach may offer a practical possibility while maintaining a favorable electron to proton beam energy ratio.

References

[1] J.R. Rees in Nuclear Instruments and Methods 96, 1971, p.149 and G. Weber et al. in Proc. 2nd ICFA Workshop on Possibilities and Limitations of Accelerators and Detectors, U. Amaldi, Ed. CERN 1980 p. 209.

[2] J. Mariner et al. in Proceedings of the 2nd European Accelerator Conference, Editions Frontieres 1990 p. 1577.

[3] Ibid., M. Harrison and R. Schmidt p.55.

[4] Ibid., R. Maier et al., p. 1580.

[5] M.B. James et al. in IEEE Trans. on Nuclear Science, Vol. NS-30, No. 4, August 1983, p.2992.

[6] H. Padamsee in Cornell report CLNS 90-1016, Cornell Univ. 1990.

[7] G. Mueller and H. Padamsee in Proc. of 1st TESLA Workshop, CLNS 90-1029, Cornell, 1990, p. 295.

THE STATUS AND DEVELOPMENT OF THE UNK PROJECT

V.A.Yarba
Institute for High Energy Physics, 142284, Protvino, Moscow region, USSR

The project of the IHEP Accelerating and Storage Complex (UNK) [1-5] envisages the possibility of accelerating protons up to 3 TeV with the beam extracted onto the fixed target and of the collision mode at 6 TeV in the c.m.s. The 1st stage of the UNK incorporating the 3 TeV machine with the system extracting the beam onto the fixed target is presently under construction.

The UNK is placed in the ∅ 5.1 m underground ring tunnel having a circumference of 20.77 km. Figure 1 shows the ring cross section with the equipment layout. The presently existing 70 GeV proton synchrotron, whose intensity is planned to be upgrades up to $5 \cdot 10^{13}$ ppp, will be the injector into the UNK. The 1st stage of the UNK, UNK-1, i.e., the 400 GeV conventional machine, is the booster for the 2nd, supersonducting stage, UNK-2, but it can also run as a storage ring. Another superconducting ring, UNK-3, is intended for 3x3 TeV proton-proton collisions. The orbits of the 1st and 2nd stages actually coincide, whereas those of UNK-2 and UNK-3 interchange periodically going from the inner wall of the tunnel to the outer one or vice versa to intersect in 4 points of Matched Straight Sections (MSS) 2, 3, 5, 6, where the detectors for colliding beams may be placed. In addition to these MSS's (2, 3, 5, 6), for the experimental setups, each 490 m long, the project also envisages another two 800-m technological sections, MSS1 and MSS4. MSS1 will house the injection, loss localization and beam abort systems as well as the accelerating stations for all the stages. MSS4 is intended for the systems of extraction and beam transfer from UNK-1 into UNK-2 and UNK-3. A part of the MSS6 space is to be occupied by the reverse beam injection from U-70 into UNK-1 in the pp-colliding beam mode.

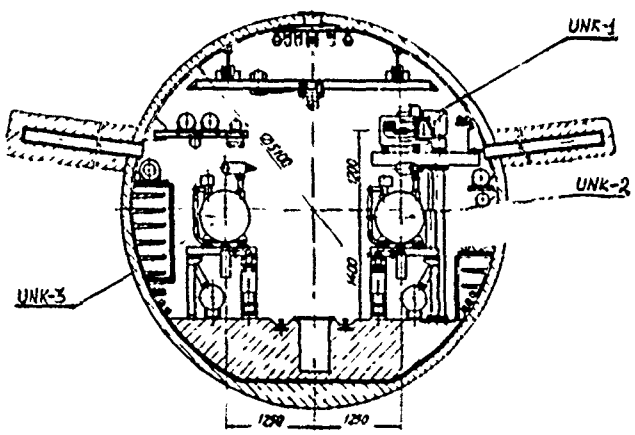


Fig. 1. The ring cross section with the equipment.

OPERATION IN THE ACCELERATION MODE

On rebunching at a frequency of the accelerating field of the UNK, 200 MHz, the U-70 beam is injected into UNK-1. Here an intensity of $6 \cdot 10^{14}$ ppp is stasked within 72 s by multiple, up to 12 times, injection. After 20-s acceleration on UNK-1 up to 400 GeV the beam is transferred into UNK-2 by single-turn injection to be accelerated further up to 3 TeV. The cycle of the superconducting stage, UNK-2, is as follows: 40-s field rise, 40-s flattop and 40-s drop. This cycle provides a mean intensity of $5 \cdot 10^{12}$ p/s. Three extraction modes from UNK-2 are foreseen: 40-s slow extraction, fast resonant extraction of 10 pulses, each lasting 2-4 ms, at an interval of 3 s and fast single-turn one for neutrino experiments. Fast resonant extraction can be carried out simultaneously with slow one. The 3d-order resonance at sextupole nonlinearity has been chosen as the operating one of the slow extraction system. The basic parameters of the fixed-target mode are presented in Table 1.

Table 1. The UNK Parameters in the Fixed-Target Mode

	UNK-1	UNK-2
Maximum energy, GeV	400	3000
Injection energy, GeV	65	400
Orbit length, m	20771.9	20771.9
Maximum field, T	0.67	5
Injection field, T	0.108	0.67
Total cycle duration, s	120	120
Acceleration time, s	20	40
Harmonic number of accelerating field	13860	13860
Total amplitude of accelerating voltage, MV	7	12
Maximum energy gain per turn, MeV	2.1	4.5
Transition energy, GeV	42	42
Betatron frequency (without special section of lattice taken into account)	36.7	36.7
Total intensity	$6 \cdot 10^{14}$	$6 \cdot 10^{14}$
Mean intensity, s^{-1}	$5 \cdot 10^{12}$	$5 \cdot 10^{12}$
Invariant transverse beam emittance, mm·mrad, not more than	150	200
Invariant longitudinal bunch emittance, MeV.m/s, not more than	100	120

In addition to beam extraction onto the external target of the experimental area, the 1st stage of the UNK envisages the experiment at the internal jet hydrogen target to be performed in MSS3 in the circulating beam of both UNK-1 and UNK-2.

COLLIDING BEAMS IN THE UNK

The further upgrading of the UNK is related to operation in the collider mode. Three different schemes of colliding beams in the UNK have been investigated: 0.4x3 TeV pp beams from UNK-1 and UNK-2 [2], 3x3 TeV $p\bar{p}$ beams in the ring of UNK-2 [4-6], and 3x3 TeV pp beams from the superconducting rings of UNK-2 and UNK-3 [3-5].

In the pp collider mode, particles are stacked according actually to the same scheme as in the acceleration mode. One of the requirements imposed on the colliding beams is that the bunch-to-bunch distance should be at least 9 m (30 ns). This can be accomplished by having inU-70 another 33 MHz recapture system (the harmonic number is 165). The frequency of the accelerating field in the UNK still remains equal to 200 MHz. Therefore when the beam is transferred into UNK-1, every sixth bucket will be filled. After UNK-2 is filled, the beam is retained there at the injection field. In UNK-1 the field polarity is reversed and other operations necessary to accelerate particles in the opposite direction are performed. After that the ring

0-7803-0135-8/91$01.00 ©IEEE

magnet is trained. According to the data available, 10-20 cycles are sufficient for that. Then the stacking procedure is repeated but the beam is injected into UNK-1 in the opposite direction with the help of the MSS6 injection system. On acceleration up to 400 GeV the beam can either be transferred into UNK-3 or used to arrange 0.4x3 TeV collision. Figure 2 shows the UNK operational scheme in this mode.

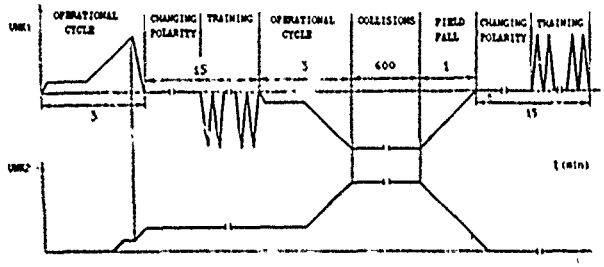


Fig. 2. Operational scheme of the 0.4x3 TeV UNK collider.

As in the accelerator mode, the U-70 beam is injected into UNK-1 12 times and is stacked there at an injection energy of 65 GeV. After that it is accelerated up to 400 GeV and injected into UNK-2 to be accelerated additionally up to 487.5 GeV and retained there for the time period required. Within this period of time field polarity reversal and other operations needed for beam acceleration in the opposite direction are carried out in UNK-1. After that a few magnetic cycles of the reverse polarity are performed to train the ring electromagnet, then the beam is injected from U-70 into UNK-1 in the opposite direction and stacked at its central orbit till the required intensity is reached. Then the beams of UNK-1 and UNK-2 are accelerated synchronously up to the maximal energy so that the ratio of their momenta at any time instant be 1:7.5. At this energy the optics of the collision ints is returned to obtain a low β-function, the beams are matched whereupon the collision mode starts. In this mode, the luminosity attainable in MSS6 can reach $1 \cdot 10^{33}$ cm^{-2}s^{-1}, where the underground experimental hall for the physics setup MMS (MultiMuon Spectrometer) is planned to be constructed. The MMS experiment is aimed primarily at the search for the t-quark at a pp-collision energy of 0.4x3 TeV (2.2 TeV in the c.m.s.). To guarantee the beam parameters required for this experiment, a special magnetic optics of MSS6 (fig.3). The chosen optics is such that the β-function in the collision area be 0.2 m in UNK-1 and 1.5 m in UNK-2. This is accomplished with the help of strong superconducting lenses Q_{39} and Q_{40}, whereas the distance between the edge ones is determined by the detector dimensions and is reduced to 16 m. To avoid having a large value of the beam envelope during injection in the lenses placed in the neighbourhood of the collision areas, the so-called "rubber optics" is applied, i.e., the gradients of the lenses are varied during the magnetic cycle.

The requirements imposed on the colliding mode are more stringent than those imposed on the fixed-target one. Therefore the UNK project has rather heavy demands on the value of the chamber coupling impedance, the level of noise in the accelerating system, injection and beam transfer mismatches.

Table 2

	UNK-1	UNK-2
Maximal energy, TeV	0.4	3
Injection energy, TeV	0.065	0.4
Number of bunches	348	348
Number of particles per bunch	$3 \cdot 10^{11}$	$3 \cdot 10^{11}$
Total number of particles per ring	$1 \cdot 10^{14}$	$1 \cdot 10^{14}$
Bunch-to-Bunch distance, m	49.5	49.5
Harmonic number of accelerating field	13860	13860
Maximal amplitude of accelerating field, MV	10	20
Beam acceleration time, s	100	100
RMS invariant beam emittance, mm·mrad	7.5	7.5
Longitudinal bunch emittance, m/ζ MeV	120	150
Minimal amplitude function at the collision point, m	0.2	1.5
RMS beam diameter at collision point, mm	0.14	0.14
Bunch length at maximal energy, cm	65	36
Beam-beam tune shift	$5 \cdot 10^{-3}$	$5 \cdot 10^{-3}$
Luminosity, cm^{-2}s^{-1}	$1 \cdot 10^{33}$	
Luminosity lifetime, h	≥ 10	
Total beam stacking and acceleration time, h	≤ 0.3	
Average number of events per collision	30	
Free area for detector, m	± 8	

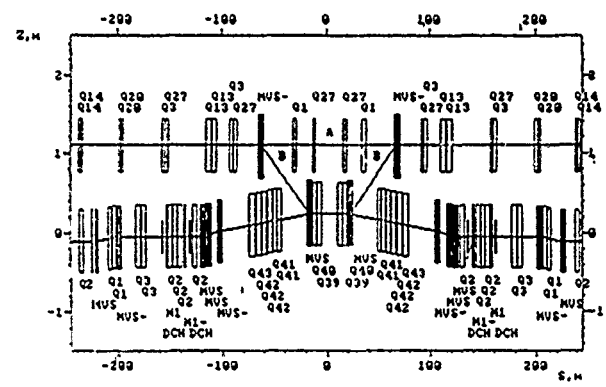


Fig. 3. Optical scheme of Matched Straight Section 6 for colliding beams.

The UNK parameters will depend essentially on the characteristics of the U-70 beam. The fixed-target mode parameters are chosen proceeding from the design characteristics of U-70 and the booster. These characteristics are now somewhat worse than required. Yet, the collider mode requires a noticeable decrease of the bunch phase volume. To attain the parameters required, the following upgrading of U-70 is planned:

- replacement of the corrugated vacuum chamber by a smooth one with a view to bring the longitudinal coupling impedance down to 10 Ohm at least;
- upgrading the power supply system for the ring electromagnet;
- upgrading the field correction system;
- development of the H^- injection system;
- an order of magnitude decrease of the injection and beam transfer mismatches.

DEVELOPMENT OF SUPERCONDUCTING MAGNETS

The superconducting ring of the UNK consists of 2192 dipoles and 474 quadrupoles. The relevant operational conditions in the acceleration and colliding beam modes impose rather stringent requirements on the value and quality of the bore field, heat load on the cryogenic system, temperature reserve necessary for the reliable operation of the UNK which must be met during the development of superconducting magnets. The nominal dipole field is chosen to be 5 T and the gradient of the quads of the regular lattice is 996.11 T/m. To ensure high-efficiency slow and fast resonant extracti-

on the good quality field in the radial direction should be at least ±3 cm. The basic characteristics of the superconducting magnets for the UNK were chosen proceeding from these requirements.

The design of dipole and quadrupole magnets has been repeatedly described and discussed [5,8]. Its basic part is a two-layer shell-type cold iron coil. Figures 4,5 show the cross sections of the dipole and quadrupole magnet for the UNK, respectively. The magnets

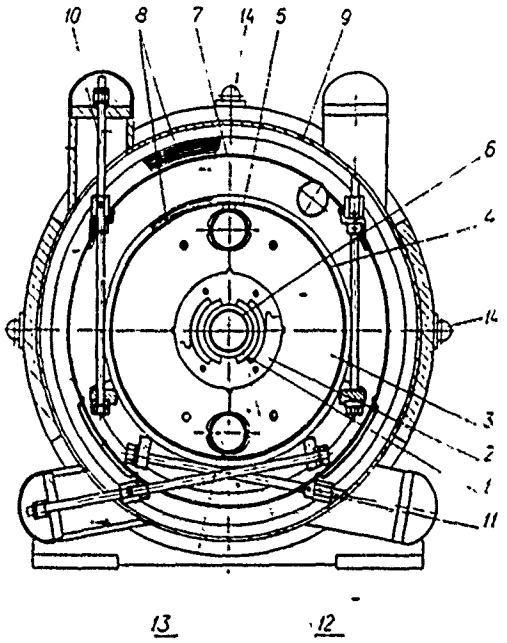


Fig. 4. Cross sectional view of a SC dipole assembled in a force-circulating cryostat: 1 - coil, 2 - collars, 3 - magnetic shield, 4 - helium vessel, 5 - two-phase helium pipe, 6 - ion pipe, 7 - thermal shield, 8 - superinsulation, 9 - vacuum vessel, 10 - suspension, 11 - extension rod, 12 - single-phase helium, 13 - two-phase helium, 14 - geodetic marks.

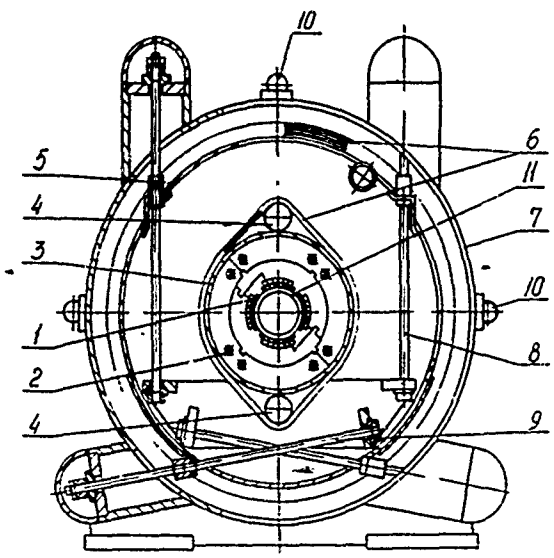


Fig. 5. Cross sectional view of a SC quad assembled in a force-circulating cryostat: 1 - coil, 2 - magnet shield, 3 - helium vessel, 4 - two-phase helium pipe, 5 - thermal shield, 6 - superinsulation, 7 - vacuum shell, 8 - suspension, 9 - extension rod, 10 - geodetic marks, 11 - ion pipe.

are produced from the same superconducting cable of "zebra" type, consisting of 19 0.85 mm in diameter strands, each containing 8910 6 thick Nb-Ti filaments embedded into a copper matrix. The critical current density at 5 T and 4.2 K is at least $2.3 \cdot 10^5$ A/cm^2.

A batch of 10 full-scale SC dipoles has been manufactured and tested. This batch was used to work out the details of the design and technology, to choose and try out the major structural materials. The collars of the magnets were manufactured from 2 mm thick sheet austenitic stainless steel of quality 05X20H15AI6 possessing a low magnetic susceptibility at helium temperatures. The magnet shield was manufactured from 3 mm thick sheet electric steel of quality 2081, havimg a lower coercive force. The collars and laminations of the shield were manufactured with the help of precision press tools of the Swiss company "Feintool".

The study of the SC dipoles manufactured of new structural materials showed the reproducibility of the basic properties from magnet to magnet.

The results on training and ramp rate properties of the SC dipoles measured in force-circulating mode of cooling with single-phase helium are given in figures 6, 7. As is seen from these figures, the critical current of the SC dipoles trained with ramp rates of up to 500 A/s exceeds the maximum operating current in the UNK cycle, i.e. 5 kA. The maximum bore field after training reaches 6.4-6.6 T.

The a heat releases in the coil and in the elements of the dipole and static heat load on the helium volume were measured. The ac loss measured in the UNK cycle for the 100 A/s ramp rate was 700 J per magnet, corresponding to the mean power in the cycle of 6 W. The total static heat influx was 5 W per magnet, out of which about 1 W accounts for that on the support system. So, the total contribution from a SC dipole into the value of the heat load on the cryogenic system does not exceed 11 W in the acceleration cycle.

Figure 8 presents the results on measuring the transfer function B/I of a full-scale dipole versus the current in the coil. As seen from the measurements, the reduction of the transfer function due to magnet shield saturation at the maximum current of 5 kA is 0.7%, which is in a good agreement with the calculations done with account of the magnet shield properties.

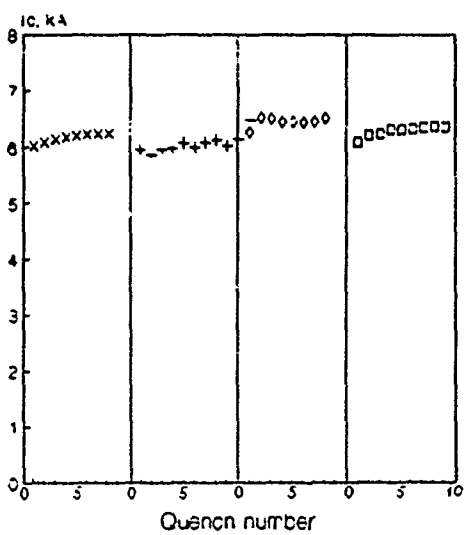


Fig. 6. Training curves for SC dipoles: ◁ - DDXB1, o - DDXB2, Δ - DDXB6.

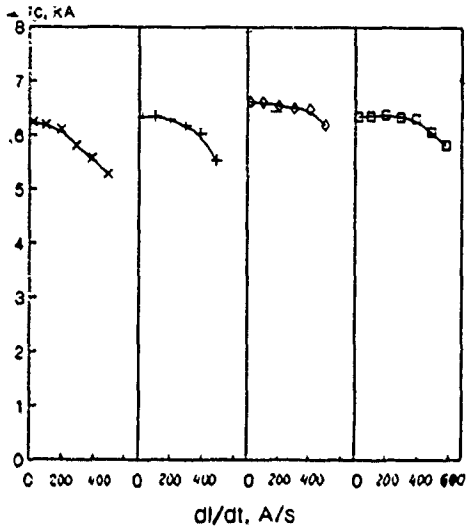


Fig. 7. Ramp rate characteristics of SC dipoles: o - DDXB2, □ - DDXB4, Δ - DDXB6.

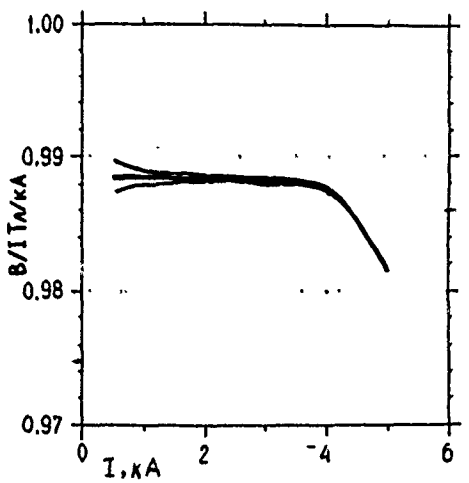


Fig. 8. Transfer function of a SC dipole versus the coil current.

Figure 9 shows the results on measuring the values of normal constituents of field nonlinearities, sextupole (C_3) and decapole (C_5), in 4 dipoles. The nonlinearities were measured at a radius of 3,5 cm versus the coil current.

As is seen from the curves, the nature of nonlinearity variation versus the value of the current is the same for all the dipoles measured. The effect of magnet shield saturation in the region of high currents corresponds to the calculation. The variation of nonlinearities in the cycle due to ponderomotive forces is within the limits of $(1\text{-}2).10^{-4}$ and is guaranteed by the optimal choice of the coil preload and of the collard rigidity. The spread in nonlinearities from magnet to magnet is within the tolerable values.

The nonzero values of C_3 and C_5 is explained by the effect of collars magnetization and deviation of the coil geometry from the design one. Since the additions caused by collars magnetization as well as the systematic errors in the coil geometry are independent of the level of the current, they will be compensated by introducing corrections into the geometry of the coils after the statistics on the results on measuring a series of SC dipoles is accumulated.

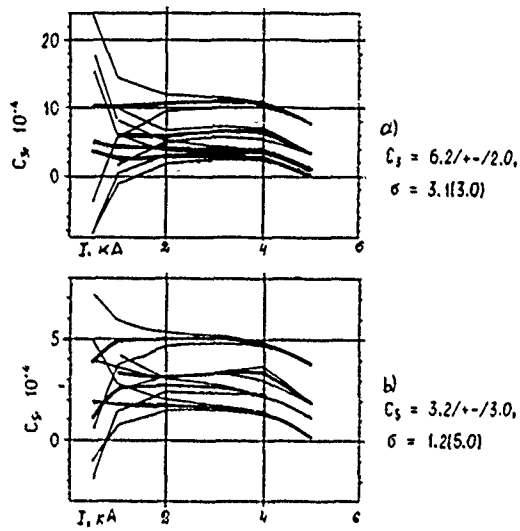


Fig. 9. Bore field nonlinearities of 4 SC dipoles at a radius of 3,5 cm versus the coil current.

The difference in the transfer function and sextupole nonlinearity during current input and output is determined by the hysteresis magnetization of the current element and is in a good agreement with the calculation.

Repeat tests of a full-scale SC dipole were done a year later after the first ones. Their results demostrated a good reproducibility of the major properties of the SC dipole for the UNK.

Three short-scale and two full-scale SC quadrupole prototype were manufactured. All models were produced of new structural materials and the SC cable having the same properties as the one used for SC dipole prototypes. Every short model was 90 cm long, that allowed one to eliminate the influence of saturation effects in the end parts of the magnet shield on the behaviour of field nonlinearities in the central cross sections.

Figures 10, 11 present the results on training and ramp rate property of a full-scale SC quad model, obtained in the force-circulating mode of cooling with single phase helium. As is seen, the critical current of such a quad exceeds essentially the maximum operating current in the UNK cycle.

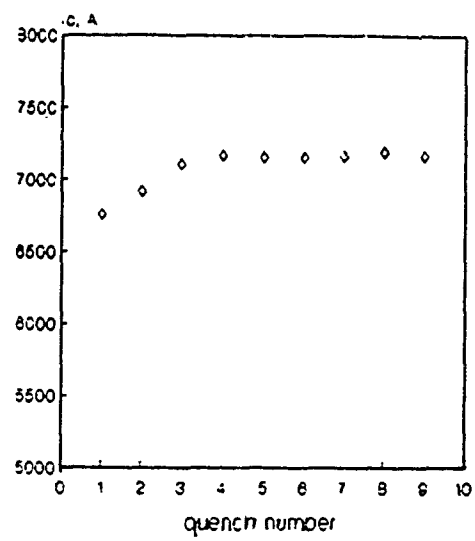


Fig. 10. Training curve of SC quad model.

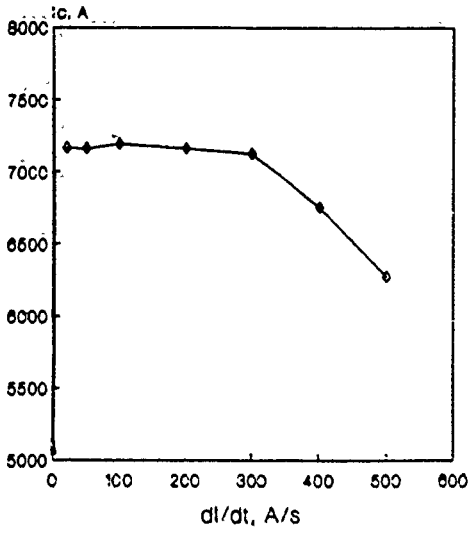


Fig. 11. Ramp rate characteristic of SC quad model.

The ac loss in a SC quad measured in the UNK cycle was 60 J/m. This means that the contribution from the ac heat release in a full-scale 3-m quad into the heat load on the cryogenic system in the UNK cycle is 1.65 W per magnet. As estimated from the results on measuring the static heat leaks in SC dipole models, the static heat leak in SC quads will make up 3 W per magnet. So, the total contribution from a SC quad into the heat load on the cryogenic system in the acceleration cycle will be about 5 W.

The measured ratio of the quad field gradient and dipole field is 19.46 m^{-1}. The variation in the ratio of the SC quad field gradient to the SC dipole field in the cycle with account of the coil magnetization and magnet shield saturation does not exceed the admissible value, $\pm 0.1\%$.

The results on measuring the bore field nonlinearities of a SC quad suggest that the effect of magnet shield saturation on variation in the values of G/I and C_6 in the range of high current is not essential and agrees with the calculations. The difference in the value of G/I and C_6 during current input and output is related to the effect of the hysteresis magnetization of the current element and is also in a good agreement with the calculations.

The systematic shift of the measured nonlinearities with respect to the design values does not exceed $2 \cdot 10^{-4}$ for C_6 and $4 \cdot 10^{-4}$ for C_{10} and is within the tolerances. The measured values of the forbidden C_n and skew S_n field nonlinearities do not exceed $\pm 2 \cdot 10^{-4}$ for $n \leq 13$ and are also within the tolerances pointing to a high quality of magnet assembling.

The SC dipoles and quads for the regular lattice of the UNK were developed as a result of the studies performed. The properties of all SC magnets satisfy the requirements imposed on the bore field value and quality, on the level of ac heat releases in the coil and elements of the design and on the value of static heat leaks into the helium vessel of the cryostat.

The analysis of the magnetic measurements show that in the operating cycle of the UNK the values of sextupole and octupole nonlinearities may be corrected by the field correction system. As to higher-order and edge nonlinearities, these are within the tolerances in the beam stacking, acceleration and extraction modes.

According to the measurement results, the heat load on the cryogenic system of the UNK in the acceleration cycle will be about 33 kW. It will be twice as low in the colliding beam mode. This means that the available power of the cryogenic system of the UNK, 60 kW, will allow us to support the operation of one superconducting ring in the acceleration mode or of two superconducting rings in the collider mode. The temperature reserve of the SC magnets allows the reliable operation of the ring SC magnet of the UNK at a liquid helium temperature of 4.4-4.6 K both in the acceleration cycle and during the e ergency removal of the energy stored.

In 1990 the production of a pilot and industrial batch of SC dipoles and quads was started with a view to attain the required reproducibility of magnets when their serial production begins. By now 10 out of 100 have been manufactured and tested. The serial production is planned to be started in 1992.

STATUS OF THE UNK CONSTRUCTION

The construction of the southern part of the ring tunnel and injection beam line is over, the work on the preparation for the equipment is underway. The construction of the surface technological buildings designed to house the power supply, cryogenic and control systems is going on.

The equipment for UNK-1 is presently in serial production. All the electromagnetic and vacuum equipment for the 2.7 km long injection beam line has been manufactured. More than 1000 warm magnets and 11000 m of the vacuum chamber have been supplied, the equipment for the accelerating system and for the power supply system of the ring electromagnet is being manufactured.

There is a special 10000 m^2 building where the equipment is tested and prepared for assembling. The assembling of the electromagnetic equipment in the injection beam line is to start at the end of this year The rate of the work being carried out confirms the feasibility of having UNK-2 constructed in 1994-1995 and of starting running it in together with the experimental setups in extracted beams in 1995-1996. The 0.4x x3 TeV colliding beams and the MMS setup running in the experimental hall of MSS6 may be ready in 1997.

REFERENCES

[1.] V.I.Balbekov et al. Proceed. of 12-th Intern. Conf. on High Energy Accel., Batavia, 1983, p. 40.
[2.] A.I.Ageyev et al. Proceed. of XIII Intern. Conf. on High on High Energy Accel., Novosibirsk, 1987, v. 2, p. 332.
[3.] A.I.Ageyev et al. Proceed. of Europ. Part. Accel. Conf., Rome, 1988, v. 1, p. 233.
[4.] K.P.Myznikov. Proceed. of Workshop on the Experimental Program at the UNK (September 14-19, 1987). Protvino, 1988, p. 13-30.
[5.] K.P.Myznikov. Proc. of Workshop "Physics at the UNK". Protvino, 1989, p. 5-15.
[6.] T.A.Vsevolozhskaya et al. - Proceed. of VII All-Union Conf. on Charged Part. Accel. Dubna, 1981, v. 1, p. 119.
[7.] V.V.Abramov et al. Study of Multimuon Events in 0.4x3 TeV p-p Collisions with Multimuon Spectrometer MMS. Preprint IHEP 90-93, Protvino, 1990.
[8.] A.I.Ageyev et al. Preprint IHEP 90-158, Protvino, 1990.

High Frequency Cascaded Resonant Transformer Rectifier Power Supply For Neutral Beam Injection*

Louis L. Reginato

Lawrence Livermore National Laboratory,
700 East Avenue
Livermore, CA 94550

ABSTRACT

Neutral beam injection for fusion requires DC megavolt power sources at several amperes. The conventional methods of using series or shunt fed multipliers cannot provide the current while the 60 Hz coupled transformer method is difficult to modularize because of size and stores excessive amounts of energy. A technique which borrows from several technologies has been investigated and shows promise for a satisfactory solution. This technique uses resonant multistage high frequency (100 kHz) series coupled ferrite transformer with rectifiers to produce megavolts at several amperes of current. Modularity, high efficiency and low energy storage are desirable features of this power source.

1. INTRODUCTION

Neutral beam injection is an essential part of the international magnetic fusion effort. The four participants in the International Thermonuclear Experimental Reactor. (ITER) have on-going programs to develop neutral beams of several amperes with 1 to MeV of energy. The Lawrence Berkeley Laboratory has been a leader in the development of neutral beams source in the 100 - 200 keV for the past two decades. The US concept for achieving megawatt neutral beams requires development or extrapolation in both the ion sources and the acceleration components (power supply). The power supply requirements for neutral beams is somewhat unique. It is required that the energy storage be as low as possible so that no damage occurs to the high voltage electrodes such as the electrostatic quadrupoles or the negative ion sources under sparkdown conditions. It is also required that it be made modular so that tap points can provide high current bias at any voltage between ground and 1.3 MV. It is also highly desirable that such a power supply be an integral part of the acceleration electrodes so that high voltage will not have to be transported long distances by cables. Above all, the efficiency of the power supply must be above 90% and must also be capable of being switched off quickly to limit the amount of energy deposition into the spark.

Low current megavolt sources are not new to the accelerator community. Megavolt DC sources of several amperes, however, are new. Traditionally, injectors for high energy accelerators have utilized "series-fed" multipliers (Cockcroft-Waltons) and "shunt-fed" multipliers (Dynamitrons) to generate megavolts at a few milliamperes of current. Series or shunt-fed high frequency multipliers, although compact, cannot provide the current required for neutral beam injectors. Multipliers or coupled transformers at 60 Hz have been used but for this application are too bulky, have excessive energy storage and are difficult to modularize. The Magnetic Fusion Energy Group at LBL has investigated the application of modular coupled ferrite transformers at high frequency (100 kHz) to generate 2.5 A of D^- at 1.3 MV A ten stage 100 kV prototype has been built and tested to investigate the feasibility of this technology.

II. CONCEPT FOR A HIGH FREQUENCY CASCADED RESONANT TRANSFORMER RECTIFIER (CRTR) DC POWER SUPPLY

The industrial market for low voltage high current power supplies has been adopting high frequency AC to DC converters for cost effective high efficiency and compactness. This technology has provided power supplies of up to a few tens of kilowatts at a few tens of kilovolts.

The high frequency is chosen for several reasons; first of all, a frequency of 100 kHz allows a considerable size reduction in the coupling transformers; size reduction allows modularity for both the accelerator and other power sources; high frequency allows usage of very efficient high resistivity ferrites made of Nickel-Zinc material making high voltage isolation and tight coupling easier; high frequency also eliminates the need for large filtering capacitors, and hence reduces considerably the energy storage. Semiconductor devices such as MOSFETS and IGBTS have achieved very high efficiencies at tens of kilohertz; the fast response of semiconductors also implies that the power sources can be turned off in less than 10μs under fault conditions eliminating the need for crowbars (a snubber core will still be required to absorb the unavoidable stray stored energy).

The transformers coupled power supplies display reactive losses due to both the leakage inductance ($L\ell$) and the magnetizing inductance (L_m). Under high current conditions, the $L\ell$ is dominant while under light loads, the L_m is of more concern. To eliminate both of the reactive losses, a series and parallel tuning has been adopted to achieve resonance. Figure 1 is a simplified schematic of the prototype accelerator power supply. The system consists of 10 each 10 kV, 1A modules that are series connected to produce 100 kV. Each module will incorporate filtering (C_f), diode protection and series limiting (RL) circuit to absorb the self stored energy

Work was performed at the Accelerator Fusion Research Division of the Lawrence Berkeley Laboratory under U.S. Department of Energy. Contract DE-AC03-76SF00098.

U.S. Government work not protected by U.S. Copyright.

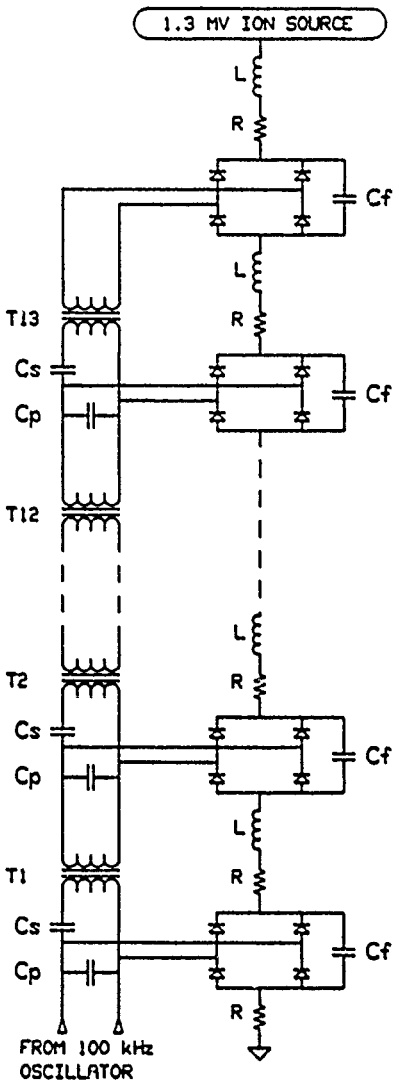


Fig. 1. Voltage multiplication using single phase cascaded resonant transformer rectifier system. (Note high resistivity ferrite cores biased by center-tap of HF transformer)

during arc-down. Each power supply module will also have the proper series and parallel capacitors (Cs, C_p) to achieve resonance as the power is transmitted in 10 kV increments. Note that even though each power supply is the same, the lower stage transformers will have to carry each individual current plus that of the power supplies above it. Computer studies of the circuit show that the tuning will also difer from stage to stage. The tuning has been chosen that under full load conditions the Q of the system will be slightly above unity. Under light load conditions, the Q will increase to greater than unity, hence the step-up per stage would increase. To maintain a constant voltage level, a feedback system is incorporated which adjusts the input voltage of the high frequency converter (Fig. 2). C_S are the series tuning capacitors and C_p are for parallel or shunt tuning. T_1 to T_{10} are the one-to-one isolation transformers. Since T_1 handles the power for all subsequent stages, it will have to wound with the appropriate wire size. T_{10} handles only the single stage power and will utilize smaller wire. At 100 kHz, close attention will have to be paid to utilizing the optimum core and winding geometries. Even though toroids were used for the 100 kV prototype, it is expected that the high power unit will utilize E-cores to maintain the low leakage at high currents (Fig. 3).

III. PROTOTYPE DESIGN AND TEST RESULTS

The proposed technique of using high frequency coupled transformers to generate megavolts at megawatts of energy looked very appealing for a number of applications. Unfortunately, lack of funds dictated that the experimental program had to be very limited and that it borrow resources from existing programs at LLNL and LBL. A number of ferrite toroids were found available from the beam research program at LLNL and some high power oscillator tubes were found at LBL. It was felt that the crucial aspect of this technique was to see if high frequency, coupled and tuned transformers could deliver high currents with an efficiency of over 90%. Computer studies were performed using a program called MICROcap II. These studies indicated that indeed under heavy load conditions the reactive losses could be tuned out. Fig. 4 shows that the output of a ten stage system would not be usable due to the reactive losses much like a series-fed

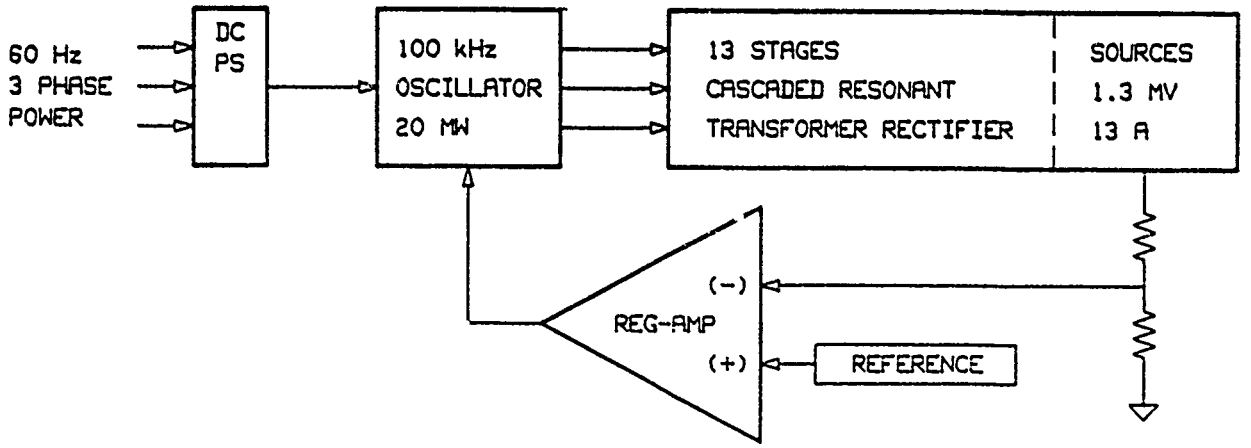


Fig. 2. Block diagram of high frequency 1.2 MV. 13A Power supply with regulation feedback system.

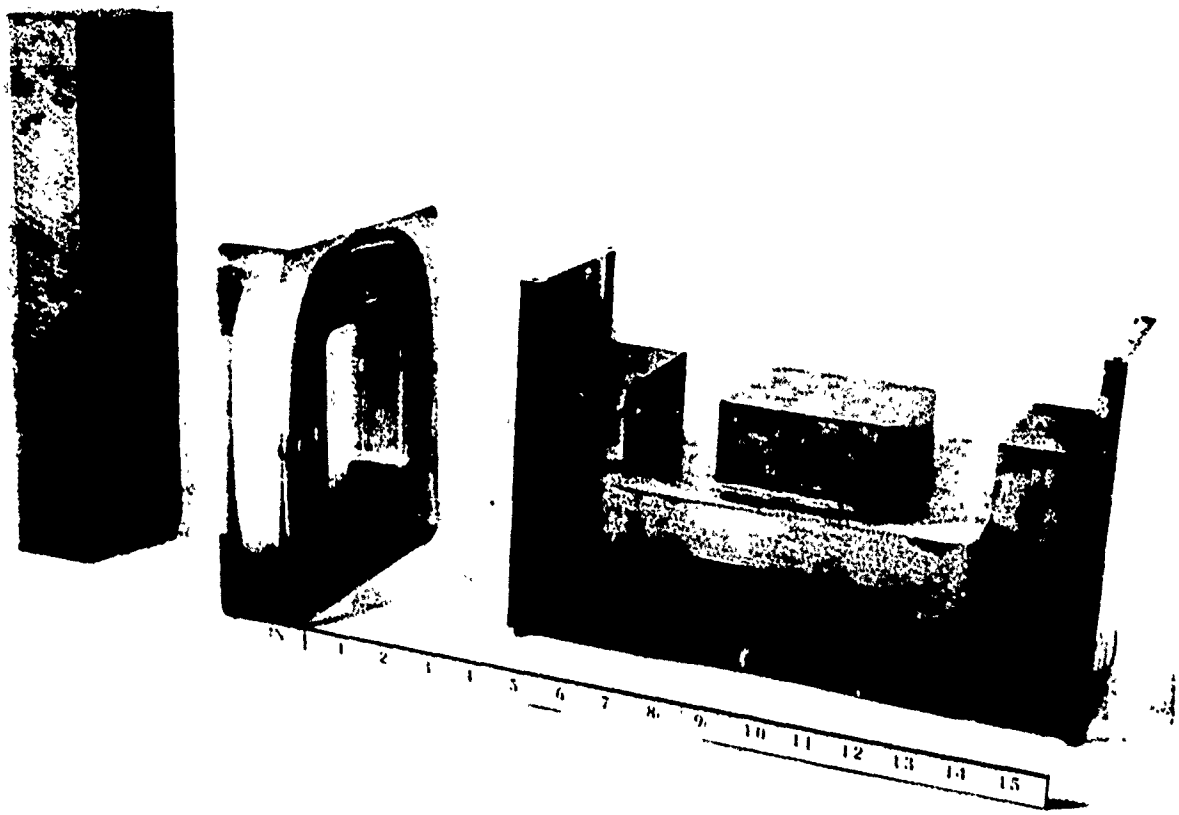


Fig. 3. Prototype E-Core for 1.3 MV high frequency cascaded transformer.

Cockcroft-Walton. Fig. 5 shows that under heavy loads the output is actually N times the input where N is the number of stages. A ten stage, 50 kHz prototype was built and tested at LBL. The impedance was chosen to be similar to that of the full voltage device so that leakage and mutual inductances have the same effective losses.

Figure 6 shows the completed prototype with the variable dummy load for testing to high power. Test results from Fig. 5 show good agreement with the computer simulation and that the output is 2Db higher than the number of stages (N = 10) times the input under full load conditions. Figure 7 shows the simplified schematic of the coupled transformers and Fig. 8 shows the output voltage under varying load conditions. It can be seen that the prototype achieved a maximum of 72 kV under light load conditions and 50 kV under full load. The design voltage of 100 kV was not achieved because of a design deficiency in the interstage transformer. Toroidal cores were used because they were readily available but it was recognized early on that this was not the best geometry for high voltage isolation and tight coupling. We incurred several failures from turn to turn arcing and winding to core shorts. Higher voltage under full load was not achieved simply because of the limited output of the 50 kHz oscillator. The frequency was lowered from 100 kHz to 50 kHz because of self resonances in the toroidal transformer. Figure 9 shows the stage voltages for varying loads. This test result shows that considerable variations in voltage occurs from stage to stage when the load is varied from 100 kΩ to

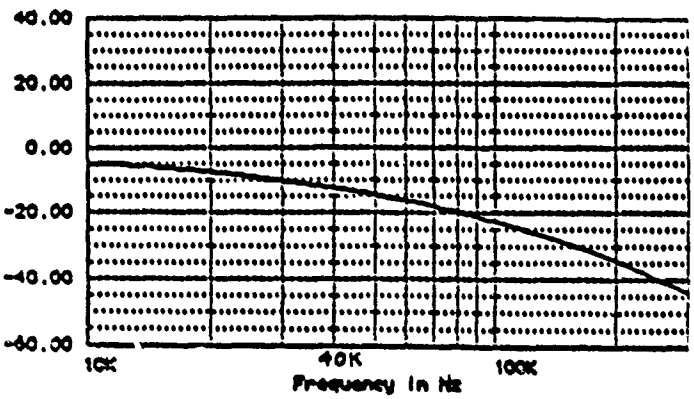


Fig. 4. Frequency Response of ten-stage high frequency transformers with resonant tuning.

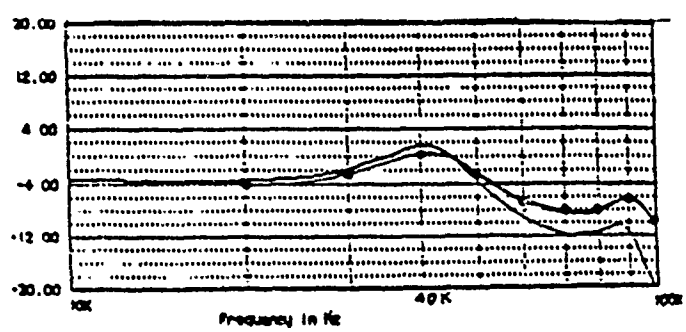


Fig. 5. Frequency Response of ten-stage high frequency transformers with resonant tuning.

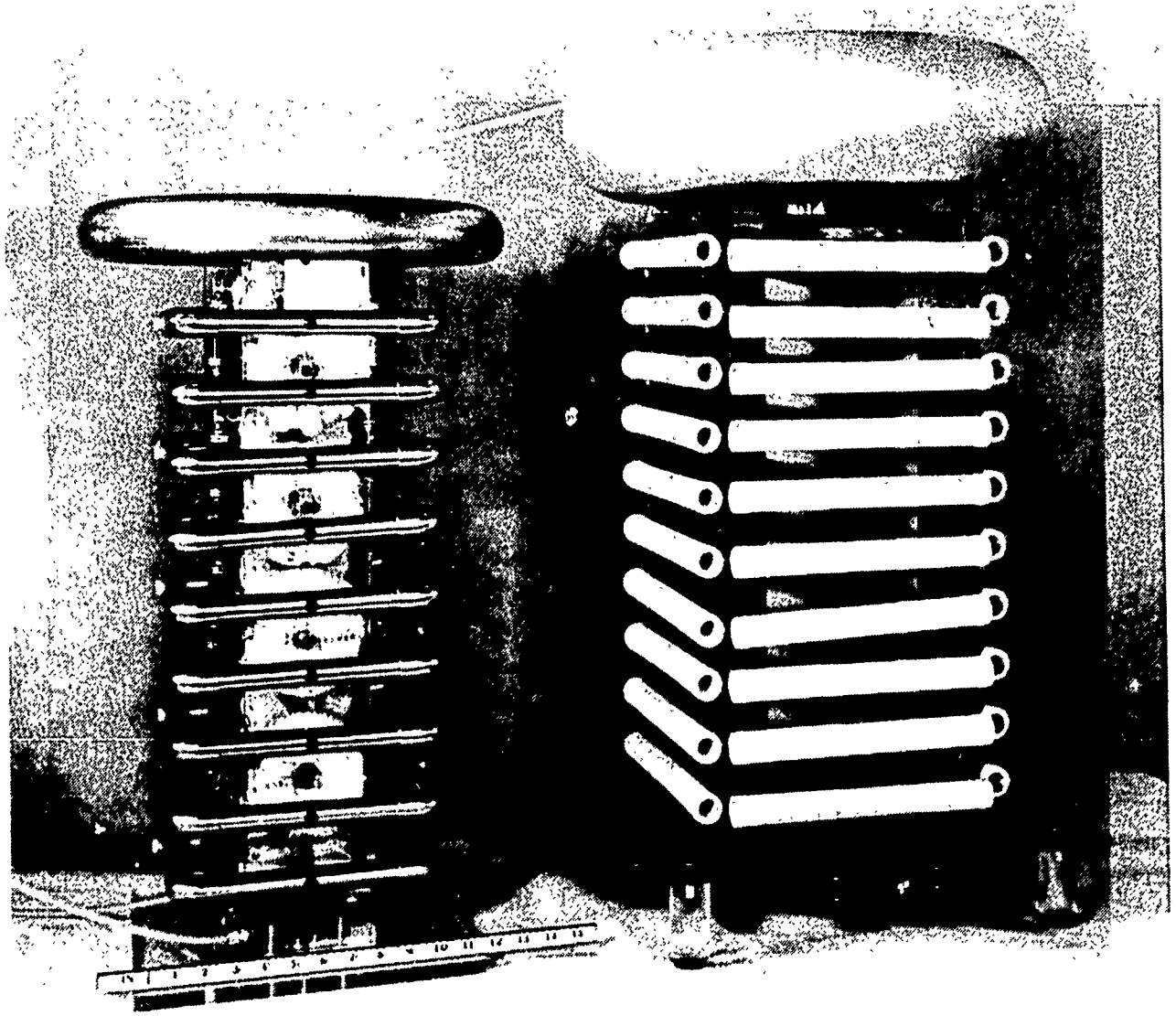


Fig. 6. Ten-stage 100 kv prototype high Frequency Cascaded Transformer Rectifier (CRTR) System with Dummy Load.

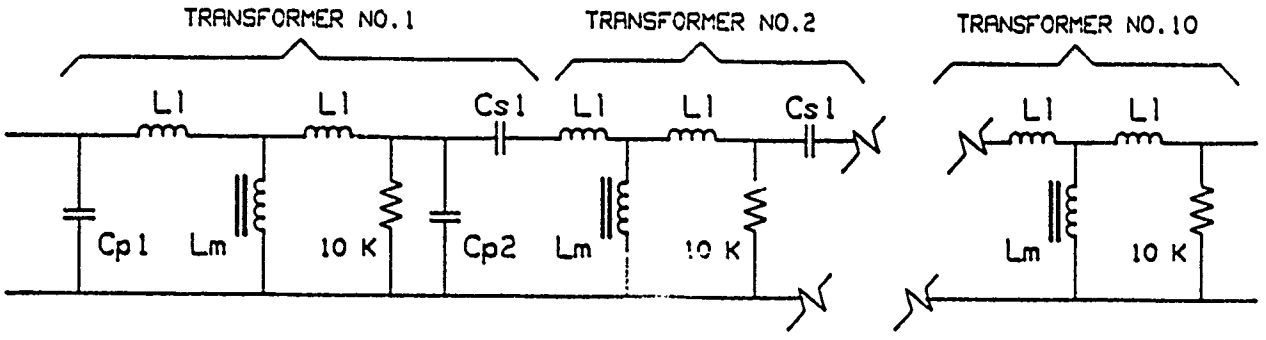


Fig. 7. Simplified Equivalent Circuit of ten-state CRTR.

700 kΩ. The Q of the tuned stages was designed to be small under full load conditions but as the load decreases the Q increases and the stage voltage changes. This is a serious consideration if tap points are required for the acceleration process. For an overall power supply where only the output is used this could offer a viable solution for a high voltage power system. Output voltage regulation can be maintained to 0.1% with a feedback system.

IV. CONCLUSION

The one tenth scale prototype of similar impedance to the final objective was quite successful in providing solid data for directing future research in this technology. It proved a number of significant point: (a) high frequency coupled transformers with tuning in only a few stage produces the desired multiplication of the input voltage, (b) tuning of a few

stages cancels the reactive losses of cascaded stages but produces some undesirable voltage division from stage to stage, (c) efficiency exceeds 90%, (d) coupled stages adapt easily to a modular system(e) high frequency clearly means compactness and low energy storage.

V. ACKNOWLEDGEMENTS

The author wishes to thank William S. Cooper for the physics and computational help; Jan G. DeVries for his engineering insight; Peter J. Rosado, G.W. Leonard and Tom A. McVeigh for their help in the assembly and testing of the prototype; Richard Heep for his overall support and coordination efforts.

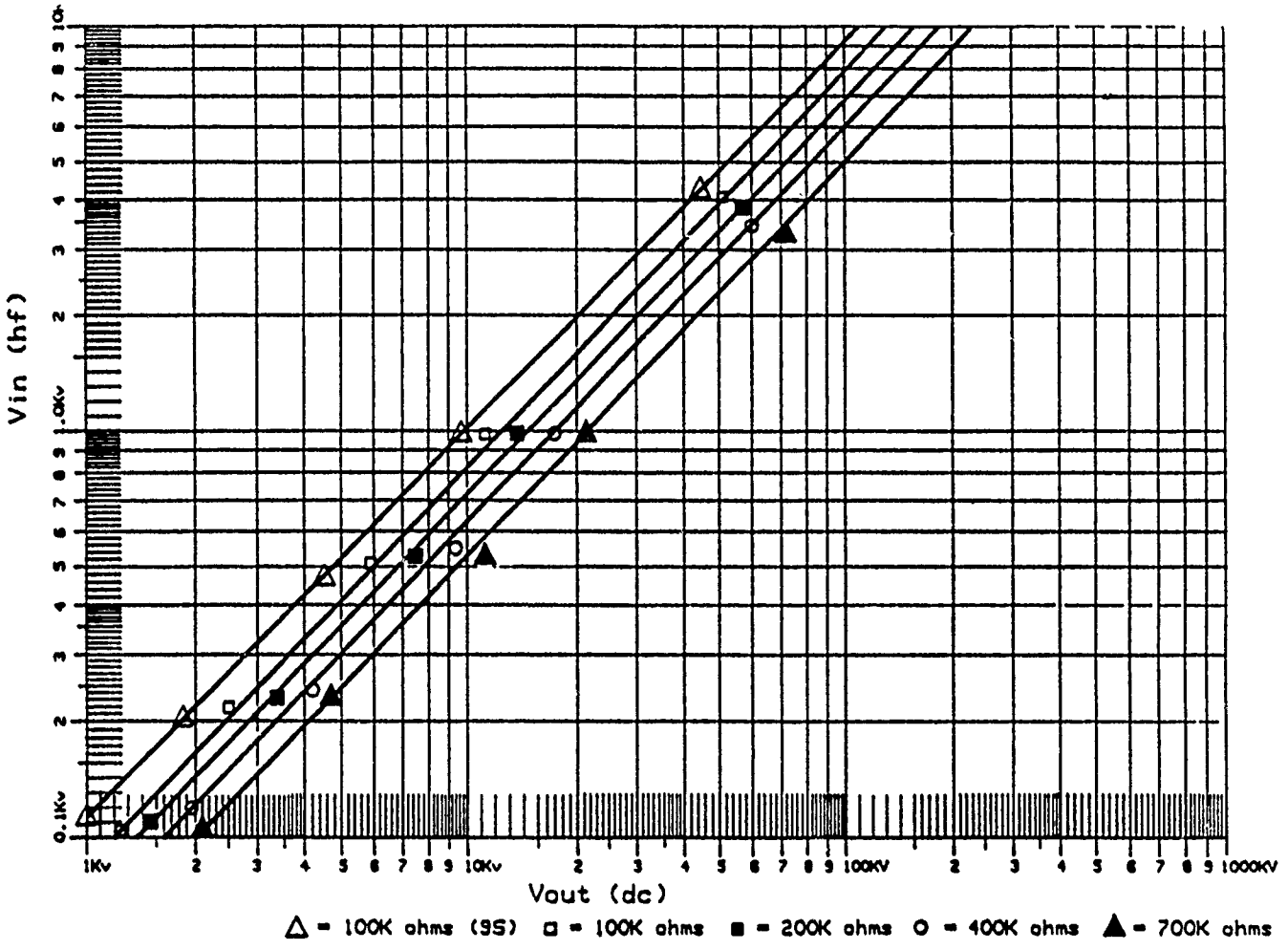


Fig. 8. Output voltage of ten-stage CRTR with various loads.

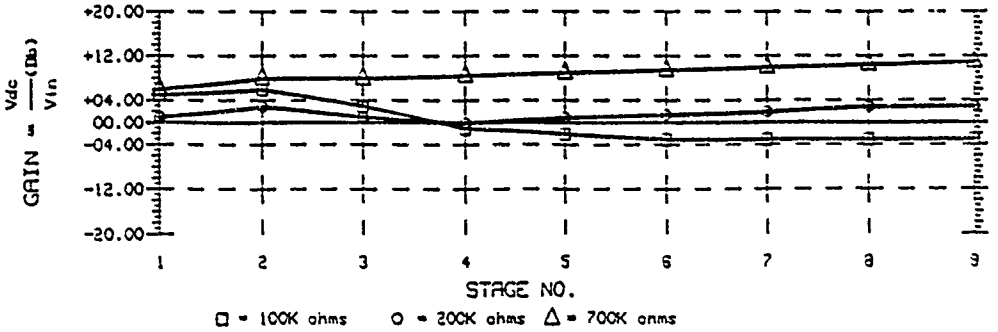


Fig. 9. Stage voltage under various load conditions.

Switching Power Supply Regulation of Storage Ring Magnets†

M.G. Billing
Floyd R. Newman Laboratory of Nuclear Studies
Wilson Synchrotron Laboratory, Dryden Road
Cornell University
Ithaca, NY 14853

INTRODUCTION

Future accelerators will require greater flexibility in the design and implementation of their optical functions. One of the most cost effective solutions for the powering of linear and non-linear focussing elements is the use of modern, high efficiency switching power supplies. These types of power supplies are in use in a number of accelerators[1,2,3] and being planned for accelerators under construction[4,5]. This paper will focus on non-resonant switching regulators and discuss the general configuration of a system of magnet power supplies, the principles of the electronic circuit designs, the typical cost of such a system and the power supply performance, including regulation, stability and reliability. It will also present some general diagnostics for systems of large numbers of power supplies and some discussion of the operational benefits from the individual powering of all focussing elements. Since 1977 this type of chopper regulator has demonstrated its excellent performance for the independent control of the quadrupole, sextupole and steering magnets in CESR (Cornell Electron Storage Ring); a number of practical considerations from this experience will be included throughout the discussion.

BASIC SYSTEM AND CIRCUIT DESIGN

A typical chopper magnet power supply system would have a set or sets of regulated DC buses providing the raw DC power to the chopper regulators located along the accelerator near the magnetic elements. Figure 1 shows the configuration in use in CESR. For each half of the ring the primary power for the magnet system is supplied from a regulated 65 VDC power supply with load and line regulation better than a few tenths of a percent. The negative side of the power supply is connected to the ground return bus and to earth ground through a fault protection circuit; due to the load current the voltage of this return bus will rise a few volts above earth ground at the far end of the ring. At a typical magnet station there are unipolar chopper regulators for the quadrupole and sextupole magnets and bipolar choppers for the steering corrector magnets. The high precision quadrupole chopper supply has a DC current transformer (DCCT) as the current regulating element, while the lower precision sextupole and steering choppers use shunts for regulation. Each chopper's connection to the positive supply bus is fused to protect against the chopper developing an internal short. The control, protection and regulation circuitry for each chopper supply is situated on a separate circuit board in a crate.

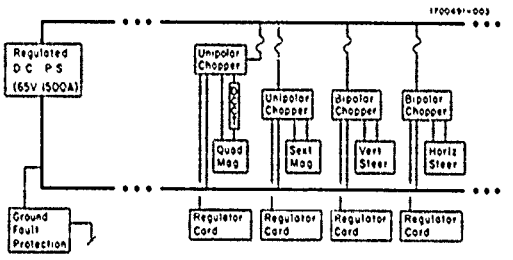


Figure 1. CESR chopper power supply system configuration.

The unipolar chopper circuit is described as a reverse biased fast recovery diode across the magnet and a switching element that periodically connects the magnet between the DC power buses. When the switch is closed, current is drawn from the DC mains through the magnet. When the switch opens, the magnet current continues to flow through the fast recovery diode. A very convenient current regulating method has the switching element operating at a fixed frequency with pulse width modulation. For conventional magnet impedances bipolar transistors or FET's are the preferred choices for the switching elements due to their low "ON" resistances. The choppers in operation in CESR are based on bipolar transistors, while the newer APS design utilizes FET's.

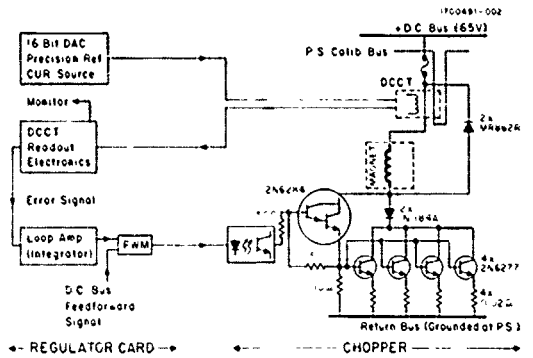


Figure 2. CESR unipolar precision DCCT regulated 100 A chopper power supply block diagram.

An example of a unipolar chopper is found in Figure 2. This is a high precision quadrupole regulator used in CESR. The regulator electronics are separated into two parts, the high power switching chopper and a regulator card with its own

† Work supported by the National Science Foundation.

0-7803-0135-8/91$03.00 ©IEEE

electrically isolated ground. This isolation is necessary because the chopper's common is connected to the return bus, possibly a few volts above ground, and generally there can be significant switching noise present on this return bus. The regulator card needs to be in a low noise environment for the best regulation performance and to permit easy control system interconnections. As shown in figure 2 to obtain the 100A maximum switching current, four 2N6277 transistors are driven as emitter followers (the emitter resistors providing current sharing) by a high current gain darlington stage. The magnet's current is is measured by a magnetically shielded DCCT, which measures the flux difference between a 1000 turn winding driven by a precision reference current and a single turn winding for the magnet's current. The DCCT is connected in the circuit at one of the DC bus potentials to minimize the EMI (electromagnetic interference) induced by the switching transients. A 16-bit DAC (digital to analog converter) provides the source for the precision reference current for the DCCT. The DCCT's error signal is detected in a sampled second harmonic demodulator circuit, which provides two independent error signals, one for monitoring and the other for regulation. To obtain improved DC stability, the loop amplifier is an integrator making use of the high open loop opamp gain at low frequency and a lag network to compensate the magnet's pole (at 0.3 Hz). The loop amplifier's signal feeds a pulse width modulator (PWM) circuit having a feedforward input from a differential bus voltage monitor. This feedforward network reduces by a factor of 100 the effect of transient changes on the DC mains at frequencies above the closed loop bandwidth of the current regulation loop. The APS design uses a Hall switch to accomplish the same wider bandwidth compensation for transients. The PWM circuit drives an opto-coupler connected to the chopper's darlington transistor stage.

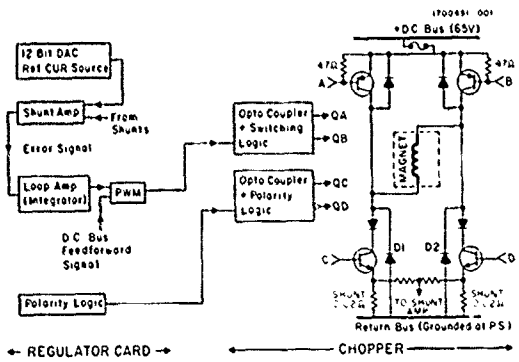


Figure 3 CESR bipolar shunt regulated chopper power supply block diagram.

The bipolar chopper regulator bears some important differences from the unipolar chopper mentioned above. Figure 3 shows the steering chopper in use in CESR; it uses a 12-bit DAC for a reference current source and a shunt for current regulation and monitoring. Aside from the additional polarity control logic the regulation loop circuitry is similar to that described above The major difference is in the chopper's circuit configuration. For an explanation choose the polarity such that the current passes through the magnet from top to bottom. Transistors labeled Q_c and Q_d are the polarity determining switches and the transistors labeled Q_a and Q_b are the switching transistors. In this case Q_c is on and Q_a and Q_d are off. Q_b is driven with the PWM switching signal so that, when Q_b is on, current is drawn from the positive bus through the magnet and through Q_c to the return bus. When Q_b switches off, the voltage at the top of the magnet swings negative causing the diode, D_2, to conduct so that current flows from the magnet through Q_c to the return bus and back to the magnet via D_2. There are two shunts at the emitters of Q_c and Q_d; these are summed with resistors to give a polarity-independent shunt signal. A pair of waveforms from an operating steering chopper is shown in figure 4. CH1 is the voltage across the magnet, while CH2 is the AC coupled magnet current displaying the current ripple in a magnet with a short L/R time constant. The bipolar chopper supply has a dynamic range of 1000 to 1.

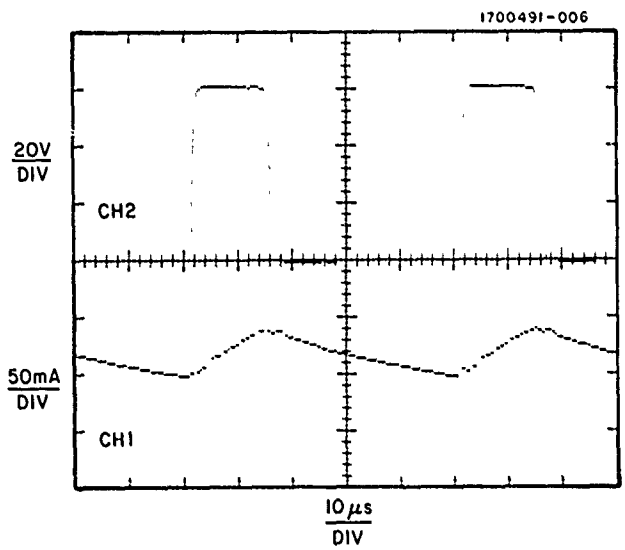


Figure 4. Switching waveforms from a CESR bipolar chopper operating at 6.25 Amps. CH1 is the voltage across the magnet and CH2 is the AC coupled magnet current ripple.

DESIGN CONSIDERATIONS AND PERFORMANCE

The fourteen years of reliable service of the more than 325 chopper power supplies in use in CESR provides a large sample of regulators with a long term operating experience. Designed in 1975 using bipolar power switching transistors, the chopper regulators have been in operation with power capacities up to 18KW. Table 1 gives some of the parameters for different unipolar and bipolar regulators in use in CESR and planned for use in APS. As table 1 indicates the chopper power supplies tend to favor higher resistance magnets, this is the case for the following reasons. First, for a given saturation voltage of the switching devices one portion of the chopper's dissipated power contribution comes from the product of the duty cycle, the magnet's current and the saturation voltage. To obtain the lowest losses and highest

efficiency, the magnet's voltage should be as large as possible for a given magnet's current. The second reason for larger magnet resistances is that practical switching devices are presently limited to total switching currents of 100-150 A per device and, to avoid having to parallel many devices, lower magnet currents are favored. In the cases of CESR and APS the quadrupole magnets have resistances in the range of 0.04 to 0.5 Ω.

Table 1. Summary of chopper regulator characteristics

Accelerator	Regulator Type	Magnet	Command Resolution	Max. I (Amps)	Max. V (Volts)
CESR	Unipolar	quadrupole	16 bit	100	60
CESR	Unipolar	transfer bend	16 bit	300	60
CESR	Unipolar	sextupole	12 bit	40	60
CESR	Bipolar	H & V steering	±12 bit	±12.5	60
APS	Unipolar	quadrupole	17 bit	468	22
APS	Unipolar	sextupole	13 bit	214	23
APS	Bipolar	H steering	±13 bit	±125	26
APS	Bipolar	V steering	±13 bit	±99-148	14-19

The maximum allowable magnetic field ripple will favor a higher chopper switching frequency and longer magnet's L/R time constant (approximately 0.5 seconds for both CESR and APS.) Additionally, due to eddy currents in the beam pipe, the effect of the magnetic field ripple will be reduced within the beam pipe; for most common beam pipes this cutoff begins at frequencies of 100 to 1000 Hz. Also at the higher frequencies the magnet itself becomes lossy from eddy currents so that the largest variation in the field will be in the region of the fringing fields, typically a small fraction of the magnetic length. The choice of a higher switching frequency for a reduction of the current ripple is counterbalanced a need to reduce the power losses due to switch transition. Since these losses are proportional to the switching frequency, lower frequencies are favored, but should be above the human audio range. With these provisions switching frequencies in the range of 20-50 KHz should continue to be favored in the future. For the case of CESR and APS both with 20 KHz switching frequency and quadrupole magnets with 0.5 second time constants, the peak to peak current ripple at a 50% duty cycle is approximately 5×10^{-5} of the magnet's current.

As mentioned earlier the two most practical choices for the switching elements in the choppers are power switching bipolar transistors and power switching FET's. The bipolar devices have been available for the last 15 to 20 years and there have been some improvements in packaging and power handling capabilities over this period. However, rapid advances in the power MOSFET technology has lead to higher current devices (e.g. 150 A MOSFETs vs. 25 A bipolars) with comparable switching speeds. The absence of the the second breakdown phenomenon in the FET's permits higher switching voltages than are practical with bipolar devices. The reproducibility of the transconductance characteristics of the MOSFET's permits a much greater control of the device's switching current and eliminates the need for emitter resistors when paralleling bipolar transistors. As an example of MOSFET advances, the CESR quadrupole chopper's driver stages and main switching transistors can be replaced with an integrated circuit capable of driving capacitive loads and a single power MOSFET, greatly simplifying the parts count and cost of future chopper systems.

One of the reasons for the excellent reliability of the CESR choppers (mentioned below) is due to the conservative design specifications. In particular, the maximum designed power dissipation in the switching devices was approximately half of the maximum specified for those devices. Also the factor of three to four allowance for degradation of the bipolar transistor's current gain over the operational lifetime of the chopper allows some margin against a significant increase in the saturation voltage of the transistors over time and the associated increase in dissipation.

Chopper power supplies are excellent power converters with the example of CESR choppers having measured efficiencies at or above 95% at full current. The efficiency can be approximately calculated from the power delivered to the load and the losses from the switching transients and from the ON-state dissipation in the switching elements. The total load power as seen by the magnet bus, P_L, is

$$P_L = I_M^2 R + \frac{1}{2} V_B I_M (\tau_R + \tau_F) F + V_{sat} I_M \tau_d F \quad (1)$$

where I_M and R are the magnet's current and resistance, V_B is the bus voltage, τ_R and τ_F are the switching element's rise and fall times, F is the switching frequency, V_{sat} is the switching element's saturation voltage drop and τ_d is the switching element's ON time. The terms in this equation are respectively the load power, the switching transient losses and the ON-state dissipation losses. The switching element's ON time is itself given by

$$\tau_d \cong \frac{I_M R}{V_B F} \quad (2)$$

and from these equations the efficiency, η, may be approximated as

$$\eta \cong 1 - \frac{V_B (\tau_R + \tau_F) F}{2 I_M R} - \frac{V_{sat}}{V_B} \quad (3)$$

From this equation it is clear that the chopper's efficiency is the highest at the maximum magnet current and that reducing the rise and fall times and saturation voltage of the switching elements improves the efficiency. One additional fact to consider about using any high efficiency power converter from a regulated source, i.e. the DC bus power supply, is that the power converters appear to the power supply as a negative resistance load. Care must then be taken to stabilize the main power supply's voltage regulation loop.

The chopper regulators in CESR have demonstrated an excellent record for stable long term performance. For the case of the high precision quadrupole choppers the measured regulation is within ±10 PPM FS (parts per million of full scale) and the maximum deviations over a 36 hour period are within 50 PPM FS. Periodic checks of the quadrupole regulators' current calibration have been undertaken using a special calibration winding built into each DCCT. The calibration system has a resolution of 40 PPM FS and found

no changes in calibrations for periods of one year above 100 PPM FS which were not due to major hardware failures.

The chopper power supplies in CESR have given very reliable service over the 14 years of operation. The performance for the calendar year 1990 is fairly typical of the chopper power supply reliability. During 1990 there were 21 failures of power supplies, 11 of these attributable to choppers, 8 to regulator cards and 2 cases in which both were replaced. This gives a failure rate of 1.75 chopper supplies per month during operations and a mean-time-to-failure of 15.5 years. Since in the early days of operations there seems to be a somewhat higher failure rate after the accelerators have been powered down several days (presumably due to the thermal cycling of components), a procedure of running all magnet supplies for 8-16 hours prior to the accelerator startup tends to induce failures in supplies suspected of early breakdowns.

The actual expenses for the assembled CESR chopper hardware in 1977 dollars was used to figure the per piece costs in Table 2. An estimate of the per piece expense for equivalent hardware in 1991 dollars is also included in Table 2. The reason that some of the 1991 costs have risen less than inflation is that prices of many of the electronic components have fallen over this period of time.

Table 2. Per piece costs of chopper regulator hardware for CESR

Component	Actual Cost in 1977 $	Estimated Cost in 1991 $
Chopper regulator chassis	$120-200	$250-333
DCCT regulator circuit card	$410	$570
Shunt regulator circuit card	$112	$235
Transductor (DCCT)	$46	$125

Before finishing chopper design considerations, some space must be devoted to the question of chopper induced EMI. It is important to realize that the CLEO detector operates with no EMI problems having magnets driven by choppers within 1.3 m of 18,000 preamps with a threshold sensitivity of 25 μV and a 10 nsec risetime. Although this has not been a very serious problem for the open frame choppers in CESR, some effort has been spent understanding and reducing the major source of EMI in the chopper circuit. The EMI occurs during the switching transients with the dominant source occuring at the time that the transistor switch begins conduction. As these transistors begin to conduct the full magnet's current and the fast recovery diodes begin to shut off, these diodes conduct a large current pulse which removes the charge stored in their junctions. In the original chopper design the switching transistors were driven into conduction rapidly with something like a factor of 3 to 4 overdrive of the base current. This permitted the diodes to conduct 300 to 400 A peak currents lasting roughly 20 nsec. This pulse effectively couples to the cables leading to the magnet which behave like a combination transmission line and antenna. The modification made to the CESR choppers was to increase the switching time of the transistors by about 50% and use the impedance of the emitter current sharing resistors with a voltage clamp on the base of the darlington driver transistors to make an effective current limiter for the drive transistors. The net effect was to reduce the peak surge current from the fast recovery diode turning off and to lengthen the duration of surge pulse, both effects reduce the EMI. One other technique is to run the magnet leads within a shielded braid, grounded at the magnet, and to AC terminate each lead of the effective twinax transmission line into its characteristic line impedance. Although the bypass capacitors do increase the rise time of the switching voltage across the magnet's coils the dominate effect is to shield and terminate the noise pulse which would have rung back and forth along the cable.

System Diagnostics in Use in CESR

The CESR chopper supplies have a number of protection circuits which will inhibit the chopper's current on a fault. These are a bus voltage monitor (trips at 80% of operating voltage), a temperature monitor on the water cooled heat sink, a transistor emitter over current trip and an over-voltage trip for the transistor collectors' saturation voltage. The latter two fault conditions were an attempt to limit the transistor's power to within the safe operating area of the transistors. As Implemented these latter two faults have generally not been too useful; future designers are likely to find success with a slightly more sophisticated transistor dissipation measurement. The first two fault circuits have been particularly useful, with the former limiting the bus surge currents during a main power supply fault and the over temperature fault sensor providing protection against a loss of cooling for the chopper (and also the magnet it services since the magnet's cooling is in series with the chopper's outlet water.)

In addition to the fault protection the CESR choppers have a magnet voltage monitor and a current regulation error tracking monitor (both having >100 Hz bandwidth); these signals are digitized by an ADC and can be accessed by the control system. The digitizing resolution of the current tracking error is 40 PPM FS for the DCCT regulated supplies and 300 PPM FS for the shunt regulated supplies. Although the CESR control system is capable of reading hundreds of voltage and regulation error signals at nearly 100 Hz in several second bursts, the obvious development for future designs would make use of the low cost of digital memory to locally provide a scrolling history of these signals.

The philosophy of the magnet power supply diagnostic software and displays at CESR has been developed with the intention of maintaining the minimum amount of "on-line" diagnostics (those which are running all the time), but to have a battery of tools available to the operator to be called on as needed. The only "on-line" diagnostic is a program which checks periodically that no chopper power supplies have tripped off; this suffices for the vast majority of problems. The most used off-line diagnostic is a window display of, for example, one of the magnet sectors; this display contains the magnets' name, set point, a bar graph of the tracking error, voltage readback and fault status. Besides finding the obvious types of errors, this diagnostic is even useful for regulators whose feedback loops have become slightly unstable: easily visible as quadrature oscillation between the tracking error and magnet voltage. Another diagnostic program reads and records the voltage and tracking error readbacks at rates up to 100 Hz in several second bursts for roughly 30 seconds, the results may be displayed as histograms of the readbacks enabling one to locate supplies that have atypical distributions (suggesting

potential regulation problems) or as FFT's of the time response to locate oscillating supplies. A third diagnostic tool is useful when there are intermittent failures in the system; this is a program that runs continuously monitoring one or more classes of magnet supplies and writing records in a file whenever any of the readbacks are outside a prescribed tolerance. When the intermittent event occurs the file may be scanned for any supplies which had failed at the same time. The last diagnostic tool to be discussed cannot be used with a stored beam since all the power supplies are turned off and a current is run in series through the special calibration winding of each of the DCCT's; the precision reference current commands are adjusted to match the tracking when the supply is regulating. In the matter of a few minutes the calibration of all precision current sources may be checked to 40 PPM FS.

OPERATIONAL BENEFITS

There are, of course, many benefits from using chopper regulators which have been mentioned above. There are several operational benefits to the freedom to have independent powering of quadrupole and sextupole magnets and three are worth mentioning. The first is the flexibility of linear and non-linear lattice design. As an example, the flexibility of the powering of the CESR quadrupoles has permitted the operation of the ring from integer tunes of 7 up to 15. The second benefit is the ability to easily locate the beam position monitors with respect to the quadrupole centers, by moving the position of the beam in the quad until it no longer steers. The final advantage of the independent powering of the quadrupole magnets is the capability of measuring and correcting the beta functions at each quadrupole. This beta correction is a standard part of the lattice loading procedure at CESR.

CONCLUSIONS

Chopper power supply regulators have demonstrated excellent performance and reliability during the 14 years of operating CESR. They are a very practical, efficient and cost effective solution for providing independent current regulation for a storage ring's linear and non-linear focussing elements.

ACKNOWLEDGEMENTS

The author would like to thank D. Rice and D. Hartill for many useful discussions about the CESR chopper system and D. McGhee for information about the APS chopper designs.

REFERENCES

[1] D.L. Hartill and D.H. Rice,"The CESR Magnet Power Supply System," IEEE Trans. on Nuc.Sci., Vol. NS-26, No. 3, pp.4078-4079, June 1979.

[2] T. Jackson, "Design and Performance of PEP Power Systems," IEEE Trans. on Nuc. Sci., Vol. NS-28, No. 3, pp. 2737-2741.

[3] H.W. Isch, A. Dupaquier, K. Fischer, R. Forrest, J. Pett, Proudlock, "Switch Mode Power Converters: Present and Future," *Proceedings of the 1989 IEEE Particle Accelerator Conference*, Chicago, IL, March 20-23, 1989, pp. 1151-1153.

[4] D. McGhee, "Status of Magnet Power Supply Development for the APS Storage Ring" *Proceedings of the 1989 IEEE Particle Accelerator Conference*, Chicago, IL, March 20-23, 1989, pp. 1925-1927.

[5] A.C. Lira, J.A. Pomilio, and D. Wisnivesky, "Power Supplies for the LNLS Magnets" *Proceedings of the 1989 IEEE Particle Accelerator Conference*, Chicago, IL, March 20-23, 1989, pp. 1922-1924.

MULTIMEGAWATT RF POWER SOURCES FOR LINEAR COLLIDERS*

G. Caryotakis
Stanford Linear Accelerator Center, Stanford University, Stanford, CA 94309 USA

Abstract

Conceptual designs for a future linear collider operating at 11.4 GHz call for peak rf power as high as 240 MW per meter, with an accelerator length of 14 km. This is an extremely high total power, which results in requirements for microwave sources that cannot be met with existing microwave tubes. While some new tube concepts are being considered, work is proceeding at several laboratories in the US and abroad on conventional 100 MW klystrons for this application. The electron beam necessary for this power to be generated, unless carefully controlled, can easily cause intrapulse melting at the klystron output circuit. This, coupled to the need for good efficiency, high production yield, and long life, poses some difficult problems to the klystron designer. Experimental klystrons at SLAC and other laboratories are approaching the goal of 100 MW in 800 nsec pulses, but much work remains to be done before a design is available which is suitable for manufacturing thousands of these tubes.

I. Power Source Options

Proposals for future linear colliders call for center-of mass-energies in the 0.5–1.0 TeV range. From studies conducted at SLAC, an attractive approach for what is referred to as the Next Linear Collider (NLC), is a 14 km machine, operating at 11.4 GHz. In Phase I of this project, a gradient of 50 MV per meter is required to reach 0.5 TeV. For Phase II, the collider would be expanded to a full TeV by doubling the gradient, i.e., quadrupling the RF power. This power calculates to 60 MW per meter for 0.5 TeV and 240 MW for the full TeV.

Despite a short pulse length (100 ns), this is a substantial concentration of power at a frequency where no conventional high power microwave tubes are available, or have ever been developed. No ground-based or ship radars using X-Band sources above one megawatt are in existence and there is no previous experience with X-Band accelerators at this power level.

The absence of an established technology for a power source has stimulated some novel approaches. The high peak powers required suggest high current, lower voltage tubes, such as a multiplicity of magnetrons or crossed field amplifiers. The numbers are impressive. If, for instance, state-of-the-art 5-megawatt crossed-field amplifiers were considered as sources, a total of almost 70,000 tubes would be required. Unit cost in these quantities could probably be lowered below the $1000 level by employing advanced automated manufacturing methods, similar to those used in the production of cooker magnetrons. Furthermore, one could aspire to triggering the CFA's with RF, eliminating the need for modulators. The combination of these possibilities is intriguing and perhaps worth pursuing. A CFA development program was, in fact, initiated at SLAC, but for tubes in the 100–200 MW level. The effort was discontinued for budgetary reasons. SLAC physicists, in collaboration with LLNL, also took a hard look at the relativistic klystron as a potential NLC source. Although a power output of 270 MW was reached (with short pulses), a decision was made against further development because of the complexity and cost of the device.

Other approaches include some tube schemes which were initially proposed several decades ago, at a time when there was DOD interest in microwave "superpower" tubes. Modern versions of these are the "cluster klystron" and the "sheet beam klystron." Such devices require a great deal of R&D work in order that some inherent problems in spurious mode control and in beam optics can be solved; but they hold promise as NLC sources if these problems could be brought under control. They are being pursued at a low level at SLAC.

Finally, there is the gyro-klystron, a "fast wave" amplifier which, in oscillator form, has been very successful as a generator of very high peak and average powers at millimetric frequencies. Significant progress has been made recently at obtaining stable gain from an X-Band gyroklystron at the University of Maryland.

Clearly then, there are several alternatives to the NLC source requirement, some of which deserve R&D efforts. However, a test accelerator is being planned now, and construction may begin within the next 2–3 years. The resulting urgent need for sources is not consistent with longer-term R&D. Consequently, the decision was made at SLAC to design and build a 100 MW klystron. The plan is to use this tube in conjunction with an RF pulse compressor which will increase peak power by a factor of about 5, while reducing the pulse length from 800 to 100 ns.

The remainder of this paper addresses the issues associated with the design of the klystron, the approaches taken at SLAC and elsewhere, the available results, and the outlook for the future.

II. The Klystron Design Problem

Output power capability in linear-beam microwave tubes scales approximately as the inverse of the square of the frequency, on the basis that maximum power is limited by the area available to dissipate beam or RF losses. Thus, the klystrons which power the SLC, producing 60 MW at 2.856 GHz with 210 Joule pulses, would scale to 3.75 MW and 13 Joules at 11.4 GHz. Of course, the power of these standard SLAC klystrons is not the limit of what can be attained at S-band. Experimental SLAC tubes have been built and operated at 150 MW. Even so, the increase in Joules per unit area, is quite considerable.

With a 100-megawatt klystron source augmented by a pulse compressor, the NLC would require about 1700 tubes for the 500 GeV Stage 1 machine. That is a prodigious number of very advanced microwave tubes, which will have to be produced with very good yield and reliability, if the economics of the machine are to be sensible. A klystron design is needed which provides an adequate margin of safety

* Work supported by Department of Energy contract DE-AC03-76SF00515.

U.S. Government work not protected by U.S. Copyright.

Table 1. 100 Megawatt Klystron Projects

	Design Voltage (kV)	Micro-Perveance	Maximum Power (MW)	RF Pulse Length (ns)	Comments
Novosibirsk [a]	1000	0.3	55	700	Gridded gun, permanent magnet focusing. Parasitic oscillations limiting power
KEK [b]	450	0.6	11	70	Failure due to output window fracture
Haimson	500	1.4	100	50	50 ns beam pulse
SLAC	440	1.8	72	100	Pulse breakup limiting output power, 1 μs beam pulse

[a] Operating frequency: 14 GHz. [b] Phase I Klystron designed for 30 MW.

electrically and thermally, and make possible production in large quantities by relatively unskilled workers.

Klystron design usually proceeds by choosing the beam voltage and current, or by selecting the "perveance" of the electron gun, defined as current/(voltage).$^{3/2}$ Simplicity, along with modulator cost and efficiency, argue for as low a beam voltage as possible, but for a linear-beam microwave tube at this frequency, conversion efficiency is known to deteriorate as the microperveance increases from, say, 1 to 2. The choice of the higher perveance and current also forces a beam of higher convergence, if the klystron cathode is to be operated at a current density and temperature consistent with long life. In turn, a higher convergence inevitably requires more precision in beam optics, with the attendant impact on reliability and cost. To provide some perspective, the SLC klystrons, which have a fine record of reliability and long life and operate at 44% efficiency, use a microperveance of 2 and an area beam convergence of 18, resulting in an average current density at the cathode of 6 amp/cm. An NLC klystron at the same perveance, efficiency and cathode loading requires a convergence of 200.

An additional argument for lower perveance is that the necessary beam confinement magnetic field can be correspondingly lower. The average output power of the NLC klystron, as postulated above, is less than 20 kW. Yet, the power consumed by the electromagnet can range from 15 to 50 kW, depending on the length of the tube and the inner diameter of the magnet. Thus a klystron electronic conversion efficiency of 40% can be degraded to an overall efficiency of 20% or less. A superconductive magnet can eliminate this need for additional power, but with considerable additional system complexity and initial cost. An alternative is permanent magnet focusing, which requires very low perveance.

There are two failure mechanisms which, together or in combination, set a limit on the power obtainable from the klystron. The first is RF breakdown in the output circuit. The second is intrapulse heating due to beam interception. The two are interrelated, with pulse heating probably the root cause of failures. In view of the above, beam control becomes a critical issue and this, more than any other consideration, is the strongest argument for lower perveances. These mechanisms need to be examined in more detail since they are at the core of the NLC klystron design problem.

In a conventional klystron RF power is extracted from the bunched beam while it traverses a resonant cavity shaped to present a short gap to the beam. The RF voltage across that gap must be equal or slightly higher than the DC beam voltage in order for the interaction between beam and circuit to be efficient. Consequently, as the beam voltage is increased, the RF gradient across the output gap may cause breakdown above a certain limit. The value of this limit is very difficult to determine because it is a function of vacuum and surface conditions in the immediate vicinity of the output gap.

Experiments at SLAC have produced some empirical values for RF breakdown in accelerator cavities with no beam present. At 2.856 GHz the gradient above which breakdown will occur was found to be approximately 3 MV/cm. It has been suggested that this threshold increases as the square root of the frequency so that at 11.4 GHz it would be almost 6 MV/cm. In fact, klystron output cavities in experimental tubes have been found to break down at a tenth or less of this value. It is clear that beam interception at the output gap or its vicinity creates the local conditions that cause RF breakdown to occur.

These local conditions arise from intrapulse heating as a result of beam interception. It can be shown that at 440 KV, where the SLAC tubes are designed to operate, 3 amperes of beam current intercepted on one square millimeter of copper surface will melt the metal within the one-microsecond beam pulse. This current is less than one percent of the klystron beam current at that voltage and consequently rather difficult to detect. If the melting occurs in the output circuit during the RF pulse it can be expected to cause some form of local plasma in which the RF field must be developed. Hence the RF breakdown.

The solution to the problem must be two-fold. First, beam optics must be excellent, particularly in the vicinity of the output circuit. Second, output circuits must be designed in which field gradients are minimized, most likely

by arranging that the interaction with the beam takes place over several gaps, rather than just one, as in the case of an ordinary klystron. This can be done with coupled resonant cavities, i.e., a standing-wave circuit, or with travelling-wave output. In both cases ordinary klystron cavities would precede the output circuit, providing RF gain and a bunched beam to drive the output.

With this background we can now review the work performed to date in this country and abroad. Four groups are addressing the problem independently: at the Novosibirsk Institute in the USSR, the VLEPP collider and its power sources are being designed to operate at 14 GHz. The other groups, at KEK, SLAC, and Haimson Research Corporation, are designing 11.4 GHz klystrons. Table 1 summarizes the approaches taken by each of the four groups.

The Soviet design is extremely ambitious, and attempts to address, in one vacuum envelope, several fundamental issues of the NLC power source. The tube consists of a klystron input section and a travelling-wave output. A probable reason for the extremely low perveance is that the tube is designed for periodic magnetic focusing. For this scheme to be effective, a long plasma wavelength in relation to the magnetic period is required. Finally, the tube is equipped with a gridded gun and an arrangement of electrodes that serve to provide the correct potential profile for beam formatior and focusing. These electrodes, which serve to distribute cathode-anode gradients more uniformly, together with the grid, offer the possibility of pulsing the klystron using a quasi-DC high voltage supply and a low voltage modulator in series with the grid.

Experimental results on the VLEPP klystron are not known with great precision. The tube has apparently produced as much as 50 MW with 700 ns pulses, but with a repetition rate of only about 1 Hz. Peak power was apparently limited by parasitic oscillations in the travelling-wave section, and not by beam interception, which is reported to be as high as 40% with full RF output.

In Japan, KEK has approached the design of a 100 MW klystron in two stages. The first tube, a microperveance 0.6 conventional klystron, was designed to produce 30 MW and was tested to 11 MW, with 70 ns RF pulses. A window failure terminated testing at that point. A full power klystron is expected to go to test later this year. It is designed to operate at 550 KV, at a microperveance of 1.2. The ouput cavity is not extended, but employs a longer interaction gap than is conventional in order to reduce surface gradients. KEK calculates a 700 KV/cm gradient for this output cavity and an efficiency of 45% for the tube.

The Haimson Research klystron employs a travelling-wave output as do the Soviets, but with a more conventional beam and focusing system. It is designed to operate at 500 KV, at a microperveance of 1.4, and is focused by an electromagnet. This tube is the only one in this survey to have produced over 100 MW. It may owe this distinction to the fact that it was operated with both high voltage and RF pulses of the order of 50 ns. The Haimson tube is also reported to have good efficiency and stability, which suggests a mature design for the output circuit.

III Experimental Results at SLAC

At SLAC three klystrons have been built and tested, though the third and last tube was damaged early in test

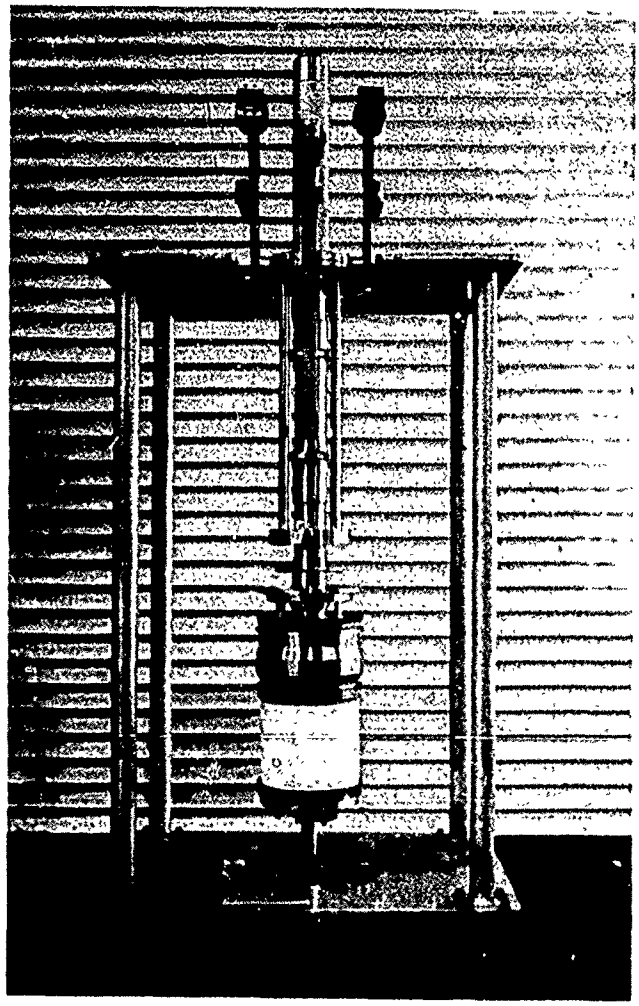


Figure 1.

and did not produce significant results. All of these tubes employed higher perveance guns than those used by the other groups, and were designed to operate at 440 KV. A conventional single-gap output cavity was used at the first of these klystrons, designated XC1 . It was calculated to have a maximum surface gradient of 1300 KV/cm at full power output. The second and third klystrons made use of a double-gap "extended interaction" cavity, operating in the 2π mode. The maximum surface field for this cavity was calculated at 750 KV/cm. A photograph of the XC2 is shown in Fig. 1 and a drawing in Fig. 2. The second SLAC klystron tested produced the best results. Four conventional cavities are used to drive the extended interaction output. The beam is formed by an electron gun with an electrostatic area convergence of 35:1. The beam is further compressed by the confining magnetic field to a total area convergence of 200:1. Two RF windows are used, which in the case of the XC-2 were of the pillbox type, with a thickness of only 30 mils. These windows failed repeatedly and the tube was repaired twice, the second time with much thicker windows.

The XC2 klystron was equipped with an isolated collector so that beam interception could be measured and the tube tested more safely. This did not turn out to be as useful as it was hoped. During test, transmission ap-

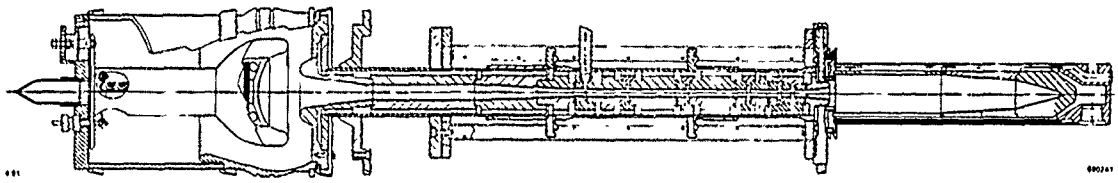


Figure 2.

peared to be perfect at all times, even with the tube operated into saturation. However, when the klystron was opened to replace a broken window and the beam tunnel was borescoped, a slight melting at the entrance of the beam tunnel and in the drift tube tips of the output cavity was observed. This was presumably due to pulse heating resulting from beam interception too small to detect by observing the difference between the cathode and collector currents.

Power output vs. beam voltage for the XC-2 is shown in Fig. 3. Note that during these tests the beam pulse width was fixed at 1 μs, while the RF drive pulse ranged from 800 ns at low levels to 100 ns at the maximum power of 72 MW. The benefits of the lower gap fields in the XC2 klystron are illustrated in Fig. 4, which compares the observed thresholds of RF breakdown as a function of pulse length for the XC1 and XC2.

The power of 72 MW, at the design voltage of 440 KV is to be compared with a value of more than 100 MW predicted by simulation. The code used allows radial motion in the beam but may not be providing sufficient detail in the simulation of electron motion due to the actual cavity fields. For the code to predict the low efficiency observed, a much smaller beam diameter must be postulated than is likely to be the case, given the damage observed at the cavity drift tube noses.

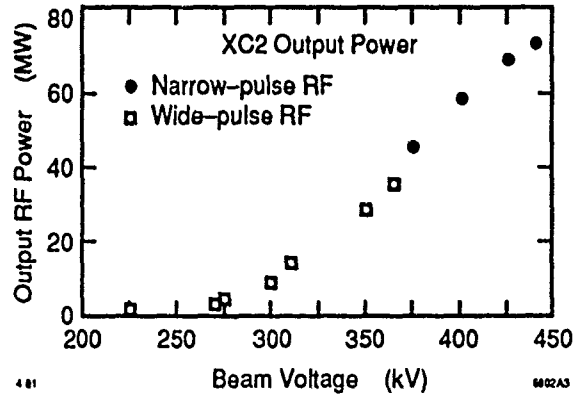


Figure 3.

The XC-2 klystron was used in a recent experiment to perform high power tests on a "binary" pulse compressor consisting of three stages, each of which combined the delayed leading half of an input RF pulse with the trailing half of the pulse. Delays were implemented by using overmoded low loss circular waveguides. The klystron was operated with an output of approximately 30 MW and 800 ns pulses, producing an input to the pulse compressor

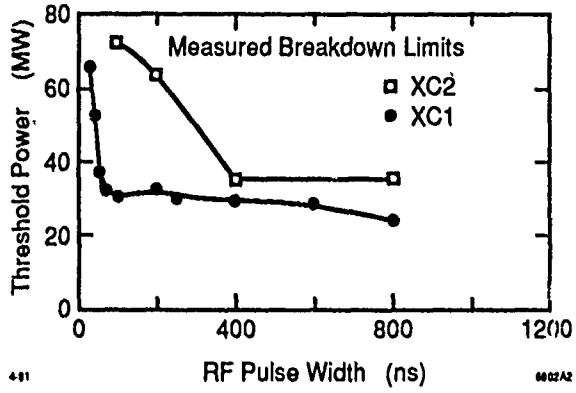


Figure 4.

of 25 MW. The result was compressed pulses of 120 MW with pulse lengths of 70 ns. The experiment is the subject of a separate paper in this conference.

IV. Future Directions at SLAC

It should be clear from the above that the design of 100 MW NLC klystron, especially one that can be produced in quantity, is a non-trivial problem. At SLAC the program for continued tube development is planned to address several issues.

The initial choice of a microperveance 1.8 beam was based on the successful SLAC S-Band work and the availability of ceramic seals and modulators for voltages below 450 KV. It now appears that for an adequate safety margin in a tube that must be produced in quantity, it would be prudent to use a lower perveance. A new test bed is being prepared which will permit operation up to 600 KV. In the meantime we plan to continue our work at 440 KV using new beam optics, without magnetic beam compression and with a total area convergence of 120, accomplished electrostatically. The purpose is to improve beam quality and to reach higher power levels without pulse breakup. During this phase of the program, klystrons will be constructed in which output circuits can be easily interchanged and a study of alternatives conducted efficiently. It is expected that standing-wave as well as traveling-wave extended interaction output circuits will be evaluated in this fashion. When the design of a new microperveance 1.2 gun and the higher voltage test bed are complete, the tube development program will continue at the lower perveance, using the same techniques of output circuit interchangability for evaluation.

In parallel with the main program of refining beam optics and selecting an optimum output circuit other klystron sub-components require development and production. Principal among those is the output window. The

windows currently used in the XC series of klystrons are 1.1 inches in diameter and 0.15 in. thick. They are not expected to be adequate for full power tubes, but will be evaluated in an X-Band resonant ring now nearing completion. Meanwhile, larger windows are being designed. Consideration is also being given to TE_{01} windows, with a transition to this mode within the tube envelope.

The core of the problem is at the output. Before a successful 1 μs, 100 MW klystron is built, it will be essential to understand, in some detail, the interaction between the beam and the fields at the output circuit. A general description of this process is provided by simulation codes which, in the "large signal" regime, predict interaction efficiency with accuracies that are of the order of perhaps 10 percentage points, as indicated above. A byproduct of this calculation is also a beam interception calculation. For the NLC klystron it is critical to evaluate the tradeoffs between efficiency and beam interception with better accuracy. A moderate uncertainty in efficiency can be tolerated, but a few percentage points of interception will destroy the circuit.

Furthermore, means must be found to detect beam interception with considerably more sensitivity than is currently available through the isolated collector. If some melting of the output circuit can occur during a single pulse, there must be provision in the modulator to remove beam voltage on a pulse-to-pulse basis. This is essential both in the development phase of the klystron, in order to reduce tube losses, as well as in the operations phase of the collider.

Finally, it will be necessary to use "beam shavers" at several locations in the tube in order to control beam scalloping. These are slight constrictions in the drift tube diameter built of a refractory metal, such as molybdenum. Molybdenum may also serve to protect drift tube noses in the output circuit.

It is expected that the combination of lower perveance, improved output circuits and the other features described above should produce successful klystron prototypes during the next year. They will be used in a Test Accelerator at SLAC whose construction should begin in the 1993-94 period.

ACKNOWLEDGMENTS

The author wishes to thank T. G. Lee, who is the engineer responsible for the XC klystron project at SLAC, and A. E. Vlieks who has supervised much of this work, for many useful discussions and for their continued dedication to a very challenging project.

THE MAGNICON:
A NEW RF POWER SOURCE FOR ACCELERATORS

Oleg A. Nezhevenko
Institute of Nuclear Physics, Novosibirsk, 630090, USSR

INTRODUCTION

In the second half of the 60th the Institute of Nuclear Physics (INP) at Novosibirsk faced the problem of creating a high-power RF generator for the electron-positron storage ring VEPP-4. In the course of research work on this problem G.I. Budker invented a new RF power source—Gyrocon. [1, 2]. The gyrocon like many other devices (..g. klystron) comprises an electron source, an input cavity for the beam modulation, a drift space and an output cavity for the electron deceleration. But unlike other RF tubes, in gyrocon the beam is not bunched, but is modulated by its circular deflection. The deflected electrons move along straight lines making a cone surface and are passed through a circular slit to the output cavity, which is a rectangular waveguide formed in a ring. With their entering point in the output cavity being continuously changed, therein the particles excite a wave travelling along the azimuth with a decelerating electric field in the point of beam passage (TE_{10} oscillations). The employment of a relativistic beam and the absence of bunching provides for the gyrocon high power and high efficiency.

Experimental parameters of all existing gyrocons are listed in Tabl. 1. The test results have proved the feasibility of RF power sources based on gyrocons and their applicability in accelerators and storage rings. At the same time there emerged problems usually arising in the course of development of a high power and high frequency gyrocon. Some of these problems are connected with overheating and breakdown of the cavities due to the decrease in their size. Another restriction is bound up with the fact that it is hard to pass a beam (in the absence of magnetic focusing) through the slits in the output cavity walls due to the narrowing of the slits and shortening of the distance between the slit edge and the beam «boundary». The problems with the beam passage make it impossible to reduce the energy of electrons (as, for example, in [5]) which could improve the cavities function.

An attempt to overcome these problems has resulted in the creation of a new RF power source with a circular deflection of the electron beam—Magnicon [6,7].

1. OPERATION PRINCIPLE OF THE MAGNICON

The magnicon design is schematically given in Fig. 1. A continuous electron beam from the electron source 1 reaches the circular deflection device 2 to be deflected there at an angle α_0 by an RF magnetic field rotating with a deflection frequency (ω). The field distribution in the cavity is shown in Fig. 2. In the drift space electrons deviate from the device axis and get into a stationary magnetic field (B_z) of the solenoid 3. While entering the magnetic field the longitudinal velocity of the electrons is transformed into a rotational transverse one, and the degree of the transformation is

Table 1

Gyrocon	Initial	CW VEPP-4	Pulsed*) VEPP-4	Pulsed Balakin's	Pulsed Los-Alamos
Frequency, MHz	430	182	430	7000	450
Power, MW	0.6	0.4	65	60	0.15
Pulse width, μs	20	10	0.7	50	
Repetition rate, pps	0.1		1	1	
Beam voltage, kV	320	240	1600	1300	82
Efficiency, %	65	60	75	25	23
Gain, dB	7	17	26	60	
References	[3]	[2]	[2]	[4]	[5]

*) In operation since 1978.

0-7803-0135-8/91$01.00 ©IEEE

characterized by the pitch angle α. Further on, travelling along a helical trajectory and steadily changing their entering point in the output cavity 4, the electrons excite a wave in the cavity travelling along the azimuth (TM_{110}) oscillation mode, Fig. 2) and transfer their energy to this wave. If the cyclotron frequency (Ω) is close to the operation one (ω) (i.e. to the circular deflection frequency, to which the cavity is also tuned) and the direction of the cyclotron rotation coincides with that of the deflection device, then the interaction can remain effective during many periods of RF oscillations.

The particle energy is transferred to the electromagnetic field in the magnicon output cavity due to the decrease in the transverse component in its velocity at a practically constant longitudinal one. It can be easily explained using as an example the deceleration of a nonrelativistic electron rotating in a homogeneous static magnetic field around the cavity axis. The fields in the cavity are known to have the following relations $Ez=-\omega r B_\perp$ (r is the radius) and in case the cyclotron frequency coincides with the operation one and, hence, the transverse velocity component is $V_\perp=\Omega r=\omega r$, then $F_z=e\ [E_z+V_\perp B_\perp]\equiv 0$. Thus, the transformation of the transverse velocity into the longitudinal one which takes place in the cavity under the action of $B_\perp$ is fully compensated by the decelerating effect E_z. As a result, the limiting electron efficiency is determined by the efficiency of the electron energy transfer into the rotational motion at the entrance into the magnetic field (i.e. by the pitch angle α) and is equal to $\eta_e\approx\sin^2\alpha$.

A long interaction and the resulting length of the output cavity lead to an essential decrease in the RF field strength, in ohmic losses and in a specific heat release. Besides, the large holes made for the beam in the centre of the cavity end walls (their diameter is equal approximately to two Larmor ones) in tandem with the «magnetic accompaniment» practically removes the problem of the current interception. Thus, the magnicon, if compared to the gyrocon, provides for attaining higher powers at shorter waves, with the high efficiency characteristic of this class of RF power sources being preserved.

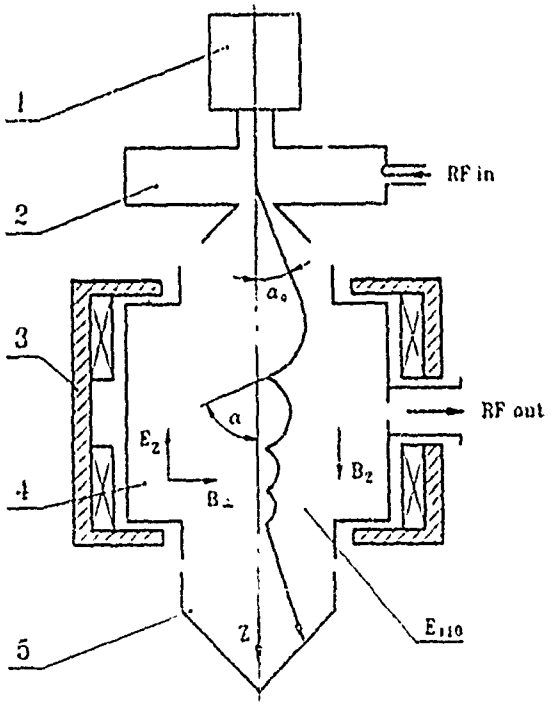


Fig. 1. Schematic of the magnicon: 1—source of electrons; 2—circular deflection cavity; 3—solenoid; 4—output cavity; 5—collector.

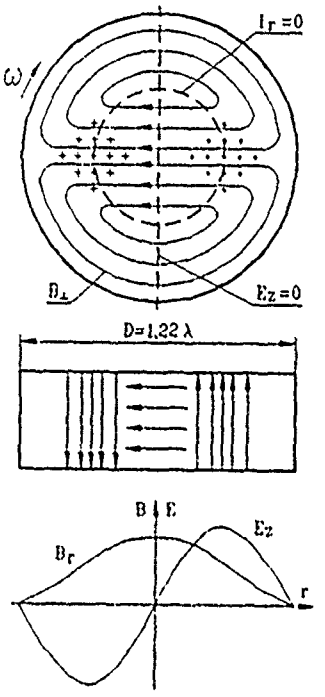


Fig. 2. Distribution of electromagnetic fields in magnicon cavities.

2. MAGNICON OUTPUT CAVITY

1. In the general case the problem cannot be solved analytically, but the interaction peculiarities can be studied while solving a simplified problem of motion of a thin nonrelativistic beam in given electromagnetic fields of a perfect (with no holes) cavity. The solution of equations of motion [7, 8] shows that the electron deceleration in a rotating wave TM_{110} at a resonant longitudinal magnetic field B_z (i.e. $\Omega=-\omega$ [1]. $\Omega=e/m_0B_z$ is the cyclotron frequency, ω is the operation frequency) is accompanied by a change only in the transverse particle velocity ($V_\perp$) while the longitudinal one (V_z) during the period of RF oscillations remains unchanged:

$$V_\perp=V_{\perp 0}\pm\Omega_{RF}\,l_\perp t,\quad l_\perp=V_{\perp 0}-(\Omega_{RF}/\Omega)\,l_\perp\sin\omega t \qquad (1)$$

[1] The sign «minus» corresponds to the coinciding direction of the electron cyclotron rotation and the wave rotation.

Here: $V_{\perp 0}=V_0\sin\alpha$, $V_{z0}=V_0\cos\alpha$, $V_0=\beta_0 c$ is the initial velocity, α is the pitch angle, $\Omega_{RF}=(e/\gamma_0 m_0)B_\perp$, $B_\perp$ is the RF magnetic field in the region of particle motion (Fig. 2).

From (1) it follows, that V_z is oscillated with an amplitude depending on the relation $B_\perp V_\perp/B_z V_{z0}$ (the lower the relation, the lower is the amplitude). From (1) it also follows, that in the course of deceleration $V_\perp$ is linearly decreased with time and the trajectory of a single particle makes a helix with a constant step and a decreasing radius. The helix axis is parallel to that of the cavity and the distance between them is equal to the initial Larmor radius R_L (Fig. 3). An instant picture of the beam position in the output cavity (Fig. 4) shows a helix with a constant radius, which axis forms an angle $\xi=\text{arctg}\,(\text{tg}\,\alpha/\theta)$ with the axis of the cavity ($\theta=\omega h/V_{z0}$ is the angle of flight of the electron in a cavity with a height h).

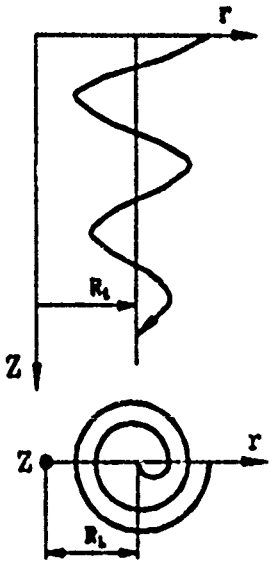


Fig. 3. Electron trajectory in the output cavity.

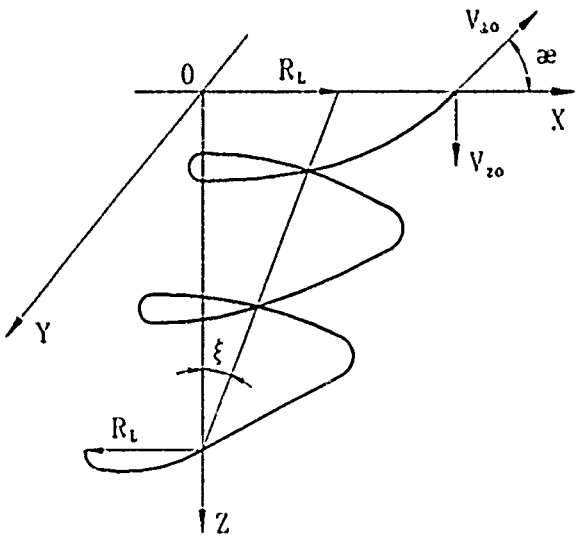


Fig. 4. The instantaneous position of the beam in the output cavity.

The RF field value optimal for deceleration can be found from (1) on condition, that by the end of passing the cavity the transverse velocity component will decrease to zero:

$$\Omega_{RF}^{opt}=(\omega V_{\perp 0}/0V_{z0})=(V_0/h)\sin\alpha. \qquad (2)$$

Expression (2) helps to calculate the optimal voltage value in the cavity. In the maximum of the electric field

$$U_{opt}=2.33(U_0/\beta_0)\sin\alpha, \qquad (3)$$

where U_0 is the beam voltage. For example, at $U_0=200$ kV and $\alpha\approx 90°$ $U_{opt}=670$ kV and is independent of the cavity height. The possibility of increasing the cavity height enables to reduce the field strength and decrease the losses in the walls[2]. The limiting cavity height is determined by the possibility of selection of parasitic modes and may exceed two wavelengths.

The magnicon can also be operated in the frequency multiplication mode, if in the output cavity the oscillations TM_{m10} are excited with a frequency $m\omega$, m times exceeding that of the deflection [8]. Many-fold multiplication of the frequency can in principle be obtained, an increase in m results in a reduction of RF fields in the region of the beam motion and of practical interest is mostly the frequency doubler. In the output cavity of the frequency doubler a TM_{210} wave is excited (Fig. 5) with a frequency two times exceeding that of the deflection system. The cyclotron rotation frequency of particles is also two times higher than that of the deflection system ($\Omega=-2\omega$). In spite of the absence of the cyclotron resonance a long time interaction takes place due to a quadruple distribution of the TM_{210} oscillation electromagnetic field. The mechanism of interaction of the electrons with the field is similar to that in the amplifier and the maximum electron efficiency is also $\eta_e\approx\sin^2\alpha$. The trajectory of a single electron is also a helix with a decreasing radius, but its axis is bent off the cavity axis [10]. The bend in the helix axis is bound up with the unlinear dependence of the electromagnetic field on the transverse coordinate. The optimal voltage in the cavity at the maximum of the electric field $U_{opt}\approx 3.1\,U_0\beta_0^{-2}$[3].

[2]The shunt impedance of the cylindrical cavity with a travelling along the azimuth wave TM_{110} [13]. $R_{sh}=122h^2[\delta(2h+d)]^{-1}$, δ is the depth of the skin layer, d is the cavity diameter.

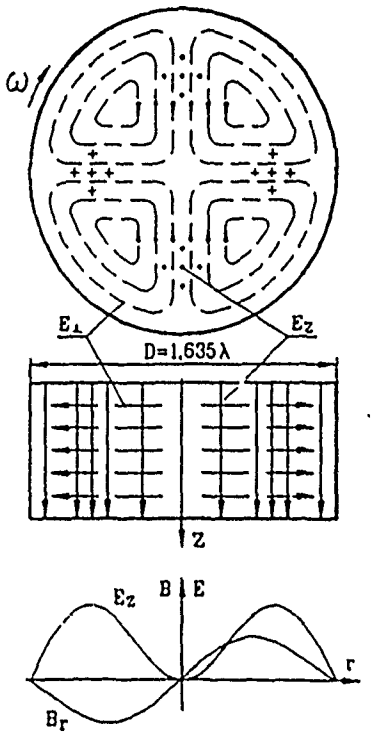


Fig. 5. Distribution of electromagnetic fields in the frequency doubler magnicon output cavity.

2. When for sustaining the synchronism a relativistic beam is used, the accompanying magnetic field ($B_z \sim \gamma$) should be decreased with deceleration. This leads to additional (uncompensated by the action of the electric RF field) transformation of the transverse momentum component into the longitudinal one and, as a result, to a decrease in the efficiency. The maximum value of η_e in this case can be estimated as:

$$\eta_e = (\gamma_0 + 1/2\gamma_0)\sin^2\alpha, \qquad (4)$$

where γ_0 is the initial value of the relative electron energy. In an ultra relativistic case η_e is easily shown to tend to 50%.

This problem can be overcome if the synchronism is sustained «in average» [8], i.e. by providing a homogeneous magnetic field in the output cavity

$$B_z \approx \omega m_0/e(\gamma_0 + 1/2) \qquad (5)$$

In this case the longitudinal component of the initial particle momentum is preserved (in average during the cyclotron revolution period), and the expression for the electron efficiency takes the form:

[3]The shunt impedance for a cavity with a TM_{210} wave equals. $R_{sh} = 96h^2[\delta(2h+D)]^{-1}$.

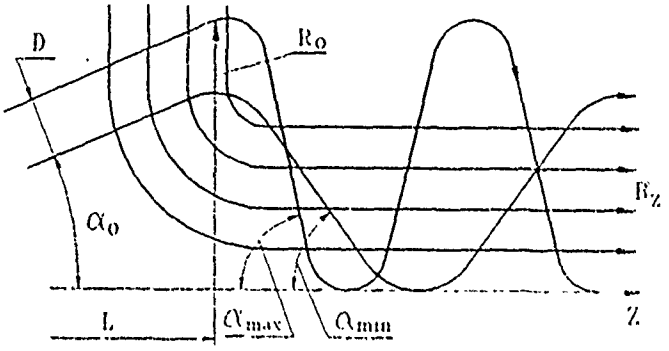


Fig. 6. The finite size beam in the magnetic field of the output cavity.

$$\eta_e = (\gamma_0 - \sqrt{\gamma_0^2 + (1-\gamma_0^2)\sin^2\alpha}\,)(\gamma_0+1)^{-1}. \qquad (6)$$

It is evident, that for $\gamma_0 \gg 1$, $\eta \approx 2\sin^2(\alpha/2)$ and large α it approaches 100%. The synchronism «in average» results in limiting the minimum value of RF fields in the cavity and some increase in the cavity voltage (in some sense, equivalent to the transit-time effect). The results of numerical simulation show, that the cavity length can exceed two wavelengths, up to $U_0 = 1-1.5$ MV, while voltage exceeds the value calculated in (3) but no more than 1.5 times.

3. The main factor reducing the efficiency and determining the magnicon power is the final beam diameter, which causes the spread of pitch angles (α_{max} and α_{min} in Fig. 6) at the entrance into the accompanying magnetic field of the output cavity and leads to an azimuthal «smearing» of the beam. The electron efficiency in this case is [8]:

$$\eta_e \approx \sin^2\alpha_{0\,av}\left[1 - \frac{D}{2R_0}\right]\left[\frac{\sin\delta\psi/2}{\psi/2}\right], \qquad (7)$$

where D and $\delta\psi$ are the radial and azimuthal beam dimensions, $R_0 = \beta_0\lambda/\pi$ is the Larmor diameter of the external particle. The beam size is first of all determined by particles deviation under the space charge effect in the drift space between the circular deflection system and the entrance to the output cavity. In fact, the drift space (L, see Fig. 6) should be reduced, i.e. α_0 should be increased, since $L = R_0 \operatorname{ctg}\alpha_0\sqrt{\sin^2\alpha - \sin^2\alpha_0}$.

The ultimate power of the magnicon is determined by the energy of electrons and the deflection angle. As a matter of fact, by setting the electron efficiency we practically impose limitations on the beam size at the entrance in the output cavity. In its turn, this size can be estimated with the help of usual relations for the envelope of a paraxial beam moving in the space free from external magnetic fields [8, 9]. Table. 2 lists the values of the ultimate beam power (P_0) at $\eta_e = 90\%$

Table 2

U_0, kV	200	300	500	800	1000
P_0, MW (at $\alpha_0=10°$)		0.1	0.5	2	4
P_0, MW (at $\alpha_0=30°$)	0.7	2	10	40	80
P_0, MW (at $\alpha_0=50°$)	4	13	52	220	500

The given estimates at ultimate powers and maximum deflection angles should be considered as approximated, as at a high perveance there will appear other restrictions for the efficiency bound up with the space charge. At the same time at $\alpha_0 \leqslant 30-50°$ the perveance is not very high and these restrictions are not decisive. While estimating η_e besides the finite beam dimensions it is necessary also to take into account the energy spread occurring in the process of circular deflection as well as an additional spread of deflection angles, taking place in the drift space under the action of the space charge. These effects, may result several percent decrease in the efficiency. The device efficiency ($\eta=P/P_0$, where P is the output power) is always lower than η_e due to the ohmic losses in the magnicon cavity walls, which might make 1—10% depending on the power and operating frequency. A due account of the mentioned above factors shows, that $\eta \approx 80\%$, which does not seem to be the limit for the magnicon, but serves a good illustration of the device abilities.

The minimum wavelength of the device is determined first of all by the breakdowns and overheating of the output cavity. For absolute deceleration of the transverse velocity component in the output cavity of the magnicon at $\gamma_0 \leqslant 2$ it is necessary to provide a RF electric field [8]:

$$E[\text{kV/cm}] \geqslant (117\eta_e^{1/2}\beta_0^2)\cdot(\lambda[\text{cm}]\sqrt{1-\eta_e(2+0.56\beta_0^2\eta_e-\gamma_0)})^{-1} \quad (8)$$

The above restriction is not very rigid. For example, for a CW magnicon at $\alpha=30$ cm and $P=3-10$ MW ($U_0=200-300$ kV) the RF field in the output cavity $E=15-20$ kV/cm, ohmic losses are 20—40 kW and the losses per surface unite are 10—20 W cm^2. In the pulsed amplifier at $\lambda=2$ cm and $U_0=500$ kV ($P\sim100$ MW) $E=300$ kV/cm, which value is essentially lower than that obtained for klystrons today [11].

3. CIRCULAR DEFLECTION SYSTEM

1. The circular deflection of an electron beam in the magnicon is performed by a RF magnetic field of a cylindrical cavity with TM_{110} oscillations (Fig. 2). The cavity is excited by an external generator to provide a circular polarization of the magnetic field in the paraxial zone crossed by the deflected electrons. This deflection method has been studied in detail in [9] and has proved reliable in the gyrocon, but the requirement of obtaining larger deflection angles in the magnicon puts forward additional problems. First, the gain coefficient drops, second, the electron beam energy spread grows, which results in the efficiency decrease. These problems have been overcome by accompanying the beam in the deflection cavity by a longitudinal stationary magnetic field, the cyclotron particle rotation in this case should coincide in direction with that of the RF field [12, 13]. The accompanying magnetic field compensates the «lag» of the particles from the rotating plane, in which the electric field

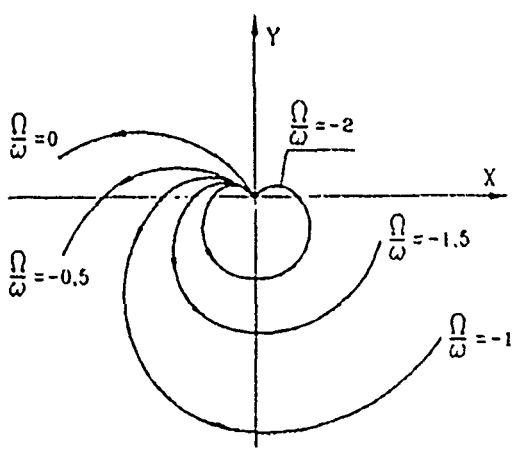


Fig. 7. Electron trajectories in the deflection cavity.

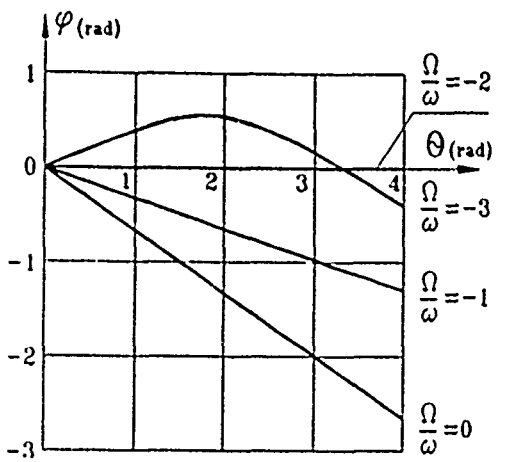


Fig. 8. Azimuth position of electrons in the rotating coordinate system.

strength of the cavity is equal to zero (Fig. 2), and the focusing effect of this field reduces the transverse beam size, and hence, the electron energy spread.

The analysis of the peculiarities of the circular deflection process can be carried out analytically in the approximation of small deflection angles [13], i.e. under the condition, that both the particle velocity in the direction of their initial motion and their energy are preserved. Shown in Fig. 7 are the projections of the particle trajectories onto the plane $x-y$ perpendicular to z. The closed cardioid in the case of $\Omega/\omega=-2$ is obtained at a flight angle $\theta=2\pi$. In Fig. 8 the particle azimuthal coordinate is given versus the flight angle. This dependence is observed in the system of coordinates rotating with a frequency ω, i.e. in synchronism with the RF field. At different values of B_z the motion takes place either in the region of the accelerating ($\varphi<0$ at $\Omega/\omega>-2$) or the decelerating ($\varphi>0$ at $\Omega/\omega<-2$) electric field of the cavity. At $\Omega/\omega=-2$ the electrons move in synchronism with the wave in the plane, where $E_z=0$ and their energy is remained unchanged. The angle of the particle deflection is:

$$\alpha_0=2\frac{\Omega_{RF}}{\omega}\frac{\sin[\theta/2(1+\Omega/\omega)]}{(1+\Omega/\omega)}=\frac{U}{U_0}\sqrt{\frac{\gamma_0-1}{\gamma_0+1}}\frac{1}{2J_1'}\frac{\sin[\theta/2(1+\Omega/\omega)]}{[(1+\Omega/\omega)\theta/2]}, \quad (9)$$

where $\Omega_{RF}=eB_\perp/\gamma_0 m_0$, U is the voltage amplitude in the cavity at the electric field maximum, $J_1'=0.582$ is the value of the Bessel function of the first kind first order in the first maximum. It should be noted, that at $\Omega/\omega=-2$ the dependence of α_0 on the flight angle (θ) is similar to that at $\Omega/\omega=0$. At $\Omega/\omega=-1$ the deflection angle is independent of θ.

To calculate the gain coefficient of the device it is necessary to calculate the losses in the cavity walls (P_R) and the power required for the beam acceleration (P_e. The sum of these powers makes the power of magnicon excitation:

$$P_{IN}=P_R+P_e=U^2/2[1/R_{sh}+\mathrm{Re}(\bar{Y}_e)] \quad (10)$$

Here U is the voltage amplitude in the cavity at the maximum electric field, R_{sh} is the shunt impedance of the cavity with a TM_{110} wave (see above), and $\mathrm{Re}(\bar{Y}_e)$ is the real part of conductivity, characterizing the beam-cavity interaction (i.e. electron conductivity). The electron conductivity [7] is:

$$\bar{Y}_e=\frac{I_0}{U_0}\frac{\gamma_0-1}{\gamma_0}\frac{1}{(J_1'\theta)^2}\frac{\omega}{\Omega}\left\{\left[\sin^2\frac{\theta}{2}-\frac{\sin^2[(1+\Omega/\omega)\theta/2]}{(1+\Omega/\omega)^2}\right]+\right.$$
$$\left.+i\frac{1}{2}\left[\sin\theta-\frac{\sin[(1+\Omega/\omega)\theta]}{(1+\Omega/\omega)^2}-\frac{\Omega/\omega\,\theta}{1+\Omega/\omega}\right]\right\}. \quad (11)$$

where I_0 and U_0 are the beam current and voltage.

The analysis shows, that for the values of the device power of practical interest the gain coefficient is maximal in the regime, when $\Omega/\omega=-2$ and the power is no more consumed for the beam acceleration ($\mathrm{Re}(\bar{Y}_e)=0$). In this case $P_{IN}=P_R$, and the flight gap is optimized for the minimum ohmic losses ($\theta_{opt}\approx\pi$). A 5-fold gain in the drive power is obtained in this case, compared to the case of a deflection device cavity without magnetic accompaniment, e.g. at $\lambda=30$ cm, $U_0=300$ kV and $P_0=3$ MW, the gain is 10—15 dB.

As it follows from (11), the beam not only loads the cavity but also detunes it. This detuning equals $\Delta\omega/\omega=0.5\rho\,\mathrm{Im}(\bar{Y}_e)$, $\mathrm{Im}(\bar{Y}_e)$ where ρ is a characteristic impedance of the cavity [9]. The beam reduces the cavity frequency, i.e. the cavity should be preliminary tuned to a frequency higher than the operating one.

In order to use the deflection system with magnetic accompaniment it is necessary to arrange the beam extraction into the drift space without essential losses in the transverse velocity. It is accomplished by placing a flux shield with a small hole for the beam to pass, which considerably limits the magnetic field in the region where the particles travel near the axis, i.e. for $\Omega/\omega=-2$, at a distance $l=(2n+1)B_z\lambda/4$ from the exit of the deflection cavity. The losses in the deflection angle at the particle extraction from a hole with a diameter d are $\Delta\alpha_0/\alpha_0=(\pi d/2\beta_z\lambda)^2$. They usually lead to a not more than 10—15% decrease in the gain [13].

2. An increase in the magnicon gain coefficient can be attained by introducing passive cavities, i.e. similar cavities, which are excited not by an external generator but by the deflected beam.

The calculation of the beam interaction with the electromagnetic field of a passive cavity is performed similarly as for the deflection cavity [13] and for the case of utmost interest ($\Omega/\omega=-2$; $\theta=\pi$) gives the following values for the deflection at the exit from the passive cavity:

$$\alpha_{out}=\sqrt{\alpha_{in}^2+\alpha_p^2-2\alpha_{in}\alpha_p\cos\psi_0}. \quad (12)$$

Here α_{in} is the deflection angle at the entrance to the passive cavity; α_p is the beam deflection angle for in the passive cavity; ψ_0 is the angle between the particle transverse velocity vector and the vector $B_\perp$ at the entrance to the passive cavity. In this case the active component[4)] of the interaction power [12] is

$$P_e=I_0U_0\sqrt{\frac{\gamma_0+1}{\gamma_0-1}}4\pi\frac{\Omega_{RF}}{\omega\lambda}\left(r_0\sin\varphi_0+\frac{2\beta_0c\alpha_{in}}{\Omega}\cos\psi_0\right), \quad (13)$$

where r_0 is the module of the particle vector radius at the entrance to the passive cavity, φ_0 is the angle between the vector radius and $B_\perp$ at the entrance of particles in the passive cavity, Ω_{RF} is calculated for $B_\perp$ in the passive cavity. R_0, φ_0, ψ_0 and the distance between the cavities l are in the following relation:

$$r_0=(2\beta_0c\alpha_{in}/\Omega\cos\theta_l), \quad \psi_0=\theta_l+\varphi_0+\pi/2, \quad (14)$$

where $\theta_l=2\pi l/\beta_0\lambda$.

Since after the deflection cavity the deflected partic-

---

4)The reactive component can be compensated by preliminary detuning the cavity.

Table 3

Operating frequency, MHz	915	Losses in the walls of the output cavity, kW	90
Beam voltage, kV	300	Losses in the walls of the passive cavity, kW	340
Beam current , A	12	Electron eificiency, %	85
Beam power, MW	3.6	RF pulse width, ms	30*)
Current pulse width, ms	50	Gain, dB	30
Repetition rate, pps	1		
Output power, MW	2.6		
Efficiency,	73		

*) This is determined by the oscillation buildup time in the passive cavity.

les move along a helix, the angular excitation rate of the passive cavity is in cyclic dependence on $l(r_0 \sim \cos\theta_l)$. Here one can distinguish two regimes which might present interest in our case: regime of maximum gain and a regime of «summing» the deflection angles (i.e. long-term interaction).

The extremum P_e, and respectively α_p, is reached at $\theta_l = \pi/2$. In this case from (12) it follows: $\alpha_{out} = \alpha_p - \alpha_{in}$. Thus, the maximum gain is achieved when the beam particles enter the cavity near the axis. In this case the gain coefficient [7] is:

$$K_p[\text{dB}] = 10 \lg \left(\frac{\alpha_{out}}{\alpha_{in}}\right)^2 = 20 \lg \left[19.8 \frac{J_0}{U_0} \frac{\gamma_0 - 1}{\gamma_0} \frac{\beta_0 \lambda}{\delta(1 + 1.22/\beta_0)} - 1\right]. \quad (15)$$

At $\lambda = 30$ cm, $U_0 = 300$ kV and $P_0 = 3$ MW, which corresponds to $K_p \approx 20$ dB; at $\lambda = 10$ cm, $U_0 = 1$ MV and $P_0 = 500$ MW, it is 47 dB. For a further increase in the gain one can use several passive cavities placed in a series along the beam motion.

The regime of «summing» the angles is realized, when $\theta_l = 0$ and $\psi_0 = \pi$ (see (13) and (14)). In this case the cavities should be placed practically close to one another, so that their excitation powers might be practically similar.

4. INITIAL MAGNICON

1. In 1985 at INP (Novosibirsk) there was built and put into operation a 915 MHz magnicon with a pulse duration of 50 μs.

A schematic of the device is shown in Fig. 9. A diode gun 2 with a LaB_6 emitter is used as the electron source. Accelerating voltage is applied to the gun from a pulsed transformer 1 placed in a tank filled with SF_6 under a pressure of 5 atm [14]. After the gun the beam is guided into a circular deflection system 3, which consists of two cavities placed in a longitudinal magnetic field ($\Omega/\omega \approx -2$).

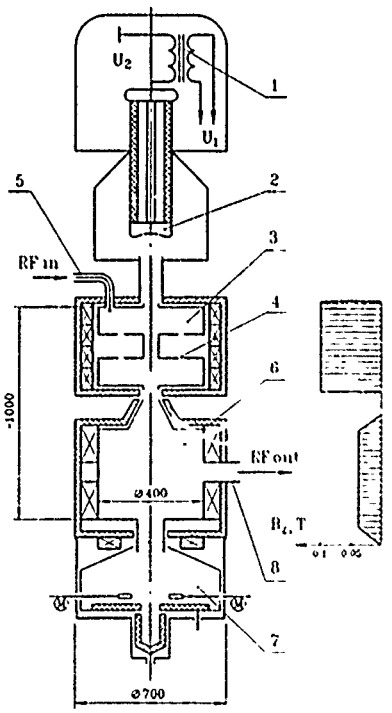


Fig. 9. Schematic of the initial magnicon.

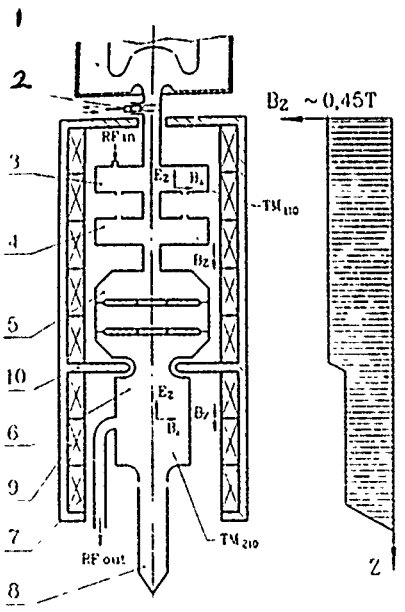


Fig. 10. Schematic of the frequency doubler.

The first cavity is excited by an external generator with the help of two couplers 5 and deflects the beam at a small angle. The second cavity (passive) is excited by a predeflected beam and provides the particle deflection at the required angle ($\alpha_0 = 30°$). The distance between the cavities $\beta_z\lambda/4$ is chosen to provide the maximum gain. The beam is extracted from the magnetic field near the device axis through a hole in the flux shield. After its flight in the drift space the beam gets into an output cavity 6 (the magnetic field distribution is shown in Fig. 9) and then into a collector section 7. The RF power is fed from the magnicon through two waveguides 8 placed at 90° along the output cavity azimuth.

The main experimentally obtained parameters of the magnicon are listed in Tabl. 3.

2. The device tuning begins with obtaining a circular deflection of the required quality. After the assemblage the cavities of the deflection system should be carefully trained to eliminate the multipactor. For this purpose the central part of the cavity is separated from its body by a circular slit cut along the nodal line of the radial current (4 in Fig. 9) and is mounted on insulators. A positive potential of 5—9 kV is applied to it, which in the presence of an accompanying magnetic field initiates a cleaning discharge in the cavity.

As is predicted by the theory, there is such a value of the accompanying magnetic field in the deflection cavity at which no power is required for the beam acceleration. The magnetic accompaniment in the deflection system essentially simplifies obtaining a deflection with a low ellipticity due to the gyrotropic properties of the magnetized beam. The gyrotropic effect develops in the form of «autostabilization» of the deflection shape, i.e. in case oscillations with elliptic polarization are excited in the cavity, then in the beam presence their ellipticity is decreased «The autostabilization coefficient» depends on the difference in conductivity of the resonance system for the following and for the meeting (with respect to the cyclotron particle rotation) wave:

$$G=(|\bar{Y}+\bar{Y}_e^M|)(|\bar{Y}+\bar{Y}_e^F|)^{-1}. \qquad (16)$$

Here $\bar{Y}$ is the cavity conductivity, while $\bar{Y}_e^F$ and $\bar{Y}_e^M$ are the electron conductivities for the following ($\Omega/\omega<0$) and the meeting ($\Omega/\omega>0$) wave, respectively (see (11)). In line with (16) the «autostabilization coefficient» is $G=6.2$ (the measured value is $G\approx 6.5$). If the deflection system comprises several cavities, their coefficients are multiplied and for our case of two cavities we have $G\approx 40$. As a result of this effect even in the case of the field ellipticity in the deflection cavity corresponding to the ratio of the ellipse axes of ~2.5 (in the absence of beam) the measured ellipticity of the deflected beam does not exceed 5%.

For attaining the maximum of the output power beside optimization of the magnetic field value and loading, there was also changed the longitudinal distribution B_z in the output cavity. In the decreasing to the end of the cavity field (−20%), as has been theoretically predicted, the interaction efficiency is lower ($\eta_e=78\%$). The maximum power and efficiency ($\eta_e=85\%$) have been obtained in the case, when the field is built up to the cavity end (+15%), i.e. when some additional longitudinal energy of particles is transferred to the transverse one The electron efficiency is determined from: $\eta_e=(P+P_{oc}+P_{pc})(P_0)^{-1}$, where P is the output power, P_{oc} are the ohmic losses in the output cavity and P_{pc} are the losses in the passive cavity walls. It should be noted, that in case the cavities are made of copper, the efficiency grows by 5%, i.e. it makes $\eta=78\%$.

The magnicon power decrease at variation of the output cavity loading is not large and makes approximately 10% at a two-fold change in the output cavity shunt iompedance. The advantage of the magnicon, which is worthy to of being mentioned, consists in the absence of the reflection of electrons in the output cavity at its deloading.

The phase and the amplitude stability of the magnicon have been studied, which turned out to be rather high. The results are given in Tabl. 4.

Table 4

$\frac{\Delta P}{\Delta U_0/U_0}$, dB/%	$\frac{\Delta P}{\Delta B_z/B_z^{*)}}$, dB/%	$\frac{\Delta\varphi}{\Delta U_0/U_0}$, deg/%	$\frac{\Delta\varphi}{\Delta B_z/B_z^{*)}}$, deg/%	$\frac{\Delta\varphi}{\Delta P_{IN}}$, deg/dB
~0.1	~0.03	~2	~3	~4

*) In the output cavity.

Table 5

Operating frequency, GHz	7	Beam current, A	240
Power, MW	60—70	Efficiency, %	60—70
Pulse duration, μs	2	Drive frequency, GHz	3.5
Repetition rate, pps	5	Gain, dB	50
Beam voltage, kV	420		

Besides the described above experiments (when the magnicon operated with damping loads) the device has been successfully tested with the accelerating structure of the racetrack microtron.

5. X-BAND PULSED MAGNICON

1. The performed above analysis proves the feasibility of a 300-1000 MW *X*-band pulsed magnicon. But the classical scheme of the device, when the main transfer of the longitudinal electron velocity in the transverse one is performed when the particles enter the accompanying magnetic field of the output cavity, requires the presence of a drift space between the deflection system and the output cavity, which limits the current and requires rather a high beam voltage ($U_0 = 1.5-2$ MV).

As a prototype for the RF power source of future linear colliders there has been developed at INP an advanced magnicon scheme providing a by an order of magnitude higher perveance compared to that of the classical one. The device is a frequency doubler, which lacks the drift space between the deflection system and the output cavity, with the deflection angle required for attaining the high efficiency being made directly in the deflection system.

2. The schematic of the device is given in Fig. 10, and its design parameters are listed in Tabl. 5. The basic elements of the device are the electron source, the cavity system, the collector and the solenoid.

The cavity system consists of a circular deflection system and an output cavity. The deflection system comprises cavity 3, in which TM_{110} oscillations are excited by the leading RF generator, and two cavities 4 and 5, excited by the electron beam. The central part of the wall between cavities 3 and 4 is insulated from the body, which makes it possible to apply to it permanent voltage for initiating the cleaning discharge and suppressing the multipactor. Cavity 5 is specially designed for obtaining a larger deflection angle at reasonable values of deflecting fields. It consists of three TM_{110} wave cavities coupled in a chain with a step $\beta_z/2$ [5)] with opposite phase oscillations in neighbouring cavities. Such a cavity provides for the use of the «angle summing» regime and for obtaining $\alpha_0 \approx 60$–$65°$ only at $E = 200$–250 kV/cm^2, required for the high efficiency.

The output cavity 6 is approximately 2λ long, which provides $E = 250$ kV/cm. The power is transferred through two connecting coupling holes shifted by 135° along the azimuth. Then it is transferred through waveguides to the load. Collector 8 is insulated from the earth for measuring the beam current. The longitudinal magnetic field ($B_z \sim 0.45$ T) is induced by a solenoid 9. Since the magnetic fields in the circular deflection system and the output cavity are somewhat different (Fig. 10) and require independent tuning for the experimental study, the solenoid is supplied with a special dividing flux shield 10. The electron source 1 contains a diode gun, a step-up pulsed transformer and a modulator. The electron gun [15] is based on a 12 cm in diameter oxide cathode. The main peculiarity of the gun is a high electrostatic compression of the beam (over 1000:1 in area). The electric field strength on the focusing electrode is approximately 140 kV/cm. For the protection of the oxide cathode during routine devacuuming of the device serves a slide vacuum valve 2 with a teflon gasket.

3. At present the electron gun has been tested. During this run there were obtained: a power $P_0 \approx 100$ MW at $U_0 = 430$ kV and $I_0 = 240$ A, a perveance of 0.82, a pulse duration of 2 μs and a repetition rate of 1 pps. The beam diameter measured in the crossover region was 4—4.5 mm. The measurements were performed by burning—through of a thin metallic foil.

Besides, there was measured the beam envelope in the magnetic field of the magnicon solenoid at $B_z = 0.45$ T. The measurements were carried out with the help of a special device with movable graphite diaphragms and metallic pipes 5.7 and 8 mm in diameter. In the course of measurements there was attained a 99% current passover of the current through a 5.7 mm in diameter and 25 mm long pipe. The measurements of the envelope showed that in the pulsation maximum the beam diameter was 3.6 mm (i.e. the area compression exceeds 1000:1), while in its minimum the beam diameter was 2.4 mm (the energy density is 5 kJ/cm^2). The measured beam parameters are close to calculated ones.

The resonance system has just been manufactured and now is being prepared for tests.

CONCLUSION

The results obtained in the course of the magnicon creation and study, as well as the calculations and the development of various schemes of the device performed have shown, that the magnicon abilities are characterized by the following parameters:

1. A power of up to 5—10 MW in the CW mode (at $U_0 = 200-300$ kV) and up to 500—1000 MW in the pulse mode (at $U_0 = 0.8-1.2$ MV).
2. An efficiency of about 60—80% (depending on the power and frequency).
3. A wave length range from 2—3 cm up to 0.5—1 m (the frequency decrease is limited by the size growth).
4. A high gain ($K = 30-60$ dB).
5. A relatively narrow frequency band ($\Delta\omega/\omega < 0.5\%$).
6. A high amplitude and phase stability.

These characteristics point out good outlooks for the magnicon application both in accelerators and other areas of microwave power engineering. As to communication systems, the utilization of the magnicon here will be reduced to the cases when it is required to have a higher power rather than a broad frequency band.

REFERENCES

[1] G.I. Budker et al. US Patent 3 885 193 (1975).
[2] G.I. Budker et al. Particle Accelerators, v. 10, 1979, pp. 41—59.
[3] O.A. Nezhevenko. Dissertation, Novosibirsk 1971.
[4] V.E. Balakin et al. Proceedings of the XthSUPAC, Dubna, 1987, v.1, pp.277-280.
[5] P.J. Tallerico. IEEE Trans. Nucl. Sci., 1983, v. NS-30, pp. 3420-3423.
[6] M.M. Karliner et al. Invent. Certificate 1110335, Sov. Bull. Inventions, N 4, 986.
[7] M.M. Karliner et al. NIM-A, v. A269, N 3, pp. 459-473, 1988.
[8] M.M. Karliner et al. Preprint INP 87-64, Novosibirsk, 1987.
[9] M.M. Karliner et al. Preprint INP 82-147, Novosibirsk, 1982.

[5)] As a matter of fact, the step is alternating, as with the particle deflection β_z decreases.

[10] V.E. Akimov et al. In Proc. of EPAC (Nice, 1990) to be published in World Sci. Pub.
[11] A.E. Vlieks et al. SLAC-PUB-4546, 1988.
[12] M.M. Karliner et al. Invent. Certificate 1043761, Sov. Bull. Inventions N 35, 1983.
[13] M.M. Karliner et al. Preprint INP 83-143, Novosibirsk, 1983.
[14] A.N.Belov et al. Preprint INP 88-66, Novosibirsk, 1988.
[15] Y.V.Baryshev et al. In Proc. BEAM'90 Conference to be published in World Sci. Pub.

AC Bias Operation of the Perpendicular Biased Ferrite Tuned Cavity for the TRIUMF KAON Factory Booster Synchrotron

R. L. Poirier and T. A. Enegren, TRIUMF,
I. B. Enchevich, Sofia University, Bulgaria.

Abstract

The rf cavity for the Booster Synchrotron requires a frequency swing from 46 MHz to 61 MHz at a repetition rate of 50 Hz and a maximum accelerating gap voltage of 65 kV. A dc biased prototype cavity built at LANL using perpendicular-biased yttrium-garnet ferrites, rather than the more conventional parallel-biased NiZn ferrites, has now undergone major reconstruction at TRIUMF for ac bias operation. RF signal level measurements have shown that the frequency swing at a repetition rate of 50 Hz can be accomplished and still handle the eddy current losses in the cavity structures with minimal effect on the magnetizing field The prototype cavity is now undergoing high power rf tests with full power ac bias operation. The results of these tests and operational experience is reported.

I. Introduction

A cross section view and a rendering of the ac bias ferrite tuned cavity are shown in Figs. 1 and 2, respectively. The

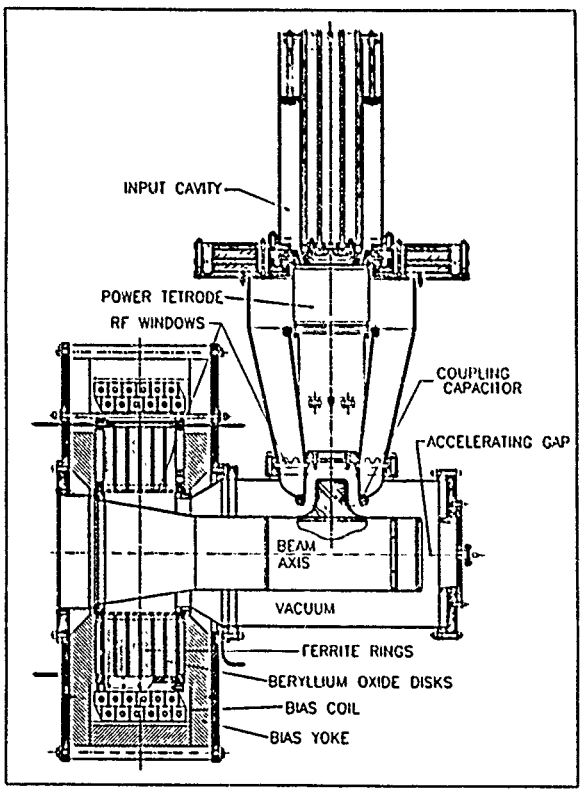


Figure 1: Cross section view of the ac biased ferrite tuner cavity.

power tetrode is capacitively coupled to the accelerating cavity and the ferrite tuner is located on the beam axis.

A toroidal magnet surrounds six yttrium garnet ferrite rings establishing a bias field in the longitudinal direction which is perpendicular to the azimuthal rf magnetic field. Beryllium oxide (BeO) cooling spacers are placed between the ferrite rings and conduct heat from the spacers to a

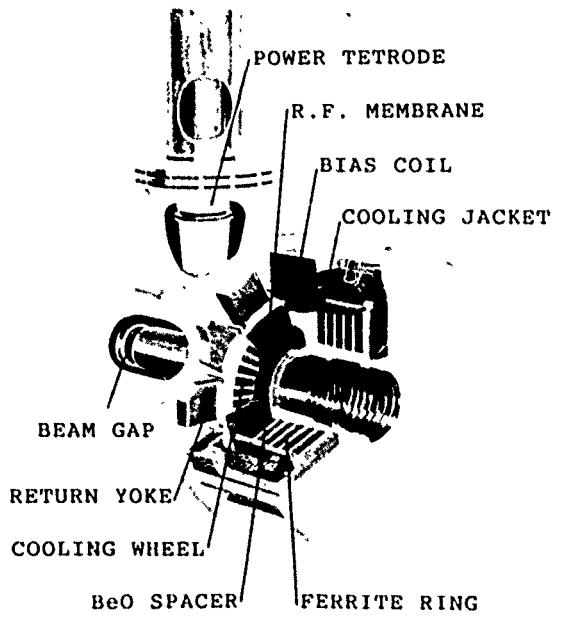


Figure 2: Rendering sketch of the ac biased ferrite tuner cavity

copper water cooling jacket at the outer radius. The return yoke for the magnetic field consists of 12 sectors which are held together by an aluminum clamping plate and a set of tie rods. The sector design allows for easy access to the various water cooling lines and provides room for the entrance and exit of the stranded cable from which the bias coil is made. The rf conducting surface of the ferrite tuner surrounding the ferrite rings is formed by the copper water cooling jacket, a tapered inner conductor and two thin rf membrane end walls. Figure 3 is a graph of the rf signal level measurements showing that the required frequency swing can be accomplished at a repetition rate of 50 Hz. Under these conditions the eddy current losses in the cavity structures are manageable and have minimal effect on the magnetizing field [1].

II. RF Conditioning

In order to test the amplifier itself for any parasitic oscillations or operational problems it was decided to first

0-7803-0135-8/91S03.00 ©IEEE

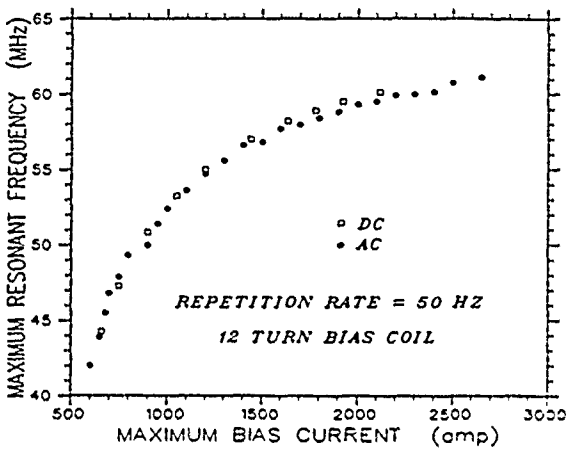


Figure 3: Frequency tuning range of the ac biased ferrite tuner.

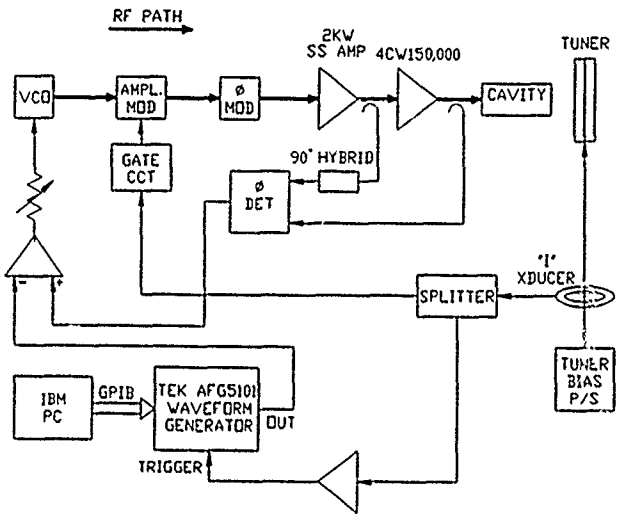


Figure 4: Block diagram of the rf controls.

assemble the cavity tuner with no ferrite rings giving a resonant frequency of 66 MHz. Limited by the use of a temporary anode power supply of 11 kV it was possible to easily overcome multipactoring and achieve 50 kV cw During this test the amplifier was generating 37 kW of rf power of which 7 kW was dissipated in the structure to develop the gap voltage and 30 kW was dissipated into a capacitively coupled 50 ohm load. With a 2% duty cycle 2 msec pulses at 65 kV were achieved at the gap, again limited by the temporary anode power supply. The above set-up also allowed the testing of the solid state driver, the input matching and the high voltage rf choke.

The cavity was then assembled with the ferrite rings installed. At a dc bias current of 800 A (49 MHz), rf conditioning through multipactoring proved to be very difficult. After 14 hours of continuous conditioning it was possible to punch through multipactoring and achieve 90 msec pulses at 25 kV with a 90% duty cycle. With further conditioning and operating in the self- excited mode it was possible to operate with 30 kV CW at the gap at 49 MHz. This represents approximately 0.2 W/cc power density in the ferrite. With a 1% duty cycle 1 msec pulses at 100 kV were achieved. A multipactoring discharge was observed in the vicinity of the narrow throat section in the outer conductor where the rf membrane makes a fingerstock connection to the outer conductor. The area of discharge was easily identified on the centre conductor and was painted with aquadag to prevent multipactoring discharge in that area. This made rf conditioning through multipactoring much easier Within one half hour it is now possible to achieve stable rf voltage on the gap either in cw or pulsed mode operation At a fixed tuner bias of 1000 A (52 MHz) the cavity has been run for several one hour intervals at 45 kV cw and at 67 kV 50% duty cycle with no adverse effects. In pulsed conditions above 67 kV we still observe a discharge in the same tuner area but not as strong as initially observed The discharge in the tuner area does not collapse the voltage at the gap but appears only as a very small perturbation on the top of the pulsed waveform. Under any of the conditions above we have not observed any discharge in air to indicate any problem with imperfect discharge at the surface of the ferrite rings.

III. High Power AC Bias Operation

High power ac bias operation requires a well synchronized rf control system to insure that the rf is switched on and off at the proper time and that the ferrite bias program is synchronized to the frequency program. For our development work, since the bias power supply program is fixed, the frequency program is synchronized to the ferrite bias program. A block diagram of the rf control system is shown in Fig. 4. The rf source is a vco driven by a programmable function generator which is programmed to follow the fixed ferrite bias program. The output of the phase detector which compares the input to output phase of the amplifier is fed to a summing junction along with the output of the programmable generator to the vco to correct the predicted program. An amplitude modulator is triggered at the beginning and end of the operating period to turn the rf on and off. Although there were many iterations under various conditions the last results are in vacuum and are shown in Fig. 5. The top trace is the voltage at the accelerating gap (65 kV) at a repetition rate of 50 Hz. The variation in voltage amplitude during the cycle is caused by the inadequate bandwith response of the low level rf components and the absence of a voltage regulating program which has yet to be incorporated. The 7 msec "on" time instead of the required 10 msecs is a function of the fixed program supplied by the power supply manufacturer and will eventually be replaced by a programmable function generator to provide the proper waveform. The bottom trace is the signal from the output of the bias power supply and the minimum and maximum bias current are

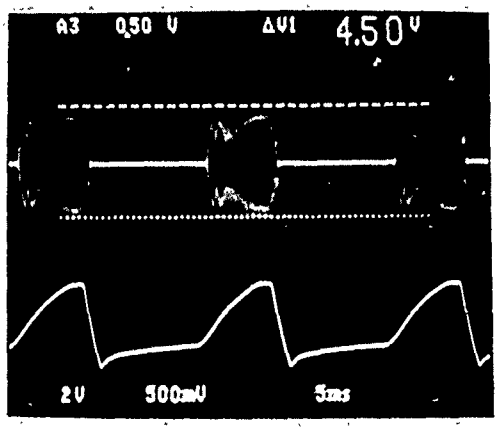


Figure 5: High power operation of the ac perpendicular biased tuner cavity. Top trace is the voltage at the accelerating gap (65 kV), and the bottom trace is the output signal from the ferrite bias power supply.

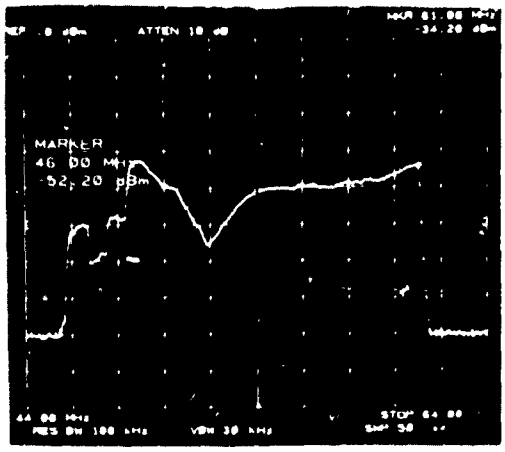


Figure 6: Spectrum analyzer measurement showing frequency swing from 46.0 MHz to 61.0 MHz.

720 A and 2520 A, respectively. Figure 6 is a measurement taken with the spectrum analyzer showing the corresponding frequency swing from 46.0 MHz to 61.0 MHz for the cycle shown in Fig. 5.

IV. Conclusions

A very important milestone in the rf development program has been reached. To the best of our knowledge this is the first time that anyone has operated a fast ac perpendicular biased yttrium garnet ferrite tuner over such a large frequency swing at high rf power levels. Hopefully in the future, ac perpendicular biased tuners will become as popular as the now well established parallel biased NiZn ferrite tuners.

V. Acknowledgements

The authors wish to acknowledge the following people for their dedicated time and effort in reaching this goal: Glen Blaker, Norm Carlson, Ken Fong, Peter Harmer, Slawomir Kwiatkowski, Joseph Lu, Amiya Mitra and Vojta Pacak. We would also wish to acknowledge the collaboration with LANL where the initial development of perpendicular biased ferrite tuners began.

VI. References

[1] R. L. Poirier *et al.*, *A Perpendicular AC Biased Ferrite Tuned Cavity for the TRIUMF KAON Factory Booster Synchrotron*, European Particle Accelerator Conference, Nice, p. 988 (1990).

RF Reference Generation for the Ground Test Accelerator*

Amy H. Regan and Peter M. Denney
MS-H827, Los Alamos National Laboratory, Los Alamos, NM 87545

Abstract

This paper describes the implementation plan for the radio-frequency (rf) reference generation subsystem of the Ground Test Accelerator (GTA). The master oscillator and most of the required components of this subsystem have been acquired and tested. Hardware descriptions and test results are cited when available. Each GTA control subsystem requires a coherent, phase-stable signal from the rf reference generation subsystem to regulate the rf field in its corresponding cavity of the accelerator. The rf reference generation subsystem is configured in a star-distribution format, originating at a master oscillator that supplies three phase-coherent frequencies harmonically related to a fixed fundamental. Phase-locked loops and Wilkinson splitters distribute these signals to many different output ports. VXI monitoring modules measure the stability of the signals being distributed. Any shift in phase of the rf reference signals from the reference generation subsystem to each cavity-control subsystem will translate directly into phase errors between cavities. The allowed tolerance on the phase error for the reference signals is +/- 0.15 degrees.

I. Subsystem Description

The rf system of the GTA operates at three harmonically-related frequencies: 425 MHz, 850 MHz, and 1700 MHz. Configured in a star-distribution network, shown in Figure 1, the rf reference generation subsystem provides coherent, phase-stable signals to each cavity field-control subsystem of the GTA. The rf transport mechanism for this network has been addressed in another report [1] and will not be covered in this paper except to note that the tested rf transport subsystem holds the phase error through 150 feet of phase-stable cables to +/- 0.036 degrees, thus allowing a +/- 0.114-degree phase error budget for the rf reference generation subsystem.

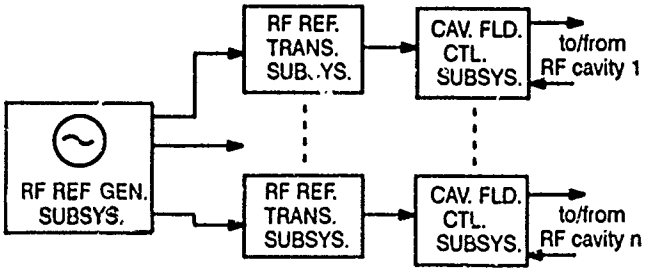


Figure 1. RF Reference Distribution Network

The master oscillator generates three fixed-frequency signals that are harmonically related to a fundamental. Each output is divided a number of times and distributed to individual cavity field-control subsystems. Figure 2 illustrates a functional block diagram of the rf reference generation subsystem.

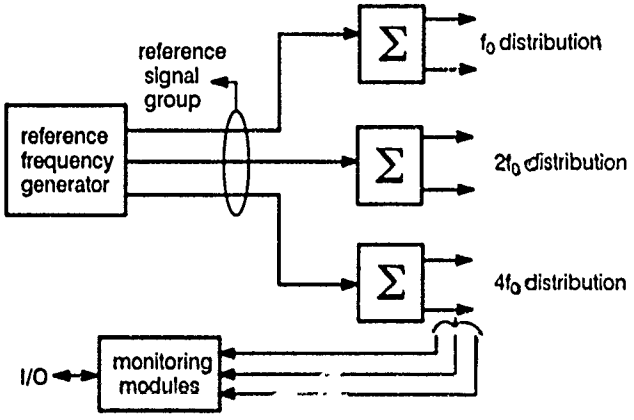


Figure 2. Functional Block Diagram of RF Reference Generation Subsystem

The rf reference generation subsystem design is based on modularity: simply by changing a few frequency-dependent components, the higher frequencies' architecture is the same as the fundamental's. The distribution requirements for the three frequencies differ such that a small number of cavities are driven at f_0 and $4f_0$ while most operate at $2f_0$. To maintain the modularity of the entire subsystem, however, each frequency leg was designed in a similar fashion with the number of outputs differing only by a binary factor. A phase-locked loop governs the phase stability of the output signals of the distribution stage relative to the input signal from the master oscillator. Figure 3 is a block diagram of the $2f_0$ leg of the rf reference generation subsystem.

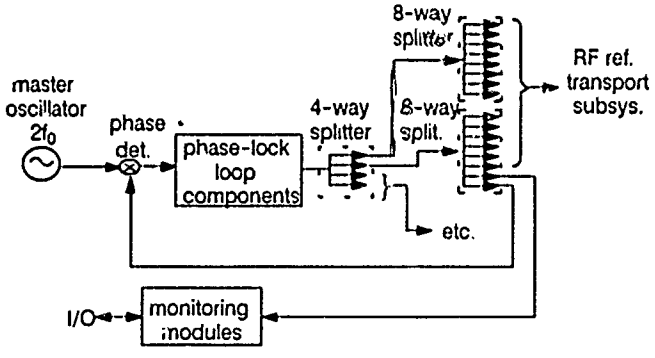


Figure 3. Block Diagram of $2f_0$ Leg

*Work supported and funded by the United States Department of Defense, Army Strategic Defense Command, under the auspices of the United States Department of Energy.

0-7803-0135-8/91$03.00 ©IEEE

II. Hardware Descriptions and Test Data

A. *Master Oscillator*

The master oscillator of the subsystem is a specially ordered continuous-wave model from Techtrol Cyclonetics, Inc. This frequency generator is a 19" rack-mount unit that utilizes an 8.5-MHz crystal as its standard. Its specifications include three internally locked, harmonically related, fixed-output frequencies (the fundamental being 425 MHz +/- 1 kHz) with a long-term frequency stability of 1×10^{-9} per day and short-term stability of 5×10^{-12} per second. The master oscillator's measured performance is presented in Table 1.

Table 1. Master Oscillator Performance

Fundamental Performance

Frequency (Hz)	425,000.0	850,000.0	1,700,000.0
Power out (dBm)	+15.0	+14.6	+15.1
Harmonics (dBc)	-44	-50	-60
Sub-har. (dBc)	<-60	<-60	-54
Spurious (dBc)	<-70	<-70	<-70

Single-Sideband (SSB) Phase Noise to Carrier Ratio (dBc/Hz)

Offset \ Freq	425 MHz	850 MHz	1700 MHz
10 Hz	-87	-81	-72
100 Hz	-107	-99	-90
1000 Hz	-128	-121	-113

B. *Phase-Locked Loop*

The output power of the final splitter stage must be +20 dBm, which means an amplifier is needed to boost each master oscillator output signal before the signal is distributed to a large number of outputs. Because the amplifier will inherently degrade the phase stability of the signal, a feedback circuit in the form of a phase-locked loop (PLL) must be incorporated to preserve phase integrity at the splitter outputs. Figure 4 depicts the phase-locked loop for the f_0 portion of the rf reference generation subsystem.

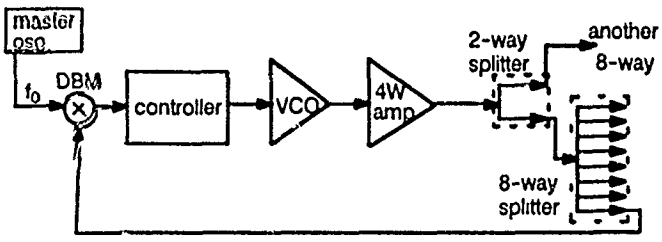


Figure 4. Phase-Locked Loop Block Diagram

The phase-locked loop incorporates a double-balanced mixer (DBM) as the phase detector, a loop controller, a voltage-controlled oscillator (VCO), a 4-watt amplifier, and Wilkinson power splitters. Each component was selected in order to minimize the phase noise of the output signal. The first component to be investigated was the VCO. A PLL is effectively a low-pass filter with respect to the phase noise of the reference signal and a high-pass filter with respect to the phase noise of the VCO [2]. The cutoff frequency in both cases is the loop bandwidth. Hence, if the phase noise specifications of the reference signal are known, a VCO is selected and the loop bandwidth chosen to provide optimum phase noise at the output of the PLL. Figure 5 illustrates the SSB phase noise specifications of the master oscillator and the varactor-tuned VCO chosen for this design. Clearly, the optimum loop bandwidth is 250 kHz.

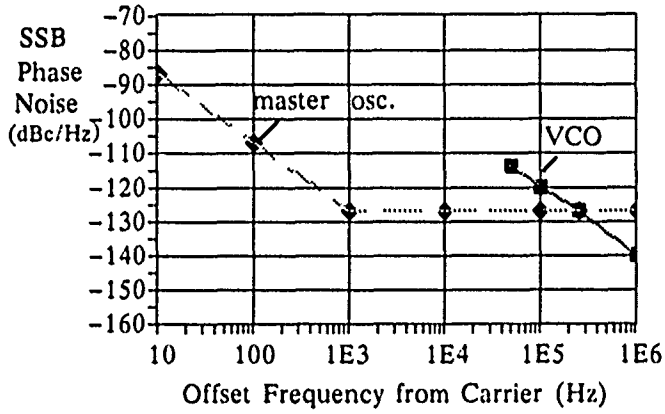


Figure 5. Phase Noise of Master Oscillator and VCO

Short-term phase jitter of the PLL output signal can be estimated from the data in Figure 5 and the following equation. [3]

$$\phi^2 = \int_{f_1}^{f_2} \frac{2N_{op}}{C} df$$

where $\phi \equiv$ phase jitter,
$N_{op} \equiv$ phase noise power density,
$C \equiv$ carrier signal power,
and $f_1 = 10$ Hz and $f_2 = 1$ MHz.

The lower frequency limit was chosen to be 10 Hz because the beam pulse in the accelerator operates near this frequency; therefore, phase changes occurring at lower frequencies can be considered long-term phase jitter. The upper frequency limit was chosen to be 1 MHz because the cavity field-control subsystem operates within a 1-MHz bandwidth. The PLL phase jitter was approximated by considering only the noise contribution of the master oscillator below 250 kHz and then adding the noise contribution of the VCO above 250 kHz. The short-term phase jitter was estimated to be 3.3×10^{-4} degrees. Obviously, noise contributions from other components within the PLL will increase the phase jitter of the output signal. The 4-watt amplifier, for example, will add to the phase noise of the VCO by an amount equal to the amplifier noise figure. This added noise will transfer to the output signal at frequencies above the loop bandwidth. On the other hand, the noise floor generated by the phase

detector and the controller will transfer to the output signal at frequencies below the loop bandwidth. For this design, a mixer and an operational amplifier have been selected that will ensure a noise floor below -128 dBc/Hz.

Long-term phase stability of the output signal is of equal importance and highly dependent on the temperature stability of the loop components. The DBM, the controller, and the splitters are the major contributors to long-term phase jitter. Because the dc offset drift of the DBM translates directly to phase error, a mixer with negligible offset drift is used. Operational amplifiers in the controller produce an input noise voltage that drifts with respect to temperature. This change in dc input voltage also translates to phase error; for this reason, low-noise operational amplifiers with good temperature stability are utilized. For additional safeguards, the circuit board containing the DBM, controller, and VCO is temperature regulated.

Once all of the components were selected and the transfer functions determined, the controller was designed using Bode analysis. A lag-lead compensator was chosen, with an integrator providing the lag compensation. The integrator ensures maximum dc gain in order to minimize long-term phase errors caused by dc drifts in the VCO. Lead compensation was used to ensure stability of the PLL. The gain of the controller was adjusted to provide a loop bandwidth of 250 kHz.

C. Splitters

The overall design of the subsystem relies strongly on the phase stability of the Wilkinson splitters. The assumption is that the phase of all of the output ports will remain constant if one output port is held constant by the phase-locked loop. Each splitter is formed by one or more stages of Wilkinson dividers designed in microstrip for application on RT/duroid 6002 dielectric. RT/duroid 6002 was chosen because of its tight permittivity tolerance and its permittivity stability with respect to temperature. Because permittivity and insertion phase are directly proportional, a stable dielectric permittivity value with respect to temperature assures stable insertion phase. Temperature chamber data of Wilkinson splitters indicate that the phase change of individual outputs relative to each other that is due to temperature changes in the 25 to 40 degree C range is negligible. For added insurance, however, all of the splitters associated with a particular phase-locked loop are mounted together on an aluminum block, creating a large thermal mass. Hence, a negligible thermal gradient is maintained.

D. Monitoring Modules

The rf reference signals are monitored through off-the-shelf VXI instruments. A power meter monitors the level of the signals out of the last stage of splitters, while a frequency counter with nine-digit resolution records the output frequency. The frequency counter uses as its reference a rubidium standard which, with a long-term stability less than 5×10^{-11}/month, is more stable than the master oscillator. Using this extremely stable external standard for the frequency counter allows the phase-locked loop output signal to be properly monitored.

In addition to these modules, two switching modules are required in order to select the various frequencies, and a custom-built phase-lock indicator module provides an interrupt should any of the phase-locked loops lose lock. All of these modules are message-based devices and are housed in a separate VXI crate in the rf reference rack.

III. SUMMARY

The rf reference generation subsystem for the GTA has been designed and individual components have been tested. The master oscillator has been delivered to Los Alamos and in-house test results have been favorable.The phase-locked loop has been designed to minimize short-term, as well as long-term, phase jitter in order to stay within the combined phase error budget of 0.114 degrees. A prototype phase-locked loop has been built and testing is currently in process. Final development of the rf reference generation subsystem is ongoing with an anticipated operational date in June 1991.

IV. ACKNOWLEDGEMENTS

The rf reference rack is a product of a team effort. The following people are recognized for their considerable contributions: M.Curtin, S. Jachim, R. Przeklasa, and A. Young.

V. REFERENCES

[1] S.P. Jachim, A.H. Regan, W.D. Gutscher, E.F. Natter, M.T. Curtin, P.M. Denney, "A Phase-Stable Transport System," *Proceedings Neutral Particle Beam Technical Symposium*, San Diego, CA, May 1990.

[2] V. Mannassewitsch, *Frequency Synthesizers: Theory and Design*, New York: John Wiley & Sons, 1987, pp. 24-27.

[3] W.P. Robins, *Phase Noise in Signal Sources (Theory and Applications)*, London: Peter Peregrinus Ltd., 1984, p. 153.

Alignment Issues of the SLC Linac Accelerating Structure*

J. T. Seeman, C. Adolphsen, F. J. Decker, G. Fischer, J. Hodgson,
R. Pennacchi, C. Perkins, and M. Pietryka
Stanford Linear Accelerator Center, Stanford, California, 94309

Introduction

The accelerating structure of the Stanford Linear Collider (SLC) is required to be aligned to 100 - 200 μm rms. Alignment at such a level will reduce transverse wakefield effects sufficiently so that only a small emittance enlargement of the beam is expected during acceleration to 50 GeV with up to 7 X 10^{10} particles per bunch. This report describes many aspects of the alignment including global alignment, local alignment, construction of the accelerating cavities, active controls of the structure alignment, external constraints, temperature and airflow effects, and alignment stability.

Laser Alignment System

The accelerator is globally aligned (every 12 m) using a laser system [1], which is housed in a 24 inch evacuated pipe which supports all the accelerator components. This system has sub-units 12 m long, called girders, with floor and wall supports and a flexible bellows at each end. A schematic view of a girder is shown in Fig. 1. A laser at one end of the accelerator illuminates Fresnel lenses which are inserted one at a time at the alignment positions. The laser spot is viewed at the other end of the accelerator. The transverse position of the laser focus indicates the position of the lenses. Local jacks are then used to correct the girder positions. The resolution of this system is about 50 - 75 microns but calibration transfer errors up to 1 mm have been seen. This system is very useful in measuring relative changes. For example, during 15 seconds of the October 1989 earthquake, settling of the accelerator occurred as well as a transverse displacement (~1 cm) of the downstream end of the accelerator [2]. See Fig. 2. The slip was fixed by placing a gentle s-bend in the accelerator over a distance of several hundred meters. A "beam based" alignment technique, discussed below, is less prone to calibration error and is used for finer girder alignment.

Telescope Alignment System

The alignment of components internal to a 12 m girder is performed using a telescope and targets mounted in 'optical' tooling holes. The holes in the thick end supports of the girder are the fiducial marks and the telescope is mounted in one of them. A target is inserted in the plate at the other end. The line between them is the survey reference for all internal components with tooling holes.

The tooling holes are part of the internal supports for the quadrupole, the aluminum strong back supporting the

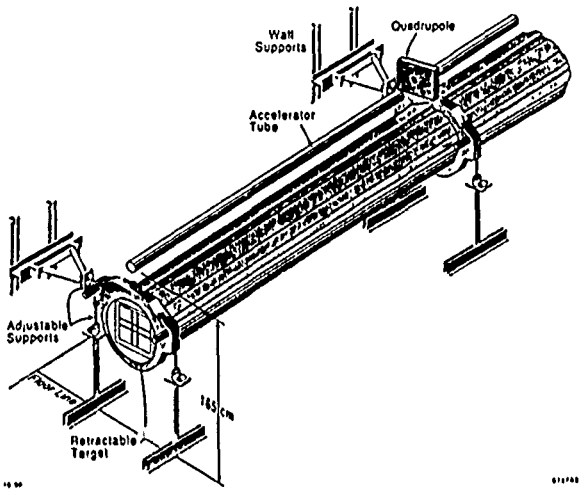


Fig. 1 Support girder for the SLC Accelerator

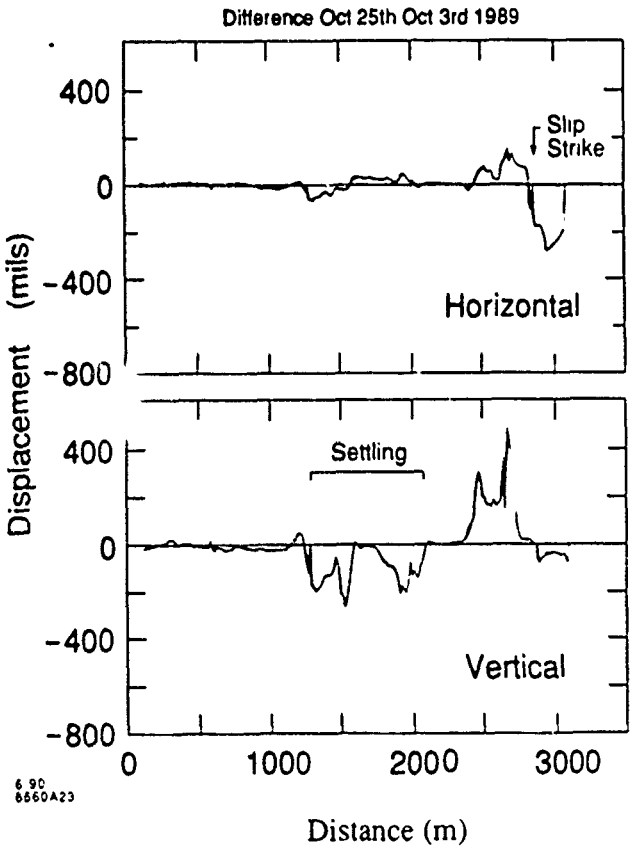


Fig. 2 Observation from the laser alignment system of the settling and shifting of the accelerating structures from the October 1989 earthquake.

* Work supported by Department of Energy contract DE-AC03-76SF00515.

U.S. Government work not protected by U.S. Copyright.

accelerator, and any beam diagnostics on that girder. The tooling holes were aligned relative to the waveguide center in the shop during the construction of the devices and pinned. The accuracy of the machined parts and alignment in the shop is quite good: 50 to 100 μm. However, this secondary reference system has the negative feature that many measurements, machining errors, clamping errors, and the like add to determine the absolute error in the placement of a component in real space. For example, aligning the copper structure with the tooling holes involves over twenty errors [3]. None of the errors are above 127 μm, but the quadratic sum is about 290 μm. Similar assembly errors arise for the quadrupoles and beam position monitors.

Beam-Based Alignment

Measurements of the trajectory of the beam along with the associated strengths of the quadrupoles and the dipole correction magnets (taken at several quadrupole settings) can be used to extract the magnetic offsets of the quadrupoles and the electrical - mechanical offsets of the position monitors [4]. The offset for each position monitor is relative to the nearby quadrupole and for each quadrupole is to the two nearest quadrupoles. With beam position monitor reading errors of order 25 μm, local offsets of 100 μm rms for quadrupoles and 80 μm rms for position monitors have been achieved. Fig. 3 shows the resulting errors of the SLC quadrupoles in the vertical plane (the horizontal plane is similar). It is difficult for this technique to remove long wavelength errors in the accelerator of the order of hundreds of meters [4]. However, the beam is expected to be insensitive to these errors.

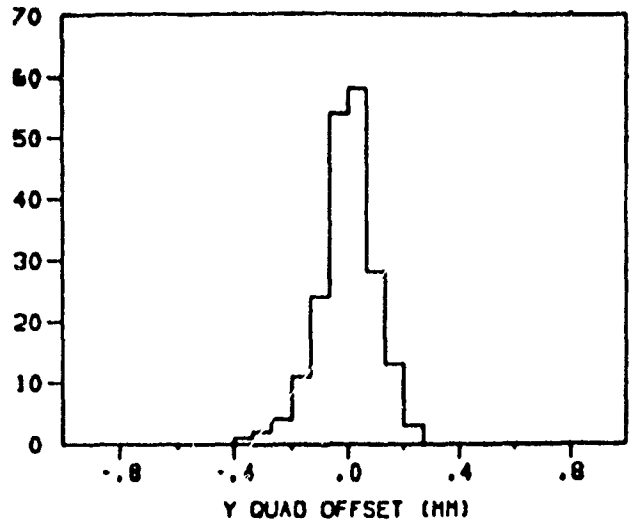


Fig. 3 Vertical residual quadrupole offsets after beam-based alignment.

Accelerator Structure Alignment

The copper accelerating structure is supported on a strongback at intervals of 1 m. These supports were adjusted 25 years ago to be straight. Some changes and settling between supports have occurred since. To align the structure, a theodolite and optical level must be used in the tunnel and many measurements taken. A typical example of the alignment data of a 12 m structure on one girder is shown in Fig. 4. The measurements took over an hour to acquire (without the complication of adjustments. (In addition, the tunnel conditions are difficult for surveyors and surveying [hot and dry]). The offsets at the supports (vertical lines in Fig. 4) can be adjusted with wrenches. Between supports, a bending device was fabricated and has been used but it's cumbersome. Less than 50 m of the 3 km linac have been realigned in this way. However, the spatial frequencies of these misaligned girders are very high (much higher than the betatron frequency) and do not contribute significantly to wakefields as positive and negative errors cancel. Whole girder offsets are the most important, because the statistical component at the betatron frequency is most harmful.

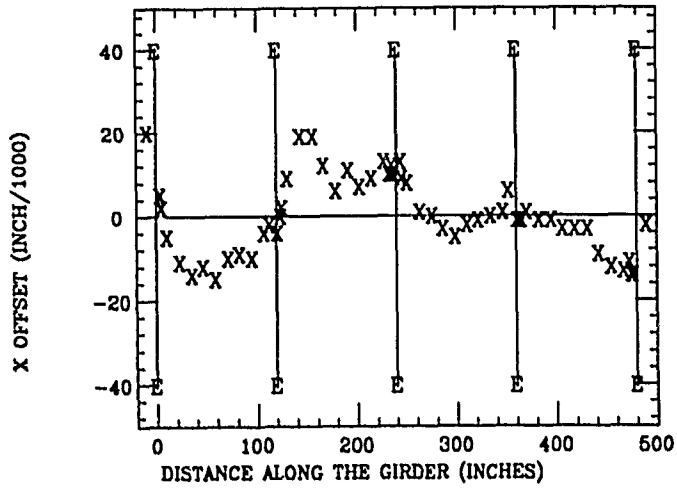


Fig. 4 Measured displacements of an accelerator structure measured every 30 cm. The symbols 'E' refer to the ends of the 10 ft assembly sections.

Active Structure Alignment Correction

A technique to actively control the accelerator offsets at the girder level has been devised [5]. Small movers are attached to the center of the girders to produce external movements of up to +/- 1 mm. The ends of the girder are held rigidly so that the quadrupoles and position monitors do not move. Small bows in many adjacent girders spaced at the betatron wavelength can easily drive wakefields in the beam. Cosine and sine like mover combinations can be devised to cancel the natural errors which affect the beam. A search is underway for an inexpensive hardware design.

Temperature and Airflow Effects

The accelerating structure is maintained internally at 113 degrees F in order to provide proper RF phasing from cell to cell. Since the structure is not insulated, heat flows from the structure towards the walls through several paths: radiant heat loss, conduction through the supports, and air convection. As a consequence, there are temperature gradients in the tunnel. The gradients have been measured [6,7] and generally give the temperature values illustrated in Fig. 5. One consequence of the temperature gradient is the refraction of the light used by the alignment telescopes. The gradient of 0.32 degrees F per 6

inches causes an unintentional vertical bow of about 20 μm in the center of the girder [7,8].

The temperature in the tunnel varies diurnally with a small air exchange from outside the tunnel. Measured temperatures over a week are shown in Fig. 6. Externally, the accelerator, H_2O piping, and the RF waveguide remain at about 111 to 113 degrees F as they are regulated. There is a relatively good thermal contact between the accelerator and its support (the strongback) which dampens the temperature variations of the strongback. The laser light pipe is not strongly coupled to the strongback and follows the variations of the surrounding air more closely. However, the lightpipe is rigidly connected to the strongback mechanically. Thus differential expansion causes bowing, checked both theoretically (ANSYS) (Fig. 7) and measured in the tunnel (Fig. 8). The bowing is 150 μm / degree F difference. Maintaining temperature conditions during alignment is very important. Alternatively, girder clamps, which hold the lightpipe center fixed, are under investigation. Also, air flow patterns from normal convection and from the nearly 600 tunnel penetrations are under study.

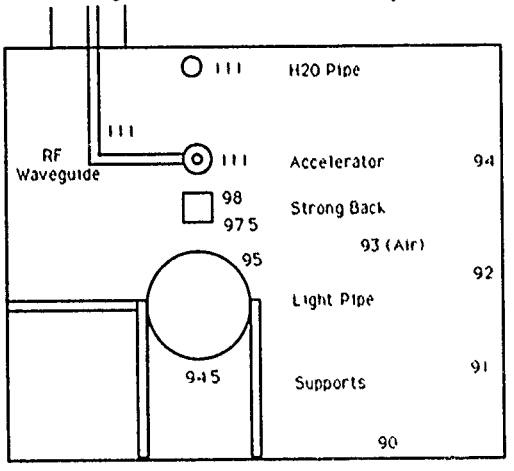


Fig. 5 Typical temperature measurements in the Linac tunnel.

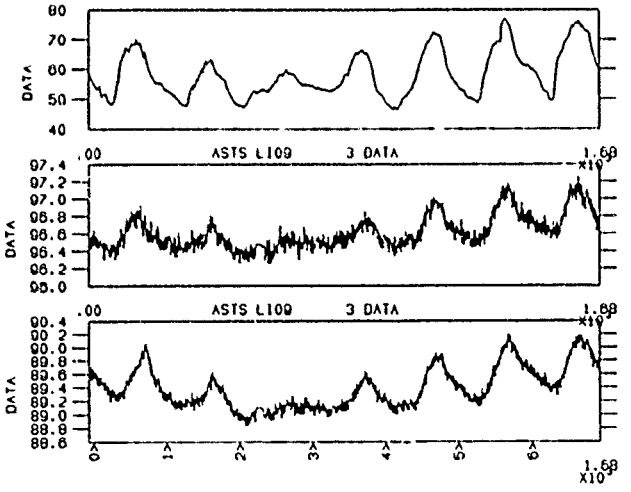


Fig. 6 Variations in temperature of the outside air (top), strongback (middle), and lightpipe (bottom) over a period of a week. The variations are correlated with a peak-to-peak variation of 25 degrees outside, 0.4 degrees for the strongback, and 1.0 degree for the lightpipe.



Fig. 7 ANSYS calculated vertical girder bowing from gradient changes. The displayed bowing over the 12 m girder is exaggerated for effect.

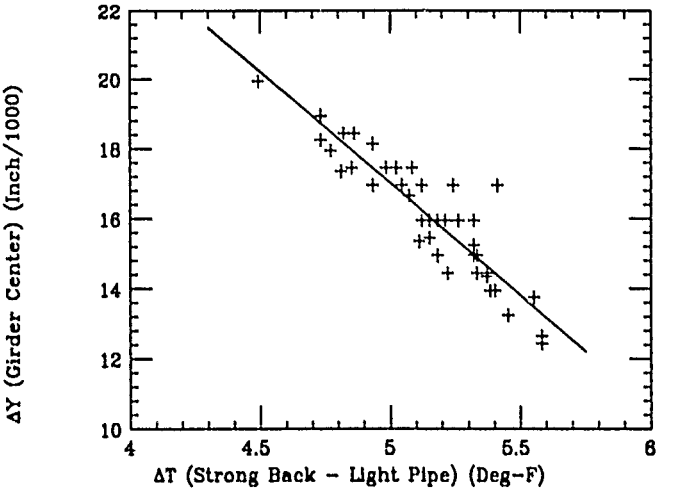


Fig. 8 Measured vertical girder bowing from gradient changes.

Acknowledgments

Many thanks are extended to the Alignment Group, Mechanical Engineering, and Operations for their help with the alignment of the linac. Conversations with A. Lisin, L. Piemontese, and K. Skarpaas have been very helpful.

References

1) W. Herrmannsfeldt, "Linac Alignment Techniques", IEEE Trans. Nucl. Sci. NS-12 No. 3, p. 9 (1965).

2) G. Fischer, "SLAC Site Geology, Ground Motion, and Some Effects of the October 17, 1989 Earthquake", SLAC-Report-358 (1990).

3) R. Sandkuhle, "Probable Error of Aligning Accelerator on the Support Girder", SLAC Engineering Note R-290501-000-007 (1966).

4) C. Adolphsen et al., 'Beam-Based Alignment Technique for the SLC Linac', IEEE 89CH2669-0 US PAC p. 977 (1989).

5) J. Seeman, 'New Compensation of Transverse Wakefield Effects in a Linac by Displacing Accelerating Structures', Proc. of 1990 Linear Accel. Conf. Albuquerque, p. 390 (1990).

6) J. Seeman et. al., "Accelerator Temperature and Girder Alignment', SLAC SLC Experimental Note 227 (1991).

7) J. Seeman et. al., "Tunnel Temperature and Alignment', SLAC SLC Experimental Note 229 (1991).

8) R. Neal, "Effects of Refraction on Optical Alignment of M Accelerator", SLAC TN-61-4 (1961).

9) L. Piemontese, "Temperatures and Heat Flow in the Linac Tunnel", SLAC SLC Experimental Note 238 (1991).

Operational History of the SPS Collider 1981 - 1990

V. Hatton
CERN, 1211 Geneva 23, Switzerland

Abstract

In June 1978 approval was given for the construction of an antiproton production and storage facility, the AA complex, and the modification of the SPS to be able to inject, accelerate and store bunches of 270 GeV protons and antiprotons with collisions in the centre of two large experimental detectors.

Two years later, after the construction of the necessary equipment and preparatory excavation of the two underground zones, the SPS fixed target operation was interrupted for nearly 12 months to complete the installations. First collisions of two bunches of protons against one bunch of antiprotons were observed on July the 10, 1981.

Since those early days the Collider performance as measured by the integrated luminosity accumulated per year (directly proportional to the number of W and Z^0 particles produced) has increased by more than two orders of magnitude. Along with the increase in the number of antiprotons produced and stored in the antiproton accumulator the smaller and smaller beam sizes in the region of the experimental detectors, the understanding and control of the collider as a complicated machine physics experiment has gradually increased.

I. MODIFICATION OF THE SPS

The initial scheme for the Collider called for the injection of three proton bunches to collide with three counter-rotating bunches of antiprotons. A new tunnel and beam transfer line, meeting up with one of the existing high energy proton extraction lines, was constructed to bring the antiprotons from the CPS to the SPS.

Particles injected into the SPS in the Fixed Target mode of operation are captured into 4620 stable buckets by the radio frequency system working at 200 MHz..There are four rf cavities through which the bunches pass; they have a travelling wave structure and are located in part of one sextant of the SPS ring; each can provide 2 MV at the nominal power. For collider operation the installation was modified so that two cavities capture and accelerate the protons while the second two units (fed in reverse direction by means of a high power coaxial switch) serve the antiprotons. The exact location of the interaction point in the detectors can be adjusted by phasing the two groups of cavities.

Extra quadrupoles were introduced around the interaction points, where the experimental detectors are located. By powering them independently from the lattice quadrupoles the beta values could be locally reduced during Collider operation only.

The vacuum system was modified to improve the average pressure by two orders of magnitude to 2 x 10^{-9} mbar. New and improved beam instrumentation was introduced. and the software used for equipment control and monitoring was improved.

II. PERFORMANCE OVERVIEW

Luminosity is determined by the energy of the colliding particles, the number of bunches per beam, the number of particles per bunch and their emittance, and by the horizontal and vertical beta values at the interaction points. The design luminosity of the SPS Collider is 10^{30} cm^{-2} s^{-1}. The integrated luminosity depends on the time variation of the above factors during the many hours when the beams are circulating; it is also a measure of the number of interesting events observable during a physics experiment in a given interval of time. An integrated luminosity of one inverse nanobarn, nb^{-1}, equals 10^{33} cm^{-2} or about 1W particle. The evolution of these two parameters over the past ten years is shown in Figure 1 (note the logarithmic scale). There was little Collider operation in 1986 during the upgrade of the antiproton accumulator and detectors.

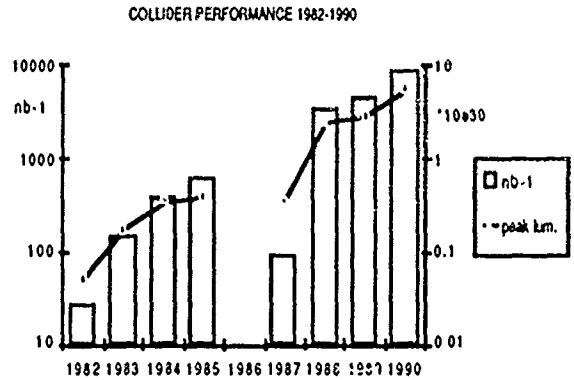


Figure 1. Collider performance from 1982-1990.

The progress from 28 nb^{-1} in the first year of operation for physics to 7240 nb^{-1} in 1990 is remarkable. The production in 1985 was greater than the total production in the four initial years; production in 1990 was close to the combined production in the two previous years with as much produced in three days of 1990 as in the whole of 1985.

The major improvements in performance have come from :

0-7803-0135-8/91$01.00 ©IEEE

- an increase from 270 to 315 GeV in particle energies from 1984,
- increased number of antiprotons available per day from the Accumulator Complex, and the change from 3 to 6 bunches
- the reduction of the beam sizes at the interaction regions by means of the low beta insertions at the experimental detectors, and
- the gradual understanding and mastering of the machine physics parameters.

III. MACHINE PERFORMANCE - LUMINOSITY - COLLISION ENERGIES

Initial operation of the Collider was limited in beam energy to 270 GeV by the ability of the water cooling system to cool the ring bending magnets and lattice quadrupoles. During the winter shut-down of early 1984 the flow rate of the cooling water was increased by more than 30% by the addition of one booster pump per SPS sextant. The cooling circuits of the power supplies were also upgraded. These modifications allowed the increase from 270 to 315 GeV during coast, limited by the temperature difference between the inlet and outlet of the dipole magnet coils.

A. Proton Bunch Intensity Limitations

Above a threshold of about 10^{11} protons per bunch there is a fast longitudinal emittance blow-up immediately after injection into the SPS caused by the vacuum chamber discontinuities. It is a microwave instability coming from the coupling of the beam to the high frequency part of the machine impedance. An optimum intensity between 1.2 - 1.5 x 10^{11} was found.

B. Production and Transfer of Antiprotons

In the first years of operation of the collider complex the antiproton accumulator (AA) produced about 6 x 10^9 pbars per hour with a maximum stored intensity of 4 x 10^{11}. The introduction of the Antiproton Collector (AC) in 1987 resulted in an increase in the production rate to 6 x 10^{10} per hour and a maximum accumulation of 1.2 x 10^{12} antiprotons.

The efficiency of transfer of antiprotons from the Accumulator to the SPS was low in the early years. Not only were two thirds of the beam lost in the process but the emittance of the antiproton bunches reaching physics energies was also increased. Over the years, careful matching of the beam lines and control of beam blow up in the injector chain and in the SPS resulted in peak transfer efficiencies of 80%. Bunch intensities of around 1.5 x 10^{10} were achieved.

The steady increase in performance in the AA in the first years of operation resulted in an increase in pbar intensities available at the time of transfer; this was usually done once per day. The operation of this delicate process, when the days production of antiprotons is transferred, is controlled by software that checks the readiness of all the equipment in the chain and synchronizes the transfer from AA to SPS. Protons were ejected from the SPS at 26 GeV and transported back to the PS along the same transfer line that the pbars would pass. Once the energy and injection oscillations of these protons in the PS were optimized the next phase was to transfer pilot pbar bunches of low intensity before finally transfering the intense bunches. Very few intense bunches of antiprotons were ever lost after the commissioning of this software. Precise measurements of the parameters of the beam down the chain were recorded automatically and analyzed after each fill thus allowing the progressive improvement in efficiency from fill to fill.

100 MHz cavities were introduced in the SPS in 1987 to allow the capture of longer bunches reducing the Laslett Q shift and giving more working space in the tune diagram; this helped fight the emittance blow-up during injection and acceleration and resulted in a higher luminosity. In addition it gave better reliability in the transfer efficiency and capture into the SPS at 26 GeV; the operation was made easier.

C. Beam Size at the Detectors

Over the history of the collider one of the major factors in the improvement in performance has been the gradual reduction in the beta values at the experiments by means of independently tuneable quadrupoles in these regions. From 7 m horizontal, 3.5 m vertical in the first year of operation the ß* has been steadily reduced to 0.6 m horizontal, 0.15 m vertical in 1990, Figure 2. The latter represent the limit of improvement since with these values the length of the bunches become comparable to the length over which the beta values are a minimum.

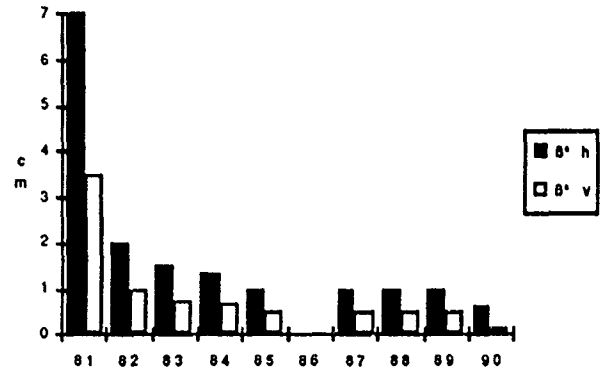


Figure 2. Evolution of beta*.

Reduction in the beta resulted stronger machine chromaticity and introduced coupling. The machine physicists were able to simulate these effects and find

suitable parameters for correction using the installed sextupoles and skew quadrupoles.

D. Beam-Beam Effect & Separation

The luminosity lifetime is mainly limited by multiple Coulomb scattering between particles in the same bunch (intra-beam scattering) which increases the emittance and by the effect of the global electromagnetic field of the particles in the opposing beam (beam-beam interaction) which causes particle losses.

The effect of one beam on the other, the so-called 'beam-beam effect', occurs when one bunch of particles passes through the other. This occurs six times around the SPS circumference when 3 proton bunches are injected with 3 antiproton bunches, and twelve times when 6 and 6 are injected. Only two of these crossings are needed for the physics programme. With the increase in particles per bunch and the number of bunches (made possible by the increase in number of antiprotons produced by the AC after 1987), it was necessary to separate the bunches at the unwanted crossing points to reduce the effect of the beam-beam interaction. A system of electrostatic separators kept the proton and antiproton bunches on different horizontal orbits during the injection and acceleration stages, and for the data-taking colliding stage keep the bunches apart except in the adjacent experimental zones and one unwanted collision point between. For the final years of operation 6 proton bunches colliding with 6 antiproton bunches was the standard operation.

E. Beam Monitoring

The introduction of new methods of beam monitoring and the development of the sensitivity of the existing systems were a vital factor in the improvement of machine performance. The introduction of the wire scanners gave an accurate means of monitoring the beam growth during a fill. The sensitive measurement of the tune of both types of particle was made possible with the Schottky pick-ups without disturbing the beam.

F. Machine Alignment

The SPS tunnel is bored out of a shale-like rock called Molasse which is intrinsically stable. When the excavation for the experimental area for UA1, ECX5, was started during normal fixed target operation we were not surprised to find a vertical displacement of the ring elements in this region especially the lattice quadrupoles. As the zone was progressively excavated, from the surface, the symmetry of forces on the tunnel was broken and the quadrupoles on each side of the ECX5 were found to move vertically upwards by over 3 mm (a tolerance of 0.15 mm was specified during the SPS construction period) Over the intervening ten years, and the introduction of the UA1 detector weighing 2000 tonnes and a non-negligible amount of concrete and steel shielding the quadrupoles have gradually returned to and past their original settings. The experimental area for UA2, ECX4, is nearly 60 metres below the surface and tunneling was the only solution. Being completely symmetric there were no movements of the quadrupoles.

IV. MACHINE PERFORMANCE-INTEGRATED LUMINOSITY

A. The Length of the Coast

The length of coast was determined by the lifetime of the beams in the SPS and the intensity of antiprotons stacked and ready to be transferred from the AA.

The design vacuum pressure for the SPS as a fixed target accelerator of 2×10^{-7} mbar. was improved by more than two orders of magnitude to avoid blow up of the beams stored for many hours. At this level the growth of the beam size due to beam-gas scattering was small and proton lifetimes of several 100 hours have been recorded.

Reduction of the noise in the low level radio-frequency system contributed significantly to the improvement of lifetime of the beams to better than 50 hours. The reduction over the years of power supply ripple and noise reduced the diffusion from the buckets induced by the beam-beam.

With such a complex operation, equipment failures resulting in the loss of coasts were inevitable. The constant efforts on the part of the engineers and technicians in the equipment groups resulted in a gradual reduction in lost coasts from 40% to less than 10% in the final year of operation, Figure 3.

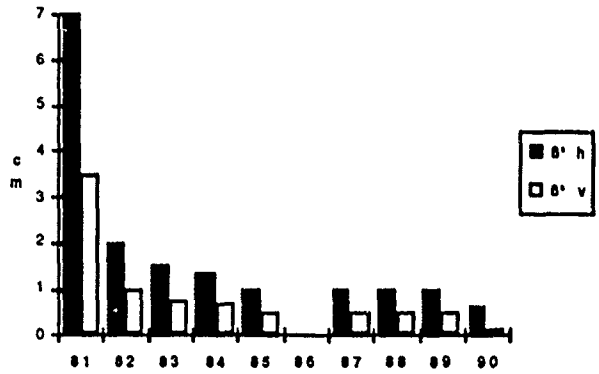


Figure 3. Number of coasts per year and percentage lost.

With the advent of the AC the number of bunches injected was doubled to 6 and the frequency of transfer changed so that by 1990 two coasts per day became routine operation.

V. ACKNOWLEDGEMENTS

The SPS Collider project was the work of large numbers of people in many Divisions of CERN, too many to mention all by name.

I would however like to thank the operations teams of Engineers in charge and Machine co-ordinators, shift leaders and control room technicians, present and past, CPS and SPS, for their enthusiasm and dedication to this project over the past ten years.

Status of the SLC Damping Ring Kicker Systems*

T. Mattison, R. Cassel, A. Donaldson, D. Gough, G. Gross, A. Harvey, D. Hutchinson, M. Nguyen
Stanford Linear Accelerator Center, Stanford CA 94309

Abstract

The damping ring kickers for the SLAC Linear Collider must meet extreme requirements on rise and fall time, flatness, time and amplitude jitter and drift, voltage, repetition rate, and reliability. After several generations of improvements to the pulsers, magnets, and controls, and evolution in the understanding of the requirements, the kicker systems are no longer a serious constraint on SLC performance. Implications for future linear colliders are discussed.

I. Early Kicker Experience

The SLAC Linear Collider (SLC) damping rings require injection and extraction kickers with rise and/or fall times of 60 nsec. The first generation SLAC-designed short-pulse kicker system [1] was adequate for commissioning the first damping ring with single bunches, but had problems with charge voltage regulation, thyratron risetime, thyratron time drift, magnet failures, load failures. Magnet pulse shape distortion would preclude kicking 2 *e-* bunches on a long flat pulse required for full SLC operation, and a group at Fermilab agreed to develop a second generation long-pulse kicker system [2]. In the meantime, more short-pulse kickers were produced for comissioning the second ring with single bunches for the first SLC beam collisions in 1987.

For the 1988 SLC physics run, the long-pulse kickers were installed in the *e-* ring, and many features of the Fermilab pulse charging system were incorporated into a SLAC pulse charging system used for all the kickers [3]. It soon became apparent that while the new magnet pulse shape was better, it was adequate for 2 *e-* bunch injection but not for extraction, which cost a factor of 2 in possible collision rate The new magnet design seemed to have a poor lifetime, and magnet failures increased dramatically as the repetition rate was raised. Thyratron time drift required constant operator intervention. The long-pulse system thyratron controls and the pulse chargers failed frequently. The kicker systems were the largest single cause of downtime in the 1988 SLC run.

A kicker improvement program was launched, with the goals of reducing down time, improving stability, and operating with 2 *e-* bunches. Experts from laboratories around the world graciously lent their experience, but many of the SLC kicker problems were unique. Sufficient progress was made [4] to allow the first SLC physics results in 1989.

II. Kicker Magnets

The damping ring straight sections are short, requiring 7 mrad kick angles, which combined with the 60 nsec risetime requires voltages up to 40KV. The kicker surrounds a 50 cm long 21 mm diameter ceramic beam pipe with a metallic coating to shield the beam from the ferrite. The magnets were designed as terminated transmission lines for optimum pulse shape. Both generations of kicker magnet design produce distorted pulse shapes and have limited service lifetimes [5]. Production yield has been improved by agitating the RTV under vacuum during degassing, and curing under pressure to redissolve bubbles. Service lifetime has been increased by evolutionary improvements to about 8 running months at 120 Hz with increasing beam intensity (and losses) [6]. Much of the improvement stems from keeping beam orbits close to the septa to minimize the kicker voltage, at some expense to ring acceptance, particularly for *e+*.

Failures in service of the original magnet design seem to depend primarily on voltage and number of pulses. Failures of the long-pulse magnets are arcs through the silicone rubber (RTV) dielectric very close to the beam pipe, and frequently occur soon after interruptions in operation. The RTV becomes brittle when radiation damaged, and thermal cycles crack it, followed by arcs in the cracks. Lifetime has been improved by flipping the injector magnets over to avoid spray from beam loss in the septum, adding heaters to prevent thermal contraction, and curing the RTV at room temperature so it is never under tension in service. Water cooled metal bars will soon be installed in the magnets to control beam-induced heating of the ceramic pipes.

The causes of pulse shape distortion in both magnet types are now understood [7]. The short-pulse magnets behave more like single LC circuits than transmission lines because flux is not prevented from flowing down the magnet. The long-pulse magnets are mismatched due to ferrite nonlinearity. Risetime has been improved by reducing the inductance with copper-on-Kapton "flux gaskets," which also help confine the grease used to prevent corona near the beam pipe.

* Work supported by US Department of Energy contract DE-AC03-76SF00515

0-7803-0135-8/91$01.00 ©IEEE

Much effort has gone into designing a third generation magnet with improved pulse shape and higher voltage capability that still fits the available space. It will use thick alumina-loaded epoxy dielectric for higher voltages and magnetic field shaping to reduce inductance for fast transit time. Epoxy requires careful processing and mold design for large volume castings with no bubbles, cracks, or debonding despite large shrinkage [8]. Magnet cells will be prepotted in shrinkable molds then potted together in a shrinkable structure. Tests of an electromagnetic mockup show good pulse performance.

III. PULSERS

Much effort has gone into improving thyratron reliability, time drift and jitter [9]. The failure-prone floating electronics package in the long pulse system was replaced completely by ferrite choke isolated rack mounted electronics, possible due to the short (150 nsec) pulse length, which have been robust and easily maintained. The more benign EEV CX-1671D thyratrons in the long-pulse systems now operate with very fast FET pulsers [10], producing RMS time jitter of as little as 100 psec and long useful life. Some of the EG&G HY-5353 tubes in the short-pulse systems perform equally well for limited times with DC keep-alive, but eventually become erratic, destroying even slow robust grid pulsers and keep-alive supplies and displaying time jumps of up to 10 nsec. Without keep-alive, the risetime is significantly degraded.

A major improvement in diagnosis and repair time was obtained by moving the pulsers and loads from the ring housings to surface buildings. The 80 foot runs of RG-220 did not degrade the rise time significantly. A third kicker pulser, load, and control system was added in each damping ring surface building to serve as a hot spare. These have occasionally been used as complete systems, but more often as sources of hot spare parts, or for adiabatic installation of engineering improvements. The pulse chargers, thyratron tanks, and loads are oil-cooled, and the oil circulation and cooling systems have been largely rebuilt for reliability and standardization. High voltage connectors on the pulser outputs facilitate the switch between pulsers [11].

III. CONTROLS AND INSTRUMENTS

The kicker timing and monitoring system [12] has evolved considerably from the original DC supply and single trigger signal. A fixed trigger rate independent of beam conditions was OR'd in with the beam-dependent trigger to prevent drifts from dynamic beam rate changes imposed by SLC machine protection systems. A hardware timing feedback module was developed to adjust the timing continuously to keep the mean thyratron delays within 100 psec of a reference trigger, independent of voltage, reservoir, or age. The timing feedback correction is read remotely and stored in a history buffer, providing a valuable diagnostic about thyratron health and allowing failure diagnosis or even prediction. Commercial time interval counters with remote readout and history of both time drift and time jitter and local continuous display of time jitter provide equally valuable information.

The thyratron pulse shape and thus magnet field at beam time varies with many parameters other than the charging voltage. Fast samplers provide information on amplitude mean and RMS for all kicker thyratron and magnet pulses (at both beam times if relevant). A remote control multiplexed oscilloscope and video camera remains the best instrument for some diagnostics of pulse to pulse variations. Each kicker installation now has a dedicated 'scope with computer assisted setup, so a single button press will display any important signal in a familar and labelled format within seconds. There is also pulse by pulse time and amplitude data for each thyratron and magnet pulse, which can be synchronized with beam position monitor information.

IV. MULTIBUNCH OPERATION

Making optimum use of the linac repetition rate requires that 2 short e- bunches 60 nsec apart in the north damping ring and 1 of the 2 e+ bunches 60 nsec apart in the south ring be injected and extracted by the kickers each machine cycle. One e- bunch collides with the e+ bunch, the other e- bunch makes e+ for collisions 2 cycles later, and the second circulating e+ bunch continues to damp before extraction the next cycle. The damping rings have loose injection kicker tolerances because errors damp out, but emittance growth from linac wakefields imposes tight (10^{-3} to 10^{-4}) tolerances on the extraction kicker. For a single bunch this is a jitter tolerance, and is fairly easy to meet by putting the beam on the peak of the pulse. For 2 bunches the tolerance applies to the difference between the kicks of the 2 e- bunches, as well as the jitter in either kick. Until 1989, the SLC operated in a mode requiring 4 linac pulses per collision, in part because the kickers could not meet the multibunch tolerences. The SLC has run with 2 e+ bunches in the south damping ring since 1989 in a 2 pulse per collision mode, and with 2 e- bunches in the north ring since 1990 in full 1 pulse per collision mode.

The 2 e- bunch extraction tolerances were met by distorting the long current pulse to compensate for the magnet imperfections [13]. This was first done with a droop inductor to produce a flatter magnet pulse, and a peaking capacitor to produce a faster rise time. The shaping was adjustable only by stopping the pulser, was done by trial and error, and was not precise enough for high beam intensity operation. The lumped pulse shaping components have now been supplemented by fine tuning devices that can be adjusted under remote control. One device is a charge line tuner that changes the second bunch kick without altering that of the first. Another is a small pulser that sends an adjustable pulse backward through the

magnet to cancel the small kick received by the second bunch on the previous turn by thyratron prepulse or early risetime [14]. Further pulse shaping devices presently constructed and ready to commission are a saturating ferrite line to filter out thyratron prepulse and sharpen the risetime, and a remotely controlled LC tuner to control the slope of the field pulse for the first bunch.

V. LESSONS FOR FUTURE COLLIDERS

Linear collider damping ring kickers are subject to far more serious constraints than most other accelerator kickers. They must run at high rates continuously and will likely be exposed to continuous beam losses. The need for fast damping leads to small rings which require fast risetimes and thus large voltages. Linac wakefields impose much tighter tolerances on extraction kicker jitter than most kicker applications, and operation with multiple bunches imposes additional difficult constraints on pulse shape.

The component in the SLC kicker systems that fell the farthest short of design performance was the magnet (both generations). The very fast risetimes require careful electromagnetic design, and the high voltages require careful electrostatic and mechanical design. For the SLC, the very short available length has made improvements very difficult, although very little damping ring performance would have been sacrificed if more space had been allocated for kickers. More length reduces the total power requirement, which can be used to lower current, voltage, or both. Multiple magnets fed in parallel would have a more favorable tradeoff between voltage and risetime, which is the basic kicker dilemma for SLC. The constraints of operating the magnet in the air outside the coated ceramic beam pipe are also large, particularly radiation damage to insulation exposed to air. It is worth re-examining the possibility of kickers inside the machine vacuum.

It has been possible to make thyratrons operate with 30 nsec risetime to 40KV and 2000A and 100 psec jitter. Time drifts are very much larger but easily corrected by feedback for constant rate operation. Optimum performance requires pulse charging and fast high voltage grid drivers and multigap tubes. Series switched circuits give better performance than Blumlein circuits because they present a higher impedance to the tube,but the plasma formation time scale sets a limit to risetime improvements. Multigap thyratrons have prepulse which can be a problem for multibunch extraction, but saturating ferrite filters can eliminate it and perhaps improve risetime as well (although not falltime).

It is very difficult to produce a passively perfect multibunch extraction kicker system. Moderate magnet imperfections can be compensated by current pulse shaping, at least for small numbers of bunches. For future colliders with trains of many closely spaced bunches it is not clear this approach remains practical. It is also possible to add independent small correction pulses at the magnet, or at other locations, to put multiple bunches on the same trajectory. This latter scheme does not compensate for jitter. Adding a second kicker $n\pi$ away in betatron phase away that receives the same pulse in parallel with an appropriate delay can compensate for both amplitude differences and jitter. However it could not compensate for kicks from other ring turns, one of the SLC problems.

VI. REFERENCES

[1] F. Bulos *et al.*, "Some Fast Beam Kicker Magnet Systems at SLAC," in *Proc. of 1987 IEEE Particle Accel. Conf.*, Wash.ington DC, Mar.ch 1987, pp. 1884-6.

[2] L. Bartelson *et al.*, "Kicker for the SLC Electron Damping Ring," in *Proc. of 1987 IEEE Particle Accel. Conf.*, Washington DC, March 1987, pp. 1582-4.

[3] R. Cassel and M. Nguyen, "Kicker Pulsed Charger", these proceedings.

[4] T. Mattison *et al.*, "Kicker Systems for the Stanford Linear Collider," in *Particle Accelerators*, vol. 30, pp. 115-20, 1990.

[5] J. Weaver *et al.*, "Design, Analysis and Measurements of Very Fast Kicker Magnets at SLAC," in *Proc. of 1989 IEEE Particle Accel. Conf.*, Chicago, IL, March 1989 pp. 411-3.

[6] T. Mattison *et al.*, "Operational Experience with SLC Damping Ring Kicker Magnets," these proceedings.

[7] R. Cassel *et al.*, "SLC Kicker Magnet Limitations," these proceedings.

[8] G. Gross *et al.*, "Development of Epoxy Potting for High Voltage Insulation at SLAC," these proceedings.

[9] A. Donaldson *et al.*, "Kicker Thyratron Experience from SLC," these proceedings.

[10] M. Nguyen and R. Cassel, "Fast Thyratron Driver," these proceedings.

[11] K. Harris *et al.*, "High Voltage Pulse Cable and Connector Experience in the Kicker Systems at SLAC," these proceedings.

[12] D. Gough *et al.*, "The Timing and Diagnostics Systems of the Kicker Magnet Pulsers for the Stanford Linear Collider," these proceedings.

[13] T. Mattison *et al.*, "Pulse Shape Adustment for the SLC Damping Ring Kickers," these proceedings.

[14] R. Cassel and T. Mattison, "Kicker Prepulse Canceller," these proceedings.

Cell Design for the DARHT Linear Induction Accelerators

M. Burns, P. Allison, L. Earley, D. Liska, C. Mockler, J. Ruhe, H. Tucker, L. Walling
Los Alamos National Laboratory, P.O. Box 1663, Los Alamos, NM 87545

Abstract

The Dual-Axis Radiographic Hydrotest (DARHT) facility will employ two linear induction accelerators to produce intense, bremsstrahlung x-ray pulses for flash radiography. The accelerator cell design for a 3-kA, 16-20 MeV, 60-ns flattop, high-brightness electron beam is presented. The cell is optimized for high-voltage stand-off while also minimizing the its transverse impedance. Measurements of high-voltage and rf characteristics are summarized.

I. INTRODUCTION

The DARHT facility at Los Alamos will generate intense bremsstrahlung x-ray pulses for radiography using two linear induction accelerators (LIA). Each LIA will produce a 3-kA, 16- to 20-MeV, 60-ns flattop, high-brightness electron beam using a 4-MeV injector and a series of 250-kV induction cells. Each cell consists of an oil-insulated ferrite core, an accelerating gap with carefully profiled electrodes and insulator, and a solenoid magnet to transport the electron beam. This paper summarizes the design of the accelerating gap region.

The cell development process included the design, fabrication, and testing of three prototype cell configurations. In chronological order, these are referred to as Mod 0, Mod 1, and Mod 2 and are shown in Fig. 1.

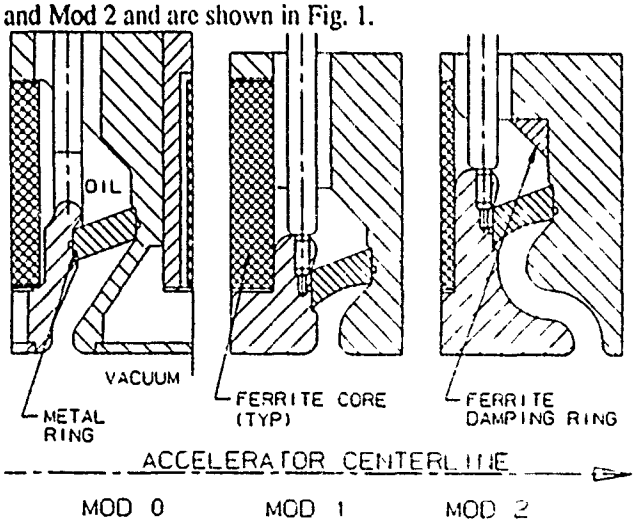


Fig. 1 Accelerating gap region of the three prototype DARHT cell designs.

The fundamental parameters of the accelerator determined the basic layout of each configuration. To provide the required pulse width while using readily available material, 11 TDK PE11B ferrite torroids (237 mm ID, 503 mm OD, 25.4 mm thick) were specified for the cell core. High-voltage breakdown of the accelerating gap is prevented by using a minimum gap width of 14.6 mm. The cell bore is 148.2 mm, which is a compromise between the large bore needed to limit growth of the beam breakup (BBU) instability and the small bore required to provide space for the solenoid magnet and to reduce costs.

The high-voltage design and breakdown measurements of these prototypes is discussed in Section 2. Section 3 deals with calculation and measurement of the transverse impedance of each configuration.

II. HIGH-VOLTAGE DESIGN

We limited the peak design electric field stress to 200 kV/cm for the type 304 stainless steel electrodes that form the accelerating gap. This condition required a minimum gap width of 14.6 mm to sustain the 292-kV gap potential generated by the failure mode in which the cell is pulsed without electron beam loading.

The design of the insulator separating the oil-filled ferrite core from the vacuum portion of the cell became the focus of the high-voltage design. Empirical electrical breakdown formulas determined the initial layout of each insulator, and then detailed electric field modeling was carried out using the two-dimensional finite-element codes POISSON and FLUX2D. The breakdown electric field was maximized by optimizing the angle between the insulator and the calculated electric potential lines. This angle should be held near 40° for the cross-linked polystyrene insulator, and to do this in the Mod 0 design required placing a conducting ring within the insulator near the negative electrode vacuum triple point. The curved vacuum-side surface of the Mod 1 and Mod 2 insulators avoids the fabrication challenges encountered with the Mod 0 insulator ring. The maximum calculated electric field stress across the Mod 2 insulator was 93 kV/cm.

Cross-linked polystyrene (trade name Rexolite) was selected for the insulator because of its low dielectric constant (ε=2.5) and excellent mechanical properties. The insulator is compressed from 0 to 0.5 mm when installed to avoid small gaps between the electrodes and the insulator, which can cause significant field enhancement.

Interaction of the electron beam with the insulator may lead to insulator charging and UV-induced breakdown. The Mod 0 design counteract this effect by partially shielding the insulator from the electron beam. The Mod 1 design ignores this feature in favor of reduced machining costs. The Mod 2 design completely shields the insulator in a way that also reduces the design's transverse impedance. Detailed modeling of the complicated Mod 2 geometry required increasing the accelerating gap width to 19.1 mm.

L.M. Earley, *et. al.* [1], have completed detailed measurements of the breakdown voltage for each cell

Work performed under the auspices of the U.S. Department of Energy

0-7803-0135-8/91$01.00 ©IEEE

configuration. Mod 0 tests were carried out with two full-sized cells driven by a low-impedance (10 Ω) Blumlein. Full-sized Mod 1 and Mod 2 geometries were investigated using a higher impedance (240 Ω) cable pulser, which avoided the cost of fabricating the ferrite core portion of the cells. The Blumlein provided a square pulse with the voltage above 90% of the peak value for about 70 ns. The square waveform from the cable pulser remained above 90% of the peak for 150 ns.

Approximately 2000 shots were recorded in testing the Mod 0 design. These included conditioning shots at lower voltages as well as shots up to the breakdown voltage. In a similar way, the cable pulser was used for 30,000 shots on Mod 1 and roughly 4000 shots on Mod 2. The high-impedance cable pulser did not drive large currents when the gaps broke down, unlike t' low-impedance Blumlein system. Thus, the cable pulser ~ ıave provided better high-voltage conditioning than the Blumlein system. The measured Mod 1 and Mod 2 breakdown voltages listed in Table 1 are the levels at which breakdown was observed for approximately half the shots at that potential. These breakdowns damaged the cells so that breakdown continued at -400 kV. No permanent damage was done to the electrodes or insulators, however, and these parts could be reused after cleaning. Mod 0 failed on the tenth shot at -350 kV, and testing was stopped at that point.

Table 1. Measured Breakdown Voltage

Design	Breakdown (kV)	Driver
Mod 0	-350 +/- 10%	Blumlein
Mod 1	-500 +/- 8%	Cable pulser
Mod 2	-520 +/- 8%	Cable pulser

III. CELL IMPEDANCE

The BBU instability results in high-frequency transverse oscillations of the electron beam, which smears the time-integrated beam spot size at the accelerator final focus. This increases the radiographic spot size and decreases the spatial resolution of the resulting radiograph. Growth of the BBU instability is dependent upon the cell transverse impedance.

Theory [2] indicates that :

$$\omega \left(\frac{cZ}{\omega}\right) = \frac{4w}{b^2}\eta \,, \qquad (1)$$

where Z is the transverse impedance (Ω/cm) of a resonant mode of angular frequency ω. The speed of light is c (cm/sec), the gap width is w (cm), and the bore radius is b (cm). η is a dimensionless constant that reflects how well the cavity modes are damped. Its value is determined by such factors as geometry and material choice. Minimizing the transverse impedance by minimizing η is the goal of the rf design of the cell.

The two-dimensional finite-difference, time-domain electromagnetic simulation code AMOS [3] was used to calculate the transverse impedance of the cell. This code is unique in that the rf absorption properties of the ferrite core are modeled. The ferrite properties were determined by measurements of small ferrite samples [4].

The low-impedance cell design process began with the Mod 0 configuration, which was an evolution of existing LIA designs. Mod 1 was a mechanical simplification of Mod 0 while also improving the cell's high voltage characteristics. Mod 2 used a "shielded gap" [5] to reduce the impedance at low frequency while also hiding the insulator from the electron beam. Our studies of these configurations with AMOS have shown that the transverse impedance can be reduced by using a low-dielectric-constant insulator material, placing the insulator close to the cell bore, avoiding gaps between the negative electrode and the ferrite core, matching rf waves into the core by controlling the amount of ferrite exposed to the cavity, using extra ferrite pieces to damp cavity modes, and properly choosing the geometry of the accelerating gap.

L. Walling, *et. al.* [6], have completed measurements of the transverse impedance of each cell design. These tests have shown that an important feature of the cell is the high-voltage drive rods attached to the negative electrode in two places 180° apart. The drive rods break the axial symmetry of the cell resulting in azimuthal variations in the impedance that cannot be modeled by AMOS. Figure 2 shows the transverse impedance measurement for the Mod 0 geometry in both the horizontal (parallel to the drive rods) and vertical (perpendicular to the drive rods) planes with the drive rods terminated in 30 Ω.

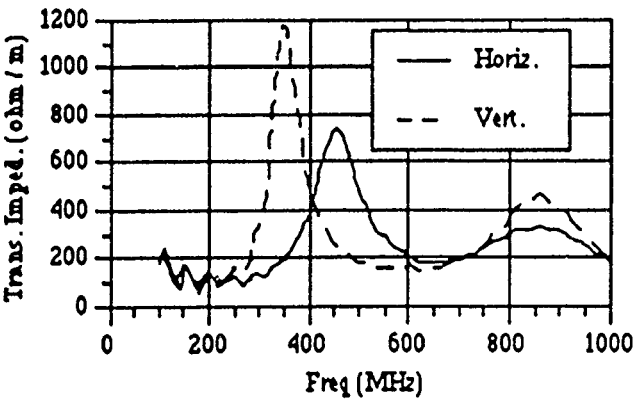


Fig. 2. Mod 0 transverse impedance in the horizontal and vertical planes.

P. Allison, *et. al.* [7], have shown that rotating pairs of cells 90° along the accelerator can take advantage of this mode splitting and reduce the effective impedance of the cell. With this installation pattern, the average of the horizontal and vertical impedances is the quantity of importance. This value should be roughly 670 Ω/m to meet the DARHT performance goals.

Figure 3 shows the average impedance vs frequency for all three cell configurations using the hollow compensation resistor discussed below. The small-amplitude oscillations in each curve are the result of calibration errors. The overall measurement accuracy is estimated to be better than 20%. The peak impedance for the Mod 0 design was 731 Ω/m at 114 MHz (η=2.29). The Mod 1 cell is much worse with a

measured peak impedance of 1275 Ω/m at 847 MHz (η=3.99). This is reduced in the Mod 2 design to 671 Ω/m at 816 MHz (η=1.61). The shielded-gap configuration has greatly reduced the magnitude of low-frequency modes. Without the damping ferrite (see Fig.1), however, measurements of the Mod 2 cell indicate that the high-frequency mode grows to 1020 Ω/m at 680 MHz.

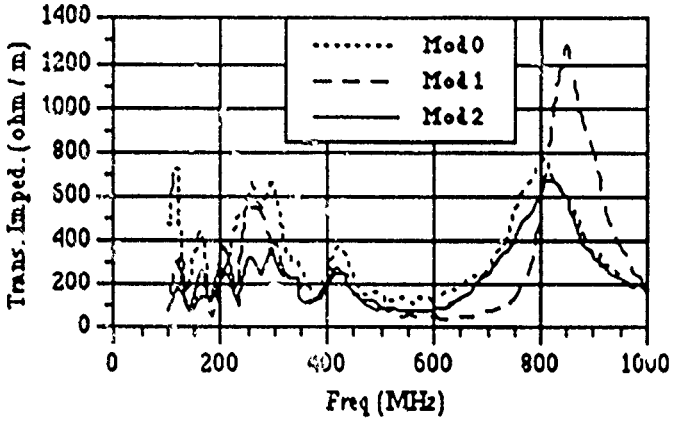


Fig. 3. Average transverse impedance vs frequency.

Attached to each side of the cell is an enclosure from which the drive rods enter the cell and in which is placed a compensation resistor. These resistors are electrically in parallel with the accelerating gap and help to reduce gap-voltage fluctuations due to electron-beam current variations.

The three enclosure/resistor designs shown in Fig. 4 were investigated in the belief that these assemblies may affect the cell impedance. In the first design, the high-voltage cable feeding the cell was connected directly to the drive rod, and a solid resistor ran along side the cable from the drive rod to ground. A hollow, cylindrical resistor was placed coaxially around the cable in the second enclosure. The third enclosure was designed to be similar to a high-power rf load. This design is referred to as the rf-horn because the resistor is surrounded by an exponential horn that maintains a constant impedance along the length of the resistor.

Shunt-resistance measurements of each enclosure design are shown in Fig. 5. The results clearly indicate that the rf-horn is the most successful design. Measurements of the accelerating cells with the various enclosures attached, however, indicate that the compensation resistor enclosure has very little effect on the transverse impedance of the cell. This result may be peculiar to the specific geometry of these designs.

IV. CONCLUSIONS

We will construct a series of Mod 2 cells for system-level integrated tests of the DARHT accelerators. This design exhibited the best high-voltage and impedance properties. The shielded gap did not significantly reduce the peak impedance compared to Mod 0, but did allow complete shielding of the insulator from the electron beam and a larger accelerating gap.

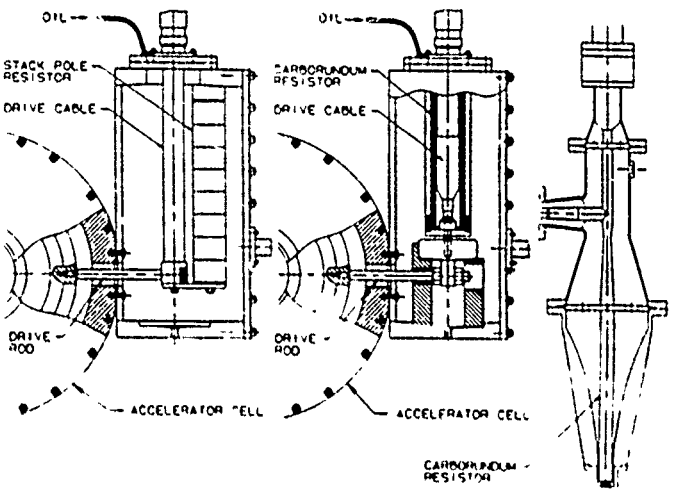


Fig. 4. Prototype compensation resistor enclosures

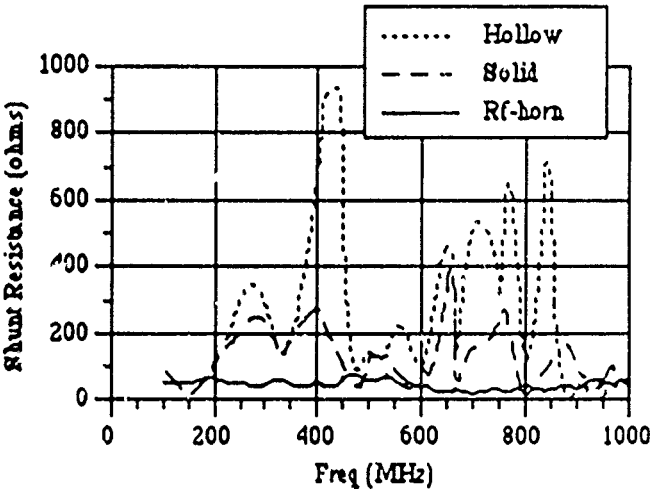


Fig. 5. Compensation resistor enclosure shunt resistance

REFERENCES

[1] L.M. Earley, "Induction Cell Insulator Experiments for the Dual Axis Radiographic Hydrotest (DARHT) Facility", *IEEE Eighth Pulsed Power Conference*, San Diego, CA, June 1991.

[2] G.J. Caporaso and A.G. Cole, "Design of Long Induction Linacs", *1990 Linear Accelerator Conference*, Albuquerque, NM, Sept. 1990.

[3] J.F. DeFord, G.D. Craig, R.R. McLeod, "The AMOS Wakefield Code", *Workshop on Accelerator Computer Codes*, Los Alamos, NM, January 1990.

[4] J.F. DeFord and G. Kamin, "Application Of Linear Magnetic Loss Model of Ferrite to Induction Cavity Simulation", *1990 Linear Accelerator Conference*, Albuquerque, NM, Sept. 1990.

[5] R.B. Miller, B.M. Marder, P.D. Coleman, "The Effect of Accelerating Gap Geometry on the Beam Breakup Instability in Linear Induction Accelerators", J. Appl. Phys., 63 ( ), Feb 1990, pp. 997-1008.

[6] L. Walling, P. Allison, M. Burns, D. Liska, D. McMurry, A. Shapiro, "Transverse Impedance Measurements of Prototype Cavities for a Dual-Axis Radiographic Hydrotest Facility (DARHT)", *IEEE 1991 Particle Accelerator Conference*, San Francisco, CA, May 1991.

[7] P. Allison, M. Burns, G. Caporaso, A. Cole, "Beam Breakup Calculations for the DARHT Accelerator", *IEEE 1991 Particle Accelerator Conference*, San Francisco, CA, May 1991.

Transverse Impedance Measurements of Prototype Cavities for a Dual-Axis Radiographic Hydrotest (DARHT) Facility*

L. Walling, Paul Allison, M. Burns, D.J. Lisk
D.E. McMurry, and A.H. Shapiro
Los Alamos National Laboratory
Los Alamos, NM 87545

I. INTRODUCTION

We have reported coupling impedance measurements on pillbox cavities [1] that were performed in preparation for studying the dual-axis radiographic hydrotest facility (DARHT) cavities. Both beadpull and wire methods were explored. From the study, we concluded that wire methods could be used to accurately measure the transverse impedance of the DARHT cavities. This report describes the results of wire measurements of several prototype DARHT cavities. References 1-2 describe in detail the measurement method.

The TM_{1n0} (or dipole) modes are deflecting modes of cavities, and the transverse coupling impedance is a measure of how efficiently the beam interacts with these modes. In this paper we will use the following definition of transverse impedance (expressed in the mks system of units):

$$Z_{\perp} = \frac{cQ[\int B_y dz]^2}{2U}$$

where c is the speed of light, Q is the quality factor, B is the magnetic field, z is the direction along the beam axis, and U is the stored energy in the cavity.

II. MEASUREMENTS

Figure 1 is a diagram of the three DARHT cavity models. The cell geometry for MOD0 is similar to a design used at Lawrence Livermore National Laboratory (LLNL) [3]. The insulator was slanted at approximately the Brewster angle to enhance the flow of rf to the ferrites, and the cavity had a corner that reflected the wave back to the ferrites. Rexolite, with a low dielectric constant close to that of the oil, was used to minimize rf reflections and to maintain a good high-voltage field profile. For all geometries AMOS [4,5] code predictions guided the designs, and the fields in the vacuum were kept below 200 kV/cm for a 250 kV accelerating voltage. The next design, MOD1, used resistive material and a smaller insulator aperture to lower the impedance and thus to improve the match at the insulator. In the MOD2 design we attempted to have a waveguide below cutoff for the TM_{110} mode and to hide the insulator from the beam. A partial ring of ferrite for the beam return current to flow through was added to absorb the TM_{120} mode. The cells are powered by two 50-Ω cables, each terminated by a 77-Ω resistor just before the drive rods enter the cell. Early in the measurements we realized that the drive rods and terminating resistors strongly affected the cavity impedance, so three types of resistors were tested on each cell. Two resistor designs, one with a carborundum resistor concentric to and enclosing the drive line and the other a stacked resistor parallel to the drive line, were built with little regard for rf considerations. The third design, a coaxial resistor in an exponential horn, was designed and tested on the assumption that its good rf properties might lower the cavity impedance. Because the rf penetration into the ferrite at the frequencies of the TM_{1n0} modes is only a few centimeters, the test cavities can be much shorter than an actual induction cell.

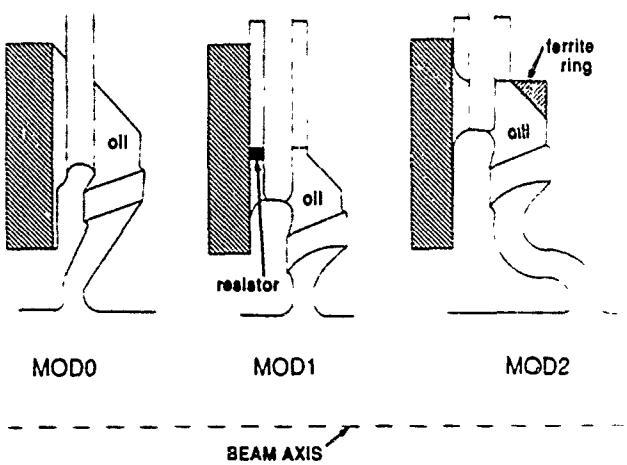


Figure 1. Geometry of three prototype DARHT cells. The three cells have cylindrical geometry except where the drive rods enter at the top and bottom of the cavity.

A. *MOD0 with Ferrites Removed*

We initially measured the cavity impedances with the ferrites removed. We modeled the cavity with MAFIA, a 3-D code that solves Maxwell's equations on a rectangular mesh. Four of the modes have dipole characteristics in the beam tube and a sextupole field configuration in the body of the cavity. This means that modes are being mixed in the cavity. URMEL-T (a 2-D code which also solves Maxwell's equations) predicted a TM_{120} mode at 1002 MHz and a TM_{310} mode at 1015 MHz. Each of these have two degenerate modes. The introduction of radial asymmetries in the cavity couple these four modes together, resulting in four mixed modes. These four mixed modes were predicted by MAFIA and closely matched the frequency and field distributions in the cavity. Table I shows the results of this measurement.

Because of MAFIA's rectangular mesh, parts of the geometry are coarsely reproduced. The TM_{310} mode has its strongest electric field in the region of the rim that connects to the drive rod. This rim is very poorly represented in the MAFIA model. Therefore it is not surprising that the impedances calculated for these mixed modes do not correspond as closely as for the TM_{110} modes.

*Work supported by the U.S. Department of Energy, Weapons Activities, GB01.

0-7803-0135-8/91S01.00 ©IEEE

Table I.
Measurement Results of DARHT Cavity
with Ferrites and Drive Rods Removed

	MAFIA		Measured	
	f(MHz)	$T^2Z_\perp/Q$ (Ω/m)	f(MHz)	$T^2Z_\perp/Q$ (Ω/m)
TM110 (H)	403	181	418	177
TM110 (V)	431	199	445	195
TM120/310 (H)	811	42	851	102
TM120/310 (V)	956	7	966	13
TM120/310 (H)	966	38	976	51
TM120/310 (V)	978	57	980	61

(H) refers to measurements in the plane of the drive rod mounts.
(V) refers to measurements in the normal plane.

B. MOD0, MOD1 and MOD2

1. AMOS Calculations

Figure 2 shows measured and calculated impedances for the three cavities with the rods removed. Both MOD0 and MOD2 were measured with and without oil, and MOD1 was measured in air only. The measured impedances plotted are $Z_\perp$ in the plane perpendicular to the plane containing the drive rods. The reason for this is that asymmetries in the cavities occur in the plane of the drive-rod mounts; therefore, the modes oriented such that the rods displace negligible field are better represented by the 2-D code. Figure 3a shows two calculated values. Originally AMOS contained a pure wave boundary condition ($Z_{boundary} = E_{||}/H_{||}$) to simulate the ferrites but has been modified to allow material with magnetic conductivity σ_m [5]. The data shown in Fig. 3b-c are calculated using only the modified version of AMOS.

Errors in the measurement are primarily due to three sources. First, the presence of the wires in the cavity locally changes the fields, thus changing the cavity impedance. This effect should be small (probably on the order of 10% or less) for the case of the DARHT cavities, because the beam pipe diameter is much greater than the wire diameter. The second source of error is the calibration itself. The measured transverse impedance is calculated from

$$Z_\perp = \frac{2Z_0 c(1 - S_{21})}{\omega \Delta^2 S_{21}}$$

where Z_0 is the characteristic impedance of the transmission line formed by the beam pipe and wires, Δ is the distance between the wires, and S_{21} is the transmission through the cavity. When S_{21} is large (as is the case for small impedances), 1- S_{21} is small, making a 1% uncertainty in S_{21} result in large errors. The third source is uncertainty in the spacing between the wires, Δ. Since the transverse impedance is as $1/\Delta^2$, uncertainties in Δ can contribute strongly to measurement errors. (The change in Z_0 due to changes in Δ is small by design.) The error bars indicated in Fig. 3 have been calculated as the square root of the sum of the squares of the expected maximum values of these three contributions. Measurements indicate that the wire spacing is constant (and known) to 2% and the calibration is kept within +/- 1%.

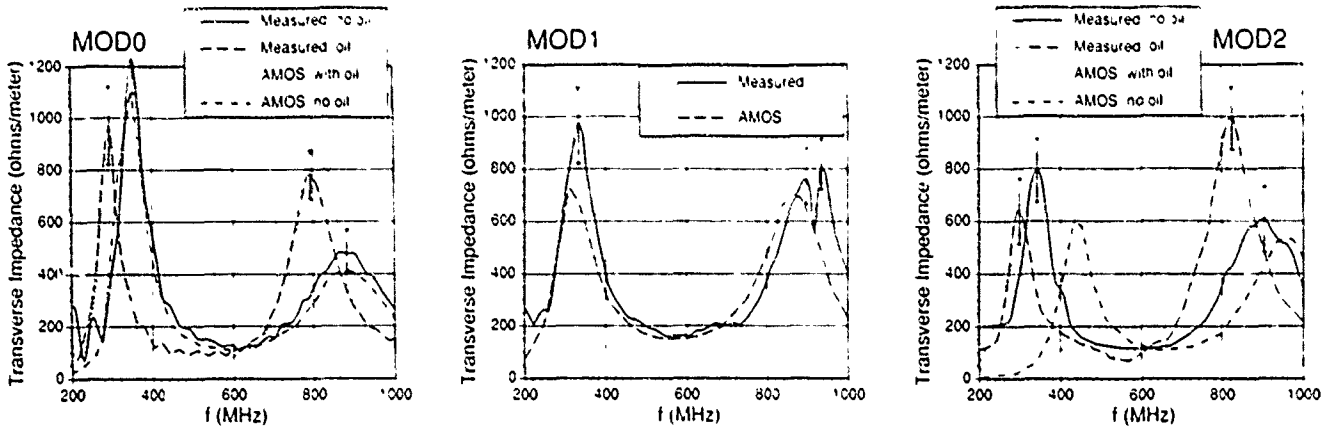


Figure 2. Comparison of measured impedances vs. AMOS predictions.

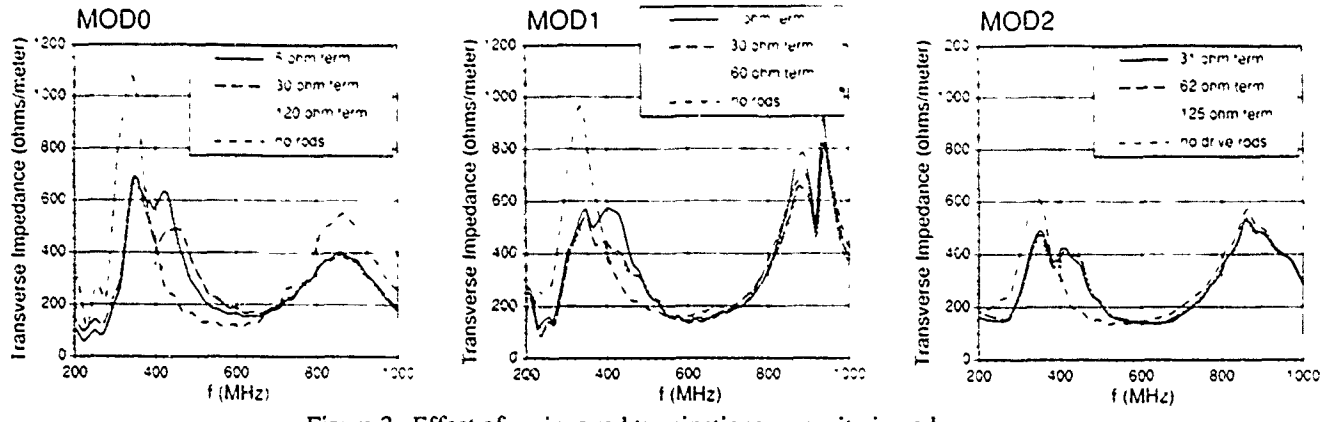


Figure 3. Effect of various rod terminations on cavity impedances.

2. Measurements With Drive Rods in Place With Various Terminations

Figure 3 shows plots of impedances measured without drive rods, and with the rods in place and terminated in various resistances. These resistors were built from two concentric rings with many parallel high-frequency resistors mounted radially. The differences in measured impedances between different terminating resisitances on the rods is generally much less than the difference between having the rod in and terminated (with anything) and having no rods in at all. In almost all cases the rods lower the mode impedances by coupling power out of the cavity.

These plots and all succeeding ones are presented as the average of the impedances measured in the planes parallel and normal to the plane containing the drive rods. The reason for this is that, because of the mode splitting caused by the drive rods, the total impedance seen by the beam can be reduced by placing half of the drive cells in one orientation (i.e., drive rods positioned horizontally) and the other half of the drive cells positioned with the drive rods vertical.

3. Measurements With Compensation Cans

The cavities must operate with the drive lines in place and loaded with compensating resistors that serve a dual purpose. First, the compensating resistor box must provide a relatively low shunt impedance in parallel with the cavity so that the drive line sees a constant input impedance in the presence of beam current and ferrite bias changes. Secondly, it is desirable that the compensating resistors provide an optimum termination to the drive rods as seen by the cavity so that the cavity modes are optimally damped. As expected, the rf resistor appeared superior. However, when the cans were mounted on the cavities and their drive lines terminated (Fig. 4), there were very small differences in the cavity impedances with different compensation cans. This finding is consistent with the results in Section 2.2.2, where the drive rods were terminated in simple resistors.

III. CONCLUSIONS

Simulations using BREAKUP [6], a code written by George Caporaso of LLNL using the beam breakup theory developed by Neil, Hall and Cooper [7], indicated that cavity impedances equal to or less than 670 W/m are acceptable for the DARHT cells. The cavity measurements indicate that we are close to that goal. In addition to the results presented, we measured impedances in MOD0 while biasing the ferrites by driving a dc through the rods. We found that the impedances were further reduced by as much as 20% when the ferrites were biased by 550 A. When this reduction is taken into consideration, we are confident that MOD0 and MOD2 will perform satisfactorily for beam breakup, although MOD2 looks slightly better and has the added benefit of shielding the insulator from the line of sight of the beam.

Although the different compensation resistors vary greatly when measured alone, when mounted on the cavities there is little difference between them. Therefore it would be reasonable to use the design that is least expensive to build.

IV. REFERENCES

[1] L. Walling, Paul Allison, and A. Shapiro, "Transverse Coupling Impedance Measurement Studies of Low-Q Cavities," 1990 Linear Accelerator Conference, Albuquerque, NM, September 1990.

[2] L.S. Walling, D.E. McMurry, D.V. Neuffer and H.A. Thiessen, "Transmission-Line Impedance Measurements for an Advanced Hadron Facility," Nucl. Inst. and Meth., Vol A281, 1989, pp. 433-447.

[3] G.D. Craig, J.F. Deford, and L. Walling, "BBU-Rings for the ETAII Induction Accelerator," 1991 IEEE Particle Accelerator Conference, San Francisco, Ca, May 1991.

[4] J.F. DeFord, G.D. Craig, and R.R. McLeod, "The AMOS Wakefield Code," Proc. Conf. Computer Codes and the Linear Accelerator Community, Los Alamos, NM, January 22-25, 1990, p. 265.

[5] J.F. DeFord and G. Kamin, "Application of Linear Magnetic Loss Model of Ferrite to Induction Cavity Simulation," 1990 Linear Accelerator Conference, Albuquerque, NM, September 1990.

[6] G.J. Caparaso, A.G. Cole, and K.W. Struve, "Beam Breakup (BBU) Instability Experiments on the Experimental Test Accelerator (ETA) and Predictions for the Advanced Test Accelerator (ATA)," IEEE Trans. Nucl. Sci., Vol. NS-30, p. 2507, 1983.

[7] V.K. Neil, L.S. Hall, and R.K. Cooper, "Further Theoretical Studies of the Beam Breakup Instability," Part. Accel.,Vol. 9, p. 213, 1979.

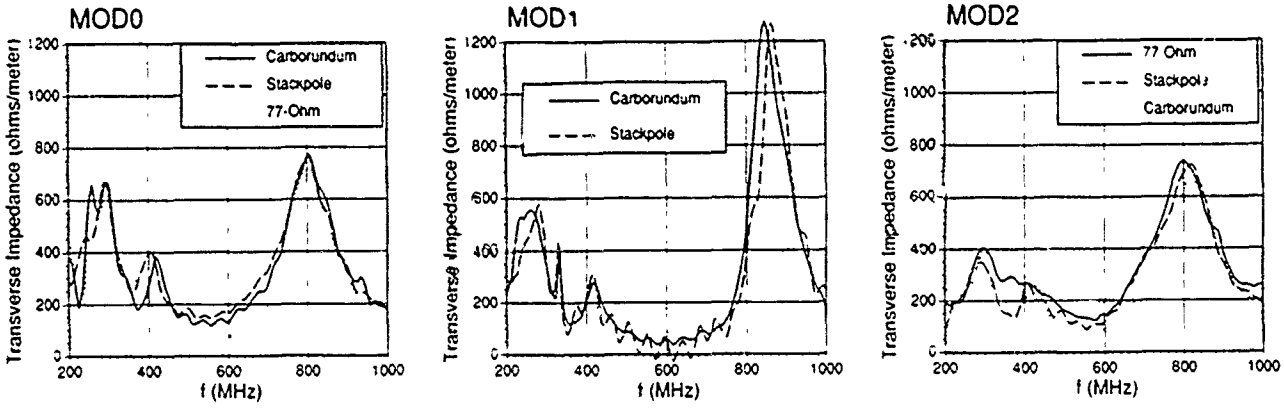


Figure 4. Effect of various compensation resistors on cavity impedances.

A New Front-End for the LEP Injector Linac

Jean-Claude Godot, Louis Rinolfi - CERN, Geneva, Switzerland
Andrea Pisent - INFN, Legnaro, Italy
Hans Braun - PSI, Villigen, Switzerland

Abstract

For improved reliability, the front-end of the LEP Injector Linac (LIL) has been replaced. The new system has been used for LEP runs, since March'91.

The experimental results presented here show a significant improvement of beam characteristics. These results also agree well with those of the simulation programs.

I. INTRODUCTION

The LIL performance figures [1] have been found to be a factor 3 above their required values for LEP physics. In order to ensure that these good performance figures are consistently obtained, a new front-end with improved reliability and which allows easier maintenance was installed. It is composed of a thermionic gun, a bunching system and a matching section to the linac. The modulator of the thermionic gun was re-designed to provide beam pulses variable in length and current from 10 to 50 ns and 0 to 15 A respectively. The beam characteristics from the gun were simulated using the EGUN code. The simulations and the optimizations of the bunching parameters were carried out using the PARMELA program. Finally, the matching section was designed with TRANSPORT. This code was also applied to the linac in order to optimize the primary beam onto the target according to the simulation results of the new front-end. A complete description is given in [2].

II. BUNCHING REQUIREMENTS FOR POSITRON PRODUCTION

The Electron Positron Accumulator (EPA), that immediately follows LIL, has an energy acceptance of $\Delta E/E = \pm 1\%$. The energy spread in the positron bunch at the end of LIL is determined by three factors, the accepted momentum spread from the production target, the microbunch length and the beam loading. The last effect can be neglected because of the low charge. The acceptance of the magnetic channel after the converter is $\Delta E = \pm 2$ MeV [3], leading to:

$$(\Delta E/E)_{converter} = \pm 0.4\%$$

at the injection into EPA.

The contribution to energy spread resulting from the microbunch length depends directly on the bunching quality. Assuming a bunch of relativistic positrons travelling on the crest of a wave, one can calculate:

$$(\Delta E/E)_{\phi} = 1 - \cos\frac{\Delta\phi}{2} \qquad (1)$$

where $\Delta\phi = \omega\Delta t$ is the phase extension of the microbunch. If a phase extension of ±8° from the bunching system is assumed, then $(\Delta E/E)_{\phi} = \pm 0.5\%$. The total energy spread, calculated using:

$$(\Delta E/E) = \sqrt{(\Delta E/E)^2_{\phi} + (\Delta E/E)^2_{converter}} \qquad (2)$$

is ±0.64%, which is well within the EPA acceptance. The number of e^- in 16° of RF phase extension was chosen as the figure of merit to evaluate the performance of the bunching system.

It is interesting to observe that the energy spectrum of the primary beam is determined by the beam loading due to the high charge needed at the converter. This does not affect the $(\Delta E/E)_{\phi}$ of the positron beam as it depends only on the microbunch length. The number of e^+ and their energy spread are, by virtue of equation (1), the best test of the bunching system efficiency.

III. BEAM DYNAMICS

Fig. 1 shows a schematic layout of the new front-end. Both the pre-buncher (PB) and the buncher work at 2.99855 GHz. The first resonator is a pill-box and the second a 2/3 π standing wave structure [4]. The gun voltage is 80 kV, and the buncher provides an additional acceleration of about 4 MeV.

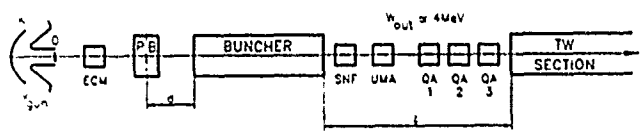


Fig. 1: Layout of the front-end

In Fig. 2, the kinetic energy of the reference particle at the end of the buncher (W_{out}) is plotted as a function of the phase ϕ_{in}; the final phase ϕ_{out} is also plotted. In the definition of these phases, there is an arbitrary offset chosen in such a way that the reference particle leaves the gun with phase equal to zero.

The two distances indicated in Fig. 1 as d and ℓ are of great importance to the longitudinal dynamics.

d is used in the pre-bunching process. The monoenergetic beam from the cathode is modulated in energy by the pre-buncher. The charge density around the reference particle is maximum after a drift space d such that:

$$\frac{d}{\lambda_{RF}} - \frac{2\pi\Delta\beta}{\beta^2} \approx 1 \qquad (3)$$

where $\Delta\beta$ is the velocity modulation amplitude. In the case of low space charge, a rather long d and a low energy modula-

0-7803-0135-8/91$01.00 ©IEEE

tion is preferred. In the case of positron production the high charge in the microbunch counteracts the bunching. A short distance and a high modulation has then to be chosen. The optimum values obtained from simulations, for a beam current of 3 A, are d = 100 mm and V_{PB} = 47.1 kV, corresponding to an average accelerating field of 1.3 MV/m.

The distance ℓ is used to improve the bunching quality after the buncher. It can be seen from Fig. 2 that the reference particle at ϕ_{ref} will correspond to a minimum of the final phase and energy curves. This e^- is at the head of the bunch (with an energy of 3.8 MeV) and it is possible to bring an e^- of 4.2 MeV from the tail of the bunch to the same phase. Since $\Delta\beta/\beta$ = 0.12%, the motion is not yet completely relativistic and after 3.5 m a bunch of 20° RF is compressed to 5° RF. This is valid to a first approximation, where space charge, energy modulation before the buncher and the non-linearity of the energy modulation were neglected. According to multi-particle simulations, the bunch of 20° rotates in phase space and has a final extension of 16°.

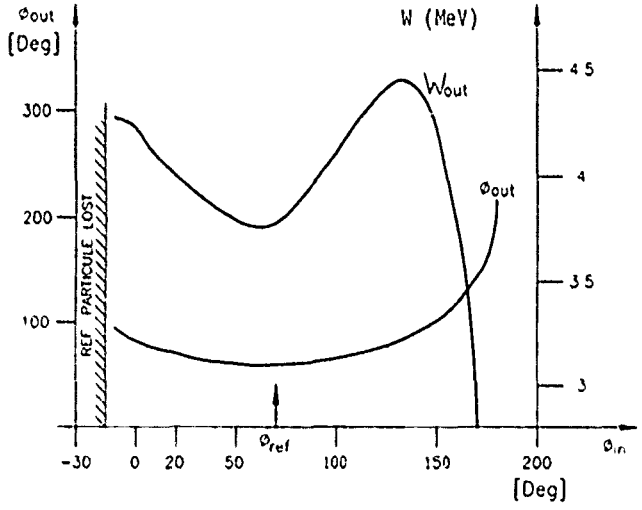


Fig. 2: Phase and kinetic energy of a single particle at buncher output versus input phase

With regard to the transverse beam dynamics, the 80 keV transport between gun and buncher is particularly delicate because of the space charge. Furthermore the surface of the cathode is spherical and the emitted current controlled by a grid, so that the emittance from the gun is of the order of 100 π mm.mrad. These problems are overcome by using a solenoidal guiding field well above the Brillouin value corresponding to 3 A of beam current. After the buncher the space charge effects become unimportant. The solenoid SNF and the triplet QA1,2,3 are used to match the beam to the first LIL accelerating section. With respect to the old front-end, the number of free parameters has been increased, so that the spot size at the converter is reduced to 1 mm (FWHH) and the maximum of the transported charge almost doubled.

Extensive calculations were performed using the three codes already mentioned. In particular for the PARMELA runs a nominal current of 3 A was chosen. Good transmission and bunching quality were found up to 9 A. Fig. 3 shows the microbunch distribution in the longitudinal phase space at the end of the matching section.

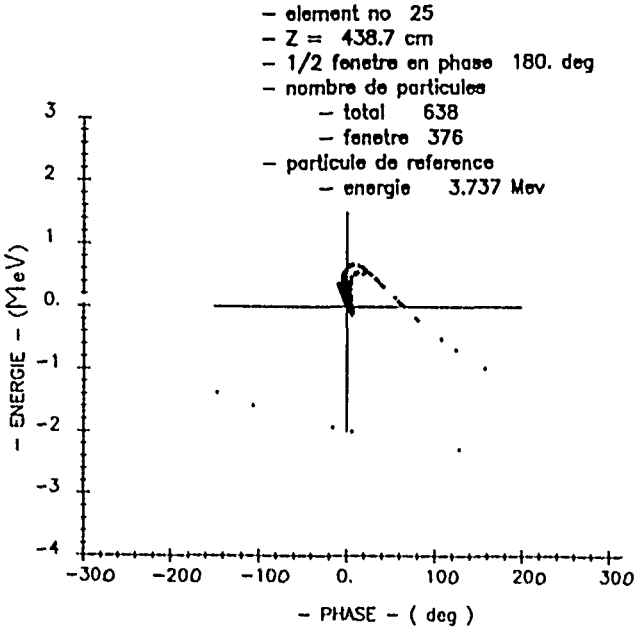


Fig. 3: Longitudinal phase space from PARMELA simulations

IV. MECHANICAL DESIGN

One of the aims of the project was to simplify mechanical design in order to have easy maintenance. This aim had to be achieved while at the same time fulfilling the quite demanding constraints imposed by the beam dynamics.

Firstly, due to the space charge effects, the distance between gun and pre-buncher has to be as short as possible.

Secondly, a standard vacuum valve is required between the gun and the pre-buncher. This valve protects the vacuum in the front-end, should the gun need to be removed, and it may also be used as a beam stopper in the safety chain.

As discussed above, the beam dynamics asks for a distance d = 100mm. To obtain this value, one side of the buncher was cut as short as possible and special bellows were welded on the pre-buncher. Finally, the buncher was mounted inside a solenoid in such a way to guarantee good continuity in the magnetic field. A spare bunching system will be realized according to this new design.

V. EXPERIMENTAL RESULTS

In order to evaluate the performance of the new front-end, the following parameters were measured. The transmission efficiencies of the bunching system and of the linac that provides the primary beam, were both measured at low and high charge values. The "non-load energy" and relative spread were measured just upstream of the target in a spectrometer line. The beam sizes were measured at the target. Finally, the yield was measured under various conditions reported in Table 1.

As already discussed in section 2, the yield measurements are, for the moment, the only data which provide a figure of merit of our bunching system. A 3 GHz RF deflector has been

installed at the buncher output, and a Tcherenkov light detector will be installed upstream of the target. This will provide a direct measure of the microbunch lengths inside the 20 ns pulse of the primary beam.

Fig. 4 displays the number of e^+ (full line) measured at the end of the linac versus the electric field in the pre-buncher.

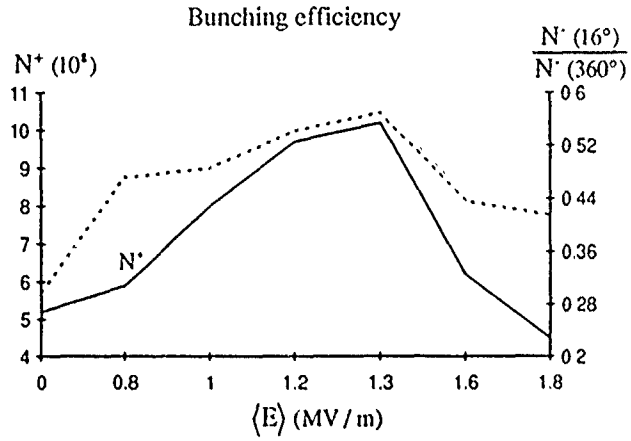


Fig. 4: Number of e^+ as a function of PB electric field

The curve is compared to the ratio N^- (16°) / N^- (360°) at the buncher output (dotted line) versus the same electric field.

The dotted line curve is obtained from PARMELA simulations and defines the bunching efficiency. The experimental and theoretical curves have their maximum at the same electric field value.

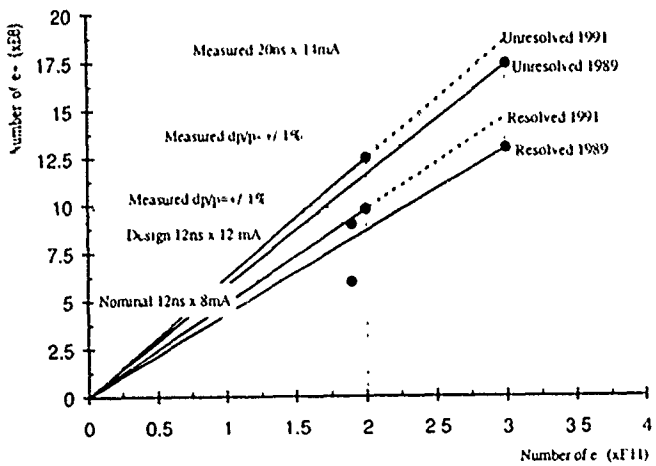


Fig. 5: LIL performance for e^+ production

The final outcome was improved reliability and increased performance figures as indicated in Fig. 5. The peak performance obtained with the old front-end [5] is compared with one experimental value obtained with the new one. The broken line is an extrapolation of expected performance with a higher primary beam charge.

Table 1: Comparison of performance

		LIL Front-End	
		1991 (New)	1989 (Peak Performance)
Gun energy	keV	80	70
Buncher output energy	MeV	4	28
No-load energy at the target	MeV	204	228
ΔE/E (full width at the base)	%	±6 6	±8
Transmission efficiency:			
- Bunching system 50 nC	%	67	66
- Bunching system 30 nC	%	72	61
- Bunching system 2 nC	%	77	56
- LIL primary beam 50 nC	%	75	76
- LIL primary beam 30 nC	%	83	83
- LIL primary beam 2 nC	%	90	90
Maximum charge at the target (e^+)	nC	83	48
For figures below, charge = 32 nC			
Beam sizes at FWHH			
- Horizontal	mm	1 0	1.0
- Vertical	mm	1 '	2 5
Unresolved yield (e^+/e^-)	10^{-3}	6.4	5 7
Resolved yield $\frac{(e^+)}{(e^-)}$, for $\frac{\Delta E}{E}=\pm 1\%$	10^{-3}	4.9	4.3
Normalized yield $\frac{(e^+)}{(e^- \times GeV)}$, for $\frac{\Delta E}{E}=\pm 1\%$	10^{-2}	2 40	1 95

VI. CONCLUSIONS

For the LIL consolidation project, a new version of the front-end was installed. Extensive simulations based on PARMELA code allowed to find an optimized configuration. The experimental and simulation results agree to within a few per cent. With respect to LIL performance, the new front-end has given a 23% higher normalized yield. The number of positrons actually produced has been increased by 14%. Both figures have been obtained for a primary beam charge of 32 nC.

VII. REFERENCES

[1] R. Bossart, J.P. Delahaye, J.C. Godot, J.H.B. Madsen, P. Pearce, A. Riche, L. Rinolfi, "The LEP Injector Linac", CERN/PS/90-56 (LP)

[2] A. Pisent, L. Rinolfi, "A New Bunching System for the LEP Injector Linac" CERN/PS/90 58 (LP)

[3] K. Hübner, "Positron Production for Particle Accelerators", CERN/PS/88-19 (LP)

[4] A. Bensussan, D.T. Tran, D. Trone "High Power Standing-Wave Tripe[illegible] structure for positron acceleration", NIM 118 (1974) 349-355.

[5] J.-P. Potier, L. Rinolfi, "LPI Peak Performance recorded in December 1989", CERN Internal Note PS/LP 90-12

Photocathode Driven Linac at UCLA for FEL* and Plasma Wakefield Acceleration Experiments

S. Hartman, F. Aghamir, W. Barletta, D. Cline, J. Dodd,
T. Katsouleas, J. Kolonko, S. Park, C. Pellegrini, J. Rosenzweig J. Smolin, J. Terrien
UCLA Dept. of Physics, 405 Hilgard Ave., Los Angeles, CA 90024

J. Davis, G. Hairapetian, C. Joshi, N. Luhmann Jr., D. McDermott
UCLA Dept. of Electrical Engineering,

Abstract

The UCLA compact 20-MeV/c electron linear accelerator is designed to produce a single electron bunch with a peak current of 200 A, an rms energy spread of 0.2% or less, and a short 1.2 picosecond rms pulse duration. The linac is also designed to minimize emittance growth down the beamline so as to obtain emittances of the order of 8πmm-mrad in the experimental region. The linac will feed two beamlines, the first will run straight into the undulator for FEL experiments while the second will be used for diagnostics, longitudinal bunch compression, and other electron beam experiments. Here we describe the considerations put into the design of the accelerating structures and the transport to the experimental areas.

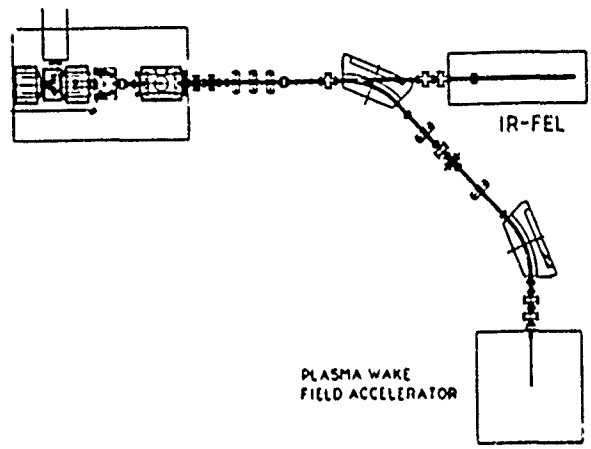


Figure 1: Beamline Layout

Introduction

In order to obtain a high-brightness electron beam we have employed an R.F. photoinjector[1] similar to that used at Brookhaven National Laboratory[2]. This photoinjector supplies a 4.5 MeV/c electron beam which is then further accelerated by a Plane Wave Transformer Linac[3] The linac brings the beam up to the desired 15-20 MeV/c momentum After the beam is accelerated it can proceed down either of two beamlines as shown in fig. 1. The transport in the straight beamline consists of the gun, a focusing solenoid, the Plane Wave Transformer, and then a series of quadrupoles to focus into the FEL undulator. The bent beamline is similar except it passes through a dipole then is focused to a horizontal and vertical waist for diagnostics. We present numerical results obtained by using the particle dynamics code PARMELA[4] to model the electron bunch dynamics through the R.F. structures. Also, we do second order TRANSPORT simulations through the beamline using the PARMELA output to study the beam transport through the remaining static elements.

Photocathode R.F. Gun

The R.F. gun is a 1.5 cell π-mode standing wave structure. It operates at the SLAC frequency of 2856 MHz and provides high peak accelerating gradients of up to 100MV/m on the photocathode. The R F gun requires 6 MW of power to accelerate electrons to 4.5 MeV/c, which will be supplied by a SLAC XK-5 klystron The high field in the cathode region minimizes the space charge emittance growth due to the space charge force when the electron beam is non-relativistic The ultra short electron bunch length can also be easily controlled by adjusting the laser pulse length, thus minimizing the energy spread in the beam and also the nonlinear emittance contribution due to a long bunch length. The photocathode is illuminated with a frequency quadrupled pulse from an Nd:YAG glass laser and can be injected at either a 70° or at 2°30′ to the axis, which will allow for enhanced photoemission using a polarized laser field parallel to the cathode or ultrashort pulsing, respectively The cathode will be initially made of copper which has a quantum efficiency $\geq 10^{-5}$

*Our group appreciates the help received from H Kirk, K Batchelor, J. Xie, J. Sheehan, G. Bennett, J Wurtele, M Allen, G Loew, and H. Hoag. This work is supported by DOE Grant no DOE-DE-AS-90ER40583 and ONR-SDIO Grant # N00014-90-J-1952.

0-7803-0135-8/91$01.00 ©IEEE

Plane Wave Transformer

The Plane Wave Transformer, PWT, which will be placed after the R.F. gun and solenoid is a π-mode standing wave structure which operates again at the SLAC frequency of 2856 Mhz and will be powered by the same klystron which powers the R.F. gun. The PWT is similar to the standard coupled cavity linac structures, accelerating the electrons in successive gaps in a π-mode field. The difference in the PWT is that it is a copper plated aluminum cylinder with washers supported $\beta\lambda/2$ apart along the axis. These washers set up the π-mode structure of the accelerating R.F. fields such that the electrons see a standard CCL field pattern. The power to the accelerating cells propagates in a TEM like mode in the outer radial region of the cylinder in a standing wave pattern which delivers power to each cell. Thus, the outer part of the structure uses the standing TEM mode to deliver and transform the power to the TM_{02}-like mode on the axis to accelerate the electrons.

PLANE WAVE TRANSFORMER

Cell Length $[cm]$	5.25
Resonant Freq. $[MHz]$	2856
Cavity Q	36,200
Shunt Impedance $[M\Omega/m]$	104

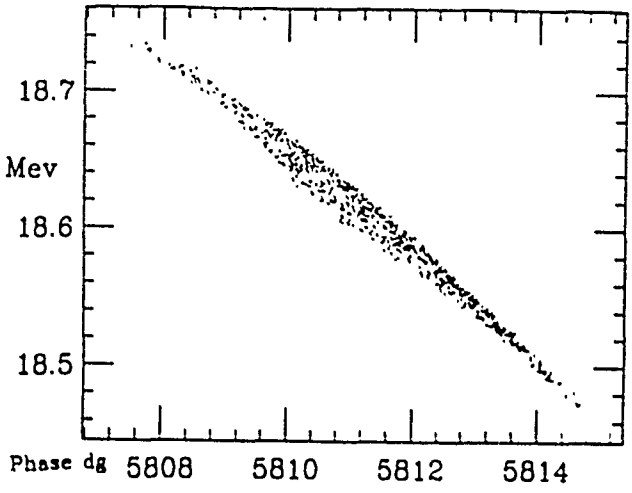


Figure 2: Longitudinal Phase Space

Linac Simulations

The gun geometry was designed and modeled with the SUPERFISH[5] code to minimize the radial nonlinear fields because any non-linear R.F. fields contribute to the emittance growth. These fields were then used as input for PARMELA simulations. PARMELA simulations were then done to model the space charge effects and also the electron dynamics in the guns' R.F. fields. For a 1nC, 4 picosecond laser pulse PARMELA gives a transverse emittance of 8πmm-mrad. Here the emittance is the transverse normalized emittance given by

$$\varepsilon_x = \frac{\pi}{m_0 c}\sqrt{< x^2 >< p_x^2 > - < x >^2 < p_x >^2} \qquad (1)$$

However at the gun exit the beam has a large rms angular divergence of 25mrad This divergence occurs because the gun exit acts like a diverging lense since the radial defocusing electric fields in the last cell of the gun are not canceled A way to remedy this divergence problem is to place a solenoid at the exit of the gun to focus the beam in the transverse direction With the solenoid in place the angular divergence can be reduced to zero or made negative thus allowing the electron beam to be focused into the following linac. However because the static magnetic field of the solenoid penetrates the R F gun some interesting additional effects are observed to take place In order to minimize the transverse emittance at the exit of the gun the initial launching phase of the photo cathode laser pulse must be shifted back in phase to 55 degrees, from its value of 65 without the solenoid. The solenoid also has the interesting effect of compressing the electron bunch length, and reducing the longitudinal emittance. The amount of compression is dependent on the launching phase. However, the transverse emittance increases when the longitudinal emittance decreases. Figure 2. shows the electron bunch longitudinal phase space at the linac exit.

PARMELA LINAC SIMULATION

Laser spot size on cathode $[\sigma mm]$	3
Laser pulse Length $[psec]$	4
Laser injection phase $[degrees]$	55
Bunch Charge $[nC]$	1
Trans. Emit $\pi mm - mrad$	8
Energy Spread %	0.2
Peak Current, I $[A]$	≥ 200
RMS Electron Bunch Length $[psec]$	1 2
Beam Energy $[MeV]$	18.6

Beam Lines

The FEL[6] beamline was designed using PARMELA to track the beam through the R.F gun, solenoid, and PWT. The output was then used as the TRANSPORT input to calculate the following beamline to second order. The main consideration for the beam transport is that the electron bunch experience no emittance growth and also that there be a 0 2mm waist at the center of the undulator so as to match well to the FEL[7] optical beam. The TRANSPORT results in figure 3. show the beam line starting at the exit of the linac.

The transport line was designed such that the electron beam has always at least an 8σ clearance in the transverse direction from the beampipe, thus insuring that most of the current will be available downstream The Plasma

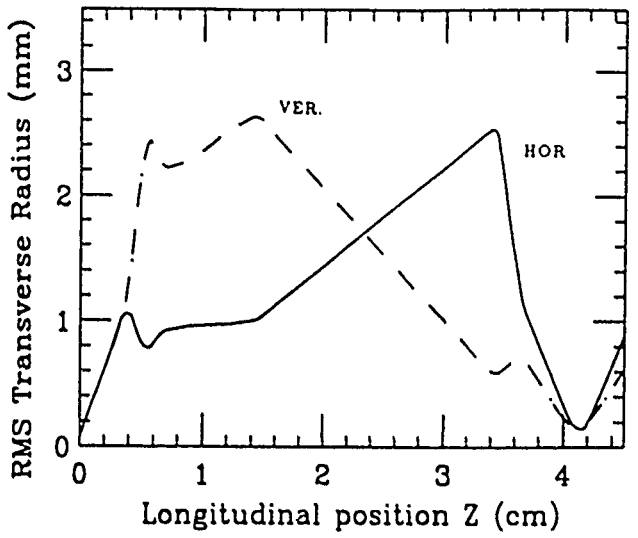


Figure 3: FEL Beam Transport Line

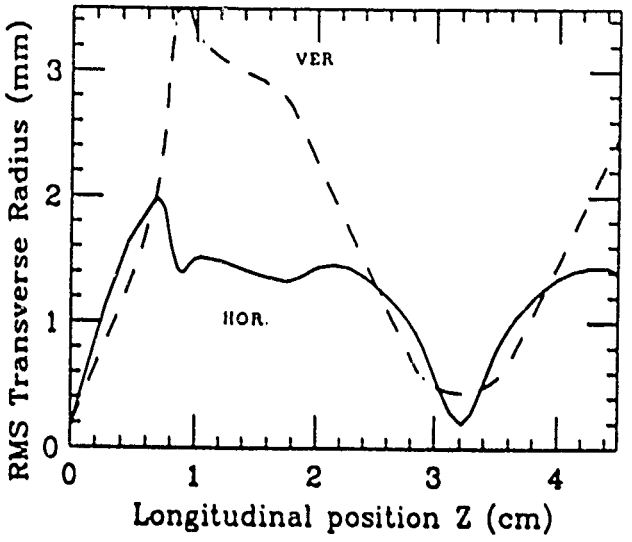


Figure 4: Diagnostic Beam Transport Line

Wakefield Accelerator[8] and diagnostic beamline, shown in figure 4., is designed such that there is a rms beam size of 0.15mm in the midpoint of the bent beamline. This will allow momentum spectrum measurements, by simply measuring beam size at the waist with a resolution of 0.1%

Beam Diagnostics

Three basic diagnostics will be used to extract information on the beam characteristics. A Faraday cup to measure the current in the beam, CCTV cameras which will measure position and profile of the beam on a phosphorous screen, and for nondestructive position and current measurements we will use stripline monitors. The beam profile monitor consists of a pneumatically actuated screen assembly which can move in and out of the beamline with high precision. The screen itself will be phosphorous coated and also electrically isolated from the beampipe so that it can be used as a faraday cup as well. The bent beamline will be utilized for the momentum analysis, and the beam profile will be monitored at the waist on a CCTV camera to measure the momentum spread. The data aquisition system will consist of a PC to control the accelerator operation and safety interlocks while recording the beam data. A frame grabber will be used to capture the beamprofile, then send it to the PC for analysis and display.

References

[1] J. Fraser and R. Scheffield, IEEE J. Quantum Electron. QE-23 (1987) 1489;
J.S. Fraser, et al ,Proc. 1987 Particle Accelerator Conf., IEEE. NS , p. 1705 (1987)

[2] K. Batchelor, H. Kirk, J. Sheehan, M. Woodle and K. McDonald, Proc, Europ. Particle Accelerator Conf., Rome, Italy,1988.
also: K. Batchelor et al., proc. 1989 Particle Accelerator Conf., Chicago IL.,p. 273.

[3] D.A. Swenson, in *Europ. Particle Accelerator Conf.*, Vol.2, 1988, Rome,Italy ed S. Tazzari, p. 1418.

[4] L. Young Los Alamos National Laboratory and modified for photo emission by K.T. McDonald, IEEE Trans. electron Devices ED-35 (1988) 2052.

[5] K. Halbach and R.F. Holsinger, Particle Accelerators 7 (1976) 213.

[6] C. Pellegrini, Nucl. Instr. & Meth. Phys. Res. A272 (1988) 364.

[7] J. Gallardo and C. Pellegrini, Optics Comm. 77 (1990) 45.

[8] J Smolin, T. Katsouleas, C. Joshi, P Davis, C Pellegrini, "Design of a Plasma Wakefield Accelerator Experiment at UCLA," Bul. Am. Phys Soc to be Pub Nov. 1990 Cf., T Katsouleas, J.J Su, W B Mori, C Joshi, J.M. Dawson, " A Compact 100 MeV Accelerator Based on Plasma Wakefields," Microwave and Particle Beam Sources and Directed Energy Concepts," H.E. Brandt, ed. Proc. SPIE 1061, pp 428-433 (1989)

Status of the LISA superconducting linac project

F. Tazzioli, A. Aragona, , R. Boni, M. Castellano, G. Di Pirro,S. Faini, M. Ferrario,
A. Gallo, S. Kulinski, C. Marchetti, M. Minestrini, P. Patteri, C. Sanelli, M. Serio,
A. Stecchi, L. Trasatti, M. Vescovi*
L. Catani, S. Tazzari #
N. Cavallo, F. Cevenini @;

* INFN, LNF, Box 13, 00044 Frascati (Italy)
\# INFN , Sez. Roma II, Tor Vergata
@ INFN Sez. Napoli

Abstract

The installation of the 25 MeV superconducting electron linac LISA is in progress at Frascati INFN National Laboratory. The installation is scheduled to be completed in Summer 1991 and commissioning will follow immediately. The status of the project is reviewed and the results of the first tests on various components are presented.

I- INTRODUCTION

The goal of the LISA project is to build a linear superconducting (SC) accelerator to acquire experience on some of the problems of SC linacs and on the generation of electron beams of high intensity and brilliance, in the mainframe of the ARES project , promoted by INFN in the field of SC radiofrequency applied to accelerators.

The design energy of the machine is 25 MeV and the beam current, averaged on a pulse duration of the order of 1 msec, is 2 mA. The repetition rate must be compatible with 1 KW average beam power.

The peak current , 5 A , is sufficient to build an infrared free electron laser (FEL). The FEL program will be carried out in collaboration with the Italian Department of Energy (ENEA).

The structure of the machine has been widely described in various conferences [1]. The only change is in the transport arc from the linac to the undulator. A layout of the machine with the arc is shown in Fig. 1 .

II - STATUS

In fall 91 the main body of the buildings and the auxilliary services have been completed, thus allowing to begin the installation of the RF, the refrigerator and the cooling plants. The construction of the SC cavities (bulk Niobium, 4 cells, with HOM suppressors) and their cryostats, entirely ordered to

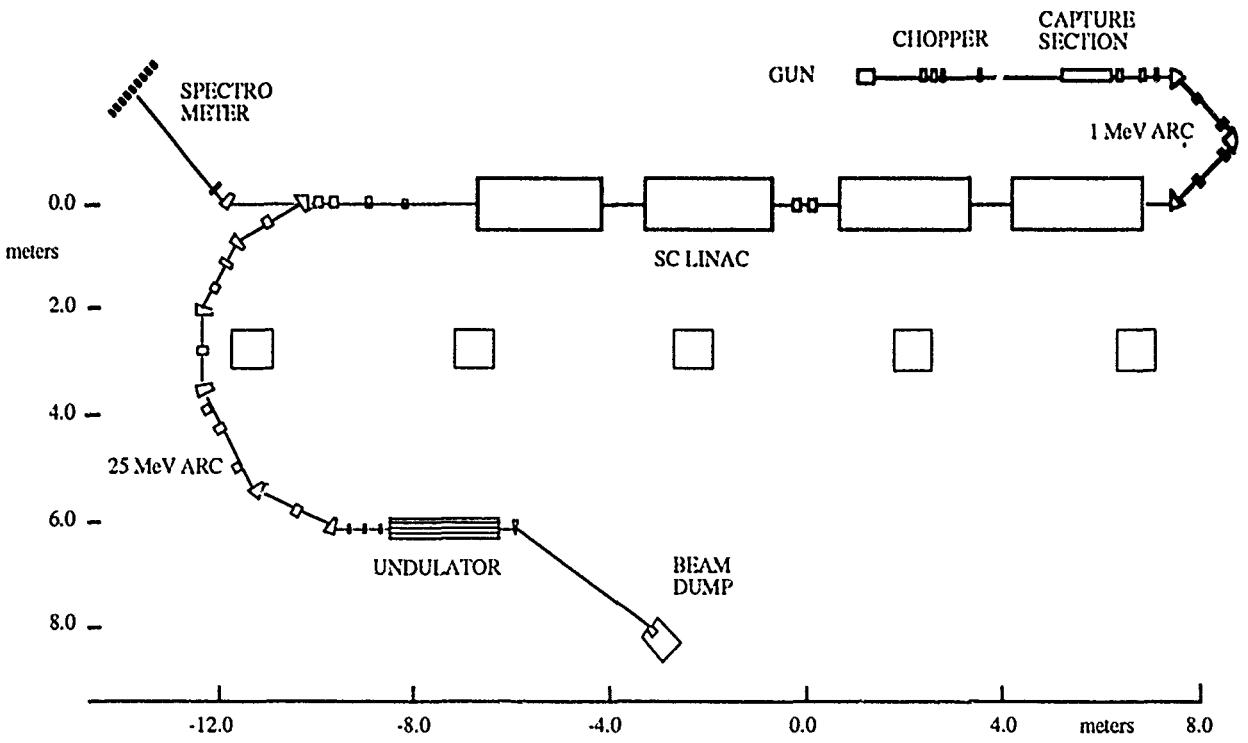


Fig. 1 - Layout of the Accelerator with the Transport Arc to the Undulator

0-7803-0135-8/91$03.00 ©IEEE

industry, has met with some minor difficulties. In particular, the first test evidenced a few design problems that needed correction. In February and April 91 two of the modules have been successfully tested at the factory and delivered. At present the useful field limit is 4 MV/m because of electron loading. However, pulsed fields of about 6 MV/m have been reached. A short period of He processing (about 30 minutes) has shown a tendency to improvement and it is foreseen that the design goal of 5 MV/m @ 2 109 will be reached after a reasonable processing period. Tab. 1 shows the results of the tests on one of the modules. The unloaded Q factor has been measured calorimetrically, driving the cavity through the main coupler at full power and measuring the flow of He gas at standard temperature and pressure.

Table 1
Measured Characteristics of a SC Module

Accelerating field (MV/m)	1.0 ; 2.2 ; 5
Cavity Q($\times 10^9$)	2.2 ; 2.0 ; 1.1
Q (main coupler)	$4.0\ 10^6$
Frequency	500.060 MHz
Tuning range / rate	± 300 KHz / 60 KHz/mm
Cryostat standby loss	5.4 W

The new arc is made of three achromatic dipole doublets. It is not isochronous, but the dispersion is very low. At the nominal energy spread $\Delta E/E \leq 2\%$ the pulse lengthening is ≈ 150 μm (i. e. ≈ 5% of the pulse length).

The lengthening due to second order terms in the trajectory equation, depending on both the transverse beam size and energy spread, have been calculated with DIMAD; their contribution, at nominal emittance and $\Delta E/E$, is smaller by one order of magnitude than that of the first order term.

The first magnet of the arc can be independently turned off allowing the beam to go straight into the spectrometer arm.

The strength of the first four quadrupoles at the linac exit is common to the spectrometer and the arc lattice, allowing simple beam switching between spectrometer or transport line. The spectrometer resolution is ≈ $5\ 10^{-4}$.

The dispersion free regions between the doublets are used to shape the optical functions for the right focus in the undulator.

The thermionic gun (nominal values of current and normalized emittance are 200 mA and $1.0\ 10^{-5}$ m rads) has been successfully tested. Emittance measurements have been made by analyzing the variations of the dimensions of the image on a fluorescent screen versus the strength of a focusing solenoid.

The screen image, given by a high linearity CCD TV camera with a resolution of 512 x 512 pixels, is digitized and memorised by a special purpose image grabber. The same instrument will be a permanent part of the machine diagnostic and control system, allowing on-line emittance measurements.

Good gun performances have been obtained up to 100 kV and 270 mA, with routine operation at 90 kV.

In Fig. 2 a 3-D elaboration of a typical beam image, obtained at 90 kV and 200 mA, is shown.

For each value of voltage and current, the square of the rms spot dimension is fitted with a parabolic function to the square of the solenoid current, and the fitted values are used to evaluate the rms emittance defined as

$$\varepsilon = \sqrt{\langle x\rangle^2\langle x'\rangle^2 - \langle x\, x'\rangle^2}.$$

In Fig. 3 the results obtained for different values of voltage and current are shown.

The space charge effect with increasing current and its dependance on beam energy are clearly visible.

At low current the experimental results show a large discrepancy with the prediction of the E-Gun code, which gives a much larger emittance. This could be due to the effect of the grid, whose effect has not yet been analysed in detail and it is not considered in the code.

A more detailed description of these measurements will be published separately.

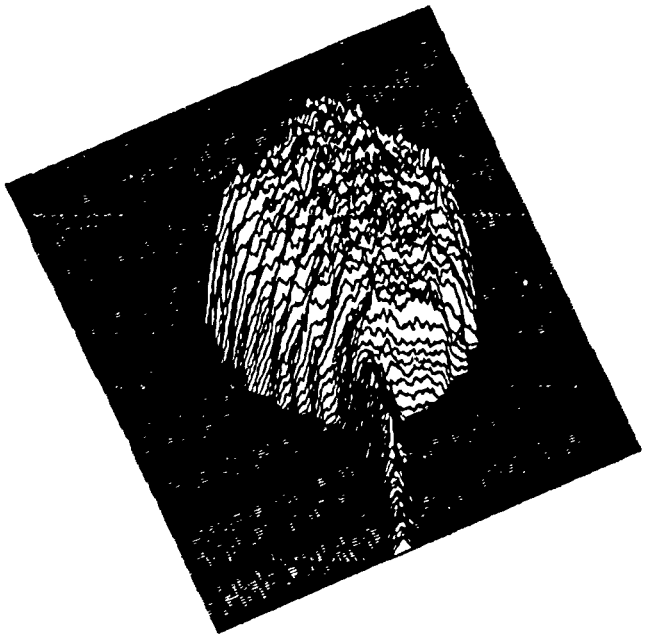


Fig. 2 - 3-D view of a beam image

At the time of this conference the auxiliary plants are practically completed and the refrigerator is ready for commissioning. Magnetic measurements on the quadrupoles have been performed and have given the expected results, while those on the dipoles are in progress. Reference points for the alignment of the accelerator have been laid down and the main parts have been positioned. A prototype of the beam position monitor has been tested and the series construction is nearly completed.

The development of the Control System [2] has followed the planned time schedule.

The communication protocols between different processor levels has been tested and most of the lowest level control codes have been written and tested.

The development of the graphic interface to the operator is in progress, following the definition of all control procedures.

The completition of the installation of the Control System is scheduled in May 91, and hardware tests will follow.

It is foreseen that the assembly of the machine will be completed in the Summer of '91.

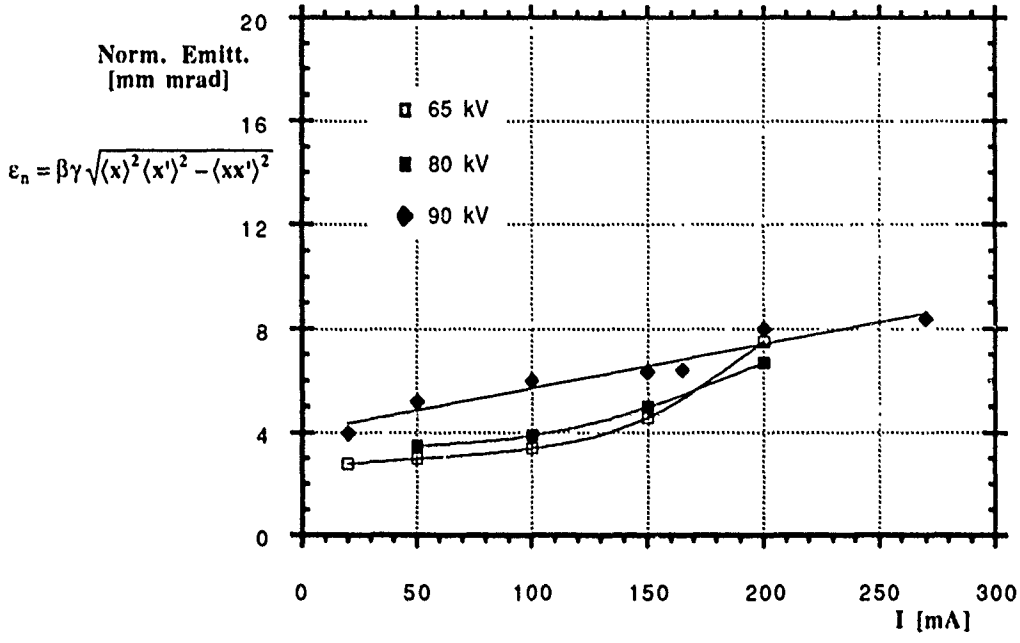


Fig. 3 - Rms Normalized Emittance vs. Gun Current and Voltage

REFERENCES

[1] A. Aragona et al.: " Status of the Lisa superconducting linac project", Proc. EPAC, 509 (1990)

[2] M. Castellano et al. : "Computer Control and Diagnostic Equipment for the LISA Project" Proc. EPAC, 866 (1990)

STATUS OF THE ARES R&D PROGRAM

R. Boni, M. Castellano, P. Fabbricatore+, M. Ferrario, A. Gallo, P. Michelato*, M. Minestrini, F. Musenich+, C. Pagani*, R. Parodi+, P. Patteri, L. Serafini*, S. Tazzari‡, F. Tazzioli.

INFN Laboratori Nazionali di Frascati, P.O. box 13, 00044 Frascati (Rome), Italy
* INFN and Università di Milano, Via Celoria 16, 20133 Milano, Italy
+ INFN Sezione di Genova, via Dodecaneso 33, 16143 Genova, Italy
‡ INFN and Università di Roma "Tor Vergata", 00173 Roma, Italy

Abstract

The ARES Superconducting Linac[1], as approved by INFN on the 15th of June 1990, together with the construction of a Φ-Factory (now called DAΦNE), asks for a three years R&D program to develop:
a) 500 MHz multicell SC cavities able to hold an accelerating field of 10 MV/m @ $Q_0 = 3 \cdot 10^9$;
b) a SC low emittance and high repetition rate injector.

The status of the program, accomplished in parallel with the completion of LISA, is given in the following.

I. CAVITY DEVELOPMENT

At present our program concerns the fabrication of prototypes of single and multicell 500 MHz SC cavities, using both bulk niobium and Nb coated copper[3]. Work on higher frequency cavities is also in progress and its development has been planned.

Bulk niobium cavities

Fabrication of a four-cell bulk niobium SC cavity is in progress, in the context of a collaboration with Italian industry (ANSALDO CO.). The process that has been developed is based on:

- deep drawing and spinning of the half cells,
- electropolishing of the cavity components,
- firing in a vacuum furnace at 700°C, inside a Ti box,
- EB welding from inside with a 90° deflected beam,
- final "metallographic" chemical treatment.

With respect to the chemical etching of the Niobium surface, we adopted the electrochemical etching (EP), mainly because of the Italian safety rules on waste disposal.

In order to test the overall cleaning procedure, we used an existing single cell, 500 MHz, Nb cavity, which was produced to develop EB welding procedures and related tooling. The results of the Q_0 vs E_{acc} are shown in Fig. 1, after three successive steps of the cleaning procedure, i.e.: electropolishing (EP), Ti box firing (HT) and final "metallographic" grain cleaning (MC).

The reported data have to be considered as promising since they were obtained in a vertical cryostat not equipped with magnetic shielding, the maximum field achieved being limited by a known defect in the equatorial region.

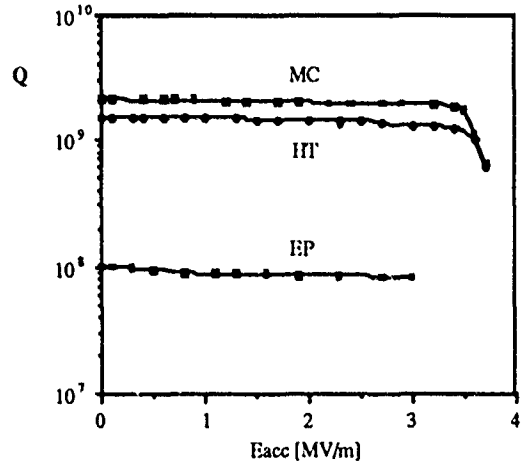


Fig. 1 - Experimental results of Q_0 vs E_{acc} for the first Nb single-cell cavity, after three successive steps of the cleaning procedure, i.e.: electropolishing (EP), Ti box firing (HT) and final "metallographic" grain cleaning (MC).

Copper, Nb coated, cavities

Following the CERN experience, we also started to develop the sputtering technique to coat Cu cavities with niobium, to profit from the good thermal conductivity of copper. Moreover this line opens the possibility to coat copper with different superconducting materials.

In the context of the collaboration with industry (ANSALDO CO.), the fabrication of a four-cell Nb coated cavity is in progress, in parallel to the realization of the bulk Nb one. The system adopted for Nb coating is the same developed at CERN, i.e. magnetron sputtering from a coaxial Nb tube placed inside the cavity.

Meanwhile the necessary equipment, both to weld cavities from the inside and to prepare the copper surface for Nb coating, have been acquired and made operational by industry.

0-7803-0135-8/91$01.00 ©IEEE

A first single cell cavity has been sputtered and tested[4]. While Q_0 at low field is satisfactory ($4 \cdot 10^9$ & 4.5 K), the behaviour of the Q_0 vs E_{acc} curve indicates that cleaning procedures and film quality were not yet optimized. A maximum field of 8 MV/m has been measured, Q_0 being $5 \cdot 10^8$.

The mechanical procedure to fabricate the half cells for copper cavities is deep drawing instead of spinning. This method, originally planned also for bulk Nb[3], has been limited to Cu because of the large number of sheets which have to be sacrificed to get a proper set of parameters for the deep drawing and a proper shape of the molds. Once optimized, the results are more reproducible and the quality of the internal surface is better.

The first four-cell cavity has been EB welded and we expect to Nb sputter the cavity in June.

As a consequence of the collaboration with a second industry (Europa Metalli-LMI), the latter has developed the technology of hydroforming copper cells and several 500 MHz single cell cavities have been realized using ETP copper to optimize the procedure. A new set of cells, produced from Cu OFHC, is now completed and they will be Nb sputtered and tested starting from June.

Work on higher frequency cavities

Following the tradition of the group from Genova, which is involved in the ARES R&D program, we measured the limiting field of some 4.5 GHz cavity, built from Nb sheets by deep drawing.

These cavities, EB welded, were chemically polished (100 μm) and annealed at high temperature (2300 K) in a vacuum furnace having residual pressure of 10^{-7} torr.

An average accelerating field of 15 MV/m without any apparent electron loading, has been measured on a batch production of 3 cavities, with an average number of 5 test for cavity. The field limitation was always a fast thermal breakdown.

This work will be continued with single and multi-cell 3 GHz cavities, whose fabrication is in progress.

An activity on 1.5 GHz coated cavities is also planned.

II. SC LOW EMITTANCE INJECTOR

According to what was anticipated in ref. [1], one major objective of the ARES R&D Program is the development of a SC low emittance RF injector. In this context, at present we are mainly working on photocathode preparation and numerical simulation. We expect to be able to design the first injector prototype during next year.

The present status of the R&D program, concerning photocathodes and simulations is outlined in the following.

Photocathode production

In collaboration with an Italian company (SAES GETTERS), a special UHV chamber, for the preparation of alkali antimonide photocathodes, has been designed. A schematic drawing of the chamber is presented in Fig. 2.

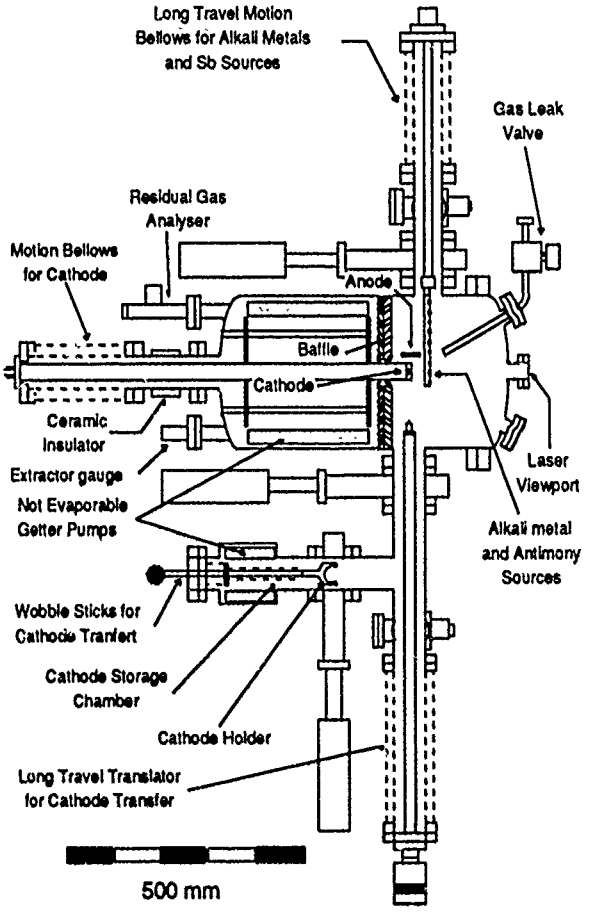


Fig.2 - Photocathode preparation chamber.

Because alkali antimonide cathodes are very sensitive to any reactive gas, 10 getter modules (SAES GETTERS-1250) are used in addition to a standard ion getter pump. The estimated ultimate pressure is in the 10^{-11} mbar range.

The alkali metals are produced by alkali metal dispensers[5] (based on alkali chromate reaction with zirconium). A new high temperature conditioning procedure of these sources ensures very low gas emission during alkali metal evaporation. Up to 8 different alkali metal sources can be assembled into the UHV chamber, enabling future developments on multi-alkali cathodes.

A load-lock system is used for introducing the source into the chamber and a special UHV transfer system[6],[7] has been developed for cathode transportation, both to surface analysis instruments or to the SC gun.

Numerical simulations

The design under study for the RF SC Gun is based on a 500 MHz 1-1/2 cell cavity[1], followed by a special single-cell resonator and a magnetic compressor[8-10].

Since in the SC Gun we expect a maximum electric field (peak) of the order of 30 MV/m, the adopted strategy is that to attain high beam brightness in two steps. The choice of a low RF frequency allows to accelerate rather long bunches and to magnetically compress them at the Gun exit once relativistic.

Because long bunches exhibit a substantial non-linear behaviour of the momentum gain with respect of the longitudinal position in the bunch, we add an especially shaped, fully decoupled and independently phased single-cell cavity downward the RF Gun cavity. This solution allows to employ cathode injection phases higher than the optimal one, while recovering the minimum value of the rms emittance and getting a more linear distributions in the longitudinal phase space[8], i.e. a more efficient magnetic compression.

The output peak current at the injector exit can be in the range of some hundreds of Amps with rms emittance of a few mm.mrad: that means a beam brightness comparable to that produced by high frequency, high peak field, RF Guns, together with a possible CW operation.

The results of the numerical simulations are summarized in Table I, where four different beams are listed, corresponding respectively to: VUV FEL (A and B), IR FEL and TESLA. The first two beams are quoted to better visualize the beam brightness enhancement produced by the decoupled cell. The parameters chosen for the TESLA beam correspond to a peak field of 50 MV/m on the cathode.

TABLE I - Numerical simulation results

	A	B	C	D
Bunch charge [nC]	.5	.5	20	5
Laser spot (σ_r) [mm]	2.	2.	3.5	2.8
Laser pulse length ($2\sigma_t$) [ps]	20	20	40	70
Laser peak power [kW]	8.7	8.7	175	87
Repetition rate [Hz]	1000	1000	30	30
RF injection phase [deg]	64	80	75	80
Output energy [MeV]	7.4	3.8	6.8	6.1
Rms energy spread [keV]	±17	±32	±170	±135
Rms bunch radius σ_x [mm]	5.2	12.7	15.	16.9
Bunch length σ_z [mm]	2.9	3.1	6.2	14.4
Rms divergence $\sigma_{x'}$ [mrad]	3.8	2.4	15.3	3.2
Rms emittance ε_n [mm·mrad]	5.9	5.5	106	15
Peak current (no compr.) [A]	19	18.5	350	35
Peak curr. (magn. compr.) [A]	125	435	2750	640
Compressed σ_z [mm]	.45	.13	.8	1.
Norm. bright.[10^{11}A/m^2·rad^2]	.45	1.8	.03	.37

In order to understand the capability of the decoupled cell to recover the rms normalized emittance, ε_n, we studied the behaviour of the total transverse momentum transfer induced by the decoupled cell[11]; as sketched in the following, the momentum transfer is found to be dependent on the injection phase and the decoupled cell acts as a RF lens.

In fact it is well known[12] that, at the gun exit, the transverse momentum of an electron, leaving the gun at a phase ϕ (with respect RF) and at a radius r, is given by:

$$p_r = \alpha k \cdot r \cdot \sin\phi \text{ [mc unit]},$$

where: $\alpha = E_o/(2kmc^2)$, $k = 2\pi/\lambda_{RF}$ and E_o is the peak field on the cathode.

When the average exit phase, $\langle\phi\rangle$, of the bunch is $\pi/2$, the increase of ε_n due to RF field is minimum. Away from the optimal value the RF contribution to ε_n is given by:

$$\Delta\varepsilon_{RF} = \alpha k \langle x^2\rangle \sqrt{(\Delta\phi^2)} |\cos\langle\phi\rangle|$$

where $\sqrt{(\Delta\phi^2)}$ is the rms bunch length [RF deg].

To recover the minimum emittance condition, a device able to induce a transverse momentum transfer strongly correlated to the injection phase is therefore used.

In a single cell cavity, for $\beta \approx 1$ particles, travelling slightly off axis, at a radius r, the transverse force produced by the accelerating TM_{010} mode can be written as:

$$F_r = e(E_r - cB_\theta) = -(er/2c)\cdot dE_z/dt$$

where $E_z(z)$ is the on axis electric field. Moreover, the transverse momentum transfer at the cavity exit is:

$$\Delta p_r = -\frac{e}{2mc^2}\int_0^t r\frac{dE_z}{dt}dt = \frac{e}{2mc^2}\int_0^L \beta_r E_z dz = \frac{\beta_r}{2mc^2}\Delta V(\phi)$$

where: $\beta_r = p_r/p_z = \text{const.}$, L is the cell length and $\Delta V(\phi)$ is the electron energy gain in the cell.

Considering now a divergent beam injected into the cell, as is the case for bunches leaving the gun, the previous equations allow to achieve a phase vs transverse momentum correlation that compensates the extra-correlation present at the gun exit when injection phases different from $\pi/2$ are used.

References

[1] The ARES Superconducting LINAC, C.Pagani, S Tazzari Eds. Report LNF-90/053(R), Frascati, May 1990.

[2] F.Tazzioli et al., "Status of the LISA Superconducting LINAC Project", presented at this conference.

[3] R.Boni et al., "Progress Report on SC Cavities for ARES", Proceeding of the 2nd EPAC Conf., p. 1067.

[4] A.Bixio et al., Report LNF-90/083(NT), Frascati, Nov. 1990.

[5] SAES GETTERS Spa, AMD 900928, Milano.

[6] R.E.Clausing et al., "Versatile UHV sample transfer system", Jurn. Vac. Sci. & Tech, 16(2), Mar/Apr, 1979.

[7] J.P.Hobson, E.V.Komelsen, "UHV technique for intervacuum sample transfer", Jurn. Vac. Sci. Tech, 16(2), Mar/Apr, 1979.

[8] L.Serafini et al., Report INFN/TC-90/10, Milano, May 1990.

[9] L.Serafini et al., "Design of the Laser Driven Injector for ARES", Proceeding of the 2nd EPAC Conf., p. 143.

[10] C.Pagani et al., "The TESLA Injector", Proc. of the 1st Int. TESLA Workshop, Cornell, July 1990.

[11] L.Serafini et al., to be published.

[12] K.J.Kim, NIM, A275 (1989), p. 201.

Preliminary Conceptual Design for a 510 MeV Electron/Positron Injector for a UCLA ϕ Factory

Glen Dahlbacka and Robert Hartline
Maxwell Laboratories, Inc., Brobeck Division
4905 Central Avenue
Richmond, California 94804

William Barletta
Lawrence Livermore National Laboratory/UCLA

Claudio Pellegrini
University of California at Los Angeles

Abstract

UCLA is proposing a compact superconducting high luminosity ($10^{32\text{-}33}$ $cm^{-2}sec^{-1}$) e^+e^- collider for a ϕ factory [1]. To achieve the required e^+e^- currents, full energy injection from a linac with intermediate storage in a Positron Accumulator Ring (PAR) is used. The elements of the linac are outlined with cost and future flexibility in mind. The preliminary conceptual design starts with a high current gun similar in design to those developed at SLAC and at ANL (for the APS). Four 4-section linac modules follow, each driven by a 60 MW klystron with a 1 μsec macropulse and an average current of 8.6 A. The first 4-section module is used to create positrons in a tungsten target at 186 MeV. The three remaining three modules are used to accelerate the e^+e^- beam to 558 MeV (no load limit) for injection into the PAR.

I. Discussion

Based on experience with linacs at SLAC, each 3-meter contoured S-band 3 GHz section can be expected to produce accelerations of approximately

$$\varepsilon = 12\sqrt{P_{MW}},$$

where ε is the particle energy in MeV
and P is the klystron power in MW.

This relationship immediately leads to a cost/benefit tradeoff in the number of sections vs. the klystron power delivered to each section.

The minimum cost for the linac occurred with one 60 MW klystron driving four 3-meter sections with a 1 μsec macropulse; this configuration is shown in figure 1. At 3 GHz, a total cluster

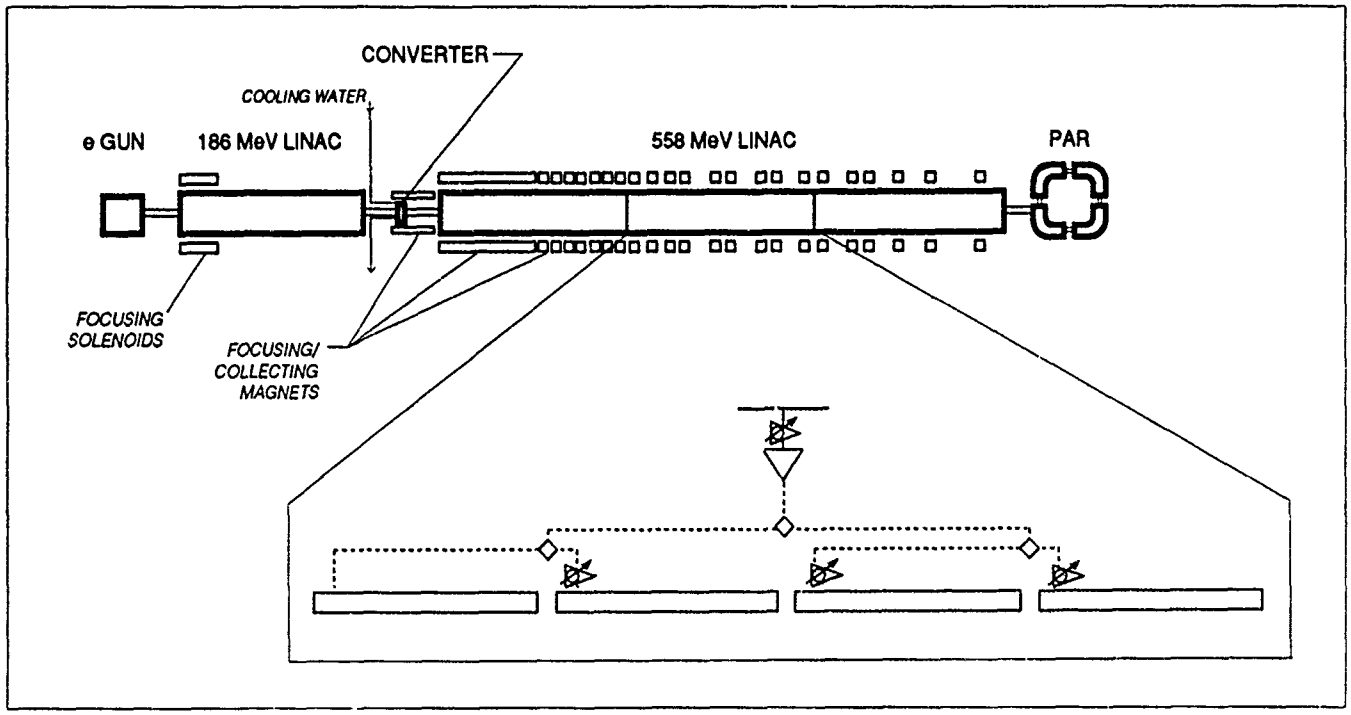


Figure 1. Components of proposed injector.

0-7803-0135-8/91$03.00 ©IEEE

charge of 9 nC (three 3 nC bunches) and an average current of 8.6 A was necessary to achieve 100 nC e^+ fill at 30 Hz in less than 6000 cycles. The sections each store 54 joules during the 1 μsec fill time. At the highest current loading, the particles extract 1.7 joules from the field. This corresponds to a 3.15% loading.

The first 4-section module is used to drive the positron convertor target, shown schematically in figure 2. It consists of a 2 m radius × 7 mm tungsten rod. The converter efficiency is estimated to be ≥ 0.04 e^+/e^-/GeV, so the extracted positron charge will be 0.06 nC/cluster (or 0.02 nC/bunch). The target will dissipate 300 W and will need to be conductively cooled by copper supports and water cooling. Details of the support structure will be computed with standard thermal analysis software, using the ANL design for the APS as guidance.

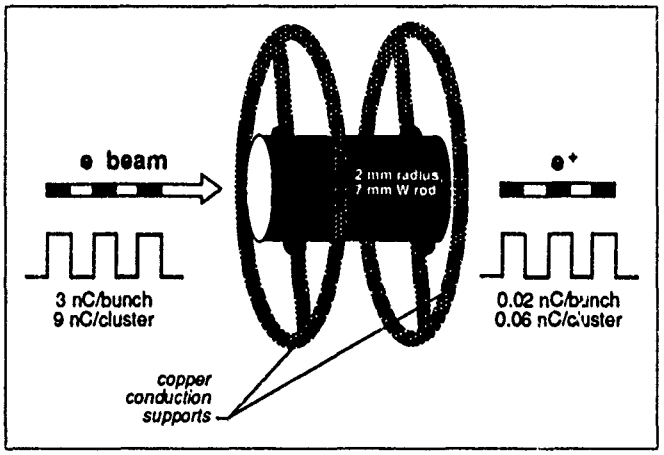


Figure 2. Tungsten converter.

After the conversion, the positrons will be collected by solenoid magnets of up to 2 meters in length. The subsequent linac in principle can accelerate particles to 558 MeV (no load), but because the additional capability will be degraded by rf window losses and loading, routine operation at 510 MeV is anticipated.

The positrons will then be injected in a damping ring, shown schematically in figure 3. A 30 kV, 60 kW rf system can drive a four dipole, 3.8 m ring with room temperature magnets of 1.3 T. The system would accept 1.4×10^{10} e^+ at 30 Hz and switch out 2×10^{12} e^+ in about 55 pulses.

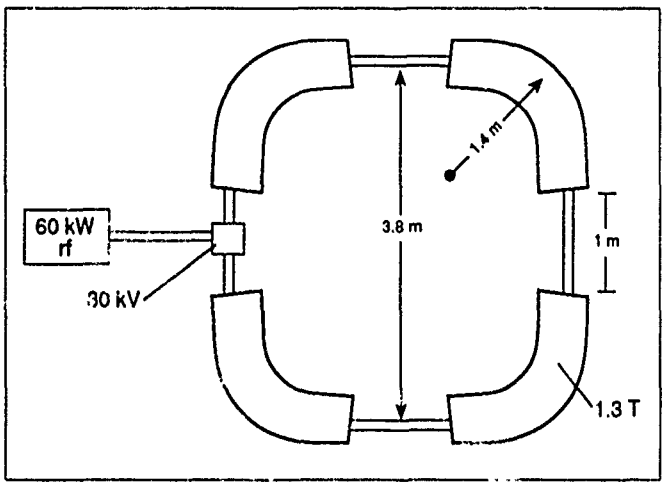


Figure 3. Positron Accumulator Ring (PAR).

II. Conclusion

In summary, the injection and positron production system for a UCLA φ factory has been considered. The system requires a high current gun that is at the state of the art. The linac and PAR are well within proven capabilities.

Operating Experience with the ALS Linac

F. Selph and D. Massoletti
Lawrence Berkeley Laboratory
Berkeley, California 94720

Introduction

The linac injector for the Advanced Light Source (ALS) at LBL was recently put into operation. Energy is 50 MeV, frequency 3 GHz. The electron gun delivers up to 6 nC in a 3.0–ns bunch at 120 kV. A train of bunches is injected into a 1-Hz booster and accelerated to 1.5 GHz for storage ring injection. A magnetic analysis system is used for optimizing the linac. Measured beam properties from the gun and after acceleration in the linac are described. Fig. 1 shows the arrangement of major linac components, and Fig. 2 is a photograph of the completed linac.

Gun

Gun performance has proved to be adequate to meet specifications. The gun contains a dispenser-type cathode, 1 cm^2 in area. Emittance at 120 kV was measured, and found to be less than the specified 4×10^{-5} π m. Normal operation for booster injection is one bunch at a 1-Hz rate, or a train of 12 bunches separated by 8 ns, also at a 1-Hz rate. The bunch width from the gun is about 3 ns FWHM. If after bunching and acceleration in the linac the energy spread is wider than the booster can accept (about 1%), some collimation at 50 MeV is done after a 40° bending magnet, where the dispersion is large.

Subharmonic Bunchers

On the basis of computer simulations it was concluded that an injection system for the linac incorporating two subharmonic bunchers would be most effective (1). The program PARMELA (2) was very useful in predicting performance. PARMELA includes longitudinal and transverse space charge effects, which are important for our bunch intensities of 4–6 nC. The engineering design (3) incorporates two subharmonic bunchers having frequencies of 125 and 500 MHz, respectively. Ideally, the bunches on reaching the first would span 90° in phase (2 ns), be compressed four times, and on reaching the second, again span 90° in phase. The gun pulse is wider than this ideal, but measurements show that the first subharmonic buncher does compress four times in phase. The second provides additional compression, as evidenced by its effect of increased linac transmission, but pulse length after this buncher cannot be measured directly.

Linac and S-Band Buncher

The linac is made in two independently driven 25–MeV sections, each 2 m long (4). The rf frequency is 2.9979 GHz. Attached to the first section is a 10–cm section of disk-loaded waveguide, designed for a phase velocity of 0.75 c, known as the s-band buncher (5). This is driven by the same klystron as the first linac section, but is provided with independent control of amplitude and phase. Although the 50–MeV energy could be achieved by one accelerating section, the two independently driven sections achieve more flexibility in operation. One important purpose involves maintaining a small energy spread with a multibunch pulse. With a 150–ns pulse, the resulting beam loading of the linac will be compensated by phase-shifting of the linac sections (6).

Transport Line and Analysis System

A ±40° switching magnet is located about 5 m from the end of the linac (Fig. 3). The bend produces dispersion so that the energy spread of the beam delivered to the booster can be controlled by an adjustable collimator 1 m downstream from the magnet. A similar collimator is placed in the analysis line, where the dispersion is the same, so that the transmitted intensity can be read on the Faraday cup. The shielded Faraday cup also serves as a beam dump within the linac cave, which is useful for linac tuning while minimizing radiation levels outside the heavily shielded linac area. The intention is to transmit to the booster only the electrons that will be accelerated to 1.5 GeV.

Instrumentation

ALS instrumentation has been described in an internal report (7). All data used in operations is digitized (8) for display on high-resolution computer monitors, and selected data can be archived on magnetic or optical recording media. This was made

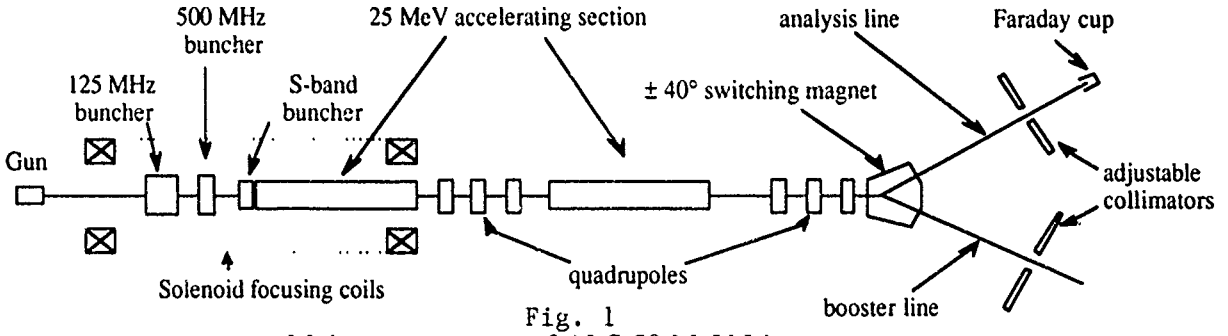


Fig. 1
Major components of ALS 50 MeV Linac

U.S. Government work not protected by U.S. Copyright.

XBL 914-785

feasible by recent advances in microprocessor and electronic instrument technology, which made the tools for accomplishing these tasks available at modest cost.

Scintillation screens mounted on remotely operated plungers are installed at a number of locations. A CCD TV camera is used to view the image of the beam profile. Although destructive, this device is very valuable as it is the only instrument that shows the beam shape. The image can be viewed directly on a TV monitor, but can also be digitized by a "frame-grabber" board in a microcomputer, and this data used for analysis.

Gun output is measured with a wall current monitor, a nondestructive pickup between the gun and the first subharmonic buncher. This device is also useful for measuring absolute bunch intensity and the time profile of bunches, and for seeing the number of bunches in the gun pulse.

A Faraday cup is used routinely in the analysis line for tuning. A deep aluminium cup is backed by a lead plug, and both are enclosed in a stainless steel shell mounted on a ceramic insulator. The shell provides the electrical connection, tapering down to a 50-ohm coupling to give a good frequency response. The purpose of using an aluminium cup is to reduce the neutron production. Additional lead shielding is provided to attenuate the gamma rays, so that less concrete is required to meet background requirements.

For nondestructive measurement of beam position two types of four-electrode capacitive pickups (BPMs) are used. Where space is at a premium, between gun and linac and between linac sections, electrodes are about 5 mm in diameter. In the transport to the booster (ltb line), the BPMs are striplines about 20 cm long and are used with steering magnets to keep the beam centered. Both types give x and y position to within 1 mm accuracy near the center of the vacuum chamber. The output of the electrodes can also be summed to give a measure of bunch intensity.

Horizontal collimators are located near a position of maximum dispersion in the booster transport line. The jaws are made of 0.5-in-thick tantalum and are remotely adjustable to provide a gap from 0 to 60 mm. In use, the gap is positioned in the center of the vacuum chamber and the transmitted fraction is used. A monoenergetic beam would have a tight waist at the collimator—about 0.6 mm—so that energy spread is almost directly proportional to collimator width. A gap of 3.3 mm allows 1% energy spread to be transmitted, which is expected to be about the limit of booster acceptance. A set of vertical collimators allows cleaning up the vertical halo before transmitting beam to the booster. These collimators have not only the useful function of reducing booster losses (since with them it is likely that nearly all beam injected will be accelerated), thus reducing the radiation level; they also provide a cleaner beam for understanding beam optics in the ltb line.

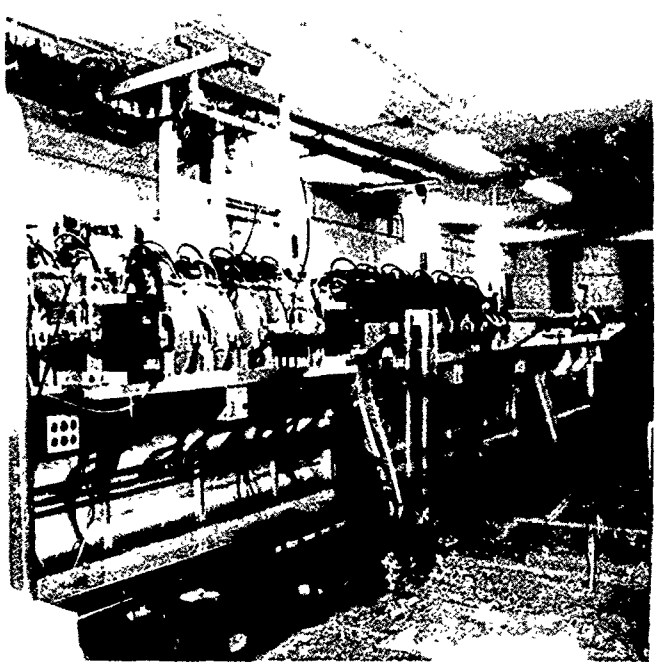


Fig. 2. The ALS linac, with the gun housing on the left. The gun-to-linac and first linac sections are surrounded by solenoid coils and supported on three rigid girders. The 3-GHz waveguide is visible at the top of the picture, and the switching magnet is at the extreme right.

An identical horizontal collimator assembly is placed in the analysis line. Using it, a narrow gap can be moved across the vacuum chamber so that a beam profile can be read with the Faraday cup. More commonly, the gap is positioned at the center of the vacuum chamber and the analysis magnet is scanned. A temperature-compensated Hall probe is installed in the analysis magnet, which gives a precise magnetic field level (hence a precise energy determination), as the current is varied.

Controls

This control system has been described in a previous paper (9). The hardware interfaces (DACs and ADCs) are contained on single-board computers called intelligent local controllers (ILCs). Each ILC is connected to one or more devices. The operator interface is a group of monitors, each driven by a personal computer. The displays are completely democratic—any available data can be shown on any display monitor. Also, since only a data link such as Ethernet is required in order to access the database, it is easy to allow other computers within the laboratory this access. The connection between the operator's computers and the ILC is another group of microprocessors. The ILCs are an LBL-designed board loaded with commercially available electronic components.

Most of the software used is available commercially. Among them are relational databases, spreadsheet programs, graphics programs, object-oriented languages, network programs, and standard PC operating systems (DOS, OS/2). So far we have found that relying on commercially available PC software has many advantages. Cost is modest, it is mostly bug-free, and is sophisticated enough to meet our needs. One computer acts as a file server and the central repository of programs used in the control system. The goal in system design was to provide a data refresh rate of 10 Hz, and so far this goal has been met. This is within human response times, thus the operator does not experience frustrating delays in the system response.

SUMMARY

Assembly of linac components was largely completed and commissioning begun in October 1990. The linac sections with their associated waveguides and loads were conditioned with rf power until a vacuum in the 10^{-8}-Torr range was achieved, before acceleration of electrons was attempted. This began in February 1991, and the first 50-MeV beam reached the Faraday cup in March. Optimization of the operation of bunchers and linac rf is continuing, but we have established that all systems work as expected. At present the intensity of beam delivered to the Faraday cup is about 0.3 nC per bunch, with 1.8% FWHM single bunch, and 4% multiple bunch energy spread.

Linac conditioning to the 50-MeV operating level was accomplished after a cumulative run time of less than 70 hours, consisting of about 25 hours of rf systems testing and conditioning and about 40 hours of actual linac operation. To date there has been about 160 hours of linac commissioning. The original cathode is still in use, with a cumulative run time of about 300 hours. Operation of the linac is restricted to off-hours while the building and facilities are under construction, which slows down the commissioning process considerably.

To avoid vacuum contamination and a protracted conditioning period, UHV practices and techniques were employed for preparation and fitting during the assembly of the rf feeds and vacuum system. Particular attention was paid to the problems of moisture and particulate contamination in the building construction environment. The engineering of the rf systems paid particular attention to the goal of providing operational simplicity. Complete control and diagnostic capabilities for rf devices are provided through the computer system, although as a prudent measure, during this commissioning period a person is always stationed near the klystron power supplies to observe any unusual behavior.

Acknowledgements

This work was supported by the Director, Office of Energy Research, Office of Basic Energy Sciences, Material Sciences Division, U.S. Department of Energy, under Contract No. DE-AC03-76SF00098.

References

1. R.H. Miller, C.H. Kim, and F.B. Selph, "Design of a Bunching Septum for a High-Intensity Electron Linac," Proceedings of the 1988 European Particle Accelerator Conf., 863 (1988).
2. "Computer Codes for Particle Acceleration Design and Analysis," 2nd ed., 137 (1990).
3. C.C. Lo. et al., "Advanced Light Source Linac Subharmonic Buncher Cavities," Proc. of the 1989 Part. Accel. Conf., 89CH2669-0, 957 (1989).
4. B. Taylor, H. Lancaster, and H. Hoag, "Engineering Design of the Injector Linac for the Advanced Light Source (ALS)," Proc. of the 1988 Linear Accel. Conf., CEBAF Report 89-001, 565 (1989).
5. R.H. Miller, R.F. Koontz, D.D. Tang, "The SLAC Injector," IEEE Trans. Nucl. Sci., N.S. 12, No. 3, 804 (1965).
6. F. Selph, "Compensation of Beam Loading in the ALS Injector Linac," Proc. of the 1988 Linear Accel. Conf., CEBAF-Report 89-001, 580 (1989).
7. J. Hinkson, "ALS Injector Diagnostics," LSEE-098, Feb 1991.
8. M. Chin, J. Hinkson, S. Magyary, "Networking Remote Instrumentation for the Advanced Light Source," Proc. of the 1989 Part. Accel. Conf., 89CH2669-0, 1648 (1989).
9. S. Magyary et al., "Advanced Light Source Control System," Proc. of the 1989 Part. Accel. Conf., 89CH2669-0, 74-98 (1989).

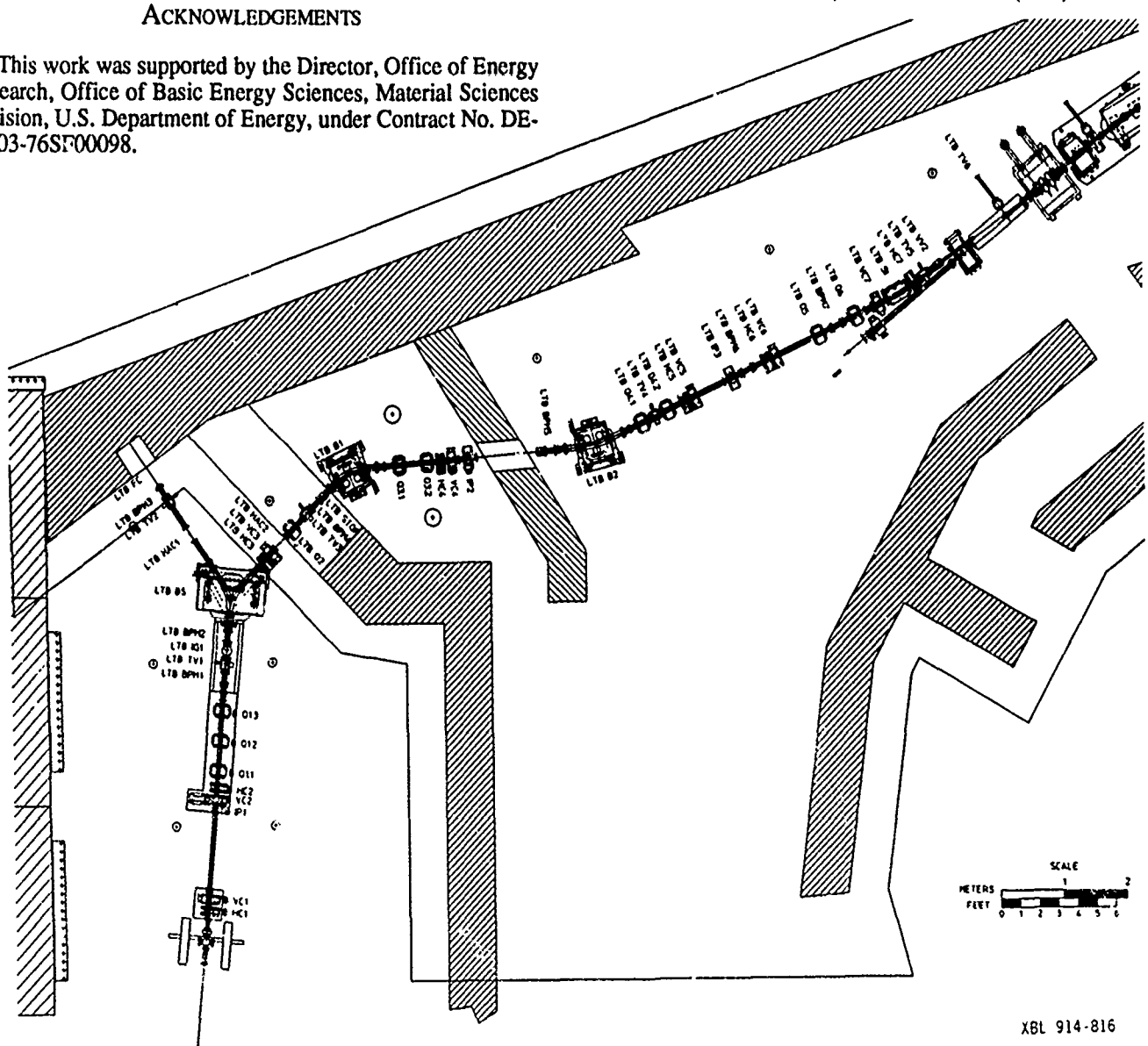


Fig. 3. Transport line from the linac to the booster.

Commissioning of the New Heavy Ion Injector at GSI

N.Angert, L.Dahl, J.Glatz, J.Klabunde, U.Ratzinger, H.Schulte, B.Wolf
GSI Darmstadt

H.Deitinghoff, J.Friedrich, H.Klein, A.Schempp
University of Frankfurt

Abstract

The Unilac has been upgraded by a new injector linac. It consists of an ECR source, a 108 MHz RFQ linac and an interdigital H-type accelerator structure. Highly charged ions (as U^{28+}) are extracted from the ion source and accelerated by the RFQ structure up to 300 keV/u. The IH tank accelerates with a very high rf efficiency up to the energy of 1.4 MeV/u. The commissioning of the new injector will be reported.

Introduction

The new GSI synchrotron SIS and storage ring ESR are in routine operation now. The Unilac is simultaneously used as injector for the SIS and to serve the low energy physics experimental area. To meet the different demands of the high and low energy experiments and to operate the accelerator facility efficiently, the scheme of time share operation has been adopted for the Unilac: beams of different ion species and currents are extracted from two injectors and accelerated to different energies on a pulse-to-pulse basis[1].

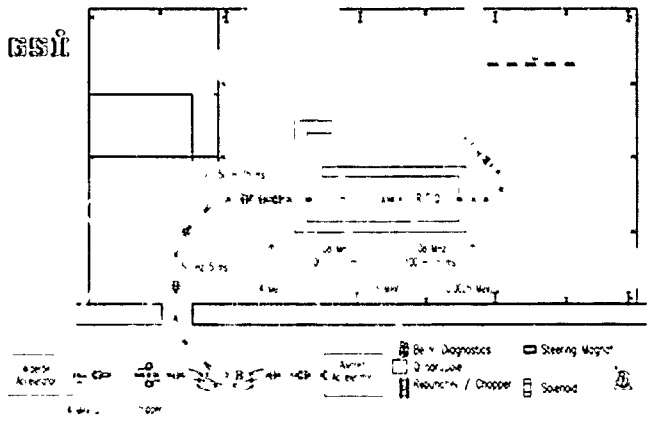


Fig. 1: Plan view of the new injector

A high charge state ion injector[2] (HLI, Hochladungsinjektor) is being commissioned presently. It is foreseen to serve low energy physics experiments and consists of an ECR (Electron-Cyclotron-Resonance) source[3], followed by a 108 MHz four rod RFQ-tank[4] and a 108 MHz interdigital H-type structure[5]. Intermediate stripping is not any longer necessary. The new injector is much shorter, has less components and needs less power than the old Wideröe accelerator and will therefore be more reliable. But it is not designed for higher beam currents.
For this reason it is planned to rebuild the old Unilac injector in order to produce higher beam currents by up to three orders of magnitude to utilize the SIS current limit.
The concept of this high current injector[6] favours a CORDIS- or a MEVVA-type ion source for single or double charged particles to be accelerated. A new 27 MHz RFQ linac substitutes the Wideröe tank 1. Due to stripping of the beam, tanks 2, 3 and 4 can be used on.

The High Charge State Injector

An ECR source[3] operating at 14.5 GHz has been developed at CEN Grenoble to deliver the same charge states of heavy ions which have been generated so far by gas stripping at 1.4 MeV/u. Test runs of the source have shown that the expectable beam currents are comparable or even higher than delivered by the existing prestripper linac (e.g. U^{28+}: 5 eμA, Pb^{25+}: 6 eμA, Xe^{17+}: 27 eμA, Ni^{8+}: 20 eμA). Such high charge states allowed an accelerator design with very efficient acceleration up to 1.4 MeV/u by application of a four rod RFQ-structure and an IH-structure (Fig. 1).
The Alvarez rf amplitude limitation conform to U^{25+} results in an extraction voltage of 23.8 kV of the ECR source to reach the input energy of 2.5 keV/u of

0-7803-0135-8/91$03.00 ©IEEE

the RFQ-structure. The expected unnormalized emittance is 200 π•mm•mrad for both planes.
Fig. 2 displays the transverse beam envelopes of the ion spectrometer. The split pole analyzing magnet has a total deflection angle of 135 degree, the angles of all pole face rotations are 25 degree vertical focusing. The inner field boundaries have a radius of 2.7 m to compensate the second order distortions. A momentum resolution of $1.3 \cdot 10^{-3}$ was obtained, Pb isotopes can be completely separated. An electrostatic chopper with a deflection voltage of 16 kV and a rise time of 10 µs converts the beam from dc to 100 Hz pulses with a duty cycle up to 50 %.

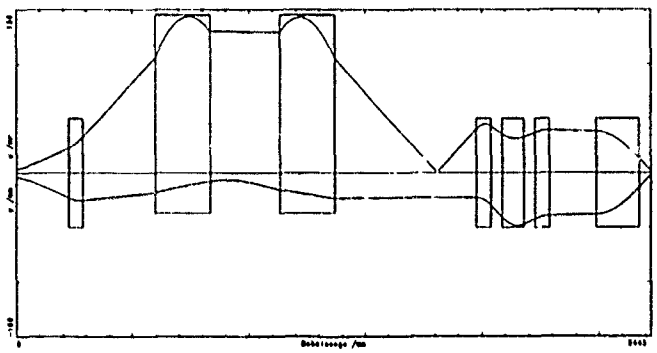


Fig. 2: Spectrometer beam envelope

The RFQ tank is about 3 m long and has a diameter of 0.5 m. For U^{25+} the maximum voltage is 78 kV (125 kW rf power) for acceleration to 0.3 MeV/u. The radial acceptance has 50 % reserve compared to the source values. The expected longitudinal emittance is 30 π•keV/u•deg at the exit.
The length of the IH-structure is 3.55 m, the diameter is 0.63 m. It contains two magnetic quadrupole tripletts, the particle output energy is 1.4 MeV/u. The very high shuntimpedance of 320 MΩ/m yields an effective voltage gain of 10.5 MV with an rf power of 109 kW. The radial acceptance is 60 π•mm•mrad unnormalized, the longitudinal acceptance 150 π•keV/u•deg.
The 180 degree beam transport line is equipped with two λ/4 coaxial type bunchers. The transverse beam optics are designed as an achromatic system. An 11 degree switching magnet with a rise time of 5 ms can deflect each other of the 100 Hz pulses for local experiments. With a 30 degree bending magnet of 35 ms field rise time one of two injector beams may be chosen for further acceleration in the Alvarez tanks working at 50 Hz pulse repetition rate.

Commissioning of the HLI

All components of the HLI are installed. Cooling water, electrical supplies, cables, RF power lines are in place. The extensively computerized controls are essentially in operating condition.

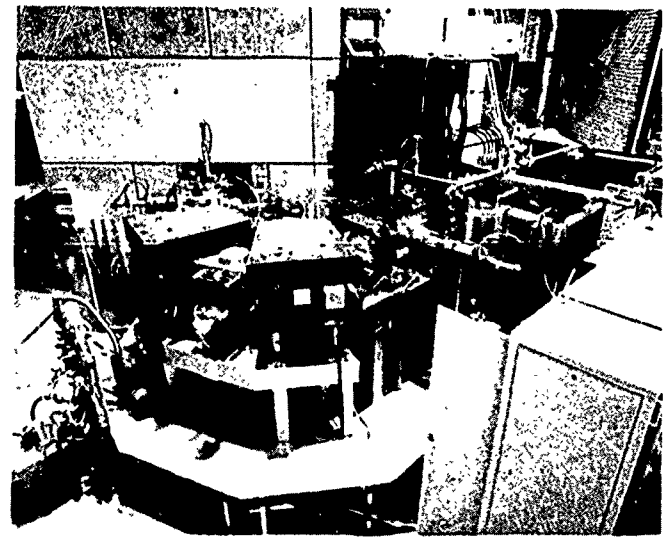


Fig. 3: Photograph of the injection beam line

The commissioning of the ECR source itself took place in Grenoble and at GSI[3]. Fig. 3 shows the source and the low energy transport system.The Xe spectrum (Fig. 4) is recorded with the new spectrometer. The isotopes are completely separated. The measured beam half width of 4 mm fits the calculations. In these tests the extraction voltage was set only to half the nominal value to avoid conditioning problems. Due to this restriction an improvement of the resolution can be expected and the designed resolution of Pb isotopes will be reached. The dispersion of the spectrometer was measured as D = 23.2 mm/%(Δp/p). The analyzed beam was transported through the following lenses and measured by an emittance measurement device. The beam properties fit the RFQ structure acceptance very well.

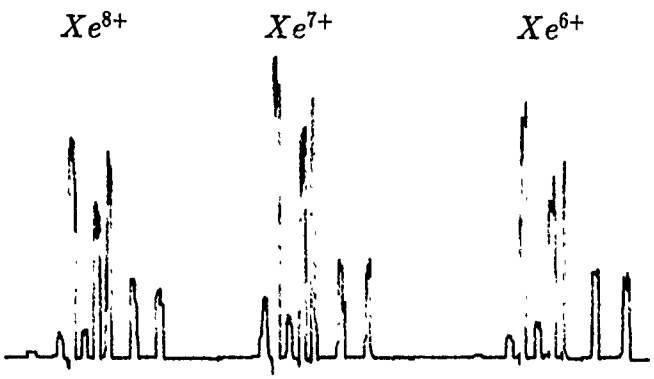


Fig. 4: Measured Xe spectrum

The RFQ structure has been developed and commissioned by the Institut für Angewandte Physik, University of Frankfurt. It is completely assembled, vacuum tested and now waiting for rf power tests. Detailed information is given in a special contribution to this conference[4]. The IH cavity was tested with low and high rf power. Fig. 5 shows the electrical field distribution recorded by a perturbation measurement. The shunt-impedance of 320 MΩ/m ± 5 % leads to a power consumption of only 109 kW for U^{25+}. The Q value is 21.500. Power tests have been carried out at following levels: P = 140 kW, 15 % duty cycle and P = 60 kW, 50 % duty cycle.

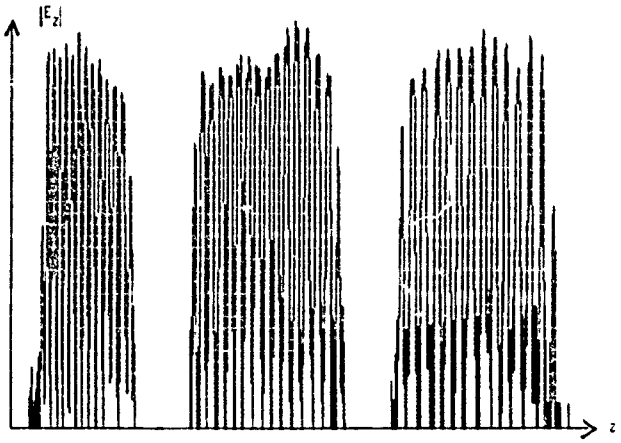


Fig. 5: Field distribution of the IH structure

For longitudinal beam matching one 108 MHz buncher cavity is installed in the intertank section and two in the 180 degree beam line. They have been tested with an rf power of 2.3 kW, 50 % duty cycle. The effective shuntimpedances are 68 and 73 MΩ/m respectively,the Q values are 6.030 and 10.050. The efficient gap voltages are 155 and 233 kV respectively.

Status and Perspectives

The HLI was scheduled to have been commissioned at the end of March. Due to other competing activities at GSI and resulting lack of manpower we are behind schedule. Commissioning of the RFQ and IH cavity with beam are now in progress, which will be followed by beam transport tests through the 180 degree bending line. Also a reproducible set of machine parameters must be worked out.
In May the rebuilding of the stripping section for pulsed operation of the matching magnets will take place. This modification will complete the efforts to establish the ion switching mode for the GSI accelerators.

References

[1] J.Glatz, "The Unilac as a Fast-Switching Variable Ion and Energy Accelerator", Proc. of the 1986 Linear Accelerator Conf., SLAC-Rep. 303, p.302, 1986.

[2] N.Angert et al., "A New 1.4 MeV/u Injector Linac for the Unilac", Proc. of the 1990 Linear Accelerator Conference, LA-12004-C, p.749, 1991.

[3] R.Geller et al., "ECR Ion Sources for Accelerators", Proc. of 1988 Linear Accelerator Conf., CEBAF-Rep.-89-001, p.455, 1989.

[4] J.Friedrich, A.Schempp, H.Deitinghoff, H.Klein (Univ.Frankfurt); N.Angert, J.Klabunde (GSI Darmstadt), "Properties of the GSI HLI-RFQ Structure, these proceedings.

[5] U.Ratzinger, "A Low Beta RF Linac-Structure of the IH-Type with Improved Radial Acceptance", Proc. of 1988 Linear Accelerator Conf.,CEBAF-Rep.-89-001, p.185, 1989.

[6] J.Klabunde, "The Unilac Upgrade Project", Proc. of 1988 Linear Accelerator Conf., CEBAF-Rep.-89-001, p.242, 1989.

DEVELOPMENT OF A RADIOACTIVE NUCLIDES ACCELERATOR AT THE MOSCOW MESON FACTORY

V.A.Andreev, V.A.Bomko*, G.N.Vjalov, S.K.Esin
D.V.Gorelov, Ju.D.Ivanov**, A.S.Iljinov, A.A.Kolomiets,
V.A.Moiseev, B.P.Murin**, P.N.Ostroumov, A.N.Zelenskij

Institute for Nuclear Research Academy of Sciences of the USSR,
117312, Moscow

*Kharkov Physical Technical Institute,310108, Kharkov
** Moscow Radiotechnical Institute,113519, Moscow

Abstract

In the Institute for Nuclear Research the new facility based on the primary proton beam of the meson factory is under development in order to obtain, separate and accelerate on-line radioactive isotopic ions up to energy of 6.5 MeV/amu with the intensity up to 10^{12} atoms/sec. In order to accelerate radioactive beam with initial ratio q/A>1/60 with good efficiency the heavy ion CW linac is considered which consists of 2 types of accelerating structures: 27.12 MHz RFQ at the energy range from 1 keV/amu to 60 keV/amu and IH-structure from 60 keV/amu to final energy of 6.5 MeV/amu.The operating frequencies of IH structure are 54.24 MHz and 108.48 MHz. The only carbon stripper at the energy of 350 keV/amu is foreseen to increase q/A up to 3/20.The last achievements in a development of RFQ and IH structures result to relatively small accelerator length - 45m and power dissipation - 1 MW.

Introduction

A new area of the nuclear matter study is opening in experiments with accelerated radionuclide beams. Experiments of that kind followed by express methods of research allow to study the properties of nuclides with short half-lives removed far from the stable β-line and being in extreme status of the nuclear matter [1,2].

Most essential advantage of the Linac for production of accelerated radioactive beams in comparison with cyclotron is a highest acceleration efficiency of ions with a minimum charge to mass ratio which is equal to 1/60. Practically ~99% of the injected beam is accepted by linac and acceleration occurs without beam losses. Successful development of the IH structures [3-9] with shunt impedances in the range of 100-300 MOm/m allows to realize the linac in CW mode. The using of stripper at the energy of 350 keV/amu does not destroy both transverse and longitudinal emittances, at the same time it allows to increase acceleration gain.

Description of the Proposed Accelerator

RFQ accelerator provides almost ~100% capture of the injected particles [10]. For the electrode voltage U=100kV the normalized acceptance is equal to 1 πmm mrad if the rf frequency is chosen f ≈ 25 MHz. Beam specifications after RFQ are $|\Delta\Phi|<20^{o}$, $|\Delta P/P|<1\%$. The using of RFQ for acceleration of ions with the ratio q/A = 1/60 up to higher energies than ~6.0 keV/amu is not efficient because it provides of the acceleration gain of ~4 keV/amu·m only, meanwhile the inter digital H- structure provides about one of ~34 keV/amu·m. Therefore at the energy range of (60-350) keV/amu for ions with q/A=1/60 the IH-structure is preferable. Main problem for ion acceleration in this range is a beam focusing. It was considered several types of beam focusing in IH-structure: 1. Alternating phase focusing; 2.The focusing with electrostatic quadrupole lenses placed inside the drift tubes; 3. Magnetic periodic focusing. The detail consideration has shown that the most efficient structure consists of magnetic guadrupole lenses placed inside the drift tubes which are alternated with the drift tubes without quadrupole lenses. To make technically achievable gradients of the lenses the drift tube length with quadrupole lens must be longer on the value of βλ. Because of the phase spread at the RFQ output is sufficiently small, the synchronous phase of IH-tank tank can be chosen equal to $\varphi=-25^{o}$. Rf field level in accelerating gaps must be determined from condition of the absence of rf breakdown in CW operation mode. Other restriction on accelerating field is the rf power dissipation per unit length P'.For the reliable operation of rf tank the value of P' is accepted equal to ~30 kW/m how it was done in Munich heavy ion post accelerator [7].The rf field in the gap is determined from expression:

$$E_{\varepsilon} = \frac{\sqrt{Z_{eff}\,P'}}{\alpha \cdot T \cdot \cos\varphi},$$

where Z_{eff} is effective shunt impedance, α is a ratio of gap width to period length. In accordance to ref [7] the optimum α value for IH-structure is .5 leading to maximum shunt impedance.

The layout of the radioactive nuclides linear accelerator is shown in fig.1. The resonant frequency of RFQ is determined by concentrated capacitance and inductance. Schematic view of the RFQ section is shown in fig.2. The calculated capacitance of each section is 68.3 pF and inductance is 490 nH that corresponds to 27 MHz frequency.

0-7803-0135-8/91$01.00 ©IEEE

The compact bunches downstream RFQ have to be accelerated up to the stripping energy of 350 keV/amu in IH-structure with magnetic quadruples periodically installed in every odd drift tube. A maximum value of gradient in focusing lenses is 10 kG/cm which corresponds to magnetic induction of 10 kG on the pole. A preliminary consideration shows that by choosing of edge shapes of the drift tubes with quadrupoles it is possible to keep the shunt impedance sufficiently high. The accelerating tank based on IH-structure in the energy range of 60-350 keV/amu consists of two sections with separate rf excitation. The power consumption of each section is expected ~150 kW.

A charge state of $^{120}Sn^{+2}$ after the passing of a carbon foil has been calculated in accordance to ref [11]. The results are presented in fig. 3. For subsequent acceleration the charge state with q = +18 was chosen. The ions with other charge states are separated and dumped using the bending magnet.

The accelerating tanks in the energy range of 350-2500 keV/amu based on IH structure designed for a synchronous phase φ=0. The phase trajectories in the plane($\tilde{\varphi}$,$\Delta\beta/\beta$) in various points along the tank with the energy from 350 keV/amu up to 2500 keV/amu are shown in , fig.4. During the acceleration the particles are moved along the phase trajectories shown in fig. 4a,c. To rotate a bunch downstream the focusing quadruplet the focusing quadruplet housing is placed in a minimum of rf field, therefore the shunt impedance of the tank is not be worsen. Due to small drift tube diameter in the accelerating region a maximum value of Z_{eff} is provided[8].

Despite of no separatrix exists in IH-structure tank calculated for synchronous acceptance in it shown in fig. 5. By suitable matching of longitudinal phase parameters of the injected beam it is possible to accelerate the bunches with $\Delta\Phi = \pm 20^{o}$ and $\Delta\beta/\beta = \pm 1.5\%$. A normalized transverse acceptance of that tank exceeding 1 πmmmrad is shown in fig. 5. The basic Linac parameters are listed in the table.

Rf power system

Basic features of the rf system are following:

1. CW rf power generation up to 150-200 kW at the three multiple frequencies.
2. A requirement of the acceleration of ions with various charge to mass ratio that results to the necessity of the output rf power variation in a wide range.
3. The absence of beam loading and CW operation mode allow to use sufficiently simple and slow feedback system.

It turns out that most suitable rf generators satisfying for specifications mentioned above except of the resonant frequencies are those developed for UNK project using the triode GU-101A as an output cascade, which can be easy modified to the lower frequency. Now 27 MHz generator is under development for the test facility.

Conclusion

The Linac for acceleration of radioactive nuclides based on RFQ and interdigital H-type structures is proposed. Basic features of the Linac are:

- CW operation;
- practically 100% capture and acceleration with minimum losses;
- small ratio q/A=1/60 of the injected ions;
- using the only stripping foil at the ion energy of 350 keV/amu;
- using IH-structure with a high value of shunt impedance resulting to a moderate rf power consumption (≈930 kW) and Linac length (~45m).

TABLE

Basic parameters of the radioactive nuclides accelerator

N of tank	1	2	3	4	5	6
Type of tank	RFQ	IH	IH	IH	IH	IH
Focusing type	RFQ	FODO	FODO	Quadruplet		
Input energy (keV/amu)	1	60	230	350	2500	4600
Output energy (keV/amu)	60	230	350	2500	4600	6500
Charge (q/A)	1/60	1/60	1/60	3/20	3/20	3/20
Operating frequency (MHz)	27	27	27	54	108	108
E_0T (kV/cm)	-	27.0	27.0	23.4	22.5	20.2
Tank length (m)	5.53	7.51	7.06	8.42	8.10	8.01
Number of accelerating cells	228	42	27	50	61	49
Synchronous phase (deg)	-90÷ ÷-30	-25	-25	0	0	0
Eff. shunt impedance (MOm/m)	-	92	50	186	168	139
Rf power consumption (kW)	44	150	150	181	188	185
Rf power loss per unit length (kW/m)	8	20	21.3	29.5	30.1	29.5

E_0 is average field on the length of $\beta\lambda/2$.

References

1. A.S.Iljinov and V.M.Lobashev. Proceedings of IVth All-Union Workshop on the Program of Experiments on Moscow Meson Factory. Moscow, 1986, p. 22. (In russian).
2. G.N.Vjalov et al. Proceedings of Workshop INES-89, Moscow, 1989, v.1, p.279.
3. V.A.Bomko et al. Study of the heavy ion accelerating structures, CNIIatominform, M., 1988. (In russian).
4. O.A.Valdner et al. VANIT, Nuclear physical researches, v.5 /5/, p.16. (In russian)
5. E.Nolte et al NIM, 158 (1979), p. 311-324.

6. E.Nolte et al NIM, 201 (1982), p. 281-285.
7. U.Ratzinger et al. NIM, A 263 (1988), p. 261-270.
8. U.Ratzinger. LINAC-88, October 3-7, 1988, p. 185.
9. T. Hattori et al, LINAC-86, June 2-6, 1986, p. 377.
10. I.M.Kapchinskij, V.A.Tepljakov, PTE, No 2, 1970, p.19.
11. M.A.Mcmaham et al. Proceedings of the 1989 IEEE PAC, No 1, Chicago, IL, p. 536.

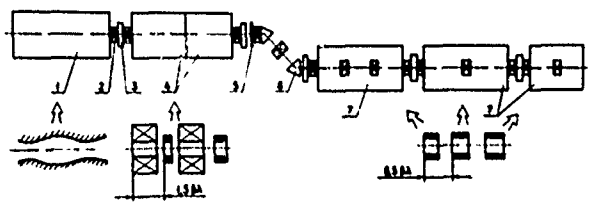


Fig.1. Schematic layout of the radioactive nuclides linear accelerator. 1 - RFQ resonator, 2 - focusing lenses, 3 - rebuncher, 4 - IH-structure tanks with magnetic periodically focusing, 5 - carbon foil, 6 - bending magnet, 7 - IH-structure with quadruplet housing.

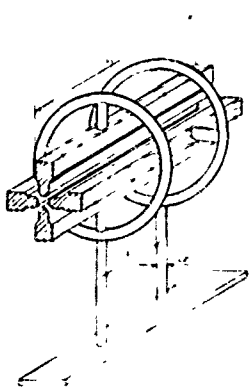


Fig.2. View of one section of the RFQ structure.

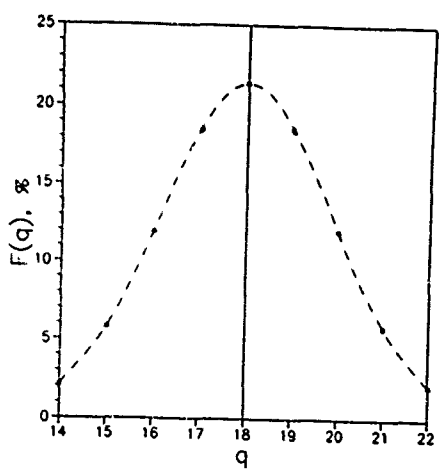
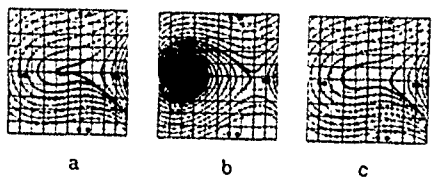
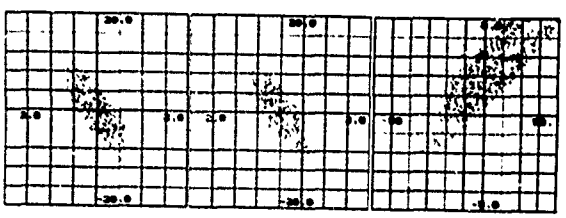


Fig.3. Charge distribution of the ^{120}Sn ions downstream the stripping foil.



a b c

Fig.4. Phase trajectories on the plane (φ, $\Delta\beta/\beta$) for IH-structure with φ_s=0 (a,c) and φ_s=-30° (b).



a b c

Fig.5. Transverse (a,b) and longitudinal (c) acceptance of the IH-structure with injection energy 350 keV/amu.

Status of the Uranium Upgrade of ATLAS

L. M. Bollinger, P. J. Billquist, J. M. Bogaty, B. E. Clifft, P. Markovich, F. H. Munson, R. C. Pardo, K. W. Shepard, and G. P. Zinkann
Argonne National Laboratory, Argonne, IL 60439

Abstract

The ATLAS Positive Ion Injector (PII) is designed to replace the tandem injector for the ATLAS heavy-ion facility. When the PII project is complete, ATLAS will be able to accelerate all ions through uranium to energies above the Coulomb barrier. PII consists of an ECR ion source on a 350 KV platform and a very low-velocity superconducting linac. The linac is composed of an independently-phased array of superconducting four-gap interdigital resonators which accelerate over a velocity range of .007c to .05c. The PII project is approximately 75% complete. Beam tests and experiments using the partially completed PII have demonstrated that the technical design goals are being met. The design, construction status, and results of recent operational experience using the PII will be discussed.

Introduction

The ATLAS superconducting linac [1] is the largest heavy-ion post-accelerators. The range of ion species which may be accelerated by ATLAS is limited to mass A < 127 by characteristics of the 9-MV tandem injector and to beam currents of typically a few particle nanoamperes for the heavier ions. The Positive Ion Injector project [2,3] will replace the ATLAS tandem electrostatic injector with a new injector which will greatly increase the beam current for all ions and extend the mass range of ATLAS to include uranium.

The Positive Ion Injector project combines an ECR source and pre-linac bunching system with a superconducting linac to produce a new class of low-velocity accelerator. The elements of PII are shown in figure 1. Design studies indicated that such a low-velocity injector would provide sufficient velocity to match the remainder of the ATLAS linac for ions of all masses. These calculations also predicted beam quality similar to that of lighter ions from the present ATLAS tandem injector.

Construction has proceeded in several phases. First, the technology for a very low-velocity superconducting linac was developed [4,5,6]. At the same time an ECR source was designed and built on a high voltage platform [7,8]. The source, beam transport and bunching system, and a small (3.5 MV) portion of the linac were completed and beam tested in early 1989 [9]. In the first half of 1990, the system was operated with 7 MV of linac installed. PII will be completed in late 1991 when the linac is enlarged to 12 MV. This final injector will accelerate uranium ions up to more than 1 MeV/A, enough for ATLAS to accept the beam and further accelerate it to ≈ 8 MeV/A.

Elements of the PII System

ECR Source and High-Voltage Platform. The ECR source is a typical 10 GHz source which was designed to operate on a 350-KV platform. Provision for radial access to the plasma region facilitates introducing solid source materials (in the form of wire, for example) into the plasma. To provide good beam bunching and longitudinal beam quality, the platform voltage must be stable to better than 1 part in 10^4.

Construction of the ECR source and high-voltage platform was completed in 1987. The source has been used since then both for beam tests and for several atomic physics experiments [7,8]. Some important results are that: 1) a variety of beams have been produced from solid samples with very high efficiency, 2) more than 1 $c\mu A$ of $^{238}U^{24+}$ has been produced, and 3) the voltage on the high voltage platform is sufficiently stable for excellent beam quality.

Beam Bunching. The two-stage bunching system is similar to that used for tandem injection of ATLAS. The first stage is a gridded-gap four-harmonic buncher with a fundamental frequency of 12.125 MHz. The amplitude of the first stage is adjusted to form a time waist about 35 m

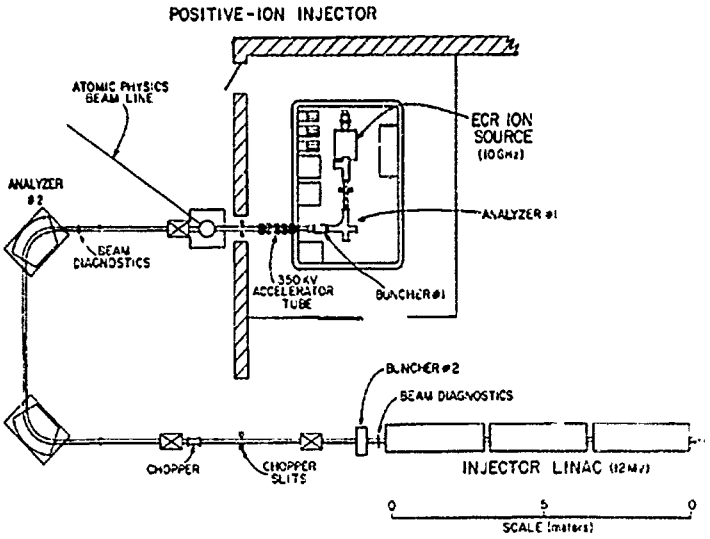


Fig. 1. Layout and major elements of the positive ion injector(PII).

U.S. Government work not protected by U.S. Copyright.

downstream, near the second stage buncher. The second buncher is a two-gap normal-conducting spiral-loaded resonator operating at 24.25 MHz, which forms a time waist ≈ 1 m downstream, near the first resonator in PII.

Development of new detection techniques[10] was necessary in order to study bunching of these low velocity ions. To date, the best bunching result is a measured 1.2-nsec FWHM for an $^{40}Ar^{12+}$ beam with the first stage buncher. The second stage buncher then formed a 130-psec bunch at a detector 55 cm downstream. This time spread is remarkably small for such a low energy beam (0.05 MeV/A).

The Injector Linac. The injector linac is formed from four types of independently-phased, four-gap accelerating structures. The linac is based on the fact that short, high-gradient superconducting accelerating structures can be closely interspersed with short, powerfully focusing superconducting solenoids. The rapid alternation of radial and longitudinal focusing elements maintains the beam in much the same way as does a Wideroe-type rf structure with magnetic lenses in the drift-tubes, but with the added flexibility of independently controlled, modular elements which allows the velocity profile to be tailored to the selected ion species.

The construction sequence of PII has been based on the flexible velocity profile of an independently-phased resonator linac. The design goal of the PII is for efficient acceleration of ions with a charge-to-mass ratio of 0.1. It was possible to configure the linac to usefully accelerate highly charged light ions with as few as five resonant cavities. This capability has allowed the features of the linac to be tested as each cryostat is completed.

At present 10 of 18 resonant cavities have been completed and are operational. Accelerating field levels obtained in off-line tests average above 4 MV/m. The average on-line level is 3 MV/m, the original design goal, but is presently limited by characteristics of the fast-tuning system and is not believed to be a fundamental limit. The lowest velocity resonator (ß = .008), has repeatedly been operated with beam at gradients above 6 MV/m.

The performance of the complete PII injector linac as a function of mass is shown in Figure 2. The different curves result from differing assumptions on charge states from the ECR ion source and, therefore, different beam currents.

Beam Tests and Operation

The highly adaptable nature of the linac has permitted a series of beam tests as construction of the low-velocity linac has proceeded. This has included several periods of actual operation of ATLAS injected with the PII system.

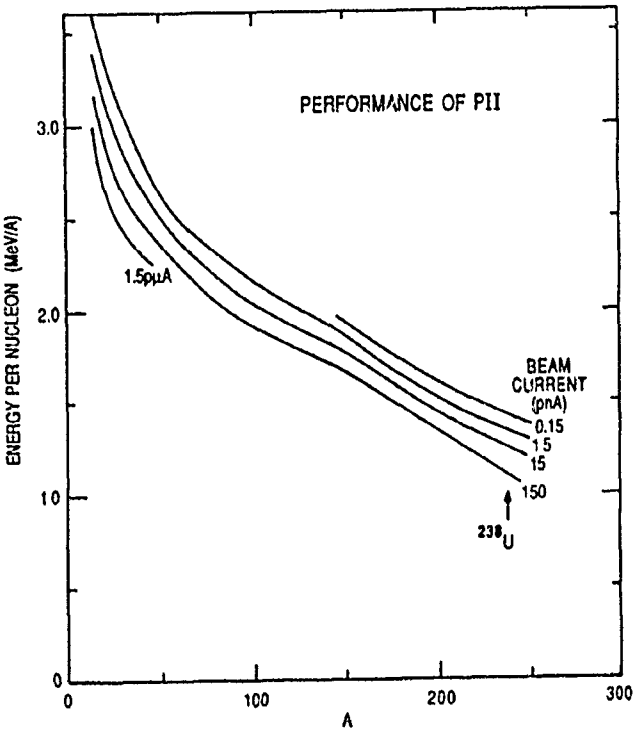


Fig. 2. Expected PII output energy as a function of mass and beam current. The different curves assume different charge states and, therefore, beam currents from the ECR ion source.

First beam through PII was obtained in February 1989, with a 3.5 MV configuration of the linac. A 1μA beam of $^{40}Ar^{12+}$ was accelerated to as much as 36 MeV. In the course of these tests the beam was injected into ATLAS, accelerated to 173 MeV, and used for a brief (6 hr) experiment. Another series of tests were performed in 1990, with a 10-resonator, 7 MV configuration of the PII linac.

A variety of beams have been accelerated with PII, including $^{3}He^{2+}$, $^{13}C^{4+}$, $^{16}O^{6+}$, $^{40}Ar^{12+,13+}$, $^{83}Kr^{17+}$, $^{86}Kr^{15+}$, and $^{92}Mo^{16+}$. In addition to beam tests of PII, the system has delivered beam to the ATLAS linac for tests and for several experiments totaling more than four weeks.

Operation of the PII system has been characterized by excellent reliability and stability. Even in these early tests, all elements of the system typically ran for extended periods, several days, with little or no operator intervention.

A primary goal for the new injector has been to achieve beam quality competitive with that of the tandem, especially in longitudinal phase space. Measured longitudinal emittance, ϵ_z, of several beams is shown in Table I. These tests demonstrate that the beams from PII

have substantially smaller longitudinal emittance than similar tandem beams, and that PII sets a new standard of quality for heavy-ion beams.

Conclusion

The results of beam tests to date indicate that all design goals for the PII system will be met. Tests of the partially completed system already demonstrate that the combination of an ECR ion source with a low-velocity superconducting linac provides an alternative to tandem electrostatic accelerators that is not only cost-effective, but can also provide improved beam quality and increased beam current.

This research was supported by the U. S. Department of Energy, Nuclear Physics Division, under contract W-31-109-ENG-38.

TABLE I
Measured Longitudinal Emittance

Ion	Stripping	ϵ_χ(keV-nsec)	
	Post-Injector	Tandem	PII
$^{3}He^{2+}$	no		$<1\pi$
$^{16}O^{6+}$	no	15π	
$^{16}O^{8+}$	yes	20π	
$^{40}Ar^{12+}$	no		5π
$^{58}Ni^{10+}$	no	30π	
$^{58}Ni^{19+}$	yes	40π	
$^{86}Kr^{15+}$	no		19π

References

[1] J. Aron, et al., Proceedings of the 1984 Linear Accelerator Conference, Seeheim, W. Germany, May 1984, GSI Report GSI-84-11, pp. 132 (1984).

[2] L. M. Bollinger and K. W. Shepard, Proceedings of the 1984 Linear Accelerator Conference, Seeheim, W. Germany, May 1984, GSI Report GSI-84-11, pp. 217 (1984).

[3] R. C. Pardo, L. M. Bollinger, and K. W. Shepard, Nucl. Instrum. and Methods B24/25, pp. 746 (1987).

[4] K. W. Shepard, Proceedings of the 1986 Linear Accelerator Conference, Stanford, California, June 1986, SLAC Report 303, pp. 269 (1986).

[5] K. W. Shepard, Proceedings of the 1987 IEEE Particle Accelerator Conference, Washington, D.C., March 1987, pp. 1812 (1987).

[6] K. W Shepard, P. K. Markovich, G P. Zinkann, B Clifft, R. Benaroya, Proceedings of the 1989 IEEE Particle Accelerator Conference, Chicago, Illinois, March 1989, pp. 974 (1989).

[7] R. C. Pardo, P. J. Billquist, and J. E. Day, Journal de Physique C1 supp. #1, pp. 695 (1989).

[8] R. C. Pardo and P. J. Billquist, Rev. Sci. Instr. 61(1), pp. 239 (1990).

[9] L. M. Bollinger, et al., Proceedings of the 1989 IEEE Particle Accelerator Conf., Chicago, Illinois, March 1989, pp. 1120 (1989).

[10] J. M. Bogaty, R. C. Pardo, and B. E. Clifft, Proc. of the 1991 Linear Accelerator Conf., Albuquerque, N.M., Sept. 1990; LA-12004-C, pp. 465 (1990).

45 MeV Linac for the 800 MeV Synchrotron Radiation Light Source

N.Kaneko,M.Yamamoto,O.Azuma,H.Iwata,T.Nakashizu and Y.Hoshi
Ishikawajima-harima Heavy Indutries.Co.,Ltd
1-15,Toyosu 3-Chome,Koto-ku,Tokyo 135 Japan

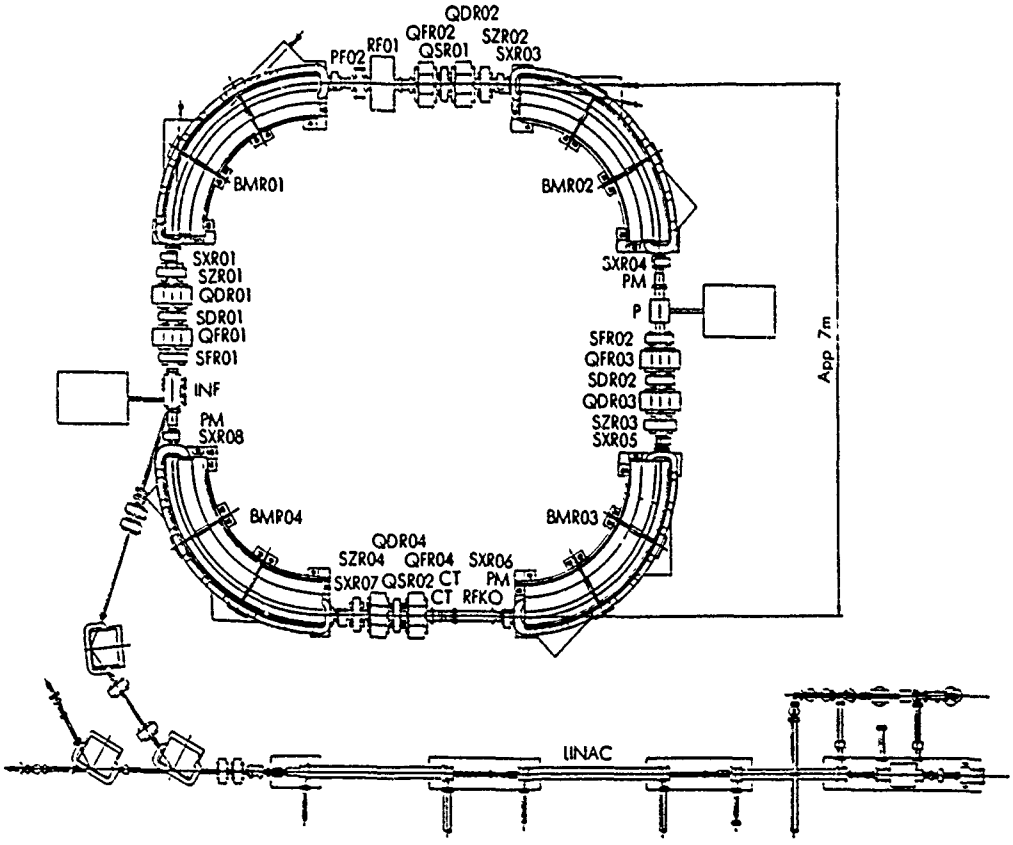
Abstract

A 45 MeV linac has been developed by Ishikawajima-harima Heavy Industries Co.,Ltd (IHI) as an injector of the compact synchrotron radiation light source. The construction of SR system, called LUNA, was completed in 1989 at Tsuchiura facility of IHI, and now several experiments for X-ray lithography are in progress. The linac is now being operated successfully. The detailed descriptions and the beam performances of the linac are described.

INTRODUCTION

Synchrotron radiation is expected to be used in various industrial applications, especially for the X-ray lithography in LSI production. The LUNA system was developed for our own use for various researches, including X-ray lithography[1].

The LUNA specifications were decided to develop "a low - cost, stable light source" in a short time. As a result, we selected the "low energy injection" method and a square ring with



(Note)

RF:	RF cavity	P:	Purturbator (Pulse magnet for injection)
SXR:	Steering magnet for horizontal direction	PM:	Position monitor
SZR:	Steering magnet for vertical direction	CT:	Current monitor
SFR, SDR:	Sextupole magnet	RFKO:	RF knock-out electrode
QSR:	Skew magnet	BMR:	Bending magnet
INF:	Inflector (Palse magnet for injection)	QFR:	Focusing quadrupole magnet
		QDR:	Defocusing quadrupole magnet

Fig. 1 Layout of Synchrotron

0-7803-0135-8/91$03.00 ©IEEE

normal conducting magnets. The ring is used both as a booster and a storage ring. The injector of LUNA is a 45 MeV linear accelerator. We choose this injection energy, for the following two points. The first one is the electron life time problem, scattering with residual gas. It is desirable to choose the higher injection energy in order to accumulate the higher beam current. The second one is compactness and cost. It is preferable to choose the lower injection energy and the shorter accelerating structure. The installation of LUNA was completed in April, 1989. Synchrotron radiation at 800MeV was observed in December, 1989. Now a days, 50mA beam current at 800MeV is obtained, and its lifetime is longer than 30 minutes. The layout of synchrotron is shown in Fig. 1.

DESCRIPTIONS OF LINAC

A. Overall configulation

Fig. 2 shows configulations of linac.The system consists of an electron gun, a 50cm buncher section, a 1.5m regular section and two 2m regular sections. Two S-band klystrons with a frequency of 2,856 MHz are used as RF sources.

B. Electron gun

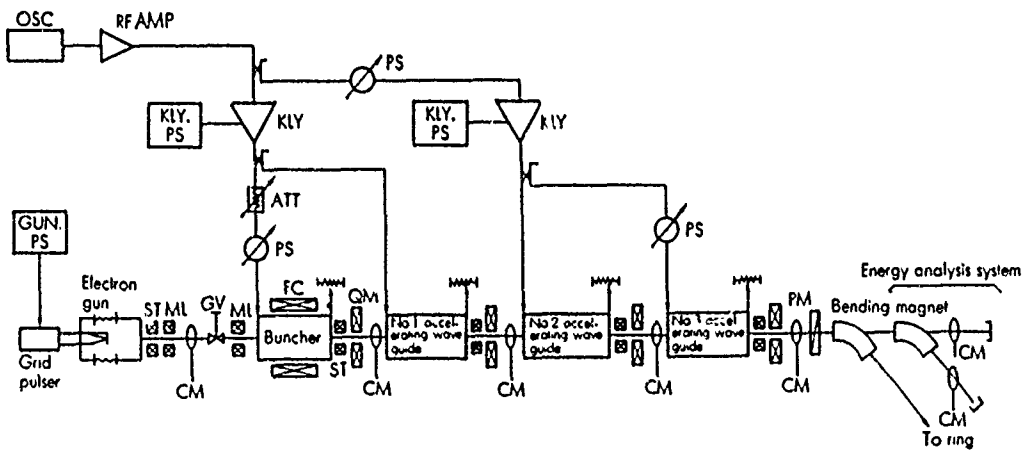
The electron gun is the triode type with grid control. The cathode is the impregnated dispenser type. Electrons are emitted by the pulse voltage 100 kV. Two type of grid pulsers are installed to produce short pulse, 40ns, and long pulse, 1.0 μ s.

C. Accelerating wave guides

Fig. 3 shows a cross-section of a regular accelerating wave guide. The specifications are shown below.

Length	1,500mm (1 wave guides)
	2,000mm (2 wave guides)
Type	2/3 π mode
	constant impedance
Shunt impedance	50 MΩ/m
Att. constant	0.28 1/m
Group velocity	0.88c
Q value	12,000
RF frequency	2,856 MHz
RF source	8 MW(peak)
	22MW(peak)

IHI has manufactured the accelerating structured at own shop. The electroforming method was used to construct them.



(Note)

PS:	Phase shifter	QM:	Quadrupole magnet
ST:	Steering magnet	PM:	Profile monitor
ML:	Magnetic lens	OSC:	Synthesizer
CM:	Current monitor	RF AMP:	RF Amplifier
CM:	Current monitor	KLY:	Klystron
GV:	Gate valve	KLY. PS:	Klystron power supply
FC:	Focusing magnet	GUN. PS:	Gun power supply
		ATT:	Attenuator

Fig. 2 Configulations of Linac

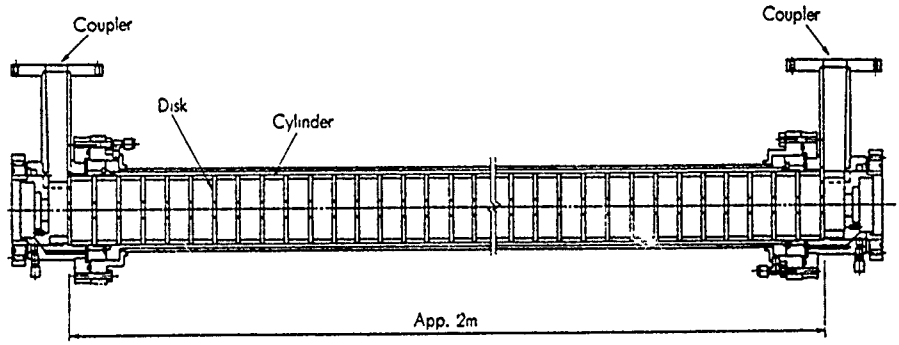


Fig. 3 Cross Section of Regular Tube

D. RF system

S-band (2856 MHz) klystron is employed because it is popular as a high power pulse klystron. The reference RF signal oscillated by a synthesizer is amplified to 2 kW by a low power pulse klystron. It is then amplified to 8 MW and 22 MW by two main klystrons.

E. Vacuum system

The vacuum system of the accelerating wave guides is designed to meet the value of 1.33 x 10 - 4 Pa (10 - 6 Torr) or less. A turbo molecular pump performs rough pumping, after which four ion pumps evacuate the accelerating wave guides with the pumping speed of 60 l/sec each.

EXPERIMENTAL PERFORMANCES

The beam energy and energy spread were measured using an energy analyzing section, which consists of a bending magnet, a slit and a current monitor. Beam energy vs. beam current curve is shown in Fig. 4. Current transformers are used as beam current monitor. They are located at each end of the accelerating wave guides. A fluorescence type screen monitor is located at the end of the linac. Emittance was also measured, following the method used at KEK (National Laboratory for High Energy Physics)[2]. Measurement was carried out by varying the focal length of the quadrupole magnet and recording the diameter of beam profile. The specifications and the performances of the linac system are summarized in Table 1. Performances satisfy the design specifications.

CONCLUSION

We have successfully developed the injector for our synchrotron light source. The measured performances fit well with the designed specifications. On the basis of this linac, we are developing the higher electrical field accelerator structure.

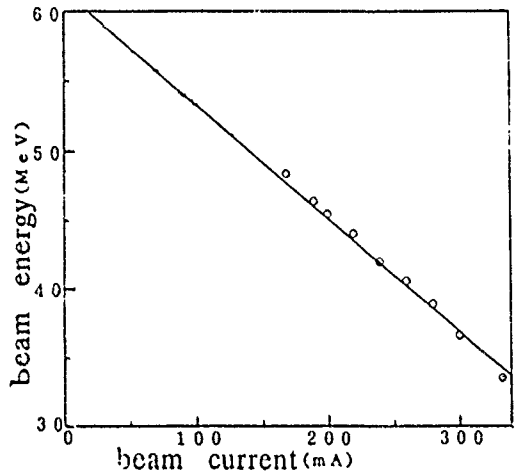


Fig.4 Beam Energy vs. Beam Current

Table 1 Specifications and Performances

	specification	result
Energy	45MeV	45MeV
Beam Current	100mA (ΔE/E <±2%)	100mA
Pulse Length	Long pulse 1μsec Short pulse 40nsec	~ 1μsec ~40nsec
Reptition Rate	1~20pps	1~20pps
Energy Spread	±2%	±1%
Emittance	10^{-5}m · rad	10^{-5}m · rad

REFERENCES

[1]S.Mandai et al.,"Development of Compact Synchrotron Light Source for X-ray Lithography", The 3rd International Conf. on Synchrotron Radiation Instr.,Tsukuba,Japan,1988

[2]S.Ohsawa et al.,"Beam emittance measurement of the positron generator at KEK",Proc.6th Symposium on Acc.Sci. and Tech.,Tokyo,Japan,Oct.1987

DESIGN STUDIES OF SSC COUPLED CAVITY LINAC

C.R. Chang, R. Bhandari, W. Funk, D. Raparia, J. Watson
SSC Laboratory *
2550 Beckleymeade Ave.
Dallas, Texas 75237

Abstract

The SSC coupled cavity linac (CCL) will be a side coupled structure operating at 1284 MHz to accelerate a nominal 25 mA H^- beam from 70 MeV to 600 MeV. We present results of both cavity design and beam dynamics studies. Each accelerating cavity is optimized by SUPERFISH, coupled cavity characteristics in the region of low-, mid- and high-energies are checked by MAFIA-3D. MAFIA-3D was also used to design the bridge coupler systems. The beam dynamics and error analysis are simulated by CCLDYN and CCLTRACE. Possible future upgrade of the CCL to 1 GeV is also discussed.

I. INTRODUCTION

The CCL provides most of the energy gain of the SSC linac. It is the least expensive per meter to fabricate, and provides the highest accelerating gradient. The side coupled type was chosen because of extensive experience at other laboratories such as LAMPF and Fermilab[1].

The SSC CCL preliminary design consists of 10 modules, each module contains 6 tanks which are resonantly coupled together by 5 bridge couplers. Each module is powered by one 20 MW klystron connected to the central bridge coupler There will be one electromagnetic quadrupole after each tank to form a FODO structure. The conceptual layout of one typical CCL module is shown in Fig.1. In the following sections we will separately discuss cavity design and beam dynamics.

II DESIGN OF ACCELERATING AND COUPLING CAVITIES

Each CCL tank is formed by brazing together 20 or 22 identical accelerating cells and 19 or 21 identical coupling cells. Every accelerating cell in a tank has the same length of $\beta\lambda/2$, where β corresponds to the mean energy of the tank. The length of each coupling cavity is chosen to be 65% of that of the accelerating cell The geometry of coupling cells should be as simple as possible since it contains almost no field They are cylindrical (R=5 cm) with two end posts for frequency fine tuning.

The geometry of accelerating cavities must be carefully designed to optimize the shunt impedance. SUPERFISH was used for this optimization. By adding capacitive loading to the center of the cavity by means of nose cones the electric field may be concentrated in the region of the beam and the transit time factor may be increased. These nose cones can also be used to fine tune the TM010 frequency. By curving the outer wall of the cavity the Q value may be increased, also improving the shunt impedance. To further reduce peak surface field which occurs at the nose cone, we adopted a double-radius nose-cone design. By enlarging the outer radius of the nose cone, the peak surface field is restricted to 32 MV/m (1.0 Kilpatrick). This corresponds to an effective on-axis accelerating gradient of 6.66 MV/m. We also chose to have the same outer radius (R=8.5 cm) and same nose cone curvatures for all accelerating cavities. The inner beam pipe radius is 1.25 cm from module 1 through 6, and is reduced to 1 cm after module 6. A typical accelerating cavity cross section is shown in Fig.2.

The SUPERFISH calculation neglects the effects of coupling slots. The actual frequency will be lower than calculated. Therefore we must design f(SUPERFISH)=1284 (MHz)+Δf, where Δf is determined from LAMPF and Fermilab data, scaled to our frequency.

The nearest-neighbour coupling k is chosen to be 5%, as a compromise of keeping high shunt impedance and minimizing the field droop caused by power flow losses. MAFIA-3D was used to calculate k. The simplest geometry we simulated includes one full accelerating cavity and two half coupling cavities, as shown in Fig.3. For this geometry we obtain four frequencies: f_o, $f_{\pi/2}$, $f_{\pi/2,\text{coupling}}$ and f_π. To eliminate the stop band, we must adjust the nose of the accelerating cell and posts of the coupling cells to bring $f_{\pi/2} = f_{\pi/2,\text{coupling}} = 1284$ MHz. We also need to adjust the length of the coupling slot to obtain the correct f_o and f_π. Then $k = (f_{\pi/2}/f_o)^2 - 1$. 3-D simulations were carried out for cavities in the low-, med- and high- energy end. Reasonable agreement has been found with SUPERFISH. Aluminium cold models to bench mark the designs for these tanks are under construction.

III. CCL BRIDGE COUPLER DESIGN

In order to provide sufficient intertank spacing for quadrupole magnets at the low energy end of the CCL, the bridge coupler length from module 1 through 5 is $5\beta\lambda/2$. After module 5, their length drops to $3\beta\lambda/2$. This keeps the length of the bridge couplers between 21.6 cm and 37.2 cm. Let R be the ratio of the length to radius of the bridge cavity. Bridge couplers in modules 1 through 3, and from module 6 to 10 will have $R < 3.7$. For these short cavities, no modes other than TM010 are in the pass band Consequently, their geometry can be made very simple. each

*Operated by the Universities Research Association, Inc., for the U.S. Department of Energy under Contract No. DE-AC02-89ER40486.
U.S. Government work not protected by U.S. Copyright.

of them consists of only one single cylindrical cavity with two end posts.

Bridge couplers in modules 4 through 5 will have $\mathcal{R} > 3.7$. For these long cavities, f(TE112,X,Y) and f(TM011) become so low that they get into the pass band and cause mode mixing problems. Currently, there are two approaches to solve this problem: (I) (LAMPF[2] and Fermilab) resonant posts are added to the bridge cavity to shift the frequencies of those unwanted modes either completely outside of the pass band or to desired values that are "symmetric" with respect to f(TM010,π/2); (II) (L. Young at LANL) disks with large apertures are used to divide a long bridge cavity into an odd number of short cavities. These short cavities will have no mode mixing problem, all modes other than TM010 are far above the pass band. A long single cavity with many posts is not mechanically simpler than a multi-cavity bridge coupler, but is electrically more difficult to tune. After trying both approaches, we prefer multi-cavity bridge couplers. Consequently, there will be two different type of bridge coupler in the CCL, 40 short ones will be of single cavity type, 10 long ones will be of multi-cavity type. Fig.4 shows a MAFIA plot of the cross section of a five-cavity bridge coupler with end tank accelerating cavities and coupling cavities.

The coupling constant between the bridge coupler and the coupling cavity was chosen to be 10%, which is much larger than the k between accelerating cavity and coupling cavity. This will make the field level in the bridge coupler much lower than that in the accelerating cavity so that the bridge coupler consumes less power.

IV. BEAM DYNAMICS AND ERROR ANALYSIS.

The drift-tube linac (DTL) that precedes the CCL operates at 428 MHz with $(E_oT) = 4$ MV/m. The CCL has $(E_oT) = 6.66$ MV/m and operates at the third harmonic of the DTL. In order to obtain a current-independent matching condition between DTL and CCL, we need to have the initial CCL accelerating gradient $(E_oT)=4/3\approx1$ MV/m. We then slowly ramp the (E_oT) across the first two tanks from 1 MV/m to 6.66 MV/m. Ramping is achieved by making the coupling constant $k_i > k_{i+1}$. We have simulated the CCL with 0 mA, 25 mA and 3×25 mA current and find the linac is approximately current independent.

The overall CCL is 117 meters in length and we need some mechanism to correct the misalignment errors. This is done by adding steering dipoles to the magnetic quadrupole after each module. The quadrupole lenses between modules will thus be different from those between tanks. Also the spacing between modules will be larger to accommodate the additional diagnostics and an isolation vacuum valve. There are two ways to get extra spacing between modules: either we make the magnetic focusing lattice non-periodic, or keep the magnetic lattice periodic but make the first and last tank in each module shorter. We chose to keep the magnetic lattice periodic, consequently tank no.1 and tank no.6 in each module have to be made shorter. This two tanks have 20 accelerating cells, while the others have 22. A shorter tank produces less RF defocusing force, which makes the overall system (quadrupole lenses + tank) non-periodic from tank to tank. However, the system is still periodic from module to module, therefore it is possible to find a matched beam solution. To minimize the maximum beam size and emittance growth, one should try to keep the average beam size in each tank approximately constant. A CCL generating code is first used to generate the tanks and calculate the required quadrupole strength to produce the desired phase advance (σ_o = 70°, G=28-33 T/m in our CCL). TRACE-3D is then used to find the matching condition. Finally CCLDYN pushes particles ($\geq$1000) through the linac. Fig.5 shows the energy spread, phase spread and x-envelop of the beam from 70 to 600 MeV. There are no particle losses in the CCL and the transverse emittance growth is about 40% ($\epsilon_{in,rms,in} = 0.194$, $\epsilon_{n,rms,out} = 0.271\ \pi$ mm-mrad).

When realistic fabrication errors are included, using CCLTRACE, the edge of the beam should stay within 60% of the bore with 95% of confidence, as show in Fig.6.

V SUMMARY AND DISCUSSION

In the simulation we observed 40% transverse emittance growth. It is caused by the fact that the bunch length is not small compared to the bucket length. Consequently the head and the tail of the bunch are experiencing different RF defocusing force. We are making an effort to reduce the emittance growth by reducing the bunch length.

We have simulated the CCL to 1 GeV by continuing the same module and magnetic lattice structure. Six more CCL modules (additional 80 meters in length) are needed. The beam is well behaved with no emittance growth or particle losses in this section The future upgrade to 1 GeV will thus be straightforward since the extra tunnel length will be built during the original construction.

The physics design of the SSC CCL is basically finished. Our next stage will be the engineering design and cold modeling.

ACKNOWLEDGEMENTS

We wish to thank R. Garnett at LANL for his help in the beam dynamics studies Many thanks to R. Noble and A. Moretti at Fermilab for many valuable discussions.

References

[1] R.J. Noble, "The FERMILAB linac upgrade", Proc. of the 1990 Linear Accel. Conf. p.26.

[2] J.M. Potter and E.A. Knapp, "Bridge coupler design and tuning experience at Los Alamos" Proc. of the 1972 Linear Accel. Conf. p.242.

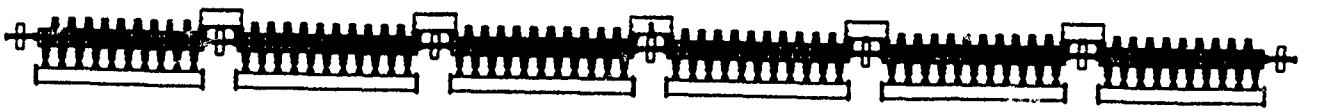


Fig.1 A typical CCL module consists of 6 tanks and 5 bridge couplers. The magnetic quadrupoles between tanks and the vacuum manifolds are also shown.

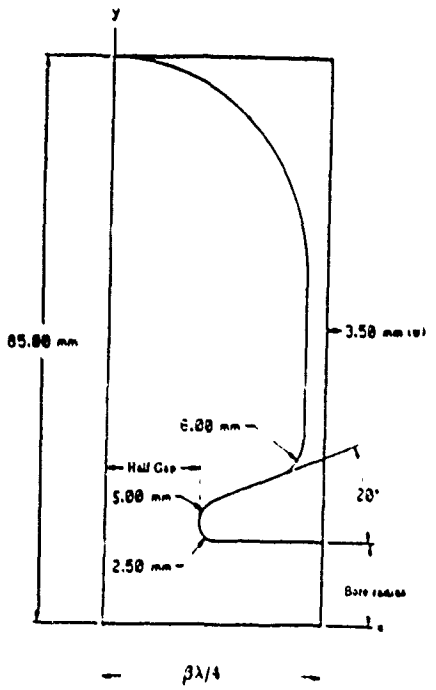


Fig.2 Cross section of a typical accelerating cavity.

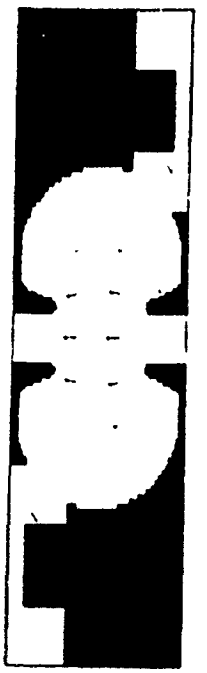


Fig.3 MAFIA simulation of one accelerating cell and two half coupling cell.

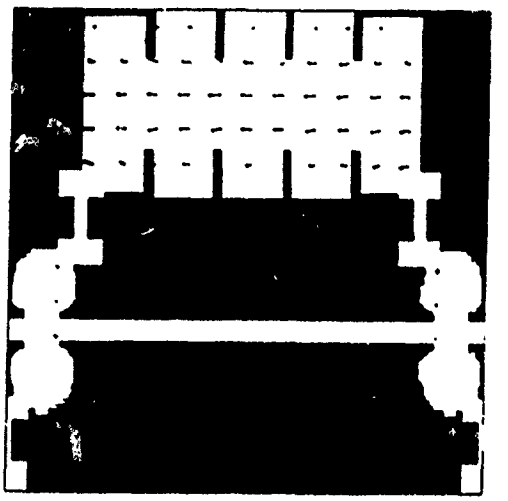


Fig.4 MAFIA simulation of multi-cavity bridge coupler.

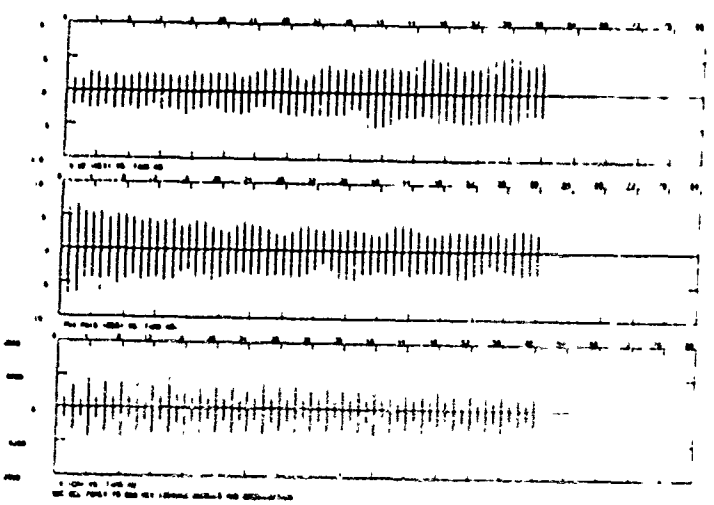


Fig.5 CCLDYN simulation results
top: energy profile
middle: phase profile
bottom: x profile.

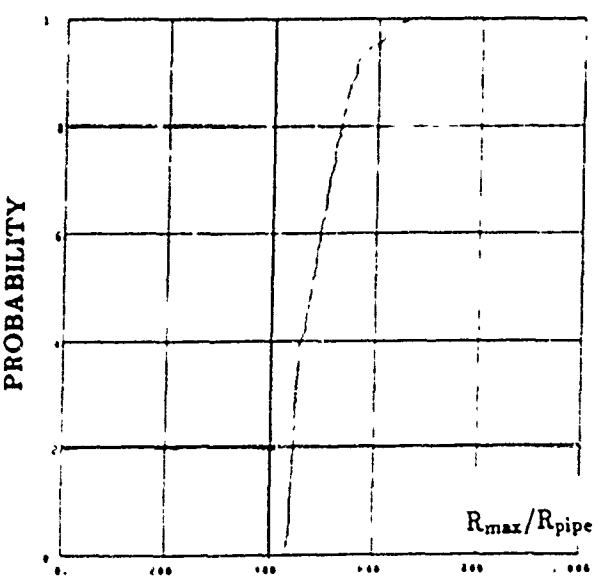


Fig.6 Results from CCLTRACE: probability vs normalized beam radius (R_{max}/R_{pipe}).

Tuning of the First 805 MHz Side-Coupled Cavity Module for the Fermilab Upgrade*

Zubao Qian, Mark Champion, Thomas G. Jurgens, Harold W. Miller, Alfred Moretti, René Padilla
Fermi National Accelerator Laboratory
P. O. Box 500, MS 306
Batavia, Illinois 60510

I. Introduction

The FNAL Linac Upgrade provides for the replacement of the last four linac drift-tube tanks with seven side-coupled cavity modules which are more efficient and will operate at higher accelerating gradient (8 MV/m). Each module is composed of four accelerating sections connected with three bridge couplers and is driven by a 12 MW, 805 MHz klystron RF power supply. Sixteen accelerating cells (main cell) and fifteen coupling cells (side cell) are brazed into an accelerating section (fig. 1).

The cavity tuning must meet several requirements for satisfactory beam dynamics. The requirements include 1) The correct frequency of the accelerating mode (805 MHz), 2) proper field flatness throughout a module, 3) Adequate shunt impedance to reach design gradient within the klystron power limits and 4) amplitude and phase stability. Beam dynamics studies indicated that the field distribution could have a ± 2% rms variation from section to section before serious degradation of the longitudinal beam emittance occurred. It was decided to make the average field agree within ± 1% of the theoretical value from section to section and to limit the rms main cell field deviation to ± 1% within any section. This is more accurate than LAMPF[1][2][3] (±2%, ±6%).

The tuning of the accelerating mode directly affects field distribution, input cavity power and stability. At the correct accelerating mode of the module, it is desirable for the TM_{010} $\pi/2$ mode of each section and the TM_{010} mode of the individual bridge couplers to agree within 2 KHz of the module accelerating mode. This minimizes reactive fields in the bridge coupling cells and provides a null signal to monitor cavity tuning changes at high power. The stability of the field distribution in the $\pi/2$ mode depends on main cell frequency errors, the relative average tuning of the accelerating and coupling cells (stopband) and the amount of power being transmitted along the structure. Stability is assured by tuning accelerating cells equally, adjusting the average coupling cell frequency higher than accelerating cell frequency (positive stopband) and proper cooling. We tune the accelerating cells to ±10 KHz and the stopband positive 50 to 100 KHz. Water cooling tubes on the edge of the accelerating cells and a programmed water temperature assure proper cooling.

The bridge coupler frequency, $3\beta\lambda/2$ section spacing and bridge coupling cell tuning are adjusted to preserve the correct section to section phase at the $\pi/2$ operating frequency of the module. To present a satisfactory standing wave ratio to the input waveguide and to insure proper field flatness throughout the module, the mode spectrum must be clear of bridge coupler resonances except for the desired TM_{010} $\pi/2$ resonance. Unwanted modes in the bridge coupler are adjusted outside of the section pass-band with tuning posts. To reduce bridge coupler losses coupling to a section is larger than between accelerating cells (7% vs. 5%). Two modes generated by the bridge coupler and coupling cells are adjusted to be symmetrical outside the section pass-band.

II. Post-Braze Section Tuning

Before brazing, the structure is tuned in a clamped configuration to 804.900 MHz. After final brazing, welding flanges and mounting the structure on a cradle, the frequency of accelerating cells and the $\pi/2$ mode are compared to the prebrazed condition. Bridge coupling cells are shorted for these measurements. For specific tuning steps see the tuning notes of Miller.[4][5] For 16 sections completed, the brazing operation, on average, shifts accelerating cells higher by about 10 KHz. The side cells, which are normally low by 2 to 5 MHz, are easy to tune equal and higher to provide a near zero stop band. From experience we preset the stopband high by about 300 KHz in air. Due to flexing of the side cells, this results in the desired positive 50 to 100KHz stopband under vacuum.

With near zero stopband, the effect of individual cell errors on the field tilt is theoretically zero. Any field deviations in a section are then caused by coupling constant errors. Before further tuning, a bead pull was done to measure the field distribution. If an individual cell field was high or low by more than 1% of the average field in the section, then an attempt was made to understand the cause and make corrections. If the correction was difficult we relied on only keeping the rms field throughout the section to <±1%. There is some indication from the first accelerator module (Prototype R) that errors in coupling of as much as 1% resulted from an offset in the side cell gap centers. This happened when we tuned some inaccessible cells from one side. This exceeds the expected coupling errors due to slot machining tolerances. To control this effect, both sides of the coupling cell are now moved equally when adjusting side cells and coupling accuracy of ±0.5% can be achieved over the length of the section.

* Operated by Universities Research Association, Inc., under contract with the United States Department of Energy.

0-7803-0135-8/91$01.00 ©IEEE

Bending of the web between acceleration cells can affect the nearest-neighbor coupling and hence can cause or correct the local tilt in the field distribution. This can also change the frequency of the two accelerating cells involved as well as the $\pi/2$ mode. Web bending has been used when one cell is higher and an adjacent cell lower than a required final tuning average. After each adjustment of the main cells the $\pi/2$ frequency is rechecked to make an assessment of the amount each accelerating cell must be increased as the structure is brought up to the desired $\pi/2$ frequency. It is important to keep the same conditions such as probe type and shorting configuration when tuning individual cells. Probe re insertion errors can easily cause frequency errors of 30KHz.

The tuning of Prototype R indicated that too large a tuning on any one cell can affect several adjacent cells by as much as 20%. Accelerating cells are therefore tuned in three or four passes. Each pass consists of raising the frequency of main cells by hammer and punch "dinging" of detentes provided on the outside surface of the cell to decrease the inductive volume. End cells are tuned by moving the accelerating nose in or out using a snap-ring groove at the section ends. End cells are properly adjusted when there is minimum energy in their adjacent side cells. Bridge coupling cells are shorted for the section tuning. As tuning progresses, the accelerating cell frequencies converge to a measured spread < 5KHz. At each step the $\pi/2$ mode, each cell frequency and Q are measured.

At the final step the mode spectrum is measured.The modes are used in a dispersion calculation with a five parameter fit to determine cell frequencies, coupling constants and stopband. The side cell $\pi/2$ mode is measured in air with the end accelerating cells shorted. Dispersion calculated and measured $\pi/2$ frequencies agree to within 20 KHz. Measurements, except for the side cell $\pi/2$ frequency are repeated with the section under vacuum to determine the five parameter fit and stopband compared to air. The accelerating $\pi/2$ mode shifts down 4KHz and the stopband shifts down by 270 KHz under vacuum. The disagreement and reduction in the $\pi/2$ mode at vacuum is in part due to a < 0.0004 inch deflection of the cavity ends which lower each end cell frequency about 32KHz. The shift in the stop band is due to deflection of the side cell walls. A stop band between 50 and 100 kHz is accepted. With experience, we have been able to preset the stopband in air so it is about +90 KHz on the first vacuum measurement. After tuning the main cells and side cells to the correct $\pi/2$ frequencies, the shorts on bridge coupling cells are removed and the end cells are tuned. An adjustable tuning cell is put on the bridge coupler ends. The tuning cell is an extended accelerating cell. The section ends are tuned by adjusting this cell and the end accelerating cell until there is zero energy in the bridge coupling cell and the adjacent side cell at the $\pi/2$ frequency. For an ideally tuned section there is no coupling cell energy at the $\pi/2$ mode.

A final bead pull is made before mounting the section on a girder. The field distribution is checked to be within specification and documented. The sections are tuned on different dates and data for atmospheric corrections are taken at different times. When all four sections are on the girder, we re measure the $\pi/2$ frequency and check for stored energy in bridge coupling and adjacent side cells. We also check for shifts due to handling. If necessary, small adjustments are made.

On Prototype R, while we were learning, we intentionally kept the section tuned low because the accelerating cell frequency is not easy to lower. It was originally planned to have individual water temperatures on each section (this may be changed in production) and each section was tuned to slightly different frequencies when corrected for vacuum at 25°C. Table 1 records the frequencies for the sections under vacuum at independent temperatures when nearly equalized. The last column shows the section $\pi/2$ frequency at 25 °C (equal water temperature on each section).

Section	Temperature T (°C)	$\pi/2$, Vac, @ T°C	$\pi/2$, Vac, @ 25°C
R-1	25.0	805.0015	805.0015
R-2	23.0	805.0013	804.9739
R-3	22.7	805.0010	804.9695
R-4	22.0	805.0020	804.9609

Table 1, Section Frequency (MHz)

III Bridge Coupler Tuning

As mentioned above, the purpose of bridge coupler tuning is to get the correct $\pi/2$ mode, phase shift and field flatness between sections with stability. The bridge couplers for the FNAL Linac are $3\beta\lambda/2$. Comparing required lengths (35 to 55 cm) with LAMPF structures and from experience with a 200 MeV prototype we expect three posts to be required for tuning. There are three modes, TE_{111Y}, TE_{111X}, and TM_{011} near the TM_{010} mode. TE_{111X} is the nearest lower mode and TM_{011} is the nearest higher mode. Both modes are out of the cavity chain passband. The two modes were adjusted to be about "symmetrical" with the $\pi/2$ mode by a post at the rear of the bridge coupler (opposite the waveguide feed iris). A fine adjustment was later made to equalize the phase shift across the bridge coupler. This was measured by switching the drive from one end to the other. An example is shown in Table 2 of the modes before and after tuning for the Module 1 section 3-4 bridge coupler.

Mode	TE_{111Y}	TE_{111X}	min,max cavity	TM_{010}	TM_{011}
No Post	744.038	782.008	785.983 835.469	804.765	864.307
Post	750.247	772.661	783.669 832.246	804.763	858.65

Table 2, Module 1 Section 3-4 Modes

The center post was not notched to allow balancing of the section to section fields. Instead, we make a differential adjustment of the end posts when they are used to adjust the TM_{010} mode. After tuning, the posts are clamped in place, marked and then taken to a shop and welded in position. Upon remounting the bridge couplers, the posts require adjusting in or out by < 1/16 inch. Snap ring like grooves

in the post are fitted with a tool for this adjustment. A small probe hole is provided at the center top of the bridge coupler to drive or pickup signals during tuning.

When tuning the four sections of a module, each pair of sections coupled with a bridge coupler were tuned first. An adjustable tuning cell, mounted on the bridge coupling cell at the end of each two section pair, was used to keep the sections $\pi/2$ frequencies equal during tuning. After tuning end bridge couplers, the adjustable cells were removed and the center bridge coupler was installed and ready to tune. The end tuning posts on the bridge coupler were roughly adjusted first so that the resulting $\pi/2$ mode frequency was close to the average of the two sections. Next the center post was adjusted in to make the TE_{111X}, and TM_{011} modes symmetrical with the TM_{010} mode and fixed. The TM_{010} mode increases slightly so the end posts are again adjusted to bring back the $\pi/2$ mode to 805 MHz ± 1KHz. A bead pull was made to check field flatness section to section. If it is not flat, differential positioning of the end posts are made. Moving one in and one out keeps the $\pi/2$ mode unchanged. Seven iterations were made to complete tuning. The posts were then marked, machined to length and welded in place.

A slot is cut in the center bridge coupler to match the power feed via the waveguide. The slot interacts fairly strongly with the above tuning and all posts have to be retuned after matching to the waveguide. For testing purposes, we slotted to match for minimum reflected power and then retuned the posts. Later it will be necessary to over couple to allow for beam loading. The phase shift was checked across the bridge coupler by driving the structure from one end and then the other while measuring at the accelerating cells nearest the bridge coupler. The bridge coupling cells were tuned to compensate this phase shift to <1 deg. Finally, under vacuum, all measurements were repeated and recorded.

IV Results and conclusions.

The Module 1 Side coupled cavity with bridge couplers was final tuned during April 1990 in the low level RF tuning lab. The $\pi/2$ frequency with power iris cut is 805.001 MHz. The stop band is +246 KHz. Driven at the waveguide port, the reflected power is -45db (VSWR = 1.01) The loaded Q is 9544. The individual cell field rms deviation from average in each section is less than 1%. The average field in each section agrees with the theoretical value calulated. The peak field decreases 0.5% over the module length due to gap spacing as ß increases. (See Fig. 2)

The four sections were checked at a single temperature (keeping the $\pi/2$ frequency constant). The field tilt from R1 end to R4 end was 5%. Changing R1,R2 down $4^{o}C$ and R3,R4 up $4^{o}C$ the $\pi/2$ frequency remained unchanged and the field tilt was 16% from the R1 end to the R4 end. Tuning experience has progressed so that by Module 3 we have been able to tune sections to agree to ± 1KHz. That plus the tilt sensitivities measured above suggest a single temperature water system will be adequate. We will decide on retuning all modules for a single water system temperature after the full power test of the prototype module.

Adequate tuning procedures have been developed for the Fermilab Linac Upgrade tuning. They continue to be improved to facilitate production and provide a simpler cooling system.

References

1. G.R. Swain, "LAMPF 805 MHz Accelerator Structure Tuning and it's Relation to Fabrication and installation." LA-791MS

2. G.R. Swain et. al., "Cavity tuning for the LAMPF 805 MHz Linac." 1972 Linac Conference.

3. James M. Potter and Edward Knapp, "Bridge coupler Design and tuning experience at Los Alamos" 1972 Linac Conference.

4. Harold W. Miller et. al., " Tuning Methods for the 805 MHz Side-Coupled Cavities in the Fermilab Linac Upgrade" 1990 Linac Conference.

5. Harold W. Miller, "Linac Cavity Upgrade Tuning Steps" Fermilab Linac Upgrade internal note, LU-180

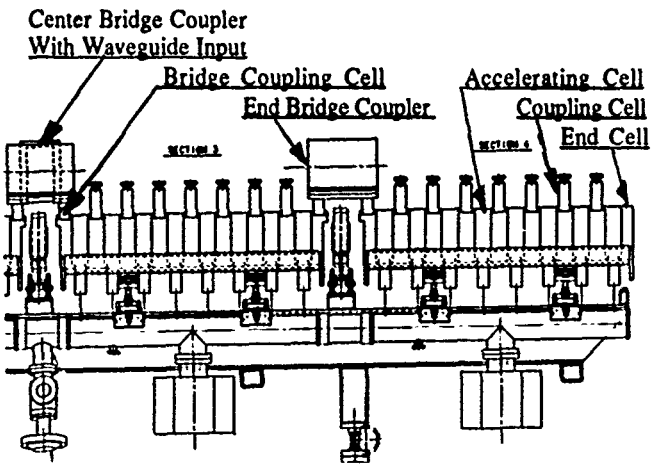


Fig.1, Module 1, Section 3&4

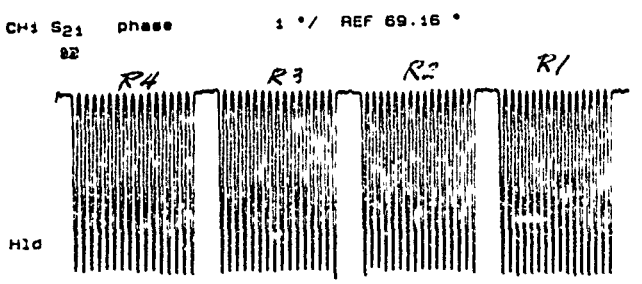


Fig.2, Module 1 Beadpull after Final Tuning

Beam Loading in a High Current Accelerating Gap*

M.J. Rhee and B.N. Ding†
Laboratory for Plasma Research and
Electrical Engineering Department
University of Maryland
College Park, Maryland 20742

Abstract

Energy exchange between a high-current beam and a source at an accelerating gap is treated with a simple transmission line theory. There exists a matching condition for which the beam energy gain is equal to the source voltage. The total energy gain in a multigap system is expressed in terms of individual source voltages and the beam current.

I. Introduction

Recently, multigap high-current accelerators[1,2] have attracted considerable attention because of their potential applications in diverse areas. Unlike a low current beam in the conventional accelerators, a high-current beam accompanies a substantial amount of field energy. Thus, as a high-current beam passes through an accelerating gap, the energy transfer takes place not only from the source to the beam but also from the beam to the source. The latter is easily ignored in the low-current accelerator systems.

In this work, the energy exchange between a beam and a source at an accelerating gap is treated with a simple transmission line theory. The beam energy gained as it passes through the accelerating gap is expressed in terms of the source voltage, the beam current, and the characteristic impedance of the transmission line. There exists a matching condition at which the accelerating voltage is equal to the source voltage. The analysis is extended to a case where the accelerating gap is shunted with a resistor. The beam energy gained in a multigap accelerator system is expressed in terms of relevant parameters.

II. Transmission Line Model

The interaction between a beam and an accelerating gap may be described with a discontinuity in a transmission line in which the beam terminates the end of the transmission line as shown in Fig. 1. As a pulse produced by a pulsed power source arrives the discontinuity, continuities are required of the voltage and current from the transmission line to the beam (Kirchhoff's voltage and current laws). We consider a case when a pulse of constant amplitude, V_S, from the source and a beam current of constant

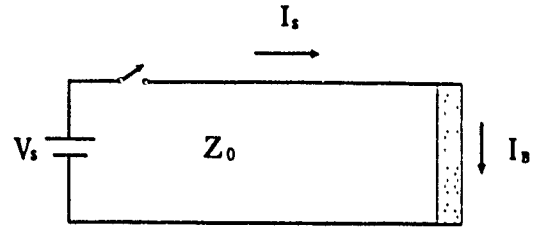


Figure 1: Schematic representation of an accelerating gap and a high-current beam.

amplitude, I_B, are arriving at the gap simultaneously. The voltage and current of the pulse are related by $V_S = I_S Z_0$ in the transmission line, where Z_0 is the characteristic impedance of the transmission line. The boundary condition that the sum of currents at the discontinuity equals zero necessitates a reflected pulse I_- such that

$$I_S + I_- = I_B, \tag{1}$$

where the voltage of the reflected pulse is given by $V_- = -I_- Z_0$. The beam experience a accelerating voltage, V_B, which is the sum of voltages of the incident and reflected pulses appearing across the gap given by

$$V_S + V_- = V_B. \tag{2}$$

Eliminating I_- and V_- from Eqs. (1) and (2), one finds

$$V_B = (2I_S - I_B)Z_0. \tag{3}$$

It is apparent from Eq. (3) that the voltage across the beam, V_B, which is the accelerating voltage, is not always equal to the source voltage $V_S = I_S Z_0$. The matching condition for which the accelerating voltage is equal to the source voltage, $V_B = V_S$, is only when

$$I_{Sm} = I_B \quad \text{or} \quad V_{Sm} = I_B Z_0, \tag{4}$$

i.e., the source voltage is equal to the beam current times the characteristic impedance. Under this condition, the full energy transfer takes place from the source to the beam. This result is illustrated in Fig. 2. It is interesting to note that when $V_S = 0$, Eq. (3) reduces to $V_B = -I_B Z_0$

*This work is supported by the U.S. Department of Energy.

†Present address: China Academy of Engineering Physics, P.O. Box 523-56, Chengdu, Sichuan, China.

0-7803-0135-8/91$01.00 ©IEEE

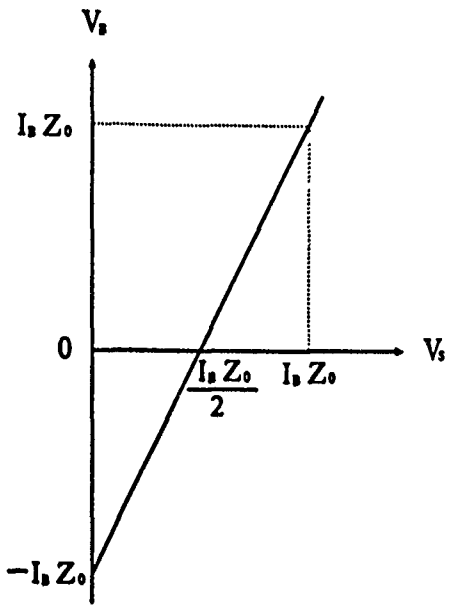


Figure 2: Accelerating voltage vs source voltage.

i.e., when the beam passes through a gap which is not powered, the beam energy is lost by the amount of the beam current times the characteristic impedance of the transmission line. Also note that when the source voltage is one-half of the matched value, $V_S = I_B Z_0/2$, the net beam energy gain is zero.

In many practical accelerator systems, a shunt resistor is employed in the accelerating gap[1] as schematically shown in Fig. 3. It is straightforward to generalize Eq. (3) to the case that includes a shunt resistance R as

$$V_B = (2I_S - I_B)Z_{\text{eff}}, \tag{5}$$

where the effective impedance is $Z_{\text{eff}} = RZ_0/(R + Z_0)$. The matching condition for which the accelerating voltage equals to the source voltage, $V_B = V_S$, is found to be

$$V_{Sm}/Z_0 = RI_B/(R - Z_0). \tag{6}$$

The results are illustrated in Fig. 4. In this case the pulse energy from the source is completely absorbed by both the beam and the shunt resistor. It is obvious from Eq. (6) that the shunt resistance R must be greater than the characteristic impedance.

III. Multigap Accelerator

In multigap accelerator, the total accelerating voltage in the system is the algebraic sum of individual accelerating voltages given by Eq. (5). Assuming identical accelerating gaps with shunt resistors and constant current through the accelerating gaps, the total beam energy in terms of individual source voltages is found by summing Eq. (5) with different $I_{si} = V_{si}/Z_0$ as

$$V_{\text{tot}} = \frac{2R}{R + Z_0} \sum_{i=1}^{n} V_{Si} - nI_B \frac{RZ_0}{R + Z_0}, \tag{7}$$

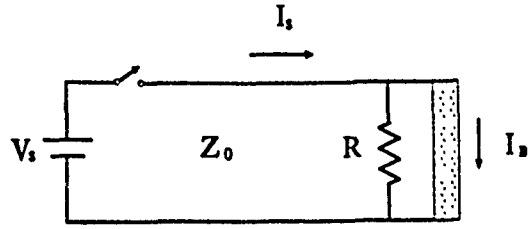


Figure 3: Schematic representation of an accelerating gap with a shunt resistor and a beam.

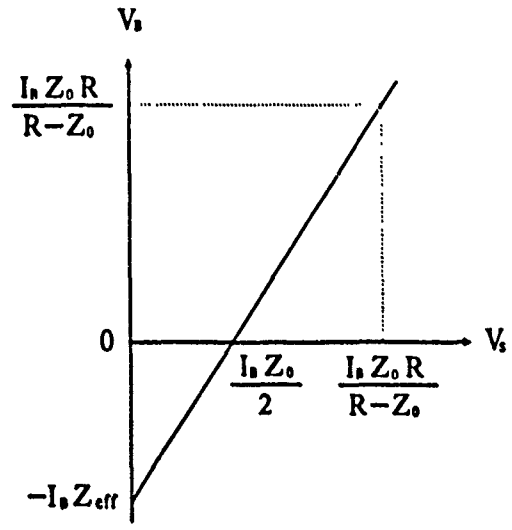


Figure 4: Accelerating voltage vs source voltage for a shunted gap.

where n is the total number of accelerating gaps. It should be noted that the total accelerating voltage is not the algebraic sum of individual source voltages. A few examples are noteworthy. If all of the accelerating gaps are not powered, the total accelerating voltage is negative, $V_{\text{tot}} = -nI_B Z_{\text{eff}}$. If one half of the gaps are not powered, $V_S = 0$, and the other half are powered with voltage, $V_S = I_B Z_0$, the net energy gain is zero. Only when every source has matched voltage, V_{Sm}, the total accelerating voltage is nV_{Sm}.

It should be noted that Eq. (5) is derived under the assumption of a constant beam current throughout the gaps such as in a relativistic electron beam accelerator. Therefore, Eq. (5) is not applicable to a low energy ion beam accelerator in which the beam current changes from gap to gap. It is also noted that since the present work assumes the beam current is a load to the transmission line, the results of present work are not applicable to a gap in which no beam is present such as that of the *voltage adder*[3].

IV. Conclusions

The beam current as it passes through an accelerating gap has been treated with a discontinuity in a transmission line. There exists a matching condition for which the accelerating voltage is equal to the source voltage and

pulse energy from the source is completely absorbed by the beam and the shunt resistor. The total beam energy gain in a multigap accelerator system is expressed in terms of individual source voltage and the beam current.

REFERENCES

[1] R. J. Briggs, D. L. Birx, G. J. Caporaso, T. J. Fesseden, R. E. Hester, R. Melendez, V. K. Neil, A. C. Paul, K. W. Struve, IEEE Trans. Nucl. Sci. **NS-28**, 3360 (1981).

[2] M. G. Mazarkis, D. L. Smith, R. B. Miller, R. S. Clark, D. E. Hasti, D. L. Johnson, J. W. Poukey, K. R. Prestwich, and S. L. Shop, IEEE Trans. Nucl. Sci. **NS-32**, 3237 (1985).

[3] T. W. L. Sanford, J. A. Halbleib, J. W. Poukey, G. T. Baldwin, G. A. Carlson, W. A. Styger, G. A. Mastin, T. Sheridan, R. Mock, J. A. Alexander, E. R. Brock, and C. O. Landron, J. Appl. Phys. **67**, 1700 (1990).

AN INTERACTIVE CODE SUPERLANS FOR EVALUATION OF RF-CAVITIES AND ACCELERATION STRUCTURES

Myakishev D.G., Yakovlev V.P.
Institute of Nuclear Physics, Novosibirsk, 630090, USSR

Abstract

The new code SUPERLANS is described. The main SUPERLANS features are: an evaluation of both the standing waves in axisymmetrical cavities and travelling waves in periodic structures; the number of modes (or dispersion curves) are calculated simultaneously in the arbitrary spectra domain. To increase the code efficiency the following modern methods are used: the isoparametric second order finite elements for the field approximation; the subspace iteration method for the determination of spectra. To increase the accuracy of calculation of the field near the axis the coordinates (Z, R^2) are used. There is code version for IBM PC/AT with the interactive dialogue data input and postprocessor with developed graphics. The code is currently used for the INP RF-system design.

INTRODUCTION

In 1979 the LANS [1] code was developed in the INP. The code used the inverse iteration method with a spectra shift for the calculation of the eigen frequencies in the arbitrary spectra domain in axisymmetrical RF-cavities. The triangular simplex elements were used in the code Then other codes MULTIMODE [2] and PRUD [3] were developed. The subspace iteration method is used for the simultaneous calculation of the number of modes in the codes. The codes also permits to calculate the dispersion curves in periodic structures. The isoparametric second order elements are used in the codes. We develop new code SUPERLANS based on the methods which are used in these codes. The main features of new code are:

- the code is made for personal computer and has interactive input-output and uses the graphical possibilities of the computer;
- the problem formulation is used, which eliminates the singularity in matrix elements on axis [2, 3],
- the coordinates (Z, R^2) are used for the increase in accuracy of field calculations near axis.

GENERAL

The code SUPERLANS was made for the calculation of azimuthally-homogeneous modes in the axisymmetrical RF cavities and periodic structures. For the evaluation of eigen modes the wave equation with respect to following function is solved. function:

$$\Pi = \begin{cases} r \cdot H_\varphi - E & \text{wave} \\ r \cdot E_\varphi - H & \text{wave} \end{cases}$$

The boundary conditions are set on axis, plane of symmetry and metallic surfaces. The metallic surfaces are supposed to have an ideal conductivity The grid with eight node isoparametric elements is used in the code The Galerkin method is used to obtain an algebraic system $(\mathbf{A} - k^2 \cdot \mathbf{B}) \cdot \Pi = 0$ Unlike [2, 3] the integration in the Galerkin method is made over the volume problem, but not over the square of the cavity crossection. In this case, the matrix coefficients haven't the singularity in integral expression:

$$a_{ij} = \int (1/x \cdot \partial\psi_i/\partial z \cdot \partial\psi_j/\partial z + \partial\psi_i/\partial x \cdot \partial\psi_j/\partial x)\, dx\, dz,$$
$$b_{ij} = \int \psi_i \cdot \psi_j / x\, dx\, dz, \quad \text{where } \nu = r^2/4$$

The Dirichlet boundary condition is set on axis, so the matrix coefficients aren't calculated for the axis nodes. The basic functions and their derivatives with respect to z for the nodes near axis are proportional to x, so the matrix coefficients haven't singularity in the integral expression on axis.

The reason of using the coordinate system $(Z, R^2/4)$ is the following. The function Π is proportional to r^2 near axis, since the field is proportional to r near axis. Isoparametric elements are closed to rectangle near axis, so, if the ordinary coordinate system is used, the r and z coordinates are proportional to the corresponding local coordinates. As a result, the function Π and r behave similarly near axis, so Π is proportional to r. Therefore, the coordinate system $(Z, R^2/4)$ is put into operation to remove this uncorrectness in the field description. In this case, we must to move the middle nodes on elements near axis for the right description of coordinates on element. The node on element side perpendicular to the axis is moved. The radius of node is found from the equation $r' = r_0^2/2$, where r_0 — the radius of corner node.

As we have said above, SUPERLANS permits to calculate the travelling waves in periodic structures. The calculation of the dispersion curves is made automatically. The Floquet theorem [4] is used for the calculation of travelling waves. The theorem permits to build the travelling wave with the phase shift θ over the structure period by two real functions. One of them is symmetrical on the period, the other is antisymmetrical. The equations for this functions are analogous to the equation for the standing wave. The functions are related on bound of period by coefficients dependent of the phase shift θ.

The code also permits the evaluation of the RF cavity with an inhomogeneous ferromagnetic and dielectric filling. For example, the one version of cavity with the retuning of frequency for the LEB [5] is shown below.

The code is realized on IBM PC/AT and the graphic possibilities of computer are widely used The interactive input-output are used with simultaneous displaying graphical information. This possibility simplifies the procedure of cavity geometry input. The logical mesh with maximum number of nodes 3000 is used for generating the finite element mesh. Ten modes can be iterating simultaneously in the arbitrary spectra domain.

The code applications are shown on some examples.

The field distributions of two modes in DAW structure [6] are shown in Figs. 1*a* and 1*b*, and dispersion curve is shown in Fig. 1*c*.

The calculation of RF cavity of VEPP-5 [7] is given in the Figs. 2*a*, 2*b*. The wide spectra domain was explored (200 modes) for this cavity. The working and one of the highest quasi-optic modes are shown in figures.

The results of cavity calculation for accelerator «Si-

0-7803-0135-8/91$01.00 ©IEEE

beria» [8] are given in Figs. 3*a*, 3*b*. In this case the modes, interacting with a beam, are shown.

The two first modes of cavity of accelerator «Li.U-10» [9] are shown in Figs. 4*a*, 4*b*. The specific feature of this cavity is that it consists of two parts. The constant voltage is applied to the internal part to suppress the multipactor.

The calculation result of the one version of cavity for the LEB with an inhomogeneous ferromagnetic and dielectric filling is shown in Fig. 5. This cavity is tuned in RF frequency within 30%.

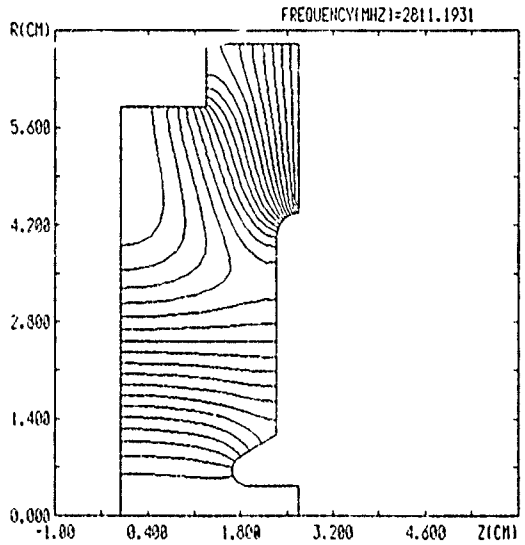


Fig. 1,a

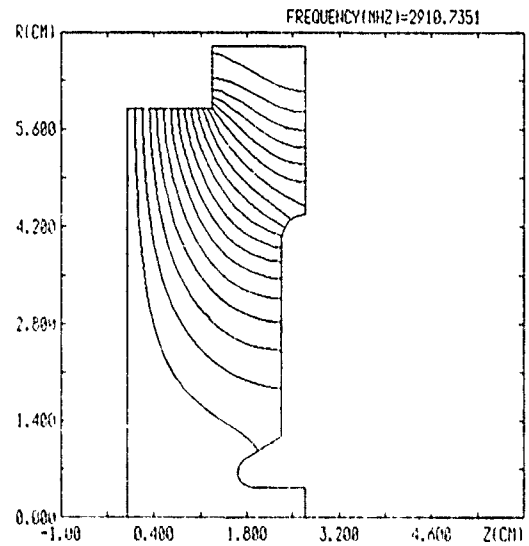


Fig. 1,b

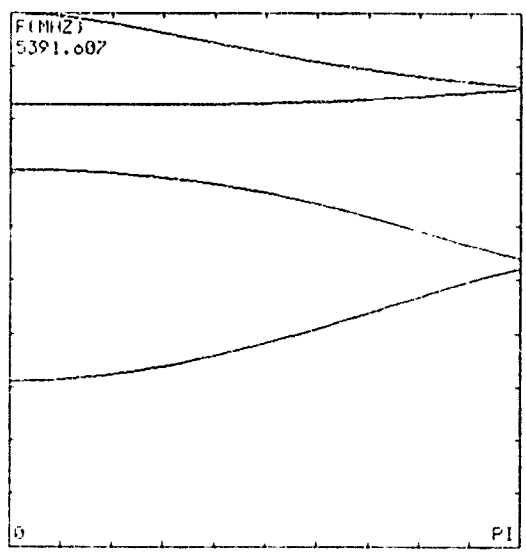


Fig 1,c

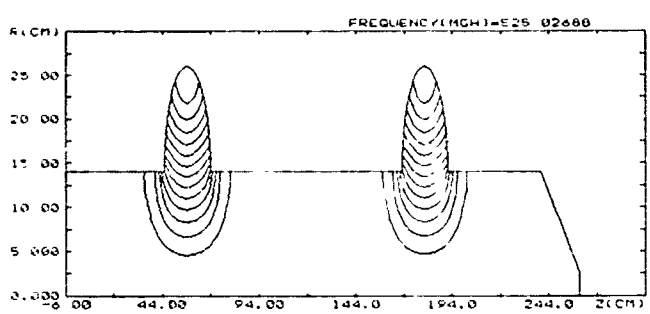


Fig 2.a

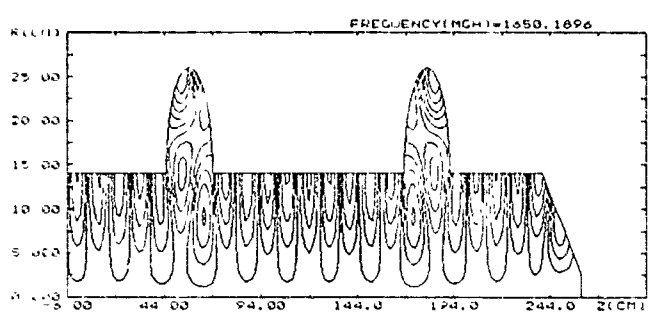


Fig 2.b

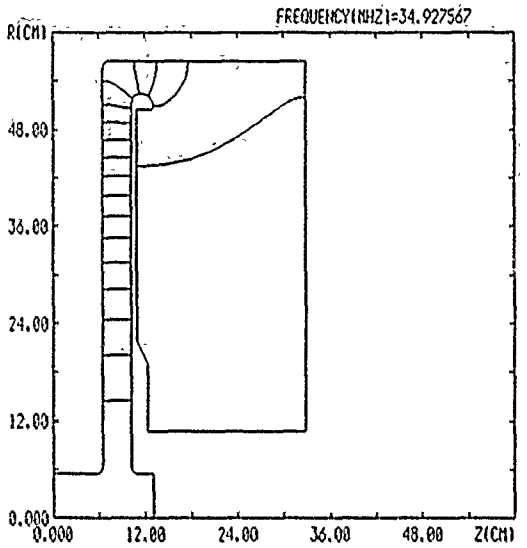


Fig. 3,a

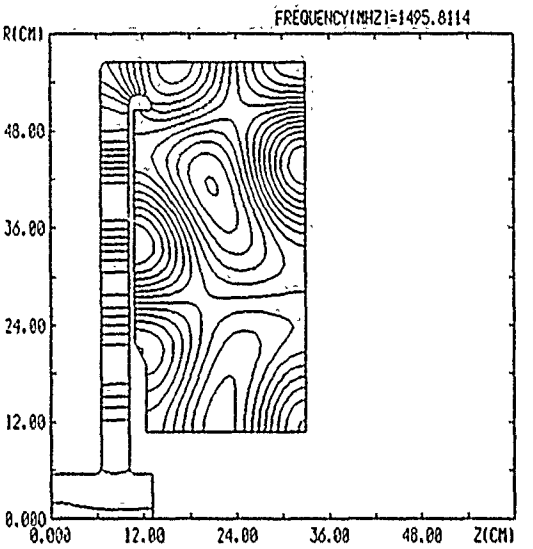


Fig. 3,b

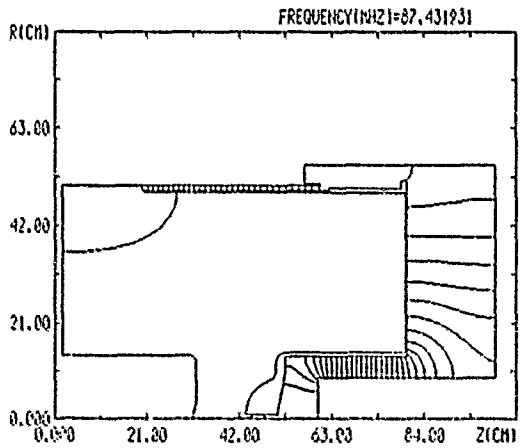


Fig. 4,a

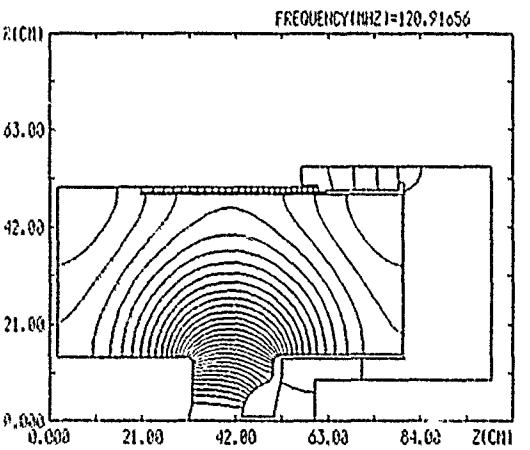


Fig. 4,b

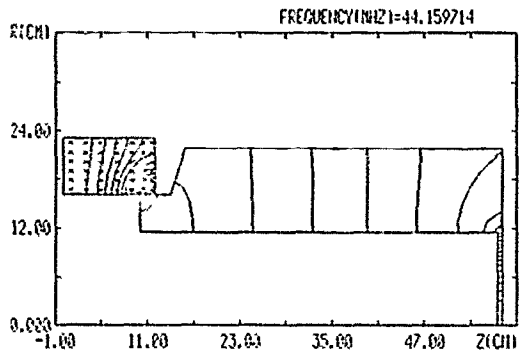


Fig. 5.

REFERENCES

[1] B.M. Fomel, V.P. Yakovlev, M.M. Karliner, P.B. Lysyansky, LANS—A New Code for Evaluation of the Electromagnetic Fields and Resonance Frequencies of Axisymmetrical RF Cavities, Particle Accelerators, N 3, 1981, vol.11, pp.173—179.

[2] M.S. Kaschiev et al. Proceedings of the 9th All-Union Conference on Charged Particle Accelerators, Dubna, USSR, 16 Oct., 1984, INIS-SU-352, CONF-8410203, Vol.1, pp.137—141.

[3] A.G. Daikovsky et al. «PRUD-W: A New Code to Compute and Design Accelerating Structures», Particle Accelerators N 1, 1986, vol.20, pp.23—43.

[4] Bell M., Dome G. CERN 73-1, Geneva, 1973.

[5] Site—Specific Conceptual Design, SSCL-SR-1056, July 1990.

[6] M.M. Karliner et al. Proc. of the EPAC, Rome, June 7—11, 1988, vol.1, pp.602—604.

[7] V.A. Lebedev et al. Proc. of the 12th All-Union Conference on Charged Particle Accelerators, Dubna, USSR, 3-5 Oct.,1990, to be published.

[8] V.V. Anashin et al. Proc. of the EPAC, Rome, June 7—11, 1988, vol.1, p.57.

[9] V.L. Auslender et al. To be Published.

The $3\pi/4$ Backward TW Structure for the ELETTRA 1.5 GeV Electron Injector

P. Girault
General Electric CGR MeV
551, rue de la Minière, BP 34, 78530 Buc, FRANCE

Summary

The $3\pi/4$ backward traveling wave (BTW) structures used for the ELETTRA 1.5 GeV Electron Injector [1] have been designed and are now under realization. These accelerating units will be fed by a TH 2132 45 MW-4.5 μs klystron coupled to a Thomson CIDR (Compresseur d'impulsion à Double Résonateur) similar to the CERN design of the SLED. The expected energy gain is equal to 33 MeV/m. This paper justifies the use of the $3\pi/4$ accelerating mode. After a description of the structure design, the choice of RF parameters leading to optimization with RF pulse compressor, evaluations of energy gain and peak field on copper based on simulations and cold tests measurements are presented. RF cold test measurements of the first unit are analysed.

Introduction

Electron linac development as injectors for light sources and the availability of several RF pulse compressor systems (SLED, LIPS etc...) renewed the interest for traveling wave accelerating structures optimized for the pulse compression mode of operation. To improve acceleration efficiency of classical forward TW units usually composed by $2\pi/3$ E-coupled cells, proposals have been made to accelerate electrons with a larger shunt impedance H-coupled backward TW structure at the $4\pi/5$ mode [2] or at the $7\pi/8$ [3] mode. Energy gain measurements of the 1.27 m $4\pi/5$ BTW section installed at LAL [4,5], associated to previous cold tests measurements on reference cells and simulations, have validated the improvement in energy expected in reference [2], i.e +23% within a 5% margin error. The high power levels reached with RF pulse compressor have also permitted to expect a good peak field behaviour of a longer unit. Finally, this new kind of BTW accelerating structure has been chosen for the ELETTRA Electron Injector [1]. In this paper, justification and characteristics of the $3\pi/4$ BTW structure are presented.

Choice of $3\pi/4$ mode

For a given cell geometry synchronous at 3 Ghz and several modes between $2\pi/3$ and π, we study variations of effective shunt impedance Z_{eff} according to the length of accelerating gap. Obviously, cell length changes for each mode to respect synchronism between wave and particule. Figure 1 shows the geometries for $3\pi/4$ and $4\pi/5$ modes. There is a value of the accelerating length gap which maximises Z_{eff} for each mode. The following table gives these maximum figures of Z_{eff} calculated with SUPERFISH for a half-cell geometry (boundary conditions corresponding to π mode).

Table 1: Optimum Z_{eff} values

mode	$2\pi/3$	$3\pi/4$	$4\pi/5$	$5\pi/6$	π
Z_{eff} Mohms/m	91.7	94.5	94.6	94.2	86.2

Optimum mode for H-coupled cells lies between $3\pi/4$ and $4\pi/5$ without the effect of magnetical coupling. Higher modes will have larger coupling slots for a same c/v_g value, and so, a larger decrease of Q factor or Z_{eff} since the ratio Z_{eff}/Q remains constant [6]. The $3\pi/4$ mode has been chosen for this reason and also because it is very simple to adjust in frequency.

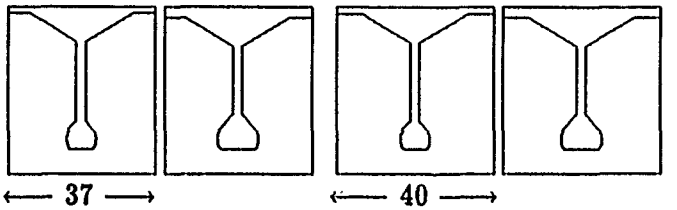


Figure 1: Variations of accelerating gap length for $3\pi/4$ and $4\pi/5$ cells

Characteristics of $3\pi/4$ BTW structure

General design

Figure 2 shows the structure which consists of 162

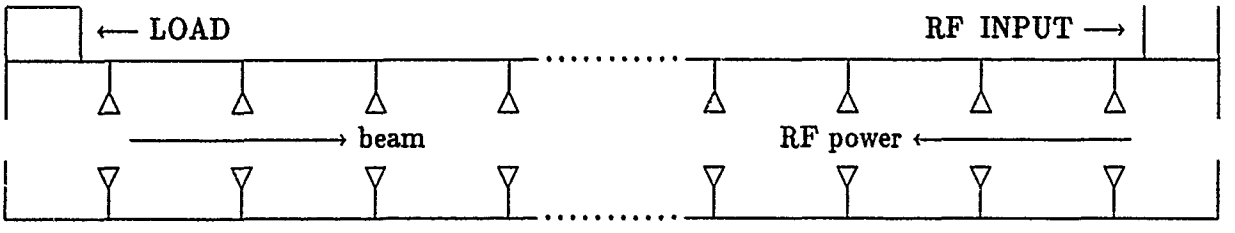


Figure 2: $3\pi/4$ BTW unit

0-7803-0135-8/91$01.00 ©IEEE

cells plus input and ouput coupler cells. These coupler cells are magnetically coupled to the RF rectangular waveguides. Operating frequency is 2998 Mhz. The total length is 6.15 m. The input coupler corresponds to beam exit to insure proper synchronism between electrons and traveling wave.

Choice of filling time structure

For ELETTRA linac, beam pulses from 10 ns to 150 ns will be accelerated at 1500 MeV. The use of RF pulse compressor gives large no-load energy variations around optimum time injection, leading to poor energy spectrum. But by advancing the phase-reversal time on one or two klystrons and by using transient beam-loading properties, energy spectrum remains inferior to $\pm$ 0.5% for jitters lower than $\pm$ 10 ns [7] (beam energies at the beginning and end of the pulse are equal). Figure 3 shows energy variations versus unit filling time for several beam pulse lengths, klystron power of 45 MW, klystron pulse length of 4.5 μs, transmission losses of 7% and CIDR cavities Q factor of 150000. Optimum for no-load energy corresponds to 0.65 μs. These variations shows that the filling time value finally adopted and equal to 0.76 μs is better for longer beam pulses.

For a compressed pulse duration of 0.76 μs, i.e a phase reversal-time occuring at 3.74 μs, the compressed power pulse amplitude varies from 259 MW (at 3.74 μs) to 88 MW (at 4.5 μs), as shown on figure 4.

The peak field

After a formation process duration of about 200 hours, high power tests of the $4\pi/5$ BTW test structure reached a peak field value on copper of 146 MV/m in good operating conditions [5]. It is important to note that it was achieved for a similar mode of operation as the $3\pi/4$ BTW unit, i.e a similar phase-reversal time (3.7 μs) and a same klystron pulse length (4.5 μs). Then, $3\pi/4$ cell geometry near axis has been chosen to limit peak field value on copper to 140 MV/m.

Cell design

Figure 5 shows the two kinds of cell composing the structure: 54 cells of type I and 108 cells of type II. Main RF parameters of each cell type is given in table 2. $\widehat{E}_s$ and $\overline{E}_a$ are respectively the peak field on copper and the average field on-axis. The ratio $\widehat{R}_{eff,tw}$ between $\widehat{E}_s$ and the effective accelerator field on-axis is related to $\widehat{R}_{tw}$ by $\widehat{R}_{eff,tw} = \widehat{R}_{tw}/T_{tw}$.

Cells of type I are placed at input coupler side to limit peak field on copper to 140 MV/m when peak power (259 MW) enters into the structure. They are replaced by cells of type II when section attenuation

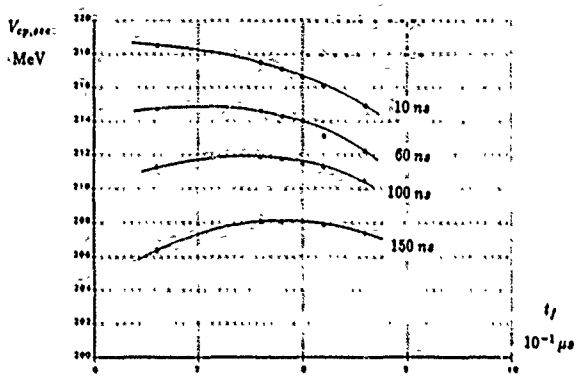


Figure 3: Variations of energy gain per section with filling time

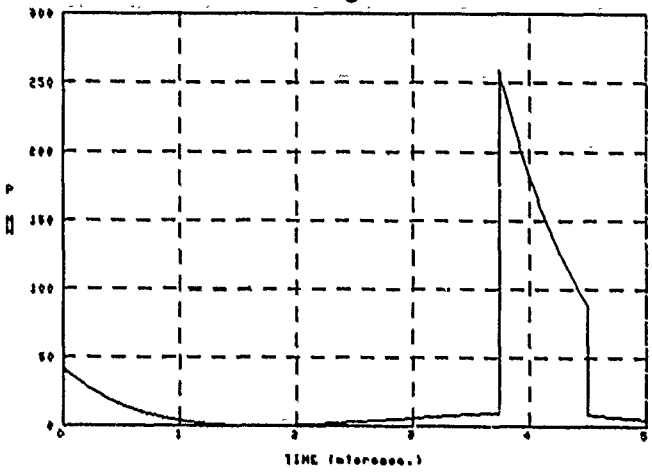


Figure 4: Power pulse amplitude after compression

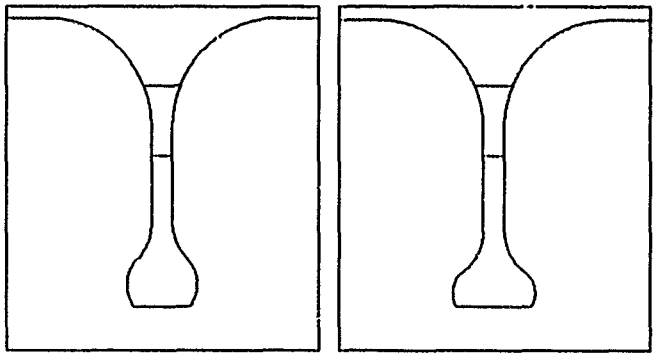


Figure 5: $3\pi/4$ H-coupled cells design

Table 2: Characteristics of $3\pi/4$ TW cells

	type I	type II
Beam clearance	10 mm	10 mm
Q	12500	12500
$Z_{eff,tw}/Q$	6195	6485
Transit time factor T_{tw}	0.856	0.860
$\widehat{R}_{tw} = \widehat{E}_s/\overline{E}_a$	1.96	2.30
c/v_g	37.1	37.1

compensates the increase of $Z_{eff,tw}/Q$ and $\widehat{R}_{tw}$ so that peak field on copper is again limited to 140 MV/m. The change of cell type increases energy gain of 2%.

Coupling slots dimension has been defined by cold measurements on test cells. Without cell cleaning, experimental Q value measured in SW has been found equal to 11500 [8]. After cleaning and brazing, one expects a final Q value higher than 11500.

Evaluations of energy gain and peak field

The following table summarises expected energy gains per section and peak fields for short and long beam pulses.

Table 3: Energy gains per section and peak field

Beam pulse ns	Energy gain per section MeV	peak field MV/m	peak field at beam time MV/m
10	217	140	88
150	207	140	91

These results give an energy gain margin of 3.5% to 8.5% with respect to the required value equal to 200 MeV. The critical point for peak field corresponds obviously to peak power injection time and not to beam injection time. It is interesting to note that for Q value equal to 11500 cited before as a preliminary pessimistic result, it decreases energy gains given in table 3 only by 2.5%.

RF cold tests measurements of the first unit

Figure 6 shows measurement of the electrical field on-axis E_z in cell mid-planes. The amplitude increase around $z = 200$ cm corresponds to the substitution of cells of type I by cells of type II. The phase-shift deviation from cell to cell with respect to the theoretical value equal to 135^o is shown on figure 7. The maximum phase-shift deviation is lower than 2^o. Before cleaning and brazing, the measured filling time has been found equal to 0.76 μs.

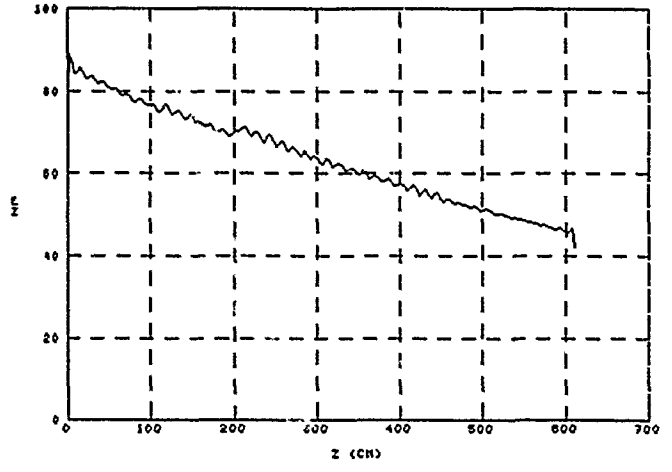


Figure 6: Electrical field on-axis in cell mid-planes

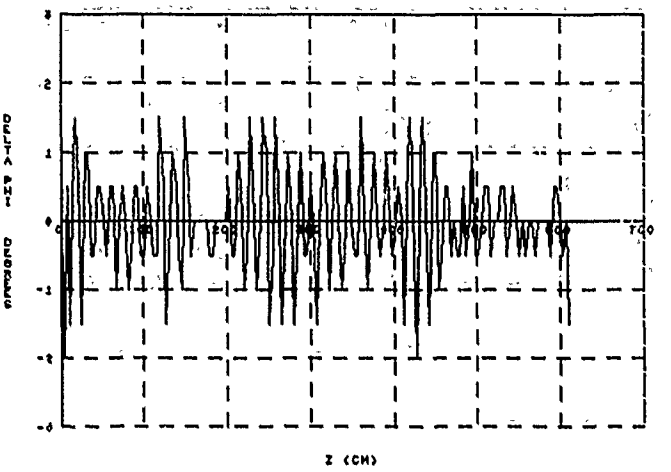


Figure 7: Phase-shift deviation from cell to cell $/^t$ 135^o

Conclusion

Preliminary RF cold tests measurements of the first $3\pi/4$ BTW structure have permitted to ascertain the tuning method validity and the filling time value with respect to optimization with RF pulse compressor. After cleaning and brazing, attenuation measurements will precise experimental Q value found in SW with no-cleaned test cells. Next power tests with RF pulse compressor will also permit to confirm the good expected peak field behaviour of the $3\pi/4$ unit.

References

[1] D. Tronc and al., The ELETTRA 1.5 GeV electron injector, this conference: XTP28.

[2] D. Tronc, Electron linac optimization for short RF and beam pulse lengths, in IEEE Trans. Nucl. Sci., NS-32, pp 3243–3245, 1985.

[3] R.H. Miller, Comparison of standing-wave and traveling-wave structures, in Proceed. of Linear Accel. Conf., SLAC, 1986, pp 200-205.

[4] P. Girault and al., $4\pi/5$ backward TW structure tested for electron linacs optimization, in Proceed. of European Part. Accel. Conf., Rome, Italy, 1988, pp 1114–1116.

[5] P. Girault and al., Power tests results of $4\pi/5$ Backward TW structure without and with SLED RF pulse compressor, in Proceed. of European Part. Accel. Conf., Nice, France, 1990, pp 37–39.

[6] P. Girault, Etude d'une nouvelle structure accélératrice à ondes progressives inverses, Université de PARIS-SUD, Orsay, France, Thesis, 1990.

[7] P. Girault, Conséquence de la fluctuation des paramètres liés au CIDR et au faisceau, General Electric CGR-MeV report, DT 18.807, April 1990.

[8] P. Girault, Mesures des cavités d'essai Trieste II, General Electric CGR-MeV report, DT 19.594, March 1991.

A NEW ELECTRON LINAC INJECTOR DESIGN UP TO 200 MeV

D.Tronc
General Electric CGR MeV
BP 34, 78 530 Buc, France

Summary

A single mechanical structure can include the on-axis components necessary for best electron bunching and acceleration up to 200 MeV in S-band. Two accelerating sections are put in serie to be seen from the RF source as one load. The sections see a backward traveling wave (BTW) at the $3\pi/4$ mode. The electrical end of the first section includes the buncher. A slight frequency change induces beam radial control keeping at the same time the energy spectrum narrow. The input/output parts near the mechanical center insure good conductance, easy focusing and dilatation. Energy figures are given at 3 GHz and at 11.4 GHz without or with mechanical integration.

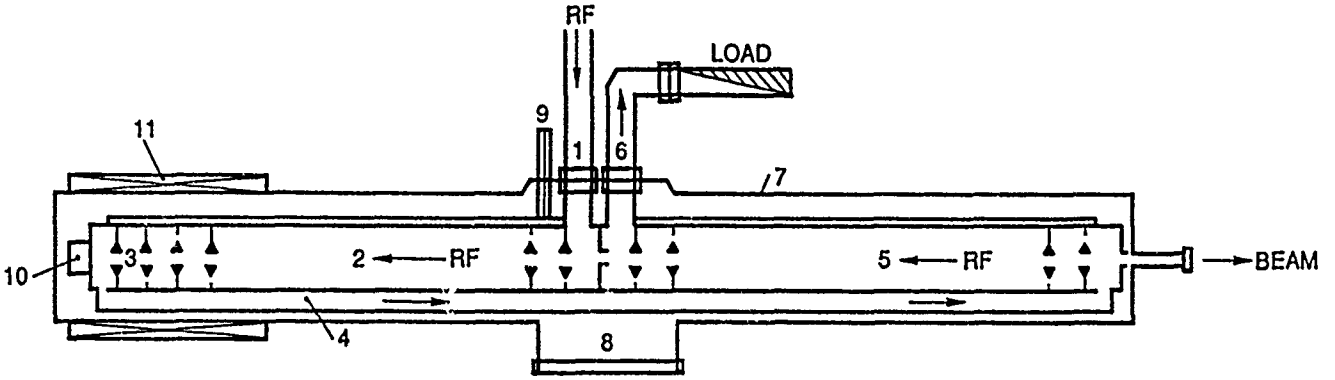
Introduction

The development of light sources asks for electron injectors from about 50 MeV to more than one GeV. Already the ELETTRA 1.5 GeV linac design takes advantage of the high shunt impedance of the backward traveling wave (BTW) to reduce the acceleration length to 30m per GeV for an expected peak RF power at 3 GHz of 225 MW at the klystron exit, before compression from 4.5μs to 0.8μs by a SLED-like system [1].

This paper presents a new design which extends the BTW use to preinjection. Feeding two BTW sections in serie, one achieves mechanical simplification, bunching integration and a simple control of the beam to RF dephasing to improve the beam radial control at low energy spread. The number of independent RF elements (sources, brazed sections, couplers) is decreased.

Backward Traveling Wave properties

The BTW had never been used until recently to accelerate [3]. It combines the advantages of traveling wave and standing wave. The forward TW electrically coupled on-axis (the classical "iris waveguide") is remarkable for its good adaptation and short filling time. The SW magnetically coupled off-axis is remarkable for its high shunt impedance. The BTW peculiarities are: (i) with reference to forward TW, the presence of noses (which insures a good shunt impedance) and the opposite directions of the beam and of the RF wave (required to accelerate), (ii) with reference to SW, the absence of the complicated coupling cells . One note that the RF input being near the beam exit and the buncher (if any) being near the RF exit, its field level depends on the line attenuation and for long pulses on the beam loading.



TWO BACKWARD TW SECTIONS IN ONE ACCELERATING STRUCTURE

Figure 1: New design for a linac on-line structure up to 200 MeV

0-7803-0135-8/91$01.00 ©IEEE

Description of the new design [2]

To bunch properly one cuts the accelerator unit in two sections and inverts them with reference to the beam. Then the bunching occurs at mid-attenuation and mid-filling time so that line attenuation, beam loading, SLED-type RF pulse length are no more critical.

Figure 1 presents the unit when the (not required) mechanical integration of the two electrical sections is achieved. The RF power enters by the coupler (1) inside a BTW periodic structure or section (2) which integrates a bunching part (3), then flows along a rectangular waveguide (4) to the next section (5) and finally leaves the section by the coupler (6) to an RF load. The electron beam created by the gun (10), crosses the buncher made of shorter cells (3), then crosses the two sections (2) and (5) before leaving the unit. Other elements includes vacuum flange (8), cooling pipes (9), eventually solenoidal focusing (11).

Electrical properties

Even without mechanical integration, the phase control capability and the recombination option are achieved:

(1) The phase is controlled in a very effective way by an RF slight frequency change. Figure 2 shows the "phase law" along the acceleration axis (in fact it is the dephasing between beam and field at the cell mid-planes, modulo $2k\pi$). It lie on-axis when there is no asynchronism. The continuous or dotted lines are obtained by a frequency change df. With N being the number of wavelengths at the group velocity vg (constant), the cumulative phase (linear) increase or decrease is:

$$d\phi/2\pi = (c/vg)\ N\ df/f$$

This means that one can switch the accelerated bucket from one side to the other of the accelerating wave sinusoid to control at the same time the radial dynamics and the energy spread as analyzed in ref. [4]. Note that strong correction occurs right at the beginning of the second section.

(2) The recombination option uses a 3db coupler to feed one downstream independantly brazed section by two upstream ones. Then identical c/vg sections can be used at similar accelerating field levels.

Mechanical properties

(1) When mechanical integration is achieved as in fig.1, the input/output components for RF, vacuum, cooling are all nearby and near the middle of the structure. This eases the gun or the solenoidal focusing set-up and gives a better pumping and cooling.

(2) The waveguide linking the two sections do not need a phasor as precise check of RF phase on the axis of the two most far away cells is part of the standard RF cold tests. No phasor is used all along the high peak power flow from klystron to load.

(3) For lengthy structures, RF and vacuum seals are separated and the waveguide is easily put inside the vacuum envelope, along the periodic structure.

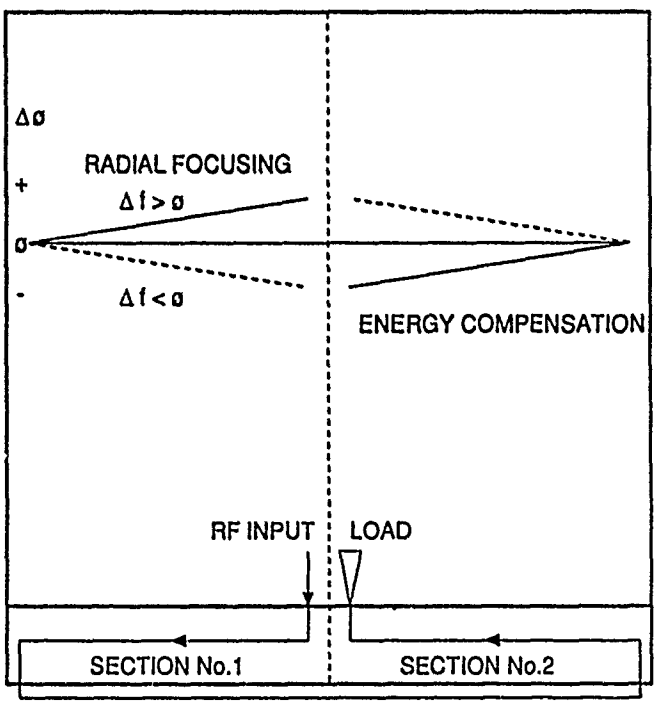


Figure 2: Dephasing control between beam and field. $\Delta\Phi$ (RF/bunch) insures best dynamics for Δf slightly positive.

Integration in linac designs

One can either use the electrical properties only, connecting in serie independant sections, or add to it the mechanical integration illustrated on fig.1. The frequency choice is not limited to S-band.

(1) The first S-band example uses two standard 6m BTW units of the ELETTRA type, put in serie, without mechanical integration [5]. The first unit will includes a buncher simply made by decreasing several $3\pi/4$ end-cell lengths. One RF source of 45 MW - 4.5 μs at the klystron, compressed by the CIDR system, feed 12.3 m at c/vg = 18.5 for 0.76 μs filling time. With the BTW geometry, such low c/vg value can be obtained without too much shunt impedance loss [3]. 280 MeV are obtained at low current. The RF circuit does not include couplers other than SLED ones nor phasor. The peak field level is moderate.

(2) Mechanical integration is of interest when shorter total length and lower energy spread for large accelerated charge are required. The peak field level characteristic of ELETTRA is reached by integration of two 3 m sections in a 6.15 m enveloppe as in fig.1, giving 200 MeV at low current.

(3) A compact injector for FEL, in the long pulse steady state mode, can use the same unit. The sections have now variable c/vg. Fed by a 30 MW - 10 μs RF source (without pulse compression), it delivers 100 MeV at low current, 70 MeV at high peak current.

(4) In X-band, at 11.4 GHz, with same lengths of 2 x 3 m and a 100 MW - 1 μs klystron pulse compressed to 400 MW - 0.2 μs [6], one obtain 470 MeV energy gain at c/vg = 10 and the type IV scaled down geometry of [7] (note that feeding with the same RF source two units of 2 x 1.5 m each, at higher c/vg, gives 514 MeV. This slight energy gain does not compensate for the complexity).

The beam clearance is then 3 mm dia. (but can be increased up to 4 mm dia. with moderate energy loss). The great number N of cells used supposes low dispersion or c/vg value. The sensitivity to frequency misadjustments depends on the N c/vg product. It remains reasonable and comparable to the S-band ELETTRA design.

Conclusion

The design presented in this paper uses backward traveling wave geometry to bunch and accelerate electrons (or positrons). This is made in the best conditions (i) as the backward propagation relieves from the very high peak field constraint at the RF input when cells are reduced in length for bunching and (ii) as the cell geometry allows precise field shaping near the particle trajectories. This is very precious to optimize the radial behaviour.

References

[1] D.Tronc and al., "The ELETTRA 1.5 GeV Electron Injector", this conference: XTP 28.

[2] French Patent 89 16566, 1989.

[3] P.Girault and al.,"$4\pi/5$ BTW structure tested for electron linacs optimization", EPAC, 1988, 1114.

[4] D.Tronc and al.,"Electron injector designs for light sources", EPAC, 1988, 487.

[5] P.Girault, "The $3\pi/4$ backward TW structure for the ELETTRA 1.5 GeV electron injector", this conference: XRA 22.

[6] R.D.Ruth, "The next Linear Collider", SLAC-PUB-5406.

[7] P.Girault, "Etude d'une nouvelle structure accélératrice à onde progressives inverses", Thèse, Orsay Univ., 1990, 123.

Quadrupole Effects in On-Axis Coupled Linacs

F.P. Adams, R.J. Burton and J. Ungrin
AECL Research
Chalk River Laboratories
Chalk River, Ontario, Canada, K0J 1J0

Abstract

Elliptical beam shapes have been seen at the exit of a number of on-axis coupled electron linacs. These non-circular shapes have been attributed to the quadrupole effects produced by the coupling slots in the cell walls. Qualitative and detailed cavity calculations predict that the quadrupole effects cancel if the coupling slots are aligned across the accelerating cavities, as opposed to rotated through 90° as has normally been the case. Two short S-band linacs, identical except for the orientation of the coupling slots, have been built to test the predictions. The results of detailed measurements of the beam profiles at the exit of the two linacs are discussed.

I. INTRODUCTION

The coupling slots of on-axis slot-coupled $\pi/2$-mode electron linear accelerator structures appear to introduce weak quadrupole fields [1,2], which perturb the accelerated beam. These fields are small relative to the accelerating field, and are therefore difficult to detect in the accelerating structure.

The rf forces affecting the beam may be expanded as

$$\vec{F}(x,y,z) = F_a(z)\hat{k} + f_r(z)\times(x\hat{i}+y\hat{j}) + f_q(z)\times(x\hat{i}-y\hat{j}) \quad (1)$$

where $F_a(z)$ is the accelerating force, $f_r(z)$ is a radially symmetric focusing force parameter and $f_q(z)$ is a parameter for a force of quadrupole symmetry. The symbols $\hat{i}$, $\hat{j}$ and $\hat{k}$ represent x, y, and z unit vectors, respectively.

For electrons moving at the speed of light, on or off axis and at any rf phase, the radially symmetric focusing forces cancel over each accelerating cavity [3]. Define on-phase and off-phase quadrupole focusing strengths

$$\Gamma' = \frac{\left\langle r_0 f_q(z)\cos\left(\frac{\pi z}{L}\right)\right\rangle_{cell}}{r_0 \times \left\langle F_a(z)\cos\left(\frac{\pi z}{L}\right)\right\rangle_{cell}} \quad (2)$$

and

$$\Gamma'' = \frac{\left\langle r_0 f_q(z)\sin\left(\frac{\pi z}{L}\right)\right\rangle_{cell}}{r_0 \times \left\langle F_a(z)\cos\left(\frac{\pi z}{L}\right)\right\rangle_{cell}}, \quad (3)$$

respectively, where r_0 is the radius at which the quadrupole force is calculated. If $\Gamma' \neq 0$, electrons at the peak accelerating phase will be focused in one plane, and de-focused in the perpendicular plane. Assuming electron trajectories in the direction of the effective accelerating force, the beam will converge in the focusing plane after a distance equal to $1/\Gamma'$.

For a particle off peak accelerating phase, the net quadrupole focusing strength is

$$\Gamma(\phi) = \Gamma' + \Gamma''\times\tan(\phi) \quad (4)$$

where ϕ is the rf phase as the electron crosses the centre of the accelerating cavity. Unless $\Gamma'' = 0$, a beam that is not well-bunched at the peak accelerating phase will be distorted by the rf phase-dependence of Γ. The beam profile will be a superposition of ellipses of varying eccentricity. The emittance of the beam will be conserved in six-dimensional phase-space, but the transverse emittance will increase.

II. NUMERICAL MODELING

The three-dimensional rf code MAFIA [4] has been used to analyze typical linac accelerating structures. The code calculates the rf fields, allowing one to determine the electric and magnetic quadrupole perturbing fields.

The initial modeling work was done at 1300 MHz. In the simplest case of a single accelerating cavity without coupling slots, no rf fields of quadrupole symmetry are predicted by the code.

The calculation was then expanded to a 2-cell linac structure (Figure 1), with coupling cavities on either side of the accelerating cavity. The coupling cavities were on-axis TM_{010} resonators, coupled by two slots in each of the cavity walls. Coupling slots were rotated 90° across both the accelerating cavity and the coupling cavities.

Significant transverse fields of quadrupole symmetry were predicted in both the accelerating cavity and in the two coupling cavities. Changes in mesh size used in the code had a negligible effect on the magnitude of these quadrupole fields.

Quadrupole forces ($\Gamma' = 5.3\times10^{-4}$ mm^{-1}) were predicted for trajectories on peak accelerating phase ($\phi = 0°$). No quadrupole forces ($\Gamma'' = 0$) were predicted for $\phi = \pm 90°$. In a multi-cell linac the transverse impulses will accumulate in successive cells and off-axis deflections of the electrons will result. Beam dynamics calculations predict that the beam profile will become elliptical, with the major axis on a line

0-7803-0135-8/91$01.00 ©IEEE

joining the slots in the output end walls of the accelerating cavities.

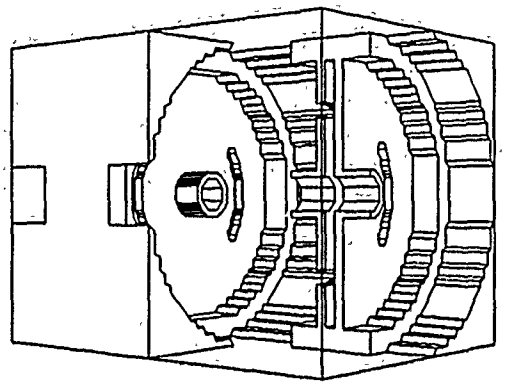


Figure 1. *Rotated slots* MAFIA model of two cells of a typical on-axis slot-coupled linac structure terminated in half-cavities. Note that coupling slots are rotated across each cavity.

An alternate accelerating structure configuration has the coupling slots in each wall of the accelerating cavities aligned. The slots are rotated across the coupling cavities to reduce second-nearest-neighbour coupling (Figure 2). A 2-cell MAFIA model of this type was developed for evaluation.

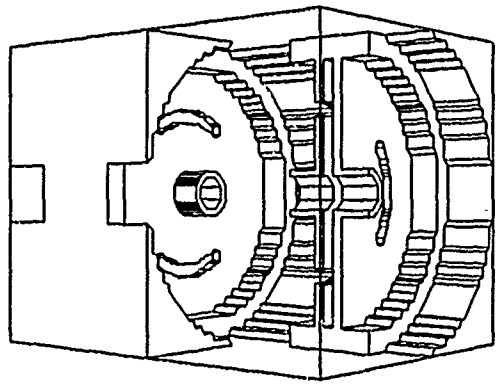


Figure 2. *Aligned slots* MAFIA model of a modified linac structure. Beam quality is improved with the coupling slots on opposite sides of the accelerating cavities aligned.

The coupling cavities contain strong quadrupole magnetic fields in this configuration, but the 90° rotation between cells results in a net cancellation. If the quadrupole components of the calculated fields for two adjacent cells are integrated, the resultant values for Γ' and Γ'' are zero. Electrons should, therefore, not be deflected, regardless of rf phase.

The MAFIA model was then reduced to a single cavity with slots in only the output end wall, to represent the first accelerating cavity of a linac. The asymmetry of the first cavity might be expected to generate large quadrupole fields. The code predicted $\Gamma' = 2.6\times10^{-4}$ mm^{-1} and $\Gamma'' = 2.0\times10^{-4}$ mm^{-1}. This value for Γ' is lower than for the regular accelerating cavities.

Several 3000 MHz linacs have been built and tested at Chalk River Laboratories and the modeling calculations with MAFIA were repeated at this frequency to predict the effects of the slots on beam shape. Numerical integration of the quadrupole perturbing forces yielded $\Gamma' = 5.0\times10^{-4}$ mm^{-1} for a rotated-slot structure.

III. EXPERIMENTS

A. Coupling-Cavity Fields

Two 1300 MHz linac segments were assembled between metal plates to form a three-cavity structure with a coupling cavity in the middle and half-cell terminations. The structure was excited in the $\pi/2$ mode and perturbation techniques were used to detect rf fields in the coupling cavity (Figure 3).

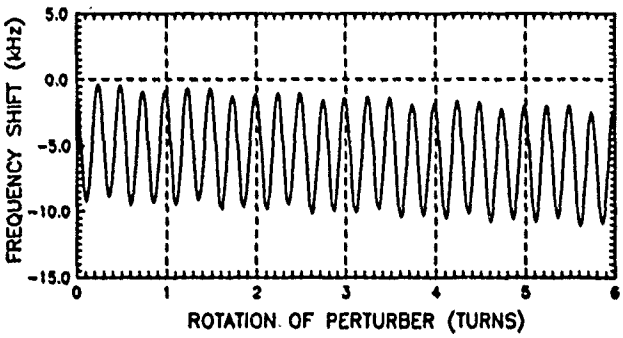


Figure 3. Frequency perturbation due to rotating a transverse dielectric rod about the axis of an on-axis coupling cavity. Four dips per revolution indicates fields with quadrupole symmetry.

The cavity was perturbed using two alumina rods 15 mm long, radially oriented and attached 180° apart to a PTFE shaft, which rotated on the axis of the coupling cavity. The outer ends of the alumina rods were 26 mm from the cavity axis. A single alumina rod in the accelerating cavity caused a frequency shift of -3.8 MHz. The -9 kHz shift in Figure 3 thus indicates a quadrupole electric field 3.4% as strong as the accelerating field.

B. Rotated-Slot Structure

A nine-cell 3000 MHz on-axis slot-coupled electron linac with rotated slots was installed and operated in a facility at Chalk River [5]:

The linac installation incorporated a triode, 24 kV, dispenser-cathode electron gun, controlled with a Wehnelt electrode biased to -3 kV. The gun pulse length was 20 - 30 μs, and the gun output was generally 350-450 mA with no on-bias applied to the Wehnelt. The gun was directly mounted on the accelerator structure without a buncher. Beam was therefore injected at all phases of the rf cycle. No focusing elements were used between the electron gun and the linac.

The 0.5 m long structure was excited by a high-power klystron and 6 μs beam pulses in the 4-6 MeV range were obtained. Beam exited the linac through a 125 μm thick titanium vacuum-air foil, which was located either 0.3 m or 2.3 m from the end of the linac. Radiation-sensitive plastic films were placed against the window to capture an image of the beam profile. Clear images were obtained using bursts of 50 to 100 beam pulses.

Typically, the rotated-slot structure accelerated 13% of the unbunched beam through the structure. The beam profile at the end of the 0.3 m drift space showed a sharp line roughly 9 mm long, parallel to a line joining the coupling slots in the output end wall of the accelerating cavity. The darkest area was at the line's midpoint. This line was crossed at its midpoint by a fainter line roughly half as long, making the central beam profile distinctly cruciform. The image was surrounded by a fainter elliptical halo, which was roughly 10 mm by 14 mm, and which was aligned with the longer arms of the central cross.

Images of the beam profile made using the 2.3 m drift pipe showed the same cruciform shape expanded to 18 mm by 29 mm. This expansion of the beam profile indicated a divergence of ±5 mrad for the ends of the longer arms.

The dependence of the quadrupole fields on rf phase can be used to explain the accelerated beam profile. Given finite Γ'', electrons far off phase will form perpendicular ellipses. Superimposing these ellipses would produce a cruciform beam profile. Numerical modeling yielded $\Gamma'' = 0$ for the rotated-slot structure, so that Γ is not phase-dependent. Equations (2) and (3) assume electrons travelling at the speed of light, so that equation (4) will not be exact in the low-energy end of the structure and Γ may be phase-dependent.

Blind slots were cut in the entrance end wall of the first accelerating cavity of the rotated-slot linac. These were aligned with the slots in the exit wall to minimize the quadrupole fields in the first cell. At the end of the 2.3 m drift space, the beam profile was unchanged.

C. Aligned-Slot Structure

A second structure with aligned slots was then assembled to test the code predictions. Except for slot orientation, this structure was identical to the first. The two interchangeable rf structures were operated with the same gun, rf supply and drift spaces for a direct comparison. The transmission through this second structure was typically 16% and was clearly and consistently greater than that of the structure with rotated slots.

The profile of the output beam was smaller and more symmetrical than that obtained with the other structure. At the end of the 0.3 m drift space, the darkest part of the image was a 1.5 mm square at the centre. This feature was surrounded by a distinct, circular halo 14 mm across.

At the end of the 2.3 m drift space the beam profile showed a central feature roughly 5 mm across. Its shape was similar to the beam from the rotated-slot structure, but smaller. Expansion of the beam profile indicated a maximum divergence of ±1 mrad for the central feature of the beam. The beam produced by the aligned-slot structure was clearly smaller, less divergent and more symmetrical than the beam produced by the rotated-slot structure. The lower beam transmission of the rotated-slot structure might result from the larger beam scraping the structure bore.

IV. CONCLUSIONS

Computer simulations indicate that on-axis slot-coupled electron linac structures should have the coupling slots in opposite accelerating cavity walls aligned. This shifts the quadrupole perturbing fields into an orientation that minimizes the perturbation of particles on or near synchronous phase. Experimental comparison of an aligned-slot linac and a rotated-slot linac confirmed the benefit of aligning the slots. The beam produced by the linac with aligned slots had a smaller size, greater symmetry and less divergence.

V. REFERENCES

[1] H. Euteneuer, private communication, 1988.

[2] M.M. Kerleyer et al., "The Influence of Electromagnetic Multipoles Produced by Resonator Coupling Slots on the Motion of Particles in a Linac," ERF SO AN, Novosibirsk, USSR, 1988. Russian-German translation by Mrs. and Mr. Kreidel, German-English translation by J. Ungrin.

[3] A.D. Vlasov, *Theory of Linear Accelerators*, Atomizdat, Moskva, translated by Z. Lerman: published for the U.S. Atomic Energy Commission and the National Science Foundation, Washington, D.C. by the Israel Program for Scientific Translations, 1968, pp. 72-74.

[4] R. Klatt et al., "MAFIA - A Three-Dimensional Electromagnetic CAD System for Magnets, RF Structures, and Transient Wake-Field Calculations," in *Proceedings of the 1986 Linear Accelerator Conference*, Stanford Linear Accelerator Center report SLAC-303 (1986 June), pp. 276-278.

[5] J. Ungrin, E.R. Gaudette and D.L. Smyth, "PHELA - A Versatile Electron-Beam Irradiation Facility," in *Accelerator Physics Branch Chalk River Laboratories Annual Technical Report*, AECL Report, AECL-10235, pp. 16-17, 1990 August.

Cavity Shape and Beam Dynamics Design for a Linac for Pions*

G. Swain
Los Alamos National Laboratory
P. O. Box 1663, MS H847
Los Alamos, NM 87545

Abstract

A linac to accelerate pions from 400 to 920 MeV kinetic energy is being designed as an upgrade to the LAMPF accelerator facility at Los Alamos. Calculations for the design of the superconducting cavity shape attempt to reduce the peak surface field needed to achieve a given accelerating gradient, yet ensure sufficient cell-to-cell coupling to maintain field stability when microphonics or other tuning errors are present. The beam dynamics design has the goal of getting the highest possible flux of pions in a narrow momentum range at the end of the linac. In order to do this, the design takes into account the survival fraction from pion decay, and optimizes the acceptance of the combination of the transport line from the pion production target to the entrance of the linac and the linac itself.

I. Introduction

A proposed linear accelerator for pions ("Pilac") would extend the capabilities of the Los Alamos Meson Physics Facility (LAMPF). Pilac is to accelerate pions from a new target on the 800 MeV proton beam line A. The pions are to be accelerated from around 380 MeV to kinetic energies up to 1120 MeV, corresponding to a momentum of 1250 Mev/c. This project has the goal of providing a flux of 10^9 pions per second at 920 MeV (1050 Mev/c momentum). The linac is to use superconducting rf cavities in order to provide large apertures and transverse acceptance, and produce high accelerating gradients without a large cost in rf power. We have chosen 805 MHz as the operating frequency in order to get the acceptance we need with cavities of practical size.

II. Cavity Shape

Our initial studies of cavity shapes for 805 MHz considered cavities which had circular arcs for the cavity profile, both at the cavity waist and at the noses where the cells join. We did a series of calculations with various cell apertures and various nose radii. The line segments between waist and nose arcs were at 10 deg from the vertical for all cases. The ratios of peak surface field Emax to accelerating gradient E0T for these shapes are summarized in Figure 1.

Subsequently, we have looked at cavities with elliptical noses. Five cases with beam apertures of 13 cm diameter are

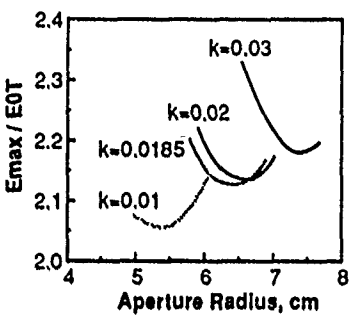


Figure 1. Peak surface field per unit accelerating gradient for cavities with circular noses for several values of cell-to-cell coupling parameter k.

listed in Table I. All of these used ellipses with 2:1 ratio of major to minor axes.

Table I
Coupling and Peak Surface Electric and Magnetic Field vs Elliptical Nose Major Axis Length

Nose MA (cm)	Coupling (%)	Emax/E0T	Hmax/E0T (A/V)
23.	1.604	1.831	4673.9
18.	2.037	1.862	4157.7
16.	2.247	1.920	3988.4
13.	2.619	2.030	3772.2
11.	2.916	2.164	3652.1

For the cavities with circular noses, the minimum Emax/E0T for 6.5 cm radius aperture was about 2.13, and for this, the nose radius was 3.5 cm and the coupling k was 1.85%. With an elliptical nose, we have less mechanical stress, and for a major axis of 13 cm, Emax/E0T is better at 2.03, and the coupling stronger at 2.6%. This is the configuration that we have chosen for Pilac. See Figure 2.

III. Linac Design

In order to evaluate alternative linac designs, we have used a figure of merit which is the product of two factors: (a) beam acceptance and (b) survival fraction. The survival fraction is the fraction of pions entering the linac that have not been lost to decay by the time they reach the linac exit. We are using the term acceptance in a specialized sense. Normally, one takes it to mean the area in energy-phase space at the start of the linac such that the particles are accelerated, such as the larger dotted area in Figure 3. For our purpose, we take acceptance to mean the area in energy-phase space for which

*Work supported by Laboratory Directed Research and Development funds from Los Alamos National Laboratory, under the auspices of the U.S. Department of Energy.

0-7803-0135-8/91$03.00 ©IEEE

the pions are within 1.5% full width momentum spread (dp/p) around the desired energy at the exit of the linac, a much smaller area. Moreover, we use the energy-phase space at the pion production target, not at the linac entrance.

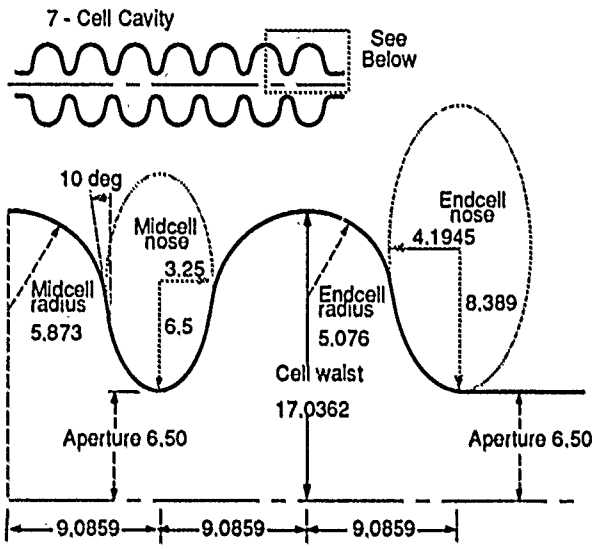


Figure 2. Pilac cavity geometry. All dimensions are in cm.

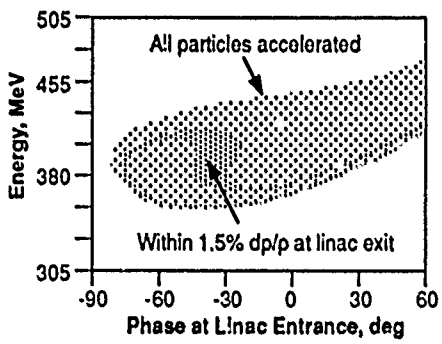


Figure 3. Acceptance areas.

We wish to capture a beam pulse at the pion production target that is 80 ps long. The beam bunch at the production target is skewed by the injection line in energy-phase space, and then rotated by the linac. In order to maximize the acceptance, we choose the rf phases of the cavities such that the beam bunch comes out narrow in energy width at the linac exit. We assume that the effect of the beam line from the pion production target to the entrance to the linac on the longitudinal phase space is approximately equivalent to a drift. The equivalent drift length for 380 MeV is 11 m.

A. Transverse Acceptance Considerations

We used 7-cell 805-MHz cavities and quadrupole doublets (30 cm effective length quads spaced 36 cm apart) in our reference design. For transverse beam acceptances of 225 π mm-mrad, and allowing space for valves, bellows, etc., this led to the configuration shown in Figure 4.

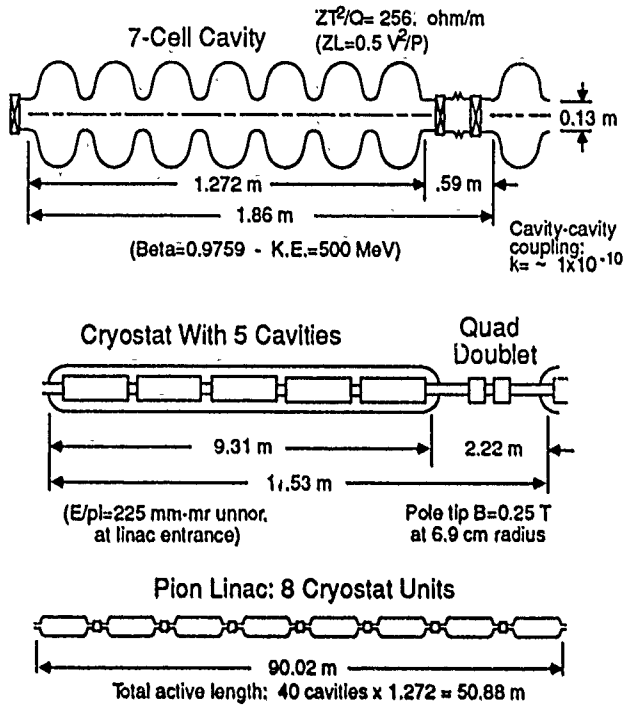


Figure 4. Reference linac configuration.

B. Longitudinal Acceptance Optimization

We chose the rf phases of the cavities in the linac such as to optimize the beam acceptance. We used the computer program LINO3 to do this. LINO3 divides a 40-cavity linac into eight sections, and adjusts the phases of the sections, and not each individual cavity phase. The optimization is done in two stages, as shown in Figure 5.

The rf phases found by the optimizer for the reference linac are given in Table II.

Table II
Design RF Phases

Section No.	Range of Cavs.	Design Phase for Section (deg)
1	1, 3	-68.06
2	4, 6	-2.049
3	7, 9	-18.23
4	10, 12	-24.85
5	13, 18	-52.55
6	19, 24	-4.904
7	25, 30	-8.891
8	31, 40	-9.913

C. Reference Case Performance

The acceptance achieved is 82 ns wide (24 deg) by 6 % FW dp/p. Figure 6 shows the result of tracing a 80 ns by 6% dp/p beam through the linac. The concave distortion introduced in the first part of the linac is largely taken out later when the bunch is rotated with the other side up [1].

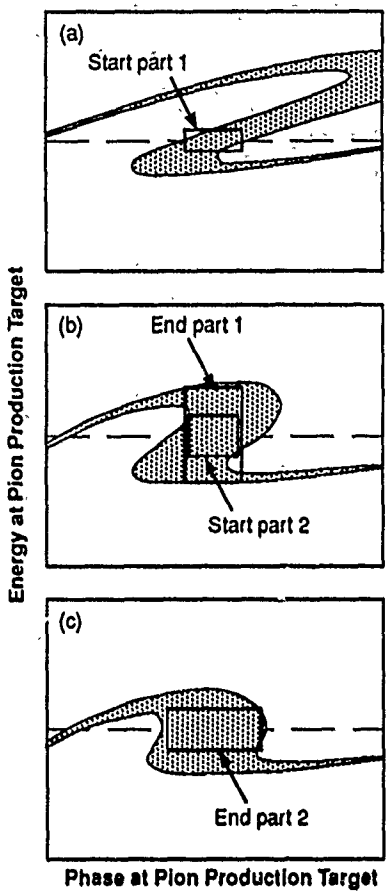


Figure 5. Part 1 of the acceptance optimization begins with uniform rf phases and expands a rectangular acceptance area in energy, (a) to (b). Part 2 expands the area in phase, (b) to (c). Each plot above is 72 deg wide by 100 MeV tall, with the 380 MeV design starting energy at the dotted line.

The variation of the transverse beam size (100% of the emittance areas) through the linac is shown in Figure 7, and stays below the 6.5 cm aperture radius.

IV. Other Cases

We have found that for acceleration from 380 to 606 MeV, we obtain 46% of the beam flux obtained at 920 MeV, and that for 380 to 821 MeV, we obtain 76%. Further studies for other exit energies are in progress.

V. Conclusions

A cavity shape with a peak surface to accelerating field ratio of 2.03 and a cell-to-cell coupling of 2.65% has been selected. An acceptance optimization procedure has led to a reference design for a 380 to 920 MeV linac. The linac uses 40 seven-cell 805-MHz cavities, and will accept a beam with 225 π mm-mrad unnormalized emittance in both transverse planes. The longitudinal acceptance has a 80 ps time width

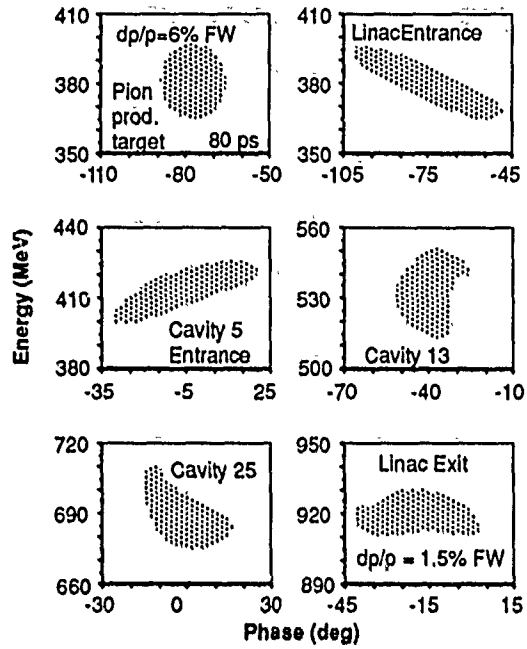


Fig. 6. Longitudinal evolution of the beam bunch.

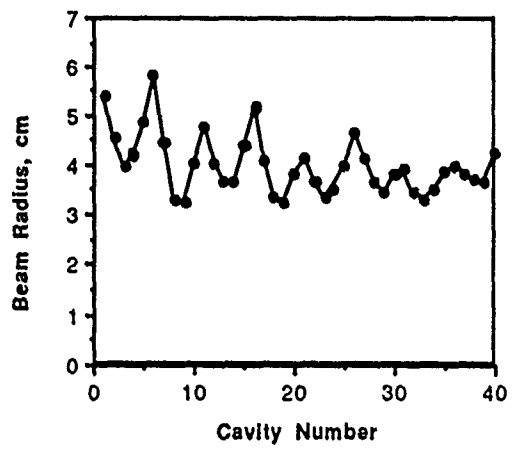


Figure 7. Maximum transverse beam size.

and 6% full width dp/p. To realize this acceptance, the injection beam line should be capable of transporting a beam with 6.6% full width dp/p.

A quadrupole doublet is used after every 5th cavity. Of the pions entering the linac, 11.6% survive at the exit for a peak accelerating gradient E0T = 12.46 MV/m.

VI. References

[1] S. Nath, G. Swain, R. Garnett, and T. P. Wangler, "Beam Dynamics Design of a Pion Linac," Proceedings of the 1990 Linear Accelerator Conference (Los Alamos Nat. Lab. report LA-12004-C), Albuquerque, NM , September 10-14, 1990, pp. 338-340.

CHARACTERIZATION OF A RAMPED GRADIENT DTL: EXPERIMENT AND THEORY*

K. F. Johnson, E. A. Wadlinger, O. R. Sander, G. P. Boicourt, G. O. Bolme, C. M. Fortgang, J. D. Gilpatrick, J. Merson, D. P. Sandoval, and V. Yuan
Los Alamos National Laboratory, Los Alamos, NM 87545

Abstract

An experimental demonstration confirming the beam-dynamics of a Ramped-Gradient Drift-Tube Linac (RGDTL) was performed at Los Alamos National Laboratory. The RGDTL was designed to optimize on the requirements of maximum beam acceleration, minimum longitudinal and transverse emittance growth, and acceptable wall power loss. At low beam energies, transverse-magnet focusing is weak and the rf defocusing must be minimized. As the beam energy increases, stronger rf defocusing can be tolerated and the rf electric field gradient can increase. A detailed comparison of theory and experiment was carried out. Beam longitudinal centroids (output energy and phase) and transverse and longitudinal emittances were measured as a function of RGDTL rf field amplitude and phase. The longitudinal centroids were also studied as functions of input beam current, energy, and degree of bunching. Comparison between experimental data and theory was in good agreement.

I. INTRODUCTION

Proton or H^- drift-tube linacs (DTLs) can achieve accelerating gradients of 4 to 5 MV/m, whereas radio-frequency quadrupoles (RFQs) achieve gradients of typically 2 MV/m. It is desirable to provide a transition region between the RFQ and the high gradient DTL, which can be accomplished by the accelerator having a field ramp that smoothly connects the two field gradients. The Los Alamos RGDTL was designed to provide this transition region [1]. It automatically matches the beam from a low-velocity, low-field gradient device (RFQ) to a high-velocity, high-gradient device (DTL). In the design procedure the requirements of maximum beam acceleration, minimum longitudinal and transverse emittance growth, and acceptable wall power loss were optimized.

The RGDTL is a 425-MHz, 1.87-m-long structure containing 29 drift tubes, 14 post couplers, 2 tuners, and 2 drive loops. It has an axial, electric-field gradient that increases from 2.0 MV/m (RFQ gradient) to 4.4 MV/m over 1.5 m for accelerating H^- from 2.07 MeV (RFQ output energy) to 6.67 MeV. The structure's mechanical design, low-power tuning, and field stabilization measurements are reported in References 2 through 5.

*Work supported and funded by the US Department of Defense, Army Strategic Defense Command, under the auspices of the US Department of Energy.

0-7803-0135-8/91$01.00 ©IEEE

An experimental demonstration validating the beam-dynamics of the RGDTL has been completed on the Accelerator Test Stand (ATS) [6]. The demonstration showed that a RGDTL with the desired stable-field distributions can be built and operated. Characterization of the RGDTL output beam confirmed that simulation codes accurately model the beam-dynamics of moderately bright beams in the RGDTL.

II. EXPERIMENTAL TECHNIQUE

The H^- input beam to the RGDTL was obtained from the ATS, 425-MHz, 2.07-MeV RFQ. The ATS was operated at a low duty factor (0.025%).

The experimental objective was to fully characterize the output beam of the RGDTL to allow for a detailed comparison to the simulation codes. To achieve this end, the output beam current, beam transmission, transverse centroids (position and angle in both planes), longitudinal centroids (beam energy and phase), and transverse and longitudinal phase-space distributions were measured for a variety of RGDTL operating conditions.

Available diagnostics for these measurements included three toroids and a Faraday cup (beam current and transmission), three capacitive probes [7] (longitudinal centroids), two pairs of slit-collectors (transverse centroids and phase-space distributions), LINDA [8] (longitudinal phase-space distribution), and an x-ray detector [9] (RGDTL rf field).

III. EXPERIMENTAL RESULTS

At low power, the RGDTL accelerating mode was tuned to 425 MHz with the desired ramped field distribution, and the field was stabilized against tuning errors. The tuning procedure is given in References 4 and 5, where the parameters to be adjusted, the goals of the adjustments, the tuning mechanisms used, and the various measurement techniques are described in detail.

The RGDTL was operated with dual rf drive loops with a master-slave configuration for amplitude control and independent phase control. The dual drive-loop coupling was determined at low power [10]. With beam, the operation of the dual rf drive system was established and shown to be stable and reliable.

The RGDTL rf electric field E_0 on axis can be determined from the energy spectrum of the x-rays generated within the cavity [9]. The x-ray energy spectra were measured versus cavity rf power. These data suggested that 470 ± 12 kW cavity power was necessary to achieve the design axial field, which is very close to the power level (460 ± 10 kW) predicted by SUPERFISH.

The RGDTL rf amplitude and phase set-points were determined using the phase-scan technique [11]. This technique utilized the capacitive probes [7] to measure the energy and phase centroids of the beam as a function of the RGDTL rf amplitude and relative rf phase. A comparison of the data to single-particle simulations provides the signature for determining the operating set-points of the RGDTL. In this procedure, it was assumed that beam centroids are unaffected by space-charge and that the centroid behavior can be predicted by single-particle simulations. Both assumptions are reasonable if the particles in the bunch experience forces that depend on the magnitude of their displacement from the synchronous particle. Figure 1 compares experiment and simulation. The data indicate that a cavity power of 448 kW gives a gap voltage near the design value (~3% high). This result is in good agreement with the x-ray data and SUPERFISH calculations.

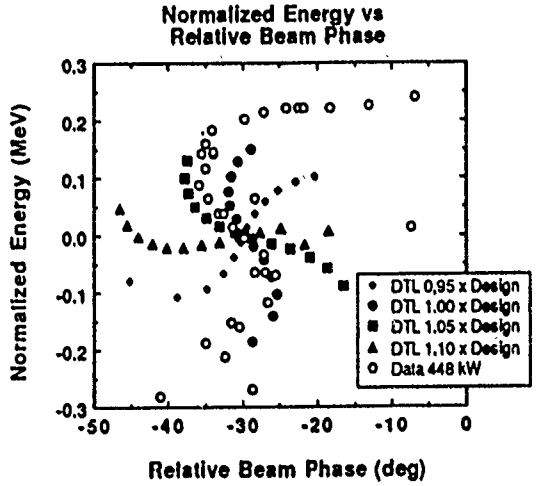


Figure 1. A comparison between RGDTL data at 448 kW and simulations at 0.95, 1.00, 1.05, and 1.10 times the design gap voltage. Relative output beam phase is used to facilitate a comparison of curve shapes. The simulations indicate that a cavity power of 448 kW gives fields that are near design specifications.

Additional phase-scans were taken where the input energy to the RGDTL was varied above and below the design input energy. This variation was accomplished by operating the ATS buncher cavity (located between the RFQ and RGDTL) in its accelerating or deaccelerating modes. The experimental results were again in good agreement with simulations.

Phase-scans were made at both low-beam currents (~20 mA) and high-beam currents (78 to 80 mA). The rf amplitude and phase set-points, as determined from the phase-scans, were independent of beam current. This result supports our assumption that beam centroids were unaffected by space charge.

Operating the RGDTL at its rf amplitude and phase set-points gave >97% beam transmission at both high- and low-beam currents which was as predicted from simulations. For quiet beams, a relative uncertainty of ~2% on beam transmission measurements was possible.

The longitudinal phase-space distributions of the RGDTL output beam were measured using LINDA [8]. These measurements were made as functions of RGDTL rf cavity power (five different levels), rf phase (three settings), and longitudinal match of the input beam. These measurements tested the RGDTL beam dynamics with different space-charge forces, external longitudinal focusing forces, and input phase-space distributions.

To study longitudinal matching to the RGDTL, data were taken with the ATS rf buncher either off or operating in its bunching, debunching, accelerating, and deaccelerating modes. The measured longitudinal Courant-Snyder (CS) parameters of the RGDTL output beam were compared to simulations using the mismatch factor (MMF) where MMF = 0 corresponds to achieving the design CS parameters. With the rf buncher off (standard ATS operation), the data and simulations are in good agreement (MMF = 0.08). For all rf-buncher modes, MMF was less than 0.2, showing that the output beam CS parameters were insensitive to the longitudinal match. In general a practical criteria of MMF < 0.3 is considered to indicate "agreement" with simulations.

The longitudinal emittance of the RGDTL output beam was measured at different RGDTL rf power levels and phases. A comparison of the rms longitudinal emittance at the optimum RGDTL power and phase set-points ($0.10 \pm 0.02\ \pi$ MeV-deg) to a previous measurement of the RFQ rms longitudinal emittance ($0.08 \pm 0.02\ \pi$ MeV-deg) indicates no longitudinal emittance growth in the RGDTL. The error on the emittance measurement is ~20% and reflects the scatter in the data. Within the limited range of RGDTL rf power and phases explored, the rms longitudinal emittance was insensitive (within experimental error) to both rf power and phase, as expected.

The RGDTL output beam transverse phase-space distributions (horizontal and vertical) were measured using a standard slit and collector technique [12]. These measurements were made as functions of RGDTL rf cavity power (five power levels), rf phase (three settings), and longitudinal match of the input beam.

Using the MMF, the measured transverse CS parameters of the RGDTL output beam were compared to simulations. At the optimum RGDTL rf power and phase set-points, there was good agreement between data and simulations. The MMF was 0.30 and 0.08 for the horizontal and vertical planes, respectively. Unlike in the longitudinal plane, large MMF (~1) were obtained in both transverse planes for non-optimum RGDTL operating conditions. As expected the output transverse CS parameters were independent of the longitudinal match of the input beam. In the ATS RGDTL experimental configuration, it was not possible to vary the transverse match of the RGDTL input beam.

The rms-normalized transverse emittances of the RGDTL output beam were measured at different RGDTL rf power levels and phases. A comparison of the rms transverse emittances at the optimum RGDTL power and phase set-

points (0.025 ± 0.002 π cm-mrad horizontal plane and $>0.022 \pm 0.002$ π cm-mrad vertical plane) to previous measurements of the RFQ rms transverse emittance ($\sim 0.026 \pm 0.002$ in both planes) indicates no transverse emittance growth in the RGDTL. The measured RGDTL vertical emittance is a lower limit because of some small beam scraping inside the capacitive probe at the RGDTL exit. The error on the emittance measurements is ~8% with background subtraction being the dominant component. Within the limited range of RGDTL rf power and phases explored, the transverse emittances were shown to be insensitive (within experimental error) to both rf power and phase, as expected.

The position and angle centroids of the RGDTL output beam were determined from the measured transverse phase-space distributions. The centroids indicated that some small mis-steering of the beam was occurring in the RGDTL. Later off-line checks of the RGDTL suggested two possible causes: (1) a misaligned quadrupole in the downstream end wall and (2) an internal braze failure that resulted in a water pressure bulge in the end wall. The bulge may have twisted or distorted the half drift-tube which supported the end wall quadrupole.

IV. SUMMARY AND CONCLUSIONS

During the commissioning process, the RGDTL performed as expected. The experimentally determined cavity power (two independent techniques) was in good agreement with the theoretical value. Beam transmission was greater than 97% with a maximum output current of 80 mA. Within experimental errors, transverse and longitudinal phase-space measurements do not indicate any emittance growth through the RGDTL. The measured output beam CS parameters are in good agreement with simulations. These results confirm the beam-dynamics predictions and thus validate the design codes and indicate that no major physics has been omitted.

The successful testing of the RGDTL has shown that compact DTLs utilizing ramped fields can be designed, built, and operated. They could be key elements in the high-brightness accelerators that are being considered in many advanced accelerator applications.

V. REFERENCES

[1] G. P. Boicourt and M. C. Vasquez, "Two New Possible Designs for the Ramped ATS-DTL," Los Alamos National Laboratory memo AT-6:85-180, November 27, 1985.

[2] D. J. Liska and L. B. Dauelsberg, "A Drift-Tube Linac Incorporating a Ramped Accelerating Field," in "Proc. 1987 IEEE Particle Accelerator Conf.," Washington, D.C., 1987, p. 1797.

[3] D. J. Liska et al., "A High-Intensity Drift-Tube Linac with Ramped Accelerating Gradient," in "Proc. 1988 Linear Accelerator Conf.," CEBAF-Report-89-001, June 1989, p. 652.

[4] J. H. Billen and A. L. Shapiro, "Post-Coupler Stabilization and Tuning of a Ramped-Gradient Drift-Tube Linac," in "Proc. 1988 Linear Accelerator Conf.," CEBAF-Report-89-001, June 1989 p. 128.

[5] J. H. Billen, "Analysis of Measured Poet-Coupler Fields in a Ramped-Gradient Drift-Tube Linac," in "Proc. 1988 Linear Accelerator Conf.," CEBAF-Report-89-001, June 1989, p. 131.

[6] O. R. Sander, et al., "Review of the Accelerator Test Stand Performance and Expectations," Los Alamos National Laboratory report LA-CP-89-489 (July 1989).

[7] J. D. Gilpatrick et al., "Synchronous Phase and Energy Measurement System for a 6. 7 MeV H- Beam," in "Proc. 1988 Linear Accelerator Conf.," CEBAF-Report-89-001, June 1989, p. 134.

[8] W. B. Cottingame et al., "Noninterceptive Technique for the Measurement of Longitudinal Parameter of Intense H^- Beams," in "Proc. 1985 Particle Accelerator Conference", IEEE Trans. Nucl. Sci., Vol. 32(5), p. 1871, 1985.

[9] G. O. Bolme et al., "Measurement of RF Accelerator Cavity Field Levels at High Power from the Characteristic X-ray Emissions," in "Proc. 1990 Linear Accelerator Conf.," Los Alamos National Laboratory report LA-12004-C, March 1991, p. 219.

[10] C. M. Fortgang and G. O. Bolme, "Dual Loop Drive on the RGDTL," Los Alamos National Laboratory memo AT-2:88-255, June 29, 1988.

[11] C. M. Fortgang et al., "Longitudinal Beam Dynamics of a 5-MeV DTL: A Comparison of Theory and Experiment," in "Proc. 1988 Linear Accelerator Conf.," CEBAF-Report-89-001, June 1989, p. 167.

[12] O. R. Sander, "Transverse Emittance: Its Definition, Applications, and Measurement," Proc. Accelerator Instrumentation, edited by E. R. Beadle and V. J. Castillo, (AIP Conf. Proc. No. 212, 1989), p. 127.

High Order Calculation of the Multipole Content of Three Dimensional Electrostatic Geometries*

Martin Berz†, William M. Fawley and Kyoung Hahn
Lawrence Berkeley Laboratory
University of California
Berkeley, CA 94720, USA

Abstract

We present an accurate and simple method of 3-D multipole decomposition of the field of arbitrary electrode geometries. The induced charge on the surface is obtained by inverting the capacity matrix. The multipole moment decomposition of the resulting potential is readily accomplished using Differential Algebra methodology. The method is applied to the focussing lattice geometry of the MBE-4 accelerator at LBL. Multipole terms of up to the order 5 are computed, and a numerical accuracy of $< 1\%$ is obtained. The effective quadrupole and dodecapole field strength are in good agreement with previous results.

1. INTRODUCTION

In many cases, the exact computation of higher order multipoles in electrostatic geometries is important. For example, in a real quadrupole-focussing geometry, multipole harmonics in addition to the wanted quadrupole one are always present to some degree. The strength of the multipole harmonics depends on the specific geometry of the electrodes, with some harmonics being eliminated or minimized by proper choice of electrode dimensions. The MBE-4, Multiple Beam Experiment at LBL, lattice has many additional multipole components besides the wanted quadrupole component. Although weak, the presence of these components, in conjunction with non-negligible transverse beam displacements, will lead to emittance growth during beam transport[1][2]. To rectify this limitation, we computed the z-dependent strength of the multipole moments using a Differential Algebra (DA) methodology to decompose the three-dimensional focussing potential. The latter is first determined by solving the capacity matrix of the actual electrode and aperture plate geometry. The choice of DA methodology was motivated by its ability to work to arbitrarily high order, with numerical accuracy limited only by that of the capacity matrix. This is in contrast to the more common method of determining the potential on a 3-dimensional mesh, where both the multipole order and numerical accuracy are limited by the mesh resolution. Our calculations show good agreement with previous determinations of the effective quadrupole lengths and dodecapole strengths and we believe that this method may prove useful wherever multipole decomposition of complicated static fields is needed.

2. POTENTIAL PROBLEM SOLUTION BY THE CAPACITY MATRIX METHOD

When a complicated boundary shape is present, a conventional field solver using FFT or SOR techniques becomes computationally expensive because of the large number of mesh points required, especially in 3-D calculations. This difficulty can be alleviated noticeably by calculating the induced charge at the boundary surface directly rather than specifying the field boundary condition. Once the boundary charge distribution is known, the field at the location of a particle can be calculated straightforwardly. Since the number of required mesh nodes is confined to where the actual charges are, *i.e.* at the boundary, substantial reduction in total mesh points is obtained.

In the capacity matrix method, the electrodes are covered with test points $\mathbf{x}_i$ (hereafter called "nodes"). Charge Q_i located at the $\mathbf{x}_i$ are determined such that the potential induced on $\mathbf{x}_i$ by all the other nodes assumes the desired value. This reduces to solving the linear system

$$\phi_j = \sum_i G(\mathbf{x}_i, \mathbf{x}_j) Q_i \qquad (1)$$

where $G(\mathbf{x}_i, \mathbf{x}_j)$ is the Green's function describing the effect of the potential of a charge at $\mathbf{x}_i$ to the point $\mathbf{x}_j$. The inverse to $G(\mathbf{x}_i, \mathbf{x}_j)$ is often called the capacity matrix $(C_{i,j})$. Once the charge Q_i are known, the potential at any point in space can be computed as

$$\phi(\mathbf{x}) = \sum_i G(\mathbf{x}_i, \mathbf{x}) Q_i. \qquad (2)$$

For non-overlapping test charges, one may use the simple Green's function of

$$G(\mathbf{x}_i, \mathbf{x}_j) = \frac{1}{|\mathbf{x}_i - \mathbf{x}_j|} \quad \text{for} \quad i \neq j. \qquad (3)$$

When computing the self-potential ($i = j$) or when the test charge width σ_i exceeds an internode spacing, the test

*Work supported by the Director, Office of Energy Research, Office of Basic Energy Sciences, Advanced Energy Projects Division, U.S Dept of Energy, under Contract No. DE-AC03-76SF00098.

†Presently at Michigan State University

0-7803-0135-8/91$01.00 ©IEEE

charge profile must be carefully considered. For the 3-D calculations discussed in Sec. 4, a triangular charge distribution was used with

$$\rho(\mathbf{x}) = \begin{cases} \frac{3}{\pi\sigma_i^3}\left(1-\frac{r_i}{\sigma_i}\right) & \text{if } r_i \le \sigma_i \\ 0 & \text{otherwise} \end{cases} \quad (4)$$

where $r_i \equiv |\mathbf{x}-\mathbf{x}_i|$. With this profile, the potential within σ_i of the test charge is given by

$$\phi(\mathbf{x}) = \frac{Q_i}{\sigma_i}\left[2 - 2\left(\frac{r_i}{\sigma_i}\right)^2 + \left(\frac{r_i}{\sigma_i}\right)^3\right] \quad (5)$$

and

$$C_{ii}^{-1} = \frac{2}{\sigma_i} \quad (6)$$

Although the particular choice of the charge profile is somewhat arbitrary, however, numerical calculations show that the determination of the mutipole harmonics is not highly sensitive to the exact charge profile. The distribution width σ_i is typically set to the internode spacing, depending on the charge distribution used. This choice prevents the self-potential from unphysically dominating the problem. Although we are representing the physically thin surface image charge by non-zero thickness spherical charges, the electric field on and near the beam transport axis should be little affected so long as the internode spacing and charge distribution width σ_i are small compared with the clear aperture between electrodes and the electrode-aperture plate separations in z.

3. MULTIPOLE EXPANSION AND DIFFERENTIAL ALGEBRA

Once the boundary surface charge has been determined (*e.g.* by the capacity matrix method of Sec. 2), the electric potential at arbitrary point in space can be computed by the summation over the charges (see equation (2)). The resulting approximate potential is infinitely differentiable, and thus its Taylor series can be computed. At interior positions where the potential varies smoothly, an approximate functional expansion can prove extremely useful in terms of computational economics. Furthermore, the expansion is quite intuitive because certain nonlinearities of the transfer map couple only with certain multipole terms. For a system such as MBE-4 where the quadrupole moment is by far the dominant component, an expansion around an aperture axis followed by a systematic multipole decomposition of the field is more convenient than the usual power series expansion.

The multipole coefficients $M_{k,l}(z)$ of the potential ϕ are defined in cylindrical coordinates system by

$$\phi(r,\theta,z) = \sum_{k=0}^{\infty}\sum_{l=0}^{\infty} M_{k,l}(z)\, r^k \cos(l\theta) \quad (7)$$

where a Fourier series expansion in θ and power series in r are used. Notice that the up-down symmetry, *i.e.* symmetric under $(y \to -y)$ transformation, of the MBE-4 geometry is implicitly assumed. No z-axis expansion is performed and $M_{k,l}(z)$ is calculated at numerous locations in z.

The source-free[1] vacuum potential ϕ satisfies the Laplace equation ($\nabla^2\phi = 0$) and thus the $M_{k,l}$ observe the following recursion relation:

$$M_{k,l} = M''_{k-2,l}/(l^2 - k^2), \quad (8)$$

where double prime denotes the second derivative with respect to z. In order that neither ϕ nor $\nabla^2\phi$ be singular at $r = 0$ and that ϕ be bounded at $z = \pm\infty$, the relation $k \ge l \ge 0$ and $k - l = even$ must be true for non-zero coefficients. The entire ensemble of multipole coefficients can then be determined from $M_{k,k}$ and its z–derivatives.

An explicit form for $M_{k,k}$ may be obtained by expressing ϕ as a Taylor series, *i.e.*

$$\phi(x,y,z) = \sum_m\sum_n \frac{x^m y^n}{m!\,n!}\left(\frac{\partial}{\partial x}\right)^m\left(\frac{\partial}{\partial y}\right)^n \phi(0,0,z) \quad (9)$$

After equating this expression with that of eqn. (7) and integrating with $\cos(k\theta)$, one finds for $k \ge 1$

$$M_{k,k}(z) = \sum_{n=0,\ even}^{k} \frac{(-1)^{(n/2)}}{2^{k-1}n!(k-n)!}\left(\frac{\partial}{\partial x}\right)^{(k-n)}\left(\frac{\partial}{\partial y}\right)^n \phi \quad (10)$$

where the up-and-down symmetry has again been used and ϕ is given by the summation over the induced boundary charges,

$$\phi(\mathbf{x}) = \sum_{i=1}^{N} \frac{Q_i}{r_i} \quad (11)$$

Here $r_i \equiv |\mathbf{x}-\mathbf{x}_i|$ and Q_i is the charge at the position of the i^{th} node. Away from the nodes this function is infinitely differentiable, and it is in principle possible (although very tedious for high orders) to compute the required derivatives $M_{k,k}^{(2i)}$ by differentiating expression (10).

To circumvent this difficulty, we use differential algebraic techniques for the computation of the higher order derivatives to machine precision without numerical errors. These techniques, which also play a key role in the high order description of optical systems, have been discussed in detail elsewhere[3][4], and the interested reader is referred to the above mentioned papers.

4. COMPUTATIONAL RESULTS

A FORTRAN code was written to evaluate the $G(\mathbf{x}_i, \mathbf{x}_j)$ of any electrode geometry, and then invert them to obtain the capacity matrix C_{ij} and the node charges Q_i.

In the case of the actual MBE-4 focussing lattice, there are a number of separate elements in the electrode: a)

[1] When beam space charge is present, it is convenient to decompose the total field as a sum of vacuum potential from the boundary charges and the free space potential of the beam charge. Hence, the relevant potential in equation (1) is the *difference* between the specified boundary potential and that due to the beam space charge in the absence of boundaries.

Quadrupole electrodes which are held at either ground or a negative voltage, b) Flat aperture plates from which the electrodes are cantilevered and through whose holes the four ion beams travel, c) A large "can" enclosure surrounding the entire focussing lattice.

The nodes were distributed uniformly over the surface of the electrode rods and with an $\sim 1/r$ dependence on the endplates. The charge distribution width σ_i was set to a constant (≈ 2.5 mm for total node number $N = 5000$), somewhat smaller than the typical internode distance in order to minimize the size effect.

Since our main interest was calculation of three-dimensional multipole components of general potential geometries, the potential at the electrostatic quadrupole electrodes was set to $\pm V_q$ rather than grounding one of the electrode pairs as in the actual case for MBE-4. We have also neglected the "can" enclosure.

In order to evaluate expression (10) numerically, higher order differential algebras were used for the computation of the derivatives of the potential ϕ. From there, the $M_{k,l}$ were computed from 0^{th} to 6^{th} order computed using expression (8).

The coefficients were made dimensionless by scaling the potential by a factor of V_q and using a normalization length of the aperture radius a, *i.e.*.

$$\phi = V_q \sum_{k=0}^{6} \sum_{l=0}^{6} M_{k,l}(z) \left(\frac{r}{a}\right)^k \cos(l\theta) \qquad (12)$$

Figure 1 shows the results for the case of N=5000. Our midplane multipole moments of $M_{2,2} = 0.9855$ and $M_{6,6} = 0.03460$ are in good agreement with 2-dimensional (*i.e.* z-independent) values of 0.9658 and 0.03461 respectively by Brady [5] using POISSON program. Meuth *et al.* [6] experimentally determined an effective quadrupole length of 10.11±0.14 cm by measuring the phase advance of the centroid motion per lattice period(σ_o), 5% shorter than our predicted effective length ($\equiv \int M_{2,2}(z)\,dz \,/\, M_{2,2}(z=0)$) of 10.60 cm (one should note that their most reliable measurement at $\sigma_o = 72°$ gave an effective quadrupole length of 9.99 cm). Our calculation, however, is quite close to the actual electrode length of 10.74 cm.

Near the endplates, the field contains large multipole field components because of the inter-digital structure of the quadrupole rods, their closeness to the endplates, and the beam aperture holes. Our numerical errors may be larger in this region because σ_i exceeds the optimal value around the aperture holes and the spherical charge shape might be a poor approximation to the true image charge distribution on the flat endplates. Thus, perhaps additional nodes and a variable charge distribution width and shape would be required in order to maintain 1% accuracy everywhere.

5. CONCLUSION AND DISCUSSION

We have presented a simple and accurate method of determining the multipole field components of electrostatic focussing system with arbitrary geometry. First the induced surface charge distribution for a given electrode potential is obtained by inverting the capacity matrix, followed by multipole decomposition of the field at the beam axis by using the DA techniques. Since the charge on the conductor surface is calculated directly in this method, the multipole harmonic amplitude can be obtained by the summation of the contributions from all the charges. Although finite size of the charge distribution at a given node poses some uncertainty of the determination of the capacity matrix, the effect can be minimized by optimally choosing the profile shape and width. Numerical experiments show that the decomposition is indeed insensitive to the the charge distribution at the nodes so long as the internode distance is much smaller than the aperture radius.

For the actual MBE-4 accelerator lattice structure, the calculated, z-dependent amplitudes of the multipole harmonics show good agreement with previous measurements in terms of effective quadrupole length and dodecapole strength.

References

[1] C. Celata, I. Haber, L. Laslett, L. Smith and M. Tiefenback, IEEE Trans. on Nucl. Sci. NS-32 (1985) 2480.

[2] S. Eylon, E. Colby, T. Fessenden, T. Garvey, K. Hahn and E. Henestroza, Part. Acc. to be published.

[3] M. Berz, IEEE Trans. Elec. Dev., 35-11 (1988) 2002.

[4] M. Berz, Part. Acc., 24 (1989) 109.

[5] V. Brady, private communication (1987).

[6] H. Meuth, S. Eylon, E. Henestroza and K. Hahn, private communication (1989).

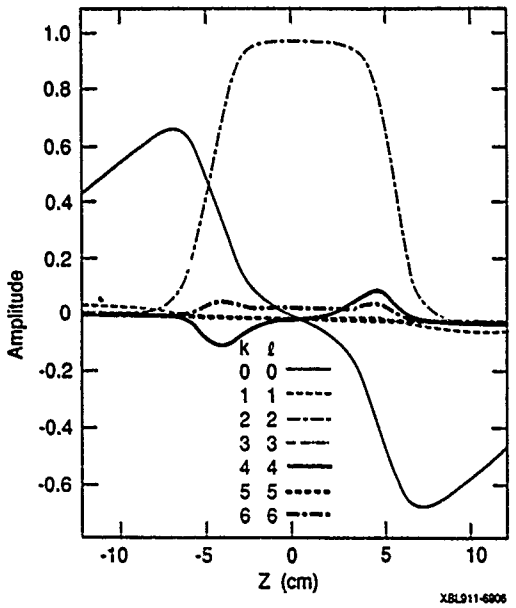


Fig 1 Multipole decomposition of the MBE-4 lattice plotted versus z for "pure" multipoles $M_{k,k}$.

Measurements on Iris-Structures with Rectangular Holes *

M. Kurz, P. Hülsmann, H. Klein, A. Schempp
Institut für Angewandte Physik
Robert-Mayer-Straße 2-4, D-6000 Frankfurt am Main, Fed. Rep. of Germany

Abstract

By replacing the irises in an electron linac by rectangular slots one gets a structure capable of focussing/defocussing an electron beam. Therefore this kind of iris-geometry could be employed alone or in combination with conventional magnetic quadrupoles for transversal focussing in future linear-colliders.

A three-cell structure with rectangular "irises" was designed and tuned to $v_{ph}=c$ at TM_{010} $2\pi/3$-mode. Perturbation measurements were performed in order to determine the fields and focussing strength of the structure.

I. INTRODUCTION

All schemes proposed for future e^+-e^--linear-colliders are featuring travelling-wave structures of iris-type for the main linac. Operating frequencies are proposed to be in the range between 11.47GHz (SLC) and 29GHz (CLIC). In this frquency regime wake field effects cannot be neglected; longitudinal wakes scaling with ω^2, transversal wakes scaling with ω^3 [1]. The final-focus luminosity needed for experiments is about $10^{33}cm^{-2}s^{-1}$. This means that beam quality has to be maintained over rather long distances (e.g. 12.5km for the CLIC main-linac) and additional transversal focussing will be required. One way to achieve the focussing is to apply external magnetic quadrupoles. The rectangular "irises" investigated in this paper could possibly be an alternative or supplement to convetional methods, combining a high accelerating gradient with the potential of considerable transverse focussing power [2, 3]. The principle is the same as in the RFQ-scheme frequently used for accelerating low-energy ions.

II. THEORETICAL ASPECTS OF RF-FOCUSSING

We assume a TM_{01}-wave travelling at v=c through a loaded waveguide operating in $\pi/2$-mode for the sake of easier understanding (see Figure 1). The results are valid for any other operating mode too.

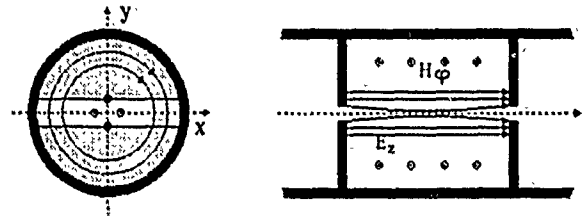


Figure 1 RF-quadrupole in $\pi/2$-mode

The iris is replaced by a narrow slit of the size of the cavity diameter oriented in X-direction. Its height is chosen such that the magnetic field behind the sceen remains undisturbed. The E_z field is assumed to be of the form

$$E_z = E_0 \cos(\omega t - kz). \qquad (1)$$

Because of the geometry of the slot $\partial H_\varphi/\partial\varphi=0$. From Maxwell's equation using cylindrical coordinates we find

$$H_\varphi = -\frac{\varepsilon r \omega}{2} E_0 \sin(\omega t - kz). \qquad (2)$$

The boundary conditions allow no X-component of the electrical field inside the screen. From divE=0 we get the Y-component of the electric field

$$E_y = -y\,k\,E_0 \sin(\omega t - kz). \qquad (3)$$

A particle travelling at $v\approx c$ and entering the structure at a certain phase Φ with respect to the RF will maintain this phase on its way through the structure. In the X-direction the particle will only experience magnetic forces; there will be additional electrical forces in the Y-direction. Finally we find

$$F_x = \frac{q\,\omega}{2\,c}\,x\,E_0 \sin(\Phi)\,, \qquad (4)$$

$$F_y = -\frac{q\,\omega}{2\,c}\,y\,E_0 \sin(\Phi),$$

and the focussing gradients

$$G_x = \frac{\omega}{2\,c^2} E_0 \sin(\Phi)\,, \qquad (5)$$

$$G_y = -G_x\,.$$

* work supported by BMFT under contract No. 055FM111

0-7803-0135-8/91$01.00 ©IEEE

An accelerating section of length l then forms a microwave-quadrupole of focal length f given by

$$f^{-1} = \frac{cGl}{U}, \qquad (6)$$

eU being the particle energy.

This derivation shows that under such idealized conditions this structure forms a rf-quadrupole.

III. EXPERIMENTS

A. Experimental setup

A three-cell structure was designed and tuned to $v_{ph} \approx c$ in the TM_{010} $2\pi/3$-mode. A sketch of the geometry used is given in Figure 2.

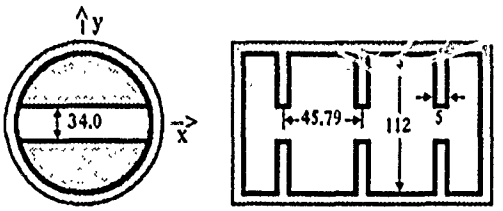


Figure 2 Structure geometry (dimensions in mm)

For the measurements a computer-controlled test stand was used, allowing for data aquisition and further processing (see Figure 3). For the reason of eliminating oscillations of the bead the cavity was moved. The catch of the bead was made adjustable on either side of the test bench in order to allow for aligning the bead with the cavity-axis.

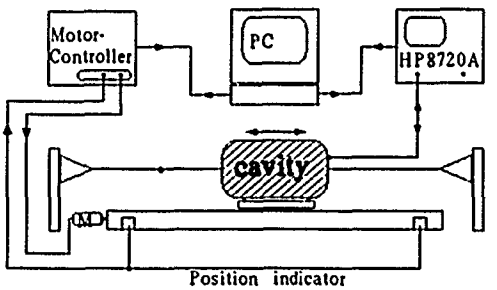


Figure 3 Experimental setup

For measuring the eletric field a thin dielectric needle (Al_2O_3) was used. The bead was first calibrated in TM_{010} pillbox cavity of well known geometry.

B. Experimental results

The cavity was tuned to $v_{ph} \approx c$ by gradually adjusting the height of the slot. The optimum was found for a 34 mm aperture.

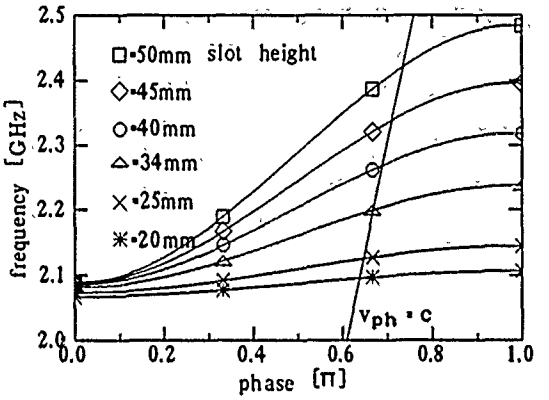


Figure 4 Brillouin-diagram of the structure for several apertures

As can be seen from the Brillouin-diagram in Figure 4 the coupling in the structure is still predominantly electric. Group velocity v_g/c is about 6.5% in the operating mode.

The E_z-field was measured on axis and for several off-axis positions in the X-Z-plane and the Y-Z-plane. The electric field is plotted versus the Z-position of the bead (see Figures 5 and 6).

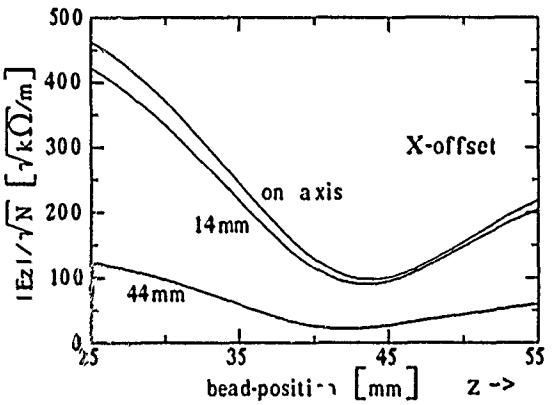


Figure 6 E-field versus bead position. Parameter: Bead offset in X-direction. The middle of screen is at z=42mm

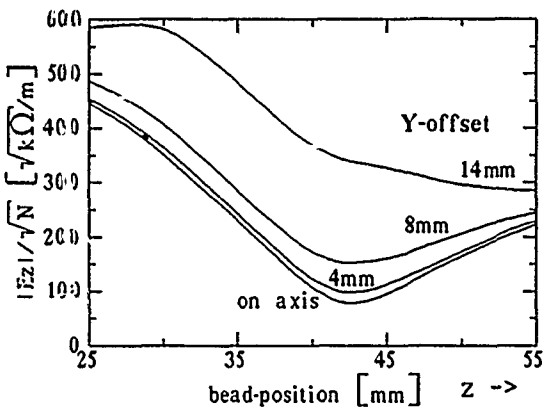


Figure 5 E-field versus bead position. Parameter: Bead offset in X-direction. The middle of screen is at z=42mm

According to the analytical approach the focussing in the X-plane is due to the magnetic field. Instead of measuring the H_φ-component we can apply to the $E_z(x)$ field which is proportional to $-H_\varphi$. In the Y-plane the relevant $E_z(z)$ field was recorded as well.

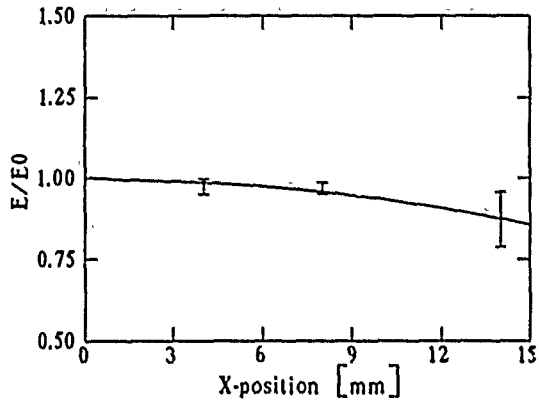


Figure 7 Normalized E_z-field vs. X-offset

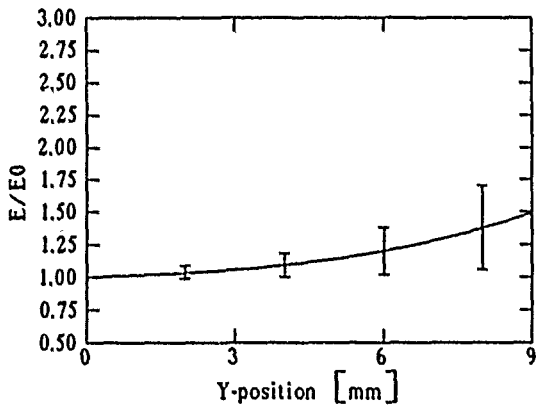


Figure 8 Normalized E_z-field vs. Y-offset

It can be seen, that the ratio E/E_0 is close to unity only for small offsets. While the change is modest for the X-offset due to the decay of the field towards the cavity wall it shows that in the Y-direction the effect of the edges causes a steeper curve.

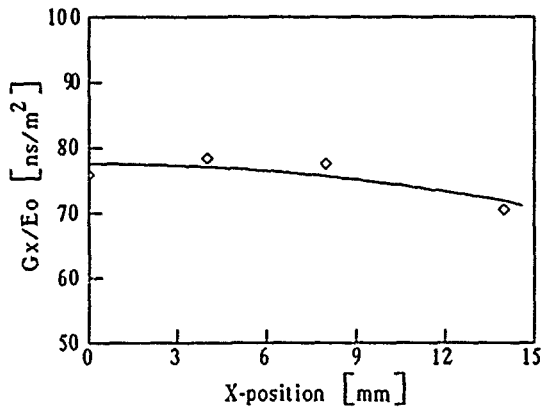


Figure 9 Normalized focussing gradient G_x/E_0

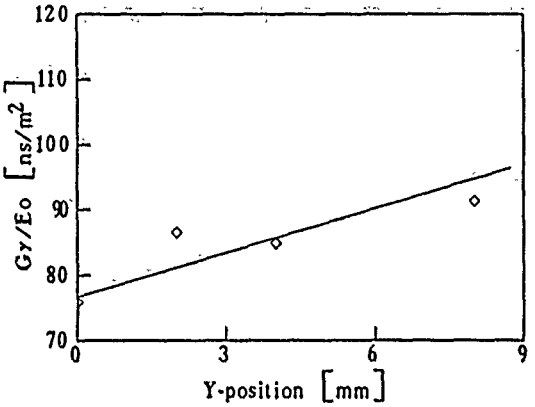


Figure 10 Normalized focussing gradient G_y/E_0

The normalized focussing gradients for the X- and Y-direction are given in Figure 9 and 10.

IV. Conclusions

The transverse focussing gradients of the examined structure match the analytical estimate [2] of 76.9ns/m^2 nearly exactly. Also the results correspond well to the ones obtained by MAFIA-calculations done by I. Wilson and H. Henke [4]. Scaled to 29GHz we find a normalized gradient of about 0.98μs/m^2 which would be equivalent to 27T/m at 20° rf-phase and 80MV/m effective accelerating field.

V. References

[1] H. Henke, CLIC Note 100, Geneva, 1989

[2] W. Schnell, CERN-LEP-RF/87-24, CLIC Note 34, Geneva, March 1987

[3] R. B. Palmer, Private Communication

[4] I. Wilson, H. Henke, CLIC Note 62, Geneva, May 1988

RF tests of a band overlap free DAW accelerating structture

R. Parodi, A.Stella
INFN GENOVA
Via Dodecaneso 33
16146 GENOVA ITALY

P.Fernandes
IMA-CNR
Via Leon Battista Alberti
Genova Italy

Abstract

Our paper deal with the results of measurements on a six cells Disk-and-Washer structure.

The RF structure operating at 3600 Mhz is optimized for a BETA =1 electron beam, trying to avoid the overlap between the band of the accelerating modes and the bands of the dangerous beam deflecting modes.

The cavity geometry was not optimized for the maximum shunt impdance, but nevertheless a characteristic shunt impedance Z/Q of 1500 ohm was obtained.

Measurements on the six cells prototype section built following our design shown a perfect agreement (in frequency and field istribution) with our computation.

The measured characteristic shunt impedance Z/Q of our prototype was 1500 ohm in agreement with our computations.

The dangerous dipole modes inducing beam break-up were(ascomputed) 40 MHz apart from the operating frequency of the structure showing the correctnessof our assumption.

INTRODUCTION

The possibility of using a Disk and Washer structure for an High intensity High gain R.F. linac was studied in many laboratories [1,2,3] due to the benefit of high shunt impedance and large bandwidth of the accelerating mode.

Nevertheless the structure is not widely used for practical applications due to the major drawback of the overlap of the accelerating and coupling TM like monopolar bands with the Hybrid dipolar bands.

This band overlap could induce serious beam unstabilities leading to beam break-up at a current lower than the design current of the accelerator.

Due to our interest for a compact, high gradient and efficient Standing Wawe linac structure to be used to build a low energy test accelerator for high energy detectors, we started a research programme on the DAW structure.

Our goal was to state whether the band overlap is a general feature of the DAW linac or that drawback can be overcome by a suitable choice of the parameters of the elementary cells of the linac structure.

We focused our attention mainly on the mode pattern of the resonant structure without attempting any optimization of the shunt impedance and efficiency of the structure itself.

We succeeded to design a DAW structure free from band overlap in the accelerating mode region, and with a reasonable shunt impedance (Z/Q) value of 1550 ohm at a frequency of 3650 Mhz

METHOD OF DESIGN

For the design of the structure we widely used computer codes for the computation of RF fields in SW-resonant structures.

We computed the first ten TE and TM monopolar modes of a linac unit cell by our OSCAR2D [4]code and the multipolar modes by the URMELT code[5] (courtesy of T.Weiland DESY).

In that way , by using a single cell of the linac and changing the boundary condition on suitable segments of the cell, we where obtain the values of the resonant frequency of the ZERO, PI and PI over TWO modes of the band pass under examination.

From those values we easily reconstructed the dispersion relation of that band pass of the structure[6]and checked whether for that geometry we have band overlap or not.

Once the right cavity shape had been found, the geometry was slightly changed till the perfect coalescence on the PI mode of the coupling mode bandpass and accelerating mode bandpass was obtained closing the stop band between the two PI modes.

After that a new complete search for the monopolar and multipolar modes was done to eventually detect a band overlap introduced by the previous geometry changes

The process converged after three iterations leading to the coalescent , band overlap free cell shown in figure 1.

From our simulations it comes thath the frequency of the accelerating and coupling monopolar TM modes is mainly related to the diameter of the outer region in the washer
zone.

0-7803-0135-8/91$01.00 ©IEEE

The frequency of the dipolar hybrid modes is more sensitive to changes in the radial dimension of the disk rergion.

Having observed this property of the unit cell of our structure, we easilly succeeded to design to design a band overlap free DAW.

Further we computed also the frequency distribution for the quadrupolar modes to be sure that also this modes does not affect the frequency spectrum of the accelerating structure inducing potentially harmful beam-break-up modes.

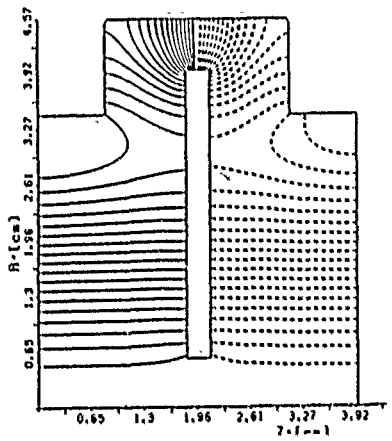


Figure 1. Prototype cell

The relevant RF properties of the cavity are reported in TABLE I.

TABLE I

GEOMETRY AND CAVITY PARAMETERS

f [MHz]	3668.	R [cm]	4.57
Z [M Ω/m]	69.	Rw [cm]	3.95
Q	19000.	Rd [cm]	3.95
T	0.725	tw [cm]	.3
ZT^2/L [M Ω /m]	50.	td [cm]	1.65
Z/Q [ohm]	1500.	r [cm]	.7

In figure 2 is reported the plot of the dispersion relation for the different band-pass showing no overlap between any multipolar mode and the accelerating one.

From that figure is straightforward to see that the accelerating mode is 40 Mhz below the frequency of the nearest dipolar mode.

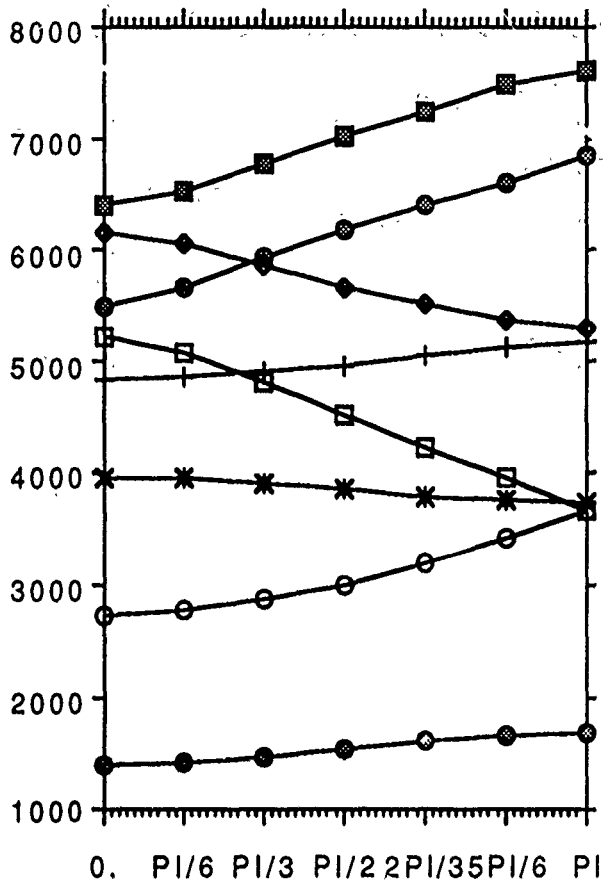


Figure 2, Dispersion plot for the infinite sructure with superimposed the measured modes of the six cells structure.

EXPERIMENT

On the basis of our computation we built a small six cell prototype operating at 3.5 GHZ shown in figure 3

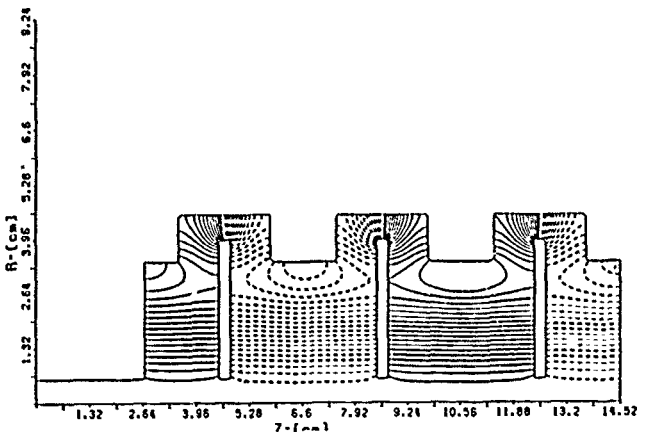


Figure 3, Half six cells ptototype structure.

For that section we measured the resonant frequencies up to eight gigahertz and using a suitable set of

rf probes we identified the bandpass of the dipolar quadrupolar and sextupolar modes.

The measured frequencies and the computed ones for the PI and ZERO modes of the model structure are reported in TABLE II together with the mode band identification.

TABLE II

computed Frequency MHz	meausred Frequency MHZ	error %	
2743	2738	0.3	
3018	2995	0.7	
3682	3640	1.1	TM monopol
4517	4464	1.1	modes
5479	4438	0.7	
6170	3133	0.9	
1645	1644	.06	
4011	4021	0.2	
4133	4134	.02	
4956	4951	0.1	Hybrid dipol.
5236	5252	0.3	modes
5698	5700	.03	
6576	6500	1.1	
7119	7175	0.8	
7759	7760	.01	
2768	2775	0.4	
2880	2872	0.3	
5029	5048	0.4	
5323	5330	0.1	Hybrid quad
6135	6143	0.1	modes
6685	6670	0.2	
7035	7045	0.2	
7962	8000	0.5	
4021	4041	0.5	
4089	4101	0.3	
6163	6116	0.8	Hybrid sext
6461	6490	0.5	modes
7297	7273	0.3	
7945	7925	0.3	

We also measured for the monopolar modes the axial field distribution and the characteristic impedance Z/Q for the accelerating one. the plot of the measured axial field is shown in figure 4; the value of the measured characteristic impedance was Z/Q=1500 Ohm in very good agreement the value of 1550 Ohm found by our computations.

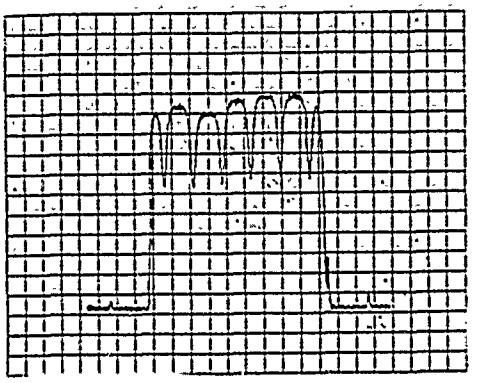


Figure 4 Axial field of the accelereting cavity on the accelerating mode

REFERENCES

[1] J.J.Manca, E.A.Knapp, D.A.Swenson; "High energy accelerating structures for High gradient proton linac applications"; IEEE Trans. Nucl. Sci., NS-24, 3, June 1977.

[2] S.Inagaki, T.Higo, K.Takata, H.Nakanishi, S.Noguchi, T.Furata, K.Kitagawa, E.Ezura, Y.Kojima, T.Takashima, "Developement of a disk and Washer cavity in KeK ", IEEE Trans. Nuc. Sci., NS-30,(4), 3752(1983).

[3] V.G.Andreev, V.M.Belugin, S.K.Esin, L.V.Kravchuk, V.V.Paramunov, parasitic modes Removal out of operating mode neibourough in the DAWaccelerating Structure" IEEE-Trans .Nucl. Sci., NS-304) 3575(1986.

4] P.Fernandes, R.Parodi,"Higher order modes computation in RF cavities" IEEE Trans. on Mag mag-24 (1) 154 (1988)

[5] U.van Rienen, T.Weiland, "Triangular discretization method for evaluation of RF fields in cylindrically symmetric cavities". IEEE Trans. Mag. Mag.21,

[6] P.Fernandes, R.Parodi, "On compensation of axial electric field unflatness in multicell accelerating structures", Particle accelerators Vol 14, (1984).

Transient Analysis of Beam-Loaded Standing Wave Accelerator Cavities

Tom Buller
Boeing Aerospace, M/S 3F-59
Seattle, Washington 98124

ABSTRACT

The time dependent response of an RF driven accelerator cavity is derived using thermodynamics. The filling and draining of stored energy without the beam present are examined, as are transients due to beam turn-on and turn-off. The analysis includes an arbitrary cavity coupling coefficient, but is restricted to constant RF source output power.

INTRODUCTION

The transient response of accelerator cavities is explored from a thermodynamic viewpoint without using circuit analogies. We examine turn-on and turn-off transients and the transients due to the appearance and disappearance of the beam. The model is general enough to include under-coupled as well as over-coupled cavities, but over-coupled cavities are emphasized because of recent interest in high average current (1 ampere) RF accelerators. Our approach is to: 1) Examine the turn-on transient with no beam, 2) Examine the transient response due to the introduction of the beam, 3) Turn the beam off and study the response and finally, 4) Examine the turn off transient without the beam.

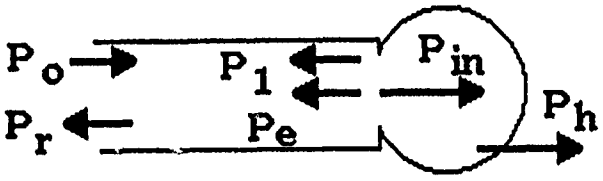
GENERAL MODEL

In our model, we consider a standing wave accelerator cavity with a constant P_0 incident upon the coupler. The coupler is characterized by a coupling coefficient B. W_0 is the steady state stored energy in the cavity with no beam and W_f is the steady state stored energy with a beam of average current I. The reverse power in the feed line (P_r) is composed of two parts; one is a time-independent component (P_1); the other is time-dependent (P_e) which is due to power re-radiating back out of the cavity toward the generator. For a cavity on resonance, P_1 and P_e are exactly out of phase. Adding the voltages vectorially gives,

$$P_r = P_1 + P_e - 2(P_1P_e)^{1/2} \quad (1)$$

It can be shown (see Appendix) that $P_1 = P_0$, therefore

$$P_r = P_0 + P_e - 2(P_0P_e)^{1/2} \quad (2)$$



$\underline{w}$ = angular frequency
P_h = heat lost in cavity
W = stored energy

$$P_c = B*P_h \quad (3)$$

$$Q_L = Q_0/(1+B) \quad (4)$$

We now apply the general model to the four cases mentioned above.

I: TURN-ON TRANSIENT (NO-BEAM)

$$P_{in} = P_h + (dW/dt) = P_0 - P_r \quad (5)$$

$$P_r = P_0 + P_e - 2(P_0P_e)^{1/2} \quad (6)$$

Combining these two equations, leads to a Bernoulli's equation of the form,

$$(dW/dt) + (\underline{w}W/Q_L) = 2(BP_0\underline{w}W/Q_0)^{1/2} \quad (7)$$

In order to solve this equation perform the substitution,

$$u = (W)^{1/2} \quad (8)$$

This yields the following,

$$(du/dt) + u(\underline{w}/2Q_L) = (BP_0\underline{w}/Q_0)^{1/2} \quad (9)$$

The general solution to this equation is,

$$u = c*\exp(-\underline{w}t/2Q_L) + (2Q_L/\underline{w})(BP_0\underline{w}/Q_0)^{1/2} \quad (10)$$

where c is an arbitrary constant. Now, impose the boundary conditions,

Work supported by USASDC contract number DASG60-90-C-0106

0-7803-0135-8/91$01.00 ©IEEE

$$u(t=0) = 0 \tag{11}$$

and,

$$u(t=\text{infinite}) = u_0 \tag{12}$$

This leads to the solution,

$$u = u_0(1 - \exp(-\underline{w}t/2Q_L)) \tag{13}$$

And the stored energy solution,

$$W = W_0(1 - \exp(-\underline{w}t/2Q_L))^2 \tag{14}$$

where,

$$W_0 = (4BP_0Q_0/\underline{w})(1+B)^{-2} \tag{15}$$

The cavity voltage behaves as,

$$V = V_0(1 - \exp(-\underline{w}t/2Q_L)) \tag{16}$$

II: TURN-ON BEAM (CURRENT = I)

$$P_{in} = P_0 - P_r = -P_e + 2(P_0P_e)^{1/2} \tag{17}$$

$$= P_h + P_b + (dW/dt) \tag{18}$$

$$P_b = I*V = I(2R_0P_h)^{1/2} \tag{19}$$

This also leads to a Bernoulli's equation,

$$(dW/dt) + (\underline{w}W/Q_L) = W^{1/2} * \{2(BP_0\underline{w}/Q_0)^{1/2} - I(2R_0\underline{w}/Q_0)^{1/2}\} \tag{20}$$

Now use the same substitution, $u = W^{1/2}$. This yields,

$$(du/dt) + (\underline{w}/2Q_L)*u = A \tag{21}$$

$$A = (BP_0\underline{w}/Q_0)^{1/2} - I(R_0\underline{w}/2Q_0)^{1/2} \tag{22}$$

The general solution to this equation is,

$$u = c*\exp(-\underline{w}t/2Q_L) + (2Q_LA/\underline{w}) \tag{23}$$

Applying the boundary conditions,
at t = 0,

$$u = W_0^{1/2} \tag{24}$$

at t = infinity,

$$u_f = W_f^{1/2} \tag{25}$$

leads to,

$$c = W_0^{1/2} - (2Q_LA/\underline{w}) \tag{26}$$

and,

$$u_f = 2Q_LA/\underline{w} \tag{27}$$

The solution is therefore,

$$u = (W_0^{1/2})\exp(-\underline{w}t/2Q_L) + (2Q_LA/\underline{w})*(1 - \exp(-\underline{w}t/2Q_L)) \tag{28}$$

$$W = W_0*\{1 - I(R_0/2BP_0)^{1/2} + I(R_0/2BP_0)^{1/2}*\exp(-\underline{w}t/2Q_L)\}^2 \tag{29}$$

The cavity voltage goes like,

$$V = V_0[1 - I(R_0/2BP_0)^{1/2} + I(R_0/2BP_0)^{1/2}*\exp(-\underline{w}t/2Q_L)] \tag{30}$$

III: TURN-OFF BEAM

This is the same differential equation (3) as the turn-on transient with no beam,

$$u = c*\exp(-\underline{w}t/2Q_L) + (2Q_L/\underline{w})*(BP_0\underline{w}/Q_0)^{1/2} \tag{31}$$

except now we have different boundary conditions.
at t = 0,

$$u = 2Q_LA/\underline{w} \tag{32}$$

This leads to,

$$c = -(2Q_L I/\underline{w})*(R_o\underline{w}/2Q_o)^{1/2} \quad (33)$$

$$u = (W_o)^{1/2} * \{1 - I(R_o/2BP_o)^{1/2} * \exp(-\underline{w}t/2Q_L)\} \quad (34)$$

$$W = W_o\{1 - I(R_o/2BP_o)^{1/2} * \exp(-\underline{w}t/2Q_L)\}^2 \quad (35)$$

$$V = V_o[1 - I(R_o/2BP_o)^{1/2} * \exp(-\underline{w}t/2Q_L)] \quad (36)$$

IV: TURN-OFF TRANSIENT (NO BEAM)

$$P_h + (dW/dt) = -P_e$$

or,

$$(dW/dt) + (\underline{w}W/Q_L) = 0 \quad (37)$$

Therefore the solution is,

$$W = W_o*\exp(-\underline{w}t/Q_L) \quad (38)$$

where,

$$W_o = 4BP_oQ_o/\underline{w}(1+B)^2 \quad (39)$$

$$V = V_o*\exp(-\underline{w}t/2Q_L) \quad (40)$$

CONCLUSIONS

In conclusion, it is seen that the accelerating voltage in the cavity does react with the characteristic fill time response in a simple exponential fashion. The response of the stored energy is not purely exponential except for the case four, which is classically how the fill time is derived [1].

ACKNOWLEDGEMENTS

I wish to thank William J. Gallagher and Arthur M. Vetter for many illuminating discussions.

APPENDIX

At steady state with no beam,

$$P_o - P_r = 4BP_o/(1+B)^2 = \underline{w}W_o/Q_o = P_h \quad (41)$$

$$P_r = P_o*\{(B-1)/(B+1)\}^2 = P_1 + P_e - 2(P_1P_e)^{1/2}$$

$$= P_1 + BP_h - 2(P_1BP_h)^{1/2}$$

$$= \{(P_1)^{1/2} - (2B/(1+B))*(P_o)^{1/2}\}^2 \quad (42)$$

Here, P_1 is the time-independent part of the reverse power, and P_e is the time dependent part. Now solving for P_1 yields two possible solutions,

$$P_1 = (P_o/(1+B)^2)*\{9B^2 - 6B + 1\} \quad (43)$$

or,

$$P_1 = (P_o/(1+B)^2)*(B+1)^2 \quad (44)$$

Therefore, $P_1 = P_o$ since the former violates conservation of energy at turn-on (t = 0) when the cavity is empty.

REFERENCES

[1] J. D. JACKSON, CLASSICAL ELECTRODYNAMICS, Second Edition New York: John Wiley and Sons, 1975 p. 357

THREE-DIMENSIONAL SPACE CHARGE AND IMAGE CHARGE EFFECTS IN RADIO-FREQUENCY-QUADRUPOLE ACCELERATORS*

F.W. Guy, SSC Laboratory

Abstract

Image charges, combined with an appropriate space-charge treatment, are one method of handling simulation of the self-fields of a charged-particle beam in a beamline partially or totally enclosed by conducting surfaces. If current density is high and if surrounding conducting surfaces are not symmetric about the beam as in an off-center beam in a cylindrical beam pipe, or if the beam comes close to a conducting surface as it does in skimming the vanes of a radio-frequency quadrupole (RFQ), then image forces can be important. A new version of PARMTEQ with 3-D space charge and an approximate image charge treatment has been written and used to simulate several high-current RFQs. This paper explains the calculational method and gives simulation results.

I. INTRODUCTION

The percentage of input beam transmitted through high-current, high-brightness RFQs is not always calculated well by the standard version of PARMTEQ. Often the code prediction is higher than experimental results. There are physics effects that could reduce transmission that have not yet been included in the code. An experimental version of PARMTEQ has been written that includes two of these physics effects, image charges and 3-D space charge. It was thought that these particular effects might be important for high-current, high-brightness RFQs because of high charge density in the beam. This paper discusses the methods that were used to include 3-D space charge and image charges in PARMTEQ, and gives some results. Only the space charge treatment is different; accelerating and focusing fields are unchanged.

II. CALCULATIONAL METHOD

A. 3-D Space Charge

The 3-D space charge is similar to that used in a modified version of PARMILA that was written to accommodate the 3-D geometry of funnel design work. It is a point-to-point non-relativistic treatment in which space-charge forces on each particle are calculated by summing repulsive forces from all other particles. Singularities in the space-charge calculation are avoided by representing particles with charge clouds rather than points. Particles in as many as five leading and following bunches can be included. With no image charges, two or three neighbor bunches are all that is necessary; more than three do not change the result. The effect of neighbor bunches is reduced by image charges because the total charge of a bunch, integrated over all particles of the bunch itself and all resulting images, is zero. It was found that a single neighbor bunch (leading and following) is sufficient when both space charge and image charges are included.

B. Image Charges

The effect of conducting boundaries is added by the image charges, which combine with bunch charges to give the total non-relativistic electric field due to the beam itself. Every particle in the beam has a primary image in each vane. There are also an infinite number of higher-order reflections but they are ignored in the code for reasons explained later. An electric potential U is generated around the vane because of this image. A particle at a certain position, the "test point," will be affected by this potential which is caused by a particle, the "point charge," at another position. The approximate image-charge calculation uses the Green's function at a test point for U caused by the image of a point charge exterior to an infinitely long conducting cylinder:

$$U(a,r,z,\Phi) = \frac{-q}{2\pi^2\varepsilon_o} \sum_{m=0}^{\infty} 2_m \cos(m\Phi) \times \int_0^{\infty} \frac{I_m(kR)\,K_m(ka)\,K_m(kr)}{K_m(kR)} \cos(kz)\,dk \qquad (1)$$

where R is the cylinder radius;
a and r are the radii of the test point and the point charge respectively, measured from the cylinder's axis;
Φ and z are the angle measured at the cylinder's axis, and axial distance, between the test point and the point charge;
I_m and K_m are modified Bessel functions;
$2_0 = 1$, $2_{m>0} = 2$.

In the numerical sum and integration, the Bessel function order m goes from zero to 30 and the integral over the wave number k goes from k=0 to k=100 in gradually increasing steps starting with Δk=0.1. These values were found to produce sufficient accuracy in the calculation.

The cylindrical approximation to the vane-tip shape is reasonably good over a single cell but in many RFQs the vane-tip radius changes gradually along the length of the vane. This change is approximated in the code by using several cylindrical vane-tip radii R during the calculation and

* Work supported and funded by the U.S. Department of Energy, Office of the Superconducting Super Collider. Work performed at Los Alamos National Laboratory.

0-7803-0135-8/91$01.00 ©IEEE

changing these radii in steps. In running a problem with the code, a four-dimensional grid for $U(a,r,z,\Phi)$ is set up for each vane-tip radius R. A new grid is read into the image-charge subroutine when R changes significantly.

The electric force on a test particle at radius a from the vane-tip axis due to the image of a charge at r is calculated by differentiating and interpolating the potential grid. The code sums over primary images (those due to first reflection) in all four vane tips but it does not take into account reflections of reflections. These higher-order reflections are much farther from the actual beam charges and they tend to cancel out because they have alternating signs and a decreasing amount of charge. Image forces on particles are strong close to a vane but decrease rapidly as distance increases; so secondary and higher-order reflections in and from other vanes will have much less effect than the primary images.

It is necessary to take vane modulations into account. This is done by stepping along the cell using (for these problems) six steps per cell. The vane surface is assumed to be parallel to the RFQ axis within each step with a vane radial distance from the RFQ axis that is the average of the actual vane radial distance over a step. The vane modulation advances 180° per cell so that a step represents a 30° advance. Because of vane modulation, the vane surface is not necessarily parallel to the axis as it would be in an unmodulated cylinder. However, during passage through two cells (a total of 360° of vane modulation) the angle at a particular radial distance averages almost to zero, so to a first approximation the effect of the non-zero surface angle is canceled.

Image-charge forces for each particle are summed over all the particles in the bunch and over corresponding particles in neighboring bunches. This is done for each of the four vanes. Finally the x', y' and energy of the particle is adjusted. This is done once per cell at the same time as the space-charge calculation.

III. RESULTS

Beam transmission percentages are shown in Table 1 for several PARMTEQ runs of 1000 particles each. Some actual RFQs studied were the ATS (Los Alamos Accelerator Test Stand), Chalk River RFQ1, and CERN RFQ2. Some unbuilt designs studied were two early versions of the SSC (Superconducting Super Collider) design (used only as an example; the final SSC design is considerably different), and the ATW (Accelerator Transmutation of Waste) design. In Table 1, input beams were matched and aligned unless otherwise noted.

Certain trends were seen in the results. Some are expected and consistent with effects that have been observed in PARMILA, or that might be expected from image charges. Trends that show up in the results are as follows:

1. The main effect of images is that beam transmission usually decreases. Particles close to the vanes are strongly attracted by image charges and are deflected out of the beam. There is a correlation between beam loss and beam charge density close to the vanes; as charge density increases, so does percentage of beam loss. The CERN RFQ did not show the transmission reduction effect, but this machine has a larger aperture than the other RFQs and the beam does not spend as much time close to the vanes.

Table 1.
Beam transmission percentages for various RFQs with different space-charge and image-charge treatments

RFQ Identity and Input Current	Transmission
ATS RFQ, 100 mA	
2-D	89.8%
3-D, no images	92.5%
3-D, with images	88.8%
Experimental results [1]	~85%
Chalk River RFQ1, 90 mA	
2-D	83.1%
3-D, no images	86.1%
3-D, with images	74.0%
Experimental results [2]	~74%
CERN RFQ2, 220 mA	
2-D	91.0%
3-D, no images	85.1%
3-D, with images	85.2%
Experimental results [3,4]	~90%
SSC RFQ (early version 4-92), 30 mA	
2-D	90.1%
3-D, no images	93.0%
3-D, with images	90.7%
SSC RFQ (early version 5-92), 50 mA	
3-D, no images, misaligned beam	81.4%
3-D, with images, misaligned beam	75.6%
SSC RFQ (early version 5-92), 70 mA	
3-D, no images, misaligned beam	73.8%
3-D, with images, misaligned beam	56.9%
3-D, with images, aligned beam	59.9%
ATW RFQ, 140 mA	
2-D	90.6%
3-D, no images	89.7%
3-D, with images	74.8%

2. Transverse emittances and Courant-Snyder parameters α, β, and γ are not much affected by image charges. A high-current, high brightness RFQ acts as a filter because the beam

fills the aperture for much of the RFQ's length. Consequently although image charges may reduce transmission and increase emittance in individual particles, output emittance change is small because lost particles are preferentially high-emittance ones.

3. The 3-D runs without image charges show a tendency toward slightly more transverse and slightly less longitudinal emittance growth than do the 2-D runs. The same tendency has been observed in PARMILA.

4. Bunch length and longitudinal emittance are usually slightly reduced by image charges. Particles at the ends of the bunch see less space-charge repulsion from the middle of the bunch because this repulsion is partially cancelled by the oppositely-charged images produced by the bunch center.

5. Misalignment or mismatch of the input beam, even if within tolerance, may cause some beam loss in the standard PARMTEQ code. Image charges tend to amplify this beam loss, probably because particles in the beam spend more time close to the vanes if the input beam is misaligned or mismatched than in a perfectly aligned and matched beam.

From the results of these few runs it is not obvious how beam loss changes with beam parameters or RFQ configuration, except that for a particular RFQ the percentage of beam loss increases with current or emittance. More study is required to understand the main factors responsible for differences in beam loss from one RFQ design to another.

High-current, high-brightness RFQs that might show a measurable image-charge effect are few, and beam measurements can be complicated and difficult. Where experimental transmission is less than the prediction of the standard PARMTEQ code, some of the discrepancy may be explained by image-charge effects such as those presented here in results from the modified code.

IV. CONCLUSIONS

The 3-D space-charge treatment made little difference in the PARMTEQ results. Image charges, on the other hand, caused significant beam loss in some cases. This effect should be taken into account in designing high-brightness, high-current RFQs. To this end, more theoretical, computational and experimental work is necessary to quantify the factors affecting image-charge beam loss.

V. ACKNOWLEDGEMENT

Thanks to Mike Pabst (KFA-Julich) for developing the Green's function for the image of a point charge outside a conducting cylinder.

VI. REFERENCES

[1] K.F. Johnson, Los Alamos National Laboratory, private communication.

[2] G.M. Arbique, B.G. Chidley, M.S. de Jong, G.E. McMichael and J.Y. Sheikh, "Beam Performance and Measurements on the RFQ1 Accelerator, *Proc. 1990 Linac Conference*, Albuquerque, NM, Sept. 10-14, 1990, pp. 677-679.

[3] J.L. Vallet, M. Vretenar and M. Weiss, "Field Adjustment, Tuning, and Beam Analysis of the High-Intensity CERN RFQ," *Proc. 2nd European Particle Accelerator Conference*, Nice, France, June 12-16, 1990, pp. 1234-1236.

[4] E. Tanke, M. Vretenar and M. Weiss, "Performance of the CERN High-Intensity Linac," *Proc. 1990 Linac Conference*, Albuquerque, NM, Sept 10-14, 1990, pp. 686-688.

Acceleration Tests of the INS 25.5-MHz Split Coaxial RFQ

S. Arai, A. Imanishi, T. Morimoto, S. Shibuya*, E. Tojyo, and N. Tokuda
Institute for Nuclear Study, University of Tokyo
Tanashi, Tokyo 188, Japan

Abstract

The INS 25.5-MHz split coaxial RFQ, a linac that accelerates ions with a charge-to-mass ratio greater than 1/30 from 1 to 45.4 keV/u, is now undergoing acceleration tests with a beam of molecular nitrogen (N_2^+) ions. Results so far obtained show that the RFQ operates in accordance with the design. Presented are preliminary results on the beam performance: emittances of the in- and output beams, output energy and its spread, and beam transmission.

I. INTRODUCTION

At the Institute for Nuclear Study (INS), we are conducting acceleration tests of a 25.5-MHz split coaxial RFQ (Radio Frequency Quadrupole) by using molecular nitrogen (N_2^+) ions. This linac accelerates ions with a charge-to-mass ratio greater than 1/30 from 1 to 45.4 keV/u. The whole cavity, 2.1 m in length and 0.90 m in inner diameter, consists of three module-cavities and has modulated vanes. The cavity underwent successfully low-power tests (frequency tuning, Q-value measurement, measurements of field strengths near the vane tips) and rf conditioning [1, 2, 3]. On January 22, 1991, the first beam acceleration was performed: N_2^+ ions were accelerated up to the design energy.

This paper describes preliminary results of acceleration tests so far conducted. Since the present low-energy beam transport line has no device for ion separation, the input beam contains ions other than N_2^+ ones. Though this prevent us from clear discussion on the beam performance, preliminary results are consistent with PARMTEQ predictions.

II. ACCELERATION TEST STAND

The setup of the acceleration test stand is shown in Fig. 1. Nitrogen ions are provided by a 2.86-GHz ECR (Electron Cyclotron Resonance) ion source. The source is a compact one, equipped with permanent magnets: six bar magnets for a sextupole field and two ring ones for a mirror field in the axial direction. Ions are extracted from the source at a potential of 28 kV.

In the low-energy beam transport line, four einzel lenses focus the beam and match its emittance with the RFQ acceptance. The voltages applied to the einzel lenses were optimized by using a computer code TRACEP, a ray tracer [4]. TRACEP simulates the particle motion in an einzel lens, whose electric field is computed by SUPERFISH. In the present system, we cannot discriminate the aimed N_2^+ ions from the contamination of other ions: N^+, N^{++}, and H_2O^+. This problem will be soon solved by installing a bending magnet between einzel lenses 2 and 3.

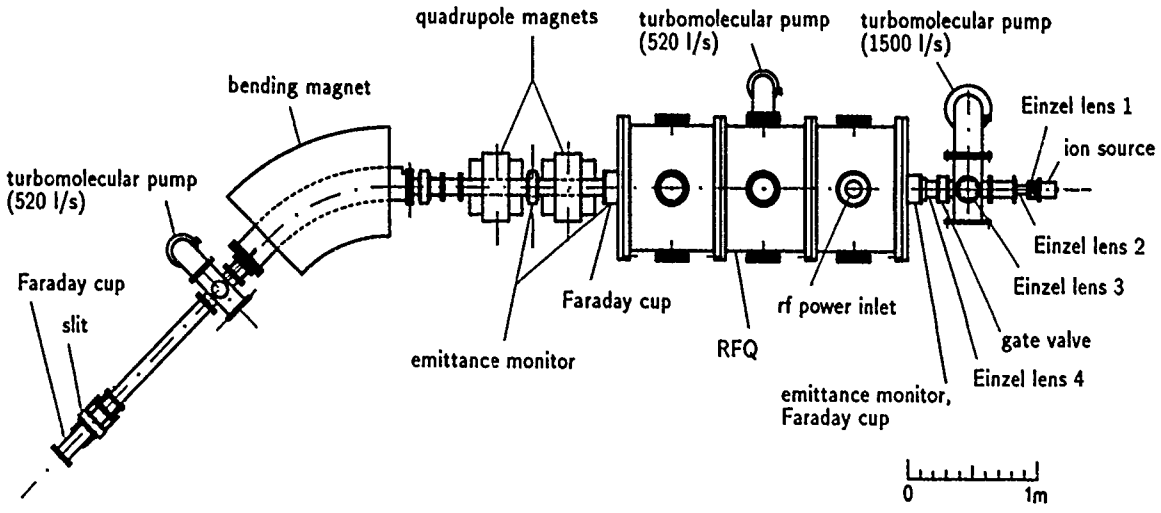


Figure 1. Setup of the acceleration test stand.

*The Graduate University for Advanced Studies, KEK, Tsukuba, Ibaraki 305, Japan

0-7803-0135-8/91$01.00 ©IEEE

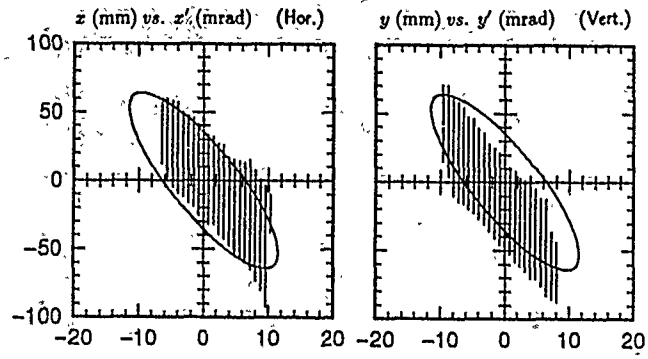


Figure 2. Emittance profiles of the input beam. The bars indicate measured profiles, and the ellipses the designed emittances matching to the RFQ acceptance ($\varepsilon_n = 0.6\ \pi$ mm·mrad).

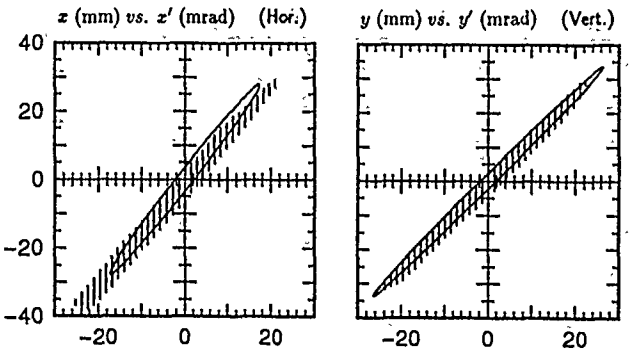


Figure 3. Emittance profiles of the output beam. The bars indicate measured profiles, and the ellipses the designed emittances ($\varepsilon_n = 0.6\ \pi$ mm·mrad).

The high-energy beam transport line was designed so as to measure the parameters of the output beam: beam currents of accelerated ions and unaccelerated ones, transverse emittances, kinetic energy and its spread. In the design, all the ions accelerated up to the design energy are focused into the Faraday cup 3 at the downstream end. For the energy-spread measurement, we set the slit in front of the Faraday cup and focus the beam onto it. The designed energy resolution $\Delta E/E$ is ±0.34%, whereas PARMTEQ predicts an energy spread of ±3.3%.

III. Acceleration Tests

A. Emittance Measurements

Figure 2 shows measured profiles of the horizontal and vertical emittances of the input beam. The profiles are the ones at the rear slit of the emittance monitor 1; the slit position is 6.9 cm up the RFQ entrance. The bars indicate profiles cut off at a threshold level, 5% of the maximum density. The ellipses indicate the emittances matching the designed RFQ acceptance. The ellipse area is 411 π mm·mrad (the normalized emittance is 0.6 π mm·mrad). The matching between the beam emittance and the RFQ acceptance is not yet perfect: the beam is slightly off the axis. For better matching, devices for the beem steering will be soon installed.

Figure 3 shows the emittance profiles of the output beam at the rear slit of the emittance monitor 2. The slit position is 71.3 cm down the vane end. The ellipses are the designed emittances. The area is 61.0 π mm·mrad, and the normalized emittance is 0.6 π mm·mrad (the normalized 90%-emittances given by PARMTEQ are 0.458 π mm·mrad in the horizontal plane and 0.470 π mm·mrad in the vertical plane). The observed emittances have larger areas. This might be attributed to the input beam: it has ions out of the acceptance ellipses and contains ions other than N_2^+ ones.

B. Beam Energy

Figure 4 shows the currents of accelerated ions as functions of the current exciting the bending magnet, and demonstrates that the ions are accelerated to the design energy. The RFQ operated at an intervane voltage V_{vv} of 109.5 kV, or a normalized intervane voltage V_n of 1.07; $V_n \equiv V_{vv}(\text{operation})/V_{vv}(\text{design})$ (= 102.0 kV). In the figure, we present the results of four measurements for ion species: N_2^+, N^+, N^{++}, and H_2O^+. At each mesurement, the currents of the quadrupole magnets were adjusted so that all accelerated ions of the aimed species might be focused into the Faraday cup 3. The slit in front of the Faraday cup was fully opened; therefore, the signal widths do not mean energy spread.

From the signal heights, the numbers of ions are in the ratio of $N_2^+ : N^+ : N^{++} : H_2O^+ = 60 : 7 : 1 : 2$. Among the observed ions, N_2^+, N^+, and H_2O^+ were produced in the ion source, but N^{++} would be created through the dissociation process of accelerated N_2^+ ions, since the intervane voltage is so high ($V_n = 4.3$ for N^{++}) that the transverse motion of the ions is instable in the RFQ (PARMTEQ predicts no transmission). If the cross section for the dissociation process is in the order of 10^{-16} cm^2, the observed amount of N^{++} ions is reasonable.

Figure 5 shows energy profiles of accelerated N_2^+ ions.

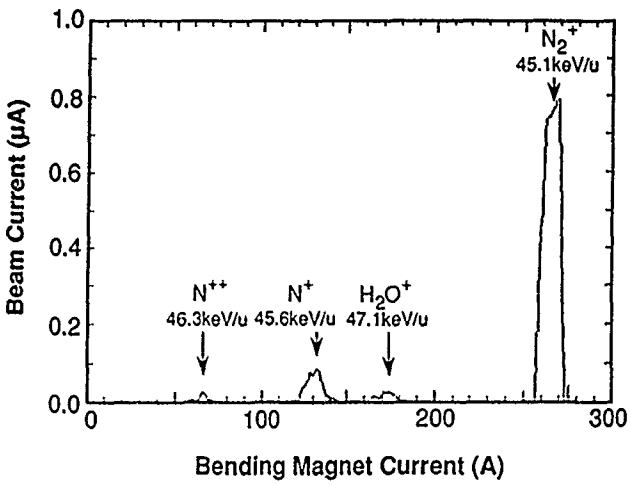


Figure 4. Beam currents measured with the Faraday cup 3 as functions of the bending-magnet current.

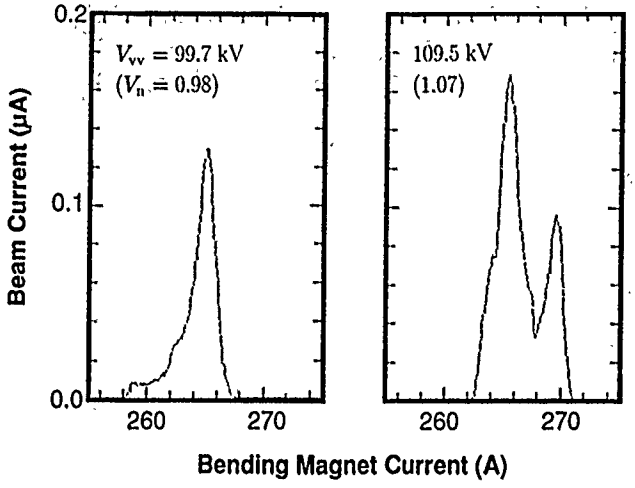


Figure 5. Energy profiles of accelerated N_2^+ ions.

In the measurements, the width of the horizontal slit in front of the Faraday cup 3 was set at ±3 mm (the estimated width of a monochromatic beam), and the intervane voltage was 99.7 kV (V_n = 0.98) or 109.5 kV (1.07). The observed full energy spreads are ±3.5% and ±3.1%, respectively. These values are almost same as PARMTEQ results.

C. Beam Transmission

The current of accelerated N_2^+ ions was measured as a function of intervane voltage. We use a notation I_i (i = 1, 2, 3) for a current measured with the Faraday cup i: I_1(all) = input beam current, comprising all of N_2^+, N^+, N^{++}, and H_2O^+ ions; I_2(all) = output beam current of accelerated and unaccelerated ions, comprising N_2^+, N^+, and H_2O^+ ions; $I_3(N_2^+)$ = current of accelerated N_2^+ ions.

Figure 6 shows current ratios I_2(all)/I_1(all) and $I_3(N_2^+)/I_1$(all) as functions of the normalized intervane voltage. At V_n = 1.1, the measured $I_3(N_2^+)/I_1$(all) is 0.6. The transmission efficiency, defined by $I_3(N_2^+)/I_1(N_2^+)$, is estimated to be higher. From the current ratio presented in the subsection B and PARMTEQ calculations yielding $I_3(N^{++})/I_1(N^{++}) = 0$ and $I_3(N^+)/I_1(N^+)$, $I_3(H_2O^+)/I_1(H_2O^+) \simeq 0.5$, we infer $I_1(N_2^+)/I_1$(all) < 0.8, and hence the transmission efficiency would be > 0.75.

The observed $I_3(N_2^+)/I_1$(all) increases with the intervane voltage. PARMTEQ, however, predicts a steeper increase: for example, $I_3(N_2^+)/I_1(N_2^+) \simeq 0.53$ at V_n = 0.9. Considering that the vanes were machined by means of the two-dimensional cutting technique (the transverse radius of curvature at the vane top is constant, $\rho_\perp = r_0$ = 0.946 cm), a possible reason for the slow increase is that, in the bunching stage, the longitudinal electric field actually generated by the vanes is weaker than that used in the PARMTEQ calculation. In other words, $A_{10} < A$. PARMTEQ uses the lowest-order two-term potential function [5]. The A parameter is the coefficient of the term that yields the longitudinal electric field. The potential function for the actual field, however, has additional higher

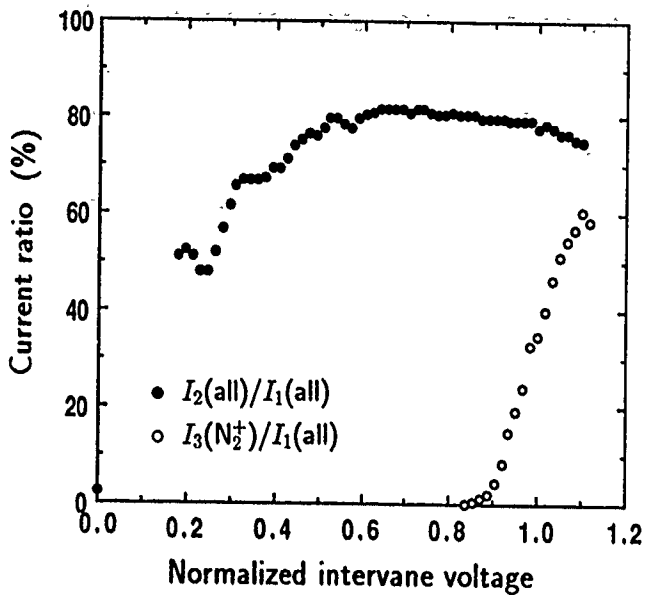


Figure 6. Current ratios I_2(all)/I_1(all) and $I_3(N_2^+)/I_1$(all) as functions of the normalized intervane voltage.

order terms; the A_{10} term is the principal one that governs the longitudinal motion. In our RFQ, the ratio A_{10}/A varies from 0.7 to 0.8 in the bunching stage [6]. The separatrix would be accordingly smaller in the capture process; as a result, the transmission efficiency might have been reduced.

Acknowledgments

The authors express their thanks to M. Kihara for his encouragement. The RFQ work is supported by the Accelerator Research Division, High Energy Physics Division, and Nuclear Physics Division of INS, and by the Grant for Scientific Research of the Ministry Education, Science and Culture. The computer works were done on FACOM M780 in the INS Computer Room.

References

[1] N. Tokuda *et al.*, *Structure and RF Characteristics of the INS 25.5-MHz Split Coaxial RFQ*, 7th Symp. on Acc. Sci. and Tech., Osaka, Japan, Dec., 1989.

[2] S. Shibuya *et al.*, *RF Tests on the INS 25.5-MHz Split Coaxial RFQ*, 1990 Linear Accelerator Conference, Albuquerque, NM, U.S.A., Sept., 1990.

[3] N. Tokuda *et al.*, *Progress Report on the INS 25.5-MHz Split Coaxial RFQ*, Int. Symp. on Heavy Ion Inertial Fusion, Monterey, CA, U.S.A., Dec., 1990.

[4] S. Yamada, *Private communications*, 1990 - 1991.

[5] K. R. Crandall *et al.*, *RF Quadrupole Beam Dynamics Design Studies*, 1979 Linear Accelerator Conference, Montauk, NY, U.S.A., March, 1979.

[6] K. R. Crandall, *Effects of Vane-Tip Geometry on the Electric Fields in Radio-Frequency Quadrupole Linacs*, Los Alamos Technical Report, LA-8595-MS, 1983.

Numerical Simulation of a Short RFQ Resonator Using the MAFIA Codes[1]

H. Wang[2] I. Ben-Zvi[3] A. Jain[4] and P. Paul
Physics Department, SUNY at Stony Brook, NY 11794-3800
and
A. Lombardi
INFN-LNL, Via Romea 4, Legnaro (PD) I-35020, Italy

Abstract

The electrical characteristics of a short ($2\beta\lambda$=0.4m) resonator with large modulation (m=4) have been studied using the three dimensional codes, MAFIA. The complete resonator, including the modulated electrodes and a complex support structure, has been simulated using $\sim$ 350,000 mesh points. Important characteristics studied include the resonant frequency, electric and magnetic fields distributions, quality factor and stored energy. The results of the numerical simulations are compared with the measurements of an actual resonator and analytical approximations.

I. INTRODUCTION

A prototype of a Superconducting RFQ (SRFQ) resonator has been designed and built at SUNY, Stony Brook [1].

The short length of the resonator is chosen to facilitate superconducting operation. This design offers many advantages for the acceleration and focussing of low β (0.01 to 0.05) heavy ion beams [2].

The SRFQ resonator has the four rod structure [3]. The short length of the SRFQ makes it possible to simulate the whole structure for a computer, including the modulation of the electrodes and the fringe field regions. We used the MAFIA codes (version 2.04) [4] to compute in detail the electrical characteristics of the resonator.

In this paper we compare the MAFIA numerical simulations with the measurements of the SRFQ resonator as well as the results of an equivalent lumped circuit analysis [5].

II. GEOMETRY DEFINITION IN MAFIA

The definition of the resonator's geometry and the mesh in MAFIA is very important for obtaining accurate results.

The most complicated objects in the SRFQ are the electrodes. Also, maximum detail in the fields is required near the electrodes. Thus we place the electrodes in the x-z and y-z planes of the simulation reference frame. The beam is along the z axis. With this particular orientation we are able to define the modulation as well as the transverse geometry of the electrode tips. The electrodes are built in slices which are one mesh step thick and are modulated along the z direction. This modulation is defined differently for each slice to account for the transverse profile. The electrode geometry in the input file format for the mesh generator code M3 has been created by a program which computes the height and modulation of each slice.

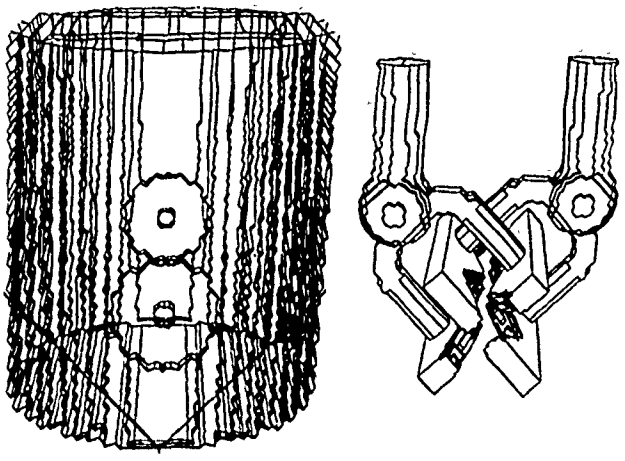


Figure 1: *SRFQ outer tank (left), inner electrodes and support structure (right) as simulated by the MAFIA M3 code*

The outer tank and the support tubes appear as inclined cylinders in the reference frame chosen. The code M3 is unable to define inclined cylinders. Therefore, these geometries have been defined by overlapping a few bricks with appropriate aspect ratios. The other components, such as the spheres, the connecting tubes and the beam ports are easy to simulate with the standard shapes available in M3. The result of this geometry simulation is shown in figure 1.

The M3 always makes structure boundaries shift to the closest mesh planes if the M3 input file doesn't define them on the mesh planes. The location of the mesh in the input must be defined very carefully in order to prevent (often unpredictable) distortion of the resonator. For the same reason, the proper position for a change in step size is on the boundaries of the structure. A high mesh density is needed in high field regions and where a high resolution boundary definition is called for. In this particular application a small mesh size was used in the beam region and around the tips of the electrodes. In this simulation the ratio between the largest and the smallest step sizes is 5.4. A smaller value is desirable, but the solution is still acceptable with this ratio.

[1] Work Supported by NSF Grant No. PHY-8902923

[2] Permanent Address : Tandem Accelerator Laboratory, Physics Department, IAE, Beijing 102413, P.R. China.

[3] Also NSLS Department, Brookhaven National Laboratory, Upton NY 11973

[4] Permanent Address : Nuclear Physics Division, BARC, Bombay 400085, India.

0-7803-0135-8/91S03.00 ©IEEE

It is also advisable to retain the symmetry of the structure in the choice of mesh densities. Otherwise similar objects may distort into different shapes. Our experience shows that detailed drawings of the structure projections on all reference planes are necessary. These drawings should show the surfaces of the structure as well as the mesh lines. This procedure is quite laborious, thus we have developed a computer program which produces the necessary drawings. The use of the auto meshing routine in the M3 is not recommended for optimum placement of mesh planes in complicated structures such as this SRFQ.

The number of mesh points required for the geometry shown in figure 1 is 347,733 (81×81×53). The average mesh density is ~1 mesh point/cm^3, the highest is 11.8/cm^3 and the lowest is 0.5/cm^3.

III. COMPUTATION AND RESULTS

Following the mesh generation we use the eigenvalue solver E31 to compute the electromagnetic fields. The E31 requires considerable memory space. Total running time depends on the availability of on-line memory. The E31 requires frequent access to large arrays, thus a lot of virtual memory storage results in excessive I/O activity. To run the E31 in fast mode with ~350,000 mesh points we need about 70 Megabytes of core memory. Since last publication [5] several improvements have been made to increase the precision of the solution. We have described the technique by which we generate the transverse profile of the electrodes. The application of this technique requires a higher mesh density in beam region and in electrode tip area. However, rounding the electrode tips leads to a better simulation of the structure. As a result, we observe an increase in the computed resonant frequency from 54.7 MHz to 56.5 MHz. The CPU time of the ~350,000 mesh point problem was about 1 hour on a CRAY 2.

The accuracy of the solution is also dependent on E31 input parameters. In this simulation the measure of the accuracy was $\nabla \times (\nabla \times \vec{E}) = 9.4 \times 10^{-4}$, $\nabla \cdot \vec{D} = 5.5 \times 10^{-14}$ and $\nabla \cdot \vec{B} = 9.1 \times 10^{-11}$ (MKS units). This precision has been obtained by using 10 resonant modes and optimizing the highest mode frequency in the computation. Other techniques [6] have also been used to improve the solution.

Table 1 lists the main electrical characteristics computed by MAFIA. The values from bead pulling measurement and those from approximate expressions derived from a lumped circuit model [5] are also given.

The experimental value of the capacitance is derived from an axial bead-pull measurement in a given cell of the SRFQ, using the following expression:

$$C_{total} = \frac{\pi}{2} a^3 \epsilon_0 k^2 A_{10}^2 (\Delta f/f)^{-1}_{peak},$$

where a is the radius of the metallic bead, $(\Delta f/f)_{peak}$ is the measured fractional peak frequency deviation, $k = 2\pi/\beta\lambda$ and A_{10} is taken as the theoretical two term potential value. Units are MKS. A better agreement should be obtained once we get A_{10} from the complete analysis of the bead-pull data.

Table 1. MAFIA Results vs Measurements and Approximate Expressions

Characteristic	MAFIA	Approx.[5]	Measure.
f (MHz)	56.493	63.4	57.372
$Q^{(1)}$	10400	8450	7200
C_{total} (pF)	41	45	53
$U^{(2)}$ (J)	3.6	3.9	4.7
Γ (Ω)	20.2	17.2	14.1
$E_a^2/U^{(3)}$ ([MV/m]^2/J)	72	62	40
$E_a^2/U^{(4)}$ ([MV/m]^2/J)	1.1	1.0	1.1
E_a/E_s	0.12	0.13	0.17
B_s^2/U (G^2/J)	7.4×10^1	3.3×10^1	3×10^1
$\Delta V/V$(%)			
Ends	4.0	3.8	—
Centre	0.04	3.8	—

Notes:
(1) For room temperature copper.
(2) At a designed inter-vane voltage of V=0.419MV [2].
(3) At the middle of a SRFQ cell.
(4) Includes transit time factor and fringe field effect.

IV. DISCUSSION

As we see in Table 1, the agreement between the MAFIA and the experiment in frequency is reasonable, considering the complexity of the structure. As mentioned above, rounding the sharp edges over the tips of the electrodes has increased the frequency by 1.8 MHz. Sharp corners lead to an anomalously high energy density which lowers the frequency. The present simulation still contains some sharp corners which do not exist in the real resonator. We estimate that by rounding the remaining electrode edges the MAFIA frequency will go up by 0.87 MHz to 57.37 MHz, in remarkable agreement to the measured value. This estimate is obtained by scaling the frequency change of 1.8 MHz by the ratio of the length of the tips and the electric energy density there to the length and energy density of the remaining sharp edges.

We can not explain the higher Q value and geometric factor Γ in MAFIA relative to the measurement. We note that similar discrepancies occur frequently between simulations and measurement. This may be the result of oxidation of the copper surface.

The electric unbalance $\Delta V/V$ [5] calculated from the MAFIA field distribution shows a difference between the ends of the electrodes and the center. This difference is due to transmission line effects along the electrodes. The approximate calculation does not include this effect.

The approximate analytical estimate for the total capacitance C_{total} in Table 1 also includes the contributions of the fringe regions and the support structure. A better estimate of the various capacitances has also improved the precision in the calculation of the $\Delta V/V$ as compared to a previous publication [5].

We also note that MAFIA calculates higher peak surface electric field E_s and magnetic field B_s than measured. This can be explained in part by sharp corners which appear in the simulation. There are several reasons for the sharp corners. First, the finite mesh density results in sharp corners at the mesh

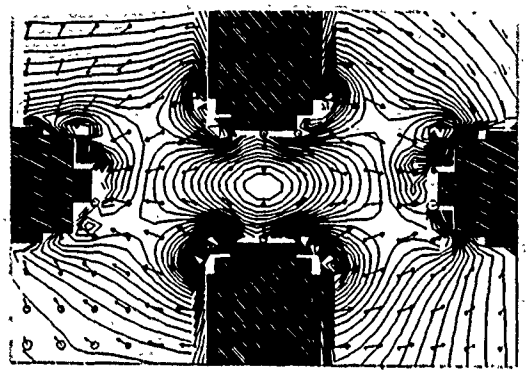


Figure 2: *Electric field (arrows) and electric energy density (contour lines) distribution at a cross section of the electrodes in the center of the resonator.*

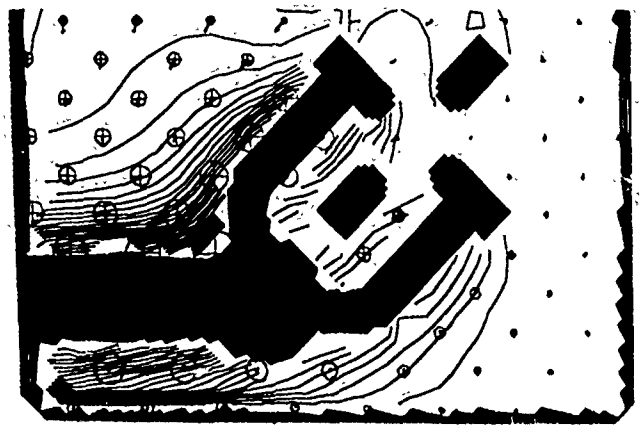


Figure 3: *The magnetic energy density (contours) and magnetic field vectors around one of the support tubes.*

cube boundaries. The second reason is that the available lattice construction elements (cylinders, spheres, blocks etc) can not match the real structure perfectly, so sharp corners may be created. For example, the support tubes, being inclined in the x-y plane had to be constructed of blocks. This resulted in sharp corners which enhance the peak surface fields. This enhancement can be estimated as approximately $\sqrt{2}$. For example, the value of B_s^2/U which appears under the MAFIA column in Table 1 is too high by approximately a factor of two. Once this correction is done the agreement becomes quite good.

The acceleration field E_a includes the transit time factor and the effect of the fringe fields. Some of the results of the MAFIA calculations are presented in another contribution to these proceedings [1]. This includes the electric energy density distribution on the beam axis and the normalized transit time factor curve. A comparison with an approximate analytic calculation and with the measurement is also shown in [1]. The electric field density has an interesting feature to which we have found no convincing explanation. The magnitude of the fringe field at high energy end of the SRFQ resonator is larger by about 20% than at the low energy end. This feature appears both in the simulation and the experiment.

Fig.2 shows the electric field and the electric energy density in the cross section of the electrodes at the center of the resonator. We expect the field to have a quadrupole symmetry, but we can see that the energy density distribution departs from this symmetry. This fact can be understood by observing the support structure as seen in Fig.1. The two pairs of U shaped tubes surround two of the four electrodes. Therefore the field on the electrodes adjacent to these tubes is changed by this asymmetric geometry. When the polarity of the electrodes is considered we find the changes are in expected direction. This may affect the peak surface electric field but should have a negligible effect on the beam dynamics. Electric unbalance $\Delta V/V$ (see Table 1) is also the result of the asymmetric internal geometry.

Another interesting feature seen in Fig.2 is that the peak energy density appears at a finite distance off the surface. This is an artifact of the MAFIA algorithm, which works with fields rather than potentials. A field value on a node is averaged with values on adjacent nodes through the solution of Maxwell's equations in a finite-difference equations [7]. Thus the value of the field on a node which is near a metal surface is reduced by the influence of the vanishing field inside the metal.

Fig.3 shows the magnetic energy density contours and magnetic field vectors around one of the support tubes. The location of the peak surface magnetic field in this resonator is next to the joint of the support tube and the tank roof, facing the tank wall.

V. ACKNOWLEDGEMENTS

The authors sincerely thank T. Barts, K.C.D. Chan, R. Wallace, of LANL and H.G. Kirk, H.C. Berry of BNL for help in the MAFIA calculations and J. Rose of Grumman Aerospace Corporation for help in the bead-pull measurements.

VI. REFERENCES

1. A. Jain, I. Ben-Zvi, P. Paul, H. Wang and A. Lombardi, *Status of the SUNY Superconducting RFQ*, these proceedings.
2. I. Ben-Zvi, A. Lombardi and P. Paul, *Design of a Superconducting RFQ Resonator*, Particle Accelerators (in press).
3. A. Schempp, M. Ferch and H. Klein, *Proc. 1987 Particle Accelerator Conf.* in IEEE Trans. Nucl. Sci. **87CH2387-9**, 267 (1987).
4. *MAFIA User Guide*, The Mafia Collaboration, DESY, LANL and KFA, 1988.
5. I. Ben-Zvi, A. Jain, A. Lombardi, and H. Wang, *Electrical Characteristics of a Short RFQ Resonator* in *Proc. 1990 Linac Conf., Albuquerque, NM*, p. 73.
6. J. Tückmantel, *Application of SAP in URMEL*, CERN/EF/RF **85-9**.
7. T. Weiland, *On the Numerical Solution of Maxwell's Equations and Applications in the Field of Accelerator Physics*, Particle Accelerators **15**, 245 (1984).

Deceleration of Antiprotons with a RFQ

A.Schempp, H. Deitinghoff, A. Firjahn-Andersch, H. Vormann
Institut für Angewandte Physik, J.W. Goethe University, Frankfurt, D-6000, Germany
M. de Saint Simon, J.Y. Hemery, C. Thibault,
Centre de Spectroscopie Nucleaire et de Spectrometrie de Masse, F-91406 Orsay, France
F. Botlo-Pilat[x]
CERN, CH-1211, Geneva, Switzerland and CSNSM, F91406 Orsay, France

Abstract

A 4-Rod-RFQ has been built for the deceleration of antiprotons which will be extracted from LEAR at 2.0 MeV and injected at 0.2 MeV into the rf-mass spectrometer built by CSNSM, Orsay for the high precision mass comparison of protons and antiprotons (PS189). The properties of the RFQ system, which should improve the counting rate by a factor of up to 10^3, the status of the project will be reported.

I. INTRODUCTION

RFQs have been built for various applications namely high current proton injectors for synchrotrons, accelerators for polarized ions, for heavy ions, and also industrial use. RFQs are unique for low energy acceleration because of the strong electric focusing with rf quadrupole fields. Input and output energies are fixed and the emittance growth can be made very small [1,2,3].

The ion source can be close to ground potential, thus allowing the use of bulky and complex ion sources like for high currents or for high charge states as well as for polarized beams and clusters. A heavy ion prestripper accelerator and e.g. LEAR (the "low energy antiproton ring" at CERN) represent bulky ion sources for which RFQs can provide efficiently post acceleration or deceleration with strong focusing and little emittance growth [4,5].

The first proposals for the deceleration of antiprotons were not realized because of the complexity and the costs involved [6,7]. A new effort by CSNSM Orsay employed a less complex RFQ structure, simpler bunching schemes, and uses only fast extraction from LEAR, thus avoiding changes in LEAR. The optimization was done for their specific experiment "Antiproton-Proton mass comparison with a radiofrequency mass- spectrometer" (PS189 [8,9.]). A layout of experiment is shown in Fig.1.

The aim of the experiment is the reduction of the present upper limit on a hyphothetical CPT theorem violation in baryon-antibaryon pairs. The experimental set-up is a specially designed radiofrequency mass spectrometer of L.G.Smith type which has been installed at the LEAR experimental area in order to make a comparison of the charge to mass ratio of an antiproton and a proton by measuring the cyclotron frequencies of antiprotons and H^- ions rotating in the same very homogenous magnetic field. The physical parameters are fitted to reach a mass comparison accuracy of 5×10^{-9} [10]. The radial acceptance of the spectrometer is extremly low: $\alpha_H = 1.$, $\alpha_V = 2.\pi$ mm×mrad and the energy spread must be smaller than $\Delta T/T = \pm 6$ eV. The kinetic energy of the particle is not allowed to exceed 0.2 MeV. The deceleration with the RFQ has to be optimized for the transmission to the spectrometer. The overall transmission is planned to be 10^{-5} to gain at least 10^2 in comparison with an energy degrading process using a foil.

II. THE DECELERATOR SYSTEM

The RFQ decelerating system has to match the spectrometer, it has to be compact and to give a high transmission to the spectrometer.
A small radial emittance growth is always important but maximizing the transmission of the RFQ in the usual way may even dilute the effective phase space. There is a buncher 1.5m

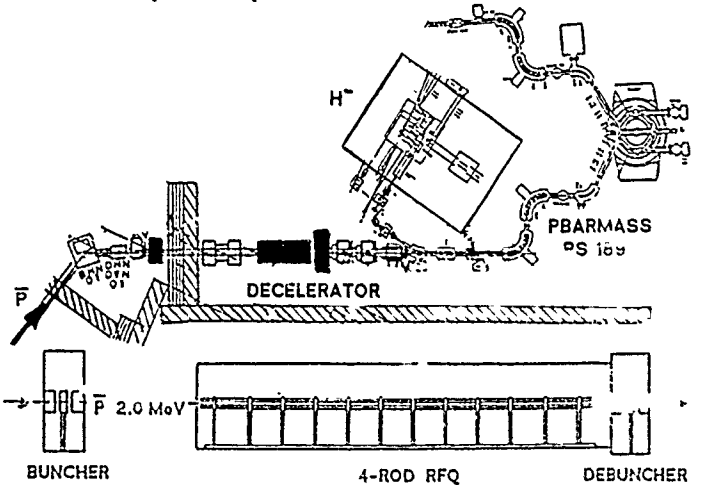


Fig.1 Layout of the experiment PS189

[x]now at SSC, Waxahachie, Tx

0-7803-0135-8/91S03.00 ©IEEE

infront of the RFQ to give a time focus at the first RFQ cell with a small energy spread. The orientation of the longitudinal output ellipse will be fine tuned with the help of a debuncher cavity attached directly to the low energy end of the RFQ because the orientation of the output ellipse is sensitive to the electrode voltage, the buncher voltage and possible energy variations of the beam. These additional degrees of freedom allow both a precise orientation of the output ellipse and some energy variation [11].

The 4-Rod RFQ resonator [12] uses an array of flat stems on a common base plate supporting the four electrodes which have a periodically changing diameter. The resonant 4-Rod insert is surrounded by a copper plated vacuum tank and driven by one loop and tuned with one plunger. Rf-stabilization is not neccessary.

A short RFQ has been designed [13] with a high electrode voltage and without an adiabatic bunching scheme, because the spectrometer accepts only the core of the beam. The beam dynamics design of the RFQ, which determines the variation of modulation, aperture and cell length along the RFQ, is characterized in fig. 2, table I gives characteristic parameters.

The bunchers are spiral loaded cavities [14]which are efficient and compact. They have been developed for application in postaccelerators and are based on $\lambda/4$ coaxial resonators in which the inner conductor is wound up to a spiral. It carries a drift tube at the open end which together with the drift tubes of a pill box cavity form two accelerting gaps for $\beta\lambda/2$-mode operation. Fig.3 shows a scheme of the spiral cavity and the the field distribution in the debuncher, table II summarizes the properties.

The beam transport system has been optimized to the small acceptance of the PS189 spectrometer. The high energy beam line with a length of 30m transports the $\bar{p}$ beam from LEAR to the entrance of the RFQ. Changes have only been made to the part after the bending magnet to avoid emittance dilution by the chromaticity. The design which can be adopted to different RFQ input matching conditions is shown in Fig.4.

The low energy beam line is about four meters long. Critical points are the transverse emittance increase of about a factor three caused by the deceleration process and the final energy spread of roughly 4%. The orientation of the longitudinal $\Delta\varphi$–ΔT ellips can be changed by the debuncher, placed as close as possible to the RFQ. Fig. 5 shows results of calculations with PARMTEQ for the deceleration of a $\bar{p}$ beam with LEAR parameters which give a transmission of 1×10^{-5} for the overall system.

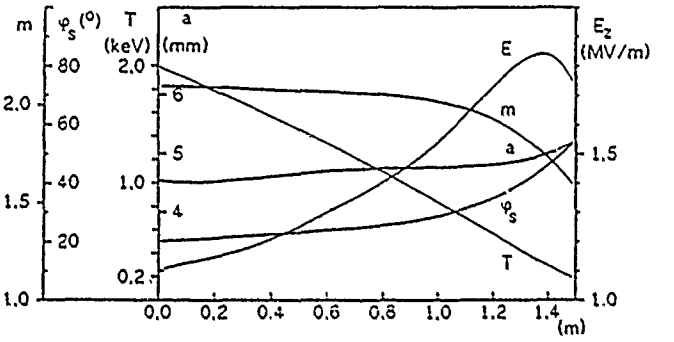


Fig.2 Electrode design of the decelerating RFQ

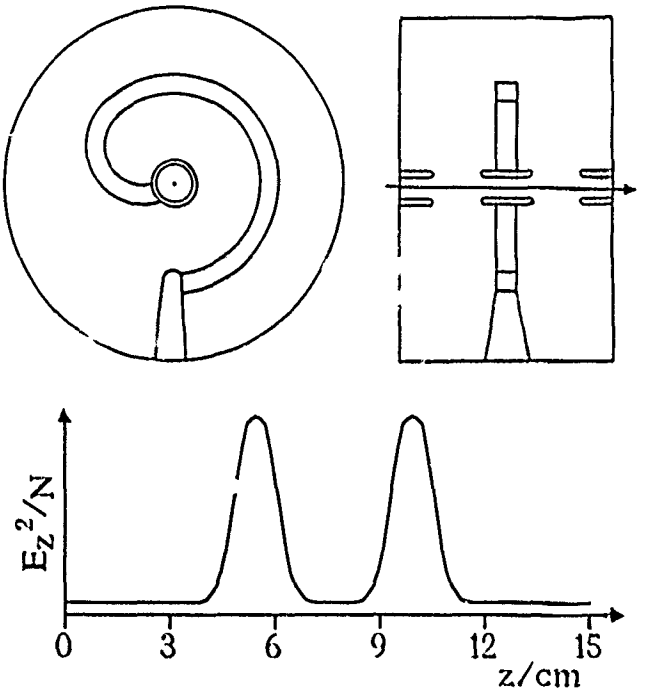


Fig.3 Scheme of spiral cavity and axial field distribution of the spiral debuncher

Table I Parameters of the decelerating RFQ

Frequency	202.5 MHz,	Electrode voltage	111kV
Input energy	2.0MeV,	Output energy	0.2MeV
Length	1.49 m,	Number of cells	46
Phase	-160 - -126°,	Aperture	4.5-5.25 mm
Modulation	2.1-1.6,	Max. field	35MV/m
Impedance R_p	57 kΩ,	Rf-power	220 kW
normalized transverse acceptance			5.0 π mmmrad

Table II Parameter of the spiral buncher/debuncher

Frequency	202.5 MHz,	Input energy	2.0/0.2MeV
Length	0.2/0.15 m,	Impedance R_p	6/4.9 MΩ
Q	4100/3900,	Aperture	25/20 mm
Rf-power	1/0.25 kW,	cavity voltage	80/35 kV

III. STATUS

The experimental set up is now near completion. The RFQ and the bunchers have been built and tuned. The RFQ-impedance has been measured to 57 kΩ and the field flatness is better than 3% which are close to theoretical values. The decelerator has been shipped to CERN and is currently being installed in the PS189 beam line. Rf-tests will be done in the first weeks of June after which a first antiproton data taking run is planned.

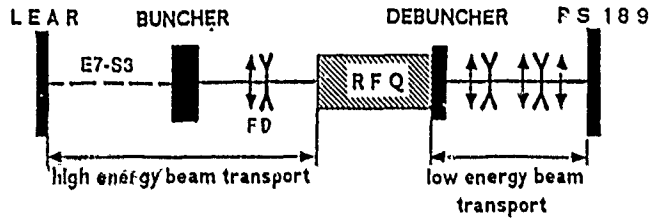


Fig. 4 Beam transport lines for PS 189

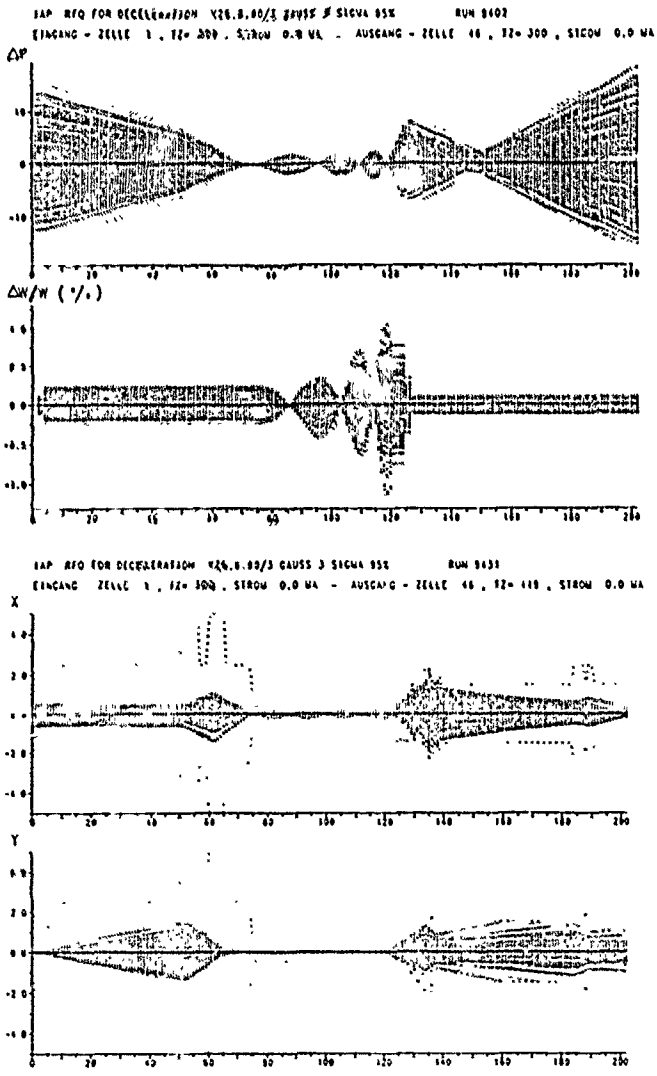


Fig. 5 PARMTEQ simulations of $\bar{p}$ deceleration

IV. REFERENCES

[1] I.M. Kapchinskij, V.A. Teplyakov, Prib. Tekh. Eksp. (1970) 17,19
[2] R. Stokes, T.Wangler, Rev.Part.Sci. 38(1988)97
[3] A. Schempp, Linac88, CEBAF-89001(1989)460
[4] A.Schempp et al., Linac84, GSI-84-11(1984)100
[5] P. Lefevre, D. Möhl, Cern PS Rep. 1984
[6] J. Billen et al., LEAR-3, Ed. Front. (1985)107
[7] C. Biscari, F. Iazzourne, LEAR-3.Ed.Front.(1985)
[8] C. Thibault et al., Nucl. Phys. B8 (1989)454
[9] M. deStSimon et al.,LEAR-4,Ed.Front.(1987)633
[10]A. Coc et al., LEAP 90, Stockholm, July 1990
[11]A. Schempp et al., Linac90, LA12004-C(1990)683
[12]A. Schempp et al., NIM B10/11(1985)831
[13]A. Schempp, EPAC 88, World. Sci. (1989)464
[14]J. Häuser et al., EPAC88, World Sci.(1889)1140

V. ACKNOWLEDGEMENTS

We want to thank H. Bernas, P. Lefevre, H.Haseroth and M. Weiss, M Zanolli, F. Nitsch, J. Friedrich and A. Kipper for support, J.P. Kapinsky for a special lecture and PET for good cooperation.

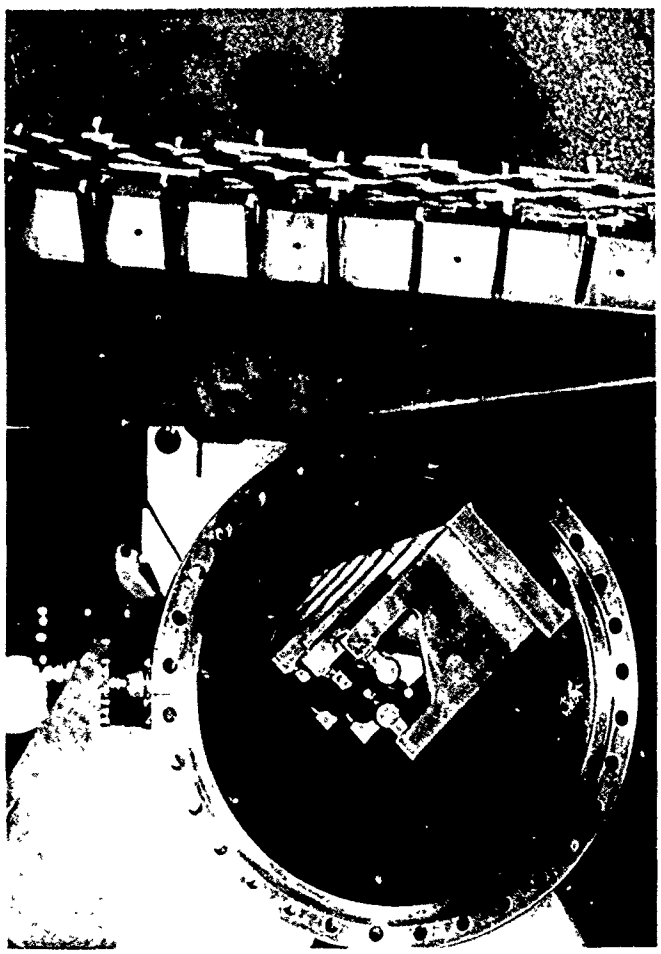


Fig. 6 Views of the decelerator RFQ

Properties of the GSI HLI-RFQ Structure*

J. Friedrich, A. Schempp, H. Deitinghoff, U. Bessler, H. Klein, R. Veith
Institut für Angewandte Physik, J.W. Goethe University
D-6000 Frankfurt 11, Germany
N. Angert, J. Klabunde,
GSI, Planckstr. 1, D-6200 Darmstadt 11, Germany

Abstract

A "High Charge State Injector (HLI)"- RFQ for the GSI, designed for the acceleration of U^{28+} from 2.5 to 300 keV/u has been built and tuned. Properties of the RFQ structure and first experimental results will be presented.

I. INTRODUCTION

The GSI accelerator facility consists of the UNILAC, the heavy ion synchrotron SIS and the storage ring ESR. The SIS synchrotron can accelerate all elements up to uranium to energies above 1 GeV/u [1,2].

To fill the SIS up to its space charge limit and to use the full potential of the new GSI accelerator complex a new high current injector in front of the UNILAC is planned which will accelerate up to 25 emA U^{2+} ions with a small duty cycle.

The development of new sources for highly charged heavy ions but lower currents (design value e.g. 5 emA instead of 25 emA) enable direct acceleration of U^{28+} ions in a new high charge state injector (HLI) for the Alvarez part of the UNILAC to supply independantly heavy ion beams for the physics program in the UNILAC experimental hall [3]. The HLI injector, which is shown schematically in Fig.1 and described in a separate paper [4], consist of an ECR source [5], an RFQ [6,7] and an IH-structure [8].

The 4-Rod RFQ will accelerate heavy ions with charge to mass ratio of $q/u \geq 0.117$ (U^{28+}) from 2.5 keV/u to 300 keV/u which corresponds to an energy gain of 2.5 MeV/q [9].

With this new injector uranium ions extracted from the ECR source will be accelerated to to 1.4 MeV/u and injected into the Alvarez structures without passing any stripper thus replacing the Wideroe/Stripper part of the UNILAC which is then dedicated to short pulse high current acceleration for SIS injection only.

II. THE 4-ROD RFQ

The 4-Rod RFQ rf-structure consists of coupled $\lambda/2$- oscillators in a linear arrangement of straight radial stems and circular rod electrodes as indicated in fig.2 [10]. Although the currents are concentrated on the stems the efficiency does not fall short compared with other RFQs. The resonator is very stable with respect to rf operation because neighbouring modes are clearly separated and all major current conducting parts can easily be cooled, which is important especially for high duty cycle operation as planned for the HLI-injector.

The design of the GSI RFQ follows the design succesfully applied for CRYRING-RFQ [11,12] but all parameters have been stringened.

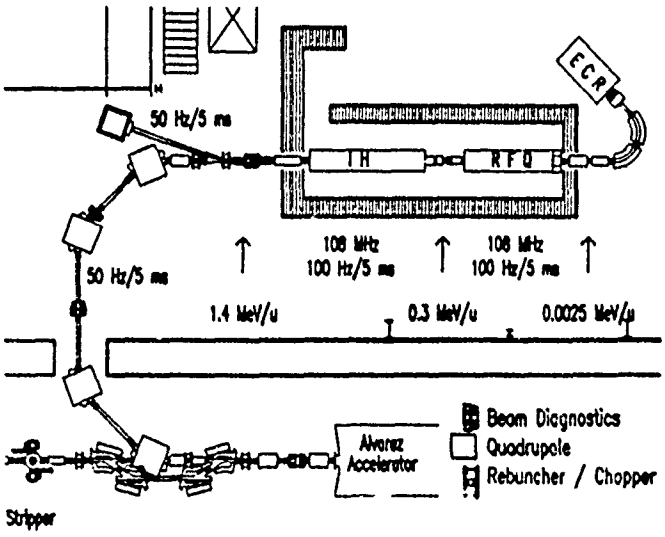


Fig. 1 Layout of the 1.4 MeV/u injector (HLI)

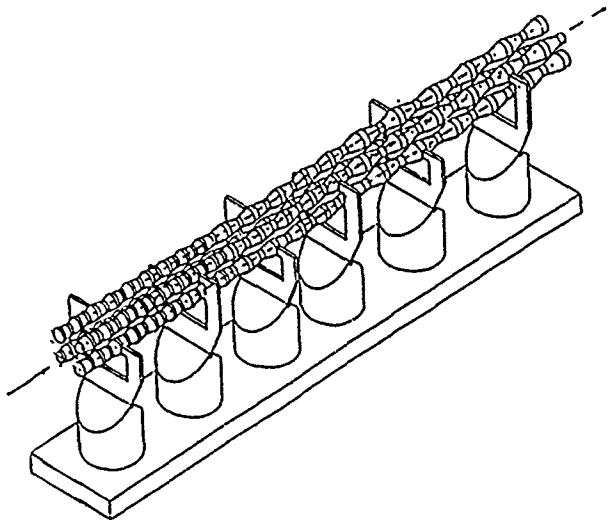


Fig. 2 Scheme of the 4-Rod RFQ structure

*Work supp. by BMFT under contract FKLA
0-7803-0135-8/91$03.00 ©IEEE

The RFQ structure should be as short as possible to save rf power and costs proportionally. When the structure frequency and electrode voltage have been chosen to give good focusing properties, the length L_S has to be optimized with respect e.g. to the beam emittance, the power consumption and the transmission, which is the ratio of d.c. input beam versus output beam.

Fig. 3 shows the final design parameters a,m, and L_i along the RFQ structure. Table I summarizes characteristic parameters. The slow increase of the ion energy T as function of the RFQ cell number N is demonstrating the fact that a significant part of the RFQ structure is required for bunching.

Results of PARMTEQ calculations [13] show a normalized radial acceptance of 1π mm mrad, for a transverse input emittance of 0.8π mm mrad the transmission is 90%. For a matched beam (α_{xy}=0.7, β_{xy}=1.6 cm/rad) and the design emittance of 0.5 π mm mrad the transmission is 99% at an emittance increase of only 10% for the full beam. Figs. 4 and 5 show the corresponding output emittances at the end of the electrodes and the phase and relative energy spectra. As can be seen from fig. 6a a few particles (about 5%) are transfered into neighboring buckets during the first stage of bunch formation. The longitudinal emittance is 10°keV/u (100%r.m.s.)

The transverse beam behaviour is plotted in fig.6 for the full beam. All calculations were done for an injected dc beam without energy spread and a transverse waterbag distribution. Fig. 7 shows results of calculations for a mismatched input beam (1mm radial displacement). While the transmission is reduced (99 to 72%) the radial output emittance is nearly constant (from ε_N=0.55 to ε_N=0.74 π mm×mrad)

Fig. 7 shows the low energy end of the cavity, which incorporates also beam diagnostic devices and indicates the coffin like design with a wide top flange along the RFQ which facilitates installation, alignment and maintenance. The RFQ has been manufactured, assembled, aligned and tuned to the operating frequency of 108.5 MHz.

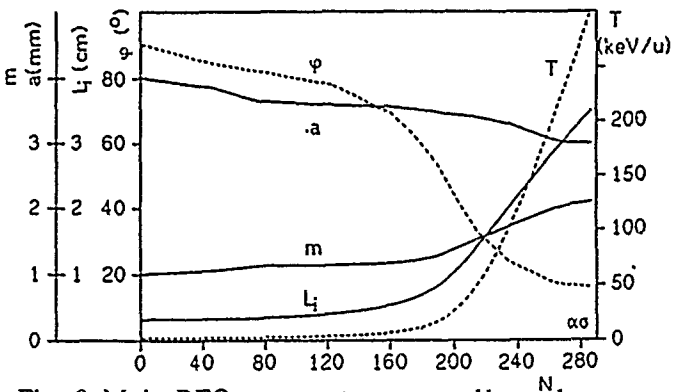


Fig. 3 Main RFQ parameters vs. cell number

The field flatness is within 5% as shown by fig.8, the Q value is Q=4150 and the impedance is R=200kΩm which means that a rf-power of 100kW is required for the design field amplitude. Fig. 9 shows views of the HLI-RFQ.

The HLI-RFQ is undergoing rf-tests now and first beam tests are planned for the week after a shut-down period in May.

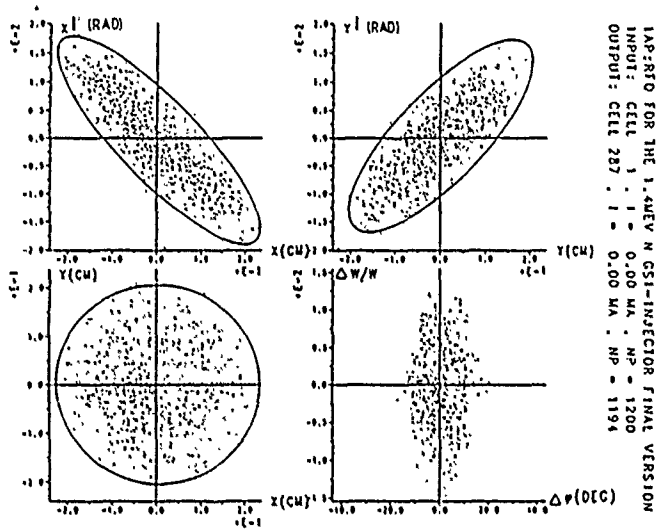


Fig. 4 Output emittances of the HLI-RFQ

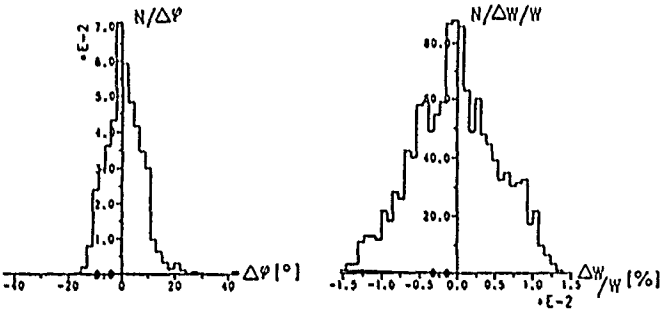


Fig. 5 Phase and energy spectra behind the RFQ

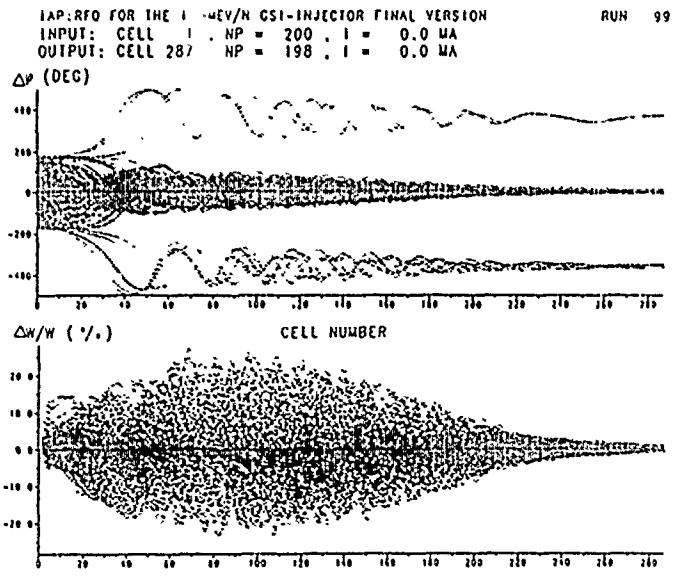


Fig. 6 Longitudinal beam behaviour along the RFQ

III. ACKNOWLEDGEMENTS

We thank those who helped and those which are patiently waiting for the completion and hope they will still be patient until everything is perfect.

IV. REFERENCES

[1] K. Blasche, D. Böhne, IEEE 89CH2669(1989) 27
[2] B. Franzke, IEEE NS 32-5(1985)3297
[3] N. Angert et al., Linac90, LA12004-C(1990)749
[4] N. Angert et al., this conf.
[5] R. Geller, PAC 89, IEEE 89CH2669(1989)1088
[6] I.M. Kapchinskiy and V. Teplyakov, Prib. Tekh.Eksp. 119, No.2(1970) 17,19
[7] A. Schempp, Linac88, CEBAF-89-001(1989)460
[8] U. Ratzinger, Linac90, LA12004-C(1990)525
[9] A. Schempp, IEEE 89CH2669(1989) 1093
[10] A. Schempp et al., NIM B10/11(1985)831
[11] A. Schempp et al., EPAC II, Ed. Front.(1990)1231
[12] A. Schempp, EPAC I, World Sci., (1988)464
[13] H. Deitinghoff et al., GSI 91-1 (1990) in print

Table I. Parameters of the HLI-RFQ

Injection/final energy	2.5 / 300 keV/u
Charge to mass ratio	28/238 - 1
Frequency, electrode voltage	108.5 MHz/80kV
Duty cycle - rep. rate	25-50%, 50-100 Hz
Aperture/modulation	3.0 mm / 1 - 2.1
Tank diameter, length	35 cm / 3.0m
Radial acceptance (norm.)	1.0 π mm mrad
Input/output emittance	0.5/0.55 π mm mrad
Longitudinal emittance r.m.s. (100%)	10° keV/u

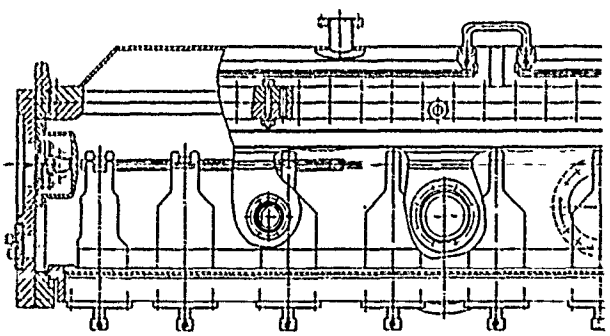


Fig. 7 Low energy end of the HLI-RFQ

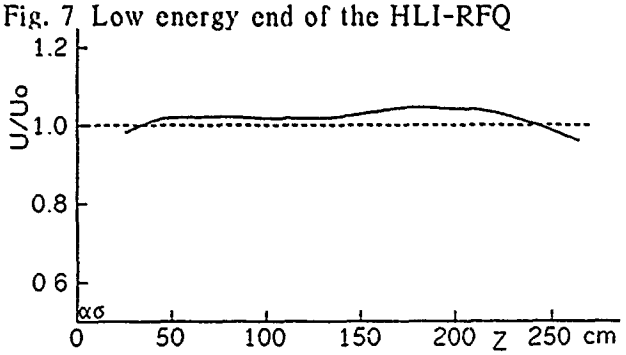


Fig. 8 Voltage distribution along the RFQ

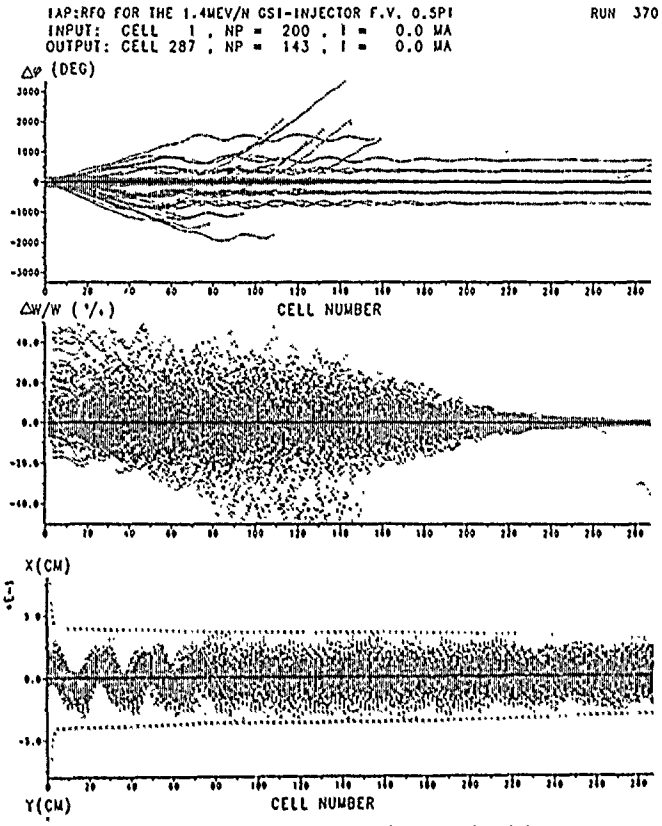


Fig. 7 Beam behaviour for a mismatched beam

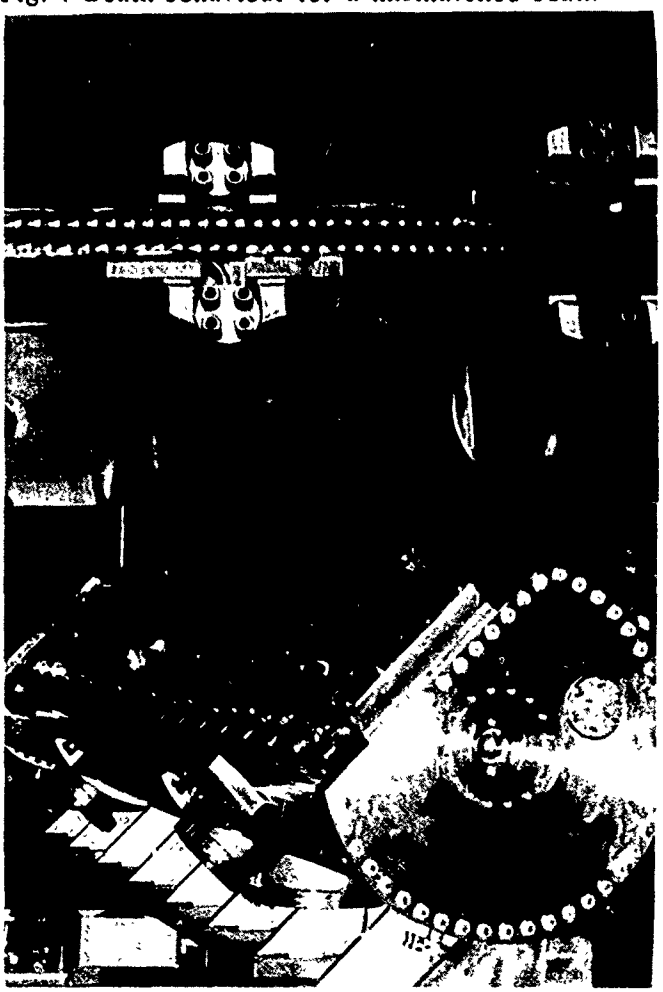


Fig. 9 Views of the HLI RFQ

New Vanes for RFQ1: Fabrication, Installation, and Tuning†

B.G. Chidley, G.E. McMichael, T. Tran-Ngoc
AECL Research, Chalk River Laboratories
Chalk River, Ontario, Canada, K0J 1J0

Abstract

The Chalk River RFQ1 accelerator was built with replaceable vanes, and the design of a new set of vanes was described at the 1990 Linear Accelerator Conference [1]. The vanes have now been fabricated. They are identified as RFQ1-1250, while the original vanes are identified as RFQ1-600. The RFQ1-600 vanes were designed with a peak surface electric field of 1.5 times Kilpatrick, which is now viewed as being too conservative. The new design uses a peak field of 1.8 Kilpatrick and a modified tip profile to increase the output energy from 0.6 MeV to 1.25 MeV. Computer simulations have been done using PARMTEQ and RFQCOEF to assess the effects of higher order harmonics of the potential on beam losses. The vanes have been machined out of GlidCop® AL-15 [2] (an alumina dispersion-strengthened copper) with the cooling channels gun drilled. Details of the fabrication, including details of the tip profile cutting, installation and tuning are described.

I. INTRODUCTION

The new vanes for RFQ1 had to be designed within constraints imposed by the existing structure. The principal changes are in the vane tip shape and modulation, but there are some changes in the vane body related to the structural material and machining techniques. The basic parameters are given in Table 1.

TABLE 1
RFQ1 Basic Parameters

Frequency	267.0 MHz
Input Energy	50 keV
Vane Length	146.88 cm
Beam Current	75 mA
Beam Emittance (rms, norm)	0.05 π cm mrad
RF Power	200 kW max
Peak Surface Electric Field	1.8 * Kp

†This work was partially supported by Los Alamos National Laboratory under contract no. 9-X5H-0578G-1.

0-7803-0135-8/91$03.00 ©IEEE

II. MECHANICAL DESIGN

The differences in cross-section shape between the RFQ1-1250 vanes, as shown in Fig. 1, and the RFQ1-600 vanes occur at the tip and at the widening near the base (hip). The hip profile adjusts the resonant frequency to compensate for the smaller beam aperture.

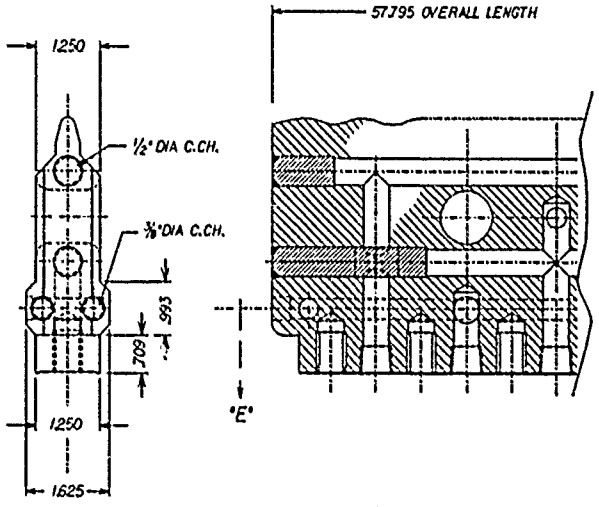


Figure 1 New vane design.

The vanes are machined from single blocks of GlidCop AL-15. The cooling channels are gun-drilled and the ends are closed with welded OFHC copper plugs [3].

III. VANE TIP PROFILE

The design procedure was as described in reference 1, except for minor changes in the final cell. The vane length is constrained to be exactly the length of the old vane. The preliminary design did not have an exact number of cells within this length and the final cell was simply truncated. It was decided to use the same final cell shape as used in the RFQ1-600 vane and this involved adjusting parameters to make the vane contain an exact number of cells. Design parameters are given in Table 2.

TABLE 2
RFQ1-1250 Design Parameters

Output Energy	1.274 MeV
Number of Cells	120
Vane Voltage	77.4 kV
Peak Field	1.75 * Kp
Transmission	87%

IV. VANE FABRICATION

RFQ1-1250 vanes were made by Westinghouse Canada Inc. on the same n/c milling machine that had been used for the RFQ1-600 vanes. Thus previous experience in coding for the milling machine was directly applicable to the new vanes.

A. Cooling Channels

Four cooling channels were gun-drilled through the full length of the vane: two 12.7 mm (½ inch) diameter holes and two 9.53 mm (⅜ inch) diameter ones. These channels have a combined water flow of 140 L/m at a velocity of 6.0 m/s.

The holes were drilled approximately halfway through from each end with a 20 mm overlap at the centre. Offset of the two holes was checked by pushing a 2 inch (50.8 mm) long standard cylindrical plug through the channel, and with an ultrasonic flaw detector. Typically, a 0.495 inch (12.57 mm) diameter plug could be pushed through the 12.7 mm holes, and a 0.364 inch (9.25 mm) one through the 9.53 mm holes.

The fact that a plug can be pushed through does not guarantee that both holes have not run out to the same side, so the wall thickness was measured ultrasonically. A special sensor was developed at Westinghouse Canada for this inspection, and calibration was done on shim stock made from GlidCop AL-15. Measurements for the worst case showed that the 12.7 mm holes meet with a 0.5 mm error and have a 0.7 mm run-out, leaving a minimum distance to the surface of 2.56 mm. The 9.53 mm holes meet with a 1.25 mm error and have a run-out of 1.6 mm, leaving a minimum distance to the surface of 1.57 mm.

The location accuracies of the cooling channels are acceptable; however, the above ultrasonic inspection results show that not enough material is left between the 9.53 mm diameter channel and the widening hip surface to allow metal to be shaved off vertically for a tuning adjustment. This will have to be done on the 45° surface above or below the channel.

The cooling channels connect to feeder channels drilled from the base of the vane and the ends of the holes are closed with welded AL-15 plugs. Experience has shown that this type of water-to-vacuum seal has high reliability.

B. Vane Coupling Rings

A pair of vane coupling rings is used similar to those of RFQ1-600. Spigots with stainless steel inserts have been used to reduce thermal conduction to the vane body, while retaining mechanical strength. This allows the rings to be soldered in-situ using a propane torch.

TIG welding of the original design of the spigot to a vane test piece failed, but a new design, as shown in Fig. 2, yielded a good joint and facilitated the job of dressing up the weld bead. Local distortion at the end of the vane after welding the spigots is in the order of 0.013 mm. This confirms that the welding operation on the vane can be done after finish machining of the vane, which would simplify fabrication.

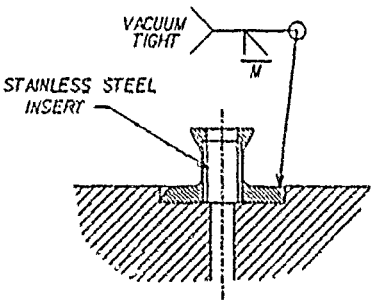


Figure 2 Welded joint between VCR spigot and vane body.

C. Mounting

The vane is mounted in the same manner as the RFQ1-600 vanes, using a copper "racetrack" gasket as a combined vacuum and rf seal. Tests indicate that AL-15 is hard enough to bite into the copper gasket and make a good seal. The holes for the mounting and adjustment bolts have HELI-COIL® inserts in them and tests have confirmed that these are suitable for the high torque used in clamping the "racetrack" gasket.

D. Tip Profile

The tip was machined with a spherical tipped end mill with a 0.5 inch (12.7 mm) radius. The cutter followed a transverse path, as indicated in Fig. 3, with longitudinal steps for the final cut of 0.5 mm. The cutter axis of rotation was inclined at 45° to avoid scuffing at the tip of the vane. The cutter radius was chosen to be the largest standard size which would not exceed the radius of curvature at the saddle point between modulation peaks. The 45° inclination of the cutter axis allows the rounding of the input end of the vane to be done, but limits the rounding at the output end to 45°. Since the rounding at the output end is arbitrary and needed only to prevent sparking, it is planned to break the sharp edge with a hand tool. The longitudinal profile has no portion where the tangent exceeds 45°, so no problems arise.

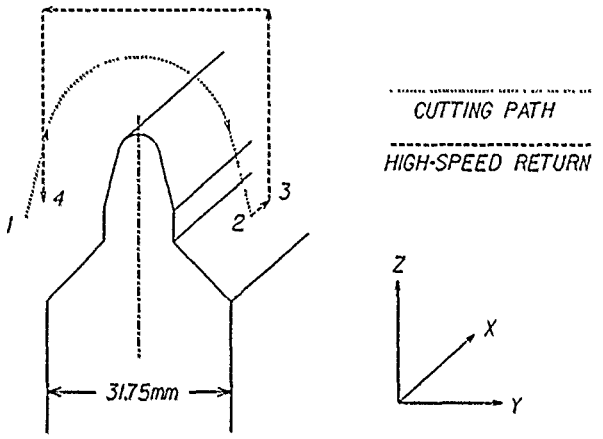


Figure 3 Path of milling machine cutter.

Eight specially made tungsten carbide tool bits had their diameters measured to the nearest 0.0025 mm. They were all within 0.025 mm and the four best were selected for the finish cuts. Machining was done using sulphur-free Sunicut 150 cutting oil at room temperature.

Milling of the vanes was completed in late April and RFQ1 has been dismantled in preparation for their installation.

V. Tip Profile Measurements

Vane tip profiles were inspected on a DEA coordinate measuring machine using a Renishaw sensor unit. The height of the vane tip at its centre-line was measured in 1 mm steps for three 50 mm long regions (at each end and at the centre) and in 5 mm steps for the remainder. The measurements were made using a 0.980 mm radius ruby sphere. The analysis program corrects for the sensor size and plots the difference between the design and measured values, as shown in Fig. 4.

Transverse profiles were measured at 5 positions corresponding to a peak or valley (where no longitudinal correction for sensor size was required). The cross section is a circular arc to within ± 0.02 mm, and agrees with the design value within the same tolerance. This confirms that the tool bit was not worn appreciably during the machining.

VI. Installation and Tuning

At the time of writing this paper, installation of the new vanes is about to begin. The procedure will be the same as used for RFQ1-600 [4,5], with the option of machining the vane hip if necessary for coarse tuning.

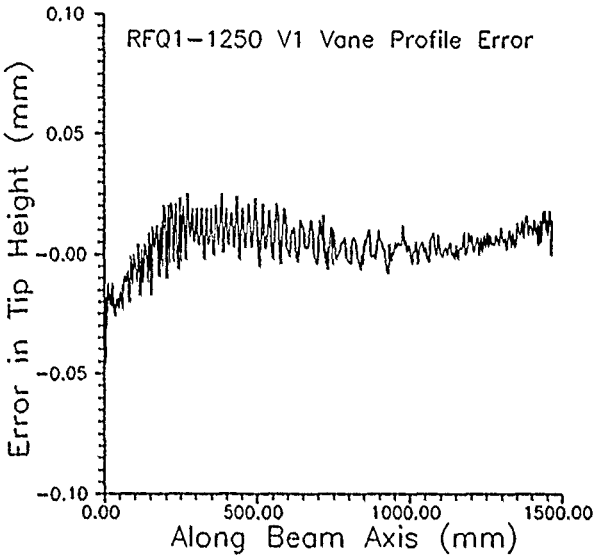


Figure 4 Vane 1 Profilometer measurements.

VII. Summary

The new vanes are within design tolerances. The AL-15 alloy appears to be a suitable material for this application as it has a conductivity near that of OFHC copper, but a much higher yield strength and good machining characteristics. Abrasion of the tool bits by the dispersed alumina is not a problem.

VIII. References

[1] B.G. Chidley et al., "New Vanes for RFQ1", 1990 Linear Accelerator Conference, LANL Report LA-12004-C, 42 (1990).

[2] GlidCop Products Information Bulletin, SCM Metal Products Inc., 1988.

[3] T. Tran-Ngoc and E. C. Douglas, "Mechanical Design of New Vanes for RFQ1",1991 Unpublished report, RC-548, available from Scientific Document Distribution Office, Chalk River Laboratories, Chalk River, Ontario K0J 1J0.

[4] G.E. McMichael et al., "RFQ1 Fabrication and Low Power Tuning", 1987 IEEE Particle Accelerator Conference, Catalog No. 87CH2387-9, 1875 (1987).

[5] R.M. Hutcheon et al., "The RF Design of a 270 MHz, CW Four Vane RFQ", 1985 Particle Accelerator Conference, IEEE Trans. Nucl. Sci., NS-32 (5), 2769 (1985).

Progress of the 473 MHz Four-Rod RFQ

Reza Kazimi, F. R. Huson, and W. W. MacKay
Department of Physics, Texas A&M University and Texas Accelerator Center†
TAC, 4800 Research Forest Dr., Bldg. 2
The Woodlands, TX 77381

Abstract

We have constructed a new four-rod type Radio Frequency Quadrupole to operate at 473 MHz. Four-rod type structures have not been used for such a high frequency before. The RFQ is designed to accelerate 10 mA of H^- ions from 30 keV to 0.5 MeV. Low rf power and high rf power measurements of the RFQ have been performed successfully. In this paper we will present our design of the RFQ and the results of tests related to low and high rf power operations such as Q and power measurements, multipactoring problems, sparking problems, vacuum performance, and cooling.

I. INTRODUCTION

The four-rod RFQ structure invented at Frankfurt [1] not only has been a viable alternative to the four-vane structure, but also offers several advantages such as simplicity of structure and elimination of the dipole mode. However, the four-rod design has not been studied extensively for frequencies much above 200 MHz. Higher frequencies (400 to 500 MHz) are desirable for pre-injectors of proton machines. We have developed a four-rod type design for these higher frequencies by introducing a small variation to the Frankfurt geometry [2,3]. After designing several simple test models, checking them using computer codes such as MAFIA [4], and obtaining desirable results from cold model measurements, we set out to make a test RFQ at 473 MHz and to accelerate a 10mA of H^- ion beam from 30 keV to 500 keV. (The reason for 473 MHz is the rf power source.) A cold model was built and tested with results which matched our theoretical calculations very well [5]. Next, we made a full beam dynamics design for a short low power RFQ. Pieces were machined and assembled and a cold test of the RFQ was done. This paper will discuss the design of the structure, the beam dynamics design, and the results of the cold and high power rf tests of the final RFQ.

II. THE STRUCTURE

The structure is made of a series of modules. Figure 1 shows two modules next to each other. Each basic module of length ℓ consists of two square plates of thickness T and width W supporting the four rods. Each supporting plate is connected to two opposing rods. Four rectangular plates cover the sides of the structure with the corners of the structure being left open to give better vacuum quality. The corners can be left open for the following reasons: First, the diagonal planes going through the opposing corners are the symmetry planes of the structure. Therefore, there should be no currents crossing these planes. In other words, the $\vec{B}$ field is perpendicular to these planes. Second, the fields are weak at the corners, so leaving the corners open should not appreciably change the resonant frequency or the Q. Figure 2 shows the magnetic field for a cross section at the middle of a module ($z = \ell/2$), showing that $\vec{B}$ is negligible at the corners.

Since the two opposing rods are attached to the same plates at many points through the structure, the dipole mode, which appears when the two opposing rods oscillate at different voltages, is not a problem. In other words, there is no mixing of unwanted dipole modes with the desired quadrupole mode. This is an advantage that all the four-rod type structures share over the four-vane types in which the mode mixing can be a serious problem.

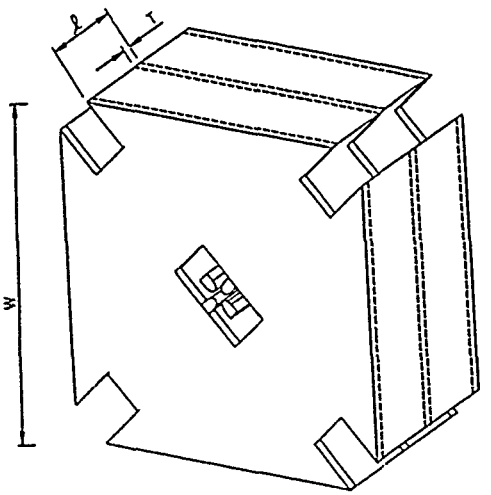


Figure 1. Two modules of the 473 MHz structure.

† TAC at HARC is a consortium of Rice University, Texas A&M University, The University of Houston, The University of Texas, Prairie View A&M university, Sam Houston State University, and the Baylor College of Medicine MR Center. This work was also supported by the SSC laboratory.

0-7803-0135-8/91$03.00 ©IEEE

All parts of the structure are bolted together and can be fully disassembled. To make it possible for the vanes to be positioned exactly in place and attached to the square plates, each plate is split diagonally into two halves. The rods are then held in place between these two halves and positioned using dowel pins. To make good rf contacts at the joints, thin annealed copper wires are squeezed in at the contact points between the plates and the sidewalls, and the rods and the plates. However, we need not worry about the quality of the joints between the two halves of the square plates; since they fall on one of the two diagonal symmetry planes which have no currents crossing them.

To design such a structure at a specific frequency, we only need to design a module using the MAFIA code. Since the structure is made of a series of identical modules it will have the same frequency, quality factor, power per unit length, etc., as a single module. Our RFQ structure is made of 10 modules. Table 1 lists the dimensions of a module for the 473 MHz structure. It also lists the frequency and Q factor predicted by MAFIA and capacitance per unit length of the vanes calculated by the CAP program, a modification of POSSION for calculating capacitance. Note that the quality factor predicted by MAFIA is not a good prediction since the Q factor also depends on other factors such as small geometrical details and surface quality, which are not taken into account by the code.

III. THE BEAM DYNAMICS DESIGN

The beam dynamics of the RFQ has been studied using the PARMTEQ program. In this design an effort has been made to keep the length of the RFQ short and the intervane voltage low, so that the total power required is below 100 kW. The input to the RFQ is 10 mA and 0.7 π mm·mrad (normalized 90%) emittance. The output beam should be about 9 mA with less than 10% emittance growth. Table 2 and Figure 3 give the parameters of the RFQ.

Table 1
Dimensions of a 473 MHz module

Length of the module(ℓ)	5.48	cm
Width of square plates (W)	18.8	cm
Thickness of the plates (T)	1.27	cm
Intervane capacitance (C_T)	107	pf/m
MAFIA Results:		
Frequency	473	MHz
Q	8500	

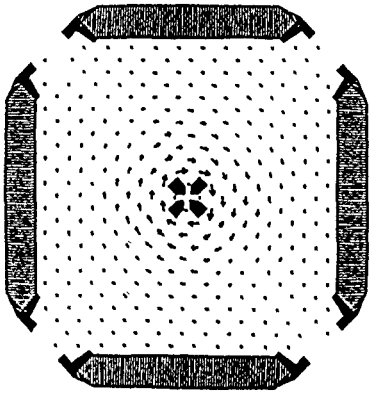


Figure 2. Plot of the magnetic field in the middle of a module. (MAFIA output)

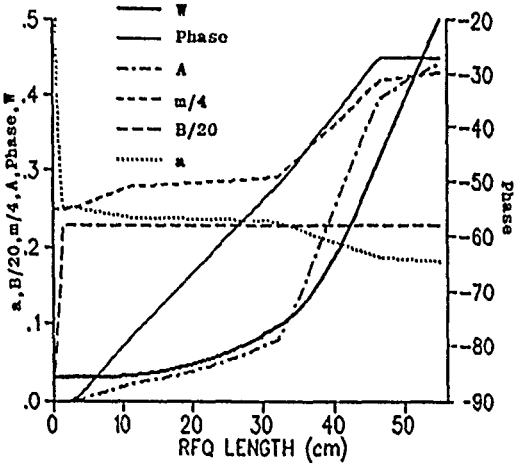


Figure 3. The RFQ parameters vs. RFQ length.

Table 2
RFQ Parameters

Ions	H^-	
Target frequency	473	MHz
Initial energy	30	keV
Final energy	500	keV
Nominal Current	10	mA
ϵ_t (norm,90%)	0.7	π mm.mrad
Transmission	95%	
Vane length	56.25	cm
Intervane voltage	67	kV
Aperture (r_0)	0.25	cm
The Cold Model:		
Frequency	473.1	MHz
Q	4400	
The RFQ:		
Frequency	470.3	MHz
Q	5000	
Power	90	kW

IV. THE RFQ

The RFQ consists of 10 modules described above. At the low energy end of the RFQ, a small single gap cavity has been added to eliminate any axial electric field at the beginning of the RFQ. The two opposite corners of the wall between this extra cavity and the first module of the RFQ have been opened wider to let the magnetic field couple the cavity to the first module of the RFQ. The resonant frequency is kept constant by decreasing the length of the first module in the RFQ from 5.48 cm to 4.1 cm.

The coordinates for machining the RFQ vane tips were calculated based on the PARMTEQ results. The transverse radius of the vane tip is 0.188 cm ($0.75 \cdot r_0$) and is kept constant through the RFQ's length. The machining of the vanes was done on a MAZAK computer controlled milling machine. A high speed cobalt tool was used to machine the modulation on the vanes which are made of tellurium copper.

V. THE TEST RESULTS

A. The low RF Power Measurements

A resonant frequency of 470.3 MHz was measured for the RFQ. This is lower than the design frequency of 473 MHz by about half a percent and can be corrected by tuning. The measured unloaded Q value is 5000, requiring a structure power of about 90 kW which is within the reach of our 100 kW rf source. Figure 4 shows the reflection coefficient versus the frequency for the RFQ. No neighboring modes are seen within 100 MHz span of the desired mode, which confirms our prediction that there should be no mode mixing.

B. The High RF Power Measurements

The RFQ was put in a vacuum chamber and pumped to less than 10^{-7} torr. The rf power is provided by an EIMAC 2KDW60LA klystrode which is capable of providing pulsed power ($\leq 100\mu s$) up to about 115 kW [6]. The RF power is delivered via a 50Ω, $1\frac{5}{8}$'' diameter coaxial line. At the klystrode with the aid of a four port directional coupler and HP 408A power meter, the amounts of power transmitted to and reflected from the RFQ are measured.

A small pickup loop in the RFQ cavity gives a sample of the RF power inside the RFQ. Knowing the attenuation factor between this pickup loop and the input transmission line gives the measurement of the RF power inside the RFQ. (The attenuation factor was measured by a HP 8753B network analyzer.) The reflected power and power inside the RFQ are monitored by a fast digital scope (Tektronix 602A.)

The RFQ was conditioned by ramping up the RF power gradually. We have seen indications of multipactoring between the RFQ vanes at power levels from ~ 200 mW to few kilowatts. However once getting to higher power levels, we did not see any indications of serious multipactoring anywhere in the cavity. The RFQ was conditioned successfully up to 112 kW with $20\mu s$ pulses and 0.1% duty factor. This is well above our 90 kW target. The RFQ is water cooled on three sides and the temperature is monitored and kept constant within one degree celsius.

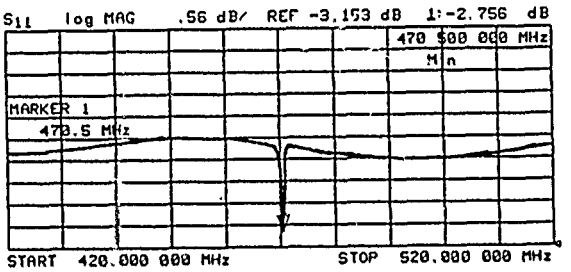


Figure 4. The reflection coefficient vs. frequency for the RFQ

VI. CONCLUSION

The cold tests and high rf power measurements of the RFQ have been accomplished, and the results are in good agreement with the calculations. The RFQ has been conditioned to 110% of the operating voltage. We are now in the process of attaching the RFQ to the ion source [7] and arranging a beam test.

VII. REFERENCES

[1] A. Schempp et al., "Zero-Mode-RFQ Development in Frankfurt," in Proceedings of the 1984 Linear Accelerator Conference, 100 (1984).

[2] R. Kazimi, "A Four-Rod Cavity RFQ," in *Proceedings of the 1988 Linear Accelerator Conference*, 140 (1988).

[3] R. Kazimi et al., "Study Of A Four-Rod RFQ Structure At 470 MHz," in *Proceedings of the 1989 IEEE Particle Accelerator Conference*, 990 (1989).

[4] R. Klatt et al., "MAFIA – A Three-Dimensional Electromagnetic CAD System for Magnets, RF Structures, and Transient Wake-Field Calculations," in *Proceedings of the 1986 Linear Accelerator conference*, 276 (1986).

[5] R. Kazimi et al., "Test of A 473 MHz Four-Rod RFQ," in *Proceedings of the 1990 Linear Accelerator Conference*, 698 (1990).

[6] W. W. MacKay et al., "Operation of A 473 MHz Pulsed Klystrode Power Source," in *Proceedings of the 1990 Linear Accelerator Conference*, 186 (1990).

[7] C.R. Meitzler et al., "Progress On The TAC Ion Source and LEBT," in *Proceedings of the 1990 Linear Accelerator Conference*, 710 (1990).

Development of a Variable Energy RFQ for Cluster Acceleration*

A.Schempp, J.Madlung, J.Dehen, H.Deitinghoff, J.Friedrich, A.Kipper
Institut für Angewandte Physik, Univ.Frankfurt, D-6000 Frankfurt 11, FRG
H.O.Moser, Institut für Mikrostrukturtechnik,
Kernforschungszentrum Karlsruhe, Postfach 3640, D-7500 Karlsruhe, FRG
G.Hadinger, M.J.Gaillard, R.Genre, J.Martin
Institut de Physique Nucleaire de Lyon, IN2P3-CRNS/Universite Claude Bernard,
43, Bd du 11 Novembre 1918, F-69622 Villeurbanne Cedex, France

Abstract

An RFQ has been designed and built as a postaccelerator for the cluster accelerator facility at the IPN, Lyon. The 4-Rod RFQ resonator is designed for variable energy by means of a variable frequency of the resonator between 80-110 MHz. The properties of the RFQ for the typical cluster mass ranges of up to 50u are discussed and the status of the project is reported.

I. Introduction

At the IPN, Lyon, a cluster ion source in combination with an electrostatic Cockroft-Walton accelerator is used for various experimental studies concerning the inner structure of clusters or the interaction of clusters with matter [1,2]. Up to now the maximum cluster energy is limited by the highest operational voltage of the Cockroft-Walton, which is 500 kV. Higher cluster velocities would increase the resolution of the measurements and widen the field of research: the comparison of effects from cluster and heavy ion impact on solids or the physics of clusters of molecules could be studied e.g.. Therefore an upgrading program of the facility was started in collaboration between IPN (Lyon), KfK (Karlsruhe) and IAP (Frankfurt) [3,4], which includes an RFQ post-accelerator and new beam lines. The RFQ accelerates clusters up to a mass of ~ 50u to energies as high as 100 keV/u and provides at the same time a sufficient transverse focusing, which is lacking in normal rf accelerators at low ion velocities. Fig. 1 shows a schematic layout of the new cluster facility.

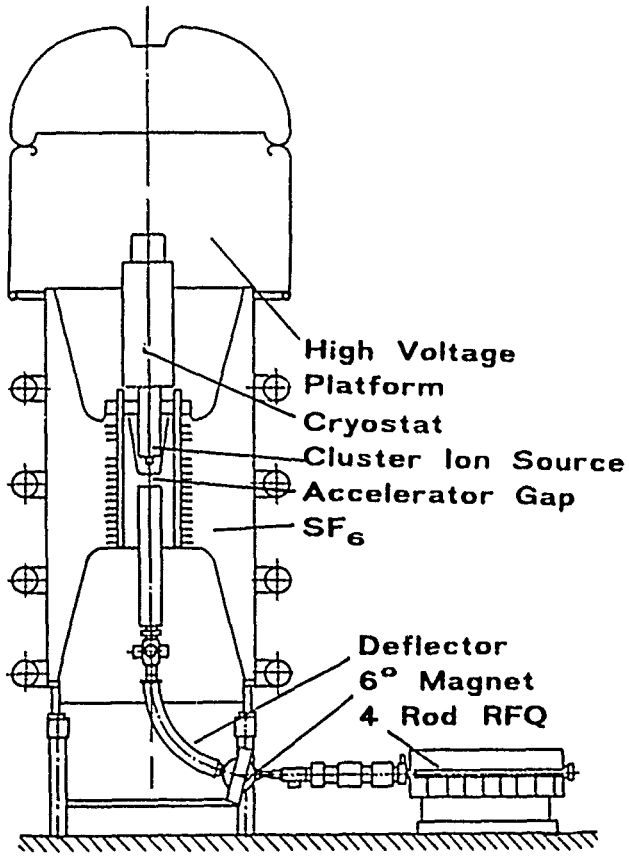


Fig. 1 : Schematic layout of the new cluster facility

II. The VE-RFQ Structure

RFQs are accelerator structures [5,6], which use electrical rf-quadrupole fields, generated by one set of electrodes, both for focusing and acceleration. But a fixed frequency accelerator is only capable to accept particles with one initial energy per nucleon and to accelerate them to one final energy per nucleon, because the velocity profile is also fixed. This can be changed by varying the cell length L_i or, as it is used in postaccelerator structures, by splitting up the structure into several individually phased units. Another way to fulfil the Wideroe resonance condition, $L_i=\beta_p\lambda_0/2=v_p/2f$, is to change the frequency f of the accelerator. Then a variation of the particle velocity v_p is possible, using the same fixed velocity profile of the electrodes : $v_p \sim f$.

The 4-Rod RFQ structure [7,8], developed in Frankfurt, has been modified such, that the frequency can be changed by a variation of the effective length of the stems and the corresponding inductivity with a movable tuning plate. Fig. 2 shows a schematic drawing of the structure.

The design of the VE-RFQ has to be made for the highest particle energy [9]. Both the input energy per nucleon E_{in} and output energy per nucleon E_{out} change with the frequency f : $E_{in}, E_{out} \sim f^2$.

*Work supported by CEC under contract SCI 0333-C(EDB) and BMFT under contract nr. 06OF186I

0-7803-0135-8/91S01.00 ©IEEE

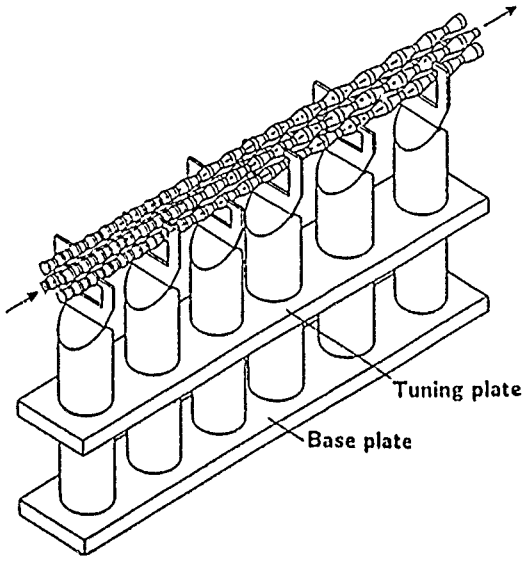


Fig. 2 : Scheme of the variable frequency 4-Rod RFQ

Consequently at a lower frequency it is possible to accelerate the same particle from a lower total input energy T_{in} with less electrode voltage U_Q : m=const → $U_Q \sim f^2$. Keeping the electrode voltage U_Q constant, heavier particles with the same input energy T_{in} can be accelerated at lower frequencies to the same total final energy T_{out} : U_Q=const → $m \sim 1/f^2$.

In table 1 the main parameters of the RFQ are summarized. For a short and compact structure the frequency should be chosen as high as possible, due to the low cluster masses < 50u and the preaccelerator voltage of 500 kV the highest operating frequency can be 110 MHz in this case. The total length is less than 2 m, the cluster energy is increased by a factor of 10. At a maximum electrode voltage of 80 kV the rf input power is less than 55 kW for 110 MHz. The designed tuning range in frequency from 80-110 MHz corresponds to a change in input and output energy by a factor of two resp., which is quite high. In addition a particle dynamics design had to be made for good beam quality taking into account the conditions mentioned before.

III. Beam Dynamics Calculations

The main design features for the RFQ have been a high acceleration rate for maximum energy gain, a short and compact structure and a low power consumption. At the input the electrode design started immediately with a modulation and a synchronous phase of 50°, the shaper part was omitted. Due to the high acceleration gradient the transverse focussing was lowered, both giving a transmission of 25% for the heaviest clusters at the highest frequency. For lower frequencies and masses the transmission is increasing to more than 70 %. The longitudinal output emittances are rather small, fig. 3 shows an example of calculated phase and energy spectra. The total phase width is about 40°, the total energy spread smaller than ~4% for the full beam [10].

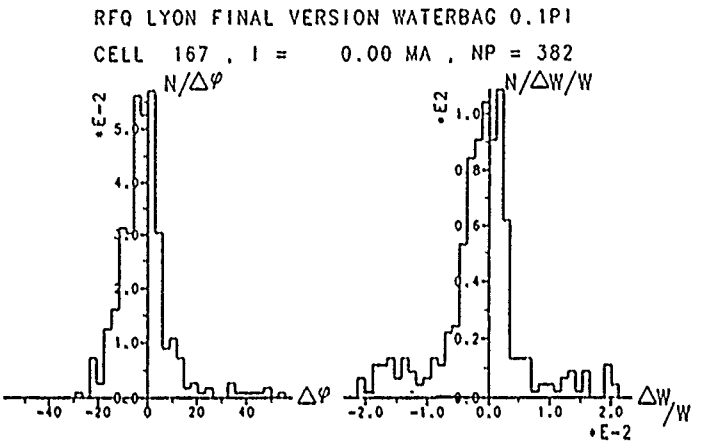


Fig. 3 : Phase and relative energy spectrum at RFQ output, mass 30, T_{out}=3 MeV, f=110 MHz

Recent work has been done on the transport of clusters through this RFQ: For masses < 10u the energy from the Cockroft-Walton is already as high as or even higher than the output energy of the RFQ. Therefore light clusters should only be transported to the target through the RFQ without loosing beam quality. The results of PARMTEQ calculations show, that this transport is possible, as long as the energy of the clusters is higher than the output or lower than the input energy of the RFQ [11]. Fig. 4 illustrates the different regions of transport and/or acceleration.

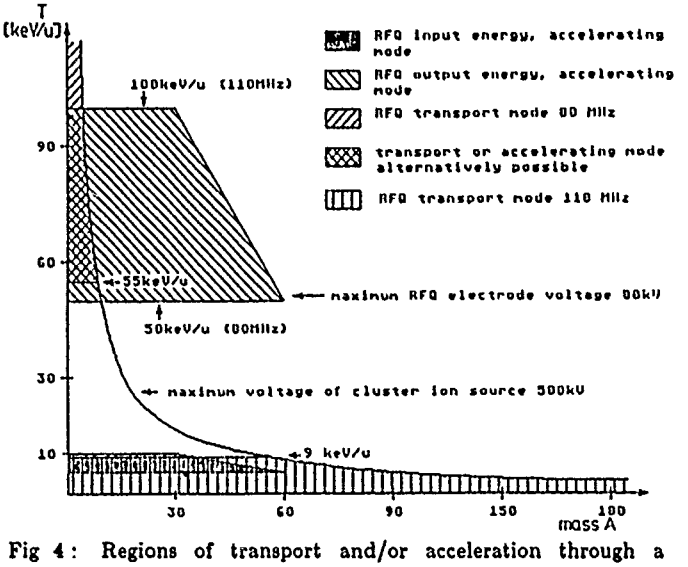


Fig 4 : Regions of transport and/or acceleration through a modulated RFQ

The transverse beam behaviour for cluster mass 5, energy 500 keV, f=80 MHz is shown in fig. 5. At a normalized emittance of 0.1 π·mm·mrad the transmission is 95% for an electrode voltage of 6 kV only, the emittance growth being 10%. For larger input emittances the voltage can be raised. By proper

adjustment of the voltage beam waists with minimum emittance growth can always be reached at the RFQ output. Depending on the voltage applied a small energy spread is introduced into the cluster beam.

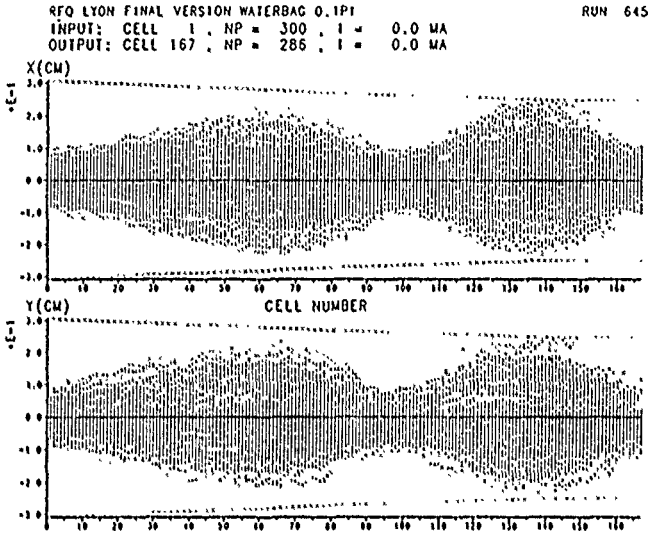


Fig. 5 : Transport of mass 5 at 500 keV through the RFQ, U_Q=6 kV, f=80 MHz

IV. First Experimental Results

First rf measurements on the completed RFQ have been carried out since the beginning of 1991. In fig. 6 the frequency is plotted as a function of the distance between the tuning plate and the base plate. The frequency range is shifted to higher values due to changes of the electrode geometry.

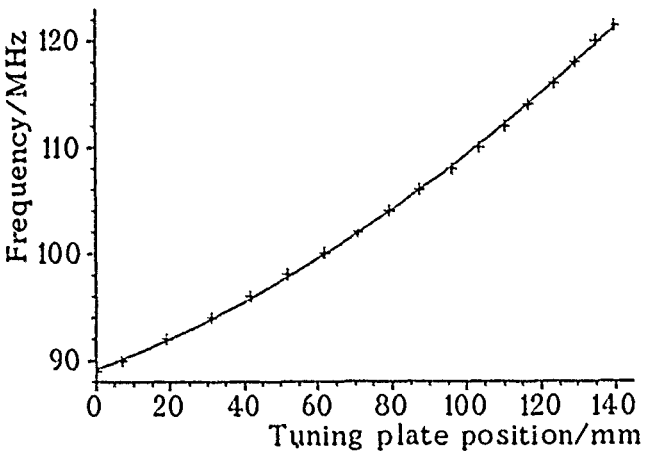


Fig. 6 : Tuning range of the resonator

The Q-value of the resonator and the Rp-value, which is a measure of the structure efficiency depend on resonator inductivity and are changed corresponding to the frequency. In fig. 7 the measured dependence of both parameters are plotted versus frequency. The curves are in good agreement with the theoretical values [4].

In first high-power tests an input power of 50 kW could be reached for a frequency of 90 MHz and a duty cycle of 1%, which is higher than required by the cluster source. First beam tests are scheduled for June.

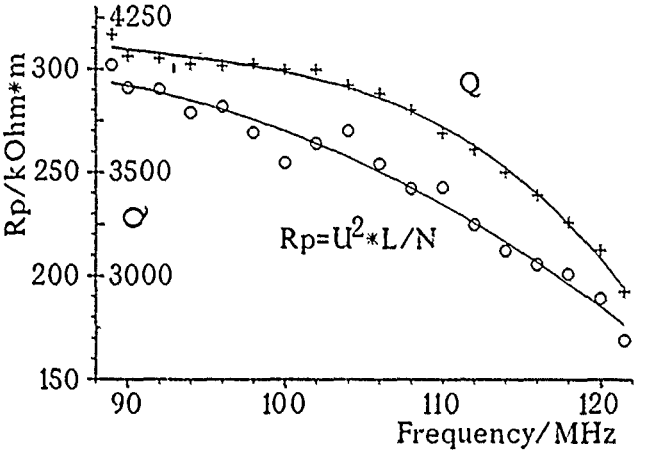


Fig. 7 : Measured Q- and Rp-values versus frequency

Table 1
RFQ parameters

Max. initial/final energy [keV/u]	10/100
Min. initial/final energy [keV/u]	5/50
Number of cells/modulation	167/1.1-1.98
Aperture [mm]	3.1-2.5
Transmission [%]	25-70
Transverse phase advance [°]	8.2-7.2
Synchronous phase [°]	50-15.5
Long. final emittances(95%)[keVnsec]	20-60
Max. electrode voltage [kV]	80
Frequency [MHz]	80-110
Length/diameter of structure [m]	2.0/0.5
Rp-value [kΩ·m]	180-300
Q-value	3000-4100

V. References

[1] M.Chevalier et al., ISSPIC 4, Aix en Provence, 1988

[2] J.P.Thomas et al., J.Physique,50-C2,pp.195,1989

[3] A.Schempp, H.O.Moser, J.Physique, 50-C2, pp.205, 1989

[4] A.Schempp et al., Proc. EPAC 2, Vol 1, Ed.Frontieres, pp.40, 1990

[5] I.M.Kapchinsky,V.Teplyakov,Prib. Tekh. Eksp.119, No.2,pp.17-19,1970

[6] K.R.Crandall, R.H.Stokes, T.P.Wangler, LINAC 79, BNL-51143,pp.20,1980

[7] A.Schempp et al. NIM B10/11,pp.831,1985

[8] A.Schempp, M.Ferch, H.Klein Proc. PAC 87, IEEE 87CH2387-9,pp.267,1987

[9] A.Schempp NIM B40/41,pp.937,1989

[10] H.Deitinghoff, A.Schempp, LINAC 1990, LA-12004-C,pp.312,1991

[11] J.Dehen, H.Deitinghoff, A.Schempp, to be published in NIM

LEAST-SQUARES FITTING PROCEDURE FOR SETTING RF PHASE AND AMPLITUDE IN DRIFT-TUBE-LINAC TANKS*

F.W. Guy, SSC Laboratory, and T.P. Wangler, Los Alamos National Laboratory

Abstract

Commissioning and operating a multi-tank drift-tube linac requires a procedure for setting phase and amplitude of the RF power in each tank. The Δ-t tuneup procedure has been extensively used for this (in LAMPF, for example). In this paper we present a complementary method using least-squares analysis of relative phase measurements. In this method bunch phases relative to RF power are measured at the input and output of the tank and at a reasonable drive distance downstream (or after the next tank with its RF off). The RF phase and amplitude are varied in a predetermined way; the resulting measured phase shifts are compared by least-squares fitting with their corresponding values from a beam-dynamics code simulation. The absolute calibration errors (assumed constant) of the phase sensors are the quantities which are varied to obtain the best fit. If these calibration errors are known, absolute values of RF phase and amplitude can be determined and the correct values set in the tank.

I. INTRODUCTION

Phase and amplitude set points must be found for the RF power in DTL (drift-tube linac) tanks when an accelerator is being first commissioned, tuned up, or restarted after a shutdown. For many years the Δ-t time-of-flight method[1,2,3] has been used quite successfully but for some accelerators it may be desirable to have an alternate or complementary method of adjusting RF power. This paper describes such a method and discusses its application. There is a brief discussion of the computer code that was written for this effort.

II. THE LEAST-SQUARES METHOD

A. *Concept and Definitions*

First, a brief description of the Δ-t method. Phase pickup sensors are required at two points downstream of the tank whose RF power is being adjusted. Usually one point is just downstream of the tank exit and the other is after the next downstream tank (whose RF power is turned off). The sensors detect beam bunch phase with respect to a reference phase. Changes in relative phase at these points, as the power in the tank is turned on and off, are converted to time-of-flight differences with and without RF power. Time-of-flight differences are also calculated by a beam-dynamics code such as PARMILA or TRACE. Experimental and calculated times-of-flight are then compared to develop information to adjust RF phase and amplitude. The RF is adjusted, then the process is repeated until the phase and amplitude are within desired tolerances.

The least-squares method also compares experimental and calculated phase measurements. There are three phase sensors (Fig. 1); one (Z_1) just upstream and one (Z_2) just downstream of the subject tank, and one (Z_3) at some appropriate drift distance further downstream. As in the Δ-t method, Z_3 can usually be placed after the next downstream tank, which is operated with no RF power. Therefore, to use this method there must be a phase sensor before the first tank, between each tank, and after a drift downstream of the last tank.

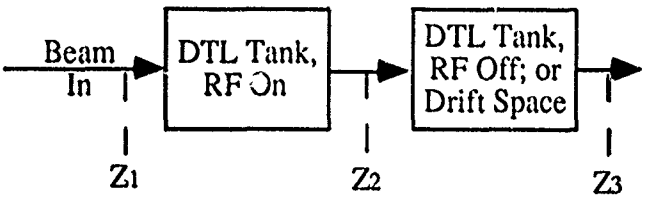


Figure 1. Placement of beam phase sensors.

The RF power is set one tank at a time starting with the lowest energy tank. The next downstream tank's RF is turned off. Beam phases Φ_1, Φ_2, and Φ_3, as measured by sensors at Z_1, Z_2, and Z_3, are defined as measured phases of the RF pickup signal from the tank when the sensor pulses induced by the beam are at their maximum. When experimental measurements are taken, the beam phase actually remains constant and the tank RF phase is adjusted. However, in this paper the tank RF phase (at the RF reference plane in the beginning of the tank) is defined as the reference phase and we assume that beam phases are measured relative to that tank phase.

Measurements of Φ_2 and Φ_3 are taken for a number of input phases Φ_1 (adjusted for Z_1 position so that beam phases at the tank bracket the input phase acceptance) and for a number of RF amplitudes (bracketing the design amplitude). Measurement of RF amplitude V, input beam energy W, and the three relative phases Φ_1, Φ_2, and Φ_3, will have unknown calibration errors which we assume will remain constant. We will henceforth refer to these constant calibration errors as offsets in the measurements. With known offsets, we can set the input phase Φ_1 and RF amplitude V to their desired values. The object of the least-squares method is to calculate the offsets from the phase-sensor measurements.

The measurements of Φ_2 and Φ_3 form a matrix covering all the input phases and RF amplitudes. One can calculate a similar matrix using a beam-dynamics code such as

* Work supported and funded by the U.S. Department of Energy, Office of the Superconducting Super Collider. Work performed at Los Alamos National Laboratory.

0-7803-9135-8/91$01.00 ©IEEE

PARMILA by running the appropriate problems. An error value, X^2, can be found from the difference between the experimental and calculated matrices. We can avoid determining the offsets in Φ_2 and Φ_3 if we use phase differences ($\Delta\Phi_2$, $\Delta\Phi_3$) due to changes in input phase ($\Delta\Phi_1$), rather than the relative phases themselves, as the quantities which are squared and summed to form X^2. Any offsets in Φ_2 and Φ_3 then cancel out.

The offsets that we need to determine, then, are $\delta\Phi_1$, the offset in the relative phase Φ_1, and δW_i, the offset in input beam energy W_i, which together with the distance between Z_1 and the tank determine the offset in the RF phase in the tank; and δV, the offset in RF amplitude V. In our code we define δW and δV as fractions of design values and $\delta\Phi$ in degrees. Offsets are added to measurements to determine true values.

$$\Phi_{1,\,true} = \Phi_{1,\,measured} + \delta\Phi$$

$$W_{i,\,true} = W_{i,\,measured} + \delta W \times W_{i,\,design} \qquad (1)$$

$$V_{true} = V_{measured} + \delta V \times V_{design}$$

These offsets are found as follows: A matrix of calculated phases Φ_2 and Φ_3 is constructed using a first guess (usually zero) at the set of offsets $\delta\Phi_1$, δW_i and δV in this way: A macroparticle representing the bunch is initiated at Z_1 with energy $W_i + \delta W_i$ at the first $\Phi_1 + \delta\Phi_1$ with the tank amplitude at the first $V + \delta V$. The macroparticle is tracked through the tank and phases at downstream sensor positions are stored. Another macroparticle with the next value of $\Phi_1 + \delta\Phi_1$ is tracked using the same W_i and V. After Φ_1 has been scanned, the scan is repeated using the next V and so on until a matrix of calculated phases has been built up using that particular set of offsets. X^2 is found by comparing the calculated matrix with the measured one:

$$X^2 = \frac{1}{2NM} \sum_{i=1}^{N} \sum_{j=1}^{M} \sum_{k=2}^{3} (\Delta\Phi_{k,calc}^{i,j} - \Delta\Phi_{k,meas}^{i,j})^2 \qquad (2)$$

where i and j indicate, respectively, RF phases and amplitudes;
N + 1 is the number of input Φ's;
N is the number of $\Delta\Phi$ measurements, $\Delta\Phi^i = \Phi^{i+1} - \Phi^i$;
M is the number of RF amplitude measurements (V's);
k is the sensor number, 2 or 3, for the Φ_k measurements,
$\Delta\Phi_{k,calc}$ is calculated by tracking through the PARMILA linac with a particular set of offsets;
$\Delta\Phi_{k,meas}$ is the corresponding measured value.

We then put in a different set of offsets, again calculate a matrix and get another value of X^2. Presumably if the second X^2 is less than the first, then the second set of assumed offsets is likely to be closer to the actual offsets in the measurements. The set of offsets that is the best fit to the actual values should produce the minimum X^2.

B. Calculational Techniques

The computer code that implements the least-squares calculation is called COMFIT. It is written in Fortran and runs in a few seconds on the Cray. The code has two subroutines that have been adapted from the PARMILA beam-dynamics code. The first uses design data on the DTL tank, previously calculated by PARMILA, at the beginning of the problem to set DTL cell parameters. The second transports a macroparticle representing the bunch through the tank and associated drifts to calculate phases at the three sensor points.

We have made several assumptions in writing this code. The first three are fundamental to the method but the others could be changed if necessary. The assumptions are:

1. The tanks are built as designed; errors in construction are ignored. Therefore given exact RF amplitude, input beam phase, and input beam energy, PARMILA can predict exact output beam phase and energy.
2. Input beam energy remains constant.
3. The macroparticle transported through the PARMILA subroutine represents the bunch centroid, and no particles are lost from the bunch during measurement. This assumption is discussed further below.
4. RF amplitude offset is the same for all amplitudes.
5. Offsets are less than about 20% in RF amplitude, 1% in beam energy and 30° in input beam phase relative to the tank.
6. Phase measurements (including Φ_1) have random jitter. The RF amplitude also jitters but remains constant during a particle transit of the tank. Jitter distribution is uniform over a specified range.

DTL tank design parameters are provided to the code in tabular form. Input data also includes sensor positions, nominal input beam energy, nominal tank voltage amplitude and synchronous Φ_1, the number of steps and step sizes in the phase scan and tank voltage (although actual values of phases and voltages could be used), and the matrix of measured phase values. There are a few other input values having to do with the fitting and plotting routines. The code first generates the DTL tank in the same way as PARMILA. It then moves into the fitting subroutine which minimizes X^2.

C. Simulated Measurements

A subroutine was included in the code to test its operation. The subroutine generates a matrix of fake "measured" phases using a specified set of offsets by running macroparticles through the tank as described above. Phase and voltage jitter can be included. The code fits this simulated data to see how closely the specified set of offsets can be reproduced. This technique was employed using a test case.

Cross-sections of the X^2 surface can be plotted by holding two of the offsets constant at specified values and plotting X^2 vs. the other offset. In the cases that have been run, these plots

have shown only one minimum in the surface in the region where the input beam and RF voltage allow the macroparticle to remain in synchronization with the RF bucket. While one cross-section may show two or more minima, cross-sections in the other directions reveal that only one is a true minimum. The code's simple slope-following minimization process works well on such a surface as long as the macroparticle remains in the bucket. Since the macro-particle represents the whole bunch, results may not be good if particles are lost from the bunch. Therefore, it is important to monitor beam current through the tank; if current is lost on any phase measurement then that measurement should not be used.

If there is no jitter in V, but some jitter in Φ in the simulated measurements, the minimum X^2 (whose units are degrees^2) is near the average value of the square of the jitter, as it should be. This provides a convenient check on the code and may be useful in estimating actual jitter.

The code has some interactive graphics capability. Various views and cross-sections of the X^2 surface can be provided and various quantities can be plotted, for instance output phase vs. output energy along lines of constant V.

D. Estimated Accuracy

Accuracy using the simulated measurements has been encouraging. A hundred or so runs were made on two different DTL tanks of 2.5 MeV and 20 MeV input energy. Input phase was scanned over $\pm 40^{\circ}$ in steps of 10° and amplitude was scanned over ±15% in steps of 5%. Many combinations of offsets and jitter amplitudes were tried. Accuracy was found to depend upon the magnitude of offsets, jitter amplitude, the number of data points in the measured matrix, and to a small extent upon details of the fitting routine. Not enough runs have been made to determine the exact nature of these dependencies, but in general for reasonable offset values (within the assumptions listed above) and jitter (within about 2° in Φ and 2% in V) the code will reproduce offsets within 1° in RF amplitude and a few tenths of a percent in V and input beam energy. For small offsets the accuracy is somewhat better. Presumably if large offsets were found in the data, corrections would be made and new data taken.

E. Some Possible Problems, Suggested Solutions and Code Improvements

If the offset in V is linear rather than constant, the code as written is inaccurate; but if such dependence is determined from other analyses, the code could easily be modified.

Some DTL tanks may be so long that if the RF power is turned off, the beam goes unstable in transiting the tank. This could occur with permanent-magnet focusing if the zero-current phase advance per focusing period approaches 90° (envelope instability) because the beam is not accelerated and the lower beam energy causes stronger focusing than the normal accelerated beam would see. This situation could cause trouble in applying the least-squares tuneup method (and indeed, any method such as Δ-t that relies on a drift space after the tank). In such a case, if there is sufficient space between the tanks perhaps two phase sensors could be placed there. In some cases it may be possible to include a phase sensor partway down the tank so that phase can be measured before the instability sets in. If enough of the bunch remains after transiting the tank to permit phase measurement, and particle loss does not cause damage to the drift tubes, perhaps the method can be used safely although particle loss may affect accuracy. Beam current could be reduced, minimizing damage and perhaps allowing instability buildup; an analysis taking into account reduced beam current should still give proper RF phase and amplitude settings although some corrections may be required and the settings may not be quite as accurate.

A more sophisticated minimization code such as MINUIT[4] might provide more information on the X^2 surface, including determination of the valid limits of the phase scan and estimation of sensitivities and jitter in all the offsets.

III. CONCLUSIONS

On the basis of the tests described above, we suggest that the least-squares method be tested with actual measurements. If no obvious uncorrectable difficulties are encountered then perhaps the method can help to determine measurement errors in the RF setting process, providing information on correct settings of RF amplitude and beam phase in DTL tanks.

IV. ACKNOWLEDGEMENT

Discussions with Ken Crandall of AccSys Corporation helped greatly in simplifying the least-squares method of DTL tuneup and in adapting the method to use phase differences, the type of experimental data that is likely to be the easiest and most accurate to measure.

V. REFERENCES

[1] K.R. Crandall, R.A. Jameson, D. Morris, and D.A. Swenson, "The Δt Turn-On Procedure," *Proc. 1972 Proton Linear Accelerator Conf.*, Los Alamos, NM, Oct 10-13, 1972, Los Alamos Scientific Report LA-5115, Nov. 1972, pp 122-125.

[2] K.R. Crandall, "The Δt Tuneup Procedure for the LAMPF 805-MHz Linac," Los Alamos Scientific Laboratory Report LA-6374-MS, June 1976.

[3] G R Swain, "Use of the Delta t Method for Setting RF Phase and Amplitude for the AHF Linac," Los Alamos National Laboratory Report LA-UR-89-1599, February 1989.

[4] F. James, "Function Minimization," *Proc. 1972 CERN Computing and Data Processing School*, Pertisau, Austria, 10-24 September, 1972 (CERN 72-21).

Production of Tightly Focused E-Beams with High-Current Accelerators*

J. W. Poukey, M. G. Mazarakis,
C. A. Frost, and J. J. Ramirez
Sandia National Laboratories
Albuquerque, NM 87185

Abstract

Using numerical modeling we study several approaches to the problem of designing an injector to produce a 3-30 kA, 2-4 mm diameter electron beam in the energy range 10-20 MeV. The cathode may be small in diameter and immersed in a strong magnetic field, producing an equilibrium beam for transport to a target (the "immersed" case). This approach appears to be the most promising for applications such as radiography, and we shall emphasize it in this paper. The alternative is the conventional "non-immersed" cathode, in which the beam from a larger-radius, cold-beam cathode is focused with magnetic lenses to a small spot on the target. Because the non-immersed case has been extensively studied, and because it has disadvantages for our purposes, we shall only discuss a few of our non-immersed-cathode injector studies, primarily for purposes of comparison.

Either type of diode is to be powered by an inductive voltage adder based on the successful SABRE/Hermes III/RADLAC (SMILE) magnetically-insulated-transmission-line design concepts.[1,2] A possible variation uses a re-entrant geometry with low electric stresses so that only the cathode face emits. We discuss issues such as dumping excess current and voltage dependence of the focus.

I. INTRODUCTION

The problem of producing small-diameter electron beams at high voltages (10-20 MV) and currents (3-30 kA) is of interest for several applications, including radiography. There are two basic issues which we will consider, namely the method for accelerating the beam, and the design of the injector. The conventional method[3,4] uses a standard multi-gap linac with a non-immersed cathode in the injector diode. Code calculations for the FXR system, including the diode, the transport and acceleration through 48 gaps, and the final focus, have been described by Boyd.[4]

In our approach to beam acceleration, we propose an MITL (magnetically insulated transmission line) voltage adder of the Hermes III/SABRE type[1,5] to apply the entire voltage (e.g., 10 MV) across a single electron-diode gap d. The primary advantages of this approach, as compared to the conventional linac, are: (1) significant reduction in cost, (2) substantial reduction in complexity, and (3) avoidance of instabilities such as BBU (beam breakup).

In our approach to injector design, we propose the immersed diode. The primary advantage of this diode, as we shall show, is relative insensitivity to variations in applied voltage and B field. Another advantage for some applications is the production of a high-current, small-radius beam in equilibrium, as opposed to a beam focused at only one axial location.

II. IMMERSED DIODES

Using the 2-D electromagnetic PIC code MAGIC, we have simulated a number of immersed diodes (see Table I). An example (Run 13) at the SABRE voltage of 10 MV is shown in Fig. 1. The idea is to create a beam from a small-radius (r_k) tip inside a large B_z field. If B_z is large and uniform enough from cathode to target, the electrons will follow the B lines and the size of the beam at the target will be about r_k.

The motivations for this approach, as opposed to non-immersed systems with magnetic lenses,[6] are: (1) The successful

*This work was supported by U.S. D.O.E.

0-7803-0135-8/91$03.00 ©IEEE

IBEX experiments[7] (see run 0 in Table I). By "successful" is meant production of a small, low-emittance beam, and agreement between MAGIC and measurement. (2) The relative insensitivity of beam parameters at the target, namely r_b (beam radius) and $\beta_\perp$ (transverse velocity), to variations in voltage V and applied B_z (see Table I). We also varied drift tube radius r_t (compare runs 13 and 15), but found almost no change in results. There is some variation with B_z, as seen in runs 9,13 and 12,17; as expected, the higher B_z results in a higher quality beam.

For comparison, we did a series of quasistatic runs using a trajectory code for a non-immersed diode with a magnetic lens. We used a large-cathode, d = 70 cm (A-K gap) system which emits from a flat velvet region of radius 6 cm. We varied V and B_z by ±10% about values for a good focus (best result: beam diameter of 2 mm), and found that the focus moves in axial position z by enough to cause increases in r_b of up to 4 mm. This does not preclude using such a diode, but one must control V and B_z to much greater precision than for our immersed cases.

Table I
Immersed Diodes for Radiography. In all cases, except 0, A-K gap d = 15 cm, and the applied B_z is uniform. In case 0, the IBEX experiment,[7] the A-K gap was d = 7 cm. The last three columns are the output beam at the target. Code: MAGIC. Run 13 is shown in Fig. 1.

					Output Beam Quality		
Run	V (MV)	r_k (mm)	r_t (mm)	B_z (kG)	I_b (kA)	$\beta_\perp$	r_b (mm)
0	3.5	1.6	30	22	12	0.17	2.1
9	10	2	40	25	39	0.15	3.1
10	12	2	40	25	51	0.16	3.5
11	13	2	40	40	49	0.14	2.0
12	10	1	20	60	37	0.14	1.1
13	10	2	10	40	35	0.07	1.7
15	10	2	40	40	35	0.07	1.8
17	10	1	10	40	42	0.10	1.7
18	12	1	10	60	47	0.07	1.4

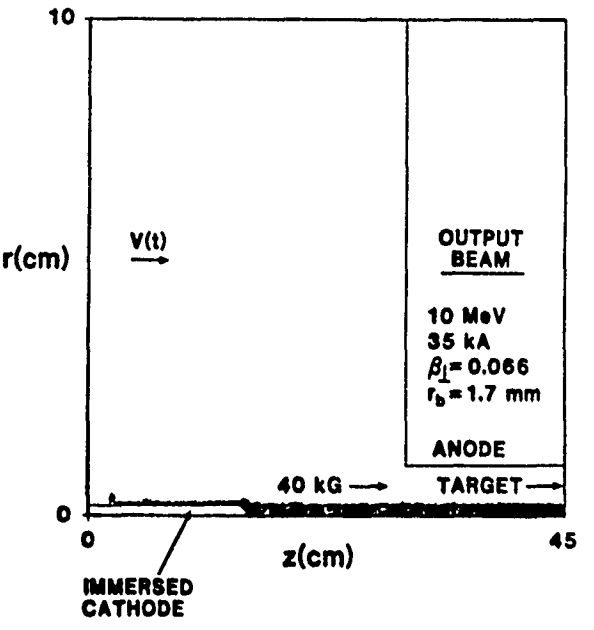


Figure 1. MAGIC simulation of immersed diode at 10 MV, 35 kA, (see run 13 of Table I). The entire diode and target (rhs) are immersed in 40 kG, yielding a high quality, small-diameter beam.

III. TRANSITION TO VOLTAGE ADDER

The input "voltage pulse" in Fig. 1 is generated by an MITL voltage-adder system such as SABRE.[5] Some simulations of the entire MITL and ten feeds have been attempted, but here we just discuss the transition from the adder to the diode. A sample run is given in Fig. 2, which includes the large outer conductor from the coaxial feed, and a truncated small-radius cathode. The coils produce 60 kG for the immersed diode, and allow over half the total of 84 kA to be "dumped" radially.

The main problem here is that the configuration inevitably yields some "halo" electrons, originating back on the cathode shank. In Fig. 2, these lead to an rms beam radius r_b on target of 2.8 mm; this is somewhat larger than desirable. Using a more gentle taper reduces this radius somewhat, but the problems of MITL sheath and shank electrons persist. Possible solutions include current-dump projections in the MITL, aperturing, and contouring the cathode to follow a flux surface.

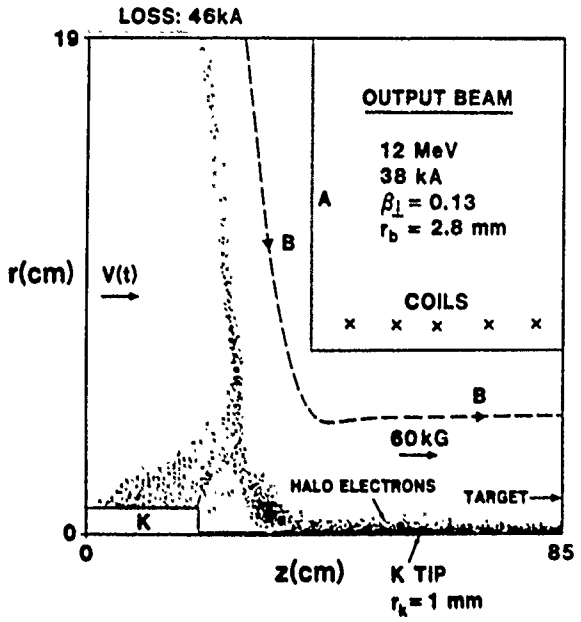


Figure 2. MAGIC run of immersed diode plus transition to voltage adder. The adder gives input voltage V(t) (modeled as TEM wave; max 12 MV). Note loss along fringing B lines.

IV. OTHER SYSTEMS

We have also studied non-immersed diodes with magnetic lenses in some detail. As discussed above, we find that such diodes are not as good as immersed ones for our purposes (e.g., radiography), due to the difficulty in maintaining a very small focal spot size over realistic voltage pulses.

An interesting variation here is a non-MITL voltage adder of the Recirculating Linear Accelerator type,[8] with a carefully designed, low-stress, non-immersed cathode and a re-entrant anode containing magnetic-field coils. Both MAGIC and trajectory-code runs show some good properties of this system, although voltage sensitivity may still be a problem. Further studies would be needed to investigate this point, and certainly to achieve a practical design.

V. SUMMARY

For the production of small-diameter electron beams in the range 10-20 MeV, we propose an inductive-voltage-adder, single (diode)-gap approach, e.g., SABRE instead of the conventional multi-gap linac. For the injector, we propose to use a small-diameter cathode immersed in a field of 40-60 kG. Our calculations predict that very high current densities can be expected, with relative insensitivity to parameter variations.

VI. REFERENCES

[1] T. W. L. Sanford et al., "Dynamics of electron flow in extended planar-anode diode operating at 19 MV and 700 kA," J. Appl. Phys., vol. 67, pp. 1700-1711, Feb. 1990.

[2] M. G. Mazarakis et al., "SMILE, a new version for the Radlac II Linac," in Proc. 1990 Linac Conf., Albuquerque, NM, Sept. 1990, pp. 438-440.

[3] T. P. Hughes et al., "Diode and transport calculations for REX, DARHT, and PHERMEX," Mission Research Report MRC/ABQ-R-1244, Feb. 1990.

[4] J. K. Boyd, "Accelerator code simulation of FXR transport," in Proc. Conference on Computer Codes and the Linac Community, Los Alamos, NM, Jan. 1990, pp. 221-232.

[5] SABRE is an upgrade of the HELIA accelerator. (D. L. Johnson and J. P. Corley, Sandia National Labs, private communication.) For HELIA and HERMES III see, e.g., Proc. 7th IEEE Pulsed Power Conf., Monterey, CA, June 1989.

[6] R. B. Miller et al., "Matching beams from relativistic electron guns into solenoidal transport systems," J. Appl. Phys., vol. 62, pp. 3535-3538, Nov. 1987.

[7] C. A. Frost et al., "High-brightness immersed source injector characterization," in Proc. 1989 IEEE Particle Accelerator Conf., Chicago, IL, March 1989, pp. 1456-1458.

[8] M. G. Mazarakis et al., "Electron diodes and cavity design for the new 4 MeV injector of the RLA," in Proc. 1990 Linac Conf., Albuquerque, NM, Sept. 1990, pp. 605-607.

LONGITUDINAL EMITTANCE MEASUREMENT OF THE 100 MeV PROTON BEAM

Yu.V.Bylinsky, A.V.Feschenko, P.N.Ostroumov
Institute for Nuclear Research,
117312 Moscow

Abstract

The results of the longitudinal emittance measurements carried out at the exit of the DTL part (100 MeV) of the 600 MeV Moscow meson factory linac are presented. A Longitudinal emittance is determined from the bunch length measurements carried out at the exit of the last DTL cavity for three different and well known values of the accelerating field amplitudes. A Bunch length is measured by means of the bunch shape monitor with the phase resolution better than 1^0 at the DTL rf frequency. The results of the emittance measurements are used for a beam longitudinal matching between the DTL and the DAW parts of the linac.

Introduction

A multiple increasing of the rf accelerating frequency in an H^+ and H^- ion linac occurs at the energy approximately 100 MeV. Therefore it is necessary to match properly the longitudinal emittance with the acceptance of the following linac stage. The longitudinal matching at the Moscow meson factory linac is provided by using 5th tank of the DTL part. This tank operates as an executive element in the feedback system to dump a longitudinal coherent oscillations of the beam. Thus, in order to tune up a longitudinal motion in the region of 100 MeV it is very important to know a longitudinal beam emittance.

Experimental setup

A method of the longitudinal emittance determination was described elsewhere [1]. It was shown, that a restoration of the phase space ellipse is possible if the bunch lengths are measured three times after the device with a linear transformation of the beam longitudinal parameters. The transformation matrices M_i (i=1,2,3) of this device must be known. A phase ellipse at the entrance of this device may be written as:

$$A\phi^2+2B\phi h+Ch^2+1=0,$$

where $\phi=\varphi-\varphi_c$, $h=(p-p_c)/p_c$, φ_c and p_c are phase and momentum of a particle at a center of the ellipse. The parameters of the ellipse may be determined from expressions [1]:

$$C = 4\frac{d(k_2-k_1)+(k_2^2-k_1^2)}{d^2(g_2^2-g_1^2)+4d(k_1g_2^2-k_2g_1^2)+4(k_1^2g_2^2-k_2^2g_1^2)},$$

$$B = Cd/2\ , \qquad A = \frac{B^2g_1^2-2Bk_1-Ck_1^2}{1+Cg_1^2},$$

$$\text{where} \qquad d = \frac{k_1^2(g_2^2-g_3^2)+k_2^2(g_3^2-g_1^2)+k_3^2(g_1^2-g_2^2)}{k_1(g_3^2-g_2^2)+k_2(g_1^2-g_3^2)+k_3(g_2^2-g_1^2)}.$$

The coefficients k_i and g_i describe the tangents $h=k_i\phi+g_i$ to the phase ellipse at the entrance of the linear device (fig.4). These coefficients are expressed through the r_{mni} elements of matrices M_i^{-1} and measured bunch lengths ΔF_i:

$$k_i = r_{221}/r_{121}\ , \qquad g_i = \frac{\Delta F_i}{2}\frac{r_{211}r_{121}-r_{111}r_{221}}{r_{121}}.$$

The fifth tank of the DTL stage of the INR linac was used as a bunch rotator for the linear transformation of a phase ellipse. Computer simulation has shown [2], that a motion of the particles with respect to each other in a bunch is kept linear in a wide range of the amplitude variation from zero up to the maximum possible value for the injection phases near -100^0. Besides it was shown, that the ΔF_i values should be measured at the lowest possible level of the phase spectrum because in this case only a longitudinal phase portrait is approximated by an ellipse satisfactory. In this case the phase ellipse being determined includes almost 100% particles. The bunch shape analyser (BSA) with the phase resolution of 1^0 at the frequency of 198.2 MHz [3,4] was used for the measurements of the bunch lengths.

Results and Discussion

During the measurements the 100 MeV stage of the linac operated with the nominal rf parameters setting. The bunchers were off and a peak current was 10 mA. The design rf field amplitude and phase in the 5th tank has been determined earlier.

The phase ellipse at the entrance of the fifth tank was restored by using the phase spectrum measurements for the following amplitudes: E=0, E=0.7E_n, E=1.3E_n, where E_n is a design value. Fig.1,2,3 show the corresponding phase spectra. The restored phase ellipse at the entrance of the bunch rotator and the tangents corresponding to the ΔF_i for the amplitudes aforementioned are presented in Fig.4. Fig.5 shows the experimental phase width vs the rf field amplitude of the bunch rotator. The same figure shows the curve corresponding to the phase widths which have been obtained by the transformation of the restored ellipse. The ellipses determined by the aforementioned technique just beyond the 5th tank operating in a nominal mode as well as at the entrance of the first DAW accelerating cavity are presented in fig.6.

Conclusion

The method for the determination of the longitudinal emittance with the aid of the phase spectra measurements is realized at the

0-7803-0135-8/91$01.00 ©IEEE

MMF linac. This method gives possibility to provide the longitudinal matching of the beam between the DTL and the DAW parts of the linac. The preliminary 100 MeV beam study has shown that the beam with 10 mA peak current can be matched successfully with the bucket of the DAW part of the linac even if the bunchers are turned off.

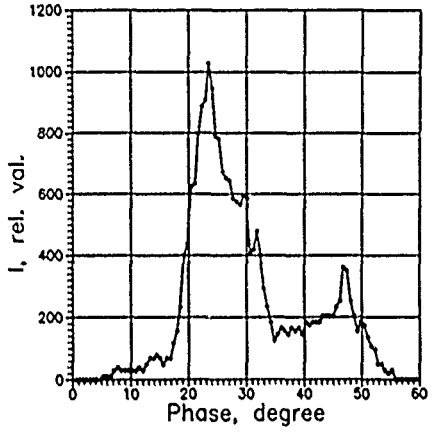


Fig.1 Phase spectrum for the rf field level of E=0 in the 5th tank

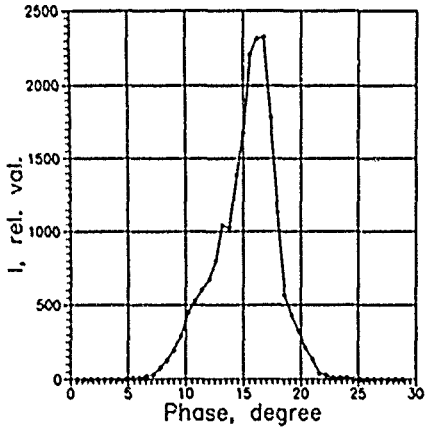


Fig.2 Phase spectrum for the rf field level of $E=0.7E_n$ in the 5th tank

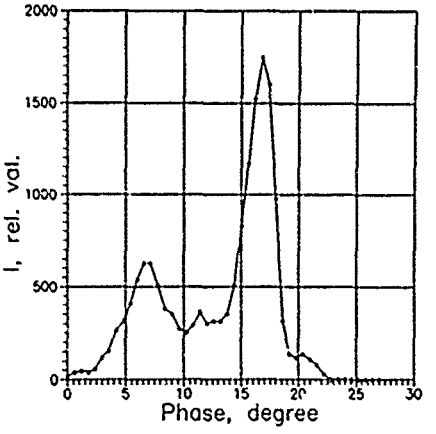


Fig.3 Phase spectrum for the rf field level of $E=1.3E_n$ in the 5th tank

References

1. A.V. Feschenko , A.M. Tron. Problems of atomic science and technology. Technique of physical experiment, Issue 3(15), Kharkov, 1983, pp. 51-53 (in russian)
2. A.V. Feschenko , P.N. Ostroumov. Preprint INR, П-0535, Moscow, 1987 (in russian).
3. A.V. Feschenko , P.N. Ostroumov. 1986 Linac Conf., Stanford, June 2-6, 1986, pp.323-327.
4. A.V. Feschenko , P.N. Ostroumov. EPAC-2, Nice, June 12-16, 1990, pp. 750-752.

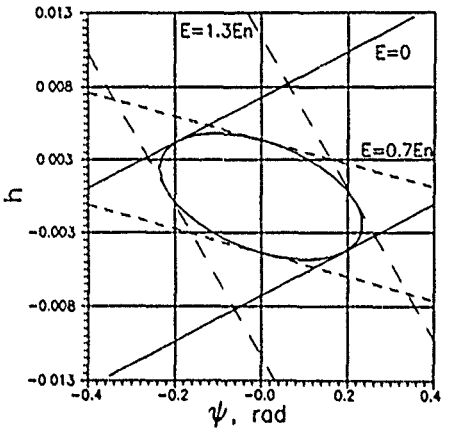


Fig.4 Phase ellipse restored and the tangents at the entrance of the 5th tank

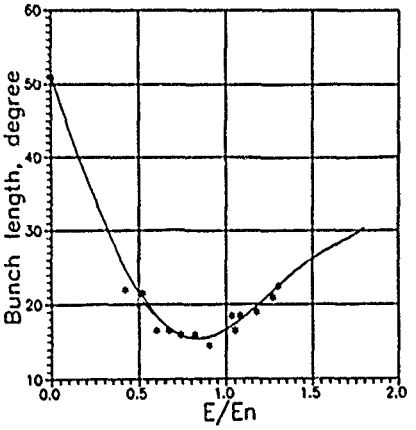


Fig.5 Bunch phase width vs 5th tank rf field amplitude

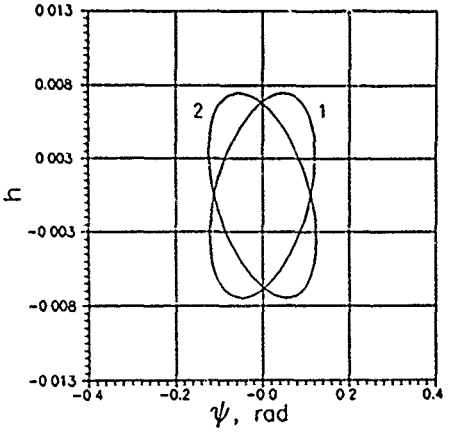


Fig.6 Phase ellipses: 1 - at the 5th tank exit, 2 -at the first DAW cavity entrance

The Delta-T Tuneup Procedure for the Fermilab Linac Upgrade

Thomas L. Owens and Elliott S. McCrory
Fermi National Accelerator Laboratory
P.O. Box 500
Batavia, Illinois 60510

Abstract

The analysis necessary to perform the delta-t procedure for setting module phase and electric field amplitude on the upgraded linac at Fermilab is described. Two distinct delta-t methods are required to tune all of the modules in the linac upgrade. The accuracy and stability of each method has been calculated as a function of linac module number. A procedure for coarse tuning of the linac is also presented. Coarse tuning is necessary to bring the module phase and amplitude into ranges where the delta-t method is accurate and reliable.

I. INTRODUCTION

The delta-t procedure is a time-of-flight technique in which beam transit time changes are recorded as rf power is turned on and off in a module. The time-of-flight changes can be used to infer phase and electric field amplitude settings within a module. The procedure was developed at the Los Alamos National Laboratory many years ago for the purpose of tuning the phase and amplitude of accelerator modules along the LAMPF linear accelerator [1]. Recently, use of the procedure has been proposed on a number of other linear accelerators [2-4].

Under current plans, the procedure will be used to set the phase and amplitude of the upgraded linear accelerator at Fermilab. The delta-t procedure will first be carried out on the existing 200 MeV linear accelerator in order to test the hardware and understand some of the practical problems associated with the procedure. Initial experiments on the existing linac were described in earlier work [4,5].

The upgraded linear accelerator, currently under construction at Fermilab, will be a 400 MeV device [6]. It will consist of seven modules, each powered by a 12 megawatt klystron. The modules are divided into 4 sections, each separated by a drift distance of $3\beta\lambda/2$. Side-coupled structures having constant cell lengths of $<\beta>\lambda/2$ make up the sections, where $<\beta>$ is the average beta for a particular section. The fundamental resonant frequency of the modules is 805 MHz.

An assumption in the theory of the delta-t procedure is that the initial phase and energy displacements from design values are small. For small displacements, the phase and energy displacements at the output of a module can be linearly related to the phase and energy displacements at the input to a module. Coarse tuning must be performed before the delta-t procedure is used in order to remain within this linear region. In addition, for some of the low energy modules, ambiguities can occur in bringing a module into tune if the initial settings deviate too much from design. A coarse tuning procedure will be described in the next section.

II. COARSE TUNING PROCEDURE

The technique for coarse tuning utilizes measurements of the energy change through a module as the module phase is varied. Energy changes can be determined from measurements of time-of-flight changes similar to those used in the delta-t procedure. Beam phase changes at two beam monitors placed after the cavity are recorded as the power to the module is alternately turned off then on. These phase changes are then converted to time-of-flight changes. The changes in velocity through a module are calculated from,

$$\frac{\Delta v}{v_i} = \left\{ \frac{1}{1 - \frac{(\Delta t_2 - \Delta t_1)}{D} v_i} - 1 \right\} \qquad (1)$$

where v_i is the velocity entering the module, D is the distance between the two beam monitors used in the measurements, and $\Delta t_{1,2}$ are the changes in the times-of-flight as rf power is turned on and off. The energy changes are calculated from equation 1 and the relation, $\Delta W = E_r \Delta\gamma$, where E_r is the rest energy of the beam particles.

As a first step in the coarse tuning procedure, the electric field amplitude within the module is increased from zero until the peak energy change through the module equals the calculated value for the design particle. The cavity phase is then set to the calculated value relative to the phase at which the peak energy change occurs. Values for the phase and energy displacement at the peak energy for the linac upgrade are given in Table I. The above procedure can bring the linac within a few degrees of final tune if the input energy displacement is zero.

Tests of the coarse tuning procedure will be made on the existing 200 MeV linac at Fermilab, before it is used on the upgraded linac. Figure 1 contains plots of the energy displacement versus module phase calculated for a module at about the middle of the existing linac. The average axial electric field on axis varies from zero to 2.6 MeV/m in the figure. The design field is 2.6 MeV/m. A sharp energy

0-7803-0135-8/91$01.00 ©IEEE

Table I
Phase and energy displacement of the peak in energy

Upgrade Module	Phase (degrees)	Energy (MeV)
1	46.07	2.57
2	47.15	3.31
3	46.91	3.99
4	45.77	4.59
5	44.37	5.13
6	43.62	5.73
7	42.26	6.15

peak and a strong sensitivity to electric field amplitude are demonstrated.

III. ACCURACY AND STABILITY OF THE DELTA-T PROCEDURE

This section provides a brief summary of results described in a much longer paper contained in the Fermilab Linac Upgrade Document File [6]. Two separate delta-t methods may be used to tune the upgraded linac. Applying Method 1, deviations from design in the changes in the times of flight through a module are measured at two positions after the module being tuned. The deviations in time-of-flight changes can be related in a linear fashion to the phase and energy displacements, as described in reference 1. Module phase is then adjusted until the output energy displacement is zero.

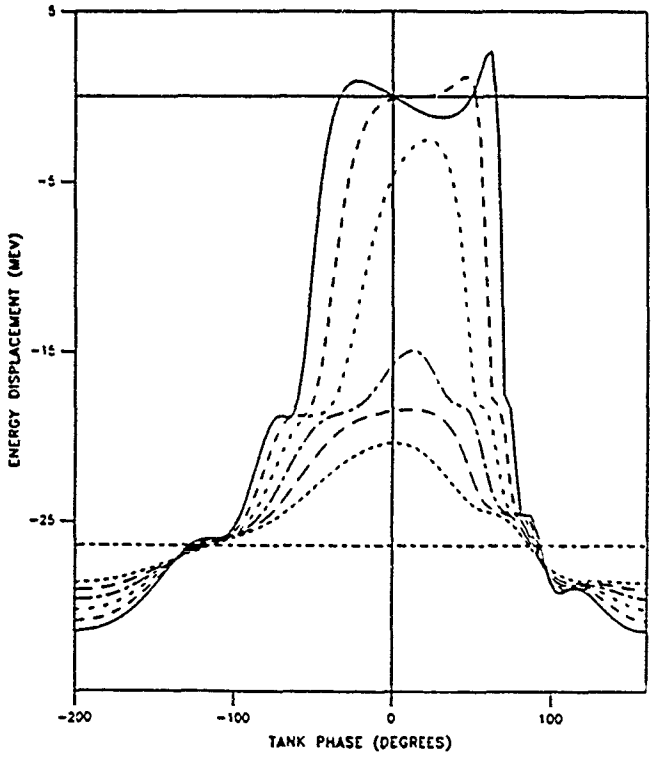


Figure 1. *Energy displacement versus tank phase for tank number 4 of the existing Fermilab Linac.*

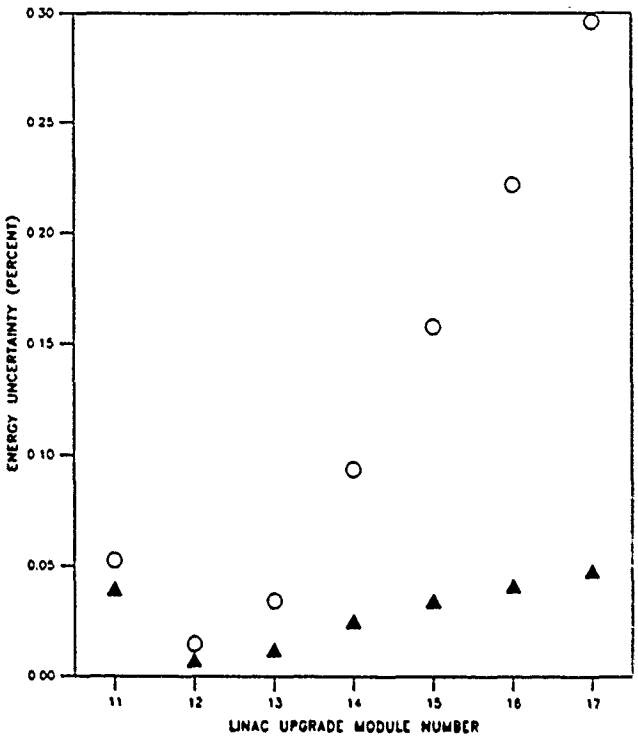


Figure 2. *Output energy uncertainty for 13.8 picosecond random error in time measurement. Circles - Method # 1 triangles - Method # 2. The two methods are described in Section III.*

This first method loses accuracy in the higher energy modules of the linac, and a second method is used to preserve accuracy. Applying Method 2, the phase of the module is adjusted until it intersects a target line which has been chosen to optimize accuracy, according to a prescription given in reference 1.

A plot of the output energy uncertainty for each of the two delta-t methods, applied to the upgraded linac at Fermilab, is shown in figure 2. A random error in the time measurement of 13.8 picosecond is assumed in thecalculations which generated figure 2. The input energy displacement is assumed to be zero. The figure shows that much greater accuracy is achieved for Method 2 after the second module in the upgraded linac. Accuracies for both methods are similar in upgrade modules 1 and 2.

In the absence of other information, it would seem logical to use Method 2 over the entire linac. Unfortunately, in the early modules of the linac, energy displacements can grow along the linac for Method 2. The process is analogous to the growth of an instability. Figure 3 demonstrates this problem, where a parameter called the stability ratio, defined in reference 1, is plotted for each of the upgraded linac modules. The stability ratio is the ratio

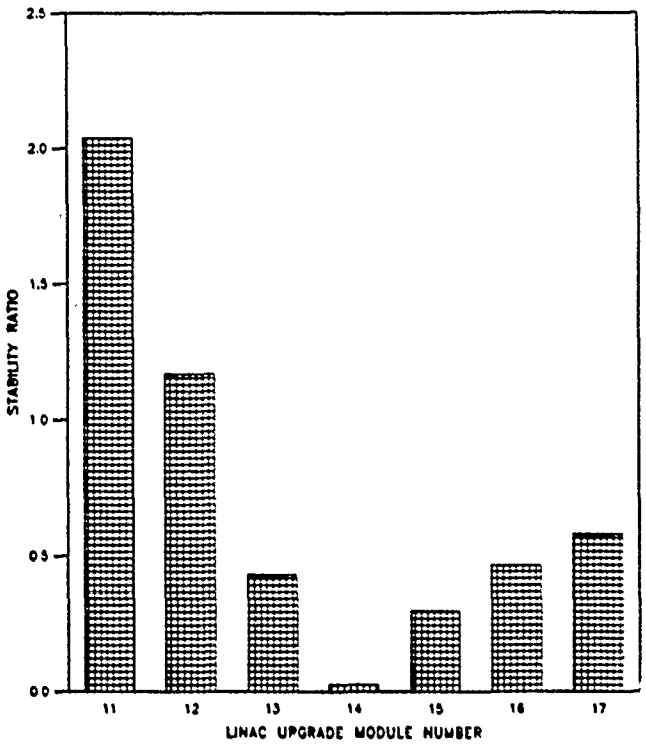


Figure 3. *Stability ratio for Method # 2 in the Fermilab Linac upgrade.*

of output energy displacement magnitude to input energy displacement magnitude multiplied by the ratio of input energy to output energy.

The stability ratio must remain less than one to insure good confinement within the longitudinal acceptance area. The stability ratio for the first two modules of the linac upgrade is greater than one. Since only two modules are involved, the "instability" acts over only a very short distance. Nonetheless, to avoid potential problems, Method 1 should probably be used over the first two modules of the linac.

IV. SUMMARY AND CONCLUSIONS

Coarse adjustment of the electric field amplitude of each module of the upgraded linac at Fermilab can be made by increasing the amplitude until the peak energy change through the module equals the calculated value for the design particle. The phase can then be set to its calculated value relative to the peak energy. Subsequently, the delta-t procedure is used to fine tune the modules. The analysis indicates that two distinct delta-t methods should be used to tune the entire upgraded linac. Method 1 should be used for modules 1 and 2, while method 2 should be used for modules 3-7.

V. REFERENCES

[1] K.R. Crandall, "The Delta-T Tuneup Procedure for the LAMPF 805 MHz Linac," LANL Report LA-6374-MS, June, 1976.

[2] G.R. Swain, "Use of the Delta-T Method For Setting RF Phase and Amplitude in the AHF Linac," in *Proceedings of the Advanced Hadron Facility Accelerator Design Workshop*, Feb. 20-25, 1989 (also LANL Report LA-11684-C).

[3] G.A. Dubinski, A.V. Reshetov, Y.U. Senichev and E.N. Shapashnikova, "New Features of the Delta-T Procedure for an Intensive Ion Linac," in *1988 Linear Accelerator Conference Proceedings*, Newport News, VA, Oct. 3-7, 1988.

[4] T. L. Owens and E.S. McCrory, "The Delta-T Tuneup Procedure for the Fermilab Linac," in *Proceedings of the 1990 Linear Accelerator Conference*, Sept. 10-14, 1990, pp. 721-723.

[5] T.L. Owens, "Phase and Amplitude Tuning Procedures for the Fermilab Linac," Fermilab Report TM-1713, Jan., 1991.

[6] R. J. Noble, "The Fermilab Linac Upgrade," in *Proceedings of the 1990 Linear Accelerator Conference*, Sept. 10-14, 1990, pp. 26-30.

[7] T.L. Owens, "The Delta-T Tuning Procedure For the Fermilab Linac Upgrade," Fermilab Linac Upgrade Document LU-177, April, 1991 (Attn: L. Lopez, mail station 307).

PROTON BEAM ACCELERATION UP TO 160 MeV AT THE MOSCOW MESON FACTORY LINAC

G.I.Batskich*, Yu.V.Bylinsky, S.K.Esin, A.P.Fedotov, A.V.Feschenko, Yu.D.Ivanov*, O.S.Korolev. L.V.Kravchuk, A.I.Kvasha*, V.A.Matveev, V.N.Michailov*,A.N.Mirzojan, N.P.Murin*, P.N.Ostroumov, S.A.Petronevich, B.A.Rubtsov*, V.L.Serov, S.I.Scharamentov, N.I.Uksusov*, S.Zy.Zyarylkapov I.A.Sagin

Institute for Nuclear Research of the Academy of Sciences of the USSR,Moscow, 117312, USSR

* Moscow Radiotechnical Institute, Moscow, 113519, USSR

Abstract

The H^+, H^- linac of the INR meson factory designed for accelerating of the 0.5 mA average current beam to the energy up to 600 MeV is under tuning in Troitsk near Moscow. The results of the tuning of the drift tube linac operating at the frequencyof 198.2 MHz with the output proton energy of 100 MeV, followed by the four disk and washer (DAW) cavities operating at the frequency of 991 MHz with the output energy of 160 MeV, are presented.

The layout and features of 160 MeV part of the linac

Recently the tuning experience of the first Alvarez tank with the output energy of 20.45 MeV was presented in ref [1].

The first stage of the linac with the output energy of 100 MeV consists of the five tanks with drift tubes operating at the frequency of 198.2MHz. The first stage is followed by the four resonant cavities with disks and washers operating at the frequency of 991 MHz, where protons are accelerated to the energy of 160 MeV.

The first four tanks of the first stage are long. For example the first of them is 3.8 longitudinal oscillation wave length long. The fifth one is a quarter wavelength long.Besides accelerating (from 94 MeV to 100 MeV the fifth tank is designed to reduce the phase length of bunches by 1.4 times (increasing respectively the momentum spread) so that the bunches should fit safely in the longitudinal acceptance of the second stage of the linac [2].

Transition from the first to the second stages of the linac is the main feature to be taken into account when tuning the accelerator.

The layout of the first and of the opening part of the second stages of the linac together with the measuring equipment is shown in fig. 1 and fig. 2. After tuning of the first stage of the linac the measuring equipment, installed at its output, was moved to the 160 MeV output.

In the course of tuning the injector was driven at 1 Hz repetition rate to avoid the excessive activation of the equipment. Tanks and resonant cavities were driven at 10 Hz.

The first 100 MeV stage of the linac.

The rf amplitude and phase setting in resonant cavities plays the major role in tuning process. For rf phase setting in a resonant cavity the dependence of the accelerated current on the rf phase difference between the tuned and the preceding resonant cavities I (φ) was used. The dependence was calculated and measured experimentally. The selection of the accelerated particles was mode with the aid of the absorbing foil which let pass through it only the particles, accelerated in the resonant cavity under tuning. Absorbing foils were placed at the output of the fifth tank.

The calculated dependencies I (φ) for the second tank for different by 5% within the range from 0.9 up to 1.1 of the nominal amplitude are shown in fig. 3. They may be used to ascertain the bucket width at a half - height level (ΔF). The nominal rf amplitude is determined by the nominal bucket width. The synchronous phase is found by the nominal rf amplitude of the calculated displacement from the front curve of phase scanning.

The aforementioned method requires the beam cutoff and may be used only for tuning at the small average beam current. Therefore the method for rf phase and amplitude setting based on the dependence of a certain harmonic of a beam current measured by the cavity monitor at the output of the accelerating cavity under tuning on the rf phase difference between this cavity and the preceding one, was proposed and used. A beam current harmonic is maximal if the bunches fit in the bucket, if the bunches exceed the bucket it is reduced due to debunching. The calculated dependence of the field level induced in the third-harmonic cavity monitor on the rf phase in the second tank is shown in fig. 4.

The accelerated beam current beyond the foil and its third harmonic were measured. The calculated and measured rf bucket width at the half-height level in the second tank got with the aid of the method based on the beam bunch harmonic monitor BHM is shown in fig.5. The rf amplitude and phase setting accuracy in the third and the fourth tanks with the aid of absorbing foils is 1% and 2° respectively. The method based on measuring of the third harmonic of the current is a bit less accurate.

The aforementioned rf amplitude and phase setting method is out suitable for the fifth short tank, in which the beam energy is just

0-7803-0135-8/91$01.00 ©IEEE

slightly increased and bunches remain compact for a wide range of phase changes and slopes of the curve I (φ) are eroded. Therefore for rf amplitude and phase setting in the fifth tank another methods ware proposed, which are based on the dependence of the transit time of particles $\Delta\Phi$ in the tank on the rf phase in it.

The layout of transit time measurement is shown in fig. 6. Results of the calculation of functions $\Delta\Phi(\varphi)$ for which $\Delta\Phi$ value corresponds to the base (BHM2 - BHM3) are shown in fig. 7. Rf amplitude ranging from zero to 1.2 of the nominal level with the step 0.2 is the parameter of the curves.

Calculated and experimental maximum phase swing of the signal, induced in BHMs between extremums as functions of the rf amplitude in the fifth tank which enable one to determine nominal rf amplitude is shown in fig. 8.

The investigation of the focusing conditions was complicated by getting out of order quadrupole lenses in the fourth and the ninth drift tube of first tank. To solve the problem gradients of the opening eight drift tubes were retuned so that the transverse phase portrait of the beam should be nominal in the center of the tenth quadrupole lens. As a result the beam in the first stage of the linac was accelerated practically without losses. The maximum accelerated current was 23 mA. The characteristic transverse profile of the beam at the output of the fifth tank is shown in fig. 9.

The 100-160 MeV stage of the linac

First of all the nominal proton beam energy (100.1).2 MeV) at the output of the first stage of the linac was accurately set by fixing the rf amplitude in the fifth tank which was roughly calculated with the bending magnet at the 160 MeV output of the linac calibrated to the energy of 94,41 MeV at the output of the fourth tank. The momentum spectrum of the particles at the output of the first linac stage is shown in fig. 10. The spectrum width at the half-height level is 0.6%. The phase spectrum of the beam bunches at the output of the first stage of the linac measured with the aid of a bunch shape monitor [3] is shown in fig. 11.

Rf amplitudes and phases in the resonant cavities NN 6-9 of the second stage of the linac were set according to the following procedure. The rf amplitude in all the cavities was determined by the power introduced in a cavity and by its shunt impedance. The rf phase setting was based on the two simultaneously measured functions: the beam current harmonic at the output of a cavity under tuning and the beam current downstream the bending magnet, both depending on the scanned rf phase in that cavity. These functions for the seventh resonant cavity are shown in fig. 12.

Summary

1. The first stage of the linac (output energy 100.1 MeV, impulse current without buncher - 23 mA) and the opening part of the second stage with the output energy 158.6 MeV (impulse current without buncher - 10 mA) have been tuned.

2. Besides traditional methods and appliances for tuning were proposed and tested new ones: rf amplitude and phase setting by phase scanning with the aid of 1) the beam current harmonic monitor together with magnetic spectrum analyzer and 2) with the aid of bunch shape monitor.

3. At the 100 ÷ 160 MeV part of the linac DAW cavities were tested successfully. The influence of parasite modes on the beam was not registered.

4. The longitudinal parameters of the beam at the output of the first stage of the linac (phase length of bunches of 13 degrees measured with the bunch length monitor and momentum spread of ± 0.76% measured with magnetic analyzer) are a bit better than designed. Therefore the beam losses due to longitudinal motion in the downstream part of the linac at the designed current of 50 mA are likely to benegligible.

Acknowledgment

Coauthors express their deep gratitude to scientists, engineers and technicians of many organizations taking part in MMF linac construction.

References

1. Ju.V.Bylinsky et al. Particle Accelerators, v.27, 1990, p. 107-112.
2. Ion Linear Accelerators, ed. by B.P.Murin, v.1,2. Moscow, 1978 (in russian).
3. A.V.Feschenko, P.N.Ostroumov. Proceedings of the 1986 Linac Conf., Stanford, June 2-6, 1986, p.323.

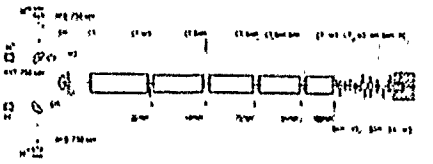


Fig. 1. The layout of the first stage of the linac with the measuring equipment.
Legend:
EM - emittance monitor, WS - wire scanner, CT - current monitor, BHM - bunch harmonic monitor, BPM - beam position monitor, HS, VS - horizontal and vertical slits, HM - halo monitor, FC - Faraday cup, BSM - bunch shape monitor, BA - beam absorbers

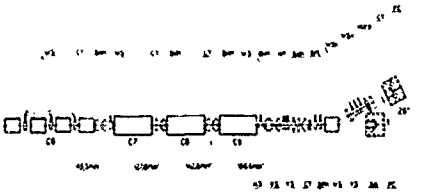


Fig. 2. The layout of the 100-160 MeV part of the linac

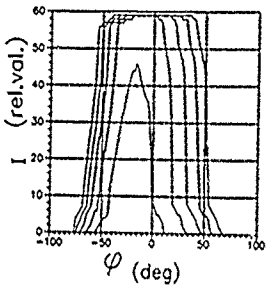


Fig.3. The beam current beyond the absorber with the cutoff energy of 43 MeV as functions of rf phase in the second tank

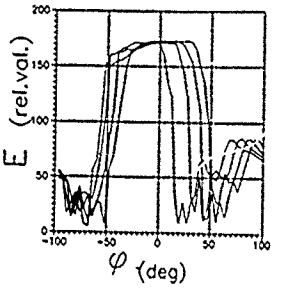


Fig.4. The dependence of the field level induced in BHM on the rf phase in the second tank

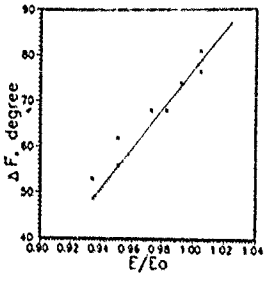


Fig 5. The second tank rf bucket width at the half-height level depending on rf amplitude
—— calculated
* experimental

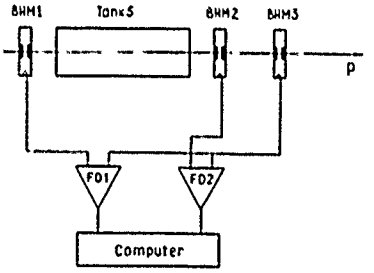


Fig. 6. The layout of time of flight measurement

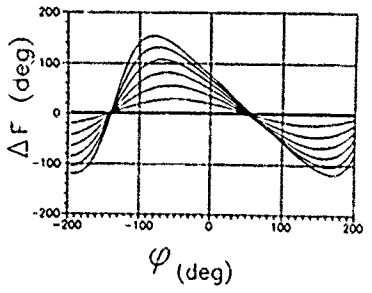


Fig. 7. The particles time of flight variation as functions of the rf phase in the fifth tank. The ΔΦ value corresponds to the phase shift between the second and the third BHM

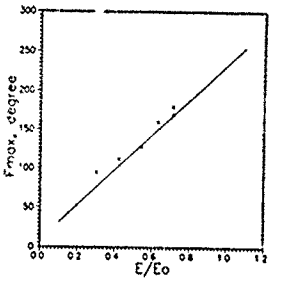


Fig.8. The phase shift of the signal, induced in BHMs between extremums as a function of the rf amplitude in the fifth tank.
—— calculated
* experimental

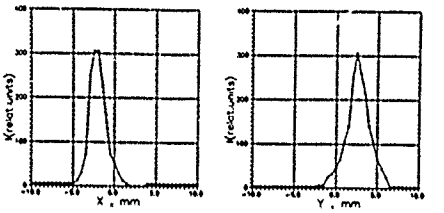


Fig. 9. Beam profiles at the energy of 100 MeV

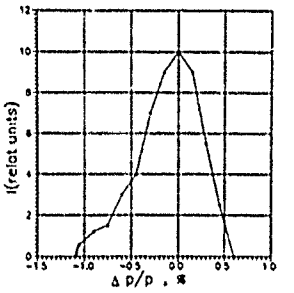


Fig.10. Momentum spectrum of the 100 Mev beam

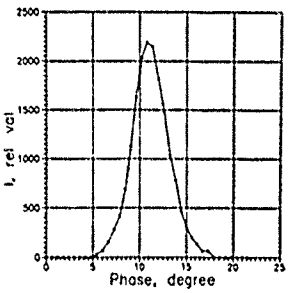


Fig.11. Phase spectrum of the 100 MeV beam

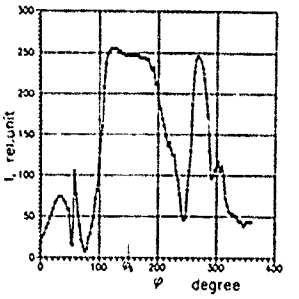


Fig.12. Phase scan by using BHM

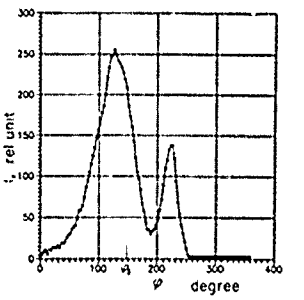


Fig.13. Phase scan by using bending magnet

Drift Compression Experiments on MBE-4 and Related Emittance Growth Phenomena*

S. Eylon, A. Faltens, W. Fawley, T. Garvey, K. Hahn, E. Henestroza, and L. Smith,
Lawrence Berkeley Laboratory, 47/112
University of California
Berkeley, CA 94720 USA

Abstract

We have recently conducted a series of experiments on the MBE-4 heavy ion accelerator in which a velocity tilt was placed on the beam in the first accelerating section beyond the injector, followed by drift compression over the remaining 11 meters. Depending upon the magnitude of the velocity tilt and the accompanying mismatch in the focusing lattice, emittance growth was observed, manifested by "butterfly" shapes in $x - x'$ phase space. We discuss various analytical limits on ion beam compression and relate them to these experiments and also to a driver for a heavy ion fusion reactor. We also present numerical simulations which investigate various aspects of compression and consequent emittance growth.

I. Introduction

MBE-4 is a multiple beam, heavy ion accelerator at LBL designed to study the physics of space-charge dominated beams and scaling thereof to a heavy ion fusion "driver". One of the major requirements for a driver is smooth and controlled compression of the heavy ion beam from a typical duration at the injector ($E \sim 2-10$ MeV) of $\sim 10\mu$sec to a duration at accelerator exit ($E \sim 5-10$ GeV) of ~ 100ns. In general, this temporal compression will involve a smaller, but not insignificant increase in line charge density also. There is an additional ~ 10x compression at nearly constant energy between the accelerator and target to bring the pulse duration to the wanted 10 ns.

In the last year, we have conducted a number of compression experiments on MBE-4 both at constant energy (*i.e.* drift compression) and with steady acceleration [1] from the injector energy of 185 kV to final energies of ~ 800 kV. In both cases, the compression is achieved via a head-to-tail velocity tilt on the beam. Of particular concern is the behavior of the ion beam transverse phase space during the longitudinal compression. Our results suggest that very strong compression ratios ($\geq 6:1$) lead to substantial emittance growth for MBE-4 beams while smaller ratios ($\leq 3:1$) generally cause little or no emittance growth. As explained in §IV, the key physics appears to be the interaction between a highly compressed and thus radially large beam and the external nonlinear dodecapole focusing forces and internal, nonlinear space charge fields.

*Work supported by the Director, Office of Energy Research, Office of Basic Energy Sciences, Advanced Energy Projects Division, U.S Dept. of Energy under Contract No. DE-AC03-76SF00098.

U.S. Government work not protected by U.S. Copyright.

II. Experimental Set-up

For the drift compression experiments described here, MBE-4 was used in a single beam mode with the 185-kV injector producing a 2.5-μs duration, 8-mA current pulse of Cs^{+1}. As the beam leaves the injector, it passes through a "matching zone" composed of a eight individual quadrupoles used for transition onto the syncopated FODo focusing lattice of the main accelerator. Within this matching zone, there is an aperture plate that absorbs the outer (and most badly aberrated) portions of the beam, reducing the current by a factor of two. In general, the matching is imperfect and the beam's radial profile shows low level hollowing oscillations between lattice period 0 (≡LP0) and LP10. The electrostatic quadrupole voltages were set to produce a single particle phase advance σ_0 of 72° per lattice period; the space-charge depressed tune σ was in the range $7 - 10°$.

The first four accelerating gaps were timed so that a nearly linear velocity tilt (ranging from 0 to $\geq 12\%$) was put on the beam. We used a numerical code **SLIDE**[1] to determine the timing and amplitude of the accelerating pulses. No further acceleration fields were applied downstream and thus the beam energy remained constant apart from the work done against the longitudinal space charge field. An energy analyzer (normally positioned at LP5) measured the temporal variation of the beam's energy with a 0.5% energy and ≤20-ns temporal resolution. At every five lattice points along the accelerator, a two-slit emittance scanner determined the $x - x'$ projection of the beam's transverse phase space. In general, the x resolution of ≈ 1.0 mm was much smaller than the typical beam radius of 5-10 mm, while the angular resolution of 0.7 mrad was comparable to the projected RMS width. The emittance scans were programmed to trace out a parallelogram in phase space with a tilt equal to that corresponding to the temporal center of the beam's phase space ellipsoid.

III. Results

Our initial drift compression experiments were with a quite vigorous acceleration schedule which resulted in a nearly 5.1 current increase by LP15, and 7.4.1 by LP20. The RMS emittance also tripled and butterfly shapes were evident in the phase space data. We then ran a number of less vigorous compression schedules to determine the sensitivity and behavior of the emittance increase.

Table 1. Emittance (ε) and beam radius (a) measurements for drift compression experiments

I_{max}/I_0	$\varepsilon^{rms}_{max}/\varepsilon^{rms}_0$	a_{max}/a_0	$\varepsilon^{\mu}_{max}/\varepsilon^{\mu}_0$	N_{max}
1:1	0.9-1.1	1.0-1.2	1.1-1.2	–
1.5:1	0.9-1.1	0.9-1.0	1.0	≥LP20
3.7:1	1.3-1.6	1.6	1.0-1.2	LP25
7.4:1	≥2.8-3.2	≥1.7-2.0	≥2.1	LP20

Table 1 presents various measured quantities summarizing the results of the different compression schedules. The "microscopic" emittance ε^{μ} is defined to be the phase space area (not necessarily contiguous) occupied by the most intense 80% fraction of the beam current. This quantity is readily extracted from the 2D map produced by the emittance scanner. ε^{μ} is expected to be a more "conserved" quantity than ε^{rms} in cases such as a simple "S" distortion of the $x-x'$ phase space. N_{max} is the lattice period at which maximum compression was measured. For the 7.4:1 compression data, it appears that portions of the beam extended outside the maximum range scanned in x, ±20 mm (the clear quadrupole aperture is 27.4 mm).

In Fig. 1 we plot $\varepsilon(z)$ for various longitudinal slices of the beam pulse in the 3.7:1 compression experiment. The slices are labeled by their charge-weighted positions in the beam with the presumption that no longitudinal overtaking has occurred. Two observations are of note: 1. Slices with little compression ($I/I_0 \leq 2.7$) suffered little emittance growth and those in free expansion near the head and tail may actually have "cooled off" with increasing z. 2. The mid-pulse slices with significant emittance growth by LP25 showed little growth at earlier positions in z where the compression was ≤ 3.0.

This first observation is also true for the 7.4:1 compression data although the sparsity of observation points (LP0-LP20 only) prevents one from drawing firm conclusions concerning the final state of the beam. Moreover, both high compression cases show that the "microscopic" transverse phase space areas of the beam increased far less than did the RMS measures. For the 3.7:1 case, the relative increase in ε^{μ} is essentially unchanged from that measured for the simple 1.1 drift case. Figure 2, which plots phase space contours of a central beam slice at LP25, shows why this is so. the phase space ellipse has developed "S"-arms which account for the increase in RMS emittance but do not result in an actual phase space dilution. By contrast, Fig. 3, which plots phase space contours for the central slice of the 7.4.1 compression case, shows a "butterfly" or bow tie shape in its wings. The butterfly wings include both a major portion ($\geq$ 30%) of the current at a given instant in time, and persist for the great majority of longitudinal slices measured at LP20. In this case, $x-x'$ phase space has been truly diluted and no simple system of lenses will reverse this degradation.

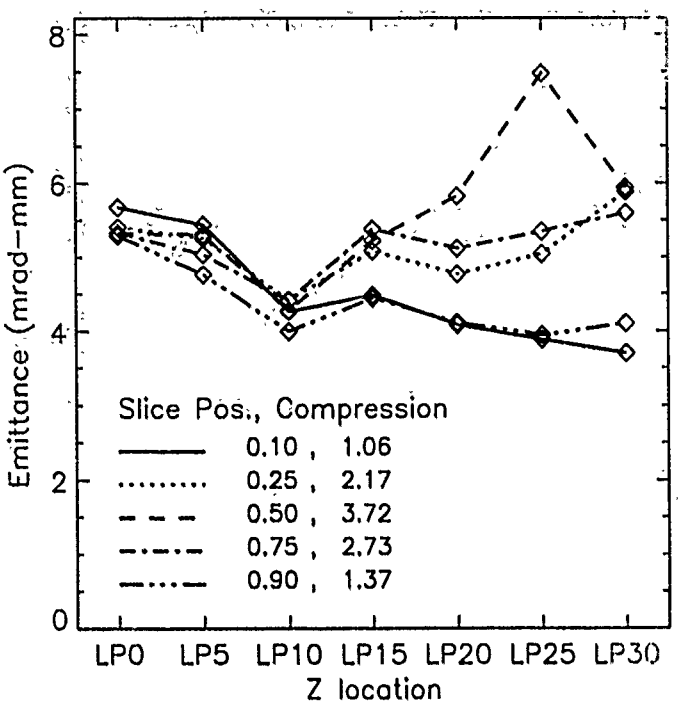


Figure 1: RMS emittance measurements for various longitudinal slices in the 3.7:1 drift compression data. The first number refers to the charge-weighted position in the beam (*i.e.* head=0, mid-pulse=0.5, tail=1) while the second refers to the maximum compression measured for a given longitudinal slice.

IV. Analysis and Discussion

After discovering the butterfly shapes in the high compression phase space data, some of us suspected that longitudinal overtaking might be occurring within the beam near the LP15-LP20 region. Supporting this view was an observed rapid temporal change in the phase space ellipsoid tilts, exceeding 90° in a time half that of the current pulse FWHM. Perhaps the butterfly shapes were actually the superposition of two beamlets of different energies whose integrated phase advance differed by $\sim 90°$. However, the **SLIDE** numerical code, which has been quite successful in predicting current waveforms for MBE-4 compressed beams, did not suggest problems with overtaking. Furthermore, energy analyzer scans taken at LP15 and LP20 do not show obvious double-valued behavior that would be a sign of longitudinal overtaking.

A related possibility is that while no longitudinal overtaking *per se* occurred, the longitudinal beam compression might have become so great in the 7.4.1 case that the *longitudinal* variation in the z-integrated phase advance for mismatch oscillations has become significant ($\geq$ 1 radian) over a quadrupole aperture radius b. If so, this allows "communication" via space charge fields between slices of different mismatch phase and might lead to relatively rapid phase mixing. For our case of $\sigma \ll \sigma_0$, we estimate the

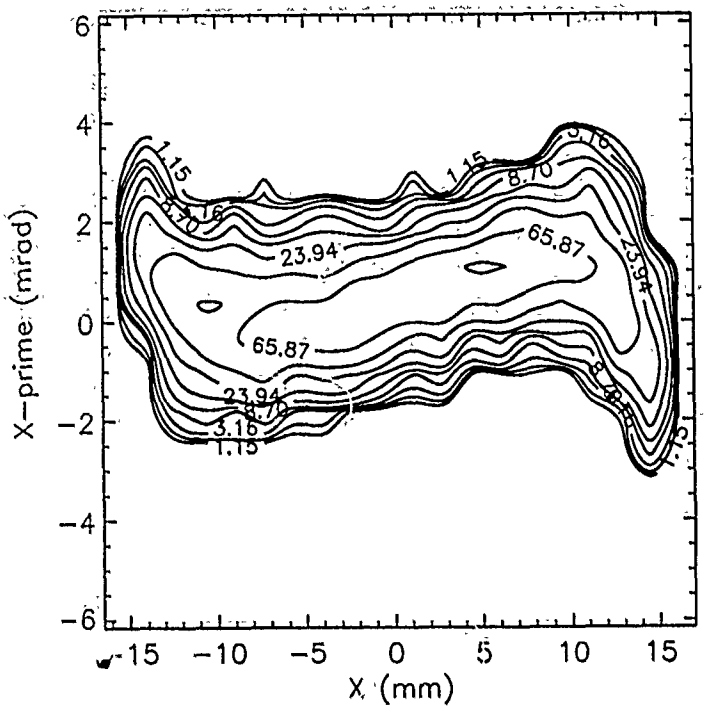


Figure 2: Phase space density contours (equi-spaced logarithmically) measured at LP25 for the central longitudinal slice of the 3.7:1 drift compression data.

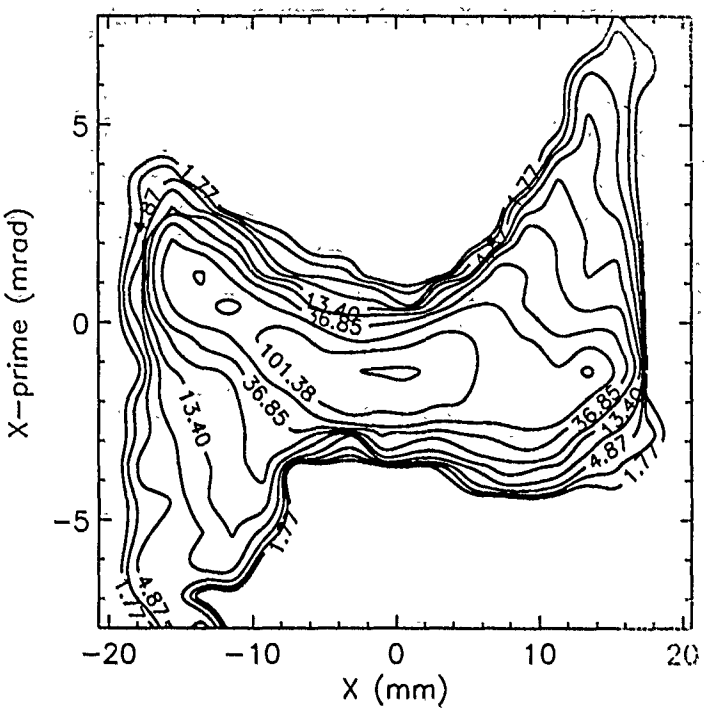


Figure 3: Phase space density contours measured at LP20 for the central longitudinal slice of the 7.4:1 drift compression data.

maximum phase advance variation as

$$\Delta\phi = \int_{LP5}^{LP20} \sqrt{2}\,\sigma_0\, dN \left|\frac{d\beta}{\beta\, dl}\right| \frac{b}{\beta_0 c} \approx 0.6\,\text{radians}\,.$$

Here N measures z in lattice periods. Given the relatively rapid (in z) reversal of the beam's compression which limits the communication time, it is unclear whether this effect and the magnitude of mismatch oscillations are sufficient to produce transverse phase space shapes such as Fig. 3.

A second suggested mechanism for emittance growth was the interaction of a compressed (and thus "fat") beam with the small ($\approx$ 10% relative to the quadrupole at the electrode surface) nonlinear dodecapole forces present in the MBE-4 lattice. Previous experiments [2] on MBE-4 have shown that dodecapole-induced phase-mixing for off-axis beams can lead to significant emittance growth. In the present experiments, however, the beam remained within $\approx \pm 0.5$mm of the axis, so simple centroid damping is ruled out. Particle simulation code runs [2] suggest that dodecapole-induced emittance growth will occur for centered, drift-compressed beams with the predicted magnitude sufficient to explain the 3.7:1 compression data. The simulation results are not as clear-cut for the 7.4:1 case, due to difficulties such as particle loss to the walls (which possibly occurred in the experiment also). D. Grote at LLNL (private communication), however, has produced butterfly shapes in a 3D simulation of MBE4 compression including dodecapole forces. Space charge non-uniformities, which appear to be quite important for $z \geq$LP10 in the 7.4:1 data, probably also affected the evolution of the transverse phase space. Such non-uniformities (both symmetric and non-symmetric) can present strong, nonlinear perturbations for highly space-charged depressed beams such as MBE-4.

Summarizing, strong (7.4:1) and rapid compression ($d\lambda/\sigma_0 dN \geq 0.1\lambda$) of the MBE-4 beam led to large emittance growth. We believe that the cause is interaction of the outer portions of the beam with nonlinear dodecapole focusing forces and possibly non-uniform space charge distributions. Weaker (3.7:1) and less rapid compression ($d\lambda/\sigma_0 dN \leq 0.05\lambda$) showed little or no RMS emittance growth. Most HIF driver designs have $d\lambda/\sigma_0 dN \leq 0.005\lambda$ within the accelerator. Hence, non-adiabatic, rapid compression problems, if they occur at all, are far more likely in the final focus section rather than within the accelerator.

References

[1] T. Garvey *et. al*,"Transverse Emittance Studies of an Induction Accelerator of Heavy Ions", Poster *XRA51*, these proceedings.

[2] S Eylon *et al.*,"Emitance Variations of Very Cold Ion Beams During Transport Through MBE-4", in *Proc Int. Symp. on Heavy Ion Inertial Fusion*, Monterey, CA, Dec., 1990, to appear in Part. Accel., 1991.

Transverse Emittance Studies of an Induction Accelerator of Heavy Ions*

T. Garvey, S. Eylon, T.J. Fessenden, K. Hahn, and E. Henestroza

Lawrence Berkeley Laboratory, University of California,
Berkeley, California 94720

Abstract

Current amplification of heavy ion beams is an integral feature of the induction linac approach to heavy ion fusion. As part of the Heavy Ion Fusion Accelerator Research program at LBL we have been studying the evolution of the transverse emittance of ion beams while they are undergoing current amplification, achieved by longitudinal bunch compression and acceleration. Experiments are conducted on MBE-4, a four beam Cs^+ induction linac. The space-charge dominated beams of MBE-4 are focused by electrostatic quadrupoles while they are accelerated from nominally 200 keV up to ~ 1 MeV by 24 accelerating gaps. Initially the beams have currents of typically 4 mA to 10 mA per beam. Early experimental results showed a growth of the normalized emittance by a factor of 2 while the beam current was amplified by up to 9 times its initial value. We will discuss the results of recent experiments in which a mild bunch length compression rate, more typical of that required by a fusion driver, has shown that the normalized emittance can be maintained at its injection value (0.03 mm-mr) during acceleration.

1. INTRODUCTION

The induction linac approach to heavy ion driven inertial fusion envisages a design in which multiple beams are employed at the low energy end of the driver with the beam current undergoing amplification as it is accelerated. Current amplification results both from the increase in particle velocity and also from longitudinal bunch compression. This compression is achieved by applying a velocity 'tilt' between the head and tail of the bunch, provided by tailored voltage waveforms applied at the accelerating gaps. MBE-4 is a four beam Cs^+ linac built to investigate longitudinal dynamics issues related to this concept. The linac is comprised of a 30 period, electrostatic, AG focusing lattice. Each doublet is followed by an accelerating gap with the exception of every fifth doublet where the gap is reserved for diagnostic access and vacuum pumping. Each lattice period (l.p.) is 45.7 cm long resulting in a linac of 13.7 metres.

Early experiments on MBE-4 concentrated on a demonstration of current amplification while maintaining control of the current profile and correcting for inevitable acceleration 'errors', which arose from the difference between ideal accelerating pulser waveforms and those waveforms achieved in practice. These experiments, in which the current was amplified from 4x10 mA to 4x90 mA and the energy increased from 200 keV (the injection value) to 900 keV, were accompanied by a growth in the normalised emittance by a factor of approximately two. This work has been reported previously and a review can be found elsewhere in these proceedings[1].

2. EXPERIMENTS

We have identified a number of mechanisms which may be responsible for emittance growth in MBE-4 including matching errors, rapid longitudinal compression (leading to a change in the space-charge electrostatic-field energy), and non-linear field effects (self-fields, image-fields, focus fields). The last of these mechanisms is particularly troublesome for off-axis beams where the edge of the beam may approach the non-linear field region of the quadrupoles[2]. For the experiments discussed here offsets are minimised by the use of steering elements at the entrance to the linac and by careful alignment of the accelerator. Proper matching of the beam phase-space to the lattice of the linac is performed by adjustment of a"matching section" consisting of eight electrostatic quadrupoles just downstream of the diode.

Recent experiments have involved the application of an acceleration schedule which results in a smaller increase in the beam line charge density between injection and full energy. In order to realise this we have reduced the extent of the applied velocity tilt in the early gaps of MBE-4 with the majority of the acceleration being provided by waveforms in which the voltage does not vary greatly during the passage of the beam pulse. The reduction in bunch compression in these experiments means that the beam pulse length is not sufficiently short for the final accelerating waveforms to completely straddle the beam pulse. Consequently the current waveforms observed in these experiments are poorer than those obtained in earlier studies, however the focus of these experiments is transverse beam dynamics.

In attempting to maintain a matched beam during acceleration we scale the strengths of the quadrupole focusing voltages, V_q, such as to keep them proportional to the beam line-charge density, λ, i.e. $V_q \sim \lambda \sim I / v$, where I and v are the beam current and velocity respectively. The beam currents and velocities used in calculating the required quadrupole voltages are determined approximately for any given acceleration schedule using a longitudinal dynamics simulation

*Work supported by the Office of Energy Research, Office of Basic Energy Sciences, U.S. Department of Energy Contract DE-AC03-76SF00098.

U.S. Government work not protected by U.S. Copyright.

code (SLID) which uses the measured beam current and energy at injection as input. The available range of quadrupole voltages is limited by breakdown and such scaling would not have been possible in the early experiments where λ was increased by a factor of ~ 4.5

Diagnostics and Data Reduction

Transverse emittance measurements are made using the familiar double slit technique with a multi-shot scanning procedure to determine the signal strength as a function of the transverse (x,x') phase space position, the charge being collected in a Faraday cup behind the downstream slit. Measurements can be made in each transverse plane in turn with typically 400 shots required to obtain one value of emittance. The charge collected through both slits is recorded many times (20 to 50) during the pulse so as to provide a time resolved measurement of the emittance. The data collected can be reduced to yield other time resolved quantities of interest such as the beam size, centroid motion and current profile integrated along the direction of the slits. A typical set of data for the beam at injection is shown in Fig.1. The four traces show the beam current (top left), beam emittance (top right), r.ms. beam size (bottom left, upper), centroid position (bottom left, lower), the r.m.s. slope of the beam (bottom right, upper) and the angular off-set of the centroid (bottom right, lower).

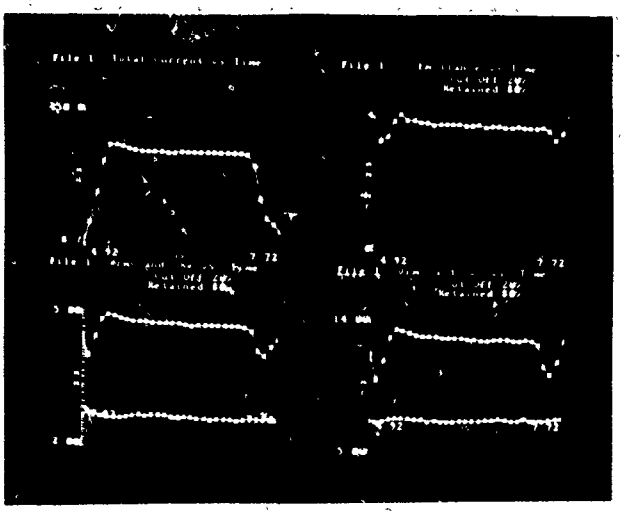


Figure 1. Time-resolved measurements of MBE-4 beam parameters. See text for explanation of traces.

Figure 2 shows a typical emittance plot at the entrance to the linac for a fixed time within the beam pulse.

In calculating the emittance we define the r.m.s. value ε_{rms} as,

$$\varepsilon_{rms}^2 = \langle (x - \langle x \rangle)^2 \rangle \langle (x' - \langle x' \rangle)^2 \rangle - \langle (x - \langle x \rangle)(x' - \langle x' \rangle) \rangle^2 , \quad (1)$$

with the normalised emittance, ε_n, being defined as,

$$\pi\varepsilon_n = 4\pi\beta\varepsilon_{rms}. \quad (2)$$

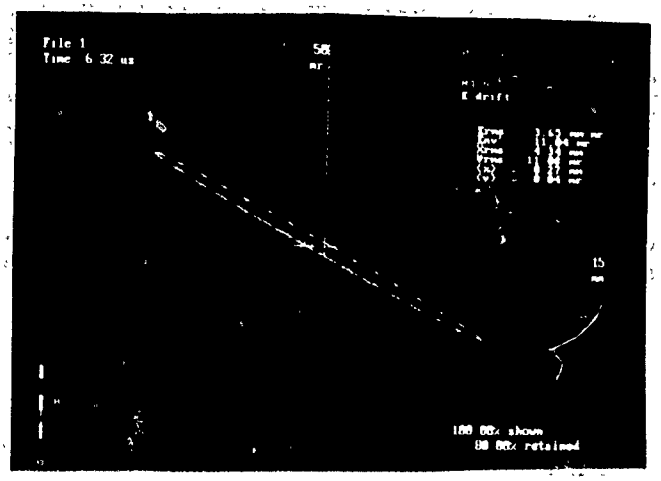


Figure 2. Phase space data at injection to the linac. The ellipse corresponds to a K-V beam of the same emittance as the measured beam.

During operation of the acceleration pulsers the signals obtained on the Faraday cups contain contributions from electrical noise which can be dominant at the edge of the phase space plots where the signal due to the beam is low. In order to exclude such effects we refer to the emittance contained in a given percentage, P, of the beam current where,

$$P = \Sigma_{i,j}\, S(x_i,x'_j,t)\; U(S(x_i,x'_j,t) - c) \,/\, \Sigma_{i,j}\, S(x_i,x'_j,t) , \quad (3)$$

In equation (3) U is a unit-step function and the constant c is is a cut-off signal level determined by iteration to correspond to the desired P. The averages used in equation (1) are calculated using only signals above the cut-off value. Typically we find that 80% values are useful for quoting the emittances of accelerated beams while 90% is usable for drift beams. Figure 3 shows a plot of the calculated emittance as a function of P where it is quite apparent that the computed value increases non-linearly with P above P = 80%.

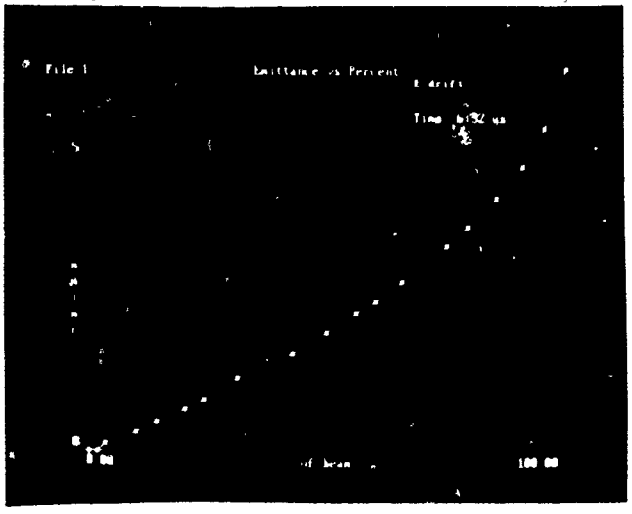


Figure 3. Emittance versus percentage of beam current.

3. RESULTS

Following the installation of a current limiting aperture we have been working with smaller beam currents (< 5 mA) which, at injection, typically have ε_n = 0.03 mm-mrad (P = 90%) [3]. The aperture was employed to remove beam particles which were over-focused due to aberrations in the diode optics. The resulting beam radius is nominally 10 mm, propagating in a transport channel of 27 mm radius. For our 'mild' acceleration schedule the measured currents and computed energies at the diagnostic stations are given in Table 1. The corresponding emittances measured under both drift and acceleration in the horizontal plane are shown in Fig. 4 for P = 80%. One can see that, within the limits of experimental error, the normalised emittance is conserved. For this schedule the energy is increased by a factor of 2.6 while λ is increased by only 18%. The 'missing' point for the acceleration data at l.p. 30 is due to faulty and irreproducible behaviour of the principal accelerating pulser in the last section of the machine.

Table 1.
Energy and current vs. l.p.

l.p.	Current (mA)	Energy (keV)
0	3.7	186
5	4.0	190
10	4.2	245
15	5.1	270
20	6.2	390
25	7.0	480

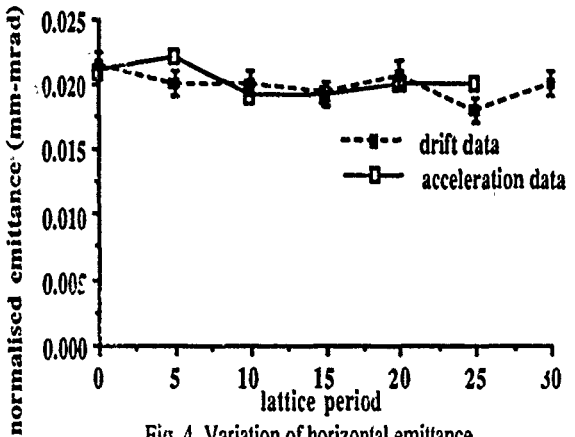


Fig. 4. Variation of horizontal emittance with l.p. for drift and acceleration.

4. DISCUSSION

We have previously reported emittance growth for our 3.7 mA beam under a stronger compression (x 3) but that data was complicated by poor matching from the injector (the matching section having been adjusted for the more usual current of 5 mA)[4]. For the data discussed in this paper the drift beam has been properly matched to the linac, however, it is apparent from measurements of the beam envelope under acceleration that the beam is becoming mismatched in the latter part of the machine. More careful matching under acceleration might require the use of accurately measured currents and energies, as opposed to the SLID calculated values, to determine the quadrupole voltages. An up-graded version of SLID (SLIDE) has been developed which gives improved agreement with the measured data and which might be used for better matching in future experiments on heavy ion induction linacs. Proper matching at injection is found to be neccessary however to minimise emittance growth for both drift and accelerated beams over the length of the linac.

Despite the mismatch under acceleration we find that, for well centered beams with sufficiently mild compression, the normalised emittance can be kept constant during acceleration. Our experiments, however, have not led us to an allowable limit for the rate of compression. Recently we have obtained data which shows that the line density can be doubled while the energy is increased by the same factor as above without much growth in the emittance. This is in contrast to early experimental data from MBE-4 where emittance growth of 75% was seen in another acceleration schedule which doubled the line density. The greater attention paid here to maintaining a well centered beam may be the beneficial factor in the new data. The maximum beam offset observed in our experiments is approximately 1.5 mm which is consistent with residual injection offsets and the limits of the alignment of the focus elements (±0.13 mm). The observed variations in emittance growth under different conditions of mis-match, beam offset and current amplification are found to be in reasonable agreement with the results of 2-D particle-in-cell simulations[1]. Thus we are confident that our computer code can accurately predict the expected growth of emittance in future induction linac designs.

5. ACKNOWLEDGEMENTS

We are indebted to L. Smith, A. Faltens and W.M. Fawley for helpful discussions.

6. REFERENCES

[1] T.J. Fessenden,"Emittance variations in current-amplifying induction linacs", invited paper in these proceedings.
[2] T. Garvey et al., "Transverse beam dynamics studies of a heavy ion induction linac", Proceedings of the 1990 Linac Conference, Albuquerque NM, September 1990, pp 752-754.
[3] T. Garvey et al., "Multiple beam induction linac studies at LBL", Proceedings of the High Power Beams Conference, Novosibirsk, July 1990, pp 1277-1282.
[4] T. Garvey et al., "Beam acceleration experiments on a heavy ion linear induction accelerator", to be published in Particle Accelerators.

Funneling Study With A Low Energy Proton Beam*

W. Barth, A. Schempp
Institut für Angewandte Physik, J.W. Goethe-Universität
D-6000 Frankfurt 11, Postfach 111932, Germany

Abstract

Funneling is a method to increase the brightness of ion beams by filling all rf-buckets in order to use the full current transport capability of an rf accelerator by frequency jumps at higher energies. This has been proposed for HIIF type drivers and neutron sources.

A simple funneling experiment is prepared at Frankfurt, using modest fields in a set up with a 50 keV proton beam and an rf deflector to study especially emittance growth effects in such funneling lines. First results will be reported.

I. Introduction

Funneling of two or more beams will drastically reduce the cost and complexity of accelerators designed to produce intense beams with brightness. Particle beams e.g. from two identical low-frequency structures are funneled into a single high frequency accelerator in such a way that every bucket of the high-frequency accelerating field is filled. For a simple two channel line the two beams have to be bunched and accelerated in identical rf accelerators at the frequency f_0, with a phase shift of 180 degrees between them (Fig. 1.).

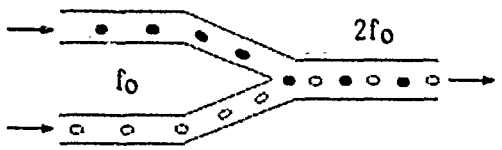


Fig. 1. Principle of a simple two channel funneling line.

A perfect funneling-line doubles the beam current and the transverse brightness at twice the frequency without any emittance growth. Applications of funneling could include accelerators for heavy ion inertial fusion (HIIF) or SNQ-type accelerators proposed for fusion material irradiation or accelerator production of tritium (APT) [1].

Funneling in a RFQ-like structure is a possibility for beam merging at low energies where electric fields are necessary to provide strong focusing. It has been shown that a single RFQ-like structure can be used to combine two ion beams [2].

For high energies funneling with discrete elements (quadrupoles, bending magnets, rebunchers, rf deflectors) is more flexible but also more expensive. A first description of such a funnel line was given by Bongardt [3] for the HIBALL. Another funnel set up for HIBALL II has been proposed at LANL [4], where also a single leg of a prototype 5-MeV funnel for light ions was sucessfully tested [5].

II. Defunneling

Experimentally there are a lot of difficulties. Therefore we investigated funnel structures at first in a different way: one bunched ion beam is devided in two displaced beams with 180° phase-shift and half repetition frequency. A perfect defunnel line devides the beam current and the transverse brightness without any emittance growth. This inversion of a funnel line allows to investigate most of the physics issues, which arise in a real funnel section. For example the design and operating of the rf deflector - the neuralgic point of every funnel - can be optimized. Furthermore we can use the defunnel line itself as an injection system for a funnel experiment, because the two output beams of the defunnel line have all the required properties.

III. Field Calculations

The deflector is a plate capacitor of length L symmetrically placed around the z-axis (the longitudinal axis of the injection accelerator) with a time varying electric field. If we neglect fringing fields at first, the electric field inside the deflector has only a homogenous and time-dependent x-component.

$$E_x(t) = A \sin(\omega t - \varphi) \qquad (1)$$

Besides the peak deflecting amplitude A, such an ideal deflector is described by its length L, the frequency ω and the phase φ.

Considering fringing fields (x-component), A is replaced by a term A(z), which depends on z. Therefore, we used a version of the SLAC166 simulation code [6,7] to calculate the potential $\Phi(x,z)$ in the deflector. From this the electric field component $E_x(z)$ on axis is obtained.

In a next step the dependence of E_x on x and also the accelerating or decelerating field component $E_z(x,z)$ is investigated. For that purpose we used the complete potential grid calculated by SLAC166 (see Fig. 2.). The actual field components

* supported by BMFT under contract no. 06 OF186 I

0-7803-0135-8/91$01.00 ©IEEE

are obtained by using the actual coordinates (x_{act}, z_{act}) of the particle (an example is shown in Fig. 3a and 3b.). This is done for every particle in the multiparticle simulations.

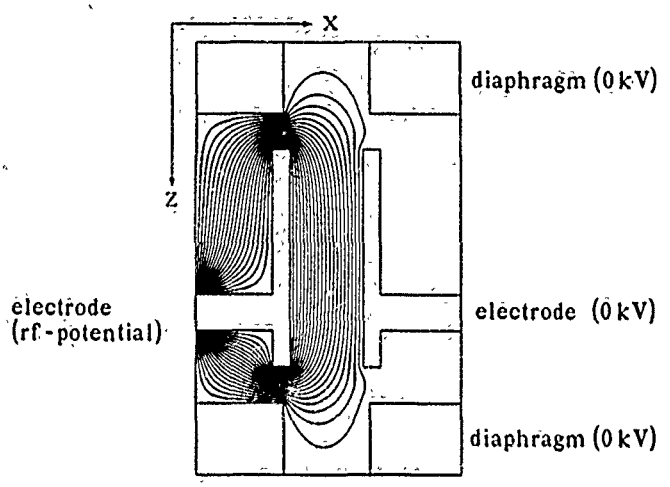


Fig. 2. The equipotential lines in the rf-deflector calculated with the SLAC166 [6;7].

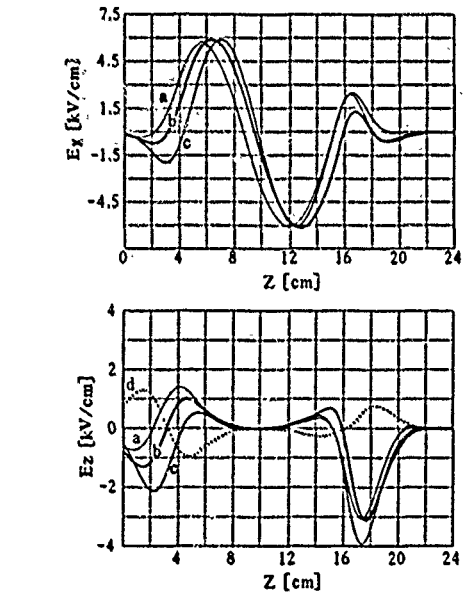


Fig. 3. a. The deflecting field component $E_x(x,z)$: E_x for a particle at the beginning (c), at the end (a) and in the center (b) of the bunch is shown. b. The longitudinal field component $E_z(x,z)$ (corresponds to Fig. 3a.); in addition E_z for a particle in the center of an adjacent bunch (d).

IV. Experimental Set Up

The experimental set up of the defunnel line is shown in Fig. 4. The injection system of the defunnel element consists of a plasma beam ion source [8], an extraction system, and a Split Coaxial-RFQ with rod electrodes [9].

With hydrogen operation the plasma beam ion source supplies a proton fraction of 90% at a max. beam current of 6 mA. The ions are extracted with an accel/decel-system at an extraction voltage of 6.5 keV. We use a solenoidal lense [10] to match the ion source beam to the 50 MHz SCR-RFQ. The SCR-RFQ accelerates the H^+-beam from 6.5 keV to 50 keV.

In the adjacent defunnel element (25 MHz) the beam is divided into parallel beams. The deflector is part of a helix-$\lambda/4$-resonator. Thus the cavity of the deflector can be very small.

For diagnostic we use faradaycups (beam current, bunchstructure), an emittance measurement device [11] and an analysing magnet for energy spectra. The parameters of the defunnel system are summarized in Tab. 1.

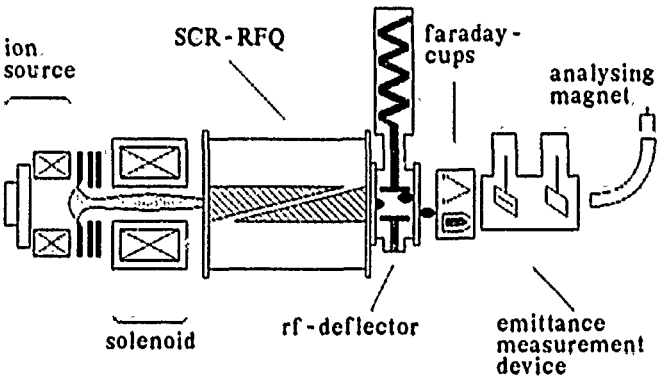


Fig. 4. The experimental set up of the defunnel line.

	SCR-RFQ	RF-Defl.
f (MHz)	50	25
Voltage (kV)	9 max.	40
Rp-value (kΩ)	180	290
Qo-value	4500	400
T_{in} (keV)	6.5	50
T_{out} (keV)	50	50
Aperture (mm)	6-4.5	42
Modulation	1.16-1.88	-
φ_s (°)	60-30	-
φ_{ot} (°)	45	-
Length (cm)	55	10 or 16
Cell number ($\beta\lambda$)	32	0.5 or 1
I_{max} (mA)	4.2	-
Displacement (mm)	-	25

Tab. 1. The parameters of the defunnel experiment.

V. Multiparticle Simulations and Experimental Results

The horizontal beam deflection and the horizontal emittance growth were measured as a function of the relative rf-phase and the deflector voltage. Fig. 5. shows the horizontal beam deflection versus deflector voltage. The asymmetric field distribution - shown in Fig. 2. - is responsible for the differences between a deflection to the left or to the right side. The agreement between measurement and simulations is excellent. The beam deflection scales with deflection voltage as expected. The emittance growth (Fig. 6.) shows a dependence on the deflector voltage which includes also terms of high order. With the rf-deflector

set at its experimentally determined optimized phase (65° for min. emittance growth) the measured displacement between the centers of the beams was 20 mm at a deflection voltage of 40 kV. This optimized phase determined by measuring the dependence of the emittance growth (deflection) on the relative rf-phase is shown in Fig. 7.

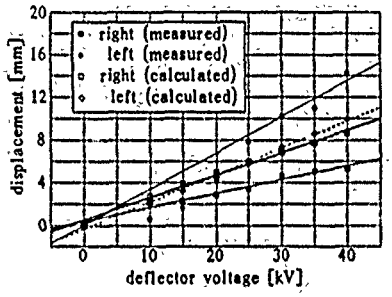


Fig. 5. The displacement as a function of the deflector voltage. The relative rf-phase φ is fixed to 65°.

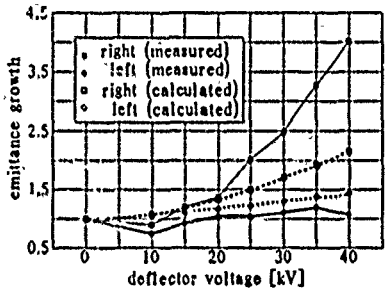


Fig. 6. The emittance growth as a function of the deflector voltage; $\varphi = 65°$.

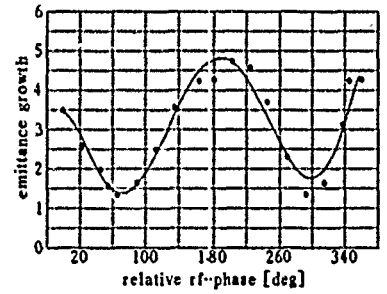


Fig. 7. The emittance growth as a function of the relative rf-phase, for a single bunch. The rf voltage has a constant value of 30 kV.

In Fig. 8. a comparison between the calculated and measured x,x'-emittance for two divided and parallel beams is shown. There are two effects which are predicted by the calculations and confirmed by the experiment: an offset in angle, which depends on the rf voltage (but independent on rf-phase) and moreover a rotation of the emittance, which is deflected to the right side. Both can be explained by the asymmetric field distribution. The value of the deflecting component of the rf-field is nearly independent on the direction of the deflection. But the longitudinal field component $E_z(x,z)$, as seen in Fig. 3b., shows a significant difference for a bunch deflected to the left or to the right side. This difference explains all asymmetrically effects, which are shown in Fig. 5-9.

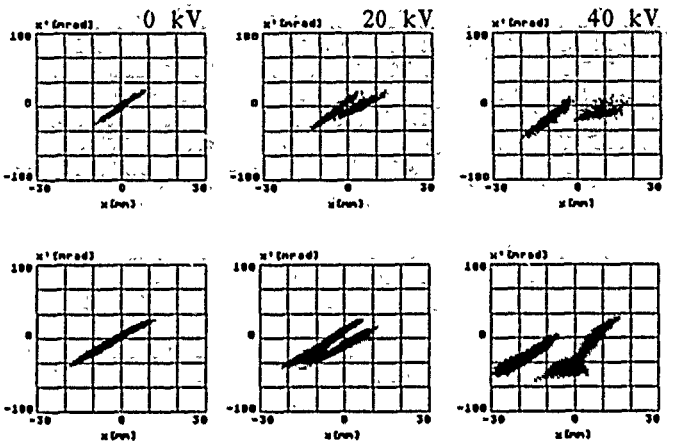


Fig. 8. The x,x'-emittance as a function of the deflector voltage. The results of the simulations are shown on the top, those of the experiments on the bottom.

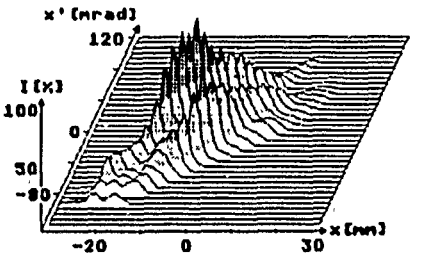


Fig. 9. The 3d x,x'-emittance at a deflector voltage of 20 kV; $\varphi = 65°$.

As a conclusion, the use of the defunnel experiments were successfull. The dependence of beam deflection and horizontal emittance growth on deflection amplitude and relative rf-phase, as well as all asymmetries were explained by the simulations.

VI. Acknowledgements

The authors thank all colleagues to their help, especially G. Hausen and I. Müller. All calculations were done at the HRZ/Frankfurt.

VII. References

[1] T.P. Wangler et. al., Linac, LA-12004-C (1990), 548.
[2] R.H. Stokes, G.N. Minerbo, IEEE, Vol. NS-32 No.5, (1985).
[3] K. Bongardt, D. Sanitz, HIIF, GSI 82-8 (1982), 224.
[4] J.F. Stovall et. al., NIM A278 (1989).
[5] K.F. Johnson et. al., Linac, LA-12004-C (1990), 701.
[6] W.B. Herrmannsfeldt, SLAC Rep. 166, (1973).
[7] W. Sinz, thesis, Univ. Frankfurt, (1985).
[8] K. Langbein, EPAC, Rome, (1988), 1228.
[9] P. Leipe, Univ. Frankfurt, thesis, (1989).
[10] A. Müller Rentz, Univ. Frankfurt, dipl. thes., (1986).
[11] G. Riehl, Univ. Frankfurt, thesis, (in prep.).
[12] W. Barth, GSI Darmstadt, rep. 91-1, in print, (1991).

LIAM - A Linear Induction Accelerator Model*

H. Brand, G. Caporaso, D. Lager, F. Coffield, and F. Chambers,
Lawrence Livermore National Laboratory

Abstract

We have developed a flexible Linear Induction Accelerator Model (LIAM) to predict both beam centroid position and the beam envelope. LIAM requires on-axis magnetic profiles and is designed to easily handle overlapping fields from multiple elements. Currently, LIAM includes solenoids, dipole steering magnets, and accelerating gaps. Other magnetic elements can be easily incorporated into LIAM due to its object-oriented design. LIAM is written in the C programming language and computes fast enough on current workstations to be used in the control room as a tuning and diagnostic aid. Combined with a non-linear least squares package, LIAM has been used to estimate beam energy at various locations within the ETA-II accelerator.

Introduction

Linear induction accelerators, such as ETA-II, are complex instruments. To obtain the best performance from such complex machines requires good, working models. Such a model must be capable of dealing with the as-built configuration of the accelerator so that actual accelerator performance can be predicted. With such a model coupled to a parameter estimation routine, and with proper beam position data taken as a function of varying magnetic element field strengths, the beam can be used as a diagnostic tool to estimate those alignment and field parameters that can not be directly measured. Once this phase of experimentation and model validation is complete, the model, now closely matched to the actual accelerator, can be used to estimate beam parameters over the entire length of the accelerator given sparse beam position data. Such prediction/estimation capabilities can greatly aid in the tuning process. In addition, these capabilities can be use to diagnose component failures and misalignments.

The LIAM Model

Motivation for LIAM

Concerned by problems in matching beam position data from early runs on ETA II to traditional matrix per element transport models [1], we began a theoretical investigation of transport models. We compared the results obtained by solving the equations of motion for a one MeV electron passing through a typical, isolated ETA-II solenoid with the results obtained using the traditional matrix-per-element approximation. Poor agreement between the two models was observed. This is due to the use of a rectangular B_z profile in the derivation of the matrix elements whereas the typical B_z profile of an ETA-II solenoid is nearly gaussian.

However, when we modified the matrix method to divide the transport region into a number of subregions, or "mini-matrices", each described by a standard solenoid matrix calculated from the solenoid's B_z field strength at the center of the subregion, we obtained better results. As the length of the subregion was decreased, the results of the matrix method rapidly approached the results obtained from solving the equations of motion until, with the subregion length of four centimeters, excellent agreement obtained.

Armed with this information, we decided to construct LIAM. LIAM was designed to be a flexible linear induction accelerator modelling code that would calculate the beam centroid position either by solving the equations of motion or by mini-matrix transport. Both beam position calculation schemes are available at the same time, and both work from the same database of electromagnetic elements. This design has proven to be very valuable. First, the method of solving the equations of motion of the beam centroid is limited only by the accuracy of the input fields. Accordingly, as better field models became available, they could be easily incorporated. Solving the equations of motion directly also eliminated the immediate need to do the sophisticated analysis required to calculate the elements of the transport matrices. Second, when the formulas for the mini-matrix transport elements were derived, they could be easily checked by direct comparision of the results from the two techniques. This capability of LIAM has proven useful on numerous occasions. Third, whenever a change was made to the code implementing one of the centroid tracking techniques, those changes could be immediately checked by comparing the results of the two techniques. And, finally, the mini-matrix approach provides roughly a

U.S. Government work not protected by U.S. Copyright.

factor of seven increased performance which is very useful when LIAM is used with a nonlinear parameter estimator where the centroid must be tracked under various conditions hundreds to thousands of times.

Capabilities of LIAM

LIAM was designed in an attempt to provide the physicist with a highly interactive tool for linear accelerator modeling. It was also designed to provide a flexible interface to the programmer and be very modular in construction by employing simple object-oriented programming techniques. It was written in the C programming language to be as portable as possible. Currently, it is being used interactively in both a standalone configuration and primarily under Common Lisp in the MAESTRO [2] environment.

Modelling As-Built Accelerator Characteristics

LIAM uses field profile parameterizations to closely match the modelled electric and magnetic fields to the actual fields within the accelerator. Nonlinear least squares parameter estimation is used to obtain the field parameterizations by fitting to either the directly measured field profile (in the case of magnetic elements), or to the theoretically calculated E_z of accelerator gaps.

For solenoids, the on-axis B_z field profile is parameterized by H, k_2, and k_4 in the equation

$$B_z(z) = H\left(p e^{(-k_2 z^2)} + (1-p)\, e^{(-k_4 z^4)}\right).$$

Dipole steering magnets ($B_x(z)$ and $B_y(z)$) are similarily parameterized. The on-axis E_z field of an acceleration gap is parametered by

$$E_z(z) = H e^{(-k_2 z^2)}$$

This simplified form was found to match the theoretically calculated field profile quite well.

LIAM has been programmed to calculate the remaining off-axis field components (e.g. B_x and B_y for a solenoid) by Taylor expansions obtained from

$$\nabla \cdot \vec{B} = \nabla \cdot \vec{E} = \nabla \times \vec{B} = \nabla \times \vec{E} = \vec{0}.$$

Using this scheme, LIAM can sum the fields $\vec{B}(x,y,z)$ and $\vec{E}(x,y,z)$ across all (contributing) accelerator elements to calculate the fields anywhere within the accelerator.

Because real accelerators are not perfect, LIAM include the formulas for handling elements that are misaligned. LIAM currently handles all three translational and all three rotational degrees of freedom for each element.

Finally, because of the large beam current and low energy used in ETA-II, the effects of images induced on the accelerator's vacuum pipe are not neglegible. Accordingly, LIAM includes code to calculate the (equivalent) fields produced by the images on the vacuum pipe, including the effects occuring at the breaks in the pipe where the accelerator gaps are located.

Beam Centroid Calculation

LIAM utilizes the LSODE [3] differential equation integration package to solve the equations of motion of the beam centroid as it moves through the electromagnetic fields of the accelerator. The LSODE package provides control over both the absolute and relative error of the solution along with automatic variable step size adjustment. LIAM treats the state variables $\left(x(z), y(z), \frac{dx}{dz}(z), \frac{dy}{dz}(z), \gamma(z)\right)$ as a system of ODEs for LSODE to solve.

LIAM utilizes in-house calculated transport matrix elements (including the first order energy correction terms) when employing the mini-matrix solution. LIAM's matrix transport can handle axial solenoidal magnetic fields overlapped by transverse dipole fields and an accelerating electric field. The matrix elements are calculated from $B_x(0,0,z_{center})$, $B_y(0,0,z_{center})$, $B_z(0,0,z_{center})$ and $E_z(0,0,z_{center})$ where the field values have been calculated using all the misalignments. (Implied here is the fact that we have found that generality of handling misalignments can be subsumed by the generality of handling overlapping fields.)

Beam Envelope Calculation

LIAM has been extended to provide for the calculation of an approximate beam radius simultaneous with the calculation of beam centroid when employing the differential equation solution technique. The extension consists of merely adding $R(z)$ and $\frac{dR}{dz}(z)$ to the vector of state variables for which LSODE solves along with the Lee-Cooper [4] envelope equation for the RMS beam radius. When calculating the beam envelope, the coupling between beam radius and beam energy is automatically included.

Usage of LIAM

LIAM is the modelling code beneath the MAESTRO system that supports daily operations in the ETA-II control room. In this role, LIAM has been used to study the effect of various solenoidal magnet field strengths upon the beam envelope prior to, or during, the use of beam emittance diagnostics. It has also been used to conduct various other theoretical studies particularily concerning various tuning strategies prior to using those strategies on ETA-II.

Another less visible, but no less valuable, use of LIAM has been as a simulator of ETA-II performance to test software changes, new software, and possible new techniques and algorithms. In this role, LIAM and some ancillary software is used to simulate the raw waveform data produced by the beam position monitors. In this way, a nearly end to end test of the MAESTRO software can be conducted.

LIAM as a Tuning and Diagnostic Aid

Before LIAM can be effectively used to tune or diagnose ETA-II, it must first be validated against the per-

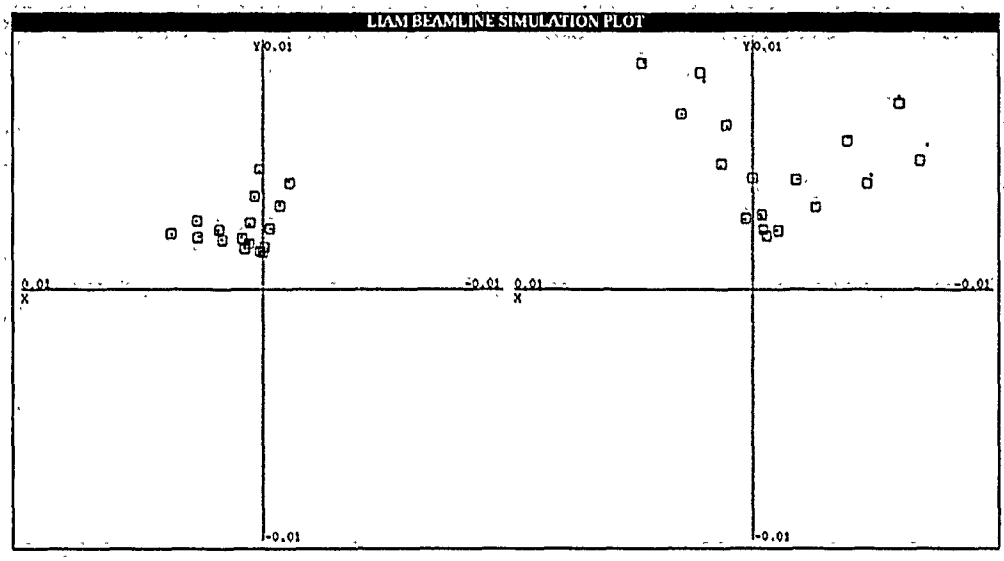


Figure 1: LIAM Fit to an ETA-II Focus-and-Steering-Sweep, note: Axes span ±0.01 meters

formance of ETA-II. During the past run period we began this process. Beam position data was collected as "focus-and-steering-sweeps" where horizontal and vertical dipole steering magnets were used to deflect the beam (to form a cross or half cross) at various values of the superimposed solenoidal field strength (see figure 1). A nonlinear parameter estimation package that closely interfaces with LIAM was used to estimate the beam launch parameters $\left(x(z_{launch}), \frac{dx}{dz}(z_{launch}), y(z_{launch}), \frac{dy}{dz}(z_{launch}), \gamma(z_{launch})\right)$ and, when necessary, various magnetic element parameters and misalignments. Initial results overestimated the beam energy by up to 80%. After much investigation, we believe we have isolated the problem to the beam position monitors and the associated signal processing of their signals. A LIAM model fit to a focus-and-steering-sweep is shown in figure 1. The measured beam position is shown as a small point, the LIAM model predicition is shown as an open square. Figure 1 depicts the focus-and-steering-halfcross deflections at two beam position monitors, the leftmost at 22 centimeters beyond the center of the dipole magnets, and the rightmost at 68 centimeters.

Another important tuning task for the ETA-II accelerator is matching the beam envelope into the Free Electron Laser (FEL) wiggler assembly. Once the LIAM model has been validated against ETA-II, and the experimental beam radius diagnostics work [5], it will be possible to include $\left(R(z_{launch}), \frac{dR}{dz}(z_{launch})\right)$ in the beam parameters estimation process. With this added information, the nonlinear parameter estimation can then be used to find appropriate field strengths to match the beam into a wiggler.

Conclusions

LIAM is a powerful modelling tool that has proved it worth in the control room of ETA-II. So far LIAM has been most valuable as a simulation tool for developing tuning techniques and algorithms that have been sucessfully used to tune ETA-II, and for developing and debugging new MAESTRO software. We plan to solve the problems we have experienced with the beam position monitors prior to the upcoming ETA-II run period. With the problems behind us, and with the introduction of the new beam radius diagnostics, LIAM should become an even more valuable addition to the ETA-II control room.

References

[1] K.L. Brown, B.K. Kear, S.K. Howry, *TRANSPORT/360, A Computer Program for Designing Charged particle Beam Transport Systems*, SLAC-91, Stanford Linear Accelerator Center, Stanford University, CA 94305, USA (1969).

[2] D.L. Lager, et. al., *MAESTRO - A Model And Expert System Tuning Resource for Operators*, Nuclear Instruments and Methods in Physics Research, North-Holland Materials Science and Engineering, Amsterdam, The Netherlands, (1990).

[3] A.C. Hindmarsh, *LSODE and LSODI, Two New Initial Value Ordinary Differential Equations Solvers*, ACM SIGNUM Newsletter, 15, No. 4 (1980), pp. 10-11.

[4] E.P. Lee, R. Cooper, *General Envelope Equations for Cylindrically Symmetric Charged-Particle Beams*, Particle Accelerators, 7, No. 83, (1976).

[5] W.E. Nexsen, private communication, (1991).

*Work performed jointly under the auspices of the US DOE by LLNL under W-7505-ENG-48 and for the DOD under SDIO/SDC MIPR No. W31-RPD-0-D4074.

Artificial Intelligence Techniques for Tuning Linear Induction Accelerators*

Darrel L. Lager, Hal R. Brand, William J. Maurer, Fred Coffield, Frank Chambers, William Turner
Lawrence Livermore National Laboratory, Livermore, CA 94550

Abstract

We have developed an expert system that acts as an intelligent assistant for tuning particle beam accelerators called MAESTRO — Model and Expert System Tuning Resource for Operators. MAESTRO maintains a knowledge base of the accelerator containing not only the interconnections of the beamline components, but also their physical attributes such as measured magnet tilts, offsets, and field profiles. MAESTRO incorporates particle trajectory and beam envelope models which are coupled to the knowledge base permitting large numbers of real-time orbit and envelope calculations in the control-room environment. To date we have used this capability in three ways: 1) to implement a tuning algorithm for minimizing transverse beam motion, 2) to produce a beam waist with arbitrary radius at the entrance to a brightness diagnostic, and 3) to measure beam energy along the accelerator by fitting orbits to focusing and steering sweeps.

I. Introduction

Particle-beam accelerators are members of a class of large, complex systems where a combination of automatic and manual techniques are required to control the system. This is especially true in a research environment where goals for understanding the physics of the machine coexist with goals for producing beams with desired characteristics. In order to satisfy these requirements we have applied Artificial Intelligence techniques to develop a Model and Expert System Tuning Resource for Operators (MAESTRO). It has been applied to tuning the Advanced Test Accelerator [1] and Experimental Test Accelerator (ETA) [2] at Lawrence Livermore National Laboratory.

MAESTRO is a metaphor for a musical conductor orchestrating the activities of control, diagnostics, physics models, and post-run analysis to control and understand the behavior of the machine. MAESTRO acts as an intelligent assistant to an operator tuning a particle-beam accelerator and contains within its framework the capability for representing the heuristic rules-of-thumb followed by human operators, rigorous physics models for computing the trajectory and envelope of the beam from knowledge of the beamline components, and a variety of displays and interfaces for automatically and manually controlling the machine.

II. The Knowledge Base

The MAESTRO architecture consists of two distinct layers, a real-time control system and a quasi-real-time layer containing the expert system, models, and operator interfaces. The real-time control (and diagnostics) system deals with events on the order of 1 second or less where a deterministic response time is a critical issue as in responding to hardware interrupts. For control it operates at level of power supplies and currents, translating requests into hardware commands for the physical supplies. The quasi-real-time layer deals with events on the scale of 1 to 30 seconds and is primarily concerned with making decisions about which supplies to control, performing computations with the model based on current supply values, and acquiring data to interpret and present to the operator. The critical issue is flexibility and capability of the software.

The interface between the two layers is the Knowledge Base (KB). It is an object-oriented database for representing the components of the beamline, their relationships, and their interconnections. The KB utilizes the concept of access-oriented programming to permit the physicist to operate at the level of fields in magnets by automatically performing, when a field value is accessed, the translations from field-in-magnet to current-in-supply to supply-powering-the-magnet to control-system-register-address-and-value. All the information needed to make the translations is in the KB, such as the measured $B_{x,y,z}(z)$ field profiles for each of the magnets. The consistentcy of the KB is automatically maintained to reflect, for example, the replacement of a power supply by one with different calibration coefficients or the insertion of a new component within the beamline.

Within the KB the machine components are represented in a class/subclass hierarchy, so the class of compensated-solenoids (assemblies with a solenoid and two steerers) is a subclass of solenoids which is a subclass of magnets. There are also classes and subclasses not only based on the component type but also the machine sections. This hierarchical structure permits dealing with the components at different levels of "granularity" making it easy to construct spread sheets, for instance, of "all the solenoids in the accelerator section".

Since some of the beamline components have data associated with them, e.g. oscilloscope traces from beam position monitors (beambugs), the KB also contains new and historical data acquired from the machine. We have developed a variety of browsers for examining not only the structure and contents of the KB but also the historical data contained within it.

III. Tuning Methods

The MAESTRO environment supports three distinct approaches to tuning particle-beam accelerators. In the first approach, "cloning the operator," the procedures and reasoning followed by the operator are encoded as faithfully as possible. A second approach, model-based tuning, exploits a near-real-time numerical simulator coupled with real-time data acquired from the machine. The third approach is to tune the machine

* Work performed jointly under the auspices of the US DOE by LLNL under W-7505-ENG-48 and for the DOD under SDIO/SDC MIPR No. W43-GBL-0-5007.

U.S. Government work not protected by U.S. Copyright.

manually, but provide the operator with more powerful tools and displays. The goal is to achieve a blend of these approaches that minimizes the tuning time and maximizes the time available for performing physics experiments. Each of these approaches is discussed below.

A. Cloning the Operator

This approach reflects two kinds of reasoning followed by the operator. In the first the operator employs a "global strategy" concerned with the overall tuning of the machine subject to constraints like "don't put the beam into the wall". The global strategy is made up of many lower-level "local strategies" concerned with the tuning of a subsection of the machine. Local strategies usually deal with a single diagnostics device (e.g. a beambug) and the components immediately upstream from it capable of correcting an error in beam position. The expert system decides which components to use based on their nearness, type, and expected effect on the beam. These strategies and how they are implemented are discussed in more detail in [1] and [3].

B. Model-Based Tuning

This approach is based on an on-line numerical model for computing the beam radius and centroid trajectory [4] given the current magnet settings and measured magnet field profiles, tilts, offsets, etc., stored in the KB. This approach hinges on bringing the models and the machine into agreement, "commissioning" [5] and has succeeded to the point where this method will be used to estimate the beam energy by fitting the computed beam behavior to the measured while sweeping focus and steering magnets over a range of values[4,3]. Ultimately the models will be used to compute an optimum set of parameters and to download those parameters onto the machine.

C. Manual Tuning

For the manual tuning approach MAESTRO presents a variety of interfaces to the operator (and physicist) to ease both the control and interpretation tasks. The interfaces are constructed from information in the KB and automatically reflect, for example, insertion or deletion of components from the beamline. An icon-based Machine Interrogation and Control Interface (MICI) presents a scaled drawing of the beamline with icons for the components. The operator uses a mouse and cursor to select components and change settings, control data acquisition, or browse historical data. Spread-sheets are particularly useful for setting and displaying magnet fields and currents. Color bargraph overlays are provided for "at a glance" monitoring of B(z) fields, discrepancies between target and measured values, and on/off status. Spread-sheets also provide a mechanism for archiving tunes and creating new tunes by cutting and pasting values from past tunes into the spread-sheet controlling the machine.

A graphical interface is provided for displaying raw and processed shot data. The operator can interact with a plot window using the mouse and control the attributes of the plot, including such things as producing a plot by grabbing points from several others.

As part of the manual interface the operator can enter commands to run various tuning algorithms. One such algorithm minimizes the transverse beam motion by sweeping the current in a steering coil over a range of values and displaying the corkscrew amplitude as a function of current. The operator then sets the current to the value producing the minimum corkscrew and repeats the procedure, sequentially optimizing all the magnets in the beamline. The algorithm is discussed in more detail in companion papers [6,2].

Commands are also available for running the models to gain insight into the machine behavior. For example, for a whole-beam brightness measurement it was desired to bring a beam with a specific radius to a waist at the face of a pepper-pot[7]. Experimentally it appeared there were certain radii where it was impossible to achieve a waist. The beam envelope model was run for a variety of settings of the two focusing solenoids upstream from the pepper pot, and the beam radius and its z derivative (r-dot) plotted for each setting, Figure 1. Since a waist occurs at r-dot=0, the figure shows that it is impossible to produce a waist for beam radii between 1 and 1.5 cm. Further simulations with the model and experiments with the machine produced changes in the transport section tune that reduced the effect of the phenomenon.

IV. Future Plans

The immediate plans for MAESTRO are to decrease the time to execute the algorithm for minimizing transverse beam motion and automate the process. Our goal is to reduce the time by a factor of 10 to 20. This will make it possible to attempt optimization of the $B_z(z)$ field profile -- during the last run period the profile was essentially fixed. Modified versions of the algorithm will be used for maximizing wiggler gain and minimizing beam radius oscillations [2].

The centroid trajectory model will be used for estimation of the beam energy at various locations down the beamline by curve fitting to focus and steering sweeps with energy as a free parameter. The beam envelope model will be used for matching the beam into an FEL wiggler as described above for matching into the pepper-pot.

V. Discussion

AI techniques have proven especially useful for tuning particle-beam accelerators, not because of any explicit "intelligence" within the system but because of the flexibility and capabilities of the environment. The unification within a single software environment of control, diagnostics, and modeling made possible the development of entirely new tuning methods and diagnostics displays. MAESTRO provided the flexibility to trade-off between the three tuning approaches as experience with the machine dictated. Having models within the environment made it relatively easy to perform pre-run simulations and gain insight into the expected effect of, for example, magnet tilts and offsets. During a run the models were used to make on-line comparisons of computed and measured behavior. And finally the models and history displays were useful for post-run analysis of the data.

The environment proved so flexible that many of the tuning algorithms and uses of the models discussed here either did not exist or were substantially refined during the run period, by

literally modifying the software as the machine was coming up each day.

VI. References

[1] D.L. Lager, H.R. Brand, W.J. Maurer, F. Coffield, and F. Chambers, "MAESTRO -- A Model and Expert System Tuning Resource for Operators", Nuclear Instruments and Methods in Physics Research, vol A293, pp480-485, 1990.

[2] W. Turner, "Control of Energy Sweep and Transverse Beam Motion in Induction Linacs", these proceedings.

[3] D.L. Lager, H.R. Brand, W.J. Maurer, "An Expert System for Tuning Particle Beam Accelerators", *in Advances in Artificial Intelligence - Applications and Theory*, J.C. Bezdek, Ed., New Jersey: World Scientific, 1990, pp 53-65.

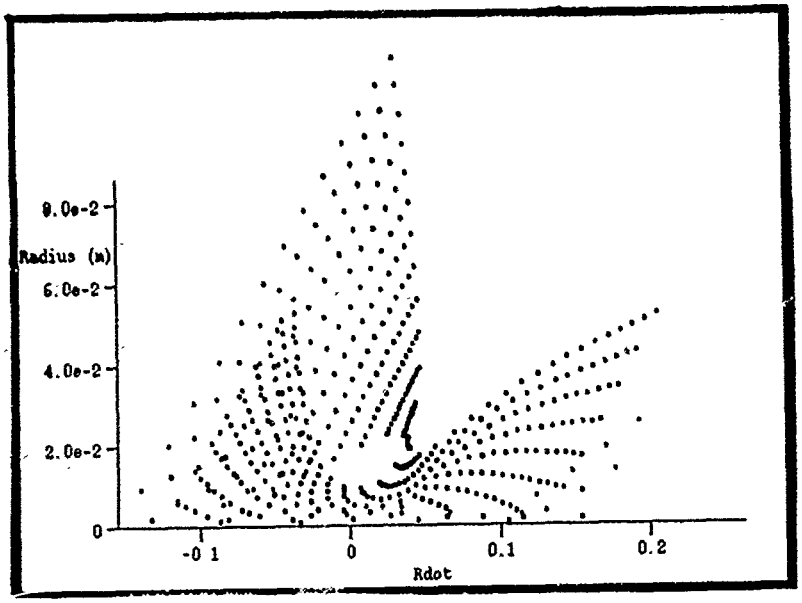
[4] H.R. Brand, et al, "LIAM - A Linear Induction Accelerator Model", these proceedings.

[5] M. Lee and S. Clearwater, "GOLD: Integraton of Model-Based Control Systems With Artificial Intelligence and Workstations", *Workshop on Model-Based Accelerator Controls*, Brookhaven National Laboratory, Upton, New York, Aug. 1987.

[6] S.L. Allen, et al, "Measurements of Reduced Corkscrew Motion on the ETA-II Linear Induction Accelerator", these proceedings.

[7] A. Paul, et al, "ETA-II Beam Brightness Measurement", these proceedings

Figure 1. Beam R vs R-dot -- Some Radii Are Unachievable for R-dot =0



Diagnostics and Data Analysis for the ETA-II Linear Induction Accelerator*

F. W. Chambers, S. L. Allen, F. J. Deadrick, W. E. Nexsen,
A. C. Paul, V. L. Renbarger, and W. C. Turner
Lawrence Livermore National Laboratory, P. O. Box 808, Livermore, CA., 94550

Abstract

The ETA-II linear induction accelerator has pulse power and beam diagnostic sensors distributed throughout the system. The accelerator consists of an injector; 20 accelerator cells arranged in two ten cell blocks; and a transport section leading to an energy analyzer. In total there are approximately 120 beam diagnostic channels and 32 pulse power signals which are recorded on six Tektronix 7912AD oscilloscopes. The analysis, display, and interpretation of this data was done using systems for scientific visualization and a simple user interface. Results from several measurements will be presented showing how the diagnostics and system were utilized.

I. INTRODUCTION

The Experimental Test Accelerator--II (ETA-II) is the latest in a series of linear induction electron accelerators constructed and operated at the Lawrence Livermore National Laboratory (LLNL) [1-3]. We have developed computerized, digitized, data acquisition systems for capturing and recording the analog trace signals and TV images generated from our diagnostic sensors. Coupled to the data acquisition are the data analysis capabilities. In this report the current data analysis capabilities for trace data will be presented with emphasis on the choices made and the underlying motivation for these decisions. A similar system is used for TV image analysis.

II. DIAGNOSTIC SENSOR LAYOUT, SIGNALS

A schematic of the ETA-II 20 accelerating cell configuration is shown in figure 1. The machine employs solenoidal transport and is configured as an injector followed by two ten cell blocks. Separating each of these major components is a pair of beam position monitors, commonly referred to as beambugs, which measure the beam current I and x,y positions as functions of time into the beam pulse. There are additional beambugs in the transport beyond the second ten cell block. There are also voltage and current diagnostics on each adjacent pair of accelerating gaps.

The machine description consists of the machine parameters (the tune) and data from the beam bugs (bugwalks), the cell probes (cprobe walks), and any other functioning diagnostics. Walks are taken sequentially in Z using six channels of Tektronix 7912 digitizers. ETA-II operates at one pulse per second; in almost all cases shot to shot reproducibility is assumed in acquiring and analyzing the data. Overall, this is a diagnostic sparse, channel poor, shot rich environment. During operations large amounts of data can be rapidly accumulated. Ways must be found to rapidly and efficiently extract and present relevant information to the physicist.

U.S. Government work not protected by U.S. Copyright.

III. GUIDING PRINCIPLES

The experimental results must be made available to the physicists in a timely and convenient manner. The system is set up to allow an intelligent person to operate it in the absence of an expert. The system works from data files; turnaround from data acquisition to data analysis is targeted to be five minutes. Since there is a large volume of data emphasis is placed on developing single page summaries of the relevant experimental results. Displays are designed to answer specific questions. Since all data analysis is fraught with danger, the raw data is displayed wherever possible, usually in a compacted form. Since printing of output over the network is often unreliable and cumbersome the system attempts to perform these functions for the physicist. Since physicists ultimately want paper and not gorgeous screen displays only black and white is used, color is not employed. Likewise, trendy scientific visualization techniques such as animation are not employed. Copious labelling is done (often making plots look cluttered) to provide the ability to identify data and analysis after the fact.

IV. THE HUMAN-MACHINE INTERFACE

The human-machine interface (HMI) screen, programmed in Interactive Data Language (IDL) running on networked VAX workstations, is shown in figure 2. This interface is inspired by the Macintosh graphical users interface (GUI); it is designed so a novice can analyze data without any typing. The upper quarter of the screen is devoted to information about the currently available data file and next file to be read. The remaining three quarters of the screen are devoted to a collection of buttons which are user selectable using the crosshairs and mouse in IDL. Buttons may be selected in any order, when they are selected a cross hatching appears. Multiple actions may be specified for sequential execution from the HMI. Buttons which cause immediate actions to take place are labelled with bold face type. The buttons are grouped in logical groupings with an indicated header. The user satisfaction with this approach has been very high. Data is typically analyzed within five minutes of its acquisition by whoever is in the control room at the time. This HMI works and earns the accolade, "user friendly".

A. File input, documentation, output

The buttons in the first column of the HMI deal with file input, data documentation, and graphical output to the printers. The first five selections under "Input file" allow the user to read in a new data file. The next two buttons under "File Info:" allow the user to print out the ASCII information contained in a single file or the file comments for a collection of files to locate relevant data. The final three buttons under "Output file:" specify if a plot file creation and destination.

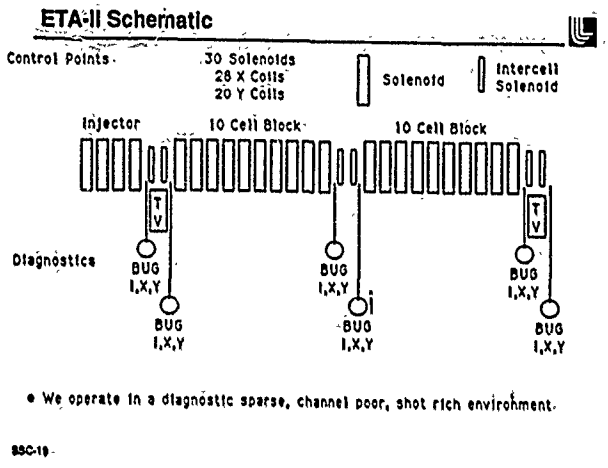


Figure 1. Schematic of the ETA-II configuration showing control and diagnostic points.

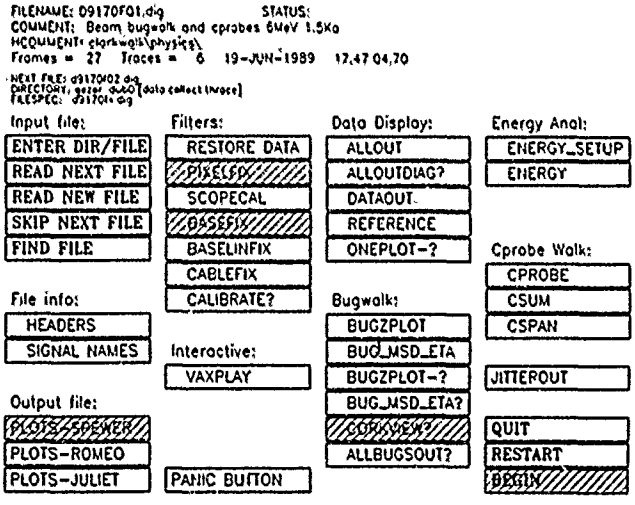


Figure 2. The Human-Machine Interface (HMI) showing data processing choices available to the user.

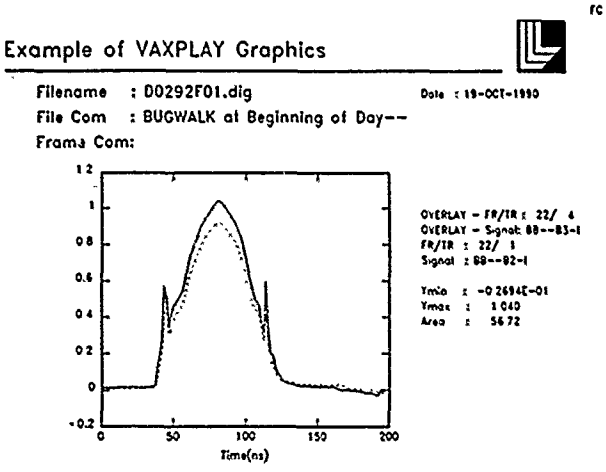


Figure 3. Example of the output of the interactive VAXPLAY data manipulation routines.

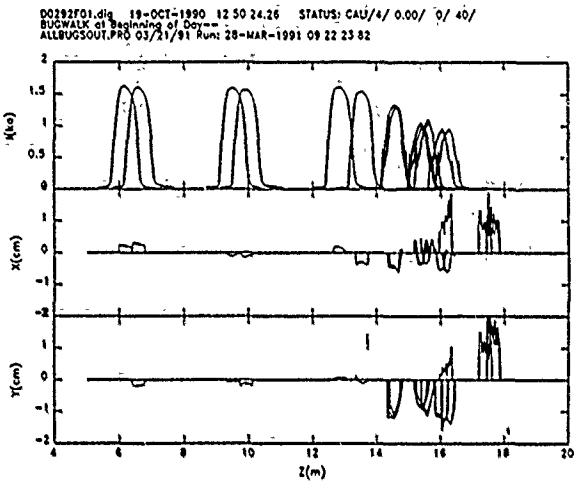


Figure 4. ALLBUGSOUT output for a bugwalk showing beam current and position for all data in a bugwalk.

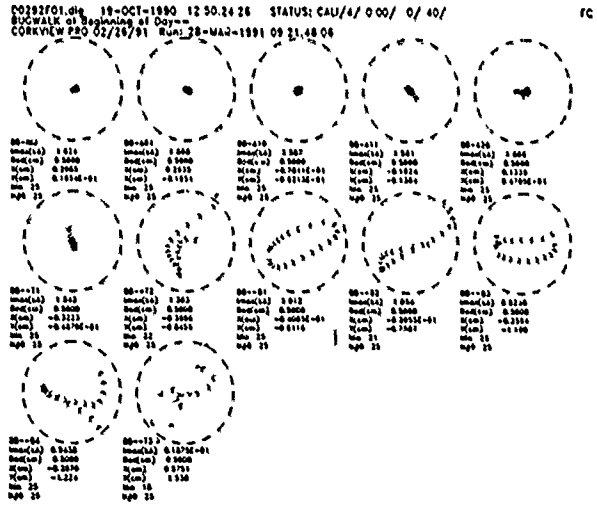


Figure 5. CORKVIEW output of beam position in x and y for all bugs in the bugwalk plotted in figure 4.

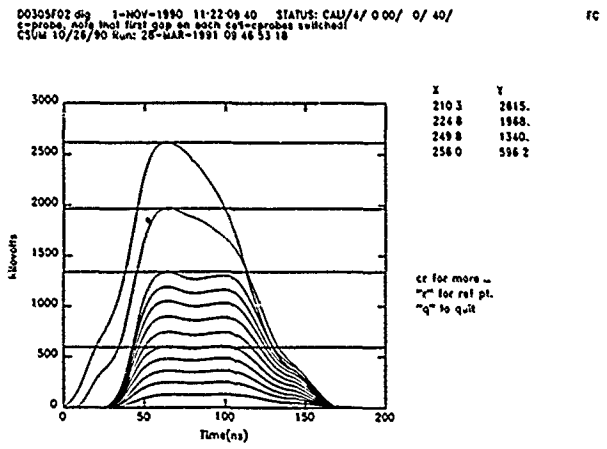


Figure 6. CSUM output of measured gap voltages showing voltages for the cell pairs and total accelerator voltage.

B. Filters

At the top of the second column the user can select filters to be applied globally to the data in the active file. PIXELFIX applies a median filter to the data to remove "bad pixels" from the data. BASEFIX and BASELINFIX apply baseline corrections to the data. The CABLEFIX filter corrects each signal for the frequency dependent cable transmission losses. CALIBRATE applies known calibration factors and algorithms to convert from the raw voltage signals to actual measured quantities. SCOPECAL uses reference channel data to determine the oscilloscope vertical gain calibrations and then to rescale the data. Several filters may be applied sequentially. When each filter is invoked it notes its actions on the file STATUS line.

C. Interactive Data Analysis

The next section is labelled, 'Interactive:'; with the button one can invoke the VAXPLAY data analysis tool. This allows one to interactively manipulate individual traces in a file using one and two letter commands. The usual manipulations such as scaling a trace, adding or subtracting traces, and plotting traces in a variety of ways are available. Under VAXPLAY the filters can be applied to individual traces. The most general data analysis capabilities reside in VAXPLAY; however the process can be slow and tedious. Hence analysis approaches are developed in VAXPLAY; then a specifically targeted data analysis routine may well be written. A sample of VAXPLAY output is shown in figure 3. VAXPLAY output is setup as a viewgraph with user specified title; this gimmick has proven quite useful.

D. Data Display

The options in the top of the third column under "Data Display:" are general purpose routines to display data in a generic fashion. These routines do not depend on the data source or format. ALLOUT will produce a full set of plots of all the data within a file; the plots are small (24 to a page). ALLOUTDIAG provides all the trace plots with printout of fundamental quantities such as mean and standard deviation. DATAOUT plots all the data on similar plots but places repeated shots on a single plot greatly compressing the data display. ONEPLOT allows one to extract a particular signal or set of signals an plot it on a user specified scale; REFERENCE extracts, plots, and analyzes the reference channel data contained in some files. Although the generic data display is useful and sometimes required, the users very quickly evolve into needing analysis tailored very specifically to the dataset and the relevant questions for that dataset.

E. Bugwalk: Data Analysis

The bugwalk data records the evolution of the time varying beam current and position in Z, the distance down the accelerator. Questions one might ask are, "Where is the current loss occurring?", "How is the corkscrew growing?", "How reproducible is the machine shot to shot?" The single page summary of a bugwalk shown in figure 4 from the ALLBUGSOUT option displays the data contained in 168 oscilloscope traces. The beam current and x,y positions are displayed in time at the various Z locations. One can see the pattern of the accelerator with the double beambugs at the ends of each cell block. Since for each bug four traces are overlayed one can see the shot to shot reproducibility is excellent. The onset of current loss is beyond the end of the accelerating section; the beam current also develops wings. Correspondingly, the beam x and y positions are now showing significant displacement and time dependent oscillations. To better view the corkscrew mode where the beam spirals around from head to tail in x and y a corkscrew plot has been developed as seen in figure 5. The x,y evolution of the beam is shown for successive beambugs down the accelerator and transport. This single page summary allows the experimentalist to quickly assess the Z growth of the corkscrew; it is easy to compare patterns from day to day.

Two other options are used in viewing beambug data. The BUGZPLOT plots single numbers parameterizations for the traces (e.g. peak current, charge, displacement) versus Z. This display is particularly useful when an instability is present; as in the study of the hose instability in beams propagating in gas. The BUG_MSD_ETA selection plots each beambug on a separate page for more detailed display.

F. Energy Measurements, C Probes

A program for analyzing the energy spectrometer data is available in the 'Energy Anal:" set of buttons. Energy analysis data appears in a companion paper [2]. The analysis of the Cprobe walks is done in the "Cprobe Walk:" section. The Cprobes are used to study the amplitude, shape, timing, and reproducibility of the applied accelerating voltage and current. With the CPROBE option the voltages from the successive diagnostics down the accelerator are plotted vertically staggered on a single plot to highlight cell to cell variations in the signals. CSPAN looks at the magnitudes of the signals from the two cellblocks. CSUM, figure 6, performs a running sum of the probes to compute the total beam kinetic energy.

V. SUMMARY

A data analysis capability has been developed which provides adequate power, flexibility, and rapid turnaround required for converting the massive amounts of data collected on all our experiments into an understanding of machine performance. The system has proven useful to users who are not proficient computer operators - a reasonably user friendly environment has been achieved. This system contributed significantly to the success of the recent experimental run.

* Performed jointly under the auspices of the US DOE by LLNL under W-7405-ENG-48 and for the DOD under SDIO/SDC MIPR No. W43-GBL-0-5007.

REFERENCES

[1] W. Turner et. al.,"Control of Energy Sweep and Transverse Beam Motion in Induction Linacs," these proceedings.

[2] S. L. Allen et. al., "Measurements of Reduced Corkscrew Motion on the ETA-II Linear Induction Accelerator," these proceedings.

[3] W. E. Nexsen et. al., 'Reduction of Energy Sweep on the ETA-II Beam,' these proceedings.

Modeling of Switching Cores for Induction Accelerators

Henry D. Shay, John F. DeFord, George D. Craig
Lawrence Livermore National Laboratory
Livermore, CA 94550

Abstract

We have successfully installed a nonlinear magnetization model in the 2 1/2-D finite difference (FDTD) electro-magnetic (EM) code AMOS. We have developed a procedure for mapping the 3-D induction cells on the 2-D AMOS mesh. These tools will be important for modeling advanced induction accelerator cells.

I. INTRODUCTION

Many future applications of induction accelerators (IA) require high quality beams and, in particular, rather small variation in beam energy. For heavy ion fusion (HIF) beams it is necessary to have an energy variation less than 0.1% so that the beams can be focussed to a small enough spot on the fusion target.[1] One of the key components in determining the energy variation of an IA beam is the ferrite or Metglas core in an induction cell. The time dependent switching of these magnetic materials determines, in part, the variation of the cell gap voltage. In order to shorten the iteration time for design of and experiments on induction cells, there are several efforts to incorporate non-linear magnetization models in finite difference codes for calculating this time varying switching. One approach is to treatment the core as one or a few lumped variable inductors in a circuit model. This approach is surely appropriate for relatively small cores, but may not properly represent the passage of switching fronts in large cores. The induction cores for HIF require moderate to high gap voltages, often for several microseconds, and so require many volt-seconds. For example, an upper limit applied to linear induction accelerators for HIF is about 0.5 volt-seconds/m[2], and so, for a cell separation of less than about 5 m at the low energy end and a maximum magnetic field swing of 3 T, HIF cores can be as large as 1 m^2 and have dimensions which are a large fraction of a meter. We have, therefore, undertaken to install a non-linear constitutive model in a 2 1/2-D , FDTD EM code, AMOS. We describe in this paper the non-linear model, its incorporation in a 1-D test-bed, its incorporation in AMOS, and a technique for mapping 3-D geometries onto a 2-D calculational mesh.

II. 3-D GEOMETRY REPRESENTATION

Induction cell are driven with a small number of cable feeds, typically two, in a geometry which is intrinsically 3-D. AMOS uses a 2-D mesh. In order to calculate the switching of an induction cell, we developed a technique for representing the 3-D geometry in a 2-D axisymmetric mesh. We have represented the coaxial drive cables by a washer-shaped object spanning the region between the inner and outer radii of the core. Its conductivity was chosen so that its impedance matched the parallel impedance of coaxial drive cables (and related load matching resistors). We have tested whether such a washer would properly describe the scattering of axisymmetric waves (azimuthal mode number, m, of zero) by conducting calculations of scattering at the junction of three coaxial cables with two of the three cables zoned in the AMOS mesh and the third represented by a washer with an equivalent impedance. The analytic solution for the three coax junction is an elementary application of S-matrix theory, and AMOS correctly predicted both the transmitted and reflected waves. In the AMOS grid of the ETA II cell, we put a current source in the mock feed in order to provide an equivalent drive and were able to reproduce simultaneously the experimentally observed voltage and current histories of the ETA II cell.

III. NONLINEAR CONSTITUTIVE MODEL

M. Hodgdon [3] has developed an empirical nonlinear constitutive model, whose equations appear below:

$$\mu^{-1} = \alpha\,\mathrm{sign}(B)\left[f(B) - \dot{H}\right] + g\left(B,\dot{B}\right) \tag{1}$$

$$f(B) = \begin{cases} A_1\tan^P(A_2B) + A_5B & \text{for } |B| \le B_{bp} \\ A_1\tan^P(A_2B_{bp}) + A_5B_{bp} + (B - B_{bp})/\mu_s & \text{for } B > B_{bp} \\ -A_1\tan^P(A_2B_{bp}) - A_5B_{bp} + (B + B_{bp})/\mu_s & \text{for } B < -B_{bp} \end{cases} \tag{2}$$

$$g\left(B,\dot{B}\right) = \begin{cases} f'(B)\left[1 - A_3c\left(\dot{B}\right)\exp\left(-\dfrac{A_4|B|}{B_{cl} - |B|}\right)\right] & \text{for } |B| < B_{cl} \\ f'(B) & \text{otherwise} \end{cases} \tag{3}$$

$$c\left(\dot{B}\right) = \begin{cases} 1 + c_1|B| & \text{for } |\dot{B}| < \dot{B}_1 \\ 1 + c_1|B_1| + c_2\left(|\dot{B}| - |B_1|\right) & \text{for } |\dot{B}| > \dot{B}_1 \end{cases} \tag{4}$$

The permeability, μ, is a function of B, H, $\dot{B}$, and the direction of the traversal of the hystersis loop, that is, the sign of $\dot{B}$. This formulation permits the consideration of major and

Work performed under the auspices of the U.S.DOE by LLNL under W-7405-ENG-48

U.S. Government work not protected by U.S. Copyright.

minor hysteresis loops. The function "f" is the inverse of the anhysteretic curve, and P, A_1, A_2, and A_5 are its fitting parameters. For |B| beyond B_{bp}, the slope of f is simply the saturation permeability of the Metglas, μ_s. As |B| approaches B_{cl}, the two halves of a hysteresis loop close at a rate determined by A_4. For |B| greater than B_{cl}, the two loops are merged. In typical parameterizations, B_{cl} and B_{bp} are nearly equal. For the DC hysteresis loop, $\dot{B}$ is zero, c is 1.0, and the width of the loop, twice the coercitivy, H_c, is determined just by the parameter A_3. For a pulsed hysteresis loop, $\dot{B}$ is not zero, and the width of the loop is c times the width of the DC loop. For most of the ferrites and Metglas under consideration, we have used piece-wise linear fits for c as a function of $\dot{B}$.

IV. 1-D FDTD SOLUTION TO MAXWELL'S EQUATIONS

Before installing this constitutive model into AMOS, we first tested it in a one 1-D test-bed. The test-bed used equations numbered (5), (6), and (7), which advance Maxwell's equations in a leap-frog scheme[4], and are substantially the same difference equations as those in AMOS. In the test-bed, we considered only the components E_x, B_y, and H_y.

$$\frac{B_{l+\frac{1}{2}}^{k+\frac{1}{2}} - B_{l+\frac{1}{2}}^{k-\frac{1}{2}}}{\Delta t} = -\frac{E_{l+1}^{k} - E_{l}^{k}}{\Delta z} \equiv \dot{B}_{l}^{k+\frac{1}{2}} \qquad (5)$$

$$H_{l+\frac{1}{2}}^{k+\frac{1}{2}} - H_{l+\frac{1}{2}}^{k-\frac{1}{2}} = \sum_{j=1}^{n} \left[\frac{\frac{1}{n}\left(B_{l+\frac{1}{2}}^{k+\frac{1}{2}} - B_{l+\frac{1}{2}}^{k-\frac{1}{2}} \right)}{\mu\left(B_{l+\frac{1}{2}}^{k-\frac{1}{2}} + \frac{j}{n}\left(B_{l+\frac{1}{2}}^{k+\frac{1}{2}} - B_{l+\frac{1}{2}}^{k-\frac{1}{2}} \right), H_{l+\frac{1}{2}}^{k-\frac{1}{2}}, \dot{B}_{l+\frac{1}{2}}^{k+\frac{1}{2}} \right)} \right] \qquad (6)$$

$$\varepsilon\left(\frac{E_{l}^{k+1} - E_{l}^{k}}{\Delta t} \right) = \frac{H_{l+\frac{1}{2}}^{k+\frac{1}{2}} - H_{l-\frac{1}{2}}^{k+\frac{1}{2}}}{\Delta z} \qquad (7)$$

Propagation is in the z-direction. The time index is k, and the z -index is i. The time step, Δt, is selected to obey the Courant condition, that is, that $\Delta t < \Delta z\sqrt{\varepsilon\mu_0}$, where Δz is the zone size. In this treatment, B serves as the independent variable advancing H via the permeability given by the constitutive model, μ as a function of B, H, and $\dot{B}$. Eq. (6) provides for n steps of sub-cycling in advancing H over each dB step on the hysteresis curve. In this sub-cycling, $\dot{B}$ is approximated as constant. In the 1-D model, we treat the conductivity of the Metglas as zero.

In addition to the formulation of the constitutive model shown above, we also tried a formulation in which all derivatives are kept continuous at B_{bp} and B_{cl} by smoothly joining the halves of f and g above and below the critical points. We found that so long as we limited the value of μ to fall within the range μ_s to about $10^5\mu_0$, we could use the simpler formulation of equations (5), (6), and (7). The limit at the high end prevented infinite slopes in the hysteresis curve ("back-bending"), which could generate pernicious numerical instabilities. For permeabilities below the lower limit, the Courant criterion would be violated, and, again, the solution would become unstable.

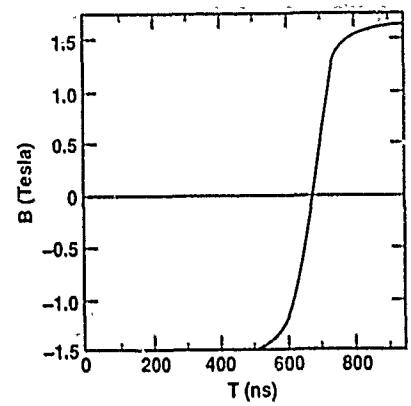


Figure 1 History of B in a thin sheet of Metglas as calculated in the 1-D test-bed.

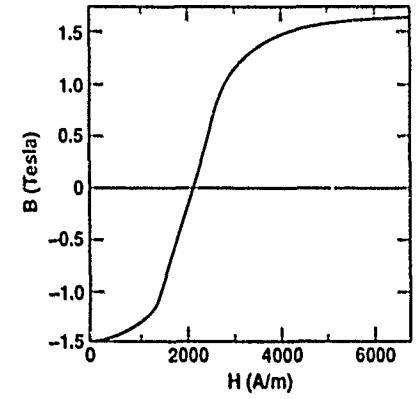


Figure 2 B-H curve for the 1D calculation of figure 1.

Sample results from 1-D test-bed calculations appear in figures 1 and 2. Both the plot of B versus time in figure 1 and the hysteresis switching curve of figure 2 have been taken from a calculation in which a plane wave impinged on a thin (1 cm) sheet of 2605SC Metglas. The right-hand-side (RHS) boundary conditions (BC) behind the Metglas sheet were those of a perfect conductor; we used a radiation BC on the LHS behind the source. The DC parameterization of the 2605SC Metglas is a modification of a parameterization provided by M. Hodgdon.[5] The c_i and $\dot{B}_i$ parameters describing the broadening of the hysteresis loop are taken from data of C. Smith of Allied Signal.[6] The two features in the model parameterizations which we were most careful to preserve were the magnetic induction at saturation and the variation of coercivity with $\dot{B}$. In this particular calculation, the sample was so small and the time scales so long that each of ten Metglas zones had nearly identical histories.

In the course of testing this magnetization model, we found that calculations with sub-cycling give virtually identical results to those without it. We therefore have not included sub-cycling in the implementation in AMOS. The use of the magnetization model did increase the running time, but not by

a prohibitive factor. Without the nonlinear model, the CPU time on an XMP CRAY spent per zone-time-step in a vectorized version of the code was 3.5μs. With the nonlinear model coded "inline" (that is, written in the same routine with differential equation solver rather than called as a subroutine - a procedure used to enable vectorization of the nonlinear model), the CPU time per zone-time-step was about 6 μs.

V. Implementation in AMOS

The AMOS code is a 2 1/2-D EM simulator for use in the design of accelerator components.[7] It is 2 1/2-D in that it uses a 2-D r-z mesh, but assumes a harmonic variation of the fields in the azimuthal (ϕ) coordinate. The user specifies the azimuthal multipole number (m) at run time, and AMOS allows spatially varying materials and a variety of BC's that support component design.

The implementation of the nonlinear model in AMOS was nearly the same as shown in eq. (5), (6), and (7) except that we did not use sub-cycling. Only the azimuthal components of magnetic induction and intensity were linked by the nonlinear model. To represent the insulation between the layers of Metglas winding, we introduced an option for anisotropic conductivity such that the conductivity in the radial direction was zero and the conductivity in the azimuthal and axial directions could be independently chosen.

In the test problems we have so far conducted with this model in AMOS, we have examined exclusively the m=0 azimuthally symmetric mode. We have configured the Metglas as a large torus around a central conductor and bounded by conductors on the back, RHS boundary, and on the outer radius. On the LHS, we had a dielectric material. We placed a magnetic current source (an additional term in the **curl E** equation) on the LHS of the dielectric material and a radiation BC on its LHS. In this manner, any reflections from the Metglas propagating to the left could leave the mesh. In the particular calculation depicted in figures 3 and 4, the Metglas torus was 10 cm long and had an inner radius of 19 cm and an outer radius of 31 cm. The temporal history of the source was a Gaussian arising to a peak at 600 ns, at which time the calculation was terminated. Figure 3 shows the B-H curves for points at inner and outer radii on the LHS of the Metglas. Because the time derivative of the magnetic induction is smaller at the outer radius, that point has a lower coercivity than the point at smaller radius, but it was not driven as fully into saturation because of the lower peak H-field. This calculation was performed with zero conductivity in all directions, and so the Metglas could support a small axial electric field, as shown in figure 4. Because of the TEM_{00} nature of the drive, it excited neither radial nor axial components of magnetic induction. As expected, the radial electric field was much larger; it rose sharply during the period of large $\dot{B}$, peaked as the Metglas began to enter saturation, and then began to fall.

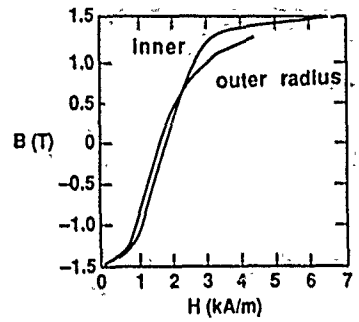


Figure 3. B-H curves from AMOS calculation of a Metglas torus

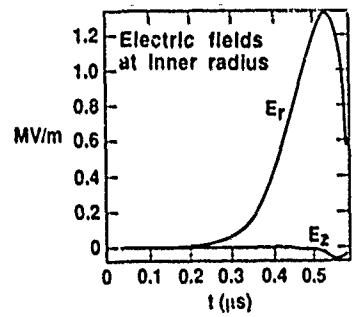


Figure 4. E fields from the AMOS calculation in figure 3.

VI. Conclusions

We have successfully installed a nonlinear magnetization model in the 2 1/2-D FDTD EM code AMOS. We have developed a procedure for mapping the 3-D induction cells on the 2-D AMOS mesh.

Future work will entail using this model for investigating several proposed HIF induction cells. We expect to install a simple vector analogue of the scalar magnetization model in AMOS and will latter implement it in a 3-D version of AMOS which is presently under development.

We gratefully acknowledge the help and advice given by M. L. Hodgdon, LANL, and C. H. Smith, Allied Signal.

References

[1] J. Hovingh, V.O. Brady, A. Faltens, D. Keefe, and E. Lee, Fusion Technology, vol. 13, p. 255, 1988.

[2] C.H. Kim and L. Smith, "A Design Procedure for Acceleration and Bunching in an Ion Induction Linac," LBL-19137, 1985.

[3] M. L.Hodgdon, "Applications of a Theory of Ferromagnetic Hysteresis," IEEE Transactions on Magnetics, vol. 24, p. 218, 1988.

[4] K. Yee, "Numerical Solution of Initial Boundary Value Problems Involving Maxwell's Equations in Isotropic Media," IEEE Antennas and Propagation, vol. 14, p.302 , 1966.

[5] M. L. Hodgdon, private communication.

[6] C H Smith, "Applications of amorphous magnetic materials at very-high magnedtiztion rates," Journal of Applied Physics, vol. 67, p. 5556, 1990.

[7] J.F. DeFord, et al., "The AMOS Wakefield Code," Proceedings of the Conference on Computer Codes and the Linear Accelerator Community, Los Alamos National Laboratory, p. 265,1990.

Modeling Magnetic Pulse Compressors*

Anthony N. Payne
Lawrence Livermore National Laboratory
Livermore, California 94550

Abstract

In this paper, we consider the problem of modeling the dynamic performance of high-average-power, high-repetition-rate magnetic pulse compressors. We are particularly concerned with developing system models suitable for studying output pulse stability in high repetition rate applications. To this end, we present a magnetic switch model suitable for system studies and discuss a modeling tool we are developing to perform these studies. We conclude with some preliminary results of our efforts to simulate the MAG1D compressor performance.

I. INTRODUCTION

Magnetic pulse compressor systems find application as drivers of linear induction accelerators that require high average power and operate at high repetition rates. An important issue in such applications is the stability of the output pulse of the compressors. In particular, the proper operation of an accelerator places stringent constraints on the pulse timing and amplitude variations during a burst of pulses [1].

The basic network configuration underlying most compressor designs is the series Melville line [2] shown in Fig. 1. While the topology of the network is relatively simple, precise analysis and design can be a difficult task because of the highly nonlinear, dynamic characteristics of the saturable inductors or magnetic switches. Moreover, pulse-to-pulse stability depends upon a complicated interaction of many dynamic factors in the compressor. The predominant factors include the energy reflections caused by mismatches between the compressor stages as well as input voltage variations and core reset point variations during the burst.

At Lawrence Livermore National Laboratory, we have been attempting to address stability issues for the MAG1D magnetic pulse compressor by way of mathematical analysis, numerical simulation, and actual experiments. The MAG1D is a three stage magnetic pulse compressor designed to deliver a nominal output voltage of 100kV with pulse width of 70nS. (The ETA-II accelerator at Livermore employs three MAG1D's to drive its 60 accelerator cells and one to drive its injector.) Our recent experimental effort in characterizing the MAG1D is summarized in [3].

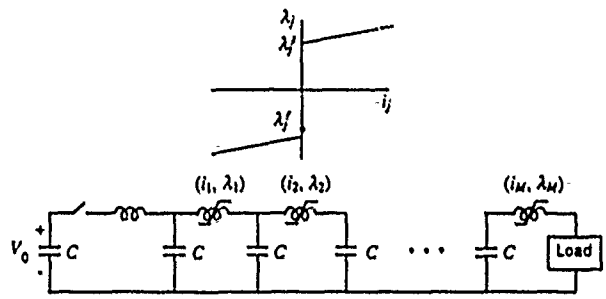


Fig. 1. An M-stage Melville line with ideal magnetic switch λ-i characteristic.

In this paper, we address the problem of modeling the dynamic performance of magnetic pulse compressors for the purpose of studying system stability. First, we present a sensitivity analysis showing the effect of input voltage regulation and magnetic switch reset variation on pulse timing stability. Next, we present a model for magnetic switches that we are using in system studies. We then discuss a general system modeling tool incorporating this model that we are using to model magnetic compressors. Finally, we summarize some preliminary results of our study of the MAG1D.

II. THE STABILITY PROBLEM

The exact nature of the stability problem is suggested by a sensitivity analysis of an ideal Melville line. Consider the M stage ideal Melville line shown in Fig. 1. Let λ_j^r be the flux reset state of switch j and let t_j denote the time at which the switch saturates. Define the arrival time of the output pulse as the time at which switch M saturates. It can then be shown that the relative variation in output pulse arrival time is well-approximated in terms of the relative variation in input voltage V_0 and the relative variation in the reset points of the magnetic switches by

$$\frac{\delta t_M}{t_M} = -\frac{1}{2}\frac{\delta V_0}{V_0} + \sum_{j=1}^{M} S_j \frac{\delta \psi_j}{\psi_j} \qquad (1)$$

where

$$S_j = (t_j - t_{j-1})/2t_M \qquad (2)$$

and

$$\psi_j = \lambda_j^s - \lambda_j^r \qquad (3)$$

* This work was performed jointly under the auspices of the U. S. Department of Energy by Lawrence Livermore National Laboratory under contract W-7405-ENG-48 for the Strategic Defense Initiative Organization and the U. S. Army Strategic Defense Command in support of SDIO/SDC MIPR No. W31RPD-00D4074.

U.S. Government work not protected by U.S. Copyright.

By design, the sequence $\{t_j - t_{j-1}\}$ is a strictly monotone decreasing sequence, so $S_1 > S_2 > \ldots > S_M$. The timing stability of the output pulse is, therefore, more sensitive to the reset variation of the earlier stages than the later stages.

While this analysis provides some insight into the problem, the behavior of actual magnetic components in a compressor deviates significantly from the idealized λ-i relation used to derive (1). Therefore, to study the effects of input voltage regulation and magnetic core reset state in an actual pulse compressor system, we require a good simulation model of the system.

III. MAGNETIC COMPONENT MODEL

The most critical elements to the construction of an overall system model are the magnetic components. These are also the most difficult to model. We present here a simple model that we have found useful for system studies.

Consider a toroidal magnetic core of cross-sectional area A with N windings. We assume that the B and H fields in the core have only azimuthal components. Furthermore, we assume that these fields can be adequately represented by their average values across the core. In the case when this assumption does not hold, it is a trivial matter to extend the results given below to a core that has been zoned into a number of concentric annuli. Let H denote the average magnetic field and M the average magnetization in the magnetic material ($B = \mu_0(H+M)$). By Faraday's law, the voltage across winding j is

$$v_j - n_j\dot{\phi}_j = 0 \tag{4}$$

The flux ϕ_j satisfies

$$\phi_j - \mu_0(A_j H l + K_s A M) = 0 \tag{5}$$

where K_s is the core stacking factor and A_j is the area enclosed by the winding. Finally, neglecting displacement currents, we obtain from Ampere's law

$$Hl - \sum_{j=1}^{N} n_j i_j = 0 \tag{6}$$

where l is the mean magnetic path length.

It remains to specify the mathematical model relating H and M (or B) in the magnetic core material. Many magnetic material models have been proposed over the last four decades (see, for example, the survey in [4]). Recently, we have devised a new model that is conceptually simple and that shows some promise for use in system studies. We merely sketch here the salient features of the model. The actual mathematical details and proofs will be the subject of a future paper.

Our model of the magnetic material consists of a set of two simultaneous differential-algebraic equations:

$$\dot{H}_a - \dot{H} + g(M, \dot{M})(H_a - H + w(M, \dot{M})) + \dot{M}\frac{\partial w(M, \dot{M})}{\partial M} = 0 \tag{7}$$

$$M - F(H_a) = 0 \tag{8}$$

Each function in (7) and (8) has a simple physical interpretation. First, the function F defines the anhysteretic curve of the magnetic material and must possess the property that

$$\lim_{H \to \pm\infty} F(H) = \pm M_s \tag{9}$$

where M_s is the saturation magnetization. Equation (7) insures that the trajectories approach the major loop defined by

$$H = F^{-1}(M) + w(M, \dot{M}) \tag{10}$$

for constant $|dM/dt|$. The function g determines the path that minor loops take, whereas the function w provides the rate-dependent loop widening and accounts for hysteretic loss in the magnetic material.

In order to apply (7) and (8), we must specify the functions F, w, and g. A simple choice is

$$F(H) = \frac{M_s H}{\alpha + |H|} \qquad \alpha > 0 \tag{11}$$

$$g(M, \dot{M}) = \gamma|\dot{M}| \qquad \gamma > 0 \tag{12}$$

$$w(M, \dot{M}) = H_c \operatorname{sgn}(\dot{M}) + k\dot{M} \tag{13}$$

In this case, the material properties are completely specified via (11)-(13) in terms of the five parameters M_s, α, γ, H_c and k. The parameter α governs the squareness of the M-H loop. The loop can be made arbitrarily square by making α sufficiently small. In (13), H_c is the dc coercive magnetic field and k determines the loop widening and, consequently, the hysteretic loss. Other functions can be used to provide a better fit to experimental data, but this will generally require that additional parameters be identified from experimental data. There is, therefore, a trade between the fidelity of the model and its facility of use.

IV. SYSTEM MODELING FRAMEWORK

We have implemented the model described above in a new network and system simulation code that is currently under development at LLNL. The code is intended to be a basis for a suite of tools being devised for pulsed power systems analysis and design optimization. At present the code possesses a collection of basic circuit component models and a free-format input language for describing the system to be simulated. It employs a sparse tableau formulation [5] of the network equations. In this formulation, the system model takes the

form of a system of simultaneous differential-algebraic equations

$$\mathbf{f}(\mathbf{x}(t), \dot{\mathbf{x}}(t), t) = 0 \quad t \geq t_0 \qquad \mathbf{x}(t_0) = \mathbf{x}_0 \tag{14}$$

The vector function **f** includes the topological constraints of the system (Kirchhoff's current and voltage laws) and the element constitutive equations. A magnetic switch or saturable reactor element consist of one or more windings and a magnetic core. The element constitutive equations that enter the tableau equations are (4)-(6) for the windings and (7)-(8) for the magnetic core. The vector **x** consists of element currents and voltages, node voltages and any other variables in the element constitutive relations (e.g., H and M for magnetic components). A stiffly stable, adaptive step-size, adaptive order solver permits the simulation of highly nonlinear and stiff dynamical systems, such as magnetically switched circuits. It also exploits the sparsity of the tableau matrix (Jacobian) of (14).

The use of a general circuit code permits changes in system topology to be made quite easily. This is an important consideration in the design of reset or bias circuits for the magnetic components. Special purpose codes written to solve the system of differential equations for a fixed topology do not enjoy this advantage.

V. MAG1D STUDIES

We have developed an end-to-end simulation model of the MAG1D compressor in our High Average Power Test Stand (HAPTS). Figure 2 depicts a simplified circuit diagram of the HAPTS system, and reference [3] gives a description of its operation.

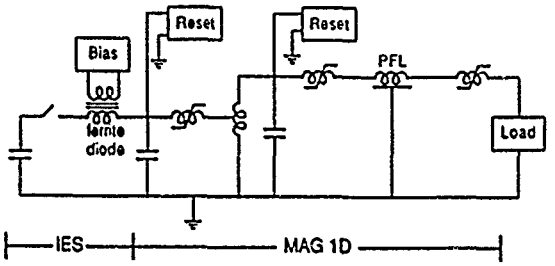


Fig. 2. Simplified circuit diagram of the MAG1D magnetic pulse compressor.

Our system model includes the nonlinear dynamics of the each of the three magnetic switches, the step-up transformer and the intermediate energy storage (IES) ferrite diode. Figure 3 shows the simulated response of the output voltage of the compressor. For comparison purposes, the actual experimentally measured output voltage is shown in Fig. 4. The qualitative agreement is good.

Presently, we are using our model to study the pulse-to-pulse stability of the system. In particular, we are analyzing the sensitivity of output pulse timing and amplitude to variations in input voltage, magnetic switch reset points and IES ferrite diode bias point. We are also presently making measurements on HAPTS that will enable us to refine and validate our model. The next step will be the design of new reset circuits that insure stable performance at high repetition rates. The results of these analyses are forthcoming.

REFERENCES

[1] W. C. Turner, D. M. Barrett, and S. E. Sampayan, "Critical system issues and modeling requirements-the problem of beam energy sweep in an electron linear accelerator," *Proc. 1990 International Magnetic Pulse Compression Workshop*, Lawrence Livermore National Laboratory, CONF-900280, April 1991.

[2] W. S. Melville, "The use of saturable reactors as discharge devices for pulse generators," *IEE Proc.*, Vol. 98, pt. 3, pp.185-207, Feb. 1951.

[3] S. E. Sampayan, W. A. Niven, C.W. Ollis, A. N. Payne, E. T. Scharlemann, W. C. Turner and J. A. Watson, "Performance characteristics of an induction linac magnetic pulse compression modulator at multi-kilohertz pulse repetition frequencies," presented at the *1991 Particle Accelerator Conference*, San Francisco, CA, May 6-9, 1991.

[4] "Working group report on network and system modeling," *Proc. 1990 International Magnetic Pulse Compression Workshop*, Lawrence Livermore National Laboratory, CONF-900280, April 1991.

[5] G. D. Hachtel, R. K. Brayton and F. G. Gustavson, "The sparse tableau approach to network analysis and design," *IEEE Trans. Circuit Theory*, Vol. CT-18, No. 1, pp. 101-113, Jan. 1971.

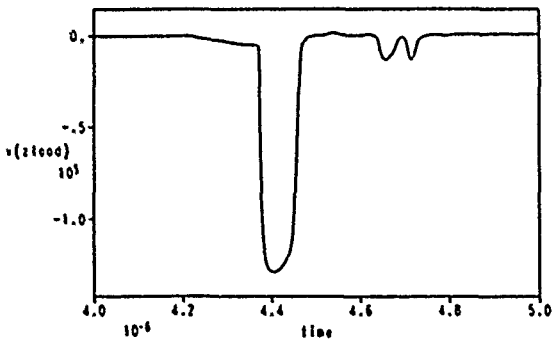
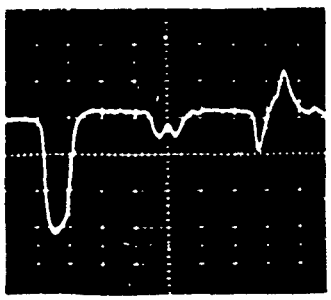


Fig. 3. Simulated output voltage waveform for the MAG1D –28kV input, 128kV peak output.



100nS/div

Fig. 4. Measured output voltage waveform for the MAG1D – 28kV input, 126kV peak output.

Measurements of Reduced Corkscrew Motion on the ETA-II Linear Induction Accelerator*

S.L. Allen, H.R. Brand, F.W. Chambers, Y.-J. Chen, F.E. Coffield, F.J. Deadrick, L.V. Griffith, D.L. Lager, W.J. Mauer, W.E. Nexsen, A.C. Paul, S. Sampayan, W.C. Turner
Lawrence Livermore National Laboratory, Livermore CA 94551

ABSTRACT

The ETA-II linear induction accelerator is used to drive a microwave free-electron laser (FEL). Corkscrew motion, which previously limited performance, has been reduced by: (1) an improved pulse distribution system which reduces energy sweep, (2) improved magnetic alignment achieved with a stretched wire alignment technique (SWAT), and (3) a unique magnetic tuning algorithm. Experiments have been carried out on a 20-cell version of ETA-II operating at 1500 A and 2.7 MeV. The measured transverse beam motion is less than 0.5 mm for 40 ns of the pulse, an improvement of a factor of 2 to 3 over previous results. Details of the computerized tuning procedure, estimates of the corkscrew phase, and relevance of these results to future FEL experiments are presented.

I. INTRODUCTION

The ETA-II is a linear induction accelerator at the Lawrence Livermore National Laboratory designed to produce a high average power electron beam for short-wavelength FELs. FEL performance in 1989 was limited to short (5-10 ns) 0.2 GW pulses at 140 GHz because of a substantial corkscrew motion (~1 cm) of the beam and the nonreproducibility of the electron beam pulse (making empirical wiggler tapering difficult). The corkscrew motion is caused by the energy sweep of the beam during the pulse, coupled with misalignments of the solenoidal transport system of the accelerator [1].

We have implemented several hardware and operational improvements and tested them on a 20-cell version of the whole (60 cell) ETA-II system. The subject of this paper is the resulting reduction of the corkscrew amplitude, and the overall improved operating performance of the ETA-II experiment (e.g., improved pulse-to-pulse reproducibility, lack of insulator damage). Discussion of improved energy flatness during the pulse [2] and a general discussion of the ETA-II system are presented elsewhere [3].

II. DESCRIPTION OF THE EXPERIMENT

A. *The ETA-II 20-Cell Experiment*

For these "prototype" experiments, ETA-II was assembled with a nine-induction-cell injector and 20 accelerator cells. The injector configuration is similar to previous experiments [4]: a common bus feeds the cells and a thermionic osmium-coated 12.7-cm-diameter dispenser cathode was operated at about 1500 A in the space-charge limited regime. A special coaxial iron shroud was added to minimize transverse magnetic fields in the region where the beam is extracted. A large Helmholtz pair was installed around the ETA-II vault and was adjusted to cancel the earth's magnetic field.

Several improvements were added to ETA-II for these experiments. A new multicable system was installed to feed the 20 cells [5] that minimizes the cell-to-cell coupling of transients. Also incorporated into this system are adjustable fluid resistors for each cell and monitors for current and voltage. The variable resistors allow impedance matching at various operating currents and electrical checkout without electron beam loading. The current and voltage monitors at each cell are coupled to a new system that stops operation in the event of an arc or overvoltage. The power supply firing sequence for the injector and the cell blocks is controlled by a new computerized feedback system. This compensates for timing drifts during the day, and also automatically varies the timing as the current and voltage are brought up at the beginning of the day.

The operating point for these experiments was selected to compensate for the inherent energy and current sweep of the injector [5]. For the ETA-II system, operating at a current of 1500 A, a cell gap voltage of 80-90 kV was shown both experimentally and theoretically to result in minimum energy sweep. This value also provides a nearly impedance-matched pulse distribution system, thereby minimizing voltage reflections and possible insulator damage.

B. *Stretched Wire Alignment Technique (SWAT)*

A Stretched Wire Alignment Technique (SWAT) [6,7] was used to magnetically align ETA-II. SWAT uses a stretched wire carefully located on the axis of the accelerator. A current pulse is propagated down the length of the wire, and any misalignments in the magnetic field cause forces on the wire that can be detected by a photoelectric sensor at the other end of the wire. The misalignments are minimized by a combination of movement of the components and adjustment of the (sine and cosine) magnetic correction coils that are an integral part of each cell. The largest correction currents were found in the intercell junctions between each 10 cell block. The SWAT technique was used to align the whole accelerator

*Performed jointly under auspices of USDOE by LLNL W-7405-ENG-48 and DOD under SDIO/SDC MIPR NO. W42-GBL-0-5007.
U.S. Government work not protected by U.S. Copyright.

including the transport section by compensating for the sag of the wire.

C. Accelerator Tuning System—MAESTRO

After the SWAT alignment, the corkscrew amplitude is further minimized directly during accelerator operations by measurements of the electron beam position as a function of time. A computerized data acquisition and control system called MAESTRO [8] acquires and processes signals from beam position monitors placed between each 10-cell block. From the calculated x and y beam positions (usually defined relative to the mean), MAESTRO can calculate the average corkscrew amplitude (A) for a specified time window:

$$A^2 = \frac{1}{\Delta t} \int_{t_1}^{t_2} (x^2 + y^2)\, dt \quad (1).$$

Because the MAESTRO system can control the current in a particular correction coil, it can determine A as a function of the correction coil current. Beam orbit calculations predict [9] a pronounced single minimum for each coil. This was verified experimentally, as shown in Fig. 1; a time window corresponding to half of the peak electron beam current was used. Note the pronounced minimum in A for each curve.

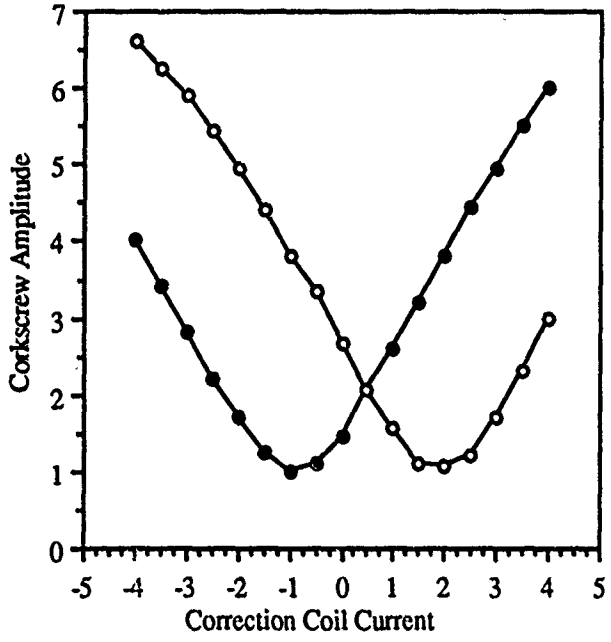


Fig. 1. Corkscrew amplitude A versus the horizontal (solid circle) and vertical (open circle) correction coil current for the last injector cell.

The MAESTRO system was used to determine the settings for the 56 correction coils in ETA-II. First, all the coils were set to the values determined by SWAT. Starting with the injector, MAESTRO then varied each horizontal and vertical compensation coil and found the current that corresponded to the minimum A. When large deviations from the SWAT values were found (or when the minimum corkscrew amplitude increased abruptly for a given coil scan), we found that repeating the previous one or two scans was necessary before the system converged. This procedure was necessary at the intercells, indicating that they are both the largest source of error and the most difficult to measure and adjust with SWAT. Once the minima were found for all of the coils, we found that subsequent passes through the system, using the beam position monitor at the end of the accelerator, resulted in no further reduction in the transverse beam motion. After the procedure was developed, the 20-cell experiment was tuned in about one day, and retuning was not necessary.

III. Experimental Results

A. Measurements of Transverse Beam Motion

The various correction coil currents are stored in the MAESTRO system, so we can easily compare the transverse beam motion with various configurations. Figure 2 compares the beam position versus time at the end of the 20 cells for three cases of correction coil currents:(a) all off, (b) the SWAT values, and (c) the values determined by minimizing A.

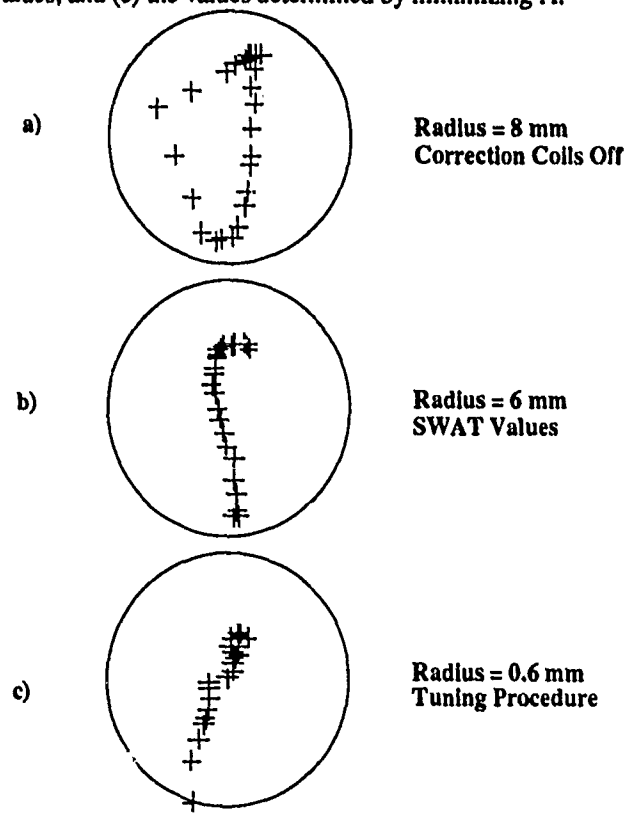


Fig. 2. Measured beam position for 40 ns with (a) all coils off, (b) SWAT values, and (c) the minimization procedure.

Figure 2 shows that there is a modest reduction in the maximum motion using the SWAT values, and nearly an order of magnitude reduction with the values obtained from the MAESTRO tuning procedure. We also determined that these results were reproducible, in that MAESTRO was used to set

the correction coil values each day and the maximum motion was nearly the same. The maximum motion (defined as the smallest circle that contains the data) as a function of the width of the pulse for the final tune of ETA-II(case c above) is shown in Fig. 3. Estimates of these 20-cell values scaled to 60 cells have been performed based on previous experimental results and theoretical models. These indicate that the amplitude should be small enough for efficient FEL operations with a 40-50 ns pulse width.

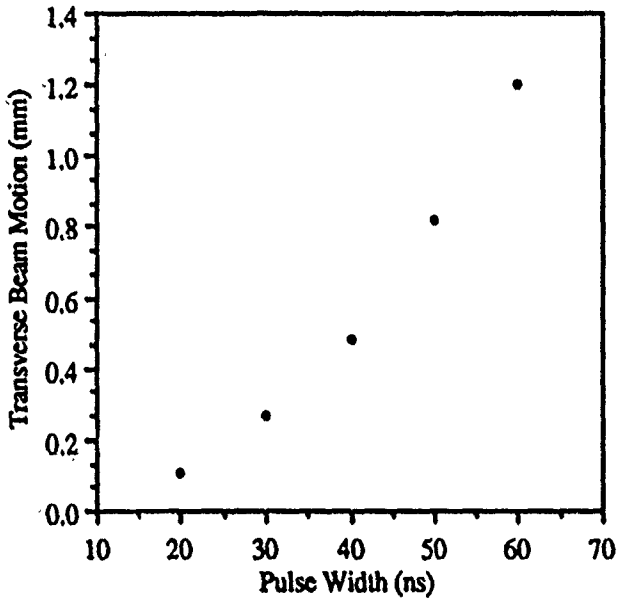


Fig. 3. Transverse beam motion versus pulse width.

B. Characterization of the Beam Motion

In an idealized case, the corkscrew motion can be described as helical motion with a fixed radius and a time-dependent phase. Becasue the phase advance depends on the energy, it is expected to be influenced by the cell voltage and the relative timing between the injector and the cell blocks. For actual experimental data, the characterization of the beam position versus time is more complicated; we have used a radius of curvature ρ defined in terms of the x and y positions and their time derivatives:

$$\rho = \frac{(\dot{x}^2 + \dot{y}^2)^{3/2}}{(\dot{x}\ddot{y} - \ddot{x}\dot{y})} .$$

The phase for a particular time period can then be defined as:

$$\Phi = \int_{t_1}^{t_2} \frac{|\dot{x}\dot{y} - \dot{x}\dot{y}|}{\rho^2} dt .$$

Using this formulation, we have compared previous 60-cell experimental data with the present 20-cell results. The major difference is that the calculated phase advance for a ~70 ns section of the pulse (i.e., between the half current points) is nearly 4π for the 60-cell data, compared with 1-2 radians for the 20-cell data. This is most likely due to the greatly decreased energy sweep during the pulse for the 20-cell experiment[2]. The ρ calculated for the 60-cell case varies during the pulse; it is large at the beginning and end (several mm) and small (less than 1 mm) in the middle of the pulse. The calculation of ρ for the 20-cell case is difficult, because the motion is nearly a straight line. (See Fig. 2c, which is a 40–ns section of the pulse.) For the 20- cell configuration, a series of experiments was carried out where the cell voltage and the relative timing between the injector and the accelerator cells was varied. The above analysis indicated that the maximum transverse motion, the radius of curvature, and the total phase advance were insensitive to these variations.

IV. DISCUSSION

We have shown that a combination of the multicable feed, SWAT alignment, and a tuning algorithm implemented with the MAESTRO control system has reduced the corkscrew amplitude for 20 cells of the ETA-II experiment to less than 0.5 mm for 40 ns of the pulse. We are now assembling the whole 60-cell experiment for use in FEL experiments with the MTX tokamak [10]. We are implementing several upgrades to further improve the system, including (1)redesigned intercell magnet support structures, (2)faster MAESTRO processing and control, and (3)improved cell block construction with Rexolite insulators assembled in a clean room. The pulsed power system is being upgraded to allow a burst of about 50 pulses at a repetition rate of ~5 kHz [11]. Burst mode FEL experiments are planned to begin late in 1991.

REFERENCES

[1] Y.-J. Chen, "Corkscrew Modes in Linear Accelerators," Nucl. Instrum. and Meth. in Phys. Res., A292, p 455-464, 1990.

[2] W. E. Nexsen et al., "Reduction of Energy Sweep of the ETA-II Beam," these proceedings.

[3] W.C. Turner, "Control of Energy Sweep and Transverse Beam Motion in Induction Linacs," these proceedings.

[4] J.C. Clark et al., "Design and Initial Operation of the ETA-II Induction Accelerator," in *Proc. 1988 Linear Accel. Conf.*, Williamsburg, VA, October 2-7, 1988.

[5] S.E. Sampayan et al., "Energy Sweep Compensation of Induction Accelerators," in *Proc. 1990 Linac Conference*, Albuquerque, NM, September 10-14, 1990.

[6] L. Griffith and F. Deadrick, "Progress in ETA-II Magnetic Field Alignment Using Stretched Wire and Low Energy Electron Beam Techniques," in *Proc. 1990 Linac Conference*, Albuquerque, NM, September 10-14, 1990.

[7] R.W. Warren, "Limitations on the Use of the Pulsed-Wire Field-Measuring Technique," presented at the *Ninth International FEL Conference*, Williamsburg, VA, 1987.

[8] Darrel L. Lager et al., "Artificial Intelligence Techniques for Tuning Linear Accelerators," these proceedings.

[9] W.C. Turner, S.L. Allen, et al., "Reduction of Beam Corkscrew Motion on the ETA-II Linear Induction Accelerator," in *Proceedings of the 1990 Linac Conference*, Albuquerque, NM, September 10-14, 1990.

[10] B.W. Stallard et al., "ECH by FEL and Gyrotron Sources on the MTX Tokamak," in *Proceedings of the 16th Symp. on Fus. Tech.*, London, Sept. 1990.

[11] S.E. Sampayan, "Performance Characteristics of an Induction Linac Magnetic Pulse Compression Modulator at Multi-Kilohertz Pulse Repetition Frequency," these proceedings.

Performance Characteristics of an Induction Linac Magnetic Pulse Compression Modulator at Multi-kilohertz Pulse Repetition Frequencies

S. E. Sampayan, F. W. Chambers, F. J. Deadrick, W. A. Niven, C. W. Ollis, A. N. Payne,
V. L. Renbarger, E. T. Scharlemann, W. C. Turner, and J. A. Watson
Lawrence Livermore National Laboratory
Livermore, CA 94550

Abstract

The ETA-II linear induction accelerator utilizes four pulse power conditioning chains. Magnetic pulse compression modulators (MAG1-Ds) form the last stage of each chain. A single power conditioning chain is used to drive the injector; the remaining three are used to drive 60 accelerator cells. Nominal parameters of the MAG1-D are an output voltage of greater than 120 kV, pulse width of 70 ns, and an output impedance of 2 ohms. Our operations goal for ETA-II is stable high average power operation at 5 kHz PRF.

We have begun upgrading and characterizing the power conditioning chain on our High Average Power Test Stand (HAPTS). On HAPTS, the pulse to pulse amplitude stability has been improved to less than 0.7% (one sigma) and of order 3 - 5 ns random jitter about a systematic timing variation. In this paper we describe the status of our work to achieve the desired performance level of the MAG1-D to allow high average power operation of ETA-II.

I. Introduction

Linear induction accelerators (LIAs) are used to produce high average power charged particle beams. These accelerators have been operated at high current (greater than 1 kA), moderate energy (order 10s of MeV) and at high repetition rates (order 5 kHz) [1-3]. Operation of the LIA depends on the time rate of change of magnetic flux through the magnetic material (typically ferrite) within the accelerator cells. The changing flux produces an acceleration gradient along the accelerator axis which imparts energy to the charged particle beam [4].

The ETA-II accelerator, in the 60 cell configuration, is nominally a 7.5 MeV, 2 kA electron beam accelerator; 1 Mev is imparted to the beam at the hot cathode injector, 6.5 MeV is imparted to the beam over 60 accelerator cells. Usable pulse width typically varies between 30-50 ns for an energy sweep, dE/E, of about 1%. Although ETA-II was designed for 5 kHz burst operation, limitations within the power conditioning chain prevented operation at full repetition rate.

The HAPTS pulse power conditioning chain was modeled after the ETA-II power conditioning chain and is used as a test bed to upgrade ETA-II systems. HAPTS consists of a capacitor bank for burst operation, a pulse power unit (PPU) and magnetic pulse compression modulator (MAG1-D) (Fig. 1). The PPU performs initial pulse conditioning and consists of a command resonant charge section (CRC) and deQ components for pulse amplitude regulation [5,6]. An intermediate energy storage section (IES), the last command-triggered switch prior to the magnetic modulator, follows the CRC. The CRC and deQ sections utilize two parallel English Electric Valve thyratrons (EEV 1826) per section because of current ratings. Four parallel thyratrons (EEV 1547) are used in the IES to minimize jitter.

High PRF operation of a thyratron required preventing immediate re-application of a reverse voltage across the tube. Ferrite diodes in both the CRC and IES loops served this purpose (Fig. 1). In the IES loop, a bias circuit is used to maintain the core in the forward saturated state. The magnetic modulator (MAG1-D) performs the final pulse conditioning prior to the induction cell [7]. This final pulse conditioning is performed with three stages of saturable magnetic cores and capacitors in a "pi" type ladder configuration, i. e. a Melville line [8]. A transformer is used in the first stage to provide a voltage gain of about 10.

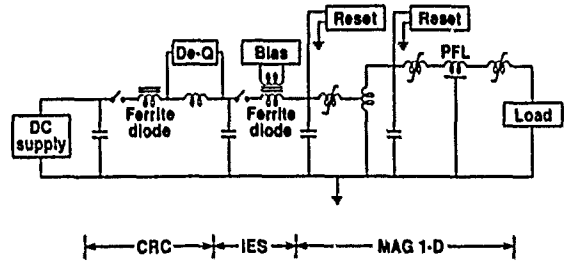


Fig. 1. HAPTS power conditioning chain.

A charge transfer time of 4 μs is required from the PPU to the MAG1-D; an output pulse of 70 ns (FWHM) with a 15 ns rise time is produced at the MAG1-D output. Overall efficiency of the MAG1-D is about 70% energy transfer into a linear load at full voltage. Typical energy output during a 50 pulse burst is on the order of 25 kJ.

The HAPTS development program has focused on minimizing random shot-to-shot and burst-to-burst pulse amplitude and timing variation. Minimizing these quantities assures reproducible beam transport and preservation of beam qualities throughout a pulse burst.

Proper beam transport and preservation of beam quality in an LIA requires minimum energy sweep over the pulse duration [9]. In a practical system, because of accelerator cell non-linearities and a non-zero pulse rise-time, the usable pulse width is somewhat less than the full pulse duration. This usable pulse duration is determined by the operating point of the accelerator which includes beam current, accelerator gap voltage, and beam to voltage pulse timing. Thus, to ensure reproducibility, either an operating point with a broad maximum must be chosen (i. e. a robust, low sensitivity operating point) [10], or stringent requirements must be placed on reproducibility of the pulse shape at the accelerator cell.

Prior to fielding the ETA-II 60 cell experiment, we began a development effort upgrading and characterizing the power

*Performed jointly under the auspices of the US DOE by LLNL under W-7405-ENG-48 and for the DOD under SDIO/SDC MIPR No. W43-GBL-0-5007.
U.S. Government work not protected by U.S. Copyright.

conditioning chain on HAPTS for eventual implementation on ETA-II. The upgrades stabilized system performance; characterizing the system allowed us to determine the most suitable operating point. We describe the progress to date here.

II. Jitter and Regulation Measurements

A. System Upgrades

Measurements on the ETA-II power conditioning chain prior to our most recent upgrades were reported earlier [11]. These past measurements indicated large voltage variations at an intermediate stage within the MAG1-D at increased PRF. Inadequate bias and reset circuit damping was understood to be the cause of these oscillations.

From these previous and additional studies, we implemented changes to both the bias and reset circuitry. These initial improvements consisted of separate IES bias and pre-compression (1st modulator stage) reset circuits. The topology of the MAG1-D reset circuits was also reconfigured and damped to allow stable reset of the saturable magnetics.

The Melville line is sensitive to input voltage fluctuations. Pulse-to-pulse stability of the MAG1-D output required a stable pulsed input voltage source, i. e. PPU output regulation. Thus, in addition to the reset and bias changes, we improved PPU regulation by implementing improved control circuitry [6]. This additional circuitry allowed for the additional delay in the ferrite diode in the CRC circuit. Typical regulation of the PPU at high PRF was measured to be on the order of 0.5%.

B. Jitter Measurements

For the purpose of this paper, we define jitter as random deviation about some systematic variation in timing. Systematic variation is easily corrected by external compensation [see for example 5]; random deviation directly impacts the accelerator operation. In this paper, one sigma variation is quoted in each quantity.

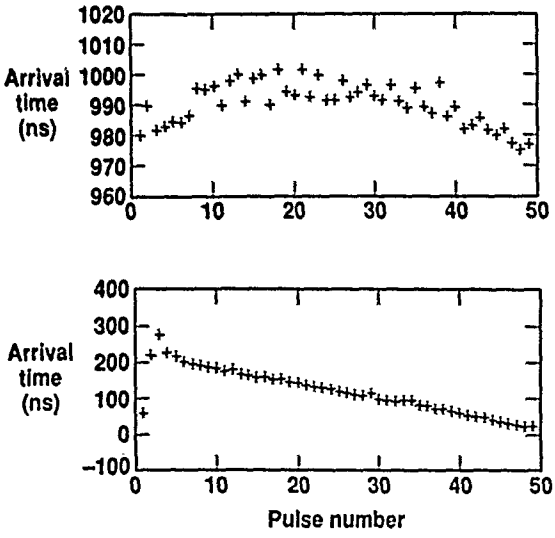


Fig. 2. MAG1-D output timing signature at: 1 kHz (top) and 5 kHz (bottom).

Typical MAG1-D output timing signatures measured at 1 and 5 kHz are shown in Figure 2. In each case, PPU jitter varied from about 6 ns at 1 kHz PRF to about 9 ns at 5 kHz PRF. Output voltage was approximately 95 kV into a linear load.

At 1 kHz, about 3 ns of random jitter accompanied a systematic variation of about 7 ns. At an increased PRF of 5 kHz, a random variation of approximately 5 ns accompanied a systematic variation of 75 ns. For a PRF between 1 and 5 kHz, the systematic variation reached a maximum of 200 ns with a more complex signature appearing at a PRF of 4 kHz.

Reproducibility of the timing signature was measured over long operational periods. An example of the reproducibility of the timing signature at 5 kHz PRF is shown in Fig. 3. Drift of the slope of a straight line fit to the timing of the last 45 pulses in a 50 pulse burst show good reproducibility over a 300,000 pulse test. For this test, the slope remains constant at 4.5 +/-0.3 ns/pulse. The random jitter component remained at about 5 ns.

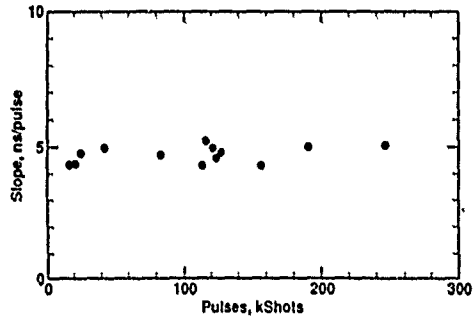


Fig. 3. Typical timing signature variation at 5 kHz PRF 50 pulse burst.

Timing variation and jitter measurements at 5 kHz were made under different cell loading conditions. Both of these quantities were found to be independent of load impedance from 2.0 (matched) to 2.7 ohm.

Growth of the timing variation and jitter was measured through the system. Jitter originated in the IES section and changed gradually through the system. Systematic variation, however, appeared to originate at the precompression or transformer stage of the MAG1-D.

C. MAG1-D Output Voltage Regulation

The output regulation characteristics of the MAG1-D were determined at several voltages, pulse repetition frequencies and load conditions. With an exception at 4 kHz, the average grouping in the output regulation was about 0.7% (one sigma pulse amplitude variation divided by the mean). Measurement resolution was 8 bit. A large variation in regulation accompanied the large timing variations at 4 kHz as mentioned in the previous section. Again, output voltage was about 95 kV into a linear load.

A 50 pulse overlay and regulation measurement taken during a typical 5 kHz, 50 pulse burst at approximately 95 kV, is shown in Fig. 4. Timing variation and jitter is not shown for clarity. The first plot shows that the reproducibility of the pulse shape during the burst was excellent.

Variation in pulse amplitude is shown in the accompanying plot. Regulation during this particular burst was 0.71% and appears to be on the order of instrument resolution.

Additional regulation measurements at 5 kHz were made under different cell loading conditions. Voltage regulation at the MAG1-D was measured to be independent of load impedance which varried from 2.0 (matched) to 2.7 ohm.

Regulation was measured at 1 and 5 kHz as a function of MAG1-D output voltage. At 1 kHz, regulation was measured to be below 0.7% for MAG1-D output voltages exceeding 110 kV. At 5 kHz, however, regulation increased to 20% above about 100 kV.

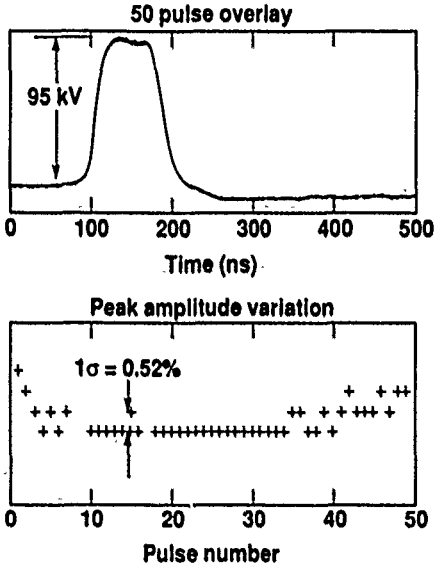


Fig. 4. Typical 5kHz regulation results.

III. Summary

We have measured the characteristics of the ETA-II power conditioning chain to 5 kHz after implementing preliminary system changes, i. e., improved reset and bias circuits and improved PPU regulation. With these changes, we found that system performance improved significantly. Timing variation ranged from about 7 ns at 1 kHz to a maximum of 200 ns at 4 kHz. At 1 and 5 kHz, random jitter was measured to be 3 to 5 ns about a reproducible variation. Pulse-to-pulse voltage regulation was measured to be approximately 0.7%. This regulation level was maintained at 1 kHz to greater than 110 kV MAG1-D output voltage and at 5 kHz to approximately 95 kV.

Additional improvements are presently being studied and implemented. Our measurements indicate that the pre-compression stage of the MAG1-D is responsible for the majority of the timing variation and also for the inadequate regulation at elevated MAG1-D output voltages. We are pursuing the addition of core material to that stage, additional stabilization of the reset circuit, and active control of core reset. To stabilize the present system further, we are also considering timing compensation as a means to remove systematic timing variation.

IV. References

1. R. J. Briggs, D. L. Birx, D. S. Prono, D. Prosnitz, and L. L. Reginato, "Induction Linac Based FELs," in Proceedings of the IEEE Particle Accelerator Conference, Washington D. C., pp. 178-182, 1987.
2. L. L. Reginato, "The Advanced Test Accelerator (ATA) a 50 MeV, 10 kA Induction Linac," presented at the 1983 Particle Accelerator Conference, Santa Fe, NM, March 1983.
3. W. A. Barletta, "Accelerating Intense Electron Beam," in Energy and Technology Review, Lawrence Livermore National Laboratory, Livermore, CA, UCRL-52000-79, September 1979.
4. S. Humphries, Principles of Charged Particle Acceleration, John Wiley and Sons, New York, 1986.
5. M. A. Newton and J. A. Watson, "Timing and Voltage Control of Magnetic Modulators on ETA-II," presented at the 7th IEEE Pulsed Power Conference, Monterey, CA, June 1989, pp. 175-177.
6. J. A. Watson, A. N. Payne, S. E. Sampayan, and C. W. Ollis, "Precision Voltage Regulation on the 5 kHz, 3.125 MW ETA-II Pulse Power System," to be presented at the 8th IEEE Pulsed Power Conference, San Diego, CA, June 1991.
7. W. C. Turner, D. M. Barrett, and S. E. Sampayan, "Critical System Issues and Modeling Requirements -the problem of Beam Energy Sweep in an Electron Linear Accelerator," presented at the International Magnetic Pulse Compression Workshop, Lake Tahoe, CA, February 1990.
8. W. S. Melville, "The Use of Saturable Reactors as Discharge Devices," IEE Proceedings (London), Part 3: Radio and Communication, vol. 98, pp. 185, 1951.
9. Y-J. Chen, "Corkscrew Modes in Linear Accelerators," Nucl. Instrum. and Meth. in Physics Research, A292, pp. 455-464 (1990).
10. S. E. Sampayan, G. J. Caporaso, Y-J. Chen, T. A. Decker, and W. C. Turner, "Energy Sweep Compensation of Induction Accelerators," presented at the 1990 Linear Accelerator Conference, Albuquerque, NM, September 1990.
11. M. A. Newton, D. M. Barrett, C. W. Ollis, and D. L. Pendleton, "Energy Flow and High Repetition Rate Issues for the ETA-II Magnetic Modulator System," presented at the 1990 Linear Accelerator Conference, Albuquerque, NM, September 1990.

Degradation of Brightness by Resonant Particle Effects *

Y.-J. Chen, G. J. Caporaso, A. G. Cole, A. C. Paul, and W. C. Turner
Lawrence Livermore National Laboratory
University of California, L-626
Livermore, California 94550

ABSTRACT

A resonance between the periodic focusing force and the envelope oscillations or the particle orbits can lead to beam halo formation and a dramatic decrease in brightness. We have developed a theoretical model for this parametric transport instability. We have also investigated the instability on the Experimental Test Accelerator II (ETA-II)[1]. The instability can be excited by altering the excitation of just one solenoid.

I. INTRODUCTION

Most accelerator configurations consist of some periodic structures such as a periodic focusing or acceleration system. The Experimental Test Accelerator-II (ETA-II)[1] is the induction linac designed to drive a 140 GHz microwave FEL. Reference 2 showed that when the envelope oscillations are in resonance with the periodic magnetic field of the first two 10-cell blocks of ETA-II, 20-25% of particles walk away from the bulk of the beam and form a halo which seriously degrades the beam brightness. The present paper aims to provide some theoretical understanding of the resonant particle effects and the cures. A theoretical model is given in Sec. II. We have investigated this parametric transport instability on ETA-II by detuning a single focusing solenoid deliberately and observing the brightness degradation. Comparisons between the simulation results and experimental data are presented in Sec. III.

II. THEORETICAL MODEL

A. *Envelope Oscillations*

In this paper, we only consider a solenoid transport system. In general, we find the matched tune for the beam by solving the envelope equation:

$$R'' + \frac{(\gamma\beta)'}{\gamma\beta}R' + \left(\frac{k_c^2}{4} - k_s^2\right)R - \frac{\mathcal{E}^2}{\gamma^2\beta^2R^3} = 0 \quad , \qquad (1)$$

where $R(z)$ is the r.m.s. beam radius and $\gamma\beta$ is the parallel beam momentum normalized by mc. Here $k_c = eB/\gamma\beta mc^2$ is the cyclotron wavenumber, $k_s^2 = I/I_o\gamma^3\beta^3R^2$ is the tune shift due to the defocusing space charge force, I is the beam current, $I_o = mc^3/e \approx 17$ kA, and $\mathcal{E}^2 = \epsilon_n^2 + P_\theta^2/c^2$ is the effective normalized emittance. P_θ and ϵ_n are the canonical angular momentum and normalized emittance of the beam. According to Eq. (1), the matched magnetic field $B_o(z)$ for a preferable slowly varying envelope $R_o(z)$ is given by

$$|B_o(z)| = \frac{2\gamma\beta mc^2}{e}\left[k_s^2 + \frac{\mathcal{E}^2}{\gamma^2\beta^2R^4} - \frac{R''}{R} - \frac{(\gamma\beta)'}{\gamma\beta}\frac{R'}{R}\right]_o^{\frac{1}{2}} \quad . \qquad (2)$$

The subscript "o" represents the matched envelope. Note that the magnetic field B_o can be both positive and negative. Hence, we can use either the continuous or the alternating solenoid field to transport the beam. Furthermore, for a smoothly varying beam envelope, the matched magnetic field B_o should also be smoothly varying except near the acceleration gaps. Let us assume that the actual magnetic field used in the machine differs from the matched magnetic field by $\delta B(z)$, and δB is much less than B_o. Then the envelope will differ from the matched value by

$$R(z) = R_o(z) + \delta R(z) \quad . \qquad (3)$$

Linearizing Eq. (1) around the matched envelope yields the following envelope oscillation equation:

$$X'' + K_e^2X = -\left(\frac{k_c^2R}{2}\right)_o\frac{\delta B}{\mathcal{B}_o} + \left(\frac{2\mathcal{E}^2}{\gamma^2\beta^2R^3}\right)_o\frac{\delta\mathcal{E}}{\mathcal{E}_o} \quad , \qquad (4)$$

where $X = \sqrt{\gamma\beta}\,\delta R$, and

$$K_e^2 = \frac{k_c^2}{4} + k_s^2 + \frac{1}{4}\left[\frac{(\gamma\beta)'}{\gamma\beta}\right]^2 - \frac{1}{2}\frac{(\gamma\beta)''}{\gamma\beta} + \frac{3\mathcal{E}^2}{\gamma^2\beta^2R^4} + \left[\frac{\partial(\gamma\beta)'}{\partial R} - \frac{(\gamma\beta)'}{\gamma\beta}\frac{\partial(\gamma\beta)}{\partial R}\right]\frac{R'}{\gamma\beta} - \left(\frac{k_c^2}{2} - 3k_s^2 - \frac{2\mathcal{E}^2}{\gamma^2\beta^2R^4}\right)\frac{R}{\gamma\beta}\frac{\partial(\gamma\beta)}{\partial R} \quad . \qquad (5)$$

There are two driving forces for the envelope oscillations [Eq. (4)]. We only consider the oscillations excited by the perturbation in the magnetic field here. We can express the magnetic driving term by a Fourier expansion, and rewrite Eq. (4) as

$$X'' + K_e^2X = \sum_{k_b} F_{k_b}e^{ik_bz} \quad . \qquad (6)$$

Note that K_e^2 is a slowly varying function. Let $X = \sum X_{k_b}e^{ik_bz}$. For $K_e \neq k_b$, the envelope oscillation does not resonate with the periodic magnetic force, and

$$X_{k_b} \approx \frac{F_{k_b}}{K_e^2 - k_b^2} \quad . \qquad (7)$$

For $K_e = k_b$, the orbits of the bulk of the beam resonate with the periodic focusing force. Then the parametric instability occurs, and

$$X_{k_b} \approx \frac{F_{k_b}}{2ik_b}z \quad . \qquad (8)$$

* Work performed jointly under the auspices of the U.S. Department of Energy by Lawrence Livermore National Laboratory under contract W-7405-ENG-48, for the Strategic Defense Initiative Organization and the U.S. Army Strategic Defense Command in support of SDIO/SDC MIPR No. W43-GBL-0-5007

U.S. Government work not protected by U.S. Copyright.

B. *Phase Mixing and Halo Formation*

A single particle orbit is given by

$$\eta'' + \left[\frac{(\gamma\beta)'}{\gamma\beta} - ik_c\right]\eta' - k_s^2(|\eta|)\eta = 0 \quad , \qquad (9)$$

where $\eta = x + iy$. Let $\eta = \eta_o + \delta\eta$. To obtain the consistent perturbation in k_s, we need to solve either the Vlasov or the continuity equation. However, for simplicity, we assume that both the perturbed and the unperturbed space charge force is linear in radius. Linearizing Eq. (9) around the unperturbed orbit yields

$$\zeta'' + K_s^2\zeta = -\sqrt{\gamma\beta}\,\eta_o e^{-i\int\frac{k_{co}}{2}dz}\left(k_{co}k_o\frac{\delta B}{B_o} + 2k_{so}^2\frac{\delta R}{R_o}\right), \qquad (10)$$

where

$$\zeta = \sqrt{\gamma\beta}\,\delta\eta\, e^{i\int k_{co}dz/2} \quad , \qquad (11)$$

$$K_s^2 = \frac{k_{co}^2}{4} - k_{so}^2 + \frac{1}{4}\left[\frac{(\gamma\beta)'}{\gamma\beta}\right]^2 - \frac{1}{2}\frac{(\gamma\beta)''}{\gamma\beta} + \frac{ik_{co}}{2}\frac{B_o'}{B_o}$$
$$+ k_{co}k_o\eta_o\left[\frac{\partial B_o/\partial\eta}{B_o} - \frac{\partial(\gamma\beta)/\partial\eta}{\gamma\beta}\right] + \frac{\partial}{\partial\eta}\left[\frac{(\gamma\beta)'}{\gamma\beta}\right], \qquad (12)$$

and $k_o \approx k_{co}/2 \pm (k_{co}^2/4 - k_{so}^2)^{1/2}$ is the betatron wavenumber for the matched beam. Solving Eq. (10) by using Eqs. (4) - (8) and (11) gives the pertubed orbit. Generally, $K_s \neq K_e + k_o - k_{co}/2$, a given Fourier component in the perturbed force can only resonate with the envelope oscillations or the particle orbits. The perturbed orbit for this single resonance case is given by

$$\frac{\delta\eta}{\eta_o} = \sum_{\substack{k_b\neq K_e \\ k_b\neq K_s-k_o+\frac{k_{co}}{2}}} \frac{k_{co}^2}{K_s^2 - (k_b + k_o - \frac{k_{co}}{2})^2} \times \left[-\frac{k_o}{k_{co}} + \frac{1}{\sqrt{\gamma\beta}}\frac{k_{so}^2}{K_e^2 - k_b^2}\right]\frac{\delta B_{k_b}}{B_o}\, e^{ik_bz}$$
$$+ \frac{k_{co}^2}{K_s^2 - (K_e + k_o - \frac{k_{co}}{2})^2}\left[\frac{k_o}{k_{co}} + \frac{i}{2\sqrt{\gamma\beta}}\frac{k_{so}^2 z}{K_e}\right]\frac{\delta B_{K_e}}{B_o}\, e^{iK_ez}$$
$$- \frac{ik_{co}^2 z}{2K_s}\left[-\frac{k_o}{k_{co}} + \frac{1}{\sqrt{\gamma\beta}}\frac{k_{so}^2}{K_e^2 - (K_s - k_o + \frac{k_{co}}{2})^2}\right] \times \frac{\delta B_{K_s-k_o+\frac{k_{co}}{2}}}{B_o}\, e^{i(K_s-k_o+\frac{k_{co}}{2})z} \qquad (13)$$

However, when $K_s = K_e + k_o - k_{co}/2$, the periodic perturbation can excite parametric instabilities simultaneously in both the envelope oscillations and the particle orbits. When the double resonance occurs, the orbit is given by

$$\frac{\delta\eta}{\eta_o} = \sum_{k_b\neq K_e} \frac{k_{co}^2}{K_s^2 - (k_b + k_o - k_{co}/2)^2} \times \left[-\frac{k_o}{k_{co}} + \frac{1}{\sqrt{\gamma\beta}}\frac{k_{so}^2}{K_e^2 - k_b^2}\right]\frac{\delta B_{k_b}}{B_o}\, e^{ik_bz}$$
$$- \frac{k_{co}^2 z}{2K_s}\left[i\frac{k_o}{k_{co}} - \frac{1}{2\sqrt{\gamma\beta}}\frac{k_{so}^2 z}{K_e}\right]\frac{\delta B_{K_e}}{B_o}\, e^{iK_ez} \qquad (14)$$

The first term in Eqs. (13) and (14) corresponds to the nonresonant orbit. The other terms in these equations describes the unstable orbits when the orbit or the envelope oscillation resonates with the B field. Equation (12) shows that K_s is a function of radius due to the space charge potential depression, and the radial dependence of the solenoidal field and the accelerating field. Hence, $\delta\eta/\eta_o$ varies in radius implicitly through $\gamma\beta$ and K_s regardless whether the particle orbit resonates with the perturbation or not. This leads to $(\delta\eta/\eta_o)'$ also varying in radius. Therefore, phase mixing occurs whenever there is an oscillatory magnetic perturbation or envelope oscillations.

Since the resonance condition is a function of radius, only the particles at certain radius can resonate with the periodic field. These particles can walk away from the bulk of the beam with an amplitude proportional to z for the single resonance case and to z^2 for the double resonance case. Eventually, a halo will be formed. Generally, $(\gamma\beta)' \approx 0$ and $B_o' \approx 0$. The resonance condition for the envelope oscillations and for the particle orbits is $k_b = K_e$ and $k_b \approx 2K_s$, respectively. Then, double resonance occurs when $k_b \approx 0.63k_{co}$ and $k_{so} \approx 0.39k_{co}$. Therefore, the double resonance can happen only if the beam is strongly space charge dominated. These double resonance conditions can be easily satisfied for the ETA-II beam since the perturbation in a single solenoid field contains many Fourier components. If the parametric instability is excited over a large distance, the quality of the beam will be damaged beyond repair.

III. EXPERIMENTS

We should choose a magnetic field B_o such that K_e does not equal an integer times the wavenumber of the periodic system. Furthermore, allowing K_e to vary along the z axis can prevent the parametric instability from growing over an extended distance. The result of particle simulations for the old ETA-II experiment reported in Ref. 2 is presented in Figs. 1 (a)-(c). As shown in Fig. 1(b), with the magnetic field of the old tune, the bulk of the beam could resonate with the periodic magnetic structure over the first 20 cells. Large envelope oscillations were excited. Hence, a halo was formed. Figures 1 (d)-(f) present the simulation results for the current ETA-II tune. The new tune is chosen so that the new beam envelope (Fig. 1(e)) is roughly the same as the old envelope (Fig. 1(b)) without the large parametric instability excitation. Comparing the envelope oscillations in Figs. 1(b) and (e) shows that the new K_e varies relatively fast in z. Therefore, it is harder for the parametric instability to ruin the beam quality.

The magnetic field of a single solenoid consists of many long wavelength Fourier components. Therefore, the instability can be excited by altering the excitation of a single solenoid. We have investigated the transport parametric instability experimentally on the newly modified version of the ETA-II. The instability was excited at the exit of the injector deliberately by detuning one focusing solenoid. The stronger space charge forces at that location allowed

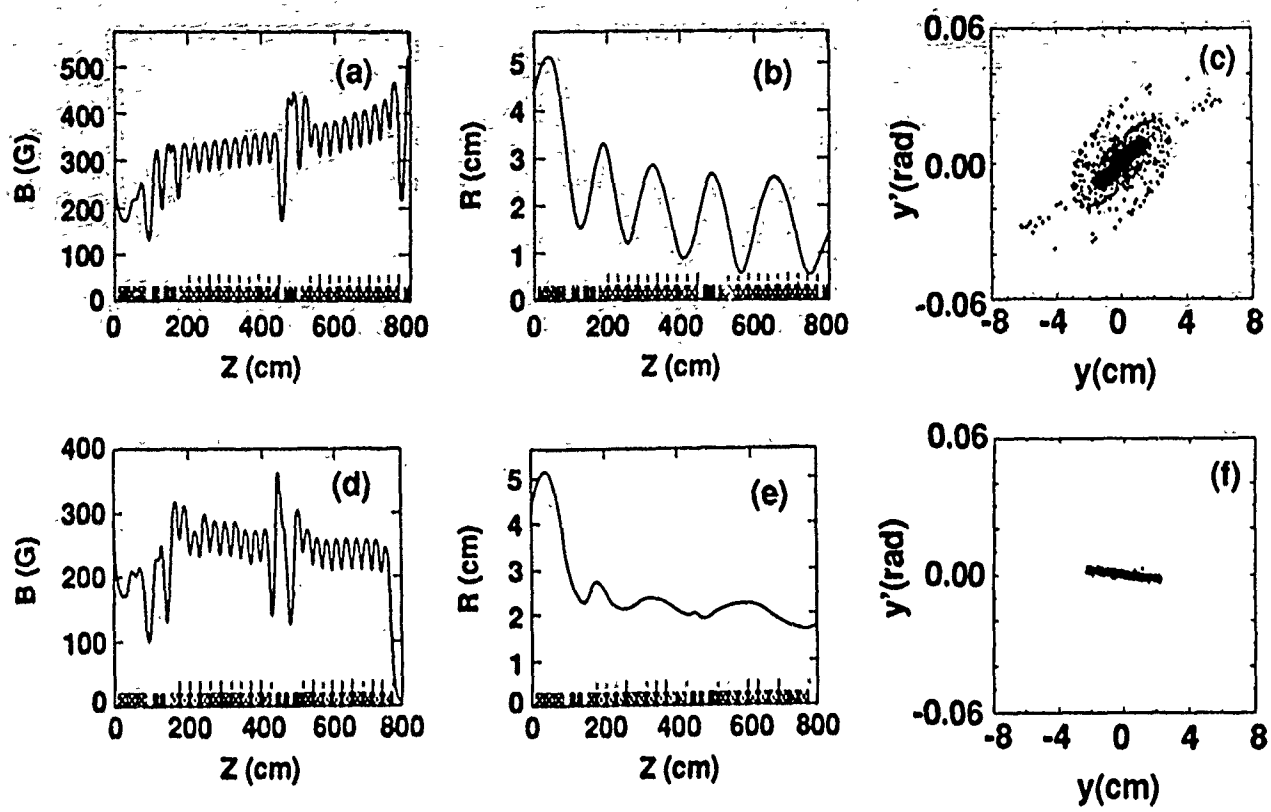


Fig. 1 Reduction of resonant degradation of brightness with choice of focusing tune. The old tune, the beam envelope and the beam phase space at the end of the 20 cells is given in (a), (b) and (c), respectively. The plots for the new tune are presented in (d), (e) and (f).

us to observe a large brightness degradation. The beam brightness was measured by using a pepper-pot emittance diagnostic[3]. Since the beam does not stay in resonance with the periodic magnetic structure over a long distance with the current ETA-II tune, a relatively large perturbation in the solenoid current excitation must be used. The nominal excitation on the first solenoid after the injector is 60.81 A. We varied the current from the nominal current to 90A. The brightness was reduced up to a factor of 3.67. The experimental data are summarized in Table I. Here, I_{C1}, I_{B4} and I_{T3} are the current excitation of the solenoid, the beam current at the pepper-pot mask, and the transmitted beam current after the mask, respectively. The intrinsic beam brightness[3] is defined as

$$J = \frac{2I}{(\pi\gamma\beta a\theta)^2} \quad , \tag{15}$$

where a is the beam radius, and θ is the intrinsic angular spread of the beam. Both the experimental and simulated brightness data are given in Table I.

IV. CONCLUSIONS

We have studied a parametric instability of envelope oscillations in a periodic solenoid focusing system. A theoretical model was developed to understand this parametric instability and its phase mixing. We have investigated the instability on ETA-II. A magnetic tune has been chosen for the ETA-II focusing system so that the envelope oscillations can not resonate with the periodicity of the focusing system over a significant distance. Therefore, it is difficult to excite this transport parametric instability and to degrade the beam quality.

Table I.
Brightness Degradation by Mismatch

I_{C1} (Amp)	I_{B4} (Amp)	I_{T3} (Amp)	J_{exp} (A/(m-rad)^2)	J_{sim} (A/(m-rad)^2)
60.81	1108	2.39	9.15×10^8	4.5×10^9
70	933	2.05	6.02×10^8	1.9×10^9
80	718	1.70	3.64×10^8	1.0×10^9
90	533	1.41	2.49×10^8	6.8×10^8

References

1. W. E. Nexsèn, et al., "The ETA-II Induction Linac as a High Average Power FEL Driver", *Proc. of the 11th Int. FEL Conf.*, Naples, FL., (August 28-Sept. 1, 1989).

2. Y.-J. Chen, et al., "Measurement and Simulation of Whole Beam Brightness on the ETA-II Linear Induction Accelerator", in *Proc. 1990 Linac Conference*, Albuquerque, NM., Sept. 10-14, 1990.

3. A. C. Paul, et al., "ETA-II Beam Brightness Measurement", this conference.

Reduction of Energy Sweep of the ETA-II Beam*

W.E. Nexsen, S.L. Allen, F.W. Chambers, R.A. Jong, A.C. Paul, S.E. Sampayan and W.C. Turner
Lawerence Livermore National Laboratory
University of California
Livermore, CA 94550

Abstract

The ETA-II electron beam will be used to drive a high power microwave frequency FEL for plasma heating experiments. For maximum FEL output power the beam energy at the entrance to the wiggler should be within ±1% of the wiggler resonance value. In initial operations the ETA-II beam energy stayed within this range for a maximum time of less than 13 ns. Much of the energy variation was due to the design of the pulsed power feeds to the accelerator induction cells. A new multicable pulsed power feed design was tested in a shortened version of ETA-II where it extended the time during which the beam energy stayed within the ±1% limits to greater than 40 ns. These design changes are now being incorporated into the full accelerator.

I. INTRODUCTION

The Experimental Test Accelerator II (ETA-II) facility is funded to develop and demonstrate the electron induction linac technology necessary for driving FELs at high average power [1]. The facility consists of the ETA-II accelerator, (the first induction linac designed specifically to drive an FEL), and several test stands for studying cathode brightness and poisoning, ferrite response, pulse-power feeds, and the operation of magnetic switches at high repetition frequency (prf). The design changes described in this report, which were tested on a shortened version of the accelerator, are now being incorporated in the full machine. When completed ETA-II will be able to supply 70 ns full-width-half-maximum pulses of 2-3 kA beam current, 6-7 Mev energy, in fifty pulse bursts at 5 kHz prf with a burst repitition rate of 0.5 Hz. As a technology demonstration we intend to use ETA-II to drive a 140 GHz FEL, the Intense Microwave Prototype (IMP) amplifier system [2]. whose output will be used for plasma heating experiments on the LLNL Microwave Tokamak Experiment (MTX).

The IMP system consists of a microwave oscillator, a quasi-optic coupler which injects the oscillator output coaxially with the beam and a wiggler which couples beam energy to the electomagnetic field. The high magnetic field and wide tunability capabilities required for the FEL are provided by a permanent magnet-laced electromagnetic wiggler with a 10-cm period and an overall length of 5.5 m.

II. ENERGY SWEEP TOLERANCES

Variation of beam energy will affect the FEL output power by two different mechanisms: through gain change as the beam energy deviates from resonance with the wiggler, and through energy sensitivity of the alignment of the beam with the axis of the wiggler. Sensitivity of beam power to off resonance operation has been calculated using the free electron laser simulation code, FRED [3,4]. For code input parameters in the expected operating range FRED predicts a 1% deviation from resonance energy reduces output power by ~6%, a 2% deviation by ~25%.

Initial misalignment of the beam with respect to the solenoidal guide field of the accelerator will result in the beam centroid following a helical path through the accelerator. Localized field errors will introduce jumps in the guiding-center radius and position along the way. If the energy is constant the beam path will be fixed in space but energy variation will modulate the cyclotron wavelength and produce a complicated sweeping in time of the beam centroid position and angle at any point including the entrance to the wiggler. This behavior, called beam "corkscrew" motion [5]-[8], imposes stringent requirements on magnetic alignment and energy sweep.

In earlier operation two beam position monitors seperated by a field free region were used to measure the spatial and angular sweep at the exit of the accelerator as the energy varied. A beam transport code was used to calculate the corresponding motion at the entrance to the wiggler and these values were used as input into FRED to determine their effect on the microwave power. For the measured corkscrew motion we estimated that a ±1% energy variation could decrease the output power by 30%, a much larger effect than merely being off resonance. Considerable improvement in magnetic alignment and reduction of corkscrew amplitude have been made since the above measurements [7] but the goal of keeping the energy variation within ±1% is still desirable. Maximizing the average FEL output power requires that the beam energy stay within these limits for a large fraction of the current pulse length. As a technology demonstration our immediate milestone has been to maintain the energy sweep within ±1% for at least 30 ns.

III. ENERGY SWEEP STUDIES

A. Beam energy measurement

Our primary beam energy diagnostic has been a magnetic spectrometer [1]. A bending magnet, located in the transport

*Performed jointly under the auspices of the US DOE by LLNL under W-7405-ENG-48 and for the DOD under SDIO/SDC MIPR No. W43-GBL-0-5007.
U.S. Government work not protected by U.S. Copyright.

section between the accelerator and the wiggler,when energized, deflects the beam into a 45° side arm.Two pairs of beam position monitors,one on the input side and the other coaxial with the side arm are used to measure the variation of the deflection angle of the beam centroid in the bending plane around the 45° central angle. The system can detect angular variations due to energy changes of~0.1% and has a 500 MHz bandwidth. The absolute energy calibration is derived from the mapping of the bending magnet's field.

B.Sources of energy variation

Energy variation may have either operational causes or be intrinsic to the design. Operational causes are those which affect shot reproducibility such as input voltage variation, timing jitter, variation of ferrite reset condition, and insulator breakdown. Such uncontrolled variation can make the accelerator almost impossible to tune and virtually useless. Two important additions were made to the ETA-II control system for the experiments described here, the first being a computer controlled feedback timing compensation system that corrects for timing drifts due to power supply variations and the second an arc and overvoltage protection system which interrupts accelerator operation when a fault occurs. The latter along with the multicable feed system modification, described below, limit the energy available for driving an arc and causing insulator damage.These changes greatly reduced uncontrolled variations and improved our ability to tune the machine. Remaining as problems are the intrinsic causes of energy variation within a shot -- time varying beam loading and cell impedence, and mismatches in the pulse-power feeds to the accelerator cells.

Measurements of beam energy variation at the output of ETA-II in its original configuration showed that the energy was within the ±1% limits for at most 13 ns [1], less than half of the period we could accept as a minimum. The source of most of this variation was traced to the cell pulse-power feeds. As originally configured, each ten-cell set was fed from its magnetic pulse compressor (MAG-1D) by a single 4 Ω water dielectric cable which connected to the input ends of a pair of busbars running parallel to the axis on opposite sides of the cell block. These provided a symetrical power feed to the individual cells which tapped into the bars along the way. The far ends of the bars were terminated to reduce reflections. Although this design provided a neat mechanical solution to the problem of pulse-power distribution, measurement and analysis soon showed that electrically it was not satisfactory. The busbars form a slow wave structure, consequently the phase of the voltage pulse with respect to the beam pulse ($\beta \approx 1$) varies with distance along the busbar. Since the beam loading modifies the applied voltage pulse, phase variation results in each gap seeing a different resultant voltage variation with time and since the final beam energy is the sum of the contributions of all of the gaps, it is not surprising that a large energy sweep was encountered.

C. Modeling the power feed.

A computer model of the pulse power feed was used to help understand its operation [9]. Experimental measurements of the injector current pulse shape, the MAG-1D voltage pulse shape and the variation of the cell leakage current with time were combined with a model of the busbar slow wave structure to calculate the time variation of each gaps voltage relative to the current pulse. The voltages were summed to give an estimate of the energy sweep of the output. The results of such a simulation are shown in Figure 1. We see that there is good agreement between the model's predictions and the experimental measurements of ±1% energy sweep for a

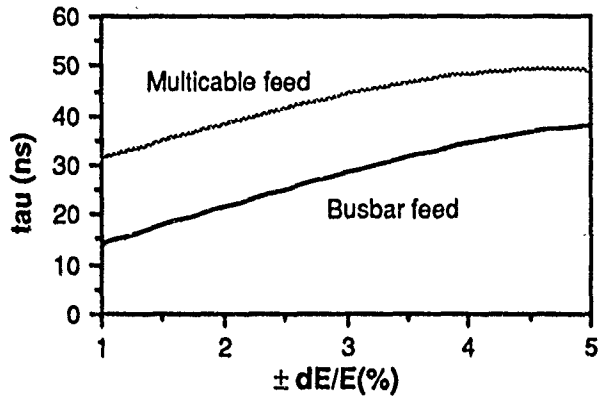


Figure 1. Time that beam energy stays within regulation range versus range (Simulation, 60 cells,E=6 Mev, I=2 kA)

maximum of 13ns with the old busbar feed.

Both experiment and modeling having shown that there was very little chance of meeting our milestone with the busbar power feed, the design of a new, multicable feed was undertaken. Such a feed system for the cells, while mechanically much more complex, allows transit time isolation from the other cells while proper choice of cable lengths insures constant phase between current pulse and gap voltages. Since it is best to feed the gaps symmetrically at two points, 180° apart, our approach was to use two 40 Ω solid dielectric cables to feed two cells in parallel. A short busbar on each side connects the high voltage electrodes of the cell pair and a cable connects to each busbar center. With this design there is ~1 ns phase difference between the two cells relative to the current pulse and some sloshing around of energy between the cell pairs during the current rise and fall when the load is not matched. Modeling of this system, detailed in reference [9], showed that this new design should enable us to meet our energy sweep milestone for the full machine for certain conditions of current, MAG-1D voltage, and timing.(Figure 1).

D. ETA-II tests.

On a test stand we developed a multicable feed system which would require minimum modification of the existing system. Each MAG-1D has two 4 Ω output cables and can

feed two ten-cell blocks. Rather than adapting the MAG-1D to the multicable feed, which would have been a major task, we installed a high voltage distribution box where transition was made from the two 4 Ω cables to twenty 40 Ω cables in parallel. The old busbar structure was replaced with the cell feed structure described above. After initial tests the new feed system was installed on the first two ten-cell blocks of ETA-II for evaluation before modifying the remainder of the accelerator. The remaining four ten-cell blocks were removed and replaced with a transport section, and the injector, whose design concentrates its voltage across the A-K gap, was left unchanged. This shortened version of ETA-II was capable of producing a 2.5-3 Mev beam.

The model was used to predict optimum values of MAG-1D voltage and relative timing between the injector and the accelerator for minimizing the energy sweep of a ~1.5 kA beam from the accelerator. Experimental measurements agreed well with predictions of the model. If we define τ as the time the beam energy has a maximum peak to peak variation of 2%, then we were able to find conditions of voltage and timing delay near the model values for which τ exceeded 40 ns. The best recorded shot is shown in Figure 2. While this shot is on the upper edge of the tau distribution the probability of

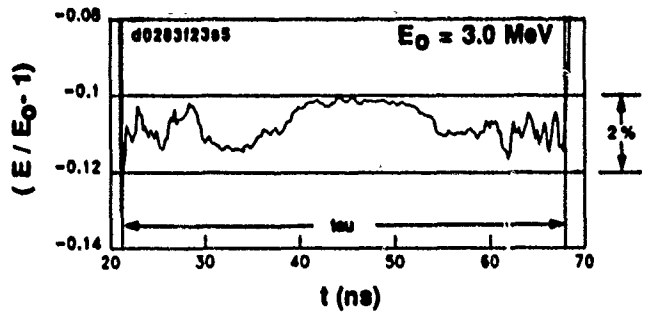


Figure 2. Beam energy variation versus time (I~1.5 kA)

exceeding the 30 ns milestone for these operating conditions was very high. Figure 3 is a histogram of the τ distribution for a set of 50 shots with the same input conditions. This data

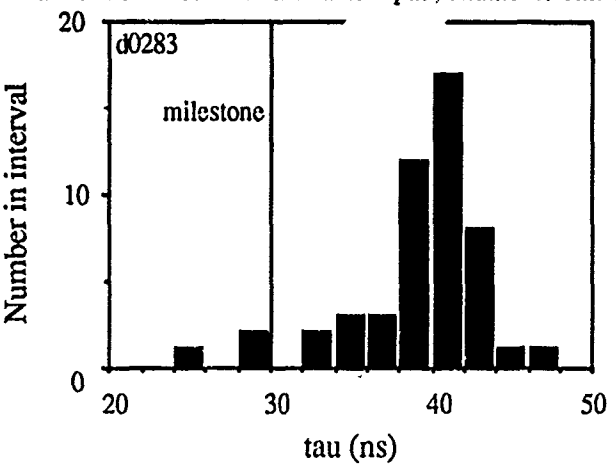


Figure 3. Histogram of tau distribution for a set of 50 shots.

was recorded as 10 shot sets at various times during a days operation. Over this period of operation the drift of the central energy value was less than 1% (Figure 4)

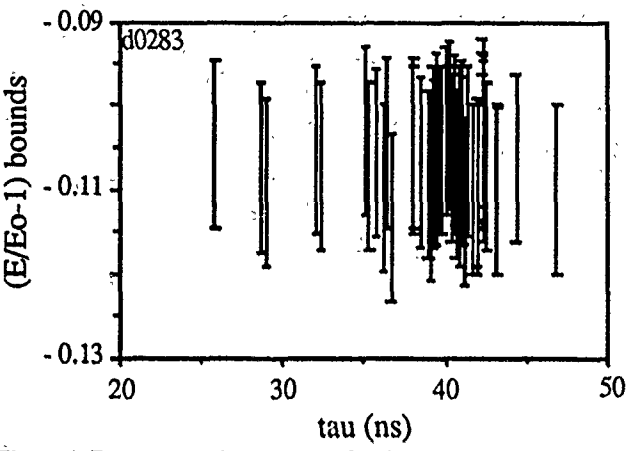


Figure 4. Energy bounds versus tau for data set.

IV. SUMMARY

In recent operation of a shortened version of ETA-II with only the injector and the first two ten-cell blocks we have been able to keep the energy sweep of the output beam to less than 2% for periods greater than 40 ns. The key ingredient of this achievement was the retrofit of a new multicable pulse power feed to the 20 cells and the development of a model for predicting optimum operating parameters. This success was perhaps a necessary but not a sufficient condition to guarantee that we will be able to maintain the same degree of regulation at higher current and with the addition of the remaining four ten-cell blocks; however, the model predicts that a retrofit of the remaining ten-cell blocks with the new feeds will lead to the desired energy regulation at full energy and higher currents.

[1] W.E. Nexsen et al., "The ETA-II Induction Linac as a High-Average-Power FEL Driver," Nucl. Instr. and Meth., A296 (1990) 54-61.

[2] R.A. Jong et al., "IMP, A Free Electron Laser Amplifier for Plasma Heating in the Microwave Tokamak Experiment," Nucl. Instr. and Meth.,A285 (1989) 379-386.

[3] T.J. Orzechowski et al., "High-Gain Free Electron Lasers using Induction Linear Accelerators," IEEE J. Quantum Electron. QE-21 (1985) 831-844.

[4] E.T. Scharlemann et al., "Comparison of the Livermore Microwave FEL Results at ELF with 2D Numerical Simulation," Nucl. Instr. and Meth.,A250 (1986) 150-158.

[5] G.J. Caparaso et al., "Beam Dynamics in the Advanced Test Accelerator (ATA)," in *Proc. 5th High Power Particle Beams Conf.*, San Francisco, CA, September, 1983,pp. 427-432.

[6] Y.J. Chen, "Corkscrew Modes in Linear Accelerators," Nucl. Instr. and Meth., A292 (1990) 455-464.

[7] S.L. Allen et al., "Measurements of Reduced Corkscrew Motion on the ETA-II Linear Induction Accelerator," these proceedings.

[8] W.C. Turner, "Control of Energy Sweep and Transverse Beam Motion in Induction Linacs," these proceedings.

[9] S.E. Sampayan et al., "Energy Sweep Compensation of Induction Accelerators,"in *Proc. 1990 Linear Accel. Conf.*, Albuquerque, NM, September, 1990.

ETA-II BEAM BRIGHTNESS MEASUREMENT*

A.C.Paul, S.L.Allen, F.W.Chambers, Y-J.Chen, F.J.Deadrick, W.C.Turner
Lawrence Livermore National Laboratory
P.O.Box 808, L626, Livermore, California, 94550

Abstract - ETA-II resumed operation in the Fall of 1990 with the injector and first two 10 cell accelerating blocks and nominal electron beam parameters of 1500 Amperes, 2.5 MeV, 70 nsec pulse width at 1 Hz PRF. The beam brightness diagnostics consisted of a Cherenkov foil view port and a pepper-pot emittance diagnostic. The Cherenkov foil experiment was used to determine the beam energy at the accelerator exit. The pepper-pot emittance diagnostic was used to determine the whole beam brightness. The brightness as a function of beam radius and time within the beam pulse was also measured. The brightness is defined as the ratio of the beam current within a given radius to the normalized four dimensional volume occupied by particles within that radius.

1. Emittance techniques

At ETA II we have used several techniques to measure the beam emittance and hence the beam brightness; 1) the two hole emittance diagnostic (TSES), [1] 2) solenoidal magnet field versus beam radius scans using Cherenkov foil light, [2] and 3) pepper-pot emittance diagnostic (PPED) using a mask and its down stream image. The TSES measures only the local beam emittance at the location of the first hole and as such does not give a whole beam measurement. For the expected operational parameters of ETA II in this low-energy space-charge dominated regime, the Cherenkov foil scan technique would be marginal for determining the whole beam emittance. For these reasons, we selected the PPED in the experiments reported here. The nominal ETA II operational parameters are expected to give a beam brightness, J, in the range $1\times10^{8} < J < 1\times10^{10}$ A/(m-rad)^2.

2. Pepper-pot emittance measurement

The pepper-pot diagnostic mask consists of a range-thick array of 0.05 cm diameter holes, spaced 0.7 cm, on a square 11 by 11 pattern. The beam incident on the mask is transmitted as a number of beamlets 80 cm down stream to a view phosphor. We measure the beam current incident on the mask, I_{B4}, and the total transmitted current, I_{T3}. The image is digitally recorded with a gated TV camera and a 512 by 480 pixel frame grabber, fig.1[1]. The time gate is adjustable and typically set to 5-10 nsec. The gate can be "walked" through the beam pulse to obtain a measurement along the 40 nsec beam flat top. The emittance of each beamlet is obtained from the expansion of the beamlet observed at the phosphor from the known beamlet size at the mask.

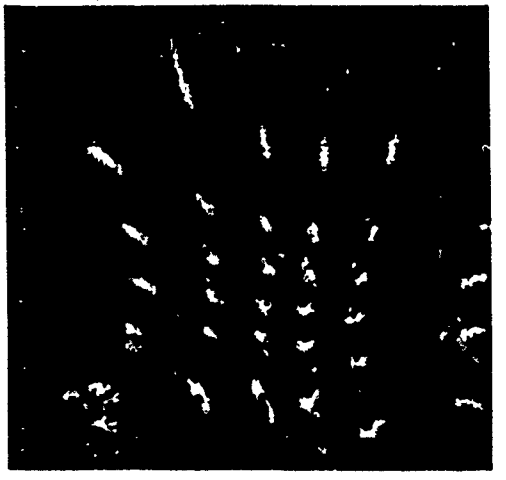


Figure 1. TV pepper-pot image showing 33 beamlets. A current of 1321 Amperes impinged on the mask, 4.72 Amperes passed to the phosphor (R0339F11.RAS).

In this work, we make no assumption about the beam being at a waist at the pepper-pot mask. We do assume the beam size at the mask, R, is large relative to the mask hole radii, r_h, fig.2. Let x_n be the measured half size of beamlet n. The angular divergence (expansion) of a beamlet in a drift of length L is given by

$$x_n' = \frac{x_n - r_h}{L} \quad . \qquad [1]$$

The horizontal hard edge beam emittance is calculated from the beamlet statistical averages as

$$\langle x^2 \rangle \equiv \sum_{n=1}^{n=2N_b} x_n^2 \quad , \quad \langle x'^2 \rangle \equiv \sum_{n=1}^{n=2N_b} x'^2_n \quad , \quad \langle x\,x' \rangle \equiv \sum_{n=1}^{n=2N_b} x_n\,x'_n \qquad [2]$$

N_b being the total number of beamlets passed by the mask. Each beamlet contributes two points two these averages, x_o, x_1' and x_o, x_2', the beamlet extremals, fig.2. The beam

* This work was performed jointly under the auspices of the US Department of Energy by Lawrence Livermore National Laboratory under W-7405-ENG-48 and for the department of Defense under SDIO/SDC MIPR No. W31RPD-8-D5005.
U.S. Government work not protected by U.S. Copyright.

[1] All figures in this paper were done with user friendly IDL graphics. *"IDL, Interactive Data Language"* Research Systems, Inc. 2021 Albion St. Denver, CO 80207

emittance given by the hard edge σ matrix representing the coefficients of the ellipse bounding all points of the beamlets[2],

$$\varepsilon_x^2 \equiv \sigma_{11}\sigma_{22} - \sigma_{12}^2 \qquad [3]$$

$$= \frac{4}{N_b^2}\left[\langle x^2\rangle\langle x'^2\rangle - \langle x\,x'\rangle^2\right] . \qquad [4]$$

Analogously in the vertical plane

$$\varepsilon_y^2 \equiv \sigma_{33}\sigma_{44} - \sigma_{34}^2 \qquad [5]$$

$$= \frac{4}{N_b^2}\left[\langle y^2\rangle\langle y'^2\rangle - \langle y\,y'\rangle^2\right] . \qquad [6]$$

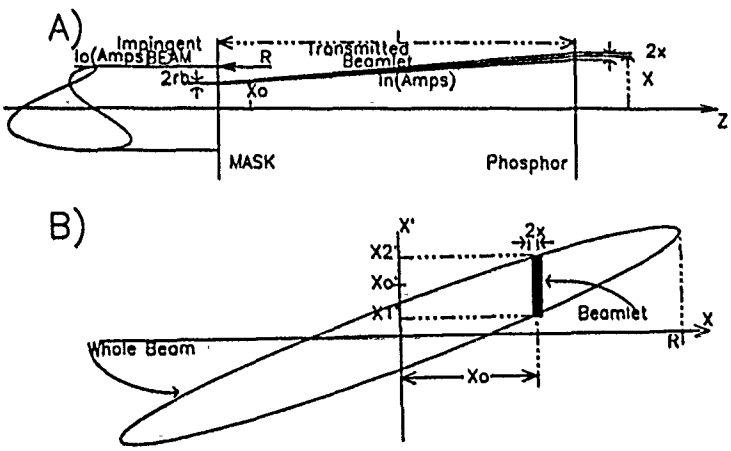


Figure 2. Pepper-pot geometry showing A) one typical beamlet, B) phase space of whole beam and beamlet at location of the mask.

At the mask, the beamlet of width $2r_h$ and angular divergence $2x_n'$ has a phase space centroid location at (X_o, X_o'):

$$X_o' = \frac{X - X_o}{L} , \qquad [7]$$

where X is the absolute location of the beamlet of width $2x_n$ at the image and X_o is the x value of the mask hole center through which this beamlet has passed.

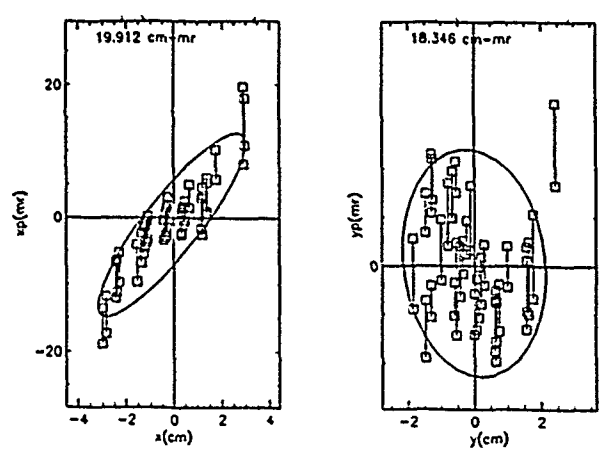


Figure 3. x-x' and y-y' phase space unfolding from expansion of beamlets for R0339F11.RAS, table 2.

[2] Note that each < > term as a factor of 2 from the sums, eq.[2] n=1.. $2N_b$, hence $\varepsilon_{x,y} = 4\,\varepsilon_{rms}$ as usual.

The elliptical contour bounding all of the beamlets may have a larger angular extent than the individual beamlets due to the inclusion of the relative beamlet-to-beamlet divergence, fig.3. This divergence can be caused by aberrations, canonical momentum from magnetic field threading the cathode, or other sources.

3. Brightness

The brightness of the n^{th} individual beamlet is

$$j_n = \frac{i_n}{(\pi\,\beta\gamma\,r_h\,\theta_n)^2} , \qquad [8]$$

θ_n is the angular divergence of the n-th beamlet, $i_n = I_{pass}\sum pixel_n/\sum pixels_{all}$ with I_{pass} taken either as the measured passed current I_{T3} or the calculated geometric current $I_{B4}\,N_b(r_h/R)^2$. The average brightness of all the beamlets is

$$J_{ave} = \frac{1}{N_b}\sum j_n . \qquad [9]$$

The whole beam brightness, J_{xy}, based on the four dimensional elliptical volume, $\pi^2\varepsilon_x\varepsilon_y/2$, is

$$J_{xy} = \frac{2\,I_{B4}}{(\pi\,\beta\gamma)^2\,\varepsilon_x\varepsilon_y} . \qquad [10]$$

If there is no phase space distortion and we correctly measure the beam radius and current impingent on the mask and the current passed by the mask, then the whole beam and average beamlet brightness would be the same. The intrinsic brightness of the beamlets can differ from the whole beam brightness by the degradations introduced by whatever whole beam phase space distortions are present.

4. Beam energy

The value of βγ used in the brightness calculation was obtained from a scan of the observed beam radius versus field of the last six focusing magnets at the end of the accelerator. Consider the beam envelope equation for a section of solenoid transport including both the emittance and space charge terms:

$$r'' + k^2 r = \frac{\varepsilon^2}{r^3} + \frac{2\,I}{I_a(\beta\gamma)^3}\,\frac{1}{r} , \qquad [11]$$

with $k = B/2(B\rho)$, $I_a = 4\pi\varepsilon_o c E_o$, E_o the beam rest energy in Volts. For electrons, I_a is 17000 Amperes. Expanding the radius, $r = r_o + a$, about the matched value r_o gives the small amplitude perturbed motion

$$a'' + 2\left[\frac{\varepsilon^2}{r_o^4} + k^2\right] a = 0 \qquad [12]$$

whose solution is

$$a = a_o \sin\left[\sqrt{2}\left[\frac{\varepsilon^2}{r_o^4} + k^2\right]^{1/2} z\right] . \qquad [13]$$

The minima occur at multiples of π. Let the number of oscillations the beam has undergone at the first minima be n. Then the number of oscillations at the second minima is (n+1)π etc. The positions of the first, second, ... minima of the observed

beam oscillations allow a solution for the value of $\beta\gamma$ by eliminating n from the above equations:

$$\beta\gamma = \frac{\Lambda}{\sqrt{2}\,\pi}\left[\left[\frac{B_2^2}{(E_o/ec)^2} + \frac{4\varepsilon_n^2}{r_o^4}\right]^{1/2} - \left[\frac{B_1^2}{(E_o/ec)^2} + \frac{4\varepsilon_n^2}{r_o^4}\right]^{1/2}\right] \quad [14]$$

B_1, B_2 being the field value at the first and second minima, Λ the length of the solenoid section, and ε_n the normalized emittance. $\beta\gamma$ is the average value inside the section of accelerator that is scanned. The final beam energy at the end of the machine will be higher by the additional acceleration produced by the last three accelerating gaps. The final beam energy compares favorably with the value deduced from reference [3].

Table 1.

Minima	Solenoid Amperes	Field kG	$\beta\gamma$ -3 gaps	E(final) MeV
B_1	73	0.489		
B_2	126	0.845	5.394	2.547
B_3	172	1.153	5.541	2.621

5. Summary of ETA-II pepper-pot beam brightness

A summary of ETA-II beam brightness for pepper-pot hole patterns of 4X4 to 11X11 with both crossover and no crossover between the mask and the view phosphor is given in table 2, below. For the beam of figures 1 and 3 the brightness is shown in fig.4.

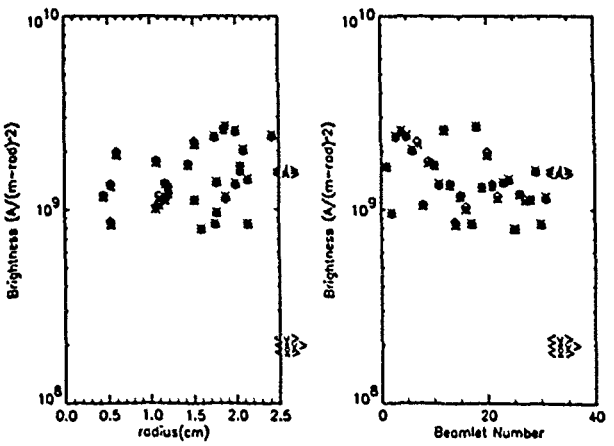


Figure 4. Brightness of beamlets of figure 1 at the location of the mask. <A> is the average of the beamlets, <xy> is the whole beam value.

Much of the scatter in brightness between the individual beamlets has resulted from the difference in the x and y emittance resulting from the elliptical shape of the image. This elliptical shape has resulted from scattering of the beamlet on passage through the mask. The brightness has been measured for 10 nsec time slots spaced every 5 nsec through the beam pulse flat top. The brightness is not a strong function of the time after correction has been made for the variation of beam energy and loading.

Table 2.

Image	I_{B4} Amps	I_{T3} Amps	N_b	J_{ave} A/(m-rad)^2	J_{xy} A/(m-rad)^2
309f07	1453	2.24	15	2.07×10^9	3.44×10^8
310f0e	1181	1.70	16	1.65×10^9	([4])
324f01	1400	25	90	1.88×10^9	2.66×10^8
333f0b	1000	3.00	110	7.69×10^8	4.16×10^8
339f1i	846	2.93	39	2.24×10^9	1.96×10^8
339f11	1321	4.72	33	1.82×10^9	2.22×10^8
341f02	1000	3.79	23	2.82×10^9	2.74×10^8
341f07	1392	4.50	33	1.68×10^9	3.60×10^8

6. Conclusions

The intrinsic beamlet brightness ($1–4\times10^9$) is about an order of magnitude higher than the observed whole beam brightness ($1–3\times10^8$). The brightness of the cathode has been previously studied [6] and is 1×10^{10}. The source of the degradation of the beam brightness is under investigation [4]. For the upcoming FEL experiments the present whole beam brightness is satisfactory. Correction for space charge and the ellipticity of the beamlet images introduced by scattering in passing through the mask will increase the beam brightness. Space charge corrections increase the brightness by about 20%. The correction for beamlet ellipticity reduces the beamlet to beamlet scatter evident in fig.4 and increases the intrinsic beamlet brightness by something less than a factor of two. These corrections to the analysis are currently being implemented.

References

[1] W. E. Nexsen et.al., "The ETA-II Induction Linac as a High-Average-Power FEL Drive," *Nuclear Instruments and Methods*, NIM-A296(1990)54-61

[2] A. C. Paul et.al., "Probing the Electron Distribution Inside the ATA Beam Pulse," *Nuclear Instruments and Methods*, NIM-A300(1991)137-150

[3] W. E. Nexsen et.al.,"Reduction of Energy Sweep of the ETA-II Beam," *Paper this conference*

[4] Y-J. Chen et.al.,"Degradation of Brightness by Resonant Particle Effects," *Paper this conference*

[5] W.C. Turner, et.al.,"High-Brightness, High-Current Density Cathode for Induction Linac FELs," 1988 Linear Accelerator Conference, Williamsburg, Virginia, Oct 2-7, 1988.

[6] W.C. Turner, et.al.,"Status of the ETA-II Linear Induction Accelerator - High Brightness Results," 1989 Particle Accelerator Conference, Chicago, Illinois, March 20-23, 1989.

[4] The whole beam value of 1.04×10^9 was for a measured I_{T3} current of 1.70 Amperes. The expected transmitted current was 5.4 Amperes.

DEVELOPMENT OF RFQ ACCELERATOR FOR THE MMF LINAC

V.A.Andreev, S.K.Esin*, I.M.Kapchinskij
D.A.Kashinskij, A.M.Kozodaev, A.A.Kolomiets,
P.N.Ostroumov*, A.M.Raskopin,
N.V.Schachrai, R.M.Vengrov
Institute for Theoretical and Experimental Physics,
Moscow, 117250, USSR
*Institute for Nuclear Research of the Academy of Sciences
of the USSR, Moscow, 117312, USSR

Abstract

The 750 keV RFQ accelerator section is under development in order to install it upstream the first drift tube cavity of the MMF Linac instead of 2-gap buncher. The using of RFQ allows to decrease accelerating tube voltage to 400 kV and to increase pulse duration two times without pulsed transformer saturation. Main features of RFQ section are discussed: sufficiently high capture efficiency (up to 67%); reasonable length of 1.3 m; beam bunching without longitudinal halo.

Introduction

The upgrade program of the Moscow Meson Factory linac [1] includes the increase of average beam current up to 1 mA by lengthening of the pulse duration up to 200 μs. This is possible if a voltage of pulsed transformer will be decreased to the 400 kV. The transportation and funneling of H^+ and H^- allows to use a whole set of channel equipment, including H^- beam chopper. If the scheme with two RFQ resonators for each type of ions in the energy range of 50 keV to 750 keV would be used there will be a complicate problem to transport and to funnel high intensity bunched beams. Therefore the RFQ booster accelerator on the frequency of 198.2 MHz is proposed to accelerate simultaneously 400 keV H^+ and H^- ions with the total peak current of 100 mA up to Alvarez tank injection energy of 750 keV.

Choice of RFQ Parameters

For the proper value of normalized acceptance of the focusing channel V_k = 1.2 π·cm·mrad, the aperture radius and the voltage between adjacent pole tips are equal to a = 16 mm and U_2 = 150 kV accordingly. A calculated value of the transverse oscillation phase advance μ_0 is 0.6 for zero current. Taking into account space charge parameter h [2] phase advance μ could be estimated as:

$$\mu = \mu_0(\sqrt{1 + h^2} - h)$$

For example, for the normalized beam emittance ε = 0.4 π·cm·mrad the ratio μ/μ_0 is sufficiently high: μ/μ_0 = 0.835.

The semi circumference pole tips with the constant radius of R_e = 8 mm is foreseen along the whole length of electrodes. A maximum value of rf field on the electrode surface is expected 265 kV/cm which corresponds to 1.8 of Kilpatrick limit and does not exceed the value normally used in accelerator practice.

Transverse matching of the axially symmetric beam being injected in RFQ is provided with using matching section of 177 mm long. The square of focusing rigidity k^2 is changed by the law:

$$k^2 \sim \sin^2(\frac{\pi \cdot z}{8 \cdot \beta\lambda})$$

For the phase density of j = 150 mA/(π·cm·mrad) the matched injected beam envelope is:

$$\sigma_x = \sigma_y = 2.774;\ \sigma'_x = \sigma'_y = -.75$$

More than 90% of the particles are contained inside an area of the phase space ellipse which overlaps with instantaneous Floke envelope. In order to match the output bunched beam consisting of approximately 60° bunches with the static quadruple channel of the Alvarez tank the output matching cell with the length of 0.33βλ is proposed. The electrode shape in this cell provides the proper changing of focusing rigidity which results to essential dropping of a time-dependence of the phase space ellipses.

Unusually high injection energy, small energy gain as well as limited RFQ size cause certain difficulties in the choice of the accelerating channel parameters. With consideration of mentioned features the accelerating channel consist of

1. A section of particle velocity modulation consisting of 4 half periods of longitudinal modulation of electrodes. The synchronous phase is equal -90°;
2. Drift section with the length of 2βλ;
3. A section of momentum spread depression with the length of 1.5 βλ. Synchronous phase is +90°. Apart the momentum spread decreasing this section allows to shorten the drift space as well as to transform the particle distribution in longitudinal phase space in such a way that in further acceleration the maximum momentum separation would be achieved for particles being inside and outside of separatrix.
4. The section of acceleration has 14βλ cells. The synchronous phase is changing from -45° to -28° along this section and the

0-7803-0135-8/91$01.00 ©IEEE

momentum width of the eparatrix of ±4% is keeping practically constant.

The RFQ parameters are presented in the table.

Table

Parameters of the RFQ resonator and beam

Parameter	Symbol	In-put	Out-put
Energy	W_s (keV)	400	750
Relative velocity	β	0.029	0.040
Average distance from electrode to the axis	R(mm)	41	8
Radius of aperture	a(mm)	41	6.85
Electrode length	l_e (mm)	1199	
Tank diameter	D(mm)	325	
Radius modulation parameter	m	1.00	1.34
Transit time factor	T	0.0	0.189
Defocusing factor	γ_s	0.00	0.061
Transverse phase advance per period in the accelerating section	μ_0	0.609	0.593
Phase width of bunches	Φ(deg)	360	60
Maximum momentum spread	$\pm\Delta p/p$(%)	0.1	3.5

A computer simulation using the code [3] has been done for injection currents in the range of 0÷100 mA. In fig. 1 the beam phase portraits along the RFQ accelerator for peak injection current of 100 mA are presented. Initial specifications result to the unusual acceleration efficiency which is equal to 67% and 60% for injection currents of 0 and 100 mA accordingly. The normalized output rms emittance on the level of 90% is 0.45 π·cm·mrad for injection current of 100 mA and emittance of 0.38 π·cm·mrad at the input of RFQ.

The rf Aspects

On the full-scale model (Fig. 2) the radio technical parameters of the RFQ have been corrected as well as the field tuning procedure has been carried out. A bead pull technique has been used. A bead has been pulled in the gap between adjacent electrodes where the electric field is more uniform than in the aperture. Therefore the errors connected with an uncertainty of the bead position are decreased.

An influence of the coupling loops installed on the resonator end plates, ring-loops electrically connecting opposite electrodes, copper plates placed perpendicular to the direction of magnetic flux as well as tuning plungers movable into the resonator volume have been studied.

It was found that design value of the rf frequency, accelerating field uniformity and satisfactory dispersion curve can be obtained if the pair of the coupling loops (on the input and output end plates) as well as tuning plungers are used.

In accordance with calculation the dissipated rf power, quality factor and shunt impedance are equal to P_m = 150 kW, Q = 6900, R_{sh} = 75 kOm accordingly. Supposing that the actual rf losses can exceed calculated value and taking into account beam loading the total rf power is estimated equal to 260 kW. Average dissipated rf power does not exceed 7 kW for 3% of duty factor.

Four driving loops are foreseen, one in each quadrant. The driving loops will be inserted in a vacuum trough the insulator disk ndow.

The resonator is made from three-layer metal (oxygen-free copper, steel, stainless steel), the electrodes are made from oxygen-free copper. The cooling channels and longitudinal holes near the aperture for alignment are foreseen in the electrodes.

References

1. Linear ion accelerators. Ed. by B.P.Murin, v.1,2, Moscow, 1978 (In russian).
2. I.M.Kapchinskij. Theory of linear resonance accelerators, Moscow, 1982 (In russian).
3. I.A.Vorobjev et al. Computer simulation of the beam dynamics in RFQ. Preprint ITEPh No 52, Moscow, 1986.

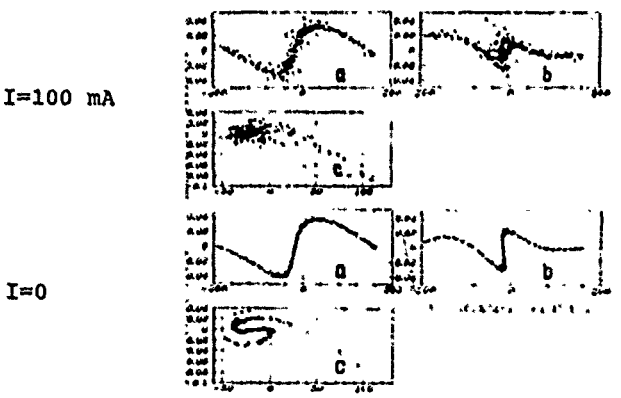


Fig. 1. Beam phase portraits at the exit of drift section (a), momentum spread depression section (b) and accelerating section (c) for peak currents of 0 and 100 mA.

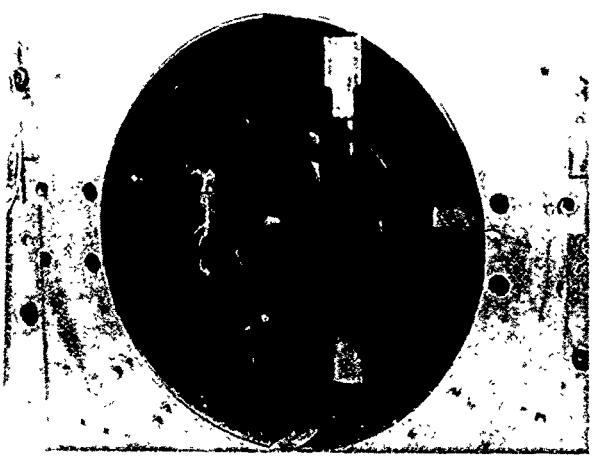


Fig. 2. Entrance view of the full-scale resonator model.

HIGH POWER MICROWAVE GENERATION IN VIRTUAL CATHODE SYSTEMS

A.N.Didenko ,V.I.Rashchikov

Moscow Physical Engineering Institute
Moscow ,115409 ,USSR

Pulsed high-power microwave generation by means of high current accelerator system has recently become an intensive area of research , the most promising among them being virtual cathode devices or vircators [1].

There are two mechanisms which lead to production of high-power microwaves in vircators [2]. The first deals with electrons , oscillating near the anode and the second with virtual cathode (VC) oscillating as a whole. Generally both mechanisms are presented, but in a given device one may dominate the other. If the anode is thick enough to absorb reflected electrons thus preventing them from reentering the diode region, the first mechanism vanished. In this paper we discuss the second mechanism, which is realized, for example, in reditron [3-4]. Anode plasma produced by high-current electron beam passing through the anode is taken into account.

The simulations were done with 2.5-dimensional fully electromagnetic and relativistic particle-in-cell code. The hollow electron beam with constant density is continuously injected into the cavity through the hole in its left side (anode of reditron). An external axial static magnetic field is imposed in all of our computer simulations. If the beam current is smaller than space-charge limiting current the VC (nought of axial electric field - E and particle density maximum - ρ) is located in the center of the cavity and no reflection of electrons occurs. When the beam current is larger than space-charge limiting current, the location of VC changes: VC moves toward anode and this distance depending upon the geometry of the cavity, external magnetic field magnitude and beam parameters. In addition to that reflected electron current appears in the cavity, its value being less than output beam current.

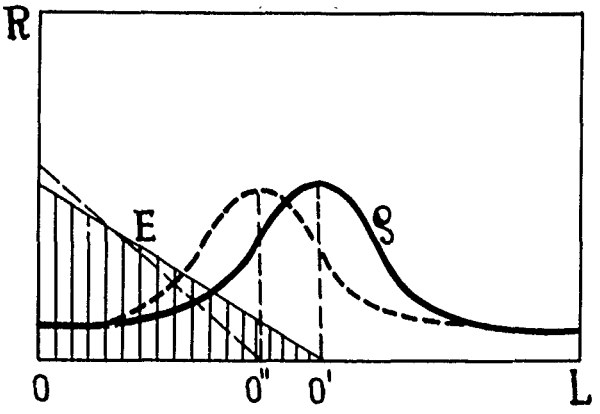


Fig.1

The mechanism of such movement can be explained by the fact, that current rise leads to increasing of potential barrier (dashed area in Fig.1), produced by cavity space charge distribution. When the kinetic energy of the particle is less than potential barrier $W < \int_0^{0'} E\,dl$, the particle is reflected from the VC and moves toward the anode. It means that VC as a whole moves toward the anode until the value of potential barrier becomes less than kinetic energy of injected particle $W > \int_0^{0''} E\,dl$. From this moment VC turns around and moves in opposite direction, oscillating around new equilibrium point. The amplitude of oscillation rise with current.

The picture varies when the beam current becomes essentially higher than space-charge limiting current. Computer simulation shows (Fig.2) that in this case VC also moves toward the anode, but the number of particles passing through the potential barrier becomes less than that of reflected ones. It leads to VC density rise up to the moment when VC practically reaches

0-7803-0135-8/91$01.00 ©IEEE

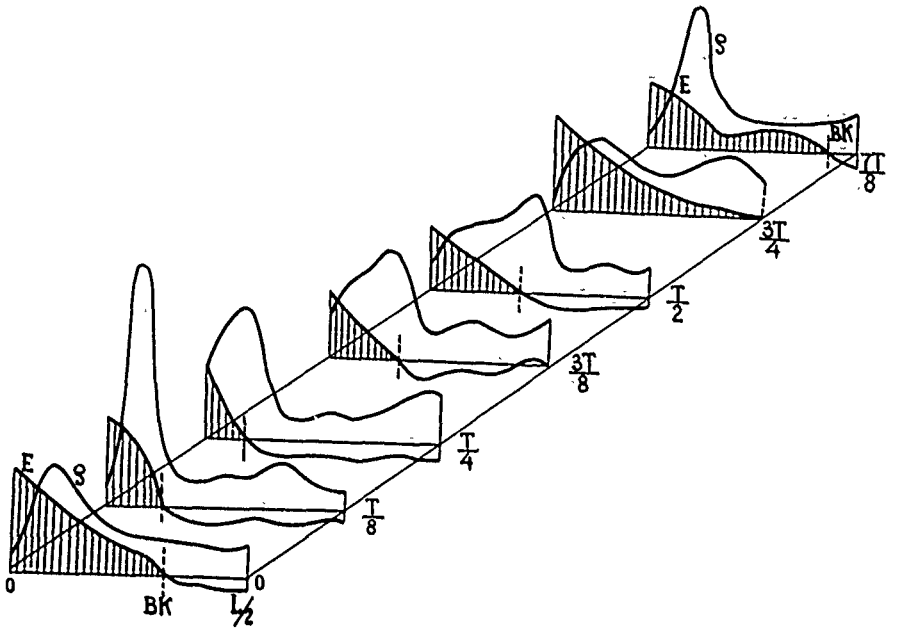


Fig.2

the anode, electrons strike it and get absorbed. The VC particle density and value of potential barrier fall down sharply and injected particles pass through it easily thus resulting in VC (particle density maximum and nought of axial electric field) moving toward the center of the cavity until the potential barrier will rise enough to stop the particles. After that the process is repeated, producing VC oscillations and strong modulation of transmitted electron current (Fig.3). This mechanism can be used for strong modulation of high-current electron beams.

Simulation shows that radiation frequency generated by electron beam is in good relation with transmitted beam frequency modulation.

In one-dimensional model VC oscillation frequency is given by [5] :

$$F = 10.2\sqrt{J/\beta\gamma} \cong 2.5\, f_p , \qquad (1)$$

where f-frequency in GHz , J-current density in kA/cm^2, f_p-plasma frequency. Computer simulation gives the value of frequency less then that in (1) , which can be explained by the fact that in reality transverse movement isn't frozen; this makes VC particle density value less than that of one dimensional model.

When high current electron beam passes through the anode , plasma is formed in anode region. Anode plasma density can be greatly changed during the beam pulse depending on beam and system parameters . We have studied the influence of anode plasma density on VC formation mechanism. When plasma density approximately equals injected beam density vircator's main characteristics (value of frequency and power generated) are practically unchanged. If plasma density is in order of magnitude higher than beam current , VC oscillation amplitude and microwave radiation frequency decrease. Since anode plasma density changes during the beam pulse, it can lead to differential changes of microwave radiation frequency and power.

Let us evaluate beam generated power in vircator. According to [6] microwave radiation power of oscillating electron is given by

$$P = \frac{1}{12}\,\frac{e^2 c}{a^2}\left[\frac{E}{m c^2}\right]^3 f(y) , \qquad (2)$$

where $f(y)$-normalized spectral function, a-amplitude of oscillation, E-total energy. In relativistic case power, generated by the electrons, oscillating around the anode or VC oscillating as a whole can be calculated from

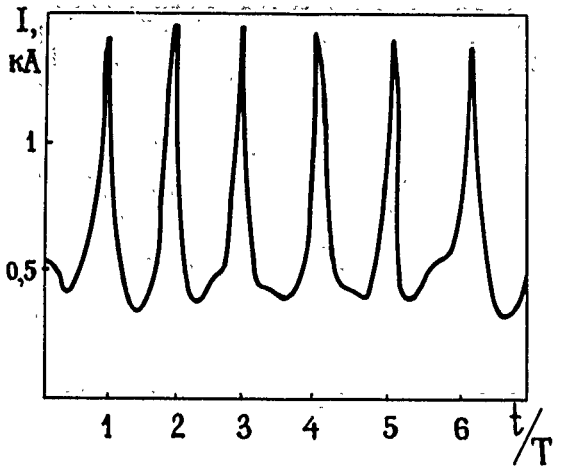


Fig.3

$$P = \frac{1}{12}\frac{e^2 c}{\alpha^2}\left[\frac{E}{m c^2}\right]^3 N^2 f(N) , \qquad (3)$$

where N-number of oscillating electrons, $f(N)$ - coherent parameter. Defining current as $I=\frac{eNc}{\alpha}$ for cavity with finite Q-factor we obtain:

$$P \cong 2.10^{-3}\gamma^3 Q\, I^2 f(N), \qquad (4)$$

where P-power generated in GW, γ-relativistic factor, I-current in kA. For typical vircator with parameters I = 10kA and γ = 2 we have in case $f(N)$=1

$$P \cong 1.6\, Q \text{ ,GW} . \qquad (5)$$

Thus we obtain output power of GW level the electron beam current being I = 10kA and Q = 1 and $P\sim$10GW if I = 100kA or Q = 10.

Radiation spectral analysis from eq.(2) showed, that besides the main harmonic, whose frequency equals electron oscillating frequency near the anode or $f\sim f_p$, higher number harmonics do appear in spectrum. Their radiation power decreasing with their number increase, the radiation is concentrated in two cones with small angular spread.

Experiments of Phys. Int.Comp. have confirmed such character of angular distribution of the relativistic vircator radiation [7]

Hence we can make the conclusion that vircator is a source of powerful microwave oscillation not only of cm but also mm and sub-mm ranges.

REFERENCES

[1]. A.N.Didenko, Ya.E.Krasik, S.F.Perelygin, G.P. Fomenko ," High - power microwave radiation of relativistic electron beam in triods," Pis'ma Zh. Tekn. Fiz,vol.5, pp.321-324,June 1976.

[2] S.C. Burkhart, R.D. Scarpetti, R.L. Lundberg," A virtual cathode reflex triode for high - power microwave generation ," J.Appl.Phys.,vol.58,pp.28-36,January 1985.

[3]. T.J.T. Kwan, H.A.Davis, R.D.Fulton, E.G. Sherwood," Effects of modulated electron beams and cavities on reditrons, " in Proceeding of the 7 International Conference on High-Power Particle Beams, Karlsruhe, Germany, July 1988,pp.447-452

[4]. A.N. Didenko,V.I. Rashchikov,"High-power microwave generation mechanism in virtual cathode systems," DAN USSR , vol.313, N3, pp.597-599, 1990.

[5]. D.J. Sullivan,J.E. Walsh, E.A. Coutsias, High- Power Microwave Sources. Edited by Granatstein and Alexeff.Massachusetts, Artech House,1987,p.484.

[6]. A.N. Didenko " Spectral and angular characteristics of relativistic oscillator radiation," DAN USSR, vol.312, N1, pp.89-92, 1990.

[7]. H. Sze, J. Benford, T.Young, D. Bromley, B. Harteneck, " A radialy and axially extracted virtual cathode oscillator," IEEE Trans.on Plasma Science, vol.PS-13, pp.492-497, 1985.

*Experimental Tests of the Power Supply and Prorotype Cell for the 1.5 MeV SLIA Acceleration Unit**

P. Corcoran, B. Bowen, V. Bailey, V. Carboni, J. Fockler, B. Chugg, and H. Nishimoto

Pulse Sciences, Inc.
San Leandro, CA 94577

ABSTRACT

The prototypes for the nominally 300 kV pulsed power supply and acceleration cell were built and tested in order to determine critical design parameters needed for their final designs. The pulsed power supply produced a 73 ns long trapezoidal pulse rising in 3 ns (10-90%) and having high frequency ripple of less than 2%. The power supply's throughput jitter measured 1.5 ns (1σ). The cell was driven by the power supply and had a resistor taking the place of the beam loading. The ferrite core material was CN-20 manufactured by Ceramic Magnetics, Inc. The cell tests showed the ferrites had a useful flux swing of 0.45 T (20.7 mV-sec) before the magnetization current pulled the cell voltage down by more than a few percent. The ferrite impedance (due to both displacement and magnetization currents) stayed in the 200 to 300-ohm range for the first 2/3 of the pulse and then dropped steadily to 60-ohms at the end of the useful pulse. The load voltage had a 5 ns risetime (with the 3 ns driver risetime) due to 550 pF cell capacitance. The prototype test results were similar to original estimates.

INTRODUCTION AND TEST OBJECTIVES

The pulsed power supply and cell were proto- types for one out of five which will comprise each 1.5 MeV SLIA acceleration unit[1]. The objective of these tests was to measure critical design parameters on a prototype system which will, in turn, provide an experimental basis for the final system design. For the power supply, the critical parameters were (1) risetime, (2) pulse length, (3) high frequency ripple (amplitude and frequency), (4) throughput jitter, and (5) high voltage integrity. For the cell, the critical parameters were (1) risetime (due to cell capacitance), (2) ferrite flux swing, (3) ferrite impedance versus time, and (4) high voltage integrity. Although some of these parameters (such as the power supply risetime, pulse length and high voltage integrity) could be accurately estimated using standard pulsed power scaling laws, other parameters (such as the ferrite flux swing and impedance variation) cannot be accurately known except by testing. The ferrite rings presented the greatest unknown since their behavior can depend on details of their fabrication (such as composition, processing and glue joints) and geometry when loaded in the cell as well as the shape and amplitude of the applied voltage pulse. The prototype power supply and cell were both needed to form a test stand for the ferrite rings. The interpretation and application of the test results for the final system design is outside the scope of this paper and will be presented at a later date.

PULSED POWER SUPPLY

The prototype power supply circuit is shown in Figure 1. The Marx was configured to have 62.5 nF and 7.5 μH so the charge time of the single PFL would roughly equal that of a 125 nF, 1.2 μH Marx charging five PFLs. The PFL output switch bias and trigger circuit was configured to mock the effect of the missing switches with its unused cables

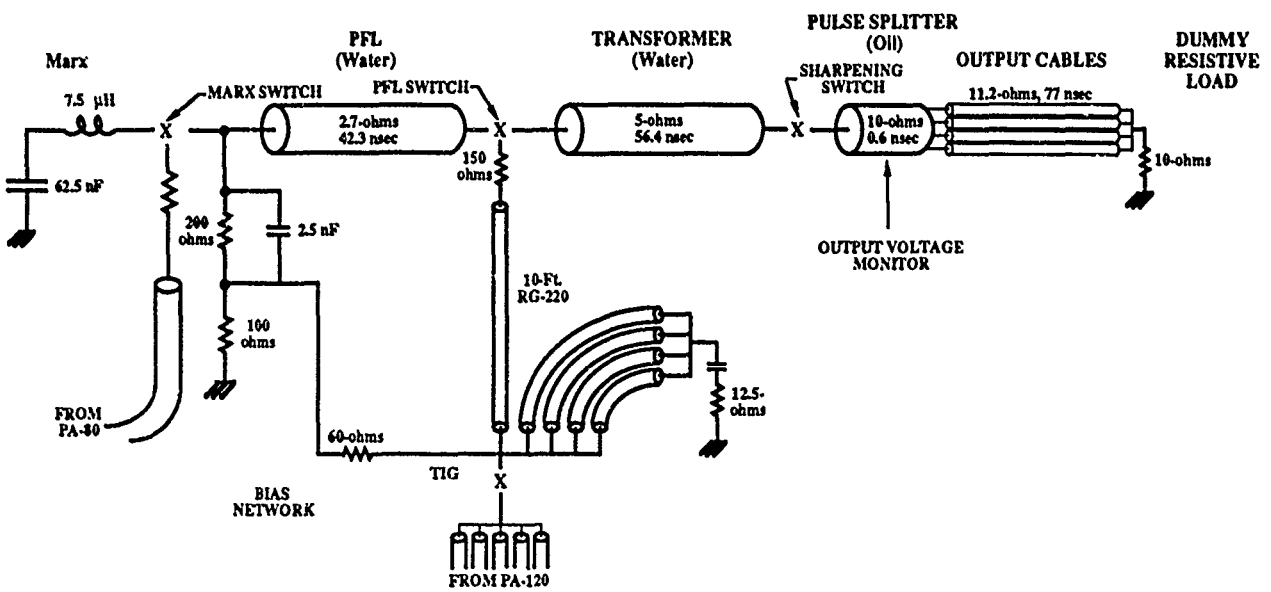


Figure 1. Prototype power supply circuit.

*Work sponsored by DARPA under Order No. 4395, Amendment 90 and by the Navy under Document N000039991 WXDZ002; monitored by the Naval Surface Warfare Center.

0-7803-0135-8/91$01.00 ©IEEE

terminated by an appropriate capacitor and resistor. The prototype PFL was built with a constant impedance along its length. The PFLs for the 1.5 MeV unit will likely have a shaped impedance profile to shape the output pulse and keep the cell voltage constant despite the variation in ferrite magnetization current. (The needed impedance profile can be calculated from the prototype cell measurements, below.)

The output pulse, measured at the entrance to the cables, is shown in Figure 2. When calibrated and corrected for monitor droop, this particular pulse had a 4.5 nsec 10-90% risetime, 306 kV mid-pulse amplitude, and 7% ramp due to PFL switch before peak charge voltage. The ± 2% ripple seen on the pulse top is comparable to the noise in the baseline which suggests that the actual ripple is somewhat less. The spike seen on the fall of the pulse is a reflection from the transition to the dummy load and not part of the forward going pulse.

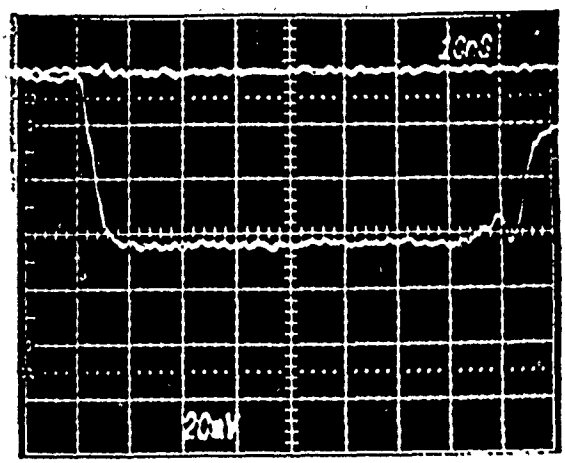


Figure 2. Power supply output voltage, shot 231 (raw).

The power supply test results were similar to the nominal design goals. The output voltage was variable between 170 and 300 kV with a minimum risetime of 3.0 ns (which is controlled by the sharpening switch pressure). The high frequency ripple was less than the ± 2% ripple also seen in the baseline (Figure 2). The pulse length was 73 ns from the beginning of the pulse (leaving the baseline) to the end of the pulse top and the throughput jitter measured 1.5 ns (1σ).

PROTOTYPE CELL

The prototype cell was driven at four (equally spaced) azimuthal locations by the prototype power supply's output cables (11.2-ohm net drive impedance). The cell was assembled in its dummy load configuration, Figure 3, which has one large diameter shielded gap on-axis and a liquid resistor (which was tested at 15 and 25-ohms) to simulate the beam loading. No extra (so-called "compensation") resistors were used in parallel to the load. (The eventual beam loading will be 30-ohms = 300 kV/10 kA.) The cell was tested at voltages ranges from 150 to 340 kV.

The large (1 meter) diameter ferrite core was made of 1.1-inch-thick rings stacked axially, as shown. The large core diameter was selected to accommodate up to seven beamlines as required in future accelerator concepts. The core was pumped down to vacuum with the rest of the cell since relatively small diameter acrylic bushings were incorporated into the drive cable feedthroughs (instead of placing the bushing in the radial waveguide). Each ring was itself made of 12 sections of CN-20 ferrite (manufactured by Ceramic Mangetics, Inc.) joined with epoxy. The 4-7 mil (each) thick joints made the core stack's flux swing dependent on how the rings were loaded in the cell. For example, a 15% larger flux swing was measured with the glue joints staggered and no axial space between the rings than with the glue joints aligned and the rings spaced 1/2-inches apart.

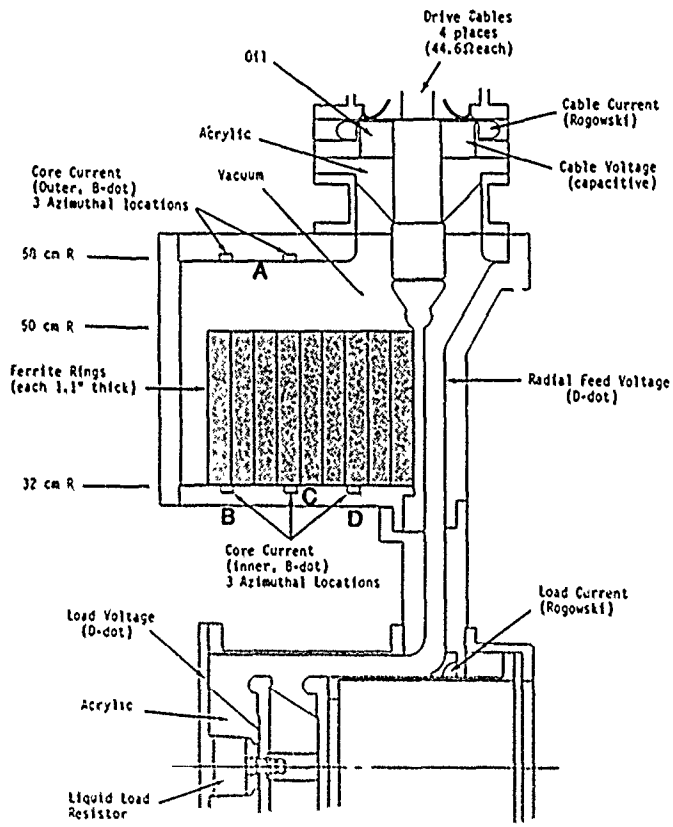


Figure 3. Prototype cell cross-section/diagnostic locations.

With the full 9-core (10.06-inch axial) stack of ferrite, the core flux swing measured 20.7 mV-sec (or 0.45 T) at the end of the useful (top) part of the pulse, shown by cable voltage B in Figure 4. The design goal was 21 mV-sec (= 300 kV x 70 ns). The full flux swing measured 23.3 mV-sec (or 0.51 T) at the zero voltage crossing point. (The cell voltage was raised above the nominal 300 kV for voltage B in order to fully saturate the core before the drive voltage reversed.) With approximately half the ferrite removed (5 cores or 5.54-inch axial remaining), the flux swing was decreased to 54% that of the full load, voltage A in Figure 4. The flux swing was thus shown to be proportional to the cross-sectional area of the ferrite despite the lower voltage of the 5-core tests. In most cases, the cores were reset through the drive cables with a 1 kA peak, 700 μs FWHM pulse which corresponded to 6.2 Oe on the inner and 4.0 Oe on the outer diameters of the ferrite

rings. A scan of reset levels showed that currents as low as 250 A peak were equally effective.

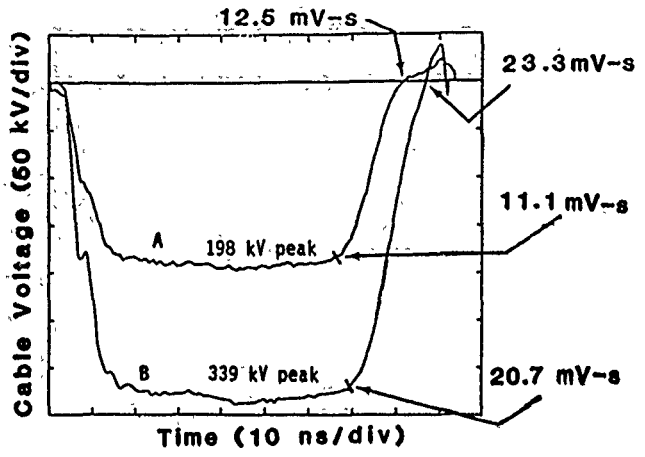


Figure 4. Core flux swing measurements (A = 5 cores, B = 9 cores).

The overall electrical behavior of the cell is shown by comparing measurements of the cable current flowing into the cell to the current flowing through the load, Figure 5. The cell voltage (not shown) was approximately 300 kV and the load resistor was 25-ohms for this particular shot. The

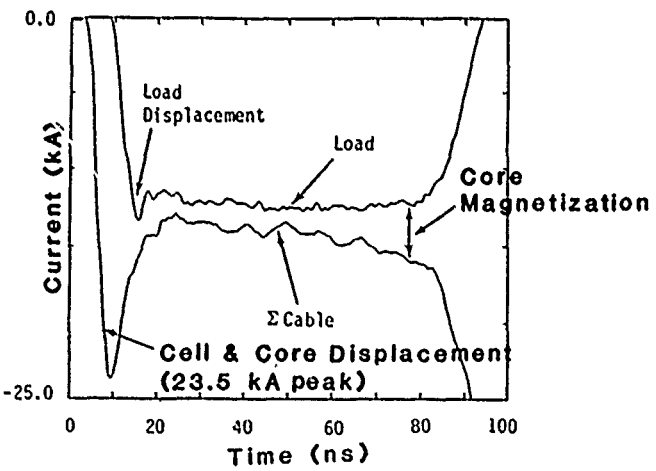


Figure 5. Cable and load current measurements.

load current monitor shows a small spike on its rise as the capcitance downstream charges; otherwise, the load current and voltage were proportional. The load voltage had a 5 ns (10-90%) risetime in response to the 3 ns drive voltage risetime. The higher amplitude, average of the four cable currents shows a 23.5 kA peak at the beginning of the pulse which occurs before the load current begins. The difference between the cable and the load current at the beginning of the pulse corresponds to the displacement current needed to charge the vacuum and ferrite filled regions of the cell between the monitor locations. A capacitance of 550 pF was calculated for the cell from the integral of the displacement current which agreed well with a capacitance value calculated from the geometry assuming a relative permitivity of 12 for the ferrite. The difference between the cable and load current during the rest of the pulse is (primarily) the core magnetization current. Unfortunately, the relatively low amplitude oscillations (a combination of noise and monitor ringing) in the current measurements make calculating the magnetization current imprecise. A better measurement of the core current was made using B-dot probes placed at various positions in the core cavity, Figure 6. The resulting current measurements show an initial displacement current on the upstream monitors which is superimposed on a bilinear magnetization current profile during the useful part of the pulse. The magnetization current has a V/I-dot = 7.3 μH and $L/L_0 = 320 (= \mu_r)$ from 0 to 55 ns and a V/I-dot = 2.2 μH and $L/L_0 = 97$ from 55 to 80 ns. (The dashed line is the average core current as measured on other shots). The impedance of the cores (including the initial displacement current) goes from 200 to 300 to 200-ohms from 0 to 55 ns, and then ramps from 200 to 60-ohms from 55 to 80 ns. The useful pulse ends at approximately 80 ns (Figure 5) when the drive pulse starts to fall and the core current rises sharply.

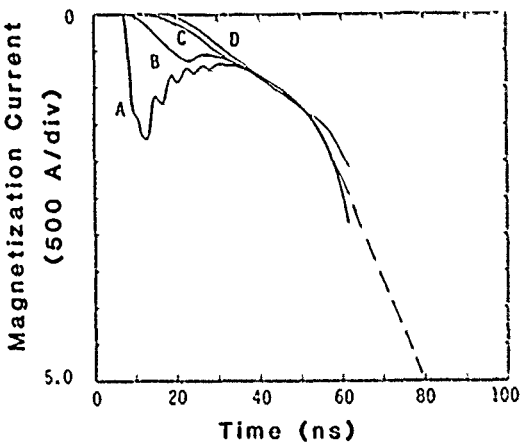


Figure 6. Core region current measurements (refer to Figure 3).

REFERENCE

[1] V. Bailey, et al., *Spiral Line Recirculating Induction Accelerator (SLIA)*, SPIE, Vol. 1061, Microwave and Particle Beam Sources and Directed Energy Concepts (1989).

Beam Breakup Considerations in the Design of Multiple Off-Axis Gaps in an Induction Accelerator Cell for *SLIA*

John Edighoffer
Pulse Sciences Inc.
600 McCormick Street
San Leandro, California 94577

Measurements of the transverse impedances of the SLIA prototype cell were performed using the bead pull technique. These measurements were compared to a computer model (BBUS) of the prototype cell. With appropriate damping, the results look very encouraging for the SLIA accelerator.

INTRODUCTION

The *SLIA POCE* experiment involves a spiral line accelerator, requiring that the accelerator cells have multiple off-axis gaps. This generates a host of potential problems with beam breakup which have several unique properties. These are off-axis excitation and gap to gap coupling. To mitigate these properties, a coaxial shielded gap was developed (see figure 1), which uncouples the gaps and symmeterizes the fields within each gap. This is because the coaxial structure cuts off nonsymmetrical fields below its TE_{11} cutoff frequency. The idea is to have the most important dipole modes and in particular the accelerating and beam loading waveforms below this symmetrical-forcing cutoff frequency. To the degree that this is true, the beam appears to be in an on-axis accelerating gap. There are typically two to five dipole modes between the coax and beam pipe cutoff frequencies. These modes must be damped to reduce the beam breakup growth rate to an acceptable level, depending on the number of gaps and the beam current being accelerated.

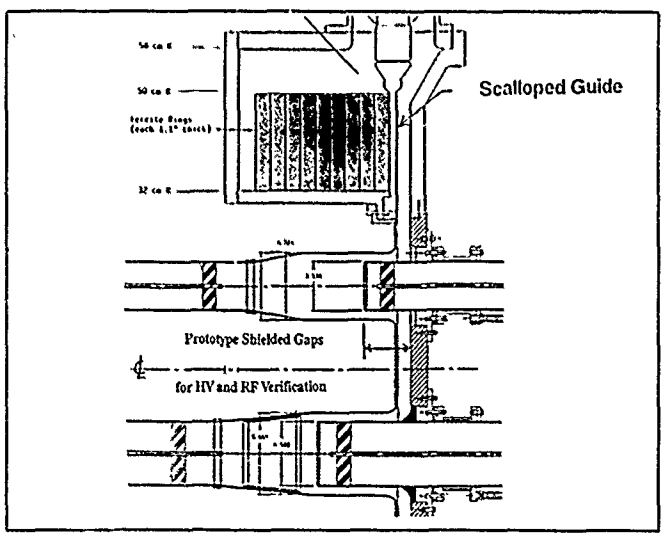


Figure 1----Prototype Cell Geometry

The beam breakup growth rate is given by

$$A_f = A_0\, e^{\Gamma} / \mathrm{Sqrt}(16\,\pi\,\Gamma)\ [1]\ , \text{ where}$$
$$\Gamma = N_{gap}\, R(\mathrm{Ohm/cm})\, I(\mathrm{kA}) / (300\, B_z(\mathrm{kG})),$$

N_{gap} is the number of acceleration gaps, I is the electron beam current, B_z is the solenoidal focusing field, t_p is the electron beam pulse width and f is the mode frequency. A_f and A_0 are the final and initial beam centroid amplitudes at the mode frequency.

The method used to determine the R and R/Q's for the *SLIA* prototype acceleration cell was a bead pull measurement, measuring the frequency shifts due to a dielectric "bead". The frequency is down shifted by an amount proportional to the square of the electric field at the bead position. By moving the "bead" across the accelerating gap, the magnitude of the electric field versus position within the gap can be determined. Thus, R/Q can then be derived.

The transit time factor is needed to correlate to the electric fields "seen" by the beam passing the gap at the speed of light to the static probe measurements. The transit time factor was arrived at by integrating the fields generated by a computer simulation(*BBUS*)[2] across the accelerating gap. Also, the "bead" measures total electric field magnitude and not its direction.

In order to address the computer model sensitivity to how the radial waveguide portion of the cell is terminated, four different choices for the model termination were used. This is because the computer model ends at the top of the radial waveguide and approximates the ferrite core absorption of RF by a factor times the free space wave impedance, with complete absorption at Zs = 1 to complete reflection at Zs = 0 or infinity. On the whole, the changes in the model termination have only a few percent effect on the R/Q determinations from the bead pull data. The data analysis uses the average value of these

Work sponsored by DARPA under Order No. 4395, Amendment 90 and by the Navy under document N00039991WXDZ002; monitored by the Naval Surface Warfare Center.

0-7803-0135-8/91$01.00 ©IEEE

four computer calculations to derive the transverse impedance from the measured frequency shifts.

The goal of this effort is to find a design with R values less than 30 ohm/cm.

R/Q DERIVATION

Starting with the basic definitions of R/Q and the Slater Perturbation Theorem, we will derive the final formula for R/Q in ohm/cm for a measured frequency shift. The basic definition of R/Q for a dipole mode is

$$R/Q_{dipole} = [\int dA_z/dx\, e^{-i\omega t}\, dz]^2 /(2\omega U) \cdot (\omega/c) \quad \text{(ohm/cm)}.^{[3]} \qquad \textit{(equation 1)}$$

For comparison, for longitudinal modes, R/Q is

$$R/Q_{long} = [\int E_z\, e^{-i\omega t}\, dz]^2 / (2\omega U) \quad \text{(ohm)}.$$

In both cases, the integrals are defined on axis from minus infinity to infinity. U is the stored energy. These integrals can be shown to be independent of the path of integration as long the path is parallel to the axis, within the pipe radius and at the speed of light (t=z/c). Taking the path integral along the pipe wall, these integrals can be truncated to just across the gap, for the relevant fields go to zero at the walls.

The basic principle of the "Slater Perturbation Theorem" is that in a standing wave, the energy is constantly oscillating between all magnetic and all electric, which means that the electric and magnetic field energies are strictly equal. If either of these field energies is modified by a probe, there will be a frequency shift to bring back the balance. The frequency shift is

$$\delta f / f = k \int (\mu H^2 - \varepsilon E^2)\, d\tau / (4\,U),^{[4]} \qquad \textit{(equation 2)}$$

where the fields are those before the perturbation, the integral is over the probe volume. The factor k is a geometrical factor which relates how the field energy is redistributed around the bead.

Starting with the definition of R/Q, equation 1, and using

$$\int dA_z/dz\, e^{-i\omega t}\, dz \,|_{axis} = (c/\omega b) \int E_z\, e^{-i\omega t}\, dz \,|_{gap} \qquad \textit{(equation 3)}$$

where b is the pipe radius, and writing

$$\int E_z e^{-i\omega t} dz = \frac{\int E_z e^{-i\omega t} dz}{\int E_z\, dz} \cdot \frac{\int E_z\, dz}{\int |E| dz} \cdot \frac{\int |E| dz}{gap} \cdot gap$$

or

$$= tf * \langle Ez/Et \rangle * \langle |E| \rangle * gap \qquad \textit{(equation 4)}$$

where we identify the first ratio as the transit time factor, tf, and the second factor as <Ez/Et>, the average direction of the electric field to the axis, and the third as the average magnitude of the electric field over the gap.

Doing the volume integral over the "bead", which is a plastic ring just under the beam pipe radius, in equation 2, we have $\delta f / f = -k\varepsilon E^2 * v/2 / (4U)$. The factor of one half is for the cosine dependence of the field over the perturbing ring volume. v is the ring volume.

Putting it all together, we have from equations 1-4 that R/Q is

$$R/Q = 240\,\pi / (k\,\varepsilon/\varepsilon_0) * gap^2 / (v/2) * [\,c/\omega b\,]^2 * [tf * \langle Ez/Et \rangle * \langle sqrt(-\delta f/f) \rangle]^2 \text{ ohm/cm} \qquad \textit{(equation 5)}$$

where <sqrt(-δf/f)> is an experimental quantity and tf and <Ez/Et> are code generated.

BEAD PULL MEASUREMENTS

The k factor is determined by fitting four measured modes in a pillbox cavity to the analytic R/Q values for those modes. The resulting k factor was then used for the other experimental geometries. The R/Q's of the pillbox were matched to an accuracy of (-7%,1%,1%,8%), and a standard deviation of 5%.

The bead pull measurements on the prototype cell were done at a series of anode pipe insertion lengths, ranging from 10.6 cm to 18 cm (see Figure 1). The most thoroughly studied geometry is the 18 cm anode insertion length. All of the results are for the upper geometry with a 4.5 cm beam pipe, 6.0 cm outer coax radius, 2.7 cm radial gap, scalloped guide, outer coax length between taper and roll up of 15.9 cm, a 2 cm roll up, 10 cm taper and the gap center line is 15 cm off the core center line. The lower gap shows the positions for the ferrite-epoxy ring and cone dampers as shaded areas near the taper and coax corner. The cone and ring are similarly mountable on the upper gap.

The average measured R/Q's for the 1 Ghz mode with a 18 cm anode insertion is 1.224 with a range of +15% -17%. The average computer model R/Q value was 1.777 with a range of +17% -20%. The experimental reproducibility has a standard deviation of 13%.. With the addition of the damping ring and cone, only an upper limit on the value of Q was obtained, allowing a prediction based on the average R/Q value of the previous bead pulls. This results R equal to about 22 ohm/cm.

The 1.8 Ghz mode for the same 18 cm anode insertion results in experimental R/Q's of .428 with a range of +20% - 25% versus the computer model of .356 +15% - 13%. With the ring and cone dampers, again only an upper limit on the Q measurement could be done, with a predicted R of 21 ohm/cm.

The Q values were measured for the 18 cm anode insertion for the cases of no ring or cone, ring only, cone only and both ring and cone, respectively, all without applied magnetic field. The Q's start at about 60 and end up somewhere less than 10 and 3, for the main modes. However, the Q's of the two main modes go up to 17 and 48 respectively in the presence of a 5.5 kG magnetic field over the ring and cone. These are the values of Q used above for predicting the resulting R values in the cases where the Q's are too low to do bead pull measurements.

Similarly, the bead pull results for anode insertion lengths of 16 cm, 14 cm, 13 cm, 12 cm, and 10.6 cm are shown in figure 2. These are the R/Q's for mode 1 at about 1 Ghz, the so called "coax mode".

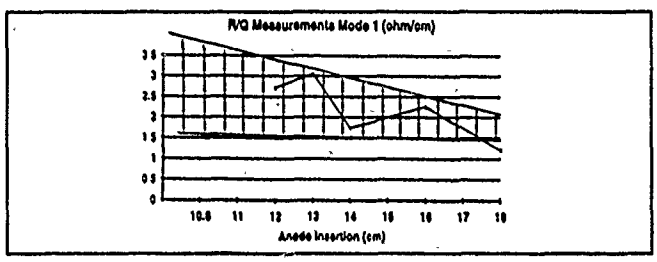


Figure 2----Mode 1 "Coax Mode" at 1.0Ghz

The standard deviation of the differences between the computer model (*BBUS*) and bead pull R/Q's for mode 1 over all anode lengths is 30%. The experimental standard deviation of mode 1 of the 18 cm case over 12 repetitions is 13%. The differences between the model and the bead pull measurement R/Q's are at about the two sigma level relative to the experimental reproducibility over all the anode lengths. The band in figure 2 is the range of computer model predictions. The points are the average bead pull R/Q's for each length.

The bead pull appears to have a stronger length dependence than the code, but the effect is at the margin of uncertainty. This effect may be due to the taper which is not modeled by the *BBUS* code. The bead pull R/Q's are within or just outside the range of values predicted by the different terminations of the radial waveguide in the *BBUS* model.

Figure 3 shows the R/Q's for mode 2 at about 1.8 Ghz, the so called "trapped mode".

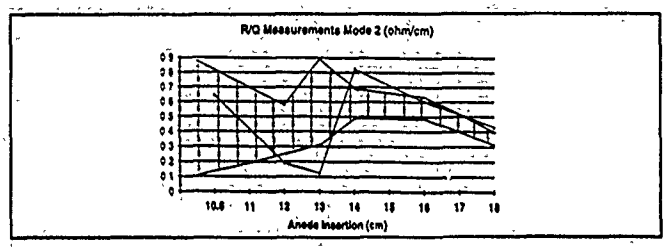


Figure 3----Mode 2 "Trapped Mode" at 1.8 Ghz

The CR-124 ferrite-epoxy, that was used to make the ring and cone, was also subjected to direct electron beam strikes of multiple pulses at 1000 A/cm, 1Mev and 100 ns with only some surface discoloration.

SUMMARY

The R/Q's measured are reasonably close to the computer model in most cases. The R can be reduced to below the design limit of 30 ohm/cm if the mode Q's can be damped to the range of less than about 23 and 70, for the main modes. With the use of the ring and cone dampers, Q's less than 17 and 48, respectively, should be achieved. Thus, the BBU problem for the difficult off-axis shielded gap geometry of the *SLIA* accelerator should be within design tolerances, even for 150 gaps. In particular, the 18 cm anode insertion choice should have transverse impedances of about 22 and 21 ohms/cm, respectively, for the main modes. For comparison, the *ATA* accelerator at Livermore has about a 12 ohm/cm transverse impedance on a 6.7 cm pipe, which roughly scaled to the *SLIA* 4.5 cm pipe would be equivalent to 27 ohm/cm.

ACKNOWLEDGMENTS

I wish to thank Heinz Lackner for his patience in doing the data collection involved in the many tedious bead pull measurements.

---

[1]V.K.Neil,L.S.Hall and R. Cooper, "Futher Theoretical Studies of the Beam Breakup Instability, UCRL-81167, May 25,1978.

[2]Tom Genoni of Mission Reasearch in Albuquerque, N.M. developed this code. It is an "analytic" model that approximates the geometry with square corners.

[3]R.J.Briggs,D.L.Birx,G.J.Caporaso and V.K.Neil, Particle Accelerators,1985, Vol. 18, pp. 41-62. (Equ.2.1.1).

[4]Ginzton,"Microwave Measurements", McGraw-Hill, 1957, p. 439, eq.10.25.

*Experimental Observations of Beam Transport in Twisted Quadrupole Fields**

J.P. Lidestri, V.L. Bailey, Jr., J.A. Edighoffer, S.D. Putnam, M.G. Tiefenback and D. Wake

Pulse Sciences, Inc.
San Leandro, CA 94577

ABSTRACT

In the course of phase space matching an electron beam from guide field focussing into a twisted quadrupole (stellarator) strong-focussing channel, we have developed Cherenkov imaging techniques to measure the profile and density distribution of the beam. We have imaged a 200 A, 850 keV electron beam (average radius ~ 4 mm) as it propagates through the transition from guide field focussing into a stellarator channel. With no matching lenses, the maximum excursion in major radius of the beam in the stellarator channel was ~ 40%. First attempts at matching reduced this excursion to the 24% level. Significant damping of these mismatched oscillations has been seen over the 2.5 meter length of the stellarator magnet channel. Emittance and profile data will be compared for the beam at the end of the channel with and without detailed matching.

INTRODUCTION

A strong focussing $\ell = 2$ is used in the SLIA (Spiral Line Induction Accelerator) bends to reduce the off-axis motion of the beam centroid for beam elements which are not at the matched energy for the bend radius and bending fields. There is then a transition between the longitudinal guide field transport in the straight sections of the SLIA and the toroidal, stellator, and vertical field transport of the bends. Theoretical calculations predict that if this transition is adiabatic then the beam will change from circular in the straight section to elliptical in the bends without significant envelope oscillations[1]. If the transition is non-adiabatic then the beam envelope oscillates. A matching scheme which uses one or two quadrupole coils plus a ring coil has been devised to take the circular beam from the solenoidal field in the straight section and provide the proper eccentricity and rotation for preservation of the elliptical beam profile in the stellarator fields[2].

BEAM DIAGNOSTICS

Current distribution measurements for the 1 MeV matching experiment were obtained with a Cherenkov[3] imaging system that has been cross-calibrated with a charge collector. The current distribution for a circular beam shown in Figure 1, was determined using two independent diagnostics. The first measurement was done by radially sampling the beam with a charge collector (2 mm resolution). The results of this measurement are plotted as charge density vs. radial position in Figure 2.

The second diagnostic used was the Cherenkov beam imaging system which allowed high resolution 2D information to be determined. With this system a typical beam profile is recorded by imaging the Cherenkov light created by the electron beam. From the digitized image shown in Figure 1, the 2D charge distribution can be reduced by normalizing the optical density of the image with the previous charge collector measurement. Figure 3 is a plot of optical density normalized to charge density vs. radial position. When the optical density of the digitized beam profile was compared over a range of film exposures a good fit was achieved as can be seen in Figure 4. Now that the imaging system is calibrated with direct charge collection data, contour plots and perspective plots can be used to determine the beam charge distribution and radii of an elliptical beam profile. Example contours and perspective plots are shown in Figures 5 and 6. These plots were generated from the circular beam profile shown in Figure 1.

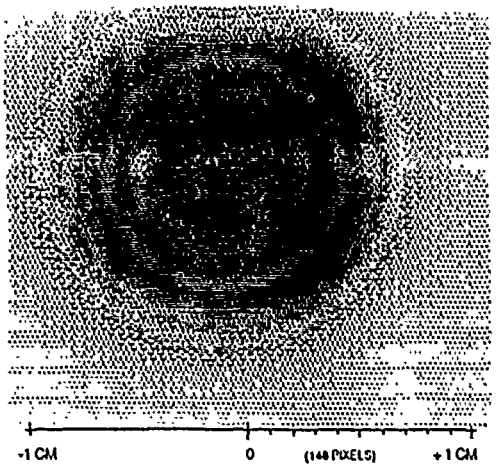


Figure 1. Digitized beam image.

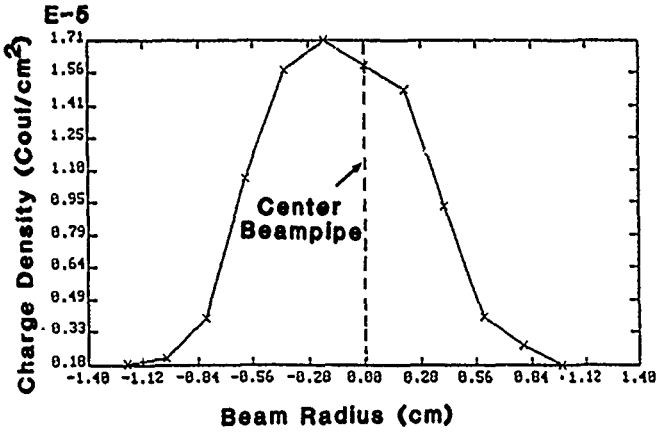


Figure 2. Radially scanned charge collector.

*Work sponsored by DARPA under Order No. 4395, Amendment 90, and by the Navy under Document N00039991 WXDZ002; monitored by the Naval Surface Warfare Center.

0-7803-0135-8/91$01.00 ©IEEE

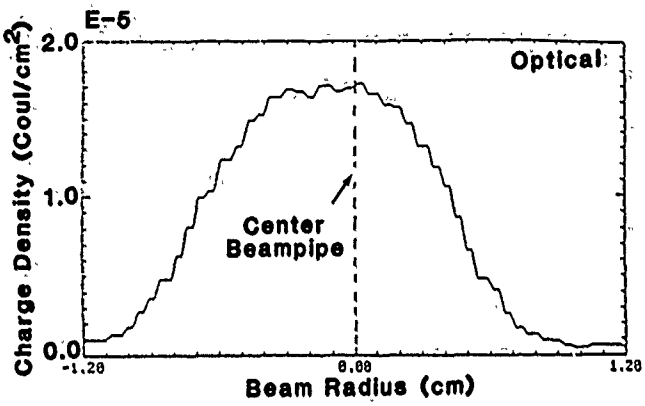


Figure 3. Line profile of Cherenkov image.

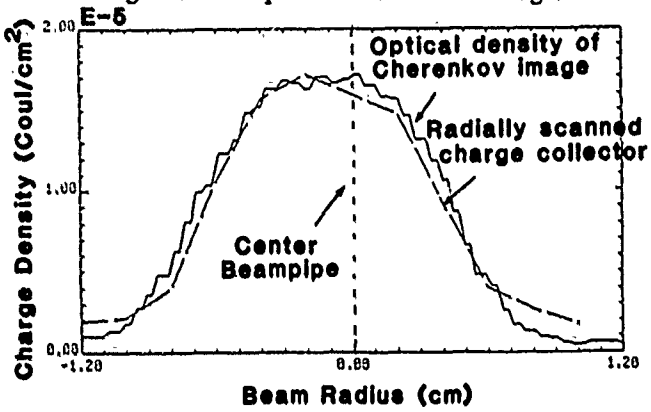


Figure 4. Otical density fit with charge density.

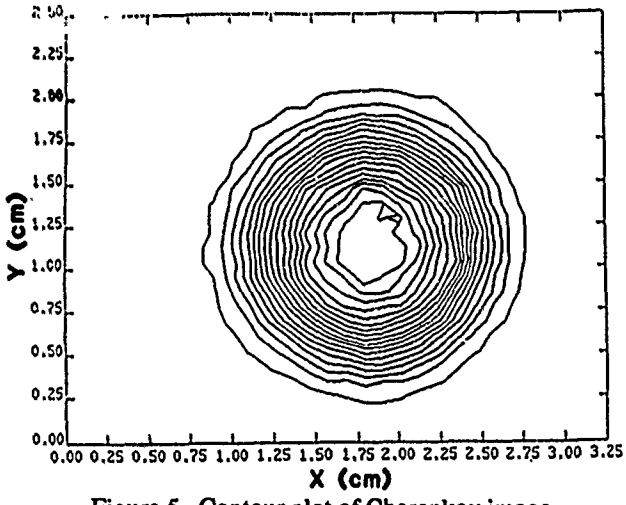


Figure 5. Contour plot of Cherenkov image.

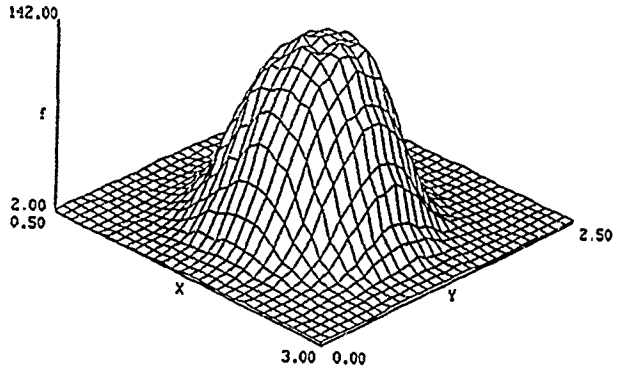


Figure 6. Perspective plot of Cherenkov image.

MATCHING EXPERIMENTS

The Cherenkov imaging technique described above has been used to investigate the beam behavior caused by the transition on and off the stellarator field both with and without matching elements. The beam kinetic energy was 848 kV and the current was 200 A. The 200 A current was chosen to simulate the beam space charge effects in the first POCE (proof-of-concept experiment) bend (4 MeV, 10 kA). The beam was extracted from a field-free diode and inserted into a short solenoid (45 cm) before entering the solenoidal (262 cm) plus stellarator field (251.3 cm) region. Another short solenoid (45 cm) was at the end of the stellarator field region. The long solenoid plus stellarator coil had the same pitch length for the windings (L = 62.83 cm) and length (4L or 251.3 cm) as the first POCE bend. The nominal solenoidal field was 1.48 kG and the on-axis stellarator field gradient was 68.5 G/cm.

No matching lenses were used in the first set of experiments shown in Figures 7 and 8. In the short straight before the stellarator field section the beam was circular and had a diameter of 6.8 mm. To first-order the beam was elliptical and rotated with the stellarator winding pitch as seen in Figure 7.

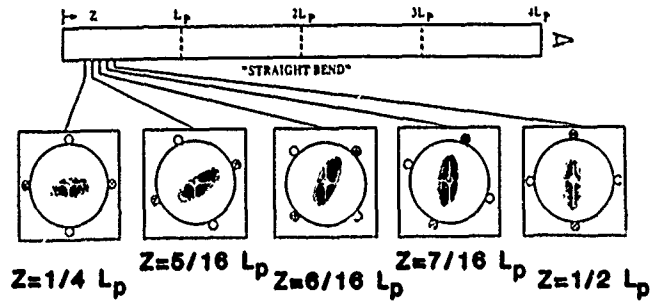


Figure 7. Beam rotation with stellarator coil.

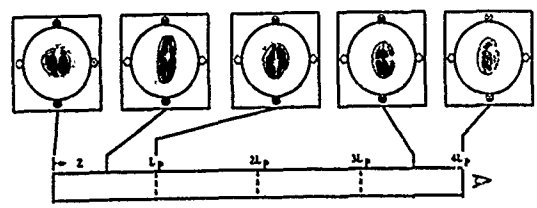


Figure 8. No matching elements.

With no matching lenses the maximum excursion in major radius of the beam in the stellarator channel during the first pitch length was ~ 40%. Significant damping of the mismatch oscillations can be observed over the 2.5 meter length of the stellarator field in Figure 8 and corresponding plot of major and minor radii in Figure 9.

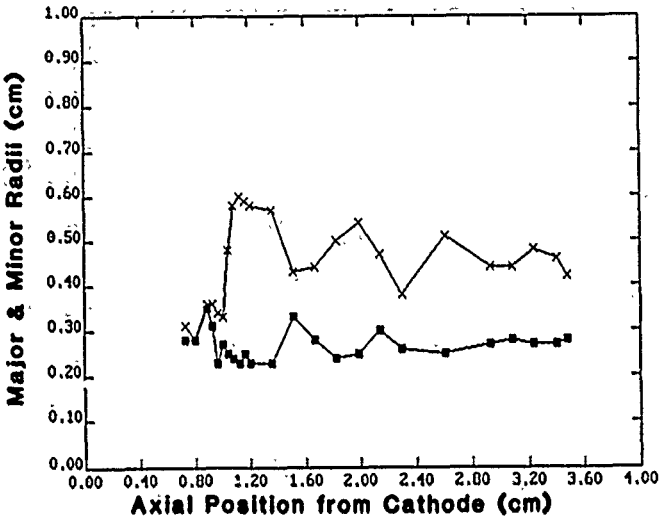


Figure 9. Radius versus position.

During the last stellarator pitch length the maximum excursion was reduced to the 10% level. When the beam exited the stellarator field, the beam remained elliptical and continued to rotate, but the rotation frequency and ellipticity was less than in the stellarator region.

The first attempt at matching used a three-element match (a ring coil and two quadrupole field coils) in the short solenoid upstream of the stellarator section. The ring coil was centered at 49.3 cm with a bucking field of - 516 G and was used to adjust the beam envelope before entering the quadrupole coils. The first quadrupole was centered at 64.3 cm with a peak gradient of 57.5 G/cm and was rotated 48.2 degrees clockwise with respect to the stellarator; the second quadrupole was centered at 75.3 cm with a peak gradient of 92.2 G/cm and was rotated 1.6 degrees clockwise. A detailed description of the derivation of these orientations is given by Tiefenback [2] in this proceeding. These matching elements reduced the oscillations in major radius in the first pitch length to the 25% level and the beam more closely followed the stellarator pitch winding as can be seen in Figure 10 and corresponding plot in Figure 11.

In the end of the stellarator region and also in the following short solenoid the beam profiles with the matching elements were almost identical to the profiles without the matching element as seen in Figures 12(a) and 12(b).

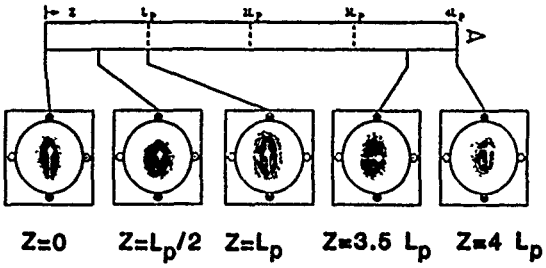


Figure 10. Three matching elements (ring, quad, quad).

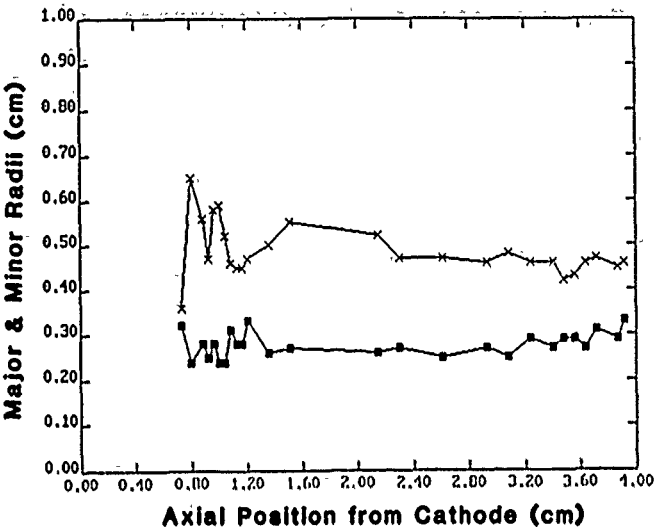


Figure 11. Radius vs. position.

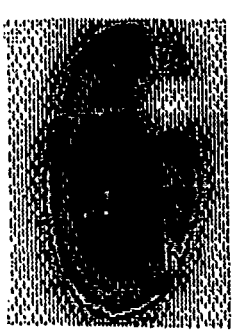


Figure 12(a). Without matching elements.

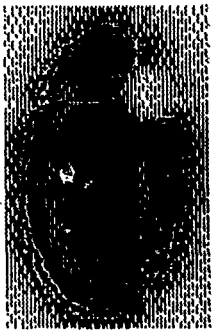


Figure 12(b). With ring and two quads.

CONCLUSION

It can be observed from Figure 9 that the use of quadrupole matching elements is not required in the first bend if the only concerns are mismatch oscillations which seemingly damp out in the 4th period of the stellarator. The issues that may require the use of a matching scheme depend on allowable emittance growth and stellarator-to-stellarator phasing. If emittance growth is observed experimentally then phase space matching can be tuned directly but if the observation of mismatch oscillations are used to achieve matching one needs to understand the damping phenomena.

REFERENCES

[1] D. Chernin, A. Mondelli, and J. Petillo, *SLIA Beamline Design Workshop*, Mission Research Corporation, Albuquerque, NM, 28 August 1989.

[2] M. Tiefenback, *Matching the Transport of Beams in a Continuously Twisted Quadrupole Channel*, Proc. of this conference.

[3] J.D. Jackson, *Classical Electrodynamics*, Wiley and Sons (1962).

*Magnet Design for SLIA Proof-of-Concept Experiment**

V. Bailey, D. Wake, R. Curry, J. Lidestri, and M. Tiefenback

Pulse Sciences, Inc.
San Leandro, CA 94577

ABSTRACT

The beam transport system for the Spiral Line Induction Accelerator (SLIA) proof-of-concept experiment (POCE - 9.5 MeV, 10 kA, 35 nsec) contains seven basic magnetic field coil configurations. The magnets are for the transition from the field-free diode into the nominal 5 kG longitudinal guide field; the transition into/out of the accelerating section; the axial field within the 1.5 MV accelerating units; the matching elements for transition on/ off stellarator fields in the bend; the toroidal, $\ell = 2$ stellarator, dipole, and quadrupole field in the 80 cm bends; the extraction of the beam from the longitudinal guide field; and the beam steering/field correction. Prototype magnet coils have been fabricated. The measured magnetic fields compared well with the predicted amplitudes, gradients, and multipole field components. Because of the large number of pulsed magnetic field coils in POCE, the shot-to-shot and day-to-day reproducibility of the magnet coil current from a PSI designed electrolytic capacitor bank was measured and found to be better than ± 0.15% for currents up to a factor of two (several kiloamperes) larger than the design values.

INTRODUCTION

An experiment to evaluate the feasibility of the spiral line induction accelerator (SLIA)[1] as a high current electron accelerator is currently underway at Pulse Sciences, Inc. The experiment involves injecting a 3.5 MeV, 10 kA electron beam into a strong focussing, two-turn, racetrack type spiral magnet transport line with two passes through each of two 1.5 MV induction accelerating units, giving a nominal 9.5 MeV output. The magnet coils which make up the magnetic transport system for the SLIA proof-of-concept experiment (POCE) are shown schematically in Figure 1. The magnet coils are grouped into the seven basic systems for the functions shown.

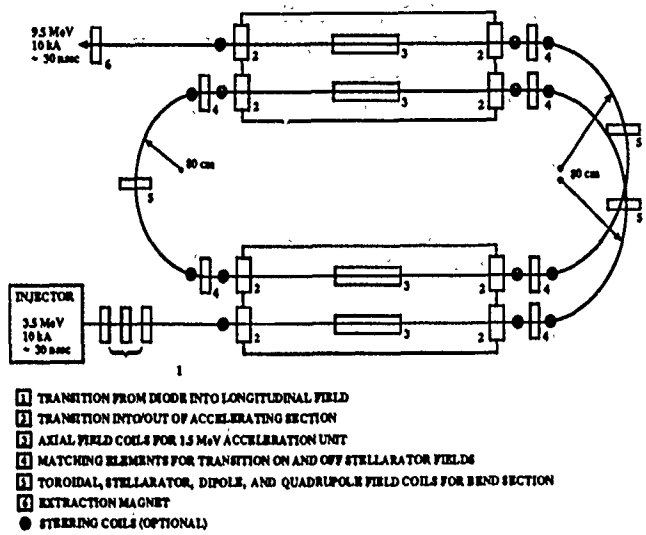


Figure 1. Magnet coils for SLIA-POCE.

UNCONVENTIONAL ASPECTS OF THE SLIA/POCE MAGNETS

Because of size and cost constraints all the SLIA-POCE magnets are pulsed. This minimizes size in that smaller conductors, without iron pole pieces, can be used to provide the desired dipole, quadrupole, stellarator, and steering fields. The electrolytic capacitor bank designed to power the SLIA-POCE magnets costs approximately 1.5 cents per watt of power delivered to the magnetic field coil as compared to the 0.5 to 1.0 dollar per watt for conventional steady-state power supplies.

The diode focussing system does not include a bucking coil to obtain a field-free cathode. Instead the focussing coil is surrounded, both radially and axially, by a magnetically thick piece of aluminum. This reduces the peak magnetic field over the emitting area of the cathode to 2.4 G which is approximately a factor of two less than could be obtained with a steady-state focussing and bucking coil which satisfy the geometrical constraints of the experiment. This removes the alignment problems and stray error fields associated with the large

*Work sponsored by DARPA under Order No. 4395, Amendment 90 and by the Navy under Document N00039991 WXDZ002; monitored by the Naval Surface Warfare Center.

0-7803-0135-8/91$01.00 ©IEEE

radius bucking coil and allows a simpler geometric and magnetic alignment procedure.

MAGNETIC SHIELD

All magnetic field coils, except at the entrance and exit, are enclosed in a magnetic shield to avoid "cross-talk" between the turns of the spiral which are separated by ~ 30 cm over most of the transport distance. Both conducting and ferromagnetic shields were evaluated. Experiments were done with aluminum (6061-T6) and low carbon steel (AISI-1024) shields to compare the bank energy efficiency, required alignment tolerances, and flux confinement times.

For the same capacitor bank energy and dimensions of interest to POCE, the solenoidal field with a low carbon steel shield was 40% larger than with an aluminum shield. For practical material thicknesses (~ 1/2-inch) and for times greater than 1 ms after excitation, the return flux was better confined with a low carbon shield. The parallelism required between the solenoid and the shield for the same percentage of transverse field error was a factor of five more stringent for the aluminum shield. Uncompensated holes in the low carbon steel of diameter up to 5 cm (in a shield of diameter 16.5 cm) caused a field perturbation of 0.1% of the solenoidal field. The field of a discrete air core quadrupole was enhanced by $\backsimeq$ 21% by the addition of a low carbon steel shield. The non-quadrupole components of the field out to a 1 cm radius, where the measurements were done, were within the experimental error bars for the Hall probe and positioning technique (a few percent).

The saturation wave velocity and rate of diffused flux were measured and used, with numerical modeling, to construct a transient ($\backsimeq$ a few ms) magnetization curve (B vs. H). The magnetization curve was used extensively in the finite element code ANSYS to carry out transient, nonlinear calculations of the predicted magnetic fields during the design of the magnet coils.

END TERMINATIONS FOR MULTIPOLE MAGNETS

The end terminations for the dipole, quadrupole, $\ell = 2$ stellarator (twisted quadrupole), and steering (two dipole magnets at 90° angles) magnets are those suggested by Laslett, Caspi, and Helm[2] (LCH). The LCH prescription for the end terminations was applied directly for the matching quadrupole magnets and steering magnets which are used on straight sections. In the case of the dipole and quadrupole magnets for the bends the LCH prescription was applied in a coordinate system which rotated with the bend. For the $\ell = 2$ stellarator winding on the bend the end terminations also included the stellarator rotation.

The purpose of the LCH end terminations is to preserve the quality of the field integrated through the entire magnet. As a test of this, the predicted focussing field for the matching quadrupole coil design, which is composed almost entirely of end terminations, was integrated from -50 cm to 50 cm along the axis of the quadrupole coil at several positions inside the 5.3 cm winding radius. The integrated focussing field followed the ideal value, linearly proportional to the radius, to within 0.26% for radii less than 3 cm.

BEND MAGNETS

The design selected for the bends of the POCE is a stellarator achromat[3] which gives an identity transformation for the beam centroid to first-order in $\Delta E/E_0$, the fractional energy variation from the mean or matched energy. With an achromat, off-energy or momentum particles all exit the bend with coordinates and velocities the same as those at the entrance. Achromat designs have been developed for all POCE bends which give (predicted) submillimeter centroid displacements for $\Delta E/E_0$ $\backsimeq \pm$ 8-10%.

The 80 cm major radius POCE bends contain four (toroidal, stellarator, dipole, and quadrupole) magnetic field coils built up radially on top of each other. The inner most magnet coil is the toroidal field coil which is composed of two helical windings of opposite pitch.

The next magnet coil in terms of radial position is the $\ell = 2$ stellarator coil which is wound on a minor radius of 5.23 cm. The toroidal M numbers ($M = 4\pi R_0/L$, where R_0 is the major radius and L is the pitch length of the winding) for the three

POCE bends are M = -16, -12, and -8, where the minus sign indicates that the Larmor rotation of the electrons is in the same sense as the rotation of the stellarator windings. Each bend has a separate M number in order to minimize the second order ($\Delta E/E_0$) effects while maintaining stable propagation for both the centroid and particle motion. The stellarator field gradient is approximately constant within the 6 cm diameter beam pipe and varies from 0.1346 G/cm/A for the first bend (M = -16) to 0.1397 G/cm/A for the third bend (M = -8). The predicted field purity is excellent at the center of the bends but has a small phase angle shift from the ideal value at the entrance and exit from the bend.

The combination of the dipole and quadrupole magnet coils on the bends provide a betatron vertical field. By controlling the current in each of the coils separately, the amplitude and field index of the betatron field can be adjusted independently. For example, in the third POCE bend the kinetic energy of the electrons, including space charge depression, will be $\simeq$ 7 MeV. For a matched bending field of 312 G and a betatron field index of 1/2 the currents in the dipole and quadrupole field coils would be 647 A and 31 A respectively.

CURRENT AND MAGNETIC FIELD REPRODUCIBILITY

Because of the large number of pulsed magnetic field coils in POCE, a series of experiments were done to determine the shot-to-shot and day-to-day reproducibility of the field and magnet coil current from a PSI designed electrolytic capacitor bank[4]. The discharge current of the capacitor bank was measured into prototype stellarator and solenoidal coils. The current density in the experiments was larger by 50% for the stellarator coil and 100% for the solenoidal coil than the design values for POCE.

The power supply set voltage was held constant during the stellarator field experiments. In a series of 23 shots taken at two-minute intervals the bank voltage varied from 397.50 to 397.89 volts, or approximately one digitization step. The current in the stellarator coil varied from 6158 A to 6148 A (± 0.08%). Two random data points were taken at 5 and 10 minute intervals following the first 23 pulses, and showed no deviation outside the range of the previous data. The following day the procedure was repeated. After five conditioning shots, the current was measured and found to be 6152 A. The power supply was then turned off for two minutes then powered up. After a five-minute warmup interval the discharge current from the bank was 6148 A which was within the ± 0.08% variation measured the previous day.

In similar experiments (17 data points at two-minute intervals) with the solenoidal coil the current varied from 4439 A to 4427 A (0.135%). Concurrent magnetic field measurements showed a ± 0.129% field variation which appeared to be random with relation to the current. The nominal 13 kG solenoidal field in these experiments was significantly above the 5.5 kG POCE design value.

SUMMARY

The conceptual design of the magnets for the beam transport system for SLIA-POCE is complete. Fabrication of the bend magnets to tolerances of $\leq$ 15 mils will be completed by mid-June 1991. The remaining magnets are either in the final engineering design phase or are being fabricated. Thirty-three independently controlled capacitor bank power supplies for the magnets have been built and tested.

REFERENCES

[1] S. Putnam, *Proc. of the 1987 IEEE Particle Accelerator Conference*, Washington, D.C., 1987, p. 887.

[2] L. J. Laslett, et al., *Part. Accel.*, 22, 1 (1987).

[3] S. Putnam, *Semi-Annual DARPA CPB Review*, Washington, D.C., April 13-14, 1989.

[4] R. Curry, et al., *Proc. of the 6th IEEE Pulsed Power Conference*, Arlington, VA, 1987, p. 248.

Experiments Investigating the Effects of the Accelerating Gap Voltage Pulse on the Ion Focused (IFR) High Current Electron Recirculators*

M. G. Mazarakis, D. L. Smith, J. W. Poukey, J. S. Wagner, L. F. Bennett,
W. R. Olson, B. N. Turman, K. R. Prestwich
Sandia National Laboratories
P. O. Box 5800
Albuquerque, NM 87185

J. Wells
Science Applications International Co.
2340 Alamo, SE
Albuquerque, NM 87106

Abstract

The lifetime of the Ion Focusing Regime (IFR) channel following the pulsing of the post-accelerating gaps is critical for an open-ended, spiral recirculating electron linear accelerator. It dictates the number of allowable beam recirculations through the gap. In the case of a racetrack configuration, it is significant but not as critical, since the presence of the electron beam focuses the ions and lengthens the lifetime of the ion channel.

It was established that pulsing the accelerating gap perturbs the IFR channel. However, for the parameters studied, the lifetime is long enough to allow at least four beam recirculations in a spiral device. In addition, cusp fields positioned upstream and downstream from the gap prevent it from perturbing the IFR channel.

INTRODUCTION

Figure 1 is a schematic diagram of our low energy Recirculating Linear Accelerator (RLA) in a closed geometry racetrack configuration. For these experiments we used the first straight section of the low-energy RLA beam line. The injector was removed, and the beam line was extended downstream from the ET-2 post accelerating cavity. It has a 1.3-MV electron injector and a single post-accelerating (ET-2) cavity with the accelerating gap located inside the IFR channel. In our RLA devices, we use a low-energy, 300-V electron beam (LEEB) to ionize a 0.1 to 0.4 mTorr argon gas. The low-energy electron beam is focused and guided along the beam line by a 200-G solenoid wrapped around the outside walls of the vacuum pipe. When the main high-energy electron beam enters the channel, the low-energy plasma electrons are expelled, leaving behind an ion channel (IFR) which electrostatically focuses and guides the beam. In the experiments reported here we energize only the post accelerating cavity. A ~ 1.2-MV voltage pulse is applied at the post accelerating gap, and the response of the preformed IFR channel is studied and analyzed.

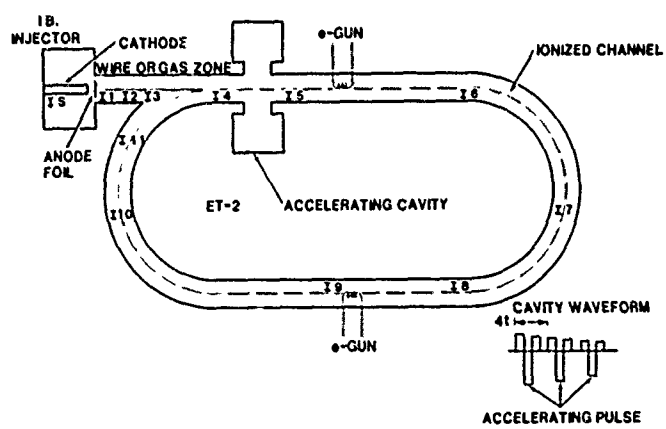


Figure 1: Schematic diagram of the low energy RLA.

EXPERIMENTAL SETUP

Figure 2 is a sketch of the actual experimental setup. Only the post-accelerating gap (ET-2) is included in the system. The IFR

*Supported by Navy SPAWAR under Space Task No. 145-SNL-1-8-1, by US DOE Contract DE-AC04-76DP00789, and DARPA Order No. 7877.

0-7803-0135-8/91$01.00 ©IEEE

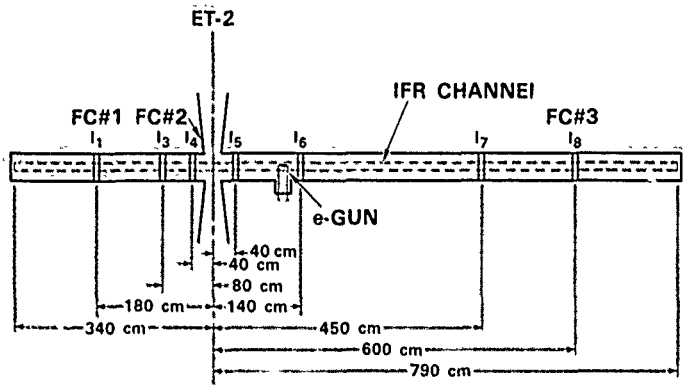


Figure 2: Experimental setup.

channel is formed using our usual technique of low-energy electron-beam ionization of a 2.5 x 10^{-4} Torr argon gas atmosphere which fills the beam transport vacuum pipes. The average channel radius is ~ 1 cm and the plasma ion density (n_i) of the order of 7 x 10^{10} ions/cm^3. The entire length of the channel is 11 m: 8 m downstream and 3 m upstream from the accelerating gap. Rogowski coils and radial Faraday cups[1] are used as diagnostics.

EXPERIMENTAL RESULTS AND ANALYSIS

Figure 3 gives samples of the current waveforms at various locations in the beam line and of the voltage pulse produced by the ET-2 cavity. Timing fiducials provide the absolute time differences of the arrival of the front of the waveform at different locations. Pulsing the gap causes the propagation of two distinct types of "disturbances," one downstream and the other upstream from the gap. The one downstream has the characteristics of an electron-beam pulse propagating with the expected maximum velocity of 2.7 x 10^{10} cm/sec (800 kV is the ET-2 first pulse) in the direction of the accelerating electric field. The other disturbance, although appearing in the Rogowski monitors as an electron-beam pulse, propagates with smaller velocities, 0.7 x 10^{10} cm/sec, and is apparently due to the upstream propagation of the sheath separating the deneutralized from the neutralized part of the IFR channel. The axial electric field created by the ion channel accelerates the channel electrons at the sheath and moves the sheath away from the accelerating gap.

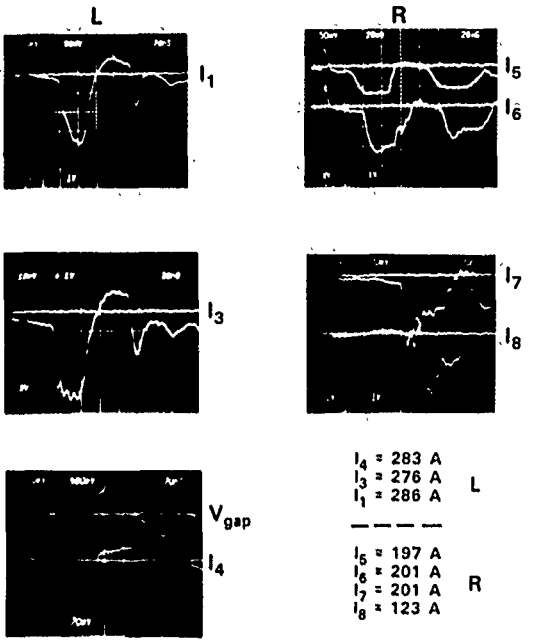


Figure 3: Samples of the current wave forms at various locations.

MAGIC[2] simulations of the beam line (Fig. 4) reproduce quite well the observed ~ 300 amps beam currents that are accelerated by the gap, the electron current accelerated by the ion column, and the propagation velocities in both directions (Table 1). Richard Hubbard arrived to the same results using his FRIEZR code.[3]

Table 1

t ns	FC#2 mA	FC#3 mA	I_3 A	I_4 A	I_7 A
6	50	0	30	222	0
12	70	0	289	282	0
18	10	0	274	274	0
24	0	0	255	268	0
30	10	0	247	259	0
36	10	0	273	262	37
	CHANGE POLARITY $\vec{E}$ OF GAP				
42	0	0	94	-76	149
48	0	0	-85	-114	133
54	0	0	-117	-114	178
60	0	0	-106	-115	132
66	0	2	-89	-105	97
72	0	4	-90	-90	71
78	0	0	-104	-94	104
84	0	0	-105	+13	116

It takes 36 ns for the deneutralizing front to reach Rogowski #7 located 3.88 m from ET-2 gap.

v_{front} = 3.88 m/36 x 10^{-9} sec = c/3

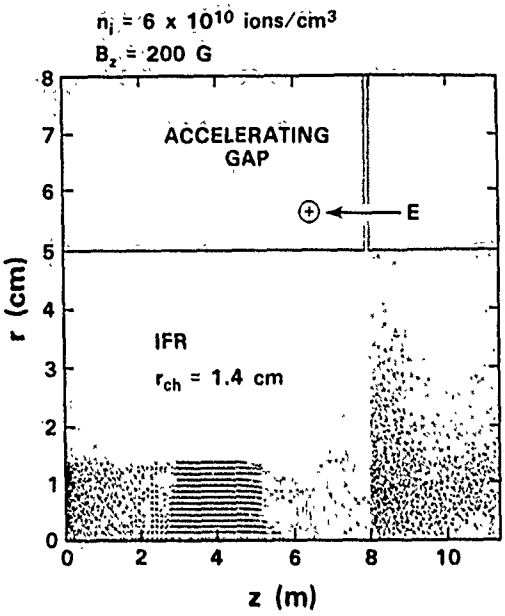


Figure 4: Electron map 24 ns following the pulsing of the ET-2 cavity.

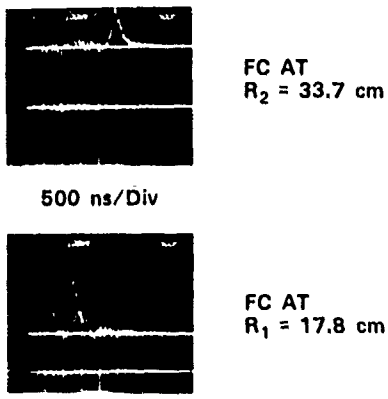


Figure 5: Time of flight measurements utilizing two Faraday cups located at different radial distances from the beam pipe axis.

Time-of-flight measurements of the ions into two Faraday cups located at different radial distances from the IFR axis (Fig. 5) gave an ion escape velocity of ~ 1.2 x 10^7 cm/sec. This velocity suggests a 400-ns escape time for the argon ions to reach the walls of the 5-cm-radius beam pipe. Numerical simulations with BUCKSHOT[4] accurately reproduced the arrival times, amplitude, and time evolution of the collected ions by the Faraday cups. Richard Hubbard with FRIEZR got the same results. For the heavier Xe ions to be used in the final device, the escape times should be ~ 600 ns.

These experimental results are encouraging, particularly for the spiral IFR version of the proposed recirculating accelerator. A Xe IFR channel could provide beam focusing for at least four recirculations (600 ns) through the post-accelerating gap. Experiments with cusp fields or transparent grids upstream and downstream from the ET-2 cap demonstrated that IFR channel can be decoupled from the gap. Electron beams or sheaths were not observed when cusp magnetic fields were utilized. It should be pointed out again that no high-energy beam was injected into the IFR channel during the experiments reported here.

CONCLUSIONS

We have established experimentally that pulsing the accelerating gap of the ET-2 cavity puts the electrons and ions of the IFR plasma channel into motion. As a result of the electron motion, two types of "disturbances" propagate axially into opposite direction: (1) electrons move to the left of the gap, and (2) a sheath moves to the right (direction of gap electric field). Both "disturbances" cause the Rogowski coils to register a 200 to 300-A current in the same direction. The argon ions of the IFR channel escape radially with velocities equal to 1.2 x 10^7 cm/sec and take 400 ns to hit the 5-cm-radius pipe. Cusp magnetic fields or possibly transparent grids upstream and downstream from the accelerating gap can decouple it from the IFR channel. The experimental observations are in very good agreement with numerical simulations.

REFERENCES

[1] K. W. Struve, et al., Mission Research Corporation, Private Communication.

[2] B. Goplen, et al., Mission Research Corp. Report MRC/WDC-R-068, 1983.

[3] R. F. Hubbard, et al., Bull. Am. Phys. Soc. 35, No. 4, p. 932 (1990).

[4] J. S. Wagner, Sandia National Laboratory Report, SAND87-2019 (1987).

RADLAC II/SMILE PERFORMANCE WITH A MAGNETICALLY INSULATED VOLTAGE ADDER*

S. L. Shope, M. G. Mazarakis, C. A. Frost, C. E. Crist
J. W. Poukey, K. R. Prestwich, and B. N. Turman
Sandia National Laboratories
Albuquerque, NM 87185

K. Struve and D. Welch
Mission Research Corporation
1720 Randolph Road, SE
Albuquerque, NM 87108

Abstract

A 12.5-m long Self Magnetically Insulated Transmission LinE (SMILE) that sums the voltages of 8, 2-MV pulse forming lines was installed in the RADLAC-II linear induction accelerator. The magnetic insulation criteria was calculated using parapotential flow theory and found to agree with MAGIC simulations. High quality annular beams with $\beta_\perp \leq 0.1$ and a radius $r_b < 2$ cm were measured for currents of 50-100-kA extracted from a magnetic immersed foilless diode. These parameters were achieved with 11 to 15-MV accelerating voltages and 6 to 16-kG diode magnetic field. The experimental results exceeded our design expectations and are in good agreement with code simulations.

INTRODUCTION

The linear induction accelerator, RADLAC II, was originally designed with eight 2 MV electrically-graded vacuum insulator stacks or envelopes. A magnetically insulated transmission line (MITL) coaxial cathode stalk was passed through the first two envelopes and used to generate a 4-MeV, 20 to 40-kA annular electron beam in a foilless diode.[1] The remaining six envelopes contained specially contoured accelerating gaps of 2 MV each that were designed to minimize radial oscillations of the beam envelope.[2] A pulsed longitudinal magnetic field, B_z, of 20 kG was used throughout the accelerator to generate and transport the annular beam through the accelerating gaps. The final beam voltage was 16 MV. The pulsed magnets proved to be unreliable with numerous mechanical failures and alignment of the magnets was extremely difficult.

To reduce the number of magnets the MITL was extended through the first four envelopes. The four-feed, 8-MV injector successfully produced a 7 to 8-MeV, 40 to 50-kA annular beam. Failures in the remaining solenoidal magnets still caused a reliability problem. We replaced the 8-MV MITL with SMILE, which added the voltages of all eight feeds to a single foilless diode. This modification eliminated all of the unreliable magnets except for one small coil, used for the foilless diode, that was located external to the accelerator. This modification provided very reliable accelerator operation and routinely produced 10 to 13-MeV, 40 to 110-kA, annular electron beams.

SMILE

The design of SMILE is similar to that of the HERMES III and HELIA accelerators.[3,4] The criteria for the self magnetic insulation was derived from Creedon's theory.[5] The radius of the accelerator insulators and interconnecting piping was fixed at R = 21.5 cm. The cathode radius needed to be r_c = 1 cm. The final design was for 110 kA and assumed 2 MV applied to each of the eight insulating stacks. Given these parameters we calculated the shank radii r_i, and operating impedances at each envelope section using Creedon's formula for the minimum current I_ℓ required to establish self-limited magnetic insulation. The current, I_ℓ is given by:

$$I_\ell = 8500\, g \gamma_\ell^3 \ell n\left[\gamma_\ell + (\gamma_\ell^2 - 1)^{1/2}\right],$$
$$\gamma_o = \gamma_\ell + (\gamma_\ell^2 - 1)^{3/2} \ell n\left[\gamma_\ell + (\gamma_\ell^2 - 1)^{1/2}\right], \quad (1)$$
$$g = [\ln R/r_i]^{-1} \text{ and } \gamma_o = V[MV]/mc^2 + 1 = \left(1 - \frac{v^2}{c^2}\right)^{-1/2}$$

The relativistic Lorentz factor, γ_ℓ, is for electrons at the boundary of the electron sheath in the minimum current case. The main criteria was to keep $I_\ell \geq 110$ kA in order to maintain magnetic

*Supported by the U.S. DOE Contract DE-AC04-76DP00789 and DARPA Order No. 7877.

0-7803-0135-8/91$01.00 ©IEEE

insulation. The final design of the 12.5-m long cathode stalk started at a radius of 10 cm and utilized seven conical steps to reduce the radius to 1 cm. The dimensions are summarized in Table I.

The design was simulated with the PIC MAGIC code.[6] Figure 1 shows an electron map of the SMILE configuration and verifies that magnetic insulation does occur. The losses near the cathode tip are due to the radial component B_r of the applied magnetic field of the foilless diode and occur when the self field B_θ is $\leq B_r$.

TABLE I.
SMILE Self-Limited Minimum Current MITL Design

MITL Segment	Optimum Segment Voltage V (MV)	Actual Cathode Radius r_c (cm)	Cathode Radius r (cm)	Vacuum Impedance Z (Ω)	Operating Impedance Z (Ω)
1	2.0	13.33	10.2	45.3	30
2	4.0	8.05	7.6	55	40
3	6.0	6.30	5.7	80	61
4	8.0	3.86	3.5	96	80
5	10.0	2.69	2.5	121	97
6	12.0	1.90	1.6	149	122
7	14.0	1.35	1.3	162	135
8	16.0	.952	1.0	180	151

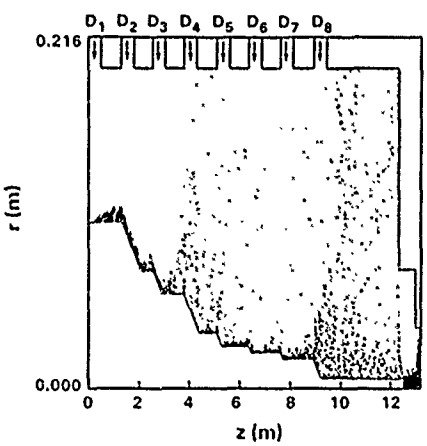


Fig. 1: Electron map simulation for SMILE showing magnetic insulation.

The 12.5-m MITL adder was cantilevered from one end of the accelerator. The adder was preloaded while it was out of the machine to compensate for gravitational droop. A diagram of SMILE is shown in Fig. 2.

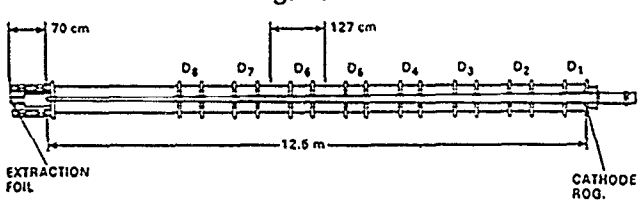


Fig. 2: SMILE configuration for RADLAC.

HIGH CURRENT BEAM GENERATION

With the SMILE modification the annular beam was still generated in a magnetic foilless diode with a small, reliable, pulsed magnet, located outside of the accelerator tank. This greatly simplifies the operation. A diagram of the foilless diode and associated beam diagnostics is shown in Fig. 3. The PIC MAGIC simulations have shown that the output current is a function of the beam loss at the divergence of the applied magnetic field at the cathode, the value of the applied field, and the anode-cathode spacing. A typical diode simulation is shown in Fig. 4. We were able to use these variables to generate high quality annular beams over a wide range, 50 to 113 kA. The voltages were 11-15 MV. Figure 5 shows voltage and current waveforms.

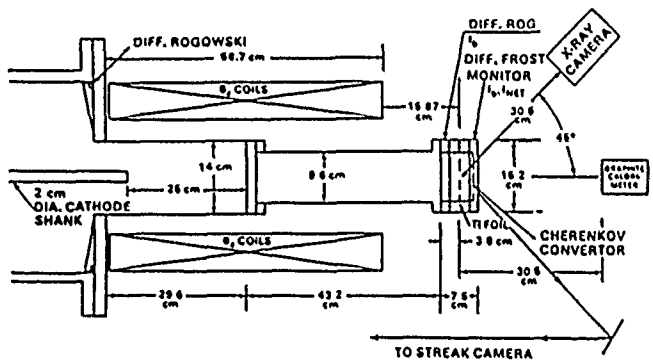


Fig. 3: Schematic diagram of the immersed foilless diode with associated diagnostics.

To determine the beam kinetic energy the voltage applied to each of the eight feeds was measured and added with appropriate time shifts to correct for electron transit time along the stack. The sum was then corrected for pulse distortion due to the MITL operation. The pulse was broadened and reduced in amplitude due to the finite inductance of the system. In addition the erosion associated with the establishment of the magnetic insulation led to a steepening of the front of the pulse. The correction typically reduced the measured peak voltage by 1-2 MV and resulted in beams with kinetic energies of 10-13 MeV.

The beam quality was measured using witness foils and time integrated x-ray and Cherenkov photos. A few shots were fired with the extraction foil and targets located in the uniform magnetic field to measure the beam radius; however, at the high current density in the

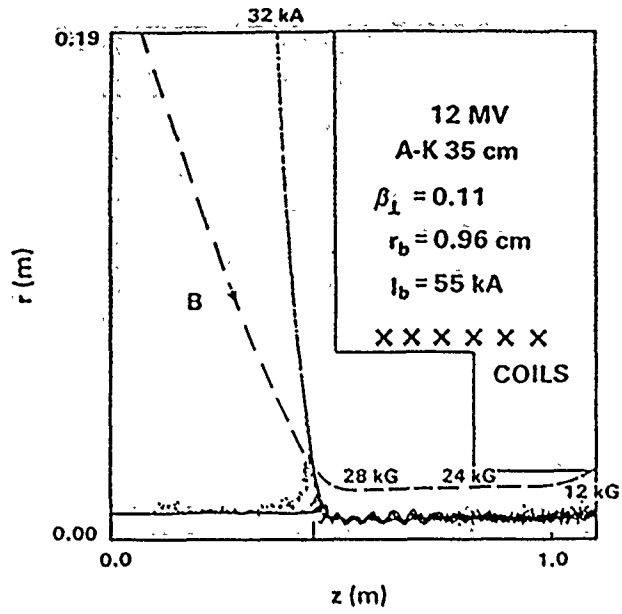


Fig. 4: PIC MAGIC simulation of typical SMILE foilless diode.

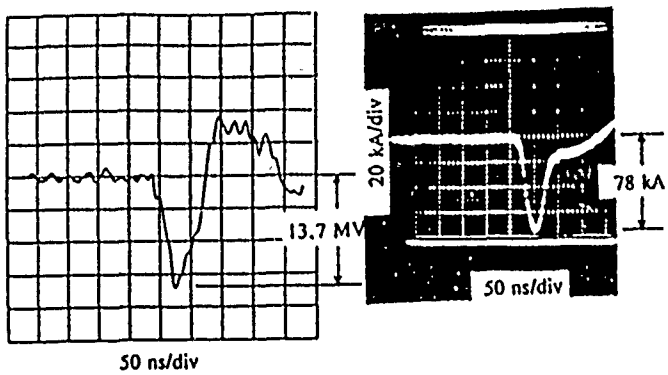


Fig. 5: Sum of voltages applied to MITL adder and extracted beam current.

annular beam the extraction foil would rupture bringing the accelerator up to air. Most of the shots were fired with the foils located in the diverging field of the magnet. This allowed the beam to adiabatically expand and reduce the current density, allowing the foils to survive.

The perpendicular thermal velocity, $v_\perp = \beta_\perp c$ is determined by measuring the spreading of the annular beam from finite Larmor radius effects. The annulus width of an x-ray pinhole camera image is a function of the width of the cathode annulus (3 mm for SMILE), the applied B_z, the beam energy, and $\beta_\perp$. Representative witness foils and x-ray pinhole photographs are shown in Fig. 6. Typical values for $\beta_\perp$ were ≤ 0.1 indicating very low emittance beams in good agreement with simulations.

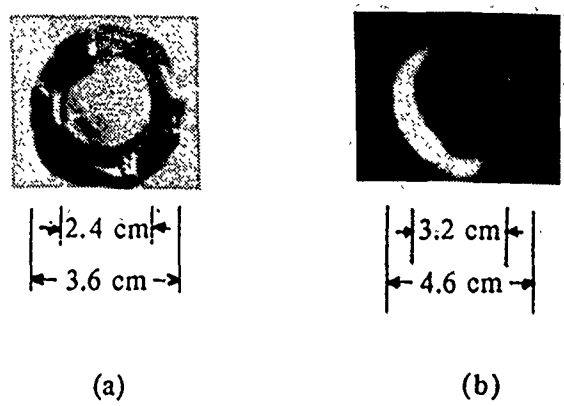


Fig. 6: (a) Witness foil of a 13 MeV, 78 kA beam that was adiabatically expanded to reduce the current density, $\beta_\perp = 0.05$. (b) X-ray pinhole photograph of a 10 MeV, 80 kA beam generated with a 2.1 cm radius cathode, $\beta_\perp = 0.07$.

CONCLUSION

The SMILE modification has resulted in a reliable and reproducible high current accelerator. Beam currents were easily varied by parameter changes predicted by MAGIC simulations. The resulting beams were of very high quality with a small transverse velocity.

REFERENCES

1. R. B. Miller, et al., J. Appl. Phys. 51, 3506 (1980).
2. S. L. Shope, et al., Proc. of the IEEE Particle Accelerator Conference, Washington, D. C., p. 978 (March 16-19, 1987).
3. R. C. Pate, et al., Proc. 6th International IEEE Pulsed Power Conference, Arlington, VA, p. 478 (June 29-July 1, 1985).
4. J. J. Ramirez, et al., Proc. 5th International IEEE Pulsed Power Conference, Arlington, VA, p. 143 (June 10-12, 1985).
5. J. H. Creedon, J. Appl. Phys. 48, p. 1070 (1977).
6. B. Goplen, et al., "Users Manual for MAGIC/Version-Sept. 1983, MRC/WDC-R/068," Mission Research Corp., Washington, D. C. (1983).

A NOVEL CONCEPT FOR A LITHIUM LENS EXCITER

G.G. Karady
Department of Electrical Engineering
Arizona State University
Tempe, AZ 85287-5706

H.A. Thiessen
Los Alamos National Laboratories
Los Alamos, NM

ABSTRACT

A particle beam is focused by the magnetic field of a lithium lens which collects particles produced in a small target. The major components are a short lithium rod and an exciter. This paper presents a new circuit concept for the exciter to produce a 100 kA current pulse with a 1 msec flat top. In every half-cycle a capacitor generates a current pulse. A thyristor-controlled rectifier charges the capacitor to the supply voltage, and a thyristor switch discharges it through a pulse transformer which supplies the lens. A zinc-oxide surge arrester, connected in parallel with the pulse transformer, produces the current flat-top. The control of a larger current pulse with a non-linear component is a new concept which improves the lens performance. The exciter can be built with commercially available components.

INTRODUCTION

The lithium lens was used in the last decade to focus particle beams on a small target. The lens consists of a lithium bar, which is supplied by a 100-150 kA current pulse. The magnetic field generated by the current pulse focuses the beam on a very small area. The dimensions of the lithium rod are, length = 10-30 cm and diameter = 0.5-2 cm. The current pulse is a half sine wave with a peak amplitude of 100-150 kA, a duration of 60-100 msec, and a repetition frequency of about 3 Hz.

Los Alamos National Laboratory investigated the feasibility of a lens with a significantly increased duty cycle. The desired current wave form is shown in Figure 1.

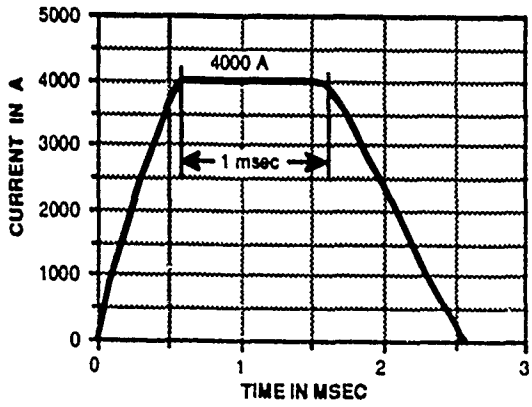


Figure 1: Current pulse for lithium lens

It can be seen that the major difference between the Los Alamos requirement and the previous designs is in the wave shape and the higher repetition frequency. The generation of the pulse with a flat top is more complicated than with a sine shape.

The purpose of this investigation is to develop a new circuit which generates a 100 kA pulse with a flat top.

BACKGROUND

The literature regarding lithium lenses was reviewed. The survey shows that the lithium lens is connected to the power supply through pulse transformers, and the current pulse is generated by a capacitor discharge. A typical system described by Bayanov et al. [1] utilizes a 100 μF low-inductance capacitor. This capacitor is charged by a rectifier and discharged by a thyristor switch through a pulse transformer having a turn ratio of 1:4. The secondary of this transformer is connected to a 50 m long co-axial cable, which is terminated by a second pulse transformer with a turns ratio of 1:6. The secondary of this transformer supplies a low-inductance strip line with a length of 6 m. The strip line is terminated by a third pulse transformer, again with a turns ratio of 1:6. The water-cooled lithium bar is mounted directly to the secondary of the last pulse transformer. The lithium bar resistance is 0.7 mohm, and its inductance is 0.05 μH. The strip line inductance is about 0.7 μH, and the co-axial cable inductance is 2 μH. The system operates at a frequency of 3 Hz and generates a sinusoidal pulse with an amplitude of 130 kA and a duration of 60 μsec. The overheating of the lithium bar limited the operation frequency and lifetime.

Sieveres et. al. [2] describe a lens using liquid lithium, supplied by a sinusoidal of 320kA current pulses. The operation frequency is 2-3 pulses per second. The lens accumulated more than 10^4 pulses in CERN.

Hojvat and Lennox [3] presented a new lens design for Fermi Laboratory. The lens was tested at CERN and survived more than 1.4 M 290-320 kA pulses.

The analysis of the results shows that: (1) all systems generate sinusiodal wave forms with no reference to a flat top; (2) the efficiency of the energy transfer is about 60% because of the losses in the pulse transformers; (3) the reduction of the number of pulse transformers is desirable; and, (4) the deterioration of the lithium bar limits the lifetime of the lens.

0-7803-0135-8/91$01.00 ©IEEE

CURRENT PULSE GENERATON WITH FLAT TOP

The standard method of generating a high-current pulse is the discharge of a charged capacitor by a thyristor switch through low-inductance line and a pulse transformer. The latter supplies the load, in our case the lens. This circuit produces a current pulse with a half sine wave shape. The generated wave shape can be modified by diverting the current, above a certain limit, to a parallel path with constant voltage in order to a produce flat top. Figure 2 shows the possible realization of this circuit.

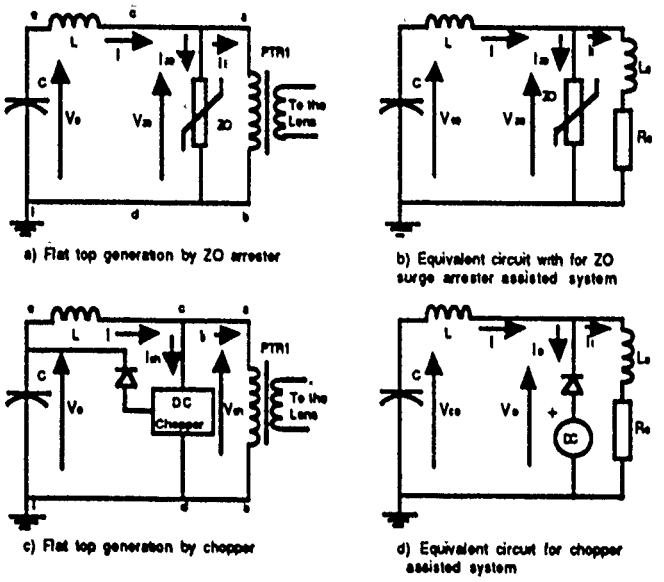


Figure 2: Current pulse forming circuit

Figure 2a diverts the current into a zinc-oxide surge arrester, which has a very non-linear current-voltage characteristic. The equivalent circuit of this system is shown in Figure 2b, where the pulse transformer and the load is represented by an equivalent impedance. The surge arrester is represented by a non-linear resistance described by equation 1:

$$V_{zo} = C_{zo}\ I_{zo}^{\alpha} \quad \text{where} \qquad (1)$$

C_{zo} and α are constants determined by the zinc-oxide material. V_{zo} and I_{zo} are the zinc-oxide device voltage and current.

This circuit was used for analytical studies and system simulation. The current and voltage wave shapes and zinc-oxide characteristics are shown in Figure 3. This figure demonstrates that this circuit generates the proper wave shape, but the zinc-oxide arrester has to absorb large amounts of energy during conduction. This requires the connection of several arresters in parallel.

Figure 2c shows another circuit realization, where a constant-voltage dc-to-dc converter is connected in parallel with the load. The equivalent circuit is shown in Figure 2d. The voltage and current wave shapes are similar to that shown in Figure 3. The converter in this circuit operates as a high-frequency chopper, produces a flat current pulse, and returns the energy to the capacitor bank during conduction.

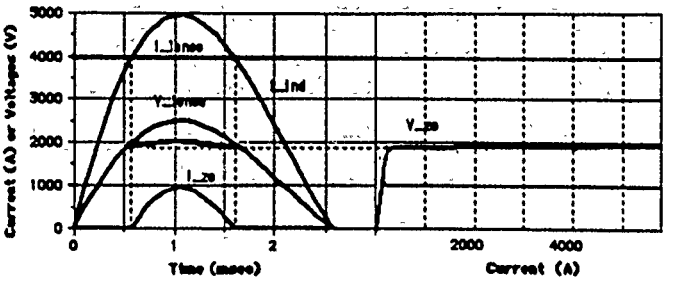


Figure 3. Current wave forming by zinc-oxide arrester

SYSTEM CONCEPT

Using the current shaping method of Figure 2a, the one-line diagram of the lens' power supply is developed and shown in Figure 4.

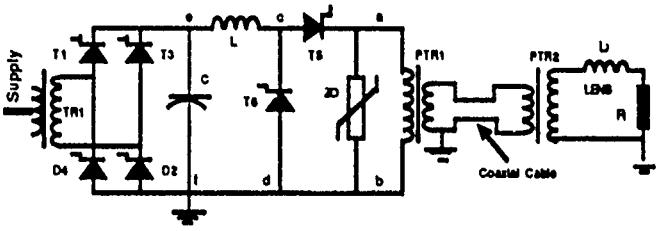


Figure 4: One-line diagram of the lithium lens power supply

The pulse transformers and lens can be replaced by an equivalent impedance.

The system operation is divided into three states. The equivalent circuit in each state is shown in Figure 5.

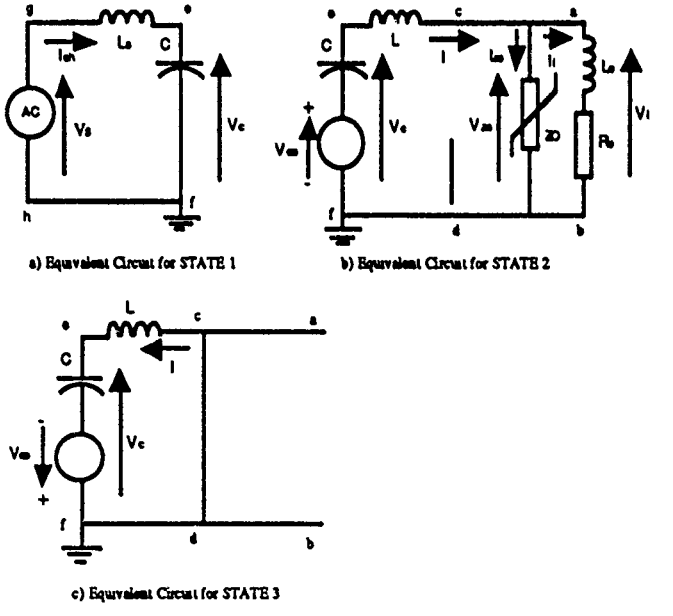


Figure 5: Equivalent circuits

State 1 - Charging (Figure 5a)

The voltage wave form is shown in Figure 6. The single-phase rectifier charges the capacitor during both the positive and negative cycles. In the positive cycle, when the source

voltage becomes equal to the capacitor voltage (point a), thyristor T5 is fired and the transformer charges the capacitor to the peak voltage (TR, D6, T5 path in Figure 4). In the negative cycle, T3 is fired and the capacitor is charged through T3, D4. When the source voltage reaches its peak value (point b), the charging is completed and the capacitor is ready for pulse generation.

State 2 - Discharge and pulse generation (Figure 5b)

Thyristor T1 is fired at any time after point b in Figure 6. This discharges the capacitor, which then generates a sinusoidal current wave as shown in Figure 7. The wave is modified by the zinc-oxide arrestor and a pulse with flat top is generated. The current of the arrestor is shown in Figure 7. This pulse is transferred to the lens through the two pulse transformers. In this process the peak current is increased from 4 kA to 100 kA. The polarity of the capacitor voltage is reversed. At the end of the discharge period, the capacitor is charged to a negative voltage (point c) which is considerably less than the peak supply voltage (point b). Nevertheless, significant energy remains in the capacitor.

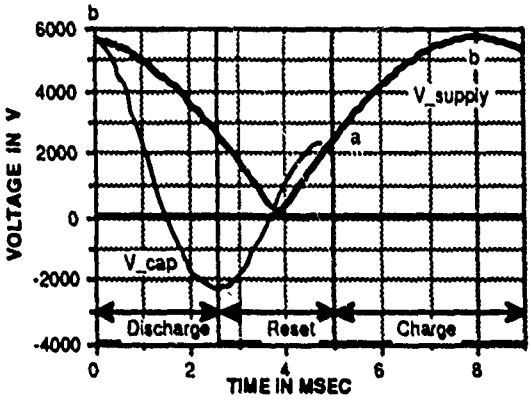


Figure 6: Voltage wave forms

State 3 - Reset period (Figure 5c)

The remaining energy is recovered by firing T_2 at point c just after T1 is turned off. The discharge of the capacitor through T2 and L reverses the capacitor voltage (point d) and recovers the energy. After that, the capacitor voltage remains constant until the charging period starts at point a.

OPERATION ANALYSIS

The system was simulated using the MICROCAP transient analysis program. For the simulation study, the system equivalent circuit was developed and shown in Figure 5. The results prove the feasibility of the circuit as shown in Figure 4. Furthermore, the results of these studies permit the selection of components and the practical design of the system.

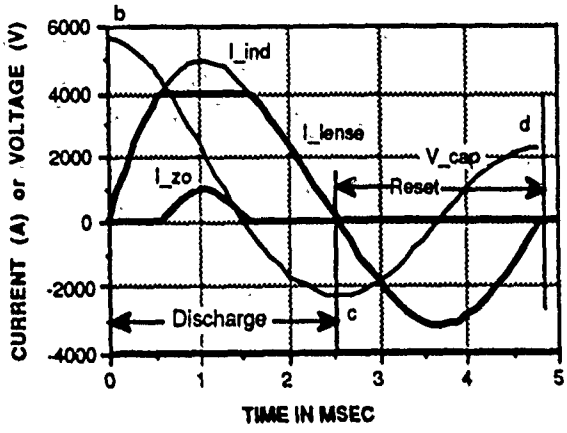


Figure 7: Current and voltage wave forms during discharge and reset

SYSTEM DESIGN

The result of the system operation analysis permits the selection of components' ratings and the determination of major requirements. Based upon the results of our preliminary analyses, the components may be selected for a future exciter. The approximate power consumption of this exciter would be 1.6 MW.

CONCLUSION

The concept of a high-power lithium lens power supply is developed. The major components are selected. The system operation analysis and computer simulation proved the feasibility of the proposed system.

REFERENCES

1. B.F. Bayanov, J.N. Petrov, G.I. Silvestrov, J.A. MacLanchlan, G.I. Nicholls, "A Lithium Lens for Axially Symmetric Focusing of High Energy Particle Beams" Nuclear Instruments and Methods, I90 (1981), pp. 9-14.
2. P. Sievers, R. Bellone, A. Ijspeert, P. Zanasco, "Development of Lithium Lenses at CERN", IEEE Trans. of Nuclear Science, Vol. NS-32, No. 5., Oct. 1985, pp. 3066-3668.
3. D.C. Fiander, C.D. Johnson, S. Murry, T.S. Sherwood, G. Dugan, C. Hojrat, A. Lennox, "Bean Test of a 2 cm Diameter Lithium Lens", IEEE Trans. Nucl. Sci., Vol. NS-32, No. 5, Oct. 1985, pp. 3063-3065.
4. G. Dugan, C. Hojvat, A.J. Lennox, G. Biallis, F. Cilio, M. Leininger, J. McCarthy, W. Sax and S. Snowdon, Mechanical and Electrical Design of the Fermilab Lithium Lens and Transformer System, IEEE Trans. Nucl. Sci, NS-30, p. 3660, 1983.

High-Intensity Flash X-Ray Source for HERMES III*

T.W.L. Sanford, J. A. Halbleib,
W. H. McAtee, and R. C. Mock

Sandia National Laboratories
Albuquerque, NM 87185

Abstract

The design of an intense source of flash x-rays that delivers a measured peak dose and dose rate of 370 krad(Si) and 3.5×10^{13} rad(Si)/s over a useful area of 80 cm^2 without target destruction is described, and measurements are compared with predictions of a numerical model. The quality of the agreement gives credibility to the measurements, validates the main assumptions of the model, and gives insight into the generation and transport of the electron/photon cascade within the source.

Introduction

HERMES III is a 19-MV, 700-kA, 25-ns pulsed electron accelerator [1] that produces intense bremsstrahlung doses and dose rates over large areas, for the study of nuclear radiation effects induced by γ-rays. The standard EPA (extended planar-anode) diode delivers peak dose and dose rate of 100 krad(Si) and 5×10^{12} rad(Si)/s over a useful area (area where the dose is greater than 50% of the peak dose) of 1000 cm^2 [2]. This diode has been used successfully as the baseline radiation source since the accelerator was commissioned 3 years ago.

In this paper, we describe a method of focusing the radiation in order to obtain much higher doses and dose rates over smaller areas. The concept is illustrated in Figure 1, where a low pressure gas cell (3 torr N_2) is introduced between the anode window and bremsstrahlung target. In the gas, the high inductive electric fields generated by the beam rapidly charge-neutralize and partially current-neutralize the incident beam, resulting in ballistic propagation. The introduction of the gas cell thus permits the annular beam to impact the target at a small radius, with little dispersion from self-fields. With this design, the radiation dispersion at the focus is minimized and the formation of an anode plasma at the upstream surface of the target due to high energy-deposition from the incident beam is no longer an issue, because the surface is inside the gas cell.

*This work was supported by the United States Department of Energy under contract DE-AC04-76 DP000789.

0-7803-0135-8/91$01.00 ©IEEE

In the following, we describe the optimization of this configuration as a function of anode-window material, target composition, gas-cell length, and beam-stabilizing mechanism. The results are compared with a two-dimensional numerical model [3] that uses the MAGIC computer code [4] to calculate the electron flow in the azimuthally symmetric AK gap and the CYLTRAN computer code of the ITS system [5] to calculate the subsequent ballistic transport in the gas cell and the electromagnetic shower in the target and downstream radiation diagnostics.

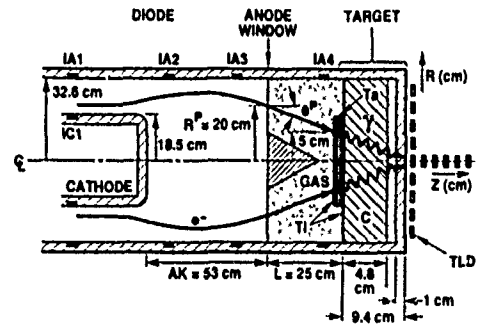


Figure 1. Schematic of high-intensity source

The experimental arrangement utilizes or modifies the existing hardware developed for the EPA diode. The operation of the accelerator and modeling are similar to that described in References 2 and 3. Briefly, sets of current shunts (IC1, IA1, · · · IA4) are used to measure current flow in the diode and gas cell, TLDs (thermoluminescent dosimeters) along the Z-axis measure the axial position of the radiation focus, and a 100-element graphite calorimeter (which replaces the target) in combination with a 48-Element TLD array at Z=0 cm are used to measure the radial energy-deposition profile and mean angle of incidence (θ^P) at the anode window and target, respectively. The model uses the time-integrated coupled radial and angular distribution at the anode window from the steady-state MAGIC simulation of electron flow at 20 MV (Figure 2), together with the measured time-integrated kinetic-energy distribution of the electrons, as input to CYLTRAN. The model calculations of dose downstream of the target are all normalized to the dose-area product measured in the TLD array at Z=0 cm.

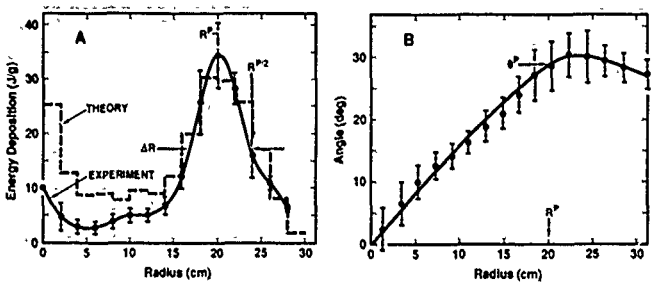


Figure 2. (A) Comparison of measured (for a 53-cm AK gap and solid cathode tip) and calculated (for a 60-cm AK gap and annular cathode tip) radial electron energy deposition at anode window. Errors correspond to RMS variation measured along ±X and ±Y axes at the same R. (B) Corresponding calculated angular distribution. Errors correspond to RMS variation in the associated 2-cm radial bin.

Anode window and target

For the high-intensity source, we use the EPA diode with a 53-cm AK gap and solid cathode tip. The gap allows the beam to enter the gas cell with a measured radius and convergence angle of 20±0.5 cm and 30±3°, respectively. Under these conditions, the incident beam imparts an energy deposition of only 30 J/g(C) at the anode window (Figure 2), which is an order of magnitude below that necessary to produce an anode plasma [6]. The solid tip minimizes the on-axis current density and concentrates the bulk of the current density at large radius [3].

At the input and exit of the gas cell, a 0.2-mm-thick aluminum anode window and a 1.5-mm-thick tantalum converter are used, respectively, to maximize the radiation dose on axis. By using the thinner window of lower Z relative to the 0.3-mm-thick titanium window of Reference 2, the multiple-Coulomb-scattering of the incident beam is kept below the intrinsic ±4° beam dispersion. Thus, scattering of the beam in the window does not contribute significantly to the dispersion of the annular beam at the target. Secondly, CYLTRAN calculations show that ~1.5 mm, instead of the 3 mm of tantalum in the Ti/Ta/C target designed for bremsstrahlung production with the EPA diode, maximizes the radiation at the focus, while still preventing primary electrons from traversing the graphite absorber. Accordingly, the tantalum thickness of the EPA target is reduced to 1.5 mm for this application.

Gas-Cell Length

The radius (R^P) of the beam measured at the target for a gas cell length of 25 cm and 30 cm coincides with that projected from the measured angle (θ^P) at the anode window (Figure 3). Accordingly, in the model, the self fields of the beam in the gas are ignored, and the propagation of the beam in the gas and subsequent electromagnetic shower in the target and downstream TLDs are modeled using CYLTRAN. This model shows that a gas-cell length (L) of ~25 to 30 cm maximizes the dose at the radiation focus, in agreement with that expected geometrically (Figure 3) and that measured (Figure 4). Additionally, the measured HWHM of the axial and radial radiation profiles (Figure 5A) are in agreement with those calculated, showing that there are no new effects contributing significantly to the dispersion of the radiation focus. The difference between measured and calculated peak doses (Figure 4) is likely due to the three-dimensional and time-dependent effects not included in the model.

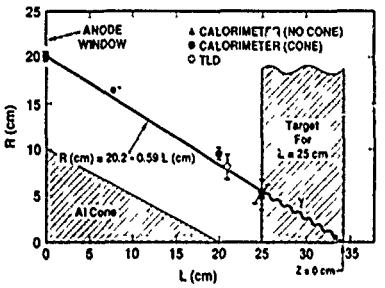


Figure 3. (•,▲) Radius of annular electron beam (R^P) measured in calorimeter as a function of gas-cell length (L). (o) Radius of annular radiation beam generated at anode window for L=0 cm and measured in TLD array 21-cm downstream of anode window.

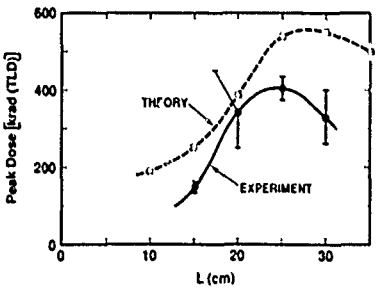


Figure 4. Comparison of measured and calculated peak dose at radiation focus as a function of gas-cell length (L).

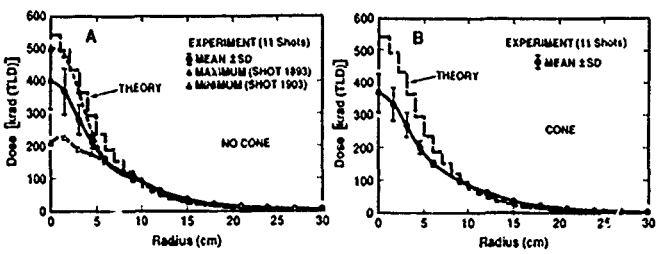


Figure 5. A comparison of measured and calculated radiation dose profile at radiation focus (Z=0) for L=25 cm. (•) mean and RMS variation about mean, ▲ maximum dose profile and △ minimum dose profile measured in radial TLD array at Z=0 for 11 shots. (A) Conical structure is not present. (B) Conical structure is present.

Such variations are observed when the calculated radial electron energy deposition is compared with that measured at the target (Figure 6). The variation measured with azimuth or between shots is more than a

factor of two times the mean at a given radius. Accordingly, the target, in order to survive, is designed to handle depositions over wide excursions. For our high-intensity source, the thickness of the tantalum laminations is reduced from the 0.051 mm thickness used in the EPA target to 0.013 mm in order to increase the threshold for spalling the tantalum from 85 J/g to 340 J/g. Under these conditions, the target has survived over 50 shots without destruction.

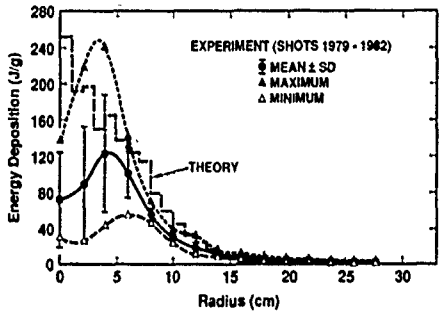


Figure 6. Comparison of measured and calculated surface energy deposition at the target as a function of radius for L=25 cm. Conical structure is in place for the measurements. (•) mean and RMS variation about mean, ▲ maximum, and △ minimum deposition for measurements made along ±X and ±Y axes at same radius for sequential shots.

Stability

At the L=25 cm optimum, a peak dose of 402±88 krad(TLD) is measured (Figure 5A). It occurs at the downstream face of the vacuum chamber as expected. The RMS variation in the peak dose is ±22%. It varies by a factor of 2.4 between extremes when measured over 11 shots. The variation in peak-dose is strongly correlated with the ±1.5 cm shot-to-shot variation in the axial position of the focus, and the magnitude of the variation in peak-dose is in rough agreement with the decrease expected when the focus occurs farther downstream. About half of the variation in the position of the axial focus is directly attributed to the variation in the mean R^P and θ^P at the input to the gas cell due to the measured ±0.3-MeV shot-to-shot variation in peak voltage. The remainder may be due to 3-D effects.

By introducing the coaxial conical structure shown in Figures 1 and 3, a weak magnetic restoring force is applied to the beam due to the induced net currents flowing on the cone. Experimentally, the application of the cone does not alter the mean position of the beam at the target (Figure 3). It does, however, reduce the RMS variation in the peak dose from 22±3.5% to 16±2.5% (Figure 5B).

Examination of Figure 4 shows that additional stability in peak-dose due to variation in focal position might be gained by adjusting the focus such that it falls a few centimeters inside the downstream face of the vacuum chamber. Because of the higher energy density at the upstream face of the target, however, the spallation threshold of the tantalum is exceeded. At present, this additional stabilizing potential is only applied minimally (Figure 3).

Conclusion

Introducing a low-pressure gas cell with a coaxial cone between the anode window and target of the EPA diode permits a peak-dose of 370 krad(Si) and corresponding peak dose-rate [7] of $\sim 3.5\times10^{13}$ rad(Si)/s (with ±16% shot-to-shot variation) to be achieved over a useful area of ~80 cm^2 without destruction of the radiation source (Figure 5B). The agreement between the radiation profiles measured and calculated gives credibility to both, as well as to the approximations made in the model.

Acknowledgments

We thank J. W. Poukey for calculating the MAGIC distribution used in the model; R. L. Westfall and the HERMES III crew for technical support; J. J. Ramirez, J. E. Maenchen, J. E. Powell, W. Beezhold, and J. R. Lee for vigorous support of this research; and D. E. Beutler for reviewing this paper.

References

[1] J. J. Ramirez, K. R. Prestwich, D. L. Johnson, J. P. Corley, G. J. Denison, J. A. Alexander, T. L. Franklin, P. J. Pankuch, T. W. L. Sanford, T. J. Sheridan, L. L. Torrison, and G. A. Zawadzkas, *Digest of Technical Papers of the 7th IEEE Pulse Power Conference,* edited by R. White and B. H. Bernstein (IEEE, New York, 1989), pp. 26-31.

[2] T.W. L. Sanford, J. A. Halbleib, and R. C. Mock, *IEEE Trans Nucl Sci,* vol.NS-37, No. 6, P. 1762, 1990.

[3] T. W. L. Sanford, J. A. Halbleib, J. W. Poukey, G. T. Baldwin, G. A. Carlson, W. A. Stygar, G. A. Mastin, T. Sheridan, R. Mock, J. A. Alexander, E. R. Brock, and C. O. Landron, *J Appl Phys,* vol. 67, p. 1700, 1990.

[4] B. Goplen, R. E. Clark, J. McDonald, W. M. Bollen, "Users Manual for MAGIC," Mission Research Corporation Report No. MRC/WDC-R-068, Alexandria, VA (September 1983).

[5] J. A. Halbleib, in *Monte Carlo Transport of Electrons and Photons,* edited by T. M. Jenkins, W. R. Nelson, and A. Rindi (Plenum Publishing Corporation, New York, 1988), pp. 249-284.

[6] T. W. L. Sanford, J. A. Halbleib, J. W. Poukey, A. L. Pregenzer, R. C. Pate, C. E. Heath, R. Mock, G. A. Mastin, D. C. Ghiglia, T. J. Roemer, P. W. Spence, and G. A. Proulx, *J Appl Phys,* vol. 66, p. 10, 1989.

[7] T. W. L. Sanford, J. A. Halbleib, D. E. Beutler, W. H. McAtee, R. C. Mock, and D. P. Knott, to be presented at 28th International Nuclear and Space Radiation Effects Conference (San Diego, CA, July 15-19, 1991).

SLC Positron Source Flux Concentrator Modulator*

J. de Lamare, A. Kulikov, R. Cassel, V. Nesterov
Stanford Linear Accelerator Center, Stanford CA 94309

Abstract

The modulator for the SLC e+ source flux concentrator provides 16 kA in a 5 μs sinusoidal half wave current for a pure inductive load, at 120 Hz. The modulator incorporates 10 EEV CX1622 thyratrons in a switching network. It provides reliable operation with acceptable thyratron lifetime.

I. DESIGN CONSIDERATIONS

Stanford Linear Collider (SLC) is an accelerator which collides electrons and positrons for particle physics research at SLAC. Such a collider requires a high yield positron source (See Reference 1 for details). The flux concentrator is a pulsed magnet that produces a focusing solenoidal magnetic field to effectively capture positrons emitted from an electron beam target (Figure 1). Positron production and capture are discussed in Reference 2. The production of a high magnetic field in the flux concentrator (up to 5.8 Tesla) requires a current pulse of 16 kA. The flux concentrator modulator provides 16 kA pulses at 120 Hz to the magnet.

Another design consideration is the system inductance. The inductance of the flux concentrator is approximately 1 μH. A more detailed description of the flux concentrator is elsewhere in these proceedings (Ref. 3). The low inductance of the magnet requires a low inductance driver to meet the system's pulse requirements. The magnet's low impedance makes efficient energy transfer to the flux concentrator difficult.

II. MODULATOR DESIGN

The flux concentrator modulator has four modules all of which charge by the same charging system composed of a high voltage power supply, a charging capacitor, and a charging inductor. Each module has two parallel charge and discharge paths. There are two forward thyratrons and one pulse cable per module. Also, two of the modules also have reverse thyratrons. There are four water cooled resistors, one per module. The four modules operate in parallel to supply the full current to the flux concentrator. The total modulator is approximately 1.5 m x 3 m x 1.5 m, and is in an interlocked high voltage room.

Because the flux concentrator modulator design requires a high current pulse into an inductive load, the system inductance was kept to a minimum. This was accomplished by building wide current paths while minimizing the current loops. Each module has a low impedance, 14 Ω, pulse cable. These cables are 15 meters long, and they are connected in parallel at the load. Creating several parallel paths reduces the system inductance and limits the average current requirements of many components; thus increasing the system reliability.

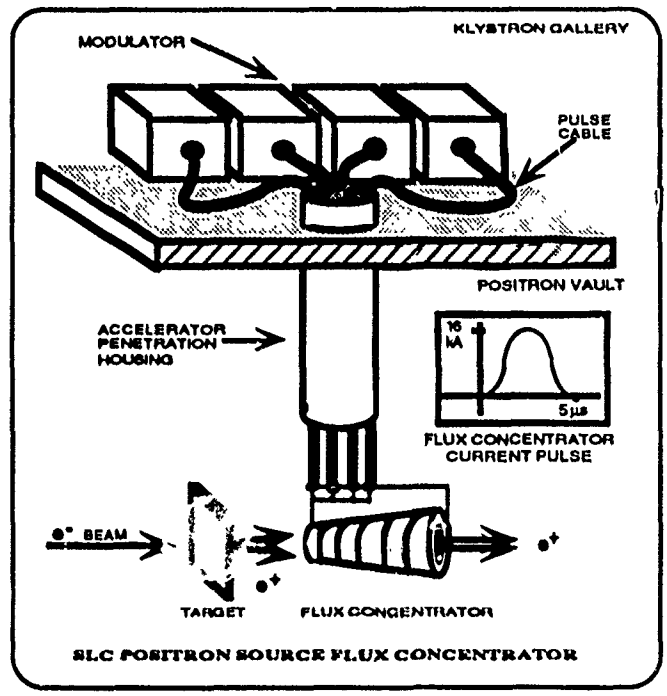


FIGURE 1: Positron Source

III. MODULATOR OPERATION

The basic modulator design is shown in Fig. 2. A 5 kV, 15 kW power supply charges the charging capacitor. This capacitor resonantly charges the parallel modulator capacitors through the charging inductor. There are eight parallel charging paths in the modulator through eight parallel charging diodes. The charging path continues through the modulator capacitors to ground via the pulse cables and the load. Each modulator capacitor has a switch to ground. These switches are EEV CX1622 thyratrons, called forward thyratrons. The forward thyratron grids are pulsed simultaneously by a grid driver. This output pulse drives a pulse transformer with eight secondaries, one per forward thyratron. Nanosecond switch jitter is ignored since the modulator current pulse is several microseconds in duration. When the forward thyratrons are switched, the positive high voltage side of the modulator capacitors are brought to ground potential, thus the parallel side of these capacitors becomes negative high voltage, and a current path is created from the modulator capacitor through the thyratron, and the load, then back to the modulator capacitor.

Before the voltage on the parallel side of the modulator capacitors swings positive, another thyratron is triggered. This tube is the reverse thyratron. It's purpose is to act as a diode such that when the voltage on the parallel side of the modulator capacitors swings positive, some of the returning energy will be dissipated through the water cooled resistor.

* Work supported by US Department of Energy contract DE-AC03-76SF00515

0-7803-0135-8/91$01.00 ©IEEE

Oscillographs of the thyratron currents are shown in Data 1. It is necessary to dissipate some of the returning energy, because after the forward thyratrons recover they are reverse biased by the modulator capacitor. EEV recommends that these thyratrons are not reverse biased above 10 kV for the first 25 microseconds after the anode pulse, because this can cause reverse conduction in the thyratron and thereby damage the tube.

After the discharge cycle is completed, the charging cycle begins again. The energy remaining in the modulator capacitors together with the energy transferred from the charging capacitor combine to swing the modulator capacitor voltage from negative to positive as seen in Data 2. The oscillograph shows the current and voltage of the charging inductor at the anode of the charging diodes. The net modulator voltage is the inverse of the recovered voltage plus twice the power supply voltage. Because the modulator recirculates some of its energy, the make-up power required from the supply is reasonable.

In series with the forward thyratron is a saturable inductor with an unsaturated inductance of 10.5μH. Because of the mismatch between the impedance of the load and the pulse cables, reflections occur up and down the cables adding an oscillation on top of the load current. The oscillations are seen on the flux concentrator current pulse at 12 kA in Data 3. The saturable inductors help to minimize these oscillations by initially slowing the rate of rise of voltage across the load.

IV. MODULATOR PERFORMANCE

The modulator has been in service since October 1989 and has 7400 hours of operating time. Thyratron lifetime has proven to be longer than expected. To this point the average thyratron lifetime in the system has been 3700 hours and 1.6 x 10^9 shots. These thyratrons have been operated at levels well below the manufacturer's specifications (See Table 1). The thyratrons show signs of aging by failing to recover after firing (latching). For the modulator to recover from a latching thyratron, the power supply is inhibited for one second when a latching current is detected. This gives time for the thyratron to recover. Then, the power supply is enabled, and the modulator returns to its normal operating levels. This recovery method is automatic, because latching may occur several times per day when the thyratrons are near their end of life. Generally, all thyratrons are replaced simultaneously so they age together.

V. INTERLOCKS

The whole positron system is comprised of several interlocks, many of which are attributed to the modulator. Besides the personnel safety interlocks, there are also interlocks for equipment protection. These include: a water flow interlock for the water cooled resistors, an over-current interlock that monitors the input current of the power supply, a frequency interlock to protect the flux concentrator from being pulsed at its mechanical resonance, and a crowbar interlock to protect the modulator from excessive charging current and charging voltage.

VI. CONCLUSIONS

A modulator for the SLC positron source flux concentrator is presently in operation at SLAC. This modulator has thus far operated at 12 kA for 7400 hours at 120 Hz and can operate at currents up to 16 kA. The modulator's switches, EEV CX1622 thyratrons, have given an average lifetime of 3700 hours and 1.6 x 10^9 shots.

VII. ACKNOWLEDGEMENTS

We would like to thank Scott Hewitt for his dedicated efforts in support of this project, as well as John Krzaszczak and the AMSS crew for their assistance in the maintenance of the modulator.

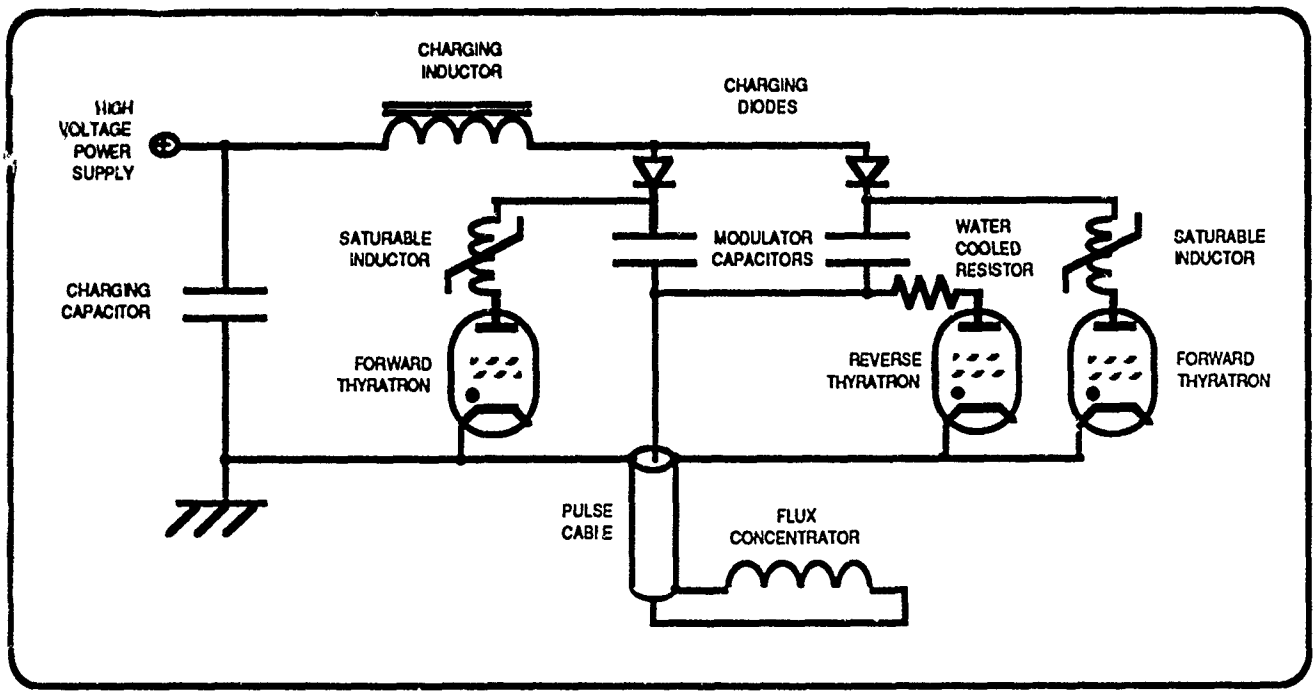


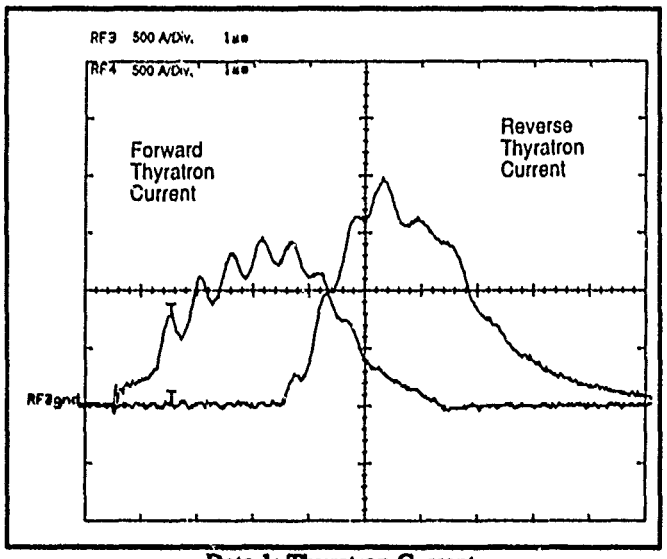
FIGURE 2 : Simplified 1/4 Modulator Schematic

SPECIFICATIONS	MFG.	FRWD. THYR.	RVRS. THYR.
Peak frwd. anode voltage	35 kV	20 kV	--
Peak rvrs. anode voltage	10 kV	12 kV	--
Peak anode current	5.0 kA	2.0 kA	3.0 kA
Average anode current	1.25 A	0.76 A	1.15 A

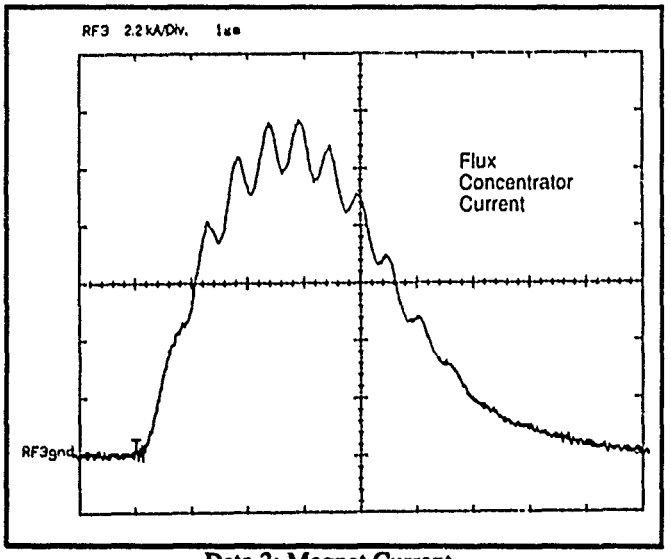
Table 1: Thyratron specifications with operation levels.

VIII. REFERENCES

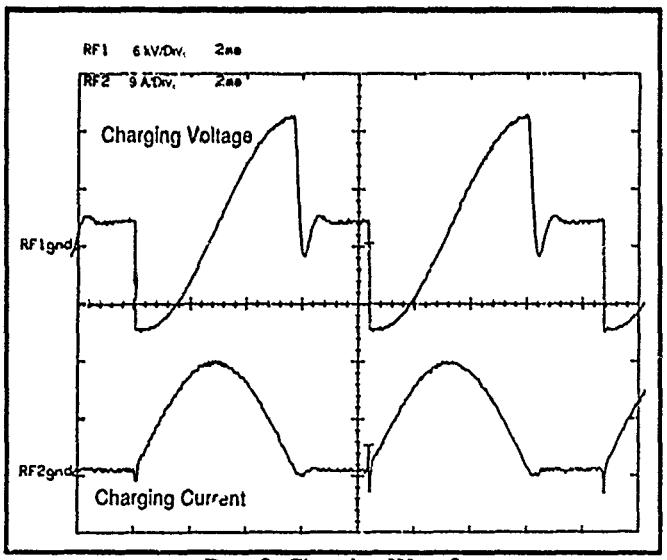
1. F. Bulos, H. De Saebler, S. Ecklund, R. Helm, H. Hoag, H. Le Boutlet, H.L. Lynch, R. Miller, K.C. Moffeit, "Design of a High Yield Positron Source," IEEE Transactions on Nuclear Science, Vol. NS-32, No. 5, Oct. 1985, pp. 1832-1834.
2. S. Ecklund, "Positrons for Linear Colliders," SLAC-Pub-4484, November 1987
3. A.V. Kulikov, "SLC Positron Source Flux Concentrator," These Proceedings



Data 1: Thyratron Current



Data 3: Magnet Current



Data 2: Charging Waveforms

FAST RISETIME MAGNETIC FIELD COIL FOR ELECTRON BEAM PROPAGATION STUDIES

D. J. Weidman,[a] W. C. Freeman, J. D. Miller, M. J. Rhee,[a)b)] R. F. Schneider,
K. T. Nguyen,[c)] and R. A. Stark
Naval Surface Warfare Center, White Oak
Silver Spring, MD 20903

Abstract

A new method for detuning the betatron frequency of an intense relativistic electron beam is investigated. The method employs a fast rising magnetic field to decrease the beam radius from the head to the tail of the beam. The magnetic field rise time is on the order of 30 ns with a peak value of about 2 kiloGauss. This method may be useful for detuning intense beam instabilities associated with betatron oscillations.

I. INTRODUCTION

Radius tailoring provides betatron detuning for reduction of the growth rate of hose instability. The betatron wavenumber is a function of beam radius R:

$$k_\beta = \left(\frac{I_b}{I_A}\right)^{\frac{1}{2}} \frac{1}{R},$$

where I_b is the beam current and I_A is the Alfven current. The equilibrium (self-pinched) beam radius R_{eq} is a function of normalized emittance $\epsilon_n^2(\zeta)$:

$$R_{eq}^2(\zeta) = \frac{\epsilon_n^2(\zeta) + P_\theta^2(\zeta)}{\gamma^2 I_b / I_A}, \qquad (2)$$

where ζ is the distance from the beam front and P_θ is the mean canonical angular momentum. Emittance tailoring, therefore, provides radius tailoring, by changing the equilibrium radius, R_{eq}, for the propagating beam.

In this experiment, a magnetic focusing field is used to confine the beam radius preferentially in the beam body and tail, while allowing the beam head to expand due to the beam space charge. This could potentially produce a controllable radius tailor in the beam, however this tailor may not survive further propagation. In order to produce a true emittance tailor the beam may then be passed through a foil to increase the transverse energy by scattering and "freeze" this emittance variation in the beam. This variation of ϵ_n in ζ guarantees the production of a tailor of $R_{eq}(\zeta)$.

The magnetic field is produced by a single turn which is energized by a high voltage pulse-forming-line. The fast variation in magnetic field occurs during the rising portion of the pulse. The risetime is in general determined by the inductance of the coil and the impedance of the pulse-forming line.

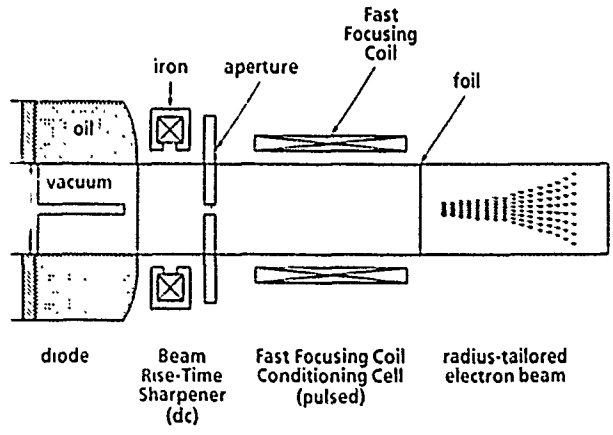


Fig. (1). Magnetic beam conditioning experiment concept.

II. EXPERIMENTAL ARRANGEMENT

Figure (1) provides an overview of the experiment: the Febetron diode, the Beam Rise-Time Sharpener[1] (BRTS), the fast focusing coil (FFC), and the foil. The Febetron

0-7803-0135-8/91$01.00 ©IEEE

705X produces a 2 MeV, 7 kA, 20 ns FWHM beam with voltage and current pulse shapes that are approximately triangular.

The BRTS consists of a dc focusing magnet and a graphite aperture: it sharpens the beam rise time to 6 ns with a 12 ns flattop at 3 kA. The operates on the principle of a magnetic lens. The magnetic field is adjusted so that only the highest energy electrons will be focussed to traverse the aperture. Since there is an instantaneously small energy spread in the beam, the lower energy, and lower current rise time portion of the electron beam will be lost.

The FFC conditioning cell consists of a nonmetallic vacuum drift chamber with axial current return bars and the external, single-turn FFC. The portion of the vacuum system surrounded by the FFC is made of glass with copper strips running axially along the inside. These strips provide a current-return path for the electron beam current and allow penetration of the FFC magnetic field to the axis of the system. The FFC is a 38 cm long, 20 cm diameter single turn to minimize inductance, thereby minimizing the rise time of the magnetic field.

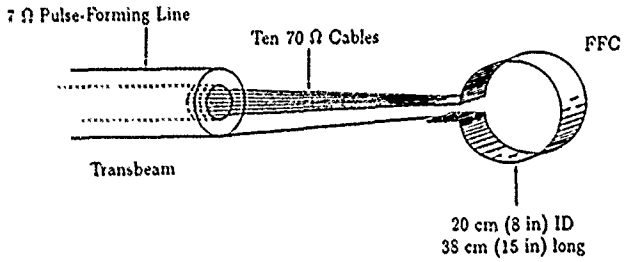


Fig. (2). Transbeam driven fast-focusing coil.

The FFC power source is Transbeam,[2] a 7-Ω machine that has been used to produce a 700 keV, 100-ns electron beam. The electron beam diode has been removed and the machine is used to drive current through the FFC. A transition section connects the end of Transbeam's 7-Ω coaxial transmission line to ten 70-Ω high-voltage (rated at 300 kV dc) coaxial cables, as shown schematically in Fig. 2. These ten cables allow flexibility in positioning the FFC relative to Transbeam. This makes it easier to use the FFC with an electron beam that is produced by another machine, such as the Febetron 705X. The ten cables are connected to the FFC, with the center conductors (#4 AWG) connected to one side of the coil and the outer conductors (braid) connected to the other side.

III. INITIAL DESIGN CALCULATIONS

The maximum magnetic field required is given by the magnetic focusing condition

$$B(kG) \geq 3.4\frac{1}{r_b}\left(\frac{\nu}{\gamma}+\frac{2\gamma T}{m_o c^2}\right)^{\frac{1}{2}} \qquad (3)$$

where r_b is the beam radius, ν is Budker's parameter, and T is the beam transverse temperature. Using the Febetron 705X parameters, the magnetic field requirement is 1.2 kG or higher.

It is straightforward to calculate the current needed for the required magnetic field. For a single-turn, long cylindrical coil, a magnetic field B is produced by a surface-current density J_s (A/m), approximately given by $B = \mu_o J_s$. The total current required is $I = J_s l = Bl/\mu_o$, where l is the length of the cylindrical coil. For B = 1.2kG, I = 40 kA.

The inductance of the FFC determines a lower limit on the rise time of the magnetic field. The inductance is approximately $L = BA/I = \mu_o A/l$ = 110nH, where A is the cross-sectional area of the coil; the lower limit on the rise time is $\tau = L/R$ = 16 ns. This is sufficiently fast to change the magnetic field during the electron beam pulse.

To predict the field-free radial expansion of the beam head, the beam envelope equation,[4]

$$\frac{d^2R}{dz^2}=\frac{I_b}{\beta^2\gamma^2 I_A R}+\frac{\epsilon_n^2}{\beta^2\gamma^2 R^3}, \qquad (4)$$

where r is the beam radius and z is the axial distance, is solved numerically. This provides a value for the radius of the beam head R_h. The radius of the beam tail R_t is confined by the FFC to the initial value of the beam radius at the diode.

The emittance tailoring ratio (the ratio of the emittance of the beam head to the emittance of the beam tail) ϵ_h/ϵ_t, after the conditioning cell, is given by

$$\frac{\epsilon_h}{\epsilon_t}=\left(\frac{\epsilon_o^2+\gamma^2\langle\theta_s^2\rangle R_h}{\epsilon_o^2+\gamma^2\langle\theta_s^2\rangle R_t}\right)^{1/2}, \qquad (5)$$

where ϵ_o is the initial beam emittance and $\langle\theta_s^2\rangle$ is the mean-square scattering angle from a foil. For our experi-

mental parameters, including a 1 mil (25 μm) titanium scattering foil and an initially cold beam, Eq. (4) can be approximated by $\epsilon_h / \epsilon_t \sim R_h / R_t$. The predicted emittance tailoring ratio for the Febetron beam with the BRTS is 4:1.

Preliminary circuit simulations have been done to model Transbeam and the fast focusing coil. The voltage and current waveforms of Transbeam in the model resemble experimental waveforms from electron beam experiments in the past. The ten 70-Ω cables were represented by a lumped circuit-element model and the single-turn FFC was modeled as a very low resistance. The results indicate that a 10 ns Transbeam rise time produces a FFC rise time of 15 to 20 ns and that 200 kA could be put through the coil. This agrees well with the analytic calculations above.

The magnetic field was measured with B-dot probes at reduced initial charging voltage. The results shown in Fig. (3), agree with the analytic calculations and circuit simulations.

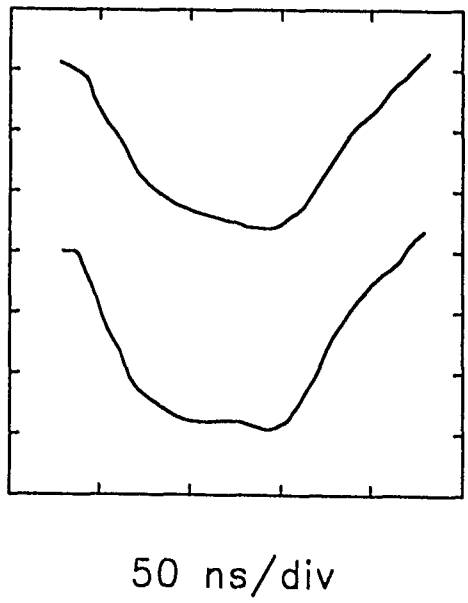


Fig. (3). Current through and magnetic field inside the fast coil. Top trace is current through the coil (10 kA/div) and bottom trace is magnetic field on axis (0.4 kG/div).

IV. STATUS

The FFC has been tested without an electron beam. Testing consists of firing Transbeam into the coil and mapping the magnetic field. The program plan is to test the FFC with an electron beam from the Febetron 705X electron beam accelerator and observe the radii of the beam head and tail. Time-resolved diagnostics will determine parameters such as the beam radius and emittance,[5] by using a slit or an array of slits, a fast detector (scintillator or Cherenkov) and a streak camera, and a segmented Faraday cup.

V. ACKNOWLEDGMENTS

We would like to thank D. R. Tejada of the U.S. Navy, and L. S. Song and B. E. Schaible of University Research Foundation for their help in constructing and in assembling parts of the experiment. We would also like to thank H. S. Uhm of Naval Surface Warfare Center and W. E. Nexsen of Lawrence Livermore National Laboratory for helpful discussions during the early phases of this work. This work has been supported by DARPA under ARPA Order No. 7792 BASIC.

VI. REFERENCES

[a] Advanced Technology and Research, Laurel, Maryland 20707
[b] Permanent address: University of Maryland, College Park, Maryland 20742
[c] Mission Research Corporation, Newington, Virginia 22122

[1] J. D. Miller, K. T. Nguyen, R. F. Schneider, K. W. Struve, H. S. Uhm, and D. J. Weidman, "Pulse-Shaping a High-Current Relativistic Electron Beam in Vacuum," Naval Surface Warfare Center Technical Report 90--268, (1990).
[2] J. R. Smith, R. F. Schneider, M. J. Rhee, H. S. Uhm, and W. Namkung, J. Appl. Phys. 60, 4119 (1986).
[3] B. Goplen, L. Ludeking, J. McDonald, G. Warren, and R. Worl, MAGIC User's Manual, (MRC, Va. 1989) Unpublished.
[4] E. P. Lee and R. K. Cooper, Part. Accel. 7, 83 (1976).
[5] R. F. Schneider, E. H. Choi, H. I. Cordova, J. R. Smith, D. J. Weidman, M. E. Moffatt, K. T. Nguyen, and H. S. Uhm, "Time-Resolved Measurement of Intense Relativistic Electron Beams," Bull. Am. Phys. Soc. 33, 1951 (1988).

LONG PULSE ELECTRON BEAMS

J. R. Smith[a] , I. R. Shokair, and K. W. Struve[b]
Sandia National Laboratories
Albuquerque, New Mexico 87185

Abstract

Pulsed power accelerators used for intense relativistic electron beam applications have generally had pulse lengths of 10 - 100 ns. There are research areas where a pulse length of several 100's of nanoseconds is required or might be advantageous (e.g. long distance propagation, microwave generation, free electron lasers). In the last 4 years several long pulse accelerators have come on line [1,2,3]. In this report the emphasis is on measurement of the parameters of a long-pulse beam. The Troll accelerator produces the beam, and a conditioning cell is used to adjust beam parameters. This system has typically been operated with the following output parameters: 2.5 MV, 1-2 kA, 0.5-1 μs.

I. SYSTEM ELEMENTS

A schematic of Troll [3] and the conditioning cell is given in Fig. 1. The basic elements of Troll are a Marx generator and a long-pulse diode. A long pulse is obtained by connecting the Marx directly to the diode without the traditional intermediate pulse forming line. The Marx output is shaped so as to obtain a relatively square pulse.

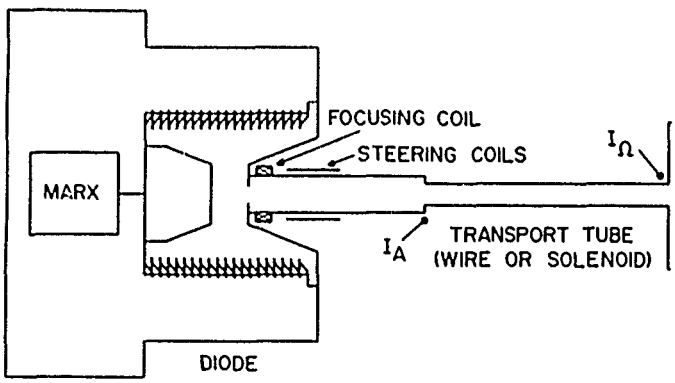


Figure 1. Troll and conditioning cell.

The pulse leading edge is adjusted with an external RC circuit, and the pulse trailing edge is defined with a crowbar switch. The Troll beam has been mainly used for long-pulse beam propagation research where beam initial conditions are frequently critical [4]. Therefore, a conditioning cell is attached at the diode output which allows adjustment of beam parameters. The conditioning cell may be divided into two regions. The first region contains a focusing coil and steering coils. The focusing coil is used to select beam size, and steering coils are used to correct minor errors in beam centering. The second region contains a transport tube, where two different modes of operation have been used. In the first mode, wire conditioning is used to improve beam quality in terms of beam centering [5]. In the second mode, solenoidal transport is used to optimize current amplitude and pulse flatness.

The long-duration, high-voltage Marx generator was supplied by Maxwell Laboratories [6]. A simplified schematic, Fig. 2, shows three major components: Marx capacitor bank, snubber network, and diverter switch. The Marx bank contains 44 stages; stage 1 consists of two 1 μF capacitors connected in parallel, stages 2 through 44 consist of two 0.5 μF capacitors connected in series through spark gaps. All 44 stages are connected in series during Marx erection, giving an open circuit voltage of 4.35 MV at the maximum capacitor charging voltage of 50 kV. The Marx capacitor bank output is connected in series with a 20 ohm resistor. This is a liquid resistor which absorbs the stored energy when the Marx is crowbarred with the diverter. Timing of the diverter trigger is adjusted to control the pulse width. Stray capacitance from the Marx generator to ground causes voltage overshoot and ringing at the pulse leading edge. The snubber network is an RC circuit which damps these oscillations. The snubber RC time constant is 140 ns. The Marx generator voltage pulse is monitored by a resistive divider.

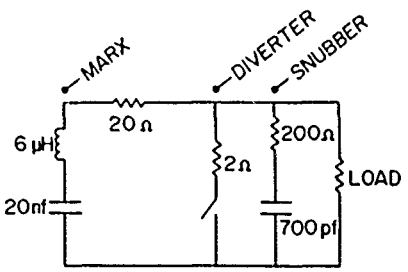


Figure 2. Troll circuit elements.

[a]Titan/Spectron
[b]Mission Research Corporation
*Work Supported by SDIO through the Naval Surface Warfare Center and the DOE at Sandia National Laboratories under contract DE-AC04-76-DP00789.

0-7803-0135-8/91$01.00 ©IEEE

The long-pulse diode was supplied by Sandia National Laboratories [7]. It is an axial stacked-ring diode.The anode-cathode gap is adjustable by attachment of cathode supports with different lengths. The results obtained in this report used a 27 cm gap setting. The electron source is a 10 cm diameter velvet disk positioned in the center of the cathode holder. The cathode holder is painted with an emission suppressant. The foilless anode has a 10 cm diameter aperture.

The focusing coil is a pancake coil which is 10 cm long with a 21 cm bore. For standard operating conditions the focusing coil is adjusted to produce a peak field on axis of 700 Gauss, which gives a 5 cm beam radius at the entrance to the transport tube. This radius was measured with an x-ray pinhole camera and represents the spot radius which contains all of the beam electrons. The corresponding Gaussian radius would be smaller. The sensitivity of beam radius to magnetic field for the focussing coil (Δ radius/Δ B-field) was measured as 3 mm/10 Gauss. The focusing coil is a pulsed coil which has a 0.5 second period. Timing is adjusted so that the beam is produced at the peak of the coil's current pulse.

The steering coils are two pairs of Helmholtz-like coils, one pair for horizontal deflection, and one pair for vertical deflection. Each coil is shaped in a rectangle, 50 cm long x 26 cm wide. For standard operating conditions it was found the beam was best centered with a vertical field of 2.5 Gauss, and a horizontal field of 0 Gauss. The steering coil fields are operated steady state.

Rogowski coils are located at the entrance and exit of the transport tube to measure beam currents I_A and I_0. Performance of the conditioning cell with wire conditioning and solenoidal conditioning is discussed in Sections III and IV.

II. WAVEFORMS

Voltage and current waveforms are given in Fig. 3. The voltage is measured at the Marx output. The current waveform is the beam current measured at the entrance to the transport tube. It has been highly repeatable over hundreds of shots.

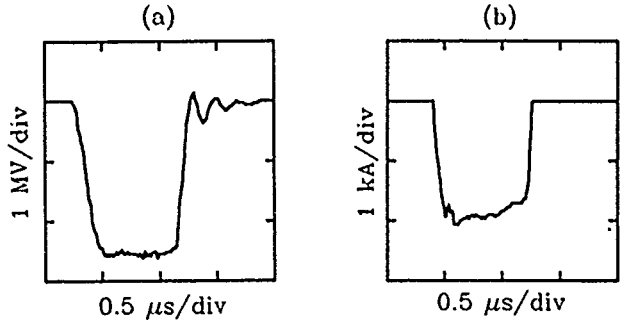


Figure 3. (a) Marx generator voltage, (b) beam current.

III. WIRE CONDITIONING MODE

For operation in the wire conditioning mode, the transport region contains a 0.1 mm diameter wire which both electrostatically focuses the beam and damps transverse oscillations. The wire is held on axis with a tripod configuration of wires at either end. Upstream, the wire was grounded to the vacuum drift tube; downstream, the wire was connected to ground through an inductor. The wire typically survives from 10 to 30 shots. Figure 4a shows the beam current, I_A, where the diverter was triggered to terminate the pulse at 500 ns. The corresponding current at the exit of the transport tube, I_0, is given in Fig 4b. Almost 50 % of the total current has been lost and pulse flatness has degraded. However, transverse oscillations were suppressed.

Beam radius was measured at the exit of the transport tube (the end of the wire) by imaging the light emitted from a Cherenkov target[4]. Beam emittance was measured by observation of radius expansion vs propagation distance for vacuum propagation. For an initial beam segment, beam radius was 3.0±0.5 cm, and beam emittance was 0.3±0.03 rad cm. The initial beam offset was ±0.4 mm, and the angular offset was less than 21 mrad.

IV. SOLENOIDAL CONDITIONING MODE

For operation in the solenoidal conditioning mode, a solenoidal magnetic field was used to confine the beam in the transport tube. The solenoid is 1.5 m long. The solenoidal field which gave optimum results was 300 Gauss. Figure 4c gives I_0 which is almost identical to I_A.

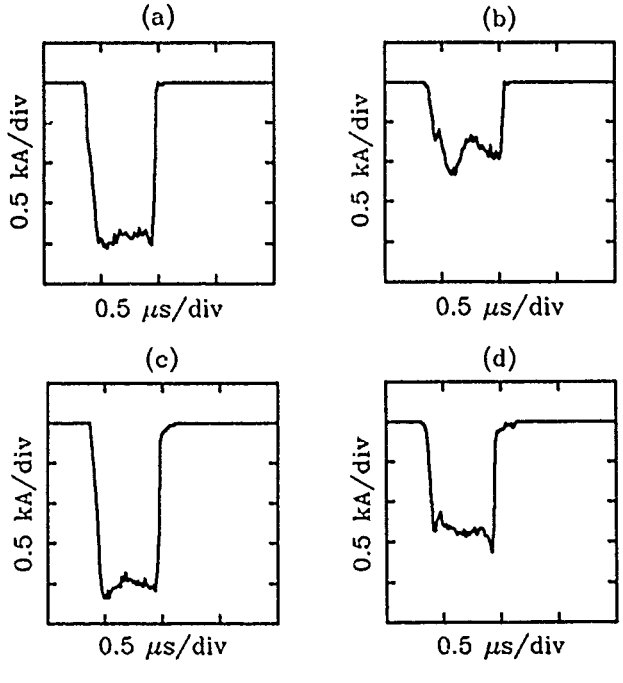


Figure 4. Beam currents: (a) I_A, (b) I_0 with wire conditioning, (c) I_0 with solenoidal conditioning, (d) I_0 with solenoidal conditioning and aperture.

For some beam propagation work it has been desirable to reduce the level of beam current. For this application an 8 cm diameter aperture was inserted near the transport tube exit. Results are shown in Fig. 4d. Using solenoidal conditioning with an aperture, and the Cherenkov target diagnostic, the initial beam radius varied between 1 and 2 cm from shot to shot. A sample of the change in beam profile throughout the pulse duration is given in Fig. 5, where beam profiles corresponding to different times into the pulse (beam slice times) are shown. A segmented Faraday cup was used to obtain this data. In the shot of Fig. 5 the beam radius decreased for later times into the pulse, although this was not noted as a general trend throughout many shots. The beam profiles do consistently fit a Gaussian distribution from shot to shot.

V. SUMMARY

Numerical results are summarized in Table I. The wire conditioning mode excels in reducing transverse oscillations and in centering the beam. The solenoidal conditioning mode offers almost 100% current transport and maintains the flat pulse shape produced by the diode. The wire mode does require increased maintenance as compared with the solenoidal mode, since the wire must be replaced at frequent intervals. The attainment of square voltage and current pulses is a stressing challenge particularly encountered in the production of long pulse electron beams, as opposed to shorter pulse beams (i.e. <100 ns). Therefore, the nearly square pulse shapes shown in Fig. 3 are significant results.

Table I. Beam parameters

	Troll	Wire Mode	Solenoid Mode	Solenoid Mode (with aperture)
Beam Current (kA)	2	1	2	1.2
Beam Radius (cm)	5[a]	~3[b]		1-2[b]

[a]time integrated, spot radius
[b]initial beam slice, Gaussian radius

VI. ACKNOWLEDGEMENTS

We gratefully acknowledge the technical support provided by P. D. Kiekel, I. Molina, and S. Hogeland.

VII. REFERENCES

[1] R. F. Schneider et al,"Thor: A microsecond intense relativistic electron beam accelerator," this conference.

[2] R.F. Lucey,Jr., R.M. Gilgenbach, J.D. Miller, J.E. Tucker and R.A. Bosch, "Transport and Stability of long-pulse relativistic electron beams in UV laser-induced ion channels," Phys. Fluids B, vol. 1, pp.430-434, February 1989.

[3] A.H. Bushnell, Y.G. Chen, and J. Shannon, "Troll: A 4-MV peak voltage pulser," in *Digest of Technical Papers, Sixth IEEE Pulsed Power Conference*, Arlington, Virginia, June 1987, pp. 390-392.

[4] R.J. Lipinski, J.R. Smith, I.R. Shokair, P. Werner, D.J. Armistead, P.D. Kiekel, I. Molina, and S. Hogeland, "Measurement of the electron-ion hose instability growth rate," Phys. Fluids B, vol. 11, pp. 2764-2778, November 1990.

[5] D.S. Prono et al, "Electron-beam guiding and phase-mix damping by an electrostatically charged wire," Phys. Rev. Lett., vol. 51, p. 723-726, August 1983.

[6] Maxwell Laboratories, Inc., 8888 Balboa Ave., San Diego, California 92123-1506

[7] R.S. Clark, M.T. Buttram, J.W. Poukey, and T.R. Lockner, "A multi-megavolt, two-microsecond electron beam diode," in *Digest of Technical Papers, Sixth IEEE Pulsed Power Conference*, Arlington, Virginia, June 1987, pp. 378-381.

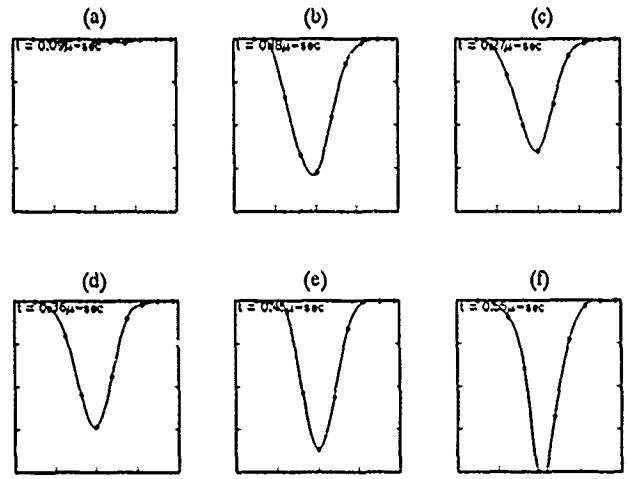


Figure 5. Beam profiles for various slice times, with solenoidal conditioning.
(a) 0.09 μs (b) 0.18 μs
(c) 0.27 μs (d) 0.36 μs
(e) 0.45 μs (f) 0.55 μs

KICKER PULSER CHARGER *

R. Cassel and M. Nguyen

Stanford Linear Accelerator Center,
Stanford, California 94309

Abstract

A highly regulated Pulsed Charging power supply was developed for the SLC damping ring kickers system to provide a kicker pulse amplitude stability of better than 0.01%. This unique supply charges the kickers cables, with capacitance of 4800 pF to 80 kV (15 J), in less than 40 usec. Operation is unaffected by intermittent kicker operation or changes in reputation rate up to the rated 180 Hz. The Charger utilizes a commercial dc regulated supply and a single SCR switch. There are three layers of regulators to insure high pulsed charging voltage stability.

Background

The SLAC, SLC requires a very will regulated damping ring kicker magnet pulse, both pulse to pulse and long term of approximately one part in ten thousand. In addition the pulsed current rise time must be less than 20 nanoseconds. This fast rise time requires a high gas pressure in the kicker pulser thyratrons which in turn infers the need to pulse charge the kicker pulser lines to avoid thyratron voltage breakdown.

Standard resonance charging of the kicker pulser line, which was first employed on the kickers, resulted in an unacceptable pulse rise time. In addition regulation of resonant charging was inadequate and irregular pulsing intervals only aggravated the regulation problems. Regulation and stability of the resonance charging system even after several improvement attempts was not better than one part in a thousand pulse to pulse and long term.

Solution

To address the rise time and regulation stability problems a pulsed charger was developed which improved the amplitude stability even with irregular pulsing intervals and repetition rates to 0.01%. and allowed for high gas pressures on the pulser thyratrons.

The design incorporates several novel approaches to achieve the desired performance. There are several items which effect the stability of charging the kicker pulser lines. as follows:

1) Impedance (capacitance) changes of the pulser line vs time related to temperature changes.

The pulser line impedance change was addressed by building a pulse charger with a low source impedance with minimal resonance charging. The source impedance of the charger is approximately 1/10 of the load impedance which results in a reduction of a factor of ten in voltage variation due to line impedance changes. The line impedance change is less than 0.1% with a water cooled line resulting in a charge voltage change of less than 0.005%.

2) Residual voltage (charge) on the pulser line resulting from reflections, leakage currents, and thyrtron turnoff variations.

The residual voltage is addressed by precharging the line to a low fixed highly regulated voltage. This voltage is less than 2% of the maximum charge voltage with a stability of 0.1% which results in less than 0.002% due to residual charge on the line.

3) Power line changes both fast and short term.

Power line changes were regulated by three layers of regulated. The first was a commercial switchmode power supply regulated to approximately 0.1%. Second a post regulator using a "bang bang" control to improve the regulation to 0.01% and Third a type of deQing circuit to proved an additional factor of two in regulation.

4) Thermal changes in monitory and control systems.

Changes in the monitory were addressed by using a low impedance temperature compensated voltage monitor directly connected to the pulser output. Because the charging is pulsed the monitor impedance could be 100 Kilohms terminated into 50 ohms which required no additional compensation to achieve the monitoring stability of 0.01% over the operation range.

The pulse charging was design to charge the 15 Joules of the pulser line in less than 40 microseconds (0.4 megawatts peak power). (Figure 1) This charging rate was fast enough to allow for the need increase in gas presser on the thyratron and at the same time slow enough to be able to reliably monitory and control the pulse amplitude to 1/10,000 and simple solid state devices.

* Work performed under U.S. Department of Energy Contract DE-AC03-76SF00515

0-7803-0135-8/91$01.00 ©IEEE

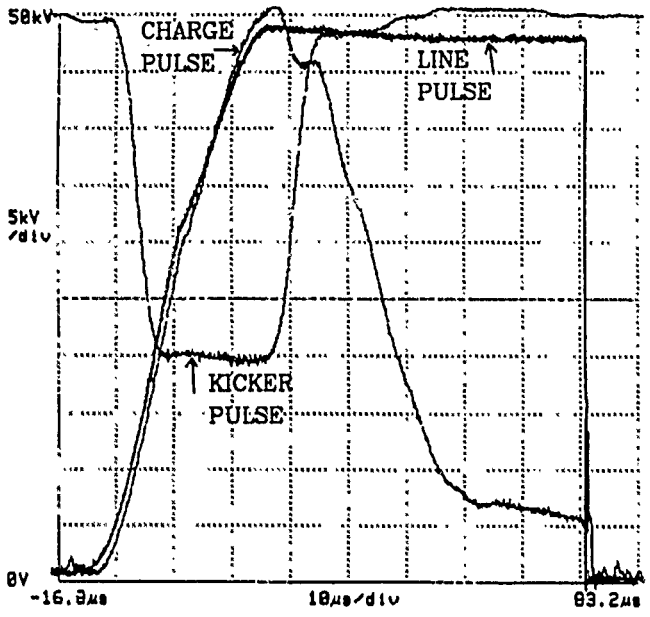


Figure 1
Pulse Charger Waveforms

Operation

The design incorporates several novel features. (Figure 2) Power is supplied by a voltage adjustable 5 kilowatt commercial switchmode power supply with a maximum voltage of 1000 Volts. The supply is connected to an energy storage capacitor C3 whose voltage changes by less than 1% during the pulse. This small voltage change allows the switching supply time to recharge the bank in the interpulse interval of 8 msec to approximately 0.5%. A shunt FET with series resistor is used as the second regulator to improve the regulation of the energy storage bank to better than 0.01% by switching on if the voltage on the capacitor is to high and off when the capacitor voltage is low. In addition to the energy storage capacitor the much smaller pulsing capacitor C7 is charge to the same voltage as the energy storage capacitor. At the pulse charging time SCR Q2 is turned on which discharges capacitor C7 through inductor L3. The system is not damped so that the discharge capacitor recharges in the opposite direction. The pulse transformer T1 which is connected between C7 and C3 steps up the voltage and generates the charging voltage for the pulser. The line capacitance reflects through the pulse transformer change the effective capacitance of the undamped ringing circuit. The negative ringing of the discharge capacitor C7 reverse biases the SCR Q2 turning it off. (Figure 3) The discharge capacitor C7 continues to ring positive again and then recharges by way of the energy storage capacitor C3. The magnetizing current of the pulse transformer helps recharge C7 to a limited voltage (approximately 50 volts) over C3 voltage determined by the flyback diodes CR1, the turns ration of T1 and the energy storage capacitor voltage. In addition to insure that the SCR is not overvoltaged diode

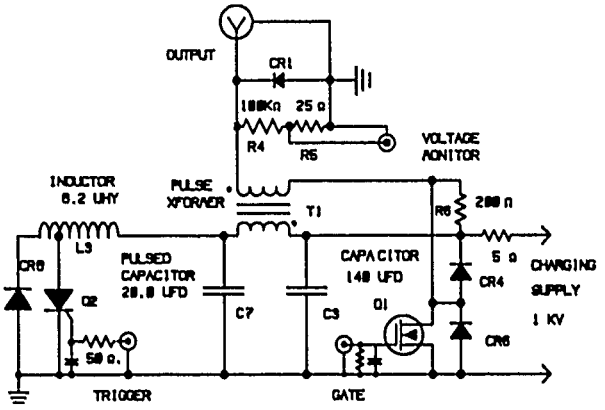


Figure 2
Simplified Schematic Diagram

CR11 forward voltage drop is used to insure that an overcharge of not more than 75 volts dose not occur. Precharging of the pulser line is accomplished by resistor R6 which connect a energy storage capacitor line to low side of the pulse transformer thereby precharging the pulser line to the regulated energy storage capacitor voltage.

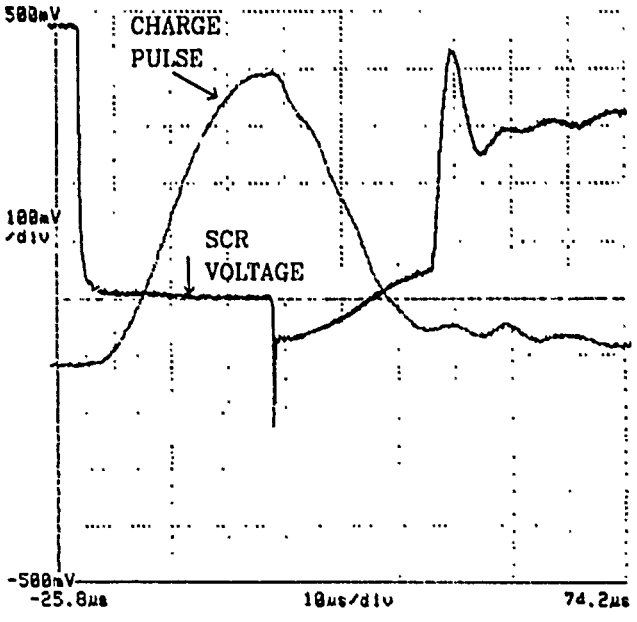


Figure 3
SCR Voltage and Charge Voltage

The final stage of regulation is accomplished by use of the FET which is connected to the low end of the pulse

transformer with diodes CR4 and CR6 insuring that the voltage dose not exceed the power supply voltage. As the line is charging diode CR6 conducts caring all of the charging current. however when the charging current is less than the power supply voltage divided by R6 the current diverts to R6 and the voltage on the FET will rise in the final 1% of the charging of the line. By turning on the FET the voltage available to charge the line is reduces by approximately 0.5%. By monitoring the peak charge voltage with the voltage divider R1 and R2 and turning on the FET the final stage of regulation is implemented. Due to the leakage inductance of the pulse transformer this last stage of regulation can only provide for pulse to pulse stability and provides only a factor of two improvement in performance. Figure 4

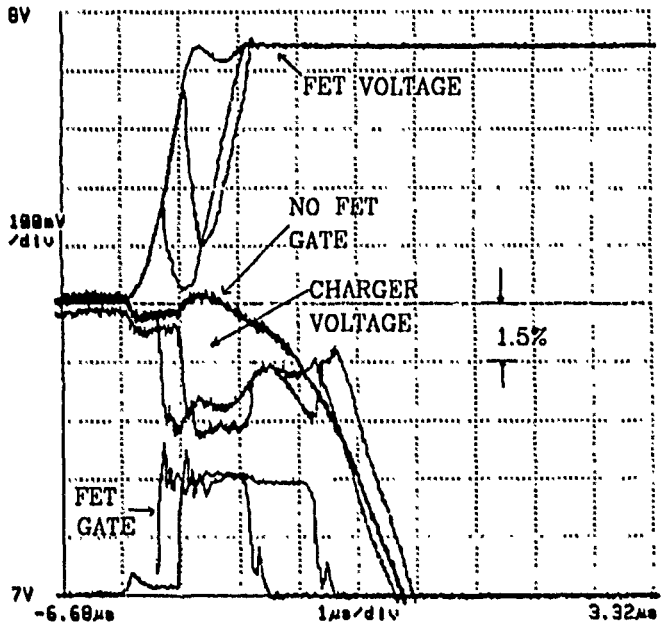


Figure 4
Final Stage Regulation

Conclusions:

A pulse charger for the SLC Damping Ring was produced which by use of several unusually technics was able to provide pulse charging regulated to 0.01% in a simple and inexpensively manor.

References

[1] F. Bulos, et al., "Some Fast Beam Kicker Magnet Systems at SLAC", Proceedings of the 1987 IEEE Particle Accelerator Conference, p. 1884.

[2] T. Mattison, et al., "Operational Experience with SLC Damping Ring Kickers", elsewhere in these Proceedings.

[3] T. Mattison, et al., "Status of the SLC Damping Ring Kickers Systems", elsewhere in these Proceedings.

PSR EXTRACTION KICKER SYSTEM IMPROVEMENTS

T. W. Hardek
Los Alamos National Laboratory, Mail Stop H852, Los Alamos, New Mexico 87545

Abstract

A program to improve the reliability of hardware required to operate the Los Alamos Proton Storage Ring has been under way for the past three years. The extraction kicker system for the PSR was identified as one candidate for improvement. Pulse modulators produce 50kV pulses 360 nsec in length at up to 24-Hz pulse repetition rate and drive two 4-meter-long stripline electrodes. Sources of difficulty with this system included short switch tube lifetime, drive cable electrical breakdown, high-voltage connector failure, and occasional electrode breakdown. This paper discusses modifications completed on this system to correct these difficulties.

1 Introduction

Extraction kickers for the Los Alamos Proton Storage Ring [1] consist of two sets of 4-meter-long electrodes pulsed to plus and minus 50 kV by Blumlein-configured transmission-line modulators. Each of the pulse modulators utilizes a single hydrogen thyratron to switch two Blumlein-configured transmission lines connected in parallel. The output connection to one of the lines is reversed to provide an inverted polarity output pulse. Ferrite cores have been added over the outer conductor of each Blumlein to increase the nominal inductance of this outer conductor to provide ground isolation for the reversed output. The system produces positive and negative output pulses that are exactly in time with each other since only one switch is used. The system suffered from fairly short main-switch-tube lifetime. In addition to short main-switch-tube lifetime the modulators utilize a pulse-charge system and the charging switch tube also suffered from short lifetime. We have replaced both switches have with EEV thyratrons.

A major part of the problem with main-switch-tube lifetime appears to have been stress from reversed current that occurs when the electrodes break down. The electrodes are 50-ohm strip lines fed at the downstream ends to take advantage of both the electric field and the magnetic field. While the basic design was good we were able to make some mechanical changes to improve the voltage holdoff capability of these structures.

Another weak point in the system was the high-voltage connection at both the modulator end and the electrode end of the drive cables. The original electrode solid connector design was replaced with a gas-insulated version. Connection to the modulator was modified to take better advantage of the insulating oil used for the modulator. In addition the original RG-218 drive cable was replaced with high quality RG-220 cable.

2 Main Switch Tube

The main switch thyratron must switch 4000 amperes in 40 nsec. This translates to a rate of rise of 100 kiloamperes per microsecond. An EGG HY-5353 was initially selected after testing several candidates. This tube cannot handle current reversal and suffered a rather short lifetime when arcing at the electrodes forced the tube to conduct in reverse. We have replaced this tube with an EEV-CX1725 [2]. The CX1725 is a hollow anode hydrogen thyratron capable of di/dt rates of 300 KA/μsec. The hollow anode design allows this tube to conduct up to 6000 amperes in reverse without damage. Arcing in our electrodes will not destroy this tube.

It is customary to supply the heater elements and the reservoir of high di/dt thyratrons with a direct current. This tends to reduce trigger jitter caused by the magnetic fields generated by heater current in the vicinity of the cathode. The CX1725 required a higher heater current than the original HY-5353 and the existing DC power supplies were unable to provide this additional output reliably. Tube specifications for the CX1725 show that one should be able to operate the heaters and reservoir from AC supplies and still achieve very low trigger jitter. Tests we conducted showed that with a large enough trigger pulse (1500 V) we in fact were able to achieve low jitter (4 to 5 nsec) but not wanting to overtax trigger circuitry we chose to use DC current. With DC-powered heaters and reservoir we achieve 1 to 2 nsec trigger jitter. We actually replaced the regulated power supplies with much simpler bridge rectifiers and filter capacitors. Regulation was obtained by installing a regulating-type line transformer ahead of the heater/reservoir supplies.

0-7803-0135-8/91$01.00 ©IEEE

3 Electrodes

Occasional arcing at the electrodes was of concern to us not only because it tended to destroy the main switch tube but also because it resulted in a missed kick which spilled beam around the ring. DC corona tests revealed two weak areas in the original mechanical design which lent themselves to improvement. We found considerable corona at the connection of the support insulators and the electrode. We also found trouble at the electrical feedthrough. An investigation into both trouble areas showed conditions in which the local vacuum might be much worse than the nominal ring vacuum of 1e-8 torr.

Fig. 1 shows the mechanical configuration of one of the extraction kicker electrodes. To optimize the kick angle the electrodes are inserted in the housing on a taper that matches the beam size. In addition to the taper one end of the electrode is offset in a direction to follow the displaced beam. To maintain a constant impedance with this taper and positional shift an impedance-adjusting tapered plate is added to the outer surface of the electrodes. Constraints imposed on the mechanical mountings by these offsets and tapers and mechanical tolerances of the housings resulted in a quite complex mechanical design.

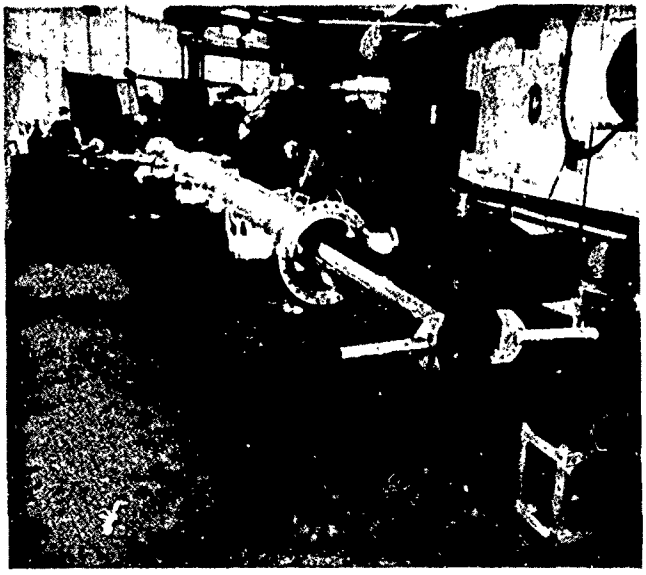


Figure 1: Extraction kicker-electrode mechanical configuration.

In the original design of the support insulators connection to the electrode was made by a U-shaped copper bracket with sharp corners. A Pin holds this piece to a copper post which is threaded into the Macor insulator. The standoff insulators were in contact with the housing and only very thin long vacuum pump-out paths were included. Several improvements were made to this design.

Fig. 2 shows details of the improved insulator support structure. We have replaced the U-shaped connecting piece with a stainless steel corona ring that extends beyond the edge of the Macor insulator. This corona ring effectively shields the triple junction at the point the end piece mates with the Macor insulator. In addition, the convolutions have been reduced in diameter, moving the Macor away from the housing and allowing better vacuum pumping. A squared-off stainless steel plug traps the rear of the insulator and the rounded corners provide alignment for this plug and the insulator. Lots of opening is afforded by this squared-off design, allowing good vacuum pumpout of the volume behind the plug.

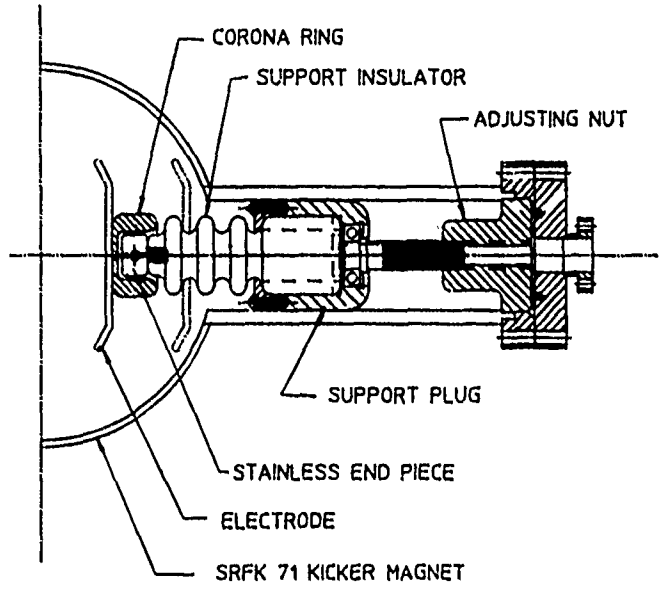


Figure 2: Support insulator.

4 Electrical Feedthrough

The original design utilized a tapered ceramic cone with a metal end cap that mated with a one-inch-diameter connecting rod. There were two major design flaws associated with this design. A corona ring originally planned for the triple junction area at the small end of the ceramic cone was never installed, and to conserve weight the connecting post was constructed as a hollow tube closed at the ends. A small pumpout port was included but was probably insufficient to really clear this volume. As shown in Fig. 3 we replaced this post with a solid titanium post which includes an integral corona ring. We have retained the rather fragile ceramic cones for the time being but plan to develop more rugged feedthroughs in the future.

5 Load Resistors

The original kicker system utilized copper sulfate load resistors. While these were excellent resistors for lab use, maintenance requirements proved to be too great for continued operation. We have replaced the copper sulfate loads with 12-inch-long 2-inch-diameter carborundum resistors immersed in oil. A water-cooled loop of copper tubing is coiled around the inside surface of the housing to obtain cooling.

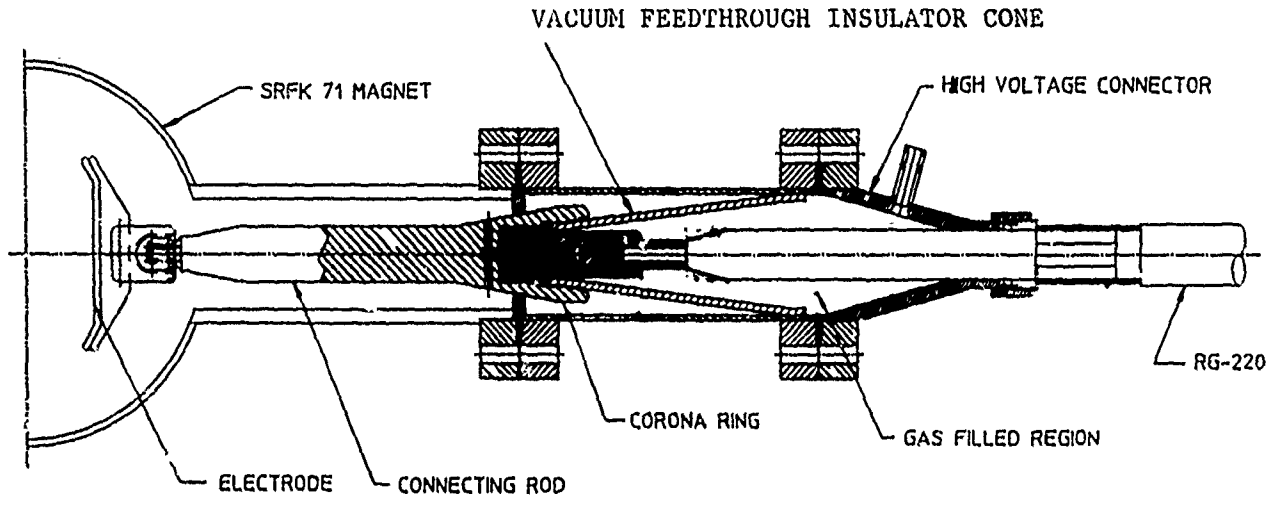


Figure 3: Electrical feedthrough.

6 Cable Connectors

Cable connection to the ceramic feedthrough was initially accomplished with a solid, rubber-filled, connector housing. The area between the air side of the ceramic feedthrough cone and a brass center conductor was filled with a rubber potting compound. The mating connector was machined from Teflon with a gentle cone shape on the mating surface. At assembly a thin coating of transformer oil is applied to the rubber and pressure on the housing deforms the potting compound excluding air. In our present connector design, the housing is filled with Freon 114, which is a high-voltage dielectric used in Tektronix high-voltage oscilloscope probes. Freon 114 provides about a factor of 3 improvement in voltage holdoff over an empty connector and we have DC tested the connectors to 70 kV. Freon 114 has a vapor pressure of 25 psi at 25 degrees centigrade so no pressurizing or manifolding is required. We simply bleed freon from a small can into the connector and close off the port valve.

While we have operated for several years with freon 114 in our connectors, concern for the environment and concern over possible hazardous compounds that could be formed during electrical breakdown have prompted us to replace the freon with dry nitrogen. Though we have not operated with the nitrogen during an actual running period we feel this will be adequate.

7 Acknowledgements

The author wishes to thank Walt Sommer, Robert Damjanovich, Michael Borden, and the MP-5 mechanical section they direct for completing the mechanical designs and providing the hardware. In addition the author wishes to thank Philip Reed, who did a majority of the electronic work.

References

[1] J. F. Power, Barbara Blind, Andrew J. Jason, "The Los Alamos Proton Storage Ring Fast-Extraction Kicker System," IEEE Transactions on Nuclear Science, NS-32 Number 5, Particle Accelerator Conference, 1985.

[2] H. Menown, C. A. Pirrie, N.S. Nicholls, "Advanced Thyratrons As Switches For the Nineties," IEEE Conference Record, Seventeenth Power Modulator Symposium, 1986.

FAST THYRATRON DRIVER*

M. N. NGUYEN AND R. L. CASSEL
Stanford Linear Accelerator Center
Stanford University, Stanford, California 94309

Abstract

A fast solid-state pulse generator used as a thyratron grid driver for kicker pulsers, has been developed and built with power MOSFETs and a transmission line transformer. The MOSFET, pulsed on and off by a pair of P-N channel HEXFETs, switches charged capacitors into the transformer connected in parallel on one end and in series on the other end to step up the voltage. The resulting output pulse parameters are 2 kilovolts peak (into 50 Ohms), 13 nanoseconds risetime (10-90%), 250 nanoseconds duration, and less than 50 picoseconds pulse-to-pulse jitter. Various methods are employed to protect the MOSFETs from thyratron arc back, including the use of TransZorbs and a magnetic diode.

Introduction

For improved performance of kicker systems, the stability and reliability of thyratron grid drivers play an important role. Earlier drivers at SLAC used SCRs as switching devices in resonant charging circuits and, although they worked well for many years, produced output pulses with slow rate of voltage rise and long throughput delay which contributed to high jitter and extended delay time of the main thyratron current. Experiments have shown that a high amplitude, low impedance and fast rise grid trigger pulse could reduce anode current time jitters.

This led to the development of a new thyratron grid driver. The circuit basically is an RC pulse generator where capacitors are charged over a long period of time and then discharged rapidly through a step-up transmission line transformer to produce an output pulse with a fast risetime and multiplied amplitude. Using a transmission line, with its frequency-independent characteristic impedance, as a transformer lead gives a high degree of coupling and virtually no delay between the transformer primary and secondary. Power MOSFETs are chosen as switching devices because they are inherently fast and the gate drive circuit is relatively simple and requires minimum drive power.

Design

A simplified schematic diagram is shown in Figure 1. The circuit consists of six identical power MOSFET switches and gate drivers, a transmission line transformer T1 and a magnetic diode X1. Only one switch and its gate drive is drawn for simplicity. The MOSFET gate driver is based on Directed Energy switching test circuit with front end (not shown) added to accommodate various interlocks and signal indicators. A TTL trigger provides input voltage for the Clock Driver DS0026 to drive the complementary P-N channel HEXFETs, IRFD9120 and IRFD110, which in turn generate the pull up and pull down for the power MOSFET gate. R1 and R2 serve to limit the HEXFETs drain voltage spike. R3 terminates Q3 gate to prevent the device from turning on in an open circuit while D1 protects it from over voltage.

The transmission line transformer consists of six strip transmission lines, each having an equal length of 24 inches and a characteristic impedance (Z_o) of about 10 Ohms, which wound around a ferrite core (Ceramic Magnetics CMD 5005). There is one turn on the first line, two turns on the second line and so forth, six turns on the sixth line. Each line in essence is a unity-coupling transformer with different impedance. One side of each line primary and secondary are then driven in parallel by charged capacitors while the other side cascaded in series with the load. The net result is that of a conventional transformer with a step-up voltage ratio of six to one and an extremely wide bandwidth. The transformer has an input impedance of: $Z_p = Z_o / 6 = 1.7$ Ohms, and an output impedance of: $Z_s = Z_p \times N^2 = 1.7 \times 6^2 = 60$ Ohms. The low-frequency cutoff is determined by: $f_l = X_L / 2 \times \pi \times L$, where $X_L = Z_o$ and $L = 0.4 \times \pi \times N^2 \times \mu \times A_c \times 10^{-8} / l$. For $N = 1$, $\mu = 2500$, $A_c = 2.58$ cm^2, and $l = 11.97$ cm, the low-frequency response is about 235 kilohertz. With given length of the line, the high-frequency cutoff predicted at one-eighth of wavelength in free space is: $f_h = 0.125 \times v / l = 61$ megahertz.

Let's consider circuit operation on the first line. A 400 volts power supply charges capacitor C2 to full voltage over time. When Q3 is turned on, C2 discharges quickly through C3, D6 and the strip line producing magnetic flux at the core and a negative voltage signal at the transformer primary. The

* Work supported by the Department of Energy, contract DE-AC03-76SF00515.

0-7803-0135-8/91$03.00 ©IEEE

signal, when propagating through the length of the line, induces an equal and opposite voltage at the transformer secondary where its negative end is bypassed to ground through C3. The induced positive end (V_{IND}) summed up with charged negative voltage apply twice the voltage across the second line with its two turns to match the impedance. Thus, the second line induced voltage now is twice the power supply voltage.

As it can be seen, the remaining four lines react in a similar manner. The sixth line finally induces a voltage that is six times the power supply voltage with a load current equals to all capacitive discharging currents. All capacitors in effect combine in parallel to provide power to the load. Moreover, the power supply negative side is floating to provide a 30 Volts negative bias voltage to the thyratron grid.

Performance

Figure 2 shows the output waveform measured into 50 Ohms resistive load. The voltage quickly rises to 2 kilovolts peak, then slowly decays with a Z_oC time constant of 0.5 microseconds where the tail collapses because of transformer core saturation. As seen, instead of six to one, the voltage ratio is closer to 5.4:1, ten percent less than the perfect condition. This loss is incurred by series impedances associated with power MOSFETs R_{DS}(on) and capacitors ESR which resulted in reducing the line charging voltage. Pulse width at half maximum (FWHM) is about 250 nanoseconds. A larger value of charge capacitors will generate a wider pulse. Since the transformer retains transmission line characteristics, the output risetime is mainly determined by the switching times of power MOSFETs and gate drivers. A risetime of 13 nanoseconds, 10 to 90 percent, is shown in Figure 3. The MOSFETs used were DE-275 501N12 from Directed Energy Inc. This device is rated at 96 Amps peak, repetitive pulses, and has a voltage rating of 500 Volts.

Throughput delay, defined as the sum of the total turn-on and the propagation delay times of each device in the signal path, is less than 100 nanoseconds.

Jitter and drift as measured with an SR620 Universal Time Interval Counter showed excellent performance. The tests, conducted with a sample size of ten thousand shots and 120 Hertz repetition rate, displayed a peak-to-peak jitter of less than 300 picoseconds with a standard deviation or rms jitter of less than 50 picoseconds.

MOSFETs Protection

Protecting the MOSFETs from failure due to drain-to-source breakdown proved to be an interesting task. High transient voltages of many kilovolts combined with low source impedance returning from the thyratron grid posed great risk to the device. Furthermore, transient pulse width also vary from ten to hundreds of nanoseconds depending on the type of thyratron breakdown. These [illegible] conditions justified a redundant MOSFET protection scheme. Referring to Figure 1, presume that a positive kick-back transient traveled through the transformer, fast recovery diode D4 turns on to clamp the voltage down. If there still is current flowing toward the MOSFET drain, snubber circuit R4-C1 along with effective series inductances reduce dv/dt and the peak transient voltage while D2 clamps the potential to the power supply voltage level. The same case applies to negative kick-back transients where D3 now provides clamping action.

Limiting transient voltages at the transformer output are TransZorbs, General Semiconductor 1.5KE200. These high peak power dissipation, extremely fast response suppressors theoretically can clamp transient voltages in less than one picosecond. However, twelve devices are needed for 2400 Volts breakdown voltage and lead inductances are in series. It results in an increase of response time to about 20 nanoseconds.

The first and probably most effective defence against the returned transients is the so-called 'magnetic diode'. As its name implies, the device can pass a large forward current while blocking it in the reverse direction by means of a saturable magnetic core. It is a transformer with one turn on the secondary and nine turns with large inductive and capacitive coupling on the primary side, wound around a high frequency ferrite core (CMD5005). A DC current applied on the primary forces the core into positive saturation. The saturated inductance impressed on the secondary is so small that it opposes little to the forward pulsed current. In the reverse direction, magnetizing inductance grows considerably to limit the transient current flow. Diode breakdown, or the ability of the transformer to stop transient current from flowing back, is determined by the Volt-second product, which is: $E \times t = 2 \times N \times B_m \times A_c \times 10^{-8}$. Where N = 1, B_m = 3300 Gausses, A_c = 1.29 cm^2, the Volt-second product is 85 kilovolts nanosecond. The applied forward bias current is about 3 Amps , determined by: $I = H \times l / 0.4 \times \pi \times N$, where H (from the core data sheet) = 10 Oers, l = 3.19 cm, and N = 9.

Conclusions

The development of this project has produced a fast voltage rise and extremely low jitter triggering source for thyratrons. Its high performance is contributing to the reliability and stability of kicker magnet systems at SLAC.

References

1. Directed Energy, "The DE-Series Fast Power MOSFET", 1988.

2. Motorola, "Gate Drive Requirements", Power MOSFET Transistor Data, 1986.

3. R. Bonebreak, "Unconventional Transformer Connections", Practical Techniques of Electronic Circuit Design, 1982.

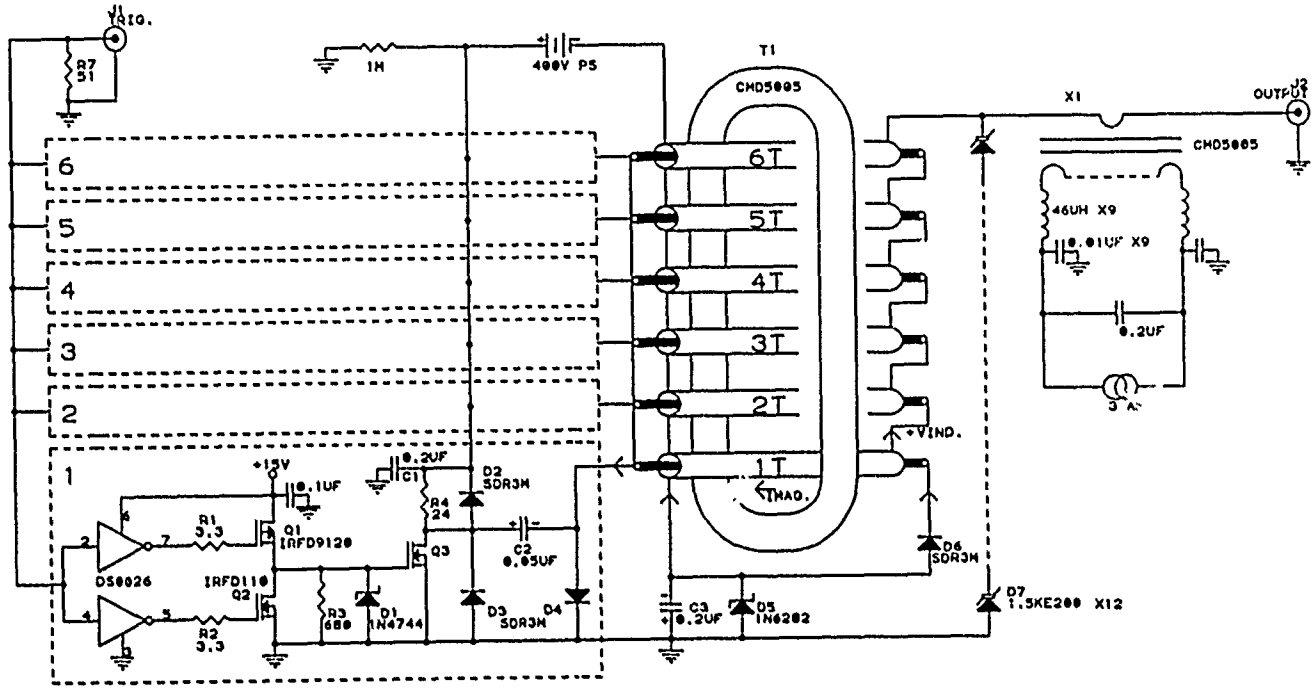


Figure 1. Simplified Schematic Diagram.

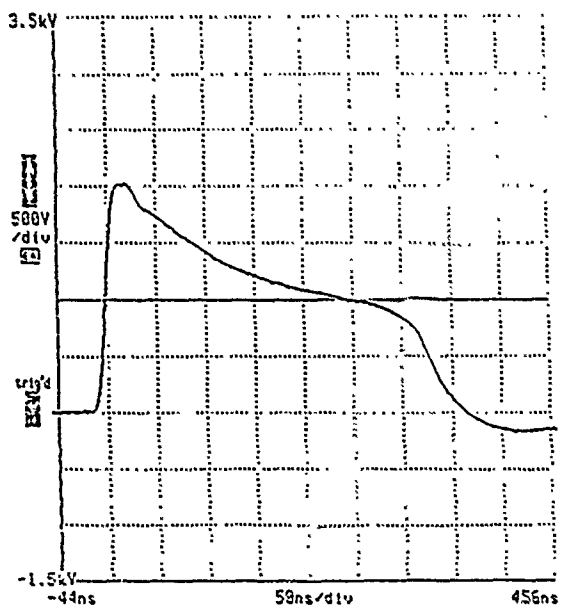


Figure 2. Output Waveform. 50 Ohms Load.

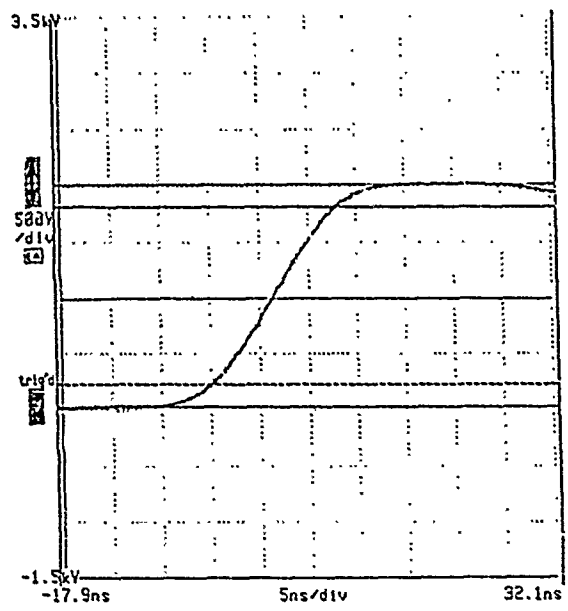


Figure 3. Voltage Rise.

Pulse Shape Adjustment for the SLC Damping Ring Kickers*

T. Mattison, R. Cassel, A. Donaldson, H. Fischer, D. Gough
Stanford Linear Accelerator Center, Stanford CA 94309

Abstract

The difficulties with damping ring kickers that prevented operation of the SLAC Linear Collider in full multiple bunch mode have been overcome by shaping the current pulse to compensate for imperfections in the magnets. The risetime was improved by a peaking capacitor, with a tunable inductor to provide a locally flat pulse. The pulse was flattened by an adjustable droop inductor. Fine adjustment was provided by pulse forming line tuners driven by stepping motors. Further risetime improvement will be obtained by a saturating ferrite pulse sharpener.

I. KICKER REQUIREMENTS AND PROBLEMS

The SLAC Linear Collider (SLC) *e-* damping ring kickers must inject and extract 2 bunches on a single pulse, one for collision and one for *e+* production, to produce full collision rate. The two bunches are 60 nsec apart, and must receive the same kick to 10^{-3} or better. The pulser risetime is marginal, and in addition the multigap thyratrons required for high voltage and fast rise time produce a series of prepulses as the gaps break down. Neither of two different magnet designs has produced a field pulse with the desired risetime and flatness for 2 *e-* bunch extraction [1]. These problems combined to prevent operation with 2 bunches in the *e-* damping ring, allowing only half of the linac pulses to be used for collisions, with the other half used for *e+* production. A program to produce a better magnet was undertaken, but progress was expected to be slow because the magnet faces additional constraints from size, high voltage, and radiation damage [2]. A parallel program was therefore undertaken to control the pulse shape.

II. SHAPING WITH LUMPED COMPONENTS

The e- extraction kicker pulser [3] uses 2 thyratrons in an oil filled tank to switch charged cables at the anodes into output cables at the floating cathodes to the magnet and its terminating load. Each thyratron switches 2 parallel 50 ohm cables, and 4 cables are paralleled at the magnet. The first method of pulse shaping was to connect inductors ("droop coils") from the cathodes to ground. The L/Z time constant was chosen so the droop in the current would approximately compensate for the rise in field due to magnet mismatch. Adjustment was provided by using a clip lead to short varying numbers of turns. The droop coils succeeded in producing equal field amplitudes for the 2 bunches, but only for a unique kicker pulse timing, which was so early that the second bunch received a significant kick on the turn before extraction.

While inductors reduce the current late in the pulse, capacitors can add current early in the pulse. A capacitor in parallel with the charge line would produce a 100% overshoot in the current, with a decay time constant fixed by the capacitor value, for ideal capacitors and switches. Experiments showed that the ZC time constant must exceed the thyratron rise time for any effect to be observed, and the di/dt is not improved even for large capacitor values, presumably being limited by the thyratron and inductances. For threshhold capacitor values the current does not overshoot but does reach the flattop value sooner. Larger values cause some overshoot (but much less than 100%) and the expected increasingly long tail. The amount of overshoot depends on the voltage, presumably because the thyratron risetime depends on voltage. Series inductance causes some ringing, but some inductance actually increases the overshoot for intermediate capacitor values by delaying capacitor discharge until the thyratron is more fully conducting. Inductance also reduces the sensitivity of the overshoot to voltage and risetime.

Ceramic capacitors were connected from thyratron anodes to ground in parallel with the charge line cables with short wires, and the capacitor value was varied for optimum performance. For large values a local maximum field early in the magnet pulse could be created, which provided a unique flat spot for the more critical first *e-* bunch, and which was early enough to avoid a large kick to the other bunch on the previous turn. The droop coil clip leads were then used to make the amplitude equal at the time of the second bunch 60 nsec later. This configuration produced a magnet pulse that was sufficiently close to ideal that 2 *e-* bunch SLC operation and 120 Hz collisions were achieved in January 1990.

Ideally the shape of the current pulse could be adjusted to make not just a local maximum in the field but a flat region of finite duration. The ideal value capacitor depends on the thyratron risetime, and 80 KV variable capacitors are not easily constructed. An alternative is a fixed capacitor with a variable

* Work supported by US Department of Energy contract DE-AC03-76SF00515

0-7803-0135-8/91$03.00 ©IEEE

inductor in series. The inductor is a short coaxial line constructed of copper pipe and rod and immersed in the thyratron tank oil, with its center conductor attached to the capacitor and outer conductor to ground. A piston with contact fingers provides a sliding short to vary the inductance. By adjusting the piston, the dB/dt can be made not only to cross zero (for a local maximum), but to be tangent to zero (for a local flat spot). Figure 1 shows this has not quite been achieved, but soon a remotely controlled version of the piston tuner should make it possible.

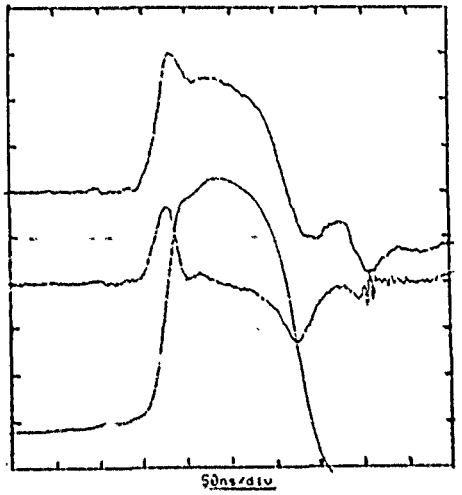


Figure 1. From top to bottom, shaped current pulse, dB/dt, and B(t) pulse.

III. ROTARY PULSE LINE TUNER

While current pulse shaping with lumped components can compensate roughly for magnet imperfections, making the adjustments requires trial and error with multiple interruptions of operations, and the proper correction would not necessarily be stable anyway. We have therefore constructed additional pulse shaping devices to provide continuous remote control of the relative *e-* kick amplitudes necessary to put the second *e-* bunch on the same orbit as the first.

The rotary pulse line tuner is designed to change the amplitude of the second bunch kick without disturbing the first bunch, and without introducing any slope to the pulse. This decouples the amplitude equality problem from the zero slope problem. The tuner is a short variable impedance transmission line inserted into the charge line cables at a distance from the thyratron. The discharge wave launched by the thyratron produces a reflection from the mismatch at one end of the tuner, and the transmitted wave produces an opposite and nearly equal reflection from the other end. The two reflections travel to the magnet where they sum to a bump of duration determined by the tuner length. The amplitude can be positive or negative depending on the mismatch, or zero if the tuner impedance is set to the line impedance. If the tuner is placed at the proper distance from the thyratron, the first bunch is not affected, and the second bunch is at the local maximum or minimum of the bump, so no slope is introduced.

The tuner high voltage conductor is a slice of 8 inch aluminum pipe, and the ground conductor is a 6 inch aluminum pipe cut in half, concentric with a .5 inch separation. They form a parallel conductor transmission line whose impedance can be varied by rotating the ground conductor. The high voltage stator is mounted on plastic standoffs approximately at the center of a 12 inch aluminum pipe, and the rotor is mounted on bearings and grounded to both end plates with sliding fingers. There are 2 RG-220 cable connectors on each end plate, and a stepping motor and readout pot on one end. One 6 foot tall oil filled tuner tank is required for each of the 2 thyratrons of the *e-* extraction pulser.

Initial scale model tests indicated that connector inductance could introduce a dip into the pulse, so the stator comes within .5 inch of the ends. The stator was also originally 180 degrees wide, giving a large maximum capacitance to the rotor that could overcome any dip. The dip in production tuners proved to be negligible, but the extra stator width caused stray capacitance to the outer pipe that made the tuning range only positive and not negative. The stator was later narrowed to 90 degrees making the range bipolar. Figure 2 shows the maximum excursion from a flat pulse is over +/- 10%, with very little perturbation at the neutral position.

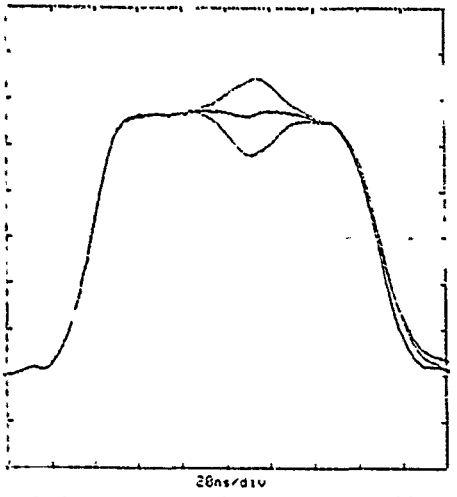


Figure 2. Current pulse at 3 rotary tuner positions

The stator operates up to 80 KV, and some arcing has occurred, mostly from the stator to the end plates, and sometimes tracking along the Delrin standoffs. Carbon tracks on the 2 inch long standoffs were traced to a layer of internal air bubbles in the raw material, apparently common in extruded Delrin. New standoffs have been made from porosity-free cast Delrin. The tuners have operated for many months with no arcs, but clearances in the tuner are small enough that air bubble, water, or other contamination of the oil can promote arcs. Arcs have caused no damage to the tuners but have destroyed charging diodes in the pulser. When one tuner

arcs it applies large forward currents to its own diodes, and reverse voltage to the diodes on the other tuner. Using a single diode string to charge both tuners, protected by a large inductor and capacitor, with smaller inductors to isolate the thyratrons during normal operation, has solved this problem.

IV. Saturating Ferrite Pulse Sharpener

Neither the lumped components nor the rotary tuners address the problem of thyratron prepulse, or poor risetime, which cause the second *e-* bunch to be kicked slightly on the turn before extraction. This cannot be corrected on the final turn because the previous turn kick is at a different betatron phase. We have developed a small pulser described elsewhere [4] to cancel the prepulse at the magnet, which in combination with the rotary tuner allows the 2 bunch orbit difference requirement to be met. However, the preferred solution is to stop the prepulse at its source. We have succeded, not only reducing the prepulse below the required level but also dramatically improving the current pulse risetime.

It is relatively common to use saturating ferrite cores to improve the rise time and reduce the commutation losses of thyratrons. Cores placed over the RG-220 output cables directly at the thyratron were found to only attenuate the prepulse by a roughly a factor of 2, and not improve the risetime, even though they had far more volt-seconds to saturation than in the observed prepulse and the early part of the rise. This was because the small amount of charge released by the prepulse raised the voltage across the ferrite to essentially the full thyratron anode voltage, which saturates the ferrite before the thyratron becomes fully conducting. There is also an equivalent shunt resistance across the ferrite cores. When a very fast voltage pulse is applied to a core, there is not only a linear rise in current to saturation, but also a prompt current approximately proportional to the voltage. This is simply the time domain manifestation of the ferrite loss tangent. Typical loss tangent vs frequency information is consistent with a simple model for an ungapped ferrite core of a shunt resistance in parallel with the unsaturated inductance that provides a time constant of a fraction of a nanosecond. For our core experiment, the resistance was comparable to the system impedance, so the prepulse was only cut by half.

This model predicts that changing the core geometry to increase the unsaturated inductance while keeping the volt-seconds to saturation constant will increase the resistance proportionately, i.e., the resistance is inversely proportional to ferrite volume at fixed cross section. This was tested by making simple inductors with 1 turn on 4 cores, 2 turns on 2 cores, and 4 turns on 1 core. The saturation volt-seconds were the same, but the 1 core inductor, with 4 times the inductance, had 1/4 the resistive current as well as 1/4 the di/dt.

Simply adding turns to a single core also increases the saturated inductance, which would increase the system rise time. The optimum solution is to make a ferrite filled coaxial structure, which has the maximum inductance and thus shunt resistance for a given volt-second saturation level, and also can be designed to match the system impedance when saturated. It should be located far enough from the thyratron that reflections do not return until the ferrite is saturated.

We tested a ferrite loaded coaxial line remote from the thyratrons and found that it transmitted no measurable prepulse, and also improved the main current pulse rise time to less than 10 nsec, as seen in Figure 2. The production device uses 20 CMD-5005 nickel-zinc cores, each 1 inch long, 1 inch ID, 1/16 inch wall thickness, on a 1 inch ID aluminum tube. The thin ferrite wall thickness was chosen to maximize the ferrite switching speed. The ferrite is separated from am outer aluminum tube by 1/8 inch of flowing oil. Enlarged ends contain chokes to either reset the ferrite (which has not proven necessary), or to pre-saturate it (to remove the pulse sharpening effect). The ends also each contain 4 RG-220 cable connectors, and the oil flow connections. It has been operated at up to 40 KV with no damage from arcs, and no arcs when the oil is flowing.

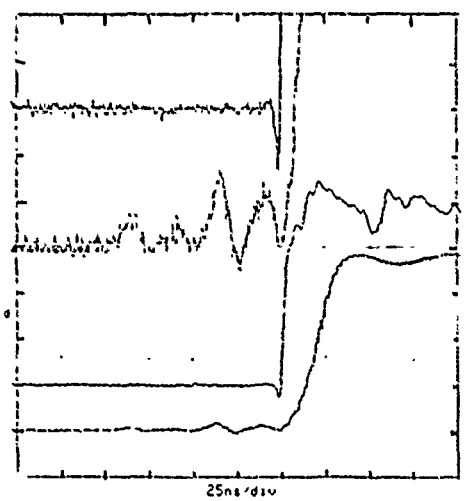


Figure 3. From bottom to top: thyratron output pulse, pulse sharpener output pulse, thyratron pulse amplified by 10 to emphasize prepulse, and same for sharpener output.

V. References

[1] R. Cassel *et al*, "SLC Kicker Magnet Limitations," these proceedings.

[2] T. Mattison *et al.*, "Operational Experience with SLC Damping Ring Kicker Magnets," these proceedings

[3] L. Bartelson *et al.*, "Kicker for the SLC Electron Damping Ring," in *Proc. of 1987 IEEE Particle Accel. Conf.*, Washington DC, March 1987, pp. 1582-4.

[4] R. Cassel and T. Mattison, "Kicker Prepulse Canceller," these proceedings.

High Voltage Pulse Cable and Connector Experience in the Kicker Systems at SLAC *

K. Harris, M. Artusy, A. Donaldson, T. Mattison
Stanford Linear Accelerator Center, Stanford CA 94309

Abstract

The SLAC 2-mile linear accelerator uses a wide variety of pulse kicker systems that require high voltage cable and connectors to deliver pulses from the drivers to the magnet loads. Many of the drivers in the SLAC kicker systems use cable lengths up to 80 feet and are required to deliver pulses up to 40 kV, with rise and fall times on the order of 20 ns. Significant pulse degradation from the cable and connector assembly cannot be tolerated. Other drivers are required to deliver up to 80 kV, 20 μs pulses over cables 20 feet long. Several combinations of an applicable high voltage cable and matching connector have been used at SLAC to determine the optimum assembly that meets the necessary specifications and is reliable.

I. SLAC KICKER SYSTEMS

There are a total of seven continuously operating kicker systems currently in use in the SLAC Linear Collider (SLC,) divided into three basic types, LC discharge kickers (for Final Focus,) Fermi-type long-pulse cable kickers, and Blumlein short-pulse kickers [1] - [4]. The primary use of the kickers are for injection and extraction of the e- and e+ bunches into the SLC damping rings, to divert e- bunches to produce e+ bunches, and to dump the beams at the final focus points. The long-pulse kickers are located in the e- north damping ring, and the short-pulse kickers are located in the e+ south damping ring and at the e+ target area, and the LC discharge kickers are for beam dumping at the final focus area. The SLC kickers systems and damping rings are described in detail in several other papers being presented at the 1991 IEEE Particle Accelerator Conference [4], [5], [7].

II. OLD KICKER CABLES AND CONNECTORS

The SLC damping ring and e+ source kickers, as previously described, are divided into two types. Figure 1 [1] shows the Blumlein short-pulse type and Figure 2 shows the Cable long-pulse type. Several types of high voltage pulse cables and connectors/connections have been used in the kicker systems at SLAC. The short-pulse kicker systems (South Damping Ring, or SDR, and the e+ source kicker) have historically used RG-220 cable that has had the outer braid terminated outside and the polyethylene tapered and terminated inside the oil Blumlein. The cables come out of the Blumlein horizontally, and there have been failures due to the air space between the outer braid and the poly as well as the awkward mechanical support of the cable.

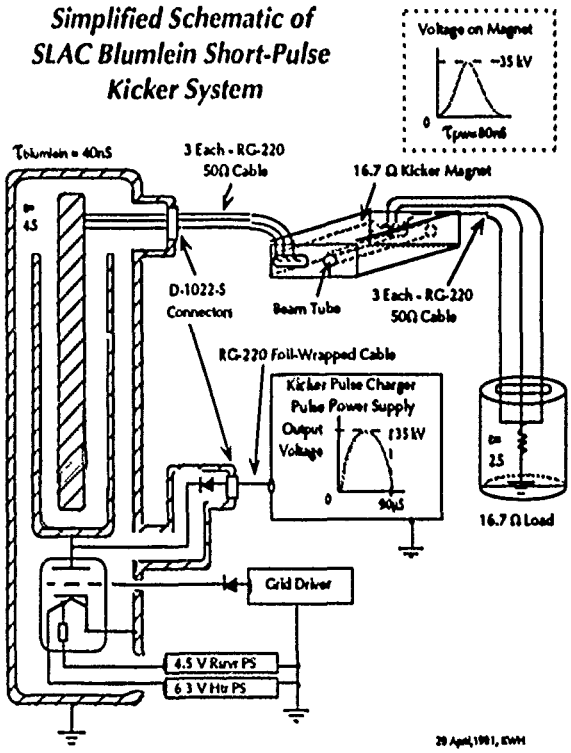


Figure 1. Short-Pulse Blumlein Kicker System.

The three cables from the Blumlein to the short-pulse kicker magnets are connected to Hugin contact bands in the magnet center conductor slab, with the ground braids clamped to cylinders on the magnet outer conductor surface. Originally the cable insulation was inserted into a cavity, formed in the RTV during magnet potting [6], without any preparation, but these connections had a high failure rate. Delrin plastic inserts are now potted into the ends to accept the cable insulation, which is tapered and greased to form an air-free connection. There have been no Delrin insert failures although there has been some corona damage. There have also been some failures in the RG-220 cables near the magnet where the ground braid

* Work supported by US Department of Energy contract DE-AC03-76SF00515

0-7803-0135-8/91$03.00 ©IEEE

has separated from the polyethylene allowing corona underneath.

The long-pulse kicker systems shown in Figure 2 (North Damping Ring, or NDR) have used Felton & Guilleaume (F&G) type HP 10.4/39.0 -50Ω/60kV coax that was very robust but difficult to obtain and quite large in diameter. RG-220 has also been used, with several types of connections. The pulsed-charger [8] cable between the thyratron tank and the pulse-charger sees ≈ 70 kV pulses with rise-times on the order of 20 μs. The standard connection has been a tapered RG-220 feed-through with o-ring seal around the PVC jacket that allows oil from the thyratron tank to wick into the outer braid. This virtually eliminates the air voids between the polyethylene and the braid, which tend to be the primary source of cable failures. The physical connection of the RG-220 to the pulse-charger tank, however, is made at a slightly upward angle, and the outer braid is terminated outside the tank. There is a short length of cable connection that is dry and exposed. This has resulted in several cable failures.

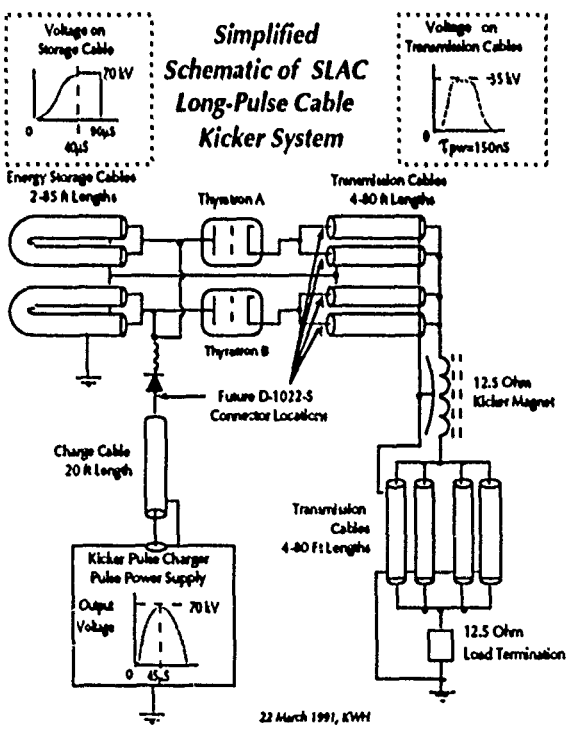


Figure 2. Long-Pulse Cable Kicker System.

The remaining long-pulse cables are currently RG-220 that are oil filled due to the just described connections. Problems associated with the cables are that oil filling is difficult, very messy, and there are almost always oil leaks from the cable that have to be dealt with. The Fermi magnets [5] associated with the long-pulse kickers are connected with four RG-220 cables at each end, with tapered and greased insulation fitting into a tapered cavity in the RTV potting of the magnet. The cable center conductors angle in to the tapered ends of the magnet center conductor and are held by setscrews accessible through holes in the RTV that are later filled with grease. There have been some failures associated with the setscrew arrangement. The cable ground braids are clamped to tubes at the magnet ends. There have been some failures due to center conductor eccentricity because the cable polyethylene gets warm from the magnet heaters and tends to flow, and the cables enter the magnet from awkward angles with tight bends.

III. New Cables And Connectors

Due to the Blumlein cable failures, an effort was made to develop a cable/connector system that was robust, reliable, compact, and as close to 50 Ω as possible for pulses up to 80 kV. Fermi and others [9], [10] have done extensive work on improving pulse coax, especially the RG-220 type. Currently, SLAC has Times AA-6778 cable installed in the short-pulse kickers between the pulse-charger and the Blumlein. AA-6778 is a version of RG-220 that has an Aluminum foil tape layer between the poly and the outer braid. This foil layer helps reduce the air pockets that cause many cable failures. Working in conjunction with Isolation Designs of Sunnyvale, CA, SLAC developed the D-1022-S connector for foil-wrapped RG-220 cable. The D-1022-S has an integrated high-voltage (HV) shield to ground to reduce field enhancement [11], oil tight Hugin type multi-lam connectors, and a tapered section for void-free poly fit. The D-1022-S is shown in Figure 3. The D-1022-S was designed using MacPoisson, a relatively simple Finite Element Analysis code on the Macintosh. The maximum field-enhancement in the connector is about 20%.

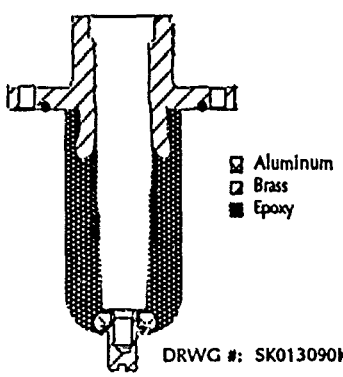


Figure 3. D-1022-S Connector for foil-wrapped RG-220.

The short length of the connector, balanced with the compromise for voltage hold-off capability, serves to preserve the coaxial impedance as much as possible, which can be important for fast pulse systems. The tapered section allows the greased (Dow-Corning 5 Compound) poly section of cable being inserted to force air bubbles out and around the poly. The cable braid is captured inside a SLAC modified UG-156 connector that is threaded onto the D-1022-S. The most probable weak link in this system is the UG-156 connector

section. Also, the eccentricity of the RG-220 type cable is very important for this connector, as is the calibration of the "pencil-sharpener" tool used to taper the poly. SLAC experience has shown that standard RG-220 cable is seldom the same size from batch to batch from most manufacturers, which has led to some problems with cable replacement.

IV. Cable And Connector Tests

The D-1022-S connector and the associated AA-6778 coax were initially tested on the output of the pulse-charger at voltages between 72 kV to 88 kV for $\approx 10^8$ shots. The output of the cable was unterminated, but a corona [12] ring was installed and the end was mounted in an oil tank. Table 1 summarizes the test results.

Table 1
D-1022-S connector and Times AA-6778
cable slow pulse tests.

Voltage	Rep-Rate	Total Hours
72 kV	60 Hz	18
75 kV	120 Hz	75.16
80 kV	60 Hz	36
80 kV	120 Hz	36
80 kV	180 Hz	69
88 kV	180 Hz	0.0167 *

Max Voltage	Max PRR	HV Hrs	Total Shots	Rise Time	Pulse Width
88 kV	180 Hz	234.18	1.0445×10^8	17 µs	≈ 50 µs

* The pulse charger failed at 88 kV.

The cable connector assemblies were also tested or a 60 Hz AC corona generator [13]. The primary testing was for corona inception voltage. Short lengths of AA-6778 cable were terminated on both ends with the D-1022-S connector, with the end of the connector immersed in oil and terminated with a corona ball of suitable diameter. Corona inception began at about 20.5 kV at the 10 pico-coulomb (pc) level. This agrees well with the MIL C-17 [14] rating of 21 kV of the AA-6778 cable. Raising the voltage to ≈ 22.8 kV, corona activity jumped to the 300 pc level. With a connector from one end of the cable removed, corona inception was at ≈ 18.6 kV. Various mechanical stresses were induced on the cable assembly, after which the inception point dropped to ≈ 13.6 kV. The assemblies also survived high-potting to 100 kV.

The D-1022-S connector was then tested by itself in a fixture designed to eliminate the cable corona from marring the connector corona results. Corona inception of the D-1022-S began at about 37 kV. At 38.6 kV, the level was in the 15 to 20 pc range, and flashover began at nearly 39 kV, which was most likely the breakdown point of the transformer oil being used in the tests.

V. Conclusions

The new cable connector assemblies being installed at SLAC will enhance maintainability and reliability. Great care in cable/connecter assembly is extremely important for good results. The MIL C-17 specification (under which AA-6778 falls) for HV coax cable appears to be sufficient for SLAC's uses. The D-1022-S/AA-6778 assemblies appear to have a high corona inception point, although more data is required. There are plans to install the D-1022-S connectors between the pulse-charger and the thyratron tank, and to and from the new pulse tuners in series with the 80 ft transmission cables.

Special Thanks to: Don Arnett, Don Williams, John Krzaszczak, Piotr Blum, Raghib Haqq, Jim Cundiff, Clive O'Conner, John Rock, Steve Pearce, and Pat Banglos of SLAC and Joseph Bianco of Isolation Designs, Sunnyvale, CA for their effort in the design, manufacturing, and testing of the described equipment.

VI. References

[1] F Bulos *et al.*, "Some Fast Kicker Magnet Systems at SLAC," in *Proc. of 1987 IEEE Particle Accel. Conf.*, Washington, D.C., March 1987.

[2] L. Bartelson *et al.*, "Kicker for the SLC Electron Damping Ring," in *Proc. of 1987 IEEE Particle Accel. Conf.*, Washington DC, March 1987, pp. 1582-4.

[3] T. Mattison *et al.*, "Kicker Systems for the Stanford Linear Collider," in *Particle Accelerators*, vol. 30, pp. 115-20, 1990.

[4] T. Mattison *et al.*, "Status of the SLC Damping Ring Kicker Systems," these proceedings.

[5] T. Mattison *et al.*, "Operational Experience with SLC Damping Ring Kicker Magnets," these proceedings.

[6] G. Gross *et al.*, "Development of Epoxy Potting for High Voltage Insulation at SLAC," these proceedings.

[7] T. Mattison *et al.*, "Pulse Shape Adjustment for the SLC Damping Ring Kickers," these proceedings.

[8] R. Cassel and M. Nguyen, "Kicker Pulsed Charger", these proceedings.

[9] J. Petter, "Improved High Voltage Coax for Antiproton Source Kicker Pulse Forming Networks and Pulse Transmission", Fermi National Accelerator Laboratory.

[10] C.A. Frost and D.B. Westenhaver, "Effects of Coaxial Cables on Fast-Risetime, High-Voltage Pulses", Joint EMP Technical Meeting, First Annual Nuclear EMP Meeting, 1973.

[11] W.J. Sarjeant and R.E. Dollinger, "High Power Electronics", Tab Books, Inc, Blue Ridge Summit, PA, pp. 171-180, 1989.

[12] E. Kuffel and W.S. Zaengl, "High Voltage Engineering", Pergamon Press, NY, NY, pp. 371, 1986.

[13] R Bartnikas and E.J. McMahon, "Engineering Dielectrics, Vol. I, Corona Measurement and Interpretation", ASTM STP 669, 1979.

[14] U.S. Military Specification, MIL-C-17F, January 1983.

KICKER PREPULSE CANCELER *

R. L. Cassel, T. S. Mattison

Stanford Linear Accelerator Center,
Stanford, California 94309

Abstract

The SLC Damping Ring extraction kicker magnets requires that the magnetic field, 58 nsec before extraction, be less than 0.1 % of the extraction field. The kicker thyratrons inherently generate prepulse currents of greater than 2 %. A Kicker Prepulse Canceler system was developed, which generates a 2.5 kV, 40 nsec wide pulse with 8 nsec rise time into 12.5 ohms, in such a manner as to cancel the kicker thyratrons prepulse current. The Prepulse Canceler has a drift of less than 5 nsec and has a jitter of less than 50 psec RMS.

Introduction

The SLAC, SLC project requires the electron damping ring to have two bunch of electrons separated in time by approximately 62 nsec. During extraction the two electron bunches must be extracted from the damping ring within one turn. The specifications require the first bunch to be kicked out with a pulse to pulse and long term stable of 1 part in 10,000 and the second bunch is to be kicked equally and stable to 1 part in 1,000. Figure 1.

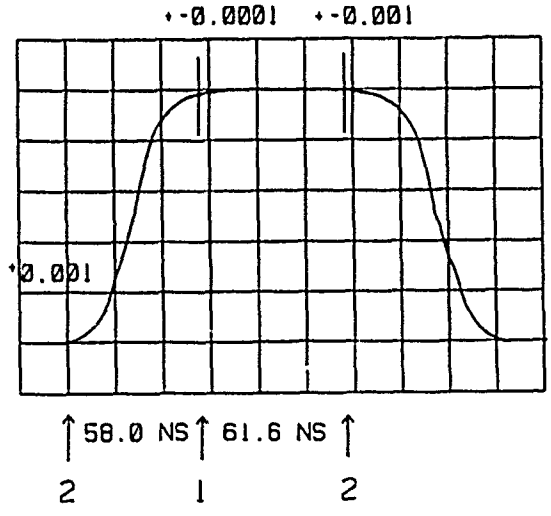


Figure 1.
Extractor Kicker requirements

In addition the second electron bunch cannot be pre-kicked by the rising edge of the kicker pulse by more than 1 parts in 1,000.

Due to the high voltages required by the kicker magnets to accomplish the nominal 58 nsec. rise time of the kicker pulse, multiple gap thyratrons were used in the kicker pulser. The multiple gap thyratrons have an inherent problems in that the individual gaps in the thyratron break down in sequence when the thyratron is triggered. The time delay between gap breakdown is unfortunately greater than 20 nsec and dependant upon the gas pressure in the thyratron. The inherent stray capacitance between thyratron grids generates a small pulse of current from the thyratron when the thyratron gaps break down. *Prepulse* is the name given to these small thyratron pre-breakdown pulses of current. Because the delay between breakdowns are long, dependent on gas presser, and are integrated by the kicker magnet, the result is an noncontrollable kick of the second bunch as it starts its last turn. This magnetic kick is large enough (approximately 1%) to be undesirable for SLC operation. Figure 2

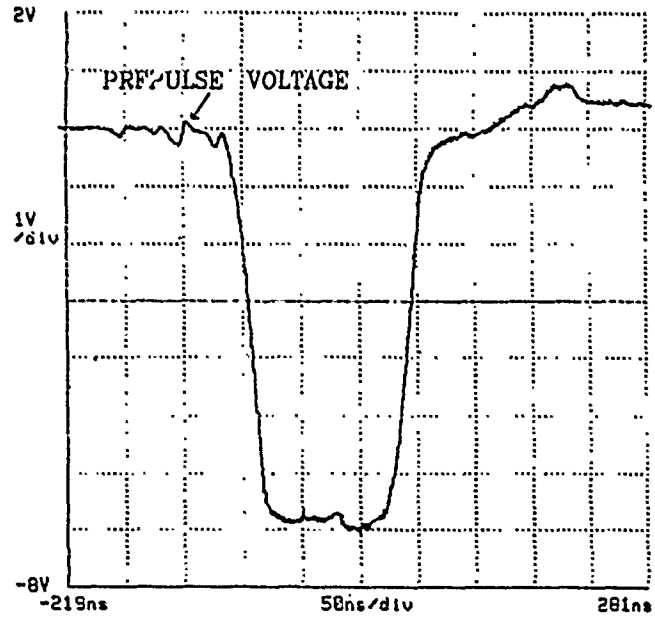


Figure 2.
Example of Thyratron Prepulse

* Work performed under U.S. Department of Energy Contract DE-AC03-76SF00515

0-7803-0135-8/91$03.00 ©IEEE

Design

To eliminate the effect of these prepulses on the second electron bunch a prepulse canceler system was developed. With the main kicker pulse being approximately 2800 amps into 12.5 ohms, it was undesirable to attempt to adjust the main pulse directly. The prepulse canceling system which was adopted was to inject a current pulse from the load side of the kicker magnet system which would start approximately the same time as the main pulse but travailing in the opposite direction toward the magnet. figure 3

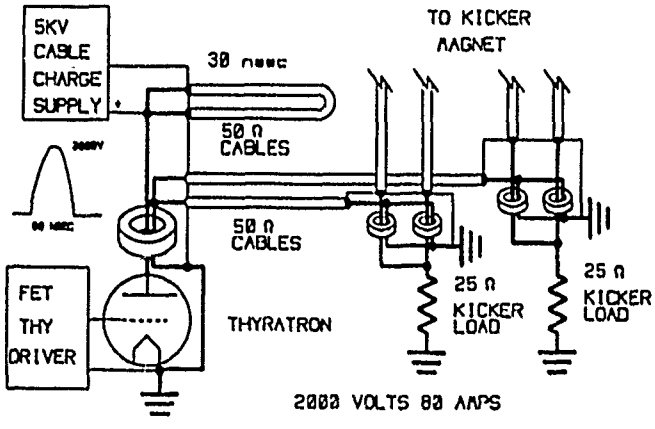


Figure 3.
Simplified Canceler Schematic

The injected current pulse is timed to reach the kicker magnet just prier to the main pulse coming from the other direction and thereby interferes or canceling the thyratron induced prepulses. Because the small prepulse was injected by way of a saturable core at the load which saturates quickly with the main pulse which then arrives much later at the load (approximately 400 nsec.) the main pulse has little effect on the prepulse canceler pulse or its pulser. Refections from the saturable core occures after extraction is over and as a result do not effect the extraction.

Saturable core transformer.

The saturable core transformer was built into the kicker loads and consists of a one turn 1" ID x 2" OD x 1" th CMD-5005 ferrite with a one turn primary coming from the prepulse canceler pulser. The resulting transformer will support a 2.5 kv 40 nsec wide prepulse canceler pulse without saturation. The cores will then saturate quickly under the present of the main pulse transmitting only a small amount of energy to the prepulse canceler pulser. The kicker loads use four cable or 12.5 ohms requiring the use of a core for each cable. figure 4

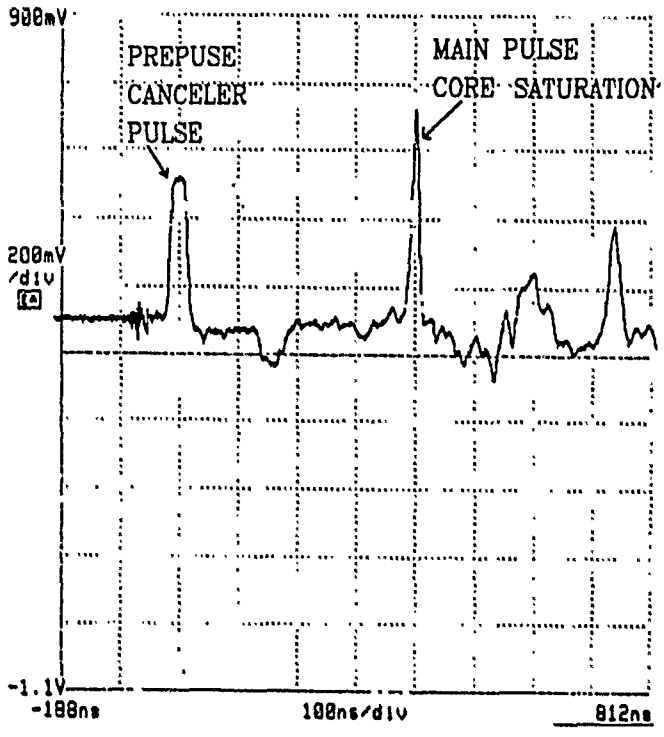


Figure 4.
Canceler Pulse & Core Saturation

Pulser design

The prepulse canceler pulser was designed to using a fast thyratron. A thyratron was chosen to reduce the possibility of problems when the main pulse reflected back to it before the saturation of the transformer core.
The thyratron chosen was a EEV CX-1588 because of it small size, high voltage capability and most of all its fast rise time. With the Thyratron being driven from a fast thyratron FET driver the rise time of the pulse is less than 5 nsec with a jitter of less than 50 psec RMS. Figure 5

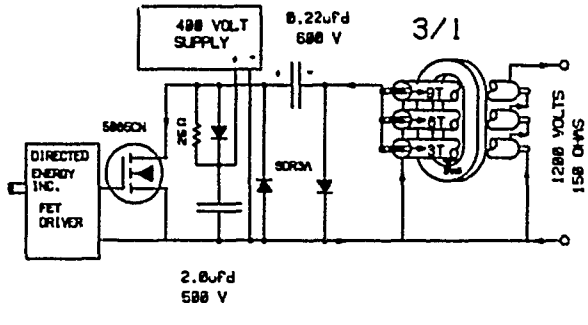


Figure 5.
Thyratron driver Schematic

The total delay of the driver and thyratron was less than 60 nsec with drift of less than 5 nsec so that no trigger time compensation was needed. The output pulse from the prepulse canceler pulser must be positive to match the canceling requirements. therefore an inverting saturable transformer consisting of two ferrite core (same material as the load transformer) provide the inversion and support the output pulse of 2.5 kv 40 nsec into 25 ohms with a 5 nsec rise time. The line for the pulser is a standard coax cable. The cable is resistance charged from a remotely controllable 5 kv power supply.

Results

The prepulse canceler pulser was fabricated and installed in the north damping ring extraction kicker system. Figure 6 & 7

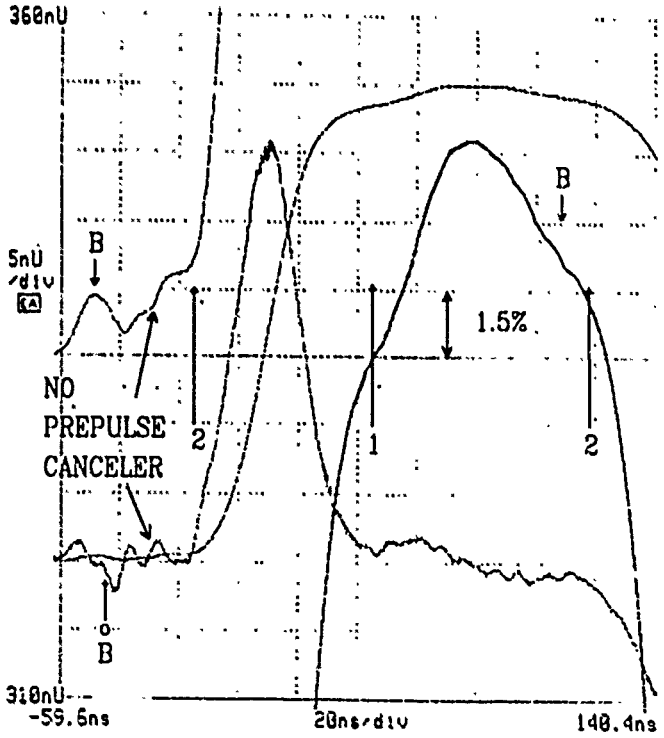


Figure 6.
Kicker Pulse without canceler

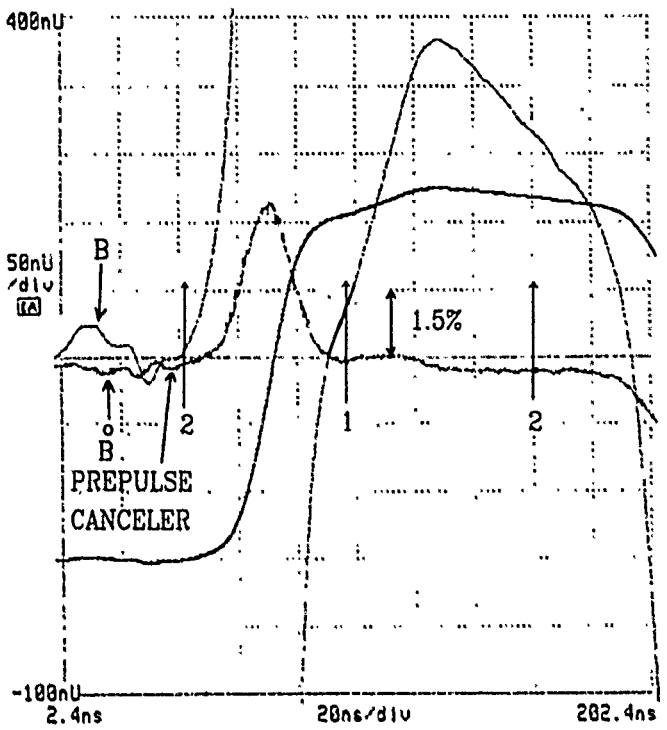


Figure 7
Kicker Pulse with canceler

References

[1] F. Bulos, et al.,"Some Fast Beam Kicker Magnet Systems at SLAC", Proceedings of the 1987 IEEE Particle Accelerator Conference, p. 1884.

Kicker Thyratron Experience from SLC*

A.R. Donaldson, R.L. Cassel, and T.S. Mattison
Stanford Linear Accelerator Center, Stanford CA 94309

L.L. Reginato
Lawrence Livermore National Laboratory, Livermore CA. 94550

Abstract

The SLAC Linear Collider has five fast kickers for the damping ring injectors, extractors, and the electron extractor for the positron target that use multi-gap Deuterium-filled thyratrons. The thyratrons operate with 30 to 70 kV anode voltages and 1 to 5 kA currents, to deliver pulses to kicker magnets with ≈ 30 ns rise times, up to ≈ 150 ns pulse widths, at 120 Hz. Operating and lifetime experience with several types of thyratrons and support electronics are discussed. Floating driver and power supply electronics were replaced by a ferrite choke isolator to allow grounding of the cathode support electronics with a commensurate increase in operating reliability. The construction of a 100 ns Blumlein enabled detailed measurements of the switching times for all SLC thyratrons under similar conditions. In the final focus area, the kickers dump the SLC beams after the e^+ e^- collisions. These thyratrons function with 15 kV anode voltages and up to 2 kA currents to produce 1/2 sine pulses with ≈ 300 ns rise times, ≈ 550 ns FWHM, at 120 Hz. Operating experience with these thyratrons will also be presented.

I. SINGLE BUNCH KICKER EXPERIENCE

The first kicker thyratron combination to operate in the SLC consisted of Blumlein configured triaxially, Z = 16.7 Ω, using castor oil as a dielectric and cooling medium for the thyratron. The first thyratron used in 1981 was an EG&G HY5333, a very compact three gap tube, rated for 50 kV and high di/dt ≈ 17 kA/μs operation. Early SLC operation required five of these pulsers. The Blumlein pulser system is still in use today in three SLC areas [1]. The thyratron is still an EG&G unit, but was upgraded in 1983 to a HY5353 which is usually operated at 35 kV, switching ≈ 4 kA with ≈ 30 ns for the 0 to 100% rise time.

The Blumlein was limited in length/height because of the intended application to about 80 ns across the base line, since the e^+ damping ring revolution time is 120 ns. These parameters dictate thyratron rise time to << 30 ns for an flattop pulse. Unfortunately, rise times were ≥ 30 ns resulting in a parabolic pulse shape, which then forces the jitter performance to << 1 ns. The HY5353's are being pushed to their limit in terms of required rise time, di/dt, and jitter performance. They were operated at high reservoir voltages in the days of resonant charging, and required frequent attention to avoid SLC down time. The typical approach was to nurse the tube until SLC Operations said, "OK, replace it." This they were reluctant to do because it could take four or five hours to accomplish. To date, HY5353 installed lifetimes are ≈ 1000 hours rather than a reasonable value, e.g., ≈ 5000 hours.

Currently a command charger [2] is used on the Blumlein, which charges the line in 50 μs and holds the charge for 50 μs before the thyratron is triggered. It allows a higher reservoir voltage, for a rise time of ≈ 25 ns, and the pulse to pulse jitter is < 1 ns. Command charging has resulted in better kicker performance with a modest increase in thyratron lifetime. The long term timing drift is canceled via a feedback system [3].

A jump increase in jitter is the first indication of a thyratron problem. Normally, jitter instability can be stopped with dc reservoir voltage adjustments, or in rare situations the dc heater voltage is increased. Decreasing the anode voltage does stop the jitter, but that also decreases the kick angle and impairs SLC operation. When the thyratron reaches the > 1000 hour stage of operation and a big jump of jitter occurs, it is more difficult to reduce or stop with heater or reservoir voltage adjustments. The HY5353 has a pre-ionization electrode or keep-alive (K-A) grid that is usually operated at ≈ 50 mA. In this regime the voltage on the electrode measures ≈ 20 V, and when a new thyratron is first installed, jitter is << 1 ns, but as the tube ages the jitter increases, and to reduce it the K-A current is removed by grounding the K-A grid through a low impedance. This improves the jitter performance for weeks and sometime months, but eventually the >>1 ns jitter reappears and forces another application of current to the K-A grid. It generally takes two or three episodes of K-A on and off before we are convinced that tube replacement is necessary. Replacement with a new or rebuilt device seems the only solution. The old unit is installed in the test Blumlein. The rejuvenation period takes about 100 hours, the anode voltage, heater, reservoir, and K-A current are varied until the thyratron stabilizes.

Occasionally the HY5353 will fire-through and can after a spate of arcing destroy the output stage of the trigger driver, which indicates operation in the spark gap mode. The trigger driver has been protected from the effects of fire-through with series diode and L-C filter. The drawback of this protection is a slower trigger rise time and consequent increase in jitter. A new output stage for the trigger generator using pulse compression has been designed and is undergoing testing. It offers a five fold speed up in the rise time from the generator while preventing reverse current from blasting the output SCR. The compressor drives the control grid with a sharper pulse to further reduce the jitter from the HY5353.

* Work supported by US D o E contract DE-AC03-76SF00515

0-7803-0135-8/91$03.00 ©IEEE

A thyratron engineer at EG&G had proposed a theory that implicated cathode hot spotting, which caused the HY5353 to exhaust an area of the cathode. It then could operate in an unstable mode until a new cathode emitting area was established [4]. Another HY5353 researcher [5] theorized that the instability was caused by grid hot spotting because of supporting evidence discovered in disassembled HY5353's. He had taken several apart and noticed bluing on the circumferences of certain control grid penetrations as if the plasma were following a specific path, which remained fixed for a period of operation until the beginning of jitter instability. He had disassembled thyratrons that had three bouts of instability and had found three different blued grid circumferences and matching polished areas on the anode. The two explanations are similar, and serve to indicate what has been observed with the HY5353's in the SLC Blumleins. However in a recent autopsy by EG&G no definite evidence for either phenomena was reported. The EG&G official version reads [6], "Gas clean-up is not evident. Cathode deterioration is causing time jitter increase with life. Cathode deterioration after 10^9 shots is normal life in our estimation." For 120 Hz operation, this translates to a 2300 hour lifetime. Fortunately, we have managed to wrest $\approx 2\times10^9$ shots based on operating hours, by nursing the thyratrons back to usability on the Blumlein test stand. Considering the total number of thyratrons consumed, the lifetime is $\approx$ 5000 hours, but since every unit has to be pulled out at $\approx$ 1000 hours for rehabilitation, once or twice, the confidence level for the HY5353 is < 50%.

II. Two Bunch Kicker Experience

The Blumlein pulser with its narrow pulse specifically for e^+ single bunch injection and extraction was ineffective for two bunch kicking in the e^- damping ring. In this ring SLC needed a kicker magnet pulse with a long flattop width for the two bunches with a 60 ns separation, and rise and fall times of $\leq$ 30 ns. The kicker uses two parallel thyratrons with each discharging a pair of 50 Ω coaxial cables [7]. Each thyratron is coaxially enclosed. Both coaxial enclosures are housed in a tank that has a mineral oil circulation system providing a filtered dielectric and thermal transfer. The thyratrons are EEV CX1671D's which when properly used are capable of $\leq$ 30 ns rise times for 10 to 90%. The anodes work at up to 70 kV, normally 60 kV and each thyratron switches 1.2 kA for a $\approx$ 150 ns pulse. These kickers are also command charged to allow high gas pressure operation for fast switching.

In the early version of this kicker (1986), the trigger driver, reservoir, heater, and prebias supplies were at the cathode potential during the pulse. The cathode electronics package was trigger and power connected to the control racks via fiber-optic cable and high frequency transformer isolation respectively. They were not reliable, hard to diagnose, and difficult to maintain without replacing the package and thyratron as an ensemble. Our early operating experience of the CX1671D is masked by the numerous false alarms caused by the triggering and supply stability problems with the electronics package.

In 1989 an isolation choke was designed so that the trigger driver, reservoir, heater, and prebias supplies could be located at ground. This choke was designed for a 5.6×10^{-3} V-sec flux swing. It consists of two stacked toroids of CMD5005 material with 2 sq. in. of area. All of the thyratron trigger, supply, and diagnostic wires and coaxial cables are bundled together with an overall jacket diameter of 1/2 inch, and then nine turns of this composite cable are wound onto the stacked toroids. The choke presents an impedance approximately 50 to 100 times the 25 Ω load on the thyratron cathode, or $\approx$ 20 A pulsed path to ground compared to the 1200 A load current. Turn to turn voltage can be as high as 4.4 kV in the circulating oil dielectric, hence a special nine holed nylon guide is placed into the toroid hole so that each turn is always physically isolated from adjacent turns. The choke is biased via an air core inductor of 100 μH connected from the cathode to ground. The core bias is $\approx$ 3.5 A, determined by the R_{dc} of the air core coil, and supplied parasitically from the dc heater supply. The resistance of the air coil was kept low to insure this 3.5 A bias. Eliminating the fiber-optic triggering reduced the jitter dramatically. The reliability of the commercial heater and reservoir supplies with hard wired diagnostics resulted in a major reduction of kicker downtime. These isolation chokes have been in use for almost two years, finally offering a true idea of the CX1671D's performance and lifetime.

Combining the early CX1671D experience with the latest data indicates the nominal is lifetime is 5500 hours with a confidence level of 70% and increasing.

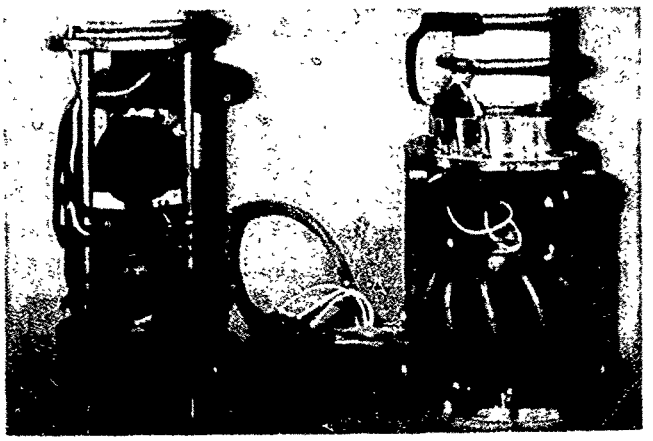


Figure 1. Comparison of the floating electronics package (left) with the isolation choke package (right).

III. Long Blumlein Results

SLC obviously needs fast and reliable thyratrons for kickers. An investigation into the suitability of our present thyratrons and a quest for better types led to the construction of a 100 ns Blumlein using water (LCW) as a dielectric to keep the physical length to a reasonable size. The Blumlein had two sets of internal electrodes, so that with a modest effort the impedance could be changed from 12.5 Ω to 25 Ω for switching point impedances of 6.25 Ω and 12.5 Ω. This would allow variation of the R in the L/R time constant. It could also offer an idea of whether the L, or the ionization time of the thyratron dominated the fall time. The thyratron was mounted

externally and coaxially beneath the line with forced air cooling to allow quick replacement and measurement access. The anode voltages were typically 25 kV, somewhat less than the actual operating voltages. The line was tested using various spark gap configurations, and then reworked to reduce the lead inductance from the center conductor to anode to 40 nH.

The data in Table 1 was taken by discharging the line into a resistive load of either 25 Ω or 12.5 Ω, and measuring the fall time (10 to 90%) at the anode of the switching device. In a few cases, no measurements were taken. The thyratrons tested were or had been used in other applications at SLAC and except for the new CX2025X, may have been previously used.

The CX1574C is the thyratron for the final focus kicker and has a 5100 hour average lifetime. It was selected for testing because of good lifetime experience, compact size (one gap), and a 15 kA current rating. The CX1536A had been used with some success in the klystron modulators on the linear accelerator where they had averaged ≈ 8000 hours. The tube is a rather compact two gap device with a 10 kA rating.

Z_{Line} =			25 Ω	12.5 Ω
SWITCH	ht."	gaps	t_{fall} in ns	t_{fall} in ns
Spark Gap	<1	1	–	12
CX1574C	8.4	1	–	42
CX1536A	12.6	2	–	60
CX1671D	13.5	3	–	60
HY5353	5.8	3	14	15 to 20
CX2025X	8.7	4	18	20

Table 1. Comparison of fall times using the Long Blumlein.

Since the CX1671D was being applied in the two bunch kicker, it could be considered a candidate for Blumlein use as well. It is a somewhat long tube with three gaps and a modest 3 kA rating, probably marginal for a 12.5 Ω Blumlein and 4 kA switching point current.

For the HY5353, we needed actual validation, since it had been in use for six years as the Blumlein thyratron. It is the shortest three gap and most compact of the thyratrons tested with a 5 kA rating for μs width pulses, and conceivably capable of 10 kA at the 100 ns width. The Blumlein was changed from 12.5 Ω to 25 Ω and the fall times for the thyratrons decreased by only 10%. This discovery indicated the fall is not L/R dominated but is mainly determined by the thyratron ionization time. Data in Table 1 implies this, since the one gap CX1574C has a two times longer fall time than the three gap HY5353. Data below in Table 2 for the HY5353 offers the same implication, i.e., increase the gas pressure and decrease the ionization time. Furthermore, the K-A grid could be prepulsed with additional reductions in fall time.

Reservoir Voltage (V)	4.0	4.5	5.0	5.5
HY5353 $t_{fall\ 10\text{-}90}$ (ns)	16	14	12	10

Table 2. Comparison of fall times vs reservoir voltage.

The CX2025X is a recent (1988) thyratron design from EEV intended as very fast, high di/dt switch, with 100 kV and 15 kA specifications. The results show it as the only serious competition for the HY5353. A redesigned thyratron housing for the SLC Blumlein with a CX2025X will permit additional testing and an eventual reliability run.

IV. Summary and Prospects

The long Blumlein tests offered a validation that the HY5353 was the only production thyratron for the single bunch kicker applications. Which unfortunately is still an SLC handicap, since it is a short lived and cranky thyratron once past the 1000 hour stage. The possible replacement a CX2025X could possibly exhibit better total performance without the eccentricities of the HY5353, once the mechanical changes to the thyratron housing on the Blumlein are accomplished. The double bunch kickers use a thyratron pair, which are far more reliable especially after the replacement of the floating electronics package, since the tubes are quite suited to kicker parameters. The final focus kickers are also correctly tubed for the present with additional work planned to reduce the reverse voltage and current for even longer lifetime.

KICKER	Units	1 bunch	2 bunch	FF 1/2 sine
Thyratron	ea	HY5353	CX1671D	CX1574C
t_{PW}	ns	80	150	540
pulse/p'lse jitter	ns	≤ 1	≤ 0.5	≤ 5
V_{Anode}	kV	35	70	+12 & -2
I_{Anode}	kA	4	1.4	+2 & - 0.4
$t_{fall\ 10\text{-}90}$	ns	25	30	300
PRR	Hz	120	120	120
Average Life	hr	5000	5500	5100
Confidence	%	< 50	70	80

Table 3. Comparison of thyratron parameters and lifetimes.

Table 3 summarizes our operating experience with the three kicker thyratrons. Based on the tests done with the long Blumlein, SLC does have the right thyratrons in the right locations. It is also possible that the Blumlein pulser can be improved by using the CX2025X in place of the HY5353.

V. Acknowledgments

The authors are indebted to the following people for quality suggestions, lively discussion, and hard work: M. Artusy, G. Aske, D. Briggs, G. Bowden, D. Gough, S. Hewitt, J. Krzaszczak, M. McCoy, and D. Williams who has patiently nursed a his share of sick and dying thyratrons.

VI. References

[1] F. Bulos *et al.*, "Some Fast Beam Kicker Magnet Systems at SLAC," PAC Record 87CH2837-9, Washington, D.C., March 1987, pp. 1884-6.

[2] R.L. Cassel and M. Nguyen, "Kicker Pulsed Charger," XTP16, this conference.

[3] D.E. Gough *et al.*, "The Timing and Diagnostics Systems of the Kicker Magnet Pulsers for SLC," XTP24, this conference.

[4] R. Caristi, Private Communication November 1988.

[5] G. McDuff, Private Communication April 1991.

[6] J. Murachver, Private Communication, August 1990.

[7] L. Bartelson *et al.*, "Kicker for the SLC Electron Damping Ring," PAC Record 87CH2837-9, Washington, D.C., March 1987, pp. 1582-4.

THE TIMING AND DIAGNOSTIC SYSTEMS OF THE KICKER MAGNET PULSERS FOR THE STANFORD LINEAR COLLIDER *

D. E. Gough, R. L. Cassel, A. R. Donaldson
D. P. Hutchinson, T. S. Mattison
Stanford Linear Accelerator Center,
Stanford, California 94309

Summary

The Stanford Linear Collider (SLC) uses several very fast thyratron pulsers to drive kicker magnets. The pulsers operate at repetition rates of between 1 and 120 pulses per second as dictated by the operational mode of the SLC. Time jitter of typically 200 psec is achieved and the longer term effect of time drift is compensated by the use of a timing feedback device. Monitoring is provided to measure and display the average time and jitter for the thyratrons and magnets. Amplitude stability of better than 10^{-3} is required and this is measured and displayed by the use of an amplitude sampler. Measurements of the individual functions of each system are provided both locally and at the Machine Control Center so that it is possible to continuously track each pulser's performance.

Introduction

The kicker magnets are located in the positron and electron damping rings with one at the 2/3 point of the linac for positron production. Each magnet is connected to a pulser located in the service building above the damping ring or in the linac klystron gallery. Both damping ring service buildings contain three complete pulser systems, two being connected to the kicker magnets whilst the third is an uncommitted standby system. To the first approximation one CAMAC crate is used for each of the pulser systems. This provides access to the SLC's comprehensive machine timing system and diagnostic monitoring capability. The magnet requirements for the two damping rings are not the same [1] and subsequently there are two pulser types used. The positron damping ring pulsers use a Blumlein with a single thyratron as the energy discharge switch. The electron damping ring pulsers are of the delay line type and use a pair of parallel connected hydrogen thyratrons as the energy discharge switch.

The analog monitoring and data storage capability of the SLC is used to provide monitoring channels of system dc voltage signals. This allows continuous access to these monitor channels and also provides the capability to obtain a history of performance.

The Timing System

The SLC beam repetition rate varies dynamically to protect certain components from damage by the beam. Thyratron anode delay can vary by tens of nsec if the pulse rate is changed, which is not tolerable. A CAMAC module provides up to 16 general use timing channels that can be programmed to generate either beam coded triggers, or base rate triggers that are unaffected by the beam code. Each channel can be adjusted in time with a step size of 8.4 nsec and a resolution of about 30 psec. Step sizes of 100 psec are available by adding a vernier delay CMAC module. Operation of the pulser at a constant repetition rate, whilst retaining the capability of being able to operate at between 1 and 120 pulses a second, is achieved by using two of the available trigger channels. One is set so that it produces a beam coded trigger and the other a base rate trigger. The base rate trigger is set so that it occurs 2 µsec after the beam coded trigger. An "or" function of these two triggers is carried out using a standard NIM module, the resultant output providing the raw trigger. This configuration provides the raw trigger pulse for the thyratron [2] and, in a similar manner, for the pulsed charger[3]. The pulsed charger trigger is set so that it occurs a nominal 100 µsec before the thyratron trigger. When a beam coded trigger is present both the pulse charger and the thyratrons are initiated at the time set by the beam coded channels. The base rate triggers that follow will have no harmful effects

Thyratron delay is also a function of filament and reservoir voltage, anode voltage, and age. A timing feedback module or stabilizer is constructed as a NIM module and one stabilizer module is used for each thyratron timing channel. The stabilizer is shown in block form at figure 1. Both input and output pulses conform to the NIM standard.

The raw trigger is patched to the stabilizer where it is used to generate a voltage ramp. The voltage ramp is compared with the voltage obtained from the DAC, which is a measure of the delay correction, to provide the delay trigger output. This trigger is routed via a NIM level convertor module to provide a TTL trigger for the thyratron trigger chassis [4]. The buffered thyratron current transformer signal is used in conjunction with a NIM discriminator to provide a time reference trigger that is patched to the stabilizer. A separate beam coded timing pulse is used to provide a reference

* Work performed under U.S. Department of Energy Contract DE-AC03-76SF00515

0-7803-0135-8/91$03.00 ©IEEE

input for the stabilizer. The reference trigger is adjusted so that the kicker magnet is powered to coincide with optimum beam performance. The time/analog convertor (TAC) produces a voltage with an amplitude determined by the time difference between the reference and feedback signals, within a range of 3 nsec. This is then compared to a reference and generates a logic control signal indicating which arrived first. The reference and feedback signals also provide a strobe pulse, provided that both signals are present. The logic control determines whether the scaler will count up or down, and the strobe initiates the process. The analog output from the DAC is set by the scaler and this provides the control voltage for the next pulse. If the time error is greater than the 3 nsec range of the TAC it is detected and flagged both locally and remotely as "out of window". The stabilizer has an active range of +/- 275 nsec, the amount of trigger delay being displayed on the front panel as well as available as a scaled analog voltage output. The stabilizer can be set to either the track or freeze mode with a logic high or low respectively. It is also possible to set the stabilizer to mid-range by a logic high pulse. Status indication is provided for out of window, out of range and track/freeze. The stabilizer is designed so that it does not introduce additional jitter into the thyratron trigger circuit by using emitter-coupled logic where appropriate.

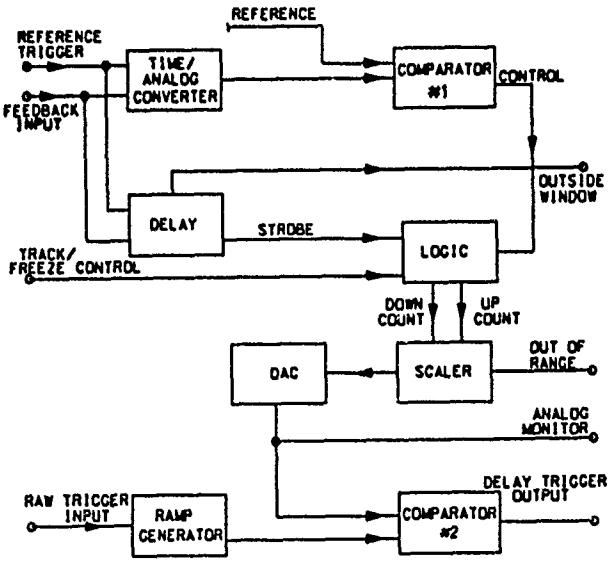


Fig.1 Stabilizer block diagram

The derived kicker timing signals from the current transformers and magnetic field obtained from the buffer module for all three systems are patched with delay lines so that they nominally coincide in time. These signals are routed to a CAMAC module TDC for system time measurement. Two of the SLC timing channels from each system are reserved for beam diagnostics and one of these trigger channels provides the TDC gate trigger.

Instrumentation is provided to monitor the performance of the timing system. The current transformer derived signal for each thyratron and the signal obtained from the magnet pick up coil are used for this. These signals are attenuated then applied to a buffer module which produces multiple outputs of each input function. The magnet pickup coil signal is integrated within the buffer module to provide monitoring capability of the kicker magnet field. One buffer module output channel for each of the thyratron current transformer signals and one magnetic field signal are applied to separate channels of a NIM module discriminator. The discriminator threshold is set so that the output pulse is independent of the input signal amplitude providing the pulser is operating above the 20% level. An output from each of the discriminator channels is connected to the "stop" control of Stanford Research Systems SR620 Time Interval Counters (TIC). A beam code trigger channel is buffered and its multiple outputs connected to each of the TIC "start" controls. This ensures that all of the TIC units are only initiated when the kickers are being operated under beam conditions and they do not respond in the standby mode. The TIC's are used to measure the time jitter and mean time over 100 machine cycles as preset at the TIC. The resultant measurements are displayed on the front panel and are also available as a scaled analog output voltage. These outputs are connected to a CAMAC module to provide data to the SLC monitoring system. The TIC can be addressed by the CAMAC crate GPIB data link so that various scale factors can be set and read remotely.

Amplitude Sampler

The heart of an amplitude sampler is a Comlinear 9400 track/hold circuit that has an input range of +/- 2 volts and a drift of about 1mV. To improve the resolution a stable voltage of 20V is subtracted when a large signal is available e.g. from a thyratron current transformer. The magnet pickup coil signal, when integrated, is small enough to send directly to the Comlinear. The block diagram at figure 2 is for the high resolution channel of the amplitude sampler for the current transformer signals; the second channel has an integrator at the input and this signal goes direct to the track/hold circuit.

The output of the track/hold is gated using a FET switch to a low droop hold circuit. A buffered time constant output provides a measurement of the average current and a buffered rms output is also provided. The trigger input signal that is used to control the operational mode of the track/hold as well as the following FET switch is obtained from a SLC beam coded trigger channel. An output from the track/hold circuit is current limited to an output connector to provide pulse to pulse amplitude measurements. All the pulse output channels from the amplitude samplers for a given damping ring are

patched to a gated ADC CAMAC module via pulse shaping capacitors. The second diagnostic timing channel provides the ADC gate command via a pulse stretcher NIM module. The gate width is set so that all of the pulse output signals can be monitored simultaneously. The amplitude signals can be measured over a number of machine cycles to give the short term amplitude stability.

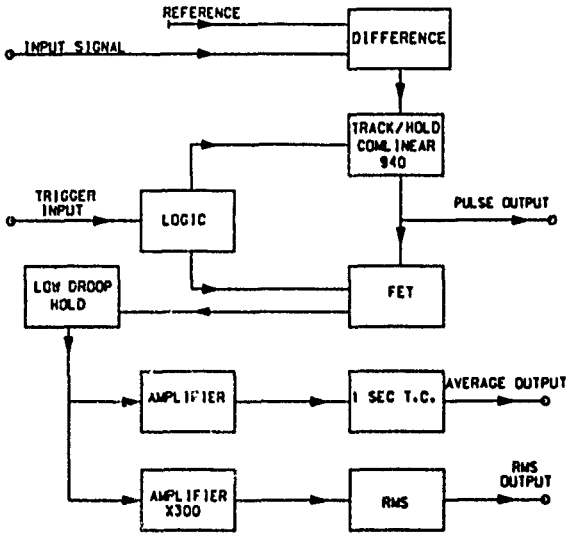


Fig.2 Amplitude sampler, high resolution channel.

Video Multiplex Oscilloscope

Pulse signal monitoring is also provided for each system. The individual monitor signals are routed to the purpose built buffer chassis which produces multiple output signals from each input signal. Each output channel is able to drive a 50 ohm load without compromising any of the similar channels. Output jacks are provided at the service building for monitoring. Another output channel of each signal is routed to a mux switch assembly. The mux output is connected to the input channels of an oscilloscope that has a video camera to provide remote monitoring. The oscilloscope and mux unit are also connected to the GPIB control system so that it is possible to select any of the mux channels with the correct oscilloscope settings. One of the beam coded trigger channels is used as a remote trigger for the oscilloscope. Dedicated function buttons on the SLC control panel are used to select the mux channel, set the trigger time, and recall a stored oscilloscope set up. A patch panel is used to match the pulser system being used for a specific kicker function so that the injection and extraction signals as seen at the display screens are correct.

Conclusions

The stabilizer, in its final form, has been operating successfully as part of the timing system since relocation of all of the electronics to the service building in 1990. A problem with electrical noise affecting the initialize control of the stabilizers used for the electron damping ring pulsers was initially encountered. This was corrected by the addition of noise rejection filters to these control lines. The original stabilizers built for this timing system used a 12 bit scaler. It was decided to develop a 16 bit version which could be used to either increase the delay range or increase the resolution. One of these modules has been built and is being tested in a development system pulser.

Installation of the amplitude samplers is now complete and final adjustments are being made to provide optimum performance. The capacitor coupling used between the pulse output monitor, which is positive polarity, and the ADC is to provide a negative signal for the ADC module.

The original intention for the high resolution amplitude sampler channels had been to use the voltage output from each current transformer and set the internal attenuators in the module to match its input voltage. We found that the voltage signal levels covered a wide range, and setting individual channels could cause problems and be confusing. It was decided to provide external attenuation of these signals where necessary so that the amplitude sampler offset is nominally 25 volts for every channel.

Initial results show that the kicker current stability obtained from the current transformers at the electron ring is a few parts in 10^4 and for the positron ring is about a part in 10^3.

Acknowledgements

We would like to acknowledge the contribution made by other members of SLC, in particular Marc Ross and Bob Noriega.

References

[1] F. Bulos, et al.,"Some Fast Beam Kicker Magnet Systems at SLAC", Proceedings of the 1987 IEEE Particle Accelerator Conference, p. 1884.

[2] A.R. Donaldson, et al., "Kicker Thyratron Experience from SLC", elsewhere in these Proceedings.

[3] R Cassel, M. Nguyen, "Kicker Pulsed Charger", elsewhere in these Proceedings.

[4] M Nguyen, R. Cassel. "Fast Thyratron Driver", elsewhere in these Proceedings.

"Fast Power Supplies for Kicker and Thin Septum Magnets in a 1.2 GeV Synchrotron Radiation Source"

B.E. Strickland, G.L. Schofield, B.L. Thomas, and W.P. White,
Maxwell Laboratories, Inc., Balboa Division,
8888 Balboa Avenue,
San Diego, CA. 92123-1506
and
B. Ng and D. Meaney
Maxwell Laboratories, Inc. Brobeck Division,
4905 Central Avenue,
Richmond, CA. 94804-5803

Abstract

The Maxwell Laboratories, Inc. (Maxwell) Model 1.2-400 Electron Storage Ring, which is being built for the LSU Center for Advanced Microstructures and Devices, is a 1.2 GeV Synchrotron which has a 200 Mev linac for injection of electrons into the storage ring. The injector section for merging the linac beam with the storage ring beam has four kicker magnets for altering the course of the stored beam and a thin septum magnet for steering the linac beam. A detailed discussion of the electrical requirements for the fast power supplies for powering the magnets, the circuits used to meet the requirements, and a comparison of the theoretical and actual data will be presented.

I. INTRODUCTION

The commercial development of Maxwell's Model 1.2-400 Electron Storage Ring, utilizes a set of four kicker magnets, a thick septum, and a thin septum to accomplish injection of charge into the storage ring from the linear accelerator. During the injection process, the incoming beam from the linear accelerator is brought in parallel, but displaced, to the stored beam by means of the thick and thin septa. The stored beam is displaced toward the incoming beam at the thin septum by kicking the stored beam with two fast pulsed kicker magnets (outer then inner) located before the thin septum. The merged beams are kicked back to the original stored beam location by two additional fast pulsed kicker magnets (inner then outer) which are identical to the first two magnets.

A set of five fast power supplies is used to generate the electrical pulses required by the four kicker magnets and the thin septum. Two identical supplies provide the pulses for each of the two inner kicker magnets and another two identical supplies provide power to each of the two outer kicker magnets. A fifth supply generates the pulse for the thin septum. A description of the requirements of the five supplies, the circuit design of the power supplies to meet the requirements, and the theoretical and measured data is presented in this paper.

II. MAGNET REQUIREMENTS

A. Kicker Magnets

The electrical waveshape required for powering each kicker magnet is identical in shape. Only the relative magnitudes of the current amplitudes between the inner and outer kicker magnets are different. By making all the waveshapes identical in shape, the pulses do not need the fast rise time rectangular pulses as generated by other kicker magnet pulsers [1,2].

The electrical pulse must have a "flattop" duration of 200 ns and the trailing edge of the pulse should fail to less than 5 percent of the flattop magnitude in approximately 370 ns. The "flattop" variation should be less than ±5.5 percent of the nominal value during a single pulse or from pulse to pulse. The pulse amplitude must be continuously adjustable from the maximum required value to 50 percent of the maximum value. The repetition rate will be approximately 1 Hz, although repetition rates of up to 10 Hz will be achievable.

For the outer kicker magnets, the maximum current required is 915 A and the nominal current amplitude is 835 A. The nominal current corresponds to an integrated field (nominal core length of 0.15 m) of 0.0012 T•m. The inner kicker magnet requires a maximum current of 230 A and a nominal current of 210 A. The nominal current for the inner magnet corresponds to an integrated field (nominal core length of 0.15 m) of 0.0003 T•m.

B. Thin Septum

Due to the short injection time of the electrons, the thin septum waveshape can be a half sinusoid, with the injected electrons only seeing the peak of the sinusoid. The maximum current required by the thin septum is 6440 A and a nominal current of 5858 A. The nominal current for the corresponds to an integrated field (nominal core length of 0.3 m) of 0.05 T•m.

The "flattop" duration should be greater than 200 ns. The maximum variation of the flattop current for a single shot and shot to shot is ≤1 percent. The current should be adjustable to 50 percent of the maximum. The nominal and maximum repetition rate for the thin septum is the same as that for the kickers, which is 1 and 10 Hz accordingly.

0-7803-0135-8/91$03.00 ©IEEE

III. CIRCUIT DESIGN

A. Kicker Magnet Fast Power Supplies

The circuit used to generate the electrical pulse for the kicker magnets is shown in Figure 1. To start current flowing in the magnet, the start switch is closed and energizes the under damped RLC circuit. The period of the under damped oscillations is made sufficiently long so that a 200 ns "flattop" (±5.5 percent of the nominal) can be realized at the top of the first oscillation. At the end of the "flattop," the crowbar switch is fired and the current through the magnet decays to within 5 percent of the flattop value in 370 ns.

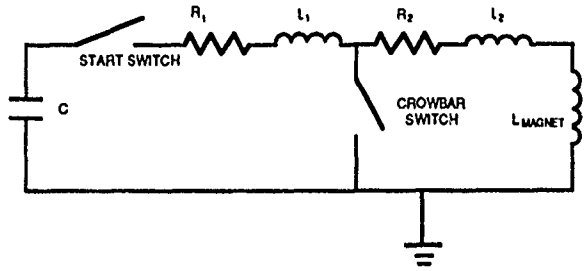


Figure 1. Circuit used for the kicker magnet supplies.

To meet the requirements of flattop and fall time, the impedances in the two loops must be carefully selected. The pulse shape for the two kicker supplies is the same, and only the relative magnitude of the required current is different. The switches in the circuit were to be implemented with thyratrons, which require a minimum voltage across them to fire reliably and have a maximum voltage which they can hold off. The limitations of the switches prevented adjusting the charge voltage of the capacitor to meet the current requirements of both inner and outer kickers. By scaling the impedances in the loops, the circuit voltages (both magnitude and shape) remain the same for both inner and outer kickers, and only the magnitude and not the shape of the current waveform is changed. Therefore, the impedances for one of the kickers had to be selected to meet the design criteria, and then the impedances were directly scaled to obtain the desired current in the other kicker. Table 1 shows the values used for the components in the drawing.

Table 1
Component values for inner and outer fast power supplies

Kicker	C	R1	L1	R2	L2
Inner	15 nF	9.4 Ω	9.6 μH	41.1 Ω	3.3 μH
Outer	60 nF	2.35 Ω	2.35 μH	11.8 Ω	0.7 μH

Once the main components were determined, extensive simulations of the circuit including the significant stray and connecting cable impedances were run using Maxwell's MAXCAP computer circuit simulation code. From the simulations it was discovered that oscillations in the output current would occur in the circuit as a result of the stray impedances in the circuit. The oscillations were eliminated by the addition of a small RC filter, consisting of a 2 nF capacitor and 10 Ω resistor, at the output of the supply to the buswork which connects the supply to the magnet. The oscillation prevention filter suppressed oscillations of the current allowing the flattop specification to be met in the simulations. An example of the simulated current for an outer kicker magnet is shown in Figure 2.

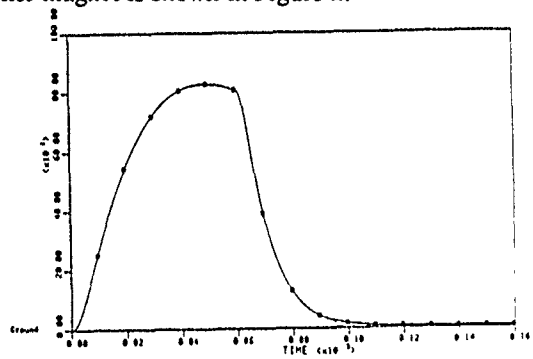


Figure 2. Simulated current in an outer kicker magnet.
(verticle 200 A/div, horiz. 200 ns/div)

B. Thin Septum Fast Power Supply

The circuit for the thin septum power supply is shown in Figure 3. To start the current pulse into the magnet, the switch is closed and the LC circuit begins to oscillate. The current through the inductance rings up. When the current begins to reverse, the switch turns off and the current flows through the diode and resistor. The circuit is now an over damped RLC circuit. The capacitor was chosen so that the period of oscillation between the inductance in the circuit and the capacitor is sufficiently long so that the "flattop" or peak of the current waveform has a variation of less than 1 percent for 200 ns. The resistance was chosen to be small enough to allow the reverse voltage on the capacitor to discharge quickly enough to allow the capacitor to be completely recharged before the next pulse is to be applied to the magnet, yet the resistance must be large enough to prevent excessive reverse current from flowing through the magnet during the reversal discharge.

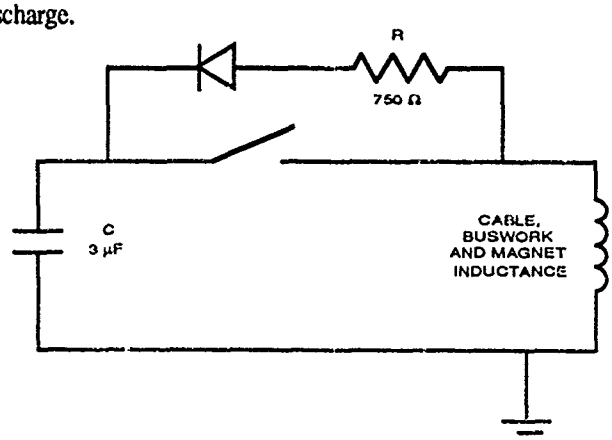


Figure 3. Thin septum circuit.

The simulations of the circuit including the strays showed small oscillations on the current waveform similar to those seen in the simulations for the kicker magnet fast power supplies. A small RC filter was placed on the buswork which connects the power supply output cable to the thin septum magnet in order to suppress the oscillations. An example of the simulated current for the thin septum magnet is shown in Figure 4.

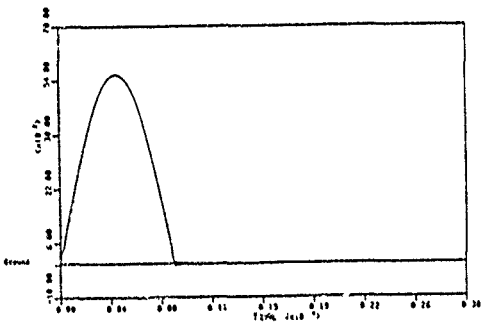


Figure 4. Simulated circuit for the thin septum magnet.
(verticle 1600 A/div, horiz. 4 μs/div)

IV. RESULTS

A. Kicker Magnet Fast Power Supplies

The kicker magnet supplies were assembled. The switches for both the start switch and crowbar switch were ITT F-130 thyratrons. An example of the current through the magnet is shown in Figure 5. The current was measured with a Pearson 5136 current probe which was mounted on the connecting buswork to the magnet. The measured waveform is as expected from the simulations, with only minor subtle differences in the waveshape. If the oscillation suppression filter is removed from the circuit, oscillation of the current waveform is seen as expected from the circuit simulations.

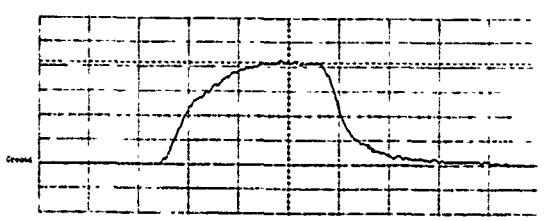


Figure 5. Measured current in an outer kicker magnet.
(verticle 200 A/div, horiz. 200 ns/div)

B. Thin Septum Fast Power Supply

The thin septum fast power supply was assembled. The main switch is a ITT F-241 thyratron. The inductance budget was very small to minimize the required operating voltage. Therefore, no additional inductance was included in the circuit other than the inductance inherent in the buswork and cabling of the system. An example of the current waveform through the thin septum magnet is shown in Figure 6. The current was measured with a Pearson 5136 current probe. The measured waveform compares well with that predicted by the theory.

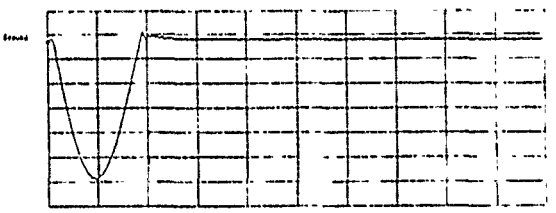


Figure 6. Measured current in the thin septum magnet.
(verticle 1000 A/div, horiz. 4 μs/div)

V. CONCLUSIONS

To meet the requirements of the fast pulsed magnets used in the injection of the linear beam for the Maxwell Model 1.2-400 Electron Storage Ring, extensive circuit simulations were run to simulate the performance of the fast power supplies. The power supplies were built, and the data obtained compares with those expected from the simulations.

VI. REFERENCES

[1] G. Nassibian, "Travelling Wave Kicker Magnets with Sharp Rise and Less Overshoot," IEEE Transactions on Nuclear Science, vol. NS-26, No. 3, pp. 4018-4020, June 1979.

[2] A. Bruckner, "Kicking Protons, Fast and Cheap," *Proc. US Particle Accelerator Conf.* Chicago, IL. 1971, p.976.

Fast TEM Kicker with MOSFET Solid State Driver

Alfredo Saab*, Michael Kogan and Tomás Russ
MIT - Bates Accelerator Center
21 Manning Rd., Middleton, MA. 01949

Abstract

The design of a fast transverse electromagnetic (TEM) kicker for use in the Bates Pulse Stretcher Ring is described. It provides a 1 mrad/m. kick for a 1GeV electron beam, with transition times below 25 ns. and a 1% flat top. The +/- 10 KV. driver uses a novel switching technique, based on MOSFET power transistors, which allows complete control over the kicker timing and simplifies the construction greatly. Calculations show that the reliability of such a driver is orders of magnitude better than present designs.

I. DESCRIPTION

The MIT-Bates Pulse Stretcher Ring is designed to expand the linac duty cycle (now < 1%) to 85% or greater. A linac pulse of 1.2 μs is injected into the ring, filling it twice. Two kicker deflectors are turned on at injection time, and then turned off very fast to minimize circulating beam losses [1].

Table 1. Kicker Specifications

Bend Angle	1 mR
Kick interval	1.33 μs
Energy range	200- 1100MeV
Repetition Rate	20 Hz. - 1000 Hz.
Active aperture	8 mm
Gap	40 mm
Available length	1.1 m.
Rise time	< 50 ns.
Fall time	< 25 ns.
Flat top	1 %

Relevant design specifications are shown in Table 1. Critical parameters are the fall time, which must stay below 25 ns., and flatness inside and outside the kicking interval, to be kept within 1% of the pulse height. This last restriction led us to consider minimum reflection schemes. Fig. 1 shows the chosen configuration: when firing, a pair of switches close and deliver complementary polarity high voltage pulses through the kicker plates into matched terminators. Because (on first order approximation) the system is perfectly matched, no reflections are produced. Energy is supplied by two DC HV power supplies with low series inductance capacitors as charge reservoirs. After the injection period, the switches open and the deflection field is abruptly removed.

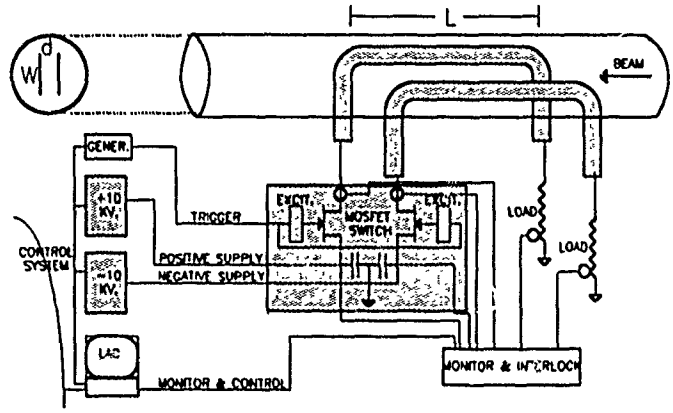


Fig. 1 - T.E.M. Kicker Block Diagram

If the kicker plates' voltage and current are related by their characteristic impedance Zo, a wave travels along them in TEM mode, producing transverse B and E fields. Electric and magnetic deflection forces are identical and, if the wave moves against the beam, additive.

II. KICKER DEFLECTION PLATES

The kicker deflection plates consist of a pair of parallel plates of width W, length L, and gap d (Fig. 1). The surrounding vacuum chamber is far enough removed from the plates to ignore its shielding effects on the electromagnetic fields inside the deflector. Maxwell's equations can be applied to calculate analytically the deflecting electric and magnetic fields for this geometry[2]. The angular deflection can be calculated to be:

$\Phi = p_T/p_L$, where pT and pL are the transverse and longitudinal momenta. For identical electrical and magnetic contributions, it is easily shown that:

$\Phi = 2.B.L.c / E(eV)$, where B is the magnetic field, E the electron beam energy, and L the length of the plates. For our case:

$\Phi = 1.10^{-3}$, L = 1 m., $E(eV) = 1.10^{+9}$, and B = 16.67 Gauss, which renders an applied force of $F = 8.10^{14}$ N, and an electric field $E = 5.10^5$ V/m. For d = 4 cm., V = 20,000 V. If Zo = 100 Ω, I = 200 A.

A plot of the deflecting magnetic field B = f(x) in the region where the beam will actually be present (+/- 8 mm.) with the vertical displacement y used as parameter shows that the B field variations are < 1.5 % within the active aperture (Fig. 2).

0-7803-0135-8/91$03.00 ©IEEE

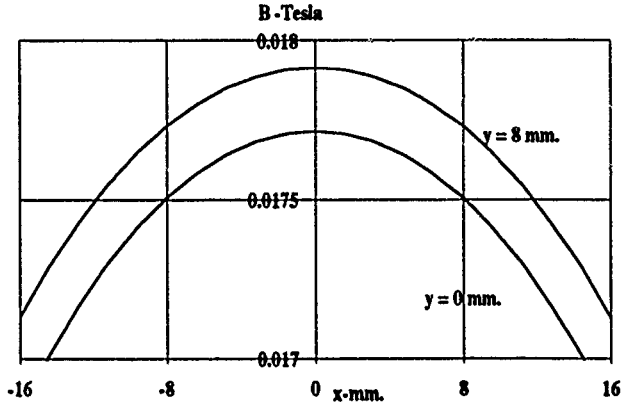


Fig. 2 - Field variations in the active region (+/- 8 mm.) of a pair of parallel kicker plates (W = 8 cm., d = 4 cm.).

Characteristic Impedance Calculations

The distributed inductance L and capacitance C can be calculated for the proposed kicker plate geometry by the analytical evaluation of the integrals for the magnetic field and for the voltage drops at x= 0 (Fig. 3). In our case, for a 100 Ω impedance d/W equals aproximately .5, justifying previous assumptions of W = 8 cm. for d = 4 cm. Notice that this differs from the standard approximation of Zo for parallel plates (377*d/W) by almost a factor of 2.

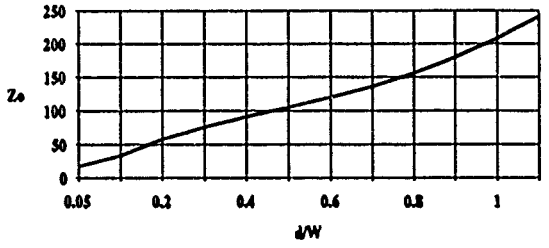


Fig. 3 - Characteristic impedance as a function of plate dimensions.

III. DRIVER SWITCH CIRCUIT

Power Section

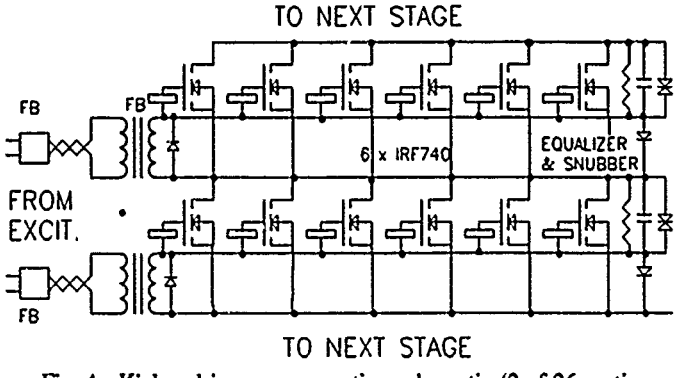


Fig. 4 - Kicker driver power section schematic (2 of 26 sections shown).

As shown in Fig.1, the kicker driver pulses the deflection plates by closing a pair of complementary polarity switches. Switch design is critical to obtain the rise time, fall time and flat top characteristics.

Given the recent availability of reliable and inexpensive power MOSFETs (Metal Oxide Semiconductor Field Effect Transistors), the switch was designed around them. MOSFETS' advantage over other devices (thyratrons, spark gaps) is that they can be turned off from the control port, without having to withdraw the main current. As majority carrier devices, MOSFETs need no charge accumulation or depletion (except for that in the oxide layer) to turn them on and off, and rise/fall times are very fast, on the order of 10/20 ns. Another crucial advantage of MOSFETs is their ability to operate at maximum voltage and current or at avalanche (voltage breakdown) without damage. Bipolar transistors suffer from well known second breakdown effects under these conditions. In any power switch, energy accumulates in the stray inductance of the circuit, causing overvoltages at turn off. MOSFETs can absorb this energy, a significant addition to system reliability. The main challenge in designing a MOSFET HV switch is that the maximum current/voltage combination for a commercial device is of about 20A. /1000 V. Therefore several devices have to be connected in parallel/series to reach 10000 V/ 200 A. as needed for each polarity switch. A "merit coefficient" for comparison was developed considering the maximum V_D and I_D, and the Miller charge for each device, to find the optimal for the switch. After analyzing all available types, a 400V. /10A. (40A. peak) device was chosen as the main component.

A switch has a total of 26 stages in series, each stage made of 6 parallel MOSFETs (see Fig. 4), giving a theoretical capacity of 10400V. / 208A. An RC and diode network equalizes the voltage among stages when the switch is off, with the diode isolating the equalizing network when the switch turns on. A protection MOV absorbs any energy spikes in each stage. Current sharing among paralleled MOSFETs is automatic due to the positive temperature coefficient of their channel resistance.

Stray inductance and capacitance on the PC board and MOSFET packaging are integrated to form a 50 Ω transmission stripline by placing the PCB at the correct distance above a ground plane.

Excitation Circuit

Each stage is driven by a pulse transformer, through a stabilizing ferrite bead. The 26 pulse tranformers have their primaries driven in parallel by a single low voltage, high current MOSFET. The design of a pulse transformer with very low leakage inductance is crucial to transporting the firing pulse to all stages. Tight coupling between primary and secondary windings with simultaneous HV isolation is obtained by using a single turn hollow conductor secondary, with the primary wound inside. The excitation circuit is shown in Fig. 5. The main MOSFET driver (IRFZ34) is moved by a push pull MOSFET stage (IRFZ10

and IRF9Z10), in turn driven by high speed-bipolar transistors. The differentiating network on the transistor bases allows them to be turned on only enough to charge the MOSFET's gate capacitance. The bipolar transistors are then turned off, avoiding storage time problems. The MOSFETs stay on thanks to the charged gate capacitance. The input trigger signal (J1) is processed by CMOS logic, all-owing for an INHIBIT signal to be connected at J2.

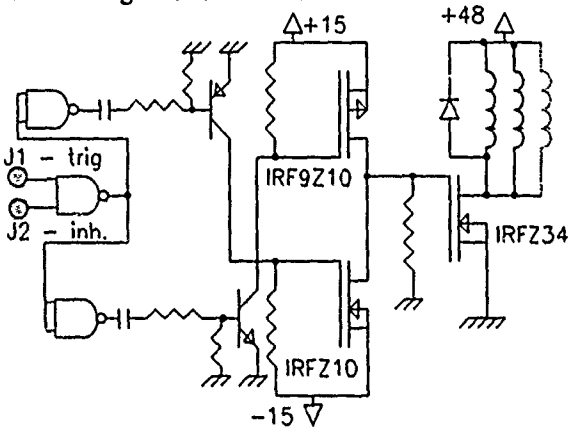


Fig. 5 - Simplified schematic of excitation circuit

Load Design

The 50 Ω/ 3 KW. terminators were designed in-house, due to the lack of available high power, high voltage loads on the market. Standard carbon composition 2W. resistors were arranged in a cylindrical configuration, as 12 stages of 6 resistors each. A connector is attached to the top of this cylinder through an impedance matching cone. The bottom of the cylinder is connected to the return tank through beryllium copper RF contacts. Dimensions of both cylinder and tank give the correct 50 Ω impedance. A voltage sampler resistor divider is brought up to the load top for monitoring purposes.The entire load is in oil to increase power handling capacity and provide HV operation. An oil circulating pump and oil/water heat exchanger will be used for continuous power operation.

IV. MEASUREMENTS

Measurements of the kicker deflection plates drive signals are shown in Fig.6 and Fig. 7, indicating that the specifications can be met with the present design. The critical fall time is around 15 ns. (from 90% to 25% of full scale). Flat top is within 1%. When operating with the kicker plates, difference in arrival time of the two pulses produce a ringing effect on the rising tedge, which is compensated by delaying slightly the beam injection until it has been damped.

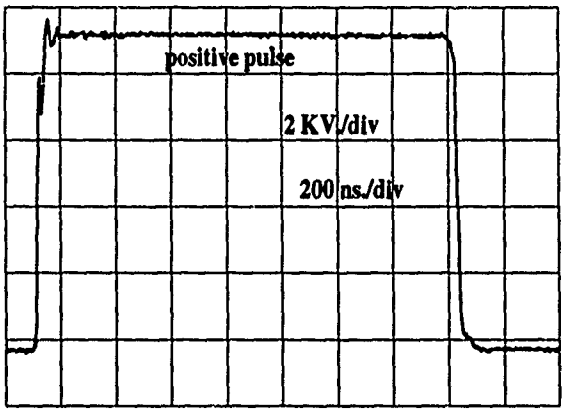


Fig. 6- Scope trace of the full positive driving pulse.

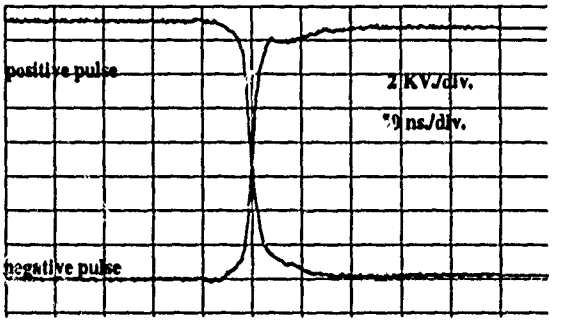


Fig. 7 - Detail of the fall time waveform for both kicker driving pulses.

V. CONCLUSIONS

A kicker design for the Bates Pulse Stretcher Ring has been shown which results in simple and reliable operation through the use of new techniques. Inexpensive MOSFET switches replace the cumbersome and complex storage line and thyratron scheme. Overall cost of each MOSFET switch hovers around US$1000, with a calculated MTBF of 50000 hrs. An interlock system has been designed and will be tested shortly. An IEEE488 controlled pulse generator and digital scope, together with a distributed power supply controller will be used to control and monitor timing and load signals through the ring control system[3].

VI. REFERENCES

[1] J. Flanz et al. "The MIT- Bates South Hall Ring", Proc. of the 1989 Particle Accelerator Conf., Chicago, Mar. 1989, pp.34

[2] T. Russ et al. " SHR Fast Kickers Design Report", Bates Internal Report., Jan. 1990.

[2] T. Russ et al. " The Bates Pulse Stretcher Ring Control System Design", Proc. of the 1989 Particle Accelerator Conf., Chicago, Mar. 1989, pp.85.

* Now with Stanford Accelerator Center.

APPLICATION OF ELECTROSTATIC UNDULATORS FOR ACCELERATION OF INTENSE ION BEAMS

E.S. Masunov, A.P. Novicov

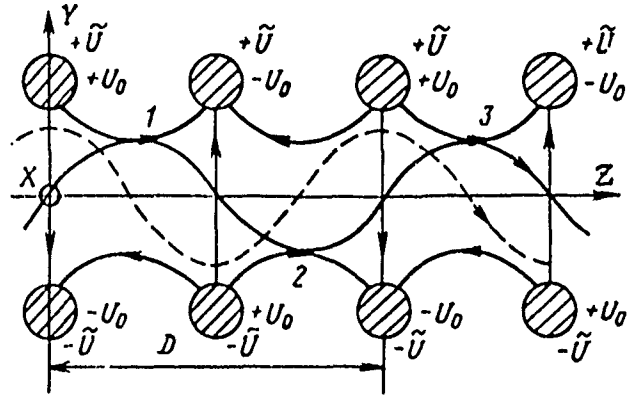
Moscow Physical Engineering Institute
115409 , Moscow , USSR

Some questions of ion beams interaction with RF and electrostatic fields in a linear undulator accelerator (lineondutron) with the plane undulator are considered. It is shown that in a lineondutron simultaneous acceleration of oppositely charged particles with the identical charge-to-mass ratio(for ex, $H^+$and H^-) may essentially increase the overall beam intensity up to a few Amp.

1. INTRODUCTION

An idea to apply undulators for acceleration of relativistic beams in a plane electromagnetic wave was discussed more than once. Various mechanisms and acceleration schemes were proposed to accelerate electrons in magnetostatic undulators and their description can be found in Refs.[1-3]. The similar principles can also be used for acceleration of non-relativistic ion beams [4]. In this case for low injection energy it is advisable to replace the magnetostatic undulator by the electrostatic one. The configuration of periodic electrostatic field can be chosen so as to provide an effective transverse particle focusing without applying additional external fields [5].

In this paper we discuss one of the possible versions of such linear accelerator, in which the ribbon ion beam is accelerated in the transverse RF- field and the field of a plane electrostatic undulator. The required field distribution is achieved by the appropriate system of electrodes, mounted in a resonator and dc-isolated between each other. Both the RF- and electrostatic potentials are supplied to adjacent electrodes, forming the accelerating channel (indicated by $\tilde{U}$ and U_0 in fig.)



The RF-frequency corresponds to the undulator space period D. Once influenced only by the RF or electrostatic field , the particle travels along the dotted curve in fig., and, as it is evident, its energy remains constant. If both the fields simultaneously influence on the charge, the particle energy doesn't vary in the transverse direction and increases in the longitudinal direction. The corresponding electrostatic field lines and particle trajectory in a combined-wave field are indicated in fig. by the solid line.

2. PARTICLE MOTION EQUATIONS

In a lineondutron scheme proposed a plane electrostatic undulator is combined with the RF-system. The electrode positions define the values of the fundamental space harmonics: the zero RF-field harmonic and the first electrostatic field harmonic, which are the working ones in our case. Higher harmonics values , in turn, depend greately on the electrode shape and size.

The field strengthes in the periodic system involved can be represented as

0-7803-0135-8/91$01.00 ©IEEE

$$a_y^v = a_v\Big(1+\sum_{n=1}^{\infty} æ_{2n}\,ch2kny\,\cos\Big(2n\int_0^z kdz\Big)\sin(\tau+\tau_0)\Big),$$

$$a_z^v = -a_v \sum_{n=1}^{\infty} æ_{2n}\,sh2kny\,\sin\Big(2n\int_0^z kdz\Big)\sin(\tau+\tau_0),$$

$$a_y^o = a_o \sum_{m=1}^{\infty} g_{2m-1}\,ch(2m-1)ky\,\cos(2m-1)\int_0^z kdz, \qquad (1)$$

$$a_z^o = -a_o \sum_{m=1}^{\infty} g_{2m-1}\,sh(2m-1)ky\,\sin(2m-1)\int_0^z kdz,$$

where $a_v = eE_v\lambda/2\pi mc^2$ and $a_o = eE_o\lambda/2\pi mc^2$ - the dimensionless amplitudes of the zero RF-field harmonic and the 1-st electrostatic field harmonic, λ-the RF-field wavelength, $\beta_s = D/\lambda$-the synchronous particle velocity, $\tau = 2\pi ct/\lambda$, $æ_{2n}$ $(n\geq 1)$, g_{2m-1} $(m\geq 2)$-the normalized higher harmonics amplitudes, which, as well as the fundamental ones, are nonsyncronous with the beam, $k = 2\pi/D(z)$ - the wavenumber.

By using the smooth approximation method one may derive the expression for the effective potential, describing the averaged particle motion

$$U_{eff} = U_o + \Delta U, \qquad (2)$$

where $U_o = a_o^2 ch(2\rho/\beta_s)/4 - a_v a_o ch(\rho/\beta_s)/2 + a_v^2/4$ the potential due to fundamental harmonics, ΔU -an addition due to the higher harmonics, $\varphi = \int_0^\xi d\xi/\beta_s - \tau + \tau_o$- the slow varying fase in a combined-wave field, $\xi = 2\pi Z/\lambda$ and $\rho = 2\pi Y/\lambda$- the normalized longitudinal and transverse coordinates in the smooth approximation.

Correspondingly, the averaged motion equations can be written as

$$\frac{d^2\xi}{d\tau^2} = -\frac{\partial U_{eff}}{\partial \xi}\,; \quad \frac{d^2\rho}{d\tau^2} = -\frac{\partial U_{eff}}{\partial \rho} \qquad (3)$$

3. FASE AND TRANSVERSE STABILITY CONDITIONS

Considering the higher harmonics, we may restrict ourselves by the harmonics, nearest to the working ones. Then near the injection plane ($\rho = 0$) the first eq. (3) yields:

$$\frac{d\,\beta_z}{d\,\tau} = \frac{b_o^2}{2\beta_s}(1+\Delta)\cos\varphi, \qquad (4)$$

where $b_o^2 = a_o\,a_v$, $\alpha = a_v/a_o$, $\Delta = æ_2/2 + æ_2\,g_3/18 - 2\,\alpha\,æ_2\sin\varphi$. When neglecting the higher harmonics, the acceleration rate is proportional to $a_o\,a_v$. An appropriate choice of the functions $a_o(\xi)$, $a_v(\xi)$ and $\varphi_s(\xi)$ turns out to supply an effective bunching and acceleration of the beam. If $\Delta = 0$ and $\rho = 0$, the potential function has the only minimum at the point $\varphi = \varphi_s$. When $æ_2$ increases, the syncronous particle energy decreases, as a rule. At the same time the phase and momentum stability region grows. With the further increase of $æ_2$ the second minimum of U_{eff}, as well as the second separatrix appear. In that case the minimum at $\varphi = \varphi_s$ becomes less pronounced and gradually disappears.

From eq.(3) one may obtain the condition of the transverse particle focusing. Taking into account the fundamental harmonics, we get

$$2\,ch\,(2\rho/\beta_s) > \alpha\,ch\,(\rho/\beta_s)\sin\varphi. \qquad (5)$$

When $\alpha\sin\varphi < 2$ for the particle fase φ $U_{eff}(\rho)$ has one minimum at $\rho = 0$. If $\alpha\sin\varphi > 2$, an intermediate maximum at $\rho = 0$ appears, and at $\rho = \pm\rho_o$, where ρ_o is a root of the equation $ch\,(\rho/\beta_s) = \alpha\sin\varphi/2$, two minimums take place. Thus, two stable trajectories of the beam, splitted spatially and located outside the plane $\rho = 0$, appear. The particle, depending on its initial conditions, can be placed on one of such trajectories, and the beam - splitted into two beams, what is undesirable.

Taking into account the effect of the higher harmonics on the transverse beam dynamics doesn't change significantly the qualitative picture, described above. However, the stability conditions are defined from

more complication equation. The analysis of the expression for ΔU showed, that with the increase of $æ_2$ the transverse oscillation frequency ω_Y decreases, and the focusing is worsed. Inversely, at $g_3 < 0$ with the increased $|g_3|$ ω_Y grows.

4. ACCELERATION OF QUASI - NEUTRAL BEAMS

All the results, obtained above, relate to acceleration of both the positive and negative ions. An interesting property of a lineondutron is that it doesn't distinguish between them. The acceleration equations are independent of the sign of charges. Therefore, under the identical ratio $(Z^{\pm}/M)$(for ex., H^+ and H^-)and the same injection conditions bunching and capture processes occur at the same resonant fase. This can allow accelerating overlapping positevely and negatively charged ion bunches , thus avoiding space-charged effects and increasing overall beam intensity. Such bunches can be made practically neutral.

The dynamics of intense beams, including space-charge effects , can be analyzed in more detail only by means of exact numerical integration studies. Numerical results confirm the conclusions, made before analytically. For the quasi-neutral bunches the results, obtained in a single- charge approximation, are found to be close enough to those obtained while taking into account intrinsic quasi-static beam fields. It takes place , even if the trajectories of the oppositely charged particles don't completely overlapp in the transverse cross-section.

The corresponding choice of the fundamentaland higher field harmonics enables to provide the focusing of quasi-neutral bunches in that case, if it exists for a single particle. The electrodes may have circular or rectangular profile. Calculations show that under the geometrical sizes of electrodes, normally used in practice, the harmonic amplitudes range as follows: $æ_2$=0÷0.2, g_3= -0.3 ÷ 0.3.

5. CONCLUSION

Simulation results of the beam dynamics and detailed study of forming the requred fields showed, that it is possible to create a lineondutron with a final energy of about 1 Mev. For example ,the parameters of $H^+$and H^-accelerator with an injection energy of 50 kev, RF- generator frequency of 150 MHz were calculated. The accelerator includes bunching and acceleration sections. On the former the field amplitudes gradually increase, and the syncronous fase decreases by the linear law. On the latter these dependencies are chosen constant. The main accelerator characteristics are the following: average acceleration rate - 0.55 Mev/m; capture coefficient- 0.8; transversal acceptance ≈ 0.1 cm.mrad; RF- and electrostatic field amplitudes - 180 kV/cm and 65 kV/cm respectively; minimum half-size of the ribbon aperture - about 4 mm.

6. REFERENCES

[1] A.A.Kolomensky and A.N.Lebedev, "Quasilinear acceleration of particles by a transverse electromagnetic wave", Zh. Eksp.Teor.Fiz, vol.50,pp.1099-1106,1966.

[2] R.B. Palmer,"Interaction of relativistic particles with free electromagnetic waves in the presence of a static helical magnet", J.Appl.Phys.,vol.50, pp. 3014-3023,1972.

[3] E.D. Courant, C. Pelligrini and W.Zakowicz,"High energy inverse free-electron laser accelerator",Phys.Rev.A, vol.32, pp.2813-2823, Nov.1985.

[4] E.S. Masunov,"Beam focusing and acceleration in a linear accelerator acceleration",in USSR Conference On Charged Particle Accelerators Proc.,Dubna,USSR, Oct.1988,pp.121-123.

[5] E.S. Masunov,"Particle dynamics in a linear undulator accelerator",Zh.Tekn. Fiz,vol.60, 8, pp.152-157,1990.

THE ELETTRA 1.5 GeV ELECTRON INJECTOR

D.Tronc, D.T.Tran, C.Bourat, P.Girault,
P.Letellier, G.Meyrand and S.Sierra,
General Electric CGR MeV,
BP 34, 78 530 Buc, France
A.Massarotti,
Sincrotrone Trieste, Italy

Summary

The ELETTRA light source will be filled at the energy of 1.5 GeV by a linac of only 60 m length. A 100 MeV preinjector includes subharmonic chopper and prebuncher, S-band prebuncher, 4 MeV buncher, two accelerating sections. A FEL mode of operation will be possible. 200 MeV accelerating units follows. Each includes a 6.15 m $3\pi/4$ backward traveling wave (BTW) section powered by a TH 2132 45 MW - 4.5 μs klystron, compressed to 0.76 μs by a Thomson CIDR (Compresseur d'impulsion à Double Résonateur) similar to the CERN design of the SLED. The main parameters choices represents a significant improvement on the RF linac state-of-art in energy gain for given length and power.

Introduction

Light source synchrotrons are filled by electron (possibly positron) beams from less than 100 MeV for lithography to more than 2 GeV. Electrons can be produced by linacs or racetrack microtrons (in the low energy cases) or by synchrotrons (in the highest energy cases). The linac has the advantage of simplicity and high accelerated charges. But its length and cost must be reduced.

We developed earlier 200 MeV linacs with an energy gain of 16.7 MeV/m [1,2]. This relatively high value combined with few long accelerating structures insured compactness. It is known that much higher gradients could be used [3]. However reliability together with the availability and cost of high peak power RF sources have limited until today very high gradients to short lengths for medical linacs of several MeV (where an energy gain of 25 MeV/m is commonly used) and for positron capture (where an energy gain of 40 MeV/m is achieved [4]).

This paper presents the ELETTRA 1.5 GeV electron injector under construction. The expected energy gain is 33.3 MeV/m in short pulse conditions (this corresponds to 30m per GeV or 35m including the focused drifts between sections). The power consumption remains reasonable, compressing the RF pulse and using new high shunt impedance cell profiles [5]. The peak RF power consumption is 225 MW per GeV (at the klystron exit for a pulse of 4.5μs before compression).

The following presentation is an overview. However the reader who wants to ascertain the critical technical points will find referenced below the useful set of the latest specific papers .

The 1.5 GeV linac

Figure 1 presents the linac which is a part of the TRIESTE ELETTRA light source [6]. It includes: (i) a 100 MeV preinjector with a long pulse FEL mode option at rather large beam current, (ii) a short pulses high energy at low current injector made of 200 MeV acccelerating units. The preinjector and the accelerating units are described in the following sections. The lengths are respectively 10m for the preinjector and 50m for the following accelerator.

The on-axis components are listed (only once for each type) from the gun (1) to the triplet (9). The off-axis ones are listed for the preinjector from the subharmonic oscillator (a) to the klystron (f) and for the accelerator first unit from the amplifier (A) to the solenoidal focusing (SF).

The backward traveling wave accelerating section at the $3\pi/4$ mode is zoomed as well as a mechanical part made of two adjacent half cells. This BTW use optimized for SLED is the design innovation.

0-7803-0135-8/91$01.00 ©IEEE

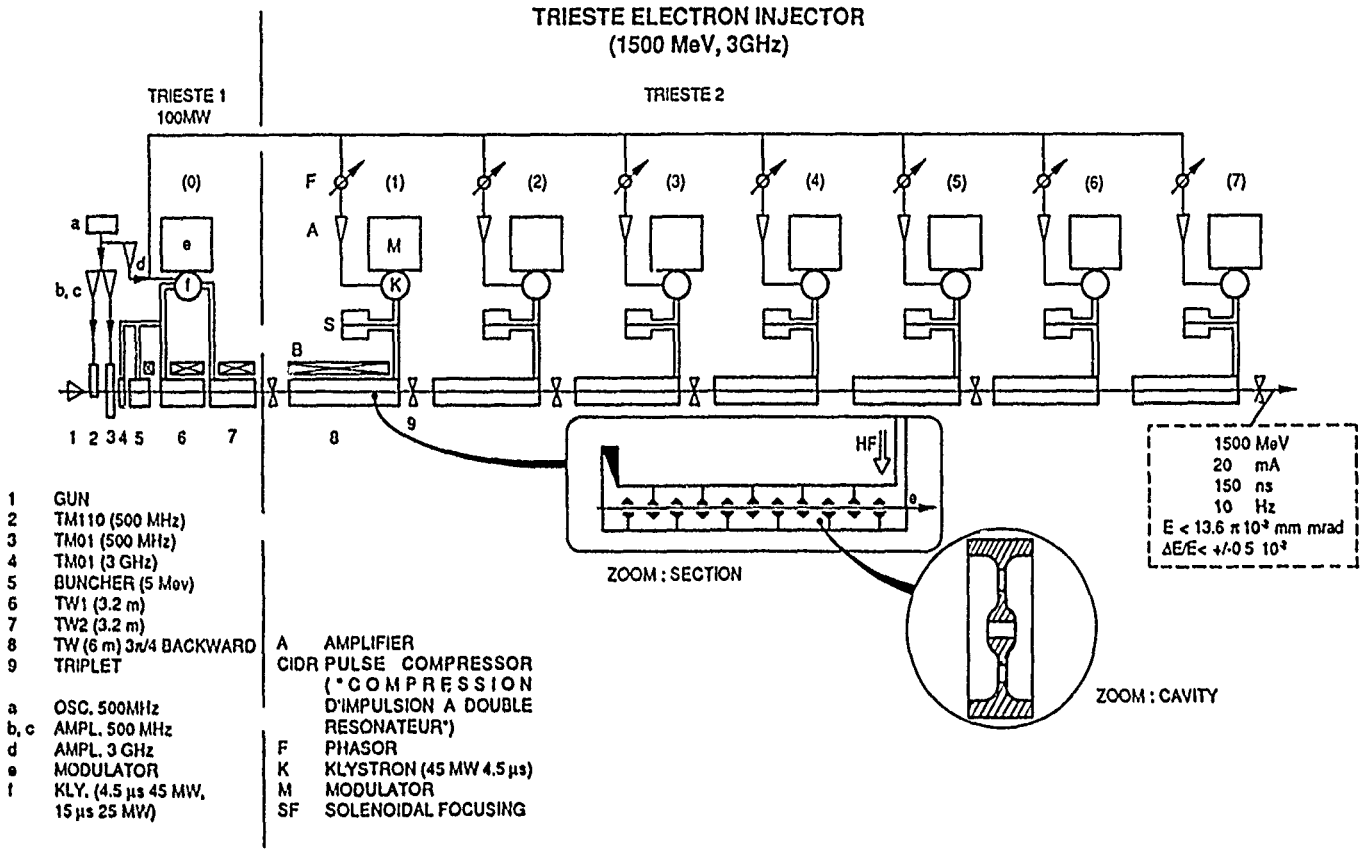


Figure 1: The TRIESTE-ELETTRA 1.5 GeV Electron injector

The expected beam characteristics are summarized in the dotted box: 20 mA will be accelerated at 1500 MeV, for pulses from 10 nanos. to 150 nanos. at 10 Hz repetition rate, within a required emittance of 0.136 m.n mrad and a 1% energy band.

The 100 MeV preinjector

Figure 2 presents this part (already built). It is made of a subharmonic chopper cell (C), a subharmonic prebuncher cell (PB5), an S-band prebuncher cell (PB3), the chopper collimator (CO), a 4 MeV buncher (B) followed by two accelerating sections (S1-2).

This preinjector has single-bunch, multi-bunch and FEL modes of operation. Ref. [9,10] analyze the three required modes of operation and simulate the FEL one. More than 0.4 nanoC is expected in the FEL mode within a bucket with a central bunch length (FWHM) of less than 10 picos. The normalized emittance is less than 200π mm mrad and the energy remains within 0.6% (the required values are 0.15 nanoC within 1%).

The 200 MeV accelerating unit

Such units follows the preinjector to rise the energy to 1500 MeV. The parameter values expected for one unit are:

Table 1: Accelerating unit parameters.

Klystron RF pulse	45 MW - 4.5 μs
Q twin compression cavities	150 000 min.
Transmission losses	7%
Compressed pulse amplitude	259 to 88 MW
Compressed pulse duration	0.76 μs
Energy for 10ns	217 MeV
Acceleration per m	35.4 MeV/m
Peak field (before beam)	139 MV/m
Peak field (at beam time)	81 MV/m
Energy for 150ns	207 MeV

Power tests made on a 1.3 meter test structure [7,8] verify that one will be able to deliver 200 MeV per unit in the 6 m structure geometry. This one is presented in details including the optimization between compression and BTW in the companion paper of this conference [5].

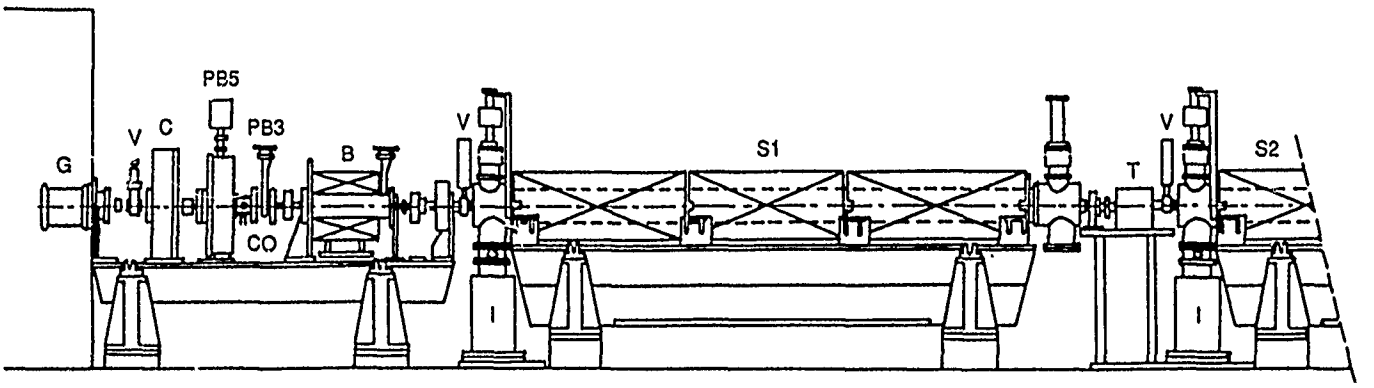


Figure 2: The ELETTRA 100 MeV preinjector beam line

The final choice of the $3\pi/4$ mode results from the (non intuitive) fact that its shunt impedance is near the highest possible value. This value lie between this mode and the $4\pi/5$ one, but NOT at higher modes nearer π: this is attributable to the decrease of Q when coupling slots becomes large. $3\pi/4$ mode is very simple to adjust in frequency.

One sees also that peak field on rounded nose is LOWER than for flat iris in the $2\pi/3$ mode for comparable energy gain. This is attributable to the large aperture at moderate c/vg value in classical iris waveguide which concentrates much field on a modest circumferal surface. The parameters values for the two geometries used along the first 2 m (at lowest peak field on nose) and then along the remaining 4 m (at greater shunt impedance) of the 6 m structure obtained with help of SUPERFISH are:

Table 2: $3\pi/4$ BTW cell parameters.

Beam clearance	10 mm dia.
c/vg	38
Q factor	12 500
Z/Q	6 195 to 6 485 Ω/m
Es/Ea (peak surface/ accelerating field)	1.96 to 2.30

This can be compared to the classical iris waveguide where for the same c/vg value, Q = 14 900, Z/Q = 3 900 Ω/m, Es/Ea = 2.07

Conclusion

The good outcome of this project will be a significant step forward in the electron linac art. The site is under construction, the preinjector has been tested with full RF power but not yet with beam, the first 6 m accelerating structure is under cold test.

References

[1] D.Tronc and al., "Electron injector designs for light sources", EPAC, 1988, 487.

[2] P.Letellier and al., "Commissioning of the 200 MeV Injector Linac for the Oxford Instr. - IBM Synchrotron light source", 1989 IEEE Part.Acc.Conf., 1082.

[3] G.Loew and J.W.Wang, "RF breakdown studies in room temperature electron linac structures", XIIIth Int.Symp. on discharges and electrical Insulation in Vacuum, Paris, 1988 / SLAC-PUB-4647 - "Progress report...", 1990, SLAC-PUB-5320.

[4] J.E.Clendenin and al., "The high-gradient S-band linac for initial acceleration of the SLC intense positron bunch", SLAB-PUB-5049, 1989.

[5] P.Girault, "The $3\pi/4$ backward TW structure for the ELETTRA 1.5 GeV electron injector", this conference: XRA 22.

[6] Sincrotrone Trieste Machine Group, "Status of the Synchrotron Light Source ELETTRA", EPAC, 1990, 478.

[7,8] P.Girault and al., "$4\pi/5$ backward TW structure .tested for electron linacs optimization", EPAC, 1988, 1114 - "Power tests results of $4\pi/5$ backward TW structure without and with SLED RF pulse compressor", EPAC, 1990, 37.

[9,10] C.Bourat, "Beam dynamics in the bunching system for ELETTRA", EPAC, 1990, 1759. - "The FEL mode beam dynamics in the linac preinjector for ELETTRA (TRIESTE)", 12th Int. Free Electron Laser Conf., 1990.

Microwave and Beam Optics Design Features of a Preinjector Linac for a Synchrotron Radiation Source

J. Haimson and B. Mecklenburg
Haimson Research Corporation
4151 Middlefield Road • Palo Alto, California 94303-4793

Abstract

This paper discusses the microwave and beam optics parameters of a chopper-prebuncher injection system and a 55MeV 2998MHz, 2.8m long accelerator waveguide assembly designed to produce inherently sharp beam energy spectra (½%) over a range of booster injection pulse periods from approximately 200 to 1½ns. The dc-biased 2998MHz chopper and prebuncher system is designed to inject into the accelerator waveguide sharply defined bunches with essentially all of the charge contained in less than 15 degrees of longitudinal phase space and with a narrow spread of electron velocities. Also, the single section, nonuniform impedance waveguide structure is designed to prevent energy spectrum broadening (typically from asymptotic off-crest bunch location during acceleration) by combining correlated energy-phase orbits with a nodal "detuned" circuit arranged to give two opposing over-the-crest phase drifts when the linac is operated at precisely six times the booster frequency. Manufacturing details are discussed, and photographs of the final fabricated equipment are shown.

INTRODUCTION

The preinjector linac was designed to operate in either (a) a stored energy short pulse mode to inject 8×10^8 accelerated electrons into the booster ring in a time interval of approximately one third of an RF cycle of the 499.65 MHz booster frequency, and with a beam energy spread of less than ±0.3 percent, or (b) a steady state linac long pulse mode in which short terminating portions of the beam pulse, over a range of 300ns, can be selected for injection into the booster ring with an energy spread of less than ±0.4 percent and at a rate of 3×10^8 electrons per booster RF cycle.

The electron gun to linac beam line comprises a low aberration, three lens optics configuration incorporating a 3GHz chopper-prebuncher system and beam collimators designed to accommodate a 140kV SLAC-type gridded electron gun that is operated over a 10:1 range of pulse currents with a maximum value, in the short pulse mode, of 1.5 A.

The traveling wave, $2\pi/3$ mode bunching and accelerating structure has an RF filling time of 780ns and is designed to operate at a loaded beam energy slightly in excess of 50MeV with a peak RF input power of 28MW. 3GHz power is transmitted from the klystron to the linac via an evacuated (10^{-8}Torr), thickwall OFHC copper rectangular waveguide network that includes three high directivity directional couplers for protection and monitoring of the klystron and for drive power to the RF chopper and prebuncher cavities.

A single RF source, short coaxial cable drive lines, and short beam drift distances consistent with the gun HV stability, ensure maintenance of a stable phase relationship between the low Q chopper and prebuncher cavity fields and the high field accelerating structure. For a given phase relationship, interaction of the velocity modulated, sharply defined (RF chopped) short bunches with the retarding standing wave electric field pattern at entry[1] to the accelerator waveguide establishes an energy-phase correlated charge distribution that is maintained during the subsequent bunching and acceleration process. Combining this correlated bunch charge with a distribution of decreasing phase velocities, arranged to give two opposing over-the-crest compensating phase drifts, results in γ convergent phase orbits and allows this single section accelerator configuration to exhibit inherent narrow energy spectrum characteristics.

General specifications of the preinjector linac are listed in Table I.

TABLE I

GENERAL SPECIFICATIONS

Linac Operating Frequency	2997.9 MHz
Klystron Peak RF Output Power	30 MW
Nominal Pulse Repetition Frequency	10 Hz
Loaded Beam Energy	50 MeV
Accelerator Waveguide RF Filling Time	780 ns
Accelerator Waveguide Stored Energy	13 joules
Normalized Geometric Beam Emittance	$<100\pi$ mm-mrad
Steady State Mode	
Pulse Length of Steady State Beam Selected for Booster Injection, adjustable up to	300 ns
Number of Electrons Injected in any Three Contiguous 3GHz RF Bunches	1.5×10^8
Steady State Beam Energy Spread	$<\pm0.4$ percent
Short Pulse Mode	
Linac Beam Pulse	1.8 ns
Number of Electrons Accelerated in a Time Interval <700ps per Pulse	8×10^8
Beam Energy Spread	$<\pm0.3$ percent
Peak Pulse Current at Entry to 3 GHz Chopper	1.1 A

CENTERLINE BEAM OPTICS

The linac injection optics elements comprise three thin lens assemblies, a relatively large diameter initial collimator to intercept the electron gun beam halo, a dc-biased chopper-prebuncher system including a water cooled chopping colli-

0-7803-0135-8/91$03.00 ©IEEE

mator located between the second and third lenses, and an injection collimator and magnetic pole piece at entry to the accelerator waveguide and associated solenoid assembly.

The three lens configuration was designed to ensure that the wide variation of electron gun beam geometry (beam divergence, waist diameter and position) associated with the 10:1 operational range of pulse currents would be matched to the requirements of the chopper-prebuncher system, especially that of maintaining a constant beam diameter at the entry plane of the chopping collimator regardless of the pulse current setting. This concept is illustrated in Figure 1 showing the beam envelope from the gun cathode through the three lens assemblies to the entry plane of the accelerator waveguide, for pulse current values of 0.15 and 1.5A. The chopper-prebuncher assembly and the chopping collimator are located between lenses 2 and 3. It can be noted that despite the wide variation of beam divergence at entry to lens 1, a constant beam diameter can be maintained at the chopper collimator with a relatively small adjustment of the lens 1 and 2 focal lengths.

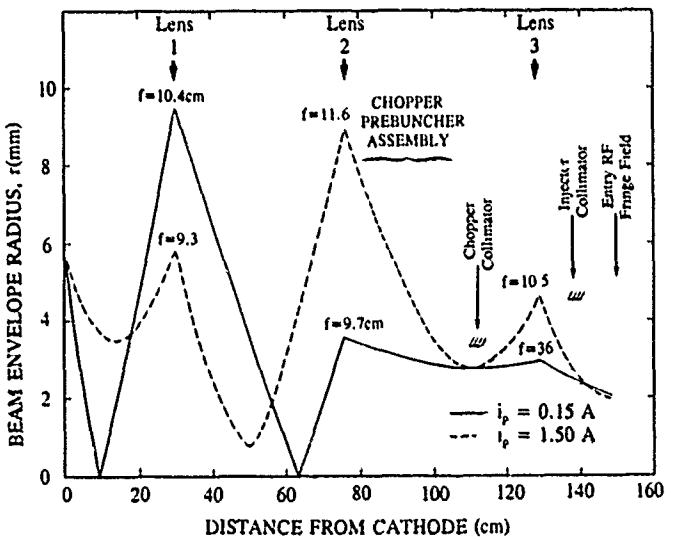


Figure 1. Beam Envelope Radius as a Function of Distance from Cathode for Pulse Current Values of 0.15 and 1.5A.

Chopper-Prebuncher System.

After passing through lens 2, the convergent beam is RF scanned in a vertical plane using a TM_{110} transverse magnetic field chopper cavity[2] and then velocity modulated using a TM_{010} prebuncher cavity. A dc magnetic dipole assembly (integrated into the chopper cavity) is used to bias the scanned beam vertically downward below the centerline so that only a fraction of the incident beam during a given (adjustable) period of each RF cycle is transmitted through the chopping collimator located on centerline downstream. With this biasing technique, the scanned beam is returned to the centerline once per RF cycle, and electrons are injected into the accelerator during a period when the RF deflection is at a maximum and passing through a reversal, i.e., when $\partial V_{RF}/\partial\omega t$, $p_\perp$ and $\partial p_\perp/\partial\omega t \rightarrow$ zero. A photograph of the linac injection system illustrating the lens and chopper-prebuncher assemblies is shown in Figure 2.

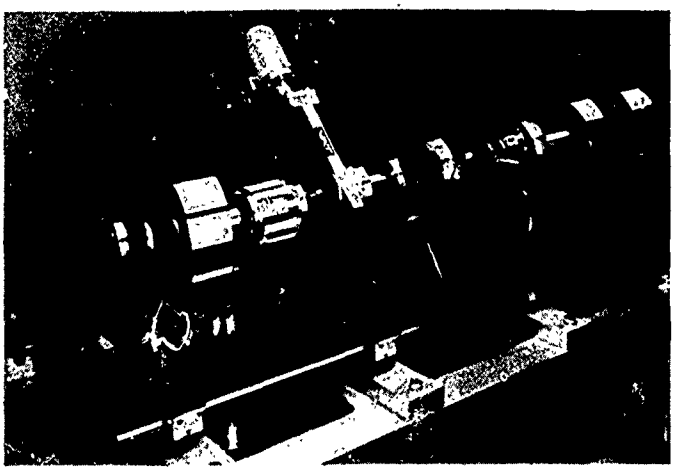


Figure 2. Linac Injection System showing the Three Lens Assemblies and the 3 GHz Chopper-Prebuncher

For the chosen design ratios of chopper collimator to beam diameter of 1.2 and RF deflection amplitude to beam diameter of 2.0, an RF chopped bunch length of 100 to 120° is transmitted through the chopper collimator when the dc bias deflection is made equal, and opposite, to the maximum RF deflection.[3]

Use of the prebuncher cavity results in an order of magnitude phase compression of the RF chopped bunch prior to injection into the linac. This is achieved by adjusting the phase relationship between the chopper and prebuncher cavities so that particles traversing the midplane of the chopper cavity at a period of maximum deflection subsequently traverse the midplane of the prebuncher cavity at a time when the velocity modulating electric field is passing through zero from a retarding to an accelerating field.[4]

Figure 3 shows a simulation of the space charge influenced kinetic energy and charge distributions within the bunch as it drifts from the chopper collimator, through the focusing lens 3, to the RF fringe field at entry to the accelerator waveguide. These chopped beam bunching computations, based on an initial prolate spheroidal nonuniform charge distribution[5] (assuming circular symmetry), indicate

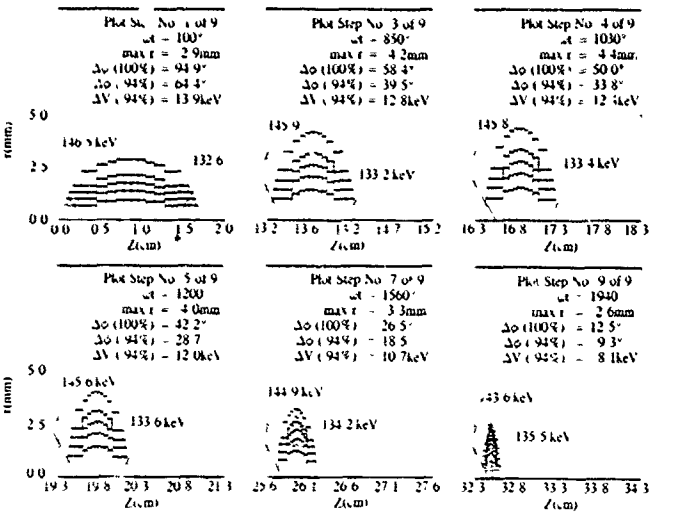


Figure 3 HRC-PRELOR Plots Showing Progressive Bunch Compression Prior to Injection into the Accelerator Waveguide (for 10^8 electrons/3GHz bunch and V_o = 140 kV).

that with 10^8 electrons per 3 GHz bunch, greater than 90 percent of the charge is injected into the accelerator with a longitudinal phase space of less than 10 degrees and a total energy spread of 8keV, i.e., less than 50 percent of the energy spread initially introduced by the prebuncher (19kV) is injected into the accelerator. The final plot steps in Figure 3 indicate that a relatively large reduction of energy spread occurs in the terminating region of the drift space where the combined action of the prebuncher and lens 3 results in a substantial radial and longitudinal compression of the bunch and a rapid growth of the space charge fields.

Accelerator Waveguide Phase Orbit Characteristics.

The accelerator waveguide input coupler cavity is designed to have a SW peak E-field of 280kV/cm at an RF input power of 28MW. The optimum injection phase at 140kV occurs for particles entering the fringe field 20 to 30 degrees after the E-field at the center of the cavity has commenced to decay from its peak retarding value. Early particles experience a greater initial reduction in energy than late arriving particles, causing the bunch width to be uniformly reduced (without phase crossovers) to approximately 2 degrees at the midplane of the cavity and producing an exit array of energy-phase correlated orbits, as indicated in Figure 4. (Particle orbit minimum energies range from 96 to 115keV and occur approximately 15mm before reaching the cavity midplane.) This correlation, with the leading phase at the lowest energy, is inverted in the sixth cavity and is then maintained along the structure; and the

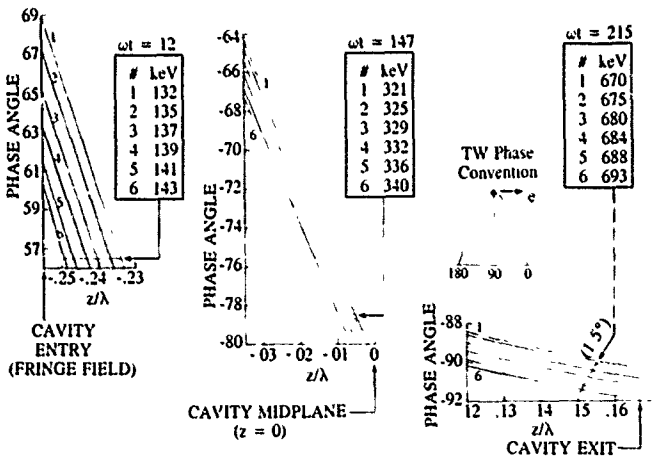


Figure 4. HRC-ELOR Input Coupler Progressive Phase Orbit Plots for the Figure 3 Injection Conditions and P_o = 28 MW.

spectral width increases and then narrows as the bunch drifts first 15 degrees behind and then 13 degrees ahead of the crest, as indicated in Figure 5. These phase drifts are achieved using a waveguide entry to exit phase velocity distribution of 0.9975 to 0.9957c. Earlier injection of the bunch, when the retarding E-field is at its maximum, produces phase crossovers and lower values of orbit minimum energy before the particles reach the input cavity midplane, causing the inherent energy spread of the emergent beam to increase. Figure 6 shows the emergent beam energy dependence on bunch entry phase for the Figure 3 injection conditions and a constant klystron voltage.

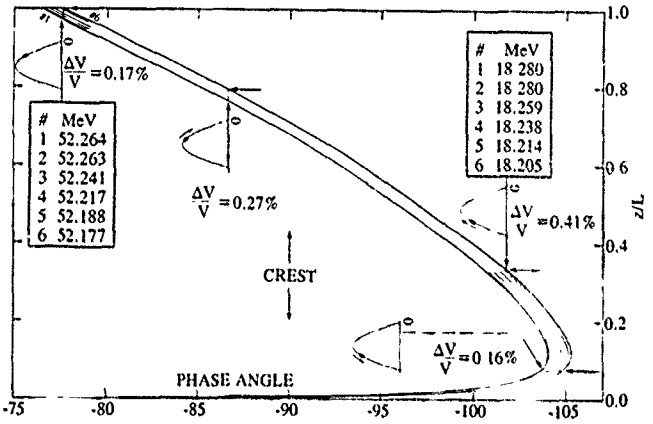


Figure 5. HRC-ELOR Phase Orbit Plots Showing Phase Drift and Reduction of Energy Spread along the Accelerator Waveguide for the Figure 3 Injection Conditions and P_o = 28MW.

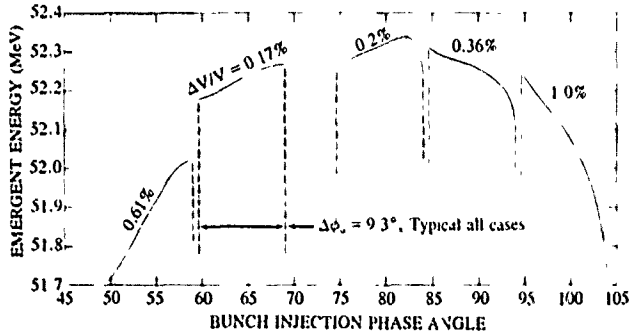


Figure 6. Emergent Energy vs Bunch Injection Phase Angle for the Figure 3 Injection Conditions and P_o = 28 MW (ΔP_o=0).

Figure 7 shows a view of the 50MeV linac centerline including the solenoids, magnetic shielding, water cooling connections and the special shear mounts used for shipping. Compact design, magnetic stainless steel internal yokes and pole pieces and the use of return shielding on all focusing elements resulted in the linac lens and solenoid assemblies having a total dissipation of less than 2 kW.



Figure 7. Overall View of the 50 MeV Linac Beam Centerline Assembly.

REFERENCES

[1] J. Haimson, "Electron Bunching in Traveling Wave Linear Accelerators," Nucl. Instr. and Meth., 39 p. 13, 1966.

[2] J. Haimson, "Optimization Criteria for SW Transverse Magnetic Deflection Cavities," Los Alamos, LA Report 3609 p. 303, Oct. 1966.

[3] Linear Accelerators, Eds P. Lapostolle and A. Septier, p. 253, North Holland Publishing Co., Amsterdam 1970.

[4] Ibid, p. 463.

[5] J. Haimson and B. Mecklenburg, "A Relativistically Corrected Three Dimensional Space Charge Analysis of Electron Bunching," IEEE Trans. Nucl. Sci., 14, p. 586, June 1967.

ELECTRON PREINJECTOR FOR SIBERIA-2 SR SOURCE

O.A. Nezhevenko, G.N. Ostreiko, B.Z. Persov,
S.I. Ruvinsky, G.V. Serdobintsev, E.N. Shaimerdenov,
M.A. Tiunov, V.P. Yakovlev, I.A. Zapryagaev
Institute of Nuclear Physics, 630060 Novosibirsk, USSR

Abstract

The 100 MeV linear accelerator operating in stored energy mode is described. It is designed to inject the electron beam (with 15 ns pulse duration and 200 mA current within 1% energy spread) into the booster ring.

The linac design is based on the 2.8 GHz DAW structure with three radial stems. The developed construction is easy for fabrication and tuning and provides a good shunt impedance of 92 MOhm/m and the working frequency domain being free of high order modes. The structure consists of a single 6 m long section.

The accelerator has a simple injection system without a special buncher. The nonbunched 40 keV beam formed by a diode gun is injected directly into the first DAW cavity.

The focusing system is simple too. It is provided both by the matching lens in front of the structure and by an RF field and has no focusing elements in the acceleration channel.

The first results of the accelerator performance are presented.

INTRODUCTION

The complex «Siberia-2», which will be built in Moscow [1] will serve to use as a SR source. It will consist of a storage ring with 2.5 GeV maximum energy as the main part and a combination of a 100 MeV electron linac and a 450 MeV booster ring «Siberia-1» as an injection part.

This report is dedicated to description of the 100 MeV linac-preinjector shown in Fig. 1.

OPERATING MODE

The booster ring «Siberia-1» will work at a single bunch mode with revolution time of 30 ns. Therefore the injector current pulse duration should not exceed 15 ns in order to avoid the influence of the injector fronts on the beam dynamics. The beam parameters required on the injector output are given in Tabl. 1.

Table 1

Beam energy	80 — 100 MeV
Energy spread	1 %
Beam current in a pulse	200 mA
Pulse duration	15 ns
Transverse emittance	0.1 mrad · cm
Repetition rate	1 pps

The modification of the DAW structure [2] with radial stems [3] was selected as an accelerating structure of the preinjector. Each washer is supported by three radial stems, which have the length close to $\lambda/4$. The use of DAW structure at the stored energy mode enables one to solve the following problems:

- because of high shunt impedance one can reach maximum energy of electrons [4];
- because of a large energy stored one can accelerate the beam with maximum current,
- because of high group velocity there is a possibility to perform an accelerating structure in the form of a single resonance section with a single power input and thus to avoid phasing of separate sections and also to simplify the requirements to accuracy of manufacturing and tuning.

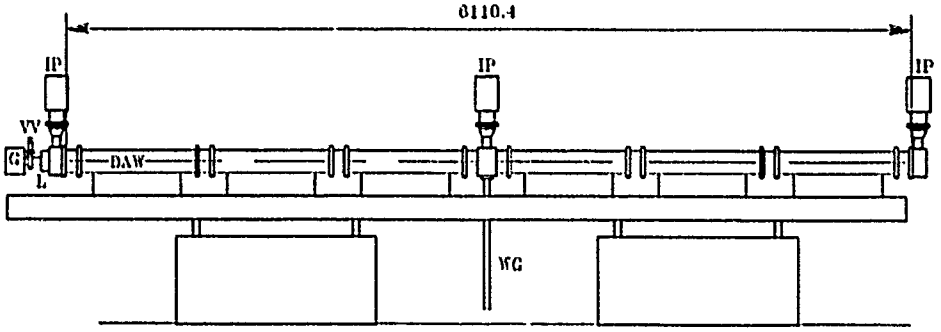


Fig. 1 The preinjector layout.

BEAM DYNAMICS

The accelerator has a single injection system without a special buncher (Fig. 2). The same injection system had been developed for the linac-positrons source of the complex VEPP-4 [5].

The nonbunched 40 keV beam formed by a diode gun is injected directly into the first resonator of the structure. The diode gun is shown in Fig. 3. The LaB_6 spherical cathode has diameter of 16.4 mm. The gun forms the parallel electron beam with the current of 4 A and with the diameter of 8 mm directly after the anode hole.

0-7803-0135-8/91$01.00 ©IEEE

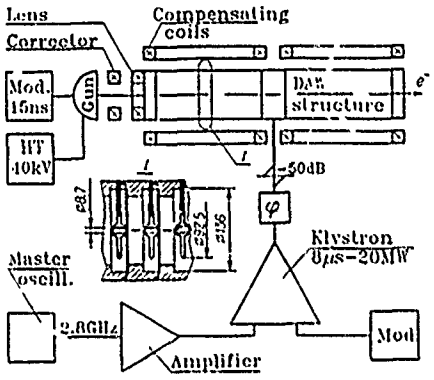


Fig. 2. The beam formmg system and RF system.

A beam bunching is realized in the first resonator, which consists of the regular halfsell with the plate front wall. The calculated beam spectrum at the accele-

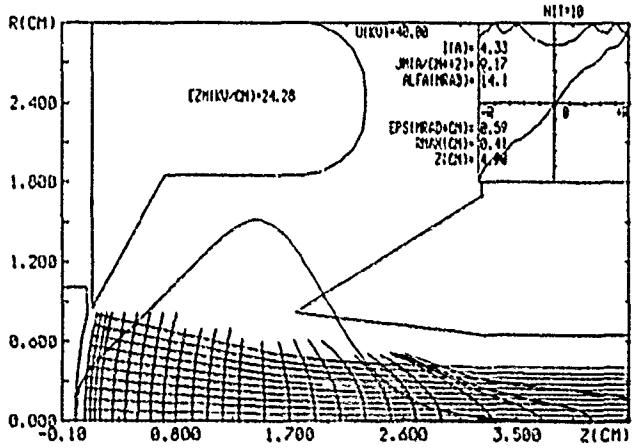


Fig. 3 The diode gun layout with beam trajectories.

rator output is shown in Fig. 4. From this figure one can see, that the beam spectrum density change at the

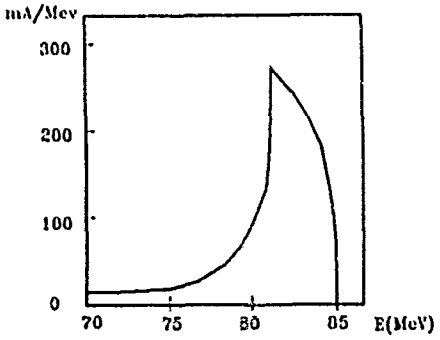


Fig. 4. The beam energy spectrum in the preinjector output.

electron energy about 80 Mev is little, within of 5% relative energy range. Because of this, one can provide the stable injection current under an unstable RF voltage.

The focusing system is simple too (Fig. 2). It is provided both by the matching lens in front of the structure and by an RF field of the first resonator. Also for a decrease in the focusing RF field influence under beam flying one must set a net in the first resonator input. It is provided essentially to decrease the beam emittance in the first resonator output and to do without additional focusing elements in the accelerating channel. Also in the beam travelling system there are a corrector for parallel shift and coils for compensating the Earth magnetic field.

The calculations by means of computer code based on the macro particle model show, that the beam emittance in the accelerator output will not exceed of $5 \cdot 10^{-2}$ mrad·cm, and the beam radius will not exceed more of 60% of the aperture.

RF SYSTEM

The preinjector RF system is shown in Fig. 2. It consists of the generator connected to accelerating structure by means of 90×45 mm^2 vacuumable rectangular waveguide. Power input is in the middle of the structure. Since we concentrated on use of the only one

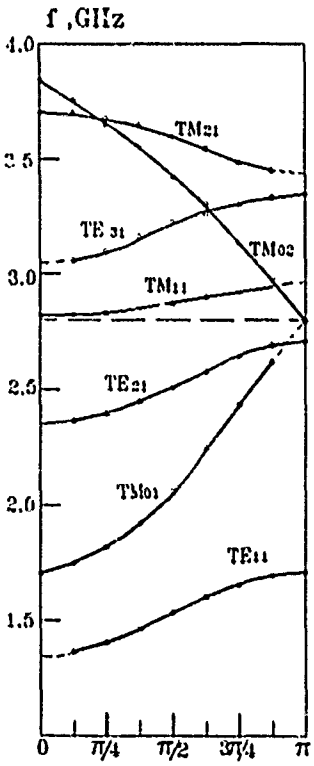


Fig. 5. The DAW structure modes spectrum.

S-band generator of 20 MW power [6] therefore the full length of the DAW structure was selected of 6 m.

As a result of numerical and experimental research [7] the optimal geometry of DAW structure provided a good shunt impedance of 92 MOhm/m and absence of high order modes within ±20 MHz concerning working mode like $-TM_{02\pi}$ was selected. The dispersion curves of the structure are given in Fig. 5.

The thermal test of the 1 m long section of structure showed that the temperature gradient of the frequency change is of 50 kHz/deg C° .

The 0.6 m long section of structure has been tested at high power [8]. The stable voltage pulse was received in 8 hours of training by means of multipacting and breaks in the leading edge. The field level received on surface of structure corresponds to accelerating gradient of 15 MeV/m.

The DAW structure parameters are given in Tabl. 2.

Table 2

Frequency,	f_{exp}	2795.7 MHz
Eff. charact. res.,	ρ	3.4 kOhm/m
Quality factor,	Q_{exp}	27 000
Overvoltage coef.,	k_0	4.0
Rel. group velocity,	β_g	0.4
Length,	L	6.1 m

CURRENT STATUS

At that time all preinjector systems had been mounted into the complex «Siberia-2» accelerating hall. The measurements of the DAW structure at low power level had been made. The shunt impedance experimental value is of 92 MOhm/m. The accelerating structure had been matched with the waveguide. In the accelerating structure and waveguide had been received vacuum.

The electron gun feed system and klystron master oscillator had been tested. At present, the preinjector is ready for operation.

CONCLUSION

From the description given above one can single out the following points of interest:

— the use of the DAW structure allowed to design the compact preinjector more efficient compared to the traditional linacs based on the disk-loaded waveguides. For example, the 100 MeV preinjector of the SR source described in report [9] requires the generator with close to twice as much power at the same full length and the more complicated prebunching system.

REFERENCES

[1] V.V. Anashin et al. Proc. of the EPAC, Rome, June 7—11, 1988, p.57.

[2] V.G. Andreev. ZhTPh, 1971, vol.41, pp.788—796.

[3] S.O. Shriber. IEEE Trans. on Nucl. Sci., NS-30, N 4, 1983, pp.3542—3544.

[4] M.M. Karliner et al. Preprint INP 86-146, Novosibirsk, 1986, p.38.

[5] G.I. Budker et al. Proc. of the 5-te All-Union Workshop on Acc., Dubna, 1977, vol.1, p.280.

[6] V.I. Beloglazov et al. Voprosy at. nauki i tehn., TPhE, 1985, vol.3(24), S.1—87, pp.8—9.

[7] M.M. Karliner et al. Proc. of the EPAC, Rome, June 7—11, 1988, vol.1, pp. 602—604.

[8] V.M. Borovikov et al. Voprosy at. nauki i tehn ,JaPhI, 1989, vol.5(5), S.1-104, pp.13—16.

[9] C. Bourat et al. Proc. of the IEEE Part. Accel Conf., Chicago, IL, March 20—23, 1989, vol.2, pp.935—937.

Fermilab Linac Upgrade Side Coupled Cavity Temperature Control System*

J. CRISP and J. SATTI,
Fermi National Accelerator Laboratory
P.O. Box 500
Batavia, Il 60510

ABSTRACT

Each cavity section has a temperature control system which maintains the resonant frequency by exploiting the 17.8 ppm/°C frequency sensitivity of the copper cavities. Each accelerating cell has a cooling tube brazed azimuthally to the outside surface. Alternate supply and return connection to the water manifolds reduce temperature gradients and maintain physical alignment of the cavity string. Special tubing with spiral inner fins and a large flow rate are used to reduce the film coefficient. Temperature is controlled by mixing chilled water with the water circulating between the cavity and the cooling skid located outside the radiation enclosure. Chilled water flow is regulated with a valve controlled by a local micro computer. The temperature loop set point will be obtained from a slower loop which corrects the phase error between the cavity section and the rf drive during normal beam loaded conditions. Time constants associated with thermal gradients induced in the cavity with the rf power require programing it to the nominal 7.1 MW level over a 1 minute interval to limit the reverse power.

INTRODUCTION

The linac upgrade project at Fermilab will replace the last 4 drift-tube linac tanks with seven side coupled cavity strings [1]. This will increase the beam energy from 200 to 400 MeV at injection into the Booster accelerator.

The main objective of the temperature loop is to control the resonant frequency of the cavity. A cavity string will consist of 4 sections connected with bridge couplers driven with a 12 MW klystron. Each section is a side coupled cavity chain consisting of 16 accelerating cells and 15 side coupling cells. For the linac upgrade, 7 full cavity strings will be used. Presently a separate temperature control system is planned for each of the 28 accelerating sections, the two transition sections, and the debuncher section.

The cavity strings will be tuned to resonance for full power beam loaded conditions. A separate frequency loop is planned that will sample the phase difference between a monitor placed in the end cell of each section and the rf drive. The frequency loop controls the set point for the temperature loop which maintains the resonant frequency through periods without beam or rf power. The frequency loop will need the intelligence required to determine under what conditions the phase error information is valid and the temperature set point should be changed.

REQUIREMENTS

The side coupled cavities will be driven at 4 times the frequency of the current linac, or about 805 MHz, and have an unloaded Q of 20,000. For a cavity constructed of a single metal, the percentage change in resonant wavelength will equal the percentage change in linear dimension which is proportional to temperature. A full cavity section had a measured temperature dependance of -14.3 KHz/°C, or 17.8 ppm/°C of 805 MHz.

If the cavity resonant frequency deviates from the drive frequency, power will be reflected from the cavity, causing standing waves within the waveguide. The klystron design specification requires it to withstand a voltage standing wave ratio, or vswr, of up to 1.5:1 at the 12 MW power level. The limit is the breakdown voltage at the ceramic window at the output of the klystron. A temperature error of about .6 °C would generate a vswr of 1.5:1. In comparison, 50 mA of beam loading will generate a vswr of 1.3:1 or require a .2 °C temperature increase with beam. The low level system should be able to maintain the .5% amplitude and .5° phase regulation required through small changes in cavity temperature.

When rf power is applied to the cavity, 200 watts per cell flows through the copper into the cooling water. The thermal resistance of the copper path results in a temperature gradient within the cell. An analysis of the transient heat flow using ANSYS was performed by Jim Olson and Terry Anderson. At 200 watts/cell, a 3.8 °C temperature gradient develops between the nose cones in the accelerating cells and the outside wall with a 1/e time constant of 34 seconds. A full cavity section was measured to have a frequency deviation of -35 KHz for 200 watts/cell of rf excitation.

The resonant frequency shift induced by the rf power could be corrected with a temperature change of -2.4 °C. It would require 62 KW of cooling to maintain the resonant frequency if the rf were abruptly switched on. If the cavity strings are kept at the temperature which provides the correct resonant frequency with nominal power, then the resonant frequency will be 35 KHz too low with no rf power

* Work supported by the Universities Research Association, Inc., under contract with the U.S. Department of Energy.

0-7803-0135-8/91$03.00 ©IEEE

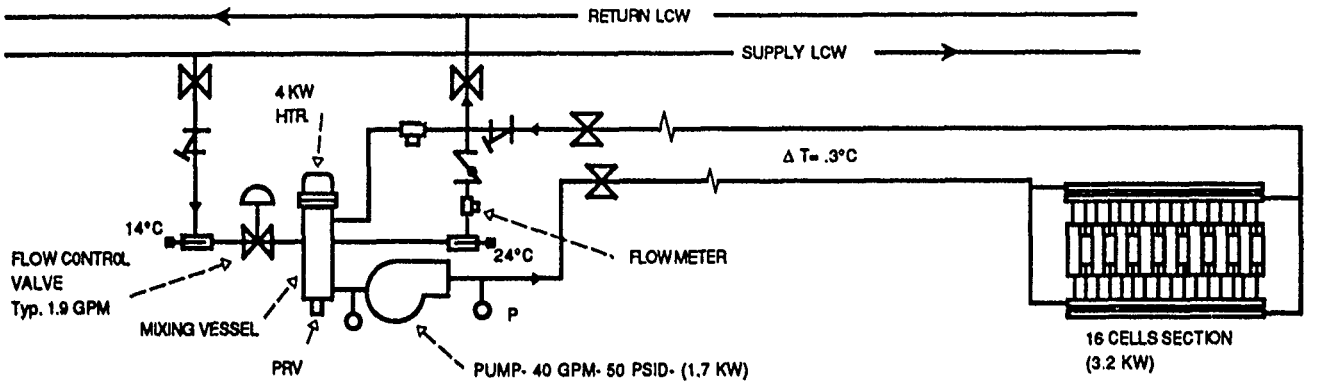


Figure 1. Schematic of typical one section cavity temperature control system.

applied. This will result in a vswr of 4.9:1, or a 3.7 MW power limit. Tom Owens used ACSL to obtain a turn on program which limits the maximum waveguide voltage to that obtained with 12 MW and a vswr of 1.5:1 while gradually increasing the power level. The cavity could reach the correct resonant frequency in about 55 seconds. This process could be automated with the local computer by monitoring the reverse power while increasing the klystron output during turn on, similar to the existing linac.

IMPLEMENTATION

Placing the cooling skids outside of the radiation enclosure has a significant impact on the design of the temperature regulation system. Figure 1 shows a typical one section cavity temperature control system. A pump circulates about 40 gpm of low conducting water, or LCW, between the cooling skid and the cavity. The temperature of the cavity will be maintained by controlling the amount of chilled water mixed with the circulating water. The cooling skids will be up to 95 feet from the cavities. The 36 gallons of water required to fill the system have a heat capacity of 574 KJ/°C compared to the 298 KJ/°C for the 1700 pounds of copper in one section. At 40 gpm, this amount of water requires 54 seconds to make one loop through the system. This delay will limit the closed loop bandwidth and complicate the use of feedforward.

The nominal rf power dissipated in the copper of the cavity will be about 3.2 KW. The water pump will contribute another 1.7 KW. With a chilled water temperature 10 °C below the cavity temperature, 1.9 gpm of chilled water will be required to extract the 4.9 KW of power. At the nominal operating power, the temperature rise across the cavity will be about .3 °C. The cavity operating temperature was chosen to be near room temperature to avoid thermally insulating the cavity.

Water has about 10 times the heat capacity and 650 times the thermal resistance of copper. The large heat capacity makes water an efficient way to transfer heat to the cavities. The thermal resistance makes it difficult to transfer heat between the water and the copper. If the water flow through the cooling tubes on the cavity is slow, little mixing will occur and a large temperature gradient will develop between the flowing water and the tube wall. Special copper tubing with spiral inner fins was used on the cavity with a turbulent flow rate selected to avoid excessive wear. From available literature, the tubing used is expected to have a film coefficient 1.5 times better than a smooth copper tube providing a thermal conductance of about 270 watts/°C per water path for a 2.4 gpm flow rate [2,3]. The time constant formed with the film coefficient of the 17 water paths and the thermal mass of the cavity is about 65 seconds.

CONTROL THEORY

A simple model, applicable to the cavity cooling system, is shown in figure 2. It consists of a container, with water flowing through it, that retains a constant volume. If we assume that the inlet water instantaneously and completely mixes in the volume, then the thermal mass C will be at the outlet temperature Tout. The change in outlet temperature will be equal to the integral of the net power flowing into the volume divided by its thermal capacitance. Assume at time t = 0 the system is in steady state, the temperature of thermal mass C is Tout = Tin, and that Tin and the chilled water flow,F , remain fixed.

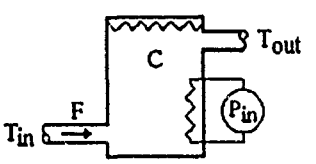


Figure 2. Simple model of cavity temperature control system.

Using Laplace transforms Tout can be found as a function of input power, Pin. Letting A = 3.814 °C-gpm/KW, the heat carrying capacity of water, and ω_0 = F/AC the relationship is provided in equation 1 below.

$$\frac{\overline{T}_{out}}{\overline{P}_{in}} = \frac{A}{F}\frac{\omega_0}{s+\omega_0} \qquad \text{equation 1}$$

For small changes in flow and temperature, Tout can be approximated with equation 2 [4].

$$\frac{\overline{T}_{out}}{\overline{F}} = \frac{\Delta T}{F}\frac{\omega_0}{s+\omega_0} \qquad \text{equation 2}$$

An integral type of controller was selected for the temperature loop because of the simplicity and the zero steady state error. Figure 3 provides a simple block diagram.

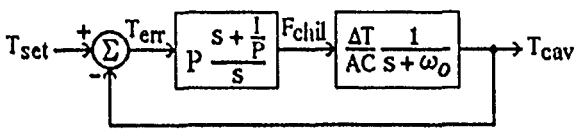


Figure 3. Simple block diagram of cavity temperature control loop.

If I/P is chosen to equal ω_0 = F/AC, then the open loop response becomes a simple integrator. The unity gain frequency of the open loop will be the closed loop corner frequency, or closed loop bandwidth ω_{cl} = P ΔT/AC. The closed loop bandwidth will be essentially constant provided the cavity temperature changes are small.

Theoretically the above system could have infinite closed loop bandwidth. Stability requires the open loop gain to be less than one when the phase shift is 180°. A conservative design would have 45° of phase margin, or only 135° of phase shift. The open loop phase shift for the case above is 90° for all frequencies. For the cavity loops, there will be additional phase shift caused by the thermal resistance of the film coefficient and the time required for the water to travel from the cooling skid to the cavity. As shown below, the closed loop bandwidth is limited to about .001 Hz.

for ω_{cl} = .001 Hz	90.0°	controller integrator
	23.4°	film coefficient, (τ = 65 sec)
	9.7°	water travel time, (27 sec)
	5.0°	cavity wall to probe, (τ = 14 sec)
	2.6°	control valve, (τ = 7.3 sec)
	0.6°	thermocouple amp, (τ = 1.6 sec)
	0.4°	computer sample time, (1 sec)
	131.7°	Total phase shift

To improve the accuracy of the chilled water control valve, a separate loop was implemented which maintains measured chilled water flow by controlling the valve. Figure 4 provides an overall block diagram. The loop improved the feedforward accuracy which greatly reduced the time required to recover from a step change in power.

Because of the thermal gradients induced in the cavity, the desired temperature at the probe changes with rf power level. The nominal temperature is chosen to be that which maintains a constant energy stored in the thermal mass of the system. This requires no heating or cooling beyond the steady state levels for changes in power. The temperature must be chosen for the correct resonant frequency at the nominal power level.

REFERENCES

1. Noble, R., "The Fermilab Linac Upgrade", Proc. of the 1990 Linac Conf., p. 26, Los Alamos Publication LA-12004-C.
2. Baumeister, T.,"Marks' Standard Handbook for Mechanical Engineers", Mcgraw-Hill,1983.
3. Chenoweth, J., "Advances in Enhanced Heat Transfer", 18th Nat. Heat Trans. Conf., San Diego Ca., 1979.
4. Crisp, J., "Temperature Control Feedback Loops for the Linac Upgrade Side Coupled Cavities at Fermilab", Fermilab TM 1698, Oct. 1990.

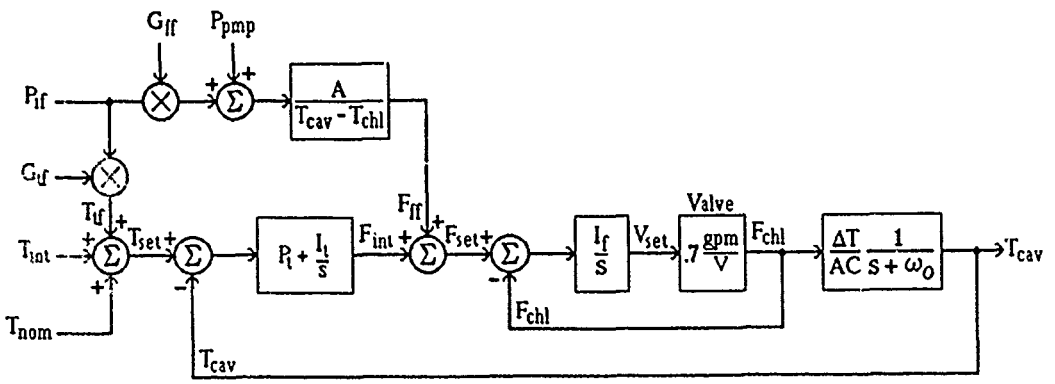


Figure 4. Block diagram of Temperature control loop.

Electron-Beam Generation, Transport, and Transverse Oscillation Experiments Using the REX Injector

R.L. Carlson, P.W. Allison, T.J. Kauppila, D.C. Moir, and R.N. Ridlon
Los Alamos National Laboratory
P.O. Box 1663
Los Alamos, New Mexico 87545

Abstract

The REX machine at LANL is being used as a prototype to generate a 4-MV, 4.5-kA, 55-ns flat-top electron beam as a source for injection into a linear induction accelerator of the 16-MeV Dual-Axis Radiographic Hydrotest facility. The pulsed-power source drives a planar velvet cathode producing a beam that is accelerated through a foilless anode aperture and transported by an air core magnetic lens for injection into the first of 48 linear induction cells. Extensive measurements of the time-resolved (<1-ns) properties of the beam using a streak camera and high-speed electronic diagnostics have been made. These parameters include beam current, voltage, current density, emittance, and transverse beam motion. The effective cathode temperature is 117 eV, corresponding to a Lapostolle emittance of 0.96 mm-rad. Transverse oscillations of the transported beam have been observed via a differenced B-dot technique to be about ±100 μm at 245 MHz. This beam motion has been correlated via detailed rf measurements of asymmetric transverse cavity modes in the A-K gap.

I. INTRODUCTION

The Relativistic Electron-Beam Experiment (REX) machine at LANL has been selected as the type of injector for the Dual-Axis Radiographic Hydrotest facility (DARHT) 16-MeV induction accelerators. This decision is based upon the detailed measurements and results previously reported [1,2]. This paper presents recent results using a smaller cathode (63.5- vs 76.2-mm diam) with a finer-structure-cloth emitting material known as "velveteen." The pulsed power source [3] has recently been modified to produce a longer (85- vs 45-ns) FWHM and flatter (±1.5 percent) electron beam pulse as required by the DARHT accelerators. Beam matching hardware and transport measurements are described along with transverse beam-motion reductions observed at the entrance to the first DARHT induction cell. This beam motion can lead to the unwanted Beam Break-Up (BBU) instability in induction accelerators containing many gaps. The 2-D particle-in-cell code ISIS [4] has been used to closely model the experimental configuration. The experimental arrangement is discussed in Section II and the data and results are presented in Section III.

Work performed under the auspices of the U.S. Department of Energy.

0-7803-0135-8/91S01.00 ©IEEE

II. EXPERIMENTS

The output end of the REX injector is shown schematically in Fig. 1 wherein the 147-mm anode-cathode (A-K) gap region is housed in a vacuum vessel cryogenically pumped to a base pressure of 6×10^{-6} torr. The electron source consists of a 63.5-mm-diam, velveteen cloth cathode recessed about 1 mm into the surface of the cathode holder and field forming assembly. The field forming electrode is centered on a 1.83-m-diam x 254-mm-thick Lucite radial insulator with embedded aluminum grading rings separating the oil-filled output transmission line from the vacuum diode region. The magnetic field used for beam extraction is generated by an air-core, bifilar-wound, solenoid extraction magnet (161-mm i.d. x 216-mm o.d. x 485-mm long) whose center is located 505 mm from the cathode surface. The extraction magnet has two additional layers containing cosine-wound dipole trim coils [5] used to null the transverse fields. The magnetic field at the edge of the cathode is likewise nulled by a 1.7-m-i.d. bucking coil centered 141 mm behind the cathode surface.

The REX pulsed power consists of a Marx generator that charges a water pulse-forming line that is switched into a glycol- and then an oil-based transmission line terminating in a liquid radial resistor with a value of 175 Ω. This resistor provides a stiff voltage source to drive the diode. Voltages and currents associated both with the pulsed power and the electron

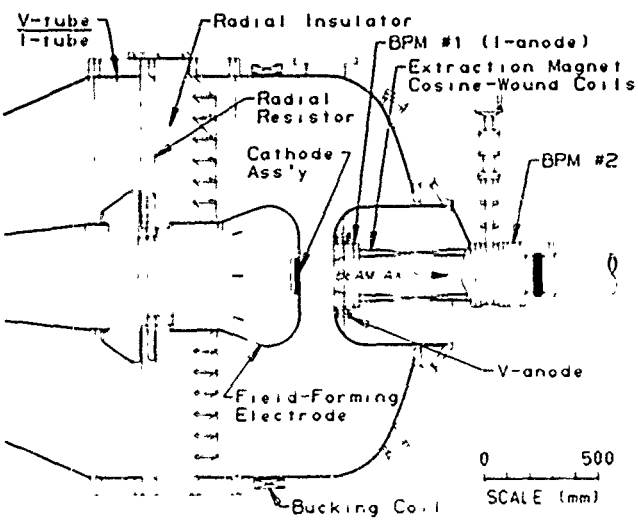


Figure 1. Schematic of REX Diode Region.

beam are measured using E-dot and B-dot type monitors integrated with passive, 1 μs time-constant, 50-Ω integrators corrected for cable loss and integrator droop. The signals are transmitted to the screen room area via 50-ns-long, Andrews, 12.7-mm-diam, Superflex foam cable. Tektronix R7103 (1-GHz) oscilloscopes are used to record the data in digital format using their DCS01 Digitizing Camera System. The diode current (Ianode) that goes through the 133.6-mm-diam anode aperture is sensed by four symmetrically located B-dots contained within the anode Beam Position Monitor (BPM #1). The BPM also contains two pairs of diametrically opposed B-dots that are used to determine the x-y coordinates of the beam position; the limiting positional resolution is 0.25 mm. The A-K gap voltage (Vanode) is measured as the sum of four equally spaced E-dots mounted flush on the flat portion of the anode.

Figure 2 shows the matching and transport section between the output of the extraction magnet and the input to the first DARHT induction cell. The extraction magnet is set to form a beam waist at the end of the transport hardware, and the steering coils are used to center the beam in the drift pipe. The beam is injected along the axis of the DARHT accelerator by the adjacent dipole steering coils.

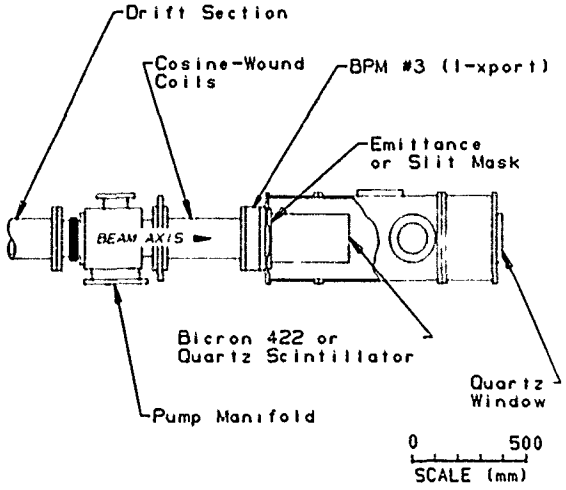


Figure 2. Rex Beam Matching Hardware

The emittance of the transported electron beam was measured by intercepting the beam with a brass mask [1,2] that was located 2.53 m from the cathode and is in the entrance plane of the first induction cell. The mask can be replaced by a 1.27-mm slit which yields the current density vs radius and time of the beam and, in particular, the modulation and energy variation of the beam. In both cases, the beam that was transmitted through the mask drifted 406 mm before striking either a 0.6-mm-thick strip of Bicron 422 or 1-mm-thick quartz plate scintillators. Light from the scintillator was imaged onto the photocathode of either an IMACON 500 or Thomson TSN-506 streak camera using a 90-mm-diam Questar telescope via two turning mirrors. Typical sweep speed for all of the measurements was 2 ns/mm.

The high-frequency transverse beam motion at the waist location was measured by using a differenced B-dot technique passively summing the opposite polarity B-dot loops of BPM #3. In an attempt to further understand the cause of this motion, a biconic transition cone from 50-Ω coax to the 53.3-Ω impedance of the REX output oil transmission line was installed. A Hewlett Packard 8753B network analyzer was used to drive this cone while either reflections or transmissions to the diode region were monitored with various shielded electric and magnetic field probes that could be rotated about the axis of the A-K gap.

III. Measurements And Analysis

Typical diode voltage and current waveforms are shown in Fig. 3. The time delay (≈ 7 ns) before the velveteen surface begins field emission corresponds to a field of 9.5 kV/mm. The current for a given voltage across the A-K gap is about 15% higher than that predicted by the ISIS code and is presently thought to be due to an even greater edge enhancement of emitted current than that calculated [1].

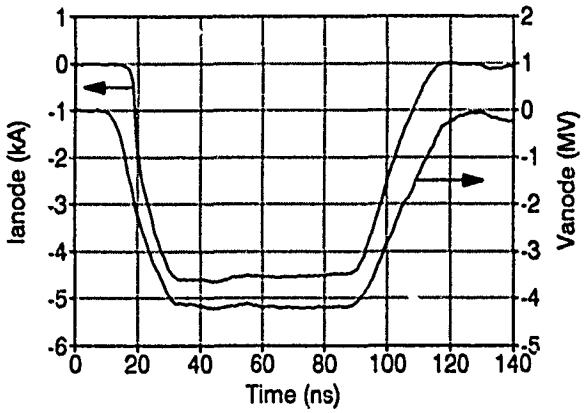


Figure 3. REX A-K Gap Voltage and Diode Current.

Streak camera slit measurements of the beam at BPM #3 with the extraction magnet set to 778G were made for comparison of the beam waist size and energy spread with the calculations as well as with the A-K gap voltage and current data of Fig. 3. Figure 4 is a slit record indicating an energy spread of ±2.5% over 55 ns as compared to the ±1.5% of Fig. 3. The cause of the increased beam diameter at ≈20 ns is still being examined. The beam edge diameter from Fig. 4 is about 62.5 mm, which is very close to the 60-mm diam calculated by ISIS.

The emittance of the beam (defocussed to 120-mm diam) at this same location was determined by fitting gaussian distributions to the beamlets of the post-processed streak camera records. These distributions were averaged over 45 ns of the flat-top portion of the pulse using 1-ns beam slices of the computer processed image. The angular spread of the center beamlet yields an effective cathode temperature of 117 eV. The Lapostolle emittance of the beam is obtained by calculating the weighted phase space area of the x-x' plot.

Since a 117-eV temperature corresponds to an emittance of 0.96 mm-rad at the cathode, the measured emittance of 1.0 mm-rad demonstrates negligible emittance growth after 2.53 m of transport.

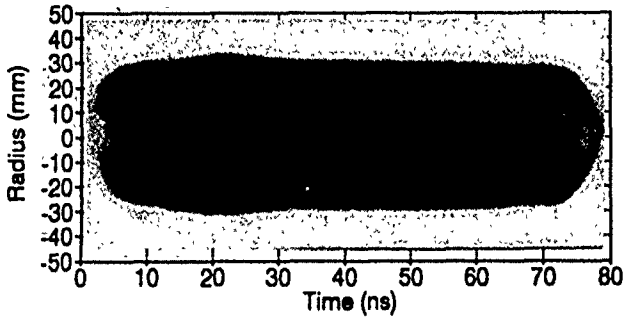


Figure 4. Slit Record of Beam Waist at 2.53 m

The transported and emitted beam current are shown overlaid on the same scales in Fig. 5 for a beam energy of 4.2 MV; the fraction transported is 90 percent. The loss of current is most likely due to high-emittance electrons that get through BPM #1 but are not transported to BPM #3. The calculated maximum size of the beam at the pole of the extraction magnet is ≈120-mm diam compared to the 161-mm diam of the magnet bore and the 148-mm diam of the propagation pipe. Figure 5 also shows that the low energy electrons associated with the rise and fall of the current pulse are over focused into the pipe walls and are not transported to the beam waist region; the beam pulse is effectively sharpened.

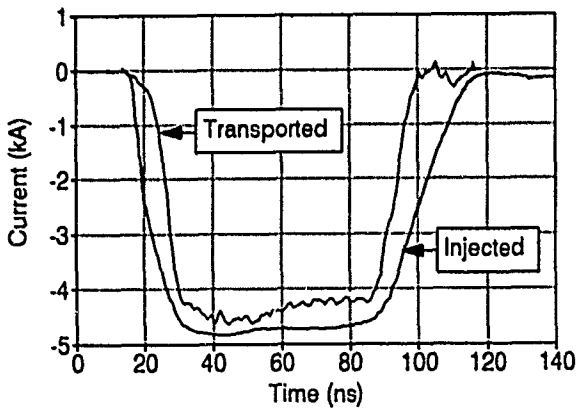


Figure 5. Emitted and Transported Beam Current

Although transverse beam motion beyond the extraction magnet has been measured on REX previously [6], the recent pulsed power modifications have reduced the motion to below the streak camera's resolution limit of ≈100 μm. Figure 6 is a typical differenced B-dot signal recorded from BPM #3 at the nominal operating conditions of 4 MV and 4.5 kA. A predominant frequency of ≈245 MHz is present and corresponds to a beam motion of ±100 μm. Since this frequency is not present in the derivatives of the pulsed power diagnostics, the code URMEL-T [7] was used to investigate the possibility of cavity modes associated with the A-K cavity region that could produce transverse fields to deflect the beam in time.

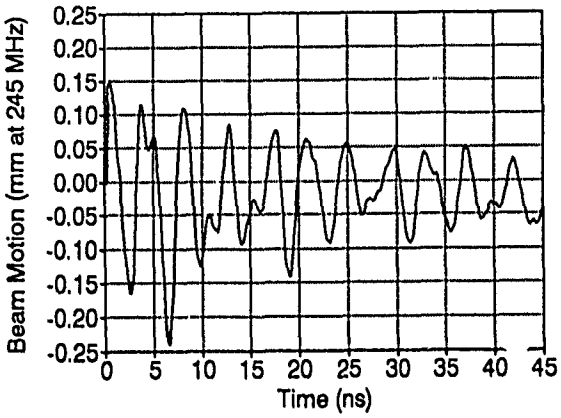


Figure 6. Differenced B-dots for Transverse Beam Motion

Accelerating (m=0) modes under 500 MHz were found at 64(67), 149(143), 310(294), 360(364), 385, and 458 MHz with URMEL-T predictions in parenthesis. Deflecting (m=1) modes were found at 254(249), 263, 335(320), 340, 380, and 437(421) MHz indicating some asymmetry either in the transmission line or in the cavity. The deflecting 254 (249)-MHz (m=1) mode was dominant and is in good agreement with the ≈245 MHz measured by the differenced B-dots. Varying the alignment of the cathode field forming electrode or of the transmission line conductor reduced the excitation only a few db. It may be that several small misalignments are causing the nominally TEM transmission-wave to have components that excite the TM_{1n0} modes of the cavity. Since this motion is where BBU gain is very low, far from the DARHT induction cell resonances, the required beam centroid stability of REX as an injector has been demonstrated.

IV. REFERENCES

[1] T. P. Hughes, R. L. Carlson, and D. C. Moir, "High-Brightness Electron-Beam Generation and Transport," J. Appl. Phys. 68 (6), pp. 2562-2571, September 1990.

[2] R. L. Carlson, L. A. Builta, T. J. Kauppila, D. C. Moir, and R. N. Ridlon, "A 4-Megavolt, 5-Kiloampere Pulsed-Power High-Brightness Electron Beam Source," *1989 IEEE Particle Accelerator Conference Proceedings*, pp. 276-278.

[3] R. L. Carlson, D. C. Moir, T. J. Kauppila, and R. N. Ridlon, "'REX' A 5-Megavolt Pulsed-Power Source for Driving High-Brightness Electron Beam Diodes," *1991 IEEE Pulsed Power Conference*, June 17-19, 1991, San Diego, Calif, and in the Proceedings to be published.

[4] ISIS was written by M. Jones, C. Snell, and G. Gisler at Los Alamos National Laboratory.

[5] G. Lawrence, A. Jason, and B. Blind, "Dipole, Quadrupole, Sextupole, and Octupole Magnetic Fields from Cosine-Wound Printed Circuit Coils," Los Alamos National Laboratory AT-3 Technical Note 86-128.

[6] L. A. Builta, R. L. Carlson, T. J. Kauppila, D. C. Moir, and R. N. Ridlon, "Pulse-Power-Induced Oscillations of the REX Electron Beam," *1989 Particle Accelerator Conference Proceedings*, pp. 322-324.

[7] U. Laustroer, U. van Rienen, T. Wilan, "Urmel and Urmel-T User Guide (Modal Analysis of Cylindrically Symmetric Cavities, Evaluation of RF-Fields in Waveguides)," DESY M-87-03, February 1987.

Matching and Transport of Beams in a Continuously Twisted Quadrupole Channel

Tiefenback, M. G., J. P. Lidestri, V. L. Bailey, Jr., and S. D. Putnam
Pulse Sciences, Inc., 600 McCormick St., San Leandro, CA 94577

Abstract

Twisted quadrupole (stellarator) focussing can reduce dispersion in the bends of a recirculating accelerator, such as the Spiral Line Induction Accelerator[1] (SLIA) under development at Pulse Sciences. Envelope oscillations caused by guide field/stellarator transitions add free energy to the beam which can couple into the beam emittance. This effect can be reduced by phase space matching of the beam at the transitions. We present experimental results on the coupled 4-D problem of envelope matching into a straight helical quadrupole channel, compare these results against envelope code predictions, and discuss expected benefits from such matching in a few-turn accelerator system.

Introduction

Helical quadrupole focussing[2] was added by Roberson, *et al.*[3], to the beam dynamics of a modified (toroidal guide field) betatron, greatly enhancing the energy mismatch tolerance over that of normal and modified betatrons. Putnam[1] adapted this focussing to an open-ended spiral geometry for multiple passes of high-current beams through common acceleration cavities, sidestepping closed-orbit injection and extraction problems. For practical reasons, quadrupole focussing is incorporated in the SLIA only within the bends. The chromatically varying envelope mismatch at uncompensated stellarator/guide field transitions can significantly increase the time-integrated transverse emittance of the beam. Envelope mismatches can also drive local emittance growth[4,5]. Mismatch mode coherence can be lost if particle oscillation frequencies vary. In the emittance-dominated limit the matched beam size scales as the square root of the emittance, and a 10% additional radial excursion of the beam can result in a 20% increase in effective emittance. Of particular concern is the relative phase of successive mismatches.

Phase space structure

The evolution of real beams can be modeled by the K-V distribution[6], in which unrealistic x'-y' correlations enforce uniformity of the beam current density. Practical beam matching involves providing the proper x-y profile and x-x'/y-y' focussing for the beam emittance. Analytical twisted quadrupole equilibria[2], including a guide field[7], exist as x-y coupled generalizations of the K-V model. These equilibria are elliptical in real space and have skew x-y'/y-x' focussing[2] and an overall rotation determined by the guide field and the total canonical angular momentum of the beam. Chernin[8] derived moment evolution equations for coupled x-y systems and provided us with Fortran coding to integrate the equations. This program was used to design a thin lens doublet to match a round, field-free beam into a stellarator channel[9] (Figure 1), showing the feasibility of nonadiabatic stellarator matching. The relevant parameters are shown in Table 1. The stellarator mouth is at z=0 cm. Consider the inverse problem of matching from a stellarator equilibrium into a solenoid. Select a quadrupole lens strength and orientation near the mouth of the stellarator to force the beam profile to be circular at some point in the following guide field (for many equilibria, no lens is necessary). At the point of roundness, place a thin quadrupole with strength and orientation chosen to zero the skew correlations of the beam and equalize the x-x'/y-y' correlations. The radial oscillations can be controlled by adjusting the $B_z(z)$ distribution For thick lenses, the cyclotron motion becomes important.

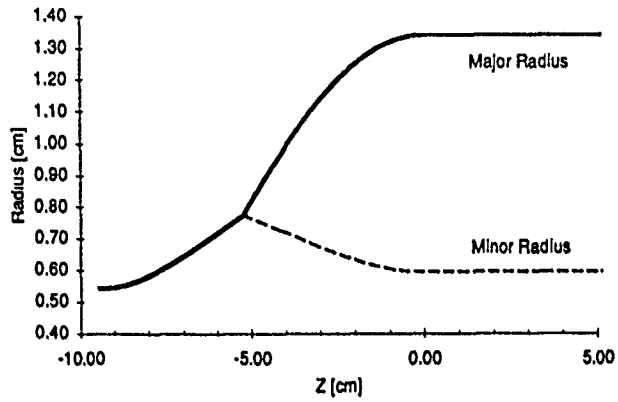


Figure 1: Matching transition between solenoid and stellarator focussing, a thin-lens existence proof.

Current:	10 kA	Energy:	3 MeV
$4\epsilon_{n,RMS}$	158 cm mrad	B_z	4666 G
R_{waist}	0.5424 cm	z_{waist}	-9.24 cm
Stel. pitch	31.42 cm	Gradient	405.5 G/cm
Lens 1 (z,G,θ)	-5.245 cm	1683 G	29.5°
Lens 2 (z,G,θ)	0 cm	10.52 G	45.0°

Table 1: Thin lens matching example parameters

*Work supported by DARPA under Order No. 4395, Amendment 90, and by the Navy under document N00039991WXDZ002, monitored by the Naval Surface Warfare Center

0-7803-0135-8/91$01.00 ©IEEE

Experimental setup

The experimental geometry is linear, referenced to the cathode at z=0 cm. Two-layer solenoid coils (average radii of 3.82 cm and 4.47cm) span from 37.8 cm to 80.0 cm for the transition section (central field 1216 G) and from 87.1 cm to 343.7 cm (central field 1476 G) for the stellarator section. Two loop coils of average radius 8.3 cm are used to adjust the $B_z(z)$ distribution. One is centered at 82.8 cm, with central field 876 G to compensate for the solenoid interruption, and the other is centered at 49.3 cm, with central field -516 G to adjust the input beam envelope. Quadrupoles are centered at 64.3 cm (peak gradient 57.5 G/cm, focussing in a plane 48.2° clockwise from vertical) and 75.3 cm (peak gradient 92.2 G/cm, focussing in a plane 1.6° degrees clockwise from vertical), of effective length ($\int B'(z)dz/B'_{max}$) 5.5 cm. A stellarator coil (right-handed, average radius 5.24 cm and pitch length 62.8 cm) spans 89.3 cm to 340.6 cm, oriented so that at its entrance the beam is defocussed in the vertical plane. The input beam passes through a waist of radius 4.7 mm at z=48.4 cm, at a guide field of 610 gauss. The beam energy is 800 keV, the current is 195 amperes, and the time-integrated normalized emittance is measured to be approximately 31 π cm mrad, using Cherenkov imaging of beamlets from a pinhole array.

The long magnet is an analogue of the 0.8 meter major radius stellarator bend currently in fabrication at Pulse Sciences, Inc., for the proof of concept experiment. The "straight bend" enabled meaningful physics measurements in energy scaled experiments, and comparison of the beam dynamics in a straight geometry with that in the bend should aid us in understanding toroidal effects. The parameters of our beam were chosen to model the 5.0 MeV, 10 kA beam expected after the first induction stage of the SLIA at Pulse Sciences. In the anticipated 10 kA system, the space-charge term in the envelope equation is much smaller than the emittance term (emittance proportional to the square of the beam size). However, the emittance is low enough in these experiments that space-charge is comparable in importance to the emittance.

Results

Our primary measurement technique is open-shutter photography of a Cherenkov convertor. A description is given in the paper by Lidestri, et al. [10], at this conference. The images are digitized with a high-resolution scanner, over a range of film exposure calibrated against mini-Faraday cup current density measurements for a dynamic range greater than 10:1. The beam radii shown here are edge radii, rather than RMS radii. We have placed a small-diameter beam stop on the front surface of the Cherenkov convertor near the center of the beam. An intensity contour is chosen surrounding the stop, of the same diameter. The intensity contour at the same level, surrounding the beam, is used to define the beam size. This protocol, while well-defined, does not yield the RMS beam profile. (We are currently working on an RMS reduction of the beam parameters.)

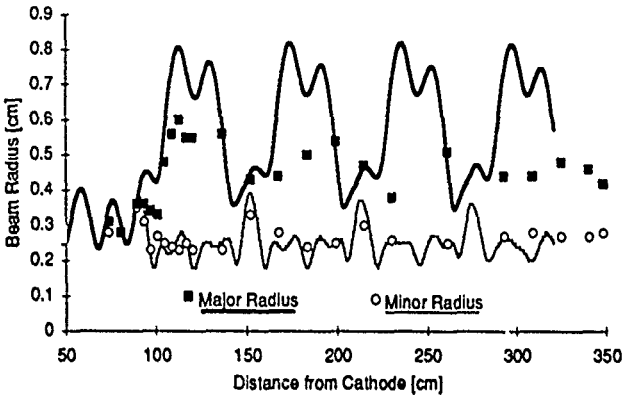


Figure 2: Beam envelope (experimental and calculated) along the channel without matching elements.

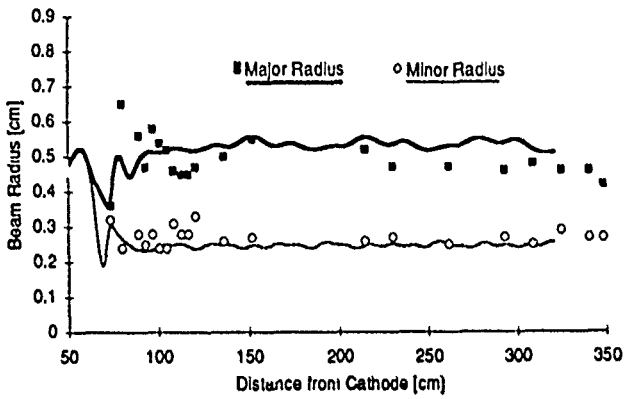


Figure 3: Beam envelope (experimental and calculated) along the channel for the nominal matched configuration of the text.

The matching fields were chosen using the measured edge radii as estimates of the RMS beam radii, and require experimental tuning.

We measured the beam envelope for the nominally matched configuration listed above, as well as for an unmatched case with neither the discrete quadrupoles nor the loop coil at 49.3 cm, and with a field strength in the transition solenoid of 1515 G. The unmatched results are shown in Fig. 2. The continuous lines show the calculated envelope. The measured major radius is systematically lower than the calculated value, which may be due to a systematic deviation of our measured edge radius from the RMS radius or to errors in the initial conditions used in the envelope calculation. The calculated major radii follow the pattern of the measured values, especially near the entrance of the channel. Two frequencies are evident at first, with the mismatch amplitude being dominated by the lower frequency mode. The initial amplitude and phase of the oscillations in the measured radii are very similar to those of the calculation, but a frequency shift and significant damping are evident downstream. The envelope model assumes a constant beam emittance, with no damping or phase-mixing of the mismatch oscillation.

Detailed matching decreases the mismatch oscillation amplitude, as shown in Fig. 3 (same scale as Fig. 2). The remaining mismatch seems to be dominated by a high fre-

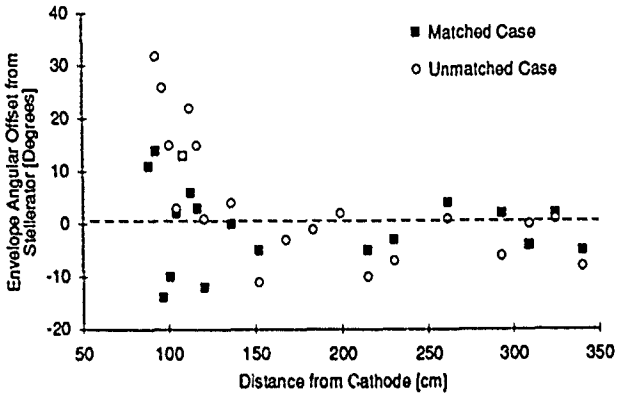


Figure 4: Orientation of the beam profile relative to the local stellarator frame.

quency mode, in contrast to the unmatched case. The beam is relatively quiescent downstream, with a measured major radius approximately 10% below the RMS radius expected from the (well known) beam current. This indicates that the edge radius we quote is probably systematically smaller than the true RMS radius, as noted above for the mismatched beam. For both configurations, the beam radii settle near the same values, dominated by the current of the beam rather than the emittance.

The orientation of the envelope ellipse relative to the local stellarator frame is shown in Figure 4, including the calculated orientation of the envelope. The deviation from the local twisted quadrupole frame is reduced significantly by matching. The envelope damping is quite rapid, with a scale length of on the order of 1 meter (5 cyclotron periods, 1.5 helix periods), and should be accompanied by an increased emittance. However, our measurements of the beam emittance at the exit of the long solenoid in the two cases are not significantly different. This is probably because our present optical diagnostic techniques do not include low-level regions of phase space.

In a report on a series of measurements of mismatch-driven emittance growth in a space-charge dominated beam of heavy ions[5], the growth was due to the development of a low-level halo of particles in phase space. Two-slit emittance measurements using direct electrical pickup of the particles had a dynamic range of greater than 200:1. The evolution of a matched beam was compared against that of a beam with a large symmetric mismatch (x and y oscillations in phase) and a beam with a large antysymmetric mismatch (x and y out of phase). In the symmetric case, only slight envelope damping was seen over ~ 6 zero-current betatron oscillation periods, with no significant growth in emittance. The antisymmetric mismatch was strongly damped, on a scale length of less than 2.5 zero-current betatron periods, and the RMS emittance grew by a factor of approximately four. Most of the increase came from regions of phase space with an intensity of less than 5% of the central peak. The peak phase space intensity dropped by only 25% with respect to that of the other beams. Such behavior would not have been resolved in our measurements to date.

Conclusions

Our present emittance measurements indicate that the central phase space density of the beam is not greatly affected by mismatches. However, the observed dispersion of the mismatch oscillations is inconsistent with zero emittance growth. As we improve our diagnostics, we should be able to resolve this anomaly. The planned two-pass SLIA system has six guide field/stellarator transitions. If each uncompensated transition caused only a 10% increase in the radial excursion of the beam, emittance growth to three times the original emittance could result, depending upon how thoroughly the mismatch were dissipated between transitions. Given the envelope damping results, it seems prudent to maintain phase space matching to avoid a large increase in the RMS emittance. Restoring the beam to a circular cross-section for guide field transport between stellarator bends also allows arbitrary choice of the phase of subsequent stellarator fields. Because of the bend, this phase is fixed when the magnet is fabricated.

References

[1] Putnam, Sidney D., "Survey of compact high current electron accelerators," in *Proc. 1987 Part. Acc. Conf.* March 16-19, Washington, D. C., pp. 887–891.

[2] Gluckstern, R. L., "Focusing of high current beams in continuously rotated quadrupole systems," in *Proc. 1979 Lin. Acc. Conf.*, Brookhaven National Laboratory. BNL-51134, pp. 245–248.

[3] Roberson, C. W., A. Mondelli, and D. Chernin *Phys. Rev. Lett.*, **50**, 1983. also *Part. Accel.*, **17**:79, 1985.

[4] Anderson, O. A. and L. Soroka, "Emittance growth in intense mismatched beams," in *Proc. 1987 Part. Acc. Conf.* March 16-19, Washington, D. C., pp. 1043–1045.

[5] Tiefenback, Michael G., "Experimental measurements of emittance growth in mismatched space-charge-dominated beams," in *Proc. 1987 Part. Acc. Conf.* March 16-19, Washington, D. C., pp. 1046–1048.

[6] Kapchinskij, I. M. and V. V. Vladimirskij, "Limitations of proton beam current in a strong focusing linear accelarator associated with the beam space charge," in *Proc. Int. Conf. on High-Energy Accel. and Inst.*, pp. 275–288, CERN, 1959.

[7] Chernin, D., "Self-consistent treatment of equilibrium space charge effects in the l=2 stellatron," in *Proc. 1985 Part. Acc. Conf.* May 13-16, Vancouver, BC, Canada, IEEE Trans. on Nuc. Sci., NS-32(5), 2504–2506.

[8] Chernin, D., "Evolution of rms beam envelopes in transport systems with linear x-y coupling," *Part. Accel.*, **24**(1), 1988.

[9] Tiefenback, M. G. November 1989. unpublished presentation to Spiral Line Induction Accelerator working group.

[10] Lidestri, J. P., et al. proceedings of this conference.

PILAC: A Pion Linac Facility for 1-GeV Pion Physics at LAMPF

Henry A. Thiessen

Los Alamos National Laboratory
Mail Stop H-847
Los Alamos, New Mexico 87545

Abstract

A design study for a Pion Linac (PILAC) at LAMPF is underway at Los Alamos. We present here a reference design for a system of pion source, linac, and high-resolution beam line and spectrometer that will provide 10^9 pions per second on target and 200-keV resolution for the (π^+,K^+) reaction at 0.92 GeV. A general-purpose beam line that delivers both positive and negative pions in the energy range 0.4-1.1 GeV is included, thus opening up the possibility of a broad experimental program as is discussed in this report. A kicker-based beam sharing system allows delivery of beam to both beamlines simultaneously with independent sign and energy control. Because the pion linac acts like an rf particle separator, all beams produced by PILAC will be free of electron (or positron) and proton contamination.

I. The Nuclear Physics Program of PILAC

There are five classes of experiments that require pions of energies up to 1.1 GeV [1]. These classes are:
1.) Λ-hypernuclear physics via the (π,K) reaction;
2.) Λ-nucleon scattering at threshold;
3.) rare decays of π and η;
4.) pion-nucleus elastic and inelastic scattering with 0.4-1.1 GeV pions; and
5.) baryon resonances.

II. PILAC Concept

A concept for the reference facility is shown in Figure 1. The reference PILAC facility requires the following items [2]:
1.) proton buncher;
2.) new target cell for zero-degree pion production;
3.) 0.38-0.53-GeV pion injection beamline;
4.) 0.38-0.92-GeV, 12.5 MeV/m gradient superconducting pion linac;
5.) kicker-based beam-sharing system;
6.) 1.1-GeV high-resolution dispersed beam line and spectrometer;
7.) general-purpose beam line with dispersed mode for existing MRS spectrometer; and
8.) experimental area and related civil engineering.

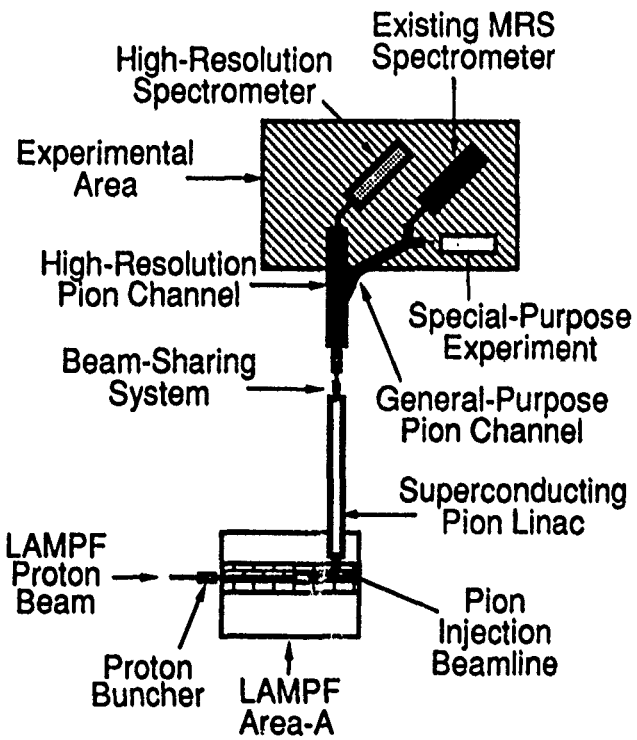


Figure 1. Concept for PILAC facility at LAMPF.

III. Proposed Development Plan for Superconducting Cavities for PILAC

The reference design requires 12.5 MeV/m cavity gradient and has negligible beam loading. We believe that this large gradient can best be achieved by use of titanium heat-treated niobium cavities [3]. In order to establish the gradient and Q that will be achieved in the PILAC cavities, it is necessary to scale up the technology to the larger, lower-frequency cavities needed and to test several prototype cavities. This requires new, larger facilities at Los Alamos. To save time, we propose to develop the heat-treatment technology in a parallel effort using existing equipment at 3 GHz. We will also take an existing 805-MHz single-cell cavity and heat-treat it in the Cornell oven.

IV. Injection Beam Line

The injection beam line proposed for PILAC consists of a matching section based on a strong quadrupole doublet placed as

0-7803-0135-8/91$01.00 ©IEEE

close as possible to the pion-production target followed by a second-order achromat. Sextupoles and octupoles correct all detrimental second- and third-order aberrations. This beam line has a solid angle of 10 msr, a momentum acceptance of 6.6%, and a transverse phase-space output of 225 π mm-mrad. In the reference version of this beam line design, 82% of the output beam is contained within the specified phase space.

We are also considering a possible design of the injection beam line that will deliver both π^+ and π^- simultaneously s is shown in Figure 2. This version of the injection line has not yet been studied thoroughly.

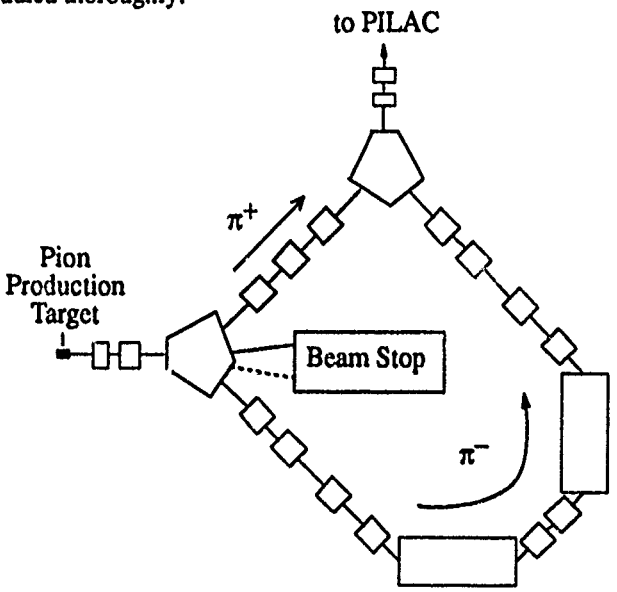


Figure 2. Possible design for simultaneous π^+ and π^- injection line for PILAC.

V. Choice of Operating Frequency for PILAC

A series of linac designs was studied to determine the optimum operating frequency for PILAC. The highest frequency that is a harmonic of the LAMPF injector and is also compatible with the required transverse phase space acceptance of 225 π mm-mrad is 805 MHz. This frequency has been chosen for the reference design.

VI. Reference Linac Design

The reference linac design is based on a study maximizing the pion intensity in the desired output phase space. A conceptual layout of this design is shown in Figure 3. The beam intensity is the product of longitudinal acceptance and pion survival in the linac. A total phase space rotation of $3\pi/4$ in the longitudinal plane maximizes the acceptancewhile minimizing the energy spread of the output beam. The layout of the linac minimizes pion decay. The number of cells per cavity was chosen to give the largest cavity that can be handled comfortably in the existing superconducting cavity lab. This results in a choice of seven cells per cavity. A total of 40 cavities is required to accelerate from 0.38-0.92 GeV. By raising the injection energy and rephasing

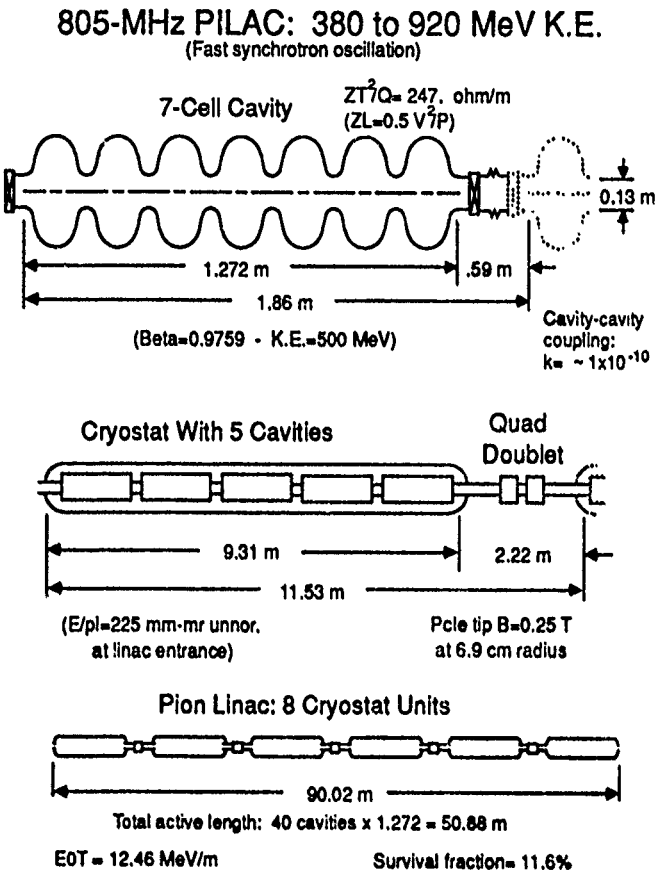


Figure 3. Reference design of pion linac.

the linac, energies up to 1.1 GeV can be provided, but at reduced intensity. Quadrupole doublets are required after each five cavities in order to contain the transverse phase space in the cavity bore. Five cavities will be mounted in a single cryostat as a module. Eight modules are combined to make the full linac. The total length of the linac is approximately 90 meters.

VII. High-Resolution Beam Line and Spectrometer

A high-resolution beam line has been designed using program MOTER [4]. This beam line, a QQQQMDMDMDMDM design with vertical bends, has a momentum dispersion of 25 cm/% and a horizontal divergence of 5 mrad full width in the horizontal planeand is shown in Figure 4. The full size of the beam spot will be 40-cm high by 10-cm wide. The momentum resolution of the high-resolution beam line calculated by MOTER

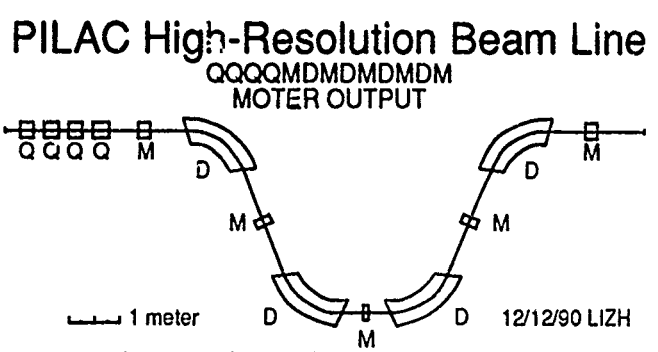


Figure 4. High resolution beam line for PILAC.

is one part in 10^4 when second- and third-order optical corrections are introduced on the dipole entrance and exit faces.

A spectrometer with acceptance matched to this beam line has also been designed and is shown in Figure 5. The design is very

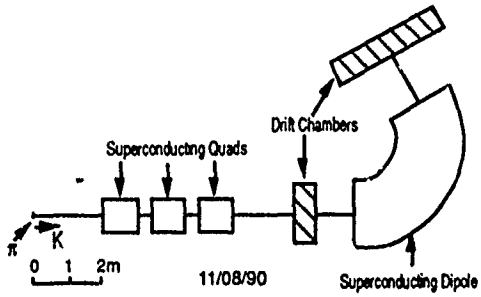


Figure 5. High-resolution spectrometer for PILAC.

similar to that of the existing EPICS spectrometer at LAMPF except that the bending magnet has been made from a single unit in order to minimize the flight path of kaons in the spectrometer. By using iron-dominated superconducting quadrupole magnets similar to those planned for the Hall-C spectrometer at CEBAF, the acceptance of the spectrometer has been increased by almost a factor of six compared with that of the existing EPICS spectrometer. The acceptance of the proposed spectrometer is 27 millisteradians for the 10-cm x 40-cm beam size of the high-resolution beam line.

VIII. General-Purpose Beam Line

A beam line capable of providing an achromatic beam spot and also 2-3 cm/% horizontal dispersion (for use with the existing MRS spectrometer) is being designed. The output beam spot and divergence in the achromatic mode will be 5-mm radius by 25 mrad (half widths). The output beam spot will be tuneable over a wide range. We are also studying a second port for the output of this line. In addition to providing beam for experimenters, the new general-purpose line will serve as a pion injector for a future linac extending the energy range of PILAC to 1600 MeV.

IX. Beam Sharing in PILAC

A kicker-based beam sharing system is envisaged for PILAC. With the kicker magnet off, the pion beam from the linac goes straight ahead into the high-resolution beam line. With kicker magnet on, the beam is deflected into the general-purpose line. The basic idea is that the kicker rise time will be comparable to the time required to switch the phase program of the linac cavities. Then the phase program and the kicker can be switched simultaneously. With simultaneous injection of π^+ and π^- into the linac, it will be possible to have independent control of the pion sign and energy delivered to each of the two beam lines.

X. PILAC Pion Yield

The pion yield expected from PILAC is $1.2\pm0.6\times10^9$ π^+ per second at 0.92 GeV. This yield is comparable to that which can be achieved in the same phase space at the proposed KAON facility and is more than an order-of-magnitude larger than can be achieved at the Brookhaven AGS with the new booster operating.

XI. Program MOTER

The program used for raytracing calculations of the high-resolution beam line and spectrometer is MOTER (Morris Klein's Optimized Tracing of Enge's rays). This program was written at Los Alamos in the early 1970s [4]. MOTER is being updated to include rf cavities in order to make possible a precision study of the optics of PILAC in a single computer program.

XII. Summary and Conclusions

PILAC is being designed to provide a beam of 10^9 pions per second at 0.92 GeV, with a future upgrade to 1.6 GeV. We have demonstrated that the system resolution of 200 keV can be achieved in a high-resolution beam line and spectrometer. In order to provide the necessary flux, the linac requires superconducting cavities that achieve a gradient of 12.5 MeV/meter. Although no linac presently operates at this high gradient, tests at laboratories around the world have shown that this gradient can be achieved by titanium heat treatment of the cavities. An R&D program is proposed to scale up the results from single-cell 1.5-3-GHz cavities to the necessary 7-cell 805-MHz cavities.

PILAC will provide an energy of 0.92 GeV with operation possible up to 1.1 GeV at reduced intensity. This energy is sufficient to optimize the yield of the (π^+,K^+) reaction and to access a broad range of interesting physics. The PILAC energy resolution, 200 keV, is more than an order-of-magnitude better than that which is available today and will give access to a wealth of information on hypernuclear physics. The PILAC beam-sharing system will allow simultaneous operation of two or more line with independent sign and energy control. The PILAC beams will be of unprecedented purity since the linac acts as a high-resolution rf separator. PILAC is cost-effective since it is by far the least expensive upgrade to LAMPF that gives access to this physics. The new superconducting cavities represent a new technology that will open up applications in other fields. Finally, PILAC is feasible only at LAMPF, since only LAMPF has the necessary tightly bunched proton beam to produce pions that can then be accelerated in a superconducting linac.

XIII. References

[1] "Physics with PILAC," Los Alamos Report, to be published.
[2] PILAC Technical Notes 1-25, Los Alamos, 1990-91 and other contributions to this conference.
[3] H. Padamsee, IEEE Cat. No. 87CH2387-9, 1691 (1987).
[4] H. A. Thiessen and M. M. Klein, Proceedings of the 4th International Conference on Magnet Technology, Brookhaven, N.Y., pp. 8-17 (1972).

HIGH VOLTAGE, HIGH POWER NESTED HIGH VOLTAGE ACCELERATOR

R.J. Adler and R.J. Richter-Sand
North Star Research Corporation 5555 Zuni, SE, Ste. 345, Albuquerque, NM, 87108

The Nested High Voltage Generator (NHVG, North Star Research Corp. patent pending) is a unique new type of accelerator based on the principle of the Faraday cage. It consists of a number of individual high voltage sections which are placed inside of the adjacent accelerator section, or 'nested' one inside the other. Electronics internal to each of the NHVG stages sets the voltage between the inner and outer Faraday cage to some voltage V. By building N stages and placing them one inside the other, we can produce a DC voltage N x V. In this paper we describe the advantages of this type of accelerator along with the results of work with the two small NHVG accelerators which we have built so far.

I. INTRODUCTION

Compact, light weight particle accelerators are desirable for a variety of applications including drivers for high power microwave generators, radiation processing, Positron Emission Tomograpy, and space based applications. The use of solid insulation is essential to reducing the size of high voltage equipment, and we believe that the NHVG is an approach which can effectively utilize solid insulation to very high (10 - 20 MV voltages). The use of solid insulation also leads to high stored energies which make pulsed operation possible as well as DC operation possible in the same device.

In this paper we first describe the fundamental principles of operation of the [illegible]ction II), and we then describe our first prototype accelerator (section III) and a tandem accelerator (section IV). We present conclusions in section V.

II. PRINCIPLE OF OPERATION

We describe the NHVG technique in more detail in this section. Figure 1 illustrates the principle of all NHVG accelerators. Topologically "nesting" high voltage systems allows us to isolate individual lower voltage systems without developing the full voltage across any one insulator. Each voltage generator is inside an adjoining generator. Reduced to it's essentials, the compact accelerator can be represented by a series of concentric conducting shells which are electrical nodes with individual voltage sources between the nodes. By the basic physics of electrostatics each of the 'generator' shells are totally isolated. This means that an observer placed between two conducting shells cannot measure the potential of the spheres relative to ground potential.

The insulation required to insulate between the two conducting shells does not depend on the total voltage of the assembly, only on the interstage voltage. This is important because a fundamental property of solid insulation is that the electric field strength which an insulator can withstand drops as the insulation gets thicker. Therefore if we break a thick insulator into a number of individual thinner sections with the voltage equally divided, significant reductions in overall thickness, and therefore in overall weight and size can be achieved. A complete conducting shell will prevent the passage of the charged particles which we wish to accelerate as well as the passage of energy. In our application, however, small holes or slots will permit particles and energy to leave or enter the shells. If the scale size of the hole in the conducting shell is r, the field due to this hole will fall off exponentially over a distance of order r. Therefore holes only compromise the integrity of the conducting shell to a limited degree.

Holes and shells are necessary for two reasons - first to allow particles to travel through the device and gain full energy as described above. We must also supply the energy required by the high voltage generators through these holes or slots. Possible techniques for supplying energy to the shells through small holes or slots include:

- Time varying magnetic fields (transformer action or inductive coupling) where the energy is allowed to pass through slots (we simply require that none of the conductors completely encircle the axis, nearly complete encirclement is allowable).
- An insulated rotating shaft with mechanical to electric generators placed inside each shell.
- Batteries which are used to power high voltage generators inside each shell. The batteries can be recharged via the particle egress hole when the generator is not in use.
- Thermoelectric converters where the system is hot.
- Cascade generators

0-7803-0135-8/91S01.00 ©IEEE

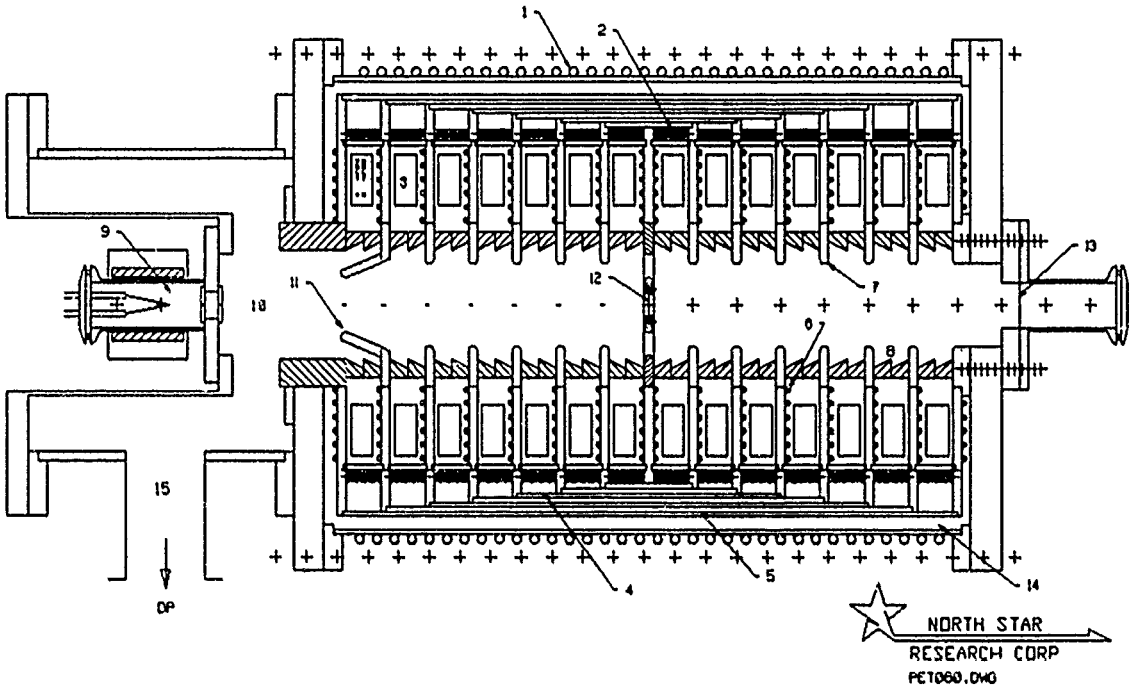


Figure 1.. Detailed schematic of the PET NHVG negative ions. 1)Primary winding 2)Secondary winding 3)Voltage multiplier 4)Conducting shell 4)Insulator 6)Conductor 7)Grading ring 8)Vacuum insulators 9)Ion Source 12)Stripping foil.

A number of practical questions are not addressed in the discussion above. The exact design of the ubiquitous interfaces between different types of insulators is not discussed. The exact geometries of the conductors for transformer coupling are also not discussed.

We believe that transformer coupling is the most effective means of providing the energy for the NHVG, and so limit the discussion to this technique, and this is the embodiment of the device shown in Figure 1. The transformer configuration consists of secondary high voltage multi-turn windings, diode/capacitor voltage multipliers. A high voltage vacuum insulator and an evacuated acceleration well through the insulator stack allows the particle beam to move from the source region at the inner most cell toward ground potential. A nearly complete conducting casing separates each pair of voltage sources. Power is supplied through an air core transformer and magnetic induction from an external oscillating field coil using a resonant circuit.

Referring also to Figure 1, the common wall between adjoining generators is arranged to be a nearly complete conductor with relatively few openings. The complete conductors are separated by oil, solid, or vacuum insulators. Openings of note are slots which allow penetration of magnetic flux without compromising the electrostatic shielding provided by the metal foil. The winding acts as a transformer secondary and converts the magnetic flux provided by the external generator into alternating electric currents which transmit power to power supplies. The power supplies, which may be as simple as capacitor --diode combinations provide a high voltage potential difference across the insulator. This insulator, which may be made of dielectric film or an insulating liquid is designed to hold-off the voltage across the module. The complete insulation afforded by the insulator is terminated by the vacuum interface which provides a separation between the insulation required for the power supply and the vacuum required for particle beam acceleration.

We outline critical issues in NHVG design below.

A) Solid Insulation

The type and voltage withstand capability of the solid insulation is critical to the design and fabrication of these devices. A slot pattern must be developed which allows flux penetration without unacceptably compromising the axial insulation. The gap between the slots should be minimized. The radius of curvature at the slot edges should be sufficiently large so that the field enhancements at the slots do not increase the field to an unacceptable degree.

B) Vacuum Insulation

The vacuum insulation issues in this accelerator are the same as those in any DC electrostatic accelerator. The design must avoid charged particle impact on insulators, and minimize accelerator length. Ion transport must be minimized since this can lead to breakdown in the accelerator. We will not elaborate on this point in this section since we did not address this problem in detail in Phase I.

C) *Transformer Coupling*

An external circuit is required to supply the magnetic flux which powers the modules. DC power is converted, by means of a switch (such as the power MOSFET) into a high frequency oscillating voltage. The coupling of an air core transformer depends on the relative primary/secondary cross-sectional area. For this reason, the coupling coefficient is small in an NHVG. The effective coupling coefficient can be increased by making the primary circuit a resonant circuit. This resonant circuit can be configured in several ways, but the simplest is to make this resonant circuit consist of the primary transformer winding and a capacitance chosen to give the desired frequency. The effective coupling coefficient is then the product of the 'Q' of the circuit, and the conventional coupling coefficient. This number can easily exceed 1. A coupling coefficient greater than 1 implies that the ratio of the output voltage to the switch voltage is greater than 1. This is a practical solution to the coupling coefficient problem.

We note that while we specify power MOSFETs in the discussion above, power grid tubes are probably the modulation technique of choice for output powers above a few kW, particularly if weight is more important than efficiency.

III. 150 KV NHVG ACCELERATOR PROTOTYPE

In order to demonstrate the fundamental principles of operation, a six module, 150 kV, 150 μA, CW/pulsed electron accelerator was constructed during an intensive 6 month effort. The resonant transformer circuit was used to inductively couple energy to step-up nested secondary coil and voltage multiplying circuits through a conductor geometry which shields electrostatic fields while it allows magnetic field penetration. Proof-of-principle experiments were conducted with a heated tantalum filament at ground potential to verify beam parameters and electron extraction.

Results obtained from the prototype device were very encouraging and verified the merits of the concept and scaling. We found no fundamental obstacles to scaling this concept to higher energies, powers, or gradients. The Phase I prototype device was still in working order when it was disassembled to assess whether any breakdowns had occurred. We anticipate that it is ultimately capable of at least 300 kV if a higher power drive system is utilized. The voltage grading achieved in the device is shown in Figure 2. We also note that one of the six sections was operated at 70 kV.

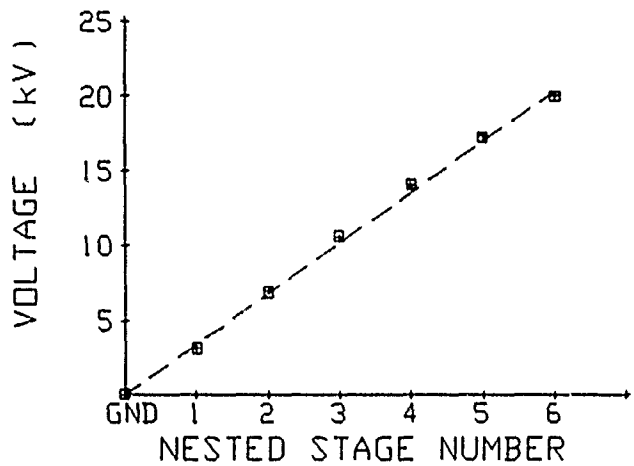


Figure 2. Accelerator voltage division. Measured across the vacuum diode and ground referenced.

The overall capacitance of this device was approximately 5 nF., and we operated the accelerator in pulsed mode by changing to a flashboard plasma electron source.

IV. TANDEM NHVG ACCELERATOR

A tandem NHVG accelerator for proton/deuteron acceleration was constructed, and reached voltages at the terminal of 215 kV (particle energies of approximately 430 kV minus the stripping cell energy, and it is still in operation. This device is 30 inches long, and approximately 1 ft. in diameter. It is capable of being considerably reduced in size.

V. CONCLUSIONS

The NHVG principle has been used to build two particle accelerators. The principle limitation to the accelerator voltage is the size of the accelerators which have been built to date, and the power available from the MOSFET based accelerators which have been used so far.

This work was supported by SDIO under contract DNA001-89-C-0114 and by DOE under grant DE-FG05-90ER80954.

LELIA : AN INDUCTION LINAC DEVELOPED FOR FEL APPLICATION

Ph. EYHARTS, J. BARDY, Ph. ANTHOUARD, P. EYL, M. THEVENOT

C.E.A - C.E.S.T.A
BP n° 2
33 114 - LE BARP (FRANCE)

Abstract

An induction linac is being studied and built at CESTA for FEL application. At first we studied the induction technology and namely the high voltage (HV) generators and the induction cells.

A HV generator designed to feed the cells with calibrated pulses (150 kV, 50 ns, ΔV/V <1 %) has been built using a charging resonant system and magnetic switches. This generator is planned for kHz repetition rate operation. A prototype induction cell has also been built and tested with a cable generator. An electron injector (1.5 MeV, 1.5 kA) has been designed and is now under completion : it uses ten induction cells and a thermoionic dispenser cathode. Numerical codes have been developed and simulations have been compared with experimental results for HV generators, induction cells and injector.

An induction accelerating module is now being studied and we plan to have the accelerator working next year at a 3 MeV energy level.

I. INTRODUCTION

The LELIA program is under development at the "Centre d'Etudes Scientifiques et Techniques d'Aquitaine" (C.E.S.T.A) since 1988. Its objective is to produce a high brightness and high average power electron beam for FEL application [1].

Such a beam will be obtained using an 1.5 MeV induction injector able to generate peak current of 1 - 2 kA.

In order to increase the beam average power, limited by the pulse time duration (~ 80 ns), we need to have it working at high repetition rate (> 1 kHz).

Moreover for FEL operation the high voltage (150 kV) pulse used to drive induction cells must be regulated to within 1 % to ensure acceptable variation in beam energy.

All these requirements led us to study and realize a HV pulse generator based on magnetic compression.

On the other hand it was an important task for us to test the induction cell technology before constructing the accelerator itself. In that way a prototype induction cell has been built and a series of experiments has been conducted in order to verify our choices in mechanical, electrical and vacuum engineering.

II. LELIA DESIGN AND EXPERIMENTS

A. *High voltage Pulse Generators*

The LELIA induction cells are designed to be driven by rectangular voltage pulse with 150 kV amplitude and 80 ns duration. Following these parameters a pulse generator has been developed at CESTA [2]. It consits of two parts :

- a Command Resonant Charging System (CRCS)
- a Pulse forming and compression device (MAG)

A cross section for this HV generator is shown in figure 1.

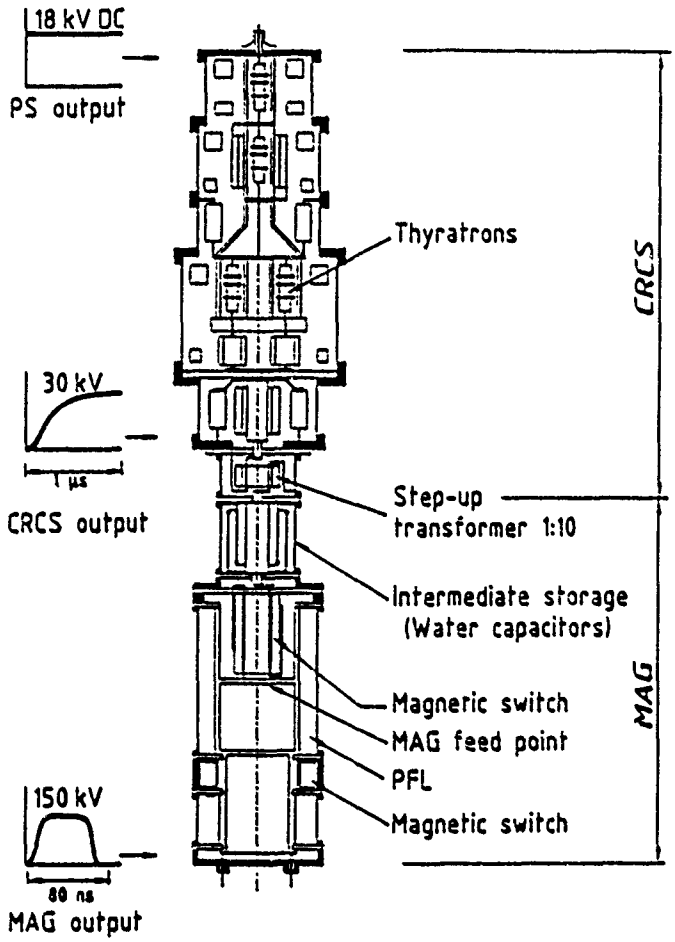


Figure 1 : Cross section of HV pulse generator.

The CRCS transforms the 25 kV DC supply into a low power sinusoidal pulse generator. It is mainly composed of thyratrons (EEV CX 1536), self-inductances and capacitors.

The output signal (30 kV/1 µs sinusoidal pulse) is amplified in a step-up transformer and used to charge the 20 nF intermediate energy storage. Then the MAG compresses this charge pulse to 80 ns and transforms it into a 150 kV rectangular pulse.

This drive pulse is delivered to the induction cells through 100 Ω coaxial cables. Each HV generator can drive 25 cells.

The MAG module is built using a coaxial water filled pulse-forming line (PFL) and magnetic switches operating

0-7803-0135-8/91$01.00 ©IEEE

as magnetic pulse compressors. PFL impedance is 2 Ω.

In a first time the HV generator has been tested with resistive load producing a 150 kV/50 ns flat top pulse. Moreover, as predicted by our numerical simulation, an improvement in the flat top quality was experimentally observed by charging the pulse forming line at the middle (**figure 2**).

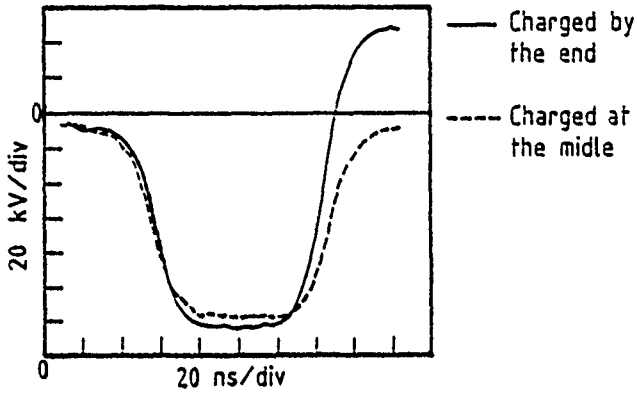


Figure 2 : MAG output voltage

Presently tests are conducted on this HV generator to verify its high repetition rate (~ 1 kHz) working ability.

B. *Prototype induction cell*

Design : LELIA prototype induction cell consists of a ferrite torroid stack housed in a non-magnetic stainless steel body connected to a vacuum pump (**figure 3**).

The value of the inner diameter of torroids is a compromise between a large diameter to minimize the Beam Break Up (BBU) instability and a small diameter to minimize the cost of the accelerator.

Cross sectional area of torroids depends upon the pulse characteristics and the ferrite magnetic properties.
It has been calculated using the relation : $V.\Delta t = S.\Delta B$ where V is the pulse voltage, Δt the pulse duration, S the cross sectional and ΔB the available flux swing of the magnetic cores.

The length of the ferrite stack has been determined from pulse width and electrical characteristics of the ferrite with the formula :

$$l \simeq \Delta t / \sqrt{\mu \epsilon}$$

where μ is the permeability and ϵ the dielectric constant of ferrite.

According to the above constraints the prototype cell has been constructed around seven PE 11 B ferrite torroids 25 mm thick, 250 mm I.D., 500 mm O.D. manufactured in Japan by T.D.K.

Oil is used as the dielectric and cooling fluid surrounding the ferrites.

Between the beam pipe and the ferrite core internal diameter is a 2 layers, 68 turns solenoid capable of producing a 2 kG axial magnetic field.

The accelerator gap is 8 mm wide and a pure alumina insulator brazed on the cell provides the vacuum-oil interface. This technology allows us to ensure a high vacuum in the beam pipe : measurements exhibit a pressure less than 5×10^{-9} torr and no presence of hydrocarbons or halogens was detected by mass spectrometer.

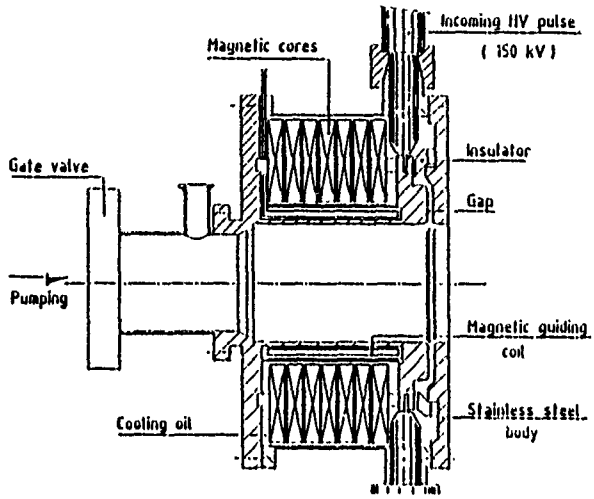


Figure 3 : Prototype induction cell

The gap profile has been designed with PALAS and AMOS numerical codes in order to minimize the BBU instability [4].

AMOS calculations have shown a dominant transverse impedance of 1250 Ω/m at 250 MHz. For utilization in an acceleration module, modifications have been made to decrease this value.

Testing : A cable generator specially developed for this application has been used to test the induction cell with applied gap voltages ranging from 10 kV to 200 kV.

The HV pulse was introduced on two opposite sides from two 100 Ω coaxial cables. No breakdown occured during these experiments.

Using an electro-optic jauge [5] we have also measured the accelerating electric field on the axis of the cell. Results have shown a good agreement between experiments and calculations obtained with FLUX 2D electrostatic numerical code (**figure 4**).

As a consequence it is important to note that the field distribution in the beam pipe is an electrostaticlike distribution.

An induction cell can be represented by the equivalent circuit model shown in **figure 5**.

The HV generator is represented by the voltage source and the transmission line to the cell by the resistor Z_0.

C_g represents the capacitance of the cell, Z_F the ferrite impedance and I_B the beam current.

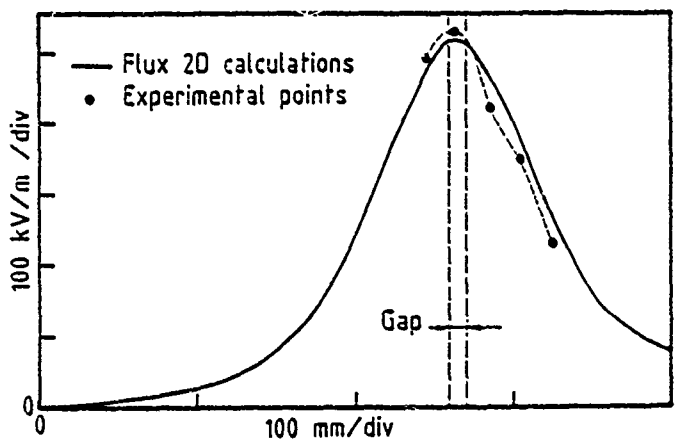


Figure 4 : Electric field profile in beam pipe

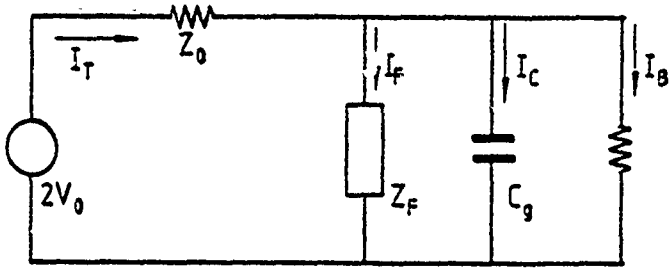


Figure 5 : Induction cell equivalent circuit

To evaluate the electrical characteristics of the prototype cell we have conducted a series of experiments with a resistive load placed on the axis of the cell to simulate the beam. A pulse voltage of 130 kV was applied to the gap ; the total cell current and resistive load current were measured. Results are shown in **figure 6.**

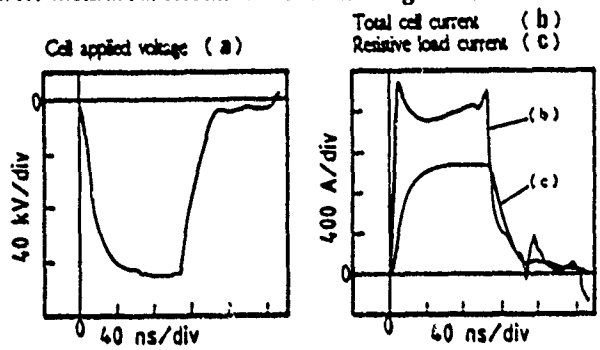


Figure 6

The displacement current I_C due to the gap capacitance can be expressed by

$$C_g \frac{dV}{dt}$$

In a first time using geometrical considerations we have calculated the gap capacitance Cg of the cell.

A value of 180 pF has been obtained.

Then it was easy to deduce I_C from **figure 6a.**

By subtracting I_C and I_B from the total cell current we have also determined the ferrite leakage current I_F.

Results of these calculations are shown in **figure 7.**

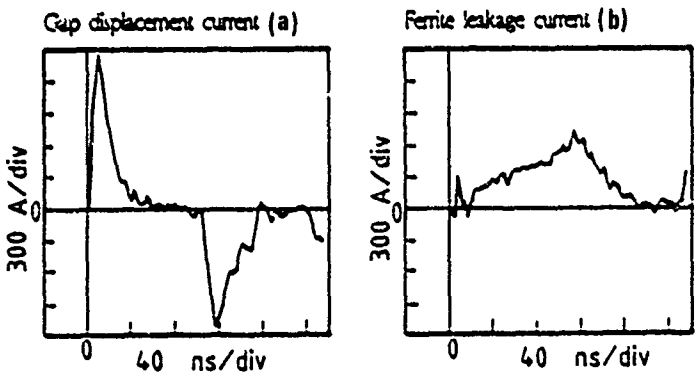


Figure 7

Examining **figure 7-a** it is obvious that the initial surge of current is essentielly due to the gap capacitance.

On the other hand it is apparent in **figure 7-b** that the ferrite reacts like a transmission line with $I_F = V\,t / L$

The slope of this trace gives an inductance L of 15µH which is in concordance with the design value.

The ferrite impedance Z_F is equal to the applied voltage divided by the ferrite current. This impedance has a constant value of 300 Ω during 40 ns.

Experimental work on the prototype cell has also permitted to verify the available flux swing ΔB in the ferrite.

Using the relation $\Delta B = \frac{1}{S}\int V dt$ we have obtained a value of 0.63 Tesla which is in concordance with the value given by the manufacturer.

C. *Injector*

An injector (1.5 MeV, 1.5 kA) has been designed and constructed at CESTA. It comprises ten induction cells similar to the prototype cell and uses a 85 mm diam. osmium dispenser cathode to produce the electron beam. The electrongun is a triode configuration (cathode surrounded by a focusing electrode, intermediate electrode and anode) optimized with SLAC and FLUX 2D numerical codes. The vacuum inside the injector is ensured by two 4500 l/s cryogenic pumps. Measurements indicate a residual pressure of 1.2×10^{-9} torr (essentially water and nitrogen).

Now the cells have been electrically tested and we plan to obtain the first beam very soonly after magnetic alignement of the guiding coils has been realized.

III. CONCLUSION

Design and construction of a HV generator and a prototype cell have permitted us to acquire, at CESTA, magnetic pulse compressors and induction technology.

From this experience we have been able to construct an injector of 1,5 MeV for FEL application (for next year construction of a 3 MeV accelerator is planned).

IV.REFERENCES

[1] J. Launspach, J.M Angles, Ph.Anthouard, J. Bardy, C. Bonnafond. H. Bottollier-Curtet, A. Devin, Ph. Eyharts, P. Eyl, J.Gardelle, G. Germain, P. Grua, J. Labrouche, J. de Mascureau, P. Le Taillandier, W. Stadnikoff, M. Thevenot, High Power Induction Linac for FEL Application at CESTA, Proc. 12th International FEL Conference, Cité Internationale, PARIS (FRANCE), September 17 - 21, 1990.

[2] M. Thevenot, P. Eyl, Ph. Anthouard ,Magnetic Compressor Studies for FEL Applications at the "Centre d'Etudes Scientifiques et Techniques d'Aquitaine", 90 International Magnetic Pulse Compression Workshop, GRANLIBAKKEN LAKE TAHOE, CALIFORNIA, Februay 12 - 14, 1990

[3] J. Bardy, Ph. Eyharts, Ph. Anthouard, F. Delaurens, P. Eyl, J. Labrouche, J. Launspach, P. Le Taillandier, J. de Mascureau, M. Thevenot, Design and Initial Operation of LELIA Induction Accelerator, Proc. 12th International FEL Conference, Cité Internationale, PARIS (FRANCE) September 17-21,1990

[4] J.F de Ford, AMOS simulation of CESTA prototype induction cell, Beam Research Program (LLNL), August 1990, Private communication.

[5] P.A Chollet, R.Gras, A. Lorin, Capteur électro-optique de champ électrique, CEN Saclay, DTA, LETI, Private communication (1990).

Effect of Wakefields on First Order Transport in the SLC Linac *

Chris Adolphsen, Karl L. F. Bane and John T. Seeman
Stanford Linear Accelerator Center, Stanford University, Stanford California 94309

Abstract

The limitation in increasing the beam current in the SLC linac comes from the emittance growth caused by wakefields. Simulations of the beam transport that model the wakefield dynamics are being done to study methods to control this growth. To verify the theoretical estimates of the wakefield strengths assumed in these simulations, data were taken which are sensitive to their effect on the first order linac transport. Specifically, the dependence of single beam loading and betatron motion on beam current was measured in the range of $0.5 \cdot 10^{10}$ to $3.5 \cdot 10^{10}$ electrons per bunch. This paper presents these data together with comparisons to results from simulations.

I. INTRODUCTION

The SLC linac accelerates bunches of particles from an energy of about 1 GeV to 47 GeV along a 3 km FODO lattice which contains 275 quadrupole magnets. Along the linac, the phase advance of the FODO cells vary ($90° \rightarrow 40°$) as does the quadrupole spacing ($3\,m \rightarrow 12\,m$). The beam is accelerated in disk-loaded waveguide structures which have an average iris radius of 1.1 cm and a cell length of 3.5 cm. The longitudinal (W_L) and transverse (W_T) wakefields generated in these structures have been computed for the m=0 and m=1 modes, respectively [1].

For an ensemble of particles, the wakefield interactions couple the particle motions. The effect can be described by treating the beam as series of longitudinal slices denoted by their longitudinal positions (s) relative to the bunch center. The energy loss and transverse angular kick per unit length (z) of each slice due to the wakefields are

$$\frac{dE}{dz}(s) = e\,I \int_s^\infty \rho(s')\, W_L(s'-s)\, ds' \qquad (1)$$

and

$$\frac{d\theta}{dz}(s) = e^2 \frac{I}{E(s)} \int_s^\infty \rho(s')\, W_T(s'-s)\, x(s')\, ds' \qquad (2)$$

where E(s) is the slice energy, I is the beam current, x is the transverse slice position relative to the waveguide axis, and $\rho(s)$ is the longitudinal charge density (unit normalization). The average energy loss and kick angle are computed by integrating these expressions over the bunch length profile.

Equation 1 shows that the beam loading is independent of the trajectories of the beam slices. Thus, a measurement of just the beam energy as a function of beam current is needed to gauge the longitudinal wakefield strength. The situation is more complicated for the angular kicks because the kick angle of one slice depends on the positions of all slices upstream of it. For the beam currents considered here, however, this is a weak effect in that the differential motion of the slices caused by the wakefield kicks over a distance of an oscillation wavelength is small compared to the oscillation amplitude. As described below, this condition can be exploited to infer the strength of the transverse wakefields from their perturbation on betatron motion.

II. BEAM PROPERTIES

To do either of these analyses requires a knowledge of the longitudinal bunch profile. In the production of the linac bunches, this shape is determined by the profile of the bunch extracted from the damping ring, and by the compression that occurs in the ring-to-linac transport line [2]. For the data taken for this study, the bunches are expected to be nearly Gaussian in shape and have an rms length (σ_s) which depends on current as

$$\sigma_s = .61 + .12 \cdot I + .0076 \cdot I^2 \qquad (3)$$

where σ_s is in units of mm and I is in units of 10^{10} electrons.

Another beam property that affects betatron motion is the energy spread of the beam. The component of energy correlated with s results from the beam loading and the sinusoidial shape of the RF accelerating waveform. The latter contribution can be computed by summing the energy gains ΔE_i from each klystron i. These have the form

$$\Delta E_i = \Delta E_{o_i} \cdot \cos(\phi_{BNS_i} + \phi_o + 2\pi s/\lambda_{RF}) \qquad (4)$$

where ΔE_{o_i} is the 'no-load' energy gain of the klystron, λ_{RF} is the RF wavelength (105 mm), ϕ_o is a phase adjustment common to all klystrons, and ϕ_{BNS_i} is a phase used to generate an energy spread to help cancel the variation in the transverse wakefield kicks along the bunch [3]. The BNS phases are constrained by the maximum energy gain possible in the linac, and by the requirement of a small energy spread at the end of the linac. As a tradeoff, a value of -20° (15°) is used in the first third (last two thirds) of the linac. Operationally, a global phase adjustment (ϕ_o) is made to minimize the energy width when the beam current is changed. For $I = 3.0 \cdot 10^{10}$, the energy width reaches a maximum of 2.5% at the end of the first third of the linac, and then gradually decreases to about 0.3% by the end of the linac. The energy spread within any slice of the beam is roughly 1%/E where E is the beam energy in GeV. This component can be ignored for this analysis without significantly changing the results.

III. SINGLE BEAM LOADING

To measure the strength of the longitudinal wakefields, the beam energy at the end of the linac was recorded for seven beam currents in the range of $0.5 \cdot 10^{10}$ to $3.5 \cdot 10^{10}$ electrons per bunch. No other tuning of the linac was done during data taking. Because only relative energy changes are well measured, a systematic adjustment was made to the values to compute the energy loss relative to the zero current energy. This adjustment was determined by finding the best overall

* Work supported by Department of Energy contract DE-AC03-76SF00515.

0-7803-0135-8/91$01.00 ©IEEE

match of the measured energy losses to the values from a simulation of these measurements. The results, expressed as fractional energy losses ($\Delta E/E$) at the end of the linac, are shown in Figure 1 for both the data and simulation.

The good agreement between the measured and simulated energy losses indicates that the longitudinal wakefields are well modeled. In the simulation, the bunch length profile was assumed to be Gaussian with a sigma given by Equation 3. The shaded area in the plot shows the range of predictions if the bunch length is changed within +/- 20% of the nominal values. The small nonlinearity in the energy loss arises mainly from the assumed bunch length dependence on current. A few percent nonlinearity also results from the phase shift caused by the beam loading in the acceleration section used for bunch compression in the ring-to-linac return line [4].

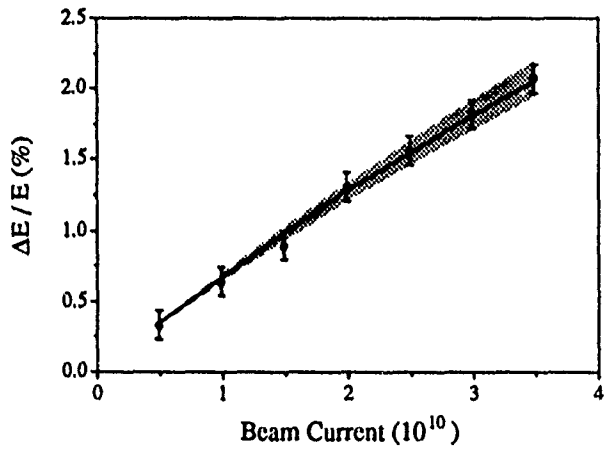


Figure 1. Measured (circles) and simulated (solid line) fractional energy loss as a function of beam current. The shaded region is described in the text.

IV. BETATRON OSCILLATIONS

The measurement of the transverse wakefield strength uses the approximation that the variation of the slice positions within a bunch undergoing betatron motion can be ignored relative to the mean oscillation amplitude. This approximation, which is independent of the amplitude of the oscillation, is valid in only certain regimes which must be determined through a simulation of the beam transport. In this regime, the equations of motion can be simplified by removing the x(s') term from the integral in Equation 2. The average kick angle in this approximation, denoted here by a subscript A, is

$$\left\langle \frac{d\theta}{dz} \right\rangle_A \equiv \alpha \frac{I}{E} \langle x \rangle \qquad (5)$$

where

$$\alpha = e^2 \int_{-\infty}^{\infty} \int_{s}^{\infty} \rho(s)\, \rho(s')\, W_T(s'-s)\, ds\, ds' \qquad (6)$$

and E is the mean beam energy. This relation has a quadrupole-like form in that the kick angle depends linearly on beam position. However, the kick is always away from the waveguide axis which leads to a lengthening of the betatron oscillation wavelength. This effect makes it appear that the beam energy is larger, which is opposite to that of beam loading.

To check the validity of this approximation, and to model any linac measurements involving betatron oscillations, a simulation program was written which treats the beam as a series of slices and transports them through the linac elements in a step wise manner. The beam profile, which was assumed Gaussian, was represented by 41 slices covering +/- 3 times the rms bunch length as given by Equation 3. The effect of wakefields was included by integrating Equations 1 and 2 for each slice over the lengths of the acceleration sections.

With this program, betatron oscillations beginning at the upstream end of the linac were simulated to check the approximation used to derive Equation 5. Specifically, the ratio

$$R \equiv \left\langle \frac{d\theta}{dz} \right\rangle \Big/ \left\langle \frac{d\theta}{dz} \right\rangle_A \qquad (7)$$

was computed at each beam position monitor (BPM) location using Equations 2 and 5 with the substitution

$$x(s) \rightarrow \bar{x}(s) \cos(\phi(s)-\phi_M) + \bar{x}'(s) \sin(\phi(s)-\phi_M) \qquad (8)$$

to make R insensitive to the phase of the oscillation. Here $\bar{x}(s)$ and $\bar{x}'(s)$ are the normalized position and slope coordinates of the slice, and $\phi(s)-\phi_M$ is the phase of the slice relative to the mean phase of the beam. If the motion of the slices remains coherent, R is unity, while for complete decoherence, $R \rightarrow \infty$. From the simulations, it was found that R remains within +/- 25% of unity in the first third of the linac for the beam currents being considered. Given this somewhat arbitrary measure of the goodness of the kick angle approximation, it was decided to limit the data analysis to only this region of the linac. Within this region, R is larger on average at low currents than at high currents although the mechanism for this is not clear.

The effect of the average kick angle described by Equation 5 can be incorporated into a first order transport matrix (in x and x') representation of the linac by including a matrix for the acceleration sections which is an integration of the kick angles over the lengths (L) of the sections. For the case of no acceleration, the 2×2 drift transport matrix is modified as

$$\begin{bmatrix} 1 & L \\ 0 & 1 \end{bmatrix} \rightarrow \begin{bmatrix} 1 & L \\ 0 & 1 \end{bmatrix} + \alpha \frac{IL^2}{2E} \begin{bmatrix} 1 & L/3 \\ 2/L & 1 \end{bmatrix} \qquad (9)$$

to first order in α (note that this correction does not apply to the propagation of beam ellipses). With this substitution, the 1,2 elements of the transport matrices computed from a corrector magnet to all downstream BPM positions should approximately match the shape of a betatron oscillation induced using that corrector. Conversely, a fit to betatron oscillation data can be made to extract the beam current dependence as specified in Equation 9. This has the advantage of allowing the effect of approximations to be absorbed into the fit current.

For this purpose, oscillation data were taken at the seven current settings used when measuring the beam loading. One corrector was used to generate an oscillation in the horizontal plane near the beginning of the linac and the resulting BPM difference orbit was recorded together with the magnets settings and the computed energy profile along the linac. The largest error in reconstructing the lattice from this information comes from the uncertainty in the energy scale. This factor,

however, can be estimated by fitting the data to a single particle trajectory with the energy scale included as a variable [5]. For this analysis, the scale factor was adjusted so the fit to the $0.5 \cdot 10^{10}$ data yielded the same result as the fit to a simulation of these data. The lowest current data were chosen because they are least affected by wakefields. A correction of about 2% was found and was applied to all seven data sets. A correction for beam loading for each current was then made using the results in Figure 1. Finally, each BPM difference orbit was fit assuming a single particle trajectory, but including the correction in Equation 9. The initial position and slope of the trajectory were allowed to vary in the fit, as was the beam current (I_{fit}) entering the correction.

The same procedure was applied to simulated BPM oscillation data for the seven beam currents. No errors were included in the BPM readings, which in the data can be ignored relative to the amplitude of the oscillations. As an example of the results, Figure 2 shows the measured and simulated BPM values, and the resulting fits for $I=3.0 \cdot 10^{10}$. In each plot there is some systematic disagreement between the fit and the BPM readings. However, an exact fit is not expected even without wakefields because a single particle trajectory does not account for incoherence effects. For the simulation, the rms of the fit residuals are 10% to 20% of the rms of the BPM values. In the data, they are 20% to 30% for all but the lowest two current settings where they are 37% and 34%, respectively. This may be due to the fact that the lower current data is more sensitive to errors in the energy profile along the linac.

The results from the current fits are shown in Figure 3 for both the data and simulation. Note that the good agreement

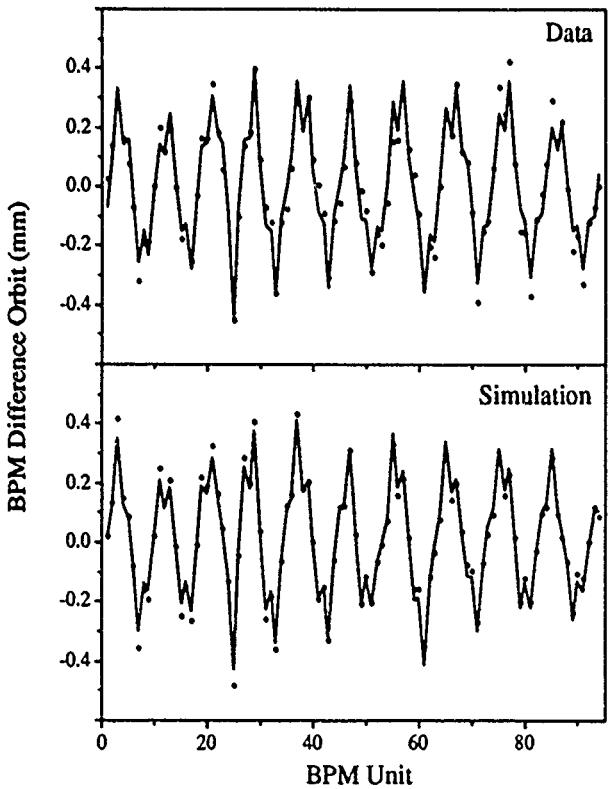


Figure 2. Measured and simulated BPM oscillations (circles) and the resulting fits (solid lines) for $I = 3.0 \cdot 10^{10}$.

for $I=0.5 \cdot 10^{10}$ is the result of the energy scale factor correction to the data. The error bars on the data correspond to a 0.2% uncertainty in the energy scale, which is a rough estimate of the error given the method in which the scale was determined. However, other types of energy profile errors are not included. The shaded region represents the range of predictions for a +/- 3° change in the global phase (ϕ_0) or a +/- 20% variation in the bunch length. The phase change was made so it affected only the energy spread and not the mean energy gain.

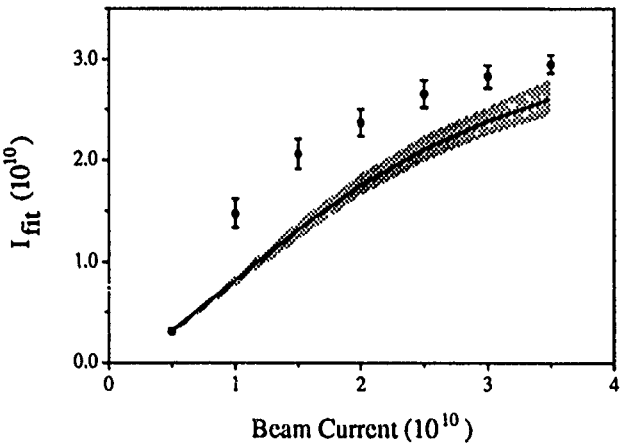


Figure 3. The fit value for the beam current from measured (circles) and simulated (solid line) BPM difference orbits as a function of the actual beam current. The shaded region is described in the text.

Given these systematic errors, the values of I_{fit} for the data are still larger than expected. Scaling the strength of the transverse wakefield function improves the agreement, although a 60% increase is necessary due in part to the decrease in the results from the simulation that also occurs with stronger wakefields. Other possible causes of the difference are errors in the energy profile along the linac, a non-Gaussian bunch length profile, or a value of R for the beam at the beginning of the oscillation which is not unity as assumed in the simulation. Repeating the measurements with a more careful setup of the linac may help eliminate some of these possibilities. In any case it is interesting to note the leveling-off of the I_{fit} values at large currents. This is most likely due to the fact that R decreases at larger currents as was noted previously. Equation 5 thus overestimates the average wakefield kick angle as the current increases.

V. REFERENCES

[1] K. Bane and P.B. Wilson, *Proc. of the 11th Int. Conf. on High Energy Accelerators*, CERN (1980), 592.

[2] K. Bane, "Simulating Longitudinal Phase Space in the SLC, from the Damping Rings to the Final Focus," SLAC/AP-80 (September 1990).

[3] V. Balakin, A. Novokhatsky and V. Smirnov, *Proc. of the 12th Int. Conf. on High Energy Accelerators*, Fermilab (1983), 119.

[4] This effect was pointed out to us by F.J. Decker.

[5] T. Himel and K. Thompson, "Energy Measurements from Betatron Oscillations," SLAC-PUB-4917 (March 1989).

Review of tolerances at the Final Focus Test Beam.*

F. Bulos, D. Burke, R. Helm, J. Irwin, G. Roy, N. Yamamoto
Stanford Linear Accelerator Center
Stanford, California 94309, USA

Abstract

We review the tolerances associated with the Final Focus Test Beam (FFTB). We have computed the acceptability window of the input beam for orbit jitter, emittance beta functions mismatch, incoming dispersion and coupling; tolerances on magnet alignment, strength and multipole content; and the initial tuneability capture of the line.

I. The Acceptability Window.

A. Bandwith and Energy.

The bandwidth is defined as the energy spread range over which the spot size at the focal point (FP) does not increase by more than 2%; it is of the order of $\pm 0.4\%$. It is expected that the beam actually delivered will have a an energy spread of the order of $\pm 0.2\%$. The tolerance on beam energy stability is then of the order of $\pm 0.2\%$ for a beam energy of $50GeV$.

B. Emittance and Beta functions.

The final horizontal spot size at the FFTB scales *linearly* with the emittance since we have to maintain the design 10σ clearance along the line and change the beta-functions accordingly. In the vertical plane, the scaling goes with the square root of the emittance up to a factor of two increase in emittance. The range of beta matching covers at least two orders of magnitude around the nominal beta functions in both horizontal and vertical planes.

C. Dispersion.

Incoming dispersion from the linac is estimated at the level of .2 to $.5\sigma$ and is linearly transformed to the focal point. The FFTB has the ability to correct as much as 7σ of dispersion at the focal point.

D. Coupling.

There are only two important coupling terms for the FFTB and it is expected that the magnitude of the incoming coupling is about 10%. We can correct at least a magnitude of 20% for both terms.

E. Position Jitter.

The position jitter at the end of the linac is estimated at the level of $.2\sigma$ and the acceptability tolerances are of the order of $.3\sigma_x$ and $.3\sigma_y$ ($150\mu m$ and $55\mu m$) for the position and $1\sigma_{x'}$ and $.3\sigma_{y'}$ ($5\mu rad$ and $.5\mu rad$) for the angles at the input. However the beam jitter should not exceed $.2\sigma$ at wire scanners in order to keep the measurement error below a 2% level.

II. Stability Tolerances.

A. Tolerance Budget.

The experience with measuring small spots at the interaction point of the SLC is that it is possible to measure a relative change of 10% in the size of the beam which translates into an ability to correct aberrations to the order of 2%. We have therefore chosen this 2% figure as the maximum allowed increase of the spot size per aberration. The total beam size growth above design is then expected to be 8% in the horizontal plane (4 contributing terms) and 14% in the vertical plane (7 contributing terms). We will also quote tolerances according to this 2% criterion for *individual elements*. We refer to the RMS tolerance as the combination in quadrature of individual tolerances to establish the design tolerance related to a given aberration.

B. Steering.

We permit beam centroid motion at the focal point to be one standard deviation ($\Delta y^* \approx \sigma_y^*$). The final quadrupole doublet (QC2 and QX1-QC1, all treated as one element) position tolerance is then $\Delta y_{fq} \approx \sigma_y^*$. Since most quadrupoles are $\pi/2+n\pi$ from the focal point, tolerances scale according to their strengths and β-functions:

$$\Delta y_q \leq \frac{1}{k_q}\sqrt{\frac{\epsilon_y}{\beta_{y_q}}}.$$

The final quadrupole position stability tolerance is therefore of the order of the final vertical spot size, 60 nm. For the other quadrupoles the β-functions and strengths put these tolerances in the range 0.4 to a few microns in the vertical plane and 1.6 to 10. μm in the horizontal plane. The RMS vertical displacement tolerance is $.2\mu m$.

C. Dispersion.

Dispersion is primarily generated at the focal point by a trajectory offset in the final quadrupole triplet. The 2% growth in spot size condition is written

$$\frac{\Delta y_{fq}}{\sigma_y^{fq}} \leq \frac{1}{5\ \delta_{rms}\ \xi_y}.$$

where ξ is the chromaticity of the doublet. This translates into a vertical position tolerance of $5\mu m$. The offset

* Work supported by the Department of Energy, contract DE-AC03-76SF00515.

0-7803-0135-8/91$01.00 ©IEEE

at the final quadrupole can be created by a direct movement of the final quadrupole or by a displacement of another quadrupole upstream steering the beam off-axis in the final lens. To study this second effect we introduce the notion of lattice multipliers defined as the amplification factor between the offset of a given quadrupole and the centroid offset in the final quadrupole.

$$\Delta y_{fq} = (k_q R^{34}_{q \to fq})\ \Delta y_q$$

Lattice multipliers depend only on the lattice structure, not on the focal point parameters or the beam properties. The greater this multiplier the tighter the dispersion tolerances on the element. Critical magnets are located at the beginning of the FT with vertical alignment tolerances between 10. and $1.5\mu m$. The quadrupole at the midpoint of the CCY has a tolerance of $2\mu m$ as it benefits from the presence of the second sextupole which compensates close to one half of the dispersion created by the final quadrupole.

D. Normal Quadrupole.

A change in the final quadrupole strength moves the waist away from the focal point, increasing the spot size at the focal point. For a 2% increase in either the horizontal or vertical spot size, the strength tolerance is

$$\frac{\Delta k}{k} \leq \frac{1}{5\ k\ \mathrm{Max}(\beta_x, \beta_y)}$$

For the final quadrupole doublet, where both strengths and beta functions are large, the tolerances are very tight: $\frac{\Delta k}{k} \leq 2.3 \times 10^{-5}$ and 2.0×10^{-4} for QC1 and QC2 respectively. For other quadrupoles the tightest tolerances occur around the sextupoles (large beta functions also): $\frac{\Delta k}{k} \leq 1.7 \times 10^{-4}$ around SD1. Taking into account all the quadrupoles in the line except the final doublet, the RMS tolerance is $\frac{\Delta k}{k} \leq 7.3 \times 10^{-5}$.

E. Skew Quadrupole.

Coupling in the optics leads to a growth of the spot size at the focal point. Because of the step function pattern of the phase advance in final focus systems, there is only one important aberration caused by quadrupole rotation and the term representing the actual rotation of the beam in the physical x-y space does not appear at a significant level. The tolerances for quadrupole rotation for the 2% increase in final spot size constraint is given by:

$$\theta \leq \frac{1}{10\ k\ \sqrt{\beta_x \beta_y}} \sqrt{\frac{\epsilon_y}{\epsilon_x}}.$$

They are of the order of 7 μrad for the final quadrupoles and 33 μrad for the rotation of all three magnets as a whole. It is a property of doublets that each quadrupole has the same rotation tolerances. The RMS value for other quadrupoles is 40 μrad.

F. Sextupole Alignment.

Waist motion and coupling also appear when the beam is horizontally or vertically offset in a sextupole, which may come from an actual displacement of the magnet or from one of the chromatic correction section (CCS) quadrupoles steering the beam off axis in the second sextupole. The same notion of multipliers applies here taking the second sextupole as the reference: $\Delta x_s = k_q\ R^{12}_{q \to s}\ \Delta x_q$. If the beam is off-axis in the first sextupole the effect is cancelled by the equal and opposite displacement in the second sextupole ($-I$ transformation). The tolerances for sextupole horizontal and vertical offsets are

$$\Delta x_s \leq \frac{1}{5\ k_s\ \mathrm{Max}(\beta_{x_s}, \beta_{y_s})},$$

$$\Delta y_s \leq \frac{1}{5\ k_s\ \sqrt{\beta_{x_s} \beta_{y_s}}} \sqrt{\frac{\epsilon_y}{\epsilon_x}}.$$

resulting in $3.5\mu m$ for the CCX sextupoles, and only $0.9\mu m$ for the CCY. The vertical tolerances are $3.5\mu m$ and $1.4\mu m$ for the CCX and CCY respectively. The multipliers for the quadrupoles inside the CCY and CCX to the second sextupoles give quadrupole horizontal alignment tolerances of $.7\mu m$ and $1\mu m$ in CCX and CCY respectively and the central quadrupole in CCX has a vertical position tolerance of $4\mu m$ while the one in CCY has to be stabilized to $0.3\mu m$.

G. Dipoles.

Dipoles located inside the CCS can steer the beam off-axis in the second sextupole: horizontally through power supply jitter and vertically through dipole rotation, giving rise to norma and skew quadrupole effects respectively. The tolerances for the stability of the power supplies and the rotation of the magnets are given by

$$\frac{\Delta B}{B} \leq \frac{1}{5\ k_s\ \overline{R_{12}}\ \theta\ \mathrm{Max}(\beta_{x_s}, \beta_{y_s})},$$

$$\Delta\phi \leq \frac{1}{5\ k_s\ \overline{R_{34}}\ \theta} \sqrt{\frac{\epsilon_y}{\epsilon_x}} \frac{1}{\sqrt{\beta_x \beta_y}}$$

The $\overline{R_{ij}}$ is the average value of the R_{ij} matrix element between the entrance and the exit of the bend. For powers supply jitter tolerances, several bending magnets connected in series are treated as one large bend. The results are $\frac{\Delta B}{B} \leq 3.3\ 10^{-5}$ for the CCX and $1.0\ 10^{-5}$ for the CCY. Rotation tolerances are of the order of 37 μrad for CCX and 14 μrad for CCY.

H. Sextupole and Skew Sextupole.

The tolerances on the normal and skew sextupole content of the quadrupoles are expressed in terms of equivalent sextupole strength and under the condition of a 2% beam size increase:

$$k_{ns} \leq \mathrm{Min}\left[\frac{\sqrt{2}}{5\sigma_x \beta_x \sqrt{1 + \frac{\sigma_y^4}{\sigma_x^4}}}\ ;\ \frac{1}{5\sigma_x \beta_y} \right]$$

and the expression for k_{ss} is obtained by exchanging σ_x for σ_y in the expression above. For FFTB the normal and skew sextupole tolerances are $k_{ns,ss} \leq .08\ m^{-2}$ for QC1 and $k_{ns,ss} \leq .004\ m^{-2}$ for QC2. The RMS values for the other quadrupoles are $k_{ns} \leq .009\ m^{-2}$ and $k_{ss} \leq .006\ m^{-2}$.

FFTB TOLERANCES

Time Scale	Final	Other Quads		Sextu-
Generator	Quads	Worst	RMS	-poles
τ_0	Δx or Δy $[\mu m]$			n/a
x'	1.	1.6	0.75	
y'	.06	.46	.18	
τ_1	Δx or Δy $[\mu m]$			n/a
$x'\delta$	50.	1.6	0.8	
$y'\delta$	4.7	1.2	.7	
τ_2	$\Delta k/k$ $[10^{-5}]$ or $\Delta\theta$ $[\mu rad]$			Δx, Δy
x'^2, y'^2	2.	17.	7.3	0.9 μm
$x'y'$	33.	110.	40.	1.4 μm
τ_3	k_s $[10^{-3}m^{-2}]$			$\Delta k/k$, $\Delta\theta$
$x'^3, x'y'^2,$	5.	12.	9.	$5.2\ 10^{-3}$
$y'^3, x'^2y',$	4.	6.	6.	0.7 *mrad*

III. The Capture and Tuning of the FFTB

We will now outline the different steps necessary to carry out the initial capture and the tuning of the FFTB in order to reach the design spot size. [1]

A. Mechanical Alignment

Early results of alignment tolerances and tuning simulations showed that it is possible to correct misalignments in the line within the alignment tolerances of 100μ horizontally and 30μ vertically. [2] The tuning involved orbit bumps to cancel the dispersion at the IP and sextupole alignment to cancel the normal and skew quadrupole effects. These figures have therefore been chosen as the goals for the initial mechanical alignment of the line.

B. Input Beam Matching

Using a different configuration of the Beta Matching section, one can analyze the incoming beam (beta functions, emittance) and match it at the entrance of the CCX. This tuning can be verified and refined at a later stage (including dispersion and coupling) using other beta minimum points in the Beta eXchanger and Final Transformer sections (BXx,BXy,FTy).

C. Beam-Based Alignment

One can determine the offset of a given quadrupole with respect to the beam by varying its strength and observing the trajectory downstream. Each quadrupole being mounted on a magnet mover it is possible to move the elements along a straight line defined by the beam. The straight section can then be hinged into alignement with other sections. With a BPM precision of $1\mu m$ all the quadrupoles can be aligned nearly to tolerances.

D. Quadrupole Tuning

Quadrupole strengths can be probed by orbit bumps launched across different sections (CCX, BX, CCY, and FT) by dipole correctors. As the sections all have π phase advance and there are always less than four effective quadrupoles per section, the sensitivity of this process is enhanced and the system is fully determined. The sensitivity in the setting of the quadrupole strengths using this method is better than the required tolerance.

E. Stability Monitoring

Dispersion appears when the beam is off-axis in an element which is a source of chromaticity. By monitoring and maintaining a constant beam position at a few locations (final doublet, sextupoles) the dispersion can be stabilized for as long as one can rely on the stability of the BPM readings. Normal and skew quadrupole aberrations arise with beam position changes at the sextupoles. After aligning the sextupoles the sum of their BPM readings can be monitored and should remain constant.

F. Global Correction

Maintaining a small spot size at the focal point will require the use of global correction techniques. A global corrector is a knob used to cancel one aberration at the focal point. One can itemize the global correctors for the FFTB according to four time scales: The first one (τ_0) corrects for position jitter in the quadrupoles displacing the final spot and is determined by the feedback system correction frequency. The second controls the dispersion originating from change of quadrupole positions and is determined by the time one can maintain the stability of the line and depends on the BPM stability at micron readings. The third set of global correctors cancels normal and skew quadrupole effects. With orbit bumps to confirm CCS alignment it may be possible to extend this time scale (τ_2) beyond the BPM stability time (τ_1). The fourth time scale (τ_3) covers remaining higher order aberrations (*e.g.* sextupole setting) and is determined by the stability of magnet power supplies. A few multi-knobs (8) finally depend on the linac running conditions and are used for the matching of the incoming beam.

IV. References

[1] F. Bulos *et al.* Beam-Based Alignment and Tuning Procedures for e^+e^- Collider Final Focus Systems, YPH5 these proceedings

[2] K. Oide, SLAC-PUB 4953

Beam-Based Alignment and Tuning Procedures for e^+e^- Collider Final Focus Systems*

F. BULOS, D. BURKE, R. HELM, J. IRWIN, A. ODIAN, G. ROY, R. RUTH, N. YAMAMOTO
Stanford Linear Accelerator Center Stanford University, Stanford, California 94309

Abstract

For future linear colliders, with very small emittances and beam sizes and demanding tolerances on final focus system alignment and magnet errors, it becomes increasingly important to use the beam as a diagnostic tool. We report here procedures we have identified and will be implemented in the Final Focus Test Beam at SLAC incorporating i) quadrupole strength changes, ii) central orbit modifications, iii) spot size measurements, and iv) beam stability monitoring.

I. ANALYSIS OF BEAM CENTROID

A. Quadrupole Alignment

Each quadrupole will be mounted on a magnet mover with vertical and horizontal range of $\pm 3mm$ and setting accuracy of $\leq 1\mu$. Alignment will be monitored by a wire alignment system, in which sensors indexed to each quadrupole will detect position relative to a system of stretched wires. The absolute positioning of the wires is expected to be $\sim \pm 100\mu$ and the location of quadrupole magnetic centers relative to the wires is expected to be $\sim \pm 10\mu$. Relative motions in the $1\,\mu$ range should be detectable. [1] If a quadrupole of inverse focal length k_i is varied by an amount $\pm\Delta k_i$, the trajectory difference at a downstream position monitor is

$$\Delta x_j = 2R_{12}^{ji}\Delta k_i x_{ci} \qquad (1)$$

where x_{ci} is the offset of the quadrupole relative to the beam and R_{12}^{ji} is the x, x' matrix element from i to j, assumed known from the optics model. The value of x_{ci} may be found by a least-squares fit to measurements of Δx_j at several monitors.

Figure 1 shows the layout of the FFTB. Beamline segments may be rotated about hinge points (HP), located at the beginning of the system or at vertices of the bends; base quadrupoles (BQ) are quadrupoles near the hinge points which will be kept fixed relative to the wire alignment system; an alignment segment is the straight line defined by a hinge point and the next base quadrupole.

Figure 2 depicts the alignment procedure. The quadrupoles in a given segment are varied one at a time and each with the exception of the base quadrupole is moved onto the beam line according to Eq. (1). Then the segment is "hinged" into alignment with the base quadrupole by steering at the hinge point and moving each quadrupole except the base quadrupole in proportion to its distance from the hinge point. The procedure is then repeated for each successive segment.

If we assume that position measurement errors are random and uncorrelated, with an rms value of $\sigma_{\rm bpm}$, then the uncertainty σ_{ci} in the determination of x_{ci} is

$$\sigma_{ci} = S_i\sigma_{\rm bpm} = \left(2\Delta k_i\Big(\sum_{j>i} R_{12}^{ji\,2}\Big)^{1/2}\right)^{-1}\sigma_{\rm bpm} \qquad (2)$$

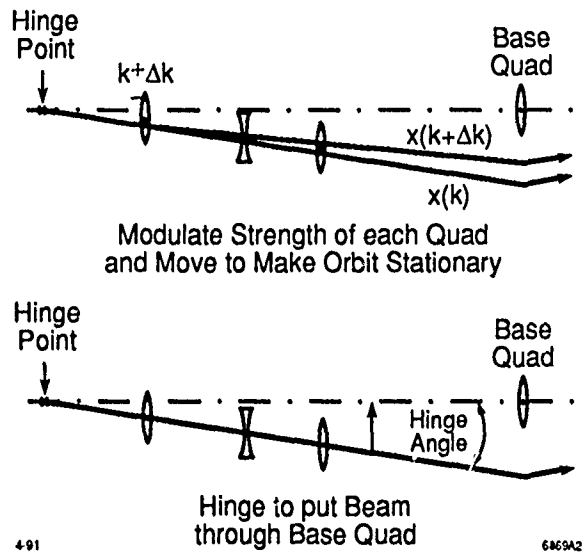


Figure 2. Quadrupole Alignment Procedure

Values of S_i for some of the most sensitive FFTB quadrupoles are compared to alignment tolerances in Table 1. The tolerance is the alignment error which would make either a 2% increase in spot size at the IP, or a 1σ maximum orbit perturbation anywhere in the lattice, whichever is smaller. We conclude that if the position monitor precision is $\sim 1\mu$ then all the quadrupoles can be aligned nearly to tolerance. The globalcorrection methods described below should then be able to compensate for residual errors.

B. Quadrupole Tuning

Quadrupole strengths can be probed by orbit bumps. The FFTB has six horizontal and six vertical dipoles for

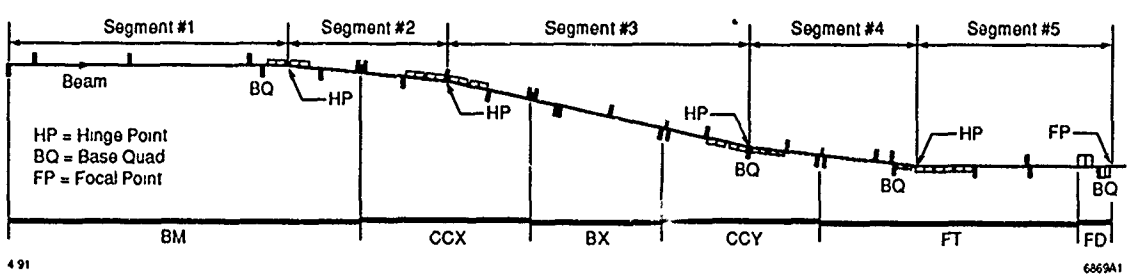


Figure 1. FFTB Alignment Segments

* Work supported by Department of Energy contract DE-AC03-76SF00515.

U.S. Government work not protected by U.S. Copyright.

Table 1. Beam-based Quadrupole Alignment Tolerances and sensitivites are given in microns.

Segment	Section	Element	Horizontal		Vertical	
			Toler.	Sensi.	Toler.	Sensi.
1	BM	Q5	110	.74	4.5	.04
		QA1	60	.42	20	.30
2	CCX	QN2	2.9	1.7	2.0	.36
		QN1	.71	.57	4.0	.63
3	BX	QT2	10	2.5	4.4	.53
		QT3	1.3	.55	30	1.9
	CCY	QM1	.65	.75	1.2	2.1
		QM2	1.1	1.3	.31	.81
4		QM1	.65	.73	1.1	2.6
	FT	QM1	1.3	.53	2.0	2.1
		QC5	4.4	.9	1.2	1.0
5	FD	QC2	15	1.5	4.8	6.8
		QC1	44	3.6	5.5	4.9

launching and terminating orbit bumps. The fact that each major subsection (CCX, BX, CCY, and FT of Fig. 1) has π phase advance enhances the sensitivity of this process. The transfer matrix between points separated by π is

$$\begin{pmatrix} -m, & 0 \\ r, & -\frac{1}{m} \end{pmatrix}$$

The linear combination of $x_1 + \frac{1}{m}x_2$ should be independent of both the initial position and slope of the beam at x_1. This condition can be checked alternately for x'-, x-, y'- and y-bumps, yielding four conditions on intermediate quadrupole strengths. Since all of these π sections have less than four contributing quadrupoles (end quadrupoles affect only the R_{21} element), the strengths of the intermediate quadrupoles can be checked. The amplitude of the bumps is chosen as large as possible subject to the constraint that the beam clear the beam-pipe by 8σ. We can check the setting error of the end quadrupoles by studying a π section between beta minimum points (see Fig. 3) for which the former end quadrupoles are now intermediate. One quadrupole located between the first dipole and the first CCX sextupole must be verified by launching a bump of known strength and requiring the appropriate displacement at the sextupole. All other quadrupoles with the exception of the final quadrupoles can be checked with the method we have described.

C. Sextupole Alignment

For a sextupole pair define $\Delta x_S = 0.5(\Delta x_1 + \Delta x_2)$ and $\Delta x_A = \Delta x_1 - \Delta x_2$. A non-zero Δx_A is equivalent to a quadrupole setting error at the sextupole position and can be detected with the same methods described above. Non-zero Δy_A creates a skew quadrupole error which can be detected if, for example, vertical motion appears in the presence of a horizontal bump.

Table 3 summarizes the sensitivity of the method in the FFTB lattice.

D. Stability Monitoring

During and following the setting of global correctors described in Sec. 4, it is important that the system remain

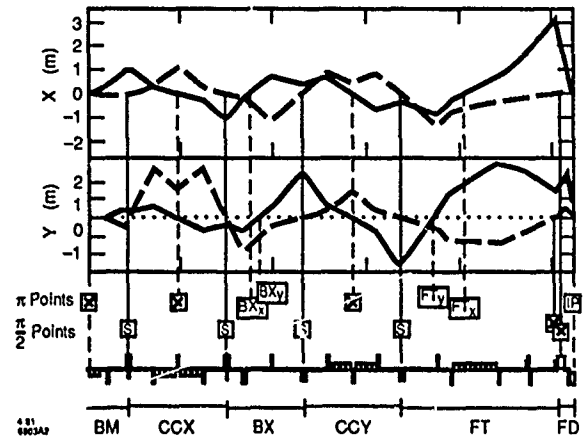


Figure 3. FFTB Orbit Bumps for Quadrupole Tuning

Table 2. Beam-based Quadrupole Tuning

Quad	Bump	$\frac{\Delta k}{k}$ Sensitivity	$\frac{\Delta k}{k}$ Tolerance
QN2	2 mm/X at SF1	6.2×10^{-4}	1.2×10^{-3}
QN1	100 μrad/X' at SF1	6.2×10^{-5}	2.1×10^{-2}
QT2	200 μrad/Y' at SF1	9.8×10^{-5}	1.5×10^{-3}
QT3	200 μrad/X' at SF1	5.6×10^{-5}	5.1×10^{-4}
QM1	0.7 mm/X at SD1	2.9×10^{-4}	6.7×10^{-4}
QM2	500 μrad/X' at SD1	2.7×10^{-4}	2.7×10^{-2}
QN3	2 mm/ X at SF1	2.5×10^{-4}	3.3×10^{-4}
QT1	2 mm/ X at SF1	1.4×10^{-4}	1.9×10^{-4}
QT4	3 mm/Y at SD1	1.7×10^{-4}	2.6×10^{-4}
QM3	3 mm/Y at SD1	5.8×10^{-5}	8.8×10^{-5}

Table 3. Beam-based Sextupole Alignment

				Vertical		
SEXT	Bump Spec	Sens.	Toler.	Bump Spec	Sens.	Toler.
SF1	2 mm/X	1.4 μ	3.5 μ	2 mm/X	2.9 μ	3.5 μ
SD1	3 mm/Y	0.9 μ	0.9 μ	3 mm/Y	0.8 μ	1.4 μ

stable. We discuss here methods to stabilize the most sensitive aberrations.

Dispersion arises whenever the beam is off axis in an element which is a source of chromaticity. By monitoring the beam at large chromatic sources, the final doublet and the sextupoles, and maintaining a constant beam position at these points, the dispersion can be stabilized for as long as one can rely on the stability of the BPM readings. For the duration of the stability time, the BPMs at the final doublet will be required to resolve a change of 2 μ for the FFTB, .2 μ for the next linear collider (NLC).

Normal and skew quadrupole aberrations arise when the beam position changes at the sextupoles. In this case it is the sum of the BPM readings at each sextupole pair which must be held constant. The sum reading of the two BPMs is quite insensitive to charge distribution because the sextupoles are at $-I$ with respect to one another and hence the beam distribution at the second sextupole is the mirror image of the distribution at the first. The precision of the BPMs must be 1 μ for the FFTB, .1 μ for NLC.[2]

II. ANALYSIS OF INTERMEDIATE SPOT SIZES

A. Matching Incoming Beam Optical Functions

Initially, the incoming β, α, and beam emittance are measured using a special configuration of quadrupole strengths in the beta match section (BM). The proper strengths for the match are then reckoned and set. This setting can be verified after the beam-based quadrupole alignment and tuning have been performed by observing the beam size at the beta minima in the BX section (π points of Fig. 3). By symmetrically varying the strength of the first and last quadrupole in the CCX section, so as not to change the dispersion function in BX, the beam size at BXx should vary according to

$$\frac{\sigma^2}{\sigma_0^2} = 1 + (\beta_Q \Delta k - \alpha_Q)^2$$

The beta match section can be adjusted until $\alpha_Q = 0$ and β_Q has the desired value.

B. Removing Incoming Dispersion

By measuring σ_0 above as either a dispersion knob or Δx_S or Δy_S defined in section 2.3 is varied, the system can be tuned so that the horizontal dispersion is zero at BXx and the vertical dispersion is zero at BXy. This is appropriate since these points are image points of the IP for their respective plane.

C. Removing Incoming Coupling

The beam delivered to a final focus system may contain coupling between the horizontal and vertical plane. Coupling at the end of the SLAC linac is thought to be about 10%. In general such a coupling may be specified with four parameters. We introduce parameters s_1 to s_4 defined by a transfer matirx or through coupling terms in the beamline Hamiltonian at the focal point,

$$V = s_1\sqrt{\beta_x^*\beta_y^*}x'y' + s_2\sqrt{\frac{\beta_x^*}{\beta_y^*}}x'y + s_3\sqrt{\frac{\beta_y^*}{\beta_x^*}}xy' + s_4\sqrt{\frac{1}{\beta_x^*\beta_y^*}}xy.$$

Note that the parameters s_i are all dimensionless. Only s_1, s_2, and s_3 affect the beam size at the IP. s_2 affects only the horizontal beam size. Since the emittance ratio, $\frac{\epsilon_y}{\epsilon_x}$, is 0.1 in the FFTB and 0.01 in the NLC, the effect of s_2 will be negligible. The term s_3 represents a rotation of the beam profile, the term s_1 represents vertical beam size blow up at the FP as shown in Fig. 4a.

At the point BXy or FTy where $\phi_x - \phi_x^* = \frac{\pi}{2} + n_x\pi$ and $\phi_y - \phi_y^* = n_y\pi$, s_1 and s_3 exchange roles as shown in the Fig. 4b. We can measure the coupling parameters s_1 and s_3 at BXy or FTy and use skew quadrupoles in the beta match section to cancel incoming coupling.

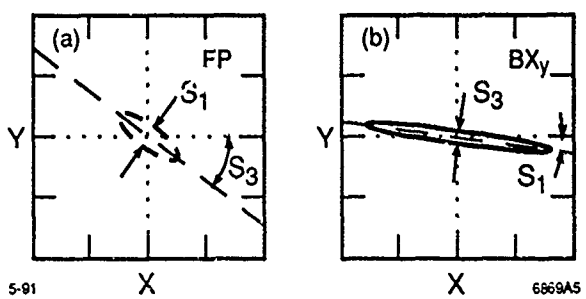


Figure 4. FFTB π Point Beam Profiles

III. ANALYSIS OF FINAL SPOT SIZE

After the foregoing techniques have been used, global correctors will be used to cancel residual aberrations at the interaction point using measurement of the position, size and orientation of the beam at the focal point. We itemize the low order aberrations still requiring correction according to four distinct time scales.

Position jitter in the quadrupole elements of the line will displace the final spot. Correction is carried out by a horizontal and vertical steering dipole placed at the final quadrupole. The time scale τ_0 is determined by feedback requirements and is estimated to be about 15 pulses.

Two steering correctors which control beam position in the final doublet are used to correct dispersion. The time τ_1 is determined by the stability time of BPMs used to maintain postion stability at the final doublet and the sextupoles.

Trim quadrupoles and a skew quadrupole at the final doublet are used to correct waist position (normal quadrupole error) in both planes and coupling (skew quadrupole error). Correction orbit bumps can be used to confirm alignment of the CCS, and with them it may be possible to extend the time scale τ_2 for normal and skew quadrupole effects beyond the BPM stability time τ_1.

The fourth time scale, τ_3, includes chromaticity correction, and two sextupoles and two skew sextupoles in the final transformer to correct sextupolar terms coming from quadrupole imperfections. These corrections are expected to be small and have a yet longer time scale ($\tau_3 \gg \tau_2$) determined by the stability of magnet power supplies.

There are a set of correctors which are used for the matching of the incoming beam from the linac into the final focus system. Four of them will perform the matching of the beta and alpha functions, two will control the dispersion function, and two will control the principal coupling terms. The time scale will depend on the stability of the linac.

IV. CONCLUSION

NLC designs exist which eliminate high order aberrations. The linear modules in these designs need to be optimized to improve tolerances associated with the appearance of low order aberrations. These tolerances are very small by present standards, and beam-based alignment and tuning techniques will be crucial in achieving them. We have described techniques which will be used for the Final Focus Text Beam now under construction at SLAC. [3] If BPMs and BSMs (beam size monitors) can be designed to operate to the required precision, we believe the procedures we have outlined can be used to successfully align and tune these systems.

REFERENCES

[1] R. Ruland and G. Fischer, The Proposed Alignment System for the Final Focus Test Beam at SLAC, SLAC-PUB-5236 (1990)

[2] G. Roy and J. Irwin, Tolerances of Two Next Generation e^+e^- Linear Collider Final Focus System Designs, Snowmass Proceedings (1990)

[3] D. Burke, The Final Focus Test Beam Project at SLAC, NGR5, These Proceedings

WAKEFIELD MEASUREMENTS OF SLAC LINAC STRUCTURES AT THE ARGONNE AATF

J. W. Wang and G. A. Loew
Stanford Linear Accelerator Center, Stanford University, Stanford, CA 94309*
and
J. Simpson, E. Chojnacki, W. Gai, R. Konecny, P. Schoessow
Argonne National Laboratory,† 9700 South Cass Avenue, Argonne, IL 60439

Abstract

Damped and detuned linac structures designed to minimize the effects of wakefields excited by $e^{\pm}$ bunch trains in future linear colliders are presently under investigation at SLAC. This paper describes the results of measurements of both longitudinal and transverse wakefields performed at the ANL Advanced Accelerator Test Facility with two SLAC-built X-Band disk-loaded waveguides: a conventional 30-cavity long constant-impedance structure and a non-conventional 50-cavity long structure along which the iris and spacer diameters have been varied so as to stagger-tune the HEM_{11} mode frequency by 37%. The results are shown to be in excellent agreement with computations made by KN7C [1], TRANSVRS [2], TBCI [3], and LINACBBU [4].

I. WAKEFIELD CALCULATION FOR FUTURE LINEAR COLLIDER STRUCTURES

Among many parameters, the design of accelerator structures for future linear colliders is constrained by undesirable effects produced by short- and long-range wakefields. These wakefields are of two types, longitudinal which produce energy spread, and transverse which produce cumulative emittance growth. The short-range fields affect particles within a single bunch while the long-range ones affect particles from bunch to bunch. In this paper, we concern ourselves with the long-range wakefields. Indeed, machines in the TeV energy range will require trains of at least 10 bunches, spread over hundreds of RF cycles per pulse, because single-bunch colliders cannot reach the desired luminosities of 10^{33}-10^{34} $cm^{-2}sec^{-1}$ unless the single-bunch populations exceed 10^{11} $e^{\pm}$. At these levels, the single-bunch effects become very difficult to control. While the short-range wakefields are only a function of the iris diameter and number of disks, the effect of long-range wakefields depends on their coherence and attenuation. At the present time, it is believed that their control will be achieved by a combination of built-in "decoherence," i.e., detuning of high-order modes (HOM), and damping by letting them escape into lossy outer regions where they can be attenuated without affecting the fundamental accelerating mode. The damping technique has been described in an earlier paper [5].

Within certain limitations, wakefields can be calculated by existing computer programs: in the time domain, via TBCI for cylindrically symmetric cavities, and MAFIA for three-dimensional cases; through field-matching techniques, via KN7C for monopoles, and TRANSVRS for higher even-poles. LINACBBU computes wakefields from an input set of mode frequencies, loss factors k, and Q's.

From these, it is possible to calculate the wake potential, i.e., the time-varying integrated effect of the wakefields of a driving bunch on a trailing test particle or another bunch. To gain confidence in these calculations, two practical SLAC-built structures were tested at the Argonne Advanced Accelerator Test Facility and the results compared with theoretical predictions.

II. THE EXPERIMENTS AT THE ARGONNE AATF

The characteristics of the two SLAC structures which were tested at the Argonne National Lab AATF are given in Table 1 and Table 2, respectively.

Table 1. Constant-Impedance Disk-Loaded Structure

Fundamental frequency (GHz)	11.424
Iris diameter 2a (cm)	0.750
Cavity diameter 2b (cm)	2.117
a/λ	0.143
Disk thickness t (cm)	0.146
Length (cm)	26.25
Phase shift per cavity	$2\pi/3$
Normalized group velocity (v_g/c)	0.033
Shunt impedance (MΩ/m)	98

Table 2. HEM_{11}-Detuned 50-cavity Disk-Loaded Structure

Iris diameter 2a range (cm)	1.22 - 0.83
Cavity diameter 2b range (cm)	2.72 - 2.01
Disk thickness (cm)	0.159
Cavity height (cm)	0.794
HOM_{11} frequency range (GHz)	11.4 - 16.7
Fractional detuning	37%

The first structure was a complete copper section which had been tested earlier in the Relativistic Klystron program at LLNL [6]. The second structure was a simple array of 50 aluminum cylinders and disks (made out of sheet metal) stacked inside a concentric S.S. vacuum pipe. The dimensions of the 50 cavities in the range given in Table 2 were chosen to fit a Gaussian HEM_{11} frequency population of the form
$p(f) \propto \exp[-(f-f_o)^2/2\sigma_f^2]$ where f_o is the center frequency (14.45 GHz) and $\sigma_f \approx 1.07$ GHz is the standard deviation. The goal of distributing the frequency population in such a manner

* Work supported by Department of Energy, contract DE-AC03-76SF00515
† Work supported by Department of Energy, contract W-31-109-ENG-38

0-7803-0135-8/91$01.00 ©IEEE

was to obtain an exponentially decaying envelope of the wake potential in the time domain. With a total number of cavities N (50), the frequency difference Δf from cavity to cavity was given by $\Delta f = (2\pi)^{1/2}\, \sigma_f/N \exp (f-f_o)^2/2\sigma_f^2$. A short program was used to calculate all the cavity dimensions centered around f_o within a $\pm 2.5\ \sigma_f$ range. Note that the resulting structure was not a true accelerator in that the fundamental mode was not fitted to be synchronous with the velocity of light. This was not important since the goal of the experiment in this case was to study the decoherence rate or decay of the HEM_{11} and other higher-order modes as a function of time.

The two experiments were carried out sequentially at Argonne within a period of several months. The AATF, which is shown schematically in Fig. 1, has been described at an earlier conference [7].

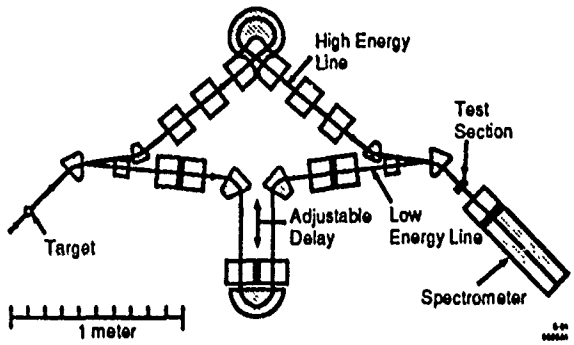


Figure 1. Plan view of the Advanced Accelerator Test Facility at Argonne. Beam line magnets are dipoles (shaded) or quadrupoles (open).

The sections to be tested are inserted, under vacuum, in the shown location, and the wake potentials are obtained by varying the time separation between the driving bunch and the witness bunch within a range of 0 and 1 nsec. A vertical-bend double-focusing spectrometer measures the energy variation of the witness bunch in the vertical plane and its horizontal position in the horizontal plane: the former yields the longitudinal wake potential, the latter gives the transverse potential as the structure is carefully swept in the horizontal plane by means of a remotely controlled carriage. The $\Delta p/p$ resolution is ~ 0.1%, the $\Delta p_\perp$ resolution is ~ 15 keV (~ 1 mrad). Fast electronic frame-grabbers digitize the beam spots in the focal plane, and a data processing program yields the analyzed data.

The experimental results for the longitudinal and transverse wake potentials of the constant-impedance structure are shown in Figs. 2 and 3 together with the computer predictions from KN7C and TRANSVRS, using 32 and 30 modes, respectively. We see that agreement is very good. For example, the measured transverse wake potential amplitude of 60 MV/nc/m^2 for a cavity with length of 0.875 cm and a full transverse offset of 0.375 cm, taking into account Gaussian bunches, gives an amplitude of 3.8V/pc/cell which is very close to the calculated value (4V/pc/cell). It is also interesting to note the excellent agreement of the experimental frequencies obtained from a Fast Fourier Transform with the calculated frequencies (see Fig. 4).

In the case of the second structure, we only show experimental data for the transverse wake potential since the structure was not designed to be an accelerator (see bottom of Fig. 5).

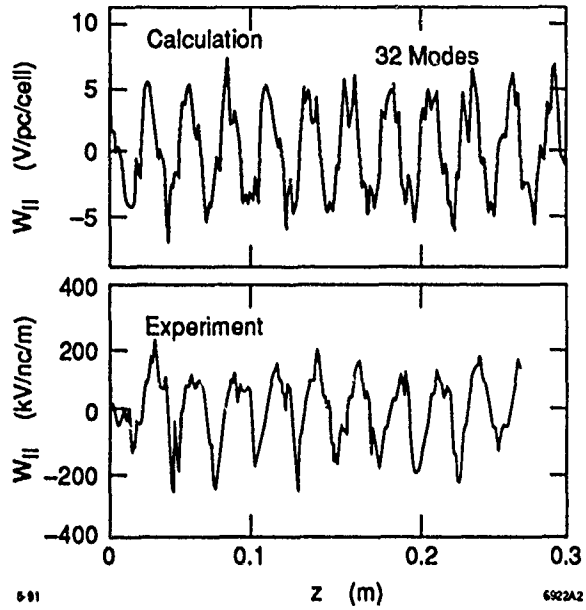


Figure 2. Longitudinal wake potential for the 30-cavity X-Band disk-loaded structure ($a/\lambda = 0.143$). TOP: Calculation by KN7C from a sum of 32 modes ($\sigma_z = 0$) for one cell. BOTTOM: Measurement result at AATF ($\sigma_z \approx 2.5$ mm) per unit length.

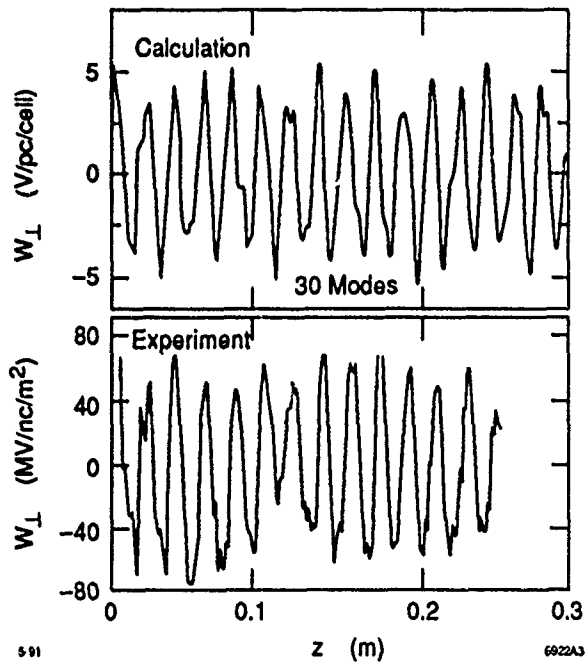


Figure 3. Transverse wake potential for the 30-cavity X-Band disk-loaded structure ($a/\lambda = 0.143$). TOP: Calculation by TRANSVRS from a sum of 30 modes ($\sigma_z = 0$, full offset = 0.375 mm) for one cell. BOTTOM: Measurement result at AATF ($\sigma_z \approx 2.5$ mm) per unit length.

The top of the figure shows the result of a theoretical calculation obtained by using LINACBBU as discussed in Ref. [8]. In this calculation, the wake function per unit length is simulated by summing the modes over the 50 frequencies present in the 50 cells. The amplitudes of all the modes are assumed to be equal. The actual propagation from cavity to cavity is neglected. Note also that in the real structure, the amplitude of the individual

wakefields increases towards the output end of the structure since the transverse fields vary as a^{-3}. Despite these shortcomings of the model, we see that the temporal agreement between theory and experiment is excellent.

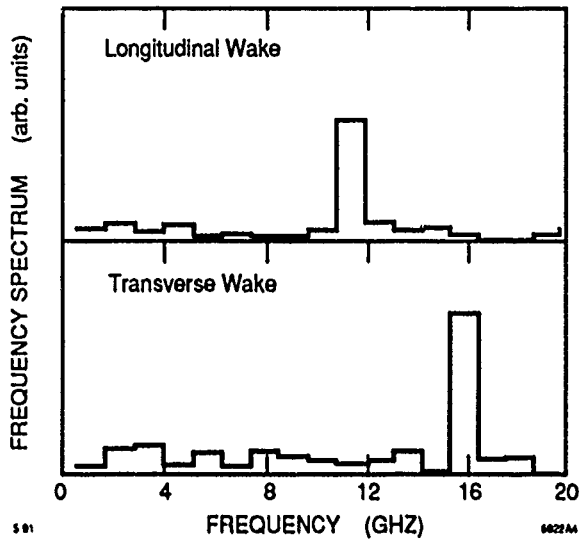


Figure 4. Frequency spectra of measured longitudinal (top) and transverse (bottom) wake potentials for the 30-cavity X-Band disk-loaded structure ($a/\lambda = 0.143$)

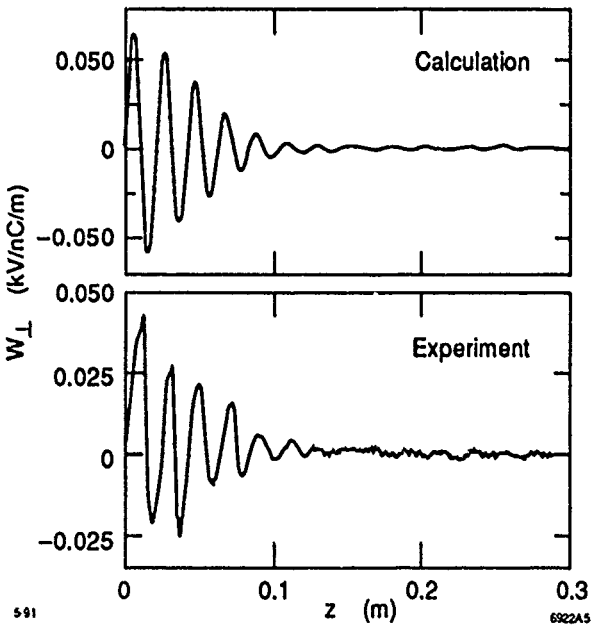


Figure 5. Transverse wake potential for the HEM_{11}-detuned 50-cavity disk-loaded structure. TOP: Calculation by LINACBBU ($\sigma_z = 0$). BOTTOM: Measurement result at AATF ($\sigma_z \approx 2.5$ mm).

III. CONCLUSIONS

The agreement between wakefield computer programs and experiments done on two SLAC structures at the Argonne AATF is very satisfying. It gives confidence in our ability to design structures and verify their behavior in a realistic physical environment. It opens the way to testing future structure designs which will incorporate both detuning and damping as well as fabrication errors, and which may therefore be too complicated to model with the required accuracy. In this regard, it would be very desirable if the AATF could be upgraded to allow an even larger time separation between the driving and the witness bunch, maybe as large as 3 nsec!

IV. ACKNOWLEDGEMENTS

The authors wish to thank R. H. Miller who participated in the first discussion leading to the SLAC/ANL collaborative effort described in this paper, and who later made useful comments.

V. REFERENCES

[1] E. Keil, Nucl. Inst. Methods, **100**, 419, (1972).

[2] K. Bane and B. Zotter, *Proc. of the 11th Int. Conf. on High Energy Accelerators*, Geneva, 59-596, (1980).

[3] T. Weiland, DESY 82-015 (1982) and Nucl. Inst. Methods, **212**, 13 (1983).

[4] K.A. Thompson and R.D. Ruth, Phys. Rev. D., **41**, 3, (Feb. 1990), SLAC-PUB-4801.

[5] H. Deruyter et al., Proc. 2nd European Particle Accelerator Conference 1990, SLAC-PUB-5263.

[6] M. Allen et al., Phys. Rev. Lett., (1989), SLAC-PUB-5039.

[7] J. Simpson et al., ANL-HEP-CP-86-46.

[8] K.A. Thompson and J.W. Wang, "Simulation of Accelerating Structures with Large Staggered Tuning," this conference.

MAINTAINING MICRON-SIZE BEAMS IN COLLISION AT THE INTERACTION POINT OF THE STANFORD LINEAR COLLIDER*

F. Rouse,[a,b], T. Gromme, W. Kozanecki, and N. Phinney
Stanford Linear Accelerator Center, Stanford University, Stanford, CA 94309 USA

Abstract

In order to maintain collisions between two micron-size beams at the interaction point of the SLC, we take advantage of the mutual electromagnetic deflection induced by one beam on the other as they cross with a nonzero relative impact parameter. We determine simultaneously the incoming and outgoing trajectory parameters of each beam on a pulse-by-pulse basis, using beam position monitors located near the IP. Comparing incoming and outgoing angles for a given beam yields the magnitude of the deflection the beam experienced during the collision from which the distance currently separating the two beams can be extracted. A simple proportional control is applied to calculate the change in upstream corrector settings to null out this distance.

INTRODUCTION

The SLAC Linear Collider (SLC) is a novel accelerator produces e^+e^- collisions at center-of-mass energies around the mass of the neutral intermediate vector boson Z^0. The collisions occur between electrons and positrons produced on every crossing, as opposed to being stored for an extended time as in electron-positron storage rings. However, since the accelerator produces fewer particles per bunch and the collision frequency is much less than at storage rings, the beams that collide in the SLC must have extremely small spot sizes in order to produce a usable number of interactions. Controlling and measuring the beam sizes and positions at the micron level is essential. We describe in this paper the performance of a feedback loop that stabilizes the transverse positions of the beams at the interaction point (IP).

BEAM-BEAM DEFLECTIONS

When electrons and positrons are brought into collisions, they mutually deflect each other due to the electromagnetic interaction between them [1,2]. We measure the deflection with Beam Position Monitors (BPMs) located upstream and downstream of the IP for both beams. The incoming and outgoing beam trajectories are fit for the electrons and positrons separately [3] with the constraint that for each beam, the incoming and outgoing orbit share a common transverse position at the IP.

Figure 1 shows an example of an observed beam-beam deflection in the x plane. The data was taken during a beam-beam scan. We scan the electron beam across the positron beam in two micron steps. Note that the positron deflection is opposite to that for electrons, as expected. The deflections are not equal, because the intensity of the electron beam is close to twice that of the positron beam.

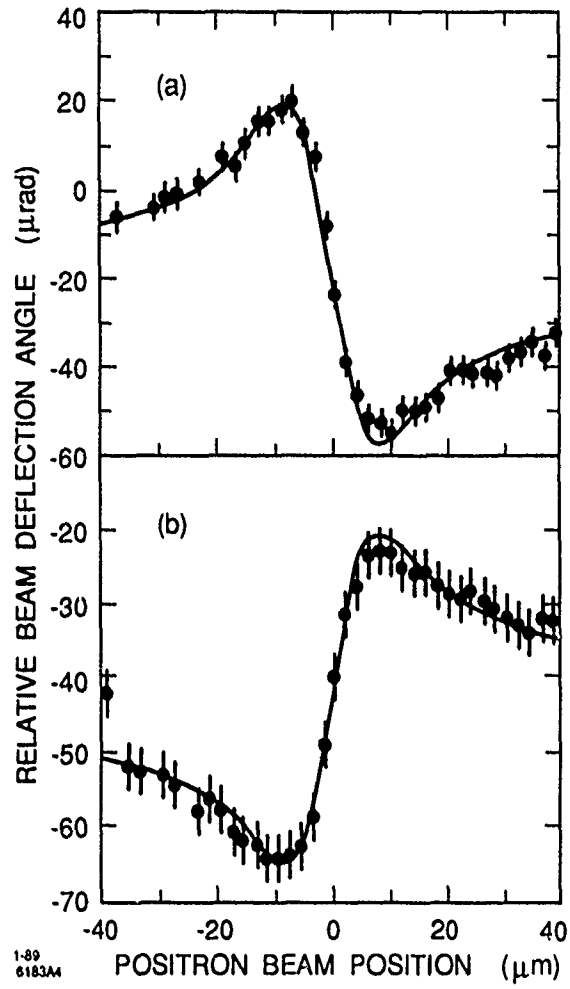


Figure 1. Deflection experienced by positrons (top) and electrons (bottom) plotted versus the transverse distance between the two beams. The curve is fit to the data in the round beam approximation. The background deflection is the value of the deflection angle at zero distance between the two beams, and is determined by a fit to the data.

PULSE-TO-PULSE MONITORING

We define the z direction as along the direction of motion of the electrons, x the horizontal axis , and y the vertical axis. Throughout this paper, we refer to the x plane; the same comments and equations apply equally to the y plane.

We parameterize the trajectory through the IP as a function of the x position at the IP, and of the incoming and deflection angles in the x plane. We then determine the least square fit to the trajectory [3]. This procedure is carried out online by an Intel 80386 microprocessor.

Figure 2 shows the deflection angles derived from the fitted electron trajectory. The expected resolution on the deflection angle, neglecting beam motion, is 2.5 μrad for a BPM position resolution of 10 μm. The resolution determined by fitting a Gaussian to the projection

* Work supported in part by Department of Energy contracts DE-AC03-76SF00515 (SLAC) and DE-AC03-76SF00098 (SLAC)

(a) University of California, Lawrence Berkeley Laboratory, Berkeley, CA 94720

(b) Present address. University of California at Davis.

0-7803-0135-8/91$01.00 ©IEEE

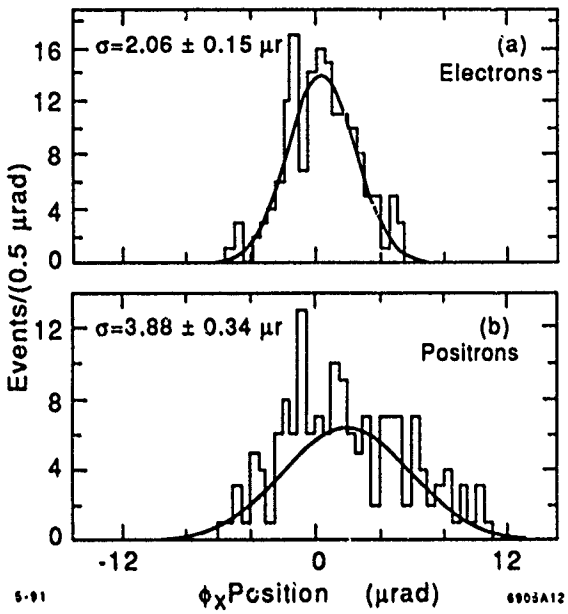


Figure 2. The distribution of deflection angles derived from then fitted electron (a) and positron (b) beam trajectories. The plot is a projection onto the y-axis of the deflection angle versus time plot.

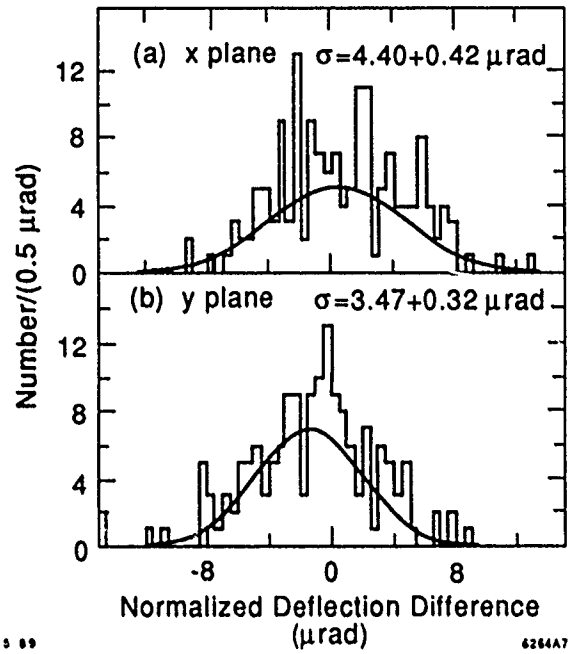


Figure 3. The difference between intensity-normalized deflections in (a) the x and (b) the y planes.

onto the y axis of reveals (a) a slightly better and (b) a slightly worse resolution. Neither result is inconsistent with expectations.

We have verified that the difference in deflections experienced by the electron and positron beams can be explained by the difference in intensity of the two beams. The deflection angle of one beam is directly proportional to the intensity of the other [1]. Therefore, we consider the intensity-normalized deflection angle difference between the electron and positron beam:

$$\text{Difference} = [(N_a\phi_{e^-})/N_{e^+}] - [(N_a\phi_{e^+})/N_{e^-}]$$

where N_{e^-} is the number of electrons, N_{e^+} is the number of positrons, and N_a is the average of the two. When we plot the distribution of differences and fit it to a Gaussian, we find the centroid of the distribution to be at zero, within errors, as shown in Fig. 3.

FEEDBACK

The deflection curve shown in Fig. 1 becomes approximately linear when the two beams are very close to one another. The slope at crossover in the horizontal plane, obtained as the first term in the Taylor expansion in the limit of small Σ_x is

$$S_x = [(-2r_eN_t)/\gamma] \times 1/[\Sigma_x(\Sigma_x + \Sigma_y)] .$$

This slope in a given plane (x or y respectively) depends strongly on the "in-plane" beam size Σ_x (Σ_y), and somewhat more weakly on the "out-of-plane" size Σ_y (Σ_x). The quantity N_t is the intensity of the target beam. We define the quantity

$$S'_x = S_x/N_t$$

as the intensity-normalized slope of the deflection curve

The beam-beam deflection is quite accurately described by a single slope parameter very close to the crossover point. This approximation breaks down as the distance between the two beams increases. However, our theoretical results have indicated that for impact parameters on the order of one beam size, the difference between the linear approximation and the actual deflection is only of the order of 10%.

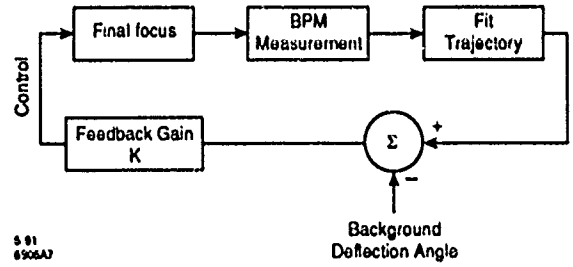


Figure 4. Conceptualization of the proportional feedback system used to maintain the beams in collisions.

We measure the intensity-normalized slope for the beam deflections periodically by performing a full-beam scan [2]. The BPMs measure the intensity of both beams pulse-by-pulse. We can therefore correct for changes in the intensity of the two beams over time We compute the distance between the two beams Δ_x by dividing the currently-determined deflection angle by the intensity-normalized slope and the measured number of particles in the target beam,

$$\Delta_x = \phi_x/(N_tS'_x)$$

RESULTS

The simple proportional feedback system illustrated in, Fig 4 shows how we maintain the beams in collision We compute the required change in magnet settings of upstream air-core correctors in order to null out any movement between the beams. The corrector magnets are extremely fast and can come to their new settings within 1/120 of a second. The magnets only have a 100 μm range, but as we can see from Fig. 1, this is sufficient to return the beams to collision over the range of deflection distances we observe.

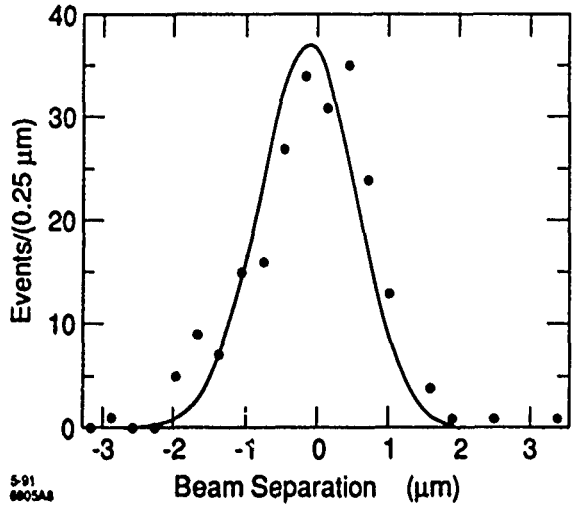


Figure 5. The distribution of beam-beam separations over a period of twenty-four seconds.

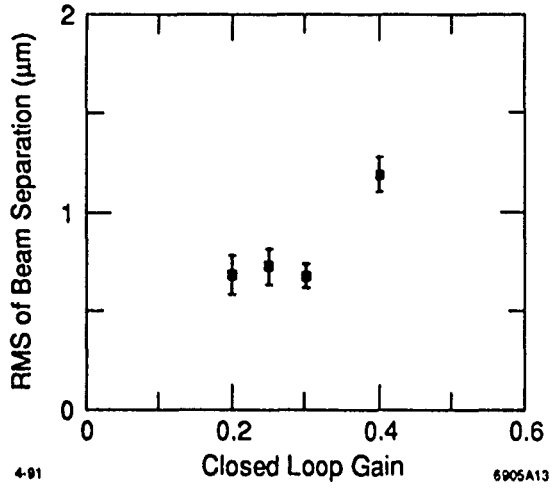


Figure 6. The average RMS of the beam-beam separations, as a function of gain.

The gain of the closed-loop feedback is the only parameter that we use to control the response of the feedback loop. We plot the distribution of distances between the beams over a twenty-four second period with a feedback gain of 0.3 in Fig. 5. If we fit this distribution to a Gaussian, plus a constant background, we find the centroid of the Gaussian is $-0.16 \pm 0.06\mu$m and the width of the Gaussian is $0.68 \pm 0.09\mu$m. The background was found to be zero, within errors. We repeated this experiment for several gains. In Fig. 6 we plot the average of the σs as a function of gain. It is obvious that at a gain of 0.4, the feedback loop has significantly worse performance than for gains between 0.2 and 0.3. We therefore conclude the optimal gain of the system is of the order of 0.3.

CONCLUSION

This paper has presented the performance of a feedback loop intended to maintain the electron and positron beams in collision at the Stanford Linear Collider. The loop was commissioned in early 1990, and was part of the usual operation by the fall. The loop brings the beams back into collision in two pulses for separations of 6 μm, with a closed loop gain of about 0.3. The width of distribution of beam-beam separation distances is about 0.6 μm, and the centroid of distances averages -0.15 μm. We estimate that this feedback loop increases the luminosity of the SLC by a factor of 20 to 30% over what it would be in the absence of the loop.

ACKNOWLEDGMENTS

The authors thank P. Bambade and R. Erikson for original ideas on the use of beam-beam deflections as a diagnostic tool. We also thank W. Koska and S.R. Wagner for their extensive theoretical and experimental work in applying those ideas to the SLC. One of the authors (F.R.) would like to thank the University of California Presidential Fellowship program for support during this work. Thanks also to L. Hendrickson for her software efforts.

REFERENCES

[1] P. Bambade et al., "Beam-Beam Deflections as an Interaction Point Diagnostic for the SLC," Phys. Rev. Lett. **62**, no. 25 (1989); SLAC-PUB-3979.

[2] W. Koska et al., "Beam-Beam Deflection as a Beam Tuning Tool at the SLAC Linear Collider," in Proc. 1989 IEEE Particle Accelerator Conf., Chicago IL; also Nucl Instrum. Methods **A286**, 32 (1990).

[3] W Koska and S Wagner, "Beam Trajectory Determination at the IP," SLAC-CN-365 (1988)

Transverse Equilibria in Linear Collider Beam-Beam Collisions

J.B. Rosenzweig
UCLA Dept. of Physics, 405 Hilgard Ave., Los Angeles, CA 90024
Pisin Chen
Stanford Linear Accelerator Center, Stanford, CA 94309

Abstract

It has been observed in simulations of the beam-beam interaction in linear colliders that a near equilibrium pinched state of the colliding beams develops when the disruption parameter is large ($D \gg 1$)[1]. In this state the beam transverse density distributions are peaked at center, with long tails. We present here an analytical model of the equilibrium approached by the beams, that of a generalized Bennett pinch[2] which develops through collisionless damping due to the strong nonlinearity of the beam-beam interaction. In order to calculate the equilibrium pinched beam size, an estimation of the rms emittance growth is made which takes into account the partial adiabaticity of the collision. This pinched beam size is used to derive the luminosity enhancement factors whose scaling is in agreement with the simulation results for both D and thermal factor $A = \sigma_z/\beta^*$ large, and explains the previously noted cubic relationship between round and flat beam enhancement factors.

Introduction

The calculation of the luminosity enhancement of linear collider beam-beam collisions due to the mutual strong focusing, or disruption, of the beams has been traditionally calculated[1] by use of particle-in-cell computer codes. These numerical calculations solve for electromagnetic fields and the motion of the particles which generate these fields self-consistently. The emergence of near equilibrium pinch confined transverse beam profiles in the limit that the disruption parameter $D_{x,y} = 2Nr_e\sigma_z/\gamma\sigma_{x,y}(\sigma_x + \sigma_y) \gg 1$ has been noted, in this regime the beam particles undergo multiple betatron oscillations during the collision. It is proposed here that these near equilibrium states are approached through collisionless damping due to mixing and filamentation in phase space, in analogy to a similar phenomena found in self-focusing beams in plasmas[3]. The expected luminosity enhancement obtained in this state is calculated in this paper. Since the approach to this equilibrium entails examining very nonlinear phase space dynamics approximations are necessary, especially with regards to the calculation of the emittance growth induced by filamentation. A model for this emittance growth, based on O. Anderson's theory of space charge induced emittance growth[4], is employed, which then allows a calculation of the luminosity enhancement which is in fairly good agreement with the values obtained by simulation.

Maxwell-Vlasov Equilibria

The equilibria we are proposing to study are of the type known as Maxwell-Vlasov equilibria, which are obtained by looking for a time independent solution of the Vlasov equation describing the beam's transverse phase space, with the forces obtained self-consistently from the Maxwell equations using the beam charge and current profiles. We begin with a flat beam ($\sigma_x \gg \sigma_y$), as these are the simplest, and most likely to be found in a linear collider. For the purpose of calculation the beams are assumed to be uniform in x and z (at least locally), and have identical profiles in y.

The vertical force on an ultra-relativistic particle is thus

$$F_y \simeq -2e|E_y| = -8\pi e^2\Sigma_b \int_0^y Y(y')dy'$$

where Y, normalized by $\int_{-\infty}^{\infty} Y dy = 1$, describes the vertical beam profile, and $\Sigma_b = N/2\pi\sigma_z\sigma_r$ is the beam surface charge density. We look for separable solutions to the time independent Vlasov equation

$$\frac{\partial f}{\partial t} = v_y\frac{\partial f}{\partial y} + F_y\frac{\partial f}{\partial p_y} = 0,$$

where $v_y = p_y/\gamma m$, i.e. solutions of the form $f = Y(y)P(p_y)$. This form is in fact approached in true thermal equilibrium. In order for this equilibrium to develop through phase space mixing, more than one nonlinear betatron oscillation must occur during collision, $D_y \simeq 2\pi r_e\Sigma_b\sigma_z^2/\sigma_y \gg 1$.

The solution to the momentum equation obtained in this manner is

$$P(p_y) = \frac{\lambda^2}{\sqrt{2\pi\gamma m}}\exp\left[-\frac{\lambda^2 p_y^2}{2\gamma m}\right]$$

which is the Maxwell Boltzmann form we should expect. The separation constant $\lambda^2 = \gamma m/\sigma_p^2$ is inversely proportional to the temperature of the system. The solution to

0-7803-0135-8/91$01.00 ©IEEE

the corresponding coordinate equation is

$$Y(y) = \frac{\alpha}{2}\mathrm{sech}^2(\alpha y), \quad \alpha = 4\pi e^2 \Sigma_b \lambda^2.$$

This profile is the one-dimensional analogue to the Bennett profile found in cylindrically symmetric Maxwell-Vlasov equilibria. The separation constant λ^2 remains to be calculated in this treatment. As a first attempt, one can use the fact that the distribution function at the origin in phase space is stationary, by symmetry, that is $\partial f/\partial t = 0$ at $(y, p_y) = (0,0)$. Thus $f(0,0)$ is a constant of the motion. Assuming an initial bi-Gaussian distribution in phase space, and equating its peak density in phase space to that of the Bennett-type profile found upon equilibration, we have

$$f(0,0) = Y(0)P(0) = \frac{\Sigma_b}{2\pi\epsilon_n mc} = (e\Sigma_b)^2\lambda^3\sqrt{\frac{2\pi}{\gamma m}}.$$

We thus have, solving directly for α,

$$\alpha = \left[\frac{8\gamma r_e \Sigma_b}{\epsilon_n^2}\right]^{1/3}$$

With this relation we can compare the luminosity that comes about by the transition to a pinch confined Bennett-like state with that of the initial Gaussian beam. At this point, we make allowance for the fact that the beams are not uniform in z and redefine $\Sigma_b \rightarrow \langle\Sigma_b^2\rangle^{1/2} = N/\sqrt{8}\pi\sigma_x\sigma_z$.

Luminosity Enhancement

The luminosity enhancement due to pinch-confinement can be calculated by taking the luminosity integrals of the two cases, assuming $A_y = \sigma_z/\beta_y^* < 1$, the depth of focus effects can be ignored, and $D_x < 1$,

$$\mathcal{L} = \frac{N^2 f_{\mathrm{rep}}}{4\pi\sigma_x\sigma_y} \rightarrow \frac{N^2 f_{\mathrm{rep}}\alpha}{6\sqrt{\pi}\sigma_x}$$

Following this prescription, the luminosity enhancement is

$$H(D_y, A_y) = \frac{4\pi^{1/2}\sigma_y}{3}\left[\frac{\gamma r_e \Sigma_b}{\epsilon_n^2}\right]^{1/3} = \frac{2}{3}(2\pi)^{1/6}\left[\frac{D_y}{A_y^2}\right]^{1/3}$$

This results of the computer simulation of luminosity enhancement by Chen and Yokoya[1] is reprinted in Figure 1. Our expression clearly has too strong a dependence on D_y and A_y to model the simulation results correctly. This is because, even though we have invoked emittance growth (phase space filamentation) as the mechanism behind collisionless approach to equilibrium, we have neglected to calculate this emittance growth.

The emittance growth can be estimated by using a method developed by Anderson to examine space-charge driven emittance growth.[4] We begin by assuming laminar flow of beam particles pinching down under the influence of the opposing beam forces which, ignoring for the moment the time dependence of the collision, is assumed to be undergoing an identical pinch. The force on the beam particles can then be written in terms of the enclosed beam current, and thus the initial transverse displacement, $F = -8\pi e^2\Sigma_b G(\xi)$, where $G(\xi) = \int_0^\xi Y(y)dy$ is a constant of the motion under laminar flow conditions. The equation of motion for the beam particles is thus $y'' + K(\xi) = 0$ ($' \equiv d/ds$), where $K(\xi) = 8\pi r_e \Sigma_b G(\xi)$. For small initial amplitudes $\xi \ll \sigma_y$ we have $K(\xi) = (8\pi r_e n_b/\gamma)\xi \equiv k_\beta^2\xi$, where $n_b = \Sigma_b/\sqrt{2\pi}\sigma_y$ is the beam density on axis. The solution for the small amplitude motion (which for small times is simple harmonic with wavenumber k_β) is thus $y = \xi[1-(k_\beta^2 s^2/2)]$, and all of the small amplitude particles focus at the wave-breaking point $s_{wb} = \sqrt{2}k_\beta^{-1}$. At wave-breaking, which corresponds to one-quarter of a beam oscillation, and after which the laminar flow assumption is violated, the rms emittance has grown explosively and can be calculated (assuming an initially parabolic beam profile of rms beam size σ_y) to be

$$\Delta\epsilon^2 = \langle y\rangle^2\langle y'\rangle^2 - \langle yy'\rangle^2 \simeq \frac{21}{8}\sigma_y^2\left[\frac{r_e N\sigma_y}{\gamma\sigma_x\sigma_z}\right]^2.$$

In fact, not all of this growth can take place, as the initial focusing occurs as the beams see a time-dependent, adiabatically increasing focusing strength. The emittance growth occurs on a length scale of k_β^{-1}, but the beam rethermalizes in a length β_y^* due to the nonlaminar effects of the finite emittance. Thus we must divide our emittance growth factor by $k_\beta\beta_y^* = (2/\pi)^{1/4}\sqrt{D_y/A_y^2}$, and in the spirit of an rms treatment, add it in squares with the initial normalized emittance ϵ_{n0}

$$\epsilon_n^2 \simeq \epsilon_{n0}^2\left[1 + \frac{3}{2}\sqrt{\frac{D_y}{A_y^2}}\right] \simeq \epsilon_{n0}^2\left[1 + \frac{8}{5}k_\beta\beta_y^*\right].$$

The adiabaticity scale length of the collision is σ_z and the initial depth of focus, or rethermalization length, is β_y^*, so

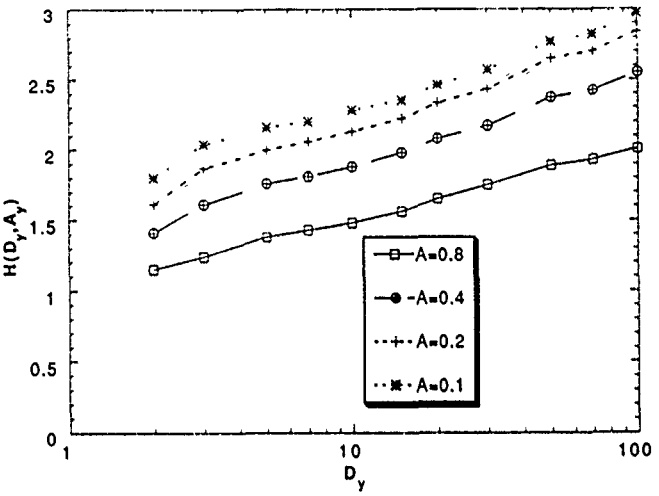


Figure 1: Luminosity enhancement as a function of D_y and A_y, found by computer simulation.

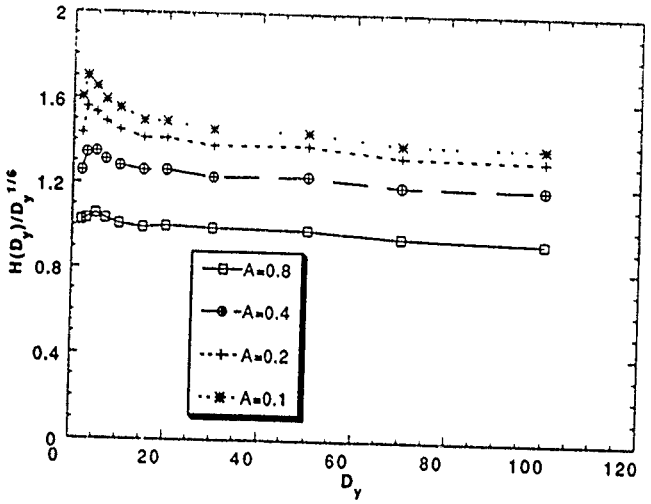


Figure 2: Luminosity enhancement as a function of D_y, multiplied by scaling factor $D_y^{-1/6}$.

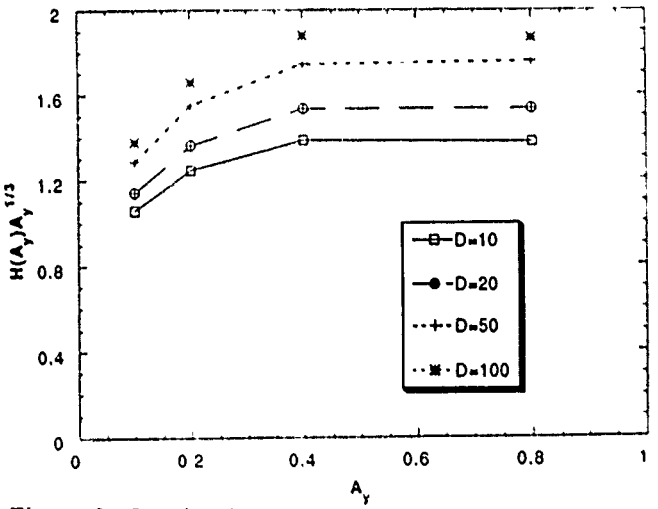


Figure 3: Luminosity enhancement as a function of A_y, multiplied by scaling factor $A_y^{1/3}$.

we must require for this model to hold that A_y be not too much smaller than unity.

Given this emittance growth factor, we can now calculate the luminosity enhancement factor to be

$$H(D_y, A_y) \simeq \frac{2}{3}\left[\frac{\sqrt{2\pi}\frac{D_y}{A_y^2}}{1+\frac{3}{2}\sqrt{\frac{D_y}{A_y^2}}}\right]^{1/3} \simeq \frac{2}{3}\left[\frac{\pi(k_\beta\beta_y^*)^2}{1+\frac{4}{3}k_\beta\beta_y^*}\right]^{1/3}.$$

In the limit of applicability ($D_y \gg 1$, $A_y \lesssim 1$), this relation approaches $H(D_y, A_y) \simeq 0.8(D_y/A_y^2)^{1/6}$. This relation yields scaling which describes the relevant data obtained in simulations quite well, as illustrated in Figs. 2 and 3. Quantitatively, one expects the best agreement when A_y and D_y are largest, and for $D_y = 100$, $A_y = 0.8$ the simulations give $H(D_y, A_y) \simeq 2$, while our scaling gives $H(D_y, A_y) \simeq 1.86$, which is in decent agreement.

The fundamental quantity which governs the luminosity enhancement is evidently $\sqrt{D_y}/A_y \simeq k_\beta\beta_y^*$. The choice of D_y, which is the square of a wave-number, to parameterized this oscillatory interaction is perhaps unfortunate, and is a historical artifact.

Round Beam Enhancement

The emittance growth process for the disruption of round beams, is beyond the scope of this short paper. The results of such a calculation have the same scaling as the flat beam case. We thus confine ourselves to considering, for the purpose of comparison to the flat beam case, the luminosity enhancement in the absence of emittance growth.

Following the treatment in Ref. [3], the Bennett profile of the pinch-confined beam system is

$$R(r) \sim \left[1+(r/a)^2\right]^{-2},$$

where $a^2 = 2\epsilon_n^2/\gamma\nu$, where the Budker parameter $\nu = Nr_e/2\sqrt{pi}\sigma_z$ (we have again taken the rms value of the charge density). The luminosity enhancement obtained in this case (*not including emittance growth*) is

$$H(D,A) = \frac{\sigma_r^2}{3a^2} = \frac{D}{12\sqrt{\pi}A^2} \sim \frac{D}{A^2}.$$

By comparing this to the equivalent flat beam expression, we see that

$$H_{\rm flat} \sim H_{\rm round}^{1/3},$$

a relationship which has been previously deduced from the simulation data[1]. This is further confirmation that our model incorporates much of the relevant physics of beam-beam disruption.

References

[1] P. Chen and K. Yokoya, *Phys. Rev. D* **38**, 987 (1988) and P. Chen, in *Physics of Particle Accelerators*, Ed. M. Month and M. Dienes, 633 (AIP, New York, 1989).

[2] W. H. Bennett, *Phys. Rev.* **45**, 890 (1934), and *Phys. Rev.* **98**, 1584 (1955).

[3] J. B. Rosenzweig, P. Schoessow, B. Cole, W. Gai, C. Ho, R. Konecny, S. Mtingwa, J. Norem, M. Rosing, and J. Simpson, *Phys. Fluids B* **2**, 1376 (1990).

[4] O.A. Anderson, *Particle Accelerators* **21**, 197 (1987).

Progress on the CLIC Final Focus System

O. Napoly*, P. Sievers, T. Taylor, B. Zotter
CERN, CH 1211 Geneva 23, Switzerland

Abstract

The Final Focus System has been adapted to the revised parameter list for CLIC [1]. It is expected that lower emittances are obtainable in the damping rings and the blowup in the main linac can be contained to 25 %. Then the luminosity is no longer limited by synchrotron radiation in the final quadrupoles, and a luminosity above $10^{33} cm^{-2} s^{-1}$ could be reached for bunches colliding head on. However, finite crossing angles are required so the disrupted beam can pass through a special aperture in the first interaction region quadrupole. The reduction of luminosity due to this crossing angle and due to unavoidable misalignments has been studied as function of bunch length with a particle tracking code. Two designs of quadrupoles are presently being evaluated, one based on permanent magnets, and the other on pulsed currents. Results of measurements on models are presented.

1 The revised beam parameters

The revised parameter list [1] assumes bunches of lower six-dimensional emittance. The normalized transverse emittances are reduced by a factor two compared to the previous assumptions

$$\begin{aligned} \epsilon_x &= 1.5 \times 10^{-6} m \\ \epsilon_y &= 0.5 \times 10^{-6} m \end{aligned} \qquad (1)$$

and the bunch is a bit shorter with

$$\sigma_z = 170 \mu m \qquad (2)$$

The energy of each particle is given by its longitudinal position in the bunch By careful balancing of the applied RF voltage and the wake potential one obtains a distribution with a spread less than 10^{-3} when asymmetric cuts are applied. [2]. Since about 15% of the particles are lost by the cuts, a total bunch population of 5.9×10^9 particles is required.

1.1 Energy profiles in DIMAD

The code DIMAD [3] allows ray-tracing of up to 10,000 (super-)particles through a beam line. Uniform and (truncated) Gaussian distributions are standard options of the program, but it has been necessary to implement more general distributions as well as the possibility to correlate particle energy with longitudinal position. Results with parabolic profiles were already reported in [4]. Non-symmetric profile functions were added by allowing asymmetric cuts of the longitudinal distribution.

1.2 Beam envelopes

The earlier lattice layout of the CLIC final focus system [4] has been retained, but the beam-envelopes were computed for the following input beta-values:

$$\begin{aligned} \beta_x^{(0)} &= 3.00\, m \\ \beta_y^{(0)} &= 3.24\, m \end{aligned} \qquad (3)$$

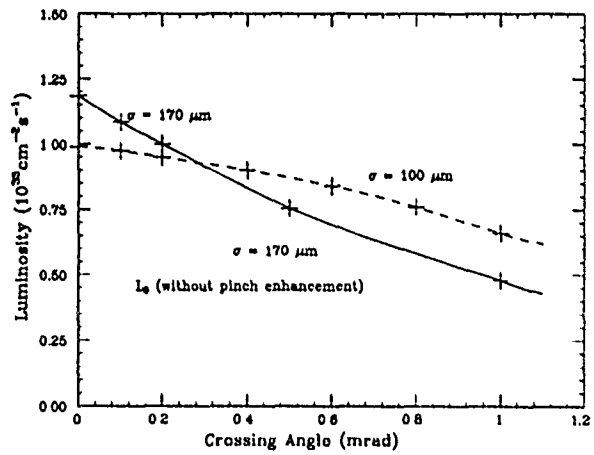


Fig.1:Luminosity dependence on crossing angle

These values correspond to the beta-values at the interaction point

$$\begin{aligned} \beta_x^* &= 4.8\, mm \\ \beta_y^* &= 0.58\, mm \end{aligned} \qquad (4)$$

and, with the emittances given in Eq.(1), to the desired spot sizes of 12 x 60 nm.

The maximum extension of the beam is $\sigma_x = 83 \mu m$ horizontally at the entrance of the last-but-one quadrupole, and $\sigma_y = 32 \mu m$ vertically at the entrance of the last one. If one fixes the aperture of both quadrupoles in such a way that the pole-tip field is $B_0 = 1.4 T$, the pole tip is at 9 σ horizontally and 15 σ vertically, which is a significant improvement with respect to the previous situation [4]

*CEN Saclay, F 91191 Gif-sur-Yvette, France

0-7803-0135-8/91$03.00 ©IEEE

2 Results from tracking simulations

The results reported in this section have been obtained by

- ray-tracing to second order with DIMAD of one or a few batches of 10,000 particles through the final focus beam line [4], taking into account synchrotron radiation in bends and quadrupoles
- processing the output distributions, split into two different beams of 5,000-particles each (electron and positron) colliding head-on, through a fast luminosity-calculation program with no beam-beam interaction
- simulating the pinch effect at collision with the CLIC beam-beam simulation program RBEAM [5]

Results for the intermediate values of beam energy, $E_0 = 250\,GeV$ and $E_0 = 500\,GeV$, have been included assuming that the normalized transverse emittances are fixed.

2.1 Optimization of the dipole strengths

The chromatic aberrations created by the final telescope are pre-corrected by sextupoles in 'chromatic correction sections' containing dipoles to create the necessary dispersion. An optimum dipole strength was found [6] by balancing the emittance growth due to synchrotron radiation, increasing with their strength, and the non-linear distortions, which decrease since the resulting higher dispersion leads to weaker sextupoles. The luminosities were computed without synchrotron radiation in the quads nor pinch enhancement since the optimal field should depend very little on both effects.

The optimization was done at three beam energies. For $E_0 = 1\,TeV$, the best field is $B_O = 245\,G$ which is the one chosen before [4]. At lower energies, where synchrotron radiation is weaker, the optimum dipole field is higher: about 340 G for 500 GeV, and almost 400 G for 250 GeV. The luminosity decreases only slightly for lower energy beams [6].

2.2 Luminosity dependence on crossing angle

For finite crossing angles, the ends of short bunches do no longer completely overlap during collision. Thus the luminosity in CLIC would decrease rapidly with increasing crossing angles as shown in Fig.1, computed with program RBEAM [5] for 2 beams of 5000 (super-)particles each tracked with DIMAD [3] through the CLIC Final Focus. With shorter bunches (e.g.$\sigma_z = 100\mu m$) the reduction is smaller, but the initial value is also reduced since the disruption is insufficient when the number of particles per bunch is kept constant.

The minimum required crossing angle is about 1 $mrad$, which yields a separation of $1.25mm$ at the face of the first quad (at $1.25m$ from the intersection), and thus permits the disrupted beam to clear the aperture of $1mm$ diameter. The disrupted beam is also larger (the emittance is increased by about one order of magnitude), and the horizontal gap needs to be widened vertically to let it pass without damage.

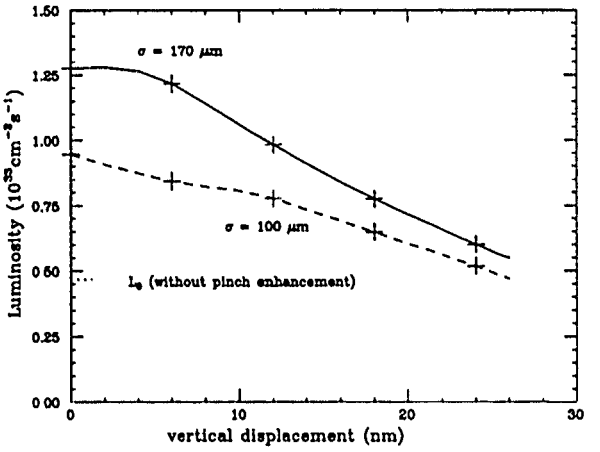


Fig.2: Luminosity dependence on displacement

For the standard bunch length of $0.17mm$, the luminosity reduction would be more than 50 %. For a slightly shorter beam of $0.1mm$, the reduction is only 35 %. A way to avoid this decrease is the use of transverse-deflecting "crab cavities" [7] which make the bunches collide over their full length even for a large crossing angle. However, the practical difficulties of keeping the required phase-stability for the deflecting modes for short bunches are considerable.

Small transverse displacements of the beam - e.g. due to jitter - are partially corrected by the attraction of the two beams as can be seen in Fig.2. However, as has been reported before [4], the inevitable misalignments of focussing elements and pick-up errors in the final focus channel will also lead to an increase of the beam size and a corresponding luminosity reduction.

3 Magnet Studies

A 25 mm long section of a permanent magnet quadrupole with iron-cobalt poles, based on a study presented previously [8], has been designed, and the components have been machined to the required sub-micron tolerances. Accurate assembly is achieved by the use of shallow precision wedges. The aperture is 1 mm in diameter, and initial results confirm the poletip field of about 1.4 T. A bench has been designed and constructed for the precise measurement of field quality and magnetic axis using the vibrating wire technique. While the model under test does not accommodate the passage of the disrupted beam entering at 1.25 mm from the axis, preliminary calculations indicate that only minor modifications would be required to achieve that goal.

commodate the passage of the disrupted beam entering at 1.25 *mm* from the axis, preliminary calculations indicate that only minor modifications would be required to achieve that goal.

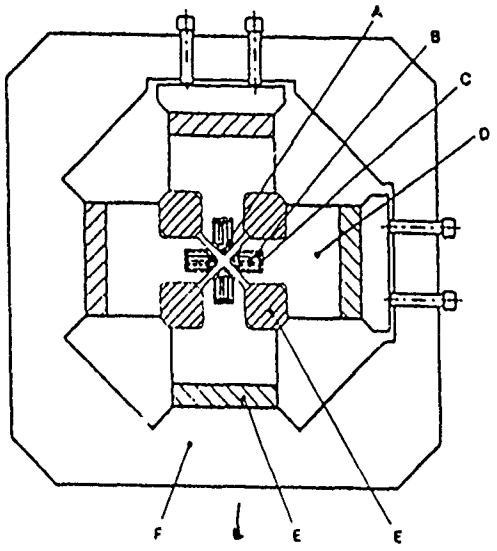


Fig.3: Cross-section of the pulsed quadrupole.
A...Copper conductor, B...Water cooling channel,
C...Stainless Steel jacket, D... Slotted SS support,
E...Ceramic spacers, F...Steel frame.

Alternatively, pulsed single conductor quadrupoles are being evaluated at CERN and elsewhere [9]. They permit higher surface fields than permanent magnets, allowing for either higher gradients, although not necessarily applicable for CLIC, or larger apertures. A scaled-up version of such a quadrupole (half aperture $A = 5\ mm$) has been built at CERN (see Fig.3) and was measured in the pulsed regime at the INP, Novosibirsk [10]

The results, given in Table 1, agree well with computations obtained by a finite element computer code [11] in the transient skin effect regime.

This table shows that sets of rather conservative parameters for single pulse operation can still be found at relatively large apertures.

The average power, at least for the elevated repetition rate of CLIC of 1.7 kHz, and thus the cooling of the quadrupole, becomes a limiting factor. A model conductor, a copper rod of 2×2 mm^2 cross-section extended into a comb-like array of cooling fins at one of its side faces has been built and its heat removal capacity been measured: a d.c. current of $I = 1.4\ kA (35 A/mm^2, 7.8\ kW/m)$ led to a modest temperature rise of the conductor above the cooling water of only 17° C. At such average powers dissipated in each conductor in the pulsed regime one can anticipate gradients of $2 \times 10^3\ T/m$ and $1 \times 10^3\ T/m$ for half- apertures of $A = 1\ mm$ and $A = 1.5\ mm$ respectively. Further problems resulting possibly from the pulsed

Table 1

Half aperture (mm)	1.0	1.0	1.5	2.0
Gradient (T/m)	1000	2000	1000	1000
Pulse duration (μs)	8	8	18	32
Peak current (kA)	4	8	9	16
Peak voltage (kV)	1.3	2.6	1.3	1.3
Energy/pulse (J)	~5.5	~22	~28	~88
Average power (kW)	9.4	37.5	48	150

Table 1: Parameters for a 1 m long quadrupole, scaled from the geometry of the tested model.

operation, like vibrations and field repeatability will have to be carefully considered. Also the passage of the opposite beams through the quadrupoles in the horizontal plane will have to be arranged, e.g. by displacing or removing the conductors in the horizontal plane [12].

4 Conclusions

Thanks to the reduced emittances in the new parameter list, luminosities in excess of $10^{33} cm^{-2} s^{-1}$ can now be reached in CLIC if the beams collide head-on. These luminosities can be maintained also at energies below 1000 GeV by slightly retuning the lenses. However, including the effects of finite crossing angles and transverse displacements of the bunches reduces the luminosities considerably. In addition to very careful alignment of the quadrupoles and pick-ups, a dynamical correction of the beam position will be required.

5 References

[1] G. Guignard, CLIC Note 135 (Jan 1991)

[2] G. Guignard and C. Fischer, CLIC Note 127 (1990)

[3] K. Brown et al., SLAC 285 (1985)

[4] O. Napoly, B. Zotter, CLIC Notes 107 and 109, also Proc.EPAC, Nice 1990, p.1408

[5] L. Wood, Program RBEAM, unpublished

[6] O. Napoly and B. Zotter, CLIC Note 129 (1990)

[7] R. Palmer, SLAC-Pub 4707 (1988)

[8] K. Egawa, T. Taylor, Proc. PAC,Chicago 1989, p.360

[9] G.I. Silvestrov et al., Proc. 14th Internat. Conf. on High Energy Accelerators, Tsukuba, Japan, 1989.

[10] M. Modena, P. Sievers et al., to be presented at the 12th Internat. Conf. on Magnet Technology, Leningrad, USSR, 24-28 June 1991.

[11] M. Modena, P. Sievers, to be presented at the COMPUMAG Conference, Sorrento, Italy, 7-11 July 1991.

[12] P. Sievers, CLIC Note 112 (1990).

Optimizing Energy Spread in the CLIC Main Linac

G. Guignard and C. Fischer
CERN, 1211 Geneva 23, Switzerland

Abstract

Making a final focus system of possible linear colliders accept the beam energy spread is an important problem. The feasibility of a certain compensation of the energy spread in a linac has already been established. This paper describes a systematic study leading to rigorous compensation of the longitudinal wake fields with the RF sinusoidal wave, using the CLIC main-linac parameters. The dependence of the energy spread on the RF voltage phase, bunch intensity and bunch length is discussed. Code parts have been written to compute the resulting energy distribution, average energy and energy spread in each case considered. Conditions were found that allow minimal tail population and somewhat narrow core size, so that at the optimum the energy spread is below 10^{-3} for $5 \cdot 10^9$ particles and satisfies final focus requirements. A new set of parameters more favourable to the CLIC performance and solving the problem initially addressed can be drawn out of the results.

I INTRODUCTION AND BASIC PRINCIPLES

The possibility of compensating the energy spread in the CLIC linac using wake potential versus RF wave has already been considered [1]. This paper reports on a systematic study of a cancellation to high orders of the longitudinal wake fields with the RF gradient [2]. Such compensation affects the energy distribution as shown for instance in ref. [3]. Proper adjustments minimize tail population and core size and make the beam's energy spread compatible with final focus acceptance, limited by the radiation in the weak dipoles as well as the sextupole strengths.

Assuming an energy E_{in} and a relative energy spread g(z) at linac entrance, the increase due to an accelerating gradient G is

$$E(z,s) = E_{in}\left[1 + g(z) + \frac{G(z)s}{E_{in}/e}\right] \qquad (1)$$

if G is the same all along the linac. The total accelerating gradient seen by a particle at position z results from the RF field diminished by the longitudinal wake, i.e.

$$G(z) = G_{RF}\cos\left(2\pi f_{RF}\frac{z}{c} - \phi_{RF}\right) - W_L(z) \qquad (2)$$

where G_{RF}, f_{RF} and ϕ_{RF} are the maximum gradient, frequency and phase of the RF wave. The longitudinal wake is given by the integral

$$W_L(z) = eN\int_{-\infty}^{z}\rho(z')W_L^{\delta}(z-z')dz' \qquad (3)$$

where the functions under the integration sign are the charge distribution, assumed to be gaussian with r.m.s. σ_z, and the wake delta-function due to a charge at z', ahead of the probe-particle ($z' \le z$). N is the number of particles in the bunch and σ_z the bunch length.

The energy distribution ν (E) has to be calculated in order to study its properties and dependence on parameters such as G_{RF}, ϕ_{RF}, σ_z, and N, and comes from

$$\nu(E) = \frac{1}{N}\frac{dN}{dE} = \frac{1}{N}\frac{dN}{dz}\frac{dz}{dE} = \frac{\rho(z)}{dE/dz} \qquad (4)$$

In principle, the derivative dE/dz can be deduced from (1). In practice, numerical estimates of it are preferred to analytical derivation. It is noticeable however that ν(E) becomes infinite when dE/dz vanishes and this is a source of numerical inaccuracies. Once the function ν(E) is known, the average energy <E> and the r.m.s energy spread σ_E are easily computable from the standard integrals. This has been done for the CLIC main linac, with systematic variations of the main parameters and search for optimum conditions.

II ENERGY DISTRIBUTION PROCESSING

Equ. [4] is used to evaluate the energy distribution ν(E). The wake field in G(z) and hence E(z) cannot be described analytically very easily and a numerical approach is preferred (section I). A detailed description of this treatment can be found in ref. [2]; basic steps are now summarized. A gaussian longitudinal bunch distribution ρ(z) considered between $\pm 4\sigma_z$, and divided into M slices or superparticles is handled under the influence of continuous external focusing, RF gradient and wake field using program LINBUNCH [4]; quantities E(z), and ρ(z) used in Equ. (4) are provided for each superparticle of index m ($1 \le m \le M$); the longitudinal coordinate z is then replaced by m and Equ. (4) becomes:

$$\nu(E,m) = \bar{\rho}(m) \bullet \Delta z / \left[E(m+1) - E(m)\right] \qquad (5)$$

with $\Delta z = 8\sigma_z/M$.

The distribution E(m) is not monotonic, as will be discussed later, and regions of same energy domain (four when the actual gradient presents two maxima) must be recombined to get a unique figure ν (E) between E and E+dE. In these regions, the initial energy bin distribution is different: the bins E(m+1) - E(m) all have different lengths, the cutting being linear along z and not in the energy domain due to the shape of the accelerating gradient; overlapping regions are therefore reshuffled into identical bin configuration before their merging is performed; the finest bin distribution found among overlapping regions is selected to rearrange the other ones. A monotonic variation ν (E) is then obtained [each pair ν(m), E(m) being unique] - examples are presented and discussed thereafter and in ref. [2]. The curves are not strictly distributions as the final energy bins do not have the same width.

0-7803-0135-8/91$03.00 ©IEEE

Statistics: Other quantities of interest such as the norm, the average energy <E> and the r.m.s. energy spread $\sigma_E/<E>$ can then be processed on the distribution $\nu(E)$, tailored according to various criteria which can be an energy threshold or a given part of the longitudinal bunch distribution selected specifying a number of r.m.s. values (σ_z).

Quality estimate: From Equ. [4] it is clear that if the distribution $\rho(z)$ is normalized to 1, this remains valid for $\nu(E)$ in the absence of cut; moreover after cuts at $\pm1\sigma_z$, $\pm2\sigma_z$ the norm values of $\nu(E)$ can be compared to the expected ones (0.6826, 0.9546); this norm evaluation is performed on $\nu(E)$ before and after the recombination process previously described; careful averaging between adjacent bins and optimization of the superparticle number M are proceeded with until the expected norm value is reached within a few 10^{-3}.

Table 1 gives some figures for cuts at $\pm1\sigma_z$, $\pm2\sigma_z$ and $\pm4\sigma_z$, and M = 701. The resulting values of <E>(normalized to the RF voltage) and $\sigma_E/<E>$ are incorporated.

	N1(*)	N2(**)	<E>	$\sigma_E/<E>$ (%)	LINBUNCH <E>	LINBUNCH $\sigma_E/<E>$ (%)
$\pm1\sigma_z$	1.0029	0.6810	.9758	.1602	.976	.156
$\pm2\sigma_z$	1.0029	0.9554	.9731	.5655	.973	.568
$\pm4\sigma_z$	1.0029	1.0007	.9717	.9408	.972	.944

(*) before rearrangement and with no cut

(**) after rearrangement

Table 1: Norm values, <E> and $\sigma_E/<E>$ for M = 701

<E> and $\sigma_E/<E>$ are also processed by LINBUNCH from the distributions $\rho(z)$, E(z) and a further consistency check is possible. Data from LINBUNCH are included for comparison.

III DEPENDENCE ON RELEVANT PARAMETERS

When the RF phase varies for previous nominal values of σ_z and N (0.2 mm and $5\cdot10^9$) the average energy is maximum when the bunch is in phase with the RF voltage ($\phi_{RF} = 0$) but the energy spread is not optimized (Fig.1). For the complete distribution ($\pm4\sigma_z$) a minimum is clearly defined near $\phi_{RF} = 4°$ which moves slightly upwards when cuts are performed as the energy distribution is not symmetrical with z.

The electric field acting on the bunch depends on ϕ_{RF}; for small values, the head (which does not experience wake fields) sees higher gradients but wakes are stronger on the rest of the bunch, lowering the resulting electric field accordingly. The best balance is for values between 4° and 6° depending on the z domain selected and corresponds to a minimum r.m.s. energy spread (Fig. 1). The bunch energy distribution shows a sharp peak at maximum energy within about 1 per mil and a very long tail; increasing the RF phase up to 6° displaces the peak towards <E> but this does not reduce the spread as the tail becomes more populated; the best compromise is for $\phi_{RF} = 4°$ when the full distribution is considered; when it is cut through, the tail is reduced accordingly and the peak moves towards the origin (<E>) (Fig. 4). The average energy is then increased as already pointed out (Fig.1).

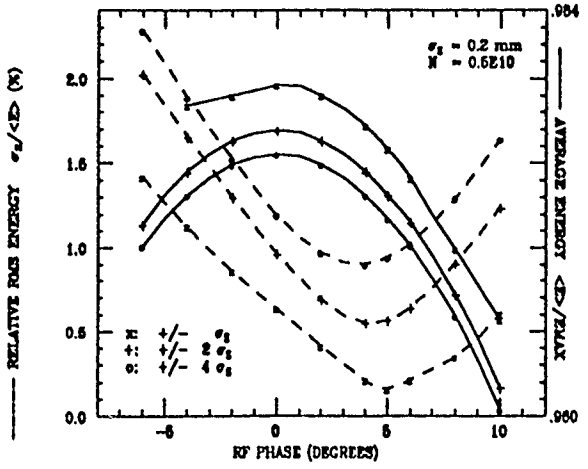


Figure 1. Dependence on RF phase of average energy and energy spread

In order to modify the energy distribution towards a denser core, the curve G(z) should be as flat as possible, likely with two local maxima. Such shapes are obtained by varying the bunch length and/or the number of particles, the RF phase being an adjustment parameter. Starting with $N = 5\cdot10^9$ and $\sigma_z = 0.2$ mm this is illustrated in Figs. 2 and 3. Fig. 2 shows the results obtained by shortening the bunch at $\phi_{RF} = 8°$ and constant intensity. Fig. 3 gives curves associated with an increasing charge N, at $\phi_{RF} = 8.5°$ and constant bunch-length . Hence the dense part of the charge distribution is centred around the average energy. However, N and σ_z are linked, in the search for a minimum of σ_E , and both must be decreased simultaneously while the fine tuning of ϕ_{RF} is small. At $N = 5\cdot10^9$ the optimum exists for $\sigma_z = 0.14$ mm and $\phi_{RF} = 7°$ giving a σ_E of ~0.5%, instead of 1% with 0.2 mm and 5°. Similarly, energy-spread optima exist for each value of N. In such optimized situations, the interesting σ_E - values are those obtained after cutting the energy distribution (lower bound at -4‰) according to final focus (FF) acceptance and the number of particles that do not contribute to the luminosity is also minimized (Table 2).

N (10^9)	σ_z (mm)	ϕ_{RF}	Fraction lost (%)	$\sigma_E/<E>$ (%)
4	0.11	7	4.5	0.156
5	0.14	7	7.7	0.157
6	0.17	8	15.1	0.097
7	0.20	8,5	22.2	0.104

Table 2: Energy spread for various parameters

Table 2 shows that the change in ϕ_{RF} for different charges is not large. However, the fraction of non-contributing particles for an FF acceptance of ±4‰ and $\sigma_E/<E>$ logically depend on N and σ_z. Variations of ϕ_{RF} by ±1° and of σ_z by ± 0.02 mm w.r.t. values of Table 2 do not degrade the energy spread by more than a factor 2.

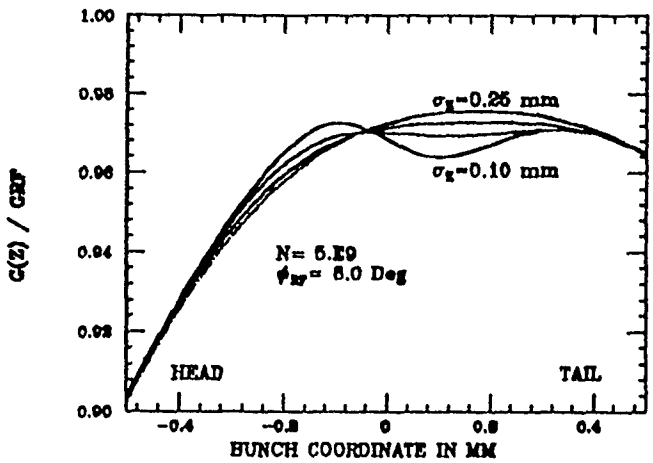


Figure 2. Gradient dependence on bunch length

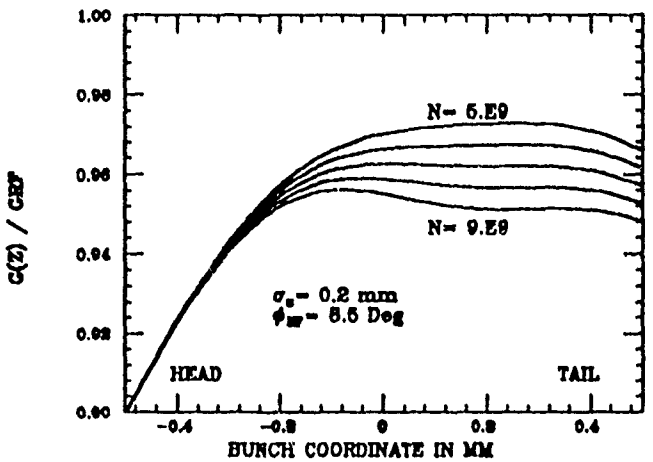


Figure 3. Gradient dependence on bunch charge

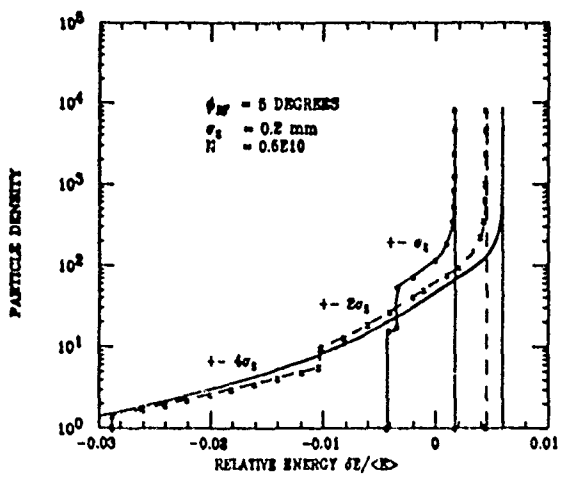


Figure 4. Energy distributions for ±1, 2 and 4σ_z cuts.

IV RESULTS AND CONCLUSIONS

With the initial values of σ_z = 0.2 mm and N = 5·10^9, the optimum phase lies between 4° and 5° (Fig.1) according to the part of the distribution that contributes to luminosity (±σ_z, ±2σ_z, ±4σ_z). The energy distributions behave as in Fig. 4. Only the case with ±σ_z is fully compatible with FF acceptance. Turning to the cases N = 5·10^9 and 6·10^9 of Table 2, the distributions have the shape given in Fig. 5, the 3 peaks corresponding to the local maxima and minimum of G(z) and the dense part being well inside the FF acceptance. Since one needs an intensity of at least 5·10^9 at the final focus to reach a luminosity of 10^{33}cm^{-2}s^{-1} and there is a minimum of σ_E in Table 2, an optimum set of parameters is given by the case N = 6·10^9 (including the 15% fraction lost). After tracking through the FF system [5], with aberrations and pinch effect, a consistent set of parameters could be found to achieve the required luminosity. The resulting list of tentative parameters is given in Table 3.

Parameters	Values	Units
Energy	1.0	TeV
Luminosity	~1.1·10^{33}	cm^{-2} s^{-1}
Enhancement factor	~2.4	
Acc. gradient	80	MVm^{-1}
RF frequency	29.985	GHz
Repetition rate	1.7	kHz
Rel. energy loss	0.32	
Critical rel. energy	0.92	
FF Beam ratio	5	
Bunch population	6·10^9	
V-emittance ($\gamma\varepsilon_y$)	0.5·10^{-6}	rad m
H-emittance ($\gamma\varepsilon_x$)	1.5·10^{-6}	rad m
FF Beam height	12	nm
Bunch length	0.17	mm
FF Beta-function (β_y)	0.576	mm

Table 3 : Main Linac tentative parameters

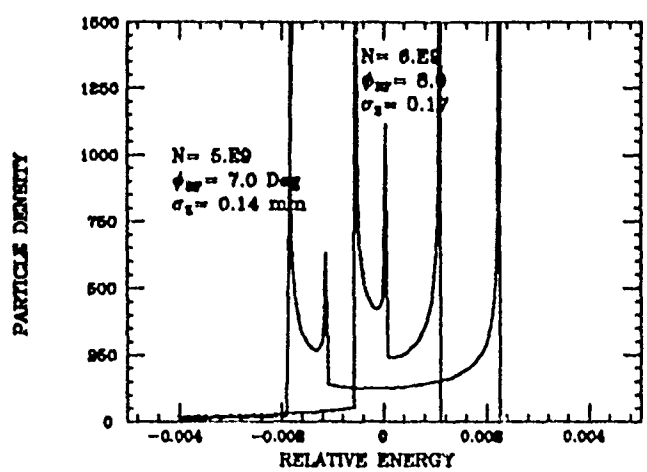


Figure 5. Energy distributions minimizing σ_E/<E>.

V REFERENCES

[1] W. Schnell, CERN, private communication.
[2] C. Fischer and G. Guignard, "Energy Spread Compensation in CLIC", CERN-SL/90-122, 1990.
[3] K.L.F Bane, "Optimizing the average longitudinal phase of the beam in the SLC linac", SLAC-AP-76, 1989.
[4] H. Henke, "Transverse Damping in a 30 GHz high energy linac", Proc. IEEE PAC 87, 1346, 1987.
[5] O. Napoly, T. Taylor, B. Zotter, this Conference.

Investigations on Beam Damping Simulations and the Associated Model of CLIC

G. Guignard, C. Fischer and A. Millich.
CERN, 1211 Geneva 23, Switzerland

Abstract

Controlling the beam stability in the CLIC main linac must be investigated numerically. Strong damping is required to cope with wake field effects and machine imperfections impose careful optics adjustments. The computation of the longitudinal and transverse wake fields has been revisited and the Green functions re-evaluated for the most recent main cavity design. BNS damping and autophasing with magnetic and microwave focusing could then be simulated and the dependence of the results on parameters such as the RF phases and voltage gradients could be studied. Since the emittance is extremely small, beam break-up is sensitive to unavoidable misalignments and algorithms of trajectory corrections have to be investigated. Simulations and beam trackings have been done under specific conditions, using the tools briefly described in this paper. Most relevant examples are presented.

I DELTA FUNCTIONS OF THE WAKE POTENTIALS

Computation of the wake field Green's functions for the disk-loaded waveguide (DLWG) of CLIC main linac is based on Ref.[1]. The delta functions of the longitudinal and transverse potentials are expressed in terms of the structure's normal modes:

$$W_L^{\delta}(\tau) = 2\sum_{n=1}^{\infty} K_{0n}\cos\omega_{0n}\tau$$

$$W_T^{\delta}(\tau) = 2\sum_{n=1}^{\infty} \frac{K_{1n}c}{\omega_{1n}a^2}\sin\omega_{1n}\tau \qquad (1)$$

where

$$K_n = \frac{\omega_n}{4}\left(\frac{R}{Q}\right)_n \qquad \text{and} \qquad \tau = \frac{z-s}{c}$$

Equ. (1) assumes small trajectory amplitudes, measured with respect to the axis of the structure as is the case in CLIC.

Using the code KN7C [2], frequencies $\omega_{on}/2\pi$ and loss factors K_{on} of the longitudinal modes synchronous with the ultrarelativistic particles have been computed for CLIC. Since this code requires a simplified input geometry with straight edges DLWG geometry is completely defined by four parameters,

the iris aperture radius	a = 2.000 mm
the cavity inner radius	b = 4.352 mm
the cavity gap width	g = 2.782 mm
the cell length, i.e. DLWG period	p = 3.332 mm

A total of 204 longitudinal modes have thus been calculated, this number being high enough for a good evaluation of the delta function, except for the very short range part. The optical model (Ref. [1] and refs therein) was included to evaluate the analytic extension giving a more correct description of the short range wake.

Transverse modes were computed with the code TRANSVRS [3]. The delta function was then evaluated according to (1), using the loss factors and frequencies of 218 modes. Figure 1 shows the longitudinal and transverse delta functions of the wake potentials (scaled with a and p when required) for the edge geometry of the CLIC structure.

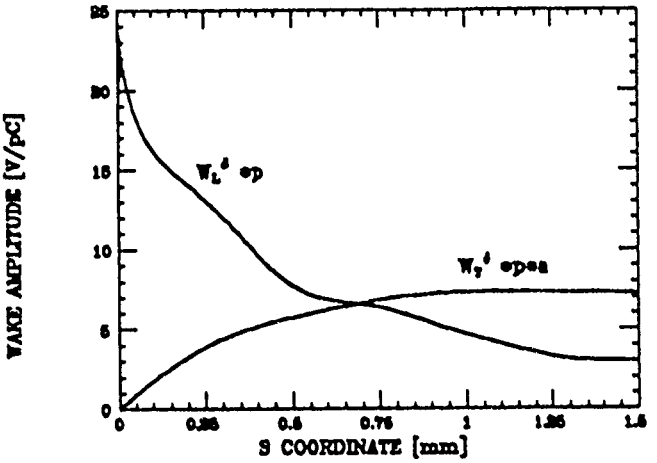


Figure 1. Green's functions of the wake fields

II BEAM STABILITY AND ONE-TO-ONE CORRECTION

Linac and beam model was revisited and the re-evaluated delta functions of the wake potentials used for the simulations. An AG focusing system with FODO lattice is assumed, with a phase advance of 90° to minimize misalignment sensitivity and $\sqrt{\gamma}$ scaling to maintain a constant stability margin (initial cell length is 5 m). Microwave quadrupoles can be added and the linac is divided into four sectors, in which the energy is multiplied by 4 going from 5 GeV to 1 TeV. BNS damping [4] and autophasing are optimized by adjustments in each sector of the RF gradient phase ϕ_{RF}, RF quadrupole phase ϕ_{RFQ} and strength. The bunch is longitudinally divided into slices, the dimensions of which are given by the emittances (unequal) and the focusing system. They are populated according to a gaussian and the total charge N is $6 \cdot 10^9$. This value, together with a bunch length $\sigma_z = 0.17$ mm and $\phi_{RF} = 7\text{-}8°$, corresponds to an optimum found in studying the compensation of the energy spread σ_E [5]. Injection off-sets of 4.2 μm and 1 μm (H and V) and random misalignments of quadrupoles and cavity-sections (1 μm and 5 μm r.m.s. in the applications) are included.

A one-to-one trajectory correction was implemented in the tracking code MTRACK [6]. Its characteristics are;

0-7803-0135-8/91$03.00 ©IEEE

1) simulation of average trajectory measurements $\langle x \rangle_{i+1}$, 2) correction of these deviations at (i+1) in moving the quadrupole i by dx; 3) introduction of random measurement and displacement errors (r.m.s. ξ_m and ξ_d), and of quadrupole misalignments δx_{i+1}. Using the coefficient m_{12} of the transfer matrix from i to i+1 (wake field kicks included) and the focal distance f, the displacement requisite to centre the beam at (i+1) in presence of errors is,

$$dx_i = \frac{\langle x \rangle_{i+1} + \xi_{m,i+1} - \delta x_{i+1}}{m_{12}/f} + \xi_{d,i} \qquad (2)$$

Tracking results presented concern three cases: *1)* a structure with conventional focusing and adjustment of ϕ_{RF} (optimum per sector at -38°, -16° - 24° and -21.5°), *2)* a structure with microwave and conventional quadrupoles (optimum at $\phi_{RFQ} = 0$ and $\phi_{RF} = 5°$, 10°, 15° and 23°), *3)* a structure as in 2) but in one sector with $\phi_{RF} = 7°$ and $\phi_{RFQ} = 7°$ to minimize σ_E. The cases differ by the way BNS damping and autophasing are achieved and the energy spread (5.6, 2.7 and 0.6% r.m.s. respectively). Blow-up is given in Figs [2] to [4] and case 3 is at the origin of the revised parameters [5]. Since the desired limit of 25% is not reached, an achromatic correction was investigated.

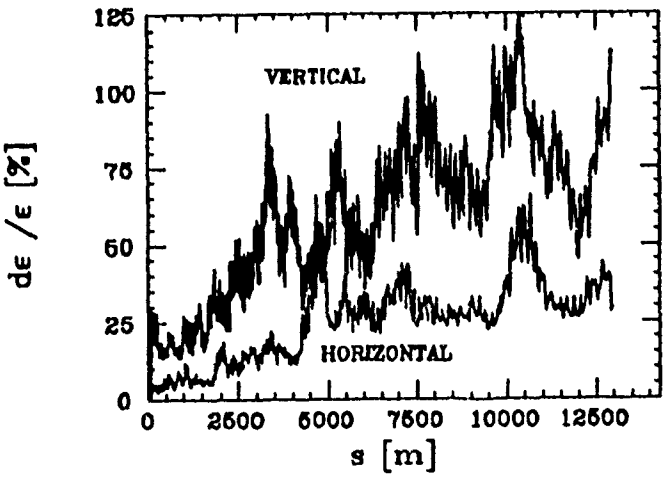


Figure 2. Blow-up with magnetic focusing only

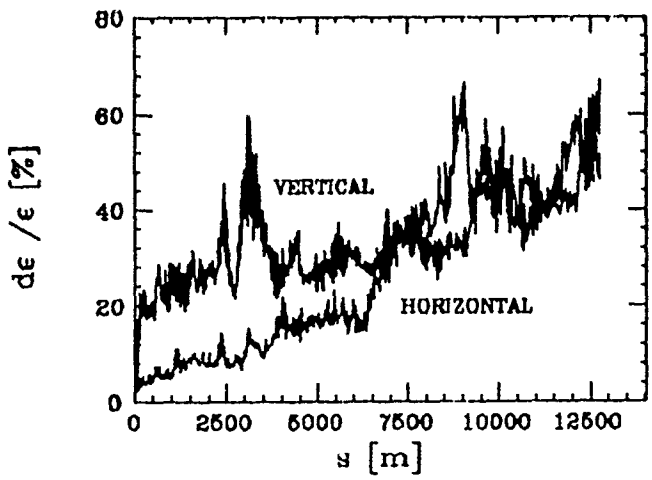


Figure 3. Blow-up with additional RFQs

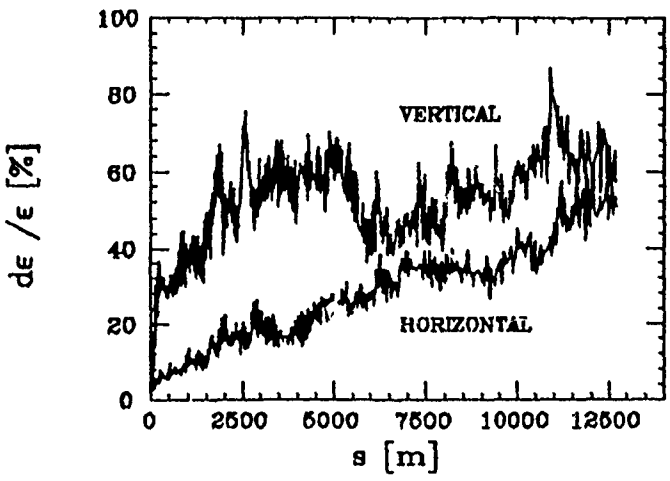


Figure 4. Blow-up for minimum σ_E.

III ACHROMATIC CORRECTION METHOD

Particles with an energy excursion $\delta = \Delta p/p_0$ have a different trajectory and will contribute to bunch dilution. Such dispersive effects can be corrected as well as the trajectory at nominal momentum p_0. One method proposed [7] leads to a minimization of the expression:

$$\phi = \sum_{j=1}^{N} \frac{(xj + Xj)^2}{\sigma_\xi^2 + \sigma_b^2} + \frac{(\Delta xj + \Delta Xj)^2}{2\sigma_\xi^2} \qquad (3)$$

xj and Xj are the measured and calculated deflections at j and for p_0, σ_ξ and σ_b are the pick-up r.m.s. precision and alignment errors. The first term is the contribution of the nominal trajectory whereas the second one describes the effect of dispersion. The quantities occurring are:

$$Xj = \sum_{i<j} R_{12}(i,j,o)\theta_i$$
$$\Delta xj = xj(\delta) - xj \qquad (4)$$

$$\Delta Xj = Xj(\delta) - Xj = \sum_{i<j} R_{12}(i,j,\delta)\frac{\theta_i}{1+\delta} - Xj \qquad (5)$$

$R_{12}(i,j,\delta)$ is the transfer matrix element which transforms a deflection θ_i at i into an excursion at j for given δ; all kicks i preceding j are considered. In Eqs. (4) and (5), Δx_j and $[R_{12}(i,j,\delta) - R_{12}(i,j,o)]$ can be developed in δ with coefficients a_n and c_n respectively; including the development of $1/(1+\delta)$ gives [8]:

$$\Delta xj = \sum_n a_n^j \delta^n \qquad (6)$$

$$\Delta Xj = \sum_{i<j}\theta_i \sum_n \left[\left(\sum_{m=1}^{n} (-1)^{n+m} c_m^{ij} \right) + (-1)^n R_{12}(i,j,o) \right] \delta^n \qquad (7)$$

To second order in δ the coefficients a_1 and a_2 are determined by measuring Δx_j for two values of δ and c_1 and c_2 are extracted from the processing of $R_{12}(i,j,\delta)$ at these two values and at $\delta = o$.

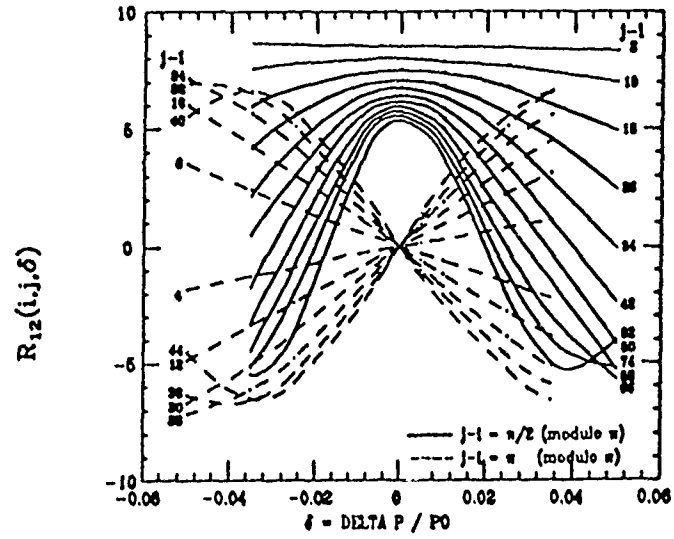


Figure 5. Variation of $R_{12}(i,j,\delta)$ with δ

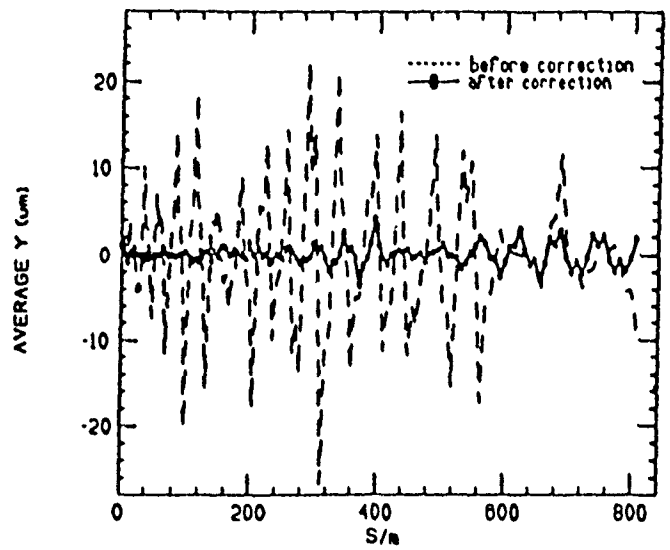


Figure 6. Correction of trajectory

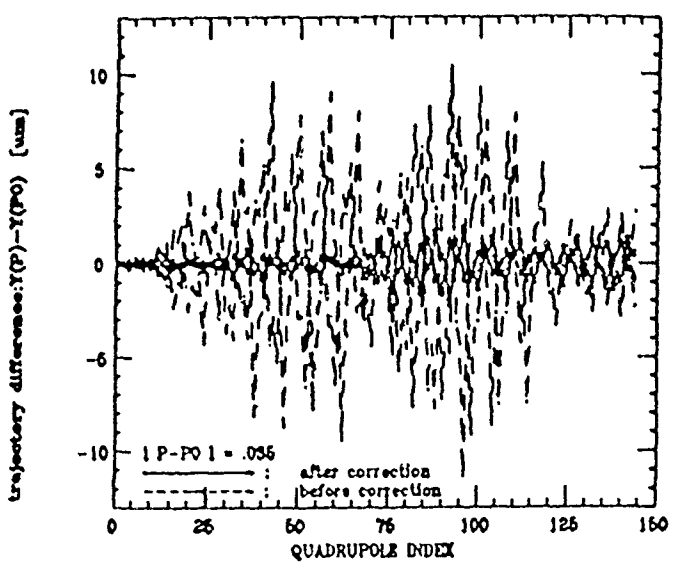


Figure 7. Correction of dispersive effect

Application to CLIC:

The exercise was tried on the CLIC structure (section II) adapting program MTRACK [6] to process trajectories and the R_{12} (i,j,δ) ; results presented there after concern the vertical plane: only QDs are considered for kick and pick-up locations.

As (j-i) increases, nonlinearities appear quickly on the R_{12} (i,j,δ) - Fig. 5. When (j-i) = $\pi/2$ (modulo π) (unbroken lines) a linear and then parabolic approximation fits for the first 2*8 pairs (i-j) (another set not represented being symmetrical around the x axis) as long as δ is limited to within ±3.5%; when (j-i) = π (modulo π) (dashed curves) the response is quasi linear up to 2*6 pairs in the same δ domain. If (j-i) or δ increase, distortions from the parabolic shape affect both families: hence for CLIC, the second order development holds well on the 26 cells (52 quadrupoles) following a kick: this has been successfully tested with a minimization algorithm based on Eqs. (3) - (7). Results in correcting trajectory, dispersion and blow-up are presented in Figs. 6, 7 and 8, for a 800 m long sector. Trajectory and dispersion are reduced by about an order of magnitude and blow-up kept below 10%, in 2 iterations.

Conclusions:

The CLIC main linac (730 quadrupoles) could then be corrected by about 10 applications of such a second order algorithm on adjacent 55 quadrupole sectors. Investigations are continuing to cover larger regions by adding higher order terms.

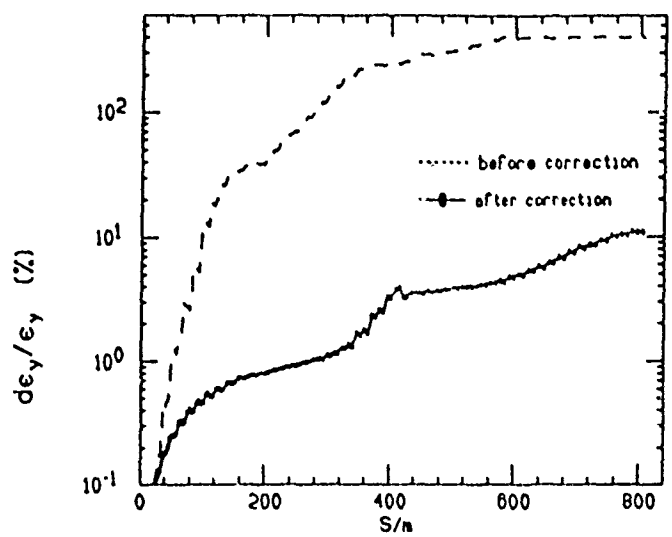


Figure 8. Achieved beam blow-up

IV REFERENCES

[1] P.B. Wilson, SLAC-PUB-4547, 1989.
[2] E. Keil , Nucl. Instr. & Methods 100, 419, 1972.
[3] D. Brandt, B. Zotter, CERN/LEP-TH/85-27, 1985.
[4] V. Balakin, A. Novokhatsky, V. Smirnov, 12th Internat. Conf. on High Energy. Accelerators, 119, 1983.
[5] G. Guignard, C. Fischer, this Conference.
[6] J. Tuckmantel, 1989 Particle Accel. Conf., Chicago, 1989.
[7] T. Raubenheimer, R. Ruth, 2nd EPAC, Nice, 1990.
[8] C. Fischer, G. Guignard, to be published.

Microwave Quadrupole Structures for the CERN Linear Collider

W. Schnell and I. Wilson
CERN, CH-1211 Geneva 23, Switzerland

Abstract

Considerable transverse focusing power can be obtained from the high-gradient RF accelerating structure of a linear collider by making either the aperture or the main cell geometry asymmetric. Such structures, acting as microwave quadrupoles, can be used to stabilize transverse wake fields by creating a spread in the transverse oscillation frequencies of the particles within a bunch. The focusing properties of both slotted-iris structures with circular cells and circular-aperture structures with asymmetric cells have been analysed using the MAFIA computer code and the results compared with the theoretically-determined limiting value obtained for an infinitely thin slit. A suitable geometry for CLIC 30 GHz structures has been established and a design based on the machine-and-braze technique is proposed.

INTRODUCTION

A relativistic beam passing off-centre through the circular aperture of an axially symmetric accelerating structure experiences no focusing at all because of exact cancellation of radial electric and azimuthal magnetic fields. The cancellation is easily removed, however, by giving the structure a suitably asymmetric shape. This creates a radio-frequency quadrupole. It turns out that the combination of high accelerating field and short wavelength of linear colliders makes it easy to obtain substantial quadrupole strength with simple (and technologically realistic) cavity shapes.

The resulting quadrupoles, arranged with alternating gradients at suitable period lengths, can be used to assist (or, in principle, even provide) the necessary transverse focusing and wake-damping [1]. Indeed, the rapid head-to-tail variation of transverse focusing within the bunch offers a powerful mechanism for either BNS damping [2] or autophasing [3]. This is qualitatively discussed below; extensive computational work on wake damping using microwave quadrupoles is reported elsewhere in this conference [4].

Other potential advantages over external magnetic quadrupoles are simultaneous acceleration and focusing (with concomitant saving of length) and the fact that precision-machined copper structures can guarantee the position and stability of the focusing axis with respect to an external reference surface with micrometre precision.

GEOMETRICAL CONFIGURATIONS FOR MICROWAVE FOCUSING

The conceptually simplest configuration is given by a narrow slit forming the beam aperture in a circular (pill-box) cavity. This is also a powerful configuration; it will be used as comparative reference for the more practical solutions described below.

As there can be no electric field parallel to a horizontal (say) slit, the horizontal force on an off-axis particle in the horizontal plane can only be due to the (azimuthal) magnetic field in the cavity. This is given by

$$B = \frac{x}{2c^2} i\omega E_z, \qquad (1)$$

where x is the horizontal displacement and E_z the peak accelerating field. It follows at once that the effective magnetic focusing gradient G_0 is given by

$$G_0 = \frac{\pi E_z}{c\lambda} \sin\varphi \qquad (2)$$

(in T/m), where φ is the RF phase angle measured backwards from the top of the accelerating wave. The situation in this plane is exactly the same as in a plasma lens, the density of axial conduction current being replaced by the displacement current density.

Since an azimuthally closed integral of radial conduction current in the end plate must equal the displacement current terminating within the integration path - and therefore remain the same as in the case of a circular aperture - it can be argued that the vertical electric field at the slit centre is doubled. Therefore, the vertical focusing due to the radial electric field generated in the aperture overcompensates the magnetic gradient of eq. (2) by exactly a factor two. The same result can be predicted by invoking the theorem that a relativistic particle can only experience quadrupole focusing - equal and opposite in both planes - as long as it does not traverse conduction current density or space charge.

COMPUTER ANALYSES

Computational analyses [5] [6] of circular cavity cells with finite width slotted apertures show surprisingly little degradation of performance below eq. (2) even for the practical range of apertures required for acceptable wake fields ($a/\lambda \approx 0.2$ for CLIC). Results from [5] are summarised below. Following a suggestion by R.B. Palmer [7] RF focusing obtained by combining a circular aperture with a flat or oval cavity has been investigated. This solution has the decisive advantage that the circular aperture which needs careful rounding and a polished surface, can be machined on a lathe.

Basic structure parameters and transverse focusing gradients of various asymmetric cavity geometries at 30 GHz have been calculated using the 3D MAFIA [8] computer program.

0-7803-0135-8/91$03.00 ©IEEE

Two types of asymmetry have been investigated:

(i) circular cavities with rectangular apertures

(ii) rectangular cavities with circular apertures.

For structures with rectangular apertures, three slot heights (3.0, 3.5 and 4.0mm) were analysed. Note that the slots extend over the full width of the iris.

For rectangular cavities with circular apertures four geometries have been investigated. The first three models had sharp cornered rectangular cross-sections with cavity heights of 6.0, 6.4 and 7.0mm. Since in practice however such geometries are difficult to machine a final calculation was made for a radiused rectangular section.

All the calculated results are for operation in the $2\pi/3$ mode and for clarity have been normalised as follows. Structure parameters are given as a fraction of the normal CLIC accelerating section values ($\kappa' = 114.8\ M\Omega/m$, $Q = 4329$, $v_g/c = 0.074$), and transverse focusing as a fraction of $\pi/c\lambda$.

Circular cavities with rectangular apertures

The results are summarised in Fig.1. It can be seen that the analytic estimate $G_0/E_Z = \pi/c\lambda$ for an infinitely thin slit only over-estimates the focusing gradients of realistic geometries by 10-20%. With the CLIC nominal accelerating field of 80 MV/m maximum transverse gradients of about 70 T/m would be obtained.

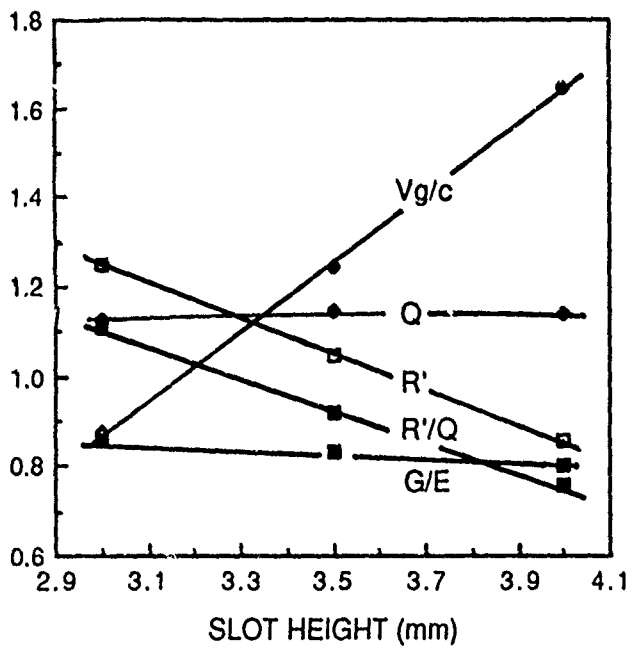


Fig.1 RF properties of slotted iris cavities

Rectangular cavities with circular apertures

The main RF characteristics are summarised in Fig.2.

For a given stored energy the maximum gradient that can be obtained $G_0 \propto (G_0/E_Z)(R'/Q)^{1/2}$. It is found however that although $(R'/Q)^{1/2}$ decreases with decreasing cavity height thelinear increase of (G_0/E_Z) produces a nett overall gain of G_0 for flatter cavities.

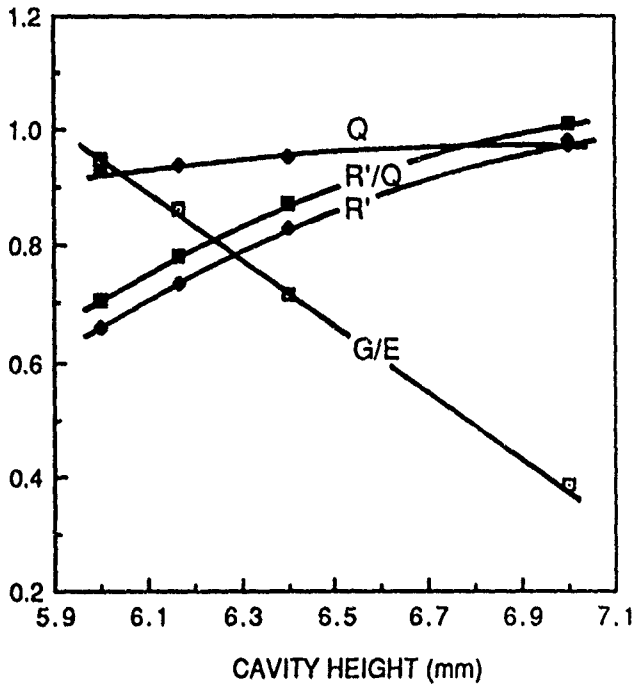


Fig.2 RF properties of rectangular cavities

Comparison of results and practical solutions

Although it is seen from the above that a circular cavity with a 3.5mm slotted iris could produce transverse focusing gradients of 85% of $\pi/c\lambda$. with little or no deterioration in the RF characteristics compared to the normal accelerating sections, it is very difficult to imagine how such a geometry could be machined to have the required radius and surface finish at the aperture for high gradient operation.

The quasi-rectangular cavity with a circular aperture on the other hand is relatively easy to machine. Several precision machined prototype pieces are shown in Fig.3. The fabrication technique is identical to that used for the discs for the normal accelerating sections except that the main body of the cavity is milled.

Transverse focusing gradients of 85% of $\pi/c\lambda$ are obtained with a cavity half height of 3.08mm but at the cost of a 25% reduction in the R' and R'/Q values. Since only about 5% of the linac structure will have asymmetric apertures this reduction is considered acceptable.

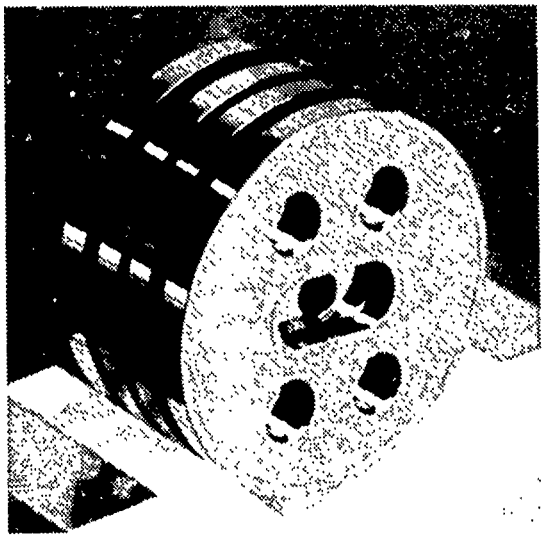


Fig.3 Precision machined discs for RF focusing sections

WAKE FIELD STABILIZATION WITH MICROWAVE QUADRUPOLES

Wakefields induced near the head of a bunch and acting back on trailing parts of the same bunch tend to produce avalanching self deflections. This instability can be stabilized by creating a gradient of transverse focusing strength along the bunch in such a way that the tail is focused more than the head. The method is named BNS damping after the inventors [2]. A linearized stability criterion is given by

$$eN\frac{\partial}{\partial s}W_{\perp} \le U\frac{\partial}{\partial s}k^2 \qquad (3)$$

where the longitudinal coordinate s is mesured from the bunch centre, eN is the bunch charge, eU the particle energy and k the transverse wave number.

In a thin-lens FODO system made of superimposed (static) external and microwave quadrupoles of focusing gradients G_e and G_{rf}, filling fractions ηe and η_{rf} of total linac length, respectively, the wave number k is given by

$$8U\sin\frac{kL}{2} = cL^2(\eta_e G_e + \eta_{rf} G_{rf}) \qquad (4)$$

where the period length L is common to both systems. The microwave transverse gradient G_{rf} may be taken as G_0 from eq. (2) times a form factor α (near unity) representing the actual cavity geometry as discussed above. Inserting this into eq. (4), differentiating with respect to s and noting that $\partial\varphi/\partial s = 2\pi/\lambda$ one finds

$$U\frac{\partial}{\partial s}k^2 = \eta_{rf}\alpha\frac{E_z}{\lambda^2}\pi^2\cos|\varphi_0|\frac{\mu_0}{\cos\frac{\mu_0}{2}} \qquad (5)$$

where φ_0 and μ_0 are the RF phase and the transverse phase advance per period (k_0L) respectively, taken at the bunch centre. This can be readily inserted into the stability criterion [3]. The particle energy cancels out. Inserting typical values (CERN Linear Collider values for example) of $N = 6 \times 10^9$, $\partial W_{\perp}/\partial s = 1.1 \times 10^{21} V/Asm^3$ (ref.[4]), $\alpha = 0.85$, $E_z = 80$ MV/m, $\lambda = 1$ cm, $\phi o = 0$ (at the top of the accelerating wave and $\mu_0 = 90°$ gives $\eta_{rf} = 0.07$ for stability - a very satisfactory result considering that the microwave quadrupole sections contribute to acceleration.

Compared with the customary method of satisfying the stability criterion by means of a (large) energy spread within the bunch this method has the advantage of not requiring special manipulations towards the end of the linac in order to reduce the energy spread to the requirement of the final focus. Also, a very large spread would be required to stabilize the CLIC wake fields. The strength of the (static) external focusing system does not explicitly appear in eq. (5). Such a system is likely to be required, however, for gaining flexibility of adjustment and in order to limit the spread of transverse phase advance μ within the bunch, given by

$$\frac{\sin\frac{\mu}{2}}{m+\sin\varphi} = \frac{\sin\frac{\mu_0}{2}}{m+\sin\varphi_0} \qquad (6)$$

with $m = \eta_e G_e/\eta_{rf} G_{rf}$.

In practice the situation is complicated by the wake fields' nonlinearity (but also the possibility of nonlinear wake field damping called "autophasing" [3]), by tolerances or misalignments and jitter of quadrupoles and accelerating sections (made severe by the rapid incoherence of oscillations associated with a large spread), and by the small energy spread required by the final focus system. A detailed treatment of these and associated problems with concomitant simulations are presented elsewhere at this conference [4].

REFERENCES

[1] W.Schnell, Microwave quadrupoles for linear colliders,CERN-LEP-RF/87-24 (1987).

[2] V.E.Balakin,A.V.Novokhatsky and V.P.Smirnov, VLEPP Transverse beam dynamics, 12th Internat. Conf. on High Energy Accelerators, Fermilab 1983 (119).

[3] V.E.Balakin, Suppression of stochastic heating of the beam in a linear collider, Institute of Nuclear Physics, Siberian Department of the USSR Academy of Sciences, Preprint 88-100, Novosibirsk (1988).

[4] G.Guignard, C.Fischer and A.Millich, Investigation on beam damping simulations and the associated model of CLIC, this conference.

[5] I.Wilson and H.Henke, Transverse fosusing strength of CLIC slotted iris accelerating structures, CLIC Note 62 (1988).

[6] H.Hanaki and N.Holtkamp, Focusing characteristics of an accelerating structure with non-circular beam holes, Orsay (1990).

[7] R.B.Palmer, Private Communication.

[8] R.Klatt et al., Proc. 1986 Linear Acc. Conf. (1986)

Design Calculations of the CLIC Transfer Structure

Erk Jensen
C E R N
CH-1211 Geneva 23
Switzerland

Abstract

The power required for acceleration in the main linac of CLIC (CERN Linear Collider, see eg. [1]) is generated by a high current, moderate energy drive beam. The transfer structure will extract this power at 30 GHz from the drive beam. A design presently under study consists simply of a circular cylindrical beam tube of relatively large diameter (16 mm) which is coupled to the wide side of one or more rectangular output waveguides through rows of coupling holes. Output waveguide cutoff and coupling hole spacing are chosen such that the beam is synchronous with the backward TE_{10} wave of the output waveguide at 30 GHz. The RF pulse length is controlled by the length of coupling sections. By placing output waveguides on both sides of the beam tube, 160 MW/m can be extracted with section lengths of 35 cm. Numerical studies show that the desired power level can be reached with small coupling holes. Excitation and propagation of parasitic higher order modes in the beam tube limit the design. The TM_{01} backward wave in the beam tube can efficiently be suppressed using "staggered coupling."

1. INTRODUCTION

Synchronism is a necessary condition for continuous interaction of the drive beam and some electromagnetic wave in the transfer structure. In a straight cylindrical tube, synchronism is impossible. Periodic disturbances or dielectrics are necessary; we use a periodic structure. In the transfer structure, the synchronism condition determines the frequency of the output signal.

The CLIC drive beam should persist over the whole accelerator length of $\simeq$13 km. In order not to deteriorate the beam over this length, not more than the required power of $\simeq$160 MW/m should be extracted, i.e. the structure should exhibit a **low beam impedance** (the drive beam current peak value is $\simeq$20 kA!). Particularly dangerous are transverse wakefields which might cause beam break-up. They scale with the inverse 3rd power of the aperture diameter. For these reasons the transfer structure should have quite a large inner cross section, and the periodic disturbance should be very shallow.

As a third condition, the output **pulse length** should be exactly 85 RF periods, because the drive beam is accelerated at the 85th sub-harmonic (at 350 MHz), and the time gaps in the drive bunch train have to be spanned by energy storage in the transfer structure. Four of these 2.8 ns bunches make up the fill time of the CLIC main linac structure.

The most obvious type of structure satisfying the above conditions is a wide circular tube with very shallow wall corrugations [2]. We have analyzed this type of structure in some detail. The output waveguide was aligned in parallel to the beam tube and coupled to it by a series of coupling holes spaced by the structure period. It turned out that the periodic disturbance caused by the coupling holes themselves is sufficient to attain the necessary power level with a beam tube diameter of 16 mm. This makes the beam tube cylindrical.

The output pulse length T (2.8 ns) is given by

$$T = \frac{L}{v_{gr}} \mp \frac{L}{c}\,, \qquad (1)$$

where L is the length of the structure and v_{gr} the group velocity of the synchronous wave. The minus (plus) sign holds for the forward (backward) wave. To attain the required pulse length with a forward wave calls for a low group velocity which seems not realizable in this case. **Backward wave operation** allows for a group velocity in the order of 0.7 c with a section length of 35 cm.

2. SIMPLIFIED MODEL

In a first, simplified model the excitation of modes in the beam tube is neglected. The field incident on the holes is just the TEM field around the beam. The coupling to the output waveguide is calculated by *Bethe* theory [3]. The contributions coupled through the holes are then just phase-shifted due to the output waveguide dispersion and added at the output.

The resulting amplitude of the TE_{10} wave at the output is simply

$$A(0) = \mathrm{j}\, I_0 \frac{\sqrt{Z_0}}{2R\lambda} \sqrt{\frac{2}{ab}}\, \frac{2}{3} r_{11}^3 \left\{ \sqrt{\frac{Z_{WG}}{Z_0}} + 2\sqrt{\frac{Z_0}{Z_{WG}}} \right\} \frac{\sin(N\,\phi(\omega))}{\sin(\phi(\omega))}\, e^{-\mathrm{j}(N-1)\phi(\omega)}\,, \qquad (2)$$

the output power is $|A(0)|^2$. The other parameters are:

I_0	*Fourier* component of beam current at ω
Z_0	$c\mu_0 = 377\,\Omega$
R	beam tube radius
a (b)	output waveguide width (height)
r_{11}	coupling hole radius
Z_{WG}	$\omega\mu_0/\beta_{WG}$
N	cells per section

0-7803-0135-8/91$03.00 ©IEEE

$\phi(\omega)$	$(\omega/c + \beta_{WG})\, p/2$
β_{WG}	$\sqrt{(\omega/c)^2 - (\pi/a)^2}$
p	structure period = cell length

The $\sin(N\phi)/\sin\phi$-term in (2) accounts for the finite length of the structure. The proportionality of the output power to the 6th power of the coupling hole radius is due to *Bethe* theory. In a refined theory [4], where also the coupling hole depth is considered, this dependence becomes even stronger.

3. MODAL ANALYSIS

Due to its large diameter the beam tube represents a waveguide well above cutoff. The field of the beam incident on the coupling holes will not only be coupled to the output waveguide, but also be scattered back into the beam tube, exciting waves in both forward and backward direction. Also, the wave in the output guide will be coupled back into the beam tube. The field thus generated in the beam tube (the wakefield) might act back on the beam and hence must not be neglected.

To account for these effects we use as a second, refined model, a modal presentation of the total field consisting of the "space charge field" around the beam plus the "wakefield" excited by the coupling holes in both the beam tube and the output waveguide. In this representation, the fields are given by

$$\begin{aligned} \vec{B} &= \sum_l A_l \vec{b}_l \,, \\ \vec{E} &= \sum_l A_l \vec{e}_l - \frac{1}{j\omega} \vec{J} \,. \end{aligned} \tag{3}$$

$\vec{e}_i$ and $\vec{b}_i$ are the normalized electric and magnetic modal fields of mode i respectively. The last term in (3) assures that only the divergence-free part of $\vec{E}$ is expanded. It remains to determine the z-dependent amplitudes A_i.

The current density $\vec{J}$ is assumed to have only a z-component and a *Gaussian* transversal distribution. If all particles move with c it is given by

$$J_z = \frac{I_0}{2\pi\sigma^2} \exp\left(-\frac{1}{2}\left(\frac{\rho}{\sigma}\right)^2 - j\,\frac{\omega}{c} z \right). \tag{4}$$

The finite beam width has been introduced here not only for a more realistic model, but also substantially improves the numerical convergence.

Sections between holes: The excitation of a mode i in a straight beam tube of length z is described by

$$\begin{aligned} A_i(z) = &\left[A_i(0) - \frac{I_0}{2} \frac{\kappa_{i0}}{j\frac{\omega}{c} - \gamma_i} \right] \exp(-\gamma_i z) \\ &+ \frac{I_0}{2} \frac{\kappa_{i0}}{j\frac{\omega}{c} - \gamma_i} \exp\left(-j\,\frac{\omega}{c} z\right). \end{aligned} \tag{5}$$

The integrals for the excitation coefficients κ_{i0} can be evaluated analytically, for TM_{0i} modes they are

$$\kappa_{i0} = \frac{\chi_{0i} B_i}{j\omega R^2 \sqrt{\pi}\, J'_0(\chi_{0i}) \sqrt{Z_i}} \,, \tag{6}$$

where the factor B_i accounts for the transverse position and shape of the beam, for a centered beam (4) it is

$$B_i = \exp\left(-\frac{1}{2}\left(\frac{\chi_{0i}\,\sigma}{R}\right)^2 \right) \tag{7}$$

for TM_{0i} modes, and zero otherwise.

The result (5) consists of a homogeneous solution with the propagation constant γ_i, and a particular solution propagating $\propto \exp(-j\omega z/c)$ with the exciting beam. The first part describes the wakefields. It is excited only at discontinuities (at the holes) and vanishes for an infinitely long beam tube. The particular solution is just the modal expansion of the TEM field of the beam.

Coupling hole sections: The wave amplitudes A_{i2} after a (short) coupling hole section are given in terms of the amplitudes A_{i1} before it by

$$A_{i2} = A_{i1} \pm \frac{j\omega}{2} \sum_k \left\{ p_e \vec{e}_k \cdot \vec{e}_{-i} + p_m \vec{b}_k \cdot \vec{b}_{-i} \right\} A_{k1} \,. \tag{8}$$

p_e and p_m are the electric and magnetic hole polarizabilities respectively. The plus (minus) sign is valid if i is a forward (backward) wave.

Matrix of a cell: If the beam is treated as another waveguide mode with amplitude I_0 and propagation constant $j\omega/c$, the results of (5) and (8) can be combined in matrix form; this is the transmission matrix of a cell of the periodic structure – its N-th power is the matrix of the transfer structure section consisting of N cells. Taking the boundary conditions into account, the overall behaviour of the structure is calculated.

4. SAMPLE RESULTS

The actual transfer structure cross section is sketched in Figure 1. Opposite coupling holes assure the suppression of unwanted dipole modes. A second pair of coupling holes is staggered by half a cell period.

Figure 2 shows as an example the inverse *Fourier* transform (time domain) output at one of the 4 output waveguides of a transfer section. The beam tube diameter is 16 mm, the coupling hole diameter 2.8 mm. The assumed drive bunch train is as foreseen for CLIC: 11 bunchlets of 160 nC each with a repetition rate of 30 GHz, repeated 4 times with a repetition rate of 350 MHz.

A power of 40 MW (76 dBW = 76 dB above 1 W) is attained. The results are in good agreement with

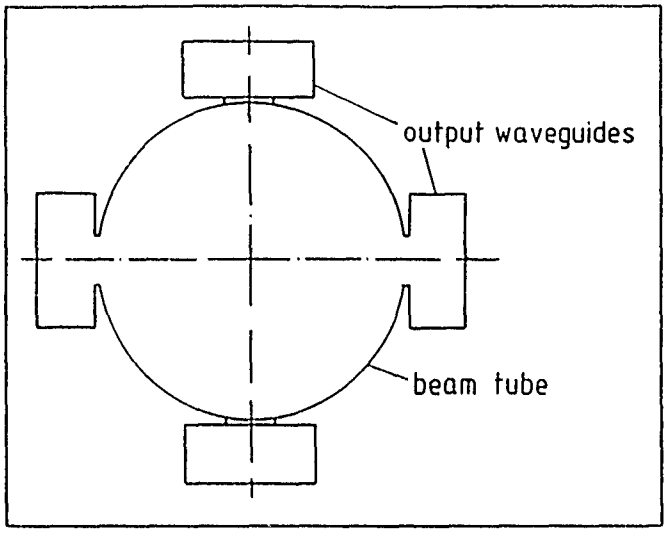


Figure 1. **Cross section of the transfer structure.** 4 output waveguides are coupled to the beam tube. One pair of coupling holes is offset from the other by half a cell length (staggered).

measurements of a scaled model [5], but predict a by about 2 dB higher output level.

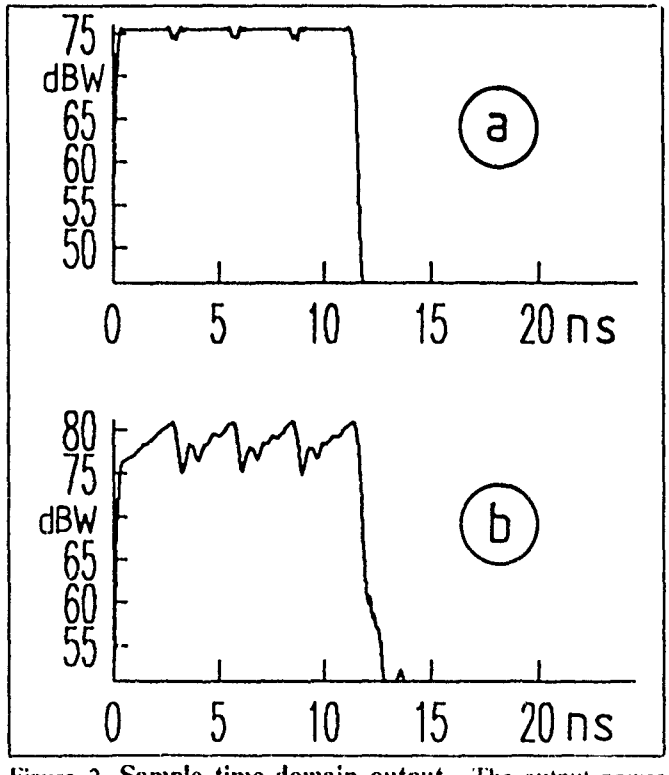


Figure 2. **Sample time domain output.** The output power in 1 of 4 waveguides is plotted versus time. Prediction by a) simplified model, and b) modal analysis

5. STAGGERED COUPLING

The most dangerous spurious mode is the TM_{01} backward wave of the beam tube. For the considered geometry, it is synchronous at about 27 GHz. The power in this mode is lost and might destroy the beam. By staggering 2 rows of coupling holes [6] as already indicated in Figure 1, the effective structure period for monopole modes inside the beam tube is halved, thus pushing their synchronous frequencies much higher. The effect of this staggering on the spectrum of the TM_{01} backward wave is sketched in Figure 3. The peak at 27 GHz vanishes completely, the peak at 30 GHz is decreased by $\simeq$15 dB.

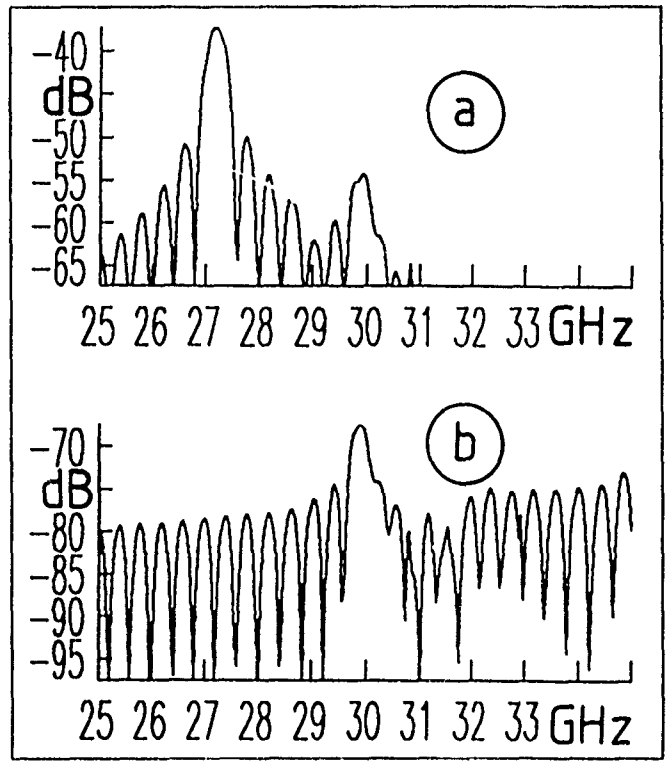


Figure 3. **Effect of staggered coupling.** The relative power in the TM_{01} backward wave plotted versus frequency. a) opposite, and b) evenly staggered coupling hole pairs.

Acknowledgement

The author wishes to thank L. Thorndahl for his help.

References

[1] S. van der Meer, "The CLIC approach to linear colliders," CERN-PS/89-50 (AR), CLIC Note 97, 1989.

[2] W. Schnell, "The drive linac for a two-stage RF linear collider," CERN-LEP/88-59 (RF), CLIC Note 85, 1988.

[3] H. A. Bethe, "Theory of diffraction by small holes," *Phys. Rev.*, vol 66, pp 163 - 182, 1944.

[4] F. Sporleder, "Erweiterte Theorie der Lochkopplung," *Dr.-Ing.-Thesis*, Technische Universitat Braunschweig, 1976.

[5] I. Thorndahl, "Model Work on a Transfer Structure for CLIC," *this conference*, 1991.

[6] W. Wunsch, private communication, 1991.

Model Work on a Transfer Structure for CLIC

L. Thorndahl
CERN, 1211 Geneva 23, Switzerland

Abstract

The structure is needed to produce for acceleration in the CLIC (CERN linear collider) main linac [1] 12 ns, 30 GHz and 40 MW RF pulses. The structure input is four trains (spaced by 2.84 ns) of 11 drive bunchlets (10^{12}e, $\sigma < 1$ mm) separated by 33.3 ps. A novel concept based on a smooth beam chamber with coupling holes into waveguides and the TEM wave associated with the drive beam bunchlets is proposed and analysed in scale models. The TEM wave is simulated with transmission lines. The structure response is measured in the frequency domain and then multiplied with the bunchlet spectrum, yielding via a subsequent inverse Fourier Transform, the amplitude and phase versus time of the resulting 30 GHz pulse.

INTRODUCTION

The non-availability of 30 GHz power tubes with appropriate power levels (~ 100 MW) for achieving acceleration in colliding linacs has prompted the use of two-beam accelerators (TBA). In a TBA a primary (or drive) beam of relatively high current and relatively low energy is used to produce the necessary high frequency power for accelerating the secondary (or driven) high energy, low current beam. The high frequency radiation is generated during the interaction of the primary beam with some "extraction" structure. The properties of the CLIC drive beam have been discussed in detail elsewhere [2] and so this paper will be concerned primarily with the results of studies of the extraction cavity, or CLIC transfer structure (CTS).

It is intended that the CLIC drive beam will be fully relativistic (~ 5 GeV) and accelerated at 350 MHz using superconducting cavities such as those planned for LEP. Generation of the desired 30 GHz power for the secondary beam will be by direct deceleration of the tightly bunched ($\sigma_z < 1$ mm) primary beam in the CTS. A fundamental requirement of the CTS is that it should exhibit a very low shunt impedance [2].

A first version [3] [4] with an aperture of 4 mm was studied both with MAFIA codes and model measurements but had to be abandoned because of its high transverse and longitudinal resistive wall impedances. To reach acceptable impedances it was considered necessary to increase the aperture to at least 12 mm[1] with the unavoidable disadvantage of overmoded beam chamber.

[1] longitudinal/transverse impedance scales approximately with the inverse linear/inverse cube of the aperture size.

DESCRIPTION OF A NEW CTS

The structure shown in Fig. 1 consists of a smooth round beam chamber containing coupling holes (at constant spacing, in the beam direction) into four rectangular waveguides. The TEM wave accompanying bunchlets has radial electrical fields and azimuthal magnetic ones at the holes causing constructive excitation of the TE_{10} backward mode in the waveguide (useful output) and non constructive excitation of the forward mode (not useful, terminated). The backward outputs from all four waveguides are intended for the acceleration in four modules of the main linac. The excitation of TE modes in the beam chamber is avoided by situating coupling holes always by pairs in symmetry with respect to the chamber axis.

The launching of TM_{01} backward waves is suppressed by offsetting in the beam direction by $\lambda/4$ the coupling holes of the top and bottom waveguides with respect to those on the left and right hand sides. Though there is no cancellation of TM_{01} forward waves, they are believed to be small in amplitude.

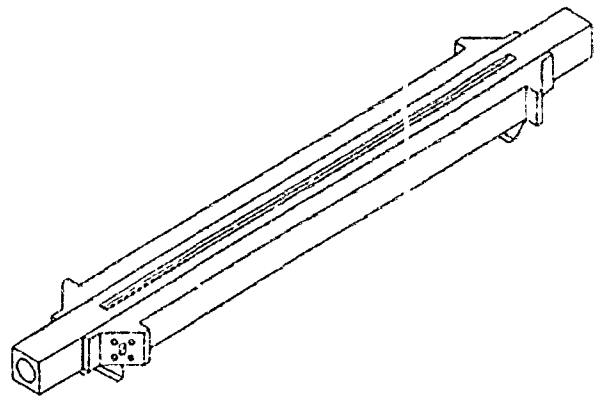


Figure 1 CTS with round beam chamber 16 mm Ø in the middle. The groove at the top is the TE_{10} waveguide with coupling holes into the beam chamber. The lids of the three other channels and an output flange are visible.

PRINCIPLE

The requirement that the structure should work as a "pulse stretcher" by extracting from a train of 11 bunchlets (lasting 333 ps) an RF pulse lasting 2.84 ns is met by using a backward wave in the waveguide as shown in Fig. 2 where a single bunchlet is followed as it crosses the structure. In the case of 11 bunchlets there is constructive superposition of 11 successive RF waves in the waveguide spaced in time by one RF period (33.3 ps) to create a rising flank (333 ps), a flat

0-7803-0135-8/91$03.00 ©IEEE

top (2.5 ns) and a falling flank (333 ps) for the output pulse. Four successive pulses create a global pulse approximately 11 ns long to fill a module of the CLIC main linac.

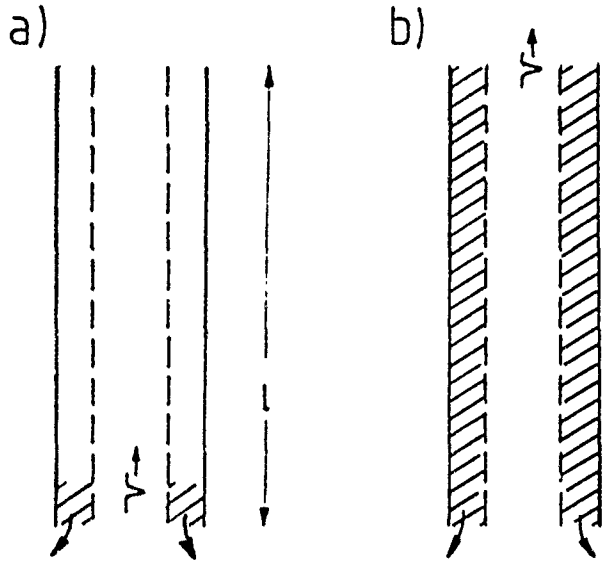


Figure 2 a) Arrival of a bunchlet at the structure. The waveguide is immediately energized and yields output power.
b) The bunchlet exits the structure ℓ/c later leaving the waveguide energized over its full length ℓ. It then empties in ℓ/β_{gr} c.
Total pulse length: $T = \ell/c(1 + 1/\beta_g)$
β_g: normalized group velocity in the waveguide.

There is a linear build-up through constructive interference of a wave sample in the waveguide as it experiences the first bunchlet through the Nth hole then the second through N-1th hole and so on up to the 11th bunchlet through the N-10th hole. The condition for constructive interference with a backward wave is:

$$\phi_b + \phi_w = 2\pi \qquad (1)$$

where ϕ_b is the spatial phase of the first longitudinal beam harmonic (at 30 GHz) and ϕ_w the phase advance of the waveguide TE_{10} mode between holes.

Phase diagram (Brillouin)

Figure 3 gives a simplified qualitative phase diagram of the CTS. The hole spacing (cell length)is chosen to fulfill the condition of constructive interference (1), as indicated by the two horizontal arrows at 30 GHz.

The two dotted arrows at about 27 GHz give the condition for constructive interference between the backward TM_{01} wave in the beam chamber and the forward TEM wave of the bunchlets.

The cut-offs of the TM_{02} and TM_{21} modes are situated above 30 GHz, the quadrupolar TM_{21} being the first one driven by the four-waveguide arrangement (but below cut-off).

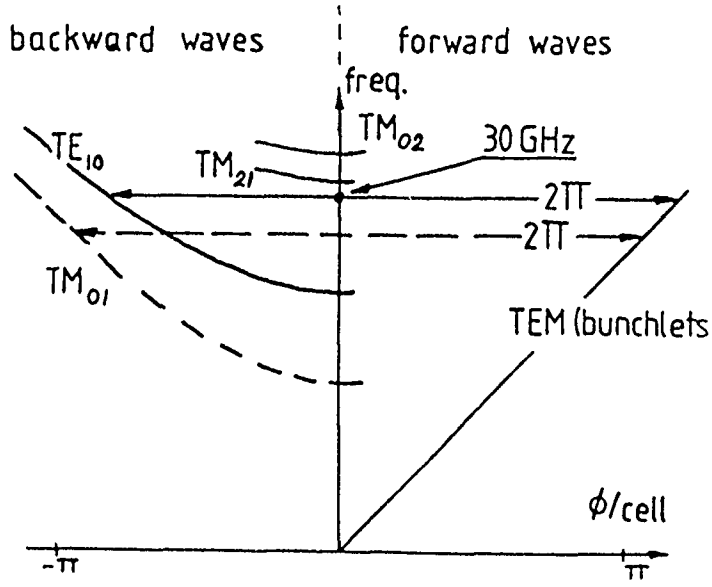


Figure 3 Simplified phase diagram for infinitely small coupling holes

MEASUREMENTS

The TEM fields of the bunchlets are simulated by two transmission lines situated near the top and bottom of the beam chamber so that their characteristic impedance is 50Ω. The lines powered in phase create at the hole positions, for a given total current on the two lines, TEM fields smaller by 24.2 dB than the same beam current situated in the middle of the chamber (See Fig. 4.). (The factor 24.2 dB was found with a separate two-dimensional resistive paper analog model.)

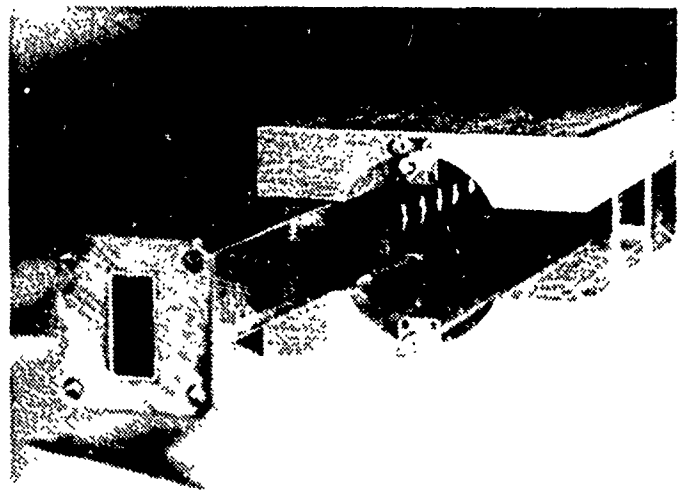


Figure 4 Simplified scaled CTS analog model with only two waveguides. TEM waves are excited with 50Ω transmission lines at top and bottom. Dimensions are larger by a factor 3.33. The operating frequency is thus 9 GHz. Hole diameter. 10.5 mm, hole spacing: 20 mm, 57 holes/waveguide, average beam chamber diameter: 53 mm.

This arrangement allows a network analyser measurement of the frequency response of the CTS, the output signal being the backward wave from the waveguide. (See Fig. 5.)

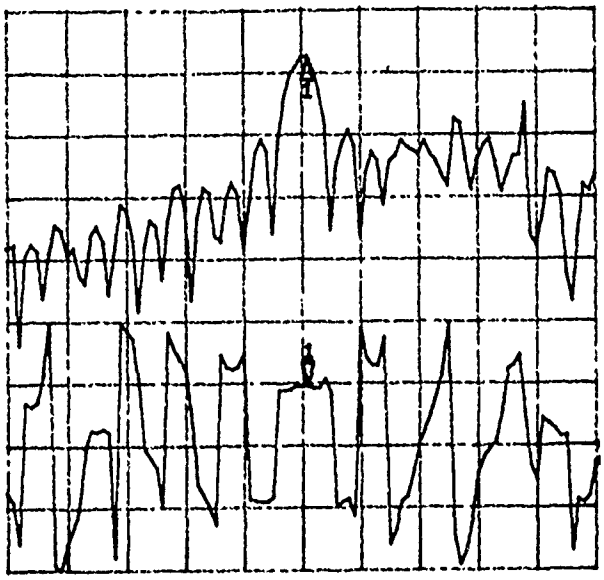


Figure 5 Frequency response of CTS model.
Amplitude 10 dB/div. and phase 90°/div.
Centre frequency 8.875 GHz, 0.2 GHz/div.

The TEM wave (from say the first bunchlet) scattering on the two rows of coupling holes inside this model creates in the beam chamber a TM_{01} backward wave containing about the same measured energy as the wave in one waveguide. This TM_{01} wave is detrimental since it interacts with the following bunchlets, creating an unwanted energy exchange. It can be suppressed by using two pairs of waveguides with coupling holes offset by $\lambda/4$, as described in the introduction and shown in Fig. 1.

Frequency scaling the measured CTS model response (9→30 GHz) and multiplying with the Fourier transform $F_b(f)$ of 11 gaussian pulses spaced by $t_0 = 33.3$ ps, charge $g = 160$ nC and $\sigma = 4$ ps,

$$F_b(f) = g e^{-2\pi\sigma^2 f^2} \sum_{N=1}^{11} e^{-2j\pi N f t_0} \qquad (2)$$

the CTS output spectrum can be calculated with an online desktop calculator.

By applying a subsequent inverse Fourier transform to the output spectrum we obtain the output pulse as a function of time, essentially a 30 GHz oscillation with a phase varying slightly with respect to an ideal 30 GHz source. (See Fig. 6.)

CONCLUSIONS

The model work and [5] show that the specified power level of 40 MW can be achieved with a simple CTS based on a smooth round chamber with coupling holes into parallel adjacent waveguides. Further work on the energy conversion efficiency and the influence of forward TE_{01} waves should by done.

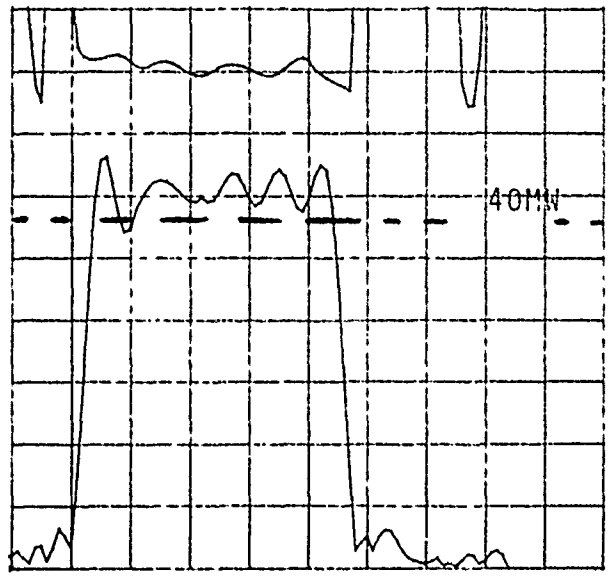


Figure 6 RF phase (20°/div) and amplitude (Amps into 50Ω, 160 A/div) of a CTS pulse caused by four trains of 11 bunchlets. The integration bandwidth for the inverse Fourier transformation is 1 GHz, corresponding approximately to the bandwidth of the driven main linac structure. The amplitude corresponding to the nominal 40 MW is indicated. Time scale 3.2 ns/div.

ACKNOWLEDGEMENTS

E. Jensen suggested the use of the backward TE_{10} wave instead of the forward one that required more structure length with more output pulse distortion. W. Wuensch solved the problems caused by the backward TM_{01} wave in the beam chamber with the proposal to annul it by having four parallel waveguides instead of two. G. Carron and C. Achard helped with model and drawing work. P. Martucci edited and typed the manuscript. Thanks to E. Jensen, W. Schnell, I. Wilson and W. Wuensch for many discussions.

REFERENCES

[1] W. Schnell, "The study of a CERN linear collider, CLIC", CERN LEP-RF/88 48, presented at the Linear Accelerator Conference, Williamsburg, October 1988.

[2] W. Schnell, "A two-stage RF linear collider using a superconducting drive linac", CERN-LEP-RF/86-06, February 1986.

[3] T. Garvey *et al.*, "Studies of a frequency scaled model transfer structure for a two-stage linear collider", Proc. New Developments in Particle Acceleration Techniques (ED. S. Turner), CERN 87-11, Orsay, 1987.

[4] T. Garvey *et al.*, "A radio-frequency transfer structure for the CERN Linear Collider", CERN-LEP-RF/89-25 and CLIC Note 92.

[5] E. Jensen, "Design calculations of the CLIC Transfer Structure", this conference.

HIGHER ORDER EFFECTS IN BEAM-BEAM DEFLECTION

Yu-Chiu Chao and Pisin Chen
Stanford Linear Accelerator Center,
Stanford, California 94309

I. INTRODUCTION

Beam-beam deflection is a useful tool for beam centering and size measurement in existing and future linear colliders [1]. It is indispensable in the Stanford Linear Collider when beam intensity becomes too strong for conventional wire scans. In future linear colliders beam-beam deflection may be one of the few viable methods from which information can be drawn about beam sizes.

Because of the importance of beam-beam deflection at higher intensity, it is crucial to address the problem of disruption. At low intensity, it is enough to use the rigid deflection formula:

$$\langle\phi\rangle_1 = \frac{-2r_eN_2}{\gamma}\frac{1}{\Delta}(1-e^{-\frac{\Delta^2}{2\Sigma^2}}) \qquad (1)$$

where $\Sigma^2 = \sigma_1^2+\sigma_2^2$, ϕ is the deflection angle , r_e the classical electron radius, Δ the impact parameter and σ the transverse RMS beam size. 1 and 2 are beam labels. The limiting cases of (1) are:

$$\langle\phi\rangle_1 = \left(-\frac{r_eN_2}{\gamma}\frac{\Delta}{\Sigma^2}\right) \qquad \Delta \ll 2.23\sigma,$$

$$\langle\phi\rangle_1 = \left(-\frac{2r_eN_2}{\gamma}\frac{1}{\Delta}\right) \qquad \Delta \gg 2.23\sigma. \qquad (2)$$

At high intensity, the bunches steer and deform each other considerably. This leads to a nonlinear deviation from the rigid formula. Below we describe some techniques attempted at modeling this effect.

II. LOWEST ORDER ANALYTICAL CALCULATION

We start with the equations relating the beam distribution and deflection of individual particles. For the 2-beam system in figure 1, a formulation of disruption with $\Delta = 0$ has been laid out in [2]. The same can be applied here except the absence of cylindrical symmetry:

With the distributions $n_0(x,y,z)$ for both beams, the effect on a particle in beam 1 by beam 2 is

$$\frac{d^2\vec{x_1}}{dt^2} = \frac{-4r_eN_2}{\gamma}n_{L2}(-2t-z_1)\int\frac{\vec{x_1}-\vec{x_2}}{|\vec{x_1}-\vec{x_2}|^2}n_{t_2}(\vec{x_2})d\vec{x_2}$$

$$= \frac{-4r_eN_2}{\gamma}n_{L2}(-2t-z_1)\vec{\nabla}_1 f_2(\vec{x_1}), \qquad (3)$$

$$f_2(\vec{x_1}) = \frac{1}{2}\int dx\ dy\ n_{t2}(x,y)\ \ \ln[(x_1-x)^2+(y_1-y)^2]$$

where $\vec{x} = (x,y), \vec{\nabla} = (\partial/\partial x, \partial/\partial y)$. The above equation is solved to the lowest order and then inverted to the same degree of accuracy to derive the change in the distribution of beam 1:

$$\delta n_{t1}(x_1,y_1,t,z_1)$$

$$= \frac{4N_2r_e}{\gamma}g(t,z_1)[n_{t01}\,\nabla_1^2 f_2 + (\vec{\nabla}_1 n_{t01})\cdot(\vec{\nabla}_1 f_2)]. \qquad (4)$$

The same formula applies to beam 2 except for a different initial distribution offset by Δ. Two terms contribute to the angular change of beam 1 : that caused by the distribution change of beam 2, and that by the change in beam 1 itself. Substituting δn_{t2} for n_{t2} and integrating over time, followed by an ensemble average over beam 1:

$$\langle\delta\phi_{1x}\rangle = \left(\frac{D_2}{\sigma_{z2}}\frac{1}{\sqrt{\pi}}\right)D_1\otimes$$
$$\left\{2\sigma_2^2\frac{1}{\Delta}\left[e^{-\frac{\Delta^2}{2(\sigma_1^2+\sigma_2^2)}}-e^{-\frac{\Delta^2}{\sigma_1^2+2\sigma_2^2}}\right]\right.$$
$$\left. - e^{-\frac{\Delta^2}{2\sigma_2^2}}2\sigma_1^2\int_0^\infty dr\frac{1}{r^2}I_1\left(\frac{r\Delta}{\sigma_2^2}\right)Q(r,\sigma_1,\sigma_2)\right\},$$

$$Q(r,\sigma_1,\sigma_2) = \left[e^{-\frac{r^2}{2\sigma_2^2}}-2e^{-\frac{r^2}{2\Sigma^2}}+e^{-\frac{r^2}{2C^2}}\right], \qquad (5)$$

$$C^2 = \left(\frac{\sigma_1^2\sigma_2^2}{\sigma_1^2+2\sigma_2^2}\right),\ D_1 = \frac{r_eN_1}{\gamma}\frac{\sigma_{z1}}{\sigma_1^2},\ D_2 = \frac{r_eN_2}{\gamma}\frac{\sigma_{z2}}{\sigma_2^2}$$

where I_1 is the Bessel function. The remaining integral is well behaved although no closed form can be found.

The contribution to $<\delta\phi_{1x}>$ due to the change in beam 1 itself is equal to (5) with the following substitutions: *interchanging* σ_1 and σ_2 and *replacing* D_1 by D_2.

*Work supported by the Department of Energy, contract DE-AC03-76SF00515.
U.S. Government work not protected by U.S. Copyright.

The total angular change is plotted in figure 2 with nominal SLC parameters ($\sigma_{1,2} = 2\mu$m, $D_{1,2} = 0.1$, $\sigma_{z1,z2} = 1$ mm). It modifies the rigid deflection formula by roughly 0.8% near $\Delta = 0$.

This method takes into account the realistic distribution and does not rely on transverse symmetry. It can be iterated to obtain progressively better results. The algebra however is formidable.

III. RIGID TWO-DISK MODEL

To focus on the nonlinear nature of the problem , we developed a conceptual model to elucidate the disruption effects at different Δ as depicted in Figure 3. The longitudinal distributions have been compressed into two δ-function peaks $2\sigma_z$ apart, each carrying a transverse Gaussian distribution with half of the total charge . The whole process of bunch crossing is concentrated in three steps corresponding to the coincidences of the "disks". At each crossing the rigid deflection formula for transverse Gaussian distributions is used to calculate the kick on each disk, which in turn is used to propagate the disk to the next crossing point. The kicks at each step are compounded towards the end. In the following D is as defined in Section II, x' is the average deflection angle .

Small impact parameter - Suppression

In this case after the 2-disk crossing is complete as in Figure 3, the compounded kick received by beam 1 is

$$x' = -\frac{1}{2}\frac{r_e N}{\gamma\sigma_\perp}\frac{\Delta}{\sigma_\perp}\left(1-\frac{1}{4}D\right). \qquad (6)$$

Thus the effect of disruption is a suppression of the rigid deflection result (2) . This can be understood since at small Δ the deflection force decreases with Δ. As disruption effect pulls the two beams closer , the deflection is reduced.

Large impact parameter - Enhancement

In the regime where the two beams are far apart transversely, we can use the second formula in (2) and get:

$$x' = -\frac{2r_e N}{\gamma\sigma_\perp}\left(\frac{\sigma_\perp}{\Delta}\right)\left[1+D\left(\frac{\sigma_\perp}{\Delta}\right)^2\right]. \qquad (7)$$

Thus the net effect is an enhancement for large Δ.

Near maximum deflection - Shift of the peak

Disruption shifts the deflection peak which can serve as a useful signature. We can calculate this from the expansion of equation (1) around the peak ($\Delta \approx 2.23\sigma$). This is then used to calculate the shift by disruption:

$$\frac{\{\text{Shift of peak}\}}{\sigma} = 0.3190D. \qquad (8)$$

These results agree with that of Section II.

IV. SEMI-RIGID TWO-DISK MODEL

The two-disk model is generalized to include changes in the second moment as well as a continuous treatment over the whole range of Δ. This is achieved via a program combining the analytical expression for single particle deflection and multiparticle tracking over a continuous range of impact parameters. The longitudinal distributions are again compressed into two δ-disks. The transverse distributions are however flexible by taking on a Gaussian distribution of particles, each allowed to move independently. The kick a particle receives from a Gaussian bunch is given by

$$\Delta\phi_{x,y} = -\frac{2r_e N}{\gamma}\frac{\Delta_{x,y}}{\Delta^2}\left(1-e^{-\frac{\Delta^2}{2\sigma^2}}\right). \qquad (9)$$

Each particle is propagated independently between crossings. Before the next kick is applied, the transverse RMS value as well as the centroid shift is calculated and substituted into (9) to obtain the next kick for each particle.

Figure 4 shows such a calculation where the rigid deflection formula (1) , the deflection of rigid 2-disks and that including second moment changes are compared. The effect of the second moment counteracts that due to the rigid 2-disk model, especially at small Δ, where the pinching of the beams enhances the deflection the most.

V. TRACKING RESULTS

Tracking has been employed to simulate the disruption effect in the realistic SLC environment. In some cases the accuracy is limited by the computer capacity we could muster. In the simulation each beam has 20000 particles meshed into a 32 × 32 grid transversely and 100 compartments longitudinally. Simulation was carried out for different disruption parameters D and different optical conditions defined by the divergence parameter A given in [2]: $A = (\sigma_z/\beta^*)$, which is a measure of the inherent divergence with β^* being the lattice beta at the collision point. Figures 5(a) and (b) show tracking results for different D and A, with $D = 0.1, A = 0.05$ corresponding to the SLC running condition. The simulation becomes difficult as Δ increases and cylindrical symmetry is thus less exact.

VI. CONCLUSION

We demonstrated different approaches in addressing disruption effects in beam-beam deflection. Short of an analytical scheme which encompasses all essential features of disruption at non-zero Δ, we settle for methods which have different emphases on the problem. The results are consistent to a large degree. Extensions of these techniques, in particular the semi-rigid disks and multi-particle tracking, are being worked on for improved understanding of this phenomenon.

REFERENCES

[1] W. Koska et al, Nucl.Inst.Meth. A286:32, 1990
R. Erickson, SLAC-PUB-4479, November 1987

[2] P. Chen and K. Yokoya, Physical Review D 38, 9871988

[3] Y. Chao and P. Chen, SLAC-PUB 5221,1990

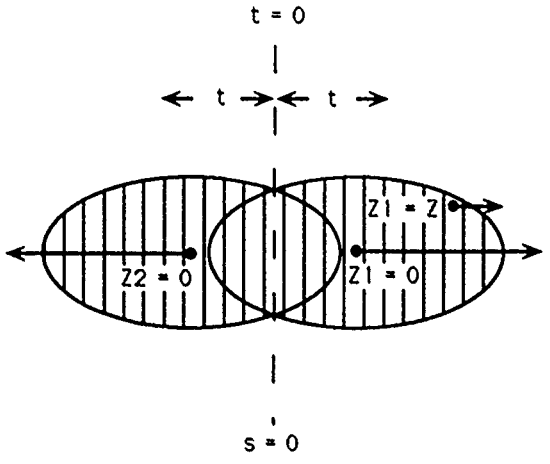


Figure 1. 2-beam system in longitudinal dimension

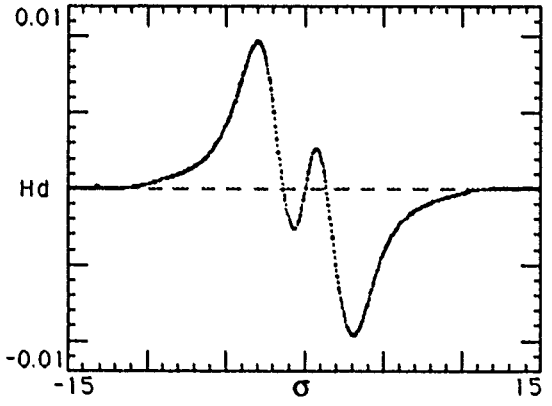


Figure 2. Net effect of disruption from analytic calc.
$Hd = (D\sigma t) / (2\,\sigma z)$

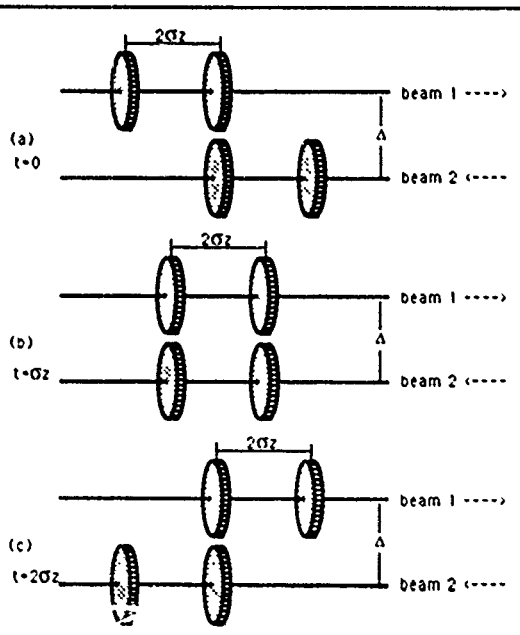


Figure 3. The conceptual 2-disk model

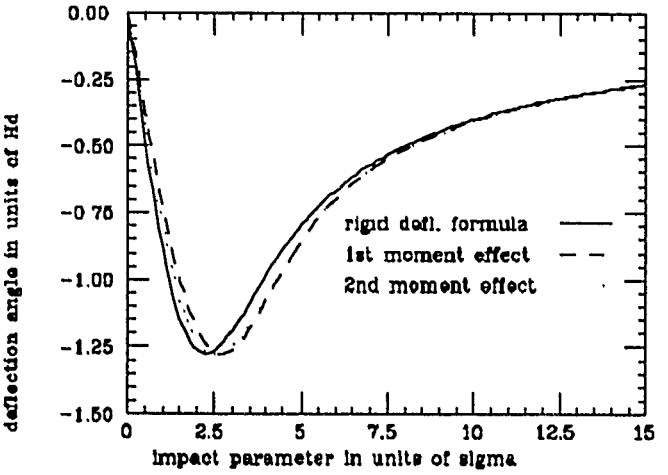


Figure 4. zero, 1st and 2nd moment disruption effect

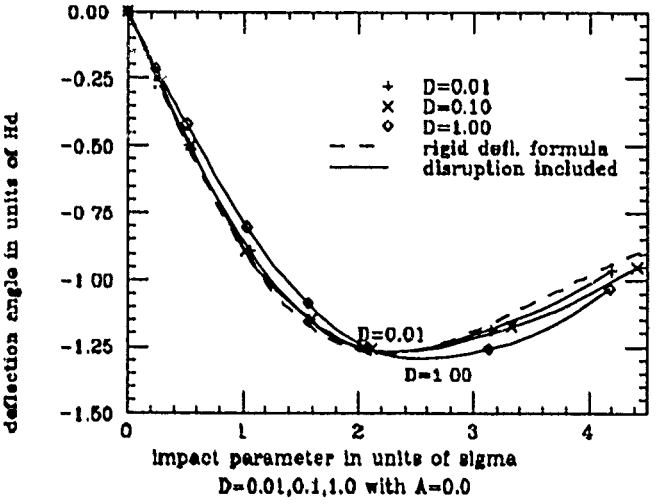


Figure 5(a).Tracking result with A=0.0

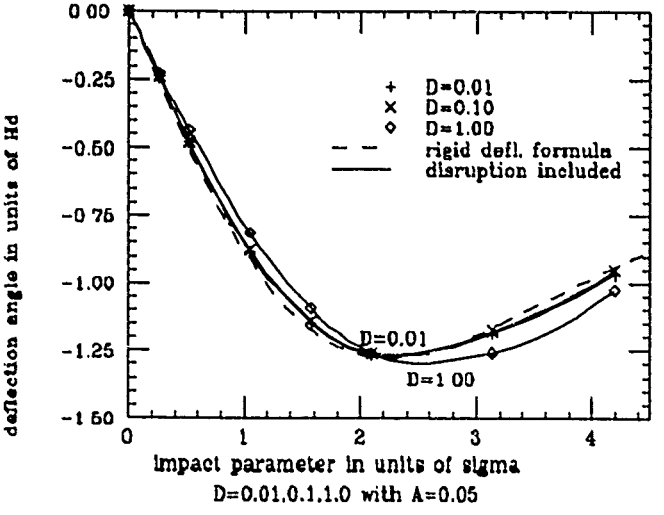


Figure 5(b).Tracking result with A=0.05

Beam-Beam Deflection and Beamstrahlung Monitor Response for Tilted Elliptic Beams*

V. Ziemann
Stanford Linear Accelerator Center, Stanford University, Stanford, CA 94309

ABSTRACT

At the interaction point of the SLC two oppositely running bunches with energies of 46 GeV and transverse extensions of a few microns are brought into collision. The strong electric and magnetic fields produced by one bunch lead to a deflection of the other bunch and to the emission of synchrotron radiation of critical energies of a few 10 MeV. This radiation, coined beamstrahlung, is detected in a Čerenkov monitor. In this paper a simulation code for the beam-beam interaction of two tilted elliptic beams is presented. A closed expression for the deflection angles is presented and the number of generated Čerenkov photons is calculated.

INTRODUCTION

At the interaction point of the SLC electron and positron bunches with a few times 10^{10} particles and bunch lengths of about 1 mm collide head on. This large number of particles in that small volume gives rise to large electromagnetic fields that the bunch carries along. Peak values of the magnetic fields in excess of 10 T occur which deflect the particles in the oppositely running bunch with deflection angles of up to 200 μrad. The effect of the fields can be characterized by a *local bending radius* ρ by which the oncoming particles are deflected. It is given by [1]

$$\frac{1}{\rho(x,y,t)} = |\Theta(x,y)| \frac{1}{\sqrt{2\pi}\sigma_z/2} \exp\left[-\frac{(ct)^2}{2(\sigma_z/2)^2}\right] , \quad (1)$$

where $\Theta(x,t)$ is the integrated deflection angle on the passage through the target bunch of length σ_z as is obvious from $|\Theta(x,y)| = \int_{-\infty}^{\infty} c\,dt/\rho(x,y,t)$. Thus the total deflection angle $\Theta(x,y)$ does not depend on the bunch length σ_z, but ρ does.

All transverse dependence of the deflection angle is buried in $\Theta(x,y)$, which for a general elliptic beam, characterized by its covariance matrix σ_{ij}, is given by [1]

$$\Theta(x,y) = \Delta y' + i\Delta x' = -\frac{2N_t r_e}{\gamma_r} F(x,y,\sigma_{ij}) , \quad (2)$$

$$F(x_1,x_2,\sigma_{ij}) = \frac{\sqrt{\pi}}{\sqrt{2(\sigma_{11}-\sigma_{22}+2i\sigma_{12})}}$$

$$\times \left\{ w\left[\frac{x_1+ix_2}{\sqrt{2(\sigma_{11}-\sigma_{22}+2i\sigma_{12})}}\right] - e^{-\frac{1}{2}\sum_{i,j}^{2}(\sigma^{-1})_{ij}x_i x_j} \right.$$

$$\left. \times\, w\left[\frac{(\sigma_{22}-i\sigma_{12})x_1 + i(\sigma_{11}+i\sigma_{12})x_2}{\sqrt{\sigma_{11}\sigma_{22}-\sigma_{12}^2}\sqrt{2(\sigma_{11}-\sigma_{22}+2i\sigma_{12})}}\right] \right\} , \quad (3)$$

where N_t is the number of particles in the target beam and γ_r is the energy of the deflected particle in units of the electrons rest mass.

* Work supported in part by Department of Energy contract DE-AC03-76SF00515

U.S. Government work not protected by U.S. Copyright.

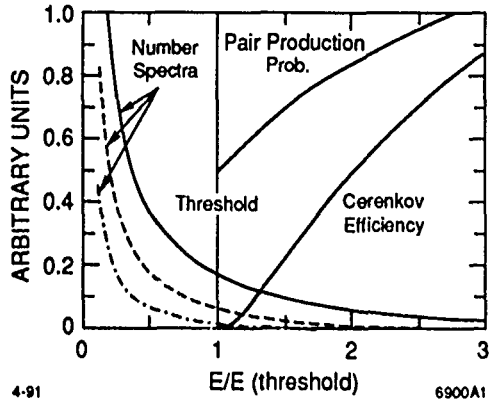


Figure 1. The pair production probability, Čerenkov photon generation efficiency and photon number spectra with critical energies of 1/2 (dotdashed), 1 (dashed) and 2 times (solid) the Čerenkov threshold. The vertical bar at 1 marks the Čerenkov threshold.

The bending radius $\rho(x,y,t)$ a particle experiences on its traversal of the oncoming bunch determines the spectrum of the emitted beamstrahlung, which is characterized by its critical energy $\varepsilon_c = 3\hbar c\gamma^3/(2\rho)$. Thus the number of beamstrahlung photons emitted per unit time and unit energy interval is given by [2]

$$\frac{dN}{d\varepsilon\,dt}\{\varepsilon, \varepsilon_c[\rho(t)]\} = \frac{1}{\sqrt{3}\pi}\frac{\alpha^2}{r_e mc}\frac{1}{\gamma^2}\int_{\varepsilon/\varepsilon_c}^{\infty} ds\, K_{5/3}(s) , \quad (4)$$

where $K_{5/3}$ is a Bessel function of fractional order [3]. Clearly, the emitted beamstrahlung spectrum depends on the local bending radius the radiating particle experiences through the critical energy ε_c. Of course the "hardest" spectrum is emitted when the bending radius is minimum at the core of the target bunch, whereas in the tails only a "soft" spectrum is emitted. Apparently, the spectrum varies as the radiating bunch traverses the target bunch. Photon number spectra for different critical energies are shown in Fig. 1.

THE BEAMSTRAHLUNG MONITOR

The beamstrahlung emanating from the interaction point is detected by a monitor about 40 m downstream. The monitor is also exposed to the radiation of a strong bending magnet and has to discriminate the photons generated in the bending magnet with critical energies of 2 MeV from the fewer photons generated in the beam-beam interaction with critical energies an order of magnitude larger.

The beamstrahlung monitor consists of a converter plate that converts the incident photons into e^+e^- pairs. This probability is given by the Heitler-Sauter cross section [4] for $\gamma \to e^+e^-$ processes which has a logarithmic dependence on the energy of the incident photon.

The generated e^+e^- pairs then travel through a gas volume made of ethylene at 1/3 atmosphere where they emit Čerenkov light. The Čerenkov photons are subsequently passed through a light channel by mirrors and are then detected by photo multiplier tubes. The threshold energy is determined by the gas and is about 25 MeV for the current monitor which leads to a $\gamma_0 \approx 50$. In Refs. [1, 5] it was shown that the number of Čerenkov photons depends on the energy of the incident photon γ_B simply according to $(1/\gamma_0 - 1/\gamma_B)^2$, as shown in Fig. 1 by the lower curve starting at the threshold. Here the energy of the photon γ_B is given in units of electron rest mass.

In order to determine how many Čerenkov photons are produced from the incident radiation characterized by its critical energy ε_c we have to integrate the number spectrum of incident photons weighted by the e^+e^- pair production probability and the probability of emitting a Čerenkov photon. This calculation has to be done for different critical energies in order to obtain a relation between the local bending radius and the number of generated Čerenkov photons per unit time [1]

$$\frac{dN_c}{dt}(x,y,t) = \Omega_0 I_0(\varepsilon_0, \varepsilon_c(x,y,t)) \,, \qquad (5)$$

where Ω_0 contains all the information about the hardware of the Čerenkov monitor. $I_0(\varepsilon_r\ \varepsilon_c)$ is given by a complicated integral that is numerically evaluated in Ref. [1]. I_0 vanishes rapidly for small $\varepsilon_c/\varepsilon_0$ due to the decreasing tail of the "soft" spectrum emitted by the particles while they traverse the tails of the target beam.

From the dependence of I_0 on $\varepsilon_c/\varepsilon_0$ we can deduce scaling relations for the beamstrahlung flux. It turns out [1] that $I_0 \propto (\varepsilon_c/\varepsilon_0)^4$ for $\varepsilon_c/\varepsilon_0 \lesssim 0.7$. Since $\varepsilon_c \propto 1/\rho$ we can use Eqs. (1)-(2) and obtain the following scaling relation for the number of Čerenkov photons

$$\int \frac{dN_c}{dt} dt \propto \frac{N_{target}^4 N_{source}}{\sigma_z^3 \gamma_{source}^4} |F(x,y,\sigma_{ij})|^4 \,, \qquad (6)$$

where all transverse dependence is buried in the function F, defined in Eq. (3).

The Simulation Algorithm

Using Eq. (5), it is easy to calculate the total number of Čerenkov photons generated during a collision by integrating dN_c/dt over t, and averaging over the transverse dimensions x and y

$$N_c = \int_{-\infty}^{\infty} dx \int_{-\infty}^{\infty} dy\, \psi_r(x,y) \int_{-\infty}^{\infty} dt\, \frac{dN_c}{dt}(x,y,t) \,, \qquad (7)$$

where $\psi_r(x,y)$ is the transverse particle distribution of the radiating beam, assumed to be Gaussian with centroid position X_i and covariance matrix $\tilde{\sigma}_{ij}$. dN_c/dt depends on the target beam distribution through the dependence of the critical energy ε_c on the local bending radius $\rho(x,y,t)$, as given by Eq. (1).

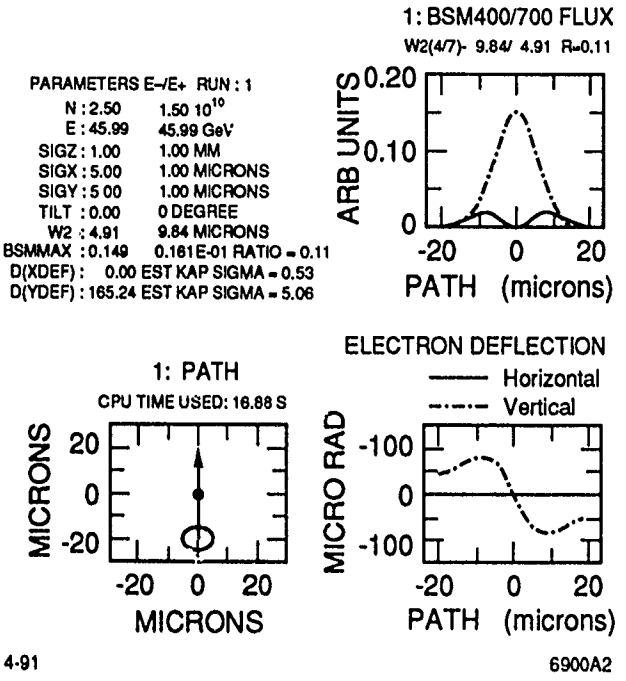


Figure 2. A typical output from the simulation code. In the upper left the input data are echoed. In the upper right the beamstrahlung fluxes are shown in arbitrary units. The solid curve is the flux from the radiating positrons on the north monitor. In the lower left depicts the path on which the scan was taken and the lower right shows the electron deflection. Here the solid curve shows the horizontal deflection and the dashed curve the vertical.

The seemingly necessary three integrations can be reduced to two by expanding I_0 into a power series in ρ_0/ρ. Using this expansion, the integral over t can be done analytically, and only two spatial integrations remain which then have to be evaluated numerically.

The beam-beam deflection angle for the centroid kick is given by the average of the deflection angle over the distribution of the kicked particles. It was evaluated in Ref. [1] in closed form, and can be written as

$$\langle\Theta\rangle = -\frac{2N_t r_e}{\gamma_r} F(X_1, X_2, \Sigma_{ij}) \,, \qquad (8)$$

where N_t is the number of particles in the target beam, and γ_r the energy of the radiating beam in units of the electron rest mass. X_1 and X_2 are the relative offsets in x and y, and Σ_{ij} is the sum of the covariance matrices of the target and the deflected beam. Since only the sum of the beam sizes appears in Eq. (8), it is not possible to determine individual beam sizes from beam-beam deflections independently.

The simulation code calculates both the deflection angles and the beamstrahlung fluxes for points along a straight path that has to be specified by the user Fig. 2 shows typical output of the code. The simulation of a typical beam-beam scan with 40 data points in which both beamstrahlung scans and the deflection curves are calculated takes about 60 s.

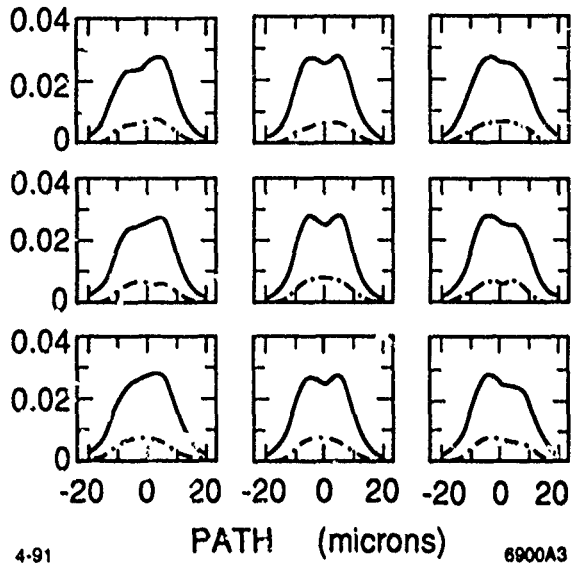


Figure 3. Vertical beamstrahlung scans for tilted beams offset with respect to each other. The beam sizes for both beams are 5×3 μm. The tilt angle is -45, 0 and $+45$ degree with respect to the horizontal axis from left to right for the positrons and top to bottom for electrons.

Round Beams

Fig. 2 shows the result where a large electron beam with $\sigma_x = 5$ μm is passed over a small positron beam with $\sigma_r = 1$ μm. The extrema of the beamstrahlung flux from the small e^+ beam (solid) coincide with the extrema of the deflection curve, because there the local bending radius the e^+ experience is largest. The deflection near the center of the target e^- beam is weaker and causes the dip. For an ideal point like e^+ source beam the dip should decrease to zero.

The radiation from the electrons (dotdashed) reflects mainly the transverse distribution of the electron beam, because only those e^- radiate that are intercepted by the fields of the positron beam, which serves as a window to view the radiating electrons.

Simulations with varying bunch sizes of 3, 4, and 5 μm for electrons and positrons confirmed the above observation [1] that the dip is always associated with the larger target beam size. This fact can be exploited as a diagnostic tool.

Tilted Elliptic Beams

At first sight it appears obvious to associate asymmetric beamstrahlung scans with tilted beams. However, if the scan is centered, the beamstrahlung scans are still symmetric, because the configuration shortly before the source beam enters the target beam is (point-) symmetric to that shortly after it exits. Therefore the fluxes are the same.

In order to break this symmetry and examine the $x-y$ coupling we have to offset the beams with respect to each other. Fig. 3 shows the results where tilted beams are scanned with 3 μm offset. Clearly now asymmetric scans are produced.

These observations can prove to be useful to diagnose tilted beams, however, only if the beams are known to be of equal size is it possible to determine the tilt direction of the individual beams [1].

Conclusions

A simulation code for the experimentally observable effects of beam-beam deflection and beamstrahlung at SLC final focus is described. In the code the interaction of general Gaussian particle distributions in the non-disruptive regime is simulated.

The simulations show that the dip in beamstrahlung scans is associated with a larger target beam size compared to the beam size of the radiating beam. Asymmetric scans turn out to be related to tilted beams that are scanned across each other with an offset.

The simulations show that it is possible to assess individual beam sizes with beamstrahlung scans whereas this is in principle not possible with deflection scans. Work based on Ref. [6] is in progress to utilize the simulation code and determine individual beam sizes quantitatively.

In the near future we hope to use these results as tools to diagnose the beams at the SLC final focus.

Acknowledgements

Discussions with C. Field and N. Toge are gratefully acknowledged. In particular discussions with E. Gero, who wrote his thesis on this subject were very helpful.

References

[1] V. Ziemann, SLAC Collider Note CN-384, 1990.

[2] A. Sokolov, I. Ternov, *Synchrotron Radiation*, Pergamon Press, New York, 1968.

[3] M. Abramowitz, I. Stegun, *Handbook of Mathematical Functions*, Dover, New York, 1972.

[4] J. Motz, H. Olsen, H. Koch, Rev. Mod Phys. 41, 581, 1969.

[5] P. Chen, SLAC AAS-Note 40, 1988.

[6] E. Gero, Ph D Thesis, Univ. of Michigan, 1991.

Simulations on Pair Creation from Beam-Beam Interaction in Linear Colliders*

P. Chen and T. Tauchi†
Stanford Linear Accelerator Center, Stanford University, Stanford, CA 94309 USA
K. Yokoya
National Laboratory for High Energy Physics, KEK, Oho, Tsukuba-shi, Ibaraki, 305, Japan

Abstract

It has been recognized that e^+e^- pair creation during the collision of intense beams in linear colliders will cause potential background problems for high energy experiments. Detailed knowledge of the angular-momentum spectrum of these low energy pairs is essential to the design of the interaction region. In this paper, we modify the computer code ABEL(Analysis of Beam-beam Effects in Linear colliders) to include the pair creation processes, using the equivalent photon approximation. Special care has been taken on the non-local nature of the virtual photon exchanges. The simulation results are then compared with known analytic formulas, and applied to the next generation colliders such as JLC.

I. INTRODUCTION

In future linear colliders, low energy e^+e^- pairs created during the beam crossing would cause background problems for the detectors. At the next generation of colliders, most such pairs will be made by *incoherent* processes, from the interactrion of individual particles (e^+, e^- or beamstrahlung γ) in the two beams. This problem was first identified by Zolotarev *et al.*[1]. At energies where the beamstrahlung parameter Υ is ≥ 1, the *coherent* production of a pair from a beamstrahlung photon interacting with the field of the oncoming beam becomes dominant, as first noted by Chen[2] The seriousness of this problem lies in the transverse momenta that the pair particles carry when leaving the interaction point(IP) with large angles. One source of transverse momentum is from the kick by the field of the oncoming beam, which results in an outgoing angle $\theta \propto 1/\sqrt{x}$, where x is the fractional energy of the particle relative to the initial beam particle energy[3]. The second source comes from the inherent scattering angles of these pairs, which may already be large when they are created. This issue was first studied in Ref.1.

In this paper we modify the ABEL[4] to include the incoherent pair creation processes using the equivalent photon approximation in the same way as Ref.1. By this simulation we can correctly take account of both the kicks and the inherent angles of the pairs. The geometric reduction is also implemented in the ABEL. The simulation results are compared with the analytic calculations with the parameters of JLC as an example of the next generation linear colliders.

II. THE ANALYTIC FORMULAS

We consider three incoherent pair creation processes, which are so-called Breit-Wheeler (BW: $\gamma\gamma \rightarrow e^+e^-$), Bethe-Heitler (BH: $e^\pm\gamma \rightarrow e^\pm e^+e^-$) and Landau-Lifshits (LL: $e^+e^- \rightarrow e^+e^-e^+e^-$) processes. In the calculations of these cross sections the basic kernal is the same using the equivalent photon approximation. For the BW process both photons are real beamstrahlung photons; for the BH process one is real and the other one is virtual; for the LL process both photons are virtual. The partial cross sections with transverse momentum (devided by γm) and outcoming angle $\theta_o \leq \theta \leq \pi - \theta_o$ are calculated by the convolution of two photon energy spectra, $n_a(y_1), n_b(y_2)$, and the differential cross section for $\gamma\gamma \rightarrow e^+e^-$, $\sigma_{\gamma\gamma}(y_1, y_2, c)$, as below.

$$\sigma(x_{\perp o}, c_o) = g \int_{-c_o}^{c_o} \int_{y_-}^{1} \int_{y_b}^{1} dc dy_2 dy_1 n_a(y_1) n_b(y_2) \sigma_{\gamma\gamma}(y_1, y_2, c), \tag{1}$$

where y_i and c are fractional photon energy and $c = \cos\theta$, respectively and g=1/4 for the BW process and 1 for both BH and LL processes. The fractional energy x of the outcoming positron(or electron) to its angle θ is expressed by

$$x = \frac{2y_1y_2}{y_1(1-c) + y_2(1+c)} \tag{2}$$

As denoted in Eq.(1), the integration regions of two photon energies are

$$1 \geq y_1 \geq y_b = \frac{y_2 y_+}{y_2 - y_-}, \quad 1 \geq y_2 \geq y_-, \tag{3}$$

$$y_\pm = \frac{x_o}{2}(1 \pm c) = \frac{x_{\perp o}}{2}\sqrt{\frac{1 \pm c}{1 \mp c}}, \tag{4}$$

where x_o and $x_{\perp o}$ are the minimum energy and the minimum transverse energy. These lower bounds are very important for the calculations because the dominant contribution comes from them. The virtual and the beamstrahlung photon spectra are given by

$$n_v(y) = \frac{2\alpha}{\pi}\frac{1}{y}\ln(\frac{1}{y}) \quad \text{and} \tag{5}$$

*Work supported by Department of Energy contract DE-AC03-76SF00515.

†Permanent address: KEK, Japan.

U.S. Government work not protected by U.S. Copyright.

$$n_b(y) = \frac{1}{\pi}\Gamma(\frac{2}{3})(\frac{\alpha\sigma_z}{\gamma\lambda_e})(3\Upsilon)^{2/3}y^{-2/3} \equiv Ay^{-2/3}, \quad (6)$$

respectively, where σ_z is the beam bunch length and λ_e is the electron Compton wavelength. Finally $\sigma_{\gamma\gamma}(y_1, y_2, c)$ is calculated by neglecting the obviously small terms $<O(\gamma^{-2})$.

$$\sigma_{\gamma\gamma}(y_1, y_2, c) = \frac{\pi r_e^2}{\gamma^2 y_1 y_2}\frac{1}{1-c^2}\left\{\frac{y_1^2(1-c)^2 + y_2^2(1+c)^2}{[y_1(1-c)+y_2(1+c)]^2}\right\} \quad (7)$$

$$\simeq \frac{\pi r_e^2}{\gamma^2 y_1 y_2}\frac{1}{1-c^2}, \quad (8)$$

where r_e is the classical electron radius. The last approximation of Eq.(8) is made due to the fact that the factor in the parenthesis (Eq.(7)) is a slowly varying function ranging from 1/2 to 1. Our estimates are therefore upper bounds, which are too big by less than a factor of 2. As we do not use this last approximation in the ABEL, this effect wil be discussed in the subsequent section. The resultant partial cross sections are[5]

$$\sigma_{BW} = 2.42\frac{r_e^2}{\gamma^2}A^2(\frac{2}{x_{\perp o}})^{\frac{4}{3}}\ln\frac{1}{\tau_o} \quad (9)$$

$$\sigma_{BH} = 5.40\frac{\alpha r_e^2}{\gamma^2}A(\frac{2}{x_{\perp o}})^{\frac{1}{3}}(\tau_o^{-\frac{1}{3}} - \tau_o^{\frac{1}{3}})(-\ln\frac{x_{\perp o}\tau_o}{2} - 0.20) \quad (10)$$

$$\sigma_{LL} = 1.27\frac{\alpha^2 r_e^2}{\gamma^2}(\frac{2}{x_{\perp o}})^2\ln\frac{1}{\tau_o}(\ln\frac{x_{\perp o}}{2\tau_o}\ln\frac{x_{\perp o}\tau_o}{2} + 3\ln\frac{x_{\perp o}}{2} + 4.44) \quad (11)$$

where $\tau_o = \tan(\theta_o/2)$. The above expressions account for only one of the two particles(say positron) in the pair. To count electron as well, we must multiply each one by 2.

III. THE ABEL SIMULATION

In the ABEL the beam bunches are described by ensembles of macro-particles. The number of macro-particles is typically 10^3 to 10^5. The whole process is divided into time slices. At each time step the bunches are further divide into longitudinal slices. For the modification of the ABEL the pairs are created in the collision between the macro-particles and the beamstrahlung photons in each logitudinal slice. There is no pair creation between the different slices, that is the incoherent pair creation processes are "local' in longitudinal direction. Then the created particles(e^+ or e^-) are tracked in the Coulomb potential which is produced by the oncoming beam. As the transverse momenta of these particles are affected by the kicks in the tracking, the partial cross sections for the processes in the ABEL are given with (x_o, θ_o) instead of $(x_{\perp o}, \theta_o)$, and there are no integrations over the beamstrahlung photon energy spectra for the BW and BH processes. Here we set θ_o=0.1 and $x_o = 10^{-5}$(5 MeV at E_{beam}=500 GeV).

$$\sigma_{BW}(y_1, y_2) = 6.28\frac{r_e^2}{\gamma^2}\frac{1}{y_1 y_2}ln\frac{1}{\tau_o} \quad (12)$$

$$\sigma_{BH}(y_1) = 4\frac{\alpha r_e^2}{\gamma^2}\frac{1}{y_1}\left\{2\ln\frac{1}{\tau_o}\{1 - \frac{1}{x_o}(\ln\frac{x_o}{2}+1)\} + (\frac{1}{y_1} - \frac{1}{x_o})\{\frac{\ln(1-c_o)}{1-c_o} + \frac{2c_o}{1-c_o^2}(\ln\frac{x_o}{2}+2)\}\right\} \quad (13)$$

$$\sigma_{LL} = 1.27\frac{\alpha^2 r_e^2}{\gamma^2}(\frac{2}{x_o})^2\left\{(\ln\frac{x_o}{2}+1)\{(\ln\frac{x_o}{2}+\frac{2}{3})(\frac{c_o}{1-c_o^2}+\ln\tau_o) + \frac{c_o\{1+\ln(1-c_o^2)\}}{1-c_o^2}\}\right\}, \quad (14)$$

y_1, y_2 are the beamstrahlung photon energies. The energy and inherent angle of the outgoing particle are calculated by Eq.(2) and (7), respectively, with y_1, y_2 satisfying the boundary conditions of Eq.(3). For the virtual photon energy, we use the distribution of Eq.(5). The transverse momentum is calculated by the energy and the final scattering angle after the kicks.

Geometric Reduction

The finite impact parameter of the interactions in these processes comes from the transverse energy($q_\perp$) of the virtual photon. The distribution of $y_\perp(\equiv q_\perp/\gamma m)$ is[6]

$$n_v(y_\perp) = \frac{y_\perp^2\, dy_\perp^2}{(y_\perp^2 + y^2/\gamma^2)^2}. \quad (15)$$

As clearly seen in the above equation, for a given equivalent photon energy y, the dominant contribution to the cross section comes from the region of small transverse momentum $y_\perp \sim y/\gamma$. In the ABEL every virtual photon has finite transverse energy($y_\perp$) according to Eq.(15). To take account of this non-local nature of virtual photon interaction, we first calculate the probability of the pair creation which is proportional to the local intensities of two beams (macro-particles or beamstrahlung photons) at a point. Defining the impact parameter(ρ) as $1/y_\perp\gamma$m,we get the non-local intensities of two beams separating by ρ in each other. Then the reduction factor can be obtained by the ratio of "non-local" intensities/ "local" ones. If the separation is far beyond the beam (transverse) size, the pair creations will be suppressed largely[1]. The ABEL creates the pairs at the position separated by ρ from the beam position and even outside the beam size.

IV. NUMERICAL COMPARISON

For the numerical comparison between the analytic calculation and the ABEL, we estimate the yields from a 1 TeV linear collider, JLC[7], where $\gamma = 10^6, \sigma_x/\sigma_y = 230/1.4\text{nm}, \sigma_z = 76\mu\text{m}, \Upsilon_{\max} = 1.12$ (we use Υ=0.39 in the analytic calculation), luminosity $L = 3.6 \times 10^{31}/\text{cm}^2/$ bunch train (10 bunches per train) and 200Hz rf pulse rate. Figure 1 shows the yields per bunch crossing calculated

[1]This *geometric reduction* effect was first observed at Novosibirsk[9], and subsequently developed theoretically by several authors[8,10].

by the partial cross sections of Eq.(9),(10),(11) and their sum as a function of $p_{\perp o} = \gamma m x_{\perp o}$ at $\theta_o = 0.1$ together with the results of the ABEL which are plotted with error bars. The yields of the analytic calculations are already multiplied by 2 for e^+ and e^-. In this figure the effect of the kicks, "correct" angular distribution (Eq.(7)) and non-local interaction in the ABEL are switched off just for the comparison. The agreement for the LL and BW processes is excellent. For the BH process the analytic calculation predicts 30% more yields than that of the ABEL, however its agreement is still good because the beamstrahlung spectrum in the analytic formulas is only approximation.

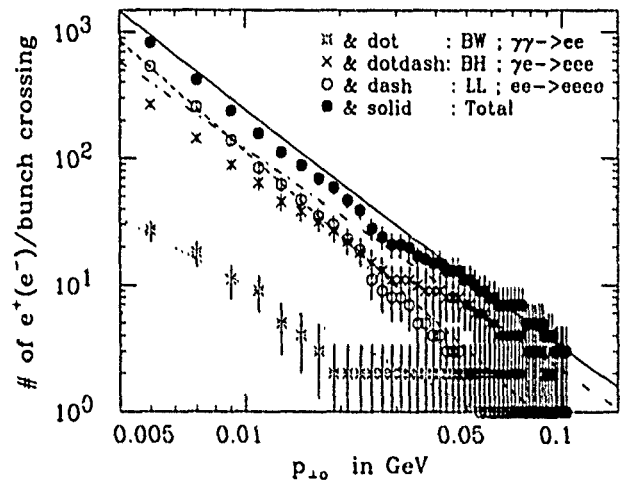


Fig. 1 Comparison between the analytic calculation and the ABEL.

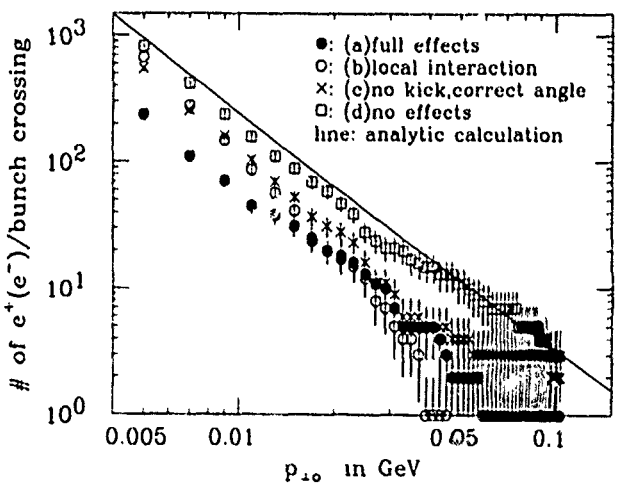


Fig. 2 The ABEL simulation results with the various effects of (a)-(d) which are explained in the text.

In addition to the large inherent angles of the pair creations, the ABEL implements the kicks. "correct" angular distribution (Eq.(7)) and the geometric reduction as described in the previous section. To see these individual effects in detail, we simulated the pairs under the four kinds of conditions, that is (a) all effects are included, (b) no geometric reduction whereas the other effects are considered, (c) only "correct" angular distribution is taken account into and (d) with no effects as described in the above comparison with the analytic calculations. The results are shown in Fig.2, where the total yields summed over the three processes are plotted in the same way as Fig.1. As clearly seen in this figure, two effects are apparent. First one is "correct" angular distribution, which reduce the yields by 35%. This effects are expected because the angular distribution of Eq.(7) has more forward-backward peaking than that of Eq.(8) which has been used in the analytic calculations. The second one is the geometric reduction. The reduction ranges from 60 to 50% for the minimum transverse momentum from 5 to 10 MeV, respectively. These values are consistent with the analytic calculation by G. L. Kotkin *et al.*[8].

REFERENCES

[1] M. S. Zolotarev, E. A. Kuraev and V. G. Serbo, Inst. Yadernoi Fiziki Preprint 81-63 (1981); SLAC TRANS-227 (1987).

[2] P. Chen, SLAC-PUB-4822(1988); appeared in *Proc. DPF Summer Study, SNOWMASS '88,* orld Scientific(1989).

[3] P. C'en and V. I. Telnov, *Phys. Rev. Lett.* **63**, 1796 (1989). P. Chen,*Particle Accelerators* **30** , 1013 (1990).

[4] K. Yokoya, ABEL,"A Computer Simulation Code for the Beam-Beam Interaction in Linear Colliders", KEK-Report-85-9, Oct. 1985, also *Nucl. Instr. Meth.* **B251**, 1 (1986).

[5] P. Chen, T. Tauchi and D. V. Schroeder, "Pair Creation at Large Inherent Angles" to appear in Snowmass'90 Proceedings.

[6] V. B. Berestetskii, E. M. Lifshitz and L. P. Pitaevskii, *Relativistic Quantum Theory* , Part 1, Pergamon Press (1971).

[7] K. Yokoya, "Beam parameters for JLC" in the proceedings of "The First Whorkshop JLC", KEK, Japan, Oct.1989.

[8] G. L. Kotkin, S. I. Polityko and V. G. Serbo, *Sov. J. Nucl. Phys.* **42** , 440, (1985).

[9] A. E. Blinov, A. E. Bondar, Yu. I. Eidelman *et al.*, *Phys. Lett* **113B**, 423 (1982). Yu. A. Tikhonov, *Candidates's Dissertation* , Inst. Nucl. Phys., Novosibirsk (1982).

[10] V. N. Baier, V. M. Katkov and V. M. Strakhovenko, *Sov. J. Nucl. Phys.* **36** , 95, (1982). A. I. Burov and Ya. S. Derbenev, INP Preprint 82-07, Novosibirsk (1982).

DIFFERENTIAL LUMINOSITY UNDER BEAMSTRAHLUNG*

Pisin Chen
Stanford Linear Accelerator Center, Stanford University, Stanford, CA 94309 USA

Abstract

For the next generation of e^+e^- linear colliders in the TeV range, the energy loss due to *beamstrahlung* during the collision of the e^+e^- beams is expected to be substantial. One consequence is that the center-of-mass energy between the colliding particles can be largely degraded from the designed value. The knowledge on the differential luminosity as a function of the center-of-mass energy is essential for particle physics analysis on the interesting events. In this paper we derive an analytic formula for such a differential luminosity, which agrees very well with computer simulations. A major characteristic of this formula is discussed.

I. INTRODUCTION

It is known that *beamstrahlung*, i.e., the synchrotron radiation from the colliding e^+e^- beams, will carry away a sbustantial fraction of beam particle energy in future linear colliders. This, for one thing, will result in a degradation of the center-of-mass energy of the colliding beams. From high energy physics point of view, it is important to know the luminosity as a function of the spreaded center-of-mass, so as to analyze the data attained from the collider.

When the average number of beamstrahlung photons radiated per beam particle is much less than unity, the energy spectrum for the final e^+ or e^- beams is simply the well-known Sokolov-Ternov spectrum [1] for the radiated photons with the fractional photon energy, $y(\equiv E_\gamma/E_0)$, replaced by the corresponding final electron (or positron) energy, $x = 1 - y$. When the condition is such that the average number of photons radiated is not much less than unity, the effect of succesive radiations becomes important. Previously, the multi-photon beamstrahlung process has been studied by Blankenbecler and Drell [2], and independently by Yokoya and Chen [3]. In this paper, we shall adopt the formulation developed in Ref. 3 as the basis for our derivation of the differential luminosity. In section 2, we will review the electron spectrum under multi-photon beamstrahlung. Section 3 will be devoted to the derivation of the differential luminosity. The characteristic feature of our formula is discussed and comparison to computer simulation is presented in the last section.

II. ELECTRON ENEERGY SPECTRUM

Let $\psi(x,t)$ be the energy spectral function of the electron for energy $x \equiv E/E_0$ at time t normalized as $\int \psi(x,t)dx = 1$. We assume that the emmision of the photon takes place in an infinitesimally short time interval. Then the evolution of the spectral function can be described by the rate equation

$$\frac{\partial\psi}{\partial t} = -\nu(x)\psi(x,t) + \int_x^\infty F(x,x')\psi(x',t)dx' \quad , \qquad (1)$$

where the first term corresponds to the *sink*, and the second term the *source*, for the evolution of $\psi(x,t)$. Here $\nu(x)$ is the average number of photons radiated per unit time and F is the spectral function of radiation, i.e., $F(x,x')dx'$ is the transition probability of an electron from energy x' to the energy interval $(x, x+dx)$ per unit time. Obviously, $F(x,x') = 0$ if $x \geq x'$. Notice, however, that F does not include the probability for electrons to remain at the same energy without photon emmision.

The spectral function of radiation can be characterized by the beamstrahlung parameter Υ, defined as

$$\Upsilon = \gamma\frac{B}{B_c} \quad , \qquad (2)$$

where B is the effective field strength of the beam, and $B_c = m^2c^3/e\hbar \sim 4.4\times10^{13}$ Gauss is the Schwinger critical field. For historical reasons, this parameter is related to the parameter ξ introduced by Sokolov and Ternov,[1] by a simple factor

$$\xi = \frac{\omega_c}{E} = \frac{3}{2}\frac{r_e\gamma^2}{\alpha\rho} = \frac{3}{2}\Upsilon \equiv \frac{x}{\kappa} \quad , \qquad (3)$$

where r_e is the classical electron radius, α the fine structure constant, ω_c the critical frequency of radiation, and ρ the instantaneous radius of curvature, which is proportional to γ. Thus the introduced parameter K is independent of energy. Since the two parameters are trivially related, one may employ either of them depending on the convenience of the situation.

The transition probability F derived by Sokolov and Ternov is

$$F(x,x') = \frac{\nu_{cl}\kappa}{xx'}f(\xi,\eta) \quad , \qquad (4)$$

$$f(\xi,\eta) = \frac{3}{5\pi}\frac{1}{1+\xi\eta}\left[\int_\eta^\infty K_{5/3}(u)du + \frac{\xi^2\eta^2}{1+\xi\eta}K_{2/3}(\eta)\right] \quad ,$$

where $\eta = \kappa[(1/x') - (1/x)]$, K_ν's are the modified Bessel functions and ν_{cl} is the number of photons per unit time calculated by the classical theory of radiation,

$$\nu_{cl} = \nu_{\eta=0} = \frac{5}{2\sqrt{3}}\frac{\alpha\gamma}{\rho} \quad . \qquad (5)$$

Note that for a given field strength ν_{cl} is independent of the particle energy. In general, however,

$$\nu(x) = \int_0^x F(x,x')dx' \equiv \nu_{cl}U_0(\xi) \quad . \qquad (6)$$

The function $U_0(\xi)$ is normalizedsuch that $U_0(0) = 1$, and can be represented by the following approximate expression:

$$U_0(\xi) = \frac{1 - 0.598\xi + 1.061\xi^{5/3}}{1 + 0.922\xi^2} \quad , \qquad (7)$$

where the relative error is within 0.7% for any ξ.

* Work supported by Department of Energy contract DE-AC03-76SF00515.

U.S. Government work not protected by U.S. Copyright.

To look for a compact analytic solution for ψ in Eq.(1), the exact Sokolov-Ternov spectral function in Eq.(4) is somewhat cumbersome. In the classical regime of radiation, i.e., $\xi \ll 1$, one can instead invoke an approximate expression to replace $f(\xi,\eta)$ in Eq.(4):

$$g(\eta) = \frac{1}{\Gamma(1/3)}\eta^{-2/3}e^{-\eta} \quad . \tag{8}$$

With this approximation, Eq.(1) can be solved by proper Laplace transformations. The details can be found from Ref. 3. The solution is

$$\psi(x,t) = e^{-N_{cl}}\left[\delta(1-x) + \frac{e^{-\eta}}{1-x}h(\eta^{1/3}N_{cl})\right] \quad , \tag{9}$$

where $N_{cl} = \nu_{cl}t$ is the average number of photons radiated up to time t, and

$$h(u) = \frac{1}{2\pi i}\int_{\lambda-i\infty}^{\lambda+i\infty}\exp(up^{-1/3}+p)dp = \sum_{n=1}^{\infty}\frac{u^n}{n!\Gamma(n/3)} \quad , \tag{10}$$

with $\lambda > 0$ and $0 \le u \le \infty$. The first term in Eq.(9) represents the electron population that suffers no radiation. The n^{th} term in the Taylor expansion of the second term corresponds to the process of n-photon emissions.

For finite values of ξ, the rate equation cannot be solved exactly since $\nu(x)$ is not constant in time any more. However, in the intermediate regime where $\xi \lesssim \mathcal{O}(10)$, $\nu(x)$ should not deviate from ν_{cl} too significantly. This suggests a solution based upon minor perturbation from the above classical result. It is found[3] that

$$\psi(x,t) = e^{-N_\gamma}\left[\delta(1-x) + \frac{e^{-\eta}}{1-x}h(\eta^{1/3}\bar{N}(t))\right] \tag{11}$$

for the intermediate regime, where

$$N_\gamma = U_0(\xi)N_{cl} \quad , \tag{12}$$

$$\bar{N} = \frac{1}{1+\xi\eta}N_{cl} + \frac{\xi\eta}{1+\xi\eta}N_\gamma \quad . \tag{13}$$

III. CENTER-OF-MASS LUMINOSITY

To find the differential luminosity $\mathcal{L}(s)$ as a function of the center-of-mass energy squared,s, one needs to convolute the energy spectrum of one beam, $\psi(x_1,t)$, with the other, $\psi(x_2,t)$. Let $t = 0$ when the e^+e^- bunches first meet. Then the first z-slice in beam #1 will always encounter a "fresh" beam #2:

$$\frac{d\mathcal{L}(0)}{dz} \propto \frac{2}{l}\int_0^{l/2} dt\psi(x_1,t)\psi(x_2,0) \quad , \tag{14}$$

where l is the total length of each bunch. A slice at z in beam #1, however, will see a beam #2 which has evolved for a time $t = z/2$:

$$\frac{d\mathcal{L}(z)}{dz} \propto \frac{2}{l}\int_0^{l/2} dt\psi(x_1,t)\psi(x_2,z/2) \quad . \tag{15}$$

Adding all z-slices in beam #1 together, we have

$$\begin{aligned}\mathcal{L} &\propto \frac{4}{l^2}\int_0^{l/2} dt\psi(x_1,t)\int_0^{l} dz\psi(x_2,z/2) \\ &= \frac{4}{l^2}\int_0^{l/2} dt\psi(x_1,t)\int_0^{l/2} dz\psi(x_2,z) \quad .\end{aligned} \tag{16}$$

Note that the above two integrals are functionally identical. Inserting the spectral function in Eq.(9), we find, for $\xi \ll 1$,

$$\begin{aligned}\phi(x) &\equiv \frac{2}{l}\int_0^{l/2} dt\psi(x,t) \\ &= \frac{1}{N_{cl}}\left[(1-e^{-N_{cl}})\delta(1-x) + \frac{e^{-\eta(x)}}{1-x}g(\eta)\right] \quad .\end{aligned} \tag{17}$$

The function $g(\eta)$ in the second term is

$$g(\eta) = \sum_{n=1}^{\infty}\frac{\eta^{n/3}}{n!\Gamma(n/3)}\gamma(n+1,N_{cl}) \quad , \tag{18}$$

where $\gamma(n+1,N_{cl})$ is the incomplete gamma function.

The center-of-mass energy squraed is $s \equiv x_1x_2$. The differential luminosity as a function of s is therefore

$$\mathcal{L}(s) = \mathcal{L}\int_s^1\int_0^1 dx_1dx_2\delta(s-x_1x_2)\phi(x_1)\phi(x_2) \quad . \tag{19}$$

It is straight forward to show that

$$\begin{aligned}\mathcal{L}(s) = \frac{\mathcal{L}}{N_{cl}^2}\Big\{&\left[1-e^{-N_{cl}}\right]^2\delta(1-s) + 2\left[1-e^{-N_{cl}}\right]\frac{e^{-\eta}}{1-s}g(\eta) \\ &+ \int_s^1 dx\frac{e^{\eta(x)-\eta(s/x)}}{(1-x)(1-s/x)}g(\eta(x))g(\eta(s/x))\Big\} \quad .\end{aligned} \tag{20}$$

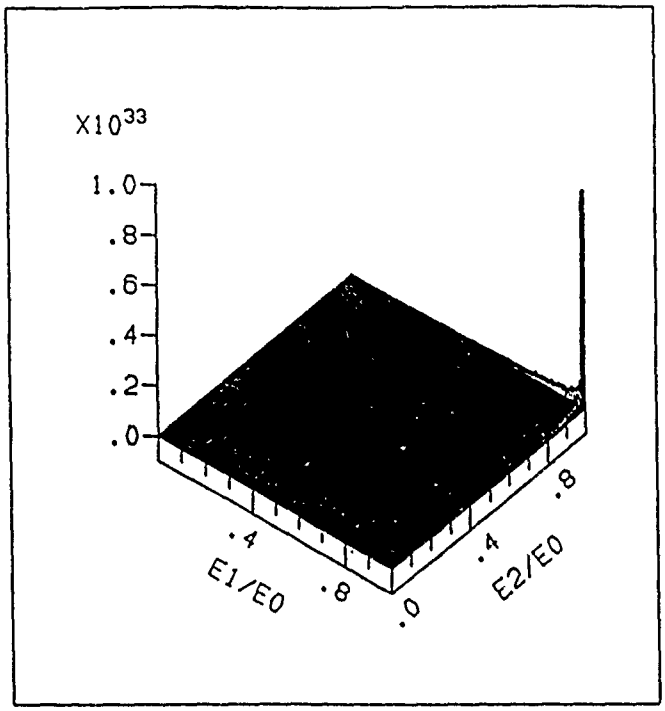


Figure 1. Two-dimensional histogram of the luminosity as a function of x_1 and x_2.

It can be shown that the last term is much smaller than unity, and is negligible. Thus

$$\mathcal{L}(s) = \frac{\mathcal{L}}{N_{el}^2}\left\{\left[1-e^{-N_{el}}\right]^2\delta(1-s)+2\left[1-e^{-N_{el}}\right]\frac{e^{-\eta}}{1-s}g(\eta)\right\}. \tag{21}$$

For the intermediate regime, the spectral function of Eq.(9) should be replaced by Eq.(11). The derivation is essentially the same, and we find

$$\mathcal{L}(s) = \frac{\mathcal{L}}{N_\gamma^2}\left\{\left[1-e^{-N_\gamma}\right]^2\delta(1-s)+2\left[1-e^{-N_\gamma}\right]\frac{e^{-\eta}}{1-s}\bar{g}(\eta)\right\}, \tag{22}$$

where

$$\bar{g}(\eta) = \sum_{n=1}^{\infty}\left(\frac{\bar{N}}{N_\gamma}\right)^n \frac{\eta^{n/3}}{n!\Gamma(n/3)}\gamma(n+1, N_\gamma) \quad . \tag{23}$$

IV. DISCUSSIONS

To confirm our theoretical formulas, we perform computer simulations using the code ABEL [4]. The parameters of a linear collider with a center-of-mass energy 1/2 TeV designed by Palmer [5] (the Machine G in Table 1) was used. The parameter $\xi = 0.45$ in this example, and the bunch length is $l = \sqrt{2\pi}\sigma_z = 0.28$ mm. A two dimansional plot of $\mathcal{L}$ as a function of x_1 and x_2 is shown in Fig. 1. We see that the most striking character of the luminosity spectrum is that, aside from the sharp delta function at the nominal machine energy, other contribution to the luminosity comes essentially from the matching between a full energy particle and a beamstrahlung degraded particle. This is evidenced by the "walls" on the edges of the 2-D plot, which corresponds to the second term in Eq.(22).

ACKNOWLEDGEMENT

The author appreciates helpful discussions with T. Barklow of SLAC.

REFERENCES

[1] A. A. Sokolov and I. M. Ternov, *Radiation from Relativistic Electrons*, AIP Trans. Series, 1986.
[2] R. Blankenbecler and S. D. Drell, Phys. Rev. Lett. 61, 2324 (1988).
[3] K. Yokoya and P. Chen, Proc. IEEE Part. Accel. Conf. 89CH2669-0, 1438 (1989).
[4] K. Yokoya, KEK Report 85-9, 1985.
[5] R. B. Palmer, Annu. Rev. Nucl. Part. Sci. 1900.40, 529 (1991).

A Practical Algorithm for Chromaticity Correction in Linear Collider Final Focus Systems

P. Krejcik
Stanford Linear Accelerator Center
Stanford University, Stanford, California 94305

Abstract

The details of a tuning algorithm are described for minimizing the chromatic error in a final focus system, using the two families of sextupoles incorporated in a chromatic correction section.The chromatic errors are characterized by the beam waist location of off-energy particles with respect to the interaction point location. It is shown that linear combinations of changes in strength to the two sextupole families can move the waist position of off-energy beams independently in the X and Y planes. Measurements at the SLC have shown that the off-energy waist position can be measured as a function of the sextupole multiknob to minimize chromaticity.

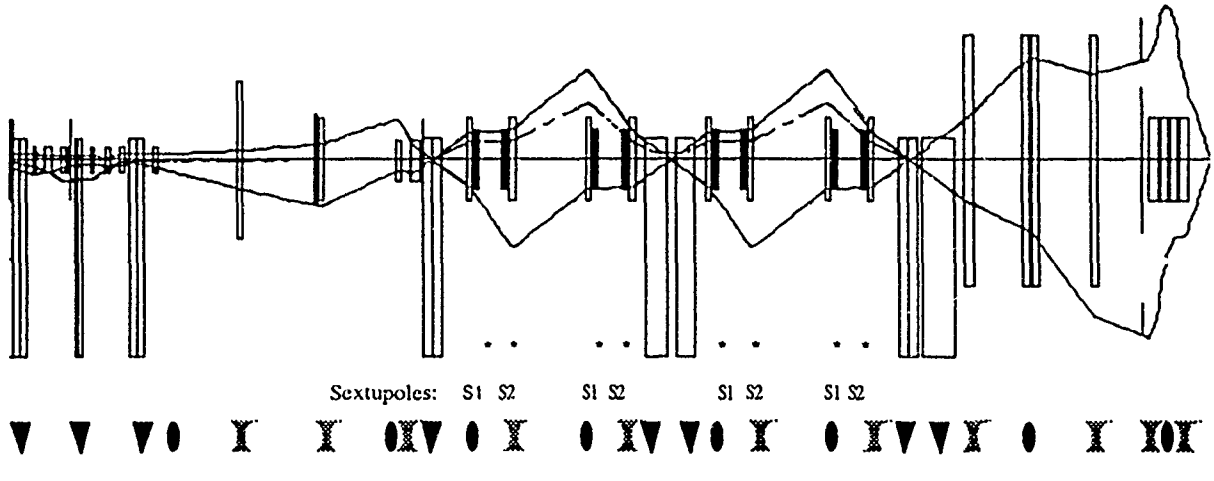
I. INTRODUCTION

In colliders the luminosity is related to the inverse square of the beam sizes at the interaction point (IP). Chromatic errors in the beam line will result in a degradation of spot size for beams with a finite energy spread. In linear colliders the beam is far from monochromatic with a typical energy spread of 0.5%. Chromatic contributions to spot size are thus very important in determining the useable luminosity.

This paper does not address so much the design of a final focus beam line nor the calculation of the contributions of all significant aberrations to spot size. Rather, it addresses the more immediate issue of how to tune the sextupoles in a given final focus beam line based on the available beam observation tools at hand. The analysis made here is of the final focus beam line of the SLC [1], using the normal conducting final triplet. The technique can be generalized to other final focus layouts, such as with the newly installed superconducting arrangement at the SLC [2].

Quantifying the chromatic effects in terms of readily observable beam parameters requires some reappraisal in a linear collider. In circular colliders the routine measurement of tunes at energies offset from the central energy reveal the change in phase advance around the ring resulting from chromatic errors. In single pass beam lines the phase advance is not easily measured, only the final beam size at the IP is measured with any degree of precision. Verifying that chromatic correction sextupoles are optimally set using only beam size data [3] requires much interpretation of the measurements and can take considerable time. The algorithm described in this paper exploits the change in the beam waist position for off energy beams as a result of chromatic errors. The chromatic correction sextupoles are scanned in a prescribed ratio to each other so that the waist position of the off energy beam changes in either the x or y plane. This type of sextupole scan has the twofold purpose of quantifying the amount of chromatic error present and allows the optimum sextupole setting to be easily implemented.

Figure 1. Beam size in x (top) and y (lower)and dispersion (dashed)in the SLC FF beam line



Work supported by the Department of Energy, Contract DE-AC03-76SF00515

0-7803-0135-8/91$03.00 ©IEEE

II. OPTICS OF THE FINAL FOCUS

Linear optics

The layout of the SLC final focus beam line is shown in fig. 1. Its design function has been covered in detail elsewhere [1]. Of interest are the two demagnifying transformers separated by a Chromatic Correction Section (CCS). In order to achieve the desired small beta functions of a few tens of millimeters at the IP the final quadrupole triplet is very strong. The strong bending of rays inside the quadrupole leads to a pronounced variation in beam waist position with energy, fig. 2, resulting in large chromatic errors.

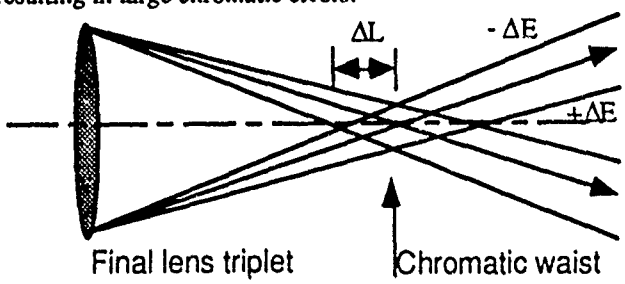


Figure 2. Simple view of the effect of chromatic errors on achievable spot size at the final focus

Chromaticity correction scheme

A string of bend dipoles generate the necessary dispersion inside the CCS where two families of sextupoles S1 and S2 are incorporated to control the chromaticity. The sextupoles act on all particles displaced from the axis of the sextupoles. The design aims at producing a correlation between this offset and energy deviation via the dispersion function but the action of the sextupoles on the beam can also arise from misalignments of the sextupole and this effect should be distinguished when evaluating the tuning algorithm.

The design strength of the sextupoles is set in order to minimize the path length integral of an off-energy ray. This is not a concept that can be easily realized in terms of tuning parameters when dealing with beam measurements. Instead, use is made of the concept of the waist motion with respect to energy deviations in the beam. Minimizing the waist motion with respect to energy can be shown to be equivalent to minimizing the path length integral [6].

III. TUNING IN THE FINAL FOCUS

First order optical tuning

Optical tuning of the beam line is a necessary precursor to chromatic correction to match to the variety of beam conditions at the entrance to the final focus beam line. The goal of the tuning is to produce the smallest beam spot compatible with the constraints of low background generation for the detector. The logical procedure in which orbits, dispersion, skew and beta matching is done so as to empirically arrive at a minimum spot size has been dealt with elsewhere [4]. Of principle interest here is the routine use of IP beam size measurements based on beam-beam deflection scans (or even wire scans for single beams) combined with systematic scans of the focal length of the final quadrupoles in what is collectively termed a *waist scan*. These waist scans reveal both the minimum spot size of the beam and the distance from the final lens at which the minimum occurs.

Tuning to minimize chromaticity

If the energy spread in the beam were to be increased then in the conceptual drawing in fig. 2 it is seen that particles of different energies cross the axis at different distances from the lens. However, all that can be observed in practice is the increase in beam size at the IP. This phenomena alone is a difficult criteria to tune the sextupoles by as it is not immediately apparent how much of the beam size is due to chromaticity, or dispersion,skew, beta mismatch etc..

If instead the centroid energy of the beam is shifted by ΔE then the waist moves by some amount ΔL in a non-chromatically corrected configuration. The amount ΔL that the waist moves with energy can be determined from a waist scan using the final quadrupoles. On the other hand the focal length of the off-energy beam can be moved with the sextupoles. The two sextupole families are scanned in a prescribed ratio to each other and one observes the off energy waist move, in much the same way as the final quadrupoles change the focal length in a conventional waist scan. A single off-energy sextupole waist scan is more expedient than conventional waist scans performed at several energies and furthermore allows the sextupoles to be directly dialled to their correct values at the completion of the scan.

Computer modelling

In order to perform the off-energy waist scans with the sextupoles it is necessary to predict the ratio in which the two sextupole families need to be changed with respect to each other. Changing the sextupole families in a prescribed ratio allows the off energy waist to be moved independantly in the x and y planes. An optics code is used in which the energy of the beam is offset and the off-energy waist position is found in each plane as each of the sextupole families are changed in turn. This immediately gives the matrix coefficients in eq. (1).

$$\begin{bmatrix} \Delta L_x \\ \Delta L_x \end{bmatrix} = \begin{bmatrix} \left(\frac{\Delta L_x}{\Delta S_x}\right)_{\Delta S_y=0} & \left(\frac{\Delta L_x}{\Delta S_y}\right)_{\Delta S_x=0} \\ \left(\frac{\Delta L_y}{\Delta S_x}\right)_{\Delta S_y=0} & \left(\frac{\Delta L_y}{\Delta S_y}\right)_{\Delta S_x=0} \end{bmatrix} \begin{bmatrix} \Delta S_x \\ \Delta S_x \end{bmatrix} \qquad (1)$$

A useful feature of this type of analysis is that the same matrix coefficients can also be found by direct measurement with the beam by observing the waist position as as each sextupole family is scanned in turn, while the beam energy is maintained with an energy offset of e.g. 0.2%.

A matrix inversion of eq. (1) gives directly the multiknob coefficients required, where the matrix coefficients in eq. (2) now indicate how much each sextupole family should be adjusted in order to move the off-energy waist by a prescribed amount.

$$\begin{bmatrix} \Delta S_x \\ \Delta S_x \end{bmatrix} = \begin{bmatrix} a_{11} a_{12} \\ a_{21} a_{22} \end{bmatrix} \begin{bmatrix} \Delta L_x \\ \Delta L_x \end{bmatrix} \qquad (2)$$

Implementation

The SLC Control Program (SCP) has a generic multiknob software capability for controlling devices, such as magnets, and keeping their strengths in a prescribed ratio. The ratios of the two sextupole families, calculated from the modelling to give orthogonal control of x and y chromaticity, are incorporated in four *chromaticity* multiknobs to allow x and y scans in each beam. The units of the multiknobs are in cm of waist motion per 100 MeV of energy offset.

IV. RESULTS OF CHROMATICITY SCANS

An example of chromaticity scan is shown in fig.3 for positrons in the south final focus. The beam energy was shifted by 100 MeV and the vertical chromaticity multiknob scanned to find the location of the off-energy waist. The graph shown is the operators output from the scan, where the square of the measured beam size is plotted as a function of the knob value. In this example the waist was found to be at B=-1.565 cm from the IP. The knob is then dialled to this value to achieve the minimum chromatic error.

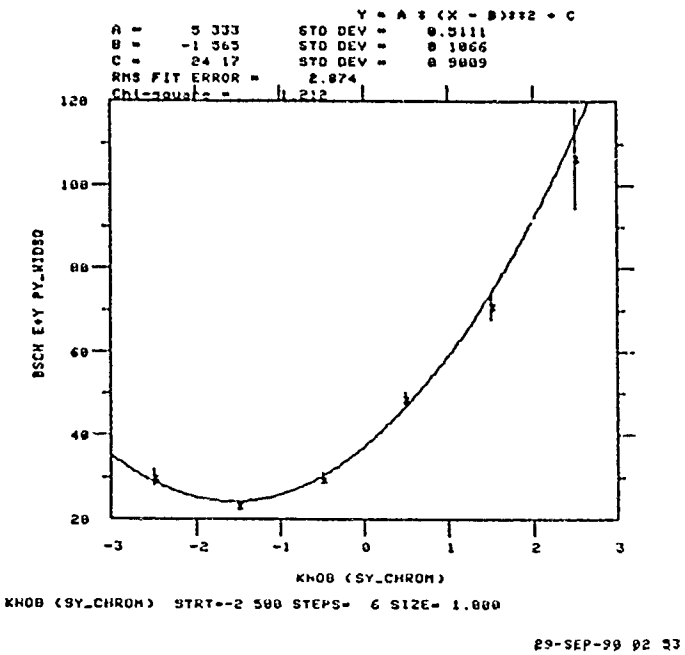


Figure 3 Measured beam waist position as a function of sextupole multiknob for the SLC beam with an energy offset of 0.2%

After implementing a chromaticity correction using this tool a normal waist scan is made (using the final quadrupoles) of the on-energy beam to check if the waist has moved. This becomes necessary if the orbit errors in the sextupoles are significant so that they add linear focusing terms to the on-energy beam. Changing the sextupoles via the chromaticity knob would in this case change the first order optics and hence the waist position. In order to distinguish between waist motion due to sextupole misalignments and true chromatic waist motion a larger energy offset for the beam is chosen so that chromatic effects become more dominant in the measurements.

V. CONCLUSION AND FUTURE OUTLOOK

The implementation of orthogonalized sextupole scans in the SLC final focus has been found to be a relatively speedy way of checking and correcting the chromaticity contribution to spot size at the IP. The procedure requires that the beam energy be briefly offset in energy by 0.5% while the sextupole multiknobs are scanned. Augmentations are possible to the technique, where the beam energy is scanned over several data points and the waist location is independantly verified by further scanning the quadrupoles in the final triplet [5].

At further reduced magnifications, such as those anticipated for the Next Linear Collider, the chromatic contribution to the final spot size becomes increasingly important. More attention has been given to the optical layout of the chromatic correction section, such as in SLAC's Final Focus Test Beam Project [6], here noninterlaced sextupole families aid in the global control of aberrations. The algorithm described in this paper is applicable to these situations and should help in matching the beam line to the variety of initial phase space conditions that one encounters in practice.

VI. ACKNOWLEDGEMENTS

Thanks are due to W. Kozanecki for passing on his experience with commissioning the SLC final focus system and to K. Brown for helpful discussions on chromatic corrections in beam lines. Also to the many people who have worked on the design and tuning of the final focus on whose experience this work was built.

VII. REFERENCES

[1] SLAC Linear Collider Design Handbook, SLAC 1984.
[2] W. Ash et al., "New Final Focus System for the SLC", these proceedings.
[3] W. Kozanecki, private communication.
[4] P. Bambade et. al., SLAC Pub. 4776, January 1989.
[5] N. Toge et. al., "Chromaticity Corrections in the SLC Final Focus System", these proceedings.
[6] K. Brown, private communication.

Linear e^+-e^- Colliders Above 1 TeV (CM)*

Alfred A. Mondelli
Science Applications International Corporation
1710 Goodridge Drive
Mc Lean, Virginia 22102

Abstract

This paper describes the scaling of the e^+-e^- linear collider beyond Next Linear Collider (NLC) to TeV-class devices. The study includes considerations of interaction-point parameters, accelerator parameters, and cost parameters, so that a complete picture of the trade-off's between the various design options can be discerned. Detailed analyses are presented for three devices: (1) the NLC at 0.5 TeV(CM) and a luminosity of $2x10^{33}$ cm^{-2}-s^{-1}, (2) the NLC Upgrade at 1.5 TeV(CM), $2x10^{34}$ cm^{-2}-s^{-1}, and (3) a 3 TeV(CM) collider at 10^{35} cm^{-2}-s^{-1}. The study shows that while the NLC device will work well at X band drive frequencies, there is an advantage to building the NLC Upgrade at K_t band, and that the 3 TeV collider should be built at K_t band to achieve reasonable operating parameters.

INTRODUCTION

This study has focused on the scaling of linear colliders beyond the Next Linear Collider (NLC) to larger colliders having center-of-mass (CM) energy up to 3 TeV. The system luminosity is scaled as the square of the energy to preserve the counting rate. Sensitivity to wake fields at the low gradient envisioned for the NLC (33 MV/m) dictates that the frequency not exceed X band (≈12 GHz). The NLC Upgrade, with ≈100 MV/m gradient, however, can operate up to K_t band (≈20 GHz), provided that the assumed SLAC structure has been modified to reduce high-order wake fields responsible for the multi-bunch beam-breakup instability. Furthermore, building the NLC Upgrade at K_t band will make it expandable to a 3 TeV (CM) collider. This last device requires an efficiency obtainable only through high-frequency operation, and therefore should be designed at ≈20 GHz.

The character of these studies has been to reduce the parameter space to a plane, using known relationships together with the specification of known quantities, and to plot curves representing "constraints" on the parameter plane. The constraint inequalities map to allowed and forbidden regions of the plane. Parameter plane analyses are carried out first for the interaction point, which is independent of the accelerator model, and then for the accelerator scaling based on a SLAC-like rf linac. Typically, the allowed region in the accelerator parameter plane is closed at high frequencies by the transverse wake-field effects and is closed at low frequencies by the ac or rf power constraints. Since the wake-field limit is a very sharp cut off, one gains by operating at high frequencies.

The results of the study indicate that the optimal operating regime for the linear collider is ≈20 GHz, where wake-field effects are still tolerable, and the collider will have the efficiency needed to reach multi-TeV energy at high luminosity.

Table 1. Interaction-Point Parameters	NLC	NLC Upgrade	3 TeV Collider
CM Energy (γmc^2) [TeV]	0.5	1.5	3.0
Luminosity (L) [cm^{-2}-s^{-1}]	$2x10^{33}$	$2x10^{34}$	$1x10^{35}$
Aspect Ratio (R)	100	100	100
Average Beam Power (P_b) [MW]	0.5	3.0	10.0
Yokoya Parameter (A)	0.2	0.2	0.2
Disruption Parameter (D)	10	20	20
Number per Bunch (N)	$1x10^{10}$	$1x10^{10}$	$2x10^{9}$

INTERACTION-POINT PARAMETERS

Eleven quantities specify the IP. They are the beam size (σ_x, σ_y, σ_z), the number per bunch (N), the bunch repetition frequency (ν), the luminosity (L), the beamstrahlung loss (δ_{BS}), the average beam power (P_b), the beam energy (γ), the disruption parameter (D), and the Yokoya parameter ($A \equiv \sigma_z/\beta^*$). The IP parameters are subject to several types of constraints. A typical study consists of specifying γ, L, $R \equiv \sigma_x/\sigma_y$, P_b, and A. Using these five choices, together with the four equations that define L, δ_{BS}, D, and P_b, reduces the original eleven-parameter space to a two-parameter space, e.g. (σ_y,σ_z). Contours of the various curves of constraint are then plotted in this parameter space, yielding regions of the (σ_y σ_z) plane that are allowed under the constraints[1].

Three different colliders have been studied, viz. the NLC, the NLC Upgrade, and a 3 TeV (CM) collider. The resulting IP parameters are summarized in Table 1.

0-7803-0135-8/91S03.00 ©IEEE

Table 2. Accelerator Model Parameters	NLC (X Band)	NLC Upgrade (X Band)	NLC Upgrade (K_t Band)	3 TeV Collider (K_t Band)
RF Frequency [GHz]	11.4	11.4	20.	20.
Average accelerating Gradient [MV/m]	33.	100.	100.	100.
σ_z [μm]	94.9	113.9	113.9	75.92
Bunches per RF Pulse	10	30	30	100
Structure Efficiency (η_S)	0.58	0.58	0.58	0.58
Total RF and Pulse Compression Efficiency (η_{RF})	0.20	0.30	0.30	0.30
a/λ	0.175	0.175	0.175	0.175
Ratio of Transverse Wake Field to Scaled-SLAC Wake Field	0.25	0.25	0.25	0.25
Length per Linac [km]	7.5	7.5	7.5	15.0
Average AC Power [MW/Linac]	13.3	79.5	26.5	88.
Peak RF Power [MW/Feed]	38.3	345.	115.	115.
Transverse Displacement (x/x_0)	<1.12	<1.12	<1.12	<1.12
Single-Bunch Energy Spread at Optimum Phase Advance	<0.005	<0.005	<0.005	<0.005
Length of RF Feed	2.	2.	0.9	0.9
Number of RF Feeds per RF Tube	8	4	8	8
Peak RF Power per Tube (before Pulse Compression) [MW]	50.	150.	100.	100.
Number of RF Tubes (both linacs)	938	1880	2080	4170
Total Capital Cost ($B)	1.7	2.2	2.3	3.7

ACCELERATOR MODEL

Accelerator Configuration

The linear collider is assumed to consist of several acceleration stages. The electron and positron bunches are injected into an S-band accelerating structure. At an energy of approximately 1 GeV they are transferred to damping rings to reduce their transverse emittances. On exiting the damping rings, the bunches must be recompressed into a single rf bucket, a process which increases the single-bunch energy spread. To control the energy spread the accelerating structure immediately following the damping ring is an S-band structure. During acceleration from the damping ring (≈1 GeV) to an energy of ≈10 GeV, adiabatic damping reduces the energy spread by ten fold. The bunches may then be further compressed from the S-band structure to a high-frequency structure (either X band or K_t band) for acceleration to the final energy.

The accelerator model considered in this study treats only the final, high-frequency structure, from nominally 10 GeV to the final energy of the collision. The accelerators for the linear collider are assumed to be based on a SLAC-type normal-conducting, traveling-wave rf linac driven by rf power amplifiers. These are assumed to be modulated rf power tubes with pulse compression to increase the peak output power per tube by a factor M_{PC}. Each rf tube, with pulse compression, is assumed to drive an accelerator module consisting of several feeds (typically 4-8 feeds per tube). The total rf efficiency is 20-30%.

Wake Field Effects

The longitudinal wake fields compete with the fundamental accelerating mode to cause energy spread within the bunch. The transverse wake fields lead to deflections of the beam from the axis, causing emittance growth. The longitudinal (monopole) wake fields scale as the square of the rf frequency, while the transverse (dipole) wake fields scale as its cube. To reduce the wake fields at high frequency, it is possible to enlarge the iris in the SLAC structure from its nominal value $a/\lambda \approx 0.11$ to $a/\lambda = 0.175$-0.20. The price of enlarging the iris is that the group velocity increases and the shunt impedance of the structure decreases, thereby requiring more rf power for a given accelerating gradient.

The effect of transverse wake fields can be controlled on a single bunch by using BNS damping[2]. The transverse wake field from bunch to bunch in a multi-bunch accelerator involves only the lowest order dipole mode (i.e. the beam-breakup mode). The structure must provide detuning for this mode so that its Q is ≈10-20, without destroying the Q or shunt impedance of the accelerating mode. Structures that meet this requirement have been designed at SLAC[3], for example. In such structures the BBU mode is essentially eliminated, and the total transverse wake field is reduced by a modest factor. For the present study the multi-bunch BBU has been neglected and the total transverse wake field has been assumed to be one-quarter of its value for a scaled SLAC structure. With this value, it is shown that BNS damping may not be required. An analytical calculation of the asymptotic bunch displacement under the influence of

transverse wake fields with external focusing and a linear head-to-tail energy spread[4] is employed in these calculations.

Selection of Accelerator Parameters

Having selected γ, N, σ_z, and P_b from the IP model, the accelerator scaling can be carried out on a parameter plane spanned by peak accelerating field (E_0) and rf wavelength (λ). The scaling is carried out, as it is for the IP, by plotting curves of constraint on the E_0-λ parameter plane. The allowed region is defined by E_0 less than the breakdown field, average AC power less than a specified maximum, peak rf power per feed less than a specified maximum, minimum energy spread less than a specified value, growth of transverse bunch displacement less than a specified value, and accelerator length less than a specified value. Table 2 shows the accelerator parameters selected for the present study.

COST MODEL

The capital cost of an rf linear collider can be expressed as the fixed cost associated with the collider (i.e. all costs that do not scale with either the length of the accelerators or the number of rf drivers), the cost per unit length of accelerator (not including the costs associated with the rf drivers), and the cost associated with the rf drivers (including the modulator, rf tube, pulse compression system, and power transfer to the linac).

The fixed costs do not enter into the cost optimization described here, but they are a significant component of the total cost of the collider. Fixed costs have been estimated at \$855M.

The costs per unit length consist mainly of the cost of the accelerator structure and vacuum system, magnets, and accelerator and klystron housings. The total of these costs has been estimated at \$25M/km.

The costs associated with the rf drivers includes the modulator and tube costs as well as the cost of the pulse compression system (which is approximately the same with either BEC[5] or SLED-II[6]). These costs are approximately \$0.5M/tube. The number of rf tubes is computed from the peak rf power per feed required together with a specification of the peak output power per tube and the power amplification factor due to pulse compression.

The results of the cost study are summarized in Table 2.

The NLC is assumed to be built at X band (11.4 GHz) and powered by rf sources with peak power of 50 MW. Since the accelerating gradient in the NLC Upgrade at X band are increased three-fold, the power requirements increase by a factor of nine over the NLC. One third of the increase has been absorbed by increasing the output power per tube from 50 MW to 150 MW.

For the K_t band NLC Upgrade the collider length is set to 7.5 km (≈100 MV/m), and the rf sources are assumed to yield 100 MW peak output power at 20 GHz. With 9.2-fold pulse compression and an output pulse duration of 0.9 μs at the rf tube, this system can drive eight 0.9 m feeds per tube. The system will consist of 2080 tubes, and will cost \$2.3B.

The 3TeV (CM) collider at K_t band is a simple expansion of the NLC Upgrade to twice the length. The performance of each rf tube is the same here as in the K_t-band Upgrade, but there are now twice as many of them. The rf costs and length-associated costs are therefore double those in the Upgrade, bringing the cost of this device to \$3.7B.

CONCLUSIONS

The scaling trends shown here lead to several interesting conclusions. The NLC will be built at X band, both because rf sources with the required power will not be available to build it at a higher frequency and because its low gradient makes it very susceptible to wake field effects at higher frequencies. Since the fixed costs are approximately 50% of the total NLC cost, it will make sense to reuse these facilities on several later upgrades.

Increasing the NLC gradient three-fold to reach the energy of the NLC Upgrade will require the installation of new rf sources with greater power and efficiency. While using 20 GHz sources for the upgrade requires that the entire X-band accelerator structure of the NLC be replaced with a K_t-band structure, this cost is offset by the saving of ≈500 tubes that is possible at 20 GHz. These two options for the NLC Upgrade are actually comparable in cost.

With the NLC Upgrade carried out at K_t band, the expansion to a 3 TeV (CM) collider will involve only the incremental costs (approximately \$1.4B) associated with its greater length. On the other hand, if the NLC Upgrade is carried out at X band, the cost of building the 3 TeV (CM) system on the NLC site will be approximately \$2.8B. On a new site, the 3 TeV device will cost \$3.7B.

ACKNOWLEDGEMENT

It is a pleasure to acknowledge many interesting discussions on these questions with David Chernin at SAIC and with Martin Reiser and Victor Granatstein at the University of Maryland.

REFERENCES

* Work supported by the U.S. Department of Energy, Division of High Energy Physics.

1 A. Mondelli and D. Chernin, Proc. 1990 Linear Accel. Conf. (Albuquerque, NM, Sept. 10-14, 1990, LA-12004-C), p. 730.

2 V. Balakin, A. Novokhatsky, and V. Smirnov, Proc. 12th Intl. Conf. on High Energy Accelerators (Fermilab, 1983), p. 119.

3 R.B. Palmer, SLAC-PUB-4542 (July, 1988).

4 D. Chernin and A. Mondelli, Part. Accel. **24**, 177 (1989).

5 Z.D. Farkas, IEEE Trans. **MTT-34**, 1036 (1986).

6 P.B. Wilson, Z.D. Farkas, and R.D. Ruth, SLAC-PUB-5330 (September, 1990).

Linac-Ring Colliders with High Disruption Parameters – a First Test of Principle*

J. R. Boyce, S. Jin, J. Kewisch, R. Li, P. K. Kloeppel,
B. Niczyporuk, R. Rossmanith, N. Sereno and R. Whitney
Continuous Electron Beam Accelerator Facility
12000 Jefferson Avenue, Newport News, VA 23606

ABSTRACT

Linac-Ring colliders are considered as one approach to an asymmetric B-factory. The beam-beam effect in a superconducting linac is different from the beam-beam effect in a storage ring or linear collider[1]. The electron beam is guided through the positron beam and disrupted. The aim of this paper is to discuss possible test facilities to study this effect.

INTRODUCTION

Recently several papers were published discussing the features of linac-ring colliders. In order to obtain luminosities of the order of 10^{34} and higher, the (positron) storage ring is operated at its linear tune shift limit of 0.05. In a practical design the number of particles in the positron bunch is 3 orders of magnitude higher than the electron bunch from the linac. As a result the disruption parameter of the electrons

$$D_e = \frac{2r_0 N_p \sigma_{pz}}{\gamma_e \sigma_{p,x} \sigma_{p,y}} \qquad (1)$$

can be about 300, and the main concern is the stability of the positron beam in the storage ring. The consequences for the electron beam are shown in Figure 1. The electrons oscillate through the positron bunch and are disrupted. In several papers,[1][2][3] it is shown that under certain circumstances the beam-beam limit can be affected by position and intensity fluctuations (random walk limit). The severity of this effect depends highly on the assumed spectrum of the random noise.

It has been proposed to test the high disruption interaction with a superconducting linac and a low energy positron storage ring. In this paper, a preliminary design of two test facilities is presented. One is a 500 MeV positron storage ring, and the other is an 85 MeV positron storage ring.

DESIGN GOALS

The electron beam from CEBAF can have up to 10^9 e^- per bunch with a normalized emittance of $10^{-6}\pi$ m-rad. The two storage rings were designed in such a way that the equilibrium transverse emittance is as small as possible to produce a high electron disruption. The lattice chosen for these two rings is the FODO cell lattice which has been widely used in the design of storage rings for its superior dynamic aperture characteristics and the ease of local chromatic correction. The design work is based on the DIMAD[4] and ZAP[5] computer codes.

*Supported by D.O.E. contract #DE-AC05-84ER40150

500 MeV STORAGE RING

The bending angle for each dipole in the 500 MeV ring is 9°. With two dipoles for each FODO cell, altogether twenty cells are needed. The minimum emittance is obtained at 144° phase advance per cell. In order to avoid excessively strong quadrupoles and sextupoles, betatron phase advances per cell of 117° for β_x and 58.5° for β_y were chosen. Some of the DIMAD output data are used in the ZAP code to find the effects of intrabeam scattering. The parameters of the 500 MeV ring are:

500 MeV Storage Ring

Energy	500 MeV
Circumference	26 m
Revolution frequency (including straight section)	10 MHz
RF	1500 MHz
Harmonic number	150
Trans. damping time	7.7 msec
Equil. emittance	10^{-8} rad-m
Equil. energy spread	4×10^{-3}
Momentum comp. factor	0.0282
Energy loss/turn	0.48 KeV
Bending angle	0.05π rad
RF voltage	800 KV
Synchrotron frequency	1.1 MHz
Tune	0.0094
Equil. bunch length	1 cm
Num. of e^+ in bunch	4×10^{11}
Max. current	1.3 A
e^- disruption D_e	116
Touschek lifetime	0.22 h

Assuming an equal-energy collision, the maximum electron disruption parameter D_e for the 500 MeV ring is 116. A schematic layout of the ring is presented in Figure 2.

85 MeV STORAGE RING

The bending angle of a dipole for the 85 MeV storage ring is 22.5°. Altogether 8 cells are needed. The betatron phase advances per cell are again 117° for β_x and 58.5° for β_y. The size of the ring is pretty small, with a diameter of about 2.44 meter. Again, some of the DIMAD output data are used in ZAP to compute the effects of intrabeam scattering.

0-7803-0135-8/91$03.00 ©IEEE

85 MeV Storage Ring

Energy	85 MeV
Circumference	7.68 m
Revolution frequency (including straight section)	20 MHz
RF	800 MHz
Harmonic number	40
Trans. damping time	400 msec
Equil. emittance	10^{-7} rad-m
Equil. energy spread	4×10^{-3}
Momentum comp. factor	0.1576
Energy loss/turn	1.2 eV
Bending angle/dipole	0.125π rad
Bending radius	0.46 m
Bending field	6.19 kG
RF voltage	800 kV
Synchrotron frequency	3.8 MHz
Tune	0.097
Equil. bunch length	1 cm
Num. of e^+ in a bunch	1.5×10^{11}
Max. current	0.5 A
e^- disruption D_e	24
Touschek lifetime	0.83 h

If the beams have equal energy, the maximum electron disruption parameter D_e is 24. A schematic layout of the 85 MeV ring is shown in Figure 3.

INTERACTION REGION FOR THE 85 MeV STORAGE RING (Equal Energy Case)

The interaction region for the 85 MeV ring consists of a missing-magnet FODO cell dispersion suppressor and a two-dimensional telescopic system.[6] The total length of the interaction region is 0.8 m, and the β function at the arc is reduced to 1 cm in both planes at the interaction point (IP). An electric septum is used to separate the electron and positron beams, and a magnetic septum bends the positron beam back to the ring. The angle of separation is 1.72°, and the length is:[7]

$$l = \frac{p\beta}{E} \tan\theta, \tag{2}$$

where β is v/c. With a maximum value of $E = 20$ kV/cm and $\theta = 1.72°$, the length of the septum for the 85 MeV storage ring is calculated to be 1.275 m. The lattice for the interaction region is shown in Figure 4.

INTERACTION REGION FOR THE 85 MeV STORAGE RING (Unequal Energy Case)

In order to achieve a higher disruption it was suggested that the 85 MeV stored positron beam collides with a 20 MeV electron beam from the linac. The electron disruption parameter in this case is 100. Based on the previous 85 MeV storage ring design, the interaction region is shown in Figure 5. A dipole and a magnetic septum are used to separate the two beams.

The bending angle θ of a dipole of length l in a uniform magnetic field B is given by

$$\sin(\frac{\theta}{2}) = \frac{lBe}{2p}, \tag{3}$$

which forms the basis for the separation of the two beams. The dipole B1 is set to bend the 85 MeV positrons approaching the interaction point (IP) $-3°$, whereas the same dipole bends the 20 MeV electron beam leaving the IP by $-12.75°$. To insure a clear separation of the two beams, an additional magnetic septum gives the electron beam a further bend of $-5.25°$ before it travels to the electron beam line. The total length of the interaction region for the positron storage ring is 2.15 meters and the length of the interaction region is 60 cm. The net bending angle for the positron beam is 22.5° taking into account B2 and B3, bending 1.5° and 24°, respectively. The two dipoles after the magnetic septum bend the electron beam by 6° and 24°, respectively.

As a summary, the β function and the dispersion functions η and η' for the whole 85 MeV ring (including the insertion for RF cavity) for unequal-energy collision are presented in Figure 6 and 7.

CONCLUSION

For the design of a Linac-Ring collider, preliminary first order optics for two storage rings of 500 MeV and 85 MeV are presented in this paper. The parameters of the rings seem well suited for the proposed experiment.

ACKNOWLEDGMENTS

The authors thank Prof. Hermann Grunder from CEBAF for continuous interest and support. In addition we thank Prof. Nathan Isgur, head of the CEBAF Theory Group, for many stimulating discussions. We finally thank Prof. Murray Tigner from Cornell for many critical remarks.

REFERENCES

[1] S. A. Heifets, G. A. Krafft, and M. Fripp, "On asymmetric collisions with large disruption parameters," Nucl. Inst. Methods in Phys. Research, A295, 286-290 (1990).

[2] Y. Baconnier, "On the stability of linac-ring colliders," CERN PS/91-02(LP).

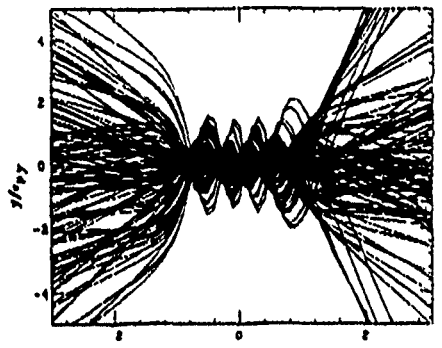
[3] P. Grosse-Wiesmann, C. D. Johnson, D. Möhl, R. Schmidt, W. Weingarten, and L. Wood, "Linac-ring-collider B-factory," p. 383, *Proc. 2nd European Particle Accelerator Conference* (Nice, 12-16 June 1990).

[4] R. V. Servranckx *et al.*, "Users' guide to the program DIMAD," SLAC Report 285, UC-28 (A), May 1985.

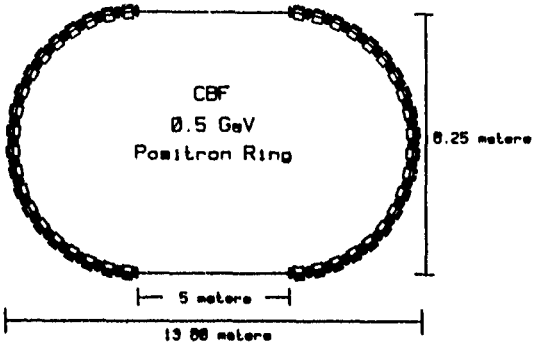
[5] M. S. Zisman, S. Chattopadhyay, and J. J. Bisognano, LBL-21270 UC-28, 1986.

[6] Karl L. Brown, Roger V. Servranckx, "First and second order charged particle optics," SLAC-PUB- 3381, July 1984.

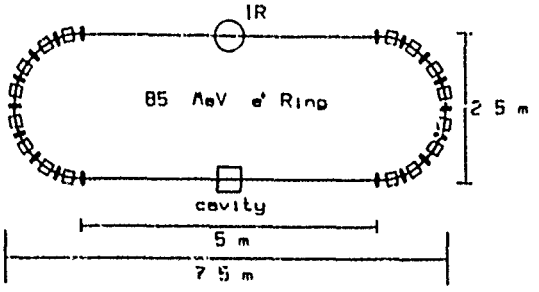
[7] C. Bovet, R. Gouiran, I. Gumowski, K. H. Reich, "A selection of formulae and data useful for the design of A.G. synchrotrons," CERN/MPS-SI/INT.DL/70/4.



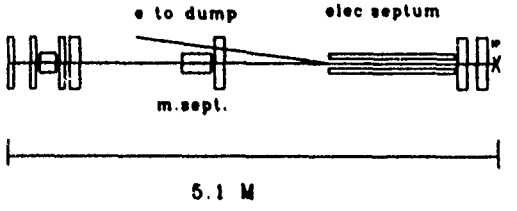
1. Disruption of the e^- beam by the $e+$ beam stored in the storage ring



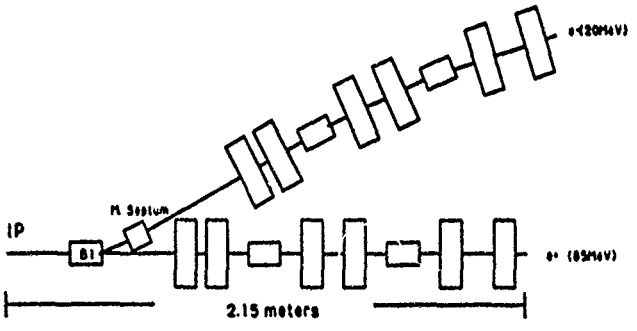
2. Schematic layout of the 500 MeV storage ring



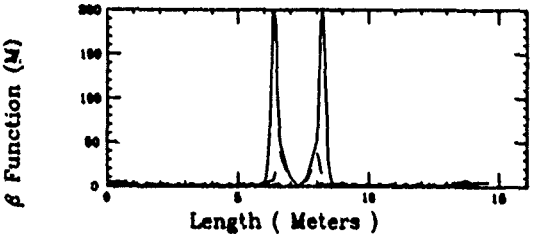
3. Schematic layout of the 85 MeV storage ring



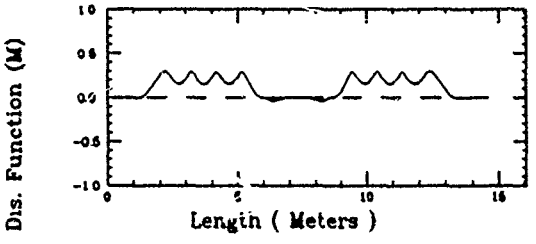
4. Interaction region of the 85 MeV storage ring



5. Asymmetric interaction region of the 85 MeV storage ring



6. β function for the 85 MeV storage ring



7. Dispersion for the 85 MeV storage ring

MISALIGNMENT STUDY OF NLC BUNCH COMPRESSOR*

R. P. Rogers, and S. A. Kheifets
Stanford Linear Accelerator Center, Stanford University, Stanford, CA 94309 USA

Abstract

Results of computer simulations of the misalignments in the 180°-bend angle second-stage bunch compressor for the NLC are described. The aim of this study was to evaluate alignment and production error tolerances. Three versions of the second stage, differing in their minimum obtainable bunch length (44 μ, 60 μ, and 86 μ) were studied. Simulations included orbit correction produced by errors and misalignments of the compressor elements. The orbit correction itself was done within some error margins. The effects of misalignments on transverse emittance growth were found. Recommendations for alleviating alignment tolerances are discussed.

I. INTRODUCTION

To diminish the effects of chromatic aberrations the NLC bunch compressor is designed to consist of two stages [1]. Small emittances in the horizontal plane, and especially in the vertical plane, are needed to achieve the desired NLC luminosity. Production and alignment errors of the system components should be kept small to preserve the emittances.

In this paper we describe the effects of misalignments on transverse emittance growth in the 180° bend angle second stage bunch compressor. Three versions of the second stage, differing in their minimum obtainable bunch length (44 μ, 60 μ, 86 μ) were studied. The found tolerances for the y-plane appear to be exceedingly tight. Measures for improving alignment tolerances are discussed.

Computer Tools

The design of the NLC bunch compressor and its operation had previously been studied using the **TRANSPORT** [2] and **TURTLE** [3] programs. However, the effects of misalignments and errors can not be studied without inclusion of an appropriate orbit correction (steering). The present study was performed with the help of the program **DIMAD** [4] chosen for its capabilities of an easy and flexible introduction of misalignments and correction.

Correction Scheme

We implemented correction of an orbit produced by randomly chosen errors and misalignments as follows: The first two half-magnets in each cell of the compressor are defined as correctors. These dipole magnets correct the beam x and y positions as read in beam position monitors (BPM) located nine elements downstream of the corrector. The corrector steers by imposing a small x or y displacement of the front end of the magnet. The exit points of the magnets remain fixed. Only one steering was made per run.

Magnets were misaligned around the tangent to the central trajectory at the midpoint of each element. The readings of the BPMs were also assumed to have errors. All error distributions were assumed to be normal cut off at two sigmas (rms). Several different runs were done with the rms displacements of magnets by 0, 25, 50, 75, and 100 μm, respectively, in x, y, and z directions, and with the rms rotations by 0, 25, 50, 75, 100 μrad about x, y, and z axes. For the BPM the corresponding rms reading error equals to 100μm.

Results

One thousand particles were tracked and analyzed per run. The particles were randomly chosen to fill a six-dimensional Gaussian distribution truncated above one sigma. The Table summarizes the results for each version of the compressor. The ratios ϵ/ϵ_0 of the emittance ϵ at the end and ϵ_0 at the beginning of the compressor are tabulated. They were found in the following way.

The beam sigma matrix [2] calculated by DIMAD from the particle distribution resulting from tracking has the form

$$\begin{matrix} \sigma_{11} & r_{12} & r_{13} & r_{14} & r_{15} & r_{16} \\ & \sigma_{22} & r_{23} & r_{24} & r_{25} & r_{26} \\ & & \sigma_{33} & r_{34} & r_{35} & r_{36} \\ & & & \sigma_{44} & r_{45} & r_{46} \\ & & & & \sigma_{55} & r_{56} \\ & & & & & \sigma_{66} \end{matrix} \qquad (1)$$

From here the emittance of each projection of the beam ellipsoid was calculated using standard formulae.

$$\epsilon_x = \sigma_{11}\sigma_{22} \times \sqrt{1 - r_{12}^2} \quad , \qquad (2)$$

$$\epsilon_y = \sigma_{33}\sigma_{44} \times \sqrt{1 - r_{34}^2} \quad , \qquad (3)$$

$$\epsilon_\delta = \sigma_{55}\sigma_{66} \times \sqrt{1 - r_{56}^2} \quad . \qquad (4)$$

The emittances ϵ_0 were calculated in a similar way from the corresponding sigma matrix at the beginning of the line. The top row of the Table gives the intrinsic emittance growth present in the aligned perfect system. Normalized emittance growth was calculated as follows:

$$\left[\frac{\epsilon/\epsilon_0}{(\epsilon/\epsilon_0)_0} - 1\right] \times 100 \quad , \qquad (5)$$

where $(\epsilon/\epsilon_0)_0$ is ϵ/ϵ_0 without misalignments for the version of the compressor being plotted, and ϵ/ϵ_0 is the emittance ratio with misalignments from the Table.

* Work supported by Department of Energy contract DE-AC03-76SF00515.

0-7803-0135-8/91$03.00 ©IEEE

Emittance growth for bunch compressor stage 2						
	86 μ Version		60 μ Version		44 μ Version	
Misalignment	ϵ_x/ϵ_{x0}	ϵ_y/ϵ_{y0}	ϵ_x/ϵ_{x0}	ϵ_y/ϵ_{y0}	ϵ_x/ϵ_{x0}	ϵ_y/ϵ_{y0}
0	1.010	1.001	1.096	1.008	1.688	0.979
dx (μ) 25	1.016	1.000	1.058	1.008	1.455	0.979
50	1.041	1.000	1.061	1.008	1.306	0.979
75	1.083	1.000	1.117	1.008	1.258	0.979
100	1.135	0.997	1.206	1.008	1.306	0.979
dx' (μrad) 25	1.010	1.147	1.096	1.068	1.687	1.047
50	1.010	1.514	1.094	1.269	1.684	1.276
75	1.009	1.994	1.093	1.572	1.678	1.614
100	1.009	2.539	1.088	1.949	1.670	2.029
dy (μ) 25	1.206	4.083	1.600	5.031	2.476	9.174
50	2.874	7.105	5.842	14.059	13.739	35.595
75	6.057	23.265	13.759	37.831	——	——
100	10.448	31.958	——	——	——	——
dy' (μrad) 25	1.009	1.000	1.092	1.008	1.679	0.979
50	1.010	1.001	1.090	1.008	1.672	0.979
75	1.012	1.000	1.088	1.008	1.665	0.979
100	1.014	1.000	1.087	1.008	1.659	0.979
dz (μ) 25	1.010	1.000	1.095	1.008	1.684	0.979
50	1.010	1.001	1.093	1.008	1.681	0.979
75	1.010	1.000	1.092	1.008	1.678	0.979
100	1.011	1.001	1.092	1.008	1.678	0.979
dz' (μrad) 25	1.010	1.009	1.096	1.020	1.688	1.004
50	1.010	1.032	1.096	1.070	1.688	1.075
75	1.010	1.066	1.096	1.168	1.688	1.186
100	1.010	1.114	1.096	1.279	1.688	1.326
$d\delta(10^{-6})$ 25	1.010	1.001	1.099	1.008	1.697	0.979
50	1.011	1.000	1.104	1.008	1.704	0.979
75	1.012	1.001	1.107	1.008	1.714	0.979
100	1.014	1.000	1.112	1.008	1.723	0.979

Figures 1–6 represent the normalized emittance growth (in percent) versus the rms magnitude of the misalignment relative to the aligned system. This removes the effects of the system intrinsic emittance growth, so that only the effects of misalignments on emittances are demonstrated. The points on the plots for the 44 μ version of the compressor stage are marked by squares, the 60 μ version by diamonds, and the 86 μ version by crosses, respectively.

More results can be found in a slightly more extensive version of this paper [5].

CONCLUSION

The results indicate that for all three versions of the compressor both the horizontal and vertical emittances exhibit sensitivity to vertical displacements and horizontal rotations. Acceptable tolerances for such misalignments appear to be on the order of several micrometers for dy and 25 μrad for dx'. For both the 60 μm and 44 μm versions of the compressor particle losses were observed starting at the vertical misalignment level of 50 μm. Other misalignments produced acceptable results up to the 100 μm or μrad level. The horizontal emittance growth seems to improve as misalignments increase. This may be due to coupling between the horizontal and vertical motion.

The alignment tolerances may be improved by using η and β matching in the compressor. Tolerances may also be improved by making use of better steering techniques. Finally, the element parameters in the designs used in the current and previous studies have been chosen with the misalignments not considered. The design of the compressor should be optimized with respect to misalignments.

REFERENCES

[1] S. A. Kheifets, R. D. Ruth, and T. M. Figuth, "Bunch Compressor for the TLC," Stanford Linear Accelerator Center preprint SLAC-PUB-5034 (1989).

[2] K. L. Brown et al., "TRANSPORT—a Computer Program for Designing Charged Particle Beam Transport Systems," Stanford Linear Accelerator Center Report SLAC-91 Rev. 2, UC-28 (1977).

[3] D. C. Carey et al., "All Purpose TURTLE," Stanford Linear Accelerator Center Report SLAC-246, UC-28 (1982).

[4] R. V. Servranckx et al., "Users Guide to the Program DIMAD," Stanford Linear Accelerator Center Report SLAC-285, UC-28 (1985).

[5] R. P. Rogers and S. A. Kheifets, "Misalignment Study of NLC Bunch Compressor," Stanford Linear Accelerator Center preprint SLAC-PUB-5501 (1991).

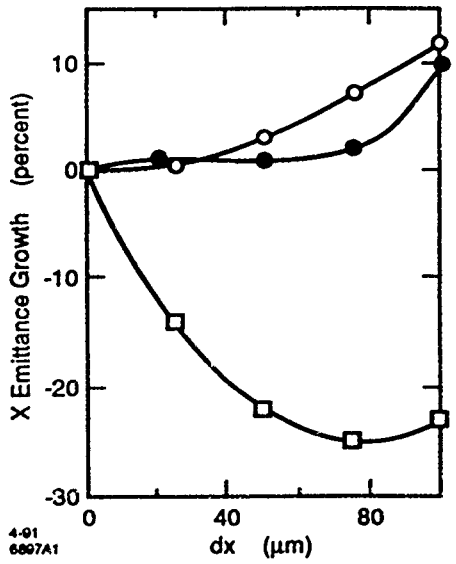


Fig. 1

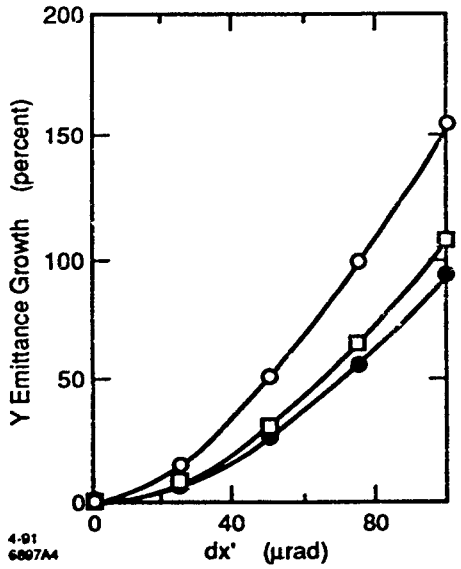


Fig. 2

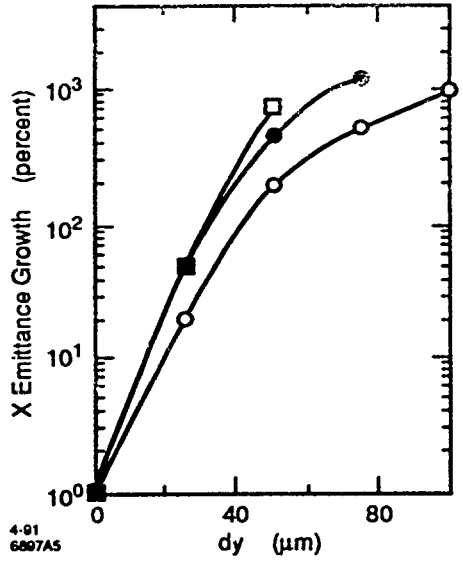


Fig. 3

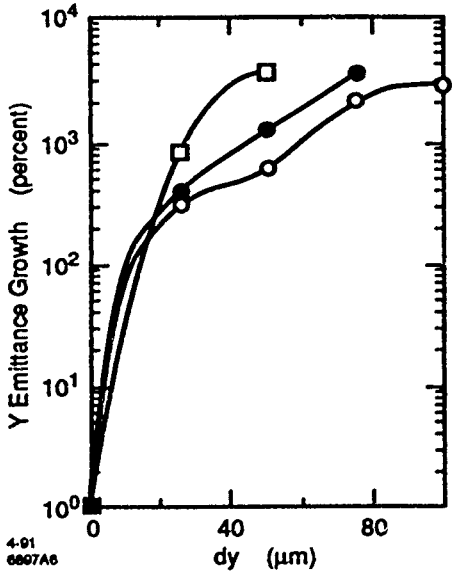


Fig. 4

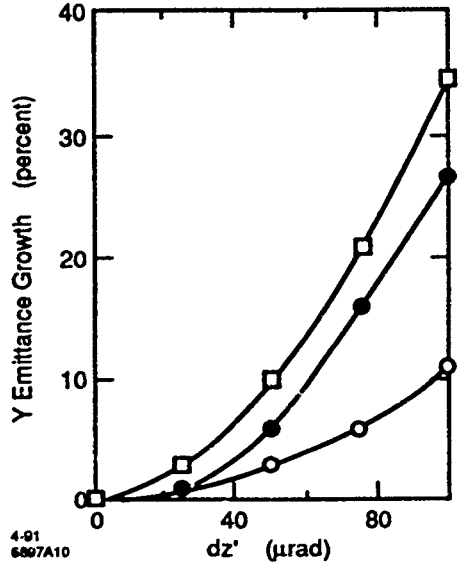


Fig. 5

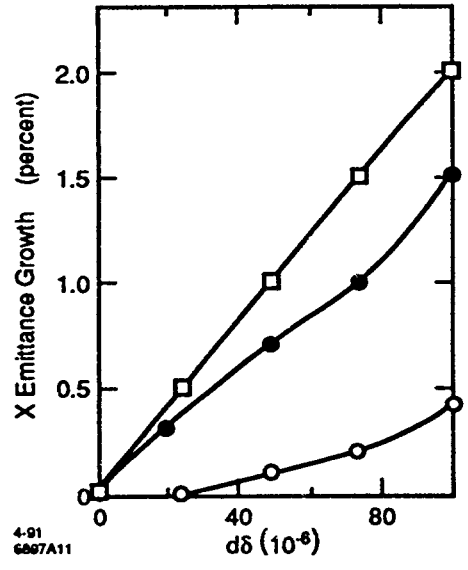


Fig. 6

High Brightness Sources for Colliders *

J.E. Spencer
Stanford Linear Accelerator Center, Stanford University
Stanford, California 94309

Abstract: Different possible sources are considered and the importance of the gun for linear colliders discussed. Low emittance electron guns suitable for SLC are available now and we discuss current work that could also provide high polarization. The relative merits of $\vec{\gamma}, \vec{e}^{\pm}$ and $\vec{p}^{\pm}$ are discussed and how the next linear collider (NLC) naturally provides both $\vec{e}^{\pm}$ and $\vec{\gamma}$. Particular emphasis was placed on stability demands of LC's without sacrificing flexibility. A general purpose, versatile source is described that can collimate and/or tailor the bunch shape. Finally, some interesting experiments for SLC are discussed that could provide good physics while testing such ideas for the next generation machine. At 0.5-1.0 TeV such a machine would be complementary and competitive with LHC.

Introduction

High energy physics has been limited to electrons and protons as primary beams because these are charged, stable and abundant. They are also direct sources of the lowest-generation, point-like fermions. With either choice, most of the physics has been derived from the outgoing, charged leptonic channels due to their cleaner signatures[1,2,3,4]. The same can be said for the incident channels with enough brightness and energy $\sqrt{s}$. Photons provide another incident channel for complementary tests of technicolor and supersymmetry for different J^{PC} states.

Laser back-scattering to provide highly polarized, high energy beams of $\gamma's$ is well know from photoproduction experiments[5]. FEL's extend the possibilities in several ways[6]. γ beams produced from high-brightness electron beams could be used directly for experiments or to make correlated $\vec{e}^{\pm}$ beams more efficiently either by thin crystals or high power lasers or FEL's rather than the usual targets whose phase volumes are larger and probably unpolarized. Then, depending on original electron bunch characteristics, the resulting pair emittances may need neither damping nor compression.

The concerns that motivated this work are based on what has been learned from SLC. Some key bottlenecks there are the stability and reliability associated with the positron production, acceleration, damping and extraction processes. This combination that ends in launching the bunch down the linac will be called the positron source. When these steps become too extended and uncoupled the difficulties are obvious. Still, the basic beam parameters are set by the source and ultimately the gun.

*Supported by U.S. Dept. of Energy contract DE-AC03-76SF00515.
U.S. Government work not protected by U.S. Copyright.

The increasing luminosity and energy required for new machines and the progressive scaling of old techniques seems increasingly impractical. The largest machines ever are proposed to learn everything about the smallest distances in the least possible time. Whether this is realistic and, if so, at what cost and with what techniques was considered elsewhere[7]. Here we extend that work with a relevant design example.

Guidelines and Parameters

The layout shown in Fig. 1 was proposed as a prototype to test the gun, accelerating structure and $\vec{e}^{\pm}$ production mechanisms but includes all the characteristics needed for such sources. Several parameters[8,9] in Table 1 are set by the LC damping rings e.g. the bunch spacing which is a problem even with an accumulator. The batch rate in LC's is limited by the modulators but two-beam schemas can go much higher. The FEL numbers are a composite that could be done now based on LANL sources[10] except for the inequalities whose limits are not currently available although 3 μ bunch lengths are possible now if not practical. Longitudinal brightness $B_{zn} = eN\beta c/\epsilon_{zn} = I_p/\delta\gamma$[8]. The numbers for SLC are what has been achieved.

Table 1: Benchmark Source Parameters for FEL's & LC's.

Parameter		FEL	NLC	SLC
RF Wavelength	cm	10.5	21.0-10.5	10.5
Rep.Rate	Hz	$\leq 10^5$	180	120
Energy	GeV	1.0	1.8	1.2
Bunches/Batch		$\leq 10^8$	10	1
Particles/Bunch	10^{10}	3	1-2	3
Bunch Spacing	ns	≥ 0.35	0.70	58.9
$\epsilon_{xn} \equiv \gamma\sigma_x^2/\beta_x$	μm	15	2.8	18(35)
ϵ_{yn}	μm	15	0.03	17(1)
$\epsilon_{zn} \equiv \gamma\frac{\delta p}{p}\sigma_z$	mm	6	19	10
σ_z	mm	> 0.25	0.10	0.50
Brightness B_{zn}	A	240	50	96

The RF Electron Gun

Of the several possibilities, very low emittance RF guns being developed for FEL's seem most promising. These typically have laser driven cathodes. RF thermionic guns at 2 MeV have been developed recently for SSRL[11] that seem to work as predicted and would be usable for SLC except for their lower bunch currents.

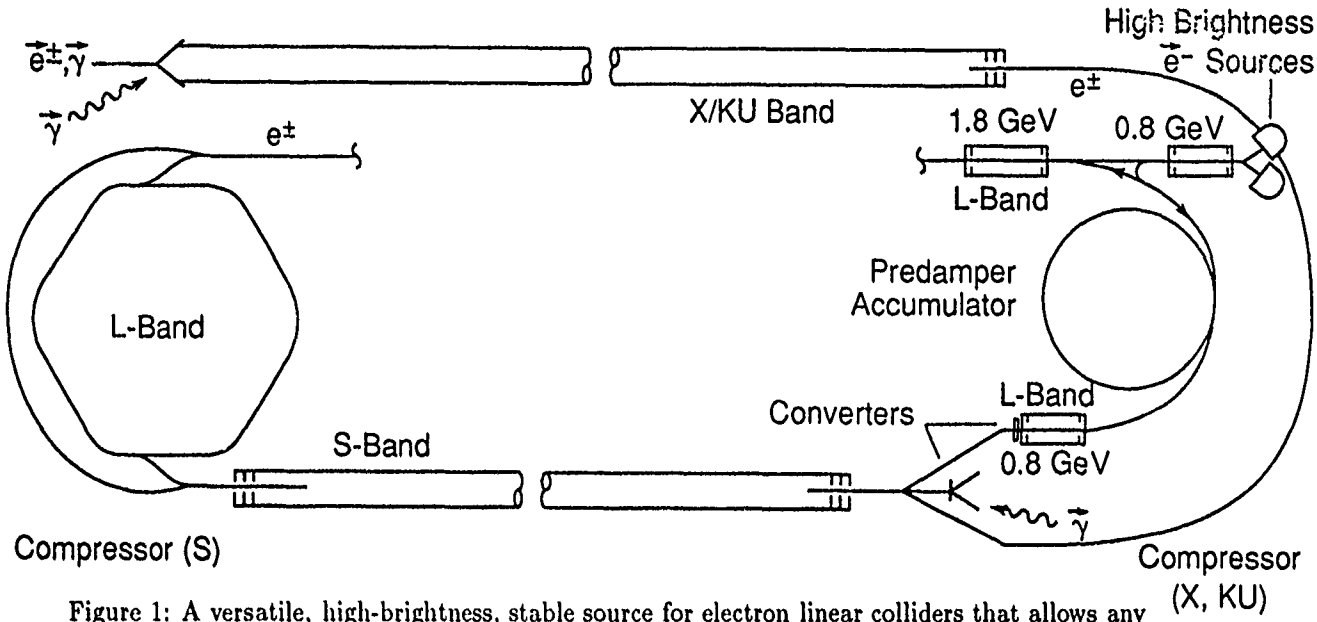


Figure 1: A versatile, high-brightness, stable source for electron linear colliders that allows any combination of $\vec{\gamma}$ and $\vec{e}^{\pm}$ experiments. The semi-circular bunch compressors at each side allow *causal* feedforward or measurements on a bunch such as transverse position or the longitudinal bunch distribution that can be used to correct or modify it before final launch into the X-band linac. Significant rate and bunch current variations are possible for both $e^{\pm}$ that would not require either the damping rings or accumulators.

Fortunately, FEL requirements for the XUV and shorter require characteristics similar to colliders[8] – high peak currents(>200 A), low emittance and energy spread(3μm and 0.1%), short micropulse lengths(1-10 ps) and minimal jitter($\ll$ pulse length). Such guns can provide SLC beams whose costs are determined by peak currents and rates for a given emittance. We also need to include high polarization 'photocathodes' as discussed in papers here and elsewhere[12] with the advantages of the RF gun. Many groups are now developing RF sources for a broad variety of applications, better performance and reliability.

Applications of 'Channeling'

Several applications of known channeling properties[13] may be useful for producing positrons e.g. by replacing conventional targets[11] or for use with high energy photons. The latter is not really channeling but using the strong fields and regular lattice as a counterpropagating beam of quasimonochromatic photons to pair produce via the Breit-Wheeler process($\gamma\gamma \rightarrow e^{\pm}$) rather than Bethe-Heitler which is less efficient[6] here for several reasons.

Scanning Transmission Ion Microscopy has been used with channeling to explore thin epitaxially grown silicon using heavy ions. Damage was observed in the channel with beams focused to 16 microns and currents of 2 nA but CSTIM has claimed 100% efficiency with negligible damage for smaller spots e.g. $\leq$200 nm[15]. High-energy, high-brightness electron or photon beams whose characteristics are matched to the lattice structure should have good gain and smaller phase volume with damage coming from wake fields, shock effects and secondaries etc.

Alternatively, lattice vibrations excited in some way could provide acceleration and focusing mechanisms with advantages over plasma schemes for fast, optimal control. Similarly, the lattice also acts as a natural collimator which would be interesting to test with a spectrometer for its effects on the beam e.g. for photorefractive or focusing effects from high fields. Taken with the production and bunch shaping steps, this could provide a more stable, well-defined beam for launch into the main accelerator.

We can define a thick, amorphous target by setting the rms pair production angle equal to the the rms multiple scattering angle and then compare this to the rms divergence of the beam at the target:

$$\sqrt{L/L_r} = m/15 = 34mr \gg \sigma_\theta$$

$$1/L_r \approx 4Nr_e^2 z(z+1)\alpha \log(183/z^{1/3})$$

where z and N are atomic number and density. For NLC, a $\beta = 10$m gives $\sigma_\theta = \sqrt{\epsilon/\beta} \leq 0.53$mr. The target thickness is about 0.1% of L_r or as thin as 4μ for tungsten which requires care but is usable and implies an equivalent wiggler with >2000 periods. This thickness limits the photon to >15 MeV where pair production is also dominant.

However, a material target isn't necessary. For SLC, $\sigma_\theta \leq 1.9$mr. For 50 GeV, Compton conversion has $\sigma_C = 3{\cdot}10^{-25}$ cm^{-2} for 3.5 eV photons. For a laser pulse with 0.1 J focused to $\sqrt{2}\mu$ we have unit probability for conversion:

$$P_C = \sigma_C n_\gamma = 1 \quad (\approx P_{BW} \text{ for } \omega_2 = 14.2eV)$$

where $n_\gamma = 3\ 10^{24} \approx 10^5 n_W$ cm^{-2} is the photon target thickness for both C and B. W conversion from Ref [6]. The outgoing Compton photon has $\omega_1 = 36$ GeV with $n_{\gamma_1} \approx 0.2 n_e$ and polarization $\vec{P}_1 > 0.9\vec{P}_{inc}$.

Bunch Shaping and Control

The goal of optimal control is to overcome K-entropy[7] with fast measurement and feedback/forward control. The problem demands in Fig. 1 are ideal. Fig. 2 shows an example of a very fast measurement of the longitudinal bunch form factor to control shape with feedback or feedforward or for measurement and control of wake fields, plasma or channel lenses or the beam-beam interaction. Coherent synchrotron radiation has been observed[16] and seems particularly well suited to a Discrete Fourier Transform in real time. We estimate this can be done now in about 10 ns using a fast multiply algorithm[17] with the response time of downstream control hardware being the problem.

In the example of Fig. 2, we can feedback to the source or forward in the compressor arcs to modulate the bunch energy for control of bunch shape. Because we can influence the same bunch that measurements were made on, it is an example of *causal feedforward*[7]. While this is easier in heavy ion colliders, it is also possible in lepton *linear* colliders but clearly imposes design constraints. Using lasers for this is consistent with the time constraints.

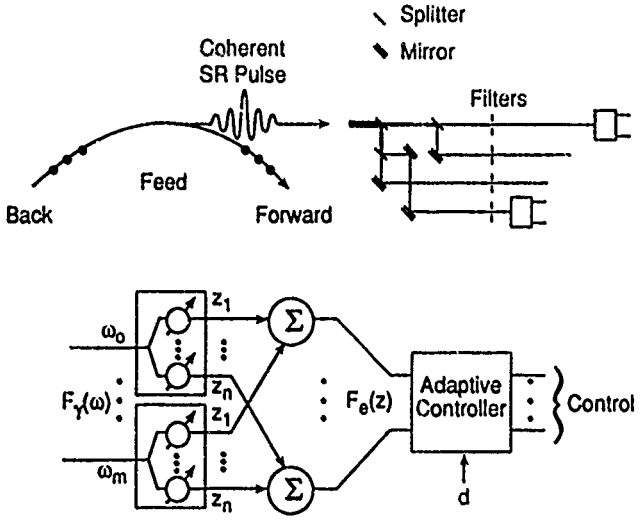


Figure 2: A Fast DFT for Bunch Shape Control.

Concluding Remarks

Conventional e^+ production uses virtual photons that produce a broad spectrum and cascade that gives a good gain in number but not entropy. Just as real photons can enhance the information rate and reduce the noise in an experiment by avoiding the low-q virtual photon divergence they can also enhance usable yields of polarized positrons.

There are many experiments where one doesn't need e^+ such as $(e\gamma \rightarrow W^-\nu)$ which could be done at SLC even though weak and nonresonant. Another e^+ production scheme[18] uses an FEL to produce 'low energy' photons converted in $0.5L_r$ of W. We would use the FEL to Compton convert or better for the direct BW process where e.g. we needed 14 eV photons in the target-free case.

References

[1] Burton Richter, Very High Energy Colliders, 1985 IEEE Part. Accel. Conf., Vol. NS-32, No.5(1985)3828.

[2] Carlo Rubbia, The 'Future' in High Energy Physics, 1988 European Part. Accel. Conf., Rome 1988, 290.

[3] Wolfgang K.H.Panofsky, A Perspective on Lepton-Photon Physics, XIVth Int'l. Symp. on Lepton-Photon Interactions, Stanford, CA(1989).

[4] C. Ahn et al., Opportunities and Requirements for Experimentation at Very High Energy $e\pm$ Colliders, SLAC-329, 1988.

[5] C.K.Sinclair, J.J.Murray, P.R.Klein and M.Rubin, IEEE Trans. on Nucl. Sci., 16, No.3(1969)1065.

[6] J.E.Spencer, Wigglers - The Newest Profession, SLAC-PUB-2677, Feb. 1981. It has been clear for a long time that higher energy photons than given by conventional lasers were needed but with comparable number densities so coherent, synchrotron radiation in undulators was suggested. The viability of different technologies for alternative incident channels, together with details on production mechanisms of the high energy photon beam or pair beams are discussed in Higher Luminosities via Alternative Incident Channels, SLAC-PUB-3645, Apr. 1985, together with references to other work.

[7] J.E.Spencer, Optimal Real-Time Control - Colliders, This Conference. This paper considers the control and stability aspects of colliders that prompted this paper.

[8] J.B.Murphy and C.Pelligrini, Editors, Proc. of ICFA Workshop, BNL 52090, March 1987.

[9] R.D.Ruth, Editor, Snowmass Linear Collider Working Group Rpts., SLAC-Report-334, March 1989.

[10] W.E.Stein et al., The Accelerator for the LANL FEL-IV, LA-UR-85-222 and L.M. Young, Compact Photoinjector Accelerators for FEL's, LA-UR-90-3332(1990).

[11] M. Borland et al., Performance of the 2 MeV Microwave Gun for the SSRL 150 MeV Linac, SLAC-PUB-5333, 1990.

[12] M.Zolotorev, Towards a High-Intensity Source of Totally Polarized Electrons, LBL-29193, May 1990.

[13] Allan H. Sorensen and Erik Uggerhoj, The Channeling of Electrons and Positrons, Sci. Am.(1989)96 and A.Belkacem et al., Phys. Rev. Lett., 58(1987)1196.

[14] F-J. Decker, Channeling Crystals for Positron Production, This Conference.

[15] M. Cholewa, BAPS, Vol. 35. No. 8(1990).

[16] T.Nakazato, et al., Phys. Rev. Lett. 63(1989)1245. See also: K.Ishi et al., to be published in Phys. Rev.

[17] A.Corneliusen et al., Computation and Control with Neural Nets, NIM A239(1990)507.

[18] V.E.Balakin and A.A.Mikhailichenko, VLEPP. The Conv. Syst. to Obtain Highly Polarized $e^{\pm}$, Proc. 12th Int'l. Conf. on High Energy Accel., Aug. 1983 and SLAC talk by V.Balakin, Sept. 1990. They use FEL's driven by 150 GeV e's to make a regenerative system.

INVESTIGATION OF SEISMIC VIBRATIONS AND RELATIVE DISPLACEMENTS OF LINEAR COLLIDER VLEPP ELEMENTS

B.A.Baklakov, P.K.Lebedev, V.V.Parkhomchuk,
A.A.Sery, A.I.Sleptsov , V.D.Shiltsev
Branch of Novosibirsk Institute of Nuclear Physics
142284 Protvino, Moscow reg., USSR

Abstract

In this work the results of seismic motion measurements in the Protvino region where VLEPP and UNK will be build are presented. Measurements of correlations and power spectrums were carried out in UNK tunnel and on the Earth surface. Factors that give main contributions to seismic motion had been investigated. Significant influence of atmospheric pressure on low frequency seismic motion was observed. This work is important for linear supercollider VLEPP design.

1. Introduction

Linear electron-positron supercolliders need very small beam transverse sizes for high luminosity [1]. For example, for luminosity of VLEPP about 10^{34} $cm^{-2}s^{-1}$ beam sizes in the interaction point should be 3*0.001 microns, and for project JLC - 0.23*0.0014 microns [2]. Precise alignment of focusing elements needs in this case. Estimations show that appreciable lens displacement from beam line is about 0.03 microns for main linac and 0.001 microns for final focus system.

During the collider run magnetic axis of lenses should be tune by feedback system working from beam position monitors. Vibro- and seismic noise levels, it's correlation properties are very important for vibration suppression system designing.

In this work the results of seismic motion measurements in the Protvino region, where VLEPP and UNK supercolliders will be build, are presented. Measurements of correlations and power spectrums were carried out in the UNK tunnel. Measurements of absolute and relative Earth surface motions, influence of atmospheric pressure on low frequency ground vibrations were carried out inside lab building. Details of this measurements could be found in INP Preprints [3,4,5].

2. Methods and instruments

Underground measurement point was situated 3 km to North from U-70 accelerator in UNK tunnel on the depth of about 30 m. Tunnel ground motion were measured in three directions by industrial seismometers SM-3KV. These probes were calibrated in the frequency range of 0.03-100 Hz. 12 bit CAMAC ADC with 700 and 80 Hz toggle frequency was used for digitizing of signals . In correlation measurements information from three probes placed at different points was simultaneously stored in CAMAC memory. For these measurements we choose probes with similar phase characteristics. Maximum distance between probes in pair correlation analysis was 140 m.

Surface measurements were made in lab building where four massive tables for VLEPP accelerating structure were installed. For absolute table vibration measurements in frequency range of 0.003-2 Hz we used seismometer SVK-D with atmospheric pressure compensation. The probe was placed on one of the tables. To measure relative movements of different tables we used tungsten wire with diameter 28 microns and length up to 14 m passing through pick-ups [3] The wire was strained by stable force of 1 4 N independent of air temperature variations Sensitivity of the probe is 10 mV/microns, one quantum of 20 bit CAMAC ADC was equal 1.0 microVolt (10^{-4} microns)

0-7803-0135-8/91$01.00 ©IEEE

3. Results of measurements

Power spectrum of vertical seismic vibrations in the UNK tunnel is shown at fig.1. These measurements were done in quiet conditions (evening of saturday).

One can see wide peak near 0.14 Hz, so called "7 second hum". The origin of this peak is usually connected with water and atmospheric activity above the ocean results in seismic waves in an earth [6]. Measurements show also that in quiet conditions vertical and horizontal spectrums are approximately equal.

Our measurements have shown that displacement due to microseismic peak does not depend on technical activity in the place of measurements. Technical noises manifest itself mainly at frequencies above 1 Hz. At weekday power spectrum at these frequencies increases more than one order of magnitude.

At frequencies greater than 10 Hz the influence of traffic activity is clearly seen. For example heavy car moving with velocity 40 km/h along the road placed of 70 m aside of measurement point results in increasing of displacements up to $(6\text{-}10)*10^{-4}$ microns, i.e. 2-3 times higher than in quiet conditions.

One can also see at fig. 1 spectrum of relative movement of two VLEPP tables measured by strained wire technique. The value of relative displacements is considerably less than absolute ground motion at frequencies below 1 Hz. At higher frequencies both spectrums are the same due to local character of vibration sources.

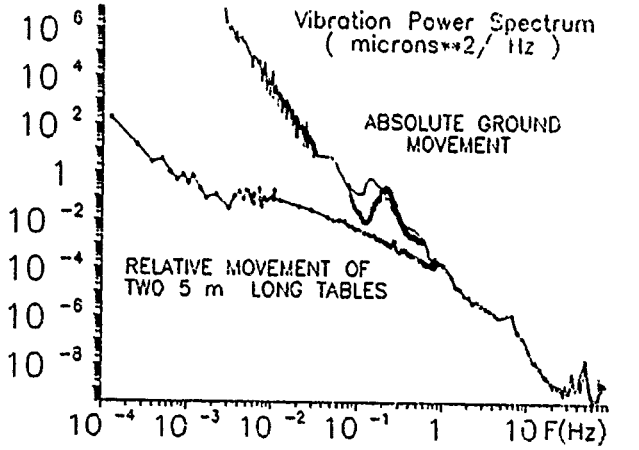


Fig.1 Power spectrums of UNK tunnel ground vibration and relative movement of two VLEPP tables

Correlation spectrums of vertical motion for distances between probes equal to 40 and 140 m are shown at fig.2 . Correlation spectrum of two signals $X(t)$ and $Y(t)$ is equal to real part of expression:

$$K(w)=\frac{<X(w)*Y^{*}(w)>}{(<|X(w)|^{2}>*<|Y(w)|^{2}>)^{1/2}} \qquad (1)$$

One can see that frequency region of high correlation decreases with increasing of distance between probes. It is also seen that for long distances high correlation exists only near the frequency of microseismic peak. The source of these peak is remote (few thousands of kilometers) and very powerful . So the correlation of two probes should be equal to unit multiplying by factor that depends on phase delay between them.

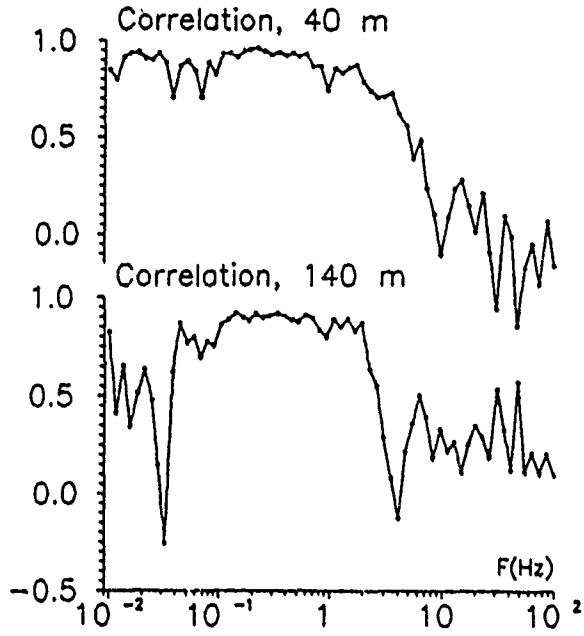


Fig.2 Spectrum of correlation for two distanced probes

4. Influence of atmospheric activity on Earth surface motion

A. Measurements

Influence of atmospheric activity on Earth motion was studying in the lab building. Absolute motion of surface, atmospheric pressure, temperature and relative displacement of VLEPP tables were measured simultaneously. Maximum distance for relative measurements was 14 m.

These measurements confirm great influence of atmospheric pressure variations on surface motions at frequencies less then 0.2-0.3 Hz . The influence can have remote or local character.

Seismic motion in the range 0.06-0.25 Hz due to "7 second hum" is an example of remote influence. In this frequency range power spectrum usually has a peak on mean frequency 0.14 Hz (fig.1). The mean frequency, shape and amplitude of peak depends on weather condition above ocean. Amplitude of peak can vary from 0.1 to 10 microns^2 /Hz. As a rule, bigger amplitude corresponds to lower mean frequency . The mean frequency of microseismic peak f can be determined from equality of mean wind velocity V to phase velocity of gravitation waves on ocean surface: $f=g/(2*\pi*V)$, where g- is the acceleration of gravity. Then for the mean frequency f=0.14 Hz we get reasonable value of wind velocity V=11 m/sec.

Local changings of atmospheric pressure and temperature influence also on motions at frequencies lower than 0.1 Hz. So we observed relative vertical displacement of two VLEPP tables equal to 30 microns during storm coming with rapid pressure changing about 15mm Hg (see fig.3).

Significant variations in atmospheric pressure result in clearly seen correlation between pressure and Earth surface motion (fig.4). The correlation has a leap due to mechanical resonance of seismometer at 0.08 Hz.

Therefore, the main contribution to ground motion in frequency region of 0.01-0.1 Hz is due to atmospheric pressure fluctuations.

B. Model of atmosphere influence on ground motion

Atmospheric flows (i.e. winds) usually have high number of Reinolds (about 10^6 and more) and high power of turbulence. For developed turbulence Kolmogorov-Obukhov law [7] gives a connection between fluctuations of flow velocity V for flow regions with sizes about λ.

$$V \simeq U*(\lambda/L)^{1/3} \qquad (2)$$

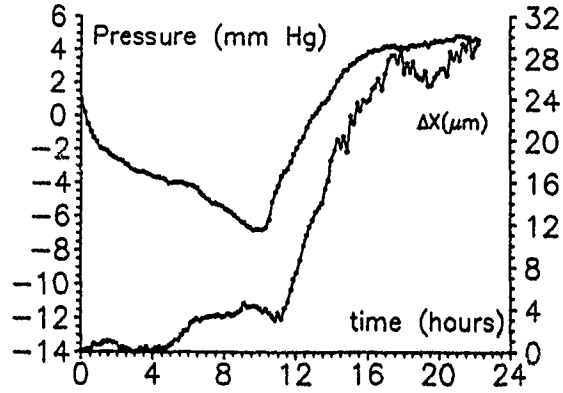


Fig.3 Pressure and relative vertical movement of two tables during cyclone passing through Protvino region at 26 of January 1991.

here U,L - main flow average velocity and size, in our case average wind velocity and thickness of atmosphere. For every size λ one can find frequency of fluctuations of flow parameters in some point of measurements:

$$f \simeq U/\lambda \ , \qquad (3)$$

and then

$$V_\lambda = V_f \simeq U^{4/3}*(f*L)^{-1/3}. \qquad (4)$$

One can estimate fluctuations of pressure:

$$P_f \simeq \rho*V_f^2/2 = \rho*U^{8/3}*(f*L)^{-2/3}/2 \qquad (5)$$

(ρ - air density) and spectrum of this fluctuations:

$$S(P)_f \simeq \frac{P_f^2}{f} = \rho^2*U^{16/3}*L^{-4/3}*f^{-7/3}/4 \qquad (6)$$

Fig.5 shows good agreement of formula (6) at L=5000 m and U=3 m/sec with measured power spectrum of atmospheric pressure fluctuations.

One can estimate absolute ground displacement X_f under the force of atmosphere pressure P_f regarding a ground as elastic homogeneous isotropic bounded medium with Youngs modulus E_f:

$$X_f \simeq P_f*\lambda/E_f = \frac{P_f*U}{E_f*f} \qquad (7)$$

Therefore, spectrum of power:

$$S(X)_f \simeq \rho^2*U^{22/3}*E_f^{-2}*L^{-4/3}*f^{-13/3}/4 \qquad (8)$$

Results of spectrum calculations according to (8) with $E=10^8$ N/m^2 are shown in fig. 5 in comparison with experimentally measured ground vibration spectrum. For infralow frequencies more reasonable consider a ground as a liquid with density ρ. In this case ground motion

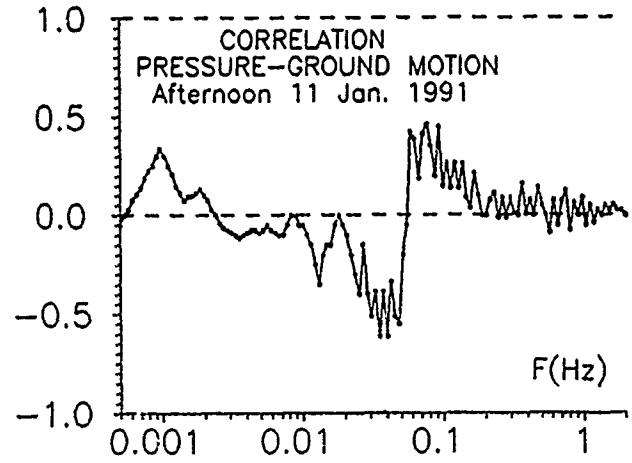


Fig. 4 Correlation between pressure and ground motion.

is frequency independent :

$$X_f \simeq P_f/(\rho * g) \qquad (9)$$

Transition from solid to liquid model corresponds to sizes :

$$\lambda_{max}/E \simeq 1/(\rho * g) \qquad (10)$$

If $E=10^8$ N/m^2 then $\lambda_{max} \simeq 3000$ m and $f_{min} \simeq 10^{-3}$Hz. In the liquid model atmospheric pressure variations of 10 mm Hg leads to maximum ground displacement of about 4 cm.

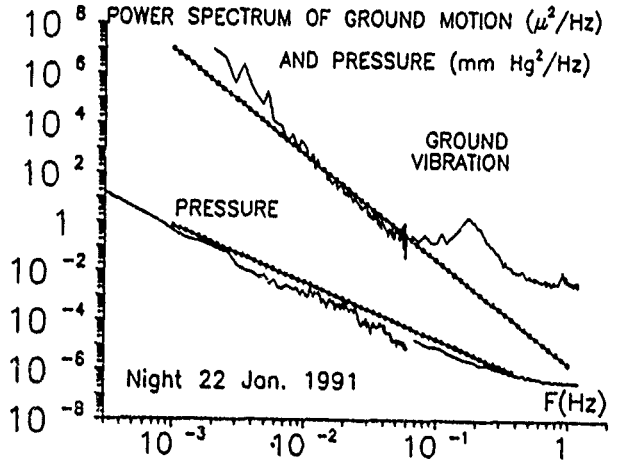


Fig.5 Comparison of vibrations and pressure spectrums with model (see text).

5. Low frequency Earth surface movements

Besides the oscillating type of motion considered above earth surface has another one like diffusion due to tension drops inside the bulk. Random character of that jumps leads to continuous diffusion of all surface.

Suggesting that the jumps probability is proportional to distance between points of surface L and time t one can make estimation of relative displacement dispersion for two points (here A - parameter of the model) :

$$\langle x^2 \rangle = A*t*L \qquad (11)$$

Results of our measurements of ground displacements using strained wire and of optical measurements in the UNK region of another group are in good agreement with the model with parameter $A=10^{-4}$ microns^2/(sec*m). 17 year studies in Stanford Linear Collider tunnel [8] show maximum vertical displacements were 15 mm and horizontal 7.5 mm and it gives $A=1.4\text{-}0.4*10^{-4}$ microns^2/(sec*m). Good agreement of data from different places points to the general character of ground motions.

Using this model one can predict displacements of the center of 20 km long VLEPP tunnel after different time (see Table 1).

Table 1

1 sec	1 min	1 hour	1 day	1 month	1 year	10 year
1.4 μm	11μm	84μm	415μm	2.3mm	7.7mm	24 mm

These displacements determine dispersions and main parameters of collider alignment feedback system.

Conclusion

In conclusion we should say that:

1. Power spectrum of seismic motion falls fast with increasing of frequency. So if there will not be strong technical sources of vibration it allows to neglect vibrations with frequency greater than 10 Hz, which amplitude is less than 0.001 microns.

Increasing of r.m.s. size of beam in interaction point due to vibrations at these frequencies :

$$\Delta X^2_f = \Delta X^2_0 * \sum_i^N \frac{\gamma_i * \beta_f}{\gamma_f * \beta_i} \simeq \Delta X^2_0 * \frac{N}{2} * \frac{\beta_f}{\beta_i}$$

where $\gamma=E/mc^2$, βi and βf beta-function in lens with number i and in interaction point. If $\beta i = 5$ m, $\beta f = 1$ mm, $N = 10^4$, then r.m.s. size would be about 0.001 microns.

2. Amplitude of motions in region 0.1 - 1 Hz is about 1 microns, and in region 1 - 10 Hz - up to 0.01 microns. These values determine requirements on speed and accuracy of feedback systems. High correlation in this case can make the requirements weaker.

3. Motions with frequencies less than 0.1 Hz determine working range of slow alignment systems. For a time of about one hour displacement can achieve 80 microns, for one year - as much as 7 mm. It means that the range of slow alignment system must be a few mm with accuracy a few microns. In this case slow alignment system would fit to the range of fast feedback.

4. It is clearly that any technical sources of vibration (highways, compressors, ventilators, etc.) should be placed far enough from the collider if possible. Another way is to suppress the vibrations from this source at the points of their creation.

The authors are grateful to Balakin V.E. for helpful discussions, to Tokmakov V.A. and Trapeznikov N.L. for seismometer handling. We also thank Molyavin V.M. for the help in preparation of measurements.

References

[1] V.E.Balakin, G.I.Budker, A.N.Skrinsky, "On the possibility of creation of super high energy electron-positron collider", VI USSR Conf. on Charge Part. Accel., Dubna, Oct. 1978, pp. 27-36.

[2] Proceedings of Intern. Workshop on Next Generation Linear Colliders, Tsukuba, Japan, 1990; KEK Internal 90-22, August 1990.

[3] V.V.Parkhomchuk, V.D.Shiltsev, "High sensitivity probe for VLEPP alignment", BINP-RD/89-02, Protvino, 1989.

[4] B.A.Baklakov. et. al., "Vibration level measurement in the UNK tunnel", Preprint INP 90-88, Novosibirsk, 1990.

[5] B.A.Baklakov et. al., "Investigation of correlation and power characteristics of earth surface motion in the UNK complex region", Preprint INP 91-15, Novosibirsk, 1991.

[6] See for example L.N.Rykunov, Microseisms, Moscow, Nauka Pub., 1967.
G.E.Fisher, "Ground motion and it's effects in accelerator design", SLAC-PUB-3392 Rev. July 1985.

[7] L.D.Landau, E.M.Lifshitz, Hydrodynamics, Moscow, 1986.

[8] G.E.Fisher, M.Mayond, "Some thoughts on linear collider alignment and mechanical stability", CERN-LEP-RF-SU-88-07, CLIC Note 61, 1988.

A Traveling Wave Accelerator With HOM Outcouplers for FEL's

R. Miller
Stanford Linear Accelerator Center
P. O. Box 4349
Stanford, CA 94305

M. Lampel
Rocketdyne Division
Rockwell International Corporation
6633 Canoga Ave., FA38
Canoga Park, CA 91303

Abstract

Electron beam brightness is a key issue in building efficient free electron lasers (FEL's), particularly for optical and shorter wavelengths. The application to FEL's of RF electron gun's [1] with laser driven photo-cathodes [2] has opened the door to developing efficient optical FEL's. The next task is to develop accelerator structures which can transport such beams with a minimum of beam degradation. A low cost approach to this is suggested in this paper: Four 1.26 meter constant gradient (CG) TW sections driven in parallel by a SLAC 5045 klystron. By using CG sections the higher order modes are incoherent due to the linearly decreasing group velocity along the structure. Together with incorporating higher order mode (HOM) outcouplers, this system is predicted to accelerate 1 nC per micropulse, 0.4 Amps per macropulse to 75 MeV from an injection energy of 5 MeV. Emittance growth is predicted to be 5 mm-mr. Rocketdyne is currently procuring these sections for testing.

[1] S. Benson, J. Schultz, B. Hooper, R. Crane, and J. Madey, Nucl. Inst. and Methods A272 (1988) 22
[2] M. Curtin, B. Bennett, R. Burke, A. Bhowmik, P Metty, S. Benson, and J. Madey, "First Demonstration of a Free-Electron Laser Driven by Electrons from a Laser Irradiated Photocathode", #EX3.4, 11'th International Conference on Free Electron Lasers, Naples, Florida

Introduction

As a next step in obtaining high brightness, high energy electron beams for FEL's low emittance accelerator sections are being fabricated for Rocketdyne by Schonberg Radiation Corporation.

This paper is organized into four sections. Section 1 looks at several different structure variations and their impact on performance, measured chiefly by maximum charge per macropulse. Section 2 then analyzes energy spread and emittance growth in some structures without HOMO's. Section 3 discusses modeling to determine the effect of HOMO's on cavity modes and Q's, and on HOM Q's of the entire structure. Section 4 summarizes the results and concludes the paper with the choice of the four 1.26 meter structures.

Section 1

The most important design specification for the linac structure is that when driven by 50 to 60 MW from a SLAC 5045 S-band klystron it must increase the beam energy by 70 MeV including the effect of beam loading. These and other specifications are listed in Table I.

TABLE I

RF Gun Energy	5 MeV
RF Power to Gun	5 MW
Linac Output Energy	75 MeV
$\Delta E/E$	<1%
RF Power to Linac	55 MW
Micropulse Charge	0.5 to 4 nC
Micropulse Spacing	1.4 ns to 21 ns
Beam Macropulse Length	>2.5 μs
Normalized Emittance	>10 $^{-}$ mm-mr
BBU Threshold Current	> 1 A

0-7803-0135-8/91$01.00 ©IEEE

We will consider two configurations of either two full 3 meter SLAC sections, or four 1.26 meter portions thereof, driven in parallel by a single 5045 klystron which must also drive the RF gun. We begin by setting the values for the parameters which determine the energy gain and fundamental mode beam loading:

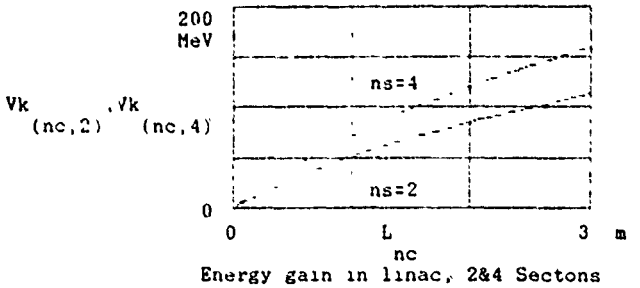
ns := 1 4 Number of sections
nc := 1 .86 Number of cells per section
$L_{nc} := .035\ nc$ m Length of each section
P := 55 MW Power to linac sections
r := 57 MΩ/m Shunt impedance

The attenuation for a section L(nc) long taken from the output end of the SLAC structure is:

$$\tau_{nc} := 5 \ln\left[711 L_{nc} + 1\right] \quad \text{Att /sect. in nepers}$$

The no load energy gain can now be calculated:

$$Vk_{nc,ns} := \left[1 - \exp\left[-2 \tau_{nc}\right]\right] ns\ P\ L_{nc}\ r$$



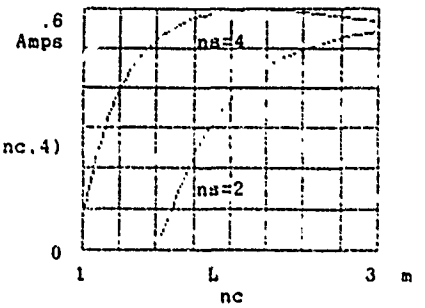
Energy gain in linac, 2&4 Sections

The next function to calculate is the beam loading derivative to determine steady state energy dependance on beam current.

$$\delta Vb_{nc,ns} := \frac{ns}{2} r\ L_{nc} \left[1 - \frac{2 \tau_{nc} \exp\left[-2 \tau_{nc}\right]}{1 - \exp\left[-2 \tau_{nc}\right]}\right]$$

The beam derivative for four short sections is 41 MeV/A, for two long sections it is 80 MeV/A. This means that the shorter sections are half as sensitive to micropulse charge fluctuations as the longer sections, possibly a critical difference in operating an FEL. The maximum current which can be run is given by

$$Imax_{nc,ns} := \frac{Vk_{nc,ns} - 70}{\delta Vb_{nc,ns}}$$



Imax , Imax
(nc,2) (nc,4)

Maximum Average Current @75 MeV
for 2 and 4 sections.

A conservative estimate of the "Good beam" pulse length is the RF pulse length minus twice the structure filling time. The variation of fill time with structure length is:

$$Tf := .722 \ln(.711 L + 1)$$

The maximum charge per macropulse, qmax, is the maximum current times the "good beam" pulse length:

$$qmax := Imax (Trf - 2 Tf)$$

The two configurations being considered transport almost identical charges, 1.1 nC each. However, Imax is lower for the four section case, and combined with the beam loading derivative this means that the four section case is much less sensitive to charge fluctuations. For example, 1% fluctuations of charge result in 0.58% energy fluctuations for the 3 m case, but only 0.22% energy fluctuations for the 1.26 m case. This is a considerable improvement for a beam with allowable rms energy spread of less than 1%.

Section 2

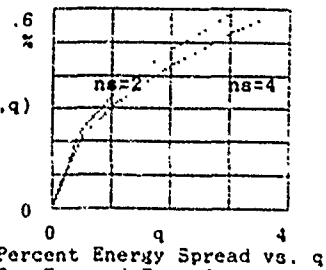
Next we must look at the energy spread and emittance growth caused by the higher order modes (HOM's). HOM frequencies are not rationally related to each other or the fundamental. Furthermore, the HOM fields decay to 1/e in a time t = Q/πf. Similarly, while the calculations by Yu and Wilson [3] assume a truly periodic structure, the actual structures are continuously tapered. For this reason it is appropriate to combine the effects of successive cells as if they were random.

First we will define and set the parameters of the problem:

nc := 36 .86		number of cells
ns := 2 ..4		number of structures
q := 0.0 5 4	nC	charge per micropulse
I := 399 I := .544		beam current
4 2		
Q := 15000		Quality factor of HOM
f := 4.3	GHz	first HOM frequency
Wl := 0.5 10^{-3}	MeV/nC/cell	Longitudinal wake potential

The percent energy spread due to the longitudinal wake is:

$$\%VHOM(nc,ns,q) := ns\ Wl \left[\frac{Q}{\pi f} nc\ q\ I_{ns}\right] \left[\frac{100}{75}\right]$$



%VHOM(36,4,q), %VHOM(86,2,q)

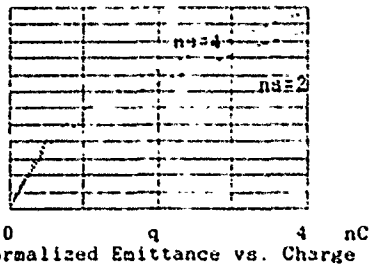
Percent Energy Spread vs. q
for Two and Four Sections

The two 3 m sections marginally outperform the four 1.26 m sections; for 1 nC it is 0.34% for 1.26 m vs. 0.30% for 3 m. With regard to single bunch beam loading Bane [7] calculates the bunch wake function for a gaussian pulse with σ_z = 1 mm. The full energy spread is 3.2 V/pC/cell, which gives a total (4σ) single bunch energy spread of 2.5% for a 4 nC bunch. Running with bunches 6 degrees forward of the crest reduces the total energy spread in each bunch to 0.4% with rms of 0.2%. The next effect we must consider is emittance growth caused by long range dipole wakefields. The parameters involved are:

r := 1	mm	rms beam radius
σx := 1	mm	rms beam centroid position
Wd := 0.5	MeV/nC	dipole wake potential/cell
a := 10	mm	accelerator disk hole radius
λ := 75	mm	first dipole mode wavelength
f := 4.3	GHz	first dipole frequency
Q := 1.5 10^{4}		first dipole mode Q
m0 := 0.511	MeV	electron rest mass

The normalized emittance growth produced by the dipole wakefields is the product of the beam radius times the transverse momentum kick of the wakefields.

$$\epsilon(nc,ns,q) := r \left[\frac{Wd}{m0}\right] \frac{\sigma x}{a} \frac{\lambda}{2\pi a} ns \left[\frac{Q}{\pi f}\right] q\ I_{ns}\ nc$$



ε(36,4,q), ε(86,2,q)

Normalized Emittance vs. Charge

Since these emittance contributions will dominate the emittance of the accelerator the structures have been designed to damp the higher order modes. It is possible to achieve a factor of 10 or more reduction in the HOM Q's. This results in at least a factor of 3 reduced emittance growth. By reducing beam centroid and rms radius by a factor of 3, emittance growth will be reduced to below 5 mm-mr

Section 3

The higher order mode outcouplers (HOMO's) are expected to reduce emittance growth by at least a factor of 3. Analysis of this has not been completed. Existing 3-d codes do not have a fine enough mesh to model the tapered structure accurately.

J. W. Wang analyzed cavities with HOMO's to determine the effects of outcouplers on the Q's of the first several modes. URMEL and KN7C were the codes used. The results for selected Q's are:

MODE	Q	Q with HOMO
TM01	13,590	13,340
HEM11	15,344	8
TM011	12,500	600

The dominant HOM is the HEM11 mode, at the lowest frequency, 4.3 GHz, and highest undamped shunt impedance at 29.3 MW/m. The mode is very nearly a π mode, which is nearly a trapped mode in the structure. However, based on Brillouin diagrams for the HEM11 mode [9, fig. 7-29, p. 221] an initial calculation of the average group velocity through the 1.26 m structure gives an upper limit of ~1,500 for the Q confirming the order of magnitude reduction expected.

Section 4

After examining the above results, the accelerator system comprised of the four 1.26 m section was chosen to be built as a driver for the Rocketdyne FEL. Although higher in cost than just using the standard SLAC sections it was felt that the advantages to be gained were worth the cost differential. In particular, the reduced sensitivity to charge fluctuations in the energy spread, and reduced emittance growth due to the HOMO's will not only allow more efficient extraction at 1 μm but also allow for attempts at operation at even shorter wavelengths down the road. Confidence is high that the calculated performance will be realized as this system is based on an incremental improvement upon the well understood 3 m section and on ongoing research at SLAC on HOMO's.

The authors would like to acknowledge and thank J. Wang, H. Deruyter, T. Roumbanis, P. Schonberg, and R. Schonberg for their helpful discussions and information. One of us (Lampel) would especially like to acknowledge the entire staff at Schonberg Radiation Corperation for support in the design and fabrication of this accelerator.

References:

1] S. Benson, J. Schultz, B. Hooper, R. Crane, and J. Madey, Nucl. Inst. & Meth. A272, pp. 22-28 (1988)
2] M. Curtin, G. Bennett, R. Burke, A. Bhowmik, P. Metty, S. Benson, and J. Madey, Nucl. Inst. & Meth. A296, pp127-133 (1990)
3] D. Yu and P. Wilson, SLAC PUB-5062
4] P. Wilson, SLAC PUB-4547
5] R. Neal, M Report No. 259, Mar 1961, Stanford University.
6] P. Wilson, SLAC PUB-2554
7] E. Bane, SLAC PUB-4165
8] G. Loew and R. Neal, SLAC DOC-108
9] R. Neal, ed., The Stanford Two-Mile Accelerator, (W.A. Benjamin, NY, 1968)

CERN PLANS FOR THE FUTURE

Carlo Rubbia
CERN
1211 Geneva 23
Switzerland

I. INTRODUCTION.

Predicting the future of a laboratory like CERN is almost like looking in a crystal ball. Since CERN is only a few kilometres away from the village where philosopher Voltaire lived it may be appropriate to quote him when he said in 1766:

"Les Philosophes qui font des systèmes sur la secrête construction de l'Univers sont comme nos voyageurs qui vont à Constantinople et qui parlent du Sérail; ils n'en ont vu que les dehors et ils prétendent savoir ce que fait le Sultan avec ses favorites!" [1] that is, translated in the language of Shakespeare: " The philosophers, with the systems they build on the hidden structure of the Universe, are like those travellers of ours, who go to visit Constantinople and come back talking of the Seraglio: they have only seen the outside, yet they claim to know what the Sultan does with his favourites! "

The goal of CERN is to provide the scientific community of the fifteen European Member States with those research facilities they may need in the field of elementary particles (HEP) and which because of their price, complexity or otherwise cannot be built on a national basis. CERN's user population is characterized by a rapid growth which can be well parametrized as an exponential with a doubling rate of about five years (another Livingston plot!, see Fig. 1). The participation of scientists from Non Member States has grown more than percentage-wise over the last decade from about 10% to about 20% of the users. It can be estimated that today CERN provides access to its facilities for over 5000 physicists, welcoming about 50% of the World's population in HEP.

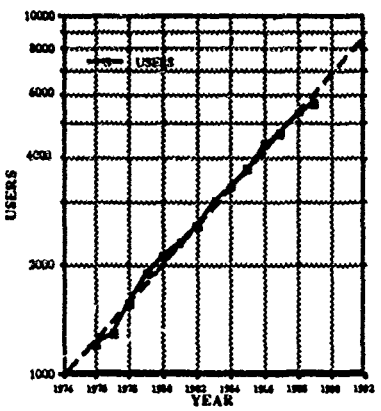


Fig. 1. Time evolution of the number of CERN users.

Amongst them there is a large, flourishing community of young physicists around the golden age of 25-35 years. On the other hand the in-house population of staff research physicists is small and it amounts to about 300 people.

CERN's goal is to provide the scientific community with the best research facilities, mostly characterized by their uniqueness, although some partial duplication with projects in other continents is unavoidable and sometimes desirable for fostering a variety of different approaches to the fundamental questions. A significant proof of the complementarity between the US and CERN's programmes is the rapid increase of "transatlantic" users which now for the first time shows balance.

The future programmes of CERN are directly connected with on-going activities and they represent in essence a further exploitation of already identified potentialities. The backbone of the CERN programme is a series of rings connected to each other by injection/transfer lines (Fig. 2). The $\bar{p}$ production and accumulation is not shown in the diagram, although low energy $\bar{p}$'s are an important part of the current CERN programmes. After a rather elaborated injection system, these rings currently accelerate beams of ions, protons, antiprotons, electrons and positrons, first injected into the CPS (R = 100 m), then transferred and accelerated in the SPS (R = 1100 m) before reaching the largest ring LEP, whose 27 km tunnel — presently limited to electron-positron collisions — is intended to house colliding protons and ions, the so-called LEP-LHC complex. Collisions between LEP and LHC will also offer high energy, high luminosity e-p collisions.

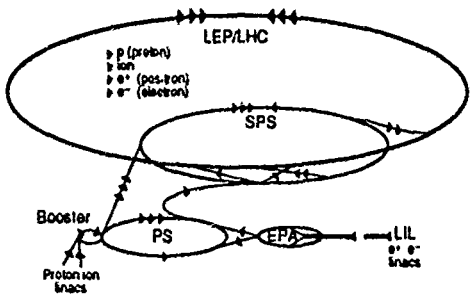


Fig. 2. Schematic view of the CERN accelerator complex.

Both CPS and SPS have extended the utilization of extracted beams. A typical CPS super-cycle (Fig. 3) shows the complexity of operation, which involves electrons, positrons, protons, antiprotons, oxygen, sulphur, etc. essentially as part of a chain process. At each new cycle within the magnetic supercycle a different type of particle is accessed and fed into the system. Antiprotons for LEAR and the antiproton accumulator (AA+ACOL), SPS feeding, PS feeding, etc., are all interrelated into an extremely complicated operation. The SPS is a similarly complex system for protons, antiprotons, electrons and positrons and various ions.

0-7803-0135-8/91$01.00 ©IEEE

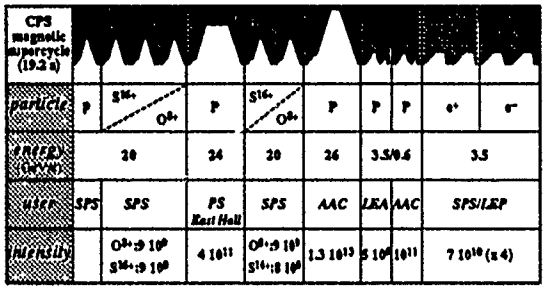


Fig. 3. Schematic display of a typical CPS super-cycle.

The wealth of facilities thus provided permits to handle a large diversity of CERN programmes which include fixed target physics and neutrino physics (19%), high energy p-$\bar{p}$ collisions at the Sp$\bar{p}$pS Collider (10%), low energy $\bar{p}$ collisions with LEAR (13%), electron-positron collisions with LEP (40%), ion physics (13%) and short-lived isotope studies with ISOLDE (5%), to name only the main subjects (figures within parenthesis provide an indication of the fraction of CERN users for each activity). At present the Sp$\bar{p}$pS collider and the synchro-cyclotron (SC) are being closed down to leave room for future programmes within a rigourously constant budget. ISOLDE will be continued by transferring it from the SC to the CPS-Booster where spare pulses are left available once they have served as injectors to the CPS.

Such a richness and variety is also exemplified by the extremes in the size of the storage devices of CERN. If the largest is by far LEP, the smallest is an antiproton trap (PS196) which has stored $\bar{p}$'s for months in a volume < 1 cm^3 (Fig. 4).

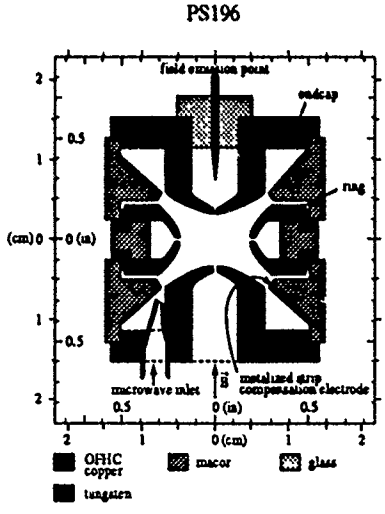


Fig. 4. Schematic view of the Penning trap

The $\bar{p}$'s are accumulated and cooled in AA+ACOL and after a transit in LEAR they are slowed down through interactions in matter to reach a momentum of about 1 KeV in a Penning trap where they are further cooled to electron volts and finally to milli-electron volts, through resistive cooling, thus reaching the temperature of the container, 4.2 K. By studying the cyclotron motion one can measure with great accuracy the ratio of the $\bar{p}$ to p mass (Fig. 5) [2]. This Penning trap method promises improvements of many orders of magnitude on several fundamental parameters of the $\bar{p}$'s.

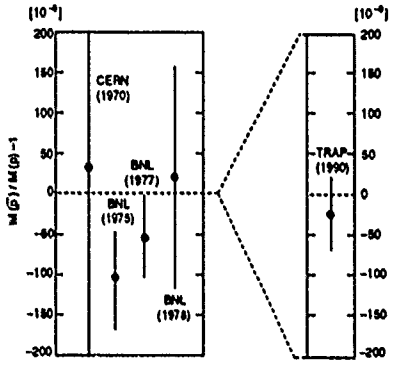


Fig. 5. Comparison with other experiments of the measurement of the ratio of the proton to antiproton masses from the Penning method.

II. FUTURE SCIENTIFIC PLANS

A. General strategy issues

It is impossible to elucidate the full extent of the future programmes of CERN within the five allotted pages. Therefore I shall focus on the high energy frontier represented by the LEP-LHC complex. A global approach is taken, in which both LEP and LHC play a parallel complementary role in the understanding of the phenomenology in the energy scale domain below 1 TeV.

Many of LEP results indicate that important discoveries may lay in the energy domain just above the one presently explored, namely the one of LEP200 and of LHC. Much of the precursory ability of LEP is due to the extraordinary precision of the results. A clear illustration appears in Fig. 6.

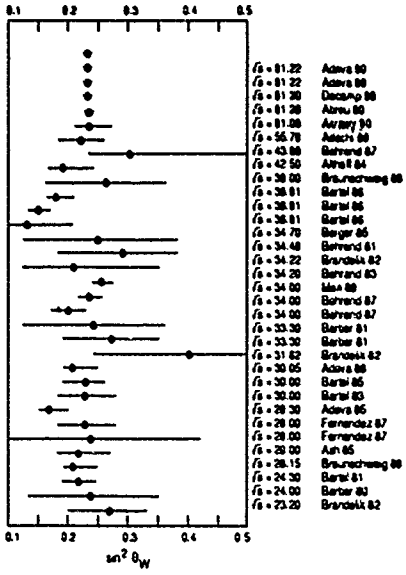


Fig. 6. History of the measurements of the electro-weak mixing parameter $\sin^2\Theta_W$. The last five points are from LEP.

The superior accuracy of LEP measurements [3] is clearly visible. A second illustration of LEP's extraordinary accuracy are the measurements of the axial and vector leptonic weak couplings, respectively g_A and g_V (Fig. 7) [4]. The line representing electro-weak expectations is also drawn. The expanded circle shows the enormous progress which occurred in the understanding of weak interactions thanks to LEP. Such a remarkable precision and the high quality of these new results permit to limit considerably the physics possibilities ahead of us and guide us in our future plans. I shall limit such considerations to a few cases:

1) *Higgs and top quark masses are related within the Standard Model.* Fig. 8 shows the constraints on the top quark and the Higgs masses, obtained taking into account the most

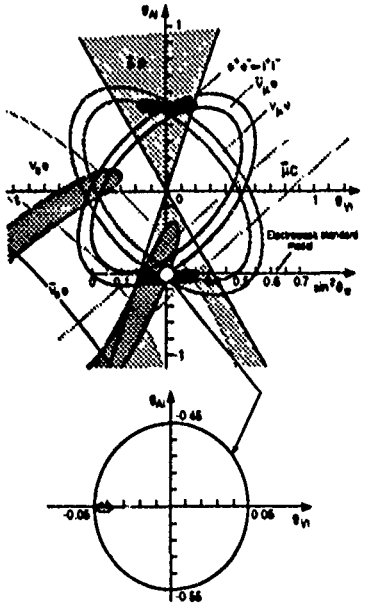


Fig. 7. Allowed region of the plane of the axial versus vector weak couplings. In order to be able to see the combined LEP results, the small white circle on the g_A axis must be expanded by a factor 10 .

recent results from LEP and the higher-order correction loops. The top quark mass should be larger than the present limits of the CDF experiment only by a factor two at most [5].

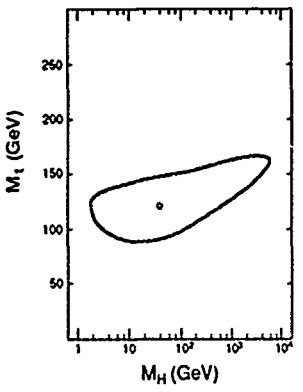


Fig. 8. Allowed contour in the m_{top}-m_{Higgs} plane at 68% C.L.

Unfortunately little or no information can be obtained about the Higgs. However the direct searches for the Higgs have given limits for the mass $\approx$ 50 GeV/c^2, substantially higher than the predictions of the expert "futurologists" [6]. This search is of extraordinary importance since the Minimal SUSY model predicts that — at least at the "tree level" — one Higgs has a mass $\leq Z^0$ mass, hence it is accessible with the planned LEP200 improvements. The top quark spectroscopy — because of its relatively "low" mass — is ideally suited for LHC, even if it is most likely beyond the range of LEP200.

2) *The Beauty complex exhibits mass oscillations in analogy to the well known K_L-K_S system thus opening the possibility for a major progress in our understanding of CP violation.* The B lifetime has been measured to be τ_B = 1.29±0.06(stat.)±0.10(syst.) ps by the ALEPH group [7]. The study of B^0–$\bar{B}^0$ mixing has started. The mixing parameter for $B_{s,d}{}^0$ is presently measured to be χ= 0.132±$0.022^{+0.027}_{-0.026}$ [8], an accuracy comparable to that of the pioneering measurements of UA1 [9], ARGUS [10] and CLEO [11]. The potentialities of LEP are evidenced by an example of a B event observed by DELPHI (Fig. 9a). Fig. 9b shows the $\mu^+\mu^-$ pair invariant mass distribution with the identification of the B decay process. Further luminosity increases of LEP and later LHC — a strong source of B mesons — will permit a systematic study of this fundamental phenomenon.

3) *Accurate measurements of the coupling strength of electro-weak and strong interactions from LEP indicate a new global picture of fundamental forces.* The Standard Model — if valid — may indeed represent the "summa summarum" of the knowledge of this century, the same way as Maxwell equations over 100 years ago. In order to accomplish it the overall unification between forces is necessary. The simplest Grand Unification Theory (GUT) is the minimal $SU(3)_C$ x $SU(2)_L$ x U(1) model with three families of matter and one Higgs doublet. The coupling constants should evolve smoothly until they become identical at the unification scale.

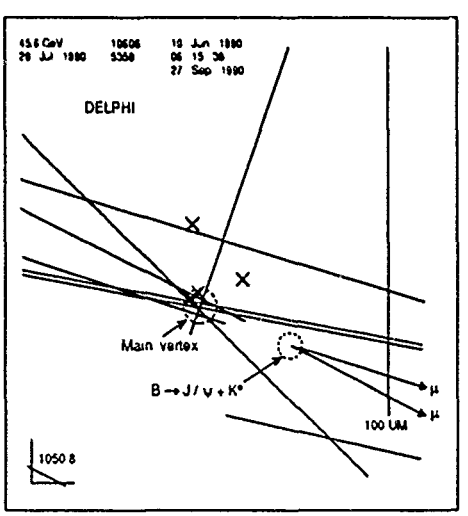


Fig. 9 a). Example of a DELPHI event in which a B decay into a J/ψ is observed.

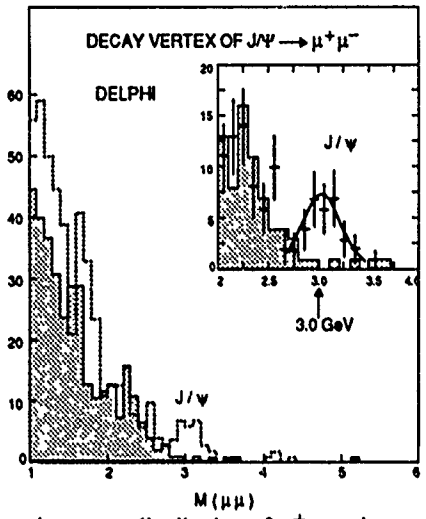


Fig. 9 b). Invariant mass distribution of $\mu^+\mu^-$ pairs as measured by DELPHI.

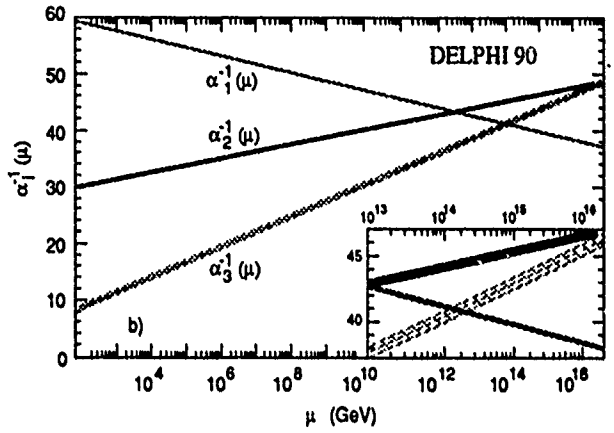


Fig. 10 Extrapolation of the fundamental coupling constants to the unification scale.

Here we make the simplifying assumption that at the unification point the couplings cross without changing slopes (the effect of this simplification for the crossing region is not large compared with the present experimental errors). Earlier data supported the idea of a minimal Standard Model with 3 families and one Higgs doublet. Note that the unification scale was then of the order of 10^{15} GeV or less. The proton lifetime, which is proportional to the fourth power of this scale, is then expected to be of the order of 10^{31} years. Present lower limits are considerably higher: $\tau_{proton} > 5.5\ 10^{32}$ years for the decay mode $p \rightarrow \pi + e$ which is expected to dominate. Therefore, both the non-observation of proton decay and the non-unification of the coupling constants independently rule out any minimal GUT, which leads to the Standard Model below the unification point.

Compared to the results of 1987 the errors coming from LEP are considerably smaller. It is clear that a single unification point can no longer be obtained within the present errors: the α_3 coupling constant misses the crossing point by more than 7 standard deviations (Fig. 10) [12].

Within the framework of GUT this non-unification implies new physics. The combination of precise data on the electroweak and strong coupling constants measured at LEP with the limits on the proton lifetime allows for stringent consistency checks of unified models. The evolution of the coupling constants within the minimal Standard Model with one Higgs doublet does not lead to Grand Unification, but if one adds five additional Higgs doublets, unification can be obtained at a scale below 10^{14} GeV. However, such a low scale is excluded by the limits on the proton lifetime.

On the contrary, the minimal super-symmetric extension of the Standard Model leads to unification at a scale of $10^{(16\pm0.3)}$ GeV (Fig. 11). Such a large unification scale is compatible with the present limits on the proton lifetime of about 10^{32} years. Note that the Plank mass (10^{19} GeV) is well above the unification scale of 10^{16} GeV, so presumably quantum gravity does not influence our results.

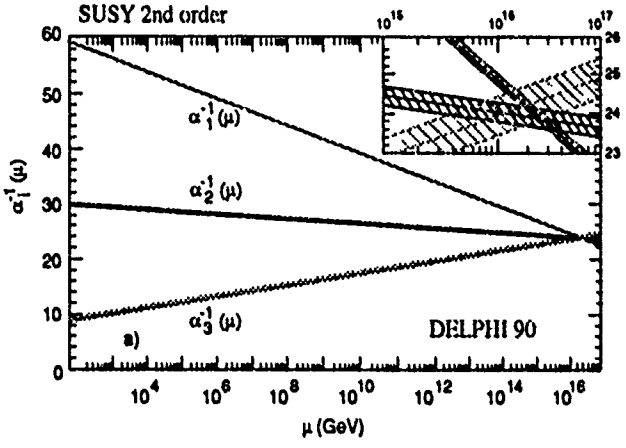


Fig. 11. Same as Fig. 10 within the framework of the minimal Supersymmetric extension of the Standard Model.

Also the non-minimal SUSY models with four or more Higgs doublets — having masses around or below the SUSY scale — can yield unification. However, once more, the unification scales are below the limits allowed by the proton decay experiments. *Therefore only the minimal SUSY model gives a unification scale which may be compatible with the proton lifetime limit.* The best fit to the allowed minimal SUSY model is obtained for a SUSY scale around 1000 GeV or more precisely, $M_{SUSY} = 10^{(3\pm1)}$ GeV, where the error mainly comes from the uncertainty in the strong coupling constant. If this minimal super-symmetric GUT describes nature, SUSY particles, which are expected to have masses of the order M_{SUSY}, could be within the reach of the present or next generation of accelerators. Likewise, proton decay at the rate $10^{(33.2\pm1.2)}$ years could be detected either in Icarus or in Superkamiokande.

As already pointed out, if minimal SUSY is correct, a Higgs particle should be essentially within the range of LEP200. Furthermore SUSY's new particle spectroscopy is presumed to be within the range of LHC.

B. Timetable

The following scenario is envisaged :

- The first step is to collect 5×10^6 Z^0 events with each LEP experiment before 1993. In order to achieve that goal the number of bunches in LEP will be increased to eight [13].

- By 1994 the energy of LEP will be pushed to the highest possible limit. This is determined by the necessity of getting as many W pairs as possible and by the interest in searching for Higgs particles at the highest possible energies. Fig. 12 shows that the total $e^+e^- \rightarrow$ hadrons cross section decreases by three orders of magnitude from the Z^0 peak to the W pair threshold region. A decision has been taken not to go by steps but to jump from the Z^0 to the highest available energy. Starting in 1994 we intend to run LEP intensively for three years in order to collect 500 pb^{-1} at the W^+W^- pair energy region.

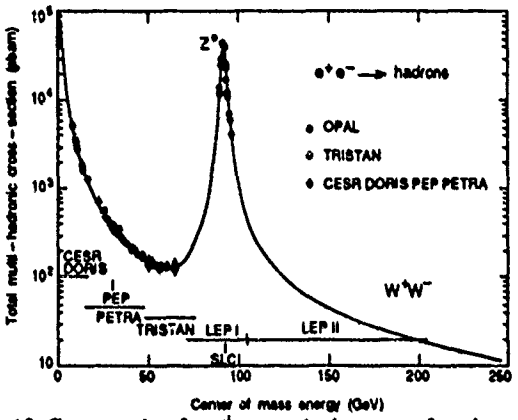


Fig. 12. Cross section for $e^+e^- \rightarrow$ hadrons as a function of $\sqrt{s}$.

- By 1998 we expect to start the LHC operation, after a one year shut-down in which LHC will be installed. Also LEP will be probably modified in order to increase the luminosity by about one order of magnitude using the "Pretzel scheme". In these conditions LEP will probably run on the Z^0 peak and longitudinal polarization will become an important added parameter.

- By the time LEP is eventually losing momentum, sometimes after the turn of the century, one or more beam crossing regions can be converted into electron-proton collisions with 7 times the HERA energies and a good luminosity.

The foreseen schedule is given in Fig. 13, with LEP running every year, except for the 1997 long shut-down and the LHC starting by 1998. However, although the schedule is well defined for LEP, for LHC it depends on its timely final approval. The reason for a cautious approach to LHC is that it is a programme aiming at a very careful design in order to obtain the most performant and most cost-effective device. A substantial gain is obtained by a twin-aperture magnet working at very low temperatures(2K). It should then be possible to reach magnetic fields perhaps as large as 10 Tesla, corresponding to $\sqrt{s}$=16 TeV and a luminosity in excess of 2.0 10^{34} cm^{-2} s^{-1} for at least three crossing points.

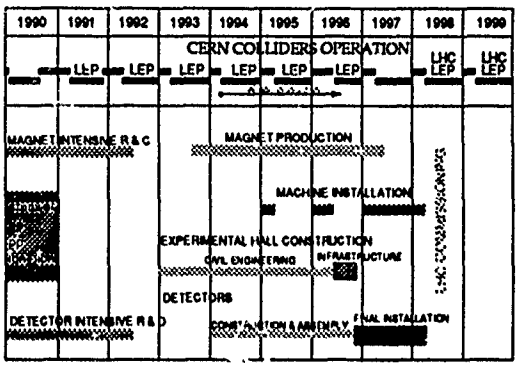


Fig. 13. Foreseen schedule for LEP operation and LHC construction.

III. CONCLUSIONS

Today CERN is playing a major role in the world community of High Energy Physics, offering services to more than one half of the world's users. Its programme is broadly diversified and it offers a large variety of particles and energies. Its chain of connected rings allows an optimum cost-effectiveness ratio. The most recent facility, LEP, has already provided an unprecedented number of Z^0's. It is a unique facility worldwide in view of its luminosity and the potentialities of energy upgrades. The full exploitation of the LEP tunnel — the so-called LEP-LHC complex — is the cornerstone of CERN's future strategy aiming at the definitive exploration of the phenomenology below 100 GeV with LEP200 and the systematic mapping of the domain up to 1 TeV with proton-proton and ion-ion collisions with the LHC.

LEP200 first and LHC later will pave the way[14] for further explorations of the 1 TeV energy scale and beyond with new linear colliders and higher energy hadronic colliders.

IV. REFERENCES

[1] Voltaire, Pensées Philosophiques, 1766.
[2] G. Gabrielse et al., Phys. Rev. Lett. 65 (1990) 1317.
[3] For a recent review see H. Burkhardt et al., CERN-PPE / 91-50, to be published in Ann. Rev. of Nucl. and Part. Sci. vol 41 (1991).
[4] F. Dydak et al., Rapporteur's talk, Proceeding of the 25th International Conference on High Energy Physics, Singapore 2 - 8 Aug. 1990, CERN-PPE-91-14.
[5] F. Abe et al., Argonne preprint ANL-HEP-PR-90-109, submitted to Phys. Rev. D.
[6] The Higgs Hunter's Guide, J. F. Gunion et al., Frontiers in Physics, Addison-Wesley (1990).
[7] D. Decamp et al., Phys. Lett. B257 (1991) 492.
[8] D. Decamp et al., Phys. Lett. B258 (1991) 236.
[9] C. Albajar et al., Phys. Lett. B186 (1987) 247; CERN PPE / 91-55. submitted to Phys. Lett.
[10] H. Albrecht et al., Phys. Lett. B192 (1987) 245.
[11] M. Artuso et al., Phys. Rev. Lett. 62 (1989) 2233.
[12] U. Amaldi, W. de Boer and H. Furstenau, Phys. Lett. B260 (1991) 447.
[13] J. P. Koutchouk, Performance of LEP, proceedings of this conference.
[14] Proceedings of "Large Hadron Collider Workshop", Aachen, 4-9 October 1990, Vol. I, II and III, CERN 90-10, ECFA 90-133.

Conference Author Index

A

Abola, A. 1347
Acharya, S. 1308, 1365
Ackerman, G. D. 1955
Adams, F. P. 795, 3011
Adler, R. J. 3201
Adolphsen, C. E. 503, 905, 1499, 2064, 2949, 3207
Advani, R. 2104
Agababian, A. G. 1579
Aghamir, F. 2967
Ahrens, L. 52, 839
Ahrens, L. A. 1273
Aiello, G. R. 988
Aikens, B. 1455
Akai, K. 2405, 2408
Akemoto, M. 1008, 1031, 1034, 1037, 1040, 2014, 2061
Akimov, V. V. 1582
Akiyama, H. 2014
Aksel, B. 2200, 2209
Alessi, J. 839
Alessi, J. G. 896, 1913
Alexandrov, V. S. 195
Alferov, V. N. 1356
Allen, A. L. 3094
Allen, C. K. 1961
Allen, M. 819, 1308, 1365
Allen, S. L. 3085, 3103, 3106
Allison, L. 2958
Allison, P. 520, 2080, 2961
Allison, P. W. 3192
Allison, S. 1419
Almeida, B. 2325
Almeida, J. 979
Althoff, K. H. 1543
Alton, G. D. 1937, 2604
Amirmadhi, F. 1115
Anami, S. 1043
Ananian, S. H. 1287, 1446, 1579
Anderson, C. 2856
Anderson, D. 863
Anderson, D. R. 2757
Anderson, K. 1946
Anderson, M. 952, 1314
Anderson, M. D. 2526
Anderson, O. A. 1955
Anderson, R. 976
Ando, A. 875
Andreev, V. A. 2984, 3109
Andrews, W. D. 1115
Anerella, M. 2164, 2167
Angert, N. 2981, 3044
Ankenbrandt, C. 87, 90, 99, 434
Annala, G. 87, 1848
Antes, K. 1958, 2008
Anthouard, P. 3204
Antoine, C. 2393
Anton, F. 1341
Antropov, V. K. 195
Aoyagi, H. 2032
Aragona, A. 2970
Arai, F. 1118
Arai, S. 3035
Araki, A. 2709
Arbique, G. M. 842, 845
Archie, C. N. 1594
Arida, M. J. 2572
Arkhipov, O. V. 195
Arnold, N. D. 1496, 2526
Artiomov, A. S. 1573, 1576
Artru, X. 2101
Artusy, M. 3159
Arutunian, S. G. 198
Asami, A. 494, 497, 1043
Ash, W. W. 2152
Ashkenazi, I. 1290
Asseev, A. A. 189
Atkins, W. H. 1522
Auerbach, E. H. 1454
Aune, B. 2393
Autin, B. 1675
Averill, R. 926
Averill, R. J. 2348
Azuma, O. 2990

B

B., Phung Ngoc 2393
Baartman, R. 1606, 1731
Baba, T. 2032
Babaian, A. Z. 2146
Bacal, M. 2011
Badier, J. 147, 1213
Bagdasarian, G. B. 2146
Bagley, P. 467
Bahrdt, J. 266
Bailey, R. 848
Bailey, V. 3114, 3123
Bailey, V. L., Jr. 3120, 3195
Baiod. R. 2506
Baird, S. 769, 1151, 1476, 2688, 2748, 2865
Bajard, M. 2799
Baklakov, B. A. 3273
Baktash, C. 2604
Balandin, V. V. 2823
Balewski, K. 1791
Ball, M. 1770
Ball, M. S. 1210
Baltay, M. 769, 926, 976, 1243, 2328, 2688
Baltay, M. M. 2369
Band, H. 834, 2152
Bane, K. L. F. 506, 1800, 2064, 3207
Bangerter, R. O. 369
Barbagelata, L. 2760
Bardy, J. 3204
Baritchi, D. 2688
Baritchi, L. 2688
Barke, A. 1359
Barklow, T. 834, 2500
Barkov, L. M. 183
Barletta, W. 982, 2856, 2967, 2976
Barletta, W. A. 2289, 2307, 2310, 2751
Barnard, J. J. 260, 2592, 2595
Barnes, M. J. 699, 964, 967, 1531, 2883
Barnes, P. 664, 678, 786, 2411, 2414, 2420, 2423, 2426
Baron, E. 594
Barr, E. 207
Barry, A. 1443
Bartalucci, S. 2850
Barth, W. 3076
Bartlett, N. W. 2182
Barton, M. Q. 284
Bashmakov, Y. A. 1681, 1684
Bassetti, M. 2850
Batskich, G. I. 3067
Batskikh, G. I. 2601, 2823
Battistella, A. 2438
Baumann, S. 2880
Bavizhev, M. D. 177, 189
Bazarko, A. 834
Bazarko, A. O. 2152
Be, S. H. 2298
Beadle, E. 1264
Beadle, E. R. 1231, 1347, 1431, 1493
Becker, K. 1115
Beckert, K. 2880
Beetz, C. P. 1981
Begg, M. 2372
Bekefi, G. 751
Bekhtev, B. V. 2601
Belomestnykh, S. A. 183
Beloshitsky, P. F. 195
Belov, V. P. 2823
Benaroya, R. 29, 2275
Bender, S. C. 2754
Bengtsson, J. 1434
Benincasa, G. 1353
Bennett, G. W. 1231
Bennett, L. F. 3126
Bennett, M. J. 1401
Benson, E. 1028
Benvenuti, C. 1023
Ben-Zvi, I. 272, 550, 1323, 2444, 3038
Berg, J. S. 1654
Berger, G. 2610
Bergher, M. 1225
Berg-Sørensen, K. 1764
Bernard, P. 1023
Bernstein, D. 5
Bertuccio, T. 952
Berz, M. 354, 884, 3020
Bessler, U. 3044
Betz, D. 619
Betzold, H. 598
Bhandari, R. 572, 2993
Bhandari, R. K. 351
Bharadwaj, V. 1255, 1258, 1458
Bharadwaj, V. K. 1830
Bhat, C. M. 831, 1773, 1946
Bhatia, T. 572
Bhatia, T. S. 1884

Biagini, M. E. 2850
Bickley, M. H. 309
Bieth, C. 2802
Bijleveld, J. 1148, 2366
Billan, J. 2122
Billen, J. H. 1884
Billing, M. 467
Billing, M. G. 2923
Billing, R. 1371
Billquist, P. J. 2987
Birx, D. L. 754
Biryukov, V. M. 177
Biscardi, R. 804, 1107, 1326, 1794, 2542, 2790
Biscari, C. 2850
Bishop, D. 964, 1531
Bisoffi, G. 1934, 2438
Bisognano, J. J. 1054, 2073, 2745
Bittner, J. 1107, 2542
Bittner, J. W. 1270
Bizek, H. 210, 2778
Black, E. L. 2375
Blas, F. 1398
Bleadon, M. E. 2134, 2477
Bleser, E. 45, 839
Blind, B. 899
Blinov, V. E. 2342
Bloess, D. 1023
Blondel, A. 147, 1213
Bloom, E. 982
Blue, R. 1163
Blumberg, L. N. 1107, 2661, 2664
Blumberg, R. 2248
Bobbs, B. 2733, 2742
Bobyleva, L. V. 195
Boer Rookhuizen, H. 2366
Boers, J. E. 275, 278
Bogacz, A. 1660, 1749
Bogacz, S. A. 1657, 1815, 1848
Bogaty, J. M. 2987
Bogdanovich, B. Y. 1048
Bogert, D. 860
Boggasch, E. 2631
Bohl, T. 848
Bohn, C. L. 1809, 1812, 2441
Boicourt, G. P. 3017
Boiko, V. A. 2601
Bollinger, L. M. 2987
Bolme, G. O. 3017
Bomko, V. A. 2984
Bong, E. 1201
Bongardt, K. 1767
Boni, R. 961, 2850, 2970, 2973
Bonin, B. 2393
Bonneau, P. 2125
Borchardt, I. 857
Bordry, F. 848
Bork, R. 1443
Borland, M. 769, 976, 1151, 1243, 2688
Bosch, R. A. 1827
Boscolo, I. 2575
Bosland, P. 2393
Bosser, J. 2509, 2832
Bossert, R. 2173, 2176, 2179, 2215
Bossert, R. C. 2182, 2185
Bossi, M. 988
Bothe, W. 932
Botlo-Pilat, F. 3041
Bouchet, B. 1186
Boulais, K. A. 479
Bourat, C. 3180
Bourianoff, G. 204, 348, 363, 383, 1302
Boussard, D. 2447
Bovet, C. 1160, 1186, 1213
Bowden, G. 996
Bowen, B. 3114
Bowling, B. 446, 1443
Boyce, J. R. 3264
Boyce, R. 973, 2328, 2688
Boyd, J. 646
Boyd, J. K. 437
Bozoki, E. 272, 1107, 2313, 2703
Bracco, R. 2712
Bragin, S. 1014
Brand, H. 3079
Brand, H. R. 3082, 3094
Brandt, J. S. 2182
Brau, C. A. 1115
Brauer, D. 857
Braun, H. 141, 1845, 2098, 2964
Brefeld, W. 2793
Brennan, J. M. 839
Brennan, S. 926, 1151, 1383, 1476
Bres, M. 772
Bricault, P. 2802
Bridges, J. 1525, 1624
Bridges, J. F. 690, 693
Bridgman, C. 1522, 2459
Briegel, C. 2520
Briggs, D. 1404, 1407
Brinker, S. 1154
Brittner, P. 1425
Brodowski, J. 1428
Brodzik, D. 1952
Brook, V. L. 1356
Broome, W. 1326, 1794
Brossard, S. 1359
Browman, A. A. 893
Brown, B. C. 2128, 2134, 2230, 2233, 2477
Brown, I. G. 1943
Brown, J. 2733
Brown, K. 834, 2058, 2067
Brown, K. A. 825
Brown, M. J. 1464
Brown, R. 1922
Brück, H. 2149
Bruhwiler, D. L. 1648
Bubp, D. 766
Buchanan, E. 1758
Buchmann, L. 1925, 2607
Buda, S. 1326
Budlong, J. 1389, 1758
Budnick, J. 923
Buhler, S. 2393
Buller, T. 3029
Bulos, F. 982, 996, 2058, 3213, 3216
Bunch, P. 2322
Bundy, R. 2381
Bunicci, J. 999, 1216
Burchat, P. 628
Burke, D. 834, 2055, 2058, 2067, 3213, 3216
Burkhardt, H. 848
Burns, A. 1186
Burns, M. 2110, 2958, 2961
Burns, M. J. 520
Burtin, G. 1160
Burton, R. J. 3011
Butler, H. S. 281
Bylinsky, Y. V. 3062, 3067
Byrd, J. M. 1080, 1842

C

Cady, R. L. 670
Cahill, K. 2523
Cai, Y. 2218
Calame, J. 658
Calderon, M. 2310
Callahan, D. A. 263
Callin, R. S. 713, 798
Calvert, J. 742, 745
Calvo, O. 946, 1467
Camas, J. 1186
Cameron, P. 681, 739
Cameron, P. R. 1216, 1273
Campbell, B. M. 1020
Campisi, I. E. 2381
Cao, X. 2435
Capista, D. 1505
Caplan, M. 763, 766
Caporaso, G. 3079
Caporaso, G. J. 520, 3100
Cappi, R. 171
Carboni, V. 3114
Carey, D. C. 1618
Carlson, R. 2107
Carlson, R. L. 245, 3192
Carlsten, B. E. 649, 2754
Carnegie, D. W. 1091
Carrieri, J. 2739
Carroll, D. 1981
Carson, J. 2173, 2176, 2185
Carson, J. A. 2182, 2227, 2233, 2236
Carter, A. 1546
Carter, H. K. 2604
Carugno, G. 1934
Cary, J. R. 1648
Caryotakis, G. 798, 2928
Cassel, R. 996, 2331, 2334, 2955, 3138, 3147, 3156
Cassel, R. L. 3153, 3162, 3165, 3168
Castellano, M. 2970, 2973
Castillo, S. 1416, 1419
Castillo, V. 1264, 1267
Castro-Garcia, P. 1213
Catani, L. 1448, 2970
Caussyn, D. D. 1770
Cavallari, G. 1023
Cavallo, N. 2970
Cavedon, J. M. 2393
Cavenago, M. 1934, 2438
Celata, C. M. 1401
Centore, A. L., II 2757
Cerino, J. 973, 1028, 1243, 2328, 2369, 2688
Cervellera, F. 1934
Cevenini, F. 2970

Cha, B.-C. K. 1314, 2526
Chabert, A. 2802
Chae, Y.-c. 1603
Chambers, F. 3079, 3082
Chambers, F. W. 3085, 3094, 3097, 3103, 3106
Champion, M. 2996
Champion, M. S. 1511
Chan, C. F. 1955
Chanel, M. 2509, 2832
Chang, C. 572
Chang, C. R. 2993
Chang, H. P. 2667
Chang, S. S. 1368
Chao, A. W. 336, 345, 360
Chao, Y. 628, 1806
Chao, Y.-C. 2152, 3246
Chargin, A. 2856
Chavis, C. 769, 2688
Chehab, R. 2101
Chel, S. 2393
Chellis, K. 2110
Chen, C. 754, 786, 2423
Chen, C.-e. 2396, 2616
Chen, P. 222, 619, 1207, 1916, 1993, 3225, 3246, 3252, 3255
Chen, S. C. 751, 2026
Chen, T. 1642
Chen, Y.-J. 3094, 3100, 3106
Cheng, Y. 1704
Chermenin, S. 857
Chernin, D. P. 312, 613
Chesnokov, Y. A. 192
Chianelli, C. 2393
Chiaveri, E. 1023
Chida, K. 875
Chidley, B. G. 845, 3047
Chin, J. 2721
Chin, Y. H. 213
Ching, H. 1827
Cho, M. 575
Cho, Y. 1624
Choi, J. 2673
Choi, J. J. 1827
Choi, M. 29, 2301
Choi, M. S. 591
Chojnacki, E. 555, 2557, 3219
Chou, P. J. 1743, 1749
Chou, T. S. 2286, 2316
Chou, W. 126, 1710
Christensen, K. E. 2263, 2453
Christiansen, J. 2631
Chu, T. S. 772
Chugg, B. 3114
Chung, Y. 1121, 1299, 1525, 2545
Chupp, W. 1975
Church, M. 108
Chursin, A. G. 2823
Ciapala, E. 1490
Ciardullo, D. J. 1344, 1347, 1431
Ciarlette, D. 1624
Ciocci, F. 2760
Clark, D. J. 2796
Claus, J. 1422
Clausen, M. 2319
Clayton, C. E. 564, 2560
Clegg, T. B. 2083
Clendenin, J. E. 500, 2098, 2284
CLIC Study Group 2052
Clifford, J. R. 2622
Clifft, B. E. 2987
Cline, D. 619, 2856, 2967
Cline, D. B. 2751
Coacolo, M. 233, 236
Coffield, F. 3079, 3082
Coffield, F. E. 3094
Cohen, S. 929
Colchester, R. J. 1160
Cole, A. G. 520, 3100
Cole, B. 204, 348, 363
Colestock, P. 1749
Colestock, P. L. 1740, 1743, 1830
Collier, P. 848, 1490
Collins, J. 1770, 1922
Colombant, D. G. 637, 1609
Colton, E. 1896
Colvin, J. 2221
Connolly, R. C. 1237
Cook, D. L. 537
Cook, J. M. 693, 2182
Cooper, W. S. 1955
Coosemans, W. 2070
Corbett, J. 1305
Corbett, W. J. 905, 1797, 2868
Corcoran, P. 3114
Cork, C. 2739
Corker, V. 1443
Cornacchia, M. 1797, 2853, 2856
Cornelis, K. 153, 848
Corredoura, P. 1404, 1806
Cottingham, G. 2164
Cottingham, J. 2167, 2239
Cottingham, J. G. 42
Coulter, K. 2173, 2179
Coulter, K. J. 2191
Coupal, D. 834
Courant, E. D. 2506, 2829
Cowles, D. N. 1401
Craddock, M. K. 57
Craig, G. D. 3088
Crandall, K. R. 401, 2583
Crawford, C. 970
Crawford, K. 2381
Crenna, F. 2760
Crisp, J. 3189
Crist, C. E. 3129
Crook, K. 1028
Crosbie, E. 210, 902, 1624, 1692, 2778
Crozon, M. 147, 1213
Cucchetti, A. 251, 1884
Culver, J. 2008
Culwick, B. B. 1481
Cummings, U. 2278
Curry, R. 3123
Curtoni, A. 2393
Cutler R. 572

D

Dabrowski, J. 2790
Daems, G. 1353
Dahl, L. 2981
Dahlbacka, G. 2976
Daibo, H. 2298
Dainelli, A. 2820
Dalbacka, G. 2856
Dale, D. 1922
D'Alsace, R. 804, 1794
Daly, R. T. 1496, 2526
Damm, R. 52
Danilov, V. D. 2613
Danilov, V. V. 183, 186, 526
Danly, B. 2026
Danly, B. G. 754, 772
Danzglock, R. 1425
Daras, T. 2610
Darrow, C. B. 564
Datte, P. 736, 1958
D'Auria, G. 710, 1978
D'Auria, J. 2607
Davies, W. G. 303
Davis, J. 2967
Davis, J. G. 2751
Davis, T. J. 728
Dawson, J. M. 564
Dawson, R. 65
De Vries, J. 1213
DeFord, J. F. 3088
DeStaebler, H. 834
Deadrick, F. J. 3085, 3094, 3097, 3106
Debiak, T. 2023
Decker, C. B. 564
Decker, F.-J. 905, 1192, 1734, 2002, 2064, 2143, 2949, 3210
Decker, G. 1525, 2545, 2790
Degèle, D. 857
Dehen, J. 3053
Dehning, B. 147, 1213
Deitinghoff, H. 2981, 3041, 3044, 3053
de Jong, M. S. 795
de Lamare, J. 3138
Delayen, J. R. 1809, 1812, 2441
Delchamps, S. 2173, 2179, 2191
Delchamps, S. W. 2185
Dell, G. F. 288, 1627
Demmel, E. 757
Demos, P. T. 601, 716, 1791
Demroff, H. P. 725
Denney, P. M. 2946
Derbenev, Y. S. 1761, 2506
Derenchuk, V. 1770, 1922
de Rijk, G. 848
Derost, J. C. 1534
de Saint Simon, M. 3041
Desavouret, E. 2477
Desforges, B. 848
Desmond, E. 1107, 1374
Desmons, M. 2393
Despe, O. D. 1461
Destler, W. W. 2578
Detlefs, W. F. 1600
Devred, A. 2480
deVries, G. J. 1955
Devynck, P. 2011
Diamond, V. T. 979
Didenko, A. N. 1860, 2775, 3111
Dikansky, N. S. 183, 523
DiMarco, J. 2215, 2480
Di Massa, G. 789
Dinev, D. 1767
Ding, B. N. 1972, 2999
Di Pirro, G. 1448, 2970
DiVergilio, W. F. 1919

Diviacco, B. 2712
Dobeck, N. 935
Dobrott, D. 1305
Dodd, J. 2967
Dodd, J. W. 2751
Doering, D. 1981
Dohan, D. A. 1350
Dolique, J.-M. 233, 236
Doll, H.-D. 1311
Donald, M. H. R. 2841, 2868
Donaldson, A. 996, 2331, 2955, 3156, 3159
Donaldson, A. R. 3165, 3168
Donasch, I. J. 1311
Dortwegt, R. 2275
Dortwegt, R. J. 29
D'Ottavio, T. 896
Douglas, D. R. 309, 443, 446, 449
Douglas, S. R. 303
Dowell, D. H. 1204
Dowling, D. T. 2604
Drachenfels, W. v. 1543
Dragt, A. J. 1621, 1630
Drozhdin, A. I. 177
Drury, M. 2381
DuPlantis, D. 1770, 1922
Dubinsky, G. A. 2823
Dubrovin, A. N. 2835
Ducar, R. J. 1552
Dunaitsev, A. F. 1356
Dutt, S. K. 360
Dutto, G. 65
Duval, M. 2802
Dwersteg, B. 2429
Dwinell, R. 742
Dyling, O. H. 1026
Dylla, H. F. 2745
Dyson, A. 2560
Dzenus, M. 2390
Dziba, A. R. 177

E

Earley, L. 2958
Early, J. W. 2754
Early, R. A. 1964
Earsom, D. L. 129
East, G. 1770
Ecklund, S. D. 500, 2005, 2098
Edighoffer, J. 3117
Edighoffer, J. A. 3120
Egawa, K. 2257, 2462
Eickhoff, H. 2880
Eidelman, Y. 269
Einfeld, D. 887, 2372
Elian, V. V. 2601
Elias, L. R. 2575, 2757
Elleaume, P. 1083
Elliott, S. M. 725
Ellison, J. A. 216
Ellison, T. 1770, 1922
Ellison, T. J. P. 1210, 1612, 2506
Emery, L. 769, 976, 1243, 1413, 1525, 1633, 1713, 2688
Emig, H. 1943
Emma, P. 905, 1284, 1549, 2064, 2500
Emma, P. J. 503
Emura, K. 2655
Enchevich, I. B. 699, 2943
Enderlein, G. 2429, 2432
Endo, K. 2257, 2462
Enegren, T. A. 2943
Eng, W. 681, 739
Enge, H. A. 1695
Engeman, G. A. 1910
Eppley, K. 719
Eppley, K. R. 1964
Erdman, K. L. 65
Erickson, R. 2152
Ermakov, V. B. 1582
Esarey, E. 2563
Escherich, K. 857
Esin, S. K. 2823, 2984, 3067, 3109
Ewald, K. 2185
Eyharts, P. 3204
Eyl, P. 3204
Eylon, S. 1975, 3070, 3073

F

Fabbricatore, P. 2399, 2973
Fabris, A. 710
Faehl, R. 649
Fagot, J. 2393
Faillon, G. 772
Faini, S. 2970
Faltens, A. 616, 1952, 3070
Fant, K. S. 798
Farias, R. H. A. 2787
Farkas, Z. D. 652
Farkhondeh, M. 634, 990, 2125, 2348
Fathizadeh, M. 917
Fauchet, A. M. 1099, 2542
Faught, E. 1308, 1365
Faugier, A. 848
Fawley, W. 3070
Fawley, W. M. 3020
Fazio, M. V. 649
Featherby, M. 2272
Fedotov, A. P. 3067
Fedotov, Y. S. 177, 189
Feinberg, B. 1401
Feinstein, J. 719
Feldman, D. W. 2754
Feldman, R. B. 2754
Fellenz, B. 1743
Fenker, H. 890, 1281
Ferede, H. 348
Ferioli, G. 1186
Fermé, J. 2802
Fernandes, P. 366, 3026
Fernow, R. C. 2572
Ferrario, M. 2970, 2973
Ferrell, J. H. 661
Ferri, G. P. 1213
Ferry, R. 29
Ferry, R. J. 2304
Feschenko, A. V. 3062, 3067
Fessenden, T. J. 586, 3073
Fiander, D. 996
Fickett, R. A. 705
Fiebig, H. J. 857
Fieguth, T. H. 503
Figley, C. 869
Figley, C. B. 964
Filippov, A. N. 183, 186
Fink, C. L. 547
Finley, D. 81, 87, 90
Fiorito, R. B. 1204
Firjahn-Andersch, A. 3041
Fischer, C. 1186, 3231, 3234
Fischer, G. 2949
Fischer, H. 3156
Fisher, A. S. 976, 2748
Fitch, J. 1028
Fitzgerald, D. 228, 1893, 1896
Fitzgerald, J. 1252
Flannigan, J. 1528, 2790
Flanz, J. 1467
Flanz, J. B. 601, 716, 1791, 2125
Flynn, T. 21
Fockler, J. 3114
Foley, M. 1743
Fong, K. 810
Forest, E. 336, 1434, 1651
Forgas, R. 923
Fortgang, C. M. 3017
Fortuna, G. 1934
Fortunato, D. 2191
Fouaidy, M. 2393
Fowkes, W. R. 713, 798
Fowler, W. B. 854
Fox, J. D. 1404, 1407
Frammery, B. 1353
Franczak, B. 2880
Frank, K. 2631
Franzke, B. 2880
Fraser, J. S. 2607
Freeman, W. C. 3141
Frey, W. W. 999
Frias, R. 1401
Friedman, A. 263, 272, 2766
Friedrich, J. 2981, 3044, 3053
Friedrichs, C. 675
Friedrichs, C. C. 643, 1020
Friedrichs, P. 1410
Friesel, D. 1770, 1922
Fripp, M. 2073
Frost, C. A. 3059, 3129
Fugitt, J. 1470
Fujimura, S. 2694
Fujino, D. 834
Fujino, T. 2402
Fujita, Y. 2682
Fukuma, H. 2257
Fulton, H. 2185
Funk, L. 572
Funk, W. 62, 2993
Furman, M. A. 300, 386, 422
Furuya, T. 2032, 2405, 2408

G

Gabella, W. E. 1591
Gabusi, J. 2266
Gai, W. 555, 1984, 2554, 2557, 3219
Gaillard, M. J. 3053
Galayda, J. 1099, 1374, 2116
Galiana, R. 1198
Gall, D. 2149

Gallardo, J. 2724
Gallardo, J. C. 2748
Gallo, A. 2850, 2970, 2973
Galluccio, F. 1669, 1672
Galyaev, N. A. 192
Gammel, G. 2023
Ganetis, G. 2164, 2167, 2239
Gao, J. 2020
Garavaglia, T. 231
Garber, M. 2164, 2167, 2239
Garcia, R. 1171, 2529
Gardner, C. 1473
Garkusha, O. V. 1570
Garnett, R. 572
Garnett, R. W. 330
Garoby, R. 171, 1398
Garoutte, R. 1028
Garren, A. 62, 2844
Garren, A. A. 2829, 2841, 2868
Garrett, J. D. 2604
Garvey, J. D. 2477
Garvey, T. 1975, 3070, 3073
Garwin, E. L. 2029, 2284
Gass, V. G. 2613
Gass, V. P. 1949
Gastebois, J. 2393
Geisik, C. 2080
Gelfand, N. 87, 105, 114
Gelfand, N. M. 81, 102
Geller, J. 2266
Gemme, G. 2399
Genin, R. D. 769
Genre, R. 3053
Gentzlinger, R. C. 2263, 2456
Gerasimov, A. 1678
Gerig, R. 123
Gerlack, R. 678
Gero, E. 1207
Gevorkov, A. K. 1573
Ghosh, A. 2164, 2167, 2239
Gilgenbach, R. M. 1827
Gilpatrick, J. D. 1136, 1139, 3017
Gioumousis, A. 1404
Girault, P. 3005, 3180
Gjaja, I. 452
Gjaja, I. M. 1621
Glaser, M. 1213
Glaskov, A. A. 2613
Glass, H. D. 2134, 2477
Glatz, J. 2981
Glazov, A. A. 1017
Glosson, R. 2134
Gluckstern, R. L. 452, 1597, 1600
Glukhikh, V. A. 2823
Gluskin, E. 1169
Götz, T. 1383
Godechot, X. 1943
Goderre, G. 81, 87, 90, 1296
Goderre, G. P. 1848
Godin, A. 2393
Godlove, T. F. 2589
Godot, J.-C. 2964
Goeppner, G. A. 29
Goetz, T. 1543
Golceff, P. 976, 2278, 2688
Goldhar, J. 239
Goldman, M. 739
Goldman, M. A. 681
Goldman, T. 2569
Goloborodko, S. G. 1356
Golubeva, N. I. 1899, 2823
Gomei, Y. 828
Gomulka, S. 2137
Gonczy, J. D. 29, 2301, 2304
Gonichon, J. 1978
Gonzalez, R. 1252
Goodman, D. L. 754
Goodwin, J. E. 294, 2506
Goodwin, R. W. 1484
Goodzeit, C. 2164, 2167
Gorelov, D. V. 2984
Goren, Y. 813
Gormley, M. 2360
Gough, D. 2955, 3156
Gough, D. E. 3168
Gougnaud, F. 2393
Gourber, J. P. 2122
Gourcy, G. 2393
Gourlay, S. 2173, 2179
Gourlay, S. A. 2227, 2233, 2236
Gournay, J. F. 2393
Grabe, H. 857
Graber, J. 2411, 2417
Granatstein, V. L. 658, 731
Grattarola, M. 2760
Gray, E. R. 1046
Gray, R. 2152
Green, M. A. 1088, 2158
Green, M. I. 2161
Greene, A. 2164, 2167, 2239
Greenwald, S. 464, 1857
Greenwald, Z. 464, 1246, 1857
Grieggs, R. J. 2459
Grieser, M. 2817
Griffin, J. 1740
Griffin, J. E. 2826
Griffith, L. V. 3094
Grishanov, B. I. 183
Gromme, A. 5
Gromme, T. 1419, 3222
Gross, G. 2331, 2334, 2955
Grote, D. P. 263
Grote, H. 324
Groves, T. 1180
Grunberg, C. 594
Grundey, T. 2450
Grunhagel, C. 1213
Gürtler, P. 2793
Gualco, G. 2760
Gualco, G. C. 2399
Gudewicz, P. 1142
Guemas, F. 2393
Guharay, S. K. 1961
Guiducci, S. 2850
Guignard, G. 3231, 3234
Gundersen, M. 619
Gundersen, M. A. 591, 1990
Gunderson, G. R. 2526
Guo, Z. 1669, 1672, 2616
Gupta, R. 2164, 2167
Gupta, R. C. 42, 2239, 2242, 2245
Gurevitch, M. 2509
Gusarov, V. N. 1860
Guy, F. W. 578, 1884, 3032, 3056
Gyles, W. 65

H

Haber, I. 263
Haberman, I. 1386
Habiger, K. W. 2622
Habs, D. 2817
Hacker, H. U. 1425
Hacker, U. 1362
Haddock, C. 2197, 2206, 2215
Hadinger, G. 3053
Haebel, E. 1023
Haenni, D. 1308
Haga, K. 440
Hagel, J. 488
Hahn, A. A. 1174, 1177, 1180
Hahn, H. 1627, 1707, 2239, 2242, 2245
Hahn, K. 3020, 3070, 3073
Hahn, R. v. 2817
Haimson, J. 646, 3183
Hairapetian, G. 2751, 2967
Halama, H. 1107, 2313, 2316
Halbach, K. 1797, 2718, 2721, 2856
Halbleib, J. A. 3135
Halemeyer, M. 2149
Hall, B. 1419
Halliwell, J. 943
Halvarsson, B. 1160
Hamilton, B. 1770
Hamilton, B. J. 1210
Hamm, M. E. 1377
Hamm, R. W. 1910, 2583
Han, H. S. 2345
Hanasaka, T. 2298
Hancock, S. 171, 174
Hand, L. 21
Hanft, R. 2227, 2230, 2233, 2480
Hanft, R. W. 2134
Hangst, J. 2360
Hangst, J. S. 1764
Hanna, B. 970
Hanna, S. M. 774
Hansen, T. A. 702
Hanus, X. 1534, 2393
Hara, M. 667, 2646
Harami, T. 707
Hardek, T. 1893, 1896
Hardek, T. W. 366, 872, 3150
Harding, D. J. 2134, 2477
Harfoush, F. 1249, 1660, 1743, 1749
Harfoush, F. A. 321, 2477, 2512
Harkay, K. 1743
Harkay, K. C. 1830
Harms, E. 1758
Harris, C. 926
Harris, K. 3159
Harris, S. 2328
Harrison, M. 96
Hartemann, F. 772
Hartill, D. L. 1246
Hartline, R. 1970, 2976
Hartman, S. 2967
Hartman, S. C. 2751
Hartung, W. 786, 2426
Harvey, A. 2331, 2955
Harwood, L. H. 446

Hassenzahl, W. V. 2721, 2736, 2739
Hatton, V. 848, 2952
Hattori, T. 875
Hauck, C. A. 1919
Hayano, H. 1008, 2061
Haydon, J. 2688
Hayes, T. 1320
Haynes, D. L. 2604
Hearty, C. 834
Heese, R. 993, 1107, 2248, 2652, 2658
Heifets, S. 458
Heine, E. 684
Heisterhagen, R. 1154
Helm, R. 219, 2058, 3213, 3216
Helm, R. H. 500, 2098
Hémery, J.-Y. 1564, 3041
Hendricks, B. 81, 87, 1293, 1296
Hendrickson, L. 1201, 1317, 1419, 1451
Henestroza, E. 1975, 3070, 3073
Henke, H. 380
Henn, K. 1362
Henrichsen, K. N. 2122
Henriot, C. 2393
Herb, S. 1222, 1276
Herr, W. 153, 1068
Herrera, J. 2164, 2167, 2239
Herrmannsfeldt, W. B. 1964
Herrup, D. 81, 1848
Herrup, D. A. 87
Hertzbach, S. 834
Hertzbach, S. S. 2152
Herzog, H. 2319
Hettel, R. 769, 926, 976, 1028, 1151, 1243, 1478, 2328, 2369, 2688
Hewett, D. W. 369, 1952, 2581, 2589
Heydari, H. 1687, 1940
Heymans, P. 1353
Hicks, J. 1922
Higo, T. 506, 1011
Hiller, M. 786, 2426
Hilleret, N. 1023
Himel, T. 1416, 1419, 1451
Himel, T. M. 1499
Hinderer, G. 2254
Hinkson, J. 1234
Hirabayashi, H. 2402
Hiramatsu, S. 165, 2625
Hirano, Y. 2298
Hirata, K. 482, 2847
Ho, C. 555
Ho, C.-H. 2554
Hodges, T. 2272
Hodgeson, J. 819
Hodgson, J. 2949
Hodgson, J. A. 1996
Hoffmann, C. R. 2337
Hofmann, I. 2492
Hogan, B. 658
Holmberg, S. P. 634, 2125
Holmes, S. D. 2477, 2896
Holz, J. 857
Honma, H. 1043
Hopkins, D. 1335
Hori, T. 2877
Horinaka, H. 2032
Horlitz, G. 2319
Horton, M. 926, 1028, 2328, 2688
Hoshi, Y. 2990
Hosseini, W. 1404, 1407
Hostetler, T. 973, 2688
Houck, T. 646, 766
Howard, D. 742, 745
Howell, J. 29, 2295, 2360
Howell, J. W. 690, 2301
Hower, N. 2278
Howry, S. 1305
Hoyer, E. 2721, 2736, 2739
Hoyt, E. W. 2284
Hoyt, M. W. 2284
Hseuh, H. C. 2266, 2292
Hsieh, H. 1107, 2119, 2248, 2316
Hsu, I. 905, 1464, 1734, 2064, 3210
Hsu, I. C. 1499
Hsu, K. T. 1157
Hsu, T.-Y. 1990
Hsue, C. S. 1704, 2667, 2670, 2697
Hsueh, S. Y. 81, 108
Hübner, K. 141, Ismann, P. 3023
Huang, Y. 374, 407, 509, 2017, 2020, 2649
Hubert, D. 857
Hughes, T. P. 245
Hui, M. 745
Hulbert, J. A. 2805
Humbert, J. C. 2477
Humphries, D. 2721
Humphries, S., Jr. 6
Hurd, J. W. 893, 2137
Hurh, P. 1177, 2360
Husmann, D. 1543
Huson, F. R. 736, 1958, 2008, 2221, 2649, 3050
Hutcheon, R. M. 795
Hutchinson, D. 2955
Hutchinson, D. P. 3168
Hutson, R. 228, 955, 1893
Hutton, A. 84

I

Ignatyev, A. P. 1048
Ikeda, M. 2402
Ikegami, K. 2694
Ikezawa, M. 1118
Iliev, A. I. 1899, 1904, 1907, 2823
Il'in, A. A. 2613
Ilinsky, N. 1014, 1722
Iljinov, A. S. 2984
Imanishi, A. 3035
In, S. R. 2298
Ingrassia, P. F. 1026
Inoue, K. 667
Ipe, N. 1028
Irwin, J. 219, 342, 1588, 2058, 3213, 3216
Isagawa, S. 757
Iselin, F. C. 327
Ishi, K. 1118
Issinsky, I. B. 2886
Itagaki, H. 2694
Itoga, K. 2032
Ivanchenkov, S. N. 2751
Ivanov, I. N. 1582
Ivanov, J. D. 2984
Ivanov, P. M. 183, 186, 523, 526
Ivanov, Y. D. 2823, 3067
Ivanov, Y. S. 2823
Ivers, J. D. 561, 2104
Iversen, K. 2390
Iwamoto, M. 2694
Iwata, H. 2990
Izawa, M. 440

J

Jablonka, J. 2393
Jablonka, M. 1534
Jablonski, E. 681
Jach, C. 816, 926, 2688
Jachim, S. P. 672, 1329
Jackson, A. 2637
Jackson, G. 1174, 1180, 1249, 1389, 1740, 1743, 1746, 1749, 1752, 1755, 1758, 2532
Jackson, R. 1359
Jacky, J. 1359
Jacobs, K. 716
Jacobs, K. D. 601, 1791
Jacobsen, R. 834, 2067
Jaeschke, E. 2817
Jaffery, T. 2215
Jaffery, T. S. 2173, 2179, 2191, 2227
Jagger, J. M. 2375, 2477
Jahnel, L. 2787
Jain, A. 2444, 3038
Jain, K. K. 1972
Jakobson, M. J. 893
Jan, G. J. 1157, 1380
Jaros, J. 834
Jayakumar, J. 2197
Jayakumar, R. 2206, 2215
Jayamanna, K. 1925
Jejcic, A. 2101
Jenkins, D. J. 702
Jenkins, T. 2310
Jenner, D. 1922
Jensen, C. 1740
Jensen, E. 3240
Jessen, P. S. 1764
Jiang, D. 2616
Jiang, H. B. 2757
Jiawen, X. 1878
Jin, S. 3264
Jöstlein, H. 2281
Jobe, R. K. 1464, 3210
Joh, K. 884
Johnson, C. D. 254
Johnson, D. E. 81, 87, 114, 120, 360, 1296, 2191
Johnson, G. 2688
Johnson, K. F. 578, 1136, 1171, 1183, 2529, 3017
Johnson, R. 1975
Johnson, R. G. 1540
Johnson, R. M. 1952
Johnson, R. P. 81, 87, 90, 93, 114, 1293, 1296

Johnson, S. 1505
Johnson, T. 1174
Johnson, W. J. D. 2754
Johnstone, C. 860
Joho, W. 141
Joly, J. M. 2393
Jones, B. 1770
Jones, C. M. 2604
Jones, F. W. 357
Jones, K. W. 893
Jong, R. A. 3103
Jordan, K. 2381
Joshel, R. 81, 87, 1293, 1296
Joshi, C. 564, 619, 2560, 2967
Joshi, C. J. 2751
Jostlein, H. 631, 2295
Joubert, A. 594, 2802
Joyce, G. 239, 242, 2563
Judin, L. I. 1166, 1279
Juillard, M. 2393
Jules, E. 1225
Jung, R. 1160, 1186, 1213
Junger, J. 2254
Junquera, T. 2393
Juras, R. C. 2604
Jurgens, T. G. 321, 2512, 2996

K

Kabe, A. 2257
Kahn, S. 2164, 2167, 2239
Kahn, S. A. 42, 2170, 2242, 2245
Kako, E. 2405, 2408
Kalbfleisch, C. 1308
Kalet, I. 1359
Kallas, N. 2197
Kalsi, S. 2119, 2248, 2652, 2658
Kaltchev, D. I. 195
Kamitsubo, H. 2646
Kamiya, Y. 2032, 2682, 2709
Kanazawa, K. 506
Kanazawa, M. 875
Kaneko, N. 2990
Kang, Y. G. 911
Kapchinskij, I. M. 3109
Karady, G. G. 949, 3132
Karantzoulis, E. 1782
Karpov, N. I. 1279
Karpov, V. A. 1681
Kasha, D. 681, 739
Kashinskij, D. A. 3109
Kasuga, T. 1338
Katayama, T. 76
Kato, R. 1118
Kato, T. 2032
Kats, J. M. 306
Katsouleas, T. 564, 619, 2967
Katsura, T. 440, 1338, 2682
Kauffmann, S. K. 339
Kauppila, T. 2107
Kauppila, T. J. 3192
Kawai, M. 828
Kawamoto, T. 1555
Kawashima, Y. 667
Kawazu, S. 707
Kazacha, V. I. 195
Kazakov, P. N. 1356
Kazarian, A. A. 1579
Kazarinov, N. Y. 195
Kazimi, R. 3050
Keane, J. 681, 774, 804, 1107, 1326, 1794
Keeley, D. 1305
Kehne, D. 248
Keil, E. 482
Keller, R. 2113
Kelley, J. P. 2381
Kellogg, N. 745
Kelly, E. 2164, 2167, 2239
Kennedy, P. 2733
Kennedy, W. L. 2441
Kerby, J. 2176, 2185
Kerns, Q. 1743
Kerslick, G. S. 561
Kettunen, L. 2140
Kewisch, J. 446, 1443, 3264
Kheifets, S. A. 3267
Khlebnikov, A. S. 2751
Khoetsian, M. Y. 1579
Kiaie, J. 1115
Kiefer, P. 2871
Kiehlmann, D. 2390
Killian, E. 2239
Kim, C. H. 2691
Kim, J. H. 1368
Kim, J. S. 1719
Kim, K. 1299
Kim, K.-J. 1088
Kim, M. S. 1368
Kim, S. H. 2375
Kim, T. 2316
Kimball, F. 2856
Kimel, I. 2757
Kimura, W. D. 558
Kincaid, B. 2721
King, A. 1305
King, Q. 1186
Kinney, W. 2173, 2179, 2191
Kipper, A. 3053
Kirchgessner, J. 21, 664, 678, 786, 2411, 2414, 2417, 2420, 2423, 2426
Kirk, H. G. 604, 2572
Kirkman-Amemiya, G. 591, 1990
Kissler, K. H. 1186
Kitamura, M. 2251
Klabunde, J. 2981, 3044
Klaisner, L. 1404, 1407
Kleffner, C. M. 2817
Klein, E. 2393
Klein, H. 2981, 3023, 3044
Klepper, O. 2880
Kloeppel, P. K. 3264
Kneisel, P. 2384, 2387
Knott, M. J. 2526
Knudsen, L. 147, 1213
Ko, I. S. 575, 1195, 2700
Ko, K. 719, 819
Kobayashi, T. 622
Kobayashi, Y. 2709
Kobliska, G. R. 2477
Kochkin, V. A. 1017
Kodera, I. 2694
Koechlin, F. 2393
Koepke, K 81, 87, 2227
Kofler, R. R. 2152
Kogan, M. 3174
Kojima, Y. 16
Koljaskin, A. D. 1949, 2613
Kolomiets, A. A. 2984, 3109
Kolonko, J. 2751, 2856, 2967
Kolte, G. 1305
Komarov, V. V. 1356
Komissarov, P. Y. 1166
Konc, J. J. 2182
Kondo, Y. 1118
Konecny, R. 555, 3219
König, W. 2880
Konovalov, V. A. 2823
Koo, Y. M. 2345
Koop, I. A. 183, 186
Koopman, J. 1186
Körber, W. 2429, 2432
Korolev, O. S. 3067
Koscielniak, S. R. 377, 696, 1725, 1728
Koska, W. 2173, 2179, 2185, 2191
Kostas, C. 312, 613
Kotov, V. I. 192
Koul, R. K. 902
Kourbanis, I. 99, 111, 1302
Koutchouk, J.-P. 147, 2891
Kowalewicz, R. 2631
Kozanecki, W. 628, 1207, 3222
Kozawa, T. 622
Kozodaev, A. M. 3109
Kponou, A. 896, 1473
Krafft, G. A. 2073, 2745
Kraimer, M. R. 1314, 1496, 2526
Krall, J. 242, 1788, 2563
Kramer, S. 1107
Krasnikov, Y. M. 1279
Krasnykh, A. K. 195
Kratz, R. 2254
Krauter, K. 1419, 1487
Kravchuk, L. V. 2823, 3067
Krejcik, P. 2067, 2500, 3258
Krieger, C. 29
Krienen, F. 2474
Krinsky, S. 11, 1096, 2542, 2676
Krisch, A. D. 2506
Krishnagopal, S. 467, 1071
Krishnaswamy, J. 1107, 2119
Kristensen, M. 1764
Krivonosov, A. I. 2613
Kroc, T. 2378
Kroes, F. 1148
Kroes, F. B. 684
Kroll, N. 719, 819, 1716
Kroll, N. M. 801
Kruse, R. W. 1145
Krycuk, A 1470
Krzywinski, J. 2149
Kubo, K. 1011, 1833, 2405, 2408
Kubo, T. 2257, 2462
Kuchar, J. 1163
Kuchnir, M. 93
Kuiper, B. 1356
Kukhtin, V. P. 2035
Kulikov, A. 1845, 3138
Kulikov, A. V. 500, 2005, 2098
Kulinski, S. 961, 2970
Kulke, B. 763, 766
Kumagai, K. 2465
Kumagai, N. 1698, 2465, 2646
Kung, P. 2688

Kunkel, W. B. 1916, 1919, 1955, 1993
Kuo, C. C. 2667, 2670, 2697
Kurakin, V. G. 2417
Kurihara, Y. 2032
Kuroda, S. 2257
Kurokawa, S. 2257
Kurokawa, S.-i. 138
Kurz, M. 3023
Kus, R. 857
Kushnick, P. 1508
Kustom, R. 1624
Kustom, R. L. 690, 693
Kuzmenko, G. A. 1860
Kuzminski, J. 2215, 2480
Kvasha, A. I. 3067
Kwan, J. W. 1955
Kwan, T. J. 649

L

Labedzki, J. 2254, 2450
Lachin, Y. Y. 2751
Lackey, J. 860, 1740
Laeger, H. 848
Lager, D. 3079
Lager, D. L. 3082, 3094
Lahti, G. 1290, 1443
Lambertson, G. 687, 819, 1404, 1407, 2537
Lamm, M. 2215
Lamm, M. J. 2173, 2179, 2191, 2227, 2233, 2236
Lamora, B. 935
Lampe, M. 242
Lampel, M. 2742, 3276
Lancaster, H. 807, 2721
Lane, S. N. 2604
Langdon, A. B. 263
Lange, R. 2319
Langstaff, R. 2272
Lankshear, R. 1695
Larkin, J. 935
Larson, D. J. 2575, 2581, 2757
Larson, J. D. 594
Larsson, A. 2008
Latham, P. E. 658, 731, 734
Latushkin, S. T. 1279
Latypov, T. A. 1582
Lau, Y. Y. 637, 1609
Laughton, C. 129
Lavender, W. 1151, 1383, 1476, 2688
Lavine, T. L. 652, 1964, 2284
Lawrence, G. P. 2598
Lawson, W. 658, 731, 734
Lax, J. 742
Laxdal, R. E. 810
LeDiberder, F. 628
Lebedev, P. K. 3273
Lebedev, V. A. 2342
Leboutet, H. 2763
Leconte, P. 2393
Lee, B. 725
Lee, E. P. 1737
Lee, G. 1249, 1758
Lee, G. C. 2182
Lee, I. Y. 2604
Lee, J. C. 2357, 2667, 2670
Lee, M. 1305, 1437
Lee, M. J. 1448
Lee, S. Y. 159, 162, 1059, 1627, 1636, 1639, 1770, 2506, 2679
Lee, T. 719, 2381, 2673
Lee, T. G. 798
Lee, T. N. 575
Lee, Y. Y. 881, 958
Lee-Whiting, G. E. 303
Leemann, C. W. 2745
Leemans, W. P. 2560
Leenen, M. 857
Legg, J. D. 725
Legg, R. 1261, 1371, 1970
Lehr, H. 2685
Lehrman, I. S. 2572
Leifete, G. 572
Leleux, G. 517
Lemeilleur, F. 1213
Lenkszus, F. R. 2526
Leonov, V. N. 2613
Leroy, J. 1534
Lessner, E. 210, 2778
Letellier, P. 3180
Leung, E. 2652
Leung, E. M. W. 2248
Leung, K. 2023, 2200
Leung, K. K. 2185
Leung, K. N. 1916, 1919, 1993, 2076
Levitt, S. 1160
Levy, C. D. P. 1925
Ley, R. 2832
Li, B. 2616
Li, C. Y. 1916, 1993
Li, K. 2616
Li, M. 371
Li, R. 452, 2616, 3264
Li, W. 2278, 2688
Li, Z. 281
Lidestri, J. 3123
Lidestri, J. P. 3120, 3195
Lienard, P. 1490
Lierl, H. 2319
Limar, V. V. 1573
Limberg, T. 1806, 2064
Lin, C. L. 2026
Lin, L. 2781, 2784, 2787
Lincoln, B. 1981
Lindner, A. 742, 745
Lindqvist, H. 425
Liou, R.-L. 1990
Lippmann, G. 598
Lipski, A. 2477
Liska, D. 2958
Liska, D. J. 2961
Littauer, R. 1130
Littauer, R. M. 1246
Liu, D. K. 1368
Liu, H. 2020, 2616
Liu, K. 2616
Liu, L. 1958
Liu, Y. 1624
Lloyd, S. 1136
Lloyd, S. C. 2456
Lo, C. C. 807
Lobanov, N. R. 2613
Loew, G. 982
Loew, G. A. 3219
Loiselet, M. 2610
Lombardi, A. 2444, 2820, 3038
Loomba, D. 2474
López, G. 392, 2203, 2212, 2224, 2468, 2471
Louie, W. 1107, 1374
Louis-Joseph, A. 1225
Low, K. 1308, 1365
Lowrey, A. R. 1204
Lu, X. 1740, 1749, 1752, 2616
Lubrano di Scampamorte, M. 2631
Lucas, P. 2523
Luccio, A. 839, 896, 1473
Luchini, K. 1371
Lucuta, P. 795
Ludewigt, B. 943
Ludgate, G. A. 1350
Ludmirsky, E. A. 189, 2146
Lueng, E. 2856
Luhmann, N., Jr. 2967
Luhmann, N. C., Jr. 766, 2751
Luijckx, G. 2366
Lujan, R. E. 2453
Lukyantsev, A. F. 1356
Lumpkin, A. H. 1204, 1967, 2754
Lundin, T. K. 129
Luo, Y. X. 575, 1195
Lyneis, C. M. 2796

M

Maas, R. 2366
MacKay, W. W. 736, 2221, 3050
MacLachlan, J. A. 1863, 2826
Macek, R. 228, 1893, 1896
Machida, S. 62, 383
Mackenzie, G. 1133
Mackenzie, G. H. 810
Madlung, J. 3053
Madura, D. 2856
Maggs, R. G. 1046
Mahale, N. K. 62, 383, 386, 389
Mahoney, K. 1470
Maier, R. 1425, 2808
Mailian, M. R. 198
Maillard, J. 2101
Main, W. 658, 731, 734
Maisheev, V. A. 189
Maki, N. 2251
Makowski, M. A. 2548
Malachov, N. A. 1582
Maldonado, J. R. 542
Malitskiy, N. D. 2823
Malyshev, O. B. 183
Malyshev, O. N. 2888
Mamaev, G. L. 1582
Mammosser, J. 2384
Mandell, S. 1273
Mane, S. R. 1585, 1690
Manfroi, T. 1978
Manglunki, D. 1198, 2509
Mann, J. 1186, 1213
Mansour, D. 1999, 2152
Mantsch, P. M. 2227, 2236
Manukian, R. H. 1287, 1446
Manz, C. 123

Mapes, M. 2292
Marc, M. R. 1115
Marchand, P. 780
Marchetti, C. 2970
Markovich, P. 2987
Marks, S. 2739
Marquardt, N. 2862
Marriner, J. 831, 1180, 1228, 1255, 1258, 1389, 1392, 1758, 1773, 1946
Marsh, K. 564
Marsh, K. A. 2560
Marshall, J. 2381
Martensson, E. 1293
Marti, F. 1163
Martin, B. 1374
Martin, D. J. 1124, 1127
Martin, J. 3053
Martin, K. 1174, 1180
Martin, P. S. 2477
Martin, S. 1767
Martinez, D. 1136
Martini, M. 171, 1890
Martinsen, G. 1365
Martirosian, Y. L. 257
Maruyama, A. 2694
Maruyama, T. 834, 2029
Marxen, H. 1311
Maschke, A. 389
Maslov, M. A. 625
Massarotti, A. 710, 3180
Massoletti, D. 2978
Masullo, M. R. 789, 2850
Masunov, E. S. 3177
Matevosian, A. R. 1446, 1579
Matheisen, A. 2429, 2432
Matrone, A. 2399, 2760
Matsuba, H. 2402
Matsuda, T. 2694
Matsuki, N. 2715
Matsumoto, H. 1008, 2061
Matsumoto, S. 908
Matthews, H. 731
Mattison, T. 982, 996, 2331, 2334, 2955, 3156, 3159
Mattison, T. S. 3162, 3165, 3168
Matveev, A. V. 2342
Matveev, V. A. 2823, 3067
Mauer, W. J. 3094
Maurer, W. J. 3082
Mavrogenes, G. 419
Maywald, H. 857
Mazarakis, M. G. 3059, 3126, 3129
Mazeline, C. 1198
Mazur, P. 2215
Mazur, P. O. 2128, 2134, 2477, 2480
McAtee, W. H. 3135
McConnell, D. 1249, 1743
McCormick, D. 1201, 1240
McCrory, E. S. 1249, 1484, 3064
McCullough, W. F. 2622
McCune, E. W. 705
McDermott, D. 2967
McDermott, D. B. 766
McDonald, D. 2023
McDonald, D. S. 1919
McDonald, M. 1925
McDowell, W. P. 1496, 2526
McGhee, D. G. 914
McGinnis, D. 1255, 1258, 1389, 1392, 1758
McGregor, J. E. 795
McInturff, A. D. 2227, 2233
McIntyre, P. M. 725
McKenna, C. M. 2088
McMichael, G. E. 845, 2093, 3047
McMurry, D. E. 2961
McNerney, A. 681
McNerney, A. J. 52, 739
Meade, A. 2164, 2239
Meadows, J. W. 547
Meads, P. F. 1767
Meaney, D. 1371, 3171
Mecklenburg, B. 646, 3183
Meddahi, M. 153
Mehta, N. 383
Meigs, M. J. 2604
Meinke, R. 2149
Meisner, K. 111
Meitzler, C. R. 1958, 2008
Mello, J. 2688
Mel'nikov, V. A. 1582
Mendelsohn, S. L. 395
Menegat, A. 652
Meng, W. 2474
Menge, P. R. 1827
Menninger, W. L. 754
Merminga, L. 2064
Merminga, N. 219, 461
Merrill, F. 2137
Merson, J. 3017
Meshcherov, R. A. 2823
Meshkov, I. N. 2888
Mestha, L. K. 783, 1332
Meth, M. 681, 739
Meuth, H. 1767
Meyer, F. 2215
Meyer, R. 1136
Meyrand, G. 3180
Miao, Y. 2221
Michailichenko, A. 458
Michailov, V. N. 3067
Michaut, C. 2011
Michel, H. 1186
Michel, W. L. 845
Michelato, P. 2973
Michelotti, L. 207, 1561, 1881
Mignardot, H. 777
Mikawa, M. 908
Mikhailov, V. A. 2886
Mikhailov, V. G. 1166
Mikheev, M. S. 1356
Mikic, Z. 1305
Milardi, C. 1448
Miles, J. 848
Miller, D. W. 532
Miller, E. 1464
Miller, H. W. 2996
Miller, J. D. 239, 3141
Miller, R. 982, 3276
Miller, R. B. 2622
Miller, R. H. 652, 769, 976, 1964, 2284
Millich, A. 3234
Mills, F. E. 2477
Mills, G. D. 2604
Milner, S. 2631
Milovanov, O. S. 2613
Milton, B. F. 65
Milton, S. 291
Milutinovic, J. 413
Minestrini, M. 2970, 2973
Minty, M. G. 1770, 2506
Mironov, V. I. 195
Mirzojan, A. N. 3067
Misek, J. 1174, 1180
Mishchenko, A. V. 2601
Mishiro, H. 1118
Mishukov, A. A. 2613
Mistry, N. B. 24
Mitchel, G. R. 979
Mitra, A. K. 938
Mitsuhashi, T. 1836
Mitsumoto, T. 2877
Mitsunobu, S. 2408
Mittig, W. 594
Miura, A. 1008
Miura, F. 2655
Miyahara, Y. 707
Mizuta, M. 2032
Mjae, E. A. 189
Mock, R. C. 3135
Mockler, C. 2110, 2958
Moffat, D. 21, 664, 678, 786, 2411, 2414, 2417, 2420, 2423, 2426
Möhl, D. 514, 2509, 2832
Moir, D. 2107
Moir, D. C. 245, 3192
Moiseev, V. A. 2984
Moisio, M. F. 1934
Mokhov, N. V. 625
Mokhtarani, A. 2227, 2230, 22[illegible]
Møller, S. P. 2811
Möller, W. D. 2429
Mølmer, K. 1764
Mondelaers, W. 2619
Mondelli, A. 312
Mondelli, A. A. 315, 613, 3261
Monteiro, S. 2307
Moore, C. 631
Morales, H. 769, 976, 1243, 2278, 2688
Moretti, A. 2996
Morgan, B. 1290
Morgan, G. 2164, 2239
Morgan, G. H. 42, 2167, 2170, 2242, 2245
Morgan, J. P. 851
Morgillo, A. 2167
Mori, W. B. 564
Mori, Y. 165
Morimoto, T. 3035
Morin, D. C. 2643
Morita, Y. 2257, 2462
Mortazavi, P. 804
Morton, P. 1407
Morton, P. L. 461, 1854, 2586
Moscatello, M. H. 2802
Moser, H. O. 3053
Moshammer, H. 905
Mosko, S. W. 2604
Mosnier, A. 2393
Mostowfi, D. 1243, 1478, 2688
Motonaga, S. 2465

Mourier, G. 772
Mouris, J. F. 2337
Mtingwa, S. 555
Mukoyama, S. 2402
Müller, G. 2417
Müller, R. 1311
Munson, F. H. 2987
Muratore, J. 2164, 2167, 2239
Murin, B. P. 2823, 2984
Murin, N. P. 3067
Murphy, J. 2248
Murphy, J. B. 1107, 1651, 2661, 2664, 2676
Musenich, F. 2973
Musenich, R. 2399
Muto, H. 875
Myakishev, D. G. 3002
Myznikov, K. P. 177

N

Nagafuchi, T. 707
Nagaitsev, S. S. 183
Nagaoka, R. 1074
Nah, Y. G. 2345
Naito, T. 1008, 2014, 2061
Nakagawa, T. 2694
Nakahara, K. 1558
Nakai, H. 2408
Nakajima, K. 622
Nakamura, N. 440
Nakamura, S. 2032, 2694
Nakamura, T. 667
Nakanishi, H. 622
Nakanishi, T. 2032, 2694
Nakano, M. 707
Nakao, K. 1043
Nakashizu, T. 2990
Nakata, S. 2694
Nakayama, H. 506
Nakazato, T. 1118
Nam, K. 2673
Namkung, W. 575, 1195, 1368
Nantista, C. 652
Napoly, O. 3228
Nassiri, A. 419
Nath, S. 485, 572
Nation, J. A. 561, 728, 2104
Natter, E. F. 1329
Naumov, I. V. 1279
Nawrocki, G. J. 1496
Nawrocky, R. 1107, 1528
Nawrocky, R. J. 2542, 2790
Nearing, J. C. 2188
Neckenig, M. 1543
Neil, G. R. 2745
Nelson, E. 719, 722
Nelson, G. 1028
Neri, F. 1597, 1630
Nesterenko, I. N. 183
Nesterov, V. 3138
Neuffer, D. 1893, 1896
Neuffer, D. V. 446, 1077
Neuschaefer, G. 485, 572, 1136, 1884
Newberger, B. S. 216
Newton, M. A. 2592, 2595
Nexsen, W. E. 3085, 3094, 3103
Nezhevenko, O. A. 2933, 3186
Ng, B. 1371, 1514, 3171
Ng, K. Y. 159, 162, 1743, 1749
Ng, K.-Y. 111, 1645
Nghiem, P. 517
Nguyen, D. 1437
Nguyen, K. T. 239, 3141
Nguyen, M. 2955, 3147
Nguyen, M. N. 3153
Nickogosian, V. T. 2146
Niczyporuk, B. 3264
Nielsen, J. S. 1764
Nielsen, R. W. 29
Niemann, R. C. 29, 2301, 2304
Niimura, N. 1118
Nikogossian, V. T. 1446
Ninomiya, S. 165
Nishida, Y. 622
Nishidono, T. 2298
Nishimoto, H. 3114
Nishimura, H. 1434
Nishinomiya, Y. 1031
Niven, W. A. 3097
Niwano, S. 1118
Noda, A. 875
Noda, K. 875
Noer, R. 21
Noguchi, S. 2405, 2408
Nolden, F. 2880
Nolen, J. A. 884, 1163
Nolker, K. 1443
Noomen, J. 1148
Norem, J. 555, 619, 1984
Novicov, A. P. 3177
Novikov, D. L. 1017
Nuhn, H.-D. 769, 973, 1151, 1410, 1476, 2688, 2748
Nuttall, J. A. 2284
Nyman, M. 943
Nyman, M. A. 1401

O

Obina, T. 1338
O'Connell, J. S. 404
O'Day, S. 2360
Odian, A. 3216
Odian, A. C. 2098
Oganessian, R. T. 2888
Oganessian, Y. T. 2888
Ogata, A. 622
Ogawa, Y. 494, 497
Ogitsu, T. 2480
Ohman, D. 5
Ohmi, K. 2847
Ohnishi, J. 2465
Ohno, H. 2715
Ohnuma, S. 371, 374, 407
Ohsaka, T. 1118
Ohsawa, Y. 2257, 2462
Ohshima, I. 1034
Ohuchi, N. 2257, 2462
Oide, K. 2058, 2488
Oikawa, Y. 2298
Okuda, S. 2694
Oleck, A. R. 2230
Ollis, C. W. 3097
Olsen, D. K. 2604
Olson, W. R. 3126
Omori, T. 2032
O'Neill, C. M. 2838
Onischenko, L. M. 195
Oram, C. 1722, 2272
Orlov, Y. 1839
Orlov, Y. F. 2838
Orrell, D. 2197
Orris, D. 2215, 2227, 2480
Orris, D. F. 2477
Ortiz, R. 1151, 1383, 1478, 2688
Orzechowski, T. 1335
Osberg, E. A. 1350
O'Shea, P. G. 2754
Ostiguy, J.-F. 2128, 2131, 2354, 2477
Ostreiko, G. N. 3186
Ostroumov, P. N. 2984, 3062, 3067, 3109
O'Sullivan, M. 935
Otake, Y. 1558
Otter, A. J. 2363
Ottonello, G. B. 2760
Owens, T. L. 3064
Oyamada, M. 1118
Ozaki, S. 2901
Ozaki, T. 2257, 2462
Ozelis, J. P. 2191

P

Pacak, V. 810
Pachnik, J. E. 2134, 2477
Padamsee, H. 21, 664, 678, 786, 2042, 2411, 2414, 2417, 2420, 2423, 2426
Padilla, R. 2996
Pagani, C. 2973
Palmer, R. B. 32
Palmieri, V. 1934
Palumbo, L. 2850
Pancella, P. V. 2506
Pang, Y. 725
Papavaritis, P. 772
Pappas, C. 863
Paramonov, V. V. 2823
Parazzoli, C. G. 2769
Pardo, R. C. 2987
Parfitt, C. P. 357
Park, E. S. 2345
Park, S. 2751, 2967
Parker, B. 1002
Parker, D. L. 725
Parkhomchuk, V. V. 529, 2888, 3273
Parodi, R. 366, 2399, 2973, 3026
Parsa, Z. 511, 1887
Parzen, G. 288, 1615, 1627, 1872, 1875
Pashenkov, A. S. 2823
Pasotti, C. 710
Pasquinelli, R. 1758
Pasquinelli, R. J. 1395
Patteri, P. 2970, 2973
Patterson, L. 2856
Paul, A. C. 3085, 3094, 3100, 3103, 3106
Paul, P. 2444, 3038

Paulson, C. C. 395
Pause, H. 1311
Paxson, V. 297
Payne, A. N. 3091, 3097
Pearce, D. 1133
Pearce, W. J. 822
Pearson, J. B. 810
Peck, S. 464
Peck, S. B. 1245
Pedersen, B. O. 2088
Pedersen, F. 2509, 2631
Peggs, S. 207, 318, 473, 476, 1302, 1458, 1657, 1660, 1848
Peggs, S. G. 2477
Pei, A. 1922
Pei, G. X. 2098
Peiniger, M. 2390
Pellegrin, J.-L. 1243, 1404, 1407
Pellegrini, C. 398, 2748, 2751, 2853, 2856, 2967, 2976
Pellico, W. 1749
Pendergast, K. D. 754
Pendleton, R. 819
Pennacchi, R. 2949
Penner, S. 351
Perelstein, E. A. 195
Perevedentsev, E. A. 183, 186, 526
Perkins, C. 2949
Perrier, J. C. 2832
Perriollat, F. 1353
Persov, B. Z. 3186
Pestrikov, D. V. 183, 523
Peters, O. 857
Peters, R. 2523
Petersen, B. 857
Peterson, D. 1228, 1758
Peterson, J. 62
Peterson, J. M. 1645
Peterson, T. 2227, 2230, 2480
Petillo, J. J. 312, 315, 613
Petit, E. 1142
Petri, H. 1922
Petronevich, S. A. 3067
Petrosian, M. L. 257
Pettersson, T. 1564
Pfister, U. 1425, 2808
Phelps, R. A. 2506
Phinney, N. 1317, 3222
Picard, M. 1383, 1543
Pieczora, K. 857
Piel, H. 2417
Pietryka, M. 2949
Pike, C. 1952
Pilat, F. 62, 204, 348, 363, 383
Pilyar, N. V. 1582
Pisent, A. 2964
Pishchulin, I. V. 1567, 1570
Pissanetzky, S. 2221
Pitthan, R. 500, 1845, 2098
Pivit, E. 774
Pjerov, S. 2248, 2316
Placidi, M. 147, 1213
Planner, C. 2272
Plate, D. 2721, 2739
Plotkin, M. 681
Plum, M. 1893, 1896
Poirier, P. 2070
Poirier, R. L. 699, 2943
Pokorny, P. 2888
Poll, D. 1389, 1758
Poloni, C. 2712
Ponomarev, O. 1890
Poole, J. 848
Popovic, M. 655, 725
Porcellato, A. M. 2438
Porter, T. 1999
Postiau, N. 2610
Potter, J. M. 1377, 1910, 2583
Potts, J. 2414
Potvin, L. 2628
Poukey, J. W. 3059, 3126, 3129
Poulsen, O. 1764
Pouryamout, J. 2417
Power, J. 1136
Powers, T. 1508, 2325
Prasuhn, D. 1425, 1767
Preble, J. 2381
Preger, M. 961
Preissner, H. 2149
Prelec, K. 1913
Prepost, R. 2029
Prestwich, K. R. 3126, 3129
Primdahl, K. 2281
Proch, D. 2414, 2429, 2432, 2435
Prodell, A. 2164, 2167, 2239
Promé, M. 2393
Pronin, A. N. 1949, 2613
Pruss, S. 87
Pruss, S. M. 294, 2128, 2340
Pugh, S. 1371, 1514
Puglisi, M. 681, 2634
Purser, K. H. 878
Pusch, G. D. 303
Putnam, S. D. 3120, 3195
Putris, F. 2351

Q

Qian, W. 2616
Qian, Y. 1692
Qian, Z. 2996
Qingwen, Q. 1878

R

Radusewicz, P. 2164, 2167
Rajagopalan, S. 222, 619
Raka, E. 1422
Rakowsky, G. 1096, 2733
Ramamoorthy, S. 2790
Ramirez, G. 1326
Ramirez, J. J. 3059
Rangarajan, G. 1621, 1630
Range, J. 2808
Rao, G. 2384
Raparia, D. 572, 2993
Rapidis, P. A. 108
Rashchikov, V. I. 3111
Raskopin, A. M. 3109
Rasmussen, N. 171
Ratner, L. G. 168, 2506
Ratti, A. 681, 739, 1803, 2820
Ratzinger, U. 567, 2981
Raubenheimer, T. O. 2503
Rawnsley, B. 1133
Read, M. E. 658
Reece, C. 1508, 2325
Reece, K. 1473
Reece, R. K. 839, 896
Rees, D. 640
Rees, D. E. 675
Reeve, P. A. 2363
Regan, A. H. 2946
Reginato, L. L. 2592, 2595, 2918, 3165
Rehak, M. 2164, 2167, 2239
Reinagel, D. J. 1537
Reinhardt, N. 591
Reinhardt-Nickulin, P. 1014, 1722
Reiniger, K. W. 920
Reiser, M. 248, 251, 658, 1818, 1821, 1961, 2497
Renbarger, V. L. 3085, 3097
Renieri, A. 2760
Renken, D. 2429
Rensfelt, K.-G. 2814
Repnow, R. 2817
Reschke, D. 2417
Reusch, M. F. 1651, 2188, 2248, 2664
Reuter, E. 1999
Reuter, E. M. 1996, 2005
Revkov, A. A. 2613
Rex, K. 1234
Rezvov, V. A. 1166
Rhee, M. J. 479, 1972, 2999, 3141
Rice, D. 464
Rice, D. H. 1246, 1857
Richardson, J. R. 48
Richert, A. 1362
Richter, R. 742, 887
Richter-Sand, R. J. 3201
Rickel, D. G. 649
Riddiford, A. 2233
Riddiford, A. W. 2236
Ridgeway, W. 742, 745
Ridlon, R. 2107
Ridlon, R. N. 3192
Riege, H. 2631
Riemer, U. 857
Rimmer, R. 687, 801, 819
Rinckel, T. 2506
Ringrose, R. 786
Rinolfi, L. 2964
Ripouteau, F. 594, 2802
Risler, R. 1359
Risselada, T. 171, 1672
Ritson, D. M. 339
Riunaud, J. P. 171
Rivkin, L. 780
Rizawa, T. 707
Rizzo, S. 2399
Robb, J. 2381
Roberts, W. 1455
Robin, D. 398, 2853, 2856
Robinson, A. L. 2640
Rocha, R. 2221, 2649
Roche, C. T. 2441
Rodgers, J. 2578
Rogers, D. 646, 766
Rogers, J. D. 661
Rogers, R. P. 3267
Rohde, D. 1758
Rohrer, E. 2164, 2239

Rohrer, E. P. 2167
Romano, T. 1107, 2724
Romano, T. J. 993
Romashkin, O. B. 1567
Romashkin, O. V. 1570
Romea, R. D. 558
Roop, B. 29, 2304
Root, L. 810
Rosas, P. 2266
Rosatelli, F. 2399, 2760
Roschin, A. A. 1166
Rose, J. 804, 1794
Rose, R. 1107, 1374
Rosenzweig, J. 619, 2967
Rosenzweig, J. B. 1776, 1779, 1987, 2751, 3225
Roser, T. 2506
Rosing, M. 555
Ross, M. 2064
Ross, M. A. 2506
Ross, M. C. 1201, 1502, 2098
Rossi, C. 710
Rossmanith, R. 3264
Röth, R. W. 2417
Rothman, J. 1107, 2542, 2790
Rouse, F. 1416, 1419, 1451, 3222
Rowen, M. 1243
Roy, G. 2058, 3213, 3216
Royet, J. M. 2155
Rubbia, C. 3279
Rubin, D. 21, 467, 664, 678, 786, 1642, 2411, 2414, 2417, 2420, 2423, 2426
Rubin, D. L. 144, 470
Rubtsov, B. A. 3067
Rück, D. M. 1943
Rudd, H. 248
Rudolph, K. 1934
Ruegg, R. 1925
Ruggiero, A. G. 413, 1422, 1869, 2820
Ruggiero, F. 1666
Ruhe, J. 2958
Rule, D. W. 1204
Rummler, J. 2146
Rumrill, R. S. 1537
Rusnak, B. 1046
Russ, T. 946, 1467, 1546, 2125, 3174
Russell, A. 207
Rusthoi, D. P. 607
Ruth, R. 2058, 3216
Ruth, R. D. 219, 1591, 1854, 2037, 2503
Rutkowski, H. L. 1952
Ruvinsky, S. I. 3186
Ryckewaert, G. 2610
Rymer, J. P. 1910
Ryne, R. 646
Ryne, R. D. 760
Rypshtein, I. 1386
Ryu, C. 575, 1195, 1368

S

Saab, A. 3174
Saadatmand, K. 1171, 1183, 2529
Sabbi, G. 366
Safa, H. 2393
Safranek, J. 769, 1104, 1151, 1243, 2278, 2369, 2688, 2865
Sagalovsky, L. 2441
Sagan, D. 1080, 1839
Sage, J. 1365, 1443
Sagin, I. A. 3067
Saito, K. 2384, 2387
Saka, T. 2032
Sakai, I. 165
Sakanaka, S. 440, 1836
Sakano, M. 2402
Sakaue, H. A. 2298
Sakharov, V. P. 1356
Salomons, R. 1401
Saltmarsh, C. 1458
Samed, Y. 786, 2423
Sampayan, S. 3094, 3097
Sampayan, S. E. 3103
Sample, J. 65
Sampson, W. 2164, 2167, 2239
Sanchez, T. 2688
Sanchez-Chopitea, L. 1201, 1284, 1317
Sandburg, J. 2266
Sander, O. R. 578, 1171, 2529, 3017
Sanders, R. T. 681, 739
Sandoval, D. 1171, 2529
Sandoval, D. P. 1237, 3017
Sanelli, C. 2970
Sanford, T. W. L. 3135
Sanok, Z. 857
Sapp, W. W. 634, 2125, 2348
Saraniti, D. 786, 2426
Saritepe, S. 81, 87, 114, 207, 225, 318, 473, 1848
Sasaki, S. 2715, 2715
Sasaki, Y. 2877
Sass, B. 1416, 1419
Sass, R. 1437
Sato, H. 165, 908
Satogata, T. 476, 1302
Satoh, K. 138
Satoh, S. 707
Satti, J. 3189
Savoy, R. 1091, 2718, 2736
Sax, W. 1999
Scandale, W. 1669, 1672, 2260
Scanlan, R. M. 2155
Schaaf, U. 2880
Schachinger, L. 297, 1434
Schachrai, N. V. 3109
Schachter, L. 561, 2104
Schaffer, G. 748
Schailey, R. 890, 985, 1281
Scharamentov, S. I. 3067
Scharlemann, E. T. 3097
Schauerte, W. 1543
Schegolev, L. M. 183
Schempp, A. 2981, 3023, 3041, 3044, 3053, 3076
Scherbakov, E. D. 1356
Schick, L. A. 144, 470
Schiffer, J. P. 1764
Schillo, M. 1543
Schindl, K. 171
Schirmer, D. 2859
Schittko, F. J. 1543
Schlachter, A. S. 2640
Schmeing, H. 979
Schmickler, H. 848
Schmidt, E. E. 2477
Schmidt, F. 1669, 1672
Schmidt, R. 147, 1186, 1213
Schmor, P. W. 65, 1925
Schmüser, P. 37, 857, 2149
Schneider, H. 2607
Schneider, H. R. 65
Schneider, J. D. 1183
Schneider, L. 863
Schneider, R. F. 239, 3141
Schneider, R. J. 878
Schneider, W. J. 2381
Schnell, W. 3237
Schnitzenbaumer, P. 2292
Schoessow, P. 555, 2557, 3219
Schofield, G. L. 3171
Schollmeier, S. 857
Schölz, F. 2432
Schönauer, H. 171
Schrage, D. L. 1046
Schuchman, J. 1107
Schuchman, J. C. 2316
Schulte, H. 2880, 2981
Schultz, D. C. 1964, 2284
Schulz, L. 2685
Schulze, M. E. 610
Schütte, W. 1219
Schütz, P. 2450
Schwandt, P. 1922
Schwarz, H. 819, 1410, 1806
Schwarz, W. 857
Schweppe, E.-G. 757
Sclyarenko, V. I. 1166
Sears, J. 21, 664, 786, 2411, 2414, 2417, 2420, 2423, 2426
Sebek, J. 769, 926, 976, 1028, 1151, 1243, 1478, 2688
Sedlyarov, I. K. 183
Seeman, J. T. 461, 905, 1201, 1499, 1734, 2064, 2949, 3207, 3210
Segall, K. 1981
Seifert, H. 757
Seifrid, P. 1758
Sekutowicz, J. 2429
Sellyey, W. C. 1145, 1204, 2769
Selph, F. 2978
Semunkin, Y. F. 2823
Sen, T. 336, 342, 345, 360
Senichev, Y. V. 1899, 1904, 2823
Senyukov, V. A. 1048
Seppi, E. 351
Serafini, L. 2973
Serdobintsev, G. V. 3186
Sereno, N. 3264
Serio, M. 2850, 2970
Serov, V. L. 3067
Serre, C. 1353
Servergin, Y. P. 2035
Servranckx, R. V. 287, 309
Sery, A. A. 529, 2888, 3273
Severgin, Y. P. 2823
Shafer, R. E. 1139
Shaimerdenov, E. N. 3186
Shapiro, A. H. 1046, 2961
Shaposhnikova, E. N. 2823

Sharma, S. 2248, 2661
Sharp, C. 935
Sharp, W. M. 260, 2592
Shatunov, Y. M. 183
Shay, H. D. 2592, 3088
Shcheulin, A. S. 1582
Shea, M. F. 1484
Shea, T. J. 1422, 1428, 1803
Sheffield, R. L. 1110, 2754
Sheikh, J. Y. 845
Shen, B. 2266, 2292
Shepard, K. W. 2987
Sherman, J. D. 2080
Sherrill, B. 1163
Sherrill, B. M. 884
Shi, J. 407
Shi, P. 1764
Shibasaki, Y. 1118
Shibata, H. 622
Shibata, Y. 1118
Shibuya, S. 3035
Shidara, T. 494, 497, 1034, 1040, 1043
Shiffler, D. 561
Shih, H.-J. 216
Shiho, M. 2625
Shiltsev, V. D. 529, 3273
Shimano, T. 2402
Shinas, M. 1171, 2529
Shintake, T. 757
Shintomi, T. 165
Shishido, T. 2405, 2408
Shoaee, H. 1416, 1419, 1437, 1451
Shokair, I. R. 3144
Shope, S. L. 3129
Shotzman, G. 2221
Shtirbu, S. 1484
Shu, Q. 21, 664, 2414
Shu, Q. S. 678, 786, 2411, 2417, 2420, 2423, 2426
Shukeilo, I. A. 2035, 2823
Shurter, R. B. 1136, 1139
Shurupov, P. B. 1949, 2613
Shutt, R. 2164, 2167, 2239
Si, H. 2616
Sibley, C. 946, 1546, 2125
Sicard, C.-H. 1353
Sidorov, V. P. 1573
Siemann, R. 467, 1071
Siemann, R. H. 2838
Siergiej, D. 81, 87, 90, 93, 1293
Sierra, S. 3180
Sievers, P. 3228
Sikora, J. P. 1130
Sikora, R. 2292
Silva, J. 2101
Sim, J. W. 2134, 2477
Simonov, E. A. 183, 523, 526
Simpson, J. 555, 2557, 3219
Simrock, S. 1470, 2515
Sims, R. 2173
Sims, W. 1264
Sinclair, C. K. 2745
Singer, H. 1425
Singh, O. V. 1528, 2542
Sissakian, A. N. 195
Skaritka, J. 2218
Skelly, J. 839, 896, 1473
Skrinsky, A. N. 183
Slater, J. M. 532
Slater, J. W. 532
Sledziewski, Z. 2011
Sleptsov, A. I. 3273
Slinker, S. 242
Sloan, T. 1770
Slobodrian, R. J. 2628
Sluijk, T. 1148
Sluijk, T. G. B. W. 684
Smedinghoff, J. 2523
Smirnov, Y. I. 195
Smith, B. H. 795
Smith, D. L. 547, 3126
Smith, G. A. 1264, 1273, 1347, 1431
Smith, H. 1028
Smith, H. V., Jr. 2080
Smith, J. 2790
Smith, J. R. 3144
Smith, J. S. 2029
Smith, L. 1064, 1737, 3070
Smith, S. A. 2206
Smith, V. 1243
Smolin, J. 2967
Smolin, J. A. 2751
Smythe, W. R. 643
Snead, C. L., Jr. 1695
Snitchler, G. 2197, 2209
Snowdon, S. C. 2477
So, I. 2790
Sobenin, N. P. 2613
Sobotta, K. 1362
Solomon, L. 1096, 2116
Solov'ev, N. G. 1567
Song, J. 2396
Song, J. J. 690
Song, J. J. H. 693
Soroka, L. 1955
Soukas, A. 839
Soukas, A. V. 940, 999, 1216
Soundranayagam, R. 625
Sowinski, J. 1922
Spädtke, P. 1943, 2880
Spalek, G. 652, 1046
Spataro, B. 961, 2850
Specht, V. 658
Spence, W. 1549, 2064
Spence, W. L. 461, 503, 905
Spencer, C. M. 1964, 2152
Spencer, J. E. 1440, 3270
Spencer, N. 5
Spencer, T. A. 1827
Sperisen, F. 2506
Spiess, W. 1425
Spigo, G. 2176, 2197
Spitz, R. 681, 739
Springer, R. W. 2754
Sredniawski, J. 2023
Sreenivas, A. 949
Stahl, S. 434, 1779
Staicu, F. 2316
Stampfer, M. 2817
Stampke, S. R. 2218
Stark, R. A. 3141
Stattel, P. 2266, 2292
Stecchi, A. 1448, 2970
Steck, M. 2817, 2880
Steele, W. F. 1955
Stefan, P. M. 1096
Stein, W. E. 2754
Steinhauer, L. C. 558
Stella, A. 3026
Stepantsov, S. V. 2888
Stephan, M. 1362
Stephenson, E. J. 2506
Stetter, M. 2631
Stever, R. 763
Stewart, M. D. 725
Stiening, R. 2149, 2480
Stillman, A. 1264
Stillman, A. N. 1189
Stitts, E. 2381
Stocker, F. 890, 1281
Stockhorst, H. 1425, 1767
Stolzenburg, C. 2149
Stover, G. 943
Stover, G. D. 1401
Stradtner, R. 943
Strait, J. 2173, 2176, 2179, 2185, 2191, 2215
Strickland, B. E. 3171
Striffler, C. D. 658, 731, 734, 2578
Stringfield, R. M. 649
Struckmeier, J. 2880
Struve, K. 3129
Struve, K. W. 3144
Studzinski, M. 713
Stuewe, R. 929
Stutzin, G. C. 1916
Su, J. J. 619
Sueno, T. 908
Sugahara, R. 2257, 2462
Sugitani, M. 2877
Sukiennicki, B. 982
Sullivan, M. 2844
Sullivan, T. 1749, 1848
Sun, D. 736
Sun, Y. 1410
Sundelin, R. 2384
Sundelin, R. M. 2381
Susta, J. 2325
Suyama, A. 1031
Suzuki, H. 707
Suzuki, T. 165
Svandrlik, M. 710
Swain, G. 3014
Swenson, C. A. 2649
Swenson, D. R. 1928, 1931
Swoboda, D. 1516
Swoyer, G. 2733
Sylvester, C. 2116
Symon, K. 1624
Syphers, M. J. 117, 129
Syresin, Y. A. 2888
Szumillo, A. 1999

T

Tajima, T. 2408
Takada, H. 2655
Takada, T. 2715
Takagi, A. 165
Takahashi, S. 2298
Takahashi, T. 2408
Takahashi, T. 1118

Takao, M. 494, 497, 506, 1011
Takasaki, E. 165
Takasaki, F. 138
Takata, K. 1011, 1034
Takayama, K. 2551, 2625
Takebe, H. 2465
Takeda, S. 1008, 1034, 1040, 2047, 2061
Takeo, T. 1338
Takeuchi, Y. 2032
Tallerico, P. 640
Tallerico, P. J. 649, 670
Tallerico, T. 1264
Talman, R. 204, 363, 383
Tanabe, Y. 707
Tanaka, H. 1698, 2694
Tanaka, M. 958
Tang, C.-M. 1788
Tang, J. 1443
Tang, J. Y. 443, 446
Tang, Z. 1946
Tantawi, S. 731
Taratin, A. M. 177
Tarovik, M. N. 2823
Tatchyn, R. 2748
Tatum, B. A. 1519, 2604
Tauchi, T. 834, 3252
Tavares, P. 2781, 2787
Taylor, B. 807
Taylor, T. 842, 2260, 3228
Tayursky, V. A. 2342
Tazzari, S. 2970, 2973
Tazzioli, F. 2970, 2973
Tecimer, M. 2757
Tekawa, M. M. 1401
Temkin, R. 2026
Temkin, R. J. 751, 754, 772
Teng, L. 210, 1624, 1692, 2679, 2778
Teng, L. C. 1603
Tepikian, S. 1627, 1636, 1639, 1707
Ter-Akopian, G. M. 2888
Teranishi, T. 1034
ter Avest, R. 2149
Terrien, J. 2967
Thern, R. 45
Thern, R. E. 1189
Thevenot, M. 3204
Thiagarajan, V. 2194
Thibault, C. 3041
Thiessen, H. 1893, 1896
Thiessen, H. A. 281, 866, 3132, 3198
Thomas, B. L. 3171
Thomas, M. 804, 1107, 2790
Thomas, R. 1344, 1347
Thompson, K. A. 431, 1404, 1407, 1854
Thompson, K. M. 2375
Thompson, P. 2164, 2167, 2239
Thompson, P. A. 2242, 2245
Thorndahl, L. 3243
Thrasher, M. H. 842
Tiefenback, M. 3123
Tiefenback, M. G. 3120, 3195
Tigner, M. 132, 786, 2423, 2910
Timakov, V. A. 2888
Tiunov, M. A. 3186
Tkatchenko, A. 517
Tkotz, R. 2631
Tlekhas, Y. I. 2613
Tobiyama, M. 1338
Toda, T. 908
Todd, A. M. M. 395
Tödten, G. 857
Toge, N. 628, 834, 2067, 2152
Tojyo, E. 3035
Tokar, R. L. 1204
Tokuda, N. 3035
Tomeoku, H. 2251
Tomimasu, T. 2655
Tomizawa, M. 875
Tomlin, R. 860
Tommassini, D. 2372
Tompkins, J. 2480
Tompkins, P. A. 1115
Tool, G. 2215
Tosi, L. 1074
Toth, K. S. 2604
Toumanian, A. R. 2146
Tourrette, T. 2393
Toyama, T. 165, 908
Trahern, C. G. 207
Tran, D. T. 3180
Tran-Ngoc, T. 3047
Tranquille, G. 2509, 2832
Trasatti, L. 1448, 2970
Trbojevic, D. 96, 99, 159, 162
Treado, T. A. 702
Trémeau, T. 772
Trimble, D. 766
Trines, D. 857
Trinks, U. 2254, 2450
Trofimov, N. N. 1356
Trombly-Freytag, K. 2134
Tronc, D. 3008, 3180
Truong, Q. V. 2802
Trzeciak, W. 1624
Trzeciak, W. S. 1088, 2643
Tsang, K. T. 312
Tsarik, S. V. 192
Tsironis, G. 1302
Tsoupas, N. 1695
Tsubata, M. 2032
Tsuchiya, K. 2257, 2462
Tsukishima, C. 2694
Tsumaki, K. 1698
Tsutaya, T. 1118
Tsutsui, Y. 2655
Tucker, H. 2958
Tucker, T. 2110
Tückmantel, J. 1023
Tumanian, A. R. 1446
Tupa, D. 1928, 1931
Turk, J. 834, 2152
Turkot, F. 2128, 2230
Turman, B. N. 3126, 3129
Turner, J. 2197, 2206
Turner, J. R. 2176
Turner, L. R. 2140
Turner, W. 3082
Turner, W. C. 581, 3085, 3094, 3097, 3100, 3103, 3106

U

Ueda, T. 622
Uher, J. 777
Uhm, H. S. 239, 455, 2566
Ungrin, J. 3011
Unser, K. 1213
Urakawa, J. 506, 1040, 1555, 2014
Urasawa, S. 1118
Uythoven, J. 1594

V

Vaganov, N. G. 1573
Valckx, F. P. G. 2011
Valdner, O. A. 1949
van Asselt, W. 839, 1216
van Asselt, W. K. 881, 1273
van de Klundert, L. J. M. 2149
Vandeplassche, D. 848, 2509
van der Linden, A. 2366
van Dyck, O. B. 1928, 1931
Vanecek, D. 1952
van Guilder, B. S. 2506
Van Maren, R. 2110
VanMaren, R. 766
Van Olst, D. 1284
van Steenbergen, A. 2724
van Zeijts, J. B. J. 1597
Van Zwienen, W. 1344, 1347
Van Zwienen, W. H. 1189
Varfolomeev, A. A. 2751
Vasas, M. 1981
Vasiliev, N. V. 1017
Vasserman, I. B. 183
Vaughn, G. D. 1522
Veith, R. 3044
Velasquez, G. 2110
Vengrov, R. M. 3109
Verdier, A. 156, 1669
Verkooijen, H. 1148
Vernon, W. 2351, 2871
Vescherevich, V. G. 183
Vescovi, M. 961, 2970
Vetrovec, J. 2730, 2742
Vetter, A. M. 1051
Veyssière, A. 2393
Viccaro, P. J. 1088, 1091
Vignola, G. 68, 961, 2850
Višnjic, V. 1701
Vjalov, G. N. 2984
Vlieks, A. E. 760, 798
Vobly, P. D. 183
Voelker, F. 687, 819
Voevodin, V. P. 1356
Volin, S. P. 1902, 2823
Volk, G. J. 2706
von Przewoski, B. 2506
von Reden, K. F. 878
Vormann, H. 3041
Vorobiev, S. A. 177
Vos, L. 1186
Voss, J. 769, 926, 1243, 2278, 2369, 2688
Vouillot, J. M. 1160
Voy, D. 1758
Vuaridel, B. 2506

Vylov, T. D. 195

W

Wachtel, J. 1326
Wadlinger, E. A. 607, 3017
Wagner, J. S. 3126
Wagner, R. 1767
Wagner, S. 834
Wait, G. D. 964, 967, 1531, 2883
Wake, D. 3120, 3123
Wake, M. 2173, 2179, 2185, 2191
Walbridge, D. G. 2134, 2477
Waldner, O. A. 2613
Walker, J. D. 2029
Walker, N. 2500
Walker, Q. 65
Walker, R. P. 2712
Wall, D. 1981
Walling, L. 1020, 2958, 2961
Walling, L. S. 643
Walther, S. R. 2088
Wanderer, P. 42, 2164, 2167, 2239
Wanderer, P. J. 2242, 2245
Wang, D. 769
Wang, D. F. 2688
Wang, D. X. 1818
Wang, D. Y. 1261, 2727
Wang, F. 985
Wang, G. 2396
Wang, H. 2444, 3038
Wang, J. 2706
Wang, J. G. 1818, 1821
Wang, J. M. 1107, 1326, 1794
Wang, J. W. 431, 3219
Wang, L. 2396
Wang, M. H. 2667, 2670, 2697
Wang, T. 1896
Wang, T.-S. 377, 1893
Wang, T.-S. F. 491
Wang, X. J. 604
Wang, X. Q. 1174, 1180, 1746, 1749
Wang, Y. 2020
Wangler, T. 251
Wangler, T P. 330, 3056
Ward, T. E. 1695
Warkentien, R. 1347
Warnock, R. L. 1591, 1654, 1824
Wartski, L. 1534
Watanabe, K. 2298
Waters, G. 964, 1531
Watson, J. 572, 2993
Watson, J. A. 3097
Watson, J. M. 1993
Weaver, J. 996, 2688
Weaver, J. N. 769, 976, 1243
Wedekind, M. 1922
Wehrle, B. 2295
Wehrle, R. B. 29
Wei, J. 1866, 1869
Weichold, M. H. 725
Weidman, D. J. 239, 3141
Weihreter, E. 2685
Weinert, A. 1362
Weingarten, W. 1023
Weintraub, B. L. 2137
Weissenburger, D. W. 2188
Welch, D. 3129
Welch, J. 467
Welch, J. J. 792, 1851, 2838
Welch, K. M. 2269
Wells, F. D. 1136, 1139
Wells, J. 3126
Wells, R. P. 1955
Weng, W. T. 52, 839, 1585
Wenzel, J. 1543
Werkema, S. 108
Wermelskirchen, C. 1151, 1383, 1476, 2688
West, C. 1290
Westenskow, G. 646, 766, 1335
White, G. R. 1540
White, W. P. 3171
Whitehead, H. 2381
Whitney, R. 3264
Wiedemann, H. 769, 976, 1104, 1243, 2278, 2369, 2688, 2727
Wienands, U. 62, 357, 2829
Wiik, B. 2910
Wiik, B. H. 2905
Wildman, D. 410
Wilks, S. C. 564
Wille, K. 1154, 2859
Willeke, F. 135, 2483, 2910
Willen, E. 2164, 2167, 2239, 2242, 2245
Williams, D. J. 2832
Williams, R. 619
Williams, T. 1848
Wills, J. S. C. 842
Wilson, E. J. N. 171
Wilson, I. 2070, 3237
Wilson, M. 863
Wilson, M. A. D. 71
Wilson, N. 2322
Wilson, N. G. 2459
Wilson, P. 1806
Wilson, P. B. 652
Winick, H. 1410, 2748
Winn, D. R. 1981, 2874
Winters, M. 2173
Wirsbinski, J. 210, 2778
Wiseman, M. 2381
Witkover, R. 839, 1428
Witkover, R. L. 1189, 1231, 1264, 1267, 1347
Wolf, B. 2981
Wolf, B. H. 1943
Wolff, D. 93
Wolff, S. 857
Won, S. 575, 1368
Wong, R. 2310
Woodle, M. 2724
Woodley, M. 1845
Woodley, M. D. 2098
Woolfe, K. 745
Wootton, P. 1359
Worden, J. 1133
Wright, D. 2284
Wright, E. L. 798
Wright, P. 1046
Wrulich, A. 2634
Wu, G. 1458
Wu, X. 62
Wu, Y. 180, 2366
Wurtele, J. 1791
Wurtele, J. S. 2026
Wüstefeld, G. 266
Wyss, C. 150

X

Xi, X. 1878
Xiao, M. 2616
Xie, J. 1323, 2017, 2020
Xie, W. 1410
Xie, Z. 2796
Xiu, L. 2008
Xu, J. 1422
Xu, Z. X. 1851

Y

Yakimenko, V. 269
Yakovlev, V. P. 3002, 3186
Yamada, R. 2131
Yamada, T. 2694
Yamamoto, A. 2402
Yamamoto, H. 2251
Yamamoto, M. Y. 2990
Yamamoto, N. 2058, 3213, 3216
Yamamoto, S. 2694
Yan, S. 2616
Yan, Y. T. 333, 336, 339, 342, 345, 360, 1663
Yang, F. 2616
Yang, J. 1151, 1383, 1476, 2688
Yang, K. M. 2542
Yang, Z. 2616
Yao, R. L. 2578
Yarba, V. A. 2913
Yazunin, I. A. 177
Yazynin, I. A. 625
Ye, W. 1174
Yen, S. 1481
Yeremian, A. D. 1964
Yeung, K. S. 783, 1332
Yin, Y. 1133, 1243, 1722
Yokouchi, S. 2298
Yokoya, K. 506, 3252
Yoon, M. 428, 2673, 2700
York, R. 363
York, R. C. 62, 383, 443, 446
York, R. L. 1928, 1931
Yoshida, M. 757, 1034
Yoshida, Y. 622
Yoshii, I. 165
Yoshioka, M. 2032
Yoshiyuki, K. 707
Yoshizawa, J. 875
Yoshizawa, M. 875
Yotam, R. 1028, 1410, 2688
Young, A. 672
Young, A. T. 1916, 1993
Young, C. 1734
Young, L. 572
Young, L. M. 1884, 2754
Young, P. E. 2586
Younger, F. C. 2727
Youngman, B. 769, 976, 1243, 2688
Yu, D. 813, 1335, 1716, 1719
Yu, J. 2616

Yu, L. H. 2542
Yu, S. 1335
Yu, S. S. 260, 2592, 2595
Yu, W. 725
Yu, X. T. 1791
Yu, Y. 2480
Yuan, J. 2616
Yuan, V. 3017
Yuan, V. W. 1171, 2529
Yue, W. K. 725
Yugami, N. 622
Yun, V. 1961
Yunn, B. 2745
Yunn, B. C. 1785
Yurkon, J. 1163

Z

Zach, M. 810
Zacharian, A. G. 2146
Zagel, J. 1174
Zaharatos, R. M. 1026
Zaltsman, A. 1320
Zangrando, D. 2712
Zapalac, G. H. 2029
Zapasek, R. 2266
Zaplatin, E. N. 1017
Zapol'sky, V. N. 192
Zapryagaev, I. A. 3186
Zbasnik, J. 2206
Zeigler, J. 2221
Zeitlin, C. 834, 2152
Zelenskiki, A. N. 2984
Zelepoukin, S. A. 1356
Zeller, A. F. 884
Zhang, B. 2396, 2399
Zhang, P. 90, 93
Zhang, R. 1323, 2020, 2616
Zhang, S. Y. 940, 999, 1005
Zhang, W. 940, 999, 1216, 1273
Zhang, X. 2676
Zhang, Z. 2616
Zhao, Z. 2396
Zhefu, Z. 2757
Zheng, H. 2480
Zholents, A. A. 2342, 2835
Zhou, J. 207
Zhou, P. 1776, 1779
Zhou, X.-H. 2805
Zhou, Y. 1371
Ziemann, V. 201, 416, 2067, 2152, 3249
Zimmermann, F. 2483
Zinin, E. I. 183
Zinkann, G. P. 2987
Ziomek, C. D. 1329
Zisman, M. S. 1, 84
Zitvogel, E. 1264, 1267
Zolfaghari, A. 601, 716, 1791
Zotter, B. 488, 491, 3228
Zu, D. 2423
Zucker, M. 1695
Zucker, M. S. 1270
Zumbro, J. D. 634, 2125, 2348
Zuo, K. 2328, 2369, 2688
Zverev, B. V. 2613
Zyarylkapov, S. Z. 3067, 3067